

UNIVERSITY OF
ILLINOIS LIBRARY
AT URBANA-CHAMPAIGN



ENGINEERING

ROOM USE ONLY



Digitized by the Internet Archive
in 2015

30.5
50

Physics

ISSN 0449-1947 — ISBN 2 902731-10-3

COLLOQUE N° 7 Supplément au Journal de Physique FASC. 7 C-7 1979

THE LIBRARY OF THE

JAN 1980

UNIVERSITY OF ILLINOIS
AT URBANA-CHAMPAIGN

205

JOURNAL **de PHYSIQUE**

**XIV^e Conférence Internationale
sur les Phénomènes d'Ionisation
dans les Gaz**

**Grenoble (France)
1979**



**PUBLICATION DE LA SOCIÉTÉ
FRANÇAISE DE PHYSIQUE
SUBVENTIONNÉE PAR LE C.N.R.S.**



EUROPHYSICS JOURNAL

VOLUME I

**XIV^e Conférence Internationale
sur les
Phénomènes d'Ionisation
dans les Gaz**

***XIVth International Conference
on Phenomena in Ionized Gases***

**Grenoble (France)
9-13 Juillet 1979**

CETTE CONFÉRENCE EST PATRONNÉE PAR/THIS CONFERENCE IS SPONSORED BY

— **Sociétés savantes/Scientific Institutions**

I.U.P.A.P. International Union of Pure and Applied Physics
 U.R.S.I. Union Radio Scientifique Internationale
 E.P.S. European Physical Society
 S.F.P. Société Française de Physique
 C.N.F.R.S. Comité National Français de Radioélectricité Scientifique
 S.E.E. Société des Electriciens et Electroniciens

— **Ministères et Organismes de Tutelle/Ministries and Sponsoring Organizations**
Ministère des Universités/Ministry of Universities

D.G.R.S.T. Délégation Générale à la Recherche Scientifique et Technique
 C.N.R.S. Centre National de la Recherche Scientifique
 D.R.E.T. Direction des Recherches, Etudes et Techniques
 C.E.A. Commissariat à l'Energie Atomique
 E.D.F. Electricité de France

— **Autorités Régionales/Local Authorities**

Conseil Général de l'Isère/General Council of Isère
 Mairie de Grenoble/Grenoble Town Hall
 Université Scientifique et Médicale de Grenoble/Scientific and Medical University of Grenoble

COMITÉ DE PATRONAGE/SPONSORING COMMITTEE

Président/Chairman : Pr Jacques YVON

M. Y. BERNARD
 D. BLANC
 C. BONET
 A. BOULLOUD
 F. CABANNES
 T. CONSOLI
 R. DAUTRAY
 J.-L. DELCROIX
 J.-F. DENISSE
 F. DENNERY
 J.-M. DOLIQUE
 H. DOUCET
 B. DREYFUS

M. FELDEN
 M. GOLDMAN
 P. GRIVET
 C. MAGNAN
 M. MAGNIEN
 J.-C. PEBAY-PEYROULA
 Y. PELENC
 J. ROBIEUX
 M. SALESSE
 E. SCHATZMAN
 M. SOUTIF
 M. TROCHERIS
 P. VALENTIN

COMITÉ SCIENTIFIQUE INTERNATIONAL/INTERNATIONAL SCIENTIFIC COMMITTEE

Président/Chairman : Pr H. MAECKER - F.R.G.

R. BALESCU Belgium
 W. BYSZEWSKI Poland
 F. W. CRAWFORD U.S.A.
 J. DUTTON U.K.
 J. LABAT Yugoslavia
 E. MOLINARI Italy

A. RUTSCHER G.D.R.
 R. S. SIGMOND Norway
 J. TAILLET France
 V. N. TSYTOVICH U.S.S.R.
 P. VIEHBOECK Austria

COMITÉ D'ORGANISATION/LOCAL ORGANIZING COMMITTEE

J. TAILLET
 C. POMOT
 M. FITAIRE
 P. HUBERT
 J.-P. BABUEL PEYRISSAC
 P. FAUCHAIS
 C. GARY
 J. PELLETIER
 M. PETIT

Président
 Secrétaire Général
 Secrétaire Scientifique
 Trésorier

AVEC LA COLLABORATION DE/WITH THE COLLABORATION OF

Grenoble Accueil - ALPES CONGRES
 Palais des Congrès de la Ville de Grenoble

PREFACE

Cet ouvrage contient les communications présentées à CIPIG 14, quatorzième conférence sur les phénomènes d'ionisation dans les gaz, tenue à Grenoble du 9 au 13 juillet 1979 sous le patronage de l'URSI, de l'IUPAP, de l'EPS, de la SFP et de la SEE en ce qui concerne les Sociétés Savantes, du Ministère des Universités, de la DGRST, de la DRET, du CNRS, du CEA et de l'EDF en ce qui concerne nos Grands Organismes Nationaux.

C'est au Professeur A. Von ENGEL que revient le mérite d'avoir perçu la nécessité d'établir, entre les Scientifiques travaillant dans tous les domaines de la décharge électrique dans les gaz et de la physique du plasma, des contacts périodiques destinés à leur permettre d'avoir une vue générale sur l'ensemble de la discipline. C'est à ses efforts que nous devons d'en avoir maintenu la tradition depuis 1953, jusqu'au moment où la relève de l'initiative personnelle s'est trouvée peu à peu confiée à des institutions stables, comme le Comité Scientifique International, avec des règles acceptées par tous pour partager de façon équitable le poids des responsabilités qu'entraîne l'organisation de nos Conférences.

Le redoutable honneur d'inviter la Communauté Scientifique Internationale à Grenoble a certes demandé à notre Comité d'Organisation un effort de longue haleine. Mais il convient de rappeler aussi que sans l'aide du Comité Scientifique International, sans les encouragements des personnalités qui forment notre Comité de Patronage, sans le travail des scientifiques qui ont bien voulu apporter leur aide à la sélection des communications, cet effort n'aurait pas pu porter ses fruits. Sans l'aide financière du Ministère des Universités, de la mairie de Grenoble, du Conseil Général de l'Isère du CNRS, du CEA, de l'EDF, de la DRET, de la DGRST et de l'IUPAP, le budget de cette manifestation n'aurait pas pu être équilibré ; sans la participation active du CNFRS qui a bien voulu accueillir dans son sein notre Comité d'Organisation, et sans l'aide matérielle apportée à ce comité par Grenoble Accueil et par l'Université Scientifique et Médicale de Grenoble, rien n'aurait été possible.

Pour terminer, il faut reconnaître l'évidence : une réunion ne vaut que ce que valent ses Conférences et ses Communications. Remercions donc les Conférenciers Invités et les auteurs des Communications pour avoir distillé pour nous la substantifique moelle qui restera dans l'esprit des participants, avec le charme de la région grenobloise et l'hospitalité de ses habitants, la justification et en même temps la récompense de l'effort de chacun.

J. TAILLET

FOREWORD

This volume contains the communications presented at ICPIG 14, the XIVe Conference on Phenomena in Ionized Gases, held in Grenoble (France) from 9th to the 13th of July 1979, under the sponsorship of URSI, IUPAP, EPS, SFP and SEE, and the patronage of the Ministry of the Universities, of DGRST, DRET, CNRS, CEA and EDF.

Professor A. Von ENGEL had the foresight to understand the necessity of establishing periodic contacts between the scientists working on all aspects of gaseous electronics and plasma physics, in order to give a general view of the whole discipline. It is thanks to his efforts that we continued this tradition from 1953 up to the moment that his personal initiative was slowly transferred to permanent institutions, such as the International Scientific Committee. They permitted the organization of our Conferences to establish rules accepted by all so as to spread in an equitable way the weight of the responsibilities.

The honor of inviting the international Scientific Community to Grenoble has imposed on our Local Committee a long and strenuous effort. But we must remember that without the help of the International Scientific Committee, without the encouragement of the people who form our Patronage Committee, without the work of the scientists who have agreed to give their aid in selecting the Communications, this effort would not have succeeded. The budget of this conference could not have been balanced without the financial aid of the Ministry of Universities, of the Grenoble City Hall, of the General Council of Isère, CNRS, CEA, EDF, DRET, DGRST and the IUPAP. Without the material aid given us by Grenoble Accueil and by the Scientific and Medical University of Grenoble, and without the guaranty of the CNFRS to our Local Committee, nothing would have been possible.

Finally, we must look at the evidence ; a scientific meeting is worth no more than the value of its conferences and its Communications. Let us therefore thank the Invited Speakers and the authors of the Communications for having distilled for us the scientific essence of this Conference. This distillation will remain in the memory of the participants along with the charm of Grenoble and the hospitality of its inhabitants, as the justification and as the recompense of the efforts of each one of us.

J. TAILLET

CONTENTS

I

- ELEMENTARY PROCESSES IN GAS DISCHARGES	
- EXCITATION AND IONIZATION	
- RECOMBINATION, ATTACHMENT AND DETACHMENT	
- ION-MOLECULE AND CHEMICAL REACTIONS	
W. WIEME, M. VANMARCKE, W. BRUYNOOGHE.- Radiative and collisional desexcitation of 3P_1 and 3P_1 resonance states in xenon	C7-3
B. DUBREUIL, A. CATHERINOT.- Excitation transfer and quenching of the $n=3$ excited states of helium in a low-pressure glow discharge.	C7-5
S. VALIGNAT, J. LEVEAU, P. DEIGAT.- Investigation of excitation mechanisms in neon with the aid of the radial distribution of excited atoms	C7-7
J.M. LABAT, J. VUKIĆEVIĆ, O. LABAT and S. DJENIŽE.- Line radiation of argon plasma in early afterglow	C7-9
J.L. MORUZZI and V.K. LAKDAWALA.- Electron attachment in SO_2	C7-11
M. CAPITELLI, M. DILONARDO and C. GORSE.- Self consistent electron energy distribution functions in non-equilibrium oxygen	C7-13
P.A.M. VAN DER KRAAN, J.W.H. DIELIS, F.J. DE HOOG.- Formation and destruction of neon molecular ions in Townsend discharges	C7-15
G.L. BRAGLIA, J.J. LOWKE.- Comparison of Monte Carlo and Boltzmann calculations of electron diffusion to an anode	C7-17
O. ANGELOV, A. BLAGOEV, Tc. POPOV.- Investigations of the electron energy distribution function in krypton afterglow plasma	C7-19
K. PESKA, E. ALGE, H. VILLINGER, H. STÖRI and W. LINDINGER.- Reactions of doubly charged ions with various neutrals	C7-21
V. VAN DER SIJDE, B.F.M. POTS, D.C. SCHRAM.- A collisional radiative model of the argon ion system tested for a large range of electron densities	C7-23
P. RANSON and J. CHAPELLE.- Calculation of the photoionization cross sections of excited levels of rare gas atoms	C7-25
N. VAN SCHAIK, L.W.G. STEENHUIJSEN, P.J.M. VAN BOMMEL and J.C.A.M. VAN DE NIEUWENHUYZEN.- Atom densities of the first excited state in low pressure neon discharges.	C7-27
J.I. LONDER, L.P. MENAHIN and K.N. ULYANOV.- Efficiency of excitation of rotational and vibrational levels in a nitrogen molecule	C7-29
Y. KAUFMAN, P. AVIVI and F. DOTHAN.- Ion clusters in the positive column of He-Co and Ar-Co discharges	C7-31
C. SANCTORUM and L. BONTE.- Time dependence of cataphoresis in a neon-argon mixture	C7-33
M. VANMARCKE and W. WIEME.- Visible line afterglow emission of a pulsed xenon discharge	C7-35
W. WIEME and J. LENAERTS.- Excimer formation in rare gas discharge afterglows	C7-37
M. VANMARCKE and W. WIEME.- Theory of resonance radiation imprisonment	C7-39
R. THOMAS, J. BARASSIN and A. BARASSIN.- Reaction $CH_4^+ + NH_3$ - Evolution des produits en fonction de la concentration de NH_3	C7-41
T. MAKABE and T. MORI.- Electron swarm having an anisotropic velocity distribution function	C7-43
M. HAYASHI.- Monte Carlo simulation of electron avalanche in hydrogen.	C7-45
S. DJENIŽE and J.M. LABAT.- Influence of perturbation of population processes of 4p argon levels	C7-47
M. NUMANO and H. ONISHI.- Excitation temperature of a rapidly varying plasma	C7-49
M. GRÖSSL, H. HELM, M. LANGENWALTER and T.D. MÄRK.- Stationary afterglow study of the singly charged atomic ions in pure Ar and Kr	C7-51
M. ABDEL-SALAM and J.L. MORUZZI.- Attachment and ion molecule reactions in SF_6 mixtures	C7-53
B. NEHMZOW, A. RUTSCHER and H.E. WAGNER.- Dissociation of water vapour in the hollow cathode glow discharge	C7-55
D. SALZMANN and S. ELIEZER.- The use of effective Feynman diagrams for atomic cross-section calculations.	C7-57
G. CERNOGORA, G. GOUSSET and A. RICARD.- $N(^2D, ^2P)$ metastable atoms production in a N_2 d.c. glow discharge	C7-59
V.I. MILJEVIĆ.- A spectroscopic study of the DC gas magnetron discharge	C7-61

- A.J. DAVIES, J. DUTTON, C.J. EVANS, A. GOODINGS and P.K. STEWART.- Monte Carlo simulations of electron drift velocities in the noble gases and their mixtures C7-63
- P. CAMBRAY.- Recombinaison de l'ion moléculaire He_2^+ à haute température C7-65
- A. LUCHES, V. NASSISI, A. PERRONE and M.R. PERRONE.- Excitation of 3^3P level of He and 4^2F level of He^+ with electron beams C7-67
- TRUONG BACH and H.W. DRAWIN.- Influence of boundary layer of a Al-seeded shock-heated plasma on the profiles of the AlI resonance lines C7-69
- T.P. GROZDANOV and R.K. JANEV.- Two electron capture processes in plasmas containing multiply charged ions C7-71
- R.R. ABDULLA, J. DUTTON and A.W. WILLIAMS.- Ionization growth in argon C7-73
- J.W.H. DIELIS, F.J. DE HOOG and D. C. SCHRAM.- Decay of metastable $\text{Ne}(^3\text{P}_2)$ -atoms C7-75
- A.V. RISBUD and M.S. NAIDU.- Ionization and attachment in water vapour and ammonia C7-77
- DARREL G. HOPPER.- Ab Initio studies of ion-molecule reactions. The $\text{N}_2\text{O}^+(\text{a}^1\text{A})$ potential energy hypersurface for the $\text{O}^+(\text{N}_2, \text{N})\text{NO}^+$ reaction C7-79
- C. FLEURIER, G. COULAUD and J. CHAPPELLE.- Effect of the ion motion at low electron densities on the profiles of the lines 4471 Å and 4922 Å of HeI C7-81
- E. ALGE, H. VILLINGER, K. PESCA, H. RAMLER, H. STÖRI and W. LINDINGER.- The influence of ion vibrational excitation on ion molecule reactions C7-83
- A. CATHERINOT and B. DUBREUIL.- Quenching of $n = 3, 4$ singlet HeI excited states by molecular nitrogen in a low-pressure glow discharge C7-85
- A.N. KLUGHAREV, A.V. LAZARENKO and V. VUJNOVIC.- The ionization rate coefficients for some radiatively excited rubidium states C7-87
- G.V. GOLUBKOV, N.M. KUZNETSOV and V. YEGOROV.- The role of single-step ionization by thermal electron-atom collisions C7-89
- Ph. GAUCHEREL, B. ROWE, J.L. QUEFFÉLEC, N. BEN JEMAA et J.C. GOMET.- Observation de l'émission de l'exciplexe Ar H^* dans des jets de plasmas d'argon-hydrogène raréfiés C7-91
- P. RANSON and J. CHAPPELLE.- Calculation of the free-bound continuum of rare gases C7-93
- L.W.G. STEENHUIJSEN, N. VAN SCHAIK, L.C.A.M. VAN DE NIEUWENHUYZEN and F.H.P. VERSPAGET.- Measurements of the production of neon 2p atoms by dissociative recombination C7-95
- N. VAN SCHAIK, L.W.G. STEENHUIJSEN, P.J.M. VAN BOMMEL and F.H.P. VERSPAGET.- Determination of the coefficients of collisional transfer between the 2p levels of neon C7-97
- D. OHEBSIAN, N. SADEGHI, C. TRASSY and J.M. MERMET.- Argon-titanium hollow cathode afterglow C7-99
- M.G. VASIL'EV, T.V. ZHIKHAREVA and G.K. TUMAKAEV.- The relative contribution of associative ionization and photoionization in xenon precursors C7-101
- A.N. VASILIEVA, I.A. GRISHINA, V.I. KITTOROV, A.S. KOVALEV and A.T. RAKHIMOV.- On the three-body electron attachment to oxygen in the plasma of a non-self-maintained discharge C7-103
- A.K. GRIGORIADY and O.I. FISUN.- On charge-exchange of ions in plasma. C7-105
- G.V. NAIDIS and V.A. SINELSHIKOV.- Determination of quenching cross-section of resonant $\text{Cs}(6\text{P})$ state by CO_2 molecules in discharge in $\text{He} - \text{CO}_2$ -Cs C7-107
- I.I. MOROZOV and V.L. TALROSE.- Molecular dissociation on bombardment by electrons of an energy lower than the ionization potential C7-109
- N.A. KERVALISHVILI and V.P. KORTKHONJIA.- Ionization average frequency in anode sheath of Penning-type high-voltage discharge C7-111
- V.I. LUKASHENKO.- Formation of $\text{K}_2(\text{A}^1\Sigma_u^+)$ molecules caused by $\text{K}(4\text{P})$ atoms in potassium discharge C7-113
- P.A. BOKHAN, V.M. KLIMKIN, A.N. MAL'TSEV, V.E. PROKOPIEV and V.G. SOKOLIKOV.- Investigation of anomalously high-speed de-excitation of Eu^+ metastable states in gas discharge plasma using modulation of induced radiation C7-115
- P.A. COXON and J.L. MORUZZI.- Positive ion mobilities in carbon dioxide C7-117
- M.S. DIMITRIJEVIĆ and P. GRUJIĆ.- A modified adiabatic theory calculation for the stark broadening of HeI ($3^1\text{P}^0 - 2^1\text{S}$) C7-119
- F. Kh. KIDRASOV.- Excitation of magnesium atoms in hollow cathode discharge C7-121

- LOW PRESSURE DISCHARGES
- POSITIVE COLUMNS
- IONIZATION WAVES AND INSTABILITIES
- NEGATIVE GLOW, HOLLOW CATHODE DISCHARGES
- RADIOFREQUENCY DISCHARGES
- TOWNSEND DISCHARGE ; BREAKDOWN AND PULSE DISCHARGES

- V.A. GODYAK and A.S. KHANNEH.- Experimental investigation of radio-frequency discharge in helium ... C7-125
- F. DOTHAN and Yu.M. KAGAN.- The composition of the positive column of a helium glow discharge at intermediate pressures C7-127
- A. ASHRAF, U.K. ROYCHOWDHURY and P. K. GHOSH.- Population densities of triplet excited states in a diffuse nitrogen plasma C7-129
- R. WINKLER, J. WILHELM, A.A. IVANOV and V.V. STARYKH.- Comparison between some macroscopic properties of the beam and glow discharge plasma in nitrogen C7-131
- P. MICHEL, S. PFAU, A. RUTSCHER and R. WINKLER.- Diffusion theory of the positive column in hydrogen glow discharges with variable degree of dissociation C7-133
- J.W. DETTMER and A. GARSADDEN.- Role of $O_2^+(a^1\Delta)$ in the oxygen plasma C7-135
- G. MUSA, A. POPESCU and N. NICULESCU.- Positive column constriction in cesium plasma discharge C7-137
- J.S. LEVINE and F.W. CRAWFORD.- Fluid theory of plasma double-layers C7-139
- P.G.A. THEUWS, H.C.W. BELJERINCK, C.E.E. PERNOT, D.C. SCHRAM and N. F. VERSTER.- Molecular beam sampling of metastable atoms from a hollow cathode arc as a probe for the electron temperature C7-141
- A.E.D. HEYLEN.- Electron-molecule collision frequencies from breakdown data in a crossed magnetic field for ethane gas C7-143
- M. AKAZAKI, K. NISHIJIMA and M. HARA.- Processes of impulse breakdown in N_2-O_2 gas mixtures and in air at low pressure C7-145
- V.A. GODYAK and A.S. KHANNEH.- Theoretical investigation of radio-frequency discharge in γ -regime.. C7-147
- W. ROZNIERSKI and J. MECHLIŃSKA-DREWKO.- The ratio of lateral diffusion coefficient to mobility for electrons in oxygen and carbon dioxide C7-149
- L. LINDBERG and S. TORVEN.- Some characteristics of an electric double layer in a magnetized plasma C7-151
- S. IMAZU, H. FUJITA, K. MIURA and T. TAKAMATSU.- Nonlinear effect of the ionization waves on the temperatures charged particles in a magnetized positive column.. C7-153
- Yu.B. GOLUBOWSKY and R. SONNENBURG.- Investigations of the contraction mechanism in a helium medium pressure discharge C7-155
- P. MICHEL, S. PFAU, A. RUTSCHER and R. WINKLER.- The positive column in the three-component mixture Ne/H_2 -experimental results in comparison with an approximative diffusion theory C7-157
- J. TAILLET.- The radio-frequency sheath in self sustained plasmas C7-159
- Yu.I. BICHKOV, V.V. OSIPOV and V.A. TELNOV.- Characteristics of the combined discharge in average pressure gas C7-161
- R.N. FRANKLIN.- Stability of the plasma-sheath C7-163
- M.E. TALAAAT.- Radiofrequency discharge tests with helium flow ... C7-165
- R.G. EARL and A. PREST.- Observations of harmonics of the discharge current in electrodeless R.F. discharges in gas mixtures C7-167
- P. KOCIAN, J.M. MAYOR and S. BOURQUARD.- Some properties of the low-pressure discharge in silane. C7-169
- C. POPOVICI, M. BALACEANU, NICU CEAUSESCU and E. AVRAM.- On the characteristics of a high voltage glow discharge C7-171
- S. IBADOV.- On the formation of plasma carbon component in the hollow cathode anomalous glow discharge..C7-173
- I. GERALD ROGOFF.- A general characteristic equation for a diffusion-controlled positive column of circular cross section with one-step and two-step ionization processes.C7-175
- V.G. VDOWIN, A.D. HAHAEV.- Experimental study on plasma nonequilibrium of high pressure metal-halide discharge C7-177
- H.T. SAELEE, M.J. COOKE and J.E. ALLEN.- E-I characteristics of an optically pumped mercury positive column C7-179
- D. GROSU and C.S. GROSU.- Remarks on the breakdown of an electric gas discharge C7-181
- V. MARTISOVITS.- Effect of collisions between the metastable atoms on their radial transport in a positive column at various spatial distributions of electrons C7-183
- V. MARTISOVITS.- Transport of metastable atoms in a positive column including radial variation of the excitation rate C7-185

- G. POPA, M. SANDULOVICIU, P. CROI-TORU and C. MOLDOVAN.- Electron beam generation by a hollow cathode discharge C7-187
- G. POPA.- The influence of the electron-neutral collisions on the ionization waves in a helium plasma C7-189
- E. BERGER and A. HEISEN.- Electron energy distribution, electric field and transport coefficients in the Faraday Darc Space C7-191
- G. CICCONE, V. MOLINARI and L. POL-LACHINI.- A nonlinear kinetic theory for HF plasma generation and electron heating C7-193
- S.Z. MOHAMAD and A.P. PETKOV.- Use of time-resolving high resolution spectroscopy in the investigation of pulse hollow-cathode discharges C7-195
- A. BOUVIER, S. ABED, B. CHARLET and A. BOUVIER.- Investigation of an early helium afterglow plasma produced by a microwave surfaguide.. C7-197
- G.A. DYUZHEV, E.A. STARTSEV and V. G. YUR'EV.- Physical processes in arc hollow cathode C7-199
- V.I. BABANIN, V.B. KAPLAN, I.N. KOLYSHKIN, V.I. KUZNETSOV, A.M. MARTSINOVSKII, A.S. MUSTAFAEV, V. I. SITNOV and A.Ya. ENDER.- Optical investigations of the spontaneous extinction of the high-current Knudsen arc discharge in Cs-Ba gas mixture C7-201
- J.T. LONDER.- A current-voltage characteristic of non-self-maintained discharge C7-203
- G.G. ARUTUNIAN and G.A. GALECHIAN.- The peculiarities of the diffusion processes in the electronegative gas plasma C7-205
- V.G. NAUMOVETS, L.L. PASECHNIK and V.V. YAGOLA.- Anomalous conductivity of low pressure HF discharge in magnetic field C7-207
- S.D. WAGNER, I.S. NISCONEN.- Electron energy distribution function and atom ionization processes in high frequency discharge mercury-argon plasma C7-209
- E.F. GORBUNOVA, A.N. EZUBCHENKO, A. I. KARCHEVSKY and Yu.A. MUROMKIN.- The separation of isotopes of noble gases in stationary high frequency discharge with travelling magnetic field C7-211
- A.I. KARCHEVSKY and E.P. POTANIN.- "Mass-diffusion" mechanism of isotope separation in gaseous discharge system with travelling magnetic field C7-213
- V.B. GIL'DENBURG, A.G. LITVAK and A.D. YUNAKOVSKY.- The dynamics of a high-frequency discharge in a wave beam C7-215
- I.R. GEKKER.- On the generation of fast electrons during interaction of microwave fields with collisionless plasma of subcritical density C7-217
- S.G. ARUTYUNYAN, I.R. GEKKER, D.M. KARFIDOV and A.A. RUCHADZE.- Ionization of gases in strong electromagnetic fields C7-219
- S. Yu. BOGDANOV, V.S. MARKOV, A.G. FRANCK and A.Z. KHODZHAEV.- Experimental study of fast reconnection of the magnetic fields through plane pinch current sheet C7-221
- P.S. LANDA, Yu.V. PONOMAREV.- Influence of the metastable atoms lifetime on the running striation excitation C7-223
- HSU HSUEH-CHI.- An investigation on the frequency characteristics of the RF discharge in Ar-Hg mixtures C7-225
- G.S. SOLNTZEV, S.A. DVININ and L.I. TSVETKOVA.- The comparison of some characteristics of electrodeless UHFD in waveguide and of DCD C7-227
- N.N. RYKALIN, A.V. NIKOLAEV and A.P. BORZHOV.- Temperature of heavy-current cylindrical hollow cathode.. C7-229
- L.M. VOLKOVA, A.M. DEVIYATOV, E.A. KRALKINA and A.V. KURALOVA.- The investigation of the fast electrons energy distribution in the positive column and negative glow of the low pressure helium discharge. C7-231

III

- HIGH PRESSURE DISCHARGES
- SPARKS, BREAKDOWN, CORONA DISCHARGE
- PROPERTIES OF ARC PLASMA ; ARC DYNAMICS
- PLASMA FLOWS
- CHEMICAL REACTORS

- A. GLEIZES, H. KAFROUNI and S. VAC-QUIE.- Mechanisms of electron disappearance in a decaying plasma arc C7-235
- H. KAFROUNI, A. GLEIZES and H. DANG DUC.- Difference between electron temperature and heavy particles temperature in arc plasma C7-237
- T. BRACKE, H.T. SOMMER and C.G. STO-JANOFF.- Numerical simulation of a decaying argon arc C7-239
- A. BOULLOUD, J. CHARRIER and R. LE NY.- Positive glow corona along a cylindrical rod between two parallel plates C7-241
- K.A. BUNTING.- The arc diameter and rate of rotation of a magnetically rotated arc with superimposed gas flow C7-243

- R.T. WATERS and E.O. SELIM.- Temporal space-charge field-changes at the cathode in negative polarity discharge C7-245
- J.M. BARONNET, J. RAKOWITZ, J.F. COUDERT, E. BOURDIN, P. FAU-CHAIS, ERCHOV and E. PAVLOV.- Spectroscopic diagnostics of A. D.C. nitrogen plasma jet C7-247
- P. BAYLE, M. BAYLE, E. MORALES.- Experimental determination of the spatio-temporal distribution of the space charge field in a breakdown C7-249
- W. HAUSCHILD and W. MOSCH.- Reasons for the dispersion of breakdown voltages in SF₆ C7-251
- E. ANTONIOS VLASTÓS.- Effect of polarity on the impulse breakdown of SF₆ C7-253
- M.M. KEKEZ and P. SAVIC.- Shock waves in spark channels, Part 1 ... C7-255
- M.M. KEKEZ, G.D. LOUGHEED and P. SAVIC.- Shock waves in spark channels, Part 2 C7-257
- H. SHINDO, S. IMIZU and T. INABA.- Electron energy relaxation effect on the dynamic characteristic of argon plasma arc C7-259
- R. WINKLER, J. WILHELM, A.A. IVANOV and V.V. STARYKH.- Kinetics of the electrons in the stationary beam discharge plasma in diatomic gases C7-261
- C.K. BHANSALI and D.M. BENENSON.- Numerical analysis of arcs in supersonic flow C7-263
- I. ABBAS and P. BAYLE.- Numerical simulation of nitrogen discharge: formation of electron shock wave. C7-265
- E.W. GRAY and J.R. PHARNEY.- Enhanced arcing as a function of organic exposure and arc current Pd and Pd/Ag electrodes C7-267
- G.R. JONES, M.R. SMITH, M. IRIE, H. L. WALMSLEY and D.C. STRACHAN.- The correlation of local voltage and cross-sectional areas for very high current gas blast arcs in air and SF₆ C7-269
- B. ELIASSON and U. KOGELSCHATZ.- Ozone production in a homogeneous oxygen discharge C7-271
- J.J. DAMELINCOURT, M. SEVIGNE, M. AUBES and L. SCOARNEC.- Axial segregation in Hg-Tl-I discharges operated at 50 Hz C7-273
- K. JAYARAM and K.H. TSUI.- Particle distributions in metal vapour-rare gas arc discharges C7-275
- K.H. GROH and S.E. WALTHER.- Operation modes of hollow cathode arcs with reduced gas flow C7-277
- J. SCHMITT and M. NEIGER.- Visible and infrared continuum radiation from a low temperature Cl₂-arc .. C7-279
- A.P. KCHUZEEV, Yu.D. KOROLEV, V.A. KUZMIN, G.A. MESYATS, V.P. ROT-SHEIN and I.A. SHEMYAKIN.- High-current diffuse discharge with the explosive cathode process.... C7-281
- J.J.A.M. VAN DER MULLEN, B.F.M. POTS, D.C. SCHRAM and B. VAN DER SIJDE.- The reduction of diffusion by plasma rotation and ion dissipative effects C7-283
- R.J. ROSADO, D.C. SCHRAM and J. LECLAIR.- Continuous emission, lowering of the ionization potential and total excitation cross-sections of an atmospheric thermal plasma..C7-285
- G.C. CRICHTON, I.W. McALLISTER and E. BREGNSBO.- Positive corona onset in atmospheric air-a multiple avalanche process C7-287
- S. VIBHOLM, A. PEDERSEN and P. THYREGOD.- Determination of low probability first breakdown voltages in compressed SF₆ C7-289
- O. HAVELKA and Z. VÁVRA.- Quantitative analysis of interaction between a high-pressure plasma column and surrounding liquid C7-291
- M. HRABOVSKY, M. KONRÅD and P. SKODA.- Theoretical model of current-zero behaviour of axially blown arc in SF₆ C7-293
- G.H. BAUER.- Spectroscopic analysis of prebreakdown-phase from positive corona into spark in N₂ C7-295
- LE GROUPE DE RECHERCHE DE SAINT-PRIVAT-D'ALLIER.- Recherches sur la foudre en France C7-297
- P. KOVITYA, J.J. LOWKE and A.D. STOKES.- Theory of arc clogging in nozzles C7-299
- E. BARRETO and H. JURENKA.- A subsonic electron fluid and the formation of small sparks C7-301
- M. SKOWRONEK, L. GIRY, VU TIEN GIA and P. ROMEAS.- Conductivity measurements of high current, high pressure discharges C7-303
- P.F. WILLIAMS, R.J. CRUMLEY and M.A. GUNDERSEN.- Studies of the basic processes responsible for laser-triggered breakdown in gases C7-305
- L.P. BRADLEY and E.L. ORHAM.- Characteristics of a high density directed plasma source C7-307
- R. MOLL and E. SCHADE.- Measurements at current zero in a SF₆ gas blast breaker C7-309
- M.S. ABOU-SEADA and KH.I.M. ALI.- Static breakdown analysis of compressed SF₆ in positive rod-to-plane gaps C7-311
- W. TILLER.- The mass flow field of the full circle arc C7-313
- J. FORT, J. BONNET, G. FOURNIER and D. PIGACHE.- Cathode density wave in an electron beam controlled discharge C7-315

- D. FIGACHE, J. BONNET, J. FORT and G. FOURNIER.- Production of hydrazine from ammonia in an atmospheric pressure electron-beam controlled discharge C7-317
- R.J. ZAHN and S. MÜLLER.- Gas temperature dependence of AC discharges between isolated electrodes C7-319
- F. KASSABJI, P. FAUCHAIS.- Heat transfer and flow in a hydrogen plasma reactor C7-321
- R.S. SIGMOND and D. LINHJELL.- The extraction of thermal energy positive ions from corona discharges in air C7-323
- H. BEYER, W. PUNK and H.G. KLOSS.- Plasma diagnostics in horizontally burning metal halide discharges C7-325
- G. BUCHET, R. HAUG and J. MAFTOUL.- CN molecular bands in a free burning metal electrodes arc C7-327
- V.F. KLIMKIN and V.V. PICKALOV.- Optical interferometry of pulsed micro-discharges C7-329
- V.D. PESKOV.- On the VUV radiation of Townsend avalanches C7-331
- V.D. PESKOV.- On the influence of electrodes on the properties of high pressure discharge C7-333
- V.D. PESKOV.- On ionization instabilities of high pressure discharges C7-335
- A.A. BOGDANOV, V.B. KAPLAN, A.M. MARTSINOVSKIY and V.G. YUR'YEV.- Plasma formation kinetic at Knudsen arc ignition C7-337
- F.G. BAKSHT, V.G. IVANOV.- Theory of low-voltage arc in noble gas.. C7-339
- F.G. BAKSHT, A.B. RYBAKOV.- Theory of hollow cathode in atmospheric arc in noble gas C7-341
- K.S. KLOPOVSKY, G.B. LOPANTSEVA, A.F. PAL, I.G. PERSIANTSEV and A.N. STAROSTIN.- Peculiarities of pulsed non-self-sustained discharges in mixtures containing CO C7-343
- A.F. PAL, I.G. PERSIANTSEV, Yu.V. PETRUSHEVITH and A.N. STAROSTIN.- On the peculiarities of passage of a low-current electron beam through gases C7-345
- V.I. GEBALOV, V.G. SAMOLOVITCH and Ju.V. FILIPPOV.- The numerical simulation of silent discharge in oxygen. Integral characteristics of discharge channel and the role of excited species reactions C7-34
- I.I. EGOROV, L.N. LESNEVSKY, G.A. POPOV, A.G. SOBOL and V.N. TURIN.- Optimisation of the characteristics of the plasma flow from a dielectric chamber C7-349
- M. LAAN, H. KORGE and K. KUDU.- The field strength and electron density calculations for the corona pulses C7-351
- Cz. KRÓLIKOWSKI, A. KAMIŃSKA-PRANKE.- An attempt to describe voltage-current characteristics of an arc when utilizing equations of magnetohydrodynamics C7-353
- J.F. COUDERT, E. BOURDIN, J.M. BARONNET, J. RAKOWITZ and P. FAUCHAIS.- Chemical kinetics study of nitrogen oxide synthesis in a D.C. plasma jet : A proposed model C7-355
- V.V. ALEXANDROV, V.A. DANILYCHEV, V. N. KOTEROV, V.V. PUSTOVALOV and A. M. SOROKA.- To the theory of electroionized discharge C7-357
- V.G. YESELEVICH, V.G. FAINSTEIN.- On expansion of the collisionless plasma into vacuum C7-359
- N.B. BOGDANOVA, B.G. PEVCHEV and V. I. POPKOV.- Electrical field strength on the positive corona electrode with the counterflow of negative ions C7-361

IV

- DISCHARGES FOR LASERS

- Irving J. BIGIO.- Electron-attaching gases in laser discharges : altered discharge parameters and negative-ion production C7-365
- A.A. KOSTYLEV, J.I. LONDER, A.P. TERENTYEV, K.N. ULYANOV and V.A. FEDOROV.- On the mechanism of glow discharge instability following the turn-off a non-self-sustained ionization source C7-367
- A.A. KOSTYLEV, V.I. PEREVODCHIKOV, A.P. TERENTYEV, K.N. ULYANOV and V.A. FEDOROV.- Investigations of instabilities in a non-self-sustained repetitively pulsed discharge. C7-369
- E.P. GLOTOV, V.A. DANILYCHEV, A.I. MILANICH and A.M. SOROKA.- Current voltage characteristics of a self-sustained electrophotoionized discharge in laser mixtures C7-371
- A. LUDMIRSKY, Ch. COHEN and Yu. KAGAN.- Kinetic processes in non-heated copper vapour laser C7-373
- H. URBÁNKOVA, L. PEKÁREK.- Long-time changes of an ionization wave in the CO₂ + N₂ + He mixture C7-375
- W.F. BAILEY and A. GARSADDEN.- Nonequilibrium dissociation phenomena C7-377
- H.J. EICHLER, H. KOCH, J. PAFFENHOLZ, J. SALK and G. SKROBOL.- Two novel HCD-structures for CuII-lasers and their performance C7-379
- M. NEIGER.- Theoretical study of negative absorption for H⁺ affinity radiation C7-381
- B. FELTS.- Réalisation et expérimentation d'un laser à vapeur de cuivre..... C7-383

- S. BOURQUARD, J.M. MAYOR and P. KOCIAN.- Measurement of the electron energy distribution in a CO₂ laser plasma C7-385
- V.A. BURTSEV, L.A. ZELENOV, A.A. KONDAKOV, R.F. KURUNOV, V.G. SMIRNOV and V.F. SHANSKY.- Optical homogeneity and molecular gas heating in a semi-self-sustained discharge C7-387
- H. AMEMIYA, T. DOTE and S. KAWAMOTO.- Relation between the striation and the stimulated emission in a He-Ne laser C7-389
- A. MARK PRELAS and G.H. MILEY.- Collisional processes in the He-CO₂ atomic carbon nuclear pumped laser 1.454 μ C7-391
- N.G. BASOV, E.P. GLOTOV, V.A. DANI-LYCHEV, A.I. MILANICH and A.M. SOROKA.- Self-sustained electro-photoionized discharge in compressed gases C7-393
- B.V. KUTEV, A.S. SMIRNOV and A.P. ZHILINSKY.- Application of RF discharge with rotating electric field for excitation of CO₂-laser C7-395
- D. AUPHELLE, F. EUVE, M. FITAIRE, A.M. POINTU, M. VIALLE and L. WARTSKY.- Study of a nitrogen-neon induced plasma C7-397
- V
- DISCHARGE AND BREAKDOWN IN VACUUM
- K. MIKKELSON, M. KRISTIANSEN and J. LIN, J. THOMPSON.- Electro-optical measurements of insulator surface flashover in vacuum C7-401
- G.N. FURSEY, V.E. PTYTSIN and N.V. EGOROV.- Influence of magnetic field on the effects preceding the transition of field emission into the vacuum breakdown C7-403
- A.S. POKROVSKAYA-SOBOLEVA, T.S. BORISOVA, G.S. GRISHUTIN and J.N. NASTITCH.- Studies of discharge phenomena during transition from breakdown in vacuum to breakdown in gas C7-405
- K. FRÖHLICH, W. WIDL.- Determination of the microscopic field enhancement factor β of prestressed vacuum interrupter contacts C7-407
- A.A. PERTSEV, V.P. SHADOV.- The experimental study of arc cathode microspots life-time by the velocity microphotography C7-409
- D.I. PROSKOUROVSKY and V.F. PUCHKAREV.- The effect of non-metallic inclusions and films on the cathode on some processes during vacuum discharges C7-411
- C.W. KIMBLIN, F.A. HOLMES, J.G. GORMAN and P.G. SLADE.- Extinction of a vacuum arc by application of a transverse magnetic field C7-413
- G.N. FURSEY, V.M. ZHUKOV, L.A. SHIROCHIN, A.F. ALEKSANDROV and S.Y. GALUSO.- Formation of high-current and density electron beam on gallium cathode with the limited emission surface C7-415
- VI
- LONG SPARKS AND LIGHTNING
- D. KOOPMAN, J. GREIG, R. PECHACEK, A. ALI and I. VITKOVITSKY, R. FERNSELER.- CO₂-laser produced channels for guiding long sparks in air ... C7-419
- P. HUBERT, G. MOUGET.- Mesure de la vitesse d'ascension du "return-stroke" en fonction de l'intensité pour deux éclairs déclenchés C7-421
- N.L. ALLEN, T.E. ALLIBONE and D. DRING.- Variation of corona inception and sparkover with positive impulse voltage in a rod/plane gap: effect of negative small ion variation C7-423
- T.E. ALLIBONE and J.C. SAUNDERSON.- Breakdown of sphere and sphere/plane gaps stressed with D.C. voltage; the effect of "conditioning" C7-425
- Henryk RYZKO.- Propagation of the leader of a long spark in air without participation of thermal ionization processes C7-427
- S. LARIGALDIE.- Linear gliding discharge over dielectric surfaces... C7-429
- VII
- SURFACE PHENOMENA
- ELECTRODE PHENOMENA
- SURFACE TREATMENT USING PLASMA (Deposition, etching, oxidation, etc...)
- S.W. TEMKO, S.K. KUZMIN, M.R. HADGY-OGGLY and T.V. IAGODOVSKAIA.- On the formation of the thin solid pellicle of nitric oxides on the liquid ozone surface in the atmosphere of smouldering discharge in nitrogen...C7-433
- P. MASSMANN, H.J. HOPMAN and J. LOS.- H₂⁺ production by interaction of a H₂⁺-ion beam with a surface C7-435

- M.G. DROUET, P. DANCER, P. KIEFFER and H. MERCURE.- Simultaneous measurements of microcrater emissions of current and copper light at the cathode of a moving arc C7-437
- E. HANTZSCHE.- Impact and resistive heat sources of cathode spots in arc discharges C7-439
- A.J. DIXON and A. VON ENGEL.- Energy spread of cluster ions from a molten metal C7-441
- A. GOLDMAN and R.S. SIGMOND.- Effects of negative air coronas on plane anode foils C7-443
- HARUO ITOH and NOBUAKI IKUTA.- Temporal increase of ionization current in N₂ gas C7-445
- S. MERCURIO.- Ablation of solid hydrogen in contact with magnetized plasmas: can the external magnetic field be the upper limit of the self consistent electric field at the solid surface? C7-447
- L. BÁRDOS and J. MUSIL.- Microwave generation of a magnetoactive oxygen plasma for oxidation C7-449
- Harald L. WITTING.- An investigation of arc starting on cold cathodes. C7-451
- G. THIELL and M. FABRY.- Etude théorique des phénomènes liés à une cathode liquide: estimation du taux d'érosion C7-453
- A. BALTOG and G. MUSA.- Surface phenomena in cesium and cesium-noble gas filled thermionic diode C7-455
- A. BALTOG and G. MUSA.- Influence of the interelectrode charge diffusion outside of the gap on the thermionic diode VI characteristics C7-457
- A.A. KUZOVNIKOV, V.L. KOVALEVSKII, V.P. SAVINOV and V.G. YAKUNIN.- The investigation of physical properties of the near electrode region of HF discharge C7-459
- M. SCHMIDT, R. SEEFELDT and G. POHLE.- Mass-spectrometric investigation of the ions in an Ar-hexamethyldisiloxane discharge C7-461
- G.A. DYUZHEV, N.K. MITROFANOV, S.M. SHKOLNIK and V.G. YUR'EV.- Anode region of high current arc discharge C7-463
- L.I. KISELEVSKII, N. Ya. KLYGIN, A.N. MAKAREVICH and D.A. SOLOVYANCHIK.- Effect of discharge radiation on electrode processes in helium C7-465
- A.I. BUSHIK.- Dynamics of the electrode processes on the reinforced materials at high-current pulsing discharge C7-467
- J. KŁOBUKOWSKA and J.S. BRZOSKO.- Note on the self-sustaining creep discharges in gas at the dielectric surface C7-469
- J.S. BRZOSKO, E. ZUKOWSKI, J. GRUDZINSKI, W. ZUKOWSKI and A. KONARZEWSKI.- Probability of the creep discharges C7-471
- E.N. ZORINA, A.V. DOBRENIN, T.O. POPOVA, T.I. PAVLASHVILI, O.V. TOLMATSHOVA, S.A. NEUSTROEV and E.B. SOKOLOV.- Some particularities of the molecular exchange in a HF flow pressure discharge C7-473

VIII

- MISCELLANEOUS DISCHARGE DEVICES

- J. FREISINGER, S. REINECK and H.W. LOEB.- The rf-ion source RIG 10 for intense hydrogen ion beams ... C7-477
- V.G. DUDNIKOV and G.I. FIKSEL'.- Surface plasma source of hydrogen atoms with an energy of hundreds eV C7-479
- N.N. KOVAL, Yu.E. KREINDEL and P.M. SHANIN.- The arc discharge of low pressure with two constricted channels and the anode plasma of large cross-section C7-481
- L.L. HATFIELD, H.C. HARJES, KRISTIANSEN, A.H. GUENTHER and K.H. SCHÖNBACH.- Laser/fiber optic breakdown of a pulse charged 90% Ar-10% N₂ gas switch C7-483
- V.A. BURTSEV, V.A. DUBYANSKI, N.P. EGOROV, M.P. KASATKINA, A.B. PRODUNOV and I.V. SHESTAKOV.- Investigation of electrical explosion of cylindrical foils in air. Coaxial high-current discharges C7-485
- M.M.B. WIJNAKKER and E.H.A. GRANNE-MAN.- A study of a weakly ionized, rotating plasma C7-487
- P. HOFFMANN, H. HÜGEL, W. SCHALL and W. SCHOCK.- Microwave discharge in a supersonic flow C7-489
- N. St.J. BRAITHWAITE and J.E. ALLEN.- Pulsed current voltage characteristics of a thermally produced plasma C7-491
- M. STIEBER and W. STERN.- The effective overvoltage of AC plasma display discharges C7-493
- V.B. KAPLAN, A.M. MARTSINOVSKIY, F.N. RASULOV and V.G. YURIEV.- Kinetic of negative grid pulse influence upon discharge plasma C7-495
- V.G. BAKSHI, A.M. MARTSINOVSKIY and V.G. YUR'YEV.- Low-voltage arc plasma in three-electrode system C7-497
- G.B. LOPANTSEVA, A.F. PAI', A.F. PEREVOZNOV, I.G. PERSIANTSEV and A.N. STAROSTIN.- Effect of gas purity on the current of a non-self sustained discharge in nitrogen C7-499

Yu. I. BEL'CHENKO and V.G. DUDNIKOV
.- Negative ion production in surface-plasma sources with unclosed electron drift discharges C7-501

M.P. RYUTOVA.- Spectrum of charge exchange neutrals from rotating plasma C7-503

A.E. BELYANKO, N.I. LIPATOV, P.P. PASHININ and A.M. PROKHOROV.- Ultraviolet radiation of the surface discharge is a preionizer of high pressure atomic-molecular impurities C7-505

N.A. KOSHILEV, N.A. STROKIN, A.A. SHKISO and A.V. MIKHALEV.- Application of the magnetic flux plasma trap to generation of current sheets in a rarefied plasma C7-507

IX

- GENERAL PLASMA THEORY
- TRANSFER PHENOMENA
- NUMERICAL METHODS

R. BALESCU and I. PAIVA-VERETENNICOFF.- Kinetic equation for a plasma in a strong high frequency electro-magnetic field C7-511

N.E. FRANKEL, K.C. HINES and R.D.B. SPEIRS.- Dielectric response and energy loss for an intermediate quantum plasma C7-513

V.A. ROZHANSKY.- Effective boundary conditions for a plasma in a magnetic field, adjacent with an electrode C7-515

LU QUAN-KANG.- A generalized Ohm's law of unsteady state in partially ionized gases C7-517

A.V. GORBATOV and E.V. SAMUILOV.- Electrophysical properties of non-equilibrium aerosol plasma C7-519

A.P. ERSHOV and A.A. KUZOVNIKOV.- Electron energy distribution function in Xe plasma in the presence of Coulomb collisions C7-521

A. Ya. ENDER and V.I. KUZNETSOV.- On the linear theory of electron processes in the collisionless diode C7-523

W. ROZMUS.- The time dependent transport coefficients for the two-component plasma C7-525

F. MANFRED.- About the generation of a "resultant drift inwards" from the boundary of a D-T-plasma by electromagnetic fields C7-527

L.L. LENGUEL.- Effect of transport processes on tokamak refueling by pellet injection C7-529

Alf H. ØIEN.- A plasma kinetic equation including strong fields and inhomogenities C7-531

TRAN NGOC AN, E. MARODE, G. FOURNIER and P. SEGUR.- Electron distribution function in a very non uniform electric field C7-533

V.C. BOFFI, V.G. MOLINARI and G. SPIGA.- Electron distribution function and ionization in space-dependent plasma theory C7-535

P.Z. CHEBOTAEV and G.E. VEKSTEIN.- The Bohm-type thermal losses from a high- plasma C7-537

P. SEGUR, S. PAREATHUMBY, M. YOUSFI and E. MARODE.- Determination of macroscopic quantities for a Townsend discharge in helium by both Boltzmann equation and Monte Carlo methods C7-539

X

- WAVES
- WAVE PROPAGATION
- WAVE-PARTICLE AND WAVE-WAVE INTERACTIONS
- INSTABILITIES
- STRONG TURBULENCE

H. AKIYAMA, T. YAMADA and S. TAKEDA.- Wave propagation in a cylindrical geometry C7-543

J.T. MENDONÇA.- Wave and particle interactions with a nonlinear dielectric perturbation in a plasma C7-545

J.E. ALLEN and L.M. WICKENS.- Hydro-magnetic rarefaction waves C7-547

J.G. TURNER and T.J.M. BOYD.- Upper hybrid solitons C7-549

T.J.M. BOYD, G.A. GARDNER and G.J. HUMPHREYS-JONES.- Self-generated magnetic fields and harmonic emission C7-551

S.S. PESIC.- Parametric decay of lower hybrid waves C7-553

ICHIRO. MORI and H.D. LEPPERT, K. WIESEMANN.- Characteristics of spatial wave echoes at the lower hybrid branch C7-555

Yu. M. ALIEV, O.M. GRADOV and V. STEFAN.- Magnetized plasma parametric resonance in non-monochromatic pump-wave C7-557

R.J. VIDMAR and F.W. CRAWFORD.- Dispersion characteristics of plasma wave-packets C7-559

T.A. DAVYDOVA and K.P. SHAMRAI.- Modulational instability and evolution of non-uniform Langmuir fields in plasmas C7-561

- B.N. BREIZMAN.- WKB model of the collapse of Langmuir waves C7-563
- N.A. ARMAND, S.A. ROGASHKOV and E. G. SHUSTIN.- Interaction of the intense microwaves with a flow of low temperature plasma (1. The experiment) C7-565
- J.P. LYNOV, P. MICHELSEN, H.L. PÉCSELI and J. JUUL RASMUSSEN.- Interaction between solitary structures in a magnetized, plasma-loaded waveguide C7-567
- T. MIKKELSEN and H.L. PÉCSELI.- Strong turbulence in partially ionized plasmas C7-569
- J.P. LYNOV, P. MICHELSEN, H.L. PÉCSELI, J. JUUL RASMUSSEN and H. SUGAI.- Nonlinear waves in a magnetized plasma waveguide C7-571
- S. IKEZAWA and Y. NAKAMURA.- A physical picture of the higher-order Landau modes of electron plasma wave C7-573
- MAGDI M. SHOUCRI.- Computer simulation of the sideband instability. C7-575
- Y. TAKEDA and M. YOKOTA.- Spiky density fluctuation and relaxation oscillation in an anomalously resistive phase C7-577
- M.T.C. FANG and S. KUHN.- On the linear stability of a collisionless single-ended Q-machine C7-579
- R. SCHRITTWIESER, E. MÄRK and S. KUHN.- Grid versus plate excitation of the electron current driven ion wave instability C7-581
- F.KH. KHAKIMOV and V.N. TSYTOVICH.- On the example of fast Langmuir solitons existence in non-equilibrium plasma C7-583
- Yu. S. SAYASOV.- Viscous damping of the magneto-acoustic oscillations, MAO, in bounded plasmas C7-585
- J. SKÁLA, J. KRÁSA and V. PEŘINA.- Two dimensional Fourier spectrum of turbulent ionization waves ... C7-587
- V.J. ŽIGMAN and B.S. MILIĆ.- On the behaviour of weakly ionized plasma with non-zero neutrals temperature placed in external D.C. electric field of moderate intensity C7-589
- C.H. SU.- Interaction of nonlinear ion-acoustic waves C7-591
- D.N. WALL and R.N. FRANKLIN.- Nonlinear interaction of beam waves and plasma waves C7-593
- MILOŠ M. SKORIĆ and BOŽIDAR V. STANIĆ.- A time domain method for transient scattering of electromagnetic waves in plasmas C7-595
- Lj. R. CANDER and B.V. STANIĆ.- Interaction of EM waves with a compressible plasma column C7-597
- P.K. CIBIN.- Influence of dissipative processes on the propagation of guided electron plasma waves on a planar plasma slab C7-599
- D.F. DUBOIS, H.A. ROSE and M.V. GOLDMAN.- A statistical theory of Langmuir turbulence C7-601
- F.P. STÖSSEL.- Electrostatic trivelpiece-gould modes in a torus C7-603
- Tu. KHIET.- Ion tail formation and saturation of the ion-acoustic instability C7-605
- A. SHIVAROVA, T. STOYCHEV.- Second order harmonic surface waves generated by one fundamental wave C7-607
- V.F. KOVALEV, V.V. PUSTOVALOV, A.B. ROMANOV and V. STEFAN.- Turbulent plasma in the field of intense high frequency radiation C7-609
- V.P. MILANTIEV and A.G. MIROSHNIKOV.- Drift motion of charged particle in resonance conditions C7-611
- V.P. MILANTIEV and P. SAIKIA.- Quasioptics in anisotropic and dispersive media C7-613
- B. LEMBEGE.- Theoretical method for predicting the properties of cyclotron harmonic waves from the perpendicular dispersion relation C7-615
- M.P. EVRARD, A.M. MESSIAEN, P.E. VANDENPLAS and G. VAN OOST.- Drift-dissipative waves and ensuing steady state of a plasma column C7-617
- L.L. PASECHNIK, L.I. ROMANYUK and N.Ye. SVAVIL'NY.- High frequency oscillations and electron beam relaxation in homogeneous gas-discharge plasma C7-619
- V.P. PAVLENKO and V.I. PETVIASHVILI.- Stability of the nonlinear periodic waves in plasma C7-621
- A.V. VOLOSEVICH, M.A. LIVSHITS and V.A. LIPEROVSKY.- Nonlinear decay interactions for the instability of Buneman-Farley C7-623
- A.V. VOLOSEVICH, M.A. LIVSHITS, V.A. LIPEROVSKY and G.A. SKURIDIN.- About the stationary turbulence regions and anomalous resistance in the magneto-sphere plasma C7-625
- M.A. LIVSHITS, V.A. LIPEROVSKY, V.M. TOMOZOV and V.N. TSYTOVICH.- The strong ion-acoustic turbulence and the electron spectrum in an electric fields C7-627
- I.A. KOL'CHUGINA, A.G. LITVAK, T.N. FEDOSEEVA and G.M. FRAIMAN.- Modulational instability of Langmuir oscillations in the field of an electromagnetic wave C7-629
- N.S. BUCHELNIKOVA and E.P. MATOCHKIN.- The instability of one-dimensional Langmuir wave. Solitons and collapse C7-631
- N.S. BUCHELNIKOVA and E.P. MATOCHKIN.- The instability and damping of the Langmuir waves with different amplitudes and phase velocities .. C7-633
- A.G. LITVAK, V.A. MIRONOV and A.M. FEIGIN.- Modulation instability and plasma electrodynamic characteristics C7-635

- A.G. LITVAK, A.M. SERGEEV and N.A. SHAKHOVA.- Self-action of quasi-optical beams in a magnetoplasma . C7-637
- G.A. MARKOV, V.A. MIRONOV and A.M. SERGEEV.- Self-trapping of lower hybrid waves at the RF breakdown of gas C7-639
- A.I. ROGASHKOVA.- Interaction of the intense microwave beam with a flow of low temperature plasma (Pt. 2. The theory) C7-641
- N.A. ARMAND, S.A. ROGASHKOV and E.G. SHUSTIN.- The UHF discharge with preliminary locally ionized gaseous medium C7-643
- A.A. PERTSEV.- Ion sound dissemination in moving plasma jet C7-645
- V.P. GERASIMOV, S.A. KAREV, V.A. OBUKHOV and G.G. SHISHKIN.- H.F. instabilities in the heterogeneous plasma of a penning discharge ion source with a hollow cathode C7-647
- S.M. MUSER, B.D. OCHIROV and A.M. RUBENCHIK.- On nonlinear stage of parametric instabilities of waves excited by localized pumping C7-649
- S.A. BEL'KOV and V.N. TSYTOVICH.- Magnetic field generation by intense Langmuir plasma waves C7-651
- F.F. ASSADULIN, G.M. BATANOV, A.A. VERTAEV, A.V. SAPOZHNIKOV and K.A. SARKSIAN.- Modulation of spectra of drift waves due to the high-frequency fields C7-653
- N. PAVLOVIĆ-BRAJUŠKOVIĆ and B. MILIĆ.- Threshold electron drift for the spontaneous excitation of non-electrostatic ion-cyclotron oscillations in weakly ionized plasmas C7-655
- G. PELLETIER.- Renormalization group method applied to large scale langmuir turbulence C7-657
- J.M. DOLIQUE.- Instabilités à faisceaux tournants multiples dans les faisceaux d'ions négatifs utilisés à la génération de faisceaux de neutres C7-659
- A.G. SITENKO.- Nonlinear wave interaction and critical fluctuations in plasmas C7-661
- V.À. ZILTSOV, P.M. KOZAREV, I.N. MAKASHIN, D.A. PANOV, A.A. SKOVORODA and A.G. SCHERBAKOV.- Study of low frequency oscillations in the open trap with minimum B magnetic field C7-663
- A.A. SKOVORODA and V.A. ZILTSOV.- ECR as a diagnostic for mirror trap plasma C7-665
- LU QUAN-KANG and CHEN ZHI-FAN.- On some properties of anisotropic plasmas C7-667
- W.N.-C SY and M. COTSAPTIS.- An equation for wave propagation in a hot nonuniform magnetized plasma C7-669

- J.C. ADAM, G. LAVAL and D. PESME.- Phase space granulation as a result of mode-mode coupling effects..... C7-671

XI

- NON IDEAL PLASMAS
- THEORY
- EXPERIMENTS
- N.P. KOZLOV, G.E. NORMAN and Yu.S. PROTASOV.- Superradiation from non-ideal plasmas in electric field .. C7-675
- S.W. TEMKO, K.W. TEMKO and S.K. KUZMIN.- On the thermodynamical stability of the plasma of gas discharge in the real gas C7-677
- K. GUNTHER, S. LANG, R. RADTKE and R. ULBRICHT.- Experimental investigation of the balmer spectrum from a dense hydrogen plasma near the photorecombination threshold C7-679
- S. HASHIGUCHI and M. INUTAKE.- Electrical conductivity of high-density shock-heated Ar and Xe plasmas ... C7-681
- A. LEYCURAS and J. LAROUR.- General expression of the drift velocity of excess electrons in dense fluid argon C7-683
- M. INUTAKE, K. SUZUKI and S. FUJIWAKA.- Sound velocity in metal-nonmetal transition region of high pressure mercury plasmas C7-685
- J. GLASSER, R. VILADROSA and J. CHAPPELLE.- Non ideality effects in a high pressure argon arc measured by infrared continuum absorption C7-687
- A. MIHAJLOV, D. DJORDJEVIĆ and M.M. POPOVIĆ.- On the modification of the quantum defect method applicable to dense plasmas C7-689
- A.N. LAGAR'KOV and A.K. SARYCHEV.- The conductivity of dense caesium plasma near the saturation line .. C7-691
- V.V. VOROBIOV, P.P. KULIK, A.V. PALLO, A.A. RAKITIN, E.K. ROZANOV and V.A. RIABYI.- Experimental investigation of the electrical and heat conductivities of alkali dense plasmas ... C7-693
- M.M. GOMBERT, C. DEUTSCH and H. MINOO.- Thermodynamical functions for dense multicomponent plasmas C7-695
- H. MINOO, M.M. GOMBERT and C. DEUTSCH.- Two particle effective potential of a dense homogeneous plasma ... C7-697

XII

- ASTROPHYSICAL PLASMAS

- T.M. ABECASIS, A.M. MOREIRA and F.M. SERRA.- On electron-coherent whistler wave interaction and particle precipitation C7-701
- H. SUGAI, K. IDO, H. NIKI and S. TAKEDA.- Propagation of whistler waves trapped in a narrow density trough C7-703
- J.G. KIRK.- Deceleration of a fast ion in an accretion column C7-705
- V.M. ČADEŽ.- Influence of toroidal magnetic field on convection in rotating star C7-707
- J. MOITY.- Experimental determination of FeII Gf-values C7-709
- S. POBERAJ.- Propagation of condensation in coronal plasma C7-711
- J.G. LOMINADZE, G.Z. MACHABELI and A.B. MIKHAILOVSKY.- Relativistic electron-positron plasma quasi-linear relaxation at the presence of magnetic bremsstrahlung C7-713
- G.Z. MACHABELI and V.V. USOV.- A plasma model of crab nebula and pulsar Np0532 radiation in roentgen and gamma ranges C7-715
- V.P. KHODNENKO, G.G. SHISHKIN and Ju.V. TRIFONOV.- Analysis of the H.F. drift instability onboard "meteor" satellite C7-717
- I.M. OJRINGEL.- Inverted population of hydrogen atoms in a turbulent cosmic plasma C7-719
- N.A. KOSHILEV, N.A. STROKIN and A.A. SHISKO.- Some properties of interaction of magnetic piston with non-magnetized plasma C7-721
- A.T. ALTYNTSEV, V.I. KRASOV, N.V. LEBEDEV and V.V. PAPERNY.- Measurements of electron energy distribution in the theta-pinch neutral sheet C7-723
- XIII
- INTERACTION OF LASER BEAMS WITH PLASMAS
- LASER-INDUCED PLASMAS (OPTICAL DISCHARGES)
- C. RICHARD NEUFELD.- Interaction of a tea-CO₂ laser pulse with a dense hydrogen plasma C7-727
- F. AMIRANOFF, R. FABBRO, E. FABRE, C. GARBAN and J. VIRMONT.- Effect of pulse shaping on interaction processes in laser produced plasmas C7-729
- A. BRUCE LANGDON.- Nonlinear inverse bremsstrahlung and heated electron distributions C7-731
- D. WRÓBLEWSKI, A. CYBULSKI and Z. SZYMANSKI.- An experimental investigation of the continuous optical discharge C7-733
- J.C. GAUTHIER, J.P. GEINDRE and N. GRANDJOUAN.- Spectroscopic study of the ionization dynamics in a CO₂ laser-produced plasma of helium .. C7-735
- J.C. GAUTHIER, J.P. GEINDRE and N. GRANDJOUAN.- Space and time resolved measurements of electron and atomic excited states densities in a CO₂ laser-produced plasma of helium .. C7-737
- M.Y. YU, P.K. SHUKLA and K.H. SPATSCHEK.- Curvature effects in laser plasma interactions C7-739
- S. CHYRCZAKOWSKI, K. MELZACKI and M. SADOWSKI.- Spectral lines emission from carbon-hydrogen plasmas generated by TEM₁₀ laser pulses C7-741
- H. BAUMHACKER, H. BRINKSCHULTE, W. RIEDMÜLLER, M. SALVAT and S. SUDO.- Ionization of isolated deuterium pellets by neodymium laser radiation C7-743
- M.J. FORREST, R.E. KIRK and N.J. PEACOCK.- A CO₂ laser-plasma interaction experiment-The scattered spectrum of Langmuir waves driven via the electron-ion decay instability C7-745
- E. CHU, R. DRUCE, M. KRISTIANSEN, M. HAGLER and R. BENGTSOEN.- Beat heating in plasmas using CO₂ lasers .. C7-747
- R.D. BLEACH, K.G. WHITNEY, J.W. SANDELIN, T.G. FINN and D.J. NAGEL.- Carbon spectra from CO₂ laser-produced plasmas C7-749
- R.D. BROOKS, Z.A. PIETRZYK and G.C. VLASES.- Multiple-pass laser heating of a short plasma column C7-751
- W.A. JANOS.- Thomson-like RF scattering by small overdense plasma particles C7-753
- N.S. KOPEIKA, T. KARCHER and C.S. IH.- Effects of space charge on the "effective cross section" C7-755
- C. CARLHOFF, J.H. SCHÄFER, K. SCHILDBACH and J. UHLENBUSCH.- High pressure optical discharges C7-757
- A.S. KOVALEV, A.M. POPOV and A.T. RAKHIMOV.- On the mechanism of breakdown of gases by the emission from a CO₂-laser near a metal surface .. C7-759
- G.I. BAKANOVICH, L.Ya. MIN'KO and A.N. CHUMAKOV.- Investigation of plasma formation dynamics and properties of underexpanded supersonic erosive laser plasma flares C7-761
- V.A. GRIBKOV, A.V. DUBROVSKY, N.V. KALACHEV, T.A. KOZLOVA and V.Ya. NIKULIN.- Dynamics of plasma phenomena in "plasma focus" under the action of powerful laser radiation C7-763
- I. APOSTOL, E. COJOCARU, M. DINESCU, V. DRĂGANESCU, Th. JULEA, I. MORJAN, M. MOLDOVAN, I.N. MIHAILESCU and V.I. KONOV.- Plasma target coupling in the case of tea-CO₂ laser produced breakdown in front of a solid target C7-765

R. BENATTAR, C. POPOVICS, R. SIGEL and J. VIRMONT.- Interferometric measurements of density profiles in laser-target interaction C7-767

F. AMIRANOFF, R. FABBRO, E. FABRE, C. GARBAN and J. VIRMONT.- Experimental investigation of transport in laser-target irradiation experiments ... C7-769

XIV

- INTERACTION OF PARTICLE BEAMS WITH PLASMAS

A.W. ALI, J.R. GREIG, I.M. VITKOVITSKY R.B. FIORITO and R.F. FERNSLER.- Interaction of an intense relativistic electron beam with the atmosphere C7-773

E.J.T. BURNS, D.J. JOHNSON, A.V. FARNWORTH, Jr., D.L. FEHL, R.J. LEEPER, L.P. MIX and G.W. KUSWA.- Diagnostics program for a magnetically insulated ion diode for inertial confinement fusion C7-775

G. FOURNIER, J. BONNET, J. BRIDET, J. FORT and D. PIGACHE.- Electron beam energy branching in oxygen C7-777

K. IMASAKI, S. MIYAMOTO, S. HIGAKI, S. NAKAI, K. NISHIHARA and C. YAMANA-NAKA.- An evidence of anomalous deposition of REB energy to the low Z target C7-779

A.I. ROGASHKOVA, T.I. SHATALOVA.- A theory of the interaction of double-beam with plasma C7-781

L.S. BOGDANKEVICH, M.V. KUZLEV and A.A. RUCHADZE.- On the theory of excitation of rippled plasma resonators by a relativistic electron beam C7-783

J. DELVAUX, A. DEVIN, A. NICOLAS, C. PEUGNET, G. WOLFF and A. KUBALA.- Expérience d'interaction électrons-matière à Valduc C7-785

XV

- DIAGNOSTIC METHODS

- PROBES

- SPECTROSCOPY

- MISCELLANEOUS

G. GOUESBET.- Laser-Doppler velocimetry in ionized gases : a review paper C7-789

M. BACAL, G.W. HAMILTON, A.M. BRUNETEAU, H.J. DOUCET and J. TAILLET.- Measurement of H^- density in a plasma by photodetachment C7-791

D. OEPTS, E.P. BARBIAN and P.J. BUSCH.- Measurement of electron density and temperature profiles by means of multiposition Thomson scattering C7-793

J. PURIĆ, I. LAKIĆEVIĆ and V. GLAVON-JIĆ.- Some regularities within the stark widths and shifts of resonance lines of neutral atoms from He to Ca C7-795

B.F.M. POTS, J.J.H. COUMANS and D.C. SCHRAM.- Collective scattering of CO_2 -laser light by the highly ionized argon plasma of a hollow cathode arc discharge C7-797

V.G. ZATSEPIN, E.A. TISHCHENKO and A.V. GOLUBEV.- Numerical methods of data processing for active submillimeter diagnostics of plasma cylinder C7-799

L.Ya. MARGOLIN, L.N. PYATNISKII and N.P. SHTERNOV.- Low-temperature plasma investigations by resonance Rayleigh scattering of weak intensity radiation C7-801

W.R. OTT, J.M. BRIDGES and J.Z. KLOSE.- The use of gas discharges as ultraviolet radiometric standards. C7-803

A. LESAGE, J. RICHOU, P. CHARIL and M. COMBIER.- An unambiguous method of electron density measurement in a shock-generated plasma, using a laser interferometer C7-805

V.A. GODYAK and S.N. OX.- Finite thickness effect of probe sheath in radio-frequency plasma probe diagnostics C7-807

V.A. GODYAK and S.N. OX.- Investigation of sheath at electrode in radio-frequency discharge C7-809

J. FLETCHER and H.A. BLEVIN.- Use of emitted photons as a probe for low pressure gas discharges C7-811

A. PIEL and F. PINNEKAMP.- The role of molecular lines in the study of plasma satellites C7-813

M. DIMITRIJEVIĆ and N. KONJEVIĆ.- On the approximative semiclassical formula for the electron-impact width of multiply ionized atom lines in plasmas C7-815

Y. ALAYLI and M. SKOWRONEK.- Etalonnage d'une chaîne de diffusion en vue du diagnostic des plasmas C7-817

C. FOURRIER, G. LEMPERIERE and J.M. POITEVIN.- Metal atom density by atomic absorption spectroscopy in a d.c. sputtering discharge C7-819

H.G. LERON and K.G. MÜLLER.- Positive ion extraction by an anodic orifice probe C7-821

- D.M. ŠULIĆ.- Measurement of electron density by electromagnetic waves which propagate on a magnetized plasma column C7-823
- M.S. DIMITRIJEVIĆ, P. GRUJIĆ and D. KOLEDIN.- Quantum mechanical calculations of the stark broadening of some He I lines from plasmas .. C7-825
- G. CICCONI, E. BLOYET, P. LEPRINCE and J. MAREC.- Microwave reflexion in rectangular waveguides by high pressure R.F. plasma columns C7-827
- K. BEHRINGER and P. THOMA.- The high power hydrogen arc as a precise standard source of continuum radiation between 53 and 92 nm C7-829
- K.U. RIEMANN.- Theory of the sheath edge in a weakly ionized collision dominated plasma C7-831
- D.G. MUIR and P.G. CAROLAN.- Faraday rotation applied to a reverse field pinch C7-833
- J. PURIĆ, I. LAKIĆEVIĆ and V. GLAVONJIĆ.- Some regularities within the stark widths and shifts of resonance lines of singly charged ions from He to Ca C7-835
- G. HIMMEL and L. SOWA.- A method of estimating the level of collective electric field fluctuations in a nonthermal plasma with a two-temperature electron gas C7-837
- V.G. VDOVIN and N.A. VDOVINA.- On determination of TL, IN, NA normal atom concentration by resonance lines broadened with mercury pressure C7-839
- T.N. TODD.- A fully automatic continuous electron temperature measurement system using a double Langmuir probe C7-841
- J.P.J. LAFON.- On plasma sheath problems C7-843
- A. PETRAKIEV, I. KOLEVA and J. GANEVA.- A spectral chronographic and equidensitometric investigation of a pulse blended discharge C7-845
- B. CHERON, J. JAROSZ and P. VERVISCH.- Mesure des probabilités de transition des raies 5^1D_2 , 6^1D_2 , 7^1D_2 + 5^1P_1 du cadmium C7-847
- G. SCHAAL and J. ZABEL.- External and internal probe measurements in discharges of luminescence lamp type C7-849
- B. VAN DER SIJDE, T. POORTERS, S. ADEMA, B.F.M. POTS and D.C. SCHRAM.- Thomson scattering with a high background level of plasma radiation C7-851
- A.V. KUPLIAUSKIENĖ and Z.J. KUPLIAUSKIS.- Rayleigh and Compton scattering cross sections of X-rays by oxygen ions C7-853
- V.V. PICKALOV and N.G. PREOBRAZHENSKY.- Restoration of two-dimensional radiation for an optically thick plasma C7-855
- V.G. ZATSEPIN, V.B. LAZAREV and E.A. TISHCHENKO.- Application of field visualization technique to SMM diagnostics of axisymmetric plasma ... C7-857
- E.A. TISHCHENKO, A.V. GOLUBEV and V.B. LAZAREV.- Radiation temperature measurement of argon arc plasma by submillimeter diagnostic techniques C7-859
- V.G. ZATSEPIN and A.V. GOLUBEV.- Determination of the ray phase for plasma cylinder using modulus of the probing radiation transmittivity.. C7-861
- E.F. PROZOROV, J.I. LONDER, K.P. NOVIKOVA and K.N. ULYANOV.- Probe diagnostic by non-self-maintained ionization C7-863
- V.G. GUDELEV, A.P. SHKADAREVICH and V.M. JASINSKII.- Laser gas-discharge plasma diagnostics based on Faraday rotation C7-865
- M.P. BRIZHINEV, S.V. EGOROV, B.G. EREMIN, A.V. KOSTROV and A.D. STEPANUSHKIN.- Measurement of electric field in turbulent plasma by the method of satellites of forbidden transitions in helium C7-867
- E.M. BARKHUDAROV, V.R. BEREZOVSKII, T.Ya. CHELIDZE, G.V. GELASHVILI, M.T. TAKTAKISHVILI and N.L. TSINTSADE.- A holographic study of laser-produced plasma at the $10.6 \mu\text{m}$ wavelength C7-869
- E.F. GIPPIUS, B.I. ILJUKHIN and V.N. KOLESNIKOV.- Some remarks on the non-equilibrium plasma diagnostics C7-871
- Yu.I. FILENKO, B.M. STEPANOV and L.S. USHAKOV.- Holographic time-differential cine-interferometry of the gas discharge plasma C7-873
- V.I. AVERIN, O.M. BREKHOV, B.S. GORBENKO, A.F. KLEPOV, G.V. KOLESOV, L.I. KONDRASHOVA, V.V. LEBEDEV, V.A. MILLER and B.M. STEPANOV.- Streak image camera "agat" with picosecond time resolution used for investigations in plasma physics C7-875
- G. THIELL, B. MEYER, M. LOUIS-JACQUET and J.C. COUTURAUD.- Spectrométrie X dans les plasmas créés par laser ; application a l'étude des phénomènes de transport de l'énergie C7-877
- AUTHOR INDEX C7-879

I

- Processus élémentaires des décharges dans les gaz
Elementary processes in gas discharges
- Excitation et ionisation
Excitation and ionization
- Recombinaison, attachement et détachement
Recombination, attachment and detachment
- Réactions ion-molécule et réactions chimiques
Ion-molecule and chemical reactions

RADIATIVE AND COLLISIONAL DESEXCITATION OF 1P_1 AND 3P_1 RESONANCE STATES IN XENON.

W. Wieme, M. Vanmarcke, W. Bruynooghe.

Laboratorium voor Natuurkunde, Rijksuniversiteit, Rozier 44 Gent, Belgium.

1. Introduction.

In the afterglow of rare gases, the intensity of the resonance radiation decays exponentially with time constant β

$$I = I_0 e^{-\beta t} \quad (1)$$

This has been verified by direct observation of the 3P_1 - 1S_0 radiation in Kr [1] and Xe [2] in the pressure range 0,1-20 Torr, and by absorption experiments of the population of the 3P_1 level in Ne, [3] and Ar [4]. The decay frequency β is given with good accuracy by the Holstein imprisonment theory, and in cylindrical geometry we find

$$\beta^{-1} = \tau_s = \frac{1}{0,205} \left(\frac{R}{\lambda}\right)^{1/2} \tau_N \quad (2)$$

Here R is the cylinder radius, λ the wavelength of the resonance line and τ_N the natural lifetime of an atom in the resonance state. In this paper we present an absorption measurement on the 3P_1 level and emission measurements of the 3P_1 - 1S_0 and 1P_1 - 1S_0 resonance radiation in Xe. It will be shown that at higher pressures collisional destruction processes become important.

2. Method.

The experimental set-up for the absorption experiment is similar to the one used in [5] except for the detection system which consist of a 1P21 photomultiplier followed by a PAR TDH-9 Waveform Eductor which allows the afterglow to be recorded in 100 channels. For the direct measurement of the resonance radiation the discharge tube was provided with a LiF window. The wavelength was selected with a McPherson 218 VUV monochromator with a 2400 l/mm grating blazed at 150 nm. Depending upon intensity, a resolution of 0,05 up to 0,5 nm was used. This was sufficient to discriminate against the well-known VUV continuum radiation of the rare gases.

The detector is a EMI-GENCOM G-26E315. The PM signal is analysed with a DATALAB DL 920 transient recorder with a time resolution of 50 ns.

3. Results.

a) Absorption

For the absorption measurement the wavelengths 492,3 nm and 491,7 nm corresponding to the transitions $6s_{1/2}$ - $7p_{3/2}$ and $6s_{1/2}$ - $6p_{3/2}$ were chosen, these being the most intense in the visible region. Assuming an exponential decay, the lifetime τ_s of the imprisoned resonance state is given by $\ln I_0 / I - t / \tau_s + \text{constant}$ where I_0 represents the intensity before and I the intensity after absorption. In the case of weak absorption ($I_0 - I \ll I_0$) this becomes

$$\ln(I_0 - I) = -\frac{t}{\tau_s} + \text{constant}.$$

The results are given in Fig.1.

The decay constant β is seen to be reasonably constant in the pressure range 0,01-10 Torr. At higher pressures some pressure dependence is observed, but these points are not taken into account for the analysis. This pressure dependence is discussed in the next paragraph. The imprisonment time is found to be: $\tau_s = 7,6 \pm 0,8 \mu s$, and, with (2) this leads to a natural lifetime

$$\tau_N = 4,3 \pm 0,5 \text{ ns}$$

or, using the relation

$$f \tau_N = \frac{m c}{8 \pi^2 e^2} \frac{g_i}{g_k} \lambda^2 \quad (3)$$

we find an oscillator strength for the 3P_1 - 1S_0 transition:

$$f = 0,226 \pm 0,025$$

These values are in good agreement with literature [2]. The lifetime of the 1P_1 resonance state could not be measured in absorption due to the low concentration of 1P_1 atoms.

b) Emission

- 147 nm emission, or $^3P_1-^1S_0$ transition. The decay consists of two components and is fitted with a computer to a curve :

$$I = A e^{-d_f t} + B e^{-d_s t} \quad (4)$$

Here d_f represents the time constant of a few μs , while d_s is a much slower decay, at least for pressures up to about 20 Torr. It can easily be demonstrated (see also ref[6]) that in Xe for pressures lower than 60 Torr we have within a 5 % accuracy :

$$d_f = \beta + \alpha_{RM} + \alpha_{RS}$$

α_{RM} represents the reaction rate constant due to collision-induced transitions from the resonance level $R(^3P_1)$ to the nearby metastable level $M(^3P_2)$, while α_{RS} indicates the formation of excimer states S through collisions of resonance states R with ground state atoms.

The measured fast decay d_f is given in Fig2 for pressures between 0,02 and 70 Torr. The points are least-square fitted to give a curve : $d_f = 1,28 \cdot 10^5 + 3330p + 27p^2$. $\beta = 1,28 \cdot 10^{-5}$ corresponds to $\tau_s = 7,8 \mu s$, in agreement with the absorption experiment. 3800 p represents collisional desexcitation of 3P_1 atoms to the 3P_2 metastable level. From detailed balancing considerations we find the collisional excitation of $Xe(^3P_2)$ to $Xe(^3P_1)$ to be 18 p. The collisional decay of 3P_2 atoms was found to be $113p + 87p^2$ [5]. It follows that the collision induced emission of $Xe(^3P_2)$ proceeds with a rate 95 p. The term $27 p^2$ represents excimer formation in three-body collisions. The re-sulting excimer can be either the O_u^+ , or the $1,3\Sigma_g^+$ states. Two-body and three-body rate constants are summarized in Table I and compared with literature.

- 129,6 nm emission, $^1P_1-^1S_0$ transition. This line has very low intensity and is fitted like (4). The slow component has not been identified. The fast component can be fitted to a curve : $v_f = 1,29 \cdot 10^5 + 1,94 \cdot 10^6 p$. At pressures above 0,8 Torr, this decay is too dependent on discharge pulse current to be taken into account. (Fig.3).

With $\beta = 1,29 \cdot 10^5$ we find for 1P_1 :

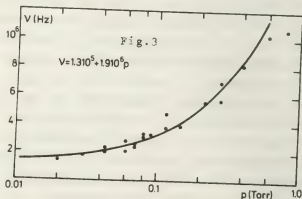
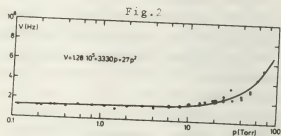
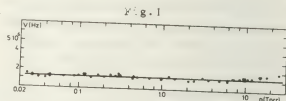
$$\tau_N = 4,1 \pm 0,6 \text{ ns} ; f = 0,181 \pm 0,036$$

The collisional desexcitation proceeds to either the lower levels, or the nearby 3S_1 .

Reaction	Rate constant	
	This work	Literature
$^3P_1 + ^1S_0 \rightarrow ^3P_2 + ^1S_0$	3330	9100 [7]
$^3P_2 + ^1S_0 \rightarrow ^3P_1 + ^1S_0$	18	49 [7]
$^3P_2 + ^1S_0 \rightarrow 2^1S_0 + h\nu$	95	71 [7]
$^3P_1 + 2^1S_0 \rightarrow Xe_2 + ^1S_0$	27	{46 [7] 99 [8]}
$^1P_1 + ^1S_0 \rightarrow ^3S_1 + ^1S_0$	$19 \cdot 10^5$	$21 \cdot 10^5$ [9]

References.

- [1] R. Turner, Phys. Rev. 158, 121, 1967.
- [2] W. Wieme, P. Mortier, Physica 65, 198, 1973.
- [3] A. V. Phelps, Phys. Rev., 114, 1011, 1959.
- [4] E. Ellis, N. D. Twiddy, J. Phys. B, 2, 1366, 1969.
- [5] W. Wieme, J. Phys. B, 4, 850, 1974.
- [6] W. Wieme, J. Lenaerts : submitted for this conference.
- [7] P. K. Lechner et al., Phys. Rev. 13, 1787, 76.
- [8] R. Brodmann, G. Zimmerer, J. Phys. B, 10, 3395, 1977.
- [9] N. Sadeghi, J. Sabbagh, Phys. Rev. 16, 2336, 77.



EXCITATION TRANSFER AND QUENCHING OF THE $n = 3$ EXCITED STATES OF HELIUM IN A LOW-PRESSURE GLOW DISCHARGE

B. Dubreuil, A. Catherinot.

Groupe de Recherches sur l'Energétique des Milieux Ionisés Université d'Orléans,
45045 Orléans Cedex, France.

I - INTRODUCTION

Excitation transfers between excited atomic states play an important part in the formation of quasi-stationary atomic excited state populations in non-L.T.E. plasmas such as low pressure and low current glow discharges. Excitation transfers by inelastic atomic or molecular collisions are responsible for lasing action in a great number of gas lasers, or on the contrary are limiting factors to the population inversion process as for the 3^1P-3^1D (95.8 μ) transition observed in a helium glow discharge (1).

In this paper we report a study of the quenching and excitation transfer mechanisms for the $n = 3$ helium sublevels in the positive column of a low-pressure glow discharge. The experimental method is based on a time resolved spectroscopic analysis of the population relaxations following a short resonant laser pulse pumping.

II - EXPERIMENT (2), (3), (4)

A tunable dye laser excited by a pulsed nitrogen laser (pulse width 4 ns, spectral width 0.2 \AA , energy/pulse $\sim 10 \mu\text{J}$, repetition rate 15 Hz) is used to induce a selective and short perturbation on the population of an helium excited state by resonant optical pumping.

The $n = 3$ states are populated in a capillary glow discharge (inner diameter 4 mm, length 60 mm). This discharge is created under continuous electrical power supply with a constant flow of helium gas (flow rate $< 1 \text{ l/h}$). Pressure P can be adjusted from 0.2 to 7 Torr and current intensity i from 10 to 40 mA. For each experimental situation (P, i), corresponding value of the electronic density n_e is measured by a high-frequency cavity perturbation method ($5 \cdot 10^9 < n_e < 5 \cdot 10^{11} \text{ cm}^{-3}$) and value of the mean electronic kinetic energy E_e is only estimated in the frame of glow discharge theory ($3 < E_e < 15 \text{ eV}$). Gas temperature is measured by means of a thermocouple in contact with the discharge tube ($T_g \sim 325 \pm 5 \text{ K}$).

After spatial filtering, the pump laser beam traverses the discharge tube. The fluorescence light emitted by a cross-section of the positive column is observed in a perpendicular direction and is imaged onto the slits of a spectrometer (resolving power ≈ 50000) and then onto a photomultiplier tube. Time dependence of the output signal is analyzed by a Boxcar averager synchronized with the pulsed laser giving on both channels A and B a time resolution of 5 ns. The fluorescence signal (channel A) is normalized to the pump laser intensity peak (channel B). Each fluorescence relaxation curve corresponds to 1.5×10^4 laser shots average.

III - MEASUREMENTS

A diagram of the $n = 3, 2$ helium energy states is shown on Fig. 1. The population variations $\Delta N_i(t)$

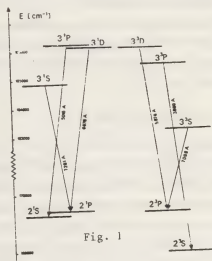


Fig. 1

of the $|i\rangle = 3^S_L$ ($S = 1, 3$; $L = S, P, D$) states induced by laser optical pumping of the transitions drawn on fig. 1 have been studied for various discharge conditions (P, i). For each pumped transition $\Delta N_i(t)$ are deduced from measurements of the time variations of the spectrally integrated resonance and sensitized fluorescence light intensities. After the laser pulse has ceased, the perturbed populations go back to their stationary values. In this laser-free relaxation mode, $\Delta N_i(t)$ are solutions of the population rate equations :

$$\frac{d \Delta N_i(t)}{dt} = a_{ii} \Delta N_i(t) + \sum_{j \neq i} a_{ij} \Delta N_j(t) \quad (1)$$

$$\Delta N_i(t_0) = \Delta N_i^0 \quad i = 1, \dots, n$$

n is the number of sublevels coupled by collisional or radiative excitation transfers. a_{ii} is the quenching coefficient of the $|i\rangle$ level (depoppingulating coefficient) whereas a_{ij} is the excitation transfer coefficient from level $|j\rangle$ to level $|i\rangle$ (populating coefficient). Generally, a_{ij} writes: $a_{ij} = \alpha_{ij} + \beta_{ij}^P n_{He} + \beta_{ij}^I n_e$ (2) where β_{ij}^P (resp. β_{ij}^I) is the rate of the excitation transfer reaction from level $|j\rangle$ to level $|i\rangle$ by collisions with ground state atoms (resp. electrons), and α_{ij} is the spontaneous radiative coefficient. a_{ii} is a negative term and satisfies the relation $a_{ii} = -\sum_{k=1}^n a_{ki} - a_{ei}$ (3) where a_{ei} is a coefficient taking into account transfer of population of the $|i\rangle$ level outside the n sublevels involved in eq. (1).

For the six different pumping experiments, and in the pressure range investigated, we observed the following transfers:

- 2^1S-3^1P pumped: $3^1P \rightleftharpoons 3^1D$ excitation transfer
- 2^1P-3^1D pumped: $3^1P \rightleftharpoons 3^1D$ excitation transfer
- 2^1P-3^1S pumped: no transfer
- 2^3S-3^3P pumped: no transfer
- 2^3P-3^3D pumped: $3^3D \rightleftharpoons 3^3P$ excitation transfer
- 2^3P-3^3S pumped: no transfer

Then the problem arises how to determine the quenching and excitation transfer coefficients a_{ij} intervening in eq. (1) from the experimental relaxation curves $\Delta N_i^{exp}(t)$.

IV - DATA ANALYSIS AND RESULTS (4)

The relaxation matrix $A = \{a_{ij}\}$ was determined from $\Delta N_i^{exp}(t)$ so as to minimize the difference between the experimental values and those calculated from the model. This method recently developed in numerical analysis and named "identification problem" (5) is equivalent to that of finding the minimum: $\inf J(A) = \inf \int_0^t \sum_{i=1}^n |\Delta N_i(t, A) - \Delta N_i^{exp}(t)|^2 dt$ where $\Delta N_i(t, A)$ is the value corresponding to $\Delta N_i^{exp}(t)$ calculated from equation (1) with the matrix A .

This problem can be solved by an iterative algorithm (gradient method): $a_{ij}^{(p)} = a_{ij}^{(p-1)} - k^{(p-1)} \frac{\partial J(A)}{\partial a_{ij}}$ $i, j = 1, \dots, n$ where p is the iteration number i and $k^{(p-1)}$ is a convergence coefficient. The functional derivative is obtained from solution of the differential adjoint problem.

An example of the identification procedure is shown on fig. 2 for the $3^1P \rightleftharpoons 3^1D$ excitation transfer processes.

For the 3^1S or 3^3S state showing no excitation transfer, solution of eq. (1) is given by

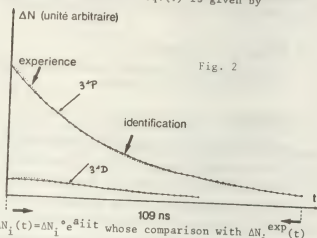


Fig. 2

leads to the quenching coefficient. Determination of the a_{ij} 's for different n_{He} and n_e values allows us to obtain the α_{ij} and β_{ij} coefficients from eq. (2) and (3) by least square linear regression. In fact no current dependence was found so that quenching and excitation transfer can be attributed to the atomic collisional processes: $He(3^1S) + He \rightarrow He(3^1L') + He + \Delta E$ to the associative ionization mechanism: $He(3^1S) + He \rightarrow He_2^+ + e + \Delta E$ and to spontaneous radiative transition: $He(3^1S) \rightarrow He(n^1L) + h\nu$. The radiative coefficients as well as the thermally averaged cross-sections σ_{ij} deduced from β_{ij} are reported below:

	radiative coef. ($10^8 s^{-1}$)	coll. quenching cross-section (\AA^2)
3^1S	0.18 \pm 0.01	3.7 \pm 0.4
3^1P	0.13 \pm 0.01	28 \pm 2
3^1D	0.63 \pm 0.04	25 \pm 2
3^3S	0.279 \pm 0.008	0.3 \pm 0.3
3^3P	0.0986 \pm 0.003	5.5 \pm 0.3
3^3D	0.656 \pm 0.007	3.6 \pm 0.3

excitation transfer cross-section (\AA^2)

$\sigma_{3^1D \rightleftharpoons 3^1S} < 0.1$	$\sigma_{3^3D \rightleftharpoons 3^3S} < 0.1$
$\sigma_{3^1P + 3^1D} : 27 \pm 2$	$\sigma_{3^3P + 3^3D} : 0.1 \pm 0.1$
$\sigma_{3^1D + 3^1P} : 10 \pm 2$	$\sigma_{3^3D + 3^3P} : 1.2 \pm 0.2$

associative ionization cross-section (\AA^2)

$\sigma_{3^1S}^{ion} < 3.7$	$\sigma_{3^3S}^{ion} < 0.3$
$\sigma_{3^1P}^{ion} : 1 \pm 1$	$\sigma_{3^3P}^{ion} < 5$
$\sigma_{3^1D}^{ion} : 15 \pm 4$	$\sigma_{3^3D}^{ion} : 2.4 \pm 0.5$

REFERENCES

1. J.S. LEVINE, A. JAVAN, Appl. Phys. Lett. 14 (1969) 348
2. B. DUBREUIL, A. CATHERINOT, Physica C93 (1978) 408
3. A. CATHERINOT, B. DUBREUIL, M. GAND, Phys. Rev. A 18, (1978) 1097.
4. B. DUBREUIL, Thèse (Université Orléans, 1979).
5. J. DELFORGE, Appl. Math. Comp. 2 (1976) 311.

INVESTIGATION OF EXCITATION MECHANISMS IN NEON WITH THE AID OF THE RADIAL DISTRIBUTION OF EXCITED ATOMS

S. Valignat, J. Leveau, F. Deigat.

E.R.A., C.N.R.S. n° 302 Laboratoire de Spectroscopie et de Luminescence, Université Claude Bernard Lyon I, 43, Bd du 11 Novembre 1918 69621 Villeurbanne, France.

The radial distribution of excited neon atoms in the $2p^5 3p$ and $2p^5 3s$ configurations are investigated under the following experimental conditions : gas pressure 0.4 to 3.1 Torr, radius of the discharge tube $R=0.5$ cm, discharge current $I=2$ to 40 mA. The absolute concentrations of excited atoms on the axis of the discharge and the electrical parameters are also determined. All these results permit us to obtain the excitation cross sections of the $2p^5 3p$ levels from the ground state and from the $2p^5 3s$ configuration. In the latter process we can, with the aid of radial distributions, differentiate the roles played by metastable and resonant states. Experimental methods. The electrical parameters are obtained with cylindrical probes. For the electron energy distribution function we use the method of probe current modulation. We deduce the intensity of the electric field from the difference between the floating potentials of two probes. The electronic mobility is calculated from the measured distribution functions. These results allow us to determine the electronic density.

The investigation of the spectral lines intensities are carried out across the axis of the discharge tube. The radial distribution of $2p^5 3p$ atoms is determined after Abel inversion and a cw tunable dye laser is used to find the radial distribution of $2p^5 3s$ atoms/1/. Putting a mirror behind the discharge tube we measure the autoabsorption and thus the density of metastable states. With the help of a calibrated lamp we obtain the absolute intensity of the radiating atoms.

Results and discussion. 1- The electron energy distribution functions exhibit a Druyvesteyn shape with electronic deficit in the energy region above the first excitation potential (Fig.1) in agreement

with other experimental results /2/.

2- The variation of the average electron energy with pressure is plotted in Fig.2. These results correspond satisfactorily with calculated data /3/.

3- The electronic density on the axis of the discharge is well represented by the following equation

$$n_e = (2.6 \pm 0.4) 10^9 I P$$

with n_e in cm^{-3} , P in Torr and I in mA.

4- The radial distribution $N(r)$ of excited atoms shows the same behaviour for all the $2p^5 3p$ states (Fig.3). In contrast the radial metastable and resonant profiles $M(r)$ are different at low pressures and become similar when the pressure is increased (Fig.4).

5- The total density of all the $2p^5 3p(\Sigma n_i)$ and all the $2p^5 3s(\Sigma m_j)$ states on the axis of the discharge tube are shown in Fig.5 as a function of pressure at different current intensities.

6- At steady state we have for the i th level of the $2p^5 3p$ configuration :

$$(1) \quad n_i \gamma_i = n_e (n Z_{0i} + \sum_j Z_{ji} m_j)$$

where n is the ground state atomic concentration, γ_i the relaxation frequency and Z_{0i} , Z_{ji} are the direct and stepwise excitation coefficients. Knowing the electron velocity distribution function $f(v)$ we may write the latter as :

$$Z_{0i} = \bar{Q}_{0i} \int_{v_i}^{\infty} v f(v) dv \quad ; \quad Z_{ji} = \bar{Q}_{ji} \int_{v_{ji}}^{\infty} v f(v) dv$$

where \bar{Q}_{0i} and \bar{Q}_{ji} are the mean cross sections corresponding to the two excitation processes.

Calling $j=1$ and $j=2$ the metastable and resonant states and assuming a zero order Bessel function $J_0(r)$ for the spatial distribution of the electronic density we obtain the following expression for the radial profile of the i th level :

$$N_i(r) = \frac{J_0(r) + b_{1i} J_0(r) M_1(r) + b_{2i} J_0(r) M_2(r)}{1 + b_{1i} + b_{2i}} \quad (2)$$

with $b_{ji} = \frac{Z_{ji} m_j(0)}{Z_{0i} n}$ $N_i(r) = \frac{n_i(r)}{n_i(0)}$

The cross sections \bar{Q}_{0i} , \bar{Q}_{1i} , \bar{Q}_{2i} are computed from equations (1) and (2) and experimental data. The results are given in Table 1. They are in good agreement with those found in /4/ (values of \bar{Q}_{0i} measured by the electron beam method) /5/ (theoretical values of \bar{Q}_{ji} calculated with the Born approximation) and /6/ (experimental values of \bar{Q}_{1i} found by optical pumping).

References.

/1/ Valignat S., Leveau J., Deigat F. et Falgon R.
Rev. Phys. Appl. 12 (1977) 1007
/2/ Rutscher A. et Pfau S.
Beitr. Plasmaphys. 7 (1967) 43
/3/ Garamoon A.A. et Ismail I.A.
J. Phys. D: Appl. Phys. 10 (1977) 991
/4/ Frish S.E. et Revald V.F.
Opt. and Spectrosc. 15 (1963) 395
/5/ Beterov I.M. et Chebotaev V.P.
Opt. and Spectrosc. 23 (1967) 467
/6/ Samson A.V.
Opt. and Spectrosc. 42 (1977) 321

2p	\bar{Q}_{0i} 10 ⁻¹⁹ cm ²	\bar{Q}_{1i} 10 ⁻¹⁶ cm ²	\bar{Q}_{2i} 10 ⁻¹⁶ cm ²
1	5		70
2	2	3	6.5
3	0.95		46
4	3.1	7.7	14
5	1.6	5.6	6.1
6	2.6	18	16
7	1.2	4.4	13
8	1	13	31
9	3.8	36	
10	1.3	16	30

Table 1

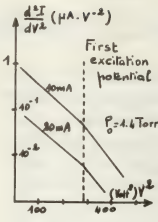


Fig 1

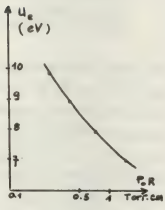


Fig 2

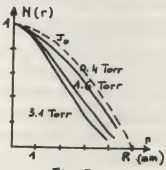
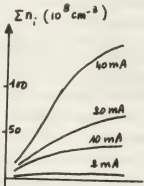


Fig 3

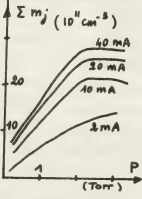


Fig 5

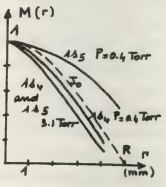


Fig 4

LINE RADIATION OF ARGON PLASMA IN EARLY AFTERGLOW

J.M. Labat, J. Vukićević, O. Labat and S. Djeniže.

Department of Physics and Meteorology and Institute of Physics, Belograd.

Spectral line radiation of a glow discharge argon plasma submitted to the short electric pulse perturbation was reported by Labat et al.⁽¹⁾. Set of spectral lines that predominantly originate from 4p to 4s levels transitions, after the perturbation have two clearly distinctive maxima. Initial rapid intensity peak during the perturbation pulse is caused by the direct excitation of atomic levels by electrons. Time the second intensity maximum appeared depends inverse proportional on the initial gas pressure and was same for all the lines observed. Decay of the second peak consists of three phases: initial rapid drop was followed by two exponential decays in succession, with time constants that suggests dissociative recombination being responsible for the 4p levels population.

Experiment. Experimental apparatus consists of U shaped discharge tube with water cooled electrodes. Discharge current was maintained constant at a value of 0.3 A for the whole range of initial gas pressure (2-15 Torr). Part of the positive column (4.5 cm length) was perturbed by a short (3 ns) high voltage (7 kV) pulse supplied by a Blumlein line. Radiation was recorded by Zeiss SPM-2 monochromator-EMI 9569B photomultiplier - Biomation 8100 waveform recorder system.

Results. Spectral lines originating from 4p to 4s levels transitions in a perturbed plasma have two intensity maxima. First that occurred right after application of electric pulse, originated from direct excitation of ground level atoms by electronic collisions. Time to reach the first intensity maximum consists of time for avalanche to develop and that of spontaneous deexcitation of higher levels to levels 4p⁽¹⁾. Decay time of this peak was found to be equal to the life time of the particular level.

Principal objectives of this report are the properties of second intensity maximum. By recording of intensity curves for

large number of spectral lines originating from 4p levels, it was found that instant t_2 the second maximum occurred does not depend on the particular line. It was always inversely proportional to the initial argon pressure, the results are given in figure 1.

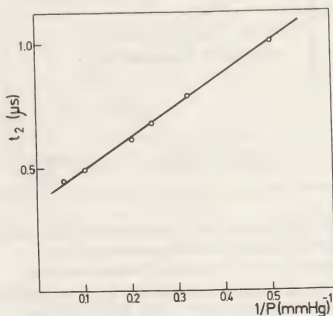


Figure 1.

This proportionality suggested that the second maximum is created by the process of ionisation, since the time constant for ionisation

$$1/\tau_i = n_{01} S^i \cdot p$$

is inversely proportional to pressure. Value n_{01} is the neutral atom density at $p=1$ Torr, S^i is the rate coefficient for collisional ionisation and p is the gas pressure in Torr. Taking for S^i values for collisional ionisation from ground level only, one obtains the results that match very well with the experiment. The ionisation process is followed by the process of molecular ions formation, in this case it is only Hornbeck-Molnar process of associative ionisation⁽²⁾, the ion conversion being negligible under conditions of the experiment. It was suggested by Lorents⁽³⁾ and indicated by the experimental results^{(4) (7)} that the argon 4p levels in a decaying

plasma are populated by the dissociative recombination of electrons and molecular ions. Further it was suggested that the decay constant of noble gases in the later afterglow is proportional to $n_2^+ \cdot n_e$ (5), (6) where n_2^+ and n_e are densities of molecular ions and electrons respectively. Typical time decay of the second intensity maximum peak is shown in figure 2.

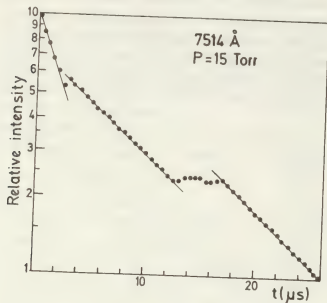


Figure 2.

Records for all the lines studied were practically equal at equal pressures. Logarithmic plot of intensity versus time have three distinct sections. First, that lasted some two microseconds, has decay constant of about 4 μ s. It was followed by the second section that lasted for next 10 μ s with time constant of 7-9 μ s. After about 4 μ s plateau follows the third exponential decay with even longer time constant 8 to 11.5 μ s. Values of three time constants versus initial pressure are given in figure 3 for 7514 Å line.

Since the pressure dependence of the time constants is rather weak, the decay is obviously caused by the recombination processes and definitely not by the diffusion.

While the first intensity drop is not easily explicable, the other two are clearly exponential and suggest that the decay process is governed by the dissociative recombination. Taking the value of dissociative recombination coefficient being

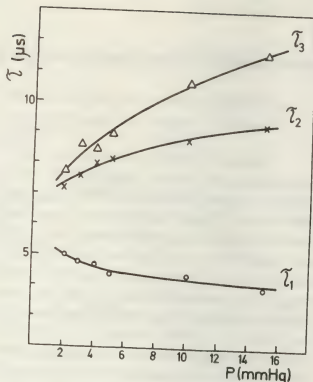


Figure 3.

$\alpha^{DR} = 9.1 \cdot 10^{-7} (300/T_e)^{0.61} \text{ cm}^3/\text{s}$ (7) one can obtain the corresponding values of electron concentration for the pressure range 2 to 15 Torr being $1.8 \cdot 10^{12}$ to $1 \cdot 10^{12} \text{ cm}^{-3}$ for τ_2 and $1.6 \cdot 10^{12}$ to $7.9 \cdot 10^{11} \text{ cm}^{-3}$ for τ_3 . Slight alteration of electron concentration during the plateau of decay is caused possibly by some dynamical processes in the plasma.

References

1. O.Labat, J.Labat, S.Djeniže, Lj.Ćirković, Contr.Papers of SPIG-78, Dubrovnik (1978)
2. O.A.Malkin: Pulse Discharge and Relaxation in Gases (in Russian) Atomizdat, Moscow, 1974
3. D.C.Lorents, Physica 82C (1976) 19
4. G.N.Gerasimov, S.Ia.Petrov, I.L.Sabirova, Optika i Spektroskopija 42 (1977) 1035
5. G.E.Veatch, H.J.Oskam, Phys.Rev.A 1 (1970) 1498
6. L.Fromhold and M.Biondi, Phys.Rev. 185 (1969) 244
7. Y.J.Shiu and M.A.Biondi, Phys.Rev. 17 (1978) 868.

ELECTRON ATTACHMENT IN SO_2

J.L. Moruzzi and V.K. Lakdawala.

Department of Electrical Engineering and Electronics, University of Liverpool, Liverpool L693BX, U.K.

INTRODUCTION

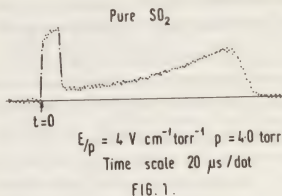
Although there has been much interest in the electrical properties of SO_2 there has been very little work carried out on the electron attaching properties of this gas, or on the mobility of the negative ion species produced as a result of attachment processes.

Some recent studies by Dupuy ⁽¹⁾ have shown that a greatly increased negative ion concentration exists in the atmosphere when SO_2 pollution is present. The present investigation has measured the attachment coefficient (α_a/p) for $1 < E/p < 80 \text{ V.cm}^{-1} \text{ torr}^{-1}$, and has found evidence for a three body attachment process for values of $E/p < 10$ and for a dissociative attachment process for values of $E/p > 10 \text{ V.cm}^{-1} \text{ torr}^{-1}$. Measurement of the mobility of the negative ions formed indicate the presence of at least three ions with reduced mobility values of 0.69, 0.62 and $0.55 \text{ cm}^2 \text{ V}^{-1} \text{ sec}^{-1}$.

APPARATUS

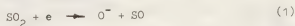
A conventional pulsed photo cathode drift-tube ⁽³⁾ was used to carry out these measurements.

A typical current waveform after signal averaging is shown in Figure 1. The attachment coefficient for the gas in the drift tube can be obtained from such waveforms by estimating the electron and ion components, of the waveforms using the area method due to Pack and Phelps ⁽³⁾. Also from data such as that shown in Figure 2 it is possible to estimate the ion transit time and thus obtain ion mobility values. Using a drift tube mass spectrometer system ⁽⁴⁾ the ion species present under various conditions were determined and will be discussed below.

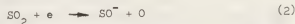


RESULTS AND CONCLUSIONS

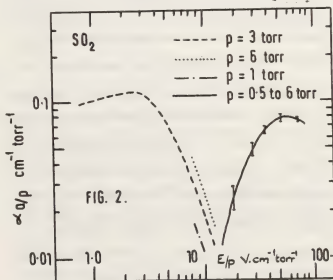
For values of $E/p > 10 \text{ V.cm}^{-1} \text{ torr}^{-1}$ the attachment process was found to be independent of pressure indicating a two body dissociative process



or



The values of α_a/p determined for this process rose from about $0.01 \text{ cm}^2 \text{ torr}^{-1}$ at $10 \text{ V.cm}^{-1} \text{ torr}^{-1}$ a peak of 0.075 at an E/p of $4 \text{ V.cm}^{-1} \text{ torr}^{-1}$ and gradually fell thereafter, see Figure 2. For values of $E/p < 10 \text{ V.cm}^{-1} \text{ torr}^{-1}$ it was found that α_a/p^2



was pressure independent indicating that a three body attachment process is occurring.

The only other recent experimental attachment study in this gas has been carried out by

Schlumbohm⁽⁵⁾ and he reports attachment coefficients in general agreement with the values reported here. A pressure squared attachment process is also reported although the E/p range over which this observed is not mentioned. Earlier work⁽⁶⁾ also indicates an attachment minimum at $\sim 10 \text{ V cm}^{-1} \text{ torr}^{-1}$.

The values of the ion mobility obtained in these experiments are shown in Figure 3. It can be seen that at least three distinct ion species are present. An important point to note in these results is that there is no distinct change in ion mobility as attachment changes from the dissociative process to the three body process. It would thus appear that the ions present are not the ions produced by the attachment process but rather ions that are clusters of SO_2 and the original ion. In order

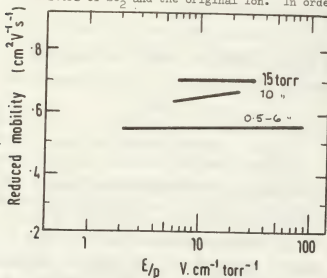


FIG. 3.

to resolve this SO_2 was studied on the mass spectrometer drift tube system used by Coxon and Moruzzi⁽⁴⁾. A spectra of the ions obtained at $p = 0.6 \text{ torr}$ and an $E/p = 8 \text{ V cm}^{-1} \text{ torr}^{-1}$ is shown in Figure 4. Under all the conditions investigated the ion at mass 144 amu tentatively identified as $\text{O}^-(\text{SO}_2)_2$, was dominant. Other ions that are readily identified are O^-SO_2 (80 amu), or O^- . (SO_2)₃ (208 amu) and $\text{SO}^-(\text{SO}_2)_2$ (176 amu).

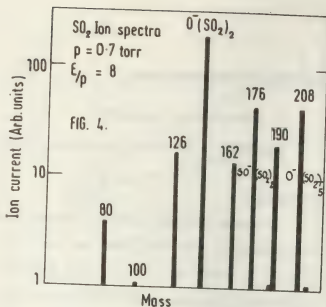


FIG. 4.

Since all three major ions appear under a given condition it must be concluded that in Figure 1 several ion species are present even though the ion current fall-off is sharp. Thus the mobility values quoted clearly refer to a family of ion species. As the pressure increases it is expected that even larger ion clusters will be formed.

- (1) Dupuy J. Private Communication (1977)
- (2) Moruzzi J.L. 1967 Rev. Sci. Instr. 38, p 1284-1285.
- (3) Chanin L., Phelps, A.V. and Biondi M.A. 1962 Phys. Rev. 128, 219-230.
- (4) Coxon P. and Moruzzi J.L. 1977 J. Phys. D. 10, 969-977.
- (5) Schlumbohm H. 1962 Z. Phys. 166, 192-206.
- (6) Bradbury N.E. and Tatel H.E. 1934 J. Chem Phys. 2 835-840.

ACKNOWLEDGEMENTS

This work was carried out at Liverpool as part of the Franco-British Collaboration on Space Charge Effects in Breakdown Phenomenon in Electro-negative Gases. We gratefully acknowledge many useful discussions with Professor J. Dupuy (University of Pau) with whom this collaborative venture is being carried out.

SELF CONSISTENT ELECTRON ENERGY DISTRIBUTION FUNCTIONS IN NON-EQUILIBRIUM OXYGEN

M. Capitelli, M. Dilonardo and C. Gorse.

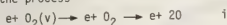
Centro di Studio per la Chimica dei Plasmi del C.N.R., Istituto di Chimica Generale dell'Università via Amendola 173-70100 Bari, Italy.

Electron energy distribution functions(edf)of molecular oxygen have been calculated by different authors[1] by solving the Boltzmann equation including both elastic and inelastic processes from the ground vibrational level(these calculations will be referred hereafter as the cold gas approximation).No work on the contrary exists on the influence of superelastic vibrational collisions and of oxygen atoms on edf in reacting oxygen. In this note we report the temporal evolution of edf during the dissociation of molecular oxygen under non-equilibrium conditions.

According to the joint vibroelectronic mechanism discussed in refs.[2,3],the dissociation rate of O_2 in electrical discharges can be written as

$$v_d \approx n_e \sum_v N_v k_d^e(v) = k_d \sum_v N_v \quad (1)$$

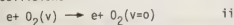
where N_v is the number density of the v th vibrational level and $k_d^e(v)$ is the rate coefficient of the process



To calculate the dissociation rate one must know both the e-D rates(i.e. the different $k_d^e(v)$'s) and the population densities of vibrational levels N_v . These last quantities can be obtained by solving a system of $v+1$ (v is the number of vibrational levels) master equations including:

- a) electron-vibration(e-V) energy exchanges
- b) vibration-vibration(V-V) and vibration-translation (V-T) energy exchanges
- c) dissociation processes induced by electron and heavy particles collisions(see refs.[2,3]).

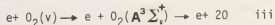
It should be noted that edf enter in the determination of N_v through the e-V and e-D rates. On the other hand the N_v populations enter in the Boltzmann equation through the superelastic vibrational collisions



and through the inelastic processes i.

At the time $t=0$ we can consider all molecules in the ground vibrational level, so that the e-V and

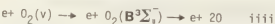
e-D rates are those calculated from edf in the cold gas approximation. As the time evolves, the population of vibrational levels achieve important values, so that the superelastic vibrational collisions can not be neglected. We must use e-V and e-D rates calculated from edf which take into account processes i, ii. A further temporal evolution brings the oxygen atoms. The Boltzmann equation must be now solved for a mixture of vibrationally excited molecules and atoms. This means that the kinetic problem should be coupled to the Boltzmann equation. This coupling has been done in the present work. Some of the results have been reported in figures 1, 2. In particular fig.1 shows edf calculated during the temporal evolution of vibrational levels and oxygen atoms ($E/N=5 \cdot 10^{-17} \text{ Vcm}^2$, $n_e=10^{11} \text{ cm}^{-3}$, $T_g=500^\circ\text{K}$, $p=5 \text{ torr}$). The production of oxygen atoms under the conditions of fig.1 is small, so that the differences in edf shown in fig.1 are due to the increased number of vibrationally excited molecules. To characterize the N_v distributions at the different times, we can say that they follow Treanor's distributions with vibrational temperatures $\vartheta_1 = E_{10}/\ln(N_0/N_1)$ assuming the values of 0,1330 and 1865°K at $t=0, 10^{-2}$ and $3.5 \cdot 10^{-2} \text{ sec}$ respectively. One can appreciate that the increase of ϑ_1 increases the tail of edf by approximately one order of magnitude. This situation propagates in the e-D rates of the process



(Herzberg continuum) as can be appreciated in fig.1, where the rate coefficients of process iii have been reported as a function of time for different vibrational levels.

Figure 2 shows the temporal evolution of edf for $E/N=9.1 \cdot 10^{-16} \text{ Vcm}^2$, $n_e=10^{12} \text{ cm}^{-3}$, $T_g=500^\circ\text{K}$ and $p=5 \text{ torr}$. The production of oxygen atoms is in this case very important, so that edf evolves from the cold molecular gas situation to an other one composed by oxygen atoms. Once more during this evolution the

e-D rates to the Herzberg continuum (upper curves in fig.2) and to the Schumann continuum (lower curves)



drastically change as can be appreciated in fig.2. It should be noted that the dissociation degree of O_2 in fig.2 is 0,042 and 1 at $t=0,2 \cdot 10^{-4}$ and $1,1 \cdot 10^{-1}$ sec respectively.

As for the dissociation kinetics, the present results obtained with e-V and e-D rates from self-consistent edf qualitatively confirm those of ref. [2,3]. These last results have been obtained with e-V and e-D rates from Maxwell edf (ref. [2]) and from the cold gas approximation (ref. [3]). In particular the present results show that k_{dj} for the conditions of fig.1 reaches at $t=3,6 \cdot 10^{-2}$ sec a value of $8,1 \cdot 10^{-3} \text{ sec}^{-1}$ which is three times greater than $k_d^e(v=0)n_e$. On the contrary for the calculations of fig.2 k_{dj} closely follows $k_d^e(v=0)n_e$, since the large concentration of oxygen atoms, because of their large V-T deactivation rates, practically destroy the vibrational content of the molecules. In these conditions one again observes the assisted recombination-dissociation mechanism discussed in ref. [3].

References

- [1] R.D.Hake and A.V.Phelps, Phys.Rev. 158, 70 (1967);
H.Myers, J.Phys. B2, 393 (1969);
K.Masek, T.Ruzicka and L.Laska, Czech.J.Phys. B27,
888 (1977)
- [2] M.Capitelli and M.Dilonardo, Chem.Phys. 30, 95
(1978)
- [3] M.Cacciatore, M.Capitelli and M.Dilonardo, Bei-
trage Aus der Plasmaphysik 18, 279 (1978)

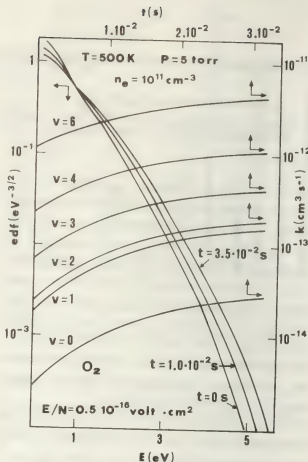


FIG.1

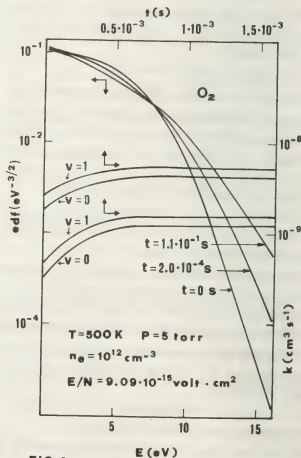


FIG.2

FORMATION AND DESTRUCTION OF NEON MOLECULAR IONS IN TOWNSEND DISCHARGES

P.A.M. Van Der Kraan, J.W.H. Dielis, F.J. de Hoog.

Eindhoven University of Technology, Eindhoven, the Netherlands.

As a part of a more comprehensive mass spectrometric study of Townsend discharges we have investigated the termolecular association reaction of atomic neon ions in their parent gas as well as the loss of the resulting molecular neon ions in dissociative collisions under various discharge conditions. Both reactions can be represented by the equation



Molecular ions are also formed by associative ionization from highly excited states of the neon atom [1].

In this contribution we will describe the discharge model used in the evaluation of the measurements. With this model we were able to determine values for the rate constants of processes (1) at various values of the reduced field strength. Finally from measured values of the dissociation rate at different swarm energies a value for the dissociation energy of Ne_2^+ was found.

Discharge model. Ion sampling from Townsend discharges between flat parallel electrodes at current densities lower than 10^{-8} A/cm^2 has the advantage that the discharge can be described by a simple model. Cumulative processes can be ruled out and only processes in which ground state atoms are involved are relevant. Space charge effects are not present. Ion sampling is therefore not hampered by space charge shielding around the sampling hole. As long as the gas density and the reduced field strength are constant, the transmission of the sampling hole for a specific ion is the same. In our model we assume that the diffusion of ions in the field direction (represented by the coordinate x), can be neglected with respect to the drift. The atomic resp. molecular ion density n^+ resp. n_2^+ obey

$$-v^+ \frac{dn^+}{dx} = \alpha_1 v^- n^-(o) e^{\alpha x} + k_d n_o n_2^+ - k_c n_o^2 n^+ \quad (2a)$$

$$-v_2^+ \frac{dn_2^+}{dx} = \alpha_2 v^- n^-(o) e^{\alpha x} - k_d n_o n_2^+ + k_c n_o^2 n^+ \quad (2b)$$

where v^+ , v_2^+ and v^- are drift velocities of atomic resp. molecular ions and electrons; The primary ionization coefficient α is split in a contribution from direct ionization α_1 and from associative ionization α_2 ; k_c and k_d are rate coefficients for the conversion and the dissociation reaction; n^- stands for the electron density.

Using the boundary conditions $n^+(d) = n_2^+(d) = 0$ at the anode, we can calculate the dependency of the ion currents at the cathode on the electrode distance d .

A general trend for the reduced ion current density i.e. the cathode ion current density divided by the discharge current density, is that for small electrode distances, where formation of ions is dominant with respect to collisional destruction, it increases with

$$1 - \exp(-\alpha d).$$

For larger distances the probability for collisional destruction of an ion increases and the reduced ion current decreases.

Experiment. The experiment was carried out in a stainless steel vessel where between a flat, gold plated cathode containing the 100 μm diameter sampling hole and a quartz anode covered with tin oxide a non-selfsustaining discharge was maintained. The usual ultra-high vacuum procedures required in ion collision studies were followed. Ion selection and detection took place with a quadrupole mass spectrometer.

In Fig. 1 the reduced ion current of neon ions vs. electrode distance at an E/N of 30.5 Td. and a pressure of 2.33 kPa is shown. From these data it was possible to evaluate the termolecular association reaction coefficient k_d by fitting the experimental points with the solution of (2). The coefficient k_d has been determined at values of E/N ranging from 9 Td. up to 30 Td. and at pressures from 2.0 kPa up to 4.0 kPa. At these values of E/N the

dissociative reaction could be neglected. Values for α_2 were taken from our own experiments on associative ionization. Drift velocities and values for α were taken from [2],[3] and [4]. The values of k_d obtained did not show a variation with E/N . In this interval the value was $(.46 \pm .04) \cdot 10^{-43} \text{ m s}^{-1}$. This is in excellent agreement with values obtained from other experiments [2],[7].

The reduced molecular ion current was measured as a function of d at pressures ranging from 270 Pa up to 930 Pa and E/N -values from 48 Td. up to 245 Td. A typical plot of this parameter vs. d is shown in Fig. 2. The value of k_c used in the analysis was from our own experiment. The values of the dissociation rate k_d , again obtained by least squares fitting of the experimental points to the solution of [2] are plotted in Fig. 3 as a function of the ion swarm energy W . This energy was taken from the driftvelocity [2] of molecular ions using Wannier's expression [5].

The dissociation energy. Since very few experimental data on the dissociation energy of neon molecular ions are known, it is worthwhile to determine a value for this energy from the behaviour of k_d as shown in Fig. 3. As a first approximation we therefore equate the swarm energy W with a kinetic temperature T as if the distribution of translational energy of the molecular ions is Maxwellian. In our case also the distribution of the molecules in the vibrational states should be taken into account. This because the swarm energy may be well above the energy difference between the vibrational states. From the measured values of k_d we can determine that for E/N up to 215 Td. the collision frequency for dissociation is at least one order of magnitude smaller than the collision frequency for elastic collisions. So we may assume that a distribution of vibrational states reflecting the kinetic temperature T is present. With help from data of Cohen and Schneider [6] we are now able to find that

$$k_d \sim (kT)^{1/2} \cdot \exp(-D/kT) \cdot \frac{\sum_v (1 + (D - E_v)/kT) \exp(-E_v/kT)}{\sum_v \exp(-E_v/kT)}. \quad (3)$$

the summation is truncated at a vibrational level 0.01 eV under the dissociation limit.

The dissociation energy found by fitting (3) to the experimental points is 1.4 ± 0.2 eV. One should note that the experimental points at higher swarm energies show deviations from the theoretical model.

Based upon the assumption that our consideration on the population of the vibrational levels will be less valid at higher swarm energies, also a fit was made for values of k_d at E/N up to 120 Td. In this case a value of $1.1 \pm .1$ eV for the depth of the potential well of the Ne_2^+ -molecule was found.

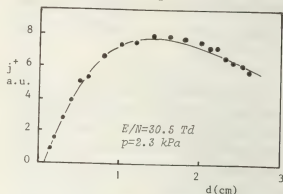


Fig.1 Reduced atomic ion current density at the cathode vs. electrode distance.

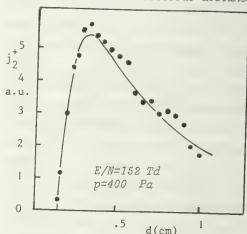


Fig.2. Reduced molecular ion current density at the cathode vs. electrode distance.

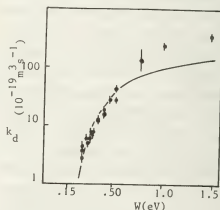


Fig.3 The dissociation rate of molecular neon ions vs. the ion swarm energy

References:

- [1] Hornbeck J.A. et al., Phys. Rev. 84 (621) 1951.
- [2] Beaty E.C. et al., Phys. Rev. 170 (116) 1968.
- [3] Hornbeck J.A., Phys. Rev. 84 (615) 1951.
- [4] Hoog F.J. de, Thesis, Eindhoven 1969.
- [5] Wannier G.H., Bell System Tech. J. 32 (170) 1953.
- [6] Cohen J. et al. J.Chem.Phys. 55 (3230) 1974.
- [7] Orient O., Chem.Phys.Lett. 23 (579) 1973.

COMPARISON OF MONTE CARLO AND BOLTZMANN CALCULATIONS OF ELECTRON DIFFUSION TO AN ANODE

G.L. Braglia*, J.J. Lowke**

*University Parma, Italy.

**University of Sydney, Australia.

Introduction: Our conception of the diffusion of electrons in a gas in which there is a uniform electric field has changed markedly in recent years.

Experimental [1] and theoretical [2,3] investigations of the diffusion of electron pulses changed the view that diffusion was isotropic and instead diffusion longitudinal and transverse to the electric field has been represented by two separate diffusion coefficients D_L and D_T [4].

Recently, however, [5], solutions of the Boltzmann equation to give the electron distribution in energy ϵ and position z for a continuous stream of electrons diffusing in a uniform electric field to an anode, showed that neither D_T or D_L was appropriate to give the electron density distribution $n(z)$. The present paper repeats this calculation using Monte Carlo methods to test the validity of the previous Boltzmann solution, which used assumptions such as an expansion in two terms in spherical harmonics of the distribution function.

Monte Carlo Calculations: Monte Carlo calculations using the methods of [6] were made for a continuous stream of electrons diffusing to an anode in a gas of atomic weight 4 at a pressure of 2.775 torr at 293°K in a uniform field of 1 V/cm. Elastic collisions only were considered using a momentum transfer cross-section $Q = 6 \cdot 10^{-16} (\epsilon/0.1)^{1/2} \text{ cm}^2$ where ϵ is electron energy in electron volts. For $Q \propto \epsilon^{1/2}$ calculations are simplified [6], but even so with 16,000 electrons, released 4 at a time, at regular intervals of $10^{-5}/4,000 \text{ S}$ over an interval of 10^{-5} S , $\sim 10^8$ collisions need to be considered. Electrons were released isotropically at a point source, 1 cm from the anode, with the equilibrium energy distribution. Any electrons crossing the anode plane were removed from the system. The speeds and radial and axial positions at the end of 10^{-5} S were used to compile the accompanying figures.

Boltzmann Calculations: The Boltzmann equation;

$$\frac{16\pi}{mM} \frac{\partial}{\partial \epsilon} \left[N \epsilon^2 Q \left(f^0 + kT \frac{\partial f^0}{\partial \epsilon} \right) + \frac{MeE}{6mN} \frac{\epsilon}{Q} \left(eE \frac{\partial f^0}{\partial \epsilon} + \frac{\partial f^0}{\partial z} \right) \right] + \frac{8\pi}{3mN} \frac{\partial}{\partial z} \left[\epsilon (eE \frac{\partial f^0}{\partial \epsilon} + \frac{\partial f^0}{\partial z}) \right] = 0$$

was solved [5] for the distribution function $f^0(\epsilon, z)$ for the above cross-section, field and pressure; m is the electron mass, M the atom mass, N the gas number density, e the electronic charge, E the electric field, k Boltzmann's constant and T the temperature. Boundary conditions were (1) at the anode, $f^0 = 0$, (2) at $\epsilon = 1 \text{ eV}$, $f^0 = 0$, (3) at $\epsilon = 0$, $eE \frac{\partial f^0}{\partial \epsilon} = - \frac{\partial f^0}{\partial z}$ and (4) at a distance far from the anode, e.g., 1 cm, f^0 equals the equilibrium energy distribution appropriate to $\partial f^0 / \partial z = 0$.

Results: are summarised in Figs. 1-4 and it is seen that there is generally good agreement between the Boltzmann and Monte Carlo solutions.

Fig. 1 indicates that the Boltzmann-Monte Carlo results for the electron density n differ substantially from the classical solutions of the continuity equation

$$\frac{\partial}{\partial z} (nW - D \frac{\partial n}{\partial z}) = 0$$

where the values of the drift velocity W and electron diffusion coefficient D are taken as constants independent of position appropriate to the value of E/N . Solutions using $D = D_L$ or $D = D_T$ underestimate and overestimate, respectively, the diffusion. The electron density gradients perturb f^0 so that W and D are really complex functions of z .

Fig. 2 indicates that the average electron energy near the anode is almost a factor of two larger than the equilibrium average energy appropriate to E/N . This increase is a result of the absence of electrons back scattered from positions in front of the electrode which would have a low energy because of their drift against the electric field. Similar

effects act to reduce the average energy in the Monte Carlo solution at the source of electrons.

In Fig. 3 the effective drift velocity W near the anode is shown to be markedly perturbed by the effect of the anode.

To obtain accurate plots of $\phi^0(\epsilon, z)$ from Monte Carlo calculations would require still more collisions than we have considered. Instead we show $\int_0^{\epsilon} \epsilon^{1/2} \phi^0 d\epsilon$ as a function of ϵ in Fig. 4 as an indication of ϕ^0 . Fig. 5 shows predicted current ratios for the Townsend-Huxley experiment. When absorption at the cathode is included, Monte Carlo ratios are at between predictions from the continuity equation using (1) isotropic diffusion, and (2) calculations using D_L and D_T [2].

Conclusion: Electron drift and diffusion in a uniform electric field cannot be represented by drift and diffusion coefficients that are independent of position. For a continuous stream of electrons absorbed at electrodes the effective longitudinal diffusion coefficient differs from that appropriate to diffusing pulses.

References:

[1] Wagner, E.B., Davis, F.J. and Hurst, G.S. J.Chem.Phys. 47, 3138 (1967).
[2] Parker, J.H., Jr. and Lowke, J.J. Phys.Rev. 181, 290 (1969).
[3] Skullerud, H.R. J.Phys.B. 2, 696 (1969).
[4] Huxley, L.G.H. and Crompton, R.W. The Diffusion and Drift of Electrons in Gases, Wiley 1974.
[5] Lowke, J.J., Parker, J.H., Jr. and Hall, C.A. Phys.Rev. A, 15, 1237 (1977).
[6] Braglia, G.L. Physica 92C, 91 (1977).

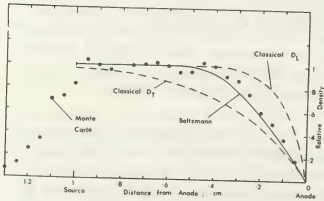


Fig. 1 Normalised Electron Density

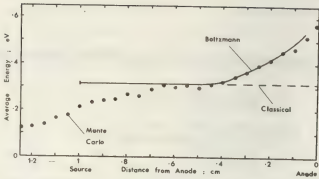


Fig. 2 Average Electron Energy

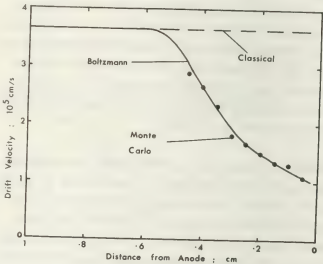


Fig. 3 Effective Drift Velocity

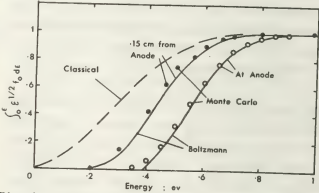


Fig. 4 Energy Integrals near Anode

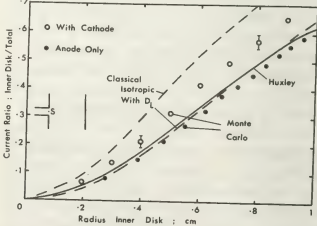


Fig. 5 Current Ratios for Townsend Huxley experiment

INVESTIGATIONS OF THE ELECTRON ENERGY DISTRIBUTION FUNCTION IN KRYPTON AFTERGLOW PLASMA

O. Angelov, A. Blagoev, Tc. Popov.

Sofia University.

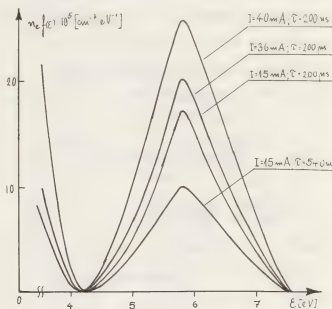
Several previous works [1-3] made in the afterglow of helium, neon and argon positive column show out that in the initial period of the plasma decay, when the quantity of the excited atoms and charged particles has not yet been substantially decreased, the electron energy distribution function (EEDF) may substantially deviate from the Maxwellian distribution function in the high energy region: 1. The fast electrons number could be many orders higher than in a Maxwellian distribution with the temperature of the main group of electrons T_e . 2. This number decreases in time much more slowly than usually presumed.

This work gives the results of similar investigations in the krypton afterglow for which no previous data exists as far as we know.

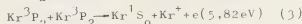
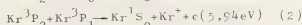
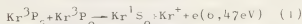
The measurements were carried out on the same experimental device, used and described in details earlier [1]. Short, rectangular voltage pulses at repetition frequency 1,5 kHz were applied on the electrodes of the discharge tube. The experimental conditions were: discharge pulse current $I = 6 + 60$ mA, gas pressure about 0,7 torr, tube diameter $r = 2,6$ cm, radius of cylindrical probe $4 \cdot 10^{-3}$ cm.

In a selected moment after the cessation of the discharge current were made both electrical probe and optical absorption measurements. As it is well known EEDF

is connected with the second derivative of the probe current $i_e''(v)$ by Drux-Bain relation. We used the time-resolving method for obtaining $i_e''(v)$ in a plasma with periodically changing parameters [1]. On fig.1 are shown experimental EEDF in absolute units measured at delay time $\tau = 200$ and 540 mks after the discharge pulse end.



The maximum at 5,8 volts is due to the electrons, created in the chemoionization reactions:



These reactions may also produce Kr_2^+ and e .

In the processes (1)-(3) the electrons are created with definite energies, but experimental maximums are broadened and fused by the influence of the finite amplitude of the imposed modulating voltage.

The density n_2 of the excited krypton

atoms Kr^3P_2 , n_1 of the Kr^3P_1 atoms and n_0 of the Kr^3P_0 atoms, which are vital for the fast electrons creation, was determined by measuring the fractional absorption of the spectral lines $Kr7694A$, $Kr5870 A$ and $Kr7854 A$ connected with these levels. The line strength values were taken from the works /4,5/.

At our experimental conditions of low gas pressure and discharge currents, the behaviour of fast electrons is governed by free diffusion towards the tube walls. In this case theoretical calculations /1/ for the EEDF give the following expression for the total density of electrons in the energy range about $\mathcal{E}_m = 5,8$ eV at the tube axis

$$S_m = \int_{(\Delta \mathcal{E}_m)} \frac{2\pi \sqrt{2}\mathcal{E}}{m^{3/2}} f(\mathcal{E}, 0) d\mathcal{E} \approx \sum_{i=0}^2 \beta_{ix} \frac{n_x n_x}{D(\mathcal{E})} \Lambda^2 \quad (4)$$

where β_{20} , β_{21} and β_{22} are the rate constants for the reactions (1), (2) and (3) respectively,

$$\frac{\beta_{ix}}{n_x n_x} = \frac{\int_0^z n_x(r) n_x(r) J_0\left(m, \frac{r}{\Lambda}\right) r dr}{\int_0^z J_0^2\left(m, \frac{r}{\Lambda}\right) r dr}$$

Λ is the diffusion length, $D(\mathcal{E})$ is the free diffusion coefficient of an electron with energy \mathcal{E} , $J_0\left(m, \frac{r}{\Lambda}\right)$ is the Bessel function.

Because of the small density of the 3P_0 and 3P_1 levels significant contribution

in the S_m have exclusively reactions including 3P_2 level, namely (1) - (3). For the determination of the rate constants of Penning ionizations were made complex measurements at 40 different discharge conditions and delay times. A system of independent equations in the form of relation (4) was set up from the results of these measurements. It was solved by the smallest square method. In this way it was found out that the rate constant for the reaction ($^3P_2, ^3P_2$) is $\beta_{22} = (9,3 + 0,4) \cdot 10^{-9} \text{ cm}^3 \text{ s}^{-1}$, for the reaction ($^3P_2, ^3P_1$) is $\beta_{21} = (1 + 0,5) \cdot 10^{-8} \text{ cm}^3 \text{ s}^{-1}$ and for the reaction ($^3P_2, ^3P_0$) is $\beta_{20} = (3,2 + 1,0) \cdot 10^{-8} \text{ cm}^3 \text{ s}^{-1}$.

The gas temperature at these small discharge currents is about 300°K, so the corresponding cross-sections for these processes at the energy 0,026 eV are: $\sigma_{22} = (2,4 + 0,1) \cdot 10^{-13} \text{ cm}^2$, $\sigma_{21} = (2,6 + 1,2) \cdot 10^{-13} \text{ cm}^2$, $\sigma_{20} = (8,3 + 2,6) \cdot 10^{-13} \text{ cm}^2$

The results strongly depend on the line strength values.

1. Blagoev A.B. et al., Zh. Tekh. Fiz., 44, 333, 338, 1974; 42, 1160, 1977.
2. Kolokolov N.B. et al., Zh. Tekh. Fiz., 48, 1044, 1832, 1978.
3. Blagoev A. and Popov Tc., Physics Letters A 66, 213, 1978; in print 79.
4. A.P. Thorne, J.E. Chamberlain, Proc. Phys. Soc., 82, 1963.
5. R.A. Lilly, JOSA, 66, 245, 1976.

REACTIONS OF DOUBLY CHARGED IONS WITH VARIOUS NEUTRALS

K. Peska, E. Alge, H. Villinger, H. Störi and W. Lindinger.

*Institut für Experimentalphysik der Leopold-Franzens-Universität Abteilung Atomphysik (Hülle),
Karl Schönherrstraße 3, A 8020 Innsbruck, Österreich.*

Recent investigations of reactions of doubly charged ions /1-5/ have shown that they occur in most of the cases via single charge transfer and that they obey a curve crossing model, developed by Landau, Zener and Stueckelberg (see Ref.1). Spears et al. /1/, who have applied this model to reactions of Mg^{++} and Ca^{++} could show, that the reactions are fast, when there is a curve crossing between the potential curve of the reactants and the coulomb repulsion curve of the products (Fig.1) at an internuclear distance of a few Å.

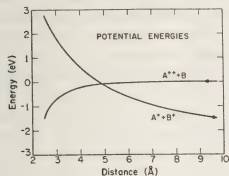


Fig.1

In order to get more insight into the mechanism of the reactions of doubly charged ions, we have investigated many of them as a function of the relative kinetic energy KE_{cm} of the reactants (thermal to a few eV) in a drift experiment /2,5/. Most of the reactions with molecular reactants turned out to be fast and independent of KE_{cm} . This is understandable due to the fact that most molecular ions have a wide variety of high lying electronic states with many vibrational levels, so

that in many combinations of doubly charged ions and molecular reactants, curve crossings occur in the proper internuclear distance, thus leading to a high reaction probability. As an example for such a case we show in Fig.2 the energy dependence of the reaction $Ne^+(^3P) + N_2$.

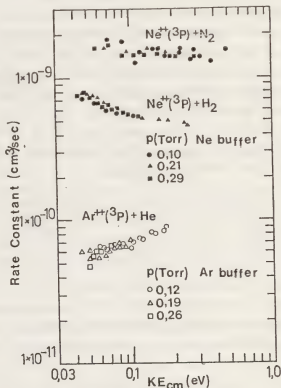


Fig.2

The situation is quite different, when H_2 or a rare gas is chosen as the neutral reactant. The H_2^+ -System has a wide range from 18.2 eV to about 28 eV in the Franck-

Condon-regime, where no electronic states exist, and the rare gas ions (singly charged) have excited states only high above the ionic ground state, so that the conditions for a curve crossing at an internuclear distance of a few Å is met only in a few cases. In the reaction $\text{Ar}^{++}({}^1\text{S}) + \text{He} \rightarrow \text{Ar}^+ + \text{He}^+$ the curve crossing occurs at 2.0 Å which is too close to allow for a high reaction probability and thus the reaction rate constant is very small ($k < 10^{-14} \text{ cm}^3 \text{ sec}^{-1}$). $\text{Ar}^{++}({}^3\text{P})$ reacts with He with a thermal rate constant of about $5.5 \times 10^{-11} \text{ cm}^3 \text{ sec}^{-1}$, the respective curve crossing being at 4.5 Å. As Fig.2 shows, there is a distinctive increase of the rate constant for this reaction with increasing relative kinetic energy KE_{cm} of the reactants. An increase of KE_{cm} means a shift of the curve crossing point to smaller internuclear distances. From these results one has to assume the maximum of the reaction probability for the above type of reaction to occur between 2 and 4.5 Å. This agrees well with result of Johnsen and Biondi, who found $\text{Ar}^{++}({}^1\text{D})$ to react quite fast ($k = 10^{-10} \text{ cm}^3 \text{ sec}^{-1}$) with He. The curve crossing is at 2.8 Å in this case.

Several more reactions will be discussed in view of the curve crossing model and results of the reactions of $\text{Ar}^{++}({}^3\text{P})$, $\text{Ar}^{++}({}^1\text{S})$ and $\text{Ne}^{++}({}^3\text{P})$ with various neutrals will be shown.

The "Österreichischer Fonds zur Förderung der wissenschaftlichen Forschung" is thanked for support through project No S 18/07.

- /1/ K.G. Spears, F.C. Fehsenfeld, M. McFarland and E.E. Ferguson, J. Chem. Phys. 56, 2562 (1972)
- /2/ H. Störi, E. Alge, H. Villinger, F. Egger and W. Lindinger, Int. J. Mass Spectrom. Ion Phys. in press (1979)

- /3/ D. Smith, D. Grief and N.G. Adams, Int.J. Mass Spectrom. Ion Phys., in press (1979)
- /4/ R. Johnsen and M.A. Biondi, Phys. Rev. A 18, 996 (1978)
- /5/ F. Howorka, J. Chem. Phys., 67, 2919 (1977)
- /6/ W. Lindinger, E. Alge, H. Störi, R.N. Varney, H. Helm, P. Holzmann and M. Pahl, Int.J. Mass Spectrom. Ion Phys. in press (1979).

A COLLISIONAL RADIATIVE MODEL OF THE ARGON ION SYSTEM TESTED FOR A LARGE RANGE OF ELECTRON DENSITIES

V. Van Der Sijde, B.F.M. Pots, D.C. Schram.

Eindhoven University of Technology, Eindhoven, the Netherlands.

Introduction. We reported earlier on a comparison between a Collisional Radiative Model (C.R.M.) for the argon ion system and density measurements of the 4s and 4p group of that system from the plasma column of a hollow cathode arc (H.C.A.) [1,2]. The literature data, available at that time, had been digested in this model; we refer to [2] for a complete description. We only mention that the 3d group had been divided into three subgroups, owing to their different nature (metastable and strongly radiative levels) and that the measurements covered an electron density range n_e from $1 \cdot 10^{18} \text{ m}^{-3}$ to $2.5 \cdot 10^{19} \text{ m}^{-3}$. It appeared that there was a factor 3 discrepancy between the model and the experimental data for the 4p group. Measurements with a new type of H.C.A. with n_e -values from $2.5 \cdot 10^{18} - 2.5 \cdot 10^{20} \text{ m}^{-3}$ showed an increasing discrepancy with the existent model with increasing density, so that it was evident that this model was not adequate to give a good explanation of the experimental behaviour of excited groups over the whole density range. We therefore decided to modify the C.R.M. and to include processes to and from the doubly ionized ground levels. Recent data of Jolly [3] were a helpful guide in this new approach.

Experimental set up. The spectroscopic measurements have been carried out by determination of the radiation of the doublet 4p group from a 10 mm radius plasma column of a steady state H.C.A. with a 0.5 m Jarrell-Ash monochromator. The discharge has a pressure of 1 mtorr, a confining axial magnetic field of 0.05 - 0.5 T and a current of 20 - 200 A. The electron temperature and -density measurements have been performed with a Thomson scattering device having a pulsed -50 J, 1.5 ms-ruby laser as a radiation source.

Results. For about 40 different plasma conditions with n_e -values from $2.5 \cdot 10^{18} - 2.5 \cdot 10^{20} \text{ m}^{-3}$ and electron temperatures T_e from 2.5 - 4.8 eV, we

measured 4p group densities from $4.7 \cdot 10^{11} - 6 \cdot 10^{13} \text{ m}^{-3}$. The conclusion is that there is - apart from experimental scatter - a reasonable agreement between the original model and the experimental data for $n_e < 2 \cdot 10^{19} \text{ m}^{-3}$ with a difference of a factor 2.5 - 3 between them. This factor was also found in Refs. [1,2]. For higher n_e -values, however, the discrepancies increase up to a factor 400, showing that this model is inadequate to describe the main physical processes in the argon ion system for this density range.

The modified model. The main changes we propose in the model in this preliminary stage are that

- 1) we diminish the excitation rate from the 3p ion ground levels to all excited groups by a factor 3 in order to obtain a better agreement at low electron densities. This adaption can be justified by the fact that in the low density case, a Corona model exists in which almost the total excitation activity comes directly from the ground levels and no other processes can cause the difference between model and experiment. Also Jolly [3] pointed out that Zapesochnyi's values [4] may be too high;
 - 2) we introduce ionization from all ion groups to the doubly ionized ground levels and recombination from these levels back to the ion system. These latter processes appeared to be of minor significance but the ionization processes appeared to be very important in diminishing the discrepancy between model and experiment for high n_e -values.
- With respect to the ionization processes, we used an ionization rate of $1 \cdot 10^{-13} \text{ s}^{-1}$ at $T_e = 3 \text{ eV}$ for the 4p doublet group, according to recent data of Jolly [3]. This rate represents a very large cross section. For other groups comparable values have been used. This stepwise ionization - or possibly excitation to highly situated groups - play an important deexciting role for the 4p group at high n_e -values. Many other (de)excitation processes between excited groups as e.g. between the

4p and 3d,4s with comparable or even larger rates do only travel the excited particles from one to another group and are not real loss processes for these groups. Processes to singly and doubly ionized ground levels can be considered as such. The latter are far more important than the first.

3) We may drop the condition that $n_e^* = n_i$ (ion density) and allow that $n_i < n_e$ according to the relation $n_e = n_i + 2n_i^{++}$. This assumption leads to further improvement between model and experiment. Calculations on the balance equation for the singly ionized particles suggest that it is necessary to allow that $n_i < n_e$ for a number of conditions in order to realize that the ionization to the doubly ionized system $n_i < n_e^{II-III}$ is smaller than or equal to that from the neutral to the singly ionized system $n_a < n_e^{I-II}$. This is necessary to maintain steady state in the case that diffusion of argon ions is negligible or is in the radial outward direction. The condition loses its significance if radial inward diffusion should exist. However, measurements of the intensity of the $\lambda = 328,6$ nm argon III line suggest for a simple Corona model for the present 4p level with a rather high transition probability value $A = 4 \cdot 10^8 s^{-1}$ and a relatively low value of the excitation cross-section of $10^{-24} m^2$, that the n_i^{++} densities are much smaller than n_i and consequently $n_i \approx n_e$. We conclude that a definite judgement on this point is not possible at this moment. We present in Fig. 1:

1) the comparison between the original model and the measurements; 2) the comparison with the model, modified according to point 1) and 2); 3) the same, modified according to point 1-3). In both modifications, there is the expected agreement with the experiment for the low n_e -values. There are still discrepancies up to a factor 25 for high n_e -values in the first modification and a factor 6 for $n_e = 5 \cdot 10^{19} m^{-3}$ in the second modification. It is in both cases suggested that still other depopulating processes are important. (In fig. 2 we show the ratio n_i/n_e as a function of n_e for all conditions to realize $n_i < n_e^{II-III} \leq n_a < n_e^{I-II}$. The smoothed curve was used for further model calculations.)

Conclusions. It is evident that for n_e -values $> 5 \cdot 10^{19} m^{-3}$, ionization to the doubly ionized system seems at least to be a partial explanation of the observed phenomena, provided that the rather large values of Jolly are used. Further improvements

can be reached if $n_i < n_e$ but the evidence of this assumption is doubtful at the moment. The measurements of Jolly with a 6 mm bore laser tube suggest that in his case $n_e \approx n_i$ to explain the large densities of excited groups.

References.

- [1] B. van der Sijde and B.F.M. Pots, Proc. 13th ICPIC, Berlin 1977, 649.
- [2] B.F.M. Pots, B. van der Sijde and D.C. Schram, Physica 94C (1978) 369.
- [3] J. Jolly, J.Q.S.R.T., 20 (1978) 503.
- [4] I.P. Zapesochnyi, Sov.Phys.JETP, 36 (1973) 1056.

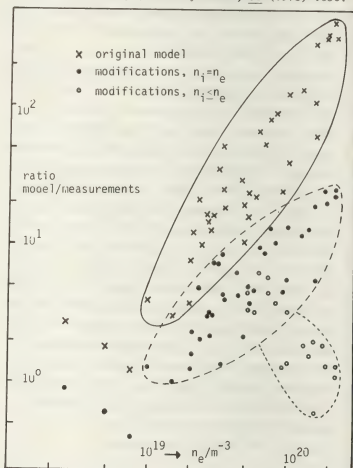


Fig. 1 Discrepancies between model and experiment

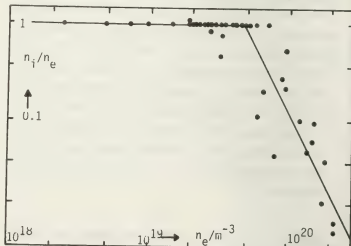


Fig. 2 n_i/n_e ratio applied in one model/experiment comparison.

CALCULATION OF THE PHOTOIONIZATION CROSS SECTIONS OF EXCITED LEVELS OF RARE GAS ATOMS

P. Ranson and J. Chapelle.

C.R.P.H.T.-C.N.R.S. Orléans, France

I- INTRODUCTION : The calculation of the photoionization cross sections of excited levels of rare gas atoms is of great interest for many problems like emission and absorption of light by plasmas or hot gases or like the determination of optimal experimental conditions for laser discharges. Ab initio calculations are generally complex and it is easier to use semi-empirical methods. One of them is the quantum defect method which permits to calculate the radial part contribution on the cross sections. Intermediate coupling is used for the angular part.

II- CALCULATION OF THE CROSS SECTION 1/

II-a- General form : With the assumption of the central field approximation, the photoionization cross section of an atom in a state i by a photon of energy $h\nu$ is given by the formulae :

$$\sigma_i^{\text{ph}}(\nu) = \frac{4\pi}{3} \alpha_0^2 \frac{h\nu}{R_{\infty}} \frac{S}{k_{\ell}^2} \quad (1)$$

$\alpha_0 = \frac{1}{137}$, a_0 Bohr radius, R_{∞} Rydberg constant, g_i statistical weight of the atom.

The transition strength S is given by

$$S = \sum_j C_{ij} \left| \int_0^{\infty} P_{n\ell}^i(r) P_{n'\ell'}^j(r) r dr \right|^2 \quad (2)$$

where $P_{n\ell}^i(r)$ et $P_{n'\ell'}^j(r)$,

except of a factor r , are the radial wave functions for bound state $i = (n, \ell)$ and for free state $j = (\epsilon = k^2, \ell')$ and where C_{ij} comes from the integration of angular part.

II-b- Calculation of radial wave function :

The quantum defect method [2] ($\mu = n - n^*$, n^* effective quantum number) based on the Coulomb approximation valid for great distances between the core and the electron allows the evaluation of radial wave function. With this approximation, for the bound states and particularly for the high ℓ states ($\ell \geq 2$), the solution of the radial Schrödinger equation diverges for small r . It is then necessary to introduce a cut-off factor with the form $f_c(\ell, r) = (1 - e^{-\alpha r})^{\ell+1}$ which gives, in the case $\mu \ll 1$, a good variation of the wave function near the origine and in the general case which permits to keep a finite wave function. The coefficient α is adjusted by the normalisation condition.

For the free states, the radial wave function is a linear combination of regular and irregular solution of the radial Schrödinger equation which gives an asymptotic form

$$(R_{\ell})^{-\frac{1}{2}} \sin(kr - \ell\pi + \frac{1}{k} \log(2kr) + \arg \Gamma(\ell + \frac{1}{k}) + \delta_{\ell}(k))$$

where the phase shift $\delta_{\ell}(k^2)$ is calculated by extrapolation of the quantum defect μ to positive energies. It is also necessary to use a cut-off factor of the same form as for the bound states for the irregular part. It is adjusted by fitting the first extremum in the irregular part with the

others and with those of regular part.

II-c- Radial matrix element : For bound states radial wave functions are calculated from the asymptotic expansion with the correction for small radius. For free states, a series expansion [3] is used. With this method, the matrix element can be calculated in analytic form. We obtain an alternate series expansion which converges only if the condition $kn^* \ll 1$ is fulfilled. The condition of convergence can be less rigid if the integration is made from 0 to R where R is calculated so as to introduce only a very small error (10^{-4}). Then, the validity of the calculation is limited to the condition $kn^* \lesssim 2$ by the increase of the term of the series.

II-d- The intermediate coupling for the rare gas

The term C_{ij} of the formulae (1) gives the angular part of the cross sections. The excited states of rare gases ($\neq \text{He}$) are not relevant of any usual coupling schemes of different orbital and spin momenta. Indeed, the appropriate coupling is intermediate between the LS coupling and the JJ or JE coupling. For this purpose, the observed energy levels are used for the decomposition of real states on the JJ states basis. For the continuum states, the computed coefficients are extrapolated from high lying levels. Then, the value of C_{ij} can be calculated via matrix algebra.

II-e- The continuum states phase shifts

The quantum defect method gives the relation between extrapolated quantum defect (in the continuum) and phase shifts of free states for a series $n\ell^5 [^2P_{3/2, 1/2}] n' \ell' [^4S, ^2P]$. However the series with same parity and same total momentum J are mutually perturbed and it is necessary to take this perturbations into account in the calculation of extrapolated quantum defects. The method proposed by Edlen [4] is used. The quantum defect of a state i belonging to the series 1 and perturbed by the states k of the series 2 is given by

$$\mu_i = \mu_i^{np} + \alpha \sum_{k \neq i} \frac{\mu_k^{-3}}{k^2} (T_i - T_k)^{-1} \quad (3)$$

T : spectral term. The unperturbed part μ^{np} can be approximated by a quadratic expansion of the energy.

III- APPLICATION TO THE LEVELS $n\ell^5 [^2P_{3/2, 1/2}] (n+1)s$; $J = 2, 1$ (S_5 and S_4 in PASCHEN NOTATION)

We have calculated the photoionization cross sections of this two levels for Ne, Ar, Kr, Xe atoms. The transitions is possible to free states with $\ell' = 1$. For the level $1S_5$ ($J = 2$) only transitions to the ionic core $^2P_{3/2}$ are allowed and the selection rules limit the transition to 5 levels ($p_{10}, p_9, p_8, p_7, p_6$). For the level $1S_4$ ($J = 1$), transitions to the two ionic cores $^2P_{3/2}, ^2P_{1/2}$ are possible and only the transitions to level p_9

are forbidden.

The figures 1a-d show the result with comparison to other theoretical works (Mc Cann-Flannery /5/, Hyman /6/, Hazi-Rescigno /7/ and Hartquist /8/). For Ne, our results are in relatively good agreement with other values (except /8/), but for Ar, important discrepancies exist and for Kr and Xe, only the results of Hartquist are in good agreement. Few experimental results are available. For Xe, the values of Rundel and al /9/ are intermediate between different theoretical results.

IV - CONCLUSION

Our method gives with a minimum of calculations the photoionization cross section including several phenomena (summation on all final states, transitions between different ionic core, mutual perturbation of series).

REFERENCES

- /1/ P. RANSON, Thesis Orléans (1978).
- /2/ A. BURGESS, M.J. SEATON, MNRAS 120, 121 (1960).
- /3/ D. SCHLUTER, Z. Fur Astrophys. 61, 67 (1965).
- /4/ B. EDLEN, Handbuch der Physik, Vol XXVII (1964).
- /5/ K.J. MC CANN, H.R. FLANNERY, Applied Phys. Let. 31, 599 (1977).
- /6/ H.A. HYMAN, Applied Phys. Let. 31, 14 (1977).
- /7/ A.V. HAZI, T.N. RESCIGNO, Phys. Rev. 16, 2376 (1977).
- /8/ R.D. RUNDEL, F.B. DUNNING, H.C. GOLDWIRE, R.F. STEBBINGS, J. of the Opt. Soc. Am. 65, 628 (1975).
- /9/ T.W. HARTQUIST, J. Phys. B, 11, 2101 (1978).

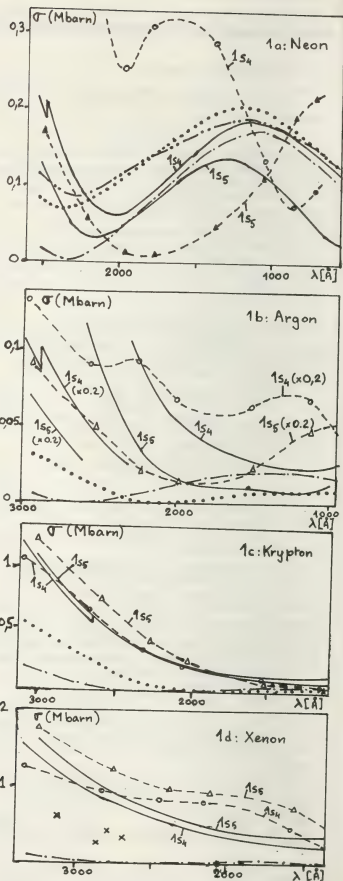


Fig. 1 : Photoionization cross sections for $1s_5$ and $1s_4$ levels. Solid curve : our results; dot-dashed curve : Mc Cann-Flannery; dashed curve : Hartquist, (O: $1s_4$), (Δ : $1s_5$).

Fig. 1a: Neon, dotted curve : Hazi-Rescigno (dipole velocity); --- Hazi-Rescigno (dipole length).

Fig. 1b: Argon, dotted curve : Hyman (note the scale change for Hartquist results and for our results nearly the threshold).

Fig. 1c: Krypton, dotted curve : Hyman.

Fig. 1d: Xenon, crosses : experimental results of Rundel and al.

ATOM DENSITIES OF THE FIRST EXCITED STATE IN LOW PRESSURE NEON DISCHARGES

N. Van Schaik, L.W.G. Steenhuisen, P.J.M. Van Bommel, J.C.A.M. Van de Nieuwenhuyzen.

Eindhoven University of Technology, Eindhoven, The Netherlands.

Introduction. The relative and absolute densities of the various neon $1s$ levels were studied, by means of optical fluorescence, in cylindrical discharge tubes ($d = 31$ mm)⁷⁾. A multi-mode CW dye laser (Spectra Physics model 370) was used as excitation source.

The relative densities and their ratio's were measured in the active discharge and in the afterglow of a neon discharge.

The absolute densities were measured in the positive column of the neon discharge by means of a modified absorption method; the absorption of the laserlight in the plasma was derived from the measured attenuation of the fluorescence signal along the path of the laser beam. In this case only that part of the laserlight spectrum that can be absorbed contributes to the measuring signal; disturbing effects at the entrance and the exit of the tube are eliminated; the accuracy is enhanced because the absorption can be measured for a large number of different path lengths in the same tube.

The relative densities. The fluorescence radiation ϕ_i originating from the $2p_2-1s_2$ transition (Paschen notation) after optical pumping of a level $1s_i$ to $2p_i$ is given by:

$$\phi_i = \sum_k J_i(\nu_k) B_{i2} n_i g_i(\nu_k) A_{22}^* / A^* \quad (1)$$

$i = M, R, S, T$ for respectively the $1s_5, 1s_4, 1s_3$ and $1s_2$ level. B_{i2} is the Einstein coefficient $1, 2, 3, 4$; n_i is the density of level $1s_i$; A_{22} is the spontaneous transition probability for the $2p_2-1s_2$ transition; A^* is the total transition probability of the level $2p_2$; $g_i(\nu_k)$ is the value at frequency ν_k of the normalised absorption profile of level $1s_i$ and $J_i(\nu_k)$ the radiative energy density in laser mode k when level $1s_i$ is irradiated. The summation is made over all laser modes. We assume that $J_i(\nu_k)$ is constant for all ν_k within

the absorption profile; this is justified because the width of the laser spectrum is about 15 times broader than the width of the absorption profile $g_i(\nu)$. Moreover we assume that the laser mode configuration does not change substantially with a change in the laser wavelength. The slight differences between the various functions $g_i(\nu)$ are neglected because of the small energy gap between the $1s$ levels. The ratio between the fluorescence radiation when $1s_5$ and $1s_4$ are irradiated is:

$$\frac{\phi_M}{\phi_R} = \frac{B_{M2} n_M A_{22} / A^* \sum_k J_M(\nu_k) g_M(\nu_k)}{B_{R2} n_R A_{22} / A^* \sum_k J_R(\nu_k) g_R(\nu_k)} = \frac{J_M(\text{tot}) B_{M2} n_M}{J_R(\text{tot}) B_{R2} n_R} \quad (2)$$

$J_M(\text{tot})$, $J_R(\text{tot})$ are the values of the laser beam power when level $1s_5$ respectively $1s_4$ is irradiated. Corresponding relations with (2) can be derived for other $1s_i$ combinations. From (2) follows that n_M/n_R can be determined from the fluorescence radiation when all other parameters of the experimental set up are kept constant. In this way we have measured for a few values of pressure and discharge current the relative densities of the $1s_5, 1s_4$ and $1s_3$ levels. This was done in the active discharge as well as in the afterglow. Figure 1 gives the ratios of the relative $1s$ densities in a 5 torr tube as function of the discharge current. At 30 mA we find $n_M/n_R = 1.6$ which is in reasonable agreement with the value 1.9 given by Soldatev⁶⁾ for a corresponding situation. Figure 2 gives the values of n_M/n_R in the afterglow for pressures 0.5, 1, 2 and 5 torr and a discharge current of 22 mA.

It must be remarked that important failures may arise if the laser mode configuration is not stable or if the laser beam power is too large. The latter condition may be checked carefully. In a number of cases we have checked the mode configuration by analysing the laser line shape with the help of a scanning Fabry-Perot interferometer.

The absolute densities. We have measured the absolute densities with the experimental set up given in figure 3. The laser beam enters the discharge tube at point 0 and may be adjusted parallel with the tube axis. Detection system DSI is fixed, but DSI I can be moved parallel to the tube axis. The distance from 0 along the tube axis is denoted by x . We will derive a relation for the ratio of the fluorescence radiation $\phi(x_2)/\phi(x_1)$. $\phi(x_2)$ and $\phi(x_1)$ are emitted simultaneously by P_2 (at $x=x_2$) and P_1 (at $x=x_1$).

The laser energy density per mode and per unit volume $J_M(v_K, x)$ is a function of x according to:

$$J_M(v_K, x) = J_M(v_K, 0) \exp(-k(v_0) g^*(v_K) \frac{v_K}{v_0} x) \quad (2)$$

with $k(v_0)$ is the absorption coefficient for the central laser frequency v_0 ; $k(v_0) = \sigma(v_0) n_M$ with $\sigma(v_0)$ is the absorption cross section at $v=v_0$; $g^*(v_K) = g(v_K)/g(v_0)$.

When $J_M(v_K, x)$ is substituted in relation (1) and using $v_K \approx v_0$ we find:

$$\ln \frac{\phi(x_2)}{\phi(x_1)} = -k(v_0)(x_2 - x_1) + \ln \frac{1 + G(x_2)}{1 + G(x_1)} \quad (4)$$

with $G(x) = 2 \int_0^x g^*(v_K) \exp(k(v_0)x(1 - g^*(v_K))) dx$.

Figure 4 gives the calculated values of

$\ln(\phi(x_2)/\phi(x_1))$ versus $(x_2 - x_1)$ for $x_1 = 0.04$ m.

Relation (4) may be approximated within 5% for $k^2(v_0)x < 2.44$ by:

$$\ln \frac{\phi(x_2)}{\phi(x_1)} = -0.707 k(v_0)(x_2 - x_1) + 0.0387 k^2(v_0)(x_2 - x_1)^2 \quad (5)$$

From the slope of $\ln(\phi(x_2)/\phi(x_1))$ at $x_2 = x_1$, we can determine the value $k(v_0)$ and from this the $1s_5$ density. Figure 5 gives a few examples of our experimental results. When the measured absorption curve is not a straight one we have $k(v_0)$ determined by curve fitting. The inaccuracy is better than 10%. It can be remarked that $k(v_0)$ depends on the used spectral transition. So it is possible to measure in the same discharge a different absorption behaviour by using different spectral transitions. Excitation of the $1s_5$ level with $\lambda = 588.2$ nm results in $k(v_0) = 21.7$, $n_M = 3.52 \cdot 10^{17} \text{ m}^{-3}$; with $\lambda = 597.5$ nm results in $k(v_0) = 7.14$, $n_M = 3.44 \cdot 10^{17} \text{ m}^{-3}$.

Figure 5 gives the absolute density with $P = 1$ torr

at various currents. They are in good agreement with measurements from Ricard ⁵⁾.

References:

- 1) Lochte-Holtgreve, Plasma diagnostics, North-Holland Publ. Co. (1968).
- 2) Mitchell and Zemansky, Resonance radiation and excited atoms, Cambridge Univ. Press (1934, 1971).
- 3) A. Corney, Atomic and Laser spectra, Clarendon Press, Oxford (1977).
- 4) S. Inatsugu et al. Phys. Rev. A11, 1, 26 (1975).
- 5) A. Ricard, Le Journal de Physique 28, 523 (1975).
- 6) A.M. Soldatev, Opt. Spect. 34, 6 (1973).
- 7) L.W.G. Steenhuijsen, thesis EUT (1979).

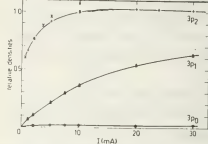


Figure 1: Measured ratio of the densities of the $1s_5, 1s_4, 1s_3$ levels in a 5 torr discharge. The crosses (x) were obtained from Ricard ⁵⁾.

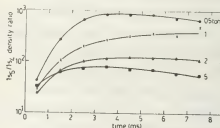


Figure 2: Values of n_1/n_0 in the afterglow for various pressures.

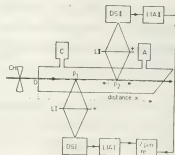


Figure 3: Experimental set up for the absorption measurements.

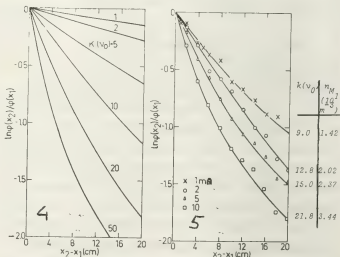


Figure 4: Calculated absorption curves for various values of $k(v_0)$.

Figure 5: Measured absorption curves for $P = 1$ torr and $\lambda = 588.2$ nm at various currents.

EFFICIENCY OF EXCITATION OF ROTATIONAL AND VIBRATIONAL LEVELS IN A NITROGEN MOLECULE

J.I. Londer, L.P. Menahin, K.N. Ulyanov.

All-Union Electrotechnical Institute, Moscow U.S.S.R.

1. Energy losses due to excitation of electrons levels in collisions of electrons with molecules may be neglected in an electrical discharge in N_2 at E/N less or about $4 \cdot 10^{16} \text{ V} \cdot \text{cm}^2/\text{U}$. Energy supplied to N_2 is transformed into heat through excitation and relaxation of rotational and vibrational levels in molecules, and also through elastic collisions of charged particles with molecules.

If ϱ_v is a fraction of energy consumed to excite vibrational levels, ϱ_e - to excite rotational levels and ϱ_{el} is the energy, dissipated through elastic collisions, we have following expression:

$$\varrho_v + \varrho_e + \varrho_{el} = 1 \quad (1)$$

Characteristic relaxation time for vibrational levels in N_2 is much greater than that for rotational levels. Therefore heating of nitrogen takes place in two ways: the rapid way by elastic collisions and rotational relaxation, and the slow way due to vibrational relaxation.

2. Experimental determination of the fraction of energy consumed by the rapid heating processes was reported in [2] when E/N was varied from 10^{-16} to $4 \cdot 10^{-16} \text{ V} \cdot \text{cm}^2$. In our paper measurements were made when E/N was varied from 10^{-17} to $10^{-16} \text{ V} \cdot \text{cm}^2$. Experiments were performed in extra pure nitrogen in a pulsed discharge, generated by an electron beam. The dimensions of the discharge chamber were $9.4 \times 2.8 \times 2.4 \text{ cm}^3$ and all measurements related to a constant volume and gas density. When energy is absorbed, pressure in the chamber changes accordingly. Pressure variations were recorded by a fast-response tensometric gauge. Typical oscillogram of a tensometric signal is given in fig.1. The envelope

shows the temporal pressure variations. Two sections of this curve can be distinguished: the initial section with a steep slope, which corresponds to rapid relaxation and a flat section, which begins after the end of the pumping pulse and which corresponds to vibrational relaxation.

3. Methods of estimating the energy consumed for rapid heating of nitrogen are based on the energy conservation law for gases at constant density:

$$\frac{\partial E_v}{\partial t} + \frac{1}{\gamma-1} \frac{\partial P}{\partial t} = W(t); \quad (t < \tau_p) \quad (2)$$

Here E_v is the vibrational energy density, W is power density absorbed by the gas, γ is adiabatic index. By integrating (2) from 0 to τ_p (where τ_p is the pulse duration) we obtain:

$$E_v(\tau_p) + \frac{\Delta P}{\gamma-1} = \varepsilon(\tau_p); \quad \varepsilon = \int_0^{\tau_p} W dt \approx W \tau_p$$

Here ΔP is the pressure increment per pulse. Expression for E_v may be written in following form:

$$\frac{\partial E_v}{\partial t} = \varrho_v W - \frac{E_v}{\tau_{vr}} \quad (4)$$

Here τ_{vr} is the characteristic relaxation time related to vibrational energy. If $\tau_p \ll \tau_{vr}$, we may obtain by integrating (4):

$$E_v(t) = \varrho_v W t (1 - \frac{t}{\tau_{vr}}); \quad t \leq \tau_p \ll \tau_{vr} \quad (5)$$

After the end of the pumping pulse rapid recombination of plasma takes place. Pressure and temperature variations will be dependent upon relaxation of vibrational levels. This process is described by equations (2) and (4) where $W=0$. The system of equations (2)-(5) can be reduced to two equations for ϱ_v and τ_{vr} .

$$\begin{aligned} \eta_v \varepsilon \left(1 - \frac{\tau_p}{2\tau_{vr}}\right) + \frac{\Delta P}{\gamma - 1} &= \varepsilon \\ \eta_v \varepsilon \left(1 - \frac{\tau_p}{2\tau_{vr}}\right) &= \frac{\tau_p P'}{\gamma - 1}; \quad P' = \frac{\partial P}{\partial t} / t = \dot{\tau}_p + 0 \quad (6) \end{aligned}$$

From (6) we derive:

$$\frac{\tau_p}{\tau_{vr}} = \frac{\tau_p P'}{\varepsilon(\gamma - 1) - \Delta P} \quad (7)$$

$$\eta_v = \left[1 - \frac{\Delta P}{\varepsilon(\gamma - 1)}\right] \left[1 - \frac{1}{2} \frac{\tau_p P'}{\varepsilon(\gamma - 1) - \Delta P}\right]^{-1} \quad (8)$$

$$\eta_z + \eta_{el} = 1 - \eta_v = \frac{\Delta P}{\varepsilon(\gamma - 1)} - \frac{1}{2} \frac{\tau_p P'}{\varepsilon(\gamma - 1) - \Delta P} \left[1 - \frac{1}{2} \frac{\tau_p P'}{\varepsilon(\gamma - 1) - \Delta P}\right]^{-1} \quad (9)$$

Expressions (7)-(9) allow to compute η_v , $\eta_z + \eta_{el}$ and τ_{vr} from the measured values of ΔP and P' . Energy input density can be determined from the mean discharge current and voltage. The cathode drop which has a value 420 ± 50 V at $P = 380$ torr and 550 ± 50 V at $P = 760$ torr should be subtracted.

In our experiments the value τ_p / τ_{vr} did not exceed 10^{-2} ; hence the equations (8)

and (9) may be simplified as follows:

$$\eta_v = 1 - \frac{\Delta P}{\varepsilon(\gamma - 1)} \quad (8a)$$

$$\eta_z + \eta_{el} = \frac{\Delta P}{\varepsilon(\gamma - 1)} \quad (9a)$$

Fraction of energy absorbed from electrons through elastic collisions is given by:

$$\eta_{el} = \frac{\tilde{\gamma}_{el}}{\varepsilon} = \tilde{\gamma}_{el} \varepsilon_e \frac{2m}{M} (eV_e E/N)^{-1} \quad (10)$$

Here $\tilde{\gamma}_{el}$ is frequency of elastic collisions (per one molecule), ε_e - mean energy of electrons, V_e - drift velocity of electrons, e - electron charge, m, M - electron and molecule masses respectively. Dependences of $\tilde{\gamma}_{el}$, V_e and ε_e on E/N were taken from [1]. According to (10) $\eta_{el} \sim 10\%$ at $E/N = 10^{-17}$ V·cm² and $\eta_{el} \sim 2\%$ at $E/N = 10^{-16}$ V·cm².

Fig. 2 shows the dependence of η_v and η_z on E/N , plotted with the use of expressions (8a), (9a) and (10). In the same figure the experimental data from [2,3] for η_z at higher values are given. It can be seen that our results are in good agreement with [2,3] at $E/N = 10^{-16}$ V·cm².

If E/N decreases, η_v decreases markedly and η_z rapidly increases.

4. A systematical error which has been made in our experiments in the determination of η_v and η_z is due to presence of a buffer volume in the discharge chamber ($\sim 10\%$) and inaccurate assessment of cathode drop value (± 50 V). This inaccuracy leads to an error in the value of η_v which is $\sim 10\%$ when $E/N = 1.5 \cdot 10^{-17}$ and $\sim 1.5\%$ when $E/N = 10^{-16}$ V·cm² at $P = 380$ torr. At $P = 760$ torr the error is less. We consider the accuracy of our results to be $\sim 15\%$.

An envelope of signals from the tensometric sensor was found to be modulated by 2.5 kHz. This oscillations modulation was connected with the generation of acoustic oscillations in the resonator, formed by the walls of the discharge chamber. Estimation of fraction of energy consumed by this oscillations, shows that their mean energy density is less than 10^{-4} J/cm². This is by 2 or 3 orders less than the total energy input density. Therefore the energy of acoustic oscillations in the energy balance was not taken into account.

Methods described above were tested in a mixture $\text{CO}_2:\text{N}_2 = 1:3$ ($P = 380$ torr) for which the vibrational energy relaxation time is known. Tensometric measurements of pressure variations performed with an accuracy of $\pm 10\%$ coincided with those, computed from the energy input density for constant volume conditions.

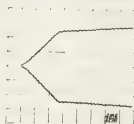


Fig. 1

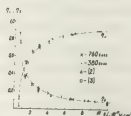


Fig. 2

References

1. A.G. Engelhardt, A.V. Phelps, C.G. Risk. Phys. Rev., 135, 6A, p. 1566 (1964).
2. A.P. Napartovich, V.G. Naumov, V.M. Shashkov DAN SSSR v. 232 p. 570 (1977).
3. R.W. Crompton, D.J. Sutton. Proc. Roy. Soc. A, v. A215, p. 467 (1952).

ION CLUSTERS IN THE POSITIVE COLUMN OF He-Co AND Ar-Co DISCHARGES

Y. Kaufman, P. Avivi and F. Dothan.

Racah Institute of Physics, The Hebrew University of Jerusalem, Jerusalem Israel.

The positive ion spectra of He-CO discharges with and without small additions of O_2 have been described in (1). Here we report on positive mass spectra in He-CO- O_2 and Ar-CO glow discharges in a wider mass range and show the presence of ion clusters having a mass of up to 188 A.M.U..

The experimental setup is described in ref.1. A Quadrupole Residual Gas Analyser was used as an ion detector. Positive ion spectra were taken from the positive column of a discharge maintained in a tube of 3.3cm inside diameter.

Fig.1 shows the positive ion spectrum from a discharge in a mixture of He-CO=7.6-0.8 torr at a current of 10.5mA. The ions are CO^+ and clusters of the type $CO^+ \cdot CO \cdot C_n$ ($n=0,1,\dots,11$).

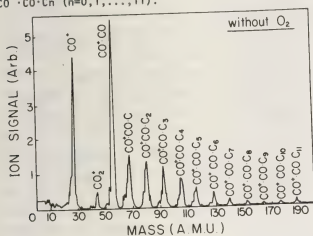


Fig. 1. He-CO- O_2 =7.6-0.8-0 torr ; I_D =10.5mA. Adding O_2 to the He-CO mixture in small amounts of 3mtorr, 6mtorr (Fig.2)

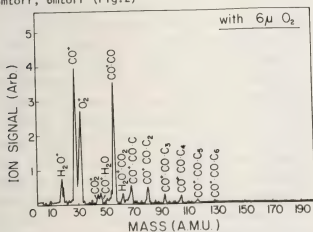


Fig. 2. He-CO- O_2 =7.6-0.8-0.006 torr ; I_D =10.5mA.

and 10mtorr, causes the disappearance of heavy clusters with $n \geq 9$, $n \geq 6$ and $n \geq 3$ respectively. With a partial pressure of 15mtorr O_2 the ion clusters disappear, while O_2^+ becomes the dominant ion (Fig. 3).

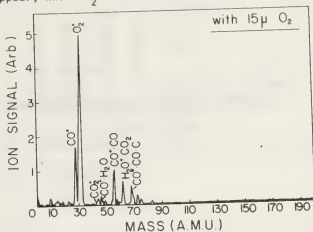


Fig. 3. He-CO- O_2 =7.6-0.8-0.015 torr ; I_D =10.5mA.

The positive ion spectra of Ar-CO discharges at a current of 25mA are given in Figs. 4-6. Figs. 4 and 5 show that addition of Ar increases the relative concentration of ion clusters. Fig. 6 shows that cooling the tube walls ($T_W=220^\circ K$) leads to the appearance of the ions $CO^+ \cdot CO \cdot C_n$ ($n=4,\dots,8$).

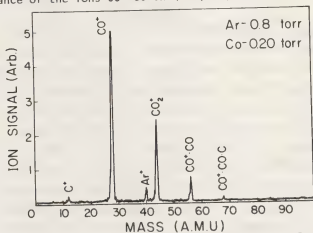


Fig. 4. Ar-CO=0.8-0.20 torr ; I_D =25mA ; $T_W=300^\circ K$. The observed change in ion composition when O_2 is added is in accordance with other authors (2,3), who argue that in the presence of oxygen the reaction $CO \rightleftharpoons C+O$ is driven preferentially to the left, thus decreasing the carbon concentration hence preventing cluster formation. Another possible process for free carbon destruction is $C+O_2^+ \rightarrow CO^+ + O$ (4,5).

The carbon loss is in agreement with our results of the disappearance of C_2 Swan bands when O_2 is added to the mixture (6). The dominance of O_2^+ ion can explain the decrease of E/N accompanying O_2 addition (1,6). The decrease of E/N results in a shift of the electron energy distribution to lower energies, thus lowering carbon production by dissociation of CO.

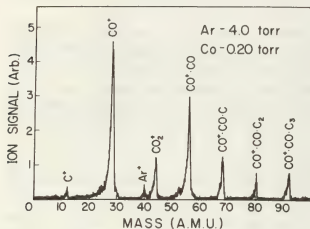


Fig. 5. Ar-Co=4.0-0.20 torr; $I_D = 25\text{mA}$; $T_W = 300^\circ\text{K}$.

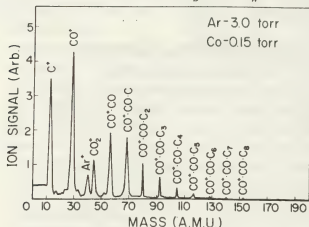


Fig. 6. Ar-Co=3.0-0.15 torr; $I_D = 25\text{mA}$; $T_W = 220^\circ\text{K}$.

The gradual disappearance of the clusters, starting with the higher mass clusters, and the monotonic decrease of their concentrations with increasing mass (Fig.1), leads to the assumption that the clusters are created one from another in the three-body process: $CO^+ \cdot CO \cdot C_{n-1} + C + M \rightarrow CO^+ \cdot CO \cdot C_n + M$ where M is an atom or a molecule. This process is consistent with Thomson's theory about ternary collisions (7,8). This theory states that the presence of a third particle M is necessary in order to remove the excess energy of two colliding particles, so that they end up in a bound state. This causes the growth of cluster density upon adding Ar to a Ar-CO mixture.

Theoretical calculations (8,9) and experiments (10) show a strong decrease (almost exponential) of cluster density with gas temperature. This is further

supported by comparing Figs. 5 and 6. Lowering the gas temperature (by cooling the tube walls) results in the appearance of five heavy clusters because of two reasons: 1) Preventing thermal destruction by detachment of the high-mass clusters. 2) Increasing sharply the formation rate constants of the clusters (8).

This work was performed with the help of a grant by the Israel Commission for Basic Research of the Israel Academy of Science which we gratefully acknowledge.

References

1. H. Keren, P. Avivi and F. Dothan, IEEE J. Quant. Electron. **QE-12**, 58 (1976).
2. M.L. Bhaumik, W.B. Lacina and M.M. Mann, IEEE J. Quant. Electron. **QE-8**, 150 (1972).
3. V.I. Volchenok, N.P. Egorov, V.N. Komarov, S.E. Kupriyanov, V.N. Ochkin, N.N. Sobolev and E.A. Truvacheev, Sov.Phys.Tech.Phys. **21**, 1500 (1976).
4. W.L. Morgan and E.R. Fisher, Research Report RIES 77-119 (1977).
5. M.B. McElory and J.C. McCovvelli, J. Geophys. Res. **76**, 6674 (1971).
6. H. Keren, P. Avivi and F. Dothan, IEEE J. Quant. Electron. **QE-11**, 590 (1975).
7. J.J. Thomson, Phil. Mag. **47**, 334 (1924).
8. B.M. Smirnov, Sov. Phys. Usp. **20**, 119 (1977).
9. R. Clappitt, 10th ICPIG, Oxford 1971, Invited Papers, p. 231.
10. V.I. Volchenok, N.P. Egorov, V.N. Komarov, S.E. Kupriyanov, V.N. Ochkin and N.N. Sobolev, Sov. Phys. Dokl. **22**, 85 (1977).

TIME DEPENDENCE OF CATAPHORESIS IN A NEON-ARGON MIXTURE.

C. Sanctorum and L. Bonte.

Laboratorium voor Natuurkunde, Fakulteit Toegepaste Wetenschappen, Rijksuniversiteit Gent, Belaique.

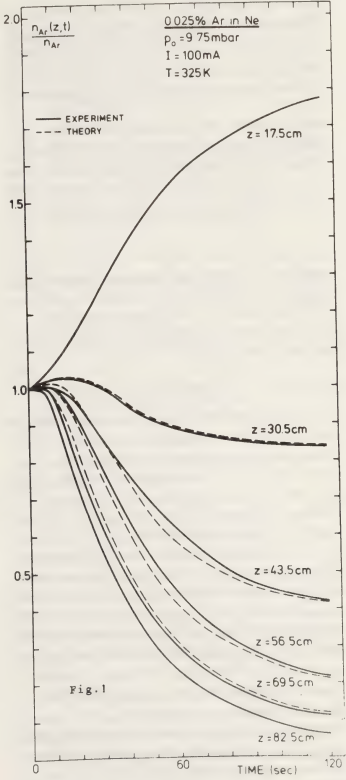
Introduction.

Within the past twenty years, the steady-state cataphoresis segregation phenomenon has been studied by numerous investigators. The time dependence of cataphoresis has received less attention.

In the present paper some data are reported of transient cataphoresis in neon containing a small amount of argon. These measurements involved time-dependent mass analysis following the initiation of the discharge (tube length 115 cm, inner diameter 2.0 cm, electrode distance 100 cm). Gas is continuously sampled through molecular leaks in the wall of the discharge tube and analyzed in a quadrupole mass spectrometer. In order to obtain a true picture of the time behaviour of the cataphoresis segregation in the discharge, the measured Ar and Ne partial pressures have been corrected for changes in gas composition caused by the gas analysis and pumping system (1). Further details concerning the discharge tube, the experimental system and the method used to determine the neutral gas constituents present in the positive column can be found elsewhere (2).

Experimental results.

For a neon-argon mixture containing 0.025 % argon, fig.1 shows the change of the relative argon density $n_{Ar}(z,t)/n_{Ar}$ with time at six different positions in the positive column. $n_{Ar}(z,t)$ is the admixture density at an axial distance z from the cathode at the time t after the initiation of the discharge. n_{Ar} is the original argon density present in the tube. The reduced pressure is 9.75 mbar and the discharge current is 100 mA. The gas temperature is 325 K. Two minutes after switching on the



discharge the steady-state cataphoresis segregation is almost reached. In fig.1 the cataphoresis segregation phenomenon is well illustrated; we observe the strong argon density increase at the cathode end of the discharge and the even stronger decrease at the anode end. In table 1 some numerical values of $n_{Ar}(z,t)/n_{Ar}$ are given.

Table 1. Experimental values of the reduced Ar-density.

time (sec)	0	20	40	60	80	100	120	∞
distance z (cm)								
82.5	1	0.722	0.407	0.231	0.145	0.090	0.060	0.046
69.5	1	0.782	0.474	0.290	0.193	0.137	0.113	0.095
56.5	1	0.911	0.641	0.444	0.319	0.254	0.217	0.200
43.5	1	0.950	0.770	0.615	0.500	0.445	0.420	0.410
30.5	1	1.020	0.944	0.886	0.854	0.843	0.835	0.835
17.5	1	1.163	1.383	1.562	1.663	1.730	1.775	1.790

Table 2. Calculated values of the reduced Ar-density.

time (sec)	0	20	40	60	80	100	120	∞
distance z (cm)								
82.5	1	0.722	0.407	0.231	0.145	0.090	0.060	0.046
69.5	1	0.815	0.502	0.303	0.204	0.144	0.119	0.095
56.5	1	0.890	0.608	0.406	0.303	0.243	0.212	0.200
43.5	1	0.951	0.742	0.574	0.488	0.439	0.416	0.410
30.5	1	1.026	0.952	0.892	0.859	0.847	0.837	0.835
17.5	1	1.163	1.383	1.562	1.663	1.730	1.775	1.790

Comparison of the experimental results with theory.

The density of the admixture as a function of place and time is given by the diffusion equation :

[1]

$$\frac{\partial}{\partial t} n_{Ar}(z,t) = D \frac{\partial^2}{\partial z^2} n_{Ar}(z,t) + K \frac{\partial}{\partial z} n_{Ar}(z,t).$$

D is the diffusion coefficient for argon in neon and the second term on the right hand accounts for the argon ion transport : $K = \mu^+ E \theta$ (3). μ^+ is the argon ion mobility in neon, E is the magnitude of the axial electric field and θ is the degree of ionization of the argon admixture.

In order to compare the experimental results with theoretical predictions, the partial differential equation [1] has been solved numerically using the finite difference method (4). For this purpose a domain was chosen bounded by the experimental argon densities for extreme z and t-values (these boundary values lie outside the dashed rectangle of table 1). The function $n_{Ar}(z,t)$ was determined that takes these argon density boundary values on the given boundary and satisfies the diffusion equation [1] within the boundary.

By successive iterations (relaxation method) the numerical values of this function within the domain are obtained. The calculations were carried out for $D = 35.4 \text{ cm}^2/\text{sec}$ (5) and $K = 1.99 \text{ cm/sec}$ (obtained from the slope of the exponential axial steady-state distribution of the argon density). The dashed curves of fig.1 show the calculated change of the argon density with time. The calculated relative argon density values corresponding with the experimental values of table 1 are shown in table 2. Comparison of calculated values with the measured values shows, that the difference in most cases is less than 5 % and in no case is larger than 10 %. This indicates that for the neon-argon mixture studied, the measured time dependence of cataphoresis appears to be consistent with theoretical predictions.

Acknowledgements.

This work has been supported by a grant from the Nationaal Fonds voor Wetenschappelijk Onderzoek, Brussels.

References.

- (1) Sullivan, J.J. and Buser, R.G., J. Vacuum Science and Technology 6 (1969) 103.
- (2) Sanctorum, C., Physica 83 B+C (1976) 367.
- (3) Oskam, H.J., Physica 40 (1969) 594.
- (4) Ames, W.F., Numerical Methods for Partial Differential Equations, Academic Press (1977).
- (5) Hogervorst, W., Physica 51 (1971) 59.

VISIBLE LINE AFTERGLOW EMISSION OF A PULSED XENON DISCHARGE

M. Vanmarcke, W. Wieme.

Laboratorium voor Natuurkunde Rijksuniversiteit, Rozier 44, Gent Belgium.

1. Introduction.

Although in recent years much work has been done on rare gas afterglows in the VUV region, the afterglow emission of the visible line spectrum has only occasionally been investigated [1][2][3]. In this paper a study of the spectral region 400-900 nm in the afterglow of a xenon discharge is described (pressure range 0,1-40 Torr).

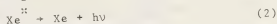
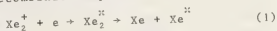
2. Method.

The discharge tube is a cylindrical pyrex vessel 40 cm long, diameter 38 mm. The discharge is struck between two nickel ring electrodes placed at 3 cm from the end windows. A side arm is provided at one end to run the discharge at low pressure without sputtering electrode material on the windows. A rectangular voltage pulse with a fall time less than 1 μ s is applied with a 807 penthode connected parallel to the discharge tube. The tube is pumped down on a UHV system and filled with high purity xenon (L'Air Liquide N47). The light is collected at the end window with a lens and focussed on the entrance slit of a monochromator. The detection system consist of a Optical Multichannel Analyser (PAR OMA 1 system) with a SIT detector. This detector can be gated to obtain a time resolution down to 100 ns. The spectral resolution is determined by the 1200 1/mm grating and was better than 0,5 nm. In this way all the principle lines of the Xenon spectrum were completely separated. The OMA system was used to obtain spectra in segments of 200 nm at selected times in the afterglow, determined by a delay generator. These spectra were recorded with a XY recorder and read out subsequently as no digital readout facilities are available at the moment.

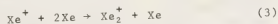
3. Results.

A typical result is shown in Fig.1. The light intensity I at first increases during the afterglow period, then decays exponentially, and finally shows a non-exponential very slow decay.

This last decay has been observed by other authors [3][4] and identified as recombination light, obtained through the dissociative recombination process :



The dimeric ions Xe_2^+ are known to be abundantly formed in the earlier part of the afterglow through the three-body process :



The recombination phenomena are governed by the rate equation

$$\frac{1}{N} \frac{dN}{dt} = -\alpha_i n_e \quad (4)$$

where α_i represents the recombination coefficient for the appropriate ion species N^+ . Therefore intensity decays due to recombination follow the law

$$I^{-1/2} = I_0^{-1/2} + \alpha_i t \quad (5)$$

This intensity decay is observed in our experiments only for the later part of the afterglow. This means obviously that in the earlier afterglow other processes have to be rate-determining.

We shall now concentrate on this earlier part. This decay can be fitted to a curve

$$I = A e^{-\alpha t} - B e^{-\beta t} \quad (6)$$

A plot of α , respectively β against p is given in Fig.2 and Fig.3. The points up to 20 Torr have been least-square fitted, to give :

$$\alpha = \frac{22}{p} + 137 p + 309 p^2 \quad (7)$$

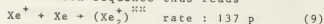
$$\beta = 5330 p \quad (8)$$

We suggest the following explanation :

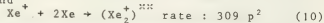
Dimeric ions are formed according to (3), with rate constant α . α then represents the conversion coefficient of atomic ions into dimeric ions. This coefficient is given in literature by several authors between $190p^2$ and $450p^2$ [5][6].

The pseudo-lifetime β can be explained as follows : the Xe_2^+ ion is formed in an excited state from which it cannot readily recombine. It decays to a lower vibrational level, possibly down to $v=0$ by collisions with neutral atoms.

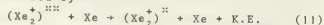
The reaction sequence thus reads



and



followed by



rate : 5330 p

and



Here $(\text{Xe}_2^+)^{***}$ represents one of possibly several higher vibrational states whereas $(\text{Xe}_2^+)^{**}$ represents a lower vibrational state, possibly $v=0$.

Process (9) has not been mentioned in literature before.

4. Comment.

Turner and Riccius [1] have performed a similar investigation in krypton. They found only an exponential decay with a rate constant 900 p for which they suggest a process similar to (11). However they failed to observe the initial formation processes (9) and/or (10). Experiments are planned in krypton to verify these results under our experimental conditions. A computer program was written to obtain the variation of the light intensity during the afterglow, taking account all forementioned processes. The shape of the intensity versus time curve is indeed nearly exponential, as observed. At low pressures (<1 Torr) diffusion effects can be expected to show up. This process can be characterized by an exponential decay; we find an ambipolar diffusion coefficient $\frac{22}{p}$, in agreement with literature [3]. At pressures above 20 Torr, the ex-

perimentally obtained α tend to be significantly lower than predicted by (7). This could mean that other processes become important, which is now further investigated.

References.

- [1] R.Turner, H.D.Riccius, J.Chem.Phys. 48, 4351, 1968.
- [2] A.Monteil et al., J Q R S T 18, 573, 1977.
- [3] A.Barbet et al., J.Phys.B, 8, 1785, 1975.
- [4] Y.J.Shui et al., Phys.Rev.A15, 494, 1977.
- [5] R.L.Fitzwilson, J.Appl.Phys., 44, 5337, 1973
- [6] A.Barbet et al., J.Phys.B, 8, 1785, 1975.

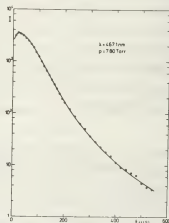


Fig. 1

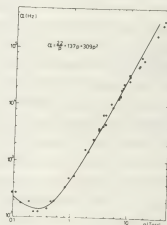


Fig. 2

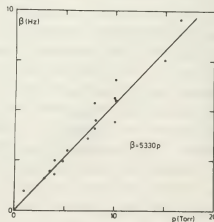


Fig. 3

EXCIMER FORMATION IN RARE GAS DISCHARGE AFTERGLOWS

W. Wieme, J. Lenaerts.

Laboratorium voor Natuurkunde, Rijksuniversiteit, Rozier 44 Gent, Belgium.

1. Introduction.

The VUV continuum in rare gases has been extensively studied with different methods.

- Discharge afterglows were mainly studied at low pressures (0,1-20 Torr). Absorption measurements on the 3P_2 metastable state established the role of three-body collisions :

$$R(^3P_2) + 2R(^1S_0) \rightarrow R_2^* + R \quad (1)$$

Reaction rates for process (1) are :

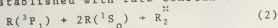
Ar:18.5 p²[1] Kr:44 p²[2] Xe:87 p²[3]

- Excitation by highly energetic particles (α source or e-beam), usually at higher pressures (100-1000 Torr). As precursors

all 4 states of the $np^5(n+1)s$ configuration have been involved. Reaction rates for (1) were stated as :

Ar : 10 p²[4] Kr : 46 p²[9] Xe : 40 p²[6]

For the 3P_1 resonant state reaction (2) has been established with rate constants :



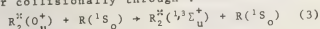
Ar : 21 p²[8] Kr : 8,45 p²[5] Xe : 46 p²[6]

- Optical excitation using synchrotron radiation has been applied to Kr and Xe [7].

This yields for reaction (2)

Kr:23 p² Xe:36 p² when R_2^* is the O_u^+ state
Kr:46 p² Xe:63 p² when R_2^* is the $^1\Sigma_g^+$ state.

The O_u^+ state can either decay radiatively, or collisionally through :



Reaction constants are :

Kr : 3,3 10⁶p Xe : 2,8 10⁶p

- Other experimental techniques are not reviewed for lack of space. Generally, we find that low pressure afterglow data tend to give reaction rates roughly twice those obtained at high pressures with other methods. Low pressure absorption measurements being the only ones where the precursors can be positively identified, we report measurements of the VUV emission in discharge afterglows at pressures between 1-150 Torr,

in an attempt to elucidate this discrepancy.

2. Theory.

In our analysis we use a four-level model. Let R represent the 3P_1 resonance state, M the 3P_2 metastable state; P and S indicate two molecular levels which can be populated through collision processes. We give no assignment to these levels, as they may stand for a multitude of vibrational levels belonging to different excimer states. We define :

β decay constant for the escape of imprisoned resonance radiation

$\alpha_{RS} \alpha_{RM} \alpha_{MP} \alpha_{SP} \alpha_{PS}$ rate coefficients for collision-induced transitions R to S, R to M, M to R, M to P, S to P, P to S, respectively. Excimers S and P decay with time constant θ and τ respectively.

The following set of differential equations results :

$$\frac{dR}{dt} = -(\beta + \alpha_{RM} + \alpha_{RS})R + \alpha_{MR}M$$

$$\frac{dM}{dt} = \alpha_{RM}R - (\alpha_{MR} + \alpha_{MP})M$$

$$\frac{dP}{dt} = -(\rho + \alpha_{PS})P + \alpha_{MP}M + \alpha_{SP}S$$

$$\frac{dS}{dt} = -(\theta + \alpha_{SP})S + \alpha_{RS}R + \alpha_{PS}P$$

We neglect backward transitions $R \rightarrow M$ and $S \rightarrow R$.

We obtain for P and S :

$$P = C_1 e^{-\sigma t} + C_2 e^{-\rho t} + C_3 e^{-d_f t} + C_4 e^{-d_s t}$$

$$S = C_5 e^{-\sigma t} + C_6 e^{-\rho t} + C_7 e^{-d_f t} + C_8 e^{-d_s t}$$

$$d_f, d_s = \frac{1}{2}[-(a+b) \pm \sqrt{(a-b)^2 + 4\alpha_{RM}\alpha_{MR}}]$$

$$\sigma, \rho = \frac{1}{2}[-(m+k) \pm \sqrt{(m-k)^2 + 4\alpha_{SP}\alpha_{PS}}]$$

$$a = \beta + \alpha_{RM} + \alpha_{RS}, \quad b = \alpha_{MR} + \alpha_{MP}$$

$$m = \beta + \alpha_{PS}, \quad k = \theta + \alpha_{SP}$$

With reaction rates known from literature, we find that for pressures up to 60 Torr, within 5 % :

$$d_f = a, \quad d_s = b$$

Simplification of σ and ρ is more difficult, as no reliable values of the coefficients $\theta, \rho, \alpha_{PS}, \alpha_{SP}$ are known. It seems however that at pressures up to about 50 Torr

we have $d_f, d_s \ll m, k$.

3. Experimental.

The discharge tube is described in [3]. It is followed by a McPherson 218 monochromator. The detector is a EMI-GENCOM G-26E315. The PM signal is analysed with a DATALAB DL 920 transient recorder with a time resolution of 50 ns. The intensity decay is fitted to a curve: $I = Ae^{-pt} + Be^{-d_f t} + Ce^{-d_s t}$. The fast decay Ae^{-pt} may include several transient processes and has not been analysed, d_f and d_s have been defined earlier.

4. Results.

We distinguish between :

a) The wavelengths adjacent to the $^3P_1-^1S_0$ resonance line (first continuum).

b) The so-called second continuum with a maximum at 170nm(Xe), 150nm(Kr) & 130nm(Ar)
No significant wavelength dependence was found throughout this second continuum. A typical result is given for Xe in Fig.1. The full line is a curve fit to the d_s values from the second continuum at pressures < 20 Torr.

In complete agreement with absorption studies, we find : Ar : $d_s = 45p + 18p^2$ (4)

$$\text{Kr} : d_s = 82p + 41p^2 \quad (5)$$

$$\text{Xe} : d_s = 113p + 87p^2 \quad (6)$$

At higher pressures the observed d_s is always slower than predicted by (4)(5) or (6). At the same time, d_s becomes highly dependent on the discharge current. This implies that interactions involving electrons become important. The points presented in Fig.1 are taken in a diffuse discharge at the lowest possible current.

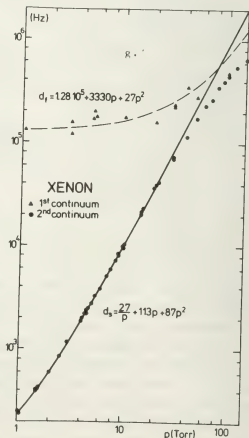
A computer simulation, including dimeric ion formation and recombination was attempted. As no precise values of electron density and temperature were available, these were treated as a parameter. The computer predicted decays show an exponential decay, corresponding to d_s , with a time constant 10 to 200 % below the full line of Fig.1, the lower n_e giving the best approximation. The first continuum has only been measured in Xe. It decays with rate constant d_f which is close to the measured decay of the 3P_1 resonance line, reported in [10](dashed line).

4. Discussion.

Our results indicate that reaction rates obtained from 3P_2 absorption measurements in Ar, Kr and Xe, are indeed reliable. The discrepancy with high pressure results is probably partly due to other precursors, partly to neglect of electron collision effects. Collision induced transitions such as (3) also become increasingly important at higher pressures.

5. References.

- [1] W.Wieme, J.Wieme-Lenaerts, Phys.Lett.47A, 37, 1974.
- [2] R.Turner, Phys.Rev.158, 121, 1967.
- [3] W.Wieme, J.Phys.B, 7, 850, 1974.
- [4] N.Thonnard, C.S.Hurst, Phys.Rev.A5, 1110, 1972.
- [5] P.K.Leichner, R.J.Ericson, Phys.Rev.A9, 251, 1974.
- [6] P.K.Leichner et al., Phys.Rev.A13, 1787, 1976.
- [7] R.Brodman, G.Zimmerer, J.Phys.B, 10, 3395, 1977.
- [8] M.Bourène et al., J.Chem.Phys.63, 1668, 75.
- [9] R.Bouciqué, P.Mortier, J.Phys.D3, 1905, 1970.
- [10] W.Wieme at al., submitted for this conference.



THEORY OF RESONANCE RADIATION IMPRISONMENT

M. Vanmarcke, W. Wieme.

Laboratorium voor Natuurkunde, Rijksuniversiteit, Herestraat 49, Gent, Belgium

1. Introduction.

The Holstein theory of resonance radiation imprisonment has been found to be in reasonably good agreement with experimental determinations of the imprisonment time at intermediate pressures (0,1-10 Torr) in rare gases [1]. Recently Payne et al. [2] claimed a discrepancy as much as a factor 3 at low pressures (0,002-0,5 Torr) in argon and they developed a theory involving the effect of correlations between absorbed and emitted frequencies. We develop here an alternative model which was constructed in order to be readily accessible for computer calculations, thereby avoiding Holstein's analytical approximations.

2. Theoretical Model for Cylindrical Geometry.

We consider $N_R(t)$ resonance atoms, symmetrically distributed in an infinite cylinder with radius R . We define the number of resonance photons emitted in the time interval dt between the distances r and $r+dr$ from the axis as (Fig.1) :

$$N_R(t)w(r,t)dr \frac{dt}{\tau_N} \quad (1)$$

Here τ_N represents the natural lifetime of the resonance state and $w(r,t)$ is the relative number of resonance photons between r and $r+dr$. For isotropic emission a fraction $[1/4\pi]\sin\theta \, d\theta \, d\phi$ is emitted between $(\theta, \theta+d\theta)$ and $(\phi, \phi+d\phi)$. The number of photons with a

frequency $(\nu, \nu+d\nu)$ is $P(\nu)d\nu$ while the probability of reaching the cylinder wall without being absorbed is given by $e^{-k_\nu \rho(r, \theta, \phi)}$, noted further as $e^{-k_\nu \rho}$
 k_ν : absorption coefficient for photons with frequency ν

ρ : distance from emission point to the wall. ($\rho = AB$ on figure 1).

The number of photons reaching the cylinder wall is given by :

$$4\pi \tau_N \frac{dN_R(t)}{dt} = - \int_0^\nu P(\nu) d\nu \int_0^R \int_0^\pi \int_0^{2\pi} w(r,t) \sin\theta e^{-k_\nu \rho} dr d\theta d\phi \quad (2)$$

We consider a non-reflecting cylinder wall, so $dN_R(t)$ represents the number of photons disappearing from the gas volume between t and $t+dt$. For an exponential decay with time constant τ_s , as is found experimentally, we have $dN_R(t) = -N_R(t) \frac{dt}{\tau_s}$ (3)

Combining (2) and (3) gives the relationship between natural lifetime τ_N and imprisonment time τ_s :

$$\frac{4\pi\tau_N}{\tau_s} = \int_0^\infty P(\nu) d\nu \int_0^R \int_0^\pi \int_0^{2\pi} w(r,t) \sin\theta e^{-k_\nu \rho} dr d\theta d\phi \quad (4)$$

It is clear that as τ_N/τ_s is a time independent quantity, then $w(r,t) = w(r)$ has to be time independent too. Quite similarly the variations of the number of resonance atoms in a cylinder with radius $s < R$, at times between $(t, t+dt)$ by summing up the loss and gain of photons (Fig.2) :

$$4\pi\tau_N d[\int_0^s N_R(t)w(r)dr] = - \int_0^\infty P(\nu) d\nu \int_0^s \int_0^\pi \int_0^{2\pi} N_R(t)w(r) dr d\theta d\phi e^{-k_\nu \rho}$$

$$\left\{ \int_0^\infty P(v) dv \int_0^R \int_{\phi_{\min}}^{\pi} \int_{\phi_{\min}}^{\phi_{\max}} N_R(t) w(r) dr dt \sin \theta d\theta d\phi \right\} \times \left\{ e^{-k_v \rho_1} - e^{-k_v \rho_2} \right\} \quad (5)$$

Because of the exponential decay of N_R and the time dependence of $w(r)$ we have :

$$d \left[\int_0^s w(r) dr N_R(t) \right] = -N_R(t) \frac{dt}{\tau_s} \int_0^s w(r) dr \quad (6)$$

In order to be able to calculate $w(r)$ we propose a parabolic density distribution for the resonance atoms :

$$n_R(r, t) = (1 - A \frac{r^2}{R^2}) n_R(0, t) \quad 0 \leq A < 1$$

Equalling (5) and (6) we find that, for any s , $w(r)$ must satisfy a relation

$$V(A, s) = G(KR, A, s) \quad (7)$$

K : absorption coefficient at the center of the resonance line.

$$V(A, s) = \int_0^s w_a(r) dr$$

$$G(\dots) = \int_0^\infty P(v) dv \int_0^R \int_{\phi_{\min}}^{\pi} \int_{\phi_{\min}}^{\phi_{\max}} w(r) \sin \theta e^{-k_v \rho} dr d\theta d\phi \}^{-1} \times$$

$$\left\{ \int_0^\infty P(v) dv \int_0^s \int_{\phi_{\min}}^{\pi} \int_{\phi_{\min}}^{\phi_{\max}} w(r) \sin \theta e^{-k_v \rho} dr d\theta d\phi - \right.$$

$$\left. \int_0^\infty P(v) dv \int_0^R \int_{\phi_{\min}}^{\pi} \int_{\phi_{\min}}^{\phi_{\max}} w(r) \sin \theta [e^{-k_v \rho_1} - e^{-k_v \rho_2}] dr d\theta d\phi \right\}$$

$$\text{and } w_a(r) = \frac{4}{2-A} \left(1 - \frac{Ar^2}{R^2} \right) \frac{r}{R^2}$$

Computer calculations of V and G with parameters A and s under the assumption of either natural and pressure broadening or doppler broadening, show that (7) can only be satisfied for one unique value A_0 of the parameter A (Fig.3). With this A_0 which remains of course function of KR , $w(r)$ is completely determined and therefore $\frac{\tau_N}{\tau_s}$ can be calculated from (4).

For $KR > 10$ we find the following formulas

a) natural and pressure broadening :

$$\frac{\tau_N}{\tau_s} = \frac{0,637}{\sqrt{KR}} \quad \text{Holstein : } \frac{\tau_N}{\tau_s} = \frac{0,629}{\sqrt{KR}}$$

b) for doppler broadening :

$$\frac{\tau_N}{\tau_s} = \frac{1,8}{KR \sqrt{\ln KR}} \quad \text{Holstein : } \frac{\tau_N}{\tau_s} = \frac{1,6}{KR \sqrt{\ln KR}}$$

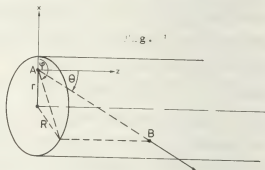
Conclusion.

Our calculations, compared to Holstein's, give about a 10 % lower imprisonment time

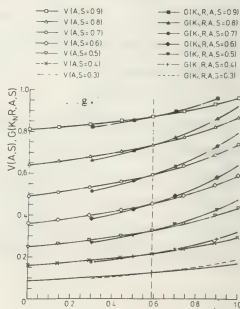
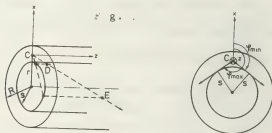
for doppler broadening, and the same results for pressure broadening. At $KR < 10$, our results can be compared to Orlov[3] and Schäfer[4]. Their assumptions (Orlov : $\rho=R$, Schäfer : homogeneous equilibrium distribution, or $A_0 = 0$) lead to some discrepancies with our more general calculations.

References.

- [1] W. Wieme, P. Mortier, Physica 65, 198, 1973.
- [2] M. G. Payne et al., Phys. Rev. 19, 1050, 1974.
- [3] L. N. Orlov, Zh. Prik. Spekt. 10, 146, 1969.
- [4] G. Schäfer, Z. Physik 261, 423, 1973.



DEFINITION OF THE DISTANCES $\rho_1 = CD$, $\rho_2 = CE$ AND THE ANGLES φ_{\min} AND φ_{\max}



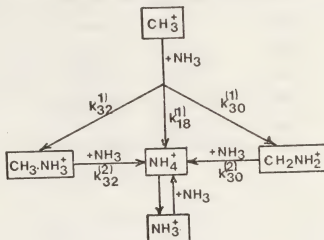
REACTION $\text{CH}_3^+ + \text{NH}_3$ - EVOLUTION DES PRODUITS EN FONCTION DE LA CONCENTRATION DE NH_3 ,R. Thomas^{*}, J. Barassin^{**}, A. Barassin^{***}.^{*}Centre de Recherches en Physique de l'Environnement terrestre et planétaire (C.R.P.E.) C.N.R.S. et C.N.R.S. 45045 Orléans, Cedex France.^{**}Laboratoire de Chimionisation. U.E.R. Sciences, Université d'Orléans. 45045 Orléans Cedex, France.^{***}Laboratoire de Chimionisation U.E.R. Sciences et Centre de Chimie de la Combustion et des Hautes Températures (C.R.C.C.H.T.) C.N.R.S., 45045 Orléans Cedex, France.

Nous avons utilisé un tube à dérive à introduction sélective (T.D.S.M.) (1) pour l'étude de la réaction $\text{CH}_3^+ + \text{NH}_3$ dans une gamme d'énergie comprise entre 0,04 eV et 1 eV. Les ions CH_3^+ sont produits à partir de CH_4 dans une source à bombardement électronique puis sélectionnés parmi les fragments ionisés à l'aide d'un spectromètre de masse avant leur introduction dans le tube à dérive d'une longueur effective de 56,5 mm. L'ammoniac est introduit dans le tube à différentes dilutions dans l'hélium utilisé comme gaz vecteur. La gamme de pression dans le tube est comprise entre 0,3 et 0,7 Torr. Afin de diminuer l'état d'excitation des ions l'introduction se fait à basse énergie (2 à 3 eV). L'énergie des électrons ionisants dans la source contribue à l'excitation des ions initiaux, elle a été abaissée à la valeur minimale compatible avec un niveau de signal suffisant (20 eV).

La constante de vitesse globale k de la réaction primaire: $\text{CH}_3^+ \xrightarrow{k} \begin{cases} \text{NH}_4^+ & k^{(1)}_{(18)} \\ \text{CH}_2\text{NH}_2^+ & k^{(1)}_{(30)} \\ \text{CH}_3\text{NH}_3^+ & k^{(1)}_{(32)} \end{cases}$

est obtenu en se plaçant dans des conditions de pseudo-premier ordre. Le temps de réaction égal au temps de transit des ions dans le tube à dérive est déduit des mobilités précédemment déterminées (2). L'analyse des ions produits permet d'atteindre les rapports de branchement et de déterminer les valeurs $k^{(1)}_{(18)}$, $k^{(1)}_{(30)}$, $k^{(1)}_{(32)}$. Du fait des réactions secondaires des ions produits avec NH_3 les constantes doivent être extrapolées pour $[\text{NH}_3] = 0$ (Figure 1). L'accord avec les valeurs de SMITH et ADAMS à 300 K est satisfaisant.

A partir de ces résultats pour expliquer l'évaluation des concentrations ioniques en fonction de la concentration en NH_3 , à température et temps de réaction constants, nous avons envisagé le modèle suivant:



Les valeurs de $k^{(2)}_{(30)}$ et $k^{(2)}_{(32)}$ ont été déterminées par comparaison entre les profils expérimentaux et les profils théoriques (Figure 2) calculés pour un temps de réaction donné égal au temps expérimental en fonction de $[\text{NH}_3]$. Ce procédé a été appliqué à différentes températures (Tableau I). L'équilibre $\text{NH}_4^+ \rightleftharpoons \text{NH}_3^+$ intervenant à haute température n'a pas été abordé.

Références:

- 1- R. THOMAS, A. BARASSIN, RR. BURKE
Int. J. Mass. Spectrom. Ion Phys. 28 (1978) 275.
- 2- R. THOMAS, J. BARASSIN, A. BARASSIN, à paraître
dans Int. J. Mass. Spectrom. Ion Phys.
- 3- D. SMITH, N.G. ADAMS, Chem. Phys. Letters 47
(1977), 145.

Tableau I

$T_{eff} (K)$	$k_{(30)}^{(2)}$ molec ⁻¹ cm ³ .s ⁻¹	$k_{(32)}^{(2)}$ molec ⁻¹ cm ³ .s ⁻¹
365	$(1 \pm 1) 10^{-10}$	$(1 \pm 1) 10^{-10}$
540	$(2 \pm 0,2)$	(2 ± 1)
800	$(2 \pm 0,2)$	(4 ± 1)
1500	$(3 \pm 0,3)$	(8 ± 1)
2500	$(5 \pm 0,5)$	(8 ± 2)
4000	$(7 \pm 0,7)$	
6000	$(8 \pm 0,8)$	

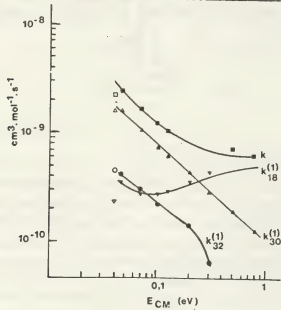


Figure 1 □ Δ ○ ▽ : Référence 3.

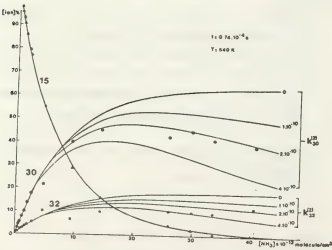


Figure 2

ELECTRON SWARM HAVING AN ANISOTROPIC VELOCITY DISTRIBUTION FUNCTION

T. Makabe, T. Mori.

Department of Electrical Engineering, Faculty of Engineering, Keio University, Yokohama, Japan.

INTRODUCTION

In recent years there has been a renewed interest in the velocity distribution function of electrons in weakly ionized gases. In this report we present the theoretical analysis of the electron swarm in a relatively high E/N , considering an anisotropy of the distribution function. The present developed theory is applied to the electron swarms in neon.

BASIC THEORY

The Boltzmann equation for the velocity distribution function $g(\mathbf{r}, \mathbf{v}, t)$ of electrons moving through a slightly ionized gas under the influence of a uniform electric field E is

$$\frac{\partial g}{\partial t} + \mathbf{v} \cdot \frac{\partial g}{\partial \mathbf{r}} + \frac{eE}{m} \frac{\partial g}{\partial v} = J(g) \quad (1)$$

where \mathbf{v} is the electron velocity, e the electronic charge, m the electron mass, and $J(g)$ the collision integral.

We express the distribution function in the form of the first three-terms of the

spherical harmonic expansion in order to

make clear the anisotropy of the function

$$g(\mathbf{r}, \mathbf{v}, t) = g_0(\mathbf{r}, \mathbf{v}, t) + g_1(\mathbf{r}, \mathbf{v}, t) \cos \theta + g_2(\mathbf{r}, \mathbf{v}, t) \frac{3 \cos^2 \theta - 1}{2} \quad (2)$$

where g_0 is the isotropic part of the distribution function, g_1 and g_2 the first and second anisotropic parts, and θ the angle between \mathbf{v} and E . When the expansion (2) is inserted into the equation (1) under the condition of one dimensional spatial

gradient along the field direction (z axis), we find the integrodifferential equation

for g_0 , g_1 , and g_2 .

$$\begin{aligned} \frac{\partial g_0}{\partial t} = & \frac{1}{v^2} \frac{\partial}{\partial v} \left[\frac{m}{M} g_0 v^4 N_0 - \frac{eE}{3m} g_1 v^2 \right] \\ & + \frac{\partial}{\partial z} \left[\frac{v}{3N_0} \frac{\partial g_0}{\partial z} + \frac{2}{5} \frac{\partial g_2}{\partial z} \right] + \frac{1}{3N_0} \frac{eE}{m} \left(\frac{\partial g_0}{\partial v} + \frac{2}{5} \frac{1}{v^3} \frac{\partial}{\partial v} (v^3 g_2) \right) \\ & - \frac{m}{M} \frac{1}{3N_0} \frac{1}{v^2} \frac{\partial}{\partial v} (g_1 v^4 (N_0 - N_0)) \\ & + \frac{1}{v} \frac{\partial}{\partial v} \int \frac{v+v_j}{v} g_0 v^2 N_0 dv \\ & + \int_{v+v_j}^{\infty} g_0 \frac{v'^2}{v} \int_{\Omega} N_0 g_1(v', v, \omega) d\Omega dv' \\ & - \int_{\Omega} g_0 \int_0^{v-v_j} \frac{v-v_j}{v} N_0 g_1(v', v, \omega) dv' d\Omega \end{aligned} \quad (3)$$

In equation (3), the first square bracket represents a divergence in velocity space, and the second square bracket shows a divergence in position space. The rest of the right side show the terms of the inelastic collisions including ionization.

Here, we may estimate g_2 as

$$g_2(r, v) = -\left(\frac{2}{3}\right)^2 \frac{1}{N_0} \left[\frac{\partial g_1}{\partial z} + \frac{eE}{m} \frac{\partial}{\partial v} \left(\frac{g_1}{v} \right) \right] \quad (4)$$

In these circumstances, the electron swarm is subject to a continuity equation of the form

$$\begin{aligned} \frac{\partial n}{\partial t} = & - \frac{\partial}{\partial z} (W(z, t) n(z, t)) + \frac{\partial^2}{\partial z^2} (D_L(z, t) n(z, t)) \\ & - \frac{\partial^3}{\partial z^3} (D_3(z, t) n(z, t)) + v_1(z, t) n(z, t) \end{aligned} \quad (5)$$

where

$$D_L = D_0 - \frac{8}{135} \frac{eE}{m} \frac{4\pi}{N_0} \frac{1}{v} \left[\frac{v^4}{N_0} \frac{\partial}{\partial v} \left(\frac{g_1}{v} \right) + \frac{\partial}{\partial v} \left(\frac{v^4}{N_0} \frac{g_1}{v} \right) \right] dv \quad (6)$$

$$D_0 = (D_T) = \frac{1}{3} \int_0^{\infty} \frac{4\pi}{N_0} v^3 dv \quad (7)$$

RESULTS and DISCUSSION

The electron energy distribution functions in neon are computed from the present theory in a range of E/N from 141.3 to 1130 Td for a steady state condition. Figure 1 and 2 show each term of the energy distribution functions $f_{\ell}(\epsilon) = \frac{4\pi}{m} \nu g_{\ell}(\nu)$ as a parameter of E/N. Also shown in these figures are the results of the usual two term Lorentz approximation for comparison. The validity of the Lorentz approximation will be judged from the direct comparison between them.

The swarm coefficients derived from the present distribution functions, especially, longitudinal and transverse diffusion coefficients are exhibited in figure 3. It is found that the gradual increase of the anisotropy with the increase of E/N.

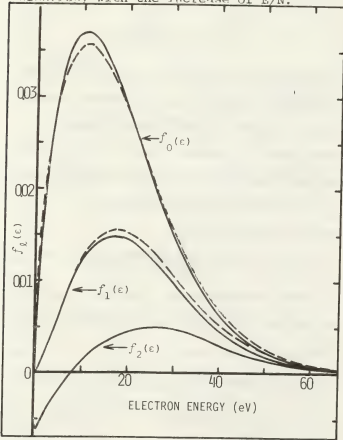


Figure 1. Theoretical isotropic and anisotropic parts of the distribution function for E/N of 282.5 Td in neon
——:three term approximation
----:Lorentz approximation

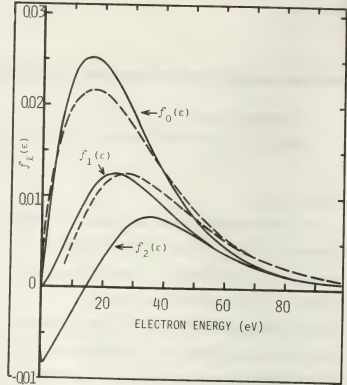


Figure 2. Theoretical isotropic and anisotropic parts of the distribution function for E/N of 706.3 Td in neon
——:three term approximation
----:Lorentz approximation.

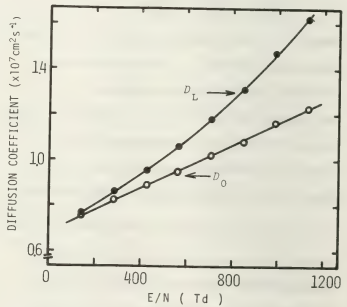


Figure 3. Longitudinal and Transverse diffusion coefficients in neon derived from the present distribution functions.

MONTE CARLO SIMULATION OF ELECTRON AVALANCHE IN HYDROGEN

M. Hayashi.

Nagoya Institut of Technology, Nagoya Japan.

In recent conference papers, we described a MCS of the behaviour of electron swarms and the properties of back scattering of electrons to the cathode in a low pressure helium, argon¹⁾ and nitrogen²⁾ gas under the influence of a uniform electric field. The properties of electron avalanches in hydrogen were studied using a same MCS technique at ratios of the electric field intensity to the gas number density E/N of from about 3 to 3000 Td.

Folkard and Haydon³⁾ Tagashira and his group⁴⁾ Saelee and Lucas⁵⁾ Hunter⁶⁾ Blevin, et al⁷⁾ have used MCS to study the electron swarm transport parameters in hydrogen.

The isotropic scattering is assumed by using the momentum transfer elastic collision cross section q_m . The good agreement of swarm parameters are confirmed between isotropic scattering model using q_m and anisotropic scattering model using q_e , where q_e is the total elastic collision cross section⁴⁾

The determination of a set of collision cross sections were very important to get the good result-

Table 1. Energy Levels of Hydrogen

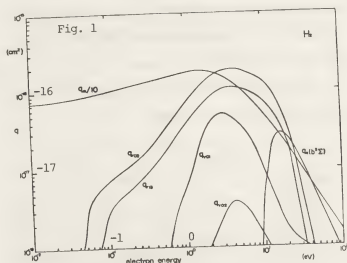
Level	Threshold (ev)	Peak Energy (ev)	μ its Xsection ($\times 10^{16}$ cm ²)
$b^3\Sigma_u^+$	8.8	16	0.28
$B^3\Sigma_u^+$	11.37	40	0.48
$c^3\Pi_u$	11.87	15	0.56
$a^3\Sigma_g^+$	11.89	15	0.09
$C^3\Pi_u$	12.40	35	0.24
$E^3\Sigma_g^+$	12.40	50	0.076
$e^3\Sigma_u^+$	13.36	16.5	0.068
$B^3\Sigma_u^+$	13.70	40	0.038
$D^3\Pi_u$	13.97	18.5	0.034
$D^3\Pi_u$	14.12	50	0.012
Ionize	15.425	70	0.972
r02	0.0439	4	1.84
r13	0.0727	4	1.07
v01	0.516	3	0.50
v02	1.003	4.3	0.040

s of wide range of E/N , and we must determined the values of q of the electron energy range up to 1000 ev.

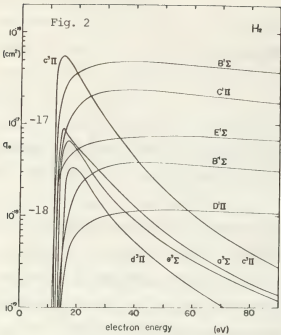
The q_m used was that obtained by Crompton, et al⁸⁾ and covers the range from 0 to 2 ev. For the region 3 to 75 ev, the q_m obtained by Srivastava, et al⁹⁾ was used, and for the region 100 to 1000 ev, we calculated q_m from the data of DCS of Fink, et al¹⁰⁾ And finally these data were connected smoothly on a curved line.

The recent calculation of electronic excitation cross sections q_e for singlet and triplet states of Chung, et al¹¹⁾ and Prok, et al¹²⁾ were used, and extrapolated to 1000 ev smoothly. We employed q_e of ten levels, and could neglect the values of q_e of the other levels that they are one or two order small.

These values are shown in Table 1 and Fig. 1 to 3.



In this MCS we must allowed for the values of q_e in order to agree with the experimental data of ionization coeff. α . These corrections were $q_e(B^3\Pi_u) \times 0.6$, $q_e(C^3\Pi_u) \times 0.4$, $q_e(C^3\Pi_u) \times 0.8$. The calculated values were almost consistent with Rose's values¹³⁾

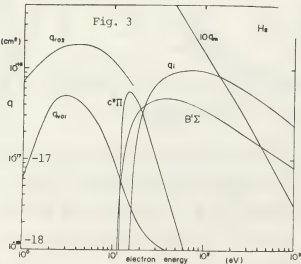


up to $E/N = 3000$ Td, which were almost coincide with our preliminary experimental values.

Fig. 4 showed the values of electron drift velocity W . At low E/N , the calculated values were larger than the experimental data.

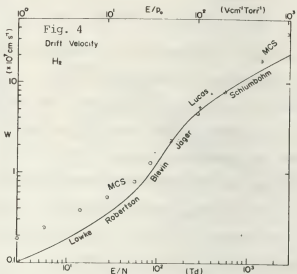
The transmission coeff. vs E/N were shown in Fig. 5 and compared with our experimental results. Good agreements were obtained if the reflection coeff. of our gold film cathode was about 0.3. The back scatterings are the phenomena of non-equilibrium region, so MCS techniques are one and only method to describe the characteristics.

The computer FACOM M-200 of the Inst. of Plasma Physics, Nagoya Univ. is used.



References

1) M. Hayashi: Gas Discharges, IEE Conf. Pub. No. 143, 195 (1976), Swansea.
2) M. Hayashi: Conf. Pub. of 4th ESCAMFIG, 61 ('78).
3) M.A. Folkard, et al: Aust. J. Phys.23, 847 ('70).



4) N. Ueno, et al: Paper of Tech. Group of Elect. Discharge, ED-72-22 (1972), in Japanese.
5) H.T. Saelee, et al: J. Phys. D, 10, 343 (1977).
6) S.R. Hunter, Aust. J. Phys. 30, 83 (1977).
7) H.A. Blevin, et al: Aust. J. Phys. 31, 299 ('78).
8) R.W. Crompton, et al: Aust.J.Phys. 22, 715 ('69).
9) S.K. Srivastava, et al: J. C. P. 63,2659 (1975).
10) M. Fink, et al: Phys. Rev. A, 12, 1374 (1975).
11) S. Chung, et al: Phys. Rev. A, 12, 1340 (1975).
12) G.M. Prok, et al: J. Quant. Spectrosc. Radiation Transfer, 9, 361 (1969).
13) D.J. Rose: Phys. Rev. 104, 273 (1956).

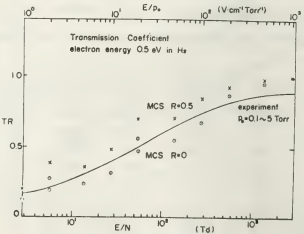


Fig. 5. Transmission coefficient vs E/N . MCS were carried out by only 100 samples of electrons at each points, so data were scattered. R is the reflection coefficient of electrons from the cathode.

INFLUENCE OF PERTURBATION ON POPULATION PROCESSES OF 4p ARGON LEVELS

S. Djeniže and J.M. Labat.

Department of Physics and Meteorology and Institute of Physics, 11000 Beograd, Yugoslavia.

Population of argon 4p levels in a decaying plasma was found to be predominantly due to the dissociative recombination of molecular argon ions⁽¹⁾⁽²⁾. This selective process of population was suggested by Lorents⁽³⁾, although no special difference between the various 4p levels has been pointed out.

An attempt was made in this study to develop the 4p levels population problem further. For this purpose four spectral lines were selected and their intensities were monitored in a DC regime as well as during the decay of a perturbed argon plasma. Rather interesting behaviour of population densities for the various perturbation energy was found, although the linear dependence of population on the gas pressure was recorded. Highest 4p level (upper level of the 7503,37 Å line) was practically under all conditions more populated in decaying plasma, what was not the case for the lower lying upper level of 8115,31 Å line.

Experiment. The main discharge was driven between the water cooled electrodes in a special U-shaped tube. Part of the positive column of 4.5 cm length was perturbed by an electric pulse applied to two ring electrodes immersed in the plasma. Short, approximately 3 ns pulses were supplied in a repetitive fashion from the Blumlein line of capacitance 2180 pF. The line was charged to 5, 6 and 8 kV, what gives, supposing about 80% of energy is transferred to plasma, the values of perturbation energies $2.2 \cdot 10^{-2}$, $3.1 \cdot 10^{-2}$ and $5.6 \cdot 10^{-2}$ Joule. Continuous flow of the spectroscopically pure argon was sustained at 16 liters per minute. Spectral lines were selected by Zeiss SPM 2 monochromator and recorded using EMI 9569B photomultiplier directly coupled to Tektronix 7704 oscilloscope, or for DC regime to galvanometer.

Results. In order to find the more detailed information on population of 4p

levels of argon, four spectral lines were selected: two of them originating from transitions between primed levels (7503,37 Å and 7948,18 Å; corresponding transitions in the Paschen notation are $1s_2-2p_1$ and $1s_3-2p_4$) and also two from the other set of levels (7514,65 Å and 8115,31 Å from transitions $1s_4-2p_5$ and $1s_5-2p_9$). Energy difference between highest $2p_1$ and lowest $2p_9$ levels is 3260 cm^{-1} or 0.404 eV.

Short perturbation pulse applied to a plasma will cause initially a rapid line intensity enhancement. This first peak lasted for some tens of nanoseconds. All the lines from 4p to 4s transitions have a second intensity maximum, 0.5 to 1 μs later depending on the pressure⁽⁴⁾. Intensity measurements were done at the second maximum. Typical results for population of the four levels in relative units versus pressure with perturbation energy as a parameter are given in figures 1 and 2.

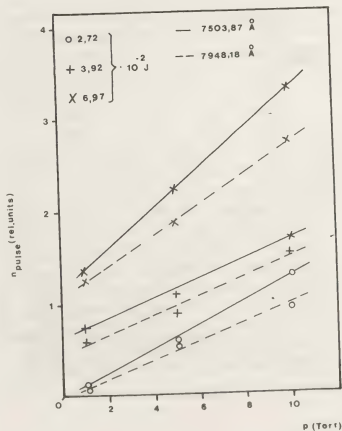


Figure 1

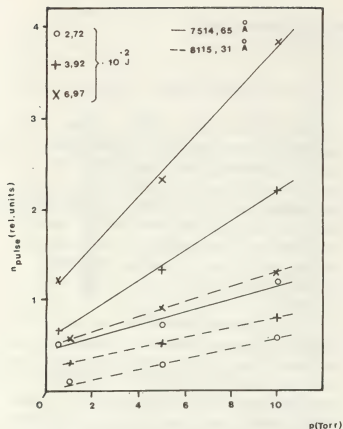


Figure 2.

Ratios of populations of highest $2p_1$ and lowest $2p_9$ levels for DC plasma and for the perturbed plasma versus pressure are given in figure 3, perturbation energy being a parameter.

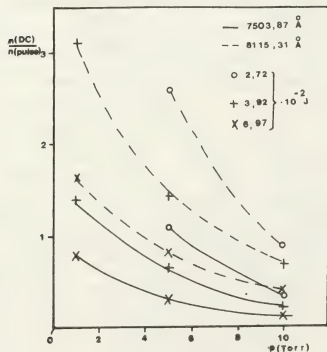


Figure 3.

While the population densities of $2p_1$ level in the whole pressure range are higher than in DC, population of low $2p_9$ level reaches the DC population just at higher pressure and maximum perturbation energy.

Ratios of DC to pulse population presented in figure 3 reveals clearly that the high $2p_1$ level is practically always more populated in a decaying plasma. There are probably the favourable conditions for molecular ions formation under these conditions. Comparison of population densities of all the $2p$ levels observed in a decaying plasma shows that $2p_5$ level becomes the highest populated level in the case of 10 Torr pressure and high perturbation energy, although in all the other cases the $2p_1$ level population is predominant.

References

1. G.N.Gerasimov, S.Ia.Petrov and I.L. Sabirova, *Optika i Spektroskopija*, 42 (1977) 1035 (in russian)
2. Y.J.Shin and M.A.Biondi *Phys.Rev.* 17 (1978) 868
3. D.C.Lorents *Physica* 82C (1976) 19
4. J.M.Labat, J.Vukićević, O. Labat and S. Djeniže (this Proceedings).

EXCITATION TEMPERATURE OF A RAPIDLY VARYING PLASMA

M. Numano and H. Onishi *

College of Engineering, University of Osaka Prefecture, Sakai, Japan.

*Mitsubishi Atomic Power Industries, Inc., Tokyo, Japan.

As is well-known, the excitation temperature, which is determined from the population distribution of excited atoms in a plasma, is not always equal to the electron temperature related to the thermal motion of electrons. The discrepancy between these two temperatures is caused by various effects /1,2,3/. Recently, it was reported that, in an expanding jet of plasma, the electron density decreases quite rapidly along the flow and that the excitation temperature differs markedly from the electron temperature /4/. When the variation of the electron density is too rapid for the population of the excited atoms to follow, the plasma may not remain in thermal equilibrium, resulting in the difference of the excitation temperature from the electron temperature.

In this report the influence of electron-density variation on the excitation temperature will be investigated. For this purpose, it is necessary to examine the variation of the population distribution of excited atoms, when the electron-density variation is given as a function of time. Here we shall consider a hydrogen plasma, and the density of atoms N_p in the excited state p is assumed to be described by

$$\begin{aligned} \frac{dN_p}{dt} = & N_e \sum_q N_q K(q,p) + \sum_q N_q A(q,p) \\ & + N_e^3 K(c,p) + N_e^2 \beta(p) \\ & - N_p \{ N_e [\sum_q K(p,q) + K(p,c)] + \sum_q A(p,q) \} \end{aligned}$$

where N_e is the electron density. The coefficient $K(p,q)$ is the rate of collisional transition from state p to state q , $K(p,c)$ is the electron impact ionization rate from state p , and $K(c,p)$ is the collisional recombination rate to state p . These coefficients are evaluated from Drawin's formulae for the cross sections of excitation and ionization due to electron collisions /5/ and the principle of detailed balance. The results are in good agreement with those of Kunc and Zgorzelski /6/. The radiative recombination coefficient $\beta(p)$ to state p is evaluated from the well-known photo-ionization cross section and the Milne relation /7/. The spontaneous transition probability $A(p,q)$ is found in reference 8.

Now let us consider a plasma which is in equilibrium for $t < 0$. At $t = 0$, the electron density begins to decrease exponentially with time as

$$N_e(t) = N_e(0) \exp(-t/t_0)$$

where $N_e(0)$ is the initial electron density and t_0 is the decay-time constant of the electron density. The electron temperature T_e is assumed to remain constant.

A few results of the numerical calculations are shown in Figs. 1-4. In these figures the population distribution and the excitation temperature are plotted against the ionization energy of excited states at the time $t = t_0$ for $N_e(0) = 10^{14} \text{ cm}^{-3}$ and $t_0 = 0.01, 0.1$ and $1 \mu\text{s}$. The excitation temperature T_{ex} was determined

from the Boltzmann plot by

$$1/T_{\text{ex}} = k \frac{d}{d\epsilon_p} \ln(N_p/g_p),$$

where k is the Boltzmann constant and g_p is the statistical weight of state p . The electron temperature was taken to be 5000K in Figs. 1 and 2 and 10000K in Figs. 3 and 4.

From these results it may be concluded that except for extremely highly excited states the excitation temperature is much lower than the electron temperature.

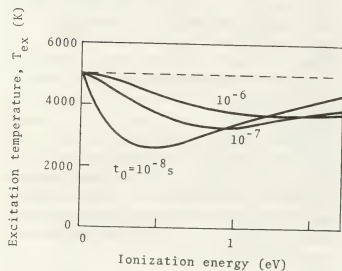


Fig. 1 Excitation temperature for $T_e = 5000\text{K}$ and $N_e(0) = 10^{14} \text{ cm}^{-3}$.

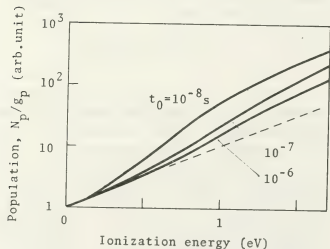


Fig. 2 Population distribution of excited atoms for $T_e = 5000\text{K}$ and $N_e(0) = 10^{14} \text{ cm}^{-3}$.

REFERENCES

1. H.R.Griem, Plasma Spectroscopy, McGraw-Hill, New York (1964).
2. M.Numano et al., JQSRT **15**, 1007 (1975).
3. M.Numano, JQSRT **20**, 227 (1978).
4. M.Abe, MS Thesis, Kyoto Univ. (1977).
5. H.W.Drawin, Report EUR-CEA-FC-383 (1966).
6. J.Kunc and M.Zgorzelski, At. Data nucl. Data Tab. **15**, 543 (1975).
7. D.R.Bates and A.Dalgarno, Atomic and Molecular Processes (Ed. by D.R.Bates), Academic Press, New York (1962).
8. W.L.Wiese et al., Atomic Transition Probabilities, Vol.I: Hydrogen through Neon, NBS, Washington,D.C. (1966).

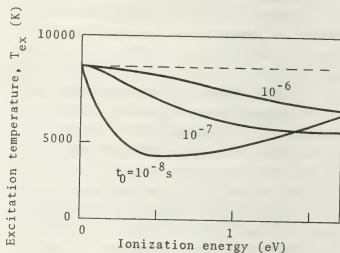


Fig. 3 Excitation temperature for $T_e = 10000\text{K}$ and $N_e(0) = 10^{14} \text{ cm}^{-3}$.

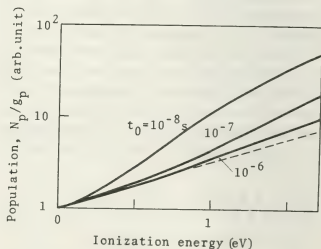


Fig. 4 Population distribution of excited atoms for $T_e = 10000\text{K}$ and $N_e(0) = 10^{14} \text{ cm}^{-3}$.

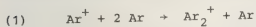
STATIONARY AFTERGLOW STUDY OF THE SINGLY CHARGED ATOMIC IONS IN PURE AR AND KR

M. Grössl, H. Helm, M. Langenwarter and T.D. Märk.

*Institut f. Experimentalphysik, Abt. F. exp Kern- und Plasmaphysik, Leopold Franzens Universität,
A 6020 Innsbruck, Österreich (Austria).*

INTRODUCTION: The transport phenomena and reaction mechanism of rare gas ions in their parent gases have been studied with different techniques by a large number of investigators. The quantitative knowledge of transport data have been improved enormously by means of precision drift tube experiments so that theories including fine structure phenomena may be tested.

Nevertheless, the understanding of the reaction mechanisms is still poor. For instance in argon values given in the literature for the effective 3-body reaction rate coefficient for the conversion of the singly charged atomic ion into the dimer ion



scatter between $0.6 \cdot 10^{-31}$ and $4.7 \cdot 10^{-31} \text{ cm}^6 \text{ s}^{-1}$. Hyatt and Knewstubb 1972 and Liu and Conway 1975 attributed an observed anomaly in the reaction behaviour of the atomic argon ions to the presence of ions in the two fine structure states, the ground state $\text{Ar}^+(^2\text{P}_{3/2})$ and the metastable state $\text{Ar}^+(^2\text{P}_{1/2})$. A definite difference in reactivity of the two fine structure states of Ne^+ and Kr^+ in their parent gases could be observed experimentally in swarm experiments by Helm and Elford 1978. As a common evidence all mentioned investigators observed a much lower destruction efficiency, due to reactions for the metastable ionic

state than for the ground state ion. In addition, a strong dependence of the metastable ion population on the neutral impurity concentration has been observed. However only one quantitative experimental result about the reactivity of the $^2\text{P}_{1/2}$ ion state is reported so far. Liu and Conway 1975 report an upper limit, because they cannot totally exclude side reactions with impurities for the destruction frequency of $\text{Ar}^+(^2\text{P}_{1/2})$ in Ar.

EXPERIMENTAL METHOD AND RESULTS: The ions were produced in a pulsed hollow cathode glow discharge and monitored with a mass spectrometer as a function of time as described elsewhere (Langenwarter et al. 1977). Careful attention was paid to minimize the impurity level in the gases used. Measurements have been made at neutral gas pressures between 0.3 and 3 Torr at 297 K.

In Ar two different exponential decays of the Ar^+ -signal could be observed at reduced gas pressures higher than 1.6 Torr, as is shown in Fig.1 for instance. From the measurements at low gas pressures (<1.5 Torr), where only one exponential decay has been observed, a value for the zero field mobility of $1.55 \text{ cm}^2/\text{Vs}$ could be deduced in very good agreement with drift tube data. Using this value effective 3-body rate coefficients for all pressures are calculated and plotted versus gas pressure

(Fig.2) in a semi-logarithmic diagram. The full dots, which are related either to the single exponential decay mode or at high pressures to the fast decay during the early afterglow, lie between $\pm 10\%$ of a mean value of the rate coefficient of $2.4 \cdot 10^{-31} \text{ cm}^6 \text{ s}^{-1}$. Evidently this loss rate corresponds to the conversion process (1) of the $^2\text{P}_{3/2}$ ground state ions. The open circles, corresponding

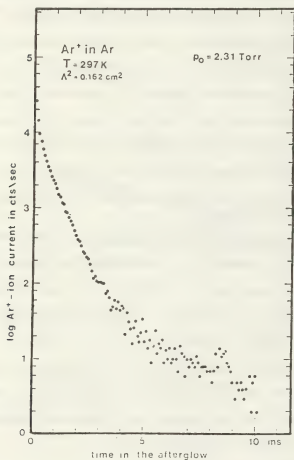


Fig.1 Measured time dependent Ar^+ ion current at high pressures: The double exponential decay curve for instance at $p_0 = 2.31 \text{ Torr}$.

to the slow decay at high pressures, show a very strong pressure dependence. This slow decay period in the late afterglow may be dominated by reactions of $\text{Ar}^+(^2\text{P}_{1/2})$ ions for which Helm and Varney 1978 proposed a reaction model. For their model the effective 3-body rate coefficients versus pressure are shown by the full line. From the pressure behaviour observed in the present experiment

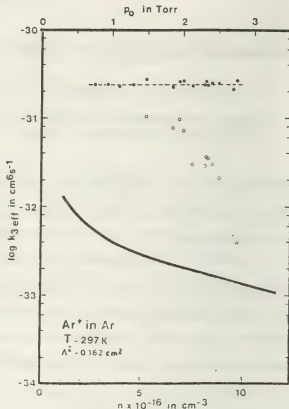


Fig.2 Effective 3-body rate coefficient as a function of gas density or pressure, calculated from the first (\bullet) and the second (\circ) decay period of the measured decay curves. Pressure dependence predicted by Helm and Varney for the metastable ion state.

we suspect an additional production process by neutral metastable-metastable collisions.

The situation in Kr is similar to Ar. The derived reduced mobility value is $0.9 \text{ cm}^2/\text{Vs}$. A 3-body rate coefficient of $2.5 \cdot 10^{-31} \text{ cm}^6 \text{ s}^{-1}$ for conversion of the ground state ion into the molecular ion has been obtained.

REFERENCES:

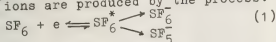
- Helm H., Varney R.N. 1978 J.Chem.Phys. 68, 5301
- Helm H., Elford M.T. 1978 private communication
- Hyatt D., Knewstubb P.F. 1972 Trans. Faraday soc. 68, 202
- Langerwalter M., Grössl M., Märk T.D. 1977 Proc. XIII I.C.P.I.G.(Ostberlin), p.45
- Liu W.F., Conway D.C. 1975 J.Chem.Phys. 62, 3070

ACKNOWLEDGMENTS:

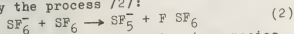
Research supported by the Österreichischer Fonds zur Förderung der wissenschaftlichen Forschung under Project Nr. S-18/05.

ATTACHEMENT AND ION MOLECULE REACTIONS IN SF₆ MIXTURESM. Abdel-Salam^{*} and J.L. Moruzzi.^{*}Department of Electrical Engineering, University of Liverpool, Liverpool L69 3BX, U.K.
^{*}Hochspannungslaboratorium TU München, Arcisstrass 21, 8 München 2, West Germany. (present address)

Introduction: SF₆ mixtures are of particular interest because of their high dielectric and thermal properties [1]. Different investigators [2] have measured the relative abundances of the negative ion species in SF₆ over a wide range of E/P. At low E/P ($\ll (E/P)_{lim}$), the SF₆⁻ ions represent 95% of the total, with about 5% SF₅⁻. For values of E/P $> (E/P)_{lim}$ the value of SF₅⁻/SF₆⁻ begins to increase with E/P. The SF₆⁻ and SF₅⁻ ions are produced by the process:



The branching ratio was found to be about 22:1 in favour of SF₆⁻. At E/P values greater than (E/P)_{lim}, SF₅⁻ was assumed to start its conversion into SF₆⁻ by the process [2]:



In this report, the negative ion species and ion-molecule reactions in various gas mixtures containing SF₆ has been studied using a drift tube mass spectrometer [3].

Results and Discussions:

a) SF₆/N₂ mixtures: The main gas flow to the drift tube was the nitrogen to which was added a titrant flow. The titrant flow was SF₆/N₂ mixture with 100/760 SF₆ content. The total pressure inside the drift tube was maintained constant at 0.9 torr and E/P was changed over the range 10-45 volt/cm.torr.

Under these conditions, only two ions were detected, SF₆⁻ and SF₅⁻. By increasing the amount of SF₆ added to the bulk nitrogen gas, it was possible to observe saturation in the number of negative ions produced, Fig. 1, indicating that all the initial electrons has been removed to form negative ions. The rate at which the negative ion signal increases with the addition of SF₆ enabled the attachment coefficient η for SF₆ to be estimated to an accuracy $\pm 20\%$:

$$d(SF_6^-) = \eta \cdot dx \cdot N_e(x), \text{ i.e.}$$

$$I_{SF_6^-} = I_0(1 - \exp(-\eta L)) \quad (3)$$

where η is for SF₆. Hence, η/P can be calculated. Over the range of E/P 10-45 v/cm.torr, η/P changes as shown in Fig. 2. Here P denotes the SF₆-pressure and P_t the total pressure of the mixture. The estimated value of η/P is in agreement with the work of Fehsenfeld [4] but very much larger than other experiments [5,6] performed on electrical discharges. It is possible that this discrepancy can be explained by invoking a detachment mechanism. Teich [7] has also obtained experimental evidence suggesting that detachment exists in SF₆.

Therefore, if this is the case, the published values [5,6] are not real attachment coefficient values but are net values [8] of η/P .

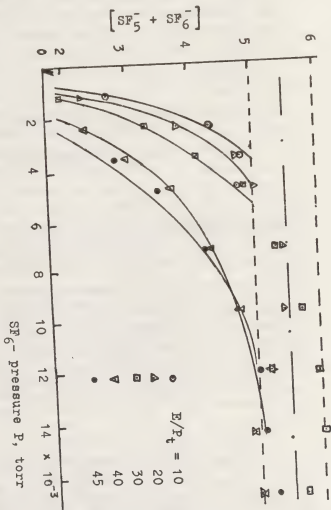


Fig.1. Total ions in the mixture at different values of E/P_t with small additions of SF₆.

The SF₅⁻ and SF₆⁻ ions at low E/P_t ($\ll (E/P_t)_{lim}$) in SF₆/N₂ mixtures are produced by the process (1) in agreement with previous measurements [2], with a branching ratio of about 11:1 in favor of SF₆⁻. At higher E/P_t values, it is interesting to observe that in the present measurements the ratio SF₅⁻/SF₆⁻ is independent of the SF₆ addition to the mixture, which contradicts the conversion process given by equation (2).

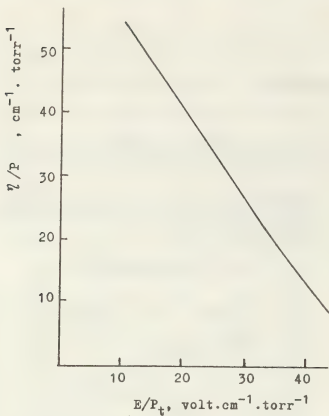
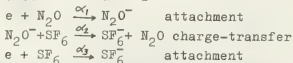


Fig. 2. η/P for SF_6 in its mixture with nitrogen.

b) $\text{SF}_6/\text{N}_2\text{O}$ mixtures: The main gas flow to the drift tube was the nitrous oxide to which was added a titrant flow. The titrant flow was $\text{SF}_6/\text{N}_2\text{O}$ mixture with 17/760 SF_6 content.

Under these conditions, seven ions were detected, $\text{N}_3\text{O}_2^+, \text{O}_4^-, \text{N}_2\text{O}_2^+, \text{NO}^-$ from N_2O against SF_6^- and SF_6^- from SF_6 . By increasing the amount of SF_6 added to the bulk N_2O gas the ion current $\text{I}_{\text{SF}_6^-}$ from SF_6 ($\Sigma \text{SF}_6^- + 2\text{SF}_5^-$) increases on the $\text{I}_{\text{SF}_6^-}$ expense of that $\text{I}_{\text{N}_2\text{O}^-}$ ($\Sigma \text{N}_3\text{O}_2^- + \text{O}_4^- + \text{N}_2\text{O}_2^- + \text{NO}^-$), Fig. 3. In an investigated scheme, the reactions leading to the formation of the negative ion currents $\text{I}_{\text{SF}_6^-}$, $\text{I}_{\text{N}_2\text{O}^-}$ are given as follows:



By solving the equations which relate the density of the ions $[\text{N}_2\text{O}^-]$ and $[\text{SF}_6^-]$, one obtains the currents $\text{I}_{\text{N}_2\text{O}^-}$ and $\text{I}_{\text{SF}_6^-}$. It was possible to obtain reasonable fit SF_6 to both the currents $\text{I}_{\text{N}_2\text{O}^-}$ and $\text{I}_{\text{SF}_6^-}$, Fig. 3 on choosing the coefficients $\alpha_1=0.1$, $\alpha_2=500.0$ and $\alpha_3=15.0$.

The high value of α_3 in comparison with α_1 as well as the very high value of α_2 the give an evidence which indicate that the large attachment coefficients observed in $\text{SF}_6/\text{N}_2\text{O}$ mixtures is not due complex ion-molecule reactions [9], but can be accounted for entirely by direct electron attachment to the SF_6 component of the mixture.

Conclusions: Within the range of the present measurements, η/P for SF_6 assumes high values than those published and do not invoke a detachment mechanism into account.

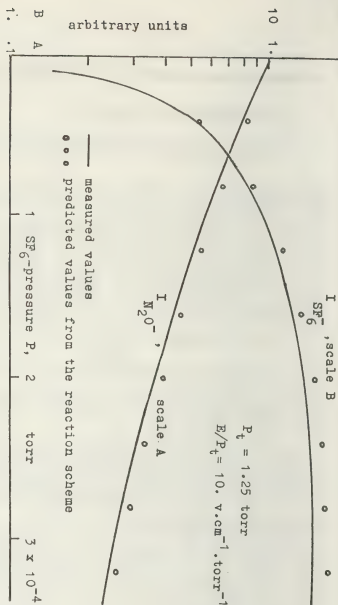


Fig. 3. Ion currents in the mixture with small addition of SF_6 .

Acknowledgment: One of the authors (MAS) is grateful to the financial support he received from the Alexander-von-Humboldt Foundation, Germany.

References:

- 1 M. Abdel-Salam and M. Abdallah, *IEEE Trans.*, Vol. IA-14, p. 516, 1978.
- 2 J.P. McGeehan et al., *J. Phys. D.*, Vol. 8, p. 153, 1975.
- 3 D.A. Price and J.L. Moruzzi, *Vacuum*, Vol. 24, p. 591, 1976.
- 4 F. Fehsenfeld, *J. Chem. Phys.*, Vol. 53, p. 2000, 1970.
- 5 M.S. Bhalla and J.D. Craggs, *Proc. Phys. Soc.*, Vol. 80, p. 151, 1962.
- 6 K.B. McAfee, *J. Chem. Phys.*, Vol. 23, p. 1435, 1955.
- 7 T.H. Teich et al., *ISH Symposium*, p. 390, 1975.
- 8 J.L. Moruzzi, *J. Phys. D.*, Vol. 1, p. 1587, 1968.
- 9 J. Dutton et al., *Vacuum*, Vol. 24, p. 609, 1976.

DISSOCIATION OF WATER VAPOUR IN THE HOLLOW CATHODE GLOW DISCHARGE

B. Nehrnow, A. Rutscher, H.E. Wagner.

Sektion Physik/Elektronik, E.M. Arndt-Universität Greifswald, D.D.R.

INTRODUCTION: During the last years much attention was given to the qualification of different types of electrical discharges for plasma chemical reactions. To realize e.g. dissociation processes under non-isothermal conditions the well-known hollow cathode glow discharge (HCGD) shows some favourable properties. Mainly these properties can be attributed to fast beam electrons accelerated in the cathode dark space. Some new papers [1/2/3] had already proved the facilities of the HCGD for the decomposition of different substances. In the following more systematic results on the production of hydrogen originated from water vapour are given [4].

EXPERIMENTAL ARRANGEMENT (Fig. 1): The water vapour produced by a calibrated evaporator flows through the HCGD (diameter 8mm) and is analysed by a gas chromatograph. A special piston compressor provides for the required high pressure at the entry of the gas chromatograph. To study the influence of the cathode wall various materials could be inserted in the device.

RESULTS AND DISCUSSION: In dependence on the essential operation parameters (pressure p /torr; power U/W ; gas flow rate v/lh^{-1} at normal conditions) the H_2 -portion x_{H_2} behind the HCGD was measured systematically. Some results (obtained with a copper cathode) are shown in Figs. 2...5. It could be noticed that high decomposition rates can be achieved. According to the gross reaction: $2H_2O \rightarrow 2H_2 + O_2$ the maximum portion of H_2 could be 66,7 vol.% at the outlet.

Of considerable interest is the fact that with regard to the reciprocal flow rate $1/v$ (Fig. 2) and the power U (Fig. 3) at high parameters liminal values are reached. Independent of the flow rate at high discharge powers an equilibrium state appears which is in the case of Fig. 3 about 30 vol%. The adjustment of such an equilibrium state seems very typical for a wide class

of non-isothermal plasma chemical reactions and should give some hints to understand the kinetic background of the conversion. Of course the exact kinetic mechanism (the totality of all elementary processes) is very complicated, even in the case of simple substances. A suitable kinetic description should collect many of these different elementary processes and should finally result in a clear formula for the calculation of the quasi equilibrium state mentioned like a mass action law.

In the frame of an overall or "macroscopic" kinetics E.N. EREMIN described plasma chemical reactions by the model of the so-called "kinetic curve" [5]. The governing discharge parameter in this model is the specific energy U/v . But frequently the other parameters of the analytic kinetic curve (the rate constants of the gross reaction) are functions of U/v , too and no generalization is possible in such a case.

We start from a balance equation of the H_2 generation which takes into account one production term (directly proportional to U) and three loss terms (one independent of U , one directly proportional to U , and one relating to the loss due to the flow rate):

$$k_E U - k_{V_0} x_{H_2} - k_{V_1} U x_{H_2} - v x_{H_2} = 0$$

The solution is: $x_{H_2}/x_{H_2\infty} = z/(1+z)$

with $z = k_{V_1} U / (k_{V_0} + v)$ and $x_{H_2\infty} = k_E / k_{V_1}$.

The systematic analysis of the experimental values shows that this clear formula is in the position to comprise analytical all the measuring points. The parameters k_E, k_{V_0}, k_{V_1} are real constants (for constant pressure) although the power U changes by the factor 250 and the flow rate v by the

factor 25. The curves in Fig. 2...5 are calculated ones using the k -values shown. That the power U can act as a governing parameter is indicated by some results belonging to other discharge operations. Fig. 5 relates to an impulse operation of the HCGD (τ : duration of the current impulse). Decisive for the rate of the H_2 production is the (mean) power of the discharge again. This was also the case for a condensed discharge as some preliminary experiments showed.

Fig. 6 contains the influence of different cathode materials on the H_2 production. There is a distinctly marked effect which can be understood if the essential process of the H_2 production is the recombination of H atoms at the cathode surface. Large recombination coefficients (e.g. Al/Al_2O_3 : 0,3/0,45) give high portions of H_2 , smaller ones (e.g. $Cu:Cu_2O$, 1 and Cu -net on glass) act inversely.

REFERENCES:

- /1/BUTYLKIN, I. P. et al. 13th ICPIG, Berlin 1977, p. 377.
- /2/METVEL, A. S., NASTYKHA, A. I., 13th ICPIG, Berlin 1977, p. 379.
- /3/MARK, T. D., Acta Physica Austria 49 (1978) 67.
- /4/NEHMZOW, B., WAGNER, H. E., Report 1977/78, Greifswald, p. 41.
- /5/EREMIN, E. N., Elementy gazovoj electrochimi, Moskau 1968.

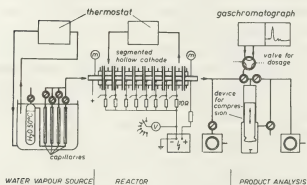


Fig. 1

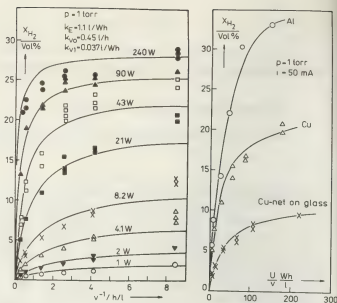


Fig. 2

Fig. 6

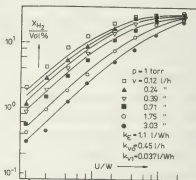


Fig. 3

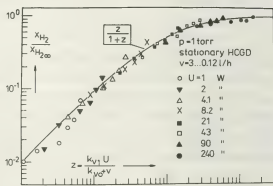


Fig. 4

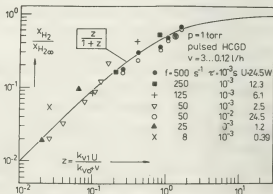


Fig. 5

THE USE OF EFFECTIVE FEYNMAN DIAGRAMS FOR ATOMIC CROSS-SECTION CALCULATIONS

D. Salzmann and S. Eliezer.

Soreq Nuclear Research Center, Yavne, Israel.

Abstract.-

In the developing research of plasma diagnostics it is necessary to know the cross-sections for many atomic processes to determine the temperature and population densities in stationary or time-dependent plasmas. The main difficulty in calculating atomic cross sections is due to the wavefunctions of the atom. We suggest a technique to overcome this difficulty by using "effective Feynman diagrams". This technique is illustrated by obtaining a simple relation between the cross-sections of electron impact excitation

$(e + X_n \rightarrow e + X_m)$ and resonant photon absorption $(h\nu + X_n \rightarrow X_m)$. The relation reads,

$$\frac{\sigma(e + X_n \rightarrow e + X_m)}{\sigma(h\nu + X_n \rightarrow X_m) \Gamma_{mn}} = \frac{\alpha}{2\pi} \frac{mc^2}{E} \frac{1}{I_{mn}} \ln Y$$

where $\alpha = 1/137$, mc^2 is the electron rest energy, E is the kinetic energy of the incoming electron, I_{mn} - the excitation energy, Γ_{mn} - the natural width and,

$$Y(u) = \frac{1 - u/2 + \sqrt{1 - u}}{1 - u/2 - \sqrt{1 - u}}, u = \frac{I_{mn}}{E}$$

Impressive agreement with experiment is found for transitions widely different in nuclear charge, degree of ionization and atomic levels. An explicit expression for the electron Gaunt factor is given.

The technique developed in this paper is a breakthrough in calculating the various electron-ion and ion-ion scattering cross-sections and the corresponding rate-coefficients.

$N(^2D, ^2P)$ METASTABLE ATOMS PRODUCTION IN A N_2 D.C. GLOW DISCHARGE.

G. Cernogora, G. Gousset, A. Ricard.

Laboratoire de Physique des Gaz et des Plasmas, Bat. 212, Université Paris Sud 91405 Orsay, France.

1) Introduction

The $N(^2D-^2P)$ metastable species are of a peculiar interest in the plasma chemistry processes with nitrogen, for example the reaction : $N(^2D-^2P) + O_2 \rightarrow NO + O$. Concentrations of $N(^2D-^2P)$ have been previously measured by Lin-Kaufman [1] in microwave discharges in order to study the quenching reactions $N(^2D-^2P) + \text{molecules}$. The overall production rates of these atomic metastable species by electrons collisions are not known at the present time. Only some cross sections for the excitation of NI spectral lines are known. In the present study we plan to determine the excitation rates of $N(^2D-^2P)$ by electron collisions in a N_2 glow discharge.

2) Experimental results

The spectral lines NI $\lambda = 1492.6 \text{ \AA}$ and $\lambda = 1742.7 \text{ \AA}$ have been chosen to determine the $N(^2D)$ and $N(^2P)$ concentrations. The Mitchell - Zemanski [2] method has been used, the coefficient $\alpha = \frac{\text{incident line broadening}}{\text{absorption line broadening}}$ has been determined in calculating the Doppler and natural broadenings in the source and the absorption tube. Temperatures are evaluated from the rotational structure of the second positive N_2 band, $\lambda = 3371 \text{ \AA}$. We have found a mean temperature of 500° K . Calculating the metastable concentrations from the absorption measurements we have taken into account the fine structure of NI lines and the instrumental broadening [3] (dissymmetrical profile with $\delta h_{1/2} = 1.3 \text{ \AA}$). The results for an absorption length $L = 50 \text{ cm}$ and a temperature $T = 500^\circ \text{ K}$ are shown in fig. 2.

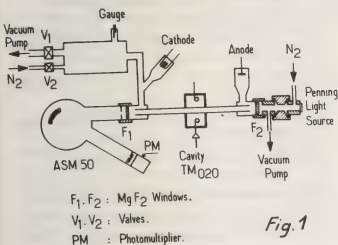


Fig. 1

The experimental arrangement is shown in fig. 1. A N_2 d-c glow discharge is produced in a 2 cm diameter, 50 cm long pyrex tube. Pressure is varying from 0.5 to 1.5 Torr and discharge current from 1 to 50 mA. The $N(^2D-^2P)$ concentrations are measured by optical absorption. The optical source is a Penning discharge in nitrogen emitting strongly the NI spectral lines. The spectral lines are analysed by means of an U.V. (Jobin-Yvon ASM 50) spectrometer with a resolution limit $\delta h = 1.3 \text{ \AA}$.

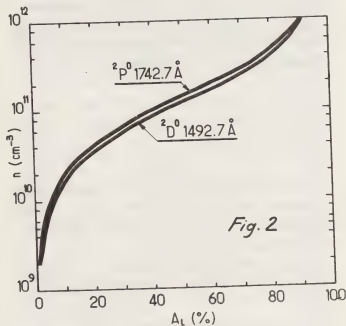


Fig. 2

Concentrations of $N(^2D, ^2P)$ metastable have been determined as functions of the discharge current for a given N_2 pressure. For $I < 10 \text{ mA}$, densities increase linearly with current. In the range $10 < I < 50 \text{ mA}$ the metastable concentrations are nearly saturated.

At 0.7 Torr, $I = 50$ mA, the saturated values are

$$\begin{aligned} n(^2D) &= 7 (\pm 1.5) \times 10^{10} \text{ cm}^{-3} \\ n(^2P) &= 12.5 (\pm 2.5) \times 10^{10} \text{ cm}^{-3} \end{aligned}$$

3) Discussion

In stationary conditions, variations of metastable concentrations are given by :

$$n_M = \frac{n_0 \quad n_e \quad C_e^M}{D_M \Lambda^2 + n_0 C_M^0 + n_e C_M^e} \quad (1)$$

where :

- n_M , n_0 , n_e are the concentrations of $N(^2D - ^2P)$ metastables, N_2 neutrals and electrons.
 - C_e^M is the excitation rate by electrons ($C_e^M = \langle \sigma_e^M w_e \rangle$, σ_e^M excitation cross section and w_e electrons velocity) C_M^0 and C_M^e are the destruction rates by electrons and N_2 molecules
 - $D_M \Lambda^2$ is the frequency of metastables diffusion and destruction on the tube wall, $\Lambda = \frac{R}{2.4}$ for a Bessel fundamental diffusion mode (R tube radius). The electron concentrations have been measured using a resonant cavity (TM 020 mode). In the present case, the shift of the resonant frequency Δf (with and without plasma) is related to the electron density by the numerical relation :

$$n_e (\text{cm}^{-3}) = 7 \times 10^8 \Delta f (\text{MHz})$$

For $I < 20$ mA and $p < 1$ Torr, we have found that the electron density is linearly dependant of the current : $n_e = bI$. Since metastables are also linearly dependent of the current for $I < 10$ mA : $n_M = aI$, we can deduce that the de-excitation by electrons ($n_e C_M^e$) can be neglected in eq. 1, and that the creation is given by :

$$C_e^M = \frac{a}{b n_0} \left[\frac{D_M}{\Lambda^2} + n_0 C_M^0 \right] \quad (2)$$

The diffusion coefficients D_M are not given in the literature. Only $D(N, N_2) = 220 \text{ cm}^2 \text{ sec}^{-1}$ has been measured by Morgan - Schiff [4]. Comparing the data in Ar- O_2 mixtures [1] :

$$\begin{aligned} D(O, Ar) &= 209 \text{ cm}^2 \text{ sec}^{-1} \quad \text{and} \\ D(O_M, Ar) &= 257 \text{ cm}^2 \text{ sec}^{-1}, \text{ we have choosen} \\ D(N_M, N_2) &= 250 \text{ cm}^2 \text{ sec}^{-1}. \end{aligned}$$

Concerning the neutrals destruction coefficient C_M^0 , we have used the data published by Slanger - Black [5] for $N(^2D)$ and Lee et Al. [6] for $N(^2P)$ and found that C_{2p}^0 can be neglected.

From measurements of a and b , we have determined the order of magnitude of

$C_e^M(^2P, ^2D) : 10^{-10} \text{ cm}^3 \text{ sec}^{-1}$. This value can be compared with previous argon metastable results [7] $C_e(^3P_2) = 2(\pm 0.7) \times 10^{-11} \text{ cm}^3 \text{ sec}^{-1}$ for $n_0 R = 10^{16} \text{ cm}^{-2}$ ($R = 1$ cm). In similar glow discharges and for analogous excitation thresholds, the electron production rates experimentally found for $N(^2D, ^2P)$ are stronger than for $Ar(^3P_2)$. This result can be interpreted as stepwise processes in the production of $N(^2D, ^2P)$ by means of the metastable molecular levels $N_2(A^3\Sigma_u^+ \pi_g)$. The argon metastable level is created by a less efficient one step process.

4) Concluding remarks

$N(^2D, ^2P)$ concentrations have been determined by optical absorption in a N_2 d-c glow discharge ($R = 1$ cm) at pressures 0.5 - 1.5 Torr and discharge currents 1 - 50 mA. The electron excitation rates are of the same order of magnitude for $N(^2D)$ and $N(^2P) : C_e^M(^2P, ^2D) = 10^{-10} \text{ cm}^3 \text{ sec}^{-1}$.

References

- [1] C.L. Lin, F. Kaufman, J. Chem. Phys. **55** (1971) 3760
- [2] A.G.G. Mitchell, M.W. Zemanski Resonance radiation and Excited atoms (Camber Un. Press NY 1961)
- [3] G. CERNOGORA - G. GOUSSET - M. POUHEY 5ème V.U.V. Conférence III (1971) 51
- [4] J.E. Morgan, H.I. Schiff, Can.J. Chem. **42** (1964) 2300
- [5] T.G. Slanger, G. Black, J. Chem Phys. **64** (1976) 4442
- [6] J.H. Lee et al., J. Chem Phys. **69** (1978) 3069
- [7] J.L. Delcroix, C.M. Ferreira, A. Ricard, Principles of Laser Plasmas, Chap. 5 - Metastable Atoms and Molecules in Ionized Gases, Ed. G. Bekefi (J. Wiley 1976).

A SPECTROSCOPIC STUDY OF THE DC GAS MAGNETRON DISCHARGE

V.I. Miljević.

Boris Kidrič Institute of Nuclear Sciences, Laboratory for Atomic Physics, 11001 Beograd, Yugoslavia.

INTRODUCTION

The properties of ionized gas in a cylindrical diode with axial magnetic field (gas magnetron diode) depends strongly on magnetic field intensity.

Under the influence of a strong magnetic field in the cylindrical diode electrons move on cycloidal paths around the cathode acquiring a velocity component in the anode direction only after collisions with gas atoms. Electron paths are considerably prolonged, thus increasing the probability of excitation and ionization.

In the case of the pulse magnetron diode, filled with argon at low pressure, it has been found that the spectrum consists of the lines which correspond to transitions from energy levels of simple and multiple ionized argon atoms, but atomic lines have not been registered (for example /1-4/).

In this paper the results of the spectroscopic study of a DC cylindrical magnetron diode, filled with argon at low pressure, are presented.

RESULTS

A cylindrical diode was used in the experiments. The anode was 30 mm long and 22 mm in diameter. The directly heated incandescent tungsten cathode, 1 mm in diameter, was placed along the cylindrical anode axis. An axial magnetic field with the maximum intensity of 1200 G was applied to the system. The experimental set up scheme is shown in Fig. 1. The working conditions were: the anode voltage $U_a = 30 - 150$ V, argon pressure $p = 10^{-4} - 10^{-2}$ torr.

Spectra were recorded with a crossed dispersion spectrograph STE 1 operated in the wavelength range of 2200 - 9000 Å with the dispersion 3,7 - 12,8 Å per mm. Relative intensities of the spectral lines have been determined by standard photographic photometry methods.

The experimental results have been obtained for the magnetic field $B_c < B < B_{cg}$, where B_c is the cut off magnetic field in a vacuum diode /5/ and B_{cg} is the cut off magnetic field in a gas magnetron diode (i.e. the critical magnetic field when the discharge current cut off occurs). The spectrum contains intense lines of ionized

argon AII, lines AIII moderate intensity, lines AIV weak intensity and atomic tungsten lines (originating from the cathode because of ion bombardment). Atomic argon lines were not formed even with prolonged exposures.

The part of the spectrum of the DC discharge with reference iron spectrum for working conditions:

- a) $p = 10^{-2}$ torr, $U_a = 30$ V, $B = 200$ G, $I_a = 3,8$ A
- b) $p = 10^{-3}$ torr, $U_a = 70$ V, $B = 200$ G, $I_a = 3,6$ A
- c) $p = 6 \cdot 10^{-4}$ torr, $U_a = 70$ V, $B = 200$ G, $I_a = 1,4$ A

is presented in Fig. 2. As it can be seen spectrum contains only argon AII lines. Also, by changing the working conditions, for constant magnetic field, only intensity of the spectral lines is changed.

Because of weak intensities of the AIII and AIV lines only the intensity of ion spectral lines AII has been analysed.

The dependence of the AII 4880 Å spectral line intensity on the square of the discharge current (solid curve) and of the discharge current on the magnetic field in the region $80 \text{ G} < B < 300 \text{ G}$ (dashed line) under the operating conditions: $U_a = 30$ V, $p = 10^{-2}$ torr is presented in Fig. 3. The dis-

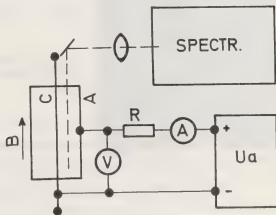
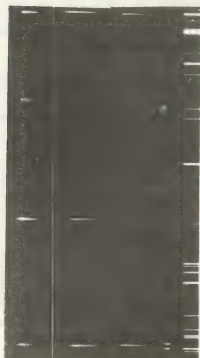


Fig.1. Experimental set-up

charge current density was about $0,2 \text{ A/cm}^2$.

The dependence of intensity on the discharge current is often used for investigation of the excitation mechanism of the spectral lines (for example /6,7/). In the case of direct excitation (cascade transitions and other processes are neglected) the dependence of spectral line intensities on the discharge current has linear character, while in the case of stepwise excitation this dependence is parabolic ($I \propto i + bi^2$).

In our case the dependence of AII 4880 A spectral line intensity on the square of the discharge current is shown in Fig.3. The low gas pressure (10^{-2}) and low discharge current density ($j=0,2 \text{ A/cm}^2$) show that intensive excitation of the ion line AII 4880 A should not be expected in stepwise collisions. However, under the influence of the radial electric and axial magnetic fields electron paths are considerably prolonged. The presence of crossed fields results in the increase of the, so called, equivalent pressure, and the electrons fulfill the conditions for stepwise collisions. In this way the probability for gas ionization and excitation is also increased.



(a) (b) (c)

Fig.2. Part of the magnetron discharge spectrum with reference iron spectrum for:

- a) $p=10^{-2}$ torr, $U_a=30 \text{ V}$, $B=200 \text{ G}$
- b) $p=10^{-3}$ torr, $U_a=70 \text{ V}$, $B=200 \text{ G}$
- c) $p=6 \cdot 10^{-4}$ torr, $U_a=70 \text{ V}$, $B=200 \text{ G}$

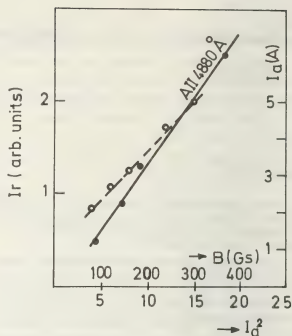


Fig.3. Dependence of the AII4880 A spectral line intensity on the square of the discharge current (solid line) and of the discharge current on the magnetic field (dashed line): $U_a=30 \text{ V}$, $p=10^{-2}$ torr, $j=0,2 \text{ A/cm}^2$.

The dependence of the AII 4880 A spectral line intensity on the discharge current when the anode voltage increase is more complex, indicating direct and stepwise excitation. This phenomenon is more expressed in the case of AII 4765 A spectral line. It may be noticed that the upper energy levels of the AII 4765 A spectral line has relatively big direct excitation cross sections.

Further work is in progress.

REFERENCES

- /1/ V.Miljević, D.Tošić, J.Appl.Phys., 4 1545(1971).
- /2/ D.Tošić, V.Miljević, Int. J. Electr., 30.175(1971).
- /3/ V.Miljević, Proc.VIII Yug.Symp.Phys.Ion. Gases,Dubrovnik,1976,p.332.
- /4/ V.Miljević, Proc.XIII Int.Conf.onPhen. Ioniz.Gases,Berlin,1977,p.171.
- /5/ A.W.Hull, Phys.Rev.,18,31(1921).
- /6/ K.I.Rozgačev, Opt.Spectr., 4,549(1958).
- /7/ V.M.Zaharova,Yu.M.Kagan, ŽETF 22,400 (1952).
- /8/ P.N.Clout, D.W.O.Heddle, J.Phys.B, 4.483(1971).

MONTE CARLO SIMULATIONS OF ELECTRON DRIFT VELOCITIES IN THE NOBLE GASES AND THEIR MIXTURES

A.J. Davies, J. Dutton, C.J. Evans, A. Goodings*, P.K. Stewart.

*Department of Physics, University College of Swansea, Singleton Park, Swansea, SA2 8PP, U.K.
*U.K.A.E.A., Winfrith, Dorset, U.K.

INTRODUCTION.

Mixtures of noble and molecular gases are widely used in neutron counters under reactor conditions. However, there are problems in their operation, concerned with radiation, electron attachment and the electrodes, which could largely be overcome by the use of noble gases alone, provided a mixture with a sufficiently high drift velocity, to give an adequate counting rate, can be found¹. This problem has stimulated the investigation of drift velocities in noble gas mixtures, the initial results of which are reported in this paper.

METHOD.

A Monte-Carlo method, originally developed in this Department by Thomas and Thomas², was modified for use at the low E/N (~ 3 Td) commonly found in neutron counters. The applied field was assumed to be uniform and the cross-sections for the various elastic, inelastic and ionization processes were taken from a number of sources³⁻¹⁰. In all simulations isotropic scattering was assumed and the step length was chosen to correspond to 0.1 of the mean free path. The initial electron energy was set at 0.01 eV and this was the minimum allowed energy of the electron during the simulation. In all calculations the gas molecules were assumed to be stationary and the pressure was taken as 1 torr. The mean energy ($\bar{\epsilon}$) of the test electron was taken to be given by its time average and was assumed to be identical with the ensemble mean energy of the electron swarm. The electron drift velocity (W) was obtained from the gradient of the distance - time (z , t) graph.

In the case of mixtures the probability of a collision with a given constituent was determined as follows. If f_1 and f_2 are the respective fractions of the two gaseous constituents in a binary mixture (i.e. $f_1 + f_2 = 1$), then the probability that any given collision involved the first constituent was taken to be:

$$P_1 = \frac{f_1 \sigma_1}{f_1 \sigma_1 + f_2 \sigma_2}$$

where σ_1 and σ_2 are the respective cross-sections of the gaseous components. Then for each collision a random number R , uniform in $\{0, 1\}$, was generated, and if R was less than P_1 the collision was taken to be with the first constituent, and if R was greater than P_1 then with the second.

RESULTS.

Figure 1 shows a typical plot of $z - (\frac{\bar{\epsilon} - \epsilon}{eE})$ vs. t for Ar, using the NAG (Numerical Algorithms Group) random number package: G05AAF(Y) for $E/N = 3.0341$ Td (i.e. $E/p = 1$ volt $\text{cm}^{-1} \text{ torr}^{-1}$ and $T = 293\text{K}$).

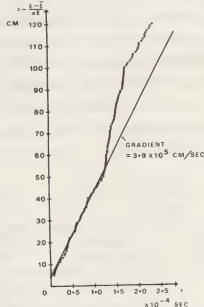


Fig. 1. Monte-Carlo (•) simulation of electrons drifting in Argon at $E/N = 3.03$ Td. Experimental Drift Velocity $\approx 4.0 \times 10^5$ cm/sec.

For clarity of presentation $z - (\frac{\bar{\epsilon} - \epsilon}{eE})$, rather than z , is plotted because this gives a curve from which the high frequency fluctuations are eliminated and for which the gradient is the same. A remarkably similar curve was recently given in the literature¹¹, where the "breakaway" in the upper part of the curve was attributed to runaway electrons occurring in the neighbourhood of the minimum in the momentum transfer cross-section. However, in the present study, it was found that, using the random number routine G05AAF(Y), breakaway occurred in all the noble gases (including even the case of a constant

cross-section, in He). This suggests that runaway electrons are not responsible. Other random number generators give different results so that it is possible that this effect is related to the random number routine. However, one cannot come to any final conclusions about this because even in the most extreme cases the results lie within the possible spread of the z, t curves resulting from diffusion. As in ref. ¹¹, good agreement was obtained, with the experimental drift velocity, using the relatively linear portion of the graph before breakaway. Since drift velocities were the prime interest in the present investigation, a random number generator was chosen which gave a long initial linear portion, of the $z - \left(\frac{e - \epsilon}{eE} \right)$ versus t curve, and such that the drift velocity computed from the gradient was in good agreement with the experimental value for He at $E/N = 3.03 \text{ Td}$. The same random number sequence, when used in He for the E/N range: $0.03 - 30.34 \text{ Td}$, gave the results in Table 1. The experimental values for the drift velocities ^{4, 12} are given for comparison and the calculated mean energies also tabulated. Good agreement with the experimental values of drift velocity ^{3, 4, 12}, was also obtained in the case of the other noble gases: Ne, Ar, Kr and Xe, for the same E/N range, given in Table 1. In all cases, approximately 8×10^5 elastic collisions were recorded.

TABLE 1

HELIUM			
E/N	$W(\text{cm/sec})$ Monte-Carlo	$W(\text{cm/sec})$ Experimental	$\bar{\epsilon}$ eV
0.03	6.97×10^4	6.31×10^4	0.02
0.15	1.78×10^5	1.82×10^5	0.09
0.30	2.71×10^5	2.65×10^5	0.18
1.52	5.96×10^5	5.97×10^5	0.81
3.03	8.48×10^5	8.57×10^5	1.64
15.17	3.34×10^6	3.5×10^6	7.38
30.34	6.87×10^6	7.3×10^6	9.16

Results for the binary noble gas mixture: He/Ar are shown in Figure 2 (again for $E/N = 3.0341 \text{ Td}$).

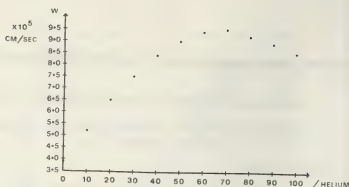


Fig. 2. Computed electron drift velocities for He/Ar mixtures at $E/N = 3.03 \text{ Td}$.

It is seen that a maximum in the value of the drift velocity occurs for a mixture of 70% He with 30% Ar, the drift velocity in this mixture being 12% greater than in helium alone. Further investigations of other mixtures are now in progress and results will be reported at the Conference.

ACKNOWLEDGEMENTS.

The work presented in this paper was carried out under a research contract financed by the United Kingdom Atomic Energy Authority. The authors would like to acknowledge the encouragement provided by the staff of C. & I. Division, AEE, Winfrith.

REFERENCES.

1. A. GOODINGS: "Experience with high temperature radiation detectors and cables for reactor instrumentation systems" IAEA-SM-226/7, 1978.
2. R. W. L. THOMAS and W. R. L. THOMAS: *J. Phys. B. (Atom. Molec. Phys.)* **2**, 562-570 (1969).
3. A. GILARDINI: "Low Energy Electron Collisions in Gases: Swarm and Plasma Methods Applied to their Study". John Wiley and Sons (1972).
4. L. G. H. HUXLEY and R. W. CROMPTON: "The Diffusion and Drift of Electrons in Gases". John Wiley & Sons (1974).
5. T. ITOH and T. MUSA: *J. Phys. Soc. Japan* **15**, 1675-1680 (1960).
6. P. LABORIE, J.-M. ROCARD and J. A. REES: "Electronic Cross-sections and Macroscopic Coefficients. I-Hydrogen and Rare Gases" Dunod: Paris (1968).
7. H. S. W. MASSEY and E. H. S. BURHOP: "Electronic and Ionic Impact Phenomena", 2nd Ed. Vol. 1, Oxford University Press (1969).
8. Y. SAKAI, H. TAGASHIRA and S. SAKAMOTO: *J. Phys. B. (Atom. Molec. Phys.)* **5**, 1010-1016 (1972).
9. Y. SAKAI, H. TAGASHIRA and S. SAKAMOTO: *J. Phys. D. (Applied Physics)* **10**, 1035-1049 (1977).
10. R. W. L. THOMAS: Ph. D. Thesis, Physics Department, University of Wales (1968).
11. H. B. MILLOY and R. O. WATTS: *Aust. J. Phys.* **30**, 73-82 (1977).
12. J. DUTTON: *J. Phys. Chem. Ref. Data* **4**, 577-856 (1975).

RECOMBINAISON DE L'ION MOLECULAIRE He_2^+ A HAUTE TEMPERATURE

P. Cambray.

Laboratoire d'Energétique et Détonique L.A. 193 du C.N.R.S. - E.N.S.M.A. - 86034 POITIERS

La plupart des études expérimentales de la recombinaison de l'ion moléculaire He_2^+ ont été faites sur des plasmas de post-décharges à la température ambiante (cf. par ex. /1/). Dans ces conditions la température électronique T_e est proche de 300 K (< 600 K) et la densité électronique n_e est généralement inférieure à $3.10^{11} \text{ cm}^{-3}$.

Les résultats présentés ici correspondent à des mesures effectuées sur un jet (de symétrie axiale) de plasma d'hélium produit par un générateur à arc soufflé à une pression de 10 Torr ($T_e \sim 1800 \text{ K}$, $n_e \sim 10^{14} \text{ cm}^{-3}$).

Nous avons mesuré, en fonction des coordonnées radiale et axiale, les grandeurs caractéristiques suivantes :

- 1) la vitesse d'écoulement (déduite du décalage des raies par effet Doppler par une méthode permettant de tenir compte des gradients axiaux /2/),
- 2) la densité électronique (à partir de l'élargissement des raies par effet Stark),
- 3) la densité de population des états excités de l'hélium atomique (par spectroscopie d'émission et d'absorption),
- 4) la température électronique (par la méthode du graphique de Boltzmann),
- 5) la densité des ions atomiques (déduite des température et densité électroniques et de la population des états de nombre quantique principal $n > 6$).

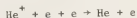
De l'ensemble de ces mesures, il résulte essentiellement que deux régions peuvent être distinguées dans le jet :

- d'une part, une région éloignée de la section d'éjection du générateur où l'écoulement peut être décrit par un modèle similaire à celui proposé par Schlichting /3/ et l'évolution des diverses espèces est principalement déterminée par la diffusion,

- d'autre part, une région proche de cette section où l'écoulement est fortement influencé par la dissipation visqueuse et dans laquelle les effets de la diffusion sont négligeables devant ceux des

processus de recombinaison.

Dans cette dernière région du jet, la densité des ions atomiques est inférieure au 1/10 de celle des électrons. L'hypothèse de neutralité macroscopique du plasma implique donc la présence d'ions positifs autres que He^+ en quantité relativement importante (densité de l'ordre de 10^{14} cm^{-3}). Après avoir vérifié que ces ions ne pouvaient être ni de l'hélium atomique He^{++} ni une quelconque impureté, nous avons conclu qu'il ne pouvait s'agir que de l'ion moléculaire He_2^+ . Compte tenu de cette hypothèse des valeurs mesurées pour les grandeurs indiquées plus haut et des taux de réaction mesurés par Deloche et al. /1/, on peut montrer que l'évolution de la densité électronique est déterminée par la réaction de recombinaison :



pour laquelle Deloche et al. /1/ proposent un taux de réaction (pour $T_e < 600 \text{ K}$) égal à :

$$\frac{dn_e}{dt} = -k_{e2} \left(\frac{T_e}{293}\right)^{-y_2} n_2 n_e^2$$

où n_2 est la densité d'ions moléculaires He_2^+ (cm^{-3}),

n_e la densité électronique (cm^{-3}),

$$k_{e2} = (4,0 \pm 0,5) \cdot 10^{-20} \text{ cm}^6/\text{s},$$

$$\text{et } y_2 = 4,0 \pm 0,5.$$

Ce qui donne pour nos conditions expérimentales ($n_2 \sim n_e$ et $T_e \sim 1800 \text{ K}$) une valeur moyenne :

$$\frac{dn_e}{dt} = -4,4 \cdot 10^{-23} n_e^3$$

alors que le taux de recombinaison que nous avons mesuré est de :

$$\frac{dn_e}{dt} = (4 \pm 0,4) \cdot 10^{-23} n_e^3$$

L'accord est donc tout à fait satisfaisant, compte tenu de l'incertitude sur l'exposant y_2 . En prenant pour k_{e2} la valeur indiquée par Deloche et al. /1/, nos mesures permettent de déterminer cet

exposant :

$$y_2 = 3,8 \pm 0,3.$$

- /1/ Deloche R., Monchicourt P., Chéret M. et Lambert F., High-pressure helium afterglow at room temperature, Phys. Rev. A., 13, 1140 (1975).
- /2/ Cambray P., Mesure de vitesse dans les jets de plasma comportant des gradients axiaux;
Troisième Symp. Int. de Chimie des Plasmas (I.U.P.A.C.), Limoges, Juillet 1977.
- /3/ Schlichting H., Boundary-layer theory, McGraw Hill (1968).

EXCITATION OF 3^3P LEVEL OF He AND 4^2F LEVEL OF He^+ WITH ELECTRON BEAMS

A. Luches, V. Nassisi, A. Perrone and M.R. Perrone

University of Lecce, Physics Department, Lecce Italy.

INTRODUCTION

As an intense electron beam drifts in rare gases, its kinetic energy is efficiently converted into electronic excitation of the gas. Excited rare gases play an important role in the development of excimer lasers. To improve efficiency of laser systems, a detailed knowledge of the various radiative and kinetic processes [1-3] which occur is necessary.

We studied the pressure dependent peak intensity and time history of the 388.9 nm radiation emitted from the $3^3P - 2^3S$ transition of He and the 468.6 nm radiation emitted from the $4^2F - 3^2D$ transition of He^+ at pressures ranging from 10^{-2} to 7500 Torr. From the decay of radiation we determined the short-lived and long-lived decay components and the values of the effective direct excitation cross-section of the 3^3P level at several gas pressures. At low pressures ($p < 4$ Torr) we also determined the quenching cross-section of the 3^3P level by ground state He collisions.

EXPERIMENTAL APPARATUS

Our electron source is a Tesla-transformer accelerator [4], which delivers a beam of 25 kA at 500 keV electrons. The beam length and density are 15 nsec (fwhm) and 3.5 kA/cm^2 , respectively.

The drift chamber (Fig.1) is separated from the field emission diode, operated below 10^{-4} Torr, by a thin ($75 \mu\text{m}$) mylar foil, supported by a perforated steel plate which acts as anode.

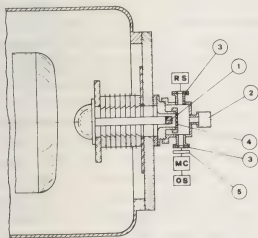


Fig.1: Experimental apparatus. 1)Cathode; 2)pressure gauge; 3)viewing port; 4)anode; 5)filter; RS-reference source; MC-monochromator; OS-oscilloscope.

About 60% of the beam emerges into the gas chamber. The photometric equipment detects light emitted perpendicularly to the beam axis. It consists of a filter system, a monochromator, a photomultiplier and an HP 184 storage oscilloscope.

EXPERIMENTAL RESULTS AND DISCUSSION

Intensity decay curves for the $3^3P - 2^3S$ and $4^2F - 3^2D$ transitions were obtained at He pressures ranging from 10^{-2} to 10^4 Torr.

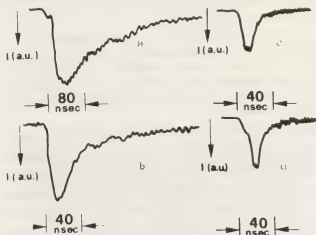


Fig.2: Traces showing photomultiplier outputs at a)0.5 Torr and 388.9 nm; b)5000 Torr and 388.9 nm; c)3000Torr and 468.6 nm; d)5000 Torr and 468.6 nm.

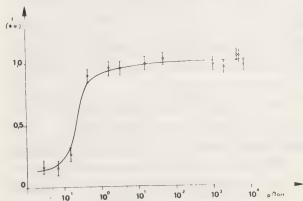


Fig.3: Peak intensity of the $3^3P - 2^3S$ transition as a function of pressure

In the range 0.03 - 0.5 Torr peak intensity exhibits a strong pressure dependence. Above 10 Torr it is almost pressure independent. In contrast, the $4^2F - 3^2D$ transition peak intensity is very weak at pres-

sures lower than a few hundred Torrs, then increases rapidly with pressure.

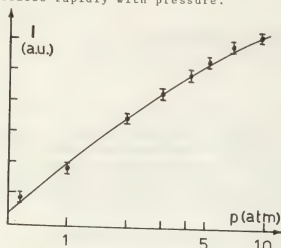


Fig. 4: Peak intensity of the $4\ 2F - 3\ 2D$ transition as a function of pressure

The decaying part of each oscilloscope trace of the photomultiplier output was fit to a curve of the form

$I(t) = I_1 \exp(-t/\tau_1) + I_2 \exp(-t/\tau_2)$ where τ_1 and τ_2 represent the short lived and long lived decay, respectively; I_1 and I_2 characterize the respective intensity amplitudes. τ_2 relates to radiative cascade contributions/2/.

p (Torr)	I_1 (a.u.)	τ_1 (n sec)	I_2 (a.u.)	τ_2 (n sec)	n^* (cm^{-3})	σ_c (10^{-24}cm^2)
0.03	0.143	100	0.025	1270	$5.7 \cdot 10^8$	266
0.07	0.118	86	0.031	7100	$4.8 \cdot 10^8$	115
0.16	0.184	82	0.092	3880	$7.6 \cdot 10^8$	78
0.50	0.485	72	0.418	282	$2.4 \cdot 10^9$	92
1.70	0.350	41	0.613	362	$1.7 \cdot 10^9$	39
3.60	0.292	25	0.630	104	$1.8 \cdot 10^9$	29
16	0.142	19	0.831	144	$1.0 \cdot 10^9$	5
55	0.186	16	0.853	135	$2.0 \cdot 10^8$	2
760	0.709	11	0.271	121	$2.9 \cdot 10^8$	0.5
1500	0.668	11	0.282	153	$2.8 \cdot 10^8$	0.2
3000	0.567	13	0.285	169	$2.8 \cdot 10^8$	0.1
5000	0.807	13	0.232	226	$3.2 \cdot 10^8$	0.07
6000	0.753	12	0.279	169	$3.1 \cdot 10^8$	0.06
7500	0.764	13	0.203	179	$3.1 \cdot 10^8$	0.05

TABLE 1: time constants and amplitudes of the $3\ 3P - 2\ 3S$ transition.

We determined the relation between the density of $3\ 3P$ states and the photomultiplier output to be $n(t=0) = n_0 = 4 \cdot 10^{16} I_0 \tau$, where I_0 is the intensity at $t=0$ (volts) and τ is the radiative meanlife.

The number density of atoms excited by direct excitation, at $t=0$ is

$$n^* = n_0 / I_0 (I_1 + I_2 \tau_1 / \tau_2)$$

The effective direct-excitation cross-section for populating the $3\ 3P$ states is

$$\sigma_{e-} = n^* / \phi p \tau_1$$

ϕ is the electron flux and p is the gas density. The values of n^* and σ_{e-} are listed in Tab.1.

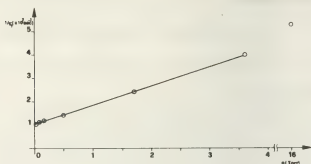
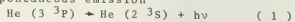
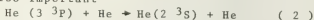


Fig. 5 : $1/\tau_1$ as a function of pressure

In the range 0.07 ± 4 Torr, $1/\tau_1$ is a linear function of gas pressure. Such behaviour could be explained as follows. For $p < 0.03$ Torr the decay is controlled only by spontaneous emission



At higher pressures ($p > 4$ Torr), collisional deactivation by ground state atomic He is also important



Since processes (1) and (2) are the most probable for $p < 4$ Torr, $1/\tau_1$ can be expressed as $1/\tau_1 = 1/\tau + kp$. k is related to the quenching cross-section σ_c by the relation $k = \sigma_c \langle v \rangle$, where $\langle v \rangle$ is the Boltzmann average velocity of He atoms. From the slope and the intercept of the graph of Fig. 5 we get $k = 2.6 \cdot 10^{-10}$ (cm^3/sec), $\tau = 98$ nsec and hence $\sigma_c = 2 \cdot 10^{-15}$ cm^2 .

For $p > 4$ Torr the last relation does not describe well our experimental results. However, we succeeded in determining the short and long lived decay components and the effective direct excitation cross-section up to 7500 Torr.

REFERENCES

- 1/-R.J.Anderson,R.H.Hughes,Phys.Rev.**A5**, 1194 (1972)
- 2/-R.J.Anderson,R.H.Hughes,J.H.Tung,S.T.Chen,Phys.Rev.**A8**, 810 (1973)
- 3/-J.E.Velazco,J.H.Kolts,D.W.Setser,J.Chem.Phys. **65**, 3468 (1976)
- 4/-I.Boscolo,M.Leo,A.Luches,L.Provenzano,Rev.Sci.Instrum. **48**, 747 (1977)

INFLUENCE OF BOUNDARY LAYER OF A Al-SEEDED SHOCK-HEATED PLASMA ON THE PROFILES OF THE Al I RESONANCE LINES

Truong Bach, H.W. Drawin*

*Observatoire de Paris-Meudon, F-92190 Meudon-France,

Association Euratom-CEA, Département de Physique du Plasma et de La Fusion Contrôlée. Centre d'Etudes Nucleaires, F-92260 Fontenay-aux-Roses.

1. INTRODUCTION

Standard electron-impact broadening theories (1,2) predict the same Stark widths for spectral lines within a given multiplet whose wavelengths are nearly the same. Differences in the measured widths of lines belonging to the same multiplet are generally assumed as being due to optical depth problems (3,4). However, the theoretically predicted property of the line widths is not verified for Ar II lines measured by Behringer and Thoma (5) who observed strong variation ($\sim 50\%$) within the $4s^2P - 4p^2P$ multiplet. One of us (6) reported recently a difference of 22% of the widths of the Al I resonance doublet $4s^2S_{1/2} - 3p^2P_{3/2}, 1/2$ ($\lambda = 3961.5 \text{ \AA} ; 3944 \text{ \AA}$). The lines were emitted by a $Al(CH_3)_3$ - seeded shock-heated argon plasma. At a temperature of $T = 9670 \text{ K}$ and an electron density of $N_e = 1.42 \times 10^{17} \text{ cm}^{-3}$ the (full) stark widths (after corrections for instrumental, Doppler and neutral gas broadening, and self-absorption assuming homogeneous plasma) were found to be $2W = 0.61 \text{ \AA} (\pm 13\%)$ and $0.50 \text{ \AA} (\pm 13\%)$ for the lines $\lambda = 3961.5 \text{ \AA}$ and 3944 \AA respectively. Fig.1 shows the densitometer recordings of the two lines and the density profiles obtained after applying a least square smoothing procedure by Fourier transform. The density profiles were converted into intensity distributions. Finally the above mentioned corrections were applied leading to different half-widths. Very recently, R ndigs and Kusch (7) reported measurement of the same lines. They found within the experimental uncertainty the same Stark width for the two lines. They particularly mentioned that "the experimental results... approach

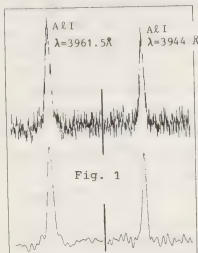


Fig. 1

the theoretical value if self-absorption contributions are taken into account". This is in contradiction to the results of (6) where self-absorption was accounted for assuming a homogeneous plasma. However, a shock-heated plasma is surrounded by a narrow but very inhomogeneous plasma region. Thus, it is still possible that differences in the half-widths are caused by the outer inhomogeneous zones near the walls.

2. PLASMA MODEL

Owing to lack of any reliable experimental data about temperature and density distributions in the boundary region of shock-heated plasmas, we have assumed that local thermodynamic equilibrium (L.T.E.) exists throughout the plasma, the boundary region included. We assumed the following temperature distribution (x = distance from wall) :

$$T(x) = T_{\infty}(1 - e^{-x/\Delta})$$

where $T_{\infty} = 9670 \text{ K}$ is the temperature in the core of the plasma. Knowing the experimentally determined values of electron density $N_{e,\infty} = 1.42 \times 10^{17} \text{ cm}^{-3}$, the density of excited Al I atoms $N_{Al,\infty}$

the total pressure $p = 4.5$ Atm, and the seeding ratio, it is possible to calculate from the equilibrium relations the relevant densities as a function of x . For the numerical calculation, an eleven-layer model is adopted. Across each layer, temperature and density are assumed to be constant.

3. LINE PROFILE CALCULATIONS

For the eleven-layer model we have solved the radiative transfer equation for the intensity $I(\Delta\lambda, x)$ as a function of wavelength $\Delta\lambda$ and distance x (i.e. as a function of layer) :

$$\frac{dI(\Delta\lambda, x)}{dx} = \epsilon(\Delta\lambda, x) - k(\Delta\lambda, x) \cdot I(\Delta\lambda, x)$$

The coefficients $\epsilon(\Delta\lambda, x)$ and $k(\Delta\lambda, x)$ are given in the wavelength scale by

$$\epsilon(\Delta\lambda, x) = \frac{1}{4\pi} \frac{hc}{\lambda_0} A N_{Al}^{(u)}(x) P(\Delta\lambda, x)$$

$$k(\Delta\lambda, x) = \frac{\pi e^2}{mc^2} \lambda_0^2 f N_{Al}^{(l)}(x) P(\Delta\lambda, x) \cdot (1 - e^{-\Delta E/kT})$$

(u = upper, l = lower level, A = Einstein coefficient $u \rightarrow l$, f = oscillator strength $l \rightarrow u$, $\Delta E = E_u - E_l$). The line profile has been approximated by a Lorentzian shape

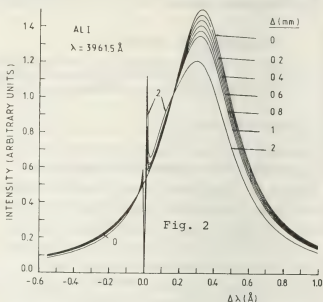
$$P(\Delta\lambda, x) = \frac{1}{\pi} \frac{W(x)}{(\Delta\lambda - d(x))^2 + W(x)^2}$$

For given values $T(x)$ and $N_e(x)$, width W and shift d have been calculated according to theory Ref. (2). For the two Al-resonance lines, the same values of W and of d are obtained. The radiative transfer equation has been solved for 200 different values of $\Delta\lambda$.

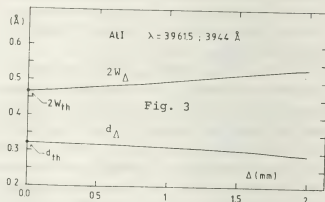
4. RESULTS

The essential results are summarized in Figs. 2-3. Fig. 2 shows how the resultant profiles change as a function of Δ . For $\Delta = 0$ (homogeneous layer) the line profile is symmetric. With increasing Δ the intensity decreases and the distortion of the blue wing increases. Quite a similar behavior is obtained for $\lambda = 3944$ Å. Fig. 3 shows the effective (full) half width $2W_\Delta$ and the effective shift d_Δ of the resultant profiles as a function of Δ . Although the two sub-levels of the ground state are differently populated, width and shift vary for both resonance lines in exactly the same manner with Δ .

Under actual conditions, the thickness δ of the thermal boundary region of a shock-heated plasma is of the order $\delta = 5 \Delta \approx 0.5$ to 1 mm. We have to conclude



that an inhomogeneous plasma region does not introduce differences in the width and shift within the frame of the model and the chosen parameter variations.



REFERENCES

- (1) H.R. GRIEM, Spectral Line Broadening Academic Press, New York (1975)
- (2) S. SAHAL-BRECHOT, Astron. Astrophys. 1, 91 (1969); 2, 322 (1969)
- (3) N. KONJEVIĆ and J.R. ROBERTS, J. Chem. Ref. Data 5, 209 (1976)
- (4) N. KONJEVIĆ and W.L. WIESE, J. Chem. Ref. Data 5, 259 (1976)
- (5) K. BEHRINGER and P. THOMA, J. Quant. Spectr. Radiat. Transf. 20, 615 (1978)
- (6) TRUONG BACH, J. Quant. Spectr. Radiat. Transf. 19, 483 (1978)
- (7) G. RÖNDIGS and H.J. KUSCH, Astron. Astrophys. 71, 44 (1979)

TWO ELECTRON CAPTURE PROCESSES IN PLASMAS CONTAINING MULTIPLY CHARGED IONS

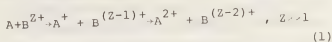
T.P. Grozdanov and R.K. Janev.

Institute of Physics, Belgrade, Yugoslavia.

It has recently been recognized that the electron transfer processes between the multicharged ions and neutral species in a crucial way influence the ionization equilibrium, energy balance, radiation and transport properties of many laboratory and astrophysical high-temperature plasmas¹⁻³. Such a role of these processes is a result of their extremely large cross sections ($\sim 10^{-14}$ cm²; $\sim vZ^q$, $q=1-2$) and the fact that highly excited states of the product ions are preferentially created by them. In Tokamak-type thermonuclear plasmas, additionally heated by neutral beams, the multicharged impurity ions play a detrimental role, which even may prevent reaching the fusion burning conditions¹. The important neutral species, which undergo charge-changing collisions with multicharged ions in the outer layers of the Tokamak plasma, are D, T and He. Almost equally important role plays the electron transfer collisions between multicharged ions and neutrals in the expanding laser produced plasmas². In such plasmas, the above mentioned processes serve as an efficient mechanism for creation of inverted population of the electronic levels of the product ions. The radiative decay of these levels is responsible for the EUV emission from laser produced plasmas.

Most of the experimental and theoretical work on the charge-changing collisions of multicharged ions with atoms has so far been done for one-electron transfer processes³⁻⁵. However, the experimental data⁶ indicate that the two-electron capture processes in these collisions have also large cross sections, being only a factor of 5 - 8 smaller than the cross sections for one-electron capture.

In the present communication we propose a model for a successive capture of two electrons in slow collision (relative velocity $v < 2 \times 10^8$ cm/s) of multiply charged ions with atoms:



The capture mechanism is supposed to be an electron funneling^{4,5} from the atomic (A) and ionic (A⁺) potential well into the "quasi-continuous" spectrum of the excited states of the ions B^{(Z-1)+} and B^{(Z-2)+}. At internuclear separation R the electron transition probability per unit time (in atomic units) is given by⁵:

$$W(R) = N^2 \frac{2\ell+1}{n} \left(\frac{n}{2}\right)^{2pn} (4R^2/Zn^3)^{2pn-1} \times \exp\left\{-\frac{R^2}{2n^3} f(\alpha) - \phi(\alpha)\right\} \quad (2)$$

$$f(\alpha) = \frac{1}{\alpha} \left[1 - \frac{\ell n(\sqrt{1+\alpha} + \sqrt{\alpha})}{\sqrt{\alpha}(1+\alpha)}\right], \quad \alpha = \frac{R}{2Zn^2}$$

$$\phi(\alpha) = 2(2pn-1) \sqrt{\frac{\alpha}{1+\alpha}} \ell n(\sqrt{1+\alpha} + \sqrt{\alpha})$$

In the above formulae $n=(2I)^{-1/2}$, I is the electron binding energy in the initial state (atom A or ion A⁺), p is the charge of the atomic (p=1) or ionic (p=2) core, ℓ is the electron initial orbital angular momentum and N is the normalization constant of the asymptotic atomic (ionic) electron wavefunction.

The method of calculation of the cross section for process (1) is in some sense iterative one. We shall neglect, in the first approximation, the capture of the second electron, and using the expression (2) with the parameters of the atom A, we can calculate the electron capture cross section from⁵:

$$\sigma = 2\pi \int_0^\infty \left[1 - \exp\left(-\frac{2}{v} \int_{\rho}^\infty \frac{W(R) R dR}{\sqrt{R^2 - \rho^2}}\right)\right] \rho d\rho \quad (3)$$

where, v is the relative velocity of the colliding particles, ρ is the impact parameter and the straight line trajectories are assumed.

Now, an effective radius R_0 of the one-electron capture process can be defined from the relation $\rho = \pi R_0^2$. Further,

we shall assume that all atoms that enter the sphere of the radius R_0 will undergo one-electron loss. The two-electron capture cross section σ_2 can be calculated from Eq.(3) in which the upper limits of the integrals are replaced by R_0 , and $W(R)$ taken from Eq. (2) with the parameters of the ion A^+ and with the substitution $Z \rightarrow Z-1$. It is clear from this procedure that σ represents the total electron capture cross section and that real one-electron cross section is given by

$$\sigma_1 = \sigma - \sigma_2.$$

We have performed the cross section calculations for the collision of He-atom with an ion of charge $Z=6$ (the only characteristics of the multiply charged ion that enters into the present theory). The parameters taken for He atom (ion) were: $N = 2.250$ (5.657), $n = 0.744$ (0.5), $p=1(2)$ and $i=0$ (0). The results of calculations are shown in Fig. 1 together with the experimental data⁶ for one and two-electron capture cross sections in He- Ar^{6+} collisions as a function of the ion impact energy E (relative velocity v). As it can be seen from the figure, the agreement of the theoretical results and the experimental data is quite satisfactory. This figure also shows that the cross section for double electron transfer for He on $Z=6$ ions is smaller only for a factor of 3-4 with respect to the one-electron capture cross section in the whole energy range investigated. Since within the proposed theory both σ_1 and σ_2 scales according to $\sigma_i \sim Z n Z$ ($i=1,2$), one can infer that the same ratio of σ_1/σ_2 approximately holds for charge-changing collisions of He with an arbitrary $Z(>6)$ - ion.

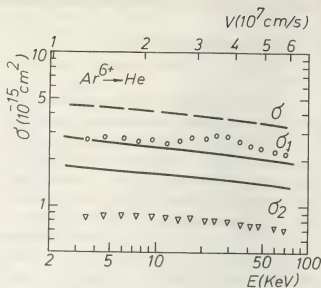


Fig. 1

References

1. C.F.Barnett, in: "The Physics of Electron. Atom. Collisions", Inv. Lectures and Progr. Repts. of IX ICPEAC, Ed.J.S. Risley and R.Geballe (University of Washington, Seattle, 1975), p.846.
2. A.V.Vinogradov and I.I.Sobel'man, Sov. Phys.- JETP, 36, 1115 (1973).
3. L.P.Presnyakov and A.D.Ulantsev, Sov. J.Quantum Electron. 4, 1320 (1975).
4. M.I.Chibisov, JETP Lett. 24, 56 (1976).
5. T.P.Grozdanov and R.K.Janev, Phys. Rev. A 17, 880 (1978).
6. A. Müller and E.Salzborn, Phys. Lett. 59A, 19 (1976).

IONIZATION GROWTH IN ARGON

R.R. Abdulla, J. Dutton and A.W. Williams

*Department of Physics, University College of Swansea, Swansea, U.K.*Introduction.

The growth of ionization currents in argon have been studied experimentally by a number of authors (1), (2), (3).

The experiments of Kruthof and Penning⁽¹⁾ and of Heylen⁽³⁾ used the standard Townsend method of measuring I as a function of d at constant E/N and gave values of the primary ionization coefficients α/N which were in agreement for purified gases. It was also shown⁽³⁾ that unpurified gas gave, as expected, higher values of α/N . There is however interest in investigating the pressure dependence of α/N to elucidate whether pressure dependent processes such as associative ionization⁽⁴⁾ are significant in ionization growth and breakdown in this gas. The only other high pressure study⁽²⁾ gave no evidence on this question because it was found that I, d curves could not be analysed to give values of α/N so that I, p curves were obtained which gave values of α/N dependent on the value of d used.

The present paper reports the initial measurements of an investigation to examine further the question of the values of the primary and secondary ionization coefficients in high pressure argon.

Apparatus.

In order to achieve the high gas purity necessary for ionization growth measurements on the rare gases the ionization chamber used in the present investigation could be evacuated to ultra high vacuum. The chamber has been described by Dutton and Powell⁽⁵⁾ and consists of a cylindrical stainless steel chamber, 50 cm in diameter and having a volume of about 40 litres. The chamber was pumped by a combination of sorption and ion pumps and could be baked at a temperature of 250°C by means of a furnace. All the taps and manifolds exterior to the furnace were degassed using heating tapes. The ultimate pressure of the system was 2×10^{-9} torr with a leak rate of $0.9 \times 10^{-6} \text{ l.}\mu\text{s}^{-1}$.

The electrodes were 15 cm diameter gold plated copper, machined to a Bruce⁽⁶⁾ profile and gave an

uniform electric field for electrode separations up to 5 cm. In the centre of the anode were drilled 37 holes 1 mm in diameter which allowed the passage of ultra-violet light on to the cathode to provide an initial current of photoelectrons.

The voltage supply was a 6 kV Fluke model 408B with a stability of 1 in 10^5 . The voltage was measured using a 4 M Ω potentiometer and ionization currents were measured by means of E.I.L. 33c vibrating reed electrometer.

In the present experiment gases of two different purities were used. With standard grade gas of 99.99% purity the ionization chamber was filled directly from the bottle while for high purity gas the bottle gas was further purified by passing it through a B.O.C. Rare Gas Purifier. The impurities in the second sample should be less than one part per million. The gas pressures were measured by means of oil and mercury manometers isolated from the chamber by sensitive bellows. All measurements were carried out at 20°C in a thermostatically controlled room.

Experimental Procedure and Analysis of Experimental Data.

In the present experiment ionization coefficients were obtained by measuring the growth of pre-breakdown ionization currents, I , as a function of inter-electrode spacing, d , for different values of E/N (electric field/gas number density). In order to overcome possible fluctuations in the initial photoelectric current, I_0 , currents $I_c = cI_0$ were measured at values of $(E/N) = (E/N)_c$ at which no ionization took place. Values of I/I_c were then obtained for different values of d .

The current growth curves were analyzed in terms of the Townsend current growth equation in the form

$$\frac{I}{I_c} = \frac{c \exp(\alpha d)}{\left[1 - \frac{\omega}{\alpha} \{ \exp(\alpha d) - 1 \} \right]}$$

where α is the ionization coefficient and ω/α a generalized secondary coefficient. The analysis

followed the method given by Crompton et al⁽⁷⁾ and Jones and Llewellyn-Jones ⁽⁸⁾.

Results.

Current growth curves have been obtained with standard grade argon (99.99% purity) at $N = 38.5 \times 10^{17} \text{ cm}^{-3}$ and for high purity argon at $N = 41.8 \times 10^{17} \text{ cm}^{-3}$, and are shown in Figure 1.

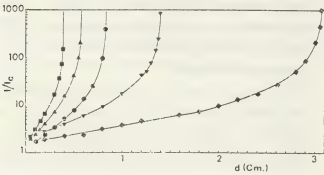


Fig. 1. High Purity Argon.
 E/N (volts cm^{-2}), \blacklozenge 3.04×10^{-16} , \blacktriangledown 3.65×10^{-16} ,
 \bullet 4.26×10^{-16} , \blacktriangle 4.86×10^{-16} , \blacksquare 5.47×10^{-16} .

The values obtained for the ionization coefficients are shown in Figure 2 and in Table 1, together with Kruthof and Penning's results for comparison. It can be seen that there is good agreement with Kruthof and Penning's results for the standard grade argon but that the coefficients are consistently about 15% lower for the high purity argon. This difference is well outside the uncertainty of about $\pm 5\%$ in the determination of α/p . This trend is to be expected as any increase in the purity of the argon would decrease the ionization coefficient.

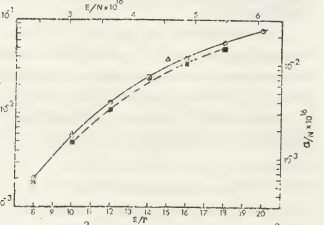


Fig. 2. α/N (cm^2) as a function of E/N (volts cm^{-2}).
--- \blacksquare --- Present experiment High Purity Argon,
($N = 41.8 \times 10^{17} \text{ cm}^{-3}$).
 Δ Present experiment Standard Grade Argon,
($N = 38.5 \times 10^{17} \text{ cm}^{-3}$).
--- \circ --- Kruthof and Penning ($0.229 \times 10^{17} \text{ cm}^{-3} < N < 53.3 \times 10^{17} \text{ cm}^{-3}$).

TABLE 1.

$\alpha/N \times 10^{18} \text{ cm}^2$ $E/N \times 10^{16} \text{ V cm}^{-2}$	High Purity	Standard Grade	Kruthof & Penning
2.43	-	0.055	0.069
3.04	0.148	0.191	0.18
3.65	0.35	0.39	0.39
4.26	0.74	-	0.73
4.56	-	1.18	-
4.86	1.06	-	1.17
5.47	1.53	-	1.68
6.08	-	2.4	2.3

This work is being continued with argon at higher pressures and with a mass spectrographic analysis of the gas samples.

References.

1. Kruthof, A.A. and Penning, F.M., 1936, Physica 3, 515-533.
2. Golden, D.E. and Fisher, L.H., 1961, Phys. Rev. 123, 1079-1086.
3. Heylen, A.E.D., 1968, Brit. J. Appl. Phys., Ser. 2, Vol. 1, 179-188.
4. Lozansky, E.D. and Robouch, B.V., 1978, Proc. 5th Int. Conf. on Gas Discharges, Liverpool, September 1978.
5. Dutton, J. and Powell, J.M., 1972, J. Phys. B. Atom. Molec. Phys. 5, 1236-1240.
6. Bruce, F.M., 1947, J. Inst. Elec. Eng., 94, 138-149.
7. Crompton, R.W., Dutton, J. and Haydon, S.C., 1956, Proc. Phys. Soc. B, 69, 2-13.
8. Jones, Eifionydd and Llewellyn-Jones, F., 1958, Proc. Phys. Soc., 62, 363-368.

DECAY OF METASTABLE Ne (3P_2)-ATOMS

J.W.H. Dielis, F.J. de Hoog and D.C. Schram.

Eindhoven University of Technology, Eindhoven, the Netherlands.

Investigations on the destruction rates of metastable atoms as a function of gas density in neon and the other noble gases have been carried out in recent years. The experimental method most frequently used is the optical absorption technique. (1,2,3, 4). A tunable dye laser was used in (5) to study non resonant fluorescence in the afterglow of a positive column in neon to determine the decay frequency of $3s$ -states. In another experiment a time resolved study of the vacuum U.V. emission of Ne (1P_1) and Ne (3P_1) states was carried out to study the Ne (3P_2) decay (6). At this moment the numerous mechanisms which govern the 3P_2 decay are fairly well understood (1,5). In the present work the afterglow of a Townsend discharge (T.D.) is used for mass spectrometrical determination of the Ne (3P_2) decay at 77 and 295 K, using the Penning ionisation of N_2 impurities as a diagnostic reaction. Current densities smaller than 10^{-6} A/cm^2 provide cumulative processes, e.g. dissociative recombination, not to take place.

Theory

Because of this low current density 3P_2 -atoms are only destroyed by i) diffusion to the wall (D), ii) excitation with a ground state atom to the nearest 3P_1 -state (a.A) and iii) three body collisions with two ground state atoms (Y). (See fig. 1). The 3P_2 decay frequency reads

$$v = \frac{D}{N\lambda^2} + \gamma N^2 + a.A.N. \left(1 - \frac{N_R}{a.N_M}\right) \quad (1)$$

with N_R and N_M the 3P_1 and 3P_2 densities, N the gas density, A the de-excitation frequency, a the ratio of excitation to de-excitation and λ the diffusion length.

Method

The Ne (3P_2) decay rate is measured by using the Penning ionisation reaction $\text{Ne } (^3P_2) + N_2 + N_2^+ + \text{Ne} + e^-$. The nitrogen density in the parent gas is so small that it does not affect the decay frequency. The rate of formation of N_2^+ ions is proportional to the

3P_2 -state density. The T.D. is pulsed from burning voltage to a lower voltage in the afterglow. N_2^+ -ions formed by the Penning reaction in the afterglow drift to the cathode which contains a small hole (10 μm). The ions are sampled, selected on mass by a Q-pole mass filter and are detected by a channeltron. The times of arrival of the N_2^+ -ions after onset of the afterglow are processed by a microprocessor. Repeatedly pulsing gives a histogram of arrival times of N_2^+ , identical to the relative density of the 3P_2 -atoms as a function of time in the afterglow and hence yield the decay frequency. The T.D., placed in a cryostat, can be cooled to liquid nitrogen temperature of 77 K. Cataphoresis of the research grade neon gas provides the impurity degree to be less than a few p.p.m. (Fig.2: exp.)

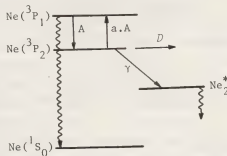


Fig 1: Diagram for the decay of $\text{Ne}(^3P_2)$ atoms.

Results

The measured decay frequencies as a function of gas density at 77 and 295 K are shown in fig. 3. By means of a nonlinear least mean square procedure eq. (1) is fitted to the data, obtaining the best values for D , A and γ , as given below

Temperature	295 K	77 K
$D(10^{20} \text{ m}^{-1} \text{ s}^{-1})$	4.8 ± 0.3	2.3 ± 0.2
$A(10^{20} \text{ m}^3 \text{ s}^{-1})$	3.2 ± 0.1	0
$\gamma(10^{-46} \text{ m}^6 \text{ s}^{-1})$	5.4 ± 0.3	0.52 ± 0.04

Diffusion coefficient

As can be seen in fig. 4 the agreement of the present data at 295 K is good, whereas at 77 K the present value is 25% larger than previous results. From potential curve considerations, showing a large insensibility of D on the shape and parameter values of the ($^3P_2 - ^1S_0$) interaction, this deviation is not disquieting.

De-excitation rate

Experimental (1,5,6,10) and theoretical (11) results on A are shown in fig. 5. The present result at 295 K is 50% smaller than previous data, but in good agreement with the theory of Cohen et al (11).

Three-body collision coefficient

The present results on γ at 77 and 300 K are in good agreement with previous experiments. The activation energy for this process is calculated to be 0.032 eV, in conformity with (12) and (13).

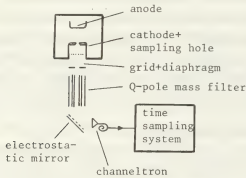


Fig 2: Experimental setup and measuring system.

Acknowledgements

The authors thank L.A.W.Gaykema and M.J.P.Vetjens for their valuable contributions and D.C.Schram and A.A.Kruithof for helpful discussions.

References

- (1) Phelps A.V., Phys. Rev. 114 (1011) 1959.
- (2) Phelps A.V. et al, Phys. Rev. 89 (1202) 1953.
- (3) Dixon J.R. et al, Phys. Rev. 107 (118) 1957.
- (4) Grant J.R. et al, Phys. Rev. 90 (59) 1953.
- (5) Steenhuysen L.W.G. et al, Proc. XIII ICPIG Berlin p. 37, 1977.
- (6) Leichner P.K. et al, Phys. Rev. A12 (2501) 1975.
- (7) Metaxas A.C. et al, J. Phys. D5 (1077) 1972.
- (8) Grant F.A., Phys. Rev. 84 (844) 1951.
- (9) Molnar J.P., Phys. Rev. 83 (945) 1951.
- (10) Biondi M.A., Phys. Rev. 88 (660) 1952.
- (11) Cohen J.S. et al, Phys. Rev. A17 (1343) 1978.
- (12) Cohen J.S. et al, J. Chem. Phys. 61 (3230) 1974.
- (13) Gritsyna V.V., Opt. Comm. 10 (320) 1974.

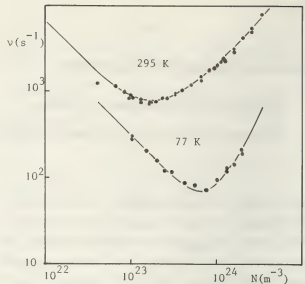


Fig 3: Decay frequency of $Ne(^2P_2)$ vs. gas density at 77 and 295 K
solid curve: least square fit of eq.1

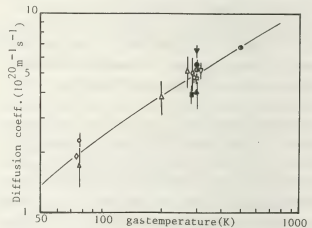


Fig 4: Diffusion coefficient vs. gas temperature. 1(●), 4(Δ), 5(□), 7(▼), 8(▲), 9(■), 10(▼), 2(○), present(○).
Solid curve: theory with 16/6-potential.

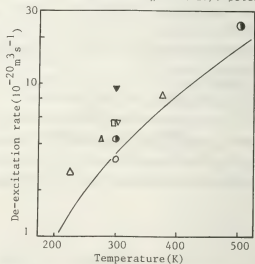


Fig 5: De-excitation rate vs. gas temperature. 1(●), 4(Δ), 10(▼), 5(□), 6(▼), present(○).
solid curve: theory/12/.

IONIZATION AND ATTACHMENT IN WATER VAPOUR AND AMMONIA

A.V. Rishbud and M.S. Naidu^{*}.^{*}Indian Institute of Science, Bangalore, India.

Presently with Eindhoven University of Technology, EEG, Group EHO, Eindhoven, The Netherlands.

Introduction. Electron attachment in water vapour has not been extensively studied as in other gases, such as, oxygen and its compounds. There are discrepancies between the existing data (1-5). The results of Parr and Moruzzi (5) are higher than those of Kuffel (1) and Ryzko (4) but are lower than those of Prasad and Craggs (2). Regarding the process of attachment, while Kuffel (1) observed it to be a three-body process at low E/N. Moruzzi and Phelps (6) did not see any attachment for $E/N \geq 33$ Td. Like wise, $\frac{\alpha}{N}$ of Prasad and Craggs (2) and Ryzko (4) also differ.

Ammonia has not been investigated for over a long time. In view of the recent interest in it (7,8), Parr and Moruzzi (5) investigated attachment processes. Only other studies made in this gas were of Bailey and Duncanson (9) and Bradbury (10). Parr and Moruzzi's n/N are 20% higher than those of Bailey and Duncanson, while those of Bradbury are ten times lower; while these discrepancies exist in n/N , there appears to be no data on the measurements of α/N .

In view of these, measurements were made in both these gases and α/N and n/N were accurately evaluated over the range $E/N = 70$ to 150 Td (for n/N) and 70 to 2400 Td ($\frac{\alpha}{N}$) over the pressure range 5 to 20 Torr (20°C) ($N = 16.5 \times 10^{16}$ to $66 \times 10^{16} \text{ cm}^{-3}$).

Experimental technique: The experimental apparatus used was of a usual form for the measurements of prebreakdown currents by the Townsend method using high vacuum techniques. Details were given by Maller and Naidu (11). Before the commencement of measurements, the ionization chamber was evacuated to 3μ Torr, the pumps were isolated and gas was leaked in (see below). The gas pressures were measured to $\pm 1\%$ using a silicone oil manometer (D.C.705). The ionization currents were read to $\pm 1\%$ (Keithley Electrometer, type 640) and the applied voltages were measured to $\pm 0.5\%$ (DM 752, Electronics Corporation of India). Under these conditions, the estimated errors in $\frac{\alpha}{N}$ and n/N were about $\pm 2\%$.

Extreme care was taken in purification and drying of the gas samples as suggested by earlier workers (5). Water vapour used was from specially prepared triply distilled deionized water, while ammonia used was purified by fractional distillation and dried using sodium. The gases were further dried before entering the ionization chamber. Care was also taken to see that the density of water vapour inside the chamber was always maintained much below its saturated vapour density at room temperature to avoid possibilities of error in pressure measurement.

Results in Water Vapour. Current growth ($\log I-d$) plots became increasingly linear for $E/N > 152$ Td indicating that n/N becomes negligible over this region. α/N and n/N obtained from these measurements are shown in figures 1 (n/N) and 2 (α/N). Fig. 1 shows that the present data of n/N are in good agreement only with those of Crompton et al (3) and differ from the data of others (1,2,4,5). α/N shown in fig. 2 agree with the data of Prasad and Craggs (2) and Ryzko (4) only to within $\pm 3\%$ over the entire range of E/N studied. n/N were found to be independent of gas pressures suggesting that attachment arises in this gas through dissociative attachment process represented as $e + \text{H}_2\text{O} \rightarrow \text{H}^- + \text{OH}$.

Results in Ammonia. Coefficients $\frac{(n-\alpha)}{N}$ and α/N measured are shown in fig. 3 and 2 respectively. The present $(n-\alpha)/N$ values are lower than those of Moruzzi and Parr (5) and Bailey (9) and are higher than those of Bradbury (10) (figure 3). Fig. 2 shows only the present data on α/N as no other data appears to be available for comparison. As was observed in water vapour, no pressure dependence of n/N was observed in this gas also indicating that attachment arises mainly through dissociative processes.

References

1. Kuffel, E., Proc. Phys. Soc., **74** (1959) 297
2. Prasad, A.N. and Craggs, J.D., Proc. Phys. Soc., **76** (1960) 223

3. Crompton, R.W., Rees, J.A. and Jory, R.L., Aust. J. Phys., 18 (1965) 541
4. Ryzko, A., Arkiv. Fys., 32 (1966) 1
5. Parr, J.E. and Moruzzi, J.L., J.Phys. D: Appl. Phys., 5(1972) 514
6. Moruzzi, J.L. and Phelps, A.V., J. Chem. Phys., 45 (1966) 4618
7. Melton, C.E., J. Chem. Phys., 45 (1966) 4414
8. Searles, S.K. and Kebabian, P., J. Phys. Chem. 72 (1968) 742
9. Bailey, V.A. and Duncanson, W.E., Phil. Mag., 2 (1930) 145
10. Bradbury, N.E., J. Chem. Phys., 2 (1934) 827
11. Maller, V.N. and Naidu, M.S., J. Phys. D: Appl. Phys., 7 (1974) 1406

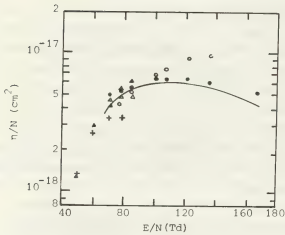


Fig. 1. Attachment coefficient (η/N) in water vapour. - present values, \blacktriangle Parr et al (5), Δ Ryzko (4), \bullet Crompton et al (3), \circ Prasad et al (2) and $+$ Kuffel (1).

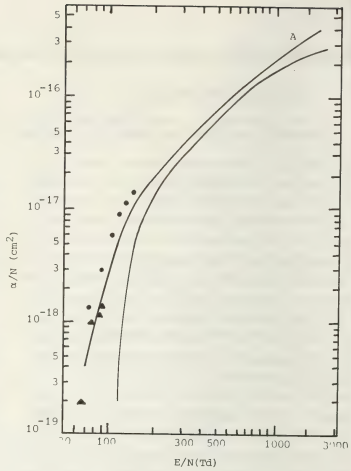


Fig. 2. Values α/N as a function of E/N in water vapour and ammonia. A present data in water vapour, B present data in ammonia, \blacktriangle Ryzko (4) and \bullet Prasad et al (2) both in water vapour.

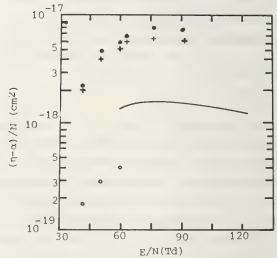


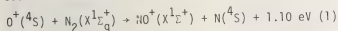
Fig. 3. Values of $(\eta-\alpha)/N$ as a function of E/N in ammonia. - Present data, \bullet Parr et al (5) \circ Bradbury (10) and $+$ Bailey et al (9)

AB INITIO STUDIES OF ION-MOLECULE REACTIONS. THE $N_2O^+(^4A'')$ POTENTIAL ENERGY HYPERSURFACE FOR THE $O^+(N_2, NNO)^+$ REACTION

Darrel G. Hopper.

Theoretical Chemistry Division, Science Applications, INC. 4124, Linden Avenue, suite 202 Dayton, Ohio 45432 U.S.A.

INTRODUCTION. It has been shown that the first electronically excited state of N_2O^+ is the $1^4A''$ bent state [1]. In this state and at about 120° this triatomic species exhibits a saddle topology with the saddle-point being very near in energy to the asymptote $O^+(^4S)$, $N_2(X^1\Sigma_g^+)$. The $1^4A''$ state lies well below the $A^2\Sigma^+$ state and in the $1^4A''$ state the molecule is predissociated in both the N-NO and NN-O coordinates. The minimum energy pathway which leads adiabatically from the 120° critical conformation to either $N(^4S)$, $NO^+(X^1\Sigma^+)$ or $O^+(^4S)$, $N_2(X^1\Sigma_g^+)$ passes through polarization wells but the minimum saddle-point appears to lie above both asymptotes at all angles [2]. An extensive ab initio survey with a double-zeta basis is being made in order to establish a first approximation to the detailed adiabatic reaction coordinate for Rxn (1)



The preliminary results of this survey are reported here in terms of the variation of the saddle-point with the valence angle A_{NNO} . The implications of these results for the N_2O^+ electronic structure and the dynamics of Rxn (1) are then discussed.

METHOD. The ab initio SCF results reported here have been obtained by use of the POLYATOM [3] integral package and BISON-MC [4]. The nitrogen and oxygen one-electron basis sets are 4s2p contractions [5] of optimized 9s5p atomic Gaussian bases [6]. The $N_2O^+(1^4A'')$ potential energy surface has been surveyed at 90° , 110° , 120° , 130° , 150° , and 170° . At each of the first five angles the nuclear separation grid is $R_{NN} = 1.0154 \text{ \AA}$ to 1.4667 \AA by 0.11282 \AA and $R_{NO} = 1.0658 \text{ \AA}$ to 1.7763 \AA

by 0.11842 \AA . At 170° the same ranges are used while the spacings are reduced to values of 0.05641 \AA and 0.05921 \AA for R_{NN} and R_{NO} , respectively. The denser grid at 170° is necessary because the near-linear avoided intersection of the $4A''(^4\Pi)$ and $4A''(^4\Sigma^-)$ potential energy hypersurfaces occurs near the $170^\circ 1^4A''$ saddle-point. **RESULTS.** The energy surface exhibits a saddle topology at all six angles. At the 170° saddle-point the wavefunction is that of the $1^4A''(^4\Pi)$ linear state component. The SCF 4s2p minimum energy saddle-point in the $N_2O^+(1^4A'')$ potential energy hypersurface occurs at 118.5° . The corresponding saddle-point value R_{NO}^* of the coordinate R_{NO} also exhibits a minimum value, $R_{NO}^* = 1.24 \text{ \AA}$, at this angle. The coordinate R_{NN} , on the other hand, exhibits a saddle-point value $R_{NN}^* = 1.28\text{--}1.29 \text{ \AA}$ over the extensive angular range $110\text{--}170^\circ$. From the results of SCF and correlated calculations of the equilibrium geometries for $N_2O(X^1\Sigma^+)$ and $N_2O^+(X^2A')$ with double-zeta quality basis sets it is estimated that the present SCF values for R_{NN}^* and R_{NO}^* are correct to within 0.03 \AA and 0.07 \AA , respectively, and that A_{NNO}^* is correct to within 9° [7].

The total energy of the minimum 4s2p SCF saddle-point, -183.1112 a.u. , is 2.9 eV below the 4s2p SCF total energy of $N_2O^+(1^4\Pi)$, -183.0061 at the $X^2\Pi$ equilibrium geometry [2]. At the latter geometry the excitation energy $X^2\Pi \rightarrow 1^4\Pi$ is $5.5 \pm 0.3 \text{ eV}$ from correlated wavefunction calculations [8]. Thus, the minimum energy saddle-point of the $1^4A''$ potential energy surface is $2.6 \pm 0.4 \text{ eV}$ above $X^2\Pi$. Using the experimental $X \rightarrow X$ ionization potential, $X^1\Sigma^+ \rightarrow 1^4A''$ is $15.5 \pm 0.4 \text{ eV}$.

From the experimental dissociation energies for N_2O^+ [9] this result places the critical energy of the reaction intermediate at about 0.2 eV above O^+, N_2 and 1.3 eV above N, NO^+ .

DISCUSSION. The key features of the potential energy surfaces have easily recognizable effects on the dynamics and energetics of chemical reactions. The qualitative projection of these effects from given surface features is a relatively straightforward application of momentum concepts from classical mechanics. In some cases classical trajectory studies have been made to verify the predicted qualitative features [10]. In the present case it is shown above that the minimum energy reaction coordinate for Rxn (1) must pass through a saddle-point $R_{NN}^* = 1.29 \pm 0.03 \text{ \AA}$, $R_{NO}^* = 1.24 \pm 0.07 \text{ \AA}$, $A_{NNO}^* = 119 \pm 9^\circ$ at an energy approximately 0.2 eV in excess of the thermal reagents. Both an energy barrier and a dynamical barrier prevent adiabatic reaction from thermal reactants. The dynamical barrier results from the fact that the value of R_{NN}^* is significantly greater than the outer anharmonic vibrational turning point, 1.18 \AA of $N_2(v=1)$, even though more than enough energy is available. Reaction (1) can proceed adiabatically only for translationally ($E_t > 0.2 \text{ eV}$) or vibrationally $N_2(v \geq 2)$ excited reagents. Both the translational and vibrational threshold effects predicted theoretically here and elsewhere [1,2] for the adiabatic reaction mechanism have been observed experimentally [11]. The low but finite thermal reactivity is, then, to be attributed to a different mechanism, which is discussed elsewhere [2,11].

At the saddle-point geometry the adiabatic ionization potential for the process $N_2O(^1\Sigma^+) \rightarrow N_2O(^1^4A'') + e$ is presently obtained

as $15.5 \pm 0.4 \text{ eV}$. This result corroborates an earlier report [1] that the first electronically excited state of N_2O^+ in the triatomic region, as well as in the atom-diatom asymptotic regions [2], is the $1^4A''$ state.

ACKNOWLEDGEMENT. This work was supported in part by the U.S. A.F. Office of Scientific Research under contract F49620-78-C-0050 with Science Applications, Inc.

REFERENCE.

1. D.G. Hopper, Chem. Phys. Lett 31(1975) 4466.
2. D.G. Hopper, J. Am. Chem. Soc. 100, 1019(1978).
3. D.B. Neuman et al. POLYATOM (Version 2), QCPE program 47, University of Indiana.
4. G. Das and A.C. Wahl, Argonne National Laboratory Report No. 7955 (1972).
5. T.H. Dunning, Jr., J. Chem. Phys. 53 (1970) 2823.
6. S. Huzinaga, J. Chem. Phys. 42 (1965) 1293.
7. D.G. Hopper, A.C. Wahl, R.L.C. Wu, and T.O. Tiernan, J. Chem. Phys. 65 (1976) 5474.
8. D.G. Hopper, unpublished results.
9. F. Gilmore, DNA 1948H, DNA Reaction Rate Handbook, 2nd ed., March 1972, Chap. 10.
10. J.C. Polanyi, Acc. Chem. Res. 5, 161 (1972).
11. For a discussion of the experimental results see Ref. [2] and E.E. Ferguson, "Ionosperic Ion-Molecule Reactions", in Interactions Between Ions and Molecules, Ed. by P. Ausloos (Plenum, New York 1975).

EFFECT OF THE ION MOTION AT LOW ELECTRON DENSITIES ON THE PROFILES OF THE LINES 4471 Å AND 4922 Å OF HeI

C. Fleuriot, G. Coulaud and J. Chapelle*

*Centre de Recherches sur la Physique des Hautes Températures C.N.R.S. 45045 Orléans Cédex.
U.E.R. Sciences Fondamentales, Université d'Orléans, 45045 Orléans Cédex.

Introduction : We have shown recently /1/ /2/ /3/ an ion mass effect on the Stark profile of the line HeI 4471 Å. These results show, for electron densities, $n_e \rightarrow 3 \times 10^{15} \text{ cm}^{-3}$, a smearing of the central structure of the line between the allowed and the forbidden components, when the reduced mass (μ) of the couple helium atom-perturbing ion decreases. The conclusion was that this effect could be imputed, reasonably, to the ion motion, because the extrapolation of our results at $\mu \rightarrow \infty$ ($V_i \sim 0$) showed an excellent agreement for the values C/P (see below, fig. 1) with the theoretical (static) predicted ones /4/ /5/. However, although this effect was clearly demonstrated, it is in contradiction with the theoretical predictions /6/ and some other theoretical estimates for which the ion motion effect is only appreciable at low electron densities ($n_e \leq 10^{15} \text{ cm}^{-3}$).

Nevertheless, there exists no clear experimental evidence of an ion effect at low densities. We can only note some theoretical attempts /7/ to obtain a better fit with experiment than the static calculations.

So, the aim of this work, is to put forth experimental evidence of an ion mass effect at low electron densities in the profiles of the lines 4471 Å of HeI, and, for further proofs, 4922 Å of HeI, for which the same effect is expected.

Methods : The lines were emitted in a conventional plasma jet with addition of a transfer anode /2/ /3/. Three different plasmas were used, each one characterized by a different reduced mass of the radiator-perturbing ion couple, specifically : $\mu = 0.8$ for the He-H plasma, $\mu = 2$ for the He-He plasma and $\mu = 3.34$ for the He-Ne plasma. The plasma composition was chosen such as more than 99 % of the ions in the plasma came from the second gas (H or Ne). The electron density was estimated from the line width of H β (plasma He-H) or by means of the Stark width of some isolated lines arising from levels $n = 5$ or 6 which suffer an important Stark broadening. The electron temperature was determined by means of the Saha law relative to high excited levels and by use of the collisional-radiative model.

The ion temperature was obtained from the Doppler width of the isolated lines of HeI arising from low energy levels.

Spectroscopic measurements were achieved on a spectrometer having a reciprocal dispersion of 4.4 Å/mm in the first order (1200 l/mm grating 1.7 m focal length). The line profiles were obtained by using an optical multichannel analyser (OMA) providing an excellent signal over noise ratio. Moreover, the light intensity was very stable (± 1 %) and the jet had an excellent cylindrical symmetry, thus, even the Abel inversion

yielded very accurate line profiles. The error was estimated to be lower than 5 % for the intensity of the line.

Results : Four parameters characterizing the line profiles were measured : the peak separation S (in Å), the ratios I/P and C/P and the halfwidth of the allowed component $\Delta\lambda$ (in Å). (Fig. 1). Our previous studies /3/ have shown that $\Delta\lambda$ and S vary only slightly with μ , within the experimental errors. In the present work, we have used $\Delta\lambda$ as a common reference parameter for comparison of the different profiles in place of n_e for which the uncertainty is about ± 15 % while for $\Delta\lambda$ this uncertainty is lower than 5 %. The peak separation S was not used as in /1/ /2/ /3/ because it varies too slowly in this range of electron density while $\Delta\lambda$ varies approximately linearly with n_e .

The results for the line 4471 Å are, partially, summed up in figs. 2 and 3 for the $\Delta\lambda$ range : $0.5 \text{ Å} \rightarrow 2 \text{ Å}$ ($n_e \sim 5 \times 10^{14} \text{ cm}^{-3}$ to $4 \times 10^{15} \text{ cm}^{-3}$). The fig. 2 shows clearly the effect of the variation of μ on the ratios I/P and C/P : the dip intensity increases while the peak intensity decreases. An example is given in Fig. 1, for $\Delta\lambda = 0.80 \text{ Å}$, where the two profiles are normalized in amplitude. Good agreement is observed between the two profiles, mainly in the allowed peak and in the wings but the central structure is smoothed in the He-H profile in comparison of the He-He profile. The observed differences between the three cases (fig. 2) for I/P, C/P (or I/P-C/P) are greater than the experimental uncertainties, so we can firmly ensure that an ion mass effect exists at low electron densities for the line 4471 Å of HeI, and also (fig. 4) for the line 4922 Å.

Finally, we have plotted (fig. 3) the ratios I/P and C/P as functions of $(\mu)^{-1/2}$ which is proportional to the ion velocity. The experimental values lie approximately on a straight line and the extrapolation (dashed lines) at an infinite reduced mass shows an excellent agreement with the theoretical static values of the ratios I/P and C/P by /4/ /5/. This feature makes us to think that the observed effect, proportional to the ion velocity, is an ion motion effect.

Discussion : These results confirm our previous measurements at higher electron densities. However we note in this experiment a variation in the ratio I/P which had no been detected (or which was within the experimental errors) at higher density. That gives an indication that the ion motion effect is more marked at low electron density, in agreement with the theoretical assumptions. Then it seems to decrease to zero up to an electron density of about 6 to $10 \times 10^{16} \text{ cm}^{-3}$ /1/.

In another connection, the comparison with the theory /7/ including a treatment of the ion dynamics, would show a best fit with our profiles than the static theories, but the corrections to the profiles given by this calculation are still too weak to perfectly fit the observed effect.

Finally, another calculation, using the model micro-field method /8/ seems to give an excellent agreement, for $n_e \leq 3.10^{15} \text{ cm}^{-3}$, with our profiles. (The results will be presented at the conference). In this model, the ion dynamic is taken into account in the same way as the electron dynamic.

References :

/1/ C. Fleurier and J. Chapelle, XIIIth ICPIG Berlin (1977).
/2/ C. Fleurier, G. Coulaud and J. Chapelle, Phys. Rev. A 18, 575 (1978).
/3/ C. Fleurier, Thèse, University of Orléans (1978).
/4/ H.R. Griem, Astrophys. J 154, 1111 (1968).
/5/ A.J. Barnard, J. Cooper and L.J. Shamey, Astron-Astrophys. 1, 28, (1969).
/6/ D.D. Burgess, J. Phys. B 3, L 67 (1970).
/7/ A.J. Barnard, J. Cooper and E.W. Smith, J.Q.S.R.T. 14, 1025 (1974).
/8/ A. Brissaud, C. Goldbach, J. Léorat, A. Mazure and G. Nollez, J. Phys. B 9, 1129 (1976).

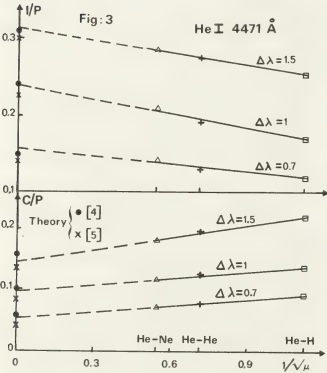


Fig.3: Variation of I/P and C/P vs $(\mu)^{1/2}$. The dashed lines represent the extrapolation of our results at $\mu \approx \infty$.

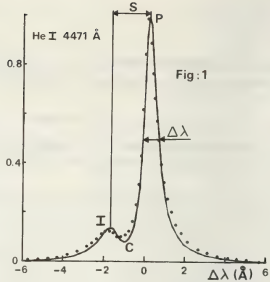


Fig.1: Profiles of the line He I 4471 Å from He-He plasma (full line) and He-H plasma (•).

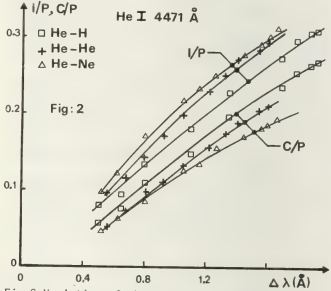


Fig.2: Variation of the ratios I/P and C/P as functions of the halfwidth $\Delta\lambda$ (proportional to n_e).

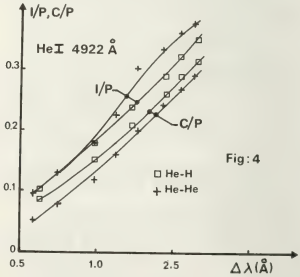


Fig.4: Variation of I/P and C/P vs $\Delta\lambda$ for the line He I 4922 Å.

THE INFLUENCE OF ION VIBRATIONAL EXCITATION ON ION MOLECULE REACTIONS

E. Alge, H. Villinger, K. Pesca, H. Ramler, H. Störi and W. Lindinger.

Institut für Experimentalphysik der Leopold Franzens Universität, Abteilung Atomphysik (Hülle), Karl Schönherstrasse 3, A 6020 Innsbruck, Österreich.

The mean kinetic energy KE_{ion} of ions drifting in a buffer gas under the influence of an electric field is well represented by the Wannier equation /1/

$$KE_{ion} = \frac{3}{2} kT + \frac{v_d^2}{2} (m_i + m_b),$$

where v_d is the drift velocity of the ions and m_i and m_b are the ion and buffer masses respectively.

On the other hand so far there only exists a qualitative picture upon the internal vibrational energy of molecular ions drifting in a buffer gas. Recent NOAA-results /2/ and results obtained in our laboratory have shown, that molecular ions such as O_2^+ and CO_2^+ are vibrationally excited more readily when drifting in an argon buffer than in a helium buffer. This was demonstrated by investigating in an argon and helium buffer the energy dependences of the rate constants of ion molecule reactions which

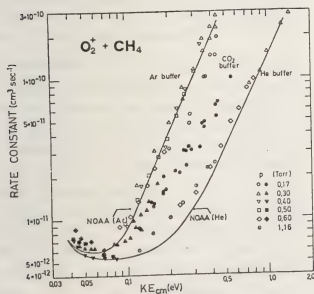


Fig. 1

strongly depend on the vibrational energy of the ions. The reaction of O_2^+ with CH_4 is slow at room temperature ($k = 6 \times 10^{-12} \text{ cm}^3 \text{ sec}^{-1}$) and has a main exothermic reaction channel into $O_2CH_3^+$, but at elevated energies (KE_{cm} , the relative kinetic energy of the reactants is obtained by conversion of the ion kinetic energy into the center of mass energy in the usual way /3/) the slightly endothermic reaction channels to CH_3^+ and CH_4^+ among other become available. According to theoretical considerations of Polanyi and coworkers /4,5/ this type of reaction should be promoted by vibrational excitation. In fact the rate constant for the reaction of O_2^+ with CH_4 shows a much stronger increase at elevated energies in an argon than in a helium buffer /6/.

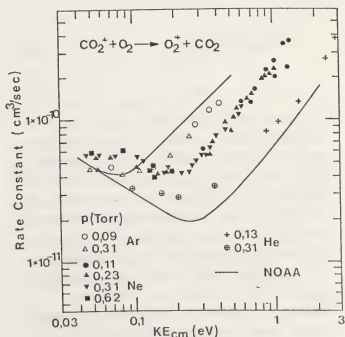


Fig. 2

In the present investigation we compare the results on the energy dependences of the reaction of O_2^+ with CH_4 obtained in a helium, an argon and a CO_2 buffer, and of the reactions of CO_2^+ with O_2 and D_2 obtained in helium, neon and argon. In the case of $O_2^+ + CH_4$ our results obtained in helium and argon agree well with the NOAA results /6/, as can be seen in Fig.1. The results obtained in CO_2 show that this buffer is less effective in vibrationally exciting O_2 than argon but is obviously more effective than helium. The results for the reaction of CO_2^+ with O_2 , which is also promoted by vibrational excitation of the reactant ion are shown in Fig.2 together with data obtained in a helium and an argon buffer at NOAA /7/. $CO_2^+ + D_2$ is a reaction, which is slowed down

The "Österreichischer Fonds zur Förderung und der wissenschaftlichen Forschung" is thanked for support under contract No. S 18/07.

- /1/ G.H. Wannier, Bell Syst. Tech. J. 32, 170 (1953)
- /2/ D.L. Albritton: NATO advanced study institute, La Baule 1978
- /3/ M.Mc Farland, D.L. Albritton, F.C. Fehsenfeld, E.E. Ferguson and A.L. Schmeltekopf, J.Chem.Phys. 59, 6620 (1973)
- /4/ J.C. Polanyi and W.H. Wong, J.Chem. Phys. 5, 1439 (1969)
- /5/ M.H. Mok and J.C. Polanyi, J.Chem. Phys. 51, 1451 (1969)
- /6/ I. Dotan, F.C. Fehsenfeld and D.L. Albritton. J.Chem.Phys. 68, 5665 (1978)
- /7/ W. Lindinger, M.Mc Farland, F.C. Fehsenfeld, D.L. Albritton, A.L. Schmeltekopf and E.E. Ferguson, J. Chem.Phys. 63, 2175 (1975).

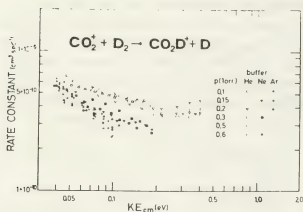


Fig. 3

by vibrational excitation and our results are shown in Fig.3. From the results of Figs. 2 and 3 one can assume, that rare gases have a higher efficiency for exciting vibrational excitation of molecular ions the heavier the atomic mass of the rare gas atoms is. This is at least the case for He, Ne, and Ar. On the other hand, when other gases instead of rare gases are used as a buffer, no such statement can be made as is seen from the examples of Fig.1.

These investigations will be carried on and will be extended to a krypton buffer.

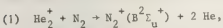
QUENCHING OF $n = 3, 4$ SINGLET HeI EXCITED STATES BY MOLECULAR NITROGEN IN A LOW-PRESSURE GLOW DISCHARGE

A. Catherinot and B. Dubreuil.

Groupe de Recherche sur l'Energétique des Milieux Ionisés, Université d'Orléans 45045 Orléans Cédex France.

I - INTRODUCTION

Electrical pumping can create rare gases excited electronic states with a good efficiency and transfer of this electronic energy to atomic and molecular radiators is a promising way to develop a wide range of laser sources in the visible and near ultra violet. Observation of intense laser emission in the N_2 first negative system at 4278 \AA (1) in (He, N_2) gaseous mixture pumped by the reaction :



has stimulated numerous studies on excitation transfers from excited helium to N_2 molecules. Measurements are generally performed in afterglow and concern only reactions involving "long life-time" HeI states (metastable and ionized atomic and molecular states (2, 3, 4, 5). On the other hand, an efficient process for the production of He_2^+ ions is associative ionization of "short life-time" (radiative) HeI excited states. Consequently these states may play an important part in laser emission in the N_2 first negative system.

In this paper, we present some preliminary experimental results concerning collisional destruction of the $n = 3, 4$ singlet HeI excited states by molecular N_2 in a low-pressure glow discharge.

II - EXPERIMENT (6, 7, 8)

A tunable dye laser excited by a pulsed nitrogen laser (pulse width 4 ns, spectral width 0.2 \AA , energy per pulse $\sim 10 \text{ \mu J}$, repetition rate 15 Hz) is used to induced a selective and short perturbation on an helium excited state by resonant optical pumping.

Excited states are populated in a capillary glow discharge (inner diameter 4 mm, length 60 mm). This discharge is created under continuous electrical power supply with a constant flow of (He, N_2) gaseous mixture (flow rate $< 1 \text{ l/h}$). Partial pressures P_{He} and P_{N_2} can be independently adjusted from 10^{-3} to 5 Torr and current intensity from 10 mA to 40 mA. Gas temperature is measured by means of a thermocouple in contact with the discharge tube ($T_g \sim 325 \pm 5 \text{ K}$). After spatial filtering, the pump laser beam traverses the discharge tube. The fluo-

rescence light emitted by a cross-section of the positive column is observed in a perpendicular direction and is imaged onto the slits of a spectrometer (resolving power ~ 100.000) and then onto a photomultiplier tube. Time dependence of the output signal is analysed by a Boxcar averager (temporal resolution $\sim 5 \text{ ns}$) and each fluorescence relaxation curve corresponds to $1.5 \cdot 10^4$ laser shoot average.

III - MEASUREMENTS

The population variation $\Delta N_i(t)$ of the $|i\rangle$ HeI state consecutive of laser optical pumping of the 2^1S-3^1P , 2^1S-4^1P , 2^1P-3^1S , 2^1P-3^1D , 2^1P-4^1S and 2^1P-4^1D radiative transitions have been studied for fixed values of the partial pressure P_{He} and various values of partial pressure P_{N_2} . For each pumped transition ($J \rightarrow i$), $\Delta N_i(t)$ is deduced from measurements of the time variations of the spectrally integrated resonance fluorescence light intensity. After the laser pulse has ceased, the perturbed populations go back to their stationary values. In this laser-free relaxation mode $\Delta N_i(t)$ is solution of the population rate equation : (9)

$$\frac{d\Delta N_i(t)}{dt} = a_{ii} \Delta N_i(t) + \sum_{J \neq i} a_{iJ} \Delta N_J(t)$$

$$\Delta N_i(t=0) = \Delta N_i^0, \quad J = 1, \dots, n$$

n is the number of sublevels coupled by collisional or radiative excitation transfers with $|i\rangle$. a_{ii} is the quenching coefficient of the $|i\rangle$ level (total depopulating coefficient) whereas a_{iJ} is the excitation transfer coefficient from $|J\rangle$ to $|i\rangle$ (populating coefficient). However, one may be note that action of a_{iJ} coefficients on $\Delta N_i(t)$ arise only after two successive reactions and so in the first phase of the relaxation and for a judicious choice of P_{He} , we can write in a first approximation :

$$\frac{d\Delta N_i(t)}{dt} = a_{ii} \Delta N_i(t)$$

$$\text{where : } a_{ii} = -(A_i + n_{\text{He}} R_{\text{He}}^i + n_{N_2} R_{N_2}^i) \quad (2)$$

A_i is the total radiative de-excitation rate, R_{He}^i and $R_{N_2}^i$ are the total de-excitation rates by collisions of the $|i\rangle$ state respectively with helium atoms (number density n_{He}) and with nitrogen molecules (number density n_{N_2}).

For each state $|i\rangle$ ($|i\rangle = 3^1S, 3^1P, 3^1D, 4^1S, 4^1P, 4^1D$) we have measured the a_{ii} coefficient as a function of P_{N_2} for a fixed value of P_{He} . Results are shown on Fig. 1 and Fig. 2.

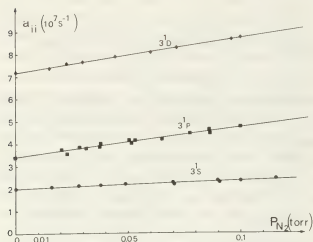


Fig. 1

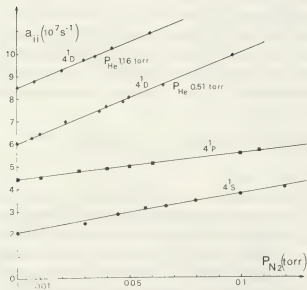


Fig. 2

RESULTS AND DISCUSSION

All measured destruction coefficients a_{ii} depend linearly on nitrogen partial pressure P_{N_2} in the nitrogen and helium partial pressure ranges we have studied. Quenching rates $R_{N_2}^i$ are deduced from relation (2) and are reported below with corresponding velocity average cross-sections $\sigma_{N_2}^i$.

level	$P_{He Torr}$	I_{mA}	$R_{N_2}^i \text{ cm}^3/\text{s}$	$\sigma_{N_2}^i \text{ cm}^2$
3^1S	0.86	30	$1.15 \cdot 10^{-9}$	$8.2 \cdot 10^{-15}$
3^1P	1.00	35	$4.4 \cdot 10^{-9}$	$3.2 \cdot 10^{-14}$
3^1D	0.83	30	$5.7 \cdot 10^{-9}$	$4.1 \cdot 10^{-14}$
4^1S	0.83	30	$5.7 \cdot 10^{-9}$	$4.1 \cdot 10^{-14}$
4^1P	0.53	35	$3.4 \cdot 10^{-9}$	$2.5 \cdot 10^{-14}$
4^1D	0.51	35	$1.35 \cdot 10^{-8}$	$9.6 \cdot 10^{-14}$

The extrapolation values of the a_{ii} at zero nitrogen partial pressure are in excellent agreement with results obtained in a pure HeI glow discharge (9, 10, 11).

On the other hand, we observe that the $R_{N_2}^{3^1S}$ quenching rate is clearly lower than the other ones, perhaps due to non resonant excitation transfers towards N_2 molecule, or to the low associative ionization probability of this 3^1S state (9, 12), in connection with the reaction (1).

Previous studies (10) of a pure helium glow-discharge have shown that for pressure greater than 1 Torr, 4^1D and 4^1P sublevels are in collisional equilibrium. Present results performed for $P_{He} = 1.16$ Torr, when the 2^1P-4^1D transition is optically pumped (Fig. 2), indicate that the 4^1P quenching rate is of the same order of magnitude than the 4^1D one.

REFERENCES

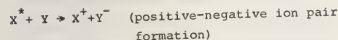
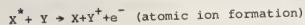
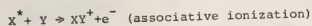
1. C.B. COLLINS, A.J. CUNNINGHAM and M. STOCKTON Appl. Phys. Lett. **25**, 344, (1974).
2. L.G. PIPER, L. GUNDEL, J.E. VELAZCO, D.W. SETSER J. Chem. Phys. **62**, 3883, (1975).
3. J.J. LEVENTHAL, J.D. EARL, and H.H. HARRIS Phys. Rev. Lett. **35**, 719 (1975).
4. G. MYERS and A.J. CUNNINGHAM J. Chem. Phys. **67**, 3352, (1977).
5. F.W. LEE, C.B. COLLINS and R.A. WALLER J. Chem. Phys. **65**, 1605 (1976)
6. B. DUBREUIL and A. CATHERINOT Physica **93C**, 408, (1978)
7. A. CATHERINOT and B. DUBREUIL Phys. Rev. A **18**, 1907, (1978)
8. A. CATHERINOT, P. PLACIET and B. DUBREUIL J. Phys. B, **11**, 3775 (1978)
9. B. DUBREUIL and A. CATHERINOT Communication presented at the XIVth CIPIG
10. A. CATHERINOT and B. DUBREUIL : communication presented at the conference : "collisions atomes-atomes aux énergies thermiques" Grenoble Décembre 1976.
11. B. DUBREUIL : Thesis (Université Orléans 1979).
12. H.F. WELLENSTEIN and W.W. ROBERTSON J. Chem. Phys. **56**, 1077 (1972)

THE IONIZATION RATE COEFFICIENTS FOR SOME RADIATIVELY EXCITED RUBIDIUM STATES

A.N. Klucharev^{*}, A.V. Lazarenko^{*}, and V. Vujnovic[†].^{*}Leningrad State University, Physical Institute, Leningrad U.S.S.R.[†]Institute of Physics, University of Zagreb, Yugoslavia.

INTRODUCTION

We studied chemiionization of the Rydberg states n^2P of rubidium, from $n = 8$ to 14. Under the chemiionization one considers ionizing collisions of two atoms, one of which, at least, is excited. The ionization proceeds by 3 channels:



Rubidium vapours at 400-560 K and at 10^{-3} - $5 \cdot 10^{-2}$ torr were irradiated by wavelengths above 280 nm, monochromatized within 0.3 nm. The source was a high-current Xenon lamp. The number of absorbed photons within an energy level and reaction volume was evaluated. By using an outer magnetic field, perpendicular to the incident light and to the collector surfaces, it was ensured that all of the produced electrons were collected.

RESULTS

A continuous background current of the electrons was found for the photon energy larger than 3.96 eV, what made possible an estimate for the ionization energy of the molecule Rb_2 equal to (3.96 ± 0.01) eV. By

using the dissociation energy of the neutral molecule, $D = (0.50 \pm 0.05)$ eV (ref.1), and assuming that the photoionization of Rb_2 started from the first vibrational level (Fig.1), we found for the dissociation energy of the molecule Rb_2^+

$$D^+ = E_i + D - 3.96 \text{ eV} = 0.72 \text{ eV}$$

E_i is the energy of ionization of Rb atom.

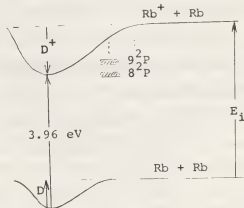


Fig.1

In our experimental conditions, the excited n^2P levels decay by chemiionization, by spontaneous emission and by collisions of 2nd kind. Radiative life times are higher for higher levels and they decay primarily by the collisional transitions. Photoionization from the levels was negligible as shown by a linear dependence of the electron current on the light intensity. The

same dependence ruled out collisions in which both atoms were excited. Therefore, our results correspond only to the chemi-ionization effected during collisions of normal and excited atoms.

For small atom concentration, a consideration of the statistical equilibrium gives the following dependence of the number of produced electrons per absorbed photon, P , versus the atom concentration in the ground level N_0 :

$$\frac{N_0}{P} = \frac{1}{\tau \langle \sigma v \rangle_i} + \frac{\langle \sigma v \rangle_i + \langle \sigma v \rangle_{P-D}}{\langle \sigma v \rangle_i} N_0$$

where τ is the radiative life time of the level, $\langle \sigma v \rangle_i$ the rate coefficient for ionization, and $\langle \sigma v \rangle_{P-D}$ the rate coefficient for mixing of n^2P and $(n-1)^2D$ states. By extrapolating $N_0 \rightarrow 0$ one determines the first term in the equation and the rate coefficient for the ionization. (The life times were taken from ref.2 and 3). The results are shown in

TABLE 1

Rb (n^2P)							
n	8	9	10	11	12	13	14
$\langle \sigma v \rangle_i$	3	7	9	14	12	11	9
($10^{10} \text{ cm}^3 \text{ s}^{-1}$)							

Theoretical description of the ionization from the high levels cannot be made in the frame of the usual model of a quasi-molecule. One should instead consider the three-body encounter between the neutral atom in normal state, a quasi-free excited

electron and the ion, formed of the atomic core left by the quasi-free electron. The collision is then treated as an interaction of the quasi-free electron with the dipole formed by the resonance charge transfer (ref.4 and 5). Transition to the ionization continuum is highly probable when the exchange energy equals the energy of ionization from the excited state. Such calculation gives a monotonically decreasing rate coefficient with increasing quantum number n . A maximum in the curve of the rate coefficient, shown in Table 1, may however result from a more elaborate treatment of the model (R.K.Janev and A.A.Mihajlov, private communication).

REFERENCES

1. D.L.Drummond and L.A.Schlie,
J.Chem.Phys. 65 (1976) 2116-25
2. F.Gounand, P.R.Fournier and I.Berlande,
Phys.Lett. 59 A (1976) 23-4
3. G. zuPutlitz and K.V.Venkataramu,
Z.f.Physik 209 (1968) 470-3
4. V.A.Smirnov and A.A.Mihajlov,
Opt.Spectrosc. (USA) 30 (1971) 525-6
5. A.Z.Devdariani, A.N.Klucharev, A.V.Lazarenko and V.A.Sheverev,
Sov.Tech.Phys.Lett. (USSR)

4 (1978) 1013-6 .

THE ROLE OF SINGLE-STEP IONIZATION BY THERMAL ELECTRON-ATOM COLLISIONS

G.V. Golubkov, N.M. Kuznetsov, V.V. Yegorov.

Institute of Chemical Physics, Academy of Sciences, Moscow, U.S.S.R.

The recombination coefficient of the reaction $A + e^- \rightarrow A^+ + e^- + e^-$ had been calculated in the diffusion approximation in ref. [1]. Energy change by an elastic collision of electrons is not characterized by a small parameter (mass ratio). The value of the ionisation rate constant (IRC) is mainly conditioned by bound elektron motion in energy region $|\epsilon| \sim T$ (T is temperature). In this energy region the average square of energy change per one elektron-elektron collision $\langle (\delta\epsilon)^2 \rangle$ has the same order of magnitude as T^2 . The diffusion approximation is correct if $\langle (\delta\epsilon)^2 \rangle / T^2 \ll 1$. Nevertheless the diffusion approximation is qualitatively true in the case $\langle (\delta\epsilon)^2 \rangle / T^2 \approx 1$ too. However the diffusion theory fails within one diffusion step $[\langle (\delta\epsilon)^2 \rangle]^{1/2}$ near the boundary $\epsilon = 0$. In this energy region a single-step ionisation (SSI) plays an important role. The SSI rate constant has a singularity at $\epsilon = 0$. Due to this singularity the distribution function $f(\epsilon)$ is considerably smaller as compared to the diffusion approximation result $f_0(\epsilon)$ in the region $|\epsilon| \lesssim T$. The IRC is obliged to change too.

The function $f(\epsilon)$ for bound electrons is described by modified Focker-Planck equation [2]:

$$g_n(\epsilon) \frac{\partial f}{\partial t} = \frac{\partial}{\partial \epsilon} \left\{ \frac{\langle (\Delta\epsilon)^2 \rangle}{2} g_n(\epsilon) \left[\frac{\partial f}{\partial t} + \frac{f}{T} \right] \right\} - K(\epsilon) f g_n(\epsilon), \quad (2)$$

$g_n(\epsilon)$ - density of states, $\langle (\Delta\epsilon)^2 \rangle$ - average square of energy change per one second, $K(\epsilon)$ - single-step IRC. In eq. (2) the term $K(\epsilon) f g_n(\epsilon)$ describes SSI. In a low temperature plasma ($T \ll I$; I - the ground state ionisation potential) hydrogen-like states of highly excited atom ($|\epsilon| \lesssim T$) play the predominant role. The density of these states is

$$g_n(\epsilon) = I_n^{3/2} \sum_+ |\epsilon|^{-5/2}, \quad (3)$$

I_n - hydrogen ionisation potential, \sum_+ - ion statistical sum. According to ref. [1] the expression of $\langle (\Delta\epsilon)^2 \rangle$ is

$$\langle (\Delta\epsilon)^2 \rangle = \frac{4}{3} (2\pi)^{1/2} e^4 m^{-1/2} \Lambda T^{-1/2} |\epsilon|, \quad \Lambda \equiv \ln(Z^2 + 1)^{1/2}, \quad (4)$$

e and m are the charge and the mass of electron, Ze - ion charge. For $K(\epsilon)$ we have $K(\epsilon) = \int_{|\epsilon|}^{\infty} \bar{\sigma}_\epsilon(E) \nu \bar{f}(E) dE$ (5) $\bar{\sigma}_\epsilon(E)$ - SSI cross section from energy level ϵ , $\nu \equiv \sqrt{2E/m}$, $\bar{f}(E)$ - free electron equilibrium distribution function.

So far there are not neither reliable theoretical nor experimental data on SSI cross section of highly excited states, which play the important role in thermal ionisation. So it is only possible to evaluate the character of the dependence and the order of magnitude of $K(\epsilon)$. As it is seen from eq. (5) $K(\epsilon)$ mainly depends on magnitude of $\bar{\sigma}_\epsilon(E)$ but not on the peculiarity of $\bar{\sigma}_\epsilon(E)$ as a function of E . The simplest estimation of $\bar{\sigma}_\epsilon(E)$ can be

made by using the Thomson classical theory [3]: $\sigma_{\epsilon}(\epsilon) \approx \frac{\sigma_m}{\pi a_0^2} \frac{\pi e^4}{E} \left(\frac{1}{|\epsilon|} - \frac{1}{E} \right)$, (6)

σ_m - the maximum SSI cross-section at $|\epsilon| = I_H$, a_0 - the Bohr radius.

The right part of eq.(2) can be expressed as the divergence of the total current $j = j_1 + j_2$, where j_1 and j_2 are the diffusion current and the SSI current:

$$j_1 = -\frac{c(\Delta \epsilon)^2}{2} \frac{g_n(\epsilon)}{\partial \epsilon} \left(\frac{\partial f}{\partial \epsilon} + \frac{f}{T} \right), \quad j_2 = \int_{-I}^{\epsilon} K(\epsilon') f(\epsilon') g_n(\epsilon') d\epsilon'. \quad (7)$$

j is equal to the rate constant if

$$\frac{\partial f}{\partial t} = 0. \text{ So we have to solve } \frac{dj}{d\epsilon} = 0 \quad (8)$$

with the boundary conditions

$$f(0) = 0, \quad f(-I) = 1/Z, \quad (9)$$

Z - atomic statistical sum.

The eq.(7)-(9) together with (3)-(6) have been solved numerically. The function $f(\epsilon)$ has been investigated near $\epsilon = 0$ analytically also. The results for f/f_0 and for IRC are shown on fig.1 and fig.2 for several values of the parameter

$$\alpha \equiv \frac{6}{15} \frac{1}{\lambda} \frac{\sigma_m}{\pi a_0^2}. \quad \text{On the figures}$$

the following notation is used: $x \equiv |\epsilon|/T$; $\theta(\alpha) \equiv j(\alpha)/j_0$; j_0 - rate constant for the diffusion approximation (see ref.[4]).

As it is seen (fig.1) $f \ll f_0$ in the region $|\epsilon| \lesssim T$. Nevertheless the increasing of j as compared to j_0 is rather small (fig.2). So the diffusion approximation for j (but not for $f(\epsilon)$ at $|\epsilon| \lesssim T$) is quite satisfactory in spite of the relatively large diffusion step for the electron-electron collisions.

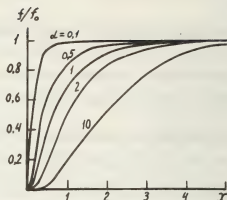


fig. 1

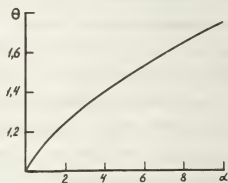


fig. 2

References

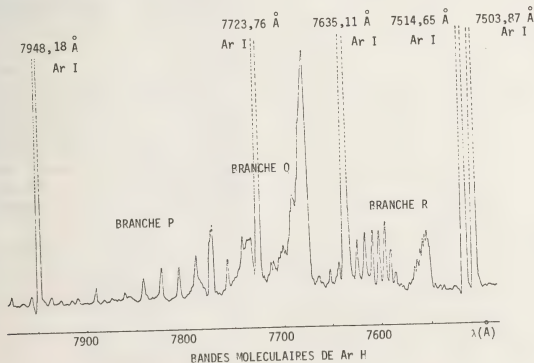
- [1] A.V.Gurevich and L.P.Pitaevskii, Zh. Eksp. Teor. Fiz. 46, 1282 (1964)
- [2] Yu.P.Denisov and N.M.Kuznetsov, Zh. Eksp. Teor. Fiz. 61, 2298 (1971)
- [3] D.R.Bates, Atomic and Molecular Processes (Academic Press, 1962)
- [4] N.M.Kuznetsov, Combustion and Explosion Phys. 5, 683 (1973), USSR

OBSERVATION DE L'EMISSION DE L'EXCIPLEXE Ar H^+ DANS DES JETS DE PLASMAS D'ARGON-HYDROGENE RAREFIESPh. Gaucherel^{*}, B. Rowe^{*}, J.L. Queffelec^{**}, N. Ben Jemaa^{**} et J.C. Gomet^{**}.^{*}Laboratoire d'Aréothermique du C.N.R.S., 4 ter route des Gardes 92190 Meudon, France.^{**}Département de Physique Atomique et Moléculaire, Université de Rennes I, avenue du Général Leclerc 35042 RENNES Cédex.

Les molécules de type excimères ou exciplexes suscitent depuis quelques années un intérêt considérable en partie lié à la possibilité de leur utilisation pour la réalisation de lasers. En ce qui concerne les exciplexes de gaz rares, les plus étudiés ont été très certainement les halogénures (Xe F , Xe Br , Kr F , Ar F etc...) et les composés alcalins gaz rares (Ar Na , Ar Cs etc...). Cependant d'autres composés sont possibles : les hydrures de gaz rares pour lesquels il existe quelques données le plus souvent théoriques, mais aussi déduites d'expériences de collisions. De façon générale, les courbes de potentiel montrent que l'état fondamental de l'hydrure neutre est répulsif et les états excités sont attractifs ; par contre l'ion moléculaire correspondant est stable [1]. Notons que pour ces hydrures, la littérature est en général plus abondante sur l'ion stable que sur la molécule neutre. C'est le cas de Ar H pour lequel il existe de nombreuses données sur Ar H^+ , par contre

les données sont relativement réduites et de plus contradictoires sur Ar H ([2], [3]). On peut d'ailleurs noter que les spectres moléculaires correspondant à la déexcitation radiative des états excités des hydrures neutres n'ont pratiquement jamais été observés. A notre connaissance, seule la transition $2\pi \rightarrow 2\Sigma$ de Ar H dont la tête de bande est observée à 7673.2 Å est actuellement attribuée à une molécule de ce type [4]. De plus dans cette dernière étude les processus de formation de cette molécule n'ont pas été étudiés.

De récentes observations effectuées dans nos laboratoires sur des jets de plasma d'argon raréfié (domaine de pression : 10^{-1} à 10 torr, température de quelques milliers de degrés) dans lesquels on injecte de l'hydrogène ou du deutérium (fig.) ont montré la présence de bandes d'émissions attribuables à Ar H ou Ar D . Les jets de plasmas étudiés sont produits par arc électrique dans un convergent



puis détendus dans un caisson basse pression. Ces plasmas sont étudiés par spectrométrie optique dans le visible et l'ultraviolet et par spectrométrie de masse quadrupolaire et sonde de Langmuir.

La densité électronique est obtenue par élargissement de raies [5] ou sonde de Langmuir, la densité des différentes espèces d'ions par spectrométrie de masse [6] et la densité de métastables par mesure d'absorption [7], la température électronique étant obtenue par sonde de Langmuir. Ces études montrent que les principales espèces présentes dans les mélanges Ar-H₂ sont :

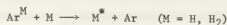
- les neutres : Ar, Ar^M, H₂ et H (où Ar^M désigne l'argon métastable ;

- les ions et électrons : Ar⁺, Ar H⁺ et e⁻.

L'émission du plasma est principalement liée à la présence d'argon métastable Ar^M par des processus du type :



où Ar^{*} désigne un atome d'argon dans un état excité radiatif, ou encore :



suivi de déexcitation radiative.

On observe donc de plus une forte émission liée à Ar H^{*} (ou Ar D^{*}) ; cette émission étant observée y compris pour les plus bas niveaux de densités ($n \approx 10^{14}$ part.cm⁻³), il existe un processus binaire de formation ne faisant pas intervenir d'états radiatifs.

Un certain nombre de processus sont envisageables dont le plus probable :

$\text{Ar}^{\text{M}} + \text{H}_2 \longrightarrow \text{Ar H}^* + \text{H}$ endothermique + 1,6 ev
d'autres possibilités existent, bien que peu probables par exemple :

$\text{Ar}^{\text{M}} + \text{Ar H}^+ \longrightarrow \text{Ar}^+ + \text{Ar H}^*$ endothermique + 2,88 ev.

L'étude des profils de densité d'électrons, d'ions et de métastables et des intensités de rayonnement permet de définir le processus prédominant ainsi que l'ordre de grandeur de sa vitesse.

[1] B. ROZEN, II Ed. Pergamon Oxford 1970, table 17

[2] M.A. CLYNE and P.B. MONKHOUSE, Chem. Phys. 28 (1978) 447-454.

[3] R.E. OLSON and B. LIU, Phys. Rev. A vol. 17, n° 5 (1968).

[4] J.W.C. JOHNS, J. of Molecular Spectroscopy 31 (1970) 488-510.

[5] J.L. QUEFFELEC et M. GIRAULT, Rev. Phys. Appl. 6 (1971) 401-407.

[6] Ph. GAUCHEREL et B. ROWE, Inst. J. of Mass Spectroscopy and ion Physics, 25 (1977) 211-227

[7] J.L. DELCROIX, C. MATOS FERREIRA et A. RICARD, Ed. du C.N.R.S. (1975), I.S.B.N. 2 222 01785.8

CALCULATION OF THE FREE-BOUND CONTINUUM OF RARE GASES

P. Ranson and J. Chapelle.

C.R.P.H.T. - C.N.R.S., 45045 Orléans Cédex, France.

The calculation of photoionization cross sections, which is the subject of a communication at this conference referred to as IM_1 is used to determine the free bound continuum. In the case of rare gas atoms (except He), if the temperature is not too high, all the ions of the plasma are in the ground state which is a doublet term $[^2P_{3/2}, ^2P_{1/2}]$ separated by a energy difference ΔE . So, it is necessary to distinguish the two channels in the relation between photoionization and recombination cross sections. The emission coefficient of recombination continuum towards a level i , is given by

$$\epsilon_i(\nu)d\nu = \frac{h\nu}{4\pi} n_e \left\{ n_{3/2}^+ \sigma_{3/2}^R(\nu_i) d\nu_i + n_{1/2}^+ \sigma_{1/2}^R(\nu_i) d\nu_i \right\}$$

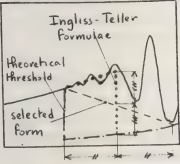
where $n_{3/2}^+$ and $n_{1/2}^+$ are the ion density for the two states, n_e the electron density, $\sigma_{3/2}^R$ and $\sigma_{1/2}^R$ are the recombination cross sections of the ion ($1 = ^2P_{3/2}, 2 = ^2P_{1/2}$) on the state i , the velocities v_1 and v_2 and the frequency ν are connected by the relation $h\nu = E_1 + \frac{1}{2}mv_1^2 = E_2 + \frac{1}{2}mv_2^2$ when E_1 and E_2 are the ionisation energies of the level i towards the two ionic states. The distribution function is assumed to be maxwellian.

Biberman and al /2/ have introduced the \mathcal{G} factor. It is defined for a wavelength λ as the ratio of the true emission coefficient to the classical emission coefficient of Kramers.

$$\epsilon(\lambda) = \frac{16\pi}{3\sqrt{3}} \frac{e^6}{mc^3} \frac{n_e^2}{(2\pi m k T)^{3/2}} (1 - e^{-\frac{h\nu}{kT}}) \mathcal{G}(\lambda, T)$$

We have calculated the \mathcal{G} factor for rare gases (except He) with the method given in 1.

It is a open question how the pseudo continuum of lines near the photoionization threshold can be taken into account. The use of the Ingliss and Teller formulae gives the position of the line for which the width is equal to the distance to the adjacent line. However, the simple application of this formulae does not remove the sudden variation



of the \mathcal{G} factor which is not observed experimentally. Therefore we prefer to use the form described by the dashed line on the figure 1. The introduction of this phenomenon implies that the \mathcal{G} factor becomes an electro-density dependent quantity.

The results of the calculated \mathcal{G} factor are shown on figures 2 for the four rare gases Ne, Ar, Kr, Xe, respectively for the spectral range 2000-10000 Å (named "visible") and for the spectral range 1-5 μm (named "infrared") and for an electron density of 10^{15} cm^{-3} . It should be noted that the influence of n_e is not the same in the visible range as in the infrared. In the visible range, the "soft" threshold is shifted towards higher wavelengths, but in the infrared, the \mathcal{G} factor is increased almost uniformly with increasing n_e .

Comparison with Schluter results /3/ and with Hofsaess results /4/ for sufficiently low n_e and $T = 8000 \text{ K}$ gives relatively good agreement in the visible range. In the infrared the results of Biberman and al /5/ are nearly equivalent to ours when the electron density is low ($\leq 10^{14} \text{ cm}^{-3}$).

References

/1/ F. RANSON, thesis Orléans (1978).
/2/ L.M. BIBERMAN, G.E. NORMAN, Optics Spect. 8, 230 (1960).
/3/ D. SCHLÜTER, Z. Astrophys. 210, 80 (1968).
/4/ D. HOFSAESS, J.Q.S.R.T., 19, 339 (1978).
/5/ L.M. BIBERMAN, G.E. NORMAN, K.N. ULYANOV, Optics Spect., 10, 297 (1961), Soviet Astron. AJ, 6, 77 (1962).

Fig. 1 : Threshold form of emission coefficient; dashed line : selected form.

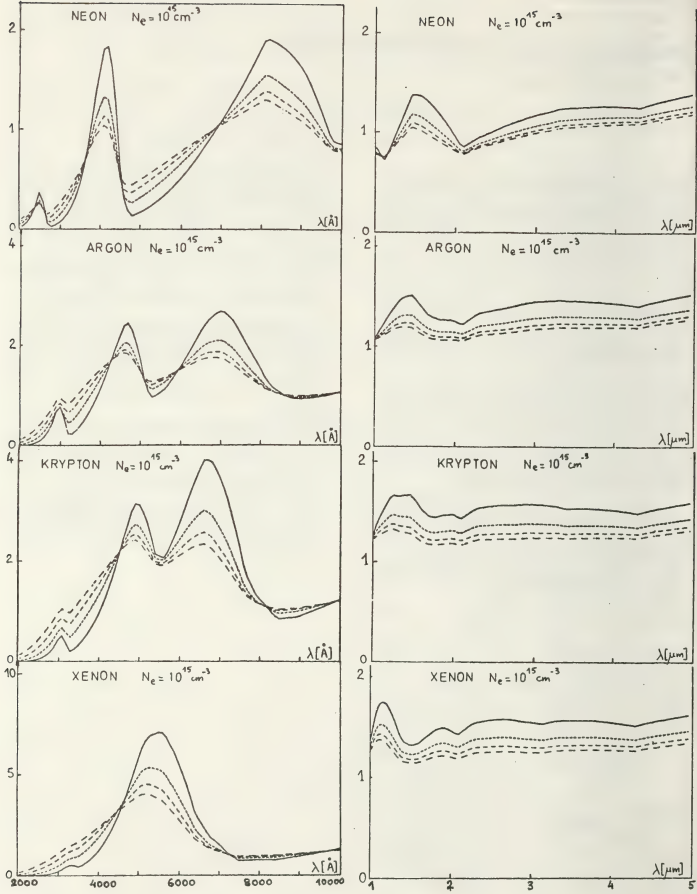


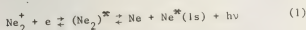
Fig. 2 : g factor for rare gases. — $T = 4000\text{ K}$,
..... $T = 6000\text{ K}$, --- $T = 8000\text{ K}$, - - - $T = 10000\text{ K}$.

MEASUREMENTS OF THE PRODUCTION OF NEON 2p ATOMS BY DISSOCIATIVE RECOMBINATION

L.W.G. Steenhuijsen, N. Van Schaik, L.C.A.M. Van de Nieuwenhuyzen, F.H.P. Verspaget.

Eindhoven University of Technology, Eindhoven, The Netherlands.

Introduction. Determined were in neon the partial recombination coefficients of the 2p levels, the relative population of the 2p levels and the recombination distribution fractions of the 1s levels. We used neon discharges with $d = 31$ nm, pressure $p = 20, 50, 100$ torr and current $I = 22$ mA. The measurements were carried out in the afterglow of the discharge ¹⁾. The afterglow radiation can be ascribed to dissociative recombination of molecular ions and electrons:



In this process highly excited atoms are produced which cascade in a stepwise manner to one of the 2p levels and from here finally deexcite by radiation to a 1s level. These last transitions cause the radiation which we have measured. The recombination coefficient α_2 can be splitted in a number of partial recombination coefficients α_{2i} , which each describe the recombination yield for each of the various 2p levels. Here we assume that transitions between the 1s levels and levels above 2p are negligible. In the afterglow the various 2p levels are populated in 2 ways: firstly from recombination as described above, secondly from atomic collisional transfer between the 2p levels. These mutual transfers prevent the possibility to determine the α_{2i} coefficients directly from the spectral distribution of the 1s-2p transitions. We have measured also the coupling coefficients K_{ij} between the 2p levels i and j . By taking the atomic coupling into account the values of α_{2i} have been determined.

Determination of the partial recombination

coefficient. In the afterglow the electron temperature decreases quickly (at 100 torr in 20 μ s) to the gas temperature. So the 2p levels are populated only by the process of dissociative recombination. Assuming that the atomic ion density can be neglected, the rate equation for each 2p level can be written as:

$$\begin{aligned} \frac{\partial p_i(t)}{\partial t} = & \alpha_{2i}(t)n_e^2(t) - A_i^* p_i(t) - \sum_{j=1}^{10} K_{ji} n_g p_i(t) \\ & + \sum_{j=1}^{10} K_{ji} n_g p_j(t) \end{aligned} \quad (2)$$

$p_i(t)$ is the density of level $2p_i$ at time t in the afterglow; A_i^* is the overall probability of spontaneous transitions to the 1s levels for level $2p_i$ ($A_i^* = \sum_{j=2}^5 A_{ij}$, with A_{ij} the spontaneous transition probability from $2p_i$ to $1s_j$); K_{ij} is the coefficient of atomic collisional transfer from level $2p_i$ to level $2p_j$; n_g is the ground state atom density.

In formula (2) we have neglected the electron coupling between the 2p levels, because of the low electron temperature. For all 2p levels together we have:

$$\sum_{i=1}^{10} \frac{\partial p_i(t)}{\partial t} = \alpha_2(t)n_e^2(t) - \sum_{i=1}^{10} A_i^* p_i(t) \quad (3)$$

The terms containing the coupling coefficients K_{ij} disappear because the influence of the "intern" transfers cancel out each other. From (3) follows:

$$n_e^2(t) = \frac{\sum_{j=1}^{10} \frac{\partial p_j(t)}{\partial t} + \sum_{j=1}^{10} A_j^* p_j(t)}{\alpha_2(t)} \quad (4)$$

In the remainder of this chapter we will omit the time indication unless it will be necessary. Substitution of n_e^2 in (2) and dividing by p_i gives:

$$\begin{aligned} \frac{1}{p_i} \frac{\partial p_i}{\partial t} + A_i^* + n_g \sum_{j=1}^{10} \{K_{ij} - K_{ji} \frac{p_j}{p_i}\} \\ \frac{\alpha_{2i}}{\alpha_2} = \frac{\sum_{j=1}^{10} \frac{1}{p_j} \frac{\partial p_j}{\partial t} + \sum_{j=1}^{10} A_j^* \frac{p_j}{p_i}}{\sum_{j=1}^{10} \frac{1}{p_j} \frac{\partial p_j}{\partial t} + \sum_{j=1}^{10} A_j^* \frac{p_j}{p_i}} \end{aligned} \quad (5)$$

We have measured in the afterglow the time courses of the relative intensities of the spectral lines originating from each individual $2p_j - 1s_1$ transition ($j = 1 \dots 10, i = 2 \dots 5$). The measured signal I_{ji} according to each of these transitions is

$$I_{ji} = \eta_{ji} A_{ji} P_j \quad (6)$$

with η_{ji} the detection coefficient of the experimental set up, which is dependent on wavelength.

Replacing in (5) p_j by $I_{ji}/\eta_{ji} A_{ji}$ gives:

$$\alpha_{2i} = \frac{\frac{1}{I_{i1}} - \frac{\partial I_{i1}}{\partial t} + A_{i1}^* + n_g \sum_{j=1}^{10} \{K_{ij} - K_{ji} \frac{\eta_{i1} A_{i1} I_{j1}}{\eta_{j1} A_{j1} I_{i1}}\}}{\sum_{j=1}^{10} \frac{\eta_{ji} A_{ji} I_{j1}}{\eta_{j1} A_{j1} I_{i1}} \left(\frac{1}{I_{j1}} - \frac{\partial I_{j1}}{\partial t} + A_{ji}^* \right)} \quad (7)$$

In relation (7) we have determined all quantities which are necessary to calculate α_{2i} . The value of $((1/I_{i1}) \cdot (\partial I_{i1}/\partial t))$ follows from our measurements of I_{i1} . However we note that these values are very small compared with the value of A_{i1}^* and so may be neglected. In (7) we need the relative values of the detection coefficients η_{ji} , which we have calibrated with the use of a tungsten ribbon lamp. From literature we have taken values for A_{i1} ⁵⁾ and α_{2i} ⁴⁾. n_g has been calculated for the tubes used. The coupling coefficients K_{ij} are measured also ³⁾. We have measured α_{2i} in a 100, 50 and 20 torr tube.

However also the disturbing terms of the atomic collisional transfer increase with the gas pressure. This is disadvantageous because in formula (7) the terms containing K_{ji} and K_{ij} are rather inaccurate. For this reason we have determined α_{2i} also at 20 torr where this effect is 5 times smaller. Table 1 gives a survey of the experimental results for α_{2i} . The inaccuracy is $\pm 15\%$.

With relation (6) we can determine the relative densities of the $2p_i$ levels:

$$\frac{P_i}{P_j} = \frac{I_{i1}}{I_{j1}} \frac{\eta_{jk} A_{jk} K_{ji}}{\eta_{ji} K_{ij} A_{i1}} \quad (8)$$

Figure 1 gives the relative densities of the $2p_i$ levels for pressures of 20, 50 and 100 torr. The inaccuracies are mainly determined by the inaccuracies of the transition probabilities ³⁾. The recombination distribution fractions give the fraction of the recombination yield produced in the levels $1s_5$, $1s_4$, $1s_3$ and $1s_2$ respectively. The fraction f_i ($i = 5, 4, 3, 2$) can be written as

$$f_i = \frac{\sum_{j=1}^{10} \frac{I_{ji}}{\eta_{ji}}}{\sum_{j=1}^{10} \sum_{i=2}^5 \frac{I_{ji}}{\eta_{ji}}} \quad (9)$$

The results are given in table 2. They are in good agreement with lit. ⁽⁵⁾.

References:

- 1) L.W.G. Steenhuijsen, thesis EUT (1979)
- 2) L.W.G. Steenhuijsen, ICPIG 14 (1979)
- 3) S. Inatsugu, Phys.Rev. A11,1,26 (1975)
- 4) L. Frommhold, Phys.Rev. 165,44, (1968)
- 5) L.W.G. Steenhuijsen et al. Proc. ICPIG 13 (1977)

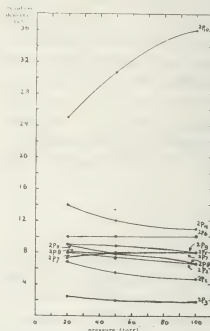


Figure 1:
Measured relative
densities of the
 $2p$ level at 60 μs
in the afterglow;
 $I = 22 \text{ mA}$

Table 1: values of $\alpha_{2i}(a_{2i})$ at various pressure

	pressures		
	20 torr	50 torr	100 torr
$2p_1$	0.10	0.08	0.07
$2p_2$	0.09	0.09	0.10
$2p_3$	0.03	0.04	0.06
$2p_4$	0.18	0.18	0.19
$2p_5$	0.08	0.07	0.05
$2p_6$	0.11	0.11	0.14
$2p_7$	0.06	0.06	0.04
$2p_8$	0.09	0.10	0.08
$2p_9$	0.13	0.18	0.24
$2p_{10}$	0.13	0.10	0.04

Table 2: Recombination distribution fractions for various pressures.

	20	50	100 torr
f_5	0.36	0.39	0.42
f_4	0.25	0.25	0.25
f_3	0.10	0.10	0.10
f_2	0.29	0.26	0.23

DETERMINATION OF THE COEFFICIENTS OF COLLISIONAL TRANSFER BETWEEN THE 2p LEVELS OF NEON

N. Van Schaik, L.W.G. Steenhuijsen, P.J.M. Van Bommel, F.H.P. Verspaget.

Eindhoven University of Technology, Eindhoven, The Netherlands.

Introduction. Transfer reactions between the various 2p levels are caused by collisions of 2p atoms with ground state atoms. The number of transfer reactions from level $2p_i$ to level $2p_j$ in unit time interval is:

$$\frac{dp_{i+j}}{dt} = K_{ij} n_g p_i \quad (1)$$

Here n_g and p_i are the densities of the levels $2p_i$ ($i = 1 \dots 10$) and the ground state level respectively; K_{ij} is the coefficient of collisional transfer between the levels p_i and p_j . Measurements on collisional transfer reactions in neon have been reported by Grandin¹⁾, Coolen²⁾ and Smits³⁾. Except Coolen they have made use of a continuous discharge. Coolen used a plasma which was generated by a proton beam. We have measured the coupling coefficients K_{ij} in the afterglow by means of selective excitation of the 2p levels from the 1s levels by irradiation with a dye laser beam. Our plasma is characterised by a) a low electron temperature, b) the population of the 2p levels is produced by dissociative recombination (no excitation from the 1s levels), c) the energy of the 2p atoms is quite large (~ 1 eV), because the dissociative recombination is a radiationless process^{4,5,6)}; the high atomic energy may have an influence on the atomic coupling directly after the recombination.

It is clear that measurements of atomic coupling in an afterglow have the advantage of the absence of electron excitation. Irradiation of the plasma with a laser beam does not influence the studied process. We performed our measurements in the afterglow period of a neon discharge ($d = 31$ mm) at gas pressures of 5,20,50 and 100 torr; the discharge current was 22 mA.

Calculation of the transfer coefficients. The decay rate of a $2p_i$ level in the undisturbed afterglow (no laser irradiation) may be described as^{2,3)}

$$\frac{\partial p_i}{\partial t} = \alpha_{2i} n_e^2 - A_i^* p_i - \sum_{j=1}^{10} K_{ji} n_g p_i + \sum_{j=1}^{10} K_{ij} n_g p_j \quad (2)$$

p_i is the density of the $2p_i$ level; α_{2i} is the partial recombination coefficient; n_e is the electron density; A_i^* is the total transition probability for the $2p_i$ level; n_g is the neutral atom density, K_{ij} is the coefficient for collisional transfer of excitation from the $2p_i$ to the $2p_j$ level; for mathematical convenience we define $K_{jj}=1$ for all $j=1, \dots, 11$. The right hand terms of (2) represent respectively the dissociative recombination, the spontaneous radiation, the collisional transfer from level $2p_i$ to level $2p_j$ and the collisional transfer of $2p_j$ to $2p_i$. We define p_i^k as the density of level $2p_i$ in case level $2p_k$ is populated extra by direct excitation of 1s atoms due to laser irradiation. The laser irradiation has no influence on the dissociative recombination which is the populating process for the 2p levels. So in the disturbed afterglow the decay of level $2p_i$ can be described as

$$\frac{\partial p_i^k}{\partial t} = \alpha_{2i} n_e^2 - A_i^* p_i^k - \sum_{j=1}^{10} K_{ji} n_g p_i^k + \sum_{j=1}^{10} K_{ji} n_g p_j^k \quad (3)$$

From our measurements we know that $\frac{1}{p_i} \frac{\partial p_i}{\partial t}$ and $\frac{1}{p_i^k} \frac{\partial p_i^k}{\partial t} \ll A_i^*$. This means in equation (2) and (3) the left terms can be taken as zero. We define $\Delta p_i^k = p_i^k - p_i$ ($i, k = 1 \dots 10$); then subtraction of (2) from (3) and subsequent dividing by Δp_i^k gives:

$$n_g \sum_{j=1}^{10} \left\{ K_{ji} \left(\frac{\Delta p_i^k}{\Delta p_k^k} \right) - K_{ij} \left(\frac{\Delta p_i^k}{\Delta p_k^k} \right) \right\} = A_i^* \left(\frac{\Delta p_i^k}{\Delta p_k^k} \right) \quad (4)$$

When I_{j1}^k is the intensity of the $2p_j$ -1s₂ transition in case level $2p_k$ is irradiated and I_{j1} is the intensity of the same transition when there is no laser irradiation then is our measured fluorescence signal given by $I_{j1}^k - I_{j1}$. From these signals we can determine the factor $\Delta p_i^k / \Delta p_k^k$ as follows:

$$\frac{\Delta p_j^k}{\Delta p_k^k} = \frac{p_j^k - p_j}{p_k^k - p_k} = \frac{\sum_{l=2}^5 (I_{jl}^k - I_{jl}^*) (A_j^* \eta_{jl})^{-1}}{\sum_{l=2}^5 (I_{kl}^k - I_{kl}^*) (A_k^* \eta_{kl})^{-1}}, \quad (5)$$

with $I_{jl} = \eta_{jl} A_{jl} p_j$, with η_{jl} is the detection efficiency for the transition $2p_j \rightarrow 1s_1$.

Relation 4 represents a system of 100 linear equations, in which the K_{ij} are the unknown. This system has been solved with the B₇₇₀₀ digital computer of EUT.

Because we did not have at our disposal a laser wavelength above 660 nm, we could not excite a 1s level to the $2p_{10}$ level. However the energy gap between the $2p_{10}$ and $2p_9$ level is so large that collisional transfer from $2p_{10}$ to $2p_9$ (or a higher 2p level) may be neglected. So we presume $K_{10j} = 0$ for $j = 2 \dots 9$; for the same reason we take $(\Delta p_j^k)/(\Delta p_{10}^k) = 0$.

Experimental realisation. The experimental set up is described in detail in lit. 7). We have measured the fluorescence radiation ΔI_{jl}^k during 3 time-intervals, with 10 μ s length each; these intervals were centered at $t = 40, 60$ and 80μ s. Every 2p level (except level $2p_{10}$) was populated extra by irradiating the plasma with the dye laser beam. Every turn the complete fluorescence was detected (with exception of the lines $\lambda = 540$ nm, 613 nm, 665 nm, 702 nm and 808 nm, which are too weak). In this way we measured the respective factors Δp_j^k ($j=1 \dots 10; k=1 \dots 9$). For solution of (4) we need $\Delta p_j^k/\Delta p_k^k$. To be able to measure Δp_j^k and Δp_k^k simultaneously we have set up two detection systems, at both sides of the discharge tube. The monochromator of one detection system is adjusted to one of the spectral lines which originate from the excited $2p_k$ level (preferably not the laser wavelength). The other detection system measured the fluorescence spectrum. In this way all fluctuations in the laser beam power and/or wavelength can be taken into account in $\Delta p_j^k/\Delta p_k^k$.

Experimental results. In table 1 the experimentally obtained values of K_{ij} are given. The given values are found as the average of the results at gas pressures 5, 20, 50 and 100 torr all at a discharge current of 22 mA. In general a dependence of K_{ij} on the gas pressure could not be determined within the accuracy boundaries. Table 2 gives the values for those coefficients in dependence of the pressure.

In table 1 we give also the influence of variations in the value of $\Delta p_j^k/\Delta p_k^k$ on the values of K_{ij} . The results are in good agreement with the results obtained by Smits 3) and Coolen 2).

References

- 1) J.P. Grandin et al., J. de Phys. 36, 787 (1975)
- 2) F.C.M. Coolen et al., Physica 93C, 131 (1978).
- 3) R.M.M. Smits, thesis EUT (1977).
- 4) M. Prins et al, proc. ICPIG 13 (1977).
- 5) A. Rogers et al., Phys. Rev. 134, A1215 (1964).
- 6) T. Conner et al., Phys. Rev. 140, A778, (1965).
- 7) L. Fromhold et al., Phys. Rev. 185, 244 (1969).
- 7) L.W.G. Steenhuijsen, thesis EUT (1979).

Table 1: Values of the atomic-scattering coefficients ($K_{ij} \pm 1 \sigma$) between the 2p-levels and their transitions. The listed values are pressure and temperature dependent.

$i \setminus j$	$2p_2$	$2p_3$	$2p_4$	$2p_5$	$2p_6$	$2p_7$	$2p_8$	$2p_9$	$2p_{10}$
$2p_2$	--	.07 $\pm .05$.21 $\pm .05$.07 $\pm .02$.05 $\pm .02$.04 $\pm .02$.02 $\pm .01$	0	.01 $\pm .01$
$2p_3$.07 $\pm .07$	--	.21 $\pm .1$.41 $\pm .30$	0	.10 $\pm .10$.05 $\pm .05$.15 $\pm .15$.10 $\pm .04$
$2p_4$.04 $\pm .03$	3.2 $\pm .2$	--	1.3 $\pm .2$.22 $\pm .03$.54 $\pm .10$.05 $\pm .03$.04 $\pm .03$	0
$2p_5$.01 $\pm .01$.05 $\pm .02$	3.5 $\pm .5$	--	.07 $\pm .02$.49 $\pm .07$.04 $\pm .02$	0	.02 $\pm .01$
$2p_6$	0 $\pm .02$.03 $\pm .005$.010 $\pm .01$.04 $\pm .01$	--	1.09 $\pm .05$.36 $\pm .5$.07 $\pm .02$.04 $\pm .02$
$2p_7$	0	0	0	0	.8 $\pm .2$	--	.72 $\pm .06$.17 $\pm .04$.12 $\pm .03$
$2p_8$	0	0	0	0	.08 $\pm .2$.16 $\pm .02$	--	2.3 $\pm .2$.80 $\pm .10$
$2p_9$	0	0	0	0	.10 $\pm .005$.06 $\pm .01$	1.3 $\pm .2$	--	4.2 $\pm .1$
$2p_{10}$	0	0	0	0	0	0	0	0	--

Table 2: The values of K_{54} , K_{76} and K_{910} ($10^{-17} m^3 s^{-1}$) in dependence of the pressure.

	100	50	20	5	Torr
K_{54}	4.0 $\pm .5$	3.6 $\pm .5$	3.3 $\pm .3$	3.2 $\pm .2$	
K_{76}	1.00 $\pm .07$.90 $\pm .08$.74 $\pm .06$.68 $\pm .06$	
K_{910}	2.9 $\pm .2$	3.2 $\pm .3$	4.6 $\pm .3$	5.6 $\pm .2$	

ARGON-TITANIUM HOLLOW CATHODE AFTERGLOW

D. Ohebsian[†], N. Sadeghi[†], C. Trassy and J.M. Mermet^{**}[†]Laboratoire de Spectrométrie Physique, Université Scientifique et Médicale de Grenoble, BP. 53, 38041 Grenoble cedex, France.^{**}Laboratoire de Physico-Chimie Industrielle I.N.S.A. 69621 Villeurbanne Cedex, France.

The mechanisms of the energy transfer between metastable and ionic species of the rare gases and metallic atoms are responsible for the laser action in rare gas-metal vapor discharge. Knowledge of the mechanisms of the production and loss of the metallic species in a rare gas plasma is therefore very important. The pulsed afterglow technique has already been used to study the excited metallic ion production in He-Cd, He-Zn (1) and He-Pb (2) discharge. In these experiments, the discharge cell containing metal pellets is placed inside an oven to produce the metal vapor at desired pressure. But this technique cannot be used for the metals having a high boiling point. For example a density of 10^{11} atoms cm^{-3} is obtained at 210°C for Zinc but at 1300°C for Titanium.

A simple way to produce these metal vapors is the hollow cathode discharge (3). The practical advantage of this process is that the metal vapor is generated by the cathode sputtering at room temperature.

In this communication we report the first results obtained in the afterglow of a Titanium hollow cathode in Argon.

Fig. (1) shows the experimental set up. The Titanium cylindrical cathode ($\phi_{\text{in}} = 9$ mm, $l = 25$ mm) is located inside a quartz cell. The Argon buffer gas pressure is varies from 0.2 to 5 torr and the gas flow is about 1 m sec^{-1} . The discharge current and duration are about 20 mA and 100 μsec respectively. The densities of the Titanium atoms and ions in their ground states and Argon metastable atoms was

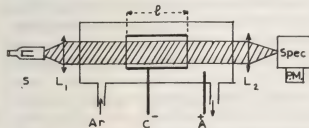
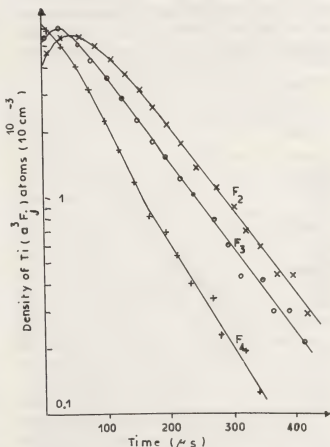


Fig. 1 : Experimental arrangement

measured by the optical absorption technique (4). For both emission intensity and absorption measurements, the photon counting and the data accumulation techniques (5) were used.

Fig. (2) shows the evolution of the population of the 3 fine structure levels a^3F_2 , a^3F_3 and a^3F_4 (at 0, 170 and 387 cm^{-1} respectively) of the Titanium ground state atoms in a 0.31 torr Argon afterglow. In this figure we can observe : i) Titanium atom density obtained is about 10^{11} atoms cm^{-3} . ii) during the discharge the populations of the three a^3F_j levels are in equilibrium by collisions with the energetic electrons of the discharge but at late afterglow they are in equilibrium by collisions with the Argon atoms at room temperature. iii) dur-

Fig. 2 : Time variation of the $\text{Ti}(a^3F_j)$ density in a 0.31 torr Argon afterglow

ing the first 100 μsec of the afterglow there is a transfer of population from the a^3F_4 to the a^3F_3 and a^3F_2 and from a^3F_3 to a^3F_2 . iv) in late afterglow the population of the a^3F_J levels decays according to an exponential law with a decay time proportional to the Argon atom density, Fig. (3). From this last observation we can conclude that the principal mechanism of the loss of the metal vapor density in the afterglow is the diffusion of the Titanium atoms across the buffer gas and their deposition on the cathode wall. The decay time (τ) of the $\text{Ti}(a^3F_J)$ atoms in Argon afterglow is $\tau = \frac{NA^2}{D_0}$, where N is the Argon atom density, A is the diffusion length and D_0 is the diffusion coefficient. From the slope of Fig. (3) we can deduce: $D_0 = 3.1 \cdot 10^{18} \text{ atoms cm}^{-1} \text{ sec}^{-1}$.

We have also observed the population of the some excited levels of Ar , Ar^+ , Ti and Ti^+ in the afterglow. Fig. (4) shows the time variation of the population of the $\text{Ar}^*(5p[5/2]_3)$, $\text{Ar}^{*+}(4p^4p^0_{7/2})$, $\text{Ti}^*(y^3G^0_3)$ and $\text{Ti}^{*+}(z^4G^0_{7/2})$ levels. The lifetime of all these levels being of the order of 10^{-8} sec , the observed time variation is that of the mechanisms responsible for the population of these levels in afterglow. For the Ti^* , Ar^* and Ar^{*+} populations, we find the well known behaviour of the electron-ion recombination populated levels, the involved ions

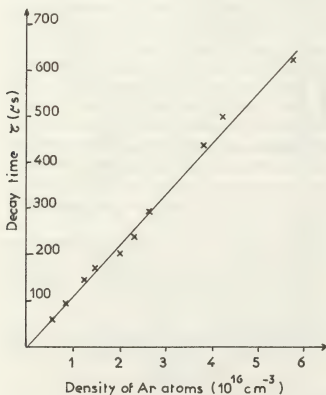


Fig. 3 : Variation of the decay time of the $\text{Ti}(a^3F_J)$ atoms versus the Argon atom density

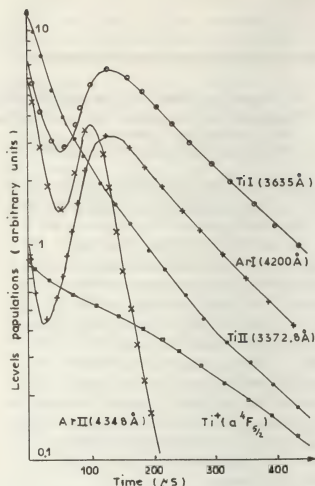


Fig. 4 : Time variation of the population of Ar^* , Ar^{*+} , Ti^* and Ti^{*+} in a 0.6 torr Argon afterglow.

being Ti^+ , Ar^+ and Ar^{++} respectively. On the other hand, the behaviour of the intensity decay of the whole Ti II transitions is entirely different and seems to show that the $(\text{Ti}^+)^*$ levels are populated by an energy transfer process. The similarity in population of all the $(\text{Ti}^+)^*$ levels seems point out that the excitation mechanism is a charge transfer process $\text{Ar}^+ + \text{Ti} \rightarrow \text{Ar} + (\text{Ti}^+)^* + \Delta E$ rather than the Penning ionization by Argon metastable atoms. The time decay of the ground state Ti^+ ions, obtained by optical absorption measurements is also shown in Fig. (4).

REFERENCES :

- (1) G.J. COLLINS, J. Appl. Phys., 44 (1973) 4633
- (2) L.A. CROSS and M.C. GOKAY, J. Appl. Phys., 49 (1978) 2639
- (3) F.J. de HOOG et al, J. Appl. Phys., 48 (1977) 3701
- (4) J. SABBAGH and N. SADEGHI, J.Q.S.R.T., 17 (1977) 297
- (5) N. SADEGHI and J. SABBAGH, Phys. Rev. A, 16 (1977) 2336.

THE RELATIVE CONTRIBUTION OF ASSOCIATIVE IONIZATION AND PHOTOIONIZATION IN XENON PRECURSORS

M.G. Vasil'ev, T.V. Zhikhareva and G.K. Tumakaev.

Ioffe Physicotechnical Institute, Academy of Sciences, Leningrad, U.S.S.R.

Abstract. The kinetics of xenon excitation and ionization and of the electron gas heating ahead of the shock front were studied theoretically for the Mach number range 14 to 20 and initial pressure $p = 5$ mm Hg. The ionization kinetics of xenon atoms was found to differ substantially from that of argon. In this case one should take simultaneously into account both associative ionization and photoionization, the latter becoming predominant in the charged particle production in xenon with increasing strength of the incident shock. The theoretical predictions for the electron density are compared with experimental values.

As has been established earlier /1,2/, photoionization in the argon precursors cannot account for experimental values of the electron density ahead of a shock even when the reflection of line and continuum radiation from the tube walls is included. The dominant mechanism of charged particle production in argon is associative ionization of the Molner-type /3/. The present work deals with a study of the kinetics of fundamental processes in the xenon precursors with the purpose of determining the predominant mechanism of ionization. The radiative and collisional processes considered xenon atoms in resonance and highly excited states in the photoexcitation of ground state atoms and their radiative and cascade transition relaxation to the ground state; (2) Photoionization of atoms from the ground and resonance states); (3) Excitation of atoms from the ground into resonance states and the processes of their de-excitation and ionization by electron impact; (4) Associative ionization involving an atom in a highly excited Rydberg state $Xe_p^* + Xe \rightarrow Xe_2^+ + e$ and dissociative recombination; (5) Ionic conversion $Xe^+ + Xe + Xe \rightleftharpoons Xe_2^+ + Xe$.

When constructing the energy balance equation for the electron gas, we included, apart from elastic and inelastic electron

collisions with atoms, also the changes in the electron gas energy involved in the photoionization, associative ionization and dissociative recombination processes.

The role of various Rydberg states of xenon atoms participating in the associative ionization reaction /4/ has also been studied. Since the oscillator strengths for the transitions into these states differ substantially from one another, the contribution of the atoms to the charged particle production is not the same. The largest and almost equal contributions come from atoms in the $6d [4\frac{1}{2}]_1^o$ and $5d' [4\frac{1}{2}]_1^o$ states, the smallest one being due to the $7d [4\frac{1}{2}]_1^o$ state. The difference in the molecular ion densities for these cases is a factor of $\sim 10^3$.

The resulting system of differential equations describing the kinetics of electron gas excitation, ionization and heating with asymptotic boundary conditions was solved numerically by the Runge-Kutta method.

The results of the computations show that while the excitation kinetics of the inert gases are the same, the ionization kinetics of xenon differs markedly from that of argon. This is due primarily to the high photoionization cross section of excited xenon atoms which exceeds by about 20 times that of argon. The photoionization cross section of the $6s [4\frac{1}{2}]_1^o$, resonance level was calculated by the method of Burgess-Seaton /5/, its value at the threshold being $3.6 \times 10^{-18} \text{ cm}^2$.

Fig.1 presents ionization rates vs. distance from the shock front in units of tube radius ($R = 5 \text{ cm}$). In contrast to argon, where the production of charged particles is determined predominantly by associative ionization while the photoionization pro-

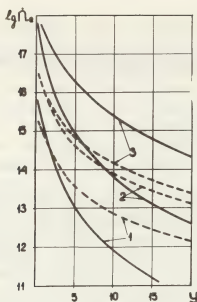


Fig. 1. Ionization rate profiles ($\text{cm}^{-3}\text{s}^{-1}$). Solid curve: excited state photoionization rate; Dashed curve: associative ionization rate. 1: $M=14$ without reflection. 2: $M=20$ without reflection. 3: $M=20$ with reflection.

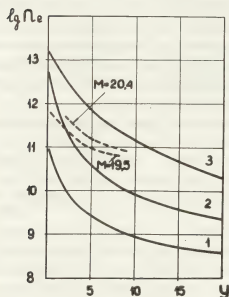


Fig. 2. Electron density profiles (cm^{-3}). Solid curves: theory for the cases in the preceding figure; Dashed curves: data obtained by microwave interferometry [6].

cesses are negligible, in xenon at $y = 1$ the probabilities of photoionization (Ph) and associative ionization (As) become comparable already at $M=14$, the (Ph) rate exceeding the (As) rate in the immediate vicinity of the shock front.

The competitive role of the photoionization of excited states compared with the process of associative ionization increases

substantially with increasing Mach number and when taking into account the reflection of radiation from the walls. Indeed, even without the inclusion of reflection, (Ph) exceeds (As) by an order of magnitude near the shock front at $M=20$. These processes become comparable here at a much larger distance from the front ($y \sim 10$) than is the case at $M=14$. Taking the reflection into account increases substantially the role of the excited state photoionization. As a result, the photoionization process becomes predominant throughout the range of y considered.

Note that as the photoionization efficiency increases, the efficiency of the atomic-to-molecular ion conversion as well as of the dissociative recombination process will likewise increase accordingly. Indeed, at $M=20$ the ion conversion rate throughout the range of y considered exceeds the associative ionization rate if the radiation reflection is considered, so that under these conditions the molecular ions should form primarily by way of conversion of atomic ions rather than in the course of the associative ionization process as was the case for $M=14$.

Fig. 2 shows the theoretical and experimental profiles of electron density. A comparison of the results indicates a satisfactory agreement between the experimental and theoretical data and a qualitatively good fit of the calculated electron densities for the case of radiation-reflecting walls to the experimental dependence on y .

References.

1. T.V. Zhikhareva, M.G. Vasil'yev, 12 Int. Conf. Phen. Ion. Gas, Eindhoven, The Netherlands, 1975.
2. T.V. Zhikhareva, M.G. Vasil'yev, Ju.G. Morozov, Zhur. Tekhn. Fiz. 45, N 3, 568 (1975).
3. A.E. Bulyshev, N.G. Preobrazhenskii, A.E. Suvorov, V.N. Yakovlev, in "Physical Gas Dynamics" (in Russian), N 6, IPTM, Novosibirsk, p.19 (1976).
4. E.E. Huffman, D.H. Katayama, J. Chem. Phys. 45, 138 (1966).
5. A. Burgess, M.J. Seaton, Mon. Not. Roy. Astron. Soc. 120, N 2 - 121 (1960).
6. D.G. Zavarin, V.V. Rozhdestvenskii, G.K. Tumakaev, Proc. I All-Union Seminar on Plasm. Conductometry, Moscow, 1977.

ON THE THREE-BODY ELECTRON ATTACHMENT TO OXYGEN IN THE PLASMA OF A NON-SELF-MAINTAINED DISCHARGE

A.N. Vasilieva, I.A. Grishina, V.I. Kitorov, A.S. Kovalev, A.T. Rakhimov.

Institute of Nuclear Physics, Moscow State University, 117234, Moscow, U.S.S.R.

The advance in the physics of lasers based on molecular gases excited by non-self-sustained discharges has made it essential to understand the elementary processes occurring in the plasma of such gases. In the working mixture of the CO₂-lasers, one can often find the molecules of oxygen, which is one of the typical electronegative gases. Accordingly, one should know the constants of electron attachment to oxygen at discharge parameters characteristic of CO₂ lasers, i.e., the E/P ratio ranging from 5 to 15 v/cm torr.

The present paper deals with the processes of electron attachment in a plasma produced by an electron beam. The beam of 100-keV electrons with current density to 400 $\mu\text{A}/\text{cm}^2$ was produced by an electron gun and injected through an aluminum foil into a quartz discharge chamber. The feeding system of the electron gun make it possible to vary the duration of the electron-beam current pulse from 0.5 to 600 μsec . While the discharge was burning and the plasma was decaying, the discharge-chamber voltage was kept constant.

Experimental results. The constants of electron attachment to oxygen were determined from the plasma decay rate. In all the experiments, plasma was produced by fast electron beam pulses of longer than

30 μsec . Such a duration is necessary for the relaxation of strata arising at the initial instant of the non-self-maintained discharge burning at $E/P \approx 11$ v/cm torr [1]. Fig. 1 shows the dependences of the inverse plasma-electron density, $1/n_e$ on the time t elapsed after the switching-off of the electron beam. The curves are constructed for gas mixtures consisting of 80% of nitrogen and 20% of oxygen at a pressure of 90 torr. The initial section of the time dependence of $1/n_e$ is on a logarithmic scale a straight line. With increasing E/P it is only the inclination of the line that is changed. A second part of the decay curve shows the slowing down of the plasma decay which is the more drastic the higher the E/P ratio becomes. Moreover, with increasing E/P, the beginning of that section shifts toward the increasing higher electron densities.

Studies of the time dependence of $1/n_e$ for the cases of decay of plasmas with various initial electron concentrations have revealed that the inclination of the initial part of the curve is independent of electron concentration, whereas the inclination of the second part shows a significant dependence on it.

To clarify the role of nitrogen and oxygen as a third body in the process of

electron attachment to the O_2 molecule, we have studied the dependence of the plasma decay rate α on oxygen concentration P_{O_2} at a given total gas pressure (Fig.2).

We have measured also the dependence of the steady-state current of the non-self-maintained discharge on the electron-beam current density j_e at $E/P=13$ v/cm torr. The discharge current has turned out to be rather accurately, proportional to the electron beam current.

Discussion. The fact that the initial part of the plasma decay curve represents, on a logarithmic scale, a straight line and that the inclination of this line is independent of initial electron concentration enables one to conclude that the initial part of the curve describes pure attachment of electrons to oxygen molecules. The decrease of relaxation rate with increasing E/P (Fig.1) and the proportionality of α/P_{O_2} to P_{O_2} suggest that the observed attachment is three-body. Fig.3 presents the dependences of the constants of the three-body electron attachment to oxygen, K_{O_2} and K_{N_2} on E/P obtained from an examination of the straight lines in fig.2. One observes a reasonable agreement with the results of [2] and [3]. An abrupt change in the character of plasma decay occurring with decreasing electron density appears to be due to a significant redistribution of the electric field and charge density during the interval after switching off the source of ionization. This is also confirmed by the fact that the character of plasma decay is entirely independent of the duration of the electron-beam pulse

when it lasts from 0.5 to 600 μ sec.

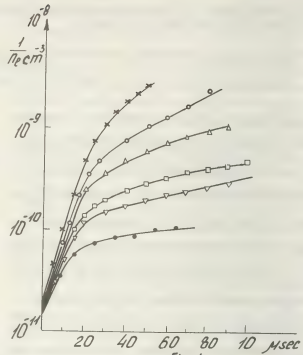


Fig. 1

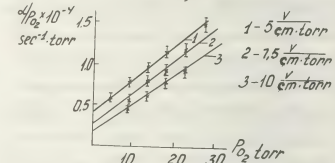


Fig. 2

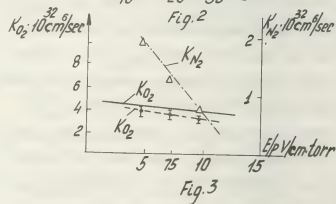


Fig. 3

References:

1. A.N.Vasilieva et al. Fizika plazmi, 2, (1979).
2. N.A.Aleksandrov. Teplofiz.visok.temperatur, 16, 719 (1978).
3. N.A.Aleksandrov. Teplofiz.visok.temperatur, 16, 231 (1978).

ON CHARGE-EXCHANGE OF IONS IN PLASMA

A.K. Grigoriady, O.I. Fisun.

Institute of Electrodynamics, Kiev 252057, U.S.S.R.

An influence of plasma particles on exchanging system is displayed in two ways. On the one hand particles at distances $r \lesssim r_0 \approx n^{-1/3}$ acting as statistically independent ones cause the appearance of an effective detuning $\langle H_0 \rangle^I$ and electron-induced charge-exchange². On the other hand exchanging system is under the action of particles being at the distances $r > r_0$. Their influence cannot be considered as statistically independent because of the strong spatial correlations.

This report deals with investigation of the effect of plasma polarization on the resonant charge-exchange. The ion entering the reaction induces a spatial charge in plasma; its potential

$$\Phi(\vec{r}, t) = -\frac{q_0}{2\pi^2} \int \frac{d\vec{k}}{k^2} \left(I - \frac{I}{\epsilon(\vec{k}, k\vec{v}_0)} \right) \cdot \exp(i\vec{k}(\vec{r} - \vec{v}_0 t)) \quad (1)$$

determines the ion-plasma interaction energy. Here ϵ is dielectric response function, \vec{v}_0 is ion velocity.

The mechanism of the effective defect formation connected with collective interactions is defined by parameter $A = \omega_p \tau$, where ω_p is the electron plasma frequency, τ is the propagation time between the critical points.

a) $A \gg 1$. Transitions between the quasimo-

lecular terms for such slow collisions are accompanied by the rebuilding of the screening cloud. One can show, that under these conditions the interaction of the exchanging couple with the near-by particles will be dominant^{1,2}.

b) $A \ll 1$. In this case transitions of the localized electron between the moving centers in the vicinity of two critical points R_{c1} and R_{c2} occur in plasma microfield with strength to depend on the velocity of ion entering the reaction. Since with the logarithmic accuracy $R_{c1} = R_{c2} = \rho_0$, we can express the energy difference between the states

$$H = q_0 \frac{\partial \Phi(\vec{r}, t)}{\partial \vec{r}} \Big|_{\vec{r}=\vec{v}_0 t} \cdot \vec{R}$$

for the critical points as

$$H(R_{c1}) = H(R_{c2}) = \frac{2q_0^2}{\pi} \sqrt{\rho_0^2 - \rho^2} \quad (2)$$

$$\cdot \int_0^1 u du \int k \operatorname{Im} \frac{I}{\epsilon(\vec{k}, k\vec{v}_0)} dk,$$

where $u = \cos(\hat{\vec{k}}, \hat{\vec{v}_0})$, ρ is the impact parameter.

The crude estimate gives us $H \sim q_0^2 \rho_0 k_d^2 \cdot L$, therefore the ratio $H/\langle H \rangle \sim 10^{-2} g^{2/3} L$ (L is Coulomb logarithm, $g = k_d^3 n^{-1}$). It follows that such plasma parameters exist where the energy difference of the quasi-molecular terms is due to the collective phenomena. Let us study this effect for se-

veral concrete conditions.

Equilibrium plasma. The response function

$$\epsilon_{eq} = 1 + \frac{k_d^2}{k^2} W\left(\frac{\omega}{k(T/m_e)^{1/2}}\right),$$

where

$$W(z) = 1 - z \exp(-z^2/2) \int_0^z dy \exp(y^2/2) + i(\pi/2)^{1/2} z \exp(-z^2/2).$$

Then

$$n = q_0^2 k_d^2 \sqrt{\rho_0^2 - \rho^2} LG(x). \quad (3)$$

Here $G(x) = (P(x) - xP'(x))/2x^2$, $P(x)$ is the integral of probability, $x = v_e/v_{Te}$.

Nonequilibrium stable plasma. Tidman-Dupree model³ for two-temperature electron gas. In this case

$$\epsilon_n(\bar{k}, \omega) = 1 + \frac{k_d^2}{k^2} \left[W\left(\frac{\omega}{k(T/m_e)^{1/2}}\right) + \frac{nT}{nT} W\left(-\frac{a\omega}{k(T/m_e)^{1/2}}\right) \right],$$

where $a = (T/T')^{1/2}$. The effective defect in this system can be written in the form

$$H_n = q_0^2 k_d^2 L \sqrt{\rho_0^2 - \rho^2} G(x) (1 + \frac{nT'}{nT} B(a, x)), \quad (4)$$

$$\text{where } B(a, x) = \frac{P(ax) - axP'(ax)}{P(x) - xP'(x)}.$$

As we can see, the magnitude of the defect is proportional to the numbers of fast particles.

Turbulent plasma. As an example of turbulent system let us consider a collisionless unmagnetized plasma with developed electrostatic turbulence. When the autocorrelation time or the field fluctuations is less than time for resonant particles to diffuse in the wave number space, the expression for a dielectric function takes a form⁴

$$\epsilon_t(\bar{k}, \omega) = 1 + \frac{k_d^2}{k^2} W(z) + \frac{k_d^4}{k^4} F(z) \cdot D, \quad (5)$$

where D is the ratio of energy density of

the random fluctuating electric field to the thermal energy density, $F(z) = W(z) \cdot (z^4 - 10z^2 + 15) + (z^2 - 7)$.

Substitution (5) into (2) gives

$$H_t = q_0^2 k_d^2 L \sqrt{\rho_0^2 - \rho^2} G(x) (1 - D \cdot B_t(x)), \quad (6)$$

where B_t is the positive functional of x .

The formula (6) follows that the random field fluctuations in turbulent plasma lead to decrease of detuning. This results from scattering of plasma electrons on the turbulent pulses reducing the test particles correlations with surroundings. In this sense an influence of fluctuations on plasma polarization properties is analogous to binary collision effects.

Let us find the plasma parameter range, where the charge-exchange process will be determined by the effect of the dynamical polarization. The adiabatic condition $H \cdot \tau \cdot \hbar^{-1} > 1$ requires the following inequality for a case of thermodynamical equilibrium

$$n > 2,6 \cdot 10^{-12} T^{3/2} \theta(x), \quad n(\text{cm}^{-3}), T(K),$$

where $\theta(x) = x G^{-1}(x)$.

This inequality together with conditions $\omega_p \tau \ll 1$, $g < 1$ restrict the plasma parameters, where this effect is possible.

References

1. Vitlina R. Z., Dyhne A. M., JETP (1973) **64**, 510.
2. Zhdahov V. P. et al., JETP (1977) **72**, 2044.
3. Tidman D., Dupree T., Phys. Fl. (1965) **8**, 1860.
4. Swami K., Sharma S., Phys. Fl. (1977) **20**, 1376.

DETERMINATION OF QUENCHING CROSS SECTION OF RESONANT Cs(6P) STATE BY CO₂ MOLECULES IN DISCHARGE IN He - CO₂ - Cs.

G.V. Naidis, V.A. Sinelshikov.

Institute of High Temperatures, U.R.S.S. Academy of Sciences, Moscow, U.S.S.R.

As molecular plasmas with alkali seedings are widely used in different devices the data on elementary processes in such plasmas are of great interest. One of the main processes in this type of plasmas which influences both energy balance and ionization balance of plasma is the collisional deactivation of resonant state of alkali atoms by molecules. In [1] a detailed review is given of experimental and theoretical data on quenching cross sections for different pairs: alkali atom + molecule. However there is no information in literature about such process for pair: cesium + carbon dioxide.

In this work the collisional deactivation cross section of resonant Cs state by CO₂ is obtained. He - CO₂ - Cs mixture was pumped with velocity $\sim 6 \cdot 10^3$ cm/sec through glass discharge tube (glow discharge current $I = 50 - 200$ mA, tube radius $R = 1.15$ cm). Partial pressures of components were $P_{\text{He}} = 20$ torr, $P_{\text{CO}_2} = 0.2 - 2$ torr. Cesium concentration N_{Cs} was changed from 10^{11} to 10^{13} cm⁻³. Because of chemical reaction between Cs and CO₂ the value of N_{Cs} is drastically changing along the discharge and so are plasma characteristics. Therefore spectral measurements were made across the discharge.

Cesium concentration in ground state was determined by total absorption of resonant cesium line $\lambda = 8521 \text{ \AA}$ ($6^2P_{3/2} - 6^2S_{1/2}$ transition), hyperfine structure was taken into account in accordance with [2]. An absolute intensity measurements of the same line were used (with account of reabsorption) for determination of the first resonant Cs(6P) state density. Simultaneously with optical measurements in the same discharge tube cross section the longitudinal electric field was measured with double electrostatic probe.

The quenching constant K was obtained from balance equation for resonant state density N_{Cs}^* . In experimental conditions convective and diffusion transfer of Cs^* and quenching of Cs^* by helium and electrons are negligible, so the balance equation is:

$$n_e N_{\text{Cs}} \langle \sigma_{e1} v_e \rangle = K \cdot N_{\text{Cs}}^* N_{\text{CO}_2} + \sum \quad (1)$$

where n_e and N_{CO_2} - densities of electrons and CO₂ molecules, $\langle \sigma_{e1} v_e \rangle$ - rate constant of Cs excitation by electrons. Term \sum contains cascades from higher Cs states and radiative deactivation of Cs^* to ground state. For determination of K the regimes were chosen where the value of \sum was less than 10% of $n_e N_{\text{Cs}} \langle \sigma_{e1} v_e \rangle$.

Radiative lifetime of Cs^* was evaluated with account of reabsorption.

The excitation rate constant $\langle \sigma_{01} v_e \rangle$ is sensitive to the form of electron energy distribution function. The use of maxwellian distribution functions for determination of $\langle \sigma_{01} v_e \rangle$ may lead to serious errors. Therefore in this work by method described in [3] electron energy distribution functions were calculated for experimental conditions. The value of $\langle \sigma_{01} v_e \rangle$ were obtained with use of excitation cross section [4]. It is worth noting that "electron temperature" $T_e = \frac{2}{3} \int_0^\infty \epsilon^{3/2} f(\epsilon) d\epsilon$ for calculated distribution functions $f(\epsilon)$ practically coincides with T_e determined from electron energy balance equation where distribution function is assumed to be maxwellian.

This coincidence was used for calculation of electron density n_e from measurements of discharge current I and electric field E . Radial distribution $n_e(r)$ was assumed to be parabolic, radial distributions $N_{\text{He}}(r)$ and $N_{\text{CO}_2}(r)$ were taken in accordance with profile of gas temperature $T(r)$. Taking into account that the main radial dependence of drift velocity V_{dr} corresponds to radial profile of gas density, for $n_e(0)$ we obtain

$$n_e(0) = \frac{I}{2TeV_{\text{dr}}(R) \int_0^R (1 - r^2/R^2) \frac{T(r)}{T(R)} dr} \quad (2)$$

where

$$V_{\text{dr}}(R) = \frac{4eE}{3\sqrt{3} T_e^{3/2} m_0} \int_0^\infty \frac{\epsilon^{3/2} \exp(-\epsilon/T_e) d\epsilon}{\nu_{\text{ea}}(\epsilon)} \quad (3)$$

e, m - charge and mass of electron, $\nu_{\text{ea}}(\epsilon)$ - transport electron - atom collision rate,

corresponding to gas density at $T(R)$. Radial profile of $T(r)$ was calculated with the help of thermal conduction equation.

From equation (1) the quenching constant K was determined, and corresponding value of quenching cross section $\sigma = 1.4 \cdot 10^{-14} \text{ cm}^2$. Square mean error of mean σ value is 7%. The measurements were made in gas temperature range 500 - 800°K. However because of the experimental error it was not possible to find temperature dependence of σ .

Radial profile of ratio $N_{\text{Cs}^*}/N_{\text{Cs}}$ which is present in equation (1) was not measured and was assumed to be uniform. This assumption led to systematic error in σ values. Estimations show that obtained value of σ may exceed true value up to 40%.

The authors are grateful to Dr. I.A. Vasilieva for helpful discussions and to V.F.Kosov for the help during the experiment.

REFERENCES

1. E.A.Andreev, E.E.Nikitin. In "Khimiya plazmy", No.3, M., Atomizdat, 1976, p.28.
2. V.A.Sinel'shikov. XIII ICPIG, Berlin, 1977, p.141.
3. A.Kh.Mnatsakanyan, G.V.Naidis. Fiz. plazmy, 2, (1976), 152.
4. S.T.Chen, A.C.Gallagher. Phys.Rev., A17, (1978), 551.

MOLECULAR DISSOCIATION ON BOMBARDMENT BY ELECTRONS OF AN ENERGY LOWER THAN THE IONIZATION POTENTIAL

I.I. Morozov, V.A. Talrose.

Institute of Chemical Physics of the Academy of Sciences of the U.S.S.R., Moscow, U.S.S.R.

One of the fundamental tasks in gas discharge is the determination of the strictly neutral dissociative elementary steps in the bombardment of molecules by low energy electrons.

Of great interest is the bombarding by electrons with energies lower than the ionization potential of the molecule, which excludes the appearance of positive ions. There is much information on generation of negative ions, but the strictly neutral ways of molecule decay are unknown.

The experimental apparatus for determination of the dependence of the relative fragmentation cross-section of gaseous products on electron energies is shown in Fig.1. The product yields of this process can also be measured by this technique.

The electron flow from filament 1 focussed by a mirror 3 bombards the gas molecules in chamber 4 through the controlling diaphragm². Some of the neutral fragments formed penetrate into chamber 7 where they are ionized by an electron beam from the second filament 8. The ions formed are extracted from the chamber by electrode 9 and focused by an electrosta-

tic lens (diaphragm 10 and 11).

With the electron energies used the positive ions do not form in the first chamber and the negative ions and electrons are trapped by grids 5 and 6. The electron current of the first chamber is modulated by a frequency of 30 Hz. The amplitude of voltage accelerating the electrons can change from 3 to 12 v and the average emission current from 50 to 300 μ A. The ionizing electron energy changes from 15 to 120 v when the 2.5 mA emission current is constant.

The modulated ion current passes from the mass analyzer to the secondary electron multiplier and is recorded by a lock-in-amplifier.

The fragmentation of C_3H_8 molecules was studied at first as it is very important for plasma chemistry. The alternating component of the ion current on modulation of the electron current in the first chamber cannot be ascribed entirely to neutral fragments. The modulated electrons in the first chamber convert some of the initial molecules to negative ions and neutral fragments and thus modulate the partial pressure of the initial gas

in the first chamber and consequently in the second. This modulation of gas density (MGD) is very weak compared to the total pressure of the gas. But its absolute value is of the same order as that for modulation of the partial pressure of neutral fragments. Fragmentation of some of the initial molecules in the first chamber results in a proportional decrease in the intensity of all mass-spectral lines of these molecules in the second chamber. Therefore MGD is synchronous and antiphase to the pressure modulation of neutral fragments. The MGD contribution to the alternating component of ion current for every mass-spectral line is proportional to the intensity of this line in an ordinary mass-spectrum. The experimental procedure was as follows: the ratio of the intensities of alternating (I_{44}^{\sim}) and direct (I_{44}^{\equiv}) ion currents in molecular propane line, m/e 44, has been determined at a fixed electron energy. This ratio was the measure of propane fragmentation in all the channels.

Fig.2 shows the relative fragmentation cross-section vs electron energy.

The fragmentation cross-section along the channel $C_3H_8 \xrightarrow{+e} C_3H_7 + H$ as a function of electron energy is given in Fig.2.1 ($\sigma_{C_3H_7}/\sigma_{fr}$ vs electron energy threshold at 5.5 eV). Comparison of the energy dependences (Fig.2.1 and 2.2) shows that C_3H_7 formation is of a resonant nature over the range 5.5-9.5 eV.

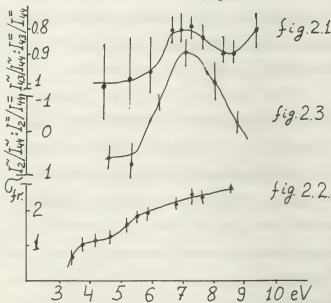
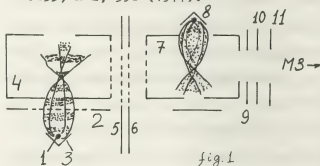
The electron energy dependence of σ_{H_2}/σ_{fr} is shown in Fig.2.3. Comparison

of the above with the energy dependence of σ_{fr} convincingly reveals that the hydrogen yield within the range 6-10 eV is of a resonant nature and its threshold is 6 eV at the maximum of 8 eV. Excitation of the triplet level with an energy of 6 eV seems to be the primary process.

The data given in the paper on propylene dissociation to neutral fragments show that dissociation occurs by excitation of triplet levels.

This technique has been used also for studying the ionization of argon metastable neutral states by electron impact at energies 20-75 eV.

1. N.I.Butkovskaya, M.N.Larichev, I.O.Leipunskii, I.I.Morozov, I.Yu.Razuvaev, V.L.Talrose, Dokl. Akad. Nauk SSSR, v.233, N 2, 398 (1977).



IONIZATION AVERAGE FREQUENCY IN ANODE SHEATH OF PENNING-TYPE HIGH-VOLTAGE DISCHARGE

N.A. Kervalishvili, V.P. Kortkhonjia.

Institute of Physics, Academy of Sciences of the Georgian SSR, Tbilisi, U.S.S.R.

Theoretical and experimental investigations of physical processes and anode sheath structure in high voltage discharge in crossed $E \perp H$ fields often require knowledge of ionization frequency dependence on anode sheath parameters. Recently, there is a lack of such data. The aim of this work was to measure the dependence of ionization average frequency on electric field strength in anode sheath.

In the "vacuum regime" in anode sheath a condition $n_i \ll n_e$ is fulfilled. The total ion current when the anode sheath thickness $d \ll \tau_a \tau_i$ is determined by the expression

$$J_i = 2\pi e l_a \int_{\tau_a}^{\tau_a + d} v_i n_e \tau d\tau = \frac{l_a \tau_a}{2} \bar{v}_i E_a$$

Hence, ionization average frequency

$$\bar{v}_i = \frac{\int_0^{\tau_a E_a} v_i d(\tau E)}{\tau_a E_a} = \frac{2 J_i}{l_a \tau_a E_a} \quad (1)$$

Electric field strength at the anode can be determined by frequency of rotational oscillations f_0 .

$$E_a = \frac{2\pi}{c} \tau_a H f_0 \quad (2)$$

where H is an external magnetic field strength.

As it is shown in [1], a fundamental mode of rotational oscillations always exists in magnetron geometry and in Pen-

ning cell in anode sheath at the anode surface.

On Fig.1 f_0 versus discharge voltage and magnetic field dependence in magnetron geometry ($\tau_a = 0.2$ cm, $l_a = 7$ cm, $\tau_c = 0.75$ cm, $p = 2 \cdot 10^{-4}$ torr, the working gas is Ar), the conditions of anode adjustment [2] are maintained. The measurement scheme is given in [1].

Ion current J_i is about 1.5 times greater than discharge current [2] and has been measured directly during the experiment.

\bar{v}_i versus φ_a is shown on the Fig. 2. As it is seen, \bar{v}_i changes approximately as square root of discharge voltage. Since values \bar{v}_i for different H and φ_a are plotted on the figure, it is possible to assume, that \bar{v}_i is proportional to the square root of potential in anode sheath.

Fig.3 illustrates \bar{v}_i versus $\frac{E_a}{H}$ dependence. For high magnetic fields, when $d \ll \tau_a$

$$\bar{v}_i \approx \frac{\int_0^{E_a} v_i(E) dE}{E_a} \quad (3)$$

It is always possible to select such dependence $v_i = f(E)$, at which \bar{v}_i calculated by (3), coincides with a measured one. I.G. in [3] an expression

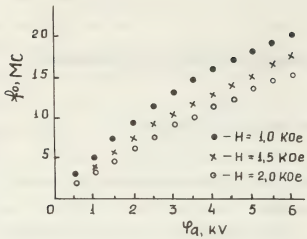


Fig.1

$$\gamma_i = \gamma_{im} \frac{2 \sqrt{\frac{W_e}{W_{e0}}}}{1 + \frac{W_e}{W_{e0}}}$$

has been used for $\gamma_i \cdot W_e =$ electron energy.

If we assume, that $T_e \ll W_e$, then

$W_e \approx \frac{mc^2}{e} \frac{E^2}{H^2}$ and we'll get

$$\gamma_i = \gamma_{im} \frac{2 \frac{E}{E_0}}{1 + \frac{E^2}{E_0^2}} \quad (4)$$

Here $E_0 = \sqrt{\frac{2W_{e0}}{mc^2}} H$

Substituting (4) into (3), we'll find

$$\bar{\gamma}_i = \gamma_{im} \frac{E_0}{E_a} \ln \left(1 + \frac{E_a^2}{E_0^2} \right)$$

This dependence for $\gamma_{im} = 1.6 \cdot 10^{-7} n_0$ and

$W_{e0} = 300 \text{ eV}$ [3] is plotted on the Fig.3 with solid line and it coincides satisfactorily with the experimental results.

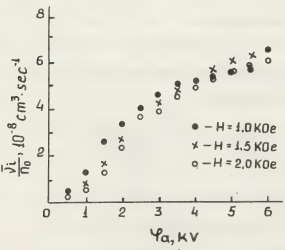


Fig.2

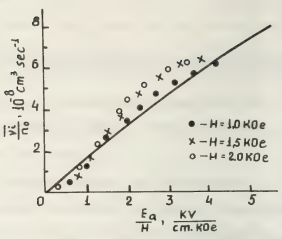


Fig.3

REFERENCES

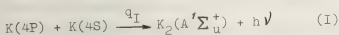
1. N.A.Kervalishvili, V.P.Kortkhonjia, XII ICPIG, part I, Lindhoven, the Netherlands, August 18-22, 1975, p.112.
2. N.A.Kervalishvili and V.P.Kortkhonjia, JIP, 42, 1905, 1973.
3. N.A.Kervalishvili, V.P.Kortkhonjia, XIII ICPIG, part II, GDR, Berlin, September 12-17, 1977, p.681.

FORMATION OF $K_2(A'\Sigma_u^+)$ MOLECULES CAUSED BY $K(4P)$ ATOMS IN POTASSIUM DISCHARGE

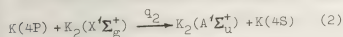
V.I. Lukashenko,

Institute of Electrodynamics, Kiev 252057, U.S.S.R.

An analysis of the generation mechanisms of the electron-excited potassium molecules $K_2(A'\Sigma_u^+)$ made in paper [1] has revealed a high efficiency of the reaction



According to [2] the collisional excitation transfer from atom to molecule may be considerable under some conditions



In present work the role of abovementioned processes in a discharge potassium plasma at medium pressures $p = (0.1 + 1.0)$ torr was investigated and the cross-sections q_1 and q_2 for reactions (1) and (2) were estimated by rather simple method.

Each of these reactions results in appearance of an electron-excited molecule in exchange for a resonant excited atom. The possibility of such "conversion" was clearly demonstrated by following experiment. A cell with potassium vapour was radiated by the resonant quanta flux from the source of special construction described previously in [1]. The total number of quanta Q absorbed by the cell and the molecular emission flux F (number of quanta emitted by the cell for second in all direc-

tions within the $A'\Sigma_u^+ - X'\Sigma_g^+$ band system) were measured. The obtained experimental dependences of F upon p are represented in Fig.1 for two magnitudes of Q .

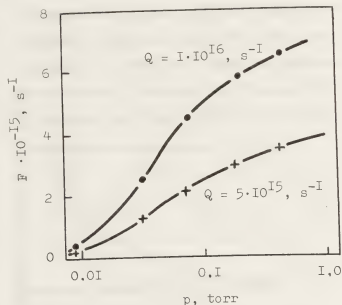


Fig.1.

The fact that at pressures $p \geq 0.3$ torr the magnitude of F exceeds the half of Q (see Fig.1) testifies to the high efficiency of the "conversion" of the $K(4P)$ atoms into the electron-excited molecules $K_2(A'\Sigma_u^+)$. The similar picture should be observed in discharge plasma, where the $K(4P)$ atoms are generated by electron impacts. To eliminate the influence of electrons upon generation and deactivation of the $K_2(A'\Sigma_u^+)$ molecules very low discharge currents ($1 + 2$) mA were used. Under these conditions

integrated over wavelength intensities of molecular band I_b and resonant lines I_l can be expressed by

$$I_b = N^* \cdot N_a \cdot q_I \cdot V_I + N^* \cdot N_m \cdot q_2 \cdot V_2 \quad (3)$$

$$I_l = N^* / \tau \quad (4)$$

Where N_a and N_m are the densities of non-excited potassium atoms and dimers, respectively [3], N^* is the concentration of the atoms K(4P), summarized over the doublet structure components, V is the relative thermal velocity of the colliding particles ($V_2/V_I \approx 0.87$), τ is the effective lifetime of potassium atom in 4P state. Experimental dependence of the magnitude I_b/I_l upon N_a is depicted in Fig.2(a).

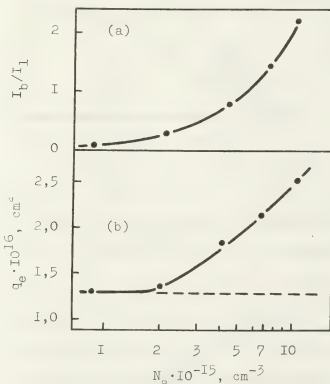


Fig.2.

As can be seen, for $N_a \geq 6 \cdot 10^{15} \text{ cm}^{-3}$ the band becomes brighter than the resonant lines and, consequently, the molecular emission becomes the main channel of the radiation loss from the discharge.

Combination of (3) and (4) gives us the expression for effective "conversion" cross-section

$$q_e = q_I \left(1 + 0.87 \frac{N_m q_2}{N_a q_I} \right) = - \frac{I_b}{I_l} \left[N_a \cdot V_I \cdot \tau \right]^{-1} \quad (5)$$

It is clear, that at low pressure, where N_m/N_a is small, q_e is equal to q_I and then it should increase with pressure due to the contribution of the process (2).

Using the data of Fig.2(a) and the value of τ for a cylindrical plasma column [4] it is easy to calculate the dependence of q_e upon N_a . The result of calculation is given in Fig.2(b). In accordance with this figure the cross-section for recombination q_I is equal to $1.3 \cdot 10^{-16} \text{ cm}^2$, that is in rather good agreement with the value $q_I = 1.6 \cdot 10^{-16} \text{ cm}^2$, obtained in paper [1]. Differences ($q_e - q_I$) in the range of $N_a \geq 5 \cdot 10^{15} \text{ cm}^{-3}$ allow us to estimate the cross section for excitation transfer q_2 .

As follows from the data of Fig.2(b) $q_2 \approx 2 \cdot 10^{-14} \text{ cm}^2$.

In conclusion it should be noted, to determine the cross-sections q_I and q_2 by described method it is required to measure the relative intensities of molecular band and resonant lines only.

References.

1. Yu. P. Korchevoi, V. I. Lukashenko, S. N. Lukashenko, *Zh. Exp. Teor. Fiz.* **75**, 846 (1978).
2. L. K. Lam et al., *J. Chem. Phys.*, **68**, 3553 (1978).
3. A. N. Nesmeyanov, *Vapour Pressure of Elements* (Academic, New York, 1963).
4. Yu. P. Korchevoi, S. N. Lukashenko, *Optica and Spectrosc.*, **43**, 826 (1977).

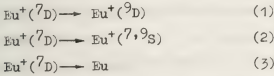
INVESTIGATION OF ANOMALOUSLY HIGH-SPEED DE-EXCITATION OF Eu^+ METASTABLE STATES
IN GAS DISCHARGE PLASMA USING MODULATION OF INDUCED RADIATION

P.A. Bokhan, V.M. Klimkin, A.N. Maltsev, V.E., Prokopiev, V.G. Sokovikov.

*The Institute of Atmospheric Optics, U.S.S.R., Academy of Sciences, Siberian Branch,
Tomsk 634055, U.S.S.R.*

1. The realization of high-speed de-excitation of metastable states is of decisive importance for excitation of continuous generation or the pulsed one with high frequency of pulse repetition in the lasers on transitions from resonance to metastable levels. The only case when quasi-continuous generation on such transitions in the ion is observed is the case of generation in Eu^+ -He mixture. In this mixture the large values of power and efficiency [1] were obtained, therefore the investigation of possible mechanisms of high-speed ($\tau \leq 10^{-7}\text{s}$) de-excitation of Eu^+ metastable states is of great interest.

2. Direct experimental study of all the processes which may determine de-excitation on ${}^7\text{D}_{1+5}$ of Eu^+ states 2 is difficult. The analysis of such processes shows that in relaxation the three paths of particle motion through excited states



are observed. Of obvious interest is the experimental determination of the particle motion path, which actually takes place, because in this case a number of reactions to be considered is much less.

In this paper the particle path was determined by the population perturbation

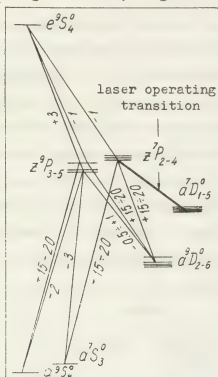
of ${}^7\text{D}_{1+5}$ Eu^+ states using transportation of particles ($\sim 20\%$ of population) from the resonance levels ${}^7\text{P}_{2+4}$, ${}^9\text{P}_5$ by stimulated emission, and by observing the response of another levels of Eu atoms and ions. In contrast to atomic spectrum the intensity modulation with the depth about $0.1\pm 20\%$ was observed on a great number of Eu ion lines. A series of the results of Eu^+ line modulation measurements is given in the table.

Table

N	Wavelength A	Transition	B, %
1	6173	${}^9\text{D}_5^0$	+13.6
2	6049	${}^9\text{D}_4^0$	+11.7
3	5966	${}^9\text{D}_3^0$	+ 6.9
4	3721	${}^9\text{S}_1$	+11.5
5	7077	${}^9\text{D}_3^0$	+ 1.15
6	7194	${}^9\text{D}_4^0$	+ 0.9
7	7370	${}^9\text{D}_5^0$	- 0.1
8	4129	${}^9\text{S}_4^0$	- 0.81
9	7217	${}^9\text{D}_2^0$	+ 0.7
10	7301	${}^9\text{D}_3^0$	+ 0.2
11	7426	${}^9\text{D}_4^0$	0
12	4205	${}^9\text{S}_4^0$	- 0.9

These results were obtained at He

pressure of 450 torr and current density $\sim 10 \text{ A/cm}^2$. The modulation coefficient $B=(J-J')/J$ where J, J' are the line intensities without generation at $\lambda=1.0019 \mu\text{m}$ and with generation of mean power 0.25 W. The simplified scheme of Eu^+ transitions, explaining the table, is given in Fig.1.



3. The results of the experiments were analyzed both qualitatively, taking into account the reabsorption effect on the intensities of spontaneous lines and lifetimes of excited states, and quantitatively, using a computer, according to the calculation procedure given in [3]. This analysis has shown:

- In this case the excitation transfer between $^9\text{P}_5$ and $^7\text{P}_{2+4}$ states occurs. The most probable transfer mechanism is the collisions of excited Eu ions with He.
- The origin of generation causes the 15-20% decrease of population of the upper operating level $^7\text{P}_4$ (and all the association of $^9\text{P}_5, ^7\text{P}_{2+4}$ levels) and 2% and 5%

increase of population of $^9\text{P}_{3,4}$ and $^9\text{D}_{1+5}$ levels, respectively.

- The reason of the $^9\text{P}_{3,4}$ populations increase is the growth of Eu^+ ground state population with activation of generation.
- Absolute values of resonance states populations are $(3+8) \cdot 10^{12} \text{ cm}^{-3}$, and those of $^9\text{D}_5$ state are $(4+7) \cdot 10^{13} \text{ cm}^{-3}$. Effective temperature of populations distribution inside the ^9D multiplet is 1100°K.

These results together with the fact of absence of modulation of spectral lines belonging to the atomic spectrum, allowed to draw a conclusion on conservation of a number of particles in considered association of levels ($^7, ^9\text{P}, ^7, ^9\text{D}, ^7, ^9\text{S}$) in the course of relaxation. It is impossible to determine the type of the path, (1) or (2), on the basis of the analysis carried out.

4. A possible mechanism of de-excitation of metastable states is, in our opinion, recombination in the displaced atomic spectrum with He with subsequent relaxation among displaced spectrum levels and with auto-ionization into the ion ground state. At present this process is not studied practically, but it is of interest not only for solving the problem of continuous generation regime on self-limiting transitions of other ions, but also for investigating processes of electron capture, recombination, analysis of particles and energy balances in ionized gases, etc.

References

- P.A.Bokhan, V.M.Klimkin, V.E.Prokopiev, S.S.Monastyrev, JETP Letters, **3**, 410, 1977.
- P.A.Bokhan, V.D.Burlakov, V.M.Klimkin, V.E.Prokopiev, The papers of 3-rd Intern. Confer. on Lasers and Applications, Dresden, GDR, 1977.
- P.A.Bokhan, A.N.Maltsev, In: Effective lasers on metal vapors, IOA SO AN SSSR, 1978, p.46

POSITIVE ION MOBILITIES IN CARBON DIOXIDE

P.A. Coxon^{*} and J.L. Moruzzi.*Department of Electrical Engineering and Electronic University of Liverpool G.B.*

Introduction - The ion drift velocities and mobilities for several positive ion species, principally in carbon dioxide, have been determined as a function of the ratio of the electric field strength to neutral particle number density E/N (Td). These measurements were made at pressures between 0.01 torr and 1 torr using a drift tube mass spectrometer which employed a secondary quadrupole mass filter to provide a mass selecting ion injection source.

Contrary to the bulk of published data on carbon dioxide, we have found that after a proper conditioning (cleaning) of the gas samples, injecting CO_2 into a drift tube containing CO_2 results in mass spectra containing only CO_2^+ and cluster ions CO_2^+CO_2 and $\text{CO}_2^+\text{CO}_2\text{CO}_2$.

Mobilities for CO_2^+ and CO_2^+CO_2 have been measured for $40 \leq E/N \leq 1400$ Td and $14 \leq E/N \leq 200$ Td respectively.

With the ion injection facility it has been possible to determine mobilities for other positive ions with ionization potentials less than that for CO_2 , in carbon dioxide :

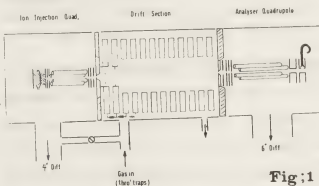
viz : O_2^+ in CO_2 : $20 \leq E/N \leq 600$ Td

NO^+ in CO_2 : $20 \leq E/N \leq 350$ Td

APPARATUS

These measurements were made on a recently constructed drift tube mass spectrometer apparatus which is represented schematically in Fig. (1). The system is unusual in that ions are not created within the drift

ION INJECTION DRIFT-TUBE (Schematic)

**Fig:1**

space, but in a separately pumped low pressure electron bombardment ionization source. After mass selection by an R.F. quadrupole mass filter the ions are injected through a small orifice into the drift tube. Injection ion energies are adjustable between 5 and 100 eV. By pulsing the source repetitive bursts of ions of known identity and with accurately defined spatial extent and temporal duration could be used for a time of flight determination of drift velocities, a histogram of arrival times being accumulated on a 1024 channel time analyser.

Drift velocities and mobilities may be determined from the mean arrival times.

RESULTS

Figure 2 shows values for the reduced mobilities K_0 for the two principal primary positive ions in carbon dioxide, namely CO_2^+ and its dimer CO_2^+CO_2 . As might be expected, the drift of CO_2^+ through CO_2 is limited by a resonant charge transfer interaction and is evidenced by the fact that the zero field mobility is

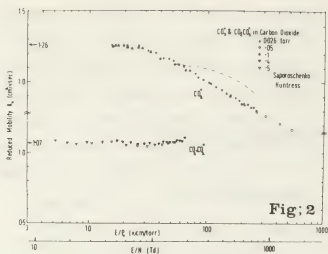


Fig. 2

considerably less than the polarization limit $1.84 \text{ cm}^2/\text{v sec.}$ and the mobility decreases with increasing ion energy. The only previous reported data for drift velocities in carbon dioxide is by Saporoschenko [1], and by Ellis, Pai, Gatland and McDaniel, and Wernlund and Cohen [2]. Saporoschenko measured mobilities for CO_2^+ and O_2^+ in CO_2 over E/P_0 range 52 to 250 v/cm torr and 20 to 250 v/cm torr respectively. However, using a glow discharge ion source he found the principal ions to be CO_2^+ , O_2^+ and O_2^+CO_2 indicating he had a considerable oxygen impurity ($\approx 100 \text{ ppm}$) which modifies the variation of mobilities with E/P .

Ellis et al studied positive and negative ion species in CO_2 but because of insufficient gas cleaning could only obtain mobilities for negative ions, the chemistry for which is uncomplicated by the presence of impurities.

Huntress [3] has determined values for the mobility of CO_2^+ in CO_2 by measuring the resonant charge transfer cross section as a function of ion energy in a pulsed ICR cell. From the cross sections he calculated ion mobilities and from the ion energy he assigned an effective E/P using the Wannier [4] equation. Although his zero field mobility is in excellent agreement with that in Fig. 1, the variation of K_0 with E/P is not. By current practice his calculation of E/P is

wrong since he used $K.E_{\text{ion}}$ instead of $K.E_{\text{cm}}$, however this does not account for the difference.

Figures 3 and 4 show the variation of ion mobility for O_2^+ and NO^+ in CO_2 with E/P . Here the interaction is probably a valence attraction since K_0 is less than K_p and both O_2^+CO_2 and NO^+CO_2 are stable, observable ion clusters.

The zero field mobilities reported here are believed to have total errors not exceeding 4%.

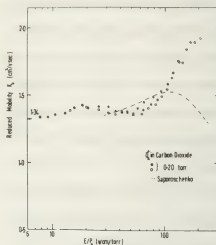
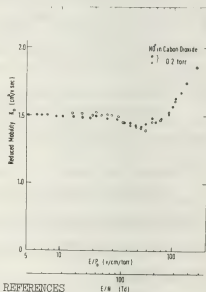


Fig. 3

Fig. 4



REFERENCES

- [1] Saporoschenko M. Phys. Rev. A., 8, 1044 (1973)
- [2] Ellis H.W., Pai R.Y., Gatland I.R., McDaniel E.W. & Wernlund R., Cohen M.J., J.Chem. Phys. 64, 3935 (1976)
- [3] Huntress W.T. J. Chem. Phys. 55, 2146 (1971)
- [4] G.H. Wannier Bell. Syst. Tech. Journal, 32, 170 (1973).

* Present address : Laboratoire d'Electricité
PAU (FRANCE)

A MODIFIED ADIABATIC THEORY CALCULATION FOR THE STARK BROADENING OF He I ($3^1P^0-2^1S$)

M.S. Dimitrijević*, P. Grujić**.

*Institute of Applied Physics, P.O. Box 24, 11001 Belgrade, Yugoslavia.

**Institute of Physics, P.O.Box 57, 11001 Belgrade, Yugoslavia.

Curvilinear trajectory adiabatic approximation for calculating Stark broadening parameters for neutral lines from plasmas, as proposed by authors,^{1,2} has been applied to HeI($3^1P^0-2^1S$) line, at $T = 5000$. K and $N_e = 10^{15} \text{ cm}^{-3}$. This line has been chosen for two reasons: (1) The quadrupole perturber-emitter interaction potential is much smaller than corresponding dipole polarization interaction, so that simple analytical calculations can be carried out; (2) Stark constant C_4 of the upper level of the transition is negative and large, so that so called defocusing effect can be distinctly demonstrated.

Within the semiclassical adiabatic theory³ half-halfwidth and shift of a line can be calculated by (we use atomic units)

$$w = 2\pi N_e \bar{v} \int_0^\infty \{1 - \cos[\eta_i(\rho) - \eta_f(\rho)]\} \rho \, d\rho$$

$$d = 2\pi N_e \bar{v} \int_0^\infty \sin[\eta_f(\rho) - \eta_i(\rho)] \cdot \rho \, d\rho$$

where N_e is the electron density, \bar{v} is the mean electron velocity, $\eta_i(\eta_f)$ is the phase shift for the elastic scattering on the initial (final) state of target atom and ρ is an impact parameter of the perturber. Phase shift $\eta(\rho)$ is evaluated along a corresponding curvilinear path,² as determined by motion of the impact electron in the long-range potential of the emitter.

In our particular case we retain only the polarization potential

$$V_P = -C_4/r^4, \quad C_4(3^1P^0) = -5.275 \cdot 10^4 \text{ au}$$

in which case one obtains for the phase shift²

$$\eta(\rho) = \xi(\tilde{\rho}) \cdot \eta^{(0)}, \quad \tilde{\rho} = (\rho/\rho_C)^4, \quad \rho_C = (-4C_4/E)^{1/4}$$

where the universal function $\xi(\tilde{\rho})$ is given by

$$\xi = \frac{16}{\pi} \tilde{\rho} \sqrt{\beta} \{E(\gamma) - \frac{8+1}{2\beta} K(\gamma)\}, \quad \beta^2 = 1 + 1/\tilde{\rho}, \quad \gamma^2 = (\beta - 1)/2\tilde{\rho}$$

E being (average) electron energy and $K(\gamma)$ $E(\gamma)$ are the elliptic integrals of first and second kind, respectively. $\eta^{(0)}$ is the usual "straight-line trajectory phase shift".³

In Figure 1 we have plotted $\eta^{(0)}$ and η for the upper level of the transition. Since the lower level Stark constant $C_4(2^1S) = 400.97 \text{ au}$ is much smaller than the absolute value of the same constant of the upper level, we neglect $\eta_f(\rho)$ in the expressions for w and d . As can be seen from Figure 1, defocusing effect of the strongly repulsive potential V_P gives rise to drastic change of behaviour of $\eta(\rho)$ at small and medium values of the impact parameter.

Evaluation of w and d has been carried out numerically, and results are

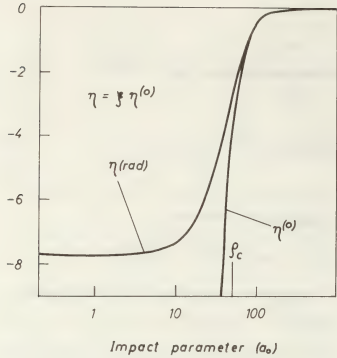


Figure 1. Semiclassical phase shifts for e - He I(3¹P) scattering, at E_e= 0.431 eV.

presented in Table 1, together with corresponding data from Griem (1974).⁴ Since in low-density plasmas Stark parameters depend practically linearly on N, it is evident from Table 1 that the defocusing effect reduces w by 12%, whereas the shift has been increased by approximately 30%.

Table 1. Half-halfwidth and shift of He I (3¹P-2¹S) line, λ = 5017 Å, multiplet 4.

	N(cm ⁻³)	T(K)	w(Å)	d(Å)
Present calc.	10 ¹⁵	5000	0.0321	-0.0361
Griem	10 ¹⁶	5000	0.3667	-0.250

As is well known,³ the very usage of the adiabatic approximation is justified if ω_{ij}⁻¹ << τ, where j corresponds to any perturbing level and τ is the collision time. If we define the latter as time

spent inside the sphere with radius R = 1.123·ρ_D, one has as an estimate for ρ=0: τ ≈ 4·10⁴ au, whereas ω⁻¹(3¹P-3¹D) ≈ 2.1·10³ au. The same holds for other impact parameters not too close to R.²

At higher temperatures inelastic collisions can not be ignored and the effect of back reaction is less prominent,⁵ as oposite to the low-temperature limit, where this effect may become dominant.¹

We conclude that, whenever there is a very close perturbing level below the upper level of the transition, defocusing effect may be noticeable at low temperatures and should be taken into account.

We are grateful to RZN of SR Serbia for the financial support.

References

1. M.S.Dimitrijević and P.V.Grujić, ESCAMPIG 1978, Essen, p. C44.
2. M.S.Dimitrijević and P.V.Grujić, to be published.
3. H.van Regemorter, 1972, in Atoms and Molecules in Astrophysics, Academic Press
4. H.R.Griem, 1974, Spectral Line Broadening by Plasmas, Academic Press, New York
5. M.S.Dimitrijević and P.Grujić, 1978, J.Q.S.R.T., 19, 407

EXCITATION OF MAGNESIUM ATOMS IN HOLLOW CATHODE DISCHARGE

F.Kh. Kidrasov.

Bashkirian State Pedagogical Institute, Ufa, U.S.S.R.

In this paper magnesium atoms triplet $k = 3^3P_0, 3^3P_1, 3^3P_2; m = 3^1P_1$. 3^3P_{012} and 4^3S_1 states excitation mechanism investigation results are presented.

The experiments were carried out at helium pressure of 0.65 Torr and discharge current ranging within 20 - 50 mA. The discharge tube construction, data of electrokinetic, spectrally-optic parameters of magnesium hollow cathode discharge filled with argon and helium were given in / 1,2 /.

Mg atoms 3^3P_{012} states considered as one state were established to be populated under our experimental conditions mainly through direct electron excitation but dominant mechanism of their decay was the stepwise transitions to 3^1P_1 resonance level and metastable states death on tube walls due to the diffusion.

Consequently for 3^3P_{012} states the balance equation can be put down as

$$\sum_k \alpha_{ok} = \sum_k (\alpha_{km} + \beta_k), \quad (1)$$

where α_{ok} is direct electron excitation rate;

α_{km} is stepwise transitions rate;

β_k is the diffusion metastable atoms escape rate.

The sum in the equation (1) means the rates one of three considered states:

The direct electron excitation rate

$$\alpha_{ok} = \frac{1}{\sqrt{2e}} \frac{1}{l_0} \bar{n}_0 \sum_j n_{ej} \int_{V_{ok}}^{\infty} Q_{ok}(V) \frac{v i_j^2(V) dV}{\int_0^{\infty} i_j^2(V) \sqrt{V} dV} \Delta l_j, \quad (2)$$

where \bar{n}_0 - averaged along the length of source ground state concentration of Mg atoms;

n_{ej} - electron concentration in the point j along the axis;

$Q_{ok}(V)$ - the direct excitation cross-section of the level k ;

Δl_j - the distance between two points j along the axis in which the second derivative curves $i_j^2(V)$ of electron current to the probe are measured.

The α_{ok} values were evaluated by using of tight-binding approximation cross-section / 3 /. Energy dependence of $Q_{ok}(V)$ to a range of greater energies was approximated by one of intercombination $\lambda = 4571 \text{ \AA}$ ($3^1S_0 - 3^3P_1$) line / 4 /. The concentration \bar{n}_0 of Mg atoms in ground state necessary for the calculation of α_{ok} is determined from self-reversed resonance $\lambda = 2852 \text{ \AA}$ ($3^1S_0 - 3^1P_1$) spectral line profile by method of / 5 /.

The stepwise transitions rate α_{km} is calculated according to the similar to (1) equation in which \bar{n}_0 is replaced

by \bar{n}_k - concentration of Mg atoms in level k , $Q_{ok}(V)$ by $Q_{km}(V)$ - a stepwise excitation cross-section and V_{ok} by $V_{km} = V_m - V_k$ - energy of transition. The stepwise excitation cross-section is obtained from Gryzinski's formula / 6 /. The concentrations of Mg atoms in 3^3P_0 , 3^3P_1 and 3^3P_2 states were determined from data of 5167, 5173 and 5184 Å lines reabsorption measurements.

The diffusion metastable atoms escape rate is

$$\beta_k = \bar{n}_k W, \quad (3)$$

where metastable states decay probability W is calculated according to the kinetic theory of gas.

The separate members of equation (1) calculation results are given in Table 1.

Table 1
The members of the balance equation (1), $10^{14} \text{ cm}^{-3} \text{ s}^{-1}$

$i, \text{ mÅ}$	$\sum_k \alpha_{ok}$	$\sum_k \beta_k$	$\sum_k \alpha_{km}$	$\sum (\beta_k + \alpha_{km})$
20	7,5	1,2	12,1	13,3
30	42,0	3,1	41,3	44,4
35	52,5	5,6	71,0	76,6
40	126,0	8,2	92,2	100,4
45	186,0	17,2	196,5	213,7
50	485,0	31,6	388,1	419,7

As it is seen from Table 1 the considered processes of population and depopulation of Mg 3^3P_{012} states take place under the conditions of our experiment, however one may remark the decay going mainly due to the transitions to 3^1P_1 resonance level.

The calculations showed that main mechanism of Mg 4^3S_1 level population is also direct electron excitation but the

depopulation takes place at the $4^3S_1 - 3^3P_{012}$ spontaneous transitions, i.e. the balance equation for $i = 4^3S_1$ may be written as

$$\alpha_{oi} = \sum_k N_{ik}, \quad (4)$$

where $k = 3^3P_0, 3^3P_1, 3^3P_2$, N_{ik} is the $4^3S_1 - 3^3P_{012}$ spontaneous transitions rate.

Table 2
The members of the balance equation (4), $10^{13} \text{ cm}^{-3} \text{ s}^{-1}$

$i, \text{ mÅ}$	N_{ik}			$\sum_k N_{ik}$
	$4^3S_1 - 3^3P_0$ 5167 Å	$4^3S_1 - 3^3P_1$ 5173 Å	$4^3S_1 - 3^3P_2$ 5184 Å	
20	8,4	1,0	3,1	4,5
30	35,4	3,5	9,3	15,4
35	46,8	5,2	15,7	24,0
40	87,5	10,8	24,2	40,4
45	119,4	17,3	50,0	79,0
50	283,1	37,6	106,0	166,0

In Table 2 one can see the results of calculations according to (4) with the use of our experimental electron energy distribution functions and data of cross-sections / 4 /. The spontaneous transitions rates N_{ik} were obtained from = 5167, 5173, 5184 Å ($4^3S_1 - 3^3P_{012}$) spectral lines absolute intensities measurements.

The balance of Mg 4^3S_1 state atoms under the investigated experimental conditions also holds good (Table 2).

REFERENCES

1. Kidrasov F.Kh., Devyatov A.M., Volkova L.M., Arkhipova L.V. XI ICPIG, Prague, 1973, 119.
2. Kidrasov F.Kh., Devyatov A.M., Volkova L.M. TBT, 12, 688, 1974.
3. Fabrikant I.I. J. Phys., B7, 91, 1974.
4. Алексанин И.С. и др. Оптика и спектр., 34, 1053, 1973.
5. Kidrasov F.Kh. VII Nat. Conf. on Spectr. with Foreigner guests Participation. Slantchev Bryag, Sept. 25-29, 1976, p. 56.
6. Gryzinski M. Phys. Rev., 115, 374, 1959; 138, 305, 322, 336, 1965.

II

- Décharges à basse pression
Low pressure discharges
- Colonnes positives
Positive columns
- Ondes d'ionisation et instabilités
Ionization waves and instabilities
- Lueur négative, décharges à cathode creuse
Negative glow, hollow cathode discharges
- Décharges à haute fréquence
Radiofrequency discharges
- Décharge de Townsend, claquage et décharges en impulsion
Townsend discharge, breakdown and pulse discharges

EXPERIMENTAL INVESTIGATION OF RADIO-FREQUENCY DISCHARGE IN HELIUM

V.A. Godyak, A.S. Kanneh.

Moscow State University, Department of Physics, Moscow, U.S.S.R.

In paper / 1 / it was noted that an increase in RF discharge voltage brought about a qualitative change in the discharge and in the discharge luminosity. In / 2,3 / it was shown that this change in regime (from α to γ) was accompanied by a sharp increase in the discharge current.

Given below are the results of the experimental investigation of plasma parameters and volt-ampere characteristics of RF discharge over a range of external conditions under which both regimes of discharge were realized. Measurements were carried out in a Helium filled cylindrical tube of radius $R = 3\text{cm}$ with two plane titanium electrodes placed inside it 7.7cm apart. The electron temperature V_e and the plasma density n were obtained from the electron branch of the volt-ampere curve of the Langmuir probe / 4 /. In calculating n the finiteness of the ratio of the probe radius ($r_p = 5 \cdot 10^{-3}\text{cm}$) to the electron mean free path was taken into account / 5 /. The discharge current was measured using a Rogovsky's coil. On increasing the discharge voltage to a critical point $V_w = V_{\gamma}$ which depends on the gas pressure P and the frequency f , a redistribution of discharge luminosity was observed. For voltages $V_w < V_{\gamma}$ (α -regime) over the range of values of V_w investigated, the axial distribution of plasma density $n(x)$ is constant, except near the boundary where it sharply decreases (Fig.1). The electron temperature was close to the temperature of the plasma in the positive column of the direct-current discharge, taking values between 6-3V depending on the pressure. The fact that

$n(x)$ here differs from the Shottky's distribution can be explained according to / 6 / by the fact that the electric field in plasma and thus the ionization frequency are functions of the x -co-ordinate. For $V_w > V_{\gamma}$ (γ -regime) the axial distribution of plasma density at pressures more than 1 torr showed a maximum near the boundary (Fig.1). If the pressure increased the maximum was observed to move towards the boundary, while its value increased and at $P = 6\text{ torr}$ the value of maximum was about 20. On going from α to the γ -regime, the electron temperature dropped to a fraction of its former value between 1.5 and 0.5V depending on the pressure (Fig.2).

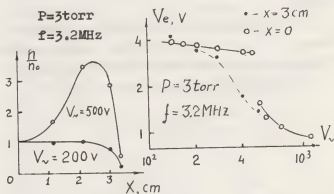


Fig.1

Fig.2

The observed changes are in accordance with the hypothesis put forward in / 1 /, according to which when V_w is large enough ($V_w > V_{\gamma}$) physical processes on the electrode and in the sheath are similar to those in the cathode fall region of the glow discharge. In this case gas ionization is mainly brought about the beam of high energy electrons injected from the sheath / 7 /. The plasma density attains a maximum near the boundary (as result of damping

of the beam) and the electron temperature is relatively low as in a non-autonomous discharge. The experimental values of the plasma density at the center n_e and the discharge current I_p , I_f are plotted in Fig. 3, 4 and 5. It can be seen here that these curves are different for α and γ -regimes. The perpendicular lines in Fig. 3, 4 show the voltage $V_{\alpha\gamma}$.

In the α -discharge, when V_{α} is not too low: $n \sim V_{\alpha} f^2$; $I_p \sim V_{\alpha}$ and decreases with increase in pressure and $I_f \sim V_{\alpha} f$.

In the γ -discharge $n(f)$, $I_p(p)$ and $I_f(f)$ practically cease to depend on their respective variables. The sharp increase of I noted in / 2, 3 / is seen here when P is large enough and f is small. According to / 7 / this takes place when the crossing over to γ -regime leads to large decrease of the sheath thickness and thus to a decrease in the discharge impedance. $V_{\alpha\gamma}$ as a function of gas pressure is shown on Fig. 6. It is seen here that this pressure dependence is similar to that of the cathode fall in the glow discharge; the minimum value of $V_{\alpha\gamma}$ is close to the normal cathode fall.

The behavior of the discharge parameters V_e , n , I and $V_{\alpha\gamma}$ agrees qualitatively with the theoretical analysis of γ -discharge carried out in / 7 /.

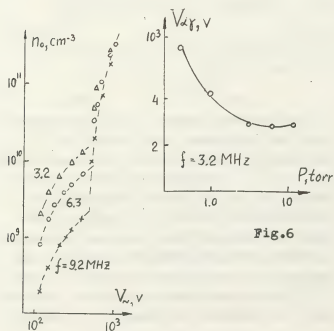


Fig. 6

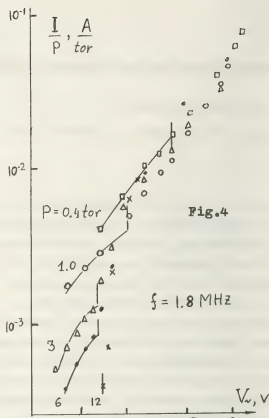
Fig. 3 ($P=3$ torr)

Fig. 4

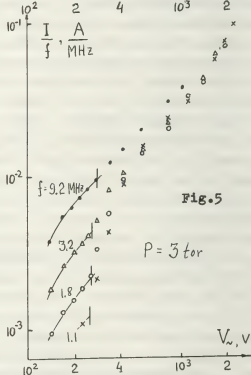


Fig. 5

1. С.М. Левитский, ЖТФ, 27, 970, 1957.
2. Г.Н. Застенкер и др., Радиотехника и электроника, 5, 1709, 1960.
3. Н.Я. Яценко, Тр. МФТИ, сер. Общ. и молек. физика, 160, 1978.
4. V.A. Godjak & all, Proc. XII Int. Conf. Phenom. Ioniz. Gases, 109, Eindhoven, 1975.
5. В.М. Захарова и др., ЖТФ, 30, 442, 1960.
6. W.P. Allis & all, Phys. Rev., 84, 519, 1951
7. Author's report in this conference.

THE COMPOSITION OF THE POSITIVE COLUMN OF A HELIUM GLOW DISCHARGE AT INTERMEDIATE PRESSURES

F. Dothan and Yu. M. Kagan

Racah Institute of Physics, The Hebrew University of Jerusalem, Jerusalem Israel.

The concentration of atomic and molecular ions and metastables is investigated for the positive column of a helium glow discharge. Recently (1,2) the system of differential equations for the helium afterglow describing the time change of these plasma parameters was written and solved. In the stationary positive column we can neglect some processes which are important in the afterglow. On the other side we must take into account processes of excitation and ionization by electron collisions which can be neglected in the afterglow.

4 equations for the concentration of the atomic and molecular ions n_1 and n_2 and metastables M_1 and M_2 on the axis of the cylindrical positive column can be written. For conditions of pressure p between 5 and 60 Torr, electron concentration n_e between 10^{10} - 10^{12} cm $^{-3}$ and electron temperature T_e between 10^4 - $4 \cdot 10^4$ OK (3), the equations can be simplified and written in the following form:

$$\alpha_{11} M_1 n_e + \frac{1}{2} X_{11} \beta_{11} M_1^2 = \left(\frac{1}{\tau_1} + \gamma N^2 \right) n_1 \quad (1)$$

$$\frac{1}{2} (1 - X_{11}) \beta_{11} M_1^2 + \gamma N^2 n_1 = \frac{1}{\tau_2} n_2 \quad (2)$$

$$d_1 \beta = \left(\frac{1}{\tau_1} n_1 + \delta N^2 + d_{11} n_e \right) M_1 + \beta_{11} M_1^2 \quad (3)$$

$$M_1 \delta N^2 = \left(\frac{1}{\tau_2} n_2 + \frac{1}{2} \beta_{12} M_1 + X_{12} n_e + d_{21} n_e \right) M_2 \quad (4)$$

These equations are balance equations for creation and disappearance of the four species per unit time and unit volume on the tube axis. In these equations d_{11} and d_{21} are the coefficients of step ionization by collisions of atomic and molecular metastables with electrons. $d_1 \beta$ gives the number of excitation of the atomic metastable level 2^3S from the ground state. γ and δ are the coefficients of conversion of atomic ions into molecular ions and atomic metastables into molecular metastables by collisions with two atoms in the ground state. $\frac{1}{\tau_1}$, $\frac{1}{\tau_2}$, $\frac{1}{\tau_{M_1}}$, $\frac{1}{\tau_{M_2}}$ are the times of diffusion of the various particles to the wall.

δ_1 is the coefficient of the collision of the second kind between molecular metastables and electrons. $\frac{1}{2} \beta_{11}$ is the coefficient of ionization by collisions between two atomic metastables; X_{11} and

$1 - X_{11}$ are proportions of atomic and molecular ions which appear by such collisions. $\frac{1}{2} \beta_{11}$ is the coefficient of ionization by collisions between atomic and molecular metastables. The coefficients X_{11} , β_{11} , β_{12} , τ_1 , τ_2 , τ_{M_1} , τ_{M_2} , δ and δ_1 are known from afterglow conditions (1,2). We must however take into account the dependence of these coefficients from T_e and gas temperature T .

To calculate the coefficients of step ionization and the number of excitations of the atomic metastable level 2^3S we need the electron energy distribution function $f_e(\epsilon)$ in the positive column of helium at intermediate pressures. For this purpose we solve the Boltzmann equation in two regions: region I where $\epsilon < \epsilon_1$ (ϵ_1 excitation energy of the first level 2^3S) and region II where $\epsilon > \epsilon_1$. The results show (3,4) that the distribution in region I is near Maxwellian with a temperature T_e while in region II it decreases much faster than a Maxwellian distribution (Figure 1).

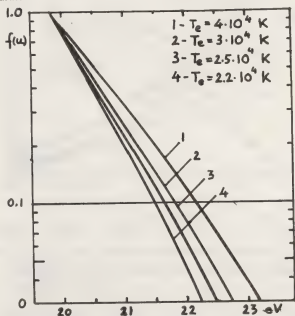


Fig.1 Electron energy distribution function for energies above 19.8 eV

Therefore for the calculation of the coefficients of step ionization d_{11} and d_{21} we used a Maxwellian distribution with the temperature T_e . For the

cross-section of stepionization we used the formula of Drawin ⁽⁵⁾. For the calculation of the number of excitations of the metastable level 2^3S from the ground state we took into account the fast decrease of the distribution function at energies $E > E_1$, and proved that it is possible to replace the number of direct excitations of the metastable level 2^3S by the quantity $d-\beta$, i.e. the difference between the total number of inelastic collisions of the first and second kind. This quantity is connected with the total cross-section of inelastic collisions and was calculated directly from the kinetic equation ⁽³⁾. For helium the calculation gives

$$d-\beta = \frac{4}{\sqrt{\pi}} n_e v_{ee} (1+\gamma u_1)^{3/2} \frac{2a-1}{2a+1} e^{-u_1} \quad (5)$$

where $u_1 = \frac{E_1}{kT_e}$; $\gamma = \frac{m v}{M v_{ee}}$; $Q^2 = \frac{q_0 u_1 N \left(\frac{2kT_e}{m} \right)^{3/2}}{2 v_{ee} (1+\gamma u_1)^{3/2}}$

v and v_{ee} are the frequencies of electron elastic collisions with atoms and of electron-electron collisions, respectively; $q_0 = 2.8 \cdot 10^{-18} \text{ cm}^2$. Some results of the solution of the equations (1)-(4) for a tube of radius $R = 1.2 \text{ cm}$. are given in the figures 2 and 3.

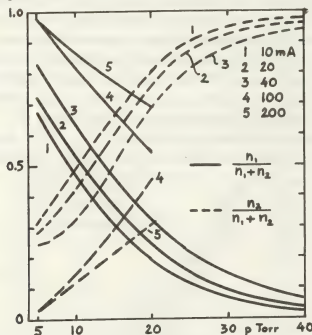


Fig.2 Proportion of atomic (n_1) and molecular ions (n_2) vs. pressure.

From Fig 2 we see that the relative number of atomic ions is maximal at the gas pressure $p=5$ Torr, increases with current and decreases with pressure. At the pressure $p=5$ Torr and currents $i \geq 100 \text{ mA}$ all ions are practically atomic ions. Even at the lowest current ($i=10 \text{ mA}$), at the pressure $p=5$ Torr, 67% of ions are atomic ions. The proportion of molecular ions decreases with current and increases with pressure. At the pressure $p=40$ Torr,

and currents $i \leq 40 \text{ mA}$ practically all ions are molecular. Their calculated concentration at $i=10 \text{ mA}$ and $p=40$ Torr is $n_2 = 7 \cdot 10^8 \text{ cm}^{-3}$. As shown in figure 3 the concentration of the atomic metastable decreases with pressure. The dependence of the concentration of the atomic metastable on the current is weak. The concentration of molecular metastables increases with pressure and decreases with current. At $i=10 \text{ mA}$ and $p=40$ Torr the concentration of molecular metastables is $M_2 = 8 \cdot 10^{10} \text{ cm}^{-3}$.

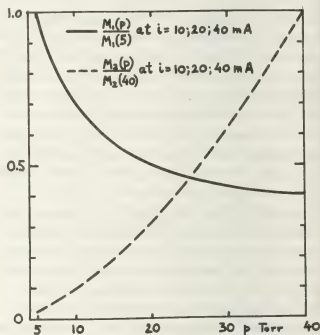


Fig.3 Normalized concentrations of atomic metastables (M_1) and molecular metastables (M_2) as a function of pressure.

References

1. R. Deloche, P. Monchicourt, M. Cheret and F. Lambert
Phys. Rev A, **13**, 1140, (1976)
2. Yu.M. Kagan, J. Phys.D (in print)
3. Yu.M. Kagan, R.J. Lyagushchenko, N. Khristov
Sov. Phys.-Techn.Phys **16**,1627,(1972)
4. Yu.B. Golubovskij, Yu.M. Kagan,R.J. Lyagushchenko
Sov. Phys.-Techn. Phys **13**,1553,(1969)
5. H.W. Drawin, Zeit. f. Phys. **164**, 513, (1961)

POPULATION DENSITIES OF TRIPLET EXCITED STATES IN A DIFFUSE NITROGEN PLASMA*

A. Ashraf, U.K. Roychowdhury† and P.K. Ghosh.

Department of Chemistry, Indian Institute of Technology Kanpur, Kanpur 208016 India.

Recently there has been much activity on line emission studies from nitrogen plasmas (1-5), primarily due to their relevance in understanding of upper atmospheric emission. But hitherto there has been little experimental work which investigates the nature of quantitative correlation between the population densities of excited states in laboratory nitrogen plasmas and cross sections of relevant electron impact processes. However, such investigations to be amenable to quantitative correlations with atomic processes, values of plasma parameters must directly be known. This is not available from earlier laboratory plasma experiments. Here we report the results of an experiment in which *in situ* measurements of electron densities (n_e) and electron temperatures (T_e) were carried out besides vibronic and rotational transition intensities from a nitrogen plasma.

Experiments were conducted at a pressure of 5 microns in a 90 cm long 2.5 cm diameter stainless steel tube and the plasma sustained by electrons injected from one end of the tube, at plasma currents (I_p) of 0.5, 1 and 2 amps. The plasma was immersed in a longitudinal magnetic field ($B=0-700$ gauss). Variation of the magnetic field resulted in a coupled variation of n_e and T_e measured at the centre of the plasma column by means of a Langmuir probe. Results of these measurements are shown in Fig. 1. The radiation from the axial region of the plasma column was taken to a 2.1/6.3 meter spectrograph (first order dispersion 3.4A per mm/1.12A per mm) through a set of angle limiting baffles. Relative intensities from the $N_2 C^3\Pi_u$ state (second positive system SPS) were measured. A typical vibrational temperature T_{vib} plot and vibrational temperatures determined from band head intensities in the n_e , T_e range of the experiment are shown in Fig.2 and Table 1 respectively. For all the SPS bands, T_{vib} increases with increase of B . In general, at a given B , it increases with I_p .

High resolution rotational spectra of SPS vibronic bands (1,0), (0,2) were photographed in 3rd order of the 6.3 meter mode of the spectrograph, and relative intensities

measured using a microdensitometer. Rotational temperatures of the ground vibrational state at $I_p=1$ amp are shown in Table 2.

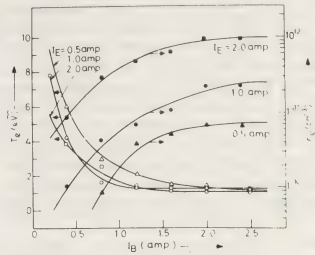


Fig.1 Plasma parameters in the magnetic field (I_p =magnet current; $B=280$ gauss/amp of I_p)

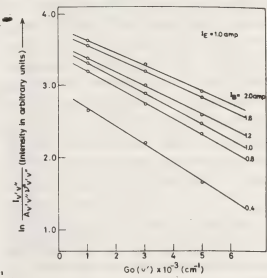


Fig.2.Vibrational temperature plot from the $N_2(0-2)$ band sequence of the Second Positive System

Table 1. Vibrational Temperatures of the $C^3\Pi_u$ state from the (0-2) sequence of the Second Positive System

I_p (amp)	I_B (amp)	0.4	0.8	1.0
0.5		4390±200	4990±300	5625±350
1.0		5660±200	6480±100	6810±100
	1.2		1.6	2.0
0.5		6260±350	6230±350	6600±250
1.0		7450±150	7760±100	8330±250

Table 2. Rotational Temperatures of the Ground Vibrational state of $C^3\Pi_u$

I_B (amp)	0.5	1.0	1.5	2.0
R_0	620±20	655±20	680±20	610±20
R_1	615±20	690±20	720±20	600±20
R_2	620±20	695±20	745±20	620±20

In the following sections we show the role of various processes in the total cross section by choosing the example of the B state, and also report results of calculations of population densities of the N_2 triplet excited states.

The total cross section of the $B^3\Pi_g$ is shown in Fig.3 for the vibrational levels $v=0-11$ with electron energy as a parameter. The cross sections are evaluated using the method from (6) and using the processes: electron impact excitation $X^1\Sigma_g^+(v''=0) \rightarrow B^3\Pi_g(v'=0-11)$, cascade processes $C^3\Pi_u \rightarrow B^3\Pi_g$, $B^1\Sigma_u^- \rightarrow B^3\Pi_g$, $W^3\Delta_u \rightarrow B^3\Pi_g$ and $A^3\Sigma_u^+ \rightarrow B^3\Pi_g$ intersystem cascade. One notes a strong dependence of the cross section on the electron energy for the lower vibrational states, unlike the higher ones. Enhanced population densities are observed beyond the $v=9$ level. Direct electron impact excitation from the ground state, $C^3\Pi_u \rightarrow B^3\Pi_g$, as well as $B^1\Sigma_u^- \rightarrow B^3\Pi_g$ contribution decrease with increasing vibrational quantum number of the $B^3\Pi_g$ state, and $W^3\Delta_u \rightarrow B^3\Pi_g$ contribution is negligible. It is the $A^3\Sigma_u^+ \rightarrow B^3\Pi_g$ intersystem cascading which increases with the vibrational quantum number of the $B^3\Pi_g$ state and accounts for increased population densities of the $B^3\Pi_g$ vibrational states beyond $v=9$. Fig.4 shows the partial contributions to the $B^3\Pi_g(v=2)$ state which has the highest Franck-Condon factor with respect to the ground state.

The collisional-radiative model used in calculation of population densities of triplet states involves the following: the ground vibrational state $v=0$ of the $X^1\Sigma_g^+$ state, vibrational levels 0-11 of $A^3\Sigma_u^+$, $v=0-12$ of $B^3\Pi_g$, $v=0-7$ of $W^3\Delta_u$, $v=0-12$ of $B^1\Sigma_u^-$ and $v=0-3$ of $C^3\Pi_u$. The following electron impact processes are considered: $X^1\Sigma_g^+ \rightarrow A^3\Sigma_u^+$, $B^3\Pi_g$, $C^3\Pi_u$, $W^3\Delta_u$, $B^1\Sigma_u^-$, radiative transitions $C^3\Pi_u \rightarrow B^3\Pi_g$, $B^3\Pi_g \rightarrow A^3\Sigma_u^+$, $B^1\Sigma_u^- \rightarrow B^3\Pi_g$, $W^3\Delta_u \rightarrow B^3\Pi_g$, and $A^3\Sigma_u^+ \rightarrow X^1\Sigma_g^+$ besides intersystem cascades $B^3\Pi_g \rightarrow B^1\Sigma_u^-$, $A^3\Sigma_u^+ \rightarrow B^3\Pi_g$, $B^3\Pi_g \rightarrow W^3\Delta_u$. The total electron impact cross sections are from (7), the method of obtaining vibrational cross sections from electronic state cross sections is from (6), and the Franck-Condon factors of various states are from (6,8,9), and transition probabilities from (10-12). The population densities calculated numerically using steady state condition, Maxwellian velocity distribution of electrons, and a constraint that the sum of population densities of all the states is equal to $1.6 \times 10^{14} \text{ cm}^{-3}$, are shown in Fig.5. It will be noted that the C state vibrational levels do not thermalize, in variance with experimental results.

References

1. F.Cramarossa et al, JQSRT 14, 419 (1974)
2. A.M.Bouchoux et al, JQSRT 16, 451 (1976)
3. J.C.Georges, J.Phys.B 9, 2153 (1976)
4. D.C.Cartwright, J.Geophys.Res. 83, 517 (1978)
5. D.C.Cartwright, J.Appl.Phys. 49, 3855 (1978)
6. W.L.Borst et al, J.Chem.Phys. 59, 5830 (1973)
7. D.C.Cartwright et al, Phys.Rev.A 16, 1041 (1977)
8. K.A.Saum et al, Phys.Rev.A 2, 1655 (1970)
9. W.Benesch et al, Ap.J. 143, 236 (1966)
10. R.Covey et al, J.O.S.A. 63, 592 (1973)
11. D.E.Shemansky et al, JQSRT 11, 1385 (1971)
12. D.E.Shemansky, J.Chem.Phys. 51, 689 (1969)

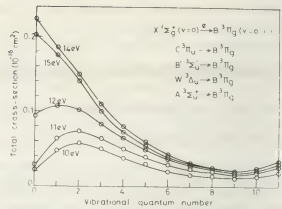


Fig.3 Total cross section of $B^3\Pi_g$

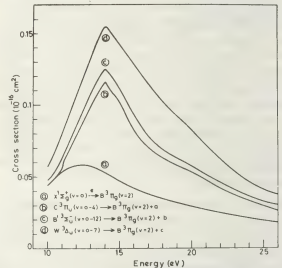


Fig.4 Partial contributions to $B^3\Pi_g(v=2)$

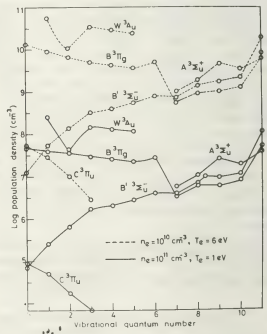


Fig.5 Population densities of N_2 triplet states for total particle density $1.6 \times 10^{14} \text{ cm}^{-3}$

* Supported by the Dept. of Atomic Energy
+ Present Address: Dept. of Chemistry,
Western Illinois University, Macomb, IL, U.S.A.

COMPARISON BETWEEN SOME MACROSCOPIC PROPERTIES OF THE BEAM AND GLOW DISCHARGE PLASMA IN NITROGEN

R. Winkler*, J. Wilhelm*, A.A. Ivanov**, V.V. Starykh**.

*Central Institute of Electron Physics Part V, Academy of Science 22 Greifswald G.D.R.
** I.V. Kurchatov Institute of Atomic Energy Moscow, U.S.S.R.

Introduction: Especially from the point of view that discharge plasma devices are being used for plasmachemical purposes it is of great interest to have sufficient knowledge, based on kinetic theory, about the behaviour of plasmas in selected molecular gases. In particular it is important to obtain information on the prevailing energy channels through which the energy, given to the electrons by different kinds of electric field, is dissipated into the several degrees of freedom of the heavy components. In this paper we calculated the electron distribution functions for the beam and glow discharge plasma in N_2 and compared important macroscopic quantities, determined by these functions, under the condition of equal power inputs per volume unit.

Kinetic equations and energy balances: We started from suitable Boltzmann equations with additional Fokker-Planck terms for the Coulomb interaction. Using the usual development of the Boltzmann equation we finally got the equations /2/

$$\left[H_{\delta} + \frac{2}{3} S_{\delta} \left(\int_0^{\hat{U}} \hat{f}_{\delta}(\hat{U}) d\hat{U} + U^{\frac{2}{3}} \int_0^{\hat{U}} \hat{f}_{\delta}(\hat{U}) d\hat{U} \right) \right] \frac{d\hat{f}_{\delta}}{d\hat{U}} + \left[6 \frac{m}{M} U^2 Q_d + S_{\delta} \left(1 - \int_0^{\hat{U}} \hat{U}^4 \hat{f}_{\delta}(\hat{U}) d\hat{U} + \frac{m}{M} \right) \right] \hat{f}_{\delta} + 3 \sum_{\mu=1}^K \int_0^{\hat{U}} \hat{U} \hat{f}_{\mu}^{in}(\hat{U}) \hat{f}_{\delta}(\hat{U}) d\hat{U} = 0 \quad (1)$$

($\delta = b$ - beam and $\delta = g$ - glow discharge plasma) for the isotropic part $f_{\delta}(U)$ of the distribution function with

$$H_b = 2 \tilde{U} U^2 \left(Q_d + \sum_{\mu=1}^K Q_{\mu}^{in} + \gamma_b U^2 \right), \quad (2a)$$

$$H_g = (E/p_0^2)^2 U / [n_0^2 (Q_d + \sum_{\mu=1}^K Q_{\mu}^{in} + \gamma_g U^2)]. \quad (2b)$$

\tilde{U} is the total turbulence energy per one electron in the beam discharge plasma, non-resonant heated by Langmuir waves, and E the electric field in the glow discharge

plasma. In (1) the first term represents the action of the turbulent or the direct electric field, the first 4 terms proportional to the Coulomb interaction of the electrons with one another and the fifth of these that between the electrons and ions. The term with the factor $6m/M$ results from the elastic collisions and the last term from the different inelastic processes. Furthermore, by appropriate analytical integration we obtained the energy balances per one electron and per pressure unit

$$\hat{P}_{\delta} = (\bar{U}^{el}/p_0)_{\delta} + (\bar{U}^{ei}/p_0)_{\delta} + \sum_{\mu=1}^K (\bar{U}_{\mu}^{in}/p_0)_{\delta} \quad (3a, b)$$

with

$$\hat{P}_b = \tilde{U} \gamma_b / p_0^b, \quad \hat{P}_g = p_0^g \gamma_g (E/p_0^g)^2. \quad (4a, b)$$

The terms in (4) represent the energy input per one electron and pressure unit by the turbulent or the direct electric field, the 3 terms on the r.h.s. of (3a, b) the energy losses in elastic collisions, by Coulomb interaction between electrons and ions and finally by the different inelastic collision processes. We chose the same cross sections for the description as in /1/. The comparison was performed under the condition

$$P_b = P_g, \quad P_b = \epsilon_0 n_0 (p_0^b)^2 (\frac{n_0}{N}) \hat{P}_b, \quad P_g = \epsilon_0 n_0 (p_0^g)^2 (\frac{n_0}{N}) \hat{P}_g \quad (5)$$

so that the energy input per unit volume was the same in both plasmas. Using (5) only 5 of the parameters $\tilde{U}, (n_0/N)_b, p_0^b, E/p_0^g, (n_0/N)_g, p_0^g$ are free. We chose E/p_0^g as determined by the other parameters. The solution was found by a threefold iterative process /2/. Especially it is necessary to select such values for the parameters which permit a comparison between both plasmas under typical conditions of their existence such as $p_0^b = 10^{-2}$, $p_0^g = 1$ Torr and the ionization degree $(n_0/N)_g = 10^{-6}$.

Results and Discussion: Fig. 1 shows the energy input $P=P_b=P_g$ as function of \tilde{U} with $(n_e/N)_b$ as parameter. The resulting energy inputs for the chosen $(n_e/N)_b$ are different from one another by about one order of magnitude for each given value of \tilde{U} and vary in the range from $\approx 10^{-2}$ to ≈ 30 W/cm³. The corresponding E/p_0^g are presented in Fig. 2 and change from ≈ 1 to ≈ 160 V/(cm Torr). In Fig. 3 an example ($\tilde{U}=1.6 \cdot 10^{-2}$ V) is given for the obtained distribution functions $f_b(U)$ and $f_g(U)$ which are adequate to one another according to (5). While the two corresponding distribution functions for $(n_e/N)_b=10^{-2}$ and therefore with $\hat{P}_b=\hat{P}_g$ are close to one another, there are very great differences in the other cases. Furthermore, we see also distinct differences in the structure. Especially from the strong vibrational excitation of the N₂ molecules in the range of 2-4 V a steplike decrease follows for $f_g(U)$. In contrast to this $f_b(U)$ is nearly Maxwellian for equal energy inputs. Finally the energy inputs \hat{P}_g and the different energy losses $(\bar{U}^{el}/p_0)_g, (\bar{U}^{elI}/p_0)_g, (\bar{U}^{VE}/p_0)_g, (\bar{U}^{EE}/p_0)_g, (\bar{U}^{DI}/p_0)_g$ and $(\bar{U}^I/p_0)_g$ for elastic and electron-ion collisions, vibrational and electronic excitation as well as dissociation and ionization are presented in Figs. 4 and 5 for $(n_e/N)_b=10^{-3}$ and 10^{-1} . We observe great differences with regard to the essential energy channels by which the greatest amount of energy input from the turbulent and the direct electric field is dissipated to the molecules and ions in the two plasma types. The obtained results show that equal energy input per one electron and pressure unit $\hat{P}_b=\hat{P}_g$ can be considered to some extent as a similarity law for the electron kinetics in various collision dominated discharge plasmas, i.e. the isotropic distribution functions of different discharge plasmas will be nearly equal in the same gas (see also Fig. 3).

References:

/1/ S. Pfau, R. Winkler, Beitr. Plasmaphys. **18** (1978) 113; **13** (1973) 273.

/2/ P. Bunkerep, U. Bunkerep, A.A. Ubanov, B. B. Cmapux, *физика плазмы* (1973) in print.

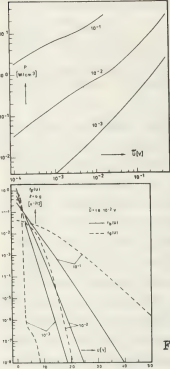


Fig. 1

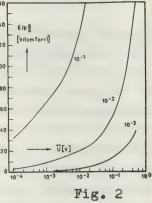


Fig. 2

Fig. 3

Fig. 4

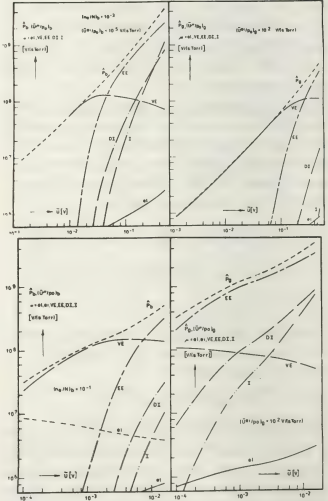


Fig. 5

DIFFUSION THEORY OF THE POSITIVE COLUMN IN HYDROGEN GLOW DISCHARGES WITH VARIABLE DEGREE OF DISSOCIATION

P. Michel, S. Pfau, A. Rutscher and R. Winkler*

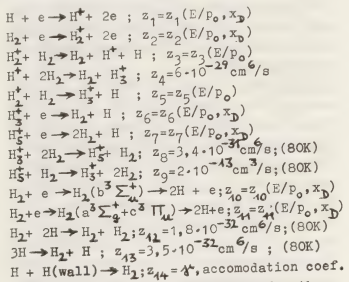
E.M.A. Universität Greifswald, Sektion Physik/Elektronik Greifswald, D.D.R.

* Akademie der Wissenschaften der DDR, Zentralinstitut für Elektronenphysik Greifswald, D.D.R.

INTRODUCTION: In connection with an increasing interest in plasma chemical reactions under non-isothermal conditions recently the classical SCHOTTKY diffusion theory of the positive column was extended to gases of varying material composition /1/. This extension resulted in a new viewpoint for the understanding of one of the most important problems in every column theory: the quantitative description of the electric characteristic of the discharge plasma. Till now the falling behaviour of the column characteristic was attributed mainly to such processes as deviations from the quasi-neutrality and the occurrence of the stepwise ionization. Now in the special case of the hydrogen discharge it was shown that the negative differential resistance of the column could be declared by the varying degree of dissociation in dependence on the discharge current. To calculate the electric characteristic on this basis a model of the discharge mechanism was used as a first step which neglected some appearing elementary processes. Now we have improved the model and extended the calculation to different gas pressures and different recombination conditions at the tube wall.

THEORETICAL MODEL: The starting-point of our calculations was the correct energy distribution function of the electrons in the H_2/H -mixture. This required the solution of the corresponding BOLTZMANN equation. Taking into account all important elastic and inelastic collisions between electrons and H_2 and H respectively (for details see /1/2/) the distribution function $f(x_D, E/p_0)$ was calculated in the frame of usual approximations for different degrees of dissociation $x_D = 0 \dots 1$ and different reduced electrical field strengths $E/p_0 = 7 \dots 100$ V/cm Torr. By this the transport coefficients and various collision rates of the electrons could be determined, too.

Contrary to /1/ in the kinetic model of the positive column now we have also considered the ion H_2^+ besides the ions H^+ , H_2^+ and H_3^+ . This expanded the process scheme altogether to the following 14 reaction channels:



The system of balance equations for the different particles H_1^+ , H_2^+ , H_3^+ and H (inclusive of some conditions for neutrality, current density and particle number) reads in differential form:

$$\begin{aligned} \text{div } r_j^+ &= n_e n_1 z_1 + n_1 n_2 z_3 - n_2^+ n_1 z_4 \\ \text{div } r_j^+ &= n_e n_2 z_2 - n_2 n_2^+ z_3 - n_2 n_2^+ z_5 \\ \text{div } r_j^+ &= n_1 n_2^+ z_6 + n_2 n_2^+ z_4 + n_2 n_2^+ z_9 - n_e n_3 z_6 - n_2 n_3^+ z_8 \\ \text{div } r_j^+ &= n_1 n_2^+ z_8 - n_e n_2^+ z_3 - n_2 n_2^+ z_9 \\ \text{with } j_k^+ &= -b^+(D_e/b_e)(n_k^+/n_e)(dn_e/dr); k=1,2,3,5 \\ n_1^+ + n_2^+ + n_3^+ + n^+ &= n_e; \text{ (neutrality condition)} \\ 2n_e n_2(z_{10} + z_{11}) + n_2 n_2^+(z_3 + z_4) + n_e n_2^+ z_6 + n_e n_2^+ z_7^+ \\ &+ (j_1^+ + j_2^+ + j_3^+) \delta(r/r_0 - 1)/r_0 = n_e n_1 z_1 + 2n_2 n_2^+ z_{12}^+ \\ &+ 2n_2^+ z_{13} + n_1 A \delta(r/r_0 - 1)/4r_0 \\ n_1 + n_2 &= p_0 n_g; \text{ (open tube, large dead space)} \\ n_1 + 2n_2 &= p_0 n_g; \text{ (closed tube, no dead space)} \\ j_D &= n_e E; \text{ (axial electric current density)} \\ (j: \text{current density; } z: \text{collision rate; } n: \text{particle concentration; } r, r_0: \text{radius coordinate, tube radius; } b: \text{mobility; } D: \text{diffusion coefficient; } n_g = 3,54 \cdot 10^{16} \text{ cm}^{-3} \text{ Torr}^{-1}; p_0: \text{reduced pressure (} ^\circ\text{C)}; p_{0g}: \text{initial pressure; } \bar{c}: \text{thermal velocity}). \end{aligned}$$

In the balance of the H atoms the terms with the delta function represent the tube wall localized production and loss processes by recombination. Radial changes of the

H and H_2 concentration are neglected. After radial averaging of the basic equations for different pressures (0,3...5 Torr) and different accommodation coefficients (10^{-7} ... 10^{-2}) the axial electric field strength E, the relative portion of the various ions $\alpha_k = \bar{n}_k^+ / \bar{n}_e$ and the degree of dissociation $x_D = n_1 / (n_1 + n_2)$ were calculated in dependence on the discharge current. At this calculation the gas temperature was set constant (80K) and we used for the radial distribution of the charge carriers a BESSEL profile.

RESULTS: Figs. 1 and 2 compare the importance of the various kinds of ions at different pressures. The H_5^+ ions are entirely insignificant at low pressures but gain considerable importance at higher pressures. On the other hand the molecular ion H_2^+ always plays only a subordinate role in the ionic budget. Fig. 3 shows the increase of the degree of dissociation with increasing current. At low pressures small currents can already produce nearly complete dissociation. At higher pressures x_D decreases but the absolute concentration of H atoms is relative independent on the pressure. Especially at low currents and relative low pressures the accommodation coefficient γ influences considerably the degree of dissociation (Fig. 4). Small values of γ relate to low temperatures at clear tube wall. Also a special coating of the wall (for instance with phosphite) reduces γ . The region of γ shown in Fig. 4 corresponds to the really occurring values under different conditions.

Finally Figs. 5 and 6 show examples of the calculated electric characteristic of the positive column in hydrogen. Contrary to all the other figures number 6 also contains results for the case of an open discharge tube (large dead space). The negative slope of the characteristic is caused by the transfer of the positive column from a prevailing molecular (H_2) discharge at low currents to states with a considerable atomic component at high currents. In consequence of the small degree of dissociation at high gas pressure the characte-

ristic remains flat in this case.

REFERENCES:

- 7/1/MICHEL, F., PFAU, S., RUTSCHER, A., WINKLER, R.
Contr. Pap. 13th ICPIG, Berlin 1977, p. 245
/2/MICHEL, F., PFAU, S., WINKLER, R., in prepar.

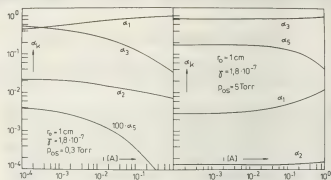


Fig. 1

Fig. 2

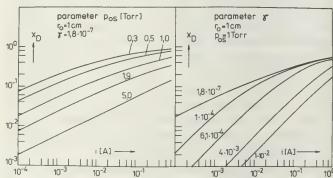


Fig. 3

Fig. 4

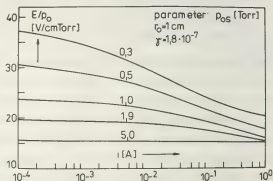


Fig. 5

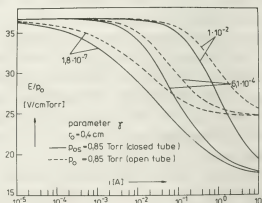


Fig. 6

ROLE OF $O_2^*(a^1\Delta)$ IN THE OXYGEN PLASMA

J.W. Dettmer and A. Garscadden

Kirtland Air Force Base, Albuquerque, New Mexico, U.S.A. 87110 and Wright-Patterson Air Force Base Ohio, U.S.A. 45433.

In this study, comparisons between experiments and mathematical models indicate that $O_2^*(a^1\Delta)$ affects the discharge in two different ways: first, two-step ionization is required to achieve the observed electron densities, and secondly, detachment by $O_2^*(a^1\Delta)$ on the negative ion, O^- , is required to match the transition points between the stable and unstable forms of the discharge.

Our experiments encompassed 1-10 torr pressure and a current density range of .35 to 35 ma/cm² in a discharge tube of 19mm diameter and 50cm length. Observations were the impedance characteristics; electric field, pressure and temperature (for determination of E/N and N); electron density; and the transition point between the stable and unstable forms of the discharge.

Our models encompassed 1 to 100 Townsends for E/N and 3.2×10^{16} to 5.6×10^{17} molecules/cc for N. A Boltzmann code with momentum transfer; rotational, vibrational and electronic excitation; dissociative attachment; ionization; dissociative ionization; and dissociation cross sections was used to determine the electron energy distribution and forward pumping rates. A chemistry code which tracked 10 neutral and charged species and utilized 69 chemical and physical reactions, including 3-species ambipolar diffusion, was used to calculate the species number densities and transition between the stable and unstable forms of the discharge.

The cross section for ionization from the

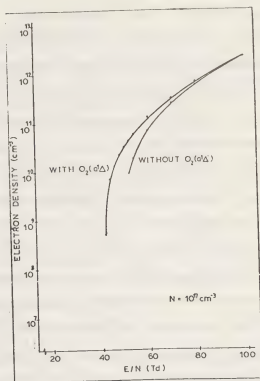
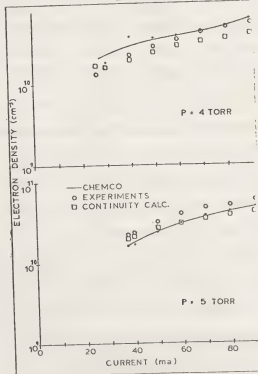
Figure 1. Effect of $O_2^*(a^1\Delta)$ on Electron Density

Figure 2. Electron Density Comparisons

$O_2^*(a^1\Delta)$ state was assumed to be the same shape and magnitude as the process from the ground level, with the onset reduced by the difference in energy between the two states. Calculations were performed by the chemistry code, with and without two-step ionization. Results for $n = 10^{17} \text{ cm}^{-3}$ are shown in Fig. 1. Figure 2 compares the calculated electron densities with experimental values determined from toroidal cavity resonance and values calculated from current continuity equations. In Fig. 2 the calculated values are the ones which include two-step ionization. For the experiments the calculated ionization densities without $O_2^*(a^1\Delta)$ ionization would be approximately an order of magnitude lower.

The oxygen discharge exists in two forms: a high-electric-field, stable form and a low-electric-field, unstable form. The latter can be described as an ionization-attachment-detachment instability. The transition between stable and unstable forms has been postulated to occur when two criteria are satisfied: first, a necessary condition is that the logarithmic derivative of the attachment coefficient with respect to E/N must dominate that of the ionization coefficient; and second, a sufficient condition is that $\frac{N_-}{N_e} > 1$. Figure 3 depicts code results of the first criterion for the two limiting conditions of all ground state and all metastable molecules. Figure 4 depicts the chemistry code calculations of the second criterion both with and without $O_2^*(a^1\Delta)$. The primary contribution of $O_2^*(a^1\Delta)$ in increasing the electron to ion ratio is as a detacher of electrons from O^- . Comparisons of the code-calculated transition points show that $O_2^*(a^1\Delta)$ must be included to match the experimental data.

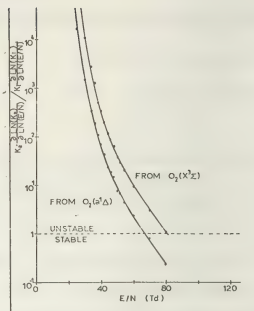


Figure 3. Stability Criterion #1

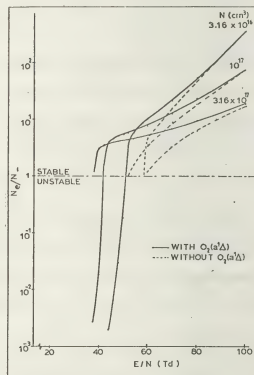


Figure 4. Electron-to-Negative Ion Ratio

*Work performed in partial fulfillment of PhD requirements at the Air Force Institute of Technology.

POSITIVE COLUMN CONSTRICTION IN CESIUM PLASMA DISCHARGE

G. Musa, A. Popescu, N. Niculescu.

Institute of Physics and Technology for Radiation Devices, P.O. Box 5207, Magurele-Bucharest, ROMANIA.

A lot of papers were published by different authors on positive column with the purpose to explain the constriction phenomena.

There are many proposed mechanisms to explain surprisingly well one and the same phenomenon - the positive column constriction.

One of the most popular explanation of the constriction is the inhomogeneous heating of the gas in the discharge tube, with the subsequent change in the radial charge density distribution /1/.

This thermal effect is considered in /2/ to be not important. Indeed, the measured pressure at which the column constriction appears for various noble gases is smaller for pulsed discharge than for the steady discharge, in spite of the fact that the thermal effects are smaller in the former.

In a previous paper /3/ we have theoretically considered the possible contribution of the atomic to molecular ion conversion process, on the radial charge density distribution in the positive column. According to our paper, due to the higher mobility of the molecular ions than that of atomic ones, the radial charge density decreases faster than Schottky distribution. The solution for the distribution of the radial charge density n , is:

$$n = n_0 \left[J_0(r) + \frac{2\gamma}{\beta\delta} J_2(r) + \frac{1}{2} \left(\frac{2\gamma}{\beta\delta} \right)^2 J_4(r) + \dots \right] \quad (1)$$

which is a fast convergent series for small values of the coefficient $2\gamma/\beta\delta$. In eq. 1, n_0 is the charge density at the positive column axis, r is the radial distance from the axis and $q = \delta \frac{r}{\beta}$. Coefficients β , γ and δ are given by the relations:

$$\beta = e(\mu_e \mu_{p1} + \mu_{p1} D_e) / (\mu_e + \mu_{p1})$$

$$\gamma = e\alpha [\mu_e / (\mu_e + \mu_{p1})] [D_{p2} - D_{p1}] / D_{p2}$$

$$\delta = \beta^{-1}(e\gamma - r)$$

where μ and D are the mobility and the diffusion coefficient, respectively, indices e , p_1 and p_2 referring to the values concerning electrons, atomic and molecular ions, respectively. The conversion frequency α is defined as $\alpha = k_c N^2$, where N is the neutral atoms density and k_c the transformation coefficient of atomic ions into molecular ions. The parameter γ_1 is the ionization frequency for atomic ions.

The conversion effect is strongly dependent on the cesium pressure and is described by the equation:

$$\frac{dN_{mol}^+}{dt} = k_c N_{at}^+ N_{at}^2 \quad (2)$$

where N_{at}^+ , N_{mol}^+ and N_{at} are respectively the densities of the atomic ions, molecular ions and neutral atoms.

In the TABLE I the values of k_c for some gases and vapours are given /4/.

TABLE I

	k_c ($10^{-31} \text{ cm}^6/\text{s}$)	p_c (torr)	$k_d \sqrt{p_c}$
He	.9	100	9.0
Ne	.7	75	6.0
Ar	2.0	13.5	7.34
Kr	2.7	9.0	8.1
Xe	3.6	5.0	8.0
Cs	150.0	2.8×10^{-2}	

with p_c the pressure above which the constriction appears, its values being taken from /2/.

We can introduce now the empirical coefficient $C = k_c \sqrt{p_c}$, which can be considered as a constant of the positive column constriction phenomena. Indeed, C has prac-

tically the same value for all gases considered. Using the value of $C=8.0$ and taking into account the value of k_c for cesium vapours, we computed the value of the expected cesium vapour pressure for the positive column constriction.

This expected value for cesium is:
 $k_c = 2.8 \times 10^{-2}$ torr.

EXPERIMENTAL SET-UP AND RESULTS.

The experimental device is shown schematically in Fig.1. The cathode is a moli-

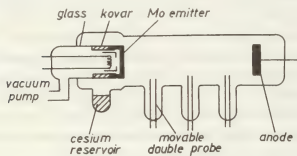


Fig.1. The experimental device

bdenum disc of 25 mm diameter heated by electron bombardment. The cathode is surrounded by a ceramic insulator, except the front planar surface. The anode is a stainless-steel disc at a distance of 300 mm from the cathode. The experimental tube is provided with a number of movable double probes. The positions of the probes were measured optically from the distance of 1.5 m from the tube.

The whole device is mounted inside an oven, which insures the necessary temperature to obtain the needed cesium vapour pressure.

In Fig.2 are given some of the obtained values for the normalized charge density versus the normalized distance r/R from the axis of the tube (where R is the radius of the tube). The charge density at the axis is n_0 . The experimental points were taken for two values of the cesium pressure: $p_1 = 2.8 \times 10^{-2}$ and $p_2 = 9 \times 10^{-2}$ torr, corresponding to the temperature of the cesium reservoir of 175 and 240°C, respectively. On the same figure are given two more curves: the Schottky curve and the computed curve for the radial charge density dis-

tribution using the equation inferred by us in /3/, but for a small conversion coef-

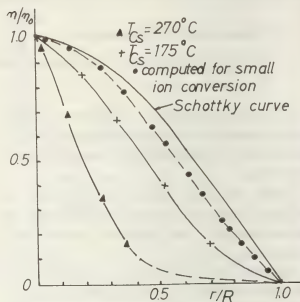


Fig.2. The normalized charge density versus the normalized distance r/R .

ficient (low pressure of the cesium vapour).

The obtained results can be compared with the value obtained for $P_C(\text{Cesium})$, according to the empirical relation $C = k_c \sqrt{P_C}$. The agreement is quite good.

We may conclude that, as it has been pointed out in our previous paper too, the ion conversion effect has to be taken into account in the explanation of the positive column constriction.

REFERENCES.

- /1/. Rohlena K., Ruzicka T., Czech. J. Phys. 828/1,50 (1978)
- Venzke D., Beitr. Pl. Phys. 18/1,65 (1978)
- /2/. Gerasimov G.N., Optika i Spectr. 43/2,209 (1977)
- /3/. Popescu A., Musa G., Phys. Letters 53A,339 (1975)
- /4/. Smirnov B.M., Ioni i vozbuždenie atomi v plazme. Moskva, Atomizdat 1974

FLUID THEORY OF PLASMA DOUBLE-LAYERS

J.S. Levine and F.W. Crawford.

Institute for Plasma Research, Stanford University, Stanford California 94305 U.S.A.

A double-layer consists of two adjacent, oppositely-charged space-charge layers, and may occur near a material boundary, or within the plasma volume (see [1]-[3] for reviews of double-layer phenomena in laboratory and space plasmas). Here, we shall analyze a steady-state double-layer separating two plasmas of different densities and temperatures, and relate its length and potential drop to the plasma parameters.

Several theoretical models have treated the double-layer as a region of high electric field and monotonic potential variation. The total potential drop is generally taken to be larger than the plasma thermal energy, and the electric field is confined to the double-layer, implying that the charge variation integrates to zero. Cold plasma, fluid, and kinetic theory approaches have been discussed [2].

THEORY

We treat the double-layer as a transition between two uniform semi-infinite plasmas; Plasma 1 at potential $\phi = 0$, and Plasma 2 at $\phi = \phi_0 > 0$. Four populations of particles are assumed (see Fig. 1): electrons, transmitted through the double-layer from Plasma 1, ions transmitted from Plasma 2, and ions in Plasma 1 and electrons in Plasma 2 that are reflected by the double-layer. The transmitted particles constituting the plasma current drift toward the double-layer, and are accelerated adiabatically; the reflected particles are reflected isothermally. We normalize charged particle densities to the transmitted electron density, and energies to the transmitted electron drift energy before acceleration,

$$\begin{aligned} N &= \frac{n_{12}}{n_{e1}}, \quad \eta_i = \frac{n_{i1}}{n_{e1}}, \quad \eta_e = \frac{n_{e2}}{n_{e1}}, \quad \tau_e = \frac{T_{e1}}{m_e v_{e1}^2}, \\ \tau_i &= \frac{T_{i2}}{m_i v_{e1}^2}, \quad \bar{U}_i = \frac{T_{i1}}{m_i v_{e1}^2}, \quad \bar{U}_e = \frac{T_{e2}}{m_e v_{e1}^2}, \\ \xi &= \frac{e\phi}{m_e v_{e1}^2}, \quad Q = \frac{1}{2} \frac{n_{i12}}{n_{e1}^2}, \quad Z = x \left(\frac{n_{e1} e^2}{m_e v_{e1}^2} \right)^{1/2}, \end{aligned} \quad (1)$$

where e is the magnitude of the electronic charge, m_α the mass of electrons or ions ($\alpha = e, i$), $n_{\alpha\beta}$ is the density, $T_{\alpha\beta}$ the temperature, and $v_{\alpha\beta}$ the drift velocity in Plasma 1 or 2 ($\beta = 1, 2$). The charge density, ρ , is given by (2) below. When $\bar{U}_i = 0$, the first exponential is 1 for $\xi = 0$, and 0 for $\xi > 0$. When $\bar{U}_e = 0$, the second exponential is 1 for $\xi = \xi_0$, and 0 for $\xi < \xi_0$.

We must solve Poisson's equation with ρ given by (2), and satisfy the conditions that ρ and the electric field, E , vanish at $\xi = 0$ and ξ_0 , and that ξ should vary monotonically from 0 to ξ_0 . These determine ξ_0 , η_e and η_i as functions of N , Q , τ_e , \bar{U}_i , \bar{U}_e and \bar{U}_1 . Typical spatial variations are shown in Fig. 1.

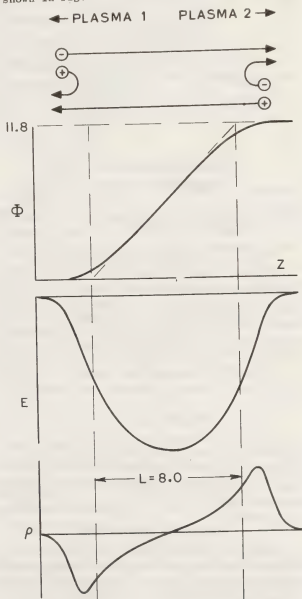


FIG. 1. SPATIAL VARIATIONS OF ϕ, E, ρ
($N=1.1$, $Q=0.8$, $\tau_e=\tau_i=\bar{U}_e=\bar{U}_1=0.1$)

$$\begin{aligned} \rho(Z) = \left\{ N \left[2(\xi_0 - \xi) + 3\tau_i + Q - \left[2(\xi_0 - \xi) + 3\tau_i + Q \right]^{1/2} / 6\tau_i \right]^{1/2} + \eta_i \exp(-\xi/\bar{U}_i) \right\} \\ - \left\{ \left[2\xi + 3\tau_e + 1 - \left[2\xi + 3\tau_e + 1 \right]^{1/2} / 6\tau_e \right]^{1/2} + \eta_e \exp(-(\xi_0 - \xi)/\bar{U}_e) \right\}. \end{aligned} \quad (2)$$

Bounds on N , Q , τ_e, τ_i, \bar{J} and \bar{J}_1 giving physically admissible solutions can be established: (a) when the reflected particles are cold ($\bar{J}_e, \bar{J}_i = 0$), ρ is discontinuous at $\phi_0 = 0, \phi_0$, and we only require

$$N^2 Q > 1 > N, \text{ or } N^2 Q < 1 < N. \quad (3)$$

(b) When $\bar{J}_e, \bar{J}_i \neq 0$, ρ is a continuous function of ϕ ; for a monotonic potential we require $d\rho/d\phi < 0$ at $\phi=0, \phi_0$. For $\phi_0 \rightarrow \infty$, these bounds simplify to

$$\bar{J}_i + 3\tau_e < 1, \bar{J}_e + 3\tau_i < Q, \quad (4)$$

which are modified Bohm conditions for collection of electrons and ions, respectively, through a sheath. More restrictive expressions obtain for finite ϕ_0 .

Solutions must satisfy $\bar{J}_1, \bar{J}_e \geq 0$. These conditions are found to be no more stringent than those already considered. For all conditions to be satisfied, reflected particles must be present on both sides of the double-layer, as we have assumed.

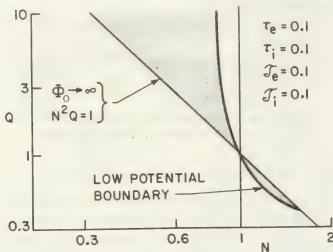


FIG. 2. CONDITIONS FOR DOUBLE-LAYER

Figure 2 shows the region of N, Q space where double-layer solutions can be found. The boundary for $\phi_0 \rightarrow \infty$, $N^2 Q = 1$, is independent of the particle temperatures. The low potential boundary moves to $N=1$ for cold particles. The potential varies along the low potential boundary, but is never less than the reflected particle temperature.

In general, Poisson's equation must be solved numerically to find ϕ_0 , but for all particles cold we obtain

$$\phi_0 = \phi_c = 2NQ(1-NQ)(N-1)/(1-N^2Q)^2. \quad (5)$$

In Fig. 3(a) the temperatures are individually increased from zero. The curves for τ_e and \bar{J}_i increase to the limit set by (4). For $\tau_i \rightarrow \infty$, $\phi_0 \rightarrow 0$. The \bar{J}_e curve decreases until no admissible solution can be found. For $N < 1$, reversing the roles of electrons and ions gives the same qualitative variations.

LENGTH OF DOUBLE-LAYER

When the reflected particles are not cold, they penetrate the double-layer, and electrical neutrality obtains only at $Z = \pm \infty$. As a criterion of the length over which most of the potential step occurs; we define L (see Fig. 1) as that distance over which the electric field evaluated at $\phi_0/2$ would have to extend to produce a step of ϕ_0 ,

$$L = \phi_0 / |E(\phi_0/2)|, \quad (6)$$

Figure 3(b) shows the temperature variation of L .

DISCUSSION

Our predictions may be compared with conditions

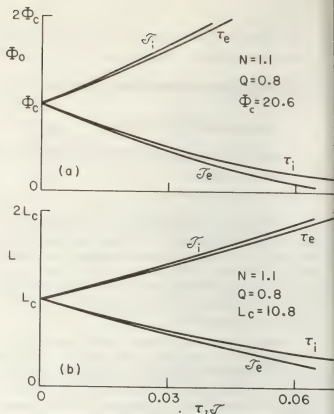


FIG. 3. TEMPERATURE VARIATION OF ϕ_0 AND L

characteristic of laboratory and space plasmas. Rough estimates for a double-layer in a double-plasma device are [4]: $N \approx 1.2$, $Q \approx 0.5$, $\tau_e \approx 0.2$, $\tau_i \approx 0.1 \approx \bar{J}_e$, $\bar{J}_i \approx 0.3$. Hence, $\phi_0 \approx 4.9$, $L \approx 5.6$. For a density of 10^{20} cm^{-3} , and electron streaming energy of 1 eV in Plasma 1, a step of 20 V, 0.8 cm long is predicted, compared with 3-15 V and 3-5 cm observed.

To compare our theory with conditions during an aurora, we assume a current of $1 \mu\text{A}/\text{m}^2$ carried by a 100 eV electron beam above the double-layer. For $N = 1.5$, $Q = 0.4$, $\tau_e = \tau_i = \bar{J}_e = \bar{J}_i = 0.1$, we predict $\phi_0 = 10.3$, $L = 7.4$, i.e. a 2 kV step in 0.7 km. The average electric field is five times greater than reported [5], but the measurements may not have been made in the center of the double-layer. If the current above the double-layer is carried by 1 keV electrons, the step increases to 20 kV, while the electric field only increases to 5.0 V/m. These potentials are of the order of magnitude necessary to account for observations of high-energy electron precipitation [3].

This work was supported by the NSF and the NASA. Thanks are due to Dr. D. B. Ilić for many fruitful discussions.

REFERENCES

- [1] Torvén, S.: *Astrophysics and Space Science Library* (in press).
- [2] Carlqvist, P.: *Astrophysics and Space Science Library* (in press).
- [3] Shawhan, S.D., Fäthammer, C.-G., and Block, L.P., *J. Geophys. Res.* **83**, 1049 (1978).
- [4] Quon, B.H., and Wong, A.Y., *Phys. Rev. Letters* **37**, 1393 (1976).
- [5] Mozer, F.S., Carlson, C.W., Hudson, M.K., Torbert, R.B., Parady, B., Yatteau, J., and Kelley, M.C., *Phys. Rev. Letters* **38**, 292 (1977).

MOLECULAR BEAM SAMPLING OF METASTABLE ATOMS FROM A HOLLOW CATHODE ARC AS A PROBE FOR THE ELECTRON TEMPERATURE

P.G.A. Theuws, H.C.W. Beijerinck, C.E.E. Pernot, D.C. Schram and N.F. Verster.

Eindhoven University of Technology, Eindhoven, The Netherlands.

Introduction. In a hollow cathode arc (HCA) discharge in noble gases fast metastable atoms are produced by electron impact and heavy particle collisions. These metastables are sampled through an orifice in the end anode. In a time-of-flight machine we have measured the centre-line intensity and the velocity distribution of the beam of metastable atoms.

Molecular beam sampling of ground state atoms gives accurate information on the ion velocity distribution and qualitative information on the ion and neutral density. The fractional intensity of the metastables relative to the intensity of the ground state atoms gives information on the electron temperature.

Experimental set up. A detailed description of the apparatus is given elsewhere ¹⁾. Fig. 1 shows a schematic of the HCA. We have measured both with a long arc (arc length $L_0 = 20$ cm) and a short arc ($L_0 = 1$ cm). Typical electron densities are $n_e = 10^{19}-10^{20} \text{ m}^{-3}$.

Theory. The general expression for the product of the centre-line intensity $I(o)$ ($\text{s}^{-1} \text{sterad}^{-1}$) and the normalized velocity distribution function $P(v)$ of the beam of metastables is given by

$$I(o) P(v) d^2\Omega dv = \left[\int_0^{L_0} n(z,v) T(z,v) A dz \right] \frac{d^2\Omega}{4\pi} dv \quad (1)$$

with A the area of the sampling orifice at $z=0$ and z the coordinate along the beam axis. The function $n(z,v)$ ($\text{m}^{-3} \text{s}^{-1} \text{m}^{-1} \text{s}$) is the production of metastables per unit volume, per unit of time and per unit of velocity and $T(z,v)$ is the transmission probability of a metastable through the plasma slice between z and $z=0$.

Fast metastable atoms are produced by charge exchange and elastic collisions with ions. We consider two processes: firstly a collision of a ground state atom with an ion followed by successive excitation by a collision with an electron and secondly a collision of a metastable with an ion with charge and excitation transfer.

The first process can be related directly to our model calculations and experimental work on the sampling of ground state atoms. For fast ground state atoms the view depth λ_n into the plasma, i.e. the mean free path, is determined mainly by elastic collisions with ground state atoms and ions and in most cases ionisation can be neglected. For metastable atoms, however, the view depth $\lambda_m = v_m / (n_e \langle Qv_e \rangle_{\text{ion},m})$ is fully determined by the deexcitation and ionisation by collisions with electrons and the relation $\lambda_m \ll \lambda_n$ holds. In this model the centre-line intensity $I(o)_m$ of metastable atoms is given by

$$I(o)_m d^2\Omega = I(o)_n P_{\text{exc}} (z \leq \lambda_m) d^2\Omega \quad (2)$$

with $I(o)_n$ the centre-line intensity of ground state atoms and $P_{\text{exc}} (z \leq \lambda_m)$ the probability that a ground state atom will be excited to a metastable state in the plasma slice with thickness λ_m in front of the end anode. We implicitly assume that $T(z,v)=1$ for $z \leq \lambda_m$ and zero elsewhere. The probability $P_{\text{exc}} (z \leq \lambda_m)$ is equal to the product of the excitation rate v_{exc} and the transit time $\tau = \lambda_m / v_n$ of the ground state atom in this plasma slice. With $v_{\text{exc}} = n_e \langle Qv_e \rangle_{\text{exc}}$ we write Eq. (2) as

$$I(o)_m d^2\Omega = I(o)_n \frac{\langle Qv_e \rangle_{\text{exc}}}{\langle Qv_e \rangle_{\text{ion},m}} d^2\Omega \quad (3)$$

where we have used $v_m = v_n$, i.e. we neglect the momentum transfer of the electron. The ratio of the reaction constants for excitation and ionisation depends strongly on the electron temperature. For argon this ratio ²⁾ is given in fig. 2. For $\langle Qv_e \rangle_{\text{exc}}$ we only consider direct excitation to a metastable state. For $\langle Qv_e \rangle_{\text{ion},m}$ we have included the 4s-4p excitation process because for electron temperatures $T_e \geq 2$ eV and electron densities $n_e \geq 10^{19} \text{ m}^{-3}$ the ionisation rate of the 4p levels is much larger than the rate of spontaneous radiative decay to the 4s levels.

The second process, i.e. charge and excitation

transfer of a metastable with an ion, has a very large cross-section Q_{exch} . No quantitative data are available, however, and we use an estimate $Q_{\text{exch}} = 500 R^2$ in analogy to the charge transfer cross-section for Cs^+ on $\text{Cs}^{(3)}$. We assume a homogeneous plasma with $T(z, v) = 1$ for $z \leq \lambda_m$ and zero elsewhere. Equation (1) is then written as

$$I(o)_m d^2\Omega = n_m n_i g Q_{\text{exch}} \frac{\lambda_m}{4\pi} d^2\Omega \quad (4)$$

with n_m and n_i the number density of the metastables and the ions, respectively. Substitution of the expression for λ_m results in

$$I(o)_m d^2\Omega = \frac{n_m v_m A}{4\pi} \left[\frac{Q_{\text{exch}} g}{\langle Qv \rangle_{e^+ \text{ ion}, m}} \right] d^2\Omega \quad (5)$$

which is the centre-line intensity of an effusive source of fast metastables multiplied by the extra factor in square brackets. The density n_m in table I has been calculated with a collisional radiative model ⁴⁾ for the plasma conditions in the upper part of table I.

In table I numerical values of the centre-line intensity $I(o)_m$ are given for the two models discussed, showing that excitation of fast ground state atoms is the dominant process of beam formation. Of course, the models used are simplified to a large extent. With the small value of $\lambda_m = 2 \cdot 10^{-4} \text{ m}$ as compared to the diameter $(4/\pi) A^2 = 5 \cdot 10^{-4} \text{ m}$ of the sampling orifice, the assumption of a homogeneous plasma is not very realistic. To explain our experimental results we also have to assume a fairly high electron temperature at this very close distance to the end anode. However, the models used do give a qualitative picture of the production and destruction processes involved.

Experimental results. Measurements have been performed for Ar and Kr for both arc configurations. In this section we will only discuss the results for Ar in the long arc configuration. In fig. 3 the measured intensities and temperatures are given for Ar in the long arc configuration as a function of the density in the source chamber n_n . The measured temperatures for the metastables are a factor 3 higher than the temperature of the fast ground state atoms ¹⁾. Our models do not explain this difference. The highest intensities are measured in case of low density, high arc current and high magnetic field. For fast ground state atoms the intensity is proportional to n_n . In fig. 4 we

give the intensity of metastables relative to the intensity of the ground state atoms as a function of n_n . Comparing this with fig. 2 results in electron temperatures varying from 2-5 eV.

For the short arc configuration we find electron temperatures varying from 3 (high density) to 7 eV (low density). Within the assumptions of our very simple model we have developed a sensitive probe for the electron temperature in front of the end anode. For further insight in the production, a better description of the plasma near the end anode is necessary.

References

- 1) P.G.A. Theuvs et al., J. Appl. Phys. **48**, 2261 (1977).
- 2) J.J.A.M. v.d. Mullen, At. Phys. Group, Rep. NT 78-01, Eindhoven University of Technology.
- 3) R.N. Bullis, as cited in "Partially ionized gases", edited by M. Mitchener and C.H. Kruger (Wiley interscience, New York, 1973), p. 109.
- 4) B.F.M. Pots and B. v.d. Sijde, private communication.

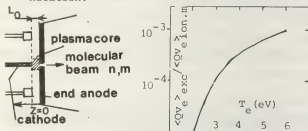


Fig. 1 Schematic of the HCA Fig. 2 The ratio of the excitation and deexcitation rates as a function of T_e .

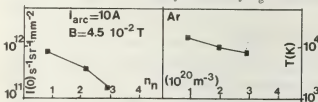


Fig. 3 Experimental results for Ar ($L_0 = 30 \text{ cm}$).

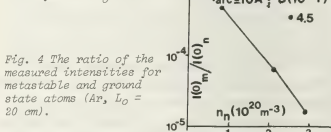


Fig. 4 The ratio of the measured intensities for metastable and ground state atoms (Ar, $L_0 = 20 \text{ cm}$).

Table 1 Plasma parameters				
n_e	$2 \cdot 10^{19} \text{ m}^{-3}$	$\langle Qv \rangle_{e^+ \text{ exc}}$	$1,7 \cdot 10^{-16} \text{ m}^3 \text{ s}^{-1}$	a)
n_n	$2 \cdot 10^{19} \text{ m}^{-3}$	$\langle Qv \rangle_{e^+ \text{ ion}, m}$	$5 \cdot 10^{-13} \text{ m}^3 \text{ s}^{-1}$	a)
T_e	3.5 eV	λ_m	$2 \cdot 10^{-4} \text{ m}$	
model 1		model 2		
$I(o)_n$	$1.3 \cdot 10^{15} \text{ b)}$	n_m	$2 \cdot 10^{16} \text{ m}^{-3}$	c)
$I(o)_m$	$2.1 \cdot 10^{12}$	$I(o)_m$	$6 \cdot 10^{19}$	

a) Ref. 2, b) Ref. 1, c) Ref. 4.

ELECTRON-MOLECULE COLLISION FREQUENCIES FROM BREAKDOWN DATA IN A CROSSED MAGNETIC FIELD FOR ETHANE GAS

A.E.D. Heylen.

Department of Electrical and Electronic Engineering, The University of Leeds, Leeds LS2 9JT West Yorkshire.

INTRODUCTION

The author has shown that for nitrogen¹, argon and hydrogen², breakdown voltages³ in a crossed magnetic field can be successfully analysed and predicted using the electron-molecule collision frequencies derived from the equivalent gas pressure times gap distance method³. A common feature of these gases is that for each gas a single collision frequency was adequate to cover the wide range of equivalent reduced electric field⁴, $(E/p)_e$, used. An exception to this general rule is ethane gas² for which the use of the derived single electron-molecule collision frequency³ did not allow good prediction of the breakdown characteristics. Since then the work of Watts⁵ has revealed collision frequencies in ethane different from those obtained by Dargan and Heylen³, but even the use of an average of Watt's lower collision frequency values did not produce good agreement between theory and experiment.

It is thus concluded that in ethane gas the collision frequency is not single-valued, but is a function of $(E/p)_e$, H/p and possibly even gas pressure, p . This is borne out by the analysis of breakdown data presented in this paper.

THEORY AND PROCEDURE

The breakdown voltage, V_s , in a crossed magnetic field is given by^{1,2}

$$V_s = \frac{B \, p d \, \sec \theta}{\ln[p(d-\delta)\sec \theta] + \ln\left[\frac{A}{\ln(1+1/\gamma_H)}\right]} \quad (1)$$

where A and B are the Townsend gas constants, $p d$ is the gas pressure times gap spacing, θ is the angle the electron avalanche makes with the electric field, δ is the gap distance required for the electrons to reach equilibrium energy and γ_H is the secondary ionization coefficient in a crossed magnetic field. In equation (1), $\sec \theta$ is given by⁴

$$\sec \theta = \left[1 + \left(\frac{e}{m} \frac{1}{v_0} \frac{H}{p} \right)^2 \right]^{\frac{1}{2}} \quad (2)$$

where e/m is the electronic charge to mass ratio, v_0 is the electron-molecule collision frequency at 1 torr and H/p the reduced magnetic field; also

$$\delta = \frac{V_i}{V_s/d} \quad (3)$$

where V_i is the ionization potential of the gas and

$$\gamma_H = \gamma_0 \left\{ 1 - \exp \left[- 8 \frac{m}{e} \frac{v_0}{(2e/m)^{\frac{1}{2}}} \frac{V_s/pd}{(H/p)^2} \right] \right\} \quad (4)$$

in which γ_0 is the secondary ionization coefficient in the absence of a magnetic field. This latter formula is due to Somerville⁶ and has been shown to apply².

By rearrangement of equation (1) as follows

$$\ln\left(1 + \frac{1}{\gamma_H}\right) \exp\left(\frac{B \, p d \, \sec \theta}{V_s}\right) = A \, p(d-\delta) \, \sec \theta \quad (5)$$

and using equations (2) to (4), it is possible to derive a value of v_0 to fit the experimental breakdown data. As no explicit expression for v_0 is available, a computer solution was used which involved a simple search and bisection technique. The values of v_0 were obtained from the breakdown data³ using equation (1) with zero magnetic field. The values of A and B are those obtained by Heylen⁷ for ethane gas and correspond to those of propane in this high E/p range.

RESULTS AND DISCUSSION

From the breakdown data for ethane gas³ and with the aid of equations (1) to (5), the v_0 values were obtained as outlined above and are shown in Fig 1. It is seen that for each gas pressure used, the collision frequency decreases with increase in $(E/p)_e$ but the values do not coincide. Again an unusual feature of ethane is that particularly at high $(E/p)_e$ the collision frequency at a given $(E/p)_e$ decreases with increase in H/p whilst in other gases the reverse has been observed⁸ in agreement with the theory for these gases. This effect has also been observed in ethane by Watts⁵ who used a pulsed Townsend technique to find v_0 . In the middle range of $(E/p)_e$, it is observed that for a given $(E/p)_e$ and H/p , where one would expect a single value of v_0 , the actual values of v_0 increase with increase in gas pressure. Although these effects are difficult to account for, it must be remembered that the present method used for determining v_0 values only samples the tail of the electron energy distribution function at values of energy above the ionization potential and small changes in the overall distribution function have a large effect on the energy tail.

It is gratifying to see that the present v_0 values tend to the constant value obtained by Dargan and Heylen³ at high gas pressure (5 to 25 torr) and that at low gas pressure the present values are in good agreement with the recent data of Watts⁵ (1.5 to 5 torr), although his values were taken at H/p magnitudes about ten times less than those of Dargan and Heylen³. A feature worth mentioning is that v_0 values obtained in the region of the left hand side of the Paschen minimum of the lowest three curves³, were large and are not shown in Fig 1. This indicates that breakdown data obtained in the apparatus³ are unreliable below the Paschen minimum because of the occurrence of long path breakdown.

Using the derived v_0 values in the Somerville equation (4), the γ_H values in the presence of a crossed magnetic field are shown in Fig 2. The γ_H values at a given E/p decrease with increase in H/p because of the increasing probability of electron recapture by the cathode. At the

highest H/p value used, the γ_H value is reduced by a factor of fourteen times, which is significant. However such a large change in γ_H has relatively little effect on the computed values of ν_0 which, it has been calculated, are reduced only by an average of about 10% at moderate H/p and 20% at high H/p when the recapture effect is neglected in the computation.

CONCLUSIONS

In ethane gas the electron molecule collision frequency at a given equivalent reduced electric field decreases with increase in the reduced magnetic field and is gas pressure dependent. Good agreement exists between present derived collision frequency values and those obtained by other authors.

ACKNOWLEDGEMENT

The author is indebted to Mr Paul Clark for carrying out the computer calculations.

REFERENCES

1. HEYLEN, A E D, 1978, Proc 5th Int. Conf. on Gas Discharges, IEE Conf. Publ. No. 165, pp 262-264
2. HEYLEN, A E D, 1979, Proc IEE, Feb. 6 p
3. DARGAN, C L, and HEYLEN, A E D, 1968, Proc IEE, 115, pp 1034-1044
4. HEYLEN, A E D, and BUNTING, K A, 1969, Int. J. Electronics, 27, pp 1-12
5. WATTS, H P, 1977, Ph.D Thesis, University of Leeds
6. SOMERVILLE, J M, 1952, Proc Phys Soc, B65, pp 620-628
7. HEYLEN, A E D, 1975, Int. J. Electronics, 39, pp 653-660
8. HEYLEN, A E D, and DARGAN, C L, 1973, Int. J. Electronics, 35, pp 433-451

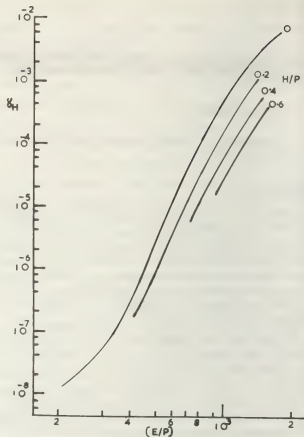


FIG 2 Townsend secondary ionization coefficient, γ_H , as a function of the reduced electric field, E/p in $V\ cm^{-1}\ torr^{-1}$, for various reduced magnetic field strengths, H/p in Tesla per torr

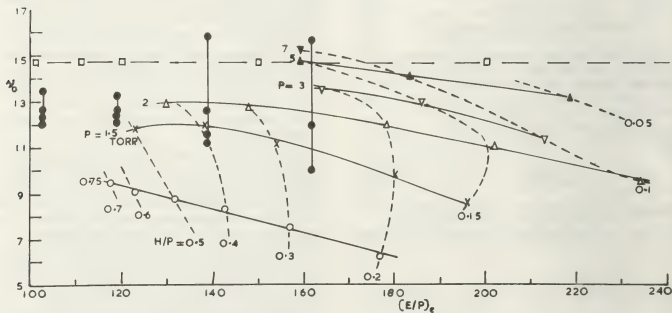


FIG 1 Computed electron-molecule collision frequency, $\nu_0 \times 10^{-9}$, in sec for ethane gas as a function of the equivalent reduced electric field $(E/p)_e$, in $V\ cm^{-1}\ torr^{-1}$ for various reduced magnetic field, H/p , in Tesla per torr and gas pressures p , in torr. Also shown: \bullet , Watts⁵, $p = 1.5$ to 5 torr; \square — \square , Dargan and Heylen³, $p = 5$ to 25 torr

PROCESSES OF IMPULSE BREAKDOWN IN N_2 - O_2 GAS MIXTURES AND IN AIR AT LOW PRESSURE

M. Akazaki, K. Nishijima and M. Hara.

Faculty of Engineering, Kyushu University, Fukuoka, Japan.

INTRODUCTION: The impulse breakdown processes were observed for N_2 - O_2 gas mixtures and for dry air at low pressure by an image converter camera. The results of time-resolved photographs are presented and the influence of the electro-negative gas O_2 on the breakdown process is discussed.

EXPERIMENTAL CONDITIONS: The tested electrode arrangement was a needlepoint (1mm tungsten rod with hemi-spherical cap) to plane (16cm brass) gap 8 cm long and was installed in a Pyrex glass cylinder of 18cm diameter and 45 cm in length. A positive impulse voltage, 1.6x150 ps, with breakdown probability between 20% and 80% was applied to the point. The gas pressure reduced to 20°C was kept at 15 torr. The gases used in the gas mixtures indicated by the oxygen content P_{O_2} were 99.995% pure for both N_2 and O_2 . Dry air was also used for comparing the results with those obtained in the gas mixtures.

RESULTS AND DISCUSSION: A) Breakdown Process The breakdown process can be divided into two types each with three phases of discharge. As the initial phase of the process, the first corona streamer (FCS), the ionizing wave (IW), secondary mid-gap streamers (cathode directed streamer (CDS) and anode directed streamer (ADS)) and the diffused luminous wave (DLW) occur in a sequence and is independent of the oxygen content. After the DLW reaches the anode glow (AG) in front of the anode, the intermediate phase of the process starts. In this phase, a positive column forms and develops from anode to cathode with the growth of discharge current. The transient positive column consists of a diffused positive column (DPC) and a

filamentary positive column (FPC). However, this phase of discharge can be divided into two distinct types of the transient glow, as shown in Fig.1(a). In the first type, for the range between P_{O_2} = 0% and 9%, no cathode streamers (CS)/1/ appear. The second type is as follows; for the range between P_{O_2} = 10% and 100%, a series of the CS advancing from the negative glow (NG) to the DPC appear. Furthermore, the breakdown process for P_{O_2} = 21% shown in Fig.1(a) becomes very similar to the one in air as shown in Fig.1(b), and the mean frequency (fs) of the CS increases from about 20kHz to 300kHz with the oxygen content in the range 10-100%, as shown in Fig.2. As the final phase of the process, the DPC reaches the NG, the discharge current increases rapidly and the transient glow changes into the transient arc without a Faraday dark space (FDS). In short, two types of the breakdown process in the N_2 - O_2 gas mixtures may be illustrated schematically as shown in Fig.3.

B) Negative Glow and Transient Positive Column Fig. 4(a) and (b) show the current density, J_N , in the NG and J_P , in the positive column obtained as a ratio of the discharge current, I , to the luminous cross section which was measured in the framing photograph. I - J_N characteristics and the values of J_N are approximately the same as those of dc glow discharge. On the other hand, the current density of the DPC in the range 0.05-2 A/cm² and the FPC in the range 2-30 A/cm² is the same as that of the positive column in dc glow discharge and the arc column in dc arc, respectively/2/. According to a spectroscopic study, 1st and 2nd positive band systems of N_2 are strong in

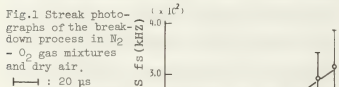
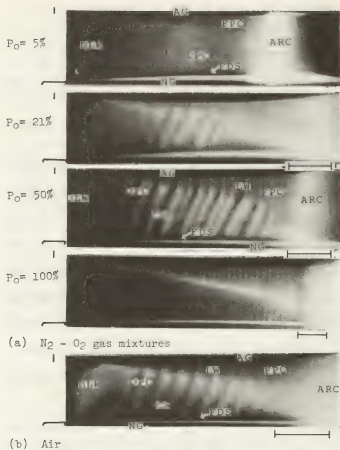


Fig.2 Mean frequencies of cathode streamer versus oxygen content

the spectra of the DPC and the CS and 1st negative band of N_2^+ becomes recognizable only in the spectra of the FPC and the Arc, in Fig.5. These results are similar to those in glow and arc discharge/3/ respectively.

CONCLUSION: (1) Discharge process in the N_2 - O_2 gas mixtures at low pressure changes significantly with the oxygen content. (2) The states in the DPC and FPC are the same as those in glow and arc discharge respectively.

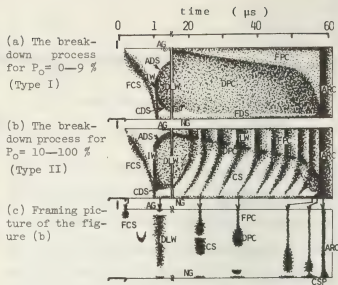


Fig.3 Conceptual figures of the breakdown processes in N_2 - O_2 gas mixtures

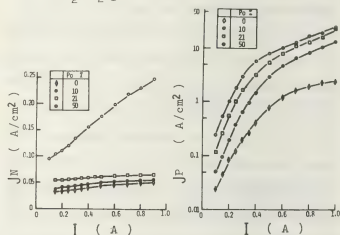


Fig.4 Discharge current versus current density in the negative glow and the positive column

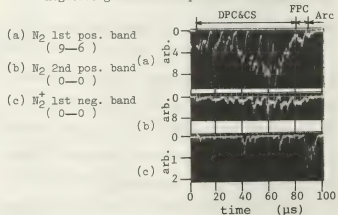


Fig.5 Relative intensity of N_2 and N_2^+ band spectra for various discharge phases at $P_O = 21\%$

REFERENCES

- /1/ T. Oshige: J. Appl. Phys., **38**, 2528 (1967)
- /2/ A. von Engel: "Ionized Gases", (2nd Edition) Clarendon Press (1965)
- /3/ K.R. Allen and K. Phillips: Proc. Phys. Soc., London, **A278**, 168 (1964)

THEORETICAL INVESTIGATION OF RADIO-FREQUENCY DISCHARGE IN γ -REGIME

V.A. Godysk, A.S. Khanneh.

Moscow State University, Department of Physics Moscow, U.S.S.R.

The existence of two different regimes of RF discharge (α and γ -regimes) was first mentioned in paper /1/. As the luminosity of the high voltage regime was observed to be similar to that of the glow discharge, the author /1/ put forward a hypothesis that secondary emission from the electrodes (γ -process) plays an important role in this regime (γ -discharge). It is presumed that γ -processes are negligible in the low voltage regime (α -discharge).

In this paper the ionization balance and the characteristics of a symmetric RF discharge taking into account γ -processes are studied.

If the ionization by the fast electron beam injected from the sheath is taken into account the ambipolar diffusion equation becomes:

$$\Delta(\mathcal{D}n) + Zn + G = 0 \quad (1)$$

$$J_i = e v_i n|_{x=\pm d} = -e \mathcal{D} \frac{dn}{dx} \Big|_{x=\pm d}$$

where n -the plasma density; Z -the ionization frequency of the plasma electrons; \mathcal{D} -the ambipolar diffusion coefficient; J_i -the ion current density at the plasma-sheath boundary ($x = \pm d$) and

G -the rate of beam ionization is given by expression:

$$G = \Gamma \frac{J_i}{e\lambda} \frac{2ch \frac{x}{\lambda}}{\exp \frac{x}{\lambda}}; \quad \Gamma = \frac{\varepsilon J_e}{\varepsilon_0 J_i}$$

where J_e -current density of the electron

beam; ε -mean beam energy; ε_0 -energy losses for one ionization; λ -the beam damping length; v_i -ion velocity at the boundary.

The solution of (1) for a cylinder with radius R and length $2d$ if $\frac{\sqrt{T_e}}{T_e} \ll \frac{\sqrt{n}}{n}$, $\lambda^2 \ll R^2, d^2$ is:

$$n(x, r) = n_0 y(x) \tilde{J}_0(2.4 \frac{r}{R})$$

$$y(x) = \cos(m \frac{x}{d}) - y_i \frac{v_i}{\mathcal{D}} \Gamma \lambda \frac{2ch \frac{x}{\lambda}}{\exp \frac{x}{\lambda}} \quad (2)$$

$$y_i = \cos m \left(1 + \frac{v_i}{\mathcal{D}} \Gamma \lambda\right)^{-1}$$

$$m \tan m = \frac{1 - \Gamma}{\Gamma} \frac{d}{\lambda}; \quad \frac{Z}{\mathcal{D}} = \left(\frac{2.4}{R}\right)^2 + \left(\frac{m}{d}\right)^2$$

where n_0 -plasma density at the centre ($x=0, r=0$); $y_i = y(\pm d)$ -its relative value at the boundary; T_e -the electron temperature. The values of m and Z as functions of Γ are shown in Fig.1 for $d = R = 10\lambda$.

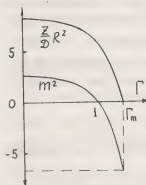


Fig.1

It can be seen (Fig.1) that when $\Gamma \gg 1$ beam ionization brings about a drop in the plasma ionization frequency ($Z \rightarrow 0$). This should lead to a decrease in the electron temperature and the effective RF field in plasma E .

When $\Gamma \ll 1$ (α -discharge) the influence of the beam ionization on the plasma is negligible. Γ is limited by the maximum value:

$$\Gamma \leq \Gamma_m = (1 - 2.4 \frac{\lambda}{R} \ln 2.4 \frac{d}{R})^{-1}$$

which follows from (2) if $Z = 0$. When $\Gamma \approx \Gamma_m$ beam ionization becomes the main process (γ -discharge). In this case Z is negligible and the axial plasma distribution is:

$$y = ch 2.4 \frac{x}{R} - y_1 \frac{v_1}{2} \Gamma \lambda \frac{2ch \frac{x}{R}}{\exp \frac{x}{\lambda}}; \quad y_1 = \frac{ch 2.4 \frac{d}{R}}{1 + \frac{v_1}{2} \Gamma \lambda} \quad (3)$$

Calculations show that when the fact that Z is a function of E and thus of x coordinate [2] is taken into account for the γ -discharge ($\Gamma = \Gamma_m$) $y(x)$ is determined by (3) only when $d < L$ (L is given below). For $d \gg R$ ($d - R > L$) in γ -discharge the axial plasma distribution is homogeneous ($y(x) \approx 1$) and $\frac{E}{\phi} = (\frac{2.4}{R})^2$ in the range $|x| < d - L$. Thus T_e and E are the same as in the plasma of the positive column (E_H) of the d.c. discharge. In the range $|x| > d - L$ the plasma distribution is

$$y' = \frac{ch 2.4 \frac{x}{R}}{ch 2.4 \frac{d}{R}} - y_1' \frac{v_1}{2} \Gamma \lambda \frac{2ch \frac{x}{R}}{\exp \frac{x}{\lambda}}; \quad y_1' = \frac{y_1}{ch 2.4 \frac{d}{R}} \quad (4)$$

Here E and T_e are comparatively low. It can be seen that in γ -discharge the maximum plasma density is at a distance of about λ from the boundary. When gas ionization in the sheath is taken into account Γ is given by

$$\Gamma = \frac{E/E_0 \cdot \gamma \langle \exp \int \alpha(x, t) dx \rangle}{\gamma + 1 - \langle \exp \int \alpha(x, t) dx \rangle} = \Gamma(u_c, PS_m, \gamma) \quad (5)$$

where γ - the electron-ion emission coefficient; α - Townsend's first ionization coefficient; S , S_m - sheath thickness and its maximum value respectively; P - the gas pressure and u_c - the amplitude of RF voltage in the sheath. According to [3] u_c and S_m are given by

$$u_c = \frac{\omega}{2\sqrt{2}} \int_0^d E dx + \left[V_c^2 - (2\sqrt{2} \int_0^d E dx)^2 \right]^{1/2} \quad (6)$$

$$S_m = (mv\omega)^{-1} 2\sqrt{2} e E_1; \quad E_1 = E(\pm d)$$

where V_c - the amplitude of the discharge voltage; ν - electron-atom collision frequency. The equation $\Gamma = \Gamma_m = 1$ leads to a PS_m - dependence at u_c which is similar to the P/E_0 - dependence at u_k (u_k , E_k - the cathode fall and the cathode fall re-

gion in the glow discharge).

Fig. 2 shows a qualitative $PS_m(u_c)$ curve, corresponding to $\Gamma = 1$. When increasing u_c to a critical value $u_{c\gamma}$ (point A in Fig. 2) Γ sharply increases from a negligible value ($\Gamma \ll 1$) to $\Gamma = 1$, indicating that a transition from α to γ discharge takes place. Further increase of u_c leads to a drop-

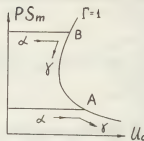


Fig. 2

ping of S_m thus to an increase in the steepness of the of the volt-ampere curve of the discharge ($J \sim \frac{u_c}{S_m}$). If PS_m in the low voltage discharge is large enough, $J(u)$ curve of the discharge may happen to be negative (a transition at point B in Fig. 2). This may be the cause of the discharge current instability. Since in γ -discharge S_m is determined by $PS_m = PS_\gamma = f(u_c)$ the current density is (sheath conduction current is neglected):

$$j_\gamma = \frac{\omega u_c}{4\pi S_\gamma} = \frac{P \omega u_c}{4\pi PS_\gamma} \quad (7)$$

The plasma density and RF field at the boundary are $n_1 = p^2 u_c (2\pi e (PS_\gamma)^2)^{-1}$; $E_1 = \frac{mv\omega S_\gamma}{2\sqrt{2}e}$

Plasma density n_0 is obtained from (3), (7)

For $d < L$; $n_0 = \frac{v_1}{2} \lambda p^2 u_c [2\pi e (PS_\gamma)^2 ch 2.4 \frac{d}{R}]^{-1}$

For $d - R > L$; $n_0 = mv\omega u_c (4\sqrt{2} \pi e S_\gamma E_H)^{-1}$

where L is defined by

$$L = \frac{R}{2.4} \ln \left(\frac{\sqrt{2} e v_1 \lambda E_H}{mv\omega S_\gamma} \right)$$

The expression for J and n in the α -discharge are qualitatively different [3]:

$$J_\alpha \sim \omega^2 u_c (E_1/p)^{-1}; \quad n_\alpha \sim \omega^2 u_c (E_1/p)^{-2}$$

Conduction current in γ -discharge sheath is negligible and plasma density is time independent ($\frac{1}{n} \frac{dn}{dt} \ll \omega$) when

$$\frac{P}{\omega} \ll (PS_\gamma)^{3/2} \left(\frac{e \lambda_1}{\pi M} p u_c \right)^{-1/2}$$

where λ_1 - ion mean free path; M - the ion mass. This defines the range of applicability of the theoretical model presented in this paper.

References:

- 1/ I. С. М. Левитский, ЖТФ, 27, 970, 1957.
- 2/ W. P. Allis & all, Phys. Rev., 84, 519, 1951.
- 3/ В. А. Голяк, Физика плазмы, 2, 141, 1976.

THE RATIO OF LATERAL DIFFUSION COEFFICIENT TO MOBILITY FOR ELECTRONS IN OXYGEN AND CARBON DIOXIDE

W. Roznerski and J. Mechlińska-Drewko.

Institute of Physics, Technical University of Gdańsk, Poland.

Abstract. The ratio of lateral diffusion coefficient to mobility D/μ in oxygen and carbon dioxide at ambient temperature has been determined for the reduced electric field E/N of $67.4 \leq E/N \leq 392.4$ Td and $15.2 \leq E/N \leq 280.9$ Td respectively.

Method. The present results have been obtained by means of Townsend and Huxley's technique [1]. The solution of the steady state electron transport equation - electron density - satisfying the boundary conditions on the surfaces of the cathode and the anode is expressed in the form of an infinite series of dipole solutions as

$$n = \sum_{k=-\infty}^{+\infty} \tau_k^{-3} (z-2kh)(\beta r_k+1) \exp(\lambda_L z - \beta r_k)$$

where

$$\tau_k = \left[(z-2kh)^2 + \frac{D_L}{D} s^2 \right]^{1/2}; \quad \lambda_L = \frac{W}{2D_L};$$

$$\beta = \lambda_L \left(1 + \frac{2\alpha'}{\lambda_L} \right)^{1/2}; \quad \alpha' = \eta - \alpha.$$

The quantities D, D_L, W, h, η and α are the lateral diffusion coefficient, the longitudinal diffusion coefficient, the drift velocity, the length of diffusion space, the attachment and the ionization coefficients respectively.

The electron current collected by the arbitrary part of the anode may be determined by the integration of current density on the anode over this surface. An expression for the fraction of total cur-

rent falling on the central disc of a divided anode results immediately from this calculation [2].

To consider the influence of negative ions in the presence of attachment processes, the procedure elaborated by Huxley and Crompton [1] has been used in this work. This procedure adopted to the present version of experiment has been described earlier [3].

For the determination of the D/μ coefficients by means of procedures mentioned above, the knowledge of the D_L/μ coefficient, the attachment coefficient η and the ionization coefficient α is necessary. Except for the D_L/μ coefficient in carbon dioxide above 182 Td, the remaining quantities are available over the investigated ranges of E/N [6, 9-13]. The limits of the variation of the D_L coefficient have been estimated on the basis of the thermodynamic treatment of anisotropic diffusion in an electric field [4].

Experiment. The experimental conditions have been described in work [5].

Results. The ratio of lateral diffusion coefficient to mobility D/μ as a function of E/N in oxygen and carbon dioxide have been illustrated in the figures 1 and 2 respectively.

The estimated values of the standard deviation of D/μ coefficients are equal 1.5% for $E/N > 182$ Td in carbon dioxide and 1% for all other values of E/N in oxygen and carbon dioxide.

Conclusion. It seems, that the procedure applied in the present work allows to determine the D/μ coefficients for the large range of reduced electric field.

References.

- [1] L.G.H.Huxley and R.W.Crompton, The Diffusion and Drift of Electrons in Gases, Wiley-Interscience, New York 1974.
- [2] W.Roznerski, J.Phys.D: Appl.Phys. **11**, L 197 (1978).
- [3] W.Roznerski and J.Mechlińska-Drewko, Phys.Letters A (accepted for publication).
- [4] R.E.Robson, Aust.J.Phys. **25**, 685 (1972).
- [5] W.Roznerski and J.Mechlińska-Drewko, Report Z.N.P.G.(Technical University of Gdańsk) - Fizyka XIX, **264**, 105 (1977).
- [6] J.J.Lowke and J.H.Parker, Phys.Rev. **181**, 302 (1969).
- [7] M.S.Naidu and A.N.Prasad, J.Phys.D: Appl.Phys. **3**, 957 (1970).
- [8] J.A.Rees, Aust.J.Phys. **17**, 462 (1964)
- [9] C.S.Lakshminarasimha, J.Lucas and N.Kontoleon, J.Phys.D: Appl.Phys. **7**, 2545 (1974).
- [10] H.Schlumbohm, Z.Physik. **184**, 492 (1965).
- [11] J.B.Freely and L.H.Fisher, Phys. Rev. **132**, A304 (1964).

- [12] M.S.Bhalla and J.D.Craggs, Proc. Phys.Soc. **76**, 369 (1960).
- [13] S.R.Alger and J.A.Rees, J.Phys.D: Appl.Phys. **9**, 2661 (1976).

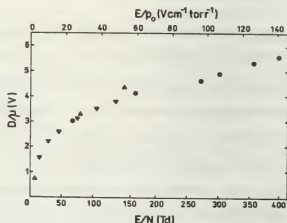


Fig.1. The D/μ coefficient in oxygen as a function of E/N . ● Present results; ▲ Lowke and Parker [6]; ▼ Naidu and Prasad [7].

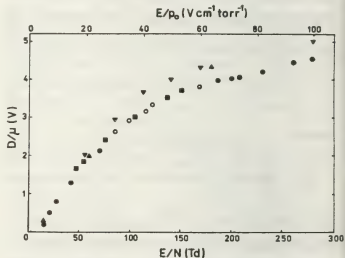


Fig.2. The D/μ values in carbon dioxide as a function of E/N . ● Present results; ○ Results of work [3]; ▼ Lakshminarasimha et al. [9]; ▲ Lowke and Parker [6]; ■ Rees [8].

SOME CHARACTERISTICS OF AN ELECTRIC DOUBLE LAYER IN A MAGNETIZED PLASMA

L. Lindberg and S. Torven.

Department of Plasma Physics, Royal Institute of Technology, S-100 44 Stockholm 70.

Electric double layers have recently attracted much interest and several new experimental results have been reported [1] [2] [3] [4] [5].

Recent reviews of the phenomenon include a general survey [6] as well as separate reviews of experiments [7] and theory [8]. Several possible applications to space and astrophysical plasmas have been discussed [9] [10] [11].

Most experiments so far have been performed in non-magnetized plasmas. Since the existence of double layers in magnetized plasmas has now been proved, much work remains to systematically investigate the properties of such double layers. The present paper reports some initial results.

The double layer studied is one with a monotonic potential variation but with a rapidly varying spatial location. It is also accompanied by a complicated spectrum of waves with frequencies from the ion acoustic regime (5 kHz) up to frequencies larger than the plasma frequency (400 MHz).

The double layer is produced in a plasma column, radially confined by an axial magnetic field (0.005-0.15 T) in the vacuum chamber between E_2 and A (Fig. 1). The plasma is maintained by a source giving inflow of plasma through an aperture in E_2 , which defines the diameter of the plasma column (1.5 cm). The plasma source is a dc arc discharge at about 1 mTorr between the mercury pool cathode C and the hollow electrode E_1 . The mercury vapour pressure in the vacuum chamber is kept typically an order of magnitude smaller than in the source. Double layers have been observed to form for electron gyro-frequencies f_{ce} in the interval $f_p/3 \leq f_{ce} \leq 5 f_p$. Here f_p is the plasma frequency. The results reported below refer to a weak magnetic field of 5 mT and a mercury atom number density of $3 \cdot 10^{18} \text{ m}^{-3}$.

As has been described previously [5], the double layer evolves from an electron rich anode sheath, when the anode potential is increased to some tens of volts (depending on the background pressure of

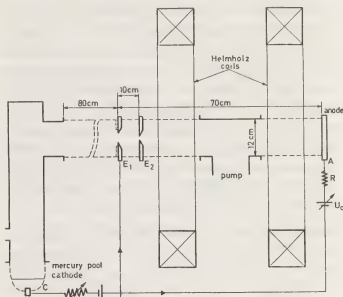


Fig. 1. Schematic picture of the discharge device. A plasma column is obtained between E_2 and A by inflow of plasma along the magnetic field through the aperture in E_2 . The plasma source is a dc arc between C and E_1 .

neutral gas) above the plasma potential. Then most of the original potential drop over the anode sheath appears over the double layer, and between the layer and the anode a new plasma (the anode plasma) is formed. The anode plasma is maintained by ionization due to electrons accelerated in the layer, whereas ionization processes are negligible in the cathode plasma owing to the low electron temperature there (2 eV). The diameter of the anode plasma column is also larger than that of the cathode plasma.

Once the layer has formed, it can be moved to any position between E_2 and A by an adjustment of the discharge current. The layer position is not stationary, but the layer moves irregularly back and forth with amplitudes somewhat larger than the layer thickness. The typical velocity in this motion (300 m/s) is much smaller than the ion acoustic speed [5]. A coincidence technique is used to reduce the effect of these fluctuations on the measurements. At a point, through which the double layer oscillates, the potential is sensed by means

of an emitting Langmuir probe and compared with a fixed value. At coincidence a short triggering pulse is produced, which is utilized for sampling of the signals from other probes. Such a sampling has also been made directly from oscillograms. Diagrams (a) and (b) in Fig. 2 show potential and electron density (expressed as a local plasma frequency) measured with movable Langmuir probes. Hot, electron emitting probes were used to measure the potential, and the density was obtained from swept characteristics of a cold probe. The sampling method reduces effects of the layer motion. However, fluctuations in the asymptotic layer voltage, in the frequency range 5 - 20 kHz, are still present as indicated ($\delta\phi$) in diagram (a). The potential level of the whole anode plasma fluctuates relative to the quiescent cathode plasma. Potential fluctuations measured simultaneously at any two positions within the anode plasma appear to be identical (within the bandwidth of the probes, 0 - 200 kHz) implying a propagation speed larger than 10^5 m/s.

Diagram (c) in Fig. 2 shows the spatial distribution of rf-power. This was picked up by an axially

movable probe consisting of an open coaxial cable of small dimensions, led into the plasma through a capillary glass tube. The power was measured by a spectrum analyzer at a frequency of 350 MHz, and such a spatial variation existed in a frequency band with a bandwidth of about 100 MHz. Electron distribution functions are being measured to correlate the observed spatial distribution of the rf-power to beam-plasma interaction. Double humped distributions have been observed on the anode side of the layer. Another rf-spectrum with an upper cut-off frequency at about 150 MHz also exists both in the anode and the cathode plasma.

The existence of the marked minimum in the electron density (Fig. 2), implying the possibility of trapping of Langmuir waves at the double layer [12], has been confirmed for a wide range of parameter values.

REFERENCES

- [1] Lutsenko, E.I., Sereda, N.D., and Kontsevoi, L.M., 1975, *Zh. Tekh. Fiz.* **45**, 789 (*Sov. Phys. Tech. Phys.* **20**, 498).
- [2] Quon, B.H. and Wong, A.Y., 1976, *Phys. Rev. Lett.* **37**, 1393.
- [3] Coakley, P., Hershkovitz, N., Hubbard, R., and Joyce, G., 1978, *Phys. Rev. Letters* **40**, 230.
- [4] Levine, J.S., Crawford, F.W., and Ilić, D.B., 1978, *Phys. Lett.* **65A**, 27.
- [5] Torvén, S. and Andersson, D., 1978, Report TRITA-EPP-78-12, Royal Inst. of Tech., Stockholm (To be published in *J. Phys. D: Appl. Phys.*).
- [6] Block, L.P., 1978, *Astrophys. Space Sci.* **55**, 59.
- [7] Torvén, S., 1978, Report TRITA-EPP-78-13, Royal Inst. Tech., Stockholm (To be published in *Wave Instabilities in Space Plasmas*, Astrophysics and Space Science Book Series, Reidel Publ. Comp., 1979).
- [8] Carlqvist, P., 1978, Report TRITA-EPP-78-15, Royal Inst. Tech., Stockholm (To be published in *Wave Instabilities in Space Plasmas*, Astrophysics and Space Science Book Series, Reidel Publ. Comp., 1979).
- [9] Fälthammar, C.-G., Akasofu, S.-I., and Alfvén, H., 1978, *Nature* **275**, 185.
- [10] Shawhan, S.D., Fälthammar, C.-G., and Block, L.P., 1978, *J. Geophys. Res.* **83**, 1049.
- [11] Alfvén, H., 1978, *Astrophys. Space Sci.*, **54**, 279.
- [12] Wahlberg, C., 1978, Report UPTC 7889R, Inst. of Techn., Uppsala University, Uppsala, Sweden.

ACKNOWLEDGEMENT

This work was supported by the Swedish Natural Science Research Council.

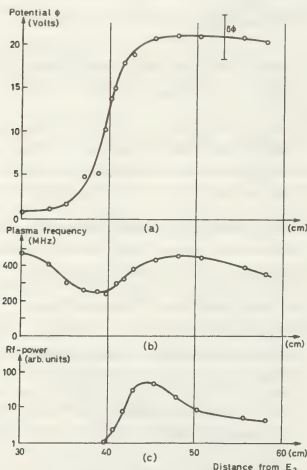


Fig. 2. The diagrams show simultaneously sampled axial profiles of the electric potential (a), the local plasma frequency (b), and the rf-power at 350 MHz (bandwidth 3 MHz).

NONLINEAR EFFECT OF THE IONIZATION WAVES ON THE TEMPERATURES OF CHARGED PARTICLES IN A MAGNETIZED POSITIVE COLUMN

S. Imazu, H. Fujita, K. Miura and T. Takamatsu.

Faculty of Engineering, Hiroshima University, Sendacho 3-8-2 Hiroshima Japan.

Introduction: The diffusion of charged particles across a magnetic field, especially the enhanced diffusion, is a problem of considerable interest. In many experiments $/1-2/$ on the positive column, a longitudinal electric field E_{0z} decreases according to the classical diffusion theory with increasing the magnetic field B . Furthermore, when B exceeds a certain critical value B_c , the helical instability starts, and then E_{0z} increases abruptly due to the enhanced diffusion. However we have experimentally found the phenomenon that, when the ionization waves start at the magnetic field slightly below B_c , E_{0z} increases to exceed the values obtained from the classical diffusion theory.

In this report, the nonlinear effect of the ionization wave on the longitudinal electric field E_{0z} is investigated for helium. Then it is found that the mean energies of the charged particles increase according to the nonlinear effect of the longitudinal perturbed electric field E_1 and, consequently, the longitudinal electric field E_{0z} increases. The theoretical values obtained are compared with experimental data, and found to be in agreement with present experiments.

Methods and results: A cylindrical symmetry is assumed in a coordinate system (r, ϕ, z) with z axis along the column, and the column is situated in a longitudinal magnetic field B . The theoretical equations are derived under the following assumptions: 1) The mean free paths of electrons and ions are small to the tube radius R . 2) The electron and ion gases have Maxwellian distributions. 3) As the metastable atoms of helium, 2^1S_1 is taken into account. 4) Molecular ions are neglected compared with atom ions. 5) The equivalent temperatures of ions at plasma edge are equal to $T_e/2$.

As basic equations, the continuity equations for the number densities of electrons, ions and metastable atoms, respectively, and the conservation equations for the energies of charged particles are used. Moreover Poisson's equation is used. (a) Steady state: We first derive the expressions for the mean energies of electrons T_e and ions T_i as a function of B for the steady state. Figure 1 shows the theoretical curves ($\gamma=0$) of T_e -vs- B and T_i -vs- B for the steady state. As shown in Fig. 1, we confirm that T_e and T_i decrease together with increasing B , according to the classical diffusion theory. Further, we obtain the expressions for the longitudinal electric field E_{0z} as a function of B for steady state, and then show the theoretical curves of E_{0z} -vs- B for $\gamma=0$ in Fig. 2, which correspond to the curves of T_e -vs- B and T_i -vs- B for $\gamma=0$ in Fig. 1. Figure 3 shows the comparison of the theoretical curve ($\gamma=0$) with experiments. As shown in Fig. 3, up to $B=B_1$ (1.25 kG) the theoretical values for $\gamma=0$ are in good agreement with experimental values. Therefore we confirm the classical diffusion theory in the region of B from 0 to B_1 . However Fig. 3

shows that the difference between the theoretical and experimental values occur above B_1 that the ionization waves develop. Although it is well known that an anomalous diffusion occurs above the critical magnetic field B_c (≈ 2.25 kG) that the helical instabilities develop.

(b) Perturbed state: We can choose a perturbation of the form $\tilde{F}_1 \cdot \exp(i\omega t - ikz)$, where k is the wave number ($k=2\pi/\lambda$), $\omega = \omega_r + i\omega_i$ the angular frequency and λ the wave length. \tilde{F}_1 is the perturbed quantity of complex number. The perturbed electric field E_1 in the longitudinal direction is derived by solving Poisson's equation, assuming the density distribution in the radial direction to be the zero order Bessel function $J_0(\alpha r)$. Where $\alpha = \sqrt{Z/D_a}$, Z is the ionization frequency and D_a the ambipolar diffusion coefficient. Here we postulate that the perturbed part of density exists in addition to steady state density. In nonlinear calculation, we can not use $\exp(i\omega t - ikz)$ and then take its real part. Putting the determinant deduced from these expressions be equal to zero, we obtain the dispersion equation for ω . We have $\omega_i < 0$, and then the amplitude of the structure exponentially with time.

(c) Effect of perturbed field E_1 : The electric field term in the energy balance equation contains the second order perturbed electric field. In the nonlinear calculation, the zero harmonic term can be written as the sum of two terms, one of which is $e\mu E_0 E_1$ for the equilibrium state. What remains is $\frac{1}{2}e\mu E_1^2$. Here μ is the mobility. The term $\frac{1}{2}e\mu E_1^2$ gives cause to increase the energies of electrons and ions when the ionization wave exists.

Figure 1 shows the curves of T_e -vs- B and T_i -vs- B for the various of γ . Where $\gamma = |E_1|/E_0$. E_0 is not equal to E_{0z} when the perturbation exists. E_{0z} is obtained from the equation of the total axial current. Here we take into account of the nonlinear effect of the electron temperature on the ionization frequency. The influence of ions on the growth of the ionization waves become to be greater than that of metastable atoms with increasing B . Figure 2 shows the curves of E_{0z} -vs- B for the various values of γ . In Fig. 3 the curve of E_{0z} -vs- B (the broken line) obtained from the conditions of ionization waves and the perturbed state mentioned above is compared with the present experimental values. In our experiments $/3/$, the discharge tube of 90 cm long and 1 cm radius, containing helium ranging from 0.5 to 1.0 Torr, was placed at the axis of a solenoid coil with the length of 70 cm. To measure the electric field E_{0z} two ring probes, P_1 and P_2 , were introduced into the middle part of the tube. Two pairs of wall probes P_3 and P_4 were mounted in a plane perpendicular to the axis of the tube. The mode m and the frequency f of the helical instability were measured with these wall probes. The wave length λ and the frequency f of the ionization waves were measured with the optical observation of the side light from the discharge tube. For typical

examples, the dependencies of λ , f and E_{0z} as a function of B are shown in Fig. 3. Here the ionization waves occur above B_1 . When B is raised further, the ionization waves coexist with the helical instabilities that start above B_C , and that E_{0z} increases rapidly.

Discussion: The theoretical curve of E_{0z} -vs- B calculated from the classical diffusion theory is indicated by the full line for $\gamma=0$ in Fig. 3. The theoretical curve below B_1 shows a satisfactory agreement between the theoretical values and experiments. Above B_1 the experimental values of E_{0z} exceed slightly the theoretical values for $\gamma=0$, and above B_C the great discrepancies between the theoretical values and experiments arise due to appearance of the helical instabilities. We attend to the results that in the region between B_1 and B_C the experimental values of E_{0z} exceed the theoretical values for $\gamma=0$. The theoretical values calculated from the nonlinear theory of ionization waves are indicated by the broken lines. This theoretical curve is in agreement with the experimental values in the region that the ionization waves appear.

We confirm that, when the ionization waves develop above B_1 , the perturbed electric field E_1 causes to increase the temperatures of electrons and ions, and then the diffusion coefficients of charged particles become more than the classical diffusion theory in the equilibrium state. Therefore the electric field E_{0z} in the axial direction increases.

We can draw the following conclusions: 1) The ionization wave near B_C is only a positive ion-guided ionization wave. 2) The ionization waves cause to increase the mean energies of electrons and ions according to nonlinear effects of waves.

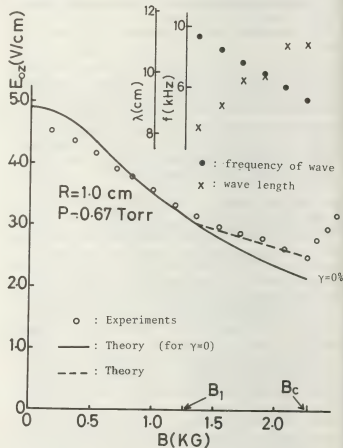
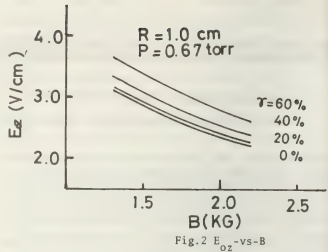


Fig. 3 Theoretical and Experimental values of E_{0z} -vs- B

References:

- /1/ B.Lehnert: 2nd UN Geneva Con. 32, 349(1958)
- /2/ B.B.Kadomtsev and A.V.Nedospasov: J. Nucl. Pt.C1, 230(1960)
- /3/ S.Imazu,K.Miura,T.Takamatsu,H.Shindo and T.Maruyama: Proc. XIII th. Int. Con. Phenom. in Ion. Gas. , Berlin (1977)295

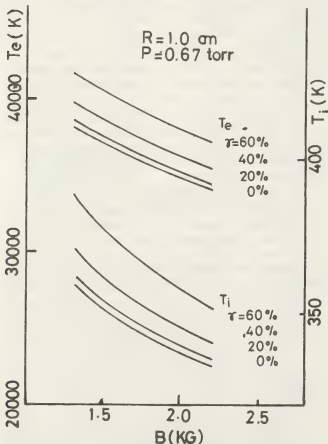


Fig.1 T_e -vs- B and T_i -vs- B

INVESTIGATIONS OF THE CONTRACTION MECHANISM IN A HELIUM MEDIUM PRESSURE DISCHARGE

Yu.B. Golubowsky and R. Sonnenburg*

Institute of Physics, Leningrad State University Department of Optics and Spectroscopy, Leningrad U.S.S.R.

*Ernst-Moritz-Arndt-Universität, Sektion Physik/Elektronik Greifswald, DDR.

Introduction In a series of publications the radial inhomogeneous heating of gas characteristic of medium pressure discharges is considered to be the reason for the contracted state of the positive column in rare-gas discharges. Experimental and theoretical investigations in argon and neon discharges at pressures of several hundred torr/1-4/ demonstrated that the abrupt contraction as well as the appearances linked to it can be explained without regarding the radial gas temperature gradient. The involvement of the energy balance of the atoms in the initial equation system, however, results in a better quantitative correlation of theory and experiment /4/. The present study investigates the contraction mechanism of the column of a helium discharge at medium pressures.

Experimental results Fig.1 shows the monotonous change of the potential gradient E (curves 1,2,3,4,5 correspond to values $p_0 R = 100, 200, 300, 500, 700$ torr cm, $R = 1$ cm) in dependence on the discharge conditions at a constant wall temperature $\theta \approx 320^\circ\text{K}$. The effective current cross section μ (a rate for the degree of contraction)
$$\mu = 2\pi \int_0^R j(r) dr$$
 $j(r)$ -current density, is $\mu \approx 0,12$ (in the case of Bessel distribution $\mu \approx 0,24$). This weak current contraction is caused by the radial inhomogeneous heating of gas. The character of discharge fundamentally changes in the case of free temperature exchange of the discharge tube with the surrounding air. The examples of E and μ in fig.2 show an abrupt change of all plasma parameters if a critical current value is reached ($p_0 R = 100$ torr cm). A weak radial contraction of the continuum radiation and a strong contraction of the line radiation is characteristic of this appearance.

Discussion The starting point for the calculation of the plasma parameters is an equation system consisting of the

balance equation of the charge carriers, the energy balance equation of the atoms and electrons and the equation for pressure and discharge current/4/. The ionization model of paper /4/ was used with I and Γ as effective rates of ionization and recombination considering the presence of atomic and molecular ions in the discharge. The experimental results can be qualitatively explained with the help of this equation system taking into account the peculiarity of the elementary processes in a helium discharge. Since the electron-atom collision frequency in the elastic range for helium does not depend on the electron velocity and thus the ionization frequency is not a nonlinear function of the electron concentration, its radial decrease is determined by a term of the kind $I \sim \exp(-eV_1/AT_e)$ with V_1 -first excitation potential, T_e - electron temperature. There are no data in the literature on the coefficient of the dissociative recombination in helium at medium pressures. Due to the position of the intersection of the potential curves of the molecular ion and the quasi-molecule in the range of the third vibrational level we can assume that the recombination of molecular ions in higher vibrational states occurs with slow electrons. On the assumption that the distribution of these ions over the vibrational levels at medium pressures is mainly determined by collisions with atoms the number of the recombination events per unit time and unit volume must contain a term $\Gamma \sim \exp(-eV_2/2\theta)$ with V_2 -potential of the vibrational level in the range of the intersection of the potential curves, θ -atom temperature. In this model the

transition to the column in the recombination range is possible which is not accompanied by a current contraction if the radial decrease of the ionization rate proceeds more planar than that of the recombination rate.

This is the case if in the ratio I/Γ

$$\frac{I}{\Gamma} = \exp \left[- \frac{eV_1}{kT_e} \left(1 - \frac{V_y T_e}{V_1 \Theta} \right) \right] \tag{1}$$

the parameter is

$$\frac{V_y T_e}{V_1 \Theta} > 1 \tag{2}$$

In the opposite case contraction will occur. Fig.3a)b) show the results of the calculations for the case of constant wall temperature $\Theta_w \approx 320^\circ\text{K}$. For these conditions we can assume that in-equation (2) is valid for all current values and the calculated monotonous current dependence of the parameters corresponds to the experimental observed. At free temperature exchange with the surrounding air the wall temperature of the discharge tube increases with increasing current and the gas temperature Θ_0 in the centre of the discharge as well. As a result of the calculations the electron temperature can be regarded as constant. At a definite current value in-equation (2) changes the symbol and thus contraction follows. The results of the corresponding calculation for increased wall temperatures for $p_0 R = 100$ torr cm are shown in fig.3c)d). The z-like characteristics(fig.3c)d)) obtained by the solution of the initial equation system correspond to the abrupt transition from the diffuse to the contracted state. The contraction appearance in a helium discharge is thus due to the inhomogeneous heating of gas.

References

/1/Golubowsky, Yu.B. et.al., Zur.Tech.Phys. 46(1976)2327
/2/Golubowsky, Yu.B. et.al., Zur.Tech.Phys. 47(1977)1852
/3/Golubowsky, Yu.B. et.al., Zur.Tech.Phys. 47(1977)1478
/4/Golubowsky, Yu.B., Sonnenburg, R. Zur.Tech.Phys.1979

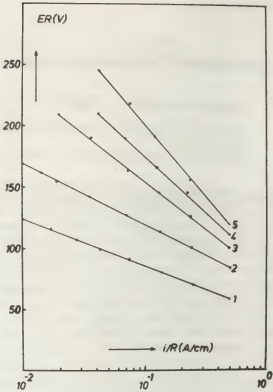


Fig.1

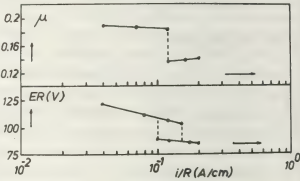


Fig.2

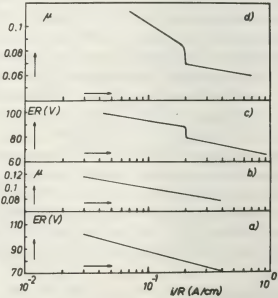


Fig.3

THE POSITIVE COLUMN IN THE THREE-COMPONENT MIXTURE Ne/H/H₂- EXPERIMENTAL RESULTS IN COMPARISON WITH AN APPROXIMATIVE DIFFUSION THEORY

P. Michel, S. Pfau, A. Rutscher and R. Winkler*.

*F.M.A. Universität Greifswald, Sektion Physik/Elektronik, Greifswald, D.D.R.
 *Akademie der Wissenschaften der DDR Zentralinstitut für Elektronenphysik Greifswald, DDR.

INTRODUCTION: During the last years the kinetic description of electrical discharges in multi-component gas mixtures had shown considerable progress. This was the consequence of an already high degree of perfection in solving the BOLTZMANN equation for electrons. Especially multi-component gas mixtures are important in LASERS and plasma chemical reactors. Typical for such devices is a more or less marked interaction between the composition of the mixture and the properties of the discharge. Analysing the dissociation of H₂ recently a first example of the influence of chemical changes (produced by the discharge itself) on the electrical characteristic was given [1]. It could be shown that the negative differential resistance of the positive column follows from increasing dissociation, which reached a considerable extent (about 100%) at high currents and low pressures. Unfortunately in pure hydrogen discharges the space and time behaviour is often complicated by standing or moving striations, fluctuations etc. More silent operation conditions are possible in mixtures of hydrogen and inert gases.

In this paper a neon/hydrogen mixture is investigated by measuring the electric characteristic and the degree of dissociation. Based on a simple theoretical model the experimental results are compared with calculated ones.

EXPERIMENTAL ARRANGEMENT: The axial electric field strength of the positive column (length: 1m, radius: 1cm) was measured via two usual static probes. To reduce the large influence of the electrodes on the degree of dissociation (effective recombination at the metallic surface) two narrow capillaries were attached in front of the electrodes. The degree of dissociation was determined using a WREDE-HARTECK-probe. In all cases the discharge tube was connected with a large dead space.

THEORETIC MODEL: Till now no solution of the BOLTZMANN equation is known for electrons in the three-component mixture Ne/H/H₂. But the discussion of this equation shows that generally the contribution of not too large Ne constituents only

plays a rather small role in the electron kinetics compared with the other terms (resulting from H and H₂) because of the small cross-sections and the large atomic mass of Ne. Neglecting all the Ne terms, the BOLTZMANN equation for electrons in the Ne/H/H₂ mixture changes to that in the H/H₂ mixture with the only difference that the actual (reduced) field strength E/p_0 is replaced by an effective one $(E/p_0)_{\text{eff}} = E/p_0(1-x_0)$; x_0 : relative concentration of Ne. In the framework of this approximation the Ne admixture in a molecular gas discharge mainly plays the role of a buffer gas. Some calculations and experiments have shown this very clearly in the Ne/N₂-mixture [2]. It could be estimated that up to $x_0 \leq 0,5$ and $(E/p_0)_{\text{eff}} \leq 20 \text{ V/cmTorr}$ the explicit influence of Ne in the H/H₂ mixture is very small. At higher Ne content the influence is noticeable, especially in the H/H₂ ionization range of the electron energy distribution function.

Taking into account Ne only as a buffer gas the diffusion theory of the positive column in the Ne/H/H₂ mixture can be formulated using the electron energy distribution functions of H/H₂, mentioned in [1]. Then the balance equations of the charge carriers, of the H atoms and of the discharge current give the basis for calculating the column characteristic, the degree of dissociation etc. With some further simplifications these equations read:

$$\begin{aligned} (\lambda/r_0)^2 (D_e/b_e) (b^+/N_0) &= x_1 z_1 + x_2 z_2 \\ x_1 x_2 z_D - x_1^2 (x_0 z_{R0} N_0 + x_1 z_{R1} N_0 + x_2 z_{R2} N_0) &+ \\ - 4 x_1 \bar{D} / 4 r_0 N_0 &= 0 \\ i &= \pi e_0 r_0^2 N_0 x_1 b_e E \\ (\lambda &= 2,405; D_e, b_e: \text{diffusion coefficient and mobility of electrons; } b^+: \text{mobility of ions;} \\ N_0: \text{total concentration of neutral particles;} &x_0, x_1, x_2: \text{relative concentrations of} \end{aligned}$$

Ne, H, and H_2 particles; z_1, z_2 : ionization rate of H and H_2 ; z_D : rate of H_2 dissoziation by electron collisions; β_2 : recombination rate by three body collisions of H atoms; γ : wall recombination coefficient of H atoms; \bar{c} : thermal velocity; r_0 : column radius; x_1 : degree of ionization). The simplifications mentioned are: Use of only one value for the mobility of the different ions H^+, H_2^+, H_3^+ (BLANCs law shows that this is correct within a failure of about 20%; $b^+ \approx 1,3 \text{ m}^2/\text{Vs}$ at 1 Torr); neglect of the ionization of Ne and neglect of the FENNING ionization of H and H_2 via meta-stable Ne atoms.

RESULTS: Fig.1 shows that with increasing Ne content x_0 the degree of dissociation $x_D = x_1/(x_1 + x_2)$ is increased too. This is the consequence of the increase of the effective field strength. Although the hydrogen component decreases by this change of the mixture ratio the absolute value of the H atom concentration remains nearly constant in the beginning (Fig.2). Fig.3 shows the degree of ionization and dissociation in dependence on the discharge current. The measured values x_D agree quite well with the theory. Finally Fig.4 compares the measured and calculated electric characteristic. The two dashed lines correspond to the limiting cases of constant chemical constitution: Ne/ H_2 (upper curve), Ne/H (lower curve). An explicit consideration of Ne in the BOLTZMANN equation of the mixture would increase these limits which roughly correspond to the experimental values. But the transit from the upper to the lower level differs considerably. Mainly this must be attributed to the neglect of the gas heating at higher currents. As a boundary condition we used $N_0 = \text{const}$ (together with $n_1 + n_2 = \text{const}$). But actually N_0 will decrease with increasing current, giving higher experimental reduced electrical field strengths than shown in Fig.4.

REFERENCES:

/1/ MICHEL, P. et.al. 13th ICPIG, Berlin 1977, p.245
14th ICPIG, Grenoble 1979
/2/ KLAGGE, S. et.al. Beitr. Plasmaphys. 7 (1977) 237

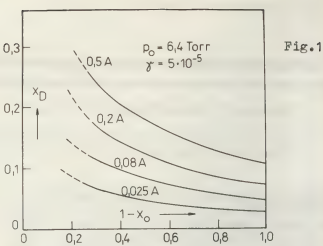


Fig.1

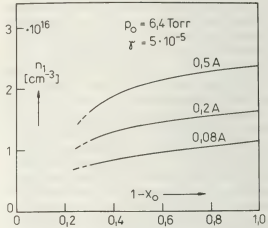


Fig.2

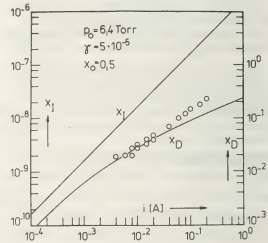


Fig.3

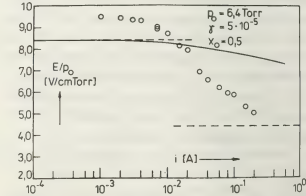


Fig.4

THE RADIO-FREQUENCY SHEATH IN SELF SUSTAINED PLASMOIDS

J. Taillet.

Office National d'Etudes et de Recherches Aéronautiques, 92320 Chatillon France.

Capacitive RF discharges are sustained by the AC current which traverses the sheaths and superimposes an AC voltage to the DC potential between plasma and electrodes/walls. When frequency is low enough, the sheath impedance is high and the peak value of the AC voltage across the sheath can be larger than the DC thermal voltage drop : this opens a gate in the potential barrier which keeps the electrons from leaving the discharge, and increases the positive space charge. Steady state is reached when the potential barrier is restituted, i.e when the plasma potential is increased up to the peak value of the AC voltage across the sheath. This effect is similar to rectification and clamping in electronic circuitry. In connection to this increase in plasma potential, sheath thickness is also increased, according to Child's law.

Described by Wood in 1920, the RF plasmoïds are localized low discharges produced at a pressure between 10^{-3} and 10^{-4} Torr by excitation at a frequency $\omega/2\pi$ between 1 and 100 MHz. They appear in shape of disks, balls, spindles floating far apart from the walls [1]. The RF plasmoïd is a resonance sustained discharge in free fall regime ; in electronegative gases, the negative ion density is much larger than the electronic density, in such a way that the plasma potential distribution is quasi-uniform and that the ion free fall velocity is related to the ionic temperature T_i and not to the electronic temperature T_e . Reference [2] gives a comprehensive survey of the corresponding literature.

The scope of this paper is the analysis of a still unexplained aspect of the behaviour of RF plasmoïds : when gas pressure is reduced, the sheath gets increasingly broader and the plasma contracts and suddenly disappears. In the present work, the unidimensional model of a slab of plasma excited between two plane electrodes is considered (fig. 1).

This model describes the plasmoïd as a discharge sustained by a resonance between sheath and plasma (the electron collision frequency ν

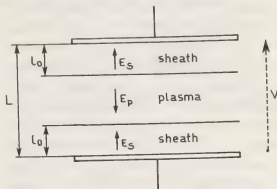


Fig. 1
Unidimensional model of the RF plasmoïd

is smaller than ω). This resonance increases both the plasma RF field E_p and the sheath RF field E_s according to the formulas :

$$(1) \quad E_p = \frac{V}{L} \frac{1}{\sqrt{(1-\theta^2 X)^2 + \theta^4 X^2 \xi^2}}$$

$$(2) \quad E_s = \frac{V}{L} \frac{\sqrt{(1-X)^2 + \theta^4 X^2 \xi^2}}{\sqrt{(1-\theta^2 X)^2 + \theta^4 X^2 \xi^2}}$$

with : V : applied RF voltage, L : electrode spacing l_0 : sheath thickness ; $\theta = (2l_0/L)^{1/2}$; $X = (\omega_p/\omega)^2$ where $\omega_p/2\pi$ is the plasma frequency $\xi = \nu/\omega$. ν is the sum of the electron-neutral collision frequency ν_0 and of an equivalent collision frequency ν' due to electron-sheath interactions [3].

$$(3) \quad \nu' = \eta \frac{\sqrt{kT_e/m}}{L(1-\theta^2)} \quad \eta < 1$$

(m : electron mass)

The sheath RF voltage is :

$$(4) \quad V_s = \frac{V}{2} \frac{\theta^2 \sqrt{(1-X)^2 + \theta^4 X^2 \xi^2}}{\sqrt{(1-\theta^2 X)^2 + \theta^4 X^2 \xi^2}}$$

and, if the thermal effect is neglected, Child's law gives :

$$(5) \quad l_0 = \frac{2}{3} \epsilon_0^{1/2} \omega_p^{-1} \cdot 2^{1/4} \cdot e (kT_e)^{-1/4} (V_S \sqrt{Z})^{3/4}$$

(e : electron charge ; ϵ_0 : permittivity of free space ; k : Boltzmann's constant).

The plasma equations are the population and the power balance equations :

$$(6) \quad \nu_i = \frac{\sqrt{kT_i/m}}{L(1-\theta^2)}$$

(ν_i : ionisation frequency. M : ion mass)

with :

$$(7) \quad \nu_i = p_0 \int_{u_i}^{\infty} P_i(u) v \cdot f(u) du$$

(p_0 : neutral pressure, v : electron velocity

P_i : ionization probability at 1 Torr

$f(u)$: energy distribution u : energy in eV)

$$\text{and : } \mathcal{L} = \mathcal{R} \quad (8)$$

$$\text{with : } \mathcal{L} = \frac{e^2}{m\omega} \left(\frac{V}{L} \right)^2 \frac{\xi}{(1-\theta^2 X)^2 + \theta^4 X^2 \xi^2}$$

$$\text{and : } \mathcal{R} = e u_i \nu_i + e \sum_n u_{en} \nu_{en} + e V_B \nu_i$$

where \mathcal{L} is the power per electron transferred from the RF field to the energy distribution and \mathcal{R} the power per electron spent in ionization, excitation, and ion wall losses.

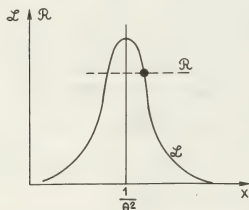


Figure 2
Energy balance

The RF plasmoid appears, around 10^{-3} Torr, with a relatively thin sheath : $\theta \ll 1$. At this pressure $v' < v_0 < \omega$ and ξ is small and proportional to pressure p_0 . The denominator of the fraction in \mathcal{L} is reduced to $(1-\theta^2 X)^2$. \mathcal{R} is essentially constant, as ν_i , when θ is small. For two sets of values of p , θ and X we can write :

$$(9) \quad \frac{1-\theta_1^2 X_1}{1-\theta_2^2 X_2} \approx \left(\frac{p_1}{p_2} \right)^{1/2}$$

and if we neglect the variations of X which are small, introducing into (5) gives :

$$(10) \quad \frac{l_{01}}{l_{02}} \approx \left(\frac{p_1}{p_2} \right)^{-3/2}$$

The sheath thickness increases, when the pressure is reduced as $p^{-3/2}$

When the size of the plasmoid is reduced, $\theta \rightarrow 1$, and ν_i increases. Fig. 2 shows that the working point is closer and closer to the dipolar resonance. The maximum of curve \mathcal{L} is

$$(11) \quad \mathcal{L}_{\max} = e^2/m\omega (V/L)^2 \xi^{-1}$$

where $\xi = v'/\omega$ when $v_0 \rightarrow 0$. ξ increases when $\theta \rightarrow 1$ and \mathcal{L}_{\max} decreases. When curve \mathcal{R} is higher than this maximum, no energy balance can be obtained and the plasmoid disappears.

A strong increase of ξ can be expected when $(1-\theta^2) L$ is of the order of the oscillation peak to peak amplitude : no plasmoid can exist with a thickness smaller than this amplitude (~ 2 cm in a typical case).

The present analysis of the decrease in size and disappearance of RF plasmoids is based on the behaviour of the RF sheath, which is considered more important than thermal effects related to Debye shielding distance. In the plasma, the presence of a large density of negative ions reduces the relevant Debye distance to a very small fraction of the plasmoid thickness in all the range of neutral pressure where it can be observed.

REFERENCES

- 1 - R.W. WOOD, Phil. Mag 8, 206 (1929)
- 2 - J. TAILLET, Am. J. Phys. 423(1969)
- 3 - J. PAVKOVICH and G. S. KIND, Proc. Vith ICPiG, Paris 3, 39, (1964).

CHARACTERISTICS OF THE COMBINED DISCHARGE IN AVERAGE PRESSURE GAS

Yu. I. Bichkov, V.V. Osipov, V.A. Telnov.

The U.S.S.R. Academy of Sciences, Siberian Branch, the High-current Electronics Institute, Tomsk.

Creating high-power CO₂-lasers by a combined excitation way that stimulated further improving of this method and further research of discharge characteristics is perspective [1,2,3,4,] The combination of both the pulse self-maintained and the main semi-self-maintained discharges are used in the combined excitation methode. The self-maintained discharge is produced by a high-voltage short time pulse source to create plasma with an electron density required. The main semi-self-maintain discharge requires lower voltage on the electrodes. Usually the large inductor being used as a decoupling element prohibits shunting of a high voltage pulse circuit by the main discharge source [2,4]. The presence of the decoupling elements makes the discharge characteristics worse. There is our concept in which two high voltage pulse sources are used, their own currents flowing in the opposite direction. It enabled us to get rid of the decoupling elements and to carry on the energetic data researches of the combine discharge at a high input energy density into nitrogen of an average pressure. The circuit scheme of this device is shown in fig. 1.

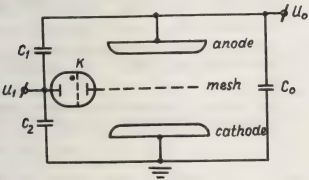


Fig. 1

A mesh was deposited into the gas gap made up with two main round electrodes with the diameter of 12 cm and with a distance of 5 cm between them. A charged 2 uFd capacitor C₀ was connected with the main electrodes, it being charged up to U₀ that was chosen less than the static breakdown voltage for the given gap. High-voltage pulses were supplied to the mesh by closing of the commutator K, each capacitor C₁ and C₂ (C₁=C₂) being discharged into the gap mesh-anode and mesh-cathode relatively producing plasma with a required electron density. The dominant amount of energy is put into the gas by means of a discharge capacitor C₀ in a regime of semi-self-maintained discharge. A spark gap as well as thyatron were used as a commutator.

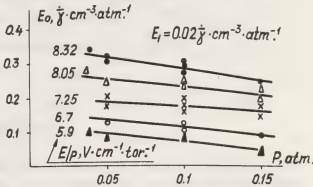


Fig. 2

Fig. 2 shows the input energy density by the main discharge into nitrogen as a function of the pressure at various values of the E/P. The pressure range P = 0.05 - 0.15 atm. at values of E/P=6-7 Vcm⁻¹ torr⁻¹ high input energy densities E₀= 0.2 - 0.3 erg·cm⁻³·atm.⁻¹ are achieved. In this range the energy density E_p=0.02 erg·cm⁻³·atm.⁻¹ put by the pulse self-maintained discharge was less than 10 percent of that put by

the main discharge. The fig. 3 shows the dependence of the energy density put by the semi-self-maintained discharge E_0 at various values of E/p as a function of the density energy put by the self-maintained discharge E_1 .

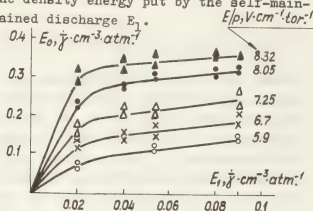


Fig. 3

Thus, the pulse self-maintained discharge using a negligible amount of energy creates the plasma with an electron density required. The time of the discharge contraction appearance as a function of the energy density E_1 is shown in fig. 4.

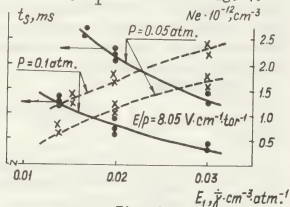


Fig. 4

The electron density "Ne" created by the pulse self-maintained discharge as a function of E_1 is represented here as well. Since the gas flow in gaps is missed in the present researches the discharge contraction was sure to occur at high energy densities put by the main discharge. The time t_s as a function of E_1 indicates the high discharge stability. Really, at $E_1 = 0.025 \text{ J·cm}^{-3} \text{ atm}^{-1}$ and $E/p = 8.05 \text{ V·cm}^{-1} \text{ torr}^{-1}$ the energy density in put by the main discharge is $E_0 = 0.25 \text{ J·cm}^{-3} \text{ atm}^{-1}$, here the discharge stability time is $t_s = 10^{-3} \text{ s}$. High stability of the discharge enables us to carry on the experiment with the

pulse self-maintained discharge repetition rate " f " = $3.5 \cdot 10^3 \text{ p·sec}^{-1}$. The average power density P in put into the main discharge and the discharge stability time t_s as a function of E/p are shown in fig. 5. At $E/p = 8 \text{ V·cm}^{-1} \text{ torr}^{-1}$ the average power density put by the main discharge reaches $P = 36 \text{ W·cm}^{-3}$, here the discharge stability time is $t_s = 6 \cdot 10^{-4} \text{ s}$.

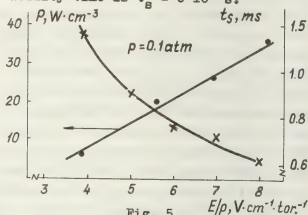


Fig. 5

The less E/p the more t_s but the average power density decreases. The represented characteristic show that the given discharge has a high stability that enables to put high energy densities per each pulse. The usage of the given excitation method in gas flow systems at relatively low gas flow speeds enables to produce the high average power density put into the gas by both the continuous discharge regime and by the regime of the discharge with a high pulse repetition rate.

References:

- 1 J.P.Reilly, J. Appl. Phys., 1972,43, N 8, 3411-3416.
- 2 A.E.Hill, Appl. Phys. Lett., 1973,22, N 15, 670-673.
- 3 N.A.Generalov, V.P.Zimakov et al. Physica plasma, 1977, t 3, v.3,626-633.
- 4 H.I.Seguin, A.K.Nam et al. Appl.Phys. Lett., 1978, 32, N 7, 418-420.

STABILITY OF THE PLASMA-SHEATH

R.N. Franklin.

The city University Northampton Square, London.

The existence, properties and structure of the sheath which forms adjacent to any surface in contact with a plasma have been studied in considerable detail in recent years. In the case of low density plasmas when the space charge dominated region is of the order of several Debye lengths thick and the charged particle motion collisionless, the requirement that the potential is monotonic leads to the Bohm criterion. This has been generalized to include an ion distribution¹. The requirement imposed relates to spatial and not temporal variations and so the stability of the solution is not investigated.

Stability analysis of the sheath is inherently complicated in comparison with situations in uniform plasma because, even in the simplest fluid model of ion motion, the charged particle densities and the ion speed are all functions of position. However, such analyses have in principle been carried out for some conventional situations. At high frequencies comparable with the electron plasma frequency studies of the Tonks-Dattner resonances both experimentally² and theoretically^{3,4} have shown that electron plasma waves undergo absorption as they propagate into the sheath and are reflected. Corresponding work at frequencies of the order of and below the ion plasma frequency has also shown that ion modes propagating on the ion "beam" which leaves the plasma and traverses the sheath are absorbed. One concludes that the conventional plasma sheath is stable.

There is a situation which arises in high temperature plasmas, e.g. fusion reactors or when the bounding surface is electron emissive which is a priori prone to instability. In this case an electron 'beam' leaves the surface and interpenetrates the ion 'beam' travelling in the opposite direction. The steady state analysis of this two stream situation has been given⁵ and is directly related to that for a hot cathode⁶. Recent extensions have been made⁷. The design of divertors depends upon whether these steady state solutions are physically significant, or as a result of instability, merely mathematical curiosities.

A complete analytical solution is impossible and so we examine an approximate model based on the following assumptions.

1. The situation is stable so that the steady state solutions for number density and particle velocities are meaningful.
2. The variation of the 'plasma' parameters is not so rapid as to render the use of uniform plasma theory corresponding to the local parameters invalid.
3. Instability will result at any frequency if a disturbance at that frequency grows sufficiently rapidly spatially as the sheath is traversed. Growth by a factor of e^3 or e^{π} is taken as a criterion.

The following equations describe the steady state

$$\begin{aligned} n_{ep} &= n_0 \exp\left(-\frac{e\phi}{kT_e}\right) && \text{for the 'plasma' electrons} \\ n_{ip} &= n_0 (1 + \alpha) \left(1 + \frac{2\eta}{u_{i0}^2}\right)^{-\frac{1}{2}} && \text{for the 'plasma' ions} \end{aligned}$$

$$n_{eb} = \alpha n_0 \left(\frac{\eta_c}{\eta_c - \eta} \right)^{\frac{1}{2}} \text{ for the 'emitted' electrons}$$

where η is the potential normalized to the electron

temperature, n_0 is the density of plasma electrons

and αn_0 the density of surface-derived electrons in the

plasma, u_{i0} is the ion speed on leaving the sheath

normalized to the ion acoustic speed $c_s = \left(\frac{kT_e}{M} \right)^{\frac{1}{2}}$,

η_c is the normalized potential difference between

plasma and surface. The equations are closed by

solving Poisson's equation with boundary conditions

$$\eta = 0 \text{ and } \frac{d\eta}{d\xi} = 0 \text{ as } \xi \rightarrow \infty.$$

For a given frequency ω the imaginary part k_i

of the wave number is determined by solving the fluid

dispersion relation

$$1 - \frac{\omega_{pep}^2}{\omega^2 - k^2 c_e^2} - \frac{\omega_{pip}^2}{(\omega - kV_i)^2} - \frac{\omega_{peb}^2}{(\omega - kV_e)^2} = 0,$$

where ω_{pep} , ω_{pip} , ω_{peb} are the local plasma

frequencies and V_i and V_e the speeds of the ion and

electron 'beams'.

The range of parameters to be examined is

determined by the fact that for any η_c there is a

limiting value of α corresponding to zero field at the

cathode. For $\eta_c = 10.0$, $\alpha^* = 0.175$.

In general the growth rates of the fastest grow-

ing mode are low for small values of η_c and of α and

the solutions are stable. A set of results for $\alpha = 0.1$

and η_c is given in Figs. 1 - 3. Figure 1 shows the

number densities and particle speeds as a function of

the distance from the cathode. Fig. 2 gives dispersion

diagrams for $\xi = 3.0$ (dashed) and $\xi = 4.6$ (solid).

Fig. 3 gives spatial growth rates as a function of

frequency and for these parameters they are sufficiently

high for the situation to be classified as marginally

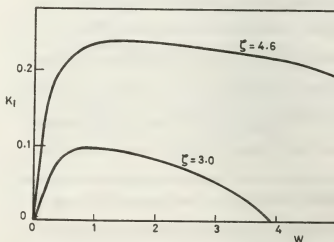
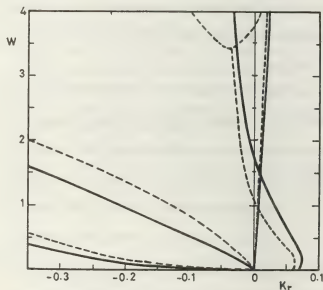
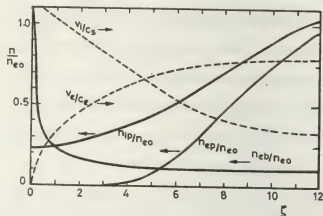
unstable.

We conclude that for high emission currents

instability can set in.

References.

1. Harrison, et al (1959) Proc. Phys. Soc. **74**, 145
2. Franklin, (1964) J. Elect. Cont. **17**, 513
3. Jackson, et al (1966) Phys. Fluids **9**, 1257
4. Ignat, (1970) Phys. Fluids (1970) **13**, 1771.
5. Weynants, et al (1973) Phys. Fluids **16**, 1962
6. Hobbs, et al (1967) Plasma Phys. **9**, 85.
7. Prewett, et al (1976) Proc. Roy. Soc. **A348**, 435
8. Harbour, UKAEA CLM - P535 (1978)



RADIOFREQUENCY DISCHARGE TESTS WITH HELIUM FLOW

M.E. Talaat.

University of Maryland, Department of Mechanical Engr. College Park, Maryland 20742, U.S.A.

Steady state eleven megacycle radiofrequency

discharge test runs were conducted with helium flowing inside a quartz tube, having an ID of 2.2 cms, at reduced pressures, $p_0 = p_{\text{gas}} (273.15/T_{\text{gas}})$, in the range of 210 to 360 torrs, flow velocities, u , in the range of 440 to 485 m/s and electric field to reduced pressure ratios, (ϵ/p_0) , in the range of 1.7 to 3.7 V/cm-Torr. External cylindrical electrodes which were wrapped around the 2.5 cm OD of the quartz tube provided the terminals for applying the radiofrequency discharge voltage. Each electrode had an axial length of about 2.4 cms and the two electrodes were separated by an axial inter-electrode distance of 2.2 cms, with one electrode being connected to the ground of an 800 watt, 11 megacycle RF power supply. The test section was fitted into the closed loop Magnetoplasmadynamic (MPD) Facility of the University of Maryland, and the system was operated with high purity helium under steady state conditions at the desired mass flow rates, pressure and temperature levels. The radiofrequency ionization of the high velocity helium was maintained by establishing a 0.1 to 0.5 ampere steady state 11 MHz discharge parallel to the flow axis of the quartz tube test section and the RF discharge current versus the applied RF voltage across the external ring electrodes were measured for each set of steady state dynamic operating conditions.

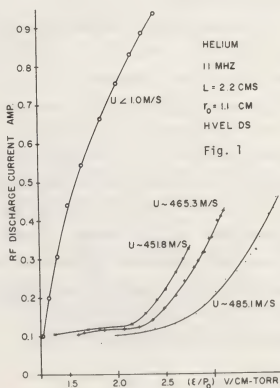
Several important observations were made, both in regard to the shape of the RF discharge and its quantitative character. In regard to the shape of the RF discharge in helium with flow:

(a) When the flow velocity was on the order of one meter per second or less (i.e., almost the static

discharge case), the RF discharge, e.g. at 0.682 ampere and $(\epsilon/p_0) = 1.89$ V/cm-torr, tended to constrict near the center and to extend, almost symmetrically, beyond the electrodes at both ends.

(b) At a helium flow velocity of about 480 meters/second, with the external high voltage electrode being upstream and the grounded electrode being downstream, the RF discharge (e.g. at 0.495 ampere and ϵ/p_0 of 3.574 volts/cm-torr) extended about 2.2 cms upstream beyond the high voltage ring electrode opposite to the direction of the gas flow, but the discharge was not constricted.

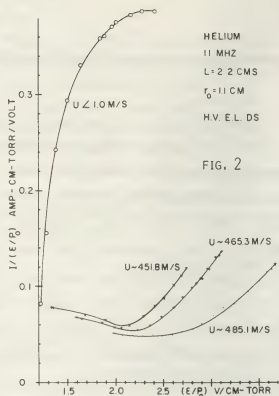
(c) At a helium flow velocity of about 465.4 meters per second, with the external high voltage electrode being downstream and the grounded electrode being upstream, the RF discharge (e.g. at 0.455 ampere and ϵ/p_0 of 3.212 volts/cm-torr) extended by about 2.2 cms downstream beyond the high voltage ring electrode in the direction of the He gas flow.



Again the discharge was not constricted.

From a quantitative viewpoint, Figure 1 gives plots of the RF discharge current, I , versus (ϵ/p_0) , for four different helium flow velocities viz. $u < 1$ meter/second (i.e., nearly the static discharge case), $u=451.8$ m/s, $u=465.3$ m/s and $u=485.1$ m/s. These curves correspond to data taken with the high voltage ring electrode being located downstream and the grounded electrode located upstream. They indicate clearly the sensitive dependence of the RF discharge current for a given value of (ϵ/p_0) on the flow velocity u . Thus, for example, at an (ϵ/p_0) value of 2.42 volts/cm-torr, the observed RF discharge current decreases substantially from a value of 0.936 ampere at a flow velocity $u < 1$ m/s to 0.194 ampere at $u=451.8$ m/s, to 0.155 ampere at $u=465.3$ m/s to 0.116 ampere at $u=485.1$ m/s. Or stated differently, we find that, for example, for an RF discharge current of 0.325 ampere, the required (ϵ/p_0) value to maintain that current increases from 1.39 V/cm-torr, for the flow velocity of less than one meter per second to 2.74 V/cm-torr for a flow velocity of 451.8 m/s to 2.92 V/cm-torr for a flow velocity of 465.3 m/s to 3.39 V/cm-torr for a flow velocity of 485.1 m/s.

Figure 2 gives plots of the quantity $I/(\epsilon/p_0)$ versus (ϵ/p_0) , for the same set of four helium flow velocities of Figure 1. The quantity $I/(\epsilon/p_0)$ gives us a measure of the electron density generated by the discharge. For example, if we consider the elastic collision frequency of the electrons to be a constant with energy of the electrons and equal for helium to $(2.55)10^9$ p₀ second⁻¹ (F. H. Reeder and S. C. Brown, Phys. Rev., Vol. 95, Nov. 4, 1954, p. 885), then the electron density n_{e0} at the center of the discharge may be obtained by multiplying the quantity $I/(\epsilon/p_0)$ in ampere-cm-torr/volt by $(9.0508)10^{18}/\gamma_n$ (A_i sq cm), where A_i is the



discharge cross sectional area in sq. cm., and γ_n is an averaging factor which depends on the radial spacial distribution of the electron density (e.g. $\gamma_n = 0.4323$ for a zero order Bessel function distribution).

We can see from Figure 2 that in order to maintain a certain value of $I/(\epsilon/p_0)$ (or the corresponding value of n_{e0}); the required electric field per torr of reduced pressure, (ϵ/p_0) , increases with increase in the flow velocity. For example, to maintain an $I/(\epsilon/p_0) = 0.12$ Amps-cm-torr/volt, the required value of (ϵ/p_0) increases from 1.24 V/cm-torr, when the flow velocity is less than one meter/sec (viz., the nearly static discharge case) to 2.74 V/cm-torr for a flow velocity of 451.8 m/s, to 2.99 V/cm-torr for a flow velocity of 465.3 m/s, to 3.63 V/cm-torr for a flow velocity of 485.1 m/s.

OBSERVATIONS OF HARMONICS OF THE DISCHARGE CURRENT
IN ELECTRODELESS R.F. DISCHARGES IN GAS MIXTURES

R.G. Earl and A. Prest.

Department of Electrical Engineering & Physical Electronics, Newcastle Upon Tyne Polytechnic,
Newcastle Upon Tyne, England.

INTRODUCTION

The effects of diatomic impurities on the electrical characteristics of the electrodeless discharge at high frequency have been studied by various workers (1,2). These measurements have concentrated on observations of breakdown stress and maintaining currents and fields. The work has been directed towards the development of non-destructive testing techniques for the gaseous purity of discharge lamps. This paper describes and accounts for harmonic generation in the discharge current which is a function of the gas composition.

EXPERIMENTAL ARRANGEMENT & MEASUREMENT PROCEDURE

Modifications have been made to the apparatus previously employed (1) to give an increased and more uniform field. The experimental arrangement is shown in Fig. 1. Electrical fields of up to 2.4 kV m⁻¹ at 3.172 MHz are attainable. Provision has been made for gas pipetting, enabling mass-spectrometer calibration to low partial pressures to be carried out. A electrical balancing procedure enables measurements of breakdown voltages and discharge currents (using current probes CP1 and CP2) to be made for several argon-nitrogen mixtures at various pressures. The technique for measurement of discharge current is similar to that reported previously (1).

The discharge current is also analysed for harmonic content using a spectrum analyser, and it is found that there are always higher order harmonics present which are generated by the discharge. Experimentally, the electric field is varied and the values of the discharge currents and their harmonics are measured. The variation of harmonic content with fundamental discharge current in a typical case is shown in Fig. 2. Generally, at higher values of discharge current, the fifth and higher order harmonics exhibit minima which are due to electron orbit effects. When an extensive set of data is examined it is possible to determine the variation of harmonic content with changes of nitrogen concentration in argon. These results are shown in Fig. 3. It is clearly evident that as the nitrogen concentration falls, so does the harmonic content. The results are taken at a discharge current of 50 mA. This choice of current is somewhat arbitrary. However, if the current selected is too high (> 90 mA) the electron orbit becomes sufficiently important to alter the harmonic structure radically. Selection of a lower current leads to a loss of resolution of the spectrum analyser. At pressures near to 40 torr, whilst the magnitude of the discharge current is dependent on the pressure, the relative harmonic content is less sensitive. Consequently, the errors indicated in Fig. 3 allow for an experimental variation in the argon base pressure

of ±8 torr. The results also suggest that the method is capable of detecting impurity concentrations down to 50 p.p.m.. This is a significant improvement on the method developed by Glancy, Clark, and Earl.

THEORY OF HARMONIC GENERATION

It is thought that the reason for the presence of the harmonics is the time variation of the electron velocity distribution function. Margenau and Hartmann (3) have shown that higher order time harmonics than the fundamental are negligible for A.C. fields when $\omega \gg \nu_{\text{coll}}$ (where ω is the angular field frequency, ν_{coll} is the fractional momentum transfer collision frequency). This inequality does not apply for the discharges we are studying. Since the distribution function is controlled by the various collision cross sections of the constituent gases in the discharge, the time variation of this function will also be uniquely determined by the gases present.

The velocity distribution function is derived from the solution of the time dependent Boltzmann equation (4):

$$\frac{\partial f}{\partial t} + \mathbf{v} \cdot \nabla f + \mathbf{a} \cdot \nabla f = \left(\frac{\partial f}{\partial t} \right)_{\text{collisions}} \quad \dots (1)$$

Since the electron drift velocity is much less than the random electron velocity, f can be approximated as:

$$f(\mathbf{v}, t) = f_0(v, t) + \frac{\mathbf{v}}{v} f_1(v, t) \quad \dots (2)$$

This approximation represents the first two terms in the expansion of $f(\mathbf{v}, t)$ in spherical harmonics, where f_0 is the isotropic term. The distribution function may be further resolved into Fourier time harmonics as:

$$f(v, t) = f_0(v) + f_1^0(v) e^{j\omega t} + f_2^0(v) e^{j2\omega t} + \dots + \frac{\mathbf{v}}{v} [f_1^1(v) e^{j\omega t} + f_1^2(v) e^{j2\omega t} + \dots] \quad \dots (3)$$

The dominant loss process in the discharge is diffusion, and since the diffusion time is long compared with a field period, the electron density cannot vary significantly within that time. Taking this into account, it can be shown that terms of the form f_n^m are zero when $(m+n)$ is odd. Consequently,

$$f(v, t) = f_0(v) + f_1^0(v) e^{j\omega t} + f_2^0(v) e^{j2\omega t} + \dots + \frac{\mathbf{v}}{v} [f_1^1(v) e^{j\omega t} + f_3^1(v) e^{j3\omega t} + \dots] \quad \dots (4)$$

The directed f_1^m terms give rise to the fundamental and harmonic currents:

$$I_1^m e^{jm\omega t} = \int_0^\infty \frac{4\pi e}{3} f_1^m e^{jm\omega t} v^3 dv \quad \dots (5)$$

FIG. 1. ELECTRICAL MEASUREMENT SYSTEM

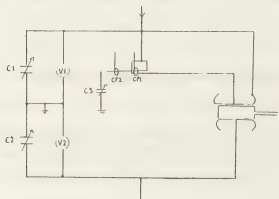


FIG. 2. VARIATION OF HARMONICS WITH FUNDAMENTAL CURRENT (49 torr Ar + 0.18% N₂)

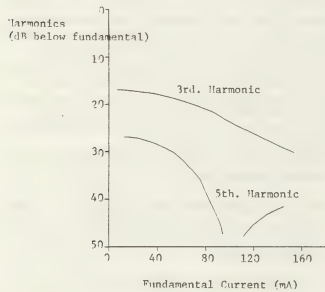
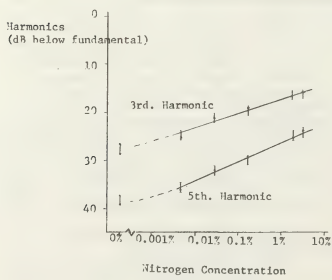


FIG. 3. VARIATION OF HARMONICS WITH NITROGEN CONCENTRATION (50 mA 42 ± 8 torr)



Substitution of equation (4) into equation (1) leads to:

$$\frac{1}{3V} \frac{d}{dV} \left(\frac{-v_a^2 v_m}{2(\omega^2 + v_a^2)} \right) \frac{\partial f_0^2}{\partial V} - \frac{1}{V} \frac{d}{dV} \left[v_a^2 v_m \left(f_0^2 + \frac{2kT}{m} \frac{\partial f_0^2}{\partial V} \right) \right] + \left(\frac{\partial f}{\partial t} \right)_{\text{inelastic}} = 0 \quad \dots (6.i)$$
$$f_1 = \left(\frac{-v_a v_m}{\omega^2 + v_a^2} \right) \frac{\partial f_0^2}{\partial V} \quad \dots (6.ii)$$

Whilst it is possible to generate the higher order equations, these become progressively more difficult to solve. However, although equations (6.i) and (6.ii) still apply in general, they can also be derived directly from equations (1) and (2), with f_0^2 and f_1 being replaced by f_0 and f_1 . An alternative approach to determine the harmonics is to solve equation (6.i) for f_0 in the steady state, and following the method of Polman (5), to increment the electric field over a complete cycle. Equation (6.ii) can then be used to find values for instantaneous current, from which the harmonics may be derived.

CONCLUSION

Experimental measurements of harmonic discharge currents as a function of nitrogen concentration in argon have been made. The production of these harmonics is expected on theoretical grounds and work is proceeding to evaluate quantitatively the effects of different gas mixtures. Of particular interest is the argon-mercury + nitrogen mixture which occurs during lamp manufacture.

REFERENCES

(1) Clancy, P.F., Clark, J.L., & Earl, R.G., I.E.E. Conf. Publ. No. 90 p.254 (1972)
No.118 p.262 (1974)
No.143 p.404 (1976)

(2) Bergman, G. Proc. XIIth. I.C.P.I.G. (1975)

(3) Margenau, H. & Hartman, L.N. Phys. Rev. 73 p.304 (1948)

(4) Shkarosky, Johnston, & Bachynski. "The Particle Kinetics of Plasmas" Addison Wesley (1966)

(5) Polman, J. Physica 54 p.305 (1971)

SOME PROPERTIES OF THE LOW-PRESSURE DISCHARGE IN SILANE

P. Kocian, J.M. Mayor, S. Bourquard.

Laboratory of Applied Physics, Federal Institut of Technology, Lausanne, Switzerland.

1. INTRODUCTION

During past several years, there has been a growing interest in the silane (SiH_4) as a material for the production of silicon and its films [1,2]. There are several methods to produce the films of Si. The deposition in a glow-discharge in silane seems to have some advantage regarding to other methods like evaporation in vacuum or cathodic sputtering [3]. Glow-discharge deposition is a complicated process which is not fully known and understood. Numerous plasmachemical reactions occur in the electric discharge in silane. To understand and to optimize the reactions it will be necessary to know the correlations between the plasmaparameters and the rates of the reactions in plasma. Unfortunately the systematic investigation of the plasmaparameters in silane was not made till now. Only the dependences of the film qualities on the pressure, on the discharge power and on the flow rate were investigated. The difficulty consist in the complexity of the molecular plasma and its diagnostics. The aim of this paper was the investigation of some basic parameters and phenomena in the low-pressure discharge in pure silane. In order to obtain informations about these properties, we have performed our measurements in a DC glow discharge, in which the diagnostics are much easier than in the generally used R.F. discharge. Contamination of the electrodes is not immediate and leaves enough time to do the measurements.

2. EXPERIMENT

The electric discharge was produced in a quartz tube 70 mm in diameter and 800 mm long. It is well known that the impurities in the discharge atmosphere influence considerably the plasmaparameters and therefore

also the plasma reactions and their products. Therefore a great precaution was taken in the purity of the gas. A vacuum of 10^{-7} torr was obtained in the tube by means of a mechanical pump in series with a turbomolecular pump. The limit pressure was measured by means of the ionization gauge. The evacuated tube was heated to outgas the discharge tube walls, the electrodes and the probes. Pure silane tapped from the cylinder passed through a flow meter to a needle valve and then entered the discharge tube. The discharge was produced between two stainless steel electrodes. Specially arranged cathode with adequate cooling minimized the contamination of the discharge atmosphere (less than 0,01%). A highly stabilized DC power supply powered the discharge.

3. MEASUREMENTS

Two basic parameters were investigated: the electric field E and the neutral gas temperature T_g . The electric field influences the electron energy and density and determines the electron energy distribution. The electric field may be measured by means of two probes placed in the positive column or by means of the mobile electrode. The knowledge of the gas temperature is important for the investigation of other plasma parameters like dissociation etc. It is necessary to note that T_g influences the gas density and therefore also the production of charged particles and transport process. There are several methods to determine the gas temperature, most of them are available at the higher pressures and at the higher currents only. In our low-pressure discharge where the temperature does

not exceed some tens of degrees the utilisation of the material thermometers seems to be the most convenient. It is necessary to note that the introducing this probe in a non isothermal plasma the measured value differs more or less from the true value. Various reactions and processes occur at the probe surface. The most of these reactions are exothermic, they relieve the heat and add a supplementary energy to the probe. The rates constants of these reactions depend on the probe surface. The convenient choice of the surface may diminish the influence of these reactions. Under suitable conditions the difference between the measured and true value does not exceed 1 % /4/.

Our measurements were realised between 0,05 and 1 torr and for plasma currents in the range 1 - 10 mA.

At the low pressure standing striations occur in the positive column. Their shape indicates that the radial electron density profile follows a Bessel function and that there are no negative ions. With increasing pressure moving striations occur and their shape is quite different, presenting an inflection point. This shape indicates a radial gaussian gradient of the electron density and a considerable concentration of negative ions. The deposited silicon at the anode and in their vicinity confirms this assumption. The discharge has quite similar properties as in organic vapours and gases /5/. The reduced electric field E/p is relatively low (less than 1 V/cm.torr) and decreases with the increasing pressure and with increasing discharge current. The detailed investigation of the electron density, electron energy and energy distribution as well as of the negative ions will be presented in other paper.

What about T_g we suppose that the gas is heated by elastic collisions of molecules, atoms and radicals with the electrons. The influence of the exothermic or endothermic reactions is neglected. Because of the low electric field the gas temperature is low.

It depends on the pressure and on the discharge current. These dependences are illustrated in Figs 1. and 2.

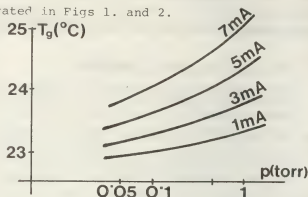


Fig. 1.: T_g in dependence on the pressure.

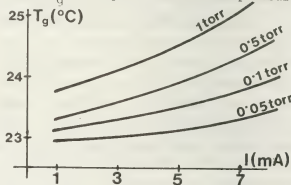


Fig. 2. : T_g in dependence on the current.

Other interesting phenomenon in the silane discharge is the deposition of silicon. We observed that under certain conditions the deposition was in form of thin film while under other conditions in form of powder. This property necessitates more detailed investigation.

As seen from this small paper the electric discharge in silane shows interesting properties which will influence undoubtedly the qualities of the deposited silicon films.

REFERENCES :

- /1/ A.L. Armizotto, Solid State Technology 1968, 43.
- /2/ H.F. Sterling, C.G. Swann, Solid State electronics 8, 653 (1965).
- /3/ R.C. Chittick, J.H. Alexander, H.F. Sterling, J. Electrochem. Soc. 116, 77 (1969).
- /4/ R. Seeliger, H. Strachler, Phys. Z. 28, 894 (1927).
- /5/ P. Kocian, Czech. J. Phys. B 16, 47 (1966).

ON THE CHARACTERISTICS OF A HIGH VOLTAGE GLOW DISCHARGE

C. Popovici, M. Balaceanu, Nicu Ceausescu and E. Avram.

Institute of Physics and Technology of Radiation Devices, Bucharest, P.O. Box 5206, Romania.

1. Introduction

Generation of energetic electron beams in high voltage (1-100 kV) and average pressure (10^{-2} - 10^{-1} torr) glow discharges presents a great importance in non-conventional technologies used in many industrial applications^{1/-/2/}. This paper deals with some characteristics of high voltage glow discharges for certain parameters specific to plasma electron sources.

2. Experiments

The electrodes system is shown in Fig.1 and Fig.2.

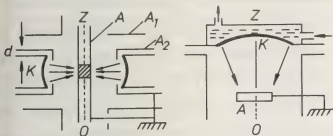


Fig.1

Fig.2

2.1 V-I Characteristics

Fig. 3 and 4 represents V-I characteristics in argon.

For discharges without central anode, it is noticed a severe decrease in the burning voltage and a strong increase in the discharge current. This discharge characteristic, well-known in the case of of torr-order pressures, is explained by the mechanism of the hollow cathode effect^{3/-/4/}. When the anode is placed in the negative glow plasma, the discharge retains the characteristics of the conventional glow discharge.

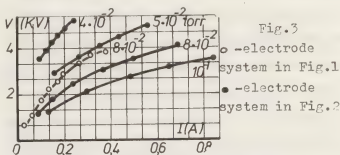


Fig.3

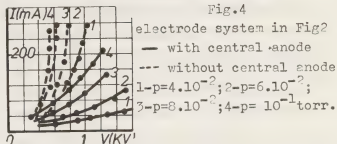


Fig.4

2.2. Thermal effects at the anode.

The thermal effects exhibited by the cathodic electrons beam in a high voltage discharge, providing the basis for a large number of practical applications of plasma electron sources, depend on discharge parameters.

In order to obtain information concerning the anode heating (the system in Fig.2) under various operation conditions, several temperature determinations of the anode have been performed after the same interval (30sec) from the discharge ignition.

Table 1.

p (torr)	U_d (V)	I_d (A)	P_d (W)	t (°C)
10^{-1}	2100	0.500	1050	1174
8.10^{-2}	2580	0.400	1032	1446
6.10^{-2}	3230	0.320	1034	1897

The data in Table 1 (where U_d, I_d, P_d and T represent voltage, current, discharge power and anode temperature, respectively) indicate that the anode heating varies substantially, although the discharge power is practically constant. This is explained by the fact that primary energetic electrons represent only a part out of the total discharge current, depending on the discharge parameters. The electron beam increases with the secondary emission coefficient (γ) of the cathode, which in its turn is an increasing function of the incident ion energy. For our experimental conditions, energy losses of the primary electrons due to inelastic collisions may be neglected. This could be seen in Table 2 which provides the following data: λ_i - mean free ionizing path; n - number of ionizing collisions in the cathode-anode space; ΔE - energy losses by inelastic collisions; $\Delta E/E$ - relative energy loss caused by inelastic collisions.

Table 2

p (torr)	E (eV)	λ_i (cm)	n	ΔE (eV)	$\Delta E/E$ (%)
10^{-1}	2100	6.36	7.7	81	4
$3 \cdot 10^{-2}$	2580	5.52	1.3	54	2
$6 \cdot 10^{-2}$	3230	14.67	1.2	36	1
$4 \cdot 10^{-2}$	4480	28.17	0.6	18	1

3. Thermal balance of the anode heating

Thermal balance of the anode heating is:

$$U_{ec} I_{ec} - P_L = J \frac{m c \Delta T}{t} \quad (1)$$

where U_{ec} - cathodic fall, I_{ec} - primary electrons current, P_L - anode power lost by radiation, conduction, etc., J - conversion constant, m - anode mass, c - specific anode heat,

ΔT - difference between final and initial temperature ($T_f - T_0$), t - time necessary to reach T_f .

For our experimental conditions, P_L may be written as:

$$P_L = \epsilon(T) \sigma T^4 S_1 + \frac{d\lambda}{dt} S_1 \quad (2)$$

where T - anode temperature (in $^{\circ}K$), $\epsilon(T)$ - anode emissivity, σ - Stefan's constant, λ - thermal conductivity of the anode - support wire, $\frac{d\lambda}{dt}$ - temperature gradient along direction of the wire, S_1 - anode area and S_2 - support wire cross-section area.

The power P_L is a complicated function of temperature (which depends on time) and therefore, the calculation from (1) of the time t necessary for the anode to reach a certain temperature is a problem which could be solved only numerically. If the temperature is not too high and the balance is far from being reached, the time t could be calculated approximately, by superestimating the power losses and considering them corresponding to the final temperature. For example, let us assume the heating (from $20^{\circ}C$ to $1300^{\circ}C$) of a tantalum disk anode (diameter=4cm, Width=0.3cm) suspended by a wolfram wire (diam.=0.1cm) in a high voltage discharge (5kV, 0.5A). Assuming $\gamma=0.35$ and $\frac{dT}{dt}=1000^{\circ}C/cm$, we obtain $t=27$ sec.

References

- /1/ R.A. Dugdale, Nature, 249, 440, (1974)
- /2/ R.A. Dugdale, J. of Materials Science, 10, 896, (1975)
- /3/ E. Bădăreanu, C. Popovici, Ann. der Physik 7, Bd. 15, 313 (1965)
- /4/ C. Popovici, M. Somegan, G. Pavelescu, Int. J. Electronics, 34, 259, (1973).

ON THE FORMATION OF PLASMA CARBON COMPONENT IN THE HOLLOW CATHODE ANOMALOUS GLOW DISCHARGE

S. Ibadov

Astrophysical Institute of the Academy of Sciences of Tazshikistan, U.S.S.R.

Plasma, containing a component of atoms and molecules of carbon, occurred in a series of important cases, for example it may appear in the laboratory high-temperature plasma, contacting with graphite /1/. At this point the situations with simultaneously bombardment of a surface by different ions in the range 100 eV remains poorly studied /2/. Cometary molecules C_2 and C_3 determine the visual diameter of cometary heads /3/ and may create the cometary atmospheres dust component directly in the environment of the cometary nucleus by condensation /4/. Laboratory investigation of the formation of solid phase in the heads of comets at the cost of action of condensation mechanism required the creation in a plasma medium an over-saturated carbon vapor phase with the concentration $n_c \gg 10^{11}$ molecule/cm³.

The use of the hollow cathode glow discharge /5-10/ is of interest for the studying of possibilities of over-saturated carbon vapor generation and also for the studying of graphite behaviour in the flow of different ions with energies ~ 100 eV. All base possibilities of formation of carbon component in plasma (evaporation and sputtering of cathode by ion bombardment; dissociation of organic molecules in plasma of discharge) are laid in such a discharge with a graphite cathode.

In the present work the results of investigations on determining of carbon component concentration in the plasma of anomalous glow discharge in the graphite hollow cathode in helium and in propan (C_3H_8) at the discharge currents $I_a = 50 - 500$ mA (the densities of ion irradiation of graphite $\sim 10^{16} - 10^{17}$ ion/cm²s) the energies of ions irradiating graphite

450 - 500 eV (He^+) and 600 - 650 eV (ions from plasma of discharge in propan), the pressure of filling gase $p_g \sim 1$ mm Hg (He) and $p_g \sim 0.1$ mm Hg (C_3H_8) are presented.

The discharge system used was a modification of the discharge part of a plasma ion source /9/. It consisted of an almost closed cylindrical hollow cathode (the radius $R = 12$ mm) and the length $L = 10$ mm) with plane ends and pivotal anode (a tungsten wire with the diameter $d_a = 1.5$ mm) introduced directly into the cathode cavity along its axis (on the length $l_a = 7-8$ mm). The whole system was inserted into homogeneous magnetic field of a coaxial coil.

The determination of the carbon vapor concentration in a plasma was carried out by measuring of the graphite layer mass ΔM , condensed on the anode pivot during certain irradiation time t_0 :

$$n_c = 4 \Delta M / \alpha m_c S_a V_T t_0 \quad (1)$$

Here α is the accommodation coefficient of carbon atoms on the anode surface; m_c is the mass of a carbon atom; S_a is the anode area corresponding to the condensate mass ΔM ; V_T and $V_T = \sqrt{8kT_c / \pi m_c}$ are the temperature and the mean thermal velocity of carbon atoms in the plasma.

The relation (1) was applied under the conditions $j < 1$ A/cm², $p_g R \sim 0.1 - 1$ mm Hg.cm when the motion of atoms in a plasma has the diffusion character and the heavy component of a plasma may be supposed isothermic: $T_c = T_g = T_w$ /11/. Here R is the linear dimension of the cathode cavity; T_g is the temperature of the filling gase; T_w is the temperature of the cathode discharge chamber wall which was measured with a thermocouple and also pirometrically. The anode temperature T_a

was also measured pirometrically .

In helium discharge the measured density of the condensation flow of carbon atoms on the anode was $J_c = 4M/S_a t_0 \approx 5(10^{-8}-10^{-7})$ g/cm²s ; for the discharge in propan J_c was approximately three times as large . The temperature of the cathode wall (of the graphite target) was in the range $T_w = 500 - 1400$ K at discharge power $I_a V_a = 20 - 300$ W .

In Fig. 1 the results of the calculations carried out by (1) for one of regimes of the discharge are given .

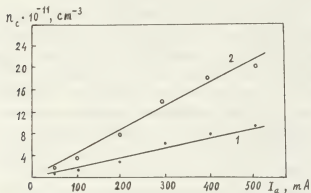


Fig. 1.- The concentration of carbon atoms in the plasma versus discharge current . 1-discharge in helium at pressure in the cathode cavity $p_{He} \approx 1$ mm Hg, discharge voltage $V_a \approx 500$ V; 2-discharge in propan : $PC_3H_8 \approx 0.3$ mm Hg, $V_a \approx 650$ V; $B_0 = 50 - 400$ Gs, V_a Const; T_a max ≈ 1500 K, $\alpha \approx 1$.

As far as the temperature $T_w \approx 2600$ K is required for the generation of carbon vapors with the concentration $n_c \sim 10^{12}$ cm⁻³, i. e. with the partial pressure $p_c \sim 10^{-4}$ mm Hg by heating of a graphite [12], the carbon vapor in the plasma is in the state of strong over-saturation and has a non-evaporation origin .

The discharge in propan with the hollow cathode in which the surface of a graphite is protected against ion irradiation by the tantalum envelope gives very small flow of carbon atoms J_c . At the same time the observed rise of the inner diameter of the cylindrical cathode surface indicates an intensive cathode sputtering process .

In the conditions of the dominating role of an ion sputtering the relation for the stationary concentration of carbon atoms in the considered plasma in the first approximation may be presented in the following

form :

$$n_c = 4sI_a / (1+\gamma) e S_{pl} V_{Tc} \quad (2)$$

Here $s = s(V_a, M^+$ etc.) is the coefficient of cathode sputtering atom/ion ; e is the charge of ion with the mass M^+ irradiating graphite; S_{pl} is the area of the plasma boundary at the cathode which owing to small thickness of near-cathode ion layer practically equals to the area of the cathode S ; $\gamma = \gamma(I_a, V_a)$ is the generalized coefficient of the secondary electron emission from cathode which may be determined experimentally [10] .

The relation (2) satisfactorily describes the curves of Fig. 1. For example in the case of the helium discharge at real values $s \approx 0$. (for $E_{He}^+ \approx 500$ eV - data of [1] are extrapolated), $I_a = 200$ mA, $\gamma \approx 2$, $S = 16$ cm², $V_{Tc} \approx 1.1 \times 10^5$ cm/s we get by (2) $n_c \approx 2 \times 10^{11}$ cm⁻³. In the case of the propan discharge an accordance between n_c from Fig. 1 with that calculated by (2) takes place at $s = 0.5 - 0.6$ atom/ion .

The author is indebted to E.M. Dubinina and O.V. Dobrovolsky for helpful discussions

References

- 1/ N.P. Busharov, E.A. Gorbатов, V.M. Gusev, M.I. Guseva and J.V. Martinenko, Phys. Plasma, USSR, 2 (1976) 588 .
- 2/ V.M. Chicherov, Atomic Energy, USSR, 44 (1978) 469 .
- 3/ O.V. Dobrovolsky, Comets, Moscow, 1966 .
- 4/ A.Z. Dolginov, Astron. J., USSR, 44 (1967) 434 .
- 5/ P.F. Little and A. Engel, Proc. Roy. Soc. A 224 (1954) 209 .
- 6/ K.G. Hernqvist, RCA Review, 19 (1958) 35 .
- 7/ A.D. White, J. Appl. Phys. 30 (1959) 711 .
- 8/ L.J. Abramovich, B.N. Klarfeld and Y.N. Nastich, J. Technic. Phys. USSR, 36 (1966) 714 .
- 9/ E.M. Dubinina and S. Ibadov, Proc. Acad. Sci. USSR, ser. Phys., 33 (1969) 548 .
- 10/ S. Ibadov, Proc. XIth Intern. Conf. on Phenomena in Ionized Gases. Prague, 1973 .
- 11/ V.L. Granovsky, Electrical Current in Gase, M., 1971 .
- 12/ A.N. Nesmejanov, Pressure of Vapor of Chemical Elements, Moscow, 1961 .

A GENERAL CHARACTERISTIC EQUATION FOR A DIFFUSION-CONTROLLED POSITIVE COLUMN OF CIRCULAR CROSS SECTION WITH ONE-STEP AND TWO-STEP IONIZATION PROCESSES

L. Gerald Rogoff.

Westinghouse Research and Development Center, Pittsburgh, Pennsylvania 15235 U.S.A.

A simple yet general equation characterizes the electrical properties of a steady-state, longitudinally-uniform positive column in which the electron density n_e is given by the continuity equation

$$D\nabla^2 n_e + \nu n_e + kn_e^2 = 0 \quad (1)$$

with the coefficients D , ν , and k independent of position and with $n_e = 0$ as the boundary condition. The general expression is derived elsewhere¹ for columns of arbitrary cross-sectional shape (including internal surfaces not connected with the outer enclosure) with the rates linear and quadratic in n_e representing various possible electron production and loss processes (i.e., ν and k positive or negative; we assume $D > 0$). That expression is

$$\left(\frac{\nu}{D}\right)A + \left(\frac{k}{D}\right)N_e = S, \quad (2)$$

where A is the cross-sectional area of the discharge space, N_e is the total number of electrons per unit length of the column, and S is a dimensionless number characteristic of the shape of the column cross section.

The quantity S is given by

$$S = - \int_a \left(\frac{\nabla_T^2 g}{g} \right) da, \quad (3)$$

where g is a normalized electron density distribution, ∇_T^2 is a normalized Laplacian, and da is a normalized element of cross-sectional area. That is, the solution of Eq. (1) is expressed in the

form $n_e = n_0 g(x/T, y/T)$, where the density n_0 is a constant representing the amplitude of the distribution and the dimensionless function g describes the spatial variation in terms of distances normalized to a scale length T transverse to the axis, i.e., T is an arbitrary reference distance which allows for a linear scaling of the size of the cross section. (Rectangular coordinates are used arbitrarily for clarity.) The operator ∇_T^2 contains derivatives with respect to the normalized distances, and the normalized area a is related to the actual area A by $aT^2 = A$.

For a discharge column described by Eq. (1), Eq. (2) is a general expression relating the coefficients, the number of electrons per unit length, the cross-sectional area, and the shape of the cross section, which is involved in the integral expression for S , Eq. (3). Since the coefficients are functions of the applied electric field, since N_e is proportional to the total electron current, and since the electron current is usually approximately equal to the total discharge current, Eq. (2) represents the voltage-current characteristic of the column.

The integral in Eq. (3) is totally normalized. Thus, if the form of g is fixed, then this integral is independent of the size of the cross section, i.e., independent of T and A . It is shown elsewhere¹ that for any given combination of signs of ν and k , the form of g is fixed if the ratio kn_0/ν and the cross-sectional shape are fixed. Thus, for

a given value of kn_0/v with the signs of v and k specified, S is a dimensionless number characteristic of the shape of the column cross section. Once S is evaluated for given discharge conditions, Eq. (2) represents a generalized characteristic for other discharge conditions corresponding to the same value of kn_0/v and same cross-sectional shape. Note that the integral in Eq. (3) is written in terms of normalized quantities to emphasize its independence of cross-sectional area. S can also be written in terms of non-normalized quantities as

$$S = - \int_A \left(\frac{v^2 n_e}{n_e} \right) dA. \quad (4)$$

We consider here the special case of a circular cross section with both v and $k > 0$. (This corresponds,¹ for example, to electron production by one-step and/or two-step electron-impact ionization.) For this case we have evaluated numerically the quantity S , and we have obtained a relationship between S and kn_0/v for all possible values of kn_0/v . The results are given in Fig. 1, where for convenience the abscissa is $kn_0/(v+kn_0) = (kn_0/v)/[1+(kn_0/v)]$. Thus, the left-most value corresponds to a linear production rate only ($k=0$) in Eq. (1) and the right-most value corresponds to a quadratic rate only ($v=0$), with all possible combinations of the two in between. Note that the left-most value can be obtained analytically¹ to be $S = (2.405)^2$. In this case Eq. (2) reduces¹ to the relationship $v/D = (2.405/R)^2$ obtained by Schottky² specifically for a circular cross section of radius R with one-step electron-impact ionization.

The terms in Eq. (1) may describe various processes. For example, the effective diffusion coefficient D may represent free or ambipolar diffusion. Similarly, the effective frequency v may include the effects of ionization by one-step

electron impact, by two-step electron impact,³ by excited state-ground state collisions, and by excited state-excited state collisions, as well as electron loss by attachment. Likewise, the effective rate coefficient k may include effects of ionization by two-step electron impact and by excited state-excited state collisions, as well as electron loss by electron-ion volume recombination.

The relationships presented here are quite general, and they may apply to a variety of types of discharges. However, they are particularly applicable to low-pressure nonequilibrium discharges.

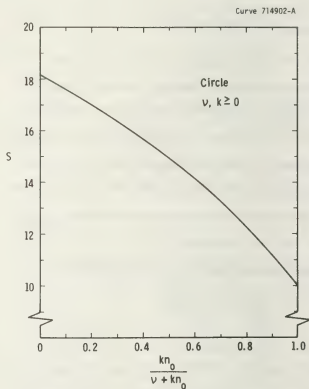


Fig. 1

References

1. G.L. Rogoff, to be published.
2. W. Schottky, Phys. Z. 25, 635 (1924).
3. For the ionization processes involving excited particles to be represented by v or k , the relevant excited particle densities must, of course, vary appropriately with n_e .

EXPERIMENTAL STUDY ON PLASMA NONEQUILIBRIUM OF HIGH PRESSURE METAL-HALIDE DISCHARGE.

V.G. Vdovin^{*}, A.D. Hahaev.^{**}^{*}All-Union Institute of Light Sources, Saransk,^{**}State University, Petrozavodsk, U.S.S.R.

In reports/1,2/ attempts are made to calculate plasma characteristics and to explain physical-chemical processes in hp mercury discharge with mh additives on the basis of LTE model. However while investigation there were noticed appreciable disagreements with experimental data. This report presents atomic plasma characteristics of ac metal-halide discharge with TlI, InI and NaI additives defined a priori on methods not based on LTE concept. Also it represents a conclusion on nonequilibrium state in practically significant conditions.

1. Heavy Particle Temperature T_g .

Starting from theoretical evaluation of contribution of different filling components to plasma polarizability authors showed buffer gas Hg generally defined it under discharge conditions/3/. Hence on the basis of holographic interferometry there was designed a method of obtaining the discharge interferogram/4/ and calculating the radial distribution of mercury density $N(r)$ /5/. With given wall temperature this enabled to find $T_g(r)$. The method takes into account the contribution of axial particle displacement into the observed band shift $S(x)$. The method activity was checked by comparison values N and T_g estimated by means of holography and radiation and resonance triplet broadening Hg 577/79 nm in purely mercury discharge for which LTE state has been proved. Figure 1 shows T_g measured in mh discharge as compared with "apparent" temperature "T" traditionally determined by radiation Hg 577/79 nm.

2. Population of Excitation Levels n_k .

By using the method of absolute radiation measurements, reabsorption of spectral lines/6/ and new Abel's inversion methods the distribution $n_k(r)$ of raw of atomic levels Tl, In, Na and Hg in mh discharge was determined in current maximum/1/ and minimum /2/ phase/7/. Measurements n_k have been carried out in the interval of dosage TlI of interest and found no appreciable changes of $\lg n_k(\varepsilon_k)$.

Fig.2 represents $\lg n_k$ as a function of level energy ε_k in phase (I) on the axis of discharge.

3. Normal Atom Concentration n_0 .

Considering the optical thickness in the center of additive resonance lines $\gg 1$ and $N \sim \text{const}$ along the tube section there was a method of determination $n_0(r)$ by full absorption of extraneous radiation in resonance line limits for the case of asymmetrical contour shape in the optically thin layer $P(v)$ /8/. While estimation $P(v)$ we used approximation in accordance with /9/. Experimental data $n_0(r=0)$ for Tl, In and Na are showed in fig2

4. Electron Concentration n_e .

Taking into account apparatus and Van der Waals broadening in the contour width of a number of lines Na and Tl, restored after Abel's inversion, Stark broadening influenced by electrons $\Delta\lambda$ were determined and $n_e(r)$ was estimated in accordance with/10/. The method of simple correction for measured line shift $\delta\lambda(x)$ to $\delta\lambda(r)$ by means of correction factor $j' = f[I_{\lambda}(x)]$ had been developed in/11/. Values $n_e(r)$ determined by δ and Δ in disc

discharge conditions are in good agreement and represented in fig.3.

5. Electron Temperature T_e .

Having discovered significant nonequilibrium in level population the theory of nonequilibrium atomic plasma was needed for T_e evaluation /12/.

Particularly using experimental values n_0 , n_e and n^+ for tallium on mh discharge axis there was estimated $n_k(\varepsilon)$ for various T_e values in discrete-diffuse approximation of the theory. Results showed that if T_e in discharge is equal to $(5-8) \times 10^3 K$ the estimated dependence $\lg n_k(\varepsilon)$ most of all describes the experimental run $\lg n_k(\varepsilon_k)$. Probably T_e forecast may be specified when evaluated the contribution of ion-molecular reactions to high excited level population.

References:

- 1.R.O.Shafner, Proc. IEEE, 59 (1971), 622.
- 2.G.Muck, H.Popp, 11-th ICPIG, Praha (1973), Cont. paper, p 231, 232.
- 3.V.G.Vdovin, A.A.Pustoshkin, N.A.Samsonova, V.S.Shlyagin: "Complete Reports of All-Union Conference on Metrology of Rapid-Running Processes", VNIIOFI, Moscow(USSR), p136 (1972).
- 4.V.G.Vdovin, A.D.Hahaev: "Complete Reports of the 1-st All-Union Conference on Photometry", VNIIOFI, Moscow (USSR), p270 (1974).
- 5.V.G.Vdovin, A.D.Hahaev: "Complete Reports of All-Union Conference on Metrology of Rapid-Running Processes", VNIIOFI, Moscow(USSR), p81(1975); Svetotekhnika, 2, page 13(1975).
- 6.L.A.Luizova, V.A.Soluanikova, A.D.Hahaev, V.G.Vdovin: "Complete Reports of the 4-th International Meeting on Plasma Physics and Technique, Karl-Marx-Stadt(GDR), ad., p37 (1974).
- 7.V.G.Vdovin, V.A.Mescheryakova, N.A.Samsonova, A.D.Hahaev: "Complete Reports of All-Union Symposium of Plasma Investigation on Spectral Line Contours", PGU, Petrozavodsk(USSR), p 156 (1974).

8.V.G.Vdovin, N.A.Samsonova: "Complete Reports of All-Union Symposium of Plasma Investigation on Spectral Line Contour", PGU, Petrozavodsk, USSR, (1974).

9.W.Funk, H-G Kloss, 11-th ICPIG, Praha, (1973), Cont. paper, p 400.

10.R.R.Griem, Plasma Spectroscopy, McGraw Hill, Co, New York, 1964.

11.V.G.Vdovin, A.D.Hahaev et al: 1-st All-Union Conference on Low-Temperature Plasma Spectroscopy Report, IGU, Leningrad, (1973).

12.L.M.Biberman, V.S.Vorobyev, I.T.Yakubov, Proc. IEEE, 59, (1971), p131; Col. MGD "Method of Electric Energy Generation", edit. Energia, Moscow (1968).

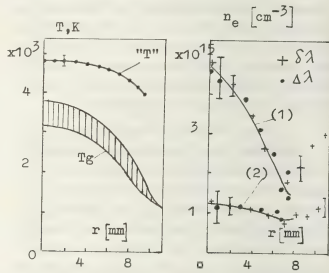


Fig.1

Fig.3

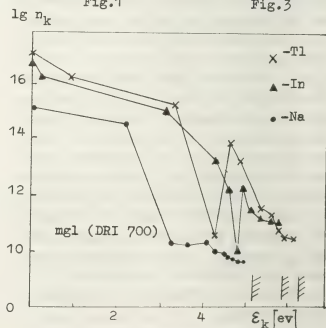


Fig.2

E-I CHARACTERISTICS OF AN OPTICALLY PUMPED MERCURY POSITIVE COLUMN

H.T. Saelee, M.J. Cooke and J.E. Allen.

Department of Engineering Science, University of Oxford, Parks Road, Oxford, U.K.

INTRODUCTION

Optically pumped discharges (OPD) have been widely used in gas lasers for population inversion. The present interest in OPD is in the context of isotope separation where a cataphoretic method has been proposed to collect the selectively excited atoms¹. However, the kinetics of an OPD has to be well known in order to operate the cataphoresis at an optimal condition.

EXPERIMENT

The experimental apparatus has been described previously². It is essentially two coaxial Hg discharges with the outer source discharge (I_{sc}) irradiating the inner cell discharge (I_{cell}). The inner cell is made of quartz glass allowing the main radiation ($6^3P_1 - 6^1S_0$) to be transmitted into the inner discharge. The excited state populations have been measured by a resonant absorption method³ and the axial electric field in the positive column by two variable probes.

RESULTS

The E-I characteristics of the positive column at a reduced pressure of 26.3 mtorr are shown in Fig. 1 for various irradiation levels ($I_{sc} = 0, 5, 10$ and 20A). The axial electric fields were measured over a range of 20.0 cm and found to be very uniform. For $I_{sc} = 0$ we have the normal E-I characteristic of a column where the axial field falls with increasing current (I_{cell}). When the column is irradiated the E-I characteristic changes completely and for $I_{sc} = 20A$ the axial field increases monotonically with I_{cell} , but at a lower absolute value. The irradiation has less effect on the column at high current ($I_{cell} > 200$ mA). With $I_{sc} = 20A$ and at low current ($I_{cell} < 50$ mA) the axial field is reduced to a negligible value.

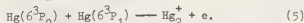
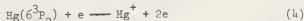
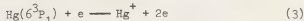
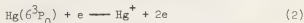
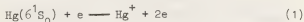
Fig. 2 shows the corresponding number density of the triplet states for the same vapour pressure as the results presented in Fig. 1. Two irradiation

levels are shown ($I_{sc} = 0$ and 10A). The densities of the 6^3P_0 and 6^3P_2 metastable states do not change much with or without irradiation. However, the density of the 6^3P_1 state increases by more than an order at low I_{cell} and less than twice at high I_{cell} (> 100 mA).

Fig. 3 shows the variations of the axial field with vapour pressure (reduced to 0°C) for two irradiation levels on two discharge currents ($I_{cell} = 10$ and 100 mA). The effect of the irradiation is greater as the pressure increases.

DISCUSSION

In a normal positive column, the charged particles gain energy from the axial electric field and dissipate it through inelastic collisions. The axial field also maintains the current continuity of the column. The loss of charged particles by recombination, both at the wall and the plasma volume is balanced by ionization processes in the plasma volume. The main ionization processes are



Other ionization processes are electron impact of the higher excited states⁴. The relative importance of electron impact ionization (1 to 4) and associative ionization (5) varies with the discharge current and the vapour pressure.

In the optically pumped column processes (3) and (5) become more important due to the increase in the density of the 6^3P_1 state. To maintain the charged particle balance, the axial field lowers (corresponding to a lower electron temperature) and ionization by electron impact, especially the ionization from the ground state becomes less important.

In a normal column the axial field increases with the pressure in order to maintain a certain fixed E/P (electric field/pressure) ratio such that the electron temperature remains constant. However, this does not apply when associative ionization becomes dominant which is the case in the optically pumped column.

A quantitative explanation can be obtained by an ion fluid model calculation since we are in the transition regime of ambipolar diffusion and free fall; this was used by Johnson et al.². We are at present extending the model to explain the E-I characteristics. This would require solving the Boltzmann equation for the electron energy distribution in order to calculate the electron drift velocity and the rate of electron impact ionization.

REFERENCES

1. Stangeby, P.C., Allen, J.E. and Fraser, D.A., Xth I.C.P.I.G. Proc., 1971, Oxford.
2. Johnson, P.C., Cooke, M.J. and Allen, J.E., J. Phys. D: Appl. Phys., Vol. 11, 1978, 1877-92.
3. Johnson, P.C., Cooke, M.J. and Allen, J.E., I.E.E. Gas Discharges Conf. Proc., 1978, Liverpool.
4. Vriens, L., Keijser, R.A.J. and Ligthart, F.A.S., J. Appl. Phys., 49(7), 1978, 3807-13.

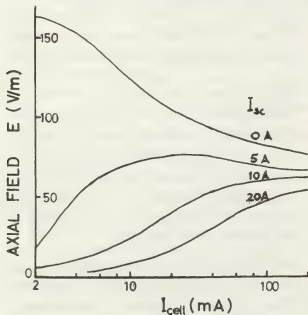


Figure 1. E-I Characteristics of the positive column.

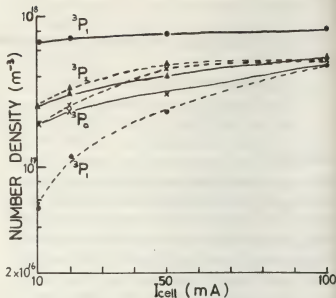


Figure 2. Excited state number densities. $^3P_0(\times)$, $^3P_1(\bullet)$, $^3P_2(\blacktriangle)$, $I_{sc} = 0A$ (----) $I_{sc} = 10A$ (—).

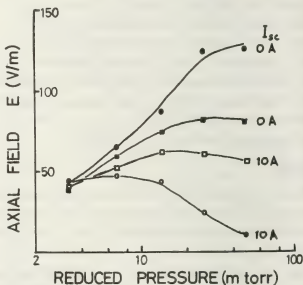


Figure 3. Axial electric field variation with pressure. $I_{cell} = 10mA$ (\bullet, \circ), $I_{cell} = 100mA$ (\blacksquare, \square).

REMARKS ON THE BREAKDOWN OF AN ELECTRIC GAS DISCHARGE

D. Grosu and C.S. Grosu.

Faculty of Physics, Jassy, Romania.

While performing our experimental study on the influence of the nature of the tube wall upon the breakdown of an electric discharge [1] we noticed, in some cases, the presence of two minima instead of one on the Paschen curve. The Paschen curves were obtained in the nitrogen, prepared by heating N_3Na , in a discharge tube like the one in Fig.1a which we called a double wall tube (DWT) or a double tube (DT). The (DWT) curves are represented in Fig.2: by dots, as function of pressure, the values of the breakdown potentials,

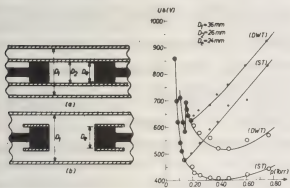


Fig.1

Fig.2

and by circles, the values of the extension potentials. We notice the presence of two minima. The lower pressure minimum is very pointed and the shift from this minimum to the maximum is achieved by a lowering of the pressure with 0.02 Torr at the most. The two curves join together in the large minimum or at lower pressure, when the discharge is intermitent. We put aside the D_2 diame-

ter tube - Fig.1b and raised again the Paschen curve. We also represented in Fig.2 the values of the breakdown and extension potentials in a single tube (S.T) The only minimum of this curve occurs at the same pressure where the pointed minimum in the (DWT) case occurs. We obtained similar results by replacing the electrode with $D_e = 24$ mm by a 16 mm one and the glass tube of $D_2 = 26$ mm by an 18 mm one. In both cases, as in all of our experimen-

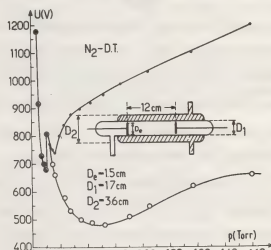


Fig.3

ts, the electrodes were of Al with a distance of 12 cm between them.

We took for granted that the walls of the two tubes influence the breakdown by polarizing the dielectric in the electric field between the electrodes. Two series of experiments were performed to prove our hypothesis.

In the first series, we introduced di-

electric liquids with a relative permittivity higher than with glass (Pyrex, $\epsilon_r = 3.6$), between the two walls of the tube in Fig.3.

In the absence of the liquid, with air between the walls, we obtained the curves in Fig.3. With water and acetone

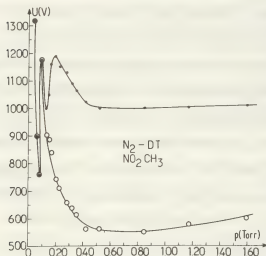


Fig.4

($\text{CH}_3\text{CO.CH}_3$) we got results similar with those of nitro-methane (NO_2CH_3) which we represented in Fig.4. By comparing these curves with ones in Fig.3 one notices an influence of the dielectric liquid upon the values of the breakdown potentials, which it rises obviously within the pressure range (0.20 - 0.50) Torr. Then the minimum for higher pressures becomes more pointed and the breakdown is more difficult. The lower pressures minimum is not influenced. A special case is represented by nitro-benzene ($\text{C}_6\text{H}_5\text{NO}_2$) in the presence of which the large minimum no longer occurs. A great number of determinations was made for each liquid, but the results remained the same.

We obtained similar results by replacing N_2 with Ne. In the Ne case the breakdown is easier and the minima are lar-

ger. The passage from the maximum to the more pointed minimum is also achieved for a decrease of the pressure by 0.02 Torr at the most; in the Ne case there is also only one minimum in the presence of nitrobenzene.

We used a simple tube (ST), like the ones in Fig.1b for the second series of experiments. With a tube of the same dimensions as those of the one in the middle of Fig.3 we got results similar to those in Fig.3. With a tube of the same dimensions as those of the inner one in Fig.3, but $D_e = 34$ mm, we obtained the Paschen curve with only one minimum. Finally, for an intermediate tube, $D_1 = 26$ mm and $D_e = 24$ mm we obtained a two minima curve, but the potential difference between the maximum and the minimum breakdown potentials was only (20 - 30) V.

We raised the Paschen curves as well as those of the extinction potentials in the O_2 case, too, prepared by heating potassium permanganate. Only one minimum was noticed in all cases.

The main results of our investigations are:

1. The revealing of the two minima Paschen curve in the case of an electric discharge breakdown in N_2 and Ne;
2. The discharge breakdown is also influenced by phenomena at the tube wall.

REFERENCES

1. D.Grosu, St.Bara and C. Bruma - XIII- th ICPIG, Contributed papers, part.I, 357, DDR, Berlin (1977).

EFFECT OF COLLISIONS BETWEEN THE METASTABLE ATOMS ON THEIR RADIAL TRANSPORT IN A POSITIVE COLUMN AT VARIOUS SPATIAL DISTRIBUTIONS OF ELECTRONS

V. Martisovits.

Institute of Physics and Biophysics, Komenský-University, 816 31 Bratislava, Mlynská Dolina, Czechoslovakia.

The purpose of the present contribution is to study the radial transport of metastables to the discharge tube wall when collisions between two metastable atoms are taken into consideration together with other destruction processes. The number density distribution of metastables across a section of the positive column and their flux to the discharge tube wall are calculated for various spatial distribution of electrons.

INTRODUCTION

In the previous papers [1,2] the transport of metastable atoms to the discharge tube wall was studied when assuming the metastables to be produced by direct excitation by electron impact and through the states optically connected with the metastable states. On the other hand only two-body and three-body collisions with ground-state atoms, and collisions with electrons were assumed as the most important volume processes that led to destruction of the metastability in a glow discharge. However, at higher concentration of metastable particles the destruction by collisions metastable-metastable is to be taken into consideration. The problem is solved for various forms for the spatial distribution of electrons $g(\mu r/R)$ assuming the rate coefficient for excitation α and destruction of metastables (β by electron impact and δ by collisions with atoms) to be independent of radius r . Here, μ is the first zero point of the Bessel function of the first kind of order zero J_0 and R the inner radius of the discharge tube.

THEORETICAL MODEL

If n_g , n , n_{e0} are the respective concentrations of ground-state, metastable atoms and the electron concentration on the axis

for a steady state we have

$$-D \frac{1}{r} \frac{d}{dr} \left(r \frac{dn}{dr} \right) = (\alpha n_g - \beta n) n_e - \delta n_g n = -\delta n^2$$

where D is the diffusion coefficient of metastables and δ coefficient for destruction of metastables by mutual collisions. The number density of electrons is given by $n_e = n_{e0} g(\mu r/R)$. Using the symmetry requirements we find that $dn/dr = 0$ at $r = 0$. To simplify the analysis the boundary condition $n_w = 0$ at the wall was used.

The equation can be normalized by putting $\xi = \mu r/R$, $y = R^2 \beta n_{e0} / \mu^2 D$, $\xi = R^2 \delta n_g / \mu^2 D$, $v = n / C y$, $\Delta = R^2 \delta C / \mu^2 D$, where $C = \alpha n_g / \beta$ is an equilibrium number density of metastables. Then we obtain the following equation

$$\frac{1}{\xi} \frac{d}{d\xi} \left(\xi \frac{dv}{d\xi} \right) = -[y g(\xi) + \xi] v + g(\xi) = -y \Delta v^2$$

with the respective boundary conditions $v_w = 0$ and $(dv/d\xi)_{\xi=0} = 0$.

RESULTS

The numerical solution was performed for y varying between 0 and 10^4 and Δ from 0 to 1000 for $\xi = 0$ (negligible destruction by collisions with atoms). The spatial distribution of electrons was descri-

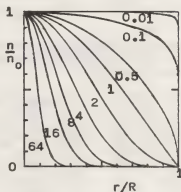


Fig.1. The spatial distribution of electrons across a section of the positive column plotted for q ranging from 0.01 to 64

bed by the function $g(x) = [j_0(x)]^q$ where $0 \leq q < \infty$. The family of curves n_e/n_{e0} against r/R is shown in figure 1. Figures 2 and 3 illustrate typical shapes of the radial distributions of metastables normalized to unity at the column axis n/n_0 for various values of the parameters q and j . The flux density of metastables to the wall is given by a formula

$$j_w = -D(dn/dr)_w = -(\mu/R)DC j'(d\nu/d\varphi)_w$$

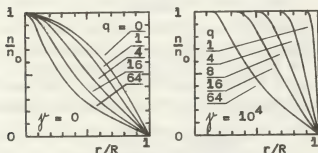
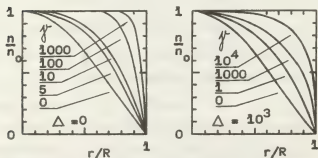
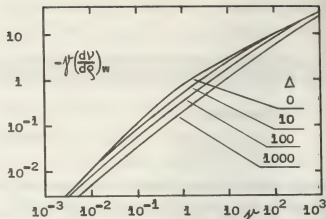
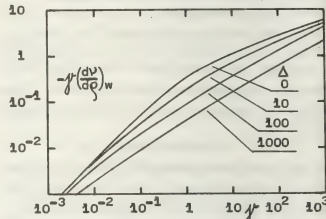
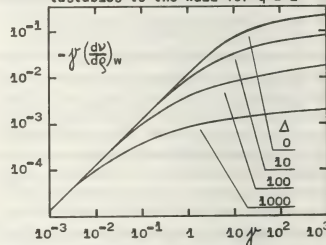
and it is shown in figures 4 - 6 (plotted $-j'(d\nu/d\varphi)_w$ only).

Representing the diffusion equation in terms of the characteristic diffusion length, the ratio of metastable number density at the axis n_0 to the equilibrium concentration C can be written as

$\frac{n_0}{C} = 2jg_0 / \{1 + jg_0 + [(1 + jg_0)^2 + 4\Delta jg_0]^{1/2}\}$
Here g_0 is a numerical factor which characterizes the influence of the higher diffusion modes. The numerical values of g_0 are presented in table 1.

Table 1.

q	0	0.5	1	2	4	8	16	64
g_0	1.45	1.18	1	0.78	0.56	0.37	0.23	0.08

Fig.2. The radial distribution of metastables for different electron density profiles and $\Delta = 0$ Fig.3. The radial distribution of metastables for $q = 1$ Fig.4. The normalized flux density of metastables to the wall for $q = 0$ Fig.5. The normalized flux density of metastables to the wall for $q = 1$ Fig.6. The normalized flux density of metastables to the wall for $q = 64$

REFERENCES

- [1] Martišovitš V., Košinár I. and Veis Š., Proc.12th Int. Conf. Phenomena in Ionized Gases, Contr. Papers, North-Holland Publ. Comp.(Amsterdam, 1975) p. 60
- [2] Košinár I., Martišovitš V. and Veis Š., Proc.13th Int. Conf. Phenomena in Ionized Gases, Contr. Papers, Phys.Soc.GDR (Berlin, 1977) p. 233

TRANSPORT OF METASTABLE ATOMS IN A POSITIVE COLUMN INCLUDING RADIAL VARIATION OF THE EXCITATION RATE

V. Martisovits.

Institute of Physics and Biophysics, Komenský-University 816 31 Bratislava, Mlynská Dolina, Czechoslovakia.

The effect of radial variation of the rate coefficient for excitation on spatial distribution of metastables across a section of the positive column and on their flux to the discharge tube wall is calculated.

INTRODUCTION

Recent investigations [1] of the radial distribution of metastable atoms in the positive column have suggested that the energy distribution function for electrons is influenced by a longitudinal magnetic field. As a result of this, the excitation rate α for production of the metastable states is dependent on radius. In order to study this problem the following model for excitation rate variation is used: $\alpha/\alpha_0 = w(\mu r/R) = [J_0(\mu r/R)]^p$ where p is a numerical factor, J_0 the Bessel function of the first kind of order zero, μ its first zero point, R the inner radius of the discharge tube, and α_0 the excitation rate at $r = 0$. The family of curves α/α_0 against r/R is shown in figure 1 for $-0.8 \leq p \leq 0.8$.

THEORY OF THE TRANSPORT

The radial transport of metastable atoms can be described by the diffusion equation for a steady state [2]

$$-D \frac{1}{r} \frac{d}{dr} \left(r \frac{dn}{dr} \right) = (\alpha n_g - \beta n) n_e$$

where n_g , n_e and n are the respective concentrations of ground-state atoms, electrons and metastable atoms. Here D is the diffusion coefficient of metastables and β coefficient for destruction of metastable atoms by electron impact. As a first approximation, the destruction of metastables by mutual collisions and by collisions with ground-state atoms is neglected. A simple boundary condition at the wall $n_w = 0$ and the electron density profile given by the zero-order Bessel function

are also supposed.

By introducing the dimensionless variables $\varrho = \mu r/R$, $\mathcal{V} = R^2 \beta n_{e0} / \mu^2 D$, $\mathcal{V} = n/C \mathcal{V}$, $C = \alpha_0 n_g / \beta$, where n_{e0} is the electron concentration on the axis, we obtain the following equation

$$\frac{1}{\varrho} \frac{d}{d\varrho} \left(\varrho \frac{d\mathcal{V}}{d\varrho} \right) + [w(\varrho) - \mathcal{V}] \mathcal{V}(\varrho) = 0$$

with the boundary conditions $\mathcal{V}_w = 0$ and $(d\mathcal{V}/d\varrho)_{\varrho=0} = 0$.

RESULTS

The numerical solution was performed for \mathcal{V} varying between 0 and 10^4 . Figure 2 illustrates the shapes of the radial distributions of metastables normalized to unity at the column axis n/n_0 . The ratio of metastable number density at the axis n_0 to the equilibrium concentration C is plotted as a function of \mathcal{V} in figure 3. The flux density of metastables to the wall is given by a formula

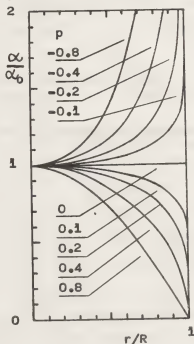


Fig.1. The radial variation of the excitation rate for production of the metastable atoms

$j_w = -D(dn/dr)_w = -(\mu/R)DC \gamma^* (d\psi/d\phi)_w$
and it is shown in figure 4 (plotted
 $-\gamma^*(d\psi/d\phi)_w$ only).

When comparing the results presented in
figures 2 - 4 it can be concluded that the
radial variation of the excitation rate
has only a small influence on the concen-
tration of metastables n_0 . On the other
hand the metastable flux density to the
wall and the radial distribution of meta-
stables are seriously changed at the same
conditions.

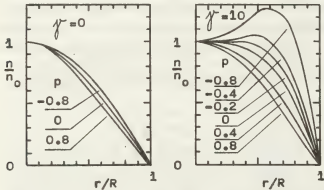


Fig.2.The radial distribution of metasta-
bles for different profiles of the
excitation rate

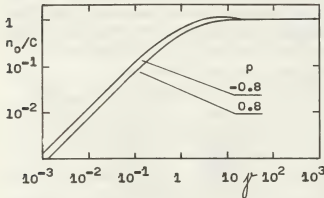


Fig.3.The relative concentration of meta-
stables at the axis

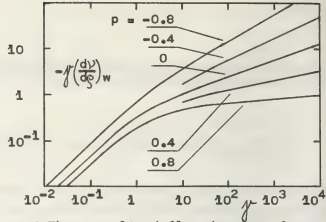


Fig.4.The normalized flux density of metasta-
bles to the wall

REFERENCES

- [1] Deutsch H., Pfau S. and Klagge S., Proc.
13th Int. Conf. Phenomena in Ionized
Gases, Contr. Papers, Phys. Soc. GDR
(Berlin, 1977) p. 239
- [2] Martišovitéš V., Paper at this conference

ELECTRON BEAM GENERATION BY A HOLLOW CATHODE DISCHARGE

G. Pops, M. Sanduloviciu^{*} and P. Croitoru, C. Moldovan^{**}.

^{*}Faculty of Physics "Al.I.Cuza" University, Iasi, Romania.

^{**}I.F.T.A.R. Bucharest, Romania.

Electrons of high energy have been produced either in a pulsed plane cathode discharge /1/ or in a frustum -plane cathode discharge /2/.

This paper reports some experimental results which show that an electron beam of high energy could be produced in a d.c. discharge with cylinder cathode which operates at low current and high voltage.

Experimental device is presented in fig. 1. The discharge was produced in a Pyrex-glass tube (T) (7.4 cm inner diameter and 40 cm long). A stainless steel cylinder of 10 cm long and 1.7 cm inner diameter was used as a cathode (C). In the cylinder there is a stainless steel movable piston (P) which allowed continuously change of the inner length of the cathode.

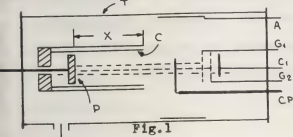


Fig.1

X is the distance between piston and front end of the cathode. The cathode was water cooling and insulated so that the internal surface only is used in the discharge. An other stainless steel cylinder of 7 cm diameter and 2.5 cm length is used as an anode (A) placed at 5 cm far from the cathode. In front of the cathode behind

of anode there is an electrostatic analyzer of 1 cm diameter made from a plane collector (C_1) and two stainless steel grids (G_1 and G_2) mesh of 50% transparency and 5 wires/mm. The distance between the grids and grid-collector was 0.5 mm.

An axially movable cylindrical tungsten probe (CP 0.2 mm diameter and 1 cm length) was placed parallel to the front edge of the cathode.

The measurements are performed in hydrogen for the pressure range of 0.1 to 0.02 mmHg and the voltage of 2 to 50 KV. A d.c. discharge was used up to 4 KV and as a pulse of 50 μ s up to 50 KV. For above range of parameters the plane cathode discharge burns in an abnormal regime without positive column and current-voltage characteristic is given by /3/:

$$J = \text{constant} \frac{V^{3/2}}{d^{5/2}} \quad (1)$$

J is the current density on the cathode, V is cathode fall measured as a floating probe potential with respect to the cathode and d is cathode fall thickness measured as the distance between cathode and probe which was always placed at the negative glow border.

In fig.2 the current voltage characteristic (1) is presented for different cathode lengths. The equation (1) is well

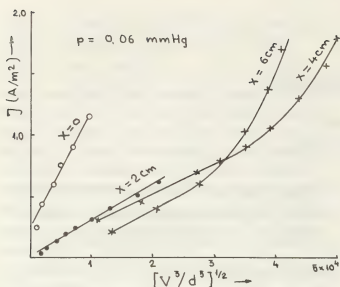


Fig. 2

verified for plane cathode. When the cylinder cathode is used the discharge still burns in an abnormal regime with well definite cathode fall and a very sharp narrow electron beam coming out from the cathode along its axis and going into negative glow. For this case the equation (1) is no more valid and experimental curves show a nonlinear increasing of the discharge current with cathode fall voltage.

The electron beam diameter was no more than 6 mm so that using the electrostatic analyser the electron beam current could be measured. In fig. 3 the both discharge current density and ratio of the beam current (I_b) to the total discharge current (I) versus cathode length are presented. It shows that a cylinder cathode is more efficient for electron beam production than a plane cathode. This efficiency increases with cathode length. An efficiency increasing was observed versus low discharge voltage and it becomes constant for higher voltage (fig. 4).

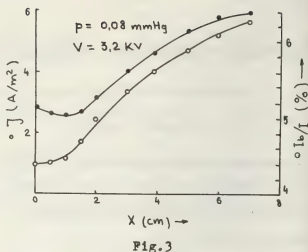


Fig. 3

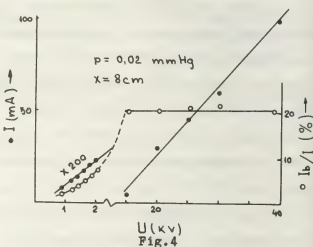


Fig. 4

References

1. G.W. McClure, Phys. Rev., **124** (1961) 969
2. G. Brătescu, E. Toader, Rev. Roum. Phys., **23** (1978), 340.
3. E. Badareu, I. Popescu, Gaz ionisés. Descharges electriques dans les gaz, Dunod-Meridiens 1965.

THE INFLUENCE OF THE ELECTRON-NEUTRAL COLLISIONS ON THE IONIZATION WAVES IN A HELIUM PLASMA

G. Popa.

Faculty of Physics "Al.I. Cuza" University, Iasi, Romania.

The general behavior of the ionization waves in a d.c. positive column have been well explained in a hydrodynamic model/1/. It shows a good agreement with experiments at high discharge currents/2/.

A more elaborated theory is a kinetic one /3/. It takes account of the spatial electron gas resonances which exist at low pressures and currents where electron-neutral collisions could not always establish a local Maxwellian distribution. The model explains remarkable aspects of the ionization waves as high ratio of the group to phase velocity and Novak's law and more wave varieties /4/. Thus the wave potential i.e. the product of the longitudinal electric field E times the optimum wavelength λ is given by :

$$U_a/E\lambda = g(1-\alpha) \quad \text{for } q = 1 \text{ or } 2 \quad (1)$$

U_a is the first excitation potential and α is the ratio of the elastic over inelastic electron energy losses in undisturbed column.

The aim of this paper is to present some experimental evidence on resonant behavior of the ionization waves and influence of the electron-neutral collisions on this resonance for the helium plasma. In a helium positive column the small coefficient

α is using /5/ given by: $\alpha = \text{const.}$

$(p/E\sqrt{U})^2$, where: p is the gas pressure, E electric field intensity and U electron energy. Therefore the equation (1) becomes for $q = 1$:

$$1 - (U_a/E\lambda) = \text{const.} (p/E\sqrt{U})^2 \quad (2)$$

which could be experimentally checked. For this purpose the electric field E , electron temperature U and optimum wavelength are measured for different helium pressure p (for helium $U_a = 19.82$ V).

Experimental device and method are presented in a previous paper /6/. The both interferometer and space time diagram methods have been used. The longitudinal electric field E and plasma parameters were measured with cylindrical probes placed near anode. The discharge was produced in a pyrex tube (60 cm long and $R = 0.5$ cm inner radius) filled with spectrally pure helium. An external sinusoidal signal which modulates the discharge current (less than 10%) was used for ionization wave excitation. The waves are detected by a photomultiplier coupled with an interferometer system and registered on XY recorder. Such interferometer traces allowed to measure the both wavelengths and space amplitude variation rates K_1

for different frequencies. In fig.1 the both dispersion and spatial amplification rate curves are presented for a constant discharge current and various gas pressures. The curves show the backward fast waves of which space amplification coefficient is larger than unity only for reduced pressure above about 1 Torr.cm.

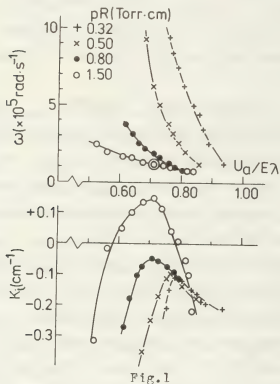


Fig.1

In such conditions the space time diagram shows a wave propagation which corresponds only to the optimum wavelength and it is also indicated by maximum of the space amplification rate curve (circle point on bottom dispersion curve fig.1). The maximum of the space amplification curves show in fig.1 the optimum wavelengths for various pressures and for the constant reduced discharge current (60 ma/cm). The longitudinal electric field and the electron temperature have been measured for undisturbed column. Their values are presented in table 1 together with the both phase (v_p) and group velocities (v_g) of the

ionization waves corresponding to the optimum wavelengths

Table 1

$n(N/m^2)$	$E(V/m)$	$U(V)$	$v_g(m/s)$	$v_p(m/s)$	v_p/v_g
85	940	6.0	16.000	1.800	8.88
133	1.000	5.6	12.600	1.270	9.92
213	1.040	5.3	3.100	800	3.87
309	1.050	4.3	540	530	1.02

In fig.2 the dependence of $\log(1-U_a/E\lambda)$ versus $\log(p/E\sqrt{U})$ is presented. It shows a straightline for experimental points up to about 1 Torr.cm, where the ratio $v_g/v_p \gg 1$.

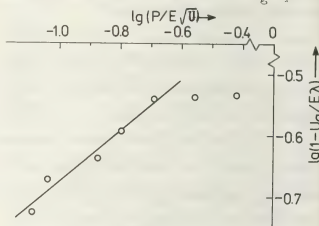


Fig.2

The above experimental results shown that at low pressure up to 1 Torr.cm a resonant behavior of the ionization waves exists. With increasing pressure for constant current the electron-neutral collision number increases, the phase and group velocities become comparable and dispersion curves become flat. It shows a transition to hydrodynamic behavior and eq.(2) is no more valid.

References

1. L. Pekárek, U.F.N. 94, (1968)463
2. K. Wojacek, Beitr. Plasmaphys., 11(1971)335
3. K. Rohlena et al. Phys. Letters 40A(1972)239
4. L. Pekárek et al. Proc. 7th SPIG, Rovinj 1974
5. V. Perina et al. Czech. J. Phys. B25(1975)660
6. G. Popa, Rev. Roum. Phys. (in print)

ELECTRON ENERGY DISTRIBUTION, ELECTRIC FIELD AND TRANSPORT COEFFICIENTS IN THE FARADAY DARK SPACE

E. Berger and A. Heisen.

Sektion Physik der Universität München, W. Germany.

The Faraday Dark Space FDS of an anomalous glow discharge is a good test object for the investigation of electron velocity distributions (EVD) in weak electric fields, because it is a transition region between the nearly field-free negative glow and the positive column.

The EVD was measured by double differentiation of a Langmuir probe characteristic /1,2/. The work function of the probe surface is influenced by the probe current. This can be eliminated by periodically potential measurement of a fixed point on the probe characteristic itself by sample and hold technics /4/.

Together with a properly matched electronic circuit this procedure allows measurements of the second derivative over more than 4 decades with high accuracy.

The reduced electric field strength E/N influences the EVD. Therefore it is possible to determine this parameter by comparison of the solutions of the Boltzmann equation

$$(1) \quad \frac{\partial f}{\partial t} + \vec{\nabla} \cdot \vec{v} f_j + \frac{e}{m} (\vec{E} + \vec{v} \times \vec{B}) \cdot \vec{\nabla}_v f_j = B(\vec{r}, \vec{v}, t)$$

with measured EVD's. We solved it for the electrons in the FDS of a H_2 glow discharge with following assumptions: stationary discharge without magnetic field; low ionization degree; use of the Lorentz approximation; maxwellian distribution for the neutral gas with temperature T_g . Numerical values of the elastic Q_m and inelastic Q_i impact cross sections with the threshold potential U_i were taken from an investigation in the E/N -range above 10 Td made by Michel and Winkler /5/. In the thermal range it was further necessary to take into account rotational excitation and deexcitation Q_{-i} cross sections /6,7/.

For the solution of the resulting differential equation system we assumed further: The EVD is in local equilibrium with the electric field

$$f_e(\vec{r}, \vec{v}) = n_e(\vec{r}) \cdot f(\vec{v})$$

and the influence of density and field gradients are negligible with respect to the determination of transport parameters evaluated from the EVD /8/.

The solutions of the resulting integro-differential equation

$$(2) \quad \left\{ \left(\frac{E}{N} \right)^2 \frac{M}{6m} \frac{U}{\Sigma Q_i} + U^2 Q_m \frac{kT_g}{e^2 g} \right\} \frac{df(U)}{dU} +$$

$$Q_m U^2 f(U) + \frac{M}{2m} SI(U) = 0 \quad \text{with}$$

$$SI(U) = \sum_i \left\{ \int_{U-U_i}^{U+U_i} Q_i(\tilde{U}) \tilde{U} f(\tilde{U}) d\tilde{U} - \int_{U-U_i}^U Q_{-i}(\tilde{U}) \tilde{U} f(\tilde{U}) d\tilde{U} \right\}$$

were compared with respect to the parameter E/N with literature values for drift velocity and characteristic energy collected by Dutton /9/. They show good agreement /10/.

From more than 300 local measurements of the EVD in the FDS performed in a bakable UHV discharge apparatus with cylindric symmetry we got the axial distribution of the different current parts shown in fig. 1.

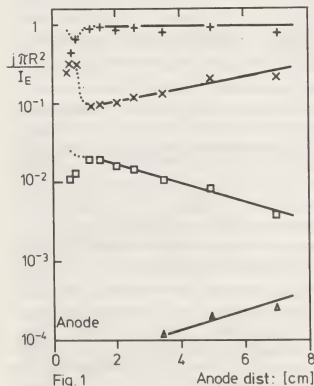


Fig. 1

- + = $e n_e b_e E_z$: electron drift current
- x = $e D_e \text{grad}(n_e)$: electron diffusion
- = $e n_e b_+ E_z$: ion drift
- Δ = $e D_+ \text{grad}(n_e)$: ion diffusion

b_+ and D_+ are the ionic transport coefficients for H_3^+ ions in H_2 . By mass spectroscopy H_3^+ was found to be the dominating ion.

Discharge parameters: tube diameter 60 mm; spherical probe, diameter 1 mm; discharge current 6.1 mA, H_2 -pressure 51 Pa.

Fig. 1 shows that the recombination loss of ions at the tube wall with the current density j_{w+}

$$(3) j_{w+} = -e D_a (E/N) (dn/dr)_R$$

D_a : ambipolar diffusion coefficient, is compensated by the drift of ions coming from the anode region. The total loss of ions is given by

$$(4) 2\pi R j_{w+} = -2\pi e \int_0^R b_+ E_z n(r) r dr$$

For approximate analytic survey we add the current transport equation ($n_0 = n(r=0)$)

$$(5) j_0 = e n_0 b_e E_z = I_E \cdot n_0 / (2\pi \int_0^R n(r) r dr)$$

and a simplified field dependence of the ambipolar diffusion coefficient $D_a(E/N)$

$$(6) N \cdot D_a(E/N) = E/N \cdot 1.6 \cdot 10^{36} [s^{-1} cm^{-1}]$$

valid near 10 Td in H_2 at 300 K and for the ion mobility of H_3^+ we use

$$(7) N \cdot b_+ = 3.01 \cdot 10^{20} [V^{-1} s^{-1} cm^{-1}]$$

The combination of (3) - (7) gives the axial dependence of the electron mobility in the FDS

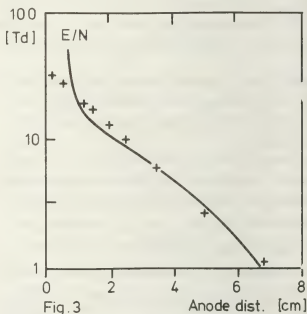
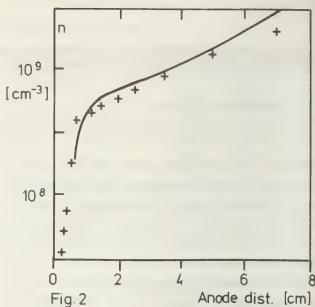
$$(8) -R^2 \cdot N \cdot \frac{d}{dz} \ln(b_e) = \text{const}$$

From this equation we conclude: The local distribution of electron mobility is the determining mechanism for the axial extension of the FDS - in contrary to the FDS-model of Ecker and Emeleus/11/. The mobility determines the axial field and, taking into account the current transport equation, the charge density, too.

With respect to the numeric dependence $D_a(E/N)$, a numeric solution gives a good agreement with the experimental data shown in figs. 2 and 3.

Especially the strong decrease of the charge density near the anode is well reproduced (fig. 2). The sharp rise of the electric field (fig. 3) in this region is not reproduced, because the assumption of local equilibrium of the EVD with the field is not valid here.

Field measurements with a transversal electron beam confirm the strong rise of the electric field.



- /1/ Druyvesteyn, M.J. 1930, Z.Phys. 64, 781-98
- /2/ Berger, E., Heisen, A. 1975, J.Phys.D 8, 629
- /3/ D'Arcy, R.J. 1974, J.Phys.D 7, 1391
- /4/ Wunderer, B.M. 1975, J.Phys.E 8, 938
- /5/ Michel, P., Winkler, R. 1976, Beitr.Plasma-phys. 17, 233
- /6/ Crompton, R.W. et al. 1969, Aust.J.Phys. 22, 715
- /7/ Gibson, D.K. 1970, Aust.J.Phys. 23, 683
- /8/ Parker, J.H. jr., Lowke, J.J. 1969, Phys.Rev. 1, 290
- /9/ Dutton, J. 1975, J.Phys.Chem.Ref.Data 4, No.3
- /10/ Berger, E. 1979, Diss. Univ. München
- /11/ Ecker, G., Emeleus, K.G. 1965, Ann.Phys. 7, No. 15, 53

A NONLINEAR KINETIC THEORY FOR HF PLASMA GENERATION AND ELECTRON HEATING.

G. Cicconi^{*}, V. Molinari^{**}, L. Pollachini^{***}.^{*}Electrical Engineering Dept. University of Genoa, Italy.^{**}Nuclear Engineering Lab., University of Bologna, Italy.^{***}C.I.S.E., Milan Italy.

Nowdays a consistent progress has been obtained in describing, by means of kinetic models, the electron kinetics of many gas discharges and plasma generation also in nonsteady state and inhomogeneous to understand the microphysics of the phenomena involved in these plasmas [1/2]. Particularly a nonlinear asymptotic analysis of the positive column [4] and the more extensive theoretical investigations on plasma column at high degree of ionization and under free fall and ambipolar diffusion regimes [5], have been considered. The replacement of the positive column of a glow discharge, by means of a plasma column produced by a HF field, was recently also proved [3]. The theory presented in this paper may be considered in this context as a first approach for a more detailed description of plasma generation and electron heating in HF discharges.

We consider a cylindrical column of ionized gas with an alternating electric field, $\vec{E}_0(\vec{r}, t)$, at a frequency ω , applied to the whole column symmetrically and directed along the axis of the cylinder. This situation could be regarded, for instance, as an idealized model of a plasma column placed in a cylindrical waveguide or resonant cavity. The presence of collisions permits the transfer of energy from the electric power to the electron gas as an effective thermalization of the energy added to the gas with a subsequent growth of ionization and plasma production. The aim of this paper is to determine the electron density and electron temperature distributions inside the column for the plasma generated by a HF field, as before sketched, when the global collision frequency of momentum transfer between electrons and other particles, ν_c , of collisional plasma satisfies the condition $\nu_c \gg \omega$.

The plasma is described by the following system of

nonlinear equations (for sake of simplicity we consider an infinite plane slab as a valid approximation of a large radius cylinder):

$$\begin{aligned} \frac{d^2 E_0}{dx^2} + k_0^2 \left(-i \frac{\pi n_0}{\omega \nu_c} \right) E_0 &= 0, & \Gamma_{ex} &= D \frac{dn}{dx} + \frac{\sigma}{e} \frac{dT_e}{dx}, \\ \frac{d\Gamma_{ex}}{dx} &= (\nu_c - \nu_n) n^2, & \Gamma_{ez} &= \frac{\sigma}{e} E_0, \\ \frac{dH_x}{dx} + \frac{\sigma}{2} E_0^2 &= M_c, & H_x &= \gamma \frac{dn}{dx} - \chi \frac{dT_e}{dx}, \\ H_z &= \beta E_0, & H_z &= \beta E_0, \end{aligned} \quad (1)$$

where the unknowns Γ_{ex} , Γ_{ez} (current densities), H_x , H_z (total energy flows), n_e , T_e (electron density and temperature) and E_0 (external electric field) are averaged in a HF period. The coefficients are:

$$\begin{aligned} D(x) &= \frac{\kappa_0 T_e(x)}{m_e \nu_c}, & \alpha(x) &= \frac{e k_0 n(x)}{m_e \nu_c}, & \gamma(x) &= \frac{5 \kappa_0^2 T_e(x)}{m_e \nu_c}, \\ \chi(x) &= \frac{5 n(x) \kappa_0^2 T_e(x)}{m_e \nu_c}, & \sigma(x) &= \frac{e^2 n(x)}{m_e \nu_c}, & \beta(x) &= \frac{5 n(x) e \kappa_0 T_e(x)}{2 m_e \nu_c}, \\ \Pi^2 &= 4 \pi e^2 n / m_e = \Pi^2(x), & & & & \\ & \text{(valid for } \omega < \nu_c \text{)}, & \kappa_0 &= \omega/c, & & \end{aligned}$$

$$\nu_c = \nu_n + N_a g \sigma_i(g) = g \sum_i \nu_i(g) = \text{const}, \quad \sigma_i = \frac{\sum_i \bar{\nu}}{N_a} = \frac{\bar{\nu}}{g},$$

where $\sigma_i(g)$ is the microscopic cross section and g the relative velocity. The collision term M_c for electron-neutral and electron-ion collision is considered as

$$M_c = M_{en} + M_{ei} = 3 n(x) \kappa_0 \left[\frac{m_e}{m_n} (T_n - T_e) \nu_n + \frac{m_e}{m_i} (T_i - T_e) \nu_i \right], \quad (2)$$

The ionization and recombination frequencies are:

$$\begin{aligned} \nu_i(T_e) &= \frac{\sigma_i}{n(x) N_a} \int_0^{T_e} \bar{\nu}_{en} d^2 c \int_0^{T_e} \bar{\nu}_{ei}(c) d^2 c = \text{const}, \\ \nu_n &= \frac{1}{n(x) N_a} \int_0^{T_e} \bar{\nu}_{en} d^2 c \int_0^{T_e} \bar{\nu}_{en}(c) d^2 c = \text{const}, \end{aligned}$$

where σ_i and σ_n are the microscopic cross sections,

$$E_i \text{ the ionization potential and } \sigma_n = \bar{\nu}/c.$$

In order to solve the system (1), for a slab of width $2a$, we assume for $n(x)$ a distribution of the type,

$$n(x) = n_0 (1 - \lambda(x) x^2 / a^2), \quad -a \leq x \leq a,$$

where $\lambda(x)$ is an unknown function. By simple algebra an equation, only dependent on λ , for the electron temperature can be obtained. Moreover it is possible to prove that if the central zone of the slab is only considered, we have $\lambda \cong \text{const}$

since λ is a very smooth function. By taking into account this hypothesis, with boundary conditions

$$T_e(0) = T_{eo}, \quad (dT_e/dx)_0 = 0,$$

the parametric equation for the electron temperature for small values of x/a , becomes

$$T_e(x, \lambda) = \frac{T_{eo} - \frac{11}{30} \frac{T_s}{\lambda^2}}{1 - \lambda^2 x^2/a^2} + \frac{T_s \lambda x^4}{30 a^4} - \frac{2}{15} \frac{T_s \lambda x^2}{a^2} + \frac{11 T_s}{30 \lambda}, \quad (3)$$

where $T_s = (\bar{v}_e - v_{te}) n_0 v_{te} m_e a^2 / k_B$ and $\bar{v}_e = \langle v_e^2 \rangle = \text{const.}$

For the electric field we obtain the solution,

$$E_0(x) = E_0(a) \exp(i\pi \eta \kappa_0 \lambda^2 / 2a) F\left(\frac{1}{4} \frac{\kappa_0 \lambda^2 a}{\eta \lambda^2}, \frac{1}{4}, \frac{1}{2}, \frac{i\pi \eta \lambda^2 \kappa_0}{a}\right), \quad (4)$$

where $F(a, b; c)$ is Gauss' confluent hypergeometric function, and

$$\eta^2 = 1 - \delta^2 = \frac{i\pi \Pi_0^2}{\omega v_{te}}, \quad \delta^2 = 1 - \frac{i\pi \Pi_0^2}{\omega v_{te}}, \quad \Pi_0^2 = \frac{4\pi n_0 e^2}{m_e}$$

$E_0(a)$ is a constant which satisfies the boundary conditions on the slab surface. For small values of x/a the (4) simply becomes

$$E_0(x) = E_0(a) \left(1 - \frac{\kappa_0^2 x^2}{2}\right),$$

which is not dependent on λ .

The equation for λ is the following:

$$\lambda = \frac{1}{5} \left(\frac{a \bar{v}_{e0}}{D_0 v_{te}} \right)^2 \left(1 + \frac{v_{eo} v_{te}}{\mu_a \lambda} \left(1 - \frac{T_{eo}}{T_s} \right) + \frac{v_{te} v_{te}}{\mu_i \lambda} \left(1 - \frac{T_{eo}}{T_s} \right) + \frac{\kappa_0 T_s}{3 m_e a^2} \frac{v_{eo}^2}{v_{te}^2} \right), \quad (5)$$

where $v_{te}^2 = \frac{3k_B T_{eo}}{m_e}$, $\bar{v}_{e0} = \frac{e E_0}{m_e}$, $D_0 = \frac{k_B T_{eo}}{m_e \mu_i}$, $\mu_a = \frac{m_a}{m_e}$, $\mu_i = \frac{m_i}{m_e}$. A diffusion length may be defined as a function of

λ as follows

$$|\lambda| = (n_0 / |\nabla^2 n|)^{1/2} = a / \sqrt{2 |\lambda|},$$

In Fig. 1 are shown the calculation results of $|\lambda|$ versus E_0 in the case of diffusion dominated plasma (DDP) for $T_s = 0$ and with T_{eo} as a parameter.

In Fig. 2 for a recombination dominated plasma (RDP) or ionization dominated plasma (IDP) are shown the

values of $|\lambda|$ versus T_s/T_{eo} with T_{eo} as a parameter.

In Fig. 3 the distribution of T_e along x/a is shown as a function of T_s/T_{eo} for $\lambda = 1$ and $\lambda = -1$.

We can conclude with the following statements:

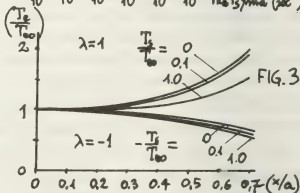
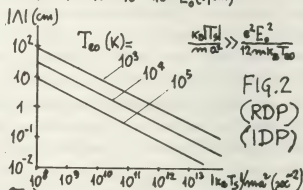
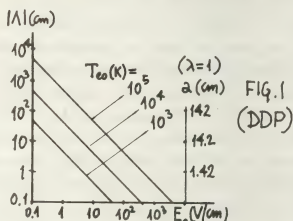
1) The gradients of $n(x)$ and $T_e(x)$ are opposite and are dependent on the source term T_s . In DDP and IDP cases ($T_s > 0$, $\lambda > 0$), on the centre of the column: $n_0 = \text{max}$ and $T_{eo} = \text{min}$. In RDP case ($T_s < 0$, $\lambda < 0$), $n_0 = \text{min}$ and $T_{eo} = \text{max}$.

2) The results are consistent with those reported

in /4//5/ and with those of the conventional theory of the positive column.

References.

- 1) A. Rutscher. Invited lecture of XIII ICPIG, Berlin, 1977, 269.
- 2) T. Růžicka and K. Rohlena. Invited lecture of XI ICPIG, Praha, 1973, 61.
- 3) M. Moisan, C. Beaudry and P. Leprince. IEEE Trans. on Plasma Science. PS-3, 1975, 55.
- 4) H. W. Friedman. The Physics of Fluids. 1967, 2053.
- 5) H.B. Valentini. Proc. of XIII ICPIG, Berlin, 1977, 225.



USE OF TIME-RESOLVING HIGH RESOLUTION SPECTROSCOPY IN THE INVESTIGATION OF PULSE HOLLOW-CATHODE DISCHARGES

S.Z. Mohamed, A.P. Petkov.

University of Sofia, Dept. of Physics, Bulgaria.

Introduction

Recently the hollow-cathode discharge with pulse supply is quite often made use for the purposes of atom-absorption spectroscopy. The time dependences of the spectral-emission characteristics of the pulse feed hollow-cathode discharge, are of a great interest (1-3). Their detailed study yields valuable information on the physical processes in the hollow-cathode source depending on the feeding regime, besides the several interesting application possibilities that it offers.

In the present work an examination is made of the dependences of the intensities and the half-width of certain spectral lines of chromium depending on parameters of the feed pulse, namely the duration of the current pulses (t_p), the duration of the pauses (T_p), the frequency of the pulses f , etc. These dependences are compared with analogous parameters in direct-current feed with current intensity variations of between 5 to 20 mA and accordingly pulse-current variations of between 100 to 400 mA. On the basis of these measurements temperature determinations of the plasma were made depending on the pulse intensity of the current and the intensity of the direct current, and on the frequency of the pulses.

Experimental

The diagram showing the principles of operation of the experimental setting is shown on Fig. 1. The hollow-cathode dis-

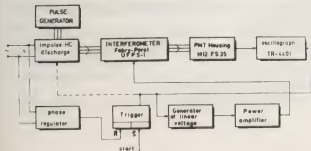


Fig. 1

charge is supplied from a pulse generator while the recording of the line and its width is done with a universal Fabry-Pérot UFP-1 interferometer "Carl-Zeiss"-Jena with piezoceramic scanning. For the recording proper an oscillograph or chart recorder is used, depending on the type of the discharge. Use was made of the G5-15 (USSR) pulse generator. The feeding of the current is done with the aid of rectangular pulses of a duration of between 5 to 10 μ sec and pauses between them of a duration is from 150 to 600 μ sec, i.e. with a repetition frequency of between 1 to 7 KHz. The d.c. bias current was 0.5 mA, and the pulse current, as much as up to 400 mA.

For the sake of obtaining correct results a detailed study was necessary of the apparatus function of the Fabry-Pérot interferometer. To that end several methods were used. The one with the use of helium-neon laser, operating in a single-mode regime, proved the best (4). In the treatment of the profiles the methods of Minkowski and Bruck (5), were used.

Results

On Fig. 2 the dependences of the intensity I of the spectral line of chromium with $\lambda = 4254 \text{ \AA}$ are shown depending on the pulse (curve 2) and direct (curve 4) currents, and depending on the half-width also on the pulse (curve 1) and direct (curve 3) currents. In these measurements the duration of the pulses $t_p = 10 \mu$ sec, and the duration of the pauses $T_p = 200 \mu$ sec, remain constant.

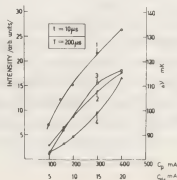


Fig. 2

On Fig.3 analogous dependences are presented, but with fixed values of $T_p=200$ μ sec and a pulse current of $C_p=300$ mA, and corresponding variations of the duration of the pulses and the direct current intensity. curves 1 and 3 give the half-width

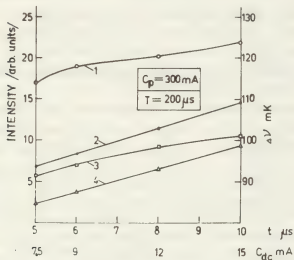


Fig.3

for a pulse and direct-current regimes, and curves 2 and 4, the intensities for pulse and direct-current regimes.

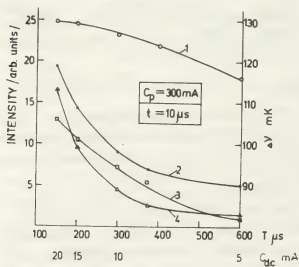


Fig.4

On Fig.4 the dependences are given of the intensity and the half-width of the same line as a function of T_p and C_{dc} with fixed values for the pulse current $C_p=300$ mA, and the duration of pulses t_p 10 μ sec. Curves 1 and 3 relate to the half widths $\Delta\nu$ of the line, and 2 and 4, to the

intensities in pulse or direct-current supply.

With the aid of the formula $\Delta\nu = 7.16 \cdot 10^{-7} \sqrt{\frac{T}{M}}$, where M is the mass of the atom of the chromium = 51.99, and assuming that the other interactions are negligibly minute and that the line has a Doppler pro-

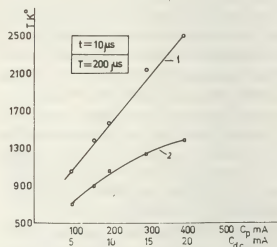


Fig.5

file, the discharge temperatures T were determined as a function of the pulse current, the intensity of the direct current and the frequency of the pulses (Fig.5,6). On both figures the curves 1 refer to pulse feed, and 2, to direct-current feed.

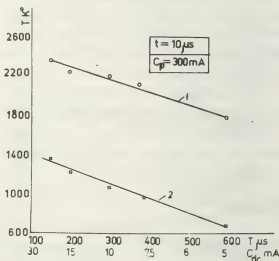


Fig.6

REFERENCES

- 1-T.Araki, T.Uchida, and Sh.Minami, Appl. Opt. 34, 150, 1977.
- 2-J.B.Dawson, D.J.Ellis, Spectrochim. Acta 23A, 565, 1967.
- 3-R.Djulgerova, Spect. Letter, 10, 727, 1977
- 4-S.Z.Mohamad, and oth., VIII Nat. Conf. on Atom. Spect., 245, 1978.
- 5-P.Minkowski, H.Bruck, ZS. Phys. 95, 27, 1935.

INVESTIGATION OF AN EARLY HELIUM AFTERGLOW PLASMA PRODUCED BY A MICROWAVE SURFAGUIDE

A. Bouvier, S. Abed, B. Charlet and A. Bouvier.

E.R.A., C.N.R.S. 308, Laboratoire de Spectroscopie et de Luminescence, Université Claude Bernard, Lyon I 43, Bd du 11 Novembre 1918 69621 Villeurbanne, France.

Abstract. Plasma is produced by a microwave surfaguide^{/1/} in a cylindric quartz cell filled with helium at a pressure of 14 torrs. A homogeneous plasma is so obtained along the axis. Spectroscopic diagnostics are used to measure during the first 100 μ s and in different parts of the cell :

- different atomic and molecular excited levels populations
- the rotational temperature of He_2 in two electronic states $e^3\Pi_g$ and $E^1\Pi_g$
- a mean electronic temperature of the class of electrons which recombine.

Introduction. Spectral investigation has shown that many atomic and molecular levels are populated during 100 μ s by recombination processes in the case of non complete Boltzmann equilibrium. To describe the variations of populations in these conditions R. Deloche and col.^{/2/} have shown that it is very important to determine the ratio T_e/T_g where T_e is the electronic temperature and T_g the neutral gas temperature, parameters we try to determine in this work.

Experimental methods. The plasma is observed end on, in a direction parallel to the axis of the cell, on a diameter, at a distance r from the axis (Fig.1). The intensity of different lines is analysed by a system (Fig.2) including, a Jobin-Yvon monochromator HRS (dispersion 12 Å/mm), a 6256 S EMI photomultiplier, a counter system Inter-technique IN 90 with a multichannel analyser and a computer using different acquisitions techniques. The single photon technique was the most adequate in this case because the time resolution could be as good as wanted.

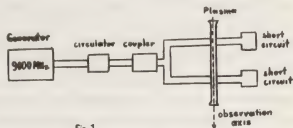


Fig. 1

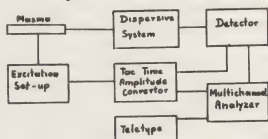


Fig. 2

- The population of different atomic and molecular levels varies with r and t (Fig. 3 and 4). Along a diameter, we obtain one minimum on the axis and two maxima on both sides of the axis. The amplitudes of the two maxima are not identical. The decay is exponential, the relaxation time varies with r and is of the same order for atomic and molecular levels.

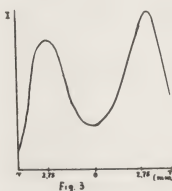


Fig. 3

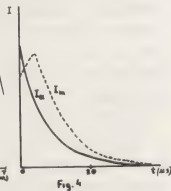
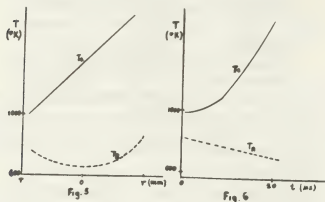


Fig. 4

- The rotational temperature is measured by considering the Boltzmann diagram. Equilibrium is realised for all the rotational numbers J except

for one J (J higher = 2) on the walls of the cell. Rotational temperature varies only a little with r and t ($\Delta t \approx 100$ K), about 700 K (Fig. 5 and 6).

3. Electronic temperature is evaluated by using theory of Griem^{/3/} and Drawin^{/4/}. A partial equilibrium is realised between electrons (for electronic density 10^{11} or 10^{12} cm^{-3}) and helium atoms in levels with quantum number higher than 5 (In fact the level 6^3D). The electronic temperature what is so measured is constant enough during the first 30 μs but increases in the cell in the part nearer the generator. This mean temperature keeps high enough (1500-2000 K) (Fig. 5 and 6). The reason is that another class of electrons with very high energy certainly exists during this interval.



Discussion. These measurements are interesting because they will permit to study recombination processes during the early afterglow when T_e is high enough and when complete Boltzmann equilibrium is not obtained. If T_R represents the temperature of the neutral gas, T_e/T_R varies a little with time, what explains the different exponential decays; but T_e and T_R vary with r what justifies the important variation of populations in the cell.

References.

/1/ M. Moisan, C. Beaudry, L. Bertrand, E. Bloyet, J.M. Gagne, P. Leprince, J. Marec, G. Mitchel, A. Ricard, Z. Zakrzewski - International Conference on Gas Discharges, Swansea, U.K. (Sept. 1976) n° 143, p.382.

/2/ R. Deloche, P. Monchicourt, M. Cheret, F. Lambert - Phys. Rev. A 13, 1140 (1976).

/3/ H.R. Griem - Plasma Spectroscopy, Ed. M. Graw-Hill Book Company, N.Y., San Francisco London (1974).

/4/ H.W. Drawin - Z. Phys. 228, 99 (1963)
Z. Phys. 225, 483 (1972).

PHYSICAL PROCESSES IN ARC HOLLOW CATHODE

G.A. Dyuzhev, E.A. Startsev and V.G. Yur'ev.

A.F. Joffe Physical Technical Institute, Academy of Sciences of the U.S.S.R., Leningrad, K-21, U.S.S.R.

Hollow cathodes, either single or multichannel, are considered now as high-current extensive lifetime electron emitters in different discharge devices. Despite the amount of works some physical processes inside hollow cathodes are still poorly understood [1]. It is caused by difficulties of detailed diagnostics of the cavity plasma in the conventional high-temperature hollow cathodes [2].

In this communication on the grounds of detailed diagnostics of the plasma in the "active zone" is carried out the investigation of ionization, current conduction, energy balance of the cavity plasma in dependence of external conditions. The experimental studies described in present paper involve highly ionized cavity plasma HC operated at arc currents from 10 to 100 A and cesium or argon pressures from 1 to 10 Torr.

The assembly used is presented in Fig.1. To maintain constant cathode temperature which is determined by auxiliary heater, the discharge is supplied by stabilized rectangular pulse of 1 msec duration and 12.5 Hz repetition rate. The measurements are performed on the end of supply pulse, when relaxation processes are terminated, by systems of gating integration (strob duration $\sim 1/\mu\text{sec}$).

Adsorption of cesium on the cathode surface diminishes its work function to as low values as $\chi_c \sim 1.3 - 1.4$ eV and allows to obtain high thermoionic current densities $j_{es} \sim 10^1 - 10^2 \text{ A/cm}^2$ at low emitter temperatures ($T_{cath} \sim 10^3 \text{ K}$)/3/.

The diagnostics of the cavity plasma is made by the probe moving axially in the HC. The evaluation of the probe data

is carried out by diffusion theory assuming charge-particle generation in the probe sheath [4]. Outside the HC the probe data are compared with optical ones.

Fig.1 shows plasma potential distribution V_0 (in respect to the cathode), electron temperature T_e (probe characteristics point that Maxwellian distribution function exist) and plasma density profiles at different points of current-voltage characteristics.

Analysis of obtained distributions show that the current conduction is determined mainly by field component of electron current $j_e \sim \sigma(T_e) E$ (where $\sigma(T_e) \sim T_e^{3/2}$ - is fully ionized plasma conductivity and E is field strength).

In Fig.2 the values of total current $I_z = j_z(z) \pi R^2$ passed through z-cross-section of HC and ionic current $I_i(z) = 2\pi R \int j_{ix}(z) dz$ ($j_{ix} = 0.43 q n \sqrt{2kT_e}$ - ionic current density) are presented. The good agreement of $I_z(0)$ with the discharge current I indicates the radial uniformity of the cavity plasma.

The linear dependence of $I_z(z)$ and $I_i(z)$ upon z is explained by the emission current constancy in the "active zone" of HC.

Some parameters that characterize the HC operation at different values of the current I are given in the Table.

Plasma penetration depth L , ionic current portion $\gamma = I_i(0)/I$ emission current density j_{es} are presented. The ratio of power, carried out by electron current from the cavity plasma, to total power and the ratio of power, carried out by ionic current, to total power are presented also.

The evolutions show that radiation losses are the most significant ones between the other losses.

I, A	L, cm	β	$j_{es}, A/cm^2$	w_i/w_0	w_d/w_0	w_i^*/w_{em}
9	0.9	0.19	11	0.29	0.33	1.2
20	1.1	0.23	18	0.31	0.37	2.0
30	1.4	0.26	22	0.32	0.38	2.9
40	1.7	0.29	25	0.32	0.38	3.8

Physical processes which occur in the HC with highly ionized plasma are well described by the equations presented in [5]. Received results show that the HC operated at constant current without auxiliary heating is heated mainly by ionic current $w_i^* = 2\pi R \int_0^L [\epsilon_{ion} - j_c + q\varphi_n(z)] j_{in}(z) dz$ and cooled by electron

emission $w_{em} = 2\pi R L j_{es} (2\kappa T_c + j_c)$ and by the heat conduction to the cathode holder.

At low current values, when $w_i^* \sim w_{em}$ the ionic current heating is balanced by the electron emission cooling. At higher currents $w_i^* > w_{em}$ that can create the important temperature gradients on the HC. The current limitation occurred at lower cesium pressures [6] is caused by the achievement of the current density which is comparable with random electron current density $j_{ian} = \frac{1}{4} q n \sqrt{\frac{8\kappa T_e}{\pi m}}$ at exit of the HC.

- /1/. J.L.Delcroix, A.R.Trindade. Adv. in Electr. and Electr. Phys. 35, 88, 1974.
- /2/. A.Brunet. Proc. XII Int. Conf. on Phen. in Ion. Gases, p.231, Eindhoven, Holland, 1975.
- /3/. G.A.Dyuzhev, E.A.Startsev, S.M.Shkolnik, V.G.Yur'ev. J. Techn. Phys. 48, 2113, 1978.
- /4/. F.G.Bakst, G.A.Dyuzhev, N.K.Mitrofanov, S.M.Shkolnik, V.G.Yur'ev. J. Techn. Phys. 43, 2574, 1973.
- /5/. F.G.Bakst, A.B.Rybakov. Proc. XIII Int. Conf. on Phen. in Ion. Gases. p.527, Berlin, G.D.R. 1977.
- /6/. G.A.Dyuzhev, E.A.Startsev, S.M.Shkolnik. J. Techn. Phys. 48, 2495, 1978.

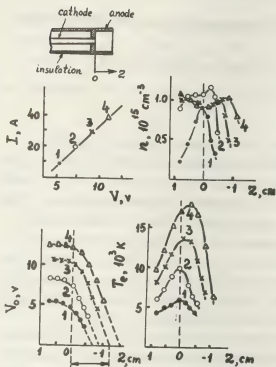


Fig. 1

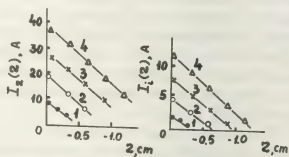


Fig. 2

OPTICAL INVESTIGATIONS OF THE SPONTANEOUS EXTINCTION OF THE HIGH-CURRENT KNUDSEN ARC DISCHARGE IN Cs-Ba GAS MIXTURE

V.I. Bebanin, V.B. Kaplan, I.N. Kolyshkin, V.I. Kuznetsov, A.M. Martynovskii, A.S. Mustafaev, V.I. Sitnov and A.Ya. Ender.

Ioffe Physical-Technical Institute of the U.S.S.R. Academy of Sciences, Leningrad, U.S.S.R.

The investigations of the spontaneous arc extinction in a switching Cs-Ba triode with a fine-mesh grid, operating in the collisionless mode, have been carried out. The use of Cs-Ba mixture, where cesium is the plasma-forming component, allowed to obtain emission currents from the cathode up to 100 A/cm^2 in Cs-pressure range 10^{-3} - 10^{-2} Torr and, thus, easily attain the limits of gas current-conduction capacity.

It is shown, that the critical current j_{crit} , preceding the spontaneous extinction of the arc (the upper current limit), doesn't depend on Ba pressure and is proportional in a wide range to Cs pressure (Fig.1). It is ascertained, that j_{crit} is the density of electron current, which can be compensated at the complete ionization of the plasma-forming atoms,

$$j_{\text{crit}} = (e \bar{V}_i / kT) P \sqrt{m_i / m_e};$$

where \bar{V}_i - average ion velocity in the plasma, m_i (m_e) - ion (electron) mass, P - gas pressure, T - temperature.

The time of existence of the arc discharge under conditions, when the critical value of the discharge current is exceeded, is inversely proportional to $\Delta j = j - j_{\text{crit}}$ (Fig.2) and is almost by an order of magnitude longer, than the similar period in the case of the inert gas discharges. Such a prolonged existence of the current conduction state may be explained by desorption of the plasma-forming atoms from the electrode surfaces. It is found, that the spontaneous arc extinction is followed by a relaxation period- the time period, in which the ignition of the arc discharge doesn't occur. This time proves to be commensurable with the time of existence of the plasma conduction state. Further, it is found, that the arc extinction is preceded by the appearance of plasma instability and the development of plasma oscillations.

In order to study the mechanism of the spontaneous arc extinction the time dependencies of the luminosity of a series of CsI, BaII and BaI lines were obtained; the luminosities of all lines investigated were measured in the subcritical (points A - C), critical (point D) and supercritical (point E) discharge modes, as well as at seven points across the interelectrode spacing (Fig.3).

Recording and processing of the experimental data were performed with the use of the multichannel measuring and calculational system, based on the computer

BESM - 4 and intended for the investigation of non-stationary periodic processes, the resolution of the order of $1 \mu\text{sec}$ being provided. All the analogue signals were being strobed simultaneously. The recording with the time resolution of $0.2 \mu\text{sec}$ was being performed by the single-channel analogue strobe-integrator. For increasing the ratio "signal-noise" the numerical averaging in the computer was employed ($N=128$). The synchronous recording of the electrical and optical relationships using the multi-channel system made possible to reveal the time shift between these relationships, as well as between optical processes at different points of the interelectrode spacing.

To determine the value of the time shift the correlation analysis was employed. The correlation function

$$K = 1/n \sum_{i=1}^n (f_1(t_i) - \bar{f}_1)(f_2(t_i - \tau) - \bar{f}_2)$$

for the luminosity relationships, obtained for the BaII line ($\lambda = 7060 \text{ \AA}$) in the cathode (point 2) and anode (point 6) regions of the discharge, is presented in Fig.4. The examination of the correlation method, being applied in our case, showed, that the measurement error of the time shift values didn't exceed 20% of the time step, i.e. was equal to $0.2 \mu\text{sec}$.

The results of data processing demonstrated, within the accuracy indicated above, the absence of time shifts during the oscillation development in the discharge modes A - D. It means, that the oscillations in the subcritical mode are not connected with the propagation of potential waves, potential jumps and other disturbances across the interelectrode spacing and are accompanied by the synchronous change of the potential at all points in the spacing. The results, obtained in the mode E, in which the spontaneous arc extinction occurs, are different. As is seen from Figs 5 and 6, under these conditions the processes are non-synchronous throughout the spacing: before the arc extinction flashes of the highly excited BaI and BaII lines radiation occur in the anode region by $3 \mu\text{sec}$ earlier, than in the cathode region, which is due to the abrupt change of the plasma potential. The spontaneous arc extinction is preceded by preparatory processes involving atom concentration depletion, manifested by the decrease of luminosity with time.

From the optical measurements it may be concluded, that the oscillatory pro-

cesses in the subcritical mode occur synchronously at all points in the spacing; these measurements confirm also the assumption about the spontaneous extinction of the high-current low-pressure discharge being due to the atom depletion in the spacing.

Thus, the arc extinction in the triode, having the fine-mesh, highly-transparent grid, is due to the high degree of atom ionization and to the escape of atoms from the spacing, while the large duration of the current pulse is determined by atom desorption from the electrode surfaces.

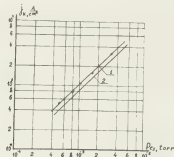


Fig. 1 Critical current density as a function of cesium pressure
1 - experiment
2 - theory

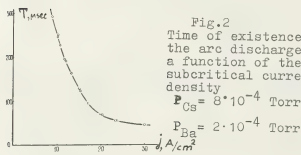


Fig. 2
Time of existence of the arc discharge as a function of the subcritical current density
 $P_{Cs} = 8 \cdot 10^{-4}$ Torr
 $P_{Ba} = 2 \cdot 10^{-4}$ Torr

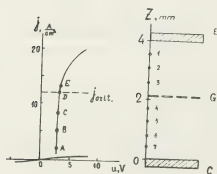


Fig. 3

Volt-ampere characteristic of the discharge and the schematic view of the interelectrode spacing

$T_k = 1660K$, $P_{Cs} = 1.1 \cdot 10^{-3}$ Torr,
 $P_{Ba} = 1 \cdot 10^{-3}$ Torr

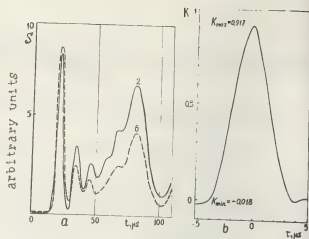


Fig. 4 a - Time dependence of the BaI line ($\lambda = 7060 \text{ \AA}$) luminosity at the points 2 and 6 in the spacing (mode B),
b - Correlation function.

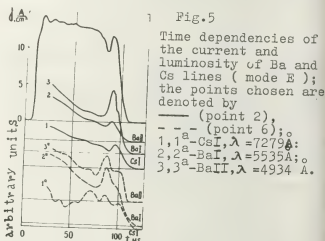


Fig. 5
Time dependencies of the current and luminosity of Ba and Cs lines (mode E); the points chosen are denoted by
— (point 2),
- - - (point 6);
1, 1a - CsI, $\lambda = 7279 \text{ \AA}$;
2, 2a - BaI, $\lambda = 5535 \text{ \AA}$;
3, 3a - BaII, $\lambda = 4934 \text{ \AA}$.

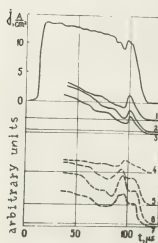


Fig. 6

Time dependencies of the current and luminosity of BaII line ($\lambda = 4934 \text{ \AA}$) at various points of the spacing (mode E)

CURRENT-VOLTAGE CHARACTERISTIC OF NON-SELF-MAINTAINED DISCHARGE.

J.I. Londer.

All-Union Electrotechnical Institute, Moscow U.S.S.R.

The analytical expression of the non-self-maintained current-voltage characteristic is obtained. The ion current flowing into cathode sheath from plasma is a potent factor in the considered model. This ion current was not taken into consideration in the classical Thomson's paper [1], when the analogous problem was solved in paper [2] the ion current from plasma was taken into consideration for construction of probe theory in non-self-maintained discharge, but the rate of ionization in the cathode sheath was not taken into account.

Let us consider the plane system of electrodes. We'll solve equations for plasma and cathode sheath separately and then make join of solutions on the plasma-sheath boundary.

2. The equations for plasma region are given by:

$$j_e = en_e \delta_e E + e \mathcal{D}_e \frac{dn_e}{dx} \quad (1)$$

$$j_i = en_i \delta_i E - e \mathcal{D}_i \frac{dn_i}{dx} \quad (2)$$

$$\frac{dj_e}{dx} = -\frac{dj_i}{dx} = e(q - \alpha_k n_e^k) \quad (3) \quad j_e + j_i = j_d \quad (4)$$

Here q is the rate of ionization created by external source, α_k is the effective recombination coefficient. Index k depends on the type of the recombination. We'll consider the cases when $k=2$ and 1. Take the origin of coordinates at the plasma-sheath boundary and introduce non-dimensional concentration N and non-dimensional length y :

$$N = \frac{n}{n_\infty}; \quad y = \frac{x}{\tau_\alpha}; \quad \tau_\alpha = \left(\frac{\mathcal{D}_\alpha}{\alpha_k n_\infty^{k-1}} \right)^{1/2} \quad (5)$$

Here is ambipolar diffusion coefficient

ent, τ_α is the recombination length, is unperturbed plasma concentration. From (1) and (2), taking into account (5), we get:

$$j_e = j_d \frac{\delta_e}{\delta_e + \delta_i} + n_\infty \frac{e \mathcal{D}_\alpha}{\tau_\alpha} N' \quad (6)$$

$$E = E_\infty N^{-1} + \frac{\mathcal{D}_e - \mathcal{D}_i}{\delta_e + \delta_i} \frac{1}{\tau_\alpha} \frac{N'}{N} \quad (7)$$

$$N' \equiv \frac{dN}{dy} = 1 - N, \quad \kappa = 1; \quad N' = (1 - N) \sqrt{\frac{2}{3(N+2)}}, \quad \kappa = 2 \quad (8)$$

Here $E_\infty = j_d / en_\infty (\delta_e + \delta_i)$ is the electric field in plasma far from boundary. Integrating (7), we can obtain the potential drop on the plasma.

$$V_p = E_\infty (L - x_0) + E_\infty \tau_\alpha \ln N_0^{-1} + \frac{\mathcal{D}_e - \mathcal{D}_i}{\delta_e + \delta_i} \ln N_0^{-1} \quad (9a)$$

($\kappa = 1$).

$$V_p = E_\infty (L - x_0) + \frac{\sqrt{2}}{2} E_\infty \tau_\alpha \ln \frac{(\sqrt{N_0 + 2} + \sqrt{2})(\sqrt{3} - \sqrt{2})}{(\sqrt{N_0 + 2} - \sqrt{2})(\sqrt{3} + \sqrt{2})} + \frac{\mathcal{D}_e - \mathcal{D}_i}{\delta_e + \delta_i} \ln N_0^{-1}; \quad (\kappa = 2). \quad (9b)$$

Here L is the anode-cathode distance, x_0 is the cathode sheath thickness, N_0 is the concentration on the plasma-sheath boundary.

3. If the heat energy of electrons is far less than the cathode drop, then electrons will be found in the sheath in the strong repulsive field and $n_1 \gg n_e$ on the whole sheath except narrow region near plasma-sheath boundary. Therefore we can neglect n_e in comparison with n_1 in Poisson's equation for sheath. The distribution of the field and n_1 must be determined from joint solution of equations:

$$\frac{dE}{dx} = \frac{e}{\epsilon_0} n_i \quad (10), \quad \frac{dj_i}{dx} = eq \quad (11), \quad j_i = en_i \delta_i E \quad (12)$$

with boundary condition $j_1(x_0) = (1 + \gamma)^{-1} j_d$. γ is the secondary emission coefficient

under bombardment of the cathode by ions.

The solutions must be joined at the plasma-sheath boundary. So, joining derivative of the field, we obtain algebraic equation for ion concentration at the boundary (N_0):

$$\frac{N_0^3}{1-N_0} \frac{e}{\epsilon_0} n_\infty = \frac{E_\infty}{\epsilon_0} + \frac{\partial e \cdot \partial i}{\partial e + \partial i} \frac{1}{\epsilon_0^2} (1-2N_0)(\kappa-1) \quad (13a)$$

$$\frac{N_0^3}{1-N_0} \frac{e}{\epsilon_0} n_\infty = \frac{E_\infty}{\epsilon_0} \sqrt{\frac{2}{3}(N_0+2)} + \frac{\partial e \cdot \partial i}{\partial e + \partial i} \frac{1}{\epsilon_0^2} \frac{N_0^2 + N_0 + 4}{3} \quad (13b)$$

Substituting the value N_0 , found from (13), in (6) and (7) we obtain values of ion current j_0 and electric field E_0 on the plasma-sheath boundary. These values j_0 and E_0 will be boundary conditions for equations (10)-(12). Introducing nondimensional field $z = E/E_0$, nondimensional coordinate $t = 1 + eqx/j_0$ and nondimensional parameter $\delta^2 = \epsilon_0 \partial e \partial i / j_0^2$, we integrate (10)-(11):

$$Z = \sqrt{\frac{t^2 - 1}{\delta^2} + 1} \quad (14) \quad X_0 = \frac{j_d(t+y)^{-1} j_0}{eq} \quad (15)$$

Now we can find the cathode drop V_c :

$$V_c = \int_0^{X_0} E dx = \frac{E_0 j_0}{eq} \int_0^{t_{\max}} Z dt; \quad t_{\max} = \frac{j_d(t+y)^{-1}}{j_0} \quad (16)$$

Substituting (14) in (16) we obtain equation of the current-voltage characteristic of the cathode sheath.

$$V_c = \frac{E_0 j_0}{2eq\delta} \left[t_{\max} \sqrt{t_{\max}^2 - 1 + \delta^2} - \delta + (\delta^2 t) \ln \frac{\sqrt{t_{\max}^2 + \delta^2 - 1} + t_{\max}}{1 + \delta} \right] \quad (17)$$

The behaviour of the expression (17) depends greatly upon the value δ . By means of (6) and (7) it can be obtained that:

$$\delta^2 = \frac{\epsilon_0 q}{e \partial e n_\infty^2} \frac{1}{N_0^2} \quad (18)$$

The value of parameter δ is less or about 1 in electropositive gases at the pressures up to several atmospheres. Under this condition it can be neglected logarithmic term in expression (17). In electronegative gases, because of strong attachment of electrons, the parameter δ can become much larger than 1. In this case it can't be neglected logarithmic term in (17). However, there are two limits, when (17) can be simplified inde-

pendently of k . The first limit takes place if:

$$t_{\max} \gg \max[t; \delta^2] \quad (19)$$

The second limit takes place if:

$$(t_{\max} - 1) \ll \min[t; \delta^2] \quad (20)$$

From (17) and (14) we obtain for cathode drop V_c and electric field E_0 near cathode: if the criterion (19) is carried out then known expressions take place [1]:

$$V_c = 0.5 j_d^2 (t+y)^{-2} (eq)^{-3/2} (\epsilon_0 \partial e)^{-1/2}; \quad E_c = j_d (t+y) (\epsilon_0 \partial e q)^{-1/2} \quad (21)$$

If the criterion (20) is carried out, then we have:

$$V_c = E_0 X_0 \left(1 + \frac{1}{2} \frac{X_0 j_0}{\epsilon_0 \partial e E_0^2} \right); \quad E_c = E_0 \left(1 + \frac{X_0 j_0}{\epsilon_0 \partial e E_0^2} \right); \quad (22)$$

4. Using (6), (15) and (16) we can obtain:

$$j_d = \left(\frac{1}{t+y} - \frac{\partial e}{\partial e + \partial i} \right) = eq(X_0 + \epsilon_0 N') \quad (23)$$

$$t_{\max} = 1 + \frac{X_0}{\epsilon_0 N_0'} \quad (24)$$

One can see from (23), that there are two characteristic lengths x_0 and $\epsilon_0 N_0'$ of forming current in considered model. Under $x_0 \gg \epsilon_0 N_0'$ the discharge current is formed mainly in the cathode sheath region, and under $x_0 \ll \epsilon_0 N_0'$ the characteristic length of forming current is $\epsilon_0 N_0'$. In the first case $t_{\max} \gg 1$ and criterion (19) can be carried out; in the second case $(t_{\max} - 1) \ll 1$ and criterion (20) can be carried out. If criterion (19) takes place, then transition region with length $\epsilon_0 N_0'$ can be neglected and the sheath can be joined with plasma without consideration j_0 and E_0 , that was made in [1]. If criterion (20) is carried out, ionization in the cathode sheath can be neglected in comparison with ionization on the length $\epsilon_0 N_0'$, that was made in [2]. And general expression (17) must be used for determining V_c in the intermediate case when the values x_0 and $\epsilon_0 N_0'$ have the same order of magnitude.

The author thanks K.N.Ulyanov for useful discussions.

References

1. J.J.Thomson, G.P.Thomson. Conduction of Electricity through Gases. v.1, chap.IV
2. K.N.Ulyanov. XIII Intern.Conf.on Phenom.in Ioniz.Gases. p.113 Berlin 1977

THE PECULIARITIES OF THE DIFFUSION PROCESSES IN THE ELECTRONEGATIVE GAS PLASMA

G.G. Arutunian, G.A. Galechian.

Jerevan State University, Research Institute of the Condensed medium Physics.

The dependence of the ambipolar diffusion coefficients of the charged particles D_e^a , D_+^a and D_-^a in the electronegative gas discharges on $\alpha = n_-/n_e$ (n_- , n_e are negative ion and electron concentrations) are considered in [1] - [3]. It is turned out in [1] that D_-^a has only positive values and slightly changes by exchange α from 10^{-3} till 10^{-4} . But it is shown in [2] that D_-^a is negative and the n_- flow in the cylindric positive column is directed from the walls of the tube to its axis.

This paper states that depending on the conditions in the discharge D_-^a may be negative, positive or equal to zero. Besides, when $D_-^a < 0$, the negative ion flow can be directed both from the plasma column axis and the opposite direction (depending on the direction of the n_- -gradient) as it is known that the n_- -distri-

bution along the radius may be both parabolic ($\nabla n_- < 0$) and two-humped [5,6] ($\nabla n_- > 0$ in the near axis region). The diffusion flow of charges in stationary electronegative gas plasma is written as follows:

$$\Gamma_+ = -D_+ \nabla n_+ + M_+ n_+ E_r \quad (1)$$

$$\Gamma_- = -D_- \nabla n_- - M_- n_- E_r \quad (2)$$

$$\Gamma_e = -D_e \nabla n_e - M_e n_e E_r \quad (3)$$

Where Γ is the particle flow density; M is the mobility; E_r is charge self consistent field; D is diffusion.

Let's take $\gamma = T_e/T_- = T_e/T_+ = T_e/T_g$. The conditions of the flow quasineutrality and equality are written as follows: $n_+ = n_e + n_-$. $\Gamma_+ = \Gamma_- + \Gamma_e$; $n_+ V_+ = n_- V_- + n_e V_e$

Having in view that $D_+ \approx D_-$ from (1)-(3) we obtain:

$$\frac{E_r(\alpha)}{E_r(0)} = \frac{1 + M_+/M_e}{1 + M_+/M_e + (1 + \alpha)M_-/M_e} \quad (4)$$

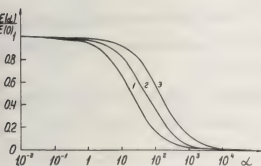


Fig.1

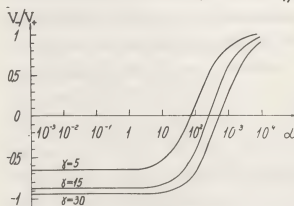


Fig.2

When $M_+ \ll M_e$ and $M_+ \approx M_-$

$$\frac{E_z(0)}{E_z(0)} = \frac{1}{1 + 2\alpha M_- / M_e} \quad (5)$$

Where $E_z(0)$ is the ambipolar field with $\alpha = 0$. From the diagrams of Fig.1 it follows that the ratio $E_z(\alpha)/E_z(0)$ in the interval $10^{-3} \leq \alpha \leq 1 \div 10$ is equal to 1, and for $1 + 10 \leq \alpha \leq 10^3 + 10^4$ this ratio sharply decreases and tends to zero. The ambipolar diffusion field per unit perturbation increases with the rise of E/P within the interval $1 + 10 \leq \alpha \leq 10^3 + 10^4$ for the given α . For Boltzmann distribution of ion concentration in the discharge (obtained experimentally in [1]) one may write:

$$\frac{\nabla n_-}{\nabla n_+} \approx \frac{\alpha}{\alpha + 1} \quad (6)$$

From the conditions of the quasineutrality and flow equality, (1)-(6), we obtain for the ion flow mean velocities:

$$\frac{V_-}{V_+} = \frac{2(1+\alpha)M_+/M_e + 1 - \gamma}{2\alpha M_- / M_e + 1 + \gamma} \quad (7)$$

Fig.2 shows the diagrams of V_-/V_+ for different γ dependent on α and calculated according to the (7). The curves of fig.1 and fig.2 are calculated for oxygen. From these diagrams it follows: 1) $V_-/V_+ = 0$, when $\alpha = \alpha_0$; 2) $V_-/V_+ < 0$, when $\alpha < \alpha_0$, i.e. n_- flow is directed to the positive column axis; 3) $V_-/V_+ > 0$, when $\alpha > \alpha_0$, i.e. n_- flow is directed to the tube's wall. For $\alpha > 10$ and $\gamma = 30$, $V_-/V_+ \approx 1$ and

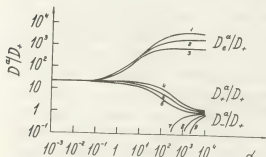


Fig.3

in case $\alpha > 10$, $V_- M_- \approx V_+ M_+$. From (1)-(3), (6) we obtain:

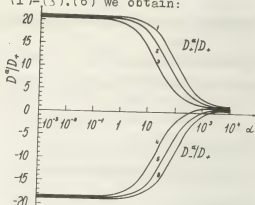


Fig.4

$$D_e^a = \frac{1 + (1 + \alpha)\gamma + \alpha\gamma M_- / M_+}{1 + (1 + \alpha)M_+ / M_e + \alpha M_+ / M_e} D_+^{(R)}$$

$$D_+^a = \frac{1 + \gamma + 2\alpha M_- / M_e}{1 + (1 + \alpha)M_+ / M_e + \alpha M_- / M_e} D_+^{(9)}$$

$$D_-^a = \frac{1 - \gamma + 2(1 + \alpha)M_+ / M_e}{1 + (1 + \alpha)M_+ / M_e + \alpha M_- / M_e} D_-^{(10)}$$

Fig.3 shows D_e^a/D_+ , D_+^a/D_+ dependent on α ; the case $E/P = 40 \text{ v/cm.tor}$ correspond to the curves 1,4; $E/P = 30 \text{ v/cm.tor}$ to the curves 2,5; $E/P = 20 \text{ v/cm.tor}$ to the curves 3,6. Fig.4 shows the dependences of D_+^a/D_+ and D_-^a/D_+ on α ; the case $E/P = 40 \text{ v/cm.tor}$ correspond to the curves 1,6; $E/P = 30 \text{ v/cm.tor}$ to the curves 2,5; $E/P = 20 \text{ v/cm.tor}$ to the curves 3,4. For $\alpha \leq 0,4$, $D_+^a = D_e^a$, like a discharge in the electropositive gases. References

1. Thompson J.B., Proc.Phys.Soc., **23**, 818 (1959).
2. Sabadil H., Beitr.Plasmaphys., **11**, 53 (1971).
3. Arutunian G.G., Galechian G.A., J.T.Phys **43**, 631 (1978).
4. Güntersulze A., Zs.f.Phys., **21**, 724 (1934).
5. Smith D., Goodall C.V., Adams N.G., J.Phys. D: Appl.Phys., **7**, 1944 (1974).
6. Galechian G.A., Izv.AN Arm.SSR, Physics, **11**, 395 (1976).

ANOMALOUS CONDUCTIVITY OF LOW PRESSURE HF DISCHARGE IN MAGNETIC FIELD

V.G. Naumovets, L.L. Pasechnik and V.V. Yagola.

Institute for Nuclear Research Ukrainian SSR Academy of Sciences Kiev, U.S.S.R.

It was established previously /1/ that in the HF discharge the superposition of the magnetic field H normal to the alternating electric field E results in a redistribution of HF voltage between the sheath and plasma. Due to this the electric field in the plasma substantially increases. Further investigations /2/ have shown that the electric field E has a maximum at some value of H , the position of the maximum being dependent on the pressure. This dependence was explained by the different influence of H on the conductivity of the plasma - σ_p and of the sheath - σ_{sh} . The calculation performed agree reasonably with the experimental dependence $E(H)$. At high magnetic fields, however, there exists some discrepancy between the measured and calculated values of E . The experimental data

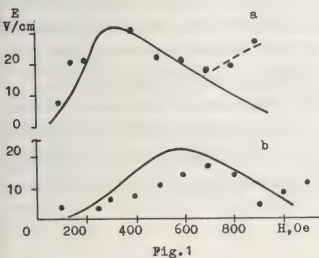


Fig.1

obtained at two pressures P of helium are presented in fig.1 by the points (a- $P = 2.10^{-2}$ mm HG; b- $P = 1.10^{-1}$ mm HG). The measurements were performed with the apparatuses described in /1,2/. The $E(H)$ - dependences calculated according to /2/ are given in fig.1 by solid lines. At the high magnetic fields these dependences are in poor agreement with the experimental data, the discrepancy being especially pronounced at the low pressures. The agreement between the experimental and calculated data can be significantly improved if one assumes at high H that the collision frequency of electrons - ν , determining the value of σ is essentially higher than the classical frequency $\nu_{ea} = 2.3 \cdot 10^9$ P /3/. The value of ν can be determined from the measurements of the phase shift - φ between the discharge HF voltage and the current in the discharge circuit. An analysis of the equivalent circuit of the discharge gap (plasma - sheath) gives for $\varphi = \arctg \left[\frac{\sigma_x}{\sigma_R} - \frac{\sigma_R^2 + \sigma_x^2}{\sigma_{sh} \cdot \sigma_R} \right]$ (1) (σ_R and σ_x - correspondingly the active and reactive components of the plasma conductivity across H , σ_{sh} - the sheath conductivity). In our experiments the electron cyclotron frequency ω_{He} is much high-

her than the frequencies of electron-atom and ion-atom collisions, ν_{ea} and ν_{ia} , and the frequency of alternate electric field - ω . Besides in our experiment the inequality is also fulfilled $E \ll E_p$, where E_p - the specific "plasma field"/4/. Under these conditions ϵ_R and ϵ_x are expressed as:

$$\epsilon_R = \frac{e^2 n \nu}{m_e \omega_{He}^2}; \quad \epsilon_x = \frac{e^2 n}{m_i \omega} \left(\frac{m_i \omega^2}{m_e \omega_{He}^2} - 1 \right)$$

(e and m_e are the electron charge and mass, n is the concentration of the charges in the plasma, m_i is the ion mass).

At high H we have usually in our experiments $|\epsilon_x| \gg \epsilon_R$. Then the expression (1) can be simplified as follows:

$$\varphi \approx \arctg \left(\frac{\epsilon_x}{\epsilon_R} \right) \approx \arctg \left(\frac{m_e \cdot \omega_{He}^2}{m_i \cdot \nu \cdot \omega} \right) \quad (2)$$

As can be seen from (2) φ is determined mainly by ν . The dependence $\varphi(H)$ which is obtained experimentally (curve 1) and calculated according to (1) under assumption that $\nu = \nu_{ea}$ (curve 2) is shown in fig.2. The discrepancy between the measured and calculated φ at high H can be eliminated by inserting instead of ν some effective frequency ν_{eff} depending on H . The values of ν_{eff} obtained by substituting the measured phase shifts φ into

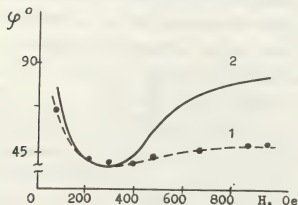


Fig.2 ($\rho - P = 4 \cdot 10^{-2}$ mm HG).

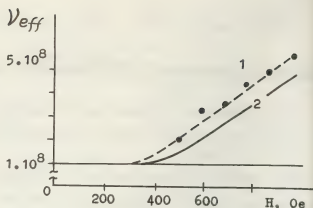


Fig.3 ($\rho - P = 4 \cdot 10^{-2}$ mm HG).

(1) and (2) are presented in fig.3 (curve 1). The calculations using ν_{eff} allow to describe correctly the behaviour of $E(H)$ in the region of the high H (fig.1, dashed curve). An analysis shows that the significant increase of ν can be due to the excitation of small-scale ion-sound oscillations on which the intense scattering of the evaluation of ν_{eff} according to /5/ is shown in fig.3 (curve 2).

References:

1. V.G. Naumovets, L.L. Pasechnik, V.V. Yagola, Proc. XIII ICPIG, Berlin, 1977, p.345-346
2. V.G. Naumovets, L.L. Pasechnik, V.V. Yagola, Fizika plazmy, 1979, 2, N°1, 187-191
3. V.E. Golant, Svershvysokochastotnye metody issledovaniya plazmy, Moskva, Nauka, 1968
4. V.L. Ginzburg, M.V. Gurevich, Uspekhi Fizicheskikh Nauk, 1960, 70, N°3, 393-428
5. L.I. Grigorieva, A.V. Loginov, A.I. Pyatak, V.L. Sizonenko, B.I. Smerdov, K.N. Stepanov, Proc. 4 Conf. Plasma Phys. Contr. Nucl. Fus. Research, Vienna, 1971, vol. III, 573-595

ELECTRON ENERGY DISTRIBUTION FUNCTION AND ATOM IONIZATION PROCESSES
IN HIGH FREQUENCY DISCHARGE MERCURY-ARGON PLASMA

S.D. Wagner, I.S. Nisconen.

Karelian Pedagogical Institute Petrozavodsk U.S.S.R.

This paper presents the results of electron energy distribution function (EEDF) measurements and calculations.

EEDF were measured by differentiating the probe currents by a radio method/1/. The probe system consisted of a cylindrical probe which could be moved across the tube radius and a large area antiprobe placed on the tube surface. The whole system was placed in the central part of the discharge tube of radius 16 mm. Voltage at 28 MHz was fed to external electrodes 26 cm apart from a generator with a symmetrical output. Measurements were made at mercury vapor pressure $2 \cdot 10^{-4}$ Torr, argon pressure 0.05 and 0.5 Torr and tube current 100 mA.

The measured EEDF differ from Maxwell functions of the same mean energy by a depletion of high energy electrons. Across the tube radius the EEDF does not change markedly, the mean electron energy decreases about two times when the argon pressure is raised from 0.05 to 0.5 Torr.

For calculating the EEDF the total energy interval was divided into three regions: the region with energies lower than the first mercury excitation potential, the region from the first mercury excitation potential to the first argon excitation potential and the region higher than the first argon excitation potential. Estimations of characteristic frequencies of electron energy losses were made for all these regions. In the first region energy losses take place mainly by elastic collisions between electrons and

argon atoms. In the second region unelastic collisions between electrons and mercury atoms are essential too. In the third region only unelastic collisions between electrons and argon atoms are essential. In all cases electron-electron interaction is negligible. A kinetic equation was worked out for every case. The equations were time-averaged/2/. The unlocal character of the EEDF was taken into account too/3/. By solving the kinetic equations the following EEDF were received for each region respectively:

$$f(\epsilon) = G - F\epsilon - Be^{-C(\epsilon+\epsilon_1)} - De^{C(\epsilon+\epsilon_1)} \quad (1),$$

$$f(\epsilon) = Be^{-C\epsilon} + De^{C\epsilon} \quad (2),$$

$$f(\epsilon) = AV\sqrt{\chi} \int_0^{2\pi} \cos^4 z K_{\frac{1}{4}} \left(\frac{\chi^2}{\cos^2 z} \right) dz \quad (3),$$

$$\chi = (\epsilon - 1) \left[\frac{3V'V_0 m W_2^3}{16e^2 E_0^2 \beta} \right]^{\frac{1}{4}}$$

where W - electron energy, W_1 - mercury atom excitation energy (4,9 eV), W_2 - argon atom excitation energy (11,5 eV),

$\epsilon = \frac{W}{W_2}$, $\epsilon_1 = \frac{W_1}{W_2}$, V' - frequency of elastic collisions between electrons and argon atoms at $\epsilon = 1$, $K_{1/4}$ - MacDonald function, E_0 - amplitude value of high frequency field strength, e , m , V - electron charge, mass and velocity, β - coefficient in the approximation for the radial potential $\varphi(r)$ in the central region of the $e\varphi(r) = \beta \left(\frac{r}{R} \right)^2$, V_0 and β - coefficients in the approximations for the frequencies of unelastic and elastic

collisions between electrons and argon atoms $\nu_2 = \nu_0 (W - W_2)$, $\nu = 8 P_2 V^3$, P_1 and P_2 - pressures of mercury and argon respectively, $C = 10^2 W_2 (\frac{P_1}{P_2})^{\frac{1}{2}} (\frac{E_0}{P_2})^{-1}$. The coefficients G , A , B , D and F are determined from the normalizing condition and the joining conditions of the EEDF and its derivative on the boundaries of the defined regions.

Constants needed for calculations were taken from the monograph/4/.

Fig. 1 and 2 present the measured and calculated EEDF. The experimental function at argon pressure 0.5 Torr is in accordance with the calculated function $E_0/P_2 = 4$ V/cm·Torr and at 0.05 Torr - with the function $E_0/P_2 = 20$ V/cm·Torr.

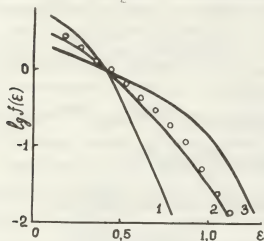


Fig. 1. $P_1 = 2 \cdot 10^{-4}$ Torr, $P_2 = 0.5$ Torr. calculation: 1 - $E_0/P_2 = 2$ V/cm·Torr, 2 - 4, 3 - 8; experiment - o.

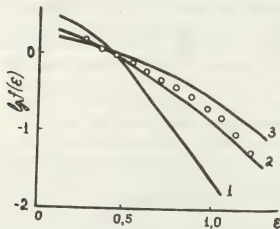


Fig. 2. $P_1 = 2 \cdot 10^{-4}$ Torr, $P_2 = 0.05$ Torr. calculation: 1 - $E_0/P_2 = 10$ V/cm·Torr, 2 - 20, 3 - 40; experiment - o.

Measured EEDF were used for determining the role of different ionization processes in the plasma. The rates of direct ionization of mercury (Z_1), stepwise ionization of mercury (Z_1) and argon (Z_2), ionization of mercury by the Penning effect (Z_P) were calculated. As all the EEDF are in the region which is lower than the direct ionization threshold of argon ionization by this process was not calculated. Calculations of stepwise ionization processes and ionization by Penning effect were made using the populations of the low excited levels of mercury and argon, which were determined by the reabsorption method. The table gives the results of calculations for a unit length of the tube.

E_2	Z_1	Z_2	Z_P	Z_S	Z_W	
Torr :		$\cdot 10^{-15}, \text{ s}^{-1}$				
0.05	: 2.8	0.04	7.5	4.9	15.2	7.5
0.5	: 0.4	0.01	5.1	4.0	9.5	6.3

The most important processes are stepwise ionization of argon and ionization of mercury by the Penning effect. A comparison of the summarized ionization (Z_S) with the value determined by the tube wall current density (Z_W) was made. The results differ no more than a factor of 1.5 - 2.

References:

- /1/ S.D.Wagner, E.K.Ignatyev, JTP(USSR), 47, 934 (1977).
- /2/ S.D.Wagner, E.K.Ignatyev, L.D.Tsendin, Proc. XIIIth Intern.Conf. Phen. Ioniz. gases, Contr. Papers, Part 1, 333, Berlin (1977).
- /3/ L.D.Tsendin, JETP(USSR), 66, 1638 (1974).
- /4/ S.C.Brown, Basic Data of Plasma Physics, Cambridge, Massachusetts, N.Y. (1959).

THE SEPARATION OF ISOTOPES OF NOBLE GASES IN STATIONARY HIGH FREQUENCY DISCHARGE WITH TRAVELLING MAGNETIC FIELD

E.F. Gorbunova, A.N. Ezubchenko, A.I. Karchevsky and Yu. A. Muromkin.

I.V. Kurchatov Institute of Atomic Energy, Moscow, U.S.S.R.

Several papers [1,3] are devoted to research of separation properties of high frequency discharge with travelling magnetic field. It is shown, that the discharge of such a kind is able to separate isotopes and gas mixtures. The separation of gas mixtures is connected in the first of all, with different ionization degree of components. The mechanism of isotope separation has not been cleared up fully yet. As probable causes of isotope separation the processes of barodiffusion and thermodiffusion were pointed out. It is proposed [2], that the observed isotope separation is connected with thermodiffusion in the neutral plasma component. The reference to the barodiffusion separation mechanism is supported by the fact that in some conditions [1,3] the coincidence of the measured enrichment coefficient \mathcal{E} with the calculated one according to the formula

$\mathcal{E} = \frac{\Delta P}{P} \ln \frac{P_2}{P_1}$, where P_2 and P_1 are pressures on the ends of the discharge chamber, M is atomic weight. It was expedient to find out how widely such simple regularity of isotope separation effect in plasma takes place. Aiming at this the comparative investigation of isotope separation of three gases, which considerably differ in their atomic weight: xenon, krypton and neon, was carried out.

The scheme of the apparatus is shown in Fig.1. The discharge was exited in the water-cooled quartz chamber (1) 110cm long and with the 6,5cm in diamet-

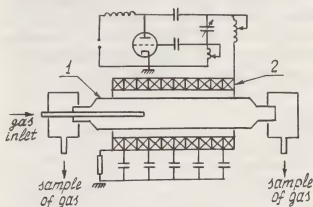


Fig.1. Experimental arrangement

er. The discharge chamber was placed in the solenoid of the delay line (2), which consisted of 60 cells. The length of the solenoid was 85cm. The phase velocity of the wave $v_{ph} = 5 \div 9 \cdot 10^6$ cm/s, frequency $f = 80 \div 460$ kHz. The amplitude of H_z -component of the magnetic field on the axis of the solenoid at varying the generator frequency in the above mentioned range decreased from 100 to 20 Oe. The power dissipated in the discharge was $2 \div 14$ kw.

The interaction of the travelling wave with plasma results in the appearance of the pressure difference $\Delta P = P_2 - P_1$ in the closed-ended chamber. The value of ΔP is in a good agreement with the formula: $\Delta P = \frac{W}{S \cdot v_{ph}}$ (W -dissipated power, S - cross-section of the chamber). In the experiments the value of ΔP reached $2,5 \cdot 10^{-1}$ mm Hg. In the discharges with the same value of ΔP the relation

$\frac{P_2}{P_1}$ can differ greatly, depending on the initial pressure P_0 and gas temperature. At constant P_0 the change of the value of $\frac{P_2}{P_1}$ is realized by means of changing the magnitude of the travelling magnetic field and, in accordance, the power dissipated in plasma. The maximum values of $\frac{P_2}{P_1}$, under which the measurements of isotope separation effect were made, were for the discharge in xenon - 140, for the discharge in krypton - 40, for the discharge in neon - 3 (stable discharge in neon was exited only under higher initial pressures than in xenon and krypton). The minimum values of $\frac{P_2}{P_1} \approx 1$ ($P_0 = 2 \text{ mm Hg}$).

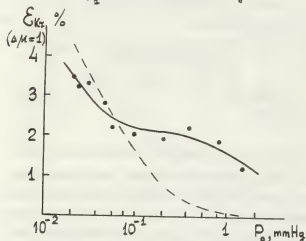


Fig. 2. Krypton enrichment coefficient versus initial pressure
 $W = 9 \div 14 \text{ kW}$, $f = 460 \text{ kHz}$

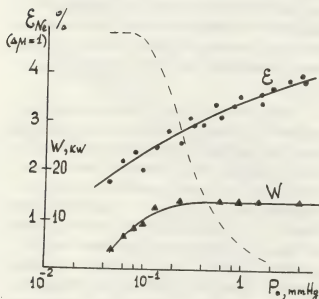


Fig. 3. Neon enrichment coefficient and dissipated power versus initial pressure. $f = 460 \text{ kHz}$

In Fig. 2, 3 the dependences of enrichment coefficients ϵ on the initial pressure Kr and Ne are shown. For comparison the values of ϵ calculated by the formula $\epsilon = \frac{1}{\mu} \ln \frac{P_2}{P_1}$ are shown in the figures in dotted lines (the values of P_2 and P_1 experimentally measured are used). The experiments show, that the quantitative coincidence of the observed isotope separation effect with the effect characteristic of barodiffusion in non-ionized gas, takes place only under some initial pressures. The effect described above can be larger as well as smaller than the barodiffusion one. The last is noticeable in the discharge in neon, $P_0 < 3 \cdot 10^{-4} \text{ mm Hg}$ (Fig. 3), and in the discharge in xenon, when the value of $P_1 \leq 1 \cdot 10^{-3} \text{ mm Hg}$.

For clearing up the contribution of thermodiffusion in isotope separation effect a cooled quartz tube with the 12mm-diameter was placed on the axis of the discharge. In the tube presence the effect decreased for 30-50 percents. But such experiments do not make it possible to estimate quantitatively the contribution of thermodiffusion. As the circulation of gas in the discharge is caused only by the radial non-uniformity of the acting force, the characteristics of the circulating flows, in the first approach, do not depend on the relatively small diameter tube being on the axis.

The absence of the quantity estimation of thermodiffusion influence hasn't made it possible to distinguish "pure" plasma isotope separation effect.

References

1. R.A. Demirkhanov, A.N. Doroshenko, V.N. Zharikov, I.J. Kadysh, A.G. Kirov, V.P. Minenko. XIII ICPIG, Contributed Papers, Part II, p. 699 (1977).
2. А. И. Карчевский, В. Л. Марцинкян, И. А. Попов, Е. П. Потанин. Физика плазмы, 3, 409 (1977).
3. Е. Ф. Горбунова, А. Н. Езубченко, А. И. Карчевский, Ю. А. Муромкин, А. П. Бабищев. Письма в ЖТФ, 3, 154 (1977); 3, 598 (1977); 4, 716 (1978).

"MASS-DIFFUSION" MECHANISM OF ISOTOPE SEPARATION IN GASEOUS DISCHARGE SYSTEM WITH TRAVELLING MAGNETIC FIELD

A.I. Karchevsky, E.P. Potanin.

I.V. Kurchatov Institute of Atomic Energy, Moscow, U.S.S.R.

The possibility of isotope enrichment in discharge system with travelling magnetic field was researched in different papers [1-3]. The separation apparatus is a long closed-ended cylinder, along the axis of which the travelling magnetic wave propagates. H.F.-electromagnetic field of the wave makes the ionization of the mixture and its acceleration in the direction of the axis. As a result a longitudinal gradient of pressure $\frac{dp}{dz}$ appears and the separation effect takes place, which consists in weighting of the mixture in the area of higher pressure and its lightening in the zone of lower pressure. The value of the experimentally measured effect in a complicated way depends on the parameters of the discharge and sort of gas. For example, in case of isotope mixture $Xe^{136} - Xe^{138}$ [3] dependence of the enrichment coefficient of mass difference per unit within the range initial pressures $P_0 = 10^{-2} - 10^{-4} \text{ torr}$ is in a good agreement with the known barodiffusion correlation [4]

$$\varepsilon = \frac{1}{m} \ln \frac{P_0}{P_0} \quad (1)$$

where P_0 and P_0 - pressures of the mixture in the areas of high and low pressure, m - averaged molecular weight. At the same for the Xe isotope mixture the experimental ε values cannot be described by (1), though their proportion to the value $\ln \frac{P_0}{P_0}$ is preserved:

$$\varepsilon = \frac{C}{m} \ln \frac{P_0}{P_0} \quad (2)$$

where C is constant ($C \leq 1$).

It should be noted that only in case of inertial field of forces the treatment of equilibrium separation effect gives the correlation (1). As in the above mentioned H.F.-system the separation process is not caused by the inertial forces and the researched diffusion phenomenon cannot be described by the correlation (1) [1,4].

In [2], the explanation of the measured effects of enrichment on the basis of the mechanism was proposed. The mechanism is connected with the transformation of radial termodiffusion effect into longitudinal one due to circulating

plasma flows. It was shown that termodiffusion should play the most important role for relatively high pressures ($P > 0.1 \text{ torr}$), when the value of circulation due to radial inhomogeneity of electromagnetic volume force $\vec{F}_E =$

$\vec{E} \cdot \vec{B}_0$ is enough for effective transportation of components in the direction of the axis. For the low initial densities ($P_0 = 10^{-2} - 10^{-4} \text{ torr}$) and remarkable electromagnetic influence on the plasma which causes the appearance in the discharge the zones of high and low pressures with different characteristics of ionization and recombination processes, there should be discharge with intensive longitudinal flow of charge particles similar to radial ambipolar diffusion one in dc-discharge. The difference in the value of friction forces which act on the neutral components of isotope mixture from the side of ions shall bring the separation process, which is in its character similar to mass-diffusion effect [5,6].

For the estimation of coefficient of binar isotope mixture enrichment which is caused by the proposed mechanism we'll use multicomponent hydrodynamic approximation. The momentum balance for each components of weakly ionized plasma (the charge of ions is one) through averaged for period values is given by [6]:

$$\begin{aligned} -\frac{dP_2}{dz} - n_2 e (E_z + \frac{v_{Em} B_m}{2}) &= n_2 v_E (n_3 \alpha_{E3} + n_4 \alpha_{E4}) \\ -\frac{dP_1}{dz} + n_1 e (E_z + \frac{v_{Em} B_m}{2}) &= n_1 v_E [n_3 (\alpha_{13} + \alpha_{13}^*) + n_4 (\alpha_{14} + \alpha_{14}^*)] \\ -\frac{dP_3}{dz} + n_3 e (E_z + \frac{v_{Em} B_m}{2}) &= n_3 v_E [n_3 (\alpha_{33} + \alpha_{33}^*) + n_4 (\alpha_{34} + \alpha_{34}^*)] \\ \frac{dP_3}{dz} &= n_3 v_E [n_3 (\alpha_{33} + \alpha_{33}^*) + n_4 \alpha_{34} v_E + n_3 \alpha_{33} v_E^2 + n_3 n_4 \alpha_{34} (v_E v_E^*)] \\ \frac{dP_4}{dz} &= n_4 v_E [n_4 (\alpha_{44} + \alpha_{44}^*) + n_3 \alpha_{43}^* + n_4 \alpha_{44} v_E + n_3 n_4 \alpha_{43} (v_E v_E^*)] \end{aligned} \quad (3)$$

where E_z - longitudinal electric field in plasma; U_i - longitudinal projection of macroscopic velocity of i-component, U_{im} - amplitude value of macroscopic velocity of charged i-sort particle in the direction of external electric field; n_i - density of i-sort particles; P_i - partial i-component pressure; α_{ij} and α'_{ij} - coefficients characterizing momentum exchange due to particle collision. Index e refers to electrons, 1 and 2 - to ions, 3 and 4 - to neutrals of both sorts relatively. Thus, the elastic scattering ion on atoms as well as the process of charge - exchange is taken into account for description of friction force of ions with neutrals of the same gas. Using the condition of absence of heavy particle flow of each sort in z direction in the steady state as well as taking into account the fact that in usual h.f. discharges electron temperature (T_e) is considerably higher the ion temperature (T_i), we get the correlation for enrichment coefficient

$$\varepsilon = \frac{1}{4m} \frac{(Q_i + 6Q^*)(Q_i - Q_n)}{(Q_i + 2Q^*)^2} \ln \frac{P_{nL}}{P_{n0}}, \quad (4)$$

where P_{nL} and P_{n0} - pressures of neutral gas in high and low pressure areas, Q_i and Q_n - diffusion elastic cross section ion and neutral atoms scattering, Q^* - charge-exchange cross section. If $\frac{dP}{d\rho} \ll \frac{dP}{d\rho}$ in the range of moderate values of $\frac{\Delta P}{\bar{P}}$ out of (4) we shall get

$$\varepsilon \approx \frac{C}{m} \frac{\Delta P}{\bar{P}}, \quad (5)$$

$$C = \frac{(Q_i + 6Q^*)(Q_i - Q_n)}{4(Q_i + 2Q^*)^2} \left(1 + \frac{P_e}{P_n} + \frac{P_i}{P_n}\right),$$

where $\Delta P = P_e - P_0$, \bar{P} - average pressure in discharge. It should be noted that equation (5) coincides with the experimentally measured dependence (2) in the range of moderate pressure difference ΔP .

But, for estimating of quantitative agreement of the experiments and theory, data about the sections Q_i , Q^* and Q_n and plasma parameters in each concrete case are necessary. Considering, for example, the average particle density in the chamber

$$n = 3 \cdot 10^{21} \frac{1}{\text{m}^3},$$

the electron density

$$n_e = 3 \cdot 10^{20} \frac{1}{\text{m}^3},$$

$$T_e = 3 \cdot 10^4 \text{ K}, \quad T_n = 10^3 \text{ K}, \quad \frac{Q_i}{Q^*} = 0.5, \quad Q_i \gg Q_n$$

we get $C \approx 0.6$.

References

1. R.A. Demirkhanov, e.a. XIII ICPIG, P. 699, 1977.
2. А.И. Карчевский, В.Л. Маршнхьян, И.А. Попов, Е.П. Потанин, Физика плазмы, 2, 409, 1977.
3. Е.Ф. Горбунова, А.Н. Езубченко, А.И. Карчевский, Ю.А. Муромкин, А.П. Бабичев, Письма ЖТФ, 3, 154, 1977; 3, 598, 1977.
4. Л.Д. Ландау, Е.М. Лифшиц, Механика сплошных сред, ГИИТЛ, 278, 1953.
5. В.М. Жданов, А.И. Карчевский, Е.П. Потанин, Письма ЖТФ, 4, 508, 1978.
6. А.И. Карчевский, Е.П. Потанин, ЖТФ, 48, в.10, 2097, 1978.

THE DYNAMICS OF A HIGH-FREQUENCY DISCHARGE IN A WAVE BEAM

V.B. Gil'denburg, A.G. Litvak and A.D. Yunakovsky.

Applied Physics Institute, Academy of Sciences of the U.S.S.R., Gorky-U.S.S.R.

One of the important problems in the theory of a high-frequency discharge in electromagnetic wave beams (optical [1], submillimeter [2] and rf [3] bands) is the study of self-consistent plasma-field evolution at the first afterbreakdown stages characterized by high electron temperature ($T_e > 10^4$ °K) and low heavy particle temperature ($T_m \sim 300$ °K). In the present paper the computer simulation results or the dynamics of such a nonequilibrium discharge in a converging wave beam are given. The analogous problem for a diverging beam was solved in [4].

The ionization by an electron impact with frequency ν_i and attachment to molecules (with frequency ν_a) were assumed to be the main processes responsible for electron balance. The frequency difference $\nu_i - \nu_a$ was considered as the given function of the field amplitude

$$\nu_i - \nu_a = \nu_a \left(\left| \frac{E}{E_c} \right|^\beta - 1 \right) \quad (1)$$

Here $\nu_a = \text{const}$; E_c is the breakdown amplitude. The plasma diffusion was assumed unessential for the discharge scales as a whole but strong enough to suppress small-scale ionization instability [6]. Under these assumptions the electric balance equation

$$\frac{\partial n}{\partial t} = (|E|^\beta - 1)n + n_i \quad (2)$$

was solved together with the parabolic equation for a "slow" field amplitude of the axisymmetric paraxial beam

$$\frac{1}{r} \frac{\partial}{\partial r} \left(r \frac{\partial E}{\partial r} \right) - 2i \left(\frac{\partial E}{\partial z} + \gamma \frac{\partial E}{\partial t} \right) = \quad (3)$$

$$= \left(1 + i \frac{\nu}{\omega} \right) n E$$

Equations (2), (3) are written in dimensionless variables: $t \rightarrow \nu_a t$, $E \rightarrow E/E_c$,

$r \rightarrow r/a_0$ (radial coordinate), $z \rightarrow z/\ell_0$ (longitudinal coordinate), $n \rightarrow n/n_0$ (electron density) using the following designations: a_0 and $\ell_0 = k a_0^2$ are the characteristic transverse and longitudinal scales of an unperturbed beam respectively ($k a_0 \gg 1$), $k = \omega/c$, ω is the field frequency, $n_0 = n_c/k \ell_0$, $n_c = m(\omega^2 + \nu^2)/4\pi e^2$ is the critical density, ν is the electron collisional frequency, n_i is the initial density defined by the intensity of an external ionizer, $\gamma = \nu_a \ell_0/c$ is the electromagnetic signal delay parameter.

Parabolic equation (3) holding when the conditions $k a_0 \gg 1$, $n \ll k \ell_0$ are satisfied describes diffraction, refraction and absorption of a beam.

The boundary conditions for equations (2), (3) are given based upon the fact that the unperturbed beam is Gaussian and focused at the distance Z_0 from the boundary

$$E(z=0) = E_0 e^{-\alpha r^2}, \quad E_0 = \frac{E_m}{\sqrt{1+Z_0^2}}, \quad \alpha = \frac{1-iZ_0(4)}{2(1+Z_0^2)}$$

E_m is the field at the centre of the focal spot. Far enough from the axis ($r = 6$) it was assumed that $E = 0$.

The initial conditions are: $n(t=0) = n_i = \text{const}$; $E(t=0) = E_1(r, z)$, where E_1 is the solution of eq. (3) with the given boundary conditions for $n = n_i$, $\gamma = 0$.

Numerical calculations were made for the values of the parameters

$$n_i = 10^{-4}, \quad z_0 = 1, \quad E_0 = 1 \quad (E_m = \sqrt{2}), \quad \beta = 4, \quad \gamma = 1$$

and for three values of parameter ν/ω : 0, 0.02 and 3. The 3-layer 11-point scheme

of the higher order of accuracy was used. The scheme parameters were chosen in such a way that when integrating over the characteristic $\xi = Z - \bar{t}$ the phase ratios were correct. The results are shown in Fig.1 as the plots of radial and axial distributions of density n and field amplitude $|E|$ for different values of time \bar{t} .

As it is seen, a rapid (avalanche-type) initial growth of the density for $\bar{t} \sim 1$ stops due to the decrease of the field amplitude and the ionization maximum begins to propagate from the focus towards the lens (breakdown wave). For sufficiently large \bar{t} the rates of the discharge evolution strongly decrease and the field value exceeding the "breakdown" one becomes small (in qualitative agreement with the stationary model assumption [7]). For small \bar{v}/ω after the first ionization maximum there occur secondary ones which are weaker and practically stop for large \bar{t} . For $\bar{v}/\omega = 3$ (in this case the beam refraction is unessential and the field dynamics is defined by absorption) the discharge quickly approaches the stationary state.

Radial profiles of density n (\bar{r}) and field $|E|$ (\bar{r}) are always monotonous for $\bar{v}/\omega = 3$. For a small \bar{v}/ω there are gaps on the axis for some \bar{t} and Z .

Based upon a qualitative analysis of eqs.(2), (3) which agree with numerical results obtained it is not difficult to show that the first maximum of electron density is of the order of magnitude (in dimensionless variables)

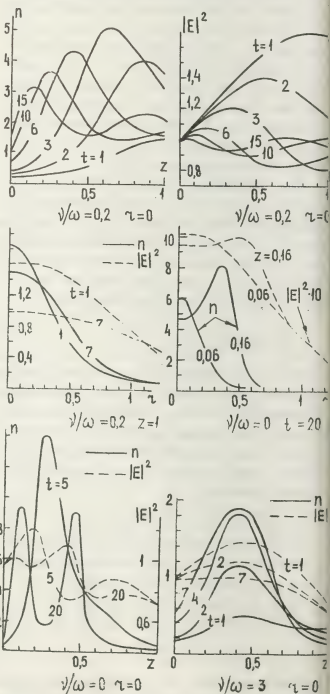
$$n_{\max} \sim \bar{n} \ln \frac{\bar{n}}{n_1}, \quad \bar{n} \sim n_c \frac{\beta \omega}{\omega + \bar{v}} \frac{1}{(ka_0)^2} \quad (5)$$

so that for sufficiently large ka_0 the initial assumption $n_{\max} \ll n_c$ is satisfied even for $\bar{v} = 0$ and rather small n_1 .

It should be emphasized that this result is correct only in the absence of small scale instability [6], which makes the discharge evolution more complicated and results in its decay into clusters with density $n \sim n_c$.

References

1. Yu.P.Raizer, Laser Spark and Discharge Propagation. "Nayka", 1974.
2. P.Woskoboinikow, W.T.Mulligan, H.C.Praddaude, D.R.Cohn. Appl.Phys. Lett., 32, 527, 1978.
3. A.V.Gurevich. Geomagn.Aeron, 12, 63, 1972.
4. M.D.Feit, T.A.Fleck, Appl.Phys.Lett. 24, 169, 1974.
5. A.D.MacDonald. Microwave Breakdown in Gases, J.Wiley, New York, 1966.
6. V.D.Gil'denburg, A.V.Kim, ZhETF, 74, 141, 1978.
7. V.D.Gil'denburg, S.V.Golubev, ZhETF, 67, 89, 1974.



ON THE GENERATION OF FAST ELECTRONS DURING INTERACTION OF MICROWAVE FIELDS WITH COLLISIONLESS PLASMA OF SUBCRITICAL DENSITY

I.R. Gekker.

Lebedev Physical Institute of the U.S.S.R. Academy of Sciences, Plasma Physics Laboratory, Moscow, U.S.S.R.

Abstract: Theoretical and experimental works on the acceleration of electrons when microwave fields act on a collisionless ($\omega > \omega_p$) isotropic plasma ($n \leq n_c = \frac{m\omega_p^2}{4\pi e^2}$) have been analyzed. In the region of rarefied plasma ($n \ll n_c$) in the absence of a critical point ($n = n_c$) the energy of suprathermal electrons decreases abruptly and, as a rule, does not exceed the maximum value of the oscillatory energy of electrons $\mathcal{E}_{\text{osc}} = \frac{e^2 E_0^2}{2m\omega^2}$ where E_0 is the amplitude of microwave field. A control experiment on the interaction of a microwave with plasma ($n \approx 0.6 n_c$) was performed in a waveguide in which accelerated electrons had been registered (see /4/).

Introduction: Electron acceleration was observed during the interaction of a microwave with an inhomogeneous isotropic /1-4/ and magnetoactive /5/ plasma. The acceleration of electrons in dense plasma ($n \geq n_c$) is usually connected with processes in the region of the critical point ($n = n_c$) /2,6/, and in rarefied plasma ($n \leq n_c$) with the development of parametric instability /4,5,7/. In Fig.1, calculated and experimental dependences $(v_e/v_{Te})_{\text{thresh}}$ are presented where $v_e = \frac{eE_0}{m\omega}$ and $v_{Te} = \sqrt{\frac{kT_e}{m}}$ - oscillatory and thermal electron velocities, n/n_c - normalized density of plasma, corresponding to "thresholds" of appearance (registration) of accelerated electrons (see /4,5/). Calculated dependences for various values of T_e/T_i taken from /7/ and from /5/ are also presented. A significant decrease in threshold values as the density approaches n_c can be seen. In Fig.2, experimental dependences of the ratio of maximum oscillatory energy of electrons in microwave field $\mathcal{E}_{\text{osc,max}}$ to maximum energy of accelerated electrons $\mathcal{E}_{\text{e,max}}$ on plasma density n/n_c are shown. It can be seen that in most of the experiments this ratio in-

creases sharply at $n/n_c \approx 1$. Calculated values $\mathcal{E}_{\text{osc,max}}/\mathcal{E}_{\text{e,max}}$ in rarefied plasma ($n/n_c \ll 1$) should not exceed 1 in the travelling wave regime when $E = E_0$ and 4 in the standing wave regime when $E = 2E_0$ (all this for $n/n_c \ll 1$). For increasing plasma density, there may take place an increase in field (for a flat layer $D = \varepsilon E$ where $\varepsilon = 1 - n/n_c$). Calculated dependences are indicated by curves 1 and 2 respectively, taking in account the field increase in plasma at $E = E_0$ and $E = 2E_0$ (Fig. 2). It can be seen that experimental curves, except for those enclosed by a dotted line /4,8/, are near the calculated. This requires explanation. From /6/,

$$\mathcal{E}_{\text{e,max}} = A e E_0 L \quad (1)$$

where the coefficient A may assume values to 2π . Then, near $n = n_c$, we have the calculated value

$$\mathcal{E}_{\text{e,max}}/\mathcal{E}_{\text{osc,max}} = 2A \frac{L\omega_0}{eE_0} = 2A \frac{L\omega_0}{8E_0} \quad (2)$$

From calculation, for $A = 2\pi$, $E_0 = 3 \text{ kV/cm}$, $\omega_0 = 10^{10} \text{ s}^{-1}$ and $L = 1 \text{ cm}$, we obtain $\mathcal{E}_{\text{e,max}}/\mathcal{E}_{\text{osc,max}} \approx 2.5 \cdot 10^2$ (decreasing E_0 to 300 V/cm gives $2.5 \cdot 10^3$), which is not so far from the experimental values presented in Fig.2.

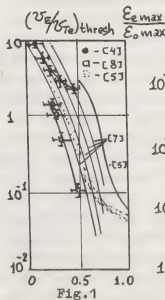


Fig.1

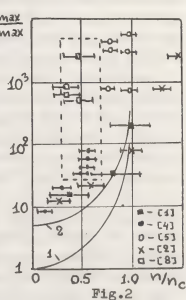


Fig.2

Experiment: Under the conditions of /4/, the generation of accelerated electrons was studied in detail and, in particular, the region of their birth was found /8/. Plasma flow with $v_e \approx 5 \cdot 10^6$ cm/s and $kT_e \approx 5$ eV, created by a mica spark injector, after 65 cm intersected a rectangular waveguide (12x6 cm) normally to its broad wall which was covered by a metallic grid (cell 0.5×0.5 mm, transparency ~ 0.5) over a length of 15 cm. A H_{10} -type wave was excited in the waveguide ($P=7$ kW, $E_0=0.5$ kV/cm, $U_e/U_0=1$, $f_0=2 \cdot 10^9$ Hz, $\tau=2$ ns, standing wave regime, $n_0=5 \cdot 10^{10}$ cm $^{-3}$, $p=5 \cdot 10^{-6}$ torr). In the opposite wall, there was a multigrid probe (MGP).

In Fig.3, curves of delay of current of accelerated electrons on the MGP, obtained for various values of E_0 at $\bar{n}/n_0=0.4$, are presented. Maximum energies reach $E_{max}=100$ –200 eV ($E_{max}/E_0 \approx 10^3$) (see Fig.2). The energy distribution of electrons for $E_0=0.035$ kV/cm is identical to the curve for $E_0=0$ ($E_{max} < 20$ eV). The field strength E_0 at which ac-

celerated electrons appear increases with decreasing n/n_0 (see Fig.1, /8/). Dependences (E_{max}/E_0) $_{th}$, /5/ are in agreement with the calculated /7/. Our data /8/ give lower values of (E_{max}/E_0) (at $E_0 \leq E_0$), which is an argument for the apparatus origin of measured "thresholds" in the appearance of accelerated electrons.

In order to determine the region of accelerated electron formation in the waveguide parallel to its broad wall, a thin plexiglass frame with fine capron grid (transparency ~ 0.25) movable along the narrow wall of the waveguide was introduced. The energy distribution and current of accelerated electrons did not change by moving the additional grid along the narrow wall of the waveguide (from 5 to 0.5 cm and then close to it). The obtained result indicates (within the limits of measurement accuracy) that noticeable electron acceleration from the volume of rarefied plasma ($\bar{n}/n_0 \leq 0.5$) inside the waveguide is absent as was noted in /4/. Observed electron acceleration apparently should be attributed to processes occurring in the region of interaction of mi-

crowave field with plasma near the metallic grid input, i.e., adopted to the method of introducing plasma into the waveguide.

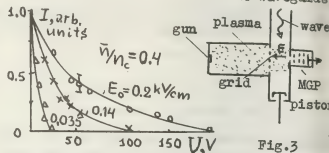


Fig.3

We shall try to elucidate the possible mechanism of electron acceleration. At the $\bar{n}/n_0 \leq 0.5$ in the waveguide and approximately twofold plasma density decrease by the metallic grid, its density directly beyond the grid (on the injector side) can reach $n/n_0 > 1$. Microwave radiation can leak into this region. Moreover, the passage through the grid of narrow "tongues" of dense plasma can maintain their original density ($n/n_0 > 1$) to distances at least of the order of the grid cell. Knowing experimental values E_{max} and E_0 from (1), we shall determine $L \approx 1$ mm, i.e. comparable with the dimension of the grid cell.

Results: Thus, it is shown that in restricted volumes ($\Delta \leq \lambda_0$) of rarefied plasma ($n/n_0 < 1$) maximum energies of accelerated electrons (far from the region $n/n_0 = 1$) do not exceed E_{osc} , i.e., the energy of oscillations of electrons in microwave field.

References:

- /1/ V.I. Barinov, I.R. Gekker, O.V. Sizukhin, E.G. Khachatryan, Short communications on physics, FIAN, 41, N2, 1971
- /2/ V.I. Barinov, I.R. Gekker, V.A. Ivanov, D.M. Karfidov, Proc. FIAN, 92, 35, "Nauka", 1977
- /3/ I.R. Gekker "Interaction of strong electromagnetic fields with plasma", "Atomizdat", 1978
- /4/ K.F. Sergeichev, V.E. Trofimov, JETP Letters, 13, 236, N5, 1971
- /5/ H. Dreicer et al., PRL, 31, 427, N7, 1973
- /6/ L.M. Kovrizhnikh, A.S. Sacharov, preprint FIAN, N118, 1978
- /7/ V.P. Silin "Parametric action of high-power radiation on plasma", "Nauka", 1973
- /8/ I.R. Gekker, T.G. Kulaeva, Plasma physics (in print)

IONIZATION OF GASES IN STRONG ELECTROMAGNETIC FIELDS

S.G. Arutyunyan, I.R. Gekker, D.M. Karfidov and A.A. Ruchadze.

Lebedev Physical Institute of the U.S.S.R. Academy of Sciences, Plasma Physics Laboratory, Moscow, U.S.S.R.

Abstract: A qualitative theory of gas breakdown had been developed for the conditions when the average energy of electron oscillations in an alternating field $\mathcal{E}_0 = \frac{e^2 E_0^2}{4m\omega_0^2}$ exceeds the ionization potential of atoms I . The dependence of the growth rate of ionization γ on \mathcal{E}_0 ($\mathcal{E}_0 = 10^2 - 10^4$ eV) is presented. Experimental investigations in the development of microwave breakdown in helium, argon and air have been conducted in the region of $E_0/\omega_0 = 1.5 \cdot 10^{-3} - 8 \cdot 10^{-7}$ V.s/cm ($\mathcal{E}_0 = 0.1 - 300$ eV) and pressures $p = 5 \cdot 10^{-4} - 10^{-3}$ torr. Satisfactory agreement between calculated and experimental dependences has been observed for $\mathcal{E}_0 \gg I$.

Introduction: In most theoretical works for weak fields (for example, see [1,2]) it is assumed that $\mathcal{E}_0 \ll kT_e \ll I$ where kT_e is the average energy of electrons (temperature). The theory of gas breakdown based on the model of average electron yields results close to those obtained within the framework of kinetic theory. In [3], an attempt was made to construct a kinetic theory of gas breakdown for arbitrary values of \mathcal{E}_0 , in particular, for $\mathcal{E}_0 \gg I$. In this case, we cannot consider solution of the kinetic equation by expansion of spherical functions sufficiently justified. In contrast to this, here we considered the question of gas ionization for $\mathcal{E}_0 \gg I$ from the standpoint of the model of average electron, and a comparison is made with experimental data.

Theory: The frequency of transport collisions of electrons is much less than frequency of ionization collisions in a strong electric field ($\mathcal{E}_0 \gg 10I$) averaged over period of oscillations. Therefore, the average energy of an electron gas turns out to be small in comparison with \mathcal{E}_0 until

the gas becomes weakly ionized. Under such conditions we shall take into account only induced motion of electrons in the field $E = E_0 \sin \omega_0 t$

$$v(t) = v_0 (\sin \omega_0 t - \sin \omega_0 t_0) \quad (1)$$
 where $v_0 = \sqrt{\frac{2\mathcal{E}_0}{m}}$. We note that the formula $\mathcal{E}_0 = \frac{e^2 E_0^2}{4m\omega_0^2}$ is valid only for $u_0^2 \gg v^2$. An electron can ionize an atom only if $v > v_i = \sqrt{\frac{2I}{m}}$. Since $v_0 \gg v_i$, secondary electrons are produced practically at arbitrary phases. After several collisions electrons may be assumed to have uniform phase distributions.

The growth rate of ionization γ can be determined from

$$\frac{dne}{dt} = n_e n_0 \bar{\sigma}_i v = n_e \gamma \quad (2)$$

where n_e and n_0 are densities of electrons and atoms, $\bar{\sigma}_i$ is the cross section of atom ionization by electron impact. Averaging over the period of electron oscillations, in the field as well as over initial phases of electron production, using the expression for $\bar{\sigma}_i(v)$ from the Born approximation $\bar{\sigma}_i(v) \approx \frac{\pi}{v^2} \ln \frac{v}{v_i}$, (3)

we obtain, within the limits of large \mathcal{E}_0 ,

$$\gamma \approx \frac{n_0 \pi \sqrt{m}}{\sqrt{\mathcal{E}_0}} \ln \frac{\mathcal{E}_0}{I} \quad (4)$$

The calculation of γ for more exact values of $\bar{\sigma}_i(v)$ taken from experiment [4] was performed on a computer. In Fig. 1, the calculated dependence $\gamma(\mathcal{E}_0)/n_0$ for helium is presented. It can be seen that at first γ/n_0 increases, reaching a maximum $\gamma_m/n_0 = 1.9 \cdot 10^{-8} \text{ cm}^3 \cdot \text{s}^{-1}$ at $\mathcal{E}_0 = 300$ eV; then, it begins to decrease, approaching the asymptotic dependence /dotted line/. The coefficient \mathcal{L} was chosen so that the curves coincide at $\mathcal{E}_0 = 10^3$ eV.

Experiment: Usually experiments (see, for example, [1,2]) have been conducted in relatively weak fields, when the characteristic parameter of breakdown of low pressures E_0/ω_0 did not exceed 10^{-8} V.s/cm (when

reby $\xi_0 < 1$). Here, we have studied the development of avalanches in a microwave field at $E_0/\omega_0 = 1.5 \cdot 10^{-8} - 8 \cdot 10^{-7} \text{ V} \cdot \text{s/cm}$ ($\xi_0 = 0.1 - 300 \text{ eV}$) in helium, argon and air. The installation consisted of a $\varnothing 20 \text{ cm}$ circular waveguide of stainless steel pumped down to $2 \cdot 10^{-6} \text{ torr}$. Experiments were conducted with a continuous flow of gas at pressure of $5 \cdot 10^{-4} - 5 \cdot 10^{-3} \text{ torr}$. The microwave generator ($\omega_0 = 10^{10} \text{ s}^{-1}$, $\tau = 10 \text{ ns}$, $\tau_p = 0.2 \text{ ns}$) excited the H_{11} -wave in waveguide.

The ionization frequency ν_i was determined from the condition of nonstationary breakdown $\gamma = \nu_i - \nu_d = t^{-1} \ln n_{ek}/n_{eo}$, where t is the measured duration of the influence of microwave radiation, ν_d is the characteristic frequency of electron losses, and n_{ek} and n_{eo} - the final and initial electron densities, the later was created during ionization of the gas by electrons emitted from heated tungsten filament ($U_a = 30 - 40 \text{ V}$) stretched across the waveguide in the antinode region of the electric field of the H_{11} standing wave (normally to \vec{E}) (Fig. 2, insertion). The value of n_{eo} reached 10^9 cm^{-3} near the filament and $kT_{eo} \approx 5 \text{ eV}$. The time constant of electron losses $t_d = \nu_d^{-1}$ was determined experimentally from a plasma decay ($t_d = 25 - 30 \text{ ns}$ for argon and air and $10 - 15 \text{ ns}$ for helium).

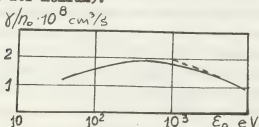


Fig. 1

The fact of "breakdown" was established by the termination of microwave transmission through the layer and by the appearance of accelerated electrons (in \vec{E} direction) when reaching critical plasma density $n_{cr} = \frac{m\omega^2}{4\pi e^2} \approx 4 \cdot 10^{10} \text{ cm}^{-3}$. The current of accelerated electrons was registered by a multigrid probe (MGP) placed on the side wall of the waveguide. In Fig. 2, the dependences on E_0 of the averaged-over-the-spectrum frequencies of ionization per atom ν_i are presented. In the region of weak fields ($\xi_0 < 1$), the values of ν_i are in

satisfactory agreement with those presented in [1, 2], and at higher fields there is agreement with the calculated dependence (Fig. 1). In curves of Fig. 2, the values E_0 are cited through a vacuum field E_0 (amplification of field on the filament can yield an increase by a factor of 2-3).

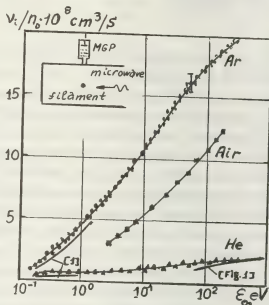


Fig. 2

The obtained dependences γ/n_0 on E_0 can be used to evaluate the maximum time for experiments with strong microwave fields. Results: Agreement has been obtained for theoretical and experimental dependences for the constant of breakdown in gases $\gamma \approx \nu_i$ in strong fields ($\xi_0 \gg 1$), i.e. in the region achieved by power pulse lasers and microwave generators [3, 5]. Continuation of experiments in the region of $E_0 = 10^3 - 10^4 \text{ eV}$ (decrease in the γ/n_0 , Fig. 1) requires the use of radiation from super-high power relativistic microwave generators [6].

References:

- 1/ A. MacDonald "Microwave breakdown in gases", "Mir", 1969
- 2/ Yu. P. Raizer "Laser spark and discharge propagation", "Nauka", 1974
- 3/ Yu. V. Afanasjev et al., JETPh, 57, 580, 1969
- 4/ L. J. Kieffer et al., Rev. M. Ph., 38, 1966
- 5/ I. R. Gekker "Interaction of strong electromagnetic fields with plasma", "Atomizdat", 1978
- 6/ N. F. Kovalev, M. I. Petelin, M. D. Raizer, et al., JETPh Letters, 18, 232, 1973

EXPERIMENTAL STUDY OF FAST RECONNECTION OF THE MAGNETIC FIELDS THROUGH PLANE PINCH CURRENT SHEET

S. Yu. Bogdanov, V.S. Markov, A.G. Franck and A.Z. Khodzhaev.

P.N. Lebedev Physics Institute, Academy of Sciences of the U.S.S.R.

Pinch current sheets are those distinguished regions in the plasma where considerable cumulation of magnetic energy and fast energy release with consequent transformation in plasma flows and high energy particles beams is possible. The study of formation and stability of the current sheets is highly essential for elucidation the nature of such astrophysical phenomena as solar flares, magnetospheric substorms and so on. The development of disruptive instabilities in tokamak plasmas is apparently results from the formation and the destruction of current sheets.

In our experiment the current pinch sheet (plane Z-pinch) was produced in the vicinity of zero (neutral) line of two-dimensional quadrupole magnetic field in argon plasma prepared by auxiliary discharge, when the electric field $E_z = 250-400$ v/cm was applied along the neutral line. The gradient of initial magnetic field was $H_z = 2-3$ kG/cm. The typical parameters of the sheet established $1 \mu\text{sec}$ after current ignition were the following: the length determined by the electrode separation was $L = 40$ cm, the width $- 2\Delta x = 6-7$ cm, the thickness $2\Delta y = 0.7$ cm, the total current $I_z = 40-60$ kA, the tangential component of the magnetic field

$H_x = 3-6$ kG, the transverse component H_y was several times less than H_x everywhere inside the sheet. During the current sheet formation plasma from the chamber volume was effectively swept into the sheet region, thus the resulting electron density of the plasma sheet reaches $N_e = 8 \cdot 10^{15} \text{cm}^{-3}$ and maintains practically uniform along the sheet width. On the contrary the density gradient in transverse direction is quite sharp reaching $\frac{\partial N_e}{\partial y} = 5 \cdot 10^{16} \text{cm}^{-4}$.

Theory predicts that the current sheet becomes unstable in respect to the tearing-mode if its width to thickness ratio exceeds $\Delta x / \Delta y > 2\pi$. However in experiment we observed the stable behaviour of the sheet during $2.5 \mu\text{sec}$ at the elongation ratio of order of 15. But if we increase the initial magnetic field gradient and decrease initial gas pressure then a new phenomenon occurs - the rapid change in magnetic field configuration of the current sheet. In $1-1.5 \mu\text{sec}$ after the current ignition we observe fast decrease of the longitudinal component of the sheet H_x and the increase of the transverse component H_y , fig. 1. Thus the fast dissipation of magnetic energy accumulated previously near the current sheet occurs through the reconnection of the antiparallel magnetic fluxes. The

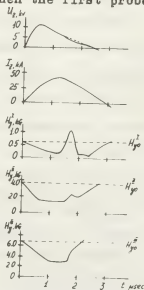
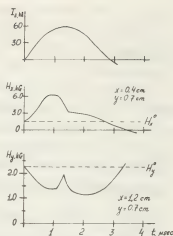
change of the longitudinal component is

$\Delta H_x = 3$ kG and the time derivative is $\partial H_x / \partial t \approx 10^{10}$ G/sec.

The current density decreases significantly in the middle of the sheet. So

far as the total current I_z does not changes, redistribution of the current along the sheet width takes place.

The dynamics of the magnetic field reconnection in the sheet was observed with three magnetic probes arranged on a line ($y=0.7$ cm, $z=15$ cm) parallel the sheet surface. The sheet formation corresponds to decrease of the transverse component H_y comparing to its value at the initial field (dashed lines, fig.2) in the time interval 0-1.4 μ sec. Then the first probe ($x^I=0.3$ cm) shows the increasing of the transverse component. Initially the change is rather smooth, $\partial H_y^I / \partial t = 6 \cdot 10^8$ G/sec. At this time the second and the third probes situated at $x^{II}=1.8$ cm and $x^{III}=3.3$ cm do not detect any change of



the signals. With the growth of magnetic field perturbation its time derivative increases approximately six folds, thus $\partial H_y^I / \partial t \approx 4 \cdot 10^9$ G/sec. During this process the transverse component reaches

the level, corresponding to the value of the initial quadrupole field, and then exceeds its essentially. The magnetic field variation reaches $(\Delta H)^I = 850$ G. The rise of the signal on the second probe is delayed in respect to the first probe signal on 0.3 μ sec, the time derivative is $\partial H_y^{II} / \partial t = 8 \cdot 10^9$ G/sec and the total variation of magnetic field reaches $(\Delta H)^{II} = 1100$ G. Thus the fast reconnection of the magnetic fluxes arising in the middle of the sheet propagates along sheet width (in x direction). If the start of the process in two spatially separated points had the time shift about 0.2-0.3 μ sec, the maximal reconnection level of order of 10^3 G can be attained with significantly reduced time shift of order 0.1 μ sec. This corresponds to the nonlinear perturbation wave propagating with the mean velocity $U_x = 1.3 \times 10^7$ cm/sec which approximately one order of magnitude exceeds characteristic Alfvén velocity for given sheet $v_A = 1.5 \times 10^6$ cm/sec. Then the perturbation of transverse component is thrown to the edge of the sheet, where the magnetic field variation reaches $(\Delta H)^{III} = 1800$ G. Therefore we can conclude that the observed phenomenon represents itself the process of fast magnetic fluxes reconnection through the current sheet, initially separated these fluxes. By another words, the fast breaking of the current sheet, having the explosive behaviour, has been produced experimentally.

INFLUENCE OF THE METASTABLE ATOMS LIFETIME ON THE RUNNING STRIATION EXCITATION

P.S. Landa, YU.V. Ponomarev.

Moscow State University, Department of Physics.

It is known that in the noble gas discharges inside a region of the running striation excitation there can be a relatively small region of currents and pressures in which there are no striation /1/. The boundaries of this region depend on the gas composition and discharge tube dimensions /2,3/. The investigation of a non-striation region is of great practical interest because the operating ranges of pressures and currents in helium-neon lasers usually overlap it /3/. In this work the presence of a non-striation region is explained by the finite lifetime of the metastable atoms.

In most of theoretical works on striation excitation, for example /4,5/, the equation for metastable atoms is not taken into account. This holds true for great currents near the Pupp boundary, where the effective lifetime of metastable atoms is small and their concentration can follow that of the electrons both in time and space. In this case the influence of metastable atoms displays itself only through the ionisation rate. In the region of small and medium currents the metastable atoms lifetime is greater or is of the same order than that of the electrons, due to which their influence becomes more considerable. The metastable atoms lifetime is determined by both the diffusion on the tube walls and their disappearance in the volume due to the processes of deexcitation and step ionization. Therefore, it is useful to introduce an effective lifetime of metastable atoms τ_{me} , which depends on the average value of the electron concentration and consequently on the discharge

current. When the current changes τ_{me} also varies in broad limits.

It is convenient to divide the whole current region, in which the striation can exist, into three parts: 1) great currents $\tau_m \gg \tau_n \gg \tau_{me}$, 2) medium currents $\tau_m \gg \tau_n \sim \tau_{me}$, 3) small currents $\tau_m \sim \tau_{me} \gg \tau_n$, (τ_n, τ_m are diffusion lifetimes of electrons and metastable atoms). In each of these regions the mechanism of the positive column instability has its distinctive peculiarities. For great and medium currents the metastable atoms diffusion on the walls is negligible and their concentration slightly depends on current. In the region of small currents the metastable atoms concentration is proportional to that of electrons and therefore considerably changes with the variations of the current.

From the known experiments one can draw a conclusion that in the regions of great and small currents two different types of striations are excited. In the region of medium currents, which is transitional, either both types of the striations are excited or they are absent. The present work is concerned with the excitation conditions and dispersion characteristics of striation in this region of current.

Hydrodynamic equations of continuity were used as initial for concentration of electrons, metastable atoms and the electron gas energy /6/. The final value of resistance of the discharge supply and boundary conditions for the positive column are taken into account /5/. The account of the positive column stability was carried out analytically at definite parameter restri-

ctions and by a computer.

To calculate stability the initial equations were linearized relatively to small deviations from the stationary values.

Without taking into account the metastable atoms diffusion these equations expressed in terms of non-dimensional variables have the form

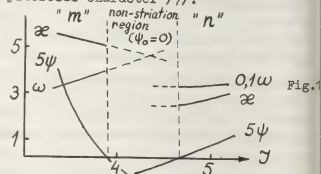
$$\begin{aligned} \frac{\partial N}{\partial \tau} - \frac{\partial^2 N}{\partial \xi^2} &= \gamma_m M + \tilde{\gamma}_T U; \quad \frac{\partial M}{\partial \tau} = P_n N - JM + JP_T U; \\ \alpha \frac{\partial U}{\partial \tau} - \beta \frac{\partial^2 U}{\partial \xi^2} - \frac{\partial N}{\partial \xi} &+ 2(N-j) + k_T U = 0; \quad (1) \\ j &= \frac{R_0}{(R_1 + R_0)\epsilon} \int_0^{\epsilon} N d\xi. \end{aligned}$$

Here M is relative deviation from the stationary value of the metastable atom concentration; J is the value proportional to the constant component of the discharge current; $\tilde{\gamma}_T$, P_n , h_m are non-dimensional temperature derivatives of the frequencies of formation of ions and metastable atoms and losses of electrons energy at collisions; γ_m is a parameter characterizing step ionization; P_n is a parameter determined by the dependence of frequency of metastable atom formation on the electrons concentration (this dependence is due to the difference of the electron distribution function from that of Maxwell /4/); other notations are the same as in /5/.

It follows from equations (1) that harmonic in time perturbation with frequency ω leads to the appearance of four waves and a syn-phase component related to the J discharge current modulation. One of these waves is basic and near the boundary of striation selfexcitation it is slightly enhanced in the direction from the cathode to anode. The other waves greatly attenuate in the propagation direction. The condition of the striation self-excitation is related to the basic wave enhancement, namely, the space amplification factor of the basic wave ψ should be greater than some boundary value ψ_0 determined by the ratio of the discharge supply resistance to the positive column resistance /5/. Near the excitation boundary at the fixed value of the discharge current J the space amplification factor ψ depends resonantly on

the wave number α , reaching its maximum value ψ_{\max} at some α . The regions of striation excitations correspond to those values of current J , for which $\psi_{\max} \geq \psi_0$. It follows from computations that these regions are mainly determined by the values of parameters P_n and P_T . Depending these parameters the conditions of striation self-excitation may be satisfied either for the whole region of medium currents, or there can be a current region which striations are absent (Fig.1), i.e. there is a non-striation region.

On both sides of the non-striation region the striation of different types with different dispersion rules should be excited: for the striation of m-type $\omega \alpha^3 = \text{const}$, for those of n-type $\omega \alpha = \text{const}$. If the non-striation region is absent the striations of m and n-types may either exist simultaneously, or a competitive depression of one of the striation types may occur. In the latter case at the current change the transition from one type of the striation to the other should be of a hysteresis character /7/.



1. S. Pfau et al. Beitr. Plasmaphys. **2**, 333, 1969
2. Н. В. Кириллова, М. И. Молчанов. Радиотехника и электроника. **23**, 2581, 1978
3. В. Е. Приволов. Квант. электр. **4**, 2085, 1977
4. К. Wojacsek. Beitr. Plasmaphys. **1**, 30, 1961; **2**, 13, 1962; **2**, 307, 1965; **6**, 319, 1966
5. П. С. Ленда, Н. В. Пономарев. Радиотехника и электроника. **21**, 2337, 1976
6. А. В. Недоспасов. УФН, **24**, 464, 1968
7. А. А. Zaitsev et al. Proc. of XII ICPIG, Eindhoven, 1975, p. 123.

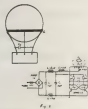
AN INVESTIGATION ON THE FREQUENCY CHARACTERISTICS OF THE RF DISCHARGE IN AR-HG MIXTURES

Hsu Hsueh-Chi.

Institute of Electric Light Source, Fudan University, Shanghai, China.

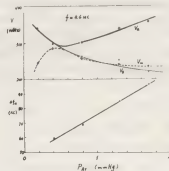
1) According to the modes of excitation, the rf electrodeless discharge may be conveniently divided into two kinds: E discharge and H discharge. These two types of discharges may exist simultaneously in the rf discharges. In weakly ionized plasma, the rf electric field may be many times greater than the toroidal electric field. Usually the H discharge may be covered up by the E discharge, especially at the breakdown stage. It is difficult to distinguish them experimentally. Therefore, they were seldom discussed. We have suggested a method of determining the frequency variation to distinguish and investigate on the rf discharges. According to the variation of frequency, we may understand the effects of E discharge and H discharge during the rf discharges.

2) For these reasons, we study the breakdown, arcing and maintenance of the rf discharge and the variation of its frequency. The discharge is created by maximum magnetic excitation in AR-HG mixtures. The rf source is a transistor push-pull power oscillator, whose power consumption is 30 watts. The discharge chamber is a spherical glass bulb 100 mm in diameter. The discharge bulb and rf source are shown in Fig.1.



We measure the rf voltages across the induction coil in order to determine the breakdown voltage V_b , arcing voltage V_a and maintainable voltage V_m at various pressures of Ar. We also record the variation of the frequency during the different stages of discharge. The results are shown in Table 1, Fig.2 and Fig.3. TABLE 1

P_{Ar} (mmHg)	0.4	0.8	1.3	1.7
V_b (kc)	—	-1	-2	-2
V_m (kc)	60	69	85	97

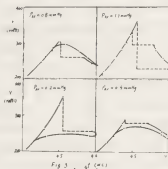


From Fig.3, we can express the relations between Δf_H and P_{Ar} as:

$$\Delta f_H = k P_{Ar} + c$$

where P_{Ar} is the pressure of Argon, k and c depend upon the discharge power and its frequency.

(3) The fact that the variation of frequency depends on the mechanism of the rf discharge may be analysed as follows. At breakdown, due to the E discharge, the



capacity of the circuit condenser would increase. This increase lowers the discharge frequency. On the other hand, after arcing, there exists the plasma, whose dielectric constant may cause a change in capacity of the circuit condenser. The inductance reflected by the discharge into the circuit also reduces the total effective inductance of the circuit, and the power absorbed by the discharge significantly increases the effective series resistances of the circuit. The result is an increase of the frequency of the oscillator in its loaded condition. It may be proved that at arcing, the increase of the frequency is

$$\Delta f_H = \frac{1}{2} \frac{f K^2}{1 + R^2 / (2\pi f L_2)^2} = F(f, K, R, L_2)$$

where f is the discharge frequency, R is the effective resistance of the plasma, $K = M^2 / L_1 L_2$, M is the mutual inductance of primary circuit and secondary plasma, L_1 and L_2 are the inductances of primary circuit and secondary plasma respectively.

From the above equation, we can see that this increase in frequency can never be negative. Therefore, we may understand clearly that both E and H discharges exist in our maximum magnetic excited rf discharges. The breakdown of the discharge is caused mainly by the rf electric field (E discharge); however, the arc is established by the ring discharge induced by the alternating magnetic field (H discharge).

From Fig.2, we can see that when the arc

is established, the voltage across the induction cell may be lowered suddenly to the maintenance voltage, whose magnitude should be related with the power coupled to the plasma directly. There is a maximum of the maintenance voltage at the pressure of Ar between 0.3 to 0.8 mmHg. In this region it provides the optimum conversion efficiency from the rf source to the plasma. The above results on the frequency variation of the rf discharge may be used to study the mechanism of that discharge and to optimize the design of the electrodeless light sources.

REFERENCES

- (1) G.Francis: Ionization Phenomena in Gases.1960,p.137
- (2) H.U.Eckert: Proc. of 4th ICPIG,1959, II A 320

THE COMPARISON OF SOME CHARACTERISTICS OF ELECTRODELESS UHFD IN WAVEGUIDE AND OF DCD

G.S. Solntzev, S.A. Dvinin and L.I. Tsvetkova.

Department of Physics, Moscow State University Moscow, U.S.S.R.

The aim of the paper is the comparison of characteristics of electrodeless UHF-discharge (UHFD) in a long tube and of DC-discharge (DCD). UHFD is excited at the frequency of 3.2 GHz in a tube of 20 mm diameter and length exceeding wavelength in the waveguide. The tube is placed at the axis of standard rectangular waveguide /1/. UHF power increasing up to 100-120 W, the discharge length also increases up to filling the whole tube. DCD is obtained in tubes of the same size. Both kinds of discharge are investigated in Xenon at pressures of 0.05-2.0 Torr. The characteristics differences could be due either to different kinds of energy supply to consequent parts of discharge or to peculiarities of charge kinetics in plasma. The electron energy gain of UHF and of DC fields may be different /2/ at $\sqrt{V} < \omega^2$, so as the maximal discrepancy must take place in gases with strong dependence of electron-atom collision frequency on velocity $V(v)$, distribution function f_e determines energy state of DCD and UHFD plasma electrons. Unfortunately, it is impossible to get volt-current characteristics (VCC) (and consequently f_e) in wide energy range because of small probes surface. Therefore electron energy state is obtained separately within two energy ranges (of course such a separation is conditional and is based on measurement methods specifics in the experiment). The average energy of bulk of electrons proportional to T_e and electron concentration n_e in DCD plasma

are measured by standard probe method with recording of probe VCC. Only ionic part and the beginning of electron part of VCC are possible to get in electrodeless UHFD plasma /3/. Therefore a hybrid method was applied to obtain the average energy of bulk mass of electrons proportional to T_e . Electron concentration n_e is obtained by MCW interferometer ($\lambda = 8$ mm) then T_e is calculated from the ionic part of VCC data. There is preliminary check of the method on the DCD plasma when average measurement is possible in wide range of electron probe current. Spectral lines intensities ratios are used for fast electrons analysis (with energies above excitation energy) in DCD and UHFD. Specific power W_{sp} in DCD is practically linear electron concentration n_e (Fig.1). W_{sp} of UHFD does not depend on n_e when incident power W_{in} rises and discharge length increases. W_{sp} increases with n_e when W_{in} exceeds the value corresponding to filling up of whole tube by UHFD, as in DCD (Fig. 1). This discrepancy is due to specifics of UHFD formation at series energy supply to different parts along the discharge; it indicates on possibility of obtaining of electrodeless UHFD of large length. The fact of W_{sp} increases with electron concentration after the tube is filled up by UHFD (as in DCD) indicates probably on minor influence of orientation of electric field strength under conditions given (we mean the field supplying the discharges). Also it is interesting that the same $W_{sp}(n_e)$ for DCD and UHFD are observed

at the same electron concentration ($2.5 \cdot 10^{12} \text{ cm}^{-3}$) and at different pressures. The intensity for two pairs of lines W_{sp} , w/cm^3

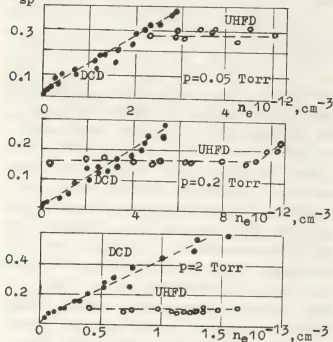


Fig. 1. The dependence of the specific power W_{sp} on the electron concentration n_e . \bullet -DCD; \circ -UHFD.

I_{4830}/I_{4501} and I_{4671}/I_{4501} for DCD (full signs) and for UHFD (empty signs) are given in Fig. 2. These intensity lines ratios for DCD (sometimes 1.5-2.0

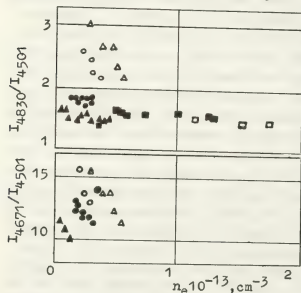


Fig. 2. The ratios of spectral lines intensity. Δ , \triangle - 0.05 Torr, \circ , \bullet - 0.2 Torr, \square , \blacksquare - 2.0 Torr

times) at pressures 0.05 and 0.2 Torr. There is no marked difference of intensity lines ratios at pressure 2.0 Torr. T_e , eV

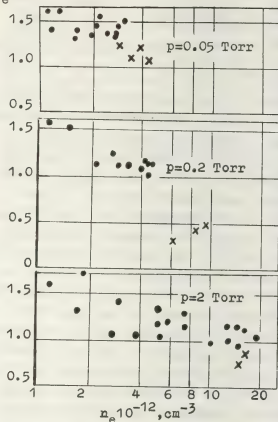


Fig. 3. T_e of the bulk of electrons. \bullet - DCD; \times - UHFD.

Therefore the fast electrons average energy in UHFD exceeds that of in DCD at low gas pressure, but they are practically the same at pressure 2.0 Torr. The average energy of bulk mass of electrons proportional to T_e in UHFD is less than DCD at pressures 0.05, 0.2 Torr but they differ scarcely at pressure 2.0 Torr (Fig 3). These results confirm suggestion of the authors [2] trying to explain observed difference of electrons of energies in UHFD and in DCD by different conditions of energy gain of electrons in these discharges when $v^2 < \omega^2$ and when $v^2 > \omega^2$. It permits to consider the application of long UHFD for spectroscopic and plasma chemistry devices as having future.

References.

- /1/ V.A.Dovzhenko; P.P.Melnichenko, G.S.Solntzev XII ICPIG, Eindhoven, 108(1975).
- /2/ Y.A.Ivanov, Y.A.Lebedev, L.S.Poljak XIII ICPIG, Berlin, 331(1977)
- /3/ V.A.Dovzhenko, G.S.Solntzev and oth. JTP 47, 2506 (1977).

TEMPERATURE OF HEAVY-CURRENT CYLINDRICAL HOLLOW CATHODE

N.N. Rykalin, A.V. Nikolaev and A.P. Borzhov.

Baikov Institute of Metallurgy Moscow U.S.S.R.

Introduction. The first papers on discharge with hollow cathode were published about twenty years ago /1,2/. The discharge of this type we used as a heavy-current source of ions. Later investigations on hollow cathode application were developed in laboratories of different countries. Physical investigations under the leadership of Prof. Delcroix /3/ and practical use of the discharge with hollow cathode by Ulvac Co. in metallurgy should be especially mentioned /4/.

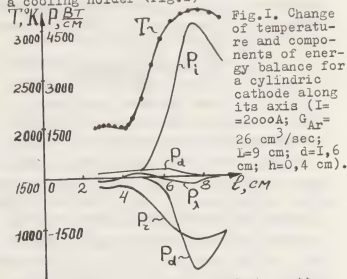
At Baikov Institute of Metallurgy experiments to study energy-physical and technological parameters of heavy-current discharge with hollow cathode are under way 5-7/. This paper presents results of temperature condition studies for cylindrical tungsten cathode. The obtained data characterize electric transfer on the cathode, its energy balance and erosion mechanism.

Experimental assembly and investigation conditions. The assembly to study cathode temperature condition consists of a cathode unit with a hollow tungsten electrode, water cooled copper anode with a crater for liquid metal, sealed chamber, d.c. power source, gas-evacuation system and measurement equipment.

Brightness temperature of the cathode providing the wave length $\lambda = 0,65$ mkm was measured in experiments. Power dissipated from cathode by heat conductivity was determined by the temperature of water cooling cathode. The arc current was in the range from 300 up to 3300 A, consumption of plasma forming gas - from 0,05 up to 0,26 cm³/sec, the cathode diameter was equal to 0,4-2 cm, the wall thickness - 0,2-0,5 cm and the cathode length - 6-12 cm. Experiments were mainly conducted in argon by pressure in the chamber of 0,4 torr. In some tests helium, nitrogen and hydrogen were used as a plasma forming gas.

Cathode temperature. By large currents two maximums of temperature are observed

on the cathode surface: the first maximum T_{1m} - in the cathode active zone, the second maximum T_{2m} - near cathode fixing in a cooling holder (Fig.1)



The typical temperature of the active zone for tungsten cathode is equal to 2900-3300°K. Value and position of the temperature maximum essentially depend on the arc current and gas consumption through cathode. By current increasing from 800 up to 3000 A the maximum temperature rises according the empiric equation

$$T_{1m} = 1750 I^{0,075} \quad (1)$$

and its position is shifted to the working end of the cathode. Providing $I = 800$ A the maximum is at a distance of 4 cm from the outlet end, and by $I = 3000$ A - 2 cm.

By varying gas consumption the maximum temperature changes negligibly. Gas consumption essentially effects the maximum position. Thus, by argon consumption through cathode of 26 and 0,5 cm³/sec its maximum temperature did not change practically and was equal to 3300°K. By gas consumption of 26 cm³/sec the maximum temperature was at the electrode tip and by consumption of 0,5 cm³/sec - at the distance of 18 mm from it. Shift of the active zone providing current and gas consumption change is obviously explained by varying pressure in the electrode cavity.

Gas type effects cathode temperature con-

dition negligibly. Thus, if plasma-forming gas is argon the temperature of outer surface was equal to 3250°K, in case of nitrogen and helium - 3270 and 3300°K correspondingly.

The second maximum near cathode fixing in the holder is obviously explained by two factors: 1) cathode is not being cooled by electron emission and 2) electrode is heated by full discharge current in this region (outside the active zone). The temperature may be determined with enough accuracy from Lenz-Joule and Stefan-Boltzmann equations

$$T_{am} = \sqrt[4]{\frac{\rho j^2}{\epsilon^2 \epsilon_0 h (2d+h)}} \quad (2)$$

Here ϵ - integral coefficient of radiation, ϵ_0 - Stefan-Boltzmann constant, ρ - specific electric resistance, d - cathode diameter and h - cathode wall thickness.

As it follows from Eq.(1) and (2) the temperature outside the spot rises more rapidly by the current than in the spot. This is the reason for limiting current of the cylindric hollow cathode caused by electrode melting near its fixing in the holder. Critical current density in the tungsten cathode body, determined experimentally by its melting, is equal to 4,6-5,6 kA/cm² (Fig.2).

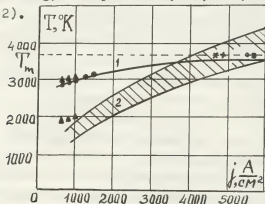


Fig.2. Change of the first (1) and second (2) temperature maximum depending on the current density in the electrode. ●, ▲ - by brightness temperature ($d=1,6-2$ cm; $h=0,4-0,5$ cm), x, +, ○, ■ - by electrode melting ($d=0,4-0,6$ cm; $h=0,2-0,3$ cm)

Cathode energy balance. Study of cathode temperature condition allowed to determine components of its energy balance. Power introduced into the cathode in the active zone consists of energy streams caused by ions energy moving to the cathode P_i and Joule heating P_d . Energy outlet oc-

curs due to radiation P_r ; electrons emission P_e , heat conductivity P and evaporation of cathode material P_v .

Power dissipated from the cathode by radiation essentially depends on the arc current and forms 45-75% of full power emerged on the cathode. Power dissipated by heat conductivity is equal to 8-14%. Power consuming on electrons thermoemission may be equal to 20-40%. The electron current part is 0,6-0,8. It rises with increasing the discharge current.

Rate of electrode erosion is satisfactorily described by Lengmouir equation and requires about 1% of the energy.

Ions moving to the cathode are the main energy source in the active zone. If the discharge current is essentially lower (in some times) than the limiting one, the power transferred by ions is equal to 85-90% of the full energy emerged in the active zone.

Cathode voltage drop calculated on the basis of energy balance in the active zone is equal to 16-20V.

Conclusion. Analysis of the temperature condition of a tungsten hollow-cathode has shown that electric current of such a cathode is provided by thermo-emission mechanism. The limiting current of a cylindric cathode has been defined experimentally. Its value is caused by electrode melting due to Joule overheating of an electrode outside the cathode spot.

References

1. Luse I.S. Proc. 2nd Int. Conf. Peaceful Uses of Atomic Energy, 1958.
2. Lidsky L.M., Rothleder S.D., Rose D.I. et al. J. Appl. Phys., 33, N 8, 1962, 2490.
3. Ferreira C.M., Delcroix J.L. J. Appl. Phys., 49(4), 1978, 2380.
4. Tokei H., Ishigami Y. Trans. of the Intern. Vac. Met. Conf. Anaheim, Calif. 1970.
5. Nikolaev A.V. et al. Fiz. i Khim. Obrab. mater., 1974, No 2.
6. Rykalin N.N., Nikolaev A.V., Borzhov A.P. Fiz. i Khim. Obrab. mater. 1977, N 2.
7. Rykalin N.N., Erokhin A.A., Nikolaev A.V. Sb. "I.P. Bardin i razvitiye metalurgii in SSSR". Izd. "Nauka", 1976, 348.

THE INVESTIGATION OF THE FAST ELECTRONS ENERGY DISTRIBUTION IN THE POSITIVE COLUMN AND NEGATIVE GLOW OF THE LOW PRESSURE HELIUM DISCHARGE

L.M. Volkova, A.M. Devyatov, E.A. Kralkina and A.V. Kuralova.

Moscow State University, U.S.S.R.

The electron energy distribution (EED) was studied in a helium hot-cathode arc discharge at pressure 0,3,0.1,0.05 and 0.025 mmHg for the discharge current 25 A. The discharge was produced in a glass tube of the length 70 cm and diameter 3 cm. The fast electrons energy distribution was deduced from the experimentally measured spectral lines intensities I in accordance with [1,2]. The spectral lines intensities were measured across the discharge tube at the different distances from the cathode. Fig 1a, 2a represent the dependence of the discharge glow intensity at the different distance from the cathode at the pressure 0.1 and 0.025 mm Hg respectively. The values of 10-16 intensities of the spectral lines, which were used for the calculation of EED $f(\varepsilon)$.

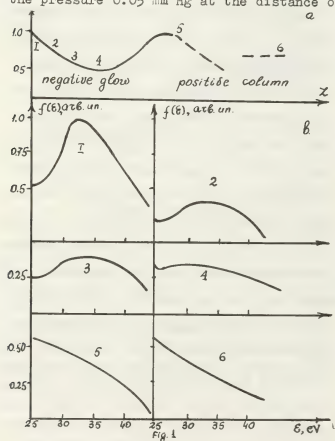
All chosen spectral lines fitted the equation

$$I(x) = C \nu(x) \int_{\varepsilon_k(x)}^{\infty} Q(x, \varepsilon) \sqrt{\varepsilon} f(\varepsilon) d\varepsilon$$

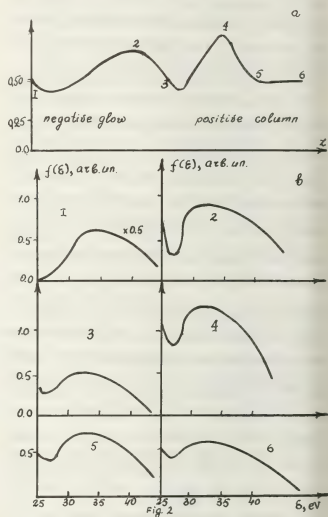
where C is const, x is the parametr, which characterises the spectral line, $\nu(x)$, $\varepsilon_k(x)$, $Q(x, \varepsilon)$ are the frequency, exitation threshold and effective excitation cross-section of the x -spectral line respectively, ε is the electron energy. All

EED were calculated in the energy interval 25-46 eV. It's pointed out in [3] that after the passage through the dark cathode space the electron impulse distribution is close to the isotropic and electron energy is near eV . Here V is the cathode drop. Consequently it was the electron energy distribution that was determined in the present work. Fig 1 shows the fast electron energy distribution calculated for different distances from the cathode at helium pressure 0.1 mm Hg. The 1st position (see Fig 1a) corresponds approximately to the middle part of the negative glow. The spectral lines intensities here are large compared to these at the other points of the negative glow and EED shows sharp maximum at 30-35 eV. While approaching the positive column (position 2-5) the maximum diminishes and in the positive column we find the smooth EED. The observed maximum on EED at 30-35 eV can hardly be attributed to the primary electrons accelerated by the cathode drop which was about 60 V in our case. The electron energy losses in the inelastic collisions are approximately equal to the excitation (~ 20 eV) and ionisation (~ 25 eV) thres-

holds, so the appearance of the secondary electrons with the energies within 35-40 eV is possible. Consequently the existence of the observed maximum on EED can be qualitatively explained by the influence of inelastic scattering of primary electrons. In the pressure 0.3 mm Hg EED shows the redundancy of fast electrons in the negative glow if compared to the positive column. The shape of EED is smooth within all investigated energy interval. At lower He pressure (0.05 and 0.025 mm Hg) the behaviour of EED in the negative glow is just the same as at 0.1 mm Hg. At the start to the positive column the amplification of the maximum occurs. This is likely connected with the presence of the striation in this part of the discharge. While moving towards the anode the maximum diminishes. There is weak plateau at the pressure 0.05 mm Hg at the distance of



the 15 cm. from anode. At 0.025 mm Hg the length of the positive column in our tube is small (10 cm) and even the anode the maximum on EED exists. (see Fig 2b).



References

- 1; A.M. Devyatov, et al. ICPIG, Prague, 1973, Contributed Papers, p. 13.
2. L.M. Volkova, et al. ICPIG XII, Eindhoven, 1975, Contributed Papers, p. 384.
3. В.Л. Грановский, "Электрический ток в газе. Установившийся ток. "Наука", 1971.

III

- Décharges à haute pression
High pressure discharges
- Etincelles, claquage, décharge corona
Sparks, breakdown, corona discharge
- Propriété du plasma des arcs et dynamique des arcs
Properties of arc plasma ; arc dynamics
- Ecoulements de plasma
Plasma flows
- Réacteurs chimiques
Chemical reactors



MECHANISMS OF ELECTRON DISAPPEARANCE IN A DECAYING PLASMA ARC

A. Gleizes, H. Kafrouni and S. Vacquie.

Centre de Physique Atomique, Laboratoire Associé au C.N.R.S. n° 277, Université Paul Sabatier, 31077 Toulouse France.

It is generally accepted that during argon plasma decay at atmospheric pressure, the disappearance of charged particles is brought about by electron-ion recombination. For a temperature of about 1 eV, recombination is partially counterbalanced by ionization. When the plasma is confined the electron losses through ambipolar diffusion are not negligible. The aim of this communication is to show the relative influence of the various processes by comparing the experimental results with theoretical estimations.

EXPERIMENTAL RESULTS. The experimental set-up is described in reference/1/. The arc is a wall stabilized one and the decay is governed by a fast thyristor.

In steady state conditions the electron number density, n_e , was determined with respect to the radius, by measuring the absolute intensity of the continuum radiation at 423 nm. The electron temperature, T_e , was deduced from relative intensity measurements of the lines.

In the extinction phase, the electron number density and the variation of the atom density n_a , were measured by laser interferometry, at two wavelengths, along the axis of the discharge. Also $n_e(r, t)$ was determined by measuring the continuum radiation (fig. 1). The values at $r=0$ are in good agreement with the results deduced from interferometry. Finally, the variations of light intensity of some Ar I lines were measured along the axis of the discharge ($r=0$). Certain results are given in another communication/2/ presented at this ICPIG: for current intensities less than 25 A, the intensity of these lines rose sharply after cutting off the current (time of increase $\sim 5 \mu s$) then fell

to zero after 250 to 300 μs . It is shown/2/ that this phenomenon is due to the rapid relaxation of the electron temperature to the gas temperature.

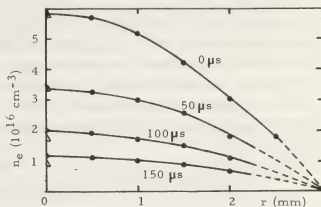


Fig. 1. Radial profile of n_e at different times after cut-off ($I=52$ A). • continuum 423 nm
Δ interferometry.

THEORETICAL ANALYSIS. In a decaying argon plasma, with cylindrical symmetry and no axial gradients, the variation of n_e is described by:

$$\frac{\partial n_e}{\partial t} + \frac{1}{r} \frac{\partial}{\partial r} (r n_e v_e) = -\alpha n_e^3 - S n_e n_1 \quad (1)$$

where v_e is the average velocity of the electrons, α the recombination coefficient, S the ionization coefficient and n_1 the density of atoms in the ground state.

The most rigorous calculation of α and S was made using a collisional radiative model/3/. For argon the deepest study was made by Katsonis/4/. In order to apply his results to equation (1), n_e , T_e , T_h and the diffusion flux must be locally known. For high values of n_e ($n_e > 10^{16} \text{ cm}^{-3}$) the plasma approaches LTE and the values of the different parameters must be known with great accuracy: for T_e and n_1 , the experimental results are not accurate enough. For this reason we developed a model which allowed us to calculate T_e , T_h , and the atom densities from experimental values of $n_e(r)$ and the axial electric field E . This model is based

on the resolution of a coupled system of balance equations for the population of each real energy level of Ar I and the electron energy balance, in the steady state plasma. For level j :

$$\begin{aligned} \bar{v}_j (n_j \bar{v}_j) = & \sum_{i=1}^{j-1} n_i n_e C_{ij} - n_j (n_e F_{ji} + \Lambda_{ij} A_{ji}) - n_j n_e S_j \\ & + \sum_{k=j+1} n_k (n_e F_{kj} + \Lambda_{kj} A_{kj}) - n_j n_e C_{jk} + n_e^3 Q_j + n_e^2 \Lambda_j R_j \end{aligned} \quad (2)$$

$$\alpha E^2 = \bar{v}_e \bar{q}_{re} + U_{inel} + K \sum_h \bar{v}_{eh} (T_e - T_h) n_e \quad (3)$$

where C_{ij} and F_{ji} are rate coefficients for collisional excitation and de-excitation; S_j the collisional ionization rate coefficient; R_j , Q_j rate coefficients for radiative and collisional recombinations; Λ_j , Λ_{ij} , escape factors of radiation. The electron energy balance (equation 3) is described in detail in 2/. For the excited levels, diffusion is negligible and we can write:

$$\frac{1}{r} \frac{\partial}{\partial r} (r n_e \bar{v}_e) = - \frac{1}{r} \frac{\partial}{\partial r} (r n_1 \bar{v}_1) \quad (4)$$

A model with such a make-up allows the calculation of T_e , T_h , n_1 , n_2 , ..., and the deduction of the ionization and recombination coefficients. The rates of these reactions are the population and depopulation rates of the ground state by collision and radiation.

As already stated, when $E \rightarrow 0$, the electron temperature drops to T_h before n_e and n_a have had the time to change. The coefficients α and S therefore must be calculated for an electron temperature equal to T_h .

COMPARISON OF THE RESULTS. The following table gives values of α and S with respect to some of the values of the (n_e, T) couple corresponding to real cases.

n_e	$8.8 \cdot 10^{+16}$	$4.0 \cdot 10^{+16}$	$1.5 \cdot 10^{+16}$	$8.0 \cdot 10^{+15}$
$T(K)$	12 500	11 000	9 500	8 400
$\alpha(1)$	$1.5 \cdot 10^{-29}$	$2.5 \cdot 10^{-29}$	$5.6 \cdot 10^{-29}$	$1.2 \cdot 10^{-28}$
$\alpha(2)$	$2.3 \cdot 10^{-30}$	$3.2 \cdot 10^{-30}$	$7.0 \cdot 10^{-30}$	$1.4 \cdot 10^{-29}$
$S(1)$	$2.7 \cdot 10^{-13}$	$5.9 \cdot 10^{-14}$	$5.7 \cdot 10^{-15}$	$8.4 \cdot 10^{-16}$
$S(2)$	4.10^{-14}	9.10^{-15}	1.10^{-15}	2.10^{-16}

(1) our values, (2) Katsonis /4/

The values of Katsonis, under the conditions of reabsorption found in the arc, are lower than ours; this is due to the choice of the excitation cross section of the first levels of Ar I.

In fig. 2 all the experimental and calculated results are presented. The 3 curves of the calculated results correspond to 3 different parameters: α is the recombination coefficient; $\gamma \equiv \alpha - S n_1 / n_e^2$, the apparent recombination coefficient and $(\partial n_e / \partial t) / n_e^3$ the electron disappearance coefficient. A good agreement is seen between the calculated and measured values of $(\partial n_e / \partial t) / n_e^3$ which would seem to justify our calculation of α and S (Katsonis' values are not in such good agreement). As the electron density increases, so do the ionization phenomena; this can be seen by comparing α and γ . Finally, the comparison between γ and $(\partial n_e / \partial t) / n_e^3$ shows the influence of diffusion which may represent 30% of the electron disappearance mechanisms.

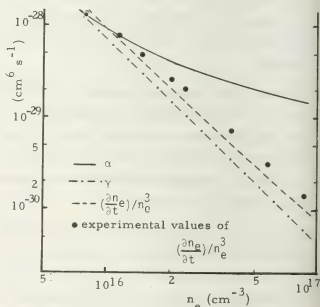


Fig. 2. Experimental and calculated values of recombination and disappearance coefficients of the electrons.

- /1/ H. Kafrouni and alii, to be published in JQSRT (1979).
- /2/ H. Kafrouni and alii, ICPIG Grenoble (1979).
- /3/ D.R. Bates and alii, Proc. Roy. Soc. London, 267, (1962), 297.
- /4/ K. Katsonis, Thèse d'état, n° 1637, Orsay (1976).

DIFFERENCE BETWEEN ELECTRON TEMPERATURE AND HEAVY PARTICLES TEMPERATURE IN ARC PLASMA

H. Kafrouni, A. Gleizes and H. Dang Duc.

Centre de Physique Atomique, Laboratoire Associé au C.N.R.S. n°277, Université Paul Sabatier, 118, route de Narbonne, 31077 Toulouse France.

Over several years various authors [1-2] have reported that the confined-arc plasma can show large deviations from Local Thermodynamic Equilibrium (LTE). These discrepancies appear under various forms : deviations from complete LTE if the pressure is considered constant, deviations from Saha law for certain atomic levels, difference between the electron temperature (T_e) and that of heavy particles (T_h). In this paper the latter question ($T_e - T_h$) will be theoretically and experimentally investigated for a plasma produced by a wall-stabilized arc burning in argon at atmospheric pressure and current intensities of between 6 and 35 A.

ANALYSIS. Let us consider a stationary plasma, the local values of electron number density (n_e) of which are known. In the absence of axial gradients, this plasma can be described by the following equations :

Equations of density conservation -

$$\frac{d}{dr}(n_j V_j) = \left(\frac{\partial n_j}{\partial t}\right)_{\text{col}}^{\text{rad}} \quad \text{for } j = 1, 2, \dots, j_M \quad (1)$$

ambipolar diffusion flux -

$$n_e V_e = -A D_A \left(\frac{dn_e}{dr}\right) \quad (2)$$

electron energy balance -

$$E^2 = 3n_e \sum_h \left(\frac{m_e}{m_h}\right) \bar{v}_{eh} k(T_e - T_h) - \frac{1}{r} \frac{d}{dr}(r \lambda_e \frac{dT_e}{dr})$$

$$\left(\epsilon_j + \frac{5}{2} kT_e\right) \frac{1}{r} \frac{d}{dr}(n_e V_e) + \bar{R} \quad (3)$$

state equation -

$$p = (n_a + n_e) k T_h + n_e k T_e \quad (4)$$

$$\text{and } n_a = \sum_{j=1}^M n_j \quad (5)$$

Equations (1) concern the densities of the real levels of Ar I. The number of unknown levels was limited to $j_M = 31$. It is assumed that the excited levels higher than j_M are in Saha equilibrium with the electrons ; $n_j V_j$ is the diffusion flux of atoms on level j :

$$n_1 V_1 = -n_e V_e \quad (\text{ground state})$$

$$n_j V_j = 0 \quad \text{for } j > 1 \quad (\text{excited states})$$

$(\partial n_j / \partial t)_{\text{col}}^{\text{rad}}$ is the balance of creations and losses, of the atoms under consideration, due to collision and radiation processes. The rates of all the envisaged reactions appear in this term : excitation and de-excitation, ionization through collision with electrons, radiative recombination and photo-ionisation, 3-body recombination, spontaneous de-excitation and photo-excitation. These reaction rates are calculated from effective experimental or theoretical cross-sections [3] by assuming that the electrons have Maxwellian distribution.

In eq. (2), D_A is the ambipolar diffusion coefficient given by Devoto [4] and A is a correction term which takes into account the atom gradient and which, at a first approximation, only depends on n_e (at constant pressure). V_e is the diffusion velocity of the electrons.

In eq. (3), E is the axial electric field measured, σ the electrical conductivity [4] and \bar{v}_{eh} the electron-heavy particle elastic collision frequencies. \bar{v}_{ea} was calculated from the effective momentum transfer cross section. λ_e is the thermal conductivity of the electrons calculated by Gorse [5]; ϵ_j is the ionization energy of Ar I and \bar{R} is the local power lost through radiation per unit volume. In order to calculate this last term, about 250 lines and the continuum radiation contribution [6] were considered taking into account the absorption of certain radiations.

Knowing $n_e(r)$ and E , rigorous resolution (eg. Runge-Kutta's method) of the system (1)-(5) is difficult : insufficient knowledge of the limit conditions ($r = R$) and often repeated calculation of the reaction rates of eq. (1). Since the resolution problems come from (dT_e/dr) , this term was used as parameter : the determination of dT_e/dr is realized

by an iterative method with 4 steps :

- i) from the $n_e(r)$ profile, a similar profile $T_e(r)$ is chosen and the values of $(dT_e/dr)_r$ deduced from it ;
- ii) using equations (2) and (3), therefore, for each value of r , the variations of T_h with T_e can be calculated $T_h = f(T_e)$;
- iii) using equations (1), (2) (4) and (5) the variations of $T_h = g(T_e)$ can be calculated for each value of r .
- iv) curves f and g cross at one point, the solution of the whole system (at point r). Thus as a function of r , all the required values can be found : T_e , T_h and the atom densities.

The solution is improved by using the new profile $T_e(r)$ as the starting point for step i).

EXPERIMENTAL METHODS AND RESULTS. The experimental set-up is described in reference /7/. In order to determine T_e , n_e is first measured by laser interferometry (at two wavelengths) and by spectroscopy (measurement of the absolute intensity of the continuum radiation /7/ : these two techniques give identical results. The $3p_8$ level density is obtained by measuring the absolute intensity of the line at 430 nm. If it is assumed that this level is in Saha equilibrium, the value of T_e can be deduced from these two measurements.

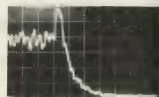
A relationship is obtained between T_e and T_h by proceeding in the following way : in the stationary state, for a fixed field value $T_e > T_h$. If the field is cut, examination of the relaxation times of the phenomena described in eq. (3) shows that while the electron temperature passes from T_e to T_h , n_e and n_a have not had the time to change. If n_j is the density of level j in Saha equilibrium :

$$n_j = n_e^2 \exp\left(\frac{E_i - E_j}{kT}\right) \quad (6)$$

As T decreases, n_j increases when n_e remains constant. Experimentally, at current intensities of less than 23 A, a sharp increase is observed in the intensity of one of the lines emitted by level j when the field E is cut (fig. 1). The relative value of the intensity increase is directly related to T_e/T_h . It should be noted that the levels under consideration are in Saha equilibrium following the resolution of system (1) and that the interferometry measurements confirmed that during the increase time

of the light intensity the changes in n_e and n_a are negligible.

Fig. 1 : Variation with time of the 696,5 nm line intensity ($I = 9$ A).



COMPARISON OF THEORETICAL AND EXPERIMENTAL RESULTS

The variations of $(T_e - T_h)$ with the electronic density are given in fig. 2. These results concern measurements and calculations at the axis of a 6 mm diameter argon arc. Under the conditions where the difference $(T_e - T_h)$ is experimentally detectable, calculation showed that the radiation loss is negligible, the energy loss due to ambipolar diffusion is low (10 % of the total) and that the diffusion of heat represents about 30 % of the total losses. The calculated values of $(T_e - T_h)$ are lightly greater than measured ones. That may be due to a systematic error of transport coefficients. Nevertheless the method used would seem interesting in the evaluation of T_h in plasmas which are a long way out of LTE.

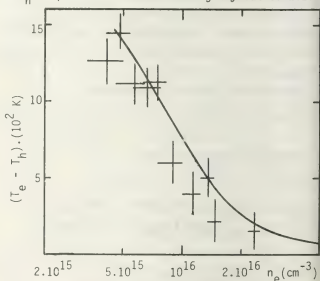


Fig. 2 : Difference between T_e and T_h versus n_e ; — calculated results, + experimental values.

- /1/ C.H. KRUGER, Phys. Fluids **13** (1970) 1737.
- /2/ J.F. UHLENBUSCH, C. FISCHER, Proc. IEEE, **59** (1971) 578.
- /3/ A. GLEIZES, H. KAFROUNI, XIII ICPIG, Berlin (1977) 35.
- /4/ R.S. DEVOTO, Phys. Fluids, **10** (1967) 354.
- /5/ GORSE, Thèse 3ème cycle, Limoges (1975) n° 75-1.
- /6/ E. SHULZ-GULDE, Z. Phys., **230** (1970) 449.
- /7/ H. KAFROUNI and alii, to be published in JQSRT (1979).

NUMERICAL SIMULATION OF A DECAYING ARGON ARC

T. Bracke, H.T. Sommer and C.G. Stojanoff.

Institut für Technische Thermodynamik, R.W.T.H. Aachen, 5100 Aachen, W. Germany.

The arc parameters of an electric arc that is subjected to rapid temporal changes of the arc current, experience temporal and spatial variations due to the effects of reaction kinetics, conduction, convection, diffusion, viscous dissipation and radiation.

The purpose of this report is to present in concise form the results of the numerical simulation of a decaying, free burning, infinitely long, axisymmetric, laminar argon arc column. The current interruption is idealized as a step function in time and the thermodynamic properties of the plasma are described by a model, which

assumes local thermodynamic equilibrium and quasi-neutrality. The transport coefficients are obtained from measurements performed on a free burning arc [5] and from kinetic calculations [3,6]. The resulting system of equations consists of the momentum (1), energy (2) and continuity (5) equations and of the conservation equation for the atoms (6) and the thermal equation of state (7).

This set of equations is supplemented with the heat flow equation (3), the particle current density equation (4) and the mass fraction definitions (8).

The dependent variables v , g , T , p and ψ_i are functions of radius and time only. An implicit finite difference method is used which has an efficient time step control

and the grid follows the developing radial solution.

$$g \frac{\partial v}{\partial t} + g v \frac{\partial v}{\partial r} = - \frac{\partial p}{\partial r} + \frac{4}{3} \frac{\partial}{\partial r} \left[\frac{\mu}{r} \frac{\partial v}{\partial r} \right] - 2 \frac{v}{r} \frac{\partial \mu}{\partial r} \quad (1)$$

$$g c_v \frac{\partial T}{\partial t} + g c_v v \frac{\partial T}{\partial r} = - \frac{1}{r} \frac{\partial}{\partial r} (r q_r) - \frac{p}{r} \frac{\partial v}{\partial r} - 4 \tilde{\epsilon} + \omega_i \epsilon^2 + \sum_i e_i \left[\frac{1}{r} \frac{\partial}{\partial r} (r J_i) - \omega_i \right] \quad (2)$$

$$q_r = - \lambda \frac{\partial T}{\partial r} + \sum_i h_i J_i \quad (3)$$

$$J_i = - g_i \Omega_i \frac{\partial \psi_i}{\partial r} \quad (4)$$

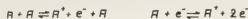
$$\frac{\partial p}{\partial t} + \frac{1}{r} \frac{\partial}{\partial r} (r g v) = 0 \quad (5)$$

$$g \frac{\partial \psi_i}{\partial t} + g v \frac{\partial \psi_i}{\partial r} = \frac{1}{r} \Omega_i \frac{\partial}{\partial r} \left(r p \frac{\partial \psi_i}{\partial r} \right) + \omega_i \quad (6)$$

$$p = g R T \quad (7); \quad \psi_i = \frac{g_i}{p} \quad (8)$$

ω_i in equation (2) is the chemical source.

The system of equations (1-8) is solved using appropriate boundary and initial conditions [1]. The chemical source terms are specified by the following reactions



The corresponding rate coefficients are taken from the literature [2, 4, 7]. The dominant diffusion processes are the inward diffusion of atoms and the outward ambipolar diffusion of charged particles.

The results of the calculations for 60 μ s after current interruption are presented in Fig. 1 - Fig. 5.

The percentage of ionization drops from 6 % to 4 % after 60 μsec and goes down to 2.5 % after 200 μsec . These results are consistent with data on the decay of the electrical conductivity. The temperature decay is linear in time and depends strongly upon the chemical reactions involved. Moreover, the present numerical analysis shows a very complex behaviour of the nonstationary arc with wave motion in the arc column starting immediately after current interruption.

References:

- /1/ Kollmann, W., Sommer, H.T., Stojanoff, C.G.: J. Non-Equilib. Thermodyn. Vol.2 1977
- /2/ Uhlenbusch, J., Fischer, E., Hackmann, J.: Bericht HMP 128, 1975
- /3/ Hirschfelder, Curtiss, Bird, John Wiley 1967
- /4/ Bond, J.W., Phys. Rev., Vol. 105, No. 6, 1957
- /5/ Stojanoff, C.G., Jahrbuch DGLR, 1971
- /6/ McDaniel, E.W. John Wiley, 1964
- /7/ Hoffert, M. Phys. of Fluids, Vol.11, No. 1, 1968

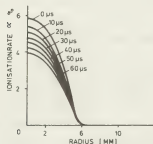


Fig.1 Radial Profiles of Degree of Ionisation

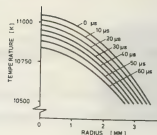


Fig.2 Radial Temperature profiles

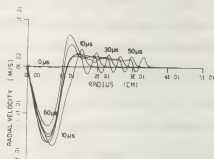


Fig.3 Radial Velocity profiles

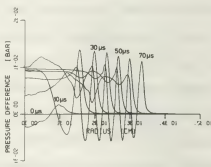


Fig.4 Radial Pressure profiles

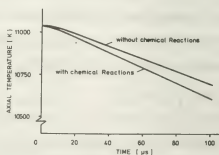


Fig.5 Decay of axial Temperature

POSITIVE GLOW CORONA ALONG A CYLINDRICAL ROD BETWEEN TWO PARALLEL PLATES

A. Boulloud, J. Charrier and R. Le Ny.

*Laboratoire de Physique Expérimentale, Institut de Physique de l'Université de Nantes,
2, rue de La Houssinière, 44072 Nantes Cedex, France.*

We have studied in room air the positive corona glow (Hermstein's glow [1]) along a stainless steel rod, 2 mm in diameter, equidistant from two parallel brass plates. The distance of the plates was 9 cm.

I/V CHARACTERISTICS.

As the rod was sustained by two rounded metal pieces, insulated from the plates and 20 cm apart, the discharge length increased with the D.C. applied voltage, because of the screening effect of these pieces. The corona current per unit length of the discharge obeys the well-known formula :

$$i = a V (V - V_s)$$

where a is a constant and V_s the threshold voltage. The length of the discharge was measured from photographs.

CURRENT RIPPLE

Ripples of the current and of the light flux from the discharge have been reported by many authors [2], [3], [4]. Their frequency is only a mean value since the period of oscillations is not really constant but fluctuates from one to another. In the investigated range (from 25 to 500 μ A) this frequency increases with the current from 115 kHz for 25 μ A and it tends towards a limit of about 440 kHz for 400-500 μ A. Previous observations with point-

to-plane gaps [4] had shown that, after a plateau, the frequency increased again.

The amplitude of oscillations varies at random. For relatively short time intervals the pattern looks like beats but for longer time intervals no regularity at all is observed. The maximum peak-to-peak variation represents 15 to 20 per cent of the mean current. This percentage tends to decrease when the current increases.

OSCILLATIONS OF THE LIGHT FLUX FROM THE DISCHARGE.

With a point-to-plane gap, the light flux from the discharge exhibits oscillations synchronized with the current ripple [4].

Two regions of the rod were imaged on slits and the intensity of the beams transmitted by the slits was studied with two photomultiplier tubes. The experimental arrangement is shown in fig. 1. The P.M.T. were in a fixed position. The optical arrangements stood on two carriages that could move along a rail for observation of various regions of the rod. An additional lens located between the mirrors and the P.M.T. reduced the beam divergence. The whole system was enclosed in a dark box in which fresh air was blown with a fan. Used air was evacuated out of the laboratory. Owing to the dimensions of the two carriages, the minimal distance between the

investigated regions of the discharge was 5 cm.

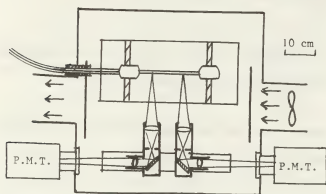


Fig. 1.— Arrangement for optical studies.

The P.M.T. currents were simultaneously observed with a 5444 dual beam Tektronix oscilloscope. A typical oscillogram is shown on fig. 2. No reproducible phase relation could be detected and a phase drift between the two traces of the same oscillogram was often observed.

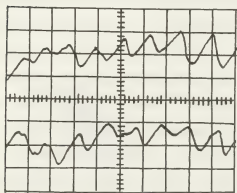


Fig. 2.— Oscillogram of the light flux from two different regions of the discharge (2 μ s per division, $i = 400\mu$ A, $V = 40,4$ kV)

Similar observations occurred when a 32 mm metal sphere located at mid-rod divided the discharge in two parts.

Thus there is no coherence between the pulsations of the discharge along the rod when the distance exceeds a few cm.

Particularly, it is obvious from these data that the frequency of the phenomenon is not regulated by the external circuit, by a quenching effect of the protective resistor for instance, and this may be easily understood: the order of magnitude of the electric charge involved during one periode is 1 nC. Owing to the capacity of the electrodes and of the H.V. cable, the voltage drop should stand below 100 V, as compared to the applied voltage (27 to 43 kV), even if Q is suddenly liberated.

Finally, our observations disagree with Beattie's and Cross's, who found that the light-flux oscillations were coherent on the surface of a relatively large sphere in a mixture of N_2 and 1 per cent of O_2 [3]. However, experimental conditions were substantially different.

REFERENCES.

- [1] W. Hermstein — Arch. für Elektr. 45, 1960, p. 209-224.
- [2] R. Fieux, M. Bouteau — E.D.F. Bull. de la Direction des Etudes et Recherches. Sér. B, 1970, N°2, p.55-88.
- [3] J.E. Beattie, J.D. Cross — 3rd Int. Conf. on Gas Discharges, London 1974 — I.E.E. Conf. Publ. N° 118, p. 279-283.
- [4] R. Le Ny, Mrs A.M. Le Ny and A. Boulloud — 4th Int. Conf. on Gas Discharges, Swansea 1976. I.E.E. Conf. Publ. N° 143, p. 246-249.

THE ARC DIAMETER AND RATE OF ROTATION OF A MAGNETICALLY ROTATED ARC WITH SUPERIMPOSED GAS FLOW

K.A. Bunting.

The Electricity Council Research Centre, Capenhurst, Nr. Chester.

Abstract

A magnetically rotated arc heater producing a uniformly heated and highly turbulent hydrogen plasma is briefly described. The effect of nozzle geometry and parameters affecting the diameter of the arc and its rate of rotation are discussed and some results are presented. It is shown that steady rotation of the arc can occur when the externally applied magnetic field is zero. The drag coefficient was determined.

1. Introduction

A magnetically rotated arc heater with hydrogen as the plasma working fluid has been developed for use in chemical processing^(1,2). A highly turbulent plasma is necessary to obtain good mixing of the reactants and, in order to satisfactorily control the rate and direction of the chemical reactions, a uniformly heated plasma is required. Both the level of turbulence and the uniformity of heating⁽³⁾ depend upon the rate of rotation of the arc and the arc diameter. It has been shown⁽¹⁾ that cathode erosion is negligible and that anode lifetime is dependent upon the rotation rate; a high arc rotation rate being required to give an acceptable lifetime. Thus, the effect of arc current, gas flow rate, cathode setback, cathode shape, nozzle geometry and magnetic flux density upon the rate of rotation of the arc have been investigated. The arc diameter, velocity, anode root velocity and the drag coefficient have also been determined.

2. Apparatus and procedure

The arc heater (Figure 1) consisted of a non-transferred d.c. plasma torch mounted on the axis of a magnetic field coil. The torch had a cylindrical outer jacket which terminated in a water cooled nozzle (anode). A water cooled rod, tipped with thoriated tungsten served as the cathode. The plasma working fluid was heated by passage through an arc generated between the electrodes which was rotated by means of a magnetic field. The gas was introduced tangentially to the plenum chamber so that the direction of swirl was in the same sense as the rotation produced by the externally applied magnetic field. The arc rotation rate was measured using differential magnetic search coils^(1,4), the resonant frequency of which was ≈ 20 MHz. The probe output was monitored oscillographically and on a frequency counter.

A mirror immersed in the plasma and screened with a jet of argon was used to take high speed cine photographs of the arc. The combination of camera aperture and optical filters was chosen so that the diameter of the arc recorded photographically was not reduced by further reductions in the amount of light collected. Synchronised photographs of the arc and the probe output were obtained using a pulse circuit to trigger the camera and a pre-framing pulse from the camera to trigger the oscilloscope.

3. Results

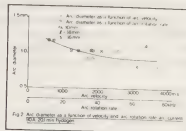
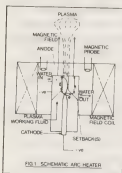


Fig. 2 Arc diameter as a function of velocity and arc rotation rate at constant current 300 A, 160 V.

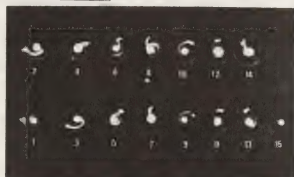


Fig. 3 Photographs of arc, 90 A, 160 V, 20 l/min. hydrogen, 200,000 p.p.s., $B = 0.0026$ Tesla, $d/A = 10$ mm, $l = 33$ mm, $s = 28$ mm, $\theta = 40^\circ$.

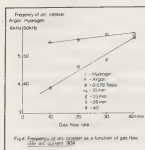


Fig. 4 Frequency of arc rotation as a function of gas flow rate at constant 300 A.

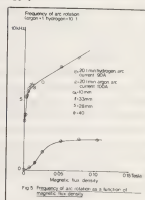


Fig. 5 Frequency of arc rotation as a function of magnetic flux density.

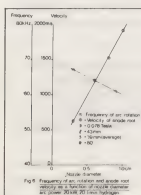


Fig. 6 Frequency of anode root velocity as a function of nozzle setback at constant 300 A, 160 V, 20 l/min. hydrogen.

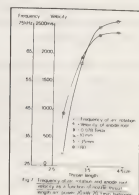


Fig. 7 Frequency of anode root velocity as a function of arc length at constant 300 A, 160 V, 20 l/min. hydrogen.

4. Discussion

It can be seen (for Figure 2 that increasing the arc velocity and rotation rate produced an increase in the convective losses from the arc and thus a reduced arc diameter. Similarly, increasing the gas flow rate or decreasing the nozzle diameter increased the convective losses and reduced the arc diameter. As the arc current increased the diameter increased approximately as $I^{2/3}$. The low viscosity and density in hydrogen lead to high convective losses as compared to argon. For example, average values of arc diameter in the range 0.65mm-1.1mm were measured for $I = 90A$ and 20 1/min. of hydrogen compared to a typical diameter of 2.5mm under similar conditions in argon. The diameter was found to be insensitive to the applied magnetic field.

Frame by frame analysis of the high speed cine films (an example is given in Figure 3) confirmed the magnetic probe readings. The rate of rotation of the arc varied from one revolution to the next but the rate, averaged over a period long compared with the period of revolution, was found to be constant. The rate of rotation increased with increasing gas flow rate (Figure 4). This is attributed to the increased thermal pinch, produced by the increased gas flow, which gives a narrower arc that is subject to smaller aerodynamic drag opposing rotation.

The rotation rate in hydrogen as a function of magnetic flux density is compared with that in argon in Figure 5. The rotation rate (n) increased with increasing magnetic flux density (B Tesla) and for hydrogen $n(kHz) = 35 + 5400B$ when $0 < B \leq 0.003$ Tesla and $n(kHz) = 56 + 62B$ when $B > 0.02$ Tesla with a transition region in between. The curve for argon exhibited a similar step but the transition region extended over a greater range of B , the slopes were smaller and the rate of rotation was approximately an order of magnitude less. The rate of rotation decreased with increasing nozzle diameter (Figure 6) and increased with increasing throat length (Figure 7). It was approximately independent of nozzle angle, setback and the angle of the cathode tip. However, for an arc current of 100A and 0.058 Tesla (other conditions as for Figure 5), the rotation rate increased from 53 to 63 kHz as the radius of curvature of the cathode tip was reduced from 6mm to 4mm. The drag coefficient for the arc for the range of Reynolds number investigated (640-1530) was found to be 0.95 and was in good agreement with results published for other arcs (5, 6, 7, 8).

The very high rates of rotation obtained in hydrogen were such as to give a uniformly heated plasma despite the small arc diameter⁽³⁾ and a highly turbulent plasma. The latter was demonstrated by injecting fine carbon particles into the flame.

It was noted that the direction of rotation in hydrogen could be with or against the direction of swirl for magnetic flux densities < 0.01 Tesla applied in the sense which produce rotation in the swirl direction. The self magnetic field of the arc is not negligible and

this effect, which was not observed in argon, is thought to originate in a spatial arc instability, the growth of which is encouraged by the resulting self-field. Depending upon the swirl direction, the spatial instability may be enhanced or suppressed by the swirl. The effect was strong enough in hydrogen to produce steady rotation rates as high as 35 kHz for zero applied field and is the explanation of the rapid initial increase in rotation rate at low magnetic flux density - the higher aerodynamic drag in argon resulting from the higher density viscosity and diameter suppresses the effect.

5. Conclusions

Very high rotation rates (≈ 80 kHz for $B = 0.08$ Tesla) have been obtained in hydrogen giving a uniformly heated and highly turbulent plasma and long electrode lifetimes. It is possible to obtain a steady and high rate of rotation in hydrogen with no externally applied magnetic field.

6. References

- (1) Bunting, K. A., "An arc heater with hydrogen as the plasma working fluid," E. C. R. C. M554, 1972.
- (2) Bunting, K. A., "Magnetically rotated arcs with superimposed gas flow," E. C. R. C. M1229, 1979.
- (3) Chen, D. C. C. and Lawton, J., "Discharge heaters based on magnetically rotated arcs," Trans. Inst. Chem. Eng., B46, No. 9, Dec. 1968.
- (4) Humphreys, J. F. and Lawton, J., "Heat transfer from magnetically rotated arc plasma," E. C. R. C. M317, 1970.
- (5) Roman, W. C. and Myers, T. W. A. R. L. 66-0191, Oct. 1966.
- (6) Winograd, Y. Y. and Klein, J. F. A. I. A. A. J., V7, No. 9, pp 1699-1703, Sept. 1969.
- (7) Adams, V. W. Aeronautical Research Council Current Papers No. 743, Parts I and II, 1964.
- (8) Nicolai, L. M. and Keuther, A. M., "Properties of magnetically balanced arcs," Phys. Fluids, V12, No. 10, pp 2072-2082, Oct., 1969.

7. Acknowledgement

The author wishes to thank Dr A. T. Churchman, Director of The Electricity Council Research Centre, Capenhurst, for permission to publish this work.

TEMPORAL SPACE-CHARGE FIELD-CHANGES AT THE CATHODE IN NEGATIVE POLARITY DISCHARGE

R.T. Waters and E.O. Selim

*Department of Physics, Electronics & Electrical Engineering, UWIST, Cardiff CF1 3NU, Wales, UK.*Introduction

Although negative-polarity corona pulses have been studied extensively by many authors,⁽¹⁾ the available data have been confined to current and light output measurements. Theoretical models and possible discharge mechanisms have therefore had to be based on these parameters. No information is available about field-changes near the cathode which are important to enable a realistic model for the discharge to be developed. This lack of data is due to difficulties in measuring field at the high-voltage electrode because of the presence of conduction current. The present paper is a brief introduction to a new technique - the field filter - for field measurements at high voltage electrodes, and demonstrates some preliminary results of measured space-charge field-changes in negative corona.

Experimental Arrangement

An inverted gap of separation 83 mm was formed between a 12.6 mm diameter hemispherically-capped rod cathode and a 250 mm diameter sphere anode, as shown in Fig. 1. The field filter was inserted into the cathode. In this application the filter took the form of an aperture of 2 mm diameter at the cathode tip, and a 6 mm diameter metallic disc which lay 2 mm beneath the aperture. This disc represents the field-sensing electrode which is connected to the output circuit and is biased with respect to the cathode (which is at earth potential) using a stabilized DC supply ± 2.5 kV maximum. A photomultiplier was used to register the total light output or the light from a defined spatial region in the gap, using a telescopic arrangement and a slit 0.1 mm wide.

The Field Filter Principle

The external field penetrating the aperture will be attenuated by the geometry of the device so that the field at the surface of the sensor (the reduced field) is proportional to the external field (Fig. 2(a)).

A reverse field is applied between the sensor and the external electrode (the cathode) in order

to prevent conduction current from reaching the sensor. This reverse field (Fig 2(b)) does not affect the charge induction process so that the effective action of the device is to filter the field changes (i.e. displacement current) from the conduction current components. The method is well suited for recording of the transient field-changes at the cathode; a biased probe for static fields has been described in an earlier paper⁽²⁾.

The sensitivity of the field filter was determined as follows: the corona inception field at the cathode was calculated to be 43 kV cm^{-1} on theoretical ground, which corresponded to an observed inception voltage of 75 kV. The field-filter signal at just below corona inception then showed the sensitivity of the field filter to be $0.056 \text{ pC (kV cm}^{-1})^{-1}$.

Results

The oscillograms of Figs. 3(a,b,c) illustrate the function of the probe in the presence of corona at the rod electrode. In the absence of the bias voltage, the recorded signal represents the sum of the integrated corona current and the transient field-changes occurring in the region of the aperture (Fig. 3(b)). When a sufficient reverse bias was applied, no conduction current was recorded, and the field changes could be seen (Fig. 3(c)). If a negative bias voltage was applied, the conduction current was much increased and the field changes are masked (Fig. 3(a)).

Between corona inception at 75 kV and 90 kV, field-changes from the mean field were always negative; a rapid reduction of field accompanied the discharge development, then the field gradually recovered to the mean field which then allowed further discharge to start. The regularity of these successive field reductions corresponds with the well-known regularity of the Trichel current pulse sequence. A plateau in the field was sometimes observed before the field recovery.

At higher voltages, a remarkable result was observed. Besides continued negative field-changes (Fig. 4(a)), positive field-changes were also seen,

(Fig. 4(b)). These were much larger than the negative field-changes, but simultaneous photomultiplier measurements showed that there was no appreciable difference in total light output accompanying either polarity of field-change. Negative field-change showed a plateau in the light output while positive change showed only a spike. Between positive and negative field-changes there was always a transition mode (Fig. 4(c)) where the negative field-change sequence was preceded by one or more smaller positive field-changes of shorter duration.

With a vertical slit aligned on the axis of the cathode (Fig. 4(d)), the photomultiplier showed no difference in the light amplitude between positive and negative field-changes. With a vertical slit aligned 3 mm off axis, the reduced light amplitudes of Fig. 4(e) were found. With the slit aligned horizontally 7.5 mm above the tip, positive field-changes accompany light amplitudes larger than those for negative field-changes (Fig. 4 (f)).

The calibration factor indicates that the maximum positive and negative field-changes were of the order of 20 MV m^{-1} and 4 MV m^{-1} respectively..

References

- (1) LOEB, L. B.: 'Electrical coronas' (Univ. Calif. Press), 1965.
- (2) SELIM, E. O. and WATERS, R. I.: 'Static probe for electrostatic field measurement in the presence of space charge', IEEE-IAS Conference Record 78CH 1346-61A, 136-141, 1978.

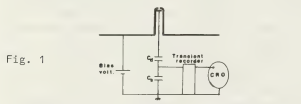


Fig. 1

Fig. 2

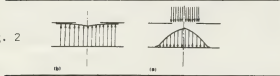


Fig. 3

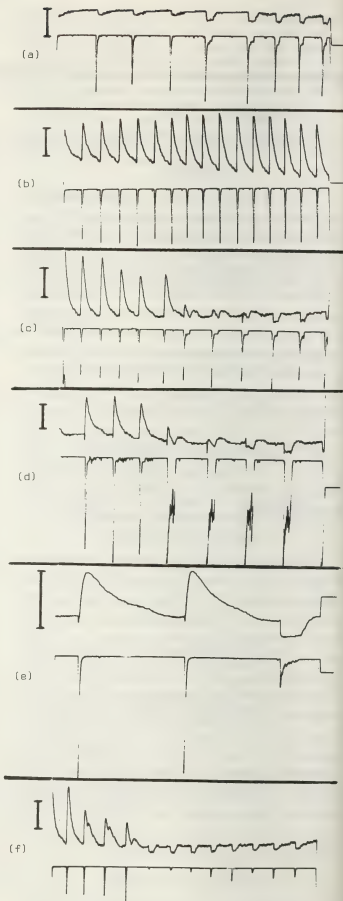


Fig. 4 Field-changes (upper traces) and optical signals (lower traces)
Sweep time $800 \mu\text{s}$ (except (e), $200 \mu\text{s}$)
Bars indicate field change of 10 MV m^{-1}

SPECTROSCOPIC DIAGNOSTICS OF A.D.C. NITROGEN PLASMA JET

J.M. Baronnet, J. Rakpitz, J.F. Coudert, E. Bourdin and P. Fauchais
Erchov* and E. Pavlov*.

*Laboratoire de Thermodynamique, Université de Limoges, 87060 Limoges Cedex France.
*Institut de Physique, Minsk, Biélorussie, U.R.S.S.

Transition probabilities, Stark broadening and shift of NI have been measured and spectroscopic diagnostics of nitrogen plasma jet have been performed.

I. EXPERIMENTAL SET-UP. The jet is produced in a closed vessel /1/. The anode arc channel is made of two parts (1)-(2) at the same electrical potential separated by a gap of 5 mm for spectroscopic observations of the arc. A BN ring (3) insulates the first anode from the second one (4). This device stabilizes the arc and permits analysis of the arc column, of the jet and of its plume.

The whole measurement : calibration, experimental data recording, and data treatment (Abel's inversion, restitution of spectral line profiles...) is performed with a data acquisition system connected to a computer.

II. TRANSITION PROBABILITIES OF NI LINES AND STARK PARAMETERS MEASURED IN THE ARC. From stark broadening of H α we have measured an electronic concentration of $1.05 \pm 0.15 \cdot 10^{17} \text{ cm}^{-3}$ on the axis of the arc - /2/ /3/; it had been previously shown that the line was not self - absorbed. We had also verified that 0.1 NI/mn of H $_2$ mixed with nitrogen (volume ratio was 5%) did not disturb the arc voltage or the microscopic properties of the plasma of interest (continuum emission at 495.5 nm and 493.5 nm line profile). Under these conditions L.C.T.E. is realized /1/ according to the criterions of DRAWIN /4/ ; consequently, starting from the equilibrium composition we have determined a temperature of $13200 \pm 400 \text{ K}$ and the concentration of NI : $3.4 \pm .4 \cdot 10^{17} \text{ cm}^{-3}$. From these measurements and those of volume emission coefficient we have determined the transition probabilities with a relative error of 50%. (table I). Our results are in good agreement with those of MOTSCHMANN /5/ and RICHTER /6/. For the lines before 550 nm our results are 20% higher than those of MOTSCHMANN, even though WIESE has increased these last measures by more than 50%. Calculations by GRIEM /8/ give results which are generally

higher than the measured values.

We have especially studied the profiles of the 746.8 nm and 493.5 nm lines and determined their neutral collision shift and broadening /1/. Resonance broadening has been included for the 746.8 nm line.

We have neglected the Doppler effect for the 493.5 nm line profile, its Stark width (2ω) and shift (d) being computed by fitting the experimental profile to a Lorentz profile. We have deduced the Stark parameters of the 746.8 nm line by comparison of the experimental profile to profiles resulting from the convolution of a Doppler profile (at the temperature of measurement) with Lorentz profiles. The results are shown in figure II, where we have also quoted the values computed by /9/ and /10/ ; for N_e between 5 and $10 \cdot 10^{16} \text{ cm}^{-3}$ and T between 11500 K and 13500 K we propose the following : $2\omega = 8.2 \cdot 10^{-3} \text{ nm}$, $d = 410^{-3} \text{ nm}$ for 746,8 nm line and $2\omega = 1,95 \cdot 10^{-2} \text{ nm}$, $d = 2,8 \cdot 10^{-3} \text{ nm}$ for 493,5 nm line.

III. PLASMA JET DIAGNOSTICS. For the study of L.T.E. in the plasma jet /4/ we have calculated the relaxation times of energy exchanges between the different degrees of freedom and we have determined the characteristic times of relaxation to chemical equilibrium. The slower process is N $_2$ dissociation ($N_2 + M \rightarrow N + N + M$); associative-ionization follows very rapidly ($N + N \rightleftharpoons N_2 + e^-$) and then charge exchange ($N_2^+ + N \rightarrow N_2 + N^+$) occurs : Ionization by electronic collision is not really significant, but even with a low concentration N $_2^+$ is of major importance.

L.C.T.E. is only realized in the core where N_e is higher than $4 \cdot 10^{15} \text{ cm}^{-3}$ ($T > 8600 \text{ K}$). Otherwise in the plume jet for example, vibration-vibration relaxation and dissociation times are great compared to hydrodynamic times. Anyhow, considering the very low relaxation times for rotation-rotation and rotation-transformation processes, rotational temperature of molecules is always equal to neutral

translational temperature.

Consequently we have developped methods for the measurement of rotational temperature /1/ and the following diagnostic method /11/ is proposed : the experimental profile is compared to theoretical profiles computed under the assumption of L.C.T.E.. Volume emission coefficients are calculated for all the rotation lines of the band under consideration (we assume that they are sufficiently narrow compared to the apparatus function and so are supposed to have a limited Dirac profile according to their intensities). We sum over the lines concerned, and perform a convolution with a triangular or Gaussian function. This is done for all of the bands of the sequence. The rotational temperature can be deduced from the rotational profile of the vibration band even if L.C.T.E. is not realized. Furthermore this method emphasises the difference between the rotational and vibrational temperatures.

CONCLUSION. A computer driven data acquisition system has permitted the measurement of the transition probabilities of NI lines and also Stark parameters of the 746,8 nm and 493,5 nm lines. Furthermore we have shown that L.C.T.E. is not realized in the plume, consequently only the rotational temperature is representative of the translational temperature of neutrals.

REFERENCES

/1/ BARONNET J.M. Thèse de Doctorat ès Sciences. Limoges (1978).
/2/ HILL R.A. J.Q.S.R.T., 7, (1963), 82.
/3/ WIESE W.E. et al., Phys. Rev., A11, (1975),1854
/4/ DRAWIN H.W., High Pressure High Temperature, 2, (1970), 359.
/5/ MOTSCHMANN H., Z. Physik, 143, (1955), 77
/6/ RICHTER J., Z. Astrophys., 51, (1961), 177.
/7/ WIESE W.L. et al., Atomic Transition Probabilities. Vol. 1. NSRDS-NBS 4 (1966)
/8/ GRIEM H.R., Plasma Spectroscopy, Mc Graw Hill (1964)
/9/ GRIEM H.R., Spectral line broadening by plasma, Academic Press (1974)
/10/ HELBIG V. et al., Phys. Rev., A14, (1976), 1082
/11/ COUDERT J.F., Thèse de 3ème cycle, Limoges, (1978).

λ nm	A_{si}	λ nm	A_{si}	λ nm	A_{si}
870.326	200.	742.364	50.	517.000	1.9
871.171	111.	744.230	102.	518.15	1.5
871.884	53.	746.831	159.	518.69	0.8
872.891	29.	946.068	25.	413.763	2.4
874.736	7.2	856.774	74.	414.342	5.1
818.485	82.	859.401	260.	415.146	9.1
818.801	125.	862.924	250.	541.188	8.9
820.036	47.	865.587	89.	540.145	4.5
821.071	48.	902.892	188.	438.440	4.2
821.632	176.	906.072	207.	439.130	9.0
822.312	214.	491.490	6.0	422.304	3.8
824.237	102.	493.503	13.3	422.474	3.7
		532.870	2.0		
		528.118	2.3		

Table I.NI transition probabilities ($A_{si} 10^5 sec^{-1}$)

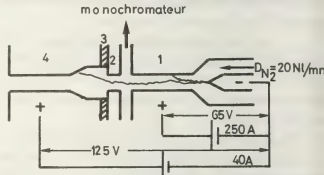


Figure 1 - Plasma device

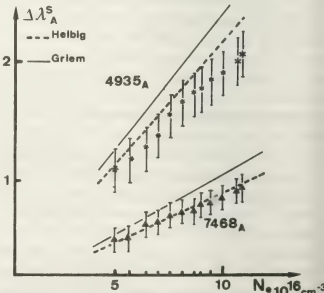


Figure II - Stark width

EXPERIMENTAL DETERMINATION OF THE SPATIO-TEMPORAL DISTRIBUTION OF THE SPACE CHARGE FIELD IN A BREAKDOWN

P. Bayle, M. Bayle, E. Morales.

Centre de Physique Atomique, Laboratoire associé au C.N.R.S. n° 277, Université Paul Sabatier, Toulouse.

Ionizing processes occurring during a breakdown are generally analysed through optical devices, photomultipliers or image converters. Though less sensitive than photomultipliers, the streak image converters have the advantage of giving a continuous spatio temporal representation of the discharge; this is particularly interesting in the case of non recurrent discharges. We have thus developed a technique to interpret streak camera records that give us the parameters governing the discharge, and in particular the space charge field. It is known that a breakdown is essentially governed by the field resulting from the superposition of the applied field and the space-charge field (1)(2).

It is possible to sort out two kinds of informations from the streak camera records :

a) information of geometric order that gives the dimension, the position of the discharge and its propagation speed (3). These are essentially qualitative informations.

b) information about the energies related to the blackening density of the film. For a film emulsion, the characteristic curve links the image density $D(x, t)$ to the luminous energy received. The blackening density $D(x, t)$ is related to the number ϕ of photons present at the corresponding point (x, t) in the discharge. As a first approximation this relation can be expressed by $D(x, t) = T L g [T \phi(x, t)]$ where Γ is the film contrast ratio and T is the transmission function of the experimental set up.

The number of photons emitted between time t and $t + dt$ at a distance x from the cathode is given by

$$d\phi(x, t) = \int_0^t n_e(x, t') \delta(x, t') v_e(x, t') \exp\left[-\frac{t-t'}{\tau}\right] dt' \quad (1)$$

τ is the mean decay time constant of excited states

$$\frac{\delta(x, t)}{\rho} = F \exp\left[-\frac{G \rho}{E(x, t)}\right]$$

is the light excitation coefficient by electrons (4)

$$v_e(x, t) = \mu \frac{E(x, t)}{\rho} \quad \text{the drift velocity}$$

$n_e(x, t)$ is the electron density distribution

$$n_e(x, t) = n_0 \exp\left[\int_0^t \alpha(x, t') v_e(x, t') dt'\right] \quad (2)$$

$$\alpha(x, t) / \rho = A \exp\left[-B \rho / E(x, t)\right]$$

As the macroscopic coefficients are functions of the electric field, we obtain from relations (1) and (2), the electric field. If $y(x, t) = E(x, t) / \rho$, we obtain.

$$\frac{dy}{dt} = \left[\frac{1}{\Gamma} \frac{\partial y}{\partial t} + \frac{\tau}{\Gamma} \left(\frac{\partial^2 y}{\partial t^2} + \frac{1}{\Gamma} \frac{\partial^2 y}{\partial t^2} \right) + \frac{\partial^2 y}{\partial t^2} - A \mu \gamma \alpha \left[\frac{y}{\Gamma} \right] \right] \left(\frac{1}{\Gamma} + \frac{C}{\Gamma} \right)^{-1}$$

Equation (3) shows the dependency of the electric (3)

field on the first derivatives of the optical density of the streak camera record. This dependency indicates important perturbations of the field that will appear at the boundaries of the light and dark areas.

A diagram of the streak camera record is given in fig. 1; analysis of the record was carried out by means of scanning microdensitometer that gives the matrix $D(x, t)$. The isodensity curve are shown in fig. 1. One can see the propagation of a cloud of electrons between the cathode and the anode. The cloud widens out and is then followed by a second discharge canal of lower speed. The impact of the electrons cloud on the anode gives rise to a return front in the direction of the cathode, where it produces a second luminous front that goes back towards the anode.

Equation (3) is solved with respect to time for each value of x . This gives us the continuous evolution of the electric field with position and time. In fig. 2 we show the analysis corresponding to the line indicated by arrows on fig. 1. The field is derived,

which amounts to neglecting memory effects on the recorded picture due to the lifetime of the excited states. We have for example in fig. 2 the evolution $E(x, t)$ of the field in time at a given point in the gap. The optical density increases in an almost monotonous manner. The first luminous front corresponds to a maximum in optical density, while the two other fronts, the anode and cathode return waves give a modification of the gradient of the optical density as a function of time (5).

Each luminous front can be associated to the propagation of a strong perturbation of the electric fields as one can see on fig. 2. The propagation of a luminous front indicates the propagation of an ionizing wave. The perturbation of the field happens in the following way : in front of the wave there exists a strong field that corresponds to a zone of high optical density gradient, this wave leaves a zone of almost neutral plasma characterized by a weak electric field behind. The wave after reflection on the anode reinforces the electric field. The arrival of the ionizing wave at anode gives rise to an intense anodic spot. The spot is related to a very strong space charge field due to the electron cloud just in front of the anode. The gradual absorption of the electrons by the anode modifies the net charge near the electrode. Once the electrons are absorbed, the cloud of remanent positive ions lowers the field at the anode, while the field towards the cathode become more strong fig. 3. This perturbation goes towards the cathode. The propagation speed of the luminous front and that of the ionizing wave are little different, because the propagation is, in fact governed by the ionizing wave. The stronger the ionization of the gas the faster is the propagation. The last wave can cross the gap (5 cm) in one nanosecond.

- (1) Yoshida (K.), Tagashira (H.) : J. Phys. D. Appl. Phys. 9, 485-490 (1976).
- (2) Davies (A. J.), Evans (C. J.), Townsend (P.), Woodison (P. M.) : Proc. IEE, Vol. 124, n° 2, 179-182 (1977).
- (3) Bayle (P.), Bayle (M.), Crokaert (M.) : J. Phys. D. Appl. Phys. 8, 2181-2189, (1975).
- (4) Legler (W.) : Zeit. Phys. 143, 173-190, (1955).
- (5) Bayle (P.), Bayle (M.), Morales (E.) : J. Phys. D. Appl. Phys. To be published.

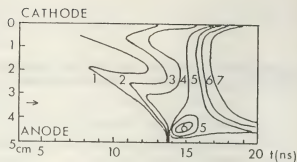


Fig. 1. Microdensitogram of streak photograph of discharge in $N_2 + CH_4$ (2.5 %),
 $P = 130$ torr, $E_o/P = 118$ V/cm. torr.

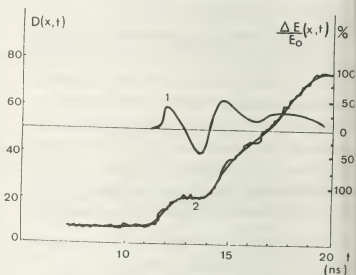


Fig. 2. Electric field (1) and optical density (2) at $x = 33.5$ mm from the cathode.

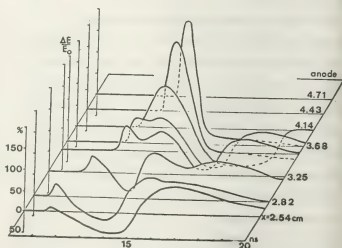


Fig. 3. Perturbation of electric field at the anode.
 $(x = \text{distance from the cathode})$.

REASONS FOR THE DISPERSION OF BREAKDOWN VOLTAGES IN SF₆

W. Hauschild and W. Mosch.

Dresden Technical University, Department for Electrical Engineering Dresden, G.D.R.

Abstract: The breakdown in SF₆ is a stochastic process, on the one hand because of the random development of electron avalanches [1] [2] [3], on the other hand because of random influences on the electrostatic field by micro-particles, micro-protrusions, or micro-discharges [1] [2] [4] [5]. It is investigated which of the random influences causes the dispersion of the breakdown voltage at different kinds of the stressing voltage.

Semi-empirical calculation of the breakdown voltage: The breakdown voltage U_d can be calculated [1] [2] according to

$$U_d = E_{di} \cdot e_h \cdot d \cdot \gamma \cdot k_t \cdot e_f = U_{di} \cdot k_t \cdot e_f, \quad (1)$$

E_{di} - intrinsic electrical strength of SF₆, measured with a stress time in the order of 1 min:

$$E_{di}/kVcm^{-1} = 890 \cdot p_{20}/MPa; \quad (2)$$

e_h - curvature factor, describing the macroscopic curvature of the electrode and calculated from the streamer theory [1] [6] (E_{dh} - maximum breakdown strength)

$$e_h = E_{dh}/E_{di} \quad (3)$$

d - gap distance;

γ - uniformity factor according to Schwaiger (E_0 - mean and E_h maximum field strength);

$$\gamma = E_0/E_h \quad (4)$$

k_t - time factor, describing the changes of the electrical strength caused by very short (impulse voltages) or very long (operation voltages) stress time;

e_f - roughness factor, describing the influences of roughness, micro-protrusions and micro-particles.

Random influences due to avalanche statistics can affect the time factor k_t , which therefore has to be considered as

a random variable. Random changes of the micro-field affect the roughness factor e_f , which is also a random variable. The distribution functions of k_t and e_f can be estimated from measured breakdown voltages. Under ideal conditions (very smooth electrodes, absolutely clean system) and d.c. or a.c. voltage ($t=1$ min), $e_f=1$ and $k_t=1$ are valid and eq.(1) delivers the maximum possible breakdown voltage $U_d = U_{di}$. Under technical conditions the expression

$$E_d = e_f \cdot k_t \cdot E_{di} \quad (5)$$

can be understood as the applicable electrical strength [1].

Time factor and avalanche statistics:

Under the assumption $e_f = 1$, according to eq.(5) the time factor k_t is a field strength related to E_{di} . For a uniform field the avalanche statistics give the breakdown probability depending on the field strength and the number of starting electrons [1] [3]. This is the distribution function of k_t (fig. 1).

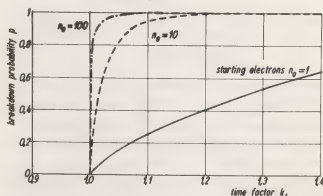


Fig. 1: Distribution function of the time factor k_t depending on the number of starting electrons (theoretically for a uniform field)

For one or a few starting electrons k_t has a large dispersion. If the number of starting electrons is high, the random

character of k_t can be neglected (see also [17]). At switching impulses (s.i.), a.c., and d.c. voltage k_t is independent of pressure and equal to one ($k_t = k_{t63} = 1$, fig. 2) or slightly smaller than one for very long stress times [17]. At lightning impulses the stress time is so short that the number of starting electrons is very limited. Now k_t is random and has to be described by its distribution function.

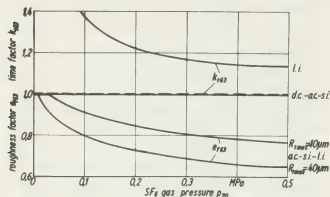


Fig. 2: Modal value of the time factor k_{t63} and of the roughness factor e_{f63} (experimentally)

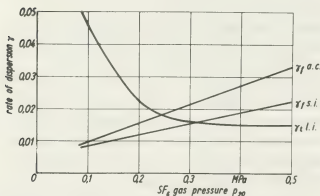


Fig. 3: Rate of dispersion γ_t for the time factor k_t and γ_f for the roughness factor e_f (experimentally)

Starting from a measured double exponential distribution for the impulse breakdown voltage [17] [27], the parameters of the double exponential distribution for the time factor k_t , the modal value k_{t63} (fig. 2, l.i.) and the rate of dispersion γ_t (fig. 3; $\gamma_{t\ l.i.}$) were calculated. Both k_{t63} and γ_t decrease with increasing gas pressure. For impulse voltages $U_d > U_{d100}$ (breakdown probability $p = 1$) the parameters k_{t63} and γ_t depend not only on the gas pressure, but also on the stress time.

Roughness factor and random changes of the micro-field: At lightning impulses the motion of micro-particles and the formation of micro-discharges cannot occur and the roughness factor has a fixed value $e_f = e_{f63} \leq 1$ (fig. 2). At a.c. voltage but also at switching impulses the micro-field near the electrode is randomly changed by moved particles, emission processes, micro-discharges at protrusions etc. from place to place and time to time. The roughness factor e_f is random now and is described by its distribution function. Because of the double-exponentially distributed breakdown voltage (a.c. and s.i. [17]) the roughness factor possesses the same distribution with the modal value e_{f63} (fig. 2) and the rate of dispersion γ_f (fig. 3). On the other hand, e_{f63} does not depend on the kind of voltage, but γ_f for a.c. is higher than for s.i. The different reasons for the dispersions γ_t and γ_f were shown by the different dependences of γ_t and γ_f on pressure (fig. 3): At lightning impulses the dispersion of the time factor is caused by the avalanche statistics and γ_t decreases with increasing pressure. At a.c. or s.i. voltage the dispersion of the roughness factor is caused by the micro-field influence of which on the breakdown process is larger at higher pressures and γ_f increases with increasing pressure.

Acknowledgement: The authors are grateful to the VEB Transformatorenwerk "Karl Liebknecht" Berlin/GDR for the support given in carrying out the investigations and to the Research Co-operation ELTRA.

References: [1] Mosch, W.; Hauschild, W.: Hochspannungsisolierungen mit Schwefelhexafluorid, VEB Verlag Technik Berlin 1979. [2] Hauschild, W.: ELEKTRIE 33 (1979) 4. [3] Mosch, W.; Hauschild, W.: IGP 13, Berlin (1977), paper 0418. [4] Bortnik, I.M.: IGP 13, Berlin (1977), paper 0428. [5] Baumgartner, R.G.: Thesis ETH Zürich 1977. [6] Pedersen, A.; Bregnsbo, E.: 2. ISH Zürich (1975), pp. 432-436. [7] Blair, D.T.A.; Crichton, B.H.; Sommerville, I.C.: ISGD Knoxville (1978), pp. 360-365.

EFFECT OF POLARITY ON THE IMPULSE BREAKDOWN OF SF₆

E. Antonios Vlastós.

The Royal Institute of Technology, S-100 44 Stockholm 70, Sweden.

Abstract: The effect of polarity on the impulse breakdown of SF₆ and the influence which a thin dielectric coating has on the impulse breakdown for both polarities was studied in the pressure range of 1-7 bar_a in a coaxial cylinder electrode configuration.

Introduction: The thought of establishing a similarity law for the breakdown of gases dates back to the end of the previous century. Paschen in this thesis, which appeared 1898, was the first to establish a relation between the breakdown voltage of a gas and the product of pressure times the electrode separation for plane parallel electrodes. The scientific scepticism about this relation, the so called Paschen's law, started to grow when experimental results from measurements with different electrode materials, electrode spacings and gases become available. Soon it became clear that the breakdown voltage of a gas, as determined experimentally, is not a monotonous single valued function of the product pressure p times the electrode separation d but shows a minimum. Further more it was found that the relation between breakdown voltage and the product pd , at values of pd , which are either lower or higher than that corresponding to Paschen's minimum, deviates from the linear one and that the deviation appears earlier for small electrode separations d . All these well known facts are summarized here to emphasize that from the beginning it was already established that the outcome from trials made to determine the breakdown voltage of a gas does not only depend on the composition and impurities of the gas but also depends on the electrodes, on their constitution, shape and surface conditions (such as roughness and oxide layers). The main reason for the influence of the electrodes on the breakdown voltage was accepted to be the electron emission from the electrode surface which appears at elevated macroscopic electric fields.

In slightly asymmetrical electric fields, such as the field produced between two coaxial cylinders, there is experimental evidence that not only the electrode shape but also the electrode surface conditions are crucial for the outcome of the measurements especially when the polarity of the electrode with the smaller radius is negative. Moreover, for electronegative gases, where the breakdown voltage is higher than that for non-electron-attaching gases the deviations from the similarity or Paschen's law were found to be larger and to appear at pressures which are lower than those corresponding to non-electron-attaching gases. The application of pressurized electronegative gases for the insulation of high voltage switchgear equipment necessitated an intensive research on the breakdown voltage of electronegative gases and especially of SF₆ which besides its favorable dielectric properties also possesses good arc quenching properties. CIGRE's study committee 15 on insulating materials has from already published work prepared a composite

Paschen's curve for SF₆ and the deviations from the Paschen's curve at different electrode spacings for essentially uniform fields [1]. The deviations from the Paschen's curve appear at a mean electrical field of about 20 kV/mm.

Results: In order to study the effect of polarity on the impulse breakdown of SF₆ and the influence which a thin dielectric coating has on the impulse breakdown for both polarities extensive measurements were performed with coaxial cylindrical electrodes with diameters of 70 and 30 mm respectively and a length over which the field was undistorted of 250 mm. Figure 1 shows the 1 % positive lightning impulse (1.2/50 μ s) breakdown voltage of SF₆ with bare polished pure aluminium and with polished and later anodized pure aluminium inner electrode as a function of the gas pressure. For comparison the 1 % breakdown voltages of air with anodized electrodes are also given. Figure 2 shows the 1 % negative lightning impulse (1.2/50 μ s) breakdown voltage of SF₆ and air with the same type of electrodes as those in figure 1. The 1 % breakdown probabilities of bare and anodized electrodes were derived by applying a hundred impulses on a new electrode pair at each voltage level and by increasing the voltage levels by small steps until the first breakdowns occurred. This measuring procedure seemed to be the most suitable since it reduces the influence of previous breakdowns on the outcome of results. The profile curve of the polished electrodes showed that the difference between the crest and bottom lines of the profile curve was about 2-4 μ m. The oxide layer thickness of the anodized aluminium electrodes was about 10 μ m and the difference between the crest and bottom lines of the profile curve of the anodized electrodes was about 1 μ m.

The results presented in figures 1 and 2 are briefly summarized as follows: (a) The 1 % impulse breakdown voltage at 1 bar_a is within the accuracy of the experiments almost equal both for bare and covered electrodes and for the two polarities. (b) At higher pressure the difference between the 1 % impulse breakdown voltage for positive and negative impulses increases. (c) The improvement due to the anodization of the electrodes is larger with negative polarity making the 1 % negative impulse breakdown voltage almost equal to that of bare electrodes with positive polarity.

A possible explanation of these results is that the great deviations between positive and negative impulse breakdown voltages in gases such as SF₆ and the deviations from Paschen's law is in one hand due to the electron emission from the surface and especially to the electron velocity distribution and on the other hand to the strong reduction of the electron attachment cross section of SF₆ at relatively low electron energies [2]. By polishing and by anodizing the electrodes the electron energy

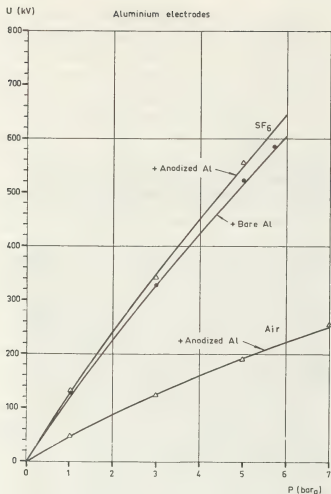


Fig. 1. Dependence on gas pressure of the 1% positive lightning impulse (1.2/50 μ s) breakdown voltage of SF₆ and air with bare polished pure aluminium and for anodized polished pure aluminium inner electrode.

distribution may change and the energy of the electrons in the tail of the distribution may be reduced so that the electrons become attached to the gas molecules and the breakdown voltage increases.

Summarizing one can conclude that the predictions of the similarity law for the breakdown voltage of gases such as SF₆ and the experimental results are not antithetical but that the basic contradiction between the predictions and the experimental results is mainly due to electrode effects and to the influence of the measuring procedure on the determination of the breakdown voltage.

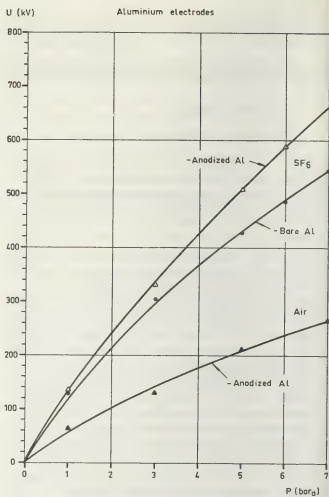


Fig. 2. Dependence on gas pressure of the 1% negative lightning impulse (1.2/50 μ s) breakdown voltage of SF₆ and air with bare polished pure aluminium and for anodized polished pure aluminium inner electrode.

Acknowledgments: The author is indebted to the Swedish Board for Technical Development for financial support, to Prof. S. Rusck for his fruitful inspiration and to Dr. A. Mikhail for the performance of the measurements.

References:

1. Rein, A., *Electra*, **32**, pp. 44-60 (1974).
2. James, D.R., Christophorou, L.G., *Proc. of Int. Symp. on Gaseous Dielectrics*, Tennessee, pp. 224-251 (1978).

SHOCK WAVES IN SPARK CHANNELS, PART 1

M.M. Kekez and P. Savic.

National Research Council, Ottawa, K1A 0R6.

INTRODUCTION

This work represents an additional step in the systematic development of the theory of spark channel formation in a series of publications [1] - [9]. It is intended to further emphasize the use of the mechanics of compressible media, in particular as related to the fields of hypersonic flow and detonation, to elucidate the problem of gas discharges. We intend to show that the paraboloidal shock front which surrounds the advancing tip of a highly conducting spark channel will degenerate into a weak discontinuity surface, i.e. a sound wave, at some distance transverse to the axis of the channel. A formula for the time of the transition from hypersonic to sonic motion is derived.

THEORY

The hypersonic analogy provides a relation between the constant-energy non-steady similar flow behind the blast wave arising, i.e. from detonation, and the steady hypersonic flow about a blunt-nosed cylinder. Its value lies in the fact that it can establish the asymptotic behaviour of the flow not just when the velocity is infinitely large but also when the properties of the flow are to be predicted at moderate supersonic speeds. Even for not too slender bodies, the drag coefficient, and other aerodynamic characteristics, remain practically unchanged for free stream Mach number greater than 3 or 4. When the Mach number of a blunt-nosed cylinder and its bow shock shape are known, then the properties at every point on the shock trajectory can be determined from cylindrical blast wave theory. The analysis of such a blast wave and its application to hypersonic flow past blunt-nosed slender cylinders, was developed by Swigart [10] to third order in inverse Mach number. We note in passing that the last two terms in the series expansion are included to improve the accuracy at later times after the initial explosions, while the first term describes a solution for the flow field during the explosion and, as such, has been used in our earlier work [1], [3] and [6].

We first briefly explain the relevance of Swigart's analysis to the theory of spark channel formation. Consideration of the processes occurring at the sharp tip leads us to assume that at every instant the energy absorbed in the tip acts like a powerful chemical heat release which drives a shock wave in all directions. The "chemical" heat is replenished by the energy of electrons heated by electric field concentration ahead of the tip, and then transferred to the heavy charged particles behind the shock front via Coulomb collisions. As the field concentration is strongest at the axis of the channel (the radius of the curvature at the tip is smallest), the preferential heating of the electrons will make the spark channel elongate mainly along the axis of the channel (in the direction of the strongest shock wave). Thus the mechanism of spark channel elongation is quite similar to the detonation of explosive materials, or to a slender body in hypersonic flight. Note that introduction of these concepts has recently provided a (satisfactory) description of a long (10 m) spark studied by Les Renardières Group (see [7] and [9]) and in addition, breakdown (U-curve, critical voltage vs distance, etc.) and related characteristics have recently been derived [8].

From Swigart we have Eq. (1)

$$\frac{R}{d} = .7951 (C_D)^{1/3} \left(\frac{z}{d} \right)^{1/3} \left[1 + \frac{1.5732}{M^2 C_D^{1/2}} \frac{z}{d} - \frac{5.8037}{M^4 C_D} \left(\frac{z}{d} \right)^2 \right] \quad (1)$$

which describes the radius of the shock front, R , about a blunt-nosed slender body hemispherical tip of diameter, d , as a function of axial distance from the nose, (z/d) , flight Mach number, M , and nose drag coefficient, C_D . (See Fig. 1.)

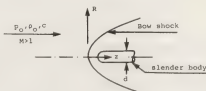


Fig. 1. Flow about a blunt-nosed in steady flight.

We introduce $R_o^2 = E/p_o$, E being the energy per unit length of the slender body, and p_o and ρ_o background pressure and density respectively and by definition the sound velocity $C^2 = \gamma p_o/\rho_o$ where γ is the ratio of specific heat.

Thanks to the hypersonic analogy we can substitute z/U_o (where U_o is the velocity of undisturbed gas with respect to the observer fixed in the body) for the time, t , thereby relating non-steady flow behind the blast wave to steady hypersonic flow. By definition the drag coefficient is

$$C_D = \frac{E}{(\pi d^2/8)\rho U^2}$$

Thus Eq. (1) becomes

$$R = \frac{1.00440}{\gamma^{\frac{1}{2}}} E_1^{\frac{1}{2}} t^{\frac{1}{2}} \left[1 + \frac{.98585}{E_1^{\frac{3}{2}}} C^2 t^{\frac{1}{2}} - \frac{2.2791}{E_1} C^2 t^{\frac{1}{2}} \gamma \right] \quad (2)$$

where $E_1 = \frac{E\gamma}{\rho_o} = C^2 R_o^2$

The velocity of the radial expansion is $\frac{\partial R}{\partial t}$, and we calculate the time when the hypersonic motion decays into a sound wave, i.e. $\frac{\partial R}{\partial t} = C$. Taking the $\gamma = 1.4$, we find from Eq. (2) that the time of the transition, t_o , is

$$t_o = \frac{.21755 E_1^{\frac{1}{2}}}{C^2}$$

Experimental verification of this theory will be attempted in our companion paper.

References

- [1] Kekez M.M. and Savic P., 1974, J. Phys. D: Appl. Phys. 7, 620
- [2] _____, 1975, 12th Int. Conf. Phon. Ion Gases, Eindhoven, 161
- [3] _____, 1976a, Proc IEE 4th Int. Conf. Gas Disch. Swansea, 129
- [4] _____, 1976b, Can. J. Phys. 54, 2216
- [5] Savic P. and Kekez M.M., 1977, Can. J. Phys. 55, 325
- [6] Kekez M.M., Makomaski A.H., and Savic P., 1977, Proc. 11th Int. Symp. Shock Tubes-Waves Seattle, 602
- [7] Kekez M.M. and Savic P., 1978, Proc. IEE 5th Int. Conf. Gas Disch., Liverpool, 336
- [8] _____, 1979a, 1979 IEEE Int. Conf. on Plasma Sci. (to be published)
- [9] _____, 1979b, J. Phys. D: Appl. Phys. (to be published)
- [10] Swigart R.G., 1960, J. Fluid Mech., 2, 613
- [11] Les Renardières Group (1975), Electra, 53, 31

SHOCK WAVES IN SPARK CHANNELS, PART 2

M.M. Kekez, G.D. Lougheed and P. Savic.

*National Research Council, Ottawa, Canada, KIA 0R6.*Experimental Evidence

In this part we attempt experimental verification of the shock theory developed in Part 1 [ref. 1]. The object of these experiments is to record the progress of the shock and sound waves associated with the spark channel for (a) the channel in process of formation and (b) the completed channel, when the shock theory is expected to apply [ref. 2].

A conventional Schlieren system was used comprising of a CW argon laser (Model 556A of Control Corp.), a 10 times expander, a Schlieren lens, knife edge (parallel to the direction of the spark channel) and a TRW (Quantrad) image converter camera. The discharge chamber was placed behind the expander. The radial expansion of the shock wave was observed through a narrow slit placed in front of the camera and perpendicular to the spark channel axis. A master trigger spark gap activated the camera via an optical pickup, while its electrical component initiated the voltage pulse to be applied to the discharge chamber. In this manner, the jitter was kept below 20 ns, and permitted good synchronisation between the streak record of the developing channel, Fig. 1a, and the voltage current wave forms, Fig. 1b, as well as between the latter and the streak record of the radially expanding shock wave, Fig. 1c. In the first set of experiments, the viewing slit was positioned about 1 mm above the cathode, whereas in the second set it was placed in the centre between two pointed electrodes made of 1 mm diameter tungsten.

For the first set of experiments using the electrode geometry and conditions of Fig. 6 in ref. 4, the energy per unit length of the developing spark channel was determined in two ways. First, it was calculated by dividing the average power, P , derived from the voltage and current wave form, Fig. 1b, by the average velocity of the channel (1.2 cm/us), and secondly it was obtained by dividing the energy, E , determined by integrations of the VI product by the length that the spark channel has traversed. These results are depicted in Fig. 2 by squares (the crosses denote error bars). While the instantaneous position of the

shock can be determined with great accuracy, velocity measurements are subject to considerable error. In Fig. 2, theoretical results are depicted by straight lines; a full line for 20°C and the broken line for 100°C neutral gas temperature. Sound velocities measured from the streak records indicate that the temperature rarely exceeds 100°C, justifying the assumption of low neutral gas temperature in the glow, as utilised in our theoretical work. This is further strengthened by the conclusions of ref. 3. In Fig. 1c, only the shock front is visible; the boundary of the channel, termed "leader" in ref. 3, corresponds to our contact surface.

In the second set of experiments, we studied the radial expansions of the channel for a completed discharge in a gap of 3.2 mm length. The voltage was varied between 11-13 kV, and the energy was stored in various condensers (8.5 - 2400 pF). (The lowest point in Fig. 2 corresponds to a capacity of 8.5 pF from a 10 cm long cable of RG 8/U type.* Such sparks are useful for testing photo-multipliers.) The discharge circuit consists of a condenser, a trigger gap and the gap under observation. An attempt was made to minimize the length of leads and the circuit inductance. In the calculation of E_1 (energy per unit length and density) we assume that this energy is a constant in the two gaps and that no energy is consumed in the leads.

In conclusion, we would point out that the transition from a shock to a sonic wave in the vicinity of the spark channel proceeds as predicted by theory, thus the concept of the hypersonic model for spark channel development is further strengthened.

References:

- [1] As in Part 1.
- [2] Freeman, R.A. and Craggs, J.D., 1969, J. Phys. D: Appl. Phys. 2 421
- [3] Kurimoto, A., Farish, O. and Tedford, D.J., 1978, Proc. IEE, 125, 767.
- [4] Kekez, M.M. and Savic, P., 1978, Proc. IEE 5th Int. Conf. Gas Discharges, Liverpool, 336.

* In this case, the gap was reduced to 1.2 mm.

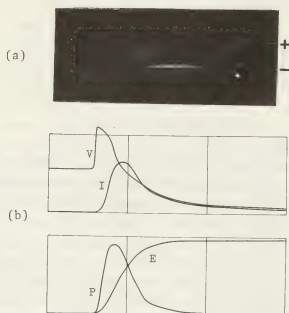


Fig. 1 (a) Streak photograph of arrested discharge in air at 250 Torr gas pressure and 2.15 cm gap length. The developing spark channel starting at the cathode was depicted as the bright area on the photograph.

(b) V-voltage waveform (20KV/div)
 I-current waveform (100A/div)
 P-calculated power (10^6 W/div)
 E-energy (2×10^6 ergs/div)

One horizontal division equals .5 μ s.
 The waveforms are synchronized with the streak photograph.

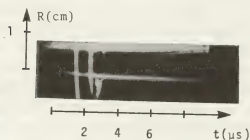


Fig. 1(c) Radial expansion of shock wave due to developing spark channel.

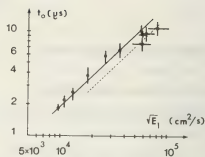


Fig. 2 Time of transition from hypersonic to sonic motion, t_0 vs (the energy per unit length and density supplied to the blast wave, E_1) $^{1/2}$. Theoretical results are depicted by straight lines.

ELECTRON ENERGY RELAXATION EFFECT ON THE DYNAMIC CHARACTERISTIC OF ARGON PLASMA ARC

H. Shindo, S. Imizu and T. Inaba^{*}.^{*}Faculty of Engineering, Hiroshima University, Hiroshima 730, Japan.

Central Research Institut of Electric Power Industry, Tokyo 180, Japan.

1. Introduction: There have been, so far, many investigations on arc dynamics, since it is important for circuit breakers. However, little work has been reported dealing with the energy relaxation effect of electrons on dynamic characteristics. The relaxation time of the electron energy is generally a strong function of the electron density and temperature. Therefore, in low electron densities and temperatures the energy relaxation time can probably dominate the arc dynamic characteristic.

The objective of the present study is to investigate experimentally the influence of the energy relaxation effect on dynamic characteristics. Argon arcs at 0.1 atm pressure, which were in the region of the electron density $5 \cdot 10^{14} \sim 10^{16} (\text{cm}^{-3})$ and the electron temperature $0.72 \sim 1.08 (\text{eV})$, were investigated.

2. Experiments: The arc source employed in this experiment is a wall-stabilized type arc which has an arc radius of 5 mm and a length of 7 cm. The inter-electrode voltage was traced when a small current was injected into the arc column burned at various constant DC currents. A small current was injected through a thyristor switch from a current source parallel with the main current source. The time history of the plasma parameter was obtained by spectroscopic measurements. In the measurements, argon gas seeded with hydrogen (0.1 % volume ratio) was partly used to determine the electron density from the H_β line width.

3. Results and Discussions: Typical plasma parameters in the central core of the arc are listed in Table I for our experimental conditions. The arc current I_s is the value before the current injection. The electron density N_e and temperature T_e were experimentally determined; namely N_e from the H_β line width and T_e from the absolute continuum radiation strength[1]. The gas temperature T_g was obtained through a kinetic formula using the measured density and temperature of electrons.

The relaxation time τ_{KE} for the electron kinetic energy is obtained by the following formula,

Table I. Typical plasma parameters in the central core of the arc at 0.1 atm pressure.

I_s (A)	N_e (cm^{-3})	T_e (eV)	T_g (eV)	τ_{KE} (μs)	τ_{IE} (ms)	N_d (cm^{-3})
30	5.0×10^{14}	0.72	0.39	23.4	5.1	1.5×10^{17}
80	2.5×10^{15}	0.82	0.64	9.9	1.2	9.5×10^{16}
150	1.3×10^{16}	1.08	1.08	2.7	0.05	2.9×10^{16}

$$\tau_{KE} = \frac{m_a}{m_e} \frac{1}{(\sigma_{ea}^0 N_e + \sigma_{ei}^0 N_i)}, \quad (1)$$

where the value reported by Devoto[2] was used for the integral Ω . The relaxation time τ_{IE} for the ionization is also calculated by the following equation,

$$\tau_{IE} = \frac{1}{\Omega_{ea}^0 N_a}, \quad (2)$$

where the value found in ref.[3] was used for the ionization cross section. It is found in Table I that τ_{IE} is more than one order higher than τ_{KE} in the same current, and that both relaxation times are strongly dependent on the electron density and temperature.

Figure 1 shows the time history of the ArI 6965 line intensity, where the value of the injected current is 20 % of the I_s value. The line intensity at first decreases from the pre-steady state value just after the current injection, resulting from the increase in the electron temperature. The time scale for changing the electron temperature is consistent with the value of τ_{KE} in Table I. Furthermore, the line intensity commences to increase after $50 \sim 100 (\mu\text{s})$ from the current injection. This time corresponded to the increase in the electron density, which was confirmed by the time variation of the H_β line profile. In Fig.1, the ionization relaxation time becomes longer at lower arc currents. In the case of $I_s = 30 (\text{A})$, the line intensity does not seem to saturate in the obser-

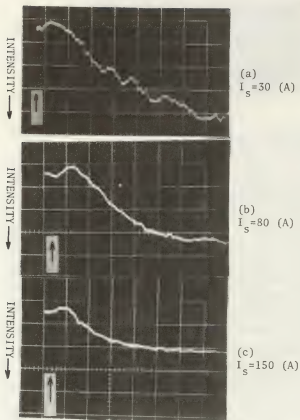


Fig.1, Time history of the ArI 6965 line intensity. Arrows indicate the time of the current injection. The time scale is 100 (μ s/div).

vation time, but it required more than 1 (ms). The figure makes clear that the ionization relaxation time becomes longer at lower electron densities and temperatures. This tendency is consistent with that in Table I. However, the absolute values differ from the values of τ_{IE} in Table I by a factor of 4 or more. The discrepancy may be due to the uncertainty in the measured values of electron temperatures, since τ_{IE} is a strong function of the temperature T_e . For example, the difference of 10 % in T_e gives an error in τ_{IE} by a factor of 3.

As mentioned above, the time for changing the electron temperature is short, but the electron density changes more gradually. These facts verify that an assumption of LTE is not valid for analyses of dynamic characteristics in low densities and temperatures. The validity of the LTE assumption was verified for the steady state at arc currents more than 150(A) [1]. The verification was made not only by spectroscopic measurements, but also by comparisons between the measured and calculated "ER-I/R" characteristics. The measured "ER-I/R" characteristics were in agreement with those calculated using the transport properties

reported by Devoto[4]. It can be concluded, from the above discussion, that LTE criteria for dynamic characteristics are more severe than those for static characteristics.

Figure 2 shows the time dependences of the inter-electrode voltages in the cases of $I_s = 30$ and 150

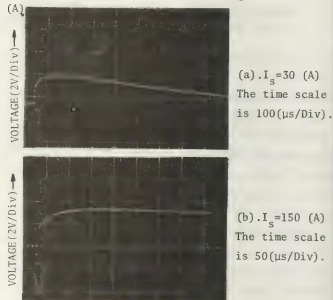


Fig.2, Voltage response. Arrows indicate the time of the current injection.

The voltage response is certainly effected by a long time constant for the ionization. In the case of $I_s = 150$ (A), the voltage transfers to the next steady state in 400(μ s). The transferring time is almost the same as that of the ArI line intensity in Fig.1(c). The voltage in the case of $I_s = 30$ (A) still does not reach the next steady state in the observing time. This behavior also corresponds to the response of the ArI line intensity in Fig.1(a). The later stage of the voltage response is found to be characterized by the relaxation time for the ionization.

4. Conclusion: Arc dynamic characteristics were investigated from the point of the electron energy relaxation time. The time for changing the electron temperature is short, but the electron density changes more slowly in low electron temperatures.

As a result, the voltage response is effected by the long time constant for the ionization.

5. References

- [1]. H. Shindo, T. Inaba, S. Imazu: Trans. IEEJ 99-A, 1 (1979), in Japanese.
- [2]. R. S. Devoto: Phys. Fluids 16, 616 (1973).
- [3]. A. von Engel: Ionized Gases, P57, Clarendon Press Oxford (1965).
- [4]. R. S. Devoto: ARL Report No. 71-0075, Appendix-C (1971).

KINETICS OF THE ELECTRONS IN THE STATIONARY BEAM DISCHARGE PLASMA IN DIATOMIC GASES

R. Winkler, J. Wilhelm, A.A. Ivanov^{*} and V.V. Sarykh[†].^{*}Central Institute of Electron Physics Part V, Academy of Science 22 Greifswald G.D.R.
[†]I.V. Kurchatov Institute of Atomic Energy, Moscow U.S.S.R.

Introduction: In recent years increasing attention has been paid to the investigations of the stationary turbulent beam discharge plasma, nonresonant heated by Langmuir waves, especially under the aspect of application in plasma chemistry [1]. Thus it is important to investigate the kinetics of the electron component of such type of discharge plasma because the energy input by the turbulent electric field occurs via the electron ensemble into the degrees of freedom of the heavy components of the plasma by binary collisions and Coulomb interaction. Within certain limits the dominance of special energy transfer channels can be optimized by variation of the discharge parameters.

Theoretical background: We started from the Boltzmann equation including turbulent heating, elastic and several direct inelastic collisions between electrons and molecules as well as the interaction of electrons with electrons and with the ions in the form of Fokker-Planck terms. The equation obtained for the isotropic part of the velocity distribution function was numerically solved for total turbulence energies per one electron \tilde{U} and degrees of ionization $(n_e/N)_0$ in a large range of values in which such beam discharge plasmas exist. The method necessary to solve the complex integro-differential equation was developed in [2, 3]. This treatment has proved suitable for calculating the quantitative behaviour of the electron component and the energy transfer situation in beam plasmas with molecular gases. In this paper we report about new results in nitrogen. For calculation we used the cross sections for impulse transfer, for vibrational and electronic excitation and

direct dissociation and ionization from [4]. This investigation in nitrogen and the comparison with the former results in hydrogen [3] allow conclusions about the specific influence of the molecular properties on the macroscopic behaviour.

Results and discussion: Because of the chosen broad intervals for \tilde{U} and n_e/N great changes in the dominant processes determining the distribution function $f_b(U)$ are to be expected. This is reflected in the behaviour of $f_b(U)$ - U momentary electron energy in V - which are shown for nitrogen and hydrogen in Fig. 1 for $n_e/N = 10^{-2}$ and $\tilde{U} = 0.16V, 0.016V, 0.0016V$ and in Fig. 2 for $\tilde{U} = 0.016V$ and $n_e/N = 10^{-1}, 10^{-2}, 10^{-3}$. From this we obtained the mean energy \bar{U}_b shown in Fig. 3 as function of \tilde{U} for $n_e/N = 10^{-1}, 10^{-2}$ and 10^{-3} . It can be easily seen that the qualitative dependence on the parameters \tilde{U} and n_e/N is the same in nitrogen and hydrogen, which suggests that the qualitative behaviour of the electron mean energy with \tilde{U} and n_e/N shows no sensitive dependence on the nature of molecular gases in the beam discharge plasma. More detailed, \bar{U}_{N_2} is smaller than \bar{U}_{H_2} in a broad medium-sized range of \tilde{U} for the same values of n_e/N due to the dominant role of the binary collisions of electrons with the molecules, especially in nitrogen with its more complicated structure concerning the vibrational levels. At very small \tilde{U} we find $\bar{U}_{N_2} > \bar{U}_{H_2}$, which is primarily due to the big energy losses in the electron-ion interaction for H_2 .

The power inputs $\hat{P}_b = \tilde{U} \cdot v_{eff}/p_0$ per one electron and per one Torr (with v_{eff}/p_0 as the normalized effective frequency for turbulent heating [2, 3]) are shown in

Fig.4. The big difference of the \hat{P} -values for very small \tilde{U} is nearly proportional to n_e/N due to the strong electron-ion interaction in H_2 in comparison with N_2 . With increased \tilde{U} both values of \hat{P} are nearly the same in a broad range of \tilde{U} and n_e/N . The small differences are connected with the different structures of the molecular gases and thus with the behaviour of the corresponding distribution functions (Figs. 1,2).

In Figs. 5,6 the energy losses \bar{U}^{el} , \bar{U}^{el} , \bar{U}^{VE} , \bar{U}^{EE} , \bar{U}^{DI} , \bar{U}^I for elastic and electron-ion interaction, vibrational and electronic excitation as well as dissociation and ionization related to the total energy loss \bar{U}^T are represented for $n_e/N=10^{-3}, 10^{-1}$. Comparing the losses in H_2 and N_2 we observe great differences with regard to the essential energy channels by which the greatest amount of energy, introduced from the turbulent field, is dissipated to the molecules. In H_2 the energy loss by electron-ion interaction prevails at low \tilde{U} , then in some range of \tilde{U} the loss by vibrational excitation and finally at high \tilde{U} the loss due to dissociation plays the dominant role. On the other hand in N_2 the vibrational energy loss is dominant nearly in the whole range of \tilde{U} and only at high \tilde{U} the excitation of electronic states prevails. Finally, with increasing n_e/N a remarkable shift of the different loss processes in H_2 as to their dominant role occurs but in N_2 there is only a change of the range of \tilde{U} in which energy losses due to vibrational and electronic excitation prevail.

References:

- /1/ A.A. Уланов, физика плазмы 1(1975)147.
- /2/ R.Winkler, J.Wilhelm, V.V.Starykh, XIII. ICPIG-1977, Contr.Pap.Part II, p. 739.
- /3/ P. Бункеев, У. Бектенов, Б.Б. Смайр, физика плазмы (1979) in print.
- /4/ S.Pfau, R.Winkler, Beitr.Plasmaphys. 18 (1978) 113; 13 (1973) 273.

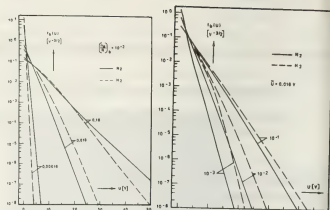


Fig. 1

Fig. 2

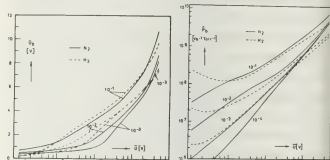


Fig. 3

Fig. 4

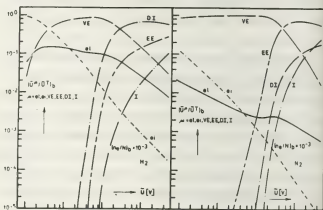


Fig. 5

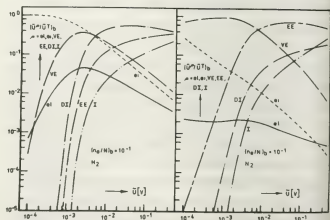


Fig. 6

NUMERICAL ANALYSIS OF ARCS IN SUPERSONIC FLOW

C.K. Bhansali and D.M. Benenson.

Laboratory for Power and Environmental Studies, Department of Electrical Engineering, State University of New York at Buffalo Amherst, New York, U.S.A.

Introduction. The complexities involved in the analysis of an arc immersed in a flowing medium have naturally led to a large number of simplified formulations including (1) the integral method /1/, (2) the one-dimensional approach /2,3/, and (3) two-zone model /4/. The present paper presents the numerical solutions of the coupled, non-linear conservation equations applied to the case of an argon arc within a converging-diverging nozzle and subjected to supersonic flow (in the downstream portion of the nozzle). An ultimate objective is the determination of the behavior of a dynamic plasma as its current ramped to current zero (and voltage ramped after current zero) - i.e., the circuit interruption problem. The present work describes the steady-state solutions obtained and needed for solution of the dynamic arc. The analysis includes real gas effects, turbulence, and (optically thin) radiation.

Formulation. The conservation equations - mass, momentum, and energy - are written, respectively

$$\frac{\partial \rho}{\partial t} + \nabla \cdot (\rho \vec{V}) = 0 \quad (1)$$

$$\frac{\partial (\rho \vec{V})}{\partial t} + \nabla \cdot (\rho \vec{V} \vec{V} - \vec{\tau}) = 0 \quad (2)$$

$$\frac{\partial (\rho e_s)}{\partial t} + \nabla \cdot (\rho e_s \vec{V} + \vec{q} - \vec{V} \cdot \vec{\tau}) = \vec{J} \cdot \vec{E} - Q_r \quad (3)$$

together with the equation of state

$$p = p(\rho, e) \quad (4)$$

and Ohm's law

$$\vec{J} = \sigma \vec{E} \quad (5)$$

where e = internal energy, $e_s = e + \frac{1}{2} V^2$, E = electric field, J = current density, p = pressure, q_r = heat flux, Q_r = radiation power density, t = time, V = velocity, ρ = density, σ = electrical conductivity, τ = stress tensor).

Turbulent effects are included through the Prandtl mixing length model with turbulent shear stress given by

$$\tau'_{zr} = \mu_t \frac{\partial u}{\partial r} \quad (6)$$

with $\mu_t = \rho \epsilon = \rho c(z - z_t) |U_{\max} - U_{\text{cold}}|$

and $\epsilon = 1.4 \times 10^{-4}$

and turbulent heat flux given by

$$q' = -k_t \frac{\partial T}{\partial r} \quad (7)$$

with $k_t = 2\rho C_p c(z - z_t) |U_{\text{cold}}|$

where C_p = specific heat at constant pressure, r = axial coordinate, u = axial velocity, U_{cold} = axial velocity outside arc, U_{\max} = axial velocity at centerline, z = axial coordinate, z_t = axial location of throat, ϵ = eddy diffusivity, μ_t = turbulent viscosity.

The arc is placed within the converging-diverging nozzle configuration shown in Fig. 1; axial location $z = 0$ represents the origin of the plasma.

Experiments are being conducted using a nozzle design similar to that shown in the figure /6/.

Solutions of the governing conservation equations are obtained using a Lax-Wendroff type two step, explicit, second order accurate finite difference method /7/, together with the concept of time splitting. A time dependent approach is employed to solve the steady-state problem (enabling essentially the same numerical procedures to be used with the dynamic, ramped plasma). Starting with assumed initial conditions, the time dependent equations are solved to obtain the steady-state solution as the asymptotic time limit of the non-steady equations. A coordinate transformation is used to transform the converging-diverging nozzle into a circular channel of constant area

$$X = z, Y = r/R(z), t = t' \quad (8)$$

(where $R(z)$ = nozzle radius).

Further, the equations in the transformed coordinates are written in conservation form

$$\frac{\partial U}{\partial t} + \frac{\partial F}{\partial X} + \frac{\partial G}{\partial Y} + S = 0 \quad (9)$$

where U , F , G , and S are four-dimensional vectors and S is the source term vector that contains all the terms that are not expressible as derivatives of the independent variables in eqn. (9).

The basic physical inputs are (1) steady-state arc current, $I = 700$ A and (2) stagnation pressure = 10 atm, which results in an exit pressure of ~ 1 atm. The mass flow is not known a priori and is obtained as part of the solution. In the present case, the argon mass flow, \dot{m} , is ~ 100 g/s.

Results. Axial distributions of centerline temperature, T_c , and centerline axial velocity u_c , are shown in Fig. 2. The initial, relatively large temperature and the subsequent reduction with axial location is associated, at least to the throat, with the small initial diameter and the resulting expansion of the column. As seen in the figure, the effect of turbulence is to reduce both the velocity and temperature as compared to the laminar case. The arc diameter, D is defined through the radial location of, say, the 5000 K isotherm. On this basis and representing the diameter in the form $D \propto z^m$, the value of m is found to be ~ 0.5 . For a nitrogen arc in a converging-diverging nozzle and using (1) a two-zone model /5/, $m \sim 0.6$ and (2) a one-dimensional model /2/, $m \sim 0.25$. Radial distributions of temperature and velocity are given in Figs. 3 and 4, respectively, at two axial locations - $z = 2.15$ cm (slightly downstream of the throat and $z = 9.6$ cm (near the exit). The expansion of the column downstream of the throat is clearly evident as is the broad, warm, but not electrically conducting, region near the exit.

References:

- /1/ M.D. Cowley, "Integral Methods of Analyzing Electric Arcs: I. Formulation," *Journal of Physics D: Applied Physics*, Vol. 17, 1974, pp. 2232-2245.
- /2/ J.J. Lowke and H.C. Ludwig, "A Simple Model for High Current Arcs Stabilized by Forced Convection," *Journal of Applied Physics*, Vol. 46, 1975, pp. 3352-3360.
- /3/ F.R. El-Akkari and D.T. Tuma, "Simulation of Transient and Zero Current Behavior of Arcs Stabilized by Forced Convection," *IEEE Transactions on Power Apparatus and Systems*, Vol. PAS-96, 1977, pp. 1784-1788.
- /4/ W. Hermann and K. Ragaller, "Theoretical Description of the Current Interrupters in HV Gas Blast Breakers," *IEEE Transactions on Power Apparatus and Systems*, Vol. PAS-96, 1977, pp. 1546-1555.
- /5/ W. Hermann and K. Ragaller, "Theoretical U. Kogelschatz, L. Niemeyer, K. Ragaller, and E. Schade, "Experimental and Theoretical Study of a Stationary High-Current Arc in a Supersonic Nozzle Flow," *J. Phys. D: Appl. Phys.*, Vol. 7, 1974, pp. 1703-1722.
- /6/ T. Bernecki, Y.C. Lau, and D.M. Benenson, "Experiments on Arcs in High Speed Flow," State University of New York at Buffalo, Buffalo, New York, in progress.
- /7/ R.W. McCormack and B.S. Baldwin, "A Numerical Method for Solving the Navier-Stokes Equations with Application to Shock-Boundary Layer Interactions," *AIAA 13th Aerospace Sciences Meeting* Pasadena, California, Paper No. 75-1, 1975.

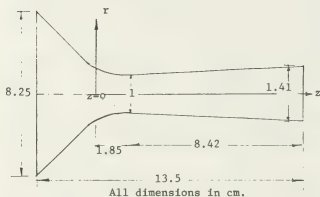


Fig. 1. Nozzle configuration.

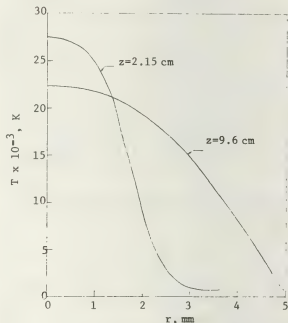
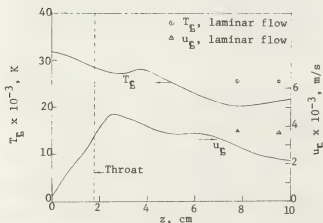
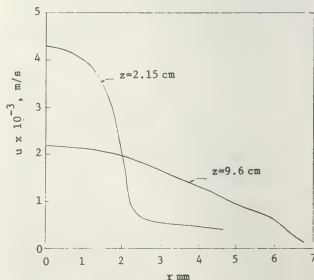
Fig. 3. Radial distributions of temperature at $z = 2.15$ and 9.6 cm.

Fig. 2. Axial distributions of centerline temperature and centerline axial velocity.

Fig. 4. Radial distributions of axial velocity at $z = 2.15$ and 9.6 cm.

NUMERICAL SIMULATION OF NITROGEN DISCHARGE : FORMATION OF ELECTRON SHOCK WAVE

I. Abbas, P. Bayle.

Centre de Physique Atomique, Laboratoire associé au C.N.R.S. n°277, Université Paul Sabatier, 31077 Toulouse Cedex, France

The formation and propagation of ionizing waves in a gas discharge under pulsed electric field is essentially governed by the space charge field that super imposes the applied field E_0 .

We aim to investigate the effect of certain parameters, namely the reduced field E_0/P and plasma initial conditions, on the structure of the resulting ionizing wave, and particularly on the formation of intensive local gradient for both the electron densities and field. This turns to be evident at the discharge tip and is a characteristic of the shock effect. It is found that the shock formation is not only related to the conditions of gas pressure and the applied electric field but it depends also upon the spatio-temporal distribution of the initiating primary electrons.

The one dimensional continuity equations describing the ionization growth are

$$\frac{\partial n_e}{\partial t} + \frac{\partial(n_e v_e)}{\partial x} = \alpha v_e n_e \quad (1)$$

$$\frac{\partial n_+}{\partial t} + \frac{\partial(n_+ v_+)}{\partial x} = \alpha v_e n_e \quad (2)$$

The calculation of the resulting space charge field in a filamentary discharge is calculated by the method of discs (1). The boundary conditions on the electrodes are the following :

$$\frac{\partial E}{\partial x} = \frac{P}{\epsilon_0} = 0 \quad \text{at the cathode } x=0$$

$$\text{at the anode } x=d$$

On the other hand, $n_+(d, t) = 0$ on the anode surface is implied by the condition $I_+(d, t) = 0$ for a continuous analysis of the discharge, but for a numerical analysis time and space discretisation introduced a better condition $n_+(d, t + \Delta t) = n_+(d, t) + \mu v_e \Delta t (1 - \nu \frac{\Delta t}{\Delta x})$ which improves both the stability and precision of the numeric solution. The boundary conditions for the electronic current on the cathode surface is

$$I_e(0, t) = I_0(t) + \int_0^d \gamma(x) \delta(x) e^{-\nu x} I_e(x, t) dx$$

$\gamma(x)$ is a function that takes into consideration the geometrical factor and the secondary effects.

Davies (2) has shown that the numerical solution of this system was improved by making use of the continuity equations for the net charge. The system was solved by the method of double characteristics for both average ($< 100\%$) and high overvoltages ($> 100\%$). To investigate the discharge at high overvoltage, the system was solved for the only part of the gas including the discharge prior to shock formation. This procedure permitted the use of smaller space increments leading to increased precision and stability without any increased computing time. The boundary conditions for the cathode were left unchanged while those for the virtual anode, assumed at distance $x = d/4$ or $d/8$ were $n_e(x, t) = n_+(x, t) = 0$. The field outside the discharge region is assumed equal to the applied field E_0 , and hence we are led to the condition

$$\frac{1}{x} \int_0^x E(y) dy = E_0$$

We investigate the influence of the initial conditions on the evolution of the discharge and particularly on the formation of the electron shock wave. The time function of the primary electrons liberated by the ultraviolet light flash from the cathode $I_0(t)$ was simulated as $I_0(t) = \frac{A}{T} \exp(-t^2/T^2)$ and the computation was carried out for different values of the parameter T , representing width of the UV flash.

We have studied the discharge in nitrogen under homogeneous applied field created by plane parallel electrodes distance 3 cm apart. The electron cloud is evolved in three successive phases (fig. 1). In the first phase the space charge effect is negligible and the electron cloud conserves its

gaussian profile. In the second phase, the space charge effects are more important and the field between the electrodes is non uniform. One observes an enlargement of the electron cloud towards the electrodes. The cloud loses its gaussian profile. Taking into consideration the role of the electric field, both velocity and amplification are not the same for all points of the profile with the result of deforming progressively the profile. The electronic density gradient increases to end towards the shock conditions. The following is a rather rough explanation for this evolution. If one considers a profile of electron density and a repartition of the field as defined on fig. 2, from equation (1) and (2), the electron density area n_1 is moving towards both cathode and anode with following speeds

$$V_1^A = v_0(\alpha_0/k + 1) \quad V_1^C = v_0(\alpha_0/k - 1)$$

V_0 is the drift velocity, first Townsend coefficient in a field near to applied field E_0 . The peak of electron density n_2 is moving with following velocities

$$V_2^A = \frac{\alpha_1 V_1 - \alpha_0 v_0}{k} + V_1 \quad V_2^C = \frac{\alpha_1 V_1 - \alpha_0 v_0}{k} - V_1$$

The result is that $V_2^A > V_1^A$ and $V_2^C > V_1^C$ which yields an important modification of the wave profile ending by a strong shock wave (see fig. 3). It is found that the shock effect is much more strong on the electronic density level than that of the electric field where the variation is less severe. Thus one can verify only partially the Albright hypothesis (3) which is realistic as much as concerning the electron density but less realistic as concerning the resultant electric field. The appearance of a shock wave is highly conditioned by the profile of the electron cloud and that is why it is very sensitive for the function $I_0(t)$. This function implies directly the same number of the cathode emitted electrons for different electron avalanche profiles. Fig. 1 shows the propagation of the maximum of electron density as function of the UV flash width measured by T until the formation of the shock. It is clear that the shock development is more fast for narrower flashes and for higher E_0/P values. We observed the same shock conditions for high overvoltages only few nanoseconds after the application of the high voltage pulse.

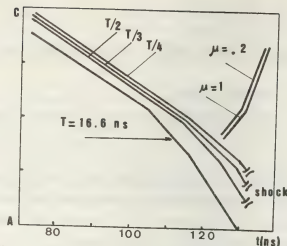


Fig. 1. Propagation of the maximum electron density with respect to width of the UV flash.

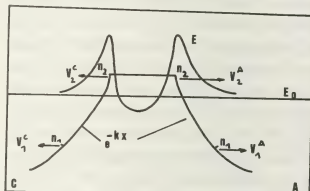


Fig. 2. Schematic diagram of electron cloud and field profile.

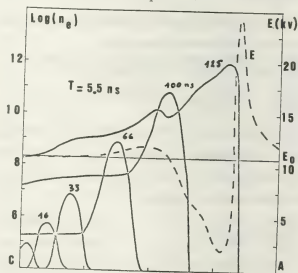


Fig. 3. Characterisation of electron shock waves.
 $E_0/P = 53 \text{ V/cm.torr}$; $P = 200 \text{ torr}$.

- (1) Davies (A. J.), Evans (C. J.) : Proc. IEE, vol. 114, n° 10, 1547-1550, (1967).
- (2) Davies (A. J.), Evans (C. J.), Woodison (P. M.) Proc. IEE, vol. 122, n° 7, 765-768, (1975).
- (3) Albright (N. W.), Tidman (D. A.) : Phys. Fluids, vol. 15, n° 1, 86-90, (1972).

**ENHANCED ARCING AS A FUNCTION OF ORGANIC EXPOSURE AND ARC CURRENT
Pd AND Pd/Ag ELECTRODES**

E.W. Gray and J.R. Pharney.

Bell Telephone Laboratories Columbus, Ohio 43213.

ABSTRACT

We report the existence of a region within which enhanced arcing (activation) exists for palladium and palladium/ silver contacts, as a function of arc current and of exposure to organic vapors. The current range where activation exists is from ~ 0.1 to ~ 1.2 A, where the range of exposures (partial pressure times time) used for diethyl phthalate was from $\sim 10^{-3}$ to ~ 10 Pa s. At very low organic exposure levels (depending upon the organic vapor and the electrode metal), arc duration statistics show an exponential behavior. Under moderate to high organic exposure levels, arc duration statistics show a log-normal distribution similar to that obtained under clean conditions when the arc current exceeds the minimum arc sustaining current. At sufficiently high currents arc duration statistics become independent of organic exposure. The envelope of the activated curves is predicted by the activation theory of Gray, Uhrig and Hohnstreiter.

THE CORRELATION OF LOCAL VOLTAGE AND CROSS-SECTIONAL AREAS FOR VERY HIGH CURRENT GAS BLAST ARCS IN AIR AND SF₆

G.R. Jones, M.R. Smith, M. Irie, H. L. Walmsley* and D.C. Strachan*.

Department of Electrical Engineering & Electronics, University of Liverpool, Liverpool L69 3BX, England.

**Shell Research Ltd., Thornton Research Centre, P.O. Box 1, Chester, England.*

1. INTRODUCTION.

Recent developments of the boundary layer integral analysis (e.g. (1)) for gas blast arc modelling have highlighted the importance of correlating the local arc voltages and the cross-sectional areas of such arc columns. This paper presents experimental results which are examined to determine whether such a simple correlation exists for very high current gas blast arcs as has already been demonstrated for current levels of a few kiloamperes (2).

2. EXPERIMENTAL CONDITIONS AND MEASUREMENTS.

The results presented are for arc discharges sustained by alternating current waveforms of frequency 80Hz and peak currents 40 - 90kA. The discharges were confined to burn in axially accelerating flows of air or SF₆ passing through a 50mm diameter, 30mm wide orifice and sustained by upstream and downstream pressures of 7.8 bar and 1 bar respectively. The upstream electrode (sintered copper-tungsten mixture) was cathodic during the arcing half cycle.

Voltages at different axial positions along the arc were measured using a 2mm diameter tungsten rod penetrating radially into the arc column, and biased electrically to draw electron current. Only a small number of local voltage measurements were taken under the present operating conditions on account of the limited probe life, combined with the limited reproducibility of the arcing conditions which necessitated a large number of

tests being performed for each representative condition.

High speed photographs of the arc were taken with a Beckman-Whitley Dynafax 350 framing camera at framing rates of $1 - 2 \times 10^4$ pps, exposure times of 1.3 - 2.6 μ s and an aperture of f/22. Adequate exposure was ensured using appropriate neutral density filters.

The arc current, overall arc voltage and upstream pressure were monitored respectively with a 0.2m Ω coaxial shunt, a Tektronix type F6015 voltage probe and a Kistler 601A pressure transducer in conjunction with a 5001 charge amplifier.

3. EXPERIMENTAL RESULTS.

Typical averaged results (10% scatter) for the axial evolution of the cross-sectional area of the luminous arc core for different instantaneous current values are shown on Fig.1 for both air and SF₆.

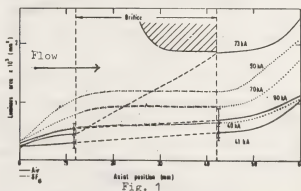


Fig. 1

Since steep temperature gradients exist at the core boundary of such arcs (e.g. (3)) the measured luminous boundaries should also approximately coincide with the electrical boundary (2),

provided there are no substantial departures from local thermal equilibrium.

The 70kA curve (Fig.1) which corresponds to an instant following the 90kA peak current curve also given on the same figure, shows an anomalous luminous area variation downstream of the nozzle exit which is due to severe evaporation of the nozzle wall caused by intense radiative heating.

The measured values of the electrical core area $G(z)$ (Fig.1) may be used in conjunction with a simple channel arc model (electrical conductivity, σ , radially constant) to give local voltage values $V(z)$ according to

$$V(z) = (i/\sigma) \int_0^z [\sigma(z)]^{-1} dz$$

where i is the instantaneous current. For a channel temperature of 2×10^4 K (3), $\sigma = 100$ (air (4)) and 105 Sm^{-1} (SF_6 (5)) being relatively insensitive to pressure ((4),(5)) and concentration of evaporated metallic impurities ((3),(6)). The resulting voltage values are generally in good agreement with the directly measured values for all currents in SF_6 (Fig.2) and for 41kA in air (Fig.3).

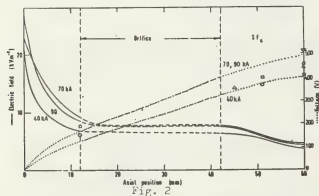


Fig. 2

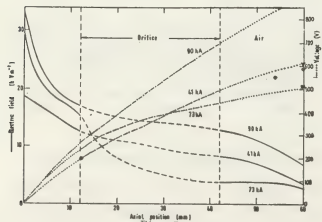


Fig. 3

Good agreement with the overall arc voltage (516V) for 70kA in air is obtained only if it is assumed that the full luminous extent, including the plasma produced by the nozzle ablation downstream of the nozzle exit, is taken into account as the electrically conducting cross-section. The derived value of overall arc voltage (900V) for the 90kA arc in air (which precedes the 70kA condition in time) is well in excess of the measured value (615V). This implies that significant nozzle ablation also occurs at 90kA although not photographically detected.

The axial variation of electrical field strength derived from the $V:z$ results shows a monotonic decrease for all currents in both air and SF_6 (Figs. 2,3).

4. ACKNOWLEDGEMENTS.

The authors are grateful to Professor J. D. Craggs for his continued encouragement and to the Science Research Council for financial support which enabled this work to be performed.

5. REFERENCES.

- 1) COWLEY M.D. J.Phys.D. Appl.Phys., **2**, 2218-2231, 1974.
- 2) WALMSLEY H.L., JONES G.R., HAJI F., STRACHAN D. J.Phys.D. Appl.Phys., **10**, 383-392, 1977.
- 3) AIREY D.R. Ph.D. Thesis, University of Bath, 1977.
- 4) LIEBERMANN R.W. and CHAN C.L. Westinghouse Report 77-1064-ARC PL - P3, May 31, 1977.
- 5) YOS J.M. AVCO Report, RAD-TM-63-7, 1967.
- 6) SHAYLER P.J. and FANG M.T.C. University of Liverpool, Arc Res. Rept., ULAF-T45, 1976.

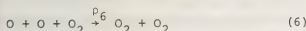
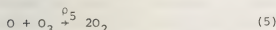
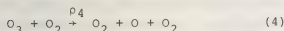
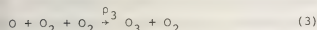
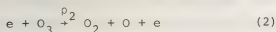
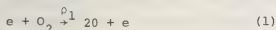
OZONE PRODUCTION IN A HOMOGENEOUS OXYGEN DISCHARGE

B. Eliasson and U. Kogelschatz.

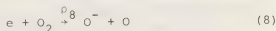
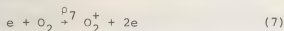
Brown Boveri Research Center, CH-5405 Baden, Switzerland.

We report on calculations of the efficiency and concentration of ozone production in a spatially homogeneous oxygen discharge. An applied electric field E accelerates electrons in a gas consisting initially of oxygen molecules O_2 . The electrons have a certain energy corresponding to the electron temperature T_e which in turn is a function of the ratio E/p where p is the gas pressure.

The electrons dissociate O_2 molecules into O atoms. Through recombination of atomic oxygen with oxygen molecules ozone is formed. The production and destruction of O and O_3 from the initial mixture of electrons and O_2 is described by the following reactions:



Along with e , O , O_2 also positive and negative ions are present. We assume that these consist predominantly of O_2^+ and O_2^- ions, respectively. These are produced according to



The rate coefficients ρ_i describing the above reactions are either known or can be calculated. They are functions of the gas temperature T_g and the electron temperature T_e . We assume that the ion temperature is equal to the gas temperature.

The time dependent balance equations for this system have been solved for two different cases: a) we assume an arbitrary initial electron concentration ($3 \times 10^{-8} \text{ cm}^{-3}$) and apply a constant electric field and b) we apply a fast voltage pulse which is high enough to cause ionization. A typical solution in case a) is shown in Fig. 1.

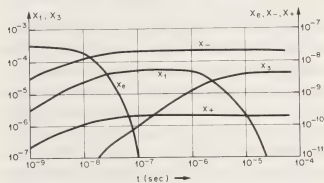


Fig. 1: particle concentrations for a constant applied electric field: $E/p = 5 \text{ V/(cm Torr)}$, $T_g = 300 \text{ K}$, $p = 1 \text{ bar}$. (The subscripts $e, 1, 2, 3, -, +$ refer to electrons, O, O_3, O, O_2^- respectively).

There are two characteristic time constants involved in the production of O and O_3 . As long as E/p is less than the breakdown value of 38 V/(cm Torr) all electrons

disappear quickly to form negative ions through dissociative attachment. The time constant of this effective attachment is $\tau_e = 1/((\rho_2 - \rho_1)n_2)$. It is of the order of some nsec for a pressure of 1 bar and is proportional to $1/p$.

The ozone concentration x_3 increases with a time constant $\tau_3 \gg \tau_e$. τ_3 is of the order of μsec at a pressure of 1 bar. It is proportional to $1/p^2$.

In Fig. 2 we show a typical solution in case of an electric pulse whose height is larger than the breakdown value. The electric field increases to the maximum value of 47 V/(cm Torr) within 50 nsec.

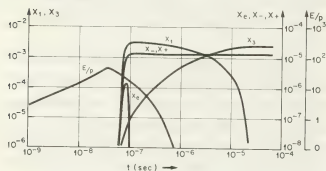


Fig. 2: Particle concentrations for a fast applied voltage pulse of the indicated shape. ($T_g = 300\text{ K}$, $p = 1\text{ bar}$)

At low electric fields all electrons are attached to atomic oxygen according to the dissociative attachment described by Eq. (8). At higher fields the ionization according to Eq. (7) dominates and we have free electrons in the gas. The free electrons exist only for ca. 30 nsec. The time constant of the increase of the ozone concentration is of the same order as before. There is a substantial difference between the results in Fig. 1 and Fig. 2 though, viz. whereas in the first case the ozone concentration is of the order of 10^{-6} in the second case the concentration reaches the very high value of $3 \cdot 10^{-3}$ in spite of the very low initial electron concentration (10^{-12} cm^{-3}). This is due to the production of an avalanche of electrons once

$E/p > 38\text{ V/(cm Torr)}$.

The number of ozone molecules produced per negative charge are shown in Fig. 3 in the case of an electric pulse as a function of E/p . Also shown is the efficiency of the ozone generation, i.e. the ratio mass of ozone produced/energy used. (An efficiency of 100% corresponds to 1220 g/kWh.)

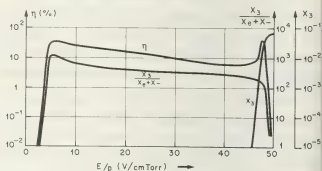


Fig. 3: Efficiency of ozone production and ozone yield per negative charge as a function of E/p . ($T_g = 300\text{ K}$, $p = 1\text{ bar}$).

There are two peaks in the efficiency curve. One around 5 V/(cm Torr) and another around 47 V/(cm Torr). The peak around 47 V/(cm Torr) is due to the increased production of electrons.

These calculations show that to obtain high efficiency and a high concentration of ozone we have to generate a fast electric pulse higher than the breakdown value of 38 V/(cm Torr). The highest pulse height obtainable is related to the rate of increase in the pulse height. The faster the pulse, the higher the applied E/p value can be.

From these calculations it also becomes apparent that a homogeneous pulsed discharge can reach efficiencies that are considerably higher than those reached in a classical ozonizer with a "silent" discharge which is inherently inhomogeneous.

AXIAL SEGREGATION IN Hg-Tl-I DISCHARGES OPERATED AT 50 Hz

J.J. Damelincourt, M. Sevigne, M. Aubes and L. Scoarnec*.

Centre de Physique Atomique, Laboratoire associé au C.N.R.S. n°277, Université Paul Sabatier, Toulouse, France.

**Centre Technique de la Compagnie des Lampes, Puteaux France.*

Both axial and radial segregation generally occurs in arcs containing mixtures of gases. In metal halide arcs used as sources of light, this phenomenon is very undesirable because the light emitted from the arc is highly non uniform.

Physical mechanisms responsible for additive segregation have been particularly studied by Fischer (1) who explains the segregation by the combined action of radial diffusion and axial convection.

In the work presented here, the experimental results for axial segregation of thallium atoms in Hg-Tl-I discharges operated at 50 Hz are compared to those calculated from a simplified model proposed by Fischer (1).

EXPERIMENTAL. Arcs are operated vertically on a 50 Hz supply with an inductance in series. The supply voltage is 300 V and discharges are 1000 w loaded. The arc tube is a quartz tube with an inner diameter of 2 cm. The distance between electrodes is 10 cm. The tube contains 50 mg of mercury and 0.3 mg (1.6 or 0.8 mg) of thallium iodide and 20 Torr of argon (at room temperature) as an ignition gas.

The instantaneous and spatially resolved arc temperatures and densities of neutral thallium atoms are obtained from side on measurements of absolute spectral radiances of 588 nm mercury line and 655 nm thallium line.

Following approximations are made :

The mercury plus argon pressure is constant along the axis of the discharge, and close to the total pressure.

Atomic ratios are radially constant and local thermodynamical equilibrium is assumed.

Corrections for absorption of spectral lines and absorption in silice tubes are obtained from relative absorption measurement assuming a unity value of plasma transparency for the 491.6 nm mercury line. Wall temperature are determined with a "710 C Ircon" pyrometer.

TEMPERATURE AND THALLIUM ATOMS DENSITIES. An iterative process allows us to obtain values of temperatures, mercury neutral atoms densities and pressures as a function of time and position.

Reference (2) gives a detailed study of the experimental apparatus and measuring method^(*). Densities of neutral thallium atoms are determined from measurements of 655 nm thallium line intensities. We used the A_{ij} value of reference (3) : $A_{ij} = 4.25 \cdot 10^6 \text{ s}^{-1}$. With experimental values of local instantaneous temperatures and neutral thallium atoms densities the thermodynamic analysis of the system Hg-Tl-I gives atomic ratios Hg/Tl.

In order to simplify the theoretical analysis we shall only consider in the following time averaged values of atomic ratios.

These results are given in fig. 1. Assuming a possible experimental error of 2 % in temperatures, the corresponding error for atomic ratio is 25 %. As it can be seen in fig. 1, the atomic ratio (Hg/Tl) varies as

$$R_0 e^{-\lambda_z}$$

with $0.18 < \lambda < 0.25$

(*) It is to be noticed that value C p. 1033 in reference (2) is $1.256 \cdot 10^{-4}$ and not $1.276 \cdot 10^{-4}$.

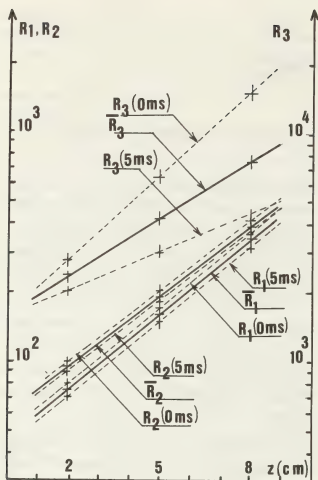


Fig. 1. atomic ratio Hg/Tl versus distance from lower electrode. Total pressure : 1.6 Atm.

COMPUTATION OF λ . The numerical procedure follows the simplified one proposed in reference (1). We shall consider only the diatomic molecule Tl I and neglect all other molecular species.

With this hypothesis the system to be solved writes as follow.

$$\frac{\partial^2 q_A}{\partial r^2} + \frac{1}{r} \frac{\partial q_A}{\partial r} + \frac{1}{2T} \frac{\partial T}{\partial r} \frac{\partial q_A}{\partial r} + \chi_A^2 q_A + \frac{v}{C_A D_0} \lambda_A \left[q_A + \left(1 - \frac{C_M}{C_A} \right) P_M G(\frac{1}{2}) \right] = 0$$

The notations are those of reference (1) and $G(\frac{1}{2})$ is a correcting factor

$$1 \ll G(\frac{1}{2}) \ll 2$$

The theoretical and experimental values obtained for the three discharges are given in table I.

TABLE I - Theoretical and experimental values of λ

lamp	filling charges (mg)		λ_{Th}	λ_{exp}
	Hg	Tl I		
1	50	3.3	0.22	0.24
2	50	1.6	0.2	0.22
3	50	0.8	0.11	0.18

Table 1 shows a reasonably good accordance between theoretical and experimental results for lamps 1 and 2 where the modulation of atomic ratio is negligible ; for lamp 3 disagreement occurs with results obtained from the steady state model.

REFERENCES.

- (1) Fischer (E.) : J. Appl. Phys., 1976, 47, 2954.
- (2) Damelincourt (J.J.), Karabourniotis (D.), Scoarnec (L.) and Herbert (P.) : J. Phys. D., Appl. Phys., 1978, 11, 1029.
- (3) Preuss (E.) : Z. Physik, 1970, 239, 133.

ARTICLE DISTRIBUTIONS IN METAL VAPOUR-RARE GAS ARC DISCHARGES

K. Jayaram and K.H. Tsui.

Instituto de Física, Universidade Federal Fluminense, Niterói, Rio de Janeiro, 24000 Brasil.

INTRODUCTION:

Study of gas discharges with contaminated metal vapour has gained importance because of the inevitable presence of metal vapour in Industrial Discharge devices. Also, the role of metal vapour impurities in fusion-type devices is being increasingly investigated. In connection with metal vapour contaminated arc discharges, it has been noted by one of the authors/1/ that substantial differences in transport properties of a plasma can arise due to the presence of metal vapour impurities. Findings of a similar nature have been reported elsewhere/2,3/. Further, in a modified type of Maecker type the collision cross section of neutral metal atoms with rare gas atoms has been determined/4/.

An arc discharge between metal electrodes is although physically simple has a number of complicated mechanisms sustaining it. In other words, while modeling an arc discharge one has to consider; radial/axial temperature and density gradients, diffusion, combination and even chemical activities. The main aim of this paper is to offer a theoretical explanation to the experimentally observed heavy particle distribution in a rare gas, metal vapour arc discharge.

STABILIZED ARC MEASUREMENTS:

Brief description of the metal vapour wall stabilized arc of special design is given in /5/. Briefly it is a simplified version of Maecker type arc with just two stabilizing discs. The arc device is designed to be evacuated so as to facilitate running in any type of gas. 10, 15 and 20A DC arcs are run between copper electrodes in a pure Helium diode at atmospheric pressure with a stabilizing electrode diameter of 6 mm. Axial electrical gradients using probes, arc current and radial temperature distributions using copper spectral line spectroscopy have been determined. Optical thinness of emitting regions for copper lines used has been verified resorting to intensities within a multiplate copper vapour pressure distribution has been determined by correlating temperature distribution and measured relative intensity of a spectral line, and different characteristics and other details have been published elsewhere/6/ and only the radial distribution of copper vapour in a 10A arc obtained in the above procedure is reproduced in Fig.1. It may be observed that neutral copper atoms appear to pile-up near the wall of the discharge. This is a peculiarity of this experiment but has been observed elsewhere/7/. With temperature attaining a

maximum in the center of the arc and assuming LTE to hold (which is probably true for $0.2 < \eta < 0.8$, η : normalized radius), this means that the ionized components are also influenced by this pile-up effect. A theoretical explanation for this effect is given.

THEORY:

Since the arc current is small, both the % ionization and magnetic pressure in the discharge are small and hence the density distribution is dominantly governed by the neutral components. Further, neutral helium gas which remains unionized due to low available thermal excitation energy fills the whole volume and neutral excited copper occupies the discharge volume; a very small fraction of the total volume. It is assumed here, that the heat produced in the ionized discharge component, namely neutral copper is transferred to and diffused by Helium. Also, neutral copper is assumed to be streaming through stationary Helium. This is a reasonable assumption, firstly because Helium is dominating and secondly the Copper coming off the electrodes must surely have a directed velocity. All components in the discharge are assumed to share the same experimentally obtained radial temperature profile. With these assumptions the momentum & energy conservation relations yield the following equations

$$\nabla p_1 = n_1 m_1 \bar{v}_1 \bar{u}_1 \dots \textcircled{1} \quad \nabla \cdot \vec{u}_1 = 0 \dots \textcircled{2} \quad n_1 m_1 \bar{v}_1 \bar{u}_1 = n_2 m_2 \bar{v}_2 \bar{u}_2$$

$$\nabla p_2 = -n_2 m_2 \bar{v}_2 \bar{u}_2 \dots \textcircled{3} \quad 0 = \nabla \cdot \vec{u}_2 \dots \textcircled{4} \quad u_1 = u_2$$

1=Helium, 2=Copper, p =Partial pressure, n =number of particles, m =mass, \bar{v} =collision frequency, Q =energy, F =friction force, λ =thermal conductivity, u =velocity and these lead to

$$\nabla(p_1 + p_2) = 0 \dots \textcircled{5}; \quad \nabla \cdot \vec{u}_1 = -u_2 F_2 \dots \textcircled{6}$$

Equations(3)&(6) reduces to $\partial p_2 / \partial r = -n_2 m_2 \bar{v}_2 u_2$

$$\frac{1}{r} \frac{\partial}{\partial r} [r \lambda_1 \frac{\partial T}{\partial r}] = -\nabla^2 T; \quad \lambda_1 = n_2 m_2 \bar{v}_2 u_2^2$$

Solving for u_2 : $u_2 = -\frac{\partial p_2}{\partial r} / [n_2 m_2 \bar{v}_2]$ &

$$\frac{\partial p_2}{\partial r} = \sqrt{\lambda_1 n_2 m_2 \bar{v}_2} (\nabla^2 T)$$

using the definition of $\lambda_1 = \frac{5}{2} \frac{k T n_1}{\bar{v}_2 m_1}$

the partial pressures of Helium and Copper are

given by $\partial p_{He} = -p_1 \sqrt{\frac{5}{2} (\nabla^2 T)}_T$ & $\partial p_{Cu} = p_1 \sqrt{\frac{5}{2} (\nabla^2 T)}_T \dots \textcircled{7}$

with $\nabla^2 T$ always negative. It is possible to find analytical expressions for p_1 and p_2 by patching a zero-order Bessel function for the temperature distribution, for example, $T(r) = T_0 J_0(K_1 r)$ where $K_1 = X_1/R$, R is the radius of the arc, where arc temperature drops to room temperature, X_1 is the first zero of J_0 and T_0 is axis temperature. By inserting seven-

ral (T,r) from experimentally obtained distribution a value of $R=2.5 \rho$, where ρ is the discharge radius was obtained. By applying Laplace's operator it is easy to approximate $\nabla^2 \frac{1}{r}$ by $-k_1^2$ and the partial pressures are then given by

$$h_1(r) = h_1(0) e^{-\sqrt{k_1} r}; \quad h_2(r) = h_2(0) + h_1(0) [1 - e^{-\sqrt{k_1} r}]$$

and the densities are given by

$$n_1(r) = \frac{n_1(0)}{J_0(k_1 r)} e^{-\sqrt{k_1} r} \quad \& \quad n_2(r) = \frac{n_2(0)}{J_0(k_1 r)} + \frac{n_1(0)}{J_0(k_1 r)} [1 - e^{-\sqrt{k_1} r}]$$

Since the arc operates at atmospheric pressure,

$$n_1(0) \pm 1.3 \times 10^{18} / \text{cm}^3 \quad n_2(0) \text{ from experiment is } \pm 10^{14} / \text{cm}^3$$

$k_1 = \frac{2.406}{2.5 \rho}$ we can obtain theoretical distributions of $n_1(r)$ & $n_2(r)$. From $n_2(r)$ applying Saha equations, the charged particle distributions can be established.

A comparison of experimental and theoretical results are made in Fig.2.

CONCLUSIONS

As can be seen from Fig.2, the theoretical and experimental curves agree only qualitatively with regard to the trend of their slopes. Probably better agreement with experiment may be obtained by numerically processing the partial pressure equations (7), rather than obtaining an analytical solution which involves additional assumptions. However, the pile-up effect is evident and this occurs at the expense of Helium accumulating at the arc center. Further, in order to understand this mechanism better it will be necessary to know the metal vapour evolution process and recombination mechanisms.

Acknowledgement

One of the authors (KJ) thanks the Australian Research Grants Committee for the PD fellowship and members of the Plasma Engineering Group of Sydney University for their participation and help. He also thanks Prof. D.W.George, Vice-Chancellor of Univ. of Newcastle for his guidance and Prof. J. Uhlenbusch of Univ. of Düsseldorf for a discussion on this topic.

References

- /1/ JAYARAM, K.: J. Phys. 271,217 (1974).
- /2/ Sakuda et al: Jap. Inst. of Elec. Engrs., Plasma Research Group report, EP-76-30,1-9 (1976).
- /3/ Airely, D.R. et al: IEEE Trans. on PAS, PAS-95, No. 1, P 1 (1975).
- /4/ Jayaram, K. & Kane, E.L.: 13th ICPIG, Berlin, 497-498 (1977).
- /5/ Miyachi, I. & Jayaram, K.: Rev. Sci. Inst. 42, 1002 (1971).
- /6/ Jayaram, K. & Kam, T.M.: Charles Kolling Res. Lab. report, Sydney Univ., T-N P-8, 1-26(1974), see also 4/above.
- /7/ Schneider, R.T. et al: App. Spectro. Vol. 24, No. 2, 253-258 (1970), see also Mack, J.M.: Thesis, Univ. Florida (1969).

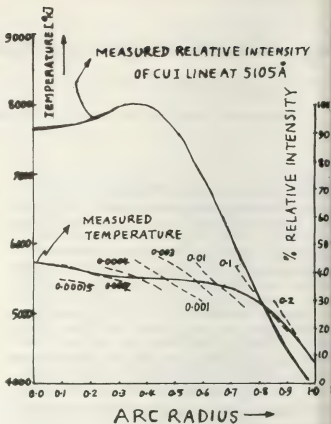


FIG. 1

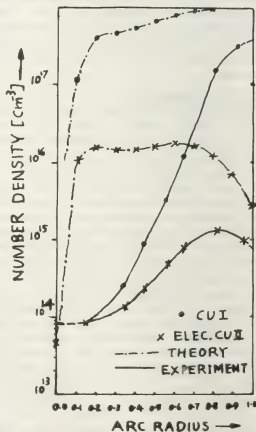


FIG. 2

OPERATION MODES OF HOLLOW CATHODE ARCS WITH REDUCED GAS FLOW

K.H. Groh and S.E. Walther^{*}.*1st Institute of Physics Gießen University, Heinrich-Buff-Ring 16, D-6300 Gießen, F.R.G.*Abstract

In 1971 the first research work on hollow cathode arcs (abbreviated HCA) started at Gießen University. Emphasis has been put on the operation of this hollow cathode arc or the ion beam neutralization of the electric propulsion unit RIT 10. In this application the HCA works as an electron source delivering electrons for main discharge starting and beam neutralization. But beside this, diagnostics have been performed dealing with the physical phenomena of HCA's. Different measurements including Langmuir probe analysis led to a simplified discharge model. The determination of the discharge current parts carried by the cathode and the electron emitter inside the cathode gave us hints to explain the observed operation modes, the plume mode, and the spot mode by assuming an electrical double sheath.

Introduction

Hollow cathodes have been developed and investigated in the scope of the research and development program of the radio frequency ion thrusters (RIT) for the use as electron source (plasma bridge neutralizer) (1). The main aspect of these activities was mechanical stability, reliable function, gas economy, and high efficiencies. The discharge mechanism has never been understood entirely and different theories have been published by various authors trying to explain the observed phenomena more or less.

For our experiments we used a hollow cathode reducing gas flow by a small orifice in the cathode disc. One can observe two operation modes, the plume mode showing a large luminous plasma region outside the cathode orifice like a plume and the spot mode where the discharge is concentrated at the cathode orifice. Between plume and spot mode there exists an unstable operation, the so-called transition mode where the discharge oscillates between plume and spot mode.

Different theories try to explain this discharge modes. Csiky and Groh (2,3) assume that the cathode space charge sheath penetrates the cathode boring which results in the change from the plume to the spot mode. According to Philip's opinion (4) the change of the electron emission from the cathode disc to the cathode interior is responsible for the change of the operation modes. However, our most recent results do not agree

with one of the mentioned theories but point to the presence of an electrical double sheath which can explain the observed plume and spot mode operation.

In the following a short description of the experiments and their interpretation will be given.

Experimental Arrangement

For the measurements we used our standardized 3 mm hollow cathode being sketched in fig. 1. The hollow cathode consists of a 3 mm molybdenum tube being enclosed for gas flow reduction purposes at the downstream end by an electron beam welded thoriated tungsten disc with a 0.3 mm diameter boring. In 2 mm distance the discharge anode is located with a centric hole of 1.5 mm diameter. At the upstream end of the hollow cathode tube the gas supply is connected, a mercury vaporizer or a gas inlet for inert gas operation.

In the cathode interior just behind the cathode disc the so-called insert is located a low work function material supply acting as electron emitter. This insert is insulated electrically against the cathode body and is connected via a feed through to an outer power supply as sketched in fig. 1, too.

The discharge is stroked by heating up the cathode to about 1100°C until a sufficient thermionic electron emission is available at an applied voltage of 150 - 200 volts between cathode and anode. If a gas flow is added in the order of magnitude of 0.02 mg/sec mercury vapour discharge ignition occurs and the discharge voltage drops to about 20 volts. Now, the cathode heater can be switched off since the discharge sustains itself heating the cathode by ion impingement.

Due to the insulated insert the discharge can be operated either between cathode and anode with floating insert or between anode and insert with floating cathode showing the below described characteristics.

Experimental Results

Operating the HCA in this manner we found that both the cathode and the insert carry the discharge current as shown in fig. 2. The main part of the discharge current is drawn from the insert at low total currents. This behaviour changes at high discharge currents when the main part is taken over by the cathode. This current distribution

^{*} Now with ERNO-Raumfahrttechnik, Bremen

depends on the pressure inside the hollow cathode which has been investigated, too. The result is graphed in fig. 3 where the discharge current parts are shown versus the hollow cathode pressure. Obviously, the current from the cathode side predominates at high gas pressures and vice versa the insert current at low pressures. That means looking at fig. 2 that the cross over point of both current graphs is shifted to lower discharge currents with increasing gas pressure.

Discussion

This behaviour of the HCA can be explained by the moving of the basic point of the discharge. The basic point or active zone of the discharge penetrates the cathode's interior more or less dependent on the pressure or the mean free path, respectively. Thus, we interpret the current sharing to cathode and insert (5).

But as we see from fig. 3 plume mode operation is possible between cathode and anode and between insert and anode. This disproves former theoretical models assuming cathode fall sheaths penetrating the cathode boring or the shift of the emission from an outer to an inner surface. Rather, we explain the observed discharge modes by an electric double sheath which appears at discontinuous cross-section reductions, as is well known (6). As a double sheath we understand a small limited area of high electrical field strength within a plasma. Such sheaths are created if the diffusion current $A \cdot j_e$ is smaller than the required current J_D . In order to deliver the needed current the charge carriers must be accelerated which happens in a double sheath as sketched in fig. 4.

In our case, the plume mode operation can be observed at low discharge pressures and/or at low discharge currents. Consequently, it follows that the drift current from the interior plasma into the cathode boring is too small and the electrons must be accelerated in a double sheath. So we identify the plume mode operation with the existence of a double sheath. The double sheath-voltage depends on the pressure and the discharge current and is in the order of magnitude of some volts.

With increasing gas pressure or increasing discharge current the diffusion current density j_e grows resulting in a higher drift current from the internal plasma. No longer, the accelerating sheath is necessary which we identify with spot mode operation. From our Langmuir probe measurements in the external discharge plasma (7) we have obtained plasma data which allow us a rough estimation of the above mentioned diffusion currents. Assuming a plasma density of $n = 10^{15} \text{ cm}^{-3}$ and an electron temperature of 10,000 K we achieve for plume mode operation at 0.3 A discharge current a drift current in the order of magnitude 0.05-0.1 amp. In accordance with our model a double sheath is required to enable the discharge current.

References

- (1) S. Walther, K. Groh, H. Loeb, AIAA-Paper No. 78-706, San Diego, 1978
- (2) G. Csiky, NASA TN D-4966, 1969
- (3) K. Groh, Doctorate Thesis, Giessen 197
- (4) D. Fearn, C. Philip, AIAA-Paper No. 72-416, Bethesda, 1973
- (5) K. Groh, S. Walther, Proc. 13. ICPG, 1978
- (6) Th. Wasserrab, "Gaselektronik II", 1978
- (7) K. Groh, S. Walther, H. Loeb, Proc. 5. IEE, Liverpool, 1978

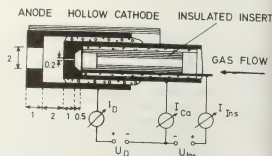


Fig. 1: Cross section of the hollow cathode

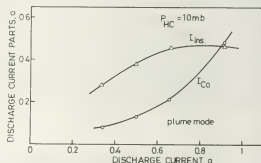


Fig. 2: Discharge current distribution to cathode J_{Ca} and insert J_{Ins}

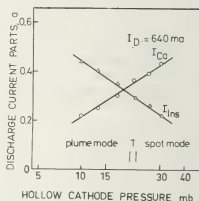


Fig. 3: Discharge current distribution to cathode J_{Ca} and insert J_{Ins} and mass flow rate in versus the gas pressure

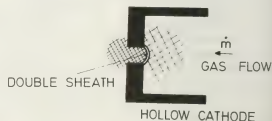


Fig. 4: Sketch of the discontinuous cross-section reduction with electrical double sheath

VISIBLE AND INFRARED CONTINUUM RADIATION FROM A LOW TEMPERATURE Cl_2 -ARC

J. Schmitt and M. Neiger.

Ruhr University Bochum, Allgemeine Elektrotechnik und Elektrooptik 4630 Bochum, F.R.G.

INTRODUCTION

Continuum visible and especially infrared emission of plasmas is of interest because of its advantages for diagnostic purposes of dense low temperature plasmas and for the investigation of properties of nonideal plasmas. Continuum radiation has been extensively studied in hydrogen and inert gases and to a lesser extent in other atmospheric gases, alkali metal vapors, mercury and the halogens [1]. In the latter case the measured visible continua were found greater than expected by factors 5-50, but the observed radia-

Fig. 1

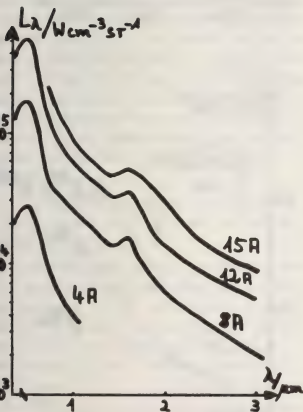
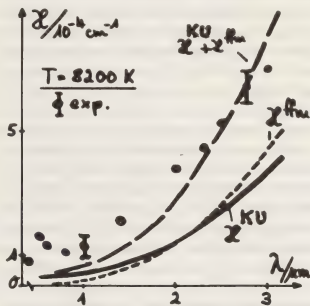


Fig. 2



tion has not been unambiguously identified [1]. It is the aim of the present work to perform quantitative measurements of the visible and infrared continuum radiation of a chlorine arc plasma.

EXPERIMENT

The Cl_2 -arc is operated in a water cooled quartz tube of 8 mm inner diameter and 10 cm length at atmospheric pressure with dc-currents of 4-15 A. Both ends of the arc are submerged in argon gas to prevent re-absorption of radiation by Cl_2 -molecules in regions of lower temperature and thus to make possible end-on observation of the arc axis. The detectors used at the exit slit of a McPherson 2051 monochromator are photomultipliers (S20, S1), a PbS - cell and a cooled InSb - photoconductive detector, whose signals are fed into a lock-in detection system. A stan-

standard carbon arc is used for absolute intensity calibration.

MEASUREMENTS

Fig. 1 shows absolute spectral continuum intensities emitted end-on from the arc axis in the wavelength range $0.4 \mu\text{m} - 3 \mu\text{m}$ for 4 different arc currents. These curves are composed from those experimental points, which seemed to be unaffected by any atomic line radiation. Simultaneous determination of the axis temperatures as a function of discharge current by absolute intensity measurements of CLI spectral lines allows conversion of the data of Fig. 1 into absolute absorption coefficients via Kirchhoffs law. The experimental points of Fig. 2 show this absorption coefficient $\kappa(\lambda, 8200 \text{ K})$.

DISCUSSION

Fig. 2 shows a comparison of absolute magnitudes and λ -dependences of our data with the calculated electron-ion contribution (Kramers-Unsöld, ξ -factor 1) κ^{KU} (solid curve) and the electron-atom bremsstrahlung (free-free-minus) κ^{ffm} (dotted curve), which was calculated according to the Hyman/Kivel approximation /2/. The sum $\kappa^{\text{KU}} + \kappa^{\text{ffm}}$ (dashed curve in Fig. 2) agrees fairly well with our data in the range $2 \mu\text{m} < \lambda < 3 \mu\text{m}$. On the other hand, fairly large differences exist for $\lambda < 2 \mu\text{m}$, especially near $\lambda \approx 1.7 \mu\text{m}$ and $\lambda \approx 0.5 \mu\text{m}$, where the experimental data lie high by factors 2 and 5 respectively. The maximum at $\lambda \approx 5300 \text{ \AA}$ may be interpreted as due to a series of electron-ion recombination thresholds into CLI $3s^2 3p^4 4p$ levels. A ξ -factor /3/ of 5 at maximum, comparable to Xe ξ -factors at 6000 \AA /4/, results from this interpretation. Moreover, the dependence $\kappa(T, 5300 \text{ \AA})$ of our data on temperature, which is shown in Fig. 3 and compared with both κ^{KU} and $5 \times \kappa^{\text{KU}}$, is also in agreement with this. Fig. 4 shows experimental data of $\kappa(T, 2.9 \mu\text{m})$ together with the contribution $\kappa^{\text{KU}} (\xi=1)$ and κ^{ffm} as a function of temperature. The steeper increase, which is observed in experiment, indicates that an additional radiation mechanism becomes important at higher temperatures. A possible process would be

strongly broadened CLI spectrum lines from energy levels close to the ionisation threshold which merge into a quasi-continuum.

LITERATURE

- /1/ H.-P. Popp: Phys. Rep. 16C, 170 (1975)
- /2/ H.A. Hyman and B. Kivel: JQSRT 13, 699 (1973)
- /3/ L.M. Bibermann and G.E. Norman: Opt. Spectr. 8, 230 (1960)
- /4/ D. Meiners and C.O. Weiss: JQSRT 16, 273 (1976)

Fig. 3

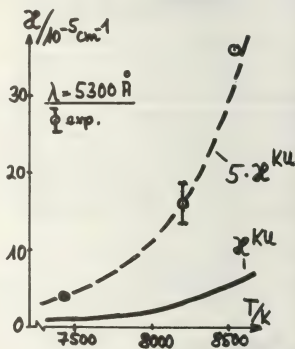
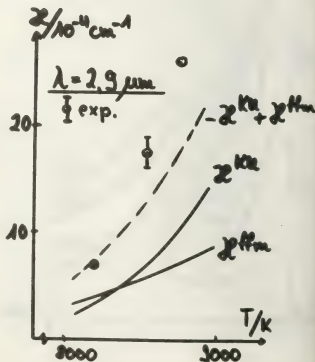


Fig. 4



HIGH-CURRENT DIFFUSE DISCHARGE WITH THE EXPLOSIVE CATHODE PROCESS

A.P. Kchuzeev, Yu.D. Korolev, V.A. Kuzmin, G.A. Mesyats, V.P. Rotshtein and I.A. Shemyakin.

The U.S.S.R. Academy of Sciences, Siberian Branch, the High-Current Electronics Institute, Tomsk.

A quasi-stable glow discharge phase is known to be characteristic for the pulse breakdown of gases by the uniform initiation of initial electrons. The papers [1-3] show that the contraction of the glow discharge can be schematized as follows. At first the cathode spot is formed on account of the cathode instability and of the explosive emission. Then the current increases in the discharge column against the cathode spot and one can observe a diffuse channel bound to the spot against a background of the glow discharge. The high-conductive contracted spark channel germinates along the diffuse channel on the cathode and the anode sides at the third stage. The investigations carried out in noble gases (Ar, Kr, Xe) and in noble gases with small additions of haloid-contained compounds (SF_6 , CCl_4) showed a great number of the cathode spots and diffuse channels to be ignited in the interelectrode volume [4,5]. These channels form a column of a homogenous plasma when igniting. The discharge involved was called a high-current diffuse discharge (H-C.D.D.). At present there are represented the results on investigations of H-C.D.D.)

1. The investigation of a charge in noble gases with additions of haloid-contained compounds

The discharge initiation was carried out by a fast electron beam with the current density of $j_{eb} = 1,5 \text{ A/cm}^2$ and with duration of 10^{-7} s . At a small storage capacitance value in the gap a quasi-stable glow discharge with ionizing multiplication burns (Fig. 1a). At a large storage capacitance value after the quasi-stable

glow discharge phase there is observed a H-C.D.D. (Fig. 1b). The photos and oscillograms of the current (Fig. 1) are obtained in the following conditions: Ar:SF_6 -100:0,13, the gap length is $d = 1,4 \text{ cm}$, an initial capacitance voltage is $U_0 = 10 \text{ kV}$, a puncture voltage is $U_p = 11,2 \text{ kV}$, a) $C = 2 \cdot 10^{-9} \text{ F}$, b) $C = 47 \cdot 10^{-9} \text{ F}$. The Fig. 2 shows the photos of the interelectrode gap and the photos of a high-current diffuse discharge spectrum section and of spark spectrum section at static gas breakdown in the mixture Ar:Xe:SF_6 . The presence of the continuum and of the electrode material lines are characteristic of the spark spectrum, while the high-current diffuse discharge spectrum is characteristic of quasi-stable glow discharge one. In mixtures $\text{Ar:Xe(Hr):SF}_6(\text{CCl}_4)$ the most bright sections correspond to luminescence bands of XeF , KrF , XeCl molecules. One of the properties of H-C.D.D. is connected with the current density constancy with invariable parameters of the electric circuit [4,5].

2. The investigation of the discharge in the nitrogen and in the air.

The problem of the H-C.D.D. ignition comes to the decision of the problem of simultaneous ignition of a great number of diffuse channels, and, secondly to the prevention of contracting, i.e. of germination of high-current channel from the cathode spot. At atmospheric pressure it wasn't succeeded in realizing such a discharge condition. However, the results of investigations at $P = 50 - 100 \text{ mm. m.c.}$ proved to be more hopeful. A quasi-stable glow discharge with the current density

of 500 A/cm^2 ignited by initiation of initial electrons by means of ultraviolet lighting. The interelectrode gap supply ($d = 0.7 \text{ cm}$) was carried out from the generator on cable lines ($\rho_g = 75 \text{ Ohm}$). The applied voltage is $U_0 = 25 \text{ kV}$. After initiating there is ignited a quasi-stable glow discharge in the gap (Fig. 3a). In 20-30 ns the emergence of cathode spots is observed (Fig. 3b). Later on the current against the spot increases. The registration of this current was carried out by the Rogovsky's belt with sectioned cathode (Fig. 3f). There was inserted wire into the cathode. If the cathode spot emerged on the wire the Rogovsky's belt registered the current accompanied the cathode spot emergence. The current oscillogram with one spot on the wire is shown in Fig. 3c. If there are appeared some spots on the cathode the transition from the diffuse channel to the contracting one became slower (Fig. 3d). The corresponding photo of the discharge is presented in (Fig. 3e). The discharge ignition duration in such a form achieved 200 ns. These experiments show a possibility of realization of the H-C.D.D. conditions in molecular gases over a great electrode surface.

REFERENCES

1. M.M.Kekez, M.R.Barrault, J.D.Craggs. J.Phys. D: Appl. Phys., 1970, Vol.3, N 12, p. 1886.
2. R.B.Baksht, Yu.D.Korolev, G.A.Mesyats. Fizika Plazma, 1977, t 3, v.3, s.652.
3. Yu.D.Korolev, V.A.Kuzmin, G.A.Mesyats, V.P.Rotshtein. JTP, 1979, t 49, v.2, s.410.
4. Yu.I.Bichkov, Yu.D.Korolev, G.A.Mesyats, A.P.Kchuzeev, I.A.Shemyakin. Pisma v JTP, 1977, t 3, v.21, s.1121.
5. Yu.I.Bichkov, Yu.D.Korolev, G.A.Mesyats, A.P.Kchuzeev, I.A.Shemyakin. Izvestiya Vuzov, "Fizika", 1978, N 7, s.72.

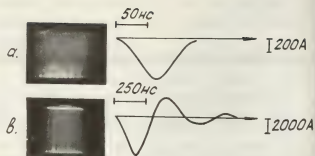


Fig. 1.

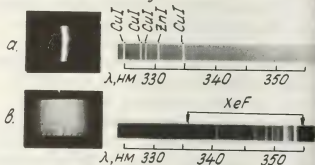


Fig. 2.

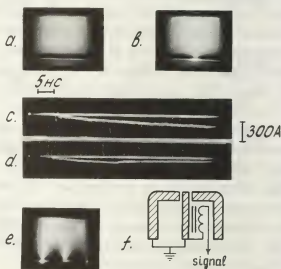


Fig. 3.

THE REDUCTION OF DIFFUSION BY PLASMA ROTATION AND ION DISSIPATIVE EFFECTS

J.J.A.M. Van der Mullen, B.F.M. Pots, D.C. Schram and B. van der Sijde.

*Eindhoven University of Technology, Eindhoven, the Netherlands.*Introduction.

Many studies have been conducted on particle transport and pressure enhancement in magnetized arcs^{1]}. The magnetic field reduces the transverse electron heat conduction and particle diffusion (at least classical), leading to higher axis values of T_e and n_e . In addition the Nernst effect reduces also the particle transport^{1]}.

In many of these treatments the effects of ion-viscosity and ion-neutral friction have been ignored. Über^{2]} realized, that in these arcs rotational velocities are relatively large and may even approach the ion thermal velocity $\frac{2kT_i}{M_i}$; the rotation (caused by radial electro field E_r) is connected with the presence of radial current. At the cathode it tends to be positive ($E_r < 0$, directed inward), at the anode negative ($E_r > 0$); the exact potential distribution depends also on geometry (cf. fig. 1). We will show that the combined effects of rotation and ion-viscosity and ion-neutral friction can reduce the particle transport substantially for positive rotation (cathode side and in our case for most of the arc length) and can enhance the transport for negative rotation (close to the anode). Consequently, there exists a weak axial gradient even in a cylindrical geometry with identical elec-

trodes : at the cathode the plasma is hotter and more dense than at the anode. It is the aim of this contribution to show, as well theoretically as experimentally that because of these effects the particle confinement may be appreciably better than "Nernst classical", i.e. classical including the Nernst-effect; in many cases the pressure-built up can be explained by the rotational confinement rather than by the Nernst effect.

Theoretical prediction.

We have investigated elongated quasi-cylindrical arcs with axial dimensions (typical gradient length L) much longer than radial dimensions (Λ). The rate of the two scale lengths is supposed to be in the order of the Hall parameter $\Omega_e \tau_e$, which is supposed to be large ($L/\Lambda \sim \Omega_e \tau_e \gg 1$; Ω_e , electroncyclotron frequency; τ_e , electron-ion collision time). The radial diffusion velocity, w_{ri}^{cl} , is much smaller than rotational velocity, $w_{\theta i}$. If we assume^{3]}, that the radial electric field is in the order of the temperature over the radial scale length Λ :

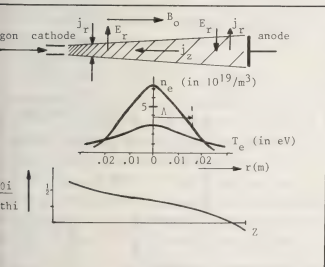
$E(\Lambda) \sim \frac{kT}{e\Lambda}$, we can estimate $w_{\theta i}$ to be: $w_{\theta i} \sim a(r)r\Omega_i$, with $a(r) \sim v_{thi}^2/\Lambda^2\Omega_i^2$. Furthermore, with $w_{ri} \sim b(r)r\Omega_i$, one can show that for classical diffusion $w_{ri}/w_{\theta i} = b(r)/a(r) \sim 1/\Omega_e \tau_e$.

The analysis of the momentum equations for ions and electrons with systematic ordering in $1/\Omega_e \tau_e$ and λ_{ii}/Λ ($\lambda_{ii} = v_{thi}^2\tau_i$), yields the following diffusion flux^{3]}:

$$nw_{ri} = \frac{1}{\Omega_e \tau_e e B_0 (1+2a)} \left\{ \left[\frac{nm_i w_{\theta i}^2}{r} + \frac{\partial}{\partial r} (p_e + p_i) - \frac{3}{2} n \frac{\partial kT}{\partial T} e + j_z B_0 \right] - \Omega_e \tau_e \left[(\nabla_i \cdot \Pi_i)_{\theta} + R_{\theta}^{ia} + M_{\theta}^S \right] \right\}$$

The second term contains contributions of viscosity $(\nabla_i \cdot \Pi_i)$, ion neutral friction, R_{θ}^{ia} , and momentum transfer connected to a finite source term M_{θ}^S ; we consider the case $\Omega_i \tau_i \leq 1$.

In the experimental case considered, we may neglect the pinch- and ion-terms in the first term of



$n_{w_{ri}}$, which can be written as $n_{w_{ri}}^{Cl} = D^{Cl} \frac{\partial n}{\partial r}$ with

$$\text{classical diffusion coefficient } D^{Cl} = \frac{kT_e}{e B_0 \Omega_e \tau_e}.$$

The second term of $n_{w_{ri}}$, "rotational diffusion", is multiplied by $\Omega_e \tau_e$ and can be very large. All three contributions depend on $w_{\theta i}$; if the ion rotation is positive (cathode side) the rotational diffusion is inward, if it is negative then the diffusion is outward. For our experimental conditions (and the estimate of $w_{\theta i}$ as above), the rotation-viscosity contribution and the ion-neutral friction are in the same order as classical transport^{3]}.

Anomalous diffusion.

For large values of $\Omega_e \tau_e$ and B_0 we observe also a high level of turbulence. These fluctuations ($k v_i / \Lambda$) may give rise to anomalous (Bohm) diffusion and enhance the transport. The anomalous diffusion coefficient, D^{an} , can be estimated as:
 $D^{an} = D^{Cl} \Omega_e \tau_e \left(\frac{\tilde{n}}{n} \right)$, if we ignore here the effect of rotation.

The turbulence level is measured^{4]} by probing the plasma-light-fluctuations with two photodiodes ($f < 1$ MHz). Of the three classes of observed waves (rotational instabilities, drift waves, ion waves, all propagating transverse to B_0) we assume that the drift waves are mainly responsible for the anomalous transport, the spectrum is relatively broadband, with $f \lesssim \Omega_i / 2\pi$, and $k \sim 1/\rho_i$. An anomalous enhancement of transport may occur for large values of $\Omega_e \tau_e$ and $\frac{\tilde{n}}{n}$.

Experimental arrangement and procedure.

We analysed the argon plasma of a hollow cathode arc (length 1.4 m, diameter .03 m). The magnetic field is varied between .05 and .4 Tesla, the plasma-current between 20A and 200 A. The electron density, n_e , and temperature, T_e , were measured with Thomson-scattering ($.2 \cdot 10^{20} < n_e < 2 \cdot 10^{20}$; $2.5 \text{ eV} < T_e < 5 \text{ eV}$). The neutral density, n_a , is obtained from line intensities (4p - 4s transition 696.5 nm) and a collisional radiative model of the Ar I-system^{5]}. Ion- and neutral temperatures follow from the Doppler broadening of Ar II and Ar I lines. For the experimental determination of the ion transport we need the source term S_i . As the axial gradients are weak and the axial component of the ion systematic velocity w_{zi} is small (though nonzero^{6]}) we may write from the ion mass balance (recombination can be neglected):

$$n_{w_{ri}}^{exp} = \frac{1}{r} \int_0^r S_i(r) dr = \frac{1}{r} \Omega_e \tau_e \langle \sigma v_e \rangle_{ion}$$

Results and discussion.

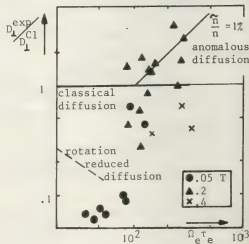
In fig. 2 the measured diffusion coefficient D^{exp} is compared with classical transport, D^{Cl} as function of the Hall parameter, $\Omega_e \tau_e$. The measurements refer to the plasma near the axis at a location halfway the electrodes. It is observed that for several conditions the diffusion is remarkably reduced as compared to classical transport. We conclude, that for these conditions rotation with ion friction improves plasma confinement appreciably. However, for large values of $\Omega_e \tau_e$ (and increasing values of the fluctuation level) the improvement deteriorates contrary to the expectations based on the rotational reduction only. The fluctuation levels are typically between $< 10^{-3}$ (for low value of $\Omega_e \tau_e$) up to $> 10^{-2}$ (for larger values of $\Omega_e \tau_e$). We observe indeed an anomalous diffusion with values which are in agreement with the expectations. We may conclude that anomalous transport takes over for large values of $(\Omega_e \tau_e) \frac{\tilde{n}}{n}$.

Acknowledgement.

We gratefully acknowledge the assistance of Mr van der Sande. This work is partly supported by the foundation FOM.

References.

- 1] G. Venus, Z. Physik 259 (1973) 437.
- 2] O. Klüber, Z. Naturforsch. 25a (1970) 1583, 27a (1972) 652.
- 3] J.J.A.M. van der Mullen, B.F.M. Pots, D.C. Schram, to be published.
- 4] B.F.M. Pots et al., Proc. 3rd Int. Conf. Waves and Instab. Plasmas, Palaiseau France, 1977, p 88-4B4.
- 5] J.J.A.M. van der Mullen et al., Proc. 13th ICPIC, Berlin, 1977, p. 323-324.
- 6] P.A.W. Tielemans, B. van der Sijde, private communications.
- 7] P. Janssen, to be published (thesis 1979).



CONTINUOUS EMISSION, LOWERING OF THE IONIZATION POTENTIAL AND TOTAL EXCITATION CROSS-SECTIONS OF AN ATMOSPHERIC THERMAL PLASMA

R.J. Rosado, D.C. Schram and J. Leclair.

Eindhoven University of Technology, Eindhoven, the Netherlands.

Introduction. A careful study of the relation between the electron density, n_e , and the electron temperature, T_e , in an atmospheric arc plasma, shows an approach to local thermodynamic equilibrium (LTE) at large values of n_e [1]. Our measurements can be interpreted in terms of a Partial LTE (PLTE) model, in which the ground state is overpopulated with respect to the other excited states. This overpopulation is shown to be caused by radiative recombination in ref. [1].

The relative overpopulation of the ground state as a function of T_e , is fairly sensitive to small variations in, both, the transition probability, A , and the value for the lowering of the ionisation potential, $\Delta\chi_0$; when an accurate value of A is available, an estimate of $\Delta\chi_0$ can be made. The total cross-section for excitation from the neutral ground state was derived from the measured degree of overpopulation. In addition we calculated the emissivity of the free-bound UV recombination radiation, which proves to be quite large in the 70-80 nm spectral range. Finally, we give some results for the continuum radiation and for the Stark parameters at $\lambda = 700$ nm.

Experimental method and data handling. The experimental method has been described in [1]. It is based on the assumption of PLTE. The source function, S , is then given by

$$S = \frac{\epsilon(\lambda)}{\kappa(\lambda)} = \frac{2hc^2}{\lambda^5} \left[\exp\left(\frac{hc}{\lambda kT_e}\right) - 1 \right]^{-1}.$$

The source function has been determined for several transitions in the Ar neutral spectrum. To this end we measured emission and absorption (λ -)profiles of selected lines (with appropriate optical thickness; $\kappa(\lambda)\lambda < 3$), at 300-1000 λ -positions over the wavelength range of the line and its adjacent continuum. The line source function proved to be constant over the line profile, and close to the continuum source function.

The experimental profiles were then fitted with

theoretical voigt profiles, for $c(\lambda)$ and $\kappa(\lambda)$, by a least squares minimisation procedure, with parameters: the source function, the optical thickness at the line center, the continuum absorption as a function of wavelength, the position of the line center, the lorentzian width of the line, and a factor accounting for the total transmissivity of the optical system. The gaussian component of the profiles was set equal to the Doppler width at T_e . Each theoretical profile was then convolved with the measured apparatus profile of the monochromator used, and compared with the measured profile. Iteratively the best fit was obtained. In this way T_e was determined using all the available information. In addition, line broadening parameters and continuum emissivities were obtained. n_e was calculated from the emission coefficient using Saha's equation. The neutral density, n_0 , followed from Dalton's law ($p = n_k T$). This value of n_0 was then compared with the value, $n_{0,s}$, obtained from LTE, in order to calculate the overpopulation of n_0 .

Results. The measurements, mainly on the 696.5 nm line, were carried out in an atmospheric, water cooled arc plasma. The channel diameter is 5.10^{-3} m and the plasma length is $9.7.10^{-2}$ m. The arc current was varied from 40 A to 250 A.

1. Influence of $\Delta\chi_0$ and A . Figure 1 is a plot of the overpopulation of the ground level, expressed in $b = n_0/n_{0,s} - 1$, which shows the expected asymptotic behaviour, approaching 0 at large values of T_e . In the calculation of $b(T_e)$ we used $A = 67 \cdot 10^5$ and $\Delta\chi_0$ from Ecker and Kroll's formula (cf. [2]). The function $b(T_e)$ is very sensitive to variations δA in A and $\delta(\Delta\chi_0)$ in $\Delta\chi_0$:

$$\delta b = \frac{n_e}{n_{0,s}} \left(\frac{\delta(\Delta\chi_0)}{kT_e} + \frac{\delta A}{A} \right).$$

In particular at high temperatures, when $n_e/n_{0,s}$ becomes large and the asymptotic behaviour of $b(T_e)$ is known, minimization of δb can provide additional

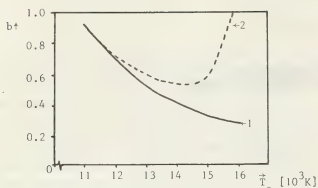


Fig. 1 Overpopulation factor $b = n_0/n_{0,s} - 1$ as a function of T_e , for Ar at 1 atm.
curve (1) with $\Delta\chi_0$ from Ecker-Kroll
curve (2) with $\Delta\chi_0$ from Unsold, Ecker-Weizel, Brunner

information on A and $\Delta\chi_0$. Assuming A to be more accurately known than $\Delta\chi_0$ we investigated the effect of different assumptions in the calculation of $\Delta\chi_0$ on $b(T_e)$. The result is given in fig. 1, in which curve 2 is the $b(T_e)$ relation obtained with the same value of A as in curve 1, but a different value of $\Delta\chi_0$: a mean value from the calculations of Unsold, Ecker-Weizel and Brunner (e.g. [2]). As can be seen curve 2 does not show the expected asymptotic behaviour, indicating that Ecker and Kroll's formula, in which the Debye length is used instead of the interparticle distance, is more satisfactory.

2. Total excitation cross-section. Assuming that radiative recombination to the ground level is the dominant mechanism causing the overpopulation in our PLTE model, we find, using the principle of detailed balancing:

$$b = \frac{n_e}{n_{0,s}} \frac{\beta_{3p}^{(2)}(T_e)}{\gamma_{3p}(T_e)}.$$

$\beta_{3p}^{(2)}(T_e)$, the radiative recombination coefficient, can easily be found from detailed balancing, using the published values for the photo-ionisation cross-section (cf. [3]). It is more difficult to obtain accurate values for $\gamma_{3p}(T_e) = \Sigma \langle \sigma v \rangle_e^{\text{exc}} + \langle \sigma v \rangle_e^{\text{ion}}$, the total excitation and ionisation cross-section from the ground level. Especially in the temperature range of interest (1-1.5 eV) the excitation cross-sections $\sigma(v_e)$ are not accurately known and depend much on the threshold behaviour, which in its turn is also not accurately known. With theoretical values for $\beta_{3p}^{(2)}(T_e)$, [3], we have determined $\gamma_{3p}(T_e)$ from the measured values of b and n_e . The result is given in fig. 2 (points). The qualitative dependence of γ_{3p} on T_e is as expected, although our values indicate that the threshold behaviour of $\gamma_{3p}(T_e)$ is

less steep than indicated in the literature.

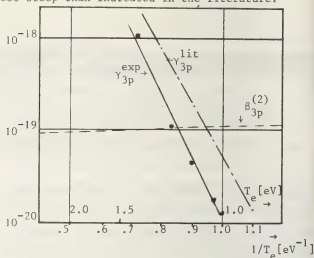


Fig. 2 Total excitation and ionisation cross-section γ_{3p} as function of T_e , for Ar at 1 atm. Also shown is the radiative recombination coef. $\beta_{3p}^{(2)}$.

γ_{3p}^{lit} : literature values for γ_{3p} .

γ_{3p}^{exp} : measured values for γ_{3p} .

3. Continuum emission and Stark parameter. Using the theoretical values for $\beta_{3p}^{(2)}$, we calculated the total power of the continuum free-bound radiation, which amounts to about 1 kW per cm arc length, for $\lambda = 72$ to 78 nm. This makes similar arcs very attractive as UV "light" sources. From our fitting procedure we also obtained the Biberman factor, ξ_{fb} (at $\lambda = 700$ nm) and the Stark broadening parameter, α . The results are summarized in table 1. The continuum absorption and the ξ_{fb} values agree with Schlüter's values [4,5]. The mean value for α , $\alpha = 7.4 \cdot 10^{-24} \text{ Å}^3$ differs by almost 40% from Griem's value, $\alpha = 12 \cdot 10^{-24} \text{ Å}^3$ [6].

Table 1.

I	T_e	n_e	K_{line}	K_{cont}	ξ_{ff}	ξ_{fb}
[Å]	[$10^3 K$]	[$10^{23} m^{-3}$]	[m^{-1}]	[m^{-1}]		
60	12.4	0.7	35.1	0.10	1.23	1.73
100	13.4	1.2	37.1	0.36	1.24	1.84
140	14.3	1.6	34.0	0.56	1.24	1.89
180	15.0	1.8	29.9	0.66	1.24	1.99
220	15.4	1.9	27.8	0.70	1.24	2.05
250	16.0	2.0	21.7	0.71	1.24	2.05

References.

- [1] Leclair, J. and Schram D.C. Proc. 13th ICPIC, Berlin (1977) p. 483.
- [2] Lochte-Holtgreven, ed., "Plasma Diagnostic" (1968) p. 157.
- [3] Katsonis, K., Thesis, Université de Paris-Sud (1962).
- [4] Schlüter, D., Z. Astrophys. 56, 43 (1962).
- [5] Schlüter, D., Z. Phys. 201 (1968), 80.
- [6] Griem, H., "Spectral line broadening by plasmas", academic Press (1974).

POSITIVE CORONA ONSET IN ATMOSPHERIC AIR- A MULTIPLE AVALANCHE PROCESS

G.C. Crichton, I.W. McAllister and E. Bregnsbo.

The Technical University, Department of Physics, Building 309B, DK 2800 Lyngby, Denmark.

Introduction: The basic assumption incorporated in the majority of models used to predict positive corona onset conditions in atmospheric air is that of a *single* electron avalanche developing to some critical magnitude, e.g. see [1,2]. The present paper describes an experimental investigation into the nature of the discharge processes leading to corona formation.

The experimental gap consisted of an inverted positive point/plane arrangement, the gap length being fixed at 150 mm. The point electrode, of overall length 200 mm, was a rod of 20-mm diameter with a hemi-ellipsoidal tip for which the minimum radius of curvature was 5 mm. The light emission associated with the discharge development was recorded by means of a photomultiplier (PM). To optimise the detection sensitivity, quartz optics were used to focus the highly stressed region of the gap, i.e. the gas volume adjacent to the point electrode tip, on to the PM photocathode. With this recording system electron avalanche activity could be detected oscillographically at ~2% below the corona onset voltage level. Measurements were performed at and below corona onset under the application of a direct voltage. The records obtained are shown in Fig.1.

Results and Discussion: At a voltage level of ~2% below the onset level, the records (Fig.1a) indicate that the ionisation activity occurring within the active volume ($E > 2.42$ kV/mm [3]) is comprised of a chain of individual electron avalanches of some 800 ns total duration. The average generation time between avalanches is some 40 ns. As the discharge gap length is 150 mm, this very short generation time indic-

ates that cathode associated phenomena cannot play an active rôle during this stage of the discharge development and consequently gas-ionising radiation is considered to be the mechanism responsible for this generation process.

As the voltage is raised towards the onset level, the records obtained (Figs. 1b & c) indicate that the individual avalanches increase in magnitude leading to a partial overlap of the pulses within each chain. The time between chains is on average several orders of magnitude greater than that of the chain duration.

At the onset voltage level the occurrence of the avalanche/corona transition is most evident; e.g. a distinctive break occurs in the trace of the photomultiplier oscillogram, see Fig.1d. These transition pulses display a consistent peak value ($\pm 3\%$) prior to the rapid development which leads to the corona discharge.

Although avalanche development can occur throughout the active volume, the greatest development will be in the proximity of the maximum field strength. Hence the resulting spatial distribution of photoelectrons together with the additive effect of the initial space-charge field will induce a self-focussing of the subsequent discharge growth. In addition, owing to the low value of the relative charge density, i.e. the ratio of positive ions to neutral molecules in the head of the initial avalanche ($< 1:10^6$), it is suggested that the subsequent avalanche space charges will fully overlap the primary space charge distribution. Thus avalanche development will occur in a field which is being continuously augmented by the accu-

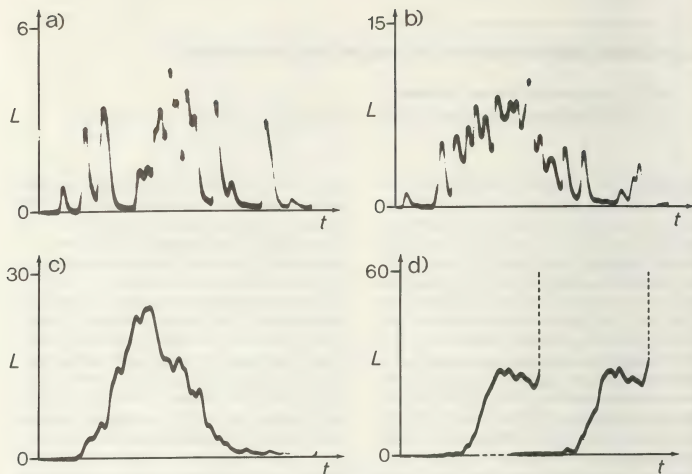


Fig.1. PM oscillograms of the electron avalanche phenomenon prior to corona onset. V_0 - corona onset voltage.

mulation of space charge until the generation process either terminates owing to avalanche statistics [4] or becomes unstable precipitating a corona discharge. A consequence of this electrostatic focusing of the avalanche generation process is that at onset the initial corona development should be located along the field line associated with the maximum field strength. A typical image intensifier record of the corona discharge in the anode region supports this viewpoint, Fig.2.

Conclusion: The experimental evidence presented illustrates that at onset the positive corona discharge in atmospheric air does not result from the formation of a single critical avalanche but from the accumulative effects of an intrinsic avalanche generation process. Thus the single avalanche concept embodied in the majority of corona onset models is at variance with these experimental observations.

L - relative light intensity.
Time scale: $\rightarrow 200$ ns
a) $98\%V_0$, b) $99\%V_0$, c) $99.8\%V_0$, d) V_0 .

References:

- 1) Les Renardières Group, *Electra* No. 23, 53 (1972).
- 2) E. Nasser et al., *J.Appl.Phys.* **45**, 3396 (1974).
- 3) H.A.Boyd et al., *Nature* **210**, 719 (1966).
- 4) H. Raether, 'Electron Avalanches and Breakdown in Gases' (Butterworths, 1964).

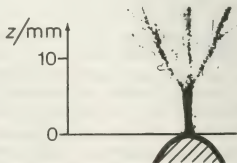


Fig.2. Image intensifier record of a positive corona discharge in atmospheric air at the onset level.

DETERMINATION OF LOW PROBABILITY FIRST BREAKDOWN VOLTAGES IN COMPRESSED SF₆S. Vibholm, A. Pedersen and P. Thyregod^{*}.

^{*}The Technical University, Department of Physics, Building 309B, DK-2800 Lyngby, Denmark.
^{*}The Technical University, IMSOR, Building 349, DK-2800 Lyngby, Denmark.

1. Introduction.

A method is described which determines the probability for the first breakdown near onset. The method is used in an analysis of the effect of surface roughness on low probability first breakdown in compressed SF₆ at positive polarity.

2. Experimental design.

A voltage level U_0 just below the withstand value is selected such that breakdown will never occur. N voltage impulses are then applied at this level. Another voltage level $U_1 = U_0 + \Delta U$ is selected and further N impulses are applied. This is continued until the first breakdown occurs at shot number n at a level $U_k = U_0 + k\Delta U$. The voltage level U_k represents the breakdown voltage for a low value fractile. The value of this fractile depends on the chosen value of ΔU and N .

3. Statistical theory.

Let $p_k(U_0, \Delta U, N, \delta, \beta)$ denote the probability for the first breakdown occurring at step number k ($k = 1, 2, \dots$) with the origin at U_0 . The parameters δ and β are, respectively, the position parameter and the scale parameter of the associated breakdown distribution. Changes in position and scale parameters can be compensated by changes in origin and step value. This means that

$$p_k(U_0, \Delta U, N, \delta, \beta) = p_k\left(\frac{U_0 - \delta}{\beta}, \frac{\Delta U}{\beta}, N, 0, 1\right) \\ = p_k(u, \Delta u, N).$$

Considering extremely low value fractiles only, it can be shown that by a suitable choice of origin and scale there is hardly any noticeable difference between the various possible probability distribu-

tions, e.g. normal, Weibull or double exponential /2/.

By choosing the normalized double exponential minimum distribution

$$F(u) = 1 - \exp(-\exp(u))$$

we obtain

$$p_k(u, \Delta u, N) = p_k(u + \ln N, \Delta u, 1).$$

As a change in N can be counteracted by shifting the position of the origin, it is sufficient to consider $N = 1$.

$$p_1(u, \Delta u) = F_0(u + \Delta u) = 1 - \exp(-\exp(u + \Delta u))$$

$$p_k(u, \Delta u) = \exp\left(-\sum_{j=1}^{k-1} \exp(u + j\Delta u)\right) F_0(u + k\Delta u) \\ k = 2, 3, \dots$$

A sequence of elementary calculations leads to the following expressions

$$p_1 = F_0(u + \Delta u) \\ p_k = [F_0(u + \eta + k\Delta u) - F_0(u + \eta + (k-1)\Delta u)] / [1 - F_0(u + \eta)]$$

$$\eta = \ln \frac{\exp(\Delta u)}{\exp(\Delta u) - 1} \quad \eta > 0 \vee \Delta u > 0$$

in which $k = 2, 3, \dots$ gives p_k in the intervals $(u + \eta + (k-1)\Delta u, u + \eta + k\Delta u)$ for a standard double exponential distribution truncated below the corrected origin $u + \eta$. The following approximations are now introduced:

1. p_1 is replaced by $F_0(u + \eta + \Delta u)$,
2. For $F_0(u + \eta)$ close to zero p_k is replaced by $[F_0(u + \eta + k\Delta u) - F_0(u + \eta + (k-1)\Delta u)]$.

This means that the non-truncated distribution is replacing the truncated distribution.

The mean value and variance of the distribution are then given by, respectively,

$$E(k) = \frac{-\gamma - \mu - \eta}{\Delta u}, \quad V(k) = \frac{\pi^2}{6(\Delta u)^2},$$

in which $\gamma = 0.5772\dots$ is Euler's constant.

Assuming that ΔU has a sufficiently small value the breakdown probability corresponding to the mean value of k will be given by

$$P = F(U_s) = F(U_0 + E(k)\Delta U)$$

$$P \approx 1 - \exp\left\{-\frac{1}{N} (1 - \exp(-\Delta u)) \exp(-\gamma)\right\}$$

$$P \approx 1 - \exp\left\{-\frac{1}{N} \Delta u \exp(-\gamma)\right\} \approx \frac{\Delta u}{N} \exp(-\gamma)$$

$$P \approx \frac{1}{N} \exp(-\gamma) \frac{\pi}{\sqrt{6}V(k)} \approx \frac{0.72}{N\sigma_k},$$

in which σ_k is the standard deviation of the step number by repeated testing.

4. Determination of low probability first breakdown in compressed SF₆.

The breakdown withstand voltage of an SF₆-insulated high voltage apparatus is largely controlled by the inherent surface roughness of the electrodes. This effect is so complex that it can only be determined experimentally.

Tests were carried out in SF₆ at a pressure of 5 bars on a system of coaxial cylinders, of which the inner cylinder was made of aluminium and had a diameter of 22.0 mm. The outer cylinder was made of stainless steel with a diameter of 59.8 mm and had suitably rounded edges. The overall length of the cylindrical part was 80 mm. The outer cylinder was used throughout the experiments, but was carefully cleaned after each individual spark, whereas the inner cylinders were discarded as soon as they had been subjected to one single spark. Repeated use of the outer cylinder is justified by the fact that the electric field near its surface is so low that no ionizing processes are possible. Five sets of inner cylinders were used, each set consisting of ten cylinders with a constant surface roughness R_a . Within each set R_a varied no more than 10%. Before testing each cylinder was carefully cleaned in an ultrasonic bath with a suitable cleaning agent. The gas was renewed after each in-

dividual breakdown. The applied voltage was a 1/2500 μ s impulse wave of positive polarity. Each of the 50 cylinders was tested according to the experimental design with $N = 100$ and $\Delta U = 2$ kV. It is essential that each sample is subjected to one breakdown only, because one single spark will inevitably change the conditions in the system.

Each voltage level must be reproducible with a high degree of accuracy. These requirements were readily met by an automatic impulse generator /3/.

For the system under consideration the theoretical breakdown voltage U_{th} for idealized electrodes is 535 kV taking into account that the compressibility factor for SF₆ at 5 bar is 0.94 /4/. The experimental results are summarized in Table 1. The values given for U_s for each individual surface roughness are based on approximately 40,000 shots.

$R_a/\mu m$	U_s/kV	$p/\%$	Confidence limits 95%/%	Roughness factor U_s/U_{th}
0.1	437	0.11	0.06 - 0.17	0.82
0.4	492	0.13	0.07 - 0.19	0.92
1	413	0.04	0.02 - 0.06	0.77
5	396	0.07	0.04 - 0.11	0.74
35	321	0.19	0.10 - 0.28	0.60

Table 1.

It is seen that even the best polished electrode surface is subjected to a considerable lowering of the first breakdown voltage due to the effect of surface roughness.

5. References.

- /1/ S. Vibholm, A. Pedersen, P. Thyregod: Proc. XIII ICPIG, Part I, p. 431-432, Berlin 1977.
- /2/ W. Hauschild, W. Bürger: Z.elekt. Inform.-u. Energietechnik 2, p. 283-295, Leipzig 1975.
- /3/ J.M. Christensen, G.C. Crichton, I. W. McAllister, A. Pedersen, S. Vibholm: ISH-Zürich, p. 128-133, 1975.
- /4/ B.H. Crichton, D.J. Tedford: J.Phys.D: Appl.Phys. 2, p. 1089-1093, 1976.

QUANTITATIVE ANALYSIS OF INTERACTION BETWEEN A HIGH-PRESSURE PLASMA COLUMN AND SURROUNDING LIQUID

O. Havelka and Z. Vávra.

Faculty of Electrical Engineering of the Technical University Brno, C.S.S.R.

If there exists a plasma column in liquid a thermal decomposition of liquid into charged particles, gases and vapour starts in the plasma-liquid boundary. If all this takes place in a closed space, the development of hot gases and vapour causes high pressure in this space. To determine this pressure it is necessary to know the energy magnitude transformed by the plasma column and the factors of liquid transformation into gases and vapour, as well.

To simplify the complicated thermodynamical and thermochemical processes in the contact area of plasma column and liquid, we assume at least quasiisothermal conditions and we express the unit volume of gases and vapour reduced to standart atmospheric pressure p_a (1 bar = 10^5 Pa) by coefficient ρ [m^3/J], from the viewpoint of usual calculation method. Then the total gas volume V_g developed from the energy Q can be estimated by the expression

$$V_g = \rho_g(Q) = \rho Q \quad (1)$$

Similarly, for the liquid volume V_e transformed into gases and vapours by energy Q , we can write

$$V_e = \rho_e(Q) = \eta Q \quad (2)$$

The dimensions of transformation factors ρ and/or η are m^3/J (m^3/Ws). They have not been perfectly known yet. As direct transformation factor measurements during the existence of plasma in liquids is practically unrealizable, the authors have designed an indirect method by combining measurements and calculation. Even though this method need not give us exact results from the viewpoint of physics (momentary temperatures of gases and vapours are not known) it provides completely satisfactory results for the purpose required, i.e. for

the calculation of pressure in a closed space with a plasma column (electric arc) under the liquid level because it emanates from the calculation method selected as well as from measurements under conditions corresponding with a real state.

Let us assume a closed chamber partially filled with liquid only, that is, with a free space the liquid level of volume W . The plasma under the liquid level liberates energy Q , pressure p is formed in the chamber, which can be calculated by applying Boyle's law

$$p = \frac{p_a \rho Q}{W + \eta Q} \quad (3)$$

In the chamber the pressure p is measured with the aid of suitable equipment simultaneously the amount of liberated energy Q . If we realize the plasma column as an electric arc we determine energy Q from the values of current i and from arc voltage u_0 either by measuring or calculating it from the relation

$$Q = \int_0^t u_0 i dt \quad (4)$$

observing the procedure [1]. Thus, from relation (3) we know all magnitudes except ρ and η . If we record all quantities in dependence upon time t during the test, we start from the intensities of pressures p_1 and energy Q_1 in different times t_1 and t_2 . Thus we get the following relations for coefficients ρ and η :

$$\begin{aligned} \rho &= \frac{p_1 p_2 W (Q_2 - Q_1)}{p_a (p_1 - p_2) Q_1 Q_2} \\ \eta &= \frac{W (p_1 Q_2 - p_2 Q_1)}{(p_1 - p_2) Q_1 Q_2} \end{aligned} \quad (5)$$

Nevertheless, the evaluation of the carried out measurements proved that there is no linear dependence between the volume of gases produced and decomposed liquid and energy Q , that means, transformation factors ρ and η are not constants as

assumed previously but power functions dependent on energy Q :

$$f = f^* Q^\epsilon; \quad \eta = \eta^* Q^\epsilon \quad (6)$$

Then

$$V_g = f Q = f^* Q^{\epsilon+1}; \quad V_g = \eta Q = \eta^* Q^{\epsilon+1} \quad (7)$$

If we substitute these modified relations into formulas (5) they become a new form:

$$f^* = \frac{p_1 W}{p_2 Q_1} \left[1 + \frac{p_1 Q_2 - p_2 Q_1}{Q_2^{\epsilon} (p_2 - p_1)} \right] \quad (8)$$

$$\eta^* = \frac{W (p_1 Q_2 - p_2 Q_1)}{(p_2 - p_1) Q_1^{\epsilon} Q_2^{\epsilon}}$$

The examination of transformation factors according to this method was carried out for transformer oil used in oil circuit breakers. The tests were carried out in a steel chamber with the plasma column length of 30 to 45 mm with an electric arc of 2000 A, 50 Hz AC. The arc burning time changed from 20 to 50 ms, the arc energy Q from 5 to 80 kJ. Measured pressures p in dependence on energy Q are represented in Fig.1.

With regard to the pressure dispersion for the given magnitude of energy it is evident that the magnitude of produced gases and vapours changes, so that their medium temperatures change correspondingly too. Then the magnitude factor f should change as well within the range given by limit curves of pressure field in Fig.1. The decomposed liquid volume remains proportional to the liberated energy so that the transformation factor η has a unique magnitude. This consideration was confirmed by calculation results obtained from a digital computer. The calculation results are the following:

$$\begin{aligned} f_{\max} &= f_{\max}^* Q^\epsilon = 2.85 \cdot 10^{-6} Q^{0.35} \\ f_{\min} &= f_{\min}^* Q^\epsilon = 1.13 \cdot 10^{-5} Q^{0.35} \\ \eta &= \eta^* Q^\epsilon = 1.00 \cdot 10^{-9} Q^{0.45} \end{aligned} \quad (9)$$

Oil transformation factors dependence on energy Q is represented graphically in Fig.2. The recalculated pressure field envelopes for $\alpha = \epsilon + 1 = 0.65$ have their courses drawn in Fig.1 in full lines and confirm the correctness of values (9).

REFERENCES:

- [1] O.Havelka: The highest energy values of intensively cooled high-pressure arc of AC with constant and variable length. 11th ICPG, Prague 1973, paper No 224
- [2] Z.Vávra: New method of measuring oil thermal decomposition with high-pressure arc in closed space. Candidate's thesis, Brno 1978.

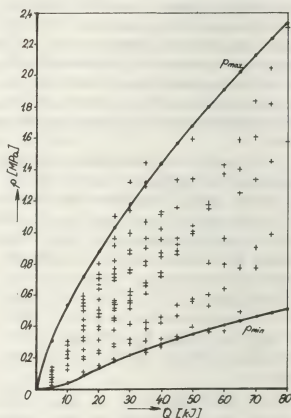


Fig. 1

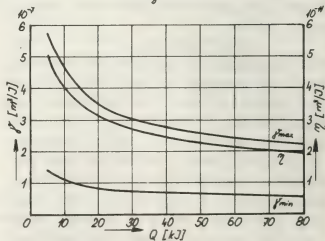


Fig. 2

THEORETICAL MODEL OF CURRENT-ZERO BEHAVIOUR OF AXIALLY BLOWN ARC IN SF₆M. Hrabovsky, M. Konrád, P. Skoda[†].Research Institute of Electrical Engineering [†]Computer Centre, OKD Praha, Prague, Czechoslovakia.Introduction

Much attention has been recently devoted to the study of current-zero behaviour of high pressure, a-c arc in supersonic nozzle flow /1-5/. Radial conduction enhanced by turbulence is the most effective energy transport mechanism within arc column in the current-zero region. In several papers /3-5/, transient behaviour of turbulence dominated arc with fixed radial temperature profile is theoretically studied, influence of electric circuit not being taken into account. We present the model of transient arc with time dependent radius of conductive core and variable temperature profile. Interaction of arc with connected electric circuit is considered in model calculations. Both the arc-circuit interaction and the temperature-profile changes are supposed to have considerable effect on resulting dynamic arc behaviour.

Model Equations and Results of Calculation

Following assumptions are used to formulate model equations:

1. The only effective energy loss mechanism is radial heat conduction due to the turbulence. The turbulence originates in the shear flow associated with the existence of strong radial temperature gradient within the arc column.
2. Arc column has cylindrical symmetry.
3. Conductive arc core of radius $r_c(t)$ is surrounded by the zone of intermediate temperature with fixed radius R , for $r=R$ the temperature reaches the temperature of cold gas. The same energy transport mechanism, as within the arc core, is effective in the intermediate zone.

The energy balance equation has then a form

$$\frac{1}{r} \frac{\partial}{\partial r} (r k_t \frac{\partial T}{\partial r}) + \sigma E^2 = \varrho C_p \frac{\partial T}{\partial t} \quad (1)$$

where effect of turbulence is described by turbulent thermal conductivity k_t /3-6/.

Conductivity k_t is given by /7/

$$k_t = \frac{\varrho C_p \mathcal{E}}{Pr_t} \quad (2)$$

where \mathcal{E} is turbulent kinematic viscosity and Pr_t is turbulent Prandtl number. To describe effect of turbulence on the arc, formulae for free turbulent shear flow were adapted /3-6/. \mathcal{E} is considered to be proportional to the axial velocity c /6/, which is equal to the velocity of sound at given temperature. Prandtl number Pr_t is constant and approximately equal to 0.5 for free turbulent flow /7/. Then from (2) we obtain $k_t = \lambda \varrho C_p c$ where λ is constant with the dimension of length. In Fig. 1 the temperature dependence of k_t/λ is given for SF₆ at 0.8 MPa, calculated from data in /3/. For the solution of (1), it is convenient to introduce turbulent heat flux potential $G = \int_0^r k_t/\lambda \, dT$ /6/ as variable instead of T . Equation (1) acquires then form

$$-\frac{\partial^2 G}{\partial r^2} + \frac{1}{r} \frac{\partial G}{\partial r} + \frac{\sigma E^2}{\lambda} = \frac{1}{\lambda c} \frac{\partial G}{\partial t} \quad (3)$$

Arc current is given by Ohm's law

$$i = 2\pi E \int_0^R r \sigma \, dr \quad (4)$$

Equations (3) and (4) with unknowns $G(r, t)$, $i(t)$, $E(t)$ can be solved using data of transport properties of the gas $\sigma(G)$, $c(G)$ together with circuit equations. The material functions $\sigma(G)$ and $c(G)$, which determine the effect of gas properties on the arc behaviour, are given in Fig. 2 for SF₆ at $p = 0.8$ MPa.

Calculations were made for the circuit with serial inductance L and parallel capacity C_1 and resistive-capacity RC_2 branches. Equations (3), (4) together with circuit equations were normalized to reduce number of independent constants. Nondimensional energy equation and Ohm's law are given by

$$\frac{\partial^2 \hat{G}}{\partial x^2} + \frac{1}{x} \frac{\partial \hat{G}}{\partial x} + \xi \hat{\sigma}^2 = \eta \frac{1}{c} \frac{\partial \hat{G}}{\partial \tau} \tag{5}$$

$$\hat{i} = \pi \hat{v} \int_0^1 x \hat{\sigma} dx \tag{6}$$

where $\hat{G}, \hat{\sigma}, \hat{c}$ are functions normalized to their axial value at $t=0$, $\hat{i}=i/i_0$, $\hat{v}=v/v_0 = E/E_0$, $x=r/R$ and $\tau=t/\tau_0$, where τ_0 is characteristic time constant. The behaviour of arc in a given circuit is determined by two nondimensional parameters

$$\xi = \frac{R^2 E_0^2 G_{a0}}{\lambda G_{a0}} \tag{7}$$

$$\eta = \frac{R^2}{\lambda \tau_0 c_{a0}} \tag{8}$$

further by the initial profile $G(x, t=0)$ and initial axial value G_{a0} , which define also the value of parameter $X = \left(\int_0^1 x \sigma(x, t=0) dx \right)^{-1}$. The Bessel profile of G within conductive core and logarithmic profile in intermediate region are supposed to occur at time $t=0$

$$\hat{G}(x, \tau=0) = \hat{G}_h + (1-\hat{G}_h) J_0(\alpha_1 x) \text{ for } x \leq x_{co} \tag{9}$$

$$\hat{G}(x, \tau=0) = \alpha_2 \ln x \text{ for } x_{co} < x \leq 1 \tag{10}$$

where x_{co} is a normalized radius of conductive core at $t=0$, $\hat{G}_h = G_h/G_{a0}$, where G_h is minimum value of G for which $\sigma \neq 0$. For given G_{a0} the values of $\hat{G}_h, x_{co}, \alpha_1$ and α_2 can be evaluated from the condition of continuity of heat flux (i.e. $\partial \hat{G} / \partial x$) at $x=x_{co}$.

Calculated waveforms of current, voltage, axial value \hat{G}_a and radius of conductive core x_c are shown in Fig. 3 for the case near the boundary for thermal reignition of arc. Fig. 4 presents the results in the Mayr's plot giving information about character of dynamic behaviour of the arc. The calculated curve is compared with the results of measurements on SF_6 arc in the same electric circuit. It can be seen that observed typical rapid changes of relative derivative of conductivity in the vicinity of current zero can be properly described by the model.

References

/1/ Hermann W. et al., IEEE Trans. PAS-95 (1976), 1165
/2/ Topham D.R., Proc. IEE 120 (1973), 1568

/3/ Swanson B.W., IEEE Trans. PAS-96 (1977) 1697
/4/ Hermann W., Ragaller K., IEEE Trans. PAS-96 (1977), 1546
/5/ El-Akkari F.R., Tuma D.T., IEEE Trans. PAS-96 (1977), 1784
/6/ Thiel H.G., Proc. IEEE 59 (1971), 508
/7/ Schlichting H., Boundary Layer Theory, New York, McGraw-Hill, 1960
/8/ Bartl J. et al., Report ÚSPE-43, 1977, Technical University Brno

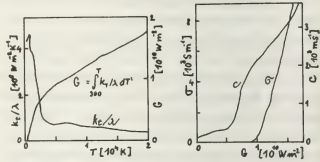


Fig. 1

Fig. 2

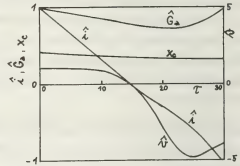


Fig. 3

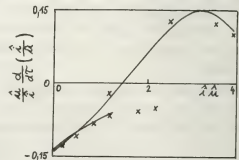


Fig. 4

SPECTROSCOPIC ANALYSIS OF PREBREAKDOWN-PHASE FROM POSITIVE CORONA INTO SPARK IN N_2

G.H. Bauer.

Institut fuer Physikalische Elektronik, Universitaet Stuttgart, F.R.G.

Abstract. The propagation of prebreakdown (streamer) from a quasistationary positive point-to-plane corona into spark in N_2 is investigated by spatial and time resolved spectroscopic methods.

Two luminous fronts, starting from the anode point, are found to traverse the gap before the bright spark occurs which is correlated to the collapse of the applied voltage.

An evaluation of the spectroscopic results and their correlation to the electric current give information about data like diameter, velocity of the first front (streamer) and its gas temperature, electron energy, electric field and number resp. density of electrons.

Experimental setup and procedure.

A high frequency coaxial cable discharge system ($>1\text{GHz}$) described in /1/, has been used to investigate the transition of a positive corona into spark. The electrodes consist of a point (Pt, radius $130\text{ }\mu\text{m}$) and a polished plane (Pt) in a distance of 18mm . The discharge tube is filled with N_2 , 53bar (impurities $<100\text{ ppm}$, mass-spectr. analysis). The predischage, which is followed by the bright spark, starts at 14.6kV (rise of voltage 1.3kV/ms), so that this process can be repeated periodically by 90 Hz .

The radiation emitted from the discharge is focused by a parabolic mirror perpendicular to the slit of a 0.3 m monochromator (grating 1200 L/mm , blazed 300 nm resp. 500 nm , $\frac{\Delta\lambda}{\lambda} \approx 2.6\text{ nm/nm}$). To the monochromator a fast photomultiplier with high gain is matched (risetime 2.5ns , cooled to -30°C).

Current measurements were made with a coaxial foil resistor/2/ (risetime $<100\text{ ps}$), which is installed in the discharge tube

system. For time scale correlation of radiation and current a pindiode was used with a risetime of 300 ps and a negligible delay. In this experiment radiation and electric current have been reproducible sufficiently, so that they could be detected either in a sampling oscilloscope (200 ps) with a connected digital averager or in a boxcar-averager (aperture time $<100\text{ ps}$).

Experimental results. The radiation occurring during this predischage, which precedes the spark, nearly exclusive originates from N_2 molecules. It mainly consists of the 2.pos. system ($C^3_{11} - E^3_{11g}$); very weak intensities of the 1.neg. system ($B^2_{1u} - X^2_{1g}$) could be observed too (about factor 10^{-2}). Both systems show a spatial-temporal development, which is interpreted as two ionizing/exciting fronts. Figure 1 and 2 show equidensities of relative radiation intensities of the two systems. These figures have been constructed out of the radiation intensities, which had been measured with axial and temporal resolution ($10\text{ }\mu\text{m}, 4\text{ns}$). This description is similar to a one wavelength concerning streak-camera-photo, that moreover does not show convolution effects of the radial profil of the discharge and the moving shutter.

Luminous fronts like these or similar ones have been detected in parallel geometry /3,4,5/ and in point-plane geometry /6,7/. The electric current corresponding to the fronts is shown in figure 3. There is a fast rise of current when the first front moves to the cathode and a sort of stagnancy in current rise when the second front moves with decreasing velocity to the plane. Additional a cathode spot can be observed.

Data for the first front. The evaluation of spectroscopic results for geometric data yields a diameter of $60\text{ }\mu\text{m}$ and a length of $(300-400)\text{ }\mu\text{m}$. The velocity at the anode is about $3 \times 10^7\text{ cm/s}$ increasing to $3 \times 10^8\text{ cm/s}$ at the cathode.

The gas temperature is determined from unresolved bands by simulating in a computer the convolution of rotational lines of all branches and the spectral profile function of the monochromator. Fitting the simulated function to the measured one yields a gas temperature of 350 K.

Electron energy is determined by measuring the relative ratios of radiative transitions of two band systems (e.g. 2.pos. and 1.neg. system). Taking into account the specific pressure dependent quenching-factor for each vibrational transition and regarding those sections of the whole band-system which had been detected, the ratios of exciting processes can be found. With an electron energy distribution (not Maxwellian!) that had been calculated by solving Boltzmann-transport-equation/8,9/ a variety of ratios for exciting processes is computed and fitted to the measured one. Thus a mean value of electron energy of $(6.5-7)\text{ eV}$ was found. The corresponding electric field is $(80-85)\text{ kV/cm}$.

The number resp. density of electrons in the first front, which now should be called streamer, is determined with data for the probability of exciting the 2.pos. system from Legler/10/. The results are shown in figure 4.

References:

- /1/ H. Albrecht et.al. BMFT-Band, Verlag TÜV Rheinland, 1973
- /2/ F. Wesner, ETZ-A, 94, 599 (1973)
- /3/ A.A. Doran, Z. Phys. 208, 472 (1968)
- /4/ K.H. Wagner, Z. Phys. 189, 465 (1966)
- /5/ P. Stritzke et. al. J. Phys. D 10, 2285 (1977)
- /6/ E. Marode, J. Appl. Phys. 46, 2005, (1975)
- /7/ T. Suzuki, J. Appl. Phys. 42, 3766, (1971)
- /8/ A.G. Angelhardt, Phys. Rev. A 135, 6A 1566, (1964)
- /9/ R. Winkler et. al., Beitr. Plasmaphys. 13, 273, (1973)
- /10/ W. Legler, Z. Phys. 173, 169, (1963)

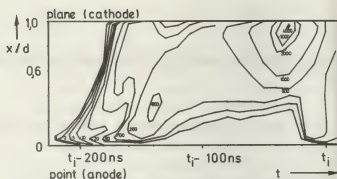


figure 1: rel. radiation intensity of the 2.pos. system in N_2 ($\lambda=337.1\text{ nm}$)

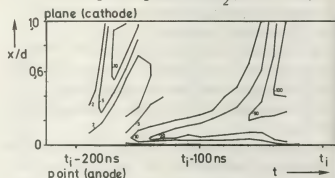


figure 2: rel. radiation intensity of the 1.neg. system in N_2 ($\lambda=391.4\text{ nm}$)

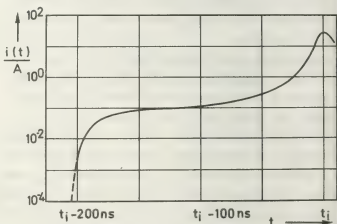


figure 3: development of discharge current

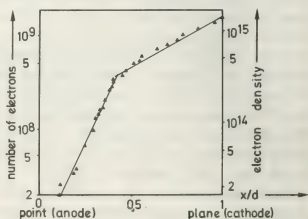


figure 4: number resp. density of electrons in the first front (streamer)

RECHERCHES SUR LA Foudre EN FRANCE

Le Groupe de Recherches de Saint-Privat-d'Allier.

Saint-Privat-d'Allier.

Une station expérimentale d'étude de la foudre a été érigée en 1973, dans le Massif Central à SAINT-PRIVAT-D'ALLIER (Haute-Loire). Sa principale originalité est le déclenchement artificiel des coups de foudre par la technique "fusée-fil" dont la validité a été démontrée avec succès par le Professeur M.M. NEWMAN.

LES OBJECTIFS

Cette station est exploitée conjointement depuis 1973 par ELECTRICITE DE FRANCE (EDF) et le Commissariat à l'Energie Atomique (CEA - Centres de GRENOBLE et de SACLAY) auxquels se sont associés en 1974 le Laboratoire de Détection et de Géophysique (CEA - LDG - BRUYERES LE CHATEL) en 1975 le Centre National d'Etudes des Télécommunications (CNET - LANNION) en 1977 l'Université de CLERMONT-FERRAND (Institut de Physique du Globe) et l'ONERA (Office National d'Etudes et de Recherches Aéronautiques - CHATILLON), et en 1978 le LPA (Laboratoire de Physique de l'Atmosphère de TOULOUSE). Cette collaboration a été établie pour tirer partie de la possibilité d'obtenir des coups de foudre en un lieu et à un instant choisis, chaque organisme ayant ses propres objectifs.

EDF étudie la protection des lignes THT contre les coups de foudre directs et les surtensions induites par les coups de foudre proches des lignes MT-BT, le CEA, intéressé par la physique de la décharge, étudie les propriétés générales des coups de foudre artificiellement déclenchés et des coups de foudre naturels; le Centre de GRENOBLE du CEA étudie pour sa part la tenue à la foudre de différents équipements. Le CNET a pour but principal la protection des lignes de télécommunication et étudie en collaboration avec le LDG la propagation des ondes électromagnétiques créées par les coups de foudre. L'ONERA effectue des recherches sur la protection des avions contre les phénomènes induits et les coups de foudre directs. L'IOPG recherche avec un radar météorologique une corrélation entre la structure des précipitations et des charges neutralisées

par la foudre. Le LPA étudie le champ électrique au sein des nuages à l'aide de ballons sondes.

LES INSTALLATIONS EXPERIMENTALES

La station expérimentale comprend essentiellement le site principal et 6 stations périphériques.

Le site principal comporte:

a) deux aires de tir: l'une à partir du sol, l'autre à partir d'un pylône, du type de ceux qu'utilise EDF pour les lignes 90 kV. L'ensemble permet de lancer 10 fusées au cours d'un orage, sans recharger les rampes de lancement.

b) Une centrale de commande, formée d'une double cage de FARADAY, qui constitue en même temps un abri sûr pour le personnel. Toutes les liaisons de commande sont effectuées par air comprimé, afin d'assurer une séparation électrique totale entre l'intérieur et l'extérieur de l'abri.

c) De nombreux équipements de mesure du courant de foudre, du champ électrique au sol, du champ électromagnétique proche, du champ acoustique, des phénomènes lumineux produits par la décharge, etc.

Les six stations périphériques, distantes de plusieurs kilomètres, permettent également des observations photographiques et optiques, des mesures du champ électromagnétique; le radar météorologique est quant à lui, installé à 12 km du site principal.

LA TECHNIQUE DE DECLenchement DE LA Foudre

La technique de tir utilisée a été mise au point par le CEA (Centre de GRENOBLE). Elle consiste à lancer vers les nuages d'orage une petite fusée du type paragrêle entraînant un mince fil métallique issu d'un dérouleur fixé au sol.

En l'absence d'un déclenchement, la fusée, freinée par le fil, est capable d'atteindre une hauteur de 700m en cinq secondes; pour des raisons de sécurité une charge explosive la détruit alors.

En présence de nuages orageux, le critère de réussite du déclenchement de la foudre est la valeur du champ électrique mesuré au sol; l'expérience a montré que le déclenchement est quasi-certain à partir d'un champ négatif (nuage négatif, sol positif) de

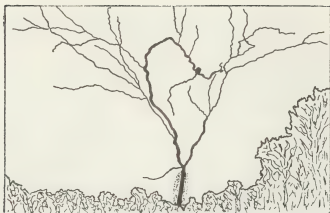


Fig.1 Photographie statique d'un coup de foudre déclenché, vu d'une distance de 2,7 km

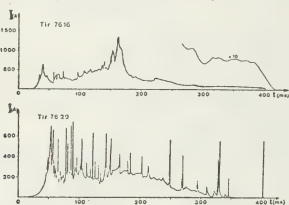


Fig.2 Composante persistante d'un coup déclenché:

- a) tir 7616 courant persistant seul
b) tir 7629 courant persistant avec impulsions superposées. (l'amplitude de ces dernières n'est pas respectée).

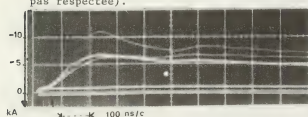


Fig.3 Impulsions de courant de foudre enregistrées avec un oscillo. à balayage rapide (tir 7716).

6 à 10 kV/m. Le coup de foudre se produit alors pour des longueurs de fil déroulé comprises entre 50 et 520m, c'est à dire bien avant que la fusée ait atteint sa hauteur maximale. Sans que la corrélation soit rigoureuse, il semblerait que le déclenchement est d'autant plus précoce que le champ au sol à l'instant du départ de la fusée est élevé. Les courants de foudre parcourent le fil, tout en le vaporisant rapidement, et peuvent être recueillis et mesurés au point d'arrimage.

LES CARACTERISTIQUES DE LA Foudre DECLENCHEE

Résultats généraux. En 6 années d'exploitation de la Station (1973-1978) 148 tirs ont été effectués au cours de 39 orages. 114 tirs se sont déroulés correctement, et 84 coups de foudre ont été déclenchés. Si on élimine les 34 échecs dus à des causes

mécaniques telles que rupture d'attelage du fil, etc on relève un taux de réussite des tirs de 73%, ce taux ayant même atteint 93% en 1978. Lorsque le tir est techniquement correct, l'échec est généralement lié à un coup de foudre naturel ayant devancé le déclenchement, ou à un champ insuffisant.

Observations optiques. Elles montrent que la foudre déclenchée artificiellement est du type ascendant (Fig.1) présentant des propriétés semblables à la foudre naturelle frappant les structures élevées.

Le coup de foudre est initié par un précurseur ascendant, se développant à partir de la fusée (upwards-leader) et progressant vers le nuage, en se ramifiant, avec une vitesse de 2 à $10 \cdot 10^4$ m/s. Lorsque ces ramifications atteignent le nuage il apparaît dans 2 cas sur 3 des réilluminations brèves et intenses, auxquelles correspondent des courants impulsionnels. On observe alors un "return-stroke" dont la vitesse mesurée en tenant compte de la longueur réelle du canal de l'éclair est comprise entre 0,5 et $2 \cdot 10^8$ m/s.

Analyse des courants. Un coup comporte toujours un courant persistant, inférieur au kA, s'écoulant pendant la décharge. Dans 2/3 des cas il s'y superpose une série d'impulsions brèves, de 10 à 20 kA et de temps de front inférieur à 0,5µs (Fig.2 & 3). Le tableau ci-dessous rassemble les données relatives à ces courants. Il indique le pourcentage des coups de foudre ayant dépassé les valeurs indiquées.

	90	50	10	MAX.
AMPLITUDE kA	2,5	12	21	42
RAIDEUR µs	0,1	0,3	1	qqqs
$\int i dt$ en Cb	7	30	120	140
$\int i^2 dt$ en A ² s	$6 \cdot 10^2$	$6 \cdot 10^3$	$5 \cdot 10^4$	$5,6 \cdot 10^4$
Nbre d'imp.	4	11	15	53
DUREE TOTALE µs	250	420	940	1070

Coups anormaux: Par un processus encore incomplètement éclairci, la foudre a quitté le fil au voisinage du sol à 14 reprises.

Comparaison avec les éclairs naturels. Semblables aux coups naturels, les coups déclenchés ont en commun avec les coups descendants les caractéristiques des impulsions secondaires mais en différent par l'absence d'une première impulsion, de forte amplitude mais de raideur moindre. Depuis deux ans les caractéristiques des éclairs naturels sont également mesurées.

En 1978 la collaboration de 8 équipes pour mieux connaître la foudre et ses effets sur divers équipements a permis d'obtenir de nombreux résultats qui seront présentés aux participants du Congrès.

THEORY OF ARC CLOGGING IN NOZZLES

P. Kovitya, J.J. Lowke and A.D. Stokes.

University of Sydney, Australia.

Introduction: Previously a simple channel model has been used to successfully predict properties of low current arcs in forced flow in a nozzle [1]. The present paper extends this treatment to large currents when mass flow through the arc is an appreciable fraction of the cold gas flow surrounding the arc. It is necessary to solve the axial momentum and mass continuity equations to obtain the axial pressure and velocity distributions. At sufficiently large currents the arc diameter equals the nozzle diameter at some axial positions. Then ablation from the nozzle wall markedly increases the pressure within the nozzle.

Theory: It is assumed that the arc plasma can be represented as a function of axial position z by area $A(z)$ and temperature $T(z)$, the arc being isothermal with radius. When the arc area attains the nozzle area it is assumed that all of the input electrical energy is absorbed at the nozzle wall either by thermal conduction or by the absorption of radiation. This energy then ablates wall material which is brought to the arc temperature and increases the plasma flow. The basic conservation equations and Ohm's law define the quantities $E(z)$, $T(z)$, $V(z)$, $V_c(z)$, $P(z)$, $A(z)$ and $\dot{m}(z)$ where E is the electric field, V and V_c the velocities of the plasma and cold gas respectively, P is the pressure and \dot{m} is the rate of mass entry into the arc in $\text{gm s}^{-1} \text{cm}^{-1}$. Ohm's Law defines the electric field for any input current I where $\sigma(T)$ is the electrical conductivity,

$$I = \sigma EA \quad (1)$$

The energy balance equation at the arc centre is

$$\rho_c C_p \frac{\partial T}{\partial t} = \sigma E^2 - U - \rho_c C_p V \frac{\partial T}{\partial z}; \quad (2)$$

ρ is the plasma density, C_p the specific heat, t the time and U the radiation emission coefficient giving net radiation emitted per unit volume at the arc centre.

The axial velocity and pressure distributions are

defined primarily by the coupled momentum and mass balance equation, i.e.,

$$\rho \frac{\partial V}{\partial t} = - \frac{\partial P}{\partial z} - \rho V \frac{\partial V}{\partial z} \quad (3)$$

$$\frac{\partial(\rho A)}{\partial t} = - \frac{\partial(\rho V A)}{\partial z} + \dot{m} \quad (4)$$

$$\frac{\partial(\rho_c (Q-A))}{\partial t} = - \frac{\partial(\rho_c V_c (Q-A))}{\partial z} - \dot{m} \quad (5)$$

Equations (4) and (5) express mass continuity for the plasma and cold gas regions respectively; the subscript c refers to the cold gas surrounding the arc and Q is the nozzle area. Rather than solve an additional equation for axial momentum for the cold gas we assume that the Mach number of the plasma equals the Mach number of the cold gas.

$$\text{Thus } V_c/a_c = V/a \quad (6)$$

where "a" is the sonic velocity.

The energy balance equation integrated over a cross section of the arc column is

$$\frac{\partial(\phi h A)}{\partial t} = \sigma E^2 - \frac{\partial(\phi h V A)}{\partial z} + \dot{m} h_c \quad (7)$$

where h is the enthalpy of the plasma. Because $h_c \ll h$ the term $\dot{m} h_c$ can be omitted. Equation (7) principally defines arc area when $A < Q$. However when the nozzle is clogged, i.e., when $A = Q$, this equation primarily determines the pressure in that for the steady state, P increases until $\phi h V Q$ at the exit equals the input electrical power. It is assumed no ablation occurs before the arc core diameter attains the nozzle diameter.

Manipulating equations (2), (4) and (7) together with the identity $\partial h / \partial t = C_p \partial T / \partial t$ it is possible to derive

$$\dot{m} = UA / (h - h_c) - UA / h \quad (8)$$

Thus we can eliminate \dot{m} from the equations and avoid using equation (7).

Equations (3-5) and (7) are expressed in the time

dependent form both to enable time dependent calculations to be made and also to provide a means of iteration on arbitrary initial values of $T(z)$, $A(z)$ and $V(z)$ to obtain steady state solutions.

In the numerical results that follow, we have assumed that σ , C_p , h , a are independent of pressure and taken values for air at 1 atmosphere. The values of U and ρ are assumed to be proportional to pressure. For cases where ablation is significant the material functions should be those of the ablated nozzle material but we have found that they differ only slightly at high temperatures from our calculations of material functions of teflon, PVC and perspex.

Results: In Fig. 1 are shown calculated arc radii as a function of axial position for various d.c. currents. In Fig. 2 the calculated pressure distributions are shown as a function of axial position. Above 2 kA, the arc restricts flow in the nozzle and the local pressure increases. In Fig. 3 the calculated axial Mach number distributions are shown for various currents. At 30 kA there is a stagnation point within the nozzle and a flow of plasma back into the high pressure tank.

The calculated volt-ampere characteristics are shown in Fig. 4, together with the temperature at the nozzle throat. Also shown is a curve calculated with the nozzle reversed, the throat then being near the exit.

Reference:

[1] Lowke, J.J. and Ludwig, H.C. J.Appl.Phys., 46, 3352 (1975).

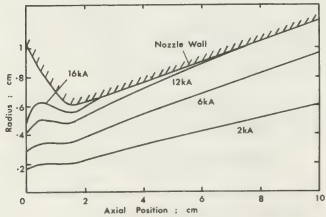


Fig. 1 Calculated arc radii as a function of current

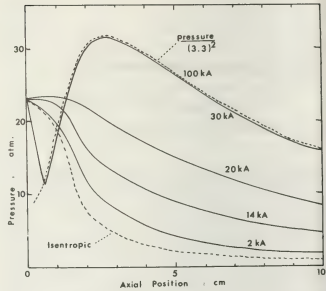


Fig. 2 Axial pressure as a function of current

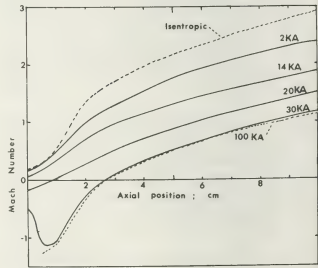


Fig. 3 Axial Mach number distribution

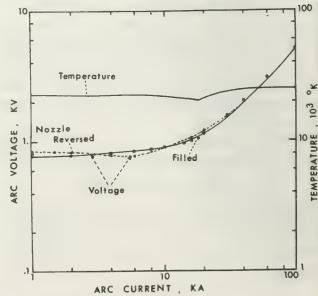


Fig. 4 Calculated V-I characteristics

A SUBSONIC ELECTRON FLUID AND THE FORMATION OF SMALL SPARKS

E. Barreto and H. Jurenka.

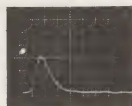
Atmospheric Sciences Research Center, State University of New York at Albany, Albany, New York 12222.

In a small high pressure discharge gap, avalanches and streamers start ionization but do not produce gas heating or a conducting bright filamentary channel. The electron density is not high enough to promote the ion-electron interaction that leads to rapid neutral gas heating. Nevertheless, long after initial ionization has subsided in a gap, a very rapid transient stage is produced. This constitutes the spark proper and changes a weakly ionized cold gas into a hot, highly conducting luminous fluid. The spark stage may incorporate very rapidly moving luminous fronts, and depending on the power supply, may lead to a much cooler arc discharge. It has been suggested many times that the spark transition can be associated with electron fluid behavior: For instance, using 2 mm long gaps we have shown that the initial ionization produces a long-lived high temperature, non-equipartition electron fluid, and that the propagation of fast luminous fronts can be associated with non-linear electron waves.¹ Here we present evidence to show that, under appropriate conditions, subsonic electron fluid behavior can also be exhibited. It is shown that heating of the gas can be accomplished by electrons that behave as a fluid and undergo subsonic turbulent mixing. From a practical point of view, the study is pertinent to problems in lightning, explosion and ignition of combustible gas mixtures, vacuum discharges and electrode erosion problems.



+ Image intensified picture -

3 amp/div



10 nsec/div

Current trace

1 μ m

Electron microscope picture of cathode spot

The figure shows an image intensified picture of a discharge produced in nitrogen using a 2 mm wide uniform field gap with a Cu cathode and a Au anode. The total energy used is 0.20 mJ and corresponds to the minimum value required to ignite a propane-air mixture in the same gap. N_2 molecules are heated because both discharges and current traces look the same. The gap is enclosed in a box with a flexible cover that allows a flow of N_2 to be maintained across the discharge region. Gas flows from top to bottom at a velocity around 100 m/sec. (The total volume flow is $58 \text{ cm}^3/\text{sec.}$) The picture illustrates two distinct discharge features that are supplemented with information from oscilloscopic recordings of the current:

a) There is an initial stage of avalanche ionization associated with the luminosity near the electrodes. The assymetry of the glow around the cathode spot shows that times are long enough to be affected by the transverse gas velocity. Current traces (procured with a large RC time) show that the initial ionization subsides in times of the order of a microsecond and consumes energy that is negligible compared to the stored 0.2 mJ. The luminosity illustrates a well known fact: the whole gap is full of ions and electrons before the spark.

b) The conical luminous region is produced long after the avalanche current has died out. The cone apex is at the cathode spot and exhibits an angle that varies between 23° and 27° . This angle is much larger than angles of the order of 3° produced by avalanches and photographed in cloud chambers. There are no streamers because of the short gap used. The current associated with the formation of the cone is recorded with a small RC time ($\sim 10^{-9}$ sec). It reaches a peak of the order of 10 A in a smooth pulse that lasts between 20

and 40 nsec. Cone luminosity is obviously unaffected by gas flow and the time intervals can only be accommodated by electron motion. The area under the current trace equals the charge in the capacitor. Hence, almost all the available energy goes into the gap during the cone formation stage. Thus the cone is identified with the spark.

Finally, there are three pertinent facts associated with the formation of a cathode spot: The first is that a spark is never produced without a spot. The second is that copious field emission is always produced by positive ions that accumulate near the metal cathode surface (e.g., in the oxide layer). The third is that time-resolved spectroscopic records² show that even smaller sparks do not exhibit metal lines away from the cathode surface for times longer than those associated with cone formation. Without getting involved in the physics of the cathode spot, we may conclude that the cone is associated with field emission from the cathode. The cone angle recorded, and its range of variation, are exactly those for a subsonic submerged jet.³ We conclude that field emitted electrons interact as a fluid with those already in the gap. Turbulent diffusive mixing between collision dominated electrons raises the overall electron energy. Additional ionization is produced in the gap and leads to the critical density for thermalization.

*Work supported by the Office of Naval Research.

References

1. Barreto, E., et al, J.Appl.Phys. 45, 3317-3327 (1974) and 48, 4510-4520 (1977)
2. Wiese, L.L. and J.A. Augis, J.Appl.Phys. 48, 4528-4535 (1977)
3. Abramovich, G.N., The Theory of Turbulent Jets, MIT Press, Cambridge, Mass. (1963)

CONDUCTIVITY MEASUREMENTS OF HIGH CURRENT, HIGH PRESSURE DISCHARGES

M. Skowronek, L. Giry, Vu Tien Gia, and P. Romeas.

Equipe "Plasmas denses" Université P. et M. Curie, Tour 12, E5, 75230 Paris Cedex 05.

1 - Introduction

A very important problem, for the heating of dense plasmas like laser produced plasmas [1] or focus type plasma [2] is the knowledge of the transport properties. Strong electrical fields or strong gradients cause the appearance of micro-turbulences and affect the conductivities. In the following paper, we describe measurements of the voltage drop over high density discharges. These measurements are in good agreement with calculations and allow the determination of the conductivity of a plasma at a density about 10^{19} cm^{-3} and a temperature about 10^7 K . Comparison is made with theory.

2 - Experimental set-up [3]

In atmospheric air, a stable ionized filament is established between two sharp needles 3 cm apart. A capacitor bank having 2.6 μF maximum capacity and a charge voltage varied from 50kV to 100 kV is discharged into the ionized channel through a spark-gap having 20 ns rise-time. The intensity is measured by means of a Rogowski coil. It reaches its maximum (100 kA to 300 kA) within 1 μs . The radial expansion of the discharge is recorded by means of an electronic camera S.T.L. used in streak mode: the temporal resolution is 4 ns/mm and the spatial resolutions is 0.1 mm. The expansion speed in the first nanoseconds is 25 km/s. A complex system of shock waves is recorded by means of a schlieren-method. The main shock propagates at Mach 12 during 1 to 2 μs . Secondary shocks overtake the main shock and accelerate it. The spectrum of the light emitted by the outer shell corresponds to a plasma whose density is 10^{21} cm^{-3} and the temperature 10^5 K .

3 - Measurements of the voltage drop

A Kerr cell is designed for this purpose. It is filled with carbon sulphur of high purity. The electrodes are 160mm x 10mm and 5mm spaced. It is transilluminated by a cw He/Ne laser. The opening of the Kerr cell is calibrated by means of square pulses of known amplitudes having 200 ns half-width.

Two pulses given by the Kerr cell are displayed on figure 1 : a) during the calibration procedure; b) with the discharge of a 0.84 μF capacitor, charged at 80 kV ; $I_{\text{max}} = 106 \text{ kA}$ at the time $t = 0.84 \mu\text{s}$. The first large pulse is due to the rise of the applied voltage. The current starts some 150 ns after. Peaks numbered from 1 to 8 corresponds to bursts in the voltage.

Another determination of the voltage drop is deduced from the analysis of the first arch of the current. It is displayed on figure 2 and a good agreement between the two determinations is obtained. On Fig.3 the calculated transmission is displayed.

The conductivity is the calculated assuming a constant temperature profile. It is about $200 \Omega^{-1} \text{ cm}^{-1}$ at the time $t = 130 \text{ ns}$.

4 - Conclusions

In order to compare the conductivity with the theory, the core plasma parameters must be known. The magnetic pressure, the kinetic pressure, the equilibrium pressure in the outer Shell are on the order of 1kbar. This gives the product NT . If we assume that N in the core is about 10^{19} cm^{-3} , T is about 10^7 K . This is also consistent with the calculated energy deposited by joule effect about 2 kJ/cm^3 .

The electric field over the discharge is rather

high, about 10^4 kv/cm. This is not far from Dreicer critical field about 310^4 v/cm. Locally it is not surprising that the electric field may exceed it. The value of the conductivity corresponds, at the best, to the formula given by Sadgeev and Galeev [4]:

$$\frac{1}{\sigma} = \frac{Z}{\epsilon_0 \omega_p} \times \frac{v_{\text{drift}}}{v_{\text{th}}} \times \frac{T_e}{T_i}; v_{\text{drift}} = \frac{j}{ne}$$

$$v_{\text{th}} = \sqrt{\frac{kT_e}{m}} \quad \omega_p: \text{plasma frequency}$$

More precision is needed in order to calculate the conductivity and to ascribe its value to microturbulence. A detailed energy balance will give also the thermal conductivity. It may be calculated also by Franz-Widemann law.

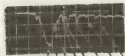
References

- 1 N.G. Basov, O.N. Krochik, 3e Conf. d'elect. quant. Paris 1963
- 2 J.W. Mather, Conf. on Plasma Phys. and Cont. fusion res. Culham, 1965.
- 3 M. Skowronek, J. Rous, A. Goldstein, F. Cabannes -Phys. Fluids **13** (1970) 378
- 4 R. Z. Sadgeev and A. A. Galeev, Non linear plasma theory. Benjamin New-York 1969

KERR CELL TRANSMISSION



a/ CALIBRATION VOLTAGE : 42KV
VERTICAL SCALE : 0.1V/div.
HORIZONTAL SCALE : 100ns/div.



PIC NUMBER: 1 2 3 4 5 6 7 8
b/ CHARGE VOLTAGE OF CONDENSATOR BANK: 80KV
VERTICAL SCALE: 0.1V/div.
HORIZONTAL SCALE: 100ns/div

Figure 1.

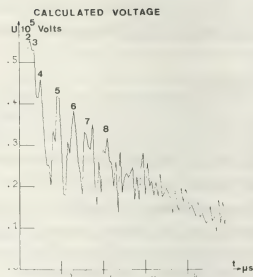


Figure 2.

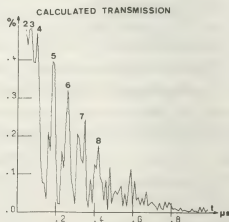


Figure 3.

STUDIES OF THE BASIC PROCESSES RESPONSIBLE FOR LASER-TRIGGERED BREAKDOWN IN GASES

P.F. Williams, R.J. Crumley and M.A. Gundersen.

Department of Electrical Engineering, Texas Tech. University Lubbock, Texas, U.S.A.

A number of technologically important applications require high voltage, high current switches which operate with low delay and jitter in the closure time. Laser-triggered spark gaps offer significant advantages for use in these applications in that the switching of 50 kV with a delay in the range of 3.0 ns. and jitter in the 0.1 ns. range has been demonstrated.¹ In this paper some experimental studies intended to elucidate the basic physical processes important in such devices are described.

In a typical laser-triggered discharge experiment a spark gap is placed in a vacuum-tight enclosure which may be filled with gas to any desired pressure up to several atmospheres. A static voltage is applied to the gap, and the gap is induced to break down by the focussed output beam of a pulsed laser. Only modest laser energy is required (~ 1 mJ.) and breakdown may be readily induced even for voltages well below the static breakdown voltage for the gap ($V \geq 0.6 V_{CB}$). Depending on the gap voltage, fill gas pressure and chemical composition, gap geometry and dimensions, and laser energy and focussing, the delay between the triggering laser and the closure of the gap may range from 1 ns. to several μ s.

In order to investigate the basic physical processes occurring in laser-induced breakdown, the experimental set-up shown in Fig. 1 was used. A spark gap consisting of two aluminum electrodes machined with a Rowgowski profile was enclosed in a stainless steel vacuum/pressure cell. Triggering was accomplished with an N_2 laser which delivered 10 ns., 5 mJ. pulses of 3361 Å radiation. The beam was focussed through a window and then a small hole in the upper gap electrode onto the lower electrode where it produced a small plasma "fireball" when tightly focussed. For all experiments we report here the gap separation was 1 cm.

A charged coaxial cable system was used to apply voltage to the gap. With careful matching of the 50 Ω load resistor a clean current pulse with no reflection-induced after-pulses was obtained. Gap current was determined by measuring the voltage across the load resistor. Optical access to the

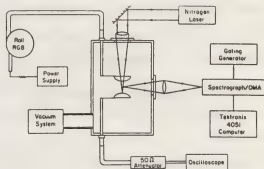


Fig. 1 Schematic drawing of experimental setup.

discharge for spectral analysis of the emission was provided by a second window transverse to the gap axis. An 0.5 m. spectrograph coupled with a computer-controlled optical multichannel analyzer was used to obtain spectra of the discharge. Gating of the SIT detector of the analyzer provided temporal resolution down to 50 ns.

Although preconditioning of the arc channel by the triggering laser probably plays a role in the breakdown process, the small plasma fireball produced by the focussed laser striking the lower electrode is primarily responsible for the gap closure. We have conducted a number of experiments designed to characterize the plasma in the fireball. In one set of experiments the vacuum cell was evacuated ($P < 1.4$) and a low voltage applied to the gap. Under these conditions the triggering laser did not cause the gap to breakdown, but a current pulse due to the plasma of the fireball was observed. Charge multiplication from ionization and other, secondary, processes was unimportant so that the integrated current of the pulse was indicative of the free charge in the fireball.

The oscillograms in Figs. 2a and 2b show the current pulses observed under these conditions with +23 and -23 volts respectively applied to the gap. The diagrams to the side of each oscillogram clarify the polarity used in each. For both polarities the integrated current is essentially the same, $\sim 2 \times 10^{-8}$ coul., supporting the contention that charge multiplication was not important in these experiments. This amount of charge is significant and strong space-charge fields, such as appear

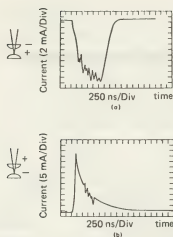


Fig. 2 Current pulses observed in an evacuated gap with ± 23 volts. Voltage polarity is indicated at the left.

necessary to explain the ability of the laser to cause gap breakdown for voltages significantly below the static breakdown voltage, can be produced in the plasma sheaths. Similar experiments have been carried out in hydrogen at pressures up to a few Torr. In these experiments for voltage polarity such that negative charges traverse the gap, clear evidence for ionization-induced current is seen even for gap voltages as low as 10 volts.

We are also carrying out a program to determine the electron density during the arc phase of laser-triggered discharges in hydrogen using Stark broadening measurements. With this technique we have obtained temporally-resolved electron density information during the arc, and for times extending to approximately 1 μ s. into the after-glow.

Electron density data obtained in this fashion are shown in Fig. 3, along with the gap current pulse, for 300 Torr of hydrogen and gap voltage approximately 80% of the static breakdown value. As might be expected, these results are similar to those observed by other workers for over-volted gaps in hydrogen.² To obtain the spectra from which these results were derived, the image of the arc was centered on the entrance slit of the spectrograph, and these densities represent, therefore, a weighted average over the diameter and length of the arc channel. Abel inversion techniques have been used to unfold the radial variation of the electron densities, and preliminary results indicate that the variations across the diameter of the luminous column are not large, being of the order of 25%. Variations along the

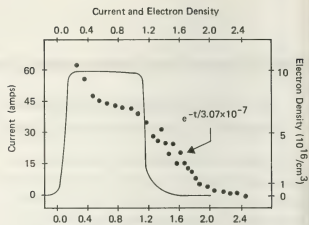


Fig. 3 Electron density (points) and gap current (solid line). 300 torr H_2 .

length of the column may be determined directly, and in our experiments the electron density displayed essentially the same time behavior at all points monitored along this dimension.

1. A.H. Guenther and J.R. Bettis, Proc. IEEE 59, 689 (1971); and references contained therein.
2. J. Meyer, Brit. J. Appl. Phys. 18, 801 (1967).

Work supported by AFOSR, and Research Corporation.

CHARACTERISTICS OF A HIGH DENSITY DIRECTED PLASMA SOURCE

L.P. Bradley and E.L. Orham.

University of California, Lawrence Livermore Laboratory, P.O. Box 5508, Livermore, California 94550.

We have developed a plasma source to produce a plasma of $10^{21}/\text{cm}^3$ particle density and project it with a velocity of 2.4 cm/ μs . This device will be used in the output spatial filter of Nova, a laser for fusion, to project a critical density plasma across the optical beam path and block target retroreflected light. The object of this paper is to describe the design of the source, present a numerical model for the plasma and discuss in detail the experimental characterization of the plasma.

A low inductance parallel capacitor bank with UV illuminated spark gaps produces a current rising at 5×10^{12} amp/sec and has 1 ns jitter. Two groups of capacitors within the bank are tuned to optimally burst a wire, thereby producing a plasma, and to magnetically propel the plasma. The wire is contained within a nozzle and has the electrodes extended in a rail gun configuration. In our application, this geometry directs the plasma across the beam path and minimizes vapor leakage toward the optics. A dump tank collects the bulk of the plasma, and baffles with an orthogonal 0.1 T magnetic field collect the plasma debris and protect the optics. The pulser, plasma source, and collectors were retrofitted into a Shiva 20 cm aperture, f/10 spatial filter and the plasma was characterized. The experimental geometry is shown in Figure 1 with expanded detail of the electrode region shown in Figure 2.

The plasma velocity was measured with Faraday cups and streak camera. The plasma divergence was recorded with witness plates and Faraday cups. These data with the known geometry permit a

determination of the plasma density. A self consistent Lagrangian numerical program modeled the pre and post burst behavior of the wire and included driving circuit parameters and magnetohydrodynamic effects. It predicted the evolution of the plasma density and temperature. The code was useful for design and optimization of the nonlinear circuit and for interpretation of the data.

A particular representative configuration used a 125 μm diameter aluminum wire sublimed by a 100 kA peak current. The measured plasma velocity was 2.4 cm/ μs , a value sufficiently fast to inject the plasma after the target directed laser pulse passed by before the retropulse returned. The plasma density assuming single ionization for aluminum exceeded 10^{21}cm^{-3} , a conservative value for blocking the 1.06 μm wavelength light. Excellent agreement was found with these data and code predictions. A probe laser was blocked as expected. The plasma volume is calculated to be sufficiently large to prevent optical burnthrough by a 10 kJ, 5 ns laser pulse. Using a radiotracer technique, we determined that less than 10^{10} atoms/ cm^2 were deposited on the optics per shot.

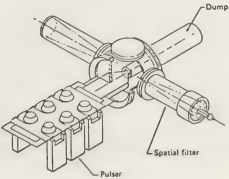


Figure 1: Plasma Shutter Experimental Configuration

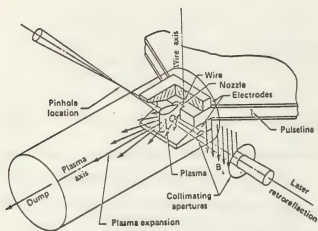


Figure 2: Plasma Source Geometry

*Work performed under the auspices of the U.S. Department of Energy by the Lawrence Livermore Laboratory under contract number W-7405-ENG-48.

MEASUREMENTS AT CURRENT ZERO IN A SF_6 GAS BLAST BREAKER

R. Moll and E. Schade.

Brown Boveri, Research Center CH-5405 Baden, Switzerland.

INTRODUCTION

Post arc current measurements are important for checking the range of validity of arc models which quantitatively predict the post arc currents in h.v. breakers according to the residual conductivity [e.g. 1]. In the case of SF_6 axially blown arcs however, such measurements place high demands on the measuring equipment because of the rapid recovery that takes place. To date only few measurements in this regime have been reported, and those were obtained under various conditions [2,3,4]. It has even been stated that SF_6 post arc currents cannot be detected. In the following report a measuring method is described which detects currents far below 1 A [5]. Tests are carried out with this measuring system (response time $\tau_r < 35$ ns) on a metal vapour-free axially blown SF_6 arc.

EXPERIMENTAL SETUP

The nozzle arrangement selected (Fig. 2) permits unrestricted optical observations except for the narrow orifice region (high speed-,schlieren photography). The vapour produced by the upstream electrode is drawn off through a small orifice in the electrode. A square-wave current pulse (1.5 kA, 5 ms) followed by a decay rate of 30 A/ μ s is generated by an LC network [6]. The arc forms a stable plasma column up-stream, while it is greatly influenced by turbulence downstream (Fig. 3).

The recovery voltage is supplied by a h.v. LC network (Fig.1). The spark gap F is fired approx. 25 μ s before the end of the 1.5 kA pulse (current injection, Fig.5,7).

The RRRV is determined by resistor R_2 . The post arc current is determined from the voltage drop across the 10 Ω shunt R_S , which is short circuited by the fast diode D before current zero.

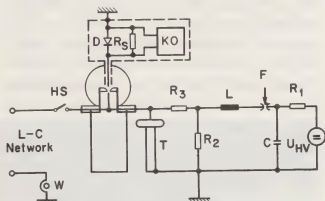


Fig. 1: HS: vacuum breaker
W : current transformer
T : resistor/capacitor divider
($\tau_r < 5$ ns)
KO: battery-powered oscilloscope

In this measuring arrangement strict coaxial design of all components must be preserved. Also the diode D consists of many coaxially arranged diodes. In addition, the diode characteristics should include a high maximum peak forward surge current, high reverse voltage in case of a restrike of the test section, low reverse currents, low junction capacitance and a short recovery time. Since it is not possible to obtain all these requirements simultaneously, the most favourable compromise must be sought for each measuring task. The response time τ_r of the post arc current measuring device is less than 35 ns.

RESULTS AND DISCUSSION

The measuring setup enabled precise post arc current investigations to be performed.

A great number of tests showed that in the case of interruption measurable post arc currents (Fig.6) occur only under conditions lying at the limit between extinction and thermal reignition. Fig. 4 shows a post arc current measurement during reignition near the critical condition. The post arc currents measured agree in amplitude and temporal evolution with theoretical values [1], although in the experiment the current decay rate is seen not to have a single constant value (Fig.5,7). To a great extent the voltage rise (0.27 kV/ μ s) at the current zero is linear. The extinction limit measured agrees with the theoretical values [1], when an average current decay rate (20 A/ μ s) is assumed. The limited observation of post arc currents leads us to be-

lieve that insulating layers are encountered which must be broken down, and that this is only possible in the vicinity of the extinction limit and often leads to re ignition. Investigations with other networks confirm this assumption, but this phenomenon should not affect the extinction limit.

- [1] Hermann W., Ragaller K., IEEE PAS-96 1546-1555 (1977)
- [2] Frind G., IEEE Conference Paper No. F 79 288-2 (1979)
- [3] Kobayashi A., et al. IEEE PAS-97 1304-1312 (1978)
- [4] Murano M., et al. IEEE PAS-94 1890-1900 (1975)
- [5] Moll R., Schade E., ISH, Milan 1979
- [6] Hermann W., et al. IEEE PAS-95 1165-1176 (1976)

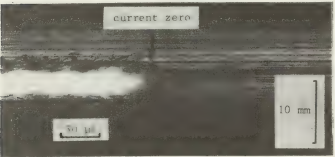


Fig. 3 Schlieren record
Reignition

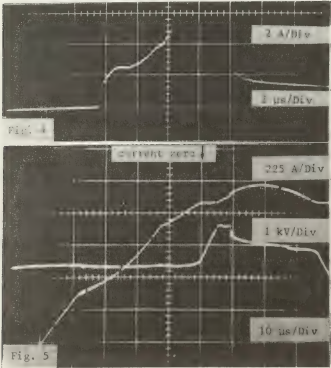


Fig. 4

Fig. 5

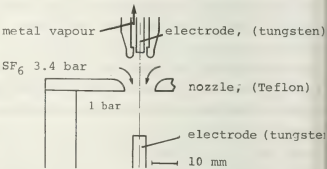


Fig. 2 Test breaker

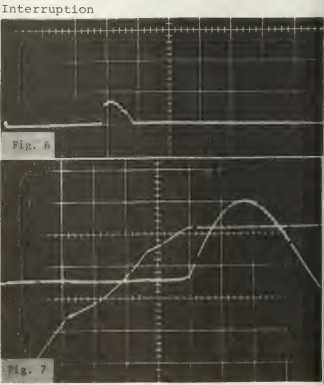


Fig. 6

Fig. 7

STATIC BREAKDOWN ANALYSIS OF COMPRESSED SF₆ IN POSITIVE ROD-TO-PLANE GAPS

M.S. Abou-Seada and KH. I. M. Ali*

*Electrical Engineering Dep., Faculty of Engineering, Cairo University, Cairo Egypt.
*Electrical Mech. Res. Inst., Ministry of Irrigation, Cairo, Egypt.

Abstract - The peculiar variation of breakdown voltage V_g with pressure P in compressed SF₆ due to corona-stabilization of the applied field is well pronounced in rod-to-plane gaps, Fig.1(a). In this paper a theoretical analysis of this stabilization effect is conducted. Accordingly a criterion is developed for computing V_g of compressed SF₆ in rod-to-plane gaps.

METHOD OF ANALYSIS

The equations of unipolar corona [1,2] are solved at each pressure at different applied voltages higher than the corona onset value V_c computed at P [3]. Solution is carried out using the saturated solution concept advised for gap configuration producing highly divergent applied field

[1]. According to this concept, the space charge ion density ρ is very high at the emitter (conductor in corona) surface and drops to a negligible value at an infinitesimal distance δ from it [1]. The resultant electric field E is assumed to rise from a practically zero value at emitter surface [1] to the corona onset value E_0 at δ [2]. E is expressed as $E = \xi E_0$, where ξ is a scalar function [1,2]. The following equations are derived for computing the ρ and E values at any finite distance s ($> \delta$) from emitter surface [1,2].

$$\frac{1}{\rho} - \frac{1}{\rho_1} = \frac{1}{\epsilon_0} \int_{\delta}^s \frac{ds}{E} \quad (1)$$

$$\xi \frac{d\xi}{ds} = \frac{\rho}{\epsilon_0} \quad (2)$$

where ρ_1 is the value of ρ at δ .

Assuming an initial approximate value ρ_{i0} for ρ_1 , equations (1) and (2) are solved simultaneously on the line of maximum

field. Integration and differentiation are replaced by finite difference relations. The field line is divided into n steps by a regularly spaced equipotentials. This gives us n reference points for computation of differences. An optimum value of n is found to be equal to 25. The distance s is measured from emitter surface as δ is negligible with respect to the length of any step. Using digital computer iterative technique the ρ and E distributions satisfying the boundary condition pertinent to the applied potential difference across the gap are computed. ρ_{i0} is taken as [2]

$$\rho_{i0} = 2(V - V_c) \int_0^V \int_0^{\phi} \frac{d\eta}{\xi^2} d\phi$$

where V is the applied voltage and ϕ is the space charge-free potential.

The ρ values are found to increase with V along the whole field line at the same pressure. Hence the mean ion charge density ρ_m , defined as $(\int_0^H \rho ds) / H$, where H is the gap length, increases with V at the same pressure. It is interesting to notice that according to the present solution concept, ρ_m of a gap at a certain P and $V \gg V_c$ comprises two values. The first, ρ_{m1} , depends on V_c . According to equation (2):

$$\int_0^{\delta} ds \xi = \frac{1}{\epsilon_0} \int_0^{\delta} \rho ds$$

As δ is infinitesimal, ξ can be assumed to remain constant inside it at its value at the emitter surface E_0 . Hence:

$$\int_0^{\delta} \rho ds = \epsilon_0 E_0 \int_0^{\delta} ds, \text{ where } E_0 = \frac{V_c}{V}$$

or $\rho_{m1} = \epsilon_0 E_0 / H$

The second value, P_{m2} depends on $(V-V_c)$.

Based on the above argument, we suggest the following breakdown criterion

$$P_{ms} = C \tag{3}$$

where P_{ms} is the value of P_m at breakdown voltage and C is a function of gap parameters and gas pressure.

A variety of gaps producing wide range of applied field divergence, for which accurate breakdown voltage measurements were reported at a wide pressure range [4, 5, 6], were considered for the determination of the function C . P_{ms} is computed for each gap in its corona-stabilized phase of breakdown using the experimentally measured breakdown voltages. Accordingly the following formulae are deduced for C .

- (i) For pressures up to that corresponding to the maximum breakdown voltage, P_m

$$C = A \sqrt{\mu P/r} \tag{4}$$

where A is a constant whose value = 0.57×10^{-4} C.M. bar^{-1/2} and μ is the ratio of the average to maximum applied fields.

- (ii) For pressures $P_m \leq P \leq P_c$, where P_c is the minimum pressure at which corona-free breakdown occurs, C remains constant at its value at P_c .

A semi-empirical formula was proposed for computing P_c [5]. This is modified to fit gaps having large rod radii. The formula suggested has the form

$$P_c e^{-P_c/r} = 0.85 \times 10^{-2}$$

where P_c in bar and r in M.

P_m is computed by substituting the value of C obtained at P_c in equation (4) and solving for P .

To compute V_g of a gap at pressure P , an approximate initial value V_0 equal to V_c at P_c is assumed for V_g . P_{ms} corresponding to V_0 is computed and compared to P_{ms} computed from equation (3). If the difference is within $\pm 0.05 P_{ms}$, V_0 re-

presents V_g , otherwise V_0 is incremented and a digital computer iterative process is performed until the condition is satisfied. Fig. 1 (a) indicates the close agreement observed between the experimentally measured values of V_g and those computed according to the suggested criterion. Fig. 1(b) depicts the P -distribution while Fig. 1 (c) to (f) display the E -distributions pertinent to V_g at different pressure values. In the E -distributions the applied field enhancement due to corona stabilization is clear

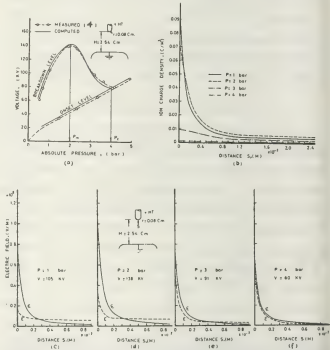


Fig.1. Breakdown characteristics of compressed SF₆ in rod-to-plane gap.

REFERENCES

[1] N.J. Felici, Direct Current, Pt. II, (Oct. 1963) 278
[2] M.P. Sarma and W. Janischawskyj, IEEE Trans., Vol. PAS-88(1969)718
[3] M.S. Abou-Seada and Kh. Ali, IEEE, IAS paper, Toronto, Ontario, Canada, (Oct. 1978)193
[4] C.N. Works and T.W. Dakin, AIEE Trans Pt. I, Vol. 72 (1952)682
[5] R. Hazel and E. Kuffel, IEEE Trans., Vol. PAS-95 (1976)178
[6] S. Sengksaard, Inter. H.V. Symposium, Zurich (1975)379.

THE MASS FLOW FIELD OF THE FULL CIRCLE ARC

W. Tiller.

Hochschule der Bundeswehr, München, F.R.G.

Introduction

As reported in former papers /1,2/ a radial free full circle arc was operated in an argon atmosphere. Due to the experimental conditions and with respect to cylindrical coordinates r, φ, z the statements $\partial/\partial t = 0$ and $\partial/\partial \varphi = 0$ hold for this arc. The mass flow in the arc cross section as a result should prove Maecker's theory /3/ of arc motion and displacement. Therefore one must know the temperature distribution. It can be measured spectroscopically as described in /2/. One has to consider that those measurements are correct only in the case of local thermal equilibrium. For arc currents greater than 50 A this condition is fulfilled.

Results of Temperature Measurements

In continuation to the measurements reported in /2/ the arc was investigated at currents between 50 A and 100 A and arc radii from 35 mm to 45 mm. As an example figure 1 shows the temperature field for an arc current $I = 75$ A and a radius of 40 mm.

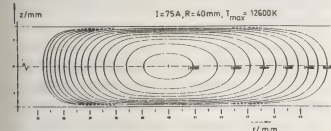


fig. 1 temperature distribution

In addition to former results figure 2 gives the correlation of the maximum temperature in the arc core with the arc current and the curvature of the arc.

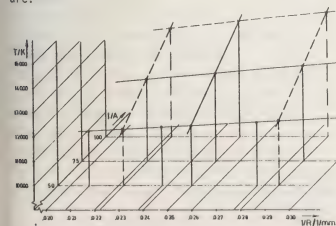


fig. 2 temperature maxima vs. current and curvature of the arc

The Mass Flow Field

By use of the known temperature distribution the velocity of the mass flow can be evaluated from the convective term of the energy equation:

$$\lambda \nabla \cdot \nabla S = \epsilon E^2 + \rho^2 S - u$$

and from the continuity equation: $\nabla \cdot \rho \vec{v} = 0$

The expressions ∇S and $\nabla^2 S$ (S = heat flux potential) are derived from the measured temperature field $T(r, z)$. The coefficients $\lambda(T)$ = thermal conductivity, $\epsilon(T)$ = electrical conductivity, $u(T)$ = specific radiation and $\rho(T)$ = mass density are taken from the literature. The electrical field strength E is measured by means of probe techniques. One has to start the evaluation in the center plane ($z=0$) which is also the plane of symmetry of the arc. There, the velocity has only a radial component v_r , that means $v_z(z=0) = 0$. Using the velocity distribution $v_r(r)$ at $z=0$ as an initial value one can compute the ρv_z and ρv_r components in small steps Δz , solving alternately the two equations mentioned above. Introducing the vector potential $\vec{\psi}$ for the mass flow by $\rho \vec{v} = \nabla \times \vec{\psi}$, the evaluation of stream lines including a constant mass flow becomes possible. Because of $\partial/\partial \varphi = 0$, the vector $\vec{\psi}$ has only an azimuthal component, and so one has only to solve a plane problem. The distance ($z_2 - z_1$) between two stream lines at a special radius r_0 is given by the integral:

$$\int_{z_1}^{z_2} (\rho v_r) dz = \psi_{r_0, z_2} - \psi_{r_0, z_1}$$

The borders z_1, z_2 have to be chosen in a way that the difference $\psi_{r_0, z_2} - \psi_{r_0, z_1}$ is constant. This evaluation was done for a constant mass flow of 0.05 mg/s per cm arc column. As a result one gets a symmetric quadrupole whirl in the arc cross section as shown in figure 3.

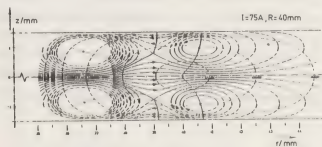


fig. 3 mass flow field in the arc cross section

In addition to the stream lines several isothermes and also the curve $\vec{\rho} \cdot \nabla S = 0$ are shown in this figure. This curve is the locus of all points without convective energy transport, i.e. there occurs only thermal conduction. By forming the limiting value, it can be shown that the temperature maximum as well as the whirl centers and the stagnation point are extraordinary points of this curve.

Interpretation of the Mass Flow Field

Discussing the conservation equation of momentum, one has a possibility to interpret the mass flow field and to verify the results. Neglecting the small temperature dependence of viscosity η in the arc, the equation of conservation of momentum reads:

$$\vec{\rho} \cdot \nabla \vec{v} = \vec{j} \times \vec{B} - \nabla p + \eta (\nabla^2 \vec{v} - \nabla \times \nabla \times \vec{v})$$

\vec{j} = electrical current density, \vec{B} = magnetic field, p = pressure. Taking the curl of the left and right hand term and neglecting the curl of the inertial force (low Reynolds number), one gets:

$$0 = \nabla \times (\vec{j} \times \vec{B}) - \eta (\nabla \times \nabla \times \nabla \times \vec{v})$$

The introduction of the vorticity by: $\vec{\omega} = \nabla \times \vec{v}$ leads to the Poisson equ.: $\nabla^2 \vec{\omega} = -\frac{1}{\eta} \nabla \times (\vec{j} \times \vec{B})$.

The curl of the Lorentz force $\nabla \times (\vec{j} \times \vec{B})$ which has azimuthal direction can be evaluated as follows: From the temperature distribution and the measured electrical field strength one knows the electrical current density. Solution of the Biot Savart equation yields the magnetic field of the arc. The external magnetic field is known from the experiment. Therefore all terms of the curl

$$\nabla \times (\vec{j} \times \vec{B}) = \vec{e}_r (B_z (\frac{\partial j_r}{\partial r} - \frac{j_r}{r}) + B_z \frac{\partial j_z}{\partial z})$$

can be computed. Because η is constant, one can take - as an analogon to the differential equation of the elastic membrane -, the curl of the Lorentz force as an area force on such a membrane. The deflection of the membrane is then proportional to the value of the vorticity $\vec{\omega}$. The curl of the Lorentz force as well as its two terms as functions of the radius for a plane $z = 0.86$ mm, which contains approximately the whirl centers and the stagnation point, is shown in figure 4.

For the same plane, figure 4 shows also the distribution of the vorticity, calculated from the mass flow field (fig. 3). A comparison of the two curves by use of the membrane model mentioned above ($(\vec{e}_r \cdot \nabla \times (\vec{j} \times \vec{B})) = \text{area force}$, $\nabla \times \vec{\omega} = \text{deflection}$) shows qualitatively (i.e. without respect to the boundary values of $\vec{\omega}$) the role of the curl

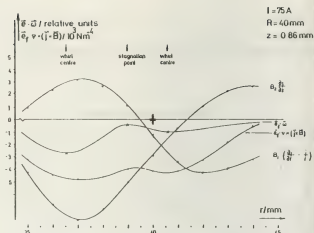


fig. 4 curl of the Lorentz force and vorticity of the Lorentz force in generating the quadrupol whirl. Moreover one realizes, evidently shown by the unsymmetry of the term $B_r (\partial j / \partial r - j/r)$ which is caused by the curvature of the arc, that just this curvature is the reason for a quadrupol whirl contrary to a double whirl as formerly expected.

Conclusion

The experiment shows, that a magnetically deflected curved arc can be fixed in a equilibrium position. This equilibrium is determined by the fact that there is a magnetohydrodynamic mass flow through the arc core which compensates the arc motion towards the center of curvature due to thermodynamic effects.

- /1/ W. Tiller, Proc. of the 11th Int. Conf. on Phen. in Ionized Gases (1973)
- /2/ W. Tiller, Proc. of the XIIth Int. Conf. on Phen. in Ionized Gases (1975)
- /3/ H. Maecker, Proc. of the IEEE 59, 439 - 449 (1971)

CATHODE DENSITY WAVE IN AN ELECTRON BEAM CONTROLLED DISCHARGE

J. Fort, J. Bonnet, G. Fournier and D. Pigache.

Office National d'Etudes et de Recherches Aéronautiques, 92320 Chatillon, France.

Introduction. The energy input in a discharge is non uniform. Transient and non uniform gas heating results in acoustic waves which propagate in and out of the discharge. If the waves yield a significant density defect, they can drive the discharge into an arc. Moderate amplitude waves can also disturb the optical quality of the medium when the discharge is used to pump a laser. Two types of perturbations can generally be identified :

- Waves propagating in a direction perpendicular to the electric field are generated by bulk heating [1, 2] .
- Waves propagating along the electric field mainly originate from the electrode vicinity, especially the cathode fall region [3, 4] .

This paper only deals with the cathode wave in a discharge where the cathode is the solid electrode. This choice is made in order to analyse a single density disturbance. Holographic interferometry is used to display the density variations. A simple model permits an estimate of energy partition between electrode and gas heating.

Experimental arrangement. A schematic diagram of the discharge set-up is given in Fig. 1. The electron beam is produced by a plasma-anode electron gun. The electric field is continuously applied between solid cathode and grid anode. Experimental conditions are :

- Gas : N_2 (chosen in order to minimize bulk heating during wave propagation).
- Pressure : 0.15 bar.
- Electron beam energy : 110 keV .
- Electron beam current density : 2 mA/cm^2 .
- Beam pulse width (FWHM) $25 \mu\text{s}$.
- Discharge voltage : 2,6 kV along a 36 mm gap.
- Cathode fall deduced from the slope break of the current voltage characteristic, $V_c \approx 440 \text{ V}$
- Discharge current : 230 A.
- Dimensions of electron window : $140 \times 60 \text{ mm}$.

The method of a reference hologram is used to obtain a real time image of the phenomena. A picture of the interferogram is taken at a given time with a fast TRW converter. [5] .

Results. The cathode wave is clearly displayed on the interferogram given in Fig. 2. The picture was

taken 50 μs after discharge initiation with an exposure time of 5 μs . The density defect close to the cathode cannot be seen with the space and time scales considered. The fringe shift of wave disturbance is less than half an interfringe. It can be noted that the main fringe pattern (at rest fringes are perpendicular to electrodes) is not changed by bulk heating of the medium and that fringe declination towards anode should be due to the propagation of the rarefaction wave resulting from the anode field-free cavity. The maximum relative variation of density $\Delta\rho/\rho_0$ (Fig. 3) is lower than 4 %. The wave speed (ratio of wave front abscissa over time) is 340 m/s.

Discussion. Those results suggest the following main assumptions :

- one-dimension model (transverse effects neglected)
- linear approximation.

In addition, it is assumed that the gas is perfect and at rest. The calculation is performed with no heat transfer to the cathode material. The appraisal of this effect will result from the comparison of the calculation with the experiment. The linear equation set is :

$$(1) \quad R(T_0 \rho' + \rho_0 T') = p'$$

$$(2) \quad \frac{\partial \rho'}{\partial t} + \rho_0 \frac{\partial u'}{\partial x} = 0$$

$$(3) \quad \rho_0 \frac{\partial u'}{\partial t} + \frac{\partial p'}{\partial x} = 0$$

$$(4) \quad \rho_0 c_v \frac{\partial T'}{\partial t} + p_0 \frac{\partial u'}{\partial x} = \dot{Q}_c$$

where T_0 , ρ_0 , p_0 and $u_0 (=0)$ are the equilibrium values for temperature, density, pressure and velocity and the primes denote the perturbations ; R is the constant of perfect gases, \dot{Q}_c is the heat input per volume and time unit in the cathode region. Initial conditions are ($t=0$)

$$(5) \quad p' = 0 \quad \text{and}$$

$$(6) \quad \frac{\partial p'}{\partial t} = (\gamma - 1) \dot{Q}_c \quad \text{in the}$$

cathode region and 0 elsewhere, where γ is the specific heat ratio.

Boundary conditions are :

$$(7) \quad \frac{\partial p'}{\partial x} = 0 \text{ at the cathode surface } (x=0) \text{ and}$$

$$p' \rightarrow 0 \text{ for } x \rightarrow \infty. \text{ The propagation equation is solved with Laplace transform in time and}$$

associated Green function for space variable [6]. Heat input is assumed to be uniform in the cathode region of length d . Time dependence is approximated by the functions (Fig. 4)

$$(8) \quad \begin{aligned} \dot{Q}_c &= \dot{Q}_0 \, t / r_m & \text{for } 0 \leq t \leq r_m \\ \dot{Q}_c &= \dot{Q}_0 & \text{for } r_m < t \leq r_m + t_p \\ \dot{Q}_c &= \dot{Q}_0 \exp(-t/\tau) & \text{for } t > r_m + t_p \end{aligned}$$

Finally, the analytic formula for the relative density variation is :

$$(9) \quad \frac{p'(x,t)}{p_0} \approx \left(\frac{y-1}{y} \cdot \frac{d}{p_0 c_0} \dot{Q}_0 \right) \left\{ \exp \left(-\frac{1}{\tau} (t - r_m - t_p - \frac{x}{c_0}) - 1 \right) \times \right. \\ \left. U \left[c_0 (t - r_m - t_p) - x \right] + \frac{1}{c_0 r_m} (c_0 t - x) U \left[c_0 t - x \right] \right. \\ \left. - \frac{1}{c_0 r_m} \left[c_0 (t - r_m) - x \right] U \left[c_0 (t - r_m) - x \right] \right\}$$

where U is the unit step function and $c_0^2 = \gamma p_0 / \rho_0$. This function is displayed in Fig. 3 for $\dot{Q}_0 d = 670 \text{ W/cm}^2$, this value being chosen in order to fit the experimental maximum of p'/ρ_0 . The corresponding electric energy input (V_c times current density) is 1200 W/cm^2 (Fig. 4). Accordingly, the electrical energy converted in gas heating is about $1/2$. Most of the remaining energy is transferred into the cathode. This energy partition limits significantly the actual gas temperature increase close to the cathode.

Conclusion. A simple model permits an appraisal of energy partition in the cathode vicinity. Two experimental data (electrical energy input and p'/ρ_0) are used to determine heat transfer into the cathode. Conversely, an appropriate model for this heat transfer would yield $\dot{Q}_0 d$ directly from a single measurement of p'/ρ_0 . More sophisticated work is in progress. In addition, the success in dealing with moderate amplitude perturbations (at short time scale and short exposure time) gives us confidence to study other problems, such as those involved in pulse repetition, with this interferometer.

REFERENCES

- [1] - W.M. CLARK, Appl. Opt. 13 (1974) 1995.
- [2] - G. FOURNIER, J. BONNET, J.L. BRUNEAU, D. PIGACHE and P.L. VIOLLET, Proceedings of 2nd Int. Symp. on Gas flow and Chemical lasers, Rhode St-

Genese (Belgium), 11-15 sept. 1978, to be published.

[3] - E.R. PUGH, J. WALLACE, J.H. JACOB, D.B. NOR-THAM and J.D. DAUGHERTY, Appl. Opt. 13 (1974) 2512.

[4] - G.L. Mc ALLISTER, V.G. DRAGGOD and R.G. EGU-CHI, Appl. Opt. 14 (1975) 1290.

[5] - J. SURGET, Proceedings of Int. Symp. on Holography Applications, Besançon, July 1970.

[6] - F.E.C. CULICK, P.I. SHEN, W.S. GRIFFIN, IEEE J. Quant. Electron. QE-12 (1976) 566.

The authors thank J. SURGET for his help with the interferometry and R. COLOMBA for his valuable technical assistance.

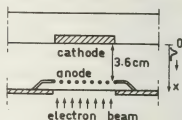


Fig. 1 : Schematic of discharge arrangement.



Fig. 2 : Interferogram taken $50 \mu\text{s}$ after discharge initiation - Exposure time $5 \mu\text{s}$.

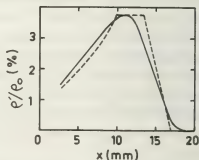


Fig. 3 : Relative density versus distance from the cathode at $t = 50 \mu\text{s}$ — experiment ---- calculation.

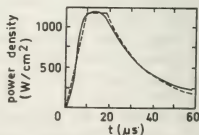


Fig. 4 : Electrical power input per cm^2 in the cathode region — experiment ---- approximation $t_m \approx 9 \mu\text{s}$, $t_p \approx 9 \mu\text{s}$, $\tau \approx 22 \mu\text{s}$.

PRODUCTION OF HYDRAZINE FROM AMMONIA IN AN ATMOSPHERIC PRESSURE ELECTRON-BEAM CONTROLLED DISCHARGE

D. Pigache, J. Bonnet, J. Fort and G. Fournier.

Office National d'Etudes et de Recherches Aérospatiales, 92320 Chatillon, France.

DC, RF and microwave discharges in ammonia have been extensively studied for the synthesis of hydrazine [1, 2, 3, 4]. Chemical and electrical efficiencies approaching economical interest have been obtained in some cases. However, as these discharges are limited in operating pressure and in size, the achievement of the high flow rates required in industry appears to be very difficult.

The electron-beam controlled discharges which have been successfully used for pumping high power lasers [5] can be operated at atmospheric pressure with good uniformity over large volume thus permitting handling of large amounts of gas in fast flow systems. Furthermore the electron average energy can be adjusted (by varying the electric field) from very low values to a maximum of the order of 2 eV (limited by breakdown); this flexibility is of special interest for plasma chemistry. Very encouraging results have already been obtained for ozone production [6] with these discharges. Preliminary results for hydrazine are presented in this paper.

Experiment. The experimental arrangement is shown in Fig. 1. The electron gun has been described previously [7]. The discharge chamber is filled with pure ammonia after being evacuated to a pressure of 10^{-1} mbar. The electron beam (120 keV, 1.3 mA/cm²) enters the chamber through a 12 μ m thick titanium foil of 15 x 5 cm². The electron-beam controlled discharge takes place between a grid which protects the electron window and the anode (aluminum alloy plate of 17 x 7 cm²). The cathode-anode spacing is 2 cm. A positive voltage is applied permanently to the anode. The discharge current flows when the gas is ionized by the electron beam (Fig. 2).

The other discharge parameters are :

- pulse duration : 100 μ s
- repetition rate : 10 Hz
- discharge current : 2.3 A
- discharge voltage : 9 kV
- pressure : 1 100 mbar
- gas flow rate (standard conditions): 7.5 cm³ s⁻¹
- ratio electric field/gas density : 1.5×10^{-16} V/cm²

The concentration ratio of hydrogen, nitrogen and ammonia are measured by gas chromatography downstream of the discharge and hydrazine is detected by a colorimetric method using p-dimethylamino-benzaldehyde [8].

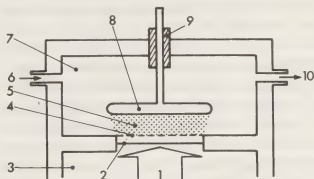


Fig. 1 - Experimental arrangement.

- 1 - 120 keV electron-beam ; 2 - Electron window (12 μ m Ti foil) ; 3 - Electron gun vacuum chamber ; 4 - discharge cathode (grid) ; 5 - Discharge zone ; 6 - Gas flow (pure ammonia) ; 7 - Discharge chamber ; 8 - Discharge anode ; 9 - Insulated feed through ; 10 - Gas flow (ammonia and products).

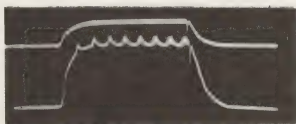


Fig. 2 - Time evolution of the electron-beam and discharge currents.

Upper trace : electron-beam current (arbitrary unit).

Lower trace : discharge current (A/cm)

Time scale : 20 μ s/cm

Results. Approximately 1,1 % of the ammonia flowing through the discharge chamber is decomposed and the hydrogen to nitrogen mole ratio is equal to 5. Assuming that hydrogen, nitrogen and hydrazine are the only products which can be formed in our experimental conditions, the hydrazine production can be calculated : the volume concentration is .37 %, the efficiency is 7g/kW-hour and the

production rate is **.144 g / hour**

After a two hours discharge run, the amount of hydrazine collected downstream the discharge by dissolving the gas output in water is one thousand times smaller than the yield calculated previously and the amount of hydrazine recovered by washing the chamber walls with water is only one hundred times smaller.

Discussion. The average residence time of the gas in the discharge chamber is 20 minutes and the surface of the aluminum alloy chamber walls is $3\ 000\text{ cm}^2$. The average deposit thickness of the hydrazine produced during a discharge run would be of the order of $1\ \mu\text{m}$. Hydrazine condensation on the chamber walls and decomposition before it can be dissolved and analysed is the most probable explanation. Another possible explanation would be the formation of other nitrogen-rich compounds such as HN_3 or N_2H_2 but these compounds are so unstable that their presence in significant amounts seems unlikely.

The discharge chamber is now being modified in order to reduce the gas residence time and to avoid as much as possible its contact with metallic surfaces.

The valuable assistance of M. ORY is acknowledged.

REFERENCES

- [1] - J.C. DEVINS and M. BURTON, J. Am. Chem. Soc. 76, 2618 (1954).
- [2] - B.A. BROWN, C.R. HOWARTH and J.D. THORNTON, Chem. Eng. Progress 112, 67, 28 (1971)
- [3] - R. BARKER, J. of the Chem. Soc., Faraday Transactions I 68 Part 2, 315 (1972).
- [4] - V.L. SIADOUK and E.N. EREMIINE, Russian J. of Phys. Chem. 49, 3, 682 (1975)
- [5] - N.G. BASOV, E.M. BELENDOV, V.A. DANILYCHÉV and A.F. SUCHKOV, Kvantovaya Elektronika 3, 121 (1971).
- [6] - D. PIGACHE, G. FOURNIER, R. LUCAS and M. LECUILLER, 13th ICPIG, Berlin, sept. 77, p. 604.
- [7] - D. PIGACHE, G. FOURNIER, J. Vac. Sci. Tech. 12, 1197 (1975).
- [8] - F.D. SNELL, Colorimetric Methods of Analysis D. Van Nostrand Co, Princeton New Jersey, p. 707.

GAS TEMPERATURE DEPENDENCE OF AC DISCHARGES BETWEEN ISOLATED ELECTRODES

R.J. Zahn and S. Müller.

Zentralinstitut für Elektronenphysik, V Akademie der Wissenschaften der D.D.R.,
D.D.R. 22 Greifswald.

Introduction: In /1/ and /2/ the transition was investigated between the bistable pulse mode, which is used in ac plasma displays, and the non-bistable continuous mode in Ne-Penning mixtures by frequency variation of the sinus wave voltage. For the transition frequency \tilde{f} of both these discharge modes there is a similarity relation with the similarity parameters f/p and pd (f -frequency of applied voltage, p -gas pressure, d -distance of the electrodes) in a wide parameter range with constant mixture ratio. The present paper deals with investigations of the influence of gas temperature on the transition between the discharge modes.

Method: The investigations were carried out between glass covered Mo-electrodes with 1 mm \varnothing and a 0.1 mm thick insulator. The distance of the electrodes was varied between 0.2 and 2.5 mm. After usual vacuum procedure the discharge vessels were filled with mixtures of Ne+1%N₂ or Ne+0.3%N₂ at pressures of $p_0=270$ torr and $p_0=450$ torr (p_0 - gas pressure at 0 °C). The frequency was varied between 10 and 1000 kHz. The gas temperature was regulated by dipping the whole discharge vessel into liquid nitrogen or cooled alcohol of -53 °C. In addition measurements were carried out at room temperature and in a heating chamber at higher temperatures. The firing voltage U_Z , minimum sustaining voltage U_L and the actual discharge current were measured. The capacitive current was nulled with a current bridge.

Results and discussion: Fig.1 shows the dependence of firing voltage and minimum sustaining voltage on frequency for $p_0=270$ torr gas pressure. The wall temperature of the discharge vessels is used as parameter.

It is shown that the transition frequency between the bistable pulse mode and the non-bistable continuous mode is characterized by a minimal frequency at which the curves of U_Z and U_L become identical. The pulse mode exists at lower frequencies but the continuous mode occurs at higher frequencies. With decreasing temperature \tilde{f} is shifting to smaller frequency values. At low frequencies ($f \leq 50$ kHz) a variation of gas temperature has a negligible effect on the firing and minimum sustaining voltage. Because the firing voltage is decreasing in the range of \tilde{f} the shift of \tilde{f} to smaller frequencies is accompanied by a decreasing bistable range. In addition to this influence on the bistable range and \tilde{f} there is also an influence on the discharge current. Fig.2 presents two diagrams, each showing the current oscillograms for two comparable discharges at $T=77$ K and 300 K but for different frequencies. When the gas density remains constant an increase in temperature leads to a shorter duration of the discharge pulses. The limited influence of gas temperature on the firing

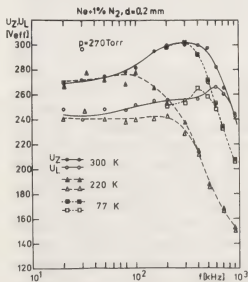
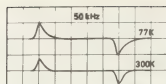
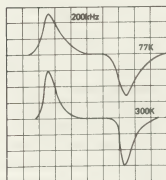


Fig. 1



Time scale:
2 μ s/div.



Time scale:
0,5 μ s/div.

Fig. 2

voltage at lower frequencies and the relatively great change of the discharge current indicate a high incidence of ionization processes by collisions of heavy particles. Such processes are collisions of excited Ne-atoms with N_2 -molecules, the Penning ionization being the main ionization mechanism. In addition, the associative ionization plays a certain role /4/. In /1/ it was demonstrated that the life time of metastable atoms is important for the existence of the continuous mode. If the life time is changed by variation of gas pressure or mixture ratio the transition frequency \tilde{f} is shifted in the same way, i.e.

$$\tilde{f}/p_0 \sim X n_g v_r Q_p \quad \text{with } v_r = \left(\frac{3kT_g}{\mu} \right)^{1/2}$$

$$\text{and } \frac{1}{\mu} = \frac{1}{m_1} + \frac{1}{m_2}$$

(X-mixture ratio, T_g - gas temperature, n_g - gas density at 1 torr and 0 °C, Q_p - cross section for Penning ionization, m_1 , m_2 - masses of gases 1 and 2). For a constant cross section Q_p , $\tilde{f}/p_0 \sim T_g^{1/2}$ results. On the other hand from the shift of \tilde{f}/p_0 the dependence of $Q_p(T)$ can be determined. Fig.3 illustrates the dependence of \tilde{f}/p_0 on $p_0 d$. Above a certain $p_0 d$ -value \tilde{f}/p_0 is independent of $p_0 d$. This break is in good correspondence with the ion transit time /1/. To the right of the break the ion transit time reaches such a value that on an average the ions are no longer swept out of the volume. The figure illustrates the shifting of \tilde{f}/p_0 (constant gas density)

at various gas temperatures for the whole $p_0 d$ range. From this shift the relative dependence of $Q(T)$ can be obtained.

Table 1

T [K]	\tilde{f}/p_0 [Hz/torr]	$Q_p \text{ rel} = \frac{Q_p(T_g)}{Q_p(300K)}$	Q_p [cm^2]
77	77	0.57	$2.85 \cdot 10^{-16}$
300	268	1	$5.0 \cdot 10^{-16}$ (from /5/)
500	395	1.14	$5.7 \cdot 10^{-16}$

By adaptation of the relative values of Q_p rel to room temperature values of other authors data can be obtained about the temperature dependence of the absolute cross sections for Penning ionization. In Table 1 Q_p has been adapted to the values of /5/.

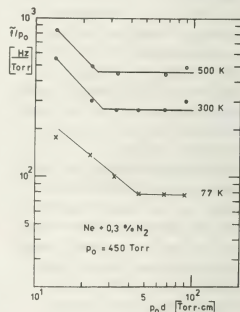


Fig. 3

References:

- /1/ Zahn, R.J., Müller, S., Beitr. Plasma-phys., in print.
- /2/ Zahn, R.J., Müller, S., XIII. ICPIG, Berlin 1977, Contr. Papers, p. 373.
- /3/ Arora, B.M., Bitzer, D.L., Slottow, H.G., Willson, R.H., 8 Nat. Symp. Inf. Display, San Francisco (1967), 1.
- /4/ West, W.P., Cook, T.B., Dunning, F.B., Rundel, R.D., Stebbings, R.F., J. Chem. Phys. 63 (1975) 1237.
- /5/ Pfau, S., Rutscher, A., Ann. Phys. 25 (1970) 321.

HEAT TRANSFER AND FLOW IN A HYDROGEN PLASMA REACTOR

F. Kassabji, P. Fauchais.

Laboratoire de Thermodynamique, U.E.R. des Sciences , 123, rue Albert Thomas, 87060 Limoges cedex, France.

I. INTRODUCTION TO THE PROBLEM.

The heat transfer from thermal plasmas to reactor walls is of major importance for the design of plasma generators or furnaces.

We propose to model a D.C. cylindrical plasma reactor working with hydrogen and defined by the following zones (figure 1).

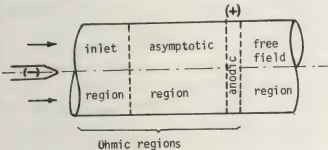


Figure 1

In the inlet region, the cold gas injected near the cathode is heated and ionised with no contact with cold walls.

The asymptotic region constitutes the region of flow development and stabilisation constricted by contact with energetically cooled walls. The increase of the ohmic energy, and therefore the gas temperature terminates in the anodic attachment zone (which we assume to be localised before the turbulent zone created by the development of plasma flow). In this zone the plasma gas transfers a part of its energy to the anode. Finally, the flow becomes steady in the free field region where the wall is cooled in a homogeneous way.

Assuming the hypothesis of the LTE we have solved the "Electro-Magneto-Dynamic" equations system /2/ by a numerically finite difference method /3/ adapted /4/ to hydrogen plasma flow in a reactor with ohmic energy contribution. The computation programme is executed on an IBM 360/91 Computer.

II. NUMERICAL RESULTS.

II-1. Evolution of temperatures in the reactor

The isotherms (figure 2) give the evolution of the temperature in a cylindrical canal of 12 mm diameter, for a current intensity of 200Amp, and a

hydrogen flow rate of 150l/min. The temperature profile in the entrance of the canal is assumed to be parabolic, but its influence is only important on first stages of flow. The temperature is maximum at the beginning and on the axis of the anodic zone where the arc strikes the wall and where the isotherms are radially attracted to the canal wall, while the hot core is growing.

After this anodic region, the plasma flows without additional heating source, the gas loses energy and cools progressively.

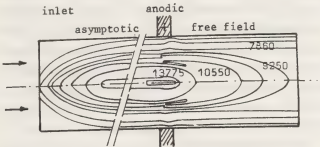


Figure 2

II-2. Electric field

The electric field in the plasma is a function of the gas nature. We notice (figure 3) that it varies only very little with the cylindrical canal diameter and almost not at all with the axial position, except at the entrance of the canal where the influence of the electrical conductivity is very important. It therefore tends to a constant asymptotic value " $E_{x,a}$ " which is independent of the gas flow rate.

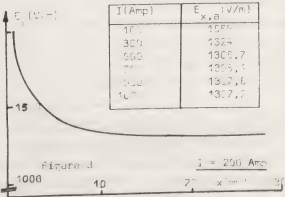


Figure 3

II-3. Thermal developed length

The "Thermal developed length L_D " is defined as the axial distance between the upstream of the cylindrical canal and the section where the average temperature reaches 90% of its asymptotic value.

This length is important for the "constrictor" design. We observe (figure 4) that it decreases with increasing current intensity; it also increases with the gas flow rate and is rather insensitive to diameter variation.

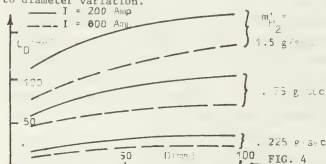


FIG. 4

II-4. Wall Heat Transfer in the ohmic heating regions.

We see that the heat flux on the wall tends to a constant value for any current intensity. The asymptotic flux " $\phi_{T,a}$ " characterises the stabilised flow in the asymptotic region. Its variation with the arc intensity and the different diameters of the canal is linear, however the influence of the hydro-gas flow rate is of little importance.

The Nusselt number in these heating regions of the constricted arc seems to be a function of the ohmic heating number "OH" /5/. It increases (figure 5) with diminution of the ohmic heating number and leads to a relatively constant value with increase of "OH". We see also its increase with arc intensity, this augmentation tends to become relatively linear for the big diameters. Moreover, Nu appears irregular at first in the upstream region of the canal but stabilises afterwards and reaches the constant values defined previously.

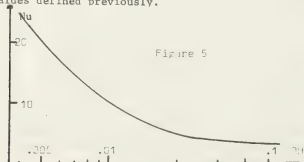


Figure 5

II-5. Wall Heat Transfer in Anodic Region.

The wall heat transfer in the anodic zone is based upon an energy balance /6/. The transfer due to the electrons have been calculated at 10000°K ac-

cording to the expression given by /7/, the terms of the ablation and of the radiation of the anode have been neglected, but the convective and radiative exchanges have been approximated by the quantity of the heat calculated at the end of the asymptotic zone.

From the expressions we have determined the anodic heat flux " ϕ_A " which increases with the intensity of the current and varies as the inverse of the diameter of the constriction canal.

Furthermore the increase of Nusselt number with arc intensity becomes more important as the diameter of the constriction canal is increased. We also observe (figure 6) its increase with the decrease of the ohmic heating number " OH_A ".

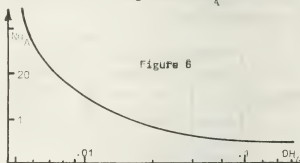


Figure 6

III. CONCLUSION.

The various calculations (by a finite difference method) for a cylindrical plasma reactor working with hydrogen for different diameters (5 to 50 mm) and different intensities of the arc current (up to 1000 Amp) have allowed the determination of the necessary parameters for the design of plasma generators or reactors working under these conditions.

REFERENCES.

- /1/ JOUKOV M.F., KOROTIEIEV A.S., OUPIOUKOV B.A., Dynamique Appliquée du Plasma Thermique (1975)
- /2/ KASSABJI F., Thèse 3ème cycle, Limoges (1975)
- /3/ SPALDING D.B. et al, Heat and mass transfer in recirculating flows, Academic Press (1969).
- /4/ FAUCHAIS P., AUBRETON J., KASSABJI F., PATEYRON B., Rapport C.E.A., SA 5323, oct. (1976)
- /5/ LUKENS L.A., INCROPERA F.P., Int. J. Heat Mass Transfer, 15, 935-951 (1972).
- /6/ SHIH K.T., PFENDER E., AIAA Jrl. 8, 211, (1970)
- /7/ WUTZKE S.A., PFENDER E., IAA Jrl. 6, 1474 (1968).

THE EXTRACTION OF THERMAL ENERGY POSITIVE IONS FROM CORONA DISCHARGES IN AIR

R.S. Sigmond and D. Linhjell.

The Norwegian Institute of Technology, Electron and Ion Physics Research Group, N-7034, Trondheim-NTH.

Abstract Thermal energy positive ions in air have been found to be very difficult to extract through holes of μm diameters in Al foils, and impossible through such holes in Au foils. Explanations are proposed and disproved.

Introduction This is not a normal type paper, it is rather a warning and an advertisement for help. We understand very little of the effects which we report upon here.

In our experimental work on positive coronas we have chosen positive ion extraction with subsequent energy and mass analysis as one of our main diagnostic tools. We expect this to give information about the gas purity (hydrated ions etc), the cathode field (through the $\text{O}_4^+/ \text{O}_2^+$ ratio), and about possible ion bunching in the space charge dominated field in the positive glow type coronas.

It was deemed essential that the extracted ions should give a true picture of the ion population arriving at the cathode plane. Thus, the extraction holes had to have diameters and lengths of the orders of some gas kinetic mean free paths or less, to avoid the formation of undercooled gas jets where ion-molecule clustering processes could occur. The mean free path in NTP air is about $.1\mu\text{m}$, and a large and quite successful effort was made to produce holes of suitable size and form in Au and Al foils of sufficient thickness to stand the pressure differential. This will be reported elsewhere. In the present work matrices of 4×4 conical holes of about $5\mu\text{m}$ smallest diameter were used, as illustrated in Figs. 1a and b.

Using such a gold foil, combined with the gold and gold plated, differentially pumped ion focussing and analyzing system of Fig. 1c, an ion current of 10^{-11}A of unharmed

positive ions was expected from a $20\mu\text{A}$ positive corona in air at pressures up to about 10kPa , according to the extraction hole area and the $j \propto \cos^5\phi$ current density distribution law of Warburg [1]. For the main ion species this is at least 10^4 times our detection limit.

Experimental results: Gold extraction foil. For the first ten happy minutes of the many months of trials, weak currents of O_2^+ and NO^+ were extracted from our $20\mu\text{A}$ pos. point-to-plane corona (dry air, 5kPa , 16mm gap width). The current then waned away. It reappeared for another 10 minutes some months later, then disappeared for good. Of course various remedies were tried, like increasing the extraction field and varying the gas pressure, but to no avail.

It is noteworthy that whenever the foil was made cathode in a negative glow discharge in the same gas, positive ions were extracted readily enough. They were the expected primary ions from ionization in air: N_2^+ , N^+ , O_2^+ , O^+ , all having energies above 100 eV .

Aluminum extraction foil Because of its insulating oxide layer, an Al foil should behave very differently from Au. As seen from Fig. 1b the Al foil holes did not get quite the desired conical shape, and, to make matters worse, we mounted the foil with the conical openings facing the discharge. However, this time the expected positive ions did come through, though with far less intensity than expected from geometrical considerations.

The following properties have been found:
1) A negative glow discharge to the foil gives primary positive ions, as with Au. But, after the glow, or even after only one positive streamer crossing to the foil sur-

face, all thermal energy ions were blocked for some tens of minutes. Then they gradually reappeared, as exemplified by Fig.2. (We have the feeling that this also happens with newly installed Au foils, with the difference that these foils do not recover). 2) Decreasing the focus electrode potential from -800 to -2200V did not change the extracted ion currents, not even at times when the ions were partly blocked due to a previous negative glow or positive streamer. Increasing the focus electrode voltage to -400V gave some 20% reduction in the extracted current. All other electrode potentials were kept adjusted for maximum extraction currents. 3) A central disk, 5mm dia., of the extraction foil including the holes was insulated electrically and the ion current to it was monitored, to check whether the disappearing ions were deflected away from the extraction hole area by surface charges accumulated during negative glows. No effect whatsoever was found.

Discussion. Our experiments have shown:

- A) The positive ion current to the part of the cathode foil containing the extraction holes is not disturbed by the effect that blocks the extraction.
- B) The extraction field is sufficient to collect a fair and field-independent part of the ions passing through the holes.
- C) A negative glow or a positive streamer to the extraction foil send >100 eV ions through the holes, but also blocks the holes for thermal energy ions for 10-20 minutes afterwards (Al foils), or indefinitely (Au foils)

The most straight-forward conclusion from these facts is that the Al surface oxide layer must be beneficial for thermal energy positive ion extraction. This means that a positive surface charge must prevent positive ions in being destroyed on the hole wall, but not prevent them in entering the holes. The higher energy ions in a negative glow must then be supposed to destroy the insulating layer, which afterwards, on Al, slowly will reform in air.

However, this explanation has serious

difficulties:

- a) At 2kPa air pressure the mean free path is about equal to the hole diameters. The only obvious effect that could block the holes is the mirror potential attraction of positive ions to the wall. Computations show, however, that this only will affect thermal velocity ions less than $.3\mu\text{m}$ from the hole wall. Thus, geometrically, an easily detectable ion current should pass at these low pressures. It does not.
- b) At high pressures, $\sim 20\text{kPa}$, the ions must diffuse in an air stream through the hole. Stationary solutions for diffusion in air streaming through a cylindrical hole of dia. and length $5\mu\text{m}$ show an ion concentration decrease by a factor of about 20, which again should leave ample ion current for our detection apparatus. It does not appear.

References [1] Warburg, E. "Handbuch der Physik" Vol.14, pp154-155. Springer 1927.

Acknowledgements We gratefully acknowledge

- The laboratory assistance of R. Dahl
- The HP97 ion path calculations by RSS' son Reier, who played it as a pinball game.

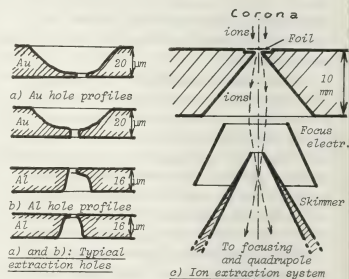


Fig.1 Electrode system and foils for ion extraction

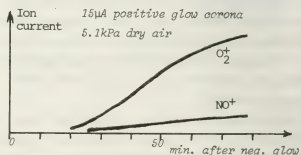


Fig.2 Recovery of ion extraction through Al foil after negative glow discharge

PLASMA DIAGNOSTICS IN HORIZONTALLY BURNING METAL HALIDE DISCHARGES

H. Beyer, W. Funk* and H.G. Kloss.

Akademy der Wissenschaften der DDR, Zentralinstitut für Elektronenphysik, IT III DDR-1017 Berlin, Warschauer Platz 5/10.

*VEB Kombinat NARVA, DDR-1017 Berlin, Ehrenbergstr. 11-14.

1. Introduction

Metal halide discharges in horizontal position show a deflection of the arc from the tube axis caused by convection. Depending on the value of this deflection more or less deviations from the cylindrical symmetry occur so that the measurements of temperature and partial pressures by means of the emission coefficient of optically thin spectral lines often can not be accomplished because in this case a cylindrical symmetry is demanded for the Abel inversion. On the other hand all the methods based on the measurement of parameters of an optically thick spectral line are suitable for the diagnostics of such non-cylindrical discharges. In this case the experimental results only depend on the conditions along the line of observation and do not depend on the geometry in the other arc zones. The methods to be recommended can be considered as being universal for this type of discharges, because from the majority of lighting additives in metal halide discharges (Na, Cs, Tl, In, Al, Sn, Sc, Fe with exception of the rare earths) optically thick spectral lines are available for measurements.

2. Experimental methods

The plasma temperature can be determined by the method developed in [1] and used for the first time in this type of discharge in [2]. In this method the temperature is measured by means of the intensity of the reversal maxima of an optically thick line, but only such spectral lines can be used the lower level of which lies sufficiently above the ground level. According to Wien's formula

$$I_{\max} = \frac{2\sqrt{3}h}{c^2} e^{-\frac{h\nu}{kT_w(0,y)}} \quad (1)$$

one can get a 'Wien's temperature' $T_w(x,y)$ according to the position $x=0$ for each intensity of the reversal maxima $I_{\max}(y)$ (x - coordinate along the line of observation; y - position of the line of observation above the tube axis; $x=0, y=0$ - coordinates of the tube axis). The real temperature maximum $T(0,y)$ along the line of observation is determined by the relation

$$T(0,y) = \frac{T_w(0,y)}{1 + \frac{k}{h\nu} T_w(0,y) \ln(MY)} \quad (2)$$

The coefficient $\ln(MY)$ essentially depends on the positions of the spectral line levels only and can be easily determined in good approximation. For instance for the Tl line 535 nm it equals to 0.85.

The distance of the line maxima $\Delta\lambda$ can be used for the determination of the partial pressures p of the lighting additives. This method was proposed in [3] for optically thick resonance lines and extended in [4] for optically thick non-resonance lines. According to [3,4] it follows

$$\Delta\lambda = a \cdot U[T(x,y)]^{1/n} \cdot p^{1/n} \quad (3)$$

a is a coefficient depending only on the spectral line under consideration and the broadening mechanism. If the broadening parameters are unknown only the relative partial pressure can be measured, n is the broadening exponent equated 1 in [3]. In our conditions (broadening of the spectral line by a foreign gas) it is better to equate $n=1.6$ [4]. The integral

$$U[T(x,y)] = \int_{-x_0}^{x_0} T^{-2}(x,y) \cdot e^{-\frac{E_n}{kT(x,y)}} dx \quad (4)$$

(E_n - energy of the lower level of the spectral line, $-x_0, +x_0$ - entrance and exit of the line of observation) has only a relatively weak dependence on the axis temperature and the form of the temperature profile. For many purposes it can be sufficiently exactly determined by assuming an approximated profile along the line of observation (for example a parabolic profile with $T_0=5000$ K and $T_w=1000$ K.)

3. Results

Metal halide discharges with various lighting additives were run in a horizontal position with d.c. and a.c., and the temperature and partial pressures in the plasma were measured by means of optically thick lines of various elements.

For example fig. 1 shows the temperature profile in an a.c. halide discharge with NaJ, TlJ and InJ as lighting additives and Hg as buffer gas for various powers in the middle of the electrodes (the distance between the electrodes $l = 42$ mm, the tube radius $R = 9,25$ mm). Using (1) and (2) the plasma temperature was

determined by means of the intensity of the reversal maxima of the Tl line 535 nm. It was found out that the deflection of the temperature maximum from the tube axis is nearly independent of the power.

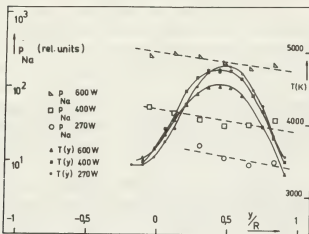


Fig. 1: Temperature and Na partial pressure in vertical direction (a.c.)

Furthermore, fig. 1 shows the dependence of the Na partial pressure in relative units on the vertical position of the line of observation within the tube which was measured from the distance of the reversed maxima of the Na lines 589,0/589,6 nm using (3). The variation of the pressure with various powers was caused by the various temperatures of the tube wall. For a certain power the Na partial pressure slowly increased from the upper wall to the tube axis, but this effect is of the order of the measuring error. In the lower part of the discharge it is not possible to get data because the discharge is cooler and there are no emission of optically thick lines.

In metal halide discharges burning in a horizontal position with d.c. strong cataphoretic effects occur [5]. This means that the partial pressure of the lighting additives rapidly decreases from the cathode to the anode while the plasma temperature increases in this direction.

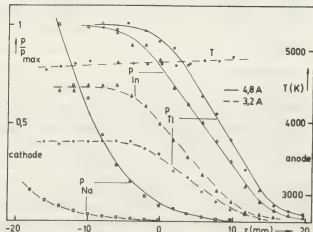


Fig. 2: Temperature and partial pressures of the lighting additives along the axis (d.c.)

Fig. 2 shows the temperature dependence in z -direction (z -coordinate in direction of the tube axis, $z = 0$ - middle between the both electrodes) for the same discharge like in fig. 1, but burning with d.c. The temperature at the centre of the deflected arc was measured by means of the intensity of the reversed Tl line 535 nm. Furthermore fig. 2 shows the variation of the partial pressures of Na, Tl and In along the z -axis obtained from the distances of their maxima of the lines 589,0/589,6, 535 and 451 nm.

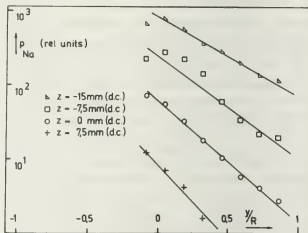


Fig. 3: Na partial pressure in vertical direction (d.c.)

The measurement of the Na partial pressure in y direction shows an effect of vertical segregation in the d.c. discharge as is demonstrated in fig. 3 for various z -positions. An explanation for this effect can be given in the following manner: There is a field-driven flow of additive ions through the arc to the cathode, a back diffusion of additive neutrals mainly through the cold gas at the bottom of the tube, and the circle is closed by the transport of the additives according to this vertical partial pressure gradient from the bottom back into the arc. For Tl and In this effect is perceptible to a smaller extent.

For Na this effect was obtained in d.c. discharges with other additives too, for example in discharges with CeJ_3 and NaJ .

In an a.c. discharge there is a sufficiently homogeneous Na distribution, while in the case of d.c. a segregation in the vertical direction occurs.

Literature

- [1] Bartels, H.; Zs. Physik 127 (1950) 243 and 128 (1950) 546
- [2] Funk, W.; Kloss, H.-G.; Serick, F.; Beitr. Plasmaphysik 13 (1973) 101
- [3] Teh-Sen Jen; Hoyaux, M.F.; Frost, L.S.; JQSRT 9 (1969) 487
- [4] Funk, W.; Kloss, H.-G.; ICPIG XIII, Berlin 1977, p. 149
- [5] Beyer, H.; Funk, W.; Kloss, H.-G.; 2nd Int. Symp. on Incoherent Light Sources, Enschede, Netherlands, 1979

CN MOLECULAR BANDS IN A FREE BURNING METAL ELECTRODES ARC

G. Buchet, R. Haug and J. Maftoul.

Laboratoire de Physique des Décharges ER 114 du C.N.R.S., Ecole Supérieure d'Electricité,
Plateau du Moulon - 91190 Gif-Sur-Yvette, France.

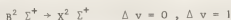
1. Introduction

The behavior of the arc, the electrode erosion and the stability depend on the material of the electrodes used and on the ambient gas. The knowledge of the arc spectrum is an important tool in order to explain the above mentioned phenomena. We have shown that a temporal correlation exists between spectral lines intensity and arc voltage fluctuations [1]. The molecular bands having a positive correlation coefficient are identified here as well as the origin of the responsible radical.

2. Experimental Techniques and Results

The spectrum of free burning arcs in air, N_2 , air + CO_2 and Ar+ O_2 mixtures has been studied. The electrodes were of different purity grades of copper. The experimental set-up is shown in fig. 1. The voltage used was 250 V with a current of 1,5 A, and a gap spacing of 2-3 mm. Under these conditions the arc is rather stable and the spectrum can be recorded for a relatively long period of time (~ 30 mm) which allows the same wavelength interval to be repeated several times. The reproducibility of the spectra is satisfactory. The photomultiplier current and the arc voltage are synchronously sampled with a frequency in the 1 KMz-1 MHz range and recorded in a wave memory recorder (2×1024 samples). The samples are then displayed on an X-Y oscilloscope (X for light and Y for voltage). The set of points statistically characterize the mentioned correlation. Fig. 2 refers to a Copper line (5153 Å) - fig. 3 refers to the head of molecular band (3883 Å) for a free burning arc in air. The comparison between figs 2 and 3 shows that the average slopes of the clouds of points are opposite. Precisely, on fig. 2 the light intensity

increases which diminishing arc voltage and inversely on fig. 3. Exploring the arc column in air with industrial copper electrodes, the violet system of molecular bands of CN in the region 3850-4216 Å was found.



To solve the problem of the origin of CN, the electrodes were replaced by ultrapure copper electrodes (99,995 %). The molecular bands were still visible (fig. 4). When arc was burning in air, but they disappeared (for both types of electrodes) when air was replaced by mixtures of Ar and O_2 (both of 99,995 % purity) as it is clear from fig. 5.

For arcs burning in an atmosphere of N_2 (99,995%) the molecular bands of nitrogen are so intense that it is impossible to detect the molecular bands of air burning CN. It is interesting to remark that in an arc with small currents (< 3 A) the molecular bands of nitrogen are not observed. For an arc burning in CO_2 enriched air we observed that the CN molecular bands intensity increased considerably (500-1000 times). This fact additionally proves an atmospheric origin of CN. The measurements of the CN molecular bands intensity allow to estimate the CO_2 -concentration.

It appears [2] that in the system C-O-N the concentration of CN radical increases with increasing gas temperature. For temperatures of $T > 6000^\circ K$ in the free burning arc in air only three types of radicals and atoms exist : CN, N, O.

3. Conclusions

The experiments show that radicals of CN found in the arc burning in air have an atmospheric origin. When metal vapour emission ceases the arc voltage increases due to decreasing conductivity and synchronously the CN band intensity increases.

4. Références

1. M.G. Drouet, R. Haug, M. Goldman,
31th Annual Gaseous Electronics Conference,
Buffalo, New York.
2. J. Amouroux,
Private Communication.

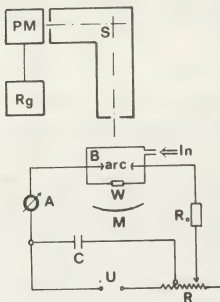


Fig. 1 Experimental setup

M - mirror, W - quartz window

In - inlet for gas injection

B - box, S - spectrometer

PM - photomultiplier, Rg - recorder

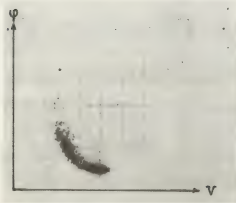


Fig. 2 Correlation between light intensity

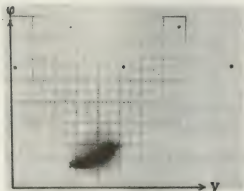
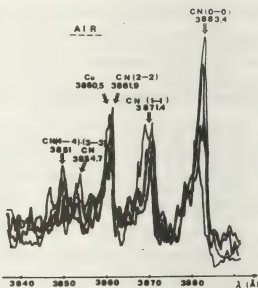
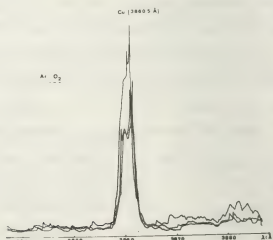
($\lambda = 5153 \text{ Å}$ - Cu - line) and arc voltage.Fig. 3 Correlation between light intensity
($\lambda = 3884 \text{ Å}$ - head of CN molecular band)
and arc voltage.

Fig. 4 Spectrum of an arc burning in air.

Fig. 5 Spectrum of an arc burning in Ar + O₂
mixtures.

OPTICAL INTERFEROMETRY OF PULSED MICRO-DISCHARGES

V.F. Klimkin and V.V. Pickalov.

Institute for Pure & Applied Mechanics Siberian Division, Academy of Science U.S.S.R., Novosibirsk 630090.

Abstract. The investigations of discharge phenomena in continuous medium are connected with the study of the objects of high density gradients, high speeds of movement $\sim 10^5$ - 10^7 cm/s, small characteristic lengths $\sim 10^{-3}$ - 10^{-2} cm. This work is devoted to the analysis of special features of microdisturbances interferometry. The objects of 10^{-2} cm sizes with stepwise density discontinuity are investigated [1].

For axial symmetry inhomogeneity the changes of refraction index connected with the shift of interferometric fringes $k(x)$ by the Abel integral equation (the refraction effects being neglected):

$$k(x) = \frac{2}{\pi} \int_x^R \frac{\Delta n(r)}{\sqrt{r^2 - x^2}} r dr. \quad (1)$$

The method of statistical regularization was used to solve this equation [2,3]. It's need to note the high influence of data errors on the accuracy of restoration. It is a first attempt of retrieval for such class of problems.

Therefore the reliability of the approximate methods of the Abel equation solution was checked up by numerical experiments on model function with stepwise discontinuity on the object's boundary

$$\Delta n(r) = \exp\left(1 - \frac{R}{r}\right). \quad (2)$$

The real experiment was simulated by introducing of random normal errors 3-10% relative to maximum of function into appropriate values of $k(x)$. The Fig.1 shows the results of restoration of the function (2) with 5% noise level (Δ). One can see that the retrieval error of discontinuity value is about 4% while the radius is dividing into 10 zones (\bullet) and not more than 1% while it's dividing into 15 zones (\circ).

The numerous series of model calculations for smooth functions show the high accuracy of the reconstruction.

The possibilities of the methods applied to microobjects with the stepwise distribution of density were determined on special set up including the Mach-Zehnder interferometer and He-Ne laser as a source of light. The object was a cylinder of melted quartz with the diameter $(0.5 \pm 2) \cdot 10^{-2}$ cm put into cell with CCl_4 . It was possible to regulate the value of refraction index changing $\Delta n = n_l - n_g$ by temperature variation of the liquid. An average refraction index of the melted quartz n_g and the temperature dependence of refraction index of CCl_4 were determined by refractometer for the wavelength of $\lambda = 632.8$ nm (the accuracy

of the measurement being $\sim 10^{-4}$), the accuracy of thermoregulation being $\sim 0.1^\circ\text{C}$.

Fringe shifts were measured by the multiplication of photography (100 or 200 times) with the help of comparator. One can see (fig.2) the results of the reconstruction of the stepwise refraction index profile ($R_q = 1.05 \cdot 10^{-2} \text{ cm}$, $\Delta n = 1.95 \cdot 10^{-2}$) by the method of statistical regularization. It is seen that the error of the shock reconstruction is about 7%. The displacement from the relation $\Delta n = \text{const}$ may be connected with the fine structure of microsamples. However an average of refraction index changing (—) is in good agreement with measured one (----).

As a result we come to conclusion about the sufficient reliability of the above method applied in interferometric study of microdisturbances appearing at the initial stages of the electric discharges in liquid dielectrics. In these experiments the ruby laser with the pulse duration of $5 \cdot 10^{-9}$ was used.

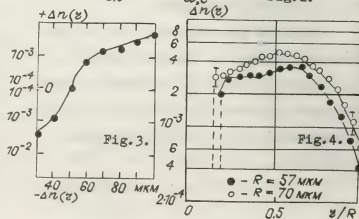
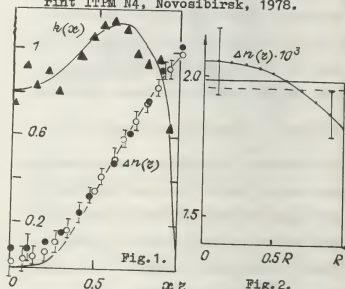
The analyses of the possible errors show that the main deviations of the shifts values obtained. In the Fig.3 one can see results of the $\Delta n(r)$ reconstruction beyond the spherical shockwave front, arising as the result of local explosion on the surface of positive electrode in distilled water. Investigations of the shock waves dynamic allowed to estimate the value of maximum pressure and energy density in the region of local discharge [4] with the help of approximate gasdy-

namic relations.

In the Fig.4 we can see the results of the $\Delta n(r)$ reconstruction for disturbances in ether ($\varepsilon \approx 4$). The reconstruction of pressure profile for similar disturbances allows to appreciate its value on the boundary of initial ionized channel in liquid (----), which is very important for understanding of physical processes connected with discharge.

REFERENCES

1. M.C.Richardson, A.J.Alcock. Appl. Phys. Lett., 1971, 18, 357.
2. V.F.Turchin, V.P.Kozlov, M.S.Malkevich. Uspekhi fiz. nauk, 1970, 102, 345.
3. V.F.Klimkin, V.V.Pickalov. In: Abel inversion and its generalization. Novosibirsk, 1978, 252.
4. V.F.Klimkin, A.G.Ponomarenko. Preprint ITPM N4, Novosibirsk, 1978.



ON THE VUV RADIATION OF TOWNSEND AVALANCHES

V.D. Peskov.

Institute for Physical Problems Moscow, U.S.S.R.

Gas scintillation counters of radiation intensively developed in last years, are advanced compared to proportional gas counters by their enhanced energy resolution [1]. In such a counters there is registered VUV radiation of the Townsend avalanches (A) in contrast to charge collecting in the conventional counters. This work concerns the study of the VUV spectra of A in rare gases and H_2 at pressures $P=0.1-30$ atm.

Method : An installation for spectra recording of a single A is presented in Fig.1. A was initiated in the cylindrical counter (7) by ^{55}Fe . Their radiation at $\lambda < 1050 \text{ \AA}$ was recorded by open counter (12) with a narrow spectral sensitivity varied from 500 to 1000 \AA by means of changing the working gas in counter and filter before the counters. Radiation with $\lambda > 1050 \text{ \AA}$ was recorded by the narrow-band counter with LiF windows (2). Spectra of the large (continuous) stream of A, initiated by ^{55}Fe (activity 0.1 c) were recorded by the vacuum spectrograph.

Fig.1 1-high pressure chamber, 2-counters with LiF window (9), 3-tap, 4-purifier, 5-calibrated source of VUV, 6-manometer, 7-scintillation counter with wire, (8), 10-spectrograph, 11-tap for gas flowing, 12-open counter, 13-differential chamber, 14-tap for flowing impurity gas.

In rare gases the accumulation of excited atoms is possible [3], so due to the step ionization the spectra of singular A and a large stream of A, in general, may be different.

Results : Constant electric field

a) Rare gases The measurement show that spectra of continuous stream of A were due to molecular radiation of the rare gas. Table 1 presents the intensity distribution of singular A radiation in relative photon numbers at different spectral intervals, measured by narrow-band counters.

Table 1

$\Delta E, \text{ eV}$	He			Ar			Xe		
	$p, \text{ atm}$			$\Delta \lambda, \text{ nm}$			$p, \text{ atm}$		
	0.1	1	25				0.1	1	10
8.5 - 12.1	0	0	200	105-125	10^6	10^4	10^3	0	0
8.5 - 14	0	$3 \cdot 10^3$	$4 \cdot 10^2$	105-155	10^6	$5 \cdot 10^4$	$3 \cdot 10^3$	10^6	10^3
8.5 - 15.8	0	$5 \cdot 10^3$	$5 \cdot 10^2$	105-200	10^6	10^5	$5 \cdot 10^3$	10^6	10^3
8.5 - 21.6	10^6	10^4	10^3	160-200	0	10^4	$3 \cdot 10^3$	0	$3 \cdot 10^3$

Comparison of these data with energy distribution in molecular spectra (see for example [2]) reveals their qualitative agreement. Therefore, A in rare gases excite preferably the molecular spectra. To explore the efficiency of the excited molecules formation and, therefore the brightness of A radiation we have measured the rates of the rare gases molecule formation in the three-particle collision processes. For this purpose there was measured the rise time of the electrical and VUV signals in the counters with a thin wire (0.01 mm) - see Fig.2. The pulse front consisted of the electron (\mathcal{T}_e) and ion (\mathcal{T}_i) components, Fast component of the VUV pulse front \mathcal{T}_g was due to formation of the excited molecules and, slow - \mathcal{T}_d - to their radiative decay. The experimental results are presented in Table 2. The rate coefficients calculated by these data are : for Ar $(4.5 \pm 2) \cdot 10^{-32} \text{ cm}^6 \text{ s}^{-1}$ and for Xe -

$$(7 \pm 2) \cdot 10^{-32} \text{ cm}^6 \text{ s}^{-1}.$$

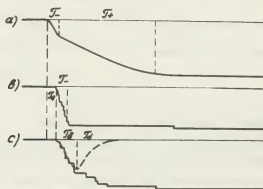


Fig.2 Electrical and light signals from counter filled with Ar+CH₄ (b) and Ar (c)

Table 2

Ar				Xe			
p, atm	T ₁ , s	T ₂ , s	T ₃ , s	T ₁ , s	T ₂ , s	T ₃ , s	
0.2	$3 \cdot 10^{-8}$	$8 \cdot 10^{-7}$	$3 \cdot 10^{-6}$	$2 \cdot 10^{-8}$	$6 \cdot 10^{-7}$	$5 \cdot 10^{-7}$	
0.3	$5 \cdot 10^{-8}$	$4 \cdot 10^{-7}$	$2 \cdot 10^{-6}$	$6 \cdot 10^{-8}$	$2 \cdot 10^{-7}$	$3 \cdot 10^{-7}$	
1	$8 \cdot 10^{-8}$	-	$5 \cdot 10^{-7}$	10^{-8}	-	10^{-7}	

Next experiment was held in a fixed volume where the excited atoms concentration was supported at a constant level. The discharge chamber with gas at pressures 1-10 torr was irradiated with ⁵⁵Fe source. This chamber was jointed to the ionization chamber. The VUV photon counter (flowing or with LiF window) were placed perpendicularly to the axis of the ionization chamber. The concentration of excited atoms and distribution of the VUV brightness was evaluated by the method, described in [3]. The constants of the excited molecule formation calculated by these data were for Ar $\sim 10^{-32} \text{ cm}^6 \text{ s}^{-1}$, for Xe $\sim 3 \cdot 10^{-32} \text{ cm}^6 \text{ s}^{-1}$.

b) H₂ Spectroscopic measurements in H₂ show that in visible and VUV regions only weak molecular spectrum is excited. On the other hand, in the H₂ counter with a thin wire (diameter 0.1 mm) the electric field strength may grow up to 10^5 V/cm and the electron energy stored at their last free path near the filament may be increased up to 100 eV. In this case the emission of the bremsstrahlung radiation from the anode, analogous to the spectrum of the electron gun, is possible. We have measured such a spectrum by means of multiwire counters [4] and discovered the weak bremsstrahlung radiation of electrons from the anode.

II Alternating electric field In the paper [5] there was described the scintillation counter with HF electric field. Such a counter advantageously differs from counters with a constant field, because it can measure simultaneously all three coordinates of the photons or particles. We have studied spectra of A both in the cavity and in the flat spark counter with a HF feeding. Electrons multiplication in the HF electric field caused the propagation of ionization wave with velocity of $10^6 - 10^7 \text{ cm/s}$ from the point of the initial ionization. The experiments with narrow-band counters show that propagation of this wave resulted from diffusion of resonance photons (at short distances) and with molecular radiation - at long distances**.

References :

- 1 A.J.P.L.Policarpo, Space Sci.Instr, 2, 77, 1977
- 2 A.N.Zaidel, E.Ya.Shreider, "Vakuumnaya spektroskopiya i ee primeneniye", Nauka 1976
- 3 V.D.Peskov, XIII ICPIG, Berlin, 2, 455 1977
- 4 I.P.Tindo, Sb."Itogi nauki", v.9, Astronomiya VINITI, M, 1974, p.173
- 5 S.Fukui, S.Hayahawa, J.Phys.Soc.Jap, 15, 532, 1960

** The principle of spherical ionization wave propagation was used to construct the X-ray detector, where the coordinates of the initial photons were determined by the VUV radiation delay time measured near the opposite edges of the counters.

ON THE INFLUENCE OF ELECTRODES ON THE PROPERTIES OF HIGH PRESSURE DISCHARGE

V.D. Peskov.

Institute for Physical Problems, Moscow, U.S.S.R.

It is known, that in the nearelectrode regions of low pressure arcs there occur a lot of exotic phenomena [1]. As for the high pressure discharges, the information about the electrode phenomena is very scanty because the intensity of visible emission is usually comparable to the radiation of nearelectrode regions.

Present work is devoted to comparison of visible and VUV spectra (500-10000 Å) of the electrodeless (EL) [2] and electrode (E) HF discharges and direct current arc (A) with W, Mo or Cu electrodes in H_2 , D_2 and rare gases at the pressures up to 30 atm with similar dimensions, power, current and other characteristics. Space distribution of the luminosity of the visible light was measured by stereoscopic system composed of two dissectors. In the VUV and ultrasoft X-ray regions we used the two-dimensional coordinate counters. In the whole spectral region (30-7000 Å) space resolution was about 0.1 mm.

1. Experiments at $p=1$ atm a) Spectra in 2000-10000 Å region. The spectra of H_2 and D_2 discharges have H^- continuum and Balmer's lines. The diameter of H^- emission region was a few mm larger compared to line emission zone. With increasing of the discharge power from 0.5 to 3 kWt the plasma parameters varied in such a way: in A - T_e from 0.8 to 1.1 eV, n_e - from $5 \cdot 10^{15}$ to 10^{17} cm^{-3} , in E - T_e from 0.7 to 0.9 eV, n_e - from $2 \cdot 10^{15}$ to 10^{16} cm^{-3} , EL - T_e from 0.7 to 1.2 eV, n_e - from $3 \cdot 10^{12}$ to 10^{15} cm^{-3} (T_e , n_e - electron temperature and density, respectively). One may conclude that in EL n_e is of some orders lesser, than equilibrium n_e calculated by Saha equation, whereas in A and E this disagreement does not exceed 2.

In EL one observes also the disagreement of about two orders with Boltzmann law for level population. Due to low density the electron energy distribution function has the "cut-tail" [3], so the impurity lines in EL with $E_{ion} > E_i$ - ionization potential of the main gas - were not excited. But even in the regims when electron densities of all the types of discharges were equal, in EL different to A and E, lines of impurities were not excited (T_e of EL was larger than in A and E). Similar results were obtained in rare gases.

b) Spectra in the range 500-2000 Å In H_2 and D_2 in A with W and Mo electrodes the highest luminosity was observed on the cathode spot with dimensions about 0.1 mm. The radiation from cathode has pulse form with a time of $\sim \mu\text{s}$, moreover in some cases we succeeded to observe by means of coordinate counters the pulse jets, flowing from the spots to column (Fig.1). Therefore we obtain in W and Mo electrodes an "explosive" mechanism of emission [1].

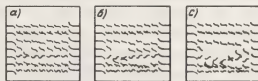


Fig.1 Oscillograms of the signals (see [4]) from two-dimensional counters observing the region of 0.5×0.5 mm a) $t=0$, b) $t=1 \mu\text{s}$, c) $t=2 \mu\text{s}$.

Electron concentration in the nearcathode region measured by the coincidence of the signals from spectrograph and coordinate counters was about 10^{18} cm^{-3} , so these jets carry the electrons and ions into the plasma column. Nearelectrode regions emitted the intense continuum spectra too. Maximum energy E_γ of the photons,

emitted from cathode measured by means of the open counter, was about 100 eV for the intensity about 1 pho/s in 4π steradn. Such radiation corresponds to the effective spot temperature about 3 eV. On the Cu cathode a so called "thermal" mechanism of emission [1] is likely to realize, because strong fluctuations in VUV and photons with $E_{\nu} \sim 100$ eV were not observed and the spot dimension was about 0.2-0.3 mm. In E discharge near the electrodes we did not observe spots, but there were registered the moving filaments about 0.1 mm in diameter and 0.3 mm in length. Electron density in the filament was about 3-5 times higher than in the background plasma, so in E there occurs an injection of the electrons ions and excited atoms from electrodes to column. A special experiment was made to check the influence of the small nearelectrode region on the density of electrons and excited atoms. We have introduced into the EL for a 1 ms the W wire perpendicularly to the electric force lines (in order not to distort the electric field). This procedure provides two or three fold increase of n_e in the pulse. Radioscopy of the discharges by means of X-ray gun and with an emission of the discharge shows, that in EL impurity concentration did not exceed $10^{-5}\%$, but in A or E it was about 0.1%. Similar results were obtained in rare gases. We did not manage to record the radiation with $E_{\nu} \sim 100$ eV in A because of the strong absorption, but in the nearelectrode region there were excited the weak ion lines. The halfwidth of HeII line (1640 Å), measured by the coincidence technique for the signals from spectrograph and coordinate counters was about 0.5 Å, i.e. temperature was about several eV. When the discharge was switched off within 0.1 μ s the spots in A disappeared approximately in the same interval, but in E - for some μ s. Afterglow time of all types of the discharges was nearly the same (about some μ s) in the visible region, and was about 10 μ s in VUV. It shows that electrodes did not strongly affect the heat balance in A and E. The cooling time similarly diminished

when we increased the speed of gas rotation in the discharge chamber.

2. Experiments at $p > 1$ atm We did not manage to distinguish VUV and visible emission of the nearelectrode regions in H_2 and D_2 at $p > 2$ atm from the background continuum radiation of the column. Visible spectra of the discharges were similar, but in EL n_e was 2-3 orders lesser, than in equilibrium. At the same time we observed the 5-10 fold deviation of the level populations from Boltzmann law. All the lines vanished in rare gases at $p > 5$ atm in spectra of EL and only continuum radiation was present. It was due to low $n_e \sim 10^{11}$ cm $^{-3}$ and the absence of the electron distribution function tail. At the same power volume density in A and in E the lines were presented. We succeeded to observe the cathode spot in A only in He at $\lambda < 1000$ Å. The intensity of this emission ^{varied} by two orders of magnitude with a characteristic time about 3-5 μ s.

Conclusion This work shows, that in A and E is always more close to equilibrium than in EL. In E and A equal n_e in contrast to EL impurities with $E_{ion} > E_i$ were always excited. Similar results were obtained in the work [5], where visible spectra of E and EL were compared. Our experiments in VUV show: that injection of the electrons, excited atoms and impurities in A and E facilitated the establishment of equilibrium.

References :

- 1 G.A.Lubimov, V.I.Rahovskiy, Uspehi Fiz. Nauk, 125, 665, 1978
- 2 D.B.Diatroptov, V.D.Peskov, ZETF, 61, 1038, 1971
- 3 J.Richter, X ICPIG, Oxford, Invited papers, 37, 1971
- 4 G.D.Bogomolov, Yu.V.Dubrovskiy, V.D. Peskov, Prib.Tech.Exper, N3, 209, 1978
- 5 V.M.Batenin, V.S.Zrodnikov, V.K. Rod-datis, V.F.Chinnow, TWT, 13, 270, 1975

ON IONIZATION INSTABILITIES OF HIGH PRESSURE DISCHARGES

V.D. Peskov.

Institute for Physical Problems, Moscow, U.S.S.R.

Recently there was discovered an instability of high pressure discharges, but the mechanism of such instability has not been studied. This report is devoted to the experimental investigation of the instability in direct current arcs and in HF discharges [4] in H_2 , D_2 and rare gases at pressures up to $P=30$ atm.

Methods : Fig.1 shows the experimental arrangement. Discharge emission was registered by means of stereoscopic system composed of two dissectors and two fast ($\sim 0.1 \mu s$) two-dimensional coordinate counters, visualizing VUV and soft X-ray radiation of plasma in narrow bands from 100 to 2000 Å with the space resolution about 0.1 mm.

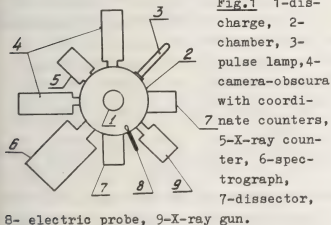


Fig.1 1-discharge, 2-chamber, 3-pulse lamp, 4-camera-obscura with coordinate counters, 5-X-ray counter, 6-spectrograph, 7-dissector, 8- electric probe, 9-X-ray gun.

Spectra were recorded by the monochromator MDR-2 and vacuum spectrograph DFS-29. Electric field distribution near the discharge was measured by the probe.

Results : Two types of the instabilities were discovered. The first one arises at $P > 3$ atm in carefully purified gases with diminishing of gas rotation speed. This instability arose in arc and electrode HF discharge in the form of disordered breakdowns near the main discharge column bended by Arhimed forces (Fig.2a). Ion lines appeared in rare gases simultaneously with breakdown. After the breakdown the visible emission vanished for some μs , but in VUV one can observe the molecular spectrum of rare gases during some tens of μs .

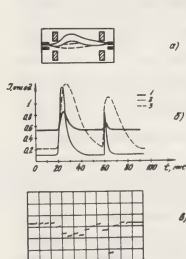


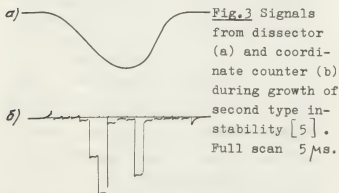
Fig.2 a) scheme of first type of instability, b) oscillograms of arc current (1), lines (2), and molecular (3) radiation at the moment of breakdown, c) oscillogram [5] of signals from coordinate counter passed 10 μs after breakdown

In electrodeless HF discharge this instability displayed as an oscillations of discharge dimension with a characteristic time about 10 μs . It was suggested [6], that such a breakdown was due to avalanche ionization of excited atoms accumulated near the main discharge

column. An attempt to calculate such a breakdown has been made in paper [7]. Our measurements with coordinate counters show, that immediately before the breakdown the intensity of molecular radiation near the discharge substantially increases that confirms the accumulation of atoms.

To demonstrate experimentally the possibility of this mechanism the following experiment was produced. When discharge came up to the surface we irradiate the region near the column by the collimated pulse of radiation with energy $E_i > E_v > E_i - E_{ex}$ and with intensity of the order of $\sim 10^{20}$ phot/s (E_i , E_{ex} - ionization potentials and first excited level of rare gas atom). Breakdown appeared simultaneously with the radiation pulse. This experiment proves the hypothesis suggested in [6] because such radiation may ionize only excited atoms, but not normal.

The second type of instability appears only in HF discharges. It was displayed in the form of rapidly growing ($1 \mu s$) filamentary regions (diameter 0,1-1 mm) intensively radiating in VUV (mainly continuum spectrum) - see Fig.3.



In the visible region continuum luminosity practically did not change, but synchrono-

usly with filament growth one can observe the weak flashes of ion lines and in D_2 weak radiation in interval up to 100 \AA . The lifetime of these filaments was about $10 \mu s$. From both the spectral distribution and its absolute brightness one can evaluate $T_e \sim 2 - 3 \text{ eV}$. Electrical probe measurements show the increase of electric field lines density near the inhomogeneities at the moments of filament growth. We can suggest the following mechanism of this instability. Electron density fluctuations provide the region of enhanced conductivity with local increase of the electric field E . As a consequence, there improves the "tail" of electron energy distribution function, increases the electron density, ratio E/p , etc.

The filament decay is likely to be connected with swelling and skinning which draw up the overheated region onto the discharge surface.

References :

- 1 V.Finkelburg, G.Maecker, "Elektricheskie dugi i termich.plasma", In.lit, 1961
- 2 J.D.Cobine, D.A.Wibbur, Journ.Appl.Phys., 22, 835, 1951
- 3 V.M.Batenin, P.V.Minaev, High Temp. - High Press, 2, 597, 1970
- 4 D.B.Diatroptov, V.D.Peskov, JETP, 61, 1038, 1971
- 5 G.D.Bogomolov, Yu.V.Dubrovskiy, V.D.Peskov, Prib.Tech.Exper., 3, 209, 1978
- 6 V.D.Peskov, Zh.Tech.Fiz., 45, 2552, 1975
- 7 J.D.Daugherty, J.A.Mangano, J.H.Jacob, Appl.Phys.Lett., 28, 581, 1976

PLASMA FORMATION KINETIC AT KNUDSEN ARC IGNITION

A.A. Bogdanov, V.B. Kaplan, A.M. Martsinovskiy, V.G. Yur'yev.

A.F. Ioffe Physical Technical Institute Academy of Sciences of the U.S.S.R., Leningrad, K.21, U.S.S.R.

In present report attempt is made to describe the whole picture of Knudsen arc ignition, that was investigated unsufficiently before /1/. The complex phenomena due to secondary cathode processes, that are inherent in break-down in cold electrode gas discharges, are absent in present situation. Therefore the discharge growth is connected with plasma creation and corresponding electrical field variation in the interelectrode gap.

The investigations were performed in device with parallel plane electrodes. Cathode with indirect heating was utilized. The gap $d \sim (1-2)$ mm. The electrode diameter $22 \sim 10$ mm. The gas filling is the cesium vapour at pressures $(10^{-3} - 10^{-2})$ torr. The discharge ignition was done by rectangular pulse with front

$0.1 \mu s$. There was no anode load in the circuit. Therefore anode voltage was constant during arc ignition. The main experimental methods are spectroscopical and probe ones. The gated integration was used with time resolution ~ 50 ns.

The discharge ignition may be divided into three stages that depends on current variation after anode voltage pulse application /2/: delay, breakdown and relaxation /Fig.1/. It is noticeable that the arc development isn't radius depending practically at all stages. It facilitates the arc investigation.

At delay stage there is no quasineutral plasma in the gap. Initial current value at $t=0$ and potential distribution is in keeping with "3/2" law, the initial electron velocities being taken into account. Ionization begins near anode. When ion concentration grows, the main potential drop moves towards cathode. The

ionization and excitation are direct. Therefore it is possible to define potential distribution in the gap by measurement of various atom excited level distributions. These results permitted to carry out the selfconsistent calculations of discharge development at delay stage /3/.

When delay stage comes to breakdown, the quasineutral plasma forms. Initially it forms near anode. After this plasma occupies all gap, the main potential drop being near cathode. Near cathode the virtual cathode is created. It regulates the discharge current magnitude at whole breakdown stage. Plasma creation is accompanied with its expansion from the gap because of ambipolar diffusion. It changes the radial line intensities distributions. Probe characteristics had only electron branch at delay stage (this branch corresponds to electron beam with cathode temperature). At breakdown stage probe characteristics have usual plasma form (Fig.2a).

When the plasma with slow electron concentration $n_e \gg n_{beam}$ is created, the excitation and ionization mechanisms change. It breaks the linear dependence of spectral lines intensity near anode upon discharge current (Fig.3). The ratio of various levels population changes also. The change of ionization mechanism is accompanied by fast increase of plasma concentration from values $n_e \sim 10^{16} cm^{-3}$ (Fig.2b). It is connected with strong plasma heating that occurs at plasma creation moment (Fig.2b). The beam relaxation by interaction with plasma oscillations may be one of possible mechanisms of such heating, the significant part of beam energy being transferred to slow plasma electrons. $\overline{I_e}$

diminution during the concentration growth may be connected with Coulomb relaxation or with cumulative ionization increase and corresponding growth of energy losses.

At the end of breakdown stage the ion concentration increases. Ions compensate the electron emission charge and virtual cathode disappears. The next current growth is relatively slow. It is connected with plasma concentration growth and with corresponding increase of Shottky effect. The degree of ionization growth is so strong that electron pressure becomes of the order of gas pressure out from the gap. Therefore the neutral atom concentration in the gap begins to diminish. Firstly it leads to variation of radial spectral line intensities (minimum of intensity occurs in center - see Fig. 1b, curves 4,5) and secondly - to diminution of plasma concentration and discharge current.

Thus the last stage is connected mainly with atom and ion balance establishment. The duration of this stage correlates well with ion diffusion (or transit) time along the gap radius.

/1/. C.J.Mullin. Phys. Rev. 70, 401 (1946).

/2/. W.B.Kaplan, A.M.Martsinovskiy, B.I.Tsirkel, V.G.Yuriev. Proc. of the IX-th Int. Conf. on Phenomena in Ionized Gases. p.199 (Bucharest, 1969).

/3/. V.I.Babanin, V.B.Kaplan, A.M.Martsinovskiy, A.Ya.Ender. Journ. Techn. Phys. 47, 1467 (1977).

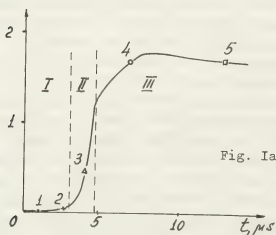


Fig. 1a

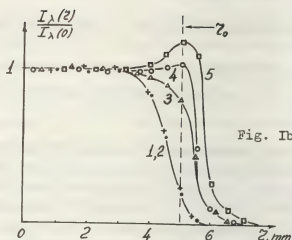


Fig. 1b

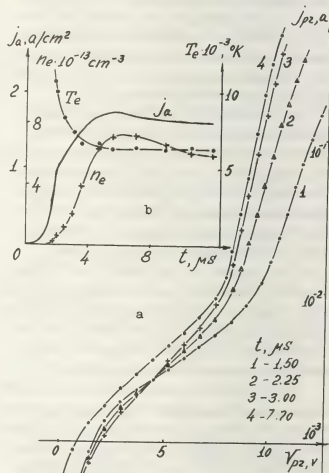


Fig. 2

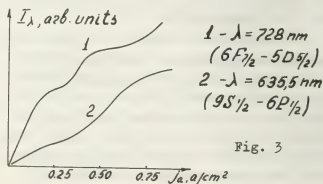


Fig. 3

THEORY OF LOW-VOLTAGE ARC IN NOBLE GAS

F.G. Baksht, V.G. Ivanov.

A.F. Ioffe Physical Technical Institute, Academy of Sciences of the U.S.S.R., Leningrad, K.21, U.S.S.R.

The most preferable ionization mechanism for low-voltage arc (LVA) is the step ionization by Maxwellian tail of electron distribution function. This mechanism provides low emitter voltage drop $\varphi_e < E_i/q$ (E_i is the excitation energy of the lowest metastable level). The mechanism of noble gas ionization was analyzed in [1]. The theoretical analysis included step and associative ionization and the reverse processes of three particle and dissociative recombination. The conversion of atomic ions into molecular ones and molecular ions dissociation were also taken into account. It was shown that LVA plasma must consist mainly of atomic ions. The small concentration of molecular ions may be calculated from the condition of ionization equilibrium, that established because of large value of dissociative recombination coefficient. The conversion of atomic ions into molecular ions, that is essential at large pl value (P is a pressure, L is a gap), may strongly diminish the concentration of atomic ions and consequently the whole plasma concentration.

The LVA plasma parameters were calculated from the following set of equations

$$j_e = -\frac{ue_a}{q} \left[q n_e \frac{d\varphi}{dx} - \kappa T_e \frac{dn}{dx} - n_e (1 + K_e^{(T)}) \kappa \frac{dT}{dx} \right] \quad (1)$$

$$j_{ia} = \frac{u_{ia}}{q} \left[q n_{ia} \frac{d\varphi}{dx} + \frac{q j_e}{u_{ei}} - \kappa T \frac{dn_{ia}}{dx} - n_{ia} \kappa \frac{dT}{dx} \right] \quad (2)$$

$$\frac{dj_{ia}}{dx} = \tilde{K}_i n_e N_o - \alpha_{ia} n_e^2 n_{ia} - K_{alm} n_{ia} N_o^2 \equiv \Gamma_{ia}, \quad (3)$$

$$S_e = \left[\left(\frac{S}{2} + K_e^{(T)} \right) \kappa T_e + q \varphi \right] j_e - \alpha_e \frac{dT_e}{dx}, \quad (4)$$

$$\frac{dS_e}{dx} = - (E_i - q\varphi) \Gamma_{ia} - \Delta S_{rad} - \Delta S_{ei} - \Delta S_{ea}, \quad (5)$$

$$\frac{d}{dx} \left(x_e \frac{dT}{dx} \right) = 0, \quad (6)$$

n_e and n_{ia} are electron and atomic ion concentration ($n_e = n_{ea} + n_{im}$). j_e and j_{ia} are electron and atomic ion fluxes. $j_e + j_{ia} = j$ (j is the arc current). N_o and T are atom concentration and temperature ($N_o = p/\kappa T$). φ and T_e are electron potential and temperature. $K_e^{(T)}$ and α_e are thermodiffusion ratio and electron thermoconductivity. u_{ea} and u_{ei} are electron mobilities in gas and fully ionized plasma. α_a is gas thermoconductivity. \tilde{K}_i , α_{ia} and K_{alm} are coefficients of ionization, recombination and conversion. E_i is ionization energy. ΔS_{rad} , ΔS_{ei} , ΔS_{ea} are electron energy losses because of radiation, electron-ion and electron-atom collisions. The molecular ion dissociation is ignored in (5) because of its small role in atomic ion balance. We utilized $\tilde{K}_i(T_e, n_e, N_o)$ value according to [1] (it must be noticed that escape of radiation and non-Maxwellian part of fast electron distribution function are essential for \tilde{K}_i value calculation).

Equation (1)-(6) were solved numerically with corresponding boundary conditions at the plasma-electrode sheathes [2]. The kinetic reflection coefficients [3] near emitter sheath and strong anisotropic component of electron distribution function near collector sheath [4] were taken into account. Results of calculation are shown at Fig.1-5. The plasma parameter values in the gap are depicted at Fig.1. (T_e , T_c , u and j_{es} are the emitter and collector temperature, arc voltage drop and emission current; φ_e and φ_c are the emitter and collector sheath voltage drops). Continuous lines correspond to $L = 0.5$ mm, dotted lines - to $L = 1$ mm. The main feature of

plasma parameter distributions is strong n_e variation across the gap because of small ℓ_i/L value (ℓ_i is ion mean free path). The distributions of atomic ion rate of generation Γ_{ia} , associative ionization rate Γ_{im} , dissociative recombination rate $\Gamma_{dz} = \alpha_{im} n_{im} n_e$, conversion rate $\Gamma_{alm} = K_{alm} n_{ia} N_0^{1/2}$ and rate of molecular ion dissociation $\Gamma_{m/a} = K_{m/a} n_{im} N_0$ are shown at Fig.2 (α_{im} is a dissociative recombination coefficient, $K_{m/a}$ is a molecular ion dissociation rate). The molecular to atomic ion concentration ratio n_{im}/n_{ia} and radiation power density W_{rad} are also shown. As it was mentioned previously, the molecular ion concentration is calculated from ionization equilibrium condition $\Gamma_{im} + \Gamma_{alm} = \Gamma_{dz} + \Gamma_{m/a}$. It may be noticed that $\sim 30\%$ of generated atomic ions are lost because of atomic to molecular ion conversion. Significant role of conversion is due to high noble gas pressure and to relatively small molecular ion dissociation rate. At Fig.3 the population of low excited levels are shown in nondimensional units $\nu_K = N_K / (N_0 g_0 e^{-E_K/kT_e})$ (g_0 and g_K are statistical weights of ground and excited levels, E_K is excitation energy, N_K is excited level population, index K corresponds to atom levels according to its energy enhancement: $K = 0, 1, 2, 3, 4$; $\nu_I \equiv \nu_1 = \nu_2$; $\nu_{II} \equiv \nu_3 = \nu_4$). Continuous lines correspond to $L = 0.5$ mm, dotted lines - to $L = 1$ mm. Increase of ν near collector is due to excited states overpopulation because of dissociative recombination of molecular ions, that are created near collector.

1. F.G.Baksht, V.G.Ivanov. Journal of the Technical Phys.(JTP) **48**, 688 (1978).
2. Thermionic Converters and Low-Temperature Plasma. ed by B.Ya.Moyzhes and G.E. Pikus (English Edition by L.A.Hansen. Techn.Inf.Center/ U.S.Department of Energy (1978)).
3. F.G.Baksht, V.G.Ivanov. JTP **40**, 218 (1970)
4. F.G.Baksht, V.G.Ivanov, B.Ya.Moyzhes. JTP **42**, 921 (1972).

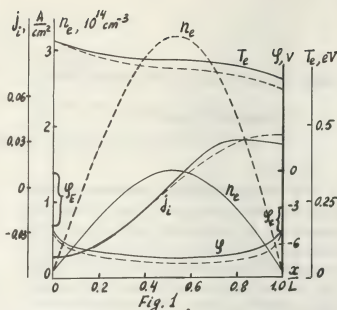


Fig. 1

$T_e = 1400^\circ K$, $T_c = 700^\circ K$, $j_{es} = 1 A/cm^2$, $\rho = 50$ torr,
 $L = 0.5$ mm : $U = 2.95$ eV, $j = 0.8 A/cm^2$
 $L = 1$ mm : $U = 3.25$ eV, $j = 0.8 A/cm^2$

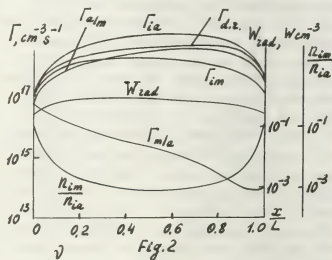


Fig. 2

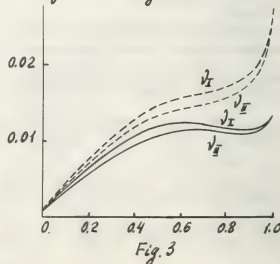


Fig. 3

THEORY OF HOLLOW CATHODE IN ATMOSPHERIC ARC IN NOBLE GAS

F.G. Baksht, A.B. Rybakov.

A.F. Ioffe Physical Technical Institute, Academy of Sciences of the U.S.S.R., Leningrad K.21 U.S.S.R.

1. The hollow arc discharge in cylindrical hollow cathode (HC) with slightly ionized noble gas plasma is considered theoretically. The approach, that was used in [1-3], is utilized below. The following inequalities are supposed to be valid: $L_L \ll \ell_i \ll \ell_i \ll R \ll L_0$ (L_L is a Langmuir sheath dimension, ℓ_i is an ion mean free path, L_i is an ionization length, $R \sim 0.1$ cm is a HC radius, L_0 is a length of HC plasma column - see Fig.1). The main potential and concentration variation along the HC radius is localized in comparatively narrow pre-electrode layers, which dimensions are L_L and L_i . In the other part of plasma column the ionization equilibrium establishes. In this part of plasma column plasma parameters are supposed to be independent on radius r . Numerical calculations were performed for Xe plasma at pressures $p = (0.3-1)$ atm., $R = 0.15$ cm, $T_e = 0.1$ eV (T_e is cathode wall temperature). Results of calculations are depicted at Fig.2-4 for $p = 1$ atm.

2. Plasma in the cavity is described by following set of equations:

$$p = N_0 k T_e \quad (1)$$

$$\frac{dI}{dz} = 2\pi R j_e = 2\pi R (j_s - j_e + j_i) \quad (2)$$

$$j_e = \frac{I}{\pi R^2} = \frac{1}{4} \frac{d\varphi}{dz} - q_e \frac{dn}{dz} - u_e n (1 + K_e^{(T)}) \kappa \frac{dT_e}{dz} \quad (3)$$

$$j_i = \frac{I}{\pi R^2} \left[\left(\frac{5}{2} + K_e^{(T)} \right) \kappa T_e - q_e \varphi \right] \quad (4)$$

$$\frac{dS_e}{dz} = \frac{2\pi R}{q_e} \left[j_s \cdot 2\kappa T_e - j_e \cdot 2\kappa T_e - j_i (\xi_i + q_e \varphi) \right] - q_e \pi R^2 \quad (5)$$

T_e is an electron temperature. n and N_0 are plasma and neutral atom concentrations. n is calculated by Saha equation at electron

temperature T_e . I is a whole electric current. j_s is an emission current from cavity wall. j_e and j_i are electron and ion currents from plasma to wall. $j_e = \frac{1}{4} q_e \frac{d\varphi}{dz}$. D_e , u_e , $K_e^{(T)}$ are electron diffusion coefficient, mobility and thermodiffusion ratio. Potential φ is counted from the cavity wall. q_e is an electron power density losses, that consist of radiation losses in spectral lines and continuum and energy losses because of electron-ion q_{ei} , and electron-atom q_{ea} collisions.

3. The Saha equation becomes invalid for plasma concentration determination at low T_e and n , when the conversion rate of atomic ions into molecular ones is comparable with or larger than the rate of three particle collisional recombination. The high rate of molecular ion recombination causes the depletion of whole plasma concentration n . It is noticeable that plasma remains in the ionization equilibrium, i.e. the whole rate of atomic and molecular ion creation is equal to the whole rate of atomic and molecular ion recombination [4]. At Fig.2 degree of ionization β_e and Saha degree of ionization $\beta_e(T_e)$ are shown as functions of T_e . It is evident that sharp depletion of plasma concentration takes place in very narrow interval of T_e variation. Therefore the critical electron temperature value T_{eo} may be defined. The degree of ionization may be sufficiently large for practical applications only if $T_e > T_{eo}$. We regarded the point $z = 0$, where $T_e = T_{eo}$, as the HC plasma column boundary.

4. The pre-electrode ionization layer ($R - z \sim L_i$) must be considered separately for j_i determination. This layer is described by the equations that take into account atomic ion generation, their diffusion and

conversion into molecular ones. The molecular ions are described by the ionization equilibrium equations. Their concentration is small because of large recombination coefficient value. Results of calculation are shown at Fig.3. $\delta = j_i / j_{i0}$ (j_{i0} is the atomic ion current value, calculated without conversion) $n_i(0)$ is plasma concentration at the boundary between the Langmuir sheath and ionization sheath. \tilde{n} - plasma concentration at the boundary of the plasma column, where ionization equilibrium exists, \tilde{n} - coincides with Saha concentration n_s at sufficiently high T_e (\tilde{n} and n_s are calculated at atom temperature $T = T_e$).

5. Atom and ion temperature T in the plasma column was found from heat balance equation:

$$-\frac{1}{2} \frac{\partial}{\partial z} (2\alpha \frac{\partial T}{\partial z}) = q_{ei} + q_{ea} \quad (6)$$

with boundary conditions

$$\left[\frac{\partial T}{\partial z} \right]_{z=0} = 0, \quad T(R) = T_c$$

6. The set of equations were integrated numerically from $z = 0$, where $T_e = T_{e0}$, $j_z = 0$. The third boundary condition along z axis was formulated at the exit of the cavity: $\left[\frac{\partial T_e}{\partial z} \right]_{z=L_0} = 0$, according to experimental situation [5,6]. At Fig.4 the calculated distributions of T_e , φ , I , radial current components j_z , j_r , j_i are shown at whole voltage drop $\varphi(L_0) = 6.2$ V ($P = 1$ atm, $j_s = 10$ A/cm², $R = 0.15$ cm).

1. F.G.Baksht, A.B.Rybakov. "Arc theory for a hollow cathode discharge in a fully ionized dense plasma" XIII Int. Conf. on Phenomena in Ionized Gases p.319-320 (Berlin, 1977).
2. F.G.Baksht, A.B.Rybakov. Journal of the Technical Phys (JTP) 48, 234 (1978).
3. F.G.Baksht, A.B.Rybakov. JTP 48, 700 (1978)
4. F.G.Baksht, V.G.Ivanov "Theory of Low-Voltage Arc in Noble Gas" (report at present conference); JTP 48, 688 (1978)
5. G.A.Djuzhev, N.K.Mitrofanov, E.A.Startsev, S.M.Shkolnik, V.G.Yuriev "Experimental Study of Arc Hollow Cathode" (A.F.Ioffe Physical-Technical Institute, Leningrad (1978)).
6. G.A.Djuzhev, N.K.Mitrofanov. JTP 48, 12 (1978).

- 1 - cathode, 2 - Langmuir sheath, 3 - plasma column.

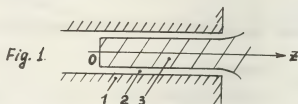


Fig. 1

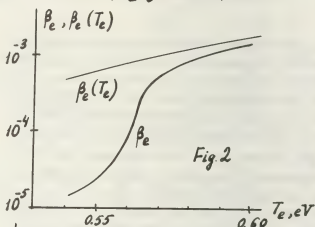


Fig. 2

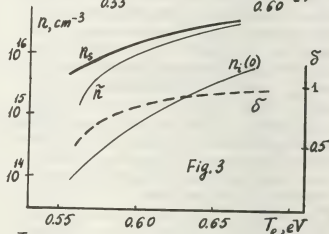


Fig. 3

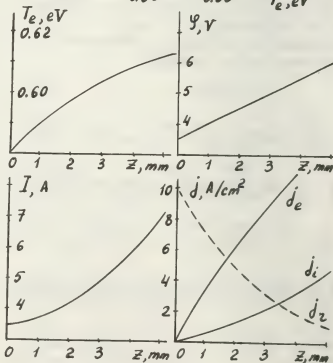


Fig. 4

PECULIARITIES OF PULSED NON-SELF-SUSTAINED DISCHARGES IN MIXTURES CONTAINING CO

K.S. Klopovsky, G.B. Lopantseva, A.F. Pal, I.G. Persiantsev and A.N. Starostin.

Institute of Nuclear Physics, Moscow State University, 117234, Moscow U.S.S.R.

We have studied pulsed non-self-sustained discharges controlled by the electron beam with the energy ~ 100 keV and a current $j_b \sim 300$ mA in gaseous mixtures containing CO with N_2 , Ar and He. The gas was pumped through a quartz discharge chamber at a rate of 1 m/sec. The electrode area was 1×1 cm², with distance $L = 1$ cm.

It has been found that at small energy inputs the discharge current j in the mixtures behaves similarly to the current in pure N_2 . As the energy input increased, the behaviour of $j(t)$ altered and one could observe a fall-off of the curve, followed by instability (fig.1). As the j_b was further enhanced, the discharge turned into an arc without the stage of j fall-off. Such a dependence of $j(t)$ was observed for all studied mixtures. No such behaviour was observed in pure N_2 and in N_2 - He mixtures.

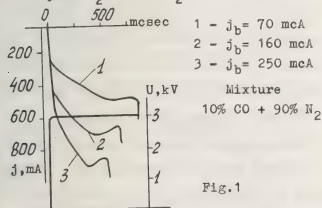


Fig.1

Fig.2 shows the dependence of $W = j_{\max} E / N_{CO}$ on the time of reaching the maximum.

The nonmonotonic behaviour of the $j(t)$

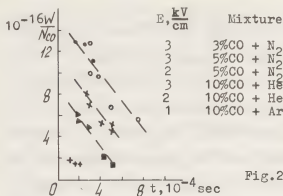
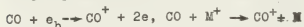


Fig.2

may be associated with a change in the rates of elementary processes during the discharge. It is well known that the dissociative attachment (d.a.) to gas molecules and the dissociative recombination (d.r.) with molecular ions proceeding via the formation of an autoionizing state have a resonance character. The cross-section for the above processes are strongly dependent upon the vibrational number.

It may be shown that as the energy input increases, the d.a. coefficient also increases, both due to electron heating caused by impact of the second kind with vibrationally excited molecules and the increase in the d.a. cross sections with the increasing vibrational number [1,2]. However, because of the strong associative detachment from CO: $O^- + CO \rightarrow CO + e$ ($k_{a.d.} \approx 4 \cdot 10^{-10}$ cm³/sec) the discharge current nonmonotonousness can not be associated with the dependence of the $k_{d.a.}$ upon T_v , whose value does not exceed 10^{-13} cm³sec⁻¹

[3]. In our experimental conditions, at sufficiently high energy inputs the main portion of energy is transferred to the vibrational degrees of freedom of the molecule (the translational temperature of plasma particles is an order of magnitude lower than the vibrational one T_v). The main channels of formation of CO^+ ions on the buffer-gas particles are as follows:



The location of the adiabatic terms $CO(X^1\Sigma^+)$ and $CO^+(X^2\Sigma^+)$ are such [4] that the transitions from the upper vibrational levels of CO to the upper one of CO^+ occur in the region allowed by the Frank-Condon principle. Therefore, CO^+ ions are formed in vibrationally excited states and their T_v may be high. Estimates show that during the recombination time $\sim 10^{-5}$ sec T_v of CO^+ ions do not relax to the gas temperature. In these conditions the form of the distribution function for vibrational states of ions and the magnitude of T_v are found to be essential for the d.r. process [5]. Assuming that the CO^+ is formed in a vibrational state^v due to the ionization of CO by the electrons of the beam (with the density n_e^b) and that the loss-channel is associated with the d.r., we find that the population of the state^v of CO^+ ion is given by

$$n^v/N^+ \approx N_{CO} (n_e/N^+) \langle \sigma_{ion}^{CO} \rangle S_v(T_v) f(\beta_v, t)_{(1)}$$

$$N^+ = \sum_v n_v = n_e$$

Here σ_{ion}^{CO} the cross section for the ionization of CO , V the relative collision velocity, $S_v(T_v)$ the Frank-Condon factor averaged over the vibrational distribution of CO , n_e the electron density in the discharge. The equation for the electron balance in the discharge has the form:

$$\frac{d n_e}{dt} = N_M n_e^b \langle \sigma_{ion}^M \rangle - n_e^2 \sum_v \beta_v \frac{n_v}{N^+} \quad (2)$$

where N_M is the gas density, β_v the coefficient of d.r. of the ion in the state^v. The total $\beta_{d.r.} = \sum_v \beta_v \frac{n_v}{N^+}$. To obtain a qualitative dependence of $\beta_{d.r.}$ on the degree of vibrational excitation of CO^+ , we use a known cross section for d.r. and assume that the distribution of ions over vibrational levels is the Boltzman distribution with the temperature T_v^i . If the capture of an electron by an ion results in the formation of only one repulsive autoionizing state

$$\beta_{d.r.} = \beta_0 \frac{T_e}{T_e - T_v^i} \exp \left\{ A \frac{T_e T_v^i}{T_e - T_v^i} \right\} \quad (3)$$

where $h\nu < T_v^i < T_e$, $h\nu$ is the vibrational quantum of the ion, T_e is the electron temperature, A is coefficient associated with the repulsive term parameters. The quasi-steady $n_e \approx \left[\langle \sigma_{ion}^M \rangle n_e^b \frac{N_M}{\beta_{d.r.}(T_v^i)} \right]^{1/2}$ (4). From (3) and (4) it follows that as T_v^i increases the n_e decreases. Thus, the typical behaviour j shown in fig.1 may be qualitatively explained by the dependence of on the energy input to the discharge.

The above considerations have a model character, because we considered only CO^+ . At $p = 1$ atm it is necessary to take into account the conversion of simple ions by triple collisions, e.g., $CO^+ + 2CO \rightarrow C_2O_2^+ + CO$. Yet, a dependence $\beta_{d.r.}$ on energy input will be observed in this case as well.

References

- [1] B.M. Smirnov "Ions and excited atoms in a plasma", Moscow, Atomizdat, (1974). [2] O. Mal ly T.F. Phys. Rev., 150, 14, (1966). [3] Yu. B. Konev et al., Preprint IAE No. 2821, Moscow, (1977). [4] A.A. Radtsig in Plasma Chemistry, 2, p.3, Moscow, Atomizdat, (1975). [5] A.V. Eletsky. These, Moscow, MFTI (1970).

ON THE PECULIARITIES OF PASSAGE OF A LOW-CURRENT ELECTRON BEAM THROUGH GASES

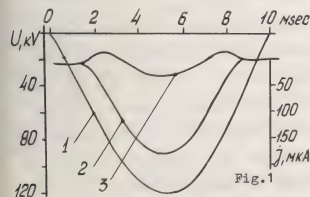
A.F. Pal, I.G. Persiantsev, Yu. V. Petrushevich and A.N. Starostin.

Institute of Nuclear Physics, Moscow State University, 117234, Moscow U.S.S.R.

In studying the non-self-sustained discharge controlled by an electron beam the current of pulsed beam is measured by means of a Rogovsky coil or an electron collector, which collects the beam passed through the evacuated discharge chamber (e.g., in [1] both methods yielded identical results). Steady-state beams are measured only with the use of the collector.

In our experiments carried out on an installation similar to that described in [2], the $1 \times 1 \text{ cm}^2$ anode of the discharge chamber, which was grounded through a resistance R_n , served as the electron collector. The beam was injected into the chamber through a grounded grid that served as the discharge-chamber cathode. The distance between the electrodes was $L=1 \text{ cm}$. The electron gun was fed by variable voltage (fig 1, osc. 1). Oscillogram 2 of fig. 1 represents the collector potential with respect to the grid, which is proportional to the current through the discharge gap filled

with the 1-atm. air. The same oscillograms have been obtained in Co_2 or a vacuum $\sim 10^{-1}$ Torr. As the beam passed through the chamber filled with Ar at the same current and voltage of the gun, oscillogram 3 of fig. 1 has been obtained. It is seen that at a low energy of the beam electrons the collector potential becomes positive, which may be associated with the passage, through the discharge gap, of a current whose direction is opposite to that of the electron beam. By decreasing the gun voltage one can obtain a positive collector potential at a maximum beam energy, i.e., a fully "reversed" current. Analogous results have been obtained when the beam passed through the nitrogen. The potential which appears on the collector grounded through the R_n and which is positive relative to the grounded grid potential may be explained by the presence of electric fields near the electrodes. These fields and the corresponding near-electrode potential jumps arise due to the redistribution of charges produced by the beam in accordance with the boundary conditions necessary for the passage of current (see fig. 2 showing schematic E-field distributions, concentration of electrons n_e and ions n_i (dashed curve) and also indicating the directions of the ion current and those of the elect-



ron-current components in the various regions).

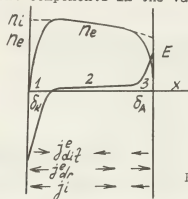


Fig.2

We now turn to the qualitative consideration of the observed phenomena. The initial set of equations has the form:

$$\frac{\partial W_e n_e}{\partial x} = q(x) - \beta n_e n_i + \frac{\partial}{\partial x} (D_L \frac{\partial n_e}{\partial x})$$

$$\frac{\partial W_i n_i}{\partial x} = q(x) - \beta n_e n_i \quad (1)$$

Here $W_e = -k_e E$ is the electron drift velocity, $W_i = k_i E$ - the ion drift velocity, D_L - the longitudinal electron-diffusion coefficient, q - the rate of generation of secondary electrons by the fast electrons of the beam. From the set (1):

$$j = e W_i n_i - e W_e n_e + e D_L \frac{\partial n_e}{\partial x} \quad (2)$$

where j is the current density in the discharge chamber. Let us divide the discharge-chamber volume into three regions (fig. 2): 1. The interval $\delta_K \sim 10^{-2}$ cm near the grid surface - the "cathode region". 2. The "positive column", which occupies the main portion of the discharge-chamber volume. 3. The "anode region" - the interval $\delta_A \sim 10^{-2}$ cm near collector.

Let us consider the experimentally observed case of the "reverse" current passing from "cathode" to "anode". Let us examine the "positive column" region. From

$$(2) \text{ it follows: } E(x) = \frac{j/e - D_L \frac{\partial n_e}{\partial x}}{k_e n_e + k_i n_i}$$

Neglecting $k_i n_i$, we have:

$$U_C = - \int_{\delta_K}^{L-\delta_A} E(x) dx \approx - (j/e k_e) L \left(\frac{1}{n_e} \right) + \frac{D_L}{k_e} \ln \frac{n_e(L-\delta_A)}{n_e(\delta_K)} \quad (3)$$

In considering the anode region we introduce the approximate boundary conditions (cf., cathode-layer theory [3])

$$n_e = 0; j_i(L-\delta_A) = 0; E(L-\delta_A) = 0; j_i(L) = j \quad (4)$$

From the set (1), taking account of (4) we obtain

$$U_A = - \int_{L-\delta_A}^L E(x) dx = - \left(\frac{\pi e q}{k_i} \right)^{1/2} \delta_A^2 = - \left(\frac{\pi}{k_i} \right)^{1/2} \frac{j^2}{(e q)^{1/2} L^2} \quad (5)$$

From the conditions at the boundary of the

"positive column" region,

$$U_K = U(\delta_K) = \frac{D_L}{k_e} \ln \frac{k_e}{k_i} \quad (6)$$

Substituting the obtained voltage-drop

into the set for external electrical circuit, we obtain $U = U_C + U_K + U_A = I R_H$; $j = I/S$; $j \beta$ (7)

Here S is the electrode area, $j \beta$ is the fast electron current density. As a result we obtain for current I :

$$I = \left(j \beta S - \frac{H(R_K + R_H)}{2} \right) + \sqrt{\left[\frac{H(R_K + R_H)}{2} \right]^2 + H \frac{D_L}{k_e} \Lambda - j \beta S H R_H} \quad (8)$$

where $R_K = \frac{L}{S e k_e} \left(\frac{1}{n_e} \right)$; $H = \left(\frac{e q \Lambda}{k_i} \right)^{1/2} S^2$;
 $\frac{D_L}{k_e} \Lambda = \left(\frac{D_L}{k_e} \right) k \left[\ln \frac{k_i}{k_e} + \left(\frac{D_L}{k_e} \right) k \ln \frac{n_e(L-\delta_A)}{n_e(\delta_K)} \right]$

Here j_A is the rate of ionization by fast electron near collector, $(D_L/k_e)k$ in the "positive column" and $(D_L/k_e)k$ in the "cathode region".

For Ar under $p=1$ atm, $E \sim 70$ keV and $j \beta = 50$ mA we have using [1] $q = 6.10^{16}$ $i/cm^3 \cdot sec$, $n_e = 10^{12} cm^{-3}$, from [4] $k_e \sim 3 \cdot 10^5 cm^2/V \cdot sec$, $D_L/k_e = 0.2$ eV and $I = 17$ mA is opposite to beam current. For air $n_e \sim 10^{10} cm^{-3}$, $k_e = 0.710^3 cm^2/V \cdot sec$ and $I = j \beta S < 0$ is equal to the beam current.

References

- [1] C. Cason, J. F. Perkins, A. H. Werkheiser, J. Duderstadt, AIAA Paper, 77-65 (1977).
- [2] E. P. Velikhov et al., Soviet JETP, 65, 543, (1973).
- [3] J. J. Lowke, D. K. Davies, J. Appl. Phys., 48, 4991, (1977).
- [4] L. G. H. Huxley and R. W. Crompton "The diffusion and drift of electrons in gases" (In Russian), Mir Publishers, Moscow 1977.

THE NUMERICAL SIMULATION OF SILENT DISCHARGE IN OXYGEN. INTEGRAL CHARACTERISTICS OF DISCHARGE CHANNEL AND THE ROLE OF EXCITED SPECIES REACTIONS

V.I. Gebalov, V.G. Samoilovitch and Ju. V. Filipov.

Department of Chemistry, Moscow State University U.S.S.R.

Using numerical simulation there have been studied physico-chemical processes during ozone synthesis in silent electric discharge. Due to the fact that ozone synthesis in question takes place in discrete short-lived discharges between dielectric plates, so-called microdischarges, the special attention has been paid to the study of the spatial-temporal distribution of microdischarge channel parameters.

Taking into account the cylinder symmetry of microdischarge channels, in earlier studies(1-5) have been studied the spatial-temporal distributions of O_2 , O_2^+ , O_2^- , O , O_3^- , O_3 and electron concentrations, on the tension of electric field and the potentials of ozonizer electrodes.

The computation of electron avalanche dynamics in microdischarge channels, as well as that of the dynamics and kinetics of the microdischarge channel constituents was made for the room temperature, taking into account the volume charge of the avalanche and the changes of anode potentials with time, but neglecting the photoionization volume. The kinetic computation was performed for the model of 24 chemical reactions (1).

The values, obtained for the time dependence of total number of particles in the channel at zero initial ozone concentration

are given in Figure 1.

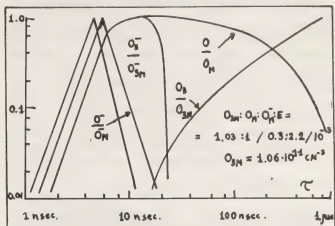


Figure 1.

The studies of microdischarge channel kinetics permitted to evaluate the importance of separate reactions at every moment of microdischarge channel existence. At the beginning of the process (4-5 nsec) the reactions of electrons with oxygen molecules predominate. After the electron avalanche reaches anode, in the microdischarge channel the reactions of negative ions take place and nearly all ozone is produced in these reactions. In 14 nsec. But beginning from 30 nsec the reactions of neutral species become most important. 97% of ozone, synthesised in microdischarge channel are produced in these reactions. Ion-molecular reactions define the configuration and power of volume channel charge and therefore only the kinetic computations of both ion-molecular reactions and neutral species reactions permit to obtain the correlation of kinetic and electric pa-

rameters for a discrete microdischarge.

Using the correlation, obtained for a discrete microdischarge, a computation has been made for ozone synthesis in an ozonizer as a whole. The characteristic feature of the kinetics of ozone synthesis in ozonizer is the existence of the stationary concentration due to the ozone decomposition reactions. The detailed study of the problem made it necessary to consider the reactions of excited species:

1. $O(^1D) + O_2 \rightarrow O_2 + O(^3P)$
2. $O(^1D) + O_3 \rightarrow O_2 + 2O(^3P)$
3. $O(^1D) + O_3 \rightarrow O_2^* + O_2$
4. $O_2^* + O_3 \rightarrow O(^1D) + 2O_2$
5. $O_2^* + O_2 \rightarrow 2O_2$

Taking account of these reactions, the change of the total amount of the constituents in microdischarge channels at the initial ozone concentration of several volume percent in as follows:

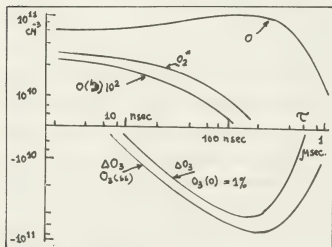


Figure 2.

The kinetics for electrons and ions does not differ in this case from the kinetics for $O_3(0) = 0$.

The computation performed permitted to obtain the dependencies of ozone concentration change by a discrete microdischarge

on the electric parameters of the latter. The analysis of this dependence has shown that the final parameters of a discrete microdischarge depend not on the pair of parameters (electrode voltage and the number of emitted electrons) but on an only parameter, namely the power of electron avalanche, that is on the largest measured number of electrons in an avalanche, or a transferred charge connected with it.

The computations made permitted to elucidate sufficiently the kinetic and electric parameters of a discrete microdischarge. The dependencies of the ozone concentration change by a discrete microdischarge on the value of transferred charge has been found. A correlation was also found between the magnitude of the transferred charge and the active power of the ozonizer.

REFERENCES

1. Gebalov V.I., Samoilovich V.G., Filippov J.V., XIII Intern. Conference on Phenomenon in Ionised Gases, Berlin, 1977, p.106.
2. В.И.Гибалов, В.Г.Самойлович, Ю.В.Филиппов. I. Коэффициенты Таунсенда. Вестн. МГУ, химия, 1977, т.18, № 3, 295.
3. В.И.Гибалов, В.Г.Самойлович, Ю.В.Филиппов. II. Температура канала микроразряда, Вестн. МГУ, химия, 1979, в печати.
4. В.И.Гибалов, В.Г.Самойлович, Ю.В.Филиппов. III. Пространственно-временные распределения в канале микроразряда. Вестн. МГУ, химия, 1979, в печати.
5. В.И.Гибалов, В.Г.Самойлович, Ю.В.Филиппов. Механизм и кинетика образования озона в озонаторах. Вестн. МГУ, химия, т.19, 1978, 549.

OPTIMISATION OF THE CHARACTERISTICS OF THE PLASMA FLOW FROM A DIELECTRIC CHAMBER

I.I. Egorov, L.N. Lesnevsky, G.A. Popov, A.G. Sobol and V.N. Turin.

Moscow U.S.S.R.

Introduction

It has been shown in [1] that the possibilities for obtaining plasma flows with high particle concentration by means of erosive source are limited. Such sources when used for technological purposes, for instance, as light source for laser-pumping, or for active space experiments [2] are required to provide heavy elements dense plasma flows (with a total particle number $N \leq 10^{20}$) at minimum energy input W by unity of mass M . To realize such plasma flows, we have chosen a source, similar to that of [3], allowing to spend a large part of the energy input to increase the number of charged and neutral particles.

For practical use of such sources, it is important to provide an effective energy utilization (the energy of the source is limited to $W \leq 20$ joule) and to obtain a minimum value of W/M for varied external parameters of the source. The purpose of the present investigations is to perfect the source of impulse plasma jets with controlled parameters for an optimal energy utilisation.

The device and experimental method

The device is shown on Fig.1. The dielectric chamber 1 is made of C_2F_4 , with a discharge channel of diameter d_0 and length l_0 .

The anode and cathode are made of Cu. The discharge is ignited by supplying a high voltage to the gap between the cathode and an intermediary electrode 4 from a special igniting source. The model was settled on a frame 6, including an electronic measurer of displacement and allowing momentum measurement (see calibration scheme on Fig.1). The optimal values of W/M were obtained by use of factor experiments [4].

According to this method, several series of experiments were provided and such a combination of the parameters was chosen that W/M was minimum. The varying factors were (the ranges of variation are shown in brackets):

1. The discharge chamber length l_0 (10-40 mm)
2. The discharge chamber diameter d_0 (2-10 mm)
3. The initial resistance of the discharge circuit R_0 ($0.5-20 \cdot 10^{-2}$ ohm)
4. The initial inductance of the discharge circuit L_0 ($2-200 \cdot 10^{-8}$ h)
5. The bank capacity C_0 (4-60 μF)

6. The initial bank voltage U_0 ($0.5-2.5 \cdot 10^3$ v)

R_0 and L_0 were measured by a "ringing circuit" method C_0 by means of a measuring bridge, the momentum P by a special momentum measurer, ΔM the erosive mass by weighting, N the number of discharges by a counter of light flashes. For every model 1000 pulses were provided at a frequency of 0.5 Hz. Experiments were achieved in a vacuum vessel at a pressure of 10 mm Hg. Furthermore, the momentum of plasma flow and the plasma velocity as a function of time were measured by means of a piezo-probe and a high-speed camera respectively.

The accuracy of all the measurement lies in the range 2-15%.

The characteristics of the plasma flow with optimal parameters

The higher described method yields an optimal value of $W = 3.08 \cdot 10^{-1}$ J/kg for $m = 6.13 \cdot 10^{-7}$ kg. It has been shown experimentally that d_0 and l_0 are limited to $d_0 \geq 2$ mm and $l_0 \geq 28$ mm because of the difficulties of initiation of long and narrow dielectric chambers. The analysis of the current and voltage oscillogram shows that during $\tau = 3$ mks, 95% of the energy stocked in the capacitor bank C_0 are supplied to the discharge, this fact demonstrating the high efficiency of the discharge circuit. Thereby, it should be noted, that the rate of energy supply essentially depends on the discharge channel diameter. For instance, when d_0 varies from 2 to 6 mm, the time of 95% energy supply varies from 6 to 1.5 mks. This has been explained as the result of the increasing of R_{act} when d_0 decreases [5]. The high-speed photography investigation shows that the plasma flow from the dielectric chamber begins at $\tau \approx 2$ mks and ends at 60 mks. Fig.3 gives the time-dependence of the plasma flow velocity. The average mass-flow velocity, determined from momentum and accelerated mass measurements is 1100 m/s, i.e. equal to the flow velocity at $\tau = 40$ mks. Fig.3 shows the plasma flow dynamics (1 - discharge current, 2 - region of charged particles flow, 3 - region of excited and neutral particles flow, 4 - region of neutral particles flow) Fig.4 and 5 show the dependency of W/M on the main geometrical parameters of the discharge chamber and on the discharge circuit parameters.

Discussion

We have optimized W/m by a factor of 3, as a result of using a planned factor experiment. In distinction from analogous experiments on metals [1] when N has been shown to be limited to $10^{16} \pm 10^{17}$ in the present case of C_2F_4 , N has been increased up to $N \approx 3 \cdot 10^{18}$ for $W \approx 20$ j.

Fig. 3 and 4 together with the high-speed photographs and the current and voltage oscillograms show that when the channel length l_0 decreases the ratio W/m increases due to increasing of the external currents behind the anode and thus of the plasma flow velocity; for $l_0/d_0 > 6$ the variation of W/m is slow, because of the increasing of R_{ad} and consequently, of the decreasing of the input power. An similar behavior is observed for W/m as a function of d_0 : at large diameters of the discharge channel we have large external currents and at small diameters, the increasing of R_{ad} decreases the rate of energy supply to dielectric chamber. It can be noted that W/m weakly depends on l_0 , C_0 and U_0 in the considered range and this fact demonstrates that the plasma flow is essentially gaso-dynamical. The significant decreasing of W/m when R_0 falls can be explained by a diminution of the energy losses in the discharge circuit. The high speed photo (Fig. 2) showing a striped structure similar to that of [1], demonstrates the discrete character of mass supply to the discharge. This phenomena requires further investigations.

The present analysis allows to recommend this kind of plasma source for utilisation when plasma clouds with a total particle number of $\sim 10^{20}$ are required.

References

1. Voronov I.D., Ivanov G.V., Lesnevsky L.N. et al. XI Inter. Conf. Phenomena in Ionized Gases, CSRS, Praga, 1973.
2. Popov G.A. et al. XXI Session COSPAR Austria, Innsbruck, 1978.
3. Андрианов А.М. и др. ЖТФ, 1969, № 3.
4. Налимов В.В., Чернова Н.А. Статистические методы планирования экстремальных экспериментов. М., "Наука", 1965.
5. W.Hart. J. Appl. Phys., 1962, v. 33, N 10.

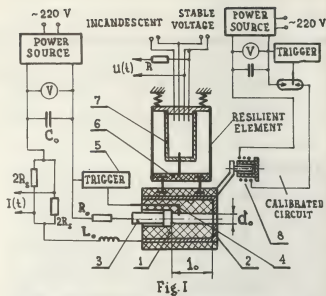


Fig. 2

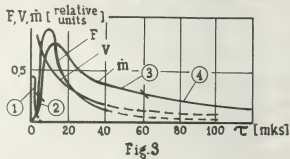


Fig. 3

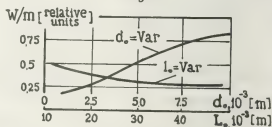


Fig. 4

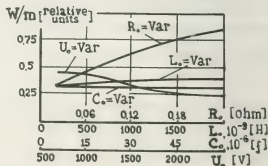


Fig. 5

THE FIELD STRENGTH AND ELECTRON DENSITY CALCULATIONS FOR THE CORONA PULSES

M. Laan, H. Korge and K. Kudu.

Tartu State University, Department of Physics, Tartu, Estonian S.S.R.

Introduction. In our previous paper [1] the spatio-temporal development of luminosity in Trichel pulses and pre-onset streamers of D.C. coronas was determined. The measurements were carried out in the point-to-plane gap in laboratory air. In this paper we are going to report about an attempt of the calculation of the main characteristics of the corona pulses on the basis of luminosity distribution measurements [1]. Such calculations for gas discharge in nitrogen in the homogeneous gap were made for the first time by Doran [2]. In our calculations the same procedure was used for the air. We supposed only two processes - ionization, and attachment - are active within the volume element under observation and that the photomultiplier current is a linear function of light intensity.

So we were able to evaluate the spatio-temporal distribution of the reduced field strength (E/p), the rate of change in the number of electrons ($dn_e/dt = d(N_+ - N_-)/dt$), and the line density of electrons (n_e). On the basis of the curves $E/p(x)$ a rough approximation of the spatio-temporal distribution of the charged particles concentration ($N_+ - N_- - N_0$) was made, using the one dimensional Poisson equation.

Trichel pulse. The calculated field distribution differs considerably from the Laplacian one. It is possible to discern two stages in the Trichel pulse development (A and B, Fig. 1). During stage A the formation of the characteristic visible regions of the discharge pulse - the negative glow, Faraday's dark space and the positive column - takes place. At the moment $t = 2$ ns the high field region is concentrated at a distance of $x \approx 0.25$ mm from the point. In this region the rate of change in the number of electrons and ions has a maximum. As a result, the positive space charge concentration maximum has shifted to $x \approx 0.05$ mm. During stage A attachment is not active and the reduction in field strength is due to the intensive generation of electrons and positive ions. During stage B, dn_e/dt reduces quickly and by the moment $t = 20$ ns attachment becomes dominant.

A streamer develops from a burst pulse when the number of electrons near the point exceeds $5 \cdot 10^6$. In this case the condition of plasma existence is fulfilled near the point electrode tip. By the moment $t = 14.5$ ns counted from the detect-

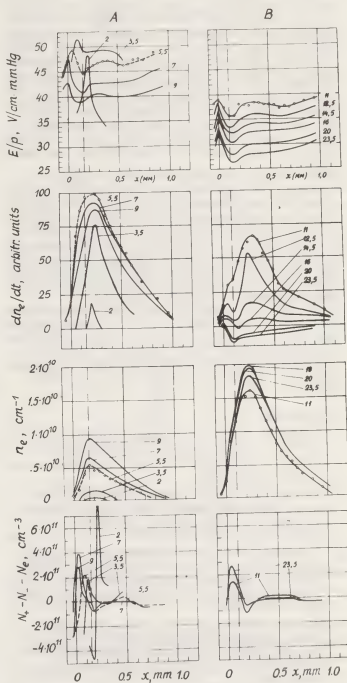


Fig.1. Trichel pulse. Spatio-temporal distribution of the E/p , dn_e/dt , n_e and $(N_+ - N_- - N_0)$, the parameters expressing time counted from the beginning of the detectable luminosity level.

able beginning typical distributions of the E/p , dn_e/dt , n_e and $(N_+ - N_- - N_e)$ have become established (Fig. 2). The characteristic regions (I - V) of a streamer have been indicated for the moment $t = 18$ ns (dotted curves). In region I avalanches arise due to photoionization. Region II of intensive ionization has a considerable spatial extent L . The increasing n_e compensates the positive space charge and produces a decrease in E/p . Supposing the streamer channel diameter is 50 μm , the electron concentration is of the order of 10^{14}cm^{-3} , which about three times exceeds the order of $(N_+ - N_- - N_e)$ for this region. Consequently, the discharge channel is quasi-neutral. In region III a decrease in field strength produces an increase of attachment and hence causes a decrease in dn_e/dt . In region IV the electron drift causes the accumulation of a negative space charge. Between the positive space charge near the point (region V) and the negative space charge the electrical field strength enhances and therefore dn_e/dt and n_e increase. The results obtained for the pre-onset streamer in the best way correspond to the model of the streamer developed by Phelps [3]. The accuracy of calculations significantly decreases for $x > 2$ mm because of the considerable deviation of the streamer branches from the discharge gap axis. In the zone near the point the distribution $(N_+ - N_- - N_e)$ may be invalid as the discharge diameter changes sharply. To verify the validity of our assumptions made above, the current of a Trichel pulse and of a pre-onset streamer was calculated in two different ways (Fig. 3) and was compared with the measured current. A more detailed analysis of this work is given in [4].

References.

1. H.Korge, K.Kudu, M.Lean. Development of D.C. Corona Pulses at Atmospheric Pressure. Proc. XIII ICPIG, Berlin, 1977, p.451-452.
2. A.A.Doran. The Propagation of a Luminous Front through a Developing Spark Discharge in N_2 . Proc. IX ICPIG, Bucharest, 1969, p. 280.
3. C.T.Phelps and R.F.Criffsiths. Dependence of Positive Corona Streamer Propagation on Air Pressure and Water Vapor Content. J. Appl. Phys., 47, 1976, pp. 2929-2934.
4. M.Lean. Calculation of the Electric Field Distribution in Direct Current Corona Pulses. Acta Comment. Univ. Tartuensis, 472, 1979, p.77-106 (in Russian).

Fig.3. Measured (solid curves) and calculated (o and x) current pulses of a Trichel pulse (a) and of a pre-onset streamer (b).

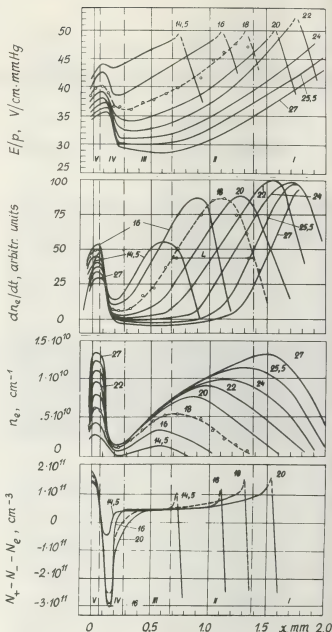
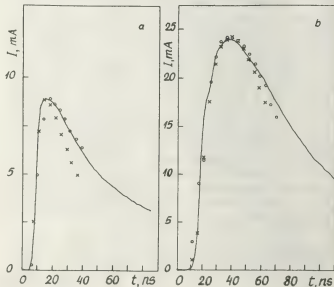


Fig. 2. Pre-onset streamer. Follow the text and Fig. 1.



AN ATTEMPT TO DESCRIBE VOLTAGE-CURRENT CHARACTERISTICS OF AN ARC WHEN UTILIZING EQUATIONS OF MAGNETOHYDRODYNAMICS

Cz. Królikowski, A. Kamińska-Pranke.

Institute of Electroenergetics, The Technical University of Poznań, Poland.

The process of obtaining low-temperature plasma by heating gas flowing through an electric arc was analysed in paper [1]. In the case of the cylindrical area flow, two regions can be assigned, the interior region and the exterior region, separated by a boundary surface with radius $r(z) = r_0$ (Fig. 1). In the interior region, i.e. for $r(z) < r_0$, gas conductance $G > 0$, whereas in the exterior region for $r(z) > r_0$, $G = 0$. In the paper, the interior flow is analysed, considering the problem of arc discharge subjected to free gas flow, parallel

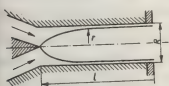


Fig. 1. Field model of flow

to the arc axis. On the basis of equations of magnetohydrodynamics, the voltage on the arc has been determined, according to the arc current, physical properties of the flowing gas and geometry of the channel. It has been assumed that in the interior of the flow the following assumptions are valid:

1. Gas flow is laminar, Mach number is much smaller than unity.
2. The flow is axially symmetric, it has not a circumferential component of speed, therefore it has no flow rotation as well.
3. The radial component of speed is much smaller than the axial component; this results in uniform pressure in the plane perpendicular to the axis of the arc.
4. The gas is in thermodynamic equilibrium.
5. Dependence of thermodynamic properties /except gas mass density/ and transport pro-

perties on pressure is negligible.

6. Axial heat transfer and radiation energy is small.

Equations of magnetohydrodynamics, presented below, describe processes occurring in the interior region of the flow:

Equation of flow continuity

$$\frac{\partial \rho}{\partial t} + \text{div}(\rho \vec{v}) = 0 \quad /1/$$

Equation of power

$$\rho \frac{d\vec{v}}{dt} = \rho \frac{\partial \vec{v}}{\partial t} + \rho(\vec{v} \cdot \nabla) \vec{v} = -\text{grad } p + \vec{j} \times \vec{B} \quad /2/$$

Equation of motion

$$\frac{\partial}{\partial t} \left[\rho \left(u + \frac{v^2}{2} \right) \right] + \text{div} \left[-\lambda \text{grad } T + \rho \vec{v} \left(h + \frac{v^2}{2} \right) \right] = \vec{j} \cdot \vec{E} \quad /3/$$

Equation of perfect gas state

$$p = \rho R_g T \quad /4/$$

Ohm's law

$$\vec{j} = \sigma \vec{E}(z) \quad /5/$$

Maxwell's electromagnetic equations

$$\text{rot } \vec{H} = \vec{j} + \frac{\partial \vec{D}}{\partial t} \quad /6/$$

$$\text{rot } \vec{E} = - \frac{\partial \vec{B}}{\partial t} \quad /7/$$

$$\text{div } \vec{D} = \rho \quad /8/$$

$$\text{div } \vec{B} = 0 \quad /9/$$

When analysing the above equations, after presenting them in cylindrical coordinates, from the point of view of assumptions 1-6, equation of power (3) can be written in the form

$$\frac{\partial}{\partial z} \left(\rho v_z C_p T \right) - v_z \frac{\partial p}{\partial z} - \frac{1}{r} \frac{\partial}{\partial r} \left(r \lambda \frac{\partial T}{\partial r} \right) = j_z E_z \quad /10/$$

In equation /10/, the coefficient of heat exchange λ occurs; it is unknown for high temperatures of the arc. On the basis of performed investigations in [2], it has been assumed that the amount of heat, carried away by means of heat conduction from the interior region to the exterior region of the flow, is proportional to the value of arc current, therefore

$$\int_0^l \int_0^1 \left(-\frac{1}{r} \frac{\partial r}{\partial r} \right) \left(r \lambda \frac{\partial T}{\partial r} \right) 2\pi r dr dx = K T \quad /11/$$

where k - proportionality constant
 l - arc length.

The flow of gas through the cylindrical channel takes place under the influence between pressure on the inlet to channel p_1 and pressure on the outlet of channel p_0 . The distribution of pressure along the channel, as investigations have shown [3], can be described by equation

$$p(z) = Bz^2 + Cz + p_1 \quad /12/$$

where $B = (p_1 - p_0)/l_k^2$; $C = -2(p_1 - p_0)/l_k$

l_k = channel length.

The flowing gas heats the region of arc discharge and after passing the way in the arc reaches the temperature of arc T_x . The coefficient of the increase in temperature Δ can be assumed as equal to $(T_x - T_0)/l_x$ - where T_0 initial temperature of being heated gas. On the basis of the equation of magnetohydrodynamics in form /1/

$$\frac{\partial}{\partial z} (r \rho v_x) = \frac{\partial}{\partial z} (\pi r^2 \rho v_x) = 0$$

we state that the mass of flowing gas through the arc column during a second is constant,

$$\pi r_0^2 \rho v_x = \text{const}$$

and depends on the total mass of gas flowing through the channel in the following way $G = G^* R_0 \rho_0 T_0 / Z \rho$ /14/

where $s = \pi r_0^2$; $F = \pi R^2$

G^* - total flow of gas through the channel.

On the basis of the above considerations, the equation of power density in the arc can be written in the form

$$\frac{G^* R_0 \rho_0 T_0}{F(Bz^2 + Cz + p_1)} \left(\rho_0 A - \frac{G^* R_0 T_0}{F(Bz^2 + Cz + p_1)} B + \right. \\ \left. - \frac{1}{r} \frac{\partial}{\partial r} \left(r \lambda \frac{\partial T}{\partial r} \right) \right) = j_z E_z \quad /15/$$

power density P_x , occurring in equation /15/,

can be determined as function of temperature, on the basis of investigated curves at different pressures. Arc temperature T_x can be expressed as voltage and arc current function on the basis of the approximate curves of conductance $G(T)$ for a definite kind of gas, whereas specific heat has a constant value for monoatomic gases and is the known function of temperature for polyatomic gases. On utilizing the above relations and equation /15/ over the arc volume, the equation was obtained which describes voltage relation on the arc in the function of arc current and takes into account physical properties of gas, as well as the geometry of the discharge channel. For arc discharge in nitrogen, the equation describing voltage current characteristics will have the form

$$3.5 F^{-1} G^* 273^{-1} R_0^2 A \left\{ \alpha \int_0^1 \int_0^1 \gamma^2 \frac{1}{\rho(z)} dr dz + \right. \\ \left. + \beta \int_0^1 \int_0^1 \gamma^2 \frac{1}{\rho(z)} dr dz \right\} - \frac{R_0 G^* A}{F} \int_0^1 \int_0^1 \gamma \frac{1}{\rho(z)} dr dz$$

where $\gamma = a + bz / \pi r^2 u$

a, b, α, β - constants of curves approximation σ/T and ρ/T

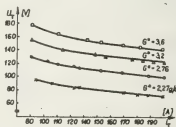


Fig.2. Voltage-current characteristics

Equation /16/ has been solved analytically by making calculations for the power channel with a radius of

4 mm and 30 mm long.

The results of calculations are presented in graphic form in fig.2. and compared with experimental data. On comparing the measured and calculated values of arc voltage with equation /16/, it has been stated that the maximum error not exceed $\pm 6\%$.

REFERENCES

1. S.N.B. Murthy. IEEE Trans. on nuclear Science, 1964.
2. Cz. Królikowski, Praca doktorska, AGH Kraków, 1964.
3. Cz. Królikowski, Zeszyty Naukowe Politechniki Poznańskiej, Elektryka 9 /34/.

CHEMICAL KINETICS STUDY OF NITROGEN OXIDE SYNTHESIS IN A D.C. PLASMA JET : A PROPOSED MODEL

J.F. Coudert, E. Bourdin, J.M. Baronnet, J. Rakowitz and P. Fauchais.

Laboratoire de Thermodynamique, 123, rue A. Thomas 87060 Limoges céder, France.

INTRODUCTION. The experimental study of nitrogen oxide synthesis in a D.C. nitrogen-oxygen plasma jet shows that the final products, after quenching, have a concentration higher than the maximum predicted by equilibrium calculations at the same pressure /1/. Departure from equilibrium can be partially explained by chemical kinetics considerations :

quenching models from high temperature equilibrium have been proposed by POLAK /2/ from /3/ and /4/ and by AMMAN /5/.

I. COMPUTING METHOD. Let us consider a mixture of I chemical species A_i reacting in J chemical reactions with reaction rate constants k_j :

$$(I) \quad \sum_{i=1}^I \nu_{ji} A_i \xrightarrow{k_j} \sum_{i=1}^I \nu'_{ji} A_i$$

The thermodynamic temperature of the system is assigned to follow a law $T = f(t)$ which is supposed to describe the temperature history of the bulk gas from entrance of the torch to the end of the reactor. The pressure is assumed to be constant all along the system.

If diffusion processes are neglected the time dependence of the chemical composition of the system is calculated by solving the following differential system.

$$(2) \quad \frac{dy_i}{dt} = w_i - \left(\frac{y_i}{\rho} \sum_{j=1}^J \nu_{ji} w_j + \frac{y_i}{T} \frac{dT}{dt} \right)$$

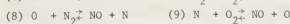
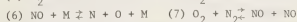
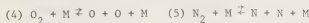
where y_i is the molar concentration of the i^{th} species, $\rho = P/kT$ and w_i the production and loss terms for i^{th} specie.

$$(3) \quad w_i = \sum_{j=1}^J k_j (\nu'_{ji} - \nu_{ji}) \prod_{i=1}^I y_i^{\nu_{ji}}$$

if the initial concentration $y_i(0)$ are known, the differential system can be solved using the appropriate predictor-corrector method proposed by WINSLOW /6/.

II. REACTIONS AND REACTION RATE CONSTANTS. We have used data gathered by PRUD'HOMME /7/, and these recommended by BAULCH /8/.

At temperature below 5000 K only the following neutral species have been considered : N_2 , O_2 , NO, N and O. They are supposed to take part in the following reactions



The selected rate constants are listed in Table I.

M is any one of the five species.

III. RESULTS. From some measurements performed on a nitrogen-oxygen plasma jet we have fitted the experimental time-temperature history along the reactor in the following manner. The temperature at each end of the reactor is 300K, the gas is heated up to 5000K in 10^{-5} sec. The initial value of the heating rate (dT/dt) is 10^9 K/s, its mean value is $5 \cdot 10^8$ K/s, the heating law is parabolic with time. A similar parabolic law is used for the quenching step during $9 \cdot 10^{-5}$ s with an initial rate -10^8 K/sec.

Molar fractions versus time are shown in figure I. Figures II and III describe respectively the time evolution of the over all production of NO ($d(NO)/dt$) and N, and the production of NO and N by each of the reactions (4) to (9).

At the very beginning of the reaction ($t < 5 \mu\text{sec}$, $T < 4000$ K) the production of NO is due mainly to reaction (7), a result which is not in agreement with the conclusions of ZEL'DOVICH /3/ and POLAK /2/ for this process. At the same time N is produced by reaction (8).

The maximum production rate of NO is reached between 8 and 12 μsec ($T = 4000 + 5000 + 4800$ K) and processes (7) (8) and (9) produce an equivalent amount of NO. The production rate of N by process (8) is equal to the loss rate by process (9) and $[N]$ is maximum. Between 12 and 18 μsec ($T = 4800 + 4200$ K) the processes (7) (8) and (9) always produce NO but with a lower rate until a zero rate is reached at 18 μsec and the process (9) destroy N. Between 18 and 60 μsec ($T = 4200 + 1500$ K) reactions (8) and (9) slightly destroy NO. The destruction of N by the process (9) is higher than the production by (8).

From $t = 60 \mu\text{sec}$ ($T < 1500$ K) the system is partially frozen especially for NO since there is no more ato-

mic nitrogen and oxygen recombines very slowly by the process (4) which governs $[O]$ during the total reaction time.

Processes (5) and (6) are significant only at high temperature ($T > 4500$ K).

CONCLUSION. At 1 atm. the frozen high temperature equilibrium predicts a maximum of $[NO]$ of 7%, the kinetics model shows that it is possible to obtain up to 11 % (a result which is in good agreement with experiment [1]).

The important role of quenching rate is shown with our model, but, as far as we know, it is the only one which points out the equally important role of heating rate. The heating rate controls the maximum concentration of NO as the quenching controls the freezing of the high temperature mixture.

REFERENCES.

- /1/ BARONNET J.M. et al, Journal de Chimie Physique **75**, (1978), 949.
- /2/ POLAK L.S. et al, Kinetics and Thermodynamics of Chemical Reaction in Low-Temperature Plasma. Moscow - Nauka (1965).
- /3/ ZEL'DOVICH Ya.B., RAIZER Y., Physics of Shocks Waves and High Temperature Hydrodynamic Phenomena, Academic Press, (1966).
- /4/ DUFF R.E. et al, J. Chem. Phys. **31**, (1959), 1018.
- /5/ AMMANN P.R., TIMMINS R.S., A.I. Ch. E. Journal **12**, (1966), 956.
- /6/ WINSLOW A.M., J. Phys. Chem., **81N**, (1977), 25
- /7/ PRUD'HOMME R. et al, Rapport O.N.E.R.A. Paris (1969).
- /8/ BAULCH D.L., High Temperature Reaction Rate Data, N° 4, Leeds (1969).

	B	α	E	References
(4)d	$3.2 \cdot 10^{19}$	-1	118000	/III.28/a/III.34/
(4)r	$5 \cdot 10^{15}$	-25	0	/III.35/
(5)d	$4.1 \cdot 10^{22}$	-1.5	224900	/III.33/a/III.37/ /III.28/
(5)r	$1.2 \cdot 10^{17}$	-5	0	/III.36/ /III.38/
(6)d	$2.9 \cdot 10^{19}$	-1	150000	/III.39/
(6)r	$4.3 \cdot 10^{20}$	-1.5	0	/III.40/
(7)d	$9.1 \cdot 10^{24}$	-2.5	128500	/III.34/
(7)r	$2.4 \cdot 10^{23}$	-2.5	85500	/III.41/
(8)d	$7 \cdot 10^{13}$	0	75500	/III.34/
(8)r	$1.3 \cdot 10^{11}$	0.5	0	/III.38/
(9)d	$1 \cdot 10^{11}$	0.5	6200	/III.42/
(9)r	$2.0 \cdot 10^{10}$	0.5	38400	/III.38/

Table I. Reaction rate constants. $k = B T^{\alpha} \exp(-E/RT)$

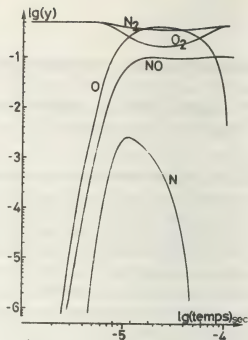
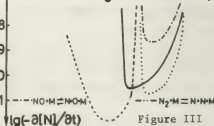
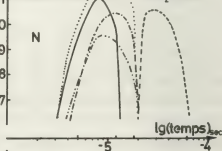
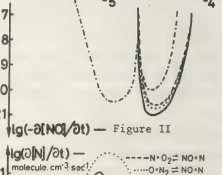
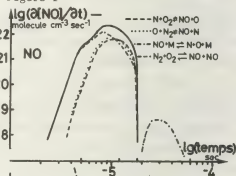


Figure I



TO THE THEORY OF ELECTROIONIZED DISCHARGE

V.V. Alexandrov, V.A. Danilychev, V.N. Koterov, V.V. Pustovalov and A.M. Soroka.

P.N. Lebedev Physical Institute, U.S.S.R. Academy of Sciences, Leninsky prospect 53, 117924, Moscow, U.S.S.R. Computer Centre of the U.S.S.R. Academy of Sciences Vavilov street 40, Moscow 117333, U.S.S.R.

The results of theoretical study of electroionized discharges are presented, which are based on the following equations /1,2/:

$$\frac{\partial n_e}{\partial t} + \frac{\partial j_e}{\partial x} = \frac{\partial n_i}{\partial t} - \frac{\partial j_i}{\partial x} = j_e L + q - \beta n_e n_i$$

$$\frac{\partial E}{\partial x} = 4\pi e | (n_e - n_i) |, j_e = \mu_e n_e \frac{E}{p}, j_i = \mu_i n_i \frac{E}{p}$$

$$j_e(0,t) = j_i(0,t), j_i(L,t) = 0, \int_0^L E dx = U \quad (1)$$

This study gives a possibility to substantiate a simple method of averaging (1) over fast time, which is determined by electron motion, instead of relation $j_e = \mu_e n_e \frac{E}{p}$ the following equality is valid:

$$n_e = \langle n_e \rangle = \frac{j}{\mu_e + \mu_i} \frac{p}{E}, j = \frac{1}{L} \int_0^L (j_e + j_i) dx \quad (2)$$

Averaged equations are valid both in the volume and in the layers.

①. A change of quasi-neutral plasma density $n = n_e = n_i$ in the discharge volume is presented by equation $\frac{\partial n}{\partial t} = q - \beta n^2$. The typical formation time for positive column resulting from this equation is $\tau_v = 1/\sqrt{q\beta}$

②. Numerical calculations /2/ of cathode layer formation have revealed four types of transition processes (Fig.1; U_c is the cathode fall). At the first stage (Fig.1; $t(0.03\mu s)$) plasma is polarized near the cathode (Fig.2a; $\rho = n_i - n_e$). This leads to an increase in the field intensity, and

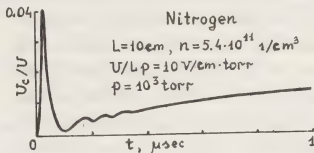


Fig. 1.

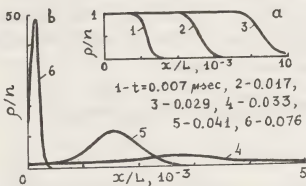


Fig. 2.

the initiation of shock ionization wave.

At the second stage (Fig.1; $0.03\mu s \leq t \leq 0.1\mu s$) the ionization wave is moving toward the cathode (Fig.2b), and forms near it a layer of positive space charge (emitting layer) where the major electron current amplification takes place due to impact gas ionization. The emitting layer is settled at the third stage (Fig.1; $0.1\mu s \leq t \leq 0.5\mu s$). At the same time there begins the charge re-distribution in the outer cathode layer. The fourth most prolonged stage determines the total time of the cathode layer

formation (Fig.1; $t > 0.1 \mu s$).

The first two fast stages are defined by non-stationary electron motion. The last two slow stages are connected with ion motion. Below are listed the basic results of an asymptotic analysis of these stages /3,4/: typical times and space scales.

③. The space charge in the emitting layer is formed mainly by the ions, the impact ionization is significantly more intense than the external ionization and recombination, and the electron motion is quasi-stationary. Emitting layer formation is accompanied by its space charge oscillations /2/, and their period and decrement may be quite well determined by a simple model /3/. The thickness of the emitting layer Δx_I and the typical time τ_I for these processes are equal :

$$\Delta x_I = \left(\frac{\mu_i}{4\pi j_v A} \right)^{1/2}, \quad \tau_I = \left[\frac{p^2}{(4\pi j_v)^3 A \mu_i} \right]^{1/4}$$

$$j_v = |e| \mu_e \bar{n} \frac{U}{L \rho}, \quad \bar{n} = L \left(\int_0^L n^{-1} dx \right)^{-1} \quad (3)$$

(at $\alpha = A p (E/p - B)^2$ approximation for the impact ionization factor).

④. The impact ionization in the external part of the layer is not significant. The dynamics of formation of the external cathode layer depends on the parameter $\alpha = \left(\frac{p \beta}{4\pi |e| \mu_i} \right)^{1/2}$. If $\alpha \ll 1$ ($\alpha \approx 0.2$ in nitrogen plasma at $p = 10^3$ torr) the process has a two-stage character. Firstly a wave of positive space charge is moving from the cathode with the damping time $\tau_w = \frac{p}{4\pi |e| n \mu_i}$ (Fig.3a). The influence of the external ionization and recombination is negligible at this stage. The space charge wave is induced by the emitting layer and may

appear repeatedly. The wave is described by the changes in the automodel form $\rho \sim \rho'(\xi)/t$, $E \sim t E'(\xi)$, $\xi \sim x/t^2$ (Fig.3b)

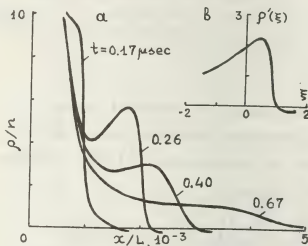


Fig. 3.

After damping of the space charge wave the plasma character is determined by the external ionization source and the recombination. With an accuracy $\rho/n \sim \alpha$ the plasma becomes quasi-neutral in the external cathode layer, and the typical thickness Δx_E and the typical time τ_E for this stage is

$$\Delta x_E = \frac{j_v}{|e| \mu_e n^2} \left(\frac{\mu_i p}{4\pi |e| \beta} \right)^{1/2}, \quad \tau_E = \frac{1}{n \beta} = \tau_v \quad (4)$$

If $\alpha \sim 1$ then the time $\tau_w \sim \tau_E$ and space charge wave are not evidently expressed.

⑤. All results described are in good agreement with numerically calculated ones /2/. Asymptotic solution for steady-state discharge /4/ leads to the same space scales. The same results are obtained from averaged equations (1,2) that confirms their validity.

References

1. N.G. Basov et al. Usp. fiz. nauk, **114**, 213 (1974); 2. V.V. Alexandrov et al. Kvantovaya elektronika, **5**, 1, 114 (1978); 3. V.V. Alexandrov et al. Dokl. Ak. Nauk, **241**, 5, 1050 (1978); 4. V.V. Alexandrov et al. Zh. vychislit. math. i math. phys., **18**, 5, 1214 (1978).

ON EXPANSION OF THE COLLISIONLESS PLASMA INTO VACUUM

V.G. Yeselevich, V.G. Fainstein.

Sibirskiy, Irkutsk 33, P.O. Box 4, U.S.S.R.

In laboratory experiments on plasma expansion into vacuum carried out till the present, the maximum recorded speeds of ion sound were several times less than the recorded velocities of accelerated ions ($C_{S_0} = (T_{e0}/m_i)^{1/2}$): $U_{\max} \approx (2+3)C_{S_0}$, $E_{\max} = \frac{m_i U_{\max}^2}{2} \approx (2 \div 4,5) T_{e0} / 1-4/$

In this paper, it is experimentally shown that at plasma expansion into vacuum, the ions may be accelerated up to velocities $U \gg C_{S_0}$. And due to instability development, the flow of electron heat from source to front providing energy supply to electrons which accelerate ions turns out to be about $10^5 + 10^6$ times less than it follows from the theory of pair collisions /5/.

The experiments were performed in a cylindrical vacuum volume with a 200 cm length, 60 cm diameter. The residual gas pressure $P \approx 5 \times 10^{-6}$ mm Hg. On one end of the chamber, a pulse source is arranged /6/, whose plasma having in space a steep front with a width $\Delta z \approx (1+5)$ cm, was expanding into the chamber. The parameters of argon plasma at the outlet of the source on front top: $T_{e0} \approx (1+5)$ eV; $T_{i0} < T_{e0}$, $n_{e0} \approx (10^7 \div 10^9) \text{ cm}^{-3}$. The duration of source operation was significantly greater than the time of passage of the plasma of the chamber length. Measurements of

electron and ion densities, electron temperature as well as of plasma front motion velocity were made with a cylindric Langmuir probe ($l = 15$ cm, $\phi = 0.05$ cm) displacing along the chamber axis.

The experiments showed that as plasma is moving from the source, the plasma density n in front top drops apparently (Fig.1) (and T_e changes comparatively little). Therefore, the value of the local Debye radius $r_D = (T_e / 4\pi n e^2)^{1/2}$ increases. The front width separated from the source by $x \leq 70$ cm, becomes of the order of $\lambda_D \approx 2\pi r_D$ and a phenomenon like dispersion is observed: density variations with a typical length $\sim \lambda_D$ lagging behind the front. At further movement, the value Δ from x changes approximately as $1/\sqrt{\pi x}$.

As ions are moving, their velocity increases continuously with increasing x to $x_{\max} = 150$ cm inclusively (Fig.2). This means that $x > 150$ cm implies further increase of the velocity U . The value of ion acceleration is determined by the gradient of electron pressure in the front and in order of magnitude agrees with the value $a \approx \frac{z T_e}{m_i} \frac{1}{n} \frac{\partial n}{\partial x} \approx \frac{z T_e}{m_i} \frac{1}{\Delta x}$ ($z = 1$ - ion charge).

The acceleration decrease with increasing x (curve inclination in Fig.2) is largely due to increasing $\Delta(x)$. Under

conditions of the experiment the maximum velocity of accelerated ions at a distance of $x_{\max} \approx 150\text{cm}$ was $\approx (15+20) C_{S0}$, which corresponds to the energy $E = (100+200) T_{e0}$.

The electron temperature gradient along the ox axis measured on a 20cm portion $\leq 0X \leq 40\text{cm}$ is about $(0.02+0.03) \frac{eV}{5\text{m}}$. The electron heat flow connected with dT_e/dx assuring electron energy restoring, energy being given to ions, is in order of magnitude $g \sim nu_e E$ (here $\Delta E \gg T_e$ is the increment of front kinetic energy on $20 \div 40\text{cm}$ portion). For this case (Figs. 1 and 2 $T_e \approx 2\text{eV}$) this value is approx. $5 \div 6$ orders less than the heat flow obtained from the theory of pair collisions [5].

As one is moving away from the source, an increase in level (up to $\frac{\hat{n}}{n} \sim 0.2$ on $0X \approx 40\text{cm}$) of electrostatic density oscillations with a typical wavelength $\sim r_D$ and frequency in the frame of reference connected with the front $\sim \omega_{0f} = (4\pi e^2 / m_1)^{1/2}$, is observed in the front region and behind.

According to [7], excitation of such a type is due to instabilities of the non-isothermic plasma with inhomogeneous temperature.

Electron scattering on oscillations leads up to a decrease in electron thermal conductivity whose calculated value [8] in order of magnitude agrees with the experimental one.

REFERENCES

1. P.F.Little, Journal of Nuclear Energy Part C, v.4, 15-22 (1962).
2. H.W.Hendel, T.T.Reboul, Phys.Fluids,
3. A.A.Plutto, N.N.Ryzhkov, A.T.Kapin, JETP, 47, 494 (1964).
4. M.A.Tyulins, JETP, 35, 511 (1965).
5. L.Jr.Spitzer, R.Härm, Phys.Rev. 89, 977 (1953).
6. V.G.Eselevich, Yu.S.Karavayev, V.I.Koroteev, V.G.Painshtein. Preprint Sib-IZMIR, 18-77 (1977).
7. D.W.Forslund, J.Geophys.Res., Space Physics, v.75, No.1, 17-27 (1970).
8. E.V.Mishin, DAN, 215, 565 (1974).

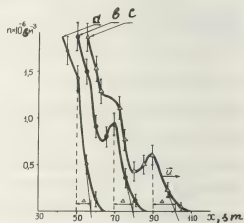


Fig.1. Spatial distribution of ion density in the front of plasma expanding into vacuum at different time moments:

- a)- $t_1 = 20 \text{ msec}$, b)- $t_2 = 26 \text{ msec}$,
c)- $t_3 = 31.5 \text{ msec}$

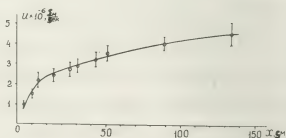


Fig.2. Change of velocity of the front of plasma expanding into vacuum, with the distance from the source.

ELECTRICAL FIELD STRENGTH ON THE POSITIVE CORONA ELECTRODE WITH THE COUNTERFLOW OF NEGATIVE IONS

N.B. Bogdanova, B.G. Pevchev and V.I. Popkov.

Krshizhanovsky Power Institute, Moscow U.S.S.R.

Introduction. To calculate the corona electrode systems including corona losses in power transmission lines, one should know the electric field strength E_c on electrode surface under corona. Recently this most important characteristic was measured directly by English as well as Soviet scientists / 1,2,3,4 /. It's clear from Soviet works / 3,4 /, that E_c remains constant, i.e. doesn't depend on applied voltage. In case of unipolar d.c. corona, the electric field strength E_c on the electrode under corona is equal to the onset strength E_0 . Various aspects of negative ion influence on discharge processes in air including corona were discussed in scientific literature for a long period of time. Possibility of such influence takes place for d.c. bipolar corona, for d.c. unipolar corona on positive electrode with negative ion injection into the gap from external ion source and also for a.c. corona when negative ions, created in the negative half cycle, return to the electrode at the next positive half cycle. Measurements of electrical field strength on the positive corona electrode, in case of counterflow of negative ions carried out in the given work, were used to determine the character of influence of

negative ions on corona discharge, to estimate the possibility of negative ion detachment and subsequent development of electron avalanches, and electrical field strength necessary for the detachment.

Measurement procedure. The measurements on d.c. and a.c. (50 Hz) corona were performed in coaxial electrode systems with the inner electrode, dia 13 mm, having a probe (an electrostatic fluxmeter) inserted therein and outer cylinder, dia 100 or 192 cm / 3,4 /. In tests with d.c. bipolar corona three wires, dia 0,08 cm, connected electrically with the external cylinder were mounted in parallel with the inner electrode (see the Scheme in Fig. 1). Three thin wires were used instead of one in order to provide the uniform distribution of negative charge over the inner electrode surface. The recording of the signal from fluxmeter was carried out by an oscilloscope or a selective nanovoltmeter. The error when measuring E_c , by means of an oscilloscope, according to our estimations, comprises 3%, in case of the nanovoltmeter - 1,5%. Experimental results. The measured field strength on the inner electrode under d.c. bipolar corona was compared with that in the case of unipolar corona

when air parameters and characteristics of the probe are constant. The forms of positive corona in both regimes are different: the unipolar corona is characterized by the appearance of streamers at overvoltages up to $n = 1,7+1,8$, for $n > 1,7+1,8$, the corona becomes uniform while the bipolar corona is uniform over the whole range of n . An example of measured field strength E on positive electrode versus applied voltage U is given in Fig. 1, where, in case of streamer unipolar corona ($n < 1,7+1,8$) the maximum values of E_c are given. As can be seen, the field strength E_c on the positive electrode at bipolar corona (for $U > U_{0 \text{ bip}}$) is also independent on U .

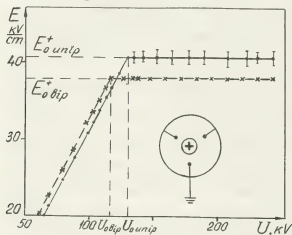


Fig. 1

However, under bipolar corona condition the value of E_c is lower than that under unipolar corona. The difference between $E_{c \text{ bip}}$ and $E_{c \text{ unip}}$ doesn't significantly exceed the measurement error and equals to $\sim 8\%$. The field strength under corona E_c^+ is equal to the onset E_0^+ in both cases. The similar decrease of the field strength on the positive corona electrode takes place also with some other methods of negative ion injection into the gap and also by returning of negative ions

at a.c. generated during a previous half cycle. The last is illustrated in Fig. 2. After the moment of corona onset in positive half cycle the field strength decreases slightly and 1,5 ms later becomes stable at $E_{c0}^+ < E_{00}^+ = E_0^+ \text{ unip}$, the difference

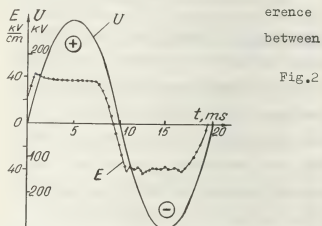


Fig. 2

E_{c0}^+ and $E_0^+ \text{ unip}$ not exceeding 5-7%. In all cases studied the existence of negative ions counterflow always results in the decrease of the field strength on the electrode with positive corona. This confirms assumptions (5,6,7) on the detachment of negative ions near the corona electrode and following formation of electron avalanches. Experimental results allow to estimate the highest potential gradients when negative ions detach. This gradient is equal to or less than the field strength $E_c^+ \text{ bip}$ on the electrode surface with positive corona at bipolar regime, i.e. $E_{\text{det}} \leq 38 \text{ kV/cm}$.

References: 1. Waters R.T., Rickard T.B., Stark W.B. Int. Symp. Hochsp. Minich, 1972, 104. 2. Waters R.T., Rickard T.B., Stark W.B. 2nd Int. Conf. on Gas Disch., London, 1972, 188. 3. Bogdanov N.B., Pevchev, B.G., Polevoy S.V. 4th Int. Conf. on Gas Disch. London, 1976. 4. Boddanova, N.B., Pevchev B.G., Polevoy S.V. Elektrichestvo, 1978, N 4, 67. 5. Kapzov N.A. Corona Discharge and its application in electrical Precipitations. Gostechizdat, 1947. 6. Popkov V.I. Izvestia of the USSR Acad. of Sci., OTN, 1948, N 4. 7. Bogdanov N.B., Pevchev B.G., Popkov V.I. Idem, "Energetika i Transport". 1978, N 1, 96.

IV

- Décharges pour lasers
Discharges for lasers



ELECTRON-ATTACHING GASES IN LASER DISCHARGES : ALTERED DISCHARGE PARAMETERS AND NEGATIVE-ION PRODUCTION

Irving J. Bigio.

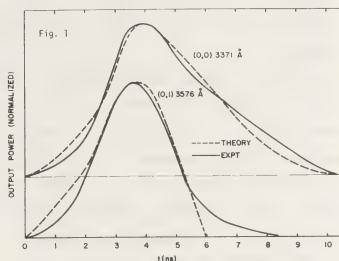
University of California, Los Alamos Scientific Laboratory, Los Alamos, NM 87545.

Two very important parameters of a laser discharge which affect the excitation rates and laser kinetics as well as the "quality" of the discharge are the electric-field-to-pressure ratio, E/P , and the preionization. The addition of an electron-attaching gas to the laser mix can strongly modify both of these parameters. By properly accounting for the changes in these discharge parameters, changes in the laser kinetics and emission can be correctly predicted. Two exemplary cases are considered: the addition of SF_6 to N_2 lasers, and preionization effects in eximer lasers.

Several authors have described the effects of adding SF_6 to the N_2 discharge laser operating on the $C^3\Pi_u \rightarrow B^3\Pi_g$ transition.¹⁻⁴ The increased power and modified pulse shapes have been variously attributed to altered kinetic mechanisms (e.g. quenching rates) and/or new excitation pathways, with contradicting explanations and experimental results.^{2,3}

In order to clarify the situation we have carried out a theoretical and experimental study which shows that the only important effect of adding SF_6 to the nitrogen discharge is the modification of electronic-state excitation rates due to the increased E/P value. (The electro-negative gas allows a higher voltage buildup before breakdown and also results in a higher impedance discharge.⁵) The Boltzman transport equation has been solved numerically for the

electron-impact excitation rates into the states of interest, for different values of E/P .⁶ The distribution among vibrational levels is determined from the Franck-Condon factors. Then by using the temporal histories of the discharge parameters, it is possible to predict the temporal history of the population inversion, hence gain, hence laser emission. Figure 1 compares the theoretical and experimental results for the case of a fast Blumlein-type discharge.



As further proof that only the E/P modification (and not any kinetic mechanism) was responsible for the laser effects, a totally different electro-negative gas was used, CF_4 , which produced very similar results to the SF_6 .

In eximer lasers pumped by a fast discharge, efficient preionization of the gas is essential for producing a uniform, arc-free discharge. Typically a strong uv flash, produced by a string of sparks, provides the preionization. However, the effectiveness of the preionization appears to

be relatively independent of the time delay between the spark pulse and the main discharge. This was surprising since the gas mixtures typically contain a few torr of F_2 , NF_3 or BCl_3 which have exceedingly fast dissociative-electron-attachment rates. Thus, essentially all the free electrons produced by the uv flash would disappear within $<10^{-7}$ seconds, whereas uniform discharges are produced even with delays exceeding one μsec .⁷

Hsia⁸ has suggested that the negative ions produced by dissociative-attachment reactions such as $F_2 + e \rightarrow F + F^-$ have a low enough electron affinity (~ 3 eV) that when the main discharge field is applied they undergo collisional detachment: $F^- + X \rightarrow F + X + e$. Thus, the negative ions themselves provide a secondary source of electrons right at the time of the main discharge.

To test this hypothesis experimentally we chose a totally different method of preionization: a radioactive emitter, americium-241. The advantages of a radioactive source for this study are that it produces no electric fields which might alter the discharge parameters, and it is much easier to estimate the electron production rate. The experimental details are described in Ref. 9. For our experimental geometry, the relation which determines the density of electrons, n_e , is

$$\frac{dn_e}{dt} = \frac{AQ}{\pi R^2 L} - \alpha n_i n_e - \beta n_e \quad (1)$$

where A is the total source activity, Q is the number of electron-ion pairs produced per alpha particle, R is the range of the alphas in the given gas, L is the length of the strip source (= the length of the laser discharge region), n_i is the ion density, while α and β are the electron-ion recombination and electron-attachment

coefficients, respectively. Since for the electronegative eximer gas mixes $\beta \gg \alpha n_i$, equation (1), at equilibrium, becomes

$$n_e = \frac{AQ}{\pi R^2 L} \cdot \frac{1}{\beta} \quad (2)$$

For our parameters equation (2) gives us a value $n_e \leq 1 \text{ cm}^{-3}$, which is obviously insufficient for stabilizing the discharge. However, since essentially all the electrons produced by the α -source result in negative ions, F^- , the density of negative ions, n_{F^-} , is determined by

$$\frac{dn_{F^-}}{dt} = \frac{AQ}{\pi R^2 L} - \alpha'(n_{F^-})^2 \quad (3)$$

where the main loss mechanism for the F^- is assumed to be three-body ion-ion recombination (rate denoted by α'): $F^- + X^+ + M \rightarrow \text{neutral products}$. Thus, we get a negative-ion density $n_{F^-} \approx 5 \times 10^8 \text{ cm}^{-3}$ at equilibrium. This density of low-affinity negative ions is sufficient to aid in stabilizing the main discharge for E/P values $\geq 100 \text{ V-cm}^{-1}\text{-torr}^{-1}$, especially if the initial voltage risetime is fast ($\sim 10^{-8} \text{ sec.}$).

In summary, whenever an electron-attaching gas is used in a laser discharge, it is wise to examine carefully the effects of increased E/P and the role of negative-ions in the discharge kinetics.

References:

1. C. S. Willet and D. M. Litynski, App. Phys. Lett. 26, 118 (1975).
2. S. N. Suchard, et al., J. Quant. Electron. QE-11, 908 (1975).
3. R. F. Atkins and S. C. Lin, App. Phys. Lett. 28, 221 (1976).
4. J. Itani, et al., App. Phys. Lett. 27, 503 (1975).
5. O. Judd, J. Quant. Electron. QE-12, 78 (1976).
6. The author is exceedingly grateful to Dr. O. P. Judd (Los Alamos Scientific Laboratory) for his assistance in providing the numerical solutions to the Boltzman transport equation.
7. T. R. Loree, et al., in *Electronic Transition Lasers II*, L. E. Wilson, et al., Eds., MIT Press, 1977.
8. J. Hsia, App. Phys. Lett. 30, 101 (1977).
9. I. J. Bigio, J. Quant. Electron. QE-14, 75 (1978).

ON THE MECHANISM OF GLOW DISCHARGE INSTABILITY FOLLOWING THE TURN-OFF A NON-SELF-SUSTAINED IONIZATION SOURCE.

A.A. Kostylev, J.I. Londer, A.P. Terentyev, K.N. Ulyanov and V.A. Fedorov.

All-Union Electrotechnical Institute, Moscow U.S.S.R.

Instabilities in a non-self-sustained glow discharge which develop when external ionisation pulse is applied have been discussed earlier in many works. According to the present dominating point of view this instability is associated with the growth of the value of self-sustained ionization function. Heating and rarefaction of gas play an important role in this case.

1. This paper reports on the measurements of gas density which were performed to clarify the mechanism of instability when the time τ_{in} exceeds the ionizer pulse duration τ_p . Experiments were carried out in a mixture of CO_2 and N_2 at atmospheric pressure. A pulsed 120keV electron beam with a current density 200 mka/cm² at the anode plane was injected into a discharge chamber through an Al-foil. The voltage across the discharge gap was maintained constant and the velocity of gas flow was 3 m/s. Change in the gas density were recorded by a laser interferometer method. Measurements were carried out with a He-Ne laser which had a three-mirror resonator [1]. The wavelength was 0.63 mkm. Optical axis of symmetry were coincident.

Typical oscillograms of a discharge current pulse and of phase overlapping are presented in Fig.1 (200 mks/cm sweep). In this case the non-ionized gas provides the main contribution to the refraction factor. A phase shift 2π corresponds to a relative change in gas density $\Delta N/N_0 = 0.016$ for the mixture $CO_2-N_2(1:2)$ and $\Delta N/N_0 = 0.018$ for the mixture (1:9), where N_0 is the initial gas density and $\Delta N = N_0 - N(t)$. The dependence of the relative density $N(t)/N_0$ on the duration of current pulse for 1:9 mix-

ture is shown in Fig.2. A point in the figure which identifies the development of instability after the termination of current pulse is marked with a cross.

2. An analytical assessment of gas rarefaction was made on the basis of a two-level model which takes into account the transfer of oscillatory energy away from the discharge zone. The continuity equations for the excited N_2 and CO_2 molecules have the form:

$$\frac{\partial N_N^*}{\partial t} + N_N^* \text{div} \vec{V} = \frac{W_N}{E_N} - \kappa(N_N^* N_C - N_C^* N_N) - \frac{N_N^*}{\tau_N} \quad (1)$$

$$\frac{\partial N_C^*}{\partial t} + N_C^* \text{div} \vec{V} = \frac{W_C}{E_C} + \kappa(N_N^* N_C - N_C^* N_N) - \frac{N_C^*}{\tau_C} \quad (2)$$

Here N_N, N_C are the densities of N_2 and CO_2 molecules in the ground state; W_N, W_C denote the power density used for the excitation of oscillatory levels in N_2 and CO_2 ; E_N, E_C are the energies of oscillatory levels in N_2 and CO_2 , κ - constant related to the oscillatory quanta exchange rate between N_2 and CO_2 ; τ_N, τ_C - relaxation time of oscillatory levels in N_2 and CO_2 . Equation (1) and (2) should be supplemented by gas dynamical equations which may be expressed for isobaric expansion of gas as follows:

$$\frac{\partial N}{\partial t} + N \text{div} \vec{V} = 0 \quad (3)$$

$$\frac{\partial E_v}{\partial t} + (E_v + \frac{\gamma}{\gamma-1} P) \text{div} \vec{V} = W \quad (4)$$

Here N is the total density of molecules in a gas mixture. The solution of system (1)-(4) may be derived with an assumption that due to the high rate of energy exchange between the N_2 and CO_2 oscillatory quanta, the establishment of equilibrium between them is practically a momentary process, i.e. that $N_N/N_C = N_N^*/N_C^* = \delta$.

The set of equations (1)-(4) may now

now be reduced to a single non-linear second-order differential equation for gas density :

$$\frac{\partial^2 n}{\partial t^2} - \left(\frac{\partial n}{\partial t} \right)^2 + [1 - B(1 - \eta)] \frac{\partial n}{\partial \tau} + B = 0$$

$$\frac{\partial n}{\partial \tau} \bigg|_{\tau=0} = B(\eta - 1); n = \frac{N}{N_0}; \tau = \frac{t}{\tau_c^*(1 + \delta)} \quad (5)$$

$$\eta = \frac{W_N + W_c}{W}, \quad \frac{1}{\tau_c^*} = \frac{1}{\tau_c} + \frac{\delta}{\tau_N}, \quad B = \frac{W \tau_c^*(1 + \delta)}{\rho \gamma} (\gamma - 1)$$

Solution of (5) is as follows :

$$n = \frac{2A \exp[1 + A - B(1 - \eta)] \tau^{\frac{1}{2}}}{[1 + A + B(1 + \eta)] \exp(A\tau) - [1 + A + B(1 - \eta)]} \quad (6)$$

$$A = 2\sqrt{B + \frac{1}{4} [1 - B(1 - \eta)]^2}$$

If $B \ll 1$, expression (6) may be simplified as follows :

$$n \approx \frac{1 + B(1 + \eta)}{1 + B + B\eta \exp[-1 - B(1 + \eta)\tau]} \exp(B\tau) \quad (6a)$$

In another limiting case when $B(1 - \eta) \gg 1$ we obtain from (6) :

$$n \approx \exp[B(\eta - 1)\tau]$$

In both cases the solution does not depend on τ_c^* . It should be noted that after termination of the pumping pulse, the gas concentration decreases for some time due to oscillatory energy relaxation. The solution of equations (1)-(4) at $W = 0$ yields :

$$n(\tau) = \frac{n^2(\tau_0)}{n(\tau) - n'(\tau_0)[1 - \exp(\tau_0 \tau)]}; \quad (\tau > \tau_0) \quad (7)$$

$$n'(\tau_0) = \frac{\partial n}{\partial \tau} \bigg|_{\tau = \tau_0}$$

To allow comparison with experimental data of $n(t)$ was computed from formulas (6a), (7) for mixture $\text{CO}_2\text{-N}_2$ (1:9) at $V_d = 3$ kV and $V_d = 5$ kV (curves 3 and 2 respectively in Fig.2). Note, that with the increase of V_d and at earlier moments of observation, the deviation from the conditional $P = \text{const}$ which is the basic approximation of the theoretical model becomes greater. Also, the discrepancy between calculation and experiment increases.

3. Discussion of results. From Fig.2 it may be seen that at $V_d = 6$ kV and 310 mks duration current pulse, instability develops at 375 mks ($\tau_{ln} > \tau_p$). By this time the gas density decreases approximately by a factor of 2.5. Comparison between the applied voltage and the static break-

down voltage of this discharge gap shows that at $n = 0.4$ the latter is three times as high as V_d .

A similar situation is true for the (1:2) mixture.

Thus the rarefaction of the gas is not a sufficient factor for the development of a static breakdown (direct Townsends ionisation). The development of instability may be associated with the growth of stepped self-sustained ionisation in the decaying plasma in an external field. In this case the increase of E/N due to gas rarefaction plays a significant role.

[1] - D.E.Ashby, D.F.Jephcott, Appl.Phys. Lett., 3, 13, 1963.

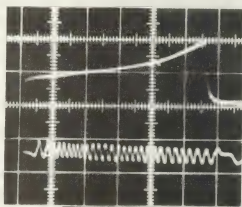


Fig.1

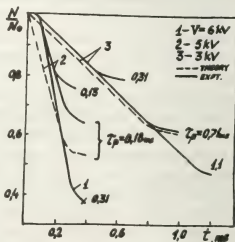


Fig.2

INVESTIGATIONS OF INSTABILITIES IN A NON-SELF-SUSTAINED REPETITIVELY PULSED DISCHARGE

A.A. Kostylev, V.I. Perevodchikov, A.P. Terentyev, K.N. Ulyanov and V.A. Fedorov.

All-Union Electrotechnical Institute, Moscow U.S.S.R.

Non-self-sustained discharges are known to be unstable. Instabilities which limit the maximum energy input in pulsed modes of operation may develop in different ways. At a sufficiently high discharge voltage an instability which occurs during a current pulse can be observed. The mechanism of this instability has already been studied in detail. At lower discharge voltages instability may develop when the external source of ionization has been turned off. As a result the discharge voltage should be decreased further. This leads to a reduced energy input per pulse in a CO_2 repetitively pulsed laser when the frequency is high or the gas velocity is small [1,2].

This paper reports on the results of experiments on instabilities occurring after turning off the ionization source of a non-self-sustained discharge when a single or two subsequent current pulses of the electron beam current were applied.

The experiments were carried out in pure N_2 or in mixture of gases $\text{CO}_2:\text{N}_2=1:9$ at atmospheric pressure. Pulsed 120 keV electron beam having a current density 200 mA/cm^2 at the anode plane was introduced through an Al-foil into a discharge chamber. Typical oscillograms of current pulse forms without instability are shown in Fig.1a, Fig.1b related to an instability developed after turning off the ionizer and Fig.1c to a case when an instability occurs when the ionizer is active. The instability development time was studied when single pulses τ_p and $2\tau_p$ or sequence of two pulses with a duration τ_p each and a period T were applied.

Dependence of instability development

time τ_a in a discharge plasma for a mixture $\text{CO}_2:\text{N}_2=1:9$ upon E/P is given in Fig.2a. It shows the time of instability development relative to the front of the current pulse after the application of a single current pulse. Points related to $\tau_p=0.3\text{ms}$, are marked (x) and those to $\tau_p=0.15\text{ms}$ -(□). Data obtained in a sequence of two pulses at $\tau_p=0.15\text{ms}$ and $T=0.75\text{ms}$ are identified by (Δ). The same figure also shows the dependence $\tau_a(E/P)$ for a case when the instability develops before the end of the current pulse i.e. when $\tau_a < \tau_p$. These experimental points are marked with 0. From the figure it may be seen that the lag of instability development in a sequence of two pulses coincides with the lag observed in a single pulse of double duration if this time is greater than 0.9ms at this value the instability is formed during the second pulse of the sequence. With further increase of E/P the instability development lag reduces slightly. When $\tau_a=0.75\text{ms}$ at $E/P=3.5\text{ kV}/\text{cm}\cdot\text{atm}$, τ_a starts again to increase rapidly. When the value τ_a diminishes to 0.15ms, the instability occurs during the first pulse.

Similar dependences were obtained in N_2 (fig.2b) with single 0.1 and 0.2ms pulses (indicated (□) and (x), respectively) and with a sequence of two pulses with $\tau_p=0.1\text{ms}$ and $T=0.9\text{ms}$ (Δ), or with $\tau_p=0.5$ and $\tau_p=1.0\text{ms}$ (■ and +) and with two pulses $\tau_p=0.5\text{ms}$ and $T=1.5\text{ms}$ (▲).

In our opinion the nature of instability at $\tau_a > \tau_p$ is the same as that observed at $\tau_a < \tau_p$. When the electron beam is interrupted the plasma starts to deionize and the current decreases. However, simultane-

ously with this process the self-sustained ionization continues to increase due to the growth of the mean energy of electrons in the applied field (E/N increases as gas concentration N decreases). Another reason is the increase of the number of fast electrons with ionizing capability. In this case $\partial N_e / \partial t$ (N_e - the electron concentration) may become positive with subsequent current and instability development. The non-self-sustained discharge transforms into a self-sustained mode. The second pulse merely accelerates this process. The time of establishment of a constant gas density after turning off the source of ionization is relatively short. It is of the order of oscillating relaxation time for the mixture of gases and corresponds to the rotational relaxation time for N_2 where the V-T relaxation time is on the contrary very long. Thus the instability will not develop after the first pulse but rather a certain stable density may be established. After the second pulse the density starts again to reduce, $\partial N_e / \partial t$ changes its sign and leads to instability. Thus, the rarefaction of the gas influences essentially the time of instability development.

Discharge voltage in lasers when an external ionizator is used for current modulation should be chosen such that E/P does not exceed the minimum value at which the instability develops, or τ_a should be greater then the time of gas transit through the discharge gap. In both cases this voltage is appreciably lower than the limiting voltage at which $\tau_a = \tau_p$, thus pumping would not be performed in the optimal conditions. It therefore appears that the most promising means of pumping would be provides anode voltage modulation in such a way that the probability of instability development be eliminated.

References

1. G.S.Dzakowic, S.A.Wutzke, J.Appl.Phys., 44,11,5061, 1973.
2. A.A.Kostylev, J.I.Londer, A.P.Terentiev, K.N.Uljanov, XIII-th Intern. Confer. on

Phenom. in Ionized gases, Berlin, 1977.

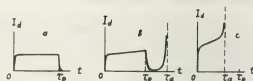


Fig.1

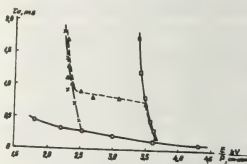


Fig.2a

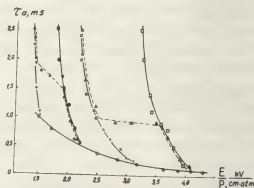


Fig.2b

CURRENT VOLTAGE CHARACTERISTICS OF A SELF-SUSTAINED ELECTROPHOTOIONIZED DISCHARGE IN LASER MIXTURES

E.P. Glotov, V.A. Danilychev, A.I. Milanich and A.M. Soroka.

Lebedev Physical Institute, U.S.S.R. Academy of Sciences Leninsky prospect 53, 117924 Moscow U.S.S.R.

Three-component compressed mixtures of rare-gas (A,R) and haloid molecules (H_2) are one of the most active media for powerful optical gas lasers [1]. In [2] a self-sustained electrophotoionized discharge (EPI-discharge) has been proposed, and the calculation for a three-component laser mixture $Ar:Xe:CCl_4=1500:50:1$ at $P=2$ atm presented. In the present paper the conditions for steady-state burning of a self-sustained EPI discharge in $A:R:H_2$ laser mixtures where the quantum energy is sufficient for photoionization of low metastable levels of the rare gas (R^*) are considered. Current-voltage calculation characteristics (CVC) are presented and the conditions for discharge stability are found. The reduced equation system for EPI-discharge in three component laser mixtures at the point approximation is:

$$\begin{aligned} \frac{dR^+}{dt} &= K_1 H_2 (F/H_2)^2 Ne - K_1 H_2 R^+ - G_1 \gamma_e R^+ + (F/\rho)^2 = \epsilon_1 K_1 H_2 / \alpha_e \rho_e D, \\ \frac{dR^-}{dt} &= G_1 \gamma_e R^+ - K_1 H_2 Ne - \beta_e AR^+ Ne, \\ \frac{dR^0}{dt} &= G_1 \gamma_e R^+ - \beta_e H^- R^+ - K_2 A^2 R^+, \\ \frac{dAR^+}{dt} &= K_2 A^2 R^+ - \beta_e H^- AR^+ - \beta_e Ne AR^+, \quad Ne + H^- = R^+ + AR^+, \\ \frac{dAR^-}{dt} &= K_1 H_2 R^+ + K_1 H_2 Ne - \epsilon_1 (K_1 H_2 / \alpha_e \rho_e D) \gamma_e R^+ - G_1 \gamma_e R^+ - G_2 AR^+ \gamma_e \end{aligned} \quad (1)$$

Here e , μ_e , are the charge and electron mobility with density n_e ; d , the part of energy spent on A^* electron level excitation with energy ε_A ; K_R , the rate constant of RH^* excimer formation at R^* and H_2 collisions; σ_i , the cross-section of photoionization R^* ; I_{ext} , the laser radiation flux

density in the resonator ($\text{cm}^2 \text{sec}^{-1}$); K_a , the rate constant for electron attachment to H_2 ; β_e , the constant of electron-ion recombination with Ar^+ molecular ions; β_i , the constant of ion-ion recombination of negative H and positive Ar^+ ions; K_t , the rate constant of molecular ion formation at triple collisions of R^+ and two A atoms; L , the active region length; and $r_{1,2}$, the reflection coefficients of the resonator mirrors, and $\bar{\sigma}_a$, the cross section of laser light absorption by Ar^+ ions. When deriving the system (1), the laser signal was assumed to be saturated.

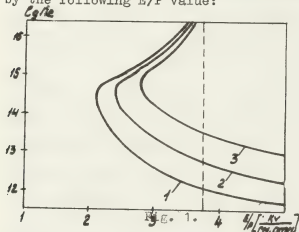
For the given optical resonator parameters and the active region length all steady-state discharge parameters are defined by E/P. The correlation between the electron density and the field intensity is

given by:

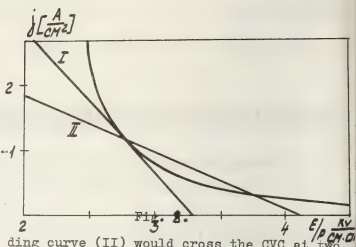
$$\begin{aligned} (E/E_0)^2 &= 1 + \frac{1}{2}y + \left\{ \frac{1}{2}y^2 + \frac{6\alpha}{5} \frac{K_F}{K_0} \frac{K_H}{\beta e n_e} [y^2 + y(\gamma+1) + \gamma] \right\}^{1/2} \\ y &= K_F A^2 / K_A H_2 + \frac{6\alpha n_0}{5} \left(1 + \frac{K_F A^2}{K_A H_2} + \beta e n_e / K_A H_2 \right)^{-1} \quad (2) \\ \gamma &= \epsilon_1 (1/n_1 \epsilon_2) \beta e (2L/5\alpha K_A H_2)^{-1} \end{aligned}$$

Figure shows the CVC of the EPI-discharge for different values of the resonator transmission. One can see the existence of the minimum $E/P(E/P)_{\min}$ parameter depending on the resonator. Starting from this value of E/P the steady-state burning of the self-sustained discharge is possible. There are two build-up and drop-down curves in the EPI-discharge CVC. The elect-

ron attachment to the haloid molecules is the main mechanism of electron loss on the drop-down curve of CVC. In the case of the build-up curve the process of dissociation recombination with AR^+ molecular ions is dominating. Since the growth of molecular ion density AR^+ is not proportional to the growth of n_e (due to the finite rate of AR^+ formation from R^+), then starting from some value E/P the electron loss would not compensate the electron origin, and no steady-state burning is possible. Note that if R^+ ion is instantly transformed into AR^+ , then the building-up CVC curve would exist at any value of E/P (instabilities connected with a stepwise ionization are not taken into account). Thus, the region where the build up curve exists is restricted from above by the following E/P value:



It is known, the drop-down CVC is unstable without the external resistance in the discharge circuit [3]. One of the CVC curves with different loading lines is presented in Fig.2. As is seen from Fig.2, there is a minimum value of external resistance for each of the points along drop-down CVC (the loading curve 1 touches CVC at this point) that makes possible the steady-state burning of EPI-discharge. When ballast resistance is $R > R_p$, the loa-



ding curve (II) would cross the CVC at two points. But the only stable crossing point is the one corresponding to a smaller E/P value. R_I is derived from:

$$\frac{R_I}{R_0} = \frac{(E/E_*)^2 - 1}{3(E/E_*)^2 + 1}, \quad R_0 = \frac{K_a}{K_r} \frac{\ell p}{e \mu_e S} \left\{ \left(\frac{E}{E_*} \right)^2 - 1 \right\}^2 \quad (4)$$

where R_0 is the resistance of a discharge gap; ℓ , the distance between electrodes, and S , the electrode area.

The existence of parasitic capacitance C_p of a discharge gap can make the drop-down curve unstable even at $R > R_I/4$. But in the case when $R C_p$ time is much smaller than the typical plasma formation time, the presence of a parasitic capacitance does not interfere the stability of discharge burning. Here the acceptable parasitic capacitance is defined by:

$$R_I C_0 = \left(1 + \frac{R_0}{R_I} \right) \left[1 + \frac{3}{(E/E_*)^2 - 1} \right] \left[1 + \frac{(E/E_*)^2}{(E/E_*)^2 - 1} \right] \frac{K_r}{K_a} \frac{4}{K_a H_2} \quad (5)$$

Under the conditions typical of excimer laser operation Eq.(5) is valid. The drop-down curve is of interest for laser applications since energy loss for photoionization is less than for buildup curve. Stimulating discussions with O.Kerimov and G.Shapiro are acknowledged.

References

1. V.Danilychev et al. Radiotekh., **12**, 1977.
2. N.Basov et al. Zh TP Letts.
3. L.Leb. Processes of Electric discharge in gases, M.-L., Gostekhizdat, 1950.
4. L.Bessonov. Theoretical Grounds of Electrotechnics, M., "Vysshaya Shkola" 1978.

KINETIC PROCESSES IN NON-HEATED COPPER VAPOUR LASER

A. Ludmirsky, Ch. Cohen and Yu. Kagan.

The Hebrew University of Jerusalem, The Racah Institute of Physics, Jerusalem, Israel.

Copper vapour lasers attracted attention owing to their high efficiency in the visible region of the spectrum. In conventional copper vapour lasers, a temperature of 1500°C is needed to achieve the required vapour pressure. A lower temperature (400°C - 600°C) is required in a double-pulse lasers using copper halides (1,2). These temperatures are usually obtained by power dissipation of the applied discharge operated at a relatively high repetition rate (3). A promising method for decreasing the working temperature of a copper vapour laser is the pulsed introduction of vapour into the working volume of the laser (4,5,6).

Copper vapour laser with inductively produced copper plasma, which is accelerated by a pulsed magnetic field, operates at room temperature in a double-pulse mode (7). The magnetic field was generated by the discharge of a capacitor ($0.7\ \mu\text{F}$, 30KV) through a solenoid mounted outside a glass tube (10cm bore and 175cm long) filled with helium.

The population densities of both the ground and $2D_{5/2}$ metastable states of copper atoms were derived from measurements of the optical absorption at 324.7nm and 510.6nm , respectively, over a wide range of the helium pressure. These measurements were made along the tube axis and across the tube to eliminate the influence of the heterogeneities of the copper vapour moving in the axis direction at the instant of vapour production.

A triggered xenon flash tube was used as the source for absorption measurements.

A lens focused the light onto the entrance slit of a 1-m monochromator equipped with $10\ \mu\text{m}$ slits and a photomultiplier tube (PMT) at the exit slit.

The PMT signal was displayed on an oscilloscope and recorded on Polaroid film.

Ground state and metastable copper densities were computed from the measured absorption by employing

the methods described by Mitchell and Zemansky (8). The absorption coefficient of the copper ground state or metastable state was obtained using the Voigt profile, which includes the effects of Doppler, natural resonance, and Van der Waals broadening. The hyper-fine structure and isotope shift were taken into account in the calculation.

The temporal variation of the temperature in the afterglow was studied by fast-scanning Fabry-Perot spectroscopy (9). The temperature of the copper vapour was determined from the Doppler broadening of the 521.8nm copper line. This line was selected in order to exclude isotope shift effects.

The temperature measurements were made across of the tube to exclude the velocity broadening effects of the moving copper vapour along the axis direction.

The temporal variation of the temperature of the copper vapour (Fig.1) was taken into account for line profile interpretation.

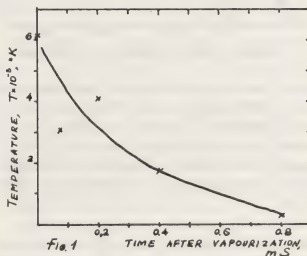


Fig. 1

The slit function was determined with the help of a copper hollow-cathode lamp. The slit function was used to calculate absorption coefficients from a

continuum radiation source.

The densities of both the ground and metastable states of copper atoms with helium at different pressures are shown in Fig. 2.

Only measurements of the ground-state densities at higher helium pressures are shown as metastable levels were not detectable.

The metastable level density decays rapidly from an initially high value while the ground-state densities exist up to 2ms. without noticeable changes.

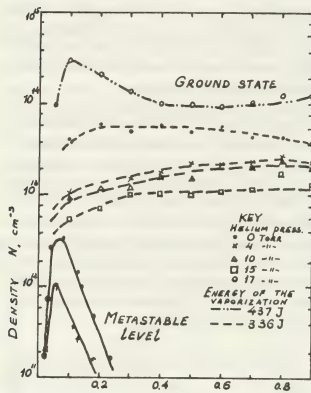


Fig. 2. TIME AFTER VAPOURIZATION PULSE, ms

In our experiments a longitudinal excitation pulse from a 3500pF capacitor charges to 30KV was applied 300-2000 μ sec after the vapour production. Lasing was obtained only with low helium pressure (2 torr), because of the difficulty of obtaining a longitudinal glow discharge between electrodes separated by 175 cm.

The maximum laser output energy was 10mJ with a pulse duration of 150nsec. Lasing on both green and yellow lines was detected. The mentioned laser energy was obtained without optimization of laser parameters.

Study of high efficiency copper lasers with pulsed production of vapour is carried out by the authors.

REFERENCES

1. C.I. Chen, N. Nerheim, and G. Russel
Appl. Phys. Lett. 23, 514 (1973)
2. I. Liberman, R. Babcock, C. Lin, T. George and I. Weaver, Appl. Phys. Lett. 25, 334 (1974)
3. A. Isarv, M. Kazaryan and G. Petrash,
ZhETF Pis. Red 16, 40, (1972)
4. G.R. Russel, N.M. Nerheim and T.J. Pivittotto,
Appl. Phys. Lett. 21, 565 (1972)
5. J.F. Asmus and N.K. Moncur, Appl. Phys. Lett.
13, 384 (1968)
6. A.M. Shukhtin, G.A. Fedotov and V.G. Mishakov,
Opt. Spectroscopy 40, 237, (1976)
7. A. Ludmirsky, Laser (file patent applic. in the
USA, N889396 from 28/3/78).
8. A.C. Mitchell and M.N. Zemanski, Resonance
Radiation and Excited Atoms (Cambridge University
Press, London, 1961)
9. A. Ludmirsky, C. Cohen and Yu. M. Kagan
Appl. Optics, Jan 1979.

LONG-TIME CHANGES OF AN IONIZATION WAVE IN THE $\text{CO}_2 + \text{N}_2 + \text{He}$ MIXTURE

H. Urbánková, L. Pekárek.

Institute of Physics, Czech. Acad. Sci., Na Slovance 2, 180 40 Prague, C.S.S.R.

For the investigation of slow changes in the composition of gas mixtures in cw CO_2 -lasers, several methods have been used: gas sample bottles for mass analysis /1,2/; side-light emission of the 4835 Å (0-1) Angstrom band of CO /3/; freezing out of the mixture in liquid nitrogen and gas chromatography /4/; mass spectrometer joined to the system /5,6/ etc. We used the changes in parameters of self-excited ionization waves /7/ for continuous registration of temporal changes of the state of the mixture of CO_2 , CO, N_2 and He. The dispersion curves of the ionization waves were taken by the method given in /8/. At the end of the experiment, i.e. when the discharge ceased to operate due to the expansion of the cathode fall almost over the whole tube, the discharge tube was connected to the manometer and to the mass spectrometer to measure the total pressure and composition of the remaining gas mixture.

The tube 2.2 cm in diameter was water cooled, made of Pyrex glass, with cylindrical nickel electrodes and the electrode distance was 70 cm. Two wire probes placed 7 and 13.6 cm from the cathode were used to measure the longitudinal electric field in the discharge positive column. The measurements were accomplished in the mixture 1 Torr $\text{CO}_2 + 1$ Torr $\text{N}_2 + 1$ Torr He at a constant current of 40 mA. The tube was sealed off before the experiment. To achieve the shortest possible lifetime of the gas fill the tube was designed with minimum ballast volume.

Fig. 1 is one example of the obtained time dependencies. The ionization wave, which is of the forward anode directed type, changes its parameters slowly until 24 hours. At this moment a point is reached where the wave converts in a relatively short time into a backward wave with cathode directed phase velocity. The bending of the frequency dependence upwards followed by change of its sign (and, hence, of the direction of phase velocity) can be attributed to growing influence of helium, which itself has only backward ionization waves /9/. In another experiment where only 1 Torr $\text{CO}_2 + 1$ Torr He mixture was used, the result was qualitatively identical, i.e. with helium-like backward waves observed in the end of the experiment. The abrupt fall in wave number as well as the falling electric field corroborate the latter

conclusion, i.e. the diminishing abundance of molecular gases.

Surprisingly, under the initial partial pressures given in Fig. 1, the total pressure in the end of the experiment was found equal to 0.26 Torr which was significantly lower than the initial partial pressure of each of the three gases including helium. As expected according to the observed wave pattern, the mass spectrometer revealed that the main remaining gas was He, with CO and/or N_2 and O_2 not exceeding their (rather strong) background measured prior to the connection of the experimental tube to the spectrometer chamber. There was no peak corresponding to CO_2 .

Comparing these results with mass spectrometer measurements of Carbone /1/, we conclude that the slow changes of the electric field, the wave number and the frequency of the forward ionization wave correspond to the known slow decrease of CO_2 during the discharge operation (CO_2 , CO and O_2 being adsorbed and chemisorbed on the tube walls and on the electrodes). The rather abrupt change around 24 hours accompanied by a drastic fall of pressure must, however, correspond to another phase of the changes in the mixture of which only the very beginning was observed /1/. Indeed, the abrupt fall of pressure begins apparently when all CO_2 molecules are dissociated and corresponding oxygen part is absorbed. Dissociation of CO molecules with further loss of oxygen then leads to the observable thin layer of carbon deposit on the tube walls near cathode. This carbone deposit in turn should cause further adsorption of helium and nitrogen ending in an appreciable lowering of the total pressure. Chemical analysis proved at the same time a considerable amount of nickel nitride formed at the cathode region.

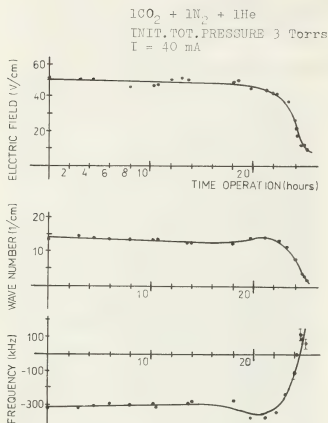


Fig.1. Time dependencies of the electric field, the wave number and the frequency of the ionization wave. The minus sign of the latter parameter designates the cathode \rightarrow anode directed phase velocity $v_p = \omega/k$. Near the $\omega = 0$ transition point (at ~ 24 hours) the frequency measurement was inaccurate due to very flat maximum of the increment curve.

REFERENCES

- /1/ R.J. Carbone, IEEE J.Quant.El. QE-3, p.373-375, Sept. 1967
- /2/ R.J. Carbone, IEEE J.Quant.El. QE-4, p.102-103
- /3/ W.J. Wiegand et al, Appl.Phys.Lett., 16, 1970, p.237-239
- /4/ E.N. Lotkova et al, Khim.vys.en. 2 (1968), p.278-283; E.S. Gasilevitch et al, Zh.T.F. 39, (1969), p.126-132
- /5/ K.M. D'Amico et al, J.Phys.D: Appl. Phys., 10, (1977), p.261
- /6/ N. Karube et al, J. Appl.Phys., 41, (1970), p.2031-2042
- /7/ L. Pekárek, Usp.fiz.n., 24, 3, (1968), p.463
- /8/ J. Skála, Czech.J.Phys. B (1973), p.284
- /9/ V. Peřina, Czech.J.Phys. B26, (1976), p.764

NON-EQUILIBRIUM DISSOCIATION PHENOMENA

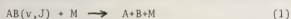
W.F. Bailey and A. Garscadden.

Air Force Aero Propulsion Laboratory, Wright-Patterson Air Force Base, Ohio, U.S.A. 45433.

A comprehensive analysis of collisionally

induced dissociation (Eqn. 1) under equilibrium and nonequilibrium conditions has been performed⁽¹⁾.

Solutions of the set of coupled non-linear differential equations (Eqn. 2) for each of the vibrational levels and the continuum, known as the Master equation, have been achieved for both steady state and time-dependent conditions.



$$\frac{dN_1}{dt} = \sum_{i,j,k} R_{j,l}^{i,k} N_j N_k - \sum_{i,j,k} R_{l,j}^{i,k} N_l N_i \quad (2)$$

N_1 denotes the concentration of molecules in state 1, and the R 's represent generalized rate coefficients for the population or depopulation of state 1 involved in collisional energy exchanges between states i , j and k . The Master equation was solved under the physically realistic assumptions that

- 1) the translational and rotational degrees of freedom are in complete Boltzmann equilibrium.
- 2) the molecules in each vibrational state are treated as separate species.
- 3) only single quantum vibrational exchanges occur.
- 4) the molecule is represented as a Morse oscillator rigid rotator system. The time dependent solution for thermal dissociation conditions (e.g., shock heating, 4000°K) has established that the vibrational energy distribution, VED, rapidly attains a pseudo-steady state (Fig. 1). This steady state distribution deviates from the equilibrium distribution because of vibrational-dissociation coupling. That is, the depletion of high level populations substantially reduces the dissociation rate from that which would be obtained if the coupling were not considered. A comparison of induction times gave good agreement except at very

high temperatures where multiple quantum V-T transitions begin to contribute. The results show that the standard ladder model predicts dissociation rates that are too low and that rotational effects must be included in the model. Agreement is further improved by including equal energy transitions involving a quasi-bound vibrational-rotational level (Fig. 2).

As an example, dissociation rates were

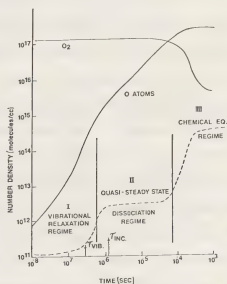


Fig. 1 Time Profiles and Uni-Directional Flux

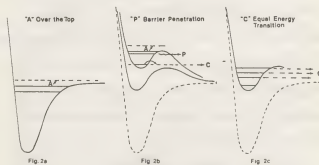


Fig. 2 Alternate Paths for Dissociation

derived for the highly non-equilibrium conditions that occur in carbon monoxide discharges. Heavy particle and electron impact dissociation have been compared (Fig. 3). The dissociation due to electron impact was derived using a steady state solution of the collisional Boltzmann equation.

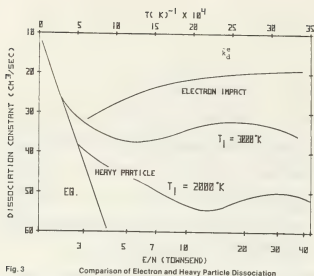


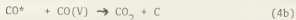
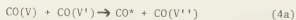
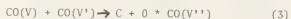
Fig. 3

Comparison of Electron and Heavy Particle Dissociation

This showed that the effective dissociation constant is a strongly increasing function of E/N and it is also enhanced by superelastic collisions and by the reduced dissociation threshold of the vibrationally excited species. Examination of the heavy particle kinetics revealed the temporal development of the three characteristic regions of the VED.

The calculated VED showed good agreement with the experimental data of Rich⁽²⁾. The predictions are that electron impact dissociation always dominates the heavy particle rate for discharges of interest in carbon monoxide. However, experiments have also been made recently on optically pumped dissociation of carbon monoxide⁽²⁾. Calculations made with the models for these conditions yielded dissociation rates that appear to be much lower than those indicated by these experiments (Fig. 4). We

therefore propose that a more efficient channel for CO dissociation must exist. Alternative processes that appear to satisfy the experimental observations are (a) multi-quantum V-V exchange and/or (b) vibrational to electronic, V-e exchange:



The observed isotopic enhancement in dissociation products, the similar dependence on the Treanor or

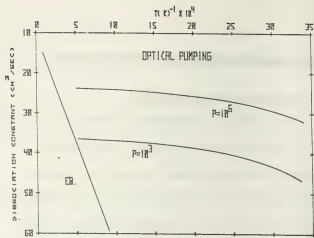


Fig. 4 Optical Pumping, Heavy Particle Dissociation Constant

plateau regions of the VED and therefore also the pumping and the temperature dependencies, will not give the relative importance of the mechanisms. However, the primary dissociation products (Eqns. (3) and (4b)) should be identifiable by mass-spectroscopy. The presence of O_2 would favor the V-V mechanism whereas the presence of CO_2 would tend to indicate the dominance of the V-e exchange. In addition, the activation energies for the V-V and V-e mechanisms differ: for the V-V, $E_V + E_V > D_0$ where $D_0 = 11\text{eV}$, while for V-e, $E_V + E_V > E^*$ where E^* is the energy of the reacting electronic state, 6.2eV for $\text{CO}(a^3\pi)$. Thus it should be possible to distinguish between the two mechanisms by titrating helium to alter the VED and simultaneously monitoring the Swan band intensity (from $\text{C} + \text{C} \rightarrow \text{C}_2^* \rightarrow \text{C}_2 + h\nu$) to establish the dependence of k_D with the location of the "knee" of the VED.

1. W. F. Bailey, PhD Thesis, US Air Force Institute of Technology, (1978).
2. Rich, J. W., R. C. Bergman, and M. J. Williams "Measurement of Kinetic Rates for Carbon Monoxide Laser System." Calspan Report No. WG-6021-A-1, November (1977).

TWO NOVEL HCD-STRUCTURES FOR CuII-LASERS AND THEIR PERFORMANCE

H.J. Eichler, H.Koch, J. Paffenholz, J. Salk and G. Skrobel.

Optisches Institut TU Berlin, Sekr. p11 Str. d. 17. Juni 135, 1000 Berlin 12.

The major problems of sputtering hollow cathode devices (HCD) for high continuous power operation of CuII-lasers /1/ are discharge instability and losses of Cu-vapour, He-Ions and light quanta.

The following constructions (fig. 1 and 3) were designed considering these criteria. The first design applies the type of HCD introduced by White /2/. The advantages of these cavity hollow cathodes (exceptionally high stability and minimum losses) can be used for CuII-laser operation by lining up the cavity hollow cathodes and connecting them by a bore which constitutes the laser tube. Two anode rods are opposing the apertures of the cavity cathodes. Both anodes and the cathode arrangement are watercooled. As this design is still in the development stage fig. 2 shows the discharge voltage and the laser output Φ vs. the discharge current I at a total pressure of 15 mb for not optimized conditions. The parameters are as follows:

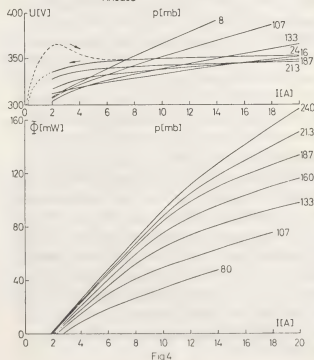
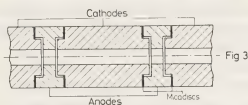
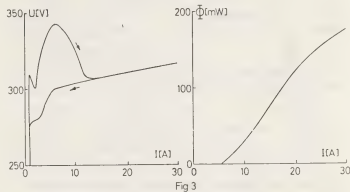
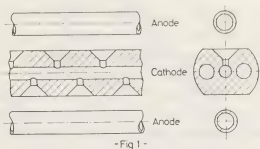
laser bore diameter: 4 mm
 laser bore length : 300 mm
 cavity aperture : 2 mm
 cavity spacing : 7,5 mm
 resonator: fully reflecting mirror and an 1 % transmittance mirror, both with radius of 2 m.
 He:Ar mixture of pressure ratio 20:1,
 total pressure: 15 mb.

Fig. 1 Cavity hollow cathode laser

Fig. 2 $U(I)$ - and $\Phi(I)$ -characteristics of the first design

Fig. 3 Cylindrical hollow cathode laser tube

Fig. 4 $U(I,p)$ - and $\Phi(I,p)$ -characteristics of the second design



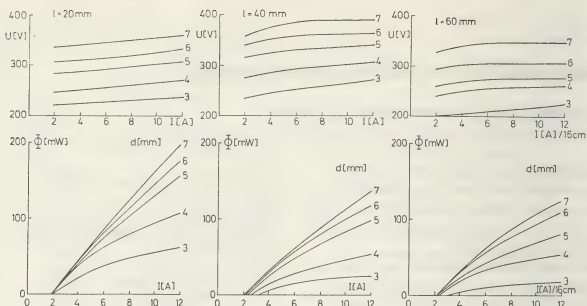


Fig 5

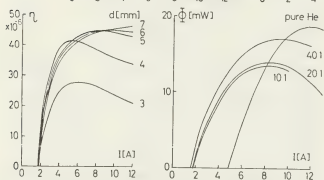


Fig 6

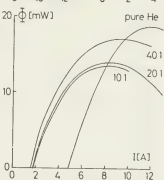


Fig 7

The second design consists of watercooled cylindrical hollow cathodes. High stability and minimization of losses were obtained with this structure by employing a small cathode-anode gap, that provides a restriction of the discharge to the laser bore only. Fig. 4 exhibits the dependences of discharge voltage U and laser multiline (740-790 nm) output Φ on the discharge current I and the total gas pressure p (He:Ar = 20:1) for an HCD-arrangement consisting of 4 cathodes with 5 mm bore diameter and 40 mm length. The $U(I)$ -characteristics display the reverse branches of the indicated full $U(I)$ -curve.

It is known, that the HCD-performance is strongly dependent on the cathode bore geometry. To our knowledge we have investigated the geometry dependence of the laser-HCD-parameters for the first time quantitatively in this high current and pressure range. Fig. 5 reveals the influence of the hollow cathode bore geometry on the $U(I)$ - and the $\Phi(I)$ -characteristics (active length 160 mm).

Fig. 5 $U(I)$ - and $\Phi(I)$ -dependence on the HCD geometry

Fig. 6 Efficiency vs. discharge current for different cathode bore diameters

Fig. 7 Laser output power saturation

Fig. 6 shows the dependence of the efficiency (e.g. laser output power divided by the product of discharge voltage and current) on the discharge current for different cathode bore diameters (8 cathodes of 20 mm length). We employed anodes of various bore lengths (2-6 mm) and bore diameters, that were equal and up to 4 mm bigger than the cathode bore diameters, without any appreciable change in discharge voltage and laser output.

Finally we were able to observe for the first time saturation of the 780,8 nm laser line at high discharge currents. With only one cathode segment of 30 mm length and 7 mm diameter it was possible to obtain 14 A discharge current without damaging the device. Fig. 7 shows measurements of the saturation of the IR-laser output for He:Ar mixtures with different pressure ratios.

References:

- /1/ B.E. Warner et al, IEEE J. Quant. Electr., Vol. QE-14, No. 8, 568 (1978)
- /2/ A.D. White, J. Appl. Phys., 30, 711 (1959)

THEORETICAL STUDY OF NEGATIVE ABSORPTION FOR H^- AFFINITY RADIATION

M. Neiger.

Ruhr University Bochum, Allgemeine Elektrotechnik und Elektrooptik, 4630 Bochum, F.R.G.

INTRODUCTION

Free-bound radiative transitions of electrons forming negative hydrogen ions are an important source of continuous radiation in dense hydrogen plasmas of low degree of ionisation /1,2/. It was first suggested in /3/ that it might be possible to obtain population inversion for this kind of phototransition. The aim of the present work is to theoretically investigate the possibility of this kind of negative absorption during the early after-glow stage of a short-circuited non-LTE hydrogen arc plasma.

ESTIMATE OF OPTICAL GAIN

The basic processes which have to be considered are absorption by photodetachment (cross-section σ_{det}^0),



and stimulated emission by induced radiative attachment,



Without assuming thermal equilibrium and with the only assumption of Maxwellian distributed kinetic particle energies the optical gain per unit length $\alpha(\lambda)$ can be expressed in terms of the photodetachment cross-section $\sigma_{\text{det}}^0(\lambda)$, the H^- binding energy EA (electron affinity), and the particle number densities n and statistical weights g respectively ($e \hat{=}$ electron, $O \hat{=}$ H-atom, $- \hat{=}$ H^- -ion):

$$\alpha = \sigma_{\text{det}}^0 \left\{ \frac{g_-}{2g_0} \frac{h^3}{(2\pi m_e k T_e)^{3/2}} n_e n_0 e^{\frac{EA - h\nu}{kT_e}} - n_- \right\}.$$

Obviously positive gain $\alpha > 0$ occurs for small enough negative ion densities n_- .

The threshold condition for "population inversion", i.e. positive gain, is

$$\{n_e/n_-\}_{\alpha>0} \geq F e^{\frac{h\nu}{kT_e}} \{n_e/n_-\}_{\text{Saha'}}$$

where $h\nu > EA$ and the factor F accounts

for absorption losses due to other radiation processes, e.g. electron-atom bremsstrahlung or electron-positive ion bremsstrahlung and photoionisation, both of which will be inevitably present. An estimate of the optical gain values expected for negligible negative ion densities in a high density, low temperature hydrogen plasma ($n_0 \approx 10^{19} \text{ cm}^{-3}$, $n_e/n_0 \approx 1\%$, $T_e \approx 1 \text{ eV}$, $\lambda = 1.3 \mu$ and $\sigma_{\text{det}}^0 = 2 \times 10^{-17} \text{ cm}^2$) yields a value of $\alpha \approx 0.01 \text{ cm}^{-1}$.

POPULATION INVERSION BY PLASMA RELAXATION

The case of an electric arc plasma is considered here. It is well known for the case of high density, low temperature hydrogen arcs ($p \approx 1-10 \text{ bar}$, $T_e \approx 1-2 \text{ eV}$) that the electron temperature T_e can exceed the heavy particle temperature T_g considerably /4/. A transient population inversion may be achieved in such a case by rapidly removing the arc maintaining electric field via a short circuit and hereby cooling down the electrons to the gas temperature T_g . If the short circuit switch is operated at time t_0 , the following plasma conditions are expected shortly before (t_0^-) and after (t_0^+) switching:

$$t_0^-: n_0, n_e = n_i, T_e > T_g,$$

$$t_0^+: - T_e \text{ drops to } T_g \text{ with a time constant } \tau \approx 10 \text{ ns} / 5.$$

$$- \text{no change of } n_0, n_e, n_i, T_g \text{ takes place for about } 100 \text{ ns} / 4/.$$

The most interesting parameter in the present case is the H^- equilibrium density $\{n_-\}_{\text{equ}}$. Calculations of rates of formation and destruction of H^- ions in a fully dissociated and partly ionized, stationary hydrogen plasma show that n_- densities are in Saha equilibrium with the electron temperature T_e for plasma conditions of interest here ($n_e \approx 10^{16} \text{ cm}^{-3}$, $n_e/n_0 \approx 1\%$,

$T_e \approx 0.5-5$ eV). Rapidly cooling down the electrons from $T_e > T_g$ to $T_e = T_g$ without a corresponding change in n_- yields "underpopulation" with respect to Saha equilibrium of negative hydrogen ion states for durations $\tau \approx 100$ ns after t_0 . The corresponding calculations yield minimum temperature ratios T_e/T_g before switching, above which transient negative absorption ($\alpha > 0$) results:

$$\left(\frac{T_e}{T_g}\right)^{3/2} = F \cdot \exp\left[FA \cdot \left(\frac{h\nu}{EA} - \frac{T_e - T_g}{T_e}\right) / (kT_g)\right].$$

Fig. 1 shows limiting curves $(T_e/T_g)_{\min}$ for $\alpha = 0$ as a function of electron temperature before switching for different loss figures F ($F = 1$ corresponds to no losses present). These curves hold for the wavelength $\lambda = 1.6 \mu$ which is close to the long wavelength threshold of the hydrogen affinity continuum. With respect to λ , a range $\lambda_{\min} < \lambda < 1.6 \mu$ exists for each ratio T_e/T_g within which positive gain is possible after switching. Fig. 2 shows such limiting curves λ_{\min} for $\alpha = 0$, $F = 1$ as a function of the temperature ratio T_e/T_g , with T_e before switching as a parameter.

CONCLUSION

It has been shown theoretically that considerable optical gain of the hydrogen affinity continuum is possible in a high density hydrogen plasma. The necessary population inversion can be achieved in a transient way by a fast short circuit of a stationary hydrogen plasma of low degree of ionisation with its temperature T_e ($T_e \approx 1-5$ eV) exceeding the heavy temperature T_g by factors 2-5. Experimental realisation of this concept seems difficult, but it would provide continuously tunable laser radiation from $\lambda = 1.6 \mu$ down to the visible region.

LITERATURE

- /1/ H.-P. Popp: Phys. Rep. 16 C, 170 (1975)
- /2/ H.-P. Popp and S. Kruse: JQSRT 16, 683 (1976).
- /3/ V.A. Kochelap: Sov. Phys. Techn. Phys. 17, 357 (1972).
- /4/ J. Jordanov and G. Kreutzberger: Proc. XIth ICPIG, p. 414, Prague (1973)

/5/ H.W. Drawin, in: "Reactions Under Plasma Conditions, Vol. I, chapt. III, Wiley, New York (1971).

Fig. 1

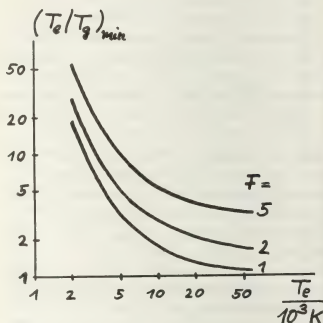
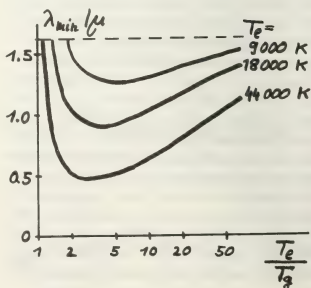


Fig. 2



REALISATION ET EXPERIMENTATION D'UN LASER A VAPEUR DE CUIVRE

B. Felts.

Laboratoire de Photoelectricite, Faculté des Sciences et Techniques de Saint-Jérôme,
13397 Marseille Cedex 4.

1. **PRINCIPE.** Les lasers à vapeur métallique sont d'un intérêt considérable en raison de leur efficacité potentielle et de leur bonne puissance de sortie en impulsions dans le spectre visible. Le laser à vapeur de cuivre est certainement l'un des plus intéressants en raison de la position privilégiée des niveaux d'énergie électroniques de l'atome de cuivre qui interviennent dans l'effet laser (fig.1).

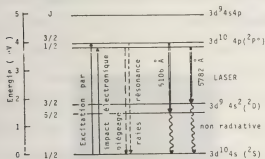


Fig.1- Diagramme d'énergie de l'atome de cuivre.

Pour obtenir l'effet laser dans la vapeur de cuivre, il faut :

1/ Disposer d'un milieu présentant une concentration en atomes de cuivre de 10^{14} à 10^{15} cm^{-3} , nécessaire au piégeage de la radiation de résonance. Ceci correspond à une pression de 0,1 torr et nécessite d'atteindre des températures de l'ordre de 1500°C si l'on utilise du cuivre pur. Si l'on fait intervenir des composés du cuivre, halogénures /1/, ou organométalliques /2/, des températures inférieures à 500°C seulement sont nécessaires.

2/ Exciter le milieu par une décharge électrique transversale ou longitudinale. Un gaz tampon sous quelques dizaines de torr favorise cette décharge.

3/ Placer le milieu actif dans une cavité laser.

Pour porter ce milieu à la température nécessaire, on peut, soit utiliser un four, soit récupérer la chaleur dissipée au cours de la décharge /4/.

Nous décrivons ci-après les expériences que nous avons réalisées avec cette deuxième solution.

2. **DISPOSITIF EXPERIMENTAL.** (fig.2). La décharge se fait entre deux électrodes annulaires, distantes de 250 mm dans un tube d'alumine. Entre les deux électrodes, une nacelle en alumine contient le cuivre. Le tube d'alumine est entouré de 3 réflecteurs en molybdène brillant, servant à diminuer les pertes de chaleur par rayonnement et à constituer ainsi un four dans la partie centrale. Ce four est contenu dans une enceinte à double paroi en acier inoxydable refroidie par eau, dans laquelle on peut faire le vide. A chaque extrémité le montage se termine par des fenêtres optiques inclinées selon l'angle de Brewster. L'anode est reliée à l'enceinte métallique et la cathode au support de fenêtre de Brewster qui sert de passage électrique.



Fig.2- Schéma du montage du laser à vapeur de cuivre.

- | | |
|--------------------------------------|---|
| (1) enceinte refroidie par eau | (2) entrée ou sortie d'eau |
| (3) support des tubes | (4) tubes d'alumine isolants |
| (5) Ecrans thermiques en polydène | (6) nacelle d'alumine contenant le cuivre |
| (7) passage électrique haute tension | (8) fenêtre de Brewster |

Le générateur d'impulsions utilise un thyatron CX 1535 selon un montage classique (fig.3). L'alimentation continue peut fournir 15 kV sous 1 A. En faisant varier les valeurs de C et L_1 , on peut travailler à des fréquences comprises entre 5 et 10 kHz. La diode D_1 sert à bloquer la surtension née entre la self et les condensateurs, la diode

D_2 et la résistance de 600Ω protègent le thyatron des impulsions inverses.

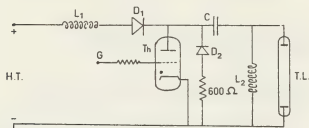


Fig.2- Schéma électrique du montage laser

L_1 : self de charge C : condensateur de charge
 D_1, D_2 : diodes L_2 : self de 0,5 mH
 Th: thyatron CX 1535 T.L.: tube laser

3. **RESULTATS.** En fonctionnement, la fréquence des impulsions est de 5 kHz, la tension continue est de 7,5 kV aux bornes de l'alimentation, ce qui donne une surtension de 15 kV sur les condensateurs. L'énergie consommée par l'alimentation est de $(2,2 \pm 0,2)$ kW.

La durée de l'impulsion électrique est de 2 μ s. Le courant crête est de l'ordre de 700 A pour une largeur à base de 200 ns. L'impulsion laser a une largeur à mi-hauteur de 20 ns. Le système émet sur les deux longueurs d'onde : verte 5105 Å et jaune 5782 Å. On peut rendre prépondérante l'une de ces deux longueurs d'onde : jaune en augmentant la tension de charge des condensateurs, verte en diminuant l'une ou l'autre, ce qui, en définitive, fait varier la température de la vapeur de cuivre.

Dans les premières expériences, nous avons mesuré une énergie par impulsion de 2 à 5 μ J pour des valeurs de la pression d'Argon de 10 à 15 Torr, l'énergie augmentant quand la pression diminue. Cette énergie est inférieure à celle que nous avons obtenue préalablement - 11,5 μ J - avec un laser chauffé à l'aide d'un four.

Nous nous proposons d'optimiser ces conditions de fonctionnement de façon à augmenter la puissance de sortie et améliorer la fiabilité du système.

REFERENCES.

- /1/ S. GARAY, I. SMILANSKI, L.A. LEVIN, G. EREZ
 IEEE J.Quant.Electronics, QE-13, n° 5, 1977, 36
- /2/ A.J. ANDREWS, C.E. WEBB, R.C. TOBIN, R. DENNING
 Opt.Comm., 22, n° 3, 1977, 272
- /3/ W.T. WALTER, N. SOLIMENC, M. PILCH, G. GOULD
 IEEE J.Quant.Electronics, QE-2, 1966, 474
- /4/ B.G. BRICKS, T.W. KARRAS, T.E. BUEZACKI,
 L.S. SPRINGER, R.S. ANDERSEN
 IEEE J.Quant.Electronics, QE-11, 1975, 570

Ce travail a bénéficié de l'aide de la DRET (Contrat 78/1069).

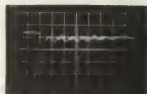


Fig.4- Visualisation de l'impulsion laser.(50ns/c ; 50mV/c)

MEASUREMENT OF THE ELECTRON ENERGY DISTRIBUTION IN A CO₂ LASER PLASMA

S. Bourquard, J.M. Mayor and P. Kocian.

*Laboratory of Applied Physics, Federal Institute of Technology, Lausanne, Switzerland.*Introduction

Much theoretical work has been carried out on CO₂ laser plasmas in order to understand the excitation mechanisms and to optimize the laser efficiency. The electron energy distribution (EED) is obtained by numerical solution of the Boltzmann equation. The different excitation rates are then obtained by a convolution of the calculated EED and the excitation cross sections. /1,2/. Direct measurement of the EED would be difficult in high pressure, high current laser discharges. However we can obtain valuable information if we perform the measurement in a D.C. glow discharge at low pressure. It turns out that the essential parameters, the reduced field E/N , the reduced current density j/N , the ratio of the electronic density to the neutral density are the same as in high pressure discharges.

Experiment

All measurements were conducted in a 2/1/1 He-N₂-CO₂ mix at 0.35 Torr, in a 80 cm long, 65 mm int. diam. Pyrex tube. The axial electric field was measured between two probes 15 cm apart. The plane Langmuir probe is situated between the two probes and is perpendicular to the axis. A thermocouple gives the temperature of the neutral gas. All probes are located 10 mm off the center of the tube. The discharge was stable for currents ranging from 80 to 500 mA. We have noticed six striations between the anode and the cathode. The last striation next to the cathode was clearer indicating decomposition of CO₂ into

CO. The electronic density could be obtained from the Langmuir probe saturation current, the values agreed within 30 % with the integral of the distribution function. This one was determined from the second derivative of the probe current, obtained with the second harmonic. The modulation frequency was 450 Hz.

Results

Two series of experiments were done, one at constant flow, the other one at constant current. The essential data and measurements of the temperature, electronic density and reduced field are reported in Table 1. The EED for each series are depicted in Fig. 1 and 2. We see that varying the current has a relative little effect on the field. On the other hand, the EED is considerably modified. This effect was also observed by Polak et al. /3/ in pure CO₂ at 2 Torr, however the low-energy part of the EED decreased with increasing current while in our case the reverse is observed. We suggest the following hypothesis: at higher current more molecules are decomposed and the resulting products then slow down the electrons. This hypothesis is confirmed when we investigate the effect of the flow for a given current. The concentration of slow electrons increases when the flow is reduced or stopped, whereas the EED becomes wider with an important flow. In the fast flow regime, the effect can still be reinforced by decreasing the current as depicted in Fig. 3.

For these conditions the electronic density is reduced by a factor of 2 and the discharge tends to vanish.

TABLE I.

Experiment No	I	II	III	IV	V	VI
flow rate (cc/min STP)	1	1	1	0	3	5
current, mA	100	150	250	250	250	250
temperature C	42	50	60	62	60	60
$E/N \cdot 10^{-16} V_{cm}^{-2}$	2.0	2.3	2.5	2.4	2.5	2.6
electronic density $\times 10^9 / cc$	2.8	5.0	5.4	4.8	3.1	2.6

Conclusion

Our measurements have shown the non-maxwellian characteristic of the EED with an important concentration of low energy electrons, as predicted by the computations. The current and the flow rate do have an important effect on the measured distributions.

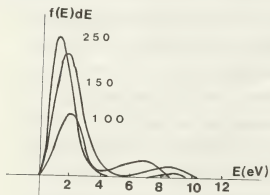


Fig. 1. Measured EED with the current (indicated in mA) as variable parameter. Flow 1 cc/min stp.

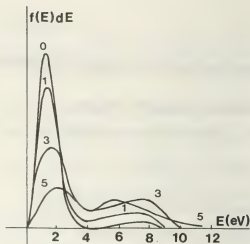
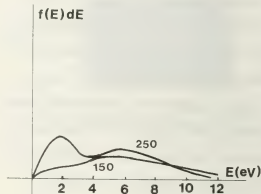


Fig. 2. Measured EED with the flow rate (indicated in cc/min stp) as variable parameter. Current 250 mA.

Fig. 3 (below). Measured EED at high flow (5cc/min) for 250 and 150 mA.



References

- /1/ W.L.Nighan, R.H.Bullis, M.C.Fowler, W.J.Wiegand, A I A A Journal 10,4,1972,407 and references cited therein.
- /2/ C.J.Eliott, O.P. Judd, A.M. Lockett, S.D.Rockwood, Los Alamos Report 5562-MS.
- /3/ L.S.Polak, Y.A. Ivanov, D.I. Slovetskii Khimiya Vysokikh Energii 5,1971,382

OPTICAL HOMOGENEITY AND MOLECULAR GAS HEATING IN A SEMI-SELF-SUSTAINED DISCHARGE

V.A. Burtsev, L.A. Zelenov, A.A. Kondakov, R.F. Kurunov, V.G. Smirnov and V.F. Shansky.

D.V. Efremov Scientific Research Institute of Electrophysical Apparatus, Leningrad, U.S.S.R.

It is known that limiting values of the specific energy removal in CO_2 lasers can be obtained if the active medium is excited up to the moment the generation drops due to gas heating up to the critical temperature. Experimental and theoretical investigation of the main molecular gas heating regularities in a semi-self-sustained discharge and relaxation dynamics when passing from vibrational energy to translational one is presented in the work. Gas temperature was determined by propagation velocity of a weak shock wave, formed due to fast Joule heating in the thin near cathode layer and propagated into the active volume to the anode region [1].

The measurements were made by means of holographic interferometry. The experimental setup to investigate the semi-self-sustained discharge regions by holographic methods is given in fig.1.

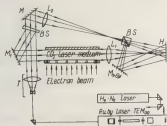


Fig.1.

Single-mode acoustic optic shutter-coherent ruby laser is used as a pulsed coherent radiation source [2-3]. The object beam diameter is 100 mm. To measure shock wave motion velocity the laser operates in a pair pulse mode at the time interval of $(1+20) \cdot 10^{-6}$ s which provides differential holograms, reflecting the state changes of the investigated inhomogeneities between two pulses. To simplify the fringe pattern treatment process at the density field

plotting in the homogeneity the holographic interferograms can be obtained simultaneously both in the bands of equal-inclination fringe and equal-thickness fringe. This was achieved by holographic image coding by means of two reference beams with the different inclination angle relative to the object one.

The active region interferograms (fig.2) and the respective spatial profiles of the neutral gas density for different time moments (fig.3) are given.

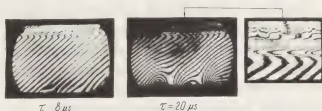
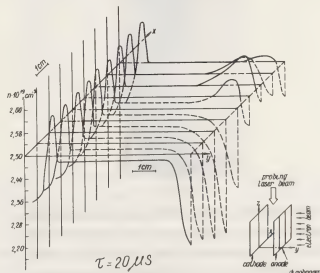
Fig.2. Specific input energy - $W = 0,5 \text{ J/cm}^3$ 

Fig.3.

It is seen that the medium remains optically homogeneous during the pumping pulse $\sim 10^{-5}$ s up to the specific input energy $\sim 1 \text{ J/cm}^3$ excluding narrow $\sim 1 \text{ cm}$

near electrode regions. Time gas temperature dependences ($\text{CO}_2:\text{N}_2:\text{He}$ mixture = 1:2:3) at different energy consumption are given in fig.4.

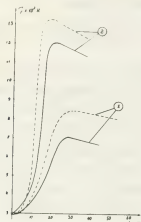


Fig.4. Dot line-calculated:

- 1) $W = 0,7 \text{ J/cm}^3$; $\frac{E}{N} = 1,5 \cdot 10^{-16} \text{ V} \cdot \text{cm}^2$
- 2) $W = 1,3 \text{ J/cm}^3$; $\frac{E}{N} = 2,76 \cdot 10^{-16} \text{ V} \cdot \text{cm}^2$

Special attention in the work is paid to investigation of the processes in the near to electrode regions resulting in passing the volume discharge stage into the contracted one. The typical interferograms of the unstable discharge stage are given in fig.5.

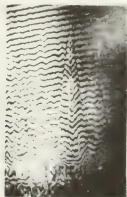


Fig.5.

To determine experimentally the definite instability development mechanism more detailed investigations and the complex gas-discharge plasma diagnostics are required.

References

1. Burtsev V.A., Kondakov A.A., Poponin V.P., Smirnov V.G., Shansky V.F. Zh.T.F., v.48, No.4, p.712.
2. Burtsev V.A., Litunovsky V.N., Smirnov A.G., Smirnov V.G. Preprint K-0291, NIIIEFA, 1976.
3. Burtsev V.A., Zelenov L.A., Kondakov A.A., Smirnov V.G., Shansky V.F. The Proceedings of the 3-d All-Union Conference on Holography. Ul'yanovsk, 1978, p.143.

RELATION BETWEEN THE STRIATION AND THE STIMULATED EMISSION IN A He-Ne LASER

H. Amemiya, T. Dote and S. Kawamoto^{*}.^{*}Institute of Physical and Chemical Research Hiroseawa, Wakoshi, Saitama, Japan.^{*}Saitama University, Saitama, Japan.

1. Introduction

The influence of discharge noise such as the striation on the gas laser performance has been studied.⁽¹⁾⁻⁽⁵⁾ One object of the present work is to reexamine if the striation would have always a damaging effect on the gas laser and to search a lasing domain free from such a wave. Another object is to study the influence of stimulated emission on the striation. We take up a He-Ne gas laser for the purpose of this investigation.

2. Experimental Apparatus

A pyrex laser tube of 4mm ϕ , L=80cm long with Brewster quartz windows was used for laser oscillations at 6328Å and 3.39 μ . As a cavity, concave mirrors with index of reflection $r=0.99$ and 1 near red and the curvature radius $R=2m$ were used for the visible light while a concave mirror with $r=0.90$ near 3 μ and $R=1m$ and an Au flat mirror with $r=1$ were used for the infrared beam. The laser intensity was detected by a photomultiplier or a liquid N₂ cooled Au-Ge semiconductor through a monochromator as a function of the discharge current. An optical fiber was driven by a motor along the laser tube to pick up the side light and obtain an interferometry of the striation. The fluctuation in the discharge was measured by a spectrum analyzer and an autocorrelator.

3. Experimental Results

Fig.1 shows the output intensity of 6328Å and 3.39 μ lasers against the discharge current I_d for some total pressures p (Torr), the pressure ratio of He and Ne being 5:1 and 8:1 respectively. Circles indicate critical currents above which the

striation was observable on the spectrum analyzer. The critical currents shifted to a higher value as p decreased. For 6328Å, the onset of striation coincided with the current giving the maximum intensity of laser output between $p=1.3$ and 1.6 Torr, but deviated from it at lower and higher values of p . In the range of I_d where the laser emission was present, the striation was well regular. With increase of I_d , the 6328Å emission disappeared. Contrary to the visible laser, the output characteristic of 3.39 μ laser showed a more gradual variation with I_d . Even after the striation increased its intensity and became turbulent, the laser oscillation persisted with a slight decreasing tendency with I_d .



Fig.1a



Fig.1b

Fig.2a shows frequency spectra of side light with I_d as a parameter. According as I_d increased, the amplitude of striation increased and the frequency spectrum varied from monochromatic to multimode and then to a broad spectrum. Fourier transformation of the autocorrelation of striation showed a change from a single peak to multiple peaks as I_d was raised. In spite of the side light modulation by the wave, the amplitude modu-

lation of 6328Å and 3.39 μ lasers by the striation was very small, although the low frequency noise like 1/f power spectrum was well observable. Fig.2b shows interferometries of the wave at each value of I_d . It is seen that the spatial coherence of the striation becomes smaller with an increase of I_d .

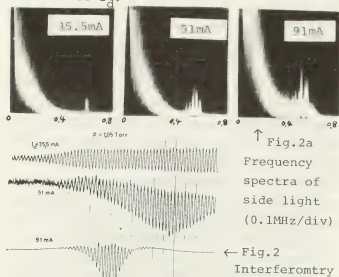


Fig.2a
Frequency
spectra of
side light
(0.1MHz/div)

Fig.2
Interferometry

Fig.3 shows a change of frequency of monochromatic striation with I_d for some total pressures ($p_{He}:p_{Ne} = 5:1$). At a constant p , the frequency of striation decreased while the wave length increased slightly with I_d .

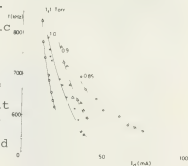


Fig.3

Finally, to investigate the effect of stimulated emission on striation the discharge current was set at a value where both monochromatic striation and 3.39 μ emission were present. When the laser was spoiled by inserting an obstruction in the cavity, a frequency shift Δf occurred in the striation spectrum and occasionally side bands appeared, as shown in Fig.4a. Fig.4b shows the frequency shift Δf vs. laser output I of 3.39 μ at $p=0.92$ Torr. It is seen that Δf has at first a linear dependence on I but then reaches a constant value at a larger I . A chopper was inserted

in the cavity to lock-in detect any variation of I_d associated with 3.39 μ emission but the change was too small to explain Δf by ΔI_d from Fig.3.

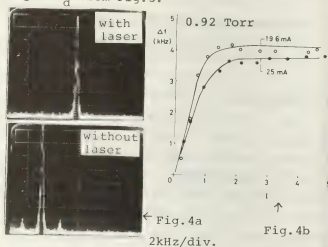


Fig.4a
2kHz/div.

Fig.4b

4. Discussion and Conclusion

One can see from Fig.1 that for 6328Å it is possible to seek a lasing domain free from the striation and any significant output drop, although the situation is less favorable for 3.39 μ . The reason why, while the 1/f power noise appear both in the side light and the laser, the striation appears much less in the latter may be as follows. The laser beam passes alternately through parts with large and small inversions whose wave length is about $l_{cm} (\ll L)$ to cancel the modulation effect. Further, the frequency is higher than the inverse life time of He(2S) and Ne(1s), etc.

On the other hand, the laser causes a frequency shift of the striation, which is not a result of a change of I_d as suggested by Fig.3, but may be due to a change of level densities in the rate equation. Thus a laser tube may become a useful tool for a microscopic study of the discharge.

References

1. A. Garscadden: Appl. Phys. Lett. 8 ('66) 85
2. A. Zeotsev et al: Sov. Phys. (T.P) 14 ('69) 575
3. T. Suzuki: Jap. J. Appl. Phys. 9 ('70) 309
4. Yu. G. Zakharenko: Opt. Spect. 37 ('74) 990
5. L. A. Malenikov et al: ibid. 38 ('75) 791
6. L. N. Guskov et al: ibid. 40 ('76) 170, 39 ('74) 528

COLLISIONAL PROCESSES IN THE He-CO_2 ATOMIC CARBON NUCLEAR PUMPED LASER 1.454 μ

A. Mark Prelas and G.H. Miley.

Nuclear Engineering Program, 214, Nuclear Engineering Laboratory, Urbana, Illinois 61801.

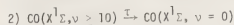
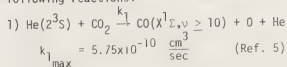
An intensive study of the kinetics of the atomic carbon nuclear pumped laser (NPL) has been undertaken because of the observation of milli-second time delays between the laser output and the neutron (i.e., excitation) input. This NPL represents the best candidate for an energy storage NPL at near atmospheric pressures discovered to date. The atomic carbon NPL on the $\text{C}(3p\ ^1P_1) - \text{C}(3s\ ^1P_1^0)$ transition @ 1.454 μ operates via the dissociation of CO_2 in He-CO_2 mixtures ($50\ T \leq P_{\text{He}} \leq 400\ T + .25\ \text{mT} \leq P_{\text{CO}_2} \leq 25\ \text{mT}$). Excitation of the laser gas is achieved by MeV alpha particles from the $^{10}\text{B}(n,\alpha)^7\text{Li}$ reaction in a thin boron coating on the inner wall of the laser tube.⁽¹⁾ This nuclear reaction is driven by a 12-ms (FWHM) pulse of thermal neutrons obtained from the Univ. of Illinois TRIGA reactor. Delays of up to 5 ms between the peak of the 1.454 μ laser signal and the thermal neutron pulse have been observed.⁽²⁾

The kinetic modeling has been derived from experimental observations involving differences in operation of the laser for various gas mixtures and for electrical excitation. A similar time delay has also been observed for the same carbon transition in Ne-CO and Ne-CO_2 gas mixtures.⁽³⁾ In contrast, in mixtures of He-CO , no significant delay is observed. In the latter case, as shown by Atkinson and Sanders,⁽⁴⁾ a single collision between the $\text{He}(2^3\text{S})$ metastable species and the CO molecule directly populates the upper laser level (ULL). However in He-CO_2 , Ne-CO and Ne-CO_2

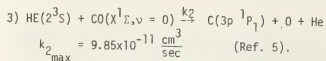
mixtures, no metastable species is sufficiently energetic to populate the upper laser level with a single collision, thereby making multiple collisions necessary.

Another important fact is that only μs delays have been observed in an electrical pumped laser (EPL) using the same mixtures but pulsed electrical discharge techniques. In EPL's, the high electron temperature during the electrical discharge destroys the ULL population in the atomic carbon, restricting lasing to the afterglow.⁽⁴⁾ In contrast, in a nuclear pumped plasma, where the average electron temperature is $\sim 0.04\ \text{eV}$, energy is transferred through the metastable or other long lived states of the buffer gas.⁽¹⁾ Consequently, nuclear pumped plasmas simulate an afterglow throughout the excitation pulse, so that the atomic carbon NPL is able to operate throughout the neutron, i.e., excitation pulse time.

A computer study demonstrates that the delays observed in the NPL experiments can be attributed to a series of slow reactions involving the $\text{He}(2^3\text{S})$ metastable species. Basically, the three step model used for the He-CO_2 NPL involves the following reactions:



$$\tau_{\text{min}} = 208 \pm 30 \mu\text{s} - \text{Torr}(\text{CO}) \quad (\text{Ref. 6})$$



Then, for example, for 100 T He + 2 mT CO₂, a delay of ~ 1 ms is predicted which compares favorably to the experimental observations.

Other mechanisms for populating the ULL have been considered; however, the two most likely, ionization-recombination and cascading to the ULL, have been eliminated based on experimental observation of select lines.⁽⁷⁾

The assumption that the dissociated CO₂ is formed in a higher vibrational state of CO (reaction 2) is essential to the above model. Thus if reaction 1 produced CO($\chi^1\Sigma, v=0$) such that reaction 3 could follow immediately, the predicted delay would be reduced to ~ 300 μs , well below experimentally observed values.

In an EPL excited with a positive column discharge, in mixtures of He-CO₂ ($5 \text{ T} \leq P_{\text{He}} \leq 40 \text{ T} + .25 \text{ mT} \leq P_{\text{CO}_2} \leq 10 \text{ mT}$), at an average power deposition ranging from 250 W/cm³ to 1500 W/cm³, and at repetition rates from 10 Hz to 100 Hz, lasing, ~ 23 μs into the afterglow was observed only after the first pulse. This behavior is attributed to the formation and accumulation of CO which in later pulses undergoes lasing via reaction 3 once the electron temperature falls to a sufficiently low value in the afterglow regime.

For applications where laser output delays on the order of 1 ms are required, such as laser feedback fusion,⁽¹⁾ such a multiple step process may prove valuable. Relatively low pressures and large volumes (possible due to the large transport distance of neutrons) of the buffer species could be used to maximize the energy storage and the delay times.

In conclusion, the long delays ($\leq 5 \text{ ms}$), ob-

served between the peak of the He-CO₂ atomic carbon NPL signal and the thermal neutron pulse, are attributed to a twostep dissociation of CO₂ with an intermediate step involving vibrational relaxation of excited CO. Computer modeling of this process gives results in agreement with experiment and with other observations including the disappearance of the delay in He-CO mixtures and EPLs.

References

- (1) Miley, G. H., "Direct Nuclear Pumped Lasers- Status and Potential Applications," Laser Interactions and Related Plasma Phenomena, H. Schwarz and H. Hora, eds., Plenum Press, N. Y., Vol. 4A, 1977, pp. 181-229.
- (2) Prelas, M. A., Akerman, M. A., Boody, F. P., and Miley, G. H., Appl. Phys. Lett., Vol. 31, Oct. 1977, p. 428.
- (3) Prelas, M. A., Anderson, J. H., Boody, F. P., Nagalingam, S. J. S., and Miley, G. H., "Nuclear Pumping of a Neutral Carbon Laser," Radiation Energy Conversion in Space, K. W. Billman, ed., Vol. 61 of Prog. in Astro. and Aero., AIAA, NY pp. 411-417 (1978).
- (4) Atkinson, J. B., Sanders, J. H., J. Phys. B (Proc. Phys. Soc.) Ser. 2, Vol. 1, p. 1171 (1968). (5) Schmeltekopf, A.
- (5) Schmeltekopf, A. L., Fehsenfeld, F., The Jour. of Chem. Phys., Vol. 53, No. 8, pp. 3173-3177, October 1970.
- (6) Willett, C. A., Introduction to Gas Lasers: Population Inversion Mechanisms, Pergamon Press, Maxwell House, Fairview Park, Elmsford, N.Y., p. 317, (1974).
- (7) Prelas, M. A., Boody, F. P., and Miley, G. H., "Recent Results with the Atomic Carbon Laser @ 1.4539 μ ," 31st Annual Gaseous Electronics Conference, Oct. 1978.

SELF-SUSTAINED ELECTROPHOTOIONIZED DISCHARGE IN COMPRESSED GASES

N.G. Basov, E.P. Glotov, V.A. Danilychev, A.I. Milanich and A.M. Soroka.

P.N. Lebedev Physical Institute, U.S.S.R. Academy of Sciences Leninsky prospect 53, 117924 Moscow, U.S.S.R.

Compressed rare gases (or mixtures of

rare gases and haloids) are the most fitting

active media for powerful lasers. Presently

the radiation power of 2 GW [1/ and 20%

efficiency can be obtained in such lasers

[2/]. Theory predicts the efficiency of 50%

[3/]. But the realization of laser potentia-

lities is impeded by strong absorption [3/

at radiation wavelengths of the existing

lasers and at possible wavelengths of new

laser systems, viz. Ar_2Cl^* , Xe_2Cl^* , Kr_2F^*

etc. The absorption is connected with

1) Ne_2^+ , Ar_2^+ , Kr_2^+ , Xe_2^+ absorption bymolecular ions ($\sigma_{\text{eff}} \approx (2.5) \cdot 10^{-17} \text{ cm}^2/4$),

2) electron photodetachment from negative

ions F^- , Cl^- ($\sigma_{\text{eff}} \approx 10^{-17} - 10^{-18} \text{ cm}^2$),

3) photoionization of low metastable le-

vels of rare gases Ar^* , Ne^* , Kr^* , Xe^* ($\sigma_{\text{eff}} \approx 10^{-17} \text{ cm}^2/5$), etc. Note that process

3) results not only in vanishing of in-

duced radiation photon (unfavourable pro-

cess for laser generation) but also in the

production of a new ion and an electron

(additional ionization), which may produce

additional photons (favourable process

for laser generation). The laser exciting

discharge may burn without the sources of

external ionization and without indepen-

dent ionization of the active medium by

electrons under the following threshold

conditions:

$$[K_1 \left(\frac{\nu_e}{\nu_e} - 1 \right) + K_2] \left(1 + \nu_e / c \sigma_{\text{eff}} X^* \right)^{-1} = 1 \quad (1)$$

Here $\frac{\nu_e}{\nu_e} - 1$ is the number of particles X^*

which excite the electron during its life-

time; K_1 , the probability of producing thelaser quantum by excited particle; K_2 ,

the probability of the photon occurrence at

electron destruction; $c \sigma_{\text{eff}} X^*$, the frequencyof X particles photoionization (c is thespeed of light; σ_{eff} , photoionization crosssection); ν_e , the speed of quantum loss in

all channels except photoionization (if

photoabsorption by all particles is insign-

ificant (excluding X^* particles), then $\nu_e = c \sigma_{\text{eff}} (4/\tau_{\text{eff}}) 2L$, where L is the length ofthe active region; τ_1, τ_2 are the reflectioncoefficients of mirrors). Value $\left(1 + \nu_e / c \sigma_{\text{eff}} X^* \right)^{-1}$

is the photoionization efficiency. The va-

lue in square brackets is equal to the num-

ber of quanta excited by electrons during

lifetime. The intensity ν_e of the excita-tion of the active particles X^* by elect-rons is a strong function of E/P parameter(E is the field intensity of the discharge, P is the pressure). As follows from Eq.(1) there exists a threshold value of E/P

starting from which there occurs burning

of EPI-discharge. It should be noted that

there exists the possibility of burning of

the self-sustained discharge in all mix-

tures where the laser quantum energy is

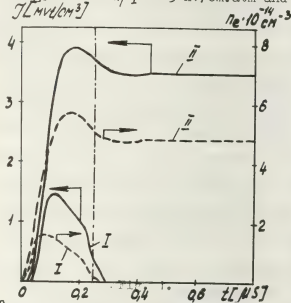
sufficient for photoionization of the excited X^* states. Technical feasibility of such a discharge requires that E/P threshold value should not exceed the field intensity which corresponds to the breakdown of the discharge gap.

The most favourable conditions for the EPI-discharge burning are realized in three-component mixtures containing rare gases and haloid molecules, where the laser quantum energy is sufficient to photoionize the low metastable levels of the rare gas R, and is not enough to photoionize the buffer gas A.

The present paper demonstrates the technical feasibility of an EPI laser pumping in $\text{Ar:Xe:CCl}_4=1500:50:1$ mixture and $P = 2$ atm. Threshold value of E/P for the EPI-discharge burning does not exceed (in this mixture) E/P values for the designed laser based on electron transitions in excimer XeCl^* molecule /6/. The laser radiation quanta of this molecule ($\lambda = 308$ nm) may ionize the low metastable energy levels of Xe^* . The following discharge geometry has been calculated: $L=50$ cm, $h(4/15)=1$, the space between electrodes $l=2$ cm; discharge volume, $V=200\text{ cm}^3$. The Kirchhoff equation has been taken into account. The power of external ionization source q_e was equivalent to an electron beam with energy $\mathcal{E}_e=150$ keV, and maximum current density $j_e \approx 6$ A/cm² (the beam has a triangular form; the rise time is 30 ns, the decay time, 220 ns). The main processes that affect kinetics of the laser mixture generation, and which have been taken into account in our calculations, are de-

tailed in /6/.

If $U/\varphi = 1.5$ kV/cm.atm (U is the applied voltage) and the ballast resistance $R = 0.1$ Ohm, then the electrons and the laser radiation disappear after cessation of the external ionization (see curves I in Fig. 1). If $U/\varphi = 3$ kV/cm.atm and $[I_{\text{MV/CM}^2}]$



$R = 0.5$ Ohm then the discharge current and the light flux density inside the resonator are available after cessation of ionization (curves II in Fig. 1). Moreover, they have the stationary values, which remain unchanged over the calculated time. Here the specific power injected into the EPI-discharge is 300 kW/cm^3 , and the power fluxes in the resonator are $J_{\text{st}} = 3.6 \text{ W/cm}^2$. Note that the discharge chain impedance determines the steady-state regime. The EPI discharge may burn rather uniformly due to "mixing" of plasma parameters inside the resonator by the radiation. Besides laser pumping, the EPI-discharge may find applications, viz., for modulation of high currents by affecting the Q-factor of the resonator.

References

1. J. Hoffman et al. Appl. Phys. Lett., 28, 1976.
2. R. Bradford, Opt. Commun., 18, 210, 1976.
3. N. Basov et al. Vestnik AN SSSR, 3, 12, 1972.
4. W. Wadt et al. Appl. Phys. Lett., 31, 572, 1977.
5. I. Sobelman. Intr. Theory Atom. Spectra, 1977.
6. N. Basov et al. ZhTF Letts, in print.

APPLICATION OF RF DISCHARGE WITH ROTATING ELECTRIC FIELD FOR EXCITATION OF CO₂-LASER

B.V. Kuteev, A.S. Smirnov and A.P. Zhilinsky.

Kalinin Polytechnical Institute, Radiophysical Department, Leningrad/U.S.S.R.

It's well known, that thermal instability leads to the constriction of glow discharge and restricts the increasing of gas pressure in CO₂-lasers. External ionisation by electron beam is one of the most effective methods of discharge stabilisation [1]. However search of another methods of instability damping is not stopped. In recent theoretical investigations [2,3] it was shown that electric field rotation with frequency exceeding the instability growth rate may lead to the stabilisation of glow discharge. This effect has been experimentally observed in stationary r.f. discharge [4]. In this communication we describe the excitation of CO₂-laser mixtures in pulsed r.f. discharge with linear and circular electric field polarisation.

The discharge takes place in cylindrical glass tube with inner diameter 1.3 cm and length 50 cm. Four electrodes 27 cm in length and 0.7 cm in width were adjusted on external surface along the tube. Electrodes were cut from the brass tube with inner diameter 1.5 cm equal to the glass tube external diameter. R.f. power supply of 1 MEGC frequency from two separate amplifiers was fed to each pair of oppositely placed electrodes.

The output power of each amplifier excited 1 kW. Phase shift between amplifier signals was varied from 0 to 180°. R.f. pulse duration was 5 msec, its period 1.6 sec. Gas mixture of CO₂:N₂:He (1:6:12 by molar concentration) have been investigated. The main discharge parameters were varied in following ranges:

gas pressure	$p=1\pm 250$ Torr
specific power	$W=1\pm 50$ W/cm ³
electric field	$E=10\pm 30$ V/cm Torr
current density	$j=5\pm 60$ mA/cm ²

Gain of test CO₂-laser radiation at $\lambda=10.6\mu$ was measured after single pass of discharge volume. Typical dependance of gain coefficient K versus time t obtained in discharge with circular polarisation of electric field in gas pressure 250 Torr is shown in fig.1. Initial gain increasing is due to set up of discharge parameters. Subsequent gain decrease can be explained by gas heating. Energy input Q has been estimated using time τ equal to positive gain duration and specific power

$$Q = \frac{W \cdot \tau}{\rho}$$

ρ - gas density

In experiments with linear electric field polarisation only one pair of elec-

trodes and one amplifier were used. The dependance of maximum gain coefficient K_{\max} versus gas pressure is shown in fig.2 (curve 1). When p exceeded 100 Torr discharge arced and luminous region occupied $1/3 \div 1/5$ of the tube length. This being the case gain vanished. Discharge was completely uniform when gas pressure was less than 30 Torr. When $30 < p < 100$ Torr streamers 0.1 cm in diameter parallel to discharge current were observed. Their origin is apparently connected with ionisation of metastable molecules [5]. The streamers didn't effect strongly on gain coefficient.

In case of circular electric field polarisation discharge arcing wasn't observed in the whole range of gas pressure. The dependance of gain coefficient versus p is shown in fig.2 (curve 2). Sometimes larger values of K_{\max} have been achieved. Values of W , τ , Q , K_{\max} obtained with a maximum gas pressure are presented in table 1. Energy input Q was approximately equal to 500 j/g. This values are close to the theoretical limit and to the data achieved in electron beam controlled discharge. Theoretical values of K_{\max} were calculated in assumption that 50% of total discharge power is spent to high-lying laser level excitation and gas temperature is equal to 300 °K. For discharge with circular polarisation calculated values of K_{\max} are in a good agreement with the experimentally observed ones. It indicates a high homogeneity and efficiency of power input in rotating field

discharge. Efficiency of linear polarisation discharge is lower. Nevertheless the the K_{\max} values achieved are of practical interest

The results presented indicate that the rotating field discharge can be successfully used for CO₂-laser excitation. This method may be useful for another gas laser excitation both alone and in combination with the external ionisation.

References:

1. E.P.Velikhov, V.D.Pismenny, A.T. Rakhimov. UFN, 122, 419, 1977.
2. G.I.Shapiro. Pisma v ZhTF, 3, 189, 1976
3. A.V.Kuteev, A.S.Smirnov. Pisma v ZhTF 4, 111, 1978.
4. A.P.Zhilinsky et al. ZhTF, 48, 2260, 1978
5. A.P.Napartovitch, A.N.Starostin. Fizika Plasmy, 2, 5, 1976.

Table 1.

Polarisation	W W/cm ³	p Torr	τ ms	Q j/g	K_{\max} %/cm	K_{\max}^{th} %/cm
linear	19	100	2	500	0.35	1.8
circular	50	250	2	500	0.5	0.8

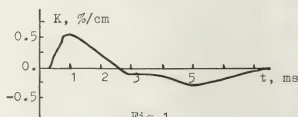


Fig.1

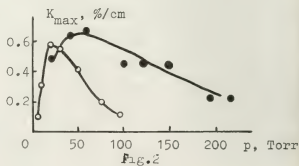


Fig.2

STUDY OF A NITROGEN-NEON NUCLEAR INDUCED PLASMA

D. Auphelle, F. Euve, M. Fitaire, A.M. Pibintu, M. Vialle and L. Wartsky*.

Laboratoire de Physique des Gaz et des Plasmas. Bâtiment 212, Université Paris-Sud, 91405 Orsay Cedex, France.

*Institut d'Electronique Fondamentale. Bâtiment 220, Université Paris-Sud, 91405 Orsay Cedex, France.

The importance of energy-transfer from neon in Ne-N₂ nuclear induced plasmas is well known. Lasing effect was observed in a Ne-N₂ mixture with a very low rate of N₂ impurity, and it was shown that lasing occurs form a Ne-N₂ energy transfer⁽¹⁾. In this communication the role of nitrogen in a stationary neon plasma induced by a 2.3 MeV proton-beam is reported. The proton-beam intensity, I_b, was varied from 0.5 to 3.5 μA. The neon pressure was in the range of 50 to 700 torrs. The nitrogen concentration-rate (10⁻⁴ to 10⁻¹) was measured with a mass-spectrometer. The influence of nitrogen on the densities of the charged particles of the plasma and an evaluation of ion-temperature are reported.

1. Ne-N₂ energy-transfer : Visible plasma spectrum was observed and first negative bands of N₂⁺ were encountered. The most intense band corresponds to a wavelength of 391.4 nm. Due to the low nitrogen concentrations the excitation of B²Σ_u⁺ state of nitrogen cannot be explained by direct proton excitation, but is the result of Ne-N₂ energy transfer. It has been established that the excitation of N₂⁺(B²Σ_u⁺) state in Ne-N₂ mixtures follows from an energy transfer from neon ions⁽²⁾. In our experiment Ne⁺ ions are produced by the proton-beam with a rate S

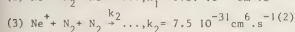
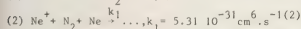
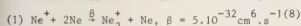
$$S = - (1/W) \cdot (dE/dx) \cdot (j/e)$$

dE/dx : proton energy-loss per unit length

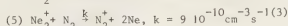
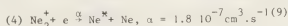
W : average energy required for an electron-ion pair production

j : proton-beam current-density

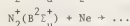
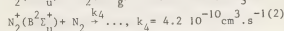
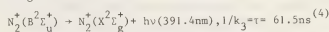
Ne⁺ ions disappear through the following reactions:



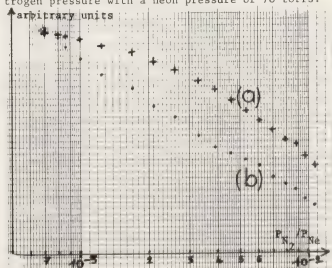
Ne₂⁺ molecular-ions created by reaction (1) disappear through the following reactions :



In the worst conditions for reaction (5) i.e. for maximum value of n_e = 10¹¹ cm⁻³ and minimum value of measured N₂ concentration [N₂] = 2 · 10¹⁶ cm⁻³ the probability of reaction (5) is 10³ higher than the probability of reaction (4). We may conclude that Ne-N₂ energy-transfer process involves Ne₂⁺ ions according to successive reactions (1) then (5). A quantitative study of these reactions taking into account measured densities of the involved species shows that N₂⁺ ions are created with a rate equal to the rate of production of Ne⁺, i.e. S. Furthermore we assume that all N₂⁺ ions are created in B²Σ_u⁺ state. The N₂⁺(B²Σ_u⁺) ion disappears owing to the following reactions :



This simple model agrees with the observed decreasing of 391.4 nm line intensity versus increasing N₂ pressure. This can be shown on figure (1) which gives the variations of 1/(k₃+k₄[N₂]) (a) and the observed 391.4 nm (b) line intensity versus nitrogen pressure with a neon pressure of 70 torrs.



2. Measurements of the $N_2^+(B^2\Sigma_u^+)$ rotational temperature :

The study of 391.4 nm R-branch rotational spectrum allows us to determine the rotational temperature, T_{rot} , of the $(B, v'=0)$ state of $N_2^+(5)$.

The following table gives the results obtained for various neon pressures and two proton-beam intensities.

P_{Ne} (torrs)	T_{rot} (K)	T_{rot} (K)
	$I_b = 2.5 \mu A$	$I_b = 0.75 \mu A$
50	520 ± 34	343 ± 10
100	497 ± 18	440 ± 23
310	528 ± 6	456 ± 11
500	527 ± 16	510 ± 40
600	558 ± 28	512 ± 14
700	516 ± 19	448 ± 20

The highly exothermal behaviour of reaction (5) explains that the N_2^+ ions temperature is much higher than the neutral gas temperature measured elsewhere (6).

3. The influence of N_2 on the electronic density and ionic equilibrium :

On measuring the electronic density, n_e , with a microwave cavity, we noticed that an increasing ratio of N_2 from 10^{-4} to 10^{-1} leads to a decreasing electronic density down to a ratio of 1/3. This ratio is roughly independent on the Ne pressure and of the beam intensity. In the experimental pressure range, the value of n_e arises from an equilibrium between the creation rate S and the recombination rate. If we assume the existence of a dominant ion with a concentration n_i , $n_i = n_e$, and $n_e = \sqrt{S/\alpha}$, where α is the recombination coefficient. At low nitrogen density the dominant ion is N_2^+ , $\alpha = \alpha_0 = 2.10^{-7} \text{ cm}^3 \cdot \text{s}^{-1(9)}$ and $n_e = n_{e0}$. Due to decreasing ratio to 1/3 of electronic density at the high N_2 densities we deduce that N_4^+ is becoming the dominant ion with : $\alpha = \alpha_1 = 2.10^{-6} \text{ cm}^3 \cdot \text{s}^{-1(9)}$. The observed electronic density n_{e1} would be consequently $n_{e1} = \sqrt{S/\alpha_1}$ and therefore $n_{e1}/n_{e0} \approx 1/3$. This agrees with previous studies made in afterglow plasmas, that indicate at least the existence of N_2^+ and N_4^+ ions in mixtures having about the same concentration that we have (7).

Thus we may conclude that even for low nitrogen concentrations the dominant ion is N_2^+ and for higher concentrations, heavier ions (N_4^+) appear.

Acknowledgements :

We would like to acknowledge E. Le Duc for his technical assistance.

This work has been supported by Direction des Recherches, études et techniques (D.R.E.T.) and by Centre National de la Recherche Scientifique.

References :

- (1) R.J. De Young, W.E. Wells, G.H. Miley, J.T. Verdeyen. Appl. Phys. Lett. 28 (1976) 519.
- (2) P. Millet, A. Birot, H. Brunet, J. Galy, J.L. Teyssier. J. Phys. B 10 (1977) 3577.
- (3) D.K. Bohme, N.G. Adams, M. Mosesman, D.B. Dunkin, E.E. Ferguson. J. Chem. Phys. 52 (1970) 5094.
- (4) F. Remy, M.N. Dumont. J. Quant. Spectrosc. Transfer 20 (1978) 217.
- (5) G. Herzberg. Spectra of diatomic molecules. Van Nostrand Reinhold Company New-York 1950.
- (6) D. Auphelle, F. Euvé, M. Fitaire, A.M. Pointu, M. Vialle (to be published).
- (7) W.H. Kasner, M.A. Biondi. Phys. Rev. A 137 (1965) 317.
- (8) A.P. Vitobis, H.J. Oskam. Phys. Rev. A5 (1972) 2618.
- (9) Principles of Laser Plasmas. G. Bekefi - John Wiley - New-York.

V

- Décharge et claquage dans le vide
Discharge and breakdown in vacuum

ELECTRO-OPTICAL MEASUREMENTS OF INSULATOR SURFACE FLASHOVER IN VACUUM*

K. Mikkelsen, M. Kristiansen, and J. Lin[†], J. Thompson[‡].[†]Department Elect. Eng., Texas Technical University, Lubbock, TX 79409 U.S.A.[‡]Department Elect. Eng., University South Carolina, Columbia, SC 29208, U.S.A.

Abstract

Electro-optical measurements of the electric field along insulator surfaces in vacuum during the few nanoseconds prior to insulator flashover have been made. The Pockels and the Kerr effect are used in conjunction with a polarization interferometer to measure the interfacial fields which have a risetime of a few ns. Insulator surface charging and cathode field enhancement occurs, followed by plasma formation near the cathode which propagates toward the anode at approximately one tenth the speed of light. Voltage collapse across the insulator occurs after the plasma formation has reached the anode.

Introduction

Surface charging of the insulator by secondary electron emission is well documented^{1,2,3}. Regions of field intensification near the cathode-vacuum-insulator triple junction causes field emission of electrons. This causes regenerative surface charging and electron multiplication with the resulting electron avalanche proceeding towards the anode.

Electro-Optical Measurements of Electric Fields

For a parallel electrode configuration, shown in Fig. 1, the phase difference $\phi(x,y) = \lambda E(x,y)$ for the Pockels effect in KDP and $\phi(x,y) = \lambda E^2(x,y)$ for the Kerr effect in nitrobenzene, where λ is the path length through the optical, active region (i.e. between the electrodes) and E is the average applied field. The phase shift ϕ is measured using a polarization analyzer (see Fig. 2), which produces a finite fringe interference pattern indicative of the phase difference between e_{11} and e_{12} , which is a function of the electric field.

A slit is positioned at the vacuum-insulator interface and the fringe pattern streaked with an image converter camera. The specific relationships between the fringe motion and interfacial

electric field strength becomes

$E_{IP}(x,t) = \text{const.} \times (\Delta y(x,t)/\delta y)$ for the Pockels effect and $E_{IK}(x,t) = \text{const.} \times [\Delta y(x,t)/\delta y]^{\frac{1}{2}}$ for the Kerr effect, where $\Delta y/\delta y = \phi/2\pi$ with δy being the uniform, or background, fringe spacing and Δy the amount of measured fringe bending⁴.

Experimental arrangement

The experimental arrangement is shown in Fig. 3. The ruby laser is used to probe the test cell and also trigger the FX-15, thereby reducing the timing problems. The only system jitter is that of the FX-15 gap, approximately 2 ns. The operating test cell pressure is 5×10^{-5} Torr.

Results

The excitation pulse to the test cell has a risetime of 2.5 ns, a 5.5 ns top which drops 5%, and a 4 ns fall time. The test cell acts as a capacitive load and charges to twice the pulse voltage.

The streaked fringe shift pattern for the KDP test cell, shown in Fig. 4, are non-uniform, indicating greater, or enhanced, electric field strength near the cathode. The maximum field is reached at the anode .6 ns before the maximum field at the cathode. This is due to continued surface charging after the applied field has peaked. The electric field as a function of anode to cathode distance shows the electric field enhancement for a specific time, (Fig. 5). Flashover occur as the excitation pulse is beginning to fall, making analysis in this area impossible. A nitrobenzene test cell with reduced risetime gave the typical streaked fringe pattern shown in Fig. 6. The previously discussed surface charging effects are again present as the fringes rise to their peaks. Note that the fringes have different slopes after peaking and that they return to the applied field value prior to flashover. The slopes indicate different surface charging rates along the insulator, corresponding to the electron avalanche propagation. The delay

* This work was supported by Sandia Laboratories.

between positive surface charging occurring at the cathode and anode is ~ 1.3 ns giving the avalanche a propagation speed of $\sim 7.7 \times 10^6$ m/s or .025c. After positive surface charging begins near the anode the field at the cathode begins to return to the applied field value at time t_3 . This phenomenon propagates across the fringe pattern in .3 ns. Sufficient energy has been deposited near the cathode to induced gas desorption from the surface³. At time t_3 the gas density reaches a point where ionization by field emitted electrons from the triple junction causes plasma formation. The number of free electrons increases significantly. These electrons cause a rapid increase in the ionization of desorbed gases and also annihilate the positive surface charge adjacent to the plasma by surface recombination. The propagation speed of the plasma formation is 3.3×10^7 m/s or 11c, while the recombination time is ~ 500 ps. After a delay of 1 ns, associated with the highly inductive stage of arc formation, the voltage across the test cell collapses.

References

1. C. H. de Tourreil et al., IEEE Trans. Elec. Insul. EI-8, 17 (1973).
2. J. P. Brainard et al., J. Appl. Phys. 45, 3262 (1974).
3. R. A. Anderson, 1974 Ann. Rep. Conf. Elec. Insul. and Dielectr. Phenom., 436 (1974).
4. J. E. Thompson et al., IEEE Trans. on Inst. and Meas. 25, 1 (1976).

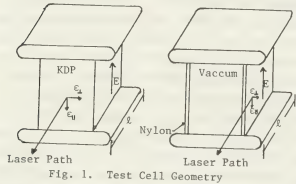


Fig. 1. Test Cell Geometry

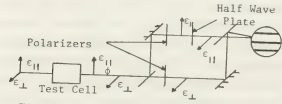


Fig. 2. Polarization Analyzer

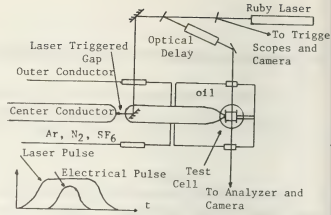


Fig. 3. Experimental Arrangement

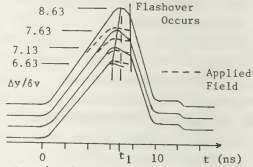


Fig. 4. Fringe Pattern for KDP Test Cell

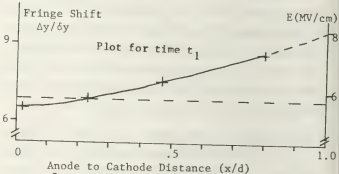


Fig. 5. Electric Field Strength for KDP Cell

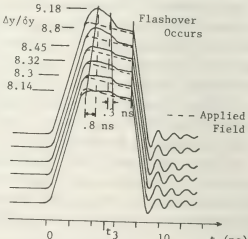


Fig. 6. Fringe Pattern for Nitro-Test Cell

INFLUENCE OF MAGNETIC FIELD ON THE EFFECTS PRECEDING THE TRANSITION OF FIELD EMISSION INTO THE VACUUM BREAKDOWN

G.N. Fursey, V.E. Ptytsin and N.V. Egorov.

The Leningrad Electrotechnical Communication Institute.

Introduction

It is known that when the field emitter is overloaded by its own emission current it explodes thus stimulating the vacuum breakdown /1/. It is also known /2,3/ that just before the explosion the field emission (FE) loses its stability and this pre-explosion state is easily identified by its specific effects: 1. the bright rings appear around the main emission image (Fig.1a); 2. the emission current spontaneously increases in time, the relative increase of current $\Delta = I_{\max}/I_0$ during the interval of the voltage pulse τ is of the order of magnitude $\approx 1.1 \div 1.5$ (Fig.1b), depending on τ and emitter geometry. Up to now these effects have no unique treatment. In the paper submitted an attempt is made to obtain additional information about pre-explosion phase of the matter by placing the emitter in external magnetic field.

Experiment was carried out in modified Müller electron microscopes in vacuum approximately equal to 5×10^{-10} Torr; the value of external magnetic field directed along the emitter axis varied in the limits (0.01÷0.4) T.

Experimental results

It is established that magnetic field influences essentially the pre-breakdown effects. Spontaneous increase of current takes place the presence of magnetic field at lower values of electric field strength. An essentially new result is the fact that Δ may reach values $\approx 5 \div 7$ during the pulse interval τ (Fig.2b, curve 1 and Fig.3a, curve 3).

At certain conditions spontaneous current increase in magnetic field is slowed down and we observed saturation of emission current.

It is established that simultaneously with large increase of current in magnetic field the "ring" effect is observed on the emission picture, the result being presented in Fig.2a. Absence of axial symmetry (that was present when $B=0$), probably, shows that processes of "ring" formation and those of main emission picture are different.

In other experiments we observed effect of "accumulation". It was shown that if the consequent single voltage pulses of constant amplitude are applied to the FE diode (the interval between the pulses being equal to ≈ 10 sec.), the amplitude of the pulses of emission current increases from pulse to pulse (Fig.3a,b). Such current increase leads to explosion of emitter, I_0 being close to the limit current $-I_{\text{lim}}$ for a given emitter. In those cases when $I_{\text{lim}} \gg I_0$, we observed a maximum of current pulse (Fig.2b, curve 1). It is worth noting that the current pulse following that with a maximum always appeared to be rectangular and of essentially smaller amplitude (Fig.2b, curve 1 and 2). It should be mentioned also that "accumulation" effect probably may not be connected with adsorption processes at the surface since the emission picture did not vary during the experiment.

Further measurements were carried out in a constant electric field. In these experiments voltage applied to the F.E. diode was chosen in such a way that

initial current density - j_0 had a value lying in the limits $10^2 \div 10^3$ A/cm². Results of our experiment are presented in Fig.4.

We established that the rate of current increase in magnetic field becomes larger with increase of initial current density. The keeping of emitter in a magnetic field without current does not influence the character of current increase with subsequent switching the electric field. It should be mentioned that decrease of current after switching off the magnetic field is going on essentially slower than the current increase. Rate of current decrease increases with initial density j_0 at $B = \text{const.}$ Slope of current increase and decrease increases with magnetic field.

A state induced by magnetic field is destroyed by heating. Minimal temperature when the induced state is destroyed is equal to $\approx 1000^\circ\text{K}$.

Main Conclusions

1. It is established that magnetic field inertially increases emitting capacity of a field emitting cathode.

2. It is shown that magnetic field essentially influences stability of a field emitter in a pre-breakdown phase and in a process of initiating vacuum breakdown.

References

1. G.N.Fursey, P.N.Vorontzov-Veliaminov. Sov.Phys., JTP, **32**, 10, 1880 (1967)
2. W.P.Dyke, J.K.Trolan. Phys. Rev., **89**, 4 (1953).
3. G.N.Fursey, V.E.Ptytsin, N.V.Egorov. Sov.Phys., Abstracts of the III Conference on High Current Emission Electronics. Tomsk, 1978.

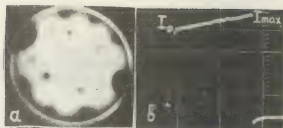


Fig.1 α -emission picture with the "ring"; $B=0$. β - pulse of current: $\tau = 400 \mu\text{sec}$, $B = 0$.

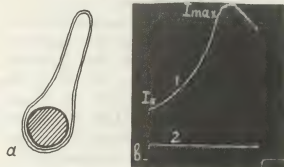


Fig.2 α - deformation of emission picture in the magnetic field at the pre-breakdown phase, $B=0,4\text{T}$; β - pulses of current, $B=0,4\text{T}$, $\tau = 1,0 \text{ msec}$.

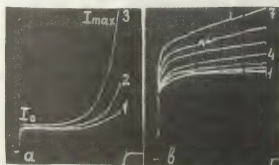


Fig.3 Effect of accumulation in a pre-breakdown phase.

α - $\tau = 500 \mu\text{sec}$, $B=0,4\text{T}$; β - $\tau = 500 \mu\text{sec}$, $B=0,04 \text{ T}$.

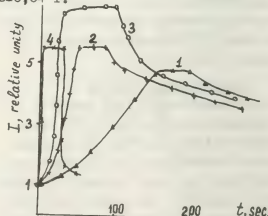


Fig.4 1. $j_0 = 3 \cdot 10^2 \text{ A/cm}^2$; 2, 4. $j_0 = 5 \cdot 10^2 \text{ A/cm}^2$; 3. $j_0 = 10^3 \text{ A/cm}^2$. In the region of current increase and saturation (for curves 1, 2, 3) B is equal to $0,04\text{T}$ and to $0,4\text{T}$ for curve 4. In the region of current decrease $B=0$ for 1-4.

STUDIES OF DISCHARGE PHENOMENA DURING TRANSITION FROM BREAKDOWN IN VACUUM TO BREAKDOWN IN GAS

A.S. Pokrovskaya-Soboleva, T.S. Borisova, G.S. Grishutin and J.N. Nastitch.

All-Union Electrotechnical Institute, Moscow U.S.S.R.

Electric strength of a vacuum gap may be described by a generalized curve of breakdown voltage as pressure $U_{br} = f(p)$ as shown in Fig.1 (curve a,b,c). It is known that the horizontal part of this curve relates to breakdown in a vacuum. The slope of the left branch of the Paschen's curve for the ignition voltage of glow discharge is connected with secondary electron emission processes initiated by positive ions excited atoms, fast neutral atoms and photons γ -processes /1/.

Of specific interest are studies of discharge phenomena in a narrow range of pressures when a transition from vacuum breakdown to glow discharge ignition takes place.

Some investigators /2/ observed maximum, in some cases, doubled electric strength values at these pressures.

Studies were performed with experimental discharge tubes to which square voltage, pulses were applied. A bipolar pulse-forming line with high-voltage hydrogen thyatron as a "switch" was used as a voltage source. Crest voltages up to 100 kV with $2 \cdot 10^{-4}$ s pulse duration were applied to the gap. The phenomena studies could be registered by an oscillograph with high voltage plates, so that the test voltage was applied directly without using a voltage divider. Pulses of fraction of a microsecond duration could be recorded.

When square voltage pulses were applied to a discharge gap of $d=0,5 + 6$ mm at pressures within $10^{-4} + 10^{-2}$ mm Hg diffuse luminescence resembling a glow discharge was observed visually. Along

with this diffuse luminescence spontaneously ruptured spark discharges accompanied by X-ray. Oscillographic records of discharge voltage and current waveforms show that the diffuse luminescence relates to a high voltage glow discharge with a rising current voltage characteristic /3/. The discharge voltage was several tens of kilovolts at currents up to 200 mA. In a high voltage glow discharge the field strength on microprotrusions is sufficient for the formation of spark discharges. They are accompanied by a local release of gases from the electrodes which in turn support the glow discharge. Oscillograms of voltage presented in Fig.2 (a, b,c) confirm that simultaneous existence of two types of discharges is possible.

The authors of /4/ also observed two concurrent types of discharges at $d=20$ mm. One of the discharges was constricted spark accompanied by an abrupt increase of current; the second was a diffused glow type discharge. The quantity of released gases is proportional to the electric charge that had passed through the gap. Thus the passage of a single elementary charge liberates two to three gas atoms. In this work a diffused discharge was observed after several constricted spark discharges appearing upon the application of a sequence of pulses. On the basis of their investigations the authors of /4/ indicated the possibility of an exchange mechanism described by Van-Atta et al. which could explain the phenomena observed. It appears to us however that regenerative sputtering of ions of opposite signs from the cathode and anode would be unlikely.

The comparison of results obtained in this paper and in previous works [1,3,5] as well as the phenomena observed by other workers [2,4] allow to represent a breakdown of a gap by a family of curves $U_{br} = f(p)$ for different gaps, as given in Fig.1.

Formation of spark discharges is a statistical phenomenon. It corresponds to the horizontal part of curve $U_{br} = f(p)$ (portion a-b) where the electric field strength is the dominant parameter. The right part is the Paschen's curve (c_1, c_2, \dots) for the ignition of glow discharge due to γ -processes.

It would be natural to assume the existence of a gradual transition from E to γ -processes in the "transitional region" (part b-c) where two types of discharges may occur simultaneously. Experiments shown that in the "transitional region" of pressures where deviations from the Paschen's curve take place, the passage of current within the discharge gap is influenced by field strength, overall voltage and pressure.

With the increase of interelectrode spacing the deviations from Paschen's law occur at higher voltages and at lower pressures. In this case a maximum of breakdown voltage appears in the "transitional region" of pressures (Fig.1, dotted line).

Thus the following pattern in the "transitional region" of pressures may be assumed. To form a high voltage glow discharge a sufficiently high gas pressure in the discharge gap is necessary. A certain amount of gas or metallic vapour may be released from the electrode due to local heating of microprotrusions by electron current during spark discharges. Subsequent pressure reduction results in the growth of voltage drop across the glow discharge. A positive space charge near the cathode increases accordingly leading to a growth of the field strength. The latter contributes to a spark initiation. A mechanism of two competitive self-

sustained discharge modes in thus suggested

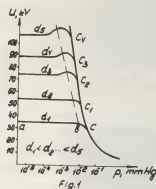


Fig.1



Fig.2

- a - high voltage glow discharge (curve c in Fig.1)
- b - spark discharges (part a-b of the curve in Fig. 1)
- c - glow discharge simultaneous with spark breakdown (part b-c of the Fig. 1)

References

1. Б.Н. Клярфельд, Л.Г. Гусева, А.С. Покровская-Соболева, МТФ, 1966, вып. 4, том 36, 704 стр.
2. Chathan M. Cooke. Second Inter. Symp. on Insulation of high voltages in Vacuum. 1966, 181 p.
3. А.С. Покровская-Соболева, Б.Н. Клярфельд, МТФ, 1957, вып. 5, т.32, 993 стр.
4. W.A. Smith, T.R. Mason, T.L.K. Childs. Discharges and electr.insulation in Vacuum. Proc. of the III-rd Intern. Symp. Paris, 1968
5. Б.Н. Клярфельд, А.С. Покровская-Соболева. Труды конференции по электронной технике. 1970, 2 (18), 101 стр.

DETERMINATION OF THE MICROSCOPIC FIELD ENHANCEMENT FACTOR β OF PRESTRESSED VACUUM INTERRUPTER CONTACTS

K. Fröhlich, W. Widl.

Chair of Switchgear, Technical University of Vienna.

Abstract - The microscopic field enhancement factor β and the field emission area a of variously prestressed vacuum interrupter contacts were investigated using the Fowler Nordheim equation. Additionally the corresponding breakdown voltage values were considered. Statistically evaluated results are shown and discussed.

INTRODUCTION

The contact surface microstructure of a vacuum interrupter is strongly affected by the type of the preceding switching operation. This causes a badly defined dielectric withstand strength of the contact gap leading to an unreliable insulating behaviour of open vacuum interrupters.

For this reason an investigation on a statistical basis was started recently in order to learn about the relevant phenomena influencing the breakdown performance of an open vacuum interrupter gap [1]. Variously prestressed contacts were tested by variously shaped voltage curves in all combinations. Beside an insight into the dielectric withstand behaviour of the gap the results also yielded conclusions about the surface microstructure and the initiating breakdown mechanisms.

In addition to this research the microscopic field enhancement factor β and the emission area a were determined after prestressing the contacts by various types of switching operations. The results are presented in this paper and yield more insight into the surface phenomena of a vacuum interrupter under actual conditions.

PROCEDURE

The tests were carried out with

- Rogowski profile shaped copper or tungsten electrodes in an experimental chamber at 10^{-8} torr (electrode diameter 40 mm, gap length 5 mm)
- a commercial vacuum interrupter valve (15.5 kV, 600 A, 12 kA); 5 mm gap length; Cu contacts

- New contacts were conditioned by 100 dc arcs (100 A, 500 ms) in order to produce clean and well defined surfaces. Then the contacts were stressed by series of one of the following switching operations:
- no load close-open operation without arcing (NL)
- no load close-open operation after one conditioning dc arc of 100 A, 100 ms (NLC operation)
- no load closing followed by a 100 A dc opening arc of 100 ms or 1000 ms duration
- no load closing followed by 50 Hz, 5 kA rms interruption (9 ms arc duration)

Fifteen seconds after each switching operation a voltage pulse was applied across the open gap rising with 20 kV/ms or 0.1 kV/ms respectively. The 20 kV/ms pulses were increased until breakdown occurred whereas the maximum voltage of the 0.1 kV/ms pulses was limited by the supply to voltage values below the breakdown voltage.

During the tests the field emission current (FEC) ≥ 100 nA was measured. The corresponding Fowler Nordheim (FN) curve was plotted by a computer

which also calculated and detracted the capacitive gap current. Finally the microscopic field enhancement factor β and the field emission area a were printed out.

RESULTS AND DISCUSSION

1. Determination of β, a after various switching operations - Table 1 shows that the surface of both the valve contacts and the Cu contacts are influenced by the preceding switching operation in the same way. After no load close-open operations preceded by a 100 A dc arc (NLC) the mean values β were highest connected with lowest mean breakdown voltages V_B . (All β - and a values were calculated using the FN equation at an assumed work function of 4.6 eV.)

A 100 A, 100 ms dc arc decreases β causing an increase of V_B . This effect is more significant, if the arc duration is extended to 1 sec. (as shown for Cu contacts). β and V_B values indicated surface smoothening by 5 kA rms interruption arcs. Repeated no load switching (NL) decreased β below the corresponding values for NLC operation. All those tendencies concerning the breakdown voltages agree with [1].

The evaluation of the FEC immediately before breakdown (critical prebreakdown current i_c) shows that i_c depends on both β and a . High β values were connected with low values of both a and i_c .

Merely after 5 kA interruption a and i_c yielded unexpectedly low values indicating that 5 kA arcs produced smaller emission sites than 100 A dc arcs at comparable charge transfer. In some cases those smaller sites were destroyed by the applied voltage causing a step in the FN curve.

contacts	type of switching operation	β	$a/\text{cm}^2 \cdot 10^{-12}$	V_B/kV	I_c/nA	$\rho(\beta, V_B)$	$E_c/10^6 \frac{\text{V}}{\text{cm}}$	test number
Cu 10^{-8} torr	NLC dc arc 100 A, 100 ms	1450	1.1	45.0	1.6	-0.39	1.3	15
	dc arc 100 A, 1 sec.	1200	1.1	57.5	4.1	-0.58	1.4	45
	NLC 5 kA rms interr.	790	4.2	79.3	11.7	-0.76	1.3	15
		885	0.8	85.3	6.7	+0.47	1.5	11
valve	NLC dc arc 100 A, 100 ms	1823	1.2	46.3	21.9	-0.51	1.7	10
	dc arc 100 A, 100 ms	1700	0.7	29.2	13.7	-0.75	1.7	11
	NLC 5 kA rms interr.	1610	1.6	50.1	22.7	-0.84	1.6	9
		1543	0.7	55.5	9.4	-0.52	1.7	20
10^{-8} torr gap length 2 mm	NLC dc arc 100 A, 30 ms	110	30	99	-	-	-	4
		139	22	109	-	-	-	8

Tab. 1

Table 1 also shows a more or less significant correlation between V_B and β manifested by a negative correlation factor $\rho(\beta, V_B)$. After 5 kA interruption, however, $\rho(\beta, V_B)$ was positive for the Cu contacts indicating the superposition of an initiating mechanism which is not governed by the FE phenomenon. In this case the peak value of the arc current was close to the threshold of anode spot formation and increasing the likelihood of particle breakdown [1]. When 5 kA were interrupted by the valve the arc certainly was in a diffuse mode but

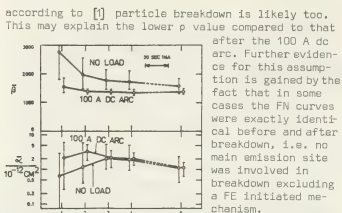


Fig.1: Change of β and α depending on the number of applied voltage pulses without any breakdown.

ent of the β value indicates that breakdown mainly is initiated by FE at a constant mean FE current density \bar{I} .

Comparable measurements with tungsten contacts yielded β values one order of magnitude less than for Cu electrodes. In this case the prebreakdown current curve showed significant microdischarge pulses which caused breakdown before the FEC reached a critical value.

2. Changes of β, α due to the applied voltage - If a series of five consecutive voltage pulses (0.1 kV/ms) were applied in intervals of 4 min. (without any breakdown) β was decreased especially after no load switching (NLC). Fig.1 shows the mean values β and α of six test series across the pulse number. Each pulse was switched off when the FEC increased to 1 mA. The corresponding FN curves started as straight lines at low currents and were bent toward lower current values at higher voltages indicating a general decrease of β during the test.

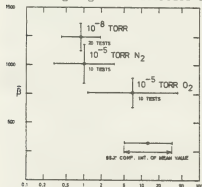


Fig.2: Influence of the residual gas pressure on β and α .

between the 4th and the 5th pulse causing 1 mA FEC yielded no further significant decrease of this saturation value.

This result shows clearly that changes of the isolating performance of a vacuum gap can be caused by the applied voltage even if no breakdown occurs.

3. Influence of pressure on β and α - If the pressure was increased to 10^{-5} torr with O_2 or N_2 the β values decreased and α values increased (Fig.2). This effect was significant if the contacts were prestressed by a 100 A dc arc especially for oxygen. However, after no load operations (NLC) the influence of pressure was negligible.

Due to the specified test procedure not de-

scribed in detail it is evident that the changes of α, β are caused by surface layer growth. The authors suppose that because of this surface layer the work function is increased [2] yielding lower calculated β values at 10^{-5} torr. It is not yet clear why this effect occurs only after arcing and not after no load switching, but it is assumed that the arc increases the surface layer growth in some way.

CONCLUSIONS

Vacuum interrupter Cu contacts show a clear correlation between the breakdown voltage and the microscopic field enhancement factor β . This indicates a mainly field emission governed breakdown mechanism. Nevertheless the probability of a particle breakdown increases after interruption of higher currents even for diffuse arcs.

The surface microstructure and the emission behaviour depends strongly on the prestress of the contacts. Obviously the amount of charge transfer by the arc as well as the number of cathode spots influence the α and β values.

The extremely high β values especially produced by no load switching call in question that the assumed work function of 4.6 eV is representative for interrupter contacts prestressed at actual conditions; particularly as the results for increased residual pressure gave the idea that the work function is influenced by the contact surface layer.

As already assumed in [1], consideration of the critical field emission current yields a rough qualitative insight into the surface microstructure of the interrupter contacts; Especially when switching low currents or performing no load operations.

The breakdown voltage of a vacuum interrupter gap is strongly influenced by the history of the contacts as well as by the applied testing voltage itself. Measurements without considering those factors can yield results which are not representative for the insulating performance the breaker would have under actual conditions [3].

The occurrence of microdischarges for tungsten electrodes not observed for Cu contacts indicates that the results obtained hitherto may not be generally valid for other materials. Further investigation is necessary in order to reveal this matter.

ACKNOWLEDGEMENT

The authors wish to thank Prof. Dr. Werner Rieder (Techn. Univ. Vienna) for the many useful discussions. The investigation was materially sponsored by the Austrian "Forschungsförderungsfonds der Gewerblichen Wirtschaft", by the "Austrian Brown Boveri Comp., Ltd." and "Metallwerk Plansee" (Austria).

REFERENCES

1. K.Fröhlich, On the Steady State Breakdown Voltage of a Vacuum Interrupter, Insul.Vac.VIII (1978) pp. E6-1...E6-14
2. K.Ashok, K.Dimoff, The effect of oxide surface layers on the breakdown voltage in metal-vacuum-metal sandwiches, Journ. of Materials Science 11(1978), pp. 150...163
3. F.Bettigala, U.Baumgärtl, G.Stock, Untersuchung beim Entwickeln und Prüfen der Vakuum-Leistungsschalter 3AF, Siemens Zeitschrift H.12 (1978), pp. 661...665

EXPERIMENTAL STUDY OF ARC CATHODE MICROSPOTS LIFE-TIME BY THE VELOCITY MICROPHOTOGRAPHY

A.A. Pertsev, V.P. Shadov.

Moscow U.S.S.R.

1. Introduction

There are two modes of cathode operation, namely diffusive and contractive in different discharge devices. For the contractive discharge current transfer through the plasma-cathode layer is provided by small cathode spots. The investigation showed (p.e. [1]), that the spots located on the cathode micro-non-informatics, consist of the array of smaller elements cathode micro-spots. The study of the cathode micro-spots development dynamics and their parameters enables one to clear the general questions of near-electrode processes and to solve connected applied problems. The life-time of the cathode microspot is one of the most important parameters. According to some investigations [1,2], the life-time of the cathode microspot ranges from few tenths of microsecond to tens microseconds. In the present work cathode microspot's life-time have been measured in the pulse arc vacuum discharges using tungsten electrodes.

2. Diagnostic technique and the experimental device

The cathode processes of arc were recorded on the photofilm by the electron-optical converter with space-time presentation of image.

The space-time four-dimensional aperture function of the process is $S(x, y, z, t)$, where S is the radionce, that was represented by 16 space two-dimensional functions $S(x, y)$, of which every other one was shifted with regard to the preceding function by $\Delta\tau$ - the exposure time. The microspot life-time can be calculated as $\tau = n \cdot \Delta\tau$ where n is the number of frames contracting a microspot. The reference grid was projected to the image of the studied process for the definition of the microspot spatial position on the cathode [3].

Fig.1 shows the principal configuration of the experimental device. Vacuum system provided the depression $\sim 10^{-6}$ Torr in the chamber (1), in which the experimental model (2) was installed. Electron-optical converter (3) with microphotographic objective (4) was used to record the arc cathode processes. For electric discharge in the experimental model the storage line (5) was used, that was triggered by the initiating device (6) with synchronization circuit (7). The experimental model (Fig.2) includes the

cathode (c) in the form of tungsten wire cut, its diameter being 1 mm; the limiting ceramic washer (w), the anode (a) and the triggering gun (t). The exposure time of the electron-optical converter varied from 0.05 to 0.5 microsecond.

3. Experimental results

Fig.3 shows the copy of the typical arc cathode process photo, the discharge current 100A. The exposure time $\Delta\tau = 0.2$ microsecond the interframe time delay can be considered in significant.

Statistical data has been obtained concerning the microspot life-time and its dynamics in pulse discharges at the cathode temperature of about 300°K.

Fig.4 shows the density distribution diagram of the microspot number via the life-time (the solid line). The picture shows, that the life-time ranges from 0.05 to 2 microsecond at the discharge duration 10 msec.

The most probable life-time is equal to 0.6 microsecond. When cathode temperature increases from 300°K to 1000°K, the distribution diagram changes very slightly, but at higher temperatures the number of microspots with short life-time decreases and the number of ones with long life-time grows (Fig.4, broken line). At temperatures up to 1500°K the microspots cluster to a single macrospot, existing during the hole discharge time.

4. Discussion

One has to note, that the measurements of the life-time were carried out by recording the light radiation duration. The cathode flame formation may be considered as the initial phase of a microspot development. The microspot life-time value, dependent on the current, will exceed the measured magnitude by the time interval needed to the microspot fixation center from the current start to its thermal explosion. According to [4] this interval is of the order of microseconds for a tungsten electrode at the current density $\sim 10^6 \text{ A/cm}^2$.

The microspot life-time measurement accuracy is limited by an electron-optical converter exposure time.

For the present case it is equal to 0.1 microsecond. That's why the accuracy of the most possible life-time measurements is limited to 20% level.

References

1. Кесаев И.Г. Катодные процессы электрической дуги. М., "Наука", 1968.
2. Раховский В.И. Физические основы коммутации электрического тока в вакууме. Москва, "Наука", 1970.
3. Богомолов Ю.А., Голубь В.Н. ТВТ, 1971, 3, 846.
4. Елинсон М.И. РИЭ, 1960, №8, 1318.

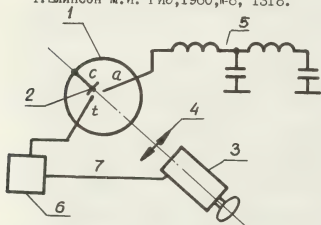


Fig. 1. The experimental unit configuration.

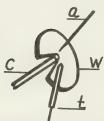


Fig. 2. The experimental model.

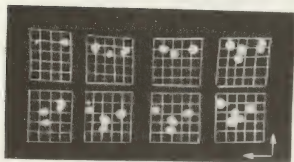


Fig. 3. The cathode microspots photo.

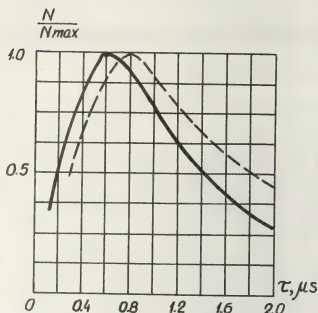


Fig. 4. The microspot distribution on the light - time.

THE EFFECT OF NON-METALLIC INCLUSIONS AND FILMS ON THE CATHODE
ON SOME PROCESSES DURING VACUUM DISCHARGES

D.I. Proskourovsky and V.F. Puchkarev.

The U.S.S.R. Academy of Sciences, Siberian Branch, the High-Current Electronics Institute, Tomsk.

Introduction. Paper [1] described the regularities of the formation of emission centers (e.c.) under the plasma of the cathode spot during the spark and the arc stages of the vacuum discharge. The comparison of experimental results with the conditions in the pre-cathode layer enabled to set the limits of realization of two possible mechanisms of new e.c. formation. The mechanism connected with the microprotrusion explosion as affected by the thermionic-field-emissive current may be realized at a distance of $r \sim 10^{-4}$ cm from the initial emission center. The mechanism connected with the breakdown of non-metallic inclusions and films enables to explain the new e.c. formation at a distance of $r \leq 10^{-2}$ cm. In the case of a spark discharge ($di/dt > 10^8$ A/s) new e.c. can emerge according to the second mechanism at distances of $r = 0.2 \pm 1$ cm at moments of spike on the current traces when the periphery plasma sections turn out to be charged up to a high ($\sim 10^3$ V) potential relative to the cathode. The results obtained in [1] may be used to explain the effects observed during vacuum discharges.

1. The motion of the vacuum arc cathode spot

The experiments with a high temporal and spacial resolution [2] detected the spots of two types: fast moving spots (the 1st type) and slow moving ones (the 2nd type). In our opinion the moving of spots of the 1st type stipulated by the decay of some fragments and by the appearance of others is explained by charging and followed by the breakdown of non-metallic inclusions and films. As it is shown in paper [3] the 1st type spots emerge only on the non-

-conditioned cathode surface. After the cathode being conditioned by the arc discharges the spots turned out to be not mobile inspite of the presence of a great number of micropoints of various dimensions on the cathode. The craters left after the spots of the 2nd type had a relatively large dimensions and a characteristic substructure. The appearance of the substructure points out that new e.c. emerged in the area of initially appeared center [4] i.e. only in this case the field-emission mechanism of e.c. formation is possible. Thus, one can suppose the spots of the 2nd type to be, in fact, the spots of the 1st type grouping in a very small area (a characteristic distance between the fragments is $\sim 10^{-4}$ cm), the consequence of this is the manifestation of additional thermal effects increasing the cathode erosion.

2. A spontaneous emergence of new cathode spots

A spontaneous emergence of new cathode spots ahead of the old ones is known to be observed at the current growth rate higher than 10^8 A/s. A radial extension of the spot front occurs only during the current growth stage, the maximum extension rate being $2 \cdot 10^6$ cm/s. The current growth in the high-voltage ignitron as was stated [5] to be accompanied by appearance of the current spikes and by formation of luminous striations between the electrodes. The formation of striations seem to be identified with the moving of more dense plasma layers from the trigger site on the cathode formed in the consequence of non-uniform cathode material arrival at plasma. The result of this is the formation of breakages in plasma with a

considerable potential drop. Comparing the data of papers [5,6] with the results of paper [1] we may assume the spontaneous emergence of the cathode spots during the spark discharge to occur according to the mechanism associated with the breakdown of non-metallic inclusions and films, and to be stipulated by the charging of the plasma periphery layers ($r > 0.2$ cm) up to a high potential. Naturally, the maximum spot front extension velocity must be determined by the cathode plasma extension velocity, i.e. it is to be equal $2 \cdot 10^6$ cm/s.

3. The cathode erosion during nanosecond vacuum discharges

The investigations of the cathode erosion at explosive emission showed that the more the e.c. on the cathode the less the material removal per one pulse. This fact is proved in [3] by the way of comparison of the surface of Mo wire cathode maintained in ultra-high and oil vacuum during nanosecond discharges. In pure vacuum conditions a small number of e.c. seem to function on the cathode in consequence of which the craters of large sizes emerged. During the cathode operation in oil vacuum the crater sizes were less that resulted in more smooth cathode surface. We also conclude from [3] that the cathode erosion in the oil vacuum is lower than that in the UHV one. We suppose this difference to be caused by the presence of the oil film on the cathode that results in appearance of a great number of e.c.

4. The appearance of double electric layers in "straight discharge" type assembly

It was stated [8], that there is appeared a double charged layer moving from the cathode at voltage applicability to the discharge gap preliminarily filled with plasma ($n \sim 10^{12} \text{ cm}^{-3}$). The reason of the appearance and of the moving of the layer is that the plasma density increases at the cathode up to the value exceeding the plasma density in the gap. However, the pre-cathode plasma formation mechanism wasn't investigated. It is shown in [9]

that the pre-cathode plasma is formed with a crucial charge density $Q = (1-5) \cdot 10^{-6} \text{ C/cm}^2$ on the surface of the dielectric films available on the cathode is created. The authors believe the plasma to be formed due to desorption and of gas ionization on the surface of these films by the electrons tunnelling through the film. In our opinion the pre-cathode plasma formation in the system of occurs due to the breakdown of non-metallic films and inclusions and of the emergence of an effective plasma source - cathode spot. As it is shown in [1], the critical surface charge density resulting in the film breakdown is $(1+5) \cdot 10^{-6} \text{ C/cm}^2$ as well.

REFERENCES

- 1 G.A.Mesyats, D.I.Proskourovsky, V.F.Puchkarev. Proc. VIII Intern. Symp. on Discharges and Electr. Insul. in Vacuum (ISDEIV), Albuquerque, USA 1978, p.C4-1.
- 2 V.I.Rakhovsky. Proc. VII ISDEIV, Novosibirsk, USSR, 1976, p.38.
- 3 I.Achert, B.Altrichter, B.Jüttner et al. Beitrage. Plasmaphys., 17, 6, 419 1977.
- 4 G.A.Mesyats, D.I.Proskourovsky, E.B.Yankelevitch. Proc. VII ISDEIV, Novosibirsk, USSR, 1976, p.230.
- 5 D.B.Cummings. IEEE Trans. Comm. and Electr. 68, 514, 1963.
- 6 A.M.Arsh, V.P.Andronova, Yu.D.Hromoy. Lett. Zh. Tekh. Fiz. 1, 1975, p.86.
- 7 G.P.Bazhenov, E.A.Litvinov, G.A.Mesya et al. Zh. Tekh. Fiz. 43, 1973, p.1262
- 8 E.I.Lutzenko, N.A.Sereda, L.M.Kontzevoy, Zh. Eksp. Teor. Fiz. 67, 1974, p.979; Zh. Tekh. Fiz. 45, 1975, p.789
- 9 V.M.Antonov, L.V.Gevorkjan, A.G.Ponomarenko, Lett. Zh. Tekh. Fiz. 4, 1978, p.995.

EXTINCTION OF A VACUUM ARC BY APPLICATION OF A TRANSVERSE MAGNETIC FIELD

C.W. Kimblin, F.A. Holmes, J.G. Gorman and P.G. Slade.

Westinghouse R&D Center Pittsburgh, Pennsylvania 15235, U.S.A.

INTRODUCTION: It has previously been shown^{1,2} that a rapidly rising magnetic field applied perpendicular to the electrode axis of a diffuse vacuum arc creates a Hall electric field and subsequent anode space charge region. With a capacitance of 50 to 200 μF connected in parallel with the arcing electrodes, and with the arc voltage rising to several kilovolts, the arc current is reduced with possible arc extinction. The present paper* is concerned with experimental observations of forced arc extinction by transverse magnetic fields at current levels to 15 kA.

EXPERIMENTAL OBSERVATION WITH AN ESSENTIALLY

LINEARLY RISING MAGNETIC FIELD: The 14 cm diameter disk shaped electrodes of an experimental vacuum device were separated a distance of 2.5 cm during the current rise of a 60 Hz half cycle. At current rest, a transverse magnetic field with an initial rate of rise of 7400 T/s was applied to the vacuum arc. This field waveform had a sinusoidal rise in 20 μs to a constant value. For current levels > 5 kA, field magnitudes > 0.03 T, and a parallel capacitance of 50 μF , the arc extinguished in less than 20 μs . We explained^{1,2} these observations in terms of the threshold field required to detach the plasma from the anode, space charge formation in the anode region, and consequent current diversion into the parallel circuit. Stefaniak³ has also observed that the arc voltage increases when fields > 0.03 T are applied to low current vacuum arcs. However, Stefaniak primarily attributes the voltage increase to cathode rather than anode sheath phenomena.

We now report that at current levels > 5 kA, and with the above experimental conditions, the arc current only approaches current zero during the

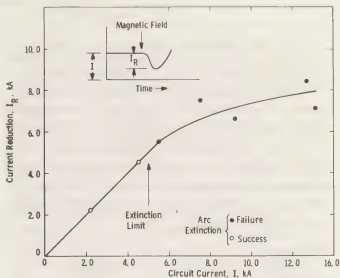


Fig. 1—Measurements of the current reduction with application of a linearly rising magnetic field. (2.5 cm electrode separation, $B = 7400$ T/s, 50 μF parallel capacitance)

first 25 μs of approximately rising field. The arc current then rises even though the field continues to increase. A plot of the current reduction versus initial current magnitude appears in Figure 1. At first we considered that the minimum in the current trace was associated with current collection from the residual plasma, and that the subsequent rise in arc current was associated with cathode spot reignition. However, analysis showed that theoretical residual current magnitudes were too low. Furthermore, there was no observable reignition peak on the voltage trace. We therefore conclude that cathode spots continue to burn throughout the period of field application.

EXPERIMENTAL OBSERVATIONS WITH AN OSCILLATING

MAGNETIC FIELD: The field coil power supply was modified to permit application of an oscillating magnetic field, and a schematic of the overall circuit appears in Figure 2. With a magnetic field frequency of 5 kHz and maximum field change of 7000 T/s, the arc was forced unstable from higher current levels in the range of 10 to 15 kA. The magnetic field, arc voltage, and arc current were recorded with a C.R.O. following field application, and representative traces are shown in Fig. 3. As expected, the arc voltage varies with

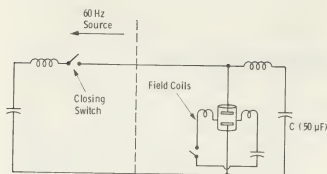


Fig. 2 - Circuit schematic

the absolute magnitude of the magnetic field. Further, it will be noted that the current is forced into oscillation and the arc is extinguished when the current reaches zero with extinction of the last cathode spot. The probability of the arc oscillating to current zero was observed to decrease when the natural frequency f_C of the capacitor circuit was \leq twice the natural frequency of the magnetic field f_B .

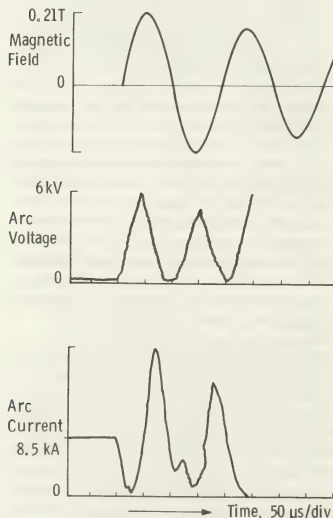


Fig. 3 - Arc extinction with an oscillating magnetic field from an initial current level of 8.5 kA

We are presently unable to calculate the detailed current evolution based on our understanding of the arc interaction with the transverse magnetic field with due consideration of the parallel circuit parameters. When, however, the arc voltage is read from the C.R.O. trace, the current passing through the vacuum arc can be calculated by just considering the local LC circuit.

PARAMETERS AFFECTING ARC EXTINCTION WITH AN

OSCILLATING MAGNETIC FIELD: Within the constraint $f_C \geq 2f_B$, the probability of arc extinction increases with increasing field amplitude and field frequency. This is consistent with previous^{1,2} observations on field magnitude and field rate of rise observed with an essentially linearly rising field. The arc should be in a diffuse mode prior to field application, with no anode spots present, and with the multiple cathode spots distributed over the total electrode surface. The effect of the initial columnar arc⁴ is not yet clear. However, we have observed arc extinctions at current levels of 11 kA when the electrodes were separated at 13 kA and the field was subsequently applied at an electrode spacing of 2 cm within 2.8 ms of electrode part. With respect to electrode spacing, in general the probability of arc extinction increases with electrode gap. A longer gap is associated with a higher dielectric recovery voltage and better arc/field interaction. However, the gap length should not be great enough to promote anode spot formation⁵ prior to magnetic field application.

CONCLUSIONS: Application of a rapidly rising transverse magnetic field to vacuum arcs results in appreciable anode space charge voltages. In the presence of a parallel capacitance and a linearly rising field, the arc current is diverted into the parallel capacitor, and arcs of ≤ 5 kA are extinguished. However, cathode spots continue to burn at higher current levels. When the anode space charge has a periodic nature due to the application of an oscillating magnetic field, the arc current oscillates with a frequency determined by the field and parallel circuit. We then observe arc extinction from initial current levels of up to 15 kA.

REFERENCES

1. P.R. Emtage et al., 13th I.C.P.I.G., p.673, 1977.
2. C.W. Kimblin et al., E.P.R.I. Report EL-393, 1977.
3. K. Stefaniak, 3rd Int. Symp. on Switching Arc Phen., Lodz, pp. 217-221, 1977.
4. J.V.R. Heberlein et al., 5th Int. Conf. on Gas Discharges, pp. 281-284, 1978.
5. C.W. Kimblin, I.E.E.E. Trans. PAS-2, 310, 1974.

FORMATION OF HIGH-CURRENT AND DENSITY ELECTRON BEAM
IN GALLIUM CATHODE WITH THE LIMITED EMISSION SURFACE

G.N. Fursey, V.M. Zhukov, L.A. Shirochin, A.F. Aleksandrov and S.Y. Galuso.

The Leningrad Electrotechnical Communication Institute.

As was shown in papers /1,2/, the explosive emission (EE) of solid and liquid gallium cathodes is characterized by high stability of EE current. The authors of paper /3/ had shown that the use of the point gallium cathodes with the limited emission surface permits to decrease the space charge in a diode and to reveal the emission properties of EE. Use of such cathodes in diodes of microsecond duration with magnetic insulation makes it possible to obtain sharply focused electron beams with a total current about 300A, energy of 150 Kev and the current density measured on the target of about 10^2 A/cm^2 /4/.

It is known /5,6,7/, that in magnetically insulated diodes the potential drop and the influence of the magnetic field of electron beam on the transporting field decrease when the ratio $\mu = \gamma/\gamma_c$ tends to unity, where γ_i and γ_c - internal and external radius of the beam. These are the beams with a weak diamagnetism, i.e. with a small ratio of transversal and the total energies of electrons. In the conventional constructions of diodes the emitting cathode surface is unlimited and the majority of electrons is emitted in the direction which is normal to magnetic force lines. It leads to greater diamagnetism in the beam.

We made the butt-ended cathode of special form (the emitting surface facing the guidance channel). In this case the transversal motion of electrons is possible because of nonuniformity of electric field near the cathode edge [$\gamma_c = (1+4) \cdot 10^{-2} \text{ cm}$] and the influence of high space charge of the beam electrons. The first factor may be diminished by deepening the cathode edge. For the width "a" of cathode ring about 10^{-2} mm , the edge sinking is of the same order of value. The second factor is decreased by limiting the emitting surface of cathode /3/.

As was noticed in /5/, processes in diode influence greatly formation and current transporting of the beam. Nevertheless versatility of processes on the cathodes with unlimited and continuously changing emitting surface makes it difficult to completely solve the problem of beam formation in a whole beam - target gap.

We supposed that in case when the butt-ended cathode with limited emitting surface is used the exact theory developed in /6,7/. may be used to describe the diode part of beam formation too. Estimates made in /6,7/ show that it is sufficient to create the magnetic field $B_i = 8 \text{ kGs}$ to provide the guidance of beam with the external radius $\gamma_c = 0.5 \text{ cm}$, energy $\gamma = 2$ beam current $I_b = 10 \text{ kA}$. It is also shown in /7/, that increase of magnetic field upto $B > B_c$ produce compressing of annular beam which results in reduction of external radius. It may be supposed that the beam which is formed in such a manner has the ratio $\mu \approx 1$ and its diameter is determined by the cathode emitting surface D_c . It makes possible to accord the diode impedance with the drift space of accelerator by varying the cathode geometry. Analysis of experimental data may be carried out basing on the results /8/, which lead to the following formula, supposing the small diamagnetism of the beam:

$$I = \frac{mc^3}{2e} (\gamma^{2/3} - 1)^{1/2} / \left(\frac{a}{2} + 2\gamma_c \gamma_c \right) (1)$$

where γ_c - radius of drift tube; γ - total electron energy; a - ring beam width.

The experimental test of validity of supposition concerning small diamagnetism of beams formed on cathodes with limited emitting surface is the subject of present paper. Fig.1 demonstrates the scheme of high voltage diode, measuring devices and gallium cathode. Total diode current I_0 , drift tube and anode electrodes current I_a , evacuated beam current I_b and accelerating voltage were fixed in experiment. The vacuum was of 10^{-5} Torr . Teflon was used as a cathode insulation. We used the cathode with $D_c = 10; 15; 22 \text{ mm}$ in diameter with the ring cathode thickness $a = 6.2 \text{ mm}$. The cathode was immersed in homogeneous magnetic field $B = 10 \text{ kGs}$. Distance between the emitting edge of cathode and the wall of drift tube was $d_{e-c} = 2 \text{ cm}$. The drift space was equal to 100 mm and its diameter was 26 mm .

Fig.2,3 give the oscillograms of current and voltage and current to voltage characteristics of the evacuated beam for different cathodes. Fig.3 gives the values of current calculated (dashed lines) by formula (1) neglecting the po-

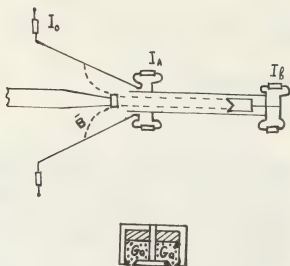


Fig.1 The scheme of high voltage diode and gallium cathode.

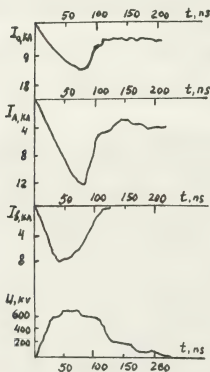


Fig.2. The oscillograms of currents and voltage.

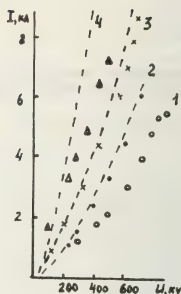


Fig.3 current to voltage characteristics. 1 - steel cathode, 2 - gallium cathode: $D_c = 10$ mm, 3 - $D_c = 15$ mm, 4 - $D_c = 22$ mm

tential drop in the beam. It corresponds to the model of "thin" annular beam, $a = 0$. For comparison, on the same figure we give the data for the steel cylindrical cathode with unlimited emitting surface. The significant difference between the evacuated beam and the calculated beam current for the cathode with $D_c = 22$ mm may be explained by the fact that electron Larmor radius in the transporting field is of the same order of value as the distance between emitting edge of cathode and drift channel wall. This results in the loss of beam in a drift space.

Thus, the use of butt-ended cathodes with limited emitting surface permits produce thin annular beams and to calculate current in diode with magnetic insulation over the whole space of formation and beam transporting by approximate formulae (1).

References

1. G.N.Fursey, V.M.Zhukov. Sov. Phys., JTP, 1974, 44, 1280.
2. I.Yu.Bartashuis, L.I.Franevichuis, G.N.Fursey. Sov. Phys., JTP, 1972, 41, 9, 1943.
3. G.N.Fursey, V.M.Zhukov. Sov. Phys., JTP, 1976, 46, 2.
4. M.S.Aksenov et al. Radiotec. and Electron. Sov. Phys., 1978, 12, 2660.
5. V.S.Voronin, A.N.Lebedev. Sov. Phys., JTP, 1973, 43, 12, 2591.
6. A.V.Agafonov, V.S.Voronin et al. JTP, 1974, 44, 9, 1909.
7. V.S.Voronin et al. Plasma Phys., 1978, 4, 3, 604.
8. L.S.Bogdankevich, A.A.Ruchadze. Uspehi Phys. Nauk, 1971, 103, 609.

VI

- Décharges longues et foudre
Long sparks and lightning

CO₂-LASER PRODUCED CHANNELS FOR GUIDING LONG SPARKS IN AIR

D. Koopman*, J. Greig, R. Pechacek, A. Ali and I. Vitkovitsky, R. Fernsler**.

*Naval Research Laboratory, Washington, D.C. 20375, U.S.A., **JACOR, Alexandria, Va., U.S.A.

*Institute for Physical Science and Technology, University of Maryland, College Park, Maryland 20742 U.S.A.

The ability of laser radiation to influence the paths of electrical discharges in gases has been previously observed^{1,2}. Excitation and ionization were believed to be active when ultraviolet³, visible⁴, or near-infrared radiation¹ from Q-switched lasers was focused to define a preferred discharge path; long duration 10.6 micron radiation in an absorbing atmosphere was noted to achieve guiding by rarefaction⁵. In our studies⁶, pulsed 10.6 micron radiation from a TEA laser has been used to produce channels in ambient air which are capable of guiding discharges nearly orthogonal to the initial E-field, over distances of 1-2 meters, at average field strengths as low as 1 KV/cm, and with average propagation velocities as high as 10^9 cm/sec. The mechanism by which these channels are produced, and the properties of the channels which influence electrical discharge processes, have been the subject of continued investigations.

A 1 KJ, 10.6 micron pulse, with a 100 nsec initial spike containing about 30% of the energy, followed by a 1.5 μ sec tail, is focused by a 3 meter f.l. lens from its original 20 cm diameter to a focal diameter of 2 cm. About 80% of the incident energy is absorbed. The channel appears as a tapered cluster of optical breakdown "beads", extending from ~ 1.2 meters from the lens to ~ 0.1 meters beyond the focal point. Detailed time-resolved diagnostic studies have shown the channel

to be formed by a complex series of events, initiated by laser ionization of aerosol particles. Spherical blast waves from the resultant plasma "beads" combine to form a nearly cylindrical shock surrounding a turbulent, low density, and partially ionized core, which expands to ~ 4 cm diameter at focus. Figure 1 presents schlieren photographs of this process. Holography confirms that the shock is a compression front, and shows the core is a region of below-atmospheric density.

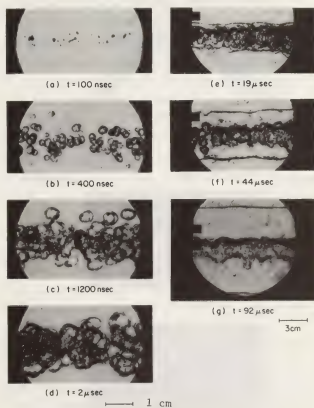


Fig. 1. Schlieren photographs of channel formation vs. time after peak of laser pulse.

Optimum guiding of discharges occurs between 5 and 300 μsec after the pulse. Spectra initially show lines of O II and N II, indicating $T \approx 30,000^\circ\text{K}$. Later a continuum spectrum, believed due to electron-neutral bremsstrahlung from the core, decays with a time constant of $\sim 10 \mu\text{sec}$. Microwave absorption measurements at $\lambda = 4 \text{ mm}$ indicate $n_e \geq 3 \times 10^{13}/\text{cm}^3$ in the core until $t \geq 50 \mu\text{sec}$. Combining the energy absorption, shock dynamics, and core expansion, we compute an average temperature of $\sim 1500^\circ\text{K}$ and near-ambient pressure within the expanded core. After 300 μsec , ambient air turbulently mixes into the core, cooling it to $\sim 500^\circ\text{K}$ by 1 msec. Using the Saha equilibrium relationship for the reaction $e + \text{O}_2 \rightarrow \text{O}_2^-$, we find that these temperatures inhibit negative ion formation, allowing the residual ioniza-

tion to exist as free electrons. In the next few msec, continued mixing drops T below 500°K , and electrons will recombine. It is the free electrons which allow electrical discharges to occur in the "return stroke" mode, explaining guiding and the fast propagation velocity. An example of guiding is shown in Figure 2, where a near -90° turn is achieved by using intersecting laser beams to define the desired spark path. This ability to direct a discharge not only to, but also away from, a designated isolated object is essential for such applications as producing the conductivity and magnetic field configuration needed to propagate relativistic e-beams to pellets in inertial fusion experiments.

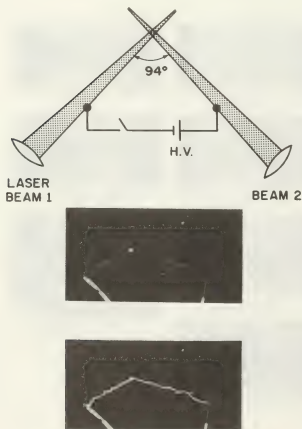


Fig. 2. A guided discharge. Top: experimental set-up; middle: laser-channels; bottom: electrical spark.

1. D. Koopman and K. Saum, J. Appl. Phys. 15 1149 (1973).
2. G. Aleksandrov, et al., Sov. Phys. Tech. Phys. 22, 1233 (1977).
3. A. Akmanov, et al., JETP Lett. 8, 258 (1968).
4. W. Pendleton and A. Guenther, R.S.I. 36, 1546 (1965).
5. K. Saum and D. Koopman, Phys. Fluids 15, 2077 (1972).
6. J. Greig, et al., Phys. Rev. Lett. 41, 174 (1978).

MESURE DE LA VITESSE D'ASCENSION DU "RETURN STROKE" EN FONCTION DE L'INTENSITE POUR DEUX ECLAIRS DECLENCHEES

P. Hubert, G. Mouget^{*}.

CEA-Saclay, Service d'Electronique Physique, B.P. N°2, 91190 Gif-Sur-Yvette.

La vitesse d'ascension de la décharge en retour (return stroke) est une caractéristique importante des coups de foudre. En effet, cette vitesse est reliée aux paramètres physiques du canal (1,2) et sa connaissance est indispensable pour interpréter les signaux électromagnétiques rayonnés à distance (3). Malheureusement, les mesures faites jusqu'à ce jour sont peu nombreuses et révèlent une large dispersion sans qu'il ait été possible d'en déduire une loi de variation en fonction des caractéristiques de l'impulsion de courant (4). Les éclairs déclenchés à St.Privat d'Allier offrent des facilités exceptionnelles pour mesurer cette vitesse dans d'excellentes conditions (5), c'est pourquoi, au cours de l'été 1978 nous avons entrepris cette étude avec une technique qui, à notre connaissance, n'avait encore jamais été utilisée avec succès.

Principe de la mesure

On utilise un appareil photographique où le film est remplacé par un écran opaque percé de deux fentes horizontales. Derrière chaque fente, un récepteur photoélectrique (diode au silicium) donne un signal qui est amplifié par une électronique appropriée. L'appareil installé à 3 km de la station foudre est orienté de telle sorte que les fentes découpent deux tranches qui définissent, à la verticale de la station, une altitude de 304 m et de 566 m au-dessus du sol, respectivement.

La mesure de la vitesse revient à connaître le temps qui sépare le front des impulsions lumineuses détectées derrière chaque fente. Pour cela, les signaux sont enregistrés sur bande magnétique en utilisant deux enregistreurs vidéo modifiés (6) qui présentent une bande passante de 3 M Hz. Comme chaque enregistreur ne possède qu'une seule voie et que la synchronisation

serait difficile on envoie sur un enregistreur le signal provenant d'une fente (fente du bas) et sur l'autre la somme des signaux des deux fentes. Il est ainsi possible de recaler les enregistrements et, par soustraction, d'identifier le signal de la fente du haut. Les photodiodes détectent le passage du précurseur descendant, puis celui du "return-stroke", ce qui donne des repères pour contrôler le sens de la progression.

Propriétés des éclairs étudiés

La mesure a réussi pour deux éclairs (tirs 7813 et 7814) qui correspondent à des déclenchements anormaux, c'est-à-dire que la décharge n'a pas suivi le fil, mais qu'elle s'est déroulée suivant un processus qui a été analysé par ailleurs (7). Cette situation est particulièrement intéressante car on se trouve pratiquement en présence d'un éclair descendant classique. L'éclair 7813 présente, en outre, l'avantage d'être tout de même tombé sur le pylône de mesure, ce qui a permis la mesure directe du courant. Cet éclair a duré 0,52 s avec 8 impulsions supérieures à 5 kA, 32 impulsions supérieures à 1 kA et une composante persistante transportant 96 Cb.

Résultats et conclusion

En ce qui concerne l'éclair 7813, la mesure de la vitesse donne des résultats clairement interprétables pour les 7 premières impulsions qui se sont produites avant l'apparition du courant persistant. Les résultats apparaissent sur la figure 1 sur laquelle on a aussi porté 4 points relatifs à l'éclair 7814, dont 1 point pour la première impulsion et 3 points pour des impulsions apparues à la fin de l'éclair après extinction du courant persistant.

* CEGEDIS - St.Brieuc

On notera que chacun des deux points correspondant à la première impulsion sont assez proches de la courbe théorique de Lundholm et Rusk, cités par K.Berger (réf.1,p.177). Par contre, les points correspondant aux impulsions subséquentes sont très éloignés de la courbe.

Il faut souligner que nos résultats tiennent compte de nombreux éléments d'information parmi lesquels nous citerons particulièrement:

- Mesure du courant par shunt résistif (tir 7813) et aussi par capteur magnétique proche (7813 et 7814).
- Photographies stéréo permettant de reconstituer le canal dans l'espace à 3 dimensions.
- Cinématographie à 700 i/s permettant d'identifier la branche correspondant à chaque amorçage.

Pour l'éclair 7813, les fentes de visée découpent une fraction du canal dont les 9/10 de la longueur appartiennent au tronc commun et qui se poursuit pour 1/10 seulement après l'intersection avec la première fourche. Dans ces conditions, le résultat n'a été que peu modifié par le phénomène de ralentissement au passage de chaque embranchement. Par contre, cette condition n'est pas remplie pour l'éclair 7814, ce qui peut expliquer une vitesse un peu plus lente.

Compte tenu de ces remarques, nous pensons que la différence entre la courbe théorique et les points expérimentaux est réelle.

Bibliographie

1. R.H.Golde, Lightning, Academic Press 1977
2. S.Szpor, Archiwum Elektrotechniki XXVI, p.279, 1977
3. M.A.Uman, D.K.Mc Lain et E.P.Krider, Am.J.Phys. 43, p.33, 1975
4. J.S.Boyle et R.E.Orville, J.Geophys.Res., 81, p.4461, 1976
5. Le Groupe de Recherches de St.Privat d'Allier, Communication à ce congrès
6. P.Hubert et G.Mouget, Rapport CEA-R-4818, 1977
7. R.Fieux et P.Hubert, Nature, 260, p.188, 1976

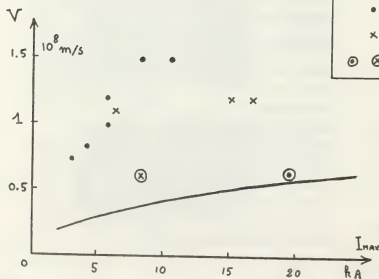


Fig. 1

- courbe théorique $I = 5 \cdot 10^5 \frac{v^2}{1-v^2}$ avec $v = \frac{V}{c}$
- éclair 7813
- x éclair 7814
- ⊗ première décharge des éclairs 7813 et 14

VARIATION OF CORONA INCEPTION AND SPARKOVER WITH POSITIVE IMPULSE VOLTAGE IN A ROD/PLANE GAP : EFFECT OF NEGATIVE SMALL ION VARIATION

N.L. Allen, T.E. Allibone and D. Dring.

Department of Electrical and Electronic Engineering, The University of Leeds, LEEDS LS2 9JT, U.K.

INTRODUCTION

The times to inception of corona and sparkover in a rod/plane gap are affected by the probability of occurrence of creation of a free electron close to the anode (1)-(4). No systematic measurements have been reported in which the sequence of events during individual impulses has been studied at a number of voltage steps between U_w and U_{100} while determining the sparkover characteristics. This paper describes measurements in which radioactive sources have been used to vary the ion density.

EXPERIMENTAL ARRANGEMENTS AND PROCEDURE

The work was carried out using a 2cm dia hemispherically-ended brass rod, 60cm above a 1m dia plane. Impulse voltages (+ 13/2000 μ s) were applied.

Background ion densities were varied by using 1mCi, 14mCi and 100mCi Cs^{137} sources each placed in its lead container level with the plane and 50cm from the axis of the rod/plane gap. A collimated γ -ray beam was pointed upwards parallel to the electrode axis, without impinging upon the electrode surfaces. The small ion densities were sampled 60cm from the axis and were measured with a Gerdien ion counter (5). Corona inception times (T_i) were obtained using a photomultiplier unit.

Sparkover characteristics were determined for each background ion density by applying 20 impulses at any one voltage setting at intervals of 20 sec.

RESULTS

Inception times to the first corona pulse are given in Table 1, and the sparkover characteristics in Fig 1 (a)-(e) were derived from the same set of results. The background negative ion density was measured with no impulses applied, and the following trends are evident:

a) Average inception times, and the earliest inception times of the range, were not signifi-

cantly reduced at constant voltage by increasing the negative ion density up to 1030 cc^{-1} . Using the 100mCi source (5200 cc^{-1}), inception times were approximately those obtained with the source in the rod ($> 80,000 cc^{-1}$).

b) Inception times were only moderately reduced with increasing voltage at constant background ion density. For the two highest densities ($> 5200 cc^{-1}$) T_i was generally reduced.

DISCUSSION

The most important feature of the results is that with the background negative small ion densities within the range 150 cc^{-1} to 1030 cc^{-1} , there was no significant change in either the corona inception time, at a given voltage, or in the sparkover characteristics. Thus, day-to-day variations in the small ion density in the atmosphere, which are well within these limits, will have no effect upon sparkover characteristics. They cannot cause the anomalous results (6) where occasional sparkover characteristics with natural background are similar to that of curve (e), since the natural ion density in this laboratory has never exceeded $\sim 400 cc^{-1}$.

At the higher densities, where the corona inception times (and hence size of corona) were significantly reduced, the slope of the sparkover characteristic increased. The condition for the increase in slope requires a background density of negative ions between 1030 and 5200 cc^{-1} .

Negative Ions and Corona Initiation

It is generally assumed that corona is initiated by electron detachment from a negative ion near the tip of the rod. However, the negative ion density immediately before each impulse would be much lower than the background values quoted here, due to combination with the large excess of positive ions produced by positive corona (5) and

sparks. Since reliable negative ion densities could not be measured during the experiments, an argument adopted earlier (7) was used to estimate their value knowing that the positive ion density before each impulse was ~ 10 times natural background. The value estimated was of the order one-tenth of background. Thus, the presence of the radioactive sources raised the negative ion densities during the experiments, but only when a background of 5200 cc^{-1} existed were they sufficient to change the corona and sparkover characteristics.

Table 1 shows that with the largest background ion densities, the earliest inception times tend towards limiting values and hence, minimum fields. This may be compared to the results of Hutzler (8) and Fieux and Hutzler (3), where a 12 cm gap, having a rod of 2 mm dia., was subjected to enhanced negative ion concentrations from a neighbouring negative corona discharge. The first "pre-onset" corona was reported to be suppressed by the enhanced negative ion concentration, and was replaced by an earlier avalanche which failed to develop a streamer. However, actual ion concentrations in the gap were not estimated.

In the present work, a transition from a streamer to an avalanche could not be observed. However, the tendency towards a limiting corona initiation time and minimum field at $> 80,000\text{ cc}^{-1}$ suggests that avalanches are not significant before this time. Taking a simple expression (1) for the axial field at the tip of the rod, $E = V/2r$, the earliest corona with all three impulse voltages studied occurred at a field of 38 kV cm^{-1} . This may be compared with minimum values of the order 30 kV cm^{-1} for inception reported by the Les

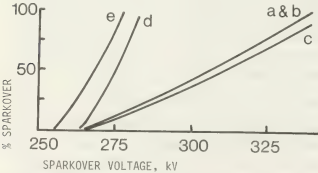


FIG 1 SPARKOVER CHARACTERISTICS

a) 150 ions cc^{-1} (natural), b) 270 ions cc^{-1} (1mCi), c) 1030 ions cc^{-1} (14mCi), d) 5200 ions cc^{-1} (100mCi), e) $> 80,000\text{ ions cc}^{-1}$ (100mCi in rod)

Renardières group (2). Minimum fields for corona inception are the subject of further work in progress in this laboratory.

REFERENCES

1. Waters R T, Jones R E and Bulcock C J; Proc IEE, 1965, 112, pp 1431-1438
2. Les Renardières Group; Electra, 1973, No 23, pp 55-157
3. Fieux R and Hutzler B; Proc Int Symp on High Voltage Technology, Munich 1972 pp 320-325
4. Somerville I C and Tedford D J; Proc 5th Int IEE Conf on Gas Discharges, Liverpool, 1978, pp 250-253
5. Allen N L, Allibone T E and Dring D; Proc IEE, 1977, 124, (2), pp 174-178
6. Allibone T E and Dring D; IEE Colloquium on Protection of Electrical Systems, May 1974
7. Allen N L, Allibone T E and Dring D; Proc 5th Int IEE Conf on Gas Discharges, Liverpool, 1978, pp 92-95
8. Hutzler B; Proc Xth Int Conf on Phenom. in Ionized Gases, Oxford 1971, p 171

Radiation Source	Small Negative Ion Density cc^{-1}	Crest Voltage kV	Inception Times	
			Range μs	Mean μs
A) No irradiation (natural background)	150	269	3.6-9.3	6.1
		284	3.5-7.4	5.6
		301	3.4-6.6	5.3
		317	3.4-8.2	5.3
		337	3.7-7.4	5.6
B) 1m-Curie Cs ¹³⁷ (50 cm from axis)	270	267	3.8-8.6	5.9
		286	3.4-8.0	5.0
		302	3.5-8.1	5.6
		317	3.8-6.7	5.6
		334	4.4-6.8	5.7
C) 14m-Curie Cs ¹³⁷ (50 cm from axis)	1030	270	4.5-8.9	6.4
		284	4.5-8.2	6.4
		301	3.9-7.9	5.7
		316	4.5-8.3	5.9
		336	3.8-7.5	5.8
D) 100m-Curie Cs ¹³⁷ (50 cm from axis)	5200	263	3.4-4.5	3.7
		269	3.4-4.7	3.9
		274	3.3-4.6	3.8
		282	3.1-4.2	3.4
E) 100m-Curie Cs ¹³⁷ (Source in Rod)	>80,000	256	3.2-3.5	3.3
		267	3.1-3.3	3.2
		276	3.0-3.3	3.1

TABLE 1 TIMES TO CORONA INCEPTION

Impulse: 13 μs to crest, 2000 μs decay to half value: 20 shots at each voltage

BREAKDOWN OF SPHERE AND SPHERE/PLANE GAPS STRESSED WITH D.C. VOLTAGE; THE EFFECT OF "CONDITIONING"

T.E. Allibone and J.C. Saunderson.

Electrical Engineering Department, The city University, London, U.K.

Introduction

Very little information has been published on the behaviour of sphere-gaps stressed with D.C. voltages, and none on the behaviour of sphere/plane gaps, and the authors have found no precise guidance as to the treatment which should be accorded to the surface of spheres before using them for voltage measurement.

Bowers and Kuntke (1937) made the first measurements of the sparkover voltages of a 1 m dia sphere-gap stressed with D.C. On negative polarity the sparkover characteristic coincided with Meador's (1934) negative impulse voltage calibration of the 1 m sphere-gap, and on positive polarity it lay some 3% below Meador's positive impulse voltage calibration, both values being lower than the A.C. calibration then quoted in the V.D.E. specification. Bowers et al made the interesting observation that, on positive polarity, sparkover can, infrequently, take place over far greater distances than the normal; e.g. at 800 kV at the 12% greater distance; at 900 kV, 30% greater and at 1000kV, 50% greater than normal.

Udo and Watanabe (1968) calibrated a 0.75 m dia sphere-gap with D.C. and found that results agreed with the present IEC calibration of such a gap under impulse voltages (IEC 52-1960) but made no reference to dispersion of sparkover values.

Colombo, Mosca and Motta (1972) calibrated 0.5 m dia, 1.0 m dia and 3.0 m dia sphere-gaps with D.C.; their calibration for the 1 m spheres lay some 5% below that of Bowers et al on positive D.C. and the standard deviation from the mean of 20 determinations at each gap setting rose to 2.5% for a spacing $S = 0.5D$. They showed that for the 3 m spheres spaced at 0.5 m, after a period > 1 day without use, sparkover began at 90% of the normal S.O.V. and rose to 98% only after some 50 sparks. For the 1 m spheres, likewise spaced at 0.5 m, a small number of "anomalous" sparks occurred at voltages below the mean by various amounts as low as 6 times the standard deviation.

No writers have commented upon the occurrence of the anomalous sparkover voltages significantly above the mean value.

Such anomalous high values were reported by Vibholm and Pedersen (1974) when applying 1.2/50µs impulses of negative polarity to a 0.45 m rod/rod gap, using brass electrodes. When the electrodes were cleaned repeatedly throughout the test, a well

defined Gaussian distribution curve of sparkover was obtained, the $V_{50\%}$ value of which was 17% higher than that obtained after the electrodes had been "conditioned" with 3000 sparks. Copper electrodes behaved similarly, but aluminium and stainless steel electrodes showed an opposite effect (details were not given). One of the present authors (Allibone and Dring 1979) has repeated this work and found a strong effect with brass electrodes stressed with switching impulses of negative polarity. The present authors (Allibone and Saunderson 1979) have found extremely large effects with a variety of rod/rod electrodes of different materials, the gaps being stressed with D.C.

In this paper the behaviour of sphere/sphere and sphere/plane gaps has been studied, the surfaces of the latter having been cleaned or, alternatively, 'conditioned'.

Apparatus

The D.C. generator is of the Cockcroft-Walton type with 7 stages of voltage multiplication and it has an output capacitance of 0.005 µF at 10^6 volts. It is connected to the sphere-gap and sphere/plane gap through a non-inductive resistance of 10^9 ohms. The whole is corona-free except for the gap under test. For voltage measurement a 10^9 ohm resistance potentiometer bridges the whole generator.

Voltage calibration

The D.C. generator was calibrated up to 300 kV against an electrostatic voltmeter (Waterton 1976) accurate to $\pm 0.25\%$; this in turn agreed to within 0.25% with the voltage recorded by the resistance voltmeter and with the 0.75 m sphere-gap at 300 kV. Calibration by this voltmeter up to 700 kV agreed with BSS 137 on both polarities to within 1.5% on negative and 3% on positive polarity.

Results

(1) Sphere-gap breakdown. Fig. 1 illustrates a difficulty encountered in the measurement of D.C. voltages. The 0.75 m spheres had been cleaned as normally recommended and, spaced at 0.3 m, were used to calibrate the set first on negative and then on positive polarity. Sparkover first occurred some 16 times at voltages below the value of - 660 kV, the BSS figure corrected for air density on the day of the test. Even after reaching - 660 kV there were several abnormally low

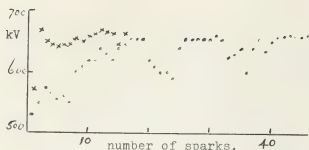


Fig 1. Sequence of sparkover voltages of a 0.5m gap between spheres of 0.75m dia.
..... Negative polarity, xxxxx positive.

breakdowns. On positive polarity there were some sparks at 5% below the anticipated value but in general at all gap spacings there were few low values, a result different from that quoted by Bowers et al.

(2) Sphere/plane breakdown. Spheres of 0.125 m, 0.25 m, and 0.5 m diameter have been used; first they were cleaned by the accepted methods and then, after test, they were extremely thoroughly cleaned with a nylon pad of the kind used in the home (e.g. a brand named Scotbrite).

The behaviour of the 0.25 m sphere/plane gap is shown in Fig. 2. The sparkover voltages on the two polarities lie between those of a rod/plane gap measured in the laboratory: these are shown as the two slanting lines. Very wide scatter was encountered on both polarities: values are shown by the vertical lines. On positive polarity scatter diminished as the gap increased to 1.5 m but on negative polarity it remained high up to 700 kV.

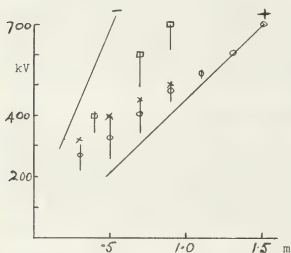


Fig. 2. Sparkover of a 0.25 m sphere/plane total range and mean positive s.o.v., sphere as normally cleaned
x sphere thoroughly cleaned
| range of negative s.o.v., sphere as normally cleaned
□ sphere thoroughly cleaned.

After the thorough scouring with nylon all sparkover values were increased and the scatter rarely exceeded 1%. The withstand voltage increased markedly; a 0.5 m gap with a breakdown ranging from +260 to 370 kV now withstood +390 kV for a one-minute test and continued sparking did not cause the breakdown voltage to fall, - in marked contrast with the behaviour of rod/plane

gaps, though no gap has so far been tested with more than 50 sparks.

It has not been possible to examine the surface to seek a cause for this improved performance but at least it can be said that normal degreasing, then the use of fine emery and then chamois leather is not sufficient to stabilise the sphere/plane sparkover mechanism.

Leader-stroke observations. In the D.C. corona, negative polarity, between sphere and plane at 1 m spacing it is possible to see leader-strokes crossing almost half of the gap from the cathode. In addition, mid-gap streamers branching both ways, as first recorded by one of the authors (Allibone and Meek 1938) can be seen at locations some 30% below the sphere.

References

- Bowers A. and Kuntke A. 1937 "A 3-million volt D.C. Generator". *Zeit. fur Tech. Phys.* **8** 209-219.
- Meador J.R. 1934 "Calibration of the sphere-gap". *Trans. Am. Inst. Elec. Eng.* **53** 942-948.
- Udo T. and Watanabe Y. 1968 "D.C. high-voltage spark-over characteristics of gaps and insulator strings" *IEEE PAS-87* 266-270.
- Colombo A., Mosca W. and Motta G. 1972 "Performance of sphere and rod/rod gaps under high D.C. voltages" *IEEE PAS-91* 501-509.
- Vibholm S. and Pedersen A. 1974 "Factors affecting breakdown voltage distribution for a rod/rod gap in air" *IEE Int. Conf. Gas Disch. London* 434-437.
- Allibone T.E. and Dring D. 1979 "Influence of electrode shape and condition on the humidity correction factor for negative polarity spark-over of rod/plane gaps". 3rd Int. Symp. H-V Engineering Milan (paper 0135).
- Allibone T.E. and Saunderson J.C. 1979 "Sparkover of rod/plane and rod/rod gaps stressed with D.C. voltages: effects of conditioning" 3rd Int. Symp. H.V. Engineering Milan (paper 0225).
- Waterton F.W. 1976 "A 300 kV electrostatic voltmeter" *Journal of Physics E. Scientific Instruments* **9** 647-650.
- Allibone T.E. and Meek J.M. 1938 "Development of the spark discharge" *Proc. Roy. Soc.* **937** 246-268.

PROPAGATION OF THE LEADER OF A LONG SPARK IN AIR WITHOUT PARTICIPATION OF THERMAL IONIZATION PROCESSES

Henryk Ryżko.

Royal Institute of Technology, S-100 44 Stockholm, Sweden.

We consider the initial stage of the leader propagation in a point-to-plane air gap at switching surge voltage (impulse voltage with front duration of some hundreds of micro-seconds). In this stage corona ahead of the leader has not reached the plane electrode so that the current of the gap is still small.

The electronic current of the leader channel is

$$i = \pi \bar{r}^2 q v N_e$$

where r - radius of the channel crosssection, in

q - elementary charge in As
 v - drift velocity of electrons in cm/s
 N_e - average electron density in cm^{-3} .

On the other hand $i = Q v$ where Q - electronic charge of the channel in As/cm.

Hence

$$N_e = \frac{Q}{\pi \bar{r}^2 q} \quad (1)$$

The value of \bar{r} depends mainly on the diffusion of the electrons, on the ionization due to the radial field of the channel and on gas expansion in the channel. As we are not able to take into account all these processes, we consider only the radial diffusion of electrons which drift along the channel axis. In this way the lower limit of \bar{r} will be calculated.

We assume as a first approximation that \bar{r} at the cathode end of the channel equals zero, further that electrons are moving in a uniform field and that a Maxwellian distribution of electron velocities is the case. Then the radius of the channel defined as the average radial displacement of electrons from the channel axis in time t is

$$\bar{r} = \left(\frac{B}{\pi} Dt \right)^{1/2}$$

where D - electron diffusion coefficient.

We substitute $D = \frac{2}{3} \bar{\epsilon} \mu$, $\mu = \frac{v}{E}$ and $t = \frac{\ell}{v}$

where $\bar{\epsilon}$ - mean random energy of electrons in V,
 μ - mobility of electrons in cm^2/Vs
 ℓ - distance of the considered cross-section of the channel from its cathode end, in cm
 E - field gradient in V/cm.

Hence finally

$$\bar{r} = \left(\frac{16}{3\pi} \frac{\bar{\epsilon} \ell}{E} \right)^{1/2} \quad (2)$$

We assume that the gas pressure in the channel is equal to atmospheric pressure (justification - see later). Using data relating $\bar{\epsilon}$ and E values we obtain numerical \bar{r} values presented in Table 1.

Table 1. Radius of the channel cross-section (lower limit), in cm.

$E(\text{kV/cm})$ \ $\ell(\text{cm})$	10	100	300
1	0.13	0.40	0.70
3	0.11	0.36	0.63
6	0.09	0.29	0.53

In order to determine the range of N_e values we assume that Q in equation (1) is equal to the positive charges per unit length of the channel, measured in 2 . The average value of this charge is 10^{-7} As/cm. Inserting this value of Q and \bar{r} values from Table 1 in equation (1) one obtains that N_e is in the range $10^{11} - 10^{13}$ electrons/ cm^3 . The actual \bar{r} values are larger than those of Table 1, because we have taken into account only the diffusion of electrons. If for instance the actual \bar{r} values are three times larger than those in Table 1, the actual density of electrons is $10^{10} - 10^{12}$ electrons/ cm^3 .

Let us now estimate the temperature of the channel under assumption that this density of electrons is produced by the thermal ionization. If the ratio of the electron density to the particle density is low and if the electrons are in thermal equilibrium with gas particles, Saha's equation can be written in the form

$$\left(\frac{N_e}{N} \right)^2 p \approx 2.4 \times 10^{-4} T^{5/2} e^{-\frac{qV_i}{KT}} \quad (3)$$

where N_e - density of electrons in cm^{-3} ,
 N - density of molecules in cm^{-3} ,
 p - gas pressure in torr,
 T - gas temperature in $^{\circ}\text{K}$,
 V_i - ionization potential of the gas in V,
 q - elementary charge in As,
 k - Boltzmann's constant in $\text{Ws}/^{\circ}\text{K}$.

As the ionization potentials of N_2 and O_2 are 15,5 V and 12,2 V respectively, we assume in this approximate calculation $V_i = 14,5$ V. Because the input current of the leader is low, the rate of rise of the channel temperature should be also low. As the channel will expand, its gas pressure cannot differ appreciably from the atmospheric one. Therefore we substitute in (3) $p = 760$ torr. With these numerical value one obtain

$$N_e = 2.7 \times 10^{19} \frac{293}{T} \text{ with units cm}^{-3} \text{ and } ^\circ\text{K}.$$

As it is shown in Fig. 1 the electron densities $10^{10} - 10^{12} \text{ cm}^{-3}$ are reached if channel temperature is around $4000 - 5000^\circ\text{K}$.

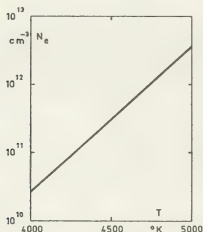


Fig. 1. Density of electrons, produced by thermal ionization in air as a function of air temperature.

We question now if the considered channel can reach these temperatures. Let us therefore compare the input energy to this channel with the loss of energy by radiation. As a degree of ionization in the channel is very low we consider these channel as unionized and consequently radiating as a black body. The loss by radiation per unit length from the channel is

$$P_r = -2\pi r \sigma T^4$$

where σ - Stefan-Boltzmann's constant.

At the temperature 4900°K ($r = 0.36 \text{ cm}$) the power loss is about 7 kW/cm . The corresponding power loss at a temperature of 4400°K ($r = 1 \text{ cm}$) is about 13 kW/cm .

The input power per unit length is

$$P_i = E Q v$$

With numerical values: $Q = 10^{-7} \text{ As/cm}$, $E = 3 \text{ kV/cm}$ and corresponding $v = 25 \times 10^5 \text{ cm/s}$ the input power per unit length is 750 W/cm .

This rough calculation indicates that in the considered conditions the thermal ionization as a source of electrons is ruled out.

Let us estimate the rate of rise of channel temperature when this temperature does not differ considerably from the temperature of the surrounding air. Because under these conditions the loss by radiation and by heat conduction are relatively low, we assume that the whole input energy is converted into heat energy of the channel. If the gas pressure in the channel is unchanged, we write

$$\frac{d\theta}{dt} = \frac{E Q v}{\pi r^2 c_p G}$$

where $\frac{d\theta}{dt}$ - rate of temperature rise of the channel in $^\circ\text{C/s}$,
 c_p - specific heat of air in $\text{Ws/g } ^\circ\text{C}$,
 G - specific weight of air in g/cm^3 .

With numerical values: $Q = 10^{-7} \text{ As/cm}$, $E = 3 \text{ kV/cm}$, $c_p = 1 \text{ Ws/g } ^\circ\text{C}$, $G = 1.3 \times 10^{-3} \text{ g/cm}^3$, one obtains

$$\frac{d\theta}{dt} = 1.4 \times 10^6 \text{ } ^\circ\text{C/s} \text{ and } 1.8 \times 10^5 \text{ } ^\circ\text{C/s} \text{ at } r = 0.36$$

and 1 cm respectively. This rough calculation indicates that even if the whole input power would cause the temperature rise, then the temperature of the channel would be not very much higher than that of the surrounding air, since the involved time intervals are in the range of tens or at most of hundreds of microseconds.

This temperature rise is sufficient to lower gas density in the channel since each new step discharge run initially along the same path.

We believe that in the considered case the leader conductivity undergoes large fluctuations. The elongation of the leader occurs when this conductivity is reduced during the step discharge manifested by a reillumination of the channel.

Conclusion: Mechanism of the long spark in air at positive switching surge voltage differs in a initial stage from that at positive impulse voltage by deficiency of the thermal ionization.

References:

- (1) L.G.H. Huxley, A.A. Zaazou, "Experimental and theoretical studies of the behaviour of slow electrons in air." *Proc. Roy. Soc. A* 196, pp. 402-426, 1949.
- (2) B. Gänger, "Elektrische Festigkeit von Luft-isolierstrecken bei hohem Schaltspannungen." *Bull. SEV*, pp. 227-236, 1971.
- (3) H. Ryžko, "Drift velocity of electrons and ions in dry and humid air and in water vapour." *Proc. Phys. Soc.*, vol. 85, pp. 1283-1295, 1965.
- (4) R.T. Waters, "Streak photography and other studies of the long spark in air." *Proc. Int. Conf. Gas Disch. and Electr. Supp. Ind.*, Leatherhead, London: Butterworth, 1962, pp. 38,53.

LINEAR GLIDING DISCHARGE OVER DIELECTRIC SURFACES

S. Larigaldie.

Office National d'Etudes et de Recherches Aéronautiques, 92320 Chatillon, France.

The analogy between gliding discharges along insulating surfaces and lightning or long gap laboratory discharges is now well known. [1]. In all these cases propagation of the discharge results from the interaction of two different electrical phenomena. A plasma channel of high conductivity, the leader, reduces the potential drop between the originating electrode and the head of the discharge. At this point, the electric field is strongly magnified and a tree-like system of many weakly ionised filaments (streamers or leader coronas) projects electrical charges in advance of the head of the leader. Reciprocally, this feeds electrical current in the leader, maintaining its ionization and conductivity. According to the present evidence, such a system could not be maintained in a stationary fashion in space; charges of one sign in front of the discharge would have the effect of shielding the electric field at the head of the leader and would lead to extinction of the discharge. The advance of the discharge is produced therefore from a sudden transformation of a portion of one of the filaments into a strongly ionized channel. This prolonged track of the leader is accompanied by a reillumination which is particularly clear in the case of the negative leader in normal air ("step leader" of lightning).

This transport phenomenon permits lightning over distances of several kilometers, when the difference of potential between a storm-cloud and the ground is only of the order of 50 megavolts. [2]

In a similar fashion, the gliding discharge along the surface of a thin dielectric disk (thickness of the order of 1 mm) can be propagated over distances greater than one meter under the effect of impulse voltages not exceeding 100 kV.

At the present time, models giving the exact mechanism for the propagation of these types of discharges appear to be incomplete and contradictory. In order to better analyse these phenomena on simple and well-defined experimental bases, an experiment on surface discharge has put set up recently at ONERA with the collaboration of CNRS ESE.

Experimental setup. Figure 1 represents schematically the experimental configuration employed. A moveable metallic comb, 1, at high voltage, is arranged opposite the dielectric slab, 2, at a distance of about 20 cm. On the other face, parallel to the comb, there is a metallic strip, 3, of width 1 cm and length 55 cm. This strip is in contact with the dielectric and is electrically connected to ground. A floating electrode, 4, passes through the dielectric near one end of the strip; this electrode is coupled to the strip via a triggered spark gap, 5. The current in the discharge is measured by a current probe, 6, with very short rise time (10 ns), which is placed around the return conductor between the strip and the triggered gap. The signal received by this probe is displayed on a high speed storage oscilloscope (frequencies up to 100 MHz). A high speed electronic image converter, 7, located in front of the experiment, permits the temporal analysis of the development of the discharge.

The converter shutter opening is actuated, with an adjustable delay, from the same impulse which triggers the spark gap. A time resolved spectroscopic analysis of the light emitted by the discharge is in process of preparation [8]. Also an experimental study of the HF and UHF radiation [9] is included for a correlation with the electromagnetic emissions of lightning.

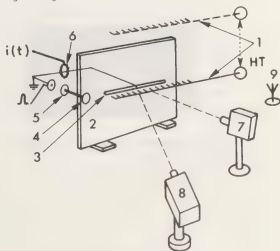


Fig. 1 - Experimental set up.

Mode of operation. Initially, the metallic comb, 1, pointing towards the strip, 3, is connected to a high voltage V (adjustable from 0 to ± 160 kV). Unipolar charging by corona discharges brings the potential of the dielectric surface and of the floating electrode close to the charging potential. The metallic comb is then removed to permit viewing of the dielectric surface by the image converter and spectroscope. As a second step, triggering the spark gap produces an almost instantaneous grounding of terminal, 4. The tangential field which appears on the charged surface induces a strong electric discharge propagating the length of the strip.

First experimental results. 1) - The discharge does not exhibit visible branching, and is guided along the strip; this is a very convenient property if optical diagnostics are to be performed; in contrast it is impossible to predict the path of three dimensional long sparks. 2) - The average current during the propagating phase of the discharge is between 30 and 1 000 A; these values are closer to the currents in lightning leaders (100 to 1000 A) [3] than to those of laboratory sparks (1 A) [4]. 3) - The mean velocity of propagation is of the order of 0.5×10^6 m/s, comparable to those of lightning leaders; the speeds of the leaders in long discharges in the laboratory are smaller by two orders of magnitude. 4) - Figures 2 and 3 represent the streak camera photographs corresponding to negative and positive polarities of the discharge. The appearance of steps (or progressions) in the discharge is visible in the two cases, the steps appear more regular with the negative polarity.

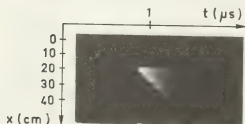


Fig. 2 : Streak camera photograph of negative gliding discharge.

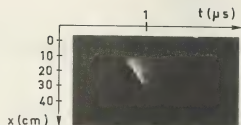


Fig. 3 : Streak camera photograph of positive gliding discharge.

Conclusion. The experimental accessibility of these gliding discharges appears markedly superior to that of other types of self-propagating discharges. This is due in particular to the possibility of rectilinearly guiding this type of discharge. The simultaneous use of several types of time-resolved diagnostics (image converter, spectroscopy, current measurement, HF and UHF emission, etc.) linked with the excellent spatial definition of Lichtenberg figures should lead to an in-depth understanding of the general mechanisms linked to the propagation of these discharges, and thence, by analogy, to a better comprehension of the mechanisms of atmospheric lightning.

Acknowledgements. It is a pleasure to acknowledge the assistance of Dr. Max GOLDMAN for his willingness to collaborate in these experiments and to assure the spectroscopic measurement.

REFERENCES

- [1] - M. TOEPLER - "Über die physikalischen Grundgesetze der in der Isolatorentechnik auftretenden elektrischen Gleiterscheinungen". Archiv für Elektrotechnik 1921.
- [2] - K. BERGER - "The earth flash" in "Lightning" vol. 1 edited by R.M. GOLDE, Academic Press 1977.
- [3] - M.A. UMAN and D.K. Mc LAIN "Radiation field and current of the lightning stepped leader", J. Geophys. Res. Vol. 75, Feb. 20 1970 pp. 1058 - 1066
- [4] - "Les Renardières Group" : "Positive discharges in long air gaps at les Renardières. 1975 Results and conclusion". International Conference on large High Voltage Electric Systems, Paris, 1977.

VII

- Phénomènes de surface
Surface phenomena
- Phénomènes aux électrodes
Electrode phenomena
- Traitements de surface par plasma (dépôt, gravure, oxydation, etc...)
Surface treatment using plasma (deposition, etching, oxidation, etc...)

ON THE FORMATION OF THE THIN SOLID PELLICLE OF NITRIC OXIDES ON THE LIQUID OZONE SURFACE IN THE ATMOSPHERE OF SMOULDERING DISCHARGE IN NITROGEN

S.W. Temko, S.K. Kuzmin^{*}, M.R. Hadgy-Ogly^{**} and T.V. Iagodovskaia^{**}.^{*}Moscow Geological Prospecting Institute (MGPI) Marx Prospect 18, Moscow K-9, U.S.S.R.^{*}Academy of Science U.S.S.R., Moscow^{**}Laboratory of Plasma Chemistry, Faculty of Chemistry, MGU, Moscow, U.S.S.R.

The present report is about processes of nitrogen oxidation in smoldering discharge on the liquid ozone surface by the temperature -196°C. Results of the experiment demonstrate, that thin solid pellicle of N_2O_5 is formed on the liquid ozone surface

Observing the yield of the reaction products we discover two stage of process:

- 1) the immediate contact of smoldering discharge with the liquid ozone surface;
- 2) the diffusion of ozone through the thin solid pellicle of N_2O_5 , which has been formed on the liquid ozone surface and covers this surface. We make experiments in the vacuum discharge installation. The initial ozone and the reaction products condense in the catch, which is been cooled down to the liquid nitrogen temperature -196°C. The construction of the discharge installation allows to realize the immediate contact of the nitric plasma with the surface of the liquid ozone pellicle. These experimental investigations have been made for the first time and are interesting for using of plasma to get new oxidizers. The theoretical explanation the processes of formation the thin solid pellicle of nitric oxides by interaction of dissociated nitrogen with the liquid ozone pellicle has been made by the authors. To do this we utilized the optimization method been developed for closed and open systems [1-6] and proposed the physical model of the process. The thin solid pellicle of nitric oxides is considered as an open limited system, for which dissociated nitrogen and liquid ozone are environment. Interaction between molecules is described by Morse potential in the pellicle [7] and by Lenard-Gones potentials [8] in gas and liquid media. The gas atmosphere consists of atomic and molecular nitrogen and molecular oxygen O_2 , which is educed by the reaction. The interaction with electrons, ions can be disregarded, because degees of ionization are negligible in consequence of low temperature -196°C and comparatively low pressure 0.4-0.6 tor. To write the stoichiometric equations of the chemical reactions the initial combinations, the intermediate and ultimate products of the reactions are to be considered. The initial combinations the intermediate and ultimate products of the reactions are consist of the next components: N, N_2 , O_3 , O_2 , NO, NO_2 , NO_3 , N_2O_5 . We are to discover such the distribution of all the components which satisfies the conditions of "non-hard normalizing" and gives the minimum of the free energy of the thin solid pellicle of nitric oxides.

The conditions of "non-hard normalizing" consist of the stoichiometric equations of the chemical reactions and the condition of balance of getting-in and getting-out nitrogen.

The method of solution. To discover the vector-density of particles we get from the equilibrium conditions the dual integral Fredholm equations of the first kind, which are to be solved jointly with the normalizing conditions for the all three mediums. The integral equations of the first kind take into account the interinfluence between the thin solid pellicle of nitric oxides and its environment. To solve the equations we use Fourier convolution has been done we do expansion in series by the Legendre or Gegenbayer polynomials. At result we get the Gilbert generalized problem [9,10] for the coefficients of the gotten series. The vector-density of particles in the pellicle of nitric oxides and its environment is the solution of the problem. Having known the vector-density of the particles we are discovering the physics values characterizing the state of the solid thin pellicle of nitric oxides, the gas and liquid mediums.

The results. The experimental results [11] include the dependence of yield N_2O_5 from the time of interaction of the nitric plasma with the pellicle of liquid ozone. We have discovered four series of the dependence of yield N_2O_5 for different initial quantities of liquid ozone O_3 (Fig. 1). The analogous dependences for the remainder of non-reacted ozone have been discovered (Fig. 2). The computation gives the picture of the distribution of the densities of the components in the three mediums: the thin solid pellicle of nitric oxides, the gas and liquid mediums.

The conclusions. The experimental investigations demonstrated, that the reaction of oxidation of active nitrogen interacting with the pellicle of liquid ozone by the temperature -196°C and the pressure 0.4-0.6 tor takes place. The ultimate product of oxidation is N_2O_5 . Having been proposed before by the authors [1-6] the statistic theory of limited clusters is applied to describe the processes in open systems. The comparison the experimental and the theoretic results demonstrates its good co-ordination.

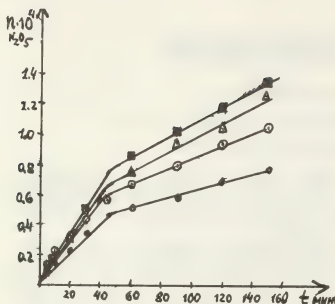


Fig. 1. Yield of N_2O_5 (in moles) as a function of time.

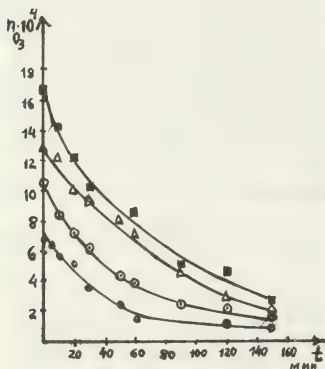


Fig. 2. Remainder of O_3 (in moles) after the reaction as a function of time.

The initial quantities of O_3 (in moles) are:

for the first (O) series $6.7 \cdot 10^{-4}$;
 for the second (◊) series $10.4 \cdot 10^{-4}$;
 for the third (Δ) series $12.9 \cdot 10^{-4}$;
 for the fourth (■) series $16.7 \cdot 10^{-4}$;

References.

- 1) K.W.Temko, S.W.Temko, DAN USSR, 166, 3, 51, 1966 (in Russian)
- 2) S.K.Kuzmin, S.W.Temko, On the stability of Many-Component Systems, JINR, P4-810, Dubna, 1974 (in Russian)
- 3) S.K.Kuzmin, On the Minimization Problem of the Many-Component Potential Theory Coll. "The Modern Problems in the Exact Sciences", Edition UDN, Moscow, 1977, p.17 (in Russian)
- 4) S.W.Temko, On the General Theory of the Stability of Macroscopic Systems, Dep. VINITI, dep. № 978-78, 21 March 1978. (in Russian)
- 5) S.K.Kuzmin, On the Many-Component Potential Theory, Dep.VINITI, dep.№2425-78, 14 July 1978 (in Russian)
- 6) S.W.Temko, S.K.Kuzmin, On the Stability of Limited Open Systems, Dep.VINITI, dep.№23110-78, 26 September 1978 (in Russian)
- 7) G.Hrzberg, The spectra and structures of simple free radicals. An introduction in molecular spectroscopy, Cornell University Press, Ithaca and London, 1971.
- 8) N.N.Bogoliubov, The Problems of the Dynamic Theory in Statistic Physics, Gostechizdat, 1946 (in Russian)
- 9) N.N.Bogoliubov, O.S.Parasiuk, DAN USSR, 109, 4, 1956 (in Russian)
- 10) O.S.Parasiuk, DAN USSR, 110, 6, 1956.
- 11) T.V.Iagodovskaia, M.R.Hadgy-Ogly, L.I. Necrasov, I.I.Volnov, GFH, 52, 1, 101, 1978 (in Russian)

NEGATIVE ION PRODUCTION BY INTERACTION OF A H_2^+ - ION BEAM WITH A SURFACE

P. Massmann, H.J. Hopman and J. Los.

Association EURATOM-FOM, FOM-Instituut voor Atoom- en Moleculafysica, Kruislaan 407, Amsterdam-Wgm., The Netherlands.

Abstract

The present measurements concerning the negative ionization of a H_2^+ -ion beam with energies between 50 and 300 eV impinging on a ThO_2 -surface. We find negative ionization efficiencies between 2 and 7%.

Retardation measurements show that the negative ions are reflected from the surface with an energy of about 0.4 times the incident beam energy. The appearing energy spread suggests that the neutralization of the incident H_2^+ -ions takes place via resonant electron capture into a repulsive state occurring before collision with the surface.

Introduction

An important method to heat thermonuclear plasmas is the injection of high energy atomic hydrogen beams. In the case of beam energies above 200 keV it is generally believed that atomic beams must be produced starting from negative ion sources [1]. One of the two presently favoured lines of development is based on direct extraction of negative hydrogen ions from surface plasma sources (SPS). There is evidence that the alkali admixture in the discharge of the SPS leads to a lowering of the workfunction of the source surfaces and that the negative ions are formed by ionization on the cathode surface.

The high conversion efficiency predicted even for low incident energies [2] and the measured efficiency values of 10% [3] suggest however also another application of the negative surface ionization process. A low workfunction surface may be used as ionizing element in an analyser for charge exchange neutrals emerging from a hydrogen plasma. Such a neutral particle analyser should operate in the low energy range <300 eV where the currently used stripping process becomes inapplicable. A similar idea has recently been proposed by others [4].

For both applications fundamental knowledge of the negative surface ionization process is desirable. In one process described by the ionization model according to Kishinevskii, reviewed in [2], the incident particles are negatively ionized during their reflection from the surface. There is evidence [5] that also sputtering of hydrogen particles adsorbed on the surface could play a role in negative ion production. Crucial for a neutral particle analyser is a good knowledge of the energy distribution of the secondary particles. Since the energy reflection decreases with increasing (normal) incident velocity [6] due to penetration effects one would like to know at which incidence angle an optimum of energy conservation and negative ion formation can be obtained.

The present measurements have been done with ThO_2 as low workfunction surface material. It was chosen because of its easy availability and its durability against air exposure.

Experimental

A positive hydrogen ion beam, consisting of 70% H_2^+ , 10% H_3^+ and 10% H^+ , with energy between 50 and 320 eV and a total current of about 5×10^{-16} A is created

by a modified sputter ion gun. The undesired beam components can be eliminated by means of a Wien filter. The interacting surface is formed by a ThO_2 - Ir ribbon. The surface temperature is 1000 K, the working (hydrogen) pressure 2×10^{-6} Torr. The ribbon is mounted at the center of a turntable allowing for adjustment of the wanted incidence angle θ . If the surface is positioned to normal incidence the primary beam current can be measured by means of a Faraday cup which is placed in front of the ribbon on the same turntable. Coaxially around the turntable different cylindrical shields can be placed with entrance slits of same dimensions in the primary beam line and exit slits of various widths defining the detection angle width $\Delta\theta$ around the angle of specular reflection. The entrance slit is chosen in such a way that for incidence angles $20^\circ < \theta < 65^\circ$ the beam fraction passing the slit is intercepted by the ribbon and for $\theta=0^\circ$ is collected by the Faraday cup. A second cup with two grids for positive V_{R+} and negative V_{R-} bias placed behind the exit slit allows detection and energy analysis of the secondary particles.

With this set up two series of measurements have been done. The first at $\theta=45^\circ$ and $\Delta\theta \approx 90^\circ$, the second at $\theta=62.5^\circ$ and $\Delta\theta \approx 6^\circ$. In the first case the undiscriminated beam has been used to measure the total negative ionization efficiency η_- as a function of incident beam voltage V_b (Fig. 1). Since η_-

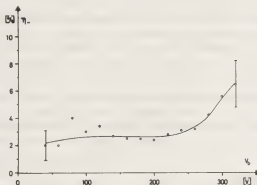


Fig. 1 - Negative ionization efficiency η_- vs incident beam voltage. Conditions: $\theta=45^\circ$; $\Delta\theta=90^\circ$; $V_{R-}=-35$ V; $V_{R+}=320$ V; from the low to the high energy part the errors vary between 55 and 25%.

is defined as the ratio of secondary over primary current the yield per incident nucleon would be about a factor of 2 lower. For these measurements V_{R+} has been applied directly to the second Faraday cup and only one negatively biased grid has been used to suppress secondary electrons. The workfunction $\phi=3.5 \pm 0.5$ eV has been determined from measurements of the thermal emission current versus surface temperature.

In the second case information about the energy distribution of the negative ions has been obtained

for $V_b = 200, 300$ V by applying a retarding voltage $0 \geq V_R \geq -300$ V to the second grid in front of the secondary Faraday cup (Fig. 2). The retardation measurements have been done with a H_2^+ -beam.

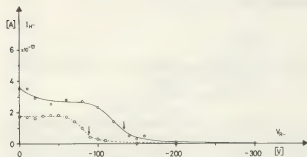


Fig. 2 - Reflected negative ion current vs negative retarding voltage. Conditions: $\square V_b = 200$ V; $\circ V_b = 300$ V, $n_- = 0.06\%$; $\theta = 62.5^\circ$; $\Delta \theta = 6^\circ$; $V_{R+} = V_b$; the arrows indicate the theoretical cut-off value.

Discussion

From Fig. 1 we see that in spite of the relatively high workfunction a negative ion yield of several per cents can be reached with ThO_2 . These values are only about a factor of 2 less than those measured by Schneider et al. [3] with a thick Cs-layer ($\phi = 1.9$ V) who also find an increase of ionization efficiency with incident energy in the considered energy range. Checks with fixed exit slit and varied incidence angle indicate however that the angular spread of the secondary particles must be large. This is the main reason why the efficiency in the case of Fig. 2 appears much lower than in Fig. 1.

Assuming classical collisions between H_2 and the oxygen atom of the ThO_2 an ideal retardation curve would have a sharp cut-off at $V_R = 0.45 V_b$. The appreciable energy spread around this cut-off value is not caused by apparatus effects. This has been confirmed by measurements with directly reflected H_2^+ yielding a spread of less than 10%. It is proposed that resonant neutralization of the H_2^+ into a repulsive state leads to the measured energy spread. In this process the dissociation energy of the molecule is spread over the two H-atoms before collision with the surface. Reflection of the atoms from an ideally flat surface predicts a width for the energy distribution which is in reasonable agreement with the measurements. The flat portion of the retardation curves suggests that no excessive penetration of the incident particles into the surface occurs and that the detected particles are negative ions reflected from the surface.

References

- [1] K.H. Berkner, R.V. Pyle, J.W. Stearns, Nucl. Fusion 15 (1975) 249
- [2] Yu.I. Bel'chenko, G.I. Dimov, V.G. Dudnikov, ICA Translations of Preprint IYaF-77-57, Philadelphia, U.S.A. (1977)
- [3] P.J. Schneider, K.H. Berkner, W.G. Graham, R.V. Pyle, J.W. Stearns, Symp. Prod. Neutralization of Neg. Hydr. Ions and Beams, Sept.(1977) p. 63
- [4] J.R. Hiskes, A.M. Karo, LLL-abstract, UCRL 80687, submitted to the Santa Fe Plasma Diagnostics meeting of the APS, March (1978)
- [5] K. Wiesemann, K. Prelec, Th. Sluyters, J. Appl. Phys. 48 (1977) 2668
- [6] O.S. Oen, M.T. Robinson, Nucl. Instr. & Meth. 132 (1976) 647

SIMULTANEOUS MEASUREMENTS OF MICROCRATER EMISSIONS OF CURRENT AND COPPER LIGHT AT THE CATHODE OF A MOVING ARC

M.G. Drouet, P. Dancer, P. Kieffer and H. Mercure.

Direction Sciences de base, Institut de Recherche de l'Hydro-Québec, Varennes, Québec, Canada, J0L 2P0.

INTRODUCTION

Numerous data have been published in the past pertaining to the erosion rate of various metal in an arc and the energies of the erosion products^{1,2}. The size of the arc footprints or the motion of the arc spots have been studied using photographic techniques, and the size of the craters has been used to estimate the current per crater and the current density^{3,4}; the micro-arc current has also been measured directly⁵. However, the mechanism of erosion is still unknown. In particular does the erosion result from a continuous evaporation during the life of the emitting site or does it result from an explosion of the site?

We present, here, simultaneous measurements at the cathode surface, of the fluctuations of the cathode current resulting from the initiation and extinction of the current from individual emitting sites and of the fluctuations of the light associated with the deexcitation of the erosion products; these results should contribute to a better understanding of the emission/erosion phenomenon at the cathode.

EXPERIMENT

The experimental arrangement is shown on Fig. 1. The 200 A arc is driven, in air at atmospheric pressure, by a transverse magnetic field between two parallel electrodes. The electrodes are separated by 2 mm; they are made of aluminium. The wire probe, made of copper, is embedded in the cathode. It is 0.3 mm in diameter. It is insulat-

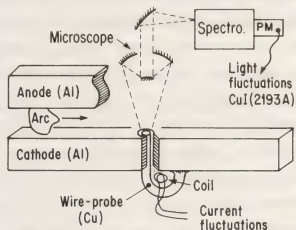


Fig. 1 Experimental arrangement.

ed from the electrode except at its end where it is soldered to it as shown on Fig. 1. It is terminated in the form of a loop so as to inductively couple the element of arc current incident on the probe surface to a small secondary coil⁵. The light emitted during the passage of the arc at the surface of the probe and corresponding to neutral and ion copper transitions is monitored using a microscope reflecting objective and a spectrometer.

RESULTS AND DISCUSSION

A typical result is reproduced on Fig. 2. The probe signal, dI/dt , gives the rate of change of the total current emitted by the copper wire probe surface⁵. The PM signal corresponds to the fluctuations, at the copper wire probe surface, of the light associated with a transition of the copper ion, Cu I 2193 Å.

As both the anode and cathode rail-electrodes are made of aluminium all the copper light emission comes from the probe surface and we may compare it

with the dI/dt signal from the probe. In fact the two signals are very similar both in duration and structure. Both the increases and decreases in the emission of light are simultaneous with those of the probe current; furthermore the high frequency fluctuations in the current associated with the initiation and extinction of individual emitting sites is also a characteristic of the light emission indicating that the emission of light is indeed associated with individual sites on the surface and not with the bulk of the plasma above the surface. Correlation of the two signals using a Biomation recorder and a PDP 11 computer has been carried out. Preliminary results indicate that the two signals are simultaneous within a μs . Correlation with a better time resolution is necessary in order to determine if the emission of light is associated with a continuous evaporation of copper during the life of the emitting site or results from an explosion of the site at the time of extinction of the current.

It is also of interest to note, on Fig. 2, the small current precursor labelled (a), 5 μs in duration, which precedes the high increase of arc current. We propose that this current may be asso-

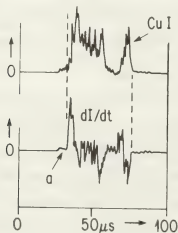


Fig. 2 Time evolution of the light emitted from the copper probe surface (Cu I, 2193 Å) and of dI/dt , the rate of change of the probe current.

ciated with the electrical polarization³ of the dielectric oxide surface by ions from the discharge as illustrated on Fig. 3. Such a polarization is necessary to induce field emission from the cathode surface³. In our case, the total charge, Fig. 2, would be approximately 10^{-7} coulomb for a probe

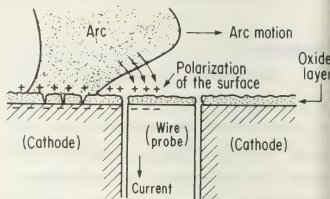


Fig. 3 Ion deposition on the oxide layer inducing the current precursor.

surface of 10^{-3} cm^2 . If this interpretation is correct, then the sharp increase in current, following this 5 μs field build-up across the oxide layer, would correspond to a breakdown through the layer and the emission of copper light would originate from the evaporation or explosion products. A small emission of copper light is also observed, on Fig. 2, simultaneously with the current-precursor.

It may be associated with the existence at the cathode surface of a copper vapor layer which, according to Leycuras⁶, would be responsible for the high current-density injection of electron in the plasma

REFERENCES

1. C.W. Kimblin, J. Appl. Phys. **44**, 3074 (1973).
2. H.C. Miller, J. Appl. Phys. **43**, 2175 (1972).
3. A.E. Guile, Proc. IEE, **121**, 1594 (1974).
4. J.E. Daalder, Ph.D Thesis, Eindhoven (1978).
5. M.G. Drouet and S. Gruber, IEEE Trans. **PAS-95**, 105 (1976).
6. A. Leycuras, J. Phys. D. **11**, 2249 (1978).

IMPACT AND RESISTIVE HEAT SOURCES OF CATHODE SPOTS IN ARC DISCHARGES

E. Hantzsché.

Zentralinstitut für Elektronenphysik der AdW der DDR, 108 Berlin, DDR, Mohrenstr. 40/41.

In developed cathode arc spots on clean metal surfaces ("type 2" spots according to Rakhovsky /1/) two regions have to be distinguished: 1) the central part, the "core" of the spot, with a high energy input that causes melting, evaporation, cratering, TF-electron emission and explosive processes, and 2) the surrounding "halo" region of interaction between the cathodic plasma and the surface with a lower energy input and without essential surface processes (compare Daalder /2/). According whether the halo is included or not, the calculated mean current densities of the arc spot i_s differ by orders of magnitude. The main cause of this bipartition is the decreasing density of the expanding plasma outside of the central crater region, and the corresponding decrease of the ion current density i_i impinging on the surface.

The ion current is the main surface heat source of the quasi-stationary arc spot. The total ion impact power within the crater area becomes

$$P_i = I_s U_c' / (1 + \chi),$$

I_s : spot current, $\chi = i_e / i_i$, $U_c' = U_c + \mathcal{E}_i - \varphi + 2kT_p / e$ (U_c : cathode fall of potential, \mathcal{E}_i : ionization potential, φ : work function, T_p : plasma ion temperature). This surface power input is diminished by elec-

tron emission cooling because of thermofield emission and ion induced secondary emission (coefficient χ_s), that results in the power

$$P_e = -I_s [(\chi - \chi_s) \bar{U}_e + \chi_s \varphi] / (1 + \chi).$$

The mean effective work function \bar{U}_e and the electron current density i_e are functions of the surface temperature T_c and the surface field strength F_c , both of which again depend mainly on i_i .

Besides of this surface source there exists a volume heat source because of the Ohmic (Joule) heating below the spot area. From the power density $q_1 = i^2 T / b_0$ (i : current density, $b_0 = T / \rho$ electric conductivity) we get by integration (applying the known current distribution and temperature distribution /3/) the total Joule power within the cathode

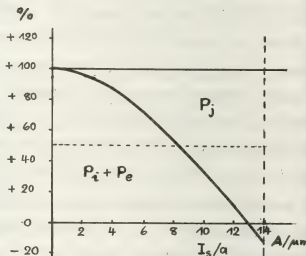
$$P_j = I_s T_0 \sqrt{\chi / b_0} \operatorname{tg} \chi + (P_i + P_e) (1 / \cos \chi - 1),$$

where T_0 is the cathode temperature far away from the spot, χ the heat conductivity of the cathode, $\chi = I_s / 4a \sqrt{\chi b_0}$, a the spot radius. The ratio $P_j / (P_i + P_e)$ depends mainly on I_s / a and weakly on I_s (or i_s). The percentages of both heat sources in the case of Cu cathodes are shown in the figure. Stationary solutions exist if $I_s / a < (I_s / a)_{\text{crit}} = 2\pi \sqrt{\chi b_0} = 13.9 \text{ A} / \mu\text{m}$ (Cu).

Models of stationary arc spots (including the evaporation flux density that limits i_1) result in $0.1 \lesssim I_s/a \lesssim 0.5$ A/ μ m (Cu cathodes, /4/). However, measurements of I_s and a (assuming crater radius = spot radius) give $2 \lesssim I_s/a \lesssim 20$ A/ μ m /5/. This discrepancy may be explained by the assumptions that 1) the cathode spot is an essential non-stationary phenomenon, 2) a large part of the current passes through the surface outside of the crater area. A discussion of non-stationary effects shows: a) the spot motion results in a reduction of Joule heating (if $I_s/a = \text{const}$); b) each kind of surface roughness increases Joule heating; c) in essentially non-stationary processes (such as explosions of protrusions, compare /6/), the critical limit $(I_s/a)_{\text{crit}}$ may be considerably exceeded, the temperature rises exponentially with time, and even in the temporal average the Joule heating dominates. The current density and the temperature in the halo region of the spot is so low, that resistive heat production is negligible. The over-all percentages of Joule heating and impact heating depend on the role of explosive processes in the spot mechanism and on the role of the halo current relative to the core (crater) current in the arc spot. Both are still unsolved problems.

References:

- /1/ V.I. Rakhovsky, IEEE Trans. Plasma Sci. PS 4 (1976), 81
- /2/ J.E. Daalder, J. Phys. D 11 (1978), 1667
- /3/ E. Hantzsche, Beitr. Plasmaphys. 12 (1972), 245
- /4/ E. Hantzsche, Beitr. Plasmaphys. 14 (1974), 135
- /5/ J.E. Daalder, IEEE Trans. Pow. App. Syst. PAS 93 (1974), 1747
- /6/ J. Mitterauer, P. Till, E. Fraunschiel, M. Häider, Proc. 4. Conf. Gas Disch. (London) 1976, 421



Percentages of surface heating ($P_i + P_e$) and of resistive heating (P_j) in a stationary cathode arc spot, current $I_s = 50$ A, as a function of I_s/a , plane Cu cathode.

ENERGY SPREAD OF CLUSTER IONS FROM A MOLTEN METAL

A. J. Dixon and A. von Engel.

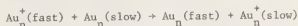
Engineering Science Dept., Oxford University.

In a recent paper (Dixon 1979) a mechanism was proposed by which the ions drawn from their molten metal by a strong electric field might have a wide spread in energy. It was concluded that the presence of a dense cloud of metal vapour close to the region from which the ions are emitted would broaden the energy spread by resonant charge exchange. Moreover, it was shown that this process will have a far greater effect on the energy spread of singly charged than of doubly charged ions because the cross section for charge exchange between a doubly charged ion and a neutral atom is relatively small.

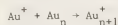
Experimental evidence for this hypothesis was provided by the work of Sudraud et al. (1979) on the energy spread of gold ions emitted from a needle of $\sim 10\mu$ tip radius wetted with molten gold by capillary flow. They observed that the ions Au^+ had a half width (F.W.H.M.) in energy of 65 eV (instrumental width unknown) and a very long tail of slower ions extending to several hundred eV below the applied voltage of 8 kV. The ions Au^{++} , on the other hand, had a half width in energy of 45 eV and no tail of slow ions.

Sudraud et al. also measured the energy spread of the cluster ions Au_2^+ , Au_3^+ , Au_4^+ , Au_5^+ , Au_3^{++} . They observed a second peak in the energy spectrum of singly charged clusters at $\sim 200\text{eV}$ below the first peak. It became more prominent (compared with the first peak) as the size of the clusters increased. The energy spread of the ions Au_3^{++} , however, displayed no second peak. This simple fact is analogous to the observations for Au^{++} (where 2 electrons

have to be exchanged) and suggests that the energy broadening of the clusters too was primarily caused by charge exchange. However, in this case the process

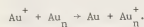


has a low probability because the number of neutral clusters in the vapour is too low. Furthermore, such charge exchange would give a single peak with a long tail rather than 2 separate peaks as observed. Another energy-broadening reaction is



but it can be ruled out because it requires thermal relative velocities to be efficient.

Of the many processes, we favour



Though non-resonant, because Au has a higher ionization potential than Au_n , it may have a large enough cross section if Au_n^+ is excited.

The surprising observation is that there are 2 peaks whose relative size varies greatly with n . This can be understood by assuming the presence of two independent sources of Au_n^+ : one is the melt, the other the vapour. The melt may be associated with the first peak. The process in the vapour is thought to represent the second peak. That the ions from the vapour have a peak at all we tentatively explain as being caused by the strong electric field (up to 10^9 V/m) which can broaden the energy levels so that the cross section of the reaction favoured above increases if only in a narrow region of the vapour.

A. J. Dixon, 1979, J.Phys.D.: to be published.

P. Sudraud, C. Colliex, J. van de Walle,

J.Physique Letts. 1979, submitted.



EFFECTS OF NEGATIVE AIR CORONAS ON PLANE ANODE FOILS

A. Goldman and R.S. Sigmond*

*Ecole Supérieure d'Electricité, Laboratoire de Physique des décharges ("LPD") du C.N.R.S.**F. 91190 Gif-sur-Yvette.***Norwegian Inst. of Technology, Electron and Ion Physics, Research Group ("Elion") N-7034 Trondheim-NTH.*

Abstract Low energy humid air ions drifting to an aluminum foil will rapidly etch cylindrical holes with diameters in the 10 μ m region. A first systematic investigation into this phenomenon is reported upon here.

Introduction We here report the first results from a joint investigation into the processes occurring at the large electrode in unipolar corona discharges. The specific case considered in this paper, negative low current point-to-plane coronas in atmospheric density air with Al or Au foil anodes, was chosen because:

- Experiments (LPD) indicated that the anode may play an important role in catalysing gas reactions in coronas.
- Preliminary studies at LPD and ELION showed that Al foil anodes of the same stock were perforated by negative coronas in Paris, but not in Trondheim.

Of necessity much work has gone into sorting out the parameters of importance to the hole formation. In this report we try to present a reasonably coherent picture of our conclusions and their experimental backing.

Properties of a "standard" corona The following corona was specified as our common starting point for systematic parameter variations:

Gas: 1 atm lab. air flow, ~50% rel. hum.

Point: Paraboloid or hyperboloid, with 75 μ m tip radius.

Plane: Al foil of 16 μ m thickness

Distance point-plane: 10 mm

Current: 50 μ A ave., neg. point, 7-9kV DC

Discharge duration: 16 h

Except where otherwise stated, this set of parameters pertains to all coronas discussed in the present paper.

This corona will burn in the Trichel pulse regime with a 2-3 μ s pulse repetition

period. As seen side-on, using photon counting or sampling, photons come from the cathode region in (Trichel) pulses of 30-40 ns duration. They all belong to the 2nd pos. band of N₂, with some contribution from the 1st neg. band. No photons from the drift or anode regions could be found. This all conforms completely with earlier observations by many authors [1].

The Al anode foil will within minutes be covered by a growing layer of glassy coating, which eventually cracks, and whitish crystals. Within some hours, holes of some μ m diameter pierce through the foil, concentrated in a (sometimes ring-shaped) region of 1-2mm radius around the corona axis, see Figs.1a - b. The holes usually are cylindrical with 90° edges in an otherwise flat, unetched foil surface. They seem to grow in numbers but not in diameter during the discharge. A glassy or scaly deposit then forms on the foil backside, covering somewhat more than the perforated area. "Worms" of a loose, white material seem to crawl out of the holes, mostly on the front side, but also on the back side of the foil.

The hole formation is not accompanied by any noticeable change in the electrical characteristics of the corona. However, a faint emission pulse of photons belonging to the 2nd pos. band of N₂ is seen coming from the backside of the foil. As shown in Fig.2, these light pulses occur 150-250 ns after the photon pulse from the cathode. They come earlier and increase in amplitude when the corona voltage and current are increased, consistent with the excitation to be expected from a pulse of cathode electrons which have traversed the gap without attachment in a space charge intensified field that increases with the current.

It is important to note that no such delayed photon pulses are found looking side-on at the gap and anode foil front.

When, however, a grid of .02-.1mm dia. wires was placed in the anode position, a spectrally similar delayed photon pulse radiated from the grid, see Fig.2a.

Storage of a foil for months in laboratory air will not destroy the delayed photon pulse emission, but soaking in water does. Likewise, no delayed radiation is seen from new Al foils perforated with a thin needle.

We have never detected any sparks on the foil surfaces or from the holes. Sparks would have told about infrequent, energetic breakdowns of insulating surface layers due to accumulating charges; a possible hole formation mechanism.

Studies of the anode foil surface.

Effects of parameter variations.

Corona polarity: No holes are formed in positive coronas (20-40 μ A current).

Foil material: No holes in Au foils.

Air humidity: No holes or pittings, no scale or crystalline deposits in P₂O₅-dried air flows. Auger microprobe analysis shows surface layer of cathode material and ^{also} indicates Al₂O₃. Holes and deposits form in the relative humidity range 30-100%, possibly with a maximum rate around 50%. (This explains why ELION at first found no holes: Trondheim air may be very dry in winter!). The deposits consist mainly of Al₂O₃ (Auger and microprobe X-ray, both sides of foil), but Debye-Scherrer photographs show no clear Al₂O₃ pattern.

Charged particle contents of electric wind:

When a grid prevents all negative particles in reaching the foil, no holes are formed. The foil collects glassy scale and a white powder giving a NH₄NO₃ Debye-Scherrer diffraction pattern.

Discharge current and duration: ~proportional influence on hole number, some on the perforated area, and ~none on hole size.

Point radius (<10-150 μ m), gap width (7-10mm)

foil thickness (10-18 μ m): Slight influence.

The hole production mechanism It is well known from semiconductor technology that surface oxidation proceeds some hundred times faster with H₂O than with O₂. In our

negative coronas in dry air the negative ions probably are neutralized by tunnelling through the thin Al₂O₃ layer without exposing the metal to further oxidation. Humid air ions make such a thick oxide layer that neutralization takes place in a few weak spots. Here oxidation is so rapid that the oxide is formed as a loose mass of little protective ability. The delayed photon pulse from the back of the foil shows that an electric field exists in or behind the holes confirming that both the front surface and the hole walls must be insulating. Thus the negative ions must be sucked to the bottom of the holes until penetration, when a new weak spot in the front oxide will take over.

References [1] M. and A. Goldman "Corona Discharges" Chapt.4 in Hirsh and Oskam (eds) "Gaseous Electronics" Vol. 1, Acad. Press 1978.

R.S. Sigmond "Corona Discharges" Chapt.4 in Meek and Craggs (eds) "Electrical Breakdown of Gases" Wiley 1978

I=50 μ A for 4h, 15 μ m Al foil, d=8mm, point 10 μ m rad.

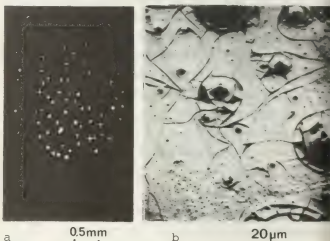


Figure 1 Al foil surface with holes

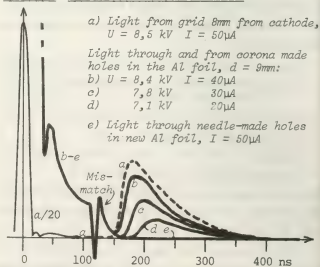


Figure 2 Light pulses from negative coronas in air

TEMPORAL INCREASE OF IONIZATION CURRENT IN N_2 GAS

Haruo Itoh and Nobuaki Ikuta.

Chiba Institute of Technology, Tokushima University.

Introduction

A consistent increase of I_m component of ionization current in N_2 for several ten minutes was observed. The after effect of ionization current flow in the gas doesn't disappear for a long time more than several hours. The current increasing rate depends on the electric field intensity, injecting electric power into the gap space, the product of pressure and gap length $p \cdot d$ and the wall-gas temperatures. In our measurement, N_2 gas is quite vivid and has a long life of activity. The phenomena of current increase are considered to be caused by the long-lived excited molecules that acts directly and indirectly for the secondary electron emission from the cathode. Current increase was also observed in other gases such as H_2 and Ar.

Experimentals

For the measurement of current, a couple of gold-plated electrodes of 10 cm in diameter, an artificial wall of 16 cm in diameter and 12 cm in height were set in a stainless steel tank of 30 cm in diameter and 50 cm in length. For the initial electron emission, a hydrogen discharge lamp was used with a quartz window. A high vacuum system and high grade N_2 gas of five nine were used to prevent erroneous results.

Results

Measurement of transient current: Transient current at the "on" or "off" of UV irradiation clarifies the behavior of secondary electron emission by meta-

stable molecules.¹⁾²⁾ The wave shapes of current at UV off are as Fig.1. Instantaneous decrease I_p is multiplied current of Photo-emitted electrons by UV. Almost exponential part shows the I_m component by metastable molecules. The time constant of which doesn't take a fixed value corresponding to gas pressure and electrode separation but varies depending on the degree of electron multiplication and it's career in the gas. The amount of I_m component I_m is a good measure of regeneration characteristics. The increase of current is almost due to the increase of I_m component.

Self-sustaining of current: When the increasing current comes near self-sustaining condition, another residual component of very long decay time appears after i_m fades out. The decay is rather linear and the rate is dependent on the ionization, activation and their career in the gas. Self-sustaining of ionization current can occur only by this long decay component I_s that grows following the build up of I_m . The decay time τ_s gradually becomes longer, and finally, self-sustaining state is achieved with infinite τ_s . After reaching to self-sustaining state, the current increases further and tends to saturate above $2 \times 10^{-7} A$ as Fig.2.

Effect of wall and gas temperature: When an artificial wall is put surrounding the electrodes, current increases in suppressed mode as shown in Fig.3,

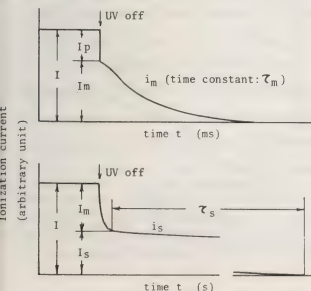


Fig.1 Transient wave forms of current after UV off.

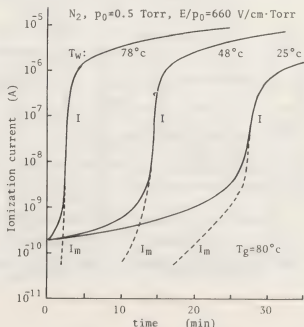


Fig.2 Wall temperature dependence of ionization current increase

and reaches to the self-sustaining state only at higher level of current. This may be caused by the efficient deactivation of metastable molecules at wall surface. Depending on the wall temperature, current increasing behavior varies as Fig.2, which shows that the deactivation of metastable molecules is strongly suffered from wall temperature, though convection flow of gas also aid the loss of metastables from discharge region. If wall temperature is changed periodically, increasing current also varies in the same phase of wall temperature as shown in Fig.4. Even in the case that wall and gas temperatures are the same, current increases faster in higher temperature condition.

Difference of voltage-current characteristics:

As the results of ionizing current flow in N_2 gas for long hours, voltage-current characteristics changes seriously as Fig.5. The change in characteristics appears consistently with a long lifetime depending on the surrounding conditions.

Discussion

The most important evidence in these experiments is that the career of ionization and activation of the gas can't be extinguished for several or several ten hours. Once ionizing current increases for a long time in N_2 gas, even after a pause of voltage application for some duration, almost instant recovery of ionization current to the same level as before is achieved. Contrary to it, if the gas is exchanged, the current starts from the initial low level. This fact shows that the activated gas has some different internal conditions from virgin gas. The dominant metastable species that give I_m component of time constant within several ten [ms] are considered to be $A^3\Sigma_u^+$ state of N_2

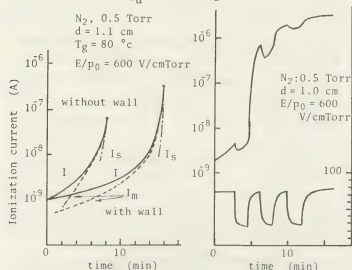


Fig.3 Difference of current increase by wall

Fig.4 Wall temperature dependence

as calculated by Molnar.¹⁾ Many researchers has given the lifetimes and collisional deactivation rate constant for this state of N_2 .³⁾⁴⁾ Using these data and supposing proper deactivation rate at the electrode surface, reasonable analysis can be obtained for the transient characteristics having various time constant. The long after-effect of activated N_2 gas is considered to be based on the vibrationally excited molecules, the radiative lifetime of which is almost infinite. That is, the collisional deactivation rate depends on the population of vibrationally excited molecules through mutual energy transfer.⁵⁾ In low gas density as this case, diffusion may be dominant loss process, where the deactivation at wall surface can give a considerable influence on the population. Consequently, temporal increase of current depends on the population distribution of excited species within the tank, and is suffered from circumstances. I_s component can be understood as the regeneration behavior of metastable species based on the vibrationally excited population in N_2 , but it is impossible for Ar. Further experimental research is needed to confirm these mechanisms with referring the collision data.

References

- 1) J.P.Molnar: Phys.Rev., **83**,933, ('51), ibid, 940, ('51)
- 2) S.C.Haydon and O.M.Williams: J.Phys.D, **9**,523, ('76)
- 3) N.P.Carleton and O.Oldenberg: J.Chem. Phys., **36**,3460
- 4) E.C.Zipf: Can.J.Chem., **47**,1863, ('69)
- 5) G.N.Hays and H.J.Oskam: J.Chem. Phys., **59**,1507, ('73)

J.F.Noxon: J.Chem. Phys., **36**, 926, ('62)

P.H.Vidaud and A.von Engel: Proc. Roy.Soc.Lond.,

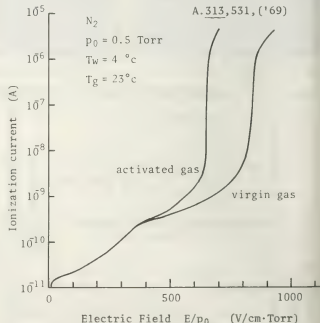


Fig.5 Field-current characteristics of activated and virgin gases

ABLATION OF SOLID HYDROGEN IN CONTACT WITH MAGNETIZED PLASMAS : CAN THE EXTERNAL MAGNETIC FIELD BE THE UPPER LIMIT OF THE SELF CONSISTENT ELECTRIC FIELD AT THE SOLID SURFACE ?

S. Mercurio.

Department of Physics, University of Wisconsin, Madison, WI, 53706 U.S.A.

Charge collectors or "probes" were first correctly used by Langmuir¹ in his studies of steady arc discharges. Later Bohm² extended their use to arcs in the presence of high magnetic fields. Probe theories even today, are quasi-steady-state theories. Behavior of charge collectors far from equilibrium are of extreme interest in research fields in which short pulses of current are collected.

In this note the ablation mechanism of solid hydrogen in contact with magnetized plasmas is discussed in terms of a transient process proper to charge collectors approaching an equilibrium.

The semiempirical approach proposed suggests a "novel" plasma-solid boundary condition, whose consequences are also found to be in excellent agreement with all experiments available to date for a variety of plasma conditions.

Since solid hydrogen has a very low binding energy, say $W=0.01$ eV, usually much less than the electron temperature, KT_e , we can safely assume that the ablation mechanism is driven by the charge and heat carried only by the electrons. The ablation front speed U , relative to the solid, just expresses the "close link" between momentum and energy transfers. The latter determines the range δ of the plasma electrons in the solid; the former, the relaxation time t^* for the transition between the initial (solid) and final (fluid-like) states of the hydrogen. The ablation front motion will be regarded here as a wave-type motion. It will be described precisely as the motion of that frame

of reference which carries along the oscillating Maxwell's Displacement field associated with ablating dielectric.

Taking δ to be equal to one mean free path of the plasma electrons of average energy in a superdense gas of number density n_0 , we have

$$\delta = \ell = (n_0 \sigma_{int})^{-1} \quad (1)$$

where σ_{int} is the interception cross section.³

The relaxation time t^* is here assumed to be the time the displacement D takes to build up and collapse. If the electron-self-collision time t_{ee} , such that $t_{ee} \ll t^* \ll t_{rec}$ (the electron-ion recombination time), then t^* will in fact be exactly the period for the heat-cycle of the electrons which have enough energy to reach the solid. Since a collapsing time is expected to be much smaller than the charging time τ , we just have $t^* = \tau$. We can easily obtain τ by integrating the following set of standard equations at any point x , with respect to time t . In one dimension the equations read

$$\frac{\partial J}{\partial x} + \frac{\partial \rho}{\partial t} = 0; \quad \frac{\partial D}{\partial x} = 4\pi\rho; \quad D = \frac{\epsilon}{\sigma} J$$

which give

$$D(t) = D_\infty [1 - \exp(-t/\tau)]; \quad D_\infty \equiv \tau \left. \frac{\partial D}{\partial t} \right|_{t=0} \quad \tau \equiv \epsilon/4\pi\sigma$$

where J is the current density, ρ the charge density, σ the electric conductivity, ϵ the dielectric constant. By identifying the initial value of the displacement current $J_d(0)$ with plasma-electron-random current $J_r = \frac{1}{4} \epsilon n_0 \bar{c}$ (at $t=0$ there is no sheath), then we have

$$\tau = D_\infty / 4\pi J_d(0) = D_\infty / \pi \epsilon n_0 \bar{c} \quad (2)$$

While $J_d(0)$ does not change when $B \neq 0$, the

ultimate value of D does change, because a solid can never be in equilibrium with a plasma. For a steady sheath to exist, the ion flow requires a "tail" in the electron velocity distribution and therefore a continuous flow exists across the sheath. The self-consistent displacement field can be obtained from an equation for dynamic equilibrium, in which the Hall's electric field has to be taken into account, that is

$$-D_{\infty}/\epsilon + E_{th} + vB/c = u/\mu \approx 0. \quad (3)$$

Where $E_{th} = kT_e/e\lambda_D$, λ_D being the Debye length and u and v two mutually perpendicular drifts across \vec{B} .

We might content ourselves with assuming that the displacement will collapse when

$$D_{\infty} = \epsilon(B + E_{th}) = \epsilon B \quad (\text{if } E_{th} \ll B) \quad (4)$$

and see whether the above assumption is able to pass some (indirect) experimental test. Deviding

(1) by (2) we obtain an expression for the ablation speed U , suitable for comparison with experiments,^{4,5,6,8} as shown in Fig. 1, that is

$$\frac{n_o U}{n_e^2} = \frac{\pi e/\sigma_{int}}{\epsilon B}$$

We now try to test (4) more directly. For instance, solid hydrogen pellets have been observed to deviate from the straight path, when injected into Risø's Puffatron. The latter produces a rotating plasma because it has strong external field. The measured⁷ average deviation is 0.2 cm. By simply using (4) to estimate the net charge on the pellet and the equation of motion for projectiles we get 0.23 cm.

We can verify that the dense ablation cloud is not so dense as to have a negligible Hall's current in the sheath, by estimating its density. By invoking mass conservation across the disassembling surface layer of thickness δ , that is:

$n_o U = n_h V$; where n_h and V are the number density and the average speed of hydrogen molecules respec-

tively, upon leaving the solid. If we now use the experimental values for U and V we get $n_h \lesssim 10^{17} \text{ cm}^{-3}$ to which correspond $\omega_c \tau_{coll} \gtrsim 1$. We note, incidentally, that by introducing (4) into the energy balance we obtain V in excellent agreement with experiment.^{4,6} In order to convince ourselves that (4) is independent of a chosen symmetry, we notice (3) can be recovered from $(D_{\infty}/\epsilon + E_{th}) \sin \theta + vB/c = u/\mu$; $v/c = uB \sin \theta / c$, for any θ , the angle between \vec{B} and \vec{J}_T . (Gaussian units have been used throughout.)

REFERENCES

1. Langmuir, I, Science 58, 290 (1923)
2. Guthrie and Wakerling, The characteristic of electrical discharge in magnetic fields (1949)
3. Brode, R.B., Review of Modern Physics 5, 263 (1953)
4. Jorgensen, L.W. et al., Plasma Physics 17, 453 (1975)
5. Foster, C.A. et al., Nuclear Fusion 17, 1067 (1977)
6. Amenda, W. et al., Fusion Fueling Workshop, Princeton, N.J. (USA)
7. Sillesen, A. (Risø, Denmark) private communication
8. Milora, S.L. et al., ORNL TM-6496, October (1978)

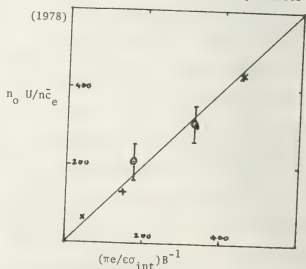


Fig. 1 o Ormak; + Puffatron; * ISX-A-Tokamak
x Pulsator; — Theory

MICROWAVE GENERATION OF A MAGNETOACTIVE OXYGEN PLASMA FOR OXIDATION

L. Bárdoš and J. Musil.

Czechoslovak Academy of Sciences, Institute of Plasma Physics, Pod voběžnou vesi 4, 180 69 Prague 8, Czechoslovakia.

1. INTRODUCTION

In recent years the plasma has growing importance for the thin solid surface film creation. Particularly, the silicon oxidation in an oxygen plasma can be in contrast to usual thermal methods favourably carried out at low temperatures. However, the basic oxidation parameters depend on plasma characteristics and therefore on the plasma generation system.

In our previous work [1], the new oxidation method using a microwave magnetoactive oxygen plasma has been described. Detailed experimental study of formation of oxide films on silicon showed that [2]

- (i) the oxide growth rate depends linearly on the plasma electron density,
- (ii) oxide films are created only in the plasma in which the floating potential (measured with respect to the ground) is $U_f \approx -10$ V.

The main aim of the present work is to describe density and potential radial profiles for two experimental arrangements differing in a way and direction of the microwave energy introduction into a discharge tube.

2. EXPERIMENTAL ARRANGEMENT AND RESULTS

The oxygen plasma was produced in the quartz tube (i.d. 75 mm) and the direction

of the static magnetic field \vec{B}_0 was parallel to the axis of the discharge tube. The plasma was generated either in the circular waveguide (the microwave energy is fed into the discharge tube along the direction of the \vec{B}_0) or by a helix slow down structure placed coaxially outside the discharge tube (the energy is fed radially, i.e. perpendicularly to the \vec{B}_0 , or quasiradially). Plasma could be also produced by the waveguide and the slow down structure operating simultaneously.

Intensity of the static magnetic field was adjustable between an electron cyclotron resonance ($\omega_{ce}/\omega = 1$) and its second harmonic ($\omega_{ce}/\omega = 2$). Experiments were carried out in oxygen at pressures of the order of 10^{-4} Torr and the incident microwave power was of the order of 1 kW ($f=2,35$ GHz). The device operated in a pulse mode with repetition frequency 50 Hz. The average plasma electron density was measured by an 8 mm interferometer, radial profiles of the saturated ion current i_+ , floating plasma potential U_f and axial component E_z of the incident wave electric field by movable probe. Typical results of our measurements are given in Fig.1, for the waveguide and the slow down structure.

3. DISCUSSION

From Fig.1 it is clearly seen that:

- (i) Radial profiles $N(r)$ almost constant in a wide vicinity of the axis can be achieved. $N(r)$ of a plasma produced by waveguide has maximum on the axis, by the structure it has minimum. In the second case the absolute value of the density is lower. ($N(r)$ produced by waveguide and structure is a sum of respective profiles).
- (ii) While the radial profile of floating potential of plasma produced by waveguide has smooth minimum on the axis, it has maximum (close to zero) on the axis for the structure generation. It is worthwhile to note that absolute values of U_f can be changed by the plasma density and for densities greater than $5 \cdot 10^{12} \text{ cm}^{-3}$ U_f in the plasma produced by the waveguide increases to zero. Moreover, regions of negative potential practically show the radial distributions of energetic electrons. These can be expected around axis in waveguide plasma and on the periphery of the discharge tube in structure plasma.
- (iii) Radial profiles of E_z fully correspond to the distribution of TE_{11} in the waveguide and radial feeding in the structure experiment.

Electron temperatures measured by a Langmuir probe on the axis of the discharge tube were 6 eV, 13 eV and 19 eV for structure, waveguide and both sources respectively.

Properties of the oxide films on Si created in this experimental arrangement are consistent with radial profiles of

$N(r)$ and $U_f(r)$. It was found that:

- (i) Homogeneity of thickness of oxide films is better in the plasma produced by the waveguide. Homogeneity better than 10% on areas of approximately 12 cm^2 can be achieved.
- (ii) In regions of strong negative potential the growth rate of films decreases.
- (iii) In the plasma generated by the structure with power above 1,5 kW edges of circular silicon samples can be strongly heated by fast electrons.

Our experiments demonstrated that the careful design of the microwave plasma reactor is very important for successful formation of the oxide films.

References:

- [1] L. Bárdoš et al., J. Phys., D8, (1975), L195
- [2] J. Musil et al., accepted in J. Phys. D, (1979).

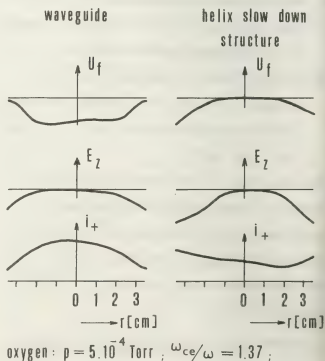


Fig.1

AN INVESTIGATION OF ARC STARTING ON COLD CATHODES

Harald L. Witting.

General Electric Company, Corporate Research and Development Schenectady N.Y., 12345 U.S.A.

The phenomena that occur when an arc is started on a cold cathode are not well understood.⁽¹⁾ We are interested in the brief period (a few sec) after breakdown when the electrode transfers from a cold cathode to a hot cathode while being heated by the arc. We have investigated this "starting period" by means of plasma probes and high speed photography.

Our electrode (Fig. 1) consists of a tungsten shank (1.2 mm dia) and a tungsten wire overwind (0.75 mm dia). A fine tungsten plasma probe is spaced 1 mm from the electrode tip. The arc tube contains argon at 2.6 kPa and mercury vapor at 0.3 Pa.

Fig. 2 shows the discharge voltage and current for a symmetrical arc tube (70 mm arc gap) in the first few ms of operation on a 60 Hz sine wave reactor, for the case where the tungsten electrodes are coated with an emission material (barium and thorium oxides). The discharge is mostly in the low-voltage arc spot mode, with brief (40 micro-sec) re-ignition and de-ignition spikes near current zero. This pattern does not change significantly for the first 1 or 2 sec of discharge operation.

Our plasma probe showed that the cathode fall is approximately 12v in the arc spot mode, and that practically all the re-ignition and de-ignition voltage drop occurs in the cathode fall.

High speed motion pictures of arc starting were taken with a Wollensak Fastax camera in 16 mm color film at 3000 pictures/sec. These showed that in the arc spot mode there is a small, bright arc spot that moves rapidly (5 m/s) over the cathode surface. The size of the arc spot has not been resolved, it appears to be less than 0.2 mm in diameter. This implies a current density exceeding 15,000 A/cm². The arc spot is surrounded by a larger (2 mm), relatively diffuse glow.

As the electrode heats up during starting (1-2 sec), the re-ignition spike gradually lengthens in duration and becomes visible in the motion pictures as a distinct mode. In this "cathode glow" mode, an intense, thin glow hugs a substantial fraction of the electrode surface without movement, and there is a definite dark space between this glow and the positive column. The cathode glow mode gradually decreases in voltage and lengthens in duration, and eventually (4-6 sec) it transfers to a diffuse, low-voltage thermionic arc mode as the electrode reaches incandescence.

With a bare tungsten electrode (no emission material), the arc spot mode is rarely observed on starting. Rather, the stationary cathode glow mode dominates, it has a high cathode fall (200v) throughout each half-cycle and heats the electrodes rapidly.

The dominant and most puzzling feature of the starting period is the arc spot mode. With a cathode fall of less than 20v, it can transfer a wide range of current (<0.1A to 5A) to cold electrodes.

This arc spot can move about a tungsten surface with scattered oxide surface layers that are less than a few microns in thickness as observed with visible and scanning electron microscopy.

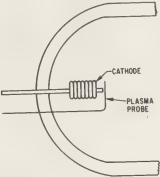


Fig. 1

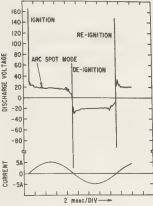


Fig. 2

We analyze the cathode arc spot on the assumption that the cathode maintains a small area on the cathode at a high temperature so that thermionic emission, enhanced by strong electric fields, can provide the required high current density. The heat conduction from the hot spot to the bulk cathode is approximately

$$P_{th} = (\pi/2) T D K$$

where T is the temperature and D the diameter of the hot spot, and K is the thermal conductivity of the cathode.

We estimate the maximum hot spot size by assuming that the conduction heat loss is supplied by all the available cathode heat, i.e., by the product of current I and cathode fall V_c, so that

$$D \leq (2/\pi) I V_c / T K$$

For example, with a hot spot temperature of 4000°K and with a tungsten substrate (K = 1.2 w/cm °K), at 1A current and 12v cathode fall we find a maximum hot spot diameter of 16 microns. The corresponding current density is 500000 A/cm². If 25% of this current is carried by positive ions that are neutralized and thermalized at the surface, then the pressure of the returning atom flux over the hot spot area A is

$$P = (2\pi M k T)^{1/2} I / 4eA = 2500 \text{ kPa.}$$

We conclude that the starting of an oxide activated, cold cathode is dominated by an arc spot mode that has the essential characteristics of a vacuum arc, namely an exceedingly small, dense, moving plasma region close to the cathode surface. The loss of ions and atoms from this plasma to the surrounding low-pressure discharge region is balanced by a flow of evaporated atoms from the surface.

Vacuum arc experiments have shown that arc ignition is practically impossible at very pure electrodes without surface effects such as produced by oxides, etc. (2) This agrees with our observation that a cathode arc spot dominates the starting on electrodes that contain an oxide emission material, while a pure tungsten electrode will start in a high-voltage glow mode.

References

1. Gaseous Electronics, M.N. Hirsh & H.J. Oskam Ed. Vol. 1, Academic Press, N.Y. 1978, p. 332.
2. G. Ecker, Ergebnisse der exakten Naturwissenschaften 33, 1-104, 1961.

ETUDE THEORIQUE DES PHENOMENES LIES A UNE CATHODE LIQUIDE : ESTIMATION DU TAUX D'EROSION

G. Thiell and M. Fabry.

Laboratoire de Physique des Milieux Ionisés, Université de Nancy I, Case Officielle 140, 54037 Nancy Cedex, France.

Le taux d'érosion de la cathode d'un arc est un paramètre important qui détermine la durée de vie de l'électrode et sa connaissance en fonction du courant d'arc est intéressante en particulier dans le cas d'une cathode à bas point de fusion. Nous utilisons les résultats déduits du diagramme d'existence de l'arc [1] appliqué à une cathode liquide (potassium) sous atmosphère d'argon pour la création de plasmas denses.

DIAGRAMME D'EXISTENCE DE L'ARC

Dans des travaux antérieurs nous avons développé un modèle de la gaine cathodique dans un arc généré à partir d'une cathode liquide en potassium dans un gaz inerte à quelques torrs. Nous avons construit le diagramme d'existence des spots constituant la tache cathodique à partir d'un bilan des échanges existant au voisinage de la cathode, en envisageant des intensités I allant jusque 100 A [2].

Ce modèle stationnaire permet de connaître la région du plan $T(j)$ où nous choisissons T , la température de la tache, en fonction de la densité de courant totale j qui la traverse, avec pour seul paramètre le courant d'arc, grandeur qui peut être facilement imposée expérimentalement. Nous avons comparé les résultats donnés par ce modèle avec les grandeurs directement accessible expérimentalement [3].

Le dispositif expérimental est décrit en 4/; la chute de la tension cathodique a été mesurée à partir d'une technique de sondes et trouvée en bon accord avec la valeur calculée. La température et la densité électronique ont été déduites de mesures spectroscopiques effectuées à quelques millimètres au dessus de la cathode: la densité électronique varie de 10^{15} à 10^{17} cm^{-3} et montre l'intérêt du dispositif pour la génération de plasmas denses.

MECANISME D'EROSION DE LA CATHODE

Pour les processus d'érosion, nous avons utilisé un modèle non-stationnaire tenant compte du mouvement des taches qui peut être représenté comme une succession de pas pendant lesquels l'arc se trouve à un certain endroit pendant un temps t_s puis à un endroit voisin déplacé d'un diamètre de spot (2a) où il opère à nouveau pendant un temps t_s . Ainsi, on suppose que les cratères sont similaires pour un courant I donné et un temps t_s . La vitesse du spot cathodique peut alors être définie:

$$v = 2a/t_s = 2(I/\pi j t_s^2)^{1/2} \quad (1)$$

et le taux d'érosion par:

$$e_r = m_c/t_s \quad (2)$$

où m_c est la masse de matière perdue par la cathode. Quand un film d'oxyde est formé, les cratères sont des hémisphères de rayon a et de forte densité de vapeur métallique. La masse de matière enlevée à partir des cratères est:

$$m_c = (2/3) \pi a^3 d \quad (3)$$

où d est la densité du matériau cathodique.

Pour une cathode de potassium liquide

$$d = 0,826 - 0,222 \cdot 10^{-3} (t - 62,4) \quad (\text{g.cm}^{-3}) \quad (^\circ\text{C})$$

et le taux d'érosion peut être écrit en fonction du taux d'évaporation $W(T)$ ($\text{g.s}^{-1} \cdot \text{cm}^{-2}$) des atomes de la cathode métallique à température T :

$$e_r = \pi a^2 W(T) \quad (4)$$

où $W(T)$ est donné pour le potassium par:

$$\log W(T) = 6,922 - 0,5 \log T - 4503/T$$

Les relations (1) à (4) donnent:

$$e_r = IW(T)/j \quad (5)$$

et la vitesse aléatoire v du spot cathodique en fonction de sa température T par:

$$v = 3W(T)/d(T) \quad (6)$$

Cette relation est représentée sur la figure 1 pour T variant de 1000 à 1500 °K.

RESULTATS

Les résultats obtenus pour les différentes quantités introduites sont présentés dans le tableau suivant, les valeurs mentionnées pour chaque courant I correspondant aux valeurs extrêmes de j et conduisant aux valeurs minimale et maximale du taux d'érosion (figure 2) en fonction de I.

j (A/m ²)	I (A)	T (°K)	m(m)	v (cm/s)	e _r (g/s)	T ₂ (K)
7,45x10 ⁸	10 ⁻²	1340	2,07x10 ⁻⁶	4,95	1,34x10 ⁻⁵	6,36x10 ⁻⁷
7,45x10 ⁸	10 ⁻⁵	1335	5,54x10 ⁻⁶	5,72	1,73x10 ⁻⁵	1,95x10 ⁻⁶
4,0x10 ⁹		1330	2,82x10 ⁻⁶	4,27	2,35x10 ⁻⁵	1,21x10 ⁻⁶
7,45x10 ⁸	1	1335	2,27x10 ⁻⁵	5,72	1,73x10 ⁻⁵	16,15x10 ⁻⁷
1,7x10 ¹⁰		1210	4,33x10 ⁻⁵	2,57	2,25x10 ⁻⁵	3,32x10 ⁻⁶
7,45x10 ⁸	10	1325	6,54x10 ⁻⁵	5,72	1,75x10 ⁻⁵	1,12x10 ⁻⁵
5,65x10 ¹⁰		1110	7,51x10 ⁻⁶	1,21	3,33x10 ⁻⁵	1,42x10 ⁻⁵
7,45x10 ⁸	100	1298	2,37x10 ⁻⁴	5,72	1,73x10 ⁻⁵	15,16x10 ⁻⁷
1,0x10 ¹¹		1125	1,78x10 ⁻⁵	1,24	1,67x10 ⁻⁵	2,67x10 ⁻⁵

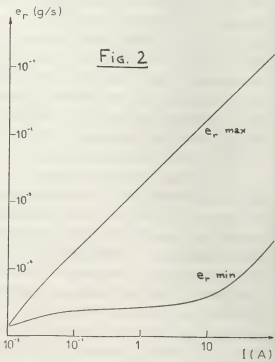
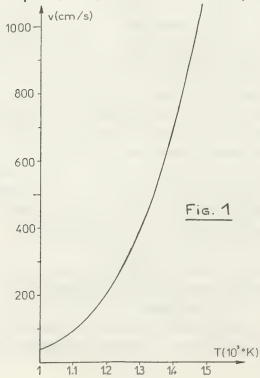
DISCUSSION

Pour essayer de justifier le fort taux d'érosion d'une cathode en métal liquide, nous considérons le bilan en énergie. Pour des courants inférieurs à 30 A et des densités j inférieures à 3.10⁹A/m², la densité d'énergie acquise par effet Joule est relativement faible devant celle perdue par l'évaporation des atomes, en accord avec l'hypothèse de la formation d'une fine couche d'oxyde. Pour des valeurs de I et j supérieures, l'effet Joule ne peut

plus être négligé mais l'érosion reste principalement due à un fort bombardement ionique de la surface cathodique. Un intense transfert de chaleur entre le plasma et la cathode provoque la croissance de zones fondues dans lesquelles se produisent des mouvements du liquide pouvant amener l'éjection de gouttelettes. Cet effet est d'ailleurs observé dans nos expériences pour des courants élevés (>30A).

Nous avons développé un modèle simple permettant d'estimer le taux d'érosion et la vitesse de déplacement des taches cathodiques à partir de l'analyse des résultats donnés par le diagramme d'existence d'un arc à cathode de potassium liquide. Toutefois, une étude plus précise de ces phénomènes devrait prendre en considération d'autres paramètres tels que la géométrie ou les parts respectives des différents composants (ions, atomes, gouttelettes) responsables de l'érosion.

11/G.ECKER Général Electric Report n°73
CRD 056 (1973).
12/G.THIELL, J.C.BRAUN Rev.Phys.Appliquée
11,609 (1976).
13/M.FABRY, G.THIELL, J.C.GEORGES J.Appl.
Phys. 47,3897 (1976).
14/G.THIELL, A.ROSSELER, M.FABRY J.Appl.
Phys. 47,1724 (1976).



SURFACE PHENOMENA IN CESIUM AND CESIUM - NOBLE GAS FILLED THERMIONIC DIODE

A. Beltoş and G. Musa.

Institute of Physics and Technology for Radiation Devices, P.O. Box 5207 Magurele-Bucharest Romania.

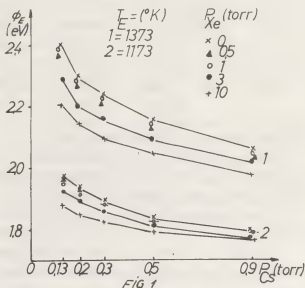
In the last years, an increased interest has been devoted to the alkali metal-noble gas mixture discharges.

The noble gas addition to the cesium thermionic diode increases the plasma density by lowering the ion loss /1/. However it is not known the influence of the presence of the noble gas on the cesium activated cathode work function. Indeed, the work function of the refractory metals in cesium vapours is given by the adsorbed cesium atoms on the surface. Because the surface coverage with adsorbed cesium atoms is established as a result of a dynamical equilibrium between evaporated and condensed atoms on the surface, an influence of the noble gas on this process is possible.

In the present paper we have studied extensively this influence for molybden-cesium system for cathode temperature $T_c = 970 - 1373^\circ\text{K}$, anode temperature $T_a = 600^\circ\text{K}$ - 1000°K , variable interelectrode gap = 0,5 - 3 mm, cesium vapour pressure $p_{Cs} = 0,08 - 0,9$ torr and xenon pressure $p_{Xe} = 0,5 - 10$ torr (residual pressure in the device 10^{-9} torr).

The work function of the molybdenum cathode has been evaluated from the value of the current for saturated mode of operation of the ignited thermionic diode /2/.

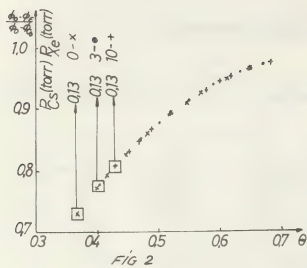
In Fig. 1 are given for two cathode temperatures the obtained results for ϕ_E versus cesium pressure for pure cesium and for cesium-xenon mixtures with various pressures of the added noble gas. Low noble gas pressure (0,5-1 torr) addition has no influence on the cathode work function. For pressures higher than 1 torr (3 torr



and 10 torr) the addition of the noble gas to the cesium diode decreases the cathode work function.

This effect is clearly evidentiated in Fig. 2, where the dependence of $(\phi_0 - \phi_E) / (\phi_0 - \phi_{Cs})$, where ϕ_0 is the bare work function of molybdenum, ϕ_E is the measured work function and ϕ_{Cs} is the work function of the cesium, is represented versus the coverage degree θ . The obtained curve in Fig. 2 incorporates the data from Fig. 1 for $T_c = 1373^\circ\text{K}$ and $T_c = 1173^\circ\text{K}$, for pure cesium and with 3 torr and 10 torr added xenon. As an example, in Fig. 2 three points corresponding to the same cesium pressure and with and without added noble gas are evidentiated. A significant change in coverage is observed, the value of θ increasing with noble gas addition.

There are three effects which can be considered as responsible for the change of the surface coverage with cesium atoms



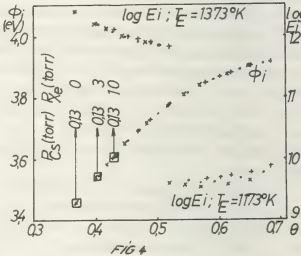
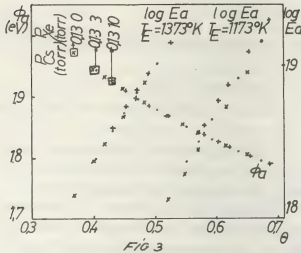
at the addition of the noble gas:

- the decrease of the cesium atoms density in the interelectrode space due to the increased thermo-diffusion;
- the decrease of the cathode temperature due to the gas thermal conductivity;
- the modification of the cesium atoms adsorption and desorption rates on the cathode surface due to the interaction at the surface level between cesium atoms and added noble gas atoms.

The first effect can only lower the coverage degree θ . The second one can explain the coverage increase only partly, because the cathode temperature is maintained at the same value.

The influence of the noble gas addition on cesium adsorption and desorption phenomena at the higher noble gas pressure can be considered as affecting the co-coverage degree. In order to evidentiate this effect, the desorption energy ϕ_a and desorption rate, $\log E_a$ for neutral cesium atoms and respectively, ϕ_i and $\log E_i$ for desorbed cesium ions (calculated using /3/) are given in Fig. 3 and Fig. 4. From these figures it results that noble gas addition determines an increase of the desorption rate for neutral cesium atoms and a slight decrease of the desorption rate for cesium ions from the cathode surface.

In conclusion, the noble gas addition



to the cesium thermionic diode above a critical pressure value changes the desorption and adsorption rates of cesium on cathode surface. Further experimental and theoretical works are necessary for detailed consideration of the observed phenomena in this experiment.

References

/1/ G. Musa et al. - Preprint P.P. 1 (1977)
/2/ N.S. Rasor - IXth Int. Conf. Ion. Gas, Bucharest (1969)
/3/ J.D. Levine, E.P. Gyftopoulos - Surface Science 1, 171;225 (1964)

INFLUENCE OF THE INTERELECTRODIC CHARGE DIFFUSION OUTSIDE OF THE GAP ON THE THERMIONIC DIODE VI CHARACTERISTICS

A. Baltog and G. Musa

Institute of Physics and Technology for Radiation Devices, P.O. Box 5207 Magurele-Bucharest Romania.

The current voltage characteristics of a thermionic diode is strongly dependent of the interelectrodic charge density. If there are no ions, the space charge is purely electronic and the VI characteristics are space charge limited. If there are ions produced by surface or volume ionization the electronic space charge is compensated (undercompensated, compensated or overcompensated). In order to evidenciate the contribution of the wall diffused charges to the interelectrodic charge density we used a special designed thermionic planar diode, with variable distance.

The cathode-anode space is surrounded (including the electrodes) by a grid, which is provided with an independent external connection. This grid can be biased positively or negatively against the cathode, the applied voltage being 0 or ± 3 V dc. For every of these voltages (V_g) applied on the grid we measured the volt-ampere characteristics of the cathode-anode space for the following experimental condition: $T_E = 1023$ - 1373°K , $d = 0,2$ - $2,5$ mm, cesium pressure $p_{Cs} = 0,13$ - $0,9$ torr. All the volt-ampere characteristics were measured again at each pressure of the added noble gas to the cesium vapours, the values of the added xenon pressure being 0; 0,5; 1; 3 and 10 torr.

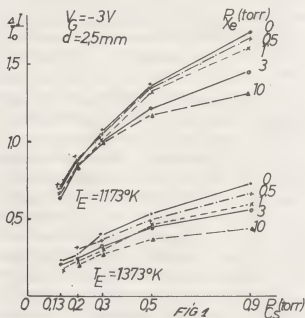
The noble gas addition has a direct effect to the charge diffusion, which must decrease with increased xenon pressure. The choice of xenon is due to the appropriate mass number of cesium and xenon.

Let us consider first the volt-ampere characteristics when there is no discharge condition in the thermionic diode. If I is

the current value right before the characteristics turn out to the discharge mode (sudden increase of the current at constant voltage) than $I_0(V_g=0 \text{ V})$ is this current value for 0 voltage on the grid, $I(V_g=\pm 3 \text{ V})$ is the current value when the grid potential is ± 3 V.

In fig. 1 are given the measured values of $(\Delta I/I_0) = [I(V_g=-3 \text{ V}) - I_0(V_g=0 \text{ V})]/I_0(V_g=0 \text{ V})$ for two emitter temperatures and previously mentioned values of the xenon pressures represented versus cesium vapour pressures

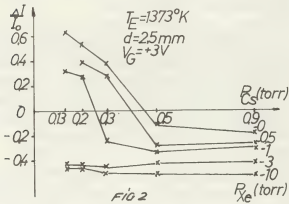
An increase of the electronic current



appears when the grid potential is -3 V, due to the repelling effect of the outside cylindrical for the diffused electrons outside of the interelectrodic gap. This effect is more evident for low emitter temperatures when surface ionization is practically negligible. In this case, due to the significant electronic space charge and nearly zero potential difference between cathode and anode,

the diffusion of electrons outside the interelectrode space is important. At higher emitter temperature there is a partial electronic space charge compensation due to surface ionization of the cesium atoms which subsequent lowering of the values of the relative diode current increase $\Delta I/I_0$. The xenon addition lower the electron diffusion due to the decrease of the mobility of the electrons.

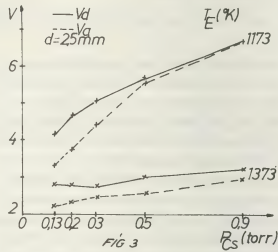
For a positive voltage (+3 V) on the grid, the behaviour of $\Delta I/I_0$ is changed drastically as it is shown in fig. 2. The main effect is the electron extraction



from the interelectrode space with subsequent reduction of the diode current. At the considered temperature of the emitter an additional effect appears as a result of the ion loss reduction which is important only at low cesium and xenon pressures. Because one ion can compensate the effect of nearly 500 electrons to the space charge, slight change in ion loss can give to significant change in the electronic current. At higher cesium or gas pressures the diffusion of ions is reduced faster than that of electrons [1].

The changes in the VI characteristics of the thermionic diode at the application of positive or negative voltages on the grid can be useful in order to define the real breakdown point. Indeed, at this point of the diode potential V_a the differences between characteristics with 0 V, -3 V and +3 V on the grid, are practically negligible, due to the anode glow which produces a potential trap in

the interelectrode gap with practically no charge diffusion outside the gap [2]. In the fig. 3, are given the value of the breakdown voltages V_d taken as usual and



the voltage V_a as before defined. Because V_a is a real appearance of anode glow fig. 3 gives us the error in the appreciation of the breakdown voltage for various parameters of the diode.

In conclusion, the use of the grid gives information on the charge loss outside the emitter collector space of thermionic diodes, pointing out the range where such losses are important. Consequently, a better geometry which lower the charge loss is a long cylindrical electrode structure.

References

/1/ G. Musa, D. Popescu, A. Baltog - Rev. Roum. Phys., 13, nr. 1, 73 (1968)
/2/ G. Musa et al. - Proc. 3rd Int. Conf. Therm. Electr. Pow. Gen., Julich(1972)

THE INVESTIGATION OF PHYSICAL PROPERTIES OF THE NEAR ELECTRODE REGION OF HF DISCHARGE

A.A. Kuzovnikov, V.L. Kovalevskii, V.P. Savinov and V.G. Yakunin.

Department of Physics, Moscow State University, U.S.S.R.

This paper is devoted to the investigation of near electrode region (NER) of High frequency discharge (HFD) of E-type. Up to now no satisfactory study has been made of the physical mechanism of such HFD, whose characteristic property is the occurrence of the DC electric fields, caused by HF-detection [1], and the streams of fast electrons [2] in the NER. HFD of the radiofrequency range in the *He*, *Ne* and *Ar* has been investigated. The discharge was produced in tubes of 40 mm diameter with flat external and internal electrodes. To investigate the NER a study was made of the spatial distribution of intensity of integral luminescence $I(x)$ and some spectral lines $I_{\lambda}(x)$. A comparative study was made of $I(x)$ and $I_{\lambda}(x)$ for HFD and the direct current glow discharge (DCGD).

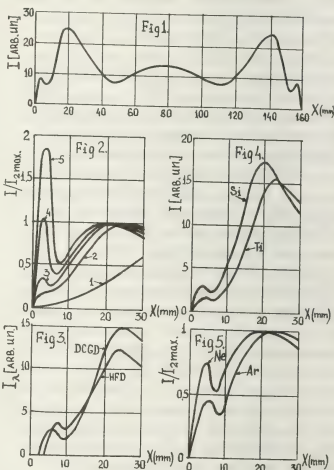
RESULTS. 1) The distribution $I(x)$ in a summetrical HFD in *He* ($p=0,25$ torr, HF voltage $V_{\omega}=400$ v, frequency $f=4$ Mc) with external electrodes is shown in Fig.1. 2) The dependence of $I(x)$ in the NER of HFD in *Ne* ($p=0,25$ torr, $f=2$ Mc) on V_{ω} is illustrated in Fig.2, where 1-100v, 2-300v, 3-600v, 4-800v, 5-1000v. 3) Fig.3 shows the spectral line *Ar* Π 4052 Å distribution $I_{\lambda}(x)$ in the NER of HFD and in the cathode region of DCGD in the same discharge tube (*Ar*, $p=0,3$ torr, $f=1,5$ Mc, $V=700$ v in both cases). 4) It is found that at $V_{\omega} \geq 400$ v the distributions $I(x)$ in HFD and DCGD are analogous and are equally dependent on the voltage supporting the discharge. 5) The dependence of $I(x)$ in HFD in *He* ($p=0,25$ torr, $f=4$ Mc, $V_{\omega}=500$ v) on the electrode material is illustrated in Fig.4. 6) The dependence of $I(x)$ on the kind of gas at the fixed re-

gime of HFD ($p=0,2$ torr, $f=2$ Mc, $V_{\omega}=500$ v) in the discharge tube with external electrodes is shown in Fig.5.

DISCUSSION. As shown in Fig.1, $I(x)$ in HFD contains in the neighbourhood of the electrode all the inhomogeneities of luminescence characteristic of the cathode fall region DCGD. The homogeneous region in the centre has the appearance of a positive column. We see in Fig.2 that the mentioned distribution $I(x)$ in HFD is formed gradually with the increase of V_{ω} . At low voltages ($V_{\omega} < 300$ v) $I(x)$ has its maximum in the centre of the discharge gap, falling monotonously to the electrodes without any characteristic structure of $I(x)$ DCGD. The monotonous fall of luminescence intensity from the centre to the electrodes corresponds to the distribution $I(x)$ in the α -type HF discharge. In this discharge the balance of charged particles is due to the volume ionisation by electrons whose energies are determined by the intensity value of HF field at the particular point of space, and by the diffusion departure of charged particles onto the walls and electrodes. As shown in Fig.3, the distribution $I_{\lambda}(x)$ for the spectral line *Ar* Π 4052 Å (as well as $I(x)$) in HFD at $V_{\omega} > 300$ v is analogous to $I_{\lambda}(x)$ in DCGD, that is, in a γ -type discharge, where the emission processes on the electrode and the electrone avalanche in the NER are the determining factors. In connection with the coincidence of $I(x)$ and $I_{\lambda}(x)$ in the NER of HFD and DCGD, one may draw analogy between the luminescing region of both discharges. It is natural to suggest that due to its physical properties the 1st luminescence

maximum region nearest to the electrode, in HFD is analogous to the "cathode luminescence" of DCGD, it is also reasonable to consider the 2nd next to the electrode maximum in the distribution $I(x)$ of HFD as an analogue of the "negative luminescence" region of DCGD. As known[3], moving from the cathode to the "cathode luminescence" region of DCGD, electrons acquire energy close to the 1st excitation potential, but lower than the gas ionization potential. Thus one may suggest that the luminescence intensity of the "cathode luminescence" region is proportional to the number of electrons emitted from the cathode. Then, the considerable increase of the amplitude of the 1st luminescence maximum with the increase of V_{\sim} shown in Fig. 2, indicates the intensification of emission processes. The distribution $I(x)$ shown in Fig. 4, 5 support this assumption. Actually, according to Fig. 4 the luminescence intensity of the quartz (Si) electrode in the NER is higher than that in the neighbourhood of the Ti-electrode. The emission ability of Si is higher than that of Ti. The emission intensity is determined by the choice of the pair "the gas - the electrode material". According to the investigation[4], the combination "Ar - glass" produces the lowest emission when it is compared with other pairs of "an inert gas - glass". Fig. 5 shows that at similar regimes of HFD in Ar the 1st luminescence maximum is considerably weaker than it is in Ne. These results show that in such HFD γ -processes play an important part. The coincidence of $I(x)$ and $I_A(x)$ in HFD and DCGD shows that the character of motion of the electrons in the NER is the same for these discharges. Hence, in the NER of the HFD concerned the electrons must perform a unidirectional rather than a vibrational motion from the electrode to the discharge center. This is possible, if in the NER the action will be performed by the electric field whose direction is constant rather than variable.

According to the mechanism of HF - detection[1], the time variation of the electrode potential relative to the space potential of plasma will represent unipolar negative pulses. These pulses must appear during negative one-half periods of HF field. When the one-half periods of HF field are positive, the electrode potential must have a small value of the order of the "floating" potential of the discharge plasma. Thus, the properties of the investigated stationary HFD are similar to the properties of the pulsed glowing direct current discharge.



References.

- [1] Butler H.S., Kino G.S., Phys. Fluids, V. 6, N. 9, (1963)/
- [2] Kuzovnikov A.A., Savinov V.P., Radio-technika and Elektronika, V. 18, N. 4, (1973).
- [3] Engel A., Ionized Gases, Oxford, (1955).
- [4] Batanov G.M., Petrov N.N., PTT, V. 1, N. 12, (1959).

MASS-SPECTROMETRIC INVESTIGATION OF THE IONS IN AN AR-HEXAMETHYLDISILOXANE DISCHARGE

M. Schmidt, R. Seefeldt and G. Pohle.

Zentralinstitut für Elektronenphysik, V Akademie der Wissenschaften der DDR, DDR 22 Greifswald.

Introduction: In gas discharges with admixtures of gaseous organic components the formation of thin dielectric films is observed /1/. This glow polymerization is very complex and for an understanding of the film growth processes it is necessary to investigate the plasma and the thin films by many different methods. In this paper results are reported of the mass spectrometric examination of the ions in the positive column of a dc glow discharge in a mixture of argon and hexamethyldisiloxane (HMDS) using the method of ambipolar effusion of charge carriers /2/. First results of mass-spectrometric investigations of a rf discharge plasma with silicon-organic admixtures (vinyltrimethylsilane) are reported by Vasile and Smolinsky /3/.

Experimental conditions: A diagram of the apparatus used in this study is shown in Fig. 1. The diameter of the discharge tube was $2R=1,5$ cm, the distance between the electrodes was 20 cm and that between anode and sampling orifice (diameter= $40\text{ }\mu\text{m}$) was 4 cm. The ions were analysed with the quadrupole mass spectrometer AMP 3. The reference potential for the acceleration voltage was given by a floating wall probe in the discharge tube opposite the sampling orifice. The argon pressure was 0.7 Torr, the pressure of the HMDS admixture varied from 1.10^{-3} – 5.10^{-2} Torr, the discharge current being 10 mA. To avoid disturbances of the mass-spectrometer by thin film formation, we did not use a flow but a closed system. The gas mixture was filled into the discharge tube and after the ignition of the discharge the ion mass spectrum was examined for 20 minutes.

Experimental results and discussion: The investigation of the mass spectrum shows that in the Ar-HMDS-discharge many different kind of ions are found (Fig. 2). The relation between the Ar^+ and Ar_2^+ -ions is similar to that in a pure argon discharge, but with increasing HMDS admixture the relative portion of Ar_2^+ -ions decreases. The ArH^+ ion current became greater than that of Ar^+ ions, and also Ar_2H^+ ions were detected. Especially at low HMDS admixtures H_3^+ -ions and ions in the mass region of 12–18 and 27–32 were observed. The time development of these ions shows that at first the concentration of the H_3^+ ions increases and then stays nearly constant, but the current of the other ions decreases (Fig.3). For higher HMDS admixtures ions are observable with higher molecular weight (Fig.2). The intensity of these ions changes periodically in dependence of the molecular weight. The distance between the maxima amounts to 14 mass units. At these higher HMDS admixtures also the current of the ions with $m/e=17$ (CH_5^+) becomes relatively intensive.

This ion population is similar to that of a methane discharge /4,5/. An remarkable change in the intensity of the ions with even and odd mass numbers as shown in /4/ was not observed. This behaviour may be due to the relatively high electron energy in the small diameter discharge tube, because Vasile and Smolinsky /5/ obtained the same results with an ion extraction from a rf discharge in methane through the electrode, where the ions were sampled from a region with higher electron energy.

The observed ion population in the argon-HMDS discharge suggests the following re-

action mechanism. After ignition thin film formation sets in. As shown through experiments in the flow system /6/ this process comes to an end within the first second. After this, there is an interaction of the plasma with the thin film on the inner surface of the discharge tube. The similarities of the ion mass spectrum to that of a methane discharge lead to the conclusion that from the thin film CH_3 -radicals or even greater particles are removed and ion molecule reactions lead to the formation of the different kinds of ions observable in the ion mass-spectrum of the discharge. As discussed in /5/, for the formation of ions with 4 and more C atoms neutral particles with 2 C atoms are necessary. Mass-spectrometric investigation of the neutral components in an argon HMDS discharge have demonstrated in addition to CH_4 the existence of C_2H_2 and C_2H_6 /6/, so that condensation reactions leading to the formation of heavier particles are possible. The concentration of the organic molecules decreases, because these particles too lead to film formation. Some of these reactions are connected with the formation of hydrogen which is accumulated in the volume.

References:

- /1/ Millard, M., "Synthesis of organic polymer films in plasmas" in "Techniques and Applications of Plasma Chemistry", Ed. Hollahan, J.R., Bell, A.T., New York 1974.
- /2/ Pahl, M., Z.Naturf. **12a**, (1957) 632.
- /3/ Vasile, M.J., Smolinsky, G., Int. J. Mass Spectrom. Ion Phys. **12**(1973)133, 147, **13** (1974) 381.
- /4/ Drost, H., et al XIII. ICPIG 1978 Contr. Paper **1**, 85
Drost, H., Physik und Technik des Plasmas III, Suhl 1972, Proc. **2** Plasmachemie p. 87, Berlin 1972.
- /5/ Vasile M.J., Smolinsky, G., Int. J. Mass Spectrom Ion Phys. **18**(1975)179.
- /6/ Schmidt M., Schulz, K.-D., Maaß, M., Proc. XIII. ICPIG, Contr.Paper **1**,381.
- /7/ Schmidt, M., Beitr. Plasmaphys. **13** (1973) 347.

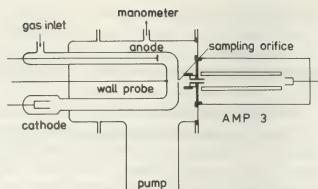


Fig.1. Experimental set up for the mass spectrometric investigations of the ions in the Ar-HMDS-discharge.

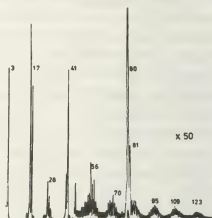


Fig.2. Mass spectrum of the ions in the Ar-HMDS discharge, $p_{\text{Ar}}=0,7$ Torr, $p_{\text{HMDS}}=3 \cdot 10^{-2}$ Torr, $i=10$ mA. For higher m/e values the sensitivity is increased by the factor 50.

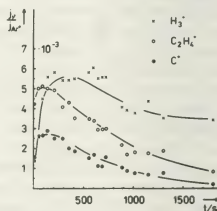


Fig.3. Time development of the relative currents of the H_3^+ , C^+ and C_2H_4^+ ions, $p_{\text{HMDS}}=1 \cdot 10^{-3}$ Torr.

ANODE REGION OF HIGH CURRENT ARC DISCHARGE

G.A. Dyuzhev, N.K. Mitrofanov, S.M. Shkolnik and V.G. Yur'ev.

A.F. Ioffe Physical-Technical Institute, Academy of Sciences of the U.S.S.R., Leningrad, K-21, U.S.S.R.

Wide applications of high current arc discharge in some plasma devices make the investigations of physical phenomena in near-electrode regions to be very important.

The experimental investigations of the anode near-electrode layer in high current arc ($I \sim 10^2 - 10^3$ A) burning freely in alkaline metal vapours at pressures $p = 10^{-2} - 10$ Torr and in noble gases at pressures 1-760 Torr have been carried out. One of methodical peculiarities of a present work is use of a low temperature erosionless multichannel cathode [1] which allows to carry high current densities ($j \sim 10^3$ A/cm²) with no contamination of near-anode plasma with cathode erosion material, which is inherent in spot operation mode. The experiments were carried out in pulse operation, a voltage stabilization taking place. This circumstance permitted to study anode sheath breakdown conditions and anode spot formation mechanism. A pulse supply of discharge (regular pulses with duration ~ 1 ms and repetition rate from 1 Hz up to 12.5 Hz and single pulses) permitted to vary a thermal regime of anode and to carry out a probe diagnostics of dense plasma (plasma concentration $n \sim 10^{13} - 10^{17}$ cm⁻³, electron temperature T_e is up to 3 eV). The plasma parameter radial distributions (n , T_e and plasma potential ϕ) were measured at various distances from anode by using the probe and spectroscopical techniques. Evaluation of probe measurement data was performed by means of a diffusion theory, assuming a charge particle production in the near-probe sheath. [2]

It was showed that at low and intermediate pressures a current transfer in

anode region has been provided by a field current component $j_{\sigma} = \sigma E$ where σ is a highly ionized plasma conductivity, E - an electric field strength. Under these conditions the spreaded at whole anode surface discharge exists with a negative anode drop (AD) in the space charge sheath. The negative AD retards an electron flow from near-anode plasma region to anode so that AD φ_a is determined by relation $-q\varphi_a/kT_e = \ln j_a/j_z$ (j_a - current density to anode, $j_z = \frac{1}{4}qn(a)\bar{v}_e(a)$ - random electron current density) (Fig.1). It is showed that the negative AD stabilizes an anode sheath in respect to a spot formation, and anode collection of a high current density can not result in change of AD sign and in anode spot rise.

The change of AD sign takes place only after near-anode plasma transition to a high ionization state if a cathode provides a sufficiently high anode current density $j_a \sim j_z$. In this case a current saturation owing to current limitation in anode region [3] is observed at current-voltage characteristics. In Fig.2 a dependence of anode saturation current on a random current density is showed. The observed deviations from proportionality which took place at high discharge currents are due to influence of own magnetic field on current transfer [3] in anode region.

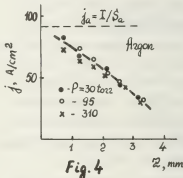
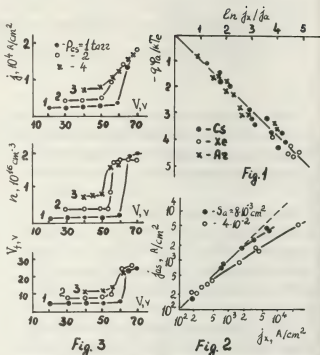
Our studies showed that discharge with a positive AD is unstable in respect to anode spot formation because an anode evaporation and following ionization of evaporised atoms results in increasing $n(a)$ and removed the current limitation mentioned above. In discharge current oscillograms a sharp current growth related

to anode sheath breakdown is observed in time interval τ after the discharge was ignited. This time interval depends on a power supplied by electron flow to anode and on thermal qualities of anode material.

In Fig. 3 the current-voltage characteristics, plasma concentration n and floating potential values V_f of the probe situated near anode are presented for $\tau = 0,5$ msec after the discharge ignition in cesium plasma at pressures $p = 1, 2$ and 4 torr. One can see that anode spot breakdown results in a sharp concentration growth and potential distribution reconstruction. In the case of the spot operation the plasma parameters are independent on p but are determined by anode material vapor pressure according to the spectroscopical data. A surface temperature evaluation of copper anode gives $T_a \sim 2300$ °K under these conditions.

The feature of high current high pressure arc ($p > 100$ torr) is a presence of a sufficiently extensive thermal layer in anode region which results in electron cooling near the anode and in diminution of plasma conductivity [4]. It results in changing of a current transfer mechanism in anode region. The current transfer to anode is produced by electron diffusion.

In Fig. 4 the diffusion current component value is represented along the discharge gap for one of the modes studied. One can see that the contribution of the diffusion current component increases near the anode so that a negative AD occurs. AD value is determined by the relation mentioned above. The change of a current transfer mechanism from a field one (in a positive arc column) to diffusion one (in anode thermal layer) leads to arc contraction near the anode which takes place at a negative AD without anode spot formation. At high discharge currents the contraction development can result in change of AD sign and in the spot formation.



- Fig. 3
- Fig. 4
- Fig. 5
- /1/. G.A.Dyuzhev, E.A.Startsev, S.M.Shkolnik, V.G.Yur'ev. J. Techn. Phys., **48**, 2113, 1978.
 - /2/. F.G.Bakst, G.A.Dyuzhev, N.K.Mitrofanov, S.M.Shkolnik, V.G.Yur'ev. J. Techn. Phys., **43**, 2574, 1973.
 - /3/. G.A.Dyuzhev, S.M.Shkolnik, V.G.Yur'ev. J. Techn. Phys., **48**, 1195, 1978.
 - /4/. L.Peretz, V.A.Nemchinsky. J. Techn. Phys., **42**, 1868, 1977.

EFFECT OF DISCHARGE RADIATION ON ELECTRODE PROCESSES IN HELIUM

L.I. Kiselevskii, N. Ya. Klygin, A.N. Makarevich and D.A. Soloviyanchik.

Institute of Physics, Byelorussian Academy of Sciences, Minsk, U.S.S.R.

The thermionic, autoelectronic and secondary ion-electron emissions are usually considered to be the main electron sources in the cathode region of electric arc and spark discharges. Some other important sources of electrons, with the photoeffect on the cathode surface among them, can be assumed to explain the current strength and cathode spot motion. However, it is extremely difficult to distinguish the role of the photoeffect in experiments, since the far-ultraviolet radiation exhibiting the photoeffect on most metals is greatly absorbed by the discharge atmosphere.

The screening effect of the atmosphere can be substantially diminished while studying a discharge in inert gases optically transparent up to short wavelengths.

Our experiments have been made in the helium atmosphere, whose transmittance is up to 400 Å /1/. This corresponds to ultimate light quantum energy of ~ 25 eV, markedly prevailing over the electron bond energy in solids. Vacuum ultraviolet quanta that pass through the atmosphere of these gases are capable of producing the photoeffect on all metals and alloys. The electric discharge between a flat polished cathode and cone-shaped anode (Cu, Mo, W) was studied under the continuous and pulse conditions with a space between electrodes being equal to ~ 10 mm. The discharge chamber at a pressure of ~ 1 atm was continuously blown through by the helium flow to remove the electrode contaminations of the atmosphere. Under steady conditions, the electrode voltage amounted to 300 V, and the current

ranged from 1 to 5 A, while in the pulse regime these were 8 kV and 100 A, respectively.

In the steady conditions, when the atmospheric purity is ensured, there appeared a discharge with a contracted column and disc cathode ~ 20-30 mm in dia /2/. The reasons for the cathode disc formation have not been earlier discussed. It is important that the cathode current covers the whole disc region and its density cannot be attributed only to the above processes. Both thermionic and autoelectronic emissions little contribute to the current density because of a low cathode surface temperature (several hundreds of degrees) and small electric current strength. The contribution of the secondary ion-electron emission is also small due to a low current density (fractions of A/cm²).

The investigations show that the most probable additional process that causes electron emission from the cathode surface outside the discharge column is photoeffect due to discharge ultraviolet light.

The above is proved by the following. The disc glow never appears in the main discharge shadow created by the dielectric screen placed into the discharge chamber. The disc glow diameter depends on the cathode material. It is greater on the metals having a higher electron work function (Fig.1). This is, probably, due to the fact that with prescribed radiative flux, a larger area is needed to produce the required current for higher electron work function.

Beyond the disc glow, small local discharge

sites shaped as a corona 0.5-3 mm in dia (Fig.2) can be generated on the cathode surface. It should be noted that these sites were registered, being partially and completely isolated from the main discharge.

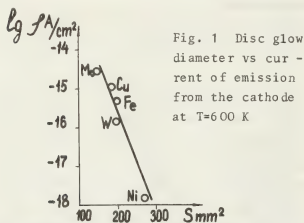


Fig. 2 Discharge with local sites

With the metal probe placed far from the discharge (up to 20 cm) where the gas is at room temperature, relatively large electric currents up to 500 μA are registered. These currents appear only when the probe is in sight of the main discharge. The probe current lasts provided that a quartz plate is mounted in front of the probe and vanishes completely when this plate is replaced by a glass one.

The kinetics of the cathode disc in the pulse regime studied by the streak-photography of glow (Fig.3) also testifies in favor of the above statement.

The data show that the speed of radial spread of the cathode disc can achieve tens of km/s, that greatly exceeds a possible expansion velocity of heated gases in the discharge. Also, we observed that glow starts first in the periphery and then covers the regions close to the discharge centre. It is also important that the cathode disc starts forming not with discharge break-down but much later when

shock waves are no longer generated in the discharge column.

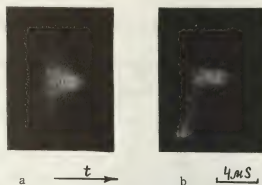


Fig. 3 Streak-photography of the cathode glow: a - symmetric cathode glow, b - asymmetric cathode glow

The formation of asymmetric cathode glow can be observed, too. In this case time variations of the shape and position of the cathode region may be considered as the well-known cathode spot moving over the cathode surface.

The experiments demonstrate that the shape and kinetics of a cathode spot in the helium discharge are affected by some processes. Of importance is also the contribution of photoprocesses on the cathode surface, namely, the cathode surface photoeffect caused by discharge ultraviolet radiation. However, a small radiation path of the vacuum ultraviolet region hampers their observation in other atmospheres.

References

1. Samson J. A. R., J. Opt. Soc. Am., 54, 876, 1964
2. Kiselevskii L. I., Klygin N. Ya., Soloviyanchik D. A., Feshchenko Z. P., Proc. XIIIth International Conference on Phenomena in Ionized Gases, Berlin, 1977, p. 713

DYNAMICS OF THE ELECTRODE PROCESSES ON THE REINFORCED MATERIALS AT HIGH-CURRENT IMPULSING DISCHARGE

A.I. Bushik.

Physical Technical Institute of the Byelorussian, Academy of Sciences, Minsk, U.S.S.R.

The field of composite materials represents a considerable source of possibilities for searching erosion resistant electrodes. The experiments have shown that erosion resistance of composite material electrodes depends upon a chain length of refractory component sintered particles that is, the longer these chains are, the more erosion resistant the material is. It is indicative of perspective application of composite materials with fibrous structure, that is, reinforced materials. Special investigation of integral erosion effect at discharge on the boundary line between two metals have first been presented in 2. It has been shown that in this case asymmetrical erosion traces form and the processes have been interpreted from the electrical erosion migration theory point of view. Up till now the dynamics of the electrode processes on reinforced materials has not been investigated

The electrode processes on reinforced materials: W-Ag, W-Cu, Fe-Al at discharges with square current pulse of 180 μ s and current amplitude of 450-1720 A have been studied by high-speed photorecording. The experiments have been carried out in air at the atmospheric pressure.

Erosion traces at unit discharge on reinforced materials in cathode and anode regimes are characterized by the presence of zones with continuous failure of wires and bonds as well as the ones with failure of wires only along the perimeter. With high density of wires the bond pressed out in the form of lugs is observed (Fig. 1a,b).

From these photographs it follows that electrode processes are of a discrete ty-

pe in space and time which is revealed in appearance and existence of separate spots providing current flow through the boundary between metal and plasma. In this case the spots on reinforced materials are of the same form as on homogeneous materials. However, their distribution due to macroinhomogeneity of reinforced materials has a number of peculiarities. As a whole discharge development

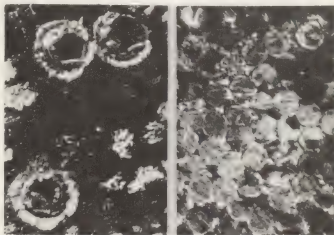


Fig. 1. Erosion trace on a reinforced electrode in the cathode regime
a) Al-Fe; b) W-Ag

occurs during several stages, their duration depending on the material composition 3. Thus in the case of a reinforced material Fe-Al the primary period of the discharge in the cathode regime is characterized by the development of weak luminescent mobile spots. The intense uniform luminescence of wires begins from about the 30th μ s and from the 70th μ s bright, less mobile spots appear. They develop along the perimeters of the wires gradually covering all the area with further transition to the Al-bond. The regions of bright luminescent spots form a bright cloud in the centre of the discharge, its area coinciding in dimensions with the

fused zone of the erosion trace. In the case of the materials W-Cu and W-Ag the process of discharge development is characterized by uniform luminescence of wires up to 20-30 μ s followed by the appearance of bright luminescent spots along the perimeters of the wires which gradually cover all the area of the wires with further transition to the bond.

Irrespective of the polarity of electrodes and alongside with the selectivity of spot appearance some delay in appearing bright luminescent spots is observed in comparison with the case of homogeneous materials. The process of discharge fading is characterized by fading firstly bright luminescent spots on the bond and in the centre of the wires. The spots on the wire periphery are the last to disappear.

The reinforced materials are characterized by a big length and random direction of boundary lines between metals with different physical properties. This influences the distribution of spots 4 in a complicated way. The refractory wires act as kernels stabilizing spots as it happens in the case of Hg-discharge.

Such a distribution of spots substantially influences the development of thermophysical processes which results in a number of peculiarities of the erosion effect. The primary peculiarity consists in the main heat load being performed by the refractory wires of the wire fitting and a more fusible component performs the function of a cooling agent. The fusible component contribution to the erosion process is determined in general by the vaporous phase because its melt is kept from throwing out by the capillary forces.

Hence it follows that the bond must possess good electrical and heat conductivity, a considerable wetting as far as the wire material is concerned. The boiling point is to be somewhat lower and comparable with the melting temperature of the wires. The vapor pressure must be somewhat larger than that of the wire material. This will condition discharge burning on

the wires with smaller density of the current than in the vapor of the wire material.

It is also important that wire sizes should be comparable with the ones of heat interaction zone of metals. This will provide the largest levelling of the heat load on the surface of the reinforced material. The delay in appearance of bright spots making the main contribution to the erosion is determined by the cooling effect of the bond. The whole complex of the above conditions provides a considerable increase of the erosion resistance of reinforced material electrodes in comparison with the ones of homogeneous materials.

R e f e r e n c e s

1. Rakhovsky V.I., Levchenko G.V., Teodorovich O.K., The Break Contact of Electrical Apparatus. Moscow, Energ., 1966.
2. Nekrashevich I.G., Bakuto I.A. Izv. AN BSSR, Ser. Fiz. Tekhn. Nauk, No.3, 1960.
3. Nekrashevich I.G., Bushik A.I., Marek B.A. Sb. The High-Current Electrical Contacts and Electrodes. Kiev, 1972.
4. Nekrashevich I.G., Bushik A.I. Izv. AN BSSR, Ser. Fiz.-Mat. Nauk No.6, 1971.

NOTE ON THE SELF-SUSTAINING CREEP DISCHARGES IN GAS AT THE DIELECTRIC SURFACE

J. Křibukowska and J.S. Brzsko.

Institute of Physics, Warsaw University Branch, Białystok, Poland.

When a thin dielectric specimen is placed between flat cylindrical electrodes of a diameter much smaller than that of the specimen and alternating voltage, $\nu = 50$ Hz is applied, creep discharges take place in the gas phase near the surface. The discharges concentrate in narrow channels oriented radially with respect to the electrode and may be registered by means of a photomultiplier (flashes) or charge amplifier (apparent charge). Study of the conditions in the plasma channel requires investigation of the discharge self-sustenance.

In this note the preliminary results are given which provide a basis for checking the validity of Paschen's law as the self-sustenance criterion. The electric field intensity near the electrode edge can be approximated by the quasi-uniform field up to the critical distance R_0 . The calculations based on the equivalent circuit method [1],[2] reveal that R is strongly dependent on the damping parameter

$$\alpha = (2\pi\nu\epsilon\eta h^{-1})^{1/2} \sim 10^3 \text{ cm}^{-1} \quad (\text{see Fig.1})$$

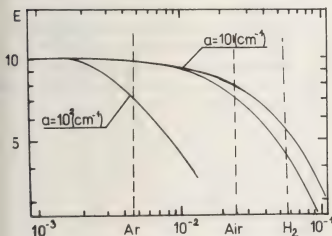


Fig.1

where ϵ and h are the permittivity and thickness of the specimen, respectively, η is the resistivity of the surface gas layer

which strongly depends on the effect of injection of carriers into the specimen [3]. The discharges were detected by means of a high sensitivity and low noise level photomultiplier or a charge amplifier working in the pulse regime. The electronic set-up (Fig.2) allowed us to measure the voltage characteristic of the discharge intensities and to determine the inception voltage U_0^{inc} .

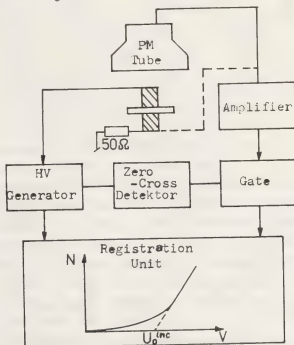


Fig.2

As inception voltage we understand the voltage for which discharges are initiated by carriers evaporated from specimen surface [3]. Measurements were done for a number of dielectric materials as plexi-PG, $\text{NH}_4\text{H}_2\text{PO}_4$ (001) - ADP and bakelite BC. The diameters of the electrode and sample were 5 mm and 20 mm, respectively. The thickness of the sample was 1 mm. A typical dependence of U_0^{inc} on gas pressure is shown in Fig.3. The calculation of the $\partial U_0^{\text{inc}} / \partial p$ ratio was based on Paschen's law,

$$U_0^{\text{inc}} = p R_0 B \ln^{-1} [A p R_0 \ln^{-1} (1 + \frac{1}{8})]$$

where p is the pressure of the specimen ambient gas, R_0 is equivalent distance between flat electrodes for the discharge channel fitted to best agreement with experimental data.

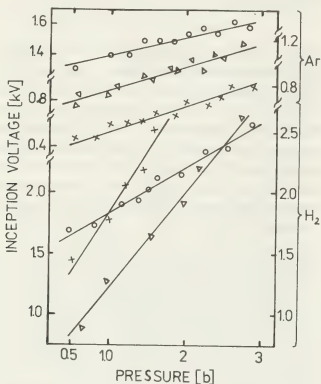


Fig.3

The coefficients A , B and γ were taken from the literature for plane geometry and the investigated gases for example from ref.[4]. The values of R_0 obtained as a result are of the order of 4×10^{-3} cm for argon, 2×10^{-2} cm for air, and 5×10^{-2} cm for hydrogen. The values of U_0^{inc} are 1 - 3 times smaller than the measured ones. Additionally the dependence of R_0 on the thickness of the sample was checked. An increase of the specimen thickness induced an increase of the range of the effective electric field, due to the lowering of the damping parameter α (see Fig.1). As a result longer sparks are allowed, what corresponds to the experimental results;

$$h = 0.22 \text{ mm and } R = 4 \times 10^{-3} \text{ cm,}$$

$$h = 1.3 \text{ mm and } R_0 = 6 \times 10^{-3} \text{ cm.}$$

The results of our measurements allow us to draw the following conclusion:

1. Paschen's law is qualitatively fulfilled for the creep sparks for pressure as well

as for spark length variation, which suggest that the discharges are self-sustaining

2. The spark length R_0 is of the order of 10^{-2} cm, which corresponds to the field intensity of the order of 10^5 Vcm^{-1} and damping parameter $10 - 100 \text{ cm}^{-2}$. As a result our quasi-uniformity assumption of the electric field is fulfilled, see Fig.1.

3. No dependence on the polarity of the electrode has been observed for the untransparent bakelite BC, see Fig.3.

4. The absolute values of U_0^{inc} are strongly dependent on the specimen material even for similar R_0 magnitudes (see Fig.3).

Taking into account that the discharge time is of the order of 10^{-8} s even for sparks 1 cm in length [5] and that U_0^{inc} is independent of polarity of the electrode we can suggest that self-sustenance is based on photoionization effects as well as exchange of carriers between the plasma channel and the specimen surface.

References:

- [1] Busch K., Report Elektrot.Z., A 92, 1971 604
- [2] Brzosko J.S., Grudziński J., Konarzewski A., Wojewódzka A., Zukowski E., J.Phys.D:Appl.Phys. 10 1977 1583
- [3] Brzosko J.S., Zukowski E., Grudziński J., Zukowski W., Konarzewski A., I.E.E.E. Transactions 1979, accepted for publication
- [4] Babikow M.A., Komarow N.S., Siergiejew A., Technika Vysokich Napraženij, Gosenergozdat, Moskva-Leningrad 1963
- [5] Kärkkäinen S., 1974 Finland Tech. Res. Centre Rep. vol.6

PROBABILITY OF THE CREEP DISCHARGES

J.S. Brzosko, E. Zukowski, J. Grudzinski, W. Zukowski and A. Konarzewski.

Institute of Physics, Warsaw University Branch, Białystok, Poland.

When a dielectric sample a few centimeters in diameter and about 1 mm thick is placed in an a.c. field of 1 kV and $f=50\text{Hz}$ between two steel electrodes of several millimeters in diameter a creep discharge occurs under normal conditions in the air at its surface. The discharges concentrate in several narrow channels oriented radially with respect to the electrode axis.

Our previous investigations as well as those presented here were conducted in fully controlled physical parameters of the gas in the experiment: the air temperature humidity and pressure were 20°C , 30% and 1 atm. respectively. The geometry of the detection system as well as electronic set-up has been similar to those published earlier [1][2]. The measurements were done for bakelite, teflon, plexiglass, the results obtained being qualitatively similar.

The aim of the present work was the continuation of the study of the statistical properties of the creep discharges.

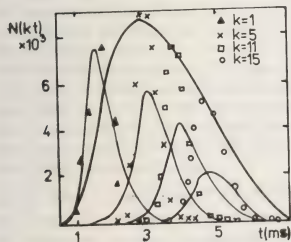


Fig.1

In the course of the investigations were done the measurements of: (i) distributions $N(kt)$ of time elapsed from the zero

cross point to the occurrence of a defined number, k , of discharges, Fig.1, (ii) the influence of the preceding discharge amplitude on the successive one A , Fig.2, (iii) the waiting time, and (iv) distribution $I(\Delta t)$ of time intervals Δt between to

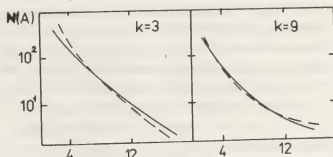


Fig.2

consecutive discharge cascades measured in number of voltage cycles, Fig.3.

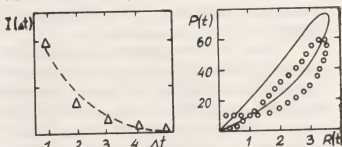


Fig.3

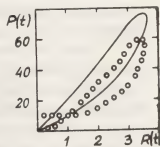


Fig.4

The results for BC sample are shown in Figs. 1-3 by way of the examples. Figs.1,2 are for the applied voltage amplitude exceeding 30% of the inception value. The results in Fig.3 were done for 2% over voltage where discharges occur in cascades of 6-10 time separated discharges with average repetition of cascades 40 ms. The dashed lines in Fig.1 and 2 represent calculations based on Poisson's distribution for variated average intensity taken from simultaneous measurements, solid line. The discharge amplitude distributions Fig.2

were measured for the k-th discharge in the cycle. We compare the amplitude distributions for small and high amplitudes of the preceding discharges, dashed and solid lines, respectively.

The discussed material reveals that the discharge probability is fully described in terms of the Poisson's statistics as well as independence of the discharge amplitude distribution for the successive discharges. This means that all parameters describing discharges are independent of the "history" of the discharges, not only those which are related to the probability of discharge initiation.

Formally the probability of the creep discharge per unit time $P(r, t)$ can be taken as proportional to the number of free electrons in the electric field operation region and to the probability (normalized to unit time) that the accelerated electron can initiate the avalanche $P_a(r, t)$ this is so the Poisson's statistic has been fulfilled

$$\partial P(r, t) = 2\pi r \partial r \bar{\sigma}_e(r, t) P_a(r, t)$$

where: $r = r + x$ is the radius of the ring at the dielectric surface which is under discussion. $\bar{\sigma}_e$ is the density of electrons in the near to the surface air layer.

It has been postulated [2], [3] that a certain number of electrons is attached to the sample surface during the discharge. In effect the electrons are liberated by way of thermal or field emission. The electron density in the gas is proportional to the frequency of detachment and exponentially decrease as a function of the time with half-time of order of 10 ms. As result of the simplification chain the probability of a discharge at time t can be written as

$$P(t) = \pi P_a \bar{\sigma}_e(t) [2r_0 R(t) + R^2(t)]$$

The effective radius of the electrical fields R can be calculated on the base of the equivalent circuit model [1].

A very simple formula describing the probability of the discharge phenomenon was obtained at the costs of introducing assumptions as to: the effective of P_a ,

the exponential character of the attachment effect, the averaging of the surface density $\bar{\sigma}_e$ and validity of equivalent circuit for description of the electrical fields.

The comparison of calculations based on above formula and experimental results reveal a good agreement Fig.4. The discrepancy is result of small knowledge about half-life of the carrier evaporation effect (in $\bar{\sigma}_e$) and preliminary carrier density parameter (in R).

References:

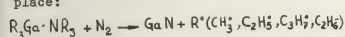
- 1 J.S.Brzosko, J.Grudziński, A.Konarzewski, E.Żukowski, A.Wojewódzka, Journal Phys.D: Appl.Phys. 10, 1977, 2201
- 2 J.S.Brzosko, E.Żukowski, J.Grudziński, W.Żukowski, A.Konarzewski, IEEE Transaction, accept for publ. in 1979
- 3 J.S.Brzosko, J.Grudziński, A.Konarzewski, A.Wojewódzka, E.Żukowski, Journ. Phys.D: Appl.Phys. 10, 1977, 1583

SOME PARTICULARITIES OF THE MOLECULAR EXCHANGE IN A HF LOW PRESSURE DISCHARGE

E.N. Zorina, A.V. Dobrenin, T.O. Popova, T.I. Pavliashvili, O.V. Tolmatshova, S.A. Neustroev and E.B. Sokolov.

The particle transport in the interelectrode space of a HF capacitor discharge is investigated in view of optimization of thin dielectric film deposition process. The concrete process investigated here consists in decomposing organo-metallic compounds and donor-acceptor complexes in the non-equilibrium plasma of a HF discharge to form a GaN film on a single-crystalline surface. As basic reactants we use organo-metallic compounds and co-ordinate complexes based on them, with low vapor pressure so that they can be injected as gases into the plasma reactor.

In the discharge column a chemical reaction of the next kind is assumed to take place:



The so-formed radicals and hydrocarbons are evacuated as gases, and GaN molecules are transported to the single-crystalline surface and are deposited on it the reaction of GaN formation takes place either in the HF plasma column, or in the electrodes spaces. To avoid nitrogen lattice discontinuities in the deposited film, the reacting mixture partial pressure sensibly exceeded the stoichiometric one. The electrical field in the discharge column varied from 50 to 500 v/cm and the plasma parameters were:

$$1 \leq T_e \leq 4 \text{ eV}; 0,1 \leq T_i \leq 0,4 \text{ eV}; 10^{10} \leq n_i \leq 10^{14} \text{ cm}^{-3}$$

Our conclusions on the character of the molecular are based on the analysis of the dependence of the deposition rate on the initial compounds partial pressure, the total pressure of the mixture, the process duration and, mainly, on the

discharge specific power. The obtained linear dependence of the deposition rate on the initial compounds partial pressure and on the total pressure of the gaseous mixture means that the process of GaN film growing is due to gaseous diffusion. Probably, the GaN formation takes place essentially in the plasma column. On dielectric surfaces (sapphire, SiO_2). The deposition rate is larger by a factor of 1,5-2 then on conducting ones. This fact can be explained as the result of an electrical field shielding by the dielectric surface.

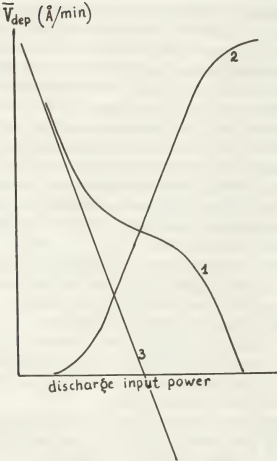
The dependence of the deposition rate on the input power is shown on fig.1 and 2. Probably two competing processes in plasma determine the film growing:

1. The GaN formation as a result of the decomposition of the initial compound.
2. The GaN desorption from the single-crystalline surface.

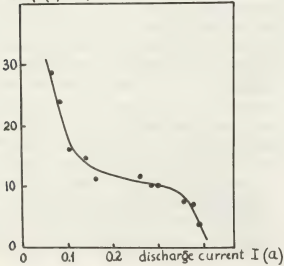
The first process should be characterized by the curve 2 of fig.1, increasing at low power input and saturated at high power input, when the initial compound entering the plasma reactor is fully decomposed within the discharge column. Since the molecule transport to the electrodes is due to diffusion it should depend entirely on the molecule concentration variation in the plasma column so that the curve 2 of fig.1 characterizes also the molecule attachment to the electrodes. The absorption and desorption processes can be characterized by the straight line 3, meaning that the increase of input power causes NGa desorption from the surface, mainly due to electron and ion bombardment. The resulting curve 1 is a conse-

quence of the simultaneous occurrence of the two processes. The experimental data obtained in the present paper and shown on fig.2 confirm the a-priori picture of fig.1.

fig.1



$\bar{V}_{dep} (\text{\AA}/\text{min})$ fig.2



VIII

- Dispositifs variés pour décharges dans les gaz
Miscellaneous discharge devices

THE RF-ION SOURCE RIG 10 FOR INTENSE HYDROGEN ION BEAMS

J. Freisinger, S. Reineck and H.W. Loeb.

1st Institute of Physics, Heinrich-Buff-Ring 16, D-6300 Giessen, F.R.G.

1. INTRODUCTION: Neutral injection is a new field of application of rf-ion sources (1). In comparison with arc discharge sources there are some advantages of our rf-plasma source called RIG 10 (Radio-Frequency-Ion-Generator of 10 cm in diameter): This type of ion source has no discharge electrodes immersed in the discharge plasma. As there are no filaments in contact with the plasma, there are no lifetime (and impurity) problems by filament deterioration. The recombination rate of atomic hydrogen ($2H \rightarrow H_2$) at quartz walls of the discharge vessel is much less ($10^{-4} \div 10^{-3}$) than on metallic ones (2). This results in a high proton fraction of about 90% (1,3). Basic investigations showed that it is possible to gain current densities of 55 ma/cm^2 at an rf-power of 1 kw. In the running experiments the discharge power is increased up to 20 kw. The profile of the plasma density and the radial distribution of the plasma temperature are measured by floating double probes in dependency of the discharge pressure, the rf-frequency, and the rf-power.

2. DESIGN AND MODE OF WORKING OF RIG 10

2.1 Definition of the Components: Concerning the mechanical set-up, the rf-plasma source RIG 10 is very simple. As shown in the half-schematic Fig. 1, it consists of the following components:

1. H_2 -inlet and regulator valve
2. Discharge vessel made of quartz (inner diam.: 10 cm)
3. Distributor: The hydrogen gas enters the discharge chamber radially. Therefore, the stay of the atoms inside the discharge region is enlarged and the probability to be ionized will be increased.
4. Rf-induction coil (air cooled)
5. Extraction system with subcomponents (extraction anode, extraction cathode, decel electrode).

2.2 Mode of Working: In radial direction the hydrogen gas enters the discharge chamber, which is surrounded by the induction coil of an rf-generator. Due to the Maxwellian laws, a high frequency magnetic field B_{rf} and in consequence an electrical rf-field E_{rf} (Fig. 2) is induced. Free electrons inside the discharge region are accelerated by the rf-field. When they have gained sufficient energy, they are able to ionize neutral atoms by inelastic collisions. Thereafter, the secondary electrons - created in this ionization process - are accelerated, too, by the same mechanism. We obtain an intense electrodeless, non-thermal rf-plasma. The beam extraction is accomplished by the conventional accel-decel-technique.

2.3 Block Diagram: Fig. 3 shows the block diagram of the power supply of RIG 10. The rf-generator consists of an rf-driver stage and an air cooled rf-amplifier. It can be tuned from 1 MHz to 30 MHz.

The maximum rf-power is 1.2 kw. The currents to the extraction electrodes and the return current are registered. - Double probes are introduced from the downstream side of the beam into the plasma in the level of the first extraction grid for measuring the plasma parameters in dependence of the radial position. The discharge pressure, the rf-power, and the rf-frequency are varied.

3. ION CURRENT DENSITY PROFILES (Experimental Results)

3.1 Pressure Dependency: In Fig. 4 you see typical ion beam density profiles. The profiles are rotationally symmetrical to the axis of the plasma source. The ion beam density increases with increasing discharge pressure (broken curves). It reaches a maximum of 55 ma/cm^2 at a discharge pressure of 13 μbar ; then the curves for the current densities (solid lines) decrease. In the shape the radial profiles are very similar. They show a plateau, and shift only in the intensity (Fig. 4). For application (1) we allow a decrease in the beam plateau of 5%. Near the walls, lower intensities must be cut-off. For the highest, the 13 μbar -curve of Fig. 4 the area usable for extraction extends out to a distance of 1.5 cm to the wall. This is a very good result - also compared with other sources. The ion beam of RIG 10 has, therefore, a usable diameter of 7 cm.

3.2 Plasma Density and Electron Temperature: The radial distribution of the plasma density (Fig. 5: broken curve) shows a similar shape as the ion current density profile. The plateau-value amounts to $2 \cdot 10^{11} \text{ cm}^{-3}$. - The electron temperature (Fig. 5: solid curve) is highest near the chamber walls, about 80,000 K. It drops to 60,000 K at the axis. This can be easily interpreted by the mode of working of the rf-plasma source (skin-effect).

3.3 Power Dependency: At a fixed discharge pressure of 13 μbar the ion current profiles for different rf-generator power values are plotted in Fig. 6. The current intensity increases almost linear with the rf-power, and reaches an ion current density of 55 ma/cm^2 at 1000 W.

3.4 Generator Frequency: The influence of the rf-generator frequency on the beam profile is relatively small. If we increase the rf-frequency from 1 to 7 MHz, the beam current density changes only about 2 ma/cm^2 . However, the operation was restricted to this small range of variation, because of ignition problems at higher and lower frequencies.

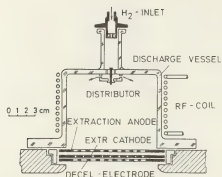


Fig. 1: Definition of the components of RIG 10

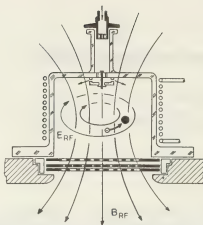


Fig. 2: Principle of rf-discharge (\ominus electron, \circ neutral atom)

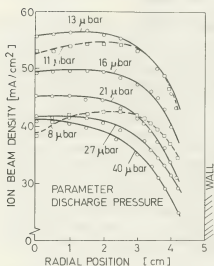


Fig. 4: Ion beam density profile as function of the radial position in the ion source. Discharge power: 1000 w

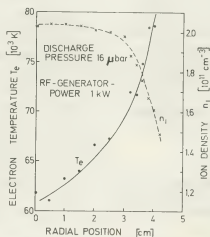


Fig. 5: Radial profile of the electron temperature and the ion density

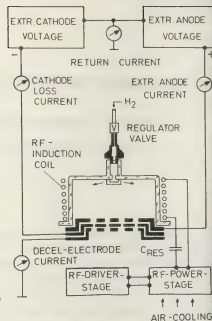


Fig. 3: Blockdiagram of the power supply of RIG 10

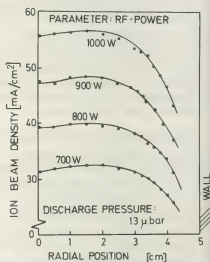


Fig. 6: Ion beam density profile in dependence on the rf-discharge power

4. CONCLUSION: In conclusion we will summarize the main results:

1. The plasma purity can be improved, because the rf-plasma source uses no filaments.
2. The proton fraction in the beam is high as the discharge chamber is made of quartz.
3. The ion density plateau extends out to a distance of 1.5 cm to the plasma chamber walls.
4. The rf-plasma source delivers a total ion beam current of 1 amp at an rf-discharge power of 1 kw. The current density amounts to 55 ma/cm².

Investigations at higher discharge (20 kw) are running, current densities of 200 to 250 ma/cm² will be realized in near future.

5. ACKNOWLEDGEMENT: This paper is based on the Doctorate Thesis of the second author. The work is supported by the Deutsche Forschungsgemeinschaft (German Research Agency).

6. REFERENCES

- (1) J. Freisinger, S. Reineck, H.W. Loeb, "An Rf-Ion Source for Neutral Injection", Proc. of the 10th Symposium on Fusion Technology, Padova, Italy, 4.-9. Sept. 1978
- (2) L. Vally, "Atom and Ion Sources", John Wiley John Wiley & Son, London 1977
- (3) S. Flügge, "Handbuch der Physik", Bd. XXXIII, "Korpuskularoptik", Springer-Verlag, Berlin-Göttingen-Heidelberg 1956, p. 80/81

SURFACE PLASMA SOURCE OF HYDROGEN ATOMS WITH AN ENERGY OF HUNDREDS eV

V.G. Dudnikov and G.I. Fiksel'.

Institute of Nuclear Physics, Novosibirsk, U.S.S.R.

1. The efficiency of accelerated particle beam production with the help of the well developed electrostatic beam-forming systems decreases significantly when accelerating voltage decreases below one kilovolt /1/. In order to produce intense beams of accelerated particles with an energy of hundreds eV, which are necessary for many applications, one can use the surface plasma method developed for production of negative ions /2/. Negative ions are formed in surface plasma sources on the bombarded surface of electrodes with a minimized work function due to the capture of electrons from the electrodes at the electron affinity level of the sputtered and reflected particles. These ions are accelerated by the near-electrode voltage drop accelerating positive ions from the discharge plasma to the electrode. In the negative ion sources the significant share of negative ions is destroyed during their movement through plasma and transformed to the directed flux of atoms with an energy of hundreds eV. One may destroy all accelerated negative ions by intensifying the destruction of them, due to thickening of the plasma and gas gap, and obtain atom fluxes with an emission density of several amperes per cm^2 .

2. To produce accelerated atom flux-

es, there were used the surface plasma sources with planotron configuration of electrodes described in detail in /3/ with a $1 \times 10 \text{ mm}^2$ emission slit and without extraction system. The source worked in a pulse mode with half-sinusoidal pulses of current up to 50 A, pulse duration up to 3 msec and repetition frequency up to 10 Hz. The fluxes of accelerated atoms and flux density distributions were detected by the secondary emission detector (SED) and by the pulse bolometer with the system of grids to remove charged particles. The bolometer used is analogous to that described in /4/: radiation of a foil preliminary heated up to 10^3 K is detected by a photodiode; the pulse heating of a foil by an atom flux leads to an increase of radiation. (Preliminary heating is introduced to shift the spectra of pulse radiation to the sensitive region of photodiode.) Bolometer sensitivity was 1 mA per joule.

3. When feeding the source with cesium the discharge voltage decreases from 600+400 V to 100+150 V and the SED and bolometer signals are sharply increased. The flux density distributions detected by the SED and the bolometer were the same.

The HWHM divergence is $\pm 10^\circ$. The flux

emission density is 1 A/cm^2 at a 5 A/cm^2 discharge current density (discharge current is 18 A). The discharge current dependence is linear when discharge voltage is fixed.

Additional experiments have shown that the fraction of discharge radiation to the SER and bolometer signals was less than 10%: the signals decreased 10+30-fold when we changed hydrogen to helium, removed the central cathode plate (Penne discharge), and closed the entrance hole of bolometer by LiF glass with a 70% transparency at a wavelength of 1200 Å.

From the 90° beam deflection in flat capacitor there were found the energy spectra of negative ions produced due to the charge exchange of accelerated atoms on a gas, outcoming from the source and on a special cesium target. (Negative ions from the source are deflected by a magnetic field and not detected.)

The spectra obtained are identical to the high-energy part of spectra of negative ions extracted from planotron sources /5/: when discharge voltage is 130 V, there were detected the particles with an energy of 90+300 eV and with maximum of spectrum at 160 eV; when discharge voltage was 300 eV, detected particles had an energy of 200+500 eV with maximum of spectrum at 330 eV.

References:

- /1/ M.D.Gabovich, Physics and Technology of Plasma Ion Sources, Moscow, Atomisdat, 1972.
- /2/ Yu.I.Bel'chenko, G.I.Dimov, V.G.Dud-

nikov, Preprint INP 77-50, Novosibirsk 1972. Proc. Symp. Production and Neutralization of Negative Ions and Beams, BNL, Upton, N.Y., 1977.

- /3/ Yu.I.Bel'chenko, G.I.Dimov, V.G.Dudnikov, ZhTF, 45, 68 (1975).
- /4/ M.G.Kagansky, S.I.Lashkul, K.G.Shakhovets, Fizika Plasmy, 3, 681 (1977).
- /5/ Yu.I.Bel'chenko, G.I.Dimov, V.G.Dudnikov, Izvestia AN SSSR, Ser. Fiz., 37, 2573 (1973).

THE ARC DISCHARGE OF LOW PRESSURE WITH TWO CONSTRICTED CHANNELS AND THE ANODE PLASMA OF LARGE CROSS-SECTION

N.N. Koval, Yu.E. Kreindel and P.M. Shanin.

The U.S.S.R. Academy of Sciences, Siberian Branch, the High-Current Electronics Institute, Tomsk.

The plasma penetration out of the constricted discharge into the expander is used for creating the plasma cathodes for getting the broad electron beams /1/. Such method of forming the emission surface permits keeping the low pressure in the accelerating spacing of the diode with the plasma emitter, securing its high electric strength but leads to the great oscillation of the diode electron current whose part doesn't exceed 30-40 p.c. of the discharge current.

In the present work there has been described the electrode system and the conditions of burning the discharge with the large cross-section anodic plasma which can be used as plasma emitter of electrons free of the above-mentioned drawbacks.

The experimental scheme is shown in Fig.1. The electrode system contains the rectangular Penning cell formed by the cold magnesium cathodes 1 and the anode 2 with the constricted hole by 1 mm diameter. The magnetic field formed between the cathodes by the permanent magnet is strained by the ferromagnetic insert in the region of the constricted hole. The second constricted electrode 3 is made

as a hollow cylinder with the diameter 200 mm and depth 100 mm, in the bottom of which, reversed to the anode 2, there is the constricted hole 1 mm coaxial with the first hole. The space between the constricted electrodes 2 and 3 is 0,6 mm. The rectangular electrode 4 is the main anode of the discharge chamber. The working gas is being injected into the cathode spacing. Thereby thanks to the little capacity of the constricted holes by the gas consumption 20-60 cm³/h, the pressure in the Penning cell was 10⁻² torr and in the electrode cavity 3, it doesn't exceed 10⁻⁴ torr.

The artificial line 5 forming the impulses with the duration 70 μs through resistance R₁ is connected between the cathodes and the constricted electrode 3. The positive voltage 2000 V is applied at the anode of the Penning cell through the resistance R₂ limiting the current to 100 μA. The grid anode is connected to the source of the direct voltage 6. The currents are measured by Rogovski belts 7-9.

The ignition of discharge with two constricted channels is initiated by the Penning discharge which due to the limiting of the current by the resistance and owing to the positive potential of the near placed electrode 3 is thrown over this electrode. As a result there is excited a known arc constricted discharge with a cold cathode in a magnetic field /2/, which is used in the plasma electron sources /3/.

The ignition voltage of such a discharge is 1-1,5 kV and the burning voltage is 50-150 V. Through the hole in this

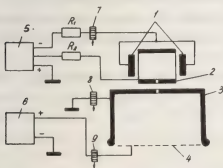


Fig.1. Diagram of the experimental arrangement.

electrode 3 in the space between this electrode and the grid anode, out of the discharge it appears plasma and electron stream accelerated in the double layer which is formed on the cathode side of the constricted hole in the electrode 2. At low potentials the grid anode operates as the probe with the current which composes 10-40 p.c. of the cathode current I_k and has high frequency modulation. However, while rising the potential U_c of the grid anode by the definite relations between this potential, current and pressure, the gas ionization in the electrode cavity 3, leads to the breakdown of the space between the plasma and the grid anode. Thus, the discharge constricted by the channels in the electrodes 2 and 3 is ignited on the grid anode. At the above indicated gas consumption the discharge ignition takes place at $U_c = 180$ V and $I_k = 15$ A. By this the current polarity in the circuit of the electrode 3 changes, the grid anode current rises up to the value near the cathode current and the current oscillations vanish. The cathode current oscillogram, the oscillograms of the corresponding current in the grid anode at two values of potential U_c and the oscillogram of

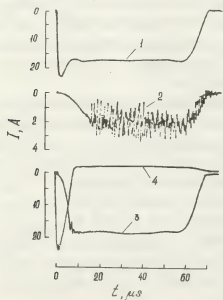


Fig.2. Oscillogram of the currents
1-cathode current, 2-grid anode current
($U_g = 100$ V), 3-grid anode current ($U_g = 200$ V)
4-electrode (3) current.

the current in the circuit of the electrode 3 are shown in Fig.2. The current increase of the grid anode after the discharge ignition and the correspondence decrease of the electrode 3 current are conditioned by the potential redistribution in the discharge, therein, as the probe measurements showed, the space between the electrode 3 and the grid anode is found to be filled in the plasma having the potential near the grid anode potential.

The characteristic peculiarity of the discharge with two constricted channels and the anode part being at low pressure is a large cross-section of the anode part with the relatively uniform distribution of density of the anode current. The burning voltage of such a discharge in the experiments didn't exceed 300 V but the current arrived at 30 A.

The examined discharge was used as an emitter for getting the broad electron beam. For this purpose the accelerating electrode was placed behind the grid anode with cells $1,6 \times 1,6$ mm² at a distance of 15 cm. The electron beam with the cross-section of 300 cm² and the current of 15 A was obtained at the accelerating voltage of 250 kV at the pressure of 10^{-4} torr and the discharge current of 16 A.

REFERENCES

- /1/ Kreindel Ju. E., Plasma electron sources., "Atomisdat," Moscow, 1977.
- /2/ Kreindel Ju. E., Nikitinski V. A., Proc. Tenth Intern. Conf. on Phenomena in Ioniz. Gases, Oxford, 217, 1971.
- /3/ Kasmin G. S. et al, Instrum. Exp. Techn (USSR), 4, 19, 1977.

LASER/FIBER OPTIC BREAKDOWN OF A PULSE CHARGED 90% Ar-10% N₂ GAS SWITCHL.L. Hatfield, H.C. Harjes^{*}, M. Kristiansen^{*}, A.H. Guenther^{*} and K.H. Schönback^{**}.^{*}Department Physics,^{*}Department Elec. Eng. Texas Technical University, Lubbock, Texas U.S.A. 79409.^{**}Technische Hochschule Darmstadt, F.R.G.

Abstract

Precise laser initiation of the breakdown in a pulse charged gas switch is described. A novel feature is the transport of the 40 ns triggering laser pulse through a 1.5 m long 1 mm diameter optical fiber. Optimization of gas breakdown characteristics was necessary as a result of the limited power transported through the fiber. Low, nanosecond delay and jitter were achieved at reduced fields approaching 180 V/cm-Torr in the overvolted gas gap through the use of 90% argon/10% nitrogen gas mixtures. The influence of laser power, gas mixture, focal point location, pressure, time of laser insertion etc. on switch performance is presented.

Laser triggered switching of high voltage spark gaps was first demonstrated more than a decade ago by Guenther and Griffin and has since been the subject of many investigations^{1,2}. The principal advantages of this type of triggering are electrical isolation of the trigger from high voltages, controllable switching delay, and subnanosecond jitter. On the other hand, optical access to the gap must be available, usually through occasionally complex system design, and care taken to avoid misalignment or environmental degradation of optical elements.

To reduce greatly the above complexity, a novel laser triggered spark gap has been constructed featuring the use of an optical fiber to transport the laser light along a circuitous route to the gap. Problems of optical alignment and the influence of the environment are all but eliminated. In addition, the use of multiple fibers illuminated by the same laser to trigger several gaps synchro-

nously, or to initiate several parallel arc channels simultaneously, appears to be trivial extensions of the technique.

The spark gap employed is a modified electrically triggered gap normally used to switch a water dielectric Blumlein line producing a 40 ns output pulse. The Blumlein is pulse charged by a Marx generator with a 250 ns erection time. The maximum voltage and energy are 250 kV and about 1 kJ. The laser beam is introduced coaxially through a 6 mm aperture in the grounded cathode and focused 1 mm inside the surface of the charged machinable tungsten anode. A schematic of the optical system is shown in Fig. 1. The lenses are U-V grade quartz and the 1.5 m long fiber is a 1 mm dia. single quartz element.

Measurements with an integrating energy meter indicate a 25% throughput efficiency in bringing the laser light into the gap. The maximum allowable laser power is determined by the permissible power density which does not cause damage to the entrance surface of the quartz fiber. This appears to be $> 5 \times 10^9$ W/cm².

The conditions for switching gas filled spark gaps with short delay and subnanosecond jitter are reviewed in references¹ and 2. The gas used should have a large secondary electron coefficient, the switch should be triggered at a large fraction of the self-breakdown voltage, the laser pulse should be longer than the switching delay, and the laser power should usually be greater than ~ 6 MW for DC charged gaps.

Since our study indicates an efficiency of ~ 25% in the overall optical system from laser output to entrance into the spark gap the requirement of 6 MW of laser power in the gap implies a rather modest input laser power of 24 MW. The intensity at the input surface of the optical fiber is then about 3×10^9 W/cm² which is below the estimated threshold for surface damage. No surface damage has been observed at the fiber at

* Supported in part by a contract from the Department of Energy, administered by Lawrence Livermore Laboratories.

this intensity, although higher intensities have produced cracks and internal damage. The efficiency of the optical system is limited by insufficient collection, reflection at the surfaces of lenses, attenuation in the fiber due to absorption and scattering, and the spreading introduced as the beam passes through the fiber. The beam emerges from the 1 mm quartz fiber with a 60 degree full-angle divergence at the e^{-1} points. To render this beam parallel would require an $f/1$ lens but as a practical compromise an $f/3$ lens is used in this system, thus lowering the efficiency. Another compromise is necessary when focusing the beam onto the anode through a hole in the cathode. As the entrance aperture in the cathode is made larger to accommodate a faster optical system the electric field in the gap becomes increasingly non-uniform. This system has a 6 mm aperture in the 10 cm diameter cathode and a $f/3$ lens is used in this case, as well. In an effort to improve the over-all throughput efficiency, the use of a fiber which introduces less divergence is being explored together with the use of anti-reflection coated optics. Results using a 0.4 mm dia. fiber which produces an output full angle of < 20 degrees will be presented.

The use of the optical fiber to transport the laser light makes simultaneous triggering of many spark gaps more attractive because it eliminates most of the optical alignment problems associated with transport of the laser beam and greatly reduces the cost. Environmental problems with the optics and personnel safety problems are also alleviated. However, if many fibers are to be illuminated with the same laser the power required could become quite large. Therefore, the optimization of gas breakdown conditions to minimize the required laser power is of great importance. Typical switch conditions employed during this study were as follows: 1 cm gap spacing; gas pressure ~ 686 Torr; gas mixture, 90% Ar-10% N_2 ; gap pulse charged to voltages < 120 kV; laser pulse length of 30-40 ns; and a laser power in the gap of 0.5-6 MW. Gas breakdown is produced in the overvoltaged gap while it is being charged by the Marx bank by firing the laser at an appropriate time after initiating erection of the Marx. With a laser power of only 2 MW in the gap we have observed nanosecond jitter and switching delay as short as 10 ns. (The reason for the good performance at this low laser power is that the gap is

pulse charged and overvolted compared to the DC breakdown voltage.³) Results as a function of laser power will be presented. The effects of changing the gas pressure and the gas mixture to 50% Ar - 50% N_2 will be discussed. The sensitivity of the triggering of the gap to the position of the focal point of the laser will also be reported.

Time integrated photographs of the gas breakdown show both single channel and multichannel modes depending on the condition of operation. Streak camera photographs of the breakdown will also be shown.

1. A. H. Guenther and J. R. Bettis, J. Phys. D. **11**, 1577 (1978).
2. Electrical Breakdown of Gases, J. M. Meeks and J. D. Craggs, Eds., John Wiley & Sons (1978) Ch. 7 and 9.
3. L. P. Bradley and T. J. Davies, IEEE JQE **QE-7**, 464 (1971) and L. P. Bradley, J. Appl. Phys. **43**, 886 (1972).

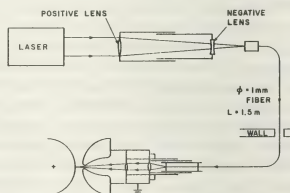


Fig. 1. Schematic Diagram of Laser/Fiber Optic Triggered High Voltage Switch Assembly.

INVESTIGATION OF ELECTRICAL EXPLOSION OF CYLINDRICAL FOILS IN AIR. COAXIAL HIGH-CURRENT DISCHARGES

V.A. Burtsev, V.A. Dubyanski, N.P. Egorov, M.P. Kasatkina, A.B. Produvnov and I.V. Shestakov.

D.V. Efremov Scientific Research Institute of Electrophysical Apparatus, Leningrad U.S.S.R.

Recently great interest has been revealed in electrical explosion of foils due to wide possibilities of its practical application. These possibilities range from foil current breakers, in which precautions are taken to suppress shunting discharge [1-3], to electric discharge light sources [4-7], in which exploding foils initiate and form high-current discharge.

The present report gives the investigation results of electrical explosion of cylindrical foils in air and explosion-initiated high-current discharge. The experiments were carried out in two regimes:

a) the exploded foil cylinder was an internal current-carrying conductor of the coaxial system (geometry of self-pressed discharge);

b) the cylinder was an external current-carrying conductor of the coaxial system (geometry of expanding discharge). In the experiments the aluminium foil cylinders, mounted on an insulating rod, were exploded. The cylinder length and perimeter ($l = 550$ mm, $b = 150$ mm) remained constant, only the foil thickness varied ($h = 6, 10, 20, 50 \mu\text{m}$). The experiments were carried out at a capacitor bank charge voltage $U_0 = 35$ kV which corresponded to a stored energy $W_0 = 180$ kJ.

In our experiments besides of the Rogovsky loop for measuring discharge current and the voltage divider on discharge gap for recording its ohmic component, number of diagnostics for studying the high-current discharge properties have been applied. They included high-speed photography of discharge, recording of plasma emission

spectrum, measurements of its brightness temperature T at various wave lengths, probe measurements of plasma magnetic fields and calorimetric measurements of radiation energy.

The experimental set-up and diagnostic methods are described in detail elsewhere [3,4].

As earlier study on electrical explosion of foils in self-pressed discharge geometry showed [3-5], electric-discharge plasma radiation in the region of wave lengths $\lambda = 270-500$ nm approaches black body radiation. Maximum brightness temperature of plasma and rate of its radial expanding do not depend on the mass of exploding foils ($T \approx 2.5$ eV, $v = 1.5 \pm 3$ km/s).

At the same time the change in foil thickness in this range leads to the significant change in $T(t)$ dependence. With the "thin" foils which serve only to initiate the discharge, plasma achieves T_{max} in a time equal roughly a quarter of the discharge circuit natural period. With the "thick foils" which serve also as commutators to switch the current into gas discharge, effect of "sharpening" of plasma radiation pulse is observed.

In fig.1a,b the results of measurements at the investigation of exploding foils in the expanding discharge geometry are given. The upper parts of fig.1 show initial curves—discharge current $I(t)$ and voltage at a discharge gap $U(t)$. Absolute and relative resistance curves $R(t)$, R/R_0 , where R_0 is the initial resistance of the foil cylinder; curves of total electric power $P = UI$ and power $p = P/m_0$ per unit of the foil mass;

curves of energy $W(t) = \int_0^t P \cdot dt$ deposited to the instant t and energy per unit of the foil mass $w = W/m_0$, these curves are calculated.

The bottom parts of fig.1 shows temporal dependences of radii r and r_s for the plasma luminous column and secondary shock wave, and of brightness temperature T measured at various wave lengths.

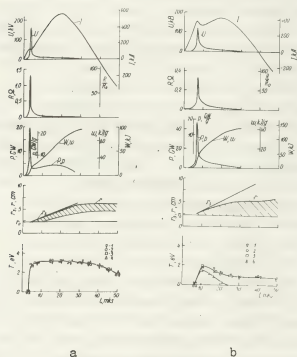


Fig.1.

h (μm) : a - 6, b - 20

λ (nm) : 1 - 490, 2 - 365, 3 - 280, 4 - 265

All regularities earlier observed in the investigations of electrical properties of exploding foils in self-pressed discharge geometry [3,4], are also valid with exploding foils in expanding discharge geometry. The largest changes were observed in the character of plasma column expanding and in the temporal behaviour of its brightness temperature.

At the explosion of thicker foils (Fig.1b) the intensively radiating plasma remains in the dielectric rod region as with self-pressed discharge. In contrast, with the thinner exploding foils (Fig.1a) electric-discharge plasma affected by the magnetic field pressure, departs from the rod and shock front ($v_s = 2$ km/c) does not practically break away from the plasma contact surface. Earlier probe measurements showed that at the plasma front an additional current layer is formed, in which the current is pumped from the main layer [6].

As for the behaviour of T , in the thin foil regime quasistationary phase with roughly constant temperature during $\sim 40 \mu\text{s}$ at rise-time of $\sim 2 \mu\text{s}$ occurs. Such a phase does not exist at the explosion of thicker foils, and in this case equilibrium radiation in the short-wave region is violated.

References

1. Andresen A.B., Burtsev V.A. et al. PTE, No.4, 146, 1973.
2. Andresen A.B., Burtsev V.A. et al. Preprint K-0292, NIIEFA, L., 1976.
3. Burtsev V.A. et al. JTP, 48, 7, 1419, 1978.
4. Burtsev V.A. et al. Preprint K-0293, NIIEFA, L., 1976.
5. Burtsev V.A. et al. JTP, 48, 9, 1845, 1978.
6. Burtsev V.A. et al. JTP, Letts, 4, 11, 654, 1978.
7. Lakutin V.A. et al. JTP, 48, 1792, 1978.

A STUDY OF A WEAKLY IONIZED, ROTATING PLASMA

M.M.B. Wijnakker and E.H.A. Granneman.

FOM-Institute for Atomic and Molecular Physics Kruislaan 407, Amsterdam, The Netherlands.

Rotating plasmas are often studied for separation of species of different mass [1,2]. If in a cylindrical system with an axial magnetic field a current is drawn between a point-like cathode (on axis) and a ring-shaped anode, the radial component of the electrical current together with the magnetic field causes a Lorentz force which drives the ionized particles in azimuthal direction. Neutrals, present in the system will be driven in the same direction due to collisions with the ions. This azimuthal velocities of ions and neutrals lead to centrifugal forces which can be used for separation of species of different mass.

In this paper measurements are given on a stationary rotating plasma with a low degree of ionization ($\sim 2\%$). The values of the rotational velocity of the neutrals are compared with values calculated from a single fluid M.H.D. theory used by Klüber [3] and Wilhelm and Hong [4], which is adapted to our experimental arrangement. Ion conduction is also included in our theoretical calculations [5]. The measurements were done in argon or xenon at filling pressures of 1 to 10 torr.

Apparatus

The main difference between the present experiment (diameter $2R=12$ cm, length L about 50 cm) and other rotating plasma experiments is that two cathode-anode configurations which face each other are used (fig.1). Calculations show that in this case the axial derivatives of the rotational velocity and the plasma potential are small in the volume between the two anodes [6]. The cylinder wall contains 24 electrically insulated stainless steel rings (2 cm thick). Two of these rings serve as anodes. Between the two anodes diagnostic ports are installed which allow optical and probe measurements in the symmetry plane of the experiment.

The rotational velocity and heavy particle temperature are determined from the Doppler shift and width of plasma spectral lines. The plasma density is determined by adding a small amount of hydrogen to the discharge and measuring the H δ Stark broadening. The pressure distribution and the separation of species of different mass are measured by means of calibrated pressure probes which are designed such that only static pressures are measured.

Theory

In the magneto-gasdynamic approximation the equation of conservation of electric charge density ($\nabla \cdot \mathbf{J}=0$) and the Navier-Stokes equation, both combined with the generalized Ohm's law give rise to the following set of equations:

$$\frac{1}{r} \frac{\partial}{\partial r} (r \frac{\partial \phi}{\partial r}) + \frac{\sigma}{\sigma_L} \frac{\partial^2 \phi}{\partial z^2} - B \frac{1}{r} \frac{\partial}{\partial r} (r v_\theta) = 0$$

$$\mu \left[\frac{\partial}{\partial r} \left(\frac{1}{r} \frac{\partial}{\partial r} (r v_\theta) \right) + \frac{\partial^2 v_\theta}{\partial z^2} \right] - \sigma_L B \left(- \frac{\partial \phi}{\partial r} + v_\theta B \right) = 0$$

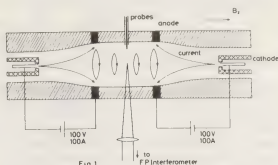


Fig 1

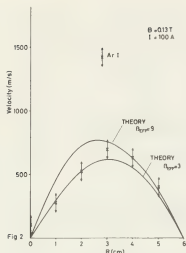
in which ϕ and v_θ are the potential and the azimuthal velocity, B the magnetic field, μ the coefficient of viscosity and σ and σ_L the electrical conductivities parallel and perpendicular to B , respectively. The plasma is assumed to be homogeneous with respect to σ , σ_L and μ . These two relations fully determine the rotational velocity v_θ and the potential ϕ as a function of r and z . Secondary flows are neglected and v_z is assumed to be zero on the walls. Wilhelm and Hong [4] showed that the solutions for v_θ and ϕ can be expressed in terms of the Hartmann number $H_L = (\sigma/\mu)^{1/2} B R$ and the Hall parameter β . In that case only electron conductivity was taken into account and consequently the Hall parameter was the electron Hall parameter β_e . In our experimental situation, however it is shown that the ion-Hall parameter β_i is of the order unity which means that the ion conduction has to be included. For that case Mitchner and Kruger [5] give the following expression for σ_L :

$$\sigma_L = \frac{(1+s)\sigma}{(1+s)^2 + \beta_e^2} = \frac{\sigma}{1+\beta_{eff}^2}$$

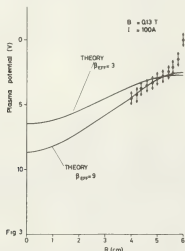
in which $s=\beta_e \beta_i$ is the so-called ion slip factor. An accurate theoretical prediction of the rotational velocity and plasma potential can be made provided $\mu, B, \sigma, \beta_{eff}$ and the electrical current I are known. It can be shown [6] that in the symmetry plane the quantity $v_\theta \mu / IB$ is only very weakly dependent on σ and β_{eff} and therefore these latter two quantities do not have to be known accurately.

Results

In fig. 2 the measured values for the rotational velocity of argon neutral particles are given at different radial positions at a filling pressure of 1 torr, magnetic field strength of 0.13 T and an electrical current of 100 A. The maximum value is about 700 m/sec; it lies about 3.5 cm outside the centre of the column. The theoretical curves are obtained as follows: For the coefficient of viscosity μ , the value $1.14 \cdot 10^{-4}$ kg m $^{-1}$ sec $^{-1}$ given by Dymond [7] for neutrals at an average temperature of 2900 K is used. In our situation for the parallel conductivity σ the Spitzer conductivity (which only depends on the electron temperature) can be taken. The electron temperature is measured in two ways:



It is determined from the line intensity ratios of neutral spectral lines (Boltzmann plot). This gives a value of 0.7 ± 0.2 eV, nearly constant with radius. This value is probably too low [8]. Besides that, two cm from the wall the electron temperature is also determined by means of a double probe. This yields a temperature of 1.0 ± 0.2 eV. Once the quantities μ, I, B, σ and β_{eff} are known one of the outputs of the calculations is the anode-cathode voltage. Feeding in the experimental anode-cathode voltage ($=18 \pm 2$ V, corrected for the cathode and anode falls), together with μ, I, B and σ gives a value for β_{eff} . For $T_e = 1.0$ eV this yields $\beta_{\text{eff}} = 3$. Because we do not know to what extent this T_e is characteristic for the whole vessel, and because usually the electron temperature of such discharges is higher [8] we also applied a value $T_e = 2.5$ eV, yielding $\beta_{\text{eff}} = 9$. Note that the differences in fig. 2 for these two cases ($T_e = 1$ eV; $\beta_{\text{eff}} = 3$ and $T_e = 2.5$ eV; $\beta_{\text{eff}} = 9$) are small. In fig. 3 the measured plasma potentials are given together with the calculated



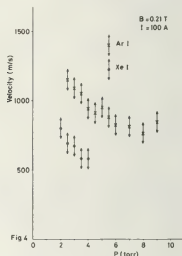
curves for the same two cases. There is a reasonable agreement between theory and experiment for the velocity as well as the potential.

The pressure enhancement from the centre of the column to the wall for the conditions mentioned in fig. 2 is approximately a factor 2.5. This rather low value is probably caused by the high heavy particle temperatures. In the centre a temperature of 5900 ± 1300 K is measured. This temperature increases with the magnetic field strength; the ratio $\frac{1}{2}mv_0^2/kT$ remains approximately constant. This latter ratio is an important quantity for the radial pressure dis-

tribution and hence for the mass separation. In a discharge in which equal amounts of Ar and Xe are present a maximum relative separation factor of 2.2 is found [6].

The velocity of the neutral particles increases linearly with the electrical current and the magnetic field strength. The neutral Xe atoms in a pure Xe discharge have about a factor 1.5-1.8 lower velocity than the neutral Ar atoms in an Ar discharge. This means that $\frac{1}{2}mv_0^2$ is approximately constant in these cases.

In a forthcoming paper we will treat this more thoroughly [9]. At higher filling pressures the velocity of neutrals decreases (fig. 4). At pressures of 10 torr for Ar and 4 torr for Xe the originally rather



uniform discharge abruptly changes character. The rotational velocities drop to values below 200 m/sec. In this situation practically no radial pressure enhancement is found. We have no quantitative explanation for this phenomenon as yet.

References

- [1] James, B.W. and Simpson, S.W., Plasma Phys. **18**, 289 (1976)
- [2] Nathrath, N., Kress, H., McClure, J., Muck, G. and Simon, M., Proc. of the Int. Conf. on Uranium Isotope Separation (London), **9** (1975)
- [3] Klüber, O., Z. Naturforsch. **25a**, 1583 (1970)
- [4] Wilhelm, H.E. and Hong, S.H., J. Appl. Phys. **48**, 2, (1977)
- [5] Mitchner, M. and Kruger, C.H., Partially Ionized Gases, Wiley, New York (1973)
- [6] Wijnakker, M.M.B. and Granneman, E.H.A. and Kistemaker, J. to be published
- [7] Dymond, J.H., J. Phys. B., Atom. Molec. Phys., **4**, 621 (1971)
- [8] Pots, B.F.M., Sijde van der, B. and Schramm, D.C. Physica Vol. **94c**, 369 (1978)
- [9] Wijnakker, M.M.B. and Granneman, E.H.A., to be published

MICROWAVE DISCHARGE IN A SUPERSONIC FLOW

P. Hoffmann, H. Hügel, W. Schall and W. Schock.

DFVR-Institute für Technische Physik, Stuttgart, Germany.

ABSTRACT

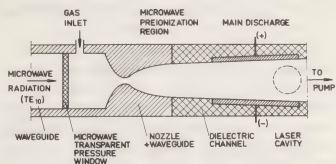
The possibility of effectively ionizing a supersonic flow by a strong microwave field within a waveguide has been demonstrated. Electron densities beyond the cut-off have been achieved at gas temperatures far below room temperature. Hence this method promises to be a good candidate to preionize and stabilize supersonic, non-selfsustained laser discharges.

INTRODUCTION

Laser discharges in supersonic flows have to satisfy several conditions: the value of the reduced field strength (E/N) should be appropriate for optimum vibrational excitation while the electron density must be sufficiently high to allow effective energy deposition into the gas. Under these conditions one must avoid having the discharge in the boundary layer and/or having it blown downstream by the supersonic flow. In addition the discharge has to be stable and spatially uniform across the channel. This can be accomplished by preionizing the flow with an e-beam¹, or by applying a pulser-sustainer discharge². However, with both concepts, technological problems arise, when one attempts to obtain true cw high power laser action. Utilizing a high frequency discharge as a preionization source or as a self-sustained main discharge, cw operation has been demonstrated³. In addition to the advantages of the rf discharge, the use of microwaves allows one to establish a desired field distribution within the channel. This contribution describes an experiment, where the dimensions of the laser channel are comparable to the wavelength with metallic walls forming a waveguide.

EXPERIMENT

The experimental setup is shown in the figure. Amplitude stabilized cw microwave radiation at 2.45 GHz, with power up to 5 kW, is propagated through a pressure window along a rectangular waveguide which



SCHEMATIC VIEW OF APPARATUS

forms both the plenum chamber and the convergent-divergent nozzle. The latter has an area ratio of 10. It merges into a flow channel made of dielectric material with flush mounted electrodes for the main discharge. An optical cavity perpendicular to the flow direction is positioned downstream of the electrode. The dimensions of the waveguide permit the exclusive propagation of the basic TE₀₁ mode. This mode's maximum electric field strength lies along the centerline of the channel with no electric fields in the vicinity of the narrow walls of the waveguide. Hence there is no ionization in the boundary layer. As the pressure rapidly decreases along the divergent part of the nozzle, conditions for breakdown are reached and a plasma with electron densities above cut-off is formed. Interferometric measurements show a decrease in electron density from 10^{11} cm^{-3} at a position 10 cm downstream of the nozzle throat to some 10^{10} cm^{-3} at 20 cm downstream of the throat. There the value of electron density is a function of the totally absorbed microwave power. Typical experimental conditions are: mass flow $\dot{m}_{\text{He}} = 5 \text{ g/s}$, $\dot{m}_{\text{CO}} = 5 \text{ g/s}$; plenum pressure $p_0 = 1 \text{ bar}$; pressure in the channel, p_c , depending on power input, from 8 to 14 mbar; gas temperature, T_c , from 60 to 120 K; i.e. only about 20 % of the input power heats the gas, with most of the energy appearing in the form of ionization, electronic and vi-

brational excitation. The theoretical microwave penetration depth into the plasma of several millimeters in flow direction was found to agree with E-field measurements. Hence the microwave field strength at the position of the main discharge, located several centimeters downstream of the throat, is negligibly small while the electron density still remains above 10^{10} cm^{-3} . Superimposing the main discharge, the E/N values vary between $1.75 \cdot 10^{-16}$ and $3 \cdot 10^{-16} \text{ V cm}^2$, only depending upon the absorbed microwave power. The power levels one can put into the main discharge without arcing are smaller than the corresponding microwave power. On the other hand a stable main discharge cannot be obtained without preionization. No laser action could be observed so far. Yet, one should take into consideration that both the expected gain would be low (some 0.1/m) and the optical path length very short, i.e. in the order of only 7 cm. Hence, one can easily be just below laser threshold.

CONCLUSIONS

It has been shown that a plasma can be effectively produced in a supersonic flow by means of microwaves. If the microwaves are used for preionization, their stabilizing effect on a superimposed main discharge is limited. On the other hand, the available energy loading of up to 0.3 eV/CO molecule, together with the molecular transit time of 100 μs through the discharge should, in principle, permit laser action.

REFERENCES

- ¹ Byron, S.R.; Klosterman, E.L. and Jones, T.G., 28th Gaseous Electronics Conference 1975, HB-6.
- ² Monson, D.J. and Srinivasan, G., Appl. Phys. Lett. 31, 828 (1977)
- ³ Schock, W.; Schall, W.; Hgel, H.; Hoffmann, P., DPG-Frhjahrstagung, Mnchen 1978, K 42.

ULSED CURRENT VOLTAGE CHARACTERISTICS OF A THERMALLY PRODUCED PLASMA

N. St. J. Braithwaite and J.E. Allen.

Department of Engineering Science, Oxford University, Oxford, England.

INTRODUCTION

The present work employs the same apparatus as that used earlier [1] - [7] in d.c. and plasma oscillation studies of collisionless and highly ionised plasmas produced by surface ionisation inside a heated cavity. D.c. analysis of the plasma [1] has shown that when a voltage is applied between the electrodes which form the cavity a field free plasma region is formed bounded by a monotonic sheath at one electrode and a double sheath at the other electrode; most of the applied potential is dropped across the monotonic sheath. If the bias voltage is applied as a voltage step there will be an interval of time during which electrons see stationary electric fields while the ions are virtually frozen, the latter responding to fields after a few ion plasma periods. This time interval is investigated here for the case when the unperturbed plasma is bounded by electron rich sheaths: rapidly applied voltages are then screened from the plasma by sheaths formed as a result of electron motion only, the plasma ions not moving appreciably on a time scale shorter than the ion inertial response time.

EXPERIMENTS

Production of the thermally ionised plasma, measurement of its temperature and a d.c. measurement of its density have been described previously [1], [6]. A caesium plasma is formed in an annular cavity between two concentric tantalum cylinders, the outer one being heated by electron bombardment to around 2200K; see eg. [1]. The cylinders, which are in radiative thermal equilibrium with each other, act as electrodes for electrical measurements. One electrode was earthed while square wave voltage pulses were applied to the other. A square wave with a rise time less than 0.5 n sec, was obtained by discharging a transmission line through the plasma, which acted as the load; current flowing through the plasma was monitored using an inductively coupled measuring circuit. Pulse durations were up to one microsecond and had a repetition rate of one kilohertz so that currents and voltages could be displayed on a double beam oscilloscope. The ion plasma period for the plasmas investigated was between one third and one microsecond.

THEORY

The analysis is carried out in planar geometry which is a reasonable approximation to the plasma cavity. The self-consistent d.c. ana-

lysis [1] assumes that half Maxwellian distributions of electrons and of ions are emitted from each electrode. The distribution of potential between the electrodes is then established by finding which of the many possible potential distributions is consistent with the half-Maxwellian inputs at the boundaries. Potentials between the electrodes for the case considered here of electron rich sheaths for no applied bias and large bias are shown in curves (a) and (b) respectively in figure 2. The potential minimum, η_1 (potential normalised to kT/e) regulates the flow of current across the device while the double layer drop, $\eta_0 - \eta_1$, adjusts the electron velocity so that the density of the electrons is equal to that of the ions in the plasma region (η_0).

For a given plasma density, n_0 , and electron emission density, n_{e0} (a function of T and ϕ) the values of η_1 and $\eta_0 - \eta_1$ are not uniquely determined, but must be related such that the electron and ion densities in the plasma are equal. The absolute values of the potential differences η_1 and $\eta_0 - \eta_1$, are determined by the variation of ion density with potential. In the d.c. case, redistribution of the ions leads to saturation of the values of η_1 and $\eta_0 - \eta_1$, for large applied voltages, and hence the current crossing the device also saturates. The ions will not respond for at least a few ion plasma periods, so that for fast rising voltage pulses the ions are assumed to have a uniform density between the electrodes, equal to the unperturbed plasma density. The self-consistent potential distribution for a constant uniform ion density, independent of potential is shown on curve (c) of figure 2. The double sheath is formed in a region formerly occupied by neutral plasma so the uniform density assumption is reasonable. The value of the potential difference $\eta_0 - \eta_1$ is obtained by requiring that there be two zeros of electric field, one at η_1 and one at η_0 . Starting from a first integration of Poisson's equation:

$$\frac{1}{2} \left(\frac{d\eta}{d\xi} \right)^2 = \int_{\eta_0}^{\eta} \frac{n_e(\eta)}{n_0} d\eta - \int_{\eta_0}^{\eta} \frac{n_0}{n_0} d\eta = Q \quad (1)$$

ξ is the distance co-ordinate normalised to a Debye length defined in terms of electron emission density n_{e0} : $\lambda_{Deo}^2 = \epsilon_0 kT / n_{e0} e^2$, $n_e(\eta)$

is discussed below; n_0 is the unperturbed plasma density; limits are for the zeros of this electric field equation. The electron distribution function to the right of the minimum in figure 1 (c) or (b) is the sum of two truncated Maxwellian distributions and has been discussed in earlier work [1]. The resulting expression for electron density, obtained by integrating over all velocities, as a function of potential is the same in d.c. and pulse cases because of the topological equivalence,

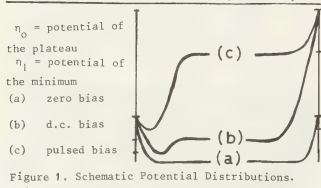


Figure 1. Schematic Potential Distributions.

see figure 1 (b) and (c).

$$\frac{n_e(\eta)}{n_{e0}} = \exp(\eta - \eta_p) \cdot (1 + \exp(\eta - \eta_p)^{1/2} + \exp(\eta) \cdot \text{erfc}(\eta - \eta_p)^{1/2}) \quad (2)$$

where

$$\text{erfc}(x) = 1 - \text{erf}(x) = 1 - \frac{2}{\sqrt{\pi}} \int_0^x \exp(-t^2) dt$$

Substituting (2) for $n_e(\eta)/n_{e0}$ and using

$n_0 = n_e(\eta_0)$ in (1) gives $\eta_0 - \eta_1 = \Delta$ as the solution of:-

$$2(1 - \Delta) \exp(\Delta - \eta_p) + (1 - \exp(-\eta_p)) \left((1 - \Delta) E(\Delta) + 2\sqrt{\frac{\Delta}{\pi}} \right) - (1 + \exp(-\eta_p)) = 0 \quad (3)$$

where $E(\Delta) = \exp(\Delta) \cdot \text{erfc}(\Delta^{1/2})$.

Approximate solution of (3) shows Δ to be almost linearly proportional to η_p for $\eta_p > 5$. Thus for the pulsed plasma, the potential is mainly developed across the double layer in contrast to the d.c. equilibrium case described above. This double layer is formed by retreat of plasma electrons in response to the applied potential and is similar to ion matrix sheath expansion in plasmas bounded by ion sheaths, although here the sheaths are electron rich.

The current crossing the device is found by considering the net electron flux in the potential distribution:

$$j = n_{e0} e \frac{c_s}{2} \exp(\eta_1) \cdot (1 - \exp(-\eta_p)) \quad (4)$$

Using (2), this current may be expressed in terms of the plasma density, n_0 , and sheath drop

$\eta_0 - \eta_1 = \Delta$, and is given in normalised form by

$$J = j \frac{2}{n_0 e c_s} = \frac{1 - \exp(-\eta_p)}{2 \exp(\Delta - \eta_p) + (1 - \exp(-\eta_p)) E(\Delta)} \quad (5)$$

In the limit of large η_p and hence large Δ , (3) can be used to show:

$$J \approx \frac{1}{2} \sqrt{\pi \Delta} \approx \frac{1}{2} \sqrt{\pi \eta_p}$$

Figure 2 shows the pulsed current voltage characteristic calculated exactly from (3) and (4).

RESULTS AND DISCUSSION

Figure 2 shows three sets of data obtained for different values of plasma density and temperature, fitted at one point to the theoretical curve of normalised current against normalised voltage. The current traces for short time scales were nearly flat topped except for the effects of stray capacitance which lead to a slight overshoot. The values of current and voltage plotted on figure 2 were read off oscilloscope traces in the flat portion after any overshoot and prior to any decay of current, observed at times approaching an ion plasma period. In practice flat topped portions were seen between 0.01 and 0.1 μsec . There is good agreement between theory and experiment for the plasma conditions studied.

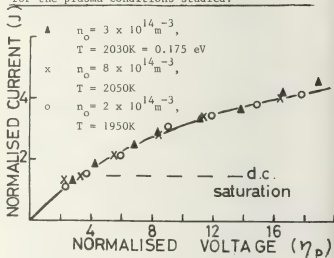


Figure 2. Normalised Current Voltage Characteristic. — Theory

In conclusion, it has been shown that currents in excess of d.c. equilibrium values can be drawn through the plasma in a pulsed mode. This is possible because of the finite response time of the ions which are essentially frozen during the early stages of the pulse. Agreement between theory and experiment is good.

REFERENCES

1. Fang, M.T.C., Fraser, D.A. and Allen, J.E., (1969), J. Phys. D 2, 229.
2. Ward, J.C. and Allen, J.E., (1970), J. Phys. E 3, 535.
3. Allen, J.E., Fang, M.T.C. and Fraser, D.A., (1971), Proc. R. Soc. Lond. A322 63.
4. Phelps, A.D.R. and Allen, J.E., (1975), Proc. XII I.C.P.I.G., 128.
5. Phelps, A.D.R. and Allen, J.E., (1976), Proc. R. Soc. Lond. A348, 221.
6. Powers, S.R., (1976), M.Sc. Dissertation, Oxford University.
7. Phelps, A.D.R. and Allen J.E., (1978), Proc. R. Soc. Lond. A360, 541.

THE EFFECTIVE OVERVOLTAGE OF AC PLASMA DISPLAY DISCHARGES

M. Stieber and W. Stern.

Zentralinstitut für Elektronenphysik, V Akademie der Wissenschaften der DDR, DDR 22 Greifswald.

Introduction: AC plasma display discharges as described in /1,2/, are particularly interesting for displays because of their memory. There are several possible memory mechanisms /3/, but the quantitative rate of these mechanisms has not yet been clarified. Memory is known to be influenced by the form of sustaining voltage signal /3,4/. Thus sine wave sustaining and square wave sustaining show a very different behaviour both in memory and in the parameters of light pulses (Figs.1,2). In the present paper the transition of square wave into sine wave sustaining and its connection with overvoltage and memory is investigated.

Method: For this purpose firing voltage U_z , minimum sustaining voltage U_L and characteristic pulse parameters of light pulses, such as peak width t_h^z , base width t_b^z , amplitude I and the logarithmic rise time constants were measured as the function of the half period $T/2$, the sustaining voltage U_s and the slope dU_s/dt_a of square wave signal (t_a time response). The used discharge cell with glazed Mo-electrodes /1,2/ (electrode distance $d=0,1\text{cm}$) was filled with 100 Torr ($\text{Ne}+0,1\%\text{Ar}$). Fig. 7 only referred to discharges in 300 Torr ($\text{Ne}+1\%\text{N}_2$). The comparison of bistable range (memory), wall voltage U_w and pulse shape can be obtained by the determination of effective overvoltage ΔV as a dominant limiting quantity for pulse shape. Two methods are used to determine ΔV and the results are compared with each other (table 1). The first method is based on the comparison with the calculated value of TOWNSEND time constant τ , which is assumed to be identical with the logarithmic rise time constant of the first

Fig. 1

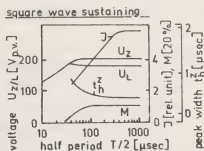


Fig. 2

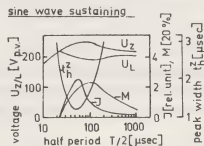


Fig. 3

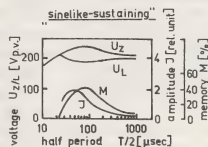


Fig. 4

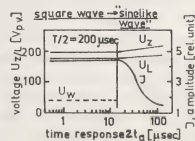
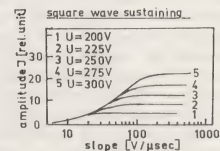


Fig. 5



phase of the light pulse. The used equation for τ was

$$\tau = (1/v_i) \{ \alpha - (1/d) \ln [1 + \beta] / \beta \}^{-1/5}$$

with v_i ion velocity, α , β TOWNSEND ionization coefficients. By the second method the wall voltage U_w , as the effective overvoltage for square wave sustaining is calculated. Fig. 6 demonstrates this method, which is based on the following assumptions:

- The wall voltage transfer down to $U_w=0$ lasts t_b^z / μ sec.
- Is the magnitude of the mean slope of sustaining voltage $S_s = U_s / t_a$ decreased so far, that amplitude of the pulse temporally agrees with the upper edge of voltage rise, the mean slope value of the wall voltage $S_w = U_w / t_b^z$ will be equal to S_s . These assumptions permit to calculate U_w , using the equation

$$U_w = t_b^z S_s = t_b^z U_s / t_a.$$

Results and discussion: The comparison of these overvoltage values is shown in table 1. The requisite data are taken from Fig. 5

Table 1: square wave sustaining

U_s [V _{pv}]	1. method τ	ΔU	2 method t_b^z	ΔU
200	0.65	24	1.6	48
225	0.5	42	1.2	78
250	0.3	95	0.9	90
300	0.19	157	0.6	150

In Fig. 4 the transition of square wave sustaining into "sinelike-sustaining" (trapeze voltage

with the same slope like sine wave) is done by lowering the slope. In fact, the parameters of discharges with "sinelike-sustaining" are comparable with sine wave sustaining, as shown in Figs. 2, 3. The example in Fig. 4 shows, that voltage U_z/L , memory $M = (U_z - U_L) / 2 / U_z$, overvoltage ΔU and pulse shape are determined by the voltage slope, if the pulse amplitude is in the voltage rise range. The lowering of the effective overvoltage ΔU with increasing voltage time response causes U_z to rise and weakens the light signal. The same behaviour is observed for sine wave sustaining. In the case of Fig. 7 linearity exists between ΔU and the slope dU/dt at the moment, at which the pulse is detected. for different frequencies and voltages.

Summary: The importance of the slope of sustaining voltages, especially for the transition of square wave into "sinelike-sustaining" is shown, and it can be confirmed, that the formalism of classical TOWNSEND theory approximately is applicable for determination of the effective mean overvoltage. In spite of the temporal development and the growth of these discharges the mean overvoltage is of practical value for interpretation of memory and pulse behaviour of ac plasma display discharges because of the superposed effects of U_s increase and U_w transfer in the course of the discharge activity.

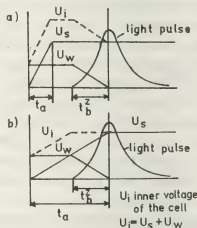


Fig. 6

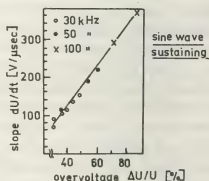


Fig. 7

References:

- /1/ Stern, W.: XIII. ICGIP, 1977, Berlin, p. 371
- /2/ Zahn, R. J., S. Mueller: XIII. ICGIP, 1977, Berlin, 373
- /3/ Weber, L. F.: Illin. Univ. Urb.-Champ. Coord. Sci. Lab. R-687
- /4/ Nakayama, N., Sh. Andoh: Proc. of the S.I.D. Vol. 13/1, 1972, p. 61-66
- /5/ Abdel-Rahman M. Zghloul, Roshdy M. Radwan Mohamed S. Abou-Seada: IEEE Transact. on Electrical Insulation, Vol. EI-11, Nov. 1, 1976, p. 28-32

DYNAMIC OF NEGATIVE GRID PULSE INFLUENCE UPON DISCHARGE PLASMA

V.B. Kaplan, A.M. Martsinovskiy, F.N. Rasulov and V.G. Yuriev.

A.F. Ioffe Physical-Technical Institute, Academy of Sciences of the U.S.S.R. Leningrad, K-21 U.S.S.R.

The grid influence upon Knudsen low-voltage arc cesium plasma was investigated in [1]. But negative grid voltage affected discharge otherwise than in [1] if negative pulse with short rise time ($\tau_f 10^{-7}$ s) is used instead of constant grid potential. The main reason of this difference is explained by the consideration of pre-electrode layers creation.

The devices and experimental technique are similar to [1].

Typical plasma parameters response on negative grid pulse is shown at Fig. 1 (T_{e1} and T_{e2} - electron temperatures in cathode and anode regions, n_1 and n_2 - plasma concentrations, φ - plasma potential, j_a and j_i - anode and grid currents, V_a , V_g - anode and grid voltages). When grid pulse is applied, the relatively small increasing of Langmuir layer occurs at time of the order of electron transit time (10^{-9} s), the ion concentration in layer being constant. Further the surplus ions are driven from nonequilibrium Langmuir layer to grid. The ion current causes the negative grid current peak (Fig. 1). Quasiequilibrium layer is created near grid wire during the ion transit time across the layer (10^{-7} s). If the decrease of electrical grid transmittance Δe_g (in consequence of Langmuir layer increasing) isn't large, the change of potential drop φ_{12} in grid plate compensates this variation. Therefore discharge current doesn't vary (Fig. 2). Current diminution begins only if grid voltage comes up to certain value V'_g . This value diminishes if the absolute value of retarding voltage φ_{12} in grid plane and plasma concentration increase.

If $V_g < V'_g$, the initial current suppres-

sion (to j'_a value) occurs during the time of quasiequilibrium layer creation (or during τ_f). It is accompanied by corresponding anode voltage increasing (Fig. 1), the main potential drop being localized in grid plane (Fig. 1b, 2). Such plasma state isn't stable. On the one hand, the increasing of Langmuir grid layer causes the increasing of grid ion current, that diminishes ion concentration near the grid (and in the cathode region) and leads to gradual decrease of transmittance and discharge current. On the other hand, electrons, that penetrate into anode region, are accelerated by the grid plane voltage

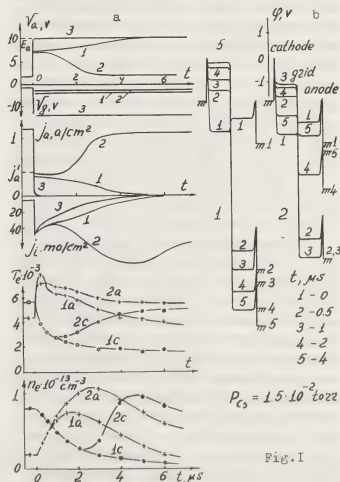
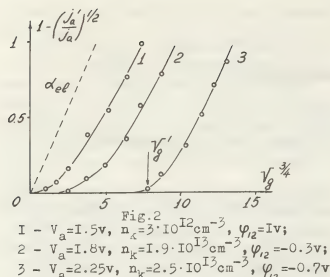
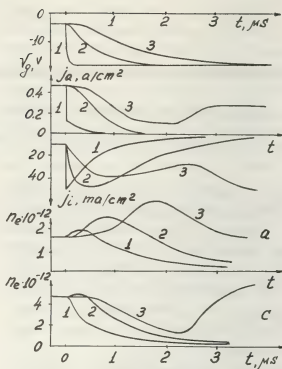


Fig. 1



drop. It causes T and n to increase (Fig. 1). The increasing of ion generation rate and their concentration in anode region compensates their departure to grid and causes the increase of grid transmittance. Therefore the opposite tendencies compete one with the others. If ion generation is insufficient for current recovery, the increasing of anode region concentration becomes slow. After maximum was obtained, anode region concentration begins to diminish, and discharge quenching occurs (curves 1 at Fig. 1a). In opposite case current recovery occurs after $(1-2)\mu s$; ion generation shifts from anode region to cathode one again. (curves 2 at Fig. 1a), and plasma passes into the state that corresponds to static grid voltage V_g .

The investigations show that inertia of cumulative ionization [2] and duration of ion transit from anode region to grid ($\sim 10^{-6}s$) promote current suppression. Both these times are longer significantly than ion transit time from the center of grid mesh to the wire. Therefore the grid pulse rise time influences significantly on discharge quenching efficiency. Fig. 3 illustrates the difference between plasma processes because of the various grid pulse rise time at constant pulse amplitude. If T_f increases, the ions generated in anode region are able to transit to the grid, the diminution of anode current being slowed down (curves 2 at Fig. 3). If T_f is sufficiently large, these ions



are able to restore the current, though grid potential continue to diminish (curves 3 at Fig. 3).

Initial current suppression may be complete if the negative grid pulse amplitude is large (curves 3 at Fig. 1a). It corresponds to coupling of pre-electrode layers of neighbour grid wires (potential quenching). But increase of pulse amplitude isn't always possible; it generates the complementary strong ionization mechanism in anode region. Discussion of this question isn't throw into this report.

References.

- /1/. F.G.Baksht, A.M.Martsinovskiy, V.G.Yuriev, report at present conference
- /2/. V.B.Kaplan, A.M.Martsinovskiy, B.I.Tsirkel, V.G.Yuriev. Proc. IXth Int. Conf. on Phenom. in Ioniz. Gases, p.199 (Bucharest, 1969).

LOW-VOLTAGE ARC PLASMA IN THREE-ELECTRODE SYSTEM

V.G. Beksht, A.M. Martsinovskiy and V.G. Yur'ev.

A.P. Ioffe Physical-Technical Institute, Academy of Sciences of the U.S.S.R., Leningrad, K-21 U.S.S.R.

Investigations of grid influence on low discharge plasma are few and not systematical [1]. There are no such investigations for high plasma concentration ($n_e \sim 10^{12} - 10^{14} \text{ cm}^{-3}$), though this problem becomes significant for practical applications [2]. The investigation of such problem in short low-voltage arc cesium plasma fills in this gap.

The experiments were performed at plane geometry devices with surface area $\sim 1 \text{ cm}^2$ and interelectrode distance $d_{ac} = (2-5) \text{ mm}$. The grids with cell dimension $\sim (100-200) \mu\text{m}$ and permeability $\alpha \sim 0.5-0.8$ were utilized. Probe and spectral plasma diagnostic methods were used together with gating integration technique. Time resolution was 50 ns [3]. When a grid is introduced in the gap, the discharge plasma dissolves to two regions with significantly various properties (cathode region and anode region - see Fig.1). In the each region electron temperature T_e , concentration n_e and plasma potential φ change little. But very sharp variation of these parameters takes place in the grid plane. If discharge is developed significantly and the whole emission current flows, the main potential drop occurs in the cathode sheath φ_1 . The electron beam from cathode loses its energy in cathode-grid region. Therefore electron temperature and plasma concentration in cathode region are higher significantly than in anode one ($T_{e1} > T_{e2}$, $n_1 \gg n_2$). Potential drop φ_{12} in the grid plane is negative, i.e. retarding for electron flow from cathode to anode region. Concentration n_2 establishes at the level sufficient for current transfer to anode (point 2 at Fig.1). When anode potential V_a diminishes, cathode potential drop φ_1 , T_{e1} , n_1 and φ_{12} diminish also, plasma parameters in anode region being unchanged (Fig.1, point 1).

When concentrations n_1 and n_2 becomes nearly equal, the grid potential drop φ_{12} changes its sign and the ion generation becomes greater in anode region than in cathode one. Discharge passes into tasitron mode, discovered in [1]. This mode of operation is the most economic because of small value of ion current to cathode ($n_1 < n_2$). Potential drop φ_{12} accelerates electrons and facilitates the current flow in the most narrow space of discharge - between the grid wires.

When V_a increases, enhancement of n_1 ceases when plasma reach the high ionization degree. If V_a continues to increase, the hot electrons penetrate into anode region. Therefore electron temperature T_{e2} and concentration n_2 increase. Concentrations in cathode and anode regions draw together and φ_{12} diminishes (point 3).

The diminution of grid potential V_g causes the enhancement of the pre-electrode layer dimension Δ near the grid wires ($\Delta^2 \sim V_g^{3/2}$). It diminishes the electrical grid permeability α_{el} and causes the enhancement of ion grid current. The pre-electrode layer is sufficiently narrow for discharge conditions that are interesting for practical applications ($n \sim 10^{15} \text{ cm}^{-3}$). Therefore permeability diminishes slowly when V_g is depleted. Moreover, if φ_{12} is retarding, α_{el} diminution is compensated by small variation of φ_{12} : $j_a \sim \alpha_{el} \times \kappa [\exp(-\frac{\varphi_{12}}{kT_{e1}}) n_1 v_{e1} - n_2 v_{e2}]$. Therefore discharge current and plasma parameters are nearly independent of V_g (Fig.2). It must be noticed that the second reason of such independence is often more significant than the first one. This phenomenon (rather than electrostatic screening) prevents grid control in high density plasma.

It is essential that the discharge quenching occurs at negative grid voltage only

if the potential drop is accelerating for electrons. Near the quenching point main ion generation is concentrated in anode region, grid permeability is small and anode current j_a is diminished appreciably. This result was obtained in experiments as well as in theoretical calculations /4/.

When load resistance R_L is in anode circuit, diminution of j_a causes V_a and φ , increasing ($V_a + j_a R_L = E_a = \text{Const}$). Therefore concentration n_i in cathode region increases. It prevents α_{eL} diminution and j_a interruption. The load resistance permit to realize the lower branch of voltage-current characteristic-branch with negative resistance. At this branch complicated oscillations occur with frequency ~ 100 kcycles. At Fig.3 the typical results of probe plasma parameters investigation in cathode (1) and anode (2) regions are shown for the conditions when oscillations occur. These are relaxation oscillations with successive ion generation transitions from one region to another.

It was also shown that grid influences upon discharge when j_a is nearly equal to random current $j_z = \frac{1}{4} n v_e$ and grid potential drop doesn't control discharge. The condition $j_a \approx j_z$ may be realized by ion concentration diminution or by increasing of anode current. The first situation may be achieved by utilization of a grid with large surface. But such grid causes the grid ion current to increase and quenching anode voltage V_a to increase also. The second situation may be achieved by effective emitter utilization, particularly in discharge with C_2 and B_a vapours. Spontaneous current interruptions arise in this situation. Possibility of grid control arises also if the dynamical effects in plasma are utilized. These two possibilities are considered in corresponding reports.

/1/ E.O.Johnson, J.Olmstead, W.H.Webster. Proc.IRE 42, 1950 (1954).

/2/ G.M.Gryaznov, V.B.Kaplan, A.M.Martsinovskiy, V.I.Serbin, V.G.Yuriev, Report on the IV-th Int.Conf.on Thermionic Power Generation (Eindhoven, Netherlands, 1975).

/3/ V.B.Kaplan, A.N.Makarov, A.M.Martsinovskiy a.o. Journ.Techn.Phys.47,247(1977).

/4/ F.G.Baksht, V.B.Kaplan, A.A.Mostin a.o. Journ.Techn. Phys. 48, 2285 (1978).

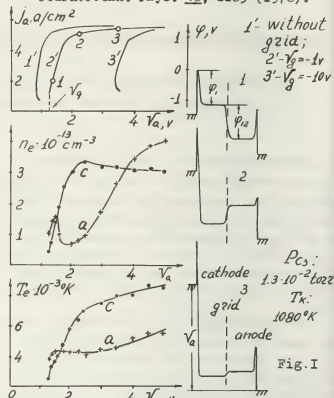


Fig. 1

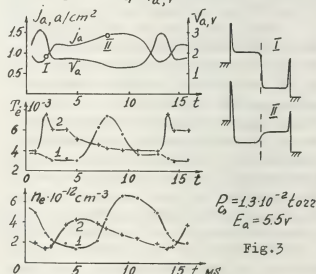


Fig. 3

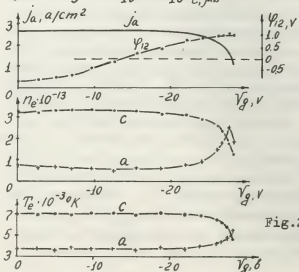


Fig. 2

EFFECT OF GAS PURITY ON THE CURRENT OF A NON-SELF SUSTAINED DISCHARGE IN NITROGEN

G.B. Lopantseva, A.F. Pal', A.F. Perevoznov, I.G. Persiantsev and A.N. Starostin.

Institute of Nuclear Physics, Moscow State University, 117234, Moscow, U.S.S.R.

Commercial nitrogen contains about 0,01 % of oxygen, whereas nitrogen of special purity (s.p.), only 0.001 %. It turns out that even so small admixtures may essentially alter the energy characteristics of the discharge. This effect is considered for a non-self-sustained discharge induced by an electron beam. At gas pressures of 1 atm, positively charged nitrogen ions N_2^+ , $N^+(1,2)$ are effectively converted in triple collisions [1] to ions N_4^+ , N_3^+ , respectively (3). Here and in follows, the number in parentheses indicates a reaction corresponding to that number in the table. The density of N_2^+ and N^+ in a discharge is 10^{16} cm^{-3} and the N_4^+ ion, which recombines with the electrons produced in the discharge (4), is the principal ion.

On the other hand, when the above amount of oxygen is present, the N_4^+ ions may disappear due to charge-exchange (5) [2]. Estimates show that at density $[O_2] = 10^{15} + 10^{16} \text{ cm}^{-3}$, the O_2^+ ion becomes (at a rate of electron production in the discharge $10^{17} \text{ cm}^{-3} \text{ sec}^{-1}$) the principal positive ion and the electron balance in the discharge will be determined by dissociative recombination on the ions of O_2 (6) [1] rather than N_2 . The effective electron-recombination coefficient is given by $\beta_{\text{eff}} = \frac{\sum [n_i] \beta_i}{\sum [n_i]}$, where $\sum [n_i]$ is the sum of

the concentrations of all positive ions in the discharge, β_i are the corresponding coefficients of recombination of the i -th ion with electrons of the discharge $\sum [n_i] = [n_e]$, $[n_e]$ is the discharge-electron density. In our case

$$\beta_{\text{eff}} = (K_4 + [O_2] K_5 / [n_e]) / (1 + [O_2] K_5 / [n_e] K_6)$$

It is seen that, if $[O_2] K_5 \ll [n_e] K_6$, β_{eff} is determined by the dissociative recombination of N_4^+ ions with the electrons. At $[O_2] K_5 > [n_e] K_6$, $\beta_{\text{eff}} \sim K_6 / (1 + [n_e] K_4 / [O_2] K_5)$ i.e., the higher the oxygen content in the gas employed, the closer the recombination coefficient to that on the O_2 molecule.

However, as the concentration of O_2 exceeds 0,1%, the conversion (8) of O_2^+ to the more complex ions [1] as well as electron attachment in the presence of a third particle (9), becomes of greater importance. The effect just mentioned have been observed on an installation described in [3].

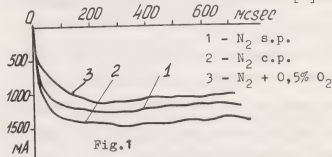


Fig.1

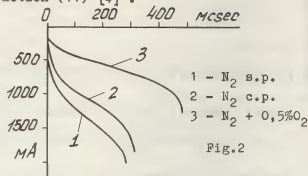
Fig.1 shows the oscillograms of the discharge current in nitrogen of various purity at a beam current of 250 mA/cm^2 and a pumping rate 100 m/sec . The highest

discharge current is observed in commercial nitrogen, the lowest in nitrogen of special purity to which 0,5% of oxygen was added.

It should be noted that, if before the field is applied the gas is subject to electron-beam radiolysis, then in the discharge gap there will accumulate atomic nitrogen whose amount is proportional to the time of electron beam operation. When the field is applied, the O_2^+ ions that appear in the discharge will partly exchange charges with nitrogen atoms, thus leading to the formation of the positive ion NO^+ (7) [4]. Since the constant for the recombination rate for the NO^+ ion (10) is about an order of magnitude lower than that of oxygen, the NO^+ ion may affect the electron balance, thereby increasing β_{eff} .

Similarly, the gas is subject to the e-beam radiolysis when the voltage is switched on at instances close to those at which the beam current is maximum if the e-beam operation time $\tau_g < L/v$ (L/v being characteristic time of passage of the gas through the discharge gap of length L). In commercial N_2 the current will be lower than in s.p. nitrogen, because the relative number of NO^+ ions in the former will be higher. This is confirmed by the experimental results presented in fig.2. Here the rate of gas flow through the discharge gap is 1-2 m/sec, $L=1$ cm, $\tau_g \sim 6 \cdot 10^{-3}$ sec. $E/N \sim 10^{-16}$ V cm², $j_g \approx 250$ mA/cm². One should mention that at low flow rates there occurs an effective occupation of the vibrational levels of the N_2 molecule. In this case, the NO^+ ions may form also in the

reaction (11) [4].



No	Reaction	Rate constant
1	$N_2 \xrightarrow{el} N_2^+ + e$	$10^{-7} \text{ cm}^3 \text{ sec}^{-1}$
2	$N_2 \xrightarrow{el} N + N$	$10^{-8} \text{ cm}^3 \text{ sec}^{-1}$
2a	$N_2 \xrightarrow{el} N^+ + N + e$	$10^{-8} \text{ cm}^3 \text{ sec}^{-1}$
3	$N_2^+ + 2N_2 \rightarrow N_4^+ + N_2$	$8 \cdot 10^{-29} \text{ cm}^6 \text{ sec}^{-1}$
4	$N_4^+ + e \rightarrow 2N_2$	$8 \cdot 10^{-8} \text{ cm}^3 \text{ sec}^{-1}$
5	$N_4^+ + O_2 \rightarrow O_2^+ + 2N_2$	$4 \cdot 10^{-10} \text{ cm}^3 \text{ sec}^{-1}$
6	$O_2^+ + e \rightarrow 2O$	$2 \cdot 10^{-8} \text{ cm}^3 \text{ sec}^{-1}$
7	$N + O_2^+ \rightarrow NO^+ + O$	$1,8 \cdot 10^{-10} \text{ cm}^3 \text{ sec}^{-1}$
8	$O_2^+ + O_2 + N_2 \rightarrow O_4^+ + N_2$	$10^{-31} \text{ cm}^6 \text{ sec}^{-1}$
9	$O_2 + e + N_2 \rightarrow O_2^- + N_2$	$10^{-31} \text{ cm}^6 \text{ sec}^{-1}$
10	$NO^+ + e \rightarrow N + O$	$1,5 \cdot 10^{-7} \text{ cm}^3 \text{ sec}^{-1}$
11	$N_2^+ + O_2^- \rightarrow NO^+ + NO$	$5 \cdot 10^{-16} \sum_v \beta_v \chi_v$

χ_v is the relative population of the vibrational levels of the molecule N_2 , β_v - the ratio of the rate constant for the level v to that for the level $v=0$.

References

- [1] B.I. Smirnov "Ions and excited atoms in plasma" Atomizdat, Moscow (1974)
- [2] T.L. McCrumb, P. Warneck. J. Chem. Phys., **66**(12), 5416, (1977).
- [3] E.P. Velikhov, S.A. Golubev, Yu.K. Zemtsov, A.F. Pal', I.G. Persiantsev, V.D. Pis'menny, A.T. Rakhimov. ZhETF, **65**, 543, (1973).
- [4] B.F. Gordiets, M.N. Markov, L.A. Shelepin "A theoretical investigation of infrared radiation in the upper atmosphere, aeronomical processes and radiation mechanisms" Preprint PIAN No.84, Moscow (1976).

NEGATIVE ION PRODUCTION IN SURFACE-PLASMA SOURCES WITH UNCLOSED ELECTRON DRIFT DISCHARGES

Yu. I. Bel'chenko, V.G. Dudnikov.

Institute of Nuclear Physics, Novosibirsk, U.S.S.R.

1. In developed variants of surface-plasma sources /2,3/ the minimum energy necessary for H^- generation is about 10^4 eV/ion. The further increase in efficiency of negative ion generation is desirable for construction of long term operation sources. The most evident way to increase the energy efficiency is the more complete utilization of negative ions emitted from electrodes /2/. In experiments presented here, more complete extraction of generated negative ions was provided with localization of the discharge near the emission slit and with geometrical focusing of negative ions emitted by a half-cylindrical cathode surface to the emission slit.

2. The diagram of the source with discharge location near the emission slit (so-called semiplanotron - SP) is shown in Fig.1.

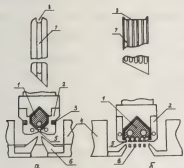


Fig.1 Semiplanotron diagram:

a - with one groove, b - with five grooves; 1 - cathode, 2 - anode, 3 - magnetic inserts, 4 - poles of magnet, 5 - emission slit, 6 - extractor, 7 - cathode groove, 8 - end cathode hollow.

Similar to the planotron /2/, the discharge takes place in a thin gap between the long cathode 1 and anode 2, which embraces the cathode. For the effective

plasma utilization, SP discharge is maintained only in a region near the emission slit. In this place the magnetic field lines are specially bent with magnetic inserts 3. The magnetic field lines two times cross the half-cylindrical cathode surface without crossing the anode, providing conditions for confinement of fast electrons emitted by cathode. These electrons oscillate in the cathode groove and drift along the emission slit sawed perpendicular to magnetic field lines. The deeper hollow 8 is made at one of the cathode end for better discharge triggering. Electromagnetic valve and heated container provide this hollow with hydrogen portions and cesium vapour. For preventing discharge in other parts of the cathode-anode gap, SP electrodes have the special shape preventing electron oscillations in these regions. Electrons in the side gaps fall quickly to the anode along the magnetic field lines. A half-cylindrical shape of the cathode operation surface provides geometrical focusing of negative ions emitted by the surface to emission slit. Extraction voltage of up to 35 kV is applied to discharge chamber, extractor 6 is under ground potential. The pulse mode of such sources was under study. An amplitude of the discharge current pulse was up to 0.2 kA, duration 1 ms, repetition rate up to 10 Hz.

3. The characteristics of high current glow discharge in SP, their dependencies on magnetic field, hydrogen and cesium density, discharge current were similar to those of planotron discharge /2/. The dependencies of extracted H^- and D^- current on discharge current are

given in Fig.2.

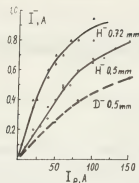


Fig.2 Current of H^- and D^- (crossed) beams as a function of discharge current. Figures near the curves - width of the emission slit. The emission slit length is 40 mm.

Maximum H^- emission density up to $3-4 A/cm^2$ was achieved with discharge current density at cathode $50 A/cm^2$. At linear plot of dependence emission H^- current density amounts to 17% of the cathode discharge current density and energy expenditure on H^- generation was ~ 5 keV/ion. It is explained by more effective plasma utilization in SP and by geometrical focusing of negative ions to emission slit. Negative ions focusing also is confirmed by intense sputtering of anode parts located opposite to the half-cylindrical cathode surface of the groove. Sputtering trace looks like a canal of 0.8 mm width.

Under the same conditions H^- current was two times less than D^- current. Because of the larger deuterium mass the leaving times are increased both for discharge positive ions and negative ions moving from cathode to emission slit. These effects can visibly intensify the D^- destruction in plasma /2/. Also, due to lower energy of bombarding deuterium particles /4/ the reduction of secondary D^- emission coefficient may play a certain role.

The five-grooves SP with multiple-aperture extraction system was tested (Fig.1b). Quite a uniform glow discharge was achieved at all the cathodes grooves with cathode current density up to $30 A/cm^2$. With large sizes of emission slit some difficulties arise for providing necessary den-

sity of hydrogen in discharge grooves. The hydrogen density gradient along the groove resulted in non-uniform discharge and brought to visible reduction of negative ions along the emission slit.

In the described versions of SP the problem of electrode cooling is quite simply solved. To this end, the channels for cooling liquid are drilled close to working parts of the cathode, anode and extractor. Note, that SP with one groove of $\sim 3 \times 15 mm^2$ is effective as compact dc source of negative ions. With discharge current $\sim 5 A$ and average power at cathode $\sim 1 kW/cm^2$ it is really to obtain dc H^- current of 0.1 A.

References:

- /1/ "Proc. Symp. on Production and Neutralization of Negative Hydrogen Ions and Beams, 1977", BNL, 50 727, N.Y.
- /2/ Yu.I.Belchenko, G.I.Dimov, V.G.Dudnikov, in /1/, p.79.
- /3/ K.Prelec, in /1/, p.111.
- /4/ P.J.Schneider, K.H.Berkner, W.G.Graham et al., in /1/, p.63.

SPECTRUM OF CHARGE EXCHANGE NEUTRALS FROM ROTATING PLASMA

M.P. Ryutova.

Institute of Nuclear Physics, Novosibirsk, U.S.S.R.

In rotating plasma experiments (see, e.g., /1-3/) it often happens that the ions are produced in a device only due to ionization of neutral gas in the crossed electric and magnetic fields (and there are no other ion sources, say, external injection). Since the ions produced from cold neutral particles by the electron impact have a negligibly small energy at the initial moment, their further motion is described by the formulae:

$$v_r = \frac{c E(r)}{H} \sin \omega_L (t - t_0) \quad (1)$$

$$v_\varphi = \frac{c E(r)}{H} [\cos \omega_L (t - t_0) - 1]$$

where $E(r)$ is a radial electric field, H is a homogeneous magnetic field (directed along the z -axis, see Fig.1), ω_L is Larmor frequency of ions. It is assumed that the Larmor radius of ion equal to $cE/H\omega_L$ is negligible as compared to the scale-length of a radial electric field which is usually of the order of the plasma radius. Since the ionization moments t_0 are distributed randomly, the distribution of ions over the phase $\psi = \omega_L (t - t_0)$ is also random.

As seen from eqs.(1), the absolute value of ion velocity $v(r) \equiv \sqrt{v_r^2(r) + v_\varphi^2(r)}$ lies within the limits from zero ($\psi = 0, 2\pi$) to $v_0(r) = 2c |E(r)/H|$ ($\psi = \pi$).

On the other hand, in off-axis measurements of charge exchange neutrals (Fig.1) the neutrals with maximum energy exceeding $\max W_0(r)$ (where $W_0(r) \equiv Mv_0^2(r)/2$) are often detected, while at small energies the spectrum of neutrals is limited not by zero but by a finite quantity which is 1.5-2 times smaller than $\max W_0$. In the present paper a simple explanation of these features of the neutral spectrum is given.

As is well known, in a resonant charge exchange event of a fast ion on a neutral

the fast neutral arises, which has just the same momentum as the initial ion. In a sufficiently dense plasma, the fast neutral has some probability to be ionized again by electron impact or by charge exchange with plasma ion before reaching the plasma boundary (in both cases the initial momentum of the ion appeared is nearly the same as the neutral momentum). This leads to the formation of the ions with non-zero initial velocities. We call them "second generation" ions (in contrast to the "first generation" ions which are produced by electron impact ionization from cold neutrals and move according to eq.(1)).

Let us first consider the properties of charge exchange neutrals produced from the first generation ions. Using eq.(1), it is easy to show that the distribution function of fast neutrals registered by a detector will be the following:

$$\frac{dI}{dW} = A \frac{n_0(\rho) n(\rho) \sigma_0(W)}{r |d\Omega(\rho)/d\rho| \sqrt{\rho^2 - r^2}} \quad (2)$$

where $n_0(r)$ and $n(r)$ are the densities of neutrals and ions respectively, $\sigma_0(W)$ is the resonant charge exchange cross section, $\Omega(r) = cE(r)/rH$ is the angular drift frequency, and ρ in (2) is considered as a function of W , defined by the following relationship:

$$\Omega(\rho) = \frac{1}{2r} \sqrt{\frac{2W}{M}} \quad (3)$$

From formulae (2) and (3) it follows an important for the experiment conclusion that in the case of "hard-body" rotation, when $\Omega(r) = \text{const}$, dI/dW is of the form of a delta-function: $dI/dW \propto \delta[W - W(r)]$; deviation of dI/dW from a delta-function is a measure of plasma motion deviation

from hard-body rotation.

The form of the function dI/dW in the cases when $\Omega(r)$ monotonely increases and monotonely decreases with radius is shown qualitatively in Fig.2. The peculiarity of the case consists in the presence of the root singularity on the lower (in the first case) and upper (in the second case) ends of the interval where dI/dW differs from zero. This makes it possible to find readily the direction of variation of the function $\Omega(r)$ from experimental data.

Thus, consideration of the first generation ions allows us to explain the presence of a lower boundary of the energy spectrum of charge exchange neutrals. As to upper boundary, in this case it cannot of course lie above $\max W_0(r)$.

For explanation of the fast neutrals formation we have to investigate the distribution function of the second generation ions. The number of these ions is determined by the ratio of ionization length λ_i to plasma radius R . Usually in experiments the condition $\lambda_i \gg R$ is fulfilled (the case when $\lambda_i \ll R$ is discussed in [4]).

Let the neutral, produced at radius r from the ion of first generation and moving at this moment at an angle α with respect to electric field, be ionized again at radius r^* . Then the velocity of thus produced second generation ion changes with time according to

$$v_r(r^*) = v \sin \psi \quad (4)$$

$$v_\varphi(r^*) = \frac{v_0}{2} + v \cos \psi$$

where

$$v = \sqrt{\frac{V_0^2(r^*)}{4} + V_0^2(r) \left[1 - \frac{\Omega(r^*)}{\Omega(r)} \right] \sin^2 \alpha} \quad (5)$$

$$\psi = \omega_0 t + \text{const}$$

Using these formulae, one can find the distribution function of neutrals, produced by charge exchange from second generation ions. However, these calculations are too cumbersome, and we shall restrict ourselves only by revealing of the maximum value of the energy of the second generation ions. From expressions (4), one can see, that the maximum (over ψ) value of the ion velocity is

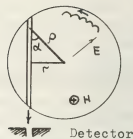


Fig.1

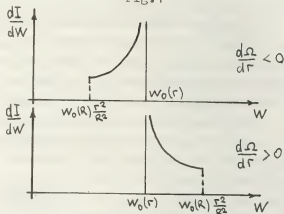


Fig.2

$$\frac{V_0(r^*)}{2} + \sqrt{\frac{V_0^2(r^*)}{4} + V_0^2(r) \sin^2 \alpha \left[1 - \frac{\Omega(r^*)}{\Omega(r)} \right]} \quad (6)$$

In the case of "hard-body" rotation the second generation ions have the same distribution function as the first generation ions, i.e. accelerated particles do not appear. The most obvious situation in which accelerated ions appear, is the following: $V_0(r)$ is the non-decreasing function of radius, $\Omega(r)$ is the decreasing one. Let, for example, $V_0(r)$ be independent of r (to judge by the results of the paper [3], V_0 can be constant in a quite large region). Then, from eqs. (5)-(6) it is easy to obtain the maximum energy of the second generation ions, which is equal to $W_0(3 + \sqrt{5})/2$, i.e. it is about 3 times higher than W_0 . One can give some examples illustrating an even more noticeable gain.

References:

- /1/ B.Lehnert, Nucl.Fusion, **11**, 485, 1971.
- /2/ B.W.James, S.W.Simpson, Phys.Lett., **46A**, 347, 1974.
- /3/ V.N.Bocharov et al., Fizika Plasmy, **4**, 488, 1978 (in Russian).
- /4/ D.D.Ryutov, T.Tange, Fizika Plasmy, **3**, 920, 1977 (in Russian).

ULTRAVIOLET RADIATION OF THE SURFACE DISCHARGE IS A PREIONIZER OF HIGH PRESSURE ATOMIC-MOLECULAR IMPURITIES

A.E. Belyanko, N.I. Lipatov, P.P. Pashinin and A.M. Prokhorov.

P.N. Lebedev Physical Institute of the U.S.S.R. Academy of Sciences, Moscow, U.S.S.R.

The results are concerned with the experimental investigation of preionized radiation of the surface discharges propagating over the substances with different values of dielectric permeability onto atomic-molecular high pressure gas impurities.

The interest to the surface discharges results from their following properties: high optical output, high power and considerable discharge aperture, comparatively ordinary bright temperature control. A specific character of the discharge interval breakdown due to strong gradients to the electric field on an interface of dielectric gas allows to make an agreement between discharge interval and accumulation without difficulties. As a result, the energy contribution rate rapidly increases and, as in consequence, a discharge plasma by their radiative properties becomes close to a black body with a surface temperature 50000°K .

It is shown that, as an ultraviolet preionization source of the atomic-molecular gas impurities it is appropriate to use over the substances the discharges with a high value $\epsilon / 10^3$ of dielectric

permeability, say, ceramics. In this case, an efficiency of the surface discharge, as a preionizer of gas impurity, which creates a great number of photoelectrons is much better than another optical sources, say, the open sparks. A compositions and pressure variations of the surrounding gas make it possible to control effectively a spectral composition and surface discharge radiation character that opens an optimal possibility (i.e. having minimum expenditure of energy) for gas medium photoionization or for photoinitiation of gas reactions. The former opens the good chances for investigations of different microscopic processes such as recombination, energy exchange between different components of gas impurities where it is easy to develop a nonequilibrium thermodynamic passing a current through a photoionized gas.

In the process of investigation of plasma discharge optical radiation the new, unknown previously, features of the light pulse behaviour were observed over the ceramics surface. A selfdamage of the overtensed surface interval favoured the short-closed line creation filled by a

dielectric with a high value of dielectric permeability. The nonlinear line losses caused by dependence of plasma filament resistance of the discharge current, under suitable conditions promoted a formation of short electromagnetic wave with the front irradiation a short / 30nsec/ pulse of hard ultraviolet radiation. On the time scale this pulse is followed by a discharge arc stage in the developing of which one realizes a main energy contribution into a discharge and the optical discharge radiation pulse is shaped with a duration on the order of magnitude exceeding an ultraviolet glow of the shock electromagnetic wave front.

As a result of the combined effect of the shock wave front radiation and that of the arc stage of a discharge the characteristic values of photoelectron density in different gas impurities were $10^8 - 10^{12} \text{ cm}^{-3}$. The energy in preionizer was 6-8j.

Photoelectrons were registered by a probe-Faraday cylinder whose constructive features made it possible to investigate a space photoelectron distribution basing of which one can conclude on a mechanism of photoionized process. As, for example, in molecular impurities $\text{CO}_2:\text{N}_2:\text{He}$ of different partial composition, a propagation of 1700\AA ultraviolet radiation which are controlled by CO_2 molecules, the photoelectrons arranged in 2-6cm out of preionization sources were conducted in con-

sequence of two-step excitation process, when two light quanta molecule absorption results in photoelectron developing.

A distinctive feature of the surface discharge operation as a preionizer compared, for example, to the open sparks is, that at gas pressure over 500 torr the photoelectron density in some gases /He, N_2 / is independent of pressure while in case of the open sparks the photoelectron concentration falls rapidly with gas pressure growth.

This specific peculiarity results from increasing of optical output of the surface discharge, the more the pressure of surrounding gas. Due to this fact, for high pressure impurity ionization it is more appropriate to use the surface discharges.

A designed qualitative model of the process investigated explains the obtained experimental results on the base of which a possible photoionization ultraviolet pumping by a discharge surface radiation of rapidly recombined atomic hydrogen plasma is discussed.

APPLICATION OF THE MAGNETIC FLUX PLASMA TRAP TO GENERATION OF CURRENT SHEETS IN A RAREFIED PLASMA

N.A. Koshilev, N.A. Strokin, A.A. Shisko and A.V. Mikhalev.

Sibizmir, Irkutsk 33, P.O. Box 4, U.S.S.R.

One simple experimental device for modelling processes occurring in neutral current sheets is θ -pinch with reverse field. In such a system for a long confinement of the neutral sheet arises a need at a required moment for sharply increasing the characteristic time of magnetic field change at the plasma boundary. Generally this problem is solved using special dischargers (crowbars). A crowbar must stand great initial strengths in the main charge circuit and be controllable at small potential difference on solenoid ends. To meet these requirements, the presence is necessary of additional electrical devices for crowbar ignition and synchronization circuits. Furthermore, crowbar applications do not exclude magnetic field distortion inside the single-turn solenoid arising due to the slot between current supplies.

This paper presents a description of a device constructed on the basis of the magnetic flux plasma trap, in which field trapping is effected by the formation of a well conducting envelope of cylindrical shape composed entirely out of plasma, and synchronization is effected without electric circuits - by variation of gas pressure in the ignition interspace.

The diagram of the device is given in

Fig. 1. Two coaxial dielectrical cylinders ($d_1=17$ cm, $L_1=35$ cm; $d_2=11$ cm, $L_2=100$ cm) provide working 2 and annular 1 volumes, each having an independent gas out/input system. The annular volume is filled with easily-ionized gas (argon).

Using system 7 of coils, a quasi-stationary initial field $H_0 \sim 150 - 600$ G, was created inside volumes 1 and 2. When H_0 reached a maximum value ($T/4 = 250 \mu\text{sec}$) with induction coils 4, initial plasma was created (density $n_0 \sim 10^{12} + 10^{14} \text{ cm}^{-3}$, $T_{i0} \approx T_{e0} \approx 0.5 + 1$ eV). After $30 + 40 \mu\text{sec}$ i.e. time required for plasma flowing along volume 2 and temperature leveling, the condenser ($C = 0.5 \mu\text{F}$, $U = 30 + 35$ kV) was connected to exciting coil 3 ($L=30$ cm). The \tilde{H} field increase time up to maximum $\tilde{H}_{\text{max}} = 1300$ G, $T/4 = 500$ nsec. When condenser discharges on coil, due to arising electric fields, gas in the annular interspace becomes ionized. Gas conductivity at initial time moments is small (the \tilde{H} magnetic field penetrates freely into the working volume), however at $t > t_0$ (Fig. 2) increases rapidly. The produced plasma forms a closed cylindrical conductor and the current flowing on the plasma, confines the field penetrated into the working volume. t_0 is controlled by changing pressure in the annular in-

terspace (Fig. 2b, c).

The magnetic flux plasma trap was used for forming current sheets in the configuration of opposite magnetic fields H_0 and \tilde{H} .

When the piston field is switched on in the working volume, a neutral current sheet is formed, which is moving towards the system axis, stops, then moves away towards the boundary of the internal volume.

On the basis of measurements of the axial magnetic fields in a working volume plasma (system of five magnetic probes located in the central cross-section of the exciting coil), the neutral sheet parameters ($\Delta = \Delta(n_0, H_0)$, $U = U(n_0, H_0)$, etc.) were determined.

The results of measurements of ion distribution functions in dynamical and static states with using eight-channel energy analyzer of charge-exchange atoms are reported.

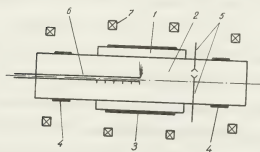


Fig. 1. Diagram of the device.

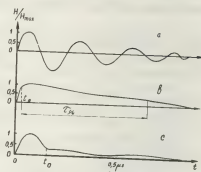


Fig. 2. Oscillograms from the magnetic probe for different pressures of argon in the annular volume / t_0 - time moment of the formation of the conducting shell/
 a - $P = 10^{-5}$ torr; b - $P = 3 \cdot 10^{-2}$ torr; c - $P = 0.7 \cdot 10^{-2}$ torr.

IX

- Théorie générale du plasma
General plasma theory
- Phénomènes de transport
Transfer phenomena
- Méthodes numériques
Numerical methods



KINETIC EQUATION FOR A PLASMA IN A STRONG HIGH FREQUENCY ELECTRO-MAGNETIC FIELD

R. Balescu and I. Paiva-Veretennicoff.*

*Faculté des Sciences, Université Libre de Bruxelles, Association Euratom-Etat Belge.

*Fakulteit der Wetenschappen, Vrije Universiteit Brussel.

Abstract.- The derivation of a correct kinetic equation for a plasma in presence of a strong electromagnetic field (e.g. a laser beam) poses two problems which, to our knowledge were never solved satisfactorily. The first is the influence of the external field on the collision process as well as on the average Vlassov field. The second is the neat separation of the rapid time- and space-scale processes from the slow ones, which are important for the transport phenomena.

The general formulation of the problem is discussed in the framework of the multiple time-scale perturbation theory of Bogoliubov-Frieman-Davidson.

The first step towards its solution is presented in detail. It involves the solution of the Vlassov equation (including longitudinal and transverse average fields) in presence of an intense external electromagnetic wave.

DIELECTRIC RESPONSE AND ENERGY LOSS FOR AN INTERMEDIATE QUANTUM PLASMA

N.E. Frankel, K.C. Hines and R.D.B. Speirs.

University of Melbourne, School of Physics, Parkville, 3052 Melbourne, Australia.

1. INTRODUCTION: With the advent of the use of laser-driven pellets to obtain thermonuclear fusion, we have in the laboratory a plasma in which the electrons have a fugacity, $Z \approx 1$, the intermediate quantum regime. When a highly compressed deuterium plasma is obtained by laser compression, the final state of the system corresponds to particle number densities of

$$\rho \approx 10^{26} - 10^{27}$$

and temperatures $T \approx 10^7 - 10^8$ /1/, /2/.

It is perhaps interesting to note that the ions in the deep interior of Jupiter correspondingly reach a fugacity regime around unity /3/. Using the above data, we find that the Fermi temperature, T_F , is virtually equal to the system's temperature, T . The temperature at which the fugacity of an electron gas reaches unity is

$T_0(Z=1) = 0.99 T_F$ /4/; thus these laser-driven fusion conditions correspond to a plasma of intermediate (partially degenerate) electrons and classical ions. What is more, the plasma parameter

$$\Gamma = e^2(4/3\pi\rho)^{1/3}/kT$$

is, for the above values, such that

$$10^{-2} \lesssim \Gamma \lesssim \frac{1}{2}.$$

Thus the particles to a first approximation are weakly coupled and also to a first approximation we can treat them using standard linear response theory.

Hore and Frankel /4/ have shown that all quantities which are thermodynamically averaged over the Fermi-Dirac distribution function can readily be expanded about the intermediate quantum region, $Z = 1$, using standard Mellin integral transform techniques. Hore and Frankel /5/ have also studied the dielectric response of the charged Bose gas about the condensation region, $Z = 1$. In this paper we report on similar calculations using the techniques of reference /5/ along with the expansions appropriate for a gas of fermions about $Z = 1$ given in reference /4/. Work up to now on this region of compelling interest in fusion research has essentially only been accessible by numerical techniques /6/, /7/.

2. RESULTS: We give here a brief summary of results obtained by the above analytical techniques for: (a) the longitudinal dielectric response function, (b) plasma dispersion relationships, (c) the

ion-acoustic sound, (d) the energy loss to collective modes, (e) the energy loss to binary collisions and (f) the electron-ion contribution to the thermal conductivity.

(a): Given the standard longitudinal dielectric response function $\epsilon(q, \omega)$ from linear RPA theory for an electron gas,

$$\epsilon(q, \omega) = 1 + \sum_{\lambda} \frac{4\pi e^2 V}{k^2 \Omega} \left[\frac{F_0(k) - F_0(k-q)}{\omega - \frac{1}{2}k \cdot q + \frac{1}{2}q^2} \right]$$

where λ is the spin, Ω the volume of the system and $F_0(p)$ the Fermi distribution function

$$F_0(k) = 1 / [Z^{-1} e^{k^2/2m\hbar^2} + 1].$$

Using the methods and techniques of references /4/ and /5/ we now expand $\epsilon(q, \omega)$ about the region $Z = 1$ to obtain small q , $T \approx T_F$, asymptotic expressions

$$\begin{aligned} \text{Re } \epsilon(q, \omega) &= 1 - \frac{\omega^2}{\omega^2 - k^2 q^2 / 4m} - \frac{q^2 k \cdot T_0}{m} \frac{\omega^2 (3\omega^2 + \frac{1}{2}k^2 q^2)}{(\omega^2 - k^2 q^2 / 4m)^3} \\ &\times \left[\frac{\gamma(5/2)}{\gamma(3/2)} + \theta \left(\frac{\gamma(2/2)}{\gamma(1/2)} - \frac{5}{3} \frac{\gamma(5/2)}{\gamma(3/2)} + O(\theta^2) \right) + \dots \right] \\ \text{Im } \epsilon(q, \omega) &= \omega^2 \frac{m^2 k T_0}{\hbar^2 \pi^2 q^2} \sinh \left(\frac{k \cdot T_0}{2\hbar \omega} \right) \exp \left(- \frac{m \omega^2}{2q^2 k T_0} \right) \times \\ &\times \left[1 + \theta \left(\frac{\gamma(3/2)}{\gamma(1/2)} - \frac{5}{3} \right) + \theta^2 \left\{ \frac{5}{9} - \frac{2}{3} \frac{\gamma(3/2)}{\gamma(1/2)} + \frac{\gamma^2(3/2)}{2\gamma^2(1/2)} \right. \right. \\ &\times \left. \left. \times \left(1 - \frac{\gamma(-1/2)}{\gamma(1/2)} \right) \right\} + O(\theta^3) + \dots \right], \end{aligned}$$

where $\mathcal{T}(s) = (1 - 2^{1-s}) \zeta(s)$, $\zeta(s)$ being the Zeta function and

$$\theta = (T_0/T)^{3/2} - 1.$$

(b): From the analytical result given in (a) we have obtained the following dispersion relationship for electron oscillations in the small q region:

$$\omega(q) = \omega_0(q) + i\gamma(q)$$

where

$$\begin{aligned} \omega_0^2 &= \omega_F^2 + \frac{3q^2 \hbar T_0}{m} \left[\frac{\gamma(5/2)}{\gamma(3/2)} + \theta \left(\frac{\gamma(3/2)}{\gamma(1/2)} - \frac{5}{3} \right) + \right. \\ &+ \theta^2 \left\{ \frac{20}{9} - \frac{\gamma(3/2)}{2\gamma(1/2)} \left(\frac{1}{3} + \frac{\gamma(3/2)\gamma(-1/2)}{\gamma^2(1/2)} \right) \right\} + \dots \Big] + \\ &+ O(q^4) \end{aligned}$$

$$\gamma = -\omega_p^2 \left(\frac{\pi}{2}\right)^{1/2} \left(\frac{2\pi}{k}\right)^{1/2} \left(\frac{m}{q}\right)^{1/2} \frac{1}{\tau^{(1/2)}} \sinh\left(\frac{k\omega_p}{2kT_e}\right) \exp\left(-\frac{\pi\omega_p^2}{2kT_e}\right) \times \\ \times \left\{ 1 - \frac{2\theta}{3} + \frac{5}{9}\theta^2 + \dots - \frac{3}{2} \frac{q^2 k T}{m \omega_p^2} \frac{\gamma^{(5/2)}}{\tau^{(5/2)}} + \theta \left(\frac{\gamma^{(3/2)} + \gamma^{(7/2)}}{\tau^{(3/2)}} \right) + O(\theta^4) + \dots \right\}.$$

(c): Defining $x = \left(\frac{m\omega}{kT}\right) - \frac{q^2 k^2}{2\lambda_{De}^2 kT}$ the expansion given in (a) above corresponds to $x \gg 1$ and $\theta \ll 1$. Now in considering ion sound modes we require $x \ll 1$. Using the appropriate asymptotic expansions for $E(q, \omega)$ for the electrons, x and θ small, and the standard form of $E(q, \omega)$ for the classical ions $\theta/8$, we then obtain for the ion sound modes

$$\omega(q) = \omega_i(q) + i\omega_{ei}(q);$$

where

$$\omega_i \approx \omega_i^* / \left[1 + \frac{\pi\omega_p^2}{q^2 k T_e} f(\theta) \right],$$

$$f(\theta) = \frac{\gamma^{(1/2)}}{\tau^{(1/2)}} + \theta \left(\frac{\gamma^{(3/2)}}{\tau^{(3/2)}} - \frac{\gamma^{(1/2)}}{3\tau^{(1/2)}} \right) + O(\theta^4);$$

$$\omega_{ei} \approx -\omega_i \left[\frac{\pi\omega_p^2}{2q^2} \left(\frac{M_i}{kT_i} \right)^{1/2} \exp\left(\frac{M_i \omega_i}{2q^2 k T_i}\right) \frac{\omega_i}{(1 + \frac{\pi\omega_p^2}{q^2 k T_e} f(\theta))} + \right. \\ \left. + \frac{\omega_i^2 \pi k T}{2q^2 k T_e} \sinh\left(\frac{k\omega_i}{2kT_e}\right) \exp\left(-\frac{\pi\omega_i^2}{2kT_e}\right) h(\theta) / \left(1 + \frac{\pi\omega_p^2}{q^2 k T_e} f(\theta) \right) \right],$$

$$h(\theta) = 1 + \theta \left(\frac{\gamma^{(3/2)}}{\tau^{(3/2)}} - \frac{2}{3} \right) + \dots$$

(d): The dielectric response function in (a) can be used to calculate the energy loss from Mev ions in a Kev electron plasma to plasmons /9/. Using the result for $(dE/dt)_{pl}$ from reference /9/, we have obtained the appropriate asymptotic expansion about $Z = 1$ ($\theta = 0$) which we give below

$$\left(\frac{dE}{dt} \right)_{pl} = -\frac{8e^2 M_i E}{3\epsilon^2 \pi} \left(\frac{1+Z}{Z} \right) (\ln \Lambda)_{pl}$$

where the analytical expansion for the prefactor $(\ln \Lambda)_{pl}$ is

$$(\ln \Lambda)_{pl} = -\left(\gamma(0) \ln \Lambda_0 + \gamma(0) [C+1] - \gamma'(0) + 2\gamma(-1) \Lambda_0 \times \right. \\ \times \ln \Lambda_0 + 2\gamma(-1) \Lambda_0 (C + \gamma_{1/2}) - 2\Lambda_0 \gamma'(-1) - \theta [2\gamma(-1) \Lambda_0 \times \\ \times \left(\frac{\gamma^{(1/2)} \tau^{(1/2)}}{\tau^{(1/2)}} \right) - \frac{5}{3} (\ln \Lambda_0 + C + \gamma_{1/2} - \frac{\gamma'(-1)}{\tau(1)}) + \dots \left. \right),$$

where $\Lambda_0 = k^2 \lambda_{De}^2 / 8\pi m_e k T$

and C is Euler's constant.

(e): We have also studied the contribution to the energy loss of an ion in an intermediate quantum electron gas due to binary collisions, $(dE/dt)_{bc}$. We have generalized the results for a classical plasma /10/ along the lines of reference /11/. We have obtained a detailed analytical expression for $(dE/dt)_{bc}$ along with the appropriate Coulomb factor $(\ln \Lambda)_{bc}$ for the laser-driven plasma.

(f): A specific expression for the electron-ion contribution to the thermal conductivity for a plasma of arbitrary degeneracy (all Z) has been given in reference /12/. We present the following

asymptotic expansion for this expression in the regime of $Z \approx 1$ ($\theta \approx 0$):

$$K_{ei} = 0.02 \frac{k_B c}{m} \left(\frac{k_B}{\lambda_e} \right)^2 \frac{T_e^*}{[\ln \Lambda^{-1} - \frac{1}{2}]} \times$$

$$x \left[1.9944 - 1.0711\theta - 1.3838\theta^2 + O(\theta^3) \right],$$

where all quantities are as in reference /12/.

3. DISCUSSION: Detailed comparison will be given of the binary collision and collective energy loss rates in the final state of a laser-driven fusion electron-ion plasma. We will also make specific comparisons for the quantities presented in (a) - (f) above with their corresponding form in the cases $Z = 0$ (classical) and $Z = \infty$ (totally degenerate).

REFERENCES:

- /1/ BRUECKNER, K.A. and JORNA, S., Rev. Mod. Phys. 46 (1974) 325.
- /2/ MINO, H., DEUTSCH, C. and HANSEN, J.P., Phys. Rev. A 14 (1976) 840.
- /3/ GEHRELS, T., editor, JUPITER (Univ. of Arizona Press, 1976).
- /4/ HORE, S.R. and FRANKEL, N.E., Phys. Rev. A 12 (1975) 1617.
- /5/ HORE, S.R. and FRANKEL, N.E., Phys. Rev. B 12 (1975) 2619.
- /6/ GOUEDARD, C. and DEUTSCH, C., J. Math. Phys. 19 (1978) 32.
- /7/ BRYSK, H., CAMPBELL, P.M. and HAMMERLING, P., Plasma Phys. 17 (1975) 473.
- /8/ ICHIMARU, S., BASIC PRINCIPLES OF PLASMA PHYSICS (W.A. Benjamin, Reading, Mass., 1973).
- /9/ SKUPSKY, S., Phys. Rev. A 16 (1977) 727.
- /10/ FRANKEL, N.E., Plasma Phys. 7 (1965) 225.
- /11/ BRYSK, H., Plasma Phys. 16 (1974) 927.
- /12/ GOUEDARD, C., J. Phys. A 10 (1977) L143.

EFFECTIVE BOUNDARY CONDITIONS FOR A PLASMA IN A MAGNETIC FIELD, ADJACENT WITH AN ELECTRODE

V.A. Rozhansky.

Kalinin Polytechnical Institute, Radiophysical Department, Leningrad, U.S.S.R.

The boundary conditions for a plasma, adjacent with an electrode usually include the surface potential distribution. Since the potential difference in the sheath must be important, it's impossible to apply these conditions for the quasi-neutral plasma equations directly. In order to receive the effective boundary conditions which are valid for the plasma equations it's necessary to express the potential difference in the sheath as a function of the particle fluxes to an electrode. In the absence of magnetic field this result was obtained in /1/ for collisionless sheath and in /2,3/ numerically for collision dominated one.

1. Collisionless sheath in a fully ionized magnetoplasma.

We shall consider the case of an electrode negatively biased with respect to plasma, the sheath scale small compared with electron cyclotron radius ρ_e and potential difference in the sheath $\varphi_c > T_e/e$. Electrons that reach an electrode must have normal energy at the sheath edge ($x=0$, $\vec{H}\vec{N}\vec{Z}$ -is parallel to an electrode) exceeding $e\varphi_c$, so that the influence of the plasma electric field on such electrons can be neglected. The corresponding orbits are almost empty, be-

cause the particle life time on these orbits $\Omega_e^{-1} = m_e c / eH$ is small compared with the time of Coulomb collisions. So the flux to an electrode is equal to the fast electron's flux to the empty region in the gamma space. The kinetic equation for the fast electrons /4/ with the zero boundary condition was solved in /5/. The corresponding flux is given by:

$$\Gamma_{e1} = 1,85 \pi^{1/2} \left(\frac{e\varphi_c}{T_e} \right)^{1/2} n_e e^{-e\varphi_c/T_e} \tilde{\rho}_e \times \quad (1)$$

$$\times \sqrt{(2m_e e\varphi_c)} \cdot \tilde{\rho}_e = \frac{m_e c}{eH} \sqrt{\frac{2e\varphi_c}{m_e}},$$

$$\sqrt{\rho} = 4\pi e^2 n m_e \Lambda / \rho^3; \quad \tilde{\rho}_e -$$

cyclotron radius of the fast electrons with the energy $e\varphi_c$.

2. Collisionless sheath in a partially ionized magnetoplasma.

Electron-neutral collisions transfer the electrons to the empty orbits and consequently lead to an additional flux to an electrode. We shall consider the case when the total cross-section is finite, so the large-angle scattering gives the main contribution to the flux. The distribution function far from the empty orbits is Maxwellian one, so we obtain /5/

$$\Gamma_{e1} = \frac{N_a}{\pi n_e T_e} \int_0^\infty dx \int_0^\pi d\theta \int_{-\infty}^\infty dQ \int dE \sqrt{2E/m_e} \frac{dG}{dE} \quad (2)$$

$$\cdot e^{-E/T_e} \left[\frac{2E}{m_e} - \left(\frac{Q}{m_e} + \Omega_e x \right)^2 \right]^{1/2}$$

N_a -neutral density G -cross-section, $Q = p_y - m_e \Omega_e x$. After intergrating we have

$$\Gamma_{e1} = \frac{\sqrt{\pi}}{2} \sqrt{e a (\sqrt{2 m_e e \psi_c})} \left(\frac{T_e}{e \psi_c} \right)^{1/2} \tilde{n} \tilde{\rho}_e e^{-e \psi_c / T_e} \quad (3)$$

$$\sqrt{e a (\sqrt{2 m_e e \psi_c})} = 1/a \sqrt{2 e \psi_c / m_e} \delta(e \psi_c)$$

The expression of the same order was obtained in /6/, but the distribution function was considered to be Maxwellian on all orbits. Result which coincides with (3) was obtained recently in /7/ by another method. The electron flux caused by electron-neutral collisions exceeds the flux connected with Coulomb collisions

$$(1) \text{ if } \sqrt{e a (\sqrt{2 m_e e \psi_c})} > \frac{e \psi_c}{T_e} \sqrt{e a (\sqrt{2 m_e e \psi_c})} \quad (4)$$

Expressions (2,3) take place if the Maxwellian distribution function far from the empty orbits is supported by the electron-electron collisions. This leads to the conditions:

$$\sqrt{e a (\sqrt{2 m_e e \psi_c})} \frac{T_e}{e \psi_c} < \frac{e \psi_c}{T_e} \sqrt{e a (\sqrt{2 m_e e \psi_c})} \quad (5)$$

If the collision frequency $\nu \sqrt{e a (\sqrt{2 m_e e \psi_c})}$ is less than given by (5) the distribution function is depleted on all orbits at $E > e \psi_c$ and the flux can be calculated as a diffusion flux of fast electrons from length of energy relaxation /1/.
3. Collision dominated sheath in a slightly ionized plasma.

Near the electrode the Boltzmann distribution for electrons is valid and the ionic flux is determined by linear density profile. After substituting the quasi-neutral solutions into Poisson's equation we obtain the distance where the space charge becomes significant

$$x^* = \left[\frac{T_e D_{in} (1 + T_e / T_i)}{4 \pi e^2 \Gamma_{in}} \right]^{1/3} \quad (6)$$

D_{in} - normal diffusion coefficient, Γ_{in} - normal ionic flux. The density in this point is given by:

$$n^* = \left[\frac{T_e \Gamma_{in}^2}{D_{in}^2 (1 + T_e / T_i)^2 4 \pi e^2} \right]^{1/3} \quad (7)$$

The potential distribution in the sheath can be obtained neglecting electron density:

$$\partial \psi / \partial x = \frac{T_e}{e} \sqrt{8 \pi e^2 T_i \Gamma_{in} |x| / T_e^2 D_{in}} \quad (8)$$

The size of the sheath is determined by condition that the electron diffusion term becomes dominant. The potential difference in the sheath is given by:

$$e \psi_c = T_e \ln \frac{6 \Gamma_{in} D_{in} T_i}{2^{1/3} \Gamma_{en} D_{in} T_e} + \frac{T_e}{3} \ln \ln \left[2 \Gamma_{in} D_{in} T_i / (\Gamma_{en} D_{in} T_e) \right] \quad (9)$$

The potential difference between the point x in plasma and sheath edge is:

$$e \psi_p(x) = T_e \ln \left\{ n(x) \left[\frac{D_{in}^2 (1 + T_e / T_i)^2 4 \pi e^2}{T_e \Gamma_{in}^2} \right]^{1/3} \right\} \quad (10)$$

Expressions (9,10) coincide with the numerical result /3/ with an accuracy $\leq 10\%$ even when $e \psi_c = T_e$.

References:

1. Thermoemission energy transfer and low temperature plasma, ed. by B.Ya.Moyzhes and G.E.Pikus, M., Nauka, 1973.
2. C.H.Su, S.H.Lam, Phys.Fluids 6, 1479, 1963.
3. I.M.Cohen, Phys.Fluids, 6, 1492, 1963; 8, 2097, 1965.
4. D.V.Sivukhin, Voprosy teorii plazmy, Atomizdat, 1964.
5. V.A.Rozhansky, L.D.Tsendin, Fizika plazmy, 4, 388, 1978.
6. I.I.Litvinov, PMTF, N1, 52, 1977.
7. F.G.Baksht, Journ.Tekhn.Phys. 48, 1782, 1978.

GENERALIZED OHM'S LAW OF UNSTEADY STATE IN PARTIALLY IONIZED GASES

Lu Guan-Kang.
Fudan University, Shanghai.

A generalized Ohm's law in fully ionized gases has been given by Spitzer, and a similar law of steady state in partially ionized gases has been derived by Cowling and Лоскунов.

We have derived a generalized Ohm's law of unsteady state in partially ionized gases, provided that the ionization and recombination processes have reached the dynamic equilibrium. It is

$$\frac{m_e}{n e^2} \frac{\partial \vec{J}}{\partial t} = \frac{\nu P_e}{n e} + \vec{E} + \frac{1}{c} \vec{v} \times \vec{B} - \frac{1}{n e c} \vec{J} \times \vec{B} - \frac{B}{n e c} (K + K_e) \vec{J}$$

$$+ \frac{1}{n e c} \left[\vec{J}_i(\omega) - \frac{m_e}{m_i} \vec{J}(\omega) \right] e^{\beta t} + \frac{K_e B}{n e c (1-\alpha)} \left[\vec{J}_i(\omega) - \frac{m_e}{m_i} \vec{J}(\omega) \right] e^{-\beta t}$$

$$+ \frac{(1-\alpha)^2 e^{\beta t}}{K_i n e c} \left\{ \int_0^{\infty} e^{\beta \tau} \left[c \nabla P_e + \vec{J} \times \vec{B} \right] d\tau \right\} \times \frac{\vec{B}}{B}, \quad (1)$$

where $\beta = \nu_e/2(1-\alpha)$, $\vec{J}_i = n e \vec{v}_i$
 $K = \nu/\omega_{ce}$ $K_e = \nu_e/\omega_{ce}$
 $K_i = \nu_i/2\omega_{ci}$ $\alpha = n/(n+n_a)$

is the ionization degree, n and n_a are the electron and atom number density respectively, ν is the mean collision frequency between an electron and an ion, ν_e is the mean collision frequency between an electron and an atom, ν_i is the mean collision frequency between an ion and an atom, v is the velocity of a plasma mass element, v_i is the relative mean velocity of ions with respect to the plasma mass element, J is the electron current density, -e is the electron charge, ω_e and ω_i are the electron and ion cyclotron frequency respectively, E and B are the electric and magnetic field strength respectively, c is the light velocity in free space, P is the pressure of plasma, and P_e is the partial pressure of the electron gas.

When K_e = 1-α, (1) reduces to a more convenient form. It is

$$\frac{m_e}{n e^2} \frac{\partial \vec{J}}{\partial t} = \frac{\nu P_e}{n e} + \vec{E} + \frac{\vec{v}}{c} \times \vec{B} - \frac{1}{n e c} \vec{J} \times \vec{B} - \frac{\vec{J}}{c} \times \vec{v}$$

$$+ \frac{(1-\alpha)}{n e c} e^{\beta t} \left[\int_0^{\infty} \nabla(P-P_e) e^{\beta \tau} d\tau \right] \times \vec{B}$$

$$- \frac{(1-\alpha)}{c} e^{-\beta t} \left[\int_0^{\infty} \vec{v}(\tau) e^{\beta \tau} d\tau \right] \times \vec{B} \quad (2)$$

where $\sigma = \frac{n e^2}{m_e (\nu + \nu_e)}$

The physical meaning of integral terms in (2) can be shown by the following integration:

$$e^{\beta t} \left[\int_0^{\infty} \vec{v}(\tau) e^{\beta \tau} d\tau \right] \times \vec{B} = [\vec{v}] \times \vec{B} (1 - e^{\beta t}) \quad (3)$$

where [v] is some middle-value of v in the interval (0,t). In (3), the middle-value theorem has been used. It is obvious, from (2) and (3), that the relaxation processes of neutral particles participating the whole movement of plasma element is expressed by the integral terms in Ohm's law.

In the limiting case β→0 (i.e. ν_e→0), by using Ohm's law (2) and Maxwell equations, it may be obtained that the speed of Alfvén's wave is v_A/√α and is not v_A, where v_A is the Alfvén speed. The physical reason of this result is obvious. As ν_e→0, the neutral atoms don't participate in the oscillations in Alfvén wave.

Similarly, if we use (2) instead of E × v × B = 0, the dispersion relation of magnetohydrodynamic wave is

$$\frac{\omega^2}{k^2} - \frac{\omega^2}{k^2} \left[V_s^2 + V_A^2 (1+\alpha) \right] + V_s^2 V_A^2 \left[\cos^2 \theta + \alpha \frac{1+\alpha \cos^2 \theta}{1+\alpha} \right] = 0 \quad (4)$$

where $A = \frac{1-\alpha}{\alpha} \frac{c \omega}{\beta + i \omega}$

φ is the angle between the wave vector k and the applied magnetic field, ω is the angular frequency, and v_s is the sound velocity.

As α=1, A→∞, (4) reduces to the result given by Alfvén and Fälthammar.

When the plasma deviates to the neutrality, the form of generalized Ohm's law has to be corrected. The form of (1) becomes

$$\frac{m_e}{n e^2} \frac{\partial \vec{J}}{\partial t} = \frac{\nu P_e}{n e} + \vec{E} + \frac{1}{c} \vec{v} \times \vec{B} - \frac{1}{n e c} \vec{J} \times \vec{B} - \frac{B(K+K_e)}{n e c} (\vec{J} - \vec{J}_e \vec{v})$$

$$+ \frac{1}{n e c} \left[\vec{J}_i(\omega) - \frac{m_e}{m_i} (\vec{J}(\omega) - \vec{J}_e \vec{v}(\omega)) \right] \times \vec{B} e^{\beta t}$$

$$+ \frac{K_e B}{n e c (1-\alpha)} \left[\vec{J}_i(\omega) - \frac{m_e}{m_i} (\vec{J}(\omega) - \vec{J}_e \vec{v}(\omega)) \right] e^{-\beta t}$$

$$+ \frac{(1-\alpha)^2}{K_i} \frac{e^{\beta t}}{n e} \left\{ \int_0^{\infty} e^{\beta \tau} \left[P d\tau + \nabla P_e + \vec{J} \times \vec{B} + \vec{J}_e \vec{v} \right] d\tau \right\} \times \frac{\vec{B}}{B},$$

where ρ_e is the electric charge density of plasma.

When the plasma approaches the steady state, (5) reduces to the form given by Любимов:

$$0 = \nabla p_e + ne(\vec{E} + \frac{1}{c} \vec{v} \times \vec{B}) - \frac{1}{c} \vec{j} \times \vec{B} - \frac{\partial}{\partial t} (k + k_e) (\vec{j} - \frac{1}{c} \vec{v}) + \frac{(1-\kappa)^2}{8\kappa^2} [\nabla p_e + \frac{1}{c} \vec{j} \times \vec{B} + \rho_e \vec{E}] \times \vec{B} \quad (6)$$

REFERENCES

- (1). L. Spitzer Jr., Phys. of Fully Ionized Gases, Interscience (1956).
- (2). T.G. Cowling, Magnetohydrodynamics, Interscience, (1957).
- (3). Любимов, ПММ 25 (1961) 611,
- (4). J.K. Lu, Acta Physica Sinica 26 (1977) 417.
- (5). H. Alfvén and C-G Fälthammar, Cosmical Electrodynamics, the Clarendon Press (1963).

ELECTROPHYSICAL PROPERTIES OF NON-EQUILIBRIUM AEROSOL PLASMA

A.V. Gorbатов and E.V. Samuilov.

The Krishniahovsky Power, Engineering Institute, Moscow U.S.S.R.

Studies on electrophysical properties of aerosol plasma (AP) with electron density, n_e , controlled exclusively by thermionic or photoelectric emission from aerosol particles, have been of interest for spacecraft development¹, MHD energy conversion², plasma chemistry and plasma-based metallurgy³. The non-equilibrium plasma whose effective electron temperature exceeds that of the carrying gas, $T_e \gg T_m$, can be produced (i) in rapidly expanding supersonic aerosol flows whose particle temperature, T_p ($T_p = (0.13-0.3)\text{eV}$), due to the time delay in the interphase heat transfer, is higher than that of the carrying gas, T_m , (ii) through the electron heating up by the applied electric field, or (iii) through the exposure of the aerosol to photons of sufficiently high energy. In our paper the determination of AP parameters is discussed taking into account the non-equilibrium mentioned.

Considered is the case of an infinite AP consisting of identical spherical particles of R_1 radius distributed in space randomly but uniformly with the concentration, N_p , and subjected to identical conditions. For simplicity it is assumed that the particles emit only thermoelect-

rons having the Maxwell velocity distribution corresponding to the quasi-stationary temperature T_p ($T_p > T_m$). The particles absorb incidenting electrons. Also, the assumption was made that electron-electron collisions could be neglected. To solve the problem, two approaches were employed, the approach selected being determined by the ratio between the mean-free-path for electron-molecule collisions λ and the action radius α of aerosol particles.

If, $\lambda \sim \alpha$, the boundary problem should be solved to determine n_e and T_e . In this problem it is assumed⁵ that any aerosol particle is located in the centre of an electrically neutral sphere of R_2 radius ($N_p^{-1} = 4\pi R_2^3/3$) and the electron distribution function ($f(\vec{V})$) should be found from the self-consistent problem, that is, from the Boltzman kinetic equation and Poisson equation written for the electric potential with corresponding boundary conditions at R_1 and R_2 . For the cases when the electric field near a particle may be considered to be Coulombian or when its influence on electrons motion is negligible ($\alpha = R_1$), the solutions can be found by the momentum method in its linear approximation ($(T_p - T_m)/T_m \ll 1$) with the allo-

wance made for the quasi-stationary charge of aerosol particles. The analysis of solution indicates that the non-isothermal AP ($T_p > T_m$) has the greater electron concentration n_e than the isothermal AP ($T_p = T_m$) at the same particle temperature, the other conditions being equal.

When $\alpha = R_1$ and $\lambda \gg R_1$, the aerosol particles may be treated as gigantic molecules emitting and absorbing electrons.

In the framework of elementary theory⁴, continuity, motion, and energy equations are used to clarify the influence of alternate uniform electric field, $E = E_0 \cos \omega t$, on AP parameters. It is assumed that field does not heat up aerosol particles significantly. The simultaneous solution of the equations was found for two extreme cases:

(i) $\tau_r \omega \ll 1$ and (ii) $\tau_r \omega \gg 1$ [$\tau_r = (\delta \bar{v}_m + \bar{v}_p)^{-1}$, $\bar{v}_m = 4\bar{v}/3\lambda$, $\bar{v}_p = \bar{v}4\pi R_1^2 N_p/3$] where τ_r - relaxation time for the electron temperature; \bar{v} - mean electron velocity; δ - average relative share of energy lost by electron having collided with a molecular. The solution obtained suggests that the field influence on electrophysical properties of AP may be neglected (the field is weak) when $E_0 \ll E_c = [T_{e,0} 3m(\omega^2 + \bar{v}_{m,0}^2)/e^2 \tau_{r,0} \bar{v}_{m,0}]^{1/5}$

On the contrary, when $E_0 \gg E_c$ (the strong field), this influence is pronounced. Here E_c is a characteristic field for the AP; $T_{e,0}$, $\bar{v}_{m,0}$, $\tau_{r,0}$ are T_e , \bar{v}_m , τ_r correspondingly at $E_0 = 0$; e and m are the electron charge and mass. If parameters of AP are those given in Ref.5, that is, $N_p \sim 10^7 \text{ cm}^{-3}$; $R_1 \sim 10^{-4} \text{ cm}$;

$T_{e,0} = T_p = T_m \sim 2.10^3 \text{ K}$, $\delta \sim 1.2 \cdot 10^{-3}$; $\bar{v}_m \sim 5.9 \cdot 10^9 \text{ s}^{-1}$ and $\omega = 23 \cdot 10^9 \text{ s}^{-1}$ is taken from Ref.6, then $E_c = 5.2 \text{ V/cm}$. These values of E_c do not appear to be excessively high as compared to fields produced by the modern radio transmitters. This along with other examples indicate that the conclusion of Ref.7 (lacking, unfortunately, affirmation by numerical estimates) according to which T_e and T_m could not differ significantly, is not sufficiently general. Heating up of electrons in the AP is followed by the decrease in n_e and change of \bar{v}_m . These two factors are responsible for the appearance of heating non-linearity at which the electrical conductivity, , becomes dependent on E_0 .

REFERENCES

1. M.S.Sodha, S.Guha. Adv. Plasma Phys., N 4, p.219, 1971
2. D.T.Helfritsch, W.A.Gustafson, J.Eng. Power, Trans. ASME, Series A, 96, N 3, p.113, 1974
3. V.A.Legasov, et al., In 'Plasma Chemistry', Atomizdat, issue 5, p.116, 1978
4. V.L.Ginzburg, The Propagation of Electromagnetic Waves in Plasmas, Pergamon Press, 1970.
5. E.G.Gibson, Phys. Fluids, 9, N 12, p.2389, 1966
6. R.T.Fante, R.G.Gamache, T.M.Yos. AIAA J. 10, N 3, p.352, 1972
7. S.Guha, A.K.Arora, Appl.Sci.Res., 22, p.176, 1970

ELECTRON ENERGY DISTRIBUTION FUNCTION IN Xe PLASMA IN THE PRESENCE OF COULOMB COLLISIONS

A.P. Ershov and A.A. Kuzovnikov.

Physics Department, Moscow State University, Moscow, U.S.S.R.

Ionization degree of positive column plasma in noble gases is usually equal to $10^{-7} - 10^{-5}$ and depending on value of E/p , (electric field to pressure ratio) the influence of coulomb collisions on plasma characteristics can be considerable /1/. However the role of this factor for Xe has been investigated neither experimentally nor theoretically.

Earlier calculations /2,3/ performed without coulomb collisions made it possible to correct the energy dependence of elastic collision cross section for electrons in Xe and to describe the dependence of the drift velocity and of the ratio of the diffusion coefficient to the mobility coefficient D_e/μ_e on value E/p for an $E/p \leq 10$ V/cm torr. However calculated values of the first Townsend ionisation coefficient α are 4-6 times larger than experimental ones /4/. This means that electron distribution function in inelastic region is determined with considerable error connected with error in inelastic cross section. Since the error in excitation cross section is more greater than error in ionizing cross section the excitation cross section was corrected to provide the agreement between calculated and experimental data for an E/p , in the range from 20 to 30 V/cm torr. At these values E/p , electron distribution has considerable value up to $V \leq 20$ eV when extrapolation mistake is not much but ionizing cross section is measured with good precision.

Electron distribution was calculated using energy dependence of electron elas-

tic cross section from /2/ and of ionizing cross section from /6/; energy dependence of excitation cross section is given by

$$S(V) = 1.8 \cdot 10^{-17} (V - 8.3) \quad [cm^2]$$

In collision integral elastic electron-atom, electron-ion, electron-electron collisions and excited and ionizing collisions were taken into account. Energy losses at inelastic collisions was assumed to be equal to the threshold of inelastic process.

The kinetic equation is solved by iteration method allowing nonlinear integro-differential equation transform to linearized recurrent differential equation

$$\frac{d}{dx} \left\{ \rho_n(x) \frac{dy_n}{dx} \right\} + \varepsilon_n(x) \frac{dy_n}{dx} - q_n(x) y_n = -f_n(x)$$

with boundary conditions

$$y_n(0) = 1 \quad y_n(1) = 0$$

and with normalization requirement

$$C \int_0^1 \sqrt{x} y_n(x) dx = 1$$

Here n - is iteration number. Energy scale is chosen in accordance with condition

$y_n(1) = 0$. This extremely task is solved by economic method /7/. The coefficients $\rho_n(x)$, $q_n(x)$, $\varepsilon_n(x)$ and $f_n(x)$ were formed with method requirements. Iterations had been performed until the difference between value of E/p , determined from balance equation

$$\mu_e E^2 = \frac{2m}{M} \langle v^2 \rangle^e V_d + \langle v^2 \rangle^{ex} V_{ex} + \langle v^2 \rangle^{ion} V_{ion}$$

and requirement value became smaller 1%.

Calculation results are given in Fig.1 - 4. Fig.1 shows examples of calculated electron energy distribution for various values E/p and p .

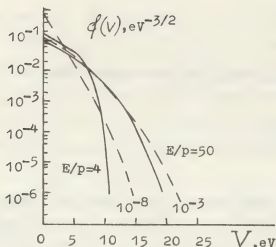


Fig.1 Electron energy distribution functions in Xe at various E/p and ionization degrees.

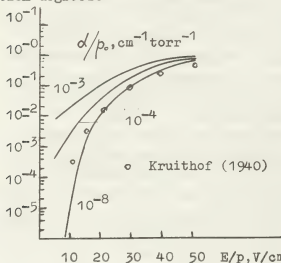


Fig.2 First Townsend ionization coefficient at various ionization degrees.

One can see that coulomb collisions increase the number both a slow and fast electrons. Significant increase of the number of fast electrons with increasing ionization degree ρ results in rapid increase of Townsend coefficient for $E/p \leq 10 \text{ V/cm torr}$ /Fig.2/. Electron distribution deformation at low energy results in strong depending of electron mobility on ionization degree /Fig.3/. This effect would be more strong without electron-ion collisions exerting influence on mobility for $\rho \geq 10^{-4}$. Whereas mean electron energy depends relatively weakly on ρ over a wide range of E/p and of ρ /Fig.4/. However D_e/μ_e ratio increasing $V_e \approx \frac{2}{3} \langle V \rangle$ significantly at small ρ depends on ρ much strongly keeping nevertheless differ

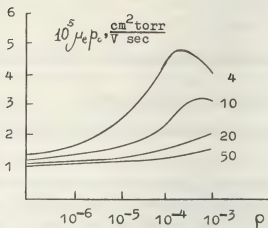


Fig.3 Electron mobility coefficient as a function of ionization degree at various E/p .

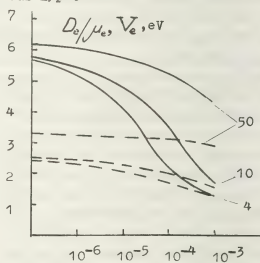


Fig.4 The ratio of the diffusion coefficient to the mobility coefficient (—) and temperature $V_e \approx \frac{2}{3} \langle V \rangle$ (---) as a function of ionization degree at various E/p .

ence from V_e even at $\rho \sim 10^{-3}$.

Results of calculation show that coulomb collisions in Xe plasma should be taken into account.

References

1. R.Winkler Beitr. Pl. Phys. 12,317,1972.
2. L.Frost,A.Phelps Ph.Rev.136,A1538,1964.
3. S.Pfau,A.Rutscher An.Phys. 22,166,1969.
4. S.Pfau,H.Scheibner Beit.Pl. 9,425,1969.
5. M.Schaper,H.Scheibner E.Pl. 9, 45,1969.
6. D.Rapp, P.Englander-Golden J. Ch.Phys. 43,1464,1965.
7. A.A.Самарский Теория разностных схем М. 1977.

ON THE LINEAR THEORY OF ELECTRON PROCESSES IN THE COLLISIONLESS DIODE

A. Ya. Ender and V.I. Kuznetsov.

Ioffe Physical-Technical Institute of the U.S.S.R. Academy of Sciences, Leningrad, U.S.S.R.

Linear electron processes will be analyzed assuming, that undisturbed potential is not negative in all the interelectrode spacing (cathode potential is taken to be zero) and the diode, being considered, has a plane-parallel geometry, with a planar emitting cathode and an absorbing anode. For such one-dimensional case the electron concentration is defined by the formula from [1]:

$$n_e(\tau, \tau) = \int_0^\infty \frac{f_e^0(\tau; u^0) u^0 du^0}{\sqrt{u^0^2 + 2\eta(\tau, \tau) + 2G(\tau, \tau, u^0)} + Q(\tau, \tau, u^0)} \quad (1)$$

Here τ^0, u^0 - time and velocity, at which an electron leaves the cathode; f_e^0 - electron distribution function on the cathode ($u^0 > 0$); G and Q are calculated using the following formulas:

$$G(\tau, \tau, u^0) = - \int_{\tau^0}^\tau \frac{\partial}{\partial \tau} \eta(t, \tau(t, u^0)) dt \quad (2)$$

$$Q(\tau, \tau, u^0) = - \int_0^\tau (\tau - \tau^0 - t) \frac{\partial}{\partial \tau} \frac{\partial}{\partial \tau} \eta(t + \tau; \tau(t + \tau; u^0)) dt$$

In these expressions the integrals are taken along the trajectory of the particle $\tau(t, u^0)$, which reached the point τ at the time τ and had left the cathode at the velocity u^0 ; the derivative with respect to τ^0 is calculated at the fixed values of t and u^0 . The function G is connected with the exchange of energy between electrons and the electric field, while the function Q expresses the change of the form of the particle number conservation law in the non-stationary electric field.

When a disturbance is imposed, the potential is $\eta(\tau, \tau) = \eta_0(\tau) + \tilde{\eta}(\tau) e^{-i\omega\tau}$. Then $G = \tilde{G}(\tau) e^{-i\omega\tau}$, $Q = \tilde{Q}(\tau) e^{-i\omega\tau}$. On linearizing (2) with respect to $\tilde{\eta}$, we get for \tilde{G} and \tilde{Q}

$$\tilde{G}(\tau, u^0) = e^{i\omega Z(\tau, u^0)} \int_0^\tau \frac{d}{dx} \tilde{\eta}(x) e^{-i\omega Z(x, u^0)} dx - \tilde{\eta}(\tau) \quad (3)$$

$$\tilde{Q}(\tau, u^0) = e^{i\omega Z(\tau, u^0)} \int_0^\tau [i\omega \frac{d}{dx} \tilde{\eta}(x) + \tilde{Q}(x, u^0) \frac{d^2}{dx^2} \eta_0(x)] \cdot$$

$$\cdot [Z(\tau, u^0) - Z(x, u^0)] u_0^{-1}(x, u^0) e^{-i\omega Z(x, u^0)} dx \quad (4)$$

Here $u_0(\tau, u^0) = \sqrt{u^0^2 + 2\eta_0(\tau)}$ - velocity of the electron on the undisturbed trajectory and $Z(\tau, u^0)$ - time of flight of the electron along the undisturbed trajectory from the cathode to the point τ

$$Z(\tau, u^0) = \tau - \tau^0 = \int_0^\tau u_0^{-1}(x, u^0) dx \quad (5)$$

In order to solve Eq. (4), we'll introduce a new function to be determined $F = \tilde{Q} e^{-i\omega Z/u^0}$. The boundary conditions for F , namely, $F(0) = 0$, $u_0^3(\tau) \frac{d}{d\tau} F(\tau) \big|_{\tau=0} = 0$ are derived from Eq. (4). Twice differentiating the equation for F and having in mind, that the energy conservation law for the undisturbed trajectory is $\eta_0(\tau) - u_0^2(\tau)/2 = \text{const}$, we reduce this equation to $\frac{d}{d\tau} (u_0^2 \frac{d}{d\tau} F) = i\omega e^{-i\omega Z(\tau)} \frac{d}{d\tau} \tilde{\eta}(\tau)$. Hence, finally we get

$$\tilde{Q}(\tau, u^0) = i\omega u_0(\tau, u^0) \int_0^\tau \frac{dx}{u_0^2(x, u^0)} \int_0^x \frac{d}{dy} \tilde{\eta}(y) e^{i\omega [Z(\tau, u^0) - Z(y, u^0)]} dy \quad (6)$$

By linearizing the Poisson equation in the vicinity of the undisturbed state and taking into account the fact, that the ion concentration is undisturbed, we obtain, using (3) and (6), the following equation:

$$\frac{d^2}{d\tau^2} \tilde{\eta} + \int_0^\infty f_e^0(u^0) u^0 du^0 \frac{e^{i\omega Z(\tau, u^0)}}{u_0(\tau, u^0)} \left[\frac{1}{u_0^2(\tau, u^0)} \int_0^\tau \frac{d}{dx} \tilde{\eta}(x) e^{-i\omega Z(x, u^0)} dx + i\omega \int_0^\tau \frac{dx}{u_0^2(x, u^0)} \int_0^x \frac{d}{dy} \tilde{\eta}(y) e^{-i\omega Z(y, u^0)} dy \right] = 0 \quad (7)$$

With the boundary conditions $\tilde{\eta}(0) = 0$, $\tilde{\eta}(\delta) = 0$, where δ - the value of the interelectrode distance in terms of the Debye radius.

In the important particular case of the electron beam $f_e^0(u^0) = N_0 \delta(u^0 - V_0)$, and (7) transforms into the equation

$$\frac{d^2}{d\tau^2} \tilde{\eta} + N_0 V_0 \frac{e^{i\omega Z(\tau)}}{u_0(\tau)} \left[\frac{1}{u_0^2(\tau)} \int_0^\tau \frac{d}{dx} \tilde{\eta}(x) e^{-i\omega Z(x)} dx + i\omega \int_0^\tau \frac{dx}{u_0^2(x)} \int_0^x \frac{d}{dy} \tilde{\eta}(y) e^{-i\omega Z(y)} dy \right] = 0 \quad (8)$$

which after the introduction of the new independent variable (5) and the new function to be determined

$$F(Z) = \int_0^\tau \frac{d}{dx} \tilde{\eta}(x) e^{-i\omega x} dx \quad (9)$$

takes the form

$$u_0 F'' - u_0' F' + N_0 V_0 F = I u_0^2 e^{-i\omega z} \quad (10)$$

with the boundary conditions

$$F(0) = 0, \quad u_0'(z) \frac{d}{dz} F(z) / z=0 = \frac{iI}{\omega} \quad (11)$$

Here I - amplitude of current disturbance. As the measurement units we choose: for time $\omega_p^{-1} = (4\pi e^2 N_0 / m)$, and for spatial coordinate $\lambda_D = V_0 / \omega_0$.

Let's find the solution of Eq.(10) for the case, when $\eta_0(\zeta) = \alpha \zeta$ (the case of the constant electric field), imposing no limitations whatever on the value α of the field. In the well-known work of Pierce (see [2]) the solution is obtained for $\alpha=0$. In the case of the constant field Eq.(10) becomes

$$(Z + V_0/\alpha) F'' - F' + N_0 V_0/\alpha F = I \alpha (Z + V_0/\alpha)^2 e^{-i\omega Z} \quad (12)$$

After the replacement of the independent variable $z = kt^k - V_0/\alpha$ and the unknown function $F = t^k y$ (in the case, being considered, $\mu = \nu = 2$, $k = \alpha/2N_0 V_0$) Eq.(12) reduces to the non-homogeneous Bessel equation

$$t^2 y'' + t y' + (t^2 - 4) y = \frac{4I V_0^3}{\alpha^2 t^2} e^{-i \frac{\omega V_0 (t^2 - \alpha^2)}{\alpha^2 t^2}} \quad (13)$$

Here $\alpha = 2V_0 \sqrt{N_0}/\alpha$, $t = \alpha \sqrt{1 + 2\alpha/\omega^2} \zeta$.

Using (11) and taking into account (9)

we get from (13) for $\tilde{\eta}(\zeta)$

$$\tilde{\eta}(\zeta) = -\frac{\pi I V_0 i}{\omega \alpha^2} \left(\int_0^t x^2 T_{12}(x, \alpha) e^{i \frac{\omega V_0 (x^2 - \alpha^2)}{\alpha^2 x^2}} dx + \frac{2\omega V_0 i}{\alpha^2} \int_0^t y^2 dy \int_0^y x^3 T_{21}(x, y) e^{i \frac{\omega V_0 (y^2 - x^2)}{\alpha^2 x^2}} dx \right) \quad (14)$$

Here $T_{ij}(x, y) = J_i(x) \cdot N_j(y) - J_j(y) \cdot N_i(x)$ and $J_i(x)$, $N_i(x)$ are Bessel and Neumann functions of the i -th order.

In the particular case of $\alpha=0$ Eq.(14) after using the asymptotic formulas for the cylindrical functions transforms into the well-known formula of Pierce

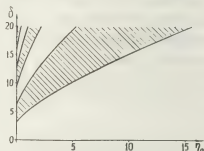
$$\tilde{\eta}(\zeta) = \frac{V_0 \sqrt{N_0}}{2\omega(N_0 - \omega^2)} \left[\frac{\omega - \sqrt{N_0}}{\omega + \sqrt{N_0}} (1 - e^{i \frac{\omega - \sqrt{N_0}}{V_0} \zeta}) - \frac{\omega + \sqrt{N_0}}{\omega - \sqrt{N_0}} (1 - e^{i \frac{\omega + \sqrt{N_0}}{V_0} \zeta}) - \frac{2\omega^2 i}{V_0 \sqrt{N_0}} \zeta \right] \quad (15)$$

The solution so obtained can be used for analyzing stability of the diode with an arbitrary undisturbed distribution of the potential in the region $\eta_0(\zeta) \neq 0$, since such a distribution can be well approximated by portions with constant, but differing values of electric field strength;

it should be noted, that at the boundaries of these portions the condition of continuity of the functions $\tilde{\eta}(\zeta)$, $\frac{d}{d\zeta} \tilde{\eta}(\zeta)$ and $\frac{d^2}{d\zeta^2} \tilde{\eta}(\zeta)$ is satisfied. The necessity to satisfy the condition $\tilde{\eta}(\delta) = 0$ leads to the dispersion relation.

In the case, being considered, i.e. $\eta_0(\zeta) = \alpha \zeta$, the dispersion relation is of the form:

$$\frac{\partial}{\partial \omega} \left(\int_0^{\alpha \sqrt{1 + 2\alpha/\omega^2}} x^2 T_{12}(x, \alpha) e^{i \frac{\omega V_0 (x^2 - \alpha^2)}{\alpha^2 x^2}} dx + \frac{2\omega V_0 i}{\alpha^2} \int_0^{\alpha \sqrt{1 + 2\alpha/\omega^2}} y^2 dy \int_0^y x^3 T_{21}(x, y) e^{i \frac{\omega V_0 (y^2 - x^2)}{\alpha^2 x^2}} dx \right) = 0 \quad (16)$$



The figure presents the regions (see hatched areas) of the aperiodic diode instability in the plane (δ, η_0) , where $\eta_0 = \alpha \delta$ - anode potential. The boundaries of these regions are defined by the equation

$$T_{22} \left(\frac{2\delta}{\eta_0} \sqrt{1 + 2\eta_0}, \frac{2\delta}{\eta_0} \right) = 0 \quad (17)$$

At $\eta_0 \rightarrow 0$ and $\eta_0 \rightarrow \infty$ the solution of (17) are $\delta \approx \pi s / (1 - 3/4 \eta_0)$ and $\delta \approx C_s \eta_0^{3/4}$, where $s = 1, 2, 3, \dots$, while C_s - constants, e.g. $C_1 = 2.1593/3$. The intercepts $(\pi(2s-1), \pi 2s)$ of the axis $\eta_0 = 0$ correspond to Pierce's instabilities. As is shown by the numerical calculations, Eq.(16) at $\text{Re } \omega \neq 0$ has no solutions. Thus, in the case $\alpha \neq 0$, as well as in the case $\alpha = 0$ the instability, which develops, when the electron beam passes through the collisionless diode, can be only aperiodic.

References:

1. V.I. Kuznetsov, A.Ya. Ender, Ioffe Ph.T.I. preprint, N 575, Leningrad, 1978.
2. J.R. Pierce, J. Appl. Phys., 15, 721, 1944.
3. E. Jahnke, F. Emde, F. Lösch, Special functions, "Nauka", 1968.

THE TIME DEPENDENT TRANSPORT COEFFICIENTS FOR THE TWO-COMPONENT PLASMA

W. Rozmus.

Institute for Nuclear Research, 00681 Warsaw, Hoza 69, Poland.

The time dependent transport coefficients for a two-component plasma /TCP/ will be found by systematic application of the projection operators technique. Similar problem was recently studied by others authors [1], [2], [3]. We consider here a weakly coupled TCP described by the Vlasov-Landau kinetic equation, linearized around the one-temperature equilibrium /without external fields/. We have found the important differences in the behaviour of the shear viscosity and friction coefficients as compared to analogous quantities from [1].

The kinetic equation, we use, can be written in the form

$$/1/ \left(I \frac{\partial}{\partial t} + S + V - \mathcal{J} - \delta \mathcal{J} \right) h(v, t) = 0$$

where, $h = \begin{bmatrix} h_s(v, t) \\ h_i(v, t) \end{bmatrix}$ stands for a vector combining the spatial Fourier transforms

of the dimensionless deviations of the both species distribution functions from

the equilibrium value, $S = \begin{bmatrix} ik_z & 0 \\ 0 & ik_z \end{bmatrix}$, V is

the linearized Vlasov operator matrix,

is the unit matrix and $\mathcal{J} = \begin{bmatrix} \mathcal{J}^{ee} & \mathcal{J}^{ei} \\ \mathcal{J}^{ie} & \mathcal{J}^{ii} \end{bmatrix}$

$\delta \mathcal{J} = \begin{bmatrix} \delta \mathcal{J}^{ee} & \delta \mathcal{J}^{ei} \\ \delta \mathcal{J}^{ie} & \delta \mathcal{J}^{ii} \end{bmatrix}$ describe collisions.

$\delta \mathcal{J}$ is the only term responsible for

coupling between electrons and ions.

By projecting eq./1/ on the ten-dimensional plasmadynamical /PD/ subspace

/cf [3] / we derive the generalized PD equations

$$/2/ \frac{\partial}{\partial t} P h(t) + P(S + V - \mathcal{J}) P h(t) - \int_0^t dt' K(t-t') P h(t-t') = R(t)$$

where P is the projector on the PD-subspace. The time dependent transport coefficients are given by the matrix

elements $K_{PF}(t)$

$$/3/ K_{PF}(t) = \int \frac{d\omega}{2\pi} e^{-i\omega t} \langle \rho | (S - \mathcal{J}) Q (-i\omega + Q(S - \mathcal{J} - \delta \mathcal{J}) Q)^{-1} Q(S - \delta \mathcal{J}) | \sigma \rangle$$

where $Q = I - P$ is the projector on the non-PD subspace, and

$$\langle \rho | f \rangle = \sum_{\alpha} \int dv \varphi_{M\alpha}^{\rho}(v) \varphi_{F\alpha}^{\rho}(v) f^{\alpha}(v)$$

In the above $\varphi_{M\alpha}^{\rho}$ is the Maxwellian distribution function, $\varphi_{F\alpha}^{\rho}$ are Hermite polynomials spanning the basis of the velocity space. An explicit evaluation of $K_{PF}/3/$ is done by perturbation method

with the accuracy up to terms proportional to the square of the wave vector.

Moreover the natural extension of the Grad 13-moments method [4] is used by

introducing the finite dimensional approximation for Q . The whole velocity space

is spanned now by 26 Hermite polynomial

tensors /13 for each species/. The inversion of the operator

$(-i\omega + Q(S - \mathcal{J} - \delta \mathcal{J}) Q)$ is now straightforward and requires

knowledge of the eigenfunctions and eigenvectors of this operator in the

finite dimensional subspace. These were calculated with required accuracy in k

expansion. Note, that we should keep elements of $(-i\omega + Q(S - \mathcal{J} - \delta \mathcal{J}) Q)^{-1}$

which are of order k and k^2 , because there are quantities like $\langle \rho | \delta \mathcal{J} | Q \rangle$ in /3/ which cannot be treated as small. They are of the zero order in the small mass ratio $\epsilon = (m_e/m_i)/$. These terms give rise to new form of the transport coefficient discussed below.

Presenting the results we restrict ourselves to the viscosity and friction coefficients, because these quantities show essential differences with those published previously [1]. For this purpose we write down explicit expression for the Laplace transform of the dissipative part of the pressure tensor $\Pi_{rs}^{\alpha}, \alpha=e,i$

$$/4/ \quad \Pi_{rs}^{\alpha} = \sum_{\beta=e,i} \eta_{rs}^{\alpha}(\omega) (i k_r q_s^{\beta}(\omega) + i k_s q_r^{\beta}(\omega) - \frac{2}{3} \delta_{rs} (k_r q_s^{\beta}(\omega)))$$

the frequency dependent shear viscosity coefficients are

$$\eta_{ii}^i(\omega) = n_0 k_B T \left[-\frac{A}{-i\omega - \Lambda_i^i} + A^2 \frac{A}{-i\omega - \Lambda_i^i} \right] + O(\epsilon^2)$$

$$/5/ \quad \eta_{ee}^e(\omega) = n_0 k_B T \left[-\frac{A}{-i\omega - \Lambda_e^e} (1-A)^2 + 2A \frac{A}{-i\omega - \Lambda_e^e} \right] + O(\epsilon)$$

$$\eta_{ee}^i(\omega) = n_0 k_B T \left[A \left(\frac{A}{-i\omega - \Lambda_e^e} - \frac{A}{-i\omega - \Lambda_i^i} \right) - A^2 \frac{A}{-i\omega - \Lambda_i^i} \right] + O(\epsilon)$$

Here $\Lambda_{ij}^{\alpha}, \alpha=e,i; j=1,2,3$, denote the matrix elements of the Landau collision operator. Explicitly

$$\Lambda_1^e = -0.14 \Lambda \quad \Lambda_1^i = -0.1 \epsilon \Lambda \quad \Lambda_3^e = 0.11 \Lambda$$

$$\Lambda_2^e = -0.22 \Lambda \quad \Lambda_2^i = -0.01 \epsilon \Lambda \quad \Lambda = (\pi/\pi)^{1/2} \lambda \ln(\lambda^{-1}) \omega_{pe}$$

$$A = \sqrt{2/3} \Lambda_3^i / (\Lambda_2^i - \Lambda_1^e)$$

where λ is the plasma parameter $\lambda = (4\pi e^2)^{1/2} / (n_e^2 / k_B^2)$ and $\omega_{pe} = (4\pi n_e^2 / m_e)^{1/2}$ is the electron plasma frequency. Expressions /5/ differ from that in [1] by terms proportional to A and A^2 .

By inspection these terms arise from the additional terms in expansion of $K_{rs}^{\alpha} / 3/$ discussed earlier

For the friction coefficient ζ_i we obtain the following formula

$$/6/ \quad \zeta_i = \sqrt{2}/12 \omega_{pe} \lambda \ln(\lambda^{-1}) - (\Lambda_3^e)^2 / (-i\omega - \Lambda_2^e)$$

The second term on the r.h.s. of /6/,

usually omitted, contains the factor $(\Lambda_3^e)^2 \sim \lambda^2$. In spite of this, this term should be kept as it produces contributions of order λ in the dispersion laws for the plasmadynamical modes [5].

References

- 1 G. Vasu, J. Plasma Phys., 16/1976/, 299,
- 2 M. Baus, Physica, 88A/1977/319, 336, 591,
- 3 R. Balescu, I. Paiva-Veretennicoff, J. Plasma Phys., 20/1978/, 231,
- 4 H. Grad, Handbuch der Physik, 1958, vol. XII
- 5 W. Rozmus, submitted in J. Plasma Phys.

ABOUT THE GENERATION OF A "RESULTANT DRIFT INWARDS" FROM THE BOUNDARY OF A D-T-PLASMA BY ELECTROMAGNETIC FIELDS

F. Manfred.

Voß, Sempetr. 25, D-8 München.

About the generation of a resultant drift inwards from the boundary of a D-T-plasma by electromagnetic fields.

Aim: The $\frac{E}{B}$ -drift at the boundary of a cylindrical plasma shall be used to generate a resultant drift inwards from the boundary of the plasma.

1) The form of equations for the motion of a charge in an E-B-field

- a) in x-y-z-coordinates,
- b) in r- ϕ -z-coordinates.

For a cylindrical plasma with a diameter of several centimeters or even meters the equations of motion in x-y-z-coordinates can formally be transformed in those for r- ϕ -z-coordinates by replacing x by r and y by ϕ , if the magnetic field B_z is strong enough or, what is in effect the same, the gyration radii are small.

There exists then a drift in a small volume, which is analogous to that in x-y-z-coordinates for E=const. and B=const.. See figures 1 and 2.

2) The solution of the equations of motion with a time-dependent magnetic field

$$B(t) = B_0 + B_1 \cdot \cos \omega t$$

and the electric fields

$$\begin{aligned} (*) \quad E_\phi(t) &= E_{0\phi} \cos \omega t + E_{1\phi} \sin \omega t \quad \text{and} \\ E_r(t) &= E_{0r} \cos \omega t + E_{1r} \sin \omega t. \end{aligned}$$

The figures 3 and 4 show the first terms of the solution $v_r(t)$ and $v_\phi(t)$, which have nonlinear terms with $\sin \omega t$, caused by the time-dependent magnetic field $B_1 \cos \omega t$. The upper long expressions are achieved by the series development of

$$e^{i \frac{\Omega_1}{\omega} \sin \omega t} \approx 1 + i \frac{\Omega_1}{\omega} \sin \omega t \quad \text{for} \quad \left| \frac{\Omega_1}{\omega} \right| \ll 1.$$

The lower expressions are achieved with the aid of the saddle point method with the collision frequency $\nu \neq 0$, here for simplicity with $\nu=0$. The constant terms in the expression for v_r represent in a time-dependent field B(t), E(t) (*) the resultant drift:

$$(**) \quad v_r \approx - \frac{1}{2B_0} \cdot \frac{E_0}{B_0} \quad , \quad \text{if} \quad 4\omega^2 \ll \Omega_0^2.$$

3) The calculation and graphic representa-

tion of useful B(t)- and E(t)-fields for the resultant drift.

For generating the resultant drift the fields B(t) and E(t) must both have terms with $\cos \omega t$, see equs. (*) and (**). That is possible, if the two fields B(t) and E(t) are themselves built up by two fields:

$$\begin{aligned} B(t) &= B_1(t) + B_2(t) \quad \text{and} \\ E(t) &= E_1(t) + E_2(t). \end{aligned}$$

Thereby should be at the boundary, where the resultant drift should exist,

$$\begin{aligned} \text{for example: } B_1(t) &\gg B_2(t) \quad \text{with} \\ E_1(t) &\ll E_2(t). \end{aligned}$$

Then the resultant drift is produced by the two fields

$$B(t) \approx B_1(t) \quad \text{and} \quad E(t) \approx E_2(t),$$

which fields are generated with desired phase by currents in two separate coils wound around the cylindrical plasma.

The figures 5 till 8 show with the aid of Fourier-Bessel-series calculated fields E(r,t) and B(r,t). By appropriate choice of the radius of the coil the electric field E(r,t) is generated in such a form, that only in the middle of the plasma, $r=0$, and at the boundary E vanishes, see figures 5 till 7. This E-field E_2 is surely greater than that E_1 in fig. 8 near the zero-point of E_1 . In the opposite the magnetic field in fig. 8 can be built up greater than that of the figures 5 till 7 near the zero-point of E_1 in fig. 8, which lies nearly at $r=1,1$ m. When the plasma reaches from $r=0$ till nearly $r=1,1$ m, at the boundary of the plasma the desired $E_2(t)$ -, $B_1(t)$ -field can be established, which causes the desired resultant drift.

The fig. 9 shows appropriate parts of the field curves for E and B.

4) Equations for $E_\phi(t)$ and $E_r(t)$ in the plasma.

If you set in v_r and v_ϕ from fig. 3 and 4 into the equations for E_r and E_ϕ from fig. 10, so you get differential equations with periodic coefficients because of the $\sin \omega t$ -terms, which can cause instabilities. If you set $\Omega_1=0$, the equation of fig. 10 for $E_\phi(t)$ with the terms A and T is established.

If further the frequency of the electromagnetic field, the plasma-frequencies $\omega_{ps}, s=e,d,t$ and the cyclotron-frequencies ω_{cs} are chosen so, that they make the term $A \ll 1$, what should be possible, then the wave length of E_0 in the plasma should nearly the same as in the vacuum. By this selection of the frequency ω it should be possible to generate in the plasma fields $E(t)$ and $B(t)$, which give the resultant drift from the boundary inwards and suppress otherwise possible instabilities.

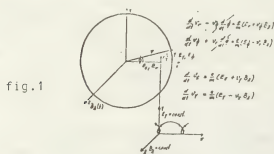


fig.1

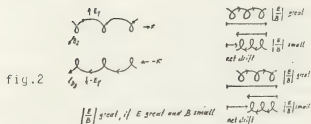


fig.2

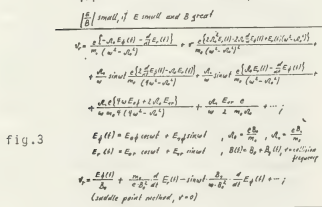


fig.3

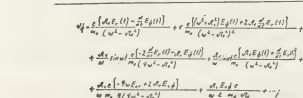


fig.4

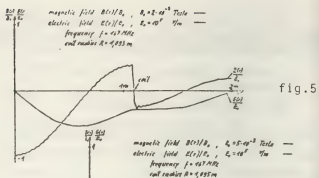
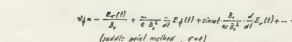


fig.5

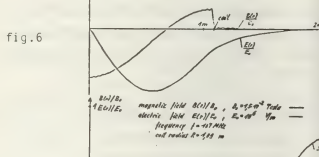


fig.6

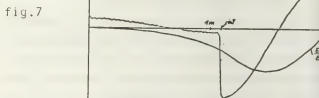


fig.7

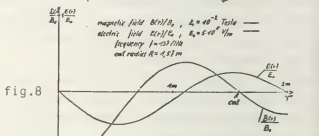


fig.8

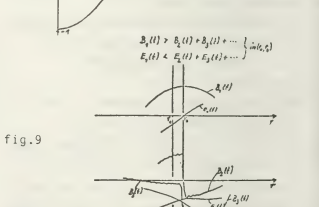


fig.9

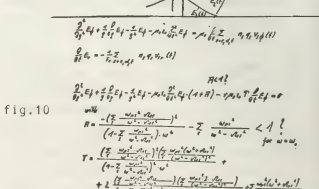


fig.10

EFFECT OF TRANSPORT PROCESSES ON TOKAMAK REFUELING BY PELLET INJECTION

L.L. Lengyel.

Max-Planck-Institut für Plasmaphysik, D-8046 Garching, EURATOM Association.

The injection of frozen hydrogen-isotope pellets into hot plasma is considered as a possible method for increasing the plasma density in tokamaks operating without divertors or for replenishing particle losses in divertor-tokamaks. The pellet entering the plasma is rapidly vaporized, the vaporization or ablation rate being a function of the energy flux incident at the pellet surface, i.e. of the temperature and density of the surrounding plasma. The ablation rate is affected by such phenomena as neutral shielding (the build-up of a high-density and relatively cold blanket around the pellet), electrostatic shielding (charging of the ablation cloud with respect to the surrounding plasma), and magnetic shielding (reduction of the energy flux carried by the incident plasma particles to the pellet by partial expulsion of the magnetic field lines from the ablation cloud). Typical ablation times are a few 10 to few 100 μ s [1]. Besides the energy transport to the pellet, the mass transport from the pellet surface is of primary importance in this problem. Since the time scale of the former process is roughly determined by the thermal velocity of the incident (hot) plasma particles, whereas the mass transport from the pellet surface (at least in its immediate neighbourhood) is determined by the thermal velocity of the cold ablated particles, the parameters of the recipient plasma are drastically affected in the vicinity of the pellet. The time necessary for smoothing (or removing) the local temperature and density gradients produced by the pellet is determined by the transport processes that dominate in the discharge regime considered. These times lie in the ms-range. Note that the transport processes also determine the characteristic magnitudes of the energy and particle losses inherent in the discharge regime considered. Hence reliable estimates concerning the pellet lifetime, the penetration depth, and particularly the pellet injection frequency required for maintaining a given average density level (for a given pellet size) can only be obtained if the relevant transport processes are accounted for. Computations based on the coup-

ling of pellet ablation models with tokamak transport codes /2, 3/, or transport models /4/, may yield completely different results, depending upon the type of transport phenomena observed and neglected in the respective numerical models.

Mense et al. /2/ performed calculations for typical fusion reactor conditions (TNS conceptual reactor design, $R=5$ m, $a_{eff}=1.6$ m, $T_i \approx 15$ keV, $n \approx 10^{20} \text{ m}^{-3}$) by neglecting ohmic heating (as compared to heating by neutral beam and alpha particles). In these calculations, the current profile was assumed to be parabolic and constant in time, and particle recycling by the wall was omitted from consideration (ideal divertor action). Neoclassical, pseudoclassical, and trapped particle effects were included in the definition of the energy and particle transport processes. However, as can be seen from the results presented by the authors, in the temperature range considered, pseudoclassical effects have little, if any, influence on the particle confinement time and other discharge characteristics; the trapped-particle modes are the dominating ones. Since the trapped particle modes strongly depend upon the amplitudes of the temperature and density gradients present in the plasma (in the trapped electron regime the diffusion coefficient scales as the square of the electron density gradient), the results of these calculations suggest that density perturbations should by all means be avoided in the bulk of the plasma. Furthermore, since adverse effects resulting from particle recycling at the wall are not present in the model considered, Mense et al. conclude that deep pellet injection is not only unnecessary but also undesirable under reactor plasma conditions.

Calculations performed for a present-day tokamak (Asdex: $R=1.65$ m, $a=0.4$ m, $T_{max} \approx 2$ keV, $n_{max} = 5 \times 10^{19} \text{ m}^{-3}$) by allowing for a wider variety of possible transport processes /3/ yield results that differ considerably from those of Mense et al. In these computations three collisional drift regimes (with Bohm diffusion as li-

miting process) and four collisionless drift regimes (trapped electron and trapped ion modes, each for two collisionalities) were taken into account. Recycling and its effects (impurity transport and charge exchange collisions) were fully accounted for. Up to eight generations of charge exchange neutrals were taken into account, the impurities were restricted to oxygen neutrals and ions (up to eight groups). The distributions of the poloidal magnetic field, current density and safety factor were calculated in a self-consistent manner. Calculations were performed with various ablation models for different pellet sizes and injection velocities. For investigating the effect of the ionization state of the ablated particles on the transport processes, the ablating pellet was considered either as an ion source or as a neutral particle source traversing the recipient plasma. The results of these calculations can be summarized as follows:

(a) The different ablation models used affect primarily the calculated ablation times (penetration depths), and only to a less extent the resulting particle confinement times and required pellet injection frequencies.

(b) The ionization state of the ablated particles plays a major role in defining the magnitude of the resulting particle losses. The pellet frequencies required for maintaining a given average density and computed in the neutral particle source approximation are an order of magnitude larger than those obtained with the ion source approximation.

(c) The rate of particles losses and thus the required re-fueling rate (pellet injection frequency) is determined by the transport processes dominating in the discharge. The results of pellet-plasma calculations depend decisively on the transport processes taken into account, or neglected, in the respective computer models.

(d) The computations performed for Asdex-conditions with recycling taken into account indicate that boundary layer fueling may require very high pellet frequencies (close to $k\text{ Hz}$) and may overload the divertor pumps. Pellet injection in the central plasma regions may become necessary.

(e) The proper modeling of pellet-plasma interactions, of the effect of charge exchange collisions in particular, may require the development of integrated ablation-transport codes.

References

- /1/ L.L. Lengyel, *Phys.Fluids* 21, 1945 - 1955 (1978)
- /2/ A.T. Mense, W.A. Houlberg, S.E. Attenberger, and S.L. Milora, ORNL/TM-6026 (April 1978)
- /3/ L.L. Lengyel and D.F. Duchs, 10th Symp. on Fusion Technology, Padova, 1978, Paper C-14
- /4/ G. Haas, M. Keilhacker, and K. Lackner, *J.Nucl. Materials* 76/77, 279-286 (1978)

PLASMA KINETIC EQUATION INCLUDING STRONG FIELDS AND INHOMOGENITIES

Alf H. Øien.

Department of Applied Mathematics, University of Bergen.

In a plasma when charged particles interact the temperature and density can be so related to the strength of the magnetic field that the helical components of the particle motions can not be neglected in the interaction process. The condition for this is roughly that $r_L < \lambda_D$, where r_L is the gyroradius and λ_D the Debye length of the charged particles. Collision integrals that are supposed to be valid under such circumstances, [1] - [4] are more complex than ordinary collision integrals for plasmas, [5] - [7], although various simplifying assumptions are made in the derivations: The homogeneity assumption is always made, force fields other than the magnetic are neglected, and the particle distribution function is taken to be isotropic in velocity space transverse the magnetic field (gyrotropic assumption). Attempts to simplify the derived collision integrals when weak, two particle collisions dominate, [2] - [4], have resulted in a rather rough estimate that the main effect of the magnetic field is to change the Coulomb logarithm from $\ln(\lambda_D/\lambda_L)$ to $\ln(r_L/\lambda_L)$ in Landau's collision integral when $\lambda_L \ll r_L (< \lambda_D)$. Here λ_L is the distance of closest approach.

The purpose of the present paper is to show the derivation of a weak-collision-integral and a kinetic equation when inhomogeneities and an electric field are taken into account and the gyrotropic assumption is not made [8]. An estimate of the relative importance of some types of collisions is also made without Fourier-transforming the relative distance of colliding particles in the collision integral.

We study a one component gas only. As starting equations we take the first two equations of the BBGKY-hierarchy, where the tripple correlation function has been neglected:

$$\begin{aligned} \frac{d}{dt} f_1 + \underline{c}_1 \cdot \frac{\partial f_1}{\partial \underline{r}_1} + \frac{e}{m} (\underline{E}_1 + \underline{c}_1 \times \underline{B}_1) \cdot \frac{\partial f_1}{\partial \underline{c}_1} = \\ = \frac{1}{m} \int d\underline{c}_2 d\underline{r}_2 \frac{\partial^2 \varphi(|\underline{r}_1 - \underline{r}_2|)}{\partial \underline{r}_1^2} \cdot \frac{\partial g}{\partial \underline{r}_1}(\underline{r}_1, \underline{r}_2, t) \quad (1) \\ \frac{d}{dt} g + \underline{c}_1 \cdot \frac{\partial g}{\partial \underline{r}_1} + \underline{c}_2 \cdot \frac{\partial g}{\partial \underline{r}_2} + \frac{e}{m} (\underline{E}_1 + \underline{c}_1 \times \underline{B}_1) \cdot \frac{\partial g}{\partial \underline{c}_1} + \end{aligned}$$

$$+ \frac{e}{m} (\underline{E}_2 + \underline{c}_2 \times \underline{B}_2) \cdot \frac{\partial g}{\partial \underline{c}_2} - \frac{1}{m} \frac{\partial^2 \varphi(|\underline{r}_1 - \underline{r}_2|)}{\partial \underline{r}_1^2} \cdot \left(\frac{\partial}{\partial \underline{c}_1} - \frac{\partial}{\partial \underline{c}_2} \right) g = \\ = - \frac{1}{m} \frac{\partial^2 \varphi(|\underline{r}_1 - \underline{r}_2|)}{\partial \underline{r}_1^2} \cdot \left(\frac{\partial}{\partial \underline{c}_1} - \frac{\partial}{\partial \underline{c}_2} \right) f_1(t) f_2(t) \quad (2)$$

Here $f(i, t) = f(\underline{r}_i, \underline{c}_i, t)$ and $g(i, j, t) = g(\underline{r}_i, \underline{c}_i, \underline{r}_j, \underline{c}_j, t)$ are the one particle distribution function and two particle correlation function. $\underline{E}_i = \underline{E}(\underline{r}_i, t)$ and $\underline{B}_i = \underline{B}(\underline{r}_i, t)$ are the electric and magnetic fields evaluated at \underline{r}_i at time t and $-\frac{\partial^2 \varphi}{\partial \underline{r}_i^2}$ is the Coulomb interaction force between particles i and j . The coupled set of equations are extremely difficult to solve in all generality. Fortunately, in Eq. (1) we need to know g only for phase space coordinates in a collision. Such a g can be found (approximately) from Eq. (2) when we take f to be given from

$$\frac{\partial f}{\partial t} + \underline{c}_i \cdot \frac{\partial f}{\partial \underline{r}_i} + \frac{e}{m} (\underline{E}_i + \underline{c}_i \times \underline{B}_i) \cdot \frac{\partial f}{\partial \underline{c}_i} = 0 \quad i=1,2. \quad (3)$$

This is due to the fact that for phase space coordinates in a collision the r. h. s. of equation (1) is small.

Thus we solve Eq. (3), then substitute the result into the r. h. s. of Eq. (2) and solve Eq. (2) and then substitute the result for g into Eq. (1), which then constitutes the kinetic equation.

We are able to solve Eq. (3) easily when \underline{E} and \underline{B} are assumed stationary and uniform on scales for a collision. Eq. (3) then gives

$$f(\underline{r}_i, \underline{c}_i, t) = S_{-t}(i) f(\underline{r}_i, \underline{c}_i, t=0) \quad (4)$$

where the operator $S_{-t}(i)$ transforms position and velocity coordinates for particle i backward in time according to the equations of motion

$$\begin{aligned} \frac{d\underline{r}_i}{dt} &= \underline{c}_i \\ \frac{d\underline{c}_i}{dt} &= \frac{e}{m} (\underline{E} + \underline{c}_i \times \underline{B}) \end{aligned} \quad (5)$$

Eq. (2) then gives for g (assuming $g(1, 2, t=0)=0$):

$$g(\underline{r}_1, \underline{r}_2, t) = (S_{-t}(1, 2) - S_{-t}(1) S_{-t}(2)) f(1, t=0) f(2, t=0) \quad (6)$$

In Eq. (6) $S_{-t}(1, 2)$ is the operator that transforms the position and velocity coordinates for particle 1 and 2 backward in time according to the equations of motion for the particles in a collision:

$$\frac{d\mathbf{c}_i}{dt} = \mathbf{c}_i \quad (7)$$

$$\frac{d\mathbf{c}_i}{dt} = \frac{e}{m} (\mathbf{E} + \mathbf{c}_i \times \mathbf{B}) - \frac{1}{m} \frac{\partial \Phi_{ij}}{\partial \mathbf{r}_i} (|\mathbf{r}_i - \mathbf{r}_j|), \quad i \neq j; i, j = 1, 2.$$

Substituting g from Eq. (6) into Eq. (1) then gives a generalized Boltzmann equation. The usefulness of that equation rests upon the solution of the dynamic equations (7), which in 3 dimensions has not been obtained, as far as the author knows. A weak interaction approximation can be found. Thus instead of the set of equations (7) we solve

$$\frac{d\mathbf{r}_i}{dt} = \mathbf{c}_i \quad (8)$$

$$\frac{d\mathbf{c}_i}{dt} = \frac{e}{m} (\mathbf{E} + \mathbf{c}_i \times \mathbf{B}) - \frac{1}{m} \sum_j (i) \sum_j (j) \frac{\partial \Phi_{ij}}{\partial \mathbf{r}_i} (|\mathbf{r}_i(0) - \mathbf{r}_j(0)|)$$

Then we expand g from Eq. (6), with respect to weak transfers and finally arrive at the following equation for f :

$$\frac{\partial f}{\partial t} + \mathbf{c}_i \cdot \frac{\partial f}{\partial \mathbf{r}_i} + \frac{e}{m} (\mathbf{E}_i + \mathbf{c}_i \times \mathbf{B}_i) \cdot \frac{\partial f}{\partial \mathbf{c}_i} = C_{ee}^V + C_{ee}^P \quad (9)$$

where

$$C_{ee}^V = \frac{1}{m} \frac{\partial}{\partial \mathbf{c}_i} \cdot \left(d\mathbf{x} d\mathbf{c}_2 \frac{\partial \Phi_{12}}{\partial \mathbf{x}} \int_0^t d\tau (S_{-i}(t) S_{-2}(\tau) \frac{1}{m} \frac{\partial \Phi_{12}}{\partial \mathbf{x}} (|\mathbf{x}|)) \right) \cdot \frac{\partial M}{\partial \mathbf{c}_i} \cdot \left(\frac{\partial}{\partial \mathbf{c}_1} - \frac{\partial}{\partial \mathbf{c}_2} \right) f(1, t) f(2, t) \quad (10)$$

$$C_{ee}^P = \frac{1}{m} \frac{\partial}{\partial \mathbf{c}_i} \cdot \left(d\mathbf{x} d\mathbf{c}_2 \frac{\partial \Phi_{12}}{\partial \mathbf{x}} \int_0^t d\tau (S_{-i}(t) S_{-2}(\tau) \frac{1}{m} \frac{\partial \Phi_{12}}{\partial \mathbf{x}} (|\mathbf{x}|)) \right) \cdot M(\tau) \cdot \left(\frac{\partial}{\partial \mathbf{r}_1} - \frac{\partial}{\partial \mathbf{r}_2} \right) f(1, t) f(2, t) \quad (11)$$

Here $\mathbf{x} = \mathbf{r}_1 - \mathbf{r}_2$ and $M(\tau)$ is the matrix

$$\begin{bmatrix} \frac{1}{\Omega} \sin \Omega \tau & \frac{1}{\Omega} (\cos \Omega \tau - 1) & 0 \\ -\frac{1}{\Omega} (\cos \Omega \tau - 1) & \frac{1}{\Omega} \sin \Omega \tau & 0 \\ 0 & 0 & \tau \end{bmatrix}$$

We observe that only when $\tau \rightarrow \infty$ in the upper τ -integration limit does C_{ee}^V correspond to the collision term of a traditional kinetic equation. Also the order of C_{ee}^P/C_{ee}^V is λ_D/L where L is the scale of the inhomogeneities. For weak inhomogeneities we can decouple f from the \mathbf{x} -integrations in Eqs. (10) and (11). We assume this below, where we make some further comments on C_{ee}^V .

The τ -integrand in C_{ee}^V can be written in the form

$$S_{-i}(t) S_{-2}(\tau) \frac{1}{m} \frac{\partial \Phi_{12}}{\partial \mathbf{x}} (|\mathbf{x}|) \cdot \frac{\partial M}{\partial \mathbf{c}_i} = -\frac{e^2}{m} \quad (12)$$

$$\cdot \frac{b b_i (X - c_{12} \tau) + [X_1 \cos \Omega \tau + X_2 \sin \Omega \tau] - [c_{12} \Omega \frac{1}{\Omega} - c_{12} \times b \frac{1}{\Omega} (\cos \Omega \tau - 1)]}{|S_{-i}(t) S_{-2}(\tau) \mathbf{x}|^3}$$

Here $b = \frac{B}{|\mathbf{B}|}$, $c_{12} = c_1 - c_2$, $\Omega = \frac{e|\mathbf{B}|}{m}$ (negative for electrons). This form seems to reveal two different ranges for

\mathbf{x} :

$$|\mathbf{x}_\perp| \gg \frac{|c_{12}|}{|\Omega|} \quad (\approx r_L) \quad (13)$$

and

$$|\mathbf{x}_\perp| \ll \frac{|c_{12}|}{|\Omega|} \quad (14)$$

In the first range we have colliding particles with trajectories that are not twined. In the second range the trajectories are intertwined. When the first of these inequalities prevails the []-parenthesis in the nominator of Eq. (12) dominates over the { }-parenthesis. Since the transverse component of Eq. (12) therefore oscillates and otherwise changes only very slowly during each oscillation, it is to be expected that the contribution to the collision integral is quite small. The remaining longitudinal component of Eq. (12) corresponds mainly as τ grows to a one dimensional collision along the magnetic field with only small collisional effects.

When the last inequality Eq. (14) prevails and in addition $|\mathbf{x}_\parallel| \lesssim r_L$ we roughly have for τ close to zero ($\tau \lesssim \frac{2\pi}{|\Omega|}$)

$$S_{-i}(t) S_{-2}(\tau) \frac{1}{m} \frac{\partial \Phi_{12}}{\partial \mathbf{x}} (|\mathbf{x}|) \cdot \frac{\partial M}{\partial \mathbf{c}_i} \approx -\frac{e^2}{m} \frac{X - c_{12} \tau}{|X - c_{12} \tau|} \quad (15)$$

i.e. almost straight line trajectories in this region. This sort of interaction is effective. When $\tau > \frac{2\pi}{|\Omega|}$ and grows while X_\perp and X_\parallel are unchanged we have an interaction that looks more and more like a one-dimensional collision along the magnetic field which has only small effects. When Eq. (14) still prevails while $|\mathbf{x}_\parallel| > |c_{12}|/|\Omega|$ the $\frac{\partial f}{\partial \mathbf{x}}$ -factor in the integrand of Eq. (10) points almost along the magnetic field. This will make the contribution from this range also small even though Eq. (12) is not mainly along the magnetic field for the strip in the $X_\parallel \tau$ -plane given by $|X_\parallel - c_{12} \tau| \lesssim r_L$.

This rough estimate may indicate when $\lambda_c \ll r_L$ ($< \lambda_D$) that the X_\perp -, X_\parallel - and τ -ranges which led to Eq. (15) are the most important ones in C_{ee}^V , i.e. the closest interaction parts of the intertwined collisions.

References.

- [1] Rostoker, N. 1960 Phys. Fluids **3**, 922.
- [2] Schram, P.P.J.M. 1969 Physica **45**, 165
- [3] Montgomery, D. et al 1974 Phys. Fluids, **17**, 954
- [4] Montgomery, D. et al 1974 Phys. Fluids, **17**, 2201
- [5] Landau, L.D. 1936 Physik. Z. Sowjetunion **10**, 154
- [6] Balescu, R. 1960 Phys. Fluids, **3**, 52
- [7] Lenard, A. 1960 Ann. Phys. (N.Y.) **3**, 390
- [8] Øien, A.H. 1979 J. Plasma Phys.

ELECTRON DISTRIBUTION FUNCTION IN A VERY NON UNIFORM ELECTRIC FIELD

Tran Ngoc An, E. Marode, G. Fournier^{*} and P. Segur^{**}.*Laboratoire de Physique des Décharges, Centre National de la Recherche Scientifique, Ecole supérieure d'Electricité, 91190 Gif-sur-Yvette, France.***Office National d'Etudes et de Recherches Aéronautiques, 92320 Chatillon, France.****Centre de Physique Atomique de Toulouse, Université Paul Sabatier, 31077 Toulouse Cedex, France.*

The usual macroscopic electron transport properties are functions of E/N only (E is the electric field and N the gas density). They are not valid if E changes significantly along a mean free path or if a boundary effect is sensitive.

These conditions occur in the dark space of a glow discharge and more generally in the cathode vicinity of many types of discharges. Only a microscopic treatment is appropriate to this situation. A solution to this problem has been published by HANTZSCHKE as soon as 1966 [1]. However, the difficulty was such that most following papers dealing with the cathode fall go on using macroscopic coefficients obtained in a uniform field. Three exceptions were the works performed independently in the authors' laboratories [2, 3, 4]. The purpose of the investigation is to obtain ionization growth in the cathode fall, energy transfer to the various processes and more generally to solve the problem of electron energy distribution in a very non uniform electric field. Since the problem is connected to many applications (gas electrical strength, laser discharges, instabilities), the three groups decided to interact and to develop the different techniques using the same set of conditions and cross-section data. The present paper intends to compare these methods. Only the electron motion within a fixed space charge distribution is analysed in this work. The common situation is the cathode fall of a glow discharge in helium [2]. At a pressure of 1 Torr (at 273 K), E varies linearly from $x=0$ (cathode) to $x=d=1.3$ cm (where $E=0$) with a voltage fall of 150 V. The electron current at the cathode is $2.84 \mu A/cm^2$. In addition, it is assumed that the distribution of the electrons emitted at the cathode is uniform between 0 and 20 eV, that scattering is isotropic for every type of collision and that the secondary electron resulting from an ionization collision appears at 0 energy.

The first method (MC) is a Monte Carlo

simulation. With respect to previous work [2], scattering has been taken into account and the numerical techniques have been much improved by using precalculated tables of collision probabilities.

The second method (referred to as BT, from Boltzmann, transfer of energy) is based on transfers between energy cells and is well developed in Ref. [3].

The third method uses a change of variables such that the Boltzmann equation becomes similar in velocity space to the equation for neutron in a spherical reactor [4]; it is referred to as BN. Then a partition of the sphere in shells yields a matrix solution of the system. The BN results were mainly obtained for a high and uniform field [4]. For a linearly decreasing field, the BN method is not yet entirely reliable, although the general variation of the parameters is in agreement with MC and BT; it is now under improvement.

Fig. 1 gives the variation in space of the ratio $M(x)$ of the current at x to that at the cathode. Fig. 2 and 3 display respectively the derivative of the current divided by the current which is an effective Townsend coefficient α and the electron density n . The discrepancies cannot be discussed in much detail here. An important fact is that the BT method is iterative in principle (unless the exact value of the backscattering at the cathode can be entered). However, a truncation is made in the backscattered distribution at some distance in order to limit to a few units the number of iterations. This results in the absence of backscattered electrons at high and moderate energy at the plasma boundary ($E=0$). Backscattering at this boundary is also excluded in the two other methods for the purpose of comparison. This explains the decrease in the density n just before $x/d=1$ since the backscattered electrons are lacking there. However the lack of backscattered electrons in the BT method begins to be sensitive from $x/d \approx 0.3$.

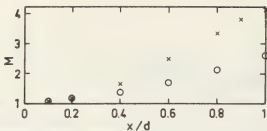


Fig. 1 - Current multiplication - \times MC method, \circ OBT method

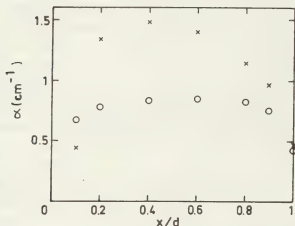


Fig. 2 - Townsend coefficient - \times MC method \circ BT method.

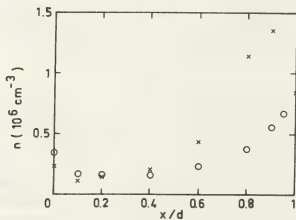


Fig. 3 - Electron density - \times MC method, \circ BT method.

As an example of energy partition over the various processes, Fig. 4 gives the variations of the excitation rates to the levels 2^3S and 2^1P . The first process dominates in the cathode layer whereas the second does in the dark space.

The three methods are not equivalent neither with respect to the computer time nor to their capabilities. It is often thought that Monte

Carlo computations are tedious and limited by computer time. However, in the present situation, considerable improvements of the numerical techniques lead to a computation probably faster than the others: A run with 1 000 particles, which is satisfactory to limit the fluctuations, requires about 2,5 minutes on a 370 IBM computer. Moreover, as already mentioned, some crude treatment of backscattering has to be made in the BT method. For a future self consistent solution of ion and electron motion via Poisson coupling, this BT method has already given preliminary results for the high field region [5] but it seems impossible to make the bridge between the high field region and the positive column. On the other hand, the other methods which can take into account electron and ion motion similarly with no assumption on backscattering seem to be appropriate in the future for a self consistent analysis including the negative glow where diffusion processes are important.

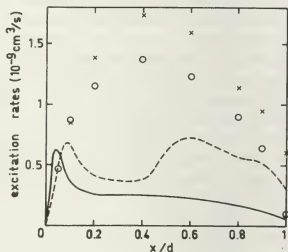


Fig. 4 - Excitation rates - \times 2^1P MC method, \circ 2^1P BT method, --- 2^3S MC method, — 2^3S BT method.

REFERENCES

- [1] - E. HANTZSCHE, Beitr. Plasmaphys. 6 (1966) 331.
- [2] - TRAN NGOC AN, E. MARODE and P.C. JOHNSON, J. Phys. D, 10 (1977) 2317.
- [3] - W.P. ALLIS, G. FOURNIER and D. PIGACHE, J. de Phys. 38 (1977) 915.
- [4] - S. PAREATHUMBY, Thèse 3ème cycle, n° 2179, Université Paul Sabatier, Nov. 1978.
- [5] - G. FOURNIER and D. PIGACHE, Proc. 13th ICPIC Berlin, sept. 12-17, 1977.

ELECTRON DISTRIBUTION FUNCTION AND IONIZATION IN SPACE-DEPENDENT PLASMA THEORY

V.C. Boffi, V.G. Molinari and G. Spiga.

Laboratorio di Ingegneria Nucleare della Università di Bologna, Bologna, Italy.

The application of a unidirectional electric field to a gas is one of the most common method for plasma production. However, also in the simplest cases, the agreement between calculations and experimental results is not yet completely satisfactory. In order to improve the situation a better understanding of all the various phenomena involved by the ionization growth would be required. This work is aimed at analyzing how a nonmaxwellian electron velocity distribution affects the ionization processes. On the other hand, it can be emphasized that the microphysical knowledge of the kinetic behaviour of electrons is a necessary basis for any progress in plasma physics⁽¹⁾. For this purpose we start with the integral form of the stationary Boltzmann equation⁽²⁻⁴⁾ that governs the distribution function $f(\bar{x}, \bar{v})$ of electrons interacting with an infinite homogeneous distribution of neutral particles, namely

$$f(\bar{x}, \bar{v}) = \int_0^\infty dt e^{-\int_0^t v(\tau') \Sigma[v(\tau')] d\tau'} \left\{ Q[\bar{x}(\tau), \bar{v}(\tau)] + \int_{R_3} d\bar{v}' k(\bar{v}' \rightarrow \bar{v}(\tau)) f[\bar{x}(\tau), \bar{v}'] \right\}. \quad (1)$$

In Eq.(1) Q is the external source, the collision frequency $v\Sigma(v) = S_r v \Sigma_r(v)$ ($r=S, R, I$) and the kernel $k(\bar{v}' \rightarrow \bar{v}) = k_S(\bar{v}' \rightarrow \bar{v}) + v_I k_I(\bar{v}' \rightarrow \bar{v})$, the subscripts S, R, I standing for scattering, recombination and ionization, respectively, and v_I being the mean number of electrons produced by ionization.

The function $\bar{x}(\tau)$ and $\bar{v}(\tau)$ are the solutions to the electron motion equation, and, in general, are given by

$$\bar{x}(\tau) = \bar{x} - \bar{x}(\tau); \quad \bar{v}(\tau) = \bar{v} - \bar{v}(\tau), \quad v(\tau) = |\bar{v}(\tau)|, \quad (2)$$

$\bar{x}(\tau)$ and $\bar{v}(\tau)$ depending on the external field.

Taking a threedimensional two-sided Laplace transform with respect to \bar{x} of both sides of Eq.(1) yields the integral equation

$$\tilde{f}(\bar{p}, \bar{v}) = \int_{R_3} e^{-\bar{p} \cdot \bar{x}} f(\bar{x}, \bar{v}) d\bar{x} = \hat{Q}(\bar{p}, \bar{v}) + \int_{R_3} \hat{k}(\bar{p}, \bar{v}' \rightarrow \bar{v}).$$

$$\cdot \tilde{f}(\bar{p}, \bar{v}') d\bar{v}', \quad (3)$$

where \hat{Q} and \hat{k} are the results of the application of the operator

$$\int_0^\infty dt e^{-\left\{ \int_0^t v(\tau') \Sigma[v(\tau')] d\tau' + \bar{p} \cdot \bar{x}(\tau) \right\}} \dots \quad (3a)$$

to $\tilde{Q}(\bar{p}, \bar{v}(\tau))$ and $k(\bar{v}' \rightarrow \bar{v}(\tau))$, respectively. If k is a kernel of finite rank n , namely

$$k(\bar{v}' \rightarrow \bar{v}) = \sum_{l=1}^n \Psi_l(\bar{v}') \hat{\Phi}_l(\bar{v}), \quad (4)$$

then we get

$$\tilde{f}(\bar{p}, \bar{v}) = \hat{Q}(\bar{p}, \bar{v}) + \sum_{l=1}^n \xi_l(\bar{p}) \hat{\Phi}_l(\bar{p}, \bar{v}), \quad (5)$$

where $\hat{\Phi}_l$ is the application of the operator, Eq.(3a), to $\Phi_l(\bar{v}(\tau))$, and

$$\xi_l(\bar{p}) = \int_{R_3} \tilde{f}(\bar{p}, \bar{v}) \Psi_l(\bar{v}) d\bar{v}. \quad (6)$$

If we define

$$A_{lm}(\bar{p}) = \int_{R_3} \Psi_l(\bar{v}) \hat{\Phi}_m(\bar{p}, \bar{v}) d\bar{v}; \quad B_l(\bar{p}) = \int_{R_3} \Psi_l(\bar{v}) \hat{Q}(\bar{p}, \bar{v}) d\bar{v}, \quad (7)$$

the coefficients ξ_l are solutions to the parametrized algebraic system

$$\xi_l(\bar{p}) = \sum_{m=1}^n A_{lm}(\bar{p}) \xi_m(\bar{p}) + B_l(\bar{p}). \quad (8)$$

The solution $\tilde{f}(\bar{p}, \bar{v})$ then follows from Eq.(5) as

$$\tilde{f}(\bar{p}, \bar{v}) = \hat{Q}(\bar{p}, \bar{v}) + \sum_{l=1}^n \hat{\Phi}_l(\bar{p}, \bar{v}) \sum_{m=1}^n (T_{lm}^{-1})_{lm}(\bar{p}) B_m(\bar{p}) \quad (9)$$

where T_{lm}^{-1} is the inverse of the matrix

$$T_{lm} = \delta_{lm} - A_{lm}(\bar{p}). \quad (10)$$

The problem is thus solved, requiring only the evaluation of the integrals in Eq.(7) according to

a suitable choice of Q , and of the two sets of linearly independent functions $\psi_1(\bar{v})$ and $\phi_1(\bar{v})$ ($Q=1, \dots, n$). In order to get the original $f(\bar{x}, \bar{v})$, its transform $\tilde{f}(\bar{p}, \bar{v})$ must finally be inverted. Then the singularities of $\hat{Q}(\bar{p}, \bar{v})$, of $\hat{\phi}_1(\bar{p}, \bar{v})$, of the vector $\underline{B}(\bar{p})$ and of the matrix $\underline{T}^{-1}(\bar{p})$ must be studied. A particular role will be played by those values of \bar{p} which are roots of $\det \underline{T}(\bar{p})=0$.

An explicit application of the theory proposed above has been processed for a monodimensional case characterized by a constant electric field, and by a simple model for collisions. This case has been chosen with the aim at exploring the existence of poles for $\underline{T}^{-1}(\bar{p})$. If a simple pole, the contribution of which will dominate asymptotically, exists, then it can be referred to as the first Townsend ionization coefficient for the physical situation considered. (for a different model of scattering and ionization, see Ref.5).

References

1. RUTSCHER, A.: Progress in Electron Kinetics of Low Pressure Discharges and Related Phenomena, XIII ICPIG, Invited Lecture, 269, Berlin 1977.
2. BOFFI, V.C. and MOLINARI, V.G.: Il Nuovo Cimento, 34B, 345 (1976).
3. BOFFI, V.C., MOLINARI V.G. and WÖNNERBERGER, W.: Il Nuovo Cimento, 45B, 109 (1978).
4. BOFFI, V.C., MOLINARI, V.G.: Il Nuovo Cimento, 49B, 77 (1979).
5. BOFFI, V.C., MOLINARI, V.G. and SPIGA, G.: 11th R.G.D. Symposium, Cannes 1978.

THE BOHM-TYPE THERMAL LOSSES FROM A HIGH- β PLASMA

P.Z. Chebotaev, G.E. Vekstein.

Institute of Nuclear Physics, Novosibirsk, U.S.S.R.

Current interest to the properties of high- β plasma is initiated by a number of proposals to use such a plasma in the fusion systems. Most often discussed possibility is the so-called "wall" (or "non-magnetic") confinement of a plasma with density $n \gtrsim 10^{17} \text{ cm}^{-3}$ /1,2/. In this confinement method the only role of the magnetic field is to reduce transverse thermal conductivity, while the mechanical equilibrium of a plasma is provided by rigid walls. So, the "wall" confinement allows us to reduce the requirements to the magnetic field strength in the solenoidal plasma systems and to obtain $\beta = 30\text{--}300$. Even more β (of the order of 10^3) may be attained in the imploding liner devices with $n \approx 10^{19}\text{--}10^{20} \text{ cm}^{-3}$ /3/. Meanwhile, the dynamics of high- β plasma cooling possesses some distinctive features /4/. The reason is that the plasma kinetic pressure must be homogeneous during the cooling process. Due to this, a hot plasma begins to flow to the walls and the high-density near-wall layer is formed. As a result, the cooling time of such a plasma can be significantly decreased /5/.

In our communication we shall consider the cooling of a hot magnetized plasma coming into contact with a cold wall. A similar problem has been recently solved

both in the numerical studies /6/ and in the experiments /7/. So, at initial moment a hot plasma with density n_0 , temperature T_0 and magnetic field H_0 fills the tube of radius R with cold walls. The magnetization parameter of a plasma $S_0 \equiv (\omega_H \tau_i)_0 \gg 1$, its thermal conductivity $\chi_0 \sim c T_0 / e H_0 S_0$. From the heat transport equation

$$\frac{3}{2} \frac{\partial(nT)}{\partial t} = -\frac{1}{r} \frac{\partial}{\partial r} r \left(\frac{5}{2} n T v - \chi \frac{\partial T}{\partial r} \right) \quad (1)$$

and the pressure homogeneity condition it follows that the whole energy flux

$$q = \frac{5}{2} n T v - \chi \frac{\partial T}{\partial r} \sim r$$

In the cold near-wall layer, where $T \ll T_0$ and the thickness of which $\Delta \ll R$, we have $q \approx \text{const}$. At the same time, $v = 0$ at the wall, so the convective heat flux is small here, and

$$q \approx -\chi \frac{\partial T}{\partial r} = \text{const} \quad (2)$$

As the thermal conductivity χ depends on the magnetic field, eq.(2) must be solved together with the equation for the magnetic field variation /8/:

$$\frac{\partial H}{\partial t} + \frac{1}{r} \frac{\partial}{\partial r} (r v H) = \frac{1}{r} \frac{\partial}{\partial r} r \left(\frac{c^2}{4\pi \sigma_L} \frac{\partial H}{\partial r} + \frac{c}{n e \beta_A} \frac{\partial T}{\partial r} \right) \quad (3)$$

A detailed analysis of eqs.(2-3) will be presented elsewhere. Here we restrict ourselves only to a qualitative explanation. In a hot region the magnetic field is frozen into the plasma and takes out with

it to the walls. If the wall is perfectly conducting, then the total magnetic flux is conserved and the magnetic field increases in the near-wall layer. In this case the plasma cooling time is $\tau_E \sim R^2/\chi_0 \delta_0^{1/3}$, by a factor of $\delta_0^{1/3}$ smaller than that for the low-pressure ($\beta \ll 1$) plasma. If the walls are non-conducting, then the magnetic flux takes out from the tube due to the Nernst effect in eq.(3) and the magnetic field near wall remains of the order of its initial value. As a result, the heat flux to the wall increases by a factor of $(\omega_{Hi}\tau_i)_0$ and τ_E reduces to the Bohm-type value: $\tau_E \sim R^2/D_b$; $D_b \sim cT_0/eH_0$. Briefly it may be explained in a following way. Hot plasma cools due to adiabatic expansion with a velocity $v_0 \sim q/n_0T_0$, and heat flux $q(t)$ may be found by taking into account the balance of particles between a hot plasma and a near-wall layer. It follows from eq.(2) that the number of particles in a near-wall layer $N_A(t) \sim R^2 \delta_0^2 \chi_0 T_0 / qR$. Because $\frac{d}{dt} N_A \sim n_0 v_0 R \sim qR/T_0$, we determine that

$$q(t) \sim n_0 T_0 (\delta_0 \chi_0 / t_0)^{1/2} \quad (4)$$

Such a dependence is valid for $t \leq \tau_E$. Now for the cooling time τ_E we have:

$$R \int_0^{\tau_E} q(t) dt \sim n_0 T_0 R^2, \quad \tau_E \sim R^2/\chi_0 \delta_0 \sim R^2/D_b \quad (5)$$

We have also carried out the numerical integration of the complete set of plasma transport equations. The plasma parameters have been chosen close to those of imploding linear devices: $n = 10^{20} \text{ cm}^{-3}$, $H_0 = 10^6 \text{ G}$, $T = 10^4 \text{ eV}$, $R = 1 \text{ cm}$; the walls are considered to be non-conducting.

The profiles of temperature, density and magnetic field while cooling are shown in Fig.1.

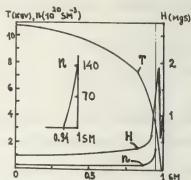


Fig.1

The cooling time τ_E is plotted in Fig.2 as a function of the magnetic field.

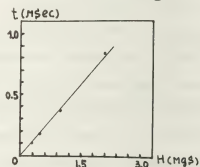


Fig.2

It is seen that this dependence is close to the linear one that corresponds to the Bohm-type law.

References:

- /1/ Budker G.I. Proc. 6th Europ. Conf., Moscow, 2, 136, 1973.
- /2/ Gross, R.A. Nuclear Fusion, 15, 729, 1975
- /3/ Velikhov, E.P. Comments on Plasma Physics, 1, 171, 1972.
- /4/ Vekstein, G.E. et al. Proc. 6th IAEA Conf., Berchtesgaden, 1976, CN-35/E-21.
- /5/ Vekstein, G.E. Sov. Phys., Doklady, 237, 295, 1977.
- /6/ Jensen, B. Phys. Fluids, 20, 373, 1977. Jablon, G., Longeon, R. Nuclear Fusion, 18, 775, 1978.
- /7/ Feinberg, B. Plasma Phys., 18, 265, 1976.
- /8/ Breginsky, S.I. In Reviews of Plasma Phys., 1, 205, 1965.

DETERMINATION OF MACROSCOPIC QUANTITIES FOR A TOWNSEND DISCHARGE IN HELIUM BY BOTH BOLTZMANN EQUATION AND MONTE CARLO METHODS

P. Segur, S. Pareathumby, M. Yousfi and E. Marode^{*}.

Laboratoire associé au C.N.R.S. N°277, Centre de Physique Atomique, 118, route de Narbonne, 31077 Toulouse Cedex.

^{*}Laboratoire de Physique des décharges, Ecole Supérieure d'Electricité Plateau du Moulon, 91190 Gif-sur-Yvette.

We compare the results obtained in the study of a weakly ionized gas for a Townsend discharge which is developed in a steady uniform field. This study has been carried out in two laboratories : firstly at the Centre de Physique Atomique de Toulouse using Boltzmann equation (1) and secondly in Paris (Ecole Supérieure d'Electricité) by Monte Carlo simulation.

A lot of papers has been devoted to the microscopic study of weakly ionized gases in steady uniform fields. However, most of them deal with homogeneous states, which are attained far from the walls i. e. when the electrons are in equilibrium with the electric field. In many cases too, these studies deal with low values of the ratio electric field upon pressure (E/P) ; we then have a great number of collisions, and the mean free paths are much smaller than the gap length. For high values of E/P , when the mean free paths are almost as great as the gap length, the methods of resolution of the Boltzmann equation normally used are no more valid. For such a case we developed a new technique based on the collision probability method well known in neutron physics. The method consists in a splitting of the phase space in spherical shells. The distribution function is assumed constant in each shell. This generates a linear system of equations in which the elements $P_{i,j}$ of the principal matrix can be considered as the collision probability that an electron, initiated in shell i , undergoes collision in shell j . If we assume the electron-atom collisions to be isotropic, the resolution of the linear system of equations gives us the isotropic part ϕ of the electron distribution function. A good number of the macroscopic quantities ruling the discharge can then be obtained

from ϕ only (Electron density n_e , mean energy E_m , excitation rates ν_k etc...). The other quantities (current J , drift velocity V_d ...) are derived from a simple quadrature of the initial Boltzmann equation.

Contrary to the Boltzmann equation approach, the same Monte Carlo method can be used for both low and high values of E/P . The program we have developed is thus valid in the two cases. The only difficulty may eventually come from the computing time which may be prohibitive in the low E/P case due to the great number of collisions involved.

To compare the two methods we choose a Townsend discharge between plane parallel plates in helium. The voltage applied is 150 volts corresponding to E/P and $P.D.$ values (D is the gap length) of 100 V.cm^{-1} , Torr^{-1} and 1 Torr.cm , respectively. We take a constant electron velocity function at the cathode of maximum energy 5 eV and we assume the anode to be perfectly absorbing.

In figure 1 we give the electron energy distribution function obtained by the two methods for the same position in the inter electrode space. The functions show similar behaviours in both cases. Fig. 2 shows the variation of the mean energy E_m with the distance. The results are in very good agreement for the two methods. The energy first increases sharply from the cathode, then oscillates around a mean value. Finally E_m grows in the proximity of the anode. This is in accordance with the continuity equation. The electron density varies inversely as V_d or E_m . Towards the anode there is a drop in density due to absorption, and thus an increase in the energy.

The $n_e(x)$ curve is displayed in fig. 3. The

density decreases near the cathode since there is no ionization, then when the electrons gain enough energy to ionize there is an increase of the density. Finally n_e decreases towards the anode due to absorption. The densities obtained by Monte Carlo are somewhat lower near the anode.

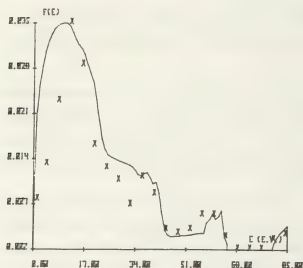


Fig. 1 - Electron energy distribution function.

— Boltzmann equation, x Monte Carlo method.

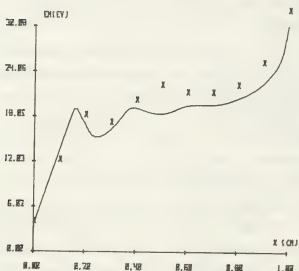


Fig. 2 - Mean energy.

— Boltzmann equation, x Monte Carlo method.

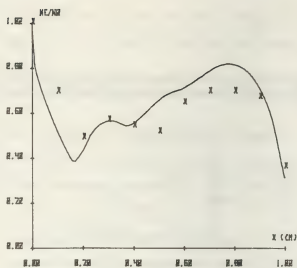


Fig. 3 - Electron density.

— Boltzmann equation, x Monte Carlo method

The variation of J/J_0 is shown in fig. 4.

Here too the discrepancies between the two amplification factors are very weak.

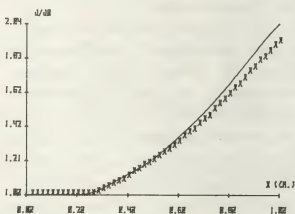


Fig. 4 - Amplification factor.

— Boltzmann equation, x Monte Carlo method

The work exposed here is the first step in a British-French collaboration on the behaviour of electronegative discharges in the neighbourhood of the walls. In the next step we intend to inject our results for heterogeneous situations in macroscopic equations used by the British team.

X

- Ondes
Waves
- Propagation des ondes
Wave propagation
- Interaction onde-particules et onde-onde
Wave-particle and wave-wave interactions
- Instabilités
Instabilities
- Turbulence forte
Strong turbulence

WAVE PROPAGATION IN A CYLINDRICAL GEOMETRY

H. Akiyama, T. Yamada and S. Takeda.

Department of Electrical Engineering, Nagoya University, Nagoya, Japan.

Abstract: The propagation of the normal modes in an ion-beam-plasma system and the ion-acoustic solitary waves is studied in a cylindrical double plasma device. After the fast ion-beam modes and ion-acoustic solitary wave concentrate at the center, density depressions emerge. These phenomena are in good agreement with the results of the computer simulation about the cylindrical ion-acoustic waves.

INTRODUCTION:

Hershkovitz et al. observed the cylindrical standing waves produced by the ion-ion beam instability (1), and the cylindrical ion-acoustic solitary waves (2). However, the report about the propagation of the cylindrical ion-beam modes is not found. About the ion-acoustic solitary waves, their experimental results of the propagation velocity and the half-width are not in agreement with the theory.

In this paper, the propagation of the cylindrical ion-beam modes and ion-acoustic solitary waves is experimentally studied, and the obtained results are compared with the theory and computer simulation.

EXPERIMENTAL DEVICE:

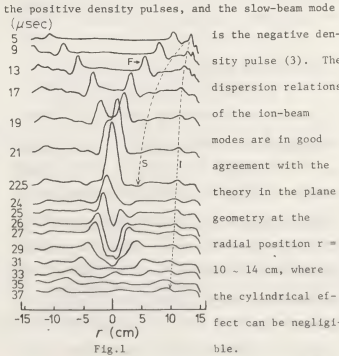
The cylindrical double plasma device used for the experiment consists of the two concentric argon plasmas separated by an mesh grid. The inner plasma of 67 cm in length and 32 cm (or 16 cm) in diameter is produced by the discharge between the several filaments and both end plates as the anode. The outer plasma is produced by the discharge between the filaments and the cylindrical mesh anode of 40

cm in diameter. The typical operating parameters are the electron temperature $T_e \approx 1$ to 2 eV, ion temperature $T_i \approx 0.1$ to 0.2 eV, plasma density $N_p \approx 10^8$ to 10^9 cm⁻³ at the pressure $P \approx 2 \times 10^{-4}$ Torr of Ar gas.

PROPAGATION OF ION-BEAM MODES:

After the steady ion-beam is injected into the inner plasma by the potential difference V between the mesh and plate anodes, the repeated pulse signals with the pulse width of 3 μ sec and amplitude of 1 V are superimposed on voltage V to excite the ion-beam modes. The steady beam velocity V_b can be varied by V .

The spatial evolution of the ion-beam modes is shown in Fig.1, where F, S and I are the fast and slow ion-beam modes, and ion-acoustic mode respectively. The fast-beam and ion-acoustic modes are



We first consider the linear theory of the ion-beam modes in the cylindrical geometry to explain the experimental results except near the center. The following formulas are readily obtained from the continuity, motion and Poisson equations,

$$V_p = V_b + \left(\frac{N_b}{N_p + N_b}\right)^{\frac{1}{2}} C_s \tag{1}$$

$$\frac{1}{n} \frac{dn}{dr} = \frac{-\frac{1}{r} \left\{1 + \left(\frac{N_b}{N_p + N_b}\right)^{\frac{3}{2}} \frac{C_s}{V_b}\right\}}{1 + \left(\frac{N_b}{N_p + N_b}\right)^{\frac{1}{2}} \frac{C_s}{V_b}} \tag{2}$$

where V_p , N_b , n and C_s are the phase velocity of the ingoing fast-beam mode, the steady density of beam ions, the perturbed density of the ion-beam mode and the ion-acoustic velocity respectively. The theoretical curves obtained from eqs.(1) and (2) are close to the experimental results for n and V_p at the radial position $r \geq 2$.

The fast-beam mode grows with the propagation, and the density depression appears at the center. This depression spreads with the outward propagation of the fast-beam mode. Then the density humps formed inside the depression are observed by the more detailed measurement from 27 μ sec till 37 μ sec. These humps with the ion-beam velocity propagate inwards and outwards finally to approach the density of the steady state.

PROPAGATION OF ION-ACOUSTIC SOLITARY WAVE:

The ion-acoustic solitary wave is excited by the positive half sine-wave pulse applied to the anode of the outer plasma, where V is nearly equal zero. The diameter of the inner plasma is changed to 16 cm. In Fig.2 is shown the dependence of the amplitude and width of the ion-acoustic solitary wave on the radial position r , where n_0 , δn and D are the steady plasma density, the perturbed density and the width of the solitary wave respectively. The solid line of $\delta n/n_0$ is the theoretical line considering the Landau damping of the solitary waves.

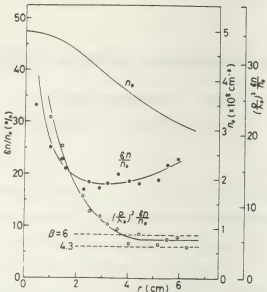


Fig.2

The product β of the maximum soliton amplitude and the square of the width is within the theoretical values ($\beta = 4.3$ for $T_i/T_e = 0.1$, $\beta = 6$ for $T_i/T_e = 0$) considering the ion temperature T_i . The velocity U of the solitary wave is $U = C_s(1 + \alpha \delta n/n_0)$. The value of α measured at the fixed radial position is nearly equal to $1/3$ predicted by the theory.

After the ion-acoustic solitary wave concentrates at the center, the density depression appears same as the fast ion-beam mode. The density humps observed in the experiment of the ion-beam modes are not observed. The spatial evolution of the solitary wave is in good agreement with the simulated results (4).

REFERENCES:

(1) T. Romesser and N. Hershkowitz: Phys. of Fluids 18 (1975) 1354.
(2) N. Hershkowitz and T. Romesser: Phys. Rev. Letters 32 (1974) 581.
(3) N. Sato, H. Sugai and R. Hatakeyama: Plasma Phys. 19 (1977) 187.
(4) T. Ogino and S. Takeda: J.Phys. Soc. Japan 41 (1976) 257.

WAVE AND PARTICLE INTERACTIONS WITH A NONLINEAR DIELECTRIC PERTURBATION IN A PLASMA

J.T. Mendonça.
Complex Interdisciplinary, Institute Superior Tecnico, Lisboa, 1, Portugal.

1. Introduction

In recent years much attention has been devoted to the problem of nonlinear susceptibilities. We discuss here two effects which are related to the susceptibility perturbation induced by a nearly monochromatic wave packet, traveling in an infinite homogeneous and isotropic plasma, due to the nonlinear motion of the particles.

From a macroscopic point of view the wave packet will behave as a dielectric perturbation moving with the group velocity, $w = (\partial\omega/\partial k)_\omega$, which can become relativistic if its main frequency ω_0 is much larger than the electron plasma frequency, ω_p . The waves which can be excited in this plasma will interact with this rapidly moving perturbation and will undergo a partial reflection. The result is very similar to the classic relativistic mirror effect, with a significant frequency upper shift of the reflected wave. On the other hand, each particle of the plasma will give rise to a nonstationary electric field when submitted to the dielectric perturbation and the result is the emission of a transition-like radiation. It is the aim of the present work to discuss these wave and particle interactions with the nonlinear dielectric perturbation induced by a strong quasi-monochromatic wave-packet.

2. Nonlinear dispersion relation

Using Maxwell's equations and the relativistic fluid equations for the electrons we can easily obtain the nonlinear dispersion relation for an electromagnetic mode (ω, \vec{k}) in the presence of a large amplitude electromagnetic wave (ω_0, \vec{k}_0) :

$$k^2 c^2 = \omega^2 - \Omega_{NL}^2 \tag{1}$$

where the nonlinear plasma frequency is given by

$$\Omega_{NL}^2 = \omega_p^2 - \omega^2 C(\omega, \omega_0) W_0 \tag{2}$$

and the coupling coefficient relating the two modes is

$$C(\omega, \omega_0) = \frac{2 e^2}{\epsilon_0 m^2 c^2} \frac{\omega_p^2}{\omega \omega_0} \left[1 + \left| \hat{a} \cdot \hat{a}_0 \right|^2 \left(2 + \frac{c^2 k_-^2}{\omega^2 \omega_0^2} + \frac{c^2 k_+^2}{\omega^2 \omega_0^2} \right) \right] \tag{3}$$

$\vec{k}_\pm = \vec{k} \pm \vec{k}_0$ and $\omega_\pm = \omega \pm \omega_0$. The dispersion relation depends on the value of the density of energy $W_0 = \frac{\epsilon_0}{2} \left| E(\omega_0, \vec{k}_0) \right|^2$ and the variation of W_0 in space and time leads to a nonstationary plasma situation.

3. Relativistic mirror

Suppose now W_0 changing rapidly in a time scale of ω^{-1} and over a distance k^{-1} . We can then assume a sharp boundary of infinitesimal thickness connecting the free plasma and the plasma submitted to the quasi-monochromatic pulse (ω_0, \vec{k}_0) . The reflection of an incident field $E_i(\omega, \vec{k})$ on the moving boundary can be calculated using a Lorentz transform to the frame boundary. In this frame we have two different media at rest, with refractive indices (see Fig. 1) :

$$N_1 = (1 - \omega_p^2 / \omega'^2)^{1/2} \quad N_2 = (1 - \Omega_{NL}^2 / \omega'^2)^{1/2} \tag{4}$$

where ω' is the Lorentz transformed frequency of the incident wave. Now we can use the Fresnel formulae to calculate the reflection coefficient, at normal incidence, and we get:

$$r = \frac{(1 - \omega k / \omega') \frac{N_1' - N_1}{N_1' + N_1} - \frac{X_{NL}}{2} \frac{\omega''^2}{\omega_0^2 + \omega''^2}}{(1 - \omega k / \omega') \frac{N_1' + N_1}{N_1' - N_1}} \tag{5}$$

where $X_{NL} \equiv C(\omega, \omega_0) W_0$, $k'' = \omega'' / c$ and ω'' is the frequency of the reflected wave in the laboratory frame:

$$\omega'' = \omega \left(1 + \frac{w^2}{c^2} - 2 \frac{wk}{\omega} \right) \left(1 - \frac{w^2}{c^2} \right)^{1/2} \tag{6}$$

Eq.(5) shows that the reflection coefficient is always of the order of the nonlinear susceptibility X_{NL} , in the laboratory frame. And we see, from eq.(6), that the frequency of the reflected wave ω'' is considerably larger than ω , if $w \approx c$.

4. Transition radiation

Let us consider now the plasma particles interacting with the moving boundary. In the moving frame each particle has velocity $\vec{v} = -\vec{w}$, if we neglect the influence of the temperature. When the particle goes from the free region, described by N'_1 , to the region described by N'_2 , it creates a nonstationary electric field whose spectrum is given by

$$E(\omega') = \frac{e}{2 \pi \epsilon_0} \frac{\beta^2}{v' k} \Theta \exp(i \frac{\omega'}{v'} \beta R) \tag{7}$$

Where $\beta = (v'/c)N'_1$ and Θ is a form factor describing the angular pattern. This expression is valid at very long distances R from the transition boundary. It can be shown from this equation that the radiation emitted by the particle has a sharp maximum in a direction nearly parallel to the particle trajectory and that significant levels of radiation can only be obtained for $\omega^2 \gg \omega_p^2$. Using eq. (7) we can deduce the following expression for the total energy radiated by a particle, in the laboratory frame:

$$W = \frac{e^2 \omega_0}{768 \pi \epsilon_0 c} \left(\frac{\Delta}{\alpha \omega_p} \right)^4 \ln \left(4 \frac{\omega_0^2}{\omega_p^2} \right) \tag{8}$$

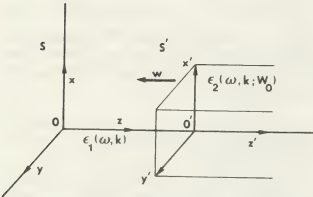


FIGURE 1 - Geometry of the problem: S is the laboratory frame; S' is the moving frame; $\epsilon_1(\omega, k)$ the linear dielectric constant of the plasma; $\epsilon_2(\omega, k; W_0)$ is the dielectric constant in the presence of the strong wave (ω_0, k_0)

Where $\Delta = \omega_0 X_{NL}(\omega_0)$ and $1 < \alpha < 3$. We see from eq.(7) that $E(\omega')$ is proportional to the electric charge and is independent of the particle mass. This means that the total energy emitted by the plasma is nearly zero, unless the plasma is slightly non-neutral. For example, suppose a plasma of density $n_0 = 10^{12} \text{ cm}^{-3}$ crossed by an electron beam of small density, $n_f \ll n_0$ and small velocity, $v_f \ll w$. The transition radiation produced by a strong electromagnetic wave-packet which is launched in this plasma is given by:

$$P_T = W_T n_f w \tag{9}$$

Even for moderately high energy W_0 , such that the nonlinear susceptibility $X_{NL}(\omega_0)$ is of the order of $(\alpha \omega_p / \omega_0)^2 \ll 1$, we get 1 m Watt of radiated power, with a very weak electron beam, $n_f / n_0 = 10^{-6}$. More detailed discussions of these can be found elsewhere^{1,2}.

References

/1/ J.T. MENDONÇA, J. of Plasma Phys. (1979); to be published
/2/ J.T. MENDONÇA, Internal. Report CEL-1/79, Lisboa (1979).

HYDROMAGNETIC RAREFACTION WAVES

J.E. Allen and L.M. Wickens.

Department of Engineering Science, The University of Oxford, Parks Road, Oxford, England.

An analytic solution for the free expansion of a collision-free strongly magnetised plasma is presented. The solution obtained is of interest in connection with solar flares and laser produced plasmas. It is shown that a wavefront develops which travels at twice the fast magneto-acoustic speed, limiting the ion emission velocity to this value. This contrasts with the case of the free expansion of an unmagnetised plasma⁽¹⁾, where the maximum ion emission velocity is determined by other effects.

The initial conditions for the problem are a quasineutral cold-ion collision-free plasma slab strongly magnetised in the z direction by a magnetic field B_0 . The source plasma electron density and temperature are n_0 and T_0 respectively (see fig. 1).

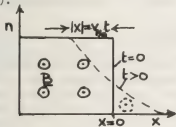


Figure 1.

Schematic of initial conditions

Neglecting electron inertia the ion momentum and continuity equations are (for $n_e = n_i = n$)

$$\frac{\partial v}{\partial t} + v \frac{\partial v}{\partial x} = -\frac{1}{nM} \left[\frac{\partial}{\partial x} \left(\frac{B^2}{2\mu_0} + Znkt \right) \right] \quad (1)$$

and

$$\frac{\partial n}{\partial t} + \frac{\partial}{\partial x} (nv) = 0 \quad (2)$$

where n and Ze/M are the ion number density and charge to mass ratio respectively; v is the ion

velocity in the x direction and all quantities are assumed to vary in the x direction alone.

For a sufficiently strong magnetic field the magnetic flux is frozen into the plasma so that

$$B/n = \text{const.} = B_0/n_0 \quad (3)$$

at a fluid particle. Since the plasma electrons are tied to the field lines thermal conduction from the source plasma is strongly inhibited and an adiabatic expansion may also be assumed so that

$$P/n^\gamma = \text{const.} \quad (4)$$

The expansion has two degrees of freedom so

$\gamma = 2$ and eqn. 4. becomes

$$kT/n = \text{const.} = kT_0/n_0 \quad (5)$$

Substituting equations 3. and 5. into eqn. 1.

then gives

$$\frac{\partial v}{\partial t} + v \frac{\partial v}{\partial x} = -\frac{v_{*}^2}{n_0} \frac{\partial n}{\partial x} \quad (6)$$

where $v_{*} = (v_{*0} + C_{*0}^2)^{1/2}$ is the fast magneto-acoustic speed and $v_{*0} = B_0/(\mu_0 M n_0)^{1/2}$, $C_{*0}^2 = (2ZkT_0/M)^{1/2}$.

We now look for self-similar solutions to the problem of the free expansion of a strongly magnetised plasma by transforming equations 2. and 6. to $\xi = x/t$ as the independent variable, giving

$$(v - \xi) \frac{dv}{d\xi} + \frac{v}{n} \frac{dn}{d\xi} = 0 \quad (7)$$

and

$$n \frac{dv}{d\xi} + (v - \xi) \frac{dn}{d\xi} = 0 \quad (8)$$

For non zero solutions to 7. and 8. we have that

$$(v - \xi) = v_{*} \quad (9)$$

and from 8. and 9. we have

$$\frac{dv}{d\xi} = -v_{*} (n_0/n) \frac{d}{d\xi} (n/n_0) \quad (10)$$

Integrating 10. from the undisturbed plasma out into the rarefaction expansion gives

$$n = (4/9)n_0 \left[1 - \xi/2v_{he} \right]^2 \quad (11)$$

The important aspect of the solution 11. is the existence of a wavefront at $\xi = 2v_{he}$, beyond which no ions exist. Figure 2. shows a normalised plot of ion density in the rarefaction expansion against $x/(v_{he}t)$. At any specified time fig.2. thus represents the ion density as a function of normalised distance. The negative values of $\xi = x/t$ correspond to a wavefront travelling back into the source plasma at the fast magneto - acoustic speed.

From equations 9. and 11. we also have

$$v = (2/3)v_{he} \left[1 + \xi/v_{he} \right] \quad (12)$$

corresponding to a linear increase in ion velocity with distance at a specified time. At the rarefaction wavefront $\xi = 2v_{he}$, so eqn. 12. then gives $2v_{he}$ as the maximum ion emission velocity. This is in marked contrast to the case of a freely expanding plasma with no magnetic field, where no maximum ion emission velocity exists. In reference (2) similar features are obtained numerically.

Finally we note that the solution obtained is analogous to that found in collision dominated gas dynamics⁽³⁾.

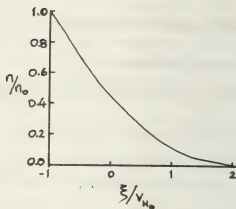


Figure 2.

Ion density in rarefaction expansion.

REFERENCES

- (1). GUREVICH, A. V., PARIISKAYA, L. V. and PITAEVSKII, L. P., 1966, J.E.T.P., 22, 449.
ALLEN, J. E. and ANDREWS, J.G., 1970, J. Plasma Phys. 4, 187.
CROW, J. E., AUER, P.L. and ALLEN, J. E., 1975, J. Plasma Phys. 14, 65.
WICKENS, L. M., ALLEN, J. E. and RUMSBY, P. T. 1978, Phys. Rev. Lett. 41, 243.
WICKENS, L. M. and ALLEN, J.E. J. Plasma Phys. - in press.
- (2). GUREVICH, A. V., PARIISKAYA, L.V. and PITAEVSKY L. V., 1973, J.E.T.P., 37, 1071.
- (3). ZELDOVICH, Ia. B. and RAIZER - 'Physics of Shock Waves...' - Vol. 1., 1966, Academic Press.

ACKNOWLEDGEMENT

This work is supported by the Rutherford Laboratory of the Science Research Council, UK.

UPPER HYBRID SOLITONS

J.G. Turner, T.J.M. Boyd*

*Polytechnic of Central London, London, U.K.
University of Wales, U.C.N.W. Bangor, Wales.

1. INTRODUCTION

Although some work has been done on soliton formation at the upper hybrid frequency using warm two-fluid theory, [1], this leaves important questions unanswered. In this work we report the results of a kinetic theoretic analysis which describes the nonlinear modulation of electrostatic upper hybrid waves in a warm magnetized plasma. The equation governing the modulation of these waves is the nonlinear Schrödinger (NLS) equation

$$i \frac{\partial \phi}{\partial \tau} + P \frac{\partial^2 \phi}{\partial x^2} + Q |\phi|^2 \phi = 0$$

in which $\phi(x,t)$ is the complex electrostatic potential, t and x denote time and space coordinates (the latter with respect to a frame of reference moving with the group velocity). The coefficient $P = \frac{1}{2} \partial^2 \omega / \partial k^2$, where ω , k are the frequency and wave number of the electrostatic carrier respectively and Q is the nonlinear frequency shift coefficient. Contributions to Q derive from three distinct nonlinear processes. One contribution describes the generation of the second harmonic ($\omega + \omega + 2\omega$); a second arises from the self-interaction between the high frequency waves ($\omega + \omega + \omega + \omega$) while the third describes the nonlinear coupling between the carrier and the slow background plasma motion (wave-particle interaction).

The stability of the soliton is determined by the sign of PQ . For $PQ > 0$ the waves are modulationally unstable while for $PQ < 0$ the modulational instability does not occur. We investigate the variation of the normalized dispersion and normalized nonlinear frequency shift with the two independent plasma parameters $\lambda = k^2 v_e^2 / \Omega^2$ and $\alpha = \omega_{pe} / \Omega$, where v_e is the electron thermal speed, Ω , the electron cyclotron frequency and ω_{pe} , the electron plasma frequency.

2. RESULTS

In order to discuss the behaviour of upper hybrid solitons, the NLS equation is cast into dimensionless form

$$i \frac{\partial \phi}{\partial \tau} + p \frac{\partial^2 \phi}{\partial \xi^2} + q |\phi|^2 \phi = 0$$

with $\tau = \Omega t$, $\xi = \Omega x / v_e$, $\phi = (2\pi e / \kappa T_e) \phi$,

$p = \Omega P / v_e^2$, $q = (m^2 v_e^4 / 4\pi^2 e^2 \Omega) Q$ where e and m are the electron charge and mass respectively and κT_e is the electron temperature. In the limit of low electron temperature and/or strong magnetic

fields ($\lambda \ll 1$), p is found to be k -independent; numerical studies indicate that this holds provided $\lambda < 0.1$. For frequencies in the range $\Omega < \omega < 2\Omega$ ($\alpha < 1.7$), the upper hybrid shows negative dispersion ($p < 0$) while for $\omega > 2\Omega$, the mode exhibits positive dispersion ($p > 0$).

In Figs. 1-3 the normalized dispersion p and nonlinear frequency shift coefficient q are plotted simultaneously vs. α , for λ in the range $0.1 \leq \alpha \leq 1.6$ for each of the three values $\lambda = 0.01, 0.1$ and 1.0 respectively. In Fig. 1 ($\lambda = 0.01$), we see that $p < 0$ and $q > 0$

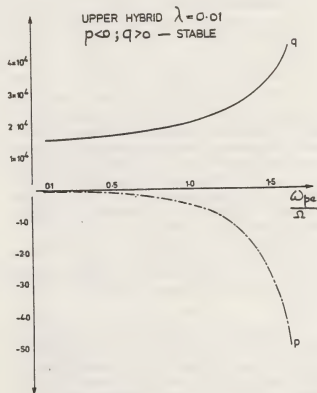


Fig. 1

throughout the range of α considered. Since $pq < 0$, the upper hybrid is therefore modulationally stable for $\lambda \leq 0.01$ and $0.1 \leq \alpha \leq 1.6$ (we disregard values of $\alpha > 1.7$ since in this regime the upper hybrid behaves as a Langmuir wave in an isotropic plasma). As λ increases and temperature effects become important, the behaviour of the p, q curves changes as shown in Fig. 2 where $\lambda = 0.1$. The important features here are the behaviour of p and q near $\alpha = 1.2$. In fact

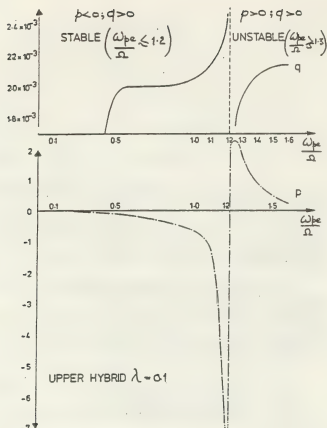


Fig. 2

p vanishes and q is discontinuous near $\alpha = 1.2$, at which point the reductive perturbation theory used breaks down. Excluding this region we can summarize the behaviour of the upper hybrid for $\lambda = 0.1$ by noting that the mode is modulationally stable (unstable) for $\alpha \leq 1.2$ ($\alpha \geq 1.3$). In Fig. 3 the corresponding plots for $\lambda = 1.0$ are presented. Again $q > 0$ throughout the range and decreases with increasing α (in contrast to the small λ limit where q increases with increasing α). We note that p changes sign from positive to negative in the region $1.0 \leq \alpha \leq 1.1$ and we deduce that the upper hybrid is modulationally unstable (stable) for $\alpha \leq 1.0$ ($\alpha \geq 1.1$).

To summarize, for the ranges of λ and α considered, it is evident from Figs. 1-3 that in general, q is positive while p is negative, predicting the general stability of the upper hybrid mode. It is when λ increases so that temperature effects become important that the upper hybrid can exhibit modulational instability, and we identify two unstable regimes: $\lambda = 0.1$, $1.3 \leq \alpha \leq 1.6$ and $\lambda = 1.0$, $\alpha \leq 1.0$. It should be noted that p decreases with increasing α for both regimes, while q respectively increases (decreases) with increasing α in the two regimes. In the unstable regime the wave amplitude and width of the soliton are proportional to $q^{-1/2}$ and $p^{1/2}$ respectively. Hence as the parameter α increases, the soliton width will decrease in both unstable regions whereas the wave amplitude will decrease (increase) for $\lambda = 0.1$ (1.0) respectively.

It is also of interest to compare the

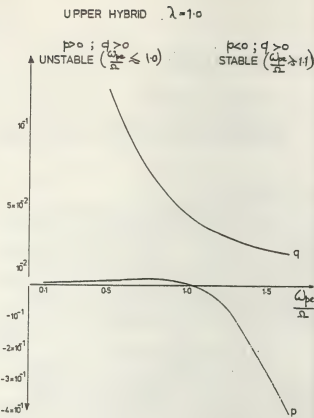


Fig. 3

contributions to the nonlinear frequency shift coefficient from the harmonic generation q_H , the self interaction q_S and the wave-particle interaction q_P ($q = q_H + q_S + q_P$) for the upper hybrid for general values of λ and α . It has been found that $|q_H| \sim |q_P|$ with $|q_S| \ll |q_H, P|$ for general values of λ and α considered.

3. DISCUSSION

The work of Porkolab and Goldman based on the warm fluid equations together with a time-averaging procedure produced a NLS equation with a nonlinear term proportional to $\delta n/n$. This term represents the reaction of the wave on the background plasma by means of a low frequency ponderomotive force which produces corresponding density changes $\delta n/n$. We have shown that this form follows explicitly from the NLS equation derived by our kinetic theory approach. In particular, we have shown [2] that the contribution to the nonlinearity from the ponderomotive force corresponds to the contribution q_P of our reductive perturbation calculation. The existence of Bernstein solitons has also been demonstrated and a corresponding analysis for the properties of Bernstein solitons as functions of λ and α has been carried out [2].

REFERENCES

- [1] M. PORKOLAB and M.V. GOLDMAN, Phys. Fluids **19**, 872 (1976).
- [2] J.G. TURNER and T.J.M. BOYD, J. Plasma Phys. (in press).

SELF-GENERATED MAGNETIC FIELDS AND HARMONIC EMISSION

T.J.M. Boyd, G.A. Gardner and G.J. Humphreys-Jones.

University of Wales, U.C.N.W., Bangor, Wales.

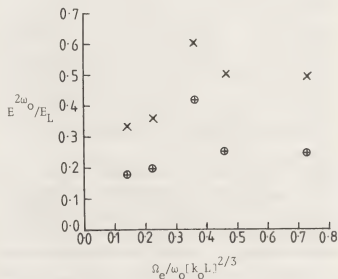
Recent observations of self-generated magnetic fields in plane target experiments [1] with high powered lasers have prompted us to look again at harmonic emission from magnetized plasmas. It is well known from the work of Fidone and his collaborators [2,3] that second harmonic generation in Tokamak plasmas has not only been observed but has proved to be a useful magnetic field diagnostic. In the experiments by Raven and his co-workers, megagauss fields were measured in the quarter-critical density region, from which one might expect that magnetic field strengths close to critical density would be very large indeed - perhaps as big as 10MG - though no measurements have yet been made in this region. In the presence of such strong magnetic fields it has been shown recently that significant absorption of normally incident laser light is possible, together with harmonic generation [4,5]. In this paper we report a theoretical study of harmonic generation together with results obtained from numerical experiments using a 1½-D code, EMPIRE. The computer experiments, in addition to providing information on harmonic emission, also indicate that a strong quasi-static magnetic field is generated in the neighbourhood of the resonance region. This field has been detected in simulations carried out independently [6].

The configuration examined in this work is the following. An electromagnetic wave propagates along Ox and is normally incident on a plasma density ramp. The electric field of the incident wave is aligned along Oy. We shall suppose that a magnetic field B_0 is applied along Oz. As the wave propagates into the plasma, the E_y field induces electron oscillations along Oy and the resultant $y \times B$ force effectively produces particle motion in the direction of propagation. Thus by charge separation along the density gradient, an electrostatic field component E_x is produced. This is of course just the extraordinary mode in the plasma. The interest in this mode stems from the fact that N_R , the density at which the wave resonates at the local upper hybrid frequency, and N_C , the cut-off density, are related by $N_C = N_R[1 - \Omega_e/\omega_0]$, where Ω_e is the electron cyclotron frequency and ω_0 , the frequency of the incident wave. Consequently if $\Omega_e \ll \omega_0$, as is certainly the case in Nd laser produced plasmas, then $N_C \approx N_R$. We then have a situation analogous to that of obliquely incident radiation in unmagnetized plasmas. The difference between the two cases is that in the latter the separation between the cut-off and resonant densities is governed by the angle of incidence of the wave, whereas in the magnetized plasma considered

here, this separation is governed effectively by the strength of the magnetic field. Thus resonant absorption of a normally incident wave is made possible by the magnetic field and has been examined both theoretically and by computer simulations.

This resonance takes the form of a plasma disturbance which produces a large localized oscillating electrostatic field. The rapid spatial variation of this field produces anharmonic oscillations of the electrons, due to their being subjected to varying electric field strengths over their excursion lengths. This electron behaviour may be represented as a series of Fourier modes at $\omega_0, 2\omega_0, 3\omega_0 \dots$ and these modes then provide a current density source with components at $2\omega_0, 3\omega_0 \dots$. The particular modes responsible for the generation of the $2\omega_0$ current density are the ω_0 and $2\omega_0$ electron oscillations. The former beats with the oscillating electron number density $N(\omega_0)$ to produce a component $eN(\omega_0)V_e(\omega_0)$ while the latter combines with the unperturbed number density to give a term $eN_0V_e(2\omega_0)$. Hence as a direct result of the resonant mechanism a current density $J(2\omega_0)$ is produced which, in turn, provides the source of second harmonic emission.

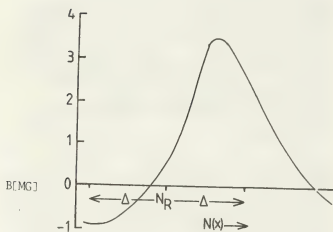
Fig. 1



⊙ - Theory ; X - Computation.

To find the relation between the power in the incident wave and that re-emitted as second harmonic, we have to determine the current density. This is then treated as "free" current and is used as a source term in the second harmonic wave equation. This relationship has been evaluated and Fig. 1 shows a comparison between the theoretical results and those obtained from computer simulations. The parameter on the abscissa is the ratio of the distance between cut-off and resonant layers and the scale of variation of the electromagnetic wave near cut-off; $k_0 = \omega_0/c$ and L is the plasma scale length, i.e. the distance between the critical density and the boundary. While there is some discrepancy between the theoretical results and those from the computer experiment, the overall agreement is quite good.

Fig. 2

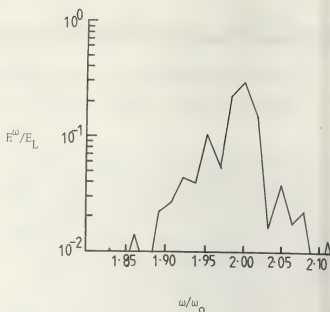


The dominant component of the resonantly induced current density lies across the density gradient, i.e. along Oy . This component is responsible for inducing a magnetic field along Oz . This field is quasi-static and, in the cold plasma limit, is restricted spatially to the plasma resonant region. However warm plasma theory predicts that the magnetic field will extend into the over-dense region, and this is observed in the computer simulations. Fig. 2 shows a plot, from our simulations, of the time-averaged magnetic field. The direction of the field reverses inside the resonant region which extends over 2Δ . Also the field extends into the over-dense plasma.

We have also examined the influence of the magnetic field effects on the harmonic line profiles. Fig. 3, taken from a run of our 1½-D fully electromagnetic code shows the line structure present on the second harmonic emission spectrum. The frequency shift of the first side band, relative to the line centre, can be seen. This is strongly dependent on magnetic field intensity.

In summary we have shown that significant harmonic emission may be produced in laser produced plasmas with strong magnetic fields. The harmonics show structure consistent with the

Fig. 3



excitation of Bernstein modes. The simulations also indicate that strong quasi-static magnetic fields are generated in the neighbourhood of the critical density.

References

1. A. Raven, O. Willi, and P.T. Rumsby, *Phys. Rev. Lett.* **41**, 554 (1978).
2. R. Cano, I. Fidone and M.J. Schwartz, *Phys. Rev. Lett.* **27**, 783 (1971).
3. T.J.M. Boyd and I. Fidone, *Phys. Fluids* **16**, 427 (1973).
4. W.L. Kroer and K. Estabrook, *Phys. Fluids* **20**, 1688 (1977).
5. W. Woo, K. Estabrook and J.S. De Groot, *Phys. Rev. Lett.* **40**, 1094 (1978).
6. W. Woo and J.S. De Groot, *Phys. Fluids* **21**, 2072, (1978).

PARAMETRIC DECAY OF LOWER HYBRID WAVES

S.S. Pesic.

Département de Physique du Plasma et la Fusion Contrôlée, Service Ign - Centre d'Etudes Nucléaires
85 X - 38041 Grenoble Cedex, France.

1 - INTRODUCTION.

The parametric instabilities induced by pump field with a driving frequency in the range of lower hybrid (LH) and electron plasma (EP) frequencies ($\omega_{ci} < \omega_0 < \min(\omega_{pe}, \omega_{ce})$) have received a great deal of attention (the present theoretical and experimental state of the art has been recently reviewed in [1]). The crucial problem of LH plasma heating is the penetration of the launched waves to the plasma core without significant pump depletion in the outer, low-density plasma layer, which can lead to a reduction of the heating efficiency. In the present paper we analyse the nature of the parametric instabilities induced in ohmically heated toroidal discharges.

2 - DISPERSION RELATION.

To approximate the physical conditions of the parametric interaction in ohmically heated toroidal discharges, we consider a two-component weakly inhomogeneous low- β cylindrical plasma confined by a magnetic field with shear. The spatial variation of the pump field and the confining magnetic field is neglected. The oscillations under consideration are assumed to be quasi-longitudinal with perpendicular wavelengths much smaller than the scale lengths of plasma inhomogeneities. Within the framework of the local wave dispersion description and the weak pump field approximation ($a_b^2 \ll 1$), the linear dispersion relation governing the parametric coupling can be represented in the well-known form [2, 3],

$$D(\vec{k}, \omega^*, r) = \epsilon(\vec{k}, \omega^*, r) + \frac{a_b^2}{4} \chi_1(\vec{k}, \omega^*, r) \{1 + \chi_e(\vec{k}, \omega^*, r)\} \\ \{\epsilon^{-1}(\vec{k}, \omega^* - \omega_0, r) + \epsilon^{-1}(\vec{k}, \omega^* + \omega_0, r)\} = 0 \quad (1)$$

where $\omega^* = \omega + i\gamma$, $\epsilon(\vec{k}, \omega, r) \equiv 1 + \sum_{\alpha} \chi_{\alpha}(\vec{k}, \omega, r)$ and $\chi_{\alpha}(\vec{k}, \omega, r)$ is the susceptibility of species α in weakly-inhomogeneous low-collisional magnetized plasma,

$$\chi_{\alpha}(\vec{k}, \omega^*, r) = \frac{1}{k^2 \lambda_{D\alpha}^2} \frac{1 + \hat{z}_{0\alpha} \phi(\lambda_{\alpha}, z_{n\alpha})}{1 + i\nu_{\alpha} \phi(\lambda_{\alpha}, z_{n\alpha}) / k_{\parallel} v_{T\alpha}} \quad (2)$$

Here $\phi(\lambda_{\alpha}, z_{n\alpha}) = \sum_n I_n(\lambda_{\alpha}) \exp(-\lambda_{\alpha})^2 Z(z_{n\alpha})$,

$$\hat{1} = 1 - \frac{\omega_{n\alpha}}{\omega + i\nu_{\alpha}} (1 + \eta_{\alpha} T_{\alpha} \frac{\partial}{\partial T_{\alpha}}), \quad \eta_{\alpha} = \frac{d \ln T_{\alpha}}{d \ln n_{\alpha}}, \quad \omega_{n\alpha} =$$

$$k v_{T\alpha}^2 \frac{d \ln n_{\alpha}}{dr}, \quad \lambda_{D\alpha}^2 = v_{T\alpha}^2 / 2 \omega_{p\alpha}^2, \quad z_{n\alpha} = (\omega^* + i\nu_{\alpha} - n\omega_{c\alpha}) /$$

$k_{\parallel} v_{T\alpha}$ and $\lambda_{\alpha} = k_{\perp}^2 v_{T\alpha}^2 / 2 \omega_{c\alpha}^2$. The components of the wave vector of oscillations in the used coordinate system are defined as :

$k_c = \cos \phi k_{\parallel} - \sin \phi k_z$, $k_{\parallel} = \cos \phi k_z + \sin \phi k_{\phi}$, where

$\phi = \angle(\vec{B}_{Oz}, \vec{B}_O)$. The finite pump wave number is included to the lowest order in the dispersion relation (1) by defining the sideband permittivity as $\epsilon(k_{\perp}, k_{\parallel} \pm k_{\parallel 0}, \omega^* \pm \omega_0, r) / 4$. Furthermore, the presence of the longitudinal plasma current is taken into account by replacing ω^* in the electron susceptibilities by $\omega^* - \vec{k} \cdot \vec{u}_D$ where u_D is the average velocity of electrons with respect to the ions. For a plane-polarized wave the coupling parameter a_b is defined by,

$$a_b^2 = (e k E_0 / m_e \omega_0^2) f(\theta, \xi, \zeta), \quad (3)$$

where $\theta = \angle(\vec{k}, \vec{B}_O)$, $\xi = \angle(\vec{E}_O, \vec{B}_O)$ and ζ is the angle between the planes (\vec{k}, \vec{B}_O) and (\vec{E}_O, \vec{B}_O) . In the present analysis the threshold electric field is minimized with respect to the angle ζ by taking the maximum value of the function $f(\theta, \xi, \zeta_m)$ for a given coupling parameter [2, 3].

3 - RESULTS.

In this section we shall present results of detailed numerical analysis of the dispersion relation (1). In the low-density plasma region ($\omega_0 / \omega_{LH} > 2$) the stability boundaries are characterized by two pronounced minima of the coupling parameter a_b . The first minimum of a_b occurs at zero detuning of the driving frequency from exact resonance, while the second, less pronounced minimum is associated with the resonant decay into an ion Bernstein or LH wave. Low minimum threshold electric fields of the resonant LH pump wave ($E_{os} \approx 50$ V/cm)

associated with the first minimum are found. Instabilities with relatively small parallel phase velocity ($k_{\parallel}^2/k^2 \gg m_e/m_i$) are preferentially excited in the low-density plasma region. The foregoing discussion is illustrated by Fig. 1 on which we have represented the variation of a_{bt} (a_{bt} is the coupling parameter corresponding to the marginal stability) and the associated normalized frequency ω/ω_{ci} with $k\lambda_D$. The variation of the normalized growth rate γ/ω_{ci} and the associated ω/ω_{ci} with a_b for different $k\lambda_D$ values is also shown. The plasma parameters chosen are relevant to the low-density plasma layer near the wave launching structure: $\omega_o/\omega_{LH} = 5$, $n_e/B_o^2 = 3.5 \times 10^{17} m^{-3} T^{-2}$, $T_e = T_i = 30$ eV and the scale length of inhomogeneities $L_{ne} = L_{Ti} = 4$ cm and $L_T = 1$ cm. Note that the level $E_{os} = 5$ kV/cm is displayed in the a_{bt} versus $k\lambda_D$ curve and is labelled by circles on the γ/ω_{ci} versus a_b curve. For pump electric field intensities of a few kV/cm the highest growth rates obtained ($\gamma = \gamma(\omega_{ci})$) are those related to the decay of the pump into a cold LH wave and an IC or nonresonant quasimode. Thus, in addition to the high-density plasma region, the decay processes involving quasimodes also dominate the decay spectrum excited for $2 < \omega_o/\omega_{LH} \lesssim 7$. Due to the presence of current in the plasma, low frequency ($\omega < \omega_{ci}$) negative energy waves, which represent parametrically driven ion cyclotron current instabilities, are excited in the longwavelength part of the decay spectrum ($k\lambda_D < 0.1$ in Fig. 1). Although a_{bt} is somewhat lower in current carrying plasma, the pump field has a stabilizing effect on the excitation of these instabilities since it eliminates the most unstable, large k_{\parallel} instabilities.

It is interesting to note that at large ω_o/ω_{LH} values and for small parallel phase velocities ($\omega/k_{\parallel} \gtrsim 0.9 v_{te}$), the derivative $\text{Re} d_{\omega}$ can become negative in a finite a_b -range, $a_{b1} \lesssim a_{bt} < a_{b2}$ (the values a_{b2} are labelled by points in Fig. 1). Therefore the expansion of the dispersion relation in a power series near the real roots (ω, k) cannot be used in the evaluation of the growth rate of quasimodes at large ω_o/ω_{LH} values. Otherwise the applicability of this expansion is limited to a narrow range of field intensities near the threshold value in which for a given k the frequency varies slightly with a_b and $\gamma \ll \omega$. Note that by increasing the collision frequency a_{bt} may become larger than a_{b2} .

For large k_z/k_{zo} values the pump wave decays into an IC quasimode and two LH waves.

This four wave decay process is followed by an abrupt increase of a_{bt} as well as by a frequency increase. There are two branches in the dispersion curves behind this $k\lambda_D$ region: the principal forward mode which is an ion Bernstein (IB) quasimode and a low-frequency ($\omega < \omega_{ci}$) nonresonant quasimode. By following the dispersion curve of the principal mode, one concludes that in the short-wavelength region ($k\lambda_D > 0.2$) and for $\omega_o/\omega_{LH} < 2$ the sideband becomes a hot IB wave. Due to their small group velocity and fast growth rates, the spatial amplification of hot IB waves dominates. An important energy transfer from the pump wave to IB waves and nonresonant quasimode leading to a bulk particle heating occurs at $\omega_o/\omega_{LH} \gtrsim 2$. In connection with this we note that for moderate pump fields the convective losses in the outer plasma layer are sufficiently large to allow an efficient wave penetration to the plasma core.

REFERENCES.

1. PORKOLAB M., Nucl. Fusion **18** (1978) 367.
2. PESIC S.S., EUR-CEA-FC 981.
3. PESIC S.S. Joint Varenna-Grenoble Symp. (1978) 16.
4. PORKOLAB M., Phys. Fluids **20** (1977) 2058.

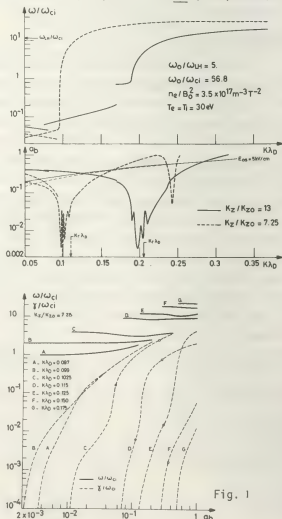


Fig. 1

CHARACTERISTICS OF SPATIAL WAVE ECHOES AT THE LOWER HYBRID BRANCH

Ichiro. Mori and H.D. Leppert^{*}, K. Wiesemann^{*}.

^{*}Department of Electric Engineering, Technical college of Tokushima University, Tokushima Japan.
^{*}Institut für experimentalphysik, Ruhr-Universität Bochum, Bochum West-Germany.

Introduction : The phenomenon of plasma wave echoes [1] in a collisionless plasma is a reversible process in which macroscopic field energy converts to particle's kinetic energy and vice versa, even in the presence of phase-mixing and Landau-damping. Therefore echoes possess great potential as diagnostic tool for investigation in the velocity space. Especially, the echoes of lower hybrid branch are interesting because of heating aspects simultaneously involving both electron-and-ion-dynamics. In this paper, comparison between the theory and the experiments on the spatial lower hybrid echoes have been made.

Model of spatial wave echo : The lower hybrid wave belongs to a ion-cyclotron wave, then the gyrating motion of particles in finite magnetic field extends the dimensions of the model automatically. The experimental plasma is, of course, of finite radial extent, but the length is long enough to consider to be infinite, so that we use here following model.

We start from the model of infinite radial extent and then the effect of finite radius is introduced by means of the restriction of perpendicular wave number. In the experiment, the background pressure is 10^{-5} Torr hydrogen, and the plasma having a electron density $n_0 \sim 3.6 \times 10^{14} \text{ m}^{-3}$ is immersed in magnetic field of 30 mT. Thus the plasma can be considered to be collisionless and Vlasov equation can be used, whereas the self-consistent fields are taken into account through Poisson's equation.

Fourier transforms of these equations are expressed

$$\begin{aligned} & i(k_{\perp} V_{Te} + k_{\perp} V_{Ti} \cos \theta - \omega) \tilde{f}_{\alpha}^{\omega} - \omega_{c\alpha} \frac{\partial \tilde{f}_{\alpha}^{\omega}}{\partial \theta} \\ & = -\frac{e q_{\alpha}}{m_{\alpha}} \tilde{E}_{\perp} \frac{\partial \tilde{f}_{\alpha}^{\omega}}{\partial v_{\perp}} + E_{\parallel} \cos \theta \frac{\partial \tilde{f}_{\alpha}^{\omega}}{\partial v_{\parallel}} - \frac{e q_{\alpha}}{m_{\alpha}} \frac{1}{(2\pi)^3} \int d\mathbf{w} \frac{d\omega_2}{d\mathbf{w}} \frac{d\omega_1}{d\mathbf{w}} \sum_{\mathbf{k}} \tilde{f}_{\alpha}^{\omega_1} \tilde{f}_{\alpha}^{\omega_2} \tilde{E}_{\perp}^{\omega} \cos \theta \\ & + E_{\parallel}^{\omega} \frac{\partial \tilde{f}_{\alpha}^{\omega}}{\partial v_{\parallel}} - E_{\parallel}^{\omega} \frac{\partial \tilde{f}_{\alpha}^{\omega}}{\partial v_{\parallel}} \frac{\sin \theta}{\omega} \frac{\partial \tilde{f}_{\alpha}^{\omega}}{\partial \theta} \dots \dots \dots (1) \\ & - k_{\perp}^2 \tilde{\Phi}^{\omega} = -\frac{|e|}{\epsilon_0} \int d\mathbf{v} \left[\tilde{f}_{\perp}^{\omega} - \tilde{f}_{\parallel}^{\omega} \right] d\mathbf{v} - k_{\perp}^2 \tilde{\Phi}_{\text{ext}}^{\omega} \dots \dots (2) \end{aligned}$$

$$\begin{aligned} \tilde{\Phi}_{\text{ext}}^{\omega}(r, z, t) &= \phi_1 g(r) \delta[k_{\perp}(z-z_1)] \cos \omega t \\ &+ \phi_2 g(r) \delta[k_{\perp}(z-z_2)] \cos \omega t \dots \dots (3) \end{aligned}$$

$$\tilde{E}^{\omega} = i \tilde{\mathcal{P}}_{\perp} \tilde{\Phi}^{\omega} \dots \dots \dots (4)$$

$$\begin{aligned} & \text{The first-order, (or linear) solution can be written as} \\ & \tilde{f}_{\alpha}^{\omega} = \tilde{f}_{\alpha}^{\omega} / D(k, \omega) \dots \dots \dots (5) \\ & D(k, \omega) = 1 + \sum_{\alpha} \frac{q_{\alpha}^2}{k_{\perp}^2} \left[1 + \frac{\omega_{c\alpha}}{k_{\perp} V_{T\alpha}} \right] \exp \left\{ - \frac{k_{\perp}^2}{k_{\perp}^2} \sum_{\alpha} \frac{\omega_{c\alpha}^2}{k_{\perp}^2} \frac{1}{V_{T\alpha}} \int_{-\infty}^{\infty} \frac{d\mathbf{v}}{v} \tilde{f}_{\alpha}^{\omega} \right\} \dots \dots \dots (6) \end{aligned}$$

Substituting Eq. (5), (6), into a non-linear part of Eq. (1), and integrate it with respect to θ , we get a second order distribution function $\tilde{f}_{\alpha}^{(2)}$ in the successive approximation. If we substitute this distribution into Poisson's equation, we can get a echo-potential in (\mathbf{r}, ω) space.

3. Calculating results : To obtain the solution, we use following assumptions. (i) We consider only a axial symmetric mode. (ii) Radial distribution of applied potential (grid potential) is uniform as $g(r)=1$. (iii) Landau-damping is not so strong, $(\omega/k) > 1$. (iv) For $\int_{-\infty}^{\infty} \tilde{f}_{\alpha}^{\omega} d\mathbf{v}$, Maxwellian distribution can be used. (v) Inequalities $\omega_{ce}^2 \gg \omega^2$, $\omega_{ce}^2 \gg k_{\perp}^2 V_{Te}^2$ are held. Under these conditions, we get finally the second order echo-potential as

$$\begin{aligned} & \tilde{\Phi}_{\text{ext}}^{(2)}(r, z, t) = \frac{1}{4\pi\epsilon_0} \frac{k_{\perp}^2}{k_{\perp}^2} \frac{k_{\perp}^2}{k_{\perp}^2} \frac{(1+\beta)(1+\beta^2)}{k_{\perp}^2} \frac{1}{k_{\perp}^2} \left\{ \frac{1}{4} \frac{V_{Te}^4}{\omega_{ce}^2 V_{Te}^2} + \frac{1}{2} \frac{V_{Te}^4}{\omega_{ce}^2 V_{Te}^2} \right\} \\ & \cdot \left\{ \tilde{f}_{\alpha}^{\omega} \tilde{f}_{\alpha}^{\omega} \cdot \tilde{J}_0(k_{\perp}^2 r^2) \cdot \left\{ 1 - \frac{1}{2} \frac{V_{Te}^2}{\omega_{ce}^2} (1+k_{\perp}^2) \omega^2 \right\} \right. \\ & \cdot \left. \sin \left\{ \frac{1}{2} (k_{\perp}^2 z - a) - \omega t \right\} \cdot \exp \left\{ -|a| z^* - |a| z_2 \right\} \dots \dots (7) \right. \end{aligned}$$

$$\begin{aligned} & W_{Te} = \frac{1}{2} m_e V_{Te}^2, \quad \tilde{f}_{\alpha}^{\omega} = \tilde{f}_{\alpha}^{\omega}, \quad \tilde{f}_{\alpha}^{\omega} = \tilde{f}_{\alpha}^{\omega}, \quad \Gamma^* = \frac{r^*}{l}, \quad z^* = \frac{z}{l} \\ & \Delta = \frac{1}{2} \frac{\sigma \tilde{f}_{\alpha}^{\omega} k_{\perp}^2}{(-\epsilon_0) m_e \tilde{f}_{\alpha}^{\omega}} \left(\frac{\omega_{ce}^2}{k_{\perp}^2 V_{Te}^2} \right) \exp \left\{ - \left(\frac{\omega_{ce}^2}{k_{\perp}^2 V_{Te}^2} \right)^2 \right\} \dots \dots (8) \end{aligned}$$

$$\Delta_{21} = \frac{1}{2} \frac{\sigma \tilde{f}_{\alpha}^{\omega} k_{\perp}^2}{(-\epsilon_0) m_e \tilde{f}_{\alpha}^{\omega}} \left\{ \frac{\omega_{ce}^2}{(k_{\perp}^2 + a) V_{Te}^2} \right\} \exp \left\{ - \left(\frac{\omega_{ce}^2}{(k_{\perp}^2 + a) V_{Te}^2} \right)^2 \right\} \dots \dots (9)$$

$$\tilde{E}_{\perp}^{\omega} = 1 - \frac{\omega_{ce}^2}{\omega^2}, \quad (\tilde{E}_{\parallel})_I = (\tilde{E}_{\parallel})_{\omega} \omega_I \text{ etc.}$$

$$\tilde{E}_{\perp}^{\omega} = 1 - \frac{\omega_{ce}^2}{\omega^2 - \omega_{ce}^2} - \frac{\omega r^2}{\omega^2 - \omega_{ce}^2}, \quad (\omega_{\perp}) = \omega_{\perp} - \omega_I$$

$$a = \sqrt{\left(\frac{\tilde{E}_{\perp}}{\tilde{E}_{\parallel}} \right) \omega_{ce} \omega_I}, \quad b = \sqrt{\left(\frac{\tilde{E}_{\perp}}{\tilde{E}_{\parallel}} \right) \omega_{ce} \omega_{\perp}}, \quad c = \sqrt{\left(\frac{\tilde{E}_{\perp}}{\tilde{E}_{\parallel}} \right) \omega_{ce} \omega_{\perp}}$$

where $\omega_{\perp} = \omega_{\perp} - \omega_I$ is the echo-frequency and the distance z^* is normalized by $l (=z_{\perp} - z_1)$, the distance between two exciting grids. A summation on k_{\perp} shows a mean with respect to an angle between the vectors \vec{k} and \vec{q} , and they related as

$$k_{\perp 1} = k_{\perp 2}$$

$$(b^2 - c^2) k_{\perp}^2 / 2b^2 - ac/b^2 + (b^2 - a^2) / 2b^2 k_{\perp} = \cos \phi$$

The effect of finite plasma-radius is taken into account by the restriction of q_{\perp} value in the integration with respect to q_{\perp} . The minimum value

of q_{\perp} is $\sim (\pi/D_p)$, where D_p is a plasma diameter, whereas the maximum value will be determined by Landau-damping. If $q_{\parallel} \sim \omega/v_{te}$ (v_{te} : electron thermal velocity), the wave will be strongly damped out. From the dispersion relation, it becomes

$$q_{\perp \max} \sim \sqrt{(-\epsilon_{\parallel}/\epsilon_{\perp})} \cdot q_{\parallel \max} = \sqrt{(-\epsilon_{\parallel}/\epsilon_{\perp})} \cdot (\omega/v_{te}).$$

4. Comparison with experiments : The experiments were performed with an apparatus previously reported [2]. The active source plasma is generated by non-resonant wave excitation by means of a waveguide-plasma-resonator arrangement [3] at 2.45 GHz.

The plasma streams into a test tube of 150 mm i.d. and 2.5 m length consisting of glass as well as stainless steel sections. The plasma is confined radially by the magnetic field and its diameter is determined by the quartz tube of the plasma generator. Figure 1 shows a typical line shape of the second-order echo at the time of $t = \pi/2\omega_m$ obtained by computer under the condition $T_e \sim 5.5$ eV, $B = 30$ mT, $n_e \sim 3.6 \times 10^{14} \text{ m}^{-3}$. Figure 2 gives the experimental curve together with the theoretical in the same condition and same scale of distance.

In Fig.2(a), upper trace gives a phase difference between test and reference signal in a linear scale showing a sawtoothed shape. Its lower end corresponds to -180° phase difference and the upper $+180^\circ$ difference. The lower trace of Fig.2(a) gives the amplitude A in a logarithmic scale. In Fig.3(a), the dependence of frequency ω_{\perp} on the maximum echo-amplitude is given, where the echo-frequency ω_m is fixed, and Fig.3(b) shows the corresponding experimental result. Figure 4 gives the spatial position of amplitude-maximum, as the frequency ω_{\perp} is varied. In this figure, the theoretical result is shown by thick line and open circles correspond to experiments.

In summary this theory of the lower-hybrid-echoes shows good agreement with the experiments.

This investigation is partly sponsored by the DFG within the Sonderforschungsbereich 162 "Plasmaphysik Bochum/Jülich". The authors thank Dr.B.Lammers for his contribution, Prof.H.Schlüter for encouragement. Thanks are also due to Mr.Kindermann for his assistance in the experimental apparatus.

5. References : [1]R.W.Gould, T.M.O'Neil and J.H. Malmberg, Phys.Rev.Lett.19 (1967) 216.

[2]H.D.Leppert et al., Phys.Lett.62A(1977)501.

[3]H.Beerwald, G. Böhm, B.Kampmann and B.Schweer, Phys.Lett.53A(1975)267.

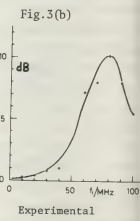
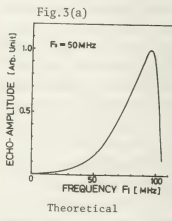
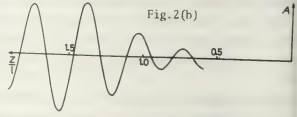
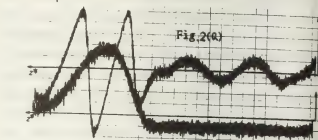
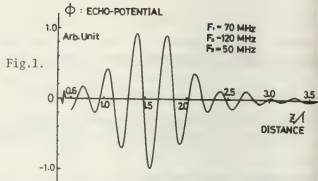
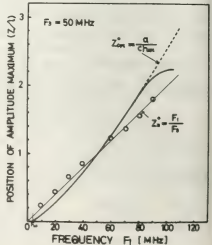


Fig.4



MAGNETIZED PLASMA PARAMETRIC RESONANCE IN NON-MONOCHROMATIC PUMP-WAVE

Yu. M. Aliev, O.M. Gradov and V. Stefan^{*}.

P.N. Lebedev Physical Institute, Academy of Sciences of the U.S.S.R., Moscow, U.S.S.R.

^{*}Boris Kidric Institute of Nuclear Sciences - Vinca, Beograd, Yugoslavia.

Parametric effects of monochromatic pump-wave interacting with plasma, in present time, are well studied [1]. On the other hand in all actual experiments dealing with an interaction of the radio or laser radiation with plasma we have signals duration of which is finite in time. Some aspects of the theory of parametric resonance in non-monochromatic pump-wave for non-magnetized plasma are given in [2-4]. In this work we represent some aspects of the finite-bandwidth parametric theory for magnetized plasma. It has been shown that the effect of finite-bandwidth leads to stabilization or facilitation of parametric growth of the turbulent noise.

We consider infinite, homogeneous, fully ionized, magnetized plasma interacting with the pump field

$$E(t) = E_0(t) \sin(\omega_0 t + \phi(t)) \quad (1)$$

where the amplitude and phase are assumed to be slow varying compared with carrier frequency ω_0 , which is chosen so to be near to the eigen-frequencies of high-frequency ($\omega_h \gg \omega_{pe}$) magnetized plasma oscillations. We also consider a set of rectangular impulses with duration τ , repetition period T and peak intensity E_0 . Note, that the conclusions presented below are valid for cases of any shape of $E_0(t)$ and $\phi(t)$ except the demand for the periodicity of $E_0(t)$ and $\phi(t)$ with the period T that must be satisfied.

Let us consider the amplitude-modulated ($\phi(t) = \phi_0$) pump wave with frequency ω_0 so that $\omega_0 \gg \omega_{pe}$ is valid in the case when the oscillation velocity of electrons is significantly less than the thermal velocity V_{Te} . In the case when the frequency of the pulse repetition $\Omega = 2\pi/T$ is much higher than all low eigen-frequencies of the magnetized plasma oscillation ($\Omega \gg \omega_s$) in the case of periodical ($\Delta > 0$) and aperiodical ($\Delta < 0, \Delta = \omega_s - \omega_h(\xi)$) instability the

following expression for the threshold is obtained

$$\frac{E_{THR}^2}{4\pi n_e T_e} = \frac{T^2}{\tau^2} \Lambda, \quad \Lambda = \frac{E_{THR, MON}^2}{4\pi n_e T_e} \quad (2)$$

Here, $E_{THR, MON}$ is the threshold for the case of monochromatic pump-wave. From (2) it is evident that the existence of the discrete external pump-wave leads to the stabilization of plasma - the increasing of the threshold $\frac{T}{\tau}$ times is apparent. Note that the wave numbers of excited oscillations are the same as in the case of monochromatic pump-wave.

With decreasing of the pulse repetition frequency the possibility for resonance $\Delta^2 \sim n^2 \Omega^2$ can be encountered which lead, in both periodical and aperiodical case, to the ion-sound instabilities. In this case the following expression for the threshold is obtained.

$$\frac{(|B_n^-|^2 + |B_n^+|^2)_{THR}}{k^2 v_{De}^2} = \frac{1}{2} \Lambda \quad (3)$$

Here:

$$B_n^\pm = \frac{\sin n\pi x}{n\pi} \eta(\omega) \exp\{-inx \pm i[\phi_0 + \phi_s]\}, \quad x = \frac{\omega t}{T}$$

$$a_0 = a_0(0 \leq t \leq \tau); \quad \phi_0 = \phi_0(0 \leq t \leq \tau)$$

The remaining notations are conventional. The wave numbers of excited oscillations are defined from $\Delta \pm n\Omega = \pm \omega_s$ in the decay case ($\tilde{\nu} < \omega_s$) or $\Delta \pm n\Omega = \pm \tilde{\nu}/\sqrt{3}$ in the nondecay case ($\tilde{\nu} > \omega_s$). The minimum threshold value from (3) is reached if $n = 1$ and $2\tau = T$. In the meantime for the positive mismatching ($\Delta > 0$) the threshold value (3) is higher than the value obtained by (2). It means that in the domain considered $\Omega \gg \omega_s$ for $\Delta > 0$ the threshold value is defined by (2) and the wave number of oscillations satisfies $\Delta = \omega_s$ in the decay case ($\omega_s > \tilde{\nu}$) or $\Delta = \tilde{\nu}/\sqrt{3}$ in the nondecay

($\omega_s \ll \tilde{\gamma}$) case. In the same time for the negative mismatching ($\Delta < 0$) the resonances $\Delta = -N\Omega$ make possible excitations of ion-sound oscillations with the threshold value given by (3) which appears to be less than the corresponding value in the case of aperiodical instabilities $\Delta = \tilde{\gamma}$.

With further decrease in the pulse repetition frequency a situation when $N\Omega \sim 2\omega_s$ can be reached (N - odd number). In the nondecay case when $\tilde{\gamma} \gg \omega_s$ is satisfied an excitation of two ion-sound modes can take place, with the threshold and increment, respectively.

$$\frac{E_{THR}^2}{4\tilde{\gamma}N\epsilon_0} = \frac{4\tilde{\gamma}\gamma_s}{\omega_h\omega_s} \frac{1}{(\tilde{\omega} - \epsilon_0)\sin\epsilon} \quad (4)$$

$$\gamma_s = \frac{\omega_s\omega_h}{4\tilde{\gamma}k^2\epsilon_0^2} \left| \sum_{m=-\infty}^{\infty} b_m b_{m-n} \right| - \gamma_s \quad (5)$$

From the expression (4) it is evident that the threshold value of the non-decay instabilities is significantly less than the corresponding value in the case of monochromatic pump-wave. The optimum value for the pulse duration, in presence of which the threshold value (4) reaches minimum, is defined from

$$\tan \epsilon_0 = \tilde{\omega} - \epsilon_0, \quad \epsilon_0 = \frac{\tilde{\omega}\tau}{T} \quad (6)$$

The wave number appearing in the right-hand side of (4) is fixed by $\Delta = \pm\tilde{\gamma}$. From here it is evident that in the case of nonmonochromatic pump-wave the decay instabilities, which are absent in the case of monochromatic pump-wave, are possible if $\Delta < 0$ is satisfied.

REFERENCES

- /1/ V.P.Silin, "Parametric Effects of High Power Radiation on Plasma", Nauka, Moscow, 1973, Chapter 3
- /2/ V.V.Pustovalov, V.P.Silin, A.A.Chernikov, Quantum Electronics (1978) 5, No 9
- /3/ Yu.M.Aliev, O.M.Gradov, D.Sünder, Beiträge aus der Plasma Physik, B.17, H.6 (1977) 353
- /4/ Yu.M.Aliev, A.A.Chernikov, O.M.Gradov, V.V.Pustovalov, V.P.Silin, V.Stefan, Eight European Conference on Controlled Fusion and Plasma Physics, Contributed papers, v.1 (1977) 146, Prague

DISPERSION CHARACTERISTICS OF PLASMA WAVE-PACKETS

R.J. Vidmar and F.W. Crawford.

Institute for Plasma Research, Stanford University, Stanford, California 94305 U.S.A.

We shall consider propagation of a wave-packet through an infinite homogeneous plasma which may be lossless, absorptive or unstable, so that the energy of the wave-packet may be conserved, dissipated, or increased as it propagates.

In 1914, Brillouin and Sommerfeld [1] determined the evolving shape of a wave-packet, and predicted the occurrence of precursors that outrun the body of the packet (see Fig. 1). The saddle-point methods they introduced have since been refined and widely used [2]. Concepts such as phase velocity, group velocity and energy velocity emerge, and are usually understood by reference to dispersion (Brillouin) diagrams showing the frequency variation (ω , real) with wavenumber (k , real). Difficulties arise for absorptive or unstable media, for which group velocity may be complex or infinite. We suggest that in such cases an observational dispersion diagram is useful, effectively describing the results of complex ω, k measurements on wave-packets. We shall use a consistent definition of group velocity to establish the form of this dispersion relation, and its dependence on the source exciting the wave-packets.

We consider two sources, both delta-functions in the direction of propagation, z : a delta-function source in time, $S_A(t, z) = \delta(z)\delta(t)$, and the switch-on of a continuous wave, $S_C(t, z) = \delta(z)H(t)\sin(\omega_0 t)$. Here, δ is a delta-function, H is a Heaviside step-function, and ω_0 is a constant frequency. These idealized sources differ by the presence (S_C) or absence (S_A) of a pole in the transform of S . They are consequently representative of sources which are either switched on and maintained indefinitely, or are pulsed.

THEORY

Although we are interested in plasmas, the wave equation may be left in general form to accommodate any medium and variable, g , that exhibits dispersive propagation. For linear propagation in one dimension we have [3],

$$P(p_{m,n}(t, z) \frac{d^{m+n}}{dt^m dz^n}) \xi(t, z) = A(a_{i,j}(t, z) \frac{d^{i+j}}{dt^i dz^j}) S(t, z), \quad (1)$$

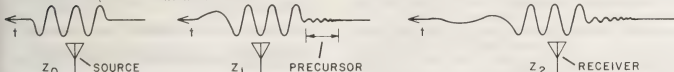
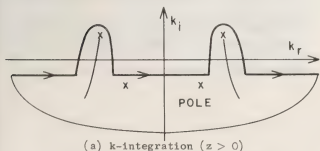
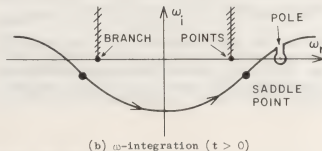
FIG. 1. DISPERSIVE PROPAGATION (Wave-packet passing fixed points, $z_0 < z_1 < z_2$)(a) k -integration ($z > 0$)(b) ω -integration ($t > 0$)

FIG. 2. INTEGRATION CONTOURS

where the coefficients $p_{m,n}$, $a_{i,j}$ describe the properties of the medium and its excitation by the source, S .

We define a Laplace transform in time, and a Fourier transform in space,

$$\xi(t, z) = \int_{-\infty-i\sigma}^{\infty-i\sigma} d\omega \int_{-\infty}^{\infty} dk \frac{\xi(\omega, k)}{(2\pi)^2} \exp[i(\omega t - kz)],$$

$$\xi(\omega, k) = \int_0^{\infty} dt \int_{-\infty}^{\infty} dz \xi(t, z) \exp[-i(\omega t - kz)]. \quad (2)$$

By assuming an initially quiescent medium, and restricting $a_{i,j}$ to constant coefficients, (1) may be transformed to

$$D(\omega, k) \xi(\omega, k) = A(\omega, k) S(\omega, k), \quad (3)$$

where $D(\omega, k)$ is the dispersion relation

To invert $\xi(\omega, k)$, the k -integration is evaluated by use of the residue theorem, taking account of the poles defined by $D(\omega, k) = 0$. Poles in the upper half-plane [see Fig. 2(a)] are included in the contour if they originate in the lower half-plane for values of ω consistent with the ω -integration along a Bromwich contour $\omega = \omega_r - i\sigma$. For further discussion, see [4].

The remaining inverse transform is of the form

$$\xi(\omega, z) = \frac{1}{2\pi} \int_{-\infty-i\sigma}^{\infty-i\sigma} d\omega F(\omega, k(\omega)) \exp[i(\omega t - k(\omega)z)], \quad (4)$$

where $k(\omega)$ is determined from $D(\omega, k) = 0$, and F is the sum of k -integral residues multiplied by the ω -transform of the source, which may contain a pole. Branch-points of function F must be avoided in the

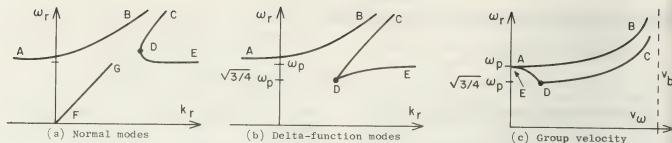


FIG. 3. BEAM-PLASMA DISPERSION DIAGRAMS AND GROUP VELOCITY

ω -plane [see Fig. 2(b)]. They result from factors in the dispersion relation such as $k^2 = a_0$ or $k^2 = d^2(\omega^2 - \omega_{\alpha}^2)$, for which branch-points occur at $\omega = 0$ and $\omega = \pm \omega_{\alpha}$, respectively.

SADDLE-POINT METHOD

We may approximate (4) by expanding the integrand about the extrema of the exponential term. The saddle-points of (4) are then required to satisfy simultaneously

$$D(\omega, k) = 0, \quad \frac{dk}{d\omega} \bigg|_{\omega_s} = \frac{1}{v} = \frac{t}{z}, \quad (5)$$

where $dk/d\omega$ must be real and positive since the contours in Fig. 2 are defined for t and z real and positive. The saddle-point, ω_s , is a function of t and z , and corresponds to the velocity, v_{ω} .

The approximation of (4) has two forms which depend on the presence or absence of a pole in F , i.e. on the nature of the source. If F is analytic, the isolated saddle-point method can be used for large z [2]. For S_A , we then have

$$\xi(t, z) \sim \sum_{\omega_s} \frac{G(\omega_s, k(\omega_s))}{z^{1/2}} \exp[i(\omega_s t - k(\omega_s)z)], \quad (6)$$

where G is a smooth function. This approximation for ξ is usually valid when z exceeds about ten wavelengths corresponding to $k(\omega_s)$.

The pole from \tilde{S}_C with $\sin \omega_0 t = \text{Im} \exp(i\omega_0 t)$ requires the simple pole singularity method [2],

$$\xi(t, z) \sim \text{Im} \sum_{\omega_s} \left\{ U(\omega_s) \exp[i(\omega_0 t - k(\omega_0)z)] \text{erfc}(\pm ib) + \frac{T(\omega_s)}{z^{1/2}} \exp[i(\omega_s t - k(\omega_s)z)] \right\}, \quad (7)$$

where $b = \{i[\omega_s - \omega_0]t - [k(\omega_s) - k(\omega_0)]z\}^{1/2}$, U and T are smooth functions, erfc is the complementary error function, and the \pm sign is chosen so that $\text{erfc} \sim 0$ for non-causal values of t and z . Precursors (see Fig. 1) are described by the $T(\omega_s)$ terms. As waves of lower v_{ω} arrive from the source, a $U(\omega_s)$ term in (7) dominates the response, after the phase of b changes sign. This phase change occurs as the real part of $\omega_s (= \omega_r + i\omega_i)$ approaches ω_0 ; erfc changes in magnitude from ~ 0 to ~ 2 . The main wave train of a source like S_C propagates with the velocity, v_{ω} , corresponding to $\text{Re}(\omega_s) = \omega_0$. Brillouin termed this "signal velocity".

DISCUSSION

The dispersion characteristics corresponding to (6) and (7) are both of the form $D(\omega, k) = 0$, but with $v = v_s$ for sources without poles (delta-function modes) and with ω real for sources with poles (normal modes). The principal distinction

between these two results is that $\omega_0 = 0$ for normal modes, but that we may have $\omega_0 \neq 0$ for delta-function excitation. For stable media, the two modes are identical. In strongly absorbing, or highly unstable media, the difference between $k(\omega_0)$ and $k(\omega_s)$ may become significant.

As an example, consider an unstable system consisting of a monoenergetic electron beam and a plasma, for which

$$D(\omega, k) = 1 - \frac{\omega_p^2}{\omega^2} - \frac{\omega_b^2}{(\omega - kv_b)^2} = 0. \quad (8)$$

Here, ω_p is the plasma frequency, ω_b is the plasma frequency of the beam, and v_b is the beam velocity. The dispersion diagrams of Figs. 3(a) and (b), for normal modes and delta-function excitation, are similar for the stable branch from A to B, but differ substantially for the branch from C to E: in the normal mode diagram, the group velocity may apparently be negative or even infinite. The delta-function modes also differ substantially below the plasma frequency, with the branch from F to G in the normal mode diagram disappearing. Values of v_{ω} corresponding to the two modes of excitation are plotted in Fig. 3(c) for comparison.

An observational dispersion diagram such as Fig. 3(b), for a pole-free source, has the advantage over a normal mode diagram such as Fig. 3(a) that it illustrates the causal group velocities, frequencies and wavenumbers that would actually be observed. Since the velocity v_{ω} of a spectral component at frequency ω has been defined as real and positive, it corresponds to the usual definition of group velocity in a stable medium, and extends that concept consistently to absorptive and unstable media. It is anticipated that the observational approach and dispersion diagram will be useful in the study of instabilities in inhomogeneous plasmas, and in ionospheric ray tracing.

This work was supported by the NASA and the NSF. The authors have benefited from discussions with Dr. K. J. Harker.

REFERENCES

- [1] Brillouin, L., Wave Propagation and Group Velocity, Academic Press (1960).
- [2] Felsen, L. B. and Marcuvitz, N., Radiation and Scattering of Waves, Prentice-Hall (1973).
- [3] Whitham, G. B., Linear and Nonlinear Waves, Wiley (1974).
- [4] Briggs, R. J., Electron-Stream Interactions with Plasmas, MIT Press (1964).

MODULATIONAL INSTABILITY AND EVOLUTION OF NON-UNIFORM LANGMUIR FIELDS IN PLASMAS

T.A. Davydova and K.P. Shamrai.

Institute for Nuclear Research, Kiev, U.S.S.R.

It has recently been observed in a set of experiments that the interaction of h.f. fields with plasmas results in a formation of cavitons, i.e. density cavities with trapped field. To interpret these experiments one adopts as a rule a modulational instability of a uniform field, which is supposed to produce cavitons in the non-linear stage. But in a majority of experiments the pump fields are essentially non-uniform through inhomogeneity and finite size of a plasma, non-uniformity of external sources of field excitation etc. Therefore it seems necessary to develop a theory of modulational instability of non-uniform fields, which differs from that of uniform field. Moreover, to investigate a possibility of caviton formation and to determine a characteristic time of a process one must examine initial stage of plasma evolution under the action of non-uniform pump field.

The evolution of some non-uniform fields was a subject of a set of numerical simulations. The present report deals with an analytic investigation of 1-dimensional initial evolution of intensive non-uniform Langmuir field in two typical cases:

- (i) localized pump field (isolated peak)
- and (ii) standing wave.

Let in the initial moment $t=0$ Langmuir

pump field $E_0 = \tilde{E}_0(x) \cos(\omega_0 t)$ is switched on "instantaneously" in a plasma. A ponderomotive force drives in plasma the coupled density and field perturbations. We shall examine a temporal evolution of this process at a linear stage, i.e. neglecting the coupling of perturbations and their influence on a pump. We use linearized system of equations by Zakharov ^{1/}.

$$\left[\frac{\partial^2}{\partial t^2} + \frac{9}{4} \omega_p^2 \tilde{r}_D^4 \left(\frac{\partial^2}{\partial x^2} + \frac{\omega_0^2 - \omega_p^2}{3 v_T^2} \right)^2 \right] \tilde{E} = \frac{3}{4} \omega_p^2 \tilde{r}_D^2 \left(\frac{\partial^2}{\partial x^2} + \frac{\omega_0^2 - \omega_p^2}{3 v_T^2} \right) \frac{\delta n}{n_0} \tilde{E}_0, \quad (1)$$

$$\left(\frac{\partial^2}{\partial t^2} - c_s^2 \frac{\partial^2}{\partial x^2} \right) \delta n = \frac{1}{8 \pi M} \frac{\partial^2}{\partial x^2} (\tilde{E}_0 \tilde{E} + \frac{1}{2} \tilde{E}_0^2), \quad (2)$$

where $\omega_p^2 = 4 \pi e^2 n_0 / m$, $v_T^2 = T_e / m$, $\tilde{r}_D^2 = v_T^2 / \omega_p^2$, $c_s^2 = T_e / M$, δn is a density perturbation and $\tilde{E}(x, t)$ is a real amplitude of field perturbation slightly depending on time.

The absolute instability exists if there are spatially bounded solutions of uniform system (1), (2), which depend on time as $\exp(-i \Omega t)$ and $\text{Im} \Omega > 0$. The threshold intensity for a standing pump wave ($\tilde{E}_0 = \tilde{E}_{\max} \sin(k_0 x)$) is determined from the equations

$$\mu_n, \nu_n = 1 + \frac{1}{2} a^2, \quad a^2 = \frac{W_{\max}}{k_0^2 \tilde{r}_D^2}, \quad W_{\max} = \frac{\tilde{E}_{\max}^2}{24 \pi n_0 T_e}$$

where $\mu_n(\frac{a^2}{2})$, $\nu_n(\frac{a^2}{2})$ ($n=2, 3, \dots$) are the eigenvalues of Mathieu equation for functions se_n and ce_n . The threshold is minimal for eigenmodes $se_2(a^2 \approx 6)$ and $ce_2(a^2 \approx 9)$.

For a localized pump field ($\tilde{C}_0 \rightarrow 0$ as $x \rightarrow \pm\infty$) the instability threshold is of order $a^2 \approx 1/2$. Here $a^2 = W_{\max} \Delta^2 / r_D^2$, where Δ is a scale of field localization region. There is a finite discrete spectrum of unstable modes both in a standing wave field and in a localized one. A number of them is determined from inequality $2n+1 < a$ (n is a whole number). The instability growth rate peaks for a ground mode and decreases monotonically as n increases.

To investigate a temporal evolution of field and density perturbations we complete system (1), (2) by initial conditions

$$\delta n(t=0) = \delta n_t(t=0) = \mathcal{E}(t=0) = \mathcal{E}_t(t=0) = 0.$$

Then it is easy to obtain the solution for small time $t < \gamma_{\max}^{-1}$. Density perturbation $\delta n / n_0 \approx (3/4) c_s^2 W_{\max} t^2$ is negative near the pump peaks and decreases in time. A ponderomotive influence of a pump field on a plasma gives rise to density cavities. Their scale is initially of order Δ (π/k_0 for a standing wave) and does not depend on pump power. At the same time the absolute value of field perturbation grows as $|\mathcal{E}| \propto t^4$.

To investigate evolution for $t > \gamma_{\max}^{-1}$ we suppose the threshold to be strongly exceeded, $W_{\max} \gg r_D^2 / \Delta^2 > m/M$ (for a standing wave here and below one must substitute Δ^{-1} for k_0). In that case $\gamma_{\max} \approx \omega_p \sqrt{W_{\max} m/M}$ and density dynamics is described by equation γ^3

$$\left(\frac{\partial^2}{\partial t^2} - c_s^2 \frac{\partial^2}{\partial x^2} - \omega_p^2 \frac{m}{M} W \right) \frac{\delta n}{n_0} = \frac{3}{2} c_s^2 W''$$

with initial conditions $\delta n(t=0) = \delta n_t(t=0) = 0$. It turned out that for $t > \gamma_{\max}^{-1}$ the excitation of a modulational instability near pump peaks results in density cavities con-

traction and deepening with growth rate

$$\gamma_{\max}^{-1} \frac{\delta n}{n_0} \approx \frac{3}{4 W_{\max}} \frac{\exp(\gamma_{\max} t)}{(\cosh(c_s t / \Delta))^{1/2}} \times \exp\left(-\frac{a}{2} \frac{x^2}{\Delta^2} \tanh \frac{c_s t}{\Delta}\right) W''\left(\frac{x}{\Delta \cosh \frac{c_s t}{\Delta}}\right).$$

The field amplitude in the centre of caviton increases with the same rate. At linear stage the density cavities scale down up to the width of the localization of the ground mode, Δ/\sqrt{a} . The duration of the contraction is determined by the most inertial process, i.e. by sound irradiation out of caviton, $t \sim \Delta/c_s$.

If the instability threshold is weakly exceeded there are few unstable modes and density profile is cusped strongly as $t \rightarrow \gamma_{\max}^{-1}$. For a localized field redundant density is squeezed out of the pump peak domain and is irradiated to infinity as sound compression waves with velocity c_s

$$\frac{\delta n}{n_0} \approx \frac{3}{2} \left\{ \frac{1}{2} [W(x - c_s t) + W(x + c_s t)] - W(x) \right\}$$

($|x| > \Delta$). For standing wave it accumulates near nodal points. Linear approximation breaks at $t \sim \gamma_{\max}^{-1} \ln a \gg \gamma_{\max}^{-1}$.

In conclusion, a linear stage of the evolution of non-uniform Langmuir pump field results in a formation near pump peaks of contracting and deepening density cavities with trapped field (cavitons).

References.

1. Zakharov V.E. (1972) Zh. eksp. teor. Fiz. 62, 1745 (Sov. Phys. JETP 35, 908).
2. Davydova T.A., Shamrai K.P. (1977) Fizika Plazmy (Sov. J. Plasma Phys.) 2, 591.
3. Davydova T.A., Shamrai K.P. (1978) Preprint Inst. Theor. Phys. 77-140P, Kiev (in Rus.).

WKB MODEL OF THE COLLAPSE OF LANGMUIR WAVES

B.N. Breizman.

Institute of Nuclear Physics, Novosibirsk, U.S.S.R.

The hypothesis on the collapse of Langmuir waves has been suggested by W.E. Zakharov in 1972 /1/. Soon afterwards, a number of attempts have been made to formulate the conditions under which the collapse takes place and to describe qualitatively its dynamics /2-5/. The basic equations in papers /1-5/ were the equations for the electric field amplitude and for the low frequency perturbation of plasma density. With such an approach the length of Langmuir wave is usually assumed to be comparable with the size of a potential well wherein the waves are trapped, i.e. it is implied that the number of eigenmodes in a well is small. This situation is very complicated for analytical study since one has to find the exact "wave functions" of Langmuir oscillations. In order to avoid this difficulty, we shall consider below a well which is wide enough and contains many eigenmodes so that WKB approximation is valid and the oscillations can be described by Liouville equation /6,7/:

$$\frac{\partial N}{\partial t} + 3\kappa \frac{\partial N}{\partial \vec{r}} - \frac{1}{2} \frac{\partial n}{\partial \vec{r}} \frac{\partial N}{\partial \kappa} = 0 \quad (1)$$

Here, the inverse plasma frequency is chosen as a unit of time, the length and the wavevector are normalized to r_D and r_D^{-1} , respectively, n is the perturbation of plasma density normalized to the unperturbed value.

In addition to eq.(1), we make use of linearized equations of hydrodynamics, which include the pressure of plasmons:

$$\frac{\partial n}{\partial t} + \text{div } \vec{V} = 0 \quad (2)$$

$$M \frac{\partial \vec{V}}{\partial t} = - \text{grad} \left(n + \int N d\vec{k} \right) \quad (3)$$

The ion velocity \vec{V} is measured here in the units of electron thermal velocity, and the ion mass - in the units of electron mass.

From the physical point of view the consideration of the collapse problem in the framework of eqs.(1)-(3) seems to be quite natural since the qualitative arguments for the two- or three-dimensional collapse and against the one-dimensional one /8/ are completely applicable to the WKB case. It should be emphasized that these arguments are not associated with whatever assumptions with respect to phase correlation. Therefore, they are valid, in particular, in the case of random phases.

The system (1)-(3) has three integrals: the number of plasmons, total momentum and energy are conserved. This system gives also the following relationship (virial theorem):

$$\begin{aligned} \frac{\partial^2}{\partial t^2} \iint \frac{r^2}{2} N d\vec{r} d\vec{k} + \frac{\partial}{\partial t} \int M n(\vec{r}) d\vec{r} = \\ = 3 \int d\vec{r} \left[\frac{n^2 + M V^2}{2} + \int (2\kappa^2 + n) N d\vec{k} \right] \end{aligned} \quad (4)$$

We shall apply it to the slow (subsonic) collapse for which the density perturbation "follows" the pressure of plasmons, i.e. $n \approx - \int N d\vec{k}$ and $\vec{V} \rightarrow 0$. With this simplifications we get

$$\frac{\partial^2}{\partial t^2} \iint N d\vec{r} d\vec{k} < 9 \int d\vec{r} \left(3 \int \kappa^2 N d\vec{k} - \frac{n^2}{2} \right) \equiv Q \quad (5)$$

The right-hand side here is constant because of the conservation of energy. Inequality (5) shows that any distribution of plasmons with negative value of Q becomes singular within a finite time. This result is similar to Talanov's theorem for the self-focusing /9/. For the spherical-symmetric problem it has been prov-

ed previously without WKB approximation /1/. In WKB case it remains true even in the absence of symmetry.

Let us now consider the supersonic collapse. It is possible to get the analytical solution of the system (1)-(3) for this case. We shall demonstrate it by the example of two-dimensional problem with axisymmetric distribution of plasma density*. In addition, we assume that the characteristic time of collapse is long as compared to the period of plasmon motion in the potential well. Then due to fast phase mixing, the spectrum of plasmons turns out to be only dependent on the angular momentum $M = K\varphi r$ and the radial adiabatic invariant

$$I = \int \left(\frac{E-n}{3} - \frac{m^2}{r^2} \right)^{1/2} dr$$

(E is the energy of plasmon). A form of the function $N(M; I)$ is determined by initial conditions.

It will be seen from what follows that for some initial states the behavior of density $n(r; t)$ is self-similar:

$$n = -(t_0 - t)^{-2} f(\rho); \quad \rho \equiv r/(t_0 - t) \quad (6)$$

This self-similarity exists not only in WKB problem of collapse but also in the exact one (see, e.g., /4/). It is important to note that if the relation (6) holds, then the boundary which separates the trapped plasmons from the untrapped ones on the plane of variables M and I , does not depend on time. Therefore, one can choose the function $N(M; I)$ being equal to some constant N_0 for trapped plasmons and to zero for untrapped ones. It is now easy to calculate the pressure of plasmons

$$\int N d\vec{k} = -\pi n \frac{N_0}{3}$$

and to derive the following equation for $f(\rho)$ from the system (2)-(3):

$$M \frac{\partial^2}{\partial \rho^2} (\rho^3 f) + \left(\frac{\pi}{3} N_0 - 1 \right) \frac{\partial}{\partial \rho} \rho \frac{\partial f}{\partial \rho} = 0 \quad (7)$$

* Similar solutions can be found for the three-dimensional spherical-symmetric case.

Whence,

$$f(\rho) = \left(\frac{M \rho^2}{\frac{\pi N_0}{3} - 1} + 1 \right)^{-3/2} \quad (8)$$

The second solution of eq.(7) is omitted since it gives the divergent space integral of n .

In the case of high enough intensity of Langmuir waves ($N_0 > 3/\pi$) formula (8) describes the collapse of initial distribution. It is easy to see that the applicability conditions for WKB approximation and for the conservation of adiabatic invariant do hold during the whole process of collapse provided they are fulfilled at the initial moment.

References:

- /1/ V.E.Zakharov. Zh. Eksp. Teor. Fiz. 62 1745, 1972.
- /2/ L.M.Degtyarev, V.E.Zakharov. Preprint N°106 Inst. of Appl. Math., Moscow, 1974.
- /3/ A.A.Galeev, P.Z.Sagdeev, Yu.S.Sigov, V.D.Shapiro, V.I.Shevchenko. Fiz. Plasmy 1, 10, 1975.
- /4/ V.E.Zakharov, A.F.Mastriyukov, V.S.Synakh. Fiz. Plasmy 1, 614, 1975.
- /5/ L.M.Degtyarev, V.E.Zakharov, L.I.Rudakov. Zh. Eksp. Teor. Fiz. 68, 115, 1975.
- /6/ A.A.Vedenov, L.I.Rudakov. Dokl. Akad. Nauk SSSR 159, 767, 1964.
- /7/ A.A.Vedenov, A.V.Gordeev, L.I.Rudakov. Plasma Phys. 2, 719, 1967.
- /8/ A.A.Galeev, P.Z.Sagdeev, V.D.Shapiro, V.I.Shevchenko. Zh. Eksp. Teor. Fiz. 73, 1352, 1977.
- /9/ S.N.Vlasov, V.A.Petrishchev, V.I.Talanov. Izv. Vuzov Radiofiz. 14, 1353, 1971.

INTERACTION OF THE INTENSE MICROWAVES WITH A FLOW OF LOW TEMPERATURE PLASMA The experiment)

N.A. Armand, S.A. Rogashkov and E.G. Shustin.

Institute of Radioengineering and Electronics, Academy of Sciences, Moscow, U.S.S.R.

The experimental study of effects arising in a course of passing a focused beam of W band microwaves across the argon plasma stream flowing out of an arc plasmatron into rarefied gas through a supersonic nozzle have been carried out. The specific parameter determining a level of the nonlinearity of plasma E/E_p $\sim 1/1$ under the experimental conditions reached the value $5+10$. The parameters of undisturbed plasma in the region of irradiation were: concentration of electrons $n_p = 10^{11}+10^{13} \text{ cm}^{-3}$, electron temperature $T_e = 0,1+0,3 \text{ eV}$, neutral gas density $N_m = 10^{14}+10^{16} \text{ cm}^{-3}$, velocity of flow $V_0 = (1+2) \cdot 10^4 \text{ cm} \cdot \text{sec}^{-1}$.

The diagnostics of plasma was carried out by means of a microwave interferometer with enhanced resolution $/2/$. The space-time distribution of a microwave field behind a plasma layer was studied with a mobile receiving antenna to determine the effects of self-action of the wave passed through plasma.

The pulse of the microwave signal of 1msec duration at frequency f_1 was mixing with the test signal of 2msec duration at the displaced frequency f_2 ($\Delta f = 0,2 \text{ gcps}$, $P_2/P_1 \sim 10^{-4}$) in a waveguide line loaded to the horn-lens antenna. The test pulse passed ahead the powerful pulse over 0,5 msec. In plasma region the microwave field represents the almost parallel beam with half-width 3cm and intensity up to 60V/cm. The intensity measurements of the test signal behind a plasma layer have made easy discrimination of the nonlinear effects against a background of the effects related to the nonhomogeneity and nonstationarity of a plasma stream and

made it possible to appreciate a character of the relaxation of the plasma disturbance caused a powerful signal.

The time-dependencies of the plasma density on the axis traverse of the microwave beam and plasma stream and the amplitude of the passed (on the frequency f_2) wave as a function of gas expenditure by plasmatron and on gas pressure in a vacuum vessel, the space-time distributions of the plasma density and wave amplitude behind plasma flow at various power levels of the microwave beam were studied.

The oscillograms (Fig.1) show a time dependence of the amplitude of the passing signal and electron concentration in a center of the microwave beam on the plasma axis in regimes in which the nonlinear interaction of a wave with plasma is observed. The regimes with nonlinear growth of the intensity of a signal on the axis of a beam (Fig.1a) are observed in the range $n_p > 0,2 \cdot 10^{12} \text{ cm}^{-3}$ and $0,12 < p < 0,25$ torr. Specific time of establishing the stationary state is varied from 1msec to 0,1+0,2msec with the increasing p and n_p . Over this period of time the level of the test beam passed through plasma becomes 2+8 times as high as the undisturbed one. As seen from the oscillograms the influence of a powerful microwave beam on plasma in these regimes leads to essential decreasing the density of plasma on the axis of a beam; this decreasing reaches 50-80% from the undisturbed density and seems to be the determining factor in the process of self-action of a powerful wave. With the increasing n_p and p the growth of intensity during a time of a powerful pulse is changed by its decreas-

ing and further by nonmonotonic time dependence. As a rule, the initial fall is changed by the more weak increasing (Fig. 1b).

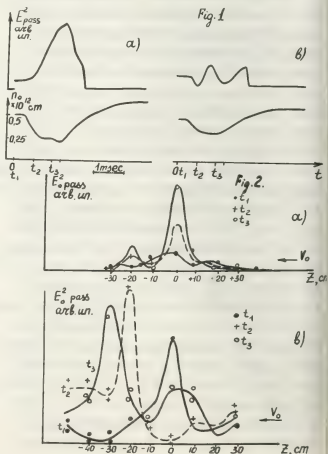
In Fig.2 are shown the space profiles of the passed wave intensity. The profiles are plotted for various periods of time after switching the powerful pulse on. The profiles of Fig.2a correspond to the regime in which the oscillograms (in Fig.1a) are recorded. In this regime narrowing the basic lobe of the directivity diagram of the antenna in the nonlinear regime (selffocusing) as well as the increasing the total power passed through plasma ("transparency enhancement" of plasma) takes place. The effect in this regime has pronounced threshold character: the decrease of power 2 times completely takes off the observed effect.

The profiles shown in Fig.2b correspond to the conditions when on the axis of a beam one can observe the fast decrease of the signal intensity in time of action of the powerful pulse or else see the oscillations of this intensity (Fig. 1b). As seen from the plotted profiles the displacement of the maximum intensity region takes place, i.e. the turn of a microwave beam in the direction of moving the plasma, i.e. the nonlinear refraction. The nonmonotonic dependence of the intensity on the axis of a microwave beam on time, as seen from this Fig. is caused by lamination of a microwave beam. The decrease of power of the basic beam leads to decreasing the velocity of the beam turn and decreasing the displacement of the region with maximum intensity from the undisturbed state. The mechanisms of the observed phenomena of the microwave-beam action on the characteristics of the test beam passed plasma may be satisfied from the analysis of the space distribution of plasma density disturbed by a powerful pulse. As seen from the interferograms taken readings in different regions of plasma flow near the axis of a microwave beam under influence of a powerful wave, the density distribution "dip" is formed.

This "dip" is smoothly lowered down on a stream and turned more or less sharply into a "hump" on moving the sensor of an interferometer up on a stream to the plasma injector. So the asymmetric nonuniformity of the plasma density distribution across the direction of the microwave beam propagation is developed. Just as the depth of disturbance so its asymmetry depend on the relations between the gas pressure, density of undisturbed plasma and stream velocity. The self-focusing of wave or the nonlinear refraction in the wave caused nonuniformity are observed on dependence on the depth of a "dip" and steepness of incline of the plasma density distribution.

REFERENCES:

1. A.V. Gurevich, A.B. Shvartsburg. The nonlinear theory of radiowave propagation in ionosphere, M., 1973.
2. E.G. Shustin, A.A. Lisitskaya. The microwave interferometer with high resolution for the study of plasma in a microwave field. Rep. on All-Union conf. on low temperature plasma physics, Kiev, 1979.



INTERACTION BETWEEN SOLITARY STRUCTURES IN A MAGNETIZED, PLASMA-LOADED WAVEGUIDE

J.P. Lynov, P. Michelsen, H.L. Pécseli and J. Juul Rasmussen.

Association EURATOM - Risø National Laboratory, DK-4000 Roskilde, Denmark.

Introduction: Two different types of non-linear electron pulses have been observed experimentally and in numerical simulations /1-2/, namely, a compressional structure corresponding to a negative potential which was identified as a Korteweg-de Vries soliton, previously observed and described by Ikezi et al. /3/, and a pulse with positive potential indicating a deficit of electrons which we refer to as an electron hole. This electron hole appears as a BGK equilibrium /4/ and our numerical simulations show that it is associated with a vortex-like configuration in phase space, thus resembling the almost stationary structures observed in a number of computer simulations of the electron two-stream instability /5/. In this paper we report observations of the mutual interaction between electron holes and their interaction with the KdV solitons.

Experiment: The experiment was conducted in the Risø Q-machine operating in the single-ended mode. A caesium plasma was produced by surface ionization on a hot tantalum plate, 3 cm in diam. A homogeneous magnetic field of 0.4 T strength confined the plasma radially. Electron and ion temperatures were ~ 0.2 eV and plasma densities were in the range 10^6 - 10^7 cm $^{-3}$. Collisions were entirely unimportant for the pulse propagation. The plasma was surrounded by a grounded cylindrical brass tube of 4 cm inner diameter acting as a waveguide. Pulses or waves were excited by means of a terminating brass tube 30 cm in length /6/. We obtained a dispersion relation for small amplitude electron oscillations /2/ that fitted very well to the Drivelpiece-Gould expression including thermal effects

$$\omega^2 = \omega_p^2 \frac{(ka)^2}{1 + (ka)^2} + 3 v_e^2 k^2, \quad (1)$$

with ω_p = the electron plasma freq., a = the plasma radius/2.4, and $v_e = \sqrt{T_e/m}$.

By exciting short negative pulses at $x = 0.3$ m with amplitudes of the order of 1 V and durations of the order of a plasma period ($= 2\pi/\omega_p$) we obtained the traces of the spatial development of the measured potential variations shown in Figs. 1 and 2. In Fig. 1 we applied two pulses ($\phi_{1,2}$) to the tube creating two solitons ($S_{1,2}$) and two holes ($H_{1,2}$). We see that S_2

passes right through H_1 causing only a phase jump of H_1 . In Fig. 2 a short pulse followed by a long tail was applied, creating two holes ($H_{1,2}$) with a small velocity difference. We see that the holes attract each other and coalesce, remaining together for the total length of the tube. If the two holes were created so that they moved against each other in the laboratory system, they were then observed to pass through each other.

Simulation: In order to make a numerical simulation of our experiment we used the program described in Ref. 7 which employs the particle-in-cell method with a leap-frog scheme for the movement of 50,000 simulation particles. The electric potential was calculated from Poisson's equation

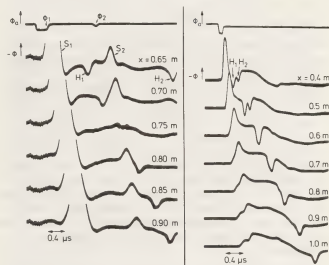


Fig. 1

Fig. 2

in the form

$$\frac{\partial^2 \phi}{\partial x^2} - \frac{\phi}{a^2} = \frac{e}{\epsilon_0} (n - n_0) \quad (2)$$

appropriate for a strongly magnetized plasma in a waveguide where only the lowest radial mode is considered. In (2), n and n_0 are the electron and ion densities respectively, where the ions are assumed to be immobile. The total energy of the system was calculated at each time step and we found energy conservation to be better than 2%. Figs. 3-4 show the temporal development of the potential variation and the phase space. Here $\phi_0 =$

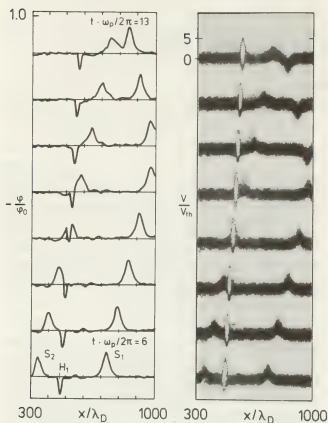


Fig. 3

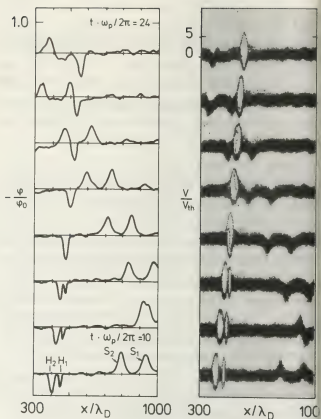


Fig. 4

$\frac{1}{2}m(\omega a)^2/e$, λ_D = the electron Debye length, and $V_{th} = (2T_e/m)^{1/2}$. In Fig. 3 the situation is similar to that in Fig. 1. We observe that the soliton S_2 passes through the hole H_1 , each being virtually unaffected. Some of our simulations indicate, however, that the hole can experience a small phase jump and velocity increase when the soliton passes through it. Fig. 4 shows a case similar to that of Fig. 2, and again we observe the attraction and coalescence of the two holes, H_1 and H_2 . As in the experiment the simulation shows that two holes pass through each other if their velocities are opposite in the laboratory system.

Conclusion: We have investigated the interaction of two different types of solitary structures, namely a KdV soliton and an electron hole, in an essentially one-dimensional system. We observed that the soliton and the hole will pass through each other with very little disturbance, similar to the case of two solitons [3]. On the other hand, two holes will coalesce if their relative velocities are small, and pass through each other for large relative velocities. Finally, we should like to point out that the electron hole may be important for the description of Langmuir turbulence in the case of strong coupling [2,8].

References:

- /1/ K. Saeki et al., Phys. Rev. Lett. (in press).
- /2/ J.P. Lynov et al., Physica Scripta (in press).
- /3/ H. Ikezi et al., Phys. Fluids **14** (1971) 1997.
- /4/ I.B. Bernstein et al., Phys. Rev. **108** (1957) 546.
- /5/ H.L. Berk et al., Phys. Fluids **13** (1970) 980.
- /6/ K. Saeki, J. Phys. Soc. Japan **35** (1973) 251.
- /7/ V. Turikov, Risø Rep. No. 380 (1978).
- /8/ T.H. Dupree, Bull. Am. Phys. Soc. **23** (1978) 869.

STRONG TURBULENCE IN PARTIALLY IONIZED PLASMAS

T. Mikkelsen and H.L. Pécseli.

Association EURATOM-Risø National Laboratory Physics Department, DK-4000 Roskilde, Denmark.

Introduction: The variation of the power spectrum of turbulent potential fluctuations in a rotating low- β plasma was investigated for varying neutral background pressures. For low pressures we find an f^{-5} spectrum. At a well-defined neutral pressure where the ion neutral collision frequency is close to the ion cyclotron frequency we observed a pronounced change in the universal part of the spectrum, resulting in an approximate $f^{-3.5}$ spectrum.

Experimental results: The experiment was conducted in a caesium plasma produced by surface ionization on a hot (~ 2000 K) spiral made of 2 mm-diameter tantalum wire. The hot filament imposed an almost parabolic potential variation across the plasma column, giving rise to an electric field, E_0 , which increased linearly with radius; the field direction being towards the center of the plasma column. Together with a homogeneous confining magnetic field, variable in the range 0.7-3 kG, this electric field gave rise to a nearly shear-free, "solid body" $E_0 \times B/B^2$ rotation of the entire

plasma column. The length of this column was ~ 1 m and its radius, $R \sim 4$ cm. Plasma densities were 10^9 - 10^{10} cm $^{-3}$ and temperatures $T_e \sim T_i \sim 0.2$ eV. Figure 1 shows the experimental set-up schematically. Figure 2a shows the radial potential profile and Fig. 2b the corresponding density variation and density fluctuations \tilde{n} at a low neutral pressure, $p = 10^{-5}$ mm Hg. For further details see refs. /1-2/. (The abscissa in Fig. 1 of ref. /2/ should be corrected as shown in Fig. 2 here). These profiles are somewhat varying with neutral pressure. Fluctuations in floating potential were detected as in ref. /2/. We obtained power spectra like those shown in Fig. 3a. Continuous spectra, indicating fully developed strong turbulence, were found. Fluctuation levels \tilde{n}/n_0 were in the range 10-40%.

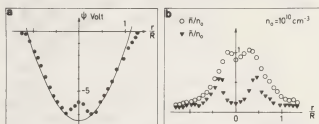
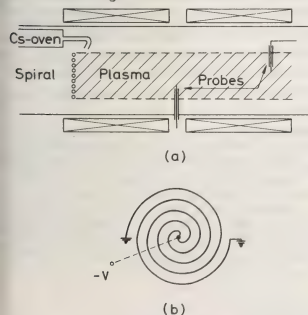


Fig. 2.

In the following we shall be concerned only with the high frequency, or "universal", part of the spectrum. Two subranges were distinguished, denoted "production" and "coupling". Recent theoretical investigations /3/ predict a wavenumber dependence k^{-3} and k^{-5} of the potential power spectrum $G(k)$ in the two subranges at low neutral pressures. (The spectrum is defined, assuming locally homogeneous and isotropic turbulence, so that $\langle \phi^2 \rangle = \int_0^\infty G(k) dk$). Due to the rapid rotation of the plasma column we may rely on Taylor's hypothesis when comparing measured frequency spectra with



theoretical wave number spectra, i.e., assume $\omega = k\bar{V}_O$, where \bar{V}_O is the magnitude of the plasma mean drift velocity at the position of the detecting probe. Spectra obtained by this assumption agree with the definition above.

After increasing the neutral background pressure, p , with argon or nitrogen we observed a change in the spectral index for the two subranges. The index variation is shown in Fig. 3b as a function of p/B or in more relevant terms v/Ω_i , where v is the ion-neutral collision frequency and Ω_i the ion cyclotron frequency. When calculating v we took a representative collision cross section $\sigma = 7 \cdot 10^{-14} \text{ cm}^2$. In reality σ varies somewhat with ion velocity, but this will not qualitatively affect our interpretation of the following.

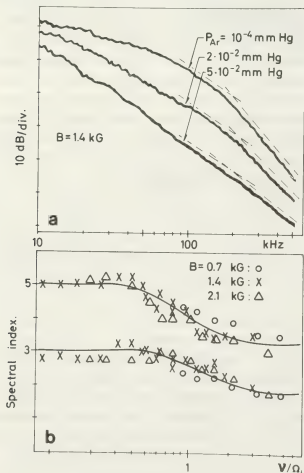


Fig. 3.

By cross-correlating the signal from two Langmuir probes across and along the plasma column we found that the perturbations were strongly field-aligned and travelled in the azimuthal direction. Filtering the

two probe signals before performing the correlation, we determined the effective dispersion relation for the fluctuations and found for the subranges in question that the propagation velocity was close to the calculated $\underline{E}_O \times \underline{B} / B^2$ rotation velocity

For low neutral pressures we identify the instability driving the turbulence as a gradient-driven "universal" instability where the "centrifugal force" on the ions enhances the growth relative to a non-rotating plasma column /4/. For higher neutral pressures (v comparable to Ω_i), theory /5/ predicts strongly field-aligned perturbations, travelling with the $\underline{E}_O \times \underline{B}$ electron velocity in agreement with our observations. The linear growth rate, Γ , for these instabilities contains two terms: i) a gradient term, and ii) a term that may give rise to instability (the Farley-Buneman instability /5/) also in uniform plasmas.

$$\Gamma = (V_{eo} - V_{io}) \frac{v_i}{\Omega_i} \frac{1}{n_O} \frac{\partial n_O}{\partial r} + \frac{v_e k^2}{\Omega_e \Omega_i} [(V_{eo} - V_{io})^2 - C_s^2].$$

By calculating $(V_{eo} - V_{io})$ at the edge of the plasma column we found that the change in spectral index sets in when $(V_{eo} - V_{io}) > C_s$, i.e., when the last term changes sign, thus enhancing the instability. We determined the ion velocity from the ion rotation frequency, ω_x , using the relation $(1 + 2 \omega_x / \Omega_i) [(\omega_E / \Omega_i) - (\omega_x / \Omega_i) - (\omega_x / \Omega_i)^2] = (\omega_x / \Omega_i) (v / \Omega_i)^2$, where ω_E is the uniform $\underline{E}_O \times \underline{B}$ rotation frequency. Note that an increase in the B -field requires a roughly proportionate increase in collision frequency v , i.e., an increase in neutral pressure, to produce the same ω_x . This is precisely what is indicated by Fig. 3b.

References:

- /1/ N. D'Angelo, H.L. Pécseli and P.I. Petersen, J. Geophys. Res. 79 (1974) 474
- /2/ T. Mikkelsen and H.L. Pécseli, Phys. Rev. Lett. 41 (1978) 951.
- /3/ C.M. Tchen, H.L. Pécseli and S.E. Larsen, Risø Rep. No. 365 (1977).
- /4/ T.K. Chu, B. Coppi, H.W. Hendel and F.W. Perkins, Phys. Fluids 12 (1969) 203.
- /5/ A. Rogister and N. D'Angelo, J. Geophys. Res. 75 (1970) 3879.

NONLINEAR WAVES IN A MAGNETIZED PLASMA WAVEGUIDE

J.P. Lynov, P. Michelsen, H.L. Pécseli, J. Juul Rasmussen and H. Sugai*

*Association EURATOM-RISØ National Laboratory Physics Department DK-4000 Roskilde-Denmark.
*Department of Electrical Engineering, Nagoya University, Nagoya-Japan.

INTRODUCTION: Theoretical investigations of nonlinear modulation of strongly dispersive electrostatic plasma oscillations /1/ have demonstrated the importance of including the effect of nonlinear Landau damping, i.e., the resonant particles at the group velocity of the wave. The contribution of these particles modify a nonlinear Schrödinger (NLS) equation for the wave envelope by a nonlocal term. For electron waves in bounded plasmas only the resonant ions are generally of importance in this connection /2/. In the present paper we report investigations of electron plasma waves in bounded plasmas where the dispersion relation is modified so that resonant electrons play the dominant role. We consider waves in a strongly magnetized ($\omega \ll \omega_{ce}$) plasma waveguide with radius r_0 . Considering the ions as a stationary uniform neutralizing background the linear dispersion relation for electron plasma waves becomes: $(\omega/k)^2 = \omega_p^2 / (k_{\perp}^2 + k_{\parallel}^2) + 3v_e^2$ where $v_e = \sqrt{T_e/m}$ while k_{\parallel} is the axial wave number and $k_{\perp} = 4/r_0$. We consider only the lowest order radial mode. For many laboratory experiments of interest $\omega/k \gg v_e$ so linear Landau damping is negligible. Moreover, particle trapping may also be ignored for weakly nonlinear waves. However for certain group velocity v_g will be close to v_e . We derive a modified NLS equation taking into account these resonant particles, and present preliminary experimental results supporting our results.

THEORY: Our basic equations are the one-dimensional electron Vlasov equation and Poisson's equation modified to take into account the finite geometry

$$v \frac{\partial f}{\partial x} + \alpha \frac{\partial \phi}{\partial x} \frac{\partial f}{\partial v} + \frac{\partial \phi}{\partial x} f'_0(v) = 0 \quad (1)$$

$$\frac{\partial \phi}{\partial x} - \phi = n-1 \quad (2)$$

with $\int f dv = n$, $\int f_0 dv = 1$ where $f_0(v)$ is the unperturbed electron velocity distribution function. The perturbed density n is normalized with n_0 , v with $u_0 = \omega_p/k_{\perp}$, t with $\tau = t/\tau_0$, x with k_{\perp}^{-1} and ϕ with $u_0^2 m/e$. The coefficient $\alpha = 0.72$ originates from the expansion in radial eigenmodes /3/ where the lowest one is considered here. To study the long time amplitude variation of electron plasma waves we use a multiple time-scale analysis and proceed in a manner very much similar to the one employed in /4/. Substituting an expansion of (f, ϕ) in powers of ϵ into (1)-(2) we obtain a set of equations for each power of ϵ . By successively removing secularly-producing terms, we finally obtain

$$i \frac{\partial a}{\partial \tau} + p \frac{\partial^2 a}{\partial \xi^2} + q a |a|^2 + a \int_{-\infty}^{\infty} \frac{v}{\xi - v} \frac{|a|^2}{\xi - v} dv = 0, \quad (3)$$

as the nonsecularity condition to third order, where $\tau = \epsilon^2 t$ and $\xi = \epsilon(x - v_g t)$. Equation (3) has the form of a modified NLS (eq.) where the nonlocal term accounts for the effect of resonant particles at v_g /1,2/. The coefficient $p \equiv \frac{1}{2} dv_g/dk$, while q and s are complicated functions of k . A NLS eq. in the cold plasma limit was derived previously /3/. The present equation differs not only in the nonlocal term but also in the significantly modified coefficient q , in particular we have a sign reversal of q even for moderately small k , see fig. 1 where q and s are shown as functions of k for the case, where $f_0(v)$ is chosen to be a Maxwellian. The dotted line shows q in the cold plasma approximation /3/.

We now introduce the real functions $\rho(\xi, \tau)$ and $\theta(\xi, \tau)$ through $a = \rho \exp(i\theta)$ and note that (3) has a plane wave solution: $\rho = \rho_0 = \text{const}$, $\theta = \theta_0 = -q \rho_0^2 \tau = \delta \omega \tau$, where $\delta \omega$ accounts for the frequency shift. Note that $\delta \omega$ is independent of s . To examine the stability of (3) we modulate this solution by introducing a small perturbation:

$$(\rho, \theta) = (\rho_0 + \delta \rho, \theta_0 + \delta \theta) \exp[i(K\xi - \Omega\tau)] + \text{c.c.}$$

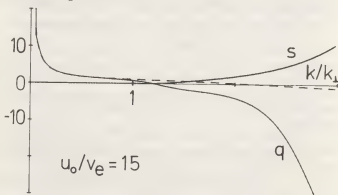


Fig. 1

The linearized dispersion relation obtained from (3) determines $\Omega = \Omega_r(K) + i\Gamma(K)$, where

$$\Omega_r^2 - \Gamma^2 = K^2 \{ p^2 K^2 - 2 \rho_0 q p \} \quad (4a)$$

$$\Omega_r \Gamma = -p \cdot s \cdot K |K| \rho_0^2 \quad (4b)$$

Eqs. (4) show that the resonant particles at v_g make the electron plasma wave unstable for any amplitude modulation, contrary to the case when this effect is absent (i.e. $s \equiv 0$), where a necessary condition for instability is $p \cdot q > 0$. In the case $s = 0$ the instability is purely growing in the group velocity frame of refer-

ence (GR), i.e., the frequency has no real part. Considering an initial-value problem where the modulation is applied at $t = 0$ with wave number K , the instability will manifest itself in the lab. frame as two growing sidebands shifted from the carrier-wave frequency by $\pm K v_g$ (Fig. 2, where only the effect of amplitude modulation is shown). However, in the case $s \neq 0$ the frequency has a real part, and for $p \cdot s < 0$ we find that $\Gamma > 0$ for disturbances with $\Omega_r/K > 0$ and $\Gamma < 0$ for $\Omega_r/K < 0$. Considering again an initial-value problem, we see that the two modes (one growing and one damping) in GR give rise to two lower- and two upper-sidebands in the laboratory frame as shown schematically in Fig. 2.

EXPERIMENT. Preliminary experimental results on the electron wave modulation were obtained in the Risø Q-machine in single-ended operation. The plasma is confined radially by a strong magnetic field ~ 0.4 T, has a density $\approx 4 \cdot 10^7 \text{ cm}^{-3}$ and $T_e \approx 0.2$ eV, i.e., $u_0/v_e \approx 15$. By applying a modulated oscillation to the floating cold end-plate, we excited an amplitude-modulated electron plasma wave. The wave propagation was investigated by an axially movable Langmuir probe connected to a capacitive amplifier. Fig. 3a shows the evolution of the frequency spectrum for a modulated wave at large amplitude (only nearest sidebands are shown). The sidebands grow with distance.

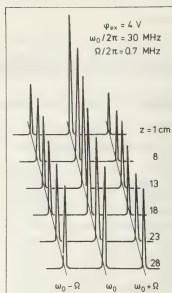


Fig. 3a

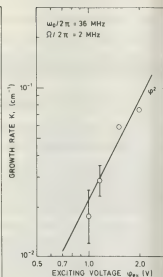


Fig. 3b

Fig. 1.

We have ensured that alternative interpretations /4,5/ can be ruled out in the present experiment.

References

- /1/ Y.H. Ichikawa and T. Taniuti, J. Phys. Soc. Jap. **34**, 513 (1973)
- /2/ K.B. Dysthe and H.L. Pécseli, Plasma Phys. **19**, 931 (1977)
- /3/ J. Juul Rasmussen, Plasma Phys. **20**, 997 (1978)
- /4/ G. van Hoven and G. Jahns, Phys. Fluids **18**, 80 (1975)
- /5/ R.N. Franklin, R.R. MacKinlay, P.D. Edgley, and D.N. Wall, Proc. R. Soc. Lond. A **360**, 229 (1978).

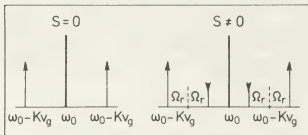


Fig. 2

The growth rate for both sidebands were found to scale roughly with the square of the applied amplitude Fig. 3b, where the growth rate of the lower sideband is plotted.

To interpret these results in terms of the presented theory, we note that (3) is more suited to an initial-value problem than to a boundary-value one applicable to the experimental situation. This is especially true because the nonlocal term must take another form when applied to the boundary-value problem. However, at least qualitatively, one should expect a k -spectrum with multiple sidebands like the ω -spectrum in Fig. 2 ($s \neq 0$). The frequency spectrum, on the other hand, consists of the two "applied" sidebands both growing in agreement with measurements (Fig. 3a). Furthermore the spatial growth rate $K_1 = \Gamma/v_g$, i.e., approximately $K_1 \propto \phi_{app}^2$ (Eq. 4b), which also agrees with the measurements. By varying the carrier frequency we found that the growth rate increased for v_g approaching v_e as expected from (4b) and

PHYSICAL PICTURE OF THE HIGHER-ORDER LANDAU MODES OF ELECTRON PLASMA WAVE

S. Ikezawa and Y. Nakamura^{*}.^{*}Chubu Institute of Technology, Kasugai (Nagoya-Shigai) 487, Japan.

Institute of Space and Aeronautical Science, University of Tokyo, 112, Japan.

Introduction: The higher-order Landau modes

are theoretically analyzed by Derfler & Monzen/1/ using a set of the plasma wave functions. In order to make clear the meaning of the individual higher-order Landau mode, we calculate the dispersion relations of the electron wave in a two-Maxwellian plasma/2/ and also in a water-bag plasma/3-4/ for $\omega/\omega_p < 1$ (electron plasma frequency), and compare them with the previous experiment/4/. It is found that the higher-order Landau mode strongly depends on the temperature in the high energy tail of the electron distribution.

Dispersion relations: In the case of the two-Maxwellian(temperature), one dimension-distribution of electrons is written as,
$$F(t, x, v) = f_{o1}(v) + f_{o2}(v) + f(t, x, v), \quad (1)$$

$$f_{o1,2} = 1, 2 (m/2\pi kT_{1,2})^{1/2} \exp(-mv^2/2kT_{1,2})$$

$$n_2/n_1 = a < 1, T_2/T_1 = b > 1.$$

f denotes the perturbed distribution, and the subscripts 1 & 2 denote the cold part of the hot part, respectively. The basic equations are the Maxwell equation approximated by the dipole excitation and the linearized-collisionless Boltzmann equation. Using the Fourier-Laplace transformation, the dispersion relation is given with the derivative of the plasma dispersion function Z' as follows;

$$Z_n'(\omega_{p1}/v_{\theta 1})^2 Z'(\omega/k_n v_{\theta 1}) + (\omega_{p2}/v_{\theta 2})^2 Z'(\omega/k_n v_{\theta 2}), \quad \omega_n^2 = \omega_{p1}^2 + \omega_{p2}^2, \quad (2)$$

where $v_{\theta 1,2} = (2kT_{1,2}/m)^{1/2}$. For $\omega_{p2} = 0$, $n=1$, and $n \geq 3$, the modes are named as the fundamental Landau mode and the higher-order Landau modes, respectively.

In the case of the water-bag model, the distribution is composed by the Maxwellian plus a water-bag due to the random motion of monoenergetic electrons. The dispersion relation is shown as follows/3-4/;

$$k_n^2 = (\omega_{p1}/v_{\theta 1})^2 Z'(\omega/k_n v_{\theta 1}) + (\omega_{pc}/v_c)^2 / [(\omega/k_n v_c)^2 - 1], \quad (3)$$

where v_c and ω_{pc} denote the truncated velocity and the water-bag plasma frequency.

The eqs.2 and 3 are calculated using the Newton-Raphson method for $a=0.1$ and $b=10$. $B = (v_c^2/v_{\theta 1}^2) = 4-50$, and shown in Figs.1 and 2, respectively. One can see in Fig.1, the two-temperature(modified fundamental Landau) modes with $4 \leq b \leq 22$ merge into the 3rd-order Landau mode($a=0$). For $23 \leq b \leq 32$, it merges into the 4th-order Landau mode, sequentially. However, as shown in Fig.2, the phase velocity can be varied arbitrarily with B in the case of the water-bag model.

Discussion: The experiment was performed using the chamber at the Institute of Space and Aeronautical Science, University of Tokyo/4/. With the high anode voltage V_a of the glow mode plasma source, a typical energy distribution and the dispersion relation are shown in Fig.3. From the inserted fog., we obtain $a=0.07$ and $b=4$ for the two-temperature model, and $B=10$ for the

water-bag model. The dispersion relations observed agree with that of the two-temperature model shown by (3) & (4) for $b=4$.

In summary, when the monoenergetic electrons are injected into the plasma for the non-Maxwellian experiment, they are assumed to be soon thermalized with the finite temperature T_2 and contribute to the higher-order Landau mode. The authors thank Prof. Y. Kawai of Kyushu University for discussion, and Prof. T. Okuda, Prof. O. Mikami and Prof. A. Kimpara for encouragements. This work was supported by Extra Research Budget of Chubu Institute of Technology.

References:

/1/ H.Derfler and T.C.Simonen: Phys. Fluids 12(1969) 269.
/2/ A.E.Aubert and N.Van Deal: CIPIG, Oxford (1971) p.96.
/3/ J.P.Treguier and D.Henry: J. Plasma Phys. 13 (1975)193.
/4/ Y.Kawai, Y.Nakamura, T.Itoh, T.Hara and T.Kawabe ;J. Phys. Soc. Japan 38(1975)876.

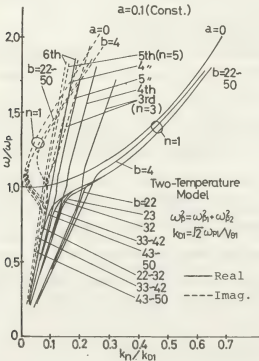


Fig.1. Dispersion relation of the two-temperature model from eq.2

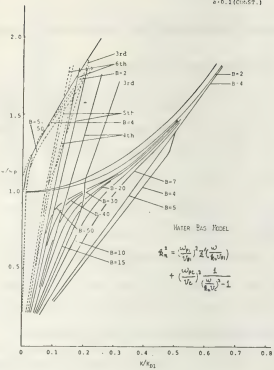


Fig.2.Dispersion relation of the water-bag model from eq.3

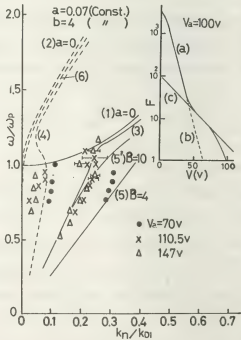


Fig.3.Comparison with the experiment/4/. The inserted figure shows an energy distribution with $T_1=7\text{eV}$, $T_2=28\text{eV}$, $a=0.07$, and the truncated potential $V_c=70\text{V}$.

COMPUTER SIMULATION OF THE SIDEBAND INSTABILITY

Magdi M. Shoucri.

Direction Sciences de base, Institut de Recherche de l'Hydro-Québec Varennes, Québec, Canada, J0L 2P0.

The physical origins of the growth of sidebands of a large amplitude wave is studied numerically, by solving the Vlasov equation in phase-space by a splitting method recently reported in the literature¹.

The pertinent equations are the Vlasov-Poisson system of equations, which are written in dimensionless form as:

$$\frac{\partial f}{\partial t} + v \frac{\partial f}{\partial x} + E(x, t) \frac{\partial f}{\partial v} = 0, \quad \frac{\partial E}{\partial x} = \int_{-\infty}^{\infty} f dv - 1$$

f is the electron distribution function; E the electric field and the other symbols have their conventional meaning. The distribution function has been initialized as:

$$f(x, v, 0) = f_0(v) \left(1 + \alpha_m \cos k_m x + \alpha \sum_{i=1}^3 (\cos k_{li} x + \cos k_{ui} x) \right)$$

and $f_0(v) = (2\pi)^{-\frac{1}{2}} \exp(-v^2/2)$. The subscripts m , l_i , u_i refer respectively to the main wave, the lower sidebands ($k_{li} < k_m$) and upper sidebands ($k_{ui} > k_m$). The length of the system is $L = 80\pi$, and $k_m = 2\pi m/L = 0.3$ with $m = 12$. We are using

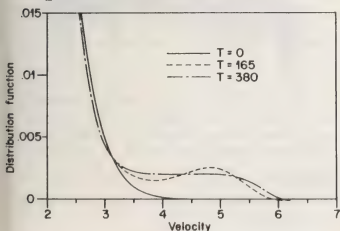
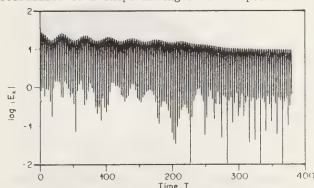
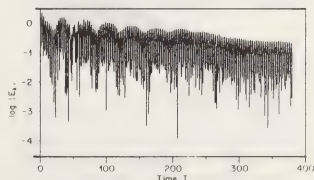


Fig. 1 Spatially averaged distribution function

128 points in space in the present simulation, and a time-step $\Delta t = 1/8\omega_p^{-1}$. The main wave is excited with a large amplitude $\alpha_m = 0.18$. This corresponds to a bounce frequency $\omega_b = (\alpha_m/2)^{\frac{1}{2}} = 0.3$. All the sidebands are excited initially with the same level $\alpha = 2 \times 10^{-3}$. For the lower sidebands $k_{l1} = 2\pi \times 11/L = 0.275$, $k_{l2} = 2\pi \times 10/L = 0.25$ and $k_{l3} = 2\pi \times 9/L = 0.225$. For the upper sidebands $k_{u1} = 2\pi \times 13/L = 0.325$, $k_{u2} = 2\pi \times 14/L = 0.35$, $k_{u3} = 2\pi \times 15/L = 0.375$. The measured asymptotic frequencies of the fundamental mode is $\omega_m = 1.142$. Figure 1 shows the spatially averaged distribution function, which at $T = 165\omega_p^{-1}$ has almost stabilized to a shape having a stable positive

Fig. 2 Time variation of the fundamental mode with $k = 0.3$ Fig. 3 Time variation of the first harmonic with $k = 0.6$

slope, while the sidebands are still growing (Figs. (4-9)). The frequencies of the lower sidebands are respectively $\omega_{l1} = 1.092$, $\omega_{l2} = 1.068$ and $\omega_{l3} = 1.033$ and $\omega_{u1} = 1.196$, $\omega_{u2} = 1.225$, and $\omega_{u3} = 1.256$. We note that $\omega_{l1} + \omega_{u1} = 2.288$, $\omega_{l2} + \omega_{u2} = 2.293$ and $\omega_{l3} + \omega_{u3} = 2.289$, while the frequency of the first harmonic is $2\omega_m = 2.284$. If in addition we note that the wavenumber of the first harmonic is $2k_m = 0.6$, and that $k_{l1} + k_{u1} = k_{l2} + k_{u2} = k_{l3} + k_{u3} = 0.6$, our results clearly points to a nonlinear coupling between the first harmonic and

the sidebands². We also note that the lower sidebands have their phase velocities ω_{li}/k_{li} on the positive side of the slope of the distribution function, which enhances their growth. The sidebands grow up to a level where the spatially averaged distribution function is distorted into a shape close to a flat plateau, as is clear from Fig. 1 at $T = 380$ p⁻¹ and the sidebands as well as the fundamental mode saturate.

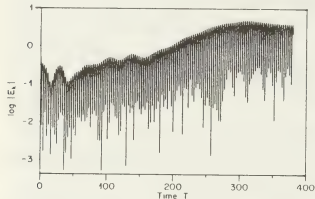


Fig. 4 Time variation of the lower sideband with $k_{l1} = 0.275$

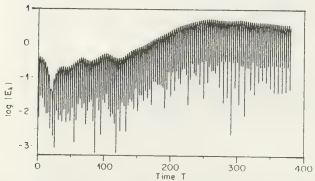


Fig. 5 Time variation of the lower sideband with $k_{l2} = 0.25$

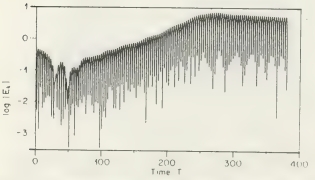


Fig. 6 Time variation of the lower sideband with $k_{l3} = 0.225$

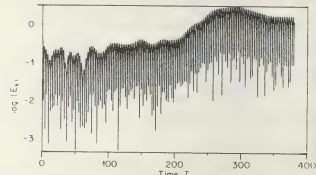


Fig. 7 Time variation of the upper sideband with $k_{u1} = 0.325$

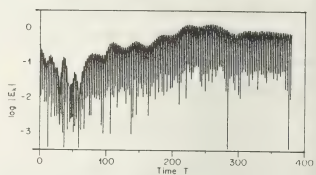


Fig. 8 Time variation of the upper sideband with $k_{u2} = 0.35$

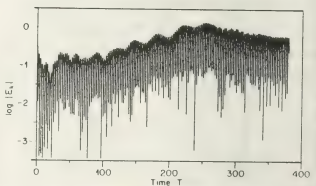


Fig. 9 Time variation of the upper sideband with $k_{u3} = 0.375$

References

1. R. Gagné and M.M. Shoucri, J. Comput. Phys. 24, 445 (1977).
2. M.M. Shoucri, Phys. Fluids 21, 1359 (1978).

SPIKY DENSITY FLUCTUATION AND RELAXATION OSCILLATION IN AN ANOMALOUSLY RESISTIVE PHASE

Y. Takeda and M. Yokota.

*Department of Physics, College of Science and Technology, Nihon University, Tokyo, Japan.*1. Introduction

Over the past decade considerable effort has been directed toward identifying the dominant physical mechanisms involved in anomalous resistivity of plasmas. The phenomena and behaviors of a plasma related with anomalous resistivity vary over a wide range depending on the nonlinear mechanism to be responsible. Detailed comparison of theory and experiments have not been possible due to the complexity and strong nonlinearity of the phenomena.

In this paper we present the first experimental observations of the anomalous resistivity which accord with behaviors predicted by the recent theoretical developments of strong Langmuir turbulence.^{1),2)} Our observation of density fluctuations by means of microwave scattering technique confirmed the numerical simulation by DeGroot et al.³⁾ which predicted the existence of large potential jumps (double layers) and localized density cavity in the strong Langmuir turbulence generated in an anomalously resistive phase.

2. Experimental Arrangements

We have carried out heating discharge experiments in a magnetic mirror with mirror ratio $R_M = 1.25$. An initial plasma was produced by a washer gun. The power of heating discharge is supplied from a capacitor of 2.2 μF with a charging voltage up to 30kV.

Main diagnostics used in the present experiment are as follows. In order to clarify the relation between the anomalous resistivity and turbulence, electrostatic fluctuations are picked up by a capacitively-coupled probe inserted radially into the discharge vessel at the center of the apparatus. A picked-up signal is passed through a high-pass filter in order to eliminate low frequency (1-2 MHz) and large

amplitude components and rough spectral

components are picked up by a capacitively-coupled probe inserted radially into the discharge vessel at the center of the apparatus. A picked-up signal is passed through a high-pass filter in order to eliminate low frequency (1-2 MHz) and large

amplitude components and rough spectral

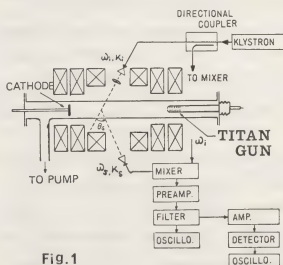


Fig.1

ge amplitude components and rough spectral

analysis of fluctuations using several band-pass

The 4mm microwave scattering system and the experimental apparatus are shown in Fig. 1. A 400 mW microwave of frequency $\omega_i/2\pi = 70 \text{ GHz}$ is launched perpendicularly to the plasma column with the wave of the magnetic field (ordinary mode). The angle θ_s is fixed at 90° .

3. Behaviors of the turbulence in the phase of anomalously high resistivity.

In Fig. 2, typical time traces are shown for (a) heating current through the filaments picked up by the C-coupled probe with pass band $18 \text{ MHz} - 145 \text{ MHz}$, (c) the filtered signals detected through band-pass filters having the center frequency of 70 MHz for the upper trace and 350 MHz for the lower trace. It must be noted that the time trace of I_p shows two dips, one in the early phase, $t = 0.4-1.8 \mu\text{S}$, and the other slightly on the flat tops, $t = 3.0-4.3 \mu\text{S}$, henceforth called the phase I and phase II respectively. The resistivity is $3 \times 10^{-2} \text{ ohm-meter}$ in the phase I, nearly twice larger than the Buneman's resistivity. Hence the early stage of the phase I is characterized by the strong two-stream instability.

As seen in Fig. 2(b), electrostatic fluctuations picked up by the C-coupled probe exhibit fast relaxation oscillations in the saturated state of the phase I, presumably demonstrating the collapse of the plasma waves into spatially localized region.^{1),2)}

The filtered video outputs of the 70 GHz microwave scattering system at $\theta_s = 90^\circ$ in the midplane show notably spiky fluctuation and a feature of relaxation oscillations. These behaviors coincide with the external measurement of turbulent waves with the C-coupled probe.

and the experimental apparatus are shown in Fig. 1. A 400 mW microwave of frequency $\omega_i/2\pi = 70 \text{ GHz}$ is launched perpendicularly to the plasma column with the wave of the magnetic field (ordinary mode). In the present experiment, the scattering

is observed in the phase of anomalously high resistivity. The time traces are shown for (a) heating current through the filaments picked up by the C-coupled probe with pass band $18 \text{ MHz} - 145 \text{ MHz}$, (c) the filtered signals detected through band-pass filters having the center frequency of 70 MHz for the upper trace and 350 MHz for the lower trace. It must be noted that the time trace of I_p shows two

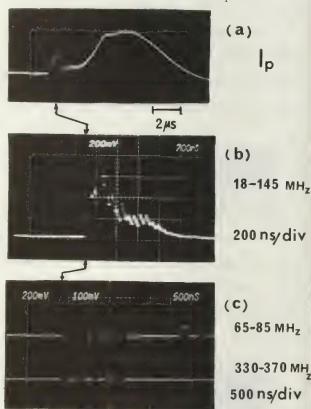


Fig.2

References

- (1) G. J. Morales and Y. C. Lee, Phys. of Fluids 19, 690 (1976)
- (2) K. Elsasser and H. Schamel, Plasma Phys. 19, 1055 (1977)
- (3) J. S. DeGroot, C. Barnes, A. E. Walstead, and O. Buneman, Phys. Rev. Lett. 38, 1283 (1977)

ON THE LINEAR STABILITY OF A COLLISIONLESS SINGLE-ENDED Q-MACHINE

M.T.C. Fang and S. Kuhn*

Department of Electrical Engineering and Electronics, University of Liverpool, Liverpool L69 3BX, England U.K.
*Institute for Theoretical Physics, University of Innsbruck, A-6020 Innsbruck, Austria.

1. Introduction. The electron-current driven "ion-acoustic" instability in collisionless single-ended Q-machines has for many years been the subject of extensive experimental investigations /1-3/. It is excited by applying a sufficiently large positive d.c. bias to the cold plate (or to some grid) and usually exhibits the character of a strongly nonlinear standing longitudinal wave localized between the hot plate and the exciting electrode. Similar oscillations have been observed in certain plasma diodes /4/.

The present work is intended as a contribution towards clarifying the onset of these oscillations. We investigate the linear stability of low-frequency, long-wavelength longitudinal waves in a collisionless single-ended Q-machine by solving Landau's dispersion relation in the appropriate limit. The time-independent state is characterized by the strongly non-Maxwellian velocity distribution functions associated with the monotonic potential distributions of a collisionless plane one-emitter diode. Apart from this choice, the bounded nature of the system is only accounted for by postulating that the wavelength equals twice the system length $L/2$.

2. Theoretical background. The steady-state velocity distribution functions (normalized to unity) are given by /5,6/

$$f_s(v) = A_s \exp(-v_s^2) U(v_s - v_{cs}), \tag{1}$$

where s denotes the particle species (e for the electrons, i for the ions), $A_s = (\pi^{1/2} a_s \cdot \text{erfc } v_{cs})^{-1}$, $a_s = (2\kappa T/m_s)^{1/2}$, κ is Boltzmann's constant, T is the hot-plate temperature, m_s is the particle mass, $\text{erfc} = 1 - \text{erf}$ is the complementary error function, $v_s = v/a_s$, $v_{cs} = v_{cs}/a_s$ is the normalized cut-off velocity, and U is the unit step function. The cutoff velocities are given by $v_{ce}^- = -(\eta_p - \eta_{cp})^{1/2}$, $v_{ci}^- = -(\eta_p)^{1/2}$ for monotonic decreasing potential distributions, and by

$v_{ce}^+ = \eta_p^{1/2}$, $v_{ci}^+ = -(\eta_{cp} - \eta_p)^{1/2}$ for monotonic increasing ones. Here, η_p and η_{cp} respectively denote the plasma potential and the cold-plate bias normalized to $\kappa T/e$, e being the magnitude of the electric elementary charge. The normalized plasma potential (as well as other quantities of interest) can be calculated from the neutral-flux density irradiating the hot plate, from the hot-plate and ionic properties, and from the applied bias /6,7/.

We are looking for small-amplitude wave perturbations proportional to $\exp[i(kx - \omega t)]$, where the (real) wavenumber k is given by π/L , and the (complex) frequency ω is to be computed from Landau's dispersion relation /8/. Using (1) and restricting ourselves to low-frequency, long-wavelength modes (i.e., neglecting $\omega/\kappa a_e$ and $k(\kappa T/4\pi n_p e^2)^{1/2}$, where n_p is the plasma density), we obtain

$$1 - \bar{v}_e/v_{ce} = Z'(v_{ci}, \zeta)/\text{erfc } v_{ci}. \tag{2}$$

Here, $\bar{v}_e = (\pi^{1/2} \text{erfc } v_{ce})^{-1} \exp(-v_{ce}^2)$ is the normalized average velocity of the electrons, $\zeta = \omega/\kappa a_i$, $Z' = \partial Z/\partial \zeta$, and Z is the incomplete plasma dispersion function as discussed by Franklin /9/.

The subsequent stability analysis is based on the steady-state results of Fig.1, which shows a section of the (η_{cp}, α) para-

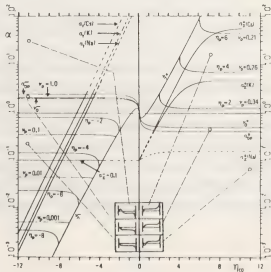


Fig. 1

meter plane for a collisionless plane one-emitter diode /5-7/. The "neutralization parameter" α is the ratio of emitted particle densities at the hot-plate surface ($\alpha = n_{10}^+/n_{e0}^+$). The figure shows type-separating curves (v_A, v_o, α_{op}), curves of constant normalized plasma density v_p (in units of n_{e0}^+), of constant normalized plasma potential η_p , of zero net electric current (α_f), and of constant normalized neutral flux (α_χ).

3. Discussion of results. To be specific, we solve the dispersion relation (2) for parameters along the α_χ -curves of Fig.1, which correspond to experimental situations where the cold-plate bias is varied, everything else being kept constant /6/. The dashed portions of these curves are outside the parameter domains for monotonic potential distributions and will not be considered here.

In the negative-bias region, Eq. (2) always yields one undamped "slow" mode (with a phase velocity lower than the ion cutoff velocity) and an infinite number of Landau-damped "fast" modes (with $\text{Re}\zeta > v_{ci}$), but no growing modes. The results for the slow mode and one of the fast modes are shown in

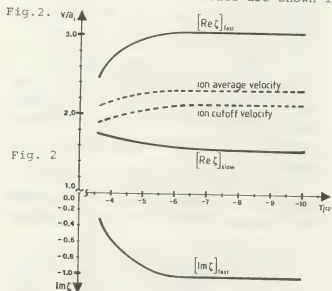


Fig. 2

In the positive-bias region considered we always find one unstable mode, cf. Fig.3. Note that for sufficiently high η_{cp} we always have $\text{Im}\zeta \gg \text{Re}\zeta$. The situation is essentially that of a Buneman two-stream instability /10/, where the large growth rate is known to be due to the resonant transfer of energy from the negative-energy, Doppler-

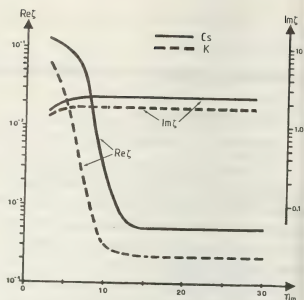


Fig. 3

shifted electron plasma oscillations to the positive-energy ion mode. The real part of the phase velocity is far too small to account for the observed oscillation frequencies /1-3/, which clearly demonstrates that the results of our linear analysis cannot be extrapolated to describe the nonlinear stage. However, our results are in qualitative agreement with experimental observations in that the growth rates are of the order of the ion-sound velocity, $(kT/m_i)^{1/2}$, /2,11/.

Acknowledgement. This work was supported by the Fonds zur Förderung der wissenschaftlichen Forschung (Austria) under grant nos 2781/S and S-18/02.

References.

- /1/ N.S.Buchel'nikova, R.A.Salimov, Sov. Phys. JETP 29 (1969) 595
- /2/ P.Michelsen et al., Plasma Phys. (1979)
- /3/ R.Schrittwieser et al., this conference
- /4/ V.I.Kuznetsov, A.Ya.Énder, Sov. Phys. Tech. Phys. 22 (1977) 1295
- /5/ W.Ott, Z. Naturforschung 22A (1967) 10
- /6/ S.Kuhn et al., Rept. UNICP-FSP78/1, Innsbruck Univ. (July 1978)
- /7/ S.Kuhn, submitted for publication
- /8/ L.D.Landau, J. Phys. USSR 10 (1946) 25
- /9/ R.N.Franklin, Proc. 10th ICPIG, Oxford (1971) 269
- /10/ T.D.Mantei et al., Plasma Phys. 18 (1976) 705
- /11/ E.Mravlag, to be published

GRID VERSUS PLATE EXCITATION OF THE ELECTRON CURRENT DRIVEN ION WAVE INSTABILITY

R. Schrittwieser, E. Märk and S. Kuhn.

*Institute for Theoretical Physics, University of Innsbruck, A-6020 Innsbruck, Austria.*Introduction:

The electron-current driven collisionless ion wave instability has been extensively investigated in the single-ended Q-machines at Innsbruck and Risø /1-4/. It is excited by applying a sufficiently large d.c. bias (ϕ_G) to an electrode (grid or plate) immersed into the plasma column and appears to be a strongly nonlinear standing wave between the hot plate (HP) and the exciting electrode.

Recent experiments have shown that the onset of the instability depends sensitively on the type of the exciting electrode. In the present contribution we report on comparative measurements in which both a grid (G) and a cold plate (CP) were used. A qualitative explanation is given.

Setup and Results:

The experiments were carried out in the Innsbruck Q-machine /1/. The plasma, produced by ionization of sodium on a hot tungsten plate ($T = 2000$ K), is contained in an axial magnetic field B of 2250 G. The exciting electrodes, whose dimensions exceed the cross section of the plasma column, are perpendicular to B and located at a distance $L = 35$ cm from HP. CP is a massive tungsten plate, whereas G is a tungsten mesh grid with wire diameter $d = 0.02$ cm, meshwidth $a = 0.2$ cm, and hence an optical transparency $\tau = 81\%$.

The dependence of the instability on the exciting d.c. bias is investigated with the "unperturbed" density (i.e. with floating electrodes) as parameter. The latter is chosen for the following reasons: (i) In the unperturbed state, the electrons have a full Maxwellian velocity distribution, so that the classical determination of densities from probe characteristics yields reliable results. This is not the case for $\phi_G > 0$ since then the electrons are drifting with non-Maxwellian velocity distributions, and additional modifications are introduced by the instability. (ii) It will be

shown below that choosing the unperturbed density as a parameter is convenient in relating our theoretical considerations to the experimental evidence.

In what follows, the instability ($f = 4-5$ kHz) is characterized by the saturation amplitude A_G and the spectral bandwidth Δf of the a.c. component of the current flowing through the exciting electrode. Fig.1 shows

the dependence of A_G and Δf in the case of grid excitation for three different densities. Each amplitude curve has two regimes: for small ϕ_G , A_G is small and grows slowly.

Above a certain point, the curve bends upwards and then increases linearly with $\sqrt{\phi_G}$, which is why we have chosen the square root scale for ϕ_G on the lower abscissa. (As $\sqrt{\phi_G}$ is proportional to the velocity with which an electron reaches the grid plane, $v_g = \sqrt{2e\phi_G/m}$, we have plotted v_g/v_e , with $v_e = \sqrt{2kT_e/m}$, on the upper abscissa.) We define the threshold of the standing ion-wave instability, ϕ_{thr} , as that value of ϕ_G at which the straight regression line of the second regime intersects the ϕ_G -axis. This definition is supported by preliminary experimental findings which seem to indicate that below this threshold the instability has the character of a travelling wave, whereas for large

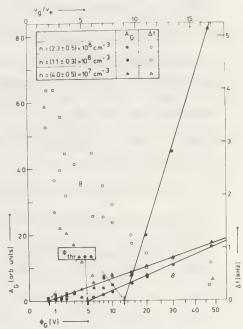


Fig.1

ϕ_G it has clearly been shown to be a standing wave /1-3/. Considering the Δf -values displayed in Fig.1 we observe that above the threshold the instability has a pronounced peak in the frequency spectrum.

As is already evident from the sample curves of Fig.1, ϕ_{thr} increases with the unperturbed density n , see Fig.2. The solid line corresponds to the linear regression $\phi_{thr} = -0.4 + 4.8 \times 10^{-8} n$.

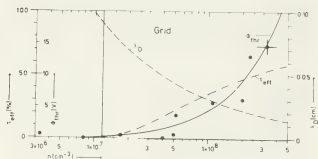


Fig.2

The results of comparative measurements where G is replaced by CP are shown in Fig.3.

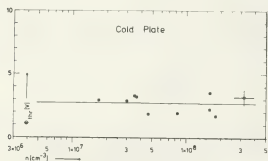


Fig.3

Note that in this case ϕ_{thr} is essentially independent of n .

Discussion:

Following Kuhn /5/, we explain the increase in ϕ_{thr} with n for grid excitation by the screening effect of the space charge sheaths around the grid wires. For small values of ϕ_G each wire is surrounded by a sheath whose thickness is of the order of the Debye length, $\lambda_D = (\kappa T_e / 4\pi n e^2)^{1/2}$. Thus we may speak of an effective grid area, which is roughly given by the geometric grid area plus the Debye sheaths. Following this argument we can define an effective transparency $\tau_{eff} = (a - \lambda_D - d/2)^2 / a^2$, which is plotted together with λ_D in Fig.2. Physically speaking, the

increase in τ_{eff} with n means that for the same ϕ_G a smaller fraction of the incoming particles is affected by G if the unperturbed density is increased. In other words, to perturb the same fraction of particles a higher bias ϕ_G is needed for higher n . This also implies that ϕ_{thr} , the grid bias at which the net electron drift is just sufficient for the onset of the instability, should increase with n . This expected behaviour is clearly reflected by the measured ϕ_{thr} -values in Fig.2

The vertical solid line in Fig.2 indicates the density where the Debye sheaths start coalescing. For lower densities, Debye shielding becomes essentially unimportant and G is equivalent to an ideal plate. In this case we expect very low values of $\phi_{thr} / 6V$, which is in accordance with Fig.2.

From the above considerations we should expect that in the case of plate excitation ϕ_{thr} should also be small and nearly independent of n . The latter feature is demonstrated by Fig.3. However, we have not yet found an explanation of the relatively large values of $\phi_{thr} \approx 2-3$ V. Future investigations will concentrate on clarifying the role of surface contamination which could be one of the reasons for this discrepancy.

Acknowledgements:

We thank Prof.F.Cap for his interest and support, and Drs.J.J.Rasmussen and G.Auer for valuable discussions. This work was supported by Fonds zur Förderung der wissenschaftlichen Forschung (Austria) under grant Nos. 2781 and S-18/o2.

References:

- /1/ N.Sato et al., Phys.Fluids **19** (1976), 70.
- /2/ R.Schrittwieser, Phys.Lett. **65A** (1978), 235.
- /3/ P.Michelsen et al., Plasma Phys.in print.
- /4/ R.Hatakeyama et al., Phys.Rev.Lett. submitted.
- /5/ S.Kuhn, Plasma Phys. submitted.
- /6/ M.T.C.Fang and S.Kuhn, submitted to this conference.

ON THE EXAMPLE OF FAST LANGMUIR SOLITONS EXISTENCE IN NON-EQUILIBRIUM PLASMA

F. KH. Khakimov and V.N. Tsytovich^{*}.^{*}Tajik State University, Dushanbe, U.S.S.R.^{*}Physical Institute of Academy of Sciences U.S.S.R., Moscow, U.S.S.R.

In present paper the example of non-maxwellian distribution at which existence of fast Langmuir solitons is presented.

Let us consider as an example the distribution of a type:

$$\Phi = \exp\left\{-\frac{v^2}{2v_T^2}\right\}^{\mu} \int \mu/\sqrt{2} \Gamma(\frac{1}{2}\mu) v_T \quad (1)$$

Nonlinear processes are determined by the following effective temperatures

$$T_{eff} = T_e \Gamma^2(\frac{\mu}{2}) / 2 \Gamma(\frac{3}{2}\mu) \Gamma(1 - \frac{1}{2}\mu)^{\mu} \quad (2)$$

$$T_{eff}^2 = T_e^2 \frac{\Gamma^3(\frac{1}{2}\mu)(3-2\mu)}{4 \Gamma^2(\frac{3}{2}\mu) \mu^2 \Gamma(2 - \frac{1}{2}\mu)} \quad (3)$$

From the expressions cited it is clear that they may be reduced to zero and even become negative. So T_{eff} and T_{eff}^2 vanish when $\mu = \frac{1}{2}$ and $\mu = \frac{3}{2}$ and diverge for small velocities when $\mu < 1/2$ and $\mu < 3/2$.

There is a unique distinguished value of $\mu = 1$ (Maxwellian solution), for which $T_{eff}^2 = T_e^2 > 0$ and integral is converging. This shows, that for higher nonlinearities Maxwellian distribution is perfectly distinguished and small deviations from Maxwellian distribution change the result qualitatively. It can be easily understood qualitatively that for cubic nonlinearities when $\mu < 1/2$ and higher nonlinearities when $\mu < 3/2$ divergence occurs because of illegitimacy of expansion in pa-

rameter $\Delta\omega/\kappa v$, for it is not determined by average particle velocity but by the velocities of those particles for which this parameter is of order of the unit. For higher nonlinearities the sensitivity of the result to the particle distribution at small velocities begins already when $\mu < 3/2$. Thus, nonlinear effects and especially higher nonlinearities may be enhanced to a large extent for nonmaxwellian distributions and besides that they may change the signs of nonlinear interactions for comparatively small changes of particle distributions.

For $\mu < 1/2$ formula (3) does not fit, and if it is supposed that distribution (1) is valid for $v > v_*$, and for $v < v_*$ there is a plateau, then for $v_* < v_T$ only a small part of low velocity particles will have distribution different from (1). For this case instead of (3) we'll have

$$T_{eff}^2 = T_e^2 \frac{\Gamma^3(\frac{1}{2}\mu)(3-2\mu)}{4 \Gamma^2(\frac{3}{2}\mu) \mu^2 (1-\mu)} \left(\frac{v_*}{v_T}\right)^{3-2\mu}, \quad (4)$$

$v_* < v_T$

If $\frac{1}{2} < \mu < 1$, T_{eff} and T_{eff}^2 are positive, but T_{eff} is $\lambda = (v_*/v_T)^{\frac{3}{2}\mu}$ times smaller than T_{eff} . For $\mu < 1/2$ sensitivity to the forming of plateau at $v < v_*$ appears for T_{eff} . Thus, if $\mu = \frac{1}{2}$ in (4), we'll obtain the case when for $M = v/v_* = 1$ higher nonlinearities give the same contribution as cu-

bic ones at

$$E^2/4\pi nT \gtrsim v_*^2/v_T^2, v_* < v_* \quad (5)$$

or, in other words, the nonlinear parameter of expansion is not $E^2/4\pi n_e m_e v_{Te}^2$ but $E^2/4\pi n_e m_e v_*^2$. At $M \gg 1$ the criterion becomes more rigid

$$\frac{E^2}{4\pi n_e T_e} \gtrsim \frac{v_*^2}{v_T^2} M^4, M \ll \sqrt{m_i} \frac{v_*}{\sqrt{T_{eH}}}, M = \frac{v_* \sqrt{m_e}}{\sqrt{T_{eH}}} \quad (6)$$

So, the appearance of fast solitons for nonequilibrium distribution when criterion (6) is valid may be expected.

Two temperature Maxwellian distributions of the type

$$\Phi = \frac{n_1/n_0}{\sqrt{2\pi} v_*} e^{-\frac{v^2}{2v_*^2}} + \frac{1}{\sqrt{2\pi} v_{Te}} e^{-\frac{v^2}{2v_{Te}^2}}; n_1 \ll n_0 \quad (7)$$

may be examined as a particular example.

Let us suppose a small part of particles to be cold $v_* < v_{Te}$. Then, for

$v_* \ll v_0 \ll v_{Te}$ we have

$$T_{eH}^{-1} = T_e^{-1} \left(1 - \frac{n_1}{n_0} \frac{v_{Te}^2}{v_*^2} + i \sqrt{\frac{\pi}{2}} \frac{v_0}{v_{Te}} \right) \quad (8)$$

Small values of T_{eH} are appearing at $\frac{v_0}{v_{Te}} \approx \sqrt{\frac{n_1}{n_0}} + \delta$; $\delta \sim n_1/n_0$, i.e. when imaginary and real parts are of the same order of magnitudes. At $\sqrt{\frac{n_1}{n_0}} \gg \delta \gg n_1/n_0$ the real part of T_{eH} dominates. It can be readily seen, that $1/T_{eH}^2$ is determined by low energy part in spite of small amounts of such particles

$$\frac{1}{T_{eH}^2} = \frac{1}{T_e^2} \left(1 + \frac{n_1}{n_0} \frac{3v_{Te}^2}{v_*^2} \right) \approx \frac{3}{T_e^2} \frac{n_1}{n_0} \quad (9)$$

Then the condition of dominating of the fifth order nonlinearity over the field be

$$\delta \sqrt{\frac{n_1}{n_0}} \left(1 - u^2 2\delta \sqrt{\frac{n_0}{n_1}} \right)^2 \ll \frac{E^2}{4\pi n_e T_e} \ll \frac{m_e}{m_i} u^2 \approx \frac{n_1}{n_0} \quad (10)$$

The last approximate inequality is valid provided soliton velocity being near the threshold $u^2 \gtrsim u_{cr}^2 \approx 4/25 \sqrt{n_1/n_0} \approx \frac{m_i}{m_e} \frac{n_1}{n_0}$ (the velocity is bigger than the sound velocity determined by effective temperature T_{eH}), at the negativity of the fifth order nonlinearity being fulfilled only under these conditions. For weak extinction the fulfillment of the condition $\frac{m_e}{m_i} \ll \frac{n_1}{n_0} \ll \left(\frac{m_e}{m_i} \right)^{2/3}$ is necessary and, therefore,

$$1 \ll u^2 < (m_i/m_e)^{4/3} \quad (11)$$

If the condition of essential over-thresholdness is fulfilled, then the analysis similar to the conducted above shows that the relation (11) remains. So when $T_{eH} \gg T_e$ and $u^2 \gg T_{eH}/T_e$ fast Langmuir solitons are described by the equation with the nonlinearity of the fifth order over the field, i.e.

$$i \frac{\partial \mathcal{E}}{\partial \tau} + \frac{\partial^2 \mathcal{E}}{\partial z^2} = -\beta |\mathcal{E}|^4 \mathcal{E}$$

$$\beta(u) = \frac{3}{4} \left(\frac{T_{eH}}{T_e} \right)^3 [u^2 - T_{eH}/T_e]^{-3} \quad (12)$$

$$v \int \frac{v_{Te}}{\sqrt{\frac{2}{3}\pi} v_{Te} - u} \frac{\partial}{\partial v} \frac{v_{Te}}{\sqrt{\frac{2}{3}\pi} v_{Te} - u} \frac{\partial \Phi}{\partial v} dv$$

which has the solution:

$$\mathcal{E} = \frac{\mathcal{E}_0 \exp \left\{ -i \Omega \tau + i \frac{u}{2} (z - u\tau) \right\}}{\sqrt{\operatorname{ch} \frac{2\sqrt{\beta}}{\sqrt{3}} (z - u\tau) \mathcal{E}_0^2}} \quad (13)$$

The shown example, in spite of its particular character demonstrates, that in nonequilibrium plasma the appearance of fast Langmuir solitons is possible.

VISCOUS DAMPING OF THE MAGNETO-ACOUSTIC OSCILLATIONS, MAO, IN BOUNDED PLASMAS

Yu. S. Sayasov.

Institute of Physics, University of Fribourg, Fribourg, Switzerland.

A sound wave reflected from a solid boundary is known to experience strong absorption connected with the fact that in a narrow boundary layer, where mass velocity \vec{v} drops quickly to zero, marked velocity gradients arise. As a result the viscous force (an example of a monoatomic gas) $\vec{F} = \eta (\Delta \vec{v} + \frac{1}{3} \text{grad div } \vec{v})$, η is viscosity coefficient, can take there big values thus influencing essentially the damping mechanism [1], §77). These considerations are certainly applicable also for MAO in bounded plasmas. However, it seems that much viscous damping of MAO in bounded plasmas due to the high velocity gradients at the boundary was never investigated. In what follows an account of theoretical results obtained in this direction in [2] is presented.

Restricting ourselves with cold, monoatomic, quasineutral, isothermal, homogeneous plasmas in a magnetic field $\vec{B}_0 = \text{const}$, one can write the MHD-equations of the one-fluid approximation, accounting for the viscous force \vec{F} , in the form:

$$\rho \frac{\partial \vec{v}}{\partial t} = \frac{1}{c} [\vec{j} \vec{B}_0] + \vec{F}, \quad \text{rot } \vec{H} = \frac{4\pi}{c} \vec{j} \\ \vec{j} = \sigma (\vec{E} + \frac{1}{c} [\vec{v} \vec{B}_0]) - \omega_{ce} [\vec{j} \vec{B}_0] / \nu B_0, \quad \text{rot } \vec{E} = -\frac{\partial \vec{H}}{\partial t} \quad (1)$$

where $\sigma = \frac{\omega_p^2}{4\pi\nu}$ is plasma conductivity, ω_p is plasma frequency, ν is electron collision frequency, ω_{ce} is electron cyclotron frequency, ρ is mass density. System (1) must satisfy at a solid boundary some constraints imposed on the mass velo-

city \vec{v} . Here are some results following from (1) for a particular case of MAO in the bounded cylindrical plasmas.

1. MAO in a long cylindrical plasma column surrounded by a dielectrical boundary of the radius a and situated in an axial magnetic field B_0 . Excitation of MAO of frequency ω is performed by a coil having the same radius and the same length as the plasma column. (These assumptions correspond to the experiments described e.g. in [3,4]). The only non-zero components of the mass velocity \vec{v} and of the high-frequency magnetic field \vec{H} are resp. the radial component v_r and axial component H_z . Solutions of (1) are defined uniquely by the boundary conditions $v_r(a) = 0$ and $H_z(a) = H_{ex}$ (field generated by the coil). Introducing dimensionless quantities $\epsilon_1 = \frac{\omega v_m}{c A}$, $\epsilon_2 = \frac{\omega v_h}{c A} (v_m = \frac{c^2}{4\pi\sigma}$, $v_h = \frac{4\pi}{3\rho}$, $c_A = \frac{B_0}{\sqrt{4\pi\rho}}$ is Alfvén velocity) and making assumptions $\epsilon_1 \ll 1$, $\epsilon_2 \ll \epsilon_1$ (weak dissipation), often fulfilled in experiments, one can formulate main result as follows. The ratio of the magnetic field amplitudes at the cylinder axis $H_z(0)$ and at the boundary H_{ex} is given by

$$\frac{H(0)}{H_{ex}} = \frac{1}{J_0(k) - i \lambda J_1(k)}, \quad k = \frac{\omega a}{c_A} (1 + \frac{1}{2} \epsilon_1) \quad (2)$$

where J_0 , J_1 are Bessel functions, $\lambda = \sqrt{\frac{\epsilon_2}{\epsilon_1}} = \sqrt{\frac{\nu k}{v_m}}$.

For the frequencies close to the frequency $\omega_0 = \frac{q_0 c_A}{a}$, $q_0 = 2,4$ ($J_0(q_0) = 0$) of the first magneto-acoustic resonance, MAR, the modulus of this

ratio can be represented in the form

$$N = \frac{|H_z(0)|}{H_{ex}} = \frac{1}{q_0 J_1(q_0 a)} \left[\left(\frac{\omega - \omega_0}{\omega_0} \right)^2 + \gamma^2 \right]^{-1/2} \quad (3)$$

where $\gamma = \frac{1}{2} \epsilon_1 + \frac{1}{q_0} \lambda = \frac{q_0 v_m}{2 c_A a} + \frac{v_h}{q_0 c_A a}$, ($\delta = \frac{\sqrt{v_h v_m}}{c_A}$ is boundary layer thickness pertaining to these MAO).

Influence of the velocity becomes appreciable according to this formula if $\frac{q_0 v_m}{2 c_A a} < \frac{v_h}{q_0 c_A a}$, i.e. for $\frac{v_h}{v_m} > 2.9 \frac{\delta}{a} \ll 1$ whereas for the infinite plasmas

the corresponding condition is much more stringent:

$\frac{v_h}{v_m} > 1$. For a fully ionized monoatomic plasma we

obtain, using expressions for the electron-ion

collision frequency ν and the ion-ion viscosity

coefficient η given in [5], the formula

$\gamma = \frac{10^6 \Lambda}{c_A a T^{3/2}} + \frac{2.4 \cdot 10^6 T^2}{A^{1/4} \Lambda n^{1/2}}$, where Λ is the Coulomb

logarithm, A is atomic weight, T is temperature in

eV and $n \text{ cm}^{-3}$ is electron density. (For $a = 5 \text{ cm}$,

$B_0 = 10^3 \text{ Gauss}$, $n = 10^{15} \text{ cm}^{-3}$, $A = 1$, viscosity be-

gins to play an essential role according to this

expression if $T > 2 \text{ eV}$). Similar conclusion can be

drawn also for plasmas with comparable concentrations of ions and neutrals.

As follows from (3) maximal value $N(\omega_0) = 0.8/\gamma$

corresponding to the first MAR is reduced in a result of the viscous effect by a factor $(1 + \frac{2\lambda}{q_0 \epsilon_1})^{-1}$.

This conclusion seems to offer a plausible explanation of a considerable reduction of the experimental values of $N(\omega_0)$ compared with those calculated without accounting for the viscous effect. (See e.g. Fig. 12 in [3], Fig. 10 in [4]).

2. MAO are generated by a short coil in a long cy-

lindrical plasma column of radius a . (Otherwise

the assumptions, corresponding to the experiments

described e.g. in [6, 7], are the same as for

case 1). As follows from the system (1), solved

under the boundary condition $v_r(0) = 0$, the at-

tribution of the axial magnetic field H_z at sufficiently long distances z from the coil follows the

formula $H_z \sim e^{-\kappa z}$, $\kappa = \text{Im} k_z$, where k_z is a root

(having smallest imaginary part) of the equation

$J_0(k_z a) - i \lambda J_1(k_z a) = 0$ and k_z is the radial

wave-number defined e.g. in [4]. (We retain here

only the members of the order $\lambda = \sqrt{\frac{\nu}{v_m}}$, neglecting

corrections to k_z which are of the order of $\frac{\nu_h}{v_m}$).

If $\frac{\omega - \omega_0}{v} \ll 1$ (usual MHD-approximation) one can

represent k_z in the form: $k_z = [q^2 - q_0^2 + i(\epsilon_1 q^2 +$

$2\lambda q_0)]^{1/2}$, $q = \frac{\omega a}{c_A}$. For ω not too close to the

frequency ω_0 of the first MAR

$\kappa = \text{Im} k_z = \frac{q^2 \epsilon_1 + 2\lambda q_0}{2\sqrt{q^2 - q_0^2}}$. According to this

expression the viscous effect leads to an addi-

tional damping with distance z described by the

factor $\exp(-\frac{\lambda q_0 z}{\sqrt{q^2 - q_0^2}})$, which can be very im-

portant for not too small values of the parameter λ .

References

- [1] L. Landau, E. Lifshits, Fluid Mechanics (Pergamon), 1960
- [2] Yu. S. Sayasov (Helv. Phys. Acta, submitted for publication)
- [3] E. Cantieni, H. Schneider, Helv. Phys. Acta 36, 993 (1963)
- [4] H. P. Elmiger et al. Helv. Phys. Acta 50, 871 (1977)
- [5] S. I. Braginskii, Rev. Plasma Phys. (Ed. M. A. Leontovich, New York 1965)
- [6] B. Lammers, Dissertation, Ruhr-Universität Bochum, 1974
- [7] B. Lammers, Z. Naturforsch. 31a, 924 (1974)

ONE-DIMENSIONAL FOURIER SPECTRUM OF TURBULENT IONIZATION WAVES

J. Skála, J. Krása and V. Peřina.

Institut of Physics, Czech. Academy of Science, 180 40 Prague 8, Na Slovance 2, Czechoslovakia.

The turbulence of unstable ionisation waves often takes place in the positive column of low current and low pressure discharge in noble gases. Experimentally, the neon discharge is abounding in various mechanisms leading to a loss of wave coherence and to the onset of strong regular wave motion [1, 2].

Lately, a great attention was paid to experiments concerning correlation motion measurements of such turbulent ionisation waves. These measurements have shown that the correlation length L_c of fully developed wave turbulence can be shorter than the mean wavelengths λ_p of the wave packets [3, 4]. In the presented contribution, measurements on turbulent ionisation waves are referred for which wave-number filter [5] was used with subsequent frequency analysis. Two-dimensional Fourier spectra $F(k, \omega)$ were obtained by this method.

The light emitted from the discharge tube $I(x, t)$ was passing through the filter composed of the stripes, whose transparence changes along the axis as $\cos(1/2(1 + m \cos(kx)))$, where m is the modulation depth and $k = 2\pi / \lambda_f$ is the wavenumber corresponding to the wavelength λ_f of the stripes, see Fig. 1. The signal from photomultiplier P , presenting the whole light, passing through is then proportional to the real part of the space Fourier spectrum

$$\langle I(x, t) \cos(kx) \rangle_L \sim \text{Re} \left[\int_{-\infty}^{\infty} I(x, t) e^{-ikx} dx \right] \quad \dots (1)$$

if we assume the integration length L to be much larger than the correlation length L_c . The frequency spectrum of the signal (I) in a conventional frequency analyser is then proportional to the absolute value of the Fourier transformation of the light fluctuations $I(x, t)$. By changing the wavelength λ_f of the filter a time-space Fourier spectrum $F(k, \omega)$ on the ω - k plane can be measured.

The space filter was realized by a loop of the film, on which a system of hyperbolic stripes was transferred photographically. In this arrangement, wavenumber scale is proportional to the

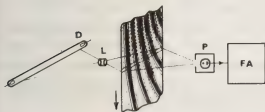


Fig. 1. Experimental arrangement: D - discharge tube, L - lens, P - photomultiplier, FA - frequency analyzer.

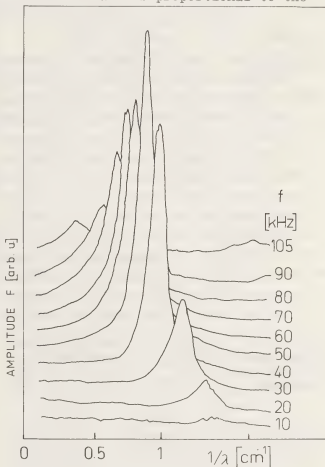


Fig. 2. Two-dimensional spectrum $F(1/\lambda, f)$ of the light fluctuations of positive column of the neon discharge ($p = 5.2$ Torr, $i = 42$ mA, tube diameter 0.6 cm). $\lambda = 2\pi / k$ and $f = \omega / 2\pi$.

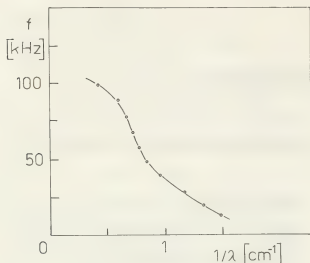


Fig. 3. Dispersion curve of the turbulent ionisation wave evaluated from Fig. 2.

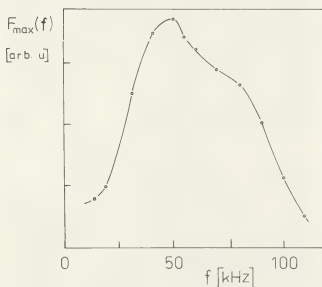


Fig. 4. The course of the maximum values of the spectrum $F_{\max}(f)$ over the dispersion curve ω_{\max} as function of the frequency.

vertical shift of the film. Another possibility for realization of the space filter is the use of two crossed lattices. In this case, the wavenumber of moiré patterns is proportional to the angle between the both lattices. The advantage of this filter is in a more genuine sinusoidal shape of the transparency.

The measurements were made in a discharge tube with the internal diameter 0.6 cm. The distance between the electrodes was 90 cm. The neon pressure was 5.2 Torr and the discharge current 42 mA. The measurements were performed in the part of the positive column, where the wave turbulence was stationary.

Fig. 2 shows a typical shape of the two-dimensional spectrum $F(k, \omega)$. The dispersion curve $\omega = \omega(k)$ which is taken to be the projection of the crest line of $F(k, \omega)$ to the ω - k plane is plotted in Fig. 3. Another important function specifying the properties of turbulent ionisation waves is the crest height over the dispersion curve. As Fig. 4 shows, the crest height exhibits an asymmetry with regard to the center wave mode for which $F(k, \omega)$ attains a maximum value. This indicates the different properties of the turbulent ionisation wave in the region of lower and higher frequencies and wavenumbers.

The shape of the frequency and/or wavenumber spectrum itself at higher frequencies or wavenumbers is markedly influenced by the second harmonics of the basic wave, the trace of which is visible in our case at the frequency 105 kHz. Nevertheless the difference between the frequency spectrum and the wavenumber spectrum is mostly given by the asymmetry of $F(k, \omega)$ along the dispersion curve.

The procedure as described above is thus suitable for an evaluation of the main characteristics of the light fluctuations caused by the turbulent ionisation waves moving down the positive column of the gas discharge.

References

- [1] Perkin R.M., Krása J. and Pekárek L., J Phys D: **8** (1975) 161
- [2] Krása J., Perkin R.M. and Pekárek L., J Phys D: **7** (1974) 2541
- [3] Grabec I. and Poberej S., Plasma Phys. **11** (1969) 519
- [4] Krása J., Peřina V. and Rothhardt L., Proc. 13th I.C.P.I.G. Berlin 1977, p.287
- [5] Skála J., Czech.J.Phys. **B23** (1973) 284
- [6] Bendat J.S., Principles and applications of random noise theory. Russ. Nauka Moscow 1965
- [7] Krása J. and Peřina V., Phys Letters **66A** (1978) 379

THE BEHAVIOUR OF WEAKLY IONIZED PLASMA WITH NON-ZERO NEUTRALS TEMPERATURE IN AN EXTERNAL D.C. ELECTRIC FIELD OF MODERATE INTENSITY

V.J. Zigman and B.S. Milić.

Institute of Physics, Department of Physics and Meteorology, Faculty of Natural and Mathematical Sciences, Belgrade, Yugoslavia.

In order to investigate further the dynamically unstable modes in weakly ionized plasmas placed in the external electric field discussed in [1], we consider here the behaviour of the modes analogous to the ones obtained in [1,2] assuming now that the applied electric field intensities (E_0) are intermediate or low, and that the effects of the non-zero temperature of the neutrals (T_n) have to be taken into account.

To this end, a new form of the electron distribution function for $T_n \neq 0$ is derived here. The Margenau-Davydov distribution was assumed as the starting point, and only elastic electron-neutral collisions were taken into account, and they were described by the billiard-ball model. The exact result for the isotropic part of this function is obtained in a straightforward way, and is of the following form:

$$f_e^{(0)}(v) = C e^{-\frac{m_e v^2}{2kT_n}} \left[\frac{4kT_n}{m_e} \frac{v^2}{v_D^4} + 1 \right] \quad (1)$$

where $v_D = \left(\frac{8mi e^2 E_0^2}{6 m_e^2 v_{10}} \right)^{1/4}$ is the characteristic Druyvesteinian velocity, and C is the normalization factor. It is clearly seen that in the limits $E_0 \rightarrow 0$ and $E_0 \rightarrow \infty$ the above function becomes a Maxwellian and a Druyvesteinian function respectively. For moderate field intensities, but still below the characteristic plasma electric field, $E_p \approx \left(\frac{6 m_e^2 kT_n v_{eff}^4}{mi e^2} \right)^{1/4}$, which is ~ 1 V/m for typical laboratory plasma, an expansion in binomial series in the

above expression is appropriate, and the following form of the electron distribution function results:

$$f_e^{(0)}(v) = C e^{-\frac{m_e v^2}{2kT_n}} \left[1 + \frac{m_e v^2}{2kT_n} + \left(\frac{1}{8} \frac{m_e^2}{k^2 T_n^2} - \frac{1}{v_D^4} \right) v^4 \right] \quad (2)$$

It can be easily seen that this approximate form of the function (1) is not suitable either for E_0 's well above the plasma electric field, or for E_0 's near zero.

The components of the plasma dielectric tensor (PDT) were then evaluated with the above form of the electron distribution function by an iterative procedure, up to the second order in \bar{u}/v_{Te} . The small terms of this order of magnitude have already been shown to be of importance if the non-potential (non-longitudinal) oscillations of the plasma are analyzed. The results for the components of the PDT generalize the expressions obtained in [1,2] and will be omitted here. The pertaining dispersion equation for the low frequency range $\frac{\omega_{pe}^2}{\omega^2} \gg \frac{\omega_{pe}^2}{k^2 v_{Te}^2}$ and for the waves propagating at right angles to the direction of E_0 has been found to be:

$$\left\{ c^2 k^2 + \omega_{pe}^2 - \omega_{pe}^2 \left[2F \frac{\bar{u}^2}{v_{Te}^2} - \frac{\omega^2}{k^2 v_{Te}^2} + 2G \frac{\omega}{k v_{Te}} - \frac{\bar{u}}{v_{Te}} \right] - \sqrt{\frac{F}{2}} k \frac{e E_0}{m_e \bar{u} k v_{Te}} + i \sqrt{\frac{F}{2}} D \frac{\omega}{k v_{Te}} \right\} \left\{ 1 - \frac{\omega_{pe}^2}{\omega^2} + \frac{1}{8} \frac{\omega_{pe}^4}{k^2 v_{Te}^2} - \frac{\bar{u}^2}{v_{Te}^2} \right\} = 0 \quad (3)$$

Here F , D , R , G denote dimensionless functionals of $f_e^{(0)}(v)$, weakly dependent on

E_0 through the small parameter $(v_N/v_D)^4$, where $v_N = (2\pi T_n/m_e)^{1/2}$, and \bar{u} and v_{Te} are the electron effective drift and thermal velocities respectively. For the function (2), these quantities are given by:

$$F = \frac{4\pi}{3} C \frac{v_{Te}^2}{\bar{u}^2} \frac{e^2 E_0}{m_e v_{Te}} \frac{1}{m_e} \left\{ \int_0^{\infty} \frac{e^{-\left(\frac{v}{v_N}\right)^2}}{v_N(v)} \left(2 \frac{v^2}{v_N^2} - \frac{1}{2} \frac{v^3}{v_N^3} \right) dv + \right. \\ \left. + \left(\frac{v_N}{v_D} \right)^4 \int_0^{\infty} \frac{e^{-\left(\frac{v}{v_N}\right)^2}}{v_N(v)} \left(-4 \frac{v^2}{v_N^2} + 4 \frac{v^5}{v_N^5} + \frac{v^3}{v_N^3} \right) dv \right\} \quad (4)$$

$$D = 3 \cdot 2^{1/2} \pi^{3/2} C \frac{v_{Te} v_N^2}{m_e} \left[1 - \frac{2}{3} \left(\frac{v_N}{v_D} \right)^4 \right] \quad (5)$$

$$R = \frac{2^{1/2} 75}{16} \pi^2 C v_{Te} \bar{u} v_N^3 \frac{m_e v_{Te}}{e E_0} \frac{1}{m_e} \left[1 - \frac{16}{15} \left(\frac{v_N}{v_D} \right)^4 \right] \quad (6)$$

$$G = 16 \pi C \frac{v_{Te}^2}{\bar{u}} \frac{e E_0}{m_e v_{Te}} \frac{1}{m_e} \left[1 - \frac{4}{3} \left(\frac{v_N}{v_D} \right)^4 \right] \quad (7)$$

$$\bar{u} = \frac{3\pi^2}{2\pi^2} C \frac{v_{Te}^3}{v_N} \frac{e E_0}{m_e v_{Te}} \frac{1}{m_e} \left[1 - \frac{4}{3} \left(\frac{v_N}{v_D} \right)^4 \right] \quad (8)$$

$$(v_{Te})^2 = \pi^{3/2} \frac{15}{4} C \frac{v_N}{m_e} \left[1 - \frac{2}{5} \left(\frac{v_N}{v_D} \right)^4 \right] \quad (9)$$

where

$$v_s(v) = 2\pi \int_0^\pi \sin^2(\nu, \theta) \left[1 - P_s(\cos \theta) \right] \sin \theta d\theta \quad (s=1,2) \quad (10)$$

and $v_1(v) = v_{Te} v$ for the billiard-ball model.

From (3), the following spectra are obtained:

$$\omega_{\pm} = -\gamma \frac{\omega_{ie} \omega_{ie}^*}{\kappa v_{Te}} \frac{\bar{u}}{v_{Te}} Q \pm \\ \pm \omega_{ie} \left[1 + \omega_{ie}^2 \left(\sqrt{\frac{2}{\pi}} R \frac{e E_0}{m_e \bar{u} \kappa v_{Te}} - 2F \frac{\bar{u}^2}{v_{Te}^2} - \right. \right. \\ \left. \left. - \gamma \frac{2 \omega_{ie}^2}{\kappa^2 v_{Te}^2} \frac{\bar{u}^2}{v_{Te}^2} + \frac{\omega_{ie}^2}{\kappa^2 v_{Te}^2} \right) Q + \gamma \frac{2 \omega_{ie}^2 \omega_{ie}^2}{\kappa^2 v_{Te}^2} \frac{\bar{u}^2}{v_{Te}^2} Q \right]^{1/2} \quad (11)$$

where

$$Q = \left[C^2 \kappa^2 + \omega_{ie}^2 + \gamma \frac{2 \omega_{ie}^2}{\kappa^2 v_{Te}^2} \frac{\bar{u}^2}{v_{Te}^2} - \frac{\omega_{ie}^2 \omega_{ie}^2}{\kappa^2 v_{Te}^2} \right]^{-1} \quad (12)$$

These two modes have been found to be weakly damped; the attenuation coefficient as determined from the $\text{Im} \omega$ is given by:

$$\gamma^{\nu} = -\frac{1}{2} \omega_{ie}^* \omega_{ie} \sqrt{\frac{2}{\pi}} R \frac{e E_0}{\kappa v_{Te}} \left[(C^2 \kappa^2 + \omega_{ie}^2) \omega_{ie}^2 - \right. \\ \left. - (2F \frac{\bar{u}^2}{v_{Te}^2} - \sqrt{\frac{2}{\pi}} R \frac{e E_0}{m_e \bar{u} \kappa v_{Te}}) \omega_{ie}^2 \omega_{ie}^* - \gamma \frac{\bar{u}^2}{\kappa v_{Te}^2} \omega_{ie}^2 \omega_{ie}^* \omega \right]^{-1} \quad (13)$$

This is in accordance with the behaviour of the analogous modes in strong electric fields for the direction of propagation perpendicular to E_0 . However, as a result of non-zero T_n and comparatively small intensities of the externally applied electric field E_0 , in the situation considered in this paper the term containing F in eq. (11) may become very large and this fact may lead to dynamic instability of these two modes. It is to be noted that the numerical values of the functionals given by eqs. (4)-(7) are all of the order of unity, as has been shown previously [1]. In the case considered here, only D , R and G are of this order of magnitude. The functional F , eq. (4), may become much larger, as can be easily verified for a typical set of plasma parameters ($T_n \sim 10^3$ K, $n_n \sim 10^{19} \text{ m}^{-3}$, $n_e \sim 10^{15} \text{ m}^{-3}$, $\phi_{en} \sim 10^{-20} \text{ m}^2$). The possibility of the development of dynamic instability with the modes considered is, hence, a specific consequence of $T_n \neq 0$ and of $E_0 \lesssim E_p$.

References

- [1] Žigman, V.J., Milić, B.S., Proc. of the VIIIth Yugoslav S.P.I.G., Dubrovnik, 1976, p. 491.
- [2] Žigman, V.J., Milić, B.S., Third International Congress on Waves and Instabilities in Plasmas, Paris, 1977, Book of Abstracts, p.175

INTERACTION OF NONLINEAR ION-ACOUSTIC WAVES

C.H. Su.

Division of Applied Mathematics, Brown University, Providence, R.I. 02912, U.S.A.

We study the head-on collisions between two solitary waves in a cold plasma described by the following equations:

$$n_t + (nu)_x = 0, \quad (1)$$

$$u_t + \left(\frac{u^2}{2} + \psi\right)_x = 0, \quad (2)$$

$$\psi_{xx} = n - e\psi, \quad (3)$$

where n, u denote density and velocity of positive ions, ψ a dimensionless potential. Equation (3), the Poisson equation, indicates that the electrons are taken to be in thermal equilibrium. The existence of solitary waves in this system has been demonstrated by Sagdeev (1966), Su and Gardner (1969). The catch-up collision of a taller wave to a smaller wave can be inferred from the elegant result for the Korteweg-deVries equation done by Gardner, Green, Kruskal and Miura (1967). Here we study head-on collisions by a perturbation method making assumption of long wave (almost quasineutrality) and small amplitudes of the colliding waves. In the first order approximation we obtain that the colliding waves have their wave fields satisfying the Korteweg-deVries equation, i.e. $aS(\xi)$ and $bS(\eta)$ where $S(\xi) = \text{sech } \frac{\xi}{2}$, a, b are constants. We have used the wave-framed coordinates system

$$\xi = \sqrt{\epsilon}k(x - C_R t) + \epsilon k\theta(\xi, \eta) \quad (4)$$

$$\eta = \sqrt{\epsilon}l(x + C_L t) + \epsilon l\theta(\xi, \eta) \quad (5)$$

where ϵ is a dimensionless parameter for small amplitude, the use of $\epsilon^{1/2}$ in Eqs.

(4), (5) makes the non-neutrality correction coming into presence same as that of nonlinearity. C_R and C_L are wave speeds, θ and ϕ phase functions for the right- and left-going waves respectively. In the second order approximation in ϵ , we obtain

- (1) Quadratic terms in S are added to the linear one.
- (2) Linear ion-acoustic wave-speeds are modified by terms which depend on wave amplitudes.
- (3) The lowest order phase functions $\theta^{(0)}(\eta)$ for $\phi^{(0)}(\xi)$ are a function of η (or ξ) alone. These functions change by a constant value as their argument varies over an infinity. After the waves suffer a collision, they have a constant amount of phase shift. The signs of these phase shifts make the arrival of the waves later than they should.

The wave fields of each wave after their collision is identical to that before, i.e. the waves preserve their identities.

In the third order of approximation, the same three corrections above show up, with the quadratic term in (1) replaced by a cubic polynomials in S . However, a salient property of the phase functions comes into place, in that $\theta^{(1)}$ and $\phi^{(1)}$ are functions of both ξ and η . Emerging from their collision, both waves now will

have a phase shift which is different at different points of the wave. The wave profiles are thus distorted from what were before the collision. Since this distorted wave field does not satisfy the equation for waves which are propagated without change in shape and speed. We study the slow-time evolution of those wave fields immediately after the collision. It is found that each of these waves splits into two parts: The main part has exactly the same profile and wave velocity as the one before collision (apart with a constant phase shift). The other part has a shape of letter N highly stretched out in horizontal direction. These secondary wavelets propagate with diminishing amplitude, in the opposite direction to the propagation of the main wave.

Our main conclusion about the effect of a head-on collision between two solitary waves are

1) Constant phase shifts. The waves get retarded during their collision. However, each wave recovers its speed and shape after collision.

2) Shedding of secondary waves. Each wave sheds a secondary wave which propagates in the opposite direction of the main wave. The amplitude of these secondary waves decrease in time due to dispersion.

Gardner, C.S., Green, J. M., Kruskal, M. I
Miura, R.M., Phys. Rev. Lett. 19, 1095-10
(1967).

Sagdeev, R.Z., Rev. of Plasma Physics.
M. A. Leontovich Ed. (Consultants Bureau
Enterprises, Inc. New York), vol. 4, p. 2
(1966).

Su, C. H., Gardner, C.S., J. of Math. Phys.
10, 536-539 (1969).

NONLINEAR INTERACTION OF BEAM WAVES AND PLASMA WAVES

D.N. Wall*, R.N. Franklin*.

Department of Engineering Science, University of Oxford.

For some time now the explosive nature of the three wave interaction in which a negative energy wave decays to two positive energy waves has been examined theoretically¹. Experimental demonstrations in plasmas, with one exception², have involved cyclotron waves^{3,4} rather than non-magnetised plasma wave modes. This paper describes measurements on an electron beam-plasma configuration demonstrating the underlying interaction but, because the experiment is carried out in space, and because the group velocities are not all in the same direction, the interaction is not one of indefinite growth in the first order approximation.

The experimental apparatus used was the Culham single-ended Q-machine ARIADNE modified by the substitution of an electron gun assembly for the cold end plate. This electron gun was part of a standard travelling-wave-tube cathode with its helical wave structure. The beam was extracted at a conventional operating voltage and subsequently slowed down by an auxiliary electrode before injection into the plasma. The plasma was formed in the usual manner in a Q-machine and typical operating conditions were with a plasma frequency of 80MHz, the ions being potassium and the plasma column diameter 2.5 cm. The density of electrons within the system was measured and the beam diameter found to be approximately 2.5 mm. The beam density depended on the beam current and voltage and could be varied up to one eighth of the plasma density.

If the beam is sufficiently fast and tenuous then

the linear beam-plasma instability can be avoided as indicated in Fig. 1. This is due to the finite radial extent of plasma and beam. The instability could be 'switched on' by operating at a sufficiently low beam speed but that regime was avoided in the work which follows.

Attempts were made to observe the decay of a beam to two plasma waves according to scheme $b \rightarrow \omega + \omega'$ indicated in Fig. 1. However, the clarity of earlier work⁵ on the scheme $\omega \rightarrow \omega' + s$ involving decay of electron waves to electron waves and ion waves could not be achieved. This was due to the competing non-linear effect in which the beam wave interacts with the beam electrons and excites sideband instabilities of the beam wave⁶. An observation of $b \rightarrow \omega + s$ has been reported recently⁷.

Accordingly the measurements were restricted to the mixing case in which two waves were injected and a third observed. The resonant nature of the process was demonstrated by fixing one frequency and varying the other to maximize the amplitude of the product wave. The process was demonstrated to occur with the injected waves both plasma waves and also for the beam wave-plasma wave case.

In order to demonstrate frequency and wave number matching the product wave frequency had to be identified and in a separate experiment under the same plasma conditions its wave length under linear conditions was measured. A comprehensive set of

data obtained in this way is shown as Fig.2, where the offset from the curve is a measure of frequency and wave number mismatch. To show the three-wave nature of the process, the product wave amplitude was measured as a function of the injected wave amplitude under fixed plasma conditions and wave frequencies.

Results given in Fig.3 indicate that until other competing non-linear effects intervene the product amplitude ϕ_3 is proportional to $\phi_1 \phi_2$.

It should be remarked that the explosive scheme $b \rightarrow b' + c''$ could not be observed in our experiment because the beam densities were not high enough nor the plasma length sufficient. Interactions were also observed in the low frequency spectrum. The waves concerned were excited by the presence of the electron beam and their frequency depended on the magnitude of the magnetic field confining the plasma column. Comparison with other work⁸ suggests that these are Bernstein waves excited by the $\underline{E} \times \underline{B}$ drift of ions at the edge of the electron beam region. Certainly the data of Fig.4 is consistent with the dispersion of such waves being excited by a beam whose speed varied as E/B , i.e. it increased with increasing electron beam density and decreased with increasing magnetic field.

The work was greatly assisted by earlier experiments of and discussions with Dr. P.D. Edgley.

*Now at UKAEA, Winfrith Heath, Dorset.

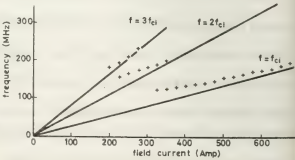
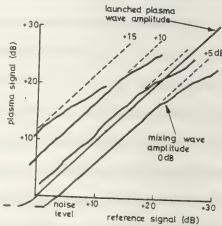
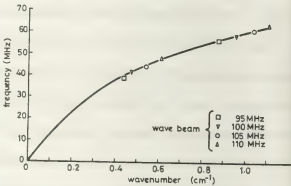
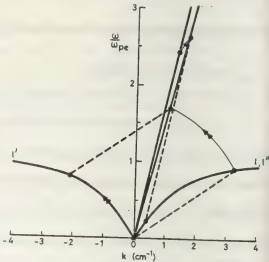
+Now at The City University, London.

References.

1. Weiland, and Wilhelmsson, 1977 Coherent Nonlinear Interaction of Waves in Plasma (Pergamon)
2. Hopman, 1971 JCIPIG X p.323
3. Sugaya, et al 1977 P.R.Litt. 39, 27
4. Sugaya, et al 1978 Phys.Lett. 69A, 265.
5. Franklin, et al 1971 ICPIG X p.324
6. van Wakeren, et al 1972 P.R.Lett. 28, 295

7. Kerst, et al 1979 Phys.Letts. 69A, 329

8. Yamada, M. et al 1977 Phys. Fluids 20, 450.



A TIME DOMAIN METHOD FOR TRANSIENT SCATTERING OF ELECTROMAGNETIC WAVES IN PLASMAS

Miloš M. Skorić and Božidar V. Stanić*

Boris Kidrić Institute of Nuclear Sciences - Vinca, POB 522, 11000 Belgrade,
Faculty of Electrical Engineering, University of Belgrade, 11000 Belgrade, Yugoslavia.

Theoretical investigations of the transient response of a cold plasma media to an electromagnetic pulse (EMP) excitation is of current interest. This class of problem has been previously considered by several methods: Fourier-Laplace transform approach, based on a frequency domain analysis /1-2/, solution of the time dependent Maxwell's equations /3-4/, and the use of the time domain multiple-scattering technique /5/.

In this contribution a new and direct time domain approach to the problem of the transient response of cold magnetoplasmas is developed. Based on a concept of a self-consistent field and Darwin-Hertree scattering formalism, space-time dependent integral equation (STIE) is formed in a simple and direct way. The proposed space-time integral equation method (STIEM), /6/, could be applied in the analysis of the transient response of an arbitrary EMP in time-varying inhomogeneous lossy magnetoplasmas of arbitrary geometrical structure.

1. SPACE-TIME INTEGRAL EQUATION METHOD

STIEM developed here is derived by the extension of the harmonic steady state Darwin-Hertree scattering method /7-8/ to the domain of transient EMP. Physical analysis and explanation of propagation and distortion of EMP in dispersive media is given in

classical papers by A. Sommerfeld and L. Brillouin /9/.

An incident wave field of an arbitrary EMP at the observation point $M(\vec{r})$ is $\vec{E}^i(\tau)$ where $\tau = \tau(\vec{r})$ is retarded time variable.

Introducing

$$\tau = \tau(\vec{r}) = t - \Psi(\vec{r}) \quad (1)$$

where t is the time variable and $\Psi(\vec{r})$ depends on a type of the incident EMP (eq. plane, spherical, etc), determining the initial condition as:

$$\tau(0) = -\Psi(0) = 0 \quad (2)$$

The wavefront of the incident EMP propagates through the plasma at the speed of light in vacuum and without distortion /9/.

Election dipole moment \vec{p} at the point $M_1(\vec{r}_1)$ in plasma caused by the transient EMP is:

$$\vec{p} = \begin{cases} \vec{p}(\vec{r}_1, \tau_1) & , \quad \tau_1 > 0 \\ 0 & , \quad \tau_1 < 0 \end{cases} \quad (3)$$

where $\tau_1 = \tau(\vec{r}_1)$.

Introducing an elementary Hertzian vector /7/, $d\vec{\Pi}_e$ at $M(\vec{r})$ scattered by the elementary plasma volume dV_1 surrounding $M_1(\vec{r}_1)$ and summing up all the contributions in the volume of plasma, the total time dependent scattered fields (self-consistent fields) are:

$$\vec{E}(\vec{r}, t) = \iiint_V \left\{ -\frac{1}{c^2} \frac{\partial^2}{\partial t^2} + \nabla \nabla \right\} \frac{\eta \vec{p}(\vec{r}_1, c\tau_1 - R)}{4\pi\epsilon_0 R} dV_1 \quad (4)$$

$$\vec{H}(\vec{r}, t) = \iiint_V \left\{ \frac{\partial}{\partial t} \nabla \times \right\} \frac{n \vec{p}(\vec{r}_1, ct_1 - R)}{4\pi \epsilon_0 R} dV_1 \quad (5)$$

where $n \equiv n(\vec{r}_1)$ is the electron density, $R = |\vec{r}_1 - \vec{r}|$, and space derivatives are applied to the coordinates of the observation point $M(\vec{r})$. $V \cap \Gamma$ is a symbol for the intersection of the plasma volume V and Γ with Γ defined as: $\Gamma: ct_1 - R \geq 0$, where $\Gamma \equiv \Gamma(\vec{r}_1)$ is different for various types of incident EMP, depending on \vec{r} and t as a parameter. Due to the space-time dependence of the volume of integration $V \cap \Gamma$, relations (4) and (5) define STIE for the scattered fields of EMP with an explicit form obtained by the substitution of the expression for \vec{p} which is derived from the electron equation of motion. In the derivation of the STIE (4), (5) we have not made any presumptions about the characteristics of the plasma media. In that way STIEM could be applied in the transient analysis of generalized cold plasma configurations.

II STIE FOR PLANE EMP SCATTERED BY AN ANISOTROPIC LOSSY PLASMA HALF SPACE

For an arbitrary plane EMP excitation one obtains: $\Gamma: ct - (\vec{r}_1 \cdot \vec{s} + R) \geq 0$ with \vec{s} as a wave normal unit vector. It is not difficult to conclude that Γ defines the interior of a paraboloid with the axis in \vec{s} direction and focus at the observation point $M(\vec{r})$.

For anisotropic stratified lossy plasma (+z direction) half space and normally incident linearly polarized plane EMP, from

the electron equation of motion one obtains:

$$\hat{p} = \frac{e^2}{m \gamma} \int_0^t \left\{ 1 - \exp(-\nu(t-t_1)) \right\} E^*(z, t_1) dt_1 \quad (6)$$

where $\hat{p} = p_x + ip_y$; $\hat{\nu} = \nu - i\omega_c$, ω_c and ν are electron cyclotron and collision frequency, and

$$E^* = E + E^\dagger.$$

Introducing a new set of variables

$v = ct - (\vec{r}_1 \cdot \vec{s} + R)$ and $u = z + v/2$ one obtains the

STIE given as:

$$E(ct - z, \frac{ct+z}{2}) = -\frac{e^2}{2m\epsilon_0 c^2} \int_0^v \int_{-\sqrt{v}}^{\sqrt{v}} n \left\{ -\nu \right\} e^{-\hat{\nu}(t-t_1)} \hat{E}_d^* \hat{t}_1 \hat{E}^* \} dv$$

$\hat{E}^* = E_{\parallel}^* + iE_{\perp}^*$ where E_{\parallel}^* and E_{\perp}^* are parallel and crosspolarized components of scattered field respectively. The above expression for the STIE is in agreement with the equation of Gray and Bowhill /10/ obtained by the use of multiple-scattering technique. For $\nu = 0$ the result agrees with /5/.

III CONCLUSION

A method of self consistent field and Darwin-Hartree microscopic scattering formalism is applied in the time domain and the space time integral equation for the scattered field is obtained. Due to the generality of the proposed method it could be applied in the transient analysis of a time-varying inhomogeneous lossy magnetoplasmas for an arbitrary EMP excitation. Transient scattering of an plane EMP in a stratified longitudinally anisotropic lossy plasma half space is considered as a special case.

REFERENCES

- /1/ C.M.Knop, Proc. IEEE, 56,1341, 1968.
- /2/ J.R.Wait, Phys. of Fluids, 12,1521,1968.
- /3/ E.Ott et.al.Can.J.Phys.46,1059,1968.
- /4/ J.C.Field, Radio Sci.,6,503,1971.
- /5/ G.K.Gray, et al, Radio Sci.,9,57,1974.
- /6/ M.M.Skorić, M.Sc.Thesis, Belgrade, 1976.
- /7/ C.G.Darwin, Trans.Camb.Phil.Soc.23,137, 1924.
- /8/ D.R.Hartree, Proc.Camb.Phil.Soc.25,97, 1929.
- /9/ L.Brillouin, "Wave prop.and Group Velocity", Acad.Press, N.Y. 1960.
- /10/ K.G.Gray, et al., Radio Sci.9, 559, 1974.

INTERACTION OF EM WAVES WITH A COMPRESSIBLE PLASMA COLUMN

Lj. R. Cander and B.V. Stanić*

*Geomagnetic Institute, Grocka,
Faculty of Electrical Engineering, University of Belgrad.

1. INTRODUCTION. The interaction of an electromagnetic wave with compressible plasma half-space or plasma column has been extensively studied in recent years [1-3]. There have, however, been very few reports with numerical results about the interaction of electromagnetic waves by an infinitely long compressible plasma column. With the recent progress in space exploration, a problem of this kind has become an important one which has some relations with space-communication technology and radio astronomical problems. The present analysis investigates the scattering of an obliquely incident plane electromagnetic wave by an infinitely long lossless plasma column. Numerical results for the differential scattering cross section are obtained for a range of acoustic velocities in electron gas.

2. FORMULATION OF THE PROBLEM. We consider the scattering problem for the case where a plane electromagnetic wave is incident on an infinitely long homogeneous lossless compressible plasma column of radius a immersed in free space. The wave vector \vec{k}_0 of an obliquely incident wave is assumed to be yz -plane and makes an angle ϕ_0 with the negative y -axis. For an incident wave whose electric field vector of magnitude E_0 makes the angle η with the x -axis, the axial components take the form

$$E_z^i = \sum_{n=-\infty}^{\infty} (-1)^n A_n^i J_n(k_{iy}r) F_n \quad (1)$$

$$H_z^i = \sum_{n=-\infty}^{\infty} (-1)^n B_n^i J_n(k_{iy}r) F_n$$

where $k_{iy} = k_0 \cos \phi_0$, $k_{iz} = k_0 \sin \phi_0$, $A_n^i = E_0 \sin \eta$, $B_n^i = -(E_0/\mu_0)^{1/2} E_0 \cos \eta$, $F_n = \exp(i n \theta + i k_{iz} z - i \omega t) \cos \phi_0$ and J_n are the Bessel functions of the first kind and order n . The axial components of the scattered wave in free space are

$$E_z^s = \sum_{n=-\infty}^{\infty} (-1)^n A_n^s H_n^{(1)}(k_{iy}r) F_n$$

$$H_z^s = \sum_{n=-\infty}^{\infty} (-1)^n i (E_0/\mu_0)^{1/2} B_n^s H_n^{(1)}(k_{iy}r) F_n \quad (2)$$

where $H_n(1)$ are the Hankel functions of the first kind and order n . A_n^s and B_n^s are scattering coefficients to be determined by the appropriate boundary conditions.

3. FORMAL SOLUTIONS. Supposing that the compressible plasma can be described by the small-signal theory and considering only the motion of electrons, the plasma column is governed by Maxwell's equations, the momentum equation and the combined equations of continuity and state [4]. A straightforward manipulation of these equations gives the following coupled second-order differential wave equations:

$$\frac{d^2 E_z}{dr^2} + \frac{1}{r} \frac{d E_z}{dr} + (p - \frac{n^2}{r^2}) E_z = -igP$$

$$\frac{d^2 H_z}{dr^2} + \frac{1}{r} \frac{d H_z}{dr} + (p - \frac{n^2}{r^2}) H_z = 0 \quad (3)$$

$$\frac{d^2 P}{dr^2} + \frac{1}{r} \frac{d P}{dr} + (q - \frac{n^2}{r^2}) P = 0$$

with

$$p = E \sin^2 \phi_0, \quad q = \frac{E}{\eta} \sin^2 \phi_0, \quad g = \frac{E \sin \phi_0}{\omega m} (\frac{\mu_0}{\epsilon_0})^{1/2} (\frac{1}{\eta} - 1),$$

$$n = \frac{u_0^2}{c^2}, \quad p = k_0^2, \quad E = 1 - \omega_p^2/\omega^2$$

ω and ω_p are, respectively, the circular frequency of the incident wave and electron plasma frequency, P is the pressure deviation from the mean and u_0 is the acoustic velocity in electron gas. The axial components E_{zn} and H_{zn} of the field and P deduced from eqn. (3) are

$$E_{zn} = \sum_{p=-\infty}^{\infty} (-1)^n \left[A_n^p J_n(p^{1/2}r) + C_n^p J_n(q^{1/2}r) \right] F_n$$

$$H_{zn} = \sum_{p=-\infty}^{\infty} (-1)^n N_n J_n(p^{1/2}r) F_n \quad (4)$$

$$P_n = \sum_{p=-\infty}^{\infty} (-1)^n C_n^p J_2(q^{1/2}r) F_n$$

with

$$J_2 = -i (\frac{E_0}{\mu_0})^{1/2} \frac{E \omega m}{\epsilon \sin \phi_0}.$$

Using the transverse field components expressed in terms of their axial components and relation for the radial component of the average velocity of electron gas

$$\nu = -\frac{i\epsilon}{\omega m} E_r - \frac{i}{\omega m n_0} \frac{\partial P}{\partial r} \quad (5)$$

one can now to satisfy the boundary conditions at the free space-homogeneous compressible plasma interface ($P_a = k_0 a$). Matching the boundary conditions gives

$$X \cdot C = Y \quad (6)$$

where X is a 5×5 square matrix, C and Y are 5×1 matrices with the elements

$$X_{12} = X_{15} = X_{31} = X_{33} = X_{34} = X_{44} = X_{51} = X_{52} = 0$$

$$X_{11} = H_n^{(1)}(x_a), X_{13} = -P J_n(\rho_a), X_{14} = -Q J_n(\rho_a)$$

$$X_{21} = -S H_n^{(1)}(x_a), X_{22} = \frac{1}{\cos \phi_0} H_n^{(1)}(x_a), X_{23} = \frac{n \sin \phi_0}{\rho_a} J_n(\rho_a)$$

$$X_{24} = \frac{-n Q}{\rho_a \sin \phi_0} J_n(\rho_a), X_{25} = i \left(\frac{\mu_0}{\epsilon_0} \right)^{1/2} \frac{1}{\rho_a} J_n'(\rho_a),$$

$$X_{32} = i \left(\frac{\epsilon_0}{\mu_0} \right)^{1/2} H_n^{(1)}(x_a), X_{35} = -J_n(\rho_a),$$

$$X_{41} = i \left(\frac{\epsilon_0}{\mu_0} \right)^{1/2} \frac{1}{\cos \phi_0} H_n^{(1)}(x_a), X_{42} = -i \left(\frac{\epsilon_0}{\mu_0} \right)^{1/2} H_n^{(1)}(x_a),$$

$$X_{43} = -i \left(\frac{\epsilon_0}{\mu_0} \right)^{1/2} \frac{1}{\rho_a} J_n'(\rho_a), X_{45} = \frac{n \sin \phi_0}{\rho_a} J_n(\rho_a), E_p = E, p$$

$$X_{53} = \frac{e \sin \phi_0}{\omega m} \rho_a^{1/2} J_n'(\rho_a), X_{54} = - \left[\frac{e}{\omega m} + \left(\frac{\epsilon_0}{\mu_0} \right)^{1/2} \frac{E}{n_0 e} \right] \frac{Q}{\sin \phi_0} J_n'(\rho_a)$$

$$X_{55} = \left(\frac{\mu_0}{\epsilon_0} \right)^{1/2} \frac{i n e}{\omega m p \rho_a} J_n(\rho_a), s = \frac{n \sin \phi_0}{\rho_a \cos^2 \phi_0}, \rho_a = \rho^{1/2} \rho_a,$$

$$C_1 = A_n^S, C_2 = B_n^S, C_3 = A_n, C_4 = C_n, C_5 = N_n$$

$$Y_1 = -E_0 J_n(x_a), Y_2 = S E_0 J_n(x_a) - \frac{i}{\cos \phi_0} H_0 J_n'(x_a)$$

$$Y_3 = \left(\frac{\epsilon_0}{\mu_0} \right)^{1/2} H_0 J_n(x_a), Y_5 = 0$$

$$Y_4 = -s \left(\frac{\epsilon_0}{\mu_0} \right)^{1/2} H_0 J_n(x_a) - \frac{i}{\cos \phi_0} E_0 \left(\frac{\epsilon_0}{\mu_0} \right)^{1/2} J_n'(x_a),$$

$$x_a = \rho_a \cos \phi_0, Q = Q \rho_a, E_0 = E_0 \sin \eta, H_0 = E_0 \cos \eta.$$

The matrix form (6) has been used for computation of the scattering coefficients A_n^S and B_n^S .

4. NUMERICAL RESULTS. We consider only the case for an E incident plane electromagnetic wave and the distribution of scattered energy in cross-polarized fields is expressed as follows

$$\frac{\partial \epsilon}{\partial d} = \frac{\lim_{r \rightarrow \infty} \hat{r} \cdot \text{Re}(\vec{E}_E^S \times \vec{H}_E^S) \cdot \vec{e}_r}{\lim_{r \rightarrow \infty} \hat{r} \cdot \text{Re}(\vec{E}_E^S \times \vec{H}_E^S) \cdot \vec{e}_r}$$

The scattered fields in above expressions are

$$\vec{E}_E^S(E_r^S, E_\theta^S, E_z^S) = \vec{E}_E^S(0, 0, E_z^S) \cdot \vec{E}_N^S(E_r^S, E_\theta^S, 0)$$

$$\vec{H}_E^S(H_r^S, H_\theta^S, H_z^S) = \vec{H}_E^S(H_r^S, H_\theta^S, 0) \cdot \vec{H}_N^S(0, 0, H_z^S)$$

Angular variation of a normalized cross-polarized components of scattering cross section for various acoustic velocities in electron gas is plotted

in Fig.1. The shapes of the curves are noticeably affected by the variation of acoustic velocity mostly in the angular interval $\Delta \theta = \pm 50^\circ$ around the lateral direction ($\theta = 180^\circ$). In the case $\beta > 0.08$ the values of \bar{C}_d^E/\bar{C}_d increases and noticeable maximum appears at $\theta = 180^\circ$, whereas it decreases for the case $0.001 < \beta < 0.08$ and the prominent minimum is seen at $\theta = 160^\circ$. These are just a few of the characteristics that can be deduced from the data given in Fig.1 and one may conclude that the angular distribution of scattered energy is very sensitive to the values of the acoustic velocities. All computations have been performed on a CDC 3600 computer.

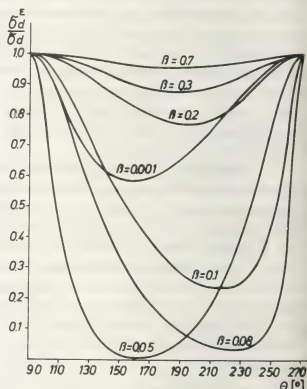


Fig.1. Normalized cross-polarized components of scattering cross section versus the azimuthal angle θ for various values of $\beta/\phi_0 = 30^\circ$, $k_0 a = 0.5$, $w_p^2/w^2 = 0.5$.

REFERENCES

- /1/ Wait, J., 1964, Can. J. Phys., 42, 1760.
- /2/ Verma, Y., and Raemer, H., 1971, Radio Sci., 6, 113.
- /3/ Kojima, T., Itakura, K., and Higashi, T., 1972, J. Appl. Phys., 43, 1309.
- /4/ Chen, H., 1974, J. Franklin Ins., 297, 221.

INFLUENCE OF DISSIPATIVE PROCESSES ON THE PROPAGATION OF GUIDED ELECTRON PLASMA WAVES ON A PLANAR PLASMA SLAB

P.K. Cibić.

Boris Kidrič Institute of Nuclear Sciences, Beograd, Yugoslavia.

The aim of this paper is to obtain the propagation and attenuation characteristics of guided electron plasma waves propagating on a planar plasma slab placed between different dielectrics in the presence of dissipative processes.

We consider a planar plasma slab of uniform density, thickness a and with the boundary planes parallel to $X-Z$ plane.

We describe plasma by equivalent permittivity

$$\epsilon_p = \epsilon_{pr} - j\epsilon_{pi} = 1 - \frac{\omega_p^2}{\omega^2 + \nu^2} - j\frac{\nu}{\omega} \frac{\omega_p^2}{\omega^2 + \nu^2} \quad (1)$$

and neighbouring dielectrics by

$$\epsilon_1 = \epsilon_{1r} - j\epsilon_{1i} = \epsilon_{1r}(1 - j \operatorname{tg} \delta_1) \quad (2)$$

$$\epsilon_2 = \epsilon_{2r} - j\epsilon_{2i} = \epsilon_{2r}(1 - j \operatorname{tg} \delta_2) \quad (3)$$

where $\operatorname{tg} \delta_1$ and $\operatorname{tg} \delta_2$ are loss tangents of the dielectrics, ω , ω_p and ν are operating, plasma and collision frequency, respectively.

In the presence of dissipative processes, guided electron plasma waves must attenuate /1-3/ and Z dependence of electromagnetic fields must be given in the form $\exp(-\alpha z - j\beta z)$, where α and β are the attenuation and propagation coefficients respectively. The introduction of this dependence into Maxwell's equations yields

$$\frac{d^2 E_z}{dy^2} + \left[(\alpha + j\beta)^2 + k_0^2 \epsilon_r \right] E_z = 0 \quad (4)$$

$$H_x = \frac{j\omega \epsilon_0 \epsilon_r}{(\alpha + j\beta)^2 + k_0^2 \epsilon_r} \frac{dE_z}{dy} \quad (5)$$

where k_0 is the wavenumber in the free space, ϵ_0 the permittivity of free space and ϵ_r the relative dielectric constant.

In the slow-wave limit /1/ we can assume that

$$|\alpha + j\beta|^2 \gg |\omega^2 \mu \epsilon| \quad (6)$$

and then the general solution of eqn.(4) is

$$E_z = \left[A \exp(-\beta y + j\alpha y) + B \exp(\beta y - j\alpha y) \right] \times \exp(-\alpha z - j\beta z) \quad (7)$$

The boundary conditions (continuity of tangential components of electric and magnetic field), with the condition that the electric and magnetic field must be finite everywhere, form set of four linear homogeneous equations for the four constants of integration. The requirement that nonzero solution of this set should exist, yields the dispersion relation

$$\exp[2a(\beta - j\alpha)] = \frac{(\epsilon_1 - \epsilon_p)(\epsilon_2 - \epsilon_p)}{(\epsilon_1 + \epsilon_p)(\epsilon_2 + \epsilon_p)} \quad (8)$$

It is evident that the propagation coefficient β and the attenuation coefficient α can be given by

$$\beta = \frac{1}{2a} \ln \frac{(\epsilon_1 - \epsilon_p)(\epsilon_2 - \epsilon_p)}{(\epsilon_1 + \epsilon_p)(\epsilon_2 + \epsilon_p)} \quad (9)$$

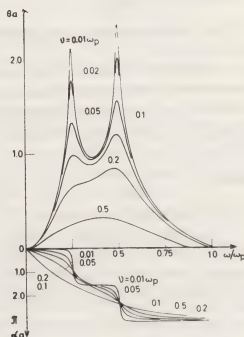


Fig. 1

$$\alpha = \frac{1}{2a} \arg \frac{(\epsilon_1 - \epsilon_p)(\epsilon_2 - \epsilon_p)}{(\epsilon_1 + \epsilon_p)(\epsilon_2 + \epsilon_p)} \quad (10)$$

If the imaginary parts of the permittivities are much smaller in magnitude than the respective real parts, the propagation coefficient β reaches the maximum values at the resonance conditions

$$\epsilon_{pr} = -\epsilon_{1r} \text{ and } \epsilon_{pr} = -\epsilon_{2r} \quad (11)$$

and these values are given by

$$\beta_m = \frac{1}{2a} \ln \left[\frac{\epsilon_{1r} + \epsilon_{2r}}{|\epsilon_{1r} - \epsilon_{2r}|} \left(\frac{\sqrt{(1 + \epsilon_{kr})^{3/2}}}{\omega_n \epsilon_{kr}} + \operatorname{tg} \delta_k \right)^{-1} \right] \quad k=1, 2, \quad (12)$$

For the lower resonance frequency the attenuation coefficient α is equal to $\pi/4a$, and for higher resonance frequency is equal to $3\pi/4a$. Between the resonances the propagation coefficient reaches the minimum value for

$$\epsilon_{pr} = -(\epsilon_{1r} + \epsilon_{2r})/2 \quad (13)$$

This minimum value is given by

$$\beta_{\min} = \frac{1}{2a} \ln \left(\frac{3(\epsilon_1^2 + \epsilon_2^2) + 10\epsilon_1\epsilon_2}{(\epsilon_1 - \epsilon_2)^2} \right) \quad (14)$$

In this case the attenuation coefficient is equal to $\pi/2a$.

The normalised propagation and attenuation characteristics are plotted for various ratios of collision and plasma frequency and $\epsilon_{1r}=15$, $\epsilon_{2r}=3$, $\operatorname{tg} \delta_1 = \operatorname{tg} \delta_2 = 0$, in fig. 1.

REFERENCES

- /1/ A.W.Trivelpiece, R.W.Gould, J.Appl.Phys. v.30(1959) 1784,
- /2/ P.J.B.Clarricoats, A.D.Olver, J.S.L. Wong, Proc. IEE, v.113(1966)755,
- /3/ B.A.Anićin, Fizika, v.1(1968)69,

A STATISTICAL THEORY OF LANGMUIR TURBULENCE

D.F. DuBois, H.A. Rose and M.V. Goldman*

*Theoretical Division, Los Alamos Scientific Laboratory.
 *University of Colorado, Boulder, Colorado.

Recent advances in the theory of "strong" Langmuir turbulence¹ have concentrated on the evolution of modulational instabilities and their relation to soliton solutions (in 1-D) and Langmuir collapse² in higher dimensions. Most of the nonlinear theories in this area have emphasized initial value or similarity solutions for the coherent nonlinear structures of interest. In many situations we can conceive of the nonlinear excitations as developing from the thermal (particle) fluctuations in the plasma in the presence of external beams or A.C. fields which drive Langmuir instabilities. Numerical studies³ have shown the birth and decay of "collapsions", new collapsions being generated from the residual fluctuation debris of previously decayed collapsions. It is not unreasonable to try to construct a statistical turbulence theory to describe such situations. The present work represents a preliminary attempt in this direction.

Our method is a generalization to the Zakharov equations¹ of the direct-interaction approximation (DIA) of Kraichnan⁴ which was originally applied to the Navier-Stokes equations. We begin with the Zakharov equations in Fourier transform space, which can be written in the compact form:

$$L_{12}N_2 = \frac{1}{2}X_{123}^{(2)}N_2N_3 + \eta_1, \quad (1)$$

where $N_1 = N_{\alpha 1}(k_1, t_1)$ is a three component vector with the discrete indices α , taking on the waves +, 0, -. Repeated indices such as 2 and 3 are understood to be summed on discrete indices α_2 , α_3 and integrated over the continuous variables k_2 , t_2 , etc. The identification of the discrete indices is: $N_+(k_1, t_1) = \phi^+(k_1, t_1)$; $N_0(k_1, t_1) = n(k_1, t_1)$; $N_-(k_1, t_1) = \phi^-(k_1, t_1)$, (2)

where $\phi^+(k_1, t_1)$, $\phi^-(k_1, t_1)$ are the spatial Fourier transforms of the envelope function of the high frequency Langmuir potential and its complex conjugate $[\phi^+(k, t)^* = \phi^-(k, t)]$ and $n(k, t)$ is the Fourier transform of the ion density deviation $[n(k, t) = n(-k, t)]$. The linear operator L_{12} is

$$\begin{bmatrix} \partial_{t_1} + \nu_e + ik_1^2 & 0 & 0 \\ 0 & \partial_{t_1}^2 + 2\nu_i \partial_{t_1} + k_1^2 & 0 \\ 0 & 0 & \partial_{t_1} + \nu_e - ik_1^2 \end{bmatrix} \cdot (2\pi)^3 \delta(k_1 - k_2) \delta(t_1 - t_2), \quad (3)$$

The only nonzero components of $X_{123}^{(2)}$ are

$$\begin{aligned} X_{+0-}^{(2)} &= -X_{-0-}^{(2)} = -i(k_1 \cdot k_3)k_1^{-2} \delta_{123}, \\ X_{+0+}^{(2)} &= -X_{-0-}^{(2)} = -i(k_1 \cdot k_2)k_1^{-2} \delta_{123}; \\ X_{0+-}^{(2)} &= X_{0+-}^{(2)} = -k_1^2(k_2 \cdot k_3) \delta_{123} \end{aligned} \quad (4)$$

$$\delta_{123} = (2\pi)^3 \delta^3(k_1 - k_2 - k_3) \delta(t_1 - t_2) \delta(t_1 - t_2).$$

Equation (1) is a general quadratically nonlinear form to which the DIA can be immediately applied,⁵ giving a set of equations coupling three important objects: the ensemble averaged (mean) fields $\langle N_i \rangle$, the infinitesimal response function⁵ (given by a functional derivative) and the covariance:

$$R_{11}, = \delta \langle N_1 \rangle / \delta \langle \eta_1 \rangle; \quad C_{11}, = \langle N_1 N_1' \rangle - \langle N_1 \rangle \langle N_1' \rangle \quad (5)$$

The equations connecting these are:

$$(L_{12} - \Sigma_{12})R_{21}, = \delta_{11}, \left[= \delta_{\alpha 1 \alpha 1}, \delta^3(k_1 - k_1') \delta(t_1 - t_1') \right], \quad (6)$$

where,

$$\Sigma_{11}, = X_{123}^{(2)}X_{23,1}, R_{22}, C_{33}, + X_{123}^{(2)} \langle N_3 \rangle, \quad (7)$$

$$L_{12} \langle N_2 \rangle = \langle \eta_1 \rangle + \frac{1}{2}X_{123}^{(2)} \langle N_2 \rangle \langle N_3 \rangle + C_{23}, \quad (8)$$

$$(L_{12} - \Sigma_{12})C_{21}, = R_{12}, + S_{12}, \quad (9)$$

$$S_{11}, = S_{11}^0, + \frac{1}{2}X_{123}^{(2)}X_{12,3}, C_{22}, C_{33}, \quad (10)$$

where S_{11}^0 is the correlation of the fluctuating part of the driving term η_1 which we can take, for example, to be white noise related to the damping decrements by a Nyquist theorem:

$$S_{11}^0, = \langle \delta \eta_1 \delta \eta_1' \rangle = \Gamma_{\alpha 1 \alpha 1}, \delta^3(k_1 - k_1') \delta(t_1 - t_1'), \quad (11)$$

$$\Gamma_{+-} = \Gamma_{-+} = 4\pi T_e \nu_e k_1^{-2}; \quad \Gamma_{00} = 3k_1^2 (m_i/m_e) \nu_i;$$

others zero. (12)

This set of nonlinear, non-Markoffian coupled equations is currently being studied by numerical analysis. The general initial value problem is difficult because of the long time histories which

must be retained in an unstably evolving system. The DIA can be shown to have the general property that the mean constants of the motion of the Zakharov equations^{1,2} $\langle N \rangle$, $\langle P \rangle$ and $\langle H \rangle$ are independent of time. These conservation properties of the complete DIA give us some confidence that these equations contain at least some of the physics important for Langmuir collapse.²

We have investigated the steady state, spatially homogeneous solutions of these equations for zero mean field. Here the $R(C)$ matrices have a diagonal (anti-diagonal) form. The explicit equations for the various components are:

$$[-i(\omega_1 - k_1^2) + \nu_e - E_{++}(k_1, \omega_1)] R_{++}(k_1, \omega_1) = 1 \quad (13a)$$

$$E_{++}(k, \omega) = (2\pi)^{-4} \int d^3 k_2 \int d\omega_2 \{ i(\underline{k}_1 \cdot \underline{k}_2)^2 k_1^{-2} k_2^2$$

$$\cdot C_{+-}(\underline{k}_2, \omega_2) R_{00}(\underline{k}_3, \omega_3) + (\underline{k}_1 \cdot \underline{k}_2)^2 k_1^{-2} k_2^{-2}$$

$$\cdot R_{++}(\underline{k}_2, \omega_2) C_{00}(\underline{k}_3, \omega_3) \} ; \quad (13b)$$

$$[-i(\omega_1 - k_1^2) + \nu_e - E_{++}(\underline{k}_1, \omega_1)] C_{+-}(\underline{k}_1, \omega_1) = R_{++}(\underline{k}_1, \omega_1) S_{+-}(\underline{k}_1, \omega_1) \quad (14a)$$

$$S_{+-}(\underline{k}_1, \omega_1) = S_{+-}^0(\underline{k}_1, \omega_1) + (2\pi)^{-4} \int d^3 k_1 \int d\omega_1 (\underline{k}_1 \cdot \underline{k}_3)^2 k_1^{-4}$$

$$\cdot C_{00}(\underline{k}_2, \omega_2) C_{+-}(\underline{k}_3, \omega_3) ; \quad (14b)$$

$$[-\omega_1^2 + 2i\omega_1 \nu_i + k_1^2 - E_{00}(\underline{k}_1, \omega_1)] R_{00}(\underline{k}_1, \omega_1) = 1, \quad (15a)$$

$$E_{00}(\underline{k}_1, \omega_1) = (2\pi)^{-4} \int d^3 k_2 \int d\omega_2 (-i)(\underline{k}_2 \cdot \underline{k}_3)^2 k_1^{-2} k_2^{-2}$$

$$\cdot [R_{++}(\underline{k}_2, \omega_2) C_{+-}(\underline{k}_3, \omega_3) - R_{--}(\underline{k}_2, \omega_2) C_{+-}(\underline{k}_3, \omega_3)] ; \quad (15b)$$

$$[-\omega_1^2 + 2i\omega_1 \nu_i + k_1^2 - E_{00}(\underline{k}_1, \omega_1)] C_{00}(\underline{k}_1, \omega_1) = R_{00}(\underline{k}_1, \omega_1) S_{00}(\underline{k}_1, \omega_1), \quad (16a)$$

$$S_{00}(\underline{k}_1, \omega_1) = S_{00}^0(\underline{k}_1, \omega_1) + (2\pi)^{-4} \int d^3 k_1 \int d\omega_1 k_1^4$$

$$\cdot (\underline{k}_2 \cdot \underline{k}_3)^2 C_{+-}(\underline{k}_2, \omega_2) C_{+-}(\underline{k}_3, \omega_3) ; \quad (16b)$$

where throughout $\underline{k}_1 = \underline{k}_2 + \underline{k}_3$, $\omega_1 = \omega_2 + \omega_3$ and $R_{--}(\underline{k}_1, \omega_1) = R_{++}(-\underline{k}_1, -\omega_1)^*$ and $C_{+-}(\underline{k}_1, \omega_1) = C_{+-}(-\underline{k}_1, -\omega_1)$.

What usually is described as weak turbulence theory is obtained from equations (14) and (16) by replacing the response functions R and everywhere by their zero order values $R_{++}^0 = [-i(\omega - k^2) + \nu_e]^{-1}$, $R_{00}^0 = [-\omega^2 + 2i\omega \nu_i + k^2]^{-1}$, $C_{+-}^0 = W(-\underline{k}) k^{-2} (2\pi)^{-4} \delta(\omega - k^2)$, etc., where $W(\underline{k})$ is the Langmuir energy density. In this approximation, it is easily seen that the two terms in E_{++} and E_{00} describe induced decay processes of the form $L + L \rightarrow S$ which lead, for example, to the well-known cascade of wave energy toward lower k .

The DIA, on the other hand, treats the self-consistent renormalization of the response functions and this renormalization is necessary to preserve

the mean constants of the motion. This renormalization has extremely important consequences: For example, if in (15b) we approximate the quantities R and C by their zero order values and then substitute the resulting E_{00} into (15a) we find that R_{00} has complex poles corresponding to the roots of the well-known modulational dispersion relation, i.e., the quantity in square brackets in (14) is just this dispersion relation generalized to the case of a broad Langmuir spectrum.⁶ Thus, in addition to the modified ion sound poles in R_{00} (modified by the decay branch of the dispersion relation) the modulational instability introduces new modulational poles in R_{00} . When this renormalization R_{00} is put into (13b), it appears that flow of Langmuir energy toward higher k becomes possible. Furthermore, C_{00} now has large components due to the modulational instability which produce a significant source term (14b) on the right-hand side of (14a). The renormalized Langmuir modes then have a finite turbulent damping in contrast to the marginally damped modes found in the usual theory of the cascade of energy toward small k .

A fully self-consistent solution of the DIA equations requires computer analysis. We will present results of 1-D numerical solutions of the DIA equations as well as a comparison of the results with direct computer solutions of the Zakharov equations. Questions concerning the spontaneous generation of a mean field at $\underline{k} = 0$ to account for the Langmuir condensation and consequent modulational instability will also be addressed.

This research was performed under the auspices of U.S. DOE and AFOSR grant #F49620-76-C-0005.

References

1. L. I. Rudakov and V. N. Tsytovich, Phys. Reports **40**, 1(1978); S. G. Thornhill and D. ter Haar, Phys. Reports **41**, (1978).
2. M. V. Goldman and D. R. Nicholson, Phys. Rev. Letters **41**, 406(1978).
3. D. R. Nicholson, M. V. Goldman, D. F. DuBois, and G. F. Reiter, "Numerical Study of Strong Langmuir Turbulence", Bull. Am. Phys. Soc. **23**, 892 (1978).
4. R. H. Kraichnan, Phys. Rev. **113**, 1181(1958).
5. D. F. DuBois and M. Espedal, Plasma Physics **20**, 1209 (1978).
6. S. Bardwell and M. V. Goldman, Ap. J. **209**, 912 (1976).
D. R. Nicholson and M. V. Goldman, Phys. Fluids **21**, 1766(1978).

ELECTROSTATIC TRIVELPIECE-GOULD MODES IN A TORUS

F.P. Stössel.

Institute for Theoretical Physics, University of Innsbruck, Innrain 52, A-6020 Innsbruck/Austria, Europe.

Abstract: Electron plasma waves are treated in a torus of square cross section with an infinitely strong azimuthal magnetic field. Eigenfrequencies and eigenfunctions are calculated numerically.

Although many experiments were performed in toroidal devices a well-developed theory of toroidal waves is not available as yet. As a step in that direction electron plasma waves are investigated in a toroidal cavity of square cross section, i.e. the same configuration as used by Swanson (1) in discussing ion cyclotron and fast waves. Cylindrical coordinates r, ϕ, z are used. The torus has a major radius R and a square of lateral length $2r_0$. The cavity is completely filled with a homogeneous plasma, and the walls are ideal conductors. In contrast to the original paper by Trivelpiece and Gould (2), where the magnetic field has only a component in the z -direction, the magnetic field here lies in the ϕ -direction. A linearized fluid description is used (3).

The magnetic field is assumed to be infinitely strong, so that the r - and z -components of the velocity can be neglected. Thus the system of linearized equations consists of the equation of continuity, the ϕ -component of the equation of motion, and Poisson's equation:

$$\frac{\partial n_1}{\partial t} + n_0 \frac{1}{r} \frac{\partial v_\phi}{\partial \phi} = 0$$

$$\frac{\partial}{\partial t} v_\phi = -\frac{a_E^2}{r} \frac{1}{r} \frac{\partial}{\partial \phi} n_1 + \frac{e}{m} n_0 \frac{1}{r} \frac{\partial}{\partial \phi} \psi$$

$$\nabla^2 \psi = 4\pi e n_1$$

$a_E = (k_B T/m)^{1/2}$ is the velocity of sound. This leads to the following equation for the electrostatic potential:

$$\frac{\partial^2}{\partial t^2} \nabla^2 \psi - \frac{a_E^2}{r^2} \frac{\partial^2}{\partial \phi^2} \nabla^2 \psi + \frac{\omega_{pe}^2}{r} \frac{\partial^2}{\partial \phi^2} \psi = 0$$

Variables can be separated by the following ansatz:

$$\psi = e^{i\omega t} e^{ik_n z} e^{im\phi} T_1(r)$$

The uniqueness-condition restricts the mode numbers m to integers; $m=0$ describes the steady-state solution. The perfectly conducting walls require that ψ vanishes at the walls, i.e. $\psi(r, z=0) = \psi(r, z=2r_0) = 0$, which results in a sinusoidal z -dependence ($\propto \sin k_n z$ with $k_n = n\pi/2r_0$) and in the conditions $\psi(r=R-r_0, z) = \psi(r=R+r_0, z) = 0$ whence we obtain boundary conditions for the radial eigenfunctions $T_1(r)$ which obey the following differential equation:

$$T_1'' + \frac{1}{r} T_1' + \left(\frac{m^2 \omega_{pe}^2}{r^2 \omega^2 - m^2 a_E^2} - \frac{m^2}{r} - k_n^2 \right) T_1 = 0$$

Primes denote derivatives with respect to r . This eigenvalue problem with ω as the eigenfrequency was solved numerically by a shooting method. Numerical values typical of large present-day experiments were chosen. E.g., the Debye-length was set equal to $7.43 \times 10^{-5} \times R$. The figures below show some examples of the eigenfunctions T_1 for an inverse

aspect ratio $a = 0.3$. The eigenfunctions are normalized by setting $dT/dr = 1$ at $r = R - r_0$. The first six modes in l ($l = 1 - 6$) are plotted one over another in each figure for $m=1, n=1$ in Fig.1, for $m=3, n=3$ in Fig.2, and for $m=5, n=5$ in Fig.3.

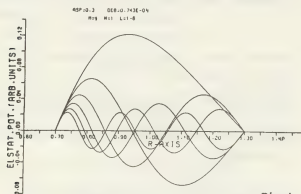


Fig.1

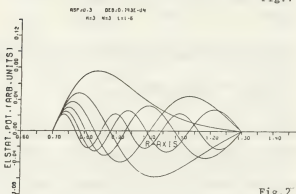


Fig.2

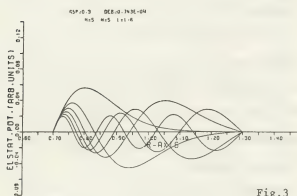


Fig.3

The eigenfrequencies ω/ω_{pe} for these cases are:

	$m=1 \quad n=1$	$m=3 \quad n=3$	$m=5 \quad n=5$
1=1	0.1387775	0.1939191	0.2101450
1=2	0.0875564	0.1602070	0.1820234
1=3	0.0620977	0.1363490	0.1636392
1=4	0.0476929	0.1164748	0.1491299
1=5	0.0385919	0.1003223	0.1359926
1=6	0.0323636	0.0874481	0.1238370

From the figures one can clearly see the deviation of the radial eigenfunctions from symmetry about $r = R$ which should obtain for linear geometries. For the appropriate linear geometry, a parallelepiped of length $2\pi R$, and side-length $2r_0$, the eigenfunctions are sinusoidal. The deviation increases with the inverse aspect ratio, i.e. with the curvature of the torus. However, as can already be suspected from the three examples given here, it turns out that the mode number n has much more influence on the shape of the eigenfunctions than the aspect ratio. On the other hand variation of m changes the eigenfrequencies but does not alter the shape of the eigenfunctions.

The eigenfrequencies for linear geometry are generally somewhat smaller than those for the torus. For the above-mentioned examples, the deviation lies within 1 - 4 % for most of the modes and reaches a maximum of 23 % for the $l=1, m=5, n=5$ mode.

This work has been supported by the Österreichischer Fonds zur Förderung der Wissenschaftlichen Forschung Grant Nr. 2781/S.

References

- (1) Swanson B.G., Phys.Fluids **17**, 1974, 2241
- (2) Trivelpiece W., Gould R.W., J.Appl.Phys. **30** 1959, 1784
- (3) Cap F.F., Handbook on Plasma Instabilities, Academic Press London, 1978, vol.2, p.817

ION TAIL FORMATION AND SATURATION OF THE ION-ACOUSTIC INSTABILITY

Tu. Khiet.

Laboratoire de Physique des Plasmas, Université de Paris XI, centre d'Orsay, Bât 212,
91405 Orsay Cédex, France.

I. INTRODUCTION

In a turbulent plasma, especially when an ion-acoustic instability is present, it has been shown experimentally ⁽¹⁾ and numerically ⁽²⁾ that the ion distribution function shows two different populations constituted by a bulk having a lower temperature and a tail corresponding to a much higher one. This phenomenon is very significant for the fusion since the most effective contribution to it comes from the high energy part of the ion population.

In this communication we shall first propose a simple method allowing to follow the time evolution of the average distribution function of a particle species. Our formalism reveals to be more powerful and more accurate than the usual quasilinear one, besides, it presents an advantage with respect to the latter in the sense that we have not to solve a diffusion equation with a diffusion coefficient depending on velocity. As an application, we subsequently consider the problem of saturation of the ion-acoustic instability driven by an electron drift current in a plasma having a large electron-to-ion temperature ratio. We then show that the two-temperature behaviour of the ion distribution function results from the exchange of energy and momentum between waves and particles; The hot component then serves to quench the instability, the spectrum and the turbulent energy of the saturated state can then be calculated within the basic assumption that enhanced ion-damping is the most efficient mechanism of absorption.

II. BASIC CONSIDERATIONS.

We consider a plasma with $T_e/T_i \gg 1$ where T_e (T_i) is the electron (ion) temperature. The electron distribution function is assumed to be a shifted Maxwellian with a drifted velocity \vec{v}_d largely ex-

ceeding in magnitude the ion-acoustic speed c_s , where $c_s = (T_e/M)^{1/2}$, M (m) being the ion (electron) mass. In these conditions, ion waves are generated with frequencies and growth-rates given by

$$\omega = k c_s / (1 + k^2 \lambda^2)^{1/2}; \quad \gamma = \gamma_e + \gamma_i$$

$$\begin{aligned} \gamma_e &= (\pi m / 8M)^{1/2} \omega^4 (k_y v_d - 1) / k^3 c_s^3 \\ \gamma_i &= -\omega_{kF_i}^4 (\omega/k) / k^3 \end{aligned} \quad (1)$$

where the notations are standard and F_i is the average distribution function of the ion species. In the early stage of the instability, ion damping is negligible but when the time grows, the waves grow in amplitude and then drive the ion to higher velocity and simultaneously heat them which in turns enhance the absorption of the waves. In order to take into account of this retro-effect, we do not try here to reduce the equation for F_i to a diffusion-like equation. In this respect, we make benefit of the relation $F(\vec{v}, t) = \langle H(\vec{v}(t)) \rangle$ where $\langle \dots \rangle$ denotes ensemble average, $H(\vec{v})$ is the value taken by F at $t=0$, $\vec{v}(t)$ is the velocity of a particle moving under the influence of the turbulent field from the point (\vec{r}, \vec{v}) at $t=0$. Using a Fourier analysis of $H(\vec{v})$ which yields $F(\vec{v}, t)$ in the form

$$F(\vec{v}, t) = \int d^3p \langle e^{i\vec{p} \cdot \vec{v}(t)} \rangle \tilde{H}(\vec{p}) \quad (2)$$

the problem is now reduced to evaluate an orbit-dependent function in a similar way as in DURREE-WEINSTOCK theory. Using a well-known technique ⁽³⁾ devoted to this formalism, the two relevant cumulants can be calculated in the lowest order as

$$\begin{aligned} \langle \Delta \vec{v} \Delta \vec{v} \rangle &= \frac{e^2}{M^2} \sum_{\vec{k}} \frac{\vec{k} \vec{k}}{k} \frac{T_e}{2k} \frac{1}{\gamma} \\ \langle \Delta \vec{v} \rangle &= -\frac{\partial}{\partial \vec{v}} \langle \Delta \vec{v} \Delta \vec{v} \rangle \end{aligned} \quad (3)$$

where $\vec{v} = \vec{v}(t) - \vec{v}$ is the velocity increment. In order to evaluate explicitly the above quantities we assume that the wave spectrum, i.e., I_k , is

nearly isotropic around the direction of v_d . Within this basic assumption, and converting the sum appearing in (3) into integral, integration over angles can be carried out to yield the results in the form

$$\langle \vec{p} \cdot \Delta \vec{v} \rangle = p U \quad (4)$$

$$\langle (\vec{p} \cdot \Delta \vec{v})^2 \rangle = p^2 a_{\parallel}^2 + p^2 a_{\perp}^2$$

in which the suffices refer to the direction of v_d and the explicit expressions of various quantities appearing in (4) are quite long to be written down here. Putting (4) into (2) and performing integration over \vec{p} -space we obtain F in the form

$$F(v, t) = \exp(-(v+U)^2/v_{\text{eff}}^2) / (\pi^{3/2} v_{\text{eff}}^3) \quad (5)$$

where $v_{\text{eff}}^2 = 2T_i/M + 4a_{\parallel}^2$; $w_{\text{eff}}^2 = 2T_i/M + 4a_{\perp}^2$ are still function of v by virtue of (3). Inspections of the analytic expressions of the various velocities appearing in (4) show that U is always negligible and the two other quantities behave as

$$v_{\text{eff}}^2 \simeq w_{\text{eff}}^2 = 2T_i(1 + \alpha T_e/T_i)/M \quad \text{for } v \ll c_s$$

$$v_{\text{eff}}^2 = (c_s^2/v_d \eta) \int_{k_*}^{\infty} dk \mathcal{E}(k) \quad \text{for } v \gg c_s/\sqrt{2}$$

$$w_{\text{eff}}^2 = (c_s^3/2v_d \eta) \int_{k_*}^{\infty} dk (1 - \frac{\omega}{k^2 v_d}) \mathcal{E}(k) \quad \text{for } v \gg c_s/\sqrt{2} \quad (6)$$

where the lower limit of integration is the non trivial solution of the equation $\omega = kv$; α is the characteristic turbulent-to-kinetic energy ratio, and $\mathcal{E}(k) = k^2 I(k)/4\pi^2$; $\eta = (\mu_m/8M)^{1/2}$

Choosing $T_e/T_i = 100$ and $\alpha = 10^{-3}$ as typical values in an ion-heating experiment we deduce from (6) that the ion-body is only slightly heated and an ion-tail is formed in the region $v \gg c_s/\sqrt{2}$

which corresponds to the resonant interaction between waves and ions.

Balancing the electron growth rate with the ion damping given by (1), using (5) and (6), we obtain at saturation

$$\frac{k^2 v_{\text{eff}}^2}{\omega^2} = \left[\text{Log} \frac{k \cdot v_d}{\eta \omega} \right]^{-1} \quad (7)$$

as a first approximation, where v_{eff} is to be calculated by (6) with $k_* = k$.

From (7) the wave spectrum results in the form

$$I(k) = \eta k^{-2} (1 + k^2 \lambda^2)^{-11/2} / \text{Log}(1/\eta)$$

the total turbulent energy is then approximately

$$\alpha = 0.25 \eta / \text{Log}(1/\eta)$$

III. CONCLUSION.

We have developed a simple method using a technique borrowed in strongly turbulent plasma theory this technique is quite general, it can be applied also to explain the existence of a non-thermal electron distribution function which plays a crucial role in a laser-produced plasma.

IV. REFERENCES.

- 1) D.S. Prono and C.B. Wharton, Plasma Phys. **15**, 253, (1973).
- 2) C.T. Dum, R. Chodura, D. Biskamp, Phys. Rev. Lett. **32**, 1231 (1974).
- 3) J. Weinstock and B. Bezzerides, Phys. Fluids **16**, 2287, (1973).

SECOND ORDER HARMONIC SURFACE WAVES GENERATED BY ONE FUNDAMENTAL WAVE

A. Shivarova, T. Stoychev.

Faculty of Physics, Sofia University, 1186 Sofia, Bulgaria.

In this report we describe experimental investigations on propagation of second order harmonic surface waves in a gas discharge plasma.

The theoretical explanation of our experimental data is based on a model given by Sato et al [1] for non-linear mixing of dispersive waves, applied in the special case of propagation of one fundamental wave of frequency ω , excited at $z=0$ in a medium with a weak nonlinearity. The optimum of the wave study by the methods used in our experiments is that when the coupler is not placed at the plasma column ends. Thus, in the theoretical model [1] we include the fact that the fundamental wave of frequency ω , phase velocity $v_{ph} = \omega/k_\omega$ and space damping rate $\tilde{\gamma}_\omega$ propagates in a direction of $z < 0$ as well as of $z > 0$ (Fig.1)

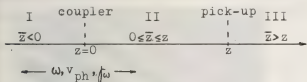


Fig. 1

Because of the non-linear plasma feature this propagating wave arouse at any $\tilde{z} \in (-\infty, +\infty)$ (Fig. 1) harmonic signals of frequency 2ω , which propagate in both directions ($z \geq \tilde{z}$ and $z < \tilde{z}$) according to the linear dispersion law with phase velocities $v_{ph} = 2\omega/k_{2\omega}$ and space damping rates $\tilde{\gamma}_{2\omega}$. If we put a pick-up at $z(z > 0)$ the total signal of frequency 2ω at this point, $A_{2\omega}(z, t)$, is a result of the interference of the waves generated by all virtual exciters \tilde{z} and reaching to the point z at the moment t :

$$A_{2\omega}(z, t) \propto M \exp(-\tilde{\gamma}_{2\omega} z) \sin(k_{2\omega} z - 2\omega t - \alpha) \\ (1) \quad - N \exp(-2\tilde{\gamma}_{2\omega} z) \sin(2k_{2\omega} z - 2\omega t - \beta)$$

where

$$M = [(C \cos \theta + B \sin \gamma)^2 + (C \sin \theta + B \sin \gamma)^2]^{1/2} \\ N = [(C \cos \theta - B \sin \gamma)^2 + (C \sin \theta - B \sin \gamma)^2]^{1/2}$$

$$\alpha = \tan^{-1} [(C \sin \theta + B \sin \gamma) / (C \cos \theta + B \cos \gamma)] \\ \beta = \tan^{-1} [(C \sin \theta - B \sin \gamma) / (C \cos \theta - B \cos \gamma)] \\ B = [(2\tilde{\gamma}_\omega + \tilde{\gamma}_{2\omega})^2 + (2k_\omega + k_{2\omega})^2]^{-1/2} \\ C = [(2\tilde{\gamma}_\omega - \tilde{\gamma}_{2\omega})^2 + (2k_\omega - k_{2\omega})^2]^{-1/2} \\ \gamma = \tan^{-1} [(2\tilde{\gamma}_\omega + \tilde{\gamma}_{2\omega}) / (2k_\omega + k_{2\omega})] \\ \theta = \tan^{-1} [(2\tilde{\gamma}_\omega - \tilde{\gamma}_{2\omega}) / (2k_\omega - k_{2\omega})]$$

If the intervals I and III whose influence is determined by B, γ are ignored, the result (1) reduces to that in [1].

Expression (1) shows that two types of harmonic waves of equal frequencies 2ω propagate simultaneously. The first one satisfies the linear dispersion relation

$$(2) \quad k' = k_{2\omega}, \quad \tilde{\gamma}' = \tilde{\gamma}_{2\omega}$$

and for the second one the conditions

$$(3) \quad k'' = 2k_\omega, \quad \tilde{\gamma}'' = 2\tilde{\gamma}_\omega$$

are valid. The interval II (Fig. 1) contributes to the amplitude of both types of waves, whereas the contribution of I increases the amplitude of the first wave and the contribution of III decreases the amplitude of the second wave, so that $M > N$.

For the high-frequency azimuthally symmetric surface waves we have $k_{2\omega} > 2k_\omega$, $\tilde{\gamma}_{2\omega} > 2\tilde{\gamma}_\omega$. We ensure experimentally the presence of interval I (Fig. 1) and we observe, in accordance with expression (1), different spatial regions (consecutively along the plasma column) of a dominant propagation of each type of harmonic waves. The propagation begins close to the coupler with a predominating of the first (shorter) wave which, however, is more attenuated. Next to this region an intermediate region follows where the two harmonic waves propagate with comparable amplitudes. When the contribution of the first wave goes down, only the propagation of the second (longer) wave which has a smaller amplitude at $z=0$ but is less attenuated, remains along the plasma column. This allows us to ob-

tain directly experimental data both for the wavenumbers and the space damping rates by relatively precise methods for wave investigations such as the methods of time-space diagrams and of phase shift measurements [2,3].

The experiments are performed on a hot-cathod neon gas discharge plasma at low pressure.

Typical instances of our experimental data for the propagation of the two types of surface harmonic waves (generated by one fundamental wave of frequency ω) obtained by phase shift measurements, are presented in Tabl. 1. The characteristics of the first (k' , f') and second (k'' , f'') types of harmonic waves are compared with the corresponding characteristics of the surface waves excited directly at the double frequency 2ω ($k_{2\omega}$, $f_{2\omega}$) and at the fundamental frequency ω (k_{ω} , f_{ω}) respectively; ω_{pe} is the electron plasma frequency. In the columns denoted as $\Delta L'$ and $\Delta L''$ the end points of the regions of dominant wave propagation are given ($z=0$ is the coupler position).

$\frac{\omega}{\omega_{pe}}$	I harmonic wave				II harmonic wave		
	$\Delta L'$ cm	k' $k_{2\omega}^{-1}$ cm	$f' \times 10^2$ $f_{2\omega}^{-1}$ cm		$\Delta L''$ cm	k'' k_{ω}^{-1} cm	$f'' \times 10^2$ f_{ω}^{-1} cm
0.19	0-55	0.53 0.51	5.0 5.2	-			
0.29	0-15	1.57 1.50	18.4 22.5	33-55	0.56 0.28	4.6 1.8	
0.35	-			3-55	0.81 0.41	6.0 2.9	

Tabl. 1

We establish that at lower frequencies ω only the first type of harmonic waves ($k' \sim k_{2\omega}$, $f' \sim f_{2\omega}$) propagates along the whole length ($L=55$ cm) of the plasma column. With the increase of the frequency the distance over which we observe a predominant propagation of this wave decreases. At higher frequencies the first type of harmonic waves attenuates considerably over a shorter distance than the plasma column length and we observe also a region of a dominant propagation of the second type of harmonic wave ($k'' \sim 2k_{\omega}$, $f'' \sim 2f_{\omega}$). The wave-

numbers measured in the intermediate region change with the distance but they are of the order of $(k'+k'')/2$ which is the wavenumber of the resulting wave obtained by the interference of the two waves with wavenumbers k' and k'' and equal amplitudes. With further increase of the frequency the region of dominant propagation of the first wave and the intermediate region vanish consecutively and the region of propagation of second wave begins to shorten. This picture of harmonic wave propagation is associated to the growing attenuation of the waves with the frequency increase. We suppose that the discrepancies from eqs (2,3) obtained above the experimental error are due to the dependences of the wave characteristics on the exciting signal amplitude. The spatial separation of the regions obtained experimentally is more strongly than the theory (formula (1)) predict. The case of the consecutive observation of the three regions is illustrated in Fig. 2a, where the time-space diagram of a harmonic wave is shown. The diagrams of the surface waves excited directly at the fundamental and double frequencies are given for comparison in Figs. 2b,c.

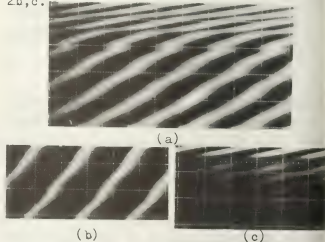


Fig. 2

References

1. Sato N., Märk E. and Popa G. (1976) Plasma Phys. **18**, 897.
2. Shivarova A., Stoychev T. and Russeva S. (1975) J.Phys.D: Appl.Phys. **8**, 383.
3. Baltova K. D., Shivarova A. P. and Stoychev T. T. (1978) Phys.Lett. **68A**, 51.

TURBULENT PLASMA IN THE FIELD OF INTENSE HIGH FREQUENCY RADIATION

V.F. Kovalev, V.V. Pustovalov, A.B. Romanov and V. Stefan*.

P.N. Lebedev Physical Institute of Academy of Sciences of the U.S.S.R., Moscow, U.S.S.R.
Boris Kidric Institute of Nuclear Sciences, Beograd Yugoslavia.

In present-day experiments dealing with the interaction of strong electromagnetic radiation with plasma high energy fluxes of the incident radiation are in use. For example, in the optical domain of frequencies the energy flux reaches the value of 10^{16} - 10^{17} W/cm² /1/. Along with this, situations when strong radiation propagates through the plasma with high level of turbulent noise are very often encountered (plasma focus /2,3/ or ionospheric plasma /4/). In the presence of the pump field turbulent plasma spectrum is affected in such a way that "failures" appear in the longwave domain when the wavelength is of the order of electron oscillation amplitude in the external field.

For the description of the homogeneous isotropic plasma interacting with the external radiation $E_0(t) = E_0 \sin \omega_0 t$ with the frequency ω_0 much higher than the electron Langmuir frequency ω_{Le} , Vlasov kinetic equation, in the form of the hydrodynamical system /5/, is used, on the base of which a nonlinear dispersion relation for the correlation function $\Psi = \langle \psi_i \psi_i^* \rangle = \frac{k^2}{2\alpha} |\phi|^2$ can be obtained

$$\begin{aligned} & \psi(k) \varepsilon_0(k) - \frac{2}{\varepsilon_0^2(k)} \int d\mathbf{k}' d\mathbf{k}'' \delta(\mathbf{k} - \mathbf{k}' - \mathbf{k}'') \psi(k') \psi(k'') \times \\ & \times \left[\alpha_1(k) \varepsilon_1^{(i)}(k, k', k'') + \frac{\beta(k) \beta(k') \beta(k'')}{\alpha_1(k) \alpha_1(k')} \varepsilon_1^{(e)}(k, k', k'') \right] \times \\ & \times \left[\alpha_1(k) \varepsilon_1^{(i)}(k, k', k'') + \frac{\beta(k) \beta(k') \beta(k'')}{\alpha_1(k) \alpha_1(k')} \varepsilon_1^{(e)}(k, k', k'') \right] - \\ & - \psi(k) \int d\mathbf{k}' d\mathbf{k}'' \delta(\mathbf{k} - \mathbf{k}' - \mathbf{k}'') \left\{ \frac{4}{\varepsilon_0(k)} \left[\alpha_1(k) \varepsilon_1^{(i)}(k, k', k'') \times \right. \right. \end{aligned} \quad (1)$$

$$\begin{aligned} & \left. \left[\alpha_1(k) \varepsilon_1^{(i)}(k, k', k'') + \frac{\beta(k) \beta(k') \beta(k'')}{\alpha_1(k) \alpha_1(k')} \varepsilon_1^{(e)}(k, k', k'') \right] \beta(k) \varepsilon_1^{(e)}(k, k', k'') \times \right. \\ & \times \left[\alpha_1(k) \varepsilon_1^{(e)}(k, k', k'') \frac{\beta(k) \beta(k')}{\alpha_1(k) \alpha_1(k')} + \frac{\beta(k) \beta(k')}{\alpha_1(k)} \varepsilon_1^{(i)}(k, k', k'') \right] - \\ & - 3\alpha_1(k) \left[\varepsilon_2^{(i)}(k, k', k'') + \frac{\beta(k) \beta(k')}{\alpha_1(k) \alpha_1(k')} \varepsilon_2^{(e)}(k, k', k'') \right] \left. \right\} \psi(k'') = 0 \\ & \alpha_1(k) = 1 + \delta \varepsilon_1(k) (1 - J_0^2(\alpha)) \alpha_1(k) - 4\alpha_1(k) (1 - J_0^2(\alpha)) \beta(k) J_0(\alpha) \\ & \varepsilon_0(k) = 1 + \delta \varepsilon_1(k) + \delta \varepsilon_2(k) + \delta \varepsilon_3(k) (1 - J_0^2(\alpha)) + \delta \varepsilon_4(k) \end{aligned}$$

Here $J_0(x)$ is Bessel function, $\delta \varepsilon_n(\omega, \mathbf{k})$ partial plasma polarizability of "n" plasma component and $\varepsilon_1^{(i)}$ and $\varepsilon_2^{(i)}$ first and second nonlinear dielectric permeability of "n" plasma component.

In equation (1) the first addendum includes the effect of high-frequency field $E_0(t)$ on plasma dielectric permeability $\varepsilon_0(k)$ /6,7/ the change of nonlinear interaction of plasma waves in the presence of the high-frequency field is included in remaining addends.

Let us consider now the process of induced scattering of the Langmuir waves on particles in the external field $E_0(t)$ when $\omega \gg k v_{Te}, \omega \gg k v_{Te} \frac{\omega - \omega_1}{|\mathbf{k} - \mathbf{k}_1|} < v_{Te}$ is satisfied. For the spectral density of oscillation energy $W(k)$ the following equation is obtained

$$\begin{aligned} & \frac{\partial W(k)}{\partial t} + \frac{dW(k)}{dk} \frac{\partial W(k)}{\partial k} = 2\gamma(k) W(k) + W(k) \int Q(k, k') W(k') dk' \\ & Q(k, k') = \frac{1}{16\pi^2} \frac{e^2}{\omega_0^2} \frac{(\mathbf{k} \cdot \mathbf{k}')^2}{(k k')^2 (\omega \omega')^2} \frac{\delta \varepsilon_3(k') (1 - \delta \varepsilon_1(k'))}{J_0^2(\alpha) \varepsilon_0(k')} \end{aligned} \quad (2)$$

In a magnetized plasma, the turbulence of the oblique Langmuir waves, excited, for example, by encountering electron beams

with velocities \vec{u}_b , parallel to magnetic field \vec{B}_0 is characterized by stationary spectral distribution /4/ which in a strong high-frequency field $a = (k\vec{r}_e) > 1$ appeared to be modulated over the frequency with the period $T_{\omega} = \omega_e^2 u_b / e E_0$.

$$W(\vec{r}) \sim \tilde{S}(\cos\theta)^2 \left(\frac{e E_0 u_b}{m_e \omega_e^2 u_b} \cos\theta \right) \sqrt{\left(k - \frac{\omega_e}{u_b} \right)} \vec{E}_0 \parallel \vec{B}_0.$$

$$\cos\theta = k\vec{B}_0 / k B_0$$

Here $\tilde{S}(\cos\theta)$ describes angle distributions of plasma turbulent noise in the presence of the external field $\vec{E}_0(t)$. The characteristic modulation of the spectral distribution $(\omega_0^2(a))$ connected with the effective amplification of nonlinear interaction of waves in a strong high frequency field, appears in the form of kernel modification $(Q(\vec{r}, \vec{r}') \sim \tau_0^{-1}(\omega))$.

Spectral distribution (3) also describes the modulation of the plasma noise in the case when instabilities arise because of the presence of electron beams in the current-carrying plasma with velocity u_b (velocity of a beam is oriented along drift velocity \vec{u} , $(\vec{u} \cdot \vec{u}_b) > 0$). The angle distribution of plasma noise in that case, certainly, has other form /8/. Let us note that modulation of plasma noise by high-frequency external field appears if intensity of external field is strong enough $E_0 \sim \frac{m_e \omega_e^2}{e k}$. So, in the above case of current carrying plasma with electron beam defined by parameters $n_e = 10^{18} \text{ cm}^{-3}$, $n_b/n_e = 10^{-3}$, $u_b = 4.2 \cdot 10^9 \text{ cm/s}$, $u = 4 \cdot 10^7 \text{ cm/s}$, $T_e = T_i = T_b = 100 \text{ keV}$ characteristic for plasma focus, oscillations with wave number

with wave number $k \sim 2 \cdot 10^4 \text{ cm}^{-1}$ could be excited. Here n_b - particle density of beam electrons, n_e - particle density of current carrying plasma electrons, $T_{e,i}$ temperature of electrons (ions) of current carrying plasma and T_b temperature of beam electrons. In the case of using CO_2 laser as source of high-frequency field, necessary value of energy flux is $q \sim 4 \cdot 10^{14} \text{ W/cm}^2$, obtainable in present time devices.

REFERENCES

- /1/ W.L.Kruer, et al, Collective behaviour in recent laser-plasma experiments, Lawrence Livermore Laboratory, June 7, Preprint UCRL 77730, (1976)
- /2/ V.A.Gribkov, et al, Works of FIAN, 85, (1976) 193,
- /3/ K.Yoneyoshi, et al, J.Phys.Jap. 41 (1976) 1081
- /4/ Yu.V.Golikov, et al, JETP Lett. 22 (1975) 3 (in russian)
- /5/ V.V.Pustovalov, et al, Lebedev Institute Report, No.12, (1976) 28,
- /6/ Yu.M.Aliev, V.P.Silin, JETP 48 (1965) 901
- /7/ V.I.Domrin, Preprint FIAN USSR, No.38, (1967)
- /8/ V.V.Pustovalov, et al, Preprint FIAN USSR, No.183, (1973)

STATIONARY MOTION OF CHARGED PARTICLE IN RESONANCE CONDITIONS

V.P. Milantiev and A.G. Miroshnikov.

Patrice Luminba University, Moscow W-302, U.S.S.R.

The relativistic dynamics of a charged particle immersed in a strong magnetic field $\vec{B}_0(\vec{r}, t)$ in the presence of H.F. quasi-monochromatic waves is considered under different resonance conditions. A slow changing "weak" /1/ electric field $\vec{E}_0(\vec{r}, t)$ is assumed. The H.F. fields are expressed as:

$$\vec{E}_\sim = \sum_s \vec{E}_s(\vec{r}, t, \omega_s, \vec{k}_s) e^{i\theta_s} + c.c. \quad (1)$$

$$\vec{B}_\sim = \sum_s \vec{B}_s(\vec{r}, t, \omega_s, \vec{k}_s) e^{i\theta_s} + c.c.$$

where c.c. represent complex conjugate.

Quantities \vec{E}_s , \vec{B}_s are assumed to be slow changing functions of coordinates and time. Fast changing wave phases $\theta_s(\vec{r}, t)$ are defined by equations:

$$\frac{d\theta_s}{dt} = -\omega_s(\vec{r}, t) + \frac{d\vec{r}}{dt} \cdot \vec{k}_s(\vec{r}, t) \quad (2)$$

$$\omega_s(\vec{r}, t) = -\frac{\partial \theta_s}{\partial t}, \quad \vec{k}_s(\vec{r}, t) = \nabla \theta_s \quad (3)$$

are the frequencies and wave vectors of the quasimonochromatic waves (1) respectively. The particle momentum is presented as follows:

$$\vec{p} = \vec{\ell}_\parallel p_\parallel + \frac{1}{2} p_\perp (\vec{\ell}_\perp e^{i\theta_0} + \vec{\ell}_\perp^* e^{-i\theta_0}) \quad (4)$$

where θ_0 - cyclotron phase rotation, $\vec{\ell}_\perp = \vec{\ell}_2 + i\vec{\ell}_3$; $\vec{\ell}_1 = \frac{\vec{B}_0}{B_0}$, $\vec{\ell}_2$, $\vec{\ell}_3$ - local unit vectors connected to the field lines of the field; p_\parallel , p_\perp - longitudinal and the transversal momentum components of the particle relative to \vec{B}_0 .

The particle motion equation in the fields \vec{E}_0 , \vec{B}_0 , \vec{E}_\sim , \vec{B}_\sim is expressed

$$\frac{d\vec{r}}{dt} = \frac{p_\parallel}{m\gamma} \vec{\ell}_\parallel + \frac{p_\perp}{2m\gamma} (\vec{\ell}_\perp e^{i\theta_0} + \vec{\ell}_\perp^* e^{-i\theta_0}) \quad (5)$$

$$\frac{dp_\parallel}{dt} = a_\parallel + \{a_1 e^{i\theta_1} + a_2 e^{2i\theta_1} + \dots + (a_{3s} e^{i\theta_s} + a_{4s} e^{i\theta_s} + a_{5s} e^{i\theta_s}) + c.c.\} = a_\parallel \quad (6)$$

$$\frac{dp_\perp}{dt} = a_\perp \quad (7)$$

$$\frac{d\theta_0}{dt} = \omega_0 + A_0 \quad (8)$$

$$\frac{d\theta_s}{dt} = \gamma_s + \frac{p_\perp}{2m\gamma} \vec{k}_s \cdot (\vec{\ell}_\perp e^{i\theta_0} + \vec{\ell}_\perp^* e^{-i\theta_0}) = \gamma_s + A_s \quad (9)$$

$$\text{where } \theta_{0s} = \theta_0 + \theta_s, \quad \omega_0 = -\frac{eB_0}{mc\gamma},$$

$$\gamma = \sqrt{1 + \frac{p_\parallel^2 + p_\perp^2}{m^2 c^2}}, \quad \gamma_s = -\omega_s(\vec{r}, t) + \vec{k}_s \cdot \vec{\ell}_\perp \frac{p_\parallel}{m\gamma}$$

Functions a_\perp , A_0 have the form of a_n with coefficients c_j and d_j respectively ($j=1, \dots, 5$). Explicit forms of the coefficients are omitted here (see /3/).

Considering resonances in functions a , A it is necessary to separate the "resonance" phase combination

$\psi_n = n_0 \theta_0 + \dots + n_M \theta_M \equiv (n_\theta, \theta_\theta)$ for which $n_0 \omega_0 + \dots + n_M \omega_M = \Delta$. Where n_θ are fixed whole numbers defined by equations (5-9). Consequently ψ_n is considered to be among the slow changing variables satisfying equation:

$$\frac{d\psi_n}{dt} = (n_\theta, \omega_\theta) + (n_\theta, A_\theta(t, x_m, \theta_j, \psi_s; \mu)) \quad (10)$$

Where $\mu = \max\{\frac{a_\perp}{L}, \frac{a_\parallel}{L}\} \ll 1$, a_\perp, a_\parallel, L are Larmor radius, particle displacement in the H.F. field and the characteristic scale length respectively /3,4/. Then averaging /3/ can be performed over

remaining fast phases in equations (5-9). In /3/ it was shown that for the case of one quasimonochromatic wave in the 1st approximation over small parameter μ the resonance phase combinations are:

$$\theta_s \pm \theta_l, 2\theta_s \pm \theta_l, 3\theta_s \pm \theta_l, \theta_s \pm 2\theta_l \quad (11)$$

In the present paper, with a set of quasimonochromatic waves (1) apart from (11) the following phase combinations are also in resonance:

$$\theta_s \pm \theta_l, \theta_s \pm \theta_s \pm \theta_l, 2\theta_s \pm \theta_s \pm \theta_l \quad (12)$$

($s \neq l$). In higher order approximations more complicated resonances are possible.

In general, the averaged equations have the form:

$$\frac{dX}{dt} = M_0 + M_1 \cos \psi + M_2 \sin \psi \quad (13)$$

$$\frac{d\psi}{dt} = (N_0, \psi_l) + N_1 + N_1 \cos \psi + N_2 \sin \psi \quad (14)$$

where $X = (\vec{R}, P_0, P_1)$; ψ - corresponding resonance phase combination.

For example, in the case of resonance between two waves ($\psi = \theta_s - \theta_l, \nu_s - \nu_l \sim \Delta$) the following equations are obtained:

$$\frac{d\vec{R}}{dt} = \frac{P_0}{m_0 \gamma} \vec{e}_l + \vec{K}_0 \quad (15)$$

$$\frac{dP_0}{dt} = L_0 + L_1 \cos \psi + L_2 \sin \psi \quad (16)$$

$$\frac{dP_1}{dt} = M_0 + M_1 \cos \psi + M_2 \sin \psi \quad (17)$$

$$\frac{d\psi}{dt} = \nu_s - \nu_l + N_0 + N_1 \cos \psi + N_2 \sin \psi \quad (18)$$

Coefficients \vec{K}_0 , L_0 , M_0 are defined by the known expressions of the drift approximation /1/. Exact forms of the remaining coefficients are very complicated. The equations are much simplified

in some particular cases. Equations (13) give the possibility to write the corresponding drift kinetic equation in resonance conditions /4/.

REFERENCES

- /1/ A.I. Morozov, L.S. Solov'ev, in Reviews of Plasma Physics, edited by M.A. Leontovich (Plenum, New York, 1966) Vol. 2.
- /2/ N.N. Bogolubov, Y.A. Mitropolski, Asymptotic method in the theory of nonlinear oscillations, Moscow, 1973.
- /3/ V.P. Milantiev, Izv. VUZov, Fizika, 8, 63, 1977.
- /4/ V.P. Milantiev, JETP, 72, 159, 1977.

OPTICS IN ANISOTROPIC AND DISPERSIVE MEDIA

V.P. Milantiev, P. Saikia.

Patrice Lumumba University, Moscow W-302 U.S.S.R.

The paper deals with the general theory of wave packets in inhomogeneous, nonstationary, anisotropic and dispersive media. Considering the second order geometrical optics approximation, we generalize the Wentzel-Fock parabolic equation [1] and obtain the energy conservation equation. It has been shown that the final expressions for these equations differ for different orderings of the field variables and the parameters of the media and depend on how we consider the inhomogeneity and nonstationarity in the material equation.

The electromagnetic field equation for an arbitrary nonmagnetic medium in the absence of external charges and currents is:

$$\text{Curl curl } \vec{E} + \frac{1}{c^2} \frac{\partial^2 \vec{D}}{\partial t^2} = 0 \quad (1)$$

The equation of energy conservation is

derived from the relation:

$$\vec{E} \frac{\partial \vec{D}}{\partial t} + \vec{B} \frac{\partial \vec{H}}{\partial t} = -c \nabla \cdot [\vec{E} \times \vec{B}] \quad (2)$$

where, we consider three material equations [2-4]

$$\vec{E}(\vec{r}, t | \alpha) = \int_{-\infty}^t dt_1 \int d\vec{r}_1 \hat{E}(\vec{r} - \vec{r}_1, t - t_1, \vec{r}_1, t_1) \vec{E}(\vec{r}_1, t_1 | \alpha) \quad (3)$$

$$\vec{E}(\vec{r}, t | \alpha) = \int_{-\infty}^t dt_1 \int d\vec{r}_1 \hat{E}(\vec{r} - \vec{r}_1, t - t_1, \frac{\vec{r} + \vec{r}_1}{2}, \frac{t + t_1}{2}) \vec{E}(\vec{r}_1, t_1 | \alpha) \quad (4)$$

$$\vec{E}(\vec{r}, t | \alpha) = \int_{-\infty}^t dt_1 \int d\vec{r}_1 \hat{E}(\vec{r} - \vec{r}_1, t - t_1, \vec{r}_1, t_1) \vec{E}(\vec{r}_1, t_1 | \alpha) \quad (5)$$

and express the field vectors \vec{E} , \vec{B} and \vec{D}

in the form

$$\vec{E}(\vec{r}, t | \alpha) = \sum_s \vec{E}(\vec{r}, t, -\frac{\partial \alpha_s}{\partial t}, \nabla \alpha_s, \dots) e^{i\alpha_s} + \text{c.c.} \quad (6)$$

where c.c. denotes the complex conjugation,

α_s - rapid phases (eikonals), amplitudes \vec{E} -

slowly varying functions of \vec{r} , t and, in general, depend on the spatial and time derivatives of the eikonal. Further, \vec{E} is supposed to depend only on the first spatial and time derivatives of the eikonal that represent the local wave vector $\vec{k}_s(\vec{r}, t)$ and the local frequency $\omega_s(\vec{r}, t)$ of the quasi-monochromatic wave (6) respectively. Now we use the geometric optics approximation $\mu = \frac{1}{|\vec{k}_s|L} \ll 1$ (7) $\frac{1}{\omega_s T} \sim \mu$ (8) where $L = |\vec{E}|/|\nabla \vec{E}|$ is the characteristic length of field inhomogeneity, $T = |\vec{E}|/|\frac{\partial \vec{E}}{\partial t}|$ - the corresponding time scale.

Let L_E, L_ω, L_k be the characteristic variation lengths of the dielectric permeability tensor, local frequency and the local wave number respectively. T_E, T_ω, T_k are the corresponding time scales.

Following orderings are considered:

$$L_E \sim L_\omega \sim L_k \sim \frac{L}{\mu}; T_E \sim T_\omega \sim T_k \sim T/\mu \quad (9)$$

$$L_E \sim L; L_\omega \sim L_k \sim \frac{L}{\mu}; T_E \sim T, T_\omega \sim T_k \sim T/\mu \quad (10)$$

$$L_E \sim L_\omega \sim L_k \sim L; T_E \sim T_\omega \sim T_k \sim T \quad (11)$$

2. The amplitude $\vec{E}(\vec{r}, t, \omega_s, \vec{k}_s) \equiv \vec{E}$ and the polarisation vector $\vec{e} = \frac{\vec{E}}{E}$; ($\vec{e} \cdot \vec{e}^* = 1$) are decomposed in the power series of the small parameter μ . Defining

$$\hat{E} \equiv \hat{E}(\vec{r}, t, \omega_s, \vec{k}_s) = \int_0^\infty d\tau \int d\vec{r}' \hat{E}(t, \vec{r}, \tau, \vec{r}') e^{i(\omega_s \tau - \vec{k}_s \cdot \vec{r}')} \quad (12)$$

$$\tau = t - t_1, \quad \vec{r}' = \vec{r} - \vec{r}_1$$

we find $\vec{D}(\vec{k}, t, \omega_s, \vec{k}_s)$ from (3), (5) and the relation

$$\vec{D}(\vec{k}, t, \omega_s, \vec{k}_s) = \frac{1}{2\pi} \int_0^{2\pi} d\alpha_s e^{-i\alpha_s(\vec{k}, t)} \vec{D}(\vec{k}, \alpha_s) \quad (13)$$

In the zeroth order approximation of the perturbation theory, orderings (9)-(11) and eqs. (3)-(5) yield the well-known eikonal equation [3].

We observe that for (9), while the equation for \vec{E} is the same, in the first order approximation, for all material equations, it differs for different material eqs. in the second order approximation.

In the first case we get

$$\frac{\partial \vec{E}_0}{\partial t} + \vec{V}_g \cdot \nabla \vec{E}_0 = \gamma \vec{E}_0 \quad (14)$$

where \vec{V}_g - group velocity, γ - damping coefficient [2] - [4]. Now onwards index "s" is dropped.

In the second case, for (3), we obtain the generalized Leontovich parabolic equation [1]:

$$\begin{aligned} \frac{\partial \vec{E}}{\partial t} + \vec{V}_g \cdot \nabla \vec{E}_1 = \gamma \vec{E}_1 + \frac{i}{2} \frac{\partial \vec{V}_g}{\partial k} : \nabla \nabla \vec{E}_0 - \left(\frac{d\omega}{dt} \frac{\partial}{\partial \omega} + \frac{d\vec{k}}{dt} \cdot \frac{\partial}{\partial \vec{k}} \right) \vec{E}_0 - i \frac{d\gamma}{dk} \cdot \nabla \vec{E}_0 + b(\vec{V}_g - \vec{V}_{g1}) \cdot \nabla \vec{E}_0 - b(\gamma - \gamma_1) \cdot \vec{E}_0 + \frac{c^2}{a} \vec{E}_0 (\vec{E}_0 \vec{E}_{0sim}^* - 2\hat{I}) : \nabla \vec{k} - \frac{\gamma}{a} \vec{E}_0 \vec{E}_0^* : \\ \left\{ \frac{\partial}{\partial \omega} (\omega^2 \hat{E}^A) + \frac{i}{2} \gamma \frac{\partial^2}{\partial \omega^2} (\omega^2 \hat{E}^H) \right\} - \frac{\vec{E}_0 \vec{E}_0^*}{a} : \\ \left\{ \frac{\partial \omega}{\partial t} + 2\omega \left(\frac{\partial}{\partial t} + \frac{\partial \omega}{\partial t} \frac{\partial}{\partial \omega} + \frac{\partial \vec{k}}{\partial t} \cdot \frac{\partial}{\partial \vec{k}} \right) + \frac{\omega^2}{2} \left(\frac{\partial \omega}{\partial t} \right. \right. \\ \left. \left. \cdot \frac{\partial^2}{\partial \omega^2} + 2 \frac{\partial \vec{k}}{\partial t} \cdot \frac{\partial^2}{\partial \vec{k} \partial \omega} - \nabla \vec{k} : \frac{\partial^2}{\partial \vec{k} \partial \vec{k}} \right) \right\} \hat{E}^H \quad (15) \end{aligned}$$

where $b = \frac{\vec{E}_0^* \vec{E}_1 : \frac{\partial}{\partial \omega} (\omega^2 \hat{E}^H)}{a}$; $a = \vec{E}_0^* \vec{E}_0 : \frac{\partial}{\partial \omega} (\omega^2 \hat{E}^H)$
 \hat{E}^H, \hat{E}^A being the hermitian and antihermitian parts of \hat{E} respectively. \vec{V}_{g1}, γ_1 are the group velocity and damping coefficient corresponding to the change of wave polarisation.

For (4), (5) some new terms appear on

the right hand side of (15). Orderings (10), (11) lead to more complicated equations for \vec{E}_0 and \vec{E}_1 .

3. The general expression for the equation of energy conservation, in the media with material equation (3) and orderings (9), (10), is written as

$$\frac{\partial W}{\partial t} + \text{div } \vec{S} - Q = - \sum_s \frac{\partial \mathcal{E}_{ij}^H}{\partial t} \frac{\mathcal{E}_i^* \mathcal{E}_j}{16\pi} + \sum_s \omega_s \left(\frac{\partial \mathcal{E}_{ij}^H}{\partial \omega_s \partial t} - \frac{\partial^2 \mathcal{E}_{ij}^H}{\partial k_s \partial \vec{k}} \right) \frac{\mathcal{E}_i^* \mathcal{E}_j}{16\pi} \quad (16)$$

W, \vec{S}, Q being the usual energy density, Poynting's vector and the energy dissipation term respectively, $\vec{E} = \vec{E}_0 + \vec{E}_1$.

In the case (11), the energy conservation equation can be obtained only if $\vec{E} = \vec{E}_0$. While for (5), it differs from (16) only by the minus sign before the last two terms on the right hand side, for (4) it does not contain the terms with second derivatives of \hat{E} .

Thus, we conclude that the equation of energy conservation is more sensitive to the form of the material equation than to the orderings.

REFERENCES

- [1] M.A. Leontovich, *Izv. Aca. Sci. U.S.S.R., ser. phys.*, **8**, 16, 1944.
- [2] Yu. L. Kravtsov, *JETP*, **55**, 1470, 1968.
- [3] B. B. Kadomtsev, "The collective phenomena in plasma", Moscow, 1976.
- [4] V. P. Silin, "An introduction to the kinetic theory of gases", Moscow, 1971.

THEORETICAL METHOD FOR PREDICTING THE PROPERTIES OF CYCLOTRON HARMONIC WAVES FROM THE PERPENDICULAR DISPERSION RELATION

B. Lembège.

Space Plasma Physics Division Space Science Department, European Space Agency, Noordwijk, The Netherlands

A theoretical method is proposed for predicting the properties of the backward propagating cyclotron harmonic waves (CHW) from the simple dispersion curve for perpendicular propagation. This method is illustrated for the frequency range $1 < \omega/\omega_c < 2$, where ω and ω_c are respectively the wave and electron cyclotron frequencies and is applicable for any plasma density conditions.

In previous experimental and theoretical study (Lembège, 1979), it was proposed a new classification of properties of CHW both in the propagation and detection plane respectively described by the normalized wave vector \vec{k}_p and the distance vector \vec{r} ; ρ is the electron gyroradius. This classification is based on the determination of two groups of values ω/ω_c separated by a certain boundary value $(\omega_{cyl}/\omega_c)_1$. Knowing a given high value of $(\omega_p/\omega_c)^2$, where ω_p is the plasma frequency, the dispersion curve for perpendicular propagation can be numerically determined (Stix, 1962); consequently the value $(\omega/\omega_c)_{P_1}$ of its inflexion point P_1 can be easily known. Then it was shown that the value $(\omega_{cyl}/\omega_c)_1$ can be quickly defined from P_1 by the numerical relation $(\omega_{cyl}/\omega_c)_1 = (\omega/\omega_c)_{P_1} - \delta_1$, where δ_1 is roughly constant for dense plasma conditions and equal to 0.145. This point $P_{cyl,1}$ was shown to present particular characteristics and to divide the frequency range $1 < \omega/\omega_c < 2$ into two groups I and II.

However, it can be shown that although the classification into two groups I and II is always applicable for any plasma conditions, the previous principle of determination of the boundary value $(\omega_{cyl}/\omega_c)_1$ cannot be simply extended to

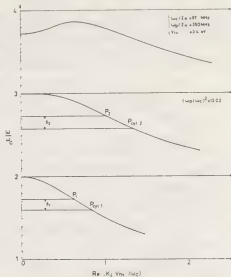


Figure 1 : Theoretical curves of the dispersion relation in the perpendicular propagation for an example of dense plasma $(\omega_p/\omega_c)^2 = 13.02$; the indexes 1 and 2 of P and P_{cyl} refer to the dispersion branches of order 1 and 2.

other plasma densities. This is due to the big variation of δ_1 with $(\omega_p/\omega_c)^2$ for mean and low plasma densities (Figure 2).

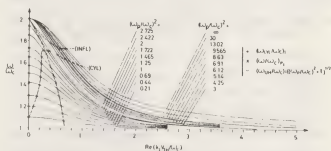


Figure 2 : Theoretical curves of the first dispersion branch in the perpendicular propagation for $(\omega_p/\omega_c)^2$ varying from infinity to very low values. The curve (CYL) (---) joins the different values of $(\omega_{cyl}/\omega_c)_1$. The curve (INFL) (---) joins the locations of the various inflexion points P_1 .

Presently, the locations of $P_{cyl,1}$ are determined for a large number of values of $(\omega_p/\omega_c)^2$ from very low to infinite plasma densities (Figure 2) ; each point $P_{cyl,1}$ is numerically defined by the frequency ω/ω_c for which the low damped part AI of the polar curves k_p has almost zero curvature with respect to the origin O (Figure 3) ; in this case $AI = A_{cyl} I_{cyl}$.

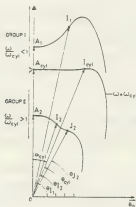


Figure 3 : Sketch of the three kinds of polar curves of the real part of k_p inside the frequency range $1 < \omega/\omega_c < 2$ (not to scale).

The ensemble of the points $P_{cyl,1}$ determines a curve (CYL) which is used as a reference curve ; this curve divides the plane $(\omega/\omega_c ; \text{Re}(k_{\perp} v_{TH}/\omega_c))$ into two areas I and II characteristic of the two groups previously defined (Figure 4).

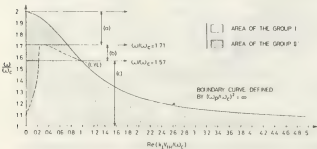


Figure 4 : Representation of the three characteristic frequency ranges (a), (b) and (c) of ω/ω_c respectively defined by (2, 1.71), (1.71, 1.57) and (1.57, 1).

The present method consists of varying the ratio ω/ω_c represented by a straight line (L) parallel to the axis $\text{Re}(k_{\perp} v_{TH}/\omega_c)$ and noting where the line (L) intersects the curve (CYL). Three different frequencies ranges of ω/ω_c , (a), (b) and (c) can be defined. It is shown that as a function of the ratio ω/ω_c , the number of intersections between (L) and (CYL), and various ranges of $(\omega_p/\omega_c)^2$ can be also defined ; in each one of these ranges, the properties of CHW can be easily obtained using the characteristics of the groups I and II. This method is shown to be extended to other dispersion branches of backward propagating CHW for perpendicular propagation.

References : - Lembège (1979), Antenna radiation pattern of cyclotron harmonic waves in a hot magnetoplasma, Rad. Science (to be published in May-June).

- Stix (1962), Theory of Plasma waves, Mc Graw Hill, New York.

DRIFT-DISSIPATIVE WAVES AND ENSUEING STEADY STATE OF A PLASMA COLUMN

M.P. Evrard, A.M. Messiaen, P.E. Vandenplas and G. Van Oost.

Laboratoire de Physique des Plasmas - Laboratorium voor Plasmafysica, Association "EURATOM-Etat belge" Associatie "Euratom-Belgische Staat", Ecole Royale Militaire - 1040 Brussels - Koninklijke Militaire School.

1. INTRODUCTION. Spontaneously excited low-frequency oscillations¹ with a frequency of the order of the characteristic drift frequency ω^* are identified as drift-dissipative waves² and are responsible for the anomalous diffusion observed in a weakly ionized helium plasma column produced by a helical microwave discharge source (see Fig. 1). Plasma parameters are : density, $5 \times 10^3 - 8 \times 10^{10} \text{ cm}^{-3}$; gas pressure, $1 - 7 \times 10^{-3}$ Torr; electron temperature T_e , 3-15 eV; ion temperature T_i , 0.2-1.4 eV; magnetic field B_0 , 850-2200 Gs.

2. THEORY. The plasma consists of hot electrons and hot ions in the presence of background neutral particles and is described by means of the linearized two-fluid equations in which T_e and T_i are introduced by scalar pressure laws and in which only electron-neutral and ion-neutral momentum transfer collisions are included. The radial temperature inhomogeneity is negligible with respect to the density inhomogeneity. The bounded plasma problem is solved in the actual cylindrical geometry.

The static fluid model is characterized by a radial Gaussian equilibrium density profile, $\langle N \rangle(r) = \langle N \rangle_0 e^{-\alpha r^2}$, where $\langle N \rangle_0$ is the equilibrium density on the column axis. Assuming quasineutrality, strong field approximation, classical ambipolar diffusion and symmetry of revolution, one obtains from the equilibrium momentum equations the radial component of the static electric field, $E_{or} = (KT_i/e\langle N \rangle)(\partial \langle N \rangle / \partial r)$. The value of E_{or} is experimentally verified and found to be negligible for the calculation of the drift wave dispersion relation. We have furthermore checked that the additional possible static effect resulting from the drift wave induced diffusion does not modify the aforesaid value of E_{or} .

Using the $e^{-i\omega t}$ perturbed linearized two-fluid continuity and momentum equations³ and the Poisson equation, we calculate the dispersion

relation for the drift waves in the quasistatic approximation. A first calculation which does not take collisions and mean particle drift velocities into account leads to

$$k_{\perp}^2 = -\left(1 - \frac{\omega_{ci}^2}{\omega^2}\right) \left(k_{\parallel}^2 - \frac{\omega^2}{V_S^2}\right) + 2\alpha n \frac{\omega_{ci}}{\omega} \quad (1)$$

where k_{\parallel} is the wavenumber parallel to \vec{B}_0 , k_{\perp} is the radial wavenumber and n/r the azimuthal one; ω_{ci} is the ion-cyclotron frequency and V_S is the ion-acoustic speed. The last term is the extra nonuniform term with respect to the dispersion relation of the ion-acoustic waves in the uniform plasma column^{4,5}. This dispersion relation provides an approximate value of k_{\perp} and when $k_{\perp}^2 V_S^2 / \omega_{ci}^2 \ll 1$, one retrieves the standard Kadomtsev dispersion relation⁶.

When we further take collisions and drift velocities into account, we then obtain a dispersion relation which can be written as a polynomial of the sixth degree in ω with complex coefficients⁷. Only one of the six complex roots satisfies the condition for drift waves: $|\omega| \ll \omega_{ci}$, $\text{Im } \omega > 0$. The behaviour of the real and imaginary parts of this root is plotted as a function of k_{\perp} in Fig. 2 and shows the existence of a region of unstable modes. The maximum of the imaginary part occurs at a k_{\perp} -value which is in good agreement with the value obtained from equation (1) when one inserts the observed most strongly excited $\text{Re } \omega$ -value of the drift wave spectrum. The importance of taking the diamagnetic drift velocity of the ions into account is very pronounced. Indeed, the neglect of the diamagnetism of the ions with respect to that of the electrons results in the disappearance of the unstable region of Fig. 2. This is demonstrated in Fig. 3 by gradually decreasing the value of the ion diamagnetic velocity by decreasing T_i , the other plasma parameters remaining constant.

The steady state density distribution in the plasma column is calculated from the diffusion equation and is given by :

$$\langle N \rangle(r, z) = \sum_{l=1}^{\infty} C_l J_0(p_l \frac{r}{d}) \exp \left(-\frac{p_l}{d} \sqrt{\frac{D_{\perp}}{D_{\parallel}}} z \right) \quad (2)$$

where p_l is the l -th root of the Bessel function J_0 , d is the radius of the metal vacuum chamber, D_{\perp} and D_{\parallel} are the anomalous diffusion coefficients the values of which are considered in the next section and C_l is a constant determined by means of the boundary condition at $z = 0$.

3. EXPERIMENTAL RESULTS. Several measurements have been carried out which identify spontaneously excited waves as drift-dissipative waves. The observed waves propagate mainly in the azimuthal direction, in the same sense as the electron diamagnetic drift velocity, and have an azimuthal mode number $n = 1$. The value of k_{\perp} derived from dispersion equation (1) is corroborated by the measurement of the radial behaviour of the wave amplitude (Fig. 4). Axially, the waves have a wavelength of the order of the length of the plasma column and they propagate from the plasma source towards the end plate, in the direction of \vec{B}_0 . Finally, the dependence of the wave frequency on T_e is in agreement with that of a drift wave. The anomalous diffusion coefficient D_{\perp} resulting from the insertion of the experimental data into the theoretical formulae⁶ and the experimental value of D_{\parallel} lead to a steady state density distribution (equation 2) of the plasma column which is in very satisfactory agreement with the measured one. The observed anomalous diffusion and the ensuing steady state density profile in the plasma column are therefore explained by means of the observed drift waves.

4. REFERENCES.

1. See e.g. Chen F.F. (1964) Phys. Fluids 7, 949.
2. See e.g. Self S.A. (1970) J. Plasma Physics, 4, 693.
3. Dubois D.M., Messiaen A.M. and Vandenplas P.E. (1972) Proceedings of the 5th European Conference on Controlled Fusion and Plasma Physics, Grenoble, France, vol. I, p. 114.
4. Messiaen A.M. and Vandenplas P.E. (1973) Plasma Phys. 15, 505.
5. Bhatnagar V.P., Van Oost G., Messiaen A.M. and Vandenplas P.E. (1976) Plasma Phys. 18, 525.
6. Kadomtsev B.B. (1965) Plasma Turbulence. Academic Press, New York.
7. Evrard M.P., Messiaen A.M., Vandenplas P.E. and Van Oost G., submitted for publication to Plasma Phys.

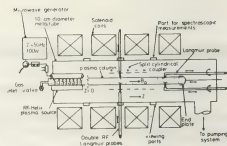


Fig.1 - Schematic diagram of the experimental apparatus.

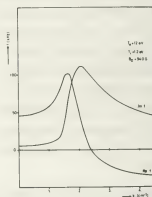


Fig.2 - Theoretically computed behaviour of the real and the imaginary part of the drift wave frequency as a function of k_{\perp} .

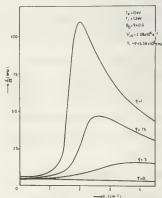


Fig.3 - Theoretically computed behaviour of the growth rate of the drift instability as a function of the ion thermal velocity.

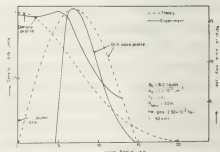


Fig.4 - Relative radial equilibrium density profile and relative axial electric field amplitude as a function of radial distance.

HIGH FREQUENCY OSCILLATIONS AND ELECTRON BEAM RELAXATION
IN HOMOGENEOUS GAS-DISCHARGE PLASMA

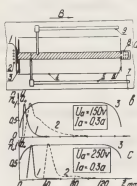
L.L. Pasechnik, L.I. Romanyuk, N. Ye. Svavil'ny.

Institute for Nuclear Research, Ukrainian Academy of Sciences, Kiev, U.S.S.R.

The account of different types of inhomogeneities in the theoretical consideration of the electron beam interaction with plasma and wave propagation in plasma allows one to observe a number of some remarkable phenomena (oscillation localization and accumulation /1,2/, rapid wave attenuation /3/). An example of the beam-plasma system, which is strongly inhomogeneous by a number of parameters is the hot cathode Penning discharge. The present report deals with results of an experimental study of the high frequency oscillations, originating in the plasma of this discharge and formation of electron velocity distribution function.

Experiments were carried out on an device with Penning cell (fig 1a). The discharge was realized in a stationary state in He (in some experiments in Ar) at a pressure $p = 8 \cdot 10^{-3} \div 5 \cdot 10^{-2}$ torr in a homogeneous magnetic field $B = 0.01 - 0.04$ T. Parameters of the beam-plasma system were varied: plasma density $n = 8 \cdot 10^{10} \div 4 \cdot 10^{11} \text{ cm}^{-3}$, primary electron velocity $v_0 = 4.5 \cdot 10^8 \div 1 \cdot 10^9 \text{ cm} \cdot \text{s}^{-1}$, ratio of beam and plasma density $\frac{n_b}{n} = 5 \cdot 10^{-4} \div 2 \cdot 10^{-2}$; the plasma electron temperature $T_e = 4 \div 8 \text{ eV}$. The con-

trol measurements were also carried out in the arc discharge plasma at the same discharge conditions (in this case electrode 6 was the anode.) This experiment showed that in both Penning discharge plasma and arc discharge plasma inside the primary electron beam intensive oscillations are generated in frequency range



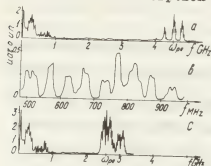
$f = 40 \text{ MHz} \div 7.5 \text{ GHz}$ whose characteristic spectrum is shown in fig 2. One can see that the most intensive oscillations are concentrated in "low frequency"

Fig. 1. Experimental device: 1-cathode, 2-auxiliary cathode, 3-diaphragm, 4-anode, 5-HF probe, 6-reflector, 7-screen, 8-stationary analyzer, 9-moving analyzer; b, c-dependences: 1- $U_{\text{HF}}(Z)$ 2- $U_{\text{LF}}(Z)$, 3- $n(Z)$.

(LF) $40 \div 1000 \text{ MHz}$ and "high frequency" (HF) $2 \div 8 \text{ GHz}$ parts of the spectrum.

The characteristic features of the obtained oscillation spectra indicated that in the studied beam-plasma system flashes ("radioimpulses") of the HF field with $\omega \approx \omega_{pe}$ are generated, which cause the plasma

potential splashes ("video pulses") with the mean statistic duration $\bar{\tau} \approx 5$ ns and the repetition period $T \approx 16 \pm 25$ ns /4/. The observed rapid selfmodulation of HF field at the present experiments is possibly connected with the peculiarity of wave generation and absorption /3/ in plasma,



which is inhomogeneous in density. The reason for the potential

Fig.2. Oscillation spectrum. a-PIG discharge; b-part of spectrum (a); c-arc discharge.

splashes may be lack of compensation of electron space charge, arising due to striction force, because of the ion inertia.

The detailed study of the space distribution of the oscillation intensity in both discharges types showed that the HF range oscillation are always localized in the inhomogeneous density plasma, adjoining to cathode (fig 1b,c, curves 1). The observed characteristics of the HF field (Z_{st} - is the coordinate of the oscillation occurrence, Z - is the half width of the HF field existence range and γ - is the space increment), agree satisfactorily with estimations from theory of the electron beam interaction with inhomogeneous density plasma /2/ (see Table I). Localization of the LF range oscillation is determined by the HF field position and primary electron beam velocity (fig 1b,c, curves 2).

According to /2/ in the HF field localization zone the transformation is possible of the excited waves in Langmuir ones with the subsequent intensive absorption of HF power by plasma electrons. Investigation of the space evolution of the electron distribution function showed that actually not only primary electron beam relaxation takes place in the HF field localization zone but also an effective

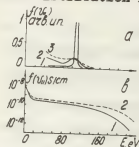


Fig.3. Electron distribution function. a-PIG discharge, 1- $Z=9$ mm, 2- $Z=17$ mm, 3- $Z=32$ mm. b-1-PIG discharge, 2-arc discharge, $Z=140$ mm, $I_a=0.3$ A, $V_a=150$ V.

heating of plasma electrons (fig 3a). Beyond the

Table I

V_a	I_a	f	Z_{st}		ΔZ		γ	
			exp	theor	exp	theor	exp	theor
B	A	GHz	mm	mm	mm	mm	cm^{-1}	cm^{-1}
150	0.05	2.56	9	13.3	80	96	4.6	6.2
150	0.1	4.3	10	11.7	40	61	6.6	7.6
150	0.3	4.94	6	6	30	30	9.2	20
250	0.3	5.6	11	12	7	15.2	8.5	37
400	0.3	4.94	24.5	32	23	91	23	4.9
150*	0.3*	3.38	4.5	4.5	5	26	>20	58

* arc discharge

spectrum practically is not changed and has an identical form in both discharges types (fig 3b).

REFERENCES:

1. Ya. B. Painberg, V. O. Shapiro, Zh. Eksp. Teor. Fiz., **47**, 1389, 1964.
2. V. Kopecky, J. Preinhaelter, Plasma Phys., **11**, 333, 1969.
3. S. M. Dikman, Pis'ma Zh. Eksp. Teor. Fiz., **27**, 429, 1978.
4. L. L. Pasechnik, L. I. Romanyuk, N. Ye. Svavil'ny, Pis'ma Zh. Tekh. Fiz., **4**, 958, 1978.

STABILITY OF THE NONLINEAR PERIODIC WAVES IN PLASMA

V.P. Pavlenko and V.I. Petviashvili.

Institute for Nuclear Research, Kiev, U.S.S.R.

It was announced in paper /1/ about observing of chains of amplitude modulated nonlinear Langmuir waves with quasi periodic space structure accompanied by corresponding density pits. From this we conclude that the amplitude modulation weakens considerably instability of monochromatic Langmuir wave. Waves like the observed ones in /1/ can exist also in plasma containing devices with condition and in auroral region of the magnetosphere where they are responsible for the anomalous resistivity.

Usually the problem of stability of periodic wave relative to infinitely small perturbations is reduced to finding of eigenvalues of linear differential eq. with periodical coefficients. In preceding studies these perturbations were expanded in inadequate system of basic functions that sometimes led to error. In present paper we expand the perturbation in integral over quasimpulses on Bloch functions the only complete basic system for eq. with periodic dependence of parameters on coordinates.

Let us consider the nonlinear Shredinger eq.(NSE). The stability problem of periodic solutions of this eq.

leads to the following dimensionless eq

$$\hat{L}_0 \hat{L}_1 f_1 = -\gamma^2 f_1 \quad (1)$$

here $\hat{L}_0 = 1 - \frac{\partial^2}{\partial x^2} - f_0^2$, $\hat{L}_1 = 1 - \frac{\partial^2}{\partial x^2} - 3f_0^2$, x is dimensionless coordinate, γ is wanted increment, f_0 is the periodic solution of the NSE that is expressed through elliptical Jacoby functions cn or dn . In dimensionless case f_0 depends only on x and \mathcal{X} , where \mathcal{X} is the modulus of elliptical functions. We expand f_1 over Bloch functions φ_k where $\varphi_k(x) = e^{ikx} u_k(x)$, $k \leq \frac{1}{2} |k_0|$, $u_k(x) = \sum_n C_{n,k} e^{in k_0 x}$, k_0 is the main wave number of periodic wave f_0^2 . After this the problem is reduced to finding of eigenvalues of the infinite matrix

$$\mathcal{L}_{mn} = \left[1 + k_0^2 (n+k)^2 \right]^2 d_{mn}^2 + 3I_2 - \left\{ 4 + k_0^2 \left[3(n+k)^2 + (m+k)^2 \right] \right\} I_1 \quad (2)$$

where $2\pi/k_0$ $I_1 = \frac{k_0}{2\pi} \int_0^2 e^{ik_0(m-n)x} dx$, $I_2 = \frac{k_0}{2\pi} \int_0^4 e^{ik_0(m-n)x} dx$

If \mathcal{X} is not too close to 1 the functions I_1 and I_2 decrease with sufficient rate with growth of $|m-n|$. Therefore it is possible to restrict ourselves with consideration of finite matrix 25×25 . We considered this matrix in the region $0 < \mathcal{X}^2 < 0.999$. The analysis of computed

data reveals the existence the instability region. The dependence of maximal increment on \mathcal{X} is given in following table

cn			dn		
\mathcal{X}	0.975	0.995	\mathcal{X}	0.985	0.995
γ	0.025. 10^{-1}	0.03 10^{-1}	γ	1.13. 10^{-1}	3.94. 10^{-2}

The more is \mathcal{X} the deeper is amplitude modulation. The according variation of energy density is small. We see that the growth of amplitude modulation causes decreasing of instability increment to the value which makes possible the existence of wave chains observed in /1/. Note that the known result on instability of periodic Langmuir wave corresponds to the case $\mathcal{X} = 0$ /2/.

The similar investigation of stability of periodic solutions of KdV eq. shows that solutions are always stable. The result is in accordance with the nonlinear consideration made in /3/ with help of the method of the reversed problem of scattering.

The KdV eq. generalized for two dimensional case has the form /4/

$$\frac{\partial}{\partial x} \left[\frac{\partial u}{\partial t} + 6u \frac{\partial u}{\partial x} + \frac{\partial^3 u}{\partial x^3} \right] = \pm \frac{\partial^2 u}{\partial y^2} \quad (3)$$

The one dimensional solutions of this eq. are expressed through cn^2 or dn^2 . Let us consider the stability of these solutions relative to two dimensional perturbations of the form $f(x, y) = \varphi(x) e^{iky + \gamma t}$

Expanding $\varphi(x)$ in the integral over Bloch functions after some transformations we get the matrix

$$\mathcal{L}_{mn} = \left[\kappa_o (\pi + \kappa) + \kappa_o^3 (\pi + \kappa)^3 \pm \frac{\kappa_y^2}{\kappa_o (\pi + \kappa)} \right] \delta_{mn} - 6 \kappa_o (\pi + \kappa) I_1$$

Diagonalisation of this matrix shows that all solutions are stable in case of negative dispersion (the lower sign in rhs of eq (3)). If the dispersion is positive all one dimensional solutions are unstable. The dependence of maximal increment on \mathcal{X} is given in following table

cn^2			dn^2		
\mathcal{X}	0.980	0.990	\mathcal{X}	0.985	0.995
γ	2.55. 10^{-1}	2.32. 10^{-1}	γ	2.08. 10^{-1}	2.07. 10^{-1}

Note that when $\kappa_y = 0$ or for big κ_y the solutions are stable.

The considered examples illustrate the proposed method for solving of stability problem of periodic solutions of other nonlinear eqs. including the solutions consisting of solitons.

It is interesting that this method gives simple way of getting zonal picture of eigenfrequencies of medium in presence of the periodic wave.

References

1. Antipov S.V., Neslin M.V., Sneshkin E. Trubnikov A.S. Zh. eksp. teor. fiz. 74, 965, 1978.
2. Zakharov V.E. Zh. eksp. teor. fiz. 62, 1745, 1972.
3. Kusnetsov E.A., Mikhailov A.V. Zh. eksp. teor. fiz. 67, 1717, 1974.
4. Kadomtsev B.B. Petviashvili V.I. Dokl. AN SSSR

NONLINEAR DECAY INTERACTIONS FOR THE INSTABILITY OF BUNEMAN-FARLEY

A.V. Volosevich, M.A. Livshits and V.A. Lipеровsky

During the magnetic disturbances the small-scale irregularities occur in the polar and equatorial electrojet along the Earth's magnetic field with the cross-dimensions from 10 cm to 10 m. These irregularities are responsible for the intense VHF radio wave scattering and in the absence of sharp gradients arise from the Buneman-Farley instability [1, 2].

The experimental studies of auroral and equatorial radar echoes revealed the discrepancies between linear theory and observations and thus posed a problem of developing nonlinear theory.

In this paper we analyse one possible nonlinear process-Buneman-Farley wave decay interaction. When the amplitude of unstable waves grows to some level these waves intensively interact so as a result of the interaction a nonlinear flow of spectral energy from the region of linear generation to the damping region can be significant.

This process is possible if the resonance conditions $\omega = \omega_1 + \omega_2$, $\vec{k} = \vec{k}_1 + \vec{k}_2$ are fulfilled. Taking into account the law of Buneman-Farley wave dispersion [3] these resonance conditions for the decay interaction in a three-dimensional case can be written as:

$$k \sin \psi = k_1 \sin \psi_1 + k_2 \sin \psi_2 \quad (1)$$

$$k \cos \psi \sin \varphi = k_1 \cos \psi_1 \sin \varphi_1 + k_2 \cos \psi_2 \sin \varphi_2 \quad (2)$$

$$k \cos \psi \cos \varphi = k_1 \cos \psi_1 \cos \varphi_1 + k_2 \cos \psi_2 \cos \varphi_2 \quad (3)$$

$$\frac{k \cos \psi \cos \varphi}{1 + \xi \sin^2 \psi + \eta k^2} = \frac{k_1 \cos \psi_1 \cos \varphi_1}{1 + \xi \sin^2 \psi_1 + \eta k_1^2} + \frac{k_2 \cos \psi_2 \cos \varphi_2}{1 + \xi \sin^2 \psi_2 + \eta k_2^2}$$

$$\vec{k} = \vec{k}(|k|, \psi, \varphi), \quad \vec{k}_1 = \vec{k}_1(|k_1|, \psi_1, \varphi_1), \quad \vec{k}_2 = \vec{k}_2(|k_2|, \psi_2, \varphi_2) \quad (4)$$

$$\eta = \frac{3R_0 v_{Te}^2}{(1+R_0) \omega_e^2}, \quad \xi = \frac{R_0 \omega_{He}^2}{(1+R_0) \omega_e^2}, \quad R_0 = \frac{\gamma_i \gamma_e}{\omega_{Hi} \omega_{He}}$$

Here φ is the angle between wave vector \vec{k} and the electrons drift velocity \vec{v}_0 , and ψ is the angle between the wave vector \vec{k} and

the plane per-

pendicular to the magnetic field.

If $k^2 \ll 1$, $\xi \sin^2 \psi \ll 1$ then the equations (1) - (4) admit the decay interaction of the Buneman-Farley waves and the above-mentioned parameters correspond to the following equations:

$$\psi_1 = (\psi \cos(y+\varphi) \pm \sqrt{\psi^2 + \psi_0^2} \sin x) (\cos(x+y+\varphi))^{-1} \quad (5)$$

$$\psi_2 = (\psi \cos(x+\varphi) \pm \sqrt{\psi^2 + \psi_0^2} \sin y) (\cos(x+y+\varphi))^{-1} \quad (6)$$

$$\psi_0^2 = \left(\frac{\xi}{\eta} \right) \frac{\cos \varphi \cos(x+y+\varphi)}{\sin^2(y-x)} \left[\sin x \sin y + 3 \cos x \cos y - \operatorname{tg} \varphi \cdot \sin(x+y) \right]$$

$x = \varphi_1 - \varphi$, $y = \varphi_2 - \varphi$
For two dimensional geometry $\psi = \psi_1 = \psi_2 = 0$ using the equations (5-6) one can draw a conclusion that the decay process for the small angle waves φ_1 and φ_2 is impossible. Thus the studies of the resonance conditions with small but not equal zero angles ψ , ψ_1 , ψ_2 bring

about the conclusion that the decay process is possible if the parameters of interacting waves correspond to certain equations. In particular there is a possibility for the decay of the linear growing wave ($\gamma > 0$) into two waves one of which spreads nearly perpendicular to the electrojet. A set of quasi-fluids equations for the electron and ion, equations of electrodynamic and equations of continuity results in the equations describing the decay process of the Buneman-Farley waves if the wave phase is fixed:

$$\frac{\partial n_R}{\partial t} - \gamma_R n_R = -i S n_R n_{R_1} \quad (7)$$

$$\frac{\partial n_{R_1}}{\partial t} - \gamma_{R_1} n_{R_1} = -i S_1 n_R n_{R_1} \quad (8)$$

$$\frac{\partial n_{R_2}}{\partial t} - \gamma_{R_2} n_{R_2} = -i S_2 n_R n_{R_1} \quad (9)$$

where the expansion of electron density takes the form:

$$n(\vec{r}, t) = \int \tilde{n}_R(\vec{r}, t) \exp\{-i(\Omega(R)t - \vec{R} \cdot \vec{r})\} d\vec{r}$$

here $\omega^e(\vec{R}) = \Omega(\vec{R}) + i\gamma_R$ is the so-

lution of the linear dispersion relation

$\mathcal{E}(\omega^e(\vec{R})) = 0$, γ_R - growth rate and

$\tilde{n}_R(\vec{r}, t) = n_R \exp(i\gamma_R t)$ is the slowly

changing amplitude of the electron density

and $\tilde{n}_{R_1} = n_{R_1} \delta(\vec{R}_1 - \vec{R}_0)$, $\tilde{n}_{R_2} = n_{R_2} \delta(\vec{R}_2 - \vec{R}_0)$

$$S = \nu_1 \nu_0 (2n_0 \omega_{H1})^{-1} \sin(\varphi_1 - \varphi) [k_1 \cos \varphi_1 - k_2 \cos \varphi]$$

$$S_1 = \nu_1 \nu_0 (2n_0 \omega_{H1})^{-1} \sin(\varphi_1 - \varphi) [k \cos \varphi_1 + k_2 \cos \varphi]$$

$$S_2 = \nu_1 \nu_0 (2n_0 \omega_{H1})^{-1} \sin(\varphi_1 - \varphi) [k_1 \cos \varphi + k \cos \varphi_1] \quad (10)$$

The solution of the equations (7)-(9)

determines the periodical transfer from one mode n_R to the modes n_{R_1} , n_{R_2} . This process will continue without damping

$\gamma_R = \gamma_{R_1} = \gamma_{R_2} = 0$. However, the greatest interest for practical purposes is the case of the stationary state. As seen from Eqs. (7)-(9) the stationary state is possible with the decay of the wave having a vector \vec{R} into the waves damp-

ing in the linear theory \vec{R}_2 , ($\gamma_{R_2} < 0$).

In this case the quasi-stationary turbulence level is determined by:

$$\rho_R^2 = \frac{|n_R|^2}{n_0^2} = \frac{|\gamma_{R_1} \gamma_{R_2}|}{|S_1 S_2|}; \quad \rho_{R_1}^2 = \frac{|\gamma_R \gamma_{R_2}|}{|S S_2|}; \quad \rho_{R_2}^2 = \frac{|\gamma_R \gamma_{R_1}|}{|S S_1|} \quad (11)$$

Taking the interacting wave parameters according to (6), the stationary state is determined by:

$$\rho_{R_2}^2 = 4 \frac{\kappa^2 \kappa_1^2 \gamma_{R_1}^2}{\gamma_{R_1}^2 \omega_{H1}^2} \frac{(\cos^2 \varphi - \beta^2)(\cos^2 \varphi_1 - \beta^2) \kappa_1^2}{[k_1 \cos \varphi_1 - k_2 \cos \varphi][k \cos \varphi - k_2 \cos \varphi_1]} \quad (12)$$

Taking the parameters for estimation: $\varphi = 0$, $\varphi_1 = 20^\circ$, $\varphi_2 = -68^\circ$, $\beta = \frac{c}{v_0} = 0.68$, $\frac{\omega^2}{\omega_{H1}^2} \sim 10^{-4}$, $\rho_{R_1}^2 \approx 10^{-3}$ and we obtain. Thus, based on the estimates one can draw a conclusion that the above-mentioned process is quite effective for the stabilization. As a result of the stationary state the wave electrostatic turbulence regions can be formed with the directions of waves are almost perpendicular to magnetic field. The given estimates correspond to experimental observations of radio-echoes from the electrostatic wave turbulence regions.

References

1. Buneman O. Exasitation of field aligned sound waves by electron streams. Phys. Rev. Lett. 1963, 10, 285-289.
2. Farley D.T. A plasma instability resulting in field aligned irregularities in the ionosphere. J. Geophys. R. 1963, 68, 6083.
3. Volosevich A.V. In Book 'Yavlenia v polarnoi ionosphere'. Nauka, Leningrad, 1979, p. 50.
4. Volosevich A.V., Liperovsky V.A. In Book 'Visokoshirotnie proyavleniya magnitosfernich processov'. Leningrad, 1978, p. 121.

ABOUT THE STATIONARY TURBULENCE REGIONS AND ANOMALOUS RESISTANCE IN THE MAGNETO-SPHERE PLASMA

A.V. Volosevich, M.A. Livshits, V.A. Liperovsky and G.A. Skuridin.

Institute for Space Research, Ac. of Sci., U.S.S.R.

The strong longitudinal currents, low frequency electrostatic waves of high level [1] and longitudinal electric fields due to anomalous resistance [2] are systematically observed in the Earth magneto-sphere plasma. So it is interesting to construct even though rough semiempiric models to describe the stationary regions of the wave electrostatic turbulence which results in anomalous resistance. We shall further restrict ourselves to the one-dimensional model of the fairly wide magnetic field tube. Let the electric field be aligned in a positive direction of Z axis along the magnetic field tube, and $T_e = T_e^*$, $T_i = T_i^0$ and the longitudinal electric field $E_{||} = E_0$ if $z = 0$. The equation describing the turbulent heating of electrons is

$$\frac{\partial n T_e}{\partial t} = \frac{3}{2} n u_0 \frac{\partial T_e}{\partial z} + n T_e \frac{\partial u_0}{\partial z} + |e| n u_0 E$$

The equation of motion is

$$m n \frac{\partial u_0}{\partial t} = - \frac{\partial n T_e}{\partial z} - |e| n E + m u_0 n \nu^*$$

where ν^* is the collective collision

frequency, u_0 is the directional velocity. If the condition $E > E_2 \approx 10^{-2} \frac{T_e m_i}{T_i m_e} \sqrt{4 \pi n T_e}$ is fulfilled, then the Sagdeev formula is valid for current in the electric field

in the homogeneous plasma stationary regime [3]: $j = e n u_0 = 10 e n c_s \left(\frac{T_i m_i}{T_e m_e} \frac{E}{\sqrt{4 \pi n T_e}} \right)^{1/2}$

The current along the magnetic force tube

$$j = \frac{4}{3} e n u_0 = \text{const} \cdot (E T_i / T_e)^{1/2}$$

where $C_s = \sqrt{T_e / m_i}$, coefficient $4/3$ is due to the pressure gradient in the equation of motion. The turbulent heating of electrons and ions can be roughly described by the set of equations assuming that the turbulence is weak and the directional velocity $v_i^0 = v_{Ti} = \sqrt{T_i / m_i}$ and $n = \text{const.}$:

$$\begin{aligned} |e| E n u_0 + \frac{3}{2} n \frac{\partial T_e}{\partial z} u_0 &= 0 \\ |e| E n C_s - \frac{3}{2} n \frac{\partial T_i}{\partial z} v_i^0 &= 0 \quad \frac{E T_i}{T_e} = \text{const} \end{aligned}$$

The solution of this system with $1 \gg \Delta z \gg t_0^2$, $t_0 = 0.87 \sqrt{T_e^* / T_i^0}$ takes the form:

$$\begin{aligned} T_e / T_e^* &= 1 - \frac{2}{3} (\Delta z)^{3/5} \\ T_i / T_e^* &= 0.55 (\Delta z)^{2/5} \\ E / E_0 &= (T_i^0 / T_e^*) (\Delta z)^{-2/3} \end{aligned}$$

Limiting of the magnetic tube length L is associated with the condition of the ion sound existence, for example, $T_e \gg 6 T_i$ and $T_e^* = 10^3$ eV, $T_i = 1$ eV, $n = 10^2$ cm $^{-3}$, $E = 3 \cdot 10^{-2}$ V/m, $m_i = 30 m_p$, the length of the tube of the field aligned current with the quasi-stationary turbulence $L \sim 1300$ km.

For the potential drop we have $U(z) - U(0) = E_0 \frac{T_i^0}{T_e^*} \frac{(\Delta z)^{3/5}}{2} \left(1 - \frac{1}{6} (\Delta z)^{3/5} \right)$ that is equal ~ 380 eV for the above written parameters. The condition of validity of the Sagdeev formula $E > E_2$ is fulfilled for the given example in the upper polar

ionosphere if the electron temperature are not too high $T_e < 5 \cdot 10^3$ eV.

The other possible case of quasistationary regime with $E_1' < E < E_2$,

$$E_1' = 10^{-2} \frac{m_e}{m_i} \sqrt{4\pi n T_e}, \quad u_0 = 10^2 \left(e E T_e / m_e \omega_{pe} \right)^{1/2}$$

is discussed in [4]. The coefficient $\lambda = \frac{1}{3}$ is due to the pressure gradient. The saturation mechanism associated with the nonlinear decay process $S \rightarrow S' + S''$ which is feasible when the wave spectrum correlation broadening is taken into account. The equations for this case [6]:

$$\frac{3}{2} \frac{\partial n T_e}{\partial z} = |e| n u_0 E + \frac{3}{2} n \frac{\partial T_e}{\partial z} u_0$$

$$\frac{3}{2} \frac{\partial n T_i}{\partial z} = |e| n E \frac{T_i}{T_e} \frac{1}{m_i} - \frac{3}{2} n \frac{\partial T_i}{\partial z} v_i$$

where it is assumed that $v_i^0 = v_{Ti} = \sqrt{T_i/m_i}$

and $n = n_0 = \text{const}$, can be solved in the stationary case: $T_i^{1/2} + \frac{2}{3} T_e^{1/2} = \text{const}$,

$$\frac{T_e}{T_i} = (1 - \alpha z)^{2/3}, \quad \frac{E}{E_0} = (1 - \alpha z)^{-1/3}, \quad \alpha = \frac{e E_0}{T_e}$$

These solutions are true with $\alpha z < 1$

For example, the stationary turbulence can exist for $z < 150$ km, in some localized region when $T^* = 5$ keV, $E = 3 \cdot 10^2$ V/m. For fairly small distances $\alpha z \ll 1$, $T_i \sim z^2$ and T_e , electric field insignificantly vary with the distance. When $\alpha z = 0.51$, $T_e/T_i \sim 6$, thus, the magnetic field tube length does not exceed 75 km with the turbulent regime [6].

For the case of external turbulization if there is a heat-removal, in the stationary case we can find the $j(E, W)$. The problem of the anomalous resistance due to strong ion-sound turbulence produced by an external source was considered in [5]. The solution of kinetic equation made it possible to find the current of nonrun-away electrons: $j_z = \int f_i(v, \theta) v_z d\vec{v} = e n u_0$

$$u_0 = \lambda v_{Te} (W/h T_e)^{1/4}, \quad \lambda = 0.1$$

The current is independent of the electric field if $E < \sqrt{h T_e (T_e/T_i)}$, $\frac{T_e}{T_i} < 10^2$

From this expression and the equation for the homogeneous state $F_* - |e| n E = 0$, $F_* = m u v_*$ one can obtain the collision effective frequency $\nu_* = \frac{|e| n E}{2 m_e v_*} \left(\frac{n T_e}{W} \right)^{1/4}$

The set of equation describing the coordinate dependence of n, u, E, T_e in stationary conditions: $n u = n_0 u_0$,

$$\frac{\partial n T_e}{\partial z} = |e| n E \left(\frac{u}{u_0} - 1 \right), \quad \frac{3}{2} n \frac{\partial T_e}{\partial z} - T_e \frac{\partial n}{\partial z} + |e| n E = 0$$

does not have solutions if $n = \text{const}$

Analogously, if $E < E_1'$

then $j = e n c_s \Lambda_i$, $\Lambda_i = \text{const}$ in the Rudakov-Korablev regime by $n = \text{const}$ there are no solution. For finding functions $E(z), n(z), u(z), T_e(z)$ the experimental information about one of these functions is needed.

References

1. R.W. Fredericks et al. JGR, 1973, **78**, 2133.
2. F.S. Moser. In "Magnetospheric Particles and Field". Holland, 1976.
3. R.S. Sagdeev. Proceedings of Symposia in Applied Mathematics **18**, 1967.
4. V.N. Tsytovich. Plasma Phys. 1971, **13**, 100.
5. M.A. Livshits, B.A. Liperovsky, V.M. Tomozov, V.N. Tsytovich. The Strong ion-acoustic Turbulence and Electron Spectrum in an Electric Field. Report on the 14th Int. Conf. on Phenomena in ionized cases.
6. V.A. Gudkova et al., In "Struktura magneto-ionosfernich avroralnich vosmuschenii". Nauka, Leningrad, 1977, p. 23.

THE STRONG ION-ACOUSTIC TURBULENCE AND THE ELECTRON SPECTRUM IN AN ELECTRIC FIELDS

M.A. Livshits, V.A. Lipеровsky, V.M. Tomozov and V.N. Tsytovich.

Institute for Space Research, Academy of Sciences of the U.S.S.R.

The problem of the ion-acoustic turbulence-plasma interaction has long been known. We shall consider the case of strong ion-acoustic turbulence.

$$\frac{m_e}{m_i} \ll \frac{W^s}{n T_e} \ll 1 \quad (1)$$

In this case the wave-particle collision integral changes significantly, that is physically related to the effect of the turbulent resonance broadening, which is determined by the effective frequency of turbulent collisions ν_{eff} [1]. The problem we consider is not self-consistent in the sense that the wave-particle interactions do not effect the spectrum and the wave energy density $W^s / n T_e$, the waves being generated by external sources.

The equation for the distribution function of electrons in the electric field with the known ion-acoustic turbulence takes the form:

$$\frac{\partial f}{\partial t} + \frac{cE}{m} \left(\cos \theta \frac{\partial f}{\partial v} - \frac{\sin \theta}{v} \frac{\partial f}{\partial \theta} \right) = \frac{1}{v^2 \sin \theta} \frac{\partial}{\partial \theta} \sin \theta \tilde{A} \frac{\partial^2 f}{\partial v^2} + I(f, \theta, t) \quad (2)$$

$$\tilde{A}(v, \theta) = \pi \left(\frac{e}{m} \right)^2 \int k_0^2 |\varphi_e|^2 \delta(\omega - \vec{k} \cdot \vec{v}) v d\vec{k} \quad (3)$$

The first term in the right-hand side in (2) describes the process of the elastic scattering of electrons. The term $I(f(v, \theta, t))$ describes the weak in-

elastic interactions of electrons with a strong ion-acoustic turbulence. This process depends on the ion-acoustic wave spectrum I_k . When ion-acoustic waves are generated in a narrow region of wave numbers near $k = k_*$ and when $k < k_*$ I_k is determined by the nonlinear scattering of waves on ions then [2]

$$I_k = \frac{W_0}{k} \ln \frac{k}{k_0} \begin{cases} 0 & k > k_* \\ 1 & k < k_* \end{cases} \quad (4)$$

If $v > v_* = \sqrt{W^s / n T_e}^{1/2}$ the collision integral $I(f(v, \theta, t))$ can be obtained via the expansion into a series of exact expressions with the parameter

$$\nu_{\text{eff}} / k v_{Te} \ll 1 \quad [3].$$

If $E = 0$, the stationary solutions of (2) are isotropic and have a power character [3]

$$\Phi = \Phi_0 v^{-\gamma} \quad (5)$$

γ being a function of the turbulent spectrum width

Table									
$\ln \frac{k_*}{k_0}$	3	4	5	6	7	8	9	10	11
γ	1,7	2,1	2,5	2,9	3,1	3,3	3,6	3,9	4,1

If $E \neq 0$, in the strict sense the exact stationary solutions of (2) over the whole velocity space in an infinite plasma do not exist; when v is high there is a stream of runaway electrons. How-

ever, we can assume that in the weak field E and if the velocities V are not very high (the appropriate criterion is given below) the electron distribution function can be written in the form

$$f(v, \theta, t) = \Phi(v, t) + f_1(v, \theta, t) \quad (6)$$

where an anisotropic addition $f_1(v, \theta, t) \ll \Phi(v, t)$ is caused by the electric field.

If the ion-acoustic turbulence is isotropic the equation for the isotropic part of the distribution function $\Phi(v, t)$ is

$$\frac{\partial \Phi}{\partial t} = M \frac{1}{v^2} \frac{\partial}{\partial v} v^5 \frac{\partial \Phi}{\partial v} + I(\Phi) \quad (7)$$

$$M = -\frac{1}{4} \left(\frac{eE}{m} \right)^2 \int_{\sin \theta}^{\sin \theta'} \cos \theta d\theta \int_{\theta}^{\theta'} \frac{\sin \theta'}{\theta} d\theta' \quad (8)$$

The anisotropic addition $f_1(v, \theta, t)$ is

$$f_1(v, \theta, t) = \left[\frac{e}{2m} \frac{E}{A} v^2 \sin \theta \frac{\partial \Phi}{\partial v} + \frac{v^3}{A} I(\Phi) \frac{\cos \theta}{\sin \theta} \right] d\theta \quad (9)$$

The solution of (7) can be found by the perturbation method. If $v \ll v_{*}$ or the electric field E is weak, the solution takes the form

$$\Phi(v) = \rho v^{-\gamma} (1 + Lv^2)$$

$$L = \frac{M \gamma (4 - \gamma)}{(\gamma - 8) [a_1 (\gamma - 7) (\gamma - 6) (\gamma - 5) - a_2 (\gamma - 7) (\gamma - 6) + a_3 (\gamma - 7) - a_4]} \quad (10)$$

The main part of (10) coincides with (5) and describes the stationary function of the electron distribution in the absence of an electric field. γ is taken from Table. The addition Lv^2 corresponds to the influence of the electric field.

a_k are the coefficients with $\Phi^{(k)}$ in $I(\Phi)$ [3]. The condition $Lv^2 \ll 1$ is fulfilled if the electric field is rather weak

$$\frac{E^2}{W^2} \ll \frac{1}{3} \left(\frac{v_{te}}{2v} \right)^2 \left(\frac{k_{*} v_{te}}{\omega_{pe}} \right)^2 \left(\frac{W}{v_{te}} \right)^2 \left\{ \ln^{-5} \frac{k_{*}}{k_0} \quad k_{*} \gg k_0 \right. \\ \left. \frac{1}{4} \quad k_{*} \approx k_0 \right\} \quad (11)$$

Writing (11) in another form, we obtain, that the solution (10) takes place if V is 'small' $v_{*} \ll v \ll v_{**}$

$$v_{**} = v_{*} \left(\frac{W^{5/2}}{E^2} \right)^{1/4} \left(\frac{k_{*} v_{te}}{\omega_{pe}} \right)^{1/4} \frac{1}{2 \cdot 3^{1/2}} \left\{ \ln^{-5/2} \frac{k_{*}}{k_0} \quad k_{*} \gg k_0 \right. \\ \left. 4^{-1/2} \quad k_{*} \approx k_0 \right\} \quad (12)$$

In the opposite case (the conditions (11) and (12) are not fulfilled) the solution takes the form

$$\Phi(v) = \frac{\rho_1}{\sqrt{v}} \left[1 - \frac{1}{24 M v} (240 a_4 - 30 a_3 + 5 a_2 - a_1) \right] \quad (13)$$

The main term in (13) coincides with the 'stationary' spectrum of [4].

The condition of validity of solutions (10) and (13) $f_1(v, \theta) \ll \Phi(v)$ is broken down at high velocities, when the first term under the integral in (9) has a predominant role. Comparison with $\Phi(v)$ results in

$$v \ll v_{**} = v_{*} \left(\frac{W^{5/2}}{E^2} \right)^{1/4} \left(\frac{k_{*} v_{te}}{\omega_{pe}} \right)^{1/4} (3\pi^2)^{1/2} \left\{ \ln^{1/2} \frac{k_{*}}{k_0} \quad k_{*} \gg k_0 \right. \\ \left. 2^{-1/4} \quad k_{*} \approx k_0 \right\} \quad (14)$$

These results can be used for the estimation of the current density in the turbulentized plasma and are important for the anomalous resistance problem.

References

1. L.I. Rudakov, V.N. Tsytovich. Plasma Physics, 13, 213, 1971.
2. V.N. Tsytovich, Theory of turbulent Plasma, Atomizdat, Moscow, 1972.
3. M.A. Livshits, V.M. Tomozov, M.V. Fedoryouk, V.N. Tsytovich. Zh. Eksp. Teor. Fiz. 72, 1414, 1977.
4. L.I. Rudakov, L.V. Korablev. Zh. Eksp. Teor. Fiz. 50, 210, 1966.

MODULATIONAL INSTABILITY OF LANGMUIR OSCILLATIONS IN THE FIELD OF AN ELECTROMAGNETIC WAVE

I.A. Kol'chugina, A.G. Litvak, T.N. Fedoseeva and G.M. Fraiman.

Institute of Applied Physics U.S.S.R., Academy of Sciences Gorky, U.S.S.R.

The paper is devoted to the analysis of modulational instability of Langmuir oscillations excited near plasma resonance region by the field of an electromagnetic wave. A detailed substantiation of quasi-static approximation equations used for numerical study of a Langmuir turbulence is presented.

Using these equations the one-dimensional Langmuir turbulence in the electric field with the given solenoidal component is numerically calculated.

1. To describe the interaction between an electromagnetic wave and plasma oscillations in an nonisothermal plasma ($T_e \gg T_i$) near plasma resonance $|\omega - \omega_p| \ll \omega_p$ we shall use a set of equations (averaged over the field period) for a slow amplitude of the electric field $\vec{E} = \vec{E}(\vec{r}, t)e^{i\omega t}$ and small electron density perturbation $n = \delta n/N_0$.

$$\frac{2i}{\omega} \frac{\partial \vec{E}}{\partial t} - \frac{c^2}{\omega^2} \text{rot rot } \vec{E} + \frac{3T_e}{m\omega^2} \nabla \text{div } \vec{E} + \varepsilon_0 \vec{E} - n \vec{E} = 0, \quad (1)$$

$$v_s \frac{\partial^2 n}{\partial t^2} - \Delta n = \Delta \frac{|\vec{E}|^2}{E_{cr}^2}. \quad (2)$$

Here $\varepsilon_0 = 1 - \omega_p^2/\omega^2$ is the linear plasma permittivity, N_0 is the unperturbed electron density, $v_s = (T_e/M)^{1/2}$ is the ion sound velocity, $E_{cr} = (16\pi N T_e)^{1/2}$ is the characteristic field of nonlinear effects.

In order the equations to be simplified we shall use the existence of two essentially different spatial scales in the problem: the electromagnetic wave length λ_t and plasma oscillation scale λ_p

$$\lambda_t \gg \lambda_p. \quad (3)$$

Since small-scale plasma oscillations are almost potential and the electromagnetic wave is almost of solenoidal character, it is possible to represent the full field as a sum of solenoidal and potential components:

$$\vec{E} = \vec{E}_s + \vec{E}_p, \text{div } \vec{E}_s = 0, \text{rot } \vec{E}_p = 0. \quad (4)$$

Substituting (4) in Eq. (1) for \vec{E}_s and \vec{E}_p we obtain the following set of equations:

$$(5)$$

$$-\frac{2i}{\omega} \text{rot } \frac{\partial \vec{E}_s}{\partial t} + \varepsilon_0 \text{rot } \vec{E}_s - \frac{c^2}{\omega^2} \text{rot rot } \vec{E}_s - \text{rot}(n \vec{E}_s) = [\nabla n \vec{E}_p],$$

$$\text{div} \left(\frac{2i}{\omega} \frac{\partial \vec{E}_p}{\partial t} + \varepsilon_0 \vec{E}_p - n \vec{E}_p + 3 \frac{c^2}{4\pi} \text{grad div } \vec{E}_p \right) = (\vec{E}_s \nabla n).$$

It is seen from (5) that solenoidal and potential oscillations are coupled due to inhomogeneous density perturbations. Therefore a solenoidal part of the field should also have a small-scale component. The amplitude of this component E_s is not difficult to be evaluated using (5)

$$E_s \ll \left(\frac{\omega^2}{c^2} \lambda_p^2 \right) n E_p \ll E_p, E_s \quad (6)$$

$\mu = \left(\frac{\omega}{c} \lambda_p \right)^2 n \ll 1$ is the basic parameter which permits to use the so-called quasi-static approximation. According to this approximation the Langmuir oscillations distribution may be found if the solenoidal (electromagnetic) field component is assumed to be known. The equation for E_s may be derived by subsequent averaging of the obtained solution over small scale oscillations.

If it is assumed that just the one-dimensional plasma oscillations are excited the problem is simplified most essentially. Under this assumption for plasma oscillations we have an equation

$$-\frac{2i}{\omega} \frac{\partial E_x}{\partial t} + (\varepsilon_0 - n) E_x + 3 \frac{c^2}{4\pi} \frac{\partial^2 E}{\partial x^2} = \frac{c^2}{\omega^2} (\text{rot rot } \vec{E})_x \quad (7)$$

where the displacement $\vec{D} = \frac{c^2}{\omega^2} \text{rot rot } \vec{E}$ is given.

Averaging of the obtained solution over a small scale enables us to introduce the effective permittivity (see [1], [2])

$$\varepsilon_{\text{eff}} = \langle (\varepsilon_0 - n) \vec{E} \rangle / \langle \vec{E} \rangle, \quad (8)$$

which defines the mean solenoidal field by the equation

$$-\frac{2i}{\omega} \frac{\partial \langle \vec{E} \rangle}{\partial t} - \frac{c^2}{\omega^2} \text{rot rot } \langle \vec{E} \rangle + \varepsilon_{\text{eff}} \langle \vec{E} \rangle = 0. \quad (9)$$

In a number of papers (see, for example, [3-5]) the problem of excitation of one-dimensional Langmuir oscillations was solved within the given full mean electric field (rather than its solenoidal component) approximation. In our opinion such a formulation is more adequate to the case of excitation of Langmuir oscillations due to stream instabilities but not to the problem of Langmuir turbulence in the field of an electromagnetic wave.

2. Let us analyse in brief the results of numerical study of a one-dimensional

Langmuir turbulence in the em wave field. The corresponding equation may be written in dimensionless form as

$$-2i \frac{\partial E}{\partial t} + \frac{\partial^2 E}{\partial x^2} + (\epsilon_0 - n)E = D, \quad (10)$$

$$\frac{\partial^2 n}{\partial t^2} - \frac{\partial^2 n}{\partial x^2} = \frac{\partial^2}{\partial x^2} |E|^2.$$

where $D = \text{const.}$

We use periodic boundary conditions and initial conditions under which the modulational instability should be realized. Numerical studies show that at the initial stage the uniform electric field E_0 (Fig.1) increases primarily up to the value exceeding the steady-state one $E_0 > D^{1/2}$. In this case the system goes out of resonance with the pump due to the nonlinear frequency shift $\sim E_0^2$. The next stage of this process without the dissipation is similar to the case of modulational instability of free Langmuir oscillations [6, 7]: the small scale component of the electric field increases and a soliton structure forms without the change in the full energy of the electric field (Fig.2). As in [6, 7] the electric field distribution is represented as a succession of equidistant solitons with essentially different amplitudes, the distance between solitons corresponding to the optimal scale of modulational instability. Despite the soliton amplitude pulsations the full energy of plasma oscillations is almost constant. The time-averaged spectra of Langmuir turbulence realizing in our calculations appear to be exponential (Fig.3). The dependence of the relaxation time versus the displacement D shown in Fig.4 is well approximated by $\tau \sim D^{1/2}$.

Note that the above considered process of modulational instability differs from that resulted from calculations with the given mean electric field [3-5] where the stationary state did not exist if the dissipation was neglected: the system came to the quasi-stationary state only when the dissipation in small scales is considerable.

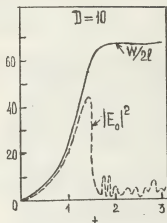


Fig.1.

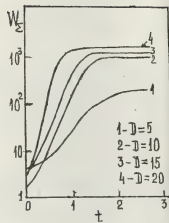


Fig.2.

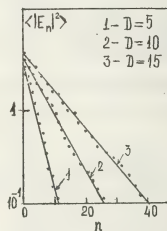


Fig.3.

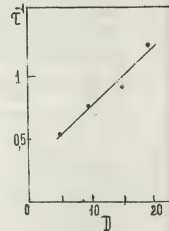


Fig.4.

References

1. A.G.Litvak, V.A.Mironov, G.M.Fraiman, *ZhETF Letters*, **22**, 368 (1975)
2. A.G.Litvak, A.M.Feigin, V.A.Mironov, Report of this Conference
3. G.J.Morales, Y.C.Lee, R.B.White, *Phys. Rev.Lett.*, **22**, 457 (1974)
4. A.A.Galeev, R.Z.Sagdeev, V.D.Shapiro, V.I.Shevchenko, *ZhETF*, **73**, 1352 (1977)
5. B.A.Al'terkop, A.S.Volokitin, V.P.Tarakanov, *Fizika Plasmy*, **3**, 59 (1977)
6. A.G.Litvak, V.Yu.Trakhtengerts, T.I.Fedosceva, G.M.Fraiman, *ZhETF Letters*, **20**, 544 (1974)
7. N.R.Pereira, R.N.Sudan, *The Phys. of Fluids*, **20**, 271 (1977).

THE INSTABILITY OF ONE-DIMENSIONAL LANGMUIR WAVE. SOLITONS AND COLLAPSE

N.S. Buchelnikova and E.P. Matochkin.

Institute of Nuclear Physics, Novosibirsk, U.S.S.R.

The numerical experiment was made to investigate the instability of one-dimensional standing Langmuir waves with amplitudes $\omega_0 = \frac{E_0^2}{8\pi nT} \gg (k_0 r_d)^2$ and phase velocities $V_{ph}/V_T \gg 1$ in the cases when plasma electron nonlinearity is negligibly small.

Case 1. $\omega_0 = 4 \cdot 10^{-2}$; $V_{ph}/V_T = 16$; $\lambda_0/r_d = 100$. In this case the modulational instability leads to the formation of two density cavities and to the concentration of the electric field in them. After some time practically all the field energy is concentrated in the cavities (Fig. 1-1, dotted line - the initial distribution). This structure is stable during a long time (Fig. 3,4). The change of electric field distribution $E(x,t)$ during plasma period T_{oe} can be described by the formula for standing soliton similar to that for Langmuir soliton [1]:

$$E(x,t) = \frac{E_{max}}{ch \frac{x}{\Delta x}} \cdot \frac{1}{2} [\sin(kx - \omega t) + \sin(kx + \omega t)]$$

$$\Delta x_{ord} = \sqrt{W_m / 12}$$

$$W_m = \frac{E_{max}^2}{8\pi nT}; \quad \frac{\tilde{n}}{n_0} = 0.5 W_m$$

Both curves are shown on Fig. 2 (dotted line - formula). The width Δx at the level $\frac{E_{max}}{e}$, the density perturbation in the cavity \tilde{n}/n_0 are equal to those of a soliton: $W_m = 6 \cdot 10^{-2}$; $\tilde{n}/n_0 = 3 \cdot 10^{-2} =$

$$= 0.5 W_m; \quad \Delta x/r_d = 27; \quad \Delta x/\lambda_0 = 0.27.$$

So the modulational instability in this case leads to the formation of quasistable standing solitons.

Case 2. $\omega_0 = 1.6$; $V_{ph}/V_T = 16$; $\lambda_0/r_d = 100$. In this case with higher initial amplitude the modulational instability also leads to electric field concentration in the cavities (Fig. 2) and to the formation of solitonlike structure (Fig. 1-2). $E(x,t)$ during plasma period changes like that of a standing soliton, but the parameters are nonequilibrium: W_m is higher and \tilde{n}/n_0 is less than those of a soliton. So the ponderomotive force must lead to the further deepening of the cavity. Really this structure is unstable and continues to contract up to the beginning of the damping (Fig. 3). At $t/T_{oe} \sim 12$ the maximum energy density $W_m = 3.9$; $\tilde{n}/n_0 = 0.3$; $\Delta x/r_d = 18$; $\Delta x/\lambda_0 = 0.18$. The damping is due to the trapping and acceleration of plasma electrons by the short wavelength modes with low phase velocities. It leads to the full absorption of the field energy. After the field absorption the cavity depth continues to increase due to ion inertia (Fig. 4). After 1-2 ion plasma periods the shock waves form on the cavity edges

and the cavity collapses.

So in this case we observe the process of collapse [2,3].

Case 3. $W_0 = 1,6$; $V_{ph}/V_T = 48$; $\lambda_0/r_d = 300$. In this case λ_0 and V_{ph} are higher than those in the case 2 and we can expect that the damping must begin much later. Really the contraction of the solitonlike structure in this case continues for a longer time up to $t/T_{oe} \sim 41$ (Fig. 3) and leads to the higher energy concentration and localization than in the case 2 (Fig. 1-3). In this case the maximum energy density $W_m = 8,8$; $\tilde{n}/n_0 = 0,3$; $\Delta x/r_d = 16,5$; $\Delta x/\lambda_0 = 0,055$. The damping like the case 2 leads to the absorption of the field energy.

So the modulational instability of onedimensional Langmuir wave leads to the formation of solitons if wave amplitude is low enough $W_0 \lesssim 3 \cdot 10^{-1}$. In other case collapse process takes place - the localization of electric field energy in the density cavities, the contraction of the cavities and increase of the energy density up to the beginning of the damping, leading to the full absorption of electric field energy by plasma electrons.

1. L.I.Rudakov Sov. Phys. Doklady 207, 821, 1972.
2. V.E.Zakharov Sov. Phys. JETP 62, 1745, 1972.
3. V.E.Zakharov, A.M.Rubenchik Sov. Phys. JETP 65, 997. 1973.

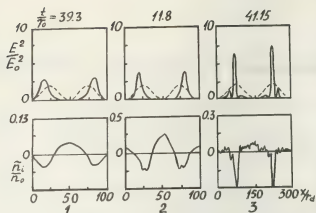


Fig. 1.

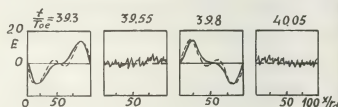


Fig. 2.

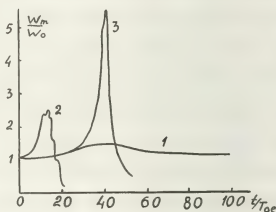


Fig. 3.

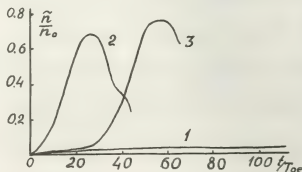


Fig. 4.

THE INSTABILITY AND DAMPING OF THE LANGMUIR WAVES WITH DIFFERENT AMPLITUDES AND PHASE VELOCITIES

N.S. Buchelnikova and E.P. Matochkin.

Institute of Nuclear Physics, Novosibirsk, U.S.S.R.

The numerical experiment was made to investigate the instability of onedimensional running Langmuir waves with high amplitudes $W_0 = \frac{E_0^2}{8\pi n T} \gg (K_0 r_d)^2$ and phase velocities $V_{ph}/V_T \gg 1$: $W_0 \sim 0,3-10^2$ ($V_{ph}/V_T = 16$); $V_{ph}/V_T \sim 3-48$ ($W_0 = 1,6$).

The increase of W_0 and decrease of V_{ph} in such range leads to the increase of plasma electron nonlinearity from the linear case up to the case of electron trapping. The linear case and the case of small nonlinearity were investigated earlier [1]. To characterize the nonlinearity the parameters $\alpha = \frac{2\sqrt{e\psi_0/m}}{V_{ph} - V_T}$ and $\alpha' = W_0 (K_0 r_d)^2$ were used. Electron nonlinearity shows itself in the increase of the perturbed electron velocity, in the sharpening of electron density perturbation and in the steepening of $E(x)$. It was shown that electron nonlinearity becomes essential if $\alpha \gtrsim 0,4$ ($\alpha' \gtrsim 10^{-3}$). The limiting case of high electron nonlinearity is the trapping of plasma electrons by the wave. The trapping becomes essential if $\alpha \gtrsim 1,3$ ($\alpha' \gtrsim 5 \cdot 10^{-2}$).

The information about numerical experiments with different amplitude waves is given in the table 1 and Fig. 1.

N	1-1	1-2	1-3	1-4	1-5	1-6
α	0,46	0,71	1,17	1,33	1,57	2,10

W_0	0,3	1,6	11	18	36	115
$\frac{\Delta N}{N} \%$	-	-	-	0,1	4,6	20
W_{max}	2,5	6,2	18,4	22,7	-	-
W_{max}/W_0	8	3,9	1,7	1,2	-	-
t_{max}/T_{oe}	37	17	4,5	4,5	-	-

In cases 1-1 - 1-4 in agreement with [1] the modulational instability with the length of perturbation $\lesssim \lambda_0$ develops and leads to the formation and contraction of the density cavity and to the concentration of the electric field in it, so that energy density $W_m = \frac{E_{max}^2}{8\pi n T}$ increases (Fig. 1). In spectral description this process shows itself in the excitation of more and more short wavelength modes with decreasing phase velocities.

When the density perturbation becomes high ($\tilde{n}/n_0 \gtrsim 10^{-2}-10^{-1}$) the conversion process $K_e \pm \beta K_i \rightarrow K_e'$ ($\beta = 1, 2, \dots, K_e, K_i$ - wave vectors) becomes essential and leads to the excitation of more and more short wavelength direct and backward modes.

The damping of the electric field begins when the modes with phase velocities low enough to trap plasma electrons are excited. The trapping and acceleration of electrons leads to the full absorption of electric field energy. The increase of initial wave amplitude leads to the increase of perturbed electron

velocity and of the addition to it due to the electron nonlinearity so that modes with higher V_{ph} begin to trap electrons and the damping starts earlier (Fig. 1, t_{max} in the table). Due to the crossing of the modes' trapping regions the electrons are accelerated up to high velocities (in the cases 1-3, 1-4 up to $V \sim V_{ph} + V_{tr}$ of the initial wave, $V_{tr} = 2\sqrt{\frac{e\phi_0}{m}}$ and forme the tail on the velocity distribution function.

If initial wave amplitude is high enough, so that $\alpha \gg 1,3$, the trapping of electrons by the initial wave becomes essential. If $\alpha \sim 1,3$ and the part of electrons $\Delta N/N_0$ trapped during first plasma period T_{oe} is small (case 1-4) the decrease of W_m due to the trapping and increase of it due to the instability are of the same order (Fig. 1). If α and $\frac{\Delta N}{N}$ increase the trapping becomes the main process (cases 1-5, 1-6). The damping rate in these cases is many orders higher than Landau damping rate. In all these cases the conversion also plays role leading to the full damping of the electric field.

The information about numerical experiments with different phase velocities is given in the table 2

N	2-1	2-2	2-3	2-4	2-5	2-6
α	0,39	0,71	0,96	1,16	1,62	2,10
V_{ph}/V_T	48	16	9,4	6,9	4,2	2,96
W_{max}	10,4	6,2	2,4	2	-	-
W_{max}/W_0	6,6	3,9	1,5	1,3	-	-
t_{max}/T_{oe}	32,7	17	5	-	-	-

The comparison of numerical experiments

with different W_0 or V_{ph} shows that the main processes are the same. The character of phenomena depends on the parameter α - in the cases of different W_0 and V_{ph} but equal α the main features of the instability and damping (including the curves $\frac{W_m(t)}{W_0}$) are similar. The increase of parameter α leads to the earlier damping of the electric field (Fig. 1). So the main processes of the Langmuir wave instability and damping are modulational instability, conversion on density perturbations and trapping of electrons by the initial wave or its modes. The electron nonlinearity doesn't influence the instability development (in agreement with theoretical results /2/) until the trapping by the initial wave becomes essential. The electron nonlinearity plays role for damping because it leads to the perturbed electron velocity increase.

1. N.S.Buchelnikova, E.P.Matochkin "Phenomena in Ionized Gases", v. II, p.831, 1977, Berlin. "Waves and Instabilities in Plasmas", p. 71, 1977, Palaiseau.
2. E.A.Kuznetsov Sov. J. Plasma Phys. 2, 327, 1976.

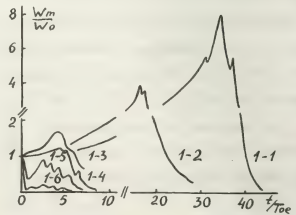


Fig. 1.

MODULATION INSTABILITY AND PLASMA ELECTRODYNAMIC CHARACTERISTICS

A.G. Litvak, V.A. Mironov and A.M. Feigin.

Applied Physics Institute, Academy of Sciences of the U.S.S.R., Gorky/U.S.S.R.

1. It is well known that the features of interaction between strong electromagnetic waves and a high density collisionless plasma is associated with modulational instability of Langmuir oscillations and further formation of Langmuir solitons. In most of papers the dynamics of plasma modulation is investigated in order to determine the anomalous absorption characterized by the effective collision frequency ν_{eff} . The other sequence is a change of the refractive index (or the real part of the permittivity) of an electromagnetic wave produced by such a small-scale structure. These effects give rise to an essential change of the field distribution and apparently alter the energy absorption in plasma. The purpose of the present report is to consider the electromagnetic wave penetration into a supercritical plasma for the case of the nonlinear changing of the refractive index.

The paper deals with a stationary selfaction of a TEM-wave in the initially homogeneous layer of a supercritical plasma. The field distribution in a layer and the dependence of the transmission coefficient on the amplitude of an incident wave have been found.

2. Let us consider the normal incidence of a plane monochromatic wave upon a plasma layer with permittivity $\epsilon_0(Z)$. It has frequency ω close to plasma frequency ω_p . In the linear approximation a wave is reflected from the region $\epsilon_0(Z) < 0$. In the nonlinear case the field can penetrate deep into the supercritical plasma. Then the complete electric field $E = E(x, z, t) \hat{x}_0$ is a superposition of the fields of an electromagnetic (vortex) and plasma (potential) waves. They have appreciably different space scales. This permits to make use of the averaging approach and solve the problem by two stages. First we shall seek the stationary distribution of plasma waves of the cross section $z = \text{const}$ excited (in the quasi-static approximation) by the given electric displacement

$D = -k_0^2 \frac{\partial^2 F}{\partial z^2} = \text{const}$. This distribution is described by the equation for a slowly varying amplitude of the electric field

$$\frac{\partial^2 a}{\partial \xi^2} + (\epsilon - a^2 + \bar{a}^2) a = d \quad (1)$$

Then, averaging (1) over the potential wave scale we have the equation which describes self-action of the mean (small-

-space average) field of a pump wave in a medium characterized by the efficacious actual permittivity ϵ_{eff} :

$$\frac{\partial^2 \bar{a}}{\partial \xi^2} - \bar{a} \left(\frac{\partial \bar{a}}{\partial \xi} \right)^2 = -d = -\epsilon_{\text{eff}}(\bar{a}) \bar{a} \quad (2)$$

$$\frac{\partial \bar{\psi}}{\partial \xi} \bar{a}^2 = C = \text{const} \quad (3)$$

In Eqs. (1)-(3) $a(\xi, z) = \frac{3M}{4m} \frac{\omega}{\omega_p} \frac{|E|}{\sqrt{6\pi N_0 T}} \psi(\xi)$ are slowly varying amplitude and phase of a wave, respectively, $\epsilon = \frac{3M}{4m} \frac{\omega^2}{\omega_p^2} \epsilon_0$,

$$d = \frac{\omega^3}{\omega_p^3} \left(\frac{3M}{4m} \right)^{3/2} \frac{D}{\sqrt{6\pi N_0 T}}, \quad \xi = \frac{2}{3} \left(\frac{m}{M} \right)^{1/2} \frac{\omega_p}{\omega} \frac{x}{r_d},$$

$$z = \left(\frac{4m}{3M} \right)^{1/2} \frac{\omega_p z}{C}$$

The line means the special averaging of stationary field distribution in the cross-section $z = \text{const}$. To find an exact value of $\epsilon_{\text{eff}} = d/\bar{a}$, one should solve the non-stationary problem. We should turn here to numerical calculations. Though the necessary detailed investigation was not made, numerical study in [2,3] show that the result of the modulational instability development is formation of a chain of solitons. We may naturally expect that in the stationary case the distance between solitons coincides with a scale of the most rapidly growing perturbation in the linearized problem. So, in [1] the stratification scale was assumed to be the same all over the instability region and is determined by the maximum value of the field at the initial moment of time ($t=0$). Estimations of the transparency parameters (penetration time and the threshold field value) obtained in this case describe rather well the experimental data [4,5] and some dependencies [6]. In the other approximation to the truth considered in this paper the local relation between the stratification scale and the electric displacement is assumed. This approach in contrast to that used in [1] permits to solve a self-consistent problem of penetration of an electromagnetic wave into a high density plasma in the general case taking account of reflection. The efficacious permittivity in such a model is defined as

$$\epsilon_{\text{eff}}(d > d_{\text{mod}}) = \frac{\sqrt{2} d}{(\text{sign } d) \pi \sqrt{3} \sqrt{2d^2/V^3} |E| - (\sqrt{2} d)^{1/3}} \quad (4)$$

At $d < d_{\text{mod}}$ ($d_{\text{mod}} = |E|^{3/2}/\sqrt{2}$ is the threshold value of displacement for modulational instability development) stratification does not occur and ϵ_{eff} is equal to the unperturbed linear value $\epsilon_{\text{eff}}(d \leq d_{\text{mod}}) = \epsilon$. It follows from (4) that in the given approximation the transparency of the initi-

ally homogeneous supercritical plasma takes place when

$$d \geq d_{th} = \left(\frac{3\pi^2}{3\pi^2 - 1} \right)^{3/2} \cdot \frac{|\epsilon|^{3/2}}{\sqrt{2}} \approx 1.17 d_{mod} \quad (5)$$

For $d < d_{th}$ the stratification of plasma is insignificant for its transparency, and the plasma remains supercritical. With the following decrease of d ϵ_{eff} grows in modulus and achieves the unperturbed value at $d = d_{mod}$.

3. Determination of ϵ_{eff} reduces the problem at the second stage to a usual electrodynamic one. Let us consider the simplest problem of such a type: viz. the normal incidence of a plane wave from vacuum to the initially homogeneous layer of a supercritical plasma with a thickness of 2ℓ , $-\ell < z < \ell$. Inside the layer, the field amplitude and phase distribution is described by a system of equations (2), (3), (4). Here the parameter C corresponds to the power flux of a wave passing through the layer. This system should be added with the boundary conditions. That is a continuity of the mean field

\bar{u} and its derivative $\partial \bar{u} / \partial z$ both at the boundaries of a layer $z = \pm \ell$ and at those points within the layer where the mean field is compared to the threshold value for the modulational instability $\bar{u}_{mod} = d_{mod} / |\epsilon|$. A solution of a system of equations (2)-(4) was investigated qualitatively by the example of integral curve behaviour on a phase plane of the system $(\bar{u}, \partial \bar{u} / \partial z)$ and determine the transmission factor T . Fig. 1 shows the dependence of T on $\theta_0 = Q_0 / \bar{u}_{mod}$ (Q_0 is the amplitude of an incident wave) for a layer of length $L = 5\lambda_0$ (λ_0 is wavelength in vacuum) with the unperturbed permittivity $\epsilon_0 = -0.1$. The dependence is of hysteric form, a complete transparency ($T=1$) being realized for the certain values of θ_0 . In Fig. 1 these resonant states are characterized by the number defined as a ratio of the layer length to the period of a nonlinear wave. Depending on the power flux C , there are two types of solutions of Eqs. (2)-(4). At $C < C^* \approx 8.4$ a layer is divided into sublayers with supercritical (unperturbed) and transparent (stratified) plasmas. At $C > C^*$ the layer becomes transparent (stratified) all over. Passing from one type of solution to the other at $C = C^*$ explains the existence of two resonant states with the same number (see Fig. 1). Note that the described dependence $T(\theta_0)$ in the resonant regions is smoother than in the case of cubic nonlinearity [7-9].

Thus, even the case of purely ohmic losses, absorption of energy of the incident radiation increases appreciably due to the essential lengthening of the region occupied by the electromagnetic field.

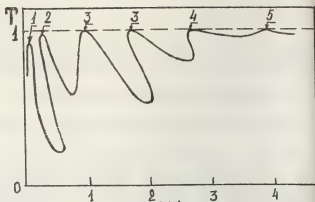


Fig. 1.

References

1. A.G.Litvak, V.A.Mironov, G.M.Fraiman, ZhETF Letters, 22, 368-371 (1975)
2. A.G.Litvak, V.Yu.Trakhtengerts, T.N.Fedoseeva, G.M.Fraiman, ZhETF Letters, 20, 544 (1974)
3. B.A.Al'terkop, A.S.Volokitin, V.P.Tarakanov, ZhTF Letters, 1, No 11, (1975)
4. Yu.Ya.Brodsky, B.G.Eremin, A.G.Litvak, Yu.A.Sakhonchik, ZhETF Letters, 13, 136 (1971)
5. G.M.Batanov, V.A.Silin, ZhETF Letters, 14, 445 (1971)
6. Yu.Ya.Brodsky, V.L.Gol'tsman, V.A.Mironov, S.I.Nechuev, ZhETF Letters, 78, 1636 (1978)
7. V.A.Mironov, Izv.VUZ-Radiofizika, 14, 1450 (1971)
8. V.B.Gil'denburg, Preprint No 57, NIRFI (1974)
9. L.M.Gorbunov, K.Zauer, Fizika Plasmy, 2, No 5 (1977)

SELF-ACTION OF QUASI-OPTICAL BEAMS IN A MAGNETOPLASMA

A.G. Litvak, A.M. Sergeev and N.A. Shakhova.

Applied Physics Institute, Academy of Sciences of the U.S.S.R., Gorky U.S.S.R.

Nonlinear effects of self-action of beams and self-modulation of electromagnetic wave packets in a magnetoactive plasma have a number of peculiarities which make them distinct from the analogous processes in an isotropic plasma. This manifests itself both in change in the nonlinearity and modification of the dispersion properties. To illustrate the said above we shall give the example of quasi-optical beams of lower hybrid waves [1, 2].

In the frequency range $\omega_{H_0} \ll \omega \ll \omega_{H_0}$ gyrotropy of the striction nonlinearity becomes essential, i.e. the expression for the averaged perturbation of plasma density δn under the action of a rf field

$$\vec{E} = \frac{1}{2} [\vec{E}(\vec{r}) e^{i\omega t - i\vec{k}_0 \cdot \vec{r}} + \text{c.c.}] \quad \text{has the form 3}$$

$$\delta n = \frac{\omega_{pe}^2}{16\pi N(T_e + T_i)} \left[\frac{1}{\omega_{H_0}^2} |E_x|^2 - \frac{1}{\omega_{H_0}^2} |E_z|^2 + \frac{1}{\omega_{H_0}^2} (E_x E_y^* - E_x^* E_y) \right] \quad (1)$$

When writing (1) one used a coordinate system depicted in Fig.1; $\omega_{pe,i}$, $\omega_{H_0,i}$ are the Langmuir and cyclotron frequencies of electrons and ions, T_e and T_i are their temperatures, N is the plasma density. If the wave dispersion is defined by the thermal motion of particles, then the equation for slow (in scale $2\pi/k_0$) complex amplitude $\mathcal{E} = E_x$ is written as follows*

$$2i \frac{\mathcal{E}_{xx} \text{tg} \theta}{K_0} \frac{\partial \mathcal{E}}{\partial \tau} = \frac{\mathcal{E}_{xx}}{K_0^2} \frac{\partial^2 \mathcal{E}}{\partial \eta^2} + \frac{3 \sin^2 2\theta}{4} \mathcal{D} \frac{\partial^2 \mathcal{E}}{\partial \xi^2} - \quad (2)$$

$$- \frac{\mathcal{E}}{16\pi N(T_e + T_i)} \left(|E|^2 + \frac{\omega_{pe}^2}{\omega_{H_0}^2} \frac{\partial}{\partial \eta} |E|^2 \right)$$

where

$$\mathcal{D} = \frac{\mathcal{E}_{zz}}{\mathcal{E}_{xx}} \left(\frac{3}{4} \frac{\omega_{pe}^2}{\omega_{H_0}^2} V_{Te}^2 + \frac{3}{4} \frac{\omega_{pi}^2}{\omega_{H_0}^2} V_{Ti}^2 \right) + \frac{\mathcal{E}_{xx}}{\mathcal{E}_{zz}} \left(\frac{3}{4} \frac{\omega_{pe}^2}{\omega_{H_0}^2} V_{Te}^2 + \frac{3}{4} \frac{\omega_{pi}^2}{\omega_{H_0}^2} V_{Ti}^2 \right),$$

$$\mathcal{E}_{xx} = 1 + \frac{\omega_{pe}^2}{\omega^2} - \frac{\omega_{pi}^2}{\omega^2} > 0, \mathcal{E}_{zz} = 1 - \frac{\omega_{pe}^2}{\omega^2} < 0,$$

*An equation with the analogous nonlinearity for the waves with frequency

$$\omega \approx \omega_{LH} = \frac{\omega_{pi}}{(1 + \omega_{pe}^2/\omega_{H_0}^2)^{1/2}}$$

was obtained in paper [4].

V_{Te} and V_{Ti} are the thermal electron and ion velocities. The nonlocal nonlinearity part may determine the self-action for sufficiently small field distribution scales. However, in case the characteristic dimension $L_{\perp} > \omega_{pe}^2/\omega_{H_0}^2 K_0$, then the last term in (2) may be neglected and one may pass to investigating the dimensionless equation

$$i \frac{\partial \mathcal{E}}{\partial \tau} = \frac{\partial^2 \mathcal{E}}{\partial \xi^2} - \frac{\partial^2 \mathcal{E}}{\partial \eta^2} + |\mathcal{E}|^2 \mathcal{E} \quad (3)$$

A similar equation which differs principally from the usual non-one-dimensional Schrödinger equation is true also for some other wave types in a magnetized plasma. Here are the examples.

1). A parabolic equation with coefficients changing their signs with the plasma characteristics is obtained in paper [5] for the wave beam propagating across the external magnetic field H_0 . In variables $u = \omega_{pe}/\omega$, $v = \omega_{pe}^2/\omega^2$ the range of interest is the parameter region between curves $u = 1 - v$ and $u = 1 - v^2$

2). Self-action of electromagnetic waves-whistlers is described by equation (3), if the angle between the central wave beam vector and the magnetic field is $\theta > \theta^*$

$$(\text{tg} \theta^* = \sqrt{2}) \quad [5]$$

3). It is easy to understand that (3) is just, considering self-modulation of packets of quasi-potential lower hybrid waves with dispersion $\omega^2 = \omega_{LH}^2 (1 + \frac{m}{M} K_z^2/K_{\perp}^2)$, where $\omega_{LH} = \omega_{pe}/(1 + \frac{\omega_{pe}^2}{\omega_{H_0}^2})^{1/2}$, K_z and K_{\perp} are the longitudinal and transverse (in relation to the magnetic field) wave vector components, m and M are the electron and ion masses, respectively (in this case coordinate z is the time variable). A similar equation may be obtained analysing the thermal dispersion of higher hybrid waves in the range $\omega_{pe}^2 > 3\omega_{H_0}^2$.

Let us discuss some peculiarities of the processes described by equation (3), resulting from the ratios for the moments of localized field distributions [2]

$$\overline{\alpha^2} = \int x^2 |E|^2 dx dy, \overline{\beta^2} = \int y^2 |E|^2 dx dy.$$

For collimated beams $\overline{\alpha^2}'(z=0) = \overline{\beta^2}'(z=0) = 0$, $\overline{\alpha^2}$ increases monotonically along the beam propagation trajectory, but $\overline{\alpha^2}$ and $(\overline{\alpha^2} \overline{\beta^2})^{1/2}$ (that corresponds to the beam cross section area) may first decrease. However, when $z \rightarrow \infty$ the beam behaviour is characterized by the transverse dimension growth. If $I = \int \left(\left| \frac{\partial \mathcal{E}}{\partial x} \right|^2 + \left| \frac{\partial \mathcal{E}}{\partial y} \right|^2 - \frac{|\mathcal{E}|^4}{2} \right) dx dy > 0$, then for

the initial amplitude distribution exten-

ded along y the beam cross section for rather great Z has the form extended along x . For $I < 0$ independently of ratio $a^2(z=0)$ and $b^2(z=0)$, beginning with some, the field distribution extends in the y -direction.

To understand the qualitative pattern of the process one may use the nonaberrational approximation [6,7] and get the equation for beam dimensions a and b in the x and y -directions, assuming its form to be constant (Gaussian, for example):

$$\frac{d^2 a}{dz^2} = \frac{1}{a^3} - \frac{\varphi}{a^2 b}, \quad \frac{d^2 b}{dz^2} = \frac{1}{b^3} + \frac{\varphi}{a b^2}, \quad (4)$$

φ characterizes the energy flux through the cross section. Within the framework of the method used one succeeds in reducing (4) to the non-autonomous differential second-order equation

$$\frac{d^2 a}{dz^2} = \frac{1}{a^3} - \frac{\varphi}{a^2 \sqrt{a^2 + \mu + \nu z^2}}, \quad (5)$$

where $\mu = b_0^2 - a_0^2$, $\nu = \frac{2\varphi}{a_0 b_0} + \frac{1}{b_0^2} - \frac{1}{a_0^2}$, a_0 and b_0 are the initial beam dimensions. In (5) the change of a is determined by the two factors: a diffractive beam divergence leading to the section widening along x and an inhomogeneous nonlinear defocusing opposed to the former. It is easy to investigate the action of the contrary tendencies in a general case using a numerical calculation, but in some cases it is possible to find an analytical solution or to point out its important features. Nonlinear self-action of beams with initial dimensions a_0, b_0 is of primary interest. Under such conditions the variables in equation (5) may be substituted $\varphi = a(\mu + \nu z^2)^{1/2}$,

$$\tau = \frac{1}{\sqrt{\mu\nu}} \arctg \sqrt{\frac{\nu}{\mu}} Z, \quad \text{making it autonomous:}$$

$$\frac{d^2 \varphi}{d\tau^2} = \frac{1}{\varphi^3} - \frac{\varphi}{\varphi^2 \sqrt{1 + \varphi^2}} - R\varphi, \quad R = \mu\nu \quad (6)$$

Analysing the phase plane of equation (6) it is easy to realize that the exact solution for a has the form

$$a = \sqrt{\mu + \nu z^2} u \left(\frac{1}{\sqrt{\mu\nu}} \arctg \sqrt{\frac{\nu}{\mu}} Z \right) \quad (7)$$

where u is the periodic function with period $T = T(u(z=0))$ determined from (6) by means of integrals. Two qualitatively different self-action regimes may be distinguished. The process of quasi-one-dimensional self-focusing of the beam along the

-direction is realized at distances $Z < Z^* = \frac{\sqrt{\mu}}{\nu} \arctg \left(\frac{\sqrt{\mu} \sqrt{1 + \varphi^2}}{\varphi} \right)_{\varphi=0}$. The beam width oscillates near the mean monotonically growing value, the amplitude of oscillations increasing with Z and their frequency decreasing; the total number of oscillations $N = \pi / (2T\sqrt{\mu\nu})$. The maximum focusing possible is determined from the one-dimensional problem $a_{\min} = a_0 / (2\varphi \frac{a_0}{b_0} - 1)$.

When $Z > Z^*$ the beam self-defocuses. Fig.2 illustrating the foregoing conclusions shows the change of the electric field amplitude $|E(x=0, y=0, z)|$ in a beam and of its dimension along the propagation trajectory Z depending on the initial distribution parameters.

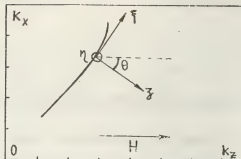


Fig.1. Wave vector surface for lower hybrid waves

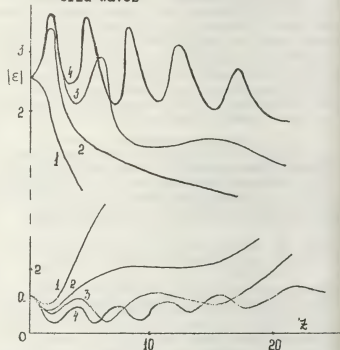


Fig.2. Some examples of beam self-defocusing. $|E(x=0, y=0, z=0)| = 2.5$; $a_0 = 1$; $b_0 = 2.5; 5; 10; 30$.

References

1. N.R. Pereira, A. Sen and A. Bers, Phys. Fluids 21, 117, 1978.
2. A.G. Litvak, A.M. Sergeev, N.A. Shakhova, ZhETF Letters, 5, No.1, 1979.
3. A.G. Litvak, Izv. VUZov-Radiofizika, 9, 900, 1966.
4. H.H. Kuehl, Phys. Fluids, 21, 2120, 1978.
5. A.G. Litvak, N.A. Shakhova, Fizika Plazmy (to be published).
6. V.I. Bespalov, A.G. Litvak, V.I. Talanov, in sb. "Nonlinear optics" (Symp. transact.), 428, "Nauka", Novosibirsk, 1968.
7. V.V. Vorob'ev, Izv. VUZov-Radiofizika, 13 1905, 1970.

SELF-TRAPPING OF LOWER HYBRID WAVES AT THE RF BREAKDOWN OF GAS

G.A. Markov, V.A. Mironov and A.M. Sergeev.

Applied Physics Institute, Academy of Sciences of the U.S.S.R., Gorky, U.S.S.R.

The study of the interaction between intense rf radiation and magnetoplasma is stimulated at present by searching for the effective methods of directed and localized field energy transfer to plasma. In this connection the possibilities of "resonance" focusing of lower hybrid waves excited in plasma by cylindrical sources (1) are of particular interest. It is evident that the role of nonlinear effects in formation of a strong field region is of great importance. In this paper the interaction between field and plasma is investigated at rf breakdown of gas near a cylindrical inductor at the frequencies of $\omega_{H_i} \ll \omega \ll \omega_{H_e}$ ($\omega_{H_{e,i}}$ are the cyclotron electron and ion frequencies). A plasma waveguide is found to be essentially isolated from walls and to trap lower hybrid waves creating it.

An air (or helium) discharge was excited with a double-coil inductor mounted coaxially with a glass balloon. The inductor was the anode load of the two-cycle generator and was placed outside the balloon walls to eliminate the inductor terminal influence. The system parameters were chosen as follows: the balloon diameter $2a=20\text{cm}$, its length $l=120\text{cm}$, the inductor diameter 6cm , its length 7cm , the operating pressure range $p=3 \cdot 10^{-2}-5 \cdot 10^{-3}$ Torr, the longitudinal magnetic field $B=500\text{Gs}$, its inhomogeneity along the axis $\approx 6\%$, the rf field frequency $f=50\text{MHz}$, the power $W=5-150\text{w}$.

To determine the plasma parameters movable cylindrical and plane probes were used. The rf potential distribution in plasma was measured by a screened pin antenna connected with the spectral analyzer. The absolute measurements of the rf field amplitude were made using the oscilloscope and the dipole antenna.

The important peculiarity of the rf discharge within the given pressure interval is the presence of a thin plasma filament extended from the inductor region along the system axis (Fig.1).

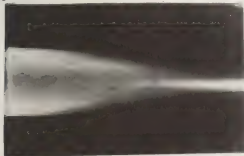


Fig.1

For $p \ll 10^{-2}$ Torr and $W \geq 10\text{w}$ the length of the filament was limited by that of the system. For comparatively small values of the rf power input $W \approx 10\text{w}$ plasma density in the filament centre $n_0 > n_c$ ($n_c = m_i^2 \pi / \ell^2$ is the critical plasma density) and is approximately the same along the axis far from the inductor. The curves of Fig.2 were obtained for $W=9.6\text{w}$, $p=10^{-2}$ Torr at different distances l from the inductor. The rf potential distribution over the discharge balloon cross section ϕ under the same experimental conditions is shown in Fig.3. The measurements of the difference between field oscillation phases at different points along the system axis indicate that the length of a wave propagating in the canal, approximately coincides with the double inductor size $\lambda \approx 14\text{cm}$. With the growth of the rf power feeding in the discharge plasma density in the filament and its thickness increase. A regime is possible when the electron density exceeds the critical value everywhere.

Passing to the interpretation of experimental data we note first of all that investigated rf potential and plasma distributions are in a quasi-static zone of the source, i.e. $\ell < \lambda_c$ where

$\lambda_c = c/f \left(1 + \frac{\omega_p^2}{\omega \omega_{H_e}}\right)^{1/2}$ is the whistler wavelength in plasma. Therefore, density and conical angle aperture measurements indicate that the pattern observed is definitely associated with excitation of the potential ionizing lower hybrid waves propagating in the consistent plasma distribution.

For a qualitative explanation of the canal structure we shall consider a simple model. It is based on the approximation of the axially symmetric plasma density and rf potential amplitude distribution being homogeneous along the magnetic field B , i.e.

$$n = n(r), \quad \varphi = \Psi(r) \exp(i\omega t - iKz)$$

where r is the distance from the balloon axis, z is the longitudinal coordinate, $K = 2\pi/\lambda$. For the rf field the Poisson equation with the longitudinal and transverse plasma permittivities

$$\epsilon_1 = 1, \epsilon_{\perp} = 1 - \frac{n}{n_c} = 1 - \frac{\omega_p^2}{\omega^2}$$

is satisfied. When writing the material equation we take into account that the electron temperature locally depends on the electric field amplitude in the discharge cross section. This permits to represent the frequency of molecule ionization at elec-

tron impact in the form $\psi_i = \psi_i(|\kappa\varphi|)$

This complicated dependence is usually approximated by the power one:

$\psi_i = \alpha|\kappa\varphi|^{2\beta}$ ($\beta > 1$) The diffusion flux on the walls and the electron adhesion to electro-negative molecules of gas are assumed to be the main factors of particle losses.

So the self-consistent distribution of rf potential of a low-hybrid wave and of plasma density is the solution of nonlinear differential equations

$$\frac{d^2\psi}{d\tau^2} + \frac{1}{\tau} \frac{d\psi}{d\tau} - \kappa^2(1 - n/n_c)\psi = 0 \quad (1)$$

$$\frac{d^2n}{d\tau^2} + \frac{1}{\tau} \frac{dn}{d\tau} + [\alpha(\kappa\varphi)^{2\beta} - \nu_a] \frac{n}{D_1} = 0$$

where D_1 is the coefficient of the ambipolar diffusion across the magnetic field, ν_a is the electron adhesion frequency.

System (1) allows the space localized solutions for which near the axis $n > n_c$, and in the peripheral region $n < n_c$ that determines an exponential decrease in the field. At the same time the density decrease is due to the adhesion action. Similar solutions correspond to the possibility of self-sustaining plasma and field distribution without the balloon wall influence.

Thus, the main result of the paper is that the localized region of field and plasma extended as a thin filament along the magnetic field is found under the rf discharge conditions. This phenomenon is explained by propagation of an ionizing lower hybrid wave in the consistent plasma distribution.

*) When describing a discharge in helium, a weak inhomogeneity of the canal along the axis should be taken into account. It leads to the same qualitative results as the adhesion in the air.

**)

Analogous solutions for electromagnetic wave beams-whistlers, propagating in the medium with the local ionization non-linearity, were considered in [2].

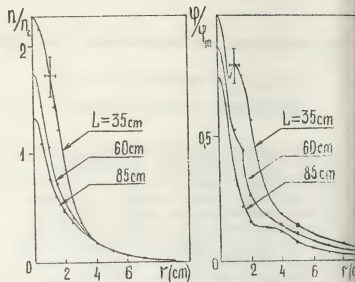


Fig. 2.

Fig. 3.

References:

1. R.L. Stenzel and W. Gekelman, Phys. Fluids 20, 108, (1977).
2. A.G. Litvak, Radiofizika 2, 629, (1966).

INTERACTION OF THE INTENSE MICROWAVE BEAM WITH A FLOW OF LOW TEMPERATURE PLASMA

2. The theory)

Al. Rogashkova.

Institute of Radioengineering and Electronics, Academy of Sciences, Moscow, U.S.S.R.

To explain the experimentally observed space distribution of the plasma stream density disturbed by the intense beam of radiowaves (1) theoretical analyses has been performed.

Let us assume that the plasma stream moves along the axis with the constant velocity V_0 . The electromagnetic wave propagates along the axis Y. Its intensity is described by the expression:

$$E^2 = A^2 \exp(-x^2/\Lambda^2), \quad (1)$$

where Λ is a characteristic dimension of the field nonuniformity.

The linearized macroscopic transfer equations for the density and temperature of electrons in the electric field are used to describe the disturbance of a stream

$$\frac{\partial^2 \psi}{\partial \theta^2} - \lambda \frac{\partial \psi}{\partial \theta} - K^2 \psi = \frac{K^2}{2} \frac{E^2}{E_p^2}, \quad (2)$$

$$\frac{\partial^2 f}{\partial \theta^2} - \frac{v_0}{V_0} \frac{\partial f}{\partial \theta} - \frac{v_0}{V_0} f = -K_T \frac{\partial^2 \psi}{\partial \theta^2} + \frac{\lambda v_0 \psi}{V_0}, \quad (3)$$

where $\psi = \frac{\Delta T}{T_e}$, $f = \frac{\Delta N}{N_e}$ is the relative variations of electron density and temperature, $\theta = x/\Lambda$, $K^2 = 3\delta \frac{\Lambda}{\ell_e} v_0 = 2\lambda_e N_e \Lambda$, λ_e - the recombination coefficient, N_e , T_e - the undisturbed values of density and temperature of plasma stream; $K_T = 0.5$ for the weakly ionized plasma. The system (1), (2) is true under following conditions: $N_e \approx N_i$ and $N_e \ll N_m$. N_i , N_m - the ion and neutral density the temperature of ions and neutrals is supposed to be unchanged.

The plasma stream is uniform in absence of the electrical field so N_e^* , T_e^* do not depend on the coordinates. The coefficient $\lambda = \frac{\partial(\lambda_e T_e^*)}{\partial(T/T_e^*)}$ is determined by the relation: $\lambda = \frac{\partial(\lambda_e T_e^*)}{\partial(T/T_e^*)}$, i.e. it characterizes the rate of dependence of the recombination coefficient and ionization frequency on the temperature; $\lambda = v_0/v_T$;

v_T is the velocity of thermodiffusion: $v_T = \frac{T_e}{m \nu_e \Lambda}$; $v_0 = \frac{\delta T_e}{2\pi \nu_e \Lambda}$. ν_i - the ion-neutral collision frequency; ℓ_e - the electron free path length; δ - the fractional lost by an electron in a collision with a neutral particle; ϵ - the plasma conductivity; E_p - the plasma field [2].

In the assumption (1) a solution of Eq (2) is:

$$\psi_{1,2} = \sqrt{\frac{\pi}{2}} \frac{K^2 A^2 / E_p^2}{\sqrt{\lambda_e^2 + K^2}} \left\{ e^{|\gamma_{1,2}|(|\theta| + \frac{1}{2} |\gamma_{1,2}|)} \left[1 - \Phi(|\theta| + \frac{1}{2} |\gamma_{1,2}|) \right] + e^{-|\gamma_{1,2}|(|\theta| - \frac{1}{2} |\gamma_{1,2}|)} \left[1 + \Phi(|\theta| - \frac{1}{2} |\gamma_{1,2}|) \right] \right\}. \quad (4)$$

The solution ψ_I is true in the region $\theta < 0$; ψ_F is true in the region $\theta > 0$; $\Phi(x)$ - the integral of errors; the constants $\gamma_{1,2} = \frac{\lambda}{2} \pm \sqrt{\frac{\lambda^2}{4} + K^2}$ determine a dimension of the plasma stream temperature disturbance.

An analytical solution of the equation (3) on the basis of an expression (4) is impossible to obtain.

However a calculation of a space pattern shows that function $\psi(\theta)$ is closely approximated by either $e^{-\gamma|\theta|}$ or $e^{-\theta^2}$ functions versus a parameters of the problem.

Suppose $\psi = A e^{-\gamma|\theta|}$. Then the solution of eq (3) takes the form:

$$\text{with } \theta < 0 \quad (a)$$

$$f = \left[\left\{ K_T + \frac{K_T x_2^2 - \beta}{(x_1 - x_2)(x_1 - x_2)} - \frac{K_T x_2^2 - \beta}{(x_1 - x_2)(x_1 - x_2)} \right\} + \frac{(K_T x_1^2 - \beta) 2\gamma e^{x_1 \theta} + f|\theta|}{(x_1 - x_2)(\gamma^2 - x_1^2)} \right] \psi; \quad (5)$$

$$\text{if } \theta > 0 \quad f = \left[\left\{ K_T - \frac{K_T x_2^2 - \beta}{(x_1 - x_2)(x_1 - x_2)} - \frac{K_T x_2^2 - \beta}{(x_1 - x_2)(x_1 - x_2)} \right\} + \frac{(K_T x_2^2 - \beta) 2\gamma e^{x_2 \theta} + f|\theta|}{(x_1 - x_2)(\gamma^2 - x_2^2)} \right] \psi; \quad \beta = \frac{\lambda v_0}{v_d}, x_{1,2} = \frac{v_0}{2v_d} \pm \sqrt{\frac{v_0^2}{4v_d^2} + \frac{v_e}{v_d}}.$$

The experiment was performed using the argon plasma for which $\delta = 3 \cdot 10^{-5}$. In the undisturbed plasma stream $N_e^* = (1.4) \cdot 10^{11} / \text{cm}^3$, $T_e^* = (1.2) \cdot 10^3 \text{ K}$, $T_e^* = 600 \text{ K}$. This

corresponds to the values of the parameters: $\kappa \in [0,05; 0,2]$, $\lambda \sim 10^{-2}$; $(v_0/v_d) \in [10^2; 10]$; $(v_e/v_d) \sim 10^{-1}$.

In Fig.1 are represented the numerical calculations of the stationary disturbances of temperature and density for $\kappa = 0,05$; $\lambda = 0,02$; $(v_0/v_d) = 50$; $(v_e/v_d) = 0,15$. It is assumed that $\lambda_e = 10^{-10}$ 1/cm²sec. The function $e^{-\theta^2}$ determining a field localization in space is denoted by a broken line. It follows from the calculations represented on Fig.1 that the sizes of disturbances introduced by a radio beam into plasma greatly exceed a radio-beam width. Under the above parameters a stream convection don't affect on the space temperature distribution curve. It is almost symmetrical in relation to the plane $\theta = 0$. The f curve is however markedly displaced in the θ - direction. It is known the parameters d , v_i , T_i are functions of the electron temperature and consequently they change in a process of an electron heating.

In Fig.2 the curves $\frac{\Delta T(\theta)}{\Delta T(0)}$ and $\frac{\Delta N}{AN_0}$ are calculated for $\gamma = 2,5$ and $(v_0/v_d) = 2$. In this case also the stream convection slightly influences upon the space distribution ψ and greatly affects on the function f : the region with an increased density is formed being displaced in space up to the injector. It is due to the convection and ambipolar diffusion velocities are approximately equal and opposite. This results in the electron accumulation.

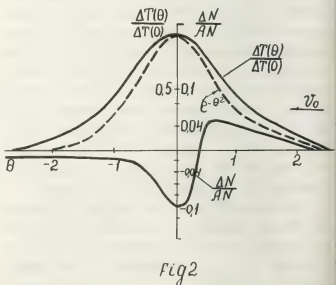
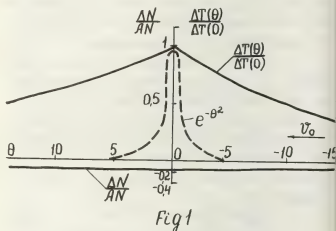
Thus the analysis shows that the plasma density decreases if the plasma stream convection velocity is much more than the diffusion velocity, the disturbance sizes exceeding field size and displacing in the direction of the stream velocity. If the convection and diffusion velocities are close both decrease and increase of the electron density take place in comparison to the undisturbed state.

The performed theoretical analysis accounts for the experimental results: the electron density disturbed distribution is assymetric; the disturbed region

size greatly exceeds the radiobeam width. This analysis explains the nature of the electron disturbed density space distribution.

REFERENCES:

1. N.A. Armand, S.A. Rogashkov, E.G. Shustin. Interaction of the microwave beam with a flow of low temperature (Part 1. Exper.) Proceedings of the XIV Conf. on PIG, 1979: Grenoble, France.
2. A.V. Gurevich, A.B. Shvartsburg. The non-linear theory of the radiowave propagation in ionosphere. "Nauka", 1973, Moscow.



THE UHF DISCHARGE WITH PRELIMINARY LOCALLY IONIZED GASEOUS MEDIUM

N.A. Armand, S.A. Rogashkov and E.G. Shustin.

Institute of Radioengineering and Electronics, Academy of Sciences, Moscow, U.S.S.R.

When studying the interaction of intense ($E \sim 50 \text{ V/cm}$) focused beams of W band microwave with a low temperature plasma stream flowing out of an electroarc plasmatron into a rarefield gas [1], it is revealed that a change of power of both passed and, especially, reflected signals has an oscillating character in the certain region of the parameters of plasma and gas (Fig.1). As a rule, oscillations begin with some delay in relation to the origin of pulse. The value of delay and period of oscillation are decreased with increasing both density of plasma and pressure of gas. The brightly luminous region ranging from the boundary of a luminous part of a plasma stream on the direction to the radiating antenna is visually observed. The more pulse duration of a microwave beam, the more distance through which the luminous region passes in this direction under other equal conditions.

The luminous region represents the area with more increased ionization moving from the stream to the source of microwave energy, i.e. the microwave discharge initiated by previous ionization in a plasma stream. This assumption is supported by direct measurements of the plasma density distribution in space between the stream axis and the antenna. The measurements are made by an interferometer with a dielectric waveguide serving as a mobile sensor [2]. On the interferograms, inside the luminous region a sharp spike corresponding to the increase of plasma density with the following slow decrease is recorded. The delay time of the spike in relation to beginning a microwave pulse increases with the displacement of the

waveguide to a radiator of microwave power

In Fig.2 is represented the plasma density space-time dependence pattern reconstructed from the oscillograms of the interferometer signal for one of the regimes in which the described phenomenon has been detected. It is seen that after switching the microwave beam on, the "hump" moving for some time towards a microwave beam is appeared on a slope of the radial profile of density distribution. Excess of concentration over the undisturbed plasma accounts for 130% (in the region of the microwave discharge origination) till 450% (at the end of a microwave pulse). With the absolute value the plasma density in the region of UHF discharge accounts for 0,7-0,9 of the critical density $n_{cr} = 1,1 \cdot 10^{12} \text{ cm}^{-3}$. It is evident that the oscillations of the reflected signal in the regimes of the initiated microwave discharge are determined by beating between the radiating and Doppler displaced (reflected from the running front of ionization) waves. So it is easy to define the front propagation velocity: $v = c\Omega/2\omega$ where Ω - the beat frequency determined from the oscillograms. The velocity of propagation of a microwave discharge is found to depend on the undisturbed ("priming") plasma parameters and to be $(0,5 \pm 3) \cdot 10^4 \text{ cm/sec}$. These data agree with the results of the measurements of the front of ionization velocity according to the delay time of peak on the interferogram corresponding to the microwave discharge on moving the sensor to the antenna.

Following Yu.P. Raiser [3], let us estimate the magnitude of the stationary

electric field for a breakdown of neutral argon under experimental conditions:

$$E^2(\text{v/cm}) = 5,7 \cdot 10^{-16} I, (\omega^2/\nu_m^2) \frac{\nu_m}{\nu_m} \Phi/\epsilon$$

where designations correspond to the accepted ones in [3]. According to our conditions in the range of pressures of 0,1-0,5 torr, this estimation defines the value of the intensity of the breakdown field $E=150\text{V/cm}$, i.e. 2,5 times more than the intensity realized in the course of the experiment. The observed phenomenon has analogs in some experiments on the optical breakdown of gases and studying the microwave discharges in waveguides [3,4].

As shown in [4], the diffusion of optical resonance radiation is responsible for the formation and propagation of the initiated microwave discharge in a waveguide. In our conditions except this mechanism, two more physical phenomena seems to be of concern. First, the change of fast free diffusion determining the particle runaway in conditions of the neutral gas breakdown by the ambipolar one (peculiar to plasma) facilitates the possibility of the avalanche breeding the particles. Second, the increase of the ionizing microwave electric field due to both "swelling" the field in the nonuniform plasma near the resonance point and reflecting the wave from the gradient of plasma concentration has great significance. The determination of a comparative importance of these mechanisms for the described phenomenon will be the subject to be investigated.

REFERENCES:

1. N.A. Armand, S.A. Rogashkov, E.G. Shustin. Interaction of the intense microwave beam with the flow of the low temperature plasma. Proceedings of the 14th Conference on FIG, Grenoble, France, 1979.
2. E.A. Shustin, A.A. Lisitskaya. The microwave interferometer with enhanced resolution for observing the plasma in a microwave field. The report of the All-Union Conference on physics of the low temperature plasma, Kiev, 1979.
3. Yu.P. Raiser. The laser spark and propagation of discharges, M., "Nauka", 1974.
4. G.W. Bettke, A.D. Ruess and oth. Phys. Fluids, 1963, v. 6, p. 594; 1966, v. 9, p. 1430; 1969, v. 12, p. 822.

Fig 1

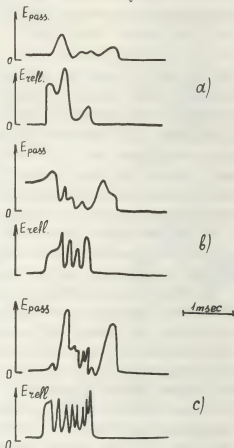
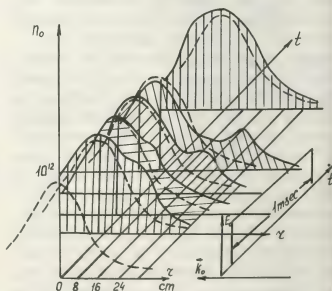


Fig 2



ION SOUND DISSEMINATION IN MOVING PLASMA JET

A.A. Pertsev.

Moscow, U.S.S.R.

1. Introduction

Beginning from some current value, critical duties, characterizing by sharp increase of value $\partial u / \partial I$ [1,2], can be reached in gas discharge high current devices with stationary supply of Li - neutral mass flow. One of the main features of critical duty is intensive potential oscillation and plasma consentration excitation [3].

Parameters of such excitation, dessemi-nating in discharge area and in moving plasma jet, were considered in this work.

2. Experimental technique

Investigations were made in gas discharge system of coaxial geometry (Fig.1). Multi-wire cathode (c) of 15 mm diameter is located on the cylindrical anode axis (a) (anode diameter is 65 mm). Li - vapours supply gasdischarge chamber through the cathode. Fixed high frequency probe (1) was installed near the anode face ($z=0$, $r=R$). Moving high frequency probe (2) traveled in the range $-(R-50 \text{ mm}) \leq r \leq (R-50 \text{ mm})$; $-40 \text{ mm} \leq z \leq 200 \text{ mm}$.

Oscillation parameters were measured by panarame spectrum analyzer (bandwidth 0.02-100 MHz), high frequency millivoltmeter (0.01-5.0 MHz) and analogue correlometer (0.05-2.0 MHz). Distributions of spectral and integral intensity oscillations were studied by spectrum analyzer and high frequency millivoltmeter, and time-space correlation functions were measured by the correlometer.

3. Experimental results

The Fig.2 shows the volt-ampere characteristic. The investigation of oscillation was carried out at the points a, b and c.

Under constant flow $\dot{m} = 4 \frac{\text{mg}}{\text{s}}$ the point a corresponds with 1 cr , the point b corresponds with 1.05 cr , the point c corresponds with 1.1 cr . Electric potential (-30 v) concerning the anode was supplied to the measurement probe. Fig.3 shows the oscillation spectrum of probe in saturation current. The fundamental oscillation frequency is $F = 0.2 \text{ MHz}$.

Fig.4 shows the space distribution of integrated intensity ion saturation current oscillation on the moving probe. Fig.5 shows space correlation functions

of ion saturation current oscillations for the probes 1 and 2 along axis z and radius r . Fig.6 and 7 shows space-time correlation function family

$$K(l, \tau) = \frac{1}{T} \int S_1(l, t) S_2(l + \Delta l, t + \Delta t) dt$$

along z ($l \sim z$) and along r ($l \sim r$) accordingly. The following calculations are based on the experimental results:

a) ion wave phase velocity along axis z - $V_z = 23 \cdot 10^3 \text{ m/s}$

and along the radius r

$$V_r = 7 \cdot 10^3 \text{ m/s}.$$

b) ion concentration disturbance wavelength $\lambda_z = 0.115 \text{ m}$, $\lambda_r = 0.035 \text{ m}$. In addition to that absence of phase shift between ion concentration and plasma potential waves was defined. The accomplished measurements show the azimuthal symmetry of discribing waves.

4. Discussion

Measured ion saturation current oscillations of probe are connected with plasma density oscillations. The plasma density in nearly completely defined by ion component density, as plasma is highly ionized in this case.

Basing on experimental data were calculated wave vectors: $K_z \approx 55 \text{ [m}^{-1}\text{]}$; $K_r \approx 170 \text{ [m}^{-1}\text{]}$, ion thermal velocity $V_{ti} \approx 2 \cdot 10^3 \text{ m/s}$, electron velocity $V_e \approx 7.5 \cdot 10^5 \text{ m/s}$

Consequently, in discribed conditions inequality $V_i \ll \frac{\omega}{K} \ll V_e$ is valid.

Assuming that discribed waves are ionic-sonic nature the damping decrement looks like:

$$\gamma = \left(\frac{\pi}{8}\right)^{\frac{1}{2}} \cdot K \left(\frac{T_e}{M_i}\right)^{\frac{1}{2}} \cdot \left\{ \left(\frac{m_e}{M_i}\right)^{\frac{1}{2}} + \left(\frac{T_e}{T_i}\right)^{\frac{3}{2}} \exp\left[-\frac{1}{2}\left(\frac{T_e}{T_i} + 3\right)\right] \right\}$$

Hence the logarithmic damping decrement may be calculated as follows

$$\theta = \gamma \cdot T = \ln \frac{A_{n+1}}{A_n} = 0.18$$

$$\text{or } \frac{A_{n+1}}{A_n} = 0.835.$$

A_{n+1} and A_n are wave amplitudes of preceding and consecutive periods accordingly. Experimental attenuation the wave length is measured to be 0.89.

Basing on the accomplished evaluations and the wave motion behaviour defined a posteriori, we can conclude, that the discribed waves indeed are the ionic-sonic waves.

References

1. Поротников А.А. В сб. "Плазменные ускорители". М., "Машиностроение", 1978.
2. Морозов А.И. Там же.
3. Глотова Н.Н. и др. "Окспериментальное исследование аномальных режимов электродинамического ускорителя плазмы". ИТФ, 1978, 48. 7.

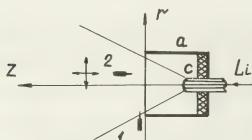


Fig.1. The experimental device.

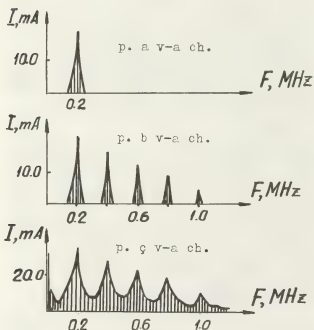


Fig.3. The ionic current oscillations spectrum in points a, b and c V-A characteristic.

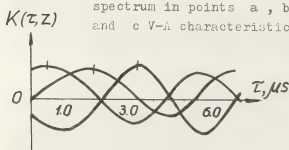


Fig.6. The space-time correlation functions of oscillations along Z-axes.

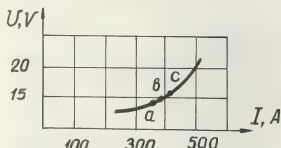


Fig.2. The volt-ampere characteristic of discharge.

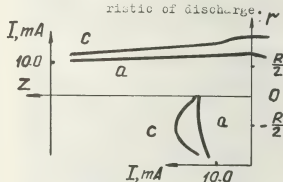


Fig.4. The distribution of integrated intensity ionic current oscillation in the plasma jet.

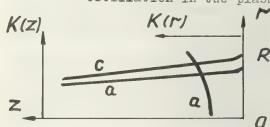


Fig.5. Space correlation function of ionic current oscillations.

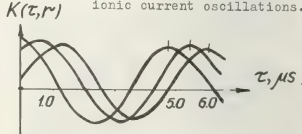


Fig.7. The space-time correlation functions of oscillations along R-axes.

HF. INSTABILITIES IN THE HETEROGENEOUS PLASMA OF A PENNING DISCHARGE ION SOURCE WITH A HOLLOW CATHODE

V.P. Gerasimov, S.A. Karev, V.A. Obukhov and G.G. Shishkin.

Moscow, U.S.S.R.

Introduction

In gaseous discharges with heterogenous distributions of electric and magnetic fields the instabilities of different types may be produced [1]. The investigation of these instabilities can possibly be used in optimization of some gaseous discharge devices. In the investigation presented herein were obtained measurements of the oscillations of the plasma potential at a number of points in the discharge chamber of the cesium ion source over range of source operating conditions. Most of the experimental tests discussed here were produced from 0.5 to 1.5 MHz.

Experimental arrangement

In this investigation the 10-Sm hollow cathode cesium ion source shown in Fig.1 was used. The magnetic field was formed by the permanent magnet mounted on the back wall of the chamber and by special ferromagnetic details. The magnetic field can be characterized as "divergence and controgated near cathode". The magnetic induction varied from 0.4 T near the cathode to 0.015 T near the screen electrode. The source was operated at the beam currents of 0.2-0.5 A. The accelerating voltage was about 1.8 kV. The discharge voltage varied from 15 to 25 V, and the discharge current was characterized by the interval of 2.0-3 A (see Fig.3). The plasma parameters like electron temperature T_e , plasma density N_e , plasma potential ϕ and electric field E were measured and calculated with the help of data which were received by using two cylindrical Langmuir's probes. Two h.f. probes were also used to record the plasma oscillations. The probes' signals were measured by spectrum analyzers and correlation receivers. All the recording systems were matched and calibrated.

Experimental results

The plasma parameters and their distributions are shown in Fig.2. From Fig.2 those skilled in art can see two areas in the discharge plasma. The first one, i.e. central plasma can be characterized as "hot and dense", while the second, i.e. preanode plasma, is more "cold and rarefied". Fig.3 shows V-A characteristics of the discharge, Fig.4 is a typical spectra which shows the relative amplitude as a function of frequency of the oscillations for a discharge current

2.2 A, discharge voltage 20V and beam current 0.42 A. This spectra has the frequencies of the dominant peaks. The first of them is on the frequency of about 40 kHz, and the second - on 0.6-0.8 MHz. In this paper the fluctuations of the second range have been investigated. Figure 5 shows the auto- and cross-correlations curves for these oscillations. The radial variation of the amplitude (at $Z=30$ mm) and axis variation of the frequency (at $r=0$) are given on the Fig.2 and 6. Figure 6 shows the dependences of the frequency of these oscillations on the discharge voltage. From Fig.2 those skilled in art can see the correlation between the amplitude of the oscillations and the plasma parameters. In order to obtain whether the oscillating area possesses convective or not the rotating velocities space-time correlations were measured. It was found that the oscillations are "in phase" both over the axial plasma area (curves 1,3 in Fig.5) and over the radial out of the area of the "hot plasma". On the contrary inside the area of the "hot plasma" the wave velocity was measured to be about 10^7 cm/s (curves 1,2 in Fig.5). It seems that this oscillation is an azimuthal wave. The frequency of this wave is slowly varying on the length (Fig.6). The magnitude of the frequency tends to increase as the flow rate of cesium and discharge voltage are increased.

Discussion of the results

In this case the plasma parameters are considerably heterogeneous on the radius as well as on the axis. That is why it is necessary to work out the theory in three-dimensional approximation. This problem could not be solved analytically. Moreover it seems to be too difficult for a numerical solution. Therefore we want to carry out a qualitative analysis. As it follows from the experiments the azimuthal wave is similar to a spoke, whose frequency is $f = Kv_y/2\pi$. According to the correlation measurements $K \approx 1/2$, where r -radius of the "hot plasma" area. If $V_y = V_{Ae} = c/B_y = 10^6 - 10^7$ m/s then $f = 0.5 - 1$ MHz. This value is in concordance with the experiments. Having experimental data on the velocity, the frequency of the wave (Fig.2,6) and the location of the maximum amplitude in every cross-section of the chamber, those skilled in art can

determine the wave's dispersion characteristics (Fig.2). It seems that considering oscillation is stipulated by heterogeneity of the distribution of the electron drift velocity. The instability of this kind have been investigated for E-H plasma accelerators with the closed-drift of electrons [2]. The conclusions of this analysis are also suitable for this case. The frequency and increment of the wave respectively are

$$\omega = K V_{dz} \pm A_{\varphi} \left(\frac{dV_{dz}}{dK} ; \frac{1}{K^2} ; \omega_{De} \right) \quad (1)$$

$$\gamma \approx \frac{K_{\varphi}}{\sqrt{K_{\varphi}^2 + K_z^2}} \frac{dV_{dz}}{dK} \quad (2)$$

It is sufficient enough to take into account only the first member of the equation (2). The character of the calculated and experimental dispersion dependences are in concordance. The spacial distribution of the oscillation amplitude can be calculated with the help of equation (2) and the expression: $K_z = \gamma / v_{dz}$. It can be showed that the maximum of the intensity of the wave is observed in the chamber area where K_z is the greatest. The presented data show that the investigated oscillation can be identified as h.f. drift waves stipulated by the slipping-stream instability.

References

1. Mikhailowsky A.B. Teoriya plazmennikh neustoyichivostey. Vol.2. Atomizdat, 1977.
2. Shishkin G.G., Gerasimov V.P. XII Internat. Conf. in ionized gases. Part I, 1975, 310. Netherlands.

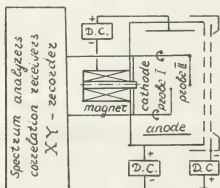


Fig 1

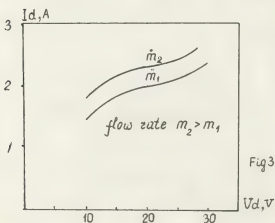
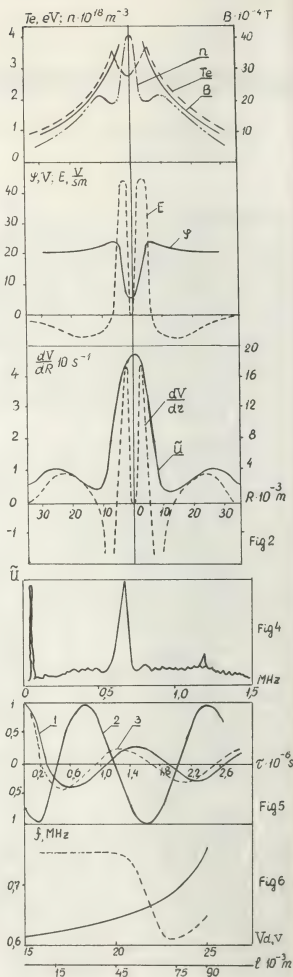


Fig 3



ON NONLINEAR STAGE OF PARAMETRIC INSTABILITIES OF WAVES EXCITED BY LOCALIZED PUMPING

S.M. Musher, B.D. Ochirov and A.M. Rubenchik.

Institute of Automation and Electrometry, Siberian Branch of the U.S.S.R. Academy of Sciences, Novosibirsk 630090 U.S.S.R.

By present time the theory of weak turbulence of homogeneous plasma has been developed well enough. It makes it possible to calculate an anomalous absorption of the electromagnetic wave via parametric instabilities. However, in real experiments the plasma or pumping waves are inhomogeneous, as a rule, and a new stabilizing mechanism, i.e. carrying out of the waves from the interaction region, arises.

The present paper considers the plasma turbulence in a homogeneous medium excited by localized pumping. Such a statement is seemed to be interesting enough. For example, in experiments on high-frequency heating of plasma in large installations the pumping wave is excited by the source of finite size and therefore is localized within well-defined resonance cone [1]. As is shown in [2], under lower hybrid heating in tokamaks just a presence of a resonance cone often defines the threshold of parametric instabilities.

To elucidate the influence of pumping localization on a nonlinear stage of the parametric instability, let us consider the excitation of Langmuir oscillations in an isotropic isothermal plasma. The equations describing the excited turbulence can be written as

$$\frac{\partial n_k}{\partial t} + \vec{v}_E \cdot \frac{\partial n_k}{\partial \vec{r}} = n_k (\gamma_p(k) - \nu_e) + \int T_{kk'} n_{k'} d\vec{k}' \quad (1)$$

Here n_k is the number of Langmuir plasmons, $\vec{v}_E = 3 \vec{v}_T (k z_d)$ is their group velocity, $T_{kk'} = \int \frac{(\omega - \omega')}{k - k'} \frac{(\vec{k} \vec{k}')^2}{k^2 k'^2} d\vec{k}'$ is the matrix element of the induced scattering on ions - the main nonlinear process, $\gamma_p(k)$ is the increment of the parametric instability and ν_e the frequency of electron-ion collisions.

In a homogeneous medium the distribution of excited oscillations is sharply anisotropic. The appearing turbulence is the succession of quasimonochromatic waves $n_k = \sum_i \mathcal{N}_i \delta(\vec{k} - \vec{k}_i)$ propagating along the electric field of the pumping wave. Their amplitudes decrease with the wave vector, and the distance between two neighbours is $\Delta k \approx k_{diff} = v_d^{-1} \sqrt{\frac{m}{M}}$

It is natural to expect that the weak inhomogeneity will not destroy a general picture of the spectrum, and we can simplify (1) turning to the satellite approximation [3] $\vec{k}_i \parallel \vec{E}_0$, $k_i = k_0 - i k_{diff}$. In dimensionless variables neglecting the difference of group velocities of the various waves, let us write down the following equations (\mathcal{N}^+ and \mathcal{N}^- are the waves propagating in the positive (\mathcal{N}^+) and

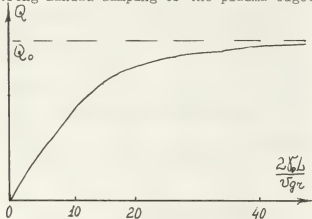
negative (ω^-) directions

$$\frac{\partial \omega_0^+}{\partial t} + v \frac{\partial \omega_0^+}{\partial x} = \omega_0^+ \left(-\frac{1}{p} + 1 - \omega_1^+ \right)$$

$$\frac{\partial \omega_i^+}{\partial t} + v \frac{\partial \omega_i^+}{\partial x} = \omega_i^+ \left(-\frac{1}{p} + \omega_{i-1}^+ - \omega_{i+1}^+ \right) \quad (2)$$

$$V = \frac{v_{Te}}{\delta_p L}; \quad p = \delta_p / \delta_{ei}$$

The behaviour of the solutions of the system (2) was investigated computationally with the use of the implicit difference scheme of the "running calculation" type. It is easy to understand that Eq.(2) has no stationary solutions. Therefore, when solving (2), we use the absorbing boundary conditions modelling the appearance of strong Landau damping or the plasma edge.



The main result of this work is presented in the Figure illustrating the flux energy to the plasma as a function of the parameter $\frac{\delta_p L}{\omega_{ge}}$, Q_0 is the energy flux in homogeneous situations. It is seen that as the pumping amplitude increases, the carrying-out of energy from the localization region quickly becomes inefficient. This result can be understood from the following considerations. In the isothermal plasma the parametric instability resulting to the exciting of oscillations is convective, and for its development it is necessary the condition $\frac{\delta_p L}{\omega_{ge}} > \Lambda$ to be valid.

Here Λ is Coulomb logarithm and

δ_p the instability increment. In the

nonlinear regime when $\delta_p / \delta_{ne} \sim 1$ the

threshold $E_0 \approx E_{th}$ is only slightly

exceeded, therefore the oscillations scatter on ions passing the length $\omega_{ge} / \delta_{ne}$.

It is seen that when the threshold is exceeded by the order of unity, the scattering length is much less than the pumping localization region. As was mentioned above, the scattering on ions is mainly back scattering. Thus the trapping of oscillations occurs, and the carrying out of energy decreases. As is shown in the Figure at

$\frac{\delta_p L}{\omega_{ge}} \sim 20$ (for the tokamak plasma $\Lambda \sim 15$) the flux energy practically coincides with the calculated one in the approximation of a homogeneous plasma.

So far excitation of oscillations was considered for an isotropic plasma. This situation is typical for laser heating. Under lower hybrid heating of plasma in tokamaks the main nonlinear process for exciting magnetized plasmons ($\omega = \omega_p \kappa_z / \kappa$) is also the induced scattering, but the oscillations are scattered at the angle about 90° . Qualitatively this situation is similar to that described above, and when calculating an anomalous absorption of the pumping wave (4), there is no need to take into account its localization in space. Thus, the resonance cone deformation due to the modulation instability of the pumping wave results to a local change of its amplitude and should be considered as a more important effect.

REFERENCES

1. P. Bellan, M. Porkolab, Phys. Fluids **17**, 1592, 1974.
2. R. Berger et al. Preprint PPPL-1307, Princeton, 1976.
3. V. Zakharov et al. JETP, **69**, 155, 1975.
4. S. Musher et al. Letters to JETP, **25**, 358, 1977.

MAGNETIC FIELD GENERATION BY INTENSE LANGMUIR PLASMA WAVES

S.A. Bel'kov and V.N. Tsytovich^{*}.^{*}Physical Technical Institute, Moscow U.S.S.R.
P.N. Lebedev Institute, Moscow U.S.S.R.

The problem of the magnetic field generation in plasma is of great importance both for explanation of the laboratory plasma's experiments, in which plasma absorbs intense electromagnetic radiation, and for astrophysical applications. The mechanisms proposed and discussed previously deal mainly with the process of amplification of a magnetic field and require also some initial magnetic field. In the present report we propose a new instability type mechanism, which results in the growth of a magnetic field from the level of the fluctuations. This instability occurs if the intense electrostatic waves in plasma are present. It is closely related with the modulation instability which was widely discussed in literature.

In the latter the growth of the density variation modulates the amplitude of the electrostatic waves, while in the mechanism proposed in the present consideration the phases of the electrostatic waves are modulated and simultaneously the magnetic fields are excited. Particles oscillate in electrostatic waves with the different phases and this results in an envelope current and hence magnetic field generation.

The appearing magnetic fields modulate the phases of waves. Thus a self-amplification of the fields takes place and the growth of the magnetic field is exponential at the initial stage. This effect has a rather general character and takes place both in collisional and collisionless plasmas. Equations which describe it in different regimes, differ one from the other. The difference between frequencies of two interacting waves serves as a criterion of the regime (collisional or collisionless). The case $\omega_1 - \omega_2 \ll \nu_e$ (ν_e is a frequency of the collision between electrons and ions) corresponds in our terminology to the collisional regime. While the case $\omega_1 - \omega_2 \gg \nu_e$ corresponds to the collisionless regime. The hydrodynamic equations can be used to find self-consistent equations for the amplitudes of a Langmuir field and generation magnetic fields. We use the method of [1] [2] to describe the excitation of the magnetic fields. Effects of excitation of the magnetic fields in this method are described by the process connected with the virtual transverse field. We write here the result for an collisional regime.

$$\vec{\nabla} \cdot \left(\frac{2i}{\omega_{pe}} \frac{\partial \vec{E}}{\partial t} + i \frac{\nu_e}{\omega_{pe}} \vec{E} + \frac{2\nu_{Te}^2}{\omega_{pe}^2} \Delta \vec{E} \right) =$$

$$= \vec{\nabla} \cdot \left(\frac{i e (\vec{E} \times \vec{B})}{m_e c \omega_{pe}} + \frac{\delta n}{n_0} \vec{E} \right) + Q_E \quad (1)$$

$$\left(\Delta - \frac{\omega_{pe}^2}{c^2 v_{te}} \frac{\partial}{\partial t} \right) \delta \vec{B} = \\ = 2.71 i e \Delta (\vec{E} \times \vec{E}^*) / 4 m_e c \omega_{pe} \quad (2)$$

$$\left(v_s^2 \Delta - \frac{\partial^2}{\partial t^2} \right) \delta n = \frac{0.27 v_{te}^2}{8 \pi m_i v_{te}} |\vec{E}|^2 \quad (3)$$

\vec{E} is the envelope of Langmuir field, $\omega_{pe} = \sqrt{\frac{4 \pi n_0 e^2}{m_e}}$, $v_{te} = \frac{T_e}{m_e}$, $v_s^2 = \frac{T_e}{m_i}$ is the pump source. The equation (3) describes the thermal modulation instability (discussed previously for the example [3]). The equation (2) is a new one. One can investigate the system of equations (1), (2), (3) for the stability problem of a monochromatic pump if we suppose that the

Q_E source compensated damping of the pump \vec{E}_0 due to collisions (which are described by term $i \frac{v_{te}}{\omega_{pe}} \vec{E}$) for a given \vec{k}_0 , ω_0 . Let us consider the case when one can neglect the variation of concentration δn . Then, the constant amplitude of monochromatic pump wave with frequency ω_0 and wave number \vec{k}_0 is unstable due to the excitation of magnetic fields (even for $\delta n = 0$). We find from (1), (2) that this instability has an threshold $2.71 |\vec{E}_0|^2 / 6 \pi n_0 T_e > \frac{c^2}{v_{te}^2} \frac{\kappa_1^2}{\kappa_d^2}$

$\kappa_d = \omega_{pe} / v_{te}$. Two cases are possible $k_0 \ll \kappa_d \left(\frac{2.71 |\vec{E}_0|^2}{8 \pi n_0 T_e} \cdot \frac{v_e}{\omega_{pe}} \right)^{1/2}$ and $\frac{v_{te}^2}{c^2} \gg \frac{v_e}{\omega_{pe}}$; then for $\kappa \gg \kappa_0$

$$\gamma = \gamma_m \omega = \frac{\kappa^2 v_{te}^2}{\omega_{pe}} \left(\frac{v_e \kappa_d^2}{\omega_{pe} \kappa^2} \right)^{1/2} \left(\frac{8.13 |\vec{E}_0|^2}{8 \pi n_0 T_e} \right)^{1/3} \equiv \gamma_1$$

and for $\kappa \ll \kappa_0$ we have $\gamma = \gamma_1 \left(\frac{\kappa}{\kappa_0} \right)^{2/3}$. On the other hand if

$$\kappa_0 \gg \kappa_d \left(\frac{2.71 |\vec{E}_0|^2 v_e}{8 \pi n_0 T_e \omega_{pe}} \right)^{1/2}$$

then for $\kappa \gg \kappa_0$ we have

$$\gamma = v_e \frac{2.71 |\vec{E}_0|^2}{6 \pi n_0 T_e} \equiv \gamma_2$$

and for $\kappa \ll \kappa_0$ we have $\gamma = \gamma_2 \left(\frac{\kappa}{\kappa_0} \right)^2$.

In collisionless regime, we should use the kinetic equation and Maxwell's equations (with nonlinear currents) in order to find equations analogous to (1), (2), (3). We obtain the following equations [2].

$$\vec{\nabla} \cdot \left(\frac{2i}{\omega_{pe}} \frac{\partial \vec{E}}{\partial t} + 3 \frac{v_{te}^2}{\omega_{pe}^2} \Delta \vec{E} \right) = \\ = \vec{\nabla} \cdot \left(i \frac{e}{m_e c} \frac{\omega_{pe}^2}{\omega_{pe}^2} (\vec{E} \times \delta \vec{B}) + \frac{\delta n_e}{n_0} \vec{E} \right) \quad (4) \\ \Delta \delta \vec{B} + (2\pi)^{3/2} \frac{\omega_{pe}^2}{c^2 v_{te}} \frac{\partial}{\partial t} \left(\delta \vec{B}(\vec{r}, t) \right) d\vec{r}' = \\ = i \frac{e}{4 m_e c \omega_{pe}} (\vec{E} \times \vec{E}^*) \quad (5)$$

$$\left(\frac{\partial^2}{\partial t^2} - v_s^2 \Delta \right) \delta n = \Delta \frac{|\vec{E}|^2}{16 \pi m_i} \quad (6)$$

The system (4-6) leads also to the instability with respect to the magnetic fields excitation for monochromatic pump wave, even if $\delta n = 0$. The threshold changes: $\frac{|\vec{E}_0|^2}{4 \pi n_0 T_e} > \frac{c^2}{v_{te}^2} \frac{v_e^2}{\omega_{pe}^2}$

The growth-rate for $\kappa \gg \kappa_0$ is $\gamma = \kappa v_{te} \left(3 |\vec{E}_0|^2 / 8 \pi n_0 T_e \right)^{1/2} \frac{v_{te}}{c}$ and reaches the maximum value for $\kappa \approx \kappa_d \left(|\vec{E}_0|^2 / 12 \pi n_0 T_e \right)^{1/2} v_{te} / c$

$$\gamma_{max} \approx \omega_{pe} \frac{v_{te}^2}{c^2} \frac{|\vec{E}_0|^2}{8 \pi n_0 T_e}$$

[1] Khakimov F. Kh. Tsytovich V. N. JETP 70, 1785 (1975)

[2] Bel'kov S. A., Tsytovich V. N. preprint Lebedev Phys. Inst. N 72 (1978)

[3] A. A. Verjaev, V. N. Tsytovich. Kratkie soobsheniya po fizike, No 4, 34 (1978)

MODULATION OF SPECTRA OF DRIFT WAVES DUE TO THE HIGH-FREQUENCY FIELDS

F.F. Assadulin, G.M. Batanov, A.A. Veriaev, A.V. Sapozhnikov and K.A. Sarkisian.

P.N. Lebedev Physical Institute Academy of Sciences, U.S.S.R.

In differ from [1-4] we shall discuss the influence of lower-hybrid pump waves $\omega_0 = (3\div 5)\omega_{UH}$, $\omega_{UH} = \omega_{pi}\omega_{ce}/\sqrt{\omega_{pe}^2 + \omega_{ce}^2}$ on the sound type ($\omega_i > \omega_{ci}$) drift waves in collisional plasma, due to drift-dissipative instability. The experimental results given below include the incomplete suppression and spectra modification of drift oscillations. Measurements were carried out at low pump fields $E_0 \leq 2 \text{ V/cm}$, when there is no parametric excitation of acoustic waves and there are no changes in macroscopic plasma parameters ($n(r), \nabla n, T_e$). The parameters of plasma [5] are the following: the length of cylindrical coulumn of plasma = 100 cm, the diameter = 4 cm, strength of stationary magnetic field, applied along the axis $B_z \approx 400$ Gauss, plasma density $n = 10^{10} \text{ cm}^{-3}$, $T_e = 6 \text{ eV}$, $Te/Ti = 10$; the pressure of nonionized gas $(Ar)p \approx 2 \cdot 10^{-4} \text{ torr}$, the size of inhomogeneity $\Delta = \left| \frac{1}{n} \frac{\partial n}{\partial r} \right| \approx 1 \text{ cm}^{-1}$; the frequencies of drift waves $\omega_i/2\pi < 100 \text{ kHz}$. High frequency field $\omega_0/2\pi = 24 \text{ MHz}$ have been excited by two semicylindrical plates 45 cm in length. There were [6] the Trivelpiece-Gould (axisymmetric modes) and dispersion for Langmuir waves $\omega_b = \omega_{pe}/\cos \theta$, where $\theta = |\vec{k} \cdot \vec{B}|$. The relations between the characteristic frequencies in the experiment is

$$\omega_{ci} < \omega_i < \omega_0 \ll \omega_{UH} \approx \omega_{pi} < \omega_b < \omega_{pe} < \omega_{ce} \quad (1)$$

(ω_{ce} - the frequency of collisions of electrons with neutrals; the other notations are standart). The latter reduces the possibilities of comparison with theoretical calculations [7], which describe the linear stage of the development of drift-dissipative instability in the presence of the field of a lower-hybrid pump wave. Figure 1 show the spectrogramms of drift waves, derived from several values

of the pump field E_0 . Figure 2 show the increase of frequency of drift waves $\Delta \omega_i$ versus field E_0 . We also measured the value of plasma noise $\delta n \cdot (\delta n)^2 \sim \int_{-\infty}^{\infty} H_i^2(\omega) d\omega$, where $\omega_s/2\pi = 100 \text{ kHz}$ which had been recorded at different values of ω_0 .

This dependence is given in figure 3. The main experimental results as it may be seen from the captures are the following:

1. There is nonthreshold modification of spectra of sound type drift waves and their incomplete suppression with the increase of E_0 fast of all on the side of higher frequencies.

2. The observable change in picks in the spectra is to the larger values of frequency without the change in values of wave vectors at low field ($E_0 \leq 3 \text{ v/cm}$) and it is such that $\Delta \omega_i/\omega_i \approx 0.01 - 0.1$.

3. With the incrcase of E_0 the intensity of drift waves decreases with an increase of pump wave frequency ω_0 .

The problem of the effect of a high frequency field on the drift instabilites (see ref. [8,9]) with the electric field perpendicular to the magnetic field is close to experimental conditions of the present work, but in our case there is a collision plasma. As that was discussed in ref. [7] from the hydrodynamic approach under the conditions $\omega_0 \geq \omega_{UH}$, $\vec{E}_0 \perp \vec{B}$, $\omega_i > \omega_{ci}$: the following dispersion equation for the branch of drift waves mentioned above has been set up

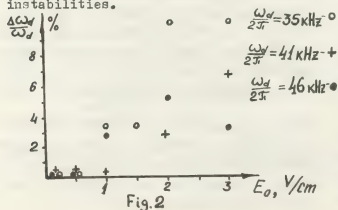
$$\omega_d^2 = K^2 v_s^2 \left(1 + i \frac{K_y \Delta v_{eff}}{K_z^2 \omega_{ce}} \right)^{-1} \quad (2)$$

where $v_{eff} = v_{ce} + 2i|E_0|^2 c^2 K_y \omega_i / B^2 \omega_{ce}^2$, $v_s^2 = T_e/m_i$. Equation (2) at the experimental conditions $\Delta K_y v_{ce} / K_z^2 \omega_{ce}^2$ and at small E_0 leads to the increase in the drift wave frequency with E_0 :

$$\Delta\omega_d/\omega_d = 10^{-4} K_1 c^2 K_2^2 \omega_{ce}/E_0 l^2 B_0^2 \omega_0^2 \& V_{ec}$$

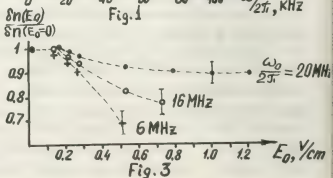
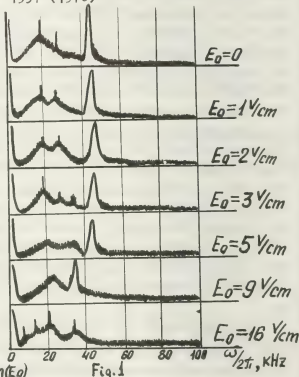
When the working fields E_0 are of the order of 1 v/cm this increase in frequency is a few percent of ω_d , what is more, the characteristic field E_* modifying spectra at large values of the drift wave frequency ω_d is smaller. The dependence of E_* from ω_0 is linear, which is in a good agreement with the experiment. The comparison of theoretical calculations with the experimental results may be only qualitative and may take place only in the region of small E_0 . One can refer (as it was done in other works ref. [2, 4]) to the increase in Landau damping of drift waves following from the increasing ω_d with E_0 as this mechanism affect the observable decrease in the amplitude of drift waves. Though this conception seems to be very ruthfal, it is necessary to carry out the theoretical investigation of the development of drift-dissipative instability in the presence of H F field with the simultaneous study of Landau damping both at the linear stage and at the stage of saturation of unstable drift waves.

Thus, experimentally observed modification of the spectra of ion-acoustic type drift waves and qualitative accordance with experimental data show that the H.F. electric field component which is perpendicular to the external magnetic field affects essentially the dynamic of drift dissipative instability and can lead to the suppression (at the process of lower-hybrid heating of plasma) of long wavelength potential (e.i. dangerous for plasma confinement in tokamaks, stellarators etc.) instabilities.



REFERENCES

1. Ya.B.Painberg, V.D.Shapiro, J.Exp. Theor. Phys. 52 293 (1967)
2. A.N.Izmailov, Ya.B.Painberg, V.K.Chelchel', V.D.Shapiro, Ukr.Phys.Journ. 13, 1215 (1968)
3. K.L.Wong, P.M.Bellan, Phys.Fluids 21, 841 (1978)
4. R.Gove, J.Grun, H.Lashinsky, Phys. Rev. Lett. 40, 1401 (1978)
5. F.F.Asadullin, G.M.Batanov, A.V.Sapozhnikov, K.A.Sarksian, Preprint Ph.Inst. Ac.Sci. N 96 (1978)
6. G.M.Batanov, et al., Preprint Ph.Inst. Ac. Sci. N 55 (1978)
7. F.F.Asadullin, G.M.Batanov, A.A.Veriaev, A.V.Sapozhnikov, K.A.Sariksian, Preprint Ph.Inst.Ac.Sci. N 231 (1978)
8. A.K.Sundaram, P.K.Kaw, Nuclear Fusion 13, 901 (1973)
9. I.Weiss, T.Morrone, Phys. Fluids 19, 1997 (1976)



THRESHOLD ELECTRON DRIFT FOR THE SPONTANEOUS EXCITATION OF NON-ELECTROSTATIC ION-CYCLOTRON OSCILLATIONS IN WEAKLY IONIZED PLASMAS

N. Pavlović-Brajković and B. Milić*

Department of Physics, Faculty of Sciences, Kragujevac, Yugoslavia,

*Department of Physics and Meteorology, Faculty of Sciences, Belgrade, Yugoslavia.

Ion-cyclotron oscillations in plasmas are generally treated as electrostatic in most theories, although it is obvious that they are of non-potential character. In this paper an attempt is made, therefore, to investigate some outstanding characteristics of these oscillations, assuming that they are not electrostatic. A uniform and infinite weakly ionized plasma is considered, and it is assumed to be placed in a homogeneous and static E_0 parallel to a constant d.c. E_0 . The ensuing anomalous Doppler effect eventually gives rise to ion- (and, of course, also electron-) cyclotron waves of growing amplitude. This fact of spontaneous excitation has been long ago observed experimentally [1], and the value of the threshold drift has been found [2] to increase with electron temperature (or rather with T_e/T_i), but the theoretical explanations [3,4] based on the assumption that the excited waves are longitudinal were not quite satisfactory.

In this paper the problem of the determination of the threshold drift has been reconsidered for the plasma described above, and for ion-cyclotron waves of non-electrostatic character. The threshold drift has been determined from the condition of marginal instability, $\text{Im } \omega = 0$, and the necessary dispersion equation is taken in the standard Fresnel (rather than Poisson) form

$$\det(k^2 \epsilon_{pq} - k_p k_q - \frac{\omega^2}{c^2} \epsilon_{pq}) = 0, \quad (1)$$

where ϵ_{pq} are the components of the plasma dielectric tensor. The latter quantities have been determined from the kinetic equations for electron and ion one-particle distribution functions, using a modified BGK collision integral for e-n and i-n elastic collisions [5], with a Maxwellian f_0^e and a shifted Maxwellian f_0^i . After the standard procedure of linearizing, applying the Fourier-Laplace transformations, evaluating the components of the complex amplitudes of the current density perturbation [6], the obtained dispersion equation yields the following expression for the threshold electron drift for the spontaneous excitation of the m th harmonic of the ion-cyclotron oscillations:

$$\frac{u_{Ti}}{v_{Ti}} = \frac{m \omega_{Bi}}{k_z v_{Ti}} + \sqrt{\frac{2}{\pi}} \frac{m_e}{m_i} \frac{v_{Te}}{v_{Ti}} \frac{m \omega_{Bi}}{v_{Te}} \times \\ \times \frac{k_z^2 v_{Te}^2}{m_i^2 \omega_{Bi}^2 \left(1 - \frac{v_{Te}^2}{\omega_{Bi}^2} \frac{k_z^2 k_{\perp}^2 v_{Te}^4}{m^4 \omega_{Bi}^4} \right)} \times \\ \times \chi(z_i), \quad (2)$$

where $\chi(z_i)$ is a rather complicated function of the argument $z_i = k_{\perp} \rho_{Li}$ (ρ_{Li} being the ion Larmor radius), which describes the effects of finite Larmor radius in the process of spontaneous excitation considered here. The approximate expressions for this function are different at $z_i \ll 1$ and at $z_i \gg 1$ (respectively, long-wave and short-wave limits, with respect to ion Larmor radius). It has been found that in the long-wave limit, the temperature dependence (appearing through the collision frequencies, thermal velocities and the variable z_i) of the threshold electron drift for the spontaneous excitation of the m th harmonic of the non-electrostatic ion-cyclotron oscillations is:

$$\frac{u_{Ti}}{v_{Ti}} \sim \frac{k_{\perp}^2 k_{\parallel}^2}{B_0^{2m-1}} T_i^{m-2} T_e^{1/2} + \frac{m \omega_{Bi}}{k_z v_{Ti}}. \quad (3)$$

In the short-wave limit, on the contrary, the threshold drift in question is practically independent of the order of the harmonic m , and it is much larger than in the former case. It is given by:

$$\frac{u_{Ti}}{v_{Ti}} \sim \sqrt{\frac{m_i}{m_e}} \frac{k_{\perp}^2}{k_{\parallel}} \left(\frac{T_e}{T_i} \right)^{3/2}. \quad (4)$$

Hence, in both short- and long-wave limits, a temperature dependence of the form $T_e^{3/2}$ is found. This is in accordance with the behaviour found in [2], which suggests that the waves excited in that experiment were not electrostatic. It would be of interest to observe experimentally the T_i -dependence of the threshold drift; in the longwave limit it should be a function of m , according to the theory developed here.

References

- [1] A.Y.WONG, R.W.MOTLEY, N.D'ANGELO, Phys. Rev. **122** A (1964) 436.
- [2] A.M.LEVINE, F.KUCKES, Phys.Fluids, **2** (1966) 2263.
- [3] W.F.DRUMMOND, M.N.ROSENBLUTH, Phys.Fluids, **5** (1962) 1507.
- [4] B.MILIC, Phys.Fluids, **15** (1972) 1630.
- [5] A.B.MIKHAILOVSKI, O.P.POGUTSE, Sov. DAN SSSR **156** (1964) 64.
- [6] N.PAVLOVIC, B.MILIC, Proc. 9th Yugoslav SPIG, Dubrovnik, 1978, p. 333.



RENORMALIZATION GROUP METHOD APPLIED TO LARGE SCALE LANGMUIR TURBULENCE

G. Pelletier.

Equipe U.S.M.G. Milieux Ionisés, Université de Grenoble I, BP 53 X, 38041 Grenoble Cedex, France.

In 1972, V.E. ZAKHAROV [1] proposed a new approach of Langmuir turbulence based on the two following equations :

$$\partial_j \left(i \frac{\partial}{\partial t} + \frac{3}{2} \omega_{pe}^2 n_D \Delta \right) E_j = \frac{\omega_{pe}}{2} \partial_j \frac{\delta n}{n_0} E_j \quad (1)$$

$$\left(\frac{\partial^2}{\partial t^2} - C_s^2 \Delta \right) \frac{\delta n}{n_0} = C_s^2 \Delta \frac{E_0 \cdot \vec{k}}{4 n_0 T_e} \quad (2)$$

In spite of its limitation to the case of small amplitude perturbations ($W \ll n_0 T$), this system exhibits strong non-linear effects, since the "Reynolds number", which can be defined as the ratio between the non-linear time scale and the linear one i.e. $R \sim \frac{W}{k^2 l_D^2 n_0 T}$, reaches large value for $k^2 l_D^2 \ll 1$.

This system has been intensively studied for its dynamical properties and to describe the various ways by which a cold Langmuir gas becomes instable.

A statistical theory of the large scale dynamics cannot be elaborated using conventional perturbations expansion, which diverges and has an "infrared catastrophe". F.Kh. KHAKIMOV and V.N. TSYTOVICH [2] proposed a first statistical theory of the Langmuir condensate, based on a double averaging technique. The "renormalization group" method, introduced by K. WILSON in 1972 [3] to describe critical phenomena was fruitfully applied in various fields of physics. Initially formulated for static problems, the method has been generalised to dynamical problems, and has been recently used with success for large scale hydrodynamic turbulence [4].

The purpose of this communication is to indicate how this new method is handled on a system close to the system (1)-(2), why it is convenient for solving the statistics of the Langmuir condensate, and what are the first few results.

We complete the two equations (1)-(2) by introducing Landau dampings and two sources of excitations : random forces in (1) and random inhomogeneities

in (2). So we are dealing with the following system, written with convenient reduced Fourier variables :

$$U_i = \lambda_1 G_1 \frac{k_i k_j}{k^2} \phi * U_j + G_1 f_i \quad (3)$$

$$\phi = \lambda_2 G_2 U_j * U_j^\dagger + G_2 \psi \quad (4)$$

G_1 is the linear Green function which propagates the Langmuir envelopes : $G_1 = [\omega - \omega_0 - \Theta k^2 + i\gamma_1(k)]^{-1}$. ω_0 is the frequency shift, equal to zero before any renormalization ; Θ describes thermal dispersion, γ_1 is the Landau damping. G_2 is the sound wave Green function : $G_2 = [k^2(\omega^2 + 2i\gamma_2\omega - ak^2)]^{-1}$. The symbol $*$ represents the convolution of the Fourier components in \vec{k} and ω . λ_1 and λ_2 are the coupling parameters. The excitations f_i and ψ have spectra which are supposed to be truncated at an ultraviolet cut-off k_0 , close to k_D . The dynamics are determined by the two Green function, the two couplings and the 2 excitation correlation functions.

A transformation T_s of the renormalization group modifies all these six functions in two steps (sometimes it can also generate new couplings). The first step consists in eliminating the small scale degrees of freedom, the wave numbers of which are in the interval $[k_0/s, k_0]$. The influence of small scale fluctuations on large scale dynamics is then described in renormalizing the six functions mentioned above, by a technique similar to that developed in ref [5]. In particular the Green functions are modified by the self-energy corrections Σ_1 and Σ_2 in accordance with Dyson equations :

$$\bar{G}_1^{-1} = G_1^{-1} - \Sigma_1 \quad (5) \quad \bar{G}_2^{-1} = G_2^{-1} - \Sigma_2 \quad (6)$$

Anyway it can be shown that the coupling parameters λ_1 and λ_2 are also changed in $\bar{\lambda}_1, \bar{\lambda}_2$; a renormalization of the excitation correlations is also necessary. The second step consists in performing scaling transformations ; changing k in $k' = sk$, the cut-off is again at k_0 . All the quantities are then changed with appropriate scaling factors which are powers of s .

The large scale properties of the system are found after many iterations of the renormalization group transformation. Obviously these properties can be found if the six above mentioned functions acquire a fixed form, with only few evolving parameters converging towards a stable limit (the fixed point).

a) Modification of the Green functions

Starting with the usual linear Landau damping in G_1 , the renormalization group generates a non-linear damping rate, which reveals the existence of a dissipation on the large wave length. There are two scattering processes which play a role : on the one hand large k sound waves modulate small k Langmuir waves, and these modulations are absorbed by the fast electrons (l-s-e scattering) ; on the second hand, a modified non-linear Landau effect causes an energy transfer towards large k , contrary to its effect in weak turbulence. So the renormalized damping rate can be expressed :

$$\gamma_1 = \gamma_0 + \nu k^2 + o(k^4) \quad (7)$$

and G_1 is characterised by four evolving parameters:

$$\omega_b, \theta, \gamma_0, \nu.$$

The usual perturbation theory would give a second order modification of G_2 which leads to the well-known oscillating-two-streams, self-modulation and decay instabilities. But the selective renormalization of large scale perturbations by small scales ones does not destabilise G_2 ; only the parameter a is modified.

b) Modification of the excitation correlations.

It can be shown that, starting from any excitation correlations, bounded in the large scale, the renormalization group generates white noise excitations, characterised by their amplitude parameters D_1 and D_2 :

$$\langle \epsilon_i(\vec{k}, \omega) \epsilon_j(\vec{k}', \omega') \rangle = 2D_1 \frac{k_i k_j}{k^2} (2\pi)^{d+1} \delta(\vec{k} + \vec{k}') \delta(\omega + \omega') \quad (8)$$

$$\langle \psi(\vec{k}, \omega) \psi(\vec{k}', \omega') \rangle = 2D_2 (2\pi)^{d+1} \delta(\vec{k} + \vec{k}') \delta(\omega + \omega') \quad (9)$$

(d is the dimension of space)

So, after several iterations, the renormalization group makes the excitation correlations evolve in simply changing D_1 and D_2 . The universal properties of the large scale proceed from that result.

c) Modification of the couplings

The renormalization group transforms the couplings simply by changing the two parameters λ_1 and λ_2 ; these modifications take properly into account differences with gaussian statistics, due to the quadratic couplings.

We indicate few results under the assumption that

the 'relevant' dynamics are subsonic for the largest wave length. Then there are two possible situations. The simplest situation is obtained when γ_0 is relevant ; it means physically that the l-s-e scattering is the main absorption for small k . The evolution of the set of parameters towards a fixed point is controlled by the following quantities :

$$\text{the "Reynolds number"} \quad y_1 = \frac{\lambda_1}{\lambda_2} \frac{D_1}{\gamma_0^2} k_0^d \quad (10)$$

$$\text{the "Kubo number"} \quad y_2 = \lambda_1^2 \frac{D_2}{\gamma_0} k_0^d \quad (11)$$

These two numbers scale as s^{-d} ; so for every positive dimension of space the couplings vanish. The dynamics are therefore asymptotically free (trivial fixed point) ; the infrared modes are gaussianly distributed, with a Rayleigh-Jeans spectrum.

Another situation is obtained when γ_0 vanishes, the dissipation being described essentially by νk^2 in (7). The convenient "Reynolds number" is now :

$$y_1 = \lambda_1 \frac{\lambda_2}{\nu} \frac{D_1}{\gamma_0} k_0^{d-4} \quad (12)$$

and the "Kubo number"

$$y_2 = \lambda_1^2 \frac{D_2}{\nu} k_0^{d-2} \quad (13)$$

But now, y_1 scales as s^{4-d} and y_2 as s^{2-d} , and then the asymptotic freedom is obtained beyond the cross over dimension $d_c = 4$, anyway y_2 vanishes for $d > 2$. In 3 dimensions, couplings are relevant and produce non gaussian fields ; but the investigation of the "non-trivial" fixed point is possible owing to an expansion in $\epsilon = 4 - d$. The detailed theory will be published later on. At the transition $\gamma_0 = 0$, the energy spectrum is like k^{d-3} and the density fluctuations is white noise, in agreement with KHAKIMOV and TSYTOVICH predictions for the condensate.

References

- [1] V.E. ZAKHAROV (1972), Soviet Phys. JETP, **35**, 908
- [2] F. Kh. KHAKIMOV, V.N. TSYTOVICH (1975), Soviet Phys. JETP, **41**, 47
- [3] K. WILSON (1972), Phys. Rev. Lett., **28**, 548
- [4] D. FORSTER, D. NELSON, M. STEPHAN (1977), Phys. Rev. A, **16**, 732
- [5] P.C. MARTIN, E.D. SIGGIA, H.A. ROSE (1973), Phys. Rev. A, **8**, 423

INSTABILITES A FAISCEAUX TOURNANTS MULTIPLES DANS LES FAISCEAUX IONS NEGATIFS UTILISES A LA GENERATION DE FAISCEAUX DE NEUTRES

J.M. Dolique.

Physique des Plasmas, Université Scientifique et Médicale de Grenoble, BP 53 X, 38041 Grenoble cedex, France.

Dans le chauffage additionnel par faisceaux de neutres des plasmas de fusion magnétique, l'énergie visée maintenant dépasse les 150 keV. La dimension et la densité de plus en plus grandes des plasmas dans les grosses machines pour la fusion, tokamaks ou miroirs, appellent en effet des énergies de plus en plus élevées, si l'on veut que le faisceau pénétre suffisamment le plasma à chauffer. A ces énergies le rendement de l'échange de charge, par lequel on passe d'un faisceau d'ions deutérium accélérés à un faisceau de neutres D^0 , est nettement plus faible si l'on neutralise des D^+ que si l'on neutralise des D^- .

C'est pourquoi un important effort est fait actuellement [1] aux Etats-Unis, en URSS, au Japon et en France, à Grenoble, au Commissariat à l'Energie Atomique, pour produire et accélérer des faisceaux intenses d'ions négatifs. Plutôt que l'extraction directe d'une source de tels ions, la méthode qui paraît la plus prometteuse est celle dite du double échange de charge : un faisceau d'ions positifs de deutérium d'énergie relativement faible (quelques keV) est transformé sur une première cellule d'échange de charge en un faisceau de D^- . Après transport sur une distance de glissement qu'on ne peut guère réduire à moins d'un mètre environ, le faisceau est accéléré à 150, 200 keV ou plus et, avant sa pénétration dans la machine de fusion, neutralisé sur une deuxième cellule d'échange de charge, en le faisceau de D^0 souhaité. Les phases de transport en espace de glissement, puis ultérieurement d'accélération, soulèvent de très difficiles problèmes tenant notamment à la nécessité de neutraliser la charge d'espace de faisceaux dont la pénétrance et facteur de courant sont élevés, sans pour autant détruire les fragiles D^- .

Une première voie explorée consiste à provoquer cette neutralisation de charge d'espace par ionisation secondaire sur le gaz résiduel maintenu, à pression moyenne ($\sim 10^{-5}$ torr) dans l'espace de

glissement. Il semble qu'on soit encore loin de maîtriser cette méthode.

Dans une seconde, proposée en 1977 [2], un très bon vide règne dans l'espace de glissement, et la charge d'espace du faisceau de D^- est neutralisée par les ions positifs qu'il entraîne depuis la cellule d'échange de charge. L'addition d'un champ magnétique axial de confinement [3] permet d'être moins exigeant sur la qualité de la neutralité en charge d'espace.

Par contre, cette introduction d'un champ magnétique pourrait donner naissance à des instabilités à faisceaux tournants multiples. C'est ce point qu'on examine ici.

A la sortie de la première cellule d'échange de charge qu'on supposera être constituée de césium, les ions entraînés par le faisceau de D^- sont des Cs^+ avec inévitablement sans doute des électrons. On peut admettre qu'il n'y a plus de D^+ . Quant aux D^0 ils ne jouent aucun rôle dans les effets de plasma étudiés.

Si $\rho = \sum_a n_a q_a$ est la densité de charge globale ($a = e, +$ pour Cs^+ , et $-$ pour D^- ; n_a densité en particules a de masse m_a et de charge q_a) une condition nécessaire et suffisante d'équilibre macroscopique pour un faisceau mixte froid de D^- , Cs^+ , e^- , radialement et axialement homogène, de rayon R_p , est :

$$\Omega_a^2 > (2q_a/\epsilon_0 m_a) \rho \quad (1)$$

où Ω_a est la gyrofréquence pour les particules a . Il suffit pour assurer (1) que $B > (2|\rho| m/\epsilon_0 e)^{1/2}$ si le faisceau est sous-neutralisé ($\rho < 0$) ou que $B > (2\rho m/\epsilon_0 e)^{1/2}$ si le faisceau est sur-neutralisé ($\rho > 0$). Pour un faisceau de D^- de 10 mA/cm² à 3 keV, ceci conduit à $B > 0,94 \sqrt{\alpha} (\alpha > 0)$ ou $B > 7,67 \sqrt{|\alpha|} (\alpha < 0)$ où $\alpha = -\rho/n_e$ et où B est en teslas.

Le champ magnétique étant suffisamment intense pour assurer cet équilibre macroscopique, il reste

à en rechercher la stabilité. En se limitant à des perturbations électrostatiques de faible amplitude, on trouve, par développement en modes normaux du système des équations macroscopiques, fermé par l'équation de POISSON, la relation de dispersion :

$$0 = D_{\ell}(k_z, \omega) \equiv f_{\ell} - (1 - \sum_{a,i} \frac{\omega_{pai}^2}{\omega_{ai}^2}) T_{\ell} R_p \frac{J_{\ell}'(T_{\ell} R_p)}{J_{\ell}(T_{\ell} R_p)} + \ell \sum_{a,i} \frac{\omega_{pai}^2 \omega_{avi}}{\omega_{ai}^2 (\omega - k_z v_{az}^0 - \ell \omega_{ai})} \quad (2)$$

où ℓ est le nombre harmonique azimutal (0, 1, 2, ...), k_z le nombre d'onde axial, ω_{ai} désigne la fréquence angulaire du rotateur rigide droit ($i = D$) ou gauche ($i = L$) : $\omega_{ai} = -(\epsilon_a \Omega_a / 2) [1 \pm [1 - 2\epsilon_a \rho / \epsilon_0 m_a \Omega_a^2]^{1/2}]$, ω_{avi} la fréquence angulaire de vortex associée, $v_{ai}^2 = (\omega - k_z v_{az}^0 - \ell \omega_{ai})^2 - \omega_{avi}^2$, $T_{\ell}^2 = -k_z^2 [1 - \sum_{a,i} \frac{\omega_{pai}^2}{\omega_{ai}^2}]^{-1} [1 - \sum_{a,i} \frac{\omega_{pai}^2}{\omega_{ai}^2}] / (\omega - k_z v_{az}^0 - \ell \omega_{ai})^2$; $\omega_{pai}^2 = n_{ai} e^2 / \epsilon_0 m_a$, où n_{ai} désigne la densité du rotateur rigide i , droit ou gauche ($\omega_{paD}^2 + \omega_{paL}^2 = \omega_{pa}^2$). J_{ℓ} est la fonction de Bessel de première espèce d'ordre ℓ . $f_{\ell} = k_z R_p [K_{\ell}(k_z R_c)] I_{\ell}'(k_z R_p) - K_{\ell}'(k_z R_p) I_{\ell}(k_z R_c)] / [K_{\ell}(k_z R_c) I_{\ell}(k_z R_p) - K_{\ell}(k_z R_p) I_{\ell}(k_z R_c)]$, où R_c est le rayon de l'en-ciente conductrice limitant radialement l'espace de glissement, K_{ℓ} et I_{ℓ} les fonctions de Bessel modifiées d'ordre ℓ . Enfin $\epsilon_a = \text{sgn } q_a$ et v_{az}^0 est la vitesse axiale d'équilibre du fluide a .

Les ions du faisceau étant produits dans la cellule d'échange de charge, on a par raison de symétrie : $\omega_{paD}^2 = \omega_{paL}^2 = \omega_{pa}^2 / 2$.

Pour les ondes longues ($k_z \ll R_p^{-1}$) qui sont les instabilités les plus dangereuses, on déduit de (2) une relation entre ℓ et la fréquence réduite $\omega / \Omega_- = x$, qui est

$$0 = D_{\ell}(x) \equiv 1 - \sum_a 4 \lambda_a \gamma_a [1 - (\frac{R_p}{R_c})^2 \ell] .$$

$$\frac{(2x + \ell \lambda_a)^2 + \lambda_a (\lambda_a - 4\gamma) \ell (\ell - 2)}{[(2x + \ell \lambda_a)^2 - \ell^2 \lambda_a (\lambda_a - 4\gamma)] [(2x + \ell \lambda_a)^2 - (\ell - 2)^2 \lambda_a (\lambda_a - 4\gamma)]} \quad (3)$$

où les $\lambda_a = \epsilon_0 m_- / m_a$ sont donnés, $\gamma_a = \rho_a / 4en_{\text{-crit}}$

où $\rho_a = n_a q_a$ et $n_{\text{-crit}} = \epsilon_0 B_0^2 / 2m_-$, $\gamma = \sum_a \gamma_a = \rho / 4en_{\text{-crit}}$.

Le domaine de stabilité est le domaine de l'espace des γ_a pour lequel les zéros de D_{ℓ} sont réels.

Dans le cas limite d'un faisceau de D^- pur, le fondamental $\ell = 1$ et le premier harmonique $\ell = 2$ sont stables. Pour $\ell > 2$, la stabilité est assurée si

$$n_- / n_{\text{-crit}} < 1 / [1 + \frac{1 - (R_p / R_c)^2 \ell}{\ell (\ell - 2)}]$$

Il suffit pour cela que

$$n_- / n_{\text{-crit}} < 1 / [1 + \frac{1 - (R_p / R_c)^6}{3}] \quad (4)$$

Comparée à la condition d'équilibre macroscopique (1), qui s'écrit encore $n_- / n_{\text{-crit}} < 1$, on voit que la stabilité exige, à champ magnétique de confinement donné, une diminution relative de la densité maximale de 25%.

Dans le cas général d'un faisceau de D^- partiellement neutralisé par des Ca^+ et pollué d'électrons, le domaine de stabilité $S(\gamma_-, \gamma_+, \gamma_e)$ est discuté en fonction de γ_- et de γ_+ / γ_e pour $\gamma = \gamma_- + \gamma_+ + \gamma_e = -1/8$ (la condition d'équilibre macroscopique est $\gamma > -1/4$).

REFERENCES

- [1] Proc. of Symp. on the Production and Neutralization of Negative Hydrogene Ions and Beams. Brookhaven 1977
- [2] J.M. DOLIQUE, ibidem, p. 215
- [3] J.M. DOLIQUE, Phys. Fluids, **22**, 194 (1979)
- [4] R. GELLER, C. JACQUOT et al., Euratom-CEA, Int. Rep. 1978

NONLINEAR WAVE INTERACTION AND CRITICAL FLUCTUATIONS IN PLASMAS

A.G. Sitenko.

Institute for Theoretical Physics, Academy of Sciences of the Ukrainian SSR, Kiev, U.S.S.R.

The spectral distribution of plasma fluctuations has a broad maximum in the low frequency domain, which is due to the random motion of the individual particles, and a set of sharp maxima at plasma eigenfrequencies. These sharp maxima are caused by the collective fluctuations, i.e. the plasma random eigen oscillations. The equilibrium collective fluctuation level is governed by the temperature; it grows essentially in nonequilibrium plasmas, especially if the plasma state approaches the kinetic instability. This growth is infinite in linear approximation, which indicates that the linear approximation is inadequate under such conditions. So one must take into account the nonlinear effects [1], which lead to the saturation of the critical fluctuations.

When investigating the nonequilibrium fluctuations it is convenient to utilize the nonlinear field equation, which follows directly from the Maxwell's equations and the microscopic density equation that describes the stochastic particle motion in plasmas. The nonlinear wave interaction is manifested most clearly when the frequencies and the wave vectors satisfy the resonance conditions. The simplest example of the resonance wave interaction is the three-wave one

that causes the decay or the explosive instabilities. In case the three-wave resonance conditions are not satisfied, the resonance interactions of four or more waves become important. One of the most significant effects that arise due to the four-wave resonance interaction is the frequency shifts of the interacting waves. In particular, the resonance interaction in plasmas causes the nonlinear shifts of the eigenfrequencies.

The nonlinear eigenfrequency shift $\Delta\omega_k$ of a longitudinal wave with the eigenfrequency ω_k and the wave vector k is a function of the wave intensity I_k and the plasma nonlinear susceptibilities:

$$\Delta\omega_k = \beta_k I_k, \quad (1)$$

$$\beta_k = \frac{1}{6\pi^2} \frac{k^3}{\partial\epsilon(\omega_k, k)/\partial\omega_k} \left\{ \frac{[\chi^{(2)}(\omega_k, k; \omega_k, k)]^2}{\epsilon(2\omega_k, 2k)} + \right. \\ \left. + 2 \frac{[\chi^{(2)}(\omega_k, k; 0, 0)]^2}{\epsilon(0, 0)} - \frac{3}{2} \chi^{(3)}(-\omega_k, -k; \omega_k, k; \omega_k, k) \right\} \quad (2)$$

The proportionality coefficient β_k is equal to zero in a cold plasma, i.e. the nonlinear wave interaction does not change the eigenfrequencies of cold plasmas.

As an example consider the Langmuir wave eigenfrequency shift in isotropic plasmas [2,3]. The hydrodynamic treatment of the electron motion in neglect

of that of ions leads to

$$\beta_k = \frac{5}{12\pi^2} \frac{e^2}{m^2} \frac{k^2 s^2}{\Omega^5} \quad (3)$$

However the hydrodynamic description is valid provided that the particle thermal velocity is small not only compared to the wave phase velocity, but also in comparison with the phase velocities of the pulsations. As the Langmuir waves do not satisfy the second condition, then the hydrodynamic approximation should not be applied when calculating the nonlinear shift. The kinetic approach results in

$$\beta_k = \frac{1}{6\pi^2} \frac{e^2}{m^2} \frac{k^2 s^2}{\Omega^5} \quad (4)$$

Note, that the kinetic β_k turns out to be zero at $T = 0$ similarly to the hydrodynamic one. However the absolute values of the nonlinear eigenfrequency shifts are different for the two approaches. The ion motion may be neglected if $\alpha^2 k^2 > \frac{m}{M}$, otherwise it must be taken into account.

The average intensity I_k of the equilibrium plasma eigenoscillations is governed by the temperature T . I_k of nonequilibrium plasma may differ essentially from the equilibrium value, thus making it very important to take into account the nonlinear eigenfrequency shifts. The spectral distribution of the electric field fluctuations in nonequilibrium plasmas is

$$\langle E^2 \rangle_{k\omega} = \pi I_k \{ \delta(\omega - \tilde{\omega}_k) + \delta(\omega + \tilde{\omega}_k) \}, \quad (5)$$

where $\tilde{\omega}_k$ is the eigenfrequency taking into account the nonlinear wave interaction, and

$$I_k = \frac{16\pi^2}{k^2 \partial \epsilon(\omega_k, k) / \partial \omega_k} \frac{\langle \beta^2 \rangle_k^0 \tilde{\omega}_k}{|J_m \epsilon(\tilde{\omega}_k, k)|} \quad (6)$$

Since the eigenfrequency $\tilde{\omega}_k$ is a function of I_k , we can use (6) as an equation for I_k , which is the fluctuation intensity in the instability region. The existence of a solution for this equation implies that the wave interaction drives the unstable plasma to some stationary state. The solution itself determines the stationary level of the critical fluctuations.

Two examples have been considered that illustrate the nonlinear saturation of the critical fluctuation level in nonequilibrium plasmas: fluctuations in a plasma with a low-density compensated particle beam [2], and those in a magnetoactive plasma with an anisotropic particle distribution [4].

1. A.G.Sitenko. Sov.J.Plasma Phys., 1, 24 (1975).
2. A.G.Sitenko. Physica Scripta, 7, 193 (1973).
3. A.G.Sitenko, V.I.Zasenkov. Ukrain.Fiz. Zh., 23, 1277(1978).
4. A.G.Sitenko, V.I.Zasenkov. Ukrain.Fiz. Zh., 23, 715 (1978).

STUDY OF LOW FREQUENCY OSCILLATIONS IN THE OPEN TRAP WITH MINIMUM B MAGNETIC FIELD

V.A. Ziltsov, P.M. Kozarev, I.N. Makashin, D.A. Panov, A.A. Skovoroda and A.G. Scherbakov.

Kurchatov Institute of Atomic Energy, Moscow, U.S.S.R.

In the minimum B open traps at the density $\omega_{ci} \leq \omega_{ci}$, when a fluid instability is damped, it has been experimentally observed the presence of low frequency drift oscillations/1,2,3/. The origins of the oscillations and there role in transport phenomena were not investigated in these references. In ref./4/ the existence of mechanism of ions transport across magnetic field due to the action of drift (LF) and ion cyclotron (HF-) oscillations was experimentally shown. In this paper the properties of LF oscillations and causes of there rise in minimum B field were investigated. The experiments were carried out with the open trap "Ogra-3B" with minimum magnet set. Magnetic field with 17 kG strength in the center was fabricated from baseball-type coil. The distance between mirrors was 70 cm. Longitudinal and radial mirror ratio were 2,06 and 2 respectively. The maximum plasma parameters in the middle of the trap were: density $2 \cdot 10^{10} \text{ cm}^{-3}$, electron temperature 0,5 keV, plasma life-time 1 sec (it was determined by charge exchange process), plasma radius 7 cm, plasma length (along Z axis) 70 cm. LF and HF oscillations were measured by the set of electrostatic antennae, disposed at the plasma midplane and along magnetic force lines. LF oscillations of "cold ion" and electron flows along force lines were measured too. Fluctuations of the electron density in the center of the trap were measured by absorption of super high frequency (SHF) electromagnetic wave at the electron cyclotron frequency /4/. The measurements of fluctuations of density and flows gave us an opportunity to obtain some of the properties of oscillations in plasma interior. Let us consider the conditions of LF waves exitation. The exitation can be "soft" at low density ($n < 1 \cdot 10^9 \text{ cm}^{-3}$), when cyclotron fluctuations are absent (Fig.1). The cyclotron oscillations, arising at the density $n > 1 \cdot 10^9 \text{ cm}^{-3}$ (threshold depends on the magnetic field value), have a burst structure. They lead to the hard exitation of low frequency oscillations (Fig.2) with E field amplitude about some tens V/cm. The bursts of HF oscillations are accompanied by the jumps of plasma potential

with an amplitude about some hundreds V. LF oscillations can be also exited after switching off the beam, when plasma density is falling down and cyclotron fluctuations are damped with help of electron heating (Fig.3). The LF oscillations spectrum, measured by the electrostatic antenna settled at the midplane (1), by an absorption of SHF wave (2) and by electron flow are similar (Fig.4). Some difference of the amplitudes of the separate constituents of spectrum is explained by the spatial localization of oscillations with different radial structure. LF oscillations are rather regular between HF bursts. During the burst sharp rebuilding of LF oscillations takes place (the time less than LF oscillations period). Time interval between the HF bursts depends on the plasma density and can be rather small (some msec.). It was possible in our experiments to receive LF spectrum during the time less than 1 msec. At the same time the oscillations of the cold ions flow (2) and the oscillations, measured by the electrostatic antenna, placed at $z=20 \text{ cm}$, have in principal lower frequency (Fig.5). For the simple model of plasma column with a parabolic radial distribution of density the dispersion relation for LF oscillations can be written as in Ref.6

$$\chi^2 = \frac{2\omega_{ci}^2 m}{\omega_{ci}^2 a^2} \left(\frac{1}{\omega} - \frac{1}{(\omega + m\omega^*)} \right)$$

where m - azimuthal mode number, a - plasma radius, ω^* - frequency of ion drift in inhomogeneous magnetic field, χ - characteristic radial wave number, determined from the boundary conditions. This equation gives two different branches of stable oscillations: electron and ion. This branches for $m=1$ are shown (the solid lines - experiment) in Fig.6. The value of ω^* in equation was taken to normalize the lowest radial mode electron branch theoretical dependence on the experimental points. Drift frequency ω^* was estimated from ion branch measurements. Experimentally the frequency values were received by help of electrostatic antenna that were disposed at the midplane. The plasma rotation in the ambipolar electric field introduces a contribution to these frequencies. The value of positive potential grows proportionally

to the density up to $1 \cdot 10^9 \text{ cm}^{-3}$. At this density the potential is about 1 kV. The frequency of plasma rotation

$$\omega \approx 10^8 \varphi / \text{s}^2 \text{B}$$

is about $1 - 1,5 \cdot 10^5 \text{ sec}^{-1}$. It rises somewhat the frequency of electron brunch and decreases that for ion brunch. Fig. 7 shows a fast scan of the electron brunch oscillations (1) at the moment when the burst of HF oscillations takes place and plasma potential changes sharply (2).

Fig. 6 shows that the electron and ion brunches of LF oscillations exist in the plasma. The dispersion of experimental points is connected with exitment of the different radial modes. Note that these brunches are neutrally stable. Electron and ion oscillations have a positive energy. When the density $n < 1 \cdot 10^9 \text{ cm}^{-3}$ the fluctuations may be excited by noises of injected beam. The measured spectrum of beam fluctuations is practically white up to the frequency about 200 kHz. An amplitude of the polarization electric field by ionization is large too. LF oscillations at $n < 1 \cdot 10^9 \text{ cm}^{-3}$ lead to an appearance of anomalous potential, discussed in [5].

If $n > 1 \cdot 10^9 \text{ cm}^{-3}$ HF oscillations arise and appearance of LF oscillations is correlated with the beginning of HF oscillations. Let us note that LF oscillations exists much more longer than HF burst (Fig. 2).

Thus LF oscillations in the frequency range up to 500 kHz take place in the open trap with minimum B. Ion and electron brunches of oscillations are observed. It is shown that they may be excited by injected beam noises and cyclotron oscillations

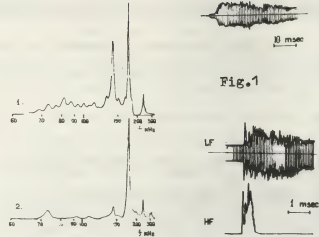


Fig. 1

Fig. 4

Fig. 2

Fig. 3

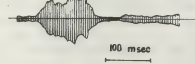


Fig. 5

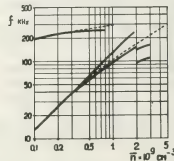
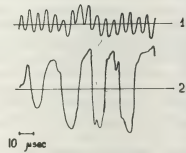


Fig. 6



Fig. 7

- /1/Artemenkov L.I. et all. *Plasm. Phys. and Contr. Nucl. Fus. Res. IAEA, Vienna, p.45, 1966.*
- /2/Damm C.C. et all. *Pl. Phys. and Con. Nucl. Fus. Res. IAEA, Vienna, p.253, 1969*
- /3/Cordey J.G. et all. *Pl. Phys. and Con. Nucl. Fus. Res. IAEA, Vienna, p.267, 1969*
- /4/Ziltsov V.A. et. al. *VII Int. Conf. Pl. Phys. and Con. Nucl. Fus. Res. IAEA-CN-37. S-2, Innsbruck, 1978*
- /5/Putvinskii S.V. Timofeev A.V. *Zh. Exp. Teor. Fiz. 69, 221 (1975)*
- /6/Kadomcev B.B. *Zh. Exp. Teor. Fiz. 40, 328 (1961)*

ECR AS A DIAGNOSTIC FOR MIRROR TRAP PLASMA

A.A. Skovoroda and V.A. Ziltsov.

Kurchatov Institute of Atomic Energy, Moscow, U.S.S.R.

When the electromagnetic (E.M.) wave propagates along the Z axis of a mirror trap and the condition $\omega_{ce} \max > \omega_{ce} \min$ is satisfied, where ω - the oscillation frequency, $\omega_{ce} \max, \min$ - maximal and minimal electron cyclotron frequencies, the electron cyclotron resonance (ECR) takes place in fixed points Z_r , where $\omega = \omega_{ce}(Z_r)$.

It is known that the transmission coefficient of right-handed polarized E.M. wave (the electric vector of the field rotates in the same direction as the electron in the magnetic field) depends on the electron density $n(Z)$ and the magnetic field gradient at the point Z_r .

It is clear that the measurement of the transmission wave power can be used for the determination of the Z local electron density. The locality of the measurement in the transverse direction (normal to the magnetic field direction) is done by employing of directional antennae.

Measurements of electron density by the method above were carried out on the mirror trap with minimum B "Ogra-3B". The plasma with density less than $2 \cdot 10^{10} \text{ cm}^{-3}$ was produced by the injection of 20 keV neutral hydrogen beam with the current 0.5 A during 1 sec. The steady magnetic field in the trap centre was less than 17 kG, the longitudinal mirror ratio was 2. The charge exchange life-time was 0.3 - 1 sec.

Two rectangular horn antennae for 8 mm E.M. waves were placed along Z axis (100 cm between horns). In this measurement the transverse locality was less than 3 cm. The longitudinal locality is equal to the dimension of the resonance zone $L(\rho_e/Z_r)^{1/2} < 1$, where $\omega_{ce}(Z) = \omega_{ce} \min (1 + Z^2/L^2)$, ρ_e - electron larmor radius. We used a plane-polarized wave, which is the superposition of oscillations with circular polarization. The left-handed polarized E.M. wave have no absorption at ECR. It is necessary take into account this fact in the experiment. At the wave propagation through a magnetic trap there are two resonance points. The presence of several resonance points can lead to the "translucence" $1/3$. We note that the experiments have revealed no "translucence" in our conditions, when $L \gg \lambda$ (λ - the distance between the resonance points, λ - the wave length) and the small fluctuations makes the wave phase stochastical.

Therefore the electron density was calculated from relation

$$t = \exp(-2\beta), \quad \beta = \frac{\pi \omega_{pe}^2 L_z}{\omega_{ce}^2} \quad ,$$

where t - the transmission power coefficient of right circularly polarized wave, ω_{pe} - the electron plasma frequency, c - light velocity, $L_z = (dB/dZ)^{-1} B_{Z=Z_r}$.

Factor two in the exponent is the result of the presence of two resonance points with the same β . In our experiment we have measured power $P = W - W_{tr}$, where W - the wave power, W_{tr} - the transmission wave power.

In the experimental conditions $\beta < 1$ and therefore $P \sim n$. The continuous measurement of P is the continuous measurement of $n(T)$, here T - time.

Fig. 1 shows the example of electron density measurement by this method in the trap centre. I_b and I_c are the injection current and the flux of cold ions along Z axis consequently. I_c is proportional to plasma and background gas densities. One can conclude from fig. 1 that the sharp change of the flux I_c after the injection switching is due to the improvement of vacuum conditions. Thus the measurement of P allows to determine not only the density, time and character of plasma build-up, but the change of the pressure of the background gas during the injection. By changing of the spatial attitude of resonance point Z_r we obtain the distribution $n(z)$, which can be used for the determination of the ion velocity distribution function. The distribution $n(z)$ was measured in the experiments continuously by means of three generators with the fixed frequencies, i.e. of the three points Z_r . The oscillation amplitude of these generators was modulated at three various frequencies (several kHz). We used one waveguide for the probing microwave signals. These measurements have shown that the distribution $n(z)$ does not depend noticeably on presence of the ion cyclotron instability, i.e. ions diffuse in the transverse direction. In addition the measurement of $n(z)$ makes it possible to draw a conclusion about the electron diffusion in the mirror trap at a instability. Fig. 2 shows the change of electron density n_e on the plasma periphery. We note that the density mag-

nitude on fig 1 is 10 times as large as on fig.2. Fig.2 shows also the amplitude of ion cyclotron oscillations A_{ic} . It is seen that the electrons appear on the periphery when the hf oscillations are absent. At the same time the plasma potential decreases up to the classical level. The density oscillations lead to the modulation of P . Fig.3 shows the spectrum of lowfrequency oscillations of electron density n in the trap center, which was measured from P . The time resolution of spectrum measurement was 10 msec. It is seen that in the beginning of the injection the oscillation frequency increases with increase of the electron density. The experiments have shown that such fluctuations correspond to the electron branch of the lowfrequency oscillations (see report of the same group). The simultaneous measurement of P and \bar{P} can be used for the determination of the density modulation $P/P \sim N/N$. The simultaneous measurement in the three points Z_r can be used for the determination of the phase velocity along the Z axis.

When the frequency of E.M. wave is less than the minimum electron cyclotron frequency the dependence $P(\Delta\omega)$ (the cyclotron absorption line) can be measured/4/. Here $\Delta\omega = \omega_{ce} \min - \omega$. In the experimental

conditions the dopler broadening of the line took place. This can be used for the determination of electron temperature T_e and the electron distribution function/2/. Fig.4 shows the continuous measurement of T_e by means of the three generators in our experiments.

Thus the measurement of the transmission of E.M. wave at ECR allows to determine the many parameters of the mirror trap plasma. The method sensitivity is enough for the measurement of the small electron density (10^7 cm^{-3} in our experiments).

where the using of the microwave interferometers is more complicated. Moreover, these measurements are local and more simple.

ECR allows to determinethe local properties of lowfrequency oscillations in plasma. The electron temperature is measured in the broad range (more than 10 eV in our experiments). The electron distribution function is restored up to the energy 4 - 5 T_e .

The method, described above, can be used for the diagnostic of plasma under the assumption of geometrical optics and when

$\omega_{ce}^2 \gg \omega_{pe}^2$. We note that the absorption $\sigma/\beta \gg 1$ is large and the measurements are difficult in such condition. But always the absorption can be decreased by changing of the spatial attitude of the resonance point Z_r or the magnitude of $\Delta\omega$.

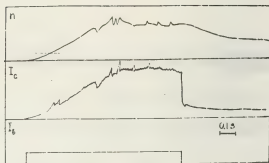


Fig.1

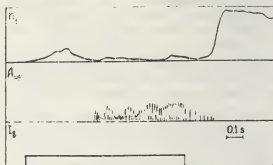


Fig.2

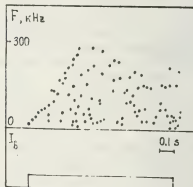


Fig.3

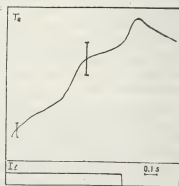


Fig.4

- /1/ Budden K.G. "Radio Waves in the Ionosphere", Cambr. Univ. Press. 1961.
- /2/ Ziltsov V.A. at all. VII Int. Conf. on Pl. Phys. and Contr. Nucl. Fus. Res., Innsbruck, 1978. IAEA-CN-37.S-2.
- /3/ Skovoroda A.A., Shvilkin B.N. Zh. Exp. Theor. Fiz. 75, 898 (1978)
- /4/ Skovoroda A.A., Shvilkin B.N. Zh. Exp. Theor. Fiz. 73, 526 (1977-)

ON SOME PROPERTIES OF ANISOTROPIC PLASMAS

Lu Guan-Kang, Chen Zhi-Fan.

Fudan University, Shanghai.

I. ELECTROSTATIC SHIELDING

The problem of electrostatic shielding potential in a plasma with anisotropic kinetic temperatures is discussed in the first part of this paper. We suppose that the applied magnetic field is along the Z axis of Cartesian coordinates. The electron distribution function may be taken as

$$f(\vec{v}) = \pi^{-3/2} |\det \vec{A}|^{1/2} \exp(-\vec{v} \cdot \vec{A} \cdot \vec{v}) \quad (1)$$

where

$$\vec{A} = \frac{m}{2} \begin{pmatrix} (K_{\perp})^{-1} & 0 & 0 \\ 0 & (K_{\perp})^{-1} & 0 \\ 0 & 0 & (K_{\parallel})^{-1} \end{pmatrix} \quad (2)$$

T_{\parallel} is the temperature along the main axis (Z axis) of tensor \vec{A} and T_{\perp} is the temperature perpendicular to it, k is the Boltzmann constant, m and \vec{v} are the electron mass and velocity respectively.

By using the integral transformation

$$F(u) = \int d\vec{v} f(\vec{v}) \delta(u - \vec{v} \cdot \vec{v} / k) \quad (3)$$

we obtain the one dimensional distribution function

$$F(u) = \left(\frac{m}{2\pi k T_{\parallel}} \right) \exp(-mu^2/2kT_{\parallel}) \quad (4)$$

where

$$T' = (k_{\perp}^2)^{-1} T_{\perp} + k_{\parallel}^2 T_{\parallel} \quad (5)$$

is the effective temperature along the \vec{k} direction, k_{\perp} and k_{\parallel} are the components of \vec{k} along and perpendicular to the Z axis respectively.

On the problem of positive charged test particle (coordinate $\vec{R}=0$ and velocity $\vec{v}=0$) shielded by electron clouds, the Coulomb forces between particles are the chief interactions. The correction of shielding effect caused by magnetic force is neglected, in other words, it is assumed that the effect of applied magnetic field is only to maintain the anisotropic of electron velocity distribution.

In this case, we obtain that the electric potential function is given by

$$V_Q(\vec{r}) = \frac{Q}{2\pi^2} \int \frac{k_{\perp}^2 K_{\perp} + k_{\parallel}^2 K_{\parallel}}{k^4 (\omega_p^2 m + k_{\perp}^2 K_{\perp} + k_{\parallel}^2 K_{\parallel})} \exp(i\vec{k} \cdot \vec{r}) d\vec{k} \quad (6)$$

where Q is the electric charge of test particle, and ω_p is the electron plasma frequency.

When $T_{\perp} \neq T_{\parallel}$, let

$$\xi = \frac{T_{\perp}}{T_{\parallel}} - 1 \quad (7)$$

As $|\xi| < 1$, integrating (7), we get

$$V_Q(\vec{r}) = \frac{Q}{R} \exp(-K_{\perp} R) + \frac{1}{2} \xi \left\{ \left[Q \cos^2 \alpha + P_2(\cos \alpha) \left(\frac{1}{R} + \frac{2}{R^2 K_{\perp}} + \frac{2}{R^3 K_{\perp}^2} \right) \right] \right. \\ \left. \exp(-K_{\perp} R) - \frac{2 P_2(\cos \alpha) Q}{R^2 K_{\perp}^2} \right\} + O(\xi^2) \quad (8)$$

where $K_{\perp} = \left(\frac{4\pi n e^2}{K_{\perp} T_{\perp}} \right)^{1/2}$, n and a are the electron density and charge respectively, $P_2(\cos \alpha)$ is the Legendre Polynomial of second order.

It can be seen that, besides the exponential decay terms, there is also a slow decay term proportional to R^{-3} in (8).

When $\alpha=0$, (8) may be reduced to

$$V_Q(R) = \frac{Q}{R} - Q K_{\perp} \int_0^{\sqrt{1/\xi}} \frac{\exp(-K_{\perp} R \varphi)}{1 - \xi \varphi^2} d\varphi \quad (9)$$

Therefore,

$$\frac{Q}{R} \exp(-K_{\perp} R) - \xi \frac{Q}{R} [1 - \exp(-K_{\perp} R)] \leq V_Q(R) \leq \frac{Q}{R} \exp(-K_{\perp} R) \quad (10)$$

where $K_{\perp} = \left(\frac{4\pi n e^2}{K_{\perp} T_{\perp}} \right)^{1/2}$, ... valids for $\infty > \xi > 0$, and ... valids for $0 > \xi > -1$.

Finally, according to the Poisson equation, the shielding electron density ρ_e given by the electron distribution function (1) is

$$\rho_e = -\frac{1}{4\pi} \nabla^2 [V_Q(\vec{r}) - \frac{Q}{R}] \\ = -\frac{1}{(2\pi)^3} \int \frac{\omega_p^2 m \exp(i\vec{k} \cdot \vec{r})}{\omega_p^2 m + k_{\perp}^2 K_{\perp} + k_{\parallel}^2 K_{\parallel}} d\vec{k} \quad (11)$$

The total shielding charge quantity is then

$$\int \rho_e d\vec{r} = -Q \int \frac{\omega_p^2 m \delta(\vec{r})}{\omega_p^2 m + k_{\perp}^2 K_{\perp} + k_{\parallel}^2 K_{\parallel}} d\vec{r} = -Q \quad (12)$$

It proves that the shielding effect is complete, therefore (1) is a rational distribution.

II. STRICT CRITERIONS OF KINETIC INSTABILITIES CAUSED BY INJECTED NEUTRAL PARTICAL BEAMS

A number of strict and general instability criterions may be obtained by analysing the geometric properties of the dispersion relations of special plasma waves.

In the second part of this paper, Nyquist diagrams of cyclotron instabilities caused by plasma streams are analysed. At first, the calculation method on instability criterions of n_b (the plasma stream density), n_s (the static plasma density), B (the applied magnetic field strength), k (the wave number), v (the stream velocity) and T (the temperature) are obtained. The numerical results of Hydrogen plasma are obtained.

Secondly, the cyclotron and electrostatic instabilities caused by two neutral plasma streams are also analysed. The numerical results of Hydrogen plasma are also given.

Finally, a necessary condition of electromagnetic instabilities caused by plasma streams is derived.

REFERENCES

- (1). G. Joyce and D. Montgomery, Phys. Fluids 10 (1967) 2017.
- (2). A.A. Vedenov and D.D. Ryutov, Rev. of Plasma Physics (Ed. Acad. M.A. Leontovich) Vol.6. (1975)

AN EQUATION FOR WAVE PROPAGATION IN A HOT NONUNIFORM MAGNETIZED PLASMA

W.N-C Sy and M. Cotsaftis.

Association Euratom-CEA sur la fusion, Département de Physique du Plasma et de la fusion contrôlée, Centre d'Études Nucléaires, Boîte Postale n°6, 92260 Fontenay-aux-Roses, France.

Plasma nonuniformities and boundary effects are usually significant for wave propagation in the lower frequency ranges in laboratory plasmas, whilst explicit incorporation of wave damping in the wave equations is necessary for a consistent calculation of resonant Q-factors of cavity modes in bounded systems. On the other hand, the existence of spatial resonances in nonuniform plasmas, such as the Alfvén wave resonance or the ion-ion hybrid resonance, exhibited mathematically by "singularities" in the basic wave equations, requires small effects such as the finite Larmor radius effect or nonlinear effects to be considered, in order to determine the fate of waves propagating in or near these "singular" regions. These factors are taken into account in the derivation of an equation for wave propagation in a hot, nonuniform magnetized plasma, with multiple ion species.

The linearized Vlasov equations, together with Maxwell's equations, are solved by a perturbation expansion in the smallness of the Larmor radius compared to characteristic scale-lengths of the plasma. Fourier transforms are taken along the uni-directional background magnetic field to retain the important kinetic effects of Landau-cyclotron damping, while differential operators are used in directions perpendicular to the magnetic field, because plasma nonuniformities and boundary effects are important in these directions. Since only waves which have counterparts in a uniform magnetized plasma are considered, the gradient terms which are associated generally with drift waves have been neglected. The resulting wave equation may be written in the form,

$$(1) \quad \nabla \times (\nabla \times \vec{E}) = -(\vec{T} + \vec{U} + \vec{W} + \vec{N}) \cdot \vec{E}$$

where \vec{T} is an algebraic tensor with the familiar structure

$$(2) \quad \vec{T} = \begin{pmatrix} A & iB & . \\ -iB & A & . \\ . & . & C \end{pmatrix}$$

The elements A, B and C contain the full plasma dispersion functions and hence explicitly incorporate Landau-cyclotron damping. They also contain summations over all species of plasma particles. The tensors \vec{U} , \vec{W} , and \vec{N} are differential operators arising respectively from the first order, second order finite Larmor radius corrections and nonlinear effects. The tensor differential operator \vec{N} is proportional to the components of the perturbed electric field. Detailed expressions of these tensors will be presented elsewhere, since they are too lengthy for this short communication. The relative magnitudes of the four

terms on RHS of (1) are in the proportions,

$$(3) \quad 1 : \epsilon : \epsilon^2 : \delta \left(1 + \frac{\omega}{c\Omega}\right),$$

where $\epsilon = \frac{\rho}{a} = \frac{v_T}{a\Omega}$ is the parameter of small Larmor radius expansion and $\delta = \frac{|\vec{B}|}{B_0}$ is ratio of perturbed to unperturbed magnetic field.

As a simple application of (1), we consider wave propagation in the ion cyclotron range of frequencies in a straight, hot, nonuniform plasma cylinder, neglecting finite Larmor radius effects and nonlinear effects. A number of authors [1] - [4] have studied this problem in connection with RF heating of laboratory plasmas. Here, the problem is considered more generally, including explicitly in the wave equation (a) multiple ion species (b) arbitrary plasma nonuniformities and (c) collisionless Landau-cyclotron damping.

On Fourier analysis in the axial and azimuthal directions in cylindrical coordinates, the reduced system of equations can be solved conveniently in the axial component of the perturbed magnetic-field.

$$(4) \quad B_z = \frac{ic}{\omega} \left\{ \frac{1}{r} \frac{d}{dr} (rE_\theta) - \frac{imEr}{r} \right\},$$

where c.g.s. - gaussian units have been used. The essential equation governing the phenomenon can be shown to be

$$(5) \quad \frac{1}{r} \frac{d}{dr} (\mathcal{D} r \frac{dB_z}{dr}) + \left(\frac{m}{r} \frac{d\mathcal{B}}{dr} - \frac{m^2 \mathcal{B}}{r^2} - 1 \right) B_z = 0,$$

where

$$(6) (7) \quad \mathcal{D} = \frac{k_\parallel^2 + A^+}{(k_\parallel^2 + A^+)^2 - B^+}, \quad \mathcal{B} = \frac{B^+}{(k_\parallel^2 + A^+)^2 - B^+}$$

The functions A^+ and B^+ are A and B appearing in (2) with the addition of harmonic cyclotron damping terms. Equation (5) has a similar structure to that found [5] for axisymmetric magnetoacoustic oscillations in a current-carrying nonuniform plasma column and it can easily be solved numerically for arbitrary temperature and density profiles.

- [1] Perkins F.W., Chance M. and Kindel J.M. (1973)
3rd Int. Symposium on Toroidal Confinement,
Garching, B8
- [2] Messiaen A.M. and Vandenplas P.E. (1974) Phys.
Lett. 49A, 475.
- [3] Adam J. and Jacquinet J. (1977) Report
EUR.CEA.FC. 886
- [4] Paoloni F.J. (1978) Nucl. Fusion 18, 359.
- [5] Sy W.N-C. (1978) Plasma Phys. 20, 33.

PHASE SPACE GRANULATION AS A RESULT OF MODE-MODE COUPLING EFFECTS

J.C. Adam, G. Laval and D. Pesme.

Centre de Physique Théorique de l'Ecole Polytechnique, Plateau de Palaiseau - 91128 Palaiseau Cedex, France.

We consider a 1.D turbulence generated by a bump-in-tail instability. Extensive numerical simulations show a time behaviour of the electric field which is inconsistent with the quasilinear theory. We compute theoretically the effect of mode-mode coupling terms, neglected in the usual quasilinear theory.

Consider a Fourier component of the electric field, with wave number k , frequency ω_k and growth rate γ_k . The resonance broadening width is $(k^2 D)^{1/3}$, where D is the quasilinear diffusion coefficient. The ratio $R \equiv (k^2 D)^{1/3} / \gamma_k$ plays the role of a Reynolds number and two regimes of turbulence have to be distinguished. If $R \ll 1$ (1), the usual quasilinear results are recovered. On the other hand, when the turbulence level is high enough for $R \gg 1$, we establish that the non-linear scattering of waves by the resonant particles is no longer negligible. Defining the resonant velocity $v(k)$ by the relation $\omega_k = k v(k)$, we show specifically the following result : the coupling of all the modes k_i which fulfill the conditions

$$k = \sum k_i \quad (3)$$

$$|v_{k_i} - k_i v(k)| \ll (k^2 D)^{1/3} \quad (4)$$

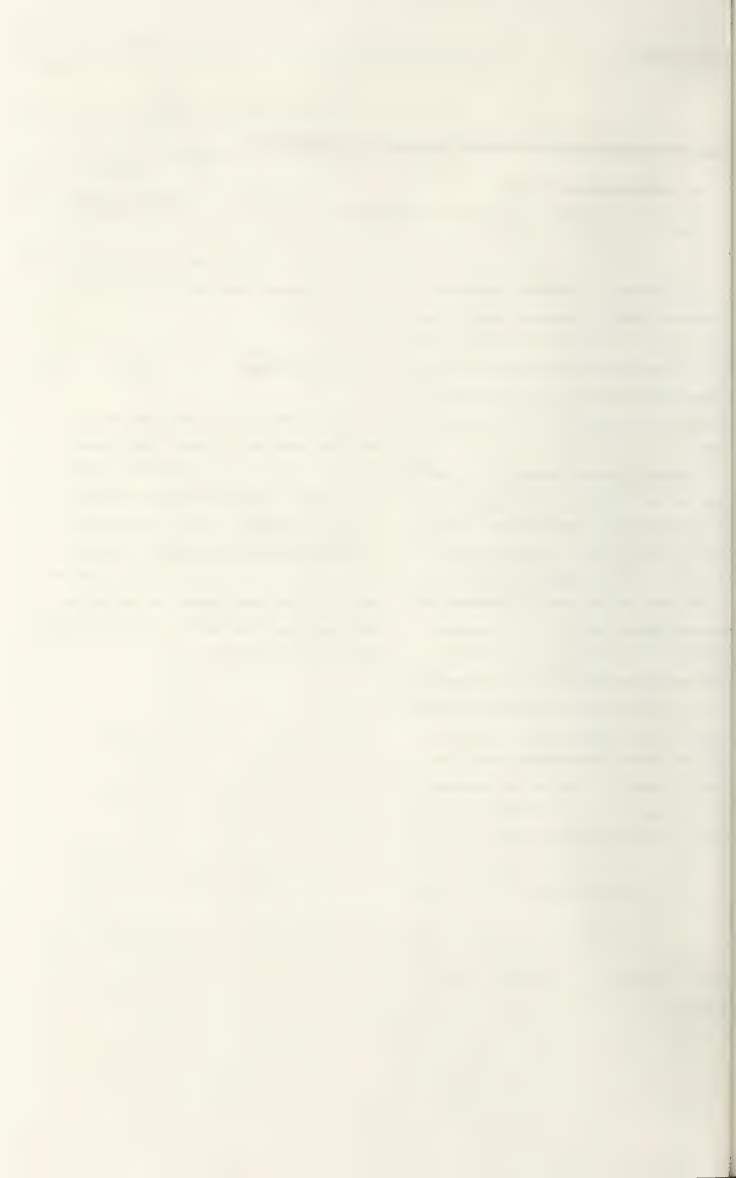
$$|v_k - \gamma_{k_i}| \ll \gamma_k \quad (5)$$

gives a contribution of the same order as the linear term.

In summary, conditions (2), (3), (4), (5) can be written :

$$\left(\frac{\partial^2 v}{\partial k^2}\right) \left[\frac{(k^2 D)^{1/3}}{v(k)}\right]^2 \ll \gamma_k \ll (k^2 D)^{1/3} \quad (6)$$

In the regime defined by (6), the usual weak - turbulence theory exhibit secularities. We show that a first summation of divergent terms leads to the so-called renormalized theories ; these last ones yield series which are not yet convergent and a second summation gives the equation describing phase space granulation as given by T.H. Dupree. We solve exactly the Dupree equation and we find that the clumps induce a supplementary stimulated emission which modifies the growth rate γ_k .



XI

- Plasma à fortes corrélations
Non-ideal plasmas
- Théorie
Theory
- Expériences
Experiments



SUPERRADIATION FROM NON-IDEAL PLASMAS IN ELECTRIC FIELD

N.P. Kozlov, G.E. Norman* and Yu. S. Protasov.

*Moscow Bauman Higher Technical School Moscow, 107005, U.S.S.R.
Institute of High Temperatures, Moscow 127412, U.S.S.R.

The effect of electric field on non-ideal plasma electrical conductivity has been experimentally investigated in [1]. A correlation between radiation intensity from non-ideal plasma and external electric field E in the same local volume has been established in this study. It is shown that the intensity becomes abnormally high with increase in E and may exceed the black body intensity at local plasma temperature.

The installation used for the experimental study of plasma-focus radiation properties was described in an earlier paper [2]. A magnetoplasma compressor operated with moderate energy inputs (discharge currents $\lesssim 500$ kA). These regimes provided stable parameters in a MHD-compression region. Plasma temperature T and electron number density n_e did not exceed 5 eV and 10^{19} cm^{-3} , respectively.

The methods used for measurements of spatial and time distributions of E , T , n_e and ion number density n_i were described in [1]. In addition n_i -distributions were determined for several regimes from absorption of ultrasoft X-rays, 10 - 12 Å. Absorption coefficients were measured for two wavelengths 6328 and

4416 Å, and continuum, 2 - 6 eV. Radiation spectra were studied in infra-red, visible and near ultra-violet regions (0,5-6,1 eV) by conventional spectral methods with high time resolution.

Special time and space-resolved diagnostic equipment was developed and built to measure energy emitted from plasma focus in a vacuum ultra-violet range: double open ionization chambers (12 - 65 eV), a quartz calorimeter ($h\nu > 6$ eV), small-time-delay bismuth bolometers (6 or 11,3 - 250 eV), a photoemission-scintillation spectrometer (10 - 350 eV).

Typical experimental results obtained are presented in fig.1, where $\mathcal{E}_{\Delta\nu}$ is an absolute value of energy emitted from plasma in spectral interval 40 - 350 eV. To emphasize the abnormally high values of $\mathcal{E}_{\Delta\nu}$ measured in the case of non-ideal plasmas ($\zeta/Z \sim 1$) the values of $\mathcal{E}_{\Delta\nu}$ in fig. 1 have been divided by energies $B_{\Delta\nu}$ emitted from the black body in the same spectral interval at plasma temperatures. As seen from fig.1 the electric fields achieved do not practically produce any effect on radiation from Debye plasmas when ζ/Z is large. The situation changes for small $\zeta/Z \sim 1$ when $\mathcal{E}_{\Delta\nu}/B_{\Delta\nu}$ rises with increase of E and exceeds unity. For

$\zeta/2 \sim 1$ the value of $\epsilon_{\Delta V}$ at maximum fields achieved is an order of magnitude higher than the limiting value $\epsilon_{\Delta V}^0 = \lim_{E \rightarrow 0} \epsilon_{\Delta V} < B_{\Delta V}$ at $E \rightarrow 0$.

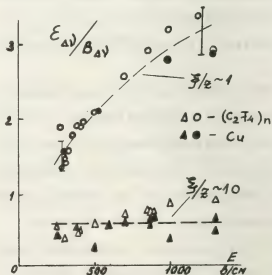
The measurements for $(C_2F_4)_n$ and Cu plasmas have shown that the dependences presented in fig.1 do not vary significantly with plasma composition. Measurements carried out for different frequency intervals have shown that radiation emitted in visible and UV spectral regions (up to 10 eV) agrees with calculations of recombination radiation and bremsstrahlung from equilibrium plasma. Radiation intensity has been observed to fall with increase in frequency up to 30 eV, which is also in qualitative agreement with theory. But for further increase of frequencies a monotonously increasing disagreement has been observed between the measured values and the theoretical predictions for equilibrium plasma.

The dependences of conductivity and radiation intensity on E show that local thermodynamic equilibrium is no longer valid for plasmas considered with increase of E . Furthermore, one can suggest that, because of $\epsilon_{\Delta V} > B_{\Delta V}$, the source of the effect observed may be a correlated spontaneous or stimulated emission of radiation. One of the possible processes may be stimulated recombination with formation of ions in the ground configuration. Then, stimulated recombination can explain the effect observed for $n_e \sim 10^{19} \text{ cm}^{-3}$ if one supposes that non-equilibrium superthermal electrons fraction α amounts $10^{-2} - 10^{-1}$

At higher α non-equilibrium electrons would influence not only conductivity and radiation, but also other plasma properties, which has not been observed as yet.

One can also suggest that the effect observed may be due to the peculiarities of the plasma generation method, that is, the effect might belong not to plasma but to the installation. Such interpretation is less probable for reasons similar to those which were pointed out in [1]. But gasdynamical conditions of the discharge considered can reduce the partial ion number densities on the lower absorbing levels compared to equilibrium, which will favour the appearance of superluminescence. Such reduction of ion lower levels number densities should be still more probable at lower densities, i.e. at higher $\zeta/2$. The absence of superluminescence in the latter case indicates that non-equilibrium super thermal electrons do not appear in Debye plasmas under such field.

1. N.P.Kozlov, G.E.Norman and Yu.S.Protasov Phys.Lett. 51A (1975) 493.
2. N.P.Kozlov, V.A.Malashchenko and Yu.S.Protasov, Zh.Priklad.Spectr.22(1975)270



ON THE THERMODYNAMICAL STABILITY OF THE PLASMA OF GAS DISCHARGE IN THE REAL GAS

S.W. Temko, K.W. Temko* and S.K. Kuzmin**.

*Moscow Geological Prospecting Institute (MGPI) Marx Prospect 18, Moscow K-9, U.S.S.R.

**MINVUZ U.S.S.R.

*Academy of Science U.S.S.R.

The present report is about discharge in weakly ionized real gas. The discharge is being kept up by the current being caused by the external source. The pressure of the plasma is balanced by the magnetic pressure being caused by the own magnetic field of the current. The discharge has the geometrical form of the ellipsoidal "cord". The plasma of the gas discharge consists of electrons, positive ions and neutrals. The interaction between the particles of the plasma is described by potential functions forming the symmetric and positive matrix. The interaction is not supposed to be weak in comparison with the average energy of chaotic movement of the particles of the plasma. We take into consideration not only the Coulomb interaction, but also the near interaction taking place when the distance between the particles is short. Accounting of the forces of near interaction is made by the Lenard-Gones potentials [1]. The state of the plasma is described by the vector-distribution of the particles. For the physical reasons the distribution function of the random vector-density of the particles of the plasma has been constructed. To discover the free energy of the plasma discharge we average internal energy and the logarithm of the probability of the random vector-density of the particles upon all possible states. The stable state of the plasma is described by the vector-density of the particles, which gives the conditional minimum of free energy. The minimum of the free energy is to be discovered under the condition of "non-hard normalizing" [2,3], which describes possibility of change of the particles from one sort to another because of chemical reactions, elastic and nonelastic interactions. The moments of the random vector-density of the particles are the corresponding distribution functions of the particles of the plasma [4]. The thermodynamical limit of the distribution functions of the particles becomes the Maxwell distributions as time becomes infinite. The solving of the problem is reduced to the generalized Gilbert problem [5,6]. Having made computer calculations we get:

- 1). the vector-density of the particles of the plasma;
- 2). the distribution function of the random vector-density of the particles;
- 3). the first moment of the random vector-density of the particles;
- 4). the average energy, the entropy and the free energy of the plasma;

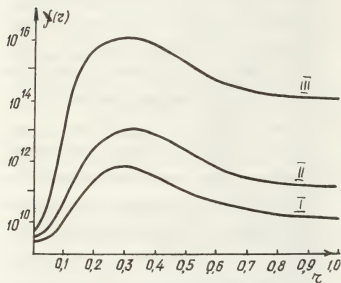
- 5). the dimensions of the gas discharge plasma "cord", when the current through the plasma is given;
 - 6). the temperatures of the electrons, the ions and the neutrals;
 - 7). the value of the numerical parameters of the Lenard-Gones potentials, which have been discovered by the method of statistical tests (the Monte-Carlo method);
 - 8). the average concentration of electrons, ions and neutrals;
 - 9). the corresponding degrees of ionizations, which depends on the average energy of the particles of the plasma, on its geometry and the character of interaction of the particles.
- The foundation of this report is the results of the authors published before [7-13]. For the closed and nearly closed systems a more general consideration is given here in comparison with published before work by one of us [14]. We considered the possibility of construction the theory of non-ideal plasma as an open system [15]. This is neither closed nor nearly closed system [16].

The method of solving the problem. Out of the equilibrium conditions and definition of the space limited plasma we get the system of the dual integral Fredholm equations of the first kind, which are to be solved in common with the normalizing conditions on the vector-density of the particles of the plasma. Having been made the necessary preliminary preparation we do Fourier convolution transform of the dual integral Fredholm equations of the first kind. Solving the generalized Gilbert problem we get the vector-density of the particles of the plasma. Knowing the vector-density of the particles we are able to examine in detail the properties the gas discharge.

The results. There are given below the results concerning the weakly ionized gas. There are given on the picture 1 the diagrams of the densities of electrons, ions and neutrals. Using the vector-density of the particles of the plasma we discover the physical values characterizing the state of the real gas discharge plasma, for example the average pressure of the plasma (picture 2).

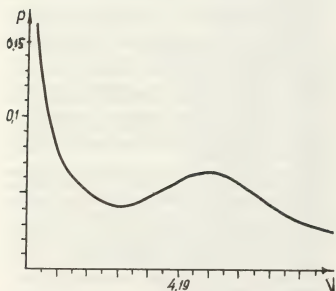
The conclusions. The authors have solved the well known problem of N.N. Bogoliubov [1]: to construct the statistical theory of plasma when interaction between the particles is described by the sum of the Coulomb potential and the Lenard-Gones potential. Having been worked by the authors the method of the statistical theory of finite clusters [7-15] gives in particular possibility to analyse completely the state of the real gas discharge

plasma in dependence of its geometry, the character of the interaction and the current going through the plasma. The consideration has been done for the real space limited plasma being assumed to be a nearly closed system. However the method of the authors is able to be used to consider the plasma as a physical finite open system. ([16]).



Picture 1. The density of ions, electrons, neutrals in the plasma.

\bar{I} . The density of ions. \bar{II} . The density of electrons. \bar{III} . The density of neutrals



Picture 2. The pressure of plasma as a function of specific volume.

References.

1. N.N.Bogoliubov, The Problems of the Dynamic Theory in the Statistic Physics. M., Gostehizdat, 1946 (in Russian).
2. S.K.Kuzmin, On the Minimization Problem of the Many-Component Potential Theory. Coll."The Modern Problems in the Exact Sciences", Edition UDN, Moscow, 1977, p.17 (in Russian).
3. S.K.Kuzmin, On the Many-Component Potential Theory, Dep. VINITI, dep. № 2425-78, 14 July 1978.(in Russian).
4. U.L. Klimantovitch, The Statistic Theory of the Nonequilibrium Processes in Plasma, Edition MGU, Moscow, 1964 (in Russian).
5. N.N.Bogoliubov, O.S.Parasiuk, DAN USSR, 109, 4, 1956 (in Russian).
6. O.S.Parasiuk, DAN USSR, 110, 6, 1956 (in Russian).
7. K.W.Temko, S.W.Temko, DAN USSR, 166, 3, 51, 1966 (in Russian).
8. S.W.Temko, K.W.Temko, Differencialnie Uravnenia, 5, 8, 1448, 1969 (in Russian).
9. S.W.Temko, PM u TPH, 1, 20, 1969 (in Russian).
10. K.S.Kuzmin, K.W.Temko, S.W.Temko, Differencialnie Uravnenia, 8, 6, 1036, 1972 (in Russian).
11. S.K.Kuzmin, S.W.Temko, On the Stability of Many-Component Systems, JINR, P4-8104, Dubna, 1974 (in Russian).
12. S.W.Temko, S.K.Kuzmin, On the Stability and Breaking of Plasma Bunches, 1977 IEEE, Troy, New York, USA, 1977.
13. S.W.Temko, S.K.Kuzmin, On the Distribution of the Particles in the Weakly Ionized Gas, 1978 IEEE, Monterey, California, USA, 1978.
14. S.W. Temko, On the General Theory of Stability of Macroscopic Systems, Dep. VINITI, dep.№ 978-78, 21 March, 1978 (in Russian).
15. S.W.Temko, S.K.Kuzmin, On the Stability of Limited Open Systems, Dep.VINITI dep. № 3110-78, 26 September, 1978 (in Russian).
16. V.E.Golant, A.P.Gilinsky, S.A.Sakharov, The Fundamentals of Plasma Physics, M., Atomizdat, 1977 (in Russian).

EXPERIMENTAL INVESTIGATION OF THE BALMER SPECTRUM FROM A DENSE HYDROGEN PLASMA NEAR THE PHOTORECOMBINATION THRESHOLD

K. Günther, S. Lang, R. Radtke and R. Ulbricht.
Akademie der Wissenschaften der DDR, Zentralinstitut für Elektronenphysik, Berlin, D.D.R.

In nearly ideal plasmas, i.e. in plasmas where the so-called non-ideality parameter $\gamma=e^2(2n_e)^{1/3}/kT$ is small compared to unity, the spectrum in the transition region from line to continuum radiation may be described by line dissolution and the statistically extended recombination continuum [1]. With increasing degree of plasma non-ideality, however, the model of the Debye shielded Coulomb potential breaks down.

In [2,3] a theory for optical properties of nonideal plasmas with $\gamma \leq 1$ was developed whose main statements consist in the following: Due to the strong electric micro-fields, the spectral lines near the photorecombination threshold disappear long before they merge in each other as predicted by Inglis and Teller. The threshold itself practically remains unshifted so that the disappearance of spectral lines consequently should lead to an intensity gap in the prethreshold region whose width is given approximately by $\Delta E=3\gamma kT$ according to [3].

In a recent paper [4] some results were noticed for the mercury spectrum in case of $\gamma = 0.056$ and 0.185 giving rise to confirm the proposed model [2,3]. From the theoretic point of view, however, it is of particular interest to know the special

distribution under nonideal circumstances for an element with a more simple atomic structure. For this purpose we investigated a pulsed hydrogen arc at elevated pressures.

The experimental arrangement for producing the hydrogen arc and the diagnostic methods used for its investigation have been described in detail in [6]. The spectral distribution of the hydrogen arc was obtained using an optical multichannel analyzer. Measurements were performed for two different pulsed arcs whose data are presented in the following table:

Arc no.	1	2
Arc temperature [K]	16700	15300
Arc pressure [atm]	2	7.5
Electron density [cm ⁻³]	$2.7 \cdot 10^{17}$	$6.2 \cdot 10^{17}$
Non-ideality parameter	0.081	0.117

The spectral distributions corresponding to the arcs listed above are shown in fig.1 for the prethreshold region. Beginning at short wavelengths, it contains the unperturbed recombination continuum, possibly followed by a region of merged lines and, for arc no. 1, the last visible hydrogen line H_{γ} . Some comparatively narrow contamination lines which were not identified unambiguously cannot influence the confidency of our following conclusions.

The intensity distribution in fig.1 suggests that the charge-carrier interaction only becomes apparent by a disappearance of spectral lines. Thus, in case of the low-pressure arc the last visible hydrogen line was H_γ , whereas in case of higher pressure we only could observe H_β yet. At the series limit an intensity gap could not be found (according to [3], for arc 2 its width should be $\Delta E \approx 0.45$ eV or $\Delta \lambda \approx 48$ nm). To confirm that the absence of this gap is not due to the high opacity of the observed plasma layer we proved in case of arc 2 that the intensity in the prethreshold region is proportional to the optical path length l_{opt} as shown in fig. 2. Shock tube experiments for a similar γ range ($\gamma = 0.102$) [5] lead to different conclusions concerning the influence of non-ideality on the radiation properties. However, we should not overestimate this discrepancy since the structure of the spectral distribution in the prethreshold region observed in [5] was within the limits of experimental error yet.

- [1] Ruzdjak, V., V. Vujnovic, *Astron. Astrophys.* 54, 751 (1977)
- [2] Kobzev, G.A. et al., *TVT* 15, 193 (1977)
- [3] Kobzev, G.A., Ju.K. Kurilenkov, *TVT* 16, 458 (1978)
- [4] Kurilenkov, Ju.K., P.V. Minaev, *ZETF* 74, 563 (1978)
- [5] Konkov, A.A. et al., *High Temp.-High Press.* 5, 405 (1973)
- [6] Radtke, R., K. Günther, *J. Phys.* 9, 1131 (1976)

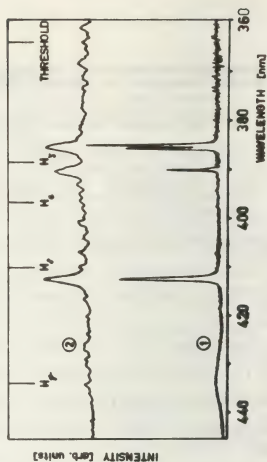


Fig.1. Spectral distribution of the arcs listed above in the prethreshold region.

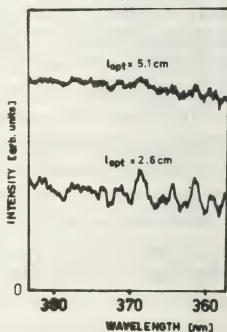


Fig.2. Radiation intensity for arc no. 2 at the threshold for different geometrical observation lengths.

ELECTRICAL CONDUCTIVITY OF HIGH-DENSITY, SHOCK-HEATED Ar AND Xe PLASMAS

S. Hashiguchi* and M. Inutake.

*Institute of Plasma Physics, Nagoya University Nagoya 464, Japan.

*Kyoto Technical University, Kyoto 606, Japan.

Abstract

Pressure, temperature, and the electrical conductivity of the plasma behind the reflected shock were measured for the range of the "plasma parameter" \mathcal{E} from 2 to 9. The electrical conductivity for Coulomb collisions, which is separated from the measured value is, on the average, 76% of Spitzer's theoretical value for Ar ($\mathcal{E}=2\sim 3$) and is 69% of it for Xe ($\mathcal{E}=5\sim 7$). The discrepancy between theory and experiment for xenon plasmas is only slightly different from the one for argon plasmas inspite of the difference of \mathcal{E} by a factor of 2.

Introduction

In the experimental study of dense, optically thick plasmas, the electron density has been determined from other parameters, say pressure and temperature since direct measurement of the electron density is difficult. The Saha equation connected by the Debye-Hückel theory is widely used to estimate the electron density. The Debye-Hückel theory, however, tends to fail with the increase in the plasma density. Slightly non-ideal plasmas to which this theory may be applied without a serious error are studied in this paper. The non-ideality of the plasma is expressed by the plasma parameter \mathcal{E} which is defined by $1/(n_e \lambda_D^3)$, where λ_D is the Debye length.

Apparatus

The shock tube is an arc-driven type

which consists of 30cm-long high pressure section and 1.8m-long low pressure section, each of which is 2cm in inner diameter.¹⁾ Figure 1 shows the schematic cross section of the shock tube near the end wall. A piezo-transducer for pressure measurement and three optical windows made of sapphire are located at the position 7mm upstream of the end wall. A coil is embedded in the end wall made of plastics (derlin or acrylite); the electrical conductivity of the plasma behind the reflected shock was measured with this coil.

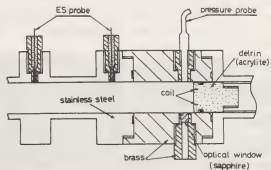


Fig.1 Schematic cross section near the end of the low pressure section

The absolute intensity of continuum radiation from the plasma and the absorption of He-Ne laser intensity across the plasma column were measured to determine temperature. In order that background plasma radiation could be eliminated the intensity of the laser light was modulated at 2MHz by an acousto-optical modulator.

The conductivity was determined from the decrease in Q-value of the coil due to

eddy currents in the plasma. The coil and a condenser forms a parallel resonance circuit. The decrease in the resonance voltage on the coil is a function of the conductivity of the plasma filled in the shock tube. This function is determined from the calibration experiment with a Sb-doped silicone cylinder of a known conductivity of 1.13×10^4 mho/m at 24°C .

Results

Time histories of the plasma conditions behind the incident and the reflected shocks are shown in Figs. 2 and 3.

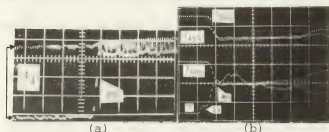


Fig.2 Oscillograms of shock-heated argon. (a) The transmitted laser intensity which was modulated with a sine wave of 2MHz. (b) From top to bottom, continuum intensities at 621nm, 450nm, and 560nm and pressure. IS and RS denote the incident and the reflected shocks, respectively. Sweep rate: 10 μ s/div.

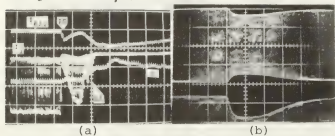


Fig.3 Oscillograms of shock-heated xenon. (a) The intensity of continuum radiation at 621nm, the transmitted laser intensity, and pressure. (b) The resonance voltage on the coil. Another trace of this oscillogram shows the same signal with increased sensitivity by a factor of 2.5. Sweep rate: 10 μ s/div.

The intensity of continuum radiation and the transmittance of the argon plasma behind the reflected shock were almost constant during the test time (40 μ s in this shot). Xenon plasmas were opaque behind the reflected shock.

Figure 4 shows the experimentally determined value of the conductivity for Coulomb collisions divided by Spitzer's theoretical value. The contribution to the conductivity for electron collisions with neutral atoms is eliminated from the measured value using the theoretical formula.²⁾ This contribution is small for the argon plasmas in this experiment. The experimental conductivity of Ar is, on the average, 76% of Spitzer's value for $\epsilon=2\sim 3$ and the one for Xe is 69% of it for $\epsilon=5\sim 7$. If the Debye length in Spitzer's formula is corrected by a numerical factor to be fitted to the experimental value, the correction factor for Xe is closer to unity than that for Ar as is found by Radtke and Günther.³⁾

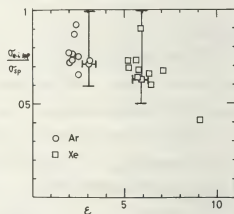


Fig.4 Experimental values of the conductivity for Coulomb collisions divided by Spitzer's value as a function of ϵ . The error mainly results from the experimental error of temperature.

References

- 1) S.Hashiguchi and M.Inutake: J.Phys. Soc. Japan **46**(1979) 285.
- 2) S.Hashiguchi, S.Sekimoto and M.Inutake: 11th Int. Shock Tube Symp., Seattle(1977) p. 622.
- 3) R.Radtke and K.Günther: Beitr. Plasma-phys. **15**(1975) 299.

GENERAL EXPRESSION OF THE DRIFT VELOCITY OF EXCESS ELECTRONS IN DENSE FLUID ARGON

A. Leycuras and J. Larour.

Université Pierre et Marie Curie - ER n°198 du C.N.R.S. T. 12, E.5, 4, Place Jussieu 75230 Paris
Cédex 06, France.

Excess electrons (e.e.) transport in dense fluid argon seems to represent the most simple situation which might happen in electron transport elsewhere than in a vacuum. In spite of this apparent simplicity electron drift velocities v_D as a function of applied electric field E exhibit complicated evolutions for different temperatures and densities. In particular the E/N parameter is no more convenient. The purpose of this paper is to establish a general expression, from a hopping model of the e.e. transport, which allows a prediction of the v_D at any field, any density, any temperature. Range limitations of the model are discussed.

A very large number of data on $e.e.v_D$ or mobilities in a quantity of dielectric fluids is available in the literature, but the most complete set of data is due to ⁽¹⁾ for e.e. in argon at densities between the triple point and the critical point. Unfortunately this remarkable work with respect of its accuracy over a wide density range, temperature effect and field effect, has not been paid enough attention by the theoreticians ⁽²⁾.

It is clear that the lack of success of the different proposed theories is due to the absence of informations relative to the form of the microscopic interaction between one electron and one argon atom surrounded by 6 nearest neighbours at distances between .4 and .5 nm. The rigorous solution of this problem is not in view apparently before a long time because it is very complicated and also because no direct scattering experiment seems possible.

We have proposed ⁽²⁾ a model, for the transfer of the electron, based on several conclusions which can be drawn from ⁽¹⁾ and

other similar experiments. The search of low field performances in ⁽¹⁾ was prompted by theoretical assumptions which assumed that it would be simpler to modify as few as possible the electron velocity distribution function. In fact "low field" is not a very convenient notion since v_D is not a linear function of the field between 0 and 25 Vcm^{-1} . At high field the situation is much more instructive since v_D reaches a constant value at $E \gg 3.10^4 \text{ Vcm}^{-1}$ ⁽³⁾ for argon, 10^4 Vcm^{-1} for xenon and 2.10^3 Vcm^{-1} for krypton in the liquid state at atmospheric pressure just above the melting point. This v_D limit versus applied field makes it clear that e.e. are not free and do not tunnel through atomic potential barriers. If we add to this observation that the values of this v_D is less than one order of magnitude larger than the sound velocity, which is related to atom velocity, it appears the most probable that the e.e. is quasi bound to an atom. The existence of such a quasi bound state has been suggested several times independently ^(4,5) but no consequence was drawn relatively to the transport process.

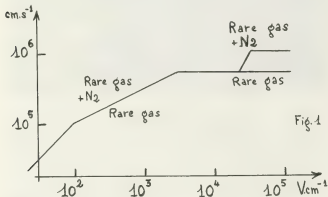
When the e.e. is orbiting on one atom its velocity is always tangent to the potential barrier in which it is trapped. Hence tunneling do not occurs even at the highest applied fields. The field modifies the e.e. trajectory which is internally tangent to a spherical envelope of radius $1/2r_E$ centered at the nucleus of the atom A. The e.e. can jump on the next atom neighbour B with respect to the field only when a collision between A and B occurs at a distance $\leq r_E$ ⁽⁶⁾. In this case the e.e. travels the mean atomic distance r_M in a time $(r_M - r_E) v_{th}^{-1}$, where v_{th} is taken as the

most probable atomic velocity. Near the critical point it is particularly clear that v_D is very small neither because v_{th} or r_M is small nor because $r_M - r_E$ is huge but because the long distance velocity correlation are important and hence the probability of collision is very low. An insight on the collision probability is given by v_S which is proportional to the probability of collision at a certain distance r_{th} . In a first approximation the collision probability $f(r_E)$ at a distance r_E is related to the one $f(r_{th})$ at r_{th} by the expression $f(r_E) = f(r_{th}) \exp - L.J.(r_E)$ where $f(r_{th})^{-1} = v_{th}/v_S (r_M/(r_M - r_{th}))$. This expression applies to short distances at least less than r_M . In fact at large E values the e.e. jumps a chain of $n(E)$ atoms distant of less than r_E and the general expression for v_D is

$$v_D = C(n(E)-1)(r_M - r_{th})(r_M - r_E)^{-1} v_S$$

$$(\exp - L.J.(r_E))^{(n(E)-1)} \quad (1)$$

C is a constant such that for $r_{th} = r_E$ $v_D = v_S$. $L.J.(r_E)$ holds for Lennard Jones potential at a distance r_E , $n(E)$ is a high order correlation function and very few is known about it. The approximation which was made in (6) on geometrical considerations can be found directly from fig.1 which reflects the main features of fig.1 in (3). The remarkable features of this curve which



have not been paid enough attention by the authors are the two changes of slope as well in the rare gases as in the mixtures before the change in slope at high field strength and the order of magnitude of the intermolecular distances. The distance between the nearest N_2 molecules is $\sim 15 \text{ \AA}$ while for the nearest argon atoms it is 4 \AA . Thus two to

three argon atoms intercalate between two N_2 molecules. It has been shown (7) that v_D at high field is larger in N_2 than in argon, this fact is certainly due to the shape of the e-argon potential $U(r)$ which is steeper at large r than the e- N_2 one. This gives some points of the $n(E)$ dependence over a wide field range and at the density of the liquid at 1 atm. This allows a better determination of $U(r)$ than in (6). From this $U(r)$ potential which is supposed in a first step to be independent of the density, v_D can be calculate for any physical condition the only limitations being that the time between collisions is longer than the lifetime of the quasi ion A^- and that the argon atoms are in the fundamental state. For a given density and a given r_E equation (1) gives very well the variation of v_D versus temperature except at the critical density. The general variation of μ_D versus density is correct but the figures differ from the experimental one by a factor two to four. The reason for this discrepancy might be due partly to the definition of r_{th} which is very sensitive to the velocity correlation of neighbouring atoms and partly because $U(r)$ is density sensitive.

- 1) Jahnke, J.A., Meyer, L. and Rice, S.A. Phys. Rev. 3A (1971) 734 - 752
- 2) Laycuras, A. and Larour, J., J. Phys. Colloques 39 CI (1978) 213-217
- 3) Yoshino, K., Sowada, U. and Schmidt, W.F. Phys. Rev. 14A (1976) 438-443
- 4) Stacey, F.D. Aust. J. Phys. 12 (1959) 105 - 108
- 5) Frommhold, L. Phys. Rev. 172 (1968) 118 - 125
- 6) Laycuras, A. and Larour, J. 4th ESCAMPIG 18-20 Sept. 1978 ESSEN West Germany.
- 7) Lowke, J.J. Aust. J. Phys. 16 (1963) 115-135

SOUND VELOCITY IN METAL-NONMETAL TRANSITION REGION OF HIGH PRESSURE MERCURY PLASMAS

M. Inutake, K. Suzuki^{*} and S. Fujiwaka.*Institute of Plasma Physics, Nagoya University, Nagoya 464, Japan.*

INTRODUCTION When the density of a weakly-ionized gas increases, the overlap between wave functions of atomic valence electrons increases and then a metal-nonmetal transition or transition from thermal ionization to pressure ionization is presumed to occur (1). It is one of the characteristic features of liquid metals that the density can be changed continuously in a wide range. Therefore, it is very interesting to investigate the electronic and thermodynamic properties of liquid metals both in the supercritical and near the critical region. Recently, the measurements of density (2), electrical conductivity (3), thermoelectric power (3), Hall coefficient (4), and Knight shift (5) have been made near the critical point of mercury ($T_{CR} = 1480^{\circ}\text{C}$, $P = 1540 \text{ kg/cm}^2$ and $\rho_{CR} = 5.5 \text{ g/cm}^3$). As for cesium ($T_{CR} = 1760^{\circ}\text{C}$, $P = 110 \text{ kg/cm}^2$, $\rho_C = 0.4 \text{ g/cm}^3$), the measurements of density, electrical conductivity, thermoelectric power have been made (6). However, a conclusive theoretical interpretation is not yet obtained for the mechanism of metal-nonmetal transition. Useful information on the mechanism would be obtained from sound velocity data, because a change in the structure of the dense fluid produces a change in the compressibility, and hence in the sound velocity.

We present the first measurements of the sound velocity of mercury up to 1600°C and 2000 kg/cm^2 . The measurements were made by means of an ultrasonic pulse transmission/echo technique, which was newly developed for such high temperature and pressure conditions (7).

EXPERIMENTAL SETUP A high pressure vessel and an ultrasonic cell are shown in Fig.1. The mercury sample is contained in the cell made of a niobium tube closed at both ends by synthetic sapphire rods. The sample between the sapphire rods is connected with a mercury reservoir through a thin channel in the inner wall of the niobium tube. The size of the sample is 1 mm in length and 10 mm in diameter. The temperature of the sample was controlled by a molybdenum-heater furnace around the cell, and measured with a Pt-30% Rh:Pt-6% Rh thermocouple. The cell was set in the high pressure

vessel made of beryllium-copper, and pressurized with argon gas (8). The pressure was measured by a Heise pressure gauge. The space between the furnace and the pressure vessel was filled as completely as possible with alumina powder in order to obtain good thermal insulation and to suppress the convection of the compressed argon. Either temperature or pressure can be controlled independently by feed-back systems of detecting the signals from the thermocouple and the pressure gauge, respectively.

The sound velocity was measured by an ultrasonic pulse transmission/echo technique. A set of quartz transducers of 20 MHz was bonded to the cold ends of the sapphire buffer-rods, use of which was essential for the success of the experiments. Sapphire has a high melting point (2050°C) and low thermal conductivity. The time required for an ultrasonic signal to traverse from one transducer to the other was measured at first. Then the time required for an echo to return from the rod/sample interface was measured for each buffer-rod. The difference between the transmission time and the average of the above two echo times gives the time required for the signal to traverse the sample. The sound velocity can be easily calculated from the sample thickness and the traverse time. It should be noted here that only the difference between the transit time and the echo times is concerned with the determination of sound velocity. Therefore the effect of the change of the sound velocity in the buffer-rods is essentially eliminated. The procedure described above was repeated for a number of different temperature and pressure. This could be carried out by adopting an electrically-controlled switching circuit.

RESULTS AND DISCUSSION The sound velocity obtained by the method described above are summarized in Fig.2. The error is $\pm 30 \text{ m/sec}$ which is shown as an error bar in Fig.2. Below the critical temperature, the sound velocity at a fixed temperature decreases with the decrease of pressure in liquid phase. It abruptly decreases to a small value in gas phase at a certain pressure. Above the critical temperature, such discontinuous change is no longer observed. Near the critical point, ultrasonic signal shows fluctuations as well as strong attenuation. The technique developed here could be successfully used to measure the change of the sound velocity near the critical point in spite of the strong attenuation (for example 40 dB/mm at 1500°C and 1500 kg/cm^2). This strong attenuation may be related to the thermodynamic anomalies near the critical point.

As the density is a measure of atomic distance, the sound velocity at a fixed supercritical pressure is plotted in Fig.3 as a function of density. The velocity and the density are normalized by the values at the triple point, respectively. This normalization is convenient for comparing

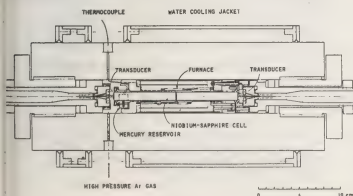


Fig.1

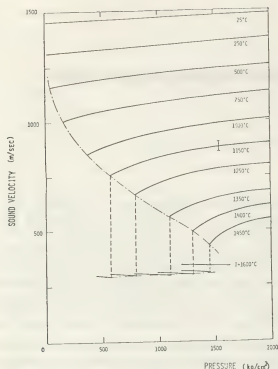


Fig. 2

the density dependence of sound velocity in mercury with that in other fluid such as argon. The density values of mercury for each set of pressure-temperature were reproduced from the compilation given by Schmutzler (9). At the density larger than 9 g/cm^3 , the sound velocity (C) varies linearly with the density (ρ). The slope ($dC/d\rho$) is $2 \times 10^4 \text{ cm}^4/\text{sec.g}$. At densities smaller than 9 g/cm^3 , the observed sound velocity deviates from the straight line. The change of the slope indicates that some change in the structure of mercury takes place at this density. It should be noted here that the onset of the metal-nonmetal transition is at the same density 9 g/cm^3 , which has been found from the measurements of electrical conductivity, thermoelectric power (3), and Hall coefficient (4). No change of the slope can be seen in nonmetallic liquid argon (10) as shown in Fig. 3. Thus the metal-nonmetal transition would be concerned with the change of the slope in sound velocity of mercury.

According to a dielectric formulation on a free electron model (11), the sound velocity in liquid metals decreases as $\rho^{1/3}$. Present results for divalent mercury plasmas do not agree with this prediction even in the metallic region. Recently, S. Nara, T. Ogawa and T. Matsubara (12) calculated the equation of state in expanded liquid metals by using a lattice model for the atomic system and Hubbard model for the electron system, and showed that the metal-nonmetal transition is accompanied with some singularity in the equation of state. It leads to a discontinuity in the slope of isothermal pressure-volume curve, i.e., to a discontinuity in the sound velocity. Our results did not show such discontinuity, but only the change of the slope at the metal-nonmetal transition.

CONCLUSION The sound velocity of high-pressure and high-temperature mercury plasmas could be measured for the first time by means of newly-developed ultrasonic technique. The dependence of the sound velocity on the density, i.e., on the interatomic distance, was observed to change at the metal-nonmetal transition (9 g/cm^3) in a supercritical-

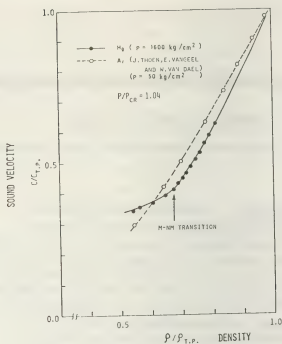


Fig. 3

pressure region. The sound velocity varies linearly with the density in the metallic region. The fluctuations and strong attenuation of the ultrasonic signal were observed near the critical point.

The authors wish to express their thank to Profs. H. Endo, M. Watabe, F. Yonezawa, H. Koshino, and Dr. K. Tsuji for many discussions. They gratefully acknowledge the encouragement of Profs. K. Takayama, H. Ikegami, and H. Isoda.

* Permanent address: College of General Education, University of Tokyo, Tokyo 153, Japan.

REFERENCES

1. G. É. Norman, Sov. Phys. JETP **33**, 912 (1971).
P. P. Kukik, Proc. 11th ICPIG, 4.6.4, Prague (1973). W. Ebeling et al., Proc. 13th ICPIG, 73, Berlin (1977).
2. F. Hensel and E. V. Frank, Rev. Mod. Phys. **40**, 697 (1968).
3. R. W. Schmutzler and F. Hensel, Phys. Lett. **35A**, 55 (1971), and Ber. Bunsenges. Phys. Chem. **76**, 531 (1972). K. Tsuji et al., J. Phys. Soc. Japan, **42**, 1594 (1977) and **44**, 1184 (1978).
4. U. Even and J. Jortner, Phil. Mag. **30**, 325 (1974).
5. U. El-Hanany and W. W. Warren, Jr., Phys. Rev. Lett. **34**, 1276 (1975).
6. V. A. Alekseev et al., JETP Letters **12**, 351 (1970). H. H. Pfeiffer et al., Phys. Letters **43A**, 111 (1973).
7. K. Suzuki, M. Inutake and S. Fujiwaka, IPPJ-310 (1977).
8. S. Fujiwaka and H. Ikezi, IPPJ-DT-47 (1975) (in Japanese).
9. R. W. Schmutzler, doctoral dissertation, Universität Karlsruhe (1971).
10. J. Thoen, E. Vangeel and W. Van Dael, Physica **45**, 339 (1969).
11. G. M. B. Webber and R. W. B. Stephens, "Physical Acoustics" (W. P. Mason ed.) Vol. 4B, Chapt. 11, Academic Press, New York (1968).
12. S. Nara, T. Ogawa and T. Matsubara, Prog. Theor. Phys. **57**, 1474 (1977).

NON IDEALITY EFFECTS IN A HIGH PRESSURE ARGON ARC MEASURED BY INFRARED CONTINUUM ABSORPTION

J. Glasser, R. Viladrosa and J. Chapelle.

CRPHT (CNRS) and GREMI (Université d'Orléans), 45045 Orléans Cédex, France.

Introduction : At the present time, non ideality effects have been measured essentially on the d.c. conductivity of plasmas produced by various types of devices. For moderately non ideal plasma (i.e. $N_D = \frac{4}{3} \pi n_e \lambda_D^3 \approx 1$, n_e electron density, λ_D Debye length), the kinetic transport theory, only applicable in principle for $N_D \gg 1$, has been prolonged down to $N_D \approx 0.5$, predicting an increase of the d.c. conductivity with decreasing N_D . Surprisingly this was not the result obtained by some authors ($1/2$) since their measured conductivity was smaller than the Spitzer one ($N_D \gg 1$). Their result is supported by other theoretical estimations $3/$. However other experimentalists $4/$ did find conductivities in accordance with the usual kinetic theory. It was thus interesting to try to clarify this puzzling problem using another approach.

Here we have used in place of the d.c. conductivity the a.c. conductivity by measurement of the infrared continuum absorption of an high pressure argon plasma. This method should be able to give at least the sense of the non ideality effect, i.e. whether it must increase or decrease the conductivity of a moderately non ideal plasma.

Estimation of the non ideality effect on the infrared continuum absorption : The infrared continuum absorption of an high pressure argon arc plasma ($1 \text{ bar} \leq p \leq 30 \text{ bars}$) is essentially due to inverse Bremsstrahlung. The absorption coefficient including induced emission can be related to the a.c. conductivity of the plasma $5/$

$$\chi' = \sigma_R (1 - \sigma_I / \omega \epsilon_0)^{-1/2} / c \epsilon_0$$

where $\tilde{\sigma}(\omega) = \sigma_R + i\sigma_I$ is the a.c. complex conductivity at angular frequency ω .

The a.c. conductivity can be calculated using Chapman Enskog kinetic theory corrected for small N_D ($\lambda = 9 \sqrt{2} N_D$). However, as we have shown in $5/$, the final formalism turns out to be much simpler than for the d.c. conductivity. Since the zeroth order of expansion is sufficient for accurate determination of the absorption coefficient, allowing also a decoupling of the electron-ion and electron neutral contribution. This is an advantage of this method since for the d.c. conductivity 3rd order is at least necessary, introducing perhaps an other cause of uncertainty. The inverse electron ion bremsstrahlung absorption coefficient can then be written as

$$\chi' = \alpha N_e^2 T_e^{-3/2} \lambda^2 G$$

The non ideal behaviour of the plasma only influences the Gaunt factor G

$$G \approx \frac{1}{3} \pi [\ln \lambda + C]$$

The coefficient C expresses the sign and magnitude of the non ideality effect. The usual kinetic theory predicts a negative C ; this means that

the Gaunt factor of a non ideal plasma must be smaller than the same quantity for an ideal plasma. The correction turns out to be of opposite direction compared to the d.c. conductivity, and also is greater, which can facilitate in principle its measurement. C can be estimated using different methods $5/$. Here for comparison we have chosen the unified theory which gives $C = 1.56$ and Kalliyugin and Norman formula which gives an opposite correction ($C > 0$) in accordance with the results of $1/$ and $2/$.

Experimental set up and diagnostic : We use the same experimental set up for plasma production as in $6/$. It is an high pressure transferred d.c. arc plasma jet. This gives a stable c.w. source with temperature of 12500 K and electron density between $1 \times 10^{17} \text{ cm}^{-3}$ and $5 \times 10^{17} \text{ cm}^{-3}$ ($2 \leq N_D \leq 4$). Spectroscopic observation and absorption measurements are made through NaCl windows. The absorption source is a low power ($\approx 5 \text{ W}$) home made c.w. CO_2 laser. Conventional infrared sources would be very difficult to use due to the intense emission of the plasma itself. The laser is also used for the Schlieren method which is exposed further. The line broadening measurements in the visible range are made with a conventional grating spectrometer. Fig. 1 shows the experimental arrangement.

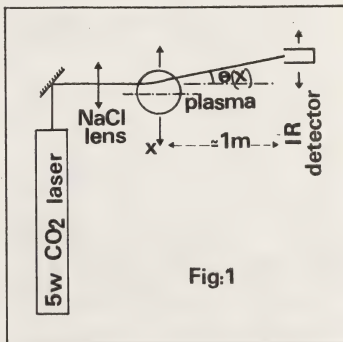


Fig.1

The infrared detector is a calorimeter type one, used only for relative measurements, since absorption does not involve calibration which is an advantage in comparison with similar emission experiments /6/.

We have shown /5/ that the real part of the refractive index of a dense plasma was not influenced by non ideality effects down to N_D 0.5. This provides a reference diagnostic method to ensure the validity of another method, like line broadening for example, which could in principle be sensitive to non ideality effects. Thus we have used an infrared Schlieren method /7/. The beam of the CO₂ laser is focalsised in the plasma and its deviation as a function of the lateral plasma coordinate is measured via the position of the calorimeter (Fig. 1). In our conditions of measurement a simple relation exists between the axis electron density and the deviation :

$$N_e(0) = (\pi A \lambda^2)^{-1} \int_0^R \theta/x \, dx$$

$A = 4.49 \times 10^{-14} \text{ cm}^{-1}$

λ : probe wavelength.

This simple method has an accuracy comparable with the one of line broadening method. It turns out that the Schlieren results agree well with the ones obtained using the AI 4159 Å line broadening parameters calculated by Griem /8/, for electron density. This is also shows that in this N_D range the line broadening seems to be insensitive to non ideality effects.

The relative radial electron density profile is determined from the relative radial continuum emission profile in the visible. Applying Abel inversion and knowing the axis electron density we can obtain the electron density profile. Temperature profile is obtained by application of Saha equation.

Results and conclusion : The absorption experiment gives us the ratio I_m/I_0 , I_m and I_0 being the intensity of the beam after and before its crossing through the plasma. Those quantities are measured as a function of the lateral coordinate x . Then the local absorption coefficient is obtained by an Abel type equation :

$$X'(r) = -1/\pi \int_r^R \frac{dx}{x^2} \ln(I_0/I_m) \frac{dx}{\sqrt{x^2 - r^2}}$$

This absorption coefficient includes three terms, the first being preponderant :

$X' = X'_{ei} + X'_{en} + X'_{ph}$
 X'_{ei} is the inverse electron ion bremsstrahlung absorption coefficient, X'_{en} the same for electron neutral interaction. X'_{ph} corresponds to photoionization. This last term comes principally from the shift of the series limit of the near infrared.

Fig. 2 gives the results obtained for the Gaunt factor at various pressures corresponding to temperatures between 11000 K and 13000 K and electron density between 1 and $4 \times 10^{17} \text{ cm}^{-3}$.

The results indicate that the Gaunt factor is smaller than in the ideal plasma case, confirming that for the d.c. conductivity the non ideality effect should increase the conductivity as predicted by the usual kinetic theory. Experiments are underway to extend those results in a wider range of electron density. This approach has thus proved to be able to give at least the sign and also a reasonable estimate of the magnitude of the effect of non ideality on the transport properties of plasmas with a small number of charged particles in the Debye sphere.

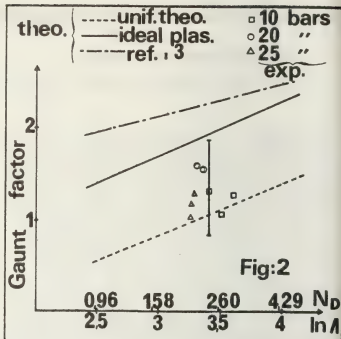


Fig:2

References

- /1/ Guenther K., Lang S., Radtke R., Popovic M. and Popovic S., Proc. of the XIIIth ICPIG VEB Buch, Leipzig, p 577 (1977).
- /2/ Goldbach C., Nollez G., Popovic S. and Popovic M., Z. Naturforsch 33a, 11 (1978).
- /3/ Kaklyugin A.S. and Norman G.E., High Temperature 11, 238 (1973).
- /4/ Bauder O.H., Appl. Phys. 9, 105 (1976).
- /5/ Glasser J. and Chapelle J., Plasma Physics 21 (in press) (1979).
- /6/ Glasser J. and Chapelle J., Proc. of the XIII ICPIG VEB Buch, Leipzig, p. 571 (1977).
- /7/ Glasser J., Villadrosa R. and Chapelle J., J. Phys. D. 11, 1703 (1978).
- /8/ Griem H.R., Spectral line broadening by plasmas (Academic Press, New-York) (1974).

ON THE MODIFICATION OF THE QUANTUM DEFECT METHOD APPLICABLE TO DENSE PLASMAS

A. Mihejlov, D. Djordjević and M.M. Popović.

Institute of Physics, Beograd Yugoslavia.

In a case that one uses the Bates and Damgaard¹ method for bound-bound transitions and Burgess and Seaton² method for the bound-free transitions, it is necessary that the outer electron and atom interaction (in a single electron approximation) has purely Coulomb behaviour for large r . In contrast to this case under the plasma conditions, the electron-atom interaction potential for both the bound and free electron states is of a finite radius of action (Debye potential or truncated Coulomb potential) and on account of that the methods mentioned, when applied to plasma would give results differing from the experiment.

Our task is to develop the method which, when applied to isolated atoms automatically gives the results of the same accuracy as Bates and Damgaard and Burgess and Seaton methods, while at the same time it can be used under the conditions characteristic of plasma.

It is well known that the condition $r_c \gg \tilde{r}_0$ is fulfilled for a wide range of plasma parameters (\tilde{r}_0 being a core effective radius and r_c a screening radius of the effective potential), and this is fact which enables us to neglect the influence of a medium on behaviour of a system outer electron+core, in a case $r \gg \tilde{r}_0$. This gives us an opportunity to determine the parameters of the effective potential, that would in an appropriate way describe the interaction of the system outer electron+core, by using the data for an isolated atom.

In choosing the effective potential we will assume, as is usual, that for $l \gg l_0$ the potential is a pure Coulomb: $V = -1/r$; for $l \leq l_0$ we will adopt the following potential:

$$V(r) = -q/r; \quad q = \begin{cases} q_0; & r < r_0 \\ 1; & r > r_0 \end{cases}$$

where l_0 is the angular quantum number of the state for which quantum defect is

negligible; q represents the effective charge which acts on the electron.

The basic task in solving the problem, reduces to the determination of r_0 and the dependence of the effective charge q on the angular quantum number l , and for a given l on the energy. The effective radius in our model depends only on the choice of l_0 , in such a way that $q(\epsilon, l_0)$ is close to unity and is of the order of magnitude of the core radius \tilde{r}_0 ; determination of q is limited by the condition that for the wave functions corresponding to the experimentally determined energy of the states the number of zero is regular.

As is usual we will take radial wave function $R_{\epsilon, l}(r)$ in the form: $R_{\epsilon, l}(r) = \frac{1}{r} P_{\epsilon, l}(x)$. For the bound states ($\epsilon = -\gamma^2/2$) function $P_{\epsilon, l}(x)$ (where $x = 2\gamma r$) satisfies the standard Whittaker equation, with parameters $\mu = q/\gamma$, $\nu = l + 1/2$, and can be expressed via its solutions $M_{\mu, \nu}(x)$ (for $r < r_0$) and $W_{\mu, \nu}(x)$ (for $r > r_0$). For the free states ($\epsilon = k^2/2$) corresponding solutions are: for $r < r_0$ - $F_l(n, \gamma)$ and for $r > r_0$ - $C_1 F_l(n, \gamma) + C_2 G_l(n, \gamma)$ where $\gamma = kr$, $n = q/k$ and are obtained from preceded solutions by using the formal substitution $\mu \rightarrow i n$, $x \rightarrow 2i\gamma$.

In the case $r = r_0$ it is necessary that the condition of continuity of the function and its derivative are fulfilled. For $\epsilon < 0$ they are satisfied with the proper choice of q and the "sewing" constant; for $\epsilon < 0$ - by choice of the coefficients C_1 and C_2 with q extrapolated from the range $\epsilon < 0$ to $\epsilon > 0$.

The phase δ_l , which is a consequence of the deviation of the effective potential from purely Coulomb one ($-1/r$ for all r) is given by:

$$\delta_l = \arctg(C_2/C_1) + j\pi \quad (1)$$

where j is an arbitrary integer.

The check of self-consistency of the method when $\epsilon \rightarrow +0$ (the equality $\delta_l(0) = \pi \nu_l(0)$ when j in eq.(1) is correspondingly

chosen), is performed by using the asymptotic expressions for the radial wave functions (ψ , $\eta \rightarrow \infty$, $\psi \rightarrow \infty$) and $\mu(0)$ - the value of quantum defect extrapolated at $\epsilon=0$.

Results:

The proposed method we tested in the case of the heavy noble gases; as an illustration we will present the results obtained for Argon.

Since in the case of Argon f states are practically hydrogenic, we adopted $l_0=3$. For r_0 we obtained the value $r_0=1.7$ which is consistent with the assumptions of the method (effective radius of the Ar^+ ion is $r_0 \approx 1.5$).

On fig.1 we presented the dependence of the effective charge q on the angular quantum number l for $r_0=1.7$ and for the main quantum number $n=4$ (which in the case of Argon corresponds to the first excited f state).

On fig.2 as an illustration, we give the 4s state wave function for $0 \leq r \leq 10$; with crosses we displayed the behaviour of the wave function for small r , obtained by using the asymptotic expression for the $P(r, l)$ function. It is obvious that the results of our calculation obtained for bound-bound transitions should be identical with ones obtained using the Bates and Dagmard method in the domain where it is applicable, if we use the same asymptotic normalization constant.

On fig.3 we presented the dependence $q(\epsilon)$ for $l=0,1,2$. On fig. 4 we give the dependence of the corresponding quantum defects $\mu(\epsilon)$ for the same l . By comparing figures 3 and 4 it becomes evident that q and μ depends on ϵ in the same way.

The phase δ_l which we obtained is in agreement with the corresponding quantity $\delta_l = \pi \mu_l$ (for $j=2$) that appears in the quantum defect method. In the range of energies in which the quantum defect method is applicable δ_l and ϵ_l in a worst case, differ by some 5%.

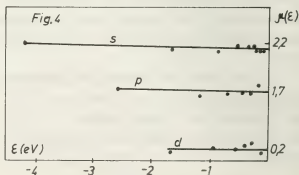
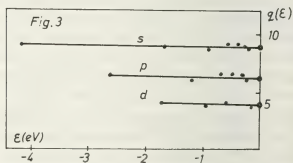
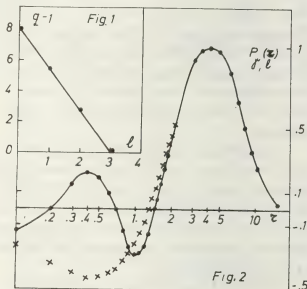
As a consequence of the results presented it is obvious that the method proposed above, in the case of isolated atoms, automatically ensures an accuracy not

smaller than that of the Bates and Dagmard method as well as Burgess and Seaton method, in a domain where they are applicable.

The advantage of the method we propose consist in the fact that, by using ones determined dependence $q(\epsilon)$ for $l \leq l_0$, it enables us to perform the calculations even under the conditions characteristic of dense plasmas when, for large r , $V(r)$ differs substantially from the Coulomb potential.

References:

1. D.R.Bates, A.Damgaard, Phyl. Trans. A242, 101 (1949)
2. A.Burgess, M.J.Seaton, Mon. Not. Roy. Astron. Soc., 121, 76 (1960).



THE CONDUCTIVITY OF DENSE CAESIUM PLASMA NEAR THE SATURATION LINE

A.N. Lagarkov, A.K. Sarychev.

Institute of High Temperatures, U.S.S.R. Academy of Sciences, Moscow, U.S.S.R.

The measurements of electrical conductivity of saturated caesium plasma¹ have demonstrated the extremely large values, exceeding the results of the usual gas-kinetic consideration by 5-6 orders of magnitude. The measurements of conductivity at 20 atm.² have shown abrupt decreasing in narrow temperature interval near saturation line and then according to the growth of temperature, relatively smooth increasing (Fig.). The anomalous behaviour of conductivity will be explained here with the formation of higher-order ionic clusters. The minimum at isobar arises due to concurrence of two processes: the ionic clusters dissociation and thermal ionization of neutral atoms.

The influence of heavy ions on conductivity for the first time was discussed by Leckenby and Robins³. They showed that the presence of the quadrumer sodium cluster would increase the conductivity of sodium vapour by an order of magnitude over that expected for the monomer. The atom of caesium has polarization constant which is larger than one for sodium. That is why the caesium vapour at high pressure has to contain more heavy ions. The structure of such ions is investigated very badly, there are no data on their role in

ionization equilibrium of plasma. The semi-conductors theory⁴ helps overcome the difficulty. Let us consider the expression for free-energy caesium vapour with ions in a centre of it. We will suppose that the concentration of particles $N(\vec{r})$ depends on co-ordinates. Such dependence is due to the strong polarization attraction of caesium atoms to the ion. In order to take into account the expression for the free energy is used which corresponds to the Van-der-Waals equation. Thus, the expression for the free energy

$$\begin{aligned} \beta F = & \int_{\Omega_1} d\vec{r} \left[N(\vec{r}) \ln \left(\frac{N(\vec{r})}{1-N(\vec{r})} \right) - N^2(\vec{r}) a \beta + \beta \frac{U(\vec{r})}{\epsilon} \right] + \\ & + (\Omega - \Omega_1) \left[N_1 \ln \left(\frac{N_1}{1-N_1} \right) - N_1^2 a \beta \right] \quad (1) \end{aligned}$$

where β is reciprocal temperature in energetic units, Ω the total volume, Ω_1 is the volume with characteristic scale of atom-ion interaction, a and b are the Van der-Waals parameters. The value N_1 is the average concentration of particles in the volume Ω_1 , $N_1 = \frac{N\Omega - \int_{\Omega_1} N(\vec{r}) d\vec{r}}{\Omega - \Omega_1}$. N is the average concentration, $U(\vec{r})$ is the potential of ion-atom interaction from calculation⁶, ϵ is dielectric permeability taking into account the decrease of potential due to dipoles interaction. According to⁵ $\epsilon = 1 + \frac{2}{3} \pi N(\vec{r}) \alpha$ where α is the polarization constant. For

C_g the value of α is 430 \AA . Let us suppose the concentration $N(\vec{r})$ is changed very strongly in the volume Ω_1 and in the volume Ω the fluctuation $c(\vec{r}) = \frac{N(\vec{r}) - N}{N} \ll 1$.

We will find such distribution of concentration in the total volume Ω , which corresponds to the minimum of free energy. For this purpose let us find the change of free energy, due to ionic cluster formation $\beta \Delta F_i \{c\} = N \int d\vec{r} \{ (c(\vec{r}) + 1) \ln \left[\frac{(c(\vec{r}) + 1) c_0}{c_0 - c} \right] - \frac{c(\vec{r})}{N \delta c_0} - \beta N c(\vec{r}) a + \beta U(\vec{r}) (c(\vec{r}) + 1) / \epsilon \}$ (2)

The optimum fluctuation is found from the condition $\delta \Delta F_i / \delta c = 0$. It satisfies the following equation

$$\tilde{c}(z) = (\exp(-\beta \tilde{U}(z)) - 1) / (1 + \exp(-\beta \tilde{U}(z)) / c_0) \quad (3)$$

where $\beta \tilde{U}(z) = \frac{\beta U(z)}{\epsilon^2} + \frac{c_0 + 1}{c_0 - \tilde{c}(z)} - \frac{1}{N \delta c_0} - 2 N a \beta \tilde{c}(z)$
 $c_0 = 1/N \delta - 1$

At small temperatures the equation (3) can have three roots. The smallest and the largest ones are realized, that corresponds to the phase transition from gas to liquid state inside the cluster. At high temperatures equation (3) has one root and there is no transition inside cluster. By means of free energy minimization we get the equation for concentration of negatively and positively charged particles. We suppose that electron-neutral atom and ion-neutral atom interaction is dominant, while electron, electron-electron, ion-electron

on interactions are negligible. So we have

$$\frac{N^+ N^-}{N} = \left(\frac{m T}{2 \pi \hbar^2} \right)^{3/2} (1 - N \delta)^{-1} \exp \left[\beta (I - \Delta I^- - \Delta I^+ + 2 N a) - \frac{N \delta}{1 - N \delta} \right]$$

where

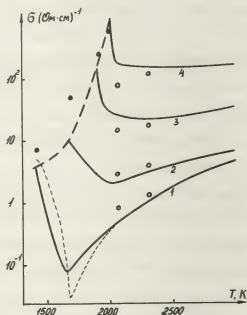
$$\beta \Delta I^+ = -N \int d\vec{r} \{ (\tilde{c} + 1) \ln \left[\frac{(\tilde{c} + 1) c_0}{c_0 - \tilde{c}} \right] - N \tilde{c}^2 a \beta - \frac{\tilde{c}(z)}{N \delta c_0} + \frac{\beta U(\tilde{c} + 1)}{\epsilon} \}$$

The quantity ΔI^+ can be written analogical-

ly. The calculations show that the concentration of negatively charged particles has a deep minimum at isobar. This minimum corresponds to the minimum of conductivity

in Fig. The same methods as in [7, 8] were used for the calculation of electrical conductivity of a dense caesium plasma. The results are shown in Fig.

1. Renkert H, Hensel F., Frank E. U. Ber. Bunsenges, Phys. Chem., 75, 507 (1971)
2. Alekseev V. A. et al. VI Inter. Conf. High. Pres. Moscow, 677 (1975)
3. Leckenby R. E., Robbins E. T., J. of Phys., 1B, 441 (1968)
4. Krivoglaз M. A. Usp. Fiz. Nauk, 111, 617 (1973)
5. Leckner T., Phys. Rev., 158, 130 (1967)
6. Valance A., J. Chem. Phys., 69, 355 (1978)
7. Lagar'kov A. N. Sarychev A. K. JETP, 68, 641 (1975).
8. Lagar'kov A. N., Sarychev A. K., Teplofiz. Vys. Temp., 16, 903 (1978).



- - experiment/1/ at saturation line, --- - experiment/2/, performed at isobar $p=20$ atm, • - experiment/1/ at 2073 K and 2273 K,
- 1 - results of present work at $p=20$ atm, 2, 3, 4 - results at $\rho_c = 0.22, 0.43, 0.75$ respectively, ρ_c - critical density, --- results at saturation line.

EXPERIMENTAL INVESTIGATION OF THE ELECTRICAL AND HEAT CONDUCTIVITIES OF ALKALI DENSE PLASMAS

V.V. Vorobiov, P.P. Kulik, A.V. Pallo, A.A. Rakin, E.K. Rozanov and V.A. Riabiy.

Moscow, U.S.S.R.

This work is a further development of the investigations [1,2] of alkali dense highly non-ideal plasma generated by pulsed high pressure (up to 1000 atm) arc discharge stabilized by a transparent capillary.

The experimental device (Fig.1) includes quartz or glass capillary between nozzle and cup electrodes, the last being made of tantalum and filled by solid alkali metal. These elements are set into an argon high pressure vessel to unload the capillary from the inner pressure and so prevent its destruction during or just after the discharge. Two tungsten floating probes allow to measure the electrical field $E = \Delta U / \Delta l$ of the arc column (ΔU being the potential drop between the probes, located at the distance Δl). The arc electrodes are connected to a capacitor bank through an inductor. The discharge is triggered either by an interelectrode wire (Fig.1) or by means of a short auxiliary discharge between the cup electrode and an additional electrode. For a capillary of diameter ~ 2 mm and length ~ 15 mm the current amplitude reaches 1 kA and the discharge lasts ~ 20 msec. The argon detention volume outside of the capillary has been increased up to ~ 70 cm (compared to 4 cm in [1-3]). This measure guarantees the discharge plasma pressure to be essentially constant and equal to initial argon static pressure in the vessel.

In this work Cs, K, Na, Li and 78% K + 22% Na eutectic alloy (weight %) have been investigated. The pressure levels adopted are 100, 300 and 1000 atm (for Cs the intermediate pressure is 250 atm). Using dual trace storage oscilloscope, ΔU (I) dependences have been recorded, which for known probe separations

$\Delta l = 1.5-4$ mm can easily be transformed into EI-characteristics. These measurements correspond to time sequences when plasma uniformly fills the interprobe space. This fact has been confirmed by speed filming of the arc column through a window (Fig.1).

Special experiments using a floating probe technique have reinforced the arguments of [1-3] for plasma purity. In particular a longitudinal array of probes, that proved the plasma potential variation along the arc column to be linear, have shown that the total electrode potential drop is localized at the cup electrode at any arc polarity. This

potential drop turned out to be more in magnitude at the normal arc polarity when the cup electrode is a cathode. Such polarity led to more intensive alkali metal evaporation and better ventilation of the discharge space than in the case of inverse polarity, so the present experiments were carried out at normal arc polarity.

Experimental EI-data were further transformed into isobars $\bar{\sigma}_s(T_{nn})$ [3] where

$$\bar{\sigma}_s = I / \alpha R^2 E, \quad T_{nn} = (EI / 2\pi R^2 \alpha)^{1/4}$$

Here R - capillary radius, α - Stephan-Boltzmann constant, T_{nn} - outer surface temperature of the arc column.

Following [2] experimental dependences

$\sigma(T)$ and $\lambda(T)$ have been obtained by solving the full inverse problem of heat conductivity based on the equations [2]:

$$T(z) = T_{nn} + E^2 \int_z^R dz / \lambda z \int_0^z \sigma \bar{\sigma} dz \quad (1)$$

$$\bar{\sigma} = 2R^2 \int_0^z \sigma \bar{\sigma} dz \quad (2)$$

where (1) is the result of integration of the Elenbaas-Heller equation for the present conditions and (2) is the expression for the average electrical conductivity. Dependences $\sigma(T)$ and $\lambda(T)$ have been found by means of a numerical variational method using a modified Monte-Carlo technique.

The results of the present investigation are shown on Fig.2 for $\sigma(T,P)$ and in the Table for $\lambda(T,P)$. Within the experimental errors these data reasonably agree with the previous results [1] for

$\sigma(T,P)$ and contain the following new information: 1) $\sigma(T)$ for $P=100$ atm; 2) $\sigma(T)$ for $T \geq 3000$ K at $P=1000$ atm; 3) $\lambda(T,P)$.

References

1. Barolskii S.G., Yermokhin N.V., Kovaliyov B.M., Kulik P.P., Riabiy V.A. Proc. XIIth ICPIG, Eindhoven, 1975, p.181.
2. Kulik P.P., Rozanov E.K., Riabiy V.A. Proc. XIIIth ICPIG, Berlin, 1977, p.585.
3. Барольский С.Г., Ермохин Н.В., Кулик П.П., Рябий В.А. ТБТ, 1976, 14, № 4, с.702.

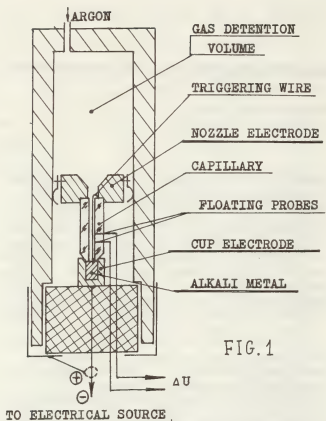
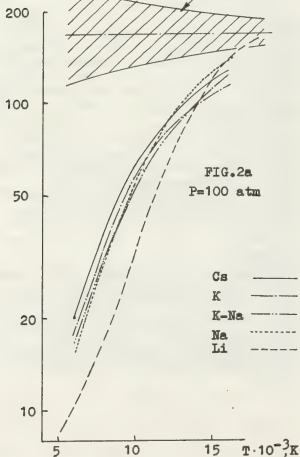
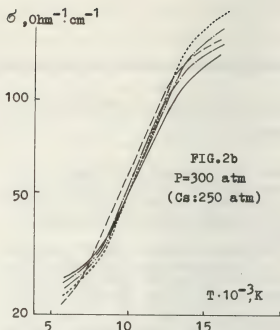
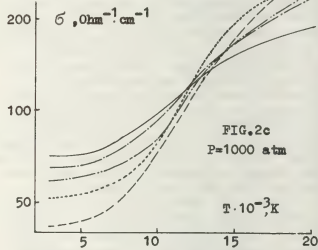


FIG.1

TO ELECTRICAL SOURCE

 $\sigma, \text{Ohm}^{-1}\text{cm}^{-1}$ FIG.2a
P=100 atm

Cs —————
 K - - - - -
 K-Na ······
 Na - · - · -
 Li - - - - -

FIG.2b
P=300 atm
(Cs:250 atm)FIG.2c
P=1000 atm

TABLE

$\lambda = \sum b_i \cdot T^{m_i}, \text{ W/cm} \cdot \text{K}; [T]=10^4 \text{ K}$
 (with accuracy of the order of factor 2)

	P,atm	b_0	m_0	b_1	m_1	b_2	m_2
Li	100	0.0590	0.45	0.4780	4.5	0.478	12
	300	0.0200	0.4	0.0730	4	0.117	9.6
	1000	0.0039	-0.4	0.0220	4.7	0.0017	11.3
Na	100	0.2080	0.32	0.7580	5.2	0.63	10
	300	0.0260	-0.5	0.1320	3.6	0.229	8
	1000	0.0055	-1.2	0.0440	3.2	0.044	7.2
K-Na	100	0.0760	0.8	0.3630	5.2	0.316	8.8
	300	0.0091	0.4	0.0760	4.4	0.1	8.8
	1000	0.0063	0.4	0.0025	4	0.014	8
K	100	0.1000	1.2	0.7500	6	0.25	12
	300	0.0190	0.48	0.1380	5	0.048	11.2
	1000	0.0910	0.6	0.0400	4.2	0.01	9.6
Cs	100	0	0	0.5000	2.2	0.229	10.4
	250	0.2000	-0.2	0.1250	3.8	0.115	10.2
	1000	0.0200	-1	0.7080	3.05	0.004	10.7

THERMODYNAMICAL FUNCTIONS FOR DENSE MULTICOMPONENT PLASMAS

M.M. Gombert, C. Deutsch and H. Minoo.

Laboratoire de Physique des Gaz et des Plasmas*, Bâtiment 212, Université Paris-Sud, Centre d'Orsay, 91405 Orsay, Cedex, France.

*Laboratoire associé au C.N.R.S.

To study plasma thermodynamics, we need an effective potential $u_{ij}(r)$ for the interaction between a particle of species i and a particle of species j . This potential takes in account the quantum effects at small relative distances^(1,2,3). For the thermodynamical calculations, we use simple analytical expressions :

$u_{ij}=z_i z_j \frac{e^2}{r} (1-\exp(-\sqrt{2\pi} \frac{r}{\kappa_{ij}}))$ for unlike particles, (1)

$u_{ii}=z_i^2 \frac{e^2}{r} (1-\exp(-\frac{\text{Log}2}{2} \frac{2}{e^{\beta}} - \sqrt{2\pi} \frac{r}{\kappa_{ii}}))$ for like particles,

with : $\kappa_{ij}=\hbar(\frac{\beta}{\mu_{ij}})^{1/2}$, μ_{ij} = reduced mass.

These potentials yield back the exact value for $r=0$ and $\beta=0$ ⁽²⁾. Log(2) takes account exchange effect of the two particles (spin=1/2). We know of a better approximation⁽⁴⁾ which reads :

$u_{ij}=z_i z_j \frac{e^2}{r} (1-\exp(-rP(r)))$ (2)

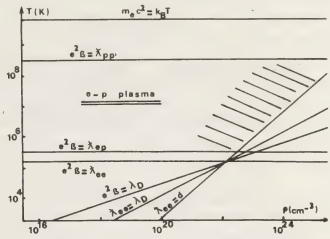
where $P(r)$ is a polynomial. For the electron-proton potential a very good approximation is :

$P(r)=A-(\frac{2}{\pi}-\frac{A^2}{2})r-A(\frac{2}{\pi}-\frac{A^2}{3})r^2$, with : $A=-\frac{u(0)}{e^2}$.

There is a maximum relative error of 0.01 at 10⁶K, 0.003 at 10⁷K and less than 0.001 at 10⁸K. With the form(1), there is a relative error of 0.1 (near $r=\kappa$). The approximations (1) or (2) always imply $e^2\beta\ll\kappa$ ($\kappa T>1\text{Ry.}$). These techniques of effective potentials are adequate for $\kappa\ll d$ (mean distance between particles). We take into account only of the exchange of two particles.

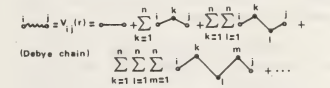
We started to study the thermodynamics with the simpler form(1) for $u(r)$. In fact, in a plasma made of electrons and several ion species, we consider the potential between two ions to be classical and we use the form(1) only for a potential between an electron and an ion or between two electrons.

Now, we can study the plasma thermodynamics, compute the correlation functions $g_{ij}(r)$ and the canonical thermodynamical functions in term of the



plasma parameter $\Lambda=e^2\beta/\lambda_D$ and a quantum parameter κ/λ_D , where λ_D is the Debye length⁽⁴⁾. We use the expansion with respect to Λ in term of nodal graphs⁽⁵⁾.

To describe the thermodynamics of multicomponent plasma, we use a matrix language⁽⁶⁾. The Debye like potential, $V_{ij}(r)$, is shown in the next figure in which the sums run over all species, and straight lines $u_{\ell k}(r)$ are the interactions (temperature dependent) between two particles.



There is the relation : $\hat{V}(k)=\hat{U}(k) \cdot [I + \hat{U}(k) \cdot C]^{-1}$ (3)

with : $\hat{U}=\begin{pmatrix} \hat{u}_{11} & \dots & \hat{u}_{n1} \\ \vdots & & \vdots \\ \hat{u}_{1n} & \dots & \hat{u}_{nn} \end{pmatrix}$, $\hat{V}=\begin{pmatrix} \hat{v}_{11} & \dots & \hat{v}_{n1} \\ \vdots & & \vdots \\ \hat{v}_{1n} & \dots & \hat{v}_{nn} \end{pmatrix}$,

(\hat{u}_{ij} and \hat{v}_{ij} denote the Fourier transforms of u_{ij} and V_{ij})

$C=\begin{pmatrix} \rho\beta C_1 & & 0 \\ & \ddots & \\ 0 & & \rho\beta C_n \end{pmatrix}$.

C_i is the i species concentration, ρC_i is the numerical density of species i . The relation (3) is si-

milar to the well known one for a one component plasma.

For an electron-proton plasma, with the potentials:

$$u_{ee}(r) = \frac{e^2}{r} (1 - \exp(-\frac{r\sqrt{2\pi}}{\lambda})) , u_{ep} = -\frac{e^2}{r} (1 - \exp(-\frac{r\sqrt{4\pi}}{\lambda}))$$

and $u_{pp}(r) = e^2/r$ ($\kappa = \kappa_{ee}$, $u_{ee}(r)$ does not take account symmetry effects), we obtain, for instance :

$$V_{ee} \approx \frac{e^2}{r} (1 + \frac{3}{2} \frac{\eta^2}{\lambda_D^2}) \left[\exp(-\frac{r}{\lambda_D} (1 + \frac{\eta^2}{4})) - \exp(-\frac{r}{\lambda} \sqrt{2\pi} (1 - \frac{\eta^2}{4})) \right],$$

$$V_{ep} \approx -\frac{e^2}{r} \left[(1 + 2\frac{\eta^2}{\lambda_D^2}) \exp(-\frac{r}{\lambda_D} (1 + \frac{\eta^2}{4})) - \frac{\eta^2}{2} \exp(-\frac{r}{\lambda} \sqrt{2\pi} (1 - \frac{\eta^2}{4})) - \exp(-\frac{r}{\lambda} \sqrt{4\pi}) \right],$$

$$V_{pp} \approx \frac{e^2}{r} \left[(1 + \frac{\eta^2}{2}) \exp(-\frac{r}{\lambda_D} (1 + \frac{\eta^2}{4})) - \frac{\eta^2}{2} \exp(-\frac{r}{\lambda} \sqrt{2\pi} (1 - \frac{\eta^2}{4})) \right],$$

with : $\eta = \kappa/\sqrt{2\pi} \lambda_D \ll 1$.

For a classical electron-proton plasma ($u(r)$ is the coulombic potential), if the number of Debye chains arriving to a nodal point is odd, the graph vanishes⁽⁷⁾. This is not right when temperature dependent potentials are needed. This is right only for the coulombic contribution to the graph but there is an additional quantum contribution. We are currently considering the electron-proton plasma and also the electron-proton-iron ion plasma at least a first order in Λ . We shall be able to give results in a short time.

(1) A.A. BARKER, J. Chem. Phys., 55, 1751 (1971).

(2) B. DAVIES and R.G. STORER, Phys. Rev., 171, 150 (1968).

(3) MINOO's communication.

(4) C. DEUTSCH and M.M. GOMBERT, J. Math. Phys., 17, 1077 (1976).

M.M. GOMBERT et C. DEUTSCH, J. de Physique (supl.), 39, C1-184 (1978).

(5) F.E. SALPETER, Ann. Phys., 5, 183 (1958).

(6) EIVIND HILS HAUGE, J. Chem. Phys., 44, 2249 (1966).

(7) C. DEUTSCH, Phys. Rev., A17, 909 (1978).

TWO PARTICLE EFFECTIVE POTENTIAL OF A DENSE HYDROGENEOUS PLASMA

H. Minoo, M.M. Gombert and C. Deutsch.

Laboratoire de Physique des Gaz et des Plasmas*, Université Paris-Sud, Centre d'Orsay, 91405 Orsay Cedex, France.

*Laboratoire associé au C.N.R.S.

1 - INTRODUCTION

In many problems dealing with thermodynamic functions and transport properties of a dense fluid or a dense plasma, it is essential to have a precise knowledge of the form of the two-particle effective potential (or binary Slater sum) and the corresponding pair correlation function. Here we consider the simplest case of a gaseous hydrogenous plasma at temperatures high enough for the hydrogen molecules to be dissociated, say about 10^5 K. In this system, the classical calculation of the pair radial distribution function $g_2(r, T)$ (r.d.f.) diverges when the distance between particles r tends toward zero, due to a singularity at $r=0$. In order to remove this singularity it is necessary to take into account the quantum effects. But, the inclusion of these effects increases considerably the difficulty of calculations. To keep these calculations analytic one has to make some simplifying approximations. Following these lines and for $k_B T > 1$ Ryd, Deutsch [1] obtained a Kramers-like pseudo-potential in the framework of the Two-Component Plasma model. In earlier works, with the inclusion of Diffraction [2] and Symmetry effects [3], some formally analogous expressions were derived, in high-temperature and dense classical electron gas within the framework of the One-Component Plasma model. References to previous works on this problem are given by Barker [4], and Davies and Storer [5].

2 - NUMERICAL COMPUTATION

At the present time, an exact calculation of the quantum-mechanical r.d.f. at any separation r is only feasible by means of heavy electronic computations. In this work, which is an extension of Barker's study [4], we are computing numerically $g_{ep}(r, T)$, $g_{ee}(r, T)$, and their corresponding effective potential at all distances and at different temperatures, with a high accuracy (errors less than one over 10^6). g_{ep} and g_{ee} are respectively electron-

proton, and electron-electron r.d.f. As two examples of these calculations : figure 1 shows variations of g_{ep} versus rT at different temperatures T ; while figure 2 illustrate the contribution of g_b and g_s to g_{ep} at $T=10^6$ K. g_b and g_s are respectively contributions to g_{ep} from bound states and scattered states of $e-p$ system. In this figure g_c is the r.d.f. corresponding to a Coulomb potential :

$$g_c = \exp(-\beta e^2/r) \quad \text{with } \beta = (k_B T)^{-1}.$$

Based on these and other results we obtained the following simple empirical expression, which reproduces quite satisfactorily the exact numerical results :

$$\ln g'_{ep}(x, \gamma) = -[(\gamma/2)^{1/2}/x] \{ \exp[-(ax + bx^2 + cx^3)] - 1 \}$$

where $x=r/\lambda$; λ is the thermal De Broglie wavelength $\lambda = h(\beta/\mu)^{1/2}$; μ is the reduced mass ;

$$a = (2\pi)^{1/2} + (\gamma/2)^{1/2} [(\pi^2/3) - \pi] + (2\gamma^2)^{1/2} [\zeta(3)(\pi/4)^{1/2} + (\pi^3/9)^{1/2} - (\pi^5/36)^{1/2}] ;$$

$$b = \frac{a^2}{2} - 2 ; c = a(\frac{a^2}{3} - 2) ; \text{ and } \gamma = 2(e^2/\hbar)^2 \mu \beta$$

3 - SMALL r REGION

The exact quantum-mechanical expression for r.d.f. can be arranged, after a lengthy calculation, in increasing power of r . The final result for g_{ep} is :

$$\begin{aligned} g_{ep}(x, \gamma) = & (\pi\gamma^3)^{1/2} [1 - (2\gamma)^{1/2} x + \gamma x^2 \\ & - \frac{2}{9} (\frac{\gamma}{2})^{3/2} x^3 (5+4D_\gamma) + \frac{\gamma^2}{72} x^4 (7 + 20 D_\gamma) \\ & - \frac{1}{225} (\frac{\gamma}{2})^{5/2} x^5 (21+140 D_\gamma + 64 D_\gamma^2) \\ & + \frac{1}{1350} \gamma^3 x^6 (\frac{11}{4} + 35D_\gamma + 56 D_\gamma^2) - O(\gamma^{7/2} x^7)] \end{aligned}$$

$$\times \left[4 \int_0^\infty \frac{k e^{-\gamma k^2} dk}{1 - e^{-\pi/k}} + \sum_{n=1}^\infty \frac{1}{n^3} \exp(\gamma/4n^2) \right].$$

where :
$$D_Y^n f(\gamma) = \frac{d^n f(\gamma)}{d\gamma^n}$$

when r is small (x << 1), the first few terms of this expression gives a satisfactory approximation of exact g_{ep}.

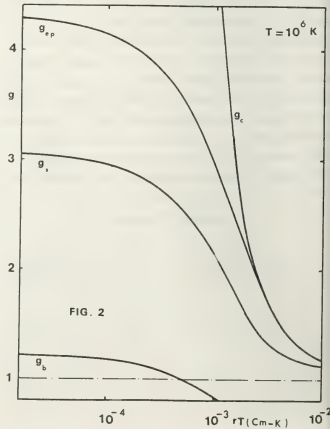
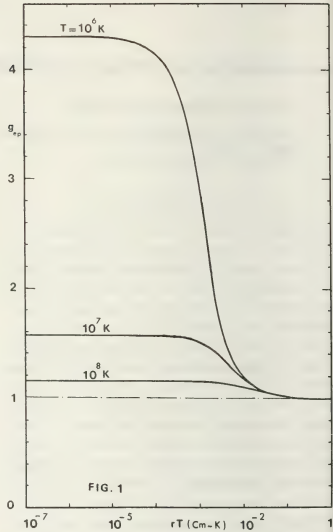
Finally, we pay attention to the very-high temperature regime, where relativistic effects become non-negligible for plasma with large Z species.

REFERENCES

[1] C. DEUTSCH, Annals of Phys. 115, 404 (1978).
[2] M.M. GOMBERT and C. DEUTSCH, Phys. Lett. 47A, 473 (1974) ; C. DEUTSCH and M.M. GOMBERT, J. Math. Phys. 17, 1077 (1976).
[3] C. DEUTSCH, M.M. GOMBERT and H. MINOO, Phys. Lett. 66A, 381 (1978).
[4] A.A. BARKER, J. Chem. Phys. 55, 1751 (1971).
[5] B. DAVIES and STORER, Phys. Rev. 171, 150 (1968).

Figure 1 - Electron-proton radial distribution function g_{ep} at different temperatures.

Figure 2 - Electron-proton radial distribution function versus rT.
g_b and g_s are respective contributions to g_{ep} from bound states and scattered states.
g_c is the r.d.f. corresponding to a Coulomb potential.



XII

- Plasmas en astrophysique
Astrophysical plasmas



ON ELECTRON-COHERENT WHISTLER WAVE INTERACTION AND PARTICLE PRECIPITATION.

T.M. Abecasis, A.M. Moreira and F.M. Serra.

*Complexo Interdisciplinar, Laboratorio de Electrodinâmica, Instituto Superior Técnico, Lisboa 1, Portugal.*Introduction

This paper describes the results related to the computational simulation of the resonant interaction between radiation belt energetic electrons and a coherent wave propagating in the whistler mode.

Due to the inhomogeneity of the geomagnetic field the electrons may be kept trapped by the field lines, depending on their pitch angle, their movement being controlled by the field; when a wave field is present the motion of these particles might be affected and, as a result of the resonant interaction with the wave, a precipitation of electrons into the ionosphere may take place due to significant changes of their pitch angles. The study of the mechanisms that lead to stimulated precipitation of electrons was the main purpose of the computational simulation. Introducing a spatially varying low-amplitude model for a whistler wave we state the importance of a cyclotron resonant mechanism by which, in a single encounter with the wave, a particle may precipitate due to a significant decrease of its v_{\perp} ; this mechanism differs considerably from the one that underlies cyclotron resonance with high amplitude whistlers that phase-trap electrons (multiple resonance) and might force its $|v_{\parallel}|$ to grow, thus leading to precipitation.

Computational Model

The simulation was performed for the magnetospheric region $L=4$ corresponding to the experiment taking place between Siple (transmitter, in Antarctica) and Roberval (receiver, in Canada).

The geomagnetic field was simulated by a dipolar field and the adopted values for the density of the cold plasma electrons in the equator varied between typical values of 10 and 10^3 el/cm^3 ; the equatorial plasma frequency is determined by this density value, and the gyrofrequency model was used to describe plasma frequency variation along a field

line / 1 /.

The equations of motion of the electrons under the simultaneous effect of the geomagnetic field (B) and of an injected coherent whistler wave

($B_w, \omega, k(z)$) are:

$$\dot{v}_{\parallel} = -v_{\perp} a \sin \phi - (v_{\perp}^2 / 2B) \frac{\partial B}{\partial z}$$

$$\dot{v}_{\perp} = a(v_{\parallel} - \frac{\omega}{k}) \sin \phi + (v_{\parallel} v_{\perp} / 2B) \frac{\partial B}{\partial z}$$

$$\dot{\phi} = k(v_{\parallel} - v_G) + \frac{a}{v_{\perp}} (v_{\parallel} - \frac{\omega}{k}) \cos \phi$$

where $(a, \omega_c) = q(B_w, B) / m$, $v_G = (\omega - \omega_c) / k$ is

the cyclotron-resonance velocity, and ϕ is the angle between \vec{B}_w and \vec{v}_{\perp} . It was then possible to track the particles, making use of fourth order Runge-Kutta formulae (in the modification due to Gill). The time step of integration was taken as $h \ll T_{NL} = 2\pi (a k v_{\perp})^{-1/2}$. Early computations were performed with constant amplitude whistlers but we noted that most of the times the final pitch angle of a particle beginning its interaction with the wave in the northern hemisphere was almost the same as in the symmetric point in the southern hemisphere, given the symmetry of the geomagnetic field and of the whistler amplitude around the equator. So we built a spatially varying amplitude model, increasing along the equator and reaching saturation values in the northern hemisphere (typically $B_w \sim 50 \text{ mT}$) corresponding to experimental values of the amplitude amplification of injected whistlers, which may reach 30 db / 2 /.

Results

We followed the cyclotron-resonance interaction from -6°N latitude to -6°S latitude. Outside this region the influence of the geomagnetic field is predominant over the whistler field.

It was possible, near resonance, to check the invariance (variation of 1 in 10000) of the parameter introduced by Karpman et al / 3 /,

$$C^2 = (v_{\perp}^2 + v_{\parallel}^2) - \frac{v_{\perp}^2}{2}$$

Depending on the initial conditions (Fig.1,table 1) the electrons might go through multiple or single resonances (the resonances in the southern hemisphere being meaningless because of the local lower amplitude of the whistler). In the simulations using low-amplitude whistlers with frequencies between 3 and 8 kHz showed that only single resonances could lead to electron precipitation.

The results for three typical electrons undergoing the interaction with a 4 kHz, $B_w \sim 50$ mV whistler are shown below; these particles^{max} had initially the same $v_{||}$ and v_{\perp} (and therefore the same α) but different ϕ ($30^\circ, 120^\circ, 210^\circ$).

For the initial values of $v_{\perp} = 5 \times 10^6$ m/s, $|v_{||}| = 2.9 \times 10^7$ m/s, $\alpha = 9.75^\circ$ at 5.7° N latitude, the following final values around latitude 6° S ($\alpha_{lc} \sim 5.45^\circ$) were obtained:

$\phi_{\text{initial}} (^{\circ})$		$ v_{\parallel} (10^7 \text{ m/s})$	$v_{\perp} (10^6 \text{ m/s})$	$\alpha (^{\circ})$
1	30	2.92	2.56	5.00
2	120	2.80	10.31	20.23
3	210	2.91	4.23	8.26

TABLE 1

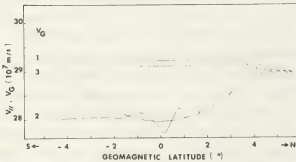


FIG.1 Evolution of $|v_G|$ and $|v_{||}|$ of the electrons (1,3-single resonances; 2-multiple resonance)

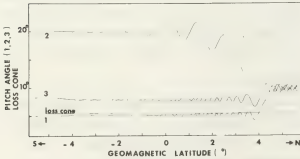


FIG.2 Evolution of loss cone and electron pitch angles

As clearly shown in FIG.2 only particle 1 precipitated ($\alpha_f < \alpha_{lc}$).

Conclusion

For particles submitted to single resonances, their pitch angle changes are mainly due to v_{\perp} variations. The Doppler-shifted frequency equals the gyrofrequency, and thus the wave fields seen by these particles rotate with the gyrofrequency as their v_{\perp} nearly do. As long as a particle is close to a resonance, which happens for a significant time interval, its v will be changed by the continuously cumulative action of the wave electric field upon the particle. It is easily seen (FIG. 3) that if $(v_{\perp} \cdot E_w) > 0$, ($0 < \phi < \pi$), v_{\perp} will decrease and if $(v_{\perp} \cdot E_w) < 0$, ($-\pi < \phi < 0$), v_{\perp} will increase. In the case of multiple resonances, although v_{\perp} oscillates, the associated particle trapping leads to a decrease of $|v_{||}|$ for electrons approaching the equator, and thus to a growth in pitch angle.

Since the adopted amplitude model leads to detrapping near the equator, in this case there is no precipitation. Note, however, that different amplitude models could lead to different conclusions. We must emphasize that, according to the adopted model, only singly resonant particles can precipitate when low amplitude whistlers are considered.

Another important result of the computation was to suggest a simplified analytical model of the cyclotron resonant interaction near $v_{||} = V_G$; integration of the equations of motion can then be simply performed. Work along these lines will be the object of future communications.



FIG. 3 Relative position of particle velocity and whistler fields.

References

/1/ - R.A. HELLIWELL, Rev. Geophys. Space Phys. 7, 281, (1969)
/2/ - R.A. HELLIWELL, Phil. Trans. R. Soc. Lond. B, 279, 213 (1977)
/3/ - KARPMAN, ISTOMIN and SHKLYAR, Plasma Physics 16, 685 (1974).

PROPAGATION OF WHISTLER WAVES TRAPPED IN A NARROW DENSITY TROUGH

H. Sugai, K. Ido, H. Niki and S. Takeda.

Department of Electrical Engineering, Nagoya University, Nagoya Japan.

Abstract: Whistler waves are observed to be trapped in the narrow density trough of width $2d \leq \lambda_{\parallel}$ (parallel wave length). The phase and amplitude profile of ducted whistlers is measured along and across the trough. The experimental results are in good agreement with the recent trapping theory.

Ducted propagation of whistler waves has been widely recognized as a mechanism guiding the wave energy along lines of magnetic field in geomagnetospheres¹. In the field-aligned density trough or hump ('duct'), whistlers are trapped somewhat in the manner of a metallic waveguide. The conventional ray theory¹ cannot be applied to the narrow duct ($2d \leq \lambda_{\parallel}$). The recent theory² solving the eigenvalue problem has predicted that whistler waves are trapped even in the narrow density trough.

In this paper we present laboratory experiments of whistler wave trapping in the narrow density trough. The details of plasma device has already been reported elsewhere³. The experiment is performed in an afterglow plasma of density $n \approx 7 \times 10^{11} \text{ cm}^{-3}$ and electron temperature $kT_e = 0.3 - 0.8 \text{ eV}$, under the magnetic field $B_0 = 100 - 200 \text{ G}$. The field-aligned density trough is artificially produced in the novel fashion where the depth and the width of the duct can be controlled arbitrarily. Whistler waves of frequency $\omega/2\pi = 100 - 500 \text{ MHz}$ are excited with an electric dipole antenna. The rf power applied to the exciter antenna is so small that the wave nonlinearity and the electron heating due to antenna actions⁴ is excluded.

While the wave energy flow diverges in the uniform density profile, the narrow density trough

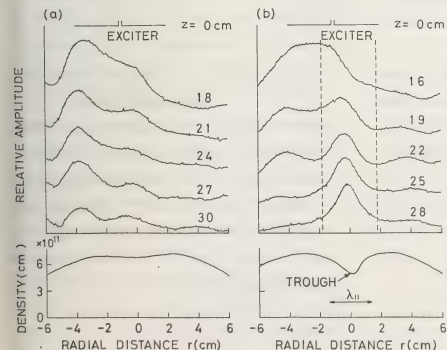


Fig.1. Relative wave amplitudes across B_0 at different axial distances from the exciter antenna, together with the density profiles in the absence (a) and the presence (b) of the narrow density trough. $\omega/\Omega = 0.70$, $\Omega/2\pi = 508 \text{ MHz}$.

confines the wave which does not broaden with increasing distance from the exciter. Figure 1 displays a comparison of the wave amplitude profiles across B_0 , in the absence [Fig.1(a)] and in the presence [Fig.1(b)] of the density trough. The perfectly ducted mode is established at $z \geq 25$ cm, while the effect of radiation broadening from the exciter antenna cannot be neglected for $z \leq 15$ cm.

The transverse profiles of wave amplitudes show the exponential decay outside the trough. The transverse decay length Λ is plotted in Fig.2, as a function of the frequency normalized by the electron cyclotron frequency Ω . The solid line in Fig.2 indicates the theoretical curve obtained in the sharp boundary model.² The experimental values of Λ become minimum around the critical frequency ω_c .

The wave length as well as the wave amplitude is modified in the presence of the density trough. The measured dispersion relations of the ducted modes well agree with the theoretical ones, as shown in Fig.3.

References

1. R.A. Helliwell, Whistlers and Related Ionospheric Phenomena (Stanford Univ., Stanford, Calif., 1965).
2. K. Mima, G. Morales, Y.C. Lee, and B.D. Fried, Research Report of Institute for Fusion Theory, Hiroshima University (1978), Hiroshima, Japan.
3. H. Sugai, M. Sato, K. Ido, and S. Takeda, J. Phys. Soc. Japan 44, 1953 (1978).
4. H. Sugai, M. Maruyama, M. Sato, and S. Takeda, Phys. Fluids 21, 690 (1978).

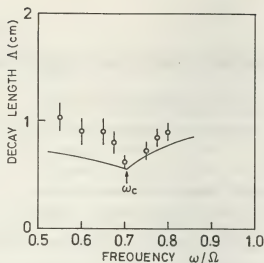


Fig.2. Experimental points and theoretical line of the transverse decay length Λ as a function of the normalized frequency ω/Ω . The density depression rate $\delta = 33\%$, and $2d = 1.4$ cm.

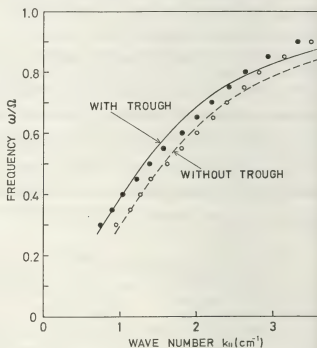


Fig.3. Comparison of the whistler wave dispersion relations in a uniform plasma and in a narrow density trough. Solid line and closed circles correspond to the case with the trough, and dashed line and open circles indicate the case without the trough. $n_1 = 6.9 \times 10^{11} \text{ cm}^{-3}$, $\Omega/2\pi = 508$ MHz, $\delta = 30\%$, and $2d = 1.4$ cm.

ACCELERATION OF A FAST ION IN AN ACCRETION COLUMN

J.G. Kirk.

Max-Planck-Institut für Physik und Astrophysik, Föhringer Ring 6, 8 München 40, FRG.

Calculations of the rate of energy deposition by a fast ion falling through the plasma above a magnetised neutron star are important in the physics of X-ray pulsars, since they play a decisive role in the question of the formation of a stand-off shock front. Treatments of spherically symmetric accretion (Alme and Wilson, 1973) used the formula for deceleration by Coulomb collisions in the absence of a magnetic field. This approach requires modification when a magnetised neutron star is considered. Basko and Syunyaev (1975) and Pavlov and Yakovlev (1976) calculated the relevant cross-sections, and estimated that the stopping length of an ion is increased by an order of magnitude over the zero-field case. However, this conclusion no longer holds when the collective effects in the plasma are included. The most important of these is the scattering of the test ion off the ion-sound waves. That such a scattering can occur is seen only when full account is taken of the orbit of the ion in the magnetic field. Even a modest level of ion-sound turbulence suffices to deflect the ion, and severely reduce the stopping length. Computer calculations of the energy and momentum deposition rates including this new effect are in progress, and it is hoped that the results will indicate whether or not a non-radiative shock can occur.

References

- Alme, M.L. and Wilson, J.R. 1973 *Astrophys. J.* **186**, 1015
Basko, M.M. and Syunyaev, R.A. 1975 *Sov. Phys. JETP* **41**, 52
Pavlov, G.G. and Yakovlev, D.G. 1976 *Sov. Phys. JETP* **43**, 489



INFLUENCE OF TOROIDAL MAGNETIC FIELD ON CONVECTION IN ROTATING STAR

V.M. Čadež.

Institute of Physics, P.O. Box 57, Yu-11001 Beograd.

We present a modified linear theory of convection in a differentially rotating magnetic star and some, relatively simple, analytical expressions regarding the criteria for the instability onset were derived.

The problem of convection in terms of standard linear theory and the normal mode analysis was widely treated under various approximations and restrictions in the literature so far [1, /3/.

In this paper, in order to investigate the convective instability in presence of a toroidal magnetic field and when a star differentially rotates, we shall apply the perturbation method and consider only those perturbations which are of the form of narrow loops [2/. The reason why such perturbations are treated is the fact that they, being in lateral total pressure equilibrium, become unstable most easily.

The fluid, we shall consider, is assumed completely ionized, ideally electrically conductive, inviscid and compressible. It satisfies the perfect gas law, its temperature field is left unspecified and it is a subject of self-gravitational attraction. In addition, the fluid is permeated by a toroidal magnetic field \vec{B}_0 and differentially rotates in such a way that the resulting tangential fluid velocity component V_θ remains constant along the field line. The whole system is therefore axially symmetric with respect to the axis of rotation. The fluid is initially stationary, in the state of equilibrium described by:

$$\frac{\partial p_0}{\partial r} + \frac{B_0}{\mu r} + \frac{B_0}{\mu} \frac{\partial B_0}{\partial r} + g_0 g - g_0 \Omega^2 r = 0 \quad (1)$$

$$\frac{1}{r} \frac{\partial p_0}{\partial \theta} + \frac{B_0 \omega \theta}{\mu r} + \frac{B_0}{\mu r} \frac{\partial B_0}{\partial \theta} - g_0 \Omega^2 r \sin \theta = 0 \quad (2)$$

Here a spherical coordinate system is introduced so that its origin coincides with the center of the star while the polar axis is oriented toward a pole.

In further analysis we shall investigate instability characteristics in the equatorial region ($\theta \approx \pi/2$) only. This restriction, however, does not exclude any of the basic physical processes involved in the instability.

From the reason of symmetry all the basic state quantities (the pressure P_0 , the fluid density ρ_0 , the temperature T_0 , the azimuthal magnetic field intensity B_0 and the angular speed of rotation Ω) have to be functions only of the coordinate r in the region near the equator. Consequently, the eq. (2) is identically satisfied there.

To investigate the behavior of the fluid when slightly perturbed adiabatically, we start from standard MHD equations:

$$\frac{\partial \rho}{\partial t} + \nabla \cdot (\rho \vec{v}) = 0$$

$$\rho \left[\frac{\partial \vec{v}}{\partial t} + \nabla \cdot \frac{\vec{v}^2}{2} - \vec{v} \times (\nabla \times \vec{v}) \right] = -\nabla p + \frac{1}{\mu} (\nabla \times \vec{B}) \times \vec{B} + \rho \vec{g}$$

$$\frac{\partial \vec{B}}{\partial t} = \nabla \times (\vec{v} \times \vec{B})$$

$$\frac{dp}{dt} = c^2 \frac{d\rho}{dt} \quad (c = \text{adiabatic sound speed})$$

All physical quantities entering as the unknowns in the above equations, have to be considered as a sum of their unperturbed, basic state, values and a small additional value due to perturbations.

Since the basic state is stationary and axially symmetric, the perturbed quantities can be expressed locally in the following form:

$$\Psi_i(r, \theta, t) = \hat{\Psi}_i(r, \theta) \exp i(m\theta - \omega t)$$

If now we consider only those perturbations which are geometrically of narrow scale in the meridional direction, i.e. if:

$$\left| \frac{1}{\Psi_i} \frac{\partial \Psi_i}{\partial \theta} \right| \gg \left| \frac{1}{\Psi_i} \frac{\partial \Psi_i}{\partial r} \right|, \quad \frac{m}{r} \quad (3)$$

then the initial set of MHD equations reduces to the following system of linearized algebraic equations:

$$i\omega^* \hat{b}_{i\varphi} - \frac{\partial}{\partial r} \ln \frac{B_0}{r} \hat{v}_{ir} + V_0 \frac{\partial}{\partial r} \ln \Omega \hat{b}_{ir} - i\omega^* \hat{\eta}_i + \frac{im}{r} \hat{v}_{i\varphi} = 0 \quad (4)$$

$$A^2 \hat{b}_{i\varphi} + \frac{\hat{p}_i}{S_0} = 0$$

$$i\omega^* \hat{v}_{ir} + \frac{im}{r} A^2 \hat{b}_{ir} - \frac{2A^2}{r} \hat{b}_{i\varphi} - g^* \hat{\eta}_i + 2\Omega \hat{v}_{i\varphi} = 0 \quad (6)$$

$$i\omega^* \hat{v}_{i\varphi} + A^2 \frac{\partial}{\partial r} \ln(B_0 r) \hat{b}_{ir} - \frac{im}{r} \frac{\hat{p}_i}{S_0} - V_0 \frac{\partial}{\partial r} \ln(\Omega r^2) \hat{v}_{ir} = 0 \quad (7)$$

$$\omega^* \hat{b}_{ir} + \frac{m}{r} \hat{v}_{ir} = 0 \quad (8)$$

$$\omega^* \frac{\hat{p}_i}{S_0} - C^2 \omega^* \hat{\eta}_i - i\mathcal{H} C^2 \hat{v}_{ir} = 0 \quad (9)$$

where: $A = \text{Alfén speed}$, $\omega^* = \omega - m\Omega$

$$\hat{b}_{ir} = \hat{B}_{ir} / B_0, \quad \hat{\eta}_i = S_i / S_0, \quad g^* = g - \Omega^2 r$$

$$\mathcal{H} \equiv \left(1 - \frac{1}{\gamma}\right) \frac{\partial}{\partial r} \ln S_0 - \frac{1}{\gamma} \frac{\partial}{\partial r} \ln T_0$$

Finally, the dispersion equation that follows from eqs. (4) - (9) is:

$$a_4 \omega^{*4} + a_2 \omega^{*2} + a_1 \omega^* + a_0 = 0 \quad (10)$$

where:

$$a_4 = A^2 + C^2$$

$$a_2 = -A^2 \left(A^2 \frac{C^2}{r^2} - A^2 \left(g^* - \frac{2C^2}{r} \right) \frac{\partial}{\partial r} \ln \frac{B_0}{S_0 r} - \frac{A^2 C^2}{r^2} \frac{\partial}{\partial r} (\Omega r^2) + C^2 \left(g^* + \frac{2A^2}{r} \right) \mathcal{H} \right)$$

$$a_1 = \frac{2m}{r} \Omega A^2 \left[C^2 \left(\frac{\partial}{\partial r} \ln \frac{B_0}{S_0 r} + \mathcal{H} \right) + g^* - \frac{2C^2}{r} - (A^2 + C^2) \frac{\partial}{\partial r} \ln(B_0 r) \right]$$

$$a_0 = \frac{A^2 m^2}{r^2} \left\{ A^2 \left[\frac{m^2 C^2}{r^2} + \left(g^* - \frac{2C^2}{r} \right) \frac{\partial}{\partial r} \ln(B_0 r) \right] + C^2 r \frac{\partial}{\partial r} \Omega^2 - C^2 g^* \mathcal{H} \right\}$$

Simple analysis of eq. (10) shows that the condition

$$a_2 > 0 \quad (11)$$

can be taken as a criterion for convective instability when a toroidal magnetic field B_0 is present and the system differentially rotates. Indeed, when $B_0, \Omega \rightarrow 0$ the criterion (11) reduces to the known condition for convection in a non magnetized and non rotating system.

It can be concluded from the condition (11) that the toroidal magnetic field will tend to reduce the convection provided that the inequality

$$\left(g^* - \frac{2C^2}{r} \right) \frac{\partial}{\partial r} \ln \frac{B_0}{S_0 r} > 0 \quad (12)$$

holds locally. For example, this can be achieved in outer regions of the stellar interior ($r > 2C^2/g^*$) if B_0 increases with r or if it decreases with r but slower than $S_0 r$. It has also to be mentioned that the presence of magnetic field affects the stability of the system by promoting other, purely magnetic, instabilities which will not be considered in this work.

As to the influence of rotation, we see that if $\frac{\partial}{\partial r} \Omega r^2 > 0$ the convection will be reduced. For example, a rigid body rotation tends to stabilize the convective instability.

/1/ "Problems of Stellar Convection", Proc. Nice, 1976, Edited by E.A. Spiegel and J.P. Zahn. Springer-Verlag Berlin.

/2/ P.A. Gilman, Ap.J. **162** (1019) 1970.

/3/ C.H. Sung, Astron. Astroph. **60** (393) 1977.

EXPERIMENTAL DETERMINATION OF FeII Gf-VALUES

J. Moity.

*Observatoire de Meudon, Département Etoiles et Galaxies, 92190 Meudon, France.*Introduction

Though the problem of the solar iron abundance has been solved owing to reliable measurements of FeI gf-values, it seems that the situation is still open to improvements with basing abundance studies on the ions FeII which are about ten times more numerous than the neutrals in the photosphere. Unfortunately, reliable measurements of FeII gf-values are scarce (Ref./1/ to /5/) and each deals with a few lines so that comparisons are not always possible. The only comprehensive experimental work is that of WARNER /6/ in which the results have been shown to depend with the upper excitation potential. Because it is the most complete set of data, these are still commonly used and SMITH /7/ has proposed a correction-formula. On the other hand, the semi-empirical calculations of KURUCZ and PEYTREMANN /8/ must be used with carefulness in abundance studies. The work we present hereafter was undertaken with a view to a future extensive study of FeII lines and to tie the various data above-mentioned together by one accurate experiment.

Experiments and results

The FeII lines were excited in a wall-stabilized arc operated in argon with 5% hydrogen for the diagnostic purpose. A continuous mixing of $\text{Fe}(\text{CO})_5$ vapour was fed into the center section of the arc by bubbling a stream of pure argon through the liquid carbonyl at slow rates (50 or 100 cm^3/mn). The FeII spectrum was photographed end-on with a 3.40 m Ebert-type spectrograph and the ArI-4300 Å and H_β lines were photoelectrically recorded. The low-current carbon arc was used as standard radiation. The physical conditions in the FeII emission zone have been varied in the ranges $[4-1.7] \times 10^{16} \text{ e}^-/\text{cm}^3$ measured from the H_β profile and $[11250 \text{ K} - 10150 \text{ K}]$ derived from LTE equations, ArI-4300 Å intensity measurement and the measured electron density.

The procedure used to derive the FeII relative gf-values is classical and they have been put on an absolute scale by using some FeI lines of known gf-values and the Saha equation. Our results are presented in the final table and compared with the other works (GHP refers to /2/, BGHR. /3/, WBW /4/ and KP /8/). The uncertainty in our relative gf-values is better than 25% for the majority of lines and it may reach 50% for the faintest lines. We think that our absolute scale is reliable to within ± 0.15 dex.

Discussion

Our values generally lie slightly above the other recent measurements but they nearly all agree to within the mutual uncertainty ranges, except for the lower multiplets of GHP who, moreover, have some doubtful results (3285.42 and 3247.17). As for the calculations of KP, their scale seems to vary with the multiplet (see mult. 7,8) but, on an average, it roughly lies at 0.25 dex below ours. The figures hereafter show that systematic errors still remain in the corrected WARNER gf-values : one with the upper excitation potential for the higher multiplets and another with the wavelength, below 3000 Å, which is here reported for the first time.

As soon as the stability of the iron concentration in the arc over periods of hours will be achieved, photoelectrical measurements will be extended to numerous other FeII lines.

References

- /1/ Roder O. : 1962, Z. Astrophys. **55**, 38.
- /2/ Grasdalén G.L., Huber M., Parkinson W.H. : 1969, Astrophys. J. **156**, 1153.
- /3/ Baschek B., Garz T., Holweger H., Richter J. : 1970, Astron. Astrophys. **4**, 229.
- /4/ Wolnick S.J., Berthel R.O., Wares G.W. : 1971, Astrophys. J. **166**, L31.

- /5/ Huber M. : 1974, Astrophys. J. 190,237.
/6/ Warner B. : 1967, Mem.R.Astr.Soc.70,
165.
/7/ Smith P.L. : 1976, Mon. Not. R. Astr.
Soc. 177, 275.
/8/ Kurucz R.L., Peytremann E. : 1975, A
table of semi-empirical gf-values,
Smithsonian Astrophys. Obs. Special
Rep. 362.

Figures : plots of $\Delta \log(gf)$, the diffe-
rence between our data and the corrected
Warner gf-values versus upper excitation
potential and wavelength.

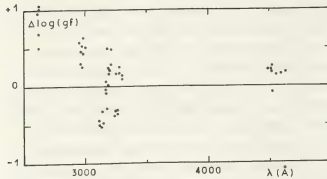
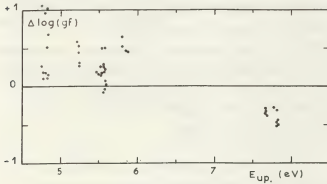


Table of results :

* Data of Warner /6/ corrected according
to Smith /7/.

Mult.	log(gf)		log(gf) : other exp.		log(gf) K.P. (1975)
	this exp.		HUBER (1974)	WARNER (*)	
UV(1)					
2599.39	0.85	0.71			0.44
2611.87	0.41	0.21			0.06
2617.62	-0.25	-0.29		-1.21	-0.48
2620.41	-1.80			-2.31	-1.75
2621.67	-0.76	-0.60		-1.45	-0.91
2585.88	0.24	0.04			-0.10
2598.37	0.33	0.15			-0.01
2607.09	0.24	0.07			-0.08
2613.82	-0.03	-0.12			-0.30
2625.66	-0.14	-0.20		-1.20	-0.43
2631.32	0.04	-0.22			-0.26
2631.05	0.06	-0.15			-0.26
2628.29	-0.14	-0.21		-1.16	-0.41

Mult.	log(gf) this exp.	log(gf) : other exp.			log(gf) K.P. (1975)
		G.H.P. (1969)	WARNER (*)		
(1)					
3277.35	-2.20	-2.79	-2.46	-2.45	
3302.86	-3.37		-3.47	-3.60	
3255.88	-2.36	-2.74	-2.53	-2.50	
3281.29	-2.56	-2.81	-2.74	-2.69	
3295.81	-2.91		-3.02	-3.00	
3303.47	-3.17		-3.32	-3.34	
3285.42	-3.25	-2.87		-3.85	
(2)					
2953.77	-1.13		-1.71	-1.51	
2970.51	-1.40		-1.93	-1.74	
2979.35	-1.80		-2.24	-2.11	
2975.94	-2.46		-2.72	-2.65	
2961.27	-2.47		-2.77	-2.66	
(6)					
3227.73	-0.74			-1.08	
3213.31	-1.00	-1.46	-1.49	-1.31	
3210.45	-1.39	-1.52	-1.68	-1.69	
3192.92	-1.71		-1.88	-1.89	
3186.74	-1.45		-1.70	-1.69	
3193.81	-1.40	-1.68	-1.62	-1.73	
3166.67	-2.91		-2.83	-2.95	
3170.34	-2.42		-2.49	-2.54	
(7)					
3196.07	-1.53	-1.72	-1.79	-2.23	
3183.11	-1.89		-2.39	-2.59	
3185.31	-2.70		-2.72	-3.30	
3163.09	-2.73		-2.70	-3.22	
(8)					
2984.83	-0.06		-0.70	-0.60	
2965.04	-1.11		-1.57	-1.47	
2964.63	-1.34		-1.79	-1.73	
3002.65	-0.57		-1.09	-1.03	
2985.54	-0.60			-1.03	
(37)		RODER (1962)	BGHR. (1970)	W.B.W. (1971)	
4629.34	-2.29	-2.10	-2.44	-2.27	-2.48
4555.89	-2.35	-2.19			-2.50
4515.34	-2.44	-2.43	-2.63	-2.35	-2.63
4491.40	-2.60				-2.82
4520.22	-2.32	-2.64	-2.76	-2.43	-3.09
(38)					
4583.83	-1.80	-1.82	-1.98	-1.85	-1.96
4549.47	-2.01	-1.89			-2.07
4522.63	-2.30	-2.08		-2.12	-2.23
4508.28	-2.27	-2.34	-2.46	-2.29	-2.41
(81)					
3259.05	-0.69		-0.79		-0.94
3258.77	-0.89		-0.98		-1.05
3247.17	-0.91		-0.69		-1.13
3237.81	-1.17		-1.38		-1.42
3237.40	-1.79				
(82)					
3177.53	-0.62			-0.34	-0.88
3135.36	-0.92			-0.61	-1.09
3114.29	-1.32			-0.88	-1.41
3144.75	-1.47			-1.00	-1.58
3116.59	-1.31			-0.82	-1.45
3133.05	-1.78			-1.26	-1.74
3114.68	-1.69			-1.18	-1.73

PROPAGATION OF CONDENSATION IN CORONAL PLASMA

S. Poberaj.

University of Ljubljana, Faculty for Electrical Engineering and J. Stefan Institute, Ljubljana, Yugoslavia.

The appearance of the luminous matter in the solar corona is in many cases due to the condensation of the coronal plasma. This relatively cool and dense matter appears as prominences inside a very hot and rarified plasma. We consider here the apparent motion of the condensations along the magnetic field.

Let us suppose that the temperature drops in some region of a hot plasma in the magnetic field. For the condensation process the number of the recombinations highly increased and so does the energy radiated into surrounding space. The temperature may drop from about 10^6 K to $2 \cdot 10^4$ K or less. Since the plasma is in the magnetic field the heat flow across the magnetic field is strongly reduced, because $\chi_{\perp} / \chi_{\parallel} \ll 1$, where χ_{\perp} and χ_{\parallel} are thermal conductivities in the directions perpendicular and parallel to the magnetic field. If the inward energy flow is low enough the cool region will spread along the magnetic field into the hot one. This problem we treat similarly as it is treated the problem of the propagation of flame above an inflammable liquid in a canal⁽¹⁾. In this case the hot region moves into the cold one.

We assume that the magnetic field is oriented along the z axis. Let Δz be

the width of the zone in which the cooling of the plasma is taking place. Δz is approximately the distance on which the temperature drops from T_1 to T_2 where T_1 is the temperature of the hot plasma and T_2 is the temperature in the condensation. The time τ_E in which the temperature drops from T_1 to T_2 is approximately equal to the energy relaxation time for the electrons flowing along the magnetic field into the condensation from the hot region. Similarly as in the problem of an inflammable liquid we get

$$\Delta z = (\chi_{\parallel}^e / \tau_E)^{1/2} \quad (1)$$

where χ_{\parallel}^e is the temperature conductivity of the electrons along the magnetic field. The thermal conductivity is given by the relation⁽²⁾

$$\chi_{\parallel}^e = \frac{k T_e^2}{e^2} \cdot \sigma_{\parallel}^e$$

σ_{\parallel}^e is the electrical conductivity parallel to the field. Treating the electron gas as an ideal one we get

$$\chi_{\parallel}^e = \frac{2}{3} \frac{k T_e^2}{e^2 n_e} \cdot \sigma_{\parallel}^e \quad (2)$$

Taking for the σ_{\parallel}^e the expression

$$\sigma_{\parallel}^e = \frac{e^2 n_e \tau_e}{m_e}$$

we get

$$v_a^e = \frac{2}{3} \frac{kT_e}{m_e} \cdot \tau_e \quad (3)$$

where τ_e is the mean collision time for the electrons. From the Eqs. (1) and (3) we get for the apparent velocity of the propagation of a condensation along the magnetic field

$$v_a = (2kT_e \cdot \tau_e / m_e \tau_E)^{1/2} \quad (4)$$

Let us use this equation to calculate the velocity v_a in a prominence in the solar corona. For T_e we take a typical value $T_e = 2 \cdot 10^4$ K. The energy relaxation time τ_E is much longer than the mean collision time τ_e . We can take for the hydrogen plasma $\tau_e / \tau_E = 10^{-2}$. For v_a we get $v_a = 45$ km/s. Velocities of similar magnitude have really been measured⁽³⁾.

If $v_a = 0$ it does not mean that the matter is flowing along the field lines. This is the velocity of the region of the enhanced radiation. In majority of the moving prominences the matter really moves along the magnetic field.

References:

- 1) Landau, L.D., and Lifshitz, E.M., Fluid Mechanics, Pergamon Press Inc., New York, 1963.
- 2) Shkarofsky, I., Bernstein, I. and Robinson B., Phys. of Fluids 6, 40 (1963).
- 3) Kaplan, S.A., Pikelner, S.B., Taytovich V.N., Plasma Physics of Solar Atmosphere, (in Russian), Nauka, Moscow 1977.

RELATIVISTIC ELECTRON-POSITRON PLASMA QUASI-LINEAR RELAXATION AT THE PRESENCE OF MAGNETIC BREMSSTRAHLUNG

J.G. Lominadze, G.Z. Machabeli and A.B. Mikhailovsky.

*Abastumani Astrophysical Observatory, Academy of Sciences GSSR, Tbilisi, U.S.S.R.,
I.V. Kurchatov Institute of Atomic Energy, Moscow, U.S.S.R.*

Recently a significant attention is paid to instabilities and non-linear phenomena, connected with them. In adopted models they may take place in pulsar magnetospheres. Such plasma specific features are determined by its ultrarelativity and very strong magnetic field ($B \sim 10^{12}$ gauss).

An ultrarelativistic particle in a strong magnetic field loses its transverse momentum due to magnetic bremsstrahlung and as a result particle distribution relaxes to a one-dimensional. By the existing notion, pulsar magnetosphere is filled up with electron-positron plasma, moving along magnetic field force line with a typical Lorentz-factor $\gamma_{\tau} \approx 10^2 - 10^3$ and with electron-positron beam with Lorentz-factor $\gamma_b \approx 10^5 - 10^7$. A beam instability [1] excited at the Cherenkov resonance of beam particles with Langmuir oscillation is generated in such plasma. Particle distribution due to quasi-linear particle interaction with the excitations, relaxes to a one-dimensional with an elongated tail. In analogy with nonrelativistic case [2] one may expect that such distribution must be unstable with respect to perturbations excited at the cyclotron resonance ($\omega - k_{\parallel} v_{\parallel} + \tilde{\omega}_p = 0$, $\tilde{\omega}_p = \frac{eB}{mc} \frac{1}{\gamma_b}$)

with beam particles, and for the real and imaginary parts of frequency

$$\omega = kc(1 - 2 \frac{\omega_p^2}{\omega_b^2} \gamma_{\tau}), \quad \Gamma = 2 \frac{n_b}{n} \frac{\omega_p^4}{\omega_b^2} \gamma_{\tau} \quad (1)$$

Here $\omega_p^2 = \frac{4\pi e^2 n}{m}$, n_b - density of beam.

Perturbations, characterized by frequency and growth rate (1) at the quasi-linear diffusion of particles lead to a transverse momentum rise. Such relaxation must complete with a magnetic bremsstrahlung, leading to a transverse momentum decrease. A competition of these two processes will determine a final form of distribution function.

The initial kinetic equation has a form

$$\frac{\partial f}{\partial t} + \frac{1}{P_{\perp}} \frac{\partial}{\partial P_{\perp}} (P_{\perp} F_{\perp} f) + \frac{\partial}{\partial P_{\parallel}} (F_{\parallel} f) = S_{QL} \quad (2)$$

Here F_{\perp}, F_{\parallel} - are transverse and longitudinal components of bremsstrahlung

force,

$$F_{\perp} = -\alpha \frac{P_{\perp}}{P_{\perp}^2}, \quad F_{\parallel} = -\alpha \left(\frac{P_{\parallel}}{mc} \right)^2, \quad \alpha = \frac{2}{3} \frac{e^2 \omega_p^2}{c^2}$$

S_{QL} - is operator of quasilinear diffusion.

$$S_{QL} = \frac{1}{P_{\perp}} \frac{\partial}{\partial P_{\perp}} \left(P_{\perp} \mathcal{D}_{\perp\perp} \frac{\partial f}{\partial P_{\perp}} \right)$$

$$\mathcal{D}_{\perp\perp} = \frac{\pi e^2 \omega_p^2}{4c \omega_b^2} \gamma_{\tau}^2 |E(k)|^2$$

Considering derivatives $\frac{\partial}{\partial P_{\perp}}$ to be greater in comparison with $\frac{\partial}{\partial t}$, $\frac{\partial}{\partial P_{\parallel}}$, we find out from (2) in a first approximation by a small parameter.

$$f_0(p_{\perp}, p_z, t) = \frac{\alpha}{P_{\perp}^2 \omega_{ce}} f_{11}(p_z, t) \times \exp \left\{ -\frac{\alpha}{P_{\perp}^2 \omega_{ce}} \frac{P_{\perp}^2}{2} \right\} \quad (3)$$

And for $f_{11}(p_z, t)$ in next approximation by a small parameter we have equation

$$\frac{\partial f_{11}}{\partial t} \approx 2 \frac{\partial}{\partial p_z} \left[\frac{p_{\perp} p_z}{m^2 c^2} f_{11} \right] \quad (4)$$

We suppose, that before the cyclotron instability outset, when noises have been thermal, the function $f_{11}(p_z, t)$ have had plateau form. If we suppose, that quasilinear relaxation lapse ($t \rightarrow \infty$) the beam decelerates completely ($f_{11}(p_z, \infty) = 0$)

$$|E(k)|^2 = \frac{4\pi m c^3 n_b}{\omega_b} \left(1 - \frac{p_z}{P_b} \right) \quad (5)$$

Using this parameter as a characteristic of noises level at relaxation stage (for finite t) we shall get an estimation for beam deceleration time $\tau = \frac{n}{n_b} \frac{\omega_b^2}{\omega_p^2} \gamma_z$

It is possible to estimate the total wave energy as

$$W_c \sim \frac{m c^2 n_b}{\gamma_z} \quad (6)$$

the rest part of beam energy is irradiated, so that

$$W = W_b = m c^2 \gamma_b n_b \quad (7)$$

It's easy to obtain from (5) an effective transverse momentum of beam particles

We have considered cyclotron instability and connected with it quasilinear relaxation of ultrarelativistic particle beam in relativistic plasma in a strong magnetic field, taking into account magnetic bremsstrahlung. Supposing that such radiation is a strong one, we have got a system of one-dimensional quasilinear equations and have found an asymptotic solution of the system for large time. It has been shown, that as a consequence of a quasilinear relaxation in a condition of strong magnetic bremsstrahlung a beam deceleration appears and beam energy transforms into the energy of radiation.

The process considered in this paper is important for pulsar magnetosphere physics.

REFERENCES

1. J.G.Lominadze, A.B.Mikhailovsky, JETP, v.76, N.3, 1979.
2. A.B.Mikhailovsky, "Teoria Plasmennikh Neustoichivostei", v.1, "Atomizdat", 1975.

A PLASMA MODEL OF CRAB NEBULA AND PULSAR Np0532 RADIATION IN ROENTGEN AND GAMMA RANGES

G.Z. Machabeli, V.V. Usov.

*Abastumani Astrophysical Observatory, Academy of Sciences, GSSR, Tbilisi, U.S.S.R.,
Space Research Institute, Academy of Sciences, U.S.S.R., Moscow, U.S.S.R.*

Lately, a significant progress in the study of processes, taking place in pulsar magnetospheres has been achieved; It allows to develop consistent pulsar radiation models. Namely, it was shown that near the pulsar surface a rapid birth of electron-positron pairs must take place.

As a result, two-component electron-positron plasma, moving from a neutron star along magnetic force lines with velocities corresponding to Lorentz-factors 10^2 - 10^3 and 10^5 - 10^7 is generated in pulsar magnetosphere.

In Np0532 case the electron-positron plasma concentration near pulsar surface attains 10^{20} cm^{-3} . Plasma particles in a strong magnetic field $B \sim 10^{12}$ quickly lose transverse momentum and the momentum distribution of particles relaxes to a one-dimensional. This one-dimensional distribution appears to be unstable with respect to oscillations, excited in electron-positron relativistic plasma. Among them the longitudinal Langmuir oscillations are characterized by the largest growth rate. Their rapid evolution leads to a plateau formation on the distribution function due to quasi-linear interaction of resonance particles with Langmuir oscillations. As a result, particle distribution relaxes to a one-dimensional one with

elongated tail without humps [1]. Such an asymmetric one-dimensional distribution appears to be unstable with respect to perturbations, excited at the cyclotron resonance with beam particles.

The instability evolution requires a number of restrictions. In particular, the condition of the lack of hose instability, smallness of damping on plasma particles and resonance condition $(\omega - k v_z - \frac{\omega_p}{\gamma} \approx 0)$

Considering also $B = B_0 (\frac{r}{r_0})^3$, $n = n_0 (\frac{r}{r_0})^3$ (B_0 , n_0 - magnetic field strength and plasma density near a neutron star surface, r_0 - star radius). In an observer's system we shall get inequality

$$\frac{\gamma^2}{\gamma_0^2} < \frac{\omega_p^2}{\omega_{B0}^2} \left(\frac{r}{r_0} \right)^3 < 1, \quad \omega_p^2 = \frac{4\pi e^2 n}{m}, \quad \omega_B = \frac{eB}{mc} \quad (1)$$

Magnetic field is slightly inhomogeneous and in the presence of velocity transverse components it can significantly influence the particle distribution character. In the weakly inhomogeneous field a force, directed transverse the magnetic field would affect a particle. This force at the relativistic character of the motion should have a form $G_{\perp} \approx -\frac{mc^2}{\gamma} \gamma_0 \psi$

Pitch-angles appearance, on account of owing quasi-linear diffusion results in magnetic bremsstrahlung and braking-by-radiation force origin. This latter one has both transverse and longitudinal compo -

nents. $\vec{F}_1 = -\alpha \psi$, $\vec{F}_2 = -\alpha \psi^2 \gamma_{\perp}^2$, $\alpha = \frac{2}{3} e^2 \omega_B^2 / c^2$

Then from kinetic equation we obtain

$$f_0(\gamma_{\perp}, \psi, \tau) \cong 2\beta f_h(\gamma_{\perp}, \tau) \times \\ \times e^{-\beta \psi^2 \left\{ 1 - \frac{3}{4} (H - E_i(\beta \psi^2)) \right\}^{(2)}}$$

Here $\beta = \frac{m^2 c^3}{2 \omega_{B1}} \gamma_{\perp}^2$,

$$f_h(\gamma_{\perp}, \tau) = \int_{\psi_{12}}^{\psi_{12}} f_0(\gamma_{\perp}, \psi, \tau) d\psi$$

H - a certain finite number. $E_i(\lambda) = \int_{\lambda}^{\infty} d\alpha$

During the cyclotron waves relaxation time τ . The beam is taken out from the region of interaction with spectrum depending only on cyclotron noises settled.

$$f_h(\gamma_{\perp}, \tau) = \frac{\text{Const}}{\gamma_{\perp} |E(\kappa)|^2} \quad (3)$$

From the energy balance equation at the proper boundary conditions we shall get

$$|E(\kappa)|^2 \cong \frac{12 \pi m^2 c^7 n_b \gamma_{\perp}^2}{e^2 \tau \omega_B \gamma_{\perp 0}}$$

$\gamma_{\perp 0}$ - is beam Lorentz-factor before the beginning of cyclotron instability evolution.

Using (2) and (3) and expressions for effective pitch-angle we obtain

$$\psi_{ess} = \left\{ 3 \pi^2 \frac{\omega_p^2}{\omega_B^2} \frac{n_b c^3}{\gamma_{\perp 0} \omega_B^3} \right\}^{1/2} \frac{1}{\gamma_{\perp}}$$

Using (3) we shall find synchrotron irradiation spectrum, which falls in roentgen and γ -ranges region $I_{\nu} \sim \nu^{-\alpha}$ where α - spectrum index appears to be ~ 1 , that is in a good accordance with observed curves. The greater part of beam energy, due to adiabatic invariant existence, is carried out beyond the light cylinder into Crab nebula and is irradiated there. Only a small part of the energy (about 1%) is irradiated directly from the pulsar with a close spectrum indice.

REFERENCES

1. Lominadze J.G., Mikhailovsky A.B., JETP, v.76, N.3, 1979.

ANALYSIS OF THE H.F. DRIFT INSTABILITY ONBOARD "METEOR" SATELLITE

V.P. Khodnenko, G.G. Shishkin and Ju. V. Trifonov.

Moscow, U.S.S.R.

I. Introduction. Hall plasma accelerators onboard the satellites /1/ can generate various types of electromagnetic noises over a wide frequency range. As evidenced by the previous theoretical and laboratory investigations /2/, /3/, /4/, noise generation in an accelerator with radial magnetic and axial electric fields results from various plasma instabilities. The paper presents the results of the "Meteor" satellite onboard measurements of HF electromagnetic fields generated by the accelerator plasma as well as comparison of the obtained data with experimental results. Onboard measurements make it possible to estimate laboratory conditions influence on development of wave processes in plasma.

2. Experimental Conditions. A Hall plasma accelerator of ring geometry with ceramic walls of the discharge channel /OD = 70 mm/ was installed onboard the Meteor satellite. A detailed description of the satellite and accelerator characteristics is presented in the earlier paper /1/, only basic data being suggested here. The Meteor satellite is a 3m high cylindrical body of about 1 m in diameter. The satellite is provided with two solar panels, more than 3 m long each, rotating along the azimuthal direction. The satellite has been put into the near-circular orbit of ~

1000 km altitude. The accelerator-ejected $150+200$ eV xenon-plasma jet had maximum particle concentration $n_{\text{max}} \sim 10^{17} \text{ m}^{-3}$ at the discharge channel section. In-flight measured the plasma jet divergence angle proved to be about 45° . To attain a discharge initiation in the accelerator, the plasma cathode was switched-on first. The receivers were connected to probes

mounted on the solar panels at about 3 m distance from the accelerator. A possibility was provided for the solar panels to move along the azimuth within angles $\varphi = -10^\circ + +40^\circ$ /Fig.1/. The measurement data were telemetered from the satellite to the ground receiving posts.

3. Experimental Results. Accelerator switching on is followed by an appreciable signal-level rise displayed on the selective micro-voltmeters. It is worth mentioning that a slight signal rise occurs when only a plasma cathode is operative /Fig.2/. Intensity of a signal increases as the probe is approaching the jet boundary though just on the plasma jet axis the electromagnetic field is weaker than that at the jet boundary. Under solar panels reversal, spatial variation in the field intensity somewhat differs from that under direct motion /Fig.2/. Electromagnetic field intensity as a function of time is plotted in Fig.3. For the sake of comparison identical measurements have been taken under laboratory conditions. Intensity of fields, generated by an accelerator of the same type in the laboratory, proved to be considerably lower than that of satellite-derived fields. Laboratory-derived time dependence of the oscillation intensity is presented in Fig. 3.

4. Discussion of Results. Comparison of the laboratory results with the satellite-derived data enables one to conclude that electromagnetic fields generation in the vicinity of a satellite in the range of ~ 30 MHz is likely to occur due to HF drift-instability analysed in papers /2/, /3/, /4/. This instability stems from a non-uniform distribution of electrons azimuthally.

thal drift velocity along the channel axis. Non-uniform density plasma, rotating in the azimuthal direction, generates closed HF currents causing electromagnetic fields in space /3/.

Time dependence of radiation intensity /4/, as evidenced by the related laboratory experiments, is associated, in general with the entire accelerator, especially its dielectric discharge channel, warm-up. Ceramics-temperature variation, effecting its conductivity, brings about a change in plasma potentials distribution which, in turn, effects the local ion flow to the walls, thereby causing a change in the local temperature. Variations in potentials distribution lead to a distortion of the associated drift-velocity distribution along the channel accompanied by variations in properties of the instability under consideration.

References:

- /1/ Morozov A.I., Snarskii R.K., Khodnenko V.P., Trifonov Ju.V. et al. Kosmicheskie issledovaniya, v.XII, N 3, (1974).
- /2/ Shishkin G.G., Gerasimov V.P. XII Internat. Conf. on Phenom. Ion. Gas (1975), 310, Netherlands
- /3/ Shishkin G.G. Internat. Conf. Gas discharge. IEE Conf. Publ. N 143, 349 (1976) England
- /4/ Gerasimov V.P., Shishkin G.G. et al. XIII Internat. Conf. on Phenom. Ion. Gas (1977) part II 771.

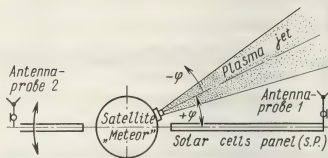


Fig. 1. Experimental arrangement

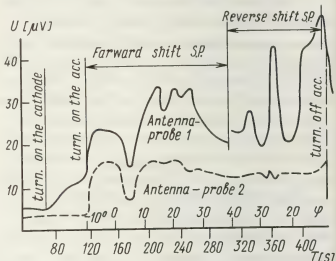


Fig. 2. Space Azimuth distribution of the electromagnetic field intensity

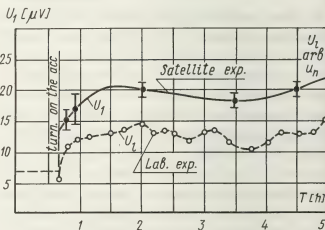


Fig. 3. Time fluctuations of the oscillations amplitude

INVERTED POPULATION OF HYDROGEN ATOMS IN A TURBULENT COSMIC PLASMA

I.M. Ojringel.

Sibirskiy, Siberian Branch, U.S.S.R. Academy of Sciences, Irkutsk.

The role of plasma effects in the emission of atomic systems was dealt with in a number of papers /1 - 6/. Part of this work was devoted to the investigation of spectral line broadening during collisions of an atom with charged particles /1 - 2/, other authors considered the effect of plasma turbulence on the processes of emission (absorption) of quanta by atoms. And both the effects of spectral line broadening by plasma turbulence /3 - 4/ and the induced processes of emission of plasmons by atoms were studied /5 - 6/.

As is well known /7/, such a state is possible in the interstellar medium when the hydrogen atoms are almost not ionized, and the electron density is enough to give an intense plasma turbulence.

In /8/, it was shown that if the hydrogen atoms are in a field of intense ultraviolet emission $\lambda \sim 1216 \div 912 \text{ \AA}$ then interaction of their spins with light quanta can produce in such a medium an inverted population with respect to the $\lambda = 21 \text{ cm}$ line emission.

Unfortunately, the criteria for the appearance of the inverted population turned out to be very strict to apply to real conditions of the interstellar medium.

In this paper it is shown that the possibility of producing inverted population

could be significantly improved if the hydrogen atoms are assumed to be in a plasma with the gyrofrequency type of wave turbulence (whistlers). As a rule, the whistler turbulence is anisotropic - let Ω be the solid angle in which the whistler wave vectors are involved. The level of whistler turbulence can be determined using the effective temperature T_{eff} which can exceed by orders of magnitude the kinetic temperature of gas or the electron temperature.

The interaction of spins of atoms, Lyman quanta and whistlers also leads up to inverted population. The consideration of this problem was performed by the same method as in /8/, but terms describing the interaction of atoms with plasma waves were added into the equations of balance. In /9/, it was shown that transitions in atoms with participation of electromagnetic waves with $\lambda = 21 \text{ cm}$ prove to be less effective than transitions with whistlers if the condition:

$$T_{\text{eff}} / T_R \gg 4 \pi \gamma_B \gamma_0^2 / 3 \Omega_B \gamma_p^3 \quad (1)$$

is valid, where T is the radiant temperature in the $\lambda = 21 \text{ cm}$ line, $\gamma_p = 9 \cdot 10^3 \sqrt{n_e} \text{ cm}^{-1}$ is Langmuir frequency, and $\gamma_0 = 1420.4 \text{ MHz}$ is the frequency of the $\lambda = 21 \text{ cm}$ line.

Plasma transitions here interconnect Zeeman sublevels of the upper level of superthin structure of the main atom's state $1H$.

When hydrogen atoms are excited by isotropic nonpolarized Lyman emission, from analysis of the equations of balance we have the following relation for spin temperatures T_{FM} of all sublevels

$$T_{4,1} = T_{4,-1} = T_{4,0} = T_* \frac{n(\nu_1) + n(\nu_2)}{[n(\nu_1) + n(\nu_2) - n(\bar{\nu}_1) - n(\bar{\nu}_2)]} \quad (2)$$

where $T_* \equiv h\nu_0/k = 0.0684^\circ K$, $n(\nu) = \lambda^2 I_\nu / 2hc$ is the phase emission density of Lyman quanta. The denotations ν_1 , ν_2 , $\bar{\nu}_1$ and $\bar{\nu}_2$ are taken from [8]; in the denominator of (2), small positive terms $\sim n(\nu)/\beta_g$ were omitted, where $\beta_g = 42n_g \frac{\Omega_g}{4\pi} \left(\frac{\nu}{\nu_B}\right)^3$ (here n_g is the whistler phase density).

From (2) it follows that with declining spectrum ($\frac{dn(\nu)}{d\nu} < 0$), the spin temperatures are positive, but already at any slowly increasing spectrum ($\frac{dn(\nu)}{d\nu} \gg \frac{n(\nu)}{\beta_g}$) the spin temperatures become negative:

$$T_{4,1} = T_{4,-1} = T_{4,0} = -T_* n(\nu) / \frac{dn(\nu)}{d\nu} \quad (3)$$

Thus, excitation of circularly and linearly polarized radio emission at $\lambda = 21$ cm occurs in this case. In calculations we disregarded collisional transitions since in turbulent plasma, transitions with participation of whistlers are more effective. Obviously, for a detailed analysis of observational data, a more complete calculation is needed with account of all possible transitions in equations of balance. In this paper, such a problem was not posed. We wished to indicate a principal possibility of producing inverted population in the $\lambda = 21$ cm line under real space conditions.

The interpretation of the available observations of 21 cm line in interstellar space in terms of our understanding of nor-

mal (not inverted) population has encountered no special difficulties so far, and this allows the question to be posed of the reality of the existence of maser enhancement in the $\lambda = 21$ cm line. In this connection, we would like to make another remark.

The determination of magnetic fields in dense clouds of interstellar gas using the observed circular polarization in the wings of the $\lambda = 21$ cm absorption line gave values of magnetic field strengths one or even two orders larger than the values of field strengths determined by other methods for average conditions in interstellar space. A conventional explanation is that in dense clouds, gas compression is followed by a respective increase in magnetic field. However, it is not excluded that maser enhancement of emission due to whistler turbulence is the case, then the magnetic field strengths thus found are overestimated.

REFERENCES

1. I.I. Sobelman, Introduction to atomic spectra theory, Fizmatgiz, 1963.
2. H.R. Griem, Spectral line broadening by plasmas, Acad. Press, 1974.
3. G.V. Sholin, DAN SSSR, 195, 589, 1970.
4. D.G. Yakovlev, ZhTF, 42, 1550, 1972.
5. I.I. Sobelman, E.L. Feinberg, JETP, 34, 494, 1958.
6. S.A. Kaplan, E.B. Kleiman, I.M. Ojringel, Astron. Zh., 49, 294, 1972.
7. S.A. Kaplan, V.N. Tsytovich, Plasma Astrophysics, M., Nauka, 1972.
8. D.A. Varshalovich, JETP, 52, 242, 1967.
9. S.A. Kaplan, E.B. Kleiman, I.M. Ojringel, Astron. Zh., 54, 1305, 1978.

SOME PROPERTIES OF INTERACTION OF MAGNETIC PISTON WITH NON-MAGNETIZED PLASMA

N.A. Koshilev, N.A. Strokin and A.A. Shisko.

Sibirián, Irkutsk 33, P.O. Box 4, U.S.S.R.

When studying phenomena with a burst nature occurring in the solar and near-terrestrial magnetospheric plasma, of interest are experiments simulating individual fragments and processes accompanying such phenomena. In particular, of crucial importance are the characteristics of current sheets arising when plasma is affected by rapidly increasing magnetic fields. A large number of experiments on transversal shock waves propagating in a rarefied plasma with a frozen-in magnetic field H_0 have shown that both structure and properties of such perturbations are determined largely by dissipative processes occurring as a result of development on the front of small-scale instabilities (Buneman, ion-acoustic, etc.). Transversal shock waves at $M_A = \frac{U}{V_A} \leq M_{ci} \approx 3$ (U - shock wave velocity, $V_A = \frac{H_0}{\sqrt{4\pi n_0 m_i}}$ - Alfvén velocity in the unperturbed plasma) have a width of $\Delta \sim 10 \frac{c}{\omega_{pe}}$ ($\omega_{pe} = \sqrt{\frac{4\pi n e^2}{m_e}}$ - Langmuir frequency) and heat predominantly the plasma electron component.

If the action time of current on plasma is less than the time necessary for the development of small-scale instabilities, laminar structures ($\Delta \sim \frac{c}{\omega_{pe}}$) are observed.

With an increase of the initial field ($H_0 \approx 0, n_0 \sim 10^{13} \text{ cm}^{-3}$) in the current sheet turbulent processes develop which lead to

electron component heating and are characterized by properties similar to those found in theory and experiments for shock waves with $M < M_{ci}$. With a decrease in initial density (at a fixed amplitude of the piston ($\tilde{H} \approx 1300 \text{ G}$) and a velocity of field increase on the plasma boundary ($4.3 \cdot 10^9 \text{ G/sec}$), due to an increase in current sheet velocity U , the time of plasma being in the transition region t_n falls and when it becomes less than the time necessary for instability excitation a quasi-stationary current sheet with a width of $\Delta_M \sim 2 \div 4 \frac{c}{\omega_{pe}}$ with parameters $\beta_H = \frac{4\pi n_0 m_i U^2}{(\Delta H)^2} \approx 0.5$, $S = \frac{2e\Delta\varphi_0}{m_e U^2} \approx 1$ indicating a full reflection of the particle flux. Before the magnetic piston, there is a sharp jump of the potential with a spatial width of $\Delta\varphi = 50 \div 100 \Gamma_d \ll \Delta_M$ which can be linked with the formation under conditions of anomalous ion viscosity of a front of the turbulent electrostatic shock wave. A detailed study of processes in the reflecting current sheet is difficult because of small typical size ($\Delta\varphi \sim 10^{-2} \text{ cm}$) however analysis of energy spectra of ions moving at various angles to front plane permits qualitative assumptions about the character of processes and comparison with other results.

MEASUREMENTS OF ELECTRON ENERGY DISTRIBUTION IN THE THETA-PINCH NEUTRAL SHEET

A.T. Altyn'tsev, V.I. Krasov, N.V. Lebedev and V.V. Paperny.

Sibizmir, Irkutsk 33, P.O. Box 4, U.S.S.R.

Dissipative processes in neutral current sheets may play an essential role in plasma heating and confinement in laboratory devices of the theta-pinch type. In addition, annihilation of the magnetic fields in the current sheet is now considered as one of the most real mechanisms of energy release in solar flares.

The experiment was performed on the "UN-Fenix" device /1/. The initial plasma (hydrogen, argon, $n_0 = 10^{12} - 10^{14} \text{ cm}^{-3}$, $T = 1-5 \text{ eV}$) was frozen in a quasi-stationary magnetic field $H_0 = 100-600 \text{ Oe}$, directed along the working volume axis ($\varnothing = 16 \text{ cm}$, $l = 1.5 \text{ m}$). The cylindrical neutral sheet with a thickness of about $10 \frac{c}{\omega_{pe}}$, converging to the volume axis is formed at a rapid compression of plasma by the magnetic piston ($H^- = 1300 \text{ Oe}$, $\tau = 1.5 \text{ sec}$), whose magnetic field was antiparallel to H_0 . The formation process and magnetic structure both are described in /1/.

In this paper, experimentally is investigated the dependence of the electron energy distribution on the plasma conductivity value in the sheet and the properties of its evolution in time and space.

The electron energy spectrum was measured by analysis of the X-ray radiation arising on the target placed into plasma /2/. Plasma conductivity and the electron tem-

perature in the sheet were measured by probe methods. In a first series of experiments, we measured the dependence of plasma conductivity on the azimuthal (current-aligned) electric field strength in the sheet. This dependence $\sigma(E_\varphi)$ is given in Fig. 1a. The measurements were for the whole range of the initial plasma parameters and showed that the conductivity values are several orders less than the Coulomb ones and are inversely proportional to the value E_φ . Such a dependence indicates the realization in the sheet of the quasilinear stage of ion-acoustic instability.

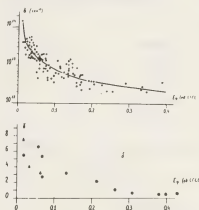


Fig. 1

Measurements of the low-energetic portion of the electron energy spectrum agree with this inference. In Fig. 2a, a solid line indicates the electron spectrum provided $n_0 = 10^{13} \text{ cm}^{-3}$, $H_0 = 230 \text{ Oe}$ within the energy range 0.5-12 keV. It is seen that the thermal part of the spectrum differs from the Maxwellian one (dash-dot line)

and is close to the distribution $\sim \exp(-\sqrt{\epsilon})$ (dash line) which must be realized at the quasilinear stage of ion-acoustic instability [3].

At the same time, one observes the pre-

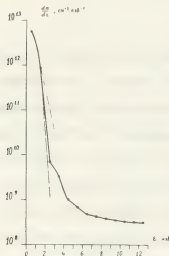


Fig. 2
spectrum may be considered as isotropic.

The measurement results of energy spectra $\frac{dN}{dE}(\epsilon)$ of electrons in the current sheet are given in Fig. 3 (a - $n_0 = 6 \cdot 10^{12} \text{ cm}^{-3}$, b - $n_0 = 10^{12} \text{ cm}^{-3}$, c - $n_0 = 4 \cdot 10^{13} \text{ cm}^{-3}$, d = 10^{14} cm^{-3}).

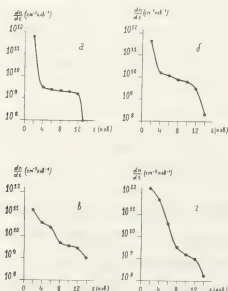


Fig. 3

It is evident that with increasing plasma density, the acceleration efficiency drops.

If the high-energetic part of the spectrum is approximated by a power function $\epsilon^{-\delta}$ within energy range 4-12 keV, one may ob-

tain the dependence of the efficiency of the acceleration mechanism determined by the value δ on the azimuthal electric field strength E_ϕ , which is shown in Fig. 1b.

High-energetic electrons are located in the vicinity of the neutral sheet. When moving away from the zero line, the index δ grows which indicates a special role of the neutral line in electron acceleration. With parallel orientation of magnetic fields of piston and initial field, the signal from X-ray detectors is absent. One may suggest the stochastic acceleration by Langmuir pulsations [4] as an acceleration mechanism.

It is of interest to study plasma heating dynamics in the neutral sheet. Plasma heating with the sheet moving towards the device axis is found to bear a relaxation character, i.e. the plasma temperature in the sheet increases periodically and then decreases. The typical time of this process is several tens of nanosec. The amplitude of temperature change is of the order of its value.

REFERENCES

1. A.T. Altyntsev, V.I. Krasov, ZhTF, 44, 2629, 1974.
2. A.T. Altyntsev, V.I. Krasov, ZhTF, 47, 44, 1977.
3. A.A. Galeev, R.Z. Sagdeev, In: "Voprosy teorii plazmy", v.7, M., p.1973.
4. V.N. Tsytovich, "Teoriya turbulentnoy plazmy", M., Atomizdat, 1971.

XIII

- Interaction des faisceaux lasers avec les plasmas
Interaction of laser beams with plasmas
Laser-induced plasmas (optical discharges)



INTERACTION OF A TEA-CO₂ LASER PULSE WITH A DENSE HYDROGEN PLASMA

C. Richard Neufeld.

Direction Sciences de base, Institut de Recherche de l'Hydro-Québec, Varennes, Québec, Canada J0L 2P0.

The physical mechanisms influencing the coupling of energy from intense laser pulses to dense plasmas are of considerable interest for the problem of laser-initiated controlled thermonuclear fusion. Studies of these phenomena in full-scale experiments involve high-speed diagnostic techniques applied to rapidly changing plasma conditions. Interest has consequently been shown¹⁻⁴ in experiments of a modest scale with somewhat relaxed physical constraints in order to simulate certain aspects of the energy coupling problem. Here we describe such a simulation study, in which a dense plasma target, created by a fast Z-pinch discharge⁵, is irradiated by a pulsed CO₂ laser.

1. The Plasma Target

The pinch discharge is produced between copper electrodes spaced 25 cm apart in a Pyrex vacuum vessel of 22.2 cm internal diameter. The current is supplied by a low-inductance energy storage bank charged to 23 kV, the oscillating discharge current reaching a maximum amplitude of approximately 500 kA. No preionization was used. The pinch was operated in hydrogen at an initial pressure of 3 Torr, maintained by continuously flushing gas from a pressurized cylinder through the discharge vessel with the aid of a mechanical vacuum pump. High-speed photographs indicate a reproducible first plasma compression (column diameter approximately 25 mm) lasting about 0.5 μs. Time-resolved spectroscopic measurements of the discharge were made, as shown on Fig. 1.

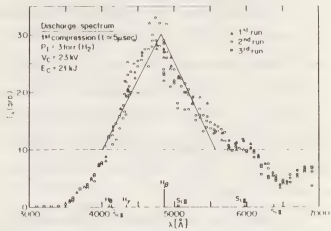


Fig. 1 Plasma emission spectrum. The dotted line indicates the assumed continuum intensity. The H_β radiation is crudely approximated by the triangular region superposed on the continuum.

The spectrum is dominated by H_β radiation (indicated crudely by the triangular region on the figure), the line being strongly Stark-broadened. The width of this line indicates an electron density of $(1 \times 10^{19} \pm 20\%) \text{ cm}^{-3}$, suitable for CO₂ laser-solid target simulation experiments.

The observed spectrum is not classical, and its analysis presents some difficulties. However, a self-consistent interpretation of the measurements, including the strong absorption of the H_α line ($\lambda_0 = 6563 \text{ Å}$) and the absence of recognizable H_γ and H_δ radiation, can be made⁶ by recognizing that substantial departures from local thermodynamic equilibrium (LTE) can exist in a plasma undergoing a rapidly-rising degree of ionization^{6,7}. This lack of LTE is not crucial to the electron density deter-

mination, but clearly precludes spectroscopic temperature measurements of the pinch plasma. On the basis of previous work by other authors^{8,9} a kinetic temperature of approximately 10 eV was assumed, a value consistent with elementary pressure balance considerations.

2. The Laser-Plasma Interaction

The plasma target was irradiated transversely by a TEA-CO₂ laser pulse, focussed to give a laser power density (measured in vacuum) of approximately 2×10^{11} W cm⁻². Visible perturbations of the plasma emission can be observed using high-speed streak photography¹⁰. In addition, quantitative measurements were made of the laser radiation backscattered from the plasma column.

A spectrum of the backscattered radiation is shown on Fig. 2. Both a broadening and a shift to longer wavelengths are evident, with essentially no signal present at the incident laser wavelength ($\Delta\lambda = 0$). In addition, the temporal behaviour of the backscattered radiation can be very complex, and often bears no apparent relation to the incident laser pulse. The results indicate that stimulated Brillouin scattering dominates the backscatter pro-

cess. This interpretation leads to a plasma kinetic temperature in excess of 200 eV during the laser-plasma interaction. At these relatively modest laser power densities only a few per cent of the incident radiation is backscattered. For the higher laser power densities proposed for laser fusion, however, the backscattered fraction may be considerably greater, especially if relatively long (> 1 ns) laser pulses are used¹¹. The plasma target described here can provide a means for checking such a hypothesis experimentally.

References

1. D.G. Steel, P.D. Rockett, D.R. Bach, and P.L. Colestock, *Rev. Sci. Instr.* **49**, 456 (1978).
2. A.A. Offenberger, A. Ng, and M.R. Cervenak, *Can. J. Phys.* **56**, 381 (1978).
3. D.R. Gray, J.D. Kilkenny, and M.S. White, *Phys. Rev. Lett.* **39**, 1270 (1977).
4. K.H. Finken, G. Bertschinger, S. Maurmann, and H.-J. Kunze, *J. Quant. Spectrosc. Radiat. Transfer* **20**, 467 (1978).
5. J. Mercier and C.R. Neufeld, *Journ. Appl. Phys.* **48**, 4498 (1977).
6. C.R. Neufeld, *Journ. Appl. Phys.* (Accepted for publication).
7. W. Engelhardt, W. Koppendörfer, and J. Sommer, *Z. Physik* **246**, 29 (1971).
8. L.A. Artsimovich, *Controlled Thermonuclear Reactions* (Gordon and Breach, New York, 1964)p. 129.
9. H. Zwickler and U. Schumacher, *Z. Phys.* **183**, 453 (1965).
10. C.R. Neufeld, P. Noth, and A. Robert, *Bull. Am. Phys. Soc.* **21**, 1139 (1976).
11. B.H. Ripin, F.C. Young, J.A. Stamper, C.M. Armstrong, R. Decoste, E.A. McLean, and S.E. Bodner, *Phys. Rev. Lett.* **39**, 611 (1977).

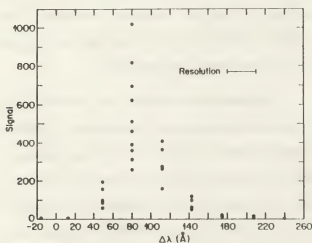


Fig. 2 Spectrum of backscattered CO₂ laser radiation shown in terms of the displacement, $\Delta\lambda$, from the incident laser wavelength ($\lambda_0 = 10.6 \mu\text{m}$).

EFFECT OF PULSE SHAPING ON INTERACTION PROCESSES IN LASER PRODUCED PLASMAS

F. Amiranoff, R. Fabbro, E. Fabre, C. Garban and J. Virmont.

Laboratoire de Physique des Milieux Ionisés, Ecole Polytechnique, 91128 Palaiseau Cedex, France.

In order to understand the effect of long shaped pulses which must be used to reach the ablative compression mode in laser fusion experiments, we have set an experiment in which we have studied the effect of the prepulse shape, added to the main pulse, on the interaction processes, and particularly on the stimulated Brillouin backscattering and on the generation of hot electrons.

The experiments were made with a Neodymium glass laser which delivers pulses of 100 GW peak power with a duration of 100 ps FWHM. A pulse stretcher permits to generate two types of pulse shape : type I is a single 100 ps pulse leading the main pulse by 500 ps and containing 10 % or 30 % of the main pulse energy, the type II is a 500 ps plateau like prepulse in front of the main pulse and containing 30 % of its energy. Beam was focused on flat aluminium targets at intensities of $2 \cdot 10^{15} \text{ W/cm}^2$.

The diagnostics are the following : optical energy balance is measured with an Ulbricht sphere; backreflection is also monitored. The spectroscopy of the specularly reflected light has been made in some experiments in the case of a 22,5 obliquely incident beam. The continuous X ray emission has been analysed with a 9 channels system using the absorber foil method. Charge collectors protected from secondary emission were used to study the fast and thermal ion emission.

The major results are given in Table I for backscattering and optical energy balance ; we observe that the backscattering is effectively increased by the prepulse, mostly in the case of the discrete prepulse, but it always remains lower than 20 %. The absorption is surprisingly constant.

The figure 1 shows the effect of prepulse on fast ions and hard X rays emissions. From these results and electron temperature measurements we have also concluded that : soft X ray emission and thermal ion production are increased ; hard X ray emission, fast ions, and T_H hot electron temperature are decreased, depending somehow on the pulse structure.

The figure 2 shows an example of the spectra of the specularly reflected light in the case of the 22°5 obliquely incidence, obtained in different experimental conditions. It appears that the spectrum is blue shifted without prepulse, is unshifted with the continuous prepulse, red shifted and very broad with the discrete prepulse.

The experimental results have been analysed by comparison with the data obtained from a 1D Lagrangian numerical simulation. Figure 3 gives the electron density profiles for the time corresponding to the maximum of the main pulse. It appears that the prepulse introduces strong modification in density profile. In the two cases of prepulse a gentle density gradient is generated in the underdense plasma at 0.6 to 0.8 n_c .

This condition is very favorable for the Brillouin instability and thus can explain the increased of the backreflection. It is interesting to note that the total level of scattered light is almost independent of pulse structure. This seems to indicate that when the prepulse is present the scattering is only more collimated as one can expect for a less inhomogeneous plasma with more gentle electron density gradient.

Numerical determination of the phase velocity of the $0.85 n_c$ surface is in agreement with the observed general behaviour of the mean spectral shift of the specular reflection. The strong spectral broadening observed in the case of the discrete prepulse can be a signature of ion turbulence in the underdense plasma. Numerical simulation confirm the possible existence of this turbulence because of the presence of very steep temperature gradients associated to the density gradients shown on the fig.3.

The second point of interest concern the reduction of the effect of hot electrons production as observed by the reduction of hard X ray and fast ion emission and the decrease of hot electron temperature. This is not clearly understood but however the smaller value of the hot electron temperature indicates that probably resonance absorption is less effective because of the longer density gradient. However, these larger density gradients will, in turn, favour collisional absorption and maintain or even increase the fractionnal absorption as shown on table I.

In conclusion, prepulse affects significantly the interaction processes. It seems that density profile modification can explain the increase of Brillouin backscattering. Hard X ray emission and consequently hot electrons production are decreased. This will be probably due to a reduction in reson-

nant absorption and enhanced classical absorption.

This work has been made as a part of the scientific program of the GRECO Interaction Laser Matter

Pulse shape	A1 0°		CH 22.5°		A1 45°	
	B.S.	Abs.	B.S.	Abs.	B.S.	Abs.
	14%	40%	6%	35%	4%	21%
	20%	41%	14%	35%	8%	22%
	17%	46%	11.5%	36%	6%	20%

Table I : Fraction of backscattered light : B.S.
Total absorption : Abs.

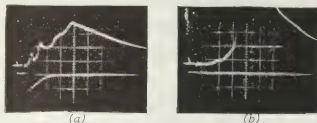


Figure 1 : Effect of a prepulse on ion (upper trace) and X ray (30Kev) (lower trace). 200ns/div.
a) without prepulse ; b) with prepulse

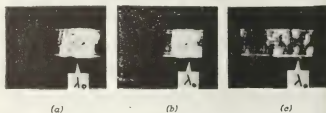


Figure 2 : Spectra of the specularly reflected light
a) without prepulse ; b) with continuous prepulse ;
c) with discrete prepulse.

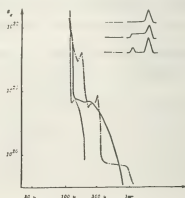


Figure 3 : electron density profiles.

NONLINEAR INVERSE BREMSSTRAHLUNG AND HEATED ELECTRON DISTRIBUTIONS

A. Bruce Langdon.

Lawrence Livermore Laboratory, P.O. Box 808 L-477, Livermore, California 94550.

In this paper we reexamine the classical collisional absorption of intense laser light in a dense plasma. We consider heating and diffusion of electrons of various energies, the evolution to a non-Maxwellian electron distribution when $Zv_0^2/v_e^2 \gtrsim 1$, and the resulting changes to transport and other properties. For example, the inverse Bremsstrahlung absorption itself is reduced by a factor of two compared to the absorption in a Maxwellian plasma of the same thermal energy density. For materials with $Z \gg 1$, this represents a more significant non-linearity than found in the many other analyses for which the relevant parameter is v_0/v_e . (Here v_0 is the peak velocity of oscillation of the electrons in the high-frequency electric field, $v_e = (T_e/m_e)^{1/2}$ is the electron thermal velocity, and Z is the ionization state.) Note also that enhanced isotropic ion fluctuations increase the scattering rate, as high Z does. The origin of this non-linearity is that, when $Zv_0^2/v_e^2 \gtrsim 1$, electron-electron collisions are not rapid enough to Maxwellianize the flat-topped velocity distribution produced by inverse Bremsstrahlung.

In the standard classical treatment, a Maxwellian electron distribution oscillates relative to the ions at frequency $\omega \gg \tau_{ei}^{-1}$, where τ_{ei} is the electron-ion scattering time. For small v_0/v_e , the absorption rate is $\propto f_e(0)$, the distribution function evaluated at $v=0$, so it seems that only the slowest electrons contribute to absorption. By an analysis which requires no $\omega \tau_{ei}$ ordering we show that the absorption is in fact proportional to f evaluated not at $v=0$ but at the velocity for which $\omega \tau_{ei}(v) \approx 1$, i.e. the oscillation period and scattering times are matched.

The equation for evolution of $f_e(v,t)$, due to inverse Bremsstrahlung and e-e collisions, is derived and integrated numerically. We consider first the effect of inverse Bremsstrahlung alone. An initially monoenergetic distribution diffuses and slows in balance so that no net gain in kinetic energy results. When electrons reach slow velocities (such that $\omega \tau_{ei}(v) \lesssim 1$) their loss of energy is slowed while upward diffusion of faster particles continues. This is the meaning of the result that the absorption depends on f_e at low velocities. By the time the electrons have gained only 10% in energy, f_e is close to its late-time form, described by a similarity solution of the form $u^{-3} \exp(-v^5/5u^5)$, with $u^5 \propto t$. For this distribution, the absorption is only 49% of what it would be if e-e collisions enforced a Maxwellian distribution, and heat flow is reduced.

For moderate values of Zv_0^2/v_e^2 , e-e collisions alter these results only slightly. For example, with $Zv_0^2/v_e^2 = 6$ the absorption is still only 49% of its Maxwellian value, and inverse Bremsstrahlung contributes equally with e-e collisions to diffusion of superthermals into the "tail" of the distribution.

*Work performed under the auspices of the U.S. Department of Energy by the Lawrence Livermore Laboratory under contract number W-7405-ENG-48.

AN EXPERIMENTAL INVESTIGATION OF THE CONTINUOUS OPTICAL DISCHARGE

D. Wróblewski, A. Cybulski and Z. Szymański.

Department of Fluid Dynamics, Institute of Fundamental Technological Research, Polish Academy of Sciences, 00-049 Warszawa, ul. Światokrzyska 21, Poland.

1. INTRODUCTION

A plasma maintained by c.w. laser beam is referred to as a continuous optical discharge /COD/. For the plasma maintenance focused radiation of powerful CO_2 lasers is used. The COD was obtained in rare gases/1,2,3,4/ and in the air /5/.

Due to large temperature gradients a convective flow is produced in the vicinity of the plasma. An interesting property of the flow is its regular oscillation with the frequency of about 25 Hz /4/.

The aim of the study, the preliminary results of which are given here, was to investigate the temperature and density distribution in the COD in argon. Spectroscopy was used to study the hot plasma core and interferometry for the neutral gas density investigation in the outer region.

2. EXPERIMENTAL ARRANGEMENT

The scheme of the experimental set-up is shown on Fig. 1. The plasma was produced inside the pressure chamber in the focus of horizontally propagating CO_2 -laser beam. The beam was focused by a spherical mirror, its power was in the range from 100 to 300 Watts. The pressure of the argon gas was 4 to 6 bars.

3. INTERFEROMETRIC MEASUREMENTS

Mach-Zehnder interferometer with a He-Ne laser as a light source was used. The pictures of the interferograms were taken with the use of a movie-camera. The exposure time was typically smaller than 2 ms. The use of the movie-camera allowed to

investigate the dynamics of the gas flow oscillations.

It was found that the fringe shift due to the electron component of the plasma was in the range of the measurement accuracy - a fraction of a fringe. Thus, the interferograms were interpreted in the terms of the neutral density only.

The interferograms exhibited pronounced vertical symmetry axis and were evaluated via the Abel transformation. The result of the transformation is the relative density distribution and in order to obtain the absolute values the density must be known in some point. The fitting at the flow boundary results in poor accuracy and therefore in our case it was made at the plasma boundary, with the use of the data obtained from the spectroscopic measurements.

As an example, the density distribu-

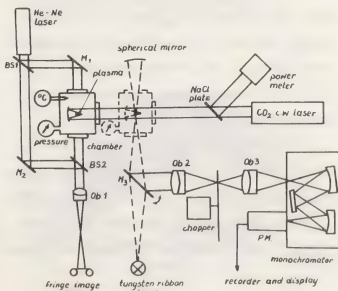


Fig. 1. Scheme of the experimental arrangement.

tions in three different phases of the oscillations, at the pressure of 4 bars, are shown on Fig. 2.

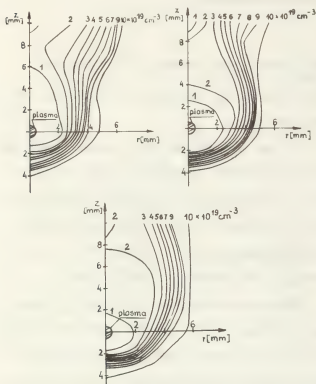


Fig. 2. Neutral density oscillations in the COD at the pressure of 4 bars. The frequency of the oscillations is 21 Hz. The time interval between the frames is 14.25 ms. The temperature on the $1 \times 10^{19} \text{ cm}^{-3}$ isodense is 2900 K.

4. SPECTROSCOPIC MEASUREMENTS

The absolute intensities of ArI 7147 Å line and the continuum at 7182 Å, 7112 Å and 4314 Å were measured. For the absolute calibration a tungsten ribbon lamp was used. As indicated on Fig. 1 a spherical mirror was used to investigate the plasma absorption at 7147 Å. The absorption was found to be negligible. Other details of the arrangement are shown on Fig. 1.

Though the plasma was found to be asymmetric, with a tail in the upward direction, the Abel inversion was used for the obtained intensities and then correction factors were introduced to account for the

change of the shape. The temperature was determined from the resulting emissivities. The results obtained from the measurement of 7147 Å line and the blue and red continua differed one from each other no more than 15 per cent.

A vertical section of the isotherms in the hot core of the plasma, at the pressure of 4 bars, is shown on Fig. 3. The displayed values represent the average from the measurements made at different wavelengths.

5. CONCLUSIONS

A complex diagnostics of the COD was performed and the temperature/density distribution was determined in the whole region influenced by the plasma presence. The influence of the convective flow on the plasma parameters was shown. The results can be used as data for hydrodynamic calculations of the gas velocity field.

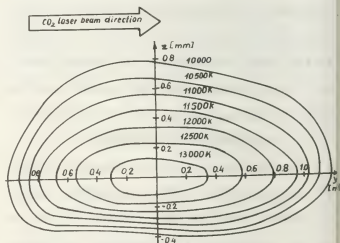


Fig. 3. Isotherms in the COD plasma as obtained from spectroscopic measurement

REFERENCES

1. N.A. Generalov et al., JETP, 61, 1434/1971
2. D.L. Franzen, J. Appl. Phys., 44, 1727/1973/
3. C.D. Moody, J. Appl. Phys., 46, 2475/1975/
4. Z. Mucha et al., Bull. Acad. Sci., 25, 362/1977/
5. M.C. Fowler, D.C. Smith, J. Appl. Phys., 46, 138/1975/

SPECTROSCOPIC STUDY OF THE IONIZATION DYNAMICS IN A CO₂ LASER-PRODUCED PLASMA OF HELIUM

J.C. Gauthier, J.P. Geindre and N. Grandjean.

Groupe d'Electronique dans les Gaz. Institut d'Electronique Fondamentale, Laboratoire associé au C.N.R.S., Université Paris-XI- Bât. 220, 91405 Orsay Cedex, France.

This paper reports on a spectroscopic study of the ionization dynamics of CO₂ laser induced plasmas in medium pressure helium gas. Previous studies have shown [1-3] that the various mechanisms of plasma evolution in space and time are not fully elucidated and may vary strongly with experimental conditions.

In this experiment, a UV preionized TEA CO₂ laser delivered approximately 1 J in a pulse which consists of an intense spike ~100 ns wide, followed by a weaker emission about 20% of the peak of some 1000 ns duration. The pulse repetition rate is 3 pulses per second. Plasma diagnostics were carried out with a high degree of precision and reliability by taking advantage of the good shot-to-shot reproducibility and of the high repetition rate of the laser. Spectroscopic measurements were made with a temporal resolution of 8 ns and a spatial resolution better than 0.1 mm in both the axial (z) and the radial (r) direction, using a computer controlled data acquisition system already described [4].

A typical time resolved spectrum taken at 1 atm. about 1mm above the focus is shown on Fig.1. Time and space-resolved measurements taken along the laser axis are shown on Figs.2a-c. They give respectively the intensity of the continuum in a spectral region free from atomic and ionic lines, the intensity of the 3³D-2³P (5076 Å) HeI transition, and the intensity of the n=4 to n=3 (4686 Å) HeII transition both corrected from their underlying continuum. The time scale origin corresponds to the beginning of the laser pulse. Results obtained over the range

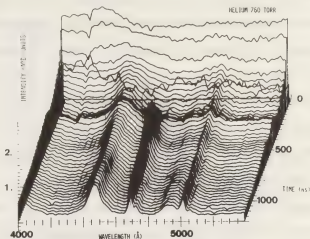
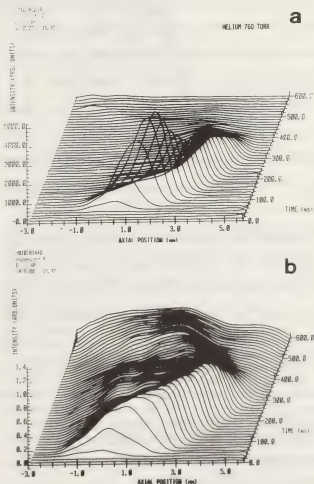


Fig.1. Time resolved spectra at 1mm above focus. Stark broadened HeI lines are prominent above the continuum. The 4686 Å HeII line appears by 300 ns.



0.7-2.5 atm. were qualitatively the same. A breakdown plasma consisting mainly of He^+ ions (only the continuum and HeI spectra are observed) appears near the focal plane ($z=0$) during the rising edge of the pulse. An expansion front with an initial velocity of 5×10^6 cm/s is observed to move in a direction opposite to that of the incident laser beam. By 300 ns the plasma velocity decreases while the trailing edge of the luminous front moves toward the focus. This period is dominated by a sharp rise of HeII emission (Fig.2c) and a strong decrease of both continuum and HeI emissions (Fig.2a-b). These results confirmed the time-resolved spectrum of Fig.1. The electron temperature increase characterized by the apparition of HeII radiation was found to be directly proportional to the fraction of laser energy contained in the tail. In addition, the initial speed of the plasma front and the time of HeII radiation appearance were also found to be proportional to the gas pressure. This rules out a radiation driven detonation mechanism [1] of expansion under the present conditions. Also, photoionization of the unheated gas ahead of the plasma front is unlikely to occur since the electron temperature deduced from the ionization state in the initial plasma is too low (4 eV). Instead, plasma evolution is governed by laser driven ionization dynamics. Radial observations shown in Figs.3a-b further substantiate this hypothesis. The hot plasma core (800 ns on Fig.3b) builds up from the bulk of the cold plasma through absorbed IR radiation from the laser tail. Indeed, experiments with a CO_2 pulse free from tail emission display a considerable reduction of the hot core size and temperature. The blast wave mechanism stated in Ref.3 is thus to be rejected. Further studies of plasma parameters under similar conditions are presented in the following paper.

- 1/ Yu.P. RAIZER - Sov. Phys. Uspekhi **8**, 650 (1966).
- 2/ N. AHMAD, B.C.GALE and M.H.KEY - Proc. Roy.Soc. **A310**, 231 (1969).

- 3/ E.V.GEORGE, G.BEFEKI and B.YA'AKOBI - Phys. Fluids **14**, 2708 (1971).
- 4/ N. GRANDJOUAN, J-C.GAUTHIER and J-P.GEINDRE - C.R. Ac. Sci. **284**, 437 (1977).

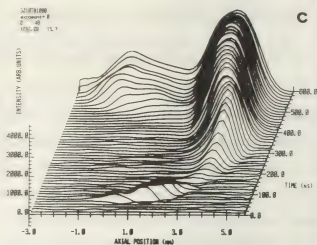


Fig.2 - Time resolved intensities along z. Laser from left to right a) continuum (4750 Å); b) HeI emission (5876 Å); c) HeII emission (4686 Å).

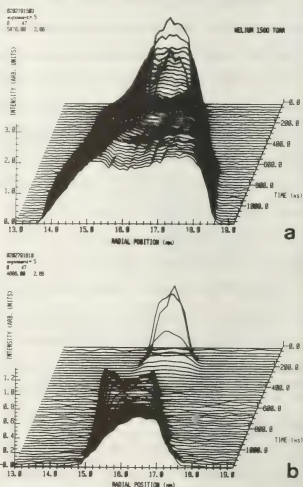


Fig.3 - Time resolved intensities along r at 1 mm above focus. a) HeI emission (5876 Å); b) HeII emission (4686 Å).

SPACE AND TIME RESOLVED MEASUREMENTS OF ELECTRON AND ATOMIC EXCITED STATES DENSITIES IN A CO₂ LASER-PRODUCED PLASMA OF HELIUM

J.C. Gauthier, J.P. Geindre and N. Grandjean.

Groupe d'Electronique dans les gaz. Institut d'Electronique Fondamentale, Laboratoire associé au C.N.R.S., Université Paris-XI- Bât. 280, 91405 Orsay Cedex, France.

Plasma spectroscopy is an efficient means to study laser induced plasmas. In a companion paper /1/ we have shown the role played by the ionization dynamics on the plasma structure through measurements of relative atomic and ionic line intensities. Here, we may extract information about electron densities and temperatures from an analysis of line widths and shifts. Also, a measure of atomic excited states populations has been obtained from the absorption of a visible, auxiliary laser.

The experimental conditions were similar to that described in Ref.1. The apparatus, already described in Ref.2, has been slightly modified to insert a nitrogen pumped dye laser for absorption measurements. The CO₂ and the dye lasers were synchronized to better than 10 ns. The probe beam diameter was about 0.2mm. Rejection of plasma light was carefully studied to allow absorption measurements down to the percent level. Radial distributions of the emission coefficient were obtained by performing an Abel inversion of the observed emission and absorption profiles using standard techniques of inversion with self absorption /3/. Typical results are shown on Fig.1. Peak absorption coefficients of 50% are seen to strongly modify the emission profile, particularly in the cold outer plasma depicted in Ref.1. This points to the uselessness of spectroscopic diagnostics in laser-created plasmas if self absorption is not properly taken into account.

Space-resolved line profiles were recorded for some HeI lines and fitted by a non-linear multipa-

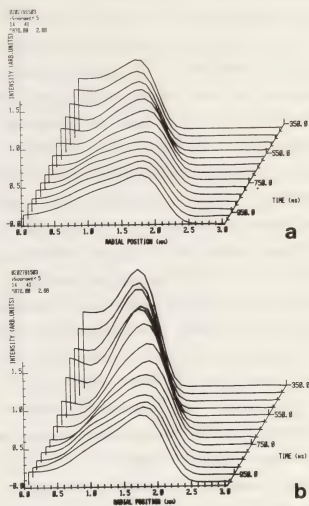


Fig.1 - Radial emissivity of HeI (5876 Å) after Abel inversion. a) direct emission ; b) true emission when measured absorption is taken into account.

rameter least squares method to Griem's Stark broadening theory /4/. This is done on Fig.2 at $z = 1$, $r = 0.5\text{mm}$ for the $3^3\text{P} - 2^3\text{S}$ He I emission at 3889 Å. Detailed agreement is remarkable, especially for the strong asymmetry of this line at elevated electron densities. From the full width of several tens of profiles such those given on Fig.2, we obtain a "map" of the time evolution of the electron density as shown on Fig.3. Results for the 6678 Å,

5876 Å and 3889 Å lines predict slightly different densities, with differences not exceeding 30% in the low density outer plasma. On axis, the results are within a factor of two at early times; the reason for the discrepancy is not yet fully understood. Similar remarks apply to the line shift for which we found the good sign and order of magnitude. The electron temperature was inferred from relative line to continuum intensities. Typical results give $T_e = 4 \pm 1$ eV in the central region and $T_e = 2.5 \pm 0.5$ eV at $r = 1.3$ mm by 500 ns, that is before plasma core heating by the laser tail (see Figs.3a-b in 1/). During laser tail-heating, the electron temperature reaches 5.8 ± 0.5 eV on axis, as deduced from Abel inverted HeII to HeI intensity ratio. From absolute absorption and emission measurements, we also obtained the absolute populations of 2^3P , 3^3P , 3^3D and 3^1D levels. Results for the 2^3P level population in units of 10^{14} cm^{-3} are given on Fig.4. Similar structure was observed for the other excited states. The internal consistency of the experiment was checked by verifying within 10% that the equal energy 3^3P and 3^1D levels were in Boltzmann equilibrium.

These results clearly show that large gradients of excited states densities (related to electron temperature gradients) may be expected in laser created plasmas. Comparison of experiment with the predictions of a one-dimensional lagrangian code /5/ including hydrodynamics, ionization dynamics and radiative transfer gives encouraging results since most of the spatial structure and temporal evolution of plasma parameters and excited states populations are well reproduced.

1/ J-C.GAUTHIER, J-P.GEINDRE, N.GRANDJOUAN : this conference.

2/ Reference 4 of the preceding paper.

3/ P.ELDER, T.JERRICK and J.W.BIRKELAND - Applied Optics 4, 589 (1965).

4/ H.R. GRIEM "Spectral line broadening by plasmas" (Academic, New York, 1975).

5/ J-C.GAUTHIER, J-P. GEINDRE (to be published).

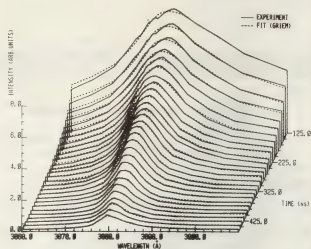


Fig.2 - Time-resolved line profile of HeI (3889 Å) emission at $z = 1$, $r = 0.5$ mm.

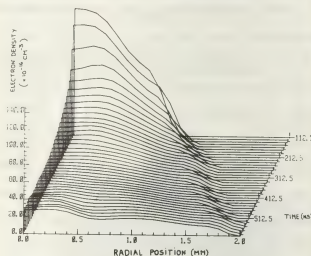


Fig.3 - Space and time resolved electron density corresponding to the raw data of Fig.2.

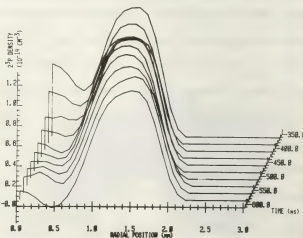


Fig.4 - 2^3P level population density as a function of space and time.

CURVATURE EFFECTS IN LASER PLASMA INTERACTIONS

M.Y. Yu, P.K. Shukla and K.H. Spatschek^{*}.^{*}Institut für Theoretische Physik, Ruhr-Universität Bochum, 4630 Bochum, F.R. Germany.^{*}Fachbereich Physik, Universität Essen, F.R. Germany.

Abstract.- In laser plasma interactions, the strong self-generated magnetic field usually has a curvature which is of the same order as the temperature and density gradients. This curvature, together with the anisotropy in the electron temperature, are shown to result in a further reduction of the already inhibited electron heat transport across the magnetic field. We show that this situation leads to hot spot formation, occurrence of Weibel type instabilities, and eventual magnetic field break-up.



SPECTRAL LINES EMISSION FROM CARBON-HYDROGEN PLASMAS GENERATED BY TEM₁₀ LASER PULSES

S. Chyrczakowski, K. Melzacki, and M. Sadowski.

*Institute of Nuclear Research, High-Temperature Plasma Physics Department.
05-400 Otwock-Swierk, Poland.*

Abstract. The plasma investigated was produced by 1 J, 40 ns, ruby laser pulses focused onto a thin polyethylene foil. Contrary to a smooth time variation of the laser pulses, in the scattered- and emitted-radiation there were observed very distinct spikes. An explanation of that effect has been proposed.

Introduction. Majority of spectroscopic investigations of laser-produced plasmas is based on time-integrated measurements those provide very limited information on the plasma dynamics. The amount and energy of respective ion species, as well as the electron temperatures at various moments can be determined on the basis of time-resolved measurements of spectral lines, e.g. [1]. Papers on this subject are not numerous, and differences in experimental conditions make difficulties to transfer the results. Therefore, it was necessary to perform detailed spectroscopic studies of a plasma generated inside the SM magnetic trap [2].

Experimental System. To produce the plasma, a ruby laser generating 1 J, 40 ns pulses was used. To study hydrodynamic effects the TEM₁₀ mode was selected. The laser pulses were focused onto a 250 μ m polyethylene foil placed perpendicular to the laser beam. All the optical studies were carried out at a pressure of 10^{-3} Pa, and without any external magnetic field. Three fast photodiodes of the BPYP-49 type were used for measurements of the incident power /signal I/, the radiation transmitted through the target /signal T/, and the light reflected back from the target into the aperture of the focusing lens /signal R/. All the

signals /I, T, and R/, alike as in the paper [3], have been observed with the same beam of the S8-12, 50 MHz, oscilloscope. Using a second input of a differential amplifier, the R signal was amplified 100 times to be comparable with the I- and T-signals.

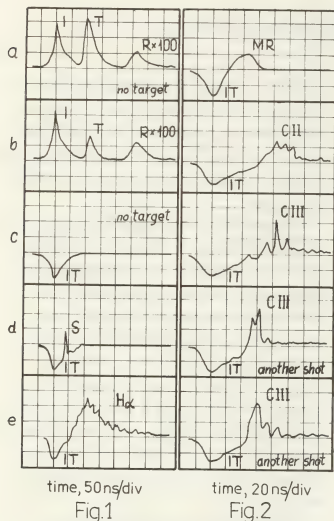
To perform spectroscopic measurements two glass monochromators equipped with the Philips-56TVP photomultipliers were applied. Those looked tangentially at the target surface and observed the same plasma region. The area of the monochromator slit projection was equal to $0.1 \times 1 \text{ mm}^2$ and localized at the distance of 0.8 - 1.0 mm from the target surface. The overlapping of the two images of the slits was checked by a photographic method. The radiation signals were registered with two S8-12 oscilloscopes triggered by the IT signal from the fourth photodiode.

The laser light scattered at the angle 90° /signal S/ was observed through the monochromator tangentially to the target surface. For a comparison, the light reflected /signal MR/ from the target turned at 45° has also been observed.

Experimental Results. The I-, T-, and R-signals normalized and those obtained with a plasma, are shown in Figs. 1a and 1b. It should be noted that the T-signals varied considerably from a shot to shot within the 15 to 95% of the I-signal. The R-signal reached only 0.4% of the I-signal and it was only slightly effected by a plasma. The possibility of the reflection within a narrow spatial-angle [4] has not however been verified.

When a plasma was generated, the T-signal

was usually delayed a few nanoseconds, and its FWHM decreased. That cannot be simply explained by a target-burn effect /5/. The S-signal was observed as a distinct peak /see Fig. 1d/, while the MR-signal had an usual shape /Fig. 2a/.



Since the laser beam was focused by the f/5.5 lens, a single laser pulse of a relatively low-power density /appr. 10^{10} Wcm^{-2} / produced a small spot of an irregular outline with numerous bubbles. Under such conditions in the focus there was generated the plasma of $T_e = 7 \text{ eV}$ and $n_e = 5 \times 10^{17} \text{ cm}^{-3}$ /2/. The time-resolved emission of $\text{H}\alpha$ 6563, CII 4267, and CIII 4647 lines from the plasma plume have been measured, /see Figs. 1e and 2b-e/. It can be seen that the lines observed /in particular CIII 4647/ reveal several distinct spikes. These spikes are relatively narrow, and their FWHM is of the order of 10 ns /while the rise time of the oscilloscope was equal to 7 ns/.

Discussion. The observations of spike emission of the carbon lines are contradictory with the results presented in other papers, e.g., Boland et al. /1/ observed smooth variations of CII - VI lines, the CVI line of the shape similar to the laser pulse, and twice longer emission of the CIII line. Also the observations of X-ray pulses emitted from targets irradiated by high-power lasers, revealed no spike structure /5/. On the other hand it is known that the power density distribution of a pulsed ruby-laser beam can be very complex and possess a number of "hot spots" those can exist a few nanoseconds /6/. Taking into account the phenomena mentioned above as well as the fact that the TEM_{10} mode was used and the laser energy was absorbed over the whole target thickness /the focal depth was 5 mm/, one can assume that a complex temperature field is obtained. This assumption is verified by the fact that the highly ionized species and fast ions are observed under the same experimental conditions /7/. If the effect discussed could be obtained at higher power, an appropriate multimode laser would be a convenient tool for the production of high-energy ion pulses. Hence, further investigations on this subject are to be continued.

The authors wish to express thanks to their colleagues of the Plasma Physics Dep. and in particular to Mr. R. Jarzęcki for assistance in the course of the experiment.

References.

1. B.C. Boland et al., J. Phys. B1, 1180 /1968/.
2. J. Baranowski et al., Proc. 8th European Conf. CFPP, Prague 1977, vol. 1, p. 106.
3. R. Sigel, Z.f.Naturforsch., 25a, 488 /1970/.
4. T.P. Donaldson et al., Phys. Rev. Lett., 37, 1348 /1976/.
5. V.A. Bojko et al., Trudy Fiz. Inst. im. Lebedeva, 76, 186 /1974/.
6. J.F. Ready, Effects of High-Power Laser Radiation /Russian Translation, Mir, Moscow 1974/, p. 28.
7. J. Baranowski /9th Europ. Conf., Oxford 1979/.

IONIZATION OF ISOLATED DEUTERIUM PELLETS BY NEODYMIUM LASER RADIATION

H. Baumhacker, H. Brinkschulte, W. Riedmüller, M. Salvat and S.Sudo.

Max-Planck-Institut für Plasmaphysik, 8046 Garching, W. Germany.

The idea of employing plasmas produced by the irradiation of solid hydrogen pellets with high power lasers for filling of magnetic confinement devices appears very attractive. It offers the possibility of creating a high energy plasma with low impurities and without any current whose magnetic field might impair the confinement of the plasma in the plasma machine. The properties of the laser produced plasma can be selected by proper choice of the pellet size and the laser parameters. For successful application of this method it is essential that the pellet be completely ionized by the laser radiation. The reason is that any potential residue material of the pellet is cold and will rapidly cool the plasma by charge exchange collisions.

We have determined experimentally the laser properties for maximum ionization of freely falling deuterium pellets. The envisaged application is to fill the Garching H II b stellarator, which calls for pellets containing 1×10^{18} deuterium atoms and - at a mean plasma energy of 100 eV - for a laser energy in the 100 J range. The pellets are formed by extruding a bar of solid deuterium through a hole in the bottom of a liquid-helium-cooled cryostat and by cutting its lower end with two ohmically heated wires. The cylindrical pellets with a diameter of 0.3 mm and a length of 0.5 mm contain $(1...2) \times 10^{18}$ deuterium atoms. After a free fall over 20 cm they are ionized in the focus of a Q-switched neodymium laser with a maximum energy of 100 J. The ionization of the pellet and the early expansion phase without magnetic field was investigated with holographic interferometry (at ruby laser wavelength) and with ion collector probes. A balance of the laser light was made in order to check the efficiency of the method with respect to transformation of laser energy into plasma energy.

It was found that less than 10 % of the pellet is ionized when the laser energy is applied in a single pulse of 25 ns duration. However, much better ionization is achieved when the laser energy is split in two successive pulses with different energies. A low power prepulse interacts with the pellet in such a way that the following main pulse finds favourable conditions for efficient ionization of the pellet material.

The influence of the following parameters which are not independent of each other, was investigated:

- a) Prepulse: At prepulse intensities of $(0.2...20) \times 10^9 \text{ W/cm}^2$ the pellet evaporates immediately after the laser shot and the pellet material expands in a predominantly gaseous state at a velocity of approximately $5 \times 10^5 \text{ m/s}$. Under these conditions best results were obtained with respect to ionization by the following main pulse.
- b) Pulse interval and laser beam diameter: At a constant prepulse intensity of $4 \times 10^9 \text{ W/cm}^2$ the time separation between the prepulse and main pulse and the diameter of the laser beam at the site of the pellet were varied. It was found that for a laser beam diameter of 3 mm the plasma production reaches a broad maximum for time intervals between 300 ns and 500 ns. For diameters of 1.5 mm and 5 mm, respectively, much less of the pellet is ionized.
- c) Energy of main laser pulse: At a prepulse intensity of $4 \times 10^9 \text{ W/cm}^2$, a laser beam diameter of 3 mm and a pulse separation of 500 ns the pellet becomes $80 \% \pm 20 \%$ ionized at the maximum main pulse energy of 100 J. However, by comparing the values for the total number of electrons with those of the ions - measured at a later time with Faraday cups - it can be concluded that a substantial portion of the plasma

recombines quite rapidly. Numerical calculations show that the ionization of the plasma drops within 200 ns to 40...70 % of its initial value and then decays very slowly.

The signals of the ion collector probes facing the plasma origin from different directions revealed that the plasma expansion is not symmetrical when the pellet is irradiated from only one direction. In this case, most of the plasma expands in the direction opposite to that of the laser beam. A much more uniform plasma cloud is formed when the laser radiation impinges on the pellet from two opposite directions. However, the total ion number does not grow with the number of laser beams. It grows only with the laser energy no matter from how many directions the pellet is irradiated.

It was demonstrated that an isolated deuterium pellet containing $(1...2) \times 10^{18}$ deuterium atoms can be completely ionized by a Q-switched neodymium laser with an energy slightly above 100 J. The process is very efficient with respect to transfer of laser energy into plasma energy: Up to 80 % of the incident laser energy is absorbed by the pellet and roughly 1/2 of this value is measured as ion kinetic energy. The averaged translational energy of the ions is typically 100...200 eV.

A CO₂ LASER-PLASMA INTERACTION EXPERIMENT- THE SCATTERED SPECTRUM OF LANGMUIR WAVES DRIVEN VIA THE ELECTRON-ION DECAY INSTABILITY

M.J. Forrest, R.E. Kirk[✉] and N.J. Peacock.

Culham Laboratory, Abingdon, Oxon, OX14 3DB, UK (Euratom/UKAEA Fusion Association).

Studies of the interaction of a pulsed CO₂ laser with a preformed high density plasma are reported. The plasma is produced in a Plasma Focus device which has been extensively diagnosed. Because of the high kinetic energy of the plasma (5 kJ cm⁻³) compared to the laser pump energy (15 joules), non-linear plasma processes can be excited without altering the basic plasma parameters.

Previous experiments⁽¹⁾ have indicated that during the compression phase of the plasma when $n_e > n_{crit}$ CO₂ = 9.94, 10¹⁸ electrons, cm⁻³ the focused laser beam is totally absorbed. The focused spot size is 500 microns and the pulse width 40 nanoseconds FWHM. Various processes have been proposed to account for this behaviour. Earlier experiments⁽²⁾ have indicated that the electron-ion decay instability, $\omega_{CO_2} \rightarrow \omega_L + \omega_{ia} \pm \delta\omega$ can contribute to the absorption process. Where ω_L and ω_{ia} are the Langmuir and ion-acoustic wave frequencies respectively and $\delta\omega$ is the permissible frequency mismatch given by

$$\delta\omega = P k_L v_e \left(\frac{m_e}{m_i} \right)^{\frac{1}{2}} / \sqrt{2}$$

P being the ratio of the pump intensity to the threshold intensity of the instability, and v_e is the electron thermal velocity. Using the analysis of Perkins and Flick (1971)⁽³⁾ for an inhomogeneous plasma where $T_e \gg T_i$, the threshold pump intensity, when the swelling of the pump wave is taken into account, is of the order of 3.10⁹ watts cm⁻². Here it is possible for Langmuir waves to be driven well above their thermal level, while the ion acoustic waves are heavily Landau damped.

A Q-switched ruby probe laser (500 MW) has been used to produce a co-operatively scattered spectrum. The probe beam is co-axial to the CO₂ pump beam and both have horizontally polarised outputs. The scattering collection optics are arranged to give a forward scattering angle of $8 \pm 2.4^\circ$, Fig. 1. This results in the scattering parameter

$$\alpha = k(\text{Debye}) / k(\text{Langmuir}) > 6$$

If $\alpha < 4$ then significant Landau damping of the Langmuir waves occurs.

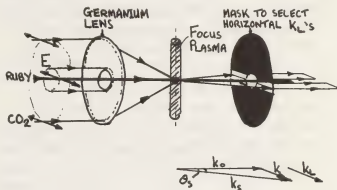


Fig.1 Schematic showing coaxial CO₂ pump beam and ruby probe beam and collection optics. The perspective vector diagram illustrates how the scattering vector k is arranged to be parallel to the excited k Langmuir's.

The scattering of these enhanced Langmuir waves results in discrete shifted electron features, each side of the ruby laser wavelength 6943 Å. This scattered spectrum is given by

$$\omega_{scat} = \omega_{ruby} \pm (\omega_{CO_2} - \omega_{ia} \pm \delta\omega)$$

Therefore the peak is displaced by $(\omega_{CO_2} - \omega_{ia}) \approx \omega_{CO_2}$ from ω_{ruby} , with a width of $2 \delta\omega$. There is, in addition, a spread in frequency due to the finite range of wave vectors accepted by the scattering optics.

A gated intensified optical multichannel analyser (OMA), in conjunction with a one metre focal length grating spectrometer, has been used to resolve the down-shifted wavelength electron feature. The experimentally derived profile was compared with theoretical predictions of amplitude and shape.

REFERENCES

1. FORREST M J et al, Phys.Rev.Letts, 37(1979) 1681-1684
2. PEACOCK N J et al, Journal de Physique (1977) Tome 38 C6 43-54
3. PERKINS F W and FLICK J, Phys. of Fluids, 14(1971) 2012-2018

*Attached from Royal Holloway College, University of London, Englefield Green, Surrey, UK.

BEAT HEATING IN PLASMAS USING CO₂ LASERS*

E. Chu, R. Druce, M. Kristiansen, M. Hagler and R. Bengtson*

*Department Electrical Engineering, Texas Tech. University, Lubbock, Texas, U.S.A. 79409.

*Department of Physics, University of Texas at Austin, Austin, Texas U.S.A. 78712.

Introduction

There has been considerable interest in beat heating as a method of heating underdense plasmas^{1,2,3}. The scheme uses two different-frequency, high-power laser beams to excite parametrically, plasma waves in the underdense plasmas. The subsequent damping of the waves is expected to heat the plasma. In order to have efficient coupling of laser energy into the plasma wave energy, the phase matching condition must be satisfied:

$$\omega_0 = \omega_1 + \omega_2$$

$$\vec{k}_0 = \vec{k}_1 + \vec{k}_2$$

where ω_0, ω_1 are the laser frequencies, ω_2 the plasma wave frequency, and \vec{k}_0, \vec{k}_1 , and \vec{k}_2 are the corresponding wave vectors.

An experiment using the 9.56 μm and 10.28 μm radiations of a CO₂ laser and a helium plasma is reported. Evidence of beat heating has been observed. However, beat heating is found to be small compared to inverse bremsstrahlung heating. Possible explanations of this observation are given.

Experimental Arrangement

A cold cathode, electron-beam controlled CO₂ laser designed for double-sided operation⁴ is used for the beat heating investigations. The pulsed laser is capable of lasing at 10.6 μm or simultaneously at 9.56 μm and 10.28 μm by the insertion of an absorption cell filled with SF₆ in the oscillator cavity. When run at 10.6 μm the laser produces 50 ns FWHM pulses with about 50 J per pulse. In the double-frequency mode, the energy per pulse is reduced by approximately 10%.

The plasma is produced by a linear discharge between two split-ring electrodes with an axial magnetic field of 2.8 T provided by a fifteen turn coil around the plasma tube, as shown in Fig. 1. The resulting plasma column is approximately 0.1 m long and 0.05 m in diameter with a density minimum

on axis. A trace of the plasma current is shown in Fig. 2. The current has a peak value of 125 kA and laser is focused into the plasma at approximately 5 μs after the initiation of the plasma current. Prior to the firing of the laser, the helium plasma has a temperature of about 4.5 eV and densities of 3.9×10^{22} - $6.5 \times 10^{22} \text{ m}^{-3}$ as the filling pressure is varied from 1.0 - 1.9 Torr.

The laser is focused by a 1 m focal length copper mirror to a spot size of approximately 0.0025 m in diameter in the center of the plasma column. A 0.5 m focal length mirror at the exit end of the plasma source refocuses the transmitted laser beam back to the same focal spot. As a result, opposite wave vectors are present at the focal spot to allow antiparallel beam beat heating investigations.

A diamagnetic loop located at the focal spot is used to measure the temperature change due to heating by the laser. The intensities of helium satellites⁵ are used to measure the amplitude of plasma waves in the plasma as a result of optical mixing.

Results

The temperature increase as measured by the diamagnetic loop under various conditions is summarized in the following table:

Filling pressure (Torr)	Temp increase with single frequency beam (eV)	Temp increase with double frequency beam (eV)
1.0	27.7 \pm 13.1	23.1 \pm 6.5
1.1	38.5 \pm 6.1	30.0 \pm 6.0
1.2	52.6 \pm 2.7	35.1 \pm 5.5
1.3	53.2 \pm 2.6	47.7 \pm 10.4
1.4	90.7 \pm 0	38.4 \pm 5.0
1.5	42.8 \pm 4.6	44.4 \pm 6.9
1.6	67.8 \pm 26.2	38.6 \pm 19.6
1.7	104.9 \pm 6.3	59.1 \pm 16.7
1.8	77.6 \pm 15.7	49.9 \pm 7.8
1.9	79.3 \pm 13.2	66.9 \pm 8.7

* This work was supported by AFOSR Grant 74-2639.

The listed figures represent the average of two or more numbers obtained under the same set of conditions. The indicated errors are the 50% confidence limits obtained by assuming the data follows the "Students" t-distribution⁶. The temperature increase with the single frequency beam which has more energy per pulse is consistently higher than that with the double frequency beam at all filling pressures except at 1.5 Torr. On applying the paired t-test to the data, this observed departure is significantly different from the rest of the measurements with a better than 99% confidence level.

As the filling pressure is varied, no significant satellite emissions associated with the $2^1P - 3^1P$ transition and the $2^1S - 3^1D$ transition are observed, indicating that no large amplitude plasma waves are present.

Discussion

The density of plasma corresponding to 1.5 Torr filling pressure is $5.3 \pm .45 \times 10^{22} \text{ m}^{-3}$ prior to the laser pulse. As a density of $5.9 \times 10^{22} \text{ m}^{-3}$ is required for resonance with the incident $9.56 \mu\text{m}$ and $10.28 \mu\text{m}$ radiations, it is likely that the observed additional heating at 1.5 Torr when the laser is running in the double frequency mode is a result of beat heating. However, this observed additional heating is insignificant compared to inverse bremsstrahlung, which may appear to be in conflict with theoretical predictions. The apparent contradiction may be resolved by the following explanation. At the resonance zone, which has a physical volume of the order of 1 mm^3 , the electrons will start to stream out of the interaction volume as soon as they are heated as a result of beat heating. Therefore, the density at the resonance zone drops and detuning from resonance may result.

Conclusion

An experiment investigating beat heating has been conducted. Additional heating at 1.5 Torr filling pressure is observed when the laser beam has both $9.56 \mu\text{m}$ and $10.28 \mu\text{m}$ radiation components. However, this additional heating is insignificant when compared to inverse bremsstrahlung heating. Absence of any significant satellite emissions indicates that no large amplitude plasma waves are present. This agrees with the small additional heating observed.

References

1. Capjack, C.E., James, C.R., Can. J. Phys. **48**, 1386 (1970).
2. Cohen, B.I., Kaufman, A.M., Watson, K.M., Phys. Rev. Lett. **29**, 581, (1972).
3. Rosenbluth, M.M., Liu, C.S., Phys. Rev. Lett. **29**, 701, (1972).
4. Jasper, J., Master Thesis, Dept. of EE, Texas Tech University, 1977.
5. Baranger, M., Mozer, B., Phys. Rev. **123**, 25 (1961).
6. Spiegel, M.R., *Theory and Problems of Statistics*, McGraw-Hill Book Company, (1961).

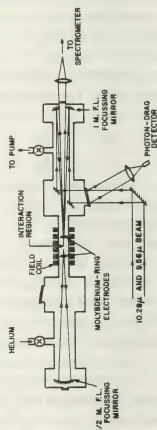


Fig. 1.
Experimental Arrangement.

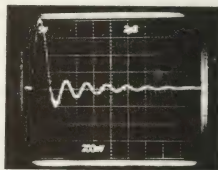


Fig. 2. Plasma Current Trace
(Vert. - 31 kA/div, Horiz. - 2 $\mu\text{s}/\text{div}$).

CARBON SPECTRA FROM CO₂ LASER-PRODUCED PLASMAS

R.D. Bleach, K.G. Whitney, J.W. Sandelin, T.G. Finn and D.J. Nagel.

Naval Research Laboratory, Washington, D.C. 20376.

Ultraviolet spectroscopy is a useful technique for the study of plasmas heated by intermediate laser power densities ($\sim 10^8$ W/cm²). In this work, the emission of solid carbon targets irradiated with 10.6 μ m laser pulses was measured and calculated.

The gain-switched pulses consisted of a 70 ns FWHM spike containing 0.4 of the energy followed by a 1 μ s tail. The focal area for normal incidence on planar graphite targets in vacuo was 1 cm². Average power densities were near 5×10^8 W/cm². The plasmas were observed parallel to the target plane with an open shutter camera and a 1 meter near-normal-incidence grating spectrograph operating in the 30-300 nm range. The time- and space-integrated spectra were recorded on Kodak 101 film. Figure 1 shows data from part of the spectral range. Strong line radiation is evident.

Standard wavelength tables were employed to identify the observed lines. Radiation from CI through CIV was noted, with most lines from the two highest ionization stages. For example, many lines from CIII triplet systems (with principal quantum numbers $n \leq 5$ and $\Delta n \leq 2$) and from CIII singlet systems ($n \leq 5$ and $\Delta n \leq 3$) were observed. CIV doublet-system lines ($n \leq 5$ and $\Delta n = 1$) were also identified. The most intense is the CIV line at 155 nm. The CIV 4d-5f and 4f-5g transitions, at 252.4 and 253 nm respectively, suggest that electrons recombined with CV (He-like) ions. The existence of CV ions implies temperatures near 10^5 K.

A stationary, local-thermodynamic-equilibrium (LTE) model was developed to compute radiation emitted from the plasma. The electron density in the excitation region ($\sim 10^{19}$ el./cm² for CO₂ lasers) and the temperatures ($> 10^4$ K) justify the use

of an LTE model. The effects of thermal conduction and radiative cooling were included, but hydrodynamic flow and radiation transport (opacity) were not computed. The time history of the total line output was calculated for each ionization stage, as shown in Figure 2 for an irradiance near 2×10^8 W/cm². During the spike of the laser pulse, a large fraction of the ions exist as CV, and the CIV radiation decreases. It recovers as the plasma cools and recombination occurs. CIII and CII emission appear sequentially. CI emission, not shown in Fig. 2, occurs late in the pulse. The computed relative intensities agree qualitatively with the measured spectra, that is, CIII and CIV are predominant.

Absorption lengths were estimated to be less than 100 μ m for CIII lines (2p-3d at 57.4 nm and 2s-2p at 97.7 nm). This indicates the need for more complex calculations, including radiation transport, in order to use line ratio techniques for temperature determinations. The analysis of the measured carbon spectrum will be discussed from the point of view of these opacity considerations and comparisons made against calculated emission spectra.

*Science Applications, Inc.

MULTIPLE-PASS LASER HEATING OF A SHORT PLASMA COLUMN

R.D. Brooks, Z.A. Pietrzyk and G.C. Vlases.

University of Washington, Seattle, Washington, 98195, U.S.A.

The heating of linear magnetically confined plasmas with pulsed CO₂ lasers was proposed as a fusion reactor scheme some time ago.⁽¹⁾ Two factors of major concern for such a device, end losses and the absorption length for the 10.6μ radiation, have led to reactor designs on the order of a kilometer in length. More recently, work has progressed on reducing end losses by several means.⁽²⁾ The multiple pass experiment reported here, which is similar to one suggested by Humphries,⁽³⁾ explores a configuration which offers the possibility of matching the effective laser absorption length to a variety of proposed shorter reactors.

Figure 1 shows a diagram of the multiple pass experimental system. The optical cavity and theta pinch are the same as previously described⁽⁴⁾ except that there is a 6" Germanium (30% ref) output coupler on the TEA laser, producing 100 Joules of output energy in about one μsec.

Diagnostics include axial viewing holographic interferometry, 90° ruby laser scattering, photon drag CO₂ radiation detectors, calorimetry, and an infrared spectrometer used to analyze the backscattered radiation.⁽⁵⁾

The performance of the non-laser heated theta pinch plasma has been analyzed using double pulse holographic interferometry. Figure 2 shows a rep-

resentative hologram and density profiles for the operating conditions chosen, assuming a 20 cm long axial uniform plasma. It can be seen that a density minimum on axis exists at times between the bounces of the plasma sheath. The numbers within the profiles are the values of b and the correlation coefficients when the central regions of the profiles are fitted to the equation: $n_e = n_{e0} + br^2$, where n_e and n_{e0} are in electrons per cm³ and r is in cm. A long plasma column with a parabolic density profile periodically re-focuses all rays that have gone through one focus. For our conditions the distance between foci associated with the observed radial density gradient is on the order of 50 cm. Thus a second focus is not realized; instead the plasma acts as a lens by re-imaging the incident focal spot. The rays exit the plasma from nearly the entire area within the density well and

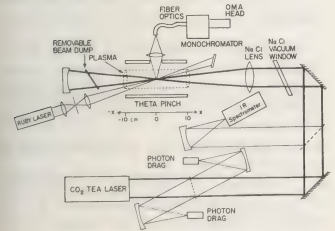


FIG. 1. Multiple-pass experimental apparatus.

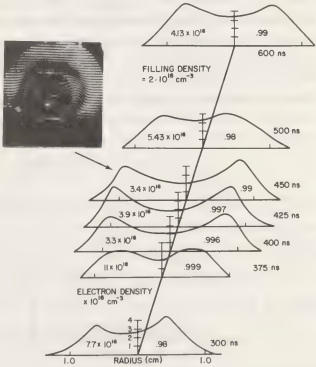


FIG. 2. Hologram and density profiles for the unheated plasma. The parameter b and the correlation coefficient are given within the profiles for a best fit of the central region to $n_e = n_{e0} + br^2$.

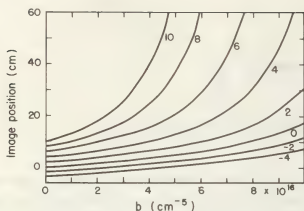


FIG. 3. Image position versus b (fit to parabolic density profile) for various input focus locations (cm). Locations are with respect to the axis in Figure 1.

appear to be coming from an image location near the center of the plasma column. Figure 3 shows the position of the focal image relative to the axis in Figure 1 versus the parameter b for various positions of the incident focus spot (shown beside the curves), for a 20 cm column. It should be pointed out that neither of these spots is where the rays actually focus but where the incident rays would focus and where the exiting rays appear to diverge from. It can be seen that for the incident focus at $X = -2$ cm, the position of the focal image is relatively constant over the range of density profiles observed in the unheated pinch. For this reason it was decided to position the incident focus here and the back mirror ($f \approx .5$ m) such that its center of curvature is at $X = +2$ cm. This should return the rays exiting the plasma back upon themselves to the plasma and along the same path through the plasma to the laser as long as the den-

sity profile does not appreciably change in the 6 ns the rays are out of the plasma.

When this modified concentric optical cavity (i.e., incorporating the return mirror) is used, the TEA laser output contains a second "spike" which is not present without a return. This second spike can be larger than the first when the first spike occurs at around 400 ns into the pinch cycle. For the first spike occurring at times between 350 and 450 ns, the temperature of the central portion of the plasma, measured by laser scattering, is shown as a function of time in Figure 4. Each point is a computer best fit to the average of a number (given beside the point) of shots. Also shown here is a representative single pass (i.e., no return mirror) laser output. It can be seen that the plasma dynamics remain important until about 700 ns, after which time the temperature becomes fairly constant. Since for inverse Bremsstrahlung absorption at constant density

$$T_f^{5/2} - T_0^{5/2} = \text{const.} \times \text{laser energy},$$

where T_f and T_0 are the final and initial temperatures, the single pass energy would have to pass through the plasma at least twice to achieve 1.3 times the temperature increase. In this manner the number of equivalent passes to achieve the multiple pass temperatures for $t > .7 \mu\text{s}$ is calculated to be 4.1, with a standard deviation of 1.3. This is consistent with what can be expected due to reflective losses at the optical surfaces of the cavity.

In conclusion, an optical cavity including the plasma as an active optical element was chosen using holography. Multiple pass heating equivalent to 4.1 ± 1.3 passes of the single pass energy was determined by ruby laser scattering.

This work was supported by the National Science Foundation.

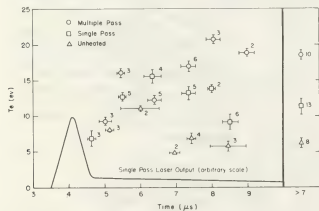


FIG. 4. Electron temperature, as determined by laser scattering, versus time into the pinch cycle. Also shown are the averaged temperatures for times greater than $.7 \mu\text{s}$.

1. J.M. Dawson, A. Hertzberg, R.E. Kidder, G.C. Vlases, H.G. Ahlstrom, and L.C. Steinhauer, in Plasma Physics and Controlled Thermonuclear Fusion (International Atomic Energy Agency, Vienna, 1971), Vol. I, p. 673.
2. L.C. Steinhauer and G.C. Vlases, Nuclear Fusion, to be published (1979).
3. S. Humphries, Jr., Plasma Phys. **16**, 623 (1974).
4. R.D. Brooks, R.G. Watt, Z.A. Pietrzyk, and G.C. Vlases, Appl. Phys. Lett. **34**, 355 (1979).
5. R.G. Watt, R.D. Brooks, and Z.A. Pietrzyk, Phys. Rev. Lett. **41**, 170 (1978).

THOMSON-LIKE RF SCATTERING BY SMALL OVERDENSE PLASMA PARTICLES

William A. Janos.

Consultant, 8381 Snowbird Drive, Huntington Beach, California 92646.

ABSTRACT

Linear perturbation theory is employed to estimate the scattering amplitude and cross section of a small overdense plasma particle of linear dimension much less than the skin depth of the incident radiation. It is shown that the scattering properties so derived are Thomson-like and can exceed the conventional sharp boundary Rayleigh-Mie results by several orders of magnitude.

INTRODUCTION

The reradiation effects giving rise to scattering of monochromatic electromagnetic waves incident on metallic or overdense plasma surfaces are generated by the free electron constituents of the plasma within a layer of thickness of the skin depth, δ_s , of the incident waves. Thicknesses much greater than this δ_s are essentially superfluous in scattering. Thus it would appear that a very thin or small scatterer, which has virtually all of its conduction electrons exposed to the incident radiation, reradiates most efficiently in terms of scattered power to mass ratio. Here we consider such a case and treat it by linear perturbation theory. Consider the scattering of an incident electromagnetic wave $\vec{E}_i(\omega)$ of frequency ω ($2\pi H_z$) by a small dense charge-neutral plasma agglomerate of characteristic length δ much less than the skin depth $\delta_s(\omega)$. More specifically, let

$$\delta \ll 2 \delta_s(\omega) \quad (1)$$

WAVE EQUATION

The time independent wave equation for the divergenceless electric vector is then

$$\left\{ \nabla^2 + k^2 (1 - i \frac{4\pi\sigma_0 H(\omega r_s)}{\omega}) \right\} \vec{E} = 0 \quad (2)$$

$k = \omega/c = 2\pi/\lambda_0$; $\sigma =$ plasma conductivity

$\Delta H(\omega r_s) = 1$ at scatterer, zero otherwise.

INTEGRAL EQUATION FOR THE SCATTERED FIELD

The integral form of (2) of interest is obtained through inversion by the free space Green's dyad.

$$\vec{E}_s(\vec{r}) = \vec{E}(\vec{r}) - \vec{E}_i(\vec{r}) = i k^2 \int d\vec{r}' \left(\frac{\sigma}{\omega} \right) \hat{\hat{z}} \times (\hat{\hat{z}} \times \vec{E}) \quad (3)$$

\vec{E}_s is the scattered field, and $\hat{\hat{z}} = (\vec{r} - \vec{r}')/|\vec{r} - \vec{r}'|$

BORN APPROXIMATION FOR A SMALL SCATTERER

The first Born Approximation, $\vec{E}_s(\vec{r})$ to the scattered field would arise by replacing $\vec{E}(\vec{r})$ in the integrand on the right of (4) by $\vec{E}_i(\vec{r}')$. Under the condition

$$\delta \ll \frac{1}{2\pi} \sqrt{\frac{c}{\sigma}} = 2 \delta_s(\omega) \quad (4)$$

namely, particle size much less than skin depth, it can be shown that the relative error in scattered field amplitude due to the first Born Approximation, neglecting all of the higher order scatterer terms is bounded as

$$\max \frac{|\vec{E}_s - \vec{E}_{s1}|}{|\vec{E}_s|} \leq \frac{\delta}{2 \delta_s(\omega) - \delta} \ll 1 \quad (5)$$

Thus with (5), the first Born Approximation applies and \vec{E} can be replaced by \vec{E}_i in the integrand on the right of (3). It also follows that all of the terms in the integrand are virtually constant over the small plasma volume. The scattered field \vec{E}_s , then takes the simplified form

$$\vec{E}_s \approx \vec{E}_{s1} = i k^2 \frac{e}{|r - r_p|} \frac{\sigma(r_p) \Delta V_p (\hat{\hat{z}}_r \times (\hat{\hat{z}}_r \times \vec{E}_i(r_p)))}{\omega} \quad (6)$$

where r_p is a mean location of the scattering volume, ΔV_p .

SCATTERING AMPLITUDE AND CROSS SECTION

The scattering amplitude A_p and cross section S_p are

$$A_p = \lim_{|r-r_p| \rightarrow 0} \left(\frac{|r-r_p| |E_s|}{|E_0|} \right) = i k \frac{\sigma \Delta V_p \sin(\theta, r, r_p)}{\omega} \quad (7)$$

$$S_p = |A_p|^2 = k^4 \left(\frac{\sigma}{\omega} \right)^2 \Delta V_p^2 \sin^2(\theta, r-r_p) \quad (8)$$

COMPARISON WITH RAYLEIGH SCATTERING

The Rayleigh-Mie scattering cross section, S_R , for an ideal conducting particle (of infinite conductivity) with the same volume is given (as in reference

$$1). \quad S_R = \frac{k^4}{(4\pi)^2} \Delta V_p^2 \sin^2(E_0, r-r_p), \quad \lambda_0 \gg \delta \quad (9)$$

Thus the ratio of the cross section (8) and (9) is

$$S_p/S_R = (4\pi)^2 (\sigma/\omega)^2 \quad (10)$$

Since for metals $\sigma \sim 10^{17} \text{ sec}^{-1}$, the above ratio can be large in the RF - microwave range.

CONCLUSION

It appears that in the limit of small particle size, much less than the skin depth of the incident radiation, the plasma electrons act collectively and additively with their individual scattering amplitudes to give rise to a composite Thomson scatterer. For high conductivity metals, of correspondingly high collision frequency ν , the total Thomson cross-section of the conduction electrons is modified by the ratio $(\omega/\nu)^2$. Application of the scattering effects considered here has been made in reference (2) and (3) to coherent forward scattering, where the estimated radio frequency permittivity of weak concentrations of small metallic scatterers has been shown to produce strong reflection, and for weaker concentrations, diluted an order of magnitude, strong absorption.

REFERENCES

1. Van den Hulst, H.C., "Light Scattering by Small Particles," J. Wiley, N.Y., 1957, Chapter 6.
2. Janos, W.A., "Microwave Reflection and Absorption by Contaminated Plasma," XII Int. Conf.

Phen. Ion. Gases, Eindhoven, 1975, 11.3.a.

3. Janos, W.A., "RF Propagation Effects of Metallic Aerosol Distributions," N.C. Christophilos Intn'l Summer School and Conf. in Plasma Phys., Spetse, Greece, July 1977.

*Partially performed at MDACW, IEC.

EFFECTS OF SPACE CHARGE ON THE "EFFECTIVE CROSS SECTION"

N.S. Kopeika[✉], T. Karcher and C.S. Ih.*Department of Electrical Engineering, University of Delaware, Newark, Delaware 19711, U.S.A.*

Recent evidence that the response of gas discharges to incident light is characterized by spectral effects and nonlinearities strikingly similar to those resulting from interaction of high intensity focused laser beams with effectively nonpreionized gases have suggested an analogy between the two phenomena.¹ In particular, it would appear that the effect of electromagnetic radiation incident on a gas discharge is to break down the gas slightly further beyond the breakdown level produced by bias currents. As a result, partial excitation or preionization of the gas by an applied current can permit observation of gas breakdown effects by small signal EM fields which could otherwise not be observed at such low intensities (microwatt order powers and lower). This can be observed at both short wavelengths such as those of light where photoionization of excited atoms takes place and at long wavelengths such as those of microwaves where electron kinetic energy enhancement by the rf electric field² and cyclotron resonance effects³ are apparent. At optical wavelengths, illumination of a Townsend discharge by low intensity light leads to actual gas breakdown at bias levels much less than those required without the light.^{4,5} The nonlinearities of ion production upon illumination of a rare gas Townsend discharge with low intensity optical radiation have been explained in a multi-inelastic collision manner analogous to multiphoton ionization phenomena in high intensity laser interaction

with gases.¹

A natural application of low intensity light interaction with gas discharges is the use of such devices to model high intensity laser gas breakdown effects. Such phenomena have been interpreted by Panarella as high energy "single-photon" photoionization through the "effective-photon" concept, based upon a spatial profile of energy per photon resulting from photon-photon interactions in high intensity focused laser beams. Application of the above analogue interaction to Panarella's experiments^{8,9} suggested that nonlinearities observed in illumination of gas discharges with low intensity light were a result of spatial gradients of excited atom densities due to electrode geometry. Accordingly, the "effective cross section" concept was introduced and shown mathematically⁹ to be analogous to Panarella's effective photon concept. The former is based upon a spatial profile of excited atom density similar to Panarella's spatial profile of photon energy. The spatial profile of actual photoionization is, in principle, the same in both cases. Indeed, experimental verification with low intensity light yielded linear ion production for relatively uniform excited atom concentration spatial profiles and nonlinear ion production for approximately Gaussian spatial profiles of excited atom concentration.⁵

In the above experiment, in order to make space charge effects relatively insignificant the dc bias was only 0.4 nA. Bias voltage was 33 V dc

about 40 V below dc breakdown. The internal gain mechanisms in discharges depend upon electron energy. Local electron energy is affected by space charge conditions. Thus, if space charge conditions are changed by the incident illumination, it could be possible that linearity of gas discharge response to light depends not on excited state concentration spatial profile but instead on space charge effects.¹⁰ In an effort to evaluate space charge effects, a parallel wire lamp similar to that in ref. 5 (electrode length ≈ 1.2 cm, electrode thickness \approx separation ≈ 0.8 cm) filled with 10 torr Ar was biased to 46 nA with a bias voltage of 80 V dc (14 V below dc breakdown). The interelectrode spacing was scanned with both 0.18 mW Ar (454.9 nm wavelength) and He-Cd (441 nm wavelength) laser beams focused to 67 μ m spot radius. The relatively flat interelectrode spatial profile of atomic excitation that characterizes low biases of such lamps was interrupted here in the middle of the interelectrode space by a hump about 62% higher in signal. The hump width was about 30% of the interelectrode separation. The 2-order of magnitude increase in bias current over the previous experiment gives rise to a noticeable excited concentration gradient as measured by both lasers which presumably is generated by space charge effects. Reduction of laser power 1-order of magnitude resulted in an almost identical spatial profile reduced about 10% in signal level, including the hump. The presence of an almost identical hump of the same width and relative height (64% here) interrupting the rather flat spatial profile indicates that such space charge effects result from the dc bias rather than from the incident laser radiation. Indeed, reduction of bias current resulted in disappearance of the hump, even when scanned by the 0.18 mW laser beams focused as

before. Consequently, linearity effects for the present experiments should be unaffected by space charge. With 80 V bias again, illumination of the non-uniform spatial profile region resulted in non-linear response to light intensity at both wavelengths while similar illumination of the uniform spatial profile region resulted in linear responses. In fact, illumination of the peak of the space charge hump, which has a flat spatial profile of excited atom concentration, also resulted in linear response. The experimental confirmation of the effective cross section concept is thus strengthened. Linearity of response seems to depend upon the predicted geometrical rather than space charge effects.

It is worthwhile noting, too, that discharge response to the Ar laser was noticeably closer to that of the He-Cd laser in the uniform as compared to non-uniform spatial profile region. This suggests possibly increased resonance radiation trapping,¹¹ which characterizes the opto-galvanic effect, in regions of non-uniform excited atom spatial profiles. It is planned to explore this further.

1. N. S. Kopeika, G. Eytan, and A. P. Kushelevsky, *J. Appl. Phys.* **50**, 11 (1979).
2. N. S. Kopeika, *IEEE Trans. Plasma Sci.* **PS-6**, 139 (1978).
3. R. Opher, J. Politch, and J. Felsteiner, *Appl. Phys. Lett.* **11**, 701 (1978).
4. N. S. Kopeika and G. Eytan, *IEEE Trans. Plasma Sci.* **PS-6**, 1 (1978).
5. N. S. Kopeika and A. P. Kushelevsky, *Appl. Opt.* **17**, 3933 (1978).
6. E. Panarella, *Found. Phys.* **4**, 227 (1974) and *Phys. Rev. Lett.* **33**, 950 (1974).
7. A. D. Allen, *Found. Phys.* **7**, 609 (1977).
8. E. Panarella, *Found. Phys.* **7**, 405 (1977) and *Phys. Rev. A* **16**, 672 (1977).
9. G. Eytan, N. S. Kopeika, and A. P. Kushelevsky, *IEEE Trans. Plasma Sci.* **PS-6**, 314 (1978).
10. G. Erez, private communication.
11. D. M. Pepper, *IEEE J. Quant. Electr.* **QE-14**, 971 (1978).

HIGH PRESSURE OPTICAL DISCHARGES

C. Carlhoff, J.H. Schäfer, K. Schildbach and J. Uhlenbusch.

Physics Institute II, University of Düsseldorf, F.R.G.

Continuous optical discharges (COD) were investigated in the past by many authors, see [1 - 7]. As a result of these experiments it was shown that in horizontal configurations beyond a critical pressure of say 30 bar COD cannot exist, whereas in vertical configurations pressures of 45 bar were reached. In our experiment discharges were sustained up to 145 bar and there is no doubt that even higher pressures are possible.

As a light source a cw - CO₂-laser with a maximum power of 1500 W is used. The laser assembly is built up as oscillator- amplifier system. The CO₂-monomode beam is vertically focussed inside of a high pressure chamber by a gold coated mirror of focal length $f = 2,5$ cm (see fig. 1). The plasma can be ignited by means of a thin tungsten wire which is moved for a short time through a region near the beam-focus. The high pressure chamber provides a conical KCl- or ZnSe-window of 20 mm thickness for entering the laser beam, which allows operation up to 1000 bar. Sapphire windows of good quality are mounted for spectroscopic observation of the plasma, for schlieren pictures and interferometric studies.

The shape of the COD is conical, if the focussed laser beam is directed as shown in fig. 1. The spatial dimension of the plasma can be altered by changing the laser power. Higher power in the laser focus blows up the plasma dimensions as can

be seen from fig. 2. As the temperature measurements under high pressure conditions in fig. 3 show, a second temperature maximum can occur, so that the plasma has a shape like a "sandglass".

Local temperature and electron density measurements in argon were performed by monitoring continuum radiation at $\lambda = 4470 \text{ \AA}$, assuming that Saha's equation is valid. Figs. 2,3 show typical temperature plots and electron density profiles achieved by side on observation of the plasma using Abel's inversion. It is interesting to note, that there is only a small increase of the electron density from $5 \times 10^{17} \text{ cm}^{-3}$ to $7 \times 10^{17} \text{ cm}^{-3}$ if the chamber pressure changes over two orders of magnitude.

The temperature profile of the plasma can be derived from the balance equations in the fluid dynamics approximation. A general two-dimensional solution of these equations is not known up to now, approximations are available as a cylindrical solution with one-dimensional flow and averaged transport processes [1], cylindrical solution with one-dimensional flow but two-dimensional heat losses [8] all assuming parallel and homogeneous laser beams. Converging beams without flow but two-dimensional heat flux distribution are considered in [3] and [9]. Introducing the heat flux potential $S = \int_{T_{\infty}}^T \chi \cdot dT$ (with χ thermal conductivity and T_{∞} temperature far away

from the plasma) the energy balance (with one-dimensional flow) reads for a Gaussian intensity distribution across the beam

$$\frac{1}{r} \frac{\partial}{\partial r} r \frac{\partial S}{\partial r} + \frac{\partial^2 S}{\partial z^2} - \lambda \frac{\partial S}{\partial z} = -\chi_r(S) \frac{2 \cdot P_0 \cdot e^{-\frac{2r^2}{w^2}}}{\pi \cdot w^2} \int_{-\infty}^{\infty} \chi_r dz$$

Here $\lambda = \frac{\rho_{\infty} \cdot c_p \cdot v_{\infty}}{\chi_{\infty}}$ with ρ_{∞} mass density, c_p specific heat capacity, χ_{∞} thermal heat conductivity, v_{∞} velocity far away from the plasma.

$w^2 = w_0^2 \left(1 + \frac{z^2}{z_R^2}\right)$ with w_0 = beam waist and z_R = Rayleigh length. A solution in the outer region without absorption is given by

$$S_{out}(r, z) \sim \frac{e^{\frac{\lambda}{2}(z - \sqrt{r^2 + z^2})}}{\sqrt{r^2 + z^2}}$$

This solution can be experimentally verified by interferometric measurements, as was done by Wroblewski, see fig. 4. For pressures in the 5 bar regime the assumption of an inner spherical absorption region (with $\chi_r \sim S$) is a good approximation. Then the energy equation can be solved inside the plasma with

$$S_{in}(r, z) \sim \frac{\lambda \ln(C \cdot \sqrt{r^2 + z^2})}{\sqrt{r^2 + z^2}} \cdot e^{\frac{\lambda}{2} z}$$

The calculated laser power to sustain a given maximum temperature as well as the temperature profile from these simple formulas are in good agreement with the experiments. A more general solution of the energy balance is in preparation.

The authors thank Dr. Byszewski, Dr. Plochocki and Mr. Wroblewski from the Polish Academy of Sciences for their support and helpful discussions.

References

- [1] Yu.P. Raizer, Sov. Phys. JETP 31, 6 1970
- [2] N.A. Generalov, Sov. Phys. JETP 34, 36 1972
- [3] G.I. Kozlov, Opt. Spectr. 37, 6 1974
- [4] D.C. Smith, M.C. Fowler, Appl. Phys. L. 22, 10 1973
- [5] D.R. Keefer, J. Appl. Phys. 46, 3 1975

- [6] C.D. Moody, J. Appl. Phys. 46, 6 1975
- [7] Z. Mucha Bull. Ac. Pol. SST 25 1977
- [8] J.H. Batte, IEEE PS 2 1974
- [9] J. Uhlenbusch, LuPP 2 Physics Inst. II, Univ. of Düsseldorf, 1973

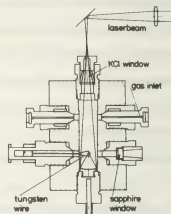


Fig.1. High pressure chamber

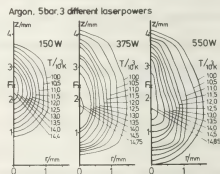


Fig.2. Temperature profiles at constant pressure

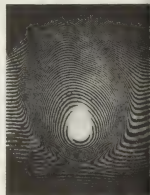
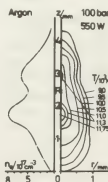


Fig.3. T and n_e at 100 bar Fig.4. Interferogram 30 bar

ON THE MECHANISM OF BREAKDOWN OF GASES BY THE EMISSION FROM A CO₂-LASER NEAR A METAL SURFACE

A.S. Kovalev, A.M. Popov and A.T. Rakhimov.

Institute of Nuclear Physics, Moscow State University, 117234, Moscow, U.S.S.R.

The effect of lowering the threshold of gas breakdown by laser emission near metal surfaces has been investigated in a large number of experimental and theoretical works. The main regularities of this phenomenon have been examined in detail in ref. /1/; they comprise the heating of the surface by laser emission to the boiling temperature, its intensive evaporation and the evolution of the breakdown in the vapours formed. In several experiments it has been found, however, that originally the breakdown appears in isolated points of the surface during the time insufficient for the heating of the surface to the boiling temperature. In ref./3/ it has been found that the recorded surface temperatures turn out to be much higher than those calculated from the measured reflection coefficients. Accordingly, the authors of /3/ has suggested that the recorded temperature characterizes not the surface temperature but the temperature of much more heated local microregions.

In what follows, we investigate a possible mechanism of optical breakdown arising in local micro-inhomogeneities of the surface.

It is known /4/ that on any polished metal surface there always are rarely distributed sharp prominences 1 or 2 μ high

and $\sim 0.1 \mu$ thick. On their tops, the external electric field is enhanced by ~ 10 times. For definiteness, we assume such a prominence to be a half-ellipsoid with semi-axes $\alpha = 1 \mu$ and $2\beta = 0.1 \mu$ at an angle $\theta = 45^\circ$ to the surface.

Consider the behaviour of such a prominence in the variable field set up by a CO₂-laser. Taking advantage of the theory of absorption of electromagnetic radiation by particles of small dimensions /5/ and substituting a uniform variable field with the intensity $E = E_0/\sqrt{2}$ for a real electric field at the surface, we obtain the following expression for energy release per unit time:

$$Q = \frac{\pi \cos^2 \theta}{3[\epsilon_n \frac{4a^3}{\beta^3} - 2]^2} (1-R)^2 \left(\frac{a}{\beta}\right)^4 \frac{1}{\lambda} \pi \beta^2 I \quad (I)$$

Here $I = \frac{c E_0^2}{8\pi}$, R is the surface reflection coefficient, $\lambda = \frac{2\pi c}{\omega}$ the radiation wavelength.

We note that formula (I) is valid provided that $4\pi\beta/\omega (\beta/a)^2 \gg 1$ (β being the conductivity). We assume that the energy is released uniformly throughout the whole volume of the prominence, the heat is removed only through its base with the area $\pi\beta^2$ and its temperature is equal to that of the surface, T_{sur} . Then the time dependence of the temperature of its top is given by

$$T - T_{\text{sur}} = \frac{Q a}{2\pi\kappa\beta^2} \left(1 - \exp\left[-\frac{\pi\kappa^2}{4a^2} t\right] \right) \quad (2)$$

where K and κ are the coefficients of thermal conductivity and diffusivity of the prominence material, respectively.

From formulas (1) and (2) it follows that the prominence is heated much faster than a smooth surface. Thus, at $k=2\frac{w}{q_{rad}cm}$, $\kappa=1$ cm²/sec, $R=0.9$ and radiation intensity $\sim 5 \cdot 10^7$ w/cm² the top of the prominence will be heated to the boiling temperature during $\sim 2 \cdot 10^{-9}$ sec, whereas the temperature of the surface itself remains practically unchanged.

After the boiling temperature is reached near the prominence top, there forms vapor with the density

$$n_n = \frac{Q_{evap}}{u_s \cdot L \cdot 2\pi\delta^2} \quad (3)$$

Here u_s is the velocity of sound in the vapor at the boiling temperature, L the heat of evaporation per single particle, $Q_{evap} = Q - 2\pi\kappa\delta^2 \frac{dT}{dt} / A$ being the portion of energy spent to evaporation. For the above parameters, $n_n \sim 10^{21}$ cm⁻³. Since in the case of the CO₂ laser the condition is fulfilled, the electric field at the top of the prominence is significantly higher than the average electric field. Assuming such a top to be a hemisphere of radius δ , the field enhancement coefficient is given by $\mu = \frac{q}{\delta}$.

Consider the behaviour of electrons in a vapour with density $\sim 10^{21}$ cm⁻³ in a volume $\sim \delta^3$ under the influence of the electric field $\mu E_0 \cdot \cos \omega t$. The equation for the electron energy \mathcal{E} will be written as

$$\frac{d\mathcal{E}}{dt} = \frac{e^2 \mu^2 E_0^2}{m(\omega^2 - \gamma^2)} \gamma - \frac{2m}{M} \mathcal{E} \cdot \gamma - D \mathcal{E} \left(\frac{\gamma}{\delta} \right)^2 \quad (4)$$

Here γ is the electron collision frequency, D the diffusion coefficient, $\bar{\mathcal{E}} \sim 5$ eV.

Since in our case, the elastic losses may be neglected, as compared with the losses to diffusion and $\gamma > \omega$, from equation (4) we obtain the condition of gas breakdown by radiation:

$$I > \frac{c}{6\pi e^2 \mu^2} \left(\frac{\pi}{\delta} \bar{\mathcal{E}} \right)^2 \quad (5)$$

In case $\mu = 20$, $\delta = 5 \cdot 10^{-6}$ cm, we have $I > 4 \cdot 10^7$ w/cm², the avalanche development time being $\sim 3 \cdot 10^{-11}$ sec. Thus, at $I \geq 5 \cdot 10^7$ w/cm² on the microscopic prominences of the surfaces there arise regions of fully ionized plasma which serve as the sources of spherical light detonation waves thus giving rise to the spreading of the discharge over the entire target surface irradiated by a laser.

References:

1. A.I. Barchukov, F.V. Bunkin, V.I. Konov, A.A. Lyubin. ZhETF, 66, 965 (1974).
2. B.E. Beverly, C.T. Walters. J. Appl. Phys. 47, 3485 (1976).
3. A.V. Bessarab, N.V. Zhidkov, S.B. Kormer, D.V. Pavlov, A.I. Funtikov. Sov. Quantum Electronics, 2, 325 (1978).
4. I.N. Slivkov. Electric insulation and discharge in vacuum. M., Atomizdat (1972).
5. L.D. Landau and E.M. Lifshitz. Electrodynamics of continuous media. M., Gos- tekhnizdat (1957).

INVESTIGATION OF PLASMA FORMATION DYNAMICS AND PROPERTIES OF UNDEREXPANDED SUPERSONIC EROSION LASER PLASMA FLARES

G.I. Bakanovich, L.Ye. Min'ko and A.N. Chumakov.

Institute of Physics, Byelorussian Academy of Sciences, Minsk, U.S.S.R.

In view of a wide laser application for obtaining moving plasmas by the effect of a free-running mode laser radiation of moderate intensities on different absorptive materials it is of great importance to examine plasma formation dynamics and heating the underexpanded supersonic erosive laser plasma flares under formation. Spectroscopic studies of the effect of free-running mode laser radiation might give us a required information only in case we use the methods providing for both space- and rather high time resolution. In the present paper this is attainable by high-speed frame-wise spectrum recording which enables the diagnostics of plasma clusters corresponding to separate laser spikes to be performed.

In the experiments a Nd glass laser with pulse energy about 500J at a half-amplitude level duration of 500 μ sec was used. Laser radiation was focused into the spot of ~ 0.2 cm diameter on the target surface. The density of laser radiation flux was about $2 \cdot 10^7$ Wt/cm², and was sufficiently enough for intensive evaporation and plasma formation under effect of every individual spike. Aluminium, brass and lead were used as plasma formation materials.

Intensive continuum and spectral lines of

atoms and ions of target material elements may be used for measurement of the main plasma parameters. For this purpose the calculation of plasma composition and the emission and absorption coefficients over a wide spectral range have been made for a wide range of electron densities at different temperatures with the Minsk-32 computer. The continuum coefficients ξ_λ have been calculated from experimentally measured space-time resolved spectral brightnesses of plasma. The electron densities have been found both by the calculated graphs $\xi_\lambda = f(N_e)$ for different temperatures and by the spectral line broadening due to the quadratic Stark effect.

The study of frames of spectrograms and streaks showed that for every plasma cluster corresponding to a separate laser spike the glow brightness amounts to maximum at some distance from the target surface (for Al 0.4-0.6mm, brass 0.5-0.8mm, Pb 0.2-0.3mm). The glow intensity distribution along the plasma cluster at different periods of time is represented in Fig.1 ("1" is the glow origin, "2" 0.15 μ sec, "3" 0.3 μ sec and "4" 0.5 μ sec; the case of the brass).

To identify the "dark space" (the weak

glow zone, detected at the target surface) one had to diagnose the nearsurface plasma formation for aluminic target. Only 6-8 frames of spectrograms corresponding to separate fragments of the flare development no later than

40 μ sec after the onset of laser effect were processed quantitatively as afterwards the spectrum

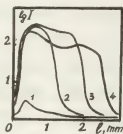


Fig. 1

nature changed sharply. Separate frames served for determination of spectral radiances along the plasma formation for 3 wavelength regions of the continuum far from intense spectrum lines. The "brightness temperature" calculated is $5 \cdot 10^3$ $^{\circ}$ K in the dark space region and increases to the height of 0.6mm. At the distance of more than 1mm from the target surface temperature was measured by relative intensities of spectral lines Al III 448nm and 451nm; the temperature values are in the range 16000-23000 $^{\circ}$ K. The analysis of radial profiles of continuum and spectral lines intensities in different cross-sections of the flare indicates an existence of pronounced temperature gradients along the plasma formation radius.

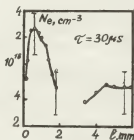


Fig. 2

Due to the usage of the technique described we succeeded in obtaining the electron distribution along the plasma formation. Fig. 2 gives the typical electron density distribution along the plasma cluster cor-

responding to a separate laser spike.

The studies show that the maximum values of the electron density ($2 \cdot 10^{18}$ cm^{-3}) and the temperature in an erosive plasma cluster are available at some distance from the target surface. This cluster area is separated from the target surface by a narrow weakly glowing zone with $T \sim 5 \cdot 10^3$ $^{\circ}$ K and $N_e \sim 10^{17}$ cm^{-3} . The detected dark space presents the zone of formation of erosive vapor cloud which absorbs laser radiation for every pulse duration. On attainment of critical flow density it results in a plasma formation at some distance above the target surface. As the time required to obtain the critical flow density is determined by the steepness of the pulse front then the dark space value depends on the pulse shape.

The dark space value l_* can be estimated by the distance covered by the vapor cloud for the time from the onset of evaporation to plasma formation (at critical flow density). The estimation yields the value of $l_* \sim 0.3$ mm which satisfactory agrees with the experimental one. The dark space value depends also on the ambient pressure and cannot exceed the value of the unidimensional expansion region where the absorption of the incident radiation is the most efficient one. Hence, with increase of the irradiation spot and with the usage of the laser pulse of the large front duration the plasma formation will occur at a considerable distance from the evaporating surface.

DYNAMICS OF PLASMA PHENOMENA IN "PLASMA FOCUS" UNDER THE ACTION OF POWERFUL LASER RADIATION

V.A. Gribkov, A.V. Dubrovsky, N.V. Kalachev, T.A. Kozlova and V.Ya. Nikulin.

P.N. Lebedev Physical Institute, U.S.S.R. Academy of Sciences, Leninsky prospect 53, 117924 Moscow, U.S.S.R.

A combined beam-laser method (CBLM) for plasma heating up to thermonuclear temperatures has been proposed in papers /1,2/. An installation of "Plasma Focus" (DPF) type has been used as the relativistic electron beam (REB) source /1/.

1. The influence of a powerful laser radiation (PLR) on plasma phenomena in the DPF at the magnetohydrodynamic stage is discussed in the present paper. Experiments have been carried out on the installation "FLORA" specially designed for CBLM investigations /3/. The DPF parameters are the following: capacitor bank energy, 50 kJ; neutron yield, $5 \cdot 10^9$ n/pulse; maximum current, 800 kA. The Nd-glass laser has the following parameters: pulse duration, 2 nsec; energy, 500 J. We have used the following diagnostic methods: simultaneous Ru-laser 5-frame interferometric and shadow photography, soft X-ray pin-hole camera, mica convex spectrograph, and the temporal evolution of hard X-ray radiation ($E > 80$ keV).

2. The typical 5-frame interferograms, pin-hole picture and shadowgram obtained during one "shot" without PLR are shown in Fig. 1.

1. Gribkov V.A., Krokhin O.N. et al. Pis'ma JETP 1973, v.18, N 9, 541.

Afanasiev Yu.V., Basov N.G. et al. Trudy FIAN (Proc. Lebedev Institute) 1978, Moscow, "Nauka", v.103, 202-230.

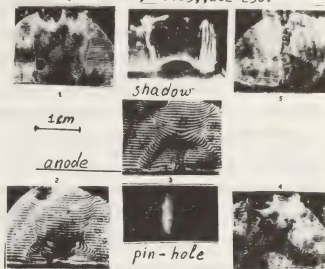


Fig. 1.

The window diameter is 4 cm.

2. Gribkov V.A. et al. JETP Lett., 1977, v.26, N 4, 209-214.
3. Veretennikov V.A., Gribkov V.A. et al. Proc. of the XIII Conf. on Phenom. in Ionized Gases, 1977, Berlin, 881-882.

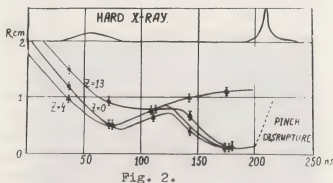


Fig. 2.

Fig. 2 presents R-t diagrams of the pinch in the DPF in respect to hard X-ray pulses. We have observed two compression

phases of the DPF with the time interval of 100 nsec. The minimum pinch radius at the moment of the first compression is about 5 mm, that is good agreement with the bright image of plasma column given by the pin-hole pictures. The electron density at this moment is $4 \times 10^{18} \text{ cm}^{-3}$. The shadowgrams show a strong anode (Cu) erosion during the first compression.

The second compression in the DPF begins with the pinch catching by the magnetic field near the anode, resulting in considerable particles' ejection to the vertical direction. In this case the linear plasma density decreases by one order of magnitude up to $3 \cdot 10^{17} \text{ cm}^{-1}$, the sharp pinch compression to the radius 1 mm takes place, and T_e appears to be in keV region, that is confirmed by the characteristics of the line impurities' spectra. At this stage the pinch life-time is about 20-30 nsec. Then, the pinch is rapidly disrupted, and the hard X-ray burst is observed.

4. Veretennikov V.A., Gribkov V.A. et al.

Proc. of IV S.U. Confer. on Plasma Accelerators and Ion Injectors, 1978
Moscow, VNTIC, 84-85.

5. Vikhrev V.V. et al. "Plasma Physics and Contr. Nucl. Fusion Res.", IAEA, 1977



Fig. 3.

Fig. 3 shows the DPF interferogram after the action of PLR focused on the anode with flux of 10^{12} W/cm^2 . Due to the action of PLR 30-50 nsec before the first compression stage there takes place the formation of the evaporated copper flare that moves vertically with the speed of $3 \cdot 10^7 \text{ cm/sec}$. In this case pin-hole picture shows the luminous "plume" 3mm in diameter, which coincides with the one on interferograms. The second compression is not observed due to PLR interaction with DPF. One may observe the rapid pinch disruption accompanying hard X-ray and neutron bursts /4/.

3. Observed pinch catching near the anode may be explained by strong anode erosion, resulting in plasma conductivity decrease. Conductivity decrease may be caused by excitation of plasma instabilities. These processes result in current sheath perturbations /5/, and are responsible for sharp pinch catching near the anode zone after PLR action. The energy of the observed Cu streams consisting of 30keV ions does not exceed 30J. Existence of such thin Cu-ion stream seems to indicate the presence of magnetic field inside the pinch of the order of 10^5 G .

In this way the performed experiments revealed PLR interaction with DPF to have essential influence on the dynamics of plasma phenomena in DPF, and may lead to new possibilities in CLBM experiments. Authors would like to express deep gratitude to Isakov A.I., Krokhin O.N., Filippova T.I. for useful discussions, and Semenov O.G., Veretennikov V.A., Korzhavin V.M., Silin P.V. for assistance in the experiments.

PLASMA TARGET COUPLING IN THE CASE OF TEA-CO₂ LASER PRODUCED BREAKDOWN IN FRONT OF A SOLID TARGET

I. Apostol, E. Cojocaru, M. Dinescu, V. Drăgănescu, Th. Julea, I. Morjan, M. Moldovan, I.N. Mihăilescu and V.I. Konov*

*Lasere Department, I.F.T.A.R., Central Institute of Physics, Bucharest, Romania.
Physical Institute "P.N. Lebedev", Moscow, U.S.S.R.

The experimental results of highly absorbant (metallic) targets irradiation by a focused TEA-CO₂ laser in air at atmospheric pressure, for incident power intensities, I , of $(10^6 \div 10^8)$ W/cm², are reported. Particularly, the coupling coefficient between the breakdown plasma and target, defined as the ratio of the thermal energy transferred to the target to the laser energy, was investigated as a function of incident intensity (laser fluence), the laser spot size and the geometry of the experiment.

As it is known [1,2] when incident laser intensity on target exceeds not only the breakdown threshold intensity, but equally another characteristic value - the laser threshold intensity for inducing a detonation wave - the breakdown plasma detaches from the target and the ionisation front propagates in a direction opposite to that of the laser beam. In this case, the plasma dimension along the laser beam exceeds considerably its transverse size. On the other hand, at lower intensities there is no detachment from the target and the plasma expands spherically into the surrounding gas. In [3] the momentum per unit energy, p/E , acting backward on the target was determined from the deflection of a ballistic pendulum. Maximum values of $(6 \div 7)$ and $(13 \div 14)$ dyn. s/J were obtained corresponding to cylindrical and spherical plasma expansions, respectively. Here E was taken to be the laser energy stored into the plasma source, $E_0(1-R)$, where E_0 is the incident laser energy and R is the time integrated loss coefficient. On the other hand, theoretical estimations performed in the same work predicted values of 7.5 and 32 dyn.s/J for the two cases.

A possible reason of such a disagreement could be the amount of energy transferred, during and after the laser pulse, from plasma to the target, which accordingly alters the denominator of the ratio p/E . We also remark the important significance of this quantity for the energy balance of the process. Such a transfer takes place through two different channels:

(a) Absorbing the plasma emitted light. As the metals exhibit high reflectivity for longer wavelengths this mechanism is efficient only for times comparable with the pulse duration when the plasma is hot enough to present an emitted spectrum with an uv maximum. As the path of the uv radiation in air is of the order of 1 mm this absorption induces only a small supplementary expansion of plasma and all laser energy goes into a spot almost equal to that of the laser beam.

(b) Thermal coupling between plasma and target. It is easy to prove that this process is developing several orders of magnitude more intensely to the target direction than in the opposite one.

This work is intended to bring a deeper insight into the transfer process mainly regarding the contribution of the two aforementioned competitive mechanisms in the case of 10.6 μ m laser radiation. To this aim experiments were performed using a double discharge TEA-CO₂ laser which was able to deliver output energies of several J in pulses of a typical shape. In view of obtaining only monomode laser emission a variable aperture diaphragm was introduced inside the resonant cavity. Beam splitters, a pyroelectric detector and a calorimeter were used to monitor the pulse shape and energy on each shot, while plasma plumes

evolution was recorded using a high speed SFR photographic camera. The targets were small pieces of copper, of different sizes, rear-thermocoupled, which were carefully cleaned after every shot. A plot of the coupling coefficient is shown in Fig.1.

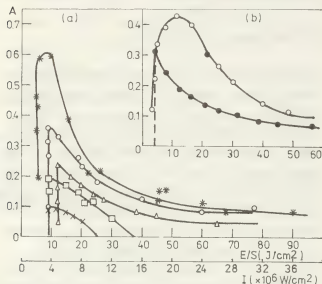


Fig.1 The coupling coefficient, A , as a function of laser fluence, E/S , and intensity, I . (a) the focus was on and after the target with laser spots: \bullet - $0.8 \cdot 10^{-2} \text{ cm}^2$; \circ - $1.3 \cdot 10^{-2} \text{ cm}^2$; Δ - $4.1 \cdot 10^{-2} \text{ cm}^2$; \square - $6.2 \cdot 10^{-2} \text{ cm}^2$; \times - $9.6 \cdot 10^{-2} \text{ cm}^2$, respectively. (b) the laser spot on target in both cases of $3 \cdot 10^{-2} \text{ cm}^2$ but the focal plane before \bullet , and after - \circ , the target.

As may be observed beyond the breakdown threshold a significant enhancement of the coupling coefficient is obtained followed by a further slow decrease. The value and the position of this maximum depends on the spot area. The largest registered value of A was of 0.6 corresponding to a laser fluence of 10 J/cm^2 and a laser spot of $0.8 \cdot 10^{-2} \text{ cm}^2$. The decrease of the coupling coefficient as the laser fluence surpasses the breakdown threshold is a result of releasing a laser absorption wave and develops more slowly for larger laser spots or target.

Such a behaviour closer agrees with the first mechanism. Thus, when the detonation wave threshold intensity is surpassed the plasma detachment from the target displaces the uv emitting region

further and further to the laser beam direction. A larger part of the emitted radiation is then absorbed by the colder plasma zones and only a small amount is reaching the target; the coupling coefficient is accordingly falling down. The reduction is slower for larger laser spot because of an increased contribution in this case of the second mechanism resulting from a raised contact surface between plasma and target.

We also put into evidence that for a same laser spot the coupling coefficient is higher when the focus was situated after the target. Such a phenomenon may be also explained by the dominance of the radiative mechanism. Thus, when the focal plane is placed before the target the hottest part of the plasma is formed at a certain distance in front of the target and a great part of the emitted uv radiation is absorbed on its path to the target.

In Fig.2 the laser intensities corresponding to maximum values of A were plotted against the laser spot area.

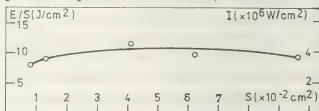


Fig.2 Incident laser intensity corresponding to maximum values of the coupling coefficient as a function of the laser spot on the target.

A very small variation may be observed which is confirming that in the range of incident laser intensity we studied both mechanisms have to be considered but the most important role is to be due to the energy transfer through uv radiation emitted by the plasma.

BIBLIOGRAPHY

- [1] I. Apostol et al, Proc. XIIth I.C.P. I.G. Eindhoven, p.337 (1975)
- [2] D. Apostol et al, Proc. XIIth I.C.P. I.G. Berlin, p. 1108 (1977)
- [3] V.P. Ageev et al, Izv. Vuz. Fiz. 11, 34 (1977)

INTERFEROMETRIC MEASUREMENTS OF DENSITY PROFILES IN LASER-TARGET INTERACTION

R. Benattar^{*}, C. Popovics^{*}, R. Sigel^{**} and J. Virmont^{*}.^{*}Laboratoire de Physique des Milieux Ionisés, Ecole Polytechnique, 91128 Palaiseau Cédex, France.^{**}On leave from Projektgruppe für Laserforschung, Max-Planck-Gesellschaft zur Förderung der Wissenschaften E.V., D-9046 Garching bei München, R.F.A.

Density profiles of the plasma created in the interaction of a high power laser with a solid target give a better knowledge of energy absorption and transport mechanisms in laser fusion experiments.

For the first time in this type of experiment, we used a polarized light interferometer based on a Wollaston prism which, by its relative simplicity and absence of alignment problems, is very convenient.

Let us recall the principle of this interferometer (Fig. 1). The object O is depicted by a high resolution lens L onto the film, with a Wollaston prism W creating two orthogonally polarized images. Interference between these two images is achieved by a pair of polarizers P1, P2, either parallel or orthogonal to each other. Two images of equal intensity and polarization are produced in the image plane which hence can interfere in the overlapping region.

The two interfering beams are two parts of the probe beam; this requires a rather good spatial coherence in the illumination field. We have applied this interferometer in two different laser plasma experiments to study the corona expansion of laser heated microspheres. Plasma production was either

with a CO₂-TEA-laser in combination with a ruby diagnostic laser ($\lambda = 0.694 \mu\text{m}$) or with a Nd-glass-laser in combination with a frequency quadrupled beam ($\lambda = 0.265 \mu\text{m}$) for interferometer illumination. Targets were microspheres with diameters in the range of 40 μm to several hundred micrometers.

In both experiments the same Wollaston prism of 30 x 30 mm cross section, with a surface flatness of $\lambda/20$, prism halves in optical contact, made of natural quartz, with $\mathcal{C} = 5 \times 10^{-3}$ rad was used. The spatial resolution obtained is 5 to 6 μm .

INTERACTION WITH CO₂ LASER EXPERIMENT ($\lambda = 10.6 \mu\text{m}$)

A CO₂ laser (40 Joule in 40 ps) illuminates a 176 μm glass microsphere.

Picture 2 in an interferogram showing plasma expansion 200 ns after the top of the CO₂ pulse. Initial surface (solid circle) and the critical electron density $N_e = 10^{19} \text{ cm}^{-3}$ (dashed circle) are indicated.

The density profile deduced by Abel inversion has two main features :

- First we can measure density as high as 10 times the CO₂ critical density i.e. 10^{20} cm^{-3} and probe

the plasma in the transport region very near the target surface.

- Moreover, the density gradient scale length is evaluated as $37 \mu\text{m}$ (between n_c and n_c/e) that is only 4 times the CO_2 laser wavelength.

INTERACTION WITH NEODYMIUM LASER ($\lambda = 1.06 \mu\text{m}$)

We study the interaction of a neodymium laser beam (5 Joules in a 100 ps pulse) with glass microspheres $70 \mu\text{m}$ diameter. The interferograms and the deduced density profiles (Fig. 3) show that spherical symmetry is rather good, for a one beam illumination.

The density profile obtained 80 ps after the top of the laser pulse has been measured in the range $2 \times 10^{19} \text{ cm}^{-3} < n_e < 4 \times 10^{20} \text{ cm}^{-3}$ and the density gradient scale length is estimated to be $20 \mu\text{m}$ in this region. The profile is compared to a numerical simulation (Fig. 3b) done with a fluid, 2 temperature, monodimensional code in which the heat flux electron is limited. As the mechanism of limitation of heat flux is not known, the limitation is done parametrically with a factor f defined by $Q = \text{Min}(\chi \nabla T, 0.6 \times f \times n_e \times v_e \times k T_e)$

The theoretical curve ($t = 150 \text{ ps}$, $f = 0.05$) is the best fit which can be found. Curves traced for $f < 0.05$ also fit well the experimental results so, we conclude that the heat flux is strongly limited producing a plasma corona strongly expanded.

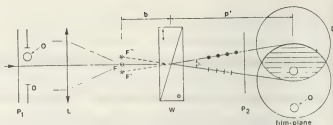


Fig. 1 - Schematic representation of the polarized light interferometer.

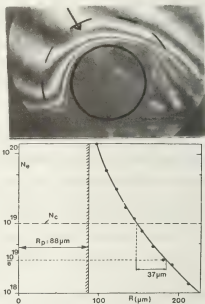


Fig. 2 - Interferogram of a glass microsphere $176 \mu\text{m}$ diameter illuminated by CO_2 laser (the plain circle is the initial sphere and the dashed line is the critical density) and deduced density profile.

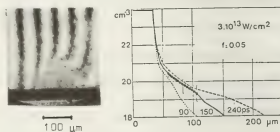


Fig. 3 - $70 \mu\text{m}$ diameter glass microsphere illuminated by a Neodymium glass laser.

- a - Interferogram measured at time $t = 160 \text{ ps}$, i.e. 80 ps after the top of the laser pulse.
- b - Experimental density profile deduced from the interferogram (3a), and calculated profiles for different times, for flux limit factor $f = 0.05$ and averaged laser intensity $\bar{I} = 3 \times 10^{13} \text{ W/cm}^2$.

EXPERIMENTAL INVESTIGATION OF TRANSPORT IN LASER-TARGET IRRADIATION EXPERIMENTS

F. Amiranoff, R. Fabbro, E. Fabre, C. Garban and J. Virmont.

Laboratoire de Physique des Milieux Ionisés, Ecole Polytechnique, 91128 Palaiseau Cedex, France.

The purpose of this work is to study by experiment the penetration depth of the heat front in a solid submitted to the strong irradiation of a laser, and also to analyse the effect of the laser wavelength on the thermal heat transport.

The target are irradiated by the output beam of a Neodymium glass laser which delivers 10 J in 80 ps at 1,06 μ wavelength, and when frequency doubled, 5 J in 80 ps at 0,53 μ . The light intensity onto the target are then $2 \cdot 10^{15}$ W/cm² at 1,06 μ and 10^{15} W/cm² at 0,53 μ . The targets employed are thin films of polystyrene whose thickness can range from 900 Å to a few microns. The diagnostics of thermal transport were the following : transmission of reflection of laser light by the target, X ray emission, thermal ion velocity in the front and the rear of the target. All measurements were made as a function of foil thickness. Depending upon the diagnostics, criteria were choosen for penetration depths characterization : 90 % foil and plasma opacity, saturation in plasma reflectivity or in X ray emission, change in the ion velocity of the thermal ions emitted on the rear side of the foil. Fig. a gives an example of foil transmission and reflection at $2 \cdot 10^{14}$ W/cm². Fig. b gives X ray emission as a function of foil thickness. Fig. c shows the effect of laser wavelength on foil transmission. In order to analyse experimental results, a numerical simu-

lation of the experiment was made with a 1D Lagrangian code, in planar geometry, and numerical determination of heat penetration was made. The table I summarizes these results and their comparison to the experiments. The column corresponds to the type of diagnostic and the row to different experimental conditions.

As a result it appears that the experimental value for heat penetration are smaller than given by the numerical simulation. This involves strong flux limitation and even with a flux limit factor of $f = 0.05$ the computed value (row a in table I) are still larger than experimental determination. It does not seem reasonable at that time to assume that the flux limit is even more smaller. One have to think of the limit of the validity of the comparison between a one ID planar simulation with the experiment which include some 2D aspect on transport. Another possibility to obtain agreement between experiment and simulation will be to reduce also the flux. However this argument must be handled with care. It is not the laser flux which should be reduced but the heat thermal flux from critical region toward the target interior. Experimental results could be interpreted by introducing some anisotropy in heat transport. Assuming for example a strong lateral conduction. The second result of this experiment is to show the more efficient transport

when plasma heating is made with a short wavelength: thermal front penetrates deeper in the target, however the interpretation of this effect does implies only that the ablation velocity is larger in the case of the short wavelengths. It appears that when comparing experiments and numerical simulation, even for the short wavelength, we must include a flux limitation which is of the same order at $0,53\mu$ and $1,06\mu$.

In conclusion, strong transport inhibition is evidenced laser target irradiation experiments. Short wavelength seems more favorable for heat penetration in solid but still subject to flux limitation problems.

This work is made as a part of the scientific program of Greco Interaction Laser Matière.

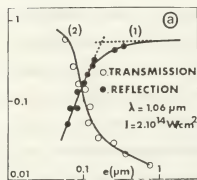


Fig. A

Reflection and transmission of the laser pulse versus foil thickness. The foil thickness corresponding to 10 % of transmission is defined as d_T ; here $d_T = 0,11\mu$.

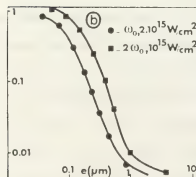


Fig. B

Variation of the transmission versus foil thickness at $1,06\mu$ and at $0,53\mu$; $d_T(\omega_0) = 0,22\mu$ and $d_T(2\omega_0) = 0,43\mu$

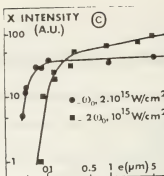


Fig. C

X-ray emission for the 1-2 keV channel versus foil thickness at $1,06\mu$ and at $0,53\mu$. The foil thickness corresponding to the saturation of the signal is defined as d_X : $d_X(\omega_0) = 0,15\mu$ and $d_X(2\omega_0) = 0,35\mu$.

		$d_T(\mu m)$	$d_{i1}(\mu m)$	$d_{i2}(\mu m)$	$d_X(\mu m)$
$2.4 \cdot 10^{14} W/cm^2$	a	0.11	0.12	0.20	0.11
	b	(0.22)	(0.22)	(0.22)	
$2.10^{15} W/cm^2$	a	0.22	0.17	0.32	0.15
	b	(0.44)	(0.46)	(0.60)	
2ω $10^{15} W/cm^2$	a	0.43	0.30	0.50	0.35
	b	(1.4)	(0.75)	(1.5)	

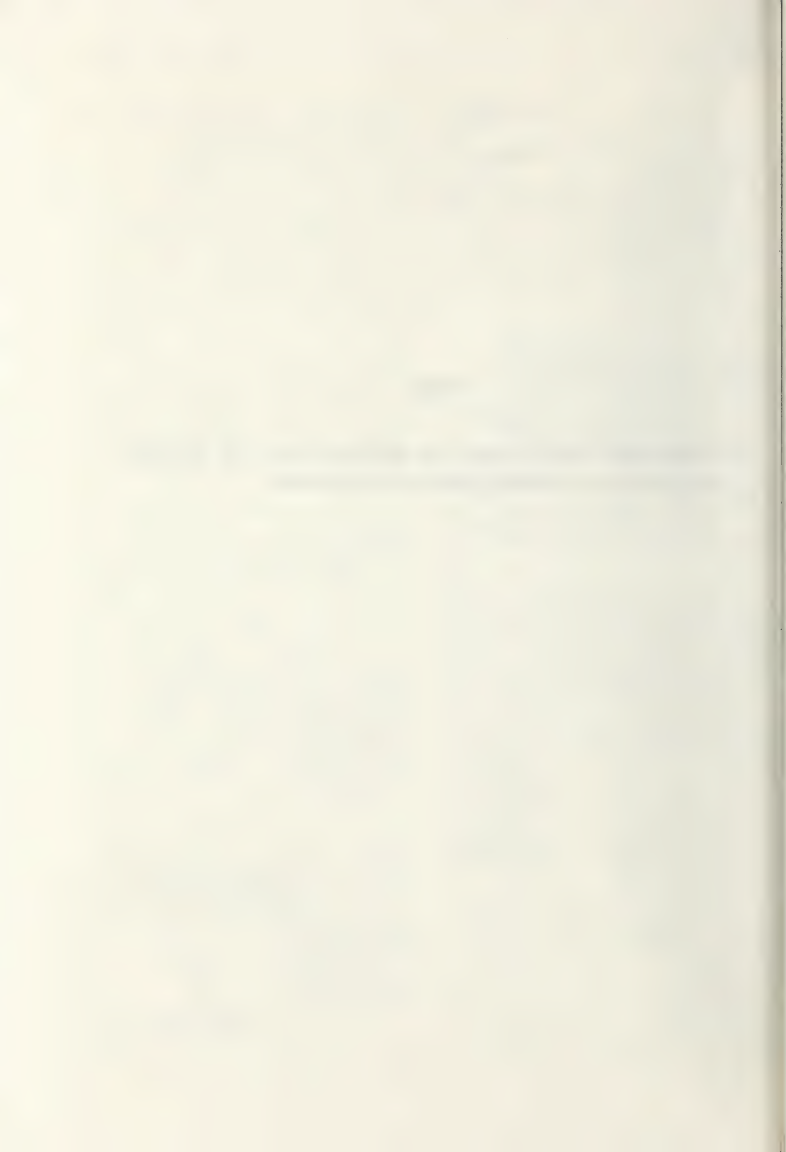
Table I

Summary of the experimental results for the characteristic foil thicknesses d_T , d_{i1} , d_{i2} , d_X . d_T and d_X have been defined in fig. A and in fig. C; d_{i1} and d_{i2} correspond respectively to the thicknesses for which the velocity of the fastest of the thermal ions and of the peak of the thermal ions in the rear side of the foil is smaller than the corresponding velocity in the front side of the foil.

The values between parenthesis are the corresponding results of the numerical simulations for two values of the flux limit factor: line a, $f = 0,05$; line b, $f = 1$.

XIV

- Interaction des faisceaux de particules avec les plasmas
Interaction of particle beams with plasmas



INTERACTION OF AN INTENSE RELATIVISTIC ELECTRON BEAM WITH THE ATMOSPHERE

A.W. Ali, J.R. Greig, I.M. Vitkovitsky, R.B. Fiorito* and R.F. Fernsler**.

Naval Research Laboratory, Washington, D.C. 20375, U.S.A.

*Naval Surface Weapons Center, White Oak, MD 20910, U.S.A.

**JAYCOR, Alexandria, VA 22304, U.S.A.

Propagation of intense relativistic electron beams (REB) in air at low^{1,2} and at atmospheric pressures,² has been studied. Such propagation depends strongly on the interaction of the beam with the atmosphere. We have studied the effect of a high current density (5-10 kA/cm²) pinched REB on the atmosphere. Beam characteristics such as radial and longitudinal beam current distribution and energy loss in the atmosphere, as well as such response of the atmosphere as the formation of ionized and excited species, were measured and compared to calculated values.

50 nsec beams with currents ≤ 60 kA and electron energies ≤ 2.5 MeV were generated using the NRL VEBA pulser. Beams were propagated in the atmosphere

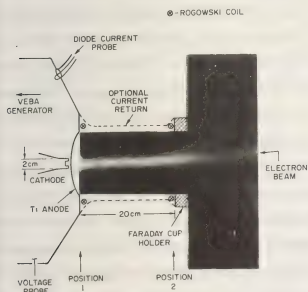


Fig.1: A REB propagating in the atmosphere.

†Work supported by the Office of Naval Research.

with and without a current return screen. Fig.1 shows the diode configuration in relation to the electron beam propagating without the current return screen. Electrical properties were measured using Rogowski loops, with diameter of 14 cm, and a variable-aperture Faraday cup (combined with a calorimeter) at positions shown in Fig.1. Exposures on thin cellophane films placed in front of the Faraday cup and an x-ray pinhole camera viewing the beam side-on (Fig.2) correlate with the radial current distribution measured by the Faraday cup. Radiation output in the visible range was measured with time-integrated photography (Fig.1) and spectroscopy ($3000 \text{ \AA} \leq \lambda \leq 6000 \text{ \AA}$). Two of the observed lines N_2 $\lambda 3371 \text{ \AA}$ and N_2^+ $\lambda 3914 \text{ \AA}$ were time-resolved and time-correlated with the beam current. No emission from oxygen nor any other species except N_2 and N_2^+ was observed. The N_2 line intensity, beam current and diode voltage are shown in Fig. 3. Beam deposi-

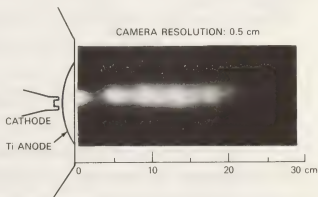


Fig.2: X-ray pinhole photograph of REB in the air.

tion in the atmosphere was inferred from dE/dx values and confirmed by estimates derived from

readings of collimated thermo-luminescent devices measuring the x-rays emitted by the atmosphere.

A typical propagated beam has maximum particle energy of 2 MeV and an injection current $I_b = 30$ kA, corresponding to a Budker parameter $v/\gamma = 0.3$. At 20 cm from the anode, the beam current density (j_b) half-width is 1.5 cm. Distances between beam foci (pinches) observed in Fig.1 and Fig.2 agree with calculated values of the betatron wave length, λ_β . The hose instability, associated with the magnetic diffusion time $\tau = \frac{\pi \sigma_0}{2c^2} = \frac{w_{pe}^2}{8vc} \frac{a^2}{c^2}$ for beam displacement¹ occurs at a distance of about 30 cm (~5% of the electron range). For the first ~25 cm of propagation, the beam is well confined with a peak current density, $j_b \sim 10$ kA/cm², $dE/dx \sim 2$ kV/cm, and ~ 1 J/cm³ is deposited into the air:

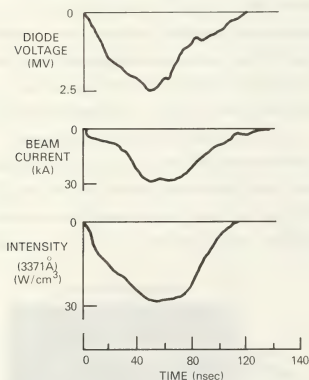


Fig.3: Time histories of selected parameters.

The response of the atmosphere to the beam is mainly through primary ionization processes (beam electrons) followed by thermalization with low energy secondary electrons. To follow these interactions, CHMAIR code, an NRL sea-level air chemistry

code, was used. The code indicates that for $j_b \sim 10$ kA/cm² and realistic current shapes, secondary electron densities of $n_e \sim 10^{16}$ cm⁻³ are achieved. Also excited state populations (N_2 and N_2^+) corresponding to excitation temperatures of ~ 5 eV are attained even though the secondary electron temperature is only ~ 0.3 eV. Thus, time histories of the visible emissions (N_2 and N_2^+) follow the current pulse shape (Fig.3) but are substantially modified by absorption at the current peak. (The indicated source intensity of ~ 30 W/cm² for the N_2 2P (0-0) band is the apparent value deduced using the optically thin approximation.) The gas temperature at the end of the current pulse is only ~ 600 K—the deposited energy being mostly stored in molecular dissociation. However, as the heated air column thermalizes and expands to pressure equilibrium, the gas temperature should approach ~ 1500 K.

The inductive field, E_z , associated with the beam rise time can set up a counterstreaming current with density $j_s = n_e e v_d$. The upper limit of j_s is ~ 3.5 kA/cm² (i.e. about 35% of j_b) for $E_z \sim 2$ kV/cm and assuming no gas breakdown. The net current, $I = I_b - I_s$, measured by the Rogowski coil at position 1, is within 10-15% of I_b measured inside the diode, suggesting that I_s is not significant. Similar measurement at position 2 (in Fig.1) shows approximately 30% lower current (within the 14 cm diameter coil). This decrease appears to be due to beam current loss from scattering, as evidenced by x-ray emission from the coil surfaces. Similarly λ_β and the identical shapes of currents in the diode, and at positions 1 and 2 suggest that I_s is small. Finally, addition of the return screen did not affect the net current measurements.

1. E.J. Lauer et al, Phys Fluids **21**, 1344-52 (1978)
2. P.E. Boldouc et al, Bull Am Phys Soc, **23**, 840 (78)

DIAGNOSTICS PROGRAM FOR A MAGNETICALLY INSULATED ION DIODE FOR INERTIAL CONFINEMENT FUSION

E.J.T. Burns, D.J. Johnson, A.V. Farnsworth, Jr., D.L. Fehl, R.J. Leeper, L.P. Mix and G.W. Kuswa.

Sandia Laboratories, Albuquerque, New Mexico, 87185.

Inertial confinement fusion (ICF) schemes require an ion power density of 10^{13} - 10^{15} watts/cm² on target.¹ At Sandia Laboratories, magnetically insulated ion diodes are being developed for possible use as a source of a suitable beam to drive ICF targets.^{2,3} The ion range in the target places an upper limit to the usable ion energy of several MeV for protons and a few tens of MeV for carbon. Both proton and carbon beams are being generated and evaluated. We describe here some of the diagnostics used to study ion beam composition and profiles from the diode, through the drift section to the target.

The proton and carbon fluence and flux are measured with carbon activation samples and biased charge collectors, respectively.^{4,5} In the activation technique, a portion of the beam is intercepted by a carbon or hydrogen target allowing the reaction $C^{12}(p,\gamma)N^{13}$ to occur. The positron decay of N^{13} is measured after irradiation allowing determination of the incident beam. Corrections for the naturally occurring deuterium must be made depending upon the beam relative voltage and current profiles. The activation technique is useful for proton energies above 460 keV and carbon energies above 6 MeV. The biased charge collectors are useful for measuring proton and carbon current densities for beam voltages greater than 100 keV. The carbon is separated from the proton beam by ion time-of-flight or filtration by thin polymer foils. The biased charge collectors and activation

technique are limited to current densities of a few hundred A/cm². Studies of beams at higher current densities require flux screen attenuation.

A time resolved x-ray pinhole camera⁶ has been used to observe the focused proton and carbon beam profiles via induced atomic excitation and thermal emission from targets, respectively. This camera used five pinholes and five independently gated CEMA detectors with effective exposure times of less than five nanoseconds. The resulting electron images were transported along a 2 kG, pulsed toroidal magnetic field, amplified in a second CEMA plate, then accelerated into a phosphor to produce visible images. These photon images were transported by a fiber optic plate directly to Polaroid film. The pinholes were covered with light tight windows which separated the vacua of the camera and target chamber. The spatial resolution of the camera in this configuration is limited by the pinhole array, typically 0.5 to 1 mm. This system was successful in observing the early time proton-induced atomic K-line excitation in an aluminum target followed by late time carbon ion heating of an expanded low density aluminum plasma.

Time resolved optical spectral measurements of the anode plasma are used to determine its temperature which is correlated to the charge state of the carbon ion accelerated. The spectrometer system is a Cerny-Turner optical spectrograph coupled to an image converter camera. The optical spectrometer is capable of viewing 70 nm between 225 and 700 nm

on a given shot. Coupled with electron density measurements from a holographic interferometer system estimates of the different carbon ion populations in the anode plasma are made. These carbon ion populations are compared with the populations measured in the drift section and target area by a Thomson parabolic mass spectrometer system.⁷

Holographic interferometry is an important tool for studying various phenomena associated with ion beam generation and the implosion of thermonuclear targets. The system in use at Sandia Laboratories employs a 3 ns ruby laser for holographic exposures. Using beam splitters and time-of-flight delays, each output pulse from the laser is divided into four colinear pulses, separated in time by as much as 28 ns, to provide interferometric data at four times. For ruby light, a free electron density of $3 \times 10^{17}/\text{cm}^2$ will produce one fringe shift in the interferogram.⁸ Interferometric measurements are being made of the diode plasma formation with the hope of reducing the divergence of ion beams through a better understanding of the formation and spatial development of anode plasmas.

Soft x-ray, vacuum ultraviolet (XUV) spectroscopy has been used to determine the response of approximately one proton range planar and cylindrical targets to an intense beam of hydrogen and carbon ions.⁹ Electron temperatures were deduced from line intensity ratios from a carbon ion heated, optically thin plasma with a high resolution, 1200 lines/mm grating, one meter grazing incidence spectrograph. Brightness temperatures and total radiated power from proton deposition were determined with a triplet array of photoelectric or x-ray diodes (XRDs). This data was used in conjunction with coupled radiation-hydrodynamic calculations to deduce the incident ion current density.

References

1. M. J. Clauser, Phys. Rev. Letts. 35, 848 (1975).
2. D. J. Johnson, A. V. Farnsworth, Jr., D. L. Fehl, R. J. Leeper, and G. W. Kuswa submitted to J. Appl. Phys.
3. D. J. Johnson, G. W. Kuswa, A. V. Farnsworth, Jr., J. P. Quintenz, R. J. Leeper, E. J. T. Burns and S. Humphries, Jr., to be published in Phys. Rev. Letts.
4. F. C. Young, J. Golden, and C. A. Kapetanakis, Rev. Sci. Instrum. 48, 432 (1977)
5. C. Eichenberger, S. Humphries, Jr., J. Maenchen, and R. N. Sudan, J. Appl. Phys. 48, 1449 (1977)
6. D. L. Fehl, J. Chang, G. W. Kuswa, and C. W. Mendel, (to be published).
7. J. N. Olsen, G. W. Kuswa, and E. D. Jones, J. Appl. Phys. 44, 2275 (1973).
8. L. P. Mix and R. W. Kessler, unpublished Sandia Report No. 77-0209.
9. E. J. T. Burns, D. J. Johnson, A. V. Farnsworth, Jr., and G. W. Kuswa, submitted to Appl. Phys. Lett.

ELECTRON BEAM ENERGY BRANCHING IN OXYGEN

G. Fournier, J. Bonnet, J. Bridet, J. Fort and D. Pigache.

Office National d'Etudes et de Recherches Aéronautiques, 92320 Chatillon, France.

Motivations. Design of lasers or chemical reactors based on an energy transfer from electrons to some gas mixture require excitation rate and efficiency data. For electrons heated by an electric field, Boltzmann codes yield the fractional power over the various inelastic processes involved [1 for O_2]. Similar results can be computed for electrons injected in a gas by an electron gun. The effects of beam propagation in any given geometry could be taken into account by a Monte Carlo simulation. The published results [2] are based on a continuous slowing-down approximation (CSDA), which can also be solved directly with the single energy variable and no boundary condition. However, the CSDA is not appropriate for obtaining the fractional powers over low energy processes [3]. The present discrete energy-loss method deals only with energy relaxation in a gas with no electric field and does not consider any boundary effect or space gradient. The energy space is divided into a few very different mesh sizes (increasing much with energy) in order to avoid a too long computer time resulting from the use of a small constant mesh size in energy up to high primary energies [3].

Formalism. The electron energy distribution function $f(u)$ is such that :

$$(1) \quad \int_0^{u_b} u^{1/2} f(u) du = 1$$

where u_b is the beam energy. The balance equation for $f(u)$ according to classical developments of Boltzmann equation at steady state is :

$$(2) \quad \begin{aligned} S(u_b)/N &= \sum_k u f(u) Q_k(u) \\ &- \sum_k' (u + u_k) f(u + u_k) Q_k(u + u_k) \\ &- \int_{2u+u_i}^{u_b} u_p f(u_p) Q'(u, u_p) du_p \\ &- \int_{u+u_i}^{2u+u_i} u_p f(u_p) Q'(u_p - u, u_p) du_p \end{aligned}$$

Here S is the source term, N is the gas density, u_k and Q_k are respectively the energy loss and the cross section for the inelastic process k , Q' is the differential ionization cross section, u_p is the energy of a primary electron, u_i is the averaged ionization energy. Attachment and ionization are not included in Q'_k but are included in Q_k . Energy transfers via elastic, superelastic and electron-electron collisions are neglected.

The processes of interest for oxygen are labeled in table 1 with their energy loss. At higher energy, the cross sections are given by the analytical formulae of Watson & al. [4]. At lower energy, a more recent cross section set of Phelps [5] is used. A single ionization process is assumed with the cross sections of Green & al. [6] but, in order to take into account various autoionization processes and ionization to ion excited states, a mean value of the ionization energy is entered; it should depend on the energy of the primaries, especially at low energy, but a simple constant is used. A value of $u_i = 19 \text{ eV}$ is chosen in order to fit the experimental data for the energy per ion pair which is 30 eV [7]. This value is a little greater than the average of the different ionization energies weighted by their cross section given in Ref. [4] which is 17 eV . The mesh sizes are 1 eV from 0 to 50 eV , 5 eV from 50 to 500 eV , 50 eV from 500 to $5\,000 \text{ eV}$ and 500 eV above. The calculation is initiated at $u = u_b$ with $f(u_b) = 1$ and energy cascading is followed step by step towards lower energies. Normalization according to Eq. (1) is made afterwards.

Results. The code has previously been run with nitrogen for which the results of Suhre & al. [8] have been checked. For oxygen, Fig. 1 gives the distribution function. Three body attachment is neglected in the following results. At energies lower than 100 eV , the distribution remains practically independent of the beam energy. Accordingly, fractional power transfer do not depend on beam energy above $1\,000 \text{ eV}$. For comparison, the distribution

function obtained by the authors from their Boltzmann code for electrons heated in an electric field

E such that $E/N = 3 \times 10^{-16} \text{ Vcm}^2$ is also shown on Fig. 1. It can be noted that the beam resulting distribution is much closer to a Maxwellian than the discharge distribution up to about 100 eV.

Fig. 2 gives the fractional power transfer over the main processes. As an example, a 6 % conversion for direct pumping of singlet oxygen is predicted. If the energy of upper levels (processes N° 12, 13 and 14) cascades into singlet states like in an electric field [9], a total fractional power transfer to singlet oxygen of 26 % is obtained. This is to be compared with the 60 % predicted and experimentally demonstrated in an electric field [9]. As an other example, it can be noted that an efficiency of 7.6 % is obtained for dissociation if it only results from processes N° 11 & 14 and that 20 % are reached if processes N° 12 and 13 also dissociate.

Conclusion. A multivalued mesh size in energy permits the computation of electron beam energy branching to be run in a short time. Detailed results are provided for oxygen. This beam code is about to be coupled with the usual Boltzmann code in order to model the electron effects in electron beam controlled discharges.

Table 1 - Electron impact processes in oxygen

Number	Identification	Energy loss (eV)
1 to 6	Three body attachment, rotation, vibration.	0.007 to 0.75
7	$a^1\Delta_g$	0.977
8	$b^1\Sigma_g^+$	1.627
9 and 10	Vibration (indirect)	0.19 and 0.38
11	Dissociative attachment	4.4
12 and 13	Various processes	4.5 and 6
14	$B^3\Sigma_u^-$	8.4
15	Rydberg series, ionization limit $X^2\Pi_g$	10
16	Ionization (average)	19
17 to 28	Rydberg series, ionization limit $a^4\Pi_u$ to B	12.7 to 22.5

REFERENCES

- [1] - K. MASEK, T. RUŽICKA & L. LÁSKA, Czech. J. Phys. B 27 (1977) 888.
- [2] - For instance K. BOYER, D.B. HENDERSON & R.L. MORSE, J. Appl. Phys. 44 (1973) 5511.
- [3] - K. SMITH & R.M. THOMSON, Computer Modeling of Gas Lasers, Plenum Press, New York, 1978, p.232.
- [4] - C.E. WATSON, V.A. DULOCK Jr., R.S. STOLARSKI & A.E.S. GREEN, J. Geophys. Res. 72 (1967) 3961.
- [5] - A.V. PHELPS, Cross section set of Nov. 3, 1977, Private Communication, 1977.
- [6] - A.E.S. GREEN & T. SAWADA, J. Atm. Terr. Phys. 37 (1972) 1719.
- [7] - L.G. CHRISTOPHOROU, Atomic and Molecular Radiation Physics, Wiley-Interscience, London, 1971.
- [8] - D.R. SUHRE & J.T. VERDEYEN, J. Appl. Phys. 47 (1976) 4484.
- [9] - S.A. LAWTON & A.V. PHELPS, J. Chem. Phys. 69 (1978) 1055.

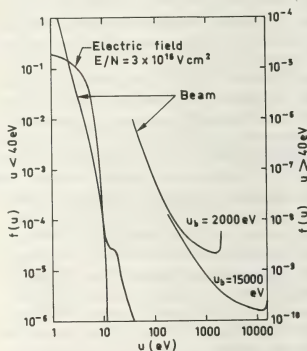


Fig. 1 : Distribution function.

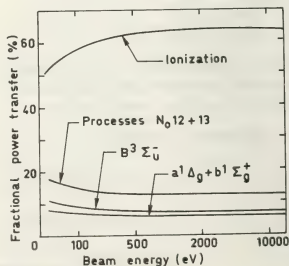


Fig. 2 : Fractional power transfer in oxygen.

AN EVIDENCE OF ANOMALOUS DEPOSITION OF REB ENERGY TO THE LOW Z TARGET

K. Imasaki, S. Miyamoto, S. Higaki, S. Nakai, K. Nishihara and C. Yamanaka.

Institute of Laser Engineering, Osaka University, Suita, Osaka, 565, Japan.

The interaction between REB and solid target is one of the most important issues in REB-ICF research because the required REB power, pellet size and structure for break-even is strongly influenced by the interaction. We report here an evidence of enhanced coupling between REB and solid target.

The experiment has been performed using 'Reiden III' REB generator. The operational power level of Reiden III is 500 keV, 100 kA. The pulse length is 80 ns. The beam is focused onto a solid target using the tungsten guide rod. The focal spot size is measured to be 1.5 mm in diameter. The 80 % of the total diode current is concentrated in the pinch region.

Using a N_2 laser, 6 ns pulse length, an interferometry and shadowgraphy of two channels were performed to measure the density profile and velocity of the blow-off plasma from the solid target irradiated by the REB. Thin foils of Ni, Ta and $(CH_2)_n$ were used as the target.

In the case of Ni foil target of 10 μ m in thickness, a symmetric blow-off was observed on both sides of the target. This fact can be explained by uniform deposition of REB energy due to the binary

collision in the target. But for the polyethylene target of 100 μ m in thickness symmetric expansion on the rear and front side was not observed, although the ρt of the target was kept the same value with the Ni target, where ρ was the mass density and t is the thickness of the target. Figure 1 shows the result of the interferometry of the polyethylene target.

This fact indicates the REB energy is absorbed in the front surface or corona region of the target and REB electron cannot penetrate the 100 μ m thick polyethylene. The same result was obtained when the polyethylene of 20 μ m in thickness was used. In the case of high Z target as Ni, this anomalous effect is suppressed.

The dynamic behavior of the target was simulated using 1-D Lagrangian code. The absorption of the REB energy to the target was assumed to be the simple classical in high Z target and anomalous in low Z target. Figure 2 shows the result of the simulation comparing with that of the experiment. They correspond quite well to each other.

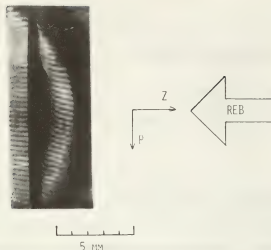


Figure 1. The interferometry of polyethylene target. The photograph was taken at 100 nsec after the pulse rise. The blow-off of the rear side did not observed in contrast with that of the front side.

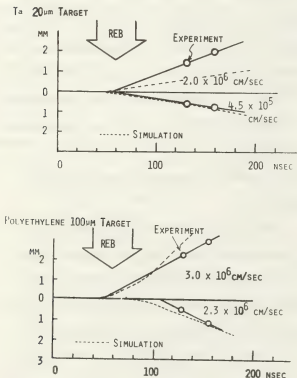


Figure 2. The simulation result with experimental data for the high Z and low Z target.

THEORY OF THE INTERACTION OF DOUBLE-BEAM WITH PLASMA

A.I. Rogashkova, T.I. Shatalova.

Institute of Radioengineering and Electronics, Academy of Sciences, Moscow, U.S.S.R.

I. In [1] is experimentally shown the instability development are considerably affected by an injection of a second beam.

A theoretical investigation of the double-beam interaction with plasma is presented in this paper in the linear and nonlinear regimes.

Two electron beams with the constant velocities v_{01} and v_{02} are assumed to move along an axis of a cylindrical metallic waveguide filled by a cold homogeneous plasma. The cross displacements is supposed to absent.

II. Suppose that the radiiuses of the beams are equal to the radius of the waveguide. The dispersion equation describing the interaction of two electron beams in plasma waveguide in the quasistatic approximation is

$$\sqrt{\frac{-\epsilon_z}{\epsilon_r}} \gamma a = \rho_0 \quad (1)$$

where a - the radius of the waveguide,

$\rho_0 = 0.5 \epsilon_z \epsilon_r$ - the axial and cross plasma per-

$$\epsilon_z = 1 - \frac{\omega_p^2}{\omega^2} - \frac{\text{mittivity} \cdot \omega_p^2 \epsilon_r}{(\omega - \gamma v_{01})^2} - \frac{\omega_p^2 \epsilon_r}{(\omega - \gamma v_{02})^2}$$

$$\epsilon_r = 1 - \frac{\omega_p^2}{(\omega - \omega_H)^2}$$

ω - a frequency, $\omega_p, \omega_{p1,2}$ - the plasma electron frequencies of plasma and beams respectively, γ - an axial wave number, ω_H - a gyrofrequency.

The dispersion equation (1) was calculated by the computer relating on (γa) in dependence on $\xi = \frac{\omega}{\omega_p}$ for different values of the parameters: $\gamma_{p1,2} = \frac{\omega_{p1,2}}{v_{01,2}} = 0.5$; $\frac{\omega_{p1,2}}{\omega_p} = 0.2$; $\omega_H = 0$.

In Fig.1 are represented dependences $\text{Re}\gamma$ and $\text{Im}\gamma$ on the normalized frequency

$$\text{for } \gamma_{p1,2} = 1, \gamma_{p1,2} = 2.25.$$

As is evident from Fig.1 the beams interact with plasma and don't interact with each other in region $\xi < 0.8$.

If $\xi > 0.8$ the branch $\text{Re}\gamma$ of an each beam is splitted into two branches that corresponds to the fast and slow space charge waves (f.s.c.w., s.s.c.w.). In region $0.9 < \xi < 1.8$ the branches describing f.s.c.w and s.s.c.w of different beams are connected in one branch, i.e. the double-beam interaction takes place.

In Fig.2 the curves of type curve 2 on Fig.1 are plotted for the following values parameters: $\gamma_{p1} = 1$; I - $\gamma_{p2} = 1.25$; II - $\gamma_{p2} = 2.75$; III - $\gamma_{p2} = 6.75$. The dotted curves described the amplification rates in the special case $\omega_p = 0$ for the same parameters γ_{p1}, γ_{p2} . From the $\text{Im}\gamma - \xi$ diagram it follows that in our system the amplification is described by the two curves. The curve 1 has the same dependence character on ξ as in case of the interaction of one beam with plasma. The curve 2 due to presence of a second beam shows the amplification is possible on the frequencies exceeding a plasma frequency. Thus the above results show that injection of a second beam into plasma greatly changes the dispersion characteristics of the plasma-beam system.

III. Let us consider $\omega_H = 0$ when the slow waves cannot propagate along the waveguide in absence of beams. It is supposed that $\omega_{p1,2} \ll \omega_p$ and the nonlinear effects in the system are only due to beams. In plane $z = 0$ the beams are modulated by a signal with the equidistant frequencies $\omega = n\Omega$. The system of equations describing a space evolution of the waves excited by one beam in the plasma waveguide is given in [2]. Generalising it in case of two beams we ob-

$$\frac{\partial^2 \Phi}{\partial \theta^2} = - \left(1 + \frac{\partial \Phi}{\partial \theta} \right) \operatorname{Re} \sum_{n=1}^{\infty} \left[\frac{q_{n1} I_{n1}}{n(1+\alpha)} + \frac{q_{n2} I_{n2}}{n} \right] e^{jn\Phi_{1,2}} \quad (2)$$

$$\Phi = \Omega t - \gamma_e z, \gamma_e = \frac{\Omega}{v_0}, v_0 = (v_{01} + v_{02})/2, I_{n1,2} = \frac{1}{n} \int_0^{2\pi} e^{-jn\Phi_{1,2}} d\gamma_e$$

$\gamma_e = \Omega t_0$ - an entrance moment of particles into space of interaction; $\Phi = \gamma_e z$ - the normalized distance; $I_{n1,2}$ - the dimensionless amplitude of current on the frequency $n\Omega$; $I_n = i_n/I_0$, $\alpha = v_{02}/v_{01}$; $q_{n1,2} = \frac{I_{n1,2}}{I_0 \omega_p^2 \epsilon_{n1,2}}$; i_n - the amplitude of current on the frequency $n\Omega$; I_0 - the constant component of current; I_n - the electron-beam-plasma frequency reduction factor [2]; f_n - the dimensionless amplitude axial component of electrical field on the frequency $n\Omega$:

$$f_n = \frac{e E_n}{m \omega v_0} e^{-jn\Phi}$$

The system (2) was calculated by the computer for 100 particles of every beam. It was solved under the following boundary conditions:

$$\begin{aligned} \frac{\partial \Phi}{\partial \theta} \Big|_{\theta=0} &= \frac{\alpha-1}{2} - \frac{1+\alpha}{2} \sum_{n=1}^{\infty} \beta_n^{(1)} \sin n\gamma_e; \\ \frac{\partial \Phi}{\partial \theta} \Big|_{\theta=0} &= \frac{1-\alpha}{2} - \frac{1+\alpha}{2} \sum_{n=1}^{\infty} \beta_n^{(2)} \sin n\gamma_e. \end{aligned} \quad (3)$$

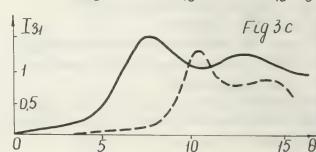
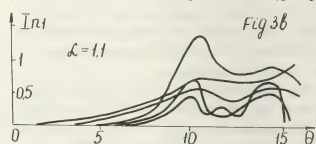
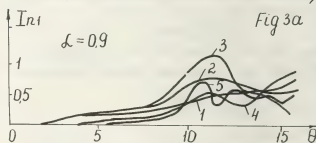
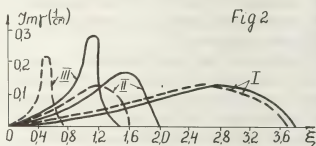
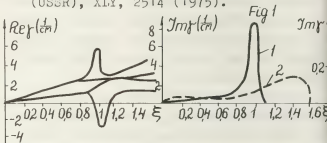
To demonstrate the influence of the second beam on the space evolution and spectrum of the excited waves the dependence of amplitude I_{n1} of the first beam for the different values of the parameters $\beta_n^{(2)}$ and α is shown in Fig.3. The calculations were held for the case $(\omega_p^2 \epsilon_2 / \omega_p^2 \epsilon_1) = 0.01$ and $\beta_n^{(1)} = 0$; $q_{n1} = -0.1$; $-0.2; -0.3; 0.2; 0.1$. From the analysis of these curves it follows that bunching the electrons of the first beam under the influence of the second one from some distance takes place and the amplitude of harmonics of the current I_{n1} increases in the space. The bunching will be more dense if the second beam moves quicker than the first one (See Fig.3a, b). The amplitude I_{31} is most, because $|q_3|$ is the largest [2]. In Fig.3c is represented the dependence I_{31} in cases when $\beta_3^{(2)} = 0.15$ and $\beta_{n \neq 3}^{(2)} = 0$ (unbroken curve) and $\beta_4^{(2)} = 0.15$, $\beta_{n \neq 4}^{(2)} = 0$ (dotted curve). It is clear that in the first case, the bunching is going much quicker and more effectively than in the first one.

IV. It is shown the injection of a second beam results in the beam plasma system becomes unstable on the frequencies exceeding the plasma frequency.

Also the second beam affect on the amplitudes and spectrum of excited waves.

REFERENCES:

1. V.D.Fedorchenko, Yu.P.Mazalov, A.S.Bakai, B.N.Rutkevich, Zh.T.F. (USSR), 65, 2225 (1973).
2. A.I.Rogashkova, M.B.Tseitlin, Zh.T.F. (USSR), XLIX, 2514 (1975).



ON THE THEORY OF EXCITATION OF RIPPLED PLASMA RESONATORS BY A RELATIVISTIC ELECTRON BEAM

L.S. Bogdankevich, M.V. Kuzelez and A.A. Ruchadze.

Lebedev Physical Institute, Moscow, U.S.S.R.

1. In this paper the problem of excitation of rippled plasma resonators by a relativistic electron beam is discussed. In the classical nonrelativistic electronics only numerical methods for solving this problem may be useful. But in the case of relativistic electron beams it may be solved analytically.

The system consists of a hollow relativistic electron beam and rippled plasma resonator (see fig.1). The length of the resonator L is more than its radius R_0 ,

which is of the same order rippled period $2\pi/K_0$ and more than the depth of ripply h , that is

$L \gg R_0 \gg 2\pi/K_0 \gg h$. The thickness of beam is less than the middle radius R_0 . The resonator is filled with cold collisionless plasma with density n_0 , which is more than the beam electron density n_b . All the system is put in strong longitudinal magnetic field B_0 and the following inequalities take place

$$R = \frac{cB_0}{4\pi n_0} \gg \omega_p, \omega_b \sqrt{\gamma}, c/R \quad (1)$$

Here $\omega_p = (4\pi e^2 n_0 / m)^{1/2}$, $\omega_b = (4\pi e^2 n_b / m)^{1/2}$, $\gamma = (1 - u^2/c^2)^{-1/2}$ and $u_{||}$, u_{\perp} are the longitudinal and transversal components respectively of beam velocity u .

In the system under the conditions (1) it can be excited by the electron beams only electromagnetic waves of E-type. Therefore below we investigate the symmetrical modes of E-waves, for which the field equations can be written in the form:

$$\begin{aligned} \frac{1}{2} \frac{\partial^2}{\partial z^2} z \frac{\partial E_z}{\partial z} - \hat{x}^2 \hat{\epsilon} E_z &= 0, \\ \hat{x}^2 E_z + iK_z \frac{\partial E_z}{\partial z} &= \hat{x}^2 B_\varphi + i \frac{\omega}{c} \frac{\partial E_z}{\partial z} = 0, \end{aligned} \quad (2)$$

where

$$\hat{\epsilon} = 1 - \frac{\omega_p^2}{\omega^2} - \frac{\omega_b^2(z) \gamma^{-2} \gamma^{-1}}{(\omega - K_z u_{||})^2}$$

$$\hat{\epsilon} = 1 - \frac{\omega_p^2}{\omega^2} - \frac{\omega_b^2(z) \gamma^{-2} \gamma^{-1}}{(\omega - K_z u_{||})^2} \quad (3)$$

The boundary conditions are

$$E_z \Big|_{z=R(z)} = \frac{E_z - K_0 h E_z \sin K_0 z}{\sqrt{1 + K_0^2 h^2 \sin^2 K_0 z}} \Big|_{z=R(z)} = 0 \quad (4)$$

Here $R(z) = R_0 + h \cos K_0 z$ represents the rippled waveguide surface equation. We also assume, that from the left edge of the resonator ($z=0$) electromagnetic waves completely reflect, but from the right edge ($z=L$) they reflect only partially and reflection coefficient is \hat{x}_{0s} .

2. The problem formulated above can simply be solved if $(h^2/R_0^2) \ll 1$, $h^2 K_0^2 \ll 1$. Below we give the solution of this problem up to the order of h^2/R_0^2 , $h^2 K_0^2$. For the field component $E_z(z)$ we can write down

$$E_z = \sum_{n=1}^{\infty} E_{zn} J_0(i\bar{x}_n z) \exp(iK_z z + i n K_0 z) \quad (5)$$

where K_z is a longitudinal wave number,

$$\begin{aligned} \bar{x}_n^2 &= x_n^2 \varepsilon_n = \left[(K_z + n K_0)^2 - \frac{\omega^2}{c^2} \right] \times \\ &\times \left\{ 1 - \frac{\omega_p^2}{\omega^2} - \frac{\omega_b^2 \gamma^{-2} \gamma^{-1} J_0^2 \Delta \mu_{0s}}{[\omega - (K_z + n K_0) u_{||}]^2} \right. \\ &\times \left. J_0^2(\mu_{0s} \frac{z_0}{R}) \right\}, \end{aligned} \quad (6)$$

and μ_{0s} is Bessel-root, $J_0(\mu_{0s}) = 0$.

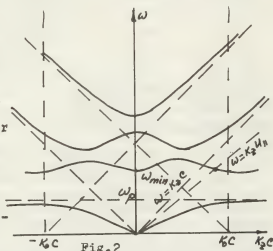
The Brouillon harmonics E_{zn} satisfy some recurrent relation, from which it follows dispersion equation for electromagnetic waves in a rippled waveguide (up to the order of h^2/R_0^2 , $h^2 K_0^2$) [1]

$$\begin{aligned} & \left[J_0(i\bar{x}_n R_0) + \frac{i h^2}{4 R_0} \bar{x}_n J_1(i\bar{x}_n R_0) \right] \left[J_0(i\bar{x}_{n-1} R_0) + \frac{i h^2}{4 R_0} \bar{x}_{n-1} J_1(i\bar{x}_{n-1} R_0) \right] \\ & \times J_1(i\bar{x}_{n-1} R_0) \left[J_0(i\bar{x}_n R_0) + \frac{i h^2}{4 R_0} \bar{x}_n J_1(i\bar{x}_n R_0) \right] + \\ & + \frac{h^2}{4} J_1(i\bar{x}_n R_0) J_1(i\bar{x}_{n-1} R_0) J_1(i\bar{x}_{n+1} R_0) \times \\ & \times \left\{ \frac{J_0(i\bar{x}_{n+1} R_0)}{J_1(i\bar{x}_{n+1} R_0)} \bar{x}_{n-1} \bar{x}_n \left[1 - \frac{K_0 (K_z + n K_0)}{\bar{x}_n^2} \right] \right. \\ & \times \left[1 + \frac{K_0 (K_z + (n-1) K_0)}{\bar{x}_{n-1}^2} \right] + \frac{J_0(i\bar{x}_n R_0)}{J_1(i\bar{x}_n R_0)} \bar{x}_{n-1} \bar{x}_n \times \\ & \times \left. \left[1 + \frac{K_0 (K_z + n K_0)}{\bar{x}_n^2} \right] \left[1 - \frac{K_0 (K_z + (n+1) K_0)}{\bar{x}_{n+1}^2} \right] \right\} = 0 \end{aligned}$$

In the first equation is write down non-correctly and only for $n=0$.

When the electron beam is absent ($\omega_p \rightarrow 0$) then from this equation we reeave the spectra of electromagnetic E-waves in a rippled waveguide ($L \rightarrow \infty$). These spectra are shown in fig.2 in the region of periodicity, $-k_0 < k_2 < +k_0$. From this figure it follows, that in the plasma waveguide there two types of E-waves: hf with $\omega > \omega_{min}$ and lf with $\omega < \omega_p$. The lf waves in origin are plasma waves and

when plasma is vanished ($\omega_p \rightarrow 0$) this waves are absent. Moreover their spectra are not due to on the ripply of waveguide. There-



fore the excitation of lf waves is identical to their excitation in smooth waveguides [2,3]

Below we investigate only excitation of hf E-waves in rippled waveguides under the condition

$$k_0 u_1 > \omega_{min} = \sqrt{\omega_p^2 + \frac{R_0^2 C^2}{R_0^2}} \quad (8)$$

when their phase velocity is less than u_1 . It must be emphasized, then in the rippled waveguides can be excited by electron beam both not only forward, but also backward waves. The group velocity of backward waves is antiparallel to their phase velocity.

It can be easily shown, that when $\omega_p < 2,4 u_1 R_0 / R_0$ then the frequencies and the growth rate of hf E-waves, excited by electron beam, are $(\omega \rightarrow \omega_0 + \delta)$,

$$\omega_0 = k_2 u_1 = u_1 \delta_{11} k_0 \left[1 \pm \frac{u_1}{C} \sqrt{1 - \left(\frac{\mu_{os} C}{k_0 u_1 \delta_{11} k_0} \right)^2} \right]$$

$$\delta = \frac{-1 + i\sqrt{3}}{2} \left(\frac{k_2^2 h^2}{8} \frac{\pi R_0 \Delta \mu_{os} \omega_0 \omega_p^2}{R_0^2 \delta_{11}^2} \right)^{1/3} \left(\frac{\mu_{os} C}{k_0 u_1 \delta_{11} k_0} \right)^{1/3}$$

$$\times \left[1 - \left(\frac{\mu_{os} C}{k_0 u_1 \delta_{11} k_0} \right)^2 \right]^{1/2} \left(\frac{\omega_0 R_0}{u_0 \delta_{11}} \right),$$

$$f(x) = \frac{1}{x} \frac{d}{dx} \ln I_0(x) \left[1 + x \frac{d}{dx} \ln \ln I_0(x) \right]$$

If $(C/u_1) > (k_0 R_0 / \mu_{os}) > (C/u_1 \delta_{11})$ then only forward waves can be excited in the system, and if $(k_0 R_0 / \mu_{os}) > (C/u_1 \delta_{11})$ then in our system can be excited backward waves also.

3. Now we can investigate the rippled resonators shown in fig.1 and their excitation by a relativistic electron beam. The frequencies of forward and backward E-waves excited by an electron beam in the resonator as in the waveguide are given by (9). But for the growth rate in the case of resonator we have [3]

$$(\omega \rightarrow \text{Re} \omega + i \text{Im} \omega \approx \omega_0 + i \text{Im} \omega):$$

$$\text{Im} \omega = \frac{\text{Im} \delta k_2^+ - \text{Im} \delta k_2^- - \frac{1}{2} \ln \alpha_{os}'}{\frac{\partial k_2^+}{\partial \omega} - \frac{\partial k_2^-}{\partial \omega}} \quad (10)$$

Here k_2^{\pm} are the wavenumbers of E-waves in the rippled waveguides, carrying energy in positive and negative \pm direction and $\text{Im} \delta k_2^{\pm}$ are their amplifier coefficients respectively.

From the dispersion equation (7) it can be shown that in the case of excitation of forward waves in the rippled resonator

$$\text{Im} \delta k_2^+ = -\frac{\text{Im} \delta}{(u_1^2 v_{g0})^{1/3}}, \quad \text{Im} \delta k_2^- = 0, \quad (11)$$

$$\frac{\partial k_2^+}{\partial \omega} = \frac{u_{11} + 2v_{g0}}{3u_{11} v_{g0}}, \quad \frac{\partial k_2^-}{\partial \omega} = -\frac{1}{v_{g0}}$$

In the case of excitation of backward waves

$$\text{Im} \delta k_2^+ = 0, \quad \text{Im} \delta k_2^- = \frac{\text{Im} \delta}{(u_1^2 v_{g0})^{1/3}}, \quad (12)$$

$$\frac{\partial k_2^+}{\partial \omega} = \frac{1}{v_{g0}}, \quad \frac{\partial k_2^-}{\partial \omega} = -\frac{u_{11} - 2v_{g0}}{3u_{11} v_{g0}}$$

Here $v_{g0} = C \sqrt{1 - \mu_{os}^2 C^2 / \omega_p^2 R_0^2}$ is the group velocity of waves in the absence of beam ($\omega_p \rightarrow 0$)

Now from the condition $\text{Im} \omega > 0$ we revise the threshold current of an electron beam for the excitation of rippled plasma resonator

$$I_{th} = \frac{34}{(k_0 h)^2} \frac{R_0 \omega_0 \mu_{os} \omega_p^2 (\mu_{os} \frac{C}{R_0})^x}{\left\{ \frac{u_{11} R_0}{C h} \left[1 - \left(\frac{\mu_{os} C}{k_0 u_{11} k_0 R_0} \right)^2 \right]^{-1} \ln \frac{1}{\alpha_{os}'} \right\}^3 K A} \quad (13)$$

In concluding we notice, that in rippled wave generators the selection of radial modes can be reached by choosing the injection radius of beam Z_0 , which must coincide with maximum of the function $E_r(z)$ for suitable radial wave number μ_{os} .

References

1. Kovaliov N.P. Sov. J. Electron. Technics, Shf electronics 3:102 (1978).
2. Bogdankevich L.S., Ruchadze A.A. Sov. Journ. ITF 47: 192 (1977).
3. Bogdankevich L.S., Kuzelez M.V., Ruchadze A.A. Sov. Journ. Plasma Physics 2: 90 (1979).

EXPERIENCE D'INTER-ACTION ELECTRONS-MATIERE A VALDUC

J. Delvaux, A. Devin, A. Nicolas, C. Peugnet, G. Wolff and A. Kubala.

Commissariat à l'Energie Atomique, Centre d'Etudes de Valduc, B.P. 14, 21120 Is-sur-Tille, France.

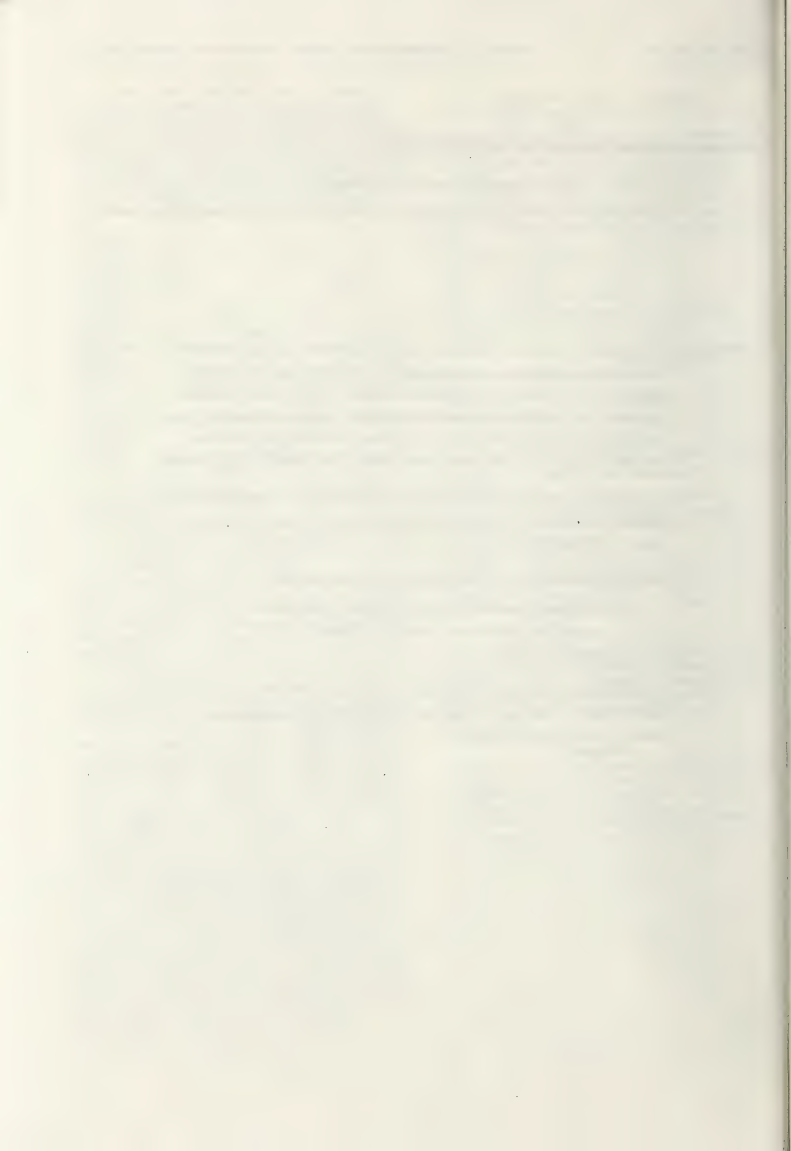
Résumé .- L'utilisation de faisceaux d'électrons pour le confinement inertiel nécessite un excellent rendement en ce qui concerne le dépôt d'énergie. Notre laboratoire a accru son effort expérimental de façon à étudier les mécanismes complexes liés au dépôt d'énergie réalisé à l'aide de cathodes à pointe. Les expériences ont été dirigées dans le sens d'une meilleure compréhension des effets du plasma anode cathode sur l'efficacité du chauffage de la feuille.

Ce travail expérimental a été réalisé avec l'aide de divers diagnostics synchronisés en temps. Les caractéristiques de l'accélérateur d'électrons sont 500 kV, 250 kA, 2 Ω .

Les principaux diagnostics utilisés dans ces expériences sont :

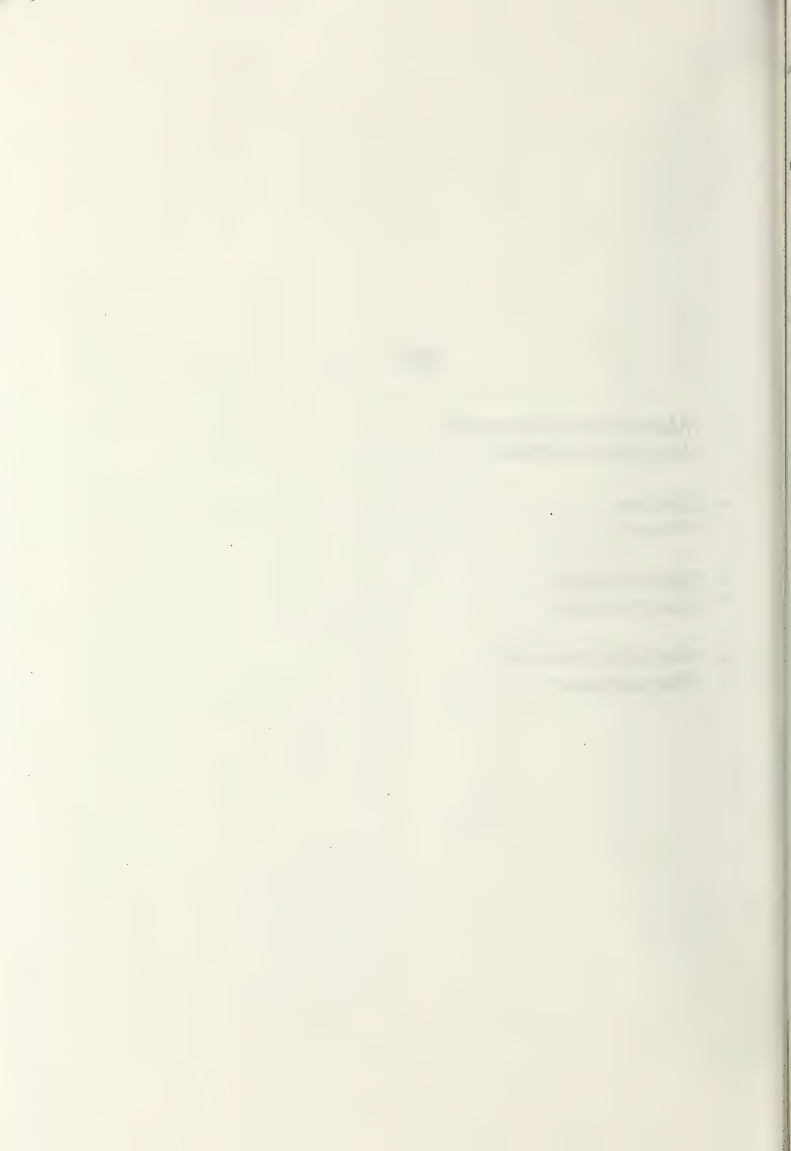
- les diodes photoélectriques X R D avec et sans filtre
- la chambre à sténopé qui visualise le plasma
- la caméra rapide

L'influence des différents paramètres sur le comportement de la diode ont été étudiés, à savoir : l'épaisseur de la feuille, la distance anode cathode, la forme de la cathode.



XV

- Méthodes de diagnostic
Diagnostic methods
- Sondes
Probes
- Spectroscopie
Spectroscopy
- Méthodes diverses
Miscellaneous



LASER - DOPPLER VELOCIMETRY IN IONIZED GASES : A REVIEW PAPER.

G. Gouesbet.

Laboratoire de Thermodynamique, associé au C.N.R.S., N°230, Faculté des Sciences et des Techniques de Rouen, 76130, Mont Saint Aignan, France.

Abstract

A review of plasmas velocities measurements by means of Laser-Doppler velocimetry is presented. Specific difficulties are pointed out. Although such experiments are until now very scarce, there is no doubt that the future will see a tremendous increase of LDV-applications to plasmas owing to its great potential.

The reader is assumed to be well aware of the LDV general theory and applications. Basic books are available (1, 2, 3).

LDV-measurements have been successively made in liquids (4), cold gases, then combustion devices. Plasmas investigations started more lately, owing to the expected difficulties : high temperatures giving rise to noise problems due to plasma and seeding particles radiations ; electromagnetic saturation of the electronic devices (r.f. torches) or electrical interference from the large current supplied to arcs ; fast evaporation of the scatter centers, coupled with difficulties to be sure that they are small enough to follow the fluid when they reach the optical probe ; thermophoresis phenomenon producing a very slow rate of data acquisition when some critical zones are studied ; sensitivity of the plasma state to the presence of possible artificial seeding particles, etc. Nevertheless, workers attempted to solve these problems in order for instance to provide a better understanding of the heat and mass transfer processes between a plasma flow and suspended particles, with emphasis on plasma chemistry.

S.A.SELF started experiments in a MHD boundary layer (5, 6, 7) with additional problems due to restricted optical access, high velocities (> 500 m/s), high spatial resolution requirements, refractive index inhomogeneity, scatter from the wall. On the other hand, temperatures were rather low ($\sim 2\,700$ K), and the fluid was more a flame than strictly speaking a plasma. Furthermore the detection used an optical Fabry-Perot system, so

without heterodyning. It was then spectroscopic measurements rather than classical LDV-ones. A laserline filter is used (10 \AA bandwidth) to remove thermal radiation and ambient light. Experiments have been then carried out with a differential-forward scatter method for sidewall measurements (8, 9). Processing was achieved through a high-speed counter linked to an P-2100 computer. Mean velocities, turbulence intensities and spectrum of velocity fluctuations have been measured.

M.R.BARRAULT et al reported about LDV-experiments in a transient (12 ms) arc circuit breaker (10). Specific problems arose plus the extra problems of transient nature of the arc, high velocities (up to $3\,000\text{ ms}^{-1}$) and drastic seeding problems. The real fringe mode optical set-up was used and forward scattering from an Ar^+ , 1.5 W, laser. The parasitic radiation was removed with a 10 \AA interference filter and associated polariser, plus a Fabry-Perot filter of 0.5 \AA bandwidth. Signal processing was achieved through an oscillographic raster display. Then improvements were made in order to cover the entire arcing period (11). But problems of interpretation remained due to the unknown size of scatter centers which did not always follow the fluid. An approximate correlation was used between signal frequencies (particle velocities) and signal amplitudes (particle sizes) in order to deduce the plasma velocity from the particle one. Such a correlation is not very reliable : as a matter of fact, big particles passing through the edges of the control volume give rise to the same signal amplitudes than small ones passing through its center. Effectively, the authors consider that the accuracy is not better than about 40 %.

Then, IRIE and BARRAULT carried out measurements using the Doppler shift of a Q-switched ruby laser radiation without foreign elements. Again, there was no heterodyne detection, so that it was spectroscopy measurements rather than LDV ones (12).

GOUESBET reported LDV-mean velocities measurements in a 4 MHz, rf torch, by means of a 5 mW

He-Ne forward real fringe system with oscillographic display of the signals (13, 14). But the exact fluid velocity was not measured due to the too large sizes of the used particles, although the disagreement was further found to be less than typically 20 %. Further experiments were carried out with a more powerful laser (Krypton, 800 mW on the 647,1 nm line) and an automatic data acquisition and processing system using a single counter (15, 16, 17, 18). The parasitic emitted light was removed by means of a monochromator (2 Å bandwidth). Seeding was achieved by means of a counter-current system supplying the plasma in $\sim 5 \mu\text{m}$, Al_2O_3 -particles, at a rate sufficiently small for not disturbing the flow. The beam was expanded before focusing to improve the S/N ratio and the spatial resolution. The spatial resolution was again increased by collecting the scattered light off-axis. The effect of the parasitic rf radiation was decreased by means of a Faraday cage and filtering the signal through rejectors. Mean velocities and 'fluctuations' have been successfully carried out. Furthermore, the atom temperatures were measured by coupling LDV- and dynamic pressures measurements.

Mme THI HIEN HO attempted measurements in a 4 MHz rf torch with a 5 mW He-Ne laser, using a real fringe mode set-up (19). Processing was achieved through a frequency tracker and a frequency analyser. Measurements were not really successful. It is suggested that a frequency tracker could be difficult to work properly owing to the small rate of particles arrival. The frequency analyser probably picked up the radio frequency of the plasma generator. Furthermore, GOUESBET's experiments showed that a 5 mW power is too critical for 'comfortable' measurements in such a situation. The photon correlation technique could be possibly successfully used.

LDV-measurements are reported from the Imperial College (London) in a DC transferred arc heater at the National Physical Laboratory (20,21). Real fringe systems were tested in forward and backward scatterings. A spectrum analyser, a frequency tracker and a frequency counter have been tested. The seeding particles were Nickel ($\sim 50 \mu\text{m}$) and alumina ones ($\sim 1 \mu\text{m}$). Velocity histograms were recorded. Alumina particles exhibit much higher velocities than nickel ones, as it could be expected from drag arguments.

The author is aware of experiments carried out in Limoges but no report has been received at time to discuss about them. Let us also mention Tiller's paper (22). Finally, preliminary plasma experiments have been made at the OHERA in 1975. A plasma work is actually now planned (Boutier, ONERA, Châtillon/Bagneux).

CONCLUSION

The previous reported experiments show that LDV can be successfully used for plasma diagnostics. The difficulties remain important, but there is now no doubt that such techniques will become a very popular tool for such experiments owing to the tremendous versatility and potential of LDV-systems.

REFERENCES

1. F.DURST, A.MELLING, J.H.WHITELAW. Principles and practice of laser-Doppler anemometry, Academic Press, 1976
2. B.M. WATRASIOWICZ, M.J.RUDD. Laser-Doppler measurements. Butterworths et Co, 1976
3. T.S.DURRANI and C.A.GREATED. Laser systems in flow measurements. Plenum Press, 1977
4. Y.YEH, H.Z.CUMMINS, Appl.Phys.Lett. **4**, 176(1964)
5. S.A.SELF, 12th Symp.on Eng.Asp.of MHD, paper III.4, Argonne (1972)
6. S.J.MORRIS, et al. 13th Symp. on Eng. Asp. of MHD, paper VI.2, Stanford (1972)
7. S.A.SELF, 14th Symp.on Eng.Asp.of MHD. Tullahoma (1974)
8. S.A.SELF, C.H.KRUGER. AIAA J.En. **1**, 25 (1977)
9. R.R.RANKIN, S.A.SELF, R.H.EUSTIS. A study of the MHD insulating wall boundary layer. Addendum to Proc.of the 16 th Symp.Eng.Asp.of MHD.Pittsburgh (1977)
10. M.R.BARRAULT et al. J.Phys.E. **7**, 663, (1974)
11. P.S.TODOROVIC et al. J.Phys.D. **9**, 423, (1976)
12. M.IRIE, M.R.BARRAULT. J.Phys.D. **10**, 1599(1977)
13. G.GOUESBET. C.R.Acad.Sci. **280B**, 597 (1975)
14. G.GOUESBET. ADL Workshop, Short Presentation. Saint-Louis, ISL, (France) Mai 1976
15. G.GOUESBET, M.TRINITE. Lett.in Heat and Mass transfer. **4**, 141-148, (1977)
16. G.GOUESBET, M.TRINITE. J.Phys.E. **10**, 1009(1977)
17. G.GOUESBET. Thèse d'Etat, Rouen, 21 dec.1977
18. G.GOUESBET et al, ADL Workshop, Purdue, (1978)
19. Mme THI HIEN HO, Thesis, McGill Univ. (1975)
20. D.F.G.DURAO, A.MELLING, Report CHT/77/2, ICST
21. BAYLISS et al, Symp.Plasm.Chem., Limoges(1977)
22. W.TILLER. Plasma-Kolloq. Aachen (1978)

MEASUREMENT OF H^- DENSITY IN A PLASMA BY PHOTODETACHMENT

M. Bacal, G.W. Hamilton*, A.M. Bruneteau, H.J. Doucet and J. Taillet*.

*Laboratoire de Physique des Milieux Ionisés**, Ecole Polytechnique, 91128 Palaiseau Cedex, France.
 **Office National d'Etudes et Recherches Aéronautiques, 92320 Chatillon, France.

Improved techniques for measuring the density of H^- or D^- in a plasma are required because of certain limitations of the techniques of Langmuir probes and mass analysis¹. Interpretation of probe data requires an assumption of the mass of positive ions and are restricted in usefulness by the Debye distance. Mass spectra measured by ion mass analyzers tend to be useful only for relative measurements unless calibration techniques are included to determine absolute ion densities. The requirement for reliable measurements of H^- and D^- is based upon the need for development of D^- ion sources suitable for neutral injection into controlled fusion devices.

Photodetachment has previously been used to measure negative ion densities in oxygen plasmas². Photodetachment consists of the detachment of the extra electron of a negative ion by a photon ($H^- + \text{photon} \rightarrow H + e$). Therefore photodetachment in a plasma produces an increase in electron density, which can be measured by probes or microwaves depending upon the geometry. The photon energy should be selected such that it is lower than the threshold energy of other photon interactions such as photoionization, photoexcitation, photoemission or photodetachment of other species. The light from a ruby laser (1.8 eV photon energy) is suitable for this purpose. The photodetachment cross-section for H^- ($4 \times 10^{-17} \text{ cm}^2$) is near its maximum at this photon energy³. We used a ruby laser capable of a 1 J pulse in a time about 30 ns.

To assure that the photodetachment signal is proportional to the density of H^- and not of other negative ions such as OH^- , O^- , or O_2^- (for which the cross-sections are one or two orders of magnitude lower) we have magnetically analyzed the nega-

tive ions extracted from the plasma and also have verified (Figure 1) that our measurements agree with the theoretical photodetachment fraction computed from the cross section for the photodetachment of H^- , but not with that for other ions :

$$\text{photodetachment fraction} = \frac{\Delta n_-}{n_-} = 1 - \exp(-\text{laser pulse energy/area} \times \sigma/h\nu) \quad (1)$$

The test of Figure 1 should be repeated whenever the experimental conditions change to authenticate the measurements.

Figure 1 shows that the photodetachment fraction $\Delta n_-/n_-$ is essentially 100 % if the laser pulse energy is more than 0.1 J. Under this condition we can determine the relative density of H^- from the change in the probe electron current density :

$$n_-/n_e = \frac{\Delta n_-}{n_e} = \frac{\Delta j_{\text{probe}}}{j_{\text{probe}}} \quad (2)$$

We found some large noise signals when the laser energy is higher than 0.2 J ; we observed an increase of these noise signals when the laser light hits a surface situated close to the probe (e.g. the stainless steel wall of a multipole). The noise signals at high laser power density (2 to 10 MW/cm²) may be due to the interaction of laser light with solid surfaces or to the onset of multiphoton effects or free-free electron interactions. This problem can be avoided by monitoring the laser pulse energy and using the data only for pulses within the range from 0.1 to 0.2 J.

We explored the photodetachment signal spatially by moving the probe in two dimensions. We found no measurable signal when the probe was completely out of the laser beam. The signal was approximately constant when the probe was moved along the

beam. Therefore when we compute the ratio of probe current densities in Eq. (2) we consider that only the section of the probe immersed in the laser beam is effective for photodetachment.

Figure 2 shows the experimental apparatus schematically. The plasma was produced in a hydrogen atmosphere of 10^{-2} Torr by thermionic electrons emitted by a cathode at a negative potential of 60 to 120 V. Densities of plasma and of gas were controlled by adjustment of the thermionic emission and of the gas feed. Light pulses from a ruby laser were injected via a reflecting prism and a 2 cm diameter glass window, and were monitored by a photomultiplier through a partially reflecting mirror. The light monitor was calibrated versus injected laser energy using a calorimeter within the vacuum chamber.

Two types of cylindrical tungsten probes were used to measure the densities of electron and ions. For absolute measurements of n_e and of n_+ it is necessary to measure the complete probe characteristic and to analyze it either by the Langmuir theory (if the probe radius is less than 3 Debye distances) or by a theory for larger probes. On the other hand, for measurements of changes in n_e and n_+ it is sufficient to use large-area probes of which the radius may be more than the Debye distance, so the probe would be self-supporting and so the pulsed probe currents would be easier to measure. The self supporting probe did not require the exposure of a supporting insulator to laser light. The best probe geometry is such that the probe axis is parallel to the laser beam, and the probe area within the laser beam is larger than the probe area outside the laser beam.

The measurements by the technique described were reproducible and independent of the probe diameter, showing n_- increasing in proportion to n_e^3 in the range of n_e between 10^9 and $2 \times 10^{10} \text{ cm}^{-3}$.

This project was performed at Ecole Polytechnique as a joint project involving three laboratories, funded by the French Commissariat à l'Energie Atomique and the U.S. Department of Energy.

* Permanent address : Lawrence Livermore Laboratory, Livermore, California, U.S.A.

** Groupe de Recherche N° 29 du Centre National de la Recherche Scientifique.

1. E. Nicolopoulou, M. Bacal and H.J. Doucet, *Le Journal de Physique*, **38**, 1399 (1977).

2. J. Taillet, *Compt. Rend., Paris*, **269**, série B, 52 (1969).

3. J. Smith and D.S. Burch, *Phys. Rev.*, **116**, 1125 (1959).

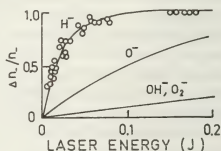


Figure 1 : Photodetachment of several negative ion species by ruby laser light as a function of laser pulse energy, according to theory of equation (1). Experimental data points are superimposed upon the theory of equation (1) for H^- , where $\sigma/h\nu \approx 139 \text{ cm}^2/\text{J}$ and the area of the laser beam is 3 cm^2 .

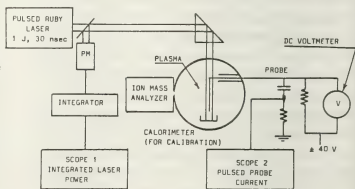


Figure 2 : Equipment diagram

MEASUREMENT OF ELECTRON DENSITY AND TEMPERATURE PROFILES BY MEANS OF MULTIPOSITION THOMSON SCATTERING

D. Oepfs, E.P. Barbier and P.J. Busch.

Association EURATOM-FOM, FOM-Instituut voor Plasmafysica, Rijnhuizen, Nieuwegein, The Netherlands.

Introduction

A shot-by-shot acquisition of data by means of Thomson scattering to establish the profiles of the density and the temperature of a plasma is laborious and forces the investigator to rely on the reproducibility of the discharge. The study of non-stationary phases during the life-time of the plasma may prove to be too difficult and certain topics might receive less attention than they deserve. A simultaneous recording of the local n_e and T_e at many positions is therefore desirable. Thomson-scattered light is available from the full length of the laser beam passing along a chord through the plasma column. This information can be subdivided into a number of elements to attain a spatial resolution in one dimension and, by shifting the laser position, the total cross-section of the plasma can be scanned. Due to the large amount of data to be collected, highly sensitive multichannel vidicon tubes have been preferred (see likewise /1/) to an extensive system of photomultipliers. The diagnostic method to be discussed here, has been developed for a medium-sized toroidal plasma apparatus, called SPICA, and first results are shown.

Plasma device

SPICA /2/ is a toroidal screw-pinch device for the study of equilibrium and stability properties of a high-beta plasma surrounded by force-free currents. Main parameters: torus major radius: 0.60 m; minor radius: 0.20 m; $T_e = 20 - 100$ eV; $n_e = 10^{21} - 10^{22} \text{ m}^{-3}$; diameter of the column: 0.05 - 0.15 m; time-scales: 1 - 100 μs .

Diagnostic device

A Q-switched ruby laser oscillator/amplifier system producing a power of 200 MW within 15 ns is employed for the 90° -scattering experiment. For observation of the Thomson-scattered light, a commercial optical multichannel analyzer is used, consisting of a vidicon camera tube (ISIT) with scanning electronics, analog-to-digital conversion and data storage. The selection of spectral and spatial elements and the data handling is performed in the way shown in Fig. 1:

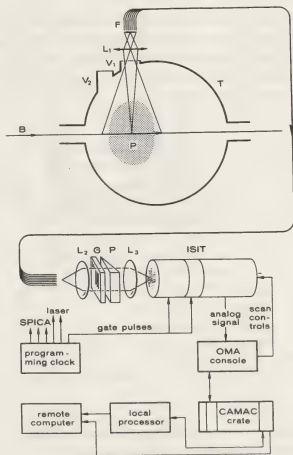


Fig. 1.

The SPICA detection system; for explanation of symbols, see text.

The laser beam (B) passes through the discharge tube (T), containing the plasma. A 150 mm long section of the laser beam is imaged by lens L_1 (35mm, $f/1.4$) through window V_1 onto a fibre-optic image guide, F. The latter consists of a linear array of 300 fibres and receives an image of $25 \times 0.065 \text{ mm}^2$. The exit face of the 12 m long bundle forms the entrance slit of a spectrometer containing a collimator lens L_2 (100 mm, $f/2$), transmission grating G (300 $\text{\AA}/\text{mm}$, $50 \times 50 \text{ mm}^2$) and prism P to obtain a non-deviating system. The condensor lens L_3 (50 mm, $f/0.95$) focusses the spectral image on the ISIT detector tube. The image is scanned in successive tracks of 500 channels each (2D mode); the signal per channel is integrated and digitized. To reduce the amount of primary data, an accumulation register has been added to the system which provides the storage of a number of spectra with a reduced spectral resolution.

Figure 2 shows an example of observed spectra. The values of the temperature and the density for an individual track are finally determined by fitting a gaussian curve to the measured points.

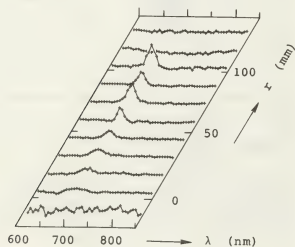


Fig. 2.

Example of observed Thomson-scattering spectra taken from different radii.

The transmission factor of the detection optics between plasma and detector amounts to only a few percent. This is mainly due to the long fibre connection and the complicated lens assemblies. The detection limit is on the order of $n_e = 5 \times 10^{20} \text{ m}^{-3}$; this density produces a signal of about 250 counts per track, collected typically from a scattering volume element which has the length of 14 mm, and a diameter determined by the beam width of 1 mm.

Conclusion

Single shot profile measurements of the plasma density and temperature have been performed by means of an optical multichannel vidicon analyzer. Care was taken to attain a suitable processing of a large number of data.

Acknowledgement

The authors are grateful to W. Kooijman for computational work and to W.J. Mastop for technical assistance.

This work was performed under the Euratom-FOM association agreement with financial support from ZWO and Euratom.

References

- /1/ N. Bretz et al., Appl. Opt. **17** (1978) 192-202.
- /2/ C. Bobeldijk et al., Nucl. Fusion, Suppl. I (1977) 493.

SOME REGULARITIES WITHIN THE STARK WIDTHS AND SHIFTS OF RESONANCE LINES OF NEUTRAL ATOMS FROM He TO Ca

J. Purić, I. Lakićević* and V. Glavonjić.

Faculty of Natural and Mathematical Sciences, Department of Physics and Meteorology and Institute of Physics, P.O. Box 550, Beograd, Yugoslavia.
 *Institute of Physics, P.O. Box 57, Beograd, Yugoslavia.

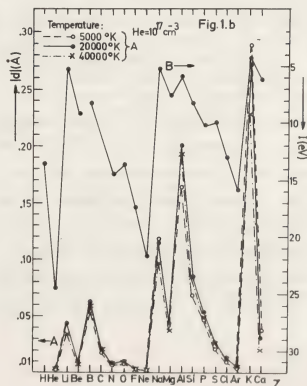
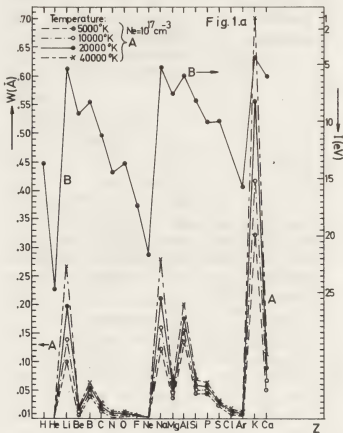
Papers published by Purić et al. /1,2/

and recently by A. Mazure and G. Wolleze /3/ have initiated interest to find possible regularities in Stark broadening and shift parameters of resonance lines of different groups of elements. In the papers /1,2/ regularities of Stark widths of the resonance lines of alkali-metals and alkali-metals and alkali-like atoms and ions have been reported and discussed. In the recently published paper /3/ the linear dependence of Stark widths and shifts of neutral resonance lines of alkali-metals on atomic parameter $|X|^{2/3}$ and $|X|^{2/3} \text{ sign} X$ respectively, has pointed out, where X is atomic polarisability.

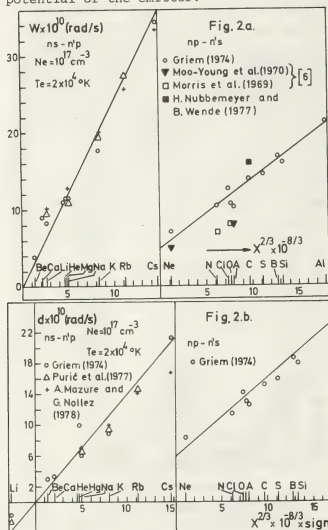
In this paper the existence of certain regularities in Stark widths and shifts values of resonance lines of neutral atoms from He to Ca available in literature have been presented and discussed. Namely, it has been found that the linear dependence of w and d values on $|X|^{2/3}$ for all resonance spectral lines of neutral atoms from He to Ca exists. Also, the periodical dependence of w and d values on atomic number Z has been noticed and discussed.

In Fig. 1 a plot of theoretical /4/ widths (a) and shifts (b), and ionization potentials I against the corresponding nuclear charge number Z is given for neutral atom lines from He to Ca. The widths and shifts have been plotted for four electron temperatures and electron density $N=10^{17} \text{ cm}^{-3}$. Analysing this figure one can conclude that a periodical behaviour of Stark

widths and shifts values along the periodic system of elements, similar to the periodical dependence of ionization potential of nuclear charge number Z , is obvious.



Furthermore, one can see that Stark widths and shifts curves have maxima for the elements with the lowest ionization potential. The minima correspond to elements with the highest ionization potential. This can be expected due to the fact that the energy gap between the nearest perturbing level and upper level of the corresponding resonance line is proportional to ionization potential of the emitter.



In Fig. 2. a and b, an example of linear dependence of w and d theoretical /4/ values on $|X|^{2/3}$ and $|X|^{2/3} \text{ sign} X$ respectively, are presented for $N = 10^{17} \text{ cm}^{-3}$ and $T = 2 \cdot 10^4 \text{ K}$. It has been found that the slope of linear trend is different for resonances originating from two types of transitions: ns-n'p and np-n's. Namely, there is one slope for He, Li, Be, Na and Mg lines (ns-n'p transition) and the other

for B, C, N, O, Ne, Al, Si, S, Cl and A lines (np-n's transition).

Theoretical and experimental w and d values are presented in Fig. 2. for the sake of comparison, but unfortunately, they are for different temperatures. Regardless of that, experimental data follow the linear trends within the estimated errors ($\pm 20\%$).

Analysing results presented in figures 1. and 2. one can draw following conclusions:

a) Periodical dependence of Stark width and shift values of resonance spectral lines on nuclear charge number Z is universal and fundamental similar to the periodical dependence of ionization potential on Z .

b) As it seems that the linear dependence of w and d values on $|X|^{2/3}$ and $|X|^{2/3} \text{ sign} X$ respectively, is valid, it may be used, firstly, to estimate the Stark widths and shifts of heavier elements lines not available so far, and secondly, as a criterion for validity of experimentally obtained data.

References

1. J. Purić, J. Labat, Lj. Ćirković, I. Lakićević and S. Djeniže, J. Phys. B, 10, 2375 (1977)
2. J. Purić, M. S. Dimitrijević and I. S. Lakićević, Phys. Lett. A, 67, 189 (1978)
3. A. Mazure and G. Nollez, Z. Nat. 33a (1978)
4. H. R. Griem, "Spectral Line Broadening by Plasmas", New York and London Acad. Press (1974)
5. N. Konjević and J. Roberts, J. of Phys. and Chem. Data, 5, 209 (1976)
6. H. Nubbemeyer and B. Wende, Phys. Rev. A, 16, No. 2, 627 (1977).

COLLECTIVE SCATTERING OF CO₂-LASER LIGHT BY THE HIGHLY IONIZED ARGON PLASMA OF A HOLLOW CATHODE ARC DISCHARGE

B.F.M. Pots, J.J.H. Coumans and D.C. Schram.

Physics Department, Eindhoven University of Technology, Eindhoven, The Netherlands.

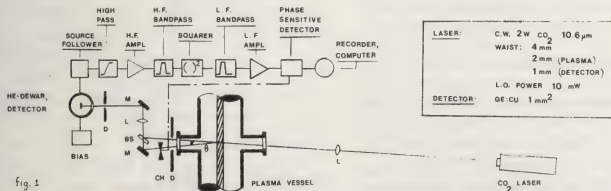
Introduction: Collective scattering of CO₂-laser radiation is an important diagnostic for the study of turbulence in plasmas. This diagnostic has obtained a lot of interest during the past few years. Most of the studies so far refer to:

a) detection of externally excited single frequency waves, b) scattering in high density plasmas (electron density $n_e \geq 10^{21} \text{ m}^{-3}$), or c) experiments with high power (pulsed or c.w.) CO₂-lasers [1,2,3,4]. We present as far as we know for the first time collective scattering measurements of spontaneously excited turbulence in a medium density plasma with a low power c.w. 2 W CO₂-laser.

Collective scattering refers to plasma scattering of electromagnetic radiation for which the so-called scattering parameter $\alpha = (k\lambda_D)^{-1} > 1$. Here $k = |k_s - k_i|$, where k_s and k_i are the wavenumbers of scattered and incident radiation respectively; λ_D is the Debye length. It is possible to obtain information about the electron density fluctuations for various wavenumbers k and angular frequencies ω . Here $\omega = \omega_s - \omega_i$, where ω_s and ω_i are the angular frequencies of the scattered and incident radiation respectively. The scattered power P_s is proportional to $n_e S(k_s - k_i, \omega_s - \omega_i)$, where $S(k, \omega)$ is the spectral density function, which represents the electron density fluctuations [5]. Mostly optical homodyne or heterodyne detection is used.

The (k, ω) -window can be varied by changing the scattering angle θ , which is proportional to k for small θ , and by changing the angular frequency ω_i of a variable bandpass filter after the optical mixer. For homodyne detection one gets $\omega_s = |\omega_i|$, so that the spectrum after the optical mixing is a direct measure of the fluctuation spectrum of the plasma.

Experimental equipment: The low power c.w. CO₂-laser is focussed in the plasma to a spot with a diameter of 2 mm (see figure 1). The plasma is created in a stationary, current driven (10-300 A), low pressure (10^{-3} torr) hollow cathode arc discharge. The plasma is cylindrical (radius 10 mm, length 0-2.5 m), magnetically confined (0-0.5 T) and highly ionized. Typical values of the plasma parameters are: electron density 10^{19} - 10^{20} m^{-3} , electron temperature 3-4 eV, ion temperature 1-2 eV, neutral density 10^{18} - 10^{19} m^{-3} , ion plasma frequency 200 MHz and Debye length 1.5 μm . A fraction of the incident laser beam is used as local oscillator (10 mW). The radiation scattered with angle θ is the signal beam, which is chopped for phase sensitive detection. Both beams are combined via a beam splitter and focussed on a liquid helium cooled Ge:Cu detector (1 mm^2 , current 1 mA). The detector is coupled via a source follower (600 Ω -50 Ω) and a high pass frequency filter (1 MHz) to broad-band low noise amplifiers (0-500



MHz, gain 40 dB). Home-made band pass filters (center frequency ν_c 1-50 MHz, bandwidth 0.1-0.3 of ν_c , 24 dB/octave) are used for spectral analysis. We can vary the scattering angle θ from 1° to 7° ($0.02 < k_D < 0.1$). We emphasized optimization of the signal to noise ratio and determination of the absolute sensitivity of the diagnostic as a whole. Both are crucial points. In optical mixing experiments it is the ambition to keep the shot noise of the local oscillator dominant with respect to other noise sources. We realized this by the use of an impedance transformer and ultra low noise active components; In this way also the local oscillator power is kept at a low level. The absolute sensitivity was determined by performing coherent and incoherent measurements with a black body and scattering from high level acoustic waves in 1 atm. argon. We are able to detect a scattered signal close to the quantum limit.

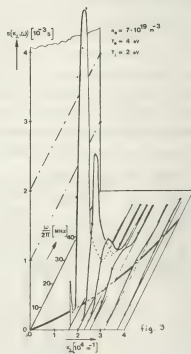
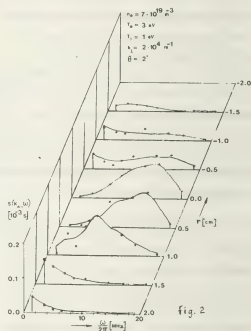
Experimental results: We used two scattering geometries: k_\perp/B and $k_\parallel B$. We found that for all plasma conditions considered the fluctuation level with k_\perp/B was close to thermal. As in this case the signals are very small we merely measured the total contents of the spectra. However, preliminary measurements indicate a maximum at the frequency-equivalent of the ion acoustic velocity. For $k_\parallel B$ we found fluctuation levels which could reach 3 orders of magnitude above thermal. In fig. 2 we show for a specific plasma condition $S(k, \omega)$ for $\theta = 2^\circ$ for various radial positions in the plasma. In fig. 3 we show $S(k, \omega)$ as functions of k_\perp and ω for a specific plasma condition for the center of the plasma. The dispersion indicates the presence of ion acoustic-like waves.

Discussion: One of the most evident result is the strong anisotropy in k -space, which indicates also the large selectivity in k -space of the collective scattering method. For k_\perp/B the level is close to thermal; for $k_\parallel B$ the level is highly non-thermal. This was contrary to our expectations for a plasma with the electron drift below but close to the critical drift for excitation of longitudinal ion acoustic waves. Perpendicularly propagating disturbances are preferred, moving with ion acoustic phase velocities, with an accumulation at long wavelengths. The frequency domain we studied so far is far above the ion cyclotron frequencies. We note, that the measurements with low frequency

optical probing indicate also a strong anisotropy in k -space and mainly perpendicularly propagating waves.

References:

- 1] Surko et al, Phys. Rev. Lett., **29** (1972) 81.
- 2] Holzhauer, Phys. Lett., **62A** (1977) 495.
- 3] Peratt et al, Phys. Fluids, **20** (1977) 1900.
- 4] Massig, Phys. Lett., **66A** (1978) 207
- 5] Sheffield, "Plasma scattering of electromagnetic radiation", Academic Press, New York, 1975.



NUMERICAL METHODS OF DATA PROCESSING FOR ACTIVE SUBMILLIMETER DIAGNOSTICS OF PLASMA CYLINDER

V.G. Zatsepin, E.A. Tishchenko and A.V. Golubev.

Institute for Physical Problems, Moscow U.S.S.R.

Abstract : We consider the numerical methods for inverse problems in active diagnostics of axisymmetric plasma under conditions of strong refraction and absorption. These methods are used to evaluate the profiles of electron density, temperature, absorption coefficient and effective collision frequency in Ar arc discharge. Results of active and passive diagnostics in submillimeter range demonstrate the applicability of equilibrium model to the investigated object.

Introduction : Modulus and phase of short wavelength probing beam are connected with plasma and diagnostic system parameters by convolution equation [1] :

$$g(\varphi) e^{-i\psi(\varphi)} = \int_{-\infty}^{\infty} K(y; \varphi) e^{-i\Phi(y)} dy \quad \left(\int_{-\infty}^{\infty} K(y) dy = 1 \right) \quad (1)$$

where φ is impact parameter of beam, $K(y; \varphi)$ is the apparatus function of the interferometer and $\Phi(y)$ is the modulation function of phase screen equivalent to plasma cylinder. In general case function $\Phi(y)$ is complex: $\Phi(y) = \text{Re}\Phi(y) + i\text{Im}\Phi(y)$. Here $\text{Re}\Phi(y)$ is the phase shift along the ray trajectory ℓ with impact parameter y :

$$\text{Re}\Phi(y) = \kappa \int_{\ell} (1 - \sqrt{\epsilon}) d\ell = 2\kappa \int_{\sqrt{a^2 - y^2}}^{\infty} \frac{\epsilon E(\xi) d\xi}{\sqrt{\xi^2 - y^2}}, \quad (2)$$

where $\epsilon(r) = \text{Re}\epsilon + i\text{Im}\epsilon$ ($|\text{Re}\epsilon| \gg |\text{Im}\epsilon|$) is a complex permittivity, $\epsilon(r) = \exp[-2E(\xi)]$ and $r = b \exp[E(\xi)]$. The function $\text{Im}\Phi(y)$ defines the integral absorption coefficient along the ray path:

$$\text{Im}\Phi(y) = \int_{\ell} \alpha d\ell = \kappa \int_{\sqrt{a^2 - y^2}}^{\infty} \frac{Q(\xi) d\xi}{\sqrt{\xi^2 - y^2}}, \quad (3)$$

where $\text{Im}\epsilon = Q(\xi) \exp[-2E(\xi)] / [1 + bE'(\xi)]$ and α is a local absorption coefficient :

$$\alpha = \frac{\kappa}{2} \frac{\text{Im}\epsilon}{\sqrt{\text{Re}\epsilon}} \approx \frac{1}{2} \frac{\nu_{\text{eff}}}{c} \frac{n_e}{n_c} \left(1 - \frac{\nu_e}{n_c} \right)^{-1/2}, \quad (\omega \gg \nu_{\text{eff}}). \quad (4)$$

If the beam width Δ is small compared to the plasma diameter $2a$ then $K(y) \rightarrow \delta(y)$, $\Psi(\varphi) \rightarrow \text{Re}\Phi(\varphi)$ and $g(\varphi) \rightarrow \exp[-i\text{Im}\Phi]$.

Abel Inversion : For axisymmetric plasma one can obtain from Abel-type equations (2) and (3) the radial distribution of electron density $n_e(r)$ and absorption coefficient $\alpha(r)$. Solving of Abel equations with due regard to refraction of radiation was made by means of series expansion of unknown and experimental functions in orthonormal set of polynomials with an optimal degree determined by regression analysis according to uncertainty of experimental function [2]. Computational tests show that accuracy of investigated functions $n_e(r)$ or $\alpha(r)$ was defined by noise of experimental functions $\text{Re}\Phi(y)$ and/or $\text{Im}\Phi(y)$ multiplied by factor $K_N \sim 2 - 3$.

Phase and Modulus Iterations : In our experiments the width of probing beam Δ was about $(5-10)\lambda \sim 1-2$ mm, plasma diameter $2a$ and maximum electron density n_0 varied in the ranges of 5-20 mm and $3 \cdot 10^{14} - 10^{16} \text{ cm}^{-3}$, respectively. Profile of measured function $\Psi(\varphi)$ is usually slightly distorted in comparison with $\Phi(y)$ because of the finite beam width. To evaluate the unknown function $\Phi(y)$ we applied the appropriate iterative procedures to the real and imaginary parts of eqn.(1) written in the algebraic notation :

$$\sum K_{ij} e^{-i\text{Im}\Phi_j} \sin(\text{Re}\Phi_i - \Psi_j - \Omega_{ij}) = 0, \quad (5)$$

$$\sum K_{ij} e^{-i\text{Im}\Phi_j} \cos(\text{Re}\Phi_i - \Psi_j - \Omega_{ij}) = g_j, \quad (6)$$

where $\sum K_{ij} e^{-i\Omega_{ij}} = 1$. Experimental function $\Psi(y)$ was taken as a zero approximation $\text{Re}\Phi_j^{(0)}$ for $\text{Re}\Phi(y)$. Iterative formula for $\text{Re}\Phi$ was chosen as follows :

$$\text{Re}\Phi_j^{(n+1)} = (\text{arcsin}[\sin(\text{Re}\Phi_j^{(n)} - \Psi_j - \Omega_{ij}) - \frac{\mathcal{C}}{K_{jj}} \sum K_{ij} \sin(\text{Re}\Phi_i^{(n)} - \Psi_j - \Omega_{ij})]) \quad (7)$$

where \mathcal{C} is a parameter which improves the convergence of iterative process. Function $\text{Im}\Phi(y)$ is determined by analogous iterative procedure :

$$\text{Im}\Phi_j^{(n)} = -\epsilon_n \left\{ e^{-\text{Im}\Phi_j^{(n)}} \sum_{K_{ij}} K_{ij} e^{-\text{Im}\Phi_j^{(n)}} \cos(\text{Re}\Phi_j - \Psi_j - \Omega_{ij}) - g_j \right\} \quad (8)$$

Computer simulation showed that noise amplification factor of these procedures did not exceed $K_N \sim 2-3$ when $2a/\Delta \gg 3$.

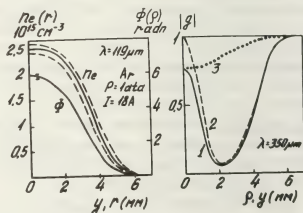
Results and Discussion: Application of these numerical methods is demonstrated on the model plasma object - d.c. arc discharge in Ar [4]. Fig.1a shows the function $\text{Re}\Phi(y)$ measured at the wavelength $\lambda = 119 \mu\text{m}$ and corresponding density profile with a 95% confidence limits defined by the input absolute errors $\Delta\Phi \sim \pm 0.1$ radn. Experimental modulus of transmission coefficient $g(\rho)$ is shown in Fig.1b (curve 1). Dotted line (2) presents the theoretical signal $g(\rho)$ calculated for refractive losses ($\text{Im}\Phi = 0$). Difference between these functions is due to dampind factor $f(y) = \exp[-\text{Im}\Phi(y)]$ -curve (3). Solving of Abel equation (3) for $\text{Im}\Phi(y)$ provides the profile of absorption coefficient $\alpha(r)$ (see Fig.2a). Temperature distribution $T_e(r)$ was evaluated from Saha equation by determined profile of $n_e(r)$. Good agreement between the experimental and calculated plasma side-on brightness $P(y)$ (Fig.2b, circles and line) confirms the applicability of equilibrium model. Theoretical function $P(y)$ was calculated employing the profiles of $\alpha(r)$ and $T(r)$ with due regard to self-absorption and refraction of plasma emission. Dotted curve in Fig.2a shows the partition of electron-ion collisions in absorption of the probing radiation. These data provide the effective collision frequencies $\nu_{ei} = 4 \cdot 10^{10}$ 1/s, $\nu_{ea} = 3 \cdot 10^{10}$ 1/s and momentum transference cross-section $\sigma_{ea} = 7.5 \cdot 10^{-16}$ cm² for Ar atoms at the temperature of $9 \cdot 10^3$ K.

The relative uncertainty of $n_e(r)$ ($\sim 5 - 10\%$) was due to the errors of experimental function $\Psi(\rho)$ ($\sim 2\%$) and the noise amplification factor $K_N \sim 2-5$ characteristic for solutions of Abel and convolution equations. We consider the accuracy of collision frequency measurements to be about 10-20% because the absorption was evaluated as a difference between the total and refractive losses. Plasma temperature calculated by means of Saha equation was in a good agree-

ment with radiative temperature T_e^r , obtained independently from measurements of the absolute intensity of plasma emission at two different wavelengths [4].

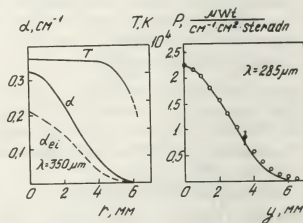
References:

- [1] L.A.Vainstein, E.A.Tishchenko, Zh. Tech.Fiz., **46**, 11, 2271 (1976)
- [2] E.L.Kosarev, Zh.Vytech.Mat. i Mat. Fiz., **13**, 6, 1591 (1973)
- [3] E.A.Tishchenko, V.V.Zav'yalov, V.G.Zatsepin, V.B.Lasarev, XIII ICPIG, Contr.papers, Berlin, p.161 (1977)
- [4] E.A.Tishchenko, A.V.Golubev, V.B.Lasarev, paper at this conference



a) Fig.1 b)

- phase function and density profile of Ar arc discharge
- experimental and theoretical (2) modulus of transmittivity and absorption factor (3)



a) Fig.2 b)

- radial distribution of absorption coefficient and temperature
- side-on spectral emissivity of plasma cylinder

LOW-TEMPERATURE PLASMA INVESTIGATIONS BY RESONANCE RAYLEIGH SCATTERING OF WEAK INTENSITY RADIATION

L. Ya. Margolin, L.N. Pyatniskii and N.P. Shternov.

Institute of High Temperature of the U.S.S.R. Academy of Sciences, Moscow U.S.S.R.

The work to be described was an attempt to determine resonance Rayleigh scattering cross sections and to investigate a plasma without a significant perturbation of level populations by incident wave field.

An estimate of the condition of weak wave field is based on equation $\tilde{G}_K \gamma_K \omega \gamma_1 \ll 1$ (see, e.g. [1]). It is equivalent to independent photon scattering by atoms (ions). In the equation \tilde{G}_K , $\hbar\omega$ and γ_1 are light intensity, photon energy and inverse lifetime of upper level 1 respectively (the incident wave frequency ω is in resonance with the electronic transition $0 \rightarrow 1$, 0 - initial state of atoms). \tilde{G}_K is the total scattering cross section defined by [2]:

$$\tilde{G}_K = \alpha \pi \tau_e^2 \frac{g_1}{g_0} \frac{\omega_0^2 \omega_K^2}{\omega^4} \frac{f_{01} f_{1K}}{(\omega - \omega_{01})^2 + \gamma_1^2/4} \quad (1)$$

Here τ_e is classical electron radius; g_1 , g_0 are statistical weights; $K=0$ or 2 , where 2 is a some intermediate state; f_{1K} are oscillator strengths; \tilde{G}_0 is the total cross section for fluorescence process and \tilde{G}_1 is the total cross section for resonance combination process. The intensity of the incident radiation is of the order 10^{14} W/cm^2 for typical conditions of the experiment.

A connection between the scattering radiation power J_K^s and incident radiation intensity J may be derived in considering of resonance light absorption and radiation kinetics. The following equation describes the connection:

$$\frac{1}{J_K^s} = C_K \left[\left(1 + \frac{g_1}{g_0} \right) + \frac{A_{1K}}{\tilde{G}_K} \frac{\omega_K}{\omega} \hbar \omega \frac{1}{J} \right] \quad (2)$$

where $K=0$ or 2 , C_K and A_{1K} are coefficient of proportionality and probability of spontaneous emission respectively. The equation gives a possibility to determine the resonance Rayleigh scattering cross sections.

Scattering light depolarisation β_K gives useful knowledge about plasma (electron states configurations, frequencies of external influences on particles, etc.). There are derivations for Rayleigh scattering depolarisation in [3]. On spreading the derivations for the case of resonance we shall get:

$$\beta_K = \frac{\sum_{M_0} \left(\begin{smallmatrix} J_1 & 1 & J_1 \\ -M_0 & 0 & M_0-1 \end{smallmatrix} \right) \left(\begin{smallmatrix} J_1 & 1 & J_1 \\ -M_0 & 0 & M_0 \end{smallmatrix} \right)^2}{\sum_{M_0} \left(\begin{smallmatrix} J_1 & 1 & J_1 \\ -M_0 & 0 & M_0 \end{smallmatrix} \right)^2 \left(\begin{smallmatrix} J_1 & 1 & J_1 \\ -M_0 & 0 & M_0 \end{smallmatrix} \right)^2} \quad (3)$$

Here $K=0$ or 2 ; J and M are quantum numbers of the states $0, 1, 2$; $\left(\begin{smallmatrix} J_1 & 1 & J_1 \\ -M_0 & 0 & M_0 \end{smallmatrix} \right) - 3j$ -symbol.

Experimental arrangement were builded by ordinary scheme which described in [4]. Plasma was probed by ion-argon laser radiation focused up to 150μ diameter. There were a polaroid and double grating monochromator DGC-12 as a spectrum analyzer. The lock-in technique was used. Plasma was created by atmospheric pressure d-c arc discharge in argon and neon with a small argon additions. The discharge current was 40 A .

In order to determine the particle level populations it is necessary a knowledge of scattering cross sections. The cross sections were measured on the basis of the equation (2). The Results of experiments with the use of incident radiation $\lambda = 5145\text{\AA}$, 4880\AA and 4765\AA are shown on Fig.1. The cross sections measuring in plasma Ne+Ar are represented in the Table 1. In argon plasma the cross sections were calculated by (1) and results of [5]. Similar calculations for plasma Ne+Ar give the values coincided with experimental results. There are the populations values of ion argon levels $4s^2P_{3/2}$ and $4s^2P_{1/2}$ in the same Table.

The results of depolarisation measurements in argon and neon plasma are represented in the Table 2. It can be seen, that there is a correlation between calculated and experimental date. However, the discrepancy between some of them exceeds experimental errors. Remember, that the relation (3) is valid for single particle scattering. So, the discrepancy is the evidence of collision influence on the depolarisation.

Thus we have show the possibility of low-temperature plasma diagnostic by resonance Rayleigh scattering of weak intensity radiation. It is of particular importance that similar measurements can be made usually without significant perturbation of the plasma.

References:

1. Н.Б.Делоне, В.П.Крайнов, УфН, т.124, с.619 (1978).
2. В.Б.Берестецкий, Е.М.Лифшиц, Л.Н.Питаевский, "Релятивистская квантовая теория", ч.1, М., Наука, 1968.

3. C.M.Penney, J.Opt.Soc.Am., v.59, p.34 (1969).

4. В.М.Батенин и др., ТВТ, т.15, с.239 (1977).

5. J.Puric, et al. Proc.XI Int.Conf.Phenom.

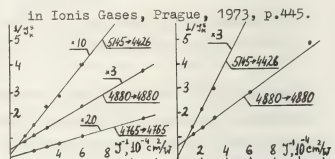


Fig.1. Experimental dependence $1/J_0^4 (1/T)$:

a) Ne+1%Ar; b) Ne+0.05%Ar

Table 1.

plasma	prob. $\lambda, \text{\AA}$	record. $\lambda, \text{\AA}$	G_{λ} $\cdot 10^{-16} \text{ cm}^2$	Population $\cdot 10^9 \text{ cm}^{-3}$
Ar	5145	4426	$0.26^{(*)}$	5.0 ± 0.6
	4880	4880	$0.9^{(*)}$	7.4 ± 0.4
	4765	4765	$0.38^{(*)}$	2.7 ± 0.5
	4765	4545	$0.12^{(*)}$	3.0 ± 0.5
Ne+ 1%Ar	5145	4426	$6.5 \pm 1.5^{(*)}$	2.1 ± 0.5
	4880	4880	$20 \pm 3^{(*)}$	2.0 ± 0.8
	4765	4765	$20 \pm 3^{(*)}$	0.9 ± 0.2

$(*)$ - Calculation by equation (1)

$(**)$ - results of experiments

Table 2

Prob. $\lambda, \text{\AA}$	Record. $\lambda, \text{\AA}$	Calc. (3)	Depolarisation		
			Experiment		
			Ar	Ne+1%Ar	Ne+0.05%Ar
5145	4426	0.46	0.45	0.46 ± 0.02	0.52 ± 0.03
4965	4727	7.0	-	5.0 ± 0.5	5.3 ± 1.2
4965	4965	0.25	-	0.33 ± 0.03	0.38 ± 0.06
4880	4880	0.46	0.56	0.34 ± 0.02	0.62 ± 0.04
4880	4228	0.46	0.40	0.25 ± 0.03	0.44 ± 0.05
4765	4765	0.25	0.15	0.31 ± 0.02	0.31 ± 0.03
4765	4545	7.0	-	4.4 ± 0.4	3.6 ± 0.4

THE USE OF GAS DISCHARGES AS ULTRAVIOLET RADIOMETRIC STANDARDS

W.R. Ott, J.M. Bridges and J.Z. Klose.

National Bureau of Standards, Atomic and Plasma Radiation Division, Washington, D.C. 20234.

This paper describes the various gas discharges used currently or under development at NBS as radiometric standards in the spectral region 110-350 nm. Some review material is included in addition to new measurements in order to provide a balanced overview of the NBS UV radiometry program. The application of such sources as a diagnostic will also be described for a few typical experiments, e.g. tokamak impurity concentration determinations, dense plasma temperature determinations, photochemical rate coefficient measurements, and uv spectro-radiometer efficiency measurements aboard space shuttle.

Six radiation sources have been investigated: 1) a hydrogen wall-stabilized arc; 2) a blackbody-limited line thermal arc plasma; 3) an argon "mini-arc"; 4) an argon "maxi-arc"; 5) a deuterium lamp; 6) a krypton dimer rf discharge lamp. Determinations of both the spectral radiance ($\text{W cm}^{-2}\text{nm}^{-1}\text{sr}^{-1}$) and the spectral irradiance (W cm^{-2}) have been undertaken.

The use of a hydrogen arc plasma as an absolute primary standard of uv spectral radiance has been described previously.¹ The optically thin Balmer continuum radiation between 360 nm and about 130 nm can be calculated to within an uncertainty of less than 3%. When operated at electron temperatures such that the radiance reaches the Larenz maximum (about $T = 20\ 000\text{K}$),

the uncertainties in the calculation are minimized since the radiance is not sensitive to the plasma diagnostics and any deviations from LTE are expected to be minimized. The spectral irradiance of the hydrogen arc has now been measured for the first time. Its potential use as a spectral irradiance standard will be discussed.

The blackbody line radiation source is similar to the one described by Boldt² and others. Contaminants of N_2 , CO_2 , and H_2 are added to a thermal argon arc plasma and the NI and CI atomic resonance lines become optically thick and in fact blackbody limited. The spectral radiance at the line centers is a function of temperature and is given by the Planck radiation law. It is used as a primary standard of spectral radiance in the spectral region 100-200 nm.

At NBS the hydrogen arc and the blackbody line arc are used as primary standards to calibrate the radiance of recently developed secondary standards such as the argon "mini-arc" and the "maxi-arc" which are easier to operate and are more portable. For example the mini-arc³ is 10 cm long, needs no ballast resistor, and can be operated with a 1 kW, 10 kg dc power supply. The spectral radiance and irradiance of both the mini-arc and the maxi-arc have been measured and are available from NBS as secondary standards in the wavelength region 110-330 nm with uncertain-

ties within 5-20% depending on wavelength. Their characteristics as standards have been extensively studied and will be described.

Commercially available low pressure deuterium lamps have been used for a number of years as secondary standards of spectral radiance in the region 165-350 nm. Measurements are now extended to shorter wavelengths (115 nm) where the many-line Lyman band dominates the spectrum. Our measurements show that the blended lines form a pseudo-continuum below 165 nm when a low resolution spectroradiometer is used for detection. The sensitivity of the spectral irradiance to the bandpass has been determined. The lamps were enclosed in a vacuum system; no change was observed in the spectral irradiance when the system was evacuated. This has special implications concerning space applications and for applications in which one desires that the radiometric standard be placed inside a vacuum system.

A commercially available krypton dimer radiation source was also tested as a potential standard of radiance and irradiance in the spectral region 125-170 nm. Its reproducibility and aging characteristics, both inside a vacuum system and at atmospheric pressure, have been measured. Operation of the lamp with other noble gases which emit continuum radiation in other wavelength bands is being investigated.

In summary, this family of gas discharges provides convenient and reliable laboratory source standards in the 110-350 nm spectral region. Calibrations of both spectral radiance and spectral irradiance are made with sources whose intensity levels cover a range of almost 6

orders of magnitude, thus allowing a variety of radiometric applications.

References

1. W. R. Ott, K. Behringer, and G. Gieres, Appl. Opt. 14, 2121 (1975).
2. G. Boldt, Space Sci. Rev. 11, 728 (1970).
3. J. M. Bridges and W. R. Ott, Appl. Opt. 16, 367 (1977).

AN UNAMBIGUOUS METHOD OF ELECTRON DENSITY MEASUREMENT IN SHOCK-GENERATED PLASMA, USING A LASER INTERFEROMETER

A. Lesage, J. Richou, P. Charil and M. Combier.

D.E.P.E.G. Observatoire de Meudon, 92190 Meudon France.

INTRODUCTION

Degree of ionisation profiles have previously been measured in shock waves by laser interferometry⁽¹⁾. The technique was however confined to incident shocks because of the difficulty in interpreting interferograms. As spectral lines tend to have better brightness behind first-and multi-reflected shock waves, it is desirable to extend this powerful method of electron-density measurement to these more highly compressed regions.

THEORY OF OPERATION

All constituents of a plasma : neutral atoms (suscript 1), ions (+), electrons(e) contribute to its refractivity :

$$(n-1) = (n-1)_1 + (n-1)_+ + (n-1)_e - (n-1)_0;$$

where $(n-1)_0$ is the refractive index of the gas before ionisation. In terms of specific refractivity K , and by noting that ions have nearly the same susceptibility as atoms :

$$(n-1) = K_1 (N_1 + N_+) + K_e N_e - K_0 N_0.$$

Because $N_0 \ll N_1$ across a shock front, and does not vary until arrival of the next front :

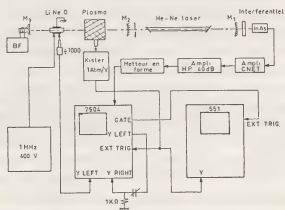
$$(n-1) = K_1 (N_1 + N_+) + K_e N_e.$$

This relationship makes it easy to compare electron and atom contribution to the refractive index. Values at two wavelengths have been computed via :

$$K_e N_e / K_1 N_1 = \frac{4.48 \cdot 10^{-4} \lambda^2}{(A' + B') / \lambda^2} \times \frac{N_e}{N_1}$$

where A' and B' are the Cauchy formula constants divided by the Loschmidt number. Behavior of the fringe pattern, when the light path's refractivity is cyclically modulated, shows how to interpret interferometric signals from shock-tube plasmas. The cyclic change is induced by a

Li Nb O₃ electro-optic crystal regularly modulated by Pockel effect⁽²⁾. A voltage proportional to the driving voltage (phase shift of the laser beam) of the crystal is fed to the y-axis of the oscilloscope (Fig.1). Modulation of the brightness of the oscilloscope trace (z-axis) produces one bright pulse for every fringe⁽³⁾. The chronology of events is recovered from the oscilloscope time base in the usual way.



The laser produces a maximum output for : $L = m\lambda$ (where m is a constant, L the initial optical-path between the two mirrors M_1, M_2 , and λ the operating wavelength). The condition for a blip on the oscilloscope is : $L + F_p(t) + f(t) = m\lambda$ (where $F_p(t)$ and $f(t)$ are the changes of path due to the cyclic modulator and the plasma respectively). Because $F_p(t)$ is proportional to the scope's y deflection, the locus of bright spots will form a bright band given by : $y = (m\lambda - 1) - f(t)$; i.e. bright bands tracing out directly the path length versus time profile. Inter-bands separation is $\lambda/2$.

APPARATUS

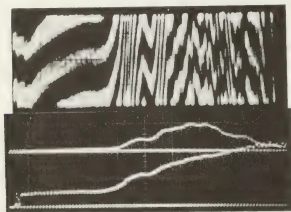
The interferometer is the same as previously described⁽¹⁾. A (15 x 5 x 1.3)mm

Li Nb O₃ crystal is located in the reference cavity (M₂, M₃) of an ASHBY-JEPH COTT interferometer ; (4) and its optical axis is parallel to the laser beam polarization. Multireflexion is used to lower the minimum modulation voltage required for a $\lambda/2$ phase shift. The mirror M₃ can be oscillated for trial purposes. The crystal modulation frequency choosen is a trade-off between the plasma index of refraction, resolution and interferometer signal amplitude. A germanium wedge in series with interference filter isolates the 3.39 μ m laser band and prevents swamping the I_{N_S} detector. The signal of the interferometer is amplified and shaped to enhance the z-axis display. When a transient (shock tube) plasma passes across the laser beam, its electron density variation perturbs the cyclic refractivity variation driven by the crystal : phase-sensitive detection is used to measure these comparatively small perturbations. The output from a quartz transducer mounted in the shock tube provides a synchronous pressure profile which facilitates interferogram interpretation.

RESULTS AND CONCLUSIONS

The method was tested first with an oscillating mirror M₃, next with incident shock waves, and finally with a succession of incident and reflected shock waves in neon (Fig. 2). In the latter case a fringe (cyclic variation) corresponds to

$$N_e = 6.6 \times 10^{16} \text{ cm}^{-3}$$



Advantages of this technique are : 1) it tracks reversals of path refractivity in an unambiguous way, 2) it detects small fluctuations not readily observed by earlier interferometric methods, and 3) it permits estimations of fraction of a fringe shift on a linear scale. The method's limitation is the interferometer modulation cut-off which limits the resolution : for transient phenomena, one would expect the display to break down if the fringing rate approached one fringe per oscillation cycle. Higher laser wavelengths and amplitudes can be used for denser or brighter plasmas. More details about these instruments can be found in reference 5.

REFERENCES

- (1) J. RICHOU and A. MOLITOR C.R. Acad.SV. Paris, t 271, p.753-756 (12 Octobre 1970).
- (2) F. POCKELS, Lehrbuch der Kristallog-
tik (Teubner, Leipzig 1906).
- (3) A. GIBSON and G.W. REID Appl. Phys
Letters, 5, 10, (1964)
- (4) D.E.T.F. ASHBY, D.F. JEPHCOTT, A.
MAZEIN and F.A. RAYNOR, J. Appl. Phys.
36, 29 (1965).
- (5) A. LESAGE, Thèse Doctorat d'Etat
Université Paris XI, 1977
(unpublished).

FINITE THICKNESS EFFECT OF PROBE SHEATH IN RADIO-FREQUENCY PLASMA PROBE DIAGNOSTICS

V.A. Godyak and S.N. Ox.

Moscow State University, Department of Physics, Moscow U.S.S.R.

It is known, that for correct probe diagnostics of RF plasma it is necessary, that RF probe potential should differ little from RF plasma potential. It is usually achieved by selection of high enough probe circuit RF impedance, which prevents from RF current to flow in this circuit /1,2,3/.

In present publication the influence of finite thickness of probe sheath upon the accuracy of RF plasma probe diagnostic is analysed. It is also shown, that the absence of RF current in the external probe circuit doesn't guarantee yet correct probe measurements.

It is convenient to illustrate the mentioned effect at the example of a plane bilateral probe, orientated normally to RF field (Fig.1). The probe plane is separated from plasma by a space charge sheath, the thickness of which S depends upon the constant negative potential V_0 . At frequencies more greater than the ion plasma one, displacement current in the sheath considerably exceeds conduction current. Then RF potential difference between probe and two plane plasma boundaries will equal to:

$$V_1(t) = -V_2(t) = S |\epsilon_P| E_P \sin \omega t \quad (1)$$

where ϵ_P and E_P are permittivity and RF field amplitude in plasma. According to (1) time average electron probe current is following:

$$\begin{aligned} \langle I_e \rangle &= \frac{J_{ec}}{2\pi} \int_0^{2\pi} \left[\frac{1}{2} \exp \frac{V_0 + V_1(t)}{V_e} + \frac{1}{2} \exp \frac{V_0 + V_2(t)}{V_e} \right] d(\omega t) = \\ &= J_{ec} e^{V_0/V_e} I_0 \left(\frac{|\epsilon_P| E_P S}{V_e} \right) = J_{ec} e^{V_0/V_e} I(\alpha) \quad (2) \end{aligned}$$

where J_{ec} - electron saturation current; V_e - electron temperature in units of potenti-

al; I_0 - modified Bessel function. In the case of $\omega^2 \gamma^2 \ll \omega_{pe}^2$, we have $|\epsilon_P| = \frac{\omega_{pe}^2}{\omega^2} \left(1 + \frac{\gamma^2}{\omega^2} \right)^{-1/2}$ and $\alpha = \alpha \frac{S}{D_e}$, where γ - frequency of electron-atom collisions; ω_{pe} - electron plasma frequency; D_e - Debye length; α - amplitude of electron oscillation in plasma. Setting the permissible probe current increase not more than 26%, correctness criterion of plane probe measurements may be obtained from (2): $\alpha \leq 1$. In plasma of self-sustained RF discharge we get $\alpha = \frac{V_{re}}{\omega} \chi^{1/2}$, and D_e of the order S ($S = K(V_e/D_e)$). Then expression for α becomes:

$$\alpha = \frac{\omega_{pe}}{\omega} \chi^{1/2} K(V_e) \quad (3)$$

As follows from (3), in RF discharge $\alpha > 1$, that may lead to considerable errors at finding plasma parameters with the plane probe (χ - effective part of energy lost by electrons).

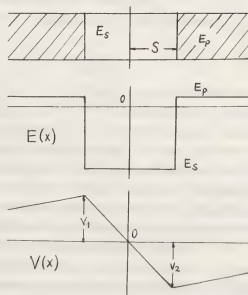


Fig.1. Distribution of RF field and RF potential in the probe sheath.

Let's consider the same problem for cylindrical probe, orientated normally to RF field. The distribution of RF potential in the probe sheath can be written as [5]:

$$V(\theta, t) = 2 \left| \frac{\mathcal{E}_p}{1 + \mathcal{E}_p} \right| E_p \frac{S^2}{r \cdot S} \cos \theta \sin \omega t$$

where r - probe radius; θ - angle between radius-vector and the direction of RF field. Then for time average electronic component of the probe current we get:

$$\langle I_e \rangle = \frac{I_{e0}}{4\pi^2} \int_0^{2\pi} d\theta \int_0^{\pi} \sin \theta d\theta \int_0^{2\pi} d\phi \frac{V_e + V(\theta, t)}{V_e} d(\omega t) =$$

$$I_{e0} e^{\frac{V_e}{V_0}} \int_0^{\frac{\pi}{2}} \left(1 + \left| \frac{\mathcal{E}_p}{1 + \mathcal{E}_p} \right| \frac{E_p}{V_e} \frac{S^2}{r \cdot S} \right) = I_{e0} e^{\frac{V_e}{V_0}} I_0^4(\beta) \quad (4)$$

As follows from (4), when $\beta \leq 1/2$ the increase of electron current doesn't exceed 13%. Unlike the plane probe, where at $\omega \ll \omega_{pe}$ probe current distortions grow with increasing of plasma density, in the case of cylindrical probe this effect is expressed weaker and distortions grow, if plasma density decreases. That's because the average RF field in the cylindrical probe sheath practically equals to RF field in plasma, while in plane probe sheath RF field increases in \mathcal{E}_p times. Nevertheless, in the case of cylindrical probe some situations are possible, in which the measured probe current will be greatly distorted ($\beta > 1/2$). It may happen, when there is a dipole resonance of cylindrical cavity in plasma at $\omega = \frac{\omega_{pe}}{\sqrt{2}}$ ($\left| \frac{\mathcal{E}_p}{1 + \mathcal{E}_p} \right| \gg 1$), and also in self-sustained RF plasma. In the last case:

$$\beta = \frac{\mathcal{E}_p^{1/2}}{\omega_{pe}} (\sqrt{2} + \omega^2)^{1/2} \frac{K^2}{V_{De} + K} \quad (5)$$

and estimations show, that $\beta > 1/2$ may be realized in rare plasma of RF discharge in molecular gases, where \mathcal{E}_p is great enough. Since the degree of probe current distortions is determined by the probe sheath thickness, it is obvious, that errors in the measurements of electron current must grow with increasing of negative probe potential. It may lead to the distortion of probe characteristics form and to the apparent enrichment of electron energy spectra by fast electrons. The dependence S from RF voltage in the sheath was neglected in deducing (2) and (4). This is admissible, if $V(t) \ll V_0$ or $a \ll D_e$ (these relations are

equivalent). In the opposite case ($a \gg D_e$), probe sheath thickness will be modulated by RF field. Time average sheath thickness $\langle S \rangle$ will grow with the increasing of RF field owing to RF voltage rectification in the sheath.

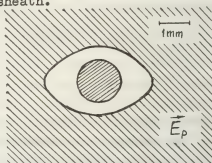


Fig.2

Such situation occurs in the sheaths at electrodes in RF discharge [4], where $\langle S \rangle \approx a$, if $a \gg D_e$. If the requirement $a \ll D_e$ is broken in the case of cylindrical probe, it will lead to unisotropic widening of probe sheath in the direction of RF field. Fig.2 shows the picture of cylindrical floating probe sheath, obtained in the air RF discharge at $\frac{\omega}{2\pi} = 3\text{MHz}$ and pressure $p = 5\text{torr}$. The observed asymmetry of probe sheath has been disappearing with the increasing of plasma density and decreasing of pressure. This fact agrees with (5).

In conclusion let's mention, that unlike the effects, studied in [1, 2, 3], the distortion of probe measurements described here can't be removed by scheme solutions. It limits on principle the sphere of using probe methods in RF plasma diagnostics.

References:

- 1/. R.R.J. Gagne, A. Cantin, J. Appl. Phys., 43, 2639, 1972
- 2/. "Плазмохимические реакции и процессы" (8. погр. ред. Л.С. Полака, М. Наука, 1977.
- 3/. В.А. Голяк, О.А. Понов, ЖТФ, 47, 766, 1977.
- 4/. В.А. Голяк, Физика плазмы, 2, 141, 1976
- 5/. von A. Sommerfeld, "Elektrodynamik", Geest & Portig K.-G., Leipzig, 1949.

INVESTIGATION OF SHEATH AT ELECTRODE IN RADIO-FREQUENCY DISCHARGE

V.A. Godyak, S.N. Ox.

Moscow State University, Department of Physics, Moscow U.S.S.R.

To construct RF discharge theory joint accounting of electrodynamic properties of quasi-neutral plasma and space charge sheath at electrode (SCSE) is needed. Let's consider the structure and electrodynamic properties of SCSE, which appear in a stationary symmetrical RF discharge between plane nonemitting electrodes in range of frequencies $\omega \gg 1/\tau$:

$$\omega_{pe}^2 \gg \omega^2 \gg \omega_{ci}^2 \quad (1); \quad \omega \gg Z; \quad \omega \gg \mathcal{A}V \quad (2)$$

where ω_{pe} and ω_{ci} - electron and ion plasma frequencies; ω - RF field frequency; V - electron-atom collision frequency; Z - ionization frequency; \mathcal{A} - effective part of energy, lost by an electron at collision. Fig. 1 shows a qualitative structure of SCSE.

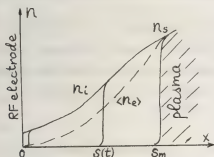


Fig. 1

Plasma ions are injected in SCSE with ion sound velocity V_s (n_s - plasma boundary density). As it follows from (1), ions are accelerated towards RF electrode by the time average component of SCSE field. At the same time electron density profile oscillates with the field frequency from S_m to RF electrode. The last requirement is fulfilled when electron oscillation amplitude at plasma boundary \mathcal{A}_s exceeds considerably the Debye radius at plasma boundary \mathcal{D}_{es} . If the electron density is step-like, then for mobile sheath

boundary we shall have: $n_e(z) = n_i(x)$. Let's set discharge current (displacement current in SCSE) as $J(t) = J_0 \cos \omega t = en \frac{d\psi}{dt}$. Time average electron density in SCSE $\langle n_e \rangle = \frac{1}{2\pi} \int_0^{2\pi} n_e(x, t) d(\omega t)$ together with stationary ion space potential determines the time average potential in SCSE - $\phi_e(z) = \langle \psi(z, t) \rangle$. Then from equations of Poisson, ion motion, RF current continuity and charge conservation for two SCSE / 1 / we shall get a system of equations. This system links together time average SCSE characteristics with set parameters $\alpha = \frac{\mathcal{D}_{es}}{\lambda_i}$ and $\mathcal{U}_c = \frac{V_c}{V_e}$ (λ_i - ion mean free path, V_c - amplitude of summary RF voltage in two SCSE, V_e - electron temperature in units of potential):

$$\frac{d^2 \eta_0}{dz^2} = y_1(z) - \langle y_0(z) \rangle$$

$$y_1(z) = \frac{e^{-\alpha z}}{\sqrt{2} \eta_0} + \alpha \int_0^z \frac{e^{-\alpha(z'-z)}}{\sqrt{2}(\eta_0 - \eta_0')} dz' + \frac{\mathcal{D}_{es}}{\Lambda} \int_0^z \langle y_0 \rangle \frac{e^{-\alpha(z'-z)}}{\sqrt{2}(\eta_0 - \eta_0')} dz'$$

$$\langle y_0(z) \rangle = \frac{y_1(z)}{\pi} \arccos \left[2 \frac{\int_0^z y_1(z') dz'}{\int_0^z y_1(z') dz'} - 1 \right]$$

$$y_1(z_1) \frac{dz_1}{dt} + y_1(z_2) \frac{dz_2}{dt} = 0$$

$$\eta_1(t) - \eta_2(t) = \mathcal{U}_c \sin \omega t$$

$\frac{\mathcal{A}}{2\pi} \int_0^{2\pi} y_1(z_{1,2}) e^{-\eta_{1,2}} d(\omega t) = 1$
where $\eta_0 = \frac{V_c}{V_e}$; $z = \frac{x}{\lambda_i}$; $y_1 = \frac{n_i}{n_s}$; $\langle y_0 \rangle = \frac{\langle n_e \rangle}{n_s}$;
 $\delta_1 = S_m/\lambda_i$; $\mathcal{A} = (M/2\pi m)^{1/2}$; η_1 and η_2 - instantaneous values of reduced RF voltages in two SCSE; Λ - characteristic dimension of quasi-neutral plasma. Point $z=0$ corresponds to plasma boundary and $z=\delta_1$ to RF electrode.

This system has been solved with computer for the large range of values $\mathcal{U}_c = 5-200$ and $\alpha = 10^{-4}-1$. Calculations showed, that the last member in the second equation

uation, linked with ionization in SCSE, at $S_m \ll \Lambda$, gives the negligible contribution to the value y_i . Time average SCSE thickness - S_0 , determining SCSE capacitive impedance was found from $\int_0^{\delta_0} y_i(z) dz = \int_0^{\delta_0} y_i(z) dz$, where $\delta_0 = S_0 / u_c$.

Fig.2 shows ion space distribution in SCSE in the case of uncollision sheath ($\alpha = 10^{-2}$, $S_0/\lambda_i = 10^{-1}$) and also when there are several collisions ($\alpha = 1$, $S_0/\lambda_i = 7$). So Fig.2 shows, that ion distribution inhomogeneity decreases while the number of collisions in SCSE increases. The same is seen from Fig.3, where dependence $y_i(\delta_i)$ at different u_c is given.

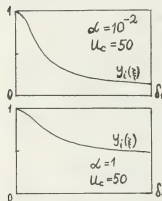


Fig.2

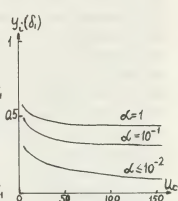


Fig.3

According to the calculations, u_c -dependences of reduced SCSE thickness δ_0 (Fig.4) and reduced time average component of RF voltage in SCSE u_0 (Fig.5) may be approximated by following expressions with accuracy to 10% :

$$\delta_0 = \ell(\alpha) u_c^{1/2} \quad (3); \quad u_0 = \frac{u_c}{3} \quad (4)$$

where parameter ℓ weakly depends upon α and may be approximated exactly enough by expression:

$$\ell(\alpha) = \frac{1.8 + \ln(1+\alpha)}{1 + \sqrt{2} \ln(1+\alpha)} \quad (5)$$

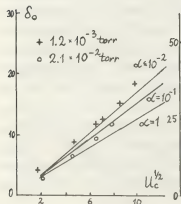


Fig.4

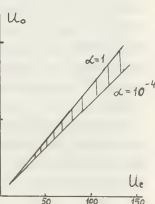


Fig.5

The results of calculations $\ell(\alpha)$ are presented at Fig.6. Approximation (5) is given by dotted line. Experimental results / 2 /, obtained in RF discharge (mercury vapour) at frequency $\frac{\omega}{2\pi} = 40.8$ MHz are given at Fig.4 and Fig.6.

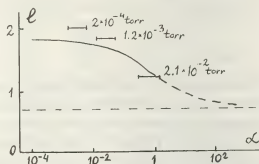


Fig.6

Let's note, that value δ_0 , and therefore the SCSE capacitive impedance, are determined by amplitude of electron oscillations at plasma boundary a_s . Actually, displacement current in SCSE is equal to conduction current in plasma due to the continuity of discharge current:

$$j_c = \frac{V_e u_c \omega}{8\pi S_0} = a_s \omega n_s; \quad ;$$

then taking into account (3) we get:

$$S_0 = 2 \ell^2 a_s$$

At high pressures ($\alpha \gg 1$) this relation, as follows from (5), takes the form: $S_0 = a_s$. This result coincides practically with results of / 1 /, where $y_i = 1$ was assumed a priori.

References:

1. В.А.Гольяк, Физика плазмы, 2, 141, 1976.
2. В.А.Годяк, О.А.Попов, А.Н.Нанна, Proc. XIII Int. Conf. Phenom. Ioniz. Gases, p. 347, Berlin, 1977.

USE OF EMITTED PHOTONS AS A PROBE FOR LOW PRESSURE GAS DISCHARGES

J. Fletcher and H.A. Blevin.

Institute for Atomic Studies, The Flinders University of South Australia, Bedford Park, 5042, South Australia.

Conventional methods of studying the behaviour of isolated electron swarms and electron streams are complicated by the effect of electrode boundaries on the variable being measured. In recent years several authors (Lowke 1962, Lucas 1966, and Skullerud 1974) have shown that the presence of metal electrodes in the region of immediate interest can modify the electron swarm parameters sufficiently for spurious results to be achieved. Indeed a further non-equilibrium effect near to the cathode due to the electron injection energy distribution being markedly different from the equilibrium distribution, does not lend itself to useful theoretical treatment and hence must be either eliminated or ignored in any experiments.

One of the few methods of obtaining information about the behaviour of electron swarms drifting through a low pressure (≈ 1 torr) gas under the influence of an electric field is to study the photon flux emitted by the swarm following electron-molecule excitation collisions. This technique was first suggested by Corrigan and von Engel (1958) and further used by Brere and von Engel (1964). The photon counting techniques used in this early work were primitive, however, resulting in poor statistics and large errors. Developments in photon detection and pulse manipulation during the intervening years have made the method a viable and indeed an accurate technique.

Details of the present experimental method have been published (Blevin et al 1976 a,b,c, 1978

a,b).

RESULTS

The crucial factor involved in these experiments is the relationship between the photon flux and the electron density integrated along the line of sight of the collimator. An exhaustive Monte-Carlo treatment of this problem in hydrogen has shown that, in hydrogen, the photon flux distribution is of the same shape as the electron density distribution although the former slightly leads the latter by a constant time interval (Hunter, 1977, Blevin *et al* 1978c). Hence the measured photon distribution may be used to calculate the drift and diffusion parameters of the electron swarm.

In order to eliminate the cathode effects an arbitrary zero position ($z = z_0$, $t = t_0$) is taken at an axial z position near the beginning of the equilibrium region, ($z \approx 3$ cms). The solution of the continuity equation given by Huxley (1972 a,b) has been modified to allow for this and gives a value of the integrated photon flux along the line of sight of the collimator N_ϕ as

$$N_\phi(y, z, t) = \frac{N_0 \exp \left[- \frac{[y^2 / (4Dt' + R^2)]}{[(4\pi Dt' + \pi R^2)(4\pi D_L t' + \pi Z^2)]^{1/2}} \right]}{\exp \left[- \frac{(z' - Wt')^2}{4D_L t' + Z^2} \right]} \quad (1)$$

In the above R and Z are the radial and longitudinal half-widths respectively at the $1/e$ height of the distribution at the arbitrary zero position, $t' = t - t_0$, $z' = z - z_0$.

For the measurement of W and D_L $y = 0$ in equation 1 i.e. on axis distributions are measured. The experimental technique is then to measure distributions at z_0 and at about six axial positions further down the drift tube. W and D_L are then obtained by curve fitting equation 1 with $y = 0$ to the experimental distribution.

Transverse diffusion coefficients can be determined by scanning the collimator across the swarm at one value of z . In this case, (Blevin *et al* 1978a).

$$\ln[N'_\phi(y, z)/N_\phi(0, z)] = -y^2/4D_L z$$

The present technique also lends itself to the measurement of ionization coefficients. (Blevin *et al* 1978a).

HYDROGEN

Data on the values of W , D_L , D_t and α/N as a function of E/N in the range $45 \leq E/N \leq 180$ Td in hydrogen along with the Monte Carlo simulations of the discharge have now been published (Blevin *et al* 1976 a,b,c, 1978 a,b,c : Hunter, 1977) and are included here for completeness.

NITROGEN

The electron drift velocity, the diffusion coefficients and the ionization coefficients have all been measured in spectroscopically pure nitrogen. These data are currently being analyzed and will be presented.

HELIUM

The present technique is currently being applied to pure helium and while only preliminary results are available at present it is evident that secondary electron emission plays an important role in the helium discharge. The progress in helium will be reported.

SECONDARY ELECTRON EMISSION

The present technique also enables a direct

study to be made of secondary electron emission from the cathode. Most previous methods have been indirect and have involved approximations in the theoretical analysis of the experimental results.

In hydrogen only two secondary mechanisms are possible, ultra-violet photon bombardment of the cathode and ion impact on the cathode. Since those secondary electrons produced by photon bombardment will occur very soon after the primary pulse ($<1.0 \mu s$) while those produced by ion impact will be released approximately one ion transit time ($\sim 20 \mu s$) later the contribution of each to the total secondary emission can be detected.

The results for hydrogen so obtained will be presented. A clear "threshold" for secondary ionization by positive ion impact is observed at $E/N \approx 200$ Td.

It is believed that this is due to the production within the discharge of H^+ ions at $E/N \leq 200$ Td and that these atomic ions are much more efficient at producing secondary electrons than the H_3^+ ions which are the only species present for $E/N < 200$ Td. Further experiments to verify this postulate are now in progress.

REFERENCES

- Blevin H.A. *et al* 1976 a,b,c J. Phys. D 9 465; Ibid 9' 1471, Ibid 9, 1671.
 Blevin H.A. *et al* 1978 a,b,c J. Phys. D 11, 2295;
 Ibid 11 1653; Austr. J. Phys. 31 299
 Hunter S.A. 1977 Austr. J. Phys. 30 83.
 Lowke J.J. 1962 Austr. J. Phys. 15 39.
 Lucas J 1966 Int. J. Electron 6 535.
 Skullerud H.R. 1974 Austr. J. Phys. 27 195.
 Huxley 1972 a,b. Austr. J. Phys. 25 43; Ibid 25, 523

THE ROLE OF MOLECULAR LINES IN THE STUDY OF PLASMA SATELLITES

A. Piel, F. Pinnekamp.

Ruhr-Universität Bochum, Institut für Experimentalphysik II, Bochum, Germany F.R.G.

The measurement of fluctuating electric fields in plasmas by means of the high frequency Stark effect has attracted much attention during the last decade. Since the intensities of the high frequency plasma satellites hardly exceed 1% of the main line intensity these structures have to be carefully separated from impurity lines. Recently Ramette and Drawin /1/ reported plasma satellites on H_{β} . Contrary to that structures on the 447.15 nm helium line measured under similar conditions by the same authors /2/ were interpreted as being due to helium molecular lines. Repeating these experiments we obtained very different results.

Experimental

The experimental set-up (fig. 1) is similar to that in ref. /1,2/. The light from the discharge tube ($l = 470\text{mm}$, $d_1 = 24\text{mm}$, Al electrodes) is observed end-on. The whole spectrum is recorded simultaneously during one shot on a 500 channel multichannel analyzer (OMA) which replaces the exit slit of a $f=1\text{m}$ grating spectrometer. The exposure time was typically $1\text{ }\mu\text{s}$ and the spectral resolution amounts to 0.024nm .

Hydrogen discharge

A typical line profile of H_{β} recorded in the afterglow $6\text{ }\mu\text{s}$ after shortcircuiting is shown in fig. 2. The discharge conditions ($I_0=600\text{A}$, $p_0=500\text{Pa}$) were very similar to those in ref. /1/. Several structures appear on the line profile which coincide with the positions of hydrogen molecular lines taken from the wavelength tables of Dieke /3/. The intensity of the structures clearly exceeds the statistical error. 25 molecular lines could be identified. In order to determine the exact positions of possible plasma satellites at $\pm \omega_p$ the plasma density was derived from Langmuir probe data and the slope of the H_{β} line wing /4/. Both methods show good agreement, yielding an electron density of $n_e = 1 \cdot 10^{21}\text{ m}^{-3}$ at the instant of exposure. Plasma satellites are therefore expected to occur at $\Delta\lambda = \pm 0.224\text{ nm}$, but weak structures at these positions are more likely to arise from molecular lines. In addition the plasma satellites should be subject to the same Stark broadening as the main line. Therefore the sharpness of the structures reported in ref. /1/ supports the interpretation as molecular lines.

Experiment ARTUR

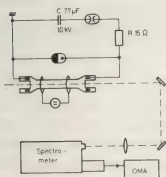


Figure 1: Experimental set-up

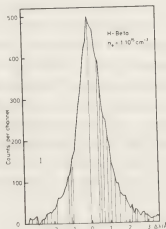


Figure 2: Hydrogen discharge

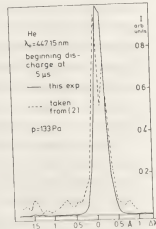


Figure 3: Helium discharge

Helium discharge

We repeated the measurements of /2/ at exactly the same discharge conditions. The profile shown in fig. 3 is an average over 80 individual shots (error bars within drawing accuracy). No structures could be registered, also at later times no structures appeared. As the peaks in /2/ were interpreted as being due to He_2 molecular lines we tried to measure optical transitions of the He_2 molecule and looked for the intense $e^3 \Pi_g^- \rightarrow a^3 \Sigma_u^+$ band at 465.0 nm. Even with an entrance slit of 1 mm width of the spectrometer and by integrating the light of the whole time of the discharge, these strong molecular lines could hardly be detected. Using a stationary RF-discharge He_2 lines are registered (fig. 4) and their intensity is shown in fig. 5 as a function of the pressure. In this discharge molecular lines in the 447.1 nm region are very weak and reach 10^{-4} of the 447.15 nm line of He at best. Therefrom we conclude that helium molecular lines do not affect the He line at 447.15 nm at pressures below 100 Pa, $n_e < 10^{20} \text{ m}^{-3}$ and $T_e \approx 4 \text{ eV}$ in this linear pulsed discharge.

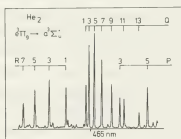


Figure 4: Helium RF-discharge

On the other hand very small amounts of hydrogen in the helium discharge change the molecular spectrum drastically. In a tube contaminated with hydrogen before the He_2 spectrum is completely suppressed at 465 nm and a strong hydrogen molecular spectrum occurs. From our experiments and the fact that practically all peaks in Drawins measurement /2/ coincide with hydrogen molecular lines, the interpretation of these structures as being due to hydrogen molecules seems to be more adequate, provided the discharge tube in /2/ has been in contact with hydrogen before.

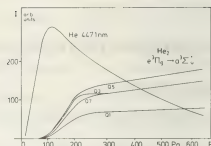


Figure 5: Intensity of helium molecular lines as a function of filling pressure

Conclusions

For this type of discharge it will be very difficult to distinguish between observations of plasma satellites and molecular lines in hydrogen discharges, since molecular lines will at least arise from boundary layers of the plasma. On the other hand we could verify that helium molecular band spectra do not affect the study of plasma satellites on helium atomic lines in helium discharges. In addition helium molecular lines will be of even less importance at lower pressures, which are typical for turbulent heating experiments. Hydrogen impurities in helium discharges, however, may be of great influence.

References

1. J. Ramette, H.W. Drawin
Z. Naturforsch. **31a**, 401 (1976)
2. H.W. Drawin, J. Ramette
Z. Naturforsch. **33a**, 1285 (1978)
3. H.M. Crosswhite, The Hydrogen Molecular Wavelength tables of Gerhard Heinrich Dieke
Wiley Intersci., New York 1972
4. A. Piel, H. Richter
accepted by Z. Naturforsch. for publication

ON THE APPROXIMATIVE SEMICLASSICAL FORMULA FOR THE ELECTRON-IMPACT WIDTH OF MULTIPLY IONIZED ATOM LINES IN PLASMAS

M. Dimitrijević and N. Konjević.

Institute of Applied Physics, 11001 Beograd, P.O. Box 24, Yugoslavia.

Introduction. For evaluation of Stark widths and shifts of non-hydrogenic spectral lines of ionized atoms, various theoretical approaches have been used (see e.g. ref. 1): semiclassical, quantum mechanical, semiempirical and approximative semiclassical. The experimental results for singly ionized atom line widths and shifts are generally in fairly good agreement (within $\pm 20\%$) with the comprehensive semiclassical calculations of Griem and coworkers¹⁾. Quantum mechanical calculations of Stark broadening parameters has been performed only for singly ionized earth alkaline metals (see e.g. ref. 1). Both theoretical approaches, semiclassical and quantum mechanical are very laborious and therefore not very practical for evaluation of large number of line widths. Tedious calculations can be avoided if one uses simple semiempirical formula¹⁾ which, for singly ionized atoms, agrees with the experiment in average within $\pm 50\%$. For multiply ionized atoms the agreement becomes worse what indicates that further theoretical effort has to be made to extend the application of this approach to higher ionization stages. Another approximative semiclassical approach has been suggested by Griem¹⁾ for the evaluation of Stark line widths of multiply ionized atoms. The theoretical results have been compared¹⁾ with the experimental results for CIII and CIV²⁾ which, at that time, were only reliable data. In the mean time a number of experimental results for the prominent lines of AlIII and AlIV³⁾, NiIII⁴⁾, OIII⁵⁾, SiIII^{6,7)} and SiIV⁷⁾ and ClIII⁸⁾ become available.

The aim of this paper is to test approximative semiclassical theoretical approach with available experimental data. It will be also proposed modification of approximative semiclassical formula and theoretical results obtained in this way are also compared with the experiment.

Theory: First, theoretical line widths were calculated from the proposed equation¹⁾ which includes lower level broadening in the weak collision terms:

$$W = N_e \tilde{v} \left[(\sigma_{\ell, \ell+1}^i + \sigma_{\ell, \ell-1}^i + \sigma_{\ell, \ell+1}^f + \sigma_{\ell, \ell-1}^f) \Delta n = 0 + \left(\sum_i \sigma_{i, i-} + \sum_f \sigma_{f, f-} \right) \Delta n \neq 0 \right] + \frac{8\pi}{3} \tilde{\lambda}^2 \frac{3n_i^4}{4Z^2} + \frac{3n_i^2}{4Z^2} \frac{kT}{E_H} \left(1 + \frac{kT}{E_H} + \frac{Z^2}{n_i^4} - 1 \right) \quad (1)$$

where N_e , T and \tilde{v} are electron concentration, temperature and average velocity respectively, $\tilde{\lambda}$ is the electron de Broglie wavelength divided by 2π , k is the Boltzman constant, E_H is the ionization energy of hydrogen, Z is the charge of the emitter which the optical electron "sees" ($Z=1$ for neutral, 2 for singly ionized atoms etc.) and n_i^* is the effective principal quantum number for initial (i) and final (f) level of the transition:

$$n_j^{*2} = Z^2 \frac{E_H}{E_{ion} - E_j} \quad (2)$$

where E_{ion} is the ionization energy for the considered series of terms and E is the energy of the level j .

First term on the right-hand side of eq. 1 are cross sections for weak collisions due to $\Delta n = 0, \ell \rightarrow \ell \pm 1$ dipole transitions, the second term gives contribution from the inelastic collisions for $\Delta n \neq 0$ perturbing levels and the last two terms are the strong collision and higher order interaction corrections:

$$\sigma_{\ell, \ell-}^j = \frac{8\pi}{3} \tilde{\lambda}^2 \left(\frac{3n_j^2}{2Z} \right)^2 \frac{\max(\ell, \ell-)}{2\ell+1} \left[n_j^{*2} - \max(\ell, \ell-) \right] v^2 \cdot \cdot \ell n \left\{ 5 - \frac{4.5}{\sqrt{Z}} + \varepsilon_{\ell, \ell-}^{-1} \left[1 + \frac{kT}{E_H} \frac{n_j^{*2}}{(Z-1)Z} \right]^{-1} \right\} \quad (3)$$

$$\varepsilon_{\ell, \ell-} = \frac{(Z-1)e^2 \omega_C}{mv^3} \quad (4)$$

$$\omega_c = \max(|\omega_L, \omega_p|), \quad \omega_p = \sqrt{\frac{4\pi N e^2}{m}}, \quad \omega_F = \frac{2Z^2 \alpha \omega_0}{3n^2}, \Delta\omega_i$$

$$= 4n^2 \left(\frac{\hbar}{mZ} \right) \left(\sum z_p^{3/2} N_p \right)^{2/3} \quad (5)$$

$$\left(\sum_{j,j'} \sigma_{jj'} \right) \Delta n \neq 0 = \frac{2\pi}{3} x^2 (n_j^2 + 3z_j^2 + 3z_j + 1) \cdot \ln(1.4 +$$

$$+ \frac{(kT_e)^{3/2}}{E_H^2 (Z-1)} \left[1 + \frac{kT_e n_j^2}{E_H (Z-1) Z^2} \right]^{-1} \quad (6)$$

where Ψ is the factor from Bates and Damgaard²⁾, ω_p is the plasma frequency, ω_F the fine structure splitting, α is fine structure constant, ω_0 is the unshifted angular frequency, $\Delta\omega_i$ is the ion splitting and Z_p and N_p are the charge and concentration of perturbing ions, respectively.

For transitions $\Delta n = 0$ in eq. 1 Gaunt factors at a threshold are taken variable ($g = 0.9-1.1/Z$) and larger than $0.2^{1)}$. We have modified weak collision term of eq. 1 (eq. 3) for $\Delta n = 0$ transitions by replacing $(5-4.5/Z)$ with the constant value of 1.4 what corresponds to the constant Gaunt factor of 0.2.

Results and discussion: The ratio of the theoretical and experimental results are given in Table 1. In this table W_u and W_m are the results obtained from unmodified and modified eq. 1. For the sake of the comparison, the results from Griem's semi-empirical formula are also given under W_{se} . From the table it is obvious that modified eq. 1 agrees best with the experiment

Table 1. Average ratios of theoretical W_u , W_m and W_{se} , and experimental halfwidths.

element	$T_e [K]$	$\left(\frac{W_u}{W_{exp}} \right)_{av.}$	$\left(\frac{W_m}{W_{exp}} \right)_{av.}$	$\left(\frac{W_{se}}{W_{exp}} \right)_{av.}$
AlII	21100	1.48	1.00	0.64
AlIV	20750	1.87	1.12	0.82
ClII	60000	0.94	0.90	0.76
ClIV	60000	1.20	0.60	0.40
SiIII	16400	2.22	1.39	0.90
SiIII	25600	2.21	1.53	0.94
SiIV	25600	2.03	1.20	0.87
OIII	25900	1.39	0.99	0.53
ClIII	24200	2.38	0.94	0.58
NIII	24300	1.58	0.10	0.62
averaged values		1.56	1.04	0.69

References:

1. Griem, H.R.: Spectral Line Broadening by Plasmas, Academic Press, London (1974)
2. Bogen, P., Z.Naturforsch. 27A, 210 (1972)
3. Platiša M., Popović, M., Dimitrijević, M., Konjević, N., Z.Naturforsch. 30A, 212 (1975)
4. Platiša, M., Popović, M., Konjević, N., Astron. Astrophys. 41, 463 (1975).
5. Platiša, M., Popović, M., Konjević, N., Astron. Astrophys. 45, 325 (1975)
6. Purić, J., Djeniže, S., Labat, J., Ćirković, Lj., Z.Phys. 267, 71 (1974)
7. Platiša, M., Dimitrijević, M., Popović, M., Konjević, N., J.Phys.B: Atom.Molec.Phys. 10, 2957 (1977)
8. Platiša, M., Dimitrijević, M., Popović, M., Konjević, N., Astron.Astrophys. 54, 837 (1977)
9. Bates, D.R. and Damgaard A., Phil.Trans.Roy. Soc., London 242A, 101 (1949).

ETALONNAGE D'UNE CHAÎNE DE DIFFUSION EN VUE DU DIAGNOSTIC DES PLASMAS

Y. Alayli* and M. Skowronek.

Laboratoire de Physique et Optique Corpusculaires (Plasmas Denses), Université Pierre et Marie Curie
Tour 12, E5, 75230 Paris, Cedex 05, France.

*Université Libanaise, Département de Physique, Beyrouth-Liban.

1 - Introduction

La diffusion Thomson d'un faisceau laser est souvent utilisée pour mesurer la densité électronique et la température des plasmas.

La température est déduite de l'élargissement Doppler de la radiation diffusée alors que la densité électronique est déduite de la mesure de l'intensité totale intégrée sur toutes les longueurs d'onde et exige une calibration absolue de la chaîne de diffusion. On utilise pour cela la diffusion Rayleigh dans les gaz dans les mêmes conditions géométriques. Cependant certaines mesures absolues de section efficace de diffusion effectuées avec un laser à rubis montrent un désaccord avec les valeurs théoriques: George et al [1] trouvent des valeurs deux fois plus grandes à 60° de la direction de propagation du faisceau laser incident, Skowronek et al [2] trouvent des valeurs deux fois plus petites à 90° et avec des impulsions lasers brèves.

Dans une récente publication [3] nous avons montré que la section efficace de diffusion Rayleigh dépend de la largeur d'impulsion Δt suivant l'expression :

$$\frac{S_{\text{exp}}}{S_{\text{th}}} = \frac{\tau_1}{\tau_0} \left(1 - \exp - \frac{\Delta t}{\tau_0} \right) \quad (1)$$

où S_{exp} et S_{th} sont respectivement les sections efficaces expérimentale et théorique,
 $\tau_1 = \frac{3}{2} \cdot \frac{\epsilon_0 m c}{\pi e^2} \cdot \lambda^2$ est le terme d'amortissement due à l'émission de la lumière et τ_0 est une constante de temps. Les résultats expérimentaux sont représentés sur la figure 1, la durée d'impulsion va de 6 ns à 200 ns.

[1] T. V. George, L. Goldstein, L. Slama, M. Yokoyama Phys. Rev., **137A**, 369 (1965)

[2] Skowronek, Y. Vitel, Y. Alayli, C. Bayer, Phys. Lett. **51 A**, 107 (1975)

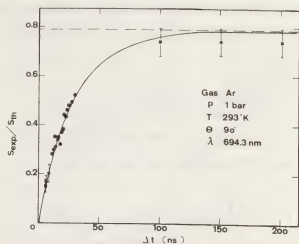


Fig. 1 : Variation de $S_{\text{exp}}/S_{\text{th}}$ avec la durée d'impulsion Δt .

La courbe représente l'expression (1)

2 - Résultats expérimentaux

Dans un premier temps, la diffusion de la lumière à 90° de la direction de propagation du faisceau laser incident a été étudiée. Les sections efficaces de diffusion ont été mesurées à différentes longueurs d'onde (651,7 nm; 594,2 nm et 481,5 nm) à l'aide d'un laser à colorants accordable; la durée des impulsions lumineuses varie peu autour de 2 ns. On a également utilisé la longueur d'onde du laser à azote de pompe (337,1 nm) dont la durée d'impulsion est de 4 ns. La forme de l'impulsion délivrée par le laser à colorants est soigneusement étudiée pour tenir compte de l'effet de la présence d'une base large qui rend difficile la définition d'une durée d'impulsion. La constante de temps τ_0 est proportionnelle au carré de la longueur d'onde comme l'est τ_1 , le rapport τ_1/τ_0 est donc indépendant de λ . Les résultats expérimentaux sont représentés sur la figure 2. Pour des impulsions de longue durée la variation en $1/\lambda^4$ de

la section efficace expérimentale est vérifiée. La variation de la section efficace de diffusion avec l'indice de réfraction a été étudiée (dans 15 gaz différents) ; la formule (1) permet de déterminer pour chaque gaz une constante de temps, elle est proportionnelle au diamètre moléculaire de Lennard-Jones. Les résultats sont représentés figure 3.

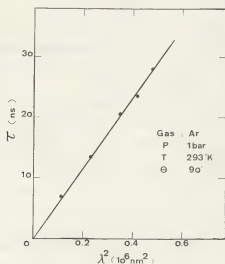


Fig. 2 : Variation de la constante de temps avec le carré de la longueur d'onde

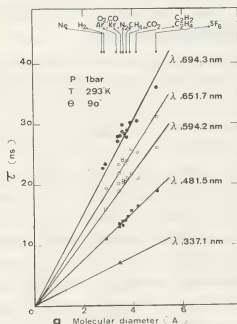


Fig. 3 : Variation de la constante de temps avec le diamètre moléculaire de Lennard-Jones

La répartition angulaire de l'intensité diffusée a été ensuite étudiée. Le gaz utilisé est l'argon et la source de lumière est le laser à rubis déclenché $\Delta t \approx 30$ ns. Le volume diffusant est proportionnel à $1/\sin\Theta$ (Θ est l'angle de diffusion) ce qui a été vérifié. L'indicatrice de diffusion déterminée par George et al [1] est recalculée en tenant compte de la correction du volume diffusant, ses résultats sont en bon accord avec les nôtres pour des durées d'impulsion longues. Pour chaque angle Θ , une constante de temps est déterminée par (1); elle est proportionnelle à $\sin\Theta/2$; les résultats sont représentés sur la figure 4.

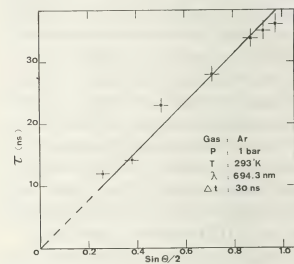


Fig. 4 : Variation de la constante de temps avec $\sin\Theta/2$.

3 - Conclusion

Nous avons étudié la diffusion de la lumière par des techniques qui nous ont permis de mettre en évidence l'influence de l'échange de quantité de mouvement entre les photons incidents et les photons diffusés.

Nous avons montré quelles sont les limitations de l'étalonnage d'une chaîne de diffusion Rayleigh, mais nous ne savons pas jusqu'à présent dans quelle mesure la diffusion Thomson elle-même est affectée par les durées brèves des impulsions des lasers de diagnostic.

[3] Y. Alayli et M. Skowronek, Symposium on Physics of Ionized Gases, Cont. pap., p. 379, Ed. Navinsek, Dubrovnik (1976)

METAL ATOM DENSITY BY ATOMIC ABSORPTION SPECTROSCOPY IN A D.C. SPUTTERING DISCHARGE

C. Fourier, G. Lempriere and J.M. Poitevin.

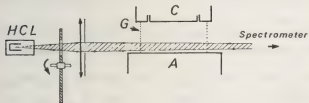
Laboratoire de Physique Corpusculaire, Institut de Physique, 2, rue de la Houssinière, 44072 Nantes Cedex, France.

INTRODUCTION — At the present time, the use of atomic absorption spectroscopy for concentration measurements of a metal vapour in sputtering glow discharges is not widely developed. We shall present here some specific problems which arise when this method is used in a d.c. sputtering discharge, and on the base of results concerning the titanium we shall show what kind of information one can obtain.

EXPERIMENTAL SET-UP — DISCHARGE CHARACTERISTICS.

The d.c. diode sputtering apparatus has been previously described [1]. The gap between the movable electrodes is 30 mm. The abnormal discharge sustained at an argon pressure of 80×10^{-3} Torr shows a well-developed cathodic glow, followed by a dark space with its boundary at ~ 9 mm from the cathode and a negative glow (NG) spreading up to the anode (A).

Fig. 1



The titanium atoms of the target (C) are ejected as a result of bombardement by gas ions from the discharge. These sputtered atoms are scattered and diffuse through the discharge chamber ($\phi = 370$ mm) most of them being deposited on the anode. The light source is a titanium hollow cathode lamp (HCL). The spectrometer has a resolving power of 0.1 \AA .

MEASUREMENTS OF THE POPULATION DENSITIES OF THE a^3F LOWER STATE — We employ the method of absorption of lines [2]

$$N_i \left[1 - \frac{g_i}{g_k} \frac{N_k}{N_i} \right] = \frac{mc}{\sqrt{\pi} e^2} \frac{V_P}{\lambda_o f_{ik}} \frac{(k_o^D \ell)}{\ell}$$

- 1) A grid (G) at the anode potential limits the diffusion zone and defines the length ℓ of the absorbing layer.
- 2) We measure the population densities N_i of the lowest triplet term a^3F_2 , a^3F_3 , a^3F_4 (0.00 ; 0.021; 0.048 eV). The small excitation temperature implies that $\frac{N_k}{N_i}$ is negligible for the observed transitions. We have measured $T_{exc} = 0.2 \text{ eV}$ at any discharge power P.
- 3) Interferometric measurements have shown that the resonance lines have no significant hyperfine structure [3].
- 4) Titanium atomic lines near the target are broadened ($\sim 0.3 \text{ \AA}$) (Most probable ejection energy = 3.3 eV). A narrowing of their width is observed through the dark space. Thus the metal atoms have a decreasing temperature from C to A. The reported measurements have been made on-axis, 5 mm from the anode where the titanium atoms are thermalized. ($T = 425 \text{ K} + V_P$).
- 5) The knowledge of α , ratio of the Doppler widths in the HCL and in the discharge is necessary for the obtention of $k_o^D \ell$. Because the radiation of the excited atoms close to A is proportional to the discharge power P [1], $k_o^D \ell$ must be proportional to P. This implies $1.4 < \alpha < 1.6$. Double path method measurements have shown that $\alpha > 1.2$ at 15 mm from C.

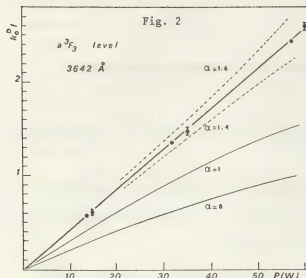
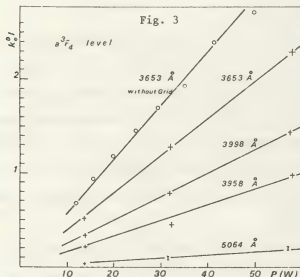


Fig.2 shows the results obtained from 3642Å and emphasizes the error made on the variation law and the population densities if one assumes $\alpha = 0$ or $\alpha = 1$.



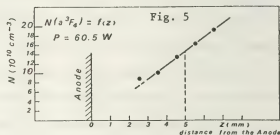
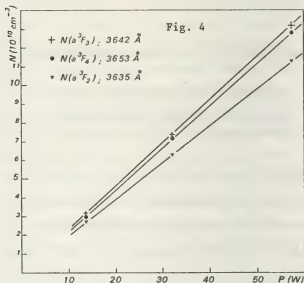
The results for a^3F_4 , obtained from several resonance lines are reported on figure 3. An identical work has been made for a^3F_2 and a^3F_3 .

6) The values of the absolute oscillator strengths f_{ik} are widely dispersed (50 to 100%). Only the $a^3F-y^3F^o$ transitions give consistent results. Using the data of Whaling [4] for these transitions we deduce other f_{ik} values from our results.

Fig. 4 gives the mean population densities. For 60W the population density of the three levels, 5 mm away from the anode reaches $\sim 4 \times 10^{11} \text{ cm}^{-3}$. Fig.5 shows the concentration gradient near the anode.

The deposition rate of ground state atoms which

can be deduced is $\sim 5 \times 10^{14} \text{ cm}^{-2} \cdot \text{s}^{-1} = 9 \times 10^{16} \text{ cm}^{-2} \cdot \text{min}^{-1}$.



Gravimetric measurements have given a deposition rate of $11-13 \times 10^{16} \text{ cm}^{-2} \cdot \text{min}^{-1}$ [1]. For $T=500\text{K}$ we would have obtained $12 \times 10^{16} \text{ cm}^{-2} \cdot \text{min}^{-1}$.

CONCLUSION - The foregoing example illustrates the difficulties to obtain accurate density values. More precisely the knowledge of the Doppler breadths of the emission line and the absorption line is needed if correct variation laws are to be deduced. We think that the limitation of the absorption length and the determination of the excitation temperature have allowed the obtention of satisfactory results concerning the correlation between the ground state atom density and the deposition rate.

REFERENCES

- [1] J.M. POITEVIN, G. LEMPERIERE, C. FOURRIER - J. Phys. D : Appl. Phys., Vol. 9, (1976) 1783.
- [2] MITCHELL and ZEMANSKY - Resonance Radiation and excited atoms. Cambridge University Press, p.122.
- [3] H.C. WAGENAAR and L. DE GALAN - Spectrochimica Acta, Vol.28 B (1973) 157.
- [4] W. WHALING, J.M. SCALO and L. TESTERMAN - The Astrophysical Journal, 212 (1977) 581.

POSITIVE ION EXTRACTION BY AN ANODIC ORIFICE PROBE

H.G. Lergon and K.G. Müller.

*Fachbereich Physik, Universität Essen-Gesamthochschule, 43 Essen, Fed. Rep. of Germany.*Abstract

From a nonthermal plasma ions are extracted by an orifice probe being anodic, i.e. positive with respect to plasma potential. In front of the orifice a secondary plasma is observed providing an intense source for ion extraction. The extraction mechanism can be explained by a potential of the secondary plasma above probe potential. The thermal energies of the ions from the secondary plasma are of the order of 1/10 eV.

Introduction

The extraction of positive ions from a plasma by an orifice probe is strongly influenced by the potential of the probe. Increasing it and thus changing from cathodic to anodic probe the extracted ion current drops to small or even negligible values, until it finally rises again (see e.g. Pahl, Lindinger, Howorka ¹). This current increase has been explained by ionization in the orifice or the adjacent region behind. A corresponding mass analysis of the ions has been recommended for the investigation of the neutral gas. In own experiments we find an increase of the collected ion current up to values an order of magnitude larger

than those for cathodic probes. Parallel to this effect the formation of an intense secondary plasma in front of the anodic probe can be observed. Apparently the secondary plasma provides an ion source. In the following the ion extraction from this ion source will be investigated.

Experiment

The nonthermal plasma of a positive column in Argon is analyzed by a combined mass spectrometer - probe diagnostic (see Lergon and Müller ²). By an orifice probe ions are extracted into a mass spectrometer allowing a retarding field analysis of ion energy. The experimental parameters are: discharge diameter 2,8 cm; pressure 0,056 mbar; discharge current 30 mA; orifice probe diameter 0,62 cm; orifice diameter 50 μ m; orifice depth 50 μ m. By this diagnostic the probe characteristic, probe current I_p versus probe voltage U_p , and the $^{40}\text{Ar}^+$ -characteristic, ion current I_+^{40} versus probe voltage U_p , are measured (see Fig.1). By a retarding voltage of a few volts the low energy component, attributed to the secondary plasma (subscript: sec) can be suppressed and thus separated from the high energy component, attributed to the main plasma (subscript:

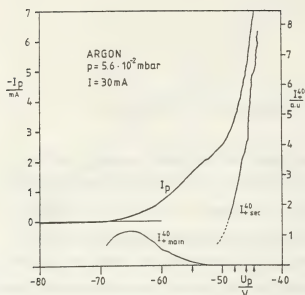


Fig. 1: Probe characteristic $I_p(U_p)$, ion characteristics $I_+^{40}(U_p)$ of high energy component (subscript: main) and low energy component (subscript: sec)

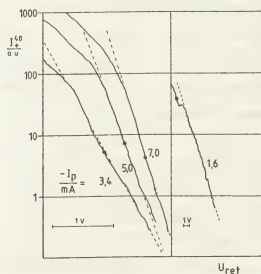


Fig. 2: Retarding field characteristics $I_+^{40}(U_{ret})$ for different probe currents I_p ; a: $U_{ret} = \text{const}$ (reference voltage).

main). For a set of probe voltages, in Fig. 1 indicated by arrows, retarding field characteristics, i.e. current I_+^{40} versus retarding voltage U_{ret} , are taken (see Fig. 2).

Discussion

The high energy component I_{+main}^{40} of Fig. 1 is attributed to ions stemming from the main plasma, being heated up in the pre-sheath in front of the wall². Their temperature agree with the electron temperature at the wall (see Table 1). The low energy component, attributed to the secondary plasma, shows temperatures in the range of 1/10 eV/k, falling with increasing U_p . Assuming a potential distribution possessing a flat maximum in the secondary plasma and a positive sheath in front of the probe the usual extraction mechanism exists. Thus for an anodic orifice probe the existence of an additional ion source, provided by the secondary plasma, has to be taken into account.

method	temperature	plasma
probe characteristic	$T_e = 1,3 \text{ eV}$	main
ion characteristic	$T_+ = 1,2 \text{ eV}$	
retarding field characteristic at $-I_p = 1,6 \text{ mA}$	$T_+ = 1,3 \text{ eV}$	
at $-I_p = 3,4 \text{ mA}$	$T_+ = 0,24 \text{ eV}$	secondary
at $-I_p = 5,0 \text{ mA}$	$T_+ = 0,16 \text{ eV}$	
at $-I_p = 7,0 \text{ mA}$	$T_+ = 0,13 \text{ eV}$	

Table 1: Ion and electron temperatures, measured by different methods²

Acknowledgements

This work has been supported by Ministerium für Wissenschaft und Forschung des Landes Nordrhein-Westfalen.

References

- 1 M. Pahl, W. Lindinger, F. Howorka, Z. Naturforsch. 27a, 678 (1972)
- 2 H.G. Lergon, K.G. Müller, Z. Naturforsch. 32a, 1093 (1977)

MEASUREMENT OF ELECTRON DENSITY BY ELECTROMAGNETIC WAVES WHICH PROPAGATE ON A MAGNETIZED PLASMA COLUMN

D.M. Šulić.

Geomagnetic Institute - Grocka, Yugoslavia.

INTRODUCTION

The determination of electron densities in plasmas from surface wave propagation data has been performed by Ilić /1/. In this paper we describe an extension of this technique to axially magnetized plasma columns.

EXPERIMENTS

Axially symmetric waves have been launched and propagated on the long positive column of a sealed-off mercury vapour diode. The tube is centered in a magnetic bench producing a nearly homogeneous axial magnetic field (Fig.1).

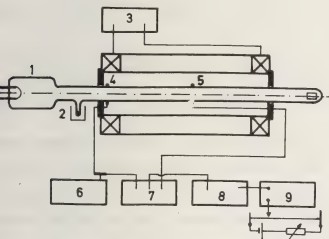


Fig.1. Discharge tube (1), Thermostatic bath (2), Power supply for magnetic bench (3), Coaxial launcher (4), Receiver (5), Signal Generator (6), Balance mixer (7), Selective amplifier (8), X-Y recorder (9).

Measurements were made at constant mercury vapour pressure of 1.2×10^{-3} torr and at various values of magnetic induction which was varied from 0 to 46,1 mT. The oscillator frequency was changed in steps of 10 MHz from 461 Gauss. The discharge current was either 50 mA or 100 mA.

The wavenumber k was determined from chart recorder plots of wave patterns obtained with the aid of an interferometer involving a balanced mixer.

THEORY AND INTERPRETATION

The dispersion relation of axially symmetric electromagnetic waves on an axially magnetized plasma column of radius a enclosed in a glass tube of outer radius b and surrounded by free space is derived from approximation and boundary conditions and reads

$$-E_1 \sqrt{-\frac{\epsilon_1}{\epsilon_1}} \frac{J_1(ak) \sqrt{\frac{\epsilon_1}{\epsilon_1}}}{J_0(ak) \sqrt{\frac{\epsilon_1}{\epsilon_1}}} = E_r \frac{K_1(ak) - \frac{K_0(ak)}{\epsilon_r - 1} \left[\frac{J_0(bk)}{J_0(bk)} + \epsilon_r \frac{J_1(bk)}{K_1(bk)} \right]}{J_0(ak) + \frac{K_0(ak)}{\epsilon_r - 1} \left[\frac{J_0(bk)}{J_0(bk)} + \epsilon_r \frac{J_1(bk)}{K_1(bk)} \right]}$$

The plasma is assumed to be cold, lossless and homogeneous. The notation is as follows: $\omega_p^2 = \frac{e^2 n}{m \epsilon_0}$ and $\Omega = \frac{e B}{m}$ are electron plasma and cyclotron frequencies, $\epsilon_1 = 1 - \frac{\omega_p^2}{\omega^2 - \Omega^2}$, $\epsilon_{\parallel} = 1 - \frac{\omega_p^2}{\omega^2}$ are respectively the normal and parallel components of the dielectric tensor, and $\epsilon_r = 4.8$ is the dielectric permittivity of the tube glass. The notation for the various Bessel functions is standard. The ratio of outer and inner glass radii b/a is 1.28.

The dispersion relation was solved by running an appropriate computer program /2/. Depending on the radial structure of the plasma, an infinite number of axially symmetric modes exist. Of these only the lowest mode is actually excited with launchers located outside the plasma. The excitation of higher axially symmetric modes would necessitate launchers within the plasma to approximate the radial variations of these modes, which involves several half wave variations along the radius.

The dispersion relation of the lowest mode is found as a family of curves of the type $\omega/\omega_p = f(ak)$ with Ω/ω_p as a parameter. The main difficulty of the method is that a change in the magnetic field causes both a change in electron density and in the parameter Ω/ω_p . This was circumvented by running an iteration process which departs from assumed values of electron density.

The consistency of the method was tested by plotting electron plasma density vs. arc current (Fig 2). With a fixed magnetic field, the electron temperature is constant and electron density should consequently be a linear function of arc current.

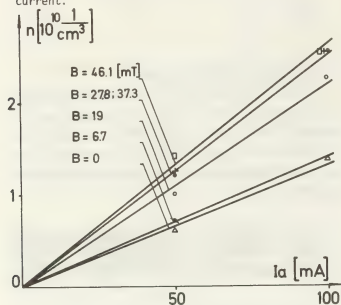


Fig 2.

Figure 3 is a plot of electron density vs. magnetic induction. This provided another check of consistency, as it was possible to prove that plasma luminosity varies with magnetic field in very much the same way.

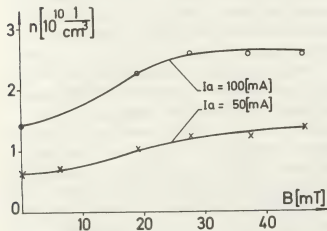


Fig 3.

CONCLUSION

In although many refinements of the interpretation of wave data could be suggested, eg. to include plasma inhomogeneity, warm and hot plasma effects it appears that the simple magneto-ionic theory in the quasistatic version reflects most of the salient features of the experiment.

ACKNOWLEDGMENTS

The author is indebted to Prof. B. Aničin of Faculty of Mechanical Engineering Belgrade for guidance in the course of the above work.

REFERENCES

1. D. Ilić, Bulletin of the Boris Kidrič Institute of Nuclear Sciences 18 Physics, N°4 (1967).
2. D. Šulić, Master Thesis, Univ. of Belgrade (1978).
3. D. Šulić, Proc. of IXth SPIG p321 (1978).
4. A.W. Trivelpiece, Slow-Wave Propagation in Plasma Waveguides, San Francisco Press, San Francisco (1967).

QUANTUM MECHANICAL CALCULATIONS OF THE STARK BROADENING OF SOME He I LINES FROM PLASMAS

M.S. Dimitrijević, P. Grujić* and D. Koledin**.

*Institute of Applied Physics, P.O. Box 24, 11001 Belgrade, Yugoslavia.

**Institute of Physics, P.O. Box 57, 11001 Belgrade, Yugoslavia.

***Department of Biophysics, Faculty of Medicine, University of Belgrade, Belgrade, Yugoslavia.

An approximative analytical method for calculating the scattering \hat{S} matrix¹ has been applied for calculating broadening of some He I ($n=3 \rightarrow n=2$) lines, making use of the quantum theory of the Stark broadening of isolated neutral lines.² We start from the standard formula³ for the half-halfwidth and shift (atomic units are used, unless otherwise stated):

$$\Delta\nu_{1/2} = \frac{\pi N}{2} \sum (-) \langle \ell + \ell' \rangle (2S^T + 1) (2L_1^T + 1) X$$

$$X = \frac{1}{L_1^T L_1^T} \left\{ \begin{matrix} L_1^T L_1^T \\ L_1^T L_1^T \end{matrix} \right\} \int f(v) dv \left[\delta_{\ell \ell'} S_1(L_1 S \ell' \frac{1}{2} L_1^T S^T, L_1^T S \ell \frac{1}{2} L_1^T S^T) S_f^{-1}(L_f S \ell' \frac{1}{2} L_f^T S^T, L_f^T S \ell \frac{1}{2} L_f^T S^T) \right] \quad (1)$$

where subscripts refer to the initial (i) and final (f) levels of the transition, superscript T to the whole perturber-emitter system and the capital letter quantum numbers to the emitter. N is the electron density, ℓ , ℓ' denote angular momentum quantum numbers before and after collision, respectively and $f(v)$ is the velocity distribution of electrons.

The diagonal \hat{S} matrix elements $S_{i,f}^{-1}$ are usually obtained by solving corresponding set of coupled integro-differential equations.⁴ If one retains only dipole terms of the direct potential matrix,⁵ neglects exchange terms and accounts for the pertur-

bing levels which belong only to $n=3$ ($n=2$) helium states, then the \hat{S} matrix can be calculated by approximate expression¹:

$$\hat{S} = \hat{K}^{1/2} e^{i\pi \ell} \hat{U} e^{i\pi \ell'} \hat{U}^{\dagger} \hat{K}^{-1/2} \quad (2)$$

where \hat{K} is a diagonal matrix of the perturber momenta, \hat{U} is a unitary matrix, defined by⁶:

$$\hat{U} + [\ell(\ell+1) - \hat{v}] \hat{U} = \mu(\mu+1), \quad (3)$$

and: $\hat{v} = \hat{v}/r^2$ is the dipole potential matrix. Diagonal matrix $\mu(\mu+1)$ determines real numbers:

$$\mu_j = \begin{cases} -\pi\mu_j, & \mu_j = \mu_j^* \\ 2\delta_j + \pi/2, & \mu_j \neq \mu_j^* \end{cases} \quad (4)$$

In case: $\mu_j = -\frac{1}{2} + i\lambda_j$, (λ_j - real), we have:

$$\tan \delta_j = \tanh(\pi\lambda_j/2) \cot(\lambda_j \ln(\tilde{k}_j/K_0)) \quad (5)$$

where K_0 is given by: $K_0^2 = 2(E-E_r)$, E being the energy of the resonance parent state and E_r denotes corresponding negative ion (in our case - He⁻). Further, we have:

$$\tilde{k}_j^2 = k_j^2 + \sum_j \Delta k_j^2, \quad U_{j,j}^2, \quad j = i', f' \quad (6)$$

$$E_i^T = \frac{1}{2} k_i^2 + \mathcal{E}_i = \frac{1}{2} k_f^2 + \mathcal{E}_f + \omega_{if} \quad (7)$$

$$K_i^2 = \overline{k_i^2} + \Delta k_i^2, \quad K_f^2 = k_f^2 + \Delta k_f^2 \quad (8)$$

where $\overline{k_j^2}$ is the arithmetic mean of two mutually most separated sublevels, \mathcal{E}_j is the energy of the substate and ω_{if} is the angular frequency of the transition.

We calculate half-halfwidth and shift for the transition : $\text{HeI}(3^3\text{P}^0-2^3\text{S})$, multiplet 2. In this particular case eg. (1) takes the form :

$$w_{id} = 6 \sqrt{2\pi} N (kT)^{-3/2} \sum_{L_i} (2L_i + 1) \times \int_0^\infty v \exp(-v^2/2kT) \left[1 - \sum_{i', f'} \exp\{i(\mathbf{r}_i - \mathbf{r}_{f'})\} \times U_{ii'}^2 - U_{ff'}^2 \right] \quad (9)$$

Quantities needed for evaluating eq. (9) are given in Table 1.

Table 1. Multiplet 2; $\lambda = 3888.7 \text{ \AA}$

Atomic state	3^3P^0	2^3S
Energy (eV)	23.006	19.812
He^- state	3^2P	2^2S
Resonant energy	22.650	19.367
K_O (au)	0.1647	0.1809

As shown in¹ applicability of the present method for evaluating \hat{S} matrix is restricted to not too small energy region and is determined by the following conditions:

$$v^2 \gg \max(\Delta k_{i'}, \Delta k_{f'}), \quad \forall i', f' \quad (10)$$

In our case, it means that calculated results are not reliable for plasma temperature below 30000. K.

Computations for the line quoted are in progress. We hope to present numerical results, as well as for some other $\text{HeI}(n=3 \rightarrow n=2)$ lines, at the Conference.

The present investigation has been carried out under the financial support from RZN of SR Serbia.

References

1. P.Grujić and D. Koledin, to be published
2. M.Baranger, Phys.Rev., 111, 481, 494, 855 (1958)
3. K.S.Barnes and G.Peach, J.Phys.B: Atom. Molec.Phys., 3, 350 (1970)
4. P.G.Burke, in Scattering Theory, ed. A.O.Barut, Gordon and Breach, New York
5. N.Feautrier and Tran Minh, J.Phys.B: Atom.Molec.Phys., 10, 3427 (1977)
6. M.J. Seaton, Proc.Phys., 77, 174 (1961)
7. D.W.O.Heddle, Proc.Roy.Soc.Lond., A, 352, 441 (1977)

MICROWAVE REFLEXION IN RECTANGULAR WAVEGUIDES BY HIGH PRESSURE R.F. PLASMA COLUMNS

G. Cicconi, E. Bloyet^{*}, P. Leprince^{*} and J. Marec^{*}.^{*}Department of Electrical Engineering, University of Genoa, Italy.

Laboratoire de Physique des Gaz et des Plasmas, Université d'Orsay, France.

The aim of this paper is the determination of some parameters of high pressure plasmas.

Principle. High pressure plasma columns can be produced by means of a surface wave generator : the Surfatron [1]. These plasmas are highly collisional (e.g. $\nu \approx 10^{10}$ Hz at 10 torr in argon) and dense (typically $n \approx 10^{14} \text{ cm}^{-3}$). Consequently we have chosen as experimental method for diagnostic, the determination of the reflexion coefficient of a microwave ($\lambda = 3 \text{ cm}$) incident on the plasma column created in very narrow quartz tubes (int. dia. about 1-2 mm), and placed as a cylindrical post in a rectangular waveguide. Then a numerical method [2] allows us to estimate some plasma parameters as, for instance, density, radial density profile, collision frequency and plasma radius, from the experimental values of modulus and phase of R. The calculated values of R are also compared with those obtained from an extension of Marcuvitz variational method [3].

Calculation. We assume for the plasma column a conventional dielectric description, where the losses are dependent on a global collision frequency ν . The radial distribution of the electron density is parabolic, as :

$$n(r) = N_{eo} \left(1 - \alpha \frac{r^2}{\rho_1^2} \right),$$

where N_{eo} is the density on the cylindrical axis, ρ_1 is the column radius and α a variable parameters of profile with $0 \leq \alpha \leq 1$. The reflexion coefficient of the plasma column in rectangular waveguide, excited in TE(1,0) mode polarized along the cylinder axis, is numerically calculated by the amplitudes of the Bessel-Fourier cylindrical modes of scattering in waveguide. The numerical code [4], for the calculation of this coefficient, solves an infinite system of linear equations obtained by the boundary conditions on the cylinder surface for the tangential components of e.m. field modes. This code was derived from an electromagnetic model where the fields are Fourier exact solutions of Maxwell's equations [2] [5]. In the cylinder, three regions may be considered: I) plasma $0 \leq r \leq \rho_1$, II) vacuum shell $\rho_1 \leq r \leq \rho_0$, III) dielectric layer $\rho_0 \leq r \leq \rho_2$.

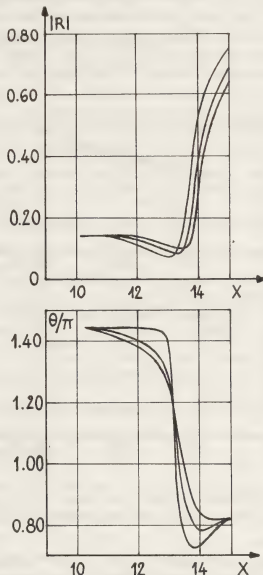


Fig.1. Theoretical variations of modulus and phase of R versus $X = \log_{10} N_{eo} (\text{cm}^{-3})$ for several collision rates.

The calculation results, for the appropriate geometry and variation range of electron density, are obtained for three values of the plasma radius $\rho_1 = 0.50, 0.65, 0.85 \text{ mm}$, $\nu/\omega = 0.0, 1.0, 2.0$ and $\alpha = 10^{-5}, 1.0$. These calculation values are practically coincident ($< 1\%$) with those obtained with the Marcuvitz variational method ($\alpha=0$) [3]. In Fig.1 are shown the results for the case $\alpha=1.0$.

Measurements. The experimental value of the reflexion coefficient modulus and phase is obtained by

VSWR measurements in standard waveguide($\lambda=3\text{cm}$).The discharge tube is pierced across the waveguide and centered in the transversal section through two holes having a diameter(6mm)twice with respect to the tube diameter(3mm),made on the waveguide large walls.The tube is centered in the holes with a precision of about 0.5mm.The systematic errors of measurement on the modulus and phase of R are respectively $\epsilon_R=\pm 6\%$ and $\epsilon_\theta=\pm 2\%$.The experimental results(argon,frequency 10GHz) are shown in Fig.2 versus RF absorbed power by the surfatron plasma(2450MHz),and for the pressure values of 10,50,150and 760 torr.

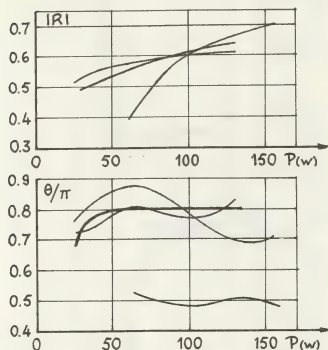


Fig.2.Variations of modulus and phase of R in Argon for several pressures versus absorbed power in plasma.

Result interpretation. The values of plasma parameters, estimated through a comparison between experimental and calculation results, are plotted in Fig3 versus pressure. The fitting is obtained within a maximum deviation of 10% for the modulus and 40% for the phase of R, without taking into account the measurement errors. The maximum value of deviation on θ/π derives essentially from the presence of the holes for tube support on the waveguide walls. If the fitting is performed by using the calculation results obtained for $\alpha=10^{-5}$, the enhancement of the calculation-experimental deviations are of the order of 15 to 20 %.

Conclusions. This study gives us the three following

information on the behaviour of surfatron plasmas : the density profile is approximately parabolic except for very high pressure (e.g. 100 torr in argon and the atmospheric pressure in neon) where the profile tends to become flat, this conclusion is also valid for RF absorbed power values higher than 100 watts; that is at the same pressure the plasma does not fill the quartz tube, the losses, expressed by the v/w term, are not proportional to the pressure. In conclusion this reflexion method can be considered as a powerful tool to estimate the plasma density and other plasma parameters. Moreover the variational Marcuvitz method is easier than the method here used but gives only an approximate averaged density value. The more important information here obtained is the estimation of the density gradient in high pressure plasmas.

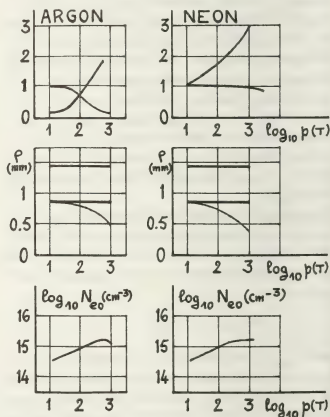


Fig.3.Comparison of Argon and Neon parameters in surfatron discharges.

- References.** 1) Leprince P. et al. 1975. IEEE Trans. Plasma Sci., PS-3, pp. 55-59.
2) Cicconi G., Molinari V., and Rosatelli, 1973, Jap. Journ. Appl. Phys. **12**, pp. 721-733.
3) Marec J. et al. 1978, J. Phys. D, **11**, pp. 1021-1027.
4) Benedetti A.P. and Poli P. 1975, CNEN RT/FIMA(75)3.
5) Cicconi G. and Rosatelli C. 1977, IEEE Trans. Microwave Theory and Tech. MTT-25, **11**, pp. 885-892.

THE HIGH POWER HYDROGEN ARC AS A PRECISE STANDARD SOURCE OF CONTINUUM RADIATION BETWEEN 53 AND 92 NM

K. Behringer and P. Thoma.

Lehrstuhl f. Techn. Elektrophysik, Techn. Universität München, Fed. Rep. of Germany.

I. Introduction: In an earlier paper /1/ it has been demonstrated, how a stationary hydrogen arc discharge can be used as a true primary source of spectral radiance in the Balmer region, i.e. between 410 and 360 nm. The method is based on the fact that the H continuum emission coefficients are calculable within a few percent, since the theoretical cross sections are exactly known. For an optically thin plasma layer, as realized in the Balmer range, the spectral radiance can be predicted with similar accuracy. In the following, an arc standard source below 100 nm will be described, now involving the optically thin Lyman resonance continuum of hydrogen. While the basic idea is very similar to the one in /1/, self-absorption problems are now much more critical and can only be overcome by a helium gas separation in the arc.

II. Experiment: A stationary plasma is generated in a cascaded arc chamber /2/ (2mm ϕ , $l=54$ mm). The arc is operated between 80 and 100 A at atmospheric pressure. The plasma column is observed end-on from two sides by two monochromators, a 2m instrument for the visible and uv range and a 1m for the far vuv. The general experimental set-up is very similar to the one in /1/, except for a three-stage differential pumping system, now connecting the arc chamber and the vacuum tank. The first capillary of this system is 0.8mm wide and located 2mm from the anodes. In the vuv, a channeltron detector is used in photon counting mode. The counting rates can be stored digitally on magnetic tape or plotted on a stripchart

recorder after D/A conversion.

Well-defined flow rates are adjusted for the gas separation of H and He. A pure He input of 800 μ /h at the anode, the vuv end of the arc, covers mainly the gas consumption of the differential pumping system, a small fraction also streaming into the discharge channel. From the other end, a mixture of H and He is forced through the arc. Both gas flows leave the channel together at a port mid-way between the electrodes. As a result the arc column consists of the H-He plasma near the cathode, the radiation of which is the subject of the present investigation, and a pure He layer near the anode. Fig. 1 shows the recorded vuv spectrum for 80 A. Below 100 nm the higher Lyman lines merge into the advanced series limit. Then follows the H resonance continuum, superimposed by some impurity lines (Ar has been used during ignition). The resonance lines of He are self-reversed in the cooler He layer at the anode. Below 50.4 nm, the He series limit, all radiation is completely reabsorbed. Thus, the hydrogen continuum radiation can be used for calibration purposes from 53 to 92 nm. The spectrum in Fig. 1 has been corrected for the vuv system response according to calculations of the H spectral radiance as described below.

III. Plasma Diagnostics: The recorded end-on spectra consist of line and continuum radiation, emitted by the H as well as the He layers of the arc. In order to isolate the H continuum (only necessary in the uv region), measurements have also been made for pure He in the whole arc. From the ratio of the He I

318.8 nm line intensities in pure He and in the above configuration, an effective He length has been derived and the respective continuum signals have been subtracted from the total. The electron density is measured from the half-widths of the lines H_β and H_γ . For the hydrogen concentration $c_H=20\%$, the result is $4 \times 10^{16} \text{ cm}^{-3}$, varying only slightly with the arc current. The electron temperature T_e is derived from the excited state population relative to the electron density (PLTE diagnostics). Again, for $c_H=20\%$, $T_e=19500 \text{ K}$ for 80 A and 21500 K for 100 A, both values decreasing with increasing hydrogen fractions. Under these conditions, the H plasma will be very close to LTE.

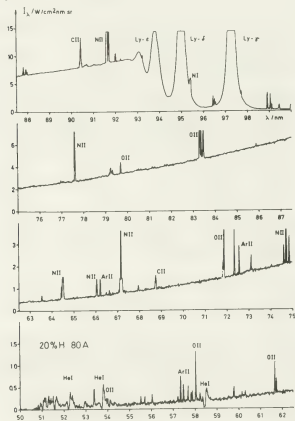


Fig. 1: Vuv arc spectrum, recorded for $I=80 \text{ A}$.

IV. Calibrations below 100 nm: A recombination of the free electrons, populating the same energy interval, leads to the Balmer continuum radiation at λ_B , when the final state is $n=2$, and to the Lyman continuum at λ_L , when $n=1$. The two wavelengths are related by $hc/\lambda_L = hc/\lambda_B + E_2$, E_2 being the excitation energy for $n=2$. The ratio of the corresponding emission coeffi-

cients must therefore be a constant, corresponding to line branching ratios. Though this simple consideration has to be corrected for the other mechanisms of continuum radiation (free-free, H^-), it can be shown that the total emission coefficients in the uv and in the far vuv are correlated by a calculable factor, which is virtually independent of temperatures and densities, if only the wavelength pairs are chosen in an appropriate way. If λ_B is to remain in the easily accessible range from 200 to 365 nm, λ_L lies between 73 and 87 nm. The above correlation must also be valid for the spectral radiances of the present arc plasma, provided that the radiation remains optically thin. A measurement of the optical thickness is therefore simply achieved by plotting the recorded vuv vs. the uv signals. The result is indeed a straight line through the origin up to $c_H \approx 25\%$. Above, an increasing influence of self-absorption is observed, which corresponds approximately to LTE estimates. Having thus excluded possible boundary or non-LTE effects, the spectral radiance in the mentioned vuv region can be calculated very accurately from a calibration of the H continuum in the uv range (uncertainty about 5%). For an application at other wavelengths the slope of the Lyman continuum must be derived from the temperature diagnostics, leading to error bars of about 15% at 53 nm. In the present experiment, this H vuv standard has already been used for measuring the continuum radiation of the pure He arc between 65 and 92 nm. An excellent consistency of these results with respective theoretical calculations confirms the validity of the described concept.

/1/ W.R. Ott, K. Behringer, and G. Gieres, Appl.

Opt. 14, 2121 (1975)

/2/ H. Maecker and S. Steinberger, Z. angew. Phys.

23, 456 (1967)

THEORY OF THE SHEATH EDGE IN A WEAKLY IONIZED COLLISION DOMINATED PLASMA

K.U. Riemann.

Institut für Theoretische Physik, Ruhr-Universität Bochum, D-4630 Bochum, Fed. Rep. Germany.

1. Introduction

Whereas the wall layer of a collisionless plasma was treated long time ago [1], there is little information on the transition from a collision dominated plasma to the collision free space charge sheath. In a former paper [2] we have given the analytic presheath and sheath solutions for a simple plasma model. These solutions refer to two distinct scales: The sheath with a typical dimension of a Debye length λ_D and the presheath on the scale of the mean free path λ . Due to the singularity of the problem, however, they cannot simply be matched to a uniformly valid potential variation.

II. Presheath and sheath

We consider a weakly ionized plasma in contact with an absorbing negative wall. The electrons are in equilibrium with the selfconsistent potential distribution. The ion kinetics is dominated by charge exchange collisions ($\lambda = \text{const}$) with cold ($T_0 < T_e$) neutrals. We refer to [2] and use dimensionless quantities

$$x = z/\lambda; \quad y = Mv^2/2kT; \quad \chi = -eU/kT_- \quad (1)$$

(z = space coordinate, plasma: $z < 0$, wall: $z = 0$; $Mv^2/2$ = ion energy; U = potential). The normalized particle densities are given by

$$n_- = e^{-\chi}; \quad n_+ = j_+ \int_{-\infty}^{\chi} \frac{e^{k(y)-k(\chi)}}{\sqrt{\chi-y}} k'(y) dy, \quad (2)$$

j_+ represents the ion current density and $k(\chi) = x$ is the inverse function of the potential variation $\chi(x)$. From Poisson's eq.

$$(\lambda_D/\lambda)^2 \chi'' = n_+ - n_- \quad (3)$$

we expect that for $\lambda_D/\lambda \rightarrow 0$ the potential is determined by the quasineutrality condition. This is true on the scale $x=O(1)$ of the presheath. From [2] we take the solution

$$x = k_0(\chi) = \ln \Phi(t_0 + \chi) \quad (\chi \leq 0) \\ \Phi(t) = \frac{c}{2\pi i} \int_{-\infty}^{i\infty} \sqrt{r(s)} e^{st} ds \\ t_0 = \frac{1}{2} \ln(\pi j_+) = 0.44636, \quad c = 0.88161 \quad (4)$$

which is shown in fig. 1. The field

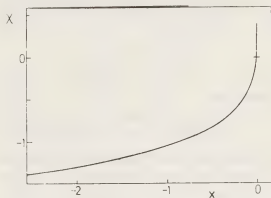


Fig. 1
singularity $k'(0)=0$ at $x = 0$ indicates the necessity of a second scale

$$\xi = x/\epsilon \quad \text{with} \quad \epsilon = j_+^{-1/2} \frac{\lambda_D}{\lambda} \quad (5)$$

representing a thin layer (sheath) where space charges are essential. The sheath solution [2]

$$\xi = \int_{\chi}^{\infty} \frac{dx}{4 \int_0^{\chi} (\sqrt{x-y} - \sqrt{y}) \Phi(t_0 - y) dy + (\bar{e}^x - 1) j_+ \frac{1}{2} \chi} \quad (6)$$

is shown in fig. 2. On this scale the quasineutral region is infinitely remote and the potential tends to $\chi=0$ for $\xi \rightarrow -\infty$. On the other hand, the sheath is "compressed" into a vertical line (corresponding to the field singularity) on the scale of the presheath.

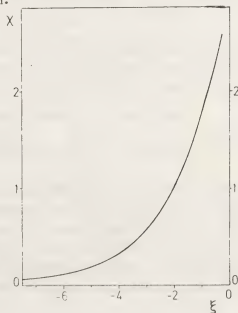


Fig. 2

III. Transition at the sheath edge

From the potential variation near the sheath edge $\chi = 0$ it is clear, that the "outer" (presheath) and "inner" (sheath) solutions cannot be matched to a sensible uniformly valid solution for small but finite values of ϵ . We have therefore to reinvestigate the problem on an intermediate scale for $\chi \rightarrow 0$ accounting for collisions and for space charge.

From eqs. (4) and (6) it follows

$$x = k_0(\chi) = -\frac{a}{2}\chi^2 + O(\chi^3) \\ \text{with } a = -\phi''(t_0) = 0.7367 \quad (7)$$

on the outer and

$$x = k_1(\chi) = \text{const} - \sqrt{\frac{15}{a}} \epsilon \chi^{-1/4} [1 + O(\chi^{1/2})] \quad (8)$$

on the inner scale. Comparing the leading terms we find the appropriate scale transformation

$$\chi = \delta w, \quad x = \frac{a}{2} \delta^2 \xi \\ \text{with } \delta = (3\epsilon^2/a^3)^{1/9} = 4.565 \epsilon^{2/9} \quad (9)$$

for the intermediate problem. Physically the transition region is dominated by slow ions emerging from charge exchange collisions: The high density contribution of these ions favours the formation of a positive space charge. On the other hand the loss of fast ions due to collisions can be neglected, to lowest order, on this scale. Consequently, collisions have nearly the same effect as an ionization process. This is the reason, why eq.(9) agrees with the corresponding scaling [3] for the collisionless Tonks-Langmuir model. The systematic development of eqs.(2) and (3) leads to the nonlinear integro-differential equation $(\kappa(w) = \xi)$

$$w'' = -\frac{\kappa''}{\kappa'^3} = \frac{3}{8} \int_{-\infty}^w \frac{\kappa'(u) - \kappa'_0(u)}{(w-u)^{1/2}} du \quad (10)$$

for the transition region. Using a simple ansatz to evaluate the integral this equation can, to a good approximation, be replaced by

$$w(\xi) = w_0(\xi) \quad \text{for } \xi < \xi_A \\ w'' = [w(\xi) - w_0(\xi_A)]^{1/2} \left(w + \frac{1}{2w} \right) \quad \text{for } \xi > \xi_A \quad (11)$$

The influence of the arbitrary limit ξ_A is only weak; $\xi_A \approx -1.6$ gives the best agreement with eq. (10). $w(\xi)$ is plotted in fig. 3. We see that it can easily be matched with the outer (w_0) and inner (w_1) solution to construct the wanted continuous potential variation. The result is shown in

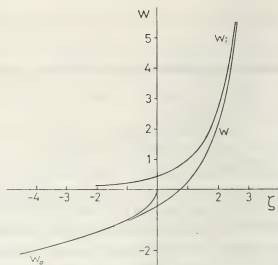
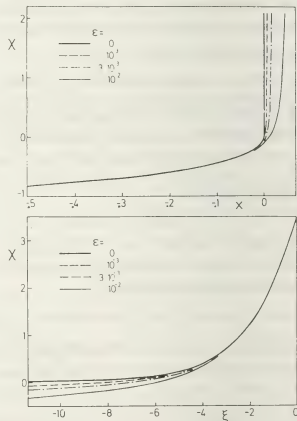


Fig. 3

figs. (4a,b) on the scale of the presheath (x) and of the sheath (ξ). The curves demonstrate the approach to the asymptotic case on both scales.



Figs. (4a,b)

References

- [1] S.A. Self, Phys. Fluids 6, 1762 (1962)
- [2] K.-U. Riemann, J. Nucl. Mat. 76 & 77, 579 (1977)
- [3] R.N. Franklin and F.R. Ockendon, J. Plasma Phys. 4, 371 (1970)

FARADAY ROTATION APPLIED TO A REVERSE FIELD PINCH

D.G. Muir* and P.G. Carolan.

Culham Laboratory, Abingdon, Oxon, OX14 3DB, UK (EURATOM/UKAEA Fusion Association).

INTRODUCTION

There are now a variety of techniques for measuring internal magnetic fields in tokamaks, that have been successfully developed, e.g. light scattering, [1][2] Zeeman splitting [3] and Faraday rotation [4]. The poloidal field, B_θ , was the quantity of interest since its distribution determines the plasma equilibrium and stability properties (the toroidal field distribution, $B_z(r)$ differs only slightly from that produced externally). In reversed field pinch plasmas, both the $B_z(r)$ and $B_\theta(r)$ field distributions are mainly generated internally and play an equal role in the plasma stability. Therefore, both B_θ and B_z are the quantities of interest.

The Faraday rotation method gives a continuous integral measurement of the internal poloidal magnetic field alone when the beam is in the vertical plane, but otherwise gives a continuous integral measurement of both internal magnetic fields. The integral is over a straight path and the measurement of the Faraday rotation angle is done by simple polarimetry external to the machine. It is proposed to use the Faraday rotation technique, employing an HCN/DCN laser ($\lambda = 337/190 \mu\text{m}$) to measure both distributions in the HBTXIA plasma.

The HBTXIA machine is a reversed field pinch (RFP) under construction at Culham. It has a major radius of 0.8m and minor radius of 0.26m. The expected plasma parameters are: $T_e \sim 50\text{-}150\text{eV}$; $n_e \sim 1.5 \times 10^{20}\text{-}4 \times 10^{20} \text{m}^{-3}$; current $\sim 400\text{kA}$; $\langle B \rangle \sim 0.5\text{T}$.

THE CHOICE OF WAVELENGTH AND SOURCE

The choice of a suitable wavelength for Faraday rotation is governed essentially by considering what sources are available, and whether this source has sufficient power for an accurate measurement of the Faraday rotation angle obtained at the source wavelength. Other important effects which have to be considered are refraction, loss of transmitted power due to turbulence [5] and degradation of the beam polarisation due to the perpendicular component of magnetic field [6][7].

We have found that because of the low toroidal magnetic field in RFP plasmas, the depolarisation effect is negligible. This is in contrast to tokamak plasmas where because of the large toroidal field, the depolarisation effect becomes important

when the Faraday rotation angle exceeds some 10° .

The rotation angle, ψ , is described by the relation:

$$\psi = \lambda^2 \int_L n_e \vec{B} \cdot d\vec{L}$$

where λ is the laser wavelength; n_e and B are the electron density and magnetic field respectively; and L is the path length. This relation is not valid when depolarisation is present.

If the plasma can be considered to be a horizontal cylinder, of radius a , with cylindrical symmetry, then for a beam of wavelength λ propagating through the plasma with an impact parameter, h , and at an angle, Ω , from the vertical plane, then the Faraday rotation angle, ψ , is found to be given by:

$$\psi = 2A\lambda^2 \left\{ \int_h^a n_e B_\theta \frac{h dr}{\sqrt{r^2 - h^2}} + \tan \Omega \int_h^a n_e B_z \frac{r dr}{\sqrt{r^2 - h^2}} \right\} \\ = \psi_\theta + \psi_z \quad (1)$$

where B_θ and B_z are the poloidal and longitudinal magnetic fields respectively; $A = 2.62 \times 10^{-13} \text{ rad tesla}^{-1}$; and ψ_θ and ψ_z are the rotation angles due to the individual magnetic fields B_θ and B_z respectively, and are given by the integral incorporating the appropriate magnetic field.

The Faraday rotation angle, therefore scales as λ^2 , as does refraction. Numerical calculations of the expected angle of rotation, and refractive deviation for various source wavelengths are given in Table I. The axial electron density used was $1.5 \times 10^{20} \text{m}^{-3}$ and the plasma current 400kA. The ratio of axial to critical electron density, n_e/n_c , is a measure of transmission of the beam. A ratio greater than 0.2 could indicate very high attenuation due to turbulence and a ratio less than 0.02 would be desirable [5]. From Table I the wavelength giving rise to the largest Faraday rotation angle with an n_e/n_c ratio of less than 0.02 and with a tolerable beam deflection is $337 \mu\text{m}$ produced by an HCN laser. At this wavelength the rotation expected is typically 10° with a beam deviation less than 5mm. The minimum measurable angle at this wavelength determined by detector and amplifier noise is about 0.1° [4]. At a higher axial electron density of $4 \times 10^{20} \text{m}^{-3}$ the DCN laser wavelength of $190 \mu\text{m}$ would also give a Faraday rotation angle of typically 10° and a beam deviation less than 5mm. The source producing rad-

iation at these wavelengths also has sufficient power for a multichannel Faraday rotation diagnostic.

DATA INVERSION

From equation (1) the Faraday rotation angle, ψ , for a beam propagating at an angle, Ω , from the vertical plane, is the sum of two rotations, ψ_θ and ψ_z , arising from the two magnetic fields B_θ and B_z . The poloidal field rotation, ψ_θ , can be measured alone when $\Omega=0$. The toroidal field rotation, ψ_z , can also be measured when $\Omega \neq 0$, but this requires that the appropriate ψ_θ be known. Therefore, for measuring the two rotation angles, we must have two beams propagating through the plasma simultaneously, at the same impact parameter, and one beam having $\Omega=0$. It is by this method that the internal magnetic fields of HBTXIA will be measured. To obtain the field profiles the diagnostic must be a multi-channel one. The pitch profile can be determined without any knowledge of the electron density, since by Abel inversion of ψ_θ and ψ_z :

$$2\lambda^2 \tan \Omega n_e B_z = -\frac{1}{\pi} \int_r^a \left(\frac{d\psi_z}{dh} \right) dh$$

$$\sqrt{h^2 - r^2}$$

$$\frac{2\lambda^2 n_e B_\theta}{r} = -\frac{1}{\pi} \int_r^a \left(\frac{d\psi_\theta}{dh} \right) dh$$

$$\sqrt{h^2 - r^2}$$

and from the definition of the pitch, $P = rB_z/B_\theta$

and the above equations:

$$P = \frac{\int_r^a \left(\frac{d\psi_z}{dh} \right) \frac{dh}{\sqrt{h^2 - r^2}}}{\tan \Omega \int_r^a \left(\frac{d\psi_\theta}{dh} \right) \frac{dh}{\sqrt{h^2 - r^2}}}$$

which does not involve the electron density. The safety factor profile is also given since $q = P/R$ where R is the plasma major radius.

CONCLUSIONS

We have concluded that a Faraday rotation diagnostic using an HCN/DCN laser is a practical diagnostic method for measuring the internal magnetic fields of a RFP and in particular the HBTXIA plasma. With the wavelengths available with this laser system, 337 μ m or 190 μ m, and the expected range of electron density ($1.5 \times 10^{20} - 4 \times 10^{20} \text{ m}^{-3}$), Faraday rotation angles of typically 10° will be observed with negligible refraction, depolarisation, or loss of transmitted power.

REFERENCES

- [1] FORREST M J, CAROLAN P G, PEACOCK N J: Nature 271 5647 (1978) 718

- [2] ALLADIO F, MARTONE M: Phys Lett, 60A, 1 (1977) 39
 [3] McCORMICK K, KIRK M, OLIVAIN J: Proc 8th Eur Conf on Controlled Fusion and Plasma Physics, Prague, 1 (1977) 140
 [4] KUNZ W: Equipe TFR, Nuc Fus, 18, 12 (1978) 1729
 [5] WORT D J H: Plasma Phys, 8 (1966) 79
 [6] CRAIG AD: Plasma Phys., 18 (1976) 777
 [7] SEGRE S E: Plasma Phys., 20 (1978) 295

TABLE I
SOURCE OF WAVELENGTHS, ROTATION AND DEFLECTION ANGLE
FOR HBTXIA

SOURCE		n_e/n_c	ψ	α
1mm	μ -wave	0.13	88°	20°
CH ₃ F	496 μ m	0.032	22°	5°
HCN	337 μ m	0.015	10°	2°
DCN	190 μ m	0.005	3°	1°
Methanol	118 μ	0.002	1°	0.3°
CD ₂	10.6 μ m	5×10^{-5}	0.01°	0.002°

$n_e = 1.5 \times 10^{20} \text{ m}^{-3}$, ψ = typical Faraday rotation angle; α = maximum deflection angle.

*Attached from Royal Holloway College, University of London

REGULARITIES WITHIN THE STARK WIDTHS AND SHIFTS OF RESONANCE LINES OF SINGLY CHARGED IONS FROM He TO Ca

J. Purić, I. Lakićević* and V. Glavonjić.

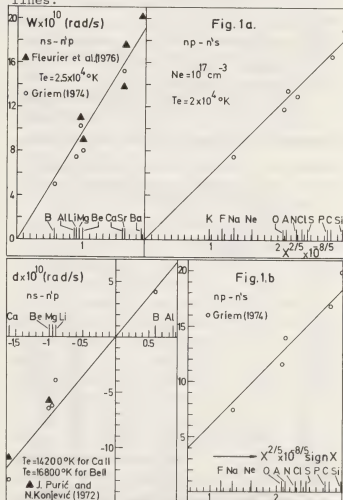
Faculty of Natural and Mathematical Sciences, Department of Physics, and Meteorology and Institute of Physics, P.O. Box 550, Beograd, Yugoslavia.

*Institute of Physics, P.O. Box 57, Beograd, Yugoslavia.

The aim of this paper is to present noticed regularities of Stark broadening and shift parameters of resonance spectral lines of singly ionized atoms from helium to calcium.

The existence of certain regularities of Stark broadening and shift parameters of neutral spectral lines of homologous groups of elements was the basis for an assumption that similar regularities may be also found for ion spectral lines. A recently published paper by Purić et al. /1/ has proved that Stark widths of alkali-like atoms and ion resonances linearly depend on the atomic charge number Z . However, in a paper given by J. Purić and V. Glavonjić /2/ periodicity of the dependence of Stark widths of resonance spectral lines of neutral and singly ionized atoms from He to Ca on atomic charge number Z has been noticed and discussed. As it was stated there, there is a lack both in theoretical and experimental data for a complete set of resonances for all ions from He to Ca. In order to complete as much as possible the set of the reliable theoretical data a new method for estimation of Stark widths and shifts of corresponding resonance lines, not given by Griem /3/, has been elaborated. The basis for this method were the expressions for Stark widths (w) and shifts (d) of ion lines given in the paper by S. Bruchoch and H. Van Regemorter /4/. Namely, they have found that w and d values linearly depend on $|X|^{2/5}$ and $|X|^{2/5} \text{ sign} X$ respectively. Actually, using available

theoretical data given by Griem /3/ as well as experimental ones obtained by Purić and Konjević /6/ and Fleurier et al. /7/, it is possible to obtain graphs similar to those in Fig. 1 a and b. From these graphs the mentioned linear dependence of w and d is obvious (within 20%) for ns-n'p and np-n's transitions. Calculating $|X|^{2/5}$ for corresponding resonance lines and using Fig. 1. a and b one can get w and d values of the lines.

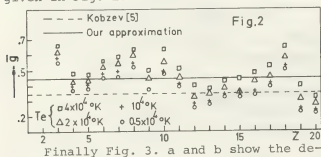


In order to check the above described

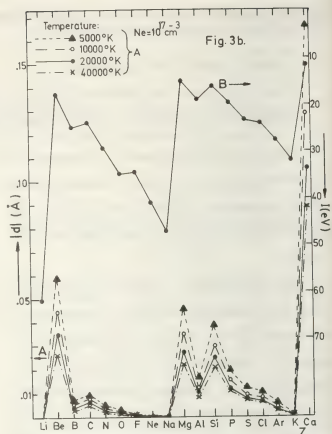
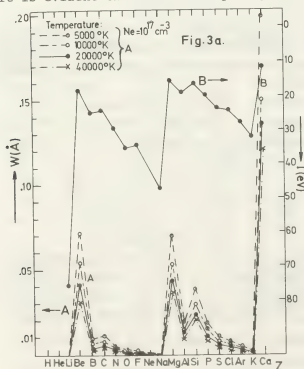
estimation for theoretical calculation

Griem's semiempirical formula for Stark widths with Gaunt factor $g=0.2$ was used in case of resonance spectral lines of all singly ionized atoms from He to Ca. The

estimated values from the trends similar to those given by Griem were consistently higher (up to 3 times) in comparison with those obtained from the semiempirical formula with $g=0.2$. In order to avoid these discrepancies the Gaunt factor has to be corrected for the corresponding ion as it is given in Fig. 2. Namely, instead of taking $g=0.2$ or even $g=0.9 - \frac{1.1}{z^*}$ as Kobzev [5] has suggested one has to take approximately $g=0.9(1 - \frac{1}{z^*})$ where $z^*=2$ for singly charged ions, for all temperatures from 5000 K to 40 000 K in order to get data following the appropriate linear trend given in Fig. 1. a and b.



pendences of w and d and of the ionization potential I on the atomic charge number Z . It is evident that w and d depend periodically



cally on Z in a similar manner as the ionization potential does.

One can expect, generally, that the calculations now in progress will show that the established linear dependence of w and d on $|x|^{5/2}$ and $|x|^{5/2} \text{sign} x$ respectively, and the corresponding periodical dependence on the atomic charge number Z are universal also for other heavier elements.

References

1. J. Purić, M. Dimitrijević and I. Lakićević, *Phys. Lett. A*, **67**, 189 (1978)
2. J. Purić and V. Glavonjić, SPiG, contributions, 273, Dubrovnik (1978)
3. H. R. Griem, "Spectral Line Broadening by Plasmas", New York and London Academic Press (1974)
4. S. Brechot and H. Van Regemorter, *Ann. d'Astr.*, **27**, 432, 739 (1964)
5. G. A. Kobzev, *Opt. Spectr. (USSR)* **30**, 106 (1971)
6. J. Purić and N. Konjević, *Z. Phys.* **249**, 440 (1972)
7. C. Fleurier, S. Sahal-Brechot and J. Chapelle, *JQSRT* **17**, 595 (1977).

METHOD OF ESTIMATING THE LEVEL OF COLLECTIVE ELECTRIC FIELD FLUCTUATIONS IN A NONTHERMAL PLASMA WITH A TWO-TEMPERATURE ELECTRON GAS

G. Himmel and L. Sowa.

Ruhr-Universität Bochum, Bochum FRG, Institut für Experimentalphysik II.

Introduction

The time averaged spectral energy density of electrostatic waves in a nonthermal plasma is one of the main ingredients which enter into a calculation of transport coefficients including collective effects. Regarding a bimaxwellian electron distribution function $1/$, characterized by the parameters $T_>/T_< \gg 1$ and $(1-\beta) = n_</n_>$ ($T_<$, $n_>$ are the temperature and the density of the thermal electrons; $n_<$, $T_>$ refer to the superthermal electrons), a strong enhancement of the level of electric field fluctuations at a frequency slightly above the electron plasma frequency is expected. Considering the HF conductivity this should give rise to marked effects compared with the thermal case $2/$. Furthermore, it is suggested, that in the Stark broadened profiles of emission lines the vicinity of the electron plasma frequency is strongly emphasized even in the case of an extremely low density of superthermal electrons $3/$. This would imply that the appearance of the so-called plasma satellites represents a sensitive indicator of a superthermal electron component. Nevertheless, a critical discussion of the real diagnostic possibilities requires a study of the effects in a wide range of parameters. Without considerably increasing the numerical efforts this may be achieved only by means of a simple approach incorporating the main features of the theory.

Basic equations

We start from the following expression for the energy density of collective electric field fluctuations

$$(1) W = C \cdot \int_0^\infty G(\Omega) d\Omega \quad C = \frac{e^2 n_>}{\pi v_{th}} \omega_p$$

$G(\Omega)$ is the spectral energy density written in dimensionless variables as in ref. 2:

$$(2) G(\Omega) = \int_{x_D}^\infty dx \sqrt{\pi} \{ \beta e^{-\Omega^2 x^2} + (1-\beta) \sqrt{\frac{T_>}{T_<}} e^{-\Omega^2 x_1^2} \} \times \{ |\epsilon(x, x_1, \Omega, \beta)|^2 \}$$

Here the following notations are used

$$\omega_p = \left\{ \frac{4\pi n_> e^2}{m} \right\}^{1/2}; \quad v_{th}^2 = \frac{k T_<}{m}$$

$$\Omega = \frac{\omega}{\omega_p}; \quad x = \{\sqrt{2} k \lambda_D\}^{-1}; \quad x_1 = \sqrt{\frac{T_<}{T_>}} x$$

$$x_D = 1/\sqrt{2}; \quad \lambda_D \text{ is the Debye length} = \frac{v_{th}}{\omega_p}$$

The integrand of equation (2) is essentially determined by the zeroes of the real part of the dielectric constant $\text{Re}(\epsilon)$. In the case of resonance the dielectric constant in the denominator may be replaced by the Landau damping decrement $\text{Im}(\epsilon)$ (binary collisions are not included in this treatment). For a given Ω the resonance is localized at $x_{\text{RES}} > x_D$ which is determined from $\text{Re}(\epsilon) = 0$. In this connection it is sufficient to use the Bohm-Gross relation for an estimate. Moreover, we realize that the following approximation holds for $\Omega \geq 1$:

$$(3) G(\Omega) \approx K \cdot \frac{2\Omega^4}{3} x_{\text{RES}}^3 \cdot \text{Im}\{\epsilon(\Omega, x_{\text{RES}})\} F(\Omega, x_{\text{RES}})$$

where $F(\Omega, x_{\text{RES}})$ is the integrand of equation (2) in the case of resonance. This approximation follows from a Taylor expansion of $\text{Re}(\epsilon)$ around x_{RES} . The width of the resonance is proportional to the extension of the region where $\text{Im}(\epsilon) > \text{Re}(\epsilon)$. In the most interesting cases it can be shown that in the vicinity of x_{RES} $\text{Im}(\epsilon)$ varies slowly compared with $\text{Re}(\epsilon)$. $K = 1.3$ is obtained by evaluating equation (2) numerically in a rigorous way. This evaluation was carried out by using two different sets of parameters: (a) the same as in ref. 3, Fig. 2; (b) $T_>/T_< = 40$, $(1-\beta) = 10^{-4}$. Applying the approximative equation (3) the numerical integration in equation (1) can be easily performed.

Results

Fig. 1 shows the electric field strength $E_0 = (8\pi W)^{1/2}$ as a function of the para-

meters T_+/T_- and $(1-\beta) = n_-/n_+$.

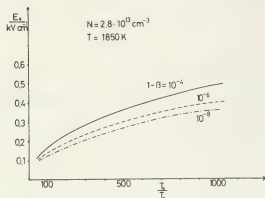


Figure 1: $E_0 = (8\pi W)^{1/2}$ vs. T_+/T_- for different values of n_-/n_+

The quoted plasma parameters referring to the bulk of thermal electrons enter only into the factor C of equation (1). Therefore it is not difficult to transfer these results to other plasma parameters. An example shall illustrate the application of the foregoing considerations. The influence of collective electric field fluctuations upon the wings of Stark broadened hydrogen lines is characterized by the ratio U, which is given by the intensity I_{nth} in the nonthermal case divided by the intensity I_{th} in the thermal case ($\beta=1$):

$$(4) U = \frac{I_{nth}}{I_{th}} = 1 + \frac{8}{3\pi} \frac{d^2 e^2 n_+}{h^2 v_{th}^2} \frac{W}{\omega_p C} \frac{P(o)}{I_{th}(\Delta\omega=\omega_p)}$$

d is the electric dipole moment (see eq. (9) of ref. 4), h Planck's constant and P(o) the central intensity, which results from a folding of all broadening mechanisms with the exclusion of the electron impact broadening. Fig. 2 shows U as a function of T_+/T_- and $(1-\beta)$. Here the example of the line P_α is chosen. The plasma parameters are the same as in Fig. 1. The detection threshold refers to the special conditions of a low density plasma, which is described in ref. 5.

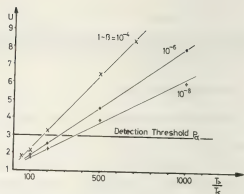


Figure 2: Enhancement of the wing intensity of the hydrogen line P_α produced by collective effects ($\Delta\omega = \omega_p$)

Conclusions

This study presents an easy method of estimating to which extent collective phenomena must be taken into consideration in the case of a bimaxwellian electron distribution. Concerning e.g. the Stark broadening of spectral lines it is shown that contrary to former conclusions there are no dramatic effects in reality. Only in extreme situations a detectable influence due to nonthermal electrons upon the line shape can be expected.

Acknowledgement

The investigations are part of the joint efforts within the Sonderforschungsbereich Plasmaphysik Bochum/Jülich.

References

- 1 D. A. Tidman, T. H. Dupree, Phys. Fluids **8**, 1860 (1965)
- 2 J. Dawson, C. Oberman, Phys. Fluids **5**, 517 (1962)
- 3 W. R. Chappell, J. Cooper, E. W. Smith, J.Q.S.R.T. **10**, 1195 (1970)
- 4 H. Griem, Ap. J. **147**, 1092 (1967)
- 5 H. Schlüter, Z. Naturforschung **18a**, 439 (1963)

ON DETERMINATION OF TL, IN, NA NORMAL ATOM CONCENTRATION BY RESONANCE LINES BROADENED WITH MERCURY PRESSURE

V.G. Vdovin and N.A. Vdovina.

All-Union Institute of Light Sources, Saransk, U.S.S.R.

To estimate the radiation while developing the light sources with metal halogenide additives it is necessary to know the additive atom concentration in the discharge and reasonably precise description of resonance line contour shapes. There were suggested some methods for determination of additive concentration $n_0(r)$: by absorption in the wing /1/, by self-reversed part of radiation contour /2/ and by full absorption in line A_G /3/. Each is based on knowledge of resonance line contour shape in optically thin layer $P(v, r)$ in the source. However the experimental determination $P(v)$ is rather difficult, therefore its estimating form is used which was obtained in various assumptions to types of broadening interaction. The agreement between the estimated $P(v)$ and real values is evaluated in this case not directly by that how exactly the estimated distribution of line intensity in radiation $I(v, x)$ and absorption $F(v, x)$ corresponds to the observed one in the source. In this work such a check is performed under conditions of non-homogeneous distribution of absorbing and radiating atoms and also the broadening component Hg that makes the subject complicated.

The above mentioned methods of n_0 determination are common for Doppler and Lorentz $P(v)$ shapes. However $P(v)$ of resonance lines, broadened by foreign gas, have rather more complicated form /4/. For this case there suggested some theories for $P(v)$ description while assuming various interaction potentials /5,6/. For pair Tl-Hg paper /7/ used the fold of dispersive contour with statistical one, obtained in assumption of Van der Waals potential.

Analogously one can have:

$$P(z) = \begin{cases} \frac{1}{\pi} \frac{\Gamma}{\gamma^2 + (z - \beta)^2}, & z > 0 \\ D \int_0^\infty \frac{t^{3/2} e^{-t} dt}{[\kappa - t(z - \beta)]^2 + (\gamma t)^2}, & z < 0 \end{cases}, \quad (1)$$

where $z = v - v_0$ - frequency, reading from the centre of unshifted line, D - normalization factor for contour in $z = 0$, ΔC_6 - the difference in force constants of Van der Waals potential for upper and lower transition levels, N - mercury atom concentration, $z :: t$, $\kappa = \frac{4\pi^3 \Delta C_6}{9\hbar} N^2$.

Paper /8/ represents Lenard-Johns potential and expression for contour shape, obtained by pressure broadening theorem, developed by Yablonsky /5/. In this case as analysis showed, $P(v)$ for our conditions may be limited by:

$$P(z) = e^{-H} [P_0(z) + H P_1(z)] \quad , \quad (2)$$

where H - number of particles in ρ radius interaction sphere for radiating (absorbing) atom, $P_0(z)$ - line contour, when there are no broadening atoms in the sphere of interaction, $P_1(z)$ - line contour, when there is one particle in the sphere of radius ρ , $P_1(z)$ - a function of potential well depth $\beta = \frac{(\Delta C_6)^2}{4\hbar \Delta C_{12}}$ and frequency shift minimum $\alpha = \frac{\Delta C_{12}}{\hbar \rho^{12}} - \frac{\Delta C_6}{\hbar \rho^6}$.

Since the investigated discharge is non-uniform according to r , $P(v)$ can be estimated in a number of source layers, with the contour being constant. Experimental data for atom temperature $T_a(r)$ and broadening atom density N /9/ were used in

layer approximation. Absorbing atom concentration at Tl $6^2P_{1/2,3/2}$, In $5^2P_{1/2,3/2}$ and Na $5^2S_{1/2}$ levels have been determined for full absorption of A_{G1} in the blue line wings, presented by the dispersive $P(v)$ form. The confidence of the obtained concentration values with error $\pm 10\%$ has been evaluated according to additive dosage taking into account the complex compound formation and besides for Tl-according to absorption in the limits of molecular band $TlI \ X^1\Sigma^+ \rightarrow A^3\Pi$. In terms of temperature $T_{exc}(r)$ the populations of Tl $7^2S_{1/2}$, In $6^2S_{1/2}$ and Na $4^2P_{1/2,3/2}$ excited states were received by modified Bartels method /10/.

In estimating $P(v)$ there used ΔC_6 calculated by London formula /11/ and ΔC_{12} obtained from experimentally measured satellite position according to Hindmarsh theory /4/. While modelling the adequacy of estimated $I(v,x)$ and $F(v,x)$ contour with experimental one the parameters, defining $P(v)$ including constants ΔC_6 and ΔC_{12} were noticed to vary.

Estimations performed with employing /1/ and /2/ showed that a

a) observed absorption contour $F(v,x)$ are satisfactorily described in Van der Waals interaction so Tl, In atom concentrations found by full absorption A_G with an error of not more than 20% and Na- not more than 10% differ from experimentally defined by absorption in blue wing and also are in good agreement with chemical analyses of filling composition in particular, for TlI molecule number, formed in Tl atom recombination during plasma decomposition ;

b) the usage of Lenard-Johns potential in $P(v)$ description does not make significant refinement in values for additive atom concentration, though improves the form adequacy of estimated $F(v,x)$ and $I(v,x)$ with experimental ones both in blue and red line wings ;

c) for more exact description of $P(v)$ in wide interval Δv probably it is needed to use another type of quasi-molecule potential $V(\rho) = \frac{C_n}{\rho^n}$ where $n \neq 6$,

and 12 ;

d) sharp difference of wing intensity in lines Tl 377 and In 410 nm is explained by superposing the electronic system of iodide absorption bands $X^1\Sigma^+ \rightarrow A^3\Pi$.

References :

1. L.A.Luizova. Optics and Spectroscopy, 38, 639, (1975).
2. V.A.Solunikova. Optics and Spectroscopy, 40, 223, (1976).
3. V.G.Vdovin, N.A.Samsonova. All-Union Symposium of Plasma Investigation on Spectral Line Contour, PGU, Petrosavodsk, (1974).
4. W.R.Hindmarsh, J.M.Farr. Collision Broadening of Spectral Lines by Neutral atoms, Pergamon, Oxford, (1972).
5. A.Jablonsky, Phys. Rev. 68, 78, (1945), Acta Phys. Polon. 23, 493, (1963); 27, 49, (1965); 34, 561, (1968).
6. R.L.Fox, H.C.Jacobson. Phys. Rev. 188, 232, (1969); A.Royer. Phys. Rev. A6, 200, 2044, (1971); G.D.Mahan. Phys. Rev. A6, 1273, (1972).
7. W.Funk, H.Kloss. Proc. XI ICPGI, Praha p 400, (1973).
8. I.Grycuc, J.Wierzbicker. Opt. Commun., 14, 384, (1975).
9. V.G.Vdovin, A.A.Pustoshkin. Compl. Rep. of All-Union Conference on Metrology of Rapid-Running Processes, VNIIOFI, M, 70, (1978).
10. I.S.Fishmann, E.M.Nurmatov. TVT, 11, 946, (1973).
11. L.N.Shabanova. Optics and Spectroscopy, 36, 23, (1974).

A FULLY AUTOMATIC CONTINUOUS ELECTRON TEMPERATURE MEASUREMENT SYSTEM USING A DOUBLE LANGMUIR PROBE

T.N. Todd.

Culham Laboratory, Abingdon, Oxon. OX14 3DB, U.K., (EURATOM/UKAEA Fusion Association).

A novel system for continuous electron temperature measurement has been developed as a plasma diagnostic on the Culham Superconducting Levitron. This system has been used to measure plasma temperatures (T_e) of between 0.1 and 20 eV and densities (n_e) in the range $5 \times 10^9 + 5 \times 10^{12}/\text{cc}$, with a response time of approximately 300 μs .

The double probe characteristic, from which electron temperature and density are derived, is best obtained by sweeping the probe with an AC voltage which only just produces current saturation. This is because the transformer coupling which electrically floats the probe causes an indefinitely maintained current saturation (ie. a DC current) in the probe windings to appear as exponentially decreasing in the current-sensing secondary winding. Thus the current signal is distorted if the probe is swept much beyond the "knees" of the characteristic. This problem arises with fixed voltage amplitude systems when the plasma temperature is low, but is overcome by this system which continuously adjusts the voltage amplitude so as to just reach saturation. Since the onset of saturation occurs at a voltage proportional to the electron temperature, precision rectification and smoothing of the driving voltage then provides a continuously varying DC voltage proportional to the electron temperature. When the current signal is similarly converted, continuous density measurements are also obtained, using the expression $n_e = \text{const} \times I_{\text{SAT}}/\sqrt{T_e}$. The system presented here achieves this effect by sweeping the probe sinusoidally and maintaining a constant proportion of third harmonic in the returned current signal (see Fig.1). This proportion is obtained by using an automatic gain-controlled amplifier (AGC) to normalise the current signal to a constant amplitude and then filtering out the third harmonic. The filter output is in turn held constant by using it as the control input of the sweep volts AGC.

High resolution equilibrium profiles of temperature and density (eg. Fig.2) are easily obtained

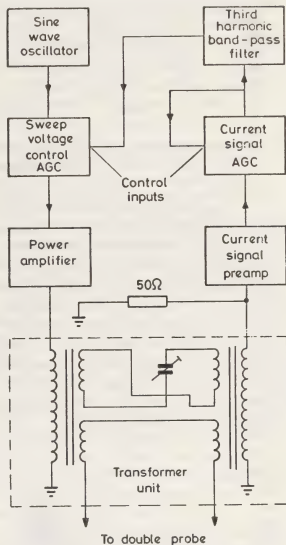


Fig.1 Schematic of system loop

by driving the probe across the plasma, so that correctly averaged comparisons can be made with the line-of-sight diagnostics. In this way average temperatures derived from the absolute intensity of the He I 5876 Å line and densities from 4 mm microwave interferometry are found to be in close agreement with those derived from the probe over a wide range of plasma parameters and despite magnetic fields of a few kilogauss.

The system usually operates with a sweep frequency of 10 kHz, which permits an AC-amplitude

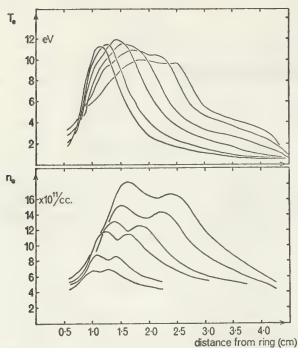


Fig.2 Plasma profiles in helium at various powers of 16 GHz microwave heating response time of approximately 200 μs , lengthened to about 400 μs by rectification and filtering. These response times can be improved by increasing the sweep frequency, but with a sacrifice in the dynamic range of the system. With 10 kHz this range is about 10,000:1 in current signal and 350:1 in voltage (ie. electron temperature), providing a system capable of tracking far into plasma decays. Fig.3 is an example of a plasma decay to which 50 Hz ohmic heating (causing a 100 Hz temperature modulation) has been added where shown.

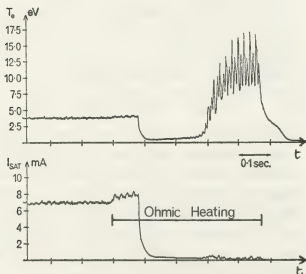


Fig.3 Microwave plasma decay with 50 Hz ohmic heating

A simple dynamic simulator of double probe characteristics has also been developed, which imitates the non-linear plasma impedance seen by the probe. It simulates plasmas of temperature $0.5 + 30$ eV and density $2 \times 10^{10} - 10^{12}/\text{cc}$, with a maximum modulation frequency of about 30 kHz. This unit provides a valuable aid in optimising and checking the temperature measurement system.

Although initially developed to follow the time dependence of Levitron plasma decays, the continuous electron temperature measurement system has become a primary diagnostic used extensively for obtaining equilibrium profiles of interest in our studies of plasma heating, containment and fluctuations.

The author acknowledges considerable contributions made to this work by D E T F Ashby and W H W Fletcher.

ON PLASMA SHEATH PROBLEMS

J.P. J. Lafon.

*Observatoire de Meudon, Département Recherches Spatiales (DESPA) C.N.R.S. L.A. 264,
92190 Meudon France.*

The analysis of a large number of geophysical and astrophysical phenomena (such as electric charging of a body in a space plasma, alteration of the characteristics of wave emission by an antenna in a hot plasma, behaviour of a plasma probe ...) requires an accurate theory of the sheath surrounding a biased conductor in a collisionless plasma. One has to solve strongly self consistent, non linear and non local integro-differential equations : the sheath depends on the potential of the body which is self consistent with the sheath structure when it is not fixed; the sheath governs the collected currents and so, sometimes, the emitted currents; all these currents may conversely control the potential of the body (and so the sheath structure) when it is not imposed (cf fig. 1). Indeed, ignoring such phenomena may lead to erroneous analyses of what occurs.

The sheath structure and the collected currents have been investigated in a number of particular cases by various authors¹ using different (physical or mathematical) approximations depending on the cases considered. Roughly speaking there are two classes of problems : those for which spherical or cylindrical symmetry can be assumed and the others. These problems can be solved using completely different formalisms. In particular problems of the second kind require the use of a still much heavier formalism. For problems of the first kind (cylindrical or spherical bodies), in non magnetized plasmas, elaborate, but also complicated theories have been developed by Bernstein and Rabinowitz², Moskalenko³, and Laframboise⁴. However surface effects are not taken into account without more or less crude approximations. On the other hand effects such as reflection or emission of particles by the body may be important; besides there are few works concerning the case of magnetized plasmas and in this case the approximations used are rather crude¹.

The equations governing the sheath structure are a Vlasov equation for the distribution function F_s of the particles of each species s together with Poisson's equation which determines the electric potential in terms of the F_s . Even in spherical or cylindrical symmetry the solution of these equations is difficult because they are strongly non linear, non local and integro-differential. Without crude approximations they can be solved only using numerical iteration in which the main problem is always the classification of the particle orbits.

Now we have found a formalism in which the problem appears to be a particular case of a general problem which consists in finding the intersection of an infinite number of domains depending on a continuous parameter in an n -dimensional space as that of a finite (small) number of domains easily delimitable^{1,5}. We have proved a general theorem and we have derived from it a systematic method for solving the problem⁶. The method is well fit for numerical computations and even reduces them to the minimum when they are necessary. In particular it is a powerful tool for solving the sheath problem completely for conductors with any surface effects as soon as the physics of these effects is known, even in some magnetized plasmas⁹.

Of course, strictly speaking, absolute self consistence requires complete radial (cylindrical or spherical) symmetry for exact solution. However, as a property of Poisson's equation which smoothes the space charge irregularities, this condition is not so important as it seems at first glance and rather strong asymmetries can be taken into account with very good accuracy^{8,11} provided that they do not disturb too much the symmetry of the electric potential (which is the only thing truly necessary).

Using our new method we have investigated the behaviour of bodies reflecting some of the particles striking them (rather different effects are produced depending on the polarization of

the body^{6,7} and that of bodies emitting photoelectrons^{8,11}. We have also investigated the case of cylindrical bodies in some weakly magnetized plasmas⁹. Of course it is not possible to discuss all the results here: they are discussed in detail elsewhere^{1,5 to 11}.

The figures shown hereafter illustrate some of the characteristics of the sheath structure under various circumstances.

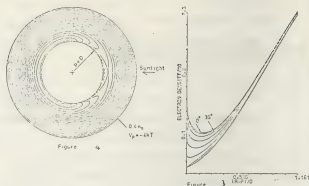
Finally there is a wide field of possible applications of the theorem and of the method, in particular for investigating all plasma sheath problems which can be stated under a similar form^{1,12}.

REFERENCES

- 1 - LAFON J.-P. J. - Etude d'une classe de systèmes obéissant à un ensemble continu de conditions dans un ensemble continu d'états. Thèse de Doctorat d'Etat ès Sciences. Université de Paris VII. 1976. Rpt Observatoire de Meudon DESPA159bis.
- 2 - BERNSTEIN I. B. and RABINOWITZ I. N. - Phys. Fluids, 1959, 2, 112-121.
- 3 - MOSKALENKO A. M. - XVth Int. Astron. Cong., Warsaw, Poland, 1959, 7/12 September 1964.
- 4 - LAFRAMBOISE J. - Theory of cylindrical and spherical Langmuir probes in a collisionless Maxwellian plasma at rest. Rpt n°100 of the Institute for aerospace studies of the University of Toronto, Canada (UTIAS100), 1966.
- 5 - LAFON J.-P. J. - Journal of Math. Phys., 18, 1977, 1178-1187.
- 6 - LAFON J.-P. J. - Plasma Phys., 17, 1975, 731-740 and 1175.
- 7 - LAFON J.-P. J. - Plasma Phys., 17, 1975, 741-756.
- 8 - LAFON J.-P. J. - Radio Science, 11, 1976, 483-493.
- 9 - LAFON J.-P. J. - Journal of Plasma Phys., 10, 1973, 383-396.
- 10 - LAFON J.-P. J. - To appear.
- 11 - LAFON J.-P. J. - To appear.

Fig. 3 - Spherical body emitting photoelectrons in a plasma. Electron density profiles in planes through the center of the sphere and at a regularly increasing angle (18° /step) with the direction of the light. $T_{\text{electrons}} = T$, radius of the body = Debye length

Fig. 4 - Spherical body emitting photoelectrons in a plasma. Iso - electron density curves: $T_{\text{electrons}} = T$, photoelectrons = γT ; Radius of the body = p (in Debye lengths)



Distribution function of the particles that leave a metallic body in a plasma:

δ_0 denotes the distribution function of the emitted particles (photoemission, secondary emission, thermionic emission ...)

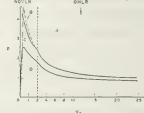
$\gamma \delta_0$ denotes the distribution function of the diffusely reflected particles (it depends on that of the particles striking the body)

γ denotes the coefficient of specular reflection

$$f(\mathbf{v}) = \frac{1}{4\pi} \left[\delta_0(\mathbf{v}) + \gamma \delta_0(-\mathbf{v}) + \gamma \delta_0(\mathbf{v}) + \gamma \delta_0(-\mathbf{v}) \right] = \frac{1}{4\pi} \left[\delta_0(\mathbf{v}) + \gamma \delta_0(-\mathbf{v}) \right]$$

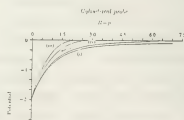
δ_0 Particles specularly reflected from the body emitted by the probe
 $\gamma \delta_0$ Particles specularly reflected from the body emitted by the probe
 $\gamma \delta_0$ Particles coming from the body and specularly reflected by the probe
 $\gamma \delta_0$ Particles coming from the body and specularly reflected by the probe
 $\gamma \delta_0$ Particles coming from the body and specularly reflected by the probe

The brackets are equal to 1 or 0 depending on the energy and the momentum of the particles.



Effect of partial reflection (reflection coefficient γ) of some of the particles striking a cylindrical body. $T_{\text{ions}} = T_{\text{electrons}} = T$, p , V_0 , q denote respectively the temperature of the particles, the radius of the body (in Debye lengths), the potential of the body (in kT) and the charge of a particle; index a for particles such that $qV_0 < 0$, b for those for which $qV_0 > 0$. The current collected is OML (Orbital Motion Limited) i.e. independent of the sheath structure in the regions indicated in the following table:

particles a	$C = 0$	D	$B + C + D$
particles b	everywhere	everywhere	OML
	$\gamma_a = 0$	$\gamma_a \neq 0$	$\gamma_a = 0$
	$\gamma_b = 0$	$\gamma_b = 0$	$\gamma_b \neq 0$



Contraction of a cylindrical sheath by an axial magnetic field. Curves 1, 2, 3 correspond respectively to the values 0, 1, 2. O.b.t. of the ratio (Debye length/axial radius) if $T_{\text{ions}} = T_{\text{electrons}} = T$; radius of the body = Debye length

A SPECTRAL CHRONOGRAPHIC AND EQUIDENSITOMETRIC INVESTIGATION OF A PULSE BLENDED DISCHARGE

A. Petrakiev, I. Koleva, J. Ganeva.

University of Sofia, Department of Physics, Chair of Optics and Spectroscopy, Bulgaria.

ABSTRACT: A method of space-and-time diagnostic of capillary pulse discharges on the basis of spectral equidensitometric investigations, is proposed.

INTRODUCTION

The specific peculiarities of the localized pulse discharges, such as the obtaining of relatively small volumes of high temperature plasma (up to 10^5 K) within very short (from μ s to ns parts) duration, good reproducibility, simplicity of the scheme, etc., have made imperative the use of such discharges on a large scale. In the field of spectroscopy capillary pulse discharges are utilized for exciting the spectra of elements which are difficult to excite, and ions with high degree of ionisation. In the process of the development, testing and calibration of standard light sources, elaborated on the basis of capillary pulse discharges [1,2], several essential features and advantages of such sources, were elucidated. The chemical composition of the plasma jet corresponds to the composition of the walls of the capillary, a fact which enables the study of the properties of such plasma of a different chemical composition. The capillary pulse discharge is characterized by a strong space-and-time heterogeneity, which makes impossible the utilization of the common spectral methods of plasma-diagnostic. In the present work an attempt is made at investigating the space-and-time development of the temperature by means of spectral-and-equidensitometric and high speed chronographic methods.

EXPERIMENTAL

The electric circuit parameters are $C=420 \mu$ F, $U=250$ kV, and $L=1.2 \mu$ H. The discharge are carried out in air at atmospheric pressure. The discharges are aperiodical, with two well-shaped half-periods of a total duration of about 180μ s. The amplitude of the current intensity at the maximum of the first half-period is up to 5 kA. The localization of the discharge channel is achieved with the aid of two 1.8 mm thick flat parallel dielectric plates with dia 2.5 mm coaxial apertures at a distance of 2 mm from one another. Since no independent discharge intervened with the voltage and the gap with which we operated, we applied a powerful brief initiating pulse, synchronized with a SFR (USSR) superhigh-speed cinema-picture camera. The latter was used in a regime of stills extension of a speed of 95000 pictures per sec in a two- and four-raster system. The linear field of the stills was of 10 mm. The combining of the SFR camera with the narrow-band interference filters has made it possible to separate and retrace in time the excitation zones of the respective spectral lines. On Fig 1 the schema of the experiment is shown. It allows to

obtain a complete space-and-time information from one single shot for the two (λ_1 and λ_2) or the four (λ_1 , λ_2 , λ_3 and λ_4) lines. The data about the lines that we have used are given on Table 1. The last column of the table shows the normal temperature values for the corresponding lines [3,4,5]

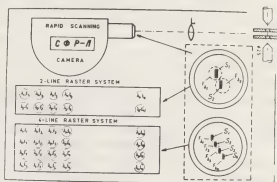


Fig.1

Table 1

	Line, nm	E_1, eV	E_2, eV	$T \times 10^{-4}, K$
λ_1	O I 604.6	10.99	13.04	1.8
λ_2	C II 437.4	24.65	27.49	3.3
λ_3	N III 409.7	27.44	30.46	4.8
λ_4	C IV 580.1	37.55	39.68	6.0

RESULTS AND DISCUSSION

The superhigh-speed photographs thus obtained, enable to retrace the structural changes in time in the discharge plasma. With pulse discharges the substance enters the interelectrode gap in the shape of vapour jets or flares. In localized pulse discharges the electrodes are stream-lined by contrary plasma jets from the channel in the direction of the electrodes. The formation of such jets is related to the evaporation of material from the walls of the capillaries in the rapid heating and expansion of the vapours. The high-speed capillary jets (Mach number up to 3) create compacted zones in the electrodes' stream-lining. Intensity pulsations are observed. This structure could be explained on the basis of the hydrodynamic phenomena arising in the outflow of supersonic speed plasma jets from a nozzle. From the stills thus obtained it can also be seen that coaxial plasma in the shape of a disk of a radius of some 4 mm is created between the capillaries. After some 20μ s after the beginning of the pulse, the bright central area ceases to grow in dimension. When we compare the stills extension of the plasma

glow of the capillary pulse discharge with use of various electrodes, great differences in the mechanism of entry of the vapours into the gap.

Spectral investigations of the discharge by zones show that in the spectrum of the central sector symmetrical to the axis there are lines of components of the composition of the capillaries, though not of the electrodes. In this area an excitation of lines with a different degree of ionization (of up to 0 V, C V), and a very good spatial distribution, are observed. The emission of lines of a different rate occurs from very narrow concentric zones of a different thickness (parts of the mm) in the area between the fronts of the bright zones and the surfaces of the plates, lines of the components forming part of the composition of the plexiglass, the air medium, and the electrodes, with a low degree of ionization, are observed.

Besides the good spatial distribution of the lines of a different frequency, a time extension is also observed. It is seen that the C IV 580.1 nm line is excited only during the first half-period, and that it achieves its maximum intensity about the 18th μ s as from the beginning of the discharge. For the N III 409.7 nm line I_{\max} is observed about the 42th μ s, for the G II 437.4 nm, about the 50th μ s, while the O I 604.6 nm line achieves a maximum value between the 64th and 70th.

The simultaneous knowledge of the intensity $I_t = F(x, y, z, t)$ of lines of a different degree of ionization has enabled us to follow up the space-and-time development of the temperature. Use was made of the temperature functions of excitation of the respective lines with such a selection as to allow to include both the high-temperature areas of the discharge channel and the peripheral zones. The temperature functions [3, 5] are determined with an accuracy of up to 15 per cent, and are normalized to unit. From the photographs obtained through the combined use of the SFR film camera and the interference filters only the stills corresponding to the maximum of the temperature functions of excitation of the respective lines (Fig. 2) were selected, and were processed by the methods of photographic equidensitometry [6, 7]

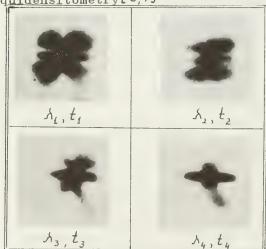


Fig. 2

All stages of the process of obtaining the Sabatier effect, were observed. A calibration of the equidensities was carried out and the blackening curves and the sensitometric properties of the photographic material utilized, were taken into account. A family of the equidensities of the lines of a different ionization rate was obtained for time instants corresponding to their normal temperatures; the difference in the blackening densities of the individual equidensities is $\Delta S = \text{const}$ (Fig. 3)

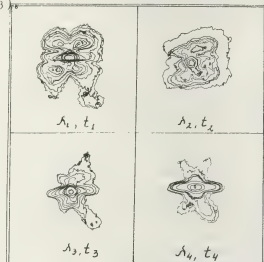


Fig. 3

By means of a numerical solution of Abel's integral equation [8] the radial distribution of the intensity was obtained. The results of space-and-time development of the temperature, obtained in the conditions of a capillary pulse discharge, is shown in Table 2.

No	equid.	604.6 nm $t_1 = 66 \mu s$		437.4 nm $t_2 = 50 \mu s$		409.7 nm $t_3 = 42 \mu s$		580.1 nm $t_4 = 18 \mu s$	
		$I(r)$ rel.	$T^\circ K$ $\times 10^{-4}$	$I(r)$ rel.	$T^\circ K$ $\times 10^{-4}$	$I(r)$ rel.	$T^\circ K$ $\times 10^{-4}$	$I(r)$ rel.	$T^\circ K$ $\times 10^{-4}$
1	15	1.8	26	3.3	35	4.8	55	6.0	
2	8.5	1.5	20	2.2	24	3.8	37	3.7	
3	5.2	1.45	13	1.5	16	3.0	26	3.4	
4	3.8	1.4	9	1.3	9	2.7	18	2.9	
5	2.9	1.3	6	1.2	6.3	2.4	14	2.8	
6	2.1	1.25	4.4	1.1	4.7	2.3	7.8	2.7	
7	1.7	1.23	3.7	1.0	3.7	2.2	6.2	2.6	
8	1.4	1.2	2.5	0.9	2.8	2.1	4.9	2.5	
9	1.2	1.15	-	-	2.4	2.0	-	-	
10	1.1	1.1	1.8	0.8	2.2	1.9	2.3	2.4	

CONCLUSIONS: The proposed method can be successfully used with plasmas, with which it is impossible, or very difficult, to determine the plasma parameters with the aid of other diagnostic methods.

- 1 Огурцова Н., Подмошнский И., ОМП, 1, 1960
- 2 Klatt H., Staatsexamensarbeit, Kiel, 1967
- 3 Larenz R., Zeit. Phys., 129, 327, 1951
- 4 Krempel H., Zeit. Phys., 167, 302, 1962
- 5 Petrakiev A., Vörös T., Spectroch. Acta 24 B, 369, 1969
- 6 Lau E., Krug W., Equidensitometry, 1968
- 7 Владимиров С., Астроном. журн., 977, 1977
- 8 Bockasten K., JOSA, 51, 9, 943, 1961

MESURE DES PROBABILITES DE TRANSITION DES RAIES 5^1D_2 , 6^1D_2 , $7^1D_2 \rightarrow 5^1P_1$ DU CADMIUMB. Cheron, J. Jarosz^{*} and P. Vervisch.

Laboratoire de Thermodynamique, L.A. C.N.R.S. N°230, Faculté des Sciences et des Techniques de Rouen, B.P. 67, 76130 Mont-Saint-Aignan, France.

^{*} I.N.S.A., avenue Albert Einstein 69621 Villeurbanne Cedex.

L'introduction d'additifs dans les flammes en vue de leur identification ou de la détermination de leurs caractéristiques physiques pose principalement à l'expérimentateur travaillant en émission, un double problème de stabilité dans le temps et dans l'espace. Dans une torche H.F., à la pression atmosphérique, la mise au point d'un système d'injection par pulvérisation ultrasonique (réf. 1) permet de répondre à cette double exigence. Des gouttelettes de diamètre 1μ sont ainsi introduites au centre d'un plasma d'argon, au niveau de la première spire d'un générateur H.F. à lignes accordées fonctionnant à 40 MHz. Un montage classique d'analyse spectroscopique permet la mesure de l'intensité des raies d'émission juste au-dessus de la dernière spire de la torche.

Des mesures préliminaires de température électronique, effectuées à partir des raies du fer, confirment que, étant donné la faible concentration des additifs dans la flamme, celui-ci varie peu avec l'élément injecté : $T_e = 5200 \pm 400^\circ K$ (fig. 1).

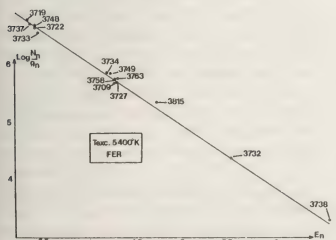


Figure 1

Les probabilités de transition données par

Laniece (réf. 2) déterminent le tracé du diagramme

de Boltzmann du cadmium (fig. 2). On déduit de celui-ci la valeur des populations des niveaux 5^1D_2 , 6^1D_2 et 7^1D_2 , et, par l'intermédiaire de la formule classique de l'intensité des raies d'émission d'un plasma mince et homogène, d'épaisseur X :

$$I_{\nu} = \frac{h\nu}{4\pi} A_{nm} N_n X,$$

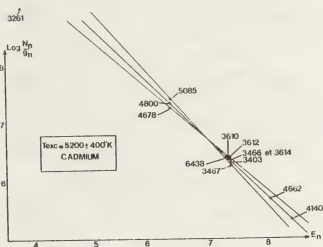


Figure 2

la valeur des probabilités de transition des raies étudiées, à savoir :

λ_{nm}	$n \rightarrow m$	$A_{nm} \cdot 10^6 s^{-1}$
6 438	$5^1D_2 \rightarrow 5^1P_1$	59 ± 6
4 662	$6^1D_2 \rightarrow 5^1P_1$	$5,5 \pm 1,2$
4 140	$7^1D_2 \rightarrow 5^1P_1$	$4,7 \pm 1,5$

Ces valeurs sont en bon accord avec les durées de vie calculées par effet Hanle (réf. 3)

Références

- (1) J.M. HERMET, J.P. ROBIN. Anal. Chem. 40, 1918, (1968)
- (2) LANIEPCE. J. Phys. 31, 439 (1970)
- (3) CHANTEPIE, COJAN, LANDAIS. J. Phys. 36, 1067 (1975).



EXTERNAL AND INTERNAL PROBE MEASUREMENTS IN DISCHARGES OF LUMINESCENCE LAMP TYPE

G. Schaal, J. Zabel.

Zentralinstitut für Elektronenphysik, V Akademie der Wissenschaften der DDR, DDR 22 Greifswald.

Introduction: Williams /1/ and Williams and Turner /2/ made experiments to determine the wall potential, the axial electric field and the electrode falls by external probes in luminescent lamp discharges. Systematic comparisons of the results of internal and external probe measurements in the same type of discharges were given in /3/ which also described statistical methods to determine the reliability of external probes. In the present paper some data are given on the mechanism of coupling the external probe to the plasma and about the accuracy with which data are obtained from axial field and floating potential measurements by this method, time resolved and with rms.

Method: In a cylindrical discharge vessel of the geometry of a 40-watt luminescent lamp without luminescent material three internal probes were introduced at a distance of 10 cm, 55 cm and 95 cm from the electrode. The tube was heated, formation of electrodes was done and it was filled with mercury and argon (3 Torr). External probes with a width of 10 cm, 4 cm, 2.4 cm and 1.2 cm were installed near the internal probe which was at a distance of 55 cm from the electrode. In another arrangement up to ten external probes were used in different regions of the tube. The measuring probes were coupled via a white cathode follower to an oscilloscope or to quadrant electrometer. In this way one could reach an input resistance of 10^9 ohms and an input capacitance of 1.6 pF.

Results: Different resistors and capacitors were connected parallel to the input of the cathode follower. The output of the cathode follower was given to the ordinate

of the oscilloscope. The signal of the internal probe was handled in the same way and given to the x-axis. From this kind of Lissajous figure it is clearly to be seen that the coupling agent to the external probe is not a resistive one but a capacitive one (Fig. 1).

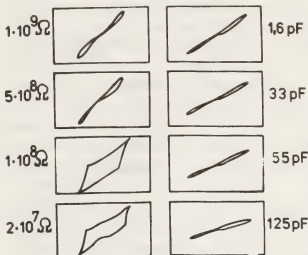


Fig.1: Response to different input impedances

From the input voltage of the cathode follower used with different input capacitors we determined the coupling capacity of the external probe (method 1). If the input of the oscilloscope with an input resistor of 10^6 ohms is connected directly to the external probe, it is possible to determine the same capacity from measuring the decay time of the probe voltage (method 2). Applying the formula of a cylindrical capacitor the value of the coupling capacity can be calculated. Table 1 shows the values obtained.

Table 1

Width of probe	Method 1	Method 2	Calculated
10 cm	330 ± 20 pf	360 pf	360 pf
4 cm	145 ± 10 pf	170 pf	144 pf
2,4 cm	93 ± 10 pf	140 pf	86 pf
1,2 cm	50 ± 8 pf	80 pf	43 pf

Taking the above mentioned second arrangement and determining rms values of the axial electrical field by internal and external probes the data obtained showed good agreement.

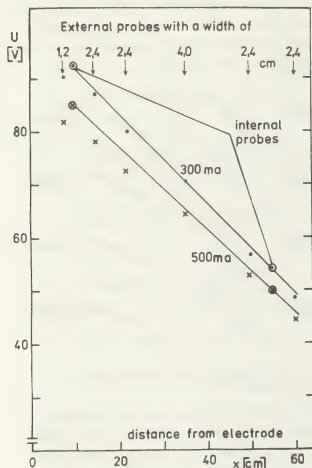


Fig.2: Floating potential determined by external and internal probes

Fig.2 shows a diagram of the measurements of floating potentials by internal and external probes against electrode distance which makes evident that the measured values of external probes are smaller than those of the internal ones. Taking into account the impact of the voltage divider, which consists of coupling capacity and input capacitance, the following corrections of the measured values have proved suitable.

Probe width

4 cm	$U = 1,01 U_{\text{measured}}$
2,4 cm	$U = 1,02 U_{\text{measured}}$
1,2 cm	$U = 1,035 U_{\text{measured}}$

Considering these corrections a good agreement of the potentials measured by both kinds of probes (Fig.3) is obtained.

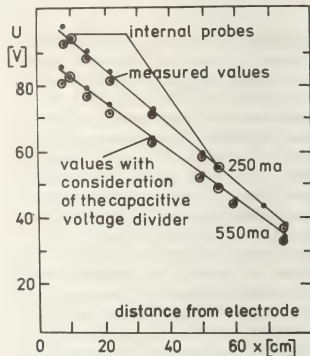


Fig.3: Influence of capacitive voltage divider

If in the system the quadrant electrometer is replaced by an oscilloscope one gets the time resolved potentials of probes. It was found that the shape of internal and external probe voltage is similar, however the amplitude of the external one is influenced by cathode follower transmission and input capacitor, whose impact can be taken into account.

Conclusions: The coupling mechanism of external probes at 50 cps is definitely of a capacitive nature. The application of high input impedance cathode followers affords a simple method to reduce deviations between the data taken from internal and external probes.

References:

- /1/ C.E. Williams, 2nd Int. Conf. Gas Discharges, London, 1972, 85-87.
- /2/ C.E. Williams, J.C. Turner, 3rd Int. Conf. Gas Discharges, London 1974, 49.
- /3/ U. Fuchert, Abschlussarbeit, Ingenieurhochschule Mittweida 1976.

THOMSON SCATTERING WITH A HIGH BACKGROUND LEVEL OF PLASMA RADIATION

B. Van der Sijde, T. Poorter, S. Adema, B.F.M. Pots and D.C. Schram.

Physics Department, Eindhoven University of Technology, Eindhoven, The Netherlands.

Introduction: Thomson scattering is nowadays a standard technique in plasma physics. Most of the experiments are carried out by using short pulse-high power lasers (e.g. a 10 ns-100 MW Q switched ruby laser). In that case the Thomson signal is mostly relatively small and there are normally minor problems with the background of plasma radiation owing to the very short pulse duration. The aim of this paper is to describe a device with a long pulse-high energy ruby laser (1.5 ms, 50 J) appropriate for measurements at small and medium electron densities. Correction for the plasma radiation (continuum and weak line radiation) and improvement of the signal to background ratio by adequate rejection of the stray light of strong lines is necessary in that case. We obtained a high rejection by using a grating in combination with an optical filter. The device built up according to this principle is a simply handling small volume system at a relatively low cost. The applicability of the device is tested with a hollow cathode arc (H.C.A.) as a plasma source; the electron density and temperature ranges of the argon plasma used were $5 \cdot 10^{18}$ – $8 \cdot 10^{20} \text{ m}^{-3}$ and 2.5–4.5 eV.

The Thomson scattering device (T.S.D.). Our aim is to develop a T.S.D. for a wide range of electron densities $n_e = 10^{18}$ – 10^{21} m^{-3} at low electron temperatures of 2.5–5 eV in the presence of a large amount of annoying plasma radiation. Laser stray light is adequately diminished by a laser- and a viewing dump. The specific problem in the case of a spectrum with a multitude of lines is to find one or more appropriate "valleys" between strong lines to place the exit channels and to clean these valleys as good as possible from the stray light of plasmaradiation. Therefore, we built a six channels polychromator with a special purpose concave holographic grating - transmission 60%, 1800 lines/mm, dispersion 1.1 nm/mm, rejection factor $1.3 \cdot 10^{-3}$ for a 1 nm bandwidth channel at

a wavelength shift of 5 nm - in combination with a four periodic 5 nm bandwidth filter - transmission at the top of 75% and of $2 \cdot 10^{-3}$ at a shift of 5 nm - to diminish the stray light still furthermore. The T.S.D. exists of a ruby laser with an incident beam focussed to a waist of 2 mm. The laser light, scattered in a volume of $1 \times 2 \times 2 \text{ mm}^3$ under 90° , is focussed on the entrance slit of polychromator with an entrance angle of $1.3 \cdot 10^{-2} \text{ sr}$. Homemade perspex light guides with 60% transmission transmit the signals to photomultipliers with a high quantum efficiency (10%). Photon counting is carried out after amplification, and discrimination with a PDP 11/20 computer system. A large entrance angle, a relatively high measured transmission factor ($1.6 \cdot 10^{-2}$), a large quantum efficiency and the application of filters is essential to get good results.

Improvement of the signal to background (S/b) ratio. We determined the rejection factor of the grating by applying Rayleigh scattering with a 20 torr argon gas sample. The rejection factor is defined here as the ratio of the counted photons in a Thomson channel (with a certain wavelength shift $\Delta\lambda$ with respect to the laser wavelength) and those in the Rayleigh channel and is as such dependent on the shift $\Delta\lambda$. These results shown in Fig.1 are valid for normalized slits equivalent to a bandwidth of 1 nm. We also indicate in the same figure the rejection factor for the combination of grating and filter for the first channel. The factor is better for the other channels. The combination improved to reject almost all stray light of strong neighbouring lines and the relative improvement in the background signals of the five channels is a factor 1.5–3.5. Additional 1 nm bandfilters appear to give no further improvement. It means that the remaining background exists of continuum and weak line radiation from the channel's wavelength itself. Application

of a polaroid filter gives a further improvement of the S/b ratio with a factor 1.2. This effect is rather small caused by the fact that the grating has a preferential transmission in the direction of the polarization of the laser light.

Measurement of the S/b ratio. The S/b ratio has been investigated for more than two decades of n_e -values at $T_e = 3.2$ -4.0 eV by application of the above mentioned equipment. In Fig.2 these ratio's are indicated. They appear to be less than 1 for all conditions and channels. Values of the S/b ratio between 0.1 and 1 are appropriate as to be used as reliable data for n_e and T_e determination. The accuracy of the n_e -values after 10 shots varies from 20% at 5.10^{18} m^{-3} to 6% at 2.10^{19} m^{-3} and 20% at 8.10^{20} m^{-3} . The calibration causes an additional error of 3%. The accuracy of T_e is 8-30% after 10 shots. In Fig.3 we show the background radiation for the high n_e -values. In channels 1 and 2 a 692.5 nm argon I line and in channels 4 and 5 a 690.1 nm argon II line is present. The influence of the first is evident at low n_e -values and that of the latter at high n_e -values. For high n_e -values $> 2.10^{20} \text{ m}^{-3}$ the increase of radiation is proportional to n_e^2 . Continuum radiation is proportional to $n_e \cdot \sum z_j^2 n_{ij} / T_e^{1/2}$, so that the measured intensity seems to be proportional to $n_e n_{i1}$ or $n_e n_{i2}$ (singly and doubly ionized particles). In [1] we point out that the n_{i2} density is not clear at this moment. The line for continuum radiation from singly ionized particles is indicated in the Fig. and shows a factor 3 discrepancy with the measured curve for the channels 1 and 2. The line for continuum radiation from doubly ionized particles has been shifted a factor 2 if Biberman and Gaunt factors are the same. If we compare the quality of this system with a 50J - 1.5 ms laser pulse with a 1J - 10 ns pulse system, it appears that on a single shot basis the accuracy of the Thomson counts in the channels are roughly as follows:

$n_e = 5.10^{18} \text{ m}^{-3}$: 50% 50 J s.; 150% 1 J s.
 $n_e = 5.10^{19} \text{ m}^{-3}$: 25% 50 J s.; 75% 1 J s.
 $n_e = 5.10^{20} \text{ m}^{-3}$: 25% 50 J s.; 25% 1 J s.

Conclusions. We conclude that for a steady state plasma with $n_e \leq 5.10^{20} \text{ m}^{-3}$ the high energy-long pulse laser system is more appropriate than a low energy short pulse laser in spite of the complication of background radiation if a valley between

strong lines can be found. A wide entrance angle, a large quantum efficiency, a good transmission, dispersion and rejection of stray light are crucial conditions.

Reference

- [1] B. van der Sijde, B.F.M. Pots, D.C. Schram, Proc. 14th ICPIG, Grenoble 1979.

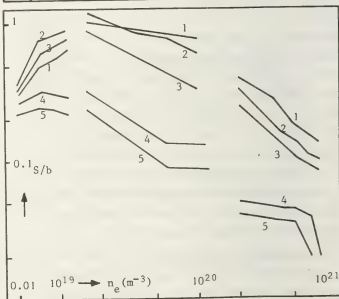
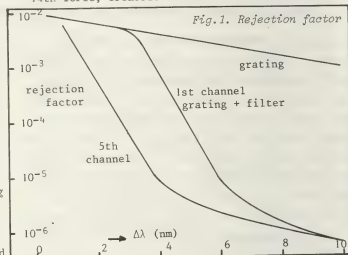


Fig. 2. Signal/background ratio's as a function of n_e .

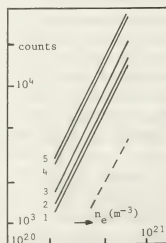


Fig. 3. Background countings as a function of n_e .

RAYLEIGH AND COMPTON SCATTERING CROSS SECTIONS OF X-RAYS BY OXYGEN IONS

A.V. Kupliauskienė and Z.J. Kupliauskis^{*}.

^{*}Institute of Physics of the Academy of Sciences of the Lithuanian SSR, Vilnius, U.S.S.R.
^{*}V. Kapsukas Vilnius State University, Vilnius, U.S.S.R.

The methods based on the photon scattering are widely used in plasma diagnostic [1]. The X-rays and gamma rays attenuation and energy absorption coefficients are proportional to the total photon interaction cross section per atom, i.e. to the sum of the cross sections of all the elementary scattering and absorption processes. The atomic cross sections for X-rays absorption at energies above 1 keV can be written as the sum of all partial cross sections for the photoelectric effect, for Rayleigh and Compton scattering. X-rays and gamma rays scattering cross sections for neutral atoms have been summarized by Hubbell et al [2,3]. The ions of different degree of ionization exist in plasma. It is therefore important to consider the change in the Rayleigh and Compton scattering cross sections when the neutral atoms are replaced by the corresponding ions.

In this paper, we report the differential and total Rayleigh and Compton scattering cross sections of X-rays by the atom and ions of oxygen. The variation of the Rayleigh scattering cross sections with the excitation and ionization of the neutral oxygen atom has been investigated in [4].

The differential Rayleigh scattering

cross sections at low incident-photon energies decrease as the degree of ionization of the atom increases at all angles. As the incident-photon energy increases, scattering cross sections at large angles do not depend on the degree of ionization whereas the scattering by outer-shell electrons is insignificant. The differential scattering cross sections decrease with increasing scattering angle and reach a minimum at scattering angles of $\pi/2 - 2\pi/3$. The reduction in the cross sections at small angles is more rapid for higher energies and the growth of the cross sections is more rapid at lower values of X-rays energy.

As the degree of ionization increases the differential Compton scattering cross sections decrease at all scattering angles and for all energies. The cross sections grow with the increasing scattering angle for small photon energies. The reduction of the cross sections is obtained in the region $\pi/2$ of the scattering angle when the X-rays energies exceed 10 keV. The differential Compton scattering cross sections of X-rays increase from zero at the zero scattering angle and reach the maximum at the scattering angle equal to π .

Table 1 lists the Rayleigh scattering cross sections, and Table 2 lists the

Table 1

The Rayleigh scattering cross
sections of X-rays (barn/atom)

E(keV)	0	0 ⁺	0 ²⁺
1	40.047	39.89	31.186
2	33.926	33.55	27.582
3	26.997	26.61	23.118
4	21.067	20.79	18.883
6	13.325	13.21	12.627
8	9.209	9.145	8.936
10	6.852	6.805	6.730
15	3.967	3.942	3.982
20	2.636	2.623	2.693
E(keV)	0 ³⁺	0 ⁴⁺	0 ⁵⁺
1	16.109	10.374	5.889
2	14.714	9.643	5.618
3	12.854	8.638	5.229
4	10.937	7.560	4.788
6	7.799	5.688	3.947
8	5.778	4.398	3.287
10	4.516	3.556	2.804
15	2.858	2.391	2.021
20	2.006	1.738	1.510

Compton scattering cross sections of X-rays by the atom and ions of oxygen. From the tables it is evident that our data are in good agreement with [2] for the neutral oxygen atom. The results listed in the tables show clearly that the Rayleigh scattering cross sections decrease while those of Compton increase for the neutral atom and all the ions investigated as the photon energy increases. The Rayleigh and Compton scattering cross sections of X-rays are very dependent on the degree of ionization. The reduction in the cross sections with the increasing degree of ionization of the atom is more

Table 2

The Compton scattering cross
sections of X-rays (barn/atom)

E(keV)	0	0 ⁺	0 ²⁺
1	0.211	0.226	0.130
2	0.721	0.756	0.494
3	1.319	1.352	0.943
4	1.867	1.886	1.379
6	2.672	2.665	2.069
8	3.152	3.139	2.514
10	3.452	3.439	2.800
15	3.873	3.864	3.208
20	4.098	4.092	3.438
E(keV)	0 ³⁺	0 ⁴⁺	0 ⁵⁺
1	0.086	0.066	0.032
2	0.310	0.239	0.117
3	0.602	0.462	0.231
4	0.895	0.680	0.348
6	1.355	1.010	0.543
8	1.645	1.211	0.682
10	1.837	1.348	0.791
15	2.143	1.592	1.012
20	2.336	1.764	1.181

significant at small energies whereas the contribution of outer-shell electrons is more important.

References

1. Properties of low energy plasma and its diagnostic (in Russian). Ed. M.F. Zhukov, Novosibirsk, Nauka Press, 1977.
2. Hubbell J.H., Veigele W.J., Briggs E.A., Brown R.T., Cromer D.T., Howerton R.J. J.Phys.Chem.Ref. Data, 4(1975) 471.
3. Hubbell J.H. Radiat.Res., 70(1977) 58.
4. Kupliauskis Z.J., Kupliauskiene A.V., Izv. VUZov SSSR.Fizika, No 4(1976) 95.

RESTORATION OF TWO-DIMENSIONAL RADIATION FOR AN OPTICALLY THICK PLASMA

V.V. Pickalov and N.G. Preobrazhensky.

Institute for Pure & Applied Mechanics, Siberian Division, Academy of Science, U.S.S.R. Novosibirsk, 630090.

Abstract. A concept of local diagnostics for an optically thick plasma without axial symmetry is proposed. It is possible to reduce the problem in two-dimensional case to the system of one-dimensional problems by decomposition in polar and cartesian coordinates.

Recently [1] the authors proposed an algorithm of data conversion to the local emissivities for an optically thick plasma of arbitrary configuration. Simulation procedure proved the reasonable accuracy for optical densities from 0 till 10 and the level of experimental errors 5-10% [2]. By decomposition technique in polar coordinates one can reduce the two-dimensional integral equation for local emissivities $\mathcal{E}(r, \theta)$ to the system of linear integral equations [2]:

$$\tilde{I}(\rho_i, \xi) = \rho_i \int_{\theta_1}^{\theta_2} \frac{\mathcal{E}_i(\theta + \xi)}{\sin^2 \theta} \times \quad (1)$$

$$\times \exp \left[- \rho_i \int_{\theta}^{\theta_1} \frac{k_i(\theta + \xi)}{\sin^2 \theta} \right] d\theta.$$

$\xi, \theta \in [0, 2\pi]$, $\rho \in [-R, R]$, $i = 1, 2, \dots$, $k_i(\theta)$ is the absorption coefficient for i-ring, $\tilde{I}(\rho_i, \xi)$ is the intensity of escaped radiation for i-ring and angle ξ . The system (1) can be solved successfully with due regard for smoothness of so-

lution as a priori assumption. If some additional information about solution is available the mathematical formulation of the problem can be efficiently simplified. E.g. the possibility of factorization in local coefficients:

$$k(x, y) = k_1(x)k_2(y), \quad \mathcal{E}(x, y) = \mathcal{E}_1(x)\mathcal{E}_2(y)$$

permits the retrieval of $\mathcal{E}(x, y)$ by means of decomposition in cartesian coordinates. In this case only two orthogonal directions are sufficient for observation and the problem comes to the system of two integral equations:

$$I_1(x) = \mathcal{E}_1(x) \cdot \int_{-\infty}^{\infty} \mathcal{E}_2(y) \exp[-k_1(x) \int_{-\infty}^y k_2(y) dy] dy,$$

$$I_2(y) = \mathcal{E}_2(y) \cdot \int_{-\infty}^{\infty} \mathcal{E}_1(x) \exp[-k_2(y) \int_{-\infty}^x k_1(x) dx] dx \quad (2)$$

Another kind of a priori information related to the form of isolines for basic plasma parameters can be prominent. In the special and the most popular axisymmetrical case (isolines are concentric circles) the problem of local diagnostics is described by one-dimensional Abel or Freeman-Katz [3] equations. In the more general case of isolines which are convex closed curves without self-intersections $\Psi(x, y, t) = 0$ one can find the spatial distribution of emissivities solving the Volterra I-st kind integral equation

$$I(\xi) = \exp \left(- \int_{t_1}^1 \mathcal{T}^+ k dt \right) \int_{t_1}^1 \mathcal{E} \left[\mathcal{T}^+ \exp \left(\int_{t_1}^t \mathcal{T}^+ k \times \right. \right.$$

$$\times dt) - \tilde{f} \exp\left(\int_{t_0}^t \tilde{f} k dt\right) \Big|_{t \in [0,1]}, k = k(t), \varepsilon = \varepsilon(t). \quad (3)$$

The "fan-shaped" measurement scheme (Fig.1a) is supposed here and the differential dS along the line of sight DL for two-place function $\alpha = \alpha(t)$ is given

$$dS \begin{cases} \tilde{f}^+(t, \xi), \frac{d\alpha}{dt} \geq 0, \\ \tilde{f}^-(t, \xi), \frac{d\alpha}{dt} < 0, \end{cases} \left(\frac{d\alpha}{dt}\right) \Big|_{t=t_1} = 0. \quad (4)$$

The case of side-on recording is easily obtained from (3); as to the special case $\tilde{f}^- = -\tilde{f}^+$ taking place for the system of shifted ellipses one comes to the generalized Freeman-Katz equation

$$I(\alpha) = 2 \exp\left(-\int_{t_1}^1 \tilde{f}^+ k dt\right) \int_{t_1}^1 \varepsilon \tilde{f}^+ \times \text{ch}\left(\int_{t_1}^t \tilde{f}^+ k dt\right) dt. \quad (5)$$

Geometrical arrangement of observation for a plasma with the known isolines is sketched in Fig.1a. The result of restoration for the model function $\varepsilon(\alpha, y) \equiv \varepsilon(t)$, t is shown in Fig.1b ($\times \times \times$) and is related to the system of shifted ellipses

$$\frac{[x - \alpha(1-t)]^2}{a^2} + \frac{y^2}{b^2} = t^2, \quad (6)$$

$a = 1.1, b = 1, \alpha = 0.4, \varphi = \xi = 0.$

Also in Fig.1b are plotted the "experimental" function $I(\alpha)$ with the noise level of 5% (oooo) and the coefficient of random error amplification $\gamma = \varepsilon / \varepsilon_1$ (----) in the method of regularization when the equation (3) is solved ($k=0$).

Fig.2 corresponds to the results of simulation in the problem of asymmetrical plasma field diagnostics for the lack of information about isolines. Modified "onion peeling" strategy [4] was used for eq. (1), maximum optical density being $\tau = 1$ and the initial noise level 1%.

Our results and theory show reason-

able accuracy for retrieval of rather complicated plasma fields as in laser explosion of targets, high temperature, tokamak or stellarator plasma etc.

REFERENCES

1. Pickalov V.V., Preobrazhensky N.G. In: Proc. XIII ICFIG, Berlin, v.1, 1977, 201.
2. Pickalov V.V. In: Abel inversion and its generalizations. Novosibirsk, 1978, 25 (in Russian).
3. Freeman M., Katz S. JOSA, 1960, 50, 826.
4. Chen F.P., Goulard R. JQSRT, 1976, 16, 819.

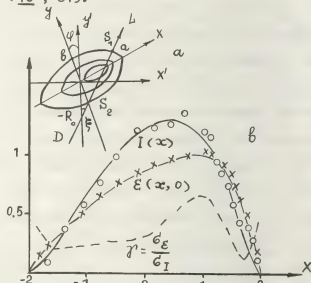


Fig.1 Geometrical arrangement of observation and the example of restoration: optically thin case.

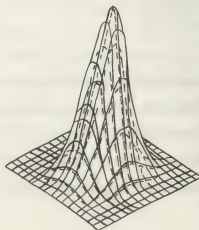


Fig.2 Modified "Onion peeling" method (layer decomposition): model function (—) and result of restoration (---); optical density $\tau = 1$.

APPLICATION OF FIELD VISUALIZATION TECHNIQUE TO SMM DIAGNOSTICS OF AXISYMMETRIC PLASMA

V.G. Zatsepin, V.B. Lazarev and E.A. Tishchenko.

Institute for Physical Problems, Moscow U.S.S.R.

Abstract : We present the development of sub-millimeter (SMM) diagnostics for inhomogeneous plasma under conditions of strong refraction [1-3], started earlier by the local probing [4] of moving UHF discharge [5]. Here is described the field visualization technique for quiescent plasma, based on registration of the probing field phase-amplitude distribution.

Experiment : Investigated discharge was situated at one of the channels of H_2O -laser ($\lambda = 119 \mu m$) interferometer (Fig.1).

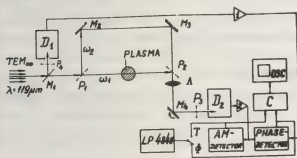


Fig.1 Scheme of experimental installation

Laser radiation consisted of two ortogonally polarised waves [6] with frequencies ω_1 and ω_2 , shifted at $\frac{\Omega}{2\pi} = \frac{\omega_1 - \omega_2}{2\pi} = 33$ kc. Detection of radiation was performed by Ge:B photoconductors [7] D_1 and D_2 at 4.2 K. To split and mix the waves ω_1 and ω_2 we used the one-dimensional wire grids P_1 - P_4 (period $20 \mu m$). P_1 reflected the reference wave ω_2 and passed the probing wave ω_1 . P_2 was crossed with P_1 . Mixers P_3 , P_4 were adjusted at 45° to polarizations. The beat signal used as a reference for the phase-voltage converter [8] was delivered by detector D_1 , coupled with laser by mylar splitter M_1 . Plasma was imaged by polyethylene lens L (diameter 54 mm, focal length $f = 280$ mm, distance to plasma and D_2 equals to $2f$) onto the horizontal

input slit (1×10 mm²) of D_2 . Image scanning was realized by rotation of the mirror M_4 with angular speed, stabilized up to 0.01%. Output voltage of the detector D_2 was proportional to the incident radiation intensity :

$$V(x) = \begin{cases} V_0(x) + |F(x)| \cos[\Omega t + \Psi(x)] & \text{with plasma} \\ V_0(x) + \alpha |M(x)| \cos[\Omega t + \Psi_0(x)] & \text{without plasma,} \end{cases}$$

where $|F(x)|e^{-i\Psi(x)}$ and $|M(x)|e^{-i\Psi_0(x)}$ are phase-amplitude distributions, α is constant coefficient, $\alpha = U/t$ and U is linear scanning speed. This signal was transmitted to the AM- and phase-detectors through a selective amplifier (2). Image field phase-amplitude distribution was registered by a storage oscilloscope and pulse analyzer LP 4840 operating in a multiscale regime. Sweep of these devices was synchronized with mirror M_4 . Parameters of the scanning system were as follows: M_4 rotation period $T_0 = 600$ ms, $U = 4\pi f/T_0 = 5.9$ mm/ms, visualized region $A = 25$ mm and number of used analyzer channels $N = 100$.

Results : Fig.2 a,b shows the phase-amplitude distributions of the probing field for filamentary UHF discharge in D_2 [5] ($P = 3.3$ ata, $W = 23$ kWt). Complex apparatus function $|K(y)|e^{-i\Omega(y)}$ (Fig.2c) of the interferometer was measured with a narrow slit in plasma plane. Phase shift introduced by plasma column was equal to $\Phi(x) = \Psi(x) - \Psi_0(x)$; modulus of transmittivity (curve (2) in Fig.4) was obtained as a ratio of the functions (2) and (1) in Fig.2a. Data processing was done by the numerical solution [9] of the convolution and Abel equations [3] with regard to refraction. Fig.3 represents the plasma electron density profile, calculated by Abel inversion of the phase function $\Phi(x)$.

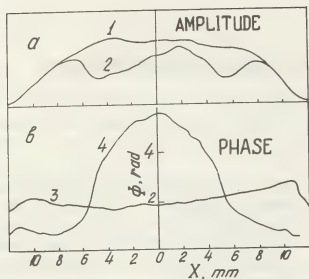


Fig. 2 a) (1) and (2) - field amplitudes $M(x)$ and $F(x)$; b) (3) and (4) - phase distributions $\Psi_0(x)$ and $\Psi(x)$; c) - plasma phase function $\Phi(x)$ (1), (2) - modulus $|H|$ and (3) - phase Ω of the apparatus function.

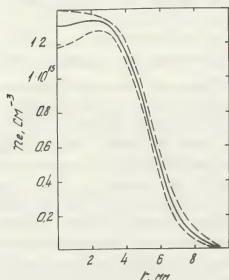


Fig. 3
Electron density profile

Dashed lines display the error limits corresponding to the absolute accuracy of the phase measurement $\Delta\Phi = \pm 0.1$ radn. Calculated modulus of transmittivity for phase function $\Phi(x)$ is shown in Fig. 4 (curve 1). Slight asymmetry of the curve is

caused by the small inclination (~ 0.04 radn) of the probing beam to the axis of the receiving system (see Fig. 2c, curve 3).

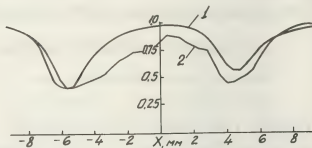


Fig. 4 Theoretical (1) and experimental (2) modulus of transmittivity

The difference between two curves is due to additional radiation loss besides refractive one. Its value in the experimental conditions was too small for application of the Abel inversion procedure to evaluate the radial distribution of the attenuation coefficient.

The authors are grateful to Academician P.L.Kapitza for the support of this work and would like to thank V.N.Sidorov for technical assistance.

References :

- [1] L.A.Vainstein, E.A.Tishchenko, Zh. Tech.Fiz, **46**, 11, 2271 (1976)
- [2] E.A.Tishchenko, L.A.Vainstein, Fiz. Plazmy, **3**, 1, 124 (1977)
- [3] E.A.Tishchenko, XIII ICPIG, Berlin, Contr.papers, p.159 (1977)
- [4] E.A.Tishchenko et al., XIII ICPIG, Berlin, Contr.papers, p.161 (1977)
- [5] P.L.Kapitza, ZETF, **57**, 1801 (1969) Sov.Phys.-JETP, **30**, 973 (1970)
- [6] V.V.Zav'yalov, G.D.Bogomolov, Pis'ma v ZETF, **20**, 393 (1974)
- [7] V.B.Lazarev, E.A.Tishchenko, Prib. Tech.Exper, 1979, to be published
- [8] V.B.Lazarev, Prib.Tech.Exper, **2**, 85 (1976)
- [9] V.G.Zatsepin, E.A.Tishchenko, A.V. Golubev, paper at this conference

RADIATION TEMPERATURE MEASUREMENT OF ARGON ARC PLASMA BY SUBMILLIMETER DIAGNOSTIC TECHNIQUES

E.A. Tishchenko, A.V. Golubev and V.B. Lazarev.

Institute for Physical Problems, Moscow U.S.S.R.

Abstract : Methods of radiation temperature measurement of the plasma filament by active and passive submillimeter diagnostic are described. The profiles of the side-on brightness of plasma thermal emission are measured at two wavelengths, one of them being selfabsorbed. These data are used to determine the radiation temperature and optical depth of plasma [1]. Simultaneous probing of the plasma filament by submillimeter radiation at two wavelengths allows to check this method and find out the degree of plasma equilibrium as well as the nature of electron collisions.

Experiment : Diagnostic installation consists of D.C. arc, heterodyne H_2O -laser ($\lambda = 119 \mu m$) [2] interferometer, homodyne backwave tube (BWT, $\lambda = 350 \mu m$) interferometer, high sensitive two-channel radio-meter and measuring apparatus.

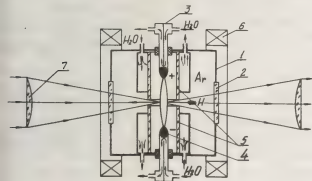


Fig.1 Arc configuration

Fig.1 shows the cross-section of D.C. arc chamber (1) ($10 \times 10 \times 10 \text{ cm}^3$). Its diagnostic windows (2) were made of crystalline quartz. The arc electrodes (50 mm apart) were cooled by water and have molibden tips (4). To facilitate the local side-on diagnostic of plasma by narrow submillimeter beams formed by the lenses (7), the plasma filament is moved with a frequency about several Hz by

oscillating magnetic field H of the coils (6).

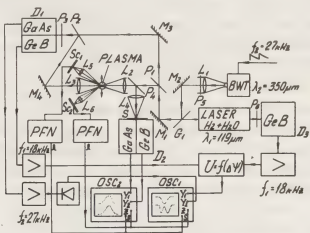


Fig.2 Diagnostic set-up : P_1 - P_6 - one-dimensional grids (period $20 \mu m$), M_1 - M_4 - metal mirrors, L_2 - L_4 - polyethylenelenses (diameter-54 mm, focal length-140 mm).

Optical system of the experimental installation (Fig.2) is a twin-wave Mach-Zehnder interferometer. H_2O -laser radiation consists of two ortogonally polarized waves with a frequency shift 18 kHz, orientated at the angles of -45° and $+45^\circ$ to the vertical. It is directed into the interferometer by means of mirror M_1 . BWT-radiation is formed in the quasioptical beam by the lens L_1 . Horizontal polarization, provided by polarizer P_5 , is directed into the interferometer by the mirrors M_1 and M_2 and grid G_1 . The frequency of BWT radiation is modulated by saw-tooth law with a frequency of 27 kHz. At the output of the interferometer there are vertically orientated polarizer P_3 and two-channel detector D_1 with photoconductors n-GaAs and Ge:B at 4.2 K. The transmittivity signal $g(p)$ ($\lambda = 350 \mu m$) is detected by n-GaAs at 27 kHz. Laser signal ($\lambda = 119 \mu m$) is detected by Ge:B at 18 kHz and employed to measure phase

shift $\Psi(\rho)$ by fast "phase-voltage" converter [3]. D_2 signal is used as the reference one. The distribution of plasma emission is measured by two-channel radiometer D_2 at $108\text{ }\mu\text{m}$ (Ge:B) and $285\text{ }\mu\text{m}$ (n-GaAs). Functions $\Psi(\rho)$, $g(\rho)$ and spectral brightnesses $I_{285}(\rho)$ and $I_{108}(\rho)$ are registered by the two-beam oscilloscopes OSC₁ and OSC₂. The impact parameter ρ is measured by the scanner system [4].

Results: Typical experimental curves are shown in Fig. 3a, b. Data processing is performed under assumption that plasma temperature gradients are negligible. In this case one obtains from radiation transfer equation the expression for $I(\nu, 0)$:

$$I(\nu, 0) = B(\nu, T_e^z) [1 - \exp(-\tau(\nu, 0))] \quad (1)$$

where $B(\nu, T_e^z)$ is blackbody spectrum, $\tau(\nu, 0)$ is plasma optical depth at $\rho=0$, T_e^z is the mean radiation electron temperature and ν is wave number. If I_1 and I_2 are the surface brightnesses at two frequencies ν_1 and ν_2 , then using eqn.(1) one can calculate the plasma optical depth at the frequency ν_1 ($\nu_2 < \nu_1$) from eqn.:

$$I_1/I_2 = \gamma \frac{1 - \exp(-\tau)}{1 - \exp(-\gamma\tau)} \quad (2)$$

where $\gamma = (\frac{\nu_1}{\nu_2})^2$ ($\gamma=0.144$ for n-GaAs and Ge:B detectors). Radiation temperature (in K) is given by the formula:

$$T_e^z = 9.9 \cdot 10^2 \frac{I_1}{1 - \exp(-\tau)} \quad (3)$$

where I_1 is brightness in $\mu\text{Wt}/\text{cm}^2 \cdot \text{cm}^{-1}$, sterad, τ is the root of eqn.(2). Plasma optical depth τ is measured independently using modulus of the complex transmittivity $g(0)$ at the frequency $\nu = 28.6\text{ cm}^{-1}$ ($\lambda = 350\text{ }\mu\text{m}$): $g(0) = \exp[-\tau(\nu, 0)/2]$

Fig. 3c shows the optical depth of the Ar arc discharge for regimes of constant current 18.2 A.

In the pressure range of 1-2.25 atm the mean radiation temperature T_e^z within experimental errors is independent on the gas pressure P and is equal to $(7.8 \pm 1.5) \cdot 10^3$ K. On the other hand, phase measurements show that electron density is proportional to $P^{1/2}$, as it must be at the equilibrium. In this case linearity of the function $\tau(P)$ gives an evidence that

electron-ion collisions dominate other collision processes. The equilibrium temperature T_e^z at $z=0$ calculated by Saha equation, is equal to $9.2 \cdot 10^3$ K, i.e. it is 10-20% higher than T_e^z .

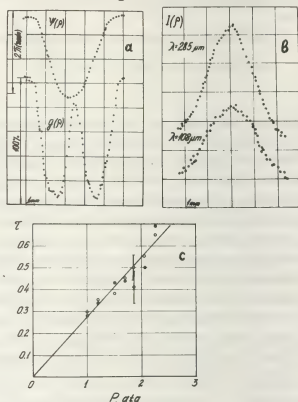


Fig. 3 Characteristics of Ar arc (discharge current equaled to 18.2 A)

- Phase $\Psi(\rho)$ ($\lambda = 119\text{ }\mu\text{m}$) and modulus $g(\rho)$ ($\lambda = 350\text{ }\mu\text{m}$) of the transmittivity.
- Plasma spectral surface brightness (top curve: $\lambda = 285\text{ }\mu\text{m}$, Y-scale - $0.54\text{ }\mu\text{Wt}/\text{cm}^2 \cdot \text{sterad} \cdot \text{cm}^{-1} \cdot \text{div}$; lower curve: $\lambda = 108\text{ }\mu\text{m}$, Y-scale - $1\text{ }\mu\text{Wt}/\text{cm}^2 \cdot \text{sterad} \cdot \text{cm}^{-1} \cdot \text{div}$)
- Optical depth τ at $\nu = 35\text{ cm}^{-1}$ ($\lambda = 285\text{ }\mu\text{m}$), clear circles - selfabsorption measurements, dark circles - active diagnostic at $\lambda = 350\text{ }\mu\text{m}$ (data converted to $\lambda = 285\text{ }\mu\text{m}$).

References:

- E.A. Tishchenko, L.A. Vainstein, Fiz. Plazmy, N1, 124 (1977)
- V.V. Zav'yalov, G.D. Bogomolov, Pis'ma v ZETF, 20, 6, 393 (1974)
- V.B. Lazarev, Prib. Tech. Exper., 2, 85, (1976)
- K.A. Zdanov et al., Prib. Tech. Exper., (1979), to be published

DETERMINATION OF THE RAY PHASE FOR PLASMA CYLINDER USING MODULUS OF THE PROBING RADIATION TRANSMITTIVITY

V.G. Zatsepin and A.V. Golubev.

Institute for Physical Problems, Moscow U.S.S.R.

Abstract : Method for determination of the phase shift along the ray trajectories in side-on probing of plasma cylinder is presented. The unknown phase function $\Phi(y)$ is restored by calculation of the first derivative $\Phi'(y)$ which is proportional to the probing beam deflection angle and defines the refractive decrease of plasma transmittivity. This method is usable under strong absorption and refraction conditions, as well as in the case when phase of the probing beam is substantially distorted.

Introduction : Modulus $g(\rho)$ and phase $\Psi(\rho)$ of the probing beam, transmitted perpendicularly to the plasma axis, are connected with apparatus function $\mathcal{K}(y)$ of the diagnostic installation and plasma phase function $\Phi(y)$ by convolution equation [1] :

$$g(\rho)e^{-i\Psi(\rho)} = \int_{-\infty}^{\infty} \mathcal{K}(y-\rho) e^{-i\Phi(y)} dy. \quad (1)$$

Experiments and computer simulations show that function $\Psi(\rho)$ is strongly distorted due to finite width of the probing beam when phase gradient $d\Phi/dy$ is too large. The measured function Ψ becomes discontinuous and differs from Φ at the value multiple to 2π if the phase increment $\Delta\Phi$ at the beam width exceeds 2π . The resulting phase distortion prevents the use of iterative methods for determination of the function $\Phi(y)$ [3]. Nevertheless, phase information may be restored by the experimental modulus of transmittivity $g(\rho)$ which is a functional of the unknown function $\Phi(y)$. Transmittivity coefficient in eqn.(1) is defined primarily by the first derivative $d\Phi/dy = K\theta$, where $K=2\pi/\lambda$ and θ is the deflection angle of the ray.

Determination of the Phase Function :

Restoration of the ray phase was performed

by means of the iterative procedure. At the n -th step of iterations we receive certain approximate solution $\Phi_n(y)$ which provides the corresponding value of the modulus $g_n(\rho)$ by eqn.(1). The functional $g(\rho) = g[\Phi(y), \Phi'(y), \dots]$ depends principally upon the first derivative $\Phi'(y)$, so one can write the finite increment of $g(\rho)$ as follows :

$$\Delta g = \frac{\partial g}{\partial \Phi'} \cdot \Delta \Phi' + \dots \quad (2)$$

It is possible to improve the function Φ'_n using eqn.(2) at the next step of iterations. Substitution of the exact and approximate values of g and Φ' in (2)

$$g(\rho) - g_n(\rho) \approx \frac{\partial g_n}{\partial \Phi'_n} [\Phi'(\rho) - \Phi'_n(\rho)] \quad (3)$$

gives the next approximation

$$\Phi'_{n+1} = \Phi'_n + (g - g_n) / (\partial g_n / \partial \Phi'_n). \quad (4)$$

This function should be closer to unknown derivative $\Phi'(y)$ because eqn.(4) takes into account the discrepancy between experimental and approximate modulus $g(\rho)$ and $g_n(\rho)$. In order to find the initial approximation Φ'_1 one can use the calibrating function :

$$g_1(\Phi') = \left| \int_{-\infty}^{\infty} \mathcal{K}(y) e^{-i\Phi' \cdot y} dy \right|, \quad (5)$$

which defines the dependence of transmittivity modulus on the angle $\theta = \Phi'/K$ of the beam deflection. Comparison of the experimental and calibrating functions permits to obtain $\Phi'_1(y)$ which is usually rather close to the unknown function $\Phi'(y)$.

Influence of Absorption : In the case of strong damping the accuracy of the phase function restoration may be substantially diminished. The influence of absorption is defined by the complex ray phase $\Phi(y) = \text{Re}\Phi(y) + i\text{Im}\Phi(y)$. If the radiation loss is vanishingly small then $\text{Im}\Phi = 0$ and the damping factor $f(y) = \exp[-\text{Im}\Phi(y)]$ is equal

to unity. Otherwise, the modulus in (4) should be calculated with regard to absorption. It is appropriate to notice, that radiation damping produces the maximum distortion of $g_n(\rho)$ when $\rho \approx 0$ (probing along the plasma diameter), meanwhile the greatest refractive losses arise at the extremums of $\Phi'(\rho)$. This peculiarity permits to find an approximate value of the absorption factor $f(\rho)$ for $\rho=0$:

$$\xi_n(0) \approx g(0)/g_n(0), \quad (6)$$

where g is the experimental function and g_n is theoretical modulus of transmittivity without absorption. If one knows the side-on distribution of the plasma emissivity $P(\rho)$ at the wavelength of probing, then profile of $f(\rho)$ may be easily determined, because function $P(\rho)$ is proportional to the product of integral absorption coefficient along the ray path and plasma temperature, which is assumed to be constant in the region of strong absorption. Function $\xi_n(\rho)$ then becomes:

$$\xi_n(\rho) = \left\{ 1 - \frac{P(\rho)}{P(0)} \left[1 - \frac{g^2(0)}{g_n^2(0)} \right] \right\}^{1/2}. \quad (7)$$

Results: The application of this procedure is illustrated in Figs.1 and 2 showing the results of the ray phase restoration for plasma of Ar arc discharge [2]. Fig.1 presents the ray phase restoration for apparatus function $X(\rho)$ and measured phase $\Psi(\rho)$ of the transmittivity coefficient with a characteristic kinks accompanying the loss of 2π in the regions where $\Phi'(\rho)$ has extremums. Function $\text{Re}\Phi(\rho)$ was obtained after seven iterations made in accordance with Eqns. (4) and (7). Experimental function $g(\rho)$ is shown in Fig.2 (circles). It agrees well with a theoretical modulus of transmittivity (solid line), calculated for restored function $\Phi(\rho)$ and absorption factor $f(\rho)$ from Eqn.(7).

The accuracy of this method is determined by the errors of the measured function $g(\rho)$ and depends on the functional connection of $g(\rho)$ and $\Phi(\rho)$. Computer simulations have shown that for concrete functions $g(\rho)$ with errors $\Delta g \sim \pm 0.01$ the accuracy of the restored function $\Phi(\rho)$ is better than 5%.

References:

- [1] L.A.Vainstein, E.A.Tishchenko, Zh.Tech. Fiz, 46, 11, 2271 (1976)
- [2] E.A.Tishchenko, A.V.Golubev and V.B.Lazarev, paper at this conference
- [3] V.G.Zatsepin, E.A.Tishchenko, A.V.Golubev, paper at this conference

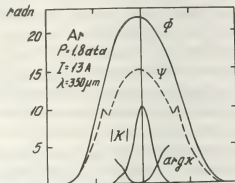


Fig.1

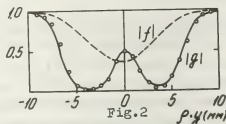


Fig.2

Fig.1 Restored (Φ) and measured (Ψ) phase of Ar arc discharge and apparatus function of the interferometer

Fig.2 Calculated (solid line) and experimental (circles) modulus of transmittivity and absorption factor ξ .

PROBE DIAGNOSTIC BY NON-SELF-MAINTAINED IONIZATION

E.F. Prozorov, J.I. Londer, K.P. Novikova and K.N. Ulyanov.

All-Union Electrotechnical Institute, Moscow U.S.S.R.

The theoretical calculation of the probe ion current for an electron beam controlled plasma is presented. The results are applicable for a case, when plasma produced ion current is more less than sheath produced ion current. The theoretically calculated probe current-voltage characteristics were compared with the experimentally measured ones.

Theory. The hydrodynamic approximation may be used for description of the movement charged particles

$$\text{div} \vec{j}_i = eq \quad (1) \quad \vec{j}_i = \rho_i \vec{v}_i \quad (2) \quad v_i = b_{ia} E^a \quad (3)$$

$$\text{div} \vec{E} = 4\pi \rho_i \quad (4) \quad \vec{E} = -\text{grad} \varphi \quad (5)$$

Analogical problem has been considered in [1] for non-self-maintained discharge, when sheath produced ion current is less, than plasma produced ion current. There are in (1)-(5) j_i - ion probe current density, q - the non-self-maintained ionization rate, a - the ion mobilities regime coefficient. The boundary conditions for (1) and (4) are: $j_i(z_0) = E(z_0) = 0$, here z_0 - the sheath - plasma margin coordinate. Introducing non-dimensional coordinate and integrating within limits from X to X_0 , we obtain

$$X_0 = (1 + \beta_m)^{\frac{1}{m+1}}; \beta_m = \frac{m+1}{eqz_p S_{pm}} I_i; I_i = j_i(z_p) S_{pm} \quad (6)$$

here $m=0,1,2$ for plane, cylindrical and spherical probe, S_{pm} - the probe area. From (4) we obtain the equation for non-dimensional field in sheath $y = E/E^* (E^* = [4\pi eqz_p^2 / b_{ia}(m+1)]^{\frac{1}{a+1}})$.

$$\frac{d}{dx} y^{a+1} + \frac{m(a+1)}{x} y^{a+1} + (a+1) \frac{X_0^{m+1} - X^{m+1}}{x} = 0; y(x) \neq 0 \quad (7)$$

Its solution is:

$$y = (a+1)^{\frac{1}{a+1}} X^{-m} \left[\frac{X_0^{m+1}}{m(a+1)} (X_0^{m(a+1)+2} - X^{m(a+1)+2}) + \frac{1}{m(a+1)+2} \left[X^{m(a+1)+2} - X_0^{m(a+1)+2} \right] \right]^{\frac{1}{a+1}} \quad (8)$$

Integrating (5) within limits from 1 to X_0 and taking into account (6) and (8), we obtain the probe current-voltage characteristic equation:

$$(1+a)^{-1} I_i (\varphi_0 - \varphi_p)^{a+1} (4\pi)^{-1} b_{ia} S_{pm} z_p^{-(a+2)} = F_{ma}(\beta_m) \quad (9)$$

$$F_{ma} = \frac{1}{m+1} \beta_m^{\frac{1}{m+1}} (1+\beta_m)^{\frac{a+3}{(a+1)(m+1)}} \int_1^{1+\beta_m} \left\{ \frac{m+1}{(ma+1)[m(a+1)+2]} - \frac{X^{-\frac{ma+1}{m+1}}}{ma+1} + \frac{X^{-\frac{m(a+1)+2}{m+1}}}{m(a+1)+2} \right\}^{\frac{1}{a+1}} dx \quad (10)$$

The right-hand part of (9) depends on β_m and the left-hand part of (9) can be calculated as a result of experiment. Thus from experimentally determining $F_{ma}(\beta_m)$ can be calculated β_m and therefore q .

Let us give specific expression of the probe current-voltage characteristic for various m and a .

Plane probe. ($m=0$). In this case (10) can be integrated in elementary functions for any a .

$$F_{0a} = 2^{-\frac{1}{a+1}} (1+a)(3+a)^{-1} \beta_0^{\frac{a+2}{a+1}} \quad (11)$$

$$I_i = \left(\frac{95}{\pi} b_{ia} \right)^{\frac{1}{a+1}} \left(\frac{eq}{a+1} \right)^{\frac{a+2}{a+1}} \left(\frac{\varphi_0 - \varphi_p}{a+3} \right)^{\frac{a+1}{a+1}} S_{p0} \quad (12)$$

This expressions have the following form for $a=1$ and $a=0.5$

$$I_i = \left(\frac{64}{\pi} \right)^{0.25} (eq)^{0.75} S_{p0} (\varphi_0 - \varphi_p)^{0.5}; \quad a=1$$

$$I_i = 3^{-\frac{5}{7}} 7^{\frac{3}{7}} \pi^{-\frac{2}{7}} b_{i0}^{\frac{2}{7}} (eq)^{\frac{5}{7}} S_{p0} (\varphi_0 - \varphi_p)^{\frac{3}{7}}; \quad a=0.5 \quad (13)$$

It will be noted that the non-self-maintained current problem has been considered in [2] for the case of plane electrodes and $a=1$.

Cylindrical probe ($m=1$). For $a=1$

$$\varphi_0 - \varphi_p = 2\alpha_p (b_{i1} L_p)^{-0.5} I_i^{0.5} F_{11};$$

$$F_{11} = 0.25 \beta_1^{-0.5} [(1+\beta_1) l_1 (1+\beta_1) - \beta_1] \quad (14)$$

for $\alpha = 0.5$:

$$\varphi_0 - \varphi_p = 3^{2/3} (I_i / \beta_{i,0})^{2/3} \zeta_p F_{1,0.5} \quad (15)$$

$$F_{1,0.5} = 0.5 \beta_{1,1}^{-2/3} (1 + \beta_1)^{7/6} \int_0^1 x^{-1/2} (2x^{-7/4} - \frac{2}{3}x + \frac{8}{21})^{2/3} dx$$

The graph of a function $F_{1,0.5}(\beta_1)$ is demonstrated in fig.1. If $\beta_1 \ll 1$, we shall come to the plane case, and $F_{1,0.5} \rightarrow \frac{3}{7} 2^{2/3} \beta_1^{3/2}$; $F_{1,1} = 0.125 \beta_1^{1/5}$. In this case the expressions (14) and (15) transform to (13).

Spherical probe. For $\alpha = 1$

$$(\varphi_0 - \varphi_p) = \sqrt{2} \left(\frac{\zeta_p I_i}{\beta_{i,1}} \right)^{0.5} F_{2,1}$$

$$F_{2,1} = 0.5 \left(\frac{3}{2\beta_2} \right)^{0.5} \left[\frac{3}{\beta_2} - (1 + \beta_2)^{2/3} + 1 \right] \quad (16)$$

For $\alpha = 0.5$:

$$(\varphi_0 - \varphi_p) = \left(\frac{3 I_i}{2 \beta_{i,0.5} \zeta_p} \right)^{2/3} \zeta_p F_{2,0.5}$$

$$F_{2,0.5} = \frac{(1 + \beta_2)^{7/9}}{3 \beta_2^{2/3}} \int_0^1 x^{-2/3} (0.2x^{-5/3} - 0.5x^{-2/3} + 0.3)^{2/3} dx \quad (17)$$

The graph of function $F_{2,0.5}(\beta_2)$ is demonstrated in fig.1. If $\beta_2 \ll 1$, we shall come to the plane case, and $F_{2,1} \rightarrow (\beta_2/6)^{3/2}$, $F_{2,0.5} \rightarrow 7.6 \cdot \beta_2^{2/3}$. The expressions (16) and (17) transform to (13).

Experiment. Ion probe current were measured in non-self-maintained pulse electron beam controlled plasma in N_2 at pressures of 25, 150 torr and $j_0 = 10^{-4} \text{ A/cm}^2$. The 95 keV electron beam was sent into the discharge volume through an Al-foil (18mkm). The measurements were taken with aid of cylindrical probe, that was placed in centre of the volume perpendicularly to the electron beam. The beam current pulse duration was $6 \cdot 10^{-3} \text{ sec}$ and it was greater than the typical recombination time (40^{-5} sec). In this case the probe current calculation problem could be considered as quasi-stationary.

The experimental current-voltage characteristics are presented in fig.2. Solid lines demonstrate the theoretical calculations for cylindrical case with account taken of direct beam current dwelling on the probe. It will be seen that there is satisfactory compliance between the theoretical curves and experimental data. Thus the probe current produced completely in the sheath.

The current-voltage characteristic expression depends on whether the probe

current is produced in the sheath or the plasma. So as to find the parameters it is necessary to proceed from an assumption to be confirmed by the estimation of the relation between I_{sh} and I_{pl} in terms of the following formula :

$$\frac{I_{sh}}{I_{pe}} = \frac{\zeta_0^{m+1} - \zeta_p^{m+1}}{\zeta_d} \Theta(\zeta_0, \zeta_d)$$

where

$$\Theta(\zeta_0, \zeta_d) = \begin{cases} [(\kappa+1)/2\kappa]^{1/2} & (m=0) \\ 2\zeta_0 K_1(\frac{\zeta_0}{\zeta_d}) / K_0(\frac{\zeta_0}{\zeta_d}) & (m=1) \\ 3\zeta_0(\zeta_0 + \zeta_d) & (m=2) \end{cases}$$

Here ζ_0 - coordinate of probe area, ζ_d - recombination length, K_n - modified Bessel function. In using the method for discharge diagnostic it will be necessary to have the sheath field exceeding the discharge field.

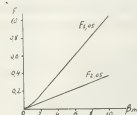


Fig. 1

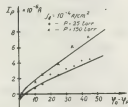


Fig. 2

- 1 - K.N.Uljanov, Proc.XIII Intern. Conf. on phenomena in ion. gases, Berlin, 1977.
- 2 - J.J.Thomson, G.P.Thomson, Conduction of electricity through gases, Cambridge, (1928).

LASER GAS-DISCHARGE PLASMA DIAGNOSTICS BASED ON FARADAY ROTATION

V.G. Gudelev, A.P. Shkadarevich and V.M. Jasinskii.

Institute of Physics, Byelorussian Academy of Sciences, Minsk, U.S.S.R.

Introduction. Faraday rotation application to plasma investigation has been known for a long time. However, new possibilities for its usage appeared with the development of lasers providing tunable radiation of high spectral density. The insertion of the medium under study into laser resonator ensures often an additional increase in sensitivity of Faraday rotation measurement. Here several definite examples of the ring laser application to determine a series of parameters of a discharge plasma placed in a longitudinal magnetic field are described.

Method. Faraday rotation angle Ψ is related to electron density N_e and magnetic field intensity H as follows ^{1/}

$$\Psi = 2,63 \cdot 10^{-17} \lambda^2 \int_0^l H N_e d\ell \quad (1)$$

where Ψ the angle in radians, λ the wavelength of probe radiation in cm, N_e in cm^{-3} , ℓ the plasma length, H in Oe. Faraday rotation, in its turn, causes counterrunning wave of a ring laser to be differed

$$\Delta\nu = \frac{C\Psi}{\pi(L + \nu \frac{dL}{d\nu})} \quad (2)$$

here, L the perimeter of the ring laser, C the light velocity, the $\nu \frac{dL}{d\nu}$ term is due to the active medium dispersion. The scaling factor of 10^6 in Ψ -dependence of $\Delta\nu$ indicates the possibility of a very

small rotation measurement by this intracavity technique.

Faraday rotation can be used also to determine spectroscopic parameters of the gas-discharge plasma having absorption or amplification lines. As was shown in ^{2/}, for this purpose it is quite promising to use Faraday rotation of linearly polarized probe radiation its frequency being in coincidence with the center of absorption line of gas-discharge plasma.

Faraday rotation usage to the purposes mentioned provides some advantages over conventional methods. In particular, the local plasma analysis is available with the magnetic field applied to definite plasma regions. In some cases by means of the magnetic field one can avoid absorption band effect of nonZeeman molecules. Finally, magnetic field permits the modulation of the measured parameter, being the important and useful factor enabling an experimental sensitivity to be increased. Naturally, an inverse problem can be solved by methods involved, i.e. using the above parameters found independently the magnetic field can be estimated.

Experimental. Experimental study was car-

ried out using a He-Ne ring laser with the wave length $\lambda = 1,15 \mu\text{m}$ and perimeter $L = 170\text{cm}$. Block diagram of the set-up is shown in Fig.1.

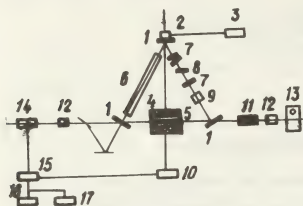


Fig. 1

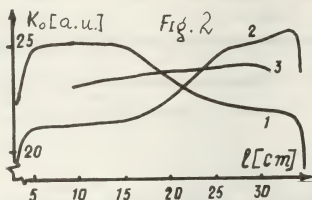
1 - mirror; 2 - piezoceramics; 3 - system of automatic frequency control; 4 - solenoid; 5 - gas-discharge plasma under study; 6 - active medium; 7 - $\lambda/4$ -plate; 8 - partial polarizer; 9 - Faraday rotator; 10 - magnetic field supply; 11 - scanning interferometer; 12 - photodetector; 13 - oscilloscope; 14 - frequency-voltage converter; 15 - lock-in amplifier; 16 - digital voltmeter; 17 - x-y-recorder.

The application of modulation technique permits us to acquire the sensitivity of the set-up used of 0,01 Hz for beating frequency measurement.

Results. Fig.2 shows the gain distribution along the active medium for gas-discharge tube obtained by local magnetic field application. The gain is found to distribute nonuniformly along the positive column of gas-discharge tube.

Curve 1 corresponds to the case when the aluminium hollow cylinder is used as a

cathode and getter body - as an anode.



For curve 2 the cylinder and getter body is exchanged their function. In both cases the gain increase has been obtained near the cathode. It demonstrates a non-uniformity of the positive column of plasma. The additional HF excitation makes the gain distribution more smooth (see curve 3). Such behaviour of gain seems to be due to the discharge stratification.

The electron density measurement has been carried out using discharge tube with length 20cm filled with helium and located into solenoid. The evaluated experiment shows that using the technique involved permits to registered the electron density as low as $10^{10}-10^{11} \text{ cm}^{-3}$. The application of probe radiation with relatively small wavelength enable the transverse gradients of plasma refractive index to be decreased significantly. Also, an optical density as low as 10^{-9} has been registered.

References.

- /1/. A.A.Dougal, et.al. Phys.Rev.Lett., **12**, 156, 1964.
- /2/. A.P.Voitovich, et.al. Doklady of Academy of Sciences of the BSSR, **20**, 801, 1977.

MEASUREMENT OF ELECTRIC FIELD IN TURBULENT PLASMA BY THE METHOD OF SATELLITES OF FORBIDDEN TRANSITIONS IN HELIUM

M.P. Brizhinev, S.V. Egorov, B.G. Eremin, A.V. Kostrov and A.D. Stepanushkin.

Institute of Applied Physics, U.S.S.R. Academy of Sciences, Gorky, U.S.S.R.

The measurement of electric fields of plasma waves is one of the important problems in experimental investigation of interaction of intense electromagnetic wave with plasma, which can give rise to a strong Langmuir turbulence [1].

In our communication we present the results of measurements of field in plasma, based on the forbidden transitions satellites method suggested by Baranger and Mozer [2].

We used the quasioptical beam of electromagnetic waves in our experiments. A plasma column with transverse dimensions $L \sim 10$ cm was placed in a constant magnetic field ($\omega_{ce} \approx 2 \cdot 10^9 \text{ sec}^{-1}$). A helium plasma was produced at pressure 10^{-2} torr with the initial electron and ion temperatures $T_e \sim 10$ eV and $T_i \sim 1$ eV respectively. An electromagnetic wave beam ($\lambda_c \approx 8$ mm) formed with a system of quasioptical converters was focused at surface of a plasma column (K H E). The maximum electric field without plasma achieved $\frac{E}{E_0} (\bar{U}/U_0 = 0.15)$. The optical emission spectra were analysed by a monochromator

DPS-12 with the instrumental halfwidth 0.2 Å sufficient for satellite resolution ($\omega_0 \approx 2 \cdot 10^{11} \text{ sec}^{-1}$). Forbidden transitions He I for three lines ($\lambda = 4026 \text{ Å}$, $\lambda = 4922 \text{ Å}$, $\lambda = 4472 \text{ Å}$) were investigated. An intense line 4922 Å was most suitable for measurements.

The line spectrum was obtained during many operation cycles of the set up.

The operating conditions of a plasma source were chosen so that during the pump wave pulse ($\tau = 200 \text{ } \mu\text{sec}$) the plasma density slowly increased passed through the critical value ($N_{cr} \approx 2 \cdot 10^{13} \text{ cm}^{-3}$). The typical emission oscillograms of the allowed line and of satellite near the critical plasma density are displayed by Fig.1. A sharp increase of the satellite emission near the critical density considerably greater than that of the allowed line points to growth of hf electric fields in plasma. In a transparent plasma ($N_e < N_{cr}$) the satellite strength was defined by the electric field of the pump wave.

Fig.2 shows three spectra of plasma emission near the line $\lambda = 4922 \text{ Å}$ of He I. Curve I represents the emission of a "cold" plasma (without pump wave) curves II and III represents the emission from plasma under the action of pump wave for undercritical ($N_e < N_{cr}$) and near critical density respectively.

The emission of a forbidden transition $23P - 43F$ in a "cold" plasma is associated with a quasi-static electric fields existing in plasma [4].

It should be noted that it is difficult to make absolute measurements of the electric field in plasma by the satellite to the allowed line intensity ratio under experimental conditions. This is due to the fact that satellites emission escapes from a small region located in a strong electric field, while the contribution to the allowed line emission was made by the whole plasma layer. Therefore the obtained experimental values for the electric field in plasma are too low.

Fig. 3 shows the electric field in plasma measured by satellites of forbidden transitions of the line $\lambda = 4922 \text{ Å}$ as a function of the electric field strength in the pump wave. In calculations we have used the linear suggested by Baranger and Mozer [2].

In a transparent plasma the electric field is linearly dependent on strength of the electric pump field. This fact supported the correctness of the field calculations made using the Baranger and Mozer linear theory. Measurements in a transparent plasma enabled us to determine the formfactor due to, as was mentioned above, the nonlocal character of optical measurements. The formfactor was found to be 3.

Near the plasma resonance ($\xi = 0$) the increase in the electric field was observed only with the pump electric field exceeding the threshold value ($E \sim 500 \text{ V/cm}$) and reached saturation for the electric pump field 2000 V/cm ($\bar{U}/U_0 \sim 8 \cdot 10^{-2}$).

The polarization of the electric field in plasma may be determined by that of satellites of the forbidden transition [5].

Polarization measurements in a transparent plasma in the presence of the focused ($L_E \sim 10 \text{ mm}$) beam of the pump wave indicated that the beam field is anisotropic with the ratio $E_x^2/E_y^2 = 4 \pm 1$ where the direction of the field components is determined with respect to the wave vector K . This result rather well corresponds to the electrodynamic estimate of the field components at the focus of the Gaussian beam.

The dependence of polarization degree on the electric field in the pump wave is shown in Fig.4. For fields $E_0 < 1000 \text{ V/cm}$ polarization measurements are difficult to be made due to the influence of unpolarized quasi-static fields. An essential anisotropy

was observed for the pump fields 1000v/cm with dominating electric field along the wave vector \vec{K} . With a further growth of the beam field the anisotropy in the electric field distribution was not observed.

Thus, in the experiments it is discovered that when the plasma is affected by an intense electromagnetic wave as a result of nonlinear interaction there appeared plasma waves with the amplitude of the electric field exceeding that of the pump wave field possibly up to the characteristic plasma fields. When the threshold field was exceeded ($E_0 > 500$ v/cm) the electric field component along the wave vector of the pump wave was increased. The maximum increase of E_{\parallel} reached 25 compared to the incident radiation. For the electric field component perpendicular to the wave vector, the enhancement of E_{\perp} amounted to 4. The increase in the longitudinal (with respect to the wave vector \vec{K}) component of the electric field in plasma is apparently due to nonlinear deformation of the plasma density profile and transformation of an electromagnetic wave into plasma one directed along the density gradient.

Reference

1. V.P.Silin. Parametric high power influence on plasma. Izd. "Nayka", 1973.
2. Baranger M., Mozer B., Phys.Rev. **123**, 25 (1961).
3. Hicks W.W., Hess R.A., Cooper W.S. Phys. Rev., **2**, 490 (1972).
4. G.Grim. Spectroscopy of plasma, Atomizdat, M., 1964.
5. Cooper W.S., Ringler H., Phys. Rev., **179**, 226 (1969).

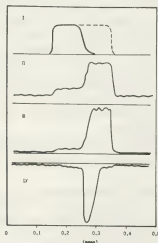


Fig.1 Oscillograms: I-Pump signal; II-Intensity of allowed transition emission; III - Satellite intensity; IV-"Fast" electron current ($W_e > 100$ ev).

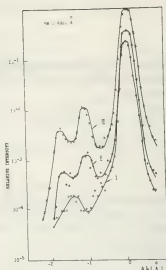


Fig.2.

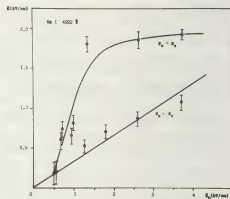


Fig.3.

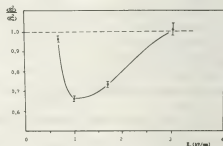


Fig.4.

A HOLOGRAPHIC STUDY OF LASER-PRODUCED PLASMA AT THE 10.6 μ m WAVELENGTH

E.M. Barkhudarov, V.R. Berezovskii, T. Ya. Chelidze, G.V. Gelashvili, M.T. Taktakishvili and N.L. Tsintsadze.

Institute of Physics, Academy of Sciences of the Georgian SSR, Institute of Physics, Academy of Sciences of the Georgian SSR, Tbilisi, U.S.S.R.

The transition from visible to infrared (IR) results in an essential increase of sensitivity of holographic interferometry as a method of electron density measurement in a plasma. In particular, the use of IR pulsed CO₂ laser radiation ($\lambda = 10.6 \mu\text{m}$) allows to study a plasma density range ($N_e L \sim 10^{15} \text{cm}^{-2}$), which is inaccessible to the interferometry in visible but is of considerable interest for studying a series of important plasma objects such as laser-produced plasma, theta-pinch, high-current diode plasma, Tokamak plasma, etc.

In our previous work [1] holograms produced by a pulsed CO₂ laser have been recorded on different thermal detectors. The highest quality holograms have been obtained on plexiglass, which has been used for the first time as a recording material.

In the present work the technique of pulsed IR holography and double-exposure holographic interferometry at 10.6 μm has been applied to studying laser-produced plasma, in particular, the laser-produced spark in air has been studied starting with a few microseconds after breakdown. Such late stages of the spark development have been chosen by two reasons: first, electron density in the spark plasma dec-

reases with the time making it advisable to operate in infrared at the stages when the density is already not high enough; second, while earlier phases (tens of nanoseconds to a few microseconds) had become formerly the subject of intense studying [2-5], in particular, by means of holographic techniques using a ruby laser [4,5], later stages of the laser-produced spark in air mentioned above remained outside the area of experimental studies.

A pulsed double-discharge TE CO₂ laser was used for obtaining IR holograms. The laser radiation energy was about 10J, being concentrated in the most part in a peak of $\tau \approx 100 \text{ ns}$ width. Holograms of the plasma were recorded using a usual double-beam scheme. Plexiglass plates of 1.5 mm thickness were used as a recording material.

A spark in air at atmospheric pressure was produced using an OGM-20 single-pulsed ruby laser (pulse energy 0.5J, pulse width 25 ns) synchronized with the pulsed CO₂ laser which served for obtaining holograms. The ruby laser radiation was focused in air by a lens of 2.5 cm focal length. Both single-exposure and double-exposure IR holograms of the laser-produced spark have been obtained for a series of times from 2 to 25 μs after breakdown.

Spark images reconstructed from single-exposure holograms allow one to trace to the dynamics of its expansion at later stages. Holographic interferograms of the spark (Fig.1) obtained by reconstruction

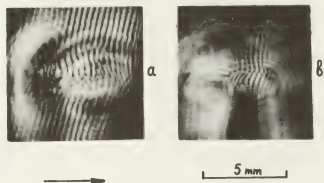


Fig.1 Holographic interferograms of the laser-produced spark.
Delay time: a - 6.2; b - 9.6 μ s.

from double-exposure holograms show interference fringe shifts to decrease with the time giving evidence of decreasing of mean electron density in the spark plasma as a result of expansion and recombination processes; this fact is also responsible for observed gradual reduction of interferogram areas where measurable fringe shifts are present corresponding to the reduction of plasma area with an electron density exceeding the sensitivity limit of holographic interferometry at 10.6 μ m. By means of a quantitative treatment of measured fringe shifts using Abel inversion the spatial and temporal distribution of electron density in decaying spark plasma was determined.

Apart from the ruby laser, a pulsed double-discharge TE CO₂ laser with the maximum radiation energy of \approx 100J was also used for plasma production. The

pulse width varied from 0.1 to 1.5 μ s depending on the gas mixture composition. The radiation was focused in air or on the surface of a solid target by a concave copper mirror or a NaCl lens of 15 cm focal length. Experiments were carried out in a stainless steel chamber at air pressures varying from atmospheric to a few Torr.

The results obtained show that at near-atmospheric pressure the CO₂ laser-produced spark has such a complicated structure that no quantitative treatment of holographic interferograms is possible. However, when air pressure is decreased the structure of the CO₂ laser-produced plasma is gradually simplified and in the pressure range 20 to a few Torr we succeeded in performing a quantitative treatment of obtained interferograms.

REFERENCES

1. E.M.Barkhudarov, V.R.Berezovskii, G.V. Gelashvili, M.I.Taktakishvili, T.Ya. Chelidze, V.V.Chichinadze. Pis'ma v Zhurn.Tekhn. Fiz., 2, 1079, 1976.
2. T.P.Evtushenko, G.M.Malishev, G.V.Ostrovskaya, V.V.Semenov, T.Ya.Chelidze. Zhurn. Tekhn.Fiz., 36, 1115, 1966.
3. A.J.Alcock, S.A.Ramsden. Appl.Phys.Letts. 8, 187, 1966.
4. A.N.Zaidel, G.V.Ostrovskaya, Yu.I.Ostrovskii, T.Ya.Chelidze. Zhurn.Tekh.Fiz., 36, 2208, 1966.
5. I.I.Komissarova, G.V.Ostrovskaya, L.L. Shapiro. Zhurn.Tekh.Fiz., 40, 1072, 1970.

SOME REMARKS ON THE NON-EQUILIBRIUM PLASMA DIAGNOSTICS

E.F. Gippius, B.I. Iljukhin and V.N. Kolesnikov.

Lebedev Physical Institute, Moscow U.S.S.R.

This report completes the list of our papers [1,2] related to the development of the physical base of non-equilibrium plasma spectroscopy. The transient dense plasma formed with the help of the high current pulse discharge in helium was chosen as an object of our investigations. The main peculiarities of such plasma diagnostics are discussed in review report [3]. In this paper we consider in addition two other problems of relatively wide interest. The first one is the effect of expansion of the PLTE model validity region in the case of unhomogeneous plasma. The second is true time of the plasma steady-state establishment.

Experimental conditions.

The coaxial discharge tube with a 1 cm inner diameter was filled with spectral pure helium at a pressure of 3 torr. The amplitude of current pulse was 4.5 kA, length being 8.5 μ sec. The details of the density measurements of electrons (N_e), ions He^+ and He^{++} as well as those of the electron temperature T_e are reported in [1]. During the time interval 2+14 μ sec N_e changed in the region $(2+6) \cdot 10^{16} \text{ cm}^{-3}$ and T_e decreased from 7.5 to 2.9 eV. The gas pressure P_w on the tube wall was also measured with the help of the piezoelectric probe.

expansion of the PLTE model validity region.

A number of effective diagnostic methods are based on the PLTE model [4,5]. Therefore it is important to know the boundary of the region where this model is valid. This boundary may be found with the help of some simple criteria inferred by Griem [4] and others from balance conditions of direct and opposite processes. However accurate calculation in which more than two processes are taken in account gives in some cases strongly narrowed validity region (Drawin [6]). We would like to note that the opposite situation, namely, the expansion of this region is also possible, if the connection between the ground and excited levels is weakened. We have observed such case in our experiments.

The ion composition of the investigated plasma is caused by strong competition of many processes [2]. The ground states are over populated because of mass transfer and diffusion. That is enough to expect the excited states to be over populated too. Fig.1 shows the expected over population degree $P_n = N_n / N_n^{eq}$ for level $n=4$ HeII as a function of time. In this calculation the electron distribution function $f_e(v)$ is usually assumed as

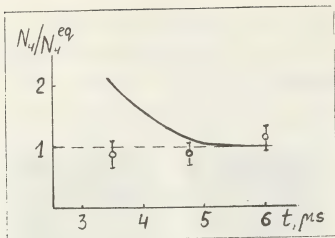


Fig. 1.

Maxwellian. The expected value of P_4 reaches 2, and PTEL model is valid for this level only at two order higher N_e than that found with the help of Griems criterion. However the experimental values of P_4 are close to 1, that is we obtain really a great expansion of the PTEL model validity region. It is possible to obtain the same result for all other atoms, the excited levels of which are strongly shifted, similar to that of HeII, to the ionisation boundary (for example H, HeI, NeI etc.). This effect can be easily explained by the non-maxwellian form of $f_e(v)$ due to plasma unhomogeneity.

The steady state establishment.

It is usually supposed that the plasma pressure becomes nearly constant along r after the time $t \sim r/w$, r being the plasma column radius, w - the velocity of shock (sound) wave. This time corresponds to that of steady state establishment. This postulate is used in dynamic models of high current pulse discharge. It is also of great importance in automodel approximation.

In our experiments $t \lesssim 1$ sec, but one

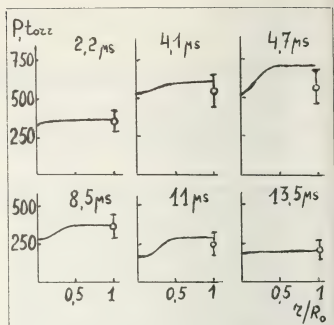


Fig. 2.

order longer time is required to achieve nearly constant pressure. Fig. 2 shows the radial distributions of total pressure $P(r)$ found from the spectroscopic data as well as the pressure P_w on the tube wall at some moments of time. Both at $P(r)$ and P_w the input of magnetic pressure is taken into account. The pressure becomes nearly constant along r only after 12 μ sec. Thus the use of automodel approximation is not valid for the analysis of plasma state during this early stages.

References.

1. E. F. Gippius, V. N. Kolesnikov. Proc. XIII-th ICPIG, Pt. 2, p. 475, Berlin, 1977; Краткие сообщ. по физике, ФИАН, №3, 17 (1977); ЖНФ, 28, 598, 1978.
2. E. F. Gippius, B. I. Iljukhin, V. N. Kolesnikov. Proc. XIII-th ICPIG, Pt. 2, p. 477, Berlin, 1977; физика плазмы, 4, 1377 (1978).
3. V. N. Kolesnikov, N. N. Sobolev. Preprint FIAN, №7 (1978).
4. H. Griem. Plasma Spectroscopy. N.-Y. 1963.
5. I. Richter. Proc. X-th ICPIG, Pt. 2, 37 (1971).
6. H. W. Drawin. In book: Progress in Plasmas and Gas Electronics. V. 1, p. 591, Berlin, 1975.

HOLOGRAPHIC TIME-DIFFERENTIAL CINE-INTERFEROMETRY OF THE GAS DISCHARGE PLASMA

Yu. I. Filenko, B.M. Stepanov and L.S. Ushakov.

Gostandard, U.S.S.R.

The methods of obtaining holographic time-differential cine-interferograms of the electric discharge in the air are considered. These are the improved methods of those described in 1,2 . The main idea of these new methods is that the reference beam is passing to a photographic plate through an opaque mask (Fig.1) with apertures placed along the spirals.



Fig.1. The mask.

When rotating such a mask some areas of the photographic plate are opened twice to pulse reference radiation, the time between exposures being multiple the radiation pulse repetition period. This multiplicity depends on the area position of the photographic plate, which enables the comparison interferograms of any pair of all recorded discharge phases to be obtained in one recording. The number of the discharge phases is equal to that of the light radiation pulses, whose repetition rate must agree with the mask rotation speed.

The block-diagram of the experiments made with the use of the soviet UIG-1M holographic instrument and the above methods is shown in Fig.2.

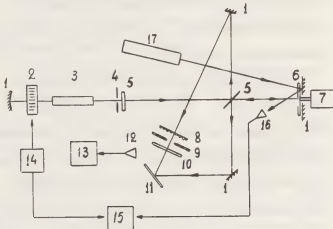


Fig.2. The block-diagram of the experiments.

The ruby laser 1,3,5 was provided with an acousto-optical modulator 2 to generate the required pulse trains. The sound wave was excited in the water cell by three symmetrical transducers. Applying about 10 kHz interruption frequency to the driving acoustic signal and choose the appropriate pumping level the stable generation of 5 giant pulse train was obtained. The rotation speed of the disk-mask 6 in the reference beam was 40 000 r.p.s. The

reference beam passed through the mask twice reflecting from the mirror 1 placed behind the mask.

To agree the mask rotation speed with the generation pulse repetition rate a He-Ne laser 17 was used, whose beam modulated by the same mask was falling onto the photodiode 16. The signals from the photodiode and the driving frequency generator 14 were directed to the two-beam oscillograph 15. Four interferograms of the successive phases of the air discharge between the electrodes 9 and all the time-differential interferograms of these discharge phases were recorded on the same photographic plate 11.

The distributions of the plasma refraction factor were evaluated in the axial approximation by computer processing. These distributions corresponding to 140 ns and 240 ns from the moment of initiation are shown in Fig. 3a,b. There are also given the error intervals whose values were caused by the errors of data obtaining and processing. In Fig. 3c the solid line denotes the changing of the refraction factor between phase A and B obtained by subtracting A curve from B curve. In this case the error interval of this dependence turns out to be so large that the zero line $n(r) - n(r) = 0$ is included into it, with such a processing one cannot be sure whether the change of n took place at all. The results of the time-differential comparison interferogram of A and B phases is shown by a dashed line in Fig. 3c.

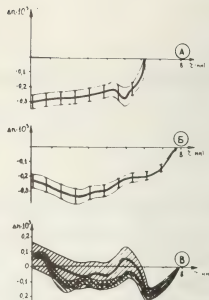


Fig. 3. The results of interferogram processing.

The error of n calculation was 19%, which allowed quantitative studies of the transition A \rightarrow B.

It should also be pointed out that due to the time-differential interferometry method the range of n change is widened to larger values. The number of fringes acceptable for the quantitative processing is limited by the obtained space resolution. When comparing successive phases with the initial phase this number determines the deviation of the object properties from the initial ones. However the time-differential interferometry methods allow such number of fringes for each comparison interferogram of the phase successive pairs resulting in the mentioned broadening.

References

1. J.C.Binder, *Nouv.Rev.d'Opt.Appl.*, v.2, N.3, 1971.
2. P.Hariharan, Z.S.Hegedus, *Opt.commun.*, v.9, N.2, 1973.

STREAK IMAGE CAMERA "AGAT" WITH PICOSECOND TIME RESOLUTION USED FOR INVESTIGATIONS IN PLASMA PHYSICS

V.I. Averin, O.M. Brekhov, B.S. Gorbenko, A.F. Klepov, G.V. Kolesov, L.I. Kondrashova, V.V. Lebedev, V.A. Miller and B.M. Stepanov.

Cosstandard, U.S.S.R.

Time-analyzing image converters FV-001 and FV-002R, developed by the All-Union Scientific Research Institute of Optical-Physical Measurements together with the Physical Institute of the Soviet Academy of Sciences, make it possible to record the pulse signals of radiation in visible and near-infrared region as well as in soft X-ray one.

A distinguishing feature of the focusing systems of the both converters consists in the small spread of electron flight times from a photocathode to the deflection systems of an electron beam thanks to high electric field intensity at the photocathode which reaches 30 kV/cm.

The image converter FV-001 has a low resistance oxygen-silver-cesium photocathode with spectral sensitivity of 300 uA/W at the wavelength 1,06 μm . An electronic shutter is arranged behind the anode in the form of two pairs of deflection plates (shutter and compensating ones), the shutter diaphragm is placed between them (the cutoff voltage of an electron beam is 400 V). Then it is followed by the wide-band deflection system for image sweep on the screen. The spatial resolution of the converter is not less than 35 mm^{-1} .

The image converter FV-002 R has a gold photocathode on a mica substrate, sensitive over the soft X-ray region. Two mutually perpendicular deflection systems, each of them is analogous to the deflection system of the image converter FV-001, are arranged behind the anode.

The calculation of the electron-optical systems of FV-001 and FV-002R is carried out with consideration for all known factors, which restrict a limiting time resolution, if the subpicosecond time resolution is ensured in the FV-001 converter and the picosecond time resolution ensured in the FV-002R converter.

The electrostatic converter PMU-I with a microchannel plate (MKP) is designed for the contact amplification of the image brightness at the output of the time-analyzing converters.

The diameters of the operating area of the photocathode and anode are equal to 40 mm, the electron-optical amplification is 1, the limiting spatial resolution is 20 mm^{-1} , the conversion coefficient at the wavelength 0,45 μm is not less than 10^4W/W .

One of the above mentioned time-analyzing converters connected with the PMU-I brightness amplifier by fiber-optical disks

may be used in a streak camera "Agat".

The image sweep at the camera output is photographed on a standard high sensitive film with the width of 35 mm by means of a contact camera attachment. The maximum dimensions of the image on the film are 10 x 40 mm at the spatial resolution up to 20 mm^{-1} . To prevent the exposure of the film by the background of the brightness amplifier, MKP is supplied by pulse voltage.

At customer's wish the camera may be also complete with a specially developed system for immediate visualization and digital processing of the recorded data.

The rest of the camera technical characteristics are given below:

- Spectral sensitivity range (Å):
 - with the image converter
PV-001 3800-12000
 - with the image converter
PV-002R 1 - 10
- Sweep duration, ns/cm 0,2; 0,5;
1,0;2,0;5,0;
10,0;20,0;
50,0;100,0;
200,0;500,0.
- Limiting time resolution,
psec 1
- Self-delay of starting,
nsec not more,
than 15
- Additional delay of starting controlled every
other nanosecond 0 - 110
- Power consumption of the
camera 220 V, 50 Hz (VA).. 90
- Overall dimensions, mm... 920x360x250
- Mass, kg not more,

than 25.

The camera "Agat" has been already used when investigating different high-speed processes, such as picosecond pulse duration generation of solid-state lasers and dye-lasers, focused laser radiation interaction with different media, development of electrical breakdown in gas and dielectric creeping discharge under the action of high-voltage nanosecond pulses.

The examples of recording high-speed processes by means of the camera "Agat" are given in Fig. 1-3.

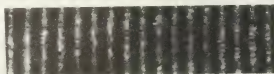


Fig. 1. Photochronogram of the internal structure of a generation spike of a Nd:glass mode-locking laser.

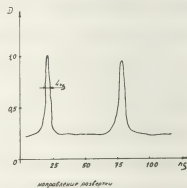


Fig. 2. Microphotogram of UV spikes of a Nd:glass laser.

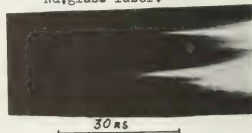


Fig. 3. Photochronographic recording of breakdown in gas between the points of the electrodes. The sweep rate is $1,3 \cdot 10^8 \text{ cm/s}$

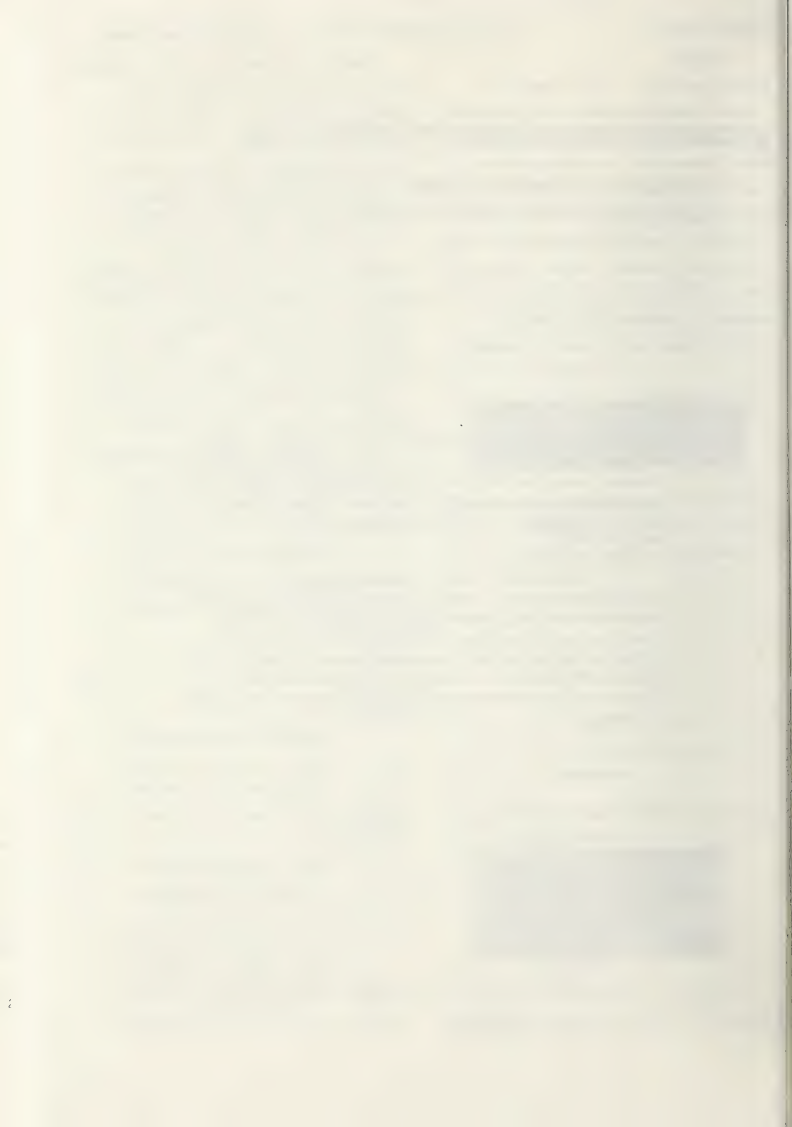
SPECTROMETRIE X DANS LES PLASMAS CREEES PAR LASER ; APPLICATION A L'ETUDE DES PHENOMENES DE TRANSPORT DE L'ENERGIE

G. Thiell, B. Meyer, M. Louis-Jacquet and J.C. Couturaud.

Commissariat à l'Energie Atomique, Centre d'Etudes de Limeil, B.P. n°27, 94190 Villeneuve-Saint-Georges, France.

Résumé.— Les études relatives aux phénomènes de transport de l'énergie sont poursuivies au CEL, dans le cadre des expériences d'implosion par rayonnement laser. Nous présentons une méthode fondée sur l'analyse spectrométrique du rayonnement X, le plasma étant créé par l'irradiation de cibles constituées d'un dépôt d'Al, d'épaisseur variable, sur un substrat de verre.

Nous décrivons d'abord le dispositif expérimental et les moyens de diagnostic utilisés pour l'étude du rayonnement X dans la gamme 4-8 Å. Après avoir précisé l'équilibre d'ionisation caractéristique d'un tel plasma, nous exposons la méthode de calcul de son émission utilisant les distributions de Te et de Ne obtenus par ailleurs à l'aide d'un code hydrodynamique lagrangien. La comparaison avec l'expérience conduit à la détermination de paramètres caractéristiques des phénomènes de transport de l'énergie.



AUTHOR INDEX

- ABBAS (I.) and BAYLE (P.).- Numerical simulation of nitrogen discharge : formation of electron shock wave C7-265
- ABECASIS (T.M.), MOREIRA (A.M.) and SERRA (F.M.).- On electron-coherent whistler wave interaction and particle precipitation C7-701
- ABED (S.).- Voir BOUVIER (A.) C7-197
- ABDEL-SALAM (M.) and MORUZZI (J.L.).- Attachment and ion molecule reaction in SF₆ mixtures.. C7-53
- ABDULLA (R.R.), DUTTON (J.) and WILLIAMS (A.W.).- Ionization growth in argon C7-73
- ABOU-SEADA (M.S.) and ALI (KH.I.M.) .- Static breakdown analysis of compressed SF₆ in a positive rod-to-plane gaps C7-311
- ADAM (J.C.), LAVAL (G.) and PESME (D.).- Phase space granulation as a result of mode-mode coupling effects C7-671
- ADEMA (S.).- Voir VAN DER SIJDE (B) C7-851
- AKAZAKI (M.), NISHIJIMA (K.) and HARA (M.).- Processes of impulse breakdown in N₂-O₂ gas mixtures and in air at low pressure C7-145
- AKIYAMA (H.), YAMADA (T.) and TAKEDA (S.).- Wave propagation in a cylindrical geometry C7-543
- ALAYLI (Y.) and SKOWRONEK (M.).- Etalonnage d'une chaîne de diffusion en vue du diagnostic des plasmas C7-817
- ALEKSANDROV (A.F.).- Voir FURSEY (G.N.) C7-415
- ALEXANDROV (V.V.), DANILYCHEV (V.A.), KOTEROV (V.N.), PUSTOVALOV (V.V.) and SOROKA (A.M.).- To the theory of electroionized discharge C7-357
- ALGE (E.).- Voir PESKA (K.) C7-21
- ALGE (E.), VILLINGER (H.), PESCA (K.), RAMLER (H.), STÖRI (H.) and LINDINGER (W.).- The influence of ion vibrational excitation on ion molecule reactions C7-83
- ALI (KH.I.M.).- Voir ABOU-SEADA (M.S.) C7-311
- ALTEV (Yu.M.), GRADOV (O.M.) and STEFAN (V.).- Magnetized plasma parametric resonance in non-monochromatic pump-wave C7-557
- ALI (A.W.), GREIG (J.R.), VITKOVITSKY (I.M.), FIORITO (R.B.) and FERNSLER (R.F.).- Interaction of an intense relativistic electron beam with the atmosphere C7-773
- ALI (A.).- Voir KOOPMAN (D.) C7-419
- ALLEN (N.L.), ALLIBONE (T.E.) and DRING (D.).- Variation of Corona inception and sparkover with positive impulse voltage in a rod/plane gap : effect of negative small ion variation C7-423
- ALLEN (J.E.).- Voir BRAITHWAITE (N.St.J.) C7-491
- ALLEN (J.E.).- Voir SAELEE (H.T.).. C7-179
- ALLEN (J.E.) and WICKENS (L.M.).- Hydromagnetic rarefaction waves.. C7-547
- ALLIBONE (T.E.).- Voir ALLEN (N.L.)..C7-423
- ALLIBONE (T.E.) and SAUNDERSON (J.C.).- Breakdown of sphere/plane gaps stressed with d.c. voltage ; the effect of "CONDITIONING"C7-425
- MCALLISTER (I.W.).- Voir CRICHTON (G.C.) C7-287
- ALTYNTSEV (A.T.), KRASOV (V.I.), LEBEDEV (N.V.) and PAPERNY (V.V.) .- Measurements of electron energy distribution in the theta-pinch neutral sheet C7-723
- AMEMIYA (H.), DOTE (T.) and KAWAMOTO (S.).- Relation between the striation and the stimulated emission in a He-Ne laser C7-389
- AMIRANOFF (F.), FABBRO (R.), FABRE (E.), GARBAN (C.) and VIRMONT (J.) .- Experimental investigation of transport in laser-target irradiation experiments C7-769
- AMIRANOFF (F.), FABBRO (R.), FABRE (E.), GARBAN (C.) and VIRMONT (J.) .- Effect of pulse shaping on interaction processes in laser produced plasmas C7-729
- ANGELOV (O.), BLAGOEV (A.) and POPOV (Tc.).- Investigations of the electron energy distribution function in krypton afterglow plasma C7-19
- ANTONIOS VLASTÓS (E.).- Effect of polarity on the impulse breakdown of SF₆ C7-253
- APOSTOL (I.), COJOCARU (E.), DINESCU (M.), DRAGANESCU (V.), JULEA (Th.), MORJAN (I.), MOLDOVAN (M.), MIHAILESCU (I.N.) and KONOV (V.I.).- Plasma target coupling in the case of tea-CO₂ laser produced breakdown in front of solid targetC7-765
- ARMAND (N.A.), ROGASHKOV (S.A.) and SHUSTIN (E.G.).- Interaction of the intense microwaves with a flow of low temperature plasma (I. The experiment)C7-565

- ARMAND (N.A.), ROGASHKOV (S.A.) and SHUSTIN (E.G.).- The UHF discharge with preliminary locally ionized gaseous medium C7-643
- ARUTUNIAN (G.G.) and GALECHIAN (G.A.).- The peculiarities of the diffusion processes in the electro-negative gas plasma C7-205
- ARUTYUNYAN (S.G.), GEKKER (I.R.), KARFIDOV (D.M.) and RUCHADZE (A. A.).- Ionization of gases in strong electromagnetic fields ... C7-219
- ASHRAF (A.), ROYCHOWDHURY (U.K.) and GHOSH (P.K.).- Population densities of triplet excited states in a diffuse nitrogen plasma C7-129
- ASSADULIN (F.F.), BATANOV (G.M.), VERIAEV (A.A.), SAPOZHNIKOV (A.V.) and SARKSIAN (K.A.).- Modulation of spectra of drift waves due to the high-frequency fields C7-653
- AUBES (M.).- Voir DAMELINCOURT (J.J.) C7-273
- AUPHELLE (D.), EUVE (F.), FITAIRE (M.), POINTU (A.M.), VIALLE (M.) and WARTSKY (L.).- Study of nitrogen-neon nuclear induced plasma . C7-397
- AVERIN (V.I.), BREKHOV (O.M.), GORBENKO (B.S.), KLEPOV (A.F.), KOLESOV (G.V.), KONDRASHOVA (L.I.), LEBEDEV (V.V.), MILLER (V.A.) and STEPANOV (B.M.).- Streak image camera "agat" with picosecond time resolution used for investigations in plasma physics C7-875
- AVIVI (P.).- Voir KAUFMAN (Y.) C7-31
- AVRAM (E.).- Voir POPOVICI (C.) ... C7-171
- BABANIN (V.I.), KAPLAN (V.B.), KOLYSHKIN (I.N.), KUZNETSOV (V.I.), MARTSINOVSKI (A.M.), MUSTAFAEV (A.S.), SITNOV (V.I.) and ENDER (A.Ya.).- Optical investigations of the spontaneous extinction of the high-current knudsen arc discharge in Cs-Ba gas mixture C7-201
- BACAL (M.), HAMILTON (G.W.), BRUNETEAU (A.M.), DOUCET (H.J.) and TAILLET (J.).- Measurement of H^- density in a plasma by photodetachment C7-791
- BAILEY (W.F.) and GARSCADDEN (A.).- Non-equilibrium dissociation phenomena C7-377
- BAKANOVICH (G.I.), MIN'KO (L.Ya.) and CHUMAKOV (A.N.).- Investigation of plasma formation dynamics and properties of underexpanded supersonic erosive laser plasma flares C7-761
- BAKSHI (F.G.) and IVANOV (V.G.).- Theory of low-voltage arc in noble gas C7-339
- BAKSHI (V.G.), MARTSINOVSKIY (A.M.) and YUR'YEV (V.G.).- Low-voltage arc plasma in three-electrode system C7-497
- BAKSHI (F.G.) and RYBAKOV (A.B.).- Theory of hollow cathode in atmospheric arc in noble gas C7-341
- BALANCEANU (M.).- Voir POPOVICI (C.) C7-171
- BALESCU (R.) and PAIVA-VERETENNICOFF (I.).- Kinetic equation for a plasma in a strong high frequency electromagnetic field C7-511
- BALTOG (A.) and MUSA (G.).- Surface phenomena in cesium and cesium - noble gas filled thermionic diode C7-455
- BALTOG (A.) and MUSA (G.).- Influence of the interelectrode charge diffusion outside of the gap on the thermionic diode VI characteristics C7-457
- BARASSIN (A.).- Voir THOMAS (R.) ... C7- 41
- BARASSIN (J.).- Voir THOMAS (R.) ... C7- 41
- BARBIAN (E.P.).- Voir OEPTS (D.) ... C7-793
- BARDOS (L.) and MUSIL (J.).- Microwave generation of a magnetoactive oxygen plasma for oxidation C7-449
- BARKHURADAROV (E.M.), BEREZOVSKIY (V.R.), CHELIDZE (T.Ya.), GELASHVILI (G.V.), TARTAKISHVILI (M.T.) and TSINTSADZE (N.L.).- A holographic study of laser-produced plasma at the 10.6 μ m wavelength C7-869
- BARONNET (J.M.).- Voir COUDERT (J.F.) C7-355
- BARONNET (J.M.), RAKOWITZ (J.), COUDERT (J.F.), BOURDIN (E.), FAUCHAIS (P.) ERCHOV and PAVLOV (E.).- Spectroscopic diagnostics of A.D.C. nitrogen plasma jet C7-247
- BARRETO (E.) and JURENKA (H.).- A subsonic electron fluid and the formation of small sparks C7-301
- BASOV (N.G.), GLOTOV (E.P.), DANILYCHEV (V.A.), MILANICH (A.I.) and SOKORA (A.M.).- Self-sustained electrophotocatalyzed discharge in compressed gases C7-393
- BATANOV (G.M.).- Voir ASSADULIN (F.F.) C7-653
- BAUER (G.H.).- Spectroscopic analysis of prebreakdown-phase from positive corona into spark in N_2 C7-295
- BAUMACKER (H.), BRINKSCHULTE (H.), RIEDMULLER (W.), SALVAT (M.) and SUDO (S.).- Ionization of isolated deuterium pellets by neodymium laser radiation C7-743
- BAYLE (P.).- Voir ABBAS (I.) C7-265
- BAYLE (M.).- Voir BAYLE (P.) C7-249
- BAYLE (P.), BAYLE (M.) and MORALES (E.).- Experimental determination of the spatio-temporal distribution of the pace charge field in a breakdown. C7-249
- BEHRINGER (K.) and THOMA (P.).- The high power hydrogen arc as a precise standard source of continuum radiation between 53 and 92 nm C7-829
- BEIJERINCK (H.C.W.).- Voir THEUWS (P.G.A.) C7-141

- BEL'CHENKO (Yu.I.) and DUDNIKOV (V.G.)
.- Negative ion production in surface-plasma sources with unclosed electron drift discharge C7-501
- BEL'KOV (S.A.) and TSYTOVICH (V.N.)
.- Magnetic field generation by intense Langmuir plasma waves ... C7-651
- BELYANKO (A.E.), LIPATOV (N.I.), PASHININ (P.P.) and PROKHOROV (A.M.)
.- Ultraviolet radiation of the surface discharge is a pre-ionizer of high pressure atomic-molecular impurities C7-505
- BENATTAR (R.), POPOVICS (C.) SIGEL (R.) and VIRMONT (J.)
.- Interferometric measurements of density profiles in laser-target interaction... C7-767
- BENENSON (D.M.)
.- Voir BHANSALI (C.K.) C7-263
- BENGSTON.
.- Voir CHU (E.) C7-747
- BEN JEMAA (N.)
.- Voir GAUCHEREL (Ph.) C7- 91
- BEREZOVSKII (V.R.)
.- Voir BARKHUDAROV (E.M.) C7-869
- BERGER (E.) and HEISEN (A.)
.- Electron energy distribution, electric field and transport coefficients in the Faraday Darc Space C7-191
- BEYER (H.), FUNK (W.) and KLOSS (H.G.)
.- Plasma diagnostics in horizontally burning metal halide discharges C7-325
- BHANSALI (C.K.) and BENENSON (D.M.)
.- Numerical analysis of arcs in supersonic flow C7-263
- BICHKOV (Yu.I.), OSIPOV (V.V.) and TELNOV (V.A.)
.- Characteristics of the combined discharge in average pressure gas C7-161
- BIGIO (I.J.)
.- Electron-attaching gases in laser discharges : altered discharge parameters and negative-ion production C7-365
- BLAGOEV (A.)
.- Voir ANGELOV (O.)... C7-19
- BLEACH (R.D.), WHITNEY (K.G.), SANDELIN (J.W.), FINN (T.G.) and NAGEL (D.J.)
.- Carbon spectra from CO₂ laser-produced plasmas C7-749
- BLEVIN (H.A.)
.- Voir FLETCHER (J.)... C7-811
- BLOYET (E.)
.- Voir CICCONI (G.) ... C7-827
- BOFFI (V.C.), MOLINARI (V.G.) and SPIGA (G.)
.- Electron distribution function and ionization in space-dependent plasma theory C7-535
- BOGDANKEVICH (L.S.), KUZELEV (M.V.) and RUCHADZE (A.A.)
.- On the theory of excitation of rippled plasma resonators by a relativistic electron beam C7-783
- BOGDANOV (A.A.), KAPLAN (V.B.), MARTSINOVSKIY and YUR'YEV (V.G.)
.- Plasma formation kinetic at knudsen arc ignition C7-337
- BOGDANOV (S. Yu.), MARKOV (V.S.), FRANCK (A.G.) and KHODZHAIEV (A.Z.)
.- Experimental study of fast reconnection of the magnetic fields through plane pinch current sheet. C7-221
- BOGDANOVA (N.B.), PEVCHIEV (B.G.) and POPKOV (V.I.)
.- Electrical field strength on the positive corona electrode with the counterflow of negative ions C7-361
- BOKHAN (P.A.), KLIMKIN (V.M.), MALTSEV (A.N.), PROKOPIEV (V.E.) and SOKOVIKOV (V.G.)
.- Investigation of anomalously high-speed de-excitation of Eu⁺ metastable states in gas discharge plasma using modulation of induced radiation... C7-115
- BONNET (J.)
.- Voir FORT (J.) C7-315
- BONNET (J.)
.- Voir FOURNIER (G.) ... C7-777
- BONNET (J.)
.- Voir PIGACHE (D.) C7-317
- BONTE (L.)
.- Voir SANCTORUM (C.) ... C7-33
- BORISOVA (T.S.)
.- Voir POKROVSKAJA-SOBOLEVA (A.S.) C7-405
- BORZHOV (A.P.)
.- Voir RYKALIN (N.N.) C7-229
- BOULLAUD (A.), CHARRIER (J.) and LE NY (R.)
.- Positive glow corona along a cylindrical rod between two parallel plates C7-241
- BOURDIN (E.)
.- Voir BARONNET (J.M.)... C7-247
- BOURDIN (E.)
.- Voir COUDERT (J.F.).. C7-355
- BOURQUARD (S.)
.- Voir KOCIAN (P.)... C7-169
- BOURQUARD (S.), MAYOR (J.M.) and KOCIAN (P.)
.- Measurement of the electron energy distribution in a CO₂ laser plasma C7-385
- BOUVIER (A.), ABED (S.), CHARLET (B.) and BOUVIER (A.)
.- Investigation of an early helium afterglow plasma produced by a microwave surfaguide C7-197
- BOUVIER (A.)
.- Voir BOUVIER (A.).... C7-197
- BOYD (T.J.M.), GARDNER (G.A.) and HUMPHREYS-JONES (G.J.)
.- Self-generated magnetic fields and harmonic emission C7-551
- BOYD (T.J.M.)
.- Voir TURNER (J.G.).. C7-549
- BRACKE (T.), SOMMER (H.T.) and STOJANOFF (C.G.)
.- Numerical simulation of a decaying argon arc C7-239
- BRADLEY (L.P.) and ORHAM (E.L.)
.- Characteristics of a high density directed plasma source C7-307
- Braglia (G.L.) and LOWKE (J.J.)
.- Comparison of Monte-Carlo and Boltzmann calculations of electron diffusion to an anode C7-17
- BRAITHWAITE (N. St.J.) and ALLEN (J.E.)
.- Pulsed current voltage characteristics of a thermally produced plasma C7-491
- BREGNSBO (E.)
.- Voir CHRICHTON (G.C.) C7-287
- BREIZMAN (B.N.)
.- WKB model of the collapse of Langmuir waves C7-563

- BREKHOV (O.M.).- Voir AVERIN C7-875
(V.I.)
- BRIDET (J.).- Voir FOURNIER (G.) .. C7-777
- BRIDGES (J.M.).- Voir OTT (W.R.)... C7-803
- BRINKSCHULTE (H.).- Voir BAUMHACKER (H.) C7-743
- BRIZHINEV (M.P.), EGOROV (S.V.), EREMIN (B.G.), KOSTROV (A.V.) and STEPANUSHKIN (A.D.).- Measurement of electric field in turbulent plasma by the method of satellites of forbidden transitions in helium C7-867
- BROOKS (R.D.), PIETRZYK (Z.A.) and VLASES (G.C.).- Multiple-pass laser heating of a short plasma column C7-751
- BRUNETEAU (A.M.).- Voir BACAL (M.). C7-791
- BRUYNOOGHE (W.).- Voir WIEME (W.)... C7- 3
- BRZOSKO (J.S.).- Voir KIOBUKOWSKA (J.) C7-469
- BRZOSKO (J.S.), ZUKOWSKI (E.), GRUDZINSKI (J.), ZUKOWSKI (W.) and KONARZEWSKI (A.).- Probability of the creep discharges C7-471
- BUCHENNIKOVA (N.S.) and MATOCHKIN (E.P.).- The instability of one-dimensional Langmuir wave. Solitons and collapse C7-631
- BUCHENNIKOVA (N.S.) and MATOCHKIN (E.P.).- The instability and damping of the Langmuir waves with different amplitudes and phase velocities C7-633
- BUCHET (G.), HAUG (R.) and MAFTOUL (J.).- CN molecular bands in a free burning metal electrodes arc C7-327
- BUNTING (K.A.).- The arc diameter and rate of rotation of a magnetically rotated arc with superimposed gas flow C7-243
- BURNS (E.J.T.), JOHNSON (D.J.), FARNSWORTH (A.V.), Jr., FEHL (D.L.), LEEPER (R.J.), MIX (L.P.) and KUSWA (G.W.).- Diagnostics program for a magnetically insulated ion diode for inertial confinement fusion C7-775
- BURTSEV (V.A.), DUBYANSKI (V.A.), EGOROV (N.P.), KASATKINA (M.P.), PRODUVNOV (A.B.) and SHESTAKOV (I.V.).- Investigation of electrical explosion of cylindrical foils in air. Coaxial high-current discharges C7-485
- BURTSEV (V.A.), ZELENOV (L.A.), KONDAKOV (A.A.), KURUNOV (R.F.), SMIRNOV (V.G.) and SHANSKY (V.F.).- Optical homogeneity and molecular gas heating in a semi-self-sustained discharge C7-387
- BUSCH (P.J.).- Voir OEPTS (D.).... C7-793
- BUSHIK (A.I.).- Dynamics of the electrode processes on the reinforced materials at high-current impulsing discharge C7-467
- CADEZ (V.M.).- Influence of toroidal magnetic field on convection in rotating star C7-707
- CAMBRAY (P.).- Recombinaison de l'ion moléculaire He⁺ à haute température C7-65
- CANDER (L.J.R.) and STANIC (B.V.).- Interaction of EM waves with a compressible plasma column C7-597
- CAPITELLI (M.), DILONARDO (M.) and GORSE (C.).- Self consistent electron energy distribution functions in nonequilibrium oxygen C7-13
- CARLHOFF (C.), SCHÄFER (J.H.), SCHILDBACH (K.) and UHLENBUSCH (J.).- High pressure optical discharges.. C7-757
- CAROLAN (P.G.).- Voir MUIR (D.G.)... C7-833
- CATHERINOT (A.) and DUBREUIL (B.).- Quenching of n = 3, 4 singlet HeI excited states by molecular nitrogen in a low-pressure glow discharge C7-85
- CATHERINOT (A.).- Voir DUBREUIL (B.). C7-5
- CEAUSCESCU (N.).- Voir POPOVICI (C.)... C7-171
- CERNOGORA (G.), GOUSSET (G.) and RICARD (A.).- N (²D,²P) metastable atoms production in a N₂ d.c. glow discharge C7-59
- CHAPELLE (J.).- Voir FLEURIER (C.).. C7-81
- CHAPELLE (J.).- Voir GLASSER (J.)... C7-687
- CHAPELLE (J.).- Voir RANSON (P.)... C7-25
- CHAPELLE (J.).- Voir RANSON (P.)... C7-93
- CHARIL (P.).- Voir LESAGE (A.) C7-805
- CHARLET (B.).- Voir BOUVIER (A.)... C7-197
- CHARRIER (J.).- Voir BOULLAUD (A.).. C7-241
- CHEBOTAEV (P.Z.) and VEKSTEIN (G.E.).- The Bohm-type thermal losses from a high-plasma C7-537
- CHELIDZE (T. Ya.).- Voir BARKHUDAROV (E.M.)..... C7-869
- CHEN ZHI-FAN.- Voir LU QUAN-KANG ... C7-667
- CHERON (B.), JAROSZ (J.) and VERVISCH (P.).- Mesure des probabilités de transition des raies 5³D₂, 6 ¹D₂, 7 ¹D₂ + 5 ¹P₁ du cadmium... C7-847
- CHU (E.), DRUCE (R.), KRISTIANSEN (M.), HAGLER (M.) and BENGTON (R.).- Beat heating in plasmas using CO₂ lasers C7-747
- CHUMAKOV (A.N.).- Voir BAKANOVICH (G.I.)..... C7-761
- CHYRCZAKOWSKI (S.), MELZACKI (K.) and SADOWSKI (M.).- Spectral lines emission from carbon-hydrogen plasmas generated by TEN₁₀ laser pulses... C7-741
- CIBIN (P.K.).- Influence of dissipative processes on the propagation of guided electron plasma waves on a planar plasma slab C7-599
- CICCONI (G.), BLOYET (E.), LEPRINCE (P.) and MAREC (J.).- Microwave reflexion in rectangular waveguides by high pressure R.F. plasma columns C7-827

- CICCONI (G.), MOLINARI (V.) and POLLACHINI (L.).- A nonlinear kinetic theory for HF plasma generation and electron heating C7-193
- COHEN (CH.).- Voir LUDMIRSKY (A.) C7-373
- COJOCARU (E.).- Voir APOSTOL (I.)... C7-765
- COMBIER (M.).- Voir LESAGE (A.)... C7-805
- COOKE (M.J.).- Voir SAELEE (H.T.). C7-179
- COTSAFTIS (M.).- Voir SY (W.N.C.) C7-669
- COUDERT (J.F.).- Voir BARONNET (J.M.) C7-247
- COUDERT (J.F.), BOURDIN (E.), BARONNET (J.M.), RAKOWITZ (J.) and FAUCHAIS (P.).- Chemical kinetics study of nitrogen oxide synthesis in a d.c. plasma jet : a proposed model C7-355
- COULAUD (G.).- Voir FLEURIER (C.).. C7-81
- COUMANS (J.J.H.).- Voir POTS (B.F.M.) C7-797
- COUTURAUD (J.C.).- Voir THIELL (G.) C7-877
- COXON (P.A.) and MORUZZI (J.L.).- Positive ion mobilities in carbon dioxide C7-117
- CRAWFORD (F.W.).- Voir LEVINE (J.S.) C7-139
- CRAWFORD (F.W.).- Voir VIDMAR (R.J.) C7-559
- CRICHTON (G.C.), McALLISTER (I.W.) and BREGNSBO (E.).- Positive corona onset in atmospheric air- a multiple avalanche process ... C7-287
- CROITORU (P.).- Voir POPA (G.).... C7-187
- CRUMLEY (R.).- Voir WILLIAMS (P.F.) C7-305
- CYBULSKI (A.).- Voir WROBLESKI (D.) C7-733
- DAMELIN COURT (J.J.), SEVIGNE (M.), AUBES (M.) and SCOARNEC (L.).- Axial segregation in Hg-Tl-I discharges operated at 50 Hz.... C7-273
- DANCER (P.).- Voir DROUET (M.G.).. C7-437
- DANG DUC (H.).- Voir KAPROUNI (H.) C7-237
- DANILYCHEV (V.A.).- ALEXANDROV (V.V.) C7-357
- DANILYCHEV (V.A.).- Voir BASOV (N.G.) C7-393
- DANILYCHEV (V.A.).- Voir GLOTOV (E.P.) C7-371
- DAVIES (A.J.), DUTTON (J.), EVANS (C.J.), GOODINGS (A.) and STEWART (P.K.).- Monte-Carlo simulations of electron drift velocities in the noble gases and their mixtures C7-63
- DAVYDOVA (T.A.) and SHAMRAI (K.P.).- Modulational instability and evolution of non-uniform Langmuir fields in plasmas C7-561
- DEIGAT (F.).- Voir VALIGNAT (S.)... C7-7
- DELVAUX (J.), DEVIN (A.), NICOLAS (A.), PEUGNET (C.), WOLFF (G.) and KUBALA (A.).- Experience d'interaction electrons-matière à Valduc C7-785
- DETTMER (J.W.) and GARSCADDEN (A.).- Role of O_2^+ ($a^1\Delta$) in the oxygen plasma C7-135
- DEUTSCH (C.).- Voir GOMBERT (M.M.). C7-695
- DEUTSCH (C.).- Voir MINOO (H.) C7-697
- DEVIN (A.).- Voir DELVAUX (J.).... C7-785
- DEVYATOV (A.M.).- Voir VOLKOVA (L.M.) C7-231
- DIELS (J.W.H.), DE HOOG (F.J.) and SCHRAM (D.C.).- Decay of metastable Ne (3^2P_2)-atoms C7-75
- DIELS (J.W.H.).- Voir VAN DER KRAAN (P.A.M.) C7-15
- DILONARDO (M.).- Voir CAPITELLI (M.) C7-13
- DIMITRIJEVIĆ (M.S.) and GRUJIĆ (P.).- A modified adiabatic theory calculation for the stark broadening of He I ($3^1P^o-2^1S$) C7-119
- DIMITRIJEVIC (M.S.), GRUJIC (P.) and KOLEDIN (D.).- Quantum mechanical calculations of the stark broadening of some He I lines from plasmas C7-825
- DIMITRIJEVIC (M.) and KONJEVIC (N.).- On the approximative semiclassical formula for the electron impact width of multiply ionized atom lines in plasmas C7-815
- DINESCU (M.).- Voir APOSTOL (I.)... C7-765
- DIXON (A.J.) and VON ENGEL (A.).- Energy spread of cluster ions from a molten metal C7-441
- DJENIŽE (S.).- Voir LABAT (J.M.)... C7-9
- DJENIŽE (S.) and LABAT (J.M.).- Influence of perturbation of population processes of 4p argon levels. C7-47
- DJORDJEVIC (D.).- Voir MIHAJLOV (A.) C7-689
- DOBRENIN (A.V.).- Voir ZORINA (E.N.) C7-473
- DOLIQUE (J.M.).- Instabilités à faisceaux tournants multiples dans les faisceaux d'ions négatifs utilisés à la génération de faisceaux de neutres C7-659
- DOTE (T.).- Voir AMEMIYA (H.) C7-389
- DOTHAN (F.) and KAGAN (Yu.M.).- The composition of the positive column of a helium glow discharge at intermediate pressures C7-127
- DOTHAN (F.).- Voir KAUFMAN (Y.) ... C7-31
- DOUCET (H.J.).- Voir BACAL (M.) ... C7-791
- DRAGANESCU (V.).- Voir APOSTOL (I.)..C7-765
- DRAWIN (H.W.).- Voir TRUONG BACH... C7-69
- DRING (G.).- Voir ALLEN (N.L.) C7-423

- DROUET (M.G.), DANCER (P.), KIEFFER (P.) and MERCURE (H.).- Simultaneous measurements of microcatheter emissions of current and copper light at the cathode of a moving arc C7-437
- DRUCE (R.).- Voir CHU (E.)..... C7-747
- DUBOIS (D.F.), ROSE (H.A.) and GOLDMAN (M.V.).- A statistical theory of Langmuir turbulence.. C7-601
- DUBREUIL (B.) and CATHERINOT (A.).- Excitation transfer and quenching of the $n = 3$ excited states of helium in a low-pressure glow discharge C7-5
- DUBREUIL (B.).- Voir CATHERINOT (A.) C7-85
- DUBROVSKY (A.V.).- Voir GRIBKOV (V.A.) C7-763
- DUBYANSKI (V.A.).- Voir BURTSSEV (V.A.) C7-485
- DUDNIKOV (V.G.).- Voir BEL'CHENKO (Yu.I.) C7-501
- DUDNIKOV (V.G.) and FIKSEL' (G.I.).- Surface plasma source of hydrogen atoms with an energy of hundreds eV C7-479
- DUTTON (J.).- Voir ABDULLA (R.R.).. C7-73
- DUTTON (J.).- Voir DAVIES (A.J.).. C7-63
- DVININ (S.A.).- Voir SOLNTSEV (G.S.) C7-227
- DYUZHNEV (G.A.), MITROFANOV (N.K.), SHKOLNIK (S.M.) and YUR'EV (V.G.).- Anode region of high current arc discharge C7-463
- DYUZHNEV (G.A.), STARTSEV (E.A.) and YUR'EV (V.G.).- Physical processes in arc hollow cathode ... C7-199
- EARL (R.G.) and PREST (A.).- Observations of harmonics of the discharge current in electrodeless R.F. discharges in gas mixtures.. C7-167
- EGOROV (I.I.), LESNEVSKY (L.N.), POPOV (G.A.), SOBOLOV (A.G.) and TURIN (V.N.).- Optimisation of the characteristics of the plasma flow from a dielectric chamber C7-349
- EGOROV (N.V.).- Voir FURSEY (G.N.).. C7-403
- EGOROV (N.P.).- Voir BURTSSEV (V.A.) C7-485
- EGOROV (S.V.).- Voir BRIZHINEV (M.P.) C7-867
- EICHLER (H.J.), KOCH (H.), PAFFENHOLZ (J.), SALK (J.) and SKROBOL (G.).- Two novel HCD-structures for Cu II-lasers and their performance C7-379
- ELIASSON (B.) and KOEGLSCHATZ (U.).- Ozone production in a homogeneous oxygen discharge C7-271
- ELIEZER (S.).- Voir SALZMANN (D.).. C7-57
- ENDER (A. Ya.).- Voir BABANIN (V.I.) C7-201
- ENDER (A. Ya.) and KUZNETSOV (V.I.).- On the linear theory of electron processes in the collisionless diode C7-523
- ERCHOV.- Voir BARONNET (J.M.) C7-247
- EREMIN (B.G.).- Voir BRIZHINEV (M.P.) C7-867
- ERSHOV (A.P.) and KUZOVNIKOV (A.A.).- Electron energy distribution function in Xe plasma in the presence of Coulomb collisions..... C7-521
- EUVE (F.).- Voir AUPHELLE (D.) C7-397
- EVANS (C.J.).- Voir DAVIES (A.J.).. C7-63
- EVARD (M.P.), MESSIAEN (A.M.), VANDENPLAS (P.E.) and VAN OOST (G.).- Drift dissipative waves and ensuing steady state of a plasma column C7-617
- EZUBCHENKO (A.N.).- Voir GORBUNOVA (E.F.).- C7-211
- FABRO (R.).- Voir AMIRANOFF (F.).. C7-729
- FABRO (R.).- Voir AMIRANOFF (F.).. C7-769
- FABRE (E.).- Voir AMIRANOFF (F.) .. C7-729
- FABRE (E.).- Voir AMIRANOFF (F.) .. C7-769
- FABRY (M.).- Voir THIELL (G.)..... C7-453
- FAINSTEIN (V.G.).- Voir YESSLEVICH (V.G.) C7-359
- FANG (M.T.C.) and KUHN (S.).- On the linear stability of a collisionless single-ended Q-machine.. C7-579
- FARNWORTH (A.V.), Jr. - Voir BURNS (E.J.T.) C7-775
- FAUCHAIS (P.).- Voir BARONNET (J.M.) C7-247
- FAUCHAIS (P.).- COUDERT (J.F.)..... C7-335
- FAUCHAIS (P.).- Voir KASSABJI (F.).. C7-321
- FEDOROV (V.A.).- Voir KOSTYLEV (A.A.) C7-367
- FEDOROV (V.A.).- Voir KOSTYLEV (A.A.) C7-369
- FEDOSEEVA (T.N.).- Voir KOL'CHUGINA (I.A.) C7-629
- FEHL (D.L.).- Voir BURNS (E.J.T.).. C7-775
- FEIGIN (A.M.).- Voir LITVAK (A.G.).. C7-635
- FELTS (B.).- Réalisation et expérimentation d'un laser à vapeur de cuivre C7-383
- FERNSLER (R.F.).- Voir ALI (A.W.).. C7-773
- FERNSLER (R.).- Voir KOOPMAN (D.).. C7-419
- FIKSEL' (G.I.).- Voir DUDNIKOV (V.G.) C7-479
- FILENKO (Yu.I.), STEPANOV (B.M.) and USHAKOV (L.S.).- Holographic time-differential cine-interferometry of the gas discharge plasma C7-873
- FILIPPOV (Ju.V.).- Voir GEBALOV (V.I.) C7-347
- FINN (T.G.).- Voir BLEACH (R.D.)... C7-749

- FIORITO (R.B.).- Voir ALI (A.W.).. C7-773
- FISUN (O.I.).- Voir GRIGORIADY (A.K.) C7-105
- FITAIRE (M.).- Voir AUPHELLE (D.). C7-397
- FLETCHER (J.) and BLEVIN (H.A.).- Use of emitted photons as a probe for low pressure gas discharge C7-811
- FLEURIER (C.), COULAUD (G.) and CHAPELLE (J.).- Effect of the ion motion at low electron densities on the profiles of the lines 4471 Å and 4922 Å of He I C7-81
- FORREST (M.J.), KIRK (R.E.) and PEACOCK (N.J.).- A CO₂ laser-plasma interaction experiment the scattered spectrum of Langmuir waves driven via the electron-ion decay instability.. C7-745
- FORT (J.), BONNET (J.), FOURNIER (G.) and PIGACHE (D.).- Cathode density wave in an electron beam controlled discharge C7-315
- FORT (J.).- Voir FOURNIER (G.) ... C7-777
- FORT (J.).- Voir PIGACHE (D.) C7-317
- FOURNIER (G.), BONNET (J.), BRIDET (J.), FORT (J.) and PIGACHE (D.).- Electron beam energy branching in oxygen C7-777
- FOURNIER (G.).- Voir FORT (J.) ... C7-315
- FOURNIER (G.).- Voir PIGACHE (D.). C7-317
- FOURNIER (G.).- Voir TRAN NGOC AN.. C7-533
- FOURRIER (C.), LEMPERIERE (G.) and POITEVIN (J.M.).- Metal atom density by atomic absorption spectroscopy in a d.c. sputtering discharge C7-819
- FRAIMAN (G.M.).- Voir KOL'CHUGINA (T.A.) C7-629
- FRANCK (A.G.).- Voir BOGDANOV (S. Yu.) C7-221
- FRANKEL (N.E.), HINES (K.C.) and SPEIRS (R.D.B.).- Dielectric response and energy loss for an intermediate quantum plasma C7-513
- FRANKLIN (R.N.).- Stability of the plasma-sheath C7-163
- FRANKLIN (R.N.).- Voir WALL (D.N.). C7-593
- FREISINGER (J.), REINECK (S.) and LOEB (H.W.).- The RF-ion source rig 10 for intense hydrogen ion beams C7-477
- FRÖHLICH (K.) and WIDL (W.).- Determination of the microscopic field enhancement factor β of prestressed vacuum interrupter contacts . C7-407
- FUJITA (H.).- Voir IMAZU (S.) C7-153
- FUJIWAKA (S.).- Voir INUTAKE (M.).. C7-685
- FUNK (W.).- Voir BEYER (H.) C7-325
- FURSEY (G.N.), PTYTSIN (V.E.) and EGOROV (N.V.).- Influence of magnetic field on the effects preceding the transition of field emission into the vacuum breakdown C7-403
- FURSEY (G.N.), ZHUKOV (V.M.), SHIROCHIN (L.A.), ALEKSANDROV (A.K.), and GALUSO (S.Y.).- Formation of high-current and density electron beam on gallium cathode with the limited emission surface C7-415
- GALECHIAN (G.A.).- Voir ARUTUNIAN (G.G.) C7-205
- GALUSO (S.Y.).- Voir FURSEY (G.N.). C7-415
- GANEVA (J.).- Voir KOLEVA (I.)..... C7-845
- GARBAN (C.).- Voir AMIRANOFF (F.).. C7-729
- GARBAN (C.).- Voir AMIRANOFF (F.). C7-769
- GARDNER (G.A.).- Voir BOYD (T.J.M.) C7-551
- GARSCADDEN (A.).- Voir BAILEY (W.F.) C7-377
- GARSCADDEN (A.).- Voir DETTMER (J.W.) C7-135
- GAUCHEREL (Ph.), ROWE (B.), QUEFFELEC (J.L.), BEN JEMAA (N.) et GOMET (J.C.).- Observation de l'émission de l'exciplexe Ar H* dans des jets de plasmas d'argon-hydrogène raréfiés C7-91
- GAUTHIER (J.C.), GEINDRE (J.P.) and GRANDJOUAN (N.).- Spectroscopic study of the ionization dynamics in a CO₂ laser-produced plasma of helium C7-735
- GAUTHIER (J.C.), GEINDRE (J.P.) and GRANDJOUAN (N.).- Space and time resolved measurements of electron and atomic excited states densities in a CO₂ laser-produced plasma of helium C7-737
- GEBALOV (V.I.), SAMOILOVITCH (V.G.) and FILIPPOV (Ju.V.).- The numerical simulation of silent discharge in oxygen. Integral characteristics of discharge channel and the role of excited species reactions C7-347
- GEINDRE (J.P.).- Voir GAUTHIER (J.C.) C7-735
- GEINDRE (J.P.).- Voir GAUTHIER (J.C.) C7-737
- GEKKER (I.R.).- On the generation of fast electrons during interaction of microwave fields with collisionless plasma of subcritical density C7-217
- GEKKER (I.R.).- Voir ARUTYUNYAN (S.G.) C7-219
- GELASHVILI (G.V.).- Voir BARKHUNDAROV (E.M.) C7-869
- GERASIMOV (V.P.), KAREV (S.A.), OBUKHOV (V.A.) and SHISHKIN (G.G.).- H.F. instabilities in the heterogeneous plasma of a penning discharge ion source with a hollow cathode C7-647
- GHOSH (P.K.).- Voir ASHRAF (A.) ... C7-129
- GIL'DENBURG (V.B.), LITVAK (A.G.) and YUNAKOVSKY (A.D.).- The dynamics of a high-frequency discharge in a wave beam C7-215

- GIPPIUS (E.F.), ILJUKHIN (B.I.) and KOLESNIKOV (V.N.).- Some remarks on the nonequilibrium plasma diagnostics C7-871
- GIRY (L.).- Voir SKOWRONEK (M.) ... C7-303
- GLASSER (J.), VILADROSA (R.) and CHAPPELLE (J.).- Non ideality effects in a high pressure argon arc measured by infrared continuum absorption C7-687
- GLAVONJIC (V.).- Voir PURIC (J.).. C7-795
- GLAVONJIC (V.).- Voir PURIC (J.).. C7-835
- GLEIZES (A.), KAFROUNI (H.) and VACQUIE (S.).- Mechanisms of electron disappearance in a decaying plasma arc C7-235
- GLEIZES (A.).- Voir KAFROUNI (H.).. C7-237
- GLOTOV (E.P.).- BASOV (N.G.) C7-393
- GLOTOV (E.P.), DANILYCHEV (V.A.), MILANICH (A.I.) and SOROKA (A.M.).- Current voltage characteristics of a self-sustained electrophotomized discharge in laser mixtures C7-371
- GODYAK (V.A.) and KHANNEH (A.S.).- Experimental investigation of radio-frequency discharge in helium C7-125
- GODYAK (V.A.) and KHANNEH (A.S.).- Theoretical investigation of radio-frequency discharge in γ -regime C7-147
- GODYAK (V.A.) and OX (S.N.).- Finite thickness effect of probe sheath in radio-frequency plasma probe diagnostics C7-807
- GODYAK (V.A.) and OX (S.N.).- Investigation of sheath at electrode in radio-frequency discharge C7-809
- GOLDMAN (M.V.).- Voir DUBOIS (D.F.) C7-601
- GOLDMAN (A.) and SIGMOND (R.S.).- Effects of negative air coronas on plane anode foils C7-443
- GOLUBEV (A.V.).- Voir TISHCHENKO (E.A.) C7-859
- GOLUBEV (A.V.).- Voir ZATSEPIN (V.G.) C7-799
- GOLUBEV (A.V.).- Voir ZATSEPIN (V.G.) C7-861
- GOLUBKOV (G.V.), KUZNETSOV (N.M.) and YEGOROV (V.V.).- The role of single-step ionization by thermal electron-atom collisions C7- 89
- GOLUBOVSKY (Yu.B.) and SONNENBURG (R.).- Investigations of the contraction mechanism in a helium medium pressure discharge C7-155
- GOMBERT (M.M.), DEUTSCH (C.) and MINOO (H.).- Thermodynamical functions for dense multicomponent plasmas C7-695
- GOMBERT (M.M.).- Voir MINOO (H.) .. C7-697
- GOMET (J.C.).- Voir GAUCHEREL (Ph.) C7- 91
- GOODINGS (A.).- Voir DAVIES (A.J.). C7- 63
- GORBATOV (A.V.) and SAMUILOV (E.V.) .- Electrophysical properties of non-equilibrium aerosol plasma .. C7-519
- GORBENKO (B.S.).- Voir AVERIN (V.I.) C7-875
- GORBUNOVA (E.F.), EZUBCHENKO (A.N.), KARCHEVSKY (A.I.) and MUROMKIN (Yu.A.).- The separation of isotopes of noble gases in stationary high frequency discharge with travelling magnetic field C7-211
- GORMAN (J.G.).- Voir KIMBLIN (C.W.) C7-413
- GORSE (C.).- Voir CAPITELLI (M.) .. C7- 13
- GOUESBET (G.).- Laser-Doppler velocimetry in ionized gases : a review paper C7-789
- GOUSSET (G.).- Voir CERNOGORA (G.) C7- 59
- GRADOV (O.M.).- Voir ALIEV (Yu.M.) C7-557
- GRANDJOUAN (N.).- Voir GAUTHIER (J.C.) C7-735
- GRANDJOUAN (N.).- Voir GAUTHIER (J.C.) C7-737
- GRANNEMAN (E.H.A.).- Voir WIJNAKKER (M.M.B.) C7-487
- GRAY (E.W.) and PHARNEY (J.R.).- Enhanced arcing as a function of organic exposure and arc current Pd and Pd/Ag electrodes C7-267
- GREIG (J.R.).- Voir ALI (A.W.) C7-773
- GREIG (J.).- Voir KOOPMAN (D.) C7-419
- GRIBKOV (V.A.), DUBROVSKY (A.V.), KALACHEV (N.V.), KOZLOVA (T.A.), and NIKULIN (V.Ya.).- Dynamics of plasma phenomena in "plasma focus" under the action of powerful laser radiation C7-763
- GRIGORIADY (A.K.) and FISUN (O.I.).- On charge - exchange of ions in plasma C7-105
- GRISHINA (I.A.).- Voir VASILIEVA (A.N.) C7-103
- GRISHUTIN (G.S.).- Voir POKROVSKAJA-SOBOLEVA (A.S.) C7-405
- GROH (K.H.) and WALTER (S.E.).- Operation modes of hollow cathode arcs with reduced gas flow C7-277
- GROSSL (M.), HELM (H.), LANGENWALTER (M.) and MARK (T.D.).- Stationary afterglow study of the singly charged atomic ions in pure Ar and Kr C7- 51
- GROSU (D.) and GROSU (C.S.).- Remarks on the breakdown of an electric gas discharge C7-181
- GROSU (C.S.).- Voir GROSU (D.) C7-181
- GROZDANOV (T.P.) and JANEV (R.K.).- Two electron capture processes in plasmas containing multiply charged ions C7 71
- GRUDZINSKI (W.).- Voir BRZOSKO (J.S.) C7-471
- GRUJIC (P.).- Voir DIMITRIJEVIC (M.S.) C7-119
- GRUJIC (P.).- Voir DIMITRIJEVIC (M.S.) C7-825

- GUDELEV (V.G.), SHKADAREVICH (A.P.) and JASINSKII (V.M.).- Laser gas-discharge plasma diagnostics based on Faraday rotation C7-865
- GUENTHER (A.H.).- Voir HATFIELD (L.L.) C7-483
- GUNDERSEN (M.A.).- Voir WILLIAMS (P.F.) C7-305
- GUNTHER (K.), LANG (S.), RADTKE (R.) and ULBRICHT (R.).- Experimental investigation of the balmer spectrum from a dense hydrogen plasma near the photorecombination threshold C7-679
- HADGY-OGLY (M.R.).- Voir TEMKO (S.W.) C7-433
- HAGLER (M.).- Voir CHU (E.) C7-747
- HAHAEV (A.D.).- Voir VDOWIN (V.G.) . C7-177
- HAMILTON (G.W.).- Voir BACAL (M.) .. C7-791
- HANTZSCHE (E.).- Impact and resistive heat sources of cathode spots in arc discharges C7-439
- HARA (M.).- Voir AKAZAKI (M.) C7-145
- HARGES (H.C.).- Voir HATFIELD (L.L.) C7-483
- HARUO ITOH and NOBUAKI IKUTA.- Temporal increase of ionization current in N_2 gas C7-445
- HASHIGUCHI (S.) and INUTAKE (M.).- Electrical conductivity of high-density, shock-heated Ar and Xe plasmas C7-681
- HATFIELD (L.L.), HARJES (H.C.), KRISTIANSEN, GUENTHER (A.H.) and SCHONBACK (K.H.).- Laser fiber optic breakdown of a pulse charged 90 % Ar - 10 % N_2 gas switch C7-483
- HAUG(R.).- Voir BUCHET (G.) C7-327
- HAUSCHILD (W.) and MOSCH (W.).- Reasons for the dispersion of breakdown voltages in SF_6 C7-251
- HÁVELKO (O.) and VÁVRA (Z.).- Quantitative analysis of interaction between a high-pressure plasma column and surrounding liquid C7-291
- HAYASHI (M.).- Monte Carlo simulation of electron avalanche in hydrogen C7- 45
- HEISEN (A.).- Voir BERGER (E.) C7-191
- HELM (H.).- Voir GROSSL (M.) C7- 51
- HEYLEN (A.E.D.).- Electron molecule collision frequencies from breakdown data in a crossed magnetic field for ethane gas C7-143
- HIGAKI (S.).- Voir IMASAKI(K.) C7-779
- HEMMEL (G.) and SOWA (L.).- A method of estimating the level of collective electric field fluctuations in a nonthermal plasma with a two-temperature electron gas C7-837
- HINES (K.C.).- Voir FRANKEL (N.E.) . C7-513
- HOFFMANN (P.), HUGEL (H.), SCHALL (W.) and SCHOCK (W.).- Microwave discharge in a supersonic flow ... C7-489
- HOLMES (F.A.).- Voir KIMBLIN (C.W.) C7-413
- DE HOOG (F.J.).- Voir DIEELS (J.W.H.) C7- 75
- DE HOOG (F.J.).- Voir VAN DER KRAAN (P.A.M.) C7- 15
- HOPMAN (H.J.).- Voir MASSMAN (P.) . C7-435
- HOPPER (D.G.).- Ab initio studies of ion-molecule reactions. The N_2O^+ (a^4A') potential energy hypersurface for the $O^+(N_2,N)NO^+$ reaction C7- 79
- HRABOVSKY (M.), KONRAD (M.) and SKODA (P.).- Theoretical model of current-zero behaviour of axially blown arc in SF_6 C7-293
- HSUEH-CHI (H.).- An investigation on the frequency characteristics of the RF discharge in Ar-Hg mixtures C7-225
- HUBERT P. and MOUGET (G.).- Mesure de la vitesse d'ascension du "Return stroke" en fonction de l'intensité pour deux éclairs déclenchés C7-421
- HUGEL (H.).- Voir HOFFMANN (P.) ... C7-489
- HUMPHREYS-JONES (G.J.).- Voir BOYD. (T.J.M.) C7-551
- IAGODOVSKAIA (T.V.).- Voir TEMKO (S.W.) C7-433
- IBADOV (S.).- On the formation of plasma carbon component in the hollow cathode anomalous glow discharge C7-173
- ICHIRO MORI, LEPPERT (H.D.) and WIESEMANN (K.).- Characteristics of spatial wave echoes at the lower hybrid branch C7-555
- IDO (K.).- Voir SUGAI (H.) C7-703
- IH (C.S.).- Voir KOPEIKA (N.S.) ... C7-755
- IKEZAWA (S.) and NAKAMURA (Y.).- A physical picture of the higher-order Landau modes of electron plasma wave C7-573
- ILJUKHIN (B.I.).- Voir GIPPIUS (E.F.) C7-871
- IMAZU (S.), FUJITA (H.), MIURA (K.) and TAKAMATSU (T.).- Nonlinear effect of the ionization waves on the temperatures charged particles in a magnetized positive column . C7-153
- IMASAKI (K.), MIYAMOTO (S.), HIGAKI (S.), NAKAI (S.), NISHIHARA (K.) and YAMANAKA (C.).- An evidence of anomalous deposition of REB energy to the low Z target C7-779
- IMIZU (S.).- Voir SHINDO (H.) C7-259
- INABA (T.).- Voir SHINDO (H.) C7-259
- INUTAKE (M.).- Voir HASHIGUCHI (S.) C7-681
- INUTAKE (M.), SUZUKI (K.) and FUJIWAKA (S.).- Sound velocity in metal-nonmetal transition region of high pressure mercury plasmas ... C7-685
- IRIE (M.).- Voir JONES (G.R.) C7-269

- IVANOV (V.G.).- Voir BAKSHT (F.G.). C7-339
- IVANOV (A.A.).- Voir WINKLER (R.). C7-131
- IVANOV (A.A.).- Voir WINKLER (R.). C7-261
- JANEV (R.K.).- Voir GROZDANOV (T.P.) C7- 71
- JANOS (W.A.).- Thomson-like RF scattering by small overdense plasma particles C7-753
- JAROSZ (J.).- Voir CHERON (B.) C7-847
- JASINSKII (V.M.).- Voir GUDELEV (V.G.) C7-865
- JAYARAM (K.) and TSUI (K.H.).- Particle distributions in metal vapour-rare gas arc discharges C7-275
- JOHNSON (D.J.).- Voir BURNS (E.J.T.) C7-775
- JONES (G.R.), SMITH (M.R.), IRIE (M.), WALMSLEY (H.L.) and STRACHAN (D.C.).- The correlation of local voltage and cross-sectional areas for very high current gas blast arcs in air and SF_6 C7-269
- JULEA (Th.).- Voir APOSTOL (I.) ... C7-765
- JURENKA (H.).- Voir BARRETO (E.) .. C7-301
- KAFROUNI (H.).- Voir GLEIZES (A.) . C7-235
- KAFROUNI (H.), GLEIZES (A.) and DANG DUC (H.).- Difference between electron temperature and heavy particles temperature in arc plasma .. C7-237
- KAGAN (Yu.M.).- Voir DOTHAN (F.) .. C7-127
- KAGAN (Yu.).- Voir LUDMIRSKY (A.) . C7-373
- KALACHEV (N.V.).- Voir GRIBKOV (V.A.) C7-763
- KAMINSKA-PRANKE (A.).- Voir KRÓLI-KÓWSKI (Cz.) C7-353
- KAPLAN (V.B.).- Voir BABANIN (V.I.) C7-201
- KAPLAN (V.B.).- Voir BOGDANOV (A.A.) C7-337
- KAPLAN (V.B.), MARTSINOVSKIY (A.M.), RASULOV (F.N.) and YURIEV (V.G.).- Kinetic of negative grid pulse influence upon discharge plasma . C7-495
- KARCHER (T.).- Voir KOPEIKA (N.S.) C7-755
- KARCHEVSKY (A.I.).- Voir GORBUNOVA (E.F.) C7-211
- KARCHEVSKY (A.I.) and POTANIN (E.P.).- "Mass-diffusion" mechanism of isotope separation in gaseous discharge system with travelling magnetic field C7-213
- KAREV (S.A.).- Voir GERASIMOV (V.P.) C7-647
- KARFIDOV (D.M.).- Voir ARUTYUNYAN (S.G.) C7-219
- KASATKINA (M.P.).- Voir BUTSEV (V.A.) C7-485
- KASSABJI (F.) and FAUCHAIS (P.).- Heat transfer and flow in a hydrogen plasma reactor C7-321
- KAUFMAN (Y.), AVIVI (P.) and DOTHAN (F.).- Ion clusters in the positive column of He-Co and Ar-Co discharges C7- 31
- KAWAMOTO (S.).- Voir AMEMIYA (H.).. C7-389
- KCHUZEVEV (A.P.), KOROLEV (Yu.D.), KUZMIN (V.A.), MESYATS (G.A.), ROTSHTEIN (V.P.) and SHEMAKIN (I.A.).- High-current diffuse discharge with the explosive cathode process C7-281
- KEKEZ (M.M.) and SAVIC (P.).- Shock waves in spark channels part I .. C7-255
- KEKEZ (M.M.), LOUGHEED (G.D.) and SAVIC (P.).- Shock waves in spark channels, part II C7-257
- KERVALISHVILI (N.A.) and KORTKHONJIA (V.P.).- Ionization average frequency in anode sheath of penning type high-voltage discharge C7-111
- KHAKIMOV (F.K.H.) and TSYTOVICH (V.N.).- On the example of fast Langmuir solitons existence in non-equilibrium plasma C7-583
- KHANNEH (A.S.).- Voir GODYAK (V.A.) C7-125
- KHANNEH (A.S.).- Voir GODYAK (V.A.) C7-147
- KHIET (Tu.).- Ion tail formation and saturation of the ion-acoustic instability C7-605
- KHODNENKO (V.P.), SHISHKIN (G.G.) and TRIFONOV (Ju.V.).- Analysis of the H.F. drift instability onboard "meteor" satellite C7-717
- KHODZHAEV (A.Z.).- Voir BOGDANOV (S.Yu.) C7-221
- KIDRASOV (F.Kh.).- Excitation of magnesium atoms in hollow cathode discharge C7-121
- KIEFFER (P.).- Voir DROUET (M.G.) . C7-437
- KIMBLIN (C.W.), HOLMES (F.A.), GORMAN (J.G.) and SLADE (P.G.).- Extinction of a vacuum arc by application of a transverse magnetic field C7-413
- KIOBUKOWSKA (J.) and BRZOSKO (J.S.).- Note on the self-sustaining creep discharges in gas at the dielectric surface C7-469
- KIRK (J.G.).- Declaration of a fast ion in an accretion column C7-705
- KIRK (R.E.).- Voir FORREST (M.J.) . C7-745
- KISELEVSKII (L.I.), KLYGIN (N.Ya.), MAKAREVICH (A.N.) and SOLOVYAN-CHIK (D.A.).- Effect of discharge radiation on electrode processes in helium C7-465
- KLEPOV (A.F.).- Voir AVERIN (V.I.) C7-875
- KLIMKIN (V.M.).- Voir BOKHAN (P.A.) C7-115
- KLIMKIN (V.F.) and PICKALOV (V.V.).- Optical interferometry of pulsed micro-discharges C7-329
- KLOPOVSKY (K.S.), LOPANTSEVA (G.B.) PAL (A.F.), PERSTANTSEV (I.G.) and STAROSTIN (A.N.).- Peculiarities of pulsed non-self-sustained discharges in mixtures containing CO C7-343

- KLOSE (J.Z.).- Voir OTT (W.R.) C7-803
- KLOSS (H.G.).- Voir BEYER (H.) C7-325
- KLUCHAREV (A.N.), LAZARENTO (A.V.) and VUJNOVIC (V.).- The ionization rate coefficients for some radiatively excited rubidium states .. C7- 87
- KLYGIN (N.Ya.).- Voir KISELEVSKII (L.I.) C7-465
- KOCH (H.).- Voir EICHLER (H.J.) ... C7-379
- KOCIAN (P.), MAYOR (J.M.) and BOURQUARD (S.).- Some properties of the low-pressure discharge in silane C7-169
- KOCIAN (P.).- Voir BOURQUARD (S.) . C7-385
- KOLEDIN (D.).- Voir DIMITRIJEVIC (M.S.) C7-825
- KOGELSCHATZ (U.).- Voir ELIASSON (B.) C7-271
- KOL'CHUGINA (I.A.), LITVAK (A.G.), FEDOSEEVA (T.N.) and FRAMIN (G.M.).- Modulational instability of Langmuir oscillations in the field of an electromagnetic wave C7-269
- KOLESNIKOV (V.N.).- Voir GIPPIUS (E.F.) C7-871
- KOLESOV (G.V.).- Voir AVERIN (V.I.) C7-875
- KOLEVA (I.).- Voir PETRAKIEV (A.) . C7-845
- KOLYSHKIN (I.N.).- Voir BABANIN (V.I.) C7-201
- KONARZEWSKI (A.).- Voir BRZOSKO (J.S.) C7-471
- KONDAKOV (A.A.).- Voir BURTSEV (V.A.) C7-387
- KONDRASHOVA (L.I.).- Voir AVERIN (V.I.) C7-875
- KONJEVIC (N.).- Voir DIMITRIJEVIC (M.) C7-815
- KÓNOV (V.I.).- Voir APOSTOL (I.) .. C7-765
- KONRAD (M.).- Voir HRABOVSKY (M.) . C7-293
- KOOPMAN (D.), GREIG (J.), PECHACEK (R.), ALI (A.), VITKOVITSKY (I.) and FERNSLER (R.).- CO₂ laser produced channels for guiding long sparks in air C7-419
- KOPEIKA (N.S.), KARCHER (T.) and IH (C.S.).- Effects of space charge on the "Effective cross-section" C7-755
- KORGE (H.).- Voir LAAN (M.) C7-351
- KOROLEV (Yu.D.).- Voir KCHUZEEV (A.P.) C7-281
- KORTKHONJIA (V.P.).- Voir KERVALISH-VILI (N.A.) C7-111
- KOSHILEV (N.A.), STROKIN (N.A.), SHISKO (A.A.) and MIKHALEV (A.V.) .- Application of the magnetic flux plasma trap to generation of current sheets in a rarefied plasma C7-507
- KOSHILEV (N.A.), STROKIN (N.A.) and SHISKO (A.A.).- Some properties of interaction of magnetic piston with non-magnetized plasma C7-721
- KOSTROV (A.V.).- Voir BRIZHINEV (M.P.) C7-867
- KOSTYLEV (A.A.), LONDER (J.I.), TERENTYEV (A.P.), ULYANOV (K.N.) and FEDOROV (V.A.) .- On the mechanism of glow discharge instability following the turn-off a non-self-sustained ionization source C7-367
- KOSTYLEV (A.A.), PEREVODCHIKOV (V.I.) TERENTYEV (A.P.), ULYANOV (K.N.) and FEDOROV (V.A.).- Investigations of instabilities in a non-self-sustained repetitively pulsed discharge C7-369
- KOTEROV (V.N.).- Voir ALEXANDROV (V.V.) C7-357
- KOVAL (N.N.), KREINDEL (Yu.E.) and SHANIN (P.M.).- The arc discharge of low pressure with two constricted channels and the anode plasma of large cross-section C7-481
- KOVALEV (A.S.).- Voir VASILIEVA (A.N.) C7-103
- KOVALEV (V.F.), PUSTOVALOV (V.V.), ROMANOV (A.B.) and STEPHAN (V.).- Turbulent plasma in the field of intense high frequency radiation . C7-609
- KOVALEV (A.S.), POPOV (A.M.) and RAKHIMOV (A.T.).- On the mechanism of breakdown of gases by the emission from a CO₂ laser near a metal surface C7-759
- KOVALEVSKII (V.L.).- Voir KUZOVNIKOV (A.A.) C7-459
- KOVITYA (P.), LOWKE (J.J.) and STOKES (A.D.).- Theory of arc clogging in nozzles C7-299
- KOZAREV (P.M.).- Voir ZILTSOV (V.A.) C7-663
- KOZLOV (N.P.), NORMAN (G.E.) and PROTASOV (Yu.S.).- Superradiation from non-ideal plasmas in electric field C7-675
- KOZLOVA (T.A.).- Voir GRIBKOV (V.A.) C7-763
- KRALIKINA (E.A.).- Voir VOLKOVA (L.M.) C7-231
- KRASA (J.).- Voir SKALA (J.) C7-587
- KRASOV (V.I.).- Voir ALTYNTSEV (A.T.) C7-723
- KREINDEL (Yu.E.).- Voir KOVAL (N.N.) C7-481
- KRISTIANSEN (M.).- Voir MIKKELSON (K.) C7-401
- KRISTIANSEN (M.).- Voir HATFIELD (L.L.) C7-483
- KRISTIANSEN (M.).- CHU (E.) C7-747
- KRÓLIKÓWSKI (Cz.), KAMIŃSKA-PRANKE (A.).- An attempt to describe voltage-current characteristics of an arc when utilizing equations of magnetohydrodynamics C7-353

KTITOROV (V.I.).- Voir VASILIEVA (A.N.)	C7-103	LANDA (P.S.) and PONOMAREV (Yu.V.).- Influence of the metastable atoms lifetime on the running striation excitation	C7-223
KUBALA (A.).- Voir DELVAUX (J.)	C7-785	LANG (S.).- Voir GUNTHER (K.)	C7-679
KUDU (K.).- Voir LAAN (M.)	C7-351	LANGDON (A.B.).- Nonlinear inverse bremsstrahlung and heated electron distributions	C7-731
KUHN (S.).- Voir FANG (M.T.C.)	C7-579	LANGENWALTER (M.).- Voir GROSSL (M.) C7-	51
KUHN (S.).- Voir SCHRITTWIESER (R.) C7-	581	LARIGALDIE (S.).- Linear gliding discharge over dielectric surfaces ..	C7-429
KULK (P.P.).- Voir VOROBIOV (V.V.) C7-	693	LAROUR (J.).- Voir LEYCURAS (A.) ...	C7-683
KUPLIAUSKIENE (A.V.) and KUPLIAUSKIS (Z.J.).- Rayleigh and Compton scattering cross-sections of X-rays by oxygen ions	C7-853	LAVAL (G.).- Voir ADAM (J.C.)	C7-671
KUPLIAUSKIS (Z.J.).- Voir KUPLIAUSKIENE (A.V.)	C7-853	LAZARENKO (A.V.).- Voir KLUCHAREV (A.N.)	C7- 87
KURALOVA (A.V.).- Voir VOLKOVA (L.M.)	C7-231	LAZAREV (V.B.).- Voir TISHCHENKO (E.A.)	C7-859
KURUNOV (R.F.).- Voir BURTSEV (V.A.) C7-	387	LAZAREV (V.B.).- Voir ZATSEPIN (V.G.) C7-	857
KUSWA (G.W.).- Voir BURNS (E.J.T.) .	C7-775	LEBEDEV (N.V.).- Voir ALTYNTSEV (A.T.)	C7-723
KUTEVA (B.V.), SMIRNOV (A.S.) and ZHILINSKY (A.P.).- Application of RF discharge with rotating electric field for excitation of CO ₂ laser	C7-395	LEBEDEV (V.V.).- Voir AVERIN (V.I.) C7-	875
KUZELEV (M.V.).- Voir BOGDANKEVICH (L.S.)	C7-783	LECLAIR (J.).- Voir ROSADO (R.J.) ..	C7-285
KUZMIN (V.A.).- Voir KCHUZEEV (A.P.) C7-	281	LEEPER (R.J.).- Voir BURNS (E.J.T.) C7-	775
KUZMIN (S.K.).- Voir TEMKO (S.W.) ..	C7-433	LE GROUPE DE RECHERCHES DE SAINT-PRIVAT-D'ALLIER.- Recherches sur la foudre en France	C7-297
KUZMIN (S.K.).- Voir TEMKO (S.W.) ..	C7-677	LEMEDGE (B.).- Theoretical method for predicting the properties of cyclotron harmonic waves from the perpendicular dispersion	C7-615
KUZNETSOV (N.M.).- Voir GOLUBKOV (G.V.)	C7- 89	LEMPERIERE (G.).- Voir FOURRIER (C.) C7-	819
KUZNETSOV (V.I.).- Voir BABANIN (V.I.)	C7-201	LENAERTS (J.).- Voir WIEME (W.)	C7- 37
KUZNETSOV (V.I.).- Voir ENDER (A.Ya) C7-	523	LENGYEL (L.L.).- Effect of transport processes on tokamak refueling by pellet injection	C7-529
KUZOVNIKOV (A.A.), KOVALEVSKII (V.L.) SAVINOV (V.P.) and YAKUNIN (V.G.).- The investigation of physical properties of the near electrode region of HF discharge	C7-459	LE NY (R.).- Voir BOULLLOUD (A.)	C7-241
KUZOVNIKOV (A.A.).- Voir ERSHOV (A.P.)	C7-521	LEPPERT (H.D.).- Voir ICHIRO MORI ..	C7-555
LAAN (M.), KORGE (H.) and KUDU (K.).- The field strength and electron density calculations for the corona pulses	C7-351	LEPRINCE (P.).- Voir CICCONI (G.) ..	C7-827
LABAT (J.M.).- Voir DJENIZÉ (S.) ...	C7- 47	LERGON (H.G.) and MÜLLER (K.G.).- Positive ion extraction by an anodic orifice probe	C7-821
LABAT (O.).- Voir LABAT (J.M.)	C7- 9	LESAGE (A.), RICHOU (J.), CHARIL (P.) and COMBIER (M.).- An unambiguous method of electron density measurement in a shock-generated plasma using a laser interferometer	C7-805
LABAT (J.M.), VUKIČEVIĆ (J.), LABAT (O.) and DJENIZÉ (S.).- Line radiation of argon plasma in early afterglow	C7- 9	LESNEVSKY (L.N.).- Voir EGOROV (I.I.) C7-	349
LAFON (J.P.J.).- On plasma sheath problems	C7-843	LEVEAU (J.).- Voir VALIGNAT (S.) ...	C7- 7
LAGAR'KOV (A.N.) and SARYCHEV (A.K.).- The conductivity of dense calcium plasma near the saturation line	C7-691	LEVINE (J.S.) and CRAWFORD (F.W.).- Fluid theory of plasma double-layers	C7-139
LAKDAWALA (V.K.).- Voir MORUZZI (J.L.)	C7- 11	LEYCURAS (A.) and LAROUR (J.).- General expression of the drift velocity of excess electrons in dense fluid argon	C7-683
LAKICEVIC (I.).- Voir PURIC (J.) ...	C7-795	LIN (J.).- Voir MIKKELSON (K.)	C7-401
LAKICEVIC (I.).- Voir PURIC (J.) ...	C7-835	LINDBERG (L.) and TORVEN (S.).- Some characteristics of an electric double layer in a magnetized plasma	C7-151

- LINDINGER (W.).- Voir ALGE (E.) ... C7- 83
- LINDINGER (W.).- Voir PESKA (K.) .. C7- 21
- LINHJELL (D.).- Voir SIGMOND (R.S.A) C7-323
- LIPATOV (N.I.).- Voir BELYANKO (A.E.) C7-505
- LIPEROVSKY (V.A.).- Voir LIVSHITS (M.A.) C7-627
- LIPEROVSKY (V.A.).- Voir VOLOSEVICH (A.V.) C7-623
- LIPEROVSKY (V.A.).- Voir VOLOSEVICH (A.V.) C7-625
- LITVAK (A.G.).- Voir GIL'DENBURG (V.B.) C7-215
- LITVAK (A.G.).- Voir KOL'CHUGINA (I.A.) C7-629
- LITVAK (A.G.), MIRONOV (V.A.) and FETGIN (A.M.).- Modulation instability and plasma electrodynamic characteristics C7-635
- LITVAK (A.G.), SERGEEV (A.M.) and SHAKHOVA (N.A.).- Self-action of quasi-optical beams in a magnetoplasma C7-637
- LIVSHITS (M.A.), LIPEROVSKY (V.A.), TOMOZOV (V.M.) and TSYTOTICH (V.N.).- The strong ion acoustic turbulence and the electron spectrum in an electric fields C7-627
- LIVSHITS (M.A.).- Voir VOLOSEVICH (A.V.) C7-623
- LIVSHITS (M.A.).- Voir VOLOSEVICH (A.V.) C7-625
- LOEB (H.W.).- Voir FREISINGER (J.)..C7-477
- LOMINADZE (J.G.), MACHABELI (G.Z.) and MIKHAILOVSKY (A.B.).- Relativistic electron-positron plasma quasi-linear relaxation at the presence of magnetic bremsstrahlung C7-713
- LONDER (J.I.).- A current-voltage characteristic of non-self-maintained discharge C7-203
- LONDER (J.I.).- Voir KOSTYLEV (A.A) C7-367
- LONDER (J.I.), MENAHIN (L.P.) and ULYANOV (K.N.).- Efficiency of excitation of rotational and vibrational levels in a nitrogen molecule C7-29
- LONDER (J.I.).- Voir PROZOROV (E.F.) C7-863
- LOPANTSEVA (G.B.).- Voir KLOPOVSKY (K.S.) C7-343
- LOPANTSEVA (G.B.), PAL' (A.F.), PEREVOZNOV (A.F.), PERSIANTSEV (I.G.) and STAROSTIN (A.N.).- Effect of gas purity on the current of a non-self sustained discharge in nitrogen C7-499
- LOS (J.).- Voir MASSMANN (P.) C7-435
- LOUGHEED (G.D.).- Voir KEKEZ (M.M.) C7-257
- LOUIS-JACQUET (M.).- Voir THIELL (G.) C7-877
- LOWKE (J.J.).- Voir BRAGLIA (G.L.) C7-17
- LOWKE (J.J.).- Voir KOVITYA (P.)... C7-299
- LUCHES (A.), NASSISI (V.), PERRONE (A.) and PERRONE (M.R.).- Excitation of 3^3P level of He and 4^2F level of He⁺ with electron beams..C7-67
- LUDMIRSKY (A.), COHEN (CH.) and KAGAN (Yu.) .- Kinetic process in non-heated copper vapour laser....C7-373
- LUKASHENKO (V.I.).- Formation of $K_2(A'^2\Sigma^+)$ molecules caused by $K(4P)$ atoms in potassium discharge C7-113
- LU QUAN-KANG.- A generalized ohm's law of unsteady state in partially ionized gases C7-517
- LU QUAN-KANG and CHEN ZHI-PAN.- On some properties of anisotropic plasmas C7-667
- LYNOV (J.P.), MICHELSEN (P.), PÉCSELI (H.L.) and RASMUSSEN (J.J.).- Interaction between solitary structures in a magnetized, plasma-loaded waveguide C7-567
- LYNOV (J.P.), MICHELSEN (P.), PÉCSELI (H.L.), RASMUSSEN (J.J.) and SUGAI (H.).- Nonlinear waves in a magnetized plasma waveguide C7-571
- MACHABELI (G.Z.).- Voir LOMINADZE (J.G.) C7-713
- MACHABELI (G.Z.) and USOV (V.V.).- A plasma model of crab nebula and pulsar Np0532 radiation in roentgen and gamma ranges C7-715
- MAFTOUL (J.).- Voir BUCHET (G.) ... C7-327
- MAKABE (T.) and MORI (T.).- Electron swarm having an anisotropic velocity distribution function C7-43
- MAKAREVICH (A.N.).- Voir KISELEVSKII (L.T.) C7-465
- MAKASHIN (I.N.).- Voir ZIL'TSOV (V.A.) C7-663
- MAL'TSEV (A.N.).- Voir BOKHAN (P.A.) C7-115
- MANFRED (F.).- About the generation of a "Resultant drift in wards" from the boundary of a D-T-plasma by electromagnetic fields C7-527
- MAREC (J.).- Voir CICCONI (G.) C7-827
- MARGOLIN (L. Ya.), PYATNISKII (L.N.) and SHTERNOV (N.P.).- Low-temperature plasma investigations by resonance Rayleigh scattering of weak intensity radiation C7-801
- MÄRK (T.D.).- Voir GRÖSSL (M.) C7-51
- MÄRK (E.).- Voir SCHRITTWIESER (R.)..C7-581
- MARKOV (V.S.).- Voir BOGDANOV (S.Yu.) C7-221
- MARKOV (G.A.), MIRONOV (V.A.) and SERGEEV (A.M.).- Self-trapping of lower hybrid waves at the RF breakdown of gas C7-639
- MARODE (E.).- Voir SEGUR (P.) C7-539
- MARODE (E.).- Voir TRAN NGOC AN ... C7-533

- MARTISOVITS (V.).- Effect of collisions between the metastable atoms on their radial transport in a positive column at various spatial distributions of electrons... C7-183
- MARTISOVITS (V.).- Transport of metastable atoms in a positive column including radial variation of the excitation rate C7-185
- MARTSINOVSKII (A.M.).- Voir BABANIN (V.I.) C7-201
- MARTSINOVSKIY (A.M.).- Voir BAKSHT (V.G.) C7-497
- MARTSINOVSKIY (A.M.).- Voir BOGDANOV (A.A.) C7-337
- MARTSINOVSKIY (A.M.).- Voir KAPLAN (V.B.) C7-495
- MASSMANN (P.), HOPMAN (H.J.) and LOS (J.).- H^- production by interaction of a H_2^+ -ion beam with a surface.. C7-435
- MATOCHKIN (E.P.).- Voir BUCHELNIKOVA (N.S.) C7-631
- MATOCHKIN (E.P.).- Voir BUCHELNIKOVA (N.S.) C7-633
- MAYOR (J.M.).- Voir BOURQUARD (S.).. C7-385
- MAYOR (J.M.).- Voir KOCIAN (P.) C7-169
- MECHLINSKA-DREWKO (J.).- Voir ROZ- NERSKI (W.) C7-149
- MELZACKI (K.).- CHYRCZAKOWSKI (S.).. C7-741
- MENAHIN (L.P.).- Voir LONDER (J.I.). C7- 29
- MENDONÇA (J.T.).- Wave and particle interactions with a nonlinear dielectric perturbation in a plasma C7-545
- MERCURE (H.).- Voir DROUET (M.G.)... C7-437
- MERCURIO (S.).- Ablation of solid hydrogen in contact with magnetized plasmas : can the external magnetic field be the upper limit of the self consistent electric field at the solid surface ? C7-447
- MERMET (J.M.).- Voir OHEBSIAN (D.).. C7- 99
- MESSIAEN (A.M.).- Voir EVRARD (M.P.) C7-617
- MESYATS (G.A.).- Voir KCHUZEEV (A.P.) C7-281
- MEYER (B.).- Voir THIELL (G.) C7-877
- MICHEL (P.), PFAU (S.), RUTSCHER (A.) and WINKLER (R.).- Diffusion theory of the positive column in hydrogen glow discharges with variable degree of dissociation... C7-133
- MICHEL (P.), PFAU (S.), RUTSCHER (A.) and WINKLER (R.).- The positive column in the three component mixture Ne/H/H₂-experimental results in comparison with an approximative diffusion theory C7-157
- MICHENSEN (P.).- Voir LYNØV (J.P.).. C7-567
- MICHENSEN (P.).- Voir LYNØV (J.P.).. C7-571
- MIHAILESCU (I.N.).- Voir APOSTOL (I.) C7-765
- MIHASLOV (A.), DJORDJEVIC (D.) and POPOVIC (M.M.).- On the modification of the quantum defect method applicable to dense plasmas C7-689
- MIKHAILOVSKY (A.B.).- Voir LOMINADZE (J.G.) C7-713
- MIKHALEV (A.V.).- Voir KOSHILEV (N.A.) C7-507
- MIKKELSEN (T.) and PECSELI (H.L.).- Strong turbulence in partially ionized plasmas C7-569
- MIKKELSON (K.), KRISTIANSEN (M.), LIN (J.) and THOMPSON (J.).- Electro-optical measurements of insulator surface flashover in vacuum C7-401
- MILANICH (A.I.).- Voir BASOV (N.G.). C7-393
- MILANICH (A.I.).- Voir GLOTOV (E.P.) C7-371
- MILANTIEV (V.P.) and MIROSHNIKOV (A.G.).- Drift motion of charged particle in resonance conditions.. C7-611
- MILANTIEV (V.P.) and SAIKA (P.).- Quasioptics in anisotropic and dispersive media C7-613
- MILEY (G.H.).- Voir PRELAS (A.M.)... C7-391
- MILIC (B.).- Voir PAVLOVIC-BRAJUS-KOVIC (N.) C7-655
- MILIC (B.S.).- Voir ZIGMAN (V.J.)... C7-589
- MILJEVIĆ (V.I.).- A spectroscopic study of the DC gas magnetron discharge C7- 61
- MILLER (V.A.).- Voir AVERIN (V.I.).. C7-875
- MIN'KO (L.Ya.).- Voir BAKANOVICH (G.I.) C7-761
- MINOO (H.).- Voir GOMBERT (M.M.)... C7-695
- MINOO (H.), GOMBERT (M.M.) and DEUTSCH (C.).- Two particle effective potential of a dense hydrogenous plasma C7-697
- MIRONOV (V.A.).- Voir LITVAK (A.G.). C7-635
- MIRONOV (V.A.).- Voir MARKOV (G.A.). C7-639
- MIROSHNIKOV (A.G.).- Voir MILANTIEV (V.P.) C7-611
- MITROFANO (N.K.).- Voir DYUZHEV (G.A.) C7-463
- MIURA (K.).- Voir IMAZU (S.) C7-153
- MIX (L.P.).- Voir BURNS (E.J.T.)... C7-775
- MIYAMOTO (S.).- Voir IMASAKI (K.) .. C7-779
- MOHAMAD (S.Z.) and PETKOV (A.P.).- Use of time-resolving high resolution spectroscopy in the investigation of pulse hollow-cathode discharges C7-195
- MOITY (J.).- Experimental determination of FeII Gf-values C7-709
- MOLDOVAN (M.).- Voir APOSTOL (I.) .. C7-765
- MOLDOVAN (C.).- Voir POPA (G.) C7-187
- MOLINARI (V.G.).- Voir BOFFI (V.C.). C7-535
- MOLINARI (V.).- Voir CICCONI (G.)... C7-193

- MOLL (R.) and SCHADE (E.).- Measurements at current zero in a SF₆ gas blast breaker C7-309
- MORALES (E.).- Voir BAYLE (P.)..... C7-249
- MOREIRA (A.M.).- Voir ABECASIS (T.M.) C7-701
- MORJAN (I.).- Voir APOSTOL (I.).... C7-765
- MORI (T.).- Voir MAKABE (T.)..... C7- 43
- MOROZOV (I.I.) and TALROSE (V.L.).- Molecular dissociation on bombardment by electrons of an energy lower than the ionization potential C7-109
- MORUZZI (J.L.).- Voir ABDEL-SALAM (M.) C7- 53
- MORUZZI (J.L.).- Voir COXON (P.A.). C7-117
- MORUZZI (J.L.) and LAKDAWALA (V.K.).- Electron attachment in SO₂.... C7- 11
- MOSCH (W.).- Voir HAUSCHILD (W.) .. C7-251
- MOUGET (G.).- Voir HUBERT (P.) C7-421
- MUIR (D.G.) and CAROLAN (P.G.).- Faraday rotation applied to a reverse field pinch C7-833
- MÜLLER (K.G.).- Voir LERGERON (H.G.). C7-821
- MÜLLER (S.).- Voir ZAHN (R.J.) C7-319
- MUROMKIN (Yu.A.).- Voir GORBUNOVA (E.F.) C7-211
- MUSA (G.).- Voir BALTOG (A.)..... C7-455
- MUSA (G.).- Voir BALTOG (A.) C7-457
- MUSA (G.), POPESCU (A.) and NICULESCU (N.).- Positive column constriction in cesium plasma discharge C7-137
- MUSIL (J.).- Voir BARDOS (L.)..... C7-449
- MUSHER (S.M.), OCHIROV (B.D.) and RUBENCHIK (A.M.).- On nonlinear stage of parametric instabilities of waves excited by localized pumping C7-649
- MUSTAFAEV (A.S.).- Voir BABANIN (V.I.) C7-201
- NAGEL (D.J.).- Voir BLEACH (R.D.).. C7-749
- NAIDIS (G.V.) and SINELSHIKOV (V.A.).- Determination of quenching cross section of resonant Cs(6P) state by CO₂ molecules in discharge in He-CO₂-Cs C7-107
- NAIDU (M.S.).- Voir RISBUD (A.V.).. C7- 77
- NAKAI (S.).- Voir IMASAKI (K.) C7-779
- NAKAMURA (Y.).- Voir IKEZAWA (S.).. C7-573
- NASSISI (V.).- Voir LUCHES (A.) ... C7- 67
- NASTITCH (J.N.).- Voir POKROVSKAJA-SOBOLEVA (A.S.) C7-405
- NAUMOVETS (V.G.), PASECHNIK (L.L.) and YAGOLA (V.V.).- Anomalous conductivity of low pressure HF discharge in magnetic field C7-207
- NEHMZOW (B.), RUTSCHER (A.) and WAGNER (H.E.).- Dissociation of water vapour in the hollow cathode glow discharge C7- 55
- NEIGER (M.).- Theoretical study of negative absorption for H⁻ affinity radiation C7-381
- NEIGER (M.).- Voir SCHMITT (J.).... C7-279
- NEUFELD (C.R.).- Interaction of a TEA-CO₂ laser pulse with a dense hydrogen plasma C7-727
- NEUSTROEV (S.A.).- Voir ZORINA (E.N.) C7-473
- NICOLAS (A.).- Voir DELVAUX (J.) ... C7-785
- NICULESCU (N.).- Voir MUSA (G.) C7-137
- NIKI (H.).- Voir SUGAI (H.) C7-703
- NIKOLAEV (A.V.).- Voir RYKALIN (N.N.) C7-229
- NIKULIN (V.Ya.).- Voir GRIBKOV (V.A.) C7-763
- NISCONEN (I.S.).- Voir WAGNER (S.D.). C7-209
- NISHIHARA (K.).- Voir IMASAKI (K.).. C7-779
- NISHIJIMA (K.).- Voir AKAZAKI (M.).. C7-145
- NOBUAKI IKUTA.- Voir HARUO ITOH.... C7-445
- NORMAN (G.E.).- Voir KOZLOV (N.P.).. C7-675
- NOVIKOVA (K.P.).- Voir PROZOROV (E.F.) C7-863
- NUMANO (M.) and ONISHI (H.).- Excitation temperature of a rapidly varying plasma C7- 49
- OBUKHOV (V.A.).- Voir GERASIMOV (V.P.) C7-647
- OCHIROV (B.D.).- Voir MUSER (S.M.). C7-649
- OEPST (D.), BARBIAN (E.P.) and BUSCH (P.J.).- Measurement of electron density and temperature profiles by means of multiposition Thomson scattering C7-793
- OHEBSTEIN (D.), SADEGHI (N.), TRASSY (C.) and MERMET (J.M.).- Argon-titanium hollow cathode afterglow. C7- 99
- ØIEN (A.H.).- A plasma kinetic equation including strong fields and inhomogeneities C7-531
- ONISHI (H.).- Voir NUMANO (M.)..... C7- 49
- ORHAM (E.L.).- Voir BRADLEY (L.P.).. C7-307
- OSIPOV (V.V.).- Voir BICHKOV (Yu.I.). C7-161
- OJRINGEL (I.M.).- Inverted population of hydrogen atoms in a turbulent cosmic plasma C7-719
- OTT (W.R.), BRIDGES (J.M.) and KLOSE (J.Z.).- The use of gas discharges as ultraviolet radiometric standards C7-803
- OX (S.N.).- Voir GODYAK (V.A.)..... C7-807
- OX (S.N.).- Voir GODYAK (V.A.) C7-809
- PAPPENHOLZ (J.).- Voir EICHLER (H.J.) C7-379
- PAIVA-VERETENNICOFF (I.).- Voir BALESCU (R.) C7-511
- PAL (A.F.).- Voir KLOPOVSKY (K.S.).. C7-343
- PAL' (A.F.).- Voir LOPATSEVA (G.B.). C7-499
- PAL (A.F.), PERSIANTSEV (I.G.), PETRUSHEVITH (Yu.V.) and STAROSTIN (A.N.).- On the peculiarities of passage of a low-current electron beam through gases C7-345

- PALLO (A.V.).- Voir VOROBIOV (V.V.).C7-693
- PANOV (D.A.).- Voir ZILTSOV (V.A.).C7-663
- PAPERNY (V.V.).- Voir ALTINTSEV (A.T.)C7-723
- PAREATHUMBY (S.).- Voir SEGUR (P.). C7-539
- PASECHNIK (L.L.).- Voir NAUMOVETS (V.G.) C7-207
- PASECHNIK (L.L.), ROMANYUK (L.I.) and SVAVIL'NY (N.Ye).- High frequency oscillations and electron beam relaxation in homogeneous gas-discharge plasma C7-619
- PASHININ (P.P.).- Voir BELYANKO (A.E.) C7-505
- PAVLENKO (V.P.) and PETIASHVILI (V.I.).- Stability of the non-linear periodic waves in plasma.. C7-621
- PAVLIASHVILI (T.I.).- Voir ZORINA (E.N.) C7-473
- PAVLOV (E.).- Voir BARONNET (J.M.).C7-247
- PAVLOVIC-BRAJUSKOVIC (N.) and MILIC (B.).- Threshold electron drift for the spontaneous excitation of non-electrostatic ion-cyclotron oscillations in weakly ionized plasmas.....C7-655
- PEACOCK (N.J.).- Voir FORREST (M.J.) C7-745
- PECHACEK (R.).- Voir KOOPMAN (D.).. C7-419
- PECSELI (H.L.).- Voir LYNOV (J.P.) C7-567
- PECSELI (H.L.).- Voir LYNOV (J.P.) C7-571
- PECSELI (H.L.).- Voir MIKKELSEN (T.) C7-569
- PEDERSEN (A.).- Voir VIBHOLM (S.) . C7-289
- PEKAREK (L.).- Voir URBANKOVA (H.) C7-375
- PELLETIER (G.).- Renormalization group method applied to large scale Langmuir turbulence C7-657
- PEREVODCHIKOV (V.I.).- Voir KOSTYLEV (A.A.) C7-369
- PEREVOZNOV (A.F.).- Voir LOPANTSEVA (G.B.) C7-499
- PÉRINA (V.).- Voir SKALA (J.) C7-587
- PERNOT (C.E.E.).- Voir THEUWS (P.G. A.) C7-141
- PERRONE (M.R.).- Voir LUCHES (A.) . C7- 67
- PERRONE (A.).- Voir LUCHES (A.) ... C7- 67
- PERSIANTSEV (I.G.).- Voir KLOPOVSKY (K.S.) C7-343
- PERSIANTSEV (I.G.).- Voir LOPANTSEVA (G.B.) C7-499
- PERSIANTSEV (I.G.).- Voir PAL (A. F.) C7-345
- PERTSEV (A.A.).- Ion sound dissemination in moving plasma jet C7-645
- PERTSEV (A.A.) and SHADOV (V.P.).- The experimental study of arc cathode microspots life-time by the velocity microphotography C7-409
- PESCA (K.).- Voir ALGE (E.) C7- 83
- PESIC (S.S.).- Parametric decay of lower hybrid waves C7-553
- PESKA (K.), ALGE (E.), VILLINGER (H.), STÖRI (H.) and LINDINGER (W.).- Reactions of doubly charged ions with various neutrals... C7- 21
- PESKOV (V.D.).- On the VUV radiation of Townsend avalanches C7-331
- PESKOV (V.D.).- On the influence of electrodes on the properties of high pressure discharge C7-333
- PESKOV (V.D.).- On ionization instabilities of high pressure discharges C7-335
- PESME (D.).- Voir ADAM (J.C.) C7-671
- PETKOV (A.P.).- Voir MOHAMAD (S.Z.).C7-195
- PETRAKIEV (A.), KOLEVA (I) and GANEVA (J.).- A spectral chronographic and equidensitometric investigation of a pulse blended discharge C7-845
- PETRUSHEVITH (Yu.V.).- Voir PAL (A.F.) C7-345
- PETVIASHVILI (V.I.).- Voir PAVLENKO (V.P.) C7-621
- PEUGNET (C.).- Voir DELVAUX (J.) .. C7-785
- PEVCEV (B.G.).- Voir BOGDANOVA (N.B.) C7-361
- PFAU (S.).- Voir MICHEL (P.) C7-133
- PFAU (S.).- Voir MICHEL (P.) C7-157
- PHARNEY (J.R.).- Voir GRAY (E.W.).. C7-267
- PICKALOV (V.V.).- Voir KLIMKIN (V.F.) C7-329
- PICKALOV (V.V.) and PREOBRAZHENSKY (N.G.).- Restoration of two-dimensional radiation for an optically thick plasma C7-855
- PIEL (A.) and A. PINNEKAMP (F.).- The role of molecular lines in the study of plasma satellites.....C7-813
- PIETRZYK (Z.A.).- Voir BROOKS (R.D.)C7-751
- PIGACHE (D.), BONNET (J.), FORT (J.) and FOURNIER (G.).- Production of hydrazine from ammonia in an atmospheric pressure electron-beam controlled dischargeC7-317
- PIGACHE (D.).- Voir FORT (J.) C7-315
- PIGACHE (D.).- Voir FOURNIER (G.).. C7-777
- PINNEKAMP (F.).- Voir PIEL (A.)... C7-813
- POBERAJ (S.).- Propagation of condensation in coronal plasma C7-711
- POHLE (G.).- Voir SCHMIDT (M.) C7-461
- POITEVIN (J.M.).- Voir FOURRIER (C.)C7-819
- POINTU (A.M.).- Voir AUPHELLE (D.). C7-397
- POKROVSKAJA-SOBOLEVA (A.S.), BORISOVA (T.S.), GRISHUTIN (G.S.) and NASTITCH (J.N.).- Studies of discharge phenomena during transition from breakdown in vacuum to breakdown in gasC7-405

- POLLACHINI (L.).- Voir CICCONI (G.) C7-193
- PONOMAREV (Yu.V.).- Voir LANDA (P.S.) C7-223
- POORTER (T.).- Voir VAN DER SIJDE (B.) C7-851
- POPA (G.).- The influence of the electron-neutral collisions on the ionization waves in a helium plasma C7-189
- POPA (G.), SANDULOVICIU (M.), CROITORU (P.) and MOLDOVAN (C.).- Electron beam generation by a hollow cathode discharge C7-187
- POPESCU (A.).- Voir MUSA (G.) C7-137
- POPKOV (V.I.).- Voir BOGDANOVA (N.B.) C7-361
- POPOV (Tc.).- Voir ANGELOV (O.) C7- 19
- POPOV (G.A.).- Voir EGOROV (I.I.).. C7-349
- POPOV (A.M.).- Voir KOVALEV (A.S.).. C7-759
- POPOVA (T.O.).- Voir ZORINA (E.N.).. C7-473
- POPOVIC (M.M.).- Voir MIHAJLOV (A.).. C7-689
- POPOVICI (C.), BALACEANU (M.), CEUSESCU (N.) and AVRAM (E.).- On the characteristics of a high voltage glow discharge C7-171
- POPOVICS (C.).- Voir BENATTAR (R.).. C7-767
- POTANIN (E.P.).- Voir KARCHEVSKY (A.I.) C7-213
- POTS (B.F.M.), COUMANS (J.J.H.) and SCHRAM (D.C.).- Collective scattering of CO₂-laser light by the highly ionized argon plasma of a hollow cathode arc discharge C7-797
- POTS (B.F.M.).- Voir VAN DER MULLEN (J.J.A.M.) C7-283
- POTS (B.F.M.).- Voir VAN DER SIJDE (V.) C7- 23
- POTS (B.F.M.).- Voir VAN DER SIJDE (B.) C7-851
- PRELAS (A.M.) and MILEY (G.H.).- Collisional processes in the He-CO₂ atomic carbon nuclear pumped laser 1.454 μ C7-391
- PREOBRAZHENSKY (N.G.).- Voir PICKALOV (V.V.) C7-855
- PRÉST (A.).- Voir EARL (R.G.) C7-167
- PRODUNOV (A.B.).- Voir BURTSEV (V.A.) C7-485
- PROKHOROV (A.M.).- Voir BELYANKO (A.E.) C7-505
- PROKOPIEV (V.E.).- Voir BOKHAN (P.A.) C7-115
- PROSKOUROVSKY (D.I.) and PUCHKAREV (V.F.).- The effect of non-metallic inclusions and films on the cathode on some processes during vacuum discharges C7-411
- PROTASOV (Yu.S.).- Voir KOZLOV (N.P.) C7-675
- PROZOROV (E.F.), LONDER (J.I.), NOVIKOVA (K.P.) and ULYANOV (K.N.) .- Prove diagnostic by non-self maintained ionization C7-863
- PTYTSIN (V.E.).- Voir FURSEY (G.N.).. C7-403
- PUCHKAREV (V.F.).- Voir PROSKOUROVSKY (D.I.) C7-411
- PURIC (J.), LAKICEVIC (I.) and GLAVONJIC (V.).- Some regularities within the stark widths and shifts of resonance lines of neutral atoms from He to Ca C7-795
- PURIC (J.), LAKICEVIC (I.) and GLAVONJIC (V.).- Some regularities within the stark widths and shifts of resonance lines of singly charged ions from He to Ca C7-835
- PUSTOVALOV (V.V.).- Voir ALEXANDROV (V.V.) C7-357
- PUSTOVALOV (V.V.).- Voir KOVALEV (V.F.) C7-609
- PYATNISKII (L.N.).- Voir MARGOLIN (L. Ya.) C7-801
- QUEFFEELEC (J.L.).- Voir GAUCHEREL (Ph.) C7- 91
- RADTKE (R.).- Voir GÜNTHER (K.) ... C7-679
- RAKHIMOV (A.T.).- Voir VASILIEVA (A.N.) C7-103
- RAKHIMOV (A.T.).- Voir KOVALEV (A.S.) C7-759
- RAKITIN (A.A.).- Voir VOROBIOV (V.V.) C7-693
- RAKOWITZ (J.).- Voir BARONNET (J.M.) C7-247
- RAKOWITZ (J.).- Voir COUDERT (J.F.).. C7-355
- RAMLER (H.).- Voir ALGE (E.) C7- 83
- RANSON (P.) and CHAPELLE (J.).- Calculation of the photoionization cross sections of excited levels of rare gas atoms C7- 25
- RANSON (P.) and CHAPELLE (J.).- Calculation of the free-bound continuum of rare gases C7- 93
- RASMUSSEN (J.J.).- Voir LYNØV (J.P.) C7-567
- RASMUSSEN (J.J.).- Voir LYNØV (J.P.) C7-571
- RASULOV (F.N.).- Voir KAPLAN (V.B.).. C7-495
- REINECK (S.).- Voir FREISINGER (J.).. C7-477
- RIABYI (V.A.).- Voir VOROBIOV (V.V.) C7-693
- RICARD (A.).- Voir CERNOGORA (G.).. C7- 59
- RICHOU (J.).- Voir LESAGE (A.) C7-805
- RIEDMÜLLER (W.).- Voir BAUMHACKER (H.) C7-743
- RIEMANN (K.U.).- Theory of the sheath edge in a weakly ionized collision dominated plasma C7-831
- RISBUD (A.V.) and NAIDU (M.S.).- Ionization and attachment in water vapour and ammonia C7- 77

- ROGASHKOV (S.A.).- Voir ARMAND (N.A.) C7-565
- ROGASHKOV (S.A.).- Voir ARMAND (N.A.) C7-643
- ROGASHKOVA (A.I.).- Interaction of the intense microwave beam with a flow of low temperature plasma. (Pt.2. The theory) C7-641
- ROGASHKOVA (A.I.) and SHATALOVA (T.I.).- A theory of the interaction of double-beam with plasma C7-781
- ROGOFF (L.G.).- A general characteristic equation for a diffusion-controlled positive column of circular cross section with one-step and two-step ionization processes C7-175
- ROMANOV (A.B.).- Voir KOVALEV (V.F.) C7-609
- ROMANYUK (L.I.).- Voir PASECHNIK (L.L.) C7-619
- ROMEAS (P.).- Voir SKOWRONEK (M.) .. C7-303
- ROSADO (R.J.), SCHRAM (D.C.) and LECLAIR (J.).- Continuous emission, lowering of the ionization potential and total excitation cross-sections of an atmospheric thermal plasma C7-285
- ROSE (H.A.).- Voir DUBOIS (D.F.)... C7-601
- ROTSHEIN (V.P.).- Voir KCHUZEEV (A.P.) C7-281
- ROWE (B.).- Voir GAUCHEREL (Ph.) .. C7- 89
- ROYCHOWDHURY (U.K.).- Voir ASHRAF (A.) C7-129
- ROZANOV (E.K.).- Voir VOROBIOV (V.V.) C7-693
- ROZHANSKY (V.A.).- Effective boundary conditions for a plasma in a magnetic field, adjacent with an electrode C7-515
- ROZMUS (W.).- The time dependent transport coefficients for the two-component plasma C7-525
- ROZNERSKI (W.) and MECHLIŃSKA-DREWKO (J.).- The ratio of lateral diffusion coefficient to mobility for electrons in oxygen and carbon dioxide C7-149
- RUBENCHIK (A.M.).- Voir MUSHER (S.M.) C7-649
- RUHADZE (A.A.).- Voir ARUTYUNYAN (S.G.) C7-219
- RUHADZE (A.A.).- Voir BOGDANKEVICH (L.S.) C7-783
- RUTSCHER (A.).- Voir NEHMZOW (B.) .. C7- 55
- RUTSCHER (A.).- Voir MICHEL (P.) .. C7-133
- RUTSCHER (A.).- Voir MICHEL (P.) .. C7-157
- RYBAKOV (A.B.).- Voir BAKSHT (F.G.)..C7-341
- RYUTOVA (M.P.).- Spectrum of charge exchange neutrals from rotating plasma C7-503
- RYKALIN (N.N.), NIKOLAEV (A.V.) and BORZHOV (A.P.).- Temperature of heavy current cylindrical hollow cathode C7-229
- RYZKO (H.).- Propagation of the leader of a long spark in air without participation of thermal ionization processes C7-427
- SADEGHI (N.).- Voir OHEBSIAN (D.).. C7- 99
- SADOWSKI (M.).- Voir CHYRCZAKOWSKI (S.) C7-741
- SAELEE (H.T.), COOKE (M.J.) and ALLEN (J.E.).- E-I characteristics of an optically pumped mercury positive column C7-179
- SAIKA (P.).- Voir MILANTIEV (V.P.).. C7-613
- SALK (J.).- Voir EICHLER (H.J.).... C7-379
- SALVAT (M.).- Voir BAUMHACKER (H.).. C7-743
- SALZMANN (D.) and ELIEZER (S.).- The use of effective Feynman diagrams for atomic cross-section calculations..... C7- 57
- SAMUILOV (E.V.).- Voir GORBATOV (A.V.) C7-519
- SANCTORUM (C.) and BONTE (L.).- Time dependence of cataphoresis in a neon-argon mixture C7- 33
- SANDELIN (J.W.).- Voir BLEACH (R.D.) C7-749
- SANDULOVICIU (M.).- Voir POPA (G.).. C7-187
- SAPOZHNIKOV (A.V.).- Voir ASSADULIN (F.F.) C7-653
- SARKSIAN (K.A.).- Voir ASSADULIN (F.F.) C7-653
- SARYCHEV (A.K.).- Voir LAGAR'KOV (A.N.) C7-691
- SAUNDERSON (J.C.).- Voir ALLIBONE (T.E.) C7-425
- SAVIC (P.).- Voir KEKEZ (M.M.) C7-255
- SAVIC (P.).- Voir KEKEZ (M.M.) C7-257
- SAVINOV (V.P.).- Voir KUZOVNIKOV (A.A.) C7-459
- SAYASOV (Yu.S.).- Viscous damping of the magneto-acoustic oscillations, MAO, in bounded plasmas C7-585
- SCHAAL (G.) and ZABEL (J.).- External and internal probe measurements in discharges of luminescence lamp type C7-849
- SCHADE (E.).- Voir MOLL (R.) C7-309
- SCHÄFER (J.H.).- Voir CARLHOFF (C.)..C7-757
- SCHALL (W.).- Voir HOFFMANN (P.)... C7-489
- SCHERBAKOV (A.G.).- Voir ZILTSOV (V.A.) C7-663
- SCHILDBACH (K.).- Voir CARLOFF (C.)..C7-757
- SCHMIDT (M.), SEEFELDT (R.) and POHLE (G.).- Mass-spectrometric investigation of the ions in an Ar-hexamethyldisiloxane discharge C7-461
- SCHMITT (J.) and NEIGER (M.).- Visible and infrared continuum radiation from a low temperature Cl₂-arc C7-279

SCHOCK (W.).- Voir HOFFMANN (P.)...	C7-489	SHISKO (A.A.).- Voir KOSHILEV (N.A.)	C7-507
SCHÖNBACK (K.H.).- Voir HATFIELD (L.L.)	C7-483	SHISKO (A.A.).- Voir KOSHILEV (N.A.)	C7-721
SCHRAM (D.C.).- Voir VAN DER SIJDE (V.)	C7- 23	SHIVAROVA (A.) and STOYCHEV (T.).- Second order harmonic surface waves generated by one fundamental wave	C7-607
SCHRAM (D.C.).- Voir DIELIS (J.W.H.)	C7- 75	SHKIADAREVICH (A.P.).- Voir GUDELEV (V.G.)	C7-865
SCHRAM (D.C.).- Voir THEUWS (P.G.A.)	C7-141	SHKOLNIK (S.M.).- Voir DYUZHEV (G.A.)	C7-463
SCHRAM (D.C.).- Voir VAN DER MULLEN (J.J.A.M.)	C7-283	SHOUCRI (M.M.).- Computer simulation of the sideband instability	C7-575
SCHRAM (D.C.).- Voir ROSADO (R.J.) ..	C7-285	SHTERNOV (N.P.).- Voir MARGOLIN (L.Ya.)	C7-801
SCHRAM (D.C.).- Voir POTS (B.F.M.) ..	C7-797	SHUKLA (P.K.).- Voir YU (M.Y.)	C7-739
SCHRAM (D.C.).- Voir VAN DER SIJDE (B.)	C7-851	SHUSTIN (E.G.).- Voir ARMAND (N.A.) ..	C7-565
SCHRITTWIESER (R.), MÄRK (E.) and KUHN (S.).- Grid versus plate excitation of the electron current driven ion wave instability.....	C7-581	SHUSTIN (E.G.).- Voir ARMAND (N.A.) ..	C7-643
SCOARNEC (L.).- Voir DAMELINCOURT (J.J.)	C7-273	SIGEL (R.).- Voir BENATTAR (R.) ...	C7-767
SEEFELDT (R.).- Voir SCHMIDT (M.)..	C7-461	SIGMOND (R.S.) and LINHJELL (D.).- The excitation of thermal energy positive ions from corona discharges in air	C7-323
SEGUR (P.).- Voir TRAN NGOC AN	C7-533	SIGMOND (R.S.).- Voir GOLDMAN (A.) ..	C7-443
SEGUR (P.), PAREATHUMBY (S.), YOUSFI (M.) and MARODE (E.).- Determination of macroscopic quantities for a Townsend discharge in helium by both Boltzmann equation and Monte Carlo methods	C7-539	SINELSHIKOV (V.A.).- Voir NAIDIS (G.V.)	C7-107
SELIM (E.O.).- Voir WATERS (R.T.)..	C7-245	SITNOV (V.I.).- Voir BABANIN (V.I.) ..	C7-201
SERGEEV (A.M.).- Voir LITVAK (A.G.)..	C7-637	SITENKO (A.G.).- Nonlinear wave interaction and critical fluctuations in plasmas	C7-661
SERGEEV (A.M.).- Voir MARKOV (G.A.)..	C7-639	SKALA (J.), KRASA (J.) and PEŘINA (V.).- Two dimensional Fourier spectrum of turbulent ionization waves	C7-587
SERRA (F.M.).- Voir ABECASIS (T.M.) ..	C7-701	SKODA (P.).- Voir HRABOVSKY (M.)...	C7-293
SEVIGNE (M.).- Voir DAMELINCOURT (J.J.)	C7-273	SKORIC (M.M.) and STANIC (B.V.).- A time domain method for transient scattering of electromagnetic waves in plasmas	C7-595
SHADOV (V.P.).- Voir PERTSEV (A.A.) ..	C7-409	SKOVORODA (A.A.).- Voir ZILTSOV (V.A.)	C7-663
SHAKHOVA (N.A.).- Voir LITVAK (A.G.)	C7-637	SKOVORODA (A.A.) and ZILTSOV (V.A.) .- ECR as a diagnostic for mirror trap plasma	C7-665
SHAMRAI (K.P.).- Voir DAVYDOVA (T.A.)	C7-561	SKOWRONEK (M.).- Voir ALAYLI (Y.)..	C7-817
SHANIN (P.M.).- Voir KOVAL (N.N.)..	C7-481	SKOWRONEK (M.), GIRY (L.), VU TIEN GIA and ROMEAS (P.).- Conductivity measurements of high current, high pressure discharges	C7-303
SHANSKY (V.F.).- Voir BURTSEV (V.A.)	C7-387	SKROBOL (G.).- Voir EICHLER (H.J.) ..	C7-379
SHATALOVA (T.I.).- Voir ROGASHKOVA (A.I.)	C7-781	SKURIDIN (G.A.).- Voir VOLOSEVICH (A.V.)	C7-625
SHEMYAKIN (I.A.).- Voir KCHUZEEV (A.P.)	C7-281	SLADE (P.G.).- Voir KIMBLIN (C.W.) ..	C7-413
SHESTAKOV (I.V.).- Voir BURTSEV (V.A.)	C7-485	SMIRNOV (V.G.).- Voir BURTSEV (V.A.)	C7-387
SHINDO (H.), IMIZU (S.) and INABA (T.).- Electron energy relaxation effect on the dynamic characteristic of argon plasma arc	C7-259	SMIRNOV (A.S.).- Voir KUTEEV (B.V.) ..	C7-395
SHIROCHIN (L.A.).- Voir FURSEY (G.N.)	C7-415		
SHISHKIN (G.G.).- Voir GERASIMOV (V.P.)	C7-647		
SHISHKIN (G.G.).- Voir KHODNENKO (V.P.)	C7-717		

- SMITH (M.R.).- Voir JONES (G.R.) ... C7-269
- SOBOL (A.G.).- Voir EGOROV (I.I.) .. C7-349
- SOKOLOV (E.B.).- Voir ZORINA (E.N.) C7-473
- SOKOVIKOV (V.G.).- Voir BOKHAN
(P.A.) C7-115
- SOLNTZEV (G.S.), DVININ (S.A.) and
TSVETKOVA (L.I.).- The comparison
of some characteristics of electro-
trodeless UHFD in waveguide and of
DCD C7-227
- SOLOVIYANCHIK (D.A.).- Voir KISELEV-
SKII (L.I.) C7-465
- SOMMER (H.T.).- Voir BRACKE (T.) ... C7-239
- SAMOILOVITCH (V.G.).- Voir GEBALOV
(V.I.) C7-347
- Sonnenburg (R.).- Voir GOLUBOWSKY
(Yu.B.) C7-155
- SOROKA (A.M.).- Voir ALEXANDROV
(V.V.) C7-357
- SOROKA (A.M.).- Voir BASOV (N.G.) .. C7-393
- SOROKA (A.M.).- Voir GLOTOV (E.P.) . C7-371
- SOWA (L.).- Voir HIMMEL (G.) C7-837
- SPATSCHKE (K.H.).- Voir YU (M.Y.) .. C7-739
- SPEIRS (R.D.B.).- Voir KRANKEL (N.E.) C7-513
- SPIGA (G.).- Voir BOFFI (V.C.) C7-535
- STANIC (B.V.).- Voir CANDER (Lj.R.) C7-597
- STANIC (B.V.).- Voir SKORIC (M.M.) . C7-595
- STAROSTIN (A.N.).- Voir KLOPOVSKY
(K.S.) C7-343
- STAROSTIN (A.N.).- Voir LOPANTSEVA
(G.B.) C7-499
- STAROSTIN (A.N.).- Voir PAL (A.F.) . C7-345
- STARTSEV (E.A.).- Voir DYUZHNEV (G.A.) C7-199
- STARYKH (V.V.).- Voir WINKLER (R.) . C7-131
- STARYKH (V.V.).- Voir WINKLER (R.) . C7-261
- STEENHUIJSEN (L.W.G.), VAN SCHAIK
(N.), VAN DE NIEUWENHUYZEN
(L.C.A.M.) and VERSAPAGET (F.H.P.)
.- Measurements of the production
of neon 2p atoms by dissociative
recombination C7- 95
- STEENHUIJSEN (L.W.G.).- Voir VAN
SCHAIK (N.) C7- 27
- STEENHUIJSEN (L.W.G.).- Voir VAN
SCHAIK (N.) C7- 97
- STEFAN (V.).- Voir ALIEV (Yu.M.) ... C7-557
- STEFAN (V.).- Voir KOVALEV (V.F.) .. C7-609
- STEPANOV (B.M.).- Voir AVERIN (V.I.) C7-875
- STEPANOV (B.M.).- Voir FILENKO (Yu.
I.) C7-873
- STEPANUSHKIN (A.D.).- Voir BRIZHINEV
(M.P.) C7-867
- STERN (W.).- Voir STIEBER (M.) C7-493
- STEWART (P.K.).- Voir DAVIES (A.J.) C7- 63
- STIEBER (M.) and STERN (W.).- The
effective overvoltage of AC plasma
display discharges C7-493
- STOJANOFF (C.G.).- Voir BRACKE (T.) . C7-239
- STOKES (A.D.).- Voir KOVITYA (P.) .. C7-299
- STÖRI (H.).- Voir ALGE (E.)..... C7- 83
- STORI (H.).- Voir PESKA (K.) C7- 21
- STOSSEL (F.P.).- Electrostatic
trivelpiece - gould modes in a
torus C7-603
- STOYCHEV (T.).- Voir SHIVAROVA (A.) C7-607
- STRACHAN (D.C.).- Voir JONES (G.R.) C7-269
- STROKIN (N.A.).- Voir KOSHILEV
(N.A.) C7-507
- STROKIN (N.A.).- Voir KOSHILEV (N.A.) C7-721
- SU (C.H.).- Interaction of nonlinear
ion-acoustic waves C7-591
- SUDO (S.).- Voir BAUMHACKER (H.) ... C7-743
- SUGAI (H.), IDO (K.), NKI (H.) and
TAKEDA (S.).- Propagation of whis-
tler waves trapped in a narrow
density trough C7-703
- SUGAI (H.).- Voir LYNNOV (J.P.) C7-571
- SULIC (D.M.).- Measurement of elec-
tron density by electromagnetic
waves which propagate on a magne-
tized plasma column C7-823
- SUZUKI (K.).- Voir INUTAKE (M.) C7-685
- SVAVIL'NY (N.Ye.).- Voir PASECHNIK
(L.L.) C7-619
- SY (W.N.C.) and COTSFTIS (M.).- An
equation for wave propagation in a
hot nonuniform magnetized plasma . C7-669
- SZYMANSKI (Z.).- Voir WROBLEWSKI
(D.) C7-733
- TAILLET (J.).- The radio frequency
sheath in self sustained plasmoids C7-159
- TAILLET (J.).- Voir BACAL (M.) C7-791
- TAKAMATSU (T.).- Voir INAZU (S.) ... C7-153
- TAKEDA (S.).- Voir AKIYAMA (H.) C7-543
- TAKEDA (S.).- Voir SUGAI (H.) C7-703
- TAKEDA (Y.) and YOKOTA (M.).- Spiky
density fluctuation and relaxation
oscillation in an anomalously re-
sistive phase C7-577
- TAKTAKISHVILI (M.T.).- Voir BARKHU-
DAROV (E.M.) C7-869
- TALAAAT (M.E.).- Radiofrequency dis-
charge tests with helium flow ... C7-165
- TALROSE (V.L.).- Voir MOROZOV (I.I.) C7-109
- TELNOV (V.A.).- Voir BICHKOV (Yu.I.) C7-161
- TEMKO (S.W.), KUZMIN (S.K.), HADGY-
OGLY (M.R.) and IAGODOVSKAYA (T.V.)
.- On the formation of the thin
solid pellicle of nitric oxides on
the liquid ozone surface in the
atmosphere of smouldering dis-
charge in nitrogen C7-433
- TEMKO (S.W.), TEMKO (K.W.) and KUZMIN
(S.K.).- On the thermodynamical
stability of the plasma of gas dis-
charge in the real gas C7-677
- TEMKO (K.W.).- Voir TEMKO (S.W.) ... C7-677

TERENTYEV (A.P.).- Voir KOSTYLEV (A.A.)	C7-367	TSYTOVICH (V.N.).- Voir BEL'KOV (S.A.)	C7-651
TERENTYEV (A.P.).- Voir KOSTYLEV (A.A.)	C7-369	TSYTOVICH (V.N.).- Voir KHAKIMOV (P.Kh.)	C7-583
THEUWS (P.G.A.), BEIJERINCK (H.C.W.) PERNOT (C.E.E.), SCHRAM (D.C.) and VERSTER (N.F.).- Molecular beam sampling of metastable atoms from a hollow cathod arc as a probe for the electron temperature	C7-141	TSYTOVICH (V.N.).- Voir LIVSHITS (M.A.)	C7-627
THIELL (G.) and FABRY (M.).- Etude théorique des phénomènes liés à une cathode liquide : estimation du taux d'érosion	C7-453	TUMAKAEV (G.K.).- Voir VASIL'EV (M. G.)	C7-101
THIELL (G.), MEYER (B.), LOUIS- JACQUET (M.) and COUTURAUD (J.C.) .- Spectrométrie X dans les plasmas créées par laser ; application à l'étude des phénomènes de trans- port de l'énergie	C7-877	TURIN (V.N.).- Voir EGOROV (I.I.) ..	C7-349
THOMAS (R.), BARASSIN (J.) and BARASSIN (A.).- Reaction $\text{CH}_3^+ + \text{NH}_3$ - évolution des produits en fonc- tion de la concentration de NH_3 ..	C7- 41	TURNER (J.G.) and BOYD (T.J.M.).- Upper hybrid solitons	C7-549
THOMA (P.).- Voir BEHRINGER (K.) ...	C7-829	UHLENBUSCH (J.).- Voir CARLHOFF (C.)	C7-757
THOMPSON (J.).- Voir MIKKELSON (K.)	C7-401	ULBRICHT (R.).- Voir GUNTHER (K.) ..	C7-679
THYREGOD (P.).- Voir VIBHOLM (S.) ..	C7-289	ULYANOV (K.N.).- Voir LONDER (J.I.)	C7- 29
TIILLER (W.).- The mass flow field of the full circle arc	C7-313	ULYANOV (K.N.).- Voir KOSTYLEV (A.A.)	C7-367
TISHCHENKO (E.A.), GOLUBEV (A.V.) and LAZAREV (V.B.).- Radiation tempe- rature measurement of argon arc plasma by submillimeter diagnostic techniques	C7-859	ULYANOV (K.N.).- Voir KOSTYLEV (A.A.)	C7-369
TISHCHENKO (E.A.).- Voir ZATSEPIN (V.G.)	C7-799	ULYANOV (K.N.).- Voir PROZOROV (E.F.)	C7-863
TISHCHENKO (E.A.).- Voir ZATSEPIN (V.G.)	C7-857	URBANKOVA (H.) and PEKÁREK (L.).- Long-time changes of an ionization wave in the $\text{CO}_2 + \text{N}_2 + \text{He}$ mixture	C7-375
TODD (T.N.).- A fully automatic con- tinuous electron temperature mea- surement system using a double Langmuir probe	C7-841	USHAKOV (L.S.).- Voir FILENKO (Yu. I.)	C7-873
TOLMATSHOVA (O.V.).- Voir ZORINA (E.N.)	C7-473	USOV (V.V.).- Voir MACHABELI (G.Z.)	C7-715
TOMOZOEV (V.M.).- Voir LIVSHITS (M.A.)	C7-627	VACQUIE (S.).- Voir GLEIZES (A.) ...	C7-235
TORVEN (S.).- Voir LINDBERG (L.) ...	C7-151	VAN BOMMEL (P.J.M.).- Voir VAN SCHAIK (N.)	C7- 27
TRAN NGOC AN, MARODE (E.), FOURNIER (G.) and SEGUR (P.).- Electron distribution function in a very non-uniform electric field	C7-533	VAN BOMMEL (P.J.M.).- Voir VAN SCHAIK (N.)	C7- 97
TRASSY (C.).- Voir OHEBSIAN (D.) ...	C7- 99	VAN DE NIEUWENHUYZEN (L.C.A.M.).- Voir STEENHUIJSEN (L.W.G.)	C7- 95
TRIPONOV (Ju.V.).- Voir KHODNENKO (V.P.)	C7-717	VAN DE NIEUWENHUYZEN (J.C.A.M.).- Voir VAN SCHAIK (N.)	C7- 27
TRUONG BACH and DRAWIN (H.W.).- In- fluence of boundary layer of a Al- seeded shock-heated plasma on the profiles of the AlI resonance lines	C7- 69	VANDENPLAS (P.E.).- Voir EVRARD (M.P.)	C7-617
TSINTSADZE (N.L.).- Voir BARKHUDAROV (E.M.)	C7-869	VAN DER KRAAN (P.A.M.), DIELIS (J.W.H.) and DE HOOG (F.J.).- For- mation and destruction of neon mo- lecular ions in Townsend dis- charges	C7- 15
TSUI (K.H.).- Voir JAYARAM (K.)	C7-275	VAN DER MULLEN (J.J.A.M.), POTS (B.F.M.), SCHRAM (D.C.) and VAN DER SIJDE (B.).- The reduction of diffusion by plasma rotation and ion dissipative effects	C7-283
TSEVTKOVA (L.I.).- Voir SOLNTZEV (G.S.)	C7-227	VAN DER SIJDE (B.), POORTER (T.), ADEMA (S.), POTS (B.F.M.) and SCHRAM (D.C.).- Thomson scattering with a high background level of plasma radiation	C7-851
		VAN DER SIJDE (V.), POTS (B.F.M.) and SCHRAM (D.C.).- A collisional radiative model of the argon ion system tested for a large range of electron densities	C7- 23
		VAN DER SIJDE (B.).- Voir VAN DER MULLEN (J.J.A.M.)	C7-283
		VALIGNAT (S.), LEVEAU (J.), DEIGAT (F.).- Investigation of excitation mechanisms in neon with the aid of the radial distribution of excited atoms	C7- 7

- VANMARCKE (M.).- Voir WIEME (W.) .. C7- 3
- VANMARCKE (M.) and WIEME (W.).- Visible line afterglow emission of a pulsed xenon discharge C7- 35
- VANMARCKE (M.) and WIEME (W.).- Theory of resonance radiation imprisonment C7- 39
- VAN OOST (G.).- Voir EVRARD (M.P.) C7-617
- VAN SCHAIK (N.).- Voir STEENHUIJSEN (L.W.G.) C7- 95
- VAN SCHAIK (N.), STEENHUIJSEN (L.W.G.), VAN BOMMEL (P.J.M.) and VAN DE NIEUWENHUYZEN (J.C.A.M.).- Atom densities of the first excited state in low pressure neon discharges C7- 27
- VAN SCHAIK (N.), STEENHUIJSEN (L.W.G.), VAN BOMMEL (P.J.M.) and VERSPAGET (F.H.P.).- Determination of the coefficients of collisional transfer between the 2p levels of neon C7- 97
- VASIL'EV (M.G.), ZHIKHAREVA (T.V.) and TUMAKAEV (G.K.).- The relative contribution of associative ionization and photoionization in xenon precursors C7-101
- VASILIEVA (A.N.), GRISHINA (I.A.), KTIKTOROV (V.I.), KOVALEV (A.S.) and RAKHIMOV (A.T.).- On the three body electron attachment to oxygen in the plasma of a non-self-maintained discharge C7-103
- VAVRA (Z.).- Voir HAVELKO (O.) C7-291
- VDOVIN (V.G.) and VDOVINA (N.A.).- On determination of TL, IN, Na normal atom concentration by resonance lines broadened with mercury pressure C7-839
- VDOVINA (N.A.).- Voir VDOVIN (V.G.) C7-839
- VDOWN (V.G.) and HAAHEV (A.D.).- Experimental study on plasma non equilibrium of high pressure metal-halide discharge C7-177
- VEKSTEIN (G.E.).- Voir CHEBOTAEV (P.Z.) C7-537
- VERIAEV (A.A.).- Voir ASSADULIN (F.F.) C7-653
- VERSPAGET (F.H.P.).- Voir VAN SCHAIK (N.) C7- 97
- VERSPAGET (F.H.P.).- Voir STEENHUIJSEN (L.W.G.) C7- 95
- VERSTER (N.F.).- Voir THEUWS (P.G.A.) C7-141
- VERVISCH (P.).- Voir CHERON (B.) .. C7-847
- VIALLE (M.).- Voir AUPHELLE (D.) .. C7-397
- VIBHOLM (S.), PEDERSEN (A.) and THYREGOD (P.).- Determination of low probability first breakdown voltages in compressed SF₆ C7-289
- VIDMAR (R.J.) and CRAWFORD (F.W.).- Dispersion characteristics of plasma wave-packets C7-559
- VILADROSA (R.).- Voir GLASSER (J.) C7-687
- VILLINGER (H.).- Voir ALGE (E.) ... C7- 83
- VILLINGER (H.).- Voir PESKA (K.) .. C7- 21
- VIRMONT (J.).- Voir AMIRANOFF (F.) C7-729
- VIRMONT (J.).- Voir AMIRANOFF (F.) C7-769
- VIRMONT (J.).- Voir BENATTAR (R.) . C7-767
- VITKOVITSKY (I.M.).- Voir ALI (A.W.) C7-773
- VITKOVITSKY (I.).- Voir KOOPMAN (D.) C7-419
- VLASES (G.S.).- Voir BROOKS (R.D.) C7-751
- VOLKOVA (L.M.), DEVYATOV (A.M.), KRALKINA (E.A.) and KURALOVA (A.V.).- The investigation of the fast electrons energy distribution in the positive column and negative glow of the low pressure helium discharge C7-231
- VOLOSEVICH (A.V.), LIVSHITS (M.A.) and LIPEROVSKY (V.A.).- Nonlinear decay interactions for the instability of buneman-Farley C7-623
- VOLOSEVICH (A.V.), LIVSHITS (M.A.), LIPEROVSKY (V.A.) and SKURIDIN (G.A.).- About the stationary turbulence regions and anomalous resistance in the magneto-sphere plasma C7-625
- VON ENGEL (A.).- Voir DIXON (A.J.) C7-441
- VOROBIOV (V.V.), KULIK (P.P.), PALLO (A.V.), RAKITIN (A.A.), ROZANOV (E.K.) and RIABYI (V.A.).- Experimental investigation of the electrical and heat conductivities of alkali dense plasmas C7-693
- VUJNOVIC (V.).- Voir KLICHAREV (A.N.) C7- 87
- VUKICEVIC (J.).- Voir LABAT (J.M.) C7- 9
- VU TIEN GIA.- Voir SKOWRONEK (M.) . C7-303
- WAGNER (H.E.).- Voir NEHMZOW (B.) . C7- 55
- WAGNER (S.D.) and NISCONEN (I.S.D.).- Electron energy distribution function and atom ionization processes in high frequency discharge mercury-argon plasma C7-209
- WALL (D.N.) and FRANKLIN (R.N.).- Nonlinear interaction of beam waves and plasma waves C7-593
- WALMSLEY (H.L.).- Voir JONES (G.R.) C7-269
- WALTHER (S.E.).- Voir GROH (K.H.) . C7-277
- WARTSKY (L.).- Voir AUPHELLE (D.) . C7-397
- WATERS (R.T.) and SELIM (E.O.).- Temporal space-charge field changes at the cathode in negative polarity discharge C7-245
- WHITNEY (K.G.).- Voir BLEACH (R.D.) C7-749
- WICKENS (L.M.).- Voir ALLEN (J.E.) C7-547
- WIEME (W.) and LENAERTS (J.).- Excimer formation in rare gas discharge afterglows C7-37
- WIEME (W.), VANMARCKE (M.) and BRUYNNOOGHE (W.).- Radiative and collisional desexcitation of ¹P₁ and ³P₁ resonance states in xenon C7- 3

- WIEME (W.).- Voir VANMARCKE (M.) .. C7- 35
- WIEME (W.).- Voir VANMARCKE (M.) .. C7- 39
- WIESEMANN (K.).- Voir ICHIRO MORI . C7-555
- WIJNAKKER (M.M.B.) and GRANNEMAN (E.H.A.).- A study of a weakly ionized, rotating plasma C7-487
- WIDL (W.).- Voir FRÖHLICH (K.) C7-407
- WILHELM (J.).- Voir WINKLER (R.) .. C7-131
- WILHELM (J.).- Voir WINKLER (R.) .. C7-261
- WILLIAMS (A.W.).- Voir ABDULLA (R. R.) C7- 73
- WILLIAMS (P.F.), CRUMLEY (R.J.) and GUNDERSEN (M.A.).- Studies of the basic processes responsible for laser-triggered breakdown in gases C7-305
- WINKLER (R.).- Voir MICHEL (P.) ... C7-133
- WINKLER (R.).- Voir MICHEL (P.) ... C7-157
- WINKLER (R.), WILHELM (J.), IVANOV (A.A.) and ST. RYKH (V.V.).- Comparison between some macroscopic properties of the beam and glow discharge plasma in nitrogen C7-131
- WINKLER (R.), WILHELM (J.), IVANOV (A.A.) and STARYKH (V.V.).- Kinetics of the electrons in the stationary beam discharge plasma in diatomic gases C7-261
- WITTING (H.L.).- An investigation of arc starting on cold cathodes C7-451
- WOLFF (G.).- Voir DELVAUX (J.) C7-785
- WROBLEMSKI (D.), CYBULSKI (A.) and SZYMANSKI (Z.).- An experimental investigation of the continuous optical discharge C7-733
- YAGOLA (V.V.).- Voir NAUMOVETS (V.G.) C7-207
- YAKUNIN (V.G.).- Voir KUZOVNIKOV (A.A.) C7-459
- YAMADA (T.).- Voir AKIYAMA (H.) ... C7-543
- YAMANAKA (C.).- Voir IMASAKI (K.) . C7-779
- YEGOROV (V.V.).- Voir GOLUBKOV (G.V.) C7- 89
- YESELEVICH (V.G.) and FAINSTEIN (V.G.).- On expansion of the collisionless plasma into vacuum .. C7-359
- YOKOTA (M.).- Voir TAKEDA (Y.) C7-577
- YOUSFI (M.).- Voir SEGUR (P.) C7-539
- YU (M.Y.), SHUKLA (P.K.) and SPATSCHEK (K.H.).- Curvature effects in laser plasma interactions C7-739
- YUNAKOVSKY (A.D.).- Voir GIL'DENBURG (V.B.) C7-215
- YUR'EV (V.G.).- Voir DYUZHEV (G.A.) C7-199
- YUR'EV (V.G.).- Voir DYUZHEV (G.A.) C7-463
- YURIEV (V.G.).- Voir KAPLAN (V.B.) C7-495
- YUR'YEV (V.G.).- Voir BAKSHT (V.G.) C7-497
- YUR'YEV (V.G.).- Voir BOGDANOV (A.A.) C7-337
- ZABEL (J.).- Voir SCHAAAL (G.) C7-849
- ZAHN (R.J.) and MÜLLER (S.).- Gas temperature dependence of AC discharges between isolated electrodes C7-319
- ZATSEPIN (V.G.) and GOLUBEV (A.V.).- Determination of the ray phase for plasma cylinder using modulus of the probing radiation transmittivity C7-861
- ZATSEPIN (V.G.), LAZAREV (V.B.) and TISHCHENKO (E.A.).- Application of field visualization technique to smm diagnostics of axisymmetric plasma C7-857
- ZATSEPIN (V.G.), TISHCHENKO (E.A.) and GOLUBEV (A.V.).- Numerical methods of data processing for active submillimeter diagnostics of plasma cylinder C7-799
- ZELENOV (L.A.).- Voir BURTSEV (V.A.) C7-387
- ZHIKHKAREVA (T.V.).- Voir VASIL'EV (M.G.) C7-101
- ZHILINSKY (A.P.).- Voir KUTEEV (B. V.) C7-395
- KHUKOV (V.M.).- Voir FURSEY (G.N.) . C7-415
- ZIGMAN (V.J.) and MILIC (B.S.).- On the behaviour of weakly ionized plasma with non-zero neutrals temperature placed in external electric field of moderate intensity . C7-589
- ZILTSOV (V.A.), KOZAREV (P.M.), MAKASHIN (I.N.), PANOV (D.A.), SKOVORODA (A.A.) and SCHERBAKOV (A.G.).- Study of low frequency oscillations in the open trap with minimum B magnetic field C7-663
- ZILTSOV (V.A.).- Voir SKOVORODA (A. A.) C7-665
- ZORINA (E.N.), DOBRENIN (A.V.), POPOVA (T.O.), PAVLIASHVILI (T.I.), TOLMATSHOVA (O.V.), NEUSTROEV (S.A.) and SOKOLOV (E.B.).- Some particularities of the molecular exchange in a HF low pressure discharge C7-473
- ZUKOWSKI (W.).- Voir BRZOSKO (J.S.) C7-471
- ZUKOWSKI (E.).- Voir BRZOSKO (J.S.) C7-471

Commission paritaire N° 26.741

© Editions de Physique 1979

Directrice de la Publication : Jeanne BERGER

Imprimé en France. — Imprimerie JOUVE, 17, rue du Louvre, 75001 PARIS
Dépôt légal : 2^e trimestre 1979

REDACTION ET ADMINISTRATION : Z.I. de Courtabœuf. — B.P. 112
91402 ORSAY — Téléphone : 907.36.88

Prix de ce Numéro : France F. 200
Etranger F. 225

THE LIBRARY OF THE

JUN 16 1980

UNIVERSITY OF ILLINOIS
URBANA-CHAMPAIGN

JOURNAL **de PHYSIQUE**

**XIV^e Conférence Internationale
sur les Phénomènes d'Ionisation
dans les Gaz**

Grenoble (France)
1979

Papiers Invités

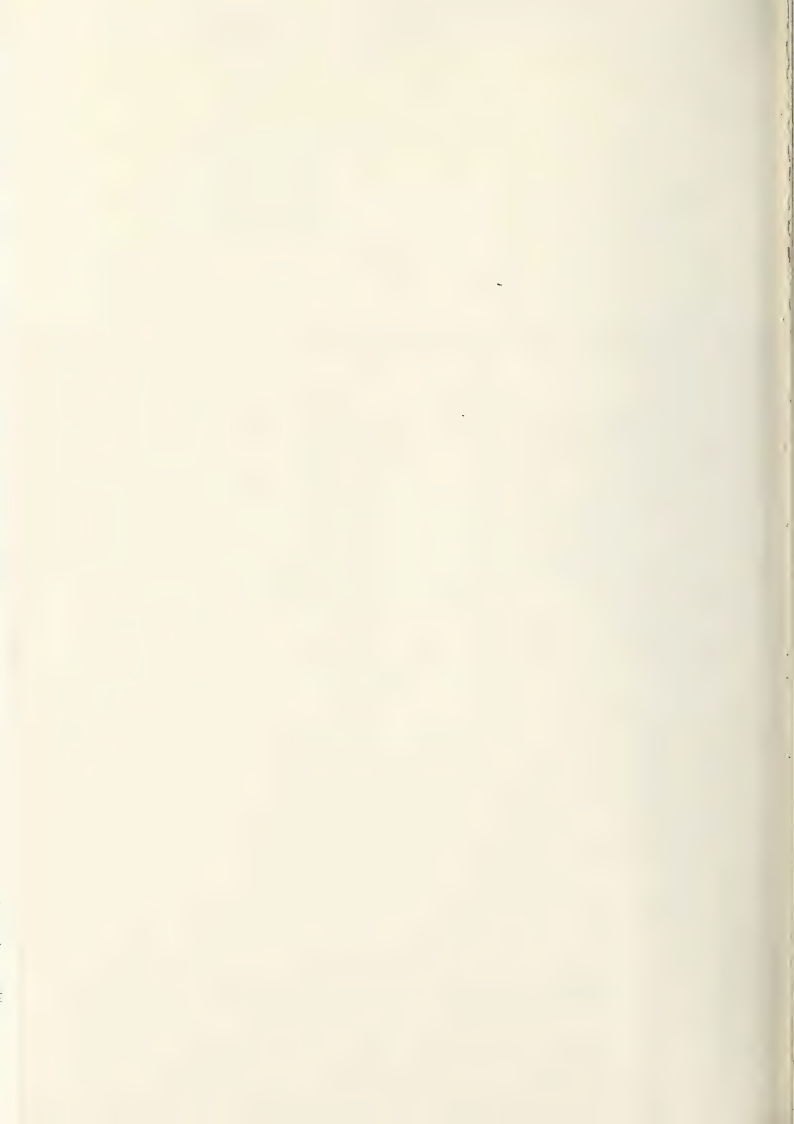


**PUBLICATION DE LA SOCIÉTÉ
FRANÇAISE DE PHYSIQUE
SUBVENTIONNÉE PAR LE C.N.R.S.**



EUROPHYSICS JOURNAL

VOLUME II



**XIV^e Conférence Internationale
sur les
Phénomènes d'Ionisations
dans les Gaz**

Papiers Invités

***XIVth International Conference
on Phenomena in Ionized Gases***

Invited Papers

Grenoble (France)
9-13 Juillet 1979

— Sociétés savantes/*Scientific Institutions*

I.U.P.A.P. International Union of Pure and Applied Physics
 U.R.S.I. Union Radio Scientifique Internationale
 E.P.S. European Physical Society
 S.F.P. Société Française de Physique
 C.N.F.R.S. Comité National Français de Radioélectricité Scientifique
 S.E.E. Société des Electriciens et Electroniciens

— Ministères et Organismes de Tutelle/*Ministries and Sponsoring Organizations*
 Ministère des Universités/*Ministry of Universities*

D.G.R.S.T. Délégation Générale à la Recherche Scientifique et Technique
 C.N.R.S. Centre National de la Recherche Scientifique
 D.R.E.T. Direction des Recherches, Etudes et Techniques
 C.E.A. Commissariat à l'Energie Atomique
 E.D.F. Electricité de France

— Autorités Régionales/*Local Authorities*

Conseil Général de l'Isère/*General Council of Isère*
 Mairie de Grenoble/*Grenoble Town Hall*
 Université Scientifique et Médicale de Grenoble/*Scientific and Medical University of Grenoble*

COMITÉ DE PATRONAGE/SPONSORING COMMITTEE

Président/*Chairman* : Pr Jacques YVON

M. Y. BERNARD
 D. BLANC
 C. BONET
 A. BOULLOUD
 F. CABANNES
 T. CONSOLI
 R. DAUTRAY
 J.-L. DELCROIX
 J.-F. DENISSE
 F. DENNERY
 J.-M. DOLIQUE
 H. DOUCET
 B. DREYFUS

M. FELDEN
 M. GOLDMAN
 P. GRIVET
 C. MAGNAN
 M. MAGNIEN
 J.-C. PEBAY-PEYROULA
 Y. PELENC
 J. ROBIEUX
 M. SALESSE
 E. SCHATZMAN
 M. SOUTIF
 M. TROCHERIS
 P. VALENTIN

COMITÉ SCIENTIFIQUE INTERNATIONAL/INTERNATIONAL SCIENTIFIC COMMITTEE

Président/*Chairman* : Pr H. MAECKER - F.R.G.

R. BALESCU Belgium
 W. BYSZEWSKI Poland
 F. W. CRAWFORD U.S.A.
 J. DUTTON U.K.
 J. LABAT Yugoslavia
 E. MOLINARI Italy

A. RUTSCHER G.D.R.
 R. S. SIGMOND Norway
 J. TAILLET France
 V. N. TSYTOVICH U.S.S.R.
 P. VIEHBOECK Austria

COMITÉ D'ORGANISATION/LOCAL ORGANIZING COMMITTEE

J. TAILLET
 C. POMOT
 M. FITAIRE
 P. HUBERT
 J.-P. BABUEL PEYRISSAC
 P. FAUCHAIS
 C. GARY
 J. PELLETIER
 M. PETIT

Président
 Secrétaire Général
 Secrétaire Scientifique
 Trésorier

AVEC LA COLLABORATION DE/WITH THE COLLABORATION OF

Grenoble Accueil - ALPES CONGRES
 Palais des Congrès de la Ville de Grenoble

PREFACE

Cet ouvrage contient les communications présentées à CIPIG 14, quatorzième conférence sur les phénomènes d'ionisation dans les gaz, tenue à Grenoble du 9 au 13 juillet 1979 sous le patronage de l'URSI, de l'IUPAP, de l'EPS, de la SFP et de la SEE en ce qui concerne les Sociétés Savantes, du Ministère des Universités, de la DGRST, de la DRET, du CNRS, du CEA et de l'EDF en ce qui concerne nos Grands Organismes Nationaux.

C'est au Professeur A. Von ENGEL que revient le mérite d'avoir perçu la nécessité d'établir, entre les Scientifiques travaillant dans tous les domaines de la décharge électrique dans les gaz et de la physique du plasma, des contacts périodiques destinés à leur permettre d'avoir une vue générale sur l'ensemble de la discipline. C'est à ses efforts que nous devons d'en avoir maintenu la tradition depuis 1953, jusqu'au moment où la relève de l'initiative personnelle s'est trouvée peu à peu confiée à des institutions stables, comme le Comité Scientifique International, avec des règles acceptées par tous pour partager de façon équitable le poids des responsabilités qu'entraîne l'organisation de nos Conférences.

Le redoutable honneur d'inviter la Communauté Scientifique Internationale à Grenoble a certes demandé à notre Comité d'Organisation un effort de longue haleine. Mais il convient de rappeler aussi que sans l'aide du Comité Scientifique International, sans les encouragements des personnalités qui forment notre Comité de Patronage, sans le travail des scientifiques qui ont bien voulu apporter leur aide à la sélection des communications, cet effort n'aurait pas pu porter ses fruits. Sans l'aide financière du Ministère des Universités, de la mairie de Grenoble, du Conseil Général de l'Isère du CNRS, du CEA, de l'EDF, de la DRET, de la DGRST et de l'IUPAP, le budget de cette manifestation n'aurait pas pu être équilibré ; sans la participation active du CNFRS qui a bien voulu accueillir dans son sein notre Comité d'Organisation, et sans l'aide matérielle apportée à ce comité par Grenoble Accueil et par l'Université Scientifique et Médicale de Grenoble, rien n'aurait été possible.

Pour terminer, il faut reconnaître l'évidence : une réunion ne vaut que ce que valent ses Conférences et ses Communications. Remercions donc les Conférenciers Invités et les auteurs des Communications pour avoir distillé pour nous la substantifique moelle qui restera dans l'esprit des participants, avec le charme de la région grenobloise et l'hospitalité de ses habitants, la justification et en même temps la récompense de l'effort de chacun.

J. TAILLET

FOREWORD

This volume contains the communications presented at ICPIG 14, the XIVe Conference on Phenomena in Ionized Gases, held in Grenoble (France) from 9th to the 13th of July 1979, under the sponsorship of URSI, IUPAP, EPS, SFP and SEE, and the patronage of the Ministry of the Universities, of DGRST, DRET, CNRS, CEA and EDF.

Professor A. Von ENGEL had the foresight to understand the necessity of establishing periodic contacts between the scientists working on all aspects of gaseous electronics and plasma physics, in order to give a general view of the whole discipline. It is thanks to his efforts that we continued this tradition from 1953 up to the moment that his personal initiative was slowly transferred to permanent institutions, such as the International Scientific Committee. They permitted the organization of our Conferences to establish rules accepted by all so as to spread in an equitable way the weight of the responsibilities.

The honor of inviting the international Scientific Community to Grenoble has imposed on our Local Committee a long and strenuous effort. But we must remember that without the help of the International Scientific Committee, without the encouragement of the people who form our Patronage Committee, without the work of the scientists who have agreed to give their aid in selecting the Communications, this effort would not have succeeded. The budget of this conference could not have been balanced without the financial aid of the Ministry of Universities, of the Grenoble City Hall, of the General Council of Isère, CNRS, CEA, EDF, DRET, DGRST and the IUPAP. Without the material aid given us by Grenoble Accueil and by the Scientific and Medical University of Grenoble, and without the guaranty of the CNFRS to our Local Committee, nothing would have been possible.

Finally, we must look at the evidence ; a scientific meeting is worth no more than the value of its conferences and its Communications. Let us therefore thank the Invited Speakers and the authors of the Communications for having distilled for us the scientific essence of this Conference. This distillation will remain in the memory of the participants along with the charm of Grenoble and the hospitality of its inhabitants, as the justification and as the recompense of the efforts of each one of us.

J. TAILLET

List of participants

ALLEMAGNE

- Funk, W.**, Kombinat Narva, 11-14 Ehrenbergstrasse, 1017 Berlin.
- Rutscher, A.**, Sektion Physik, Domstrasse 10, 22 Greifswald.
- Wilhelm, J.**, Zentral Inst. Elektronenphysik 5, 8-10 R Blum Strasset, 226 Greifswald.
- Bauer, G.-H.**, Institut fuer Physik. Elektr., 72 Boeblingerstrasse, D-7000 Stuttgart 1.
- Behringer, K.**, Lehrstuhl F. Techn. Elektrophy, 21 Arcisstrasse, D-8000 Muenchen.
- Berger, E.**, Sektion Physik der Univesitaet, 4 Schellingstrasse, 8000 Muenchen 40.
- Brinkschvete, H.**, MPI f. Plasmaphysik, 8046 Garching.
- Behringer, K.**, Lehrstuhl f. Techn. Elektrophy, 21 Arcisstrasse, D-8000 Muenchen.
- Grieger, G.**, Max-Planck-Inst. f. Plasmaphysik, D-8046 Garchin.
- Groh, K.**, 1 Institute of Physics, Heine-Buffring 16, D-6300 Giessen.
- Grosse-Wilde, H.**, Siemens AG FL Plas, 2 Guenther-Scharowsky-STR, 8520 Erlangen.
- Gundel, H.**, Zentralinstitut fuer Elektronen, 40 Mohrenstrasse, 108 Berlin.
- Himmel, G.**, Inst. exp. Physik 2 Ruhr-Univ., Universitaetsstrasse, 4630 Bochum.
- Klein, W. J.**, DFVLR, Linder Hoehe, 5000 Koeln 90.
- Koch, H.**, Opt. Institut Techn. Univ. Berlin, Stasse des 17 Juni 135, 1000 Berlin 12.
- Lengyel, L.**, Max-Planck-Inst. f. Plasmaphysik, D-8046 Garching.
- Lergon, G.**, University of Essen, FB Physic, 43 Essen.
- Maecker, H.**, Lehrstuhl fuer Technoelektrophys, Arcisstr 21, 8000 Muenchen.
- Maly, R. R.**, Institut fuer Physik. Elektro, 72 Boeblingerstrasse, D-7000 Stuttgart 1.
- Mueller, K. G.**, University of Essen, 5 Universitaet STR, 43 Essen.
- Neiger, N.**, Univ. Bochum Electrooptics Dept. Universitaet Strasse 150, D-4630 Bochum.
- Petelski, E. F.**, Institut fuer Astrophysik, Auf dem Huegel 71, D-53 Bonn.
- Piel, A.**, Universitaet Bochum, Querenburgerstr, D-4630 Bochum.
- Pinnekamp, F.**, Universitaet Bochum, Querenburger Strasse, D-4630 Bochum.
- Riemann, K. U.**, Inst. Theor. Phys. Univ. Bochum, Universitaetsstr. 150, D-4630 Bochum.
- Salvat, M.**, Ippgarching, MP I Physplasma, 8046 Garching.
- Sommer, H. T.**, Inst. Techn. Thermodynamik, 5100 Aachen.
- Sowa, L.**, Inst. Exp. Physik II Ruhr-Univ., Universitaetstr, 4630 Bochum.
- Staeblein, H. G.**, Lehrst. f. Techn. Elektrophysik, 21 Arcisstrasse, D-8000 Muenchen 2.
- Sucky, K.**, Inst. Theorphysics, Uduesseldorf, 1, Universitaetsstrasse, D-4000 Duesseldorf 1.
- Tiller, W.**, Hochschule der Bundeswehr, Nerner Heisenberg Weg, 8014 Neubiberg.

- Uhlenbusch, J. F.**, Phys. Inst. II Univ. Duesseldorf, Universitaetsstrasse 1, 4 Dvesseldorf.
- Voss, M. F.**, Gesamthochschule Paderborn, Semperstr. 25, 8 Muenchen 85.
- Waelbroeck, F. G.**, KFA Juelich, Kernforschungsanlage GMBH, 5170 Juelich.
- Woldemar, B.**, Institut fuer Plasmaphysik, Universitaet Hannover Callin 18, 3000 Hannover.
- Yu, M.**, Theor. Physik 1, Ruhr Uni-Bochu, 4630 Bochum 1.
- Zimmermann, B.**, Bocham Electrotechnik, Universitaet Strasse 150, 4630 Bochum.

AUSTRALIE

- Fletcher, J.**, Flinders University, Sturt Road, Bedford Park 5042.
- Frankel, N. E.**, School of Physics, University of Melbourne, Parkville, Melbourne Australia, 3052 Melbourne.
- Hines, K. C.**, School of Physics, University of Melbourne, Parkville, Melbourne Victoria, 3052 Melbourne.
- Luwke, J. J.**, Dept. Electrical Engineering, University of Sydney, NSW 2006.

AUTRICHE

- Cap, F. F.**, University of Innsbruck, Innerebnerstrasse .40, A-6020 Innsbruck.
- Grossl, M.**, Inst. f. Experimentalphys. ABT F, 3 Karl Schoneraerrstrasse, A-6020 Innsbruck.
- Kuhn, S.**, Inst. for Theoretical Physics, Innrain 52, A-6020 Innsbruck.
- Maerk, E.**, Inst. fuer Theoretical Physics, Innrain 52, A-6020 Innsbruck.
- Peska, K.**, Institut fuer Experimentalphys., 3 Karl Schonberstrasse, 6020 Innsbruck.
- Rieder, W.**, Techn. University Vienna, Gusshausstr. 25, A-1040 Vienna.
- Schrittwieser, R.**, Inst. Theor. Phys., University, Innrain 52, A-6020 Innsbruck.
- Stoessel, F.**, Inst. for Theoretical Physics, Innrain 52, A-6020 Innsbruck.

BELGIQUE

- Balescu, R.**, Université Libre Bruxelles, Campus Plaine ULB, 1050 Bruxelles.
- Bruynooghe, W.**, Laboratorium voor Natuurkunde, 44 Rozier, B-9000 Gent.
- David, I. Ch.**, Laboratoire de Physique des Plasmas, ERM, rue de la Renaissance, 1040 Bruxelles.
- Lenaerts, J.**, Laboratorium voor Natuurkunde, Ledeganckstraat 35, B-9000 Gent.
- Paiva-Veretennicoff, I.**, Departement Natuurkunde VUB, Plein LAAN2, B-1050 Brussels.
- Prohorof, S.**, CP 165, LPP Université Libre Bruxelles, 50, avenue F.-Roosevelt, B-1050 Bruxelles.

Sanctorum, C., Laboratorium voor Natuurkunde, 44 Rozier, B-9000 Gent.

Van Oost, G., Labo. Plasmafysica KMS-ERM, Renaissance LAAN30, 1040 Brussel.

Vanmarcke, M., Laboratorium voor Natuurkunde, Rozier 44, 9000 Gent.

Verkenne, Ch., Service de Mesures Electriques, Inst. d'Electricité Montefiore, Bât. B28, 4000 Liège.

Wieme, W., Laboratorium voor Natuurkunde, Rozier 44, B-9000 Gent.

CANADA

Kekez, M. M., National Research Council, BLDG MO, Montreal RD, Ottawa Ontario KIA 0R6.

Shoucri, M. M., Hydro-Quebec IREQ, Montee Ste Julie, Varennes JO-2PO.

CHINE

Hsu, H. C., Inst. Electric. Light Sources, Fudan University, 201903 Shanghai.

Lu Q. K., Department of Physics, Fudan University, 201903 Shanghai.

Wei, X. R., Nanjing, Institute of Technology, Nanjing.

DANEMARK

Crichton, G., Callum Department of Physics Sect. 2, Danmarks Tekniske Højskole, 2800 Lyngby.

Lynov, J. P., Riso National Laboratory, DK-4000 Roskilde.

Michelsen, P., Riso National Laboratory, DK-4000 Roskilde.

Pecseli, H. L., Riso National Laboratory, DK-4000 Roskilde.

Rasmussen, J. J., Riso National Laboratory, DK-4000 Roskilde.

Surensen, G., Institute of Physics, Ny Munkegade, 8240 Risskov.

Vibholm, S., Department of Physics, Sect. 2, BLD 309, The Techn. University, DK-2800 Lyngby.

EGYPT

Khalil Ibrahim, M. A., Electromechanical Res. Instit., Shiekh Rehan Street, Cairo, Egypt., Ministry of Irrigation.

FRANCE

Abbas, L., Centre Physique Atomique, 118, Route de Narbonne, 31077 Toulouse Cedex.

Allis, W., Phelps Laboratoire de Physique des Plasmas, Université de Paris-Sud, 91405 Orsay.

Amberg, R., Physique des Milieux Ionisés, Domaine Universitaire, 38041 Grenoble Cedex 53.

Aubes, M., Centre de Physique Atomique, 118, Route de Narbonne, 31077 Toulouse.

Aubret, Th., Thermodynamique, 123, rue Albert-Thomas, 87060 Limoges.

Babuel-Peyrissac, J. P., Centre Etude de Limeil, 5, avenue Mariville, 94100 Saint Maurice.

Bacal, M., Physique des Milieux Ionisés, Ecole Polytechnique, 91128 Palaiseau Cedex.

Barassin, A., Chimionisation U.E.R. Sciences, 45045 Orléans Cedex.

Baronnet, J. M., Thermodynamique, 123, rue Albert-Thomas, 87060 Limoges.

Batal, A., Physicochimie Industrielle, 20, avenue A.-Einstein, 69621 Villeurbanne Cedex.

Bayle, P., Centre Physique Atomique, 118, Route de Narbonne, 31077 Toulouse Cedex.

Bernard, J., Centre d'Etude de Limeil, CEA, BP 27, 94190 Ville-neuve Saint Georges.

Blanc, D., Centre de Physique Atomique, 118, Route de Narbonne, 31077 Toulouse Cedex.

Bobin, J. L., Commissariat à l'Energie Atomique, BP 27, 94190 Ville-neuve Saint Georges.

Bouloud, A., Laboratoire de Physique Expérimentale, 2, rue de la Houssinière, 44072 Nantes Cedex.

Bourdard, G., Commissariat Energie Atomique 29, rue de la Fédération, 75015 Paris.

Bourdin, E., Thermodynamique, 123, rue Albert-Thomas, 87100 Limoges.

Bouvier, A., Laboratoire Spectroscopie et Luminescence, 43, bd du 11 Novembre 1918, 69621 Villeurbanne.

Brunet, A., ONERA, 29, avenue de la Division Leclerc, 92320 Châtillon.

Cambray, P., L.A. 193 (CNRS), rue Guillaume VII, 86036 Poitiers Cedex.

Caron, M., Direction Scientifique PUK, 23, rue Balzac, BP 78708, 75360 Paris Cedex 08.

Catherinot, A., GREMI, UER Sciences Université, 45045 Orléans Cedex.

Cernogora, P., Physique des Plasmas, Bât. 212, Université Paris-Sud, 91405 Orsay Cedex.

Chapelle, J., Centre Recherche Physique Hautes Températures, 10, avenue de la Recherche Scientifique, 45045 Orléans Cedex.

Chenevier, P., Physique des Milieux Ionisés, Domaine Universitaire, 38041 Grenoble Cedex 53.

Cheron, B., Thermodynamique LA 230 28665, Faculté des Sciences de Rouen, 76130 Mont Saint Aignan.

Cojan, C., Thermodynamique LA 230, BP 67, 76130 Mont Saint Aignan.

Collobert, D., CNET, Route de Trégastel, 22301 Lannion.

Coxon, P. A., Groupe d'Electricité, avenue Philippon, 64000 Pau.

Delcroix, J. L., Physique des Plasmas, Université Paris XI, 91405 Orsay.

Dennerly, F. M., Société l'Air Liquide, 75, quai d'Orsay, 75007 Paris.

Deutsch, C., Plasmas Orsay, 91405 Orsay.

Dotique, P., Physique des Plasmas, Université de Grenoble, 38041 Grenoble Cedex 53.

Doucet, H. J., Laboratoire Physique Milieux Ionisés, Ecole Polytechnique, 91128 Palaiseau Cedex.

Drawin, H. W., Association EURATOM-CEA, Centre d'Etudes Nucléaires, 92260 Fontenay aux Roses.

Dubreuil, B., Gremi UER Sciences, Université d'Orléans, 45045 Orléans Cedex.

Dumas, J. L., Centre d'Etudes Cryogéniques, BP 15, 38360 Sas-senage.

Escande, D. F., PMI Ecole Polytechnique, 91128 Palaiseau Cedex.

Fabry, M., Laboratoire Physique des Milieux Ionisés, Univ. Nancy I, Case off. 140, 54037 Nancy Cedex.

Fain, A., CEA Centre d'Etudes de Limeil, BP 27, 94190 Ville-neuve Saint Georges.

Fauchais, P., Thermodynamique, 123, rue Albert-Thomas, 87100 Limoges.

Faure, C., CEA, BP 27, 94190 Villeneuve Saint Georges.

Felts, B., Photoélectricité, rue Henri-Poincaré, 13397 Marseille Cedex 4.

Fitaire, M., Physique Plasmas, Bât. 212, 91405 Orsay.

Fleurier, Cl., CRPHT CNRS, 45045 Orléans Cedex.

- Fort, J.**, ONERA, 29, avenue de la Division Leclerc, 92320 Châtillon.
- Fournier, G.**, ONERA, 29, avenue de la Division Leclerc, 92320 Châtillon.
- Fourrier, C.**, Physique Corpusculaire, 2, Chemin de la Houssinière, 44072 Nantes Cedex.
- Garaude, F.**, CEL, BP 27, 94190 Villeneuve Saint Georges.
- Gary, C. H.**, Electricité de France, 1, avenue Général de Gaulle, 92141 Clamart.
- Gaucherol, P.**, Aérodynamique, 4^{ter}, Route des Gardes, 92190 Meudon.
- Glasser, J.**, CRPHT CNRS, 10, avenue de la Recherche Scientifique, 45045 Orléans Cedex.
- Gleizes, A.**, Centre de Physique Atomique, 118, Route de Narbonne, 31077 Toulouse Cedex.
- Goldman, A.**, Laboratoire Physique des Décharges, ESE Plateau du Moulon, 91190 Gif sur Yvette.
- Goldman, M.**, Laboratoire Physique des Décharges, Plateau du Moulon, 91190 Gif sur Yvette.
- Gombert, M. M.**, Laboratoire de Physique des Plasmas, Université de Paris XI, 91405 Orsay Cedex.
- Gouard, P.**, CEL, BP 27, 94190 Villeneuve Saint Georges.
- Gouesbet, G.**, LA 230, BP 67, 76130 Mont Saint Aignan.
- Gousset, G.**, CRPHT CNRS, 10, avenue de la Recherche Scientifique, 45100 Orléans.
- Grandjouan, N.**, Inst. Electronique Fondamentale, Bât. 220, Faculté Sciences Orsay, 91405 Orsay.
- Hamelin, CRPE CNET CNRS**, avenue de la Recherche Scientifique, 45045 Orléans Cedex.
- Haug, R.**, Laboratoire Physique des Décharges, Plateau du Moulon, 91190 Gif sur Yvette.
- Heyvaerts**, Observatoire de Meudon, 92190 Meudon.
- Hubert, P.**, DPHEP CEA, Saclay, BP 2, 91190 Gif sur Yvette.
- Hutzler, B.**, Electricité de France, 1, avenue du Général de Gaulle, 92141 Clamart.
- Ilunga, M. U.**, DAPHE, Observatoire de Meudon, 92190 Meudon.
- Jacquot, C.**, Fusion CENG, Chemin des Martyrs, 38000 Grenoble.
- Jaroszy, J.**, Physicochimie Industrielle, 20, avenue A. Einstein, 69621 Villeurbanne Cedex.
- Kafrouni, H.**, Centre de Physique Atomique, 118, Route de Narbonne, 31077 Toulouse Cedex.
- Kassabji, F.**, Laboratoire de Thermodynamique, 123, rue Albert-Thomas, 87060 Limoges Cedex.
- Lafon, J. P.**, Observatoire de Meudon (DESPA), Place Janssen, 92190 Meudon.
- Larigaldie, S.**, ONERA, 29, avenue de la Division Leclerc, 92320 Châtillon.
- Larour, J.**, LPOC, tour 12, 5^e étage, Université Paris VI^e, place Jussieu, 75230 Paris Cedex 05.
- Le Breton, J. P.**, CEA Centre d'Etude de Limeil, BP 27, 94190 Villeneuve Saint Georges.
- Lembege, B.**, CRPE CNET/CNRS, 3, avenue de la République, 92131 Issy les Moulineaux.
- Leprince, P.**, Physique des Plasmas, Bât. 210, 91405 Orsay Cedex.
- Lesage, A.**, DEPEG, Observatoire de Meudon, 92190 Meudon.
- Lezard, J. M.**, Commissariat Energie Atomique, 33, rue de la Fédération, 75000 Paris.
- Louvet, F.**, DRET, 26, bd Victor, 75996 Paris Armées.
- Maftoul, J.**, Laboratoire Physique des Décharges, Plateau du Moulon, 91190 Gif sur Yvette.
- Manuel, P.**, DER-EDF, 1, avenue du Général de Gaulle, 92141 Clamart Cedex.
- Marec, J.**, Physique des Gaz et des Plasmas, Bât. 212, Université Paris-Sud, 91405 Orsay.
- Marode, E.**, Laboratoire Physique des Décharges, CNRS, Plateau du Moulon, 91190 Gif sur Yvette.
- Misguich, J. H.**, STGI-CEA, BP 6, 92260 Fontenay aux Roses.
- Moity, J.**, Observatoire de Meudon, Place Janssen, 92190 Meudon.
- Mourier, G.**, THOMSON-CSF, 38, rue Vauthier, 92100 Boulogne.
- Nguyen, D. N.**, Claude SA, 27-29 rue de Sèvres, 92103 Boulogne Billancourt.
- Pateyron, B.**, Thermodynamique, 123, rue Albert-Thomas, 87060 Limoges.
- Pebay-Peyroula, J. C.**, Laboratoire de Spectrométrie Physique, Domaine Univ. BP 53, 38041 Grenoble.
- Pelletier, J.**, USMG, Physique des Milieux Ionisés, BP 53X, 38400 Saint Martin d'Hères.
- Pelletier, G.**, Physique des Milieux Ionisés, Domaine Universitaire, 38041 Grenoble Cedex 53.
- Pesic, S. S.**, DPH-PFC-SIG, CEN-G 85X, 38041 Grenoble Cedex.
- Pesme, D.**, Ecole Polytechnique, 91128 Palaiseau.
- Pigache, D.**, ONERA, 29, avenue de la Division Leclerc, 92320 Châtillon.
- Pointu, A. M.**, Laboratoire Physique Plasmas, Bât. 212, Université Paris XI, 91405 Orsay.
- Pomathion, P.**, CRPE CNET/CNRS, avenue de la Recherche Scientifique, 45045 Orléans Cedex.
- Pomot, C.**, Physique des Milieux Ionisés, Domaine Universitaire, 38041 Grenoble Cedex 53.
- Popovics, C.**, Physique des Milieux Ionisés, Ecole Polytechnique, 91128 Palaiseau Cedex.
- Povey, M.**, Physique des Plasmas, Bât. 212, JPS, 91405 Orsay.
- Queflec, J. L.**, Physique Moléculaire, avenue Général-Leclerc, 35042 Rennes Cedex.
- Ranson, P.**, Centre Recherche Physique Hautes Températures, 1D, avenue Recherche Scientifique, 45045 Orléans.
- Reisse, C.**, Centre d'Etude de Limeil CEA, BP 27, 94190 Villeneuve Saint Georges.
- Ricard, A.**, Physique Plasmas, Bât. 212, Université Paris-Sud, 91405 Orsay.
- Riou, J. P. A.**, Aérospatiale ISSAC, BP 11, 33160 Saint Médard en Jalles.
- Roche, M.**, CEA Valduc, BP 14, 21120 Is sur Tille.
- Rowe, B.**, Aérodynamique, 4^{ter}, Route des Gardes, 92190 Meudon.
- Sadeghi, N.**, Laboratoire Spectrométrie Physique, BP 53, 38041 Grenoble Cedex.
- Saubignac, C.**, Commissariat Energie Atomique, Le Barp, BP 2, 33220 Belin Bellet.
- Segur, P.**, CPAT, 118, Route de Narbonne, 31077 Toulouse.
- Skowronek, M.**, Plasmas Denses, Université P.-et-M.-Curie, tour 12, 5^e étage, 4, Place Jussieu, 75230 Paris Cedex 05.
- Speller, C.**, Laboratoire de Physique des Plasmas, Université de Paris-Sud, 91405 Orsay.
- Sy, W.**, Association EURATOM-CEA DPH-PFC, BP 6, 92260 Fontenay aux Roses.
- Taillet, J.**, ONERA, 29, avenue de la Division Leclerc, 92320 Châtillon.
- Thiell, CEA Centre d'Etudes de Limeil**, BP 27, 94190 Villeneuve Saint Georges.
- Truong-Bach, DEPEG-Spectroscopie des Plasmas**, Observatoire de Meudon, 92190 Meudon.

Tu, K., Laboratoire Physique des Plasmas, Université Paris-Sud, 91405.

Vacquie, S., Centre de Physique Atomique, 118, Route de Narbonne, 31077 Toulouse Cedex.

Valignat, S., Spectroscopie ERA CNRS 302, 43, bd du 11 Novembre, 69621 Villeurbanne.

Vervisch, P., Thermodynamique LA 230 28665, Faculté des Sciences de Rouen, 76130 Mont Saint Aignan.

Vialle, M., Laboratoire Physique des Plasmas, 91405 Orsay.

Zadworny, F., Physique des Plasmas, BP 53X, Bât. Chimie Recherche du DU, 38041 Grenoble Saint Martin d'Hères.

GRANDE-BRETAGNE

Allen, J. E., University of Oxford, Dept. Engineering Sciences, Oxford.

Braithwaite, N. S. J., Dept. Engineering Sciences, University of Oxford, Parks RD, Oxford OX1 3PJ.

Bunting, K. A., Electricity Council Research CE, Capenhurst Chester.

Carolan, P. G., Culham Laboratory, Abingdon Oxon.

Chandrakar, K., Department of Electrical Engineer, University of Salford, Salford M 54WT.

Dixon, A., Dept. of Engineering Oxford, Parks RD, Oxford.

Dutton, J., Department of Physics, Singleton Park, Swansea SA 28PP, Wales.

Earl, R. G., Newcastle on Tyne Polytechnic, Ellison Building Ellison PL, Newcastle on Tyne NE1 8ST.

Forrest, M. J., Culham Laboratory, UKAEA, Abingdon Oxon.

Franklin, R. N., City University, Northampton SA, London EC1V 0HB.

Humphreys, J. G. J., UCNW Bangor School of Mathematics, University College of Wales, Bangor Gwynedd LL 57 2DG.

Clayton, J. J. D., Department of Physics, the Univ. Pengais, Aberystwyth Dyfed SY 23 3BZ.

Jones, J. D. C., Department of Physics, the Univ. Pengais, Aberystwyth Dyfed SY 23 3BZ.

Llewellyn-Jones, F., Physics Dept., Singleton Park, Swansea SA 2 SPP.

Mason, J. W., High Voltage Laboratory, Riverside House, Beresford ST Woolwich, London SE 18 6BU.

Massey, H. S., University College, Dept. Physics Gower Street, London WC 1ELBT.

Mellis, J., Physics Dept. University of St Andrews, North Haugh, St Andrews KY 16 955.

Moruzzi, J. L., Dept. Electrical Engineering, Liverpool L 693BX.

Murray, G. A., Physics Dept. University of St Andrews, North Haugh, St Andrews KY 16 955.

Nicolas, D., Rutherford Laboratory, Chilton, Didcot Oxfordshire, OX1 10X.

Phelps, A. D. R., Natural Philosophy Dept., Strathclyde University, Glasgow G 4ONG.

Prest, A., Newcastle on Tyne Polytechnic, Ellison Building Ellison PL, Newcastle NE1 8ST.

Quillin, M. C., RSRE, St Andrews RD Malver England, WR 14 3P.

Saelee, H. T., Dept. of Engineering Sciences, Parks Road, Oxford OX1 3PJ.

Smith, A. L. S., Physics Dept. University of St Andrews, North Haugh, St Andrews KY 16 955.

Todd, T. N., Golham Laboratory, Abingdon Oxon OX 14 3DB.

Von Engel, A., Engineering Sciences, Parks RD, Oxford.

Wharmby, D. J., Thorn Lighting, Melton Road, Leicester.

HONGRIE

Janossy, M., Central Research Inst. of Physic, Konkoly Thege UT, POB 49, H-1525 Budapest.

INDES

Suryaprasad, G., Physical Research Laboratory Navrangpura, Ahmedabad 380009.

IRLANDE

Sexton, M. C., University College, Cork.

ISRAEL

Andrei, B. A., Physics Dep. Ben-Gurion Univ., Beer-Sheva.

Dothan, F., Inst. of Physics Hebrew University, Jerusalem.

Fruchtmann, A., Racah Inst. of Physics, Hebrew Univ. Givat RAM, Jerusalem.

Kagan, Y., Racah Inst. of Physics, Givat RAM Hebrew University, Jerusalem.

Kaufman, Y., Racah Institute of Physics, Hebrew University Givat RAM, Jerusalem.

Levron, D., Laser Division NRCN, PO BOX 9001, Beer Sheva.

Salzmann, D., Soreq Nuclear Research Centre, Yavneh.

ITALIE

Braglia, G. L., Università di Parma, Ist Fisica, Via d'Azeglio 85, 43100 Parma.

Capitelli, M., Istituto Chimica Delluniversit, 173 Via Amendola, 70100 Bari.

Cicconi, G., Electr. Eng. Dep. University, 13 F Causa, 16145 Genova.

De Benedictis, S., Centro Studi Chimica Plasm CNR Via Amendola 173, 70100 Bari.

Luches, A., Istituto di Fisica, Via Arnesano, 73100 Lecce.

Mercurio, S., Physics Dept. University of Wis, Riazza Vittorio Veneto, 20 Palermo 90143.

Molinari, E., Istituto di Chimica Università, Citta Universitaria, 00100 Roma.

Perrone, M. R., Istituto di Fisica, Via Arnesano, 73100 Lecce.

Pollachini, L., Cise, PO BOX 3986, 20100 Milano.

Realini, G., CCR-EURATOM, 21020 Ispra (Varese).

Rosatelli, C., Electr. Eng. Dep. University, 13 F Causa, 16145 Genova.

Ventura, G., Iroe, Via Panciatichi 64, 50127 Firenze.

JAPON

Fukuyama, A., Okayama University, Tsushima, 700 Okayama.

Haruo, S., Hiroshima University, Senda-Cho 3, Hiroshima-Shi, 730 Hiroshima-City.

Hayashi, M., Nagoya Institute of Technology, Gokiso-Cho, Syowa-Ku, 466 Nagoya.

Hiddenori, A., Nagoya University, Furocho, Chikusaku, Nagoya.

Hiroshi, A., Institute of Phys. Chem. Research, Hiroasawa Wakoshi Saitama, 351.

Ikezawa, Chubu Institute of Technology, 1200 Matsumoto, 487 Kasugai.

Ikuta, Technical College Tokushima, Minamijosanjima, 110 Tokushima.

Imazu, S., Hiroshima University, Senda-Cho 3-8-2 Hiroshima, 730.

Inutake, M., Institute of Plasma Physics, Furocho, Nagoya 464.

Itoh, H., Chiba Institute of Technology, Tsudanuma 2-17-1, 275 Narashino-Shi. Chiba.

Makabe, T., Department of Electrical Eng., Keio University, 3-14-1 Hiyos, I-Cho, Yokohama 223.

Mori, I. J., Depart. Electric Engtokusima Uni, Minamami Josanjima, 770 Tokusima.

Nakai, S., Institute of Laser Engineering, Osata Univ. Yamada-Kami, 565 Suita.

Nishijima, K., Department of Electrical Engineering, Kyushu University, Hakozaki Higshi-Ku, Fukuoka 812.

Suganomata, S., Yamanashi University, Takeda-4, 400 Kofu.

Suzuki, K., College of General Education, Komaba Meguroko, 153 Tokyo.

Takeda, Y., Department of Physics Nihon Univ., Kanda-Suvugadai, Chiyoda-Ku, Tokyo 101.

Ueda, Mitsubishi Electric Corpora, 80 Nakano Minamishimizu, Amagasaki Hyogo 661.

NORVÈGE

Sigmono, R. S., Phys. Dept. Norw. Inst. of Techn., N-7034 Trondheim-NTH.

PAYS-BAS

Barbian, E., Fom Rijnhuizen Nieuwegein/Holl., Rijnhuizen, 3430 AA.

Beyerinck, H. C. N., Eindhoven, University of Technology, PO BOX 513, Eindhoven.

Borgh, C. Q., Eindhoven, University of Technology, Den Dolech, PO BOX 513, Eindhoven.

Coppoolse, Holec Switchgeargroup, 61 Tuindorpstraat POB 23, 7550 AA Hengeld.

Coumans, J. J. H., Eindhoven, University of Technology, Den Dolech, PO BOX 513, Eindhoven.

Depts, D., Fom Instituut voor Plasmafysic, Rynhuizen, 3430 AA Nieuwegein.

Dielis, J., Eindhoven, University of Technology, Den Dolech 2, 5612 AZ Eindhoven.

Flinsenbergh, H., Eindhoven, University of Technology, Den Dolech, PO BOX 513, Eindhoven.

Massmann, P., Fom Instituut voor Atoom EN, Kruislaan 487 PON BUS 41883, 1009 D3 Amsterdam.

Van Schaik, N., Eindhoven, University of Technology, PO BOX 513, Eindhoven.

Schellekens, H., Holec Research Department, Tuindorpstraat 61, Hengelo (OV).

Schram, D., Eindhoven, University, Den Dolech 2, 5600 MB Eindhoven.

Stoop, T., NV KEMA, Utrechtseweg 310, 6800 ET Arnhem.

Theuvs, P. G. A., Phys. Dept. Einoh, University of Technology, Den Dolech 2, Eindhoven.

Van der Mullen, J., Physics Department, Eindhoven, Den Dolech, Eindhoven.

Van der Sijde, B., Physics Department, Eindhoven, Den Dolech 2, 5600 MB Eindhoven.

Verheyen, M. J., TH Eindhoven, Den Dolech 2, Eindhoven.

Verster, N. F., Phys. Dept. Einoh, University of Technology, Den Dolech 2, Eindhoven.

Vriens, L., Philips Research Laboratories, Eindhoven.

Weysenfeld, C., Philips Research Laboratories, Holstlaan. Eindhoven.

Wynakker, M. M. B., Fom Instituut, Kruislaan 487, PO BUS 41883, 1009 DB Amsterdam.

POLOGNE

Gryzinski, M., Institute of Nuclear Research, Swierk, 05-400 Otwock.

Krolkowski, C., Instytut Elektroenergetyki, Piotrowo SA, 60965 Poznan.

Roznerski, W., Institute of Physics, 11, Majakowskiego, 80-952 Gdansk.

Stachorska, H. D., Institute de la Physique UMCS, 10 Nowotki, 20031 Lublin.

Wolowski, J., Inst. Plasma Phys. Laser, Bemowo PO BOX 49, 00-908 Warszawa.

Wroblewski, J., Swietokrzyska 21, 00-049 Warszawa.

PORTUGAL

Matos-Ferreira, C., Centro de Electrodinamica, Ist. av. Rovisco Pais. Lisbonne.

Mendonca, J. T., Instituto Superior Tecnico, av. Rovisco Pais 1, 1000 Lisboa.

Serra, F. M., Electrodinamica, 1 S Tecnico, av. Rovisco Pais 1, 1000 Lisboa.

ROUMANIE

Baltok, A., Inst. Phys. and Tech., Bucarest Magurele, BP 5206.

Popa, G., Faculty of Physics Iasi, 23 August 11, R-6600 Iasi.

SUÈDE

Alfven, H., Plasma Physics Royal Inst. Tech., Stockholm, 10044 Stockholm.

Handel, S. K., Institute of Physics, BOX 530, Univ. of Uppsala, S-751 21 Uppsala.

Lindberg, L. V., Royal Institute of Technology, Dept. of Plasma Physics, S-10044 Stockholm.

Rysko, H., Royal Institute of Technology, Teknikringen 33, S-10044 Stockholm.

Torven, S., Royal Institute of Technology, Dept. of Plasma Physics, S-10044 Stockholm 70.

Vlastos, A. E., Royal Institute of Technology, Tecnicringen 33, S-10044 Stockholm 70.

SUISSE

Adam, B., Brown Boveri and CO LTD, Research Center KLR, CH-5405 Baden Daettwil.

Berger, K., 31 Gstadtstrasse, CH 8702.

Bourquard, S., Physique Appliquée EPF Lausanne, Ruchonnet 2, 1003 Lausanne.

Brand, K. P., Brown Boveri Research Center, CH-5405 Baden-Daettwil.

Buxbaum, C., BBC DEP EKR, 5400 Baden.

Kucian, P., Ecole Polytechnique Fédérale, Ruchonnet 2, 1003 Lausanne.

Kogelschatz, U., Brown Boveri, Research Center, Baden-Daettwil CH 5405.

Mayor, I. M., Physique Appliquée EPF Lausanne, Ruchonnet 2, 1003 Lausanne.

Means, R., CRPP, 21, avenue des Bains, 1004 Lausanne.

Niemeyer, L., Brown Boveri Research Center, CH 5405 Baden.

Paris, P., CRPP, 21, avenue des Bains, 1007 Lausanne.

Sayasov, Y., Institute of Physics, Perolles Univ. Fribourg, CH-1700 Fribourg.

Schade, E., BBC Research Center CH-5405 Baden.

Schoetzau, H. J., Sprecher Schuh AG, CH-5001 Aarau.
 Sturzenegger, C., Sprecher Schuh AG, CH-5001 Aarau.
 Webb, A. P., Universitat Zurich, Winterthurerstrasse 190,
 8057 Zurich.

TCHÉCOSLOVAQUIE

Bardos, L., Institute of Plasma Physics, POD Vodarenskoo Vezi 4,
 18069 Prague.
 Havelka, O., Chair of El Machines and Apparatus, 10 TR Obranco
 MSRU, 66243 Brno.
 Nenicka, V., Institute of Electr. Engineer, Vavalske Namesti 55,
 11690 Prague.
 Urbankova, H., Institute of Physics CZ AC SCI, 2 NA Slovance,
 19100 Prague.

U.R.S.S.

Assinovski, E., Institute of High Temperatures, Moscow Koro-
 vinskoye Chausse, Moscow 127412.
 Belchenko, J., Nuclear Physics Institute, NP Hayku 11,
 630090 Novosibirsk.
 Breizman, Institute of Nuclear Physics, 630090 Novosibirsk.
 Bugzova, Moscow Radio Institute, Moscow.
 Chistyakov, P., Moscow Ing. Phys. Institute, USSR Moscow
 Kashirskoe Shosse, Moscow.
 Chutov, J., Kiev State University, Kiev Shevchenko University,
 Kiev.
 Dudnikov, V., Nuclear Physics Institute, Prospekt Nayki 11,
 630090 Novosibirsk 90.
 Fursey, G. N., Institut Communication, Nbreznaja Moiky 61,
 Leningrad.
 Gekker, I., Lebedev Physical Institute, Lenin avenue 53,
 117333 Moscow.
 Gurevich, A. V., Lebedev Physical Institute, 53 Leninsky Prosp.,
 117333 Moscow.
 Iouriev, V., Phys. Techn. Inst. Leningrad, Leningrad Politechnic 26,
 Leningrad.
 Jilinskii, Kalinin Politechnical Institute, Leningrad Politechnic
 Street, Leningrad.
 Khakinov, F., Tadjik State University, 17 Lenin, Dushanbe.
 Khorasanov, G., Sukhumi Physical Technical Ins., 384914 Suk-
 humi PO 14.
 Kisselevskii, L., Spectroscopy Minsk USSR, Leninski PN 70,
 220602 Minsk.
 Klimontovich, Y., Fac. Physique Université Moscou, MTS Lénine,
 Moscou.
 Klopov, I., Leningrad Institute Aviation E, Leningrad Gercen
 Street 65, Leningrad.
 Kolesnikov, V. V., Lebedev Physical Institute, 53 Leninsky Prosp.,
 117333 Moscow.
 Kortkhonija, V., Tbilisi Academi Scinces USSR, Gouramishvili
 STR 6, Tbilisi.
 Kravchenko, S. K., Heat Mass Transfer Inst., Podlesna 15,
 220078 Minsk.
 Kudu, K., Tartu State University, 18 Ulikooli STR, 202400 Tartu.
 Lesnevskii, L. N., University, Moscow Leninsky Cory, Moscow.
 Lysoivan, A., Physico Techn. Inst. Ukrainian, Academy of Sciences,
 Karkuf, 108 Akademicheskaya.
 Milantiev, Patrice Lumumba University, 3 Ordjonikidze, Moscow
 W-302.
 Nikolaev, A. V., Institut of Metallugi an SSSR, 49 Leninski Prospect,
 117333 Moscow.

Passtchnik, L., Kiev Institute Nuclear Research, Kiev Prospect
 Nauki 119, 252650 Kiev.
 Preobrajenski, N., 630090 Novosibirsk ITPM, Prospect Nayki 4,
 630090 Novosibirsk.
 Presniakov, L. P., Lebedev Physical Institute, Leninsky Prospect 53,
 117924 Moscow.
 Protasov, Y. S., MHTS Baumas, Bauman, 107005 Moscow.
 Rachimov, A., Moscow University, USSR Moscow Leninskii Gory,
 Moscow.
 Roukhadze, A., Lebedev Physical Institute, Lenin avenue 53,
 117333 Moscow.
 Shishkin, G. G., Academy Science USSR, Moscow.
 Sholin, G., Kurchatov Institute of Atomic, Energy Kurchatov
 Square, 123182 Moscow.
 Sigov, Y. S., Keldysh Institute of Appl. Math., Miusskaya Square 4,
 125047 Moscow A-47.
 Smirnov, V., Leningrad Elektro Physical, Aparatus, 188631 Lenin-
 grad N-042.
 Sokolov, Moscow Power Engineering Inst., 14 Krasnokazar-
 mennaya, Moscow E-250.
 Soloviantchik, D., Spectroscopy Minsk USSR, Leninsky Pros-
 pect 70, 220602 Minsk.
 Tolstoukhina, Secret de Délégation Russe, Moscou.
 Tsytoich, V. N., Lebedev Institut, 53 Leninsky Prospect, Moscow.

U.S.A.

Ahlstrom, H., Lawrence Livermore Laboratory, Alameda,
 PO BOX 5508 L-481.
 Bailly, W. M. F., Air Force Aéro Propulsion, BLDG 18 AREA B,
 Wright Patterson AFB Ohio.
 Davies, D. K., Westinghouse Rand D Center, Beulah Road, Pitts-
 burgh PA 15235.
 Djeu, N., Naval Research Laboratory, 4555 Overlook AVE SW,
 Washington DC 20375.
 Dubois, D. F., Los Alamos Scientific Laboratory, Los Alamos
 New Mexico.
 Elton, R. C., US Naval Research Laboratory, Code 5504, Washing-
 ton DC 20315.
 Ernesto, B., ASRC Stat. Univ. of NY, 1400 Washington avenue,
 Albany, NY 12222.
 Fiorito, R., White oak Code R 41, Silver Spring, Maryland.
 Frazer, W., Dept. of Electrical Engineer, Texas Tech. University,
 Lubbock, Texas 19409.
 Garscadden, A., Air Force Aero Propulsion Laboratory, Wright-
 Patterson AFB, Dayton 0410 45433.
 Bhaumik, M. L., Northrop Research of Technology, I, Research
 Park, Palos Verdes, California.
 Bigio, I. J., Los Alamos Scientific Laboratory, Group L-I, MS-548,
 Los Alamos, New Mexico 8754.
 Bleach, R. D., Naval Research Laboratory, Code 6680, Washing-
 ton DC.
 Boehmer, H., University of California, Department of Physics,
 Irvine CA 92717.
 Bradley, L. P., Lawrence Livermore Laboratory, PO BOX 5508,
 Livermore, California 94550.
 Burns, E. J. T., Sandia Laboratories, Organization 4242, Albu-
 querque NM 87185.
 Clauser, M. J., Sandia Laboratories, Albuquerque, NM 87185.
 Crawford, F. W., Institute for Plasma Research, Via Crespo,
 Stanford Univ., Stanford CA 94305.

- Kimblin, C. W.**, Westinghouse Research Center, 1310 Beulah Road, Pittsburgh, Pennsylvania.
- Kristiansen, M.**, Dept. Electrical Engineering, Texas Tech. University, PO BOX 4439, Lubbock, Texas.
- Langdon, A. B.**, Lawrence Livermore Laboratory, BOX 808, Livermore 94550.
- Manheimer, W. M.**, Code 6190, Naval Research Laboratory, Washington DC 20315.
- Miller, M. H.**, University of Maryland, 1133 Hampton Road RT 4, Annapolis MD 21401.
- Mosher, D.**, Naval Research Laboratory, Washington DC 20375.
- Okada, Plasma Physics Laboratory, Univ.**, PO BOX 451, Princeton, 08544 New Jersey.
- Ott, W. R.**, National Bureau of Standards, Washington DC 20234.
- Gray, E. W.**, Bell Labs, 6200 East Broad Street, Columbus Ohio 43213.
- Greig, J. R.**, Naval Research Laboratory, Overlook, avenue, Washington DC 20375.
- Guenther, A. H.**, Air Force Weapons Laboratory, Kirtland AFB, NM 87117.
- Hernquist, K.**, RCA Laboratories, Princeton NJ.
- Hill, R. A.**, Hughes Aircraft CO MSGC-129, Centinella and Teale 5750, 90230 Culver City, California.
- Hiskes, J. R.**, Lawrence Livermore Laboratory, PO BOX 808, Livermore CA 94550.
- Kapetanacos, C. A.**, Naval Research Laboratory, Code 6761, Washington DC 20375.
- Kassel, S.**, The Rand Corporation, 2100 M Street NW, Washington DC.
- Pietrzyk, A.**, University of Washington, Seattle WA 98195.
- Rogoff, G. L.**, Westinghouse RTD Center, 1310 Beulah Road, Pittsburgh PA 15235.
- Rose, M. F.**, Naval Surface Weapons Center, Dahlgren Laboratory F 102, Dahlgren, Virginia 22448.
- Sambis, J. G.**, Naval Research Laboratory, Code 6740, Washington DC 20375.
- Stallings, C.**, Physics INT CO, 2700 Merced ST, San Leandro, California.
- Trenchard, E. A.**, Westinghouse Electric Corp, BOX 1521 MS 3714, Baltimore MD 21203.
- Tuma, D.**, Dept. Elec. Eng., Carnegie Mellon Univ., Pittsburgh PA 15213.
- Venugopalan, M.**, Western Illinois University, Currens Hall 301, Macomb, Illinois 61455.
- Vitkovitsky, T. M.**, Naval Research Laboratory, Washington DC 20375.
- Witting, H. L.**, General Electric Corp Res. and Dev., K-1 Rad Box 8, Schenectady NY 12301.
- YUGOSLAVIE**
- Bozidar, S.**, Fac. of Electrical Engineer, 13, bd Revolucije, 11000 Beograd.
- Cadez, V. M.**, Institute of Physics, Studentski TRG 12/V, YU-11001 Beograd.
- Cander, L.**, Geomagnetic Institute, 11306 Grocka.
- Cibin, Boris**, Kidrio Institute POB 522, 11001 Beograd.
- Cirkovic, L. M.**, Dept. of Physics and Meteorology, PO BOX 550, 11001 Beograd.
- Grozdanov, T. P.**, Institute of Physics, 12/V Studentski TRG, 11001 Beograd.
- Grujic, Our**, for Theoretical Physics, 12/V Studentski TRG, 11000 Beograd.
- Labat, J. M.**, Dept. of Physics and Meteorolog., PO BOX 550, 11001 Beograd.
- Lakicevic, S. I.**, Institute of Physics, Studentski TRG 12/V, PO BOX 57, 11000 Beograd.
- Milan, D.**, Institute of Applied Physics, Marsala Birjzova 14, 11001 Beograd PO BOX 24.
- Miljevic, V.**, Atomic Physics Laboratory, Vinca PO BOX 522, 11001 Beograd.
- Pavlovic-Bradjukovic, N.**, Dept. Physics, University Kraguj, 34000 Kragujevac.
- Poberaj, Faculty** for Electrical Engineer, 25 Trzaska, 61000 Ljubljana.
- Popovic, M. M.**, Institut de Physique, BP 57, Studentski TRG 16, 11001 Beograd.
- Puric-Jagos, Institute** of Physics, Studentski TRG 12/5, 11000 Beograd.
- Sulic, D.**, Geomagnetic Institute, 11306 Grocka.
- Vujnovic, V.**, Institute of Physics of the University, Bijenicka 46, PO BOX 304, 41001 Zagreb.
- Vukicevic, J.**, Institute of Physics, 12/V Studentski TRG, 11001 Beograd.
- Zigman, V.**, Institute of Physics, Fac. of Sci., Studentski TRG 16, 11000 Beograd.

CONTENTS

H. ALFVÉN. — Plasma in laboratory and space.....	C7-1	Yu. P. RAIZER. — Optical discharges.....	C7-141
H. S. W. MASSEY. — Ionic reactions with laboratory and in planetary atmospheres.....	C7-21	H. W. DRAWIN. — Plasma properties and atomic processes at medium and high pressures.....	C7-149
J. HEYVAERTS. — Plasma and solar physics. The solar flare phenomenon.....	C7-37	M. GRYSINSKI. — Theoretical description of collisions in plasma : classical methods.....	C7-171
F. LLEWELLYN-JONES. — Contact electrode processes and microplasma diagnostics.....	C7-47	J. R. HISKES. — Formation of hydrogen negative ions by surface and volume processes with application to negative ion sources.....	C7-179
K. BERGER. — Survey on actual knowledge and physical problems.....	C7-57	I. GALLIMBERTI. — The mechanism of the long spark formation.....	C7-193
Yu. S. SIGOV and V. E. ZAKHAROV. — Strong turbulence and its computer simulation.....	C7-63	J. WILHELM and R. WINKLER. — Progress in the kinetic description of non-stationary behaviour of the electron ensemble in non-isothermal plasmas.....	C7-251
M. J. CLAUSER, E. J. T. BURNS, J. CHANG, A. V. FARNSWORTH, S. A. GOLDSTEIN, D. J. JOHNSON, G. W. KUSWA, T. A. MEHLHORN, C. W. MENDEL, L. P. MIX, J. W. POUKEY, J. P. QUIN-TENZ, M. A. SWEENEY, J. P. VANDEVENDER and M. M. WIDNER. — Particle beam interactions with plasmas and their application to inertial fusion..	C7-81	W. M. MANHEIMER. — Anomalous transport from plasma waves.....	C7-269
G. GRIEGER. — Progress in toroidal magnetic confinement.....	C7-87	L. P. PRESNYAKOV and A. M. URNOV. — X-ray plasma diagnostics.....	C7-279
H. G. AHLSTROM. — Progress of laser fusion at Lawrence Livermore Laboratory.....	C7-97	P. FAUCHAIS and J. RAKOWITZ. — Physics on plasma chemistry.....	C7-289
Yu. L. KLIMONTOVICH. — Kinetic theory of spectral line broadening in a non-equilibrium plasma.....	C7-113	F. WAELBROECK, I. ALI-KHAN, K. J. DIETZ and P. WIENHOLD. — Surface problems in magnetic confinement systems.....	C7-313
W. H. LONG Jr. and M. L. BHAUMIK. — Electric discharge pumping of excimer lasers.....	C7-127	F. W. CRAWFORD. — Phenomena in ionized gases : some reflections on the XIVth ICPIG.....	C7-317
		Author index.....	C7-323

Plasma in laboratory and space

H. Alfvén

Royal Institute of Technology, Department of Plasma Physics, S-100 44 Stockholm, Sweden

Résumé. — On étudie les phénomènes du plasma en laboratoire, dans les magnétosphères, et dans les régions astrophysiques les plus lointaines. Il est probable que les qualités de base des plasmas sont partout les mêmes, mais la translation des connaissances entre les régions exige des lois d'échelle d'un facteur allant jusqu'à 10^{27} (= la proportion entre la distance Hubble 10^{28} cm et les dimensions du laboratoire, disons 10 cm).

Les phénomènes du plasma sont compliqués et on ne peut les comprendre qu'au moyen de diagnostics sophistiqués. Jusqu'à présent, les diagnostics en laboratoire ont été développés avec succès et la physique du plasma dans l'espace doit se baser sur un flux de connaissances du laboratoire. Cependant, les mesures *in situ* dans les magnétosphères (y compris l'héliosphère = la magnétosphère solaire) ont atteint un tel niveau de sophistication qu'en quelque sorte, la physique du plasma magnétosphérique devance la physique du plasma en laboratoire.

Ainsi l'exploration des régions astrophysiques (définies comme les régions non encore accessibles aux mesures *in situ*) doit se baser sur une translation des connaissances non seulement à partir de la physique de laboratoire, mais aussi à partir de la physique de la magnétosphère. De plus, une translation des connaissances des magnétosphères au laboratoire peut rajeunir les recherches de la fusion. Les recherches magnétosphériques ont démontré qu'il y a des régions du plasma de deux sortes :

- les régions du plasma passives, lesquelles peuvent être décrites par la théorie classique de l'hydrodynamique. Elles transmettent des ondes et des particules chargées de haute énergie, mais si les courants de champ-aligné dépassent une certaine valeur elles sont transférées dans :

- les régions du plasma actives. Celles-ci transportent les courants de champ-aligné qui leur donnent une structure de filament ou de feuille d'une épaisseur allant jusqu'à quelques rayons cyclotroniques (ioniques ou électroniques). Elles transmettent l'énergie d'une région à une autre, et produisent des doubles couches électriques qui accélèrent les particules à hautes énergies. On ne peut pas décrire les régions actives par les théories hydromagnétiques. Des conditions limites sont essentielles, et peuvent être introduites par une théorie des circuits. Un traitement équivoque des conditions limites est souvent inévitable dans les théories de fusion magnétique.

La translation des connaissances à partir du laboratoire et des magnétosphères engendre désormais une révolution dans l'astrophysique. Par exemple, la théorie de la formation du système solaire peut se baser sur l'extrapolation de ce que l'on sait de la physique magnétosphérique et de la physique du plasma en laboratoire. Cependant, il y a deux sortes de plasmas qui sont importants en astrophysique et qu'on ne peut pas encore étudier ni en laboratoire ni dans les magnétosphères : les plasmas poudreux, d'importance dans les nuages interstellaires, et les ambiplasmas (se composant de la matière aussi bien que de l'antimatière), d'importance dans le débat cosmologique.

Abstract. — Plasma phenomena are studied in the laboratory, in the magnetospheres, and in more distant astrophysical regions. The basic properties of plasmas are likely to be the same everywhere but the transfer of knowledge between the regions requires laws of scaling by a factor of up to 10^{27} (= ratio between Hubble distance 10^{28} cm and laboratory dimensions, say 10 cm).

Plasma phenomena are complicated and can be understood only with the help of a very sophisticated diagnostics. Up to recently, diagnostics in the laboratory was best developed and space plasma physics must be based on a flow of knowledge from the laboratory. However, *in situ* measurements in the magnetospheres (including the heliosphere = the solar magnetosphere) has now reached such a sophistication that in some respects magnetospheric plasma physics is ahead of laboratory plasma physics.

Hence the exploration of astrophysical regions (defined as those regions not yet accessible to *in situ* measurements) must be based on a transfer of knowledge not only from laboratory physics but also from magnetospheric physics. Further, a transfer of knowledge from the magnetospheres to the laboratory may rejuvenate fusion research.

Magnetospheric research has demonstrated that there are plasma regions of two different kinds :

- passive plasma regions, which can be described by classical hydrodynamic theory. They transmit waves and high energy charged particles but if the field-aligned currents exceed a certain value they are transferred into.

- active plasma regions. These carry field-aligned currents which give them a filamentary or sheet structure with thickness down to a few cyclotron radii (ionic or even electronic). They transmit energy from one region to another and produce electric double layers which accelerate particles to high energies. Active regions cannot be described by hydromagnetic theories. Boundary conditions are essential and may be introduced by circuit theory. (Erroneous treatment of boundary conditions is often fatal in magnetic merging theories.)

Transfer of knowledge from the laboratory and the magnetospheres is now starting a revolution in astrophysics. For example the theory of formation of the solar system can be based on extrapolation of what is known from magnetospheric and laboratory plasma physics.

However, there are two kinds of astrophysically important plasmas which cannot yet be studied in the laboratory or in the magnetospheres : *dusty plasmas*, of importance in interstellar clouds, and *ambiplasmas* (consisting of both matter and antimatter), of importance in the cosmological discussion.

Introduction : The importance of translation. —

Translation is difficult. You realize this when you attend a meeting in English in a French-speaking country, especially if your mother tongue is neither English nor French. To use another great language for a moment, the Italians say : traduttore-traditore (a translator is a traitor). Also, the types of translation we shall discuss in this paper are not always exact.

In modern plasma physics translation is very important in several respects. Plasmas are studied

both in the laboratory and in space, and there are good reasons to believe that in several important respects the basic properties of laboratory plasmas and space plasmas are the same. But as the linear scale of laboratory experiments is — say — 10 cm, a scaling by a factor of 10^9 to 10^{12} is necessary in order to apply the laboratory results to planetary magnetospheres or to the solar magnetosphere (heliosphere or interplanetary space). Furthermore to apply the results to galactic and intergalactic — including cosmological — problems we have to

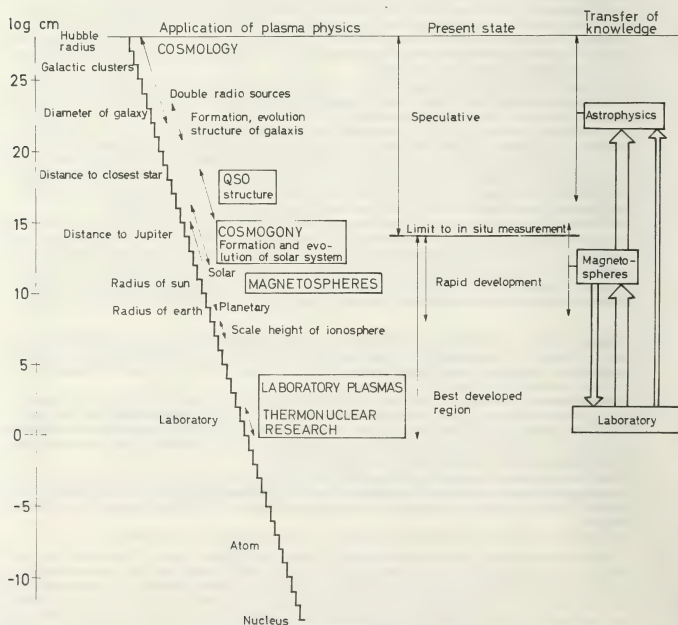


Fig. 1. — Plasmas in laboratory and in cosmos.

scale up by another factor of 10^9 to 10^{12} or more. As different plasma parameters obey different scaling laws, translation from one region to another is often difficult.

Figure 1 gives a survey of some important plasma phenomena. Probably several of them are closely related although a scaling by a very large factor is essential in order to realize this. Hence important progress in plasma physics can be expected if we succeed in unifying the different fields. However, this can only be done if we study the very difficult field of scaling plasma phenomena. Hence we shall devote § 2.1 to scaling laws.

There is another translation which also is very important : the translation between a *magnetic field description* and a *current description* of plasma phenomena. Space measurements of magnetic fields are relatively easy, whereas direct measurements of electric currents are very difficult, in many cases impossible. Hence it is natural to present the results of space exploration (by spacecrafts and by astrophysical observations) by pictures of the magnetic field configuration. Furthermore, in magnetohydrodynamic theories, it is convenient to eliminate the current (\mathbf{i} = current density) and represent electric currents by $\text{curl } \mathbf{B}$. This method is acceptable in the treatment of a number of phenomena (see Fig. 2).

However there are also a number of phenomena which cannot be treated in this way but require an approach in which the electric current is taken account of explicitly (see Fig. 2). The translation between the magnetic field description and the electric current description is made by the help of Maxwell's first equation

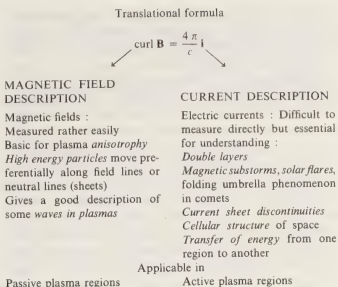
$$\text{curl } \mathbf{B} = \frac{4\pi}{c} \mathbf{i} + \frac{1}{c} \frac{\partial \mathbf{D}}{\partial t} \quad (1)$$

where the displacement current usually can be neglected.

As is shown in figure 2 some kinds of plasma phenomena should be described by the field picture and others by the current picture. Attempts to describe a certain group of phenomena with the wrong formalism often lead to erroneous results (see Alfvén, 1977a). We shall discuss this further in Part II.

1. Part I. Passive and active plasmas. — 1.1

EXPERIMENTAL AND THEORETICAL APPROACH TO PLASMA PHYSICS. — Plasma physics has started along two parallel lines. One is the hundred years old investigations in what was called *electrical discharges in gases*. To a high degree this approach was experimental and phenomenological, and only very slowly it reached some degree of theoretical sophistication. Most theoretical physicists looked down on this field, which was complicated and awkward. The plasma exhibited striations and double-layers, the electron distribution was sometimes very far from



The plasma dualism is somewhat analogous to the general particle-field dualism in physics.

The current description requires a new formalism with **ELECTRIC CIRCUITS** as an important ingredient. This is somewhat analogous to the necessity of introducing a new formalism when the importance of quantum phenomena was discovered.

Fig. 2. — Dualism in plasma physics.

Maxwellian, there were all sorts of oscillations and instabilities. In short, it was a field which was not at all suited for mathematically elegant theories.

The other approach came from the highly developed kinetic theory of ordinary gases. It was thought that with a limited amount of work this field could be extended to include also ionized gases. The theories were mathematically elegant and claimed to derive all the properties of a plasma from first principles. In reality this was not true. Because of the complexity of the problem a number of approximations were necessary which were not always appropriate. The theories had very little contact with experimental plasma physics, and all the awkward and complicated phenomena which had been observed in the study of discharges in gases were simply neglected.

In cosmic plasma physics the experimental approach was initiated by Birkeland, who was the first one to try to connect laboratory plasma physics and cosmic plasma physics. (Neither of the terms was used at that time !) Birkeland observed aurorae and magnetic storms in nature, and tried to understand them through his famous terrella experiment. He found that when his terrella was immersed in a plasma, luminous rings around the poles were produced (under certain conditions). Birkeland identified these rings with the auroral zones. As we know today, this was essentially correct. Further he constructed a model of the polar magnetic storms, supposing that the auroral electrojet was closed through vertical currents (along the magnetic field lines). This idea also is essentially correct. Hence although Birkeland

could not know very much about the complicated structure of the magnetosphere, research today follows essentially Birkeland's lines, of course supplemented by space measurements.

Unfortunately, the progress along these lines was disrupted. Theories about plasmas — at that time called ionized gases — were developed without any contact with the laboratory plasma work. In spite of this — or perhaps because of this — the belief in them was so strong that they were applied directly to space. One of the results was the Chapman-Ferraro theory, which soon got generally accepted to such an extent that Birkeland's approach was almost completely forgotten. For thirty or forty years it was often not even mentioned in text books and surveys, and all attempts to revive it and develop it were neglected.

1.1.1.1 *Confrontation between theory and experiments.* — The crushing victory of the theoretical approach over the experimental approach lasted as long as a confrontation with reality could be avoided. However, from the theoretical approach, it was concluded that plasmas could easily be confined in magnetic fields and heated to such temperatures as to make thermonuclear release of energy possible. When attempts were made to construct thermonuclear reactors, a confrontation between the theories and reality was unavoidable. The result was catastrophic. Although the theories were generally accepted the plasma itself refused to believe in them. Instead the plasma showed a large number of important effects, which were not included in the theory. It was slowly realized that one had to build up new theories but this time in close contact with experiments.

The thermonuclear crisis did not affect cosmic plasma physics very much. The development of the theories went on because they largely dealt with phenomena in regions of space where no real check was possible. The fact that the basis of several of the theories had been proved to be false in the laboratory had very little effect: one said that this did not necessarily prove that they must be false also in cosmos!

The second confrontation, however, came when space missions made the magnetosphere and interplanetary space accessible to physical instruments. The first results were interpreted in terms of the generally accepted theories, or new theories were built up on the same basis. However, when the observational technique became more advanced, it became obvious that these theories were not applicable. The plasma in space is just as complicated as laboratory plasmas.

A survey of what is known about the magnetospheric plasmas is given for example in a recent report from the Alpbach Symposium on *Magnetospheric Boundary Phenomena* (Battrick, 1979).

1.2 PRESENT STATE OF THE CLASSICAL THEORY. — The classical theory, the foundation of which is due to Chapman and Cowling, has been very successful in accounting for all those phenomena which according to figure 2 are related to the field description. The propagation of waves in plasmas belongs to this category, and so does the motion of high energy charged particles and the drift of low energy particles, including mirror effects. However, a real plasma has many properties which are not easy to describe by the classical formalism. Certainly it is possible to produce externally heated plasmas (e.g. cesium-plasmas) which are completely quiescent, and in these the classical formalism seems to give a good description. For references see for example Motley 1975.

However, as soon as an electric current is passed through the quiescent plasma a number of complicated phenomena are produced which require an extensive development of classical theory, sometimes even a new approach (Clark and Hamberger, 1979).

The most important of these *anomalous* properties are:

a) Sometimes the plasma becomes more *noisy* than expected theoretically, sometimes less.

b) The energy distribution becomes strongly *non-Maxwellian*; there is a considerable — sometimes very large — excess of high energy particles. The velocity distribution is very often highly anisotropic.

c) The electron temperature may be orders of magnitude larger than the ion temperature which may be considerably higher than the neutral gas temperature, which again may differ from the wall temperature or the temperature of the dust (in case the plasma is *dusty*).

1.2.1 *Instabilities.* — There are a very large number of phenomena which often are referred to as *instabilities*. Examples of such phenomena are:

d) At sufficiently large current density the plasma may contract into *filaments* (Marklund, 1978).

e) In case the plasma consists of a gas mixture, plasma phenomena often *separate* its components (Marklund, 1979).

f) When the electron drift velocity exceeds the thermal velocity, *double layers* may be produced (Torvén, 1978). Under certain conditions these may explode and produce violent current surges and lead to the acceleration of plasma particles, sometimes up to extremely high energies, even cosmic ray energies (Carlqvist, 1969, 1972, 1973).

g) It is also possible that at current densities above a certain limit the resistivity of the plasma increases by orders or magnitude (*anomalous resistivity*) but arguments for the occurrence of such a phenomenon are still not convincing. (In several cases the forma-

tion of double layers may have been interpreted as anomalous resistivity.)

h) When β (= the ratio between gas pressure and magnetostatic pressure) approaches unity, the geometrical confinement of a plasma may be deformed. The long list of such instabilities include the *kink instability*, and *sausage instability*.

1.3 BOUNDARY CONDITIONS. CIRCUIT DEPENDENCE.

— When applying the classical theory and its modern development, it is often not observed how important the boundary conditions are. Infinite plasma models or models with static boundary condition are often applied to problems with variable boundary conditions. This often gives completely erroneous results: In many theories it is taken for granted that the behaviour of a plasma depends *only* on the local parameters (e.g. density, temperature, magnetic field). This is often seriously misleading. As an example, in a non-curlfree (= current carrying) plasma the properties of the plasma are not only a function of the local parameters but also of the outer *circuit*, in which the current I closes. For references see Alfvén 1977a, Torvén 1978. Figure 3 shows how is a simple circuit, consisting of an electromotive force V , a resistor R and an inductance L . By changing R or/and L the behaviour of the plasma may be changed in a drastic way. The value of R decides whether the plasma is relatively stable or oscillating. If the plasma contains a double layer, which explodes, the circuit energy $\frac{1}{2}LI^2$ is released in this. Hence the violence of the plasma explosion is determined largely by the circuit.

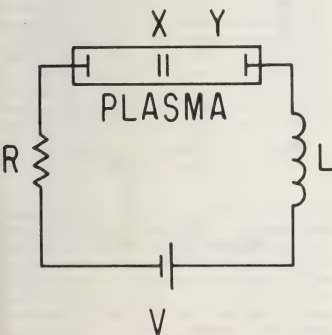


Fig. 3. — If a current flows in a plasma, the plasma phenomena depend partially on the outer circuit. If the resistance R is smaller than the negative resistance of the double layer X , the current becomes unstable.

The influence of the *circuit* is essential not only in a laboratory experiment but also in space. In this case the total volume in which the current flows affects the behaviour of the plasma in every point. In many cases it is convenient to introduce the boundary conditions by drawing an *equivalent circuit* (see 1.6).

1.4 TRANSLATION FROM MAGNETIC FIELDS INTO ELECTRIC CURRENT DESCRIPTION. — Hydromagnetic phenomena can be described either by using a magnetic field or an electric current picture. The translation is given by eq. (1).

Especially in plasma astrophysics the magnetic field description has been used almost exclusively and the current has not been given explicitly. This is dangerous because there are a number of current-dependent phenomena which cannot be accounted for and in several cases it leads to serious mistakes (see Alfvén, 1977a). Phenomena which cannot be understood without explicitly accounting for the current are:

- A) Energy transfer from one region to another.
- B) Formation of double layers (already mentioned under f)).
- C) The occurrence of explosive events such as solar flares, magnetic substorms, *folding umbrella* phenomenon in comets, and stellar flares.
- D) Double layer violation of the Ferraro corotation. Establishing *partial corotation* is essential for the understanding of some features of the solar system (Alfvén and Arrhenius, 1976).
- E) Formation of filaments in the aurora, the solar atmosphere and nebulae (already mentioned under d)) perhaps also in the Cytherean ionosphere (see Russell, Elphic and Slavin, 1979).
- F) Production of hydromagnetic waves (at least one mechanism which may be the most important one).
- G) Formation of current sheets which may give space a *cellular* structure and hence allow the existence of antimatter in the universe (Fälthammar, Akasofu and Alfvén, 1978).

1.5 DOUBLE LAYERS. — In a low density plasma localized space charge regions may build up large potential drops over distances of the order of some tens of the Debye length. Such regions have been called *electric double layers* since an electric double layer is the simplest space charge distribution that gives a potential drop in the layer and a vanishing electric field on each side of the layer. In the laboratory double layers have been studied for half a century, but their importance in cosmical plasmas has not been generally recognized until recently.

Recent reviews of the phenomenon include a general survey (Block, 1978) as well as separate

reviews of experiments (Torvén, 1978) and theory (Carlqvist, 1979). Recent experiments (Coakley *et al.*, 1979; Torvén and Andersson, 1979) have also demonstrated the existence of double layers in magnetized laboratory plasmas. Electric field measurements in satellite orbit have shown the existence of double layer structures above the auroral zone (Mozer *et al.*, 1977; Shawhan *et al.*, 1978).

A double layer can be formed in several ways. An important case is that a double layer is produced when the drift velocity of electrons exceed the thermal velocity.

If the plasma contains a double layer, a strong interaction with the external circuit (Fig. 3) can be produced, because the layer voltage can be strongly fluctuating (Torvén, 1978). *Exploding* double layers were first discovered in mercury rectifiers used in d.c. high power transmission circuits. The phenomenon is likely to be basic for the understanding of solar flares, magnetic substorms and related phenomena. Then the layer voltage is mainly given by $-L \, dI/dt$, which may exceed the normal double layer voltage V_0

by several orders of magnitude. The process may continue until I vanishes, and then the energy $\frac{1}{2} L I_0^2$ (I_0 is the initial current) has been released in the double layer, mainly in the form of kinetic energy of ions and electrons.

Measurements at a double layer in a magnetized laboratory plasma (Coakley *et al.*, 1979) show that the equipotential surfaces, which are perpendicular to the magnetic field in the layer, curve at the plasma boundary, where they become parallel to the magnetic field. In this way the plasmas on each side of the layer become surrounded by regions with a strong radial electric field, perpendicular to the magnetic field. This radial field is directed inward on the low potential side of the layer and outward on the high potential side. The situation resembles the situation when two cables are connected by a double layer.

1.6 FIELD ALIGNED CURRENTS AS CABLES. — The discovery that the aurora often is produced by highly anisotropic and almost monochromatic electrons is a strong indication of the existence of electrostatic

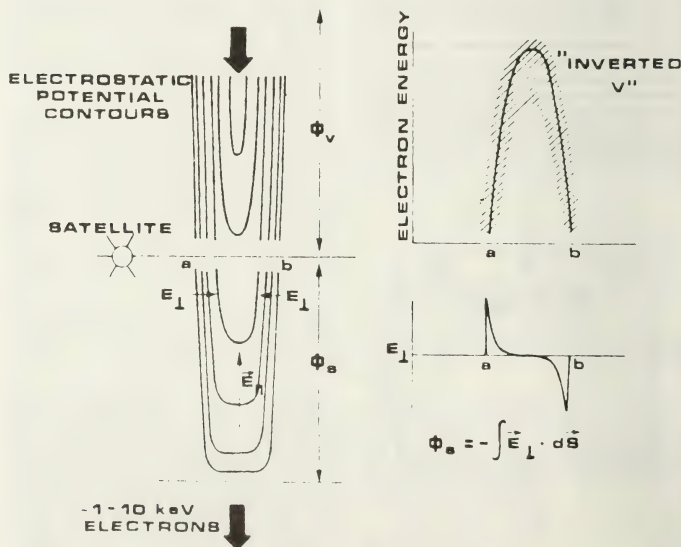


Fig. 4. — (Left) Electrostatic potential distribution according to Gurnett (1972). The magnetic field is vertical. The current-carrying flux tube is insulated from the surrounding plasma by a thin cylindrical shell of rotating plasma, which produces a voltage drop which equals the electrostatic drop in the layer. (Right) Observed inverted V events confirm the theory.

double layers in the lower magnetosphere. However the electron mirror effect is a competing mechanism for the electron acceleration (Block and Fälthammar, 1976; Fälthammar, 1977, 1978a, 1978b). It is also possible — as suggested by Lennartsson (1977) — that both mechanisms are combined, the mirror effect being the primary cause which gives rise to one or several double layers.

A double layer produces primarily equipotential surfaces perpendicular to the magnetic field. An important problem is how these continue. The inverted V events and the detection of very strong electric fields perpendicular to \mathbf{B} indicate a possible solution (see Fig. 4). A filamentary or sheet current in the auroral region is *insulated* by such electric fields from the surrounding plasma in which it produces a limited perturbation. There is a similarity with an electric cable in the ocean which carries a strong current in a low resistance metal wire. This is insulated from the conducting water surrounding it by a rubber cylinder, in which the electric field is similar to the radial electric field surrounding the field aligned current in the magnetosphere.

Laboratory plasma experiments have demonstrated a similar phenomenon (Coakley *et al.*, 1979). Often two *cables* are produced, one on each side of a double layer.

If we combine these results with the general tendency of field aligned currents to flow in filaments, we may conclude that *electric currents in plasmas have a tendency to flow in cables*. These are *insulated* from the surrounding plasma by sometimes very strong electric field in the same way as in underwater cables the electric conductor is insulated from the surrounding water. Hence a plasma cable may transfer power over large distances with a limited amount of perturbation of the surrounding plasma.

In the same way as two high power transmission cables connect a generator and a *consumer*, a pair of plasma cables may connect a generator and a *consumer*. The generator often consists of a plasma moving with a velocity component perpendicular to the magnetic field \mathbf{B} and hence generating an e.m.f.

$$V = \frac{1}{c} \int \mathbf{v} \times \mathbf{B} \, ds$$

where the integral is taken between the ends of the two cables. The consumer may be a double layer accelerating charged particles which later produce light or synchrotron radiation. The consumer may also be a *motor* putting plasma in motion in a distant region. As an example, in the auroral circuit the generator is located in the solar wind and the *consumers* are double layers accelerating high energy particles which later illuminate the night sky in the auroral zone, or a *motor* producing the sun-ward drift in the magnetosphere. (See Fig. 5 and cf. Alfvén, 1979a.)

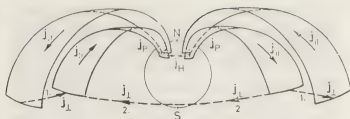


Fig. 5a. — Large-scale Birkeland current sheets shown schematically for a dipolar geometry with alternative closure paths for the lower latitude sheet currents.

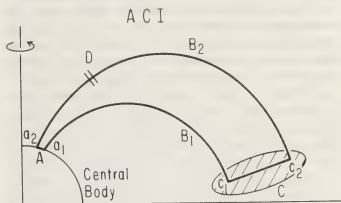


Fig. 5b. — Auroral Circuit I. Currents along the magnetic field lines B_1 and B_2 close through the upper atmosphere at A and through the magnetospheric plasma at C. The e.m.f. is produced by motion at A and C. The current may produce one or more electrostatic double layers D.

The tendency of electric currents to flow in cables makes the circuit approach a reasonable first approximation to many plasma problems.

1.7 DIFFERENT TYPES OF PLASMA REGIONS. — What has been said above might be summarized and elaborated in the following way: it seems that at least in low density cosmic plasmas there are three different types of regions.

1.8 « PASSIVE » PLASMA REGIONS. — These regions may transmit different kinds of plasma waves and flow of high energy particles. There may be transient currents perpendicular to the magnetic field changing the state of motion of the plasma but not necessarily associated with strong electric fields and currents parallel to the magnetic field. A plasma of this kind fills most of space.

If in an initially homogeneous plasma the parameters in one region are changed above a certain limit the plasma often reacts by setting up a discontinuous interphase. Instead of a continuous space variation of the parameters the plasma *prefers* to produce a discontinuity interphase separating two almost homogeneous regions. This may sometimes be the origin of *double layers*, taking up voltage differences, and *current sheets*, separating regions of different magnetization, temperature, and density.

1.9 « ACTIVE » PLASMA REGIONS. — Besides the passive plasma regions there are also small but very important regions where filamentary and sheet currents flow (Alfvén, 1977a). By transferring energy and producing sharp borders between different regions of passive plasmas, they are of decisive importance to the overall behaviour of plasmas in space. There are two different — but somewhat related — types of such regions which we shall call *plasma cables* and *boundary current sheets*.

1.9.1 *Plasma cables*. — Plasma cables seem to be reasonably stable formations which could be considered as entities which are important for the understanding of plasma phenomena. (Of course their interior structure should be described by classical theory.) The plasma cables are either filaments or *flattened filaments*, sheets with not very large extension. They carry an electric current parallel to the magnetic field, and this is the primary cause of their properties. They are often very efficient in transferring electromagnetic power from one region to another. The cables are embedded in passive plasmas, which have essentially the same properties in all directions around them. They are *insulated* from the surrounding by a thin cylindrical electrostatic sheath (or double layer) which reduces the interaction with the surrounding. In the magnetosphere and upper ionosphere the density in the cable is sometimes lower than in the surrounding (Block and Fälthammar, 1968). In other cases the density in the cable may be much larger than in the surrounding, because ionized matter is pumped into the cable from the surrounding (Marklund, 1979). By doing so selectively, the chemical composition in the cable may differ from that of its surrounding. Besides the cylindrical electrostatic sheath there are often longitudinal *double layers*, in which a considerable part of the power which the cable transmits may be converted into high energy particle energy. The double layers sometimes explode, and this produces excessively high energy particles (Carlqvist, 1978). Then the current in the cable may be disrupted and switched into another circuit (Boström, 1974, 1975). Such plasma cables have been discovered (or are likely to exist) in several places :

(a) *The auroral current system* consists of plasma cables, sometimes filaments — possibly associated with auroral rays — and more frequently sheets — possibly associated with auroral arcs. The inverted V events are likely to be produced by cables (Block, 1978). In the auroral zone such cables transfer energy from the equatorial plane to the auroral zone, and double layers are likely to be the direct cause of some types of luminous aurorae.

(b) *Solar prominences*. The electromotive force is due to motions in the photosphere in combination with the photospheric magnetic fields (Fig. 6). The prominences are often filaments but sometimes sheet-

like (quiescent prominences). Double layers are often produced, and when they explode, they cause solar flares. *Spicules* are probably small scale versions of the same phenomenon.

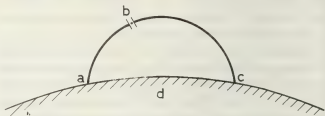


Fig. 6. — Prominence circuit consisting of a magnetic field tube abc and a subphotospheric connection cda. The

$$\text{e.m.f.} = \int_a^c \mathbf{v} \times \mathbf{B} \cdot d\mathbf{s}$$

is produced by motions with velocity \mathbf{v} in the presence of a solar magnetic field \mathbf{B} . It produces a current in the solar corona which collects matter from the surrounding (Marklund, 1978, 1979). If the current density exceeds a certain limit a double layer b is formed. If it explodes the inductive energy $\frac{1}{2} L I^2$ in the circuit is very rapidly released at the point of disruption. Note that the prominence circuit is a simplified version of the well-known auroral circuit, which makes it possible to construct it with a high degree of certainty.

(c) *Coronal streamers and polar plumes*. As we expect that the heliospheric large current system should connect with the sun in the polar regions and in the equatorial region, it seems likely that these

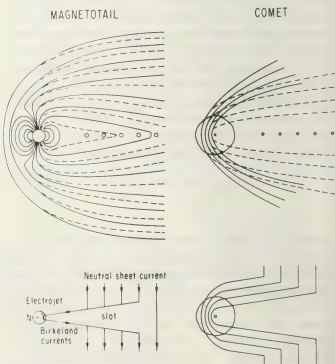


Fig. 7. — Similarity between the magnetosphere and a comet (Ip and Mendis, 1976). Current disruption which causes repetitive substorms in the magnetosphere also causes the *folding umbrella* phenomenon in comets, and simultaneous brightening of the coma.

phenomena are basically similar to the solar prominences. The main difference is that the prominences are produced in a photospheric circuit, whereas the streamers and plumes are caused by the large heliospheric current system.

(d) The filamentary structure in *cometary tails* (Mendis, 1978; see Fig. 7), and in *interstellar nebulae* may be caused in the same way. *Stellar flares* are probably due to the same mechanism as solar flares. It has also been suggested that the transfer of energy to the *double radio sources* from the galaxy which normally is located half the way between them is due to a plasma cable of this type (Alfvén, 1978a).

Filaments are more easily seen at large distances whereas sheets are more easily detected from spacecrafts.

1.9.2 Ionospheric projection of active and passive plasma regions.— The drastic difference between active and passive plasma regions is visualized by a look at the ionosphere. The auroral zones are those

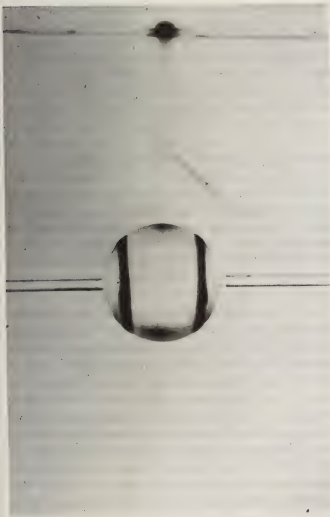


Fig. 8. — The auroral zones. If a terrella is placed in a plasma, the terrella is dark in the regions where the field lines connect with passive plasma regions (polar caps and low latitudes) but luminous in the regions which connect with active plasma regions (auroral ovals). The figure shows a modern version (Block, 1955) of Birkeland's experiment. Space photographs of the night side of the earth are similar (although usually perturbed locally).

regions of the ionosphere which connect magnetically to active regions in the magnetosphere. The rest of the ionosphere connects with passive plasma regions, and hence receives very little energy from above (Fig. 8).

It is tempting to identify the different auroral patterns with the different active structures in the magnetosphere: auroral rays may derive from active filaments, arcs from sheets, draperies from perturbed sheets. However there are quite a few rather complicated phenomena in the transitional region between the magnetosphere and the ionosphere. Further, there are horizontal currents in the upper ionosphere, which also may produce luminous effects. Hence the relation between the structure of the active plasma in the magnetosphere and the visually observed aurora is very complicated.

1.9.3 Boundary current sheets.— In striking contrast to the current layer we have discussed above, there is another type of current layers which form boundaries between two regions of plasma which have drastically different parameters. The basic difference is that the cables we have discussed carry such small currents that their magnetic field is small compared to the exterior field, whereas in the boundary current sheets the current is large enough to change the surrounding field very much. In the magnetosphere there are three such layers (see Alfvén, 1979a; Heikkilä, 1975; Heikkilä and Block, 1977):

The magnetopause, which often is a very thin current layer (a few cyclotron radii thick) and separates two regions with opposite magnetic fields (directed northward and southward), but with other parameters (pressure, density) not necessarily very different (Fig. 9).

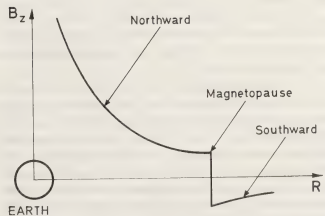


Fig. 9. — Magnetic field reversal in the magnetopause.

In many cases a spacecraft passing the region of the magnetopause observes more than one magnetic discontinuity. This is usually interpreted as an indication that the magnetopause moves very rapidly out and in. The data can probably also be interpreted as a *folding* of the magnetopause current layer. Auroral

draperies are often observed to fold so that they become S-shaped. This process may continue, resulting in a triple layer. Similarly the heliospheric boundary layer is known to be wavy. By analogy it is quite reasonable that the magnetospheric current layer is folded so that a spacecraft traverses it three times. A model of this has been given by Smith (1979). The current layer may be very thin (a few cyclotron radii) and need not necessarily move. *The neutral sheet in the tail* also separates two regions with opposite magnetic field (directed towards and away from the Earth). Other parameters are usually similar. It is believed that the magnetic field often has a small northward magnetic field superimposed.

Further there is a *current layer in the front* of the magnetopause which separates a region of very weak magnetic field in the solar wind from a much stronger field (three times or more) between the front current and the magnetopause. This current layer is usually referred to as the *bow shock*. It transforms a large part of the solar wind kinetic energy into electromagnetic energy (Alfvén, 1979).

In the *heliosphere* there is a very extended current layer in the *equatorial plane*, waving up and down, which separates an inward magnetic field from an outward directed field (Fig. 10) (Alfvén, 1977a; Akasofu, Lee and Gray, 1979).

Current layers similar to those in the magnetotail and heliosphere have also been discovered in the *Jovian magnetosphere* and in *other magnetospheres*, and theoretically inferred in the *tails of comets*.

The magnetotail current sheet is likely to produce explosive double layers (Carlqvist, 1978; Kan *et al.*, 1978) causing magnetic substorms, and the cometary current sheet probably does the same, causing the folding umbrella phenomenon (Mendis, 1978). Whether other current sheets have the same property is not known.

There are a number of theories of each of these current layers but unfortunately a general theory covering all these very important phenomena seems still to be lacking.

The discovery of these layers (the first one, the plasmopause, discovered by Cahill) looks to many as the most sensational of all space research discoveries (although Dungey (1961, 1964) had predicted them to some extent). No one had guessed that such current layers had such a remarkable stability. The existence of such layers change our views of the structure of space plasmas (Fälthammar *et al.*, 1978). As of course it is impossible to claim that such layers exist only in those regions where spacecrafts have made *in situ* measurements, we must drastically revise our views of the structure of space. The existence of such boundary layers are likely to lead to the conclusion that space everywhere (interstellar space and intergalactic space) has a *cellular structure*. We shall discuss the consequences of this later, especially in 2.5.1.

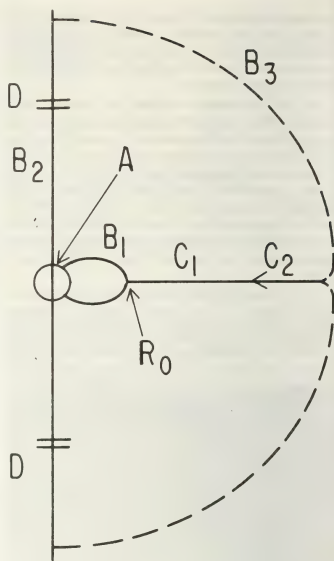


Fig. 10. — Heliospheric Circuit. The Sun acts as a unipolar inductor (A) producing a current which goes outwards along the axis (B_2) and inwards in the equatorial plane C_2 , C_1 and along the magnetic field lines B_1 . The current closes at large distances (B_3).

1.10 FINE STRUCTURE OF ACTIVE PLASMA REGIONS.

— It is a matter of controversy how thin the active plasma regions are. The auroral zone has an extension of a few degrees (= some 10^7 cm). However the thickness of an auroral arc or ray is often of the order 10^5 cm, sometimes perhaps even smaller. Measurements of the thickness of magnetopause current layers are often interpreted as indicating a thickness of a few orders of magnitude more than the ion cyclotron radius. However there are also many measurements giving thicknesses of only a few cyclotron radii. Hence active plasma regions may have a *fine* structure of the order of a few cyclotron radii which are the basic elements which determine the basic properties of active plasmas.

Solar prominences are supposed to be 10^8 or 10^9 cm in diameter, but in many cases a filamentary fine structure is observed in the prominence, indicating that the prominence should be considered as a *rope*

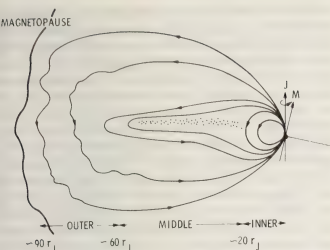


Fig. 11. — Jovian magnetosphere (Smith, 1979).

consisting of a multitude of small wires. It is possible that also the smallest observed filamentary structure in the sun (some 10^7 cm) consists of still smaller filaments, perhaps going down to 10^5 cm structures like those observed in the ionosphere.

Hence it seems doubtful whether a deeper understanding of the properties of a plasma is possible before we are able to study its fine structure. Hence the study of active plasma regions according to the principles we have discussed may very well be an important step forward but should not be regarded as the final step.

An important discovery of small scale current ropes (diameter 10^6 cm) was made recently by the Pioneer Venus Orbiter (Russel, Elphic, Slavin, 1979). The Cytherean ionosphere is penetrated by a large number of twisted magnetic filaments of the same kind as recently studied theoretically by Marklund (1978). They differ from the auroral rays of our ionosphere in the respect that they are magnetically contracted. It is possible that the observed phenomenon is the long sought-for filamentary structure which should be the basic constituent of filamentary currents in prominences, coronal streamers etc., perhaps also in cometary tails, and cosmic plasmas in general.

1.11 DISCUSSION : DUSTY PLASMA, AMBIPLASMA.

— We have here described three typical regions of plasma : *passive plasmas*, which seem to be the most common type in the magnetospheres of the planets and the sun, *cables* which are found in the auroral zones, and *boundary current sheets*, of which the magnetopause is the best studied example. However it is quite likely that there are many cases which are intermediate between these three types. A detailed analysis is needed before it is possible to decide this.

Another important fact is that cosmic plasmas very often are *dusty*. Interstellar clouds are typical examples. It is likely that the solar system was formed out of

such a cloud, which means that our solar system should be a product of the evolution of a dusty plasma (Alfvén and Carlqvist, 1978). Although the largest part of a dusty cloud consists of a *dusty passive plasma*, the small *dusty active plasma regions* are likely to be of decisive importance for the evolution of the cloud into a solar system.

As the dust particles usually are charged — especially in the active plasma regions — the motion of small dust grains (up to 10^{-3} cm or in certain cases even more) may be dominated by magnetic field, so that they constitute superheavy plasma particles. In the active plasma regions, where there are many high energy electrons, the grains may have high electrostatic potentials (1 000 V or more) so that they are more efficiently trapped.

As it seems possible that the universe is symmetric with respect to matter and antimatter, plasmas consisting of protons, antiprotons, electrons and positrons should also be investigated. The study of the evolution of such an *ambiplasma* is important for the cosmological discussion. See 2.5.1.

1.12 CHEMICAL DIFFERENTIATION IN A PLASMA. —

There are a number of plasma processes producing chemical differentiation (Arrhenius, 1976; Alfvén and Arrhenius, 1976). One important mechanism is the following. In a partially ionized plasma, the elements with low ionization potentials, which in general are the heavy elements, may be completely ionized, whereas the elements with high ionization potentials, such as H, O, and especially the noble gases, are completely non-ionized. As electromagnetic forces act exclusively on the former group, a chemical separation may be achieved.

Chemical separation in cosmic plasmas have actually been observed (Schoeler *et al.*, 1979). It seems likely that the mentioned process is responsible for the separation, but there seems also to be other separating processes.

Also, the dynamics of the dust in the plasma differs from the gas component, which means that the laws of motion of the chemical substances condensed as grain differs from the non-condensed components.

It has been claimed that a cosmic plasma necessarily must have a uniform chemical composition because of *turbulence*, and for a long time there has been a general belief that *cosmical abundances* of chemical elements could be defined which represent an invariable chemical composition of cosmic matter everywhere. This belief is now decisively contradicted by observations. In part it had originated because of a semantic mistake. When large non-thermal Doppler broadening was observed this was called *turbulence* and it was thought that a chemical mixing must take place. In reality the Doppler broadening can often be attributed to the passage through the plasma of non-mixing waves. As another example — if a spacecraft passes a region with *filamentary*

structure, it will register rapidly varying density and magnetic field, but it is misleading to call the region *turbulent* and conclude that chemical mixing takes place. Instead — as we have seen — in a region with filamentary structure chemical differentiation may take place.

2 Part II. Scaling and application. — 2.1 SCALING PROCEDURES. — As it is likely that the basic properties of a plasma are the same in the *laboratory*, the *magnetospheres*, and in more distant *astrophysical regions* a transfer of knowledge between these regions may help us to understand plasma phenomena.

The advance of thermonuclear research has resulted in a better knowledge of plasma phenomena in the laboratory, and much of this knowledge can be transferred to space problems. However thermonuclear investigations are increasingly focussed on those problems which are believed to be of technical interest, and they are not necessarily those which are most interesting in cosmical physics. Hence for the contact between the different fields of plasma physics, it is essential to make *laboratory experiments especially designed for simulation of cosmic problems*. A survey of such experiments has been given by Fälthammar (1974), and by Block (1976). Further it is now possible to make active experiments out in space. As Fälthammar summarizes it, this means that the era of active experiments in the magnetosphere may bring a new importance to space-related laboratory experiments. This is a consequence of the shift of emphasis from exploratory measurements in the early space age to an increasingly sophisticated physics-oriented effort. In such an effort, certain types of laboratory experiments can enhance the fruitfulness of the experiments in space by improving the understanding of basic plasma physical processes of importance in the space environment.

Laboratory experiments for studying space phenomena have traditionally been of a type which we may refer to as *configuration simulation*, i.e., they have aimed at simulating, if only in some limited sense, the actual configuration of a system (e.g., the whole magnetosphere) as well as some of the physical processes taking place within it. The basic difficulty in configuration simulation stems from the large scaling ratio. It puts very severe limits on the possibilities of scaling in a strict sense and necessitates compromises which lead to what may be called qualitative scaling. In spite of these constraints, interesting results have been achieved in a number of cases using model experiments of the terrella type. The magnetic neutral sheet in the nightside magnetosphere is such a system, for which interesting simulation experiments have been performed.

Another type of experiments, which should be considered, may be referred to as *process simulation*. The knowledge gained from direct observations in

space has shown that the real magnetospheric plasma behaves in a considerably more complicated way than the simple models of it that have been extensively used. This necessitated a new approach, where the actual behaviour of real plasmas had to be determined experimentally and accounted for, even where not well understood theoretically. In the case of the magnetosphere, it is more difficult, and in some cases impossible, to make a corresponding consolidation of the experimental basis. Usually, measurements can be made only at a single point at a time, and in an orbit-governed time-space sequence, which is often far from optimum. Even within these limits, the costs of space missions imposes further serious constraints. The advent of active experiments in space is one important step towards a better understanding of the real space plasma. However, the fruitfulness of this activity should be greatly enhanced if combined with suitably designed laboratory experiments. Such experiments need not necessarily simulate the actual configuration of a phenomenon in space, but they should adequately simulate the plasma physical process in question (e.g. collisionless resistivity). We may refer to simulation of this kind as *process simulation*. In many cases this involves simulating only the local behaviour of a plasma, and then the problem of huge scaling factors disappears.

The relevance of laboratory plasma experiments is not limited to simulation. In the past, essential concepts such as Birkeland currents, electric fields along magnetic field lines, electrostatic particle acceleration, and the role of current filamentation and non-homogeneity in general were conceived as a result of close contacts with laboratory plasma experience in general. In the future, too, it can be expected that progress in space plasma physics can benefit from laboratory plasma experiments in a much broader sense than that of simulation (Fälthammar, 1974).

Experiments have been made by Podgorny and Sagdeev (1970), Podgorny (1976) and by Danielsson and Lindberg (1964, 1965).

Theoretical laws for scaling are well-known since long ago (summarized e.g. in Alfvén and Fälthammar, 1963). A recent detailed survey is given by Siscoe (1979). However it should be remembered that scaling laws depend on a theoretical formalism which probably is applicable to passive plasmas, but it has not yet been clarified how a scaling between active plasma regions should be made.

Predictions of what could be expected at the first space mission to a planet have so far not been very successful.

(Traduttore-traditore !) The predictions are of course based on generally accepted theories, and almost every new space mission has demonstrated that our understanding of space plasmas is still not very good.

2.2 CURRENT MODELS. — As pointed out in 1.4 a systematic translation from the usual magnetic field models to electric current models should be made. We shall here discuss a few attempts to such translation, which demonstrate what new aspects can be obtained from current models.

2.2.1 *Auroral circuit.* — Zmuda and Armstrong (1974) made magnetic field observations in the auroral region, and derived the electric current system from these, which was also discussed by Rostoker and Boström (1976). A simplified model is shown in figure 5. The electromotive force is produced by the sunward convection in the equatorial plane. A current flows in the circuit $C_1 B_1 A_1 A_2 B_2 C_2$ and transfers power to a double layer D, which accelerates charged particles. The circuit describes the conversion of (1) kinetic energy (of the convection) into (2) electromagnetic energy (of the circuit), further into (3) electrostatic energy (in the double layer) and into (4) kinetic energy of beams of particles, and finally into (5) light and ionisation (in the auroral ionosphere). (See Alfvén, 1977a.)

2.2.2 *Heliospheric circuit.* — The magnetic data from space measurements in the solar wind can be used for construction of the heliographic circuit (Alfvén, 1977a). The result is shown in figure 10. The translation alone leads to the following conclusions :

- (a) There must be essentially radial currents of 1.5×10^9 A in each of the polar regions of the sun.
- (b) The currents must close through the sun, which acts as an unipolar generator which excites the circuit.
- (c) Coronal streamers and polar plumes are likely to be filaments produced by the current system.

A more detailed analysis of the circuit, including a computer model of heliospheric currents and magnetic fields has been done by Akasofu, Lee and Gray (1979).

2.2.3 *Magnetospheric circuit.* — Because of the complicated geometry of the magnetosphere, a direct construction of a current model of the magnetosphere

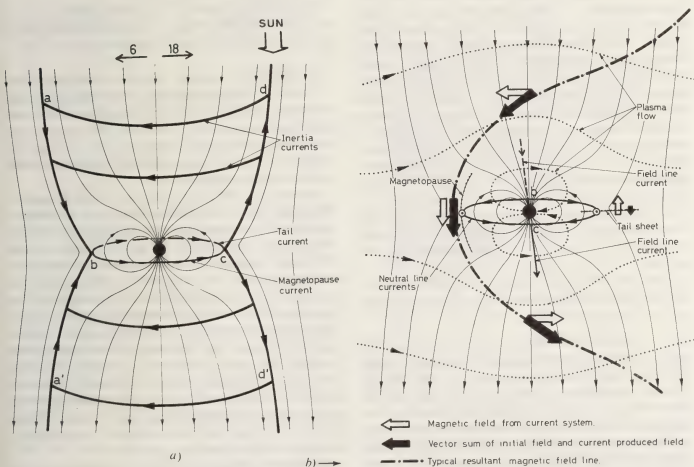


Fig. 12. — Because the magnetospheric circuit has a more complicated geometry than the auroral circuit or the heliospheric circuit, it is more difficult to construct it. Figure 12a shows a first approximation in which the magnetic field consists of the earth's dipole field and a homogeneous southward interplanetary field. The solar wind produces an electromotive force, which gives rise to the current system shown in the figure (seen from the sun). If the magnetic field from this current is added to the first approximation field a second approximation field is obtained (Fig. 12b), which gives the shape of a typical magnetic field line (---), the magnetopause (.....) and the tail sheet (.....). Also the bow shock is derived (not shown in the figure). The current system transfers the kinetic energy of the solar wind to the auroral circuit (which is a part of the large scale circuit) where it produces high energy particles and ultimately ionisation and light in the auroral ionosphere.

is difficult. An attempt has been made to reach such a model by successive approximations (Alfvén and Fälthammar, 1971; Alfvén, 1979). Figure 12a shows the first approximation in which the magnetic field is supposed to be a dipole field superimposed by a southward interplanetary field. The solar wind produces an e.m.f. which gives rise to the current system of figure 12a. If the magnetic field from this is added to the original field we obtain a second approximation (Fig. 12b). The model describes the structure of the magnetopause, the tail current sheet, and the general shape of the magnetic field lines.

Especially important is that the energy transfer from the solar wind to the magnetopause turns out to be a straight-forward and simple process. Further, the auroral circuit of 2.2.1 is part of the circuit, and so is Boström's model of magnetic substorms which can be explained by an exploding double layer formed in the tail current sheet. (*Magnetic merging* theories of magnetic substorms are likely to be erroneous because of neglect of the boundary conditions, see 1.3 and Heikkilä, 1978a, b and Heikkilä and Block, 1977.)

2.2.4 Current systems of Jupiter, comets and other magnetospheres. — The conditions in the Jovian magnetosphere are not yet very well clarified. Preliminary results from Pioneer 10 and 11 indicate that the Jovian magnetosphere in some respects is more similar to the heliosphere than the terrestrial magnetosphere. The magnetic field close to Jupiter is a dipole field, but further out there is a strong current in the equatorial plane which to some extent is similar to the heliospheric current in the equatorial plane (Smith, 1979, see Fig. 11). However, the strong asymmetry of the Jovian field and the presence of Io makes the conditions highly asymmetric (Dessler, 1979).

A possible current system in cometary tails has been constructed by Mendis (1978), but unfortunately *in situ* measurements of cometary plasmas are still lacking.

Space measurements from some other magnetospheres may allow the construction of current systems (see i.e. Dolginov, 1978).

2.2.5 Solar prominence circuit. — As the sun is still outside the reach of spacecrafts, a detailed diagnostics of solar plasmas is impossible, and theories of solar phenomena will necessarily remain speculative. However we have enough solar observations to be able to extrapolate our knowledge of carefully investigated space plasmas with a rather good confidence (Alfvén, 1977a).

Hence we conclude that a solar prominence is due to a current in a circuit similar to the auroral circuit but simpler: it consists of a magnetic flux tube intersecting the solar surface in two points, and a photospheric or subphoto-spheric connection between these points. The electromotive force is produced, by motions in the photosphere in the presence of magnetic

fields. The size of a prominence circuit is comparable to that of the auroral circuit, but the currents are much larger ($\sim 10^{12}$ A) because of the higher conductivity (the high resistivity in the upper ionosphere is replaced by a low resistivity due to the high temperature).

Like in the auroral circuit a double layer may be produced. The auroral double layer is often rapidly fluctuating, giving rise to the rapid variability of auroral phenomena. The prominence double layer is still more variable; indeed it can explode, producing solar flares. A quantitatively consistent theory of solar flares as due to such a current disruption has been worked out by Carlqvist (1969).

Much work has been spent on attempts to explain solar flares by a magnetic field formalism. (A survey is given by Heyvaerts in his lecture at this conference.) For reasons given in the introduction and in 1.4 (cf. Fig. 2) this is inadequate. More specifically, in the magnetic merging theories of solar flares the boundary conditions are not correctly introduced and hence these theories cannot explain the rapid concentration of the inductive energy of the whole circuit to the point of disruption.

2.2.6 Possible scaling to galactic dimensions. — An attempt has been made to scale up the heliospheric current system to galactic dimensions (see 2.5.4).

2.3 ROTATING MAGNETIZED BODY SURROUNDED BY A PLASMA. — A basic problem in astrophysics is the interaction between a rotating magnetized body and a surrounding plasma. (The body has of course a gravitational field.) The simplest case is when the magnetization is homogeneous and parallel (or antiparallel) to the rotational axis.

In the idealized case when only hydromagnetic effects are active, the plasma will attain a Ferraro corotation. However, this is unrealistic for a number of reasons. There is always an outer limit to the corotation because of the limitations of the surrounding plasma. In the case of the Earth the synchronous radius is comparable with the limits of the magnetosphere, outside which we cannot expect corotation. Even closer to the dipole there is a general sunward plasma drift, showing that the corotation is restricted to the plasmasphere. Further out the difference in angular velocity necessarily produces an e.m.f. (which tends to establish corotation) but this is taken up by electrostatic double layers. Hence the double layers produce a *decoupling* which allows a violation of the Ferraro theorem.

In the solar magnetosphere (= heliosphere or interplanetary space) the solar wind prevents the establishment of a corotation. Instead a thin current sheet in the equatorial plane is generated. The heliospheric current system has been discussed in 2.2.2. The knowledge we can gain from studying the transfer of angular momentum to a surrounding plasma should serve as a basis for the approach to the *cos-*

mogonic problem how the sun transferred angular momentum to the planets when they were formed and how the planets did the same to their satellite systems. The main difference from the present state is that the plasma density in the surrounding is likely to be much larger. The currents which would be required to establish a Ferraro corotation are so large that they are likely to produce double layers which decouple the surrounding plasma to a certain degree. The state which we should expect (*partial corotation of free-wheeling plasma*) is given by an equilibrium between the gravitation and centrifugal force which because of the geometry of the magnetic field should give the plasma an angular velocity of $(2/3)^{1/2}$ of the Kepler velocity (see Alfvén and Arrhenius, 1976).

Similar phenomena may be decisive for the evolution of galaxies. The angular momentum of the interstellar medium may be transferred to the intergalactic medium, and its kinetic energy transmitted in plasma cables to the surrounding (Alfvén, 1978a). See 2.5.4.

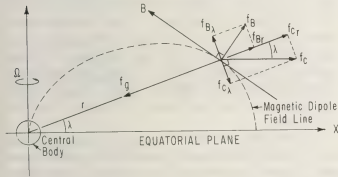


Fig. 13. — Partial corotation.

2.4 APPLICATION TO COSMOGONY. — Plasma phenomena were of decisive importance at the origin of the solar system and at the early phases of its evolution. The present chemical and dynamical structure of the planetary and satellite systems is to a large extent a product of such plasma processes.

There are good reasons for believing that the solar system originated from a primeval solar nebula which may have had a very low but certainly not negligible degree of ionization. It is likely to have had a structure which is normal to what all cosmic plasmas seem to have according to Part I; most of its volume was filled by a *passive* plasma which probably was very cool (perhaps 50 K) and very dusty. This was interlaced by a network of *active* plasma regions: current carrying filaments and sheets, which were energized ultimately from the gravitational energy released when the nebula contracted. Their activity was of decisive importance to the dynamical and chemical evolution of the cloud.

There seems to have been three plasma processes which have been important for the present structure of the solar system.

2.4.1 Chemical differentiation at the early phases. This has been discussed in 1.12.

2.4.2 Critical velocity. — A very pronounced feature of the solar system is its *band structure* (Fig. 14). For a number of reasons it seemed likely that this was produced when clouds with different chemical composition fell in towards a central body (sun or planet) and were stopped when they reached a certain *critical velocity* given by

$$v_{crit} = \left(\frac{2 e V_{ion}}{m_a} \right)^{1/2}$$

(V_{ion} = ionization potential, m = atomic mass).

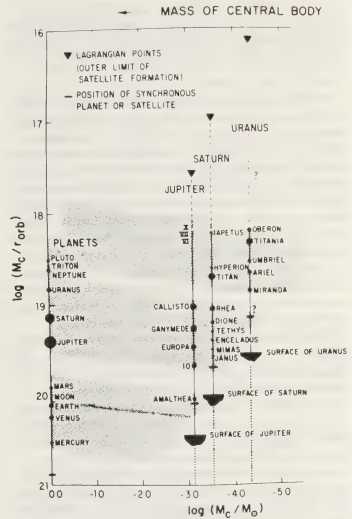


Fig. 14. — Band structure of Solar System.

This theoretical conjecture lacked empirical support, but as soon as the thermonuclear plasma technique became available, experiments were started in order to investigate the theoretically predicted phenomenon. The experiments confirmed the theoretical predictions and led to the discovery of a sharp — actually unexpectedly sharp — limit, given by eq. (2), for the relative velocity between a neutral gas and a magnetized plasma.

The critical velocity has now been subject to extensive experimental and theoretical investigations for

20 years (Danielsson, 1973; Sherman, 1973; Himmel *et al.*, 1973, 1976, 1977; Danielsson and Brenning, 1975; Axnäs, 1978; Raadu, 1978; Piel *et al.*, 1978; Petelski, 1978). It is an example of a plasma phenomenon which was predicted on the basis of a cosmogonic theory which initially was considered to be rather speculative.

There is not yet any unquestionable experimental demonstration of the critical velocity under present cosmical conditions but there are some indications that it has been observed (Srňka, 1977). Experiments to demonstrate the critical velocity under cosmical conditions have been suggested by Möbius, Boswell, Piel and Henry (1979).

2.4.3 Transfer of angular momentum and partial rotation. — This is the third plasma phenomenon which probably was of decisive importance for giving our solar system its present structure. See 2.3.

2.5 COSMOLOGICAL APPLICATIONS. — 2.5.1 Cellular structure of space and the existence of antimatter.

— A basic cosmological problem is whether the Universe is symmetric with regard to matter-antimatter. As long as the interstellar (and intergalactic) medium was considered to be homogeneous, it was rather difficult to accept the existence of antimatter, because matter and antimatter could not be mixed but must occupy different regions. Theoretically this is possible if there are *Leidenfrost layers* separating regions of antimatter from regions of koinomatter (= ordinary matter). A model of such layers was worked out (Lehnert, 1977, 1978). However, it was not obvious whether such a layer was stable.

The discovery of the cellular structure of space plasmas has drastically changed the situation. We know now that in the magnetospheres there are stable current sheets, separating plasma regions with different magnetization, temperature, density, etc. It is easy to imagine that in principle similar sheets might separate regions of different kinds of matter as shown by Lehnert (1976, 1977).

A Leidenfrost sheet must be surrounded on both the koino- and antimatter side by fully ionized layers, but these are not necessarily more than about one mean free path thick. At that distance there could very well be a sudden transition to a plasma with very low ionization. Such abrupt transitions are often observed in plasma experiments and are well understood theoretically (Lehnert, 1976).

Hence a region of passive koinoplasma and a region of passive antiplasma could coexist close to each other and a cosmically very thin and unnoticable layer of active plasma will separate them.

2.5.2 Properties of an ambiplasma. — The possible existence of antimatter makes the theoretical study of an *ambiplasma* (consisting of a mixture of koinomatter and antimatter) a challenging problem. The plasma should consist not only of protons and

antiprotons but also of high energy (10^8 eV) electrons and positrons.

A thorough analysis of the properties of an ambiplasma (separation of matter and antimatter, production of Leidenfrost-layers, energy release and radiation, etc.) is essential for a deeper understanding of a symmetric Universe.

2.5.3 Theory of QSOs. — The enormous energy release in QSOs is one of the headaches in modern astrophysics and a serious difficulty to the Big-Bang hypothesis. As the energy release is much larger than what can reasonably be supplied by nuclear reactions, there are only two energy sources left, viz. gravitation (*black holes*) and annihilation. For a number of reasons the latter alternative seems to be preferable (Alfvén, 1979a, b).

2.5.4 Double radio sources. — As one more example of the transfer of knowledge to astrophysics from magnetospheric and laboratory investigations we should mention the problem of double radio sources. The strong synchrotron emission from the pair may either originate from a *hidden* energy source in each of the sources — but no such source has been found — or derive from the galaxy often located exactly half way between the sources — which is more reasonable. However, the mechanism of transfer of energy has been a riddle. Theories about ejection of clouds have met a number of serious difficulties.

It seems that transfer of energy by electric currents of the type we are familiar with in the auroral region may give a solution of this problem. This means that the circuit transferring energy from a generator to a double layer in the laboratory, when scaled up by a linear factor of 10^9 explains the transfer of energy to the auroral double layers, and when scaled up again by a similar very large factor may account for the energy transfer to double radio sources (Alfvén, 1978a) (Fig. 15).

2.6 TRANSFER OF KNOWLEDGE FROM MAGNETOSPHERIC PLASMAS TO LABORATORY PLASMAS. — Thermonuclear research derives its origin from a transfer of knowledge — or at least inspiration — from cosmical physics. Names like *stellarator* and *astron* testify this. Laboratory physics has generously paid back this debt by introducing new concepts like double layers, current disruption and critical velocity into cosmical physics. Also the current description and the use of circuit diagrams for representing cosmical phenomena of course originate from the laboratory. The rapid development of very sophisticated diagnostics in magnetospheric research may lead us to expect that a transfer of knowledge from cosmical physics to laboratory physics may be fruitful.

Of special interest is that the stability problem which is a major obstacle in thermonuclear research, seems not to be so serious in cosmical physics. Compli-

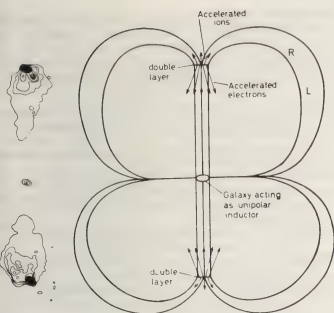


Fig. 15. — Galactic circuit extrapolated from heliospheric circuit. Radio astronomic observations by Current 10^{17} A and double layer voltage 10^{18} V.

cated plasma configurations, like solar prominences, coronal streamers, and the magnetopause seem to be so long-lived that one would guess that they represent stable, or at least semi-stable, configurations.

This may inspire thermonuclear research to consider new approaches to the thermonuclear problem. Further, there are a number of plasma phenomena which are nowadays more easily studied in space than in the laboratory. For example, transients with the electron gyro frequency in a cosmic plasma of 10^{-4} G have a time constant of 10^{-2} s, which is easily measurable — whereas in a thermonuclear plasma of 10^4 G it is 10^{-10} s, far below what can be measured in a comfortable way.

So this shows again how important it is to integrate the different domains of plasma physics.

Acknowledgments. — This paper was written during my stay at the Royal Institute of Technology with kind support by the chairman of the Department of Plasma Physics, Professor C.-G. Fälthammar. It is a result of numerous discussions with him and with a number of other members of the Department, especially Drs L. Block, P. Carlqvist, L. Lindberg, M. Raadu and S. Torvén. I have also profited from discussions with Professor B. Lehnert and Drs B. Bonnevier and D. Ohlson of the Department of Plasma Physics and Fusion Research. Mrs K. Vikbladh, E. Florman, K. Forsberg and S. Lilliesköld have kindly helped me with the editing.

References

- AKASOFU, S.-I., What is a Magnetospheric Substorm? *Space Sci. Revs.* for the Chapman Conference, 1979.
- AKASOFU, S.-I., LEE, L. C. and GRAY, P. C., A Model of the Interplanetary Magnetic Field Configuration (private communication) 1979.
- ALFVÉN, H., Electric Current Structure of the Magnetosphere. In *Physics of the Hot Plasma in the Magnetosphere*, B. Hultqvist and L. Stenflo, Ed. (Plenum Publ. Co, New York) 1975a.
- ALFVÉN, H., Relations between Cosmic and Laboratory Plasma Physics, *Ann. of the New York Academy of Sci.* **257** (1975b) 179.
- ALFVÉN, H., Electric Currents in Cosmic Plasmas, *Rev. of Geophys. and Space Phys.* **15** (1977a) n° 3.
- ALFVÉN, H., Is the Universe Matter-Antimatter Symmetric? *Antinucleon-Nucleon Interactions*, Wenner-Gren Volume 29, G. Eksping and S. Nilsson, Ed. (Pergamon Press, Oxford and New York) 1977b.
- ALFVÉN, H., Double Radio Sources, *Astrophys. Sp. Sci.* **54** (1978a) 279.
- ALFVÉN, H., The Band Structure of the Solar System. In *The Origin of the Solar System*, S. F. Dermott, Ed. (J. Wiley, New York), 1978b.
- ALFVÉN, H., Electric Current Model of Magnetosphere, TRITA-EPP-79-09, Royal Inst. of Technology, Stockholm and in Proceedings of the Chapman Conference on Magnetospheric Boundary Layers, Alpbach June 11-15, 1979 (to be published by European Space Agency), 1979a.
- ALFVÉN, H., Annihilation Model of the QSOs, TRITA-EPP-79-08, Royal Inst. of Technology, Stockholm (to be published in *Astrophys. Space Sci.*) 1979b.
- ALFVÉN, H. and ARRHENIUS, G., Evolution of the Solar System, NASA SP-345, Washington D.C., 1976.
- ALFVÉN, H., ARRHENIUS, G. and MENDIS, D. A., The Role of Plasma in the Primeval Nebula. In *Comets, Asteroids, Meteorites, Interrelations, Evolution and Origins*, Proc. 39th Int. Coll. IAU, Lyon, France 1976, Univ. of Toledo, Ohio, USA 1977, 1976.
- ALFVÉN, H. and CARLQVIST, P., Interstellar Clouds and the Formation of Stars, *Astrophys. Space Sci.* **55** (1978) 487.
- ALFVÉN, H. and FÄLTHAMMAR, C.-G., *Cosmical Electrodynamics*, Int. Series of Monographs on Physics (Clarendon Press, Oxford), 1963.
- ALFVÉN, H. and FÄLTHAMMAR, C.-G., A New Approach to the Theory of the Magnetosphere, *Cosmic Electrodynamics* **2** (1971) 78.
- ARRHENIUS, G., Chemical Aspects of the Formation of the Solar System. In *Origin of the Solar System*, S. F. Dermott, Ed. (J. Wiley, New York), 1976, p. 522.
- AXNÄS, I., Experimental Investigations of the Critical Ionization Velocity in Gas Mixtures, *Astrophys. Space Sci.* **55** (1978a) 139.
- AXNÄS, I., Experimental Comparison of the Critical Ionization Velocity in Atomic and Molecular Gases, TRITA-EPP-78-04, Royal Inst. of Technology, Stockholm, 1978b.
- BATTRICK, B., Proc. of the Chapman Conference on Magnetospheric Boundary Layers, Alpbach, June 11-15, 1979 (to be published by European Space Agency), 1979.
- BLOCK, L. P., Interpretation of Laboratory Experiments of Interest to Space Physics. Proc. AGU Int. Symp. on Solar-Terrestrial Phys., Boulder, Col., 1976, D. J. Williams, Ed. (Am. Geophys. Union), 1976, p. 255.

- BLOCK, L. P., A Double Layer Review, *Astrophys. Space Sci.* **55** (1978) 59.
- BLOCK, L. P. and FALTHAMMAR, C.-G., Effects of Field-Aligned Currents on the Structure of the Ionosphere, *J. Geophys. Res.* **73** (1968) 4807.
- BLOCK, L. P. and FALTHAMMAR, C.-G., Mechanisms that May Support Magnetic-Field-Aligned Electric Fields in the Magnetosphere, *Ann. Geophys.* **32** (1976) 161.
- BOSTRÖM, R., Ionosphere-Magnetosphere Coupling. In *Magnetospheric Physics*, B. M. McCormac, Ed. (D. Reidel Publ. Co, Dordrecht, Holland), 1974, p. 45.
- BOSTRÖM, R., Mechanisms for Driving Birkeland Currents. In *Physics of the Hot Plasma in the Magnetosphere*, B. Hultqvist and L. Stenflo, Ed. (Plenum Press, New York), 1975.
- CARLQVIST, P., Current Limitation and Solar Flares, *Solar Physics* **7** (1969) 377.
- CARLQVIST, P., On the Formation of Double Layers in Plasmas, *Cosmic Electrodynamics* **3** (1972) 377.
- CARLQVIST, P., Double Layers and Two-Stream Instability in the Solar Flares, TRITA-EPP-73-05, Royal Inst. of Technology, Stockholm, 1973.
- CARLQVIST, P., Some Theoretical Aspects of Electrostatic Double Layers, TRITA-EPP-78-15, Royal Inst. of Technology, Stockholm (to be published in Wave Instabilities in Space Plasmas, URSI XIX General Assembly, Astrophys. Space Science Book Series (Reidel Publ. Co.), 1979) 1978.
- CLARK, W. H. M. and HAMBERGER, S. M., Anomalous Conductivity and Electron Heating in a Plasma Unstable to the Two-Stream Instability, CLM-P531, Culham Lab., Abingdon, Oxfordshire, England, 1979.
- COAKLEY, P., JOHNSON, L. and HERSHKOWITZ, N., Strong Laboratory Double Layers in the Presence of a Magnetic Field, *Phys. Lett.* **70A** (1979) 425.
- DANIELSSON, L., Review of the Critical Velocity of Gas-Plasma Interaction. I : Experimental Observations, *Astrophys. Space Sci.* **24** (1973) 459.
- DANIELSSON, L. and BRENNING, N., Experiment on the Interaction between a Plasma and a Neutral Gas II, *Phys. Fluids* **18** (1975) 661.
- DANIELSSON, L. and LINDBERG, L., Plasma Flow through a Magnetic Dipole Field, *Phys. Fluids* **7** (1964) 1878.
- DANIELSSON, L. and LINDBERG, L., Experimental Study of the Flow of a Magnetized Plasma through a Magnetic Dipole Field, *Arkiv för Fysik* **28** (1965) 1.
- DESSLER, A. J., Comparison of Voyager Flyby Data with the Magnetic-Anomaly Model of Jupiter-Magnetopause Effects. Proc. of the Chapman Conference on Magnetospheric Boundary Layers, Alpbach, June 11-15, 1979 (to be published by European Space Agency), 1979.
- DOLGINOV, S. S., Magnetic Fields in the Vicinity of Venus According to «Venera» and «Mariner» Data, report presented at the Symp. on the Origin of Planetary Magnetism, Houston, Texas, USA, Nov. 8-11, 1978.
- DUNGEY, J. W., Interplanetary Magnetic Field and the Auroral Zones, *Phys. Rev. Lett.* **6** (1961) 47.
- DUNGEY, J. W., Null points in Space Plasma. In Proc. Plasma Space Sci. Symp., C. C. Chang and S. S. Huang, Ed. (D. Reidel Publ. Co, Dordrecht, Holland), 1965.
- EATHER, R. H., MENDE, S. B. and WEBER, E. J., Cusp Aurora and Substorm Current Systems. Proc. of the Chapman Conference on Magnetospheric Boundary Layers, Alpbach, June 11-15, 1979 (to be published by European Space Agency), 1979.
- FALTHAMMAR, C.-G., Laboratory Experiments of Magnetospheric Interest, *Space Sci. Rev.* **15** (1974) 803.
- FALTHAMMAR, C.-G., Problems Related to Macroscopic Electric Fields in the Magnetosphere, *Rev. Geophys. and Space Phys.* **15** (1977) no 4, 457.
- FALTHAMMAR, C.-G., Generation Mechanisms for Magnetic-Field-Aligned Electric Fields in the Magnetosphere, *J. Geomag. Geoelectr.* **30** (1978a) 419.
- FALTHAMMAR, C.-G., Non-Resistive Electric Potential Drops in Cosmical Plasmas, TRITA-EPP-78-17, Royal Inst. of Technology Stockholm, 1978b.
- FALTHAMMAR, C.-G., AKASOFU, S.-I. and ALFVÉN, H., The Significance of Magnetospheric Research for Progress in Astrophysics, *Nature* **275** (1978) 185.
- GURNETT, D. A., Electric Field and Plasma Observations in the Magnetosphere. In *Critical Problems of Magnetospheric Physics*, E. R. Dyer, Ed., p. 123, Inter-Union Committee on Solar-Terrestrial Physics, National Academy of Sciences, Washington, D.C., USA, 1972.
- HEIKKILÄ, W. J., Magnetospheric Plasma Regions and Boundaries. In *Physics of the Hot Plasma in the Magnetosphere*, B. Hultqvist and L. Stenflo, Ed. (Plenum Publ. Co, New York), 1975.
- HEIKKILÄ, W. J., Criticism of Reconnection Models of the Magnetosphere, *Planet. Space Sci.* **26** (1978a) 121.
- HEIKKILÄ, W. J., Electric Field Topology Near the Dayside Magnetopause, *J. Geophys. Res.* **83** (1978b) 1071.
- HEIKKILÄ, W. J., BLOCK, L. P., Review of Magnetospheric Boundary Layer Phenomena and Relations to Current Theories, *Geophysica*, **14** : 2 (1977).
- HIMMEL, G. and PIEL, A., The Velocity Limitation in a Rotating Plasma Device of the Homopolar Type, *J. Phys. D : Appl. Phys.* **6** (1973).
- HIMMEL, G., MOBIUS, E. and PIEL, A., Investigation of the Structure and the Plasma Parameters in a Critical Velocity Rotating Plasma, *Z. Naturforsch.* **31a** (1976) 934.
- HIMMEL, G., MOBIUS, E. and PIEL, A., Investigation of Particle Velocities in a Critical Velocity Rotating Plasma, *Z. Naturforsch.* **32a** (1977) 577.
- KAN, J. R., AKASOFU, S.-I. and LEE, L. C., Physical Processes for the Onset of Magnetospheric Substorms, *Space Sci. Rev.*, for the Chapman Conference on Magnetospheric Substorms, 1978.
- KAWASHIMA, N., Characteristics of Intruding Plasma in a Simulated Magnetosphere, *Cosmic Electrodynamics* **1** (1971) 415.
- LEHNERT, B., Element Separation Effects in the Boundary Region of a Plasma Surrounded by Neutral Gas, *Astrophys. Space Sci.* **40** (1976) 225.
- LEHNERT, B., Problems of Matter-Antimatter Boundary Layers, *Astrophys. Space Sci.* **46** (1977) 61.
- LEHNERT, B., Matter-Antimatter Boundary Layers with a Magnetic Neutral Sheet, *Astrophys. Space Sci.* **53** (1978) 459.
- LENNARTSSON, W., On the Role of Magnetic Mirroring in the Auroral Phenomena, *Astrophys. Space Sci.* **51** (1977) 461.
- MARKLUND, G., Steady State Models for Filamentary Plasma Structures Associated with Force-Free Magnetic Fields, TRITA-EPP-78-09, Royal Inst. of Technology, Stockholm, 1978.
- MARKLUND, G., Plasma Convection in Force-Free magnetic Fields as a Mechanism for Chemical Separation in Cosmical Plasmas, *Nature* **277** (1979) 370.
- MENDIS, D. A., on the Hydromagnetic Model of Comets, *The Moon, and the Planets*, **18** (1978) 361.
- MOTLEY, R. W., *Q-Machines* (Academic Press, New York), 1975.
- MOZER, F. S., CARLSON, C. N., HUDSON, M. K., TORBERT, R. B., PARADY, B., YATTEAU, J. and KELLEY, M. C., Observations of Paired Electrostatic Shocks in the Polar Magnetosphere, *Phys. Rev. Lett.* **38** (1977) 292.
- MOBIUS, E., PIEL, A. and HIMMEL, G., Evaluation of the Plasma-parameters and the Nonthermal Field Fluctuations in a Critical Velocity Rotating Plasma, Report 78-M2-036, Inst. für Experimentalphysik II, Ruhr-Universität Bochum, 1978.
- MOBIUS, E., PIEL, A. and HIMMEL, G., Determination of the Plasma-parameters and the Suprathermal Microfields in a Critical Velocity Rotating Plasma, *Z. Naturforsch.* **34a** (1979a).
- MOBIUS, E., BOSWELL, R. W., PIEL, A. and HENRY, D., A Spacelab Experiment on the Critical Ionization Velocity, *Geophys. Res. Lett.* **6** (1979b) 29.

- PETELSKI, E., Critical Ionization Velocity and the Interaction of Stellar Winds with the Stellar Medium. IVth Solar Wind Conf., Burghausen, Germany 1978.
- PIEL, A., MOBIUS, E. and HIMMEL, G., The Origin of Turbulent Heating in a Critical Velocity Rotating Plasma, Report 78-M2-037, Inst. für Experimentalphysik II der Ruhr-Universität Bochum, 1978.
- PODGORNY, I. M. and SAGDEEV, R. Z., Physics of Interplanetary Plasma and Laboratory Experiments, *Soviet Phys. Uspekhi* **12** (1970) 445.
- PODGORNY, I. M., Laboratory Experiments (Plasma Intrusion into the Magnetic Field), In Proc. Int. Symp. on Solar-Terrestrial Physics, Boulder, Colorado, June 7-18, 1976.
- RAADU, M., The Role of Electrostatic Instabilities in the Critical Velocity Mechanism, *Astrophys. Space Sci.* **55** (1978) 125.
- ROSTOKER, G. and BOSTROM, R., A Mechanism for Driving the Gross Birkeland Current Configuration in the Auroral Oval, *J. Geophys. Res.* **81** (1976) 235.
- RUSSELL, C. T., ELPHIC, R. C. and SLAVIN, J. A., The Solar Wind Interaction with Venus. Proc. on the Chapman Conf. on Magnetospheric Boundary Layers, Alpbach, June 11-15, 1979 (to be published by European Space Agency), 1979.
- SCHOLER, M., HOVESTADT, D., KLECKER, B. and GLOEKLER, G., The Composition of Energetic Particles in Corotating Events, *Astrophys. J.* **227** (1979) 323.
- SHAWHAN, S. D., FALTHAMMAR, C.-G. and BLOCK, L. P., On the Nature of Large Auroral Zone Electric Fields at 1- R_E Altitude, *J. Geophys. Res.* **83** (1978) 1049.
- SHERMAN, J. C., Review of the Critical Velocity of Gas-Plasma Interaction II : Theory. *Astrophys. Space Sci.* **24** (1973) 487.
- SISCOE, G. L., Scaling Relations and Planetary Magnetospheres. In Proc. of the Chapman Conf. on Magnetospheric Boundary Layers, Alpbach, June 11-15, 1979 (to be published by European Space Agency), 1979.
- SMITH, E., Jupiter's Magnetosphere. In Proc. of the Chapman Conf. on Magnetospheric Boundary Layers, Alpbach, June 11-15, 1979 (to be published by European Space Agency), 1979.
- SRNKA, L. J., Critical velocity and the LTP. *Phys. Earth Planet. Inter.* **14** (1977) 321.
- TORVÉN, S., Formation of Double Layers in Laboratory Plasmas, TRITA-EPP-78-13, Royal Inst. of Technology, Stockholm (to be published in Wave Instabilities in Space Plasmas, URSI XIX General Assembly, Astrophys. and Space Sci. Book Series (Reidel Publ. Co.) 1979 1979, 1978).
- TORVÉN, S. and ANDERSSON, D., Observations of Electric Double Layers in a Magnetized Plasma, *J. Phys. D. : Appl. Phys.* **12** (1979) 717.
- ZMUDA, A. J. and ARMSTRONG, J. C., The Diurnal Flow Pattern of Field-Aligned Currents, *J. Geophys. Res.* **79** (1974) 4611.

Ionic reactions in the laboratory and in planetary atmospheres

H. S. W. Massey, F. R. S.

Department of Physics and Astronomy, University College London, U.K.

Abstract. — A detailed understanding of the ionospheres of the Earth and planets requires knowledge of the rates of many ionic reactions as well as of electron recombination coefficients and photoionization cross sections. These must be obtained primarily by laboratory measurements but it is often difficult to provide data applicable under the atmospheric conditions, especially of translational and vibrational temperature. An account is given of the present situation for the main terrestrial ionosphere taking account of the availability of extensive data from the Atmospheric Explorer satellites, for the ionospheres of Venus and Mars in the light of recent data obtained with planetary probes and for the lower ionosphere of the Earth taking account of rocket data.

Introduction. — Very soon after the discovery of the earth's ionosphere it was realized that a knowledge of the rates of certain atomic collision processes would be required in order to understand the behaviour of this region. It was early realized that at least a large fraction of the free electrons which were responsible for reflecting radiowaves back to earth were produced through photoionization by ultraviolet, and possibly even shorter, electromagnetic radiation from the Sun. To determine the electron concentration at any time and place, it was necessary to know also what processes are responsible for loss of free electrons. The choice seemed to be between recombination to positive ions or attachment to neutral molecules — massive negative ions would have little effect on the transmission of radio waves. As at the time, in the early 1930's, little or nothing was known about the rates of these processes, the matter was fiercely debated. However, it was shown in 1942 [Massey and Bates, 1942] that photodetachment by sunlight is so rapid that, in the main ionosphere, negative ions must be of negligible importance during the day. The search for a sufficiently fast recombination process took some time until Bates and Massey in 1947 produced arguments to show that it must be dissociative recombination. At that time there was little theoretical and no experimental evidence about this process but it is now very well established as we shall see. Since recombination is only effective with positive molecular ions it follows that much depends on the rates of ionic reactions which take place after the initial process of photoionization. The importance of reliable information about these rates for an understanding of the behaviour of the terrestrial ionosphere is clear. This is true not only for the main ionosphere but also *a fortiori* for the lower fringe, the D region and below, which extends down to quite low altitudes. Here the pressure is so high that many more reaction possibilities arise involving negative as well as positive ions.

Similar considerations apply to the ionospheres of Mars and Venus which are already being investigated from planetary probes. In the near future there will be a demand for information about reaction rates

involving more exotic molecular neutral and ionized systems in order to interpret data about the Jovian ionosphere. Before much longer this will extend to still other cases including Saturn, certain planetary satellites such as Titan, and certain comets.

The problem of carrying out experimental measurements of electronic and ionic collision rates for application to these large scale atmospheric environments is by no means straightforward. It is essential that the conditions under which the laboratory data are obtained reproduce those prevailing in the regions of the ionosphere to which they are being applied. To achieve this is much more difficult than would appear at first and it is largely responsible for the fact that, although a considerable fraction of research in atomic and molecular physics since the last war has been especially devoted towards obtaining such data, it is only now that the information is sufficiently comprehensive and reliable for use with confidence.

The dynamical temperature T_g of the neutral gas in the earth's atmosphere increases with altitude in the main part of the ionosphere from about 200 K at 100 km to over 1 000 K at 300 km. Moreover, the electron and ion temperatures T_e and T_i respectively at any particular height are in general substantially different from each other and from T_g . This means that the rates of the relevant ionic reactions are needed as functions of these temperatures over quite a wide range, extending well beyond room temperature. While this is difficult in any case it is aggravated by the fact that, when molecular systems are involved, internal excitation of the reactants is likely to have a major effect on the reaction rate. It cannot be presumed that the vibrational temperature of ambient ions will be the same as the translational.

In the main terrestrial ionosphere the atmospheric tides produce ionospheric motion and the consequent interaction with the earth's magnetic field leads to drift motions of the ions which may affect the energetics of the reactions involved as well as complicating the analysis of observed data in terms of electron loss rates.

A further important matter which is particularly

significant in dealing with relatively high pressure situations is the state of aggregation of the ambient ions. Cluster formation was the bugbear of early measurements of ionic mobilities and it is very important in the lower ionosphere.

Advances in technique which we shall shortly summarize have made it possible to provide usefully applicable information but the whole situation has been greatly simplified by the development of space research techniques. These have made possible *in situ* measurements of ionospheric properties in so comprehensive a fashion that a self-consistent check of reaction rates derived from laboratory experiment is already practicable, at least for the main ionosphere. The combination of laboratory and space techniques is a very powerful one and, as we shall see, a remarkably complete picture of the mean behaviour of the main regions of the ionosphere in terms of ionic and dissociative recombination reaction rates can now be built up.

Requirements for a complete theory of the mean ionosphere. — The ionosphere varies with latitude, longitude, time of day, epoch in the solar cycle and condition of the Sun. We shall not attempt to discuss the variability in any detail but refer to a *mean* ionosphere, at a temperate latitude and quiet phase in the solar cycle and usually in day time equilibrium. We shall say only a little about the behaviour at night.

For a complete theory of the behaviour of this mean ionosphere we need to know :

- (a) the composition and concentration of the neutral atmosphere as a function of height,
- (b) the spectrum of the solar radiation in the XUV region which is of sufficient quantum energy to produce photoionization of atmospheric atoms and/or molecules, and
- (c) the drift velocities and diffusion rates of the ions as functions of height.

In principle given these data and knowledge of the cross sections for ionization of atmospheric atoms and molecules by XUV radiation and by electrons with energies characteristic of the photoelectrons produced in these processes, for dissociative recombination of electrons with atmospheric molecular ions as a function of electron and gas temperature, and for all relevant reactions involving neutral and ionized atmospheric molecular systems as functions of translational and vibrational temperatures.

It would be possible to calculate the electron and ion concentrations and temperatures and the ion composition as a function of height. In fact laboratory data are always to some extent incomplete and it is much more effective if information is available by direct *in situ* measurements using space techniques of electron and ion concentration and temperature and

of ion composition. It is then relatively easy to check for self-consistency. This is the situation reached at present with the main region of the earth's ionosphere, at least in the mean as we have defined it.

To interpret the variable aspects of the main ionosphere is more complicated because it is necessary to take account of ionization due to solar corpuscular streams and to variations in the solar XUV radiation. Although we shall not discuss these aspects for the main ionosphere we shall say something about the relation of the disturbances observed in the lower ionosphere to the various relevant reaction rates.

Relevant ionospheric measurements by space techniques. — Because of the variability of the ionosphere and indeed of the factors producing it, *in situ* measurements should be made at the same time and place of *all* the relevant quantities. Figure 1 shows a mean ionospheric profile of electron concentration. Particular interest attaches to the region below 250 km as it is in this region that photochemical equilibrium, in day time, is relatively unaffected by drift and diffusion effects. However the lifetime of an artificial satellite decreases rapidly as the perigee distance

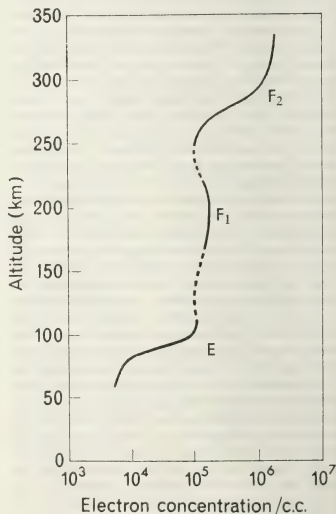


Fig. 1. — Schematic representation of the variation of the electron concentration with height in the undisturbed terrestrial ionosphere.

alls below this value. For this reason it is only recently that continuous and comprehensive data have become available from satellite-borne instruments. This has been achieved through the Atmospheric Explorer satellites (AE) C, D and E.

These satellites have been launched into highly eccentric orbits, the apogee distance being of the order 4 000 km and the perigee close to 150 km. With this perigee distance the apogee distance would decrease at a rapid rate (initially about 300 km a month) but by means of auxiliary propulsion this is avoided so that the satellite lifetime is adequate. Excursions to lower perigee distances for a limited number of orbits is also possible. The limit in this case is the maximum pressure at which the onboard instruments can function effectively.

The second important feature of the Atmospheric Explorer is the comprehensive range of instruments carried so that simultaneous measurements may be made continuously of all important ionospheric quantities. Thus AEC, the first to be launched (Dec. 1973), carries an open [Nier *et al.*, 1973] and a closed [Pelz *et al.*, 1973] source neutral mass spectrometer to measure the composition of the neutral atmosphere in the mass range from 1 to 46 a.m.u., a velocity distribution analyser [Spencer *et al.*, 1973] to measure the neutral gas temperature, a cold-cathode gauge and capacitance manometer [Rice *et al.*, 1973] to measure the total atmospheric density, accelerometers [Champion and Marcos, 1973] to measure the total atmospheric density at altitudes below 400 km, a magnetic [Hoffman *et al.*, 1973] and a Bennett type [Brinton *et al.*, 1973] ion mass spectrometer to measure ion composition and concentration up to 46 a.m.u., a retarding potential analyser [Hanson *et al.*, 1973] to measure ion mass, temperature, concentration and drift velocity, a cylindrical Langmuir probe [Brace *et al.*, 1973] to measure electron temperature and concentration as well as ion concentration, a solar EUV spectrophotometer [Hinteregger *et al.*, 1973] to measure the solar energy in the wavelength range 14 to 185 nm, a solar EUV filter photometer [Heath and Osantowski, 1973] to measure the solar energy in bands from 4 to 135 nm, a UV spectrometer [Barth *et al.*, 1973] to measure the altitude distribution of NO between 80 and 250 km, a photoelectron spectrometer [Doering *et al.*, 1973] to measure the flux of photoelectrons and fast electrons with energies between 2 and 500 eV, a visible airglow photometer [Hays *et al.*, 1973] to measure the intensities of the airglow at wavelengths of 630, 557.3, 427.8, 337.1, 52.0 and 731.9 to 733.0 nm, a low energy ion and electron detector [Hoffman *et al.*, 1973] to measure particle fluxes in the energy range 0.2 to 25 keV, as well as a three-axis fluxgate magnetometer [Armstrong and Zmuda, 1973].

With this remarkable automatic laboratory in space not only are all the important ionospheric parameters observed continuously but there is a

considerable degree of redundancy so that measurements made by one instrument may be checked or calibrated against those made by others. The only special problem which is at all important for applications to ionospheric photochemistry is that of measuring the concentration of atomic and molecular oxygen. Above 100-120 km the atmospheric oxygen is mainly monatomic and hence highly reactive. With a closed source mass spectrometer most of the atomic oxygen will react on the surfaces before ionization. There is strong evidence that if the surfaces to which the incoming atoms are exposed are gold-plated quantitative conversion to O_2 occurs, so that the sum $[O_2] + \frac{1}{2}[O]$ is measured, [] denoting concentration of. In an open source instrument the position is not so clear. It seems, however, that in this case with surfaces only briefly exposed to low pressure conditions, as in rocket flights, most of the atomic oxygen reaches the ionizing chamber without reaction. For surfaces exposed over a long period as in satellite observations this no longer applies and effectively all of the atoms recombine to form O_2 just as in the closed source case. This means that, at altitudes well above 120 km both types of instrument yield $[O]$ with reasonable accuracy because $[O_2]$ is relatively small. However it is important also to determine $[O_2]$. [Nier *et al.*, 1974] were able to adapt their open source instrument to do this, distinguishing the ambient O_2 from that derived by recombination of ambient O, by the possession of a velocity relative to the collector equal to the satellite velocity. This was only possible when the satellite was operated in a spinning mode.

Remarks on the measurement of ionic reaction rates.

— A great step forward in experimental techniques for measurement of ionic reaction rates under thermal conditions was taken with the introduction of the flowing afterglow technique [Ferguson *et al.*, 1964]. This method has been applied with great success to the measurement at room temperature of a great variety of reaction rates of importance in planetary ionospheres. Recently a further variant known as the selected ion flow tube (SIFT) technique has been introduced [Adams and Smith, 1976a]. In this the ions under study are not produced by an electric discharge in the flowing gas but by injection of a mass-selected beam of ions into the flow tube. This has the advantage of eliminating a number of other ionic species as well as electrons, photons and excited atoms and molecules from the reacting system. The identification of product ions and the determination of branching ratios is thereby facilitated while it becomes possible to study reactions involving ions in metastable states.

Both the original flowing afterglow technique and this modification are very effective at room temperatures but it is more difficult to extend the temperature range of the observations. With some diffi-

culty, in a flowing afterglow tube measurements may be made up to a temperature of 900 K, but not higher.

For these reasons a great deal of effort has been devoted to the use of drift tube techniques in which the ions are accelerated to superthermal energies by application of an electric field. By an ingenious extension of techniques for measurement of ion mobilities McDaniel and his collaborators [McDaniel, 1968] have been able to measure ionic reaction rates $k(T_g, F/N)$ as a function of the ratio F/N of electric field strength F to the concentration N of the main (buffer) gas through which the ions drift, at room temperature T_g . The problem is to convert $k(T_g, F/N)$, to $k(T)$ which is the reaction rate when all the degrees of freedom of the reactants are in thermal equilibrium at temperature T .

The usual procedure is to assume that the mean kinetic energy E_{lab} of the ions is given by Wannier's expression (Wannier, 1953), valid when the collision frequency is constant,

$$E_{lab} = \frac{1}{2} M_i v_d^2 + \frac{1}{2} M_n v_n^2 + \frac{3}{2} \kappa T \quad (1)$$

where M_i , M_n are the masses of the ion and neutral gas atom respectively, v_d is the ion drift velocity and T the gas temperature. The mean kinetic energy E_{cm} , in the CM system, for the interacting systems is given by

$$E_{cm} = \frac{1}{2} (M_i M_n / M_i + M_n) (v_i^2 + v_n^2), \quad (2)$$

where v_i^2 and v_n^2 are the mean square thermal velocities of the ions and neutral atoms respectively.

Since

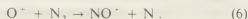
$$v_n^2 = 3 \kappa T / M_n, \quad v_i^2 = 2 E_{lab} / M_i, \quad (3)$$

$$E_{cm} = (M_n / M_i + M_n) (E_{lab} - \frac{3}{2} \kappa T) + \frac{3}{2} \kappa T. \quad (4)$$

$k(T_g, F/N)$ is then taken to be $k(T_{eff})$ where

$$\frac{3}{2} \kappa T_{eff} = E_{cm}. \quad (5)$$

Strong support for the validity of this procedure, when both reacting systems are atomic and the variation of the reaction rate with temperature is not too rapid, has recently been provided by a theoretical study due to Viehland and Mason (1977). They develop a systematic procedure for determining T_{eff} . The first approximation in this procedure is a good one under the conditions stated and it is just (5) with E_{cm} given by (4). At the same time Lin and Bardsley (1977) carried out a Monte Carlo simulation of ion motion in drift tubes which again showed that (5) is a good approximation under these conditions. On the other hand, their results showed clearly that indiscriminate use of the approximation could lead to unsatisfactory data about the variation of the reaction rate coefficient with temperature. A particular example of interest in the present context is the reaction



This was studied experimentally by Allbritton *et al.* (1977) together with two other reactions with the special aim of checking the conclusions of Viehland and Mason and of Lin and Bardsley. For this purpose they used a flow drift tube [McFarland *et al.*, 1973a] which combines the versatility of the flowing afterglow technique with the drift tube for obtaining higher energy ions. They measured rate coefficients, $k(T_g, F/N)$ using two different buffer gases He and Ar. From these results they derived $k(T_{eff})$ using (5).

Figure 2 shows that different results are obtained for the two buffer gases arising from differences in the ion velocity distributions in the two cases. This is confirmed by using the velocity distributions calculated by Lin and Bardsley (1977) first to unfold the reaction cross sections as a function of ion energy for the helium data and then to derive the reaction rate for argon as a function of T_{eff} . This agrees well with the observed results (see Fig. 2). The helium observations also agree with those calculated assuming Maxwellian distributions about T_{eff} (Fig. 2).

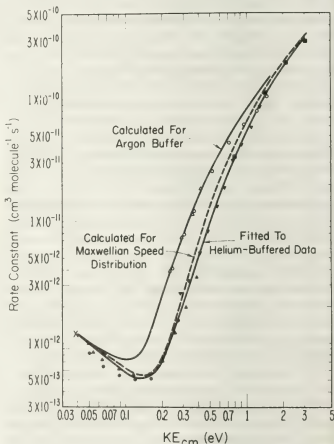


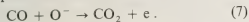
Fig. 2. — Rate coefficients for the reaction $O^+ + N_2 \rightarrow NO^+ + N$ measured by Allbritton *et al.* (1977) using the flow drift technique with different gases as indicated. $\circ \triangle$ argon at pressures of 0.112 and 0.206 torr respectively; $\blacksquare \blacktriangle \bullet$ helium at pressures of 0.206, 0.395, 0.410 and 0.810 torr respectively; \times measured by the flowing afterglow method at room temperature (Dunkin *et al.*, 1968). The rate coefficients are given using E_{cm} as defined by (4).

This reaction is an extreme case in which the variation with temperature is rapid. An experimental check on the validity of (5) in other cases may be carried out by verifying that the resultant $k(T_{eff})$

curve is independent of the buffer gas. If not it is necessary to use higher approximations in the Viehland and Mason procedure to obtain the correct curve.

Strictly speaking these considerations only apply when both reactants are atomic so no complications arise from internal degrees of freedom. So far it has been necessary to assume in the case of molecular reactants that they are in their lowest vibrational states. As the reaction rate may well depend quite strongly on the degree of vibrational excitation this may introduce considerable uncertainty into the application of experimental data. Attention must always be paid to this question, particularly when the ions are molecular because their mode of production may well lead preferentially to formation in excited vibrational states. In such cases the reaction rate will depend on the age of the ions and this may be used to check whether excited states are contributing to the results. The problem of application to large scale systems may be aggravated by absence of knowledge of the state of internal excitation of some of the molecular constituents in such systems.

Incidentally, a considerable step forward has recently been made in solving the related problem of determining the degree of excitation of the products. Thus Bierbaum *et al.* (1977) have succeeded in observing infrared radiation arising from vibrationally excited CO_2 produced in the reaction



From observations of this kind the vibrational energy distribution of the CO_2 may be obtained.

Measurement of dissociative recombination coefficients. — Although electron-ion recombination is not usually thought of as an ionic reaction it plays so central a role in atmospheric photochemistry that we must pay some attention here to the problems involved in its measurement.

Until the introduction [Biondi and Brown, 1949] of the microwave probing of discharge afterglows to monitor the rate of loss of electrons there was no direct experimental information available about recombination rates. To obtain definite results for ions in well defined states, as a function of electron and of ion temperature, proved to be a very difficult task. Particular interest for atmospheric applications attaches to recombination to N_2^+ , O_2^+ and NO^+ .

In experiments involving discharge afterglows one major problem is that of ensuring that the ions to which the electrons are recombining are indeed those which are under study and not other more complex ions which are readily formed in afterglow conditions. This must be achieved while at the same time ensuring that recombination and not diffusion to the container walls is the dominant loss process for electrons.

Kasner and Biondi (1968) found these conditions were achieved for N_2^+ ions in an afterglow in neon

at a pressure between 15 and 40 torr containing a partial pressure of N_2 between 5×10^{-5} and 10^{-3} torr. However the state of vibrational excitation of these ions remained uncertain. Measurements were then made of the recombination coefficient at room temperature and extended by Mehr and Biondi (1969) to electron temperatures as high as 4000 K by using microwave heating. These latter measurements continued to refer, however, to neutral gas at room temperature.

Merging beam techniques have not yet proved accurate enough at low relative kinetic energies to provide a check on afterglow measurements but Walls and Dunn (1974) have used the ion storage technique to measure recombination cross sections for slow electrons with NO^+ and O_2^+ which may be compared with the afterglow measurements for these ions. Walls and Dunn contained the ions under study in a cylindrical quadrupole ion trap [Byrne and Farago, 1965], the containing fields being a large homogeneous magnetic field parallel to the axis and an electrostatic field of potential proportional to $r^2 - 2z^2$ where r, z are the usual cylindrical coordinates. In such a combination of fields each ion has a characteristic frequency of oscillation in the z direction and this was used to detect each ion species through the noise power spectrum of the image currents induced at one end of the trap [Dehmelt and Walls, 1968]. Electrons of well defined energy from 0.045 eV up to 10 eV were fired into the trap along magnetic field lines and the rate of loss of ions observed.

With residence times attainable for NO^+ of 40 min it seems very probable that the recombination measurements referred to ions in their ground electronic and vibrational states. For O_2^+ on the other hand the vibrational lifetimes are expected to be very much longer and the distribution of vibrational excitation is likely to be that determined by their mode of formation.

Walls and Dunn measured cross sections as functions of electron energy and these must be averaged over Maxwellian energy distributions to obtain recombination coefficients as functions of electron temperature. Some ambiguity arises in this procedure because of the uncertain extrapolation of the cross section data to zero electron energy. This is unimportant for O_2^+ and figure 3 shows remarkably good agreement with the results obtained in afterglow experiments over a very wide range of electron temperatures. The indications are that, despite all the uncertainties, the O_2^+ under study has indeed been in the ground electronic and vibrational states.

For NO^+ there is greater ambiguity in deriving recombination coefficients from the cross section data as seen from figure 4. Nevertheless there is quite good agreement with the afterglow data, supporting again the assumption that the ions are in their ground states.

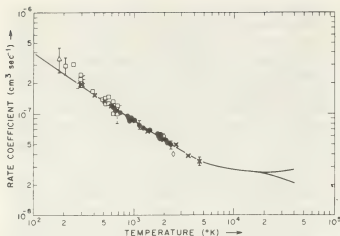


Fig. 3.—Rate coefficients for dissociative recombination of electrons to O_2^+ , measured as functions of electron temperature by different observers. \times Mehr and Biondi (1969); Kasner and Biondi (1968); Plumb *et al.* (1972); Cunningham and Hobson (1972); Stein *et al.* (1964); Mahdavi *et al.* (1971). — derived from the cross section measurements of Wills and Dunn (1974).

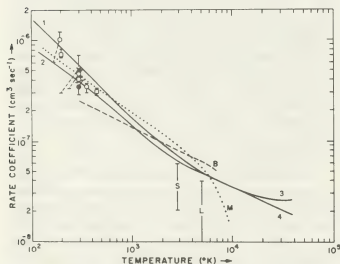


Fig. 4.—Rate coefficients for dissociative recombination of electrons to NO^+ measured as functions of electron temperature by different observers. \square Weller and Biondi (1968); \diamond Gunton and Shaw (1965); \times Young and St-John (1966); \circ Mahdavi *et al.* (1971); S Stein *et al.* (1964); L Lin and Teare (1963). The full line curves are derived from the cross section measurements of Wills and Dunn (1974) using different extrapolations of these measurements to lower (1 and 2) and higher (3 and 4) energies respectively. ----- calculated by Bardsley (1968); calculated by Michels (1973).

Ionic reactions and dissociative recombination in the ionosphere.—Figure 5 shows the height distribution of electrons and of the main positive ions in the terrestrial ionosphere near sunspot minimum derived from analysis of observations over many years with rocket-borne instruments. It will be seen that NO^+ is dominant at altitudes below 180 km whereas NO is a minor constituent. The reverse

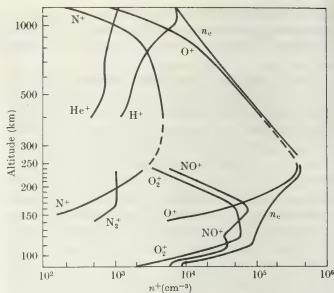


Fig. 5.—Variation with altitude in the earth's ionosphere of the concentrations of electrons and of the main varieties of positive ions near sunspot minimum, derived from analysis over many years of observations made with rocket borne instruments.

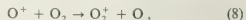
situation applies to N_2^+ which is a minor ion derived from a major neutral constituent.

Between altitudes of 130 and 250 km the major neutral constituents are N_2 and O . Thus at 160 km the concentrations of O , N_2 and O_2 are typically 4×10^{15} , 9×10^{15} and $6 \times 10^{14} \text{ m}^{-3}$ while at 220 km the corresponding values are 7.5×10^{14} , 6×10^{14} and 3×10^{13} . The ions primarily produced by the solar radiation are, in this altitude range, very largely N_2^+ and O^+ . It is clear by reference to figure 5 that ionic reactions must play a vital part in redistributing this ionization.

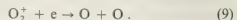
A great deal of analysis of these reactions is now possible by working with a combination of laboratory data with data obtained from the Atmospheric Explorer satellites. We shall analyse in this way the equilibrium concentrations of O_2^+ , N_2^+ and NO^+ , checking particularly the self-consistency of the schemes developed.

The O_2^+ Chemistry.—The AEC data were first discussed in this connexion by Oppenheimer *et al.* (1976a).

In the neighbourhood of the 200 km level, where the concentration of O_2 is relatively small, the main source of O_2^+ is the charge transfer reaction



direct production by photoionization of O_2 being very small. At the same time the only important loss process is dissociative recombination



The equilibrium concentration $[O_2^+]$ of O_2^+ is then determined from

$$k_1[O^+][O_2] = \alpha[O_2^+][e], \quad (10)$$

where k_1 is the rate coefficient for (8) and α is the recombination coefficient for (9). The latter is thus given by

$$\alpha = \frac{k_1[O^+][O_2]}{[O_2^+][e]}. \quad (11)$$

Torr *et al.* (1977) applied these considerations to data obtained from AEC in the day time at altitudes between 190 and 240 km for which they should be valid. For k_1 they assumed the value measured by McFarland *et al.* (1973) using the flow drift tube method, namely

$$k_1 = (2.0 \pm 0.2) \times 10^{-17} (T/300)^{-0.4 \pm 0.14} \text{ m}^3 \text{ s}^{-1}, \\ T < 1800 \text{ K}, \quad (12)$$

T being the reduced temperature

$$(M_i M_n)/(M_i + M_n) (T_n/M_n + T_i/M_i),$$

M_i, M_n being respectively the ion and neutral molecule masses, T_i, T_n the corresponding temperatures.

$[O^+]$ and $[O_2^+]$ were obtained directly from the mass spectrometer measurements and $[O_2]$ from the open source neutral mass spectrometer using the technique developed by Nier *et al.* (1974) referred to earlier. The total ion density and electron temperature were measured by the cylindrical electrostatic

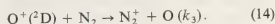
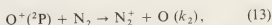
probe, and neutral temperatures inferred from the scale height of the N_2 .

To avoid any contribution to ionization via auroral excitation data used were limited to latitudes less than 55° .

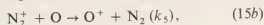
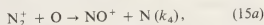
Figure 6 shows the derived value of α as a function of electron temperature compared with the measurement of Walls and Dunn (1974) discussed earlier. The agreement is remarkably good and suggests that the measured values of both k_1 and α are close to the truth. It is interesting to note that the analysis is independent of knowledge of the EUV spectrum of the sun.

Oppenheimer *et al.* (1976) were primarily concerned with deriving $[O_2]$ from observed concentrations of $[O_2^+]$ and they took into account a number of minor sources and sinks for O_2^+ , using experimental values for reaction rates. The O_2 concentrations which they derived were checked against measured data and found to be consistent.

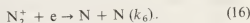
The N_2^+ Chemistry. — In the daytime N_2^+ is produced primarily through photoionization, ionization by energetic photoelectrons and by charge transfer reactions with metastable O^+ ions, namely



Loss of N_2^+ occurs mainly through the ionic reactions



and by dissociative recombination

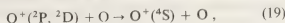
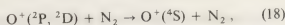


The equilibrium concentration $[N_2^+]$ of N_2^+ is then given by

$$[N_2^+] = \{ q_1 + q_2 + k_2[O^+(^2P)] + k_3[O^+(^2D)] \} \times \\ \times [N_2]/(k_4 + k_5)[O] + k_6[e] \quad (17)$$

q_1 and q_2 are the respective rates of production by photoionization and by photoelectron ionization of N_2 .

Oppenheimer *et al.* (1976) made a preliminary comprehensive study in which they considered in detail the sources and sinks of the metastable O^+ ions over the altitude range from 160 to 380 km. Below 240 km the only important sinks are found to be the reactions (13) and (14) respectively but at greater altitudes the quenching reactions



become important.

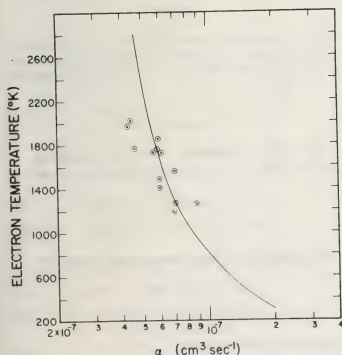


Fig. 6. — Rate coefficient for dissociative recombination of electrons with O_2^+ as a function of electron temperature, — derived from the measurements of Walls and Dunn (1974) (see Fig. 3) and \square obtained by Torr *et al.* (1976) from analysis of Atmospheric Explorer C data.

Using available measured values for rate constants, supplemented by information on quenching rates available from measurements of the airglow emission at 731.9 nm [Walker *et al.*, 1975; Rusch *et al.*, 1975] and theoretical values for rates of electron deactivation of the metastable ions, together with AEC data on the EUV solar spectrum and laboratory and theoretical information about photoionization and photoelectron ionization rates, Oppenheimer *et al.* (1976) derived $[N_2^+]$ as a function of altitude for a number of orbital passes. Their results are compared in figure 7 with observed values for a particular orbit. The calculated results depend, above 240 km, on assumptions made about the unmeasured reaction rates for the reactions (18), (19). For $O^+(^2P)$ the best fit was obtained with reaction rates for quenching by N_2 and by O respectively of 4.0×10^{-16} and $1.0 \times 10^{-16} \text{ m}^3 \text{ s}^{-1}$ and for quenching of $O^+(^2D)$ by O of $1.0 \times 10^{-16} \text{ m}^3 \text{ s}^{-1}$. Although these are very preliminary and probably not definite values they show that, with further refinement, data on reactions very difficult to study in the laboratory may be obtained from observations in space.

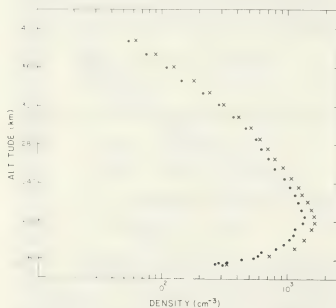


Fig. 7. — Variation of N_2^+ concentration with altitude: ● observed with magnetic ion mass spectrometer on Atmospheric Explorer C during the upleg of a particular orbit; × calculated by Oppenheimer *et al.* (1976) from the ion chemistry of N_2^+ .

Torr *et al.* (1977) took advantage of the fact that the reactions (18) and (19) are unimportant below 240 km. In that case all $O^+(^2P)$ and $O^+(^2D)$ primarily formed by photoionization will be ultimately converted to N_2^+ . Furthermore, below 210 km the contribution to N_2^+ loss by recombination is small. Under these conditions (17) reduces to

$$[N_2^+] = (q_1 + q_2 + q_3 \beta + q_4 \beta) (k_4 + k_5) [O]. \quad (20)$$

Here q_3 and q_4 are the rates of production of $O^+(^2P)$

and $O^+(^2D)$ by photoionization and photoelectron ionization respectively and $\beta = [O]/[N_2]$.

Using measured values for $[N_2]$ and $[O]$ made by the open source mass spectrometer, values were found for k_4 and k_5 increasing gradually from $1.03 \times 10^{-16} \text{ m}^3 \text{ s}^{-1}$ at an ion temperature of 600 K to $1.19 \times 10^{-16} \text{ m}^3 \text{ s}^{-1}$ at 900 K. The lowest value agrees very well with that measured by McFarland *et al.* (1974) using the flow drift tube method, but the laboratory values decrease as the effective temperature rises. The opposite result found by Torr *et al.* can be ascribed to neglect of recombination which becomes increasingly important at the higher altitudes as may be seen from figure 8. Detailed analysis of the recombination contribution is complicated by inadequate evidence about the influence of vibrational excitation on the rate but the order of magnitude seems to be quite close to that measured by Mehr and Biondi (1969).

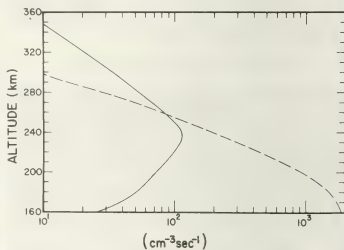
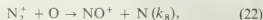
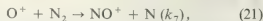
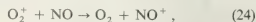
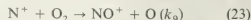


Fig. 8. — Comparison of loss rates of N_2^+ in the ionosphere at different altitudes: — due to dissociative recombination; --- due to the ionic reaction $N_2^+ + O \rightarrow NO^+ + N$ (from Torr *et al.*, 1977a).

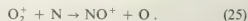
The NO^+ Chemistry. — NO^+ is produced, at altitudes above 150 km, mainly through the reactions,



while appreciable contributions also come from



and, below 200 km, from



Dissociative recombination (coefficient α) is the only effective loss process at these altitudes.

At altitudes above 240 km there is no significant contribution from (24) or (25) so that in equilibrium, in day time,

$$[\text{NO}^+] = k_7[\text{O}^+][\text{N}_2] + k_8[\text{N}_2^+][\text{O}] + k_6[\text{N}^+][\text{O}_2]/\alpha(T_e)[c]. \quad (26)$$

[Torr *et al.*, 1977c] used this relation to analyse AEC data for altitudes below 350 km so as to avoid complications due to vertical transport of NO^+ . k_7 was obtained from the analysis of the $[\text{N}_2^+]$ chemistry. Conditions were chosen in which the contribution from (22) was negligible while a major contribution comes from (21). It was found that, over the ion temperature range from 500 to 1 200 K, good agreement with (26) is obtained if k_7 is taken to be that measured by Albritton *et al.* (1977) as described earlier and $\alpha(T_e)$ is taken from the observations of Walls and Dunn [1974].

As an interesting illustration of the importance of ion drift motion under certain conditions Torr *et al.* also analysed night time data for which case no contribution comes from (22) or (23). Figure 9 shows a comparison between the values of k_7 consistent with the night time data and those derived from the day time observations. It is seen that, at ion temperatures greater than 750 K, the night time values rise rapidly with increasing ion temperature whereas for the day time, in agreement with laboratory experiment, they continue to fall slowly, at least up to 1 000 K. The difference can be ascribed to the possession by the ions at night of a large drift velocity, as measured by the retarding potential analyser.

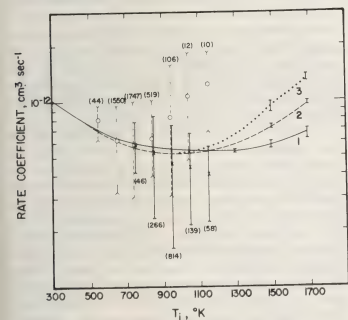
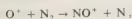


Fig. 9. — The rate coefficient for the reaction



observed as a function of ion temperature T_i by Torr *et al.* (1977), from observations made by instruments aboard Atmospheric Explorer C: \bullet derived from day time observations; \circ derived from night time observations. The numbers refer to the number of samples used. Curves 1, 2, 3, calculated for the ionospheric conditions using the measurements of Albritton *et al.* (1977) and different assumed ion velocity distributions.

During day time the production of NO^+ is so much greater that in any case the influence of drift motion on the NO^+ distribution is relatively unimportant.

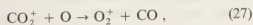
Ionic reactions in the ionospheres of Mars and Venus.

— A considerable amount of information is already available about the atmosphere of Mars and about the Martian ionosphere. The Viking project which successfully landed two instrumented packages on the Martian surface in July 1976 greatly expanded the information already available from the earlier Mariner missions. During entry through the atmosphere observations were made with a mass spectrometer of the atmospheric composition [Nier and McElroy, 1977], and with a retarding potential analyser of ionospheric properties [Hanson *et al.*, 1977], including the ion composition, concentration and temperature.

The atmosphere of Mars is much more tenuous than that of the earth, the pressure at ground being only 6×10^{-2} times as large. It is composed very largely of CO_2 . Measurements with the mass spectrometers on the two Viking landers show that at 130 km altitude the concentrations of CO_2 , N_2 , CO and O_2 are roughly, in m^{-3} , 3×10^{16} , 10^{15} , 4×10^{14} and 10^{14} respectively. At 160 km the values differ somewhat between the two landers. From the one which landed on 3 September 1976, the respective values are 5×10^{14} , 5×10^{13} , 2×10^{13} and 10^{12} . The concentrations of atomic oxygen were not measured but from estimates based on photochemical information it is likely that at 130 km the concentration is of the order $2 \times 10^{14} \text{ m}^{-3}$, falling by a factor of ten in the next 40 km.

Measurements with the retarding potential analysers on the two landers show that the peak electron concentration in day time is very close to 10^{11} m^{-3} , occurring at an altitude of 130 km, falling to 10^9 in the next 120 km. The main positive ion over this range is O_2^+ . The next most abundant ion, CO_2^+ , is about ten times less abundant at altitudes above the maximum and increasingly less so at lower altitudes — at 110 km its concentration is only about 1 % of that of the O_2^+ .

The ion chemistry responsible for this situation is quite simple. CO_2^+ ions primarily produced by solar photoionization are converted to O_2^+ through the reaction



the rate of which has been measured at room temperature by Fehsenfeld *et al.* (1970) as

$$1.0 \times 10^{-16} \text{ m}^3 \text{ s}^{-1}.$$

McElroy *et al.* (1977) have considered other reactions in a preliminary analysis which yields values for the concentrations of O_2^+ and CO_2^+ in quite good agreement with the observed data.

An unexpected major difference between the terrestrial and Martian ionospheres is that the latter exhibits no F region (see Fig. 1). This region arises because at altitudes from 300 to 800 km or more the main neutral constituent in the earth's atmosphere is atomic oxygen. The primary O^+ ions can only recombine through conversion, in some ionic reaction, to a molecular ion, a process which must necessarily be very slow at altitudes where few neutral molecules are present. This means that the effective rate of loss of electrons is very low and hence the equilibrium electron concentration is large.

It was expected that a similar situation would apply to Mars. Just as the terrestrial O_2 is dissociated by sunlight and at sufficiently great height the atomic oxygen floats above the denser N_2 , so on Mars the CO_2 should be photodissociated to form CO and O. In this case once again the O should dominate in the neutral atmosphere at high altitudes so that recombination would be very slow and the equilibrium electron concentration high. It is still not clear why this does not occur.

We must expect that the ion chemistry of an atmosphere which is predominantly composed of CO_2 will also be appropriate for the ionosphere of Venus. The atmosphere of this planet is known from early probing missions to be composed mainly of CO_2 with about a 5% admixture of N_2 , a result confirmed by the recent Pioneer and Venera lander and orbital missions. On the other hand the pressure at ground level is about 90 times larger than on the earth. The electron concentration-altitude profile of the ionosphere [Bauer *et al.*, 1977] has been derived from observations made in the Mariner 10 occultation experiment. The day time maximum of $4 \times 10^{11} \text{ m}^{-3}$ occurs at 130-140 km altitude. Remarkably enough, considering the very different pressure and dynamical conditions compared to Mars, the Venus ionosphere also shows no F region. Information about the ion composition is just now becoming available from observations made in the latest U.S. and Russian missions. Taken together with data obtained in the same missions on the composition of the neutral atmosphere, sufficient material will be available for an analysis of the ion chemistry taking account of laboratory data.

A remarkable feature of the ionosphere of Venus is the persistence of an electron concentration which, at the maximum, is of order of 10^{10} m^{-3} on the night side. This is despite the fact that the rotation period of the planet is as long as 244.3 days. Any explanation must clearly depend in some form or other on ionic reactions.

It is clear that there will be demands for new measurements to be carried out in the laboratory on reactions which have only become important in the atmospheric context because of the possibility of extending the terrestrial studies to other planets. These demands will increase and embrace even more

exotic reactants in the near future when data on the composition of the atmospheres and ionospheres of the outer planets become available. Already electron concentration profiles of the Jovian ionosphere have been obtained. Saturn is well within range as is also its remarkable satellite Titan which certainly possesses an atmosphere. In addition to the planets many problems arise in connexion with the ionospheres at the cores of comets [Mendis and Ip, 1977]. The position here is that even the source of the ionization is not known. A cometary fly-by is likely to help in resolving such questions and raising others about the origin of the constituent positive ions which will certainly call for further laboratory studies of ionic reactions.

The lower ionosphere of the earth.—We now consider the reactions involved in the region of the earth's atmosphere at heights below 100 km. Although this represents only a lower fringe of the ionosphere it is of considerable importance in practice. Thus, because of the relatively high collision frequency at these altitudes, electromagnetic waves suffer absorption which can become serious for radio propagation if the electron concentration is not too low. In fact the concentration is subject to considerable variations not only due to solar flares but also at certain periods during the year, as we shall see.

It is also of interest to trace out the downward prolongation of the ionosphere into the stratosphere and below. Thus it is conceivable that some ionic reactions may be of importance in the chemistry of minor constituents in these atmospheric regions, a subject which is now actively studied in relation to environmental problems. Again it may well be that ions form the nucleation centres for the noctilucent clouds observed in middle latitudes in the region of the temperature minimum near 85 km.

In many ways the problem of understanding the ion chemistry of the atmosphere below 100 km is more difficult than for the upper atmosphere. As the pressure increases many more reactions become possible while minor neutral constituents such as H_2O , NO , metastable $O_2(^1\Delta_g)$ molecules, CO_2 , O_3 , etc., play important, and sometimes major, roles. At the same time the altitudes are too low for artificial satellites to circulate for useful times. However, vertical sounding rockets may still be used to provide uniquely valuable data albeit discontinuously and at a much slower rate. It is perhaps ironic that the bugbear of early experimental work on ionic mobilities, cluster formation of ions with water molecules, is a matter of much importance and interest at altitudes below 85 km. This has led to a revival of the study of ion clustering and presents many challenging experimental problems.

Below 70 km account must be taken of negative ions which at higher altitudes are quite unimportant.

Figure 10 shows the temperature distribution in the atmosphere below 100 km with the various regions indicated. The temperature minimum near 85 km is noteworthy.

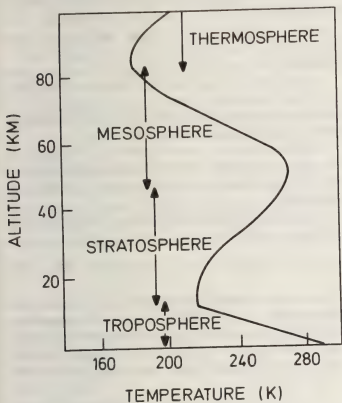


Fig. 10.— Variation of the temperature with altitude in the middle and lower atmosphere, in equatorial regions.

Figure 11 shows the observations made by Narcisi *et al.* (1971) of the positive ion composition at altitudes below 90 km using a mass spectrometer. Above 85 km the main ions, of mass 32 and 30 a.m.u., are O_2^+ and NO^+ respectively, but very shortly

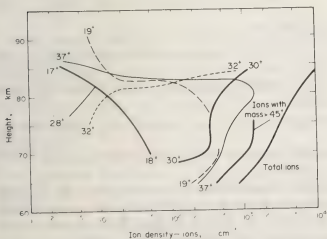


Fig. 11.— Ion composition in the terrestrial atmosphere at altitudes below 90 km observed by Narcisi *et al.* (1971) using rocket borne instruments. The numbers give the ion mass in a.m.u.

below 85 km ions of mass 19 and 37 a.m.u., as well as with mass 55 a.m.u., become dominant. In all cases these ions may be identified as hydrated protons H_3O^+ , $H_3O^+ \cdot H_2O$ and $H_3O^+ \cdot 2H_2O$ respectively.

Later observations have confirmed these results and indicate that even heavier clusters may be present. It is difficult to detect these because the last water molecules are so weakly bound as to be lost in the sampling process.

As mentioned earlier, negative ions predominate over electrons at altitudes below 70 km but analysis of the negative ion composition with rocket-borne equipment is very difficult. This is because, in flight, the rocket charges up negatively with respect to the ambient atmosphere so that the problem of drawing in negative ions in a non-selective manner for sampling is a complicated one. However, some observations have been made. Narcisi *et al.* (1971, 1972) found, in particular, among the dominant species, a series beginning at mass 80 a.m.u. and extending up to 152 a.m.u. in stages of 18 a.m.u. These were identified as $NO_3^-(H_2O)_n$ with n ranging from 0 to 5. Ions with mass 60 and 76 were probably CO_3^- and CO_4^- . Arnold *et al.* (1971) on the other hand observed ions with masses 111 ± 1 and 125 ± 1 as the most abundant. These were identified tentatively as $CO_4^-(H_2O)_2$, or $NO_2^-(HNO_2) \cdot H_2O$, and $NO_3^-(HNO_3)$ respectively. Unclustered CO_3^- , NO_3^- , HCO_3^- , O_2^- and Cl^- were

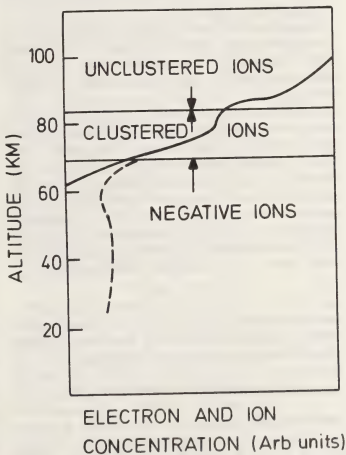


Fig. 12.— Schematic representation of the variation of electron and of positive ion (—) concentration with altitude below 100 km

also observed but none of the clustered ions observed by Narcisi *et al.*

Figure 12 shows schematically the different regions of ionization below 100 km on the basis of rocket and other observations. It must be remembered that this diagram as well as most of the remarks above refer to the undisturbed region. We shall conclude the discussion of the lower ionosphere with some brief description of the disturbed conditions as far as they are concerned with ionic reactions.

Discussion of the ion chemistry in the undisturbed lower ionosphere must begin by considering the source of the ionization. Solar radiation with quantum energy sufficient to ionize the main atmospheric constituents is absorbed above 90 km. However Ly α radiation with a quantum energy of 10.4 eV can penetrate through an absorption window down to 80 km and even lower. This radiation can ionize NO, which while a minor constituent is present in sufficient concentration to provide the observed NO⁺ as a primary ion. This conclusion has been derived from rocket measurements of the NO concentration and the solar spectrum, taken together with laboratory measurement of the recombination rate to NO⁺.

The source of the O₂⁺ ions is less obvious but it is more generally ascribed to ionization of O₂ (¹ Δ_g) metastable molecules by radiation in the wavelength range between 102.7 and 111.8 nm.

At altitudes below 70 km most of the ionization must be due to cosmic radiation, with N₂⁺ and O₂⁺ as the primary ions.

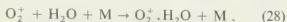
Given that NO⁺ and O₂⁺ are the primary ions at the altitude where hydronium cluster formation first occurs and that NO⁺ is produced at the more rapid rate what reactions are responsible for producing these clusters?

A great amount of laboratory effort has been spent in the past few years in measuring rates of cluster formation and break-up. There seems to be no difficulty in tracing out the sequences which lead from O₂⁺ to the hydronium clusters but for NO⁺ the situation is still not clear. In considering possible sequences account must be taken of the rate at which cluster ions recombine. Measurements by Lin *et al.* (1973) of dissociative recombination coefficients to water cluster ions show that values as high as

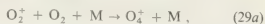
$$3 \times 10^{-12} \text{ m}^3 \text{ s}^{-1}$$

are to be expected.

For formation from O₂⁺, O₂⁺.H₂O is first formed, either through the three body reaction,



or through the sequence



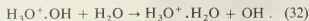
Subsequently the O₂⁺.H₂O reacts either directly with water to produce H₃O⁺



or, more probably as judged from measured reaction rates, via



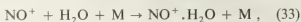
followed by



Further three body reactions with H₂O then produce higher degrees of hydration.

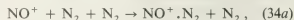
Measurements of reaction rates by Fehsenfeld *et al.* (1971) and Good *et al.* (1970) using quite different techniques indicate that these reaction sequences are acceptable.

With NO⁺ the basic difficulty is that the process analogous to (28)

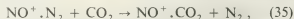


which could initiate the sequence, is far too slow (Fehsenfeld *et al.*, 1971). Alternative suggestions involving the formation of intermediate cluster ions NO⁺.N₂ and/or NO⁺.CO₂ were made [Dunkin *et al.*, 1971; Heimerl and Vanderhoff, 1971; Niles *et al.*, 1972].

It seems likely that these intermediates do play a key role but there is still no certainty about the relative importance of the different possibilities. The sequence



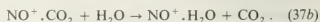
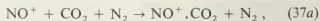
does not seem likely because of the high rate of the backward reaction in (34a), N₂ being only weakly bound to NO⁺. An alternative possibility involves the reaction



followed by



A still further possibility involves NO⁺.CO₂ alone viz :



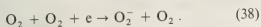
The measurement of reaction rates by flowing afterglow drift tube and SIFT methods is very difficult because of the low binding energies of some of the complexes. This requires that a sufficient concentration of a highly reactive scavenger is present to react totally with the weakly bound complex and produce a more stable detectable ion before the

weakly bound complex can be broken up. Values of the rate coefficient for (37a) at 200 K differ by a factor of ten. The most recent measurements [Smith *et al.*, 1977] using the SIFT method and paying special attention to the scavenging technique yield a high value. If this is correct then both the sequences (35), (36) and (37a), (37b) are likely to be significant in producing $\text{NO}^+ \cdot \text{H}_2\text{O}$.

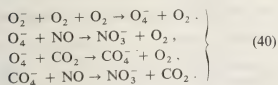
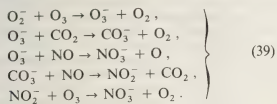
Even when this stage is reached it is far from clear what series of reactions leads thence to hydrated protons.

Until these complex reaction sequences are unraveled it is not possible to develop a detailed ion chemistry at those altitudes for which cluster ions are dominant.

Considerable attention has also been paid to determining the reaction paths followed in producing negative ions which predominate over the electrons below 70 km. The primary ion in these cases is almost certainly O_2^- formed by the three body reaction



A series of ionic reactions ultimately leads to the production of NO_3^- which, because of the high electron affinity of NO_3 [3.8 eV, Refaey and Franklin, 1974; Ferguson *et al.*, 1972], is the terminal ion. One sequence which proceeds via O_3^- and one via O_4^- are as follows



The rates of these reactions have been measured by flowing afterglow techniques [Massey, 1976] and they provide at least plausible reaction paths. However, the further stages which lead to hydration are less well understood and progress is hindered by the paucity of *in situ* observations of the negative ion composition.

In the region in which negative ions predominate over electrons ionization loss is by mutual neutralization. A number of measurements of mutual neutralization rates have been made [see for example Church and Smith, 1977; Smith *et al.*, 1976, 1977] using the flowing afterglow technique. The rate coefficient is not sensitive to the nature of the reactant ions being close to $5 \times 10^{-14} \text{ m}^3 \text{ s}^{-1}$ at room temperature for both clustered and unclustered ions.

Turco (1977) has considered in some detail the production of Cl^- ions in the lower ionosphere and finds that these ions are likely to depend strongly on the local concentrations of NO and H_2O . Under certain conditions they may well constitute as much as 10 % of the negative ion population. This is consistent with the *in situ* observations of Arnold *et al.* (1971) referred to earlier.

Although a great deal of work has been done in measuring rates of relevant ionic reactions the situation is so complex that much remains to be done before the ion chemistry is thoroughly understood.

The disturbed lower ionosphere. — At the time of a solar flare the X-ray emission from the Sun is enhanced, especially at the short wave end of the spectrum. These hard X-rays penetrate to the lower ionosphere where they ionize the main gases N_2 and O_2 . A similar increase in ionization at these levels occurs at polar latitudes (Polar Cap Absorption, PCA, events) when the flux of energetic charged particles entering the atmosphere from the sun is increased. It is found that during these disturbances the level at which ion clustering becomes important is depressed by more than 10 km during the day time.

Mitra (1975) has considered how the ion composition changes during flares and PCA events in terms of ionic reaction rates and showed that the reduction in the altitude at which clustering occurs would be expected in both cases.

The same feature is present during the so-called winter anomaly [Appleton, 1937] in ionospheric absorption — on most winter days at latitudes above 35° the h.f. ionospheric absorption is often larger than on summer days at midday. Measurements from rockets have shown that this is due to increased electron concentration in the height range 80-90 km [Mechtly and Sharke, 1968; Beynon and Williams, 1970; Dickinson *et al.*, 1976]. Beynon *et al.* (1976) have found, in further rocket experiments, that during an anomaly day the concentration of NO^+ is increased relative to O_2^+ so that it is by far the most abundant ion above 72 km, well below the altitude at which ion clusters normally dominate. It appears that the anomaly is due to increase in the NO concentration in the lower ionosphere.

Noctilucent clouds. — The highest cloud formations observed are the so called noctilucent clouds which are visible at high latitudes for a few months in the summer near twilight. As long ago as 1888 Jesse showed by triangulation that these clouds are located at altitudes close to 85 km, the height of the temperature minimum in the mesosphere, which is at its lowest in the summer at these latitudes. Recently, evidence from satellite observations [Donahue *et al.*, 1972] suggests that the noctilucent cloud displays are a nearly permanent feature at high latitudes in summer.

Almost all suggested mechanisms for formation of these clouds assume the presence of water vapour and suitable condensation nuclei [Castleman, 1974]. The possibility that these nuclei may be ions rather than dust particles was raised by Witt (1969). Direct evidence in support of this has been obtained by Goldberg and Witt (1977). They launched rockets containing identical payloads one from a mid-latitude station (Wallops Island, Virginia) and one at a higher latitude (Kiruna, Sweden), in the day time, following a visual sighting of noctilucent clouds the previous midnight. Each payload contained a quadrupole ion mass spectrometer, a probe to measure total ion density, and Faraday rotation experiments to measure electron concentration.

The mid-latitude launch produced data on positive ion composition of the normal type, consisting mainly of hydronium cluster ions and cluster ions of NO. While these ions were also observed in the high latitude launch they were much less prominent than heavy ions with masses between 90 and

145 a.m.u., observed in groups 18 a.m.u. apart. A plausible identification of these ions is that they are hydrates of Fe^+ or FeO^+ which it is then suggested provide the nuclei for the noctilucent cloud formation.

Metallic ions arising from ablation of meteors are observed at altitudes in this region. They lead to formation of so called sporadic E ionization.

It may well be that ion clustering is indeed of major importance in the formation of noctilucent clouds, in which case much may be learned about the process of nucleation from laboratory studies of clustered ions.

Acknowledgments. — My sincere thanks are due to my secretary, Mrs M. Burton, for assistance in preparing the manuscript and in many other ways and to Mr. D. Rooks for the preparation of slides and figures. Miss Una Campbell has also helped in providing line drawings.

References

- [1] ADAMS, N. G. and SMITH, D., *J. Phys.* **B** 9 (1976a) 1349.
- [2] ALBRITTON, D. L., DOTAN, I., LINDINGER, W., MCFARLAND, M., TELLINGHUISEN, J. and FEHSENFELD, F. C., *J. Chem. Phys.* **66** (1977) 410.
- [3] APPLETON, E. V., *Proc. R. Soc. A* **162** (1937) 451.
- [4] ARMSTRONG, J. C. and ZMUDA, A. J., *Radio Science* **8** (1973) 401.
- [5] ARNO, D. F., KESSEL, J., KRANKOWSKY, D., WIEDER, H. and ZÄHRINGER, J., *J. Atmos. Terr. Phys.* **33** (1971) 1169.
- [6] BARTH, C. A., RUSCH, D. W. and STEWART, A. I., *Radio Science* **8** (1973) 379.
- [7] BATES, D. R. and MASSEY, H. S. W., *Proc. R. Soc. A* **192** (1947) 1.
- [8] BAUER, S. J., BRACE, L. H., HUNTER, D. M., INTRILIGATOR, D. S., KNUDSEN, W. C., NAGY, A. F., RUSSEL, C. T., SCARF, F. L. and WOLFE, J. H., *Space Sci. Rev.* **20** (1977) 413.
- [9] BEYON, W. J. G. and WILLIAMS, E. R., *J. Atmos. Terr. Phys.* **32** (1970) 1325.
- [10] BEYON, W. J. G., WILLIAMS, E. R., ARNOLD, F., KRANKOWSKY, D., BAIN, W. C. and DICKINSON, P. H. G., *Nature* **261** (1976) 118.
- [11] BIERBAUM, V. M., ELLISON, G. B., FUTRELL, J. H. and LEONE, S. R., *J. Chem. Phys.* **67** (1977) 2376.
- [12] BIONDI, M. A. and BROWN, S. C., *Phys. Rev.* **75** (1949) 1700.
- [13] BRACE, C. H., THEIS, R. F. and DALGARNO, A., *Radio Science* **8** (1973), 341.
- [14] BRINTON, H. C., SCOTT, L. R., PHARO, M. W. and COULSON, J. T., *Radio Science* **8** (1973) 323.
- [15] BYRNE, J. and FARAGO, P. S., *Proc. Phys. Soc.* **86** (1965) 801.
- [16] CASTLEMAN, A. W., *Space Sci. Rev.* **15** (1974) 547.
- [17] CHAMPTION, K. S. W. and MARCOS, F. A., *Radio Science* **8** (1973) 297.
- [18] CHURCH, M. J. and SMITH, D., *Int. J. Mass Spectrom. Ion Phys.* **23** (1977) 137.
- [19] CUNNINGHAM, A. J. and HOBSON, R. M., *Proc. Phys. Soc.* **B** 5 (1972) 2320.
- [20] DEHMELT, H. G. and WALLS, F. L., *Phys. Rev. Lett.* **21** (1968) 127.
- [21] DICKINSON, P. H. G., HALL, J. E. and BENNETT, F. D. G., *J. Atmos. Terr. Phys.* **38** (1976) 163.
- [22] DOERING, J. P., BOSTROM, C. O. and ARMSTRONG, J. C., *Radio Science* **8** (1973) 387.
- [23] DONAHUE, T. M., GUENTHER, B. and BLAMONT, J. E., *J. Atmos. Sci.* **29** (1972) 1205.
- [24] DUNKIN, D. B., FEHSENFELD, F. C., SCHMELTEKOPF, A. C. and FERGUSON, E. E., *J. Chem. Phys.* **54** (1971) 3817.
- [25] FEHSENFELD, F. C., DUNKIN, D. B. and FERGUSON, E. E., *Planet. Space Sci.* **18** (1970) 1267.
- [26] FEHSENFELD, F. C., MOSEMAN, M. and FERGUSON, E. E., *J. Chem. Phys.* **55** (1971) 2115.
- [27] FERGUSON, E. E., DUNKIN, D. B. and FEHSENFELD, F. C., *J. Chem. Phys.* **57** (1972) 1459.
- [28] FERGUSON, E. E., FEHSENFELD, F. C., DUNKIN, D. B., SCHMELTEKOPF, A. L. and SCHIFF, H. I., *Planet. Space Sci.* **12** (1964) 1169.
- [29] GOLDBERG, R. A. and WITT, G., *J. Geophys. Res.* **82** (1977) 2619.
- [30] GOOD, A., DURDEN, D. A. and KEBARLE, P., *J. Chem. Phys.* **55** (1971) 3627.
- [31] GUNTUN, R. C. and SHAW, T. M., *Phys. Rev. A* **140** (1965) 756.
- [32] HANSON, W. B., SANATANI, S. and ZUCCARO, D. R., *J. Geophys. Res.* **82** (1977) 4351.
- [33] HANSON, W. B., ZUCCARO, D. R., LIPPINCOTT, C. R. and SANATANI, S., *Radio Science* **8** (1973) 333.
- [34] HAYS, P. B., CARIGNAN, G., KENNEDY, B. C., SHEPHERD, G. G. and WALKER, J. C. G., *Radio Science* **8** (1973) 369.
- [35] HEATH, D. F. and OSANTOWSKI, J. F., *Radio Science* **8** (1973) 361.
- [36] HEIMEL, J. M. and VANDERHOFF, J. A., *EOS Trans. AGU* **52** (1971) 870.
- [37] HINTEREGGER, N. E., BEDO, D. E. and MANSON, J. E., *Radio Science* **8** (1973) 349.
- [38] HOFFMAN, J. H., HANSON, W. B., LIPPINCOTT, C. R. and FERGUSON, E. E., *Radio Science* **8** (1973a) 315.
- [39] HOFFMAN, R. A., BURCH, J. L., JANETZKE, R. W., MCCHESENEY, J. F., WAY, S. H. and EVANS, D. S., *Radio Science* **8** (1973) 393.
- [40] JESSE, O., *Astron. Nachr.* **140** (1896) 161.
- [41] JOHNSON, C. Y., *J. Geophys. Res.* **71** (1966) 330.
- [42] KASNER, W. H. and BIONDI, M. A., *Phys. Rev.* **174** (1968) 139.
- [43] LEU, M. T., BIONDI, M. A. and JOHNSON, R., *Phys. Rev. A* **7** (1973) 292.
- [44] LIN, S. C. and TEARE, J. D., *Phys. Fluids* **6** (1963) 355.

- [45] LIN, S. L. and BARDSLEY, J. N., *J. Chem. Phys.* **66** (1977) 435.
- [46] McDANIEL, E. W., MARTIN, D. W. and BARNES, W. S., *Rev. Sci. Instrum.* **33** (1962) 2.
- [47] McELROY, M. B., KONG, T. Y. and YUNG, Y. L., *J. Geophys. Res.* **82** (1977) 4379.
- [48] MCFARLAND, M., ALBRITTON, D. L., FEHSENFELD, F. C., FERGUSON, E. E. and SCHMELTEKOPF, A. L., *J. Chem. Phys.* **59** (1974) 6629.
- [49] MCFARLAND, M., ALBRITTON, D. L., FEHSENFELD, F. C., FERGUSON, E. E. and SCHMELTEKOPF, A. L., *J. Geophys. Res.* **79** (1974) 2925.
- [50] MAHDAVI, M., HASTED, J. B. and NAKSHBANDI, M. M., *Proc. Phys. Soc. B* **4** (1971) 1726.
- [51] MASSEY, H. S. W. and BATES, D. R., *Rept. Prog. Phys.* **9** (1942) 62.
- [52] MASSEY, H. S. W., *Negative Ions* (Camb. Univ. Press), 1976, 3rd Edition, pp. 541-78.
- [53] MECHTLY, E. A. and SHRIKE, J. S., *J. Geophys. Res.* **73** (1968) 6243.
- [54] MEHR, F. J. and BIONDI, M. A., *Phys. Rev.* **181** (1969) 264.
- [55] MENDIS, D. A. and IP, W.-H., *Space Sci. Rev.* **20** (1977) 145.
- [56] MITRA, A. P., *J. Atmos. Terr. Phys.* **37** (1975) 895.
- [57] NARCISI, R. S., BAILEY, A. D., DELLA LUCCA, L., SHERMAN, C. and THOMAS, D. M., *J. Atmos. Terr. Phys.* **33** (1971) 1147.
- [58] NARCISI, R. S., BAILEY, A. D., WLODYKA, L. E. and PHILBRICK, C. R., *J. Atmos. Terr. Phys.* **34** (1972) 647.
- [59] NIER, A. O., POTTER, W. E., HICKMAN, D. R. and MAUERSBERGER, K., *Radio Science* **8** (1973) 271.
- [60] NIER, A. O., POTTER, W. E., KAYSER, D. C. and FINSTAD, R. G., *Geophys. Res. Lett.* **1** (1974) 197.
- [61] NIER, A. O. and McELROY, M. B., *J. Geophys. Res.* **82** (1977) 4341.
- [62] NILES, F. E., HEMERL, J. M. and KELLER, G. E., *EOS Trans. AGU* **53** (1972) 456.
- [63] OPPENHEIMER, M., DALGARN, A. and BRINTON, H. C., *J. Geophys. Res.* **81** (1976a) 4678.
- [64] OPPENHEIMER, M., DALGARN, A. and BRINTON, H. C., *J. Geophys. Res.* **81** (1976b) 3762.
- [65] PELZ, D. T., REBER, C. A., HEDIN, A. E. and CARIGNAN, G. R., *Radio Science* **8** (1973) 277.
- [66] PLUMB, I. C., SMITH, D. and ADAMS, N. G., *Proc. Phys. Soc. B* **5** (1972) 1762.
- [67] REFAEY, R. M. A. and FRANKLIN, J. L., *J. Chem. Phys.* **61** (1974) 733.
- [68] REID, G. C., *J. Atmos. Sci.* **32** (1975) 523.
- [69] RICE, C. J., CARTER, V. L., LA VALLE, S. R., CHATER, W. T., JONES, D. A., KING, C. G. and NELSON, D. F., *Radio Science* **8** (1973) 305.
- [70] RUSCH, D. W., TORR, D. G., HAYS, P. B., WALKER, J. C. C. and NIER, A. O., *EOS Trans. AGU* **56** (1975) 1037.
- [71] SMITH, D., ADAMS, N. G. and CHURCH, M. J., *Planet. Space Sci.* **24** (1976) 697.
- [72] SMITH, D., ADAMS, N. G. and GRIEF, D., *J. Atmos. Terr. Phys.* **39** (1977a) 513.
- [73] SMITH, D., CHURCH, M. J. and MILLER, T. M., *J. Chem. Phys.* **68** (1977) 1224.
- [74] SPENSER, N. W., NIEMANN, H. B. and CARIGNAN, G. R., *Radio Science* **8** (1973) 287.
- [75] STEIN, R. P., SCHICK, M., SYVERSON, M. W., SHAW, T. M. and GUNTON, R. C., *Phys. Fluids* **7** (1964) 1641.
- [76] TORR, D. G., TORR, M. R., WALKER, J. C. G., NIER, A. O., BRACE, L. H. and BRINTON, H. C., *J. Geophys. Res.* **81** (1976) 5578.
- [77] TORR, D. G., ORSINI, D., TORR, M. R., HANSON, W. B., HOFFMAN, J. H. and WALKER, J. C. G., *J. Geophys. Res.* **82** (1977b) 1631.
- [78] TORR, M. R., ST-MAURICE, J. P. and TORR, D. G., *J. Geophys. Res.* **82** (1977a) 3287.
- [79] TURCO, R. P., *J. Geophys. Res.* **82** (1977) 3585.
- [80] VIEHLAND, L. A. and MASON, E. A., *J. Chem. Phys.* **66** (1977) 422.
- [81] WALKER, J. C. G., TORR, D. G., HAYS, P. B., RUSCH, D. W., DOCKEN, K., VICTOR, G. and OPPENHEIMER, M., *J. Geophys. Res.* **80** (1975) 1026.
- [82] WALLS, F. and DUNN, G. H., *J. Geophys. Res.* **79** (1974) 1911.
- [83] WANNIER, G. H., *Bell. Syst. Tech. J.* **32** (1953) 160.
- [84] WELLER, C. S. and BIONDI, M. A., *Phys. Rev.* **172** (1968) 198.
- [85] WITT, G., *Space Res.* **9** (1969) 157.
- [86] YOUNG, R. A. and ST-JOHN, G., *Phys. Rev.* **152** (1966) 25.

Plasma and solar physics. The solar flare phenomenon

J. Heyvaerts

Observatoire de Paris-Meudon and Université de Paris VII

Résumé. — Les principaux aspects de la physique solaire ayant trait à la physique des plasmas sont rapidement présentés. Le phénomène d'éruption solaire est décrit et certaines théories actuelles concernant l'état pré-éruptif et le mécanisme de déclenchement passées en revue, à savoir : la théorie de l'existence d'un point de retournement dans les états d'équilibre possible et la théorie basée sur l'analogie avec les instabilités résistives observées dans les Tokomaks. La microphysique qui, croit-on, permet le confinement turbulent d'un plasma de 100 millions de K dans le plasma coronal est évoquée, et on montre enfin qu'une turbulence cyclotron ionique dans la région éruptive possède une signature assez caractéristique dans les abondances isotopiques et états de charges des ions accélérés.

Abstract. — The main topics of solar physics to which plasma physics is relevant are briefly presented. The solar flare phenomenon is described and some present theories concerning the preflare state and flare triggering reviewed, namely the theory based on the existence of a turning point in the set of possible preflare equilibria and the theory based on an analogy with resistive instabilities observed in Tokomaks. The microphysics which is believed to be responsible of the confinement by turbulent processes of a 10^8 K plasma in the coronal plasma is evoked and it is finally shown that ion cyclotron turbulence in the flaring region is evidenced by a characteristic signature in isotopic abundances and charge states of accelerated ions.

This communication is intended to be a short survey of our present state of knowledge and partial understanding of the solar flare phenomenon.

The reader may not be very familiar with solar physics, and so I shall first make a rapid description of the sun as a whole. This will give me the opportunity to allude to some plasma physics problems of interest far solar physicists other than the flare problem.

The sun is a normal typical star, that is a self gravitating sphere of hot plasma which sustains its energy output by the nuclear conversion of hydrogen into helium in an interior core, very hot (15×10^6 K) and very dense (120 g cm^{-3} , or $7 \times 10^{25} \text{ cm}^{-3}$). The plasma there is a strongly coupled plasma. The largest part of the rest of the sun up to near the surface is made of a similar type of plasma. The energy liberated inside is radiatively transferred outwards, very slowly of course because the opacity of the solar matter is very large there. The physics of energy transport changes somewhat near the surface because the radiative model predicts sharp temperature gradients there. It turns out that in this model the opaque region just below the visible surface of the sun should be unstable to convective motions, or in other terms the gravity-wave modes become purely growing. One gets then a convective superficial layer which is certainly turbulent.

The convection manifests itself at the photosphere (the visible outer layer of the sun in ordinary white light) in the form of the so-called granulation. The granulation is shown in figure one. Bright regions represent slightly hotter ascending pieces of plasmas,

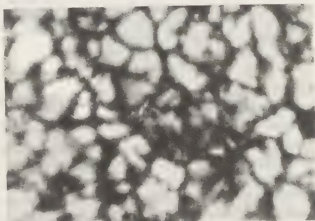


Fig. 1. — The solar granulation. The size of each granule is typically 700 km.

while in the cooler, darker interstices the matter is sinking again downwards. Granules are small (700 km). The theory of convection in a system in which a strong density difference exists between the top and the bottom and where magnetic fields exist and are even perhaps generated is not at all in a satisfactory state now. This convective flow transport energy to an overlying static radiatively stable thin layer above, which is what is properly called the sun's atmosphere. It also exists there a number of waves which propagate upward and represent an outgoing flux of mechanical energy.

Superposed to the granular motion one has been able to detect another type of cellular motion too, the supergranulation. The size of a supergranule is much larger than that of a granule (30 000 km) and

its life time, is some 10 hrs. The supergranular motion sweeps the magnetic field and concentrates it on the boundaries of the cells. Figure 2 represents an artist view of granular and supergranular motions. In the atmosphere itself, the mean temperature decreases with height up to a certain point, where it reaches 4 300 K. For definiteness we shall consider here that this is the surface of the interior sun. Above this point the temperature raises again as a result of the dissipation of the mechanical flux of energy driven in the outer atmosphere by the convection zone. The theory of the generation, propagation in the outer layers, and dissipation of waves in the solar atmosphere is also a difficult aspect of solar physics which will not be our point today. Ideally it would involve a theory of compressive convection turbulence, in the presence of a magnetic field, of the propagation of resulting waves in a strongly inhomogeneous medium and its ultimate dissipation in the very rarefied medium which constitutes the outer layers: the chromosphere and the corona. The

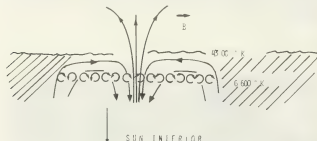


Fig. 2. — A schematic drawing of granular and super granular motions and solar magnetic fields.

chromosphere above the surface is a tenuous medium (density 10^{11} - 10^{12} cm^{-3}) at a temperature of 10^4 K. It cannot be seen in full light in normal non eclipse conditions, but may easily be photographed at wavelengthes of lines which form in these regions, in particular the $H\alpha$ line of hydrogen and a violet line of ionized calcium (K line). Figure 3 is a picture of the sun in this latter radiation. The granular aspect is the chromospheric counter part of the supergra-

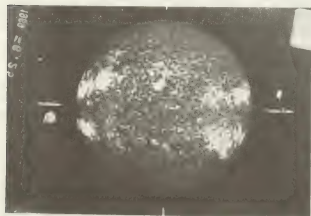


Fig. 3. — Calcium II K line photograph of the sun. Brighter regions coincide with magnetic field enhancement.

nulation pattern and bright patches are regions of enhanced magnetic field. The magnetic field dominates the higher chromosphere as can be seen on $H\alpha$ photographs which show a hairy structure of magnetic field lines.

The chromosphere is in contact on its upper boundary with the corona, an even more tenuous medium (10^9 cm^{-3}) also heated by the mechanical energy flux, it is thought, though this is far less evident than for the chromosphere. The temperature of the corona is between 1 and several million degrees. The contact between these two regions is characterized by very strong temperature gradient. It is called the transition region. The corona is perhaps an even more structured region than the chromosphere, as you can see on the eclipse photograph shown in figure 4.

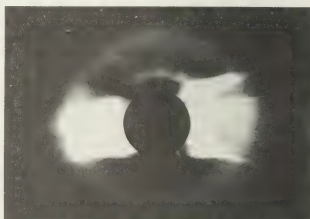


Fig. 4. — The solar corona as seen in white light eclipse photograph.

Active regions appear as concentration of magnetic flux around special regions, the sunspots, like the ones shown in the picture (Fig. 5). In these spots, the average field may range from 500 to several 1 000 G, and the extension of the spot in the nearby region, the penumbra, shows that one could conceive the spot as a bundle of magnetic fibers. I shall leave apart also in this brief survey the extremely interesting and difficult problem related to the dynamo action of the photosphere and the creation of the sun's magnetic field. It is quite probable of course that the

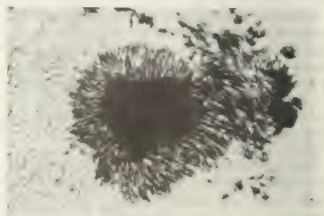


Fig. 5. — A white light photograph of two sunspots.

origin of this field is intimately related to the convective motions rather deep in the sun, as evidenced in the fact that fields are patterned by the supergranular motions, and in the fact that spots grow at corners of supergranules. Active region flux concentrations exert a strong influence on the neighbouring corona which we can now see even against the disk by soft X ray imaging. The thermal radiation of the hot corona is detected by this instrumentation, and the following picture (Fig. 6) shows essentially map of the corona which is sensible to both density and temperatures. It is seen that the corona is threaded by a system of loops of all sizes, presumably underlying the magnetic structure. We have also observed «holes» which are regions of open magnetic fields, with lower densities or temperatures, and which must be

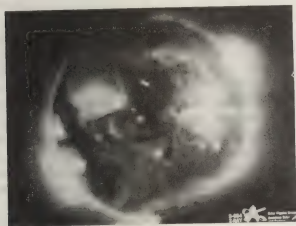


Fig. 6. — X ray picture of the solar corona.

considered as the source of the solar wind. Magnetic flux in the form of flux tubes emerge in the outer atmosphere, presumably because of buoyancy forces exerted on them on the photosphere, in which they are also at smaller pressure, but at equal temperature because of the effectiveness of radiative energy transport. They are then lighter and suffer vertical buoyant forces. When popping up in the atmosphere they create short lived X ray bright point, which are seen on figure 7, by their interaction with the ambient fields, or perhaps by their own internal dynamics.

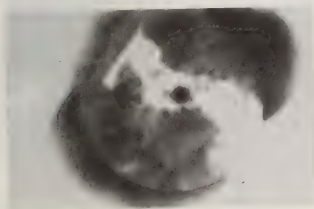


Fig. 7. — Negative of an X ray picture of the solar corona showing X ray bright points (black dots).

A more dramatic energy release event is the solar flare which instead of being a very local energy release in a rather quiet environment occurs in an active region. Obviously the energetics of a solar flare cannot be accounted for only on the basis of the energy of the emerging magnetic field. The event releases some 10^{32} ergs in some 100 to 1 000 s depending on the importance of the event. An $H\alpha$ photograph of a flare at its full development is shown in figure 8.

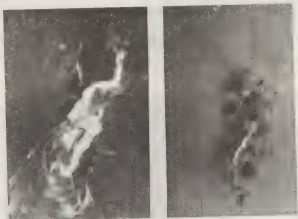


Fig. 8. — A fully developed two ribbon solar flare as it appears in $H\alpha$ light (left) and in white light (right). The fact that white light emission is detectable is rare and characteristic of very large events only.

We can sketch the observable manifestations of a flare as follows :

- 1) The phenomenon occurs always very close to a line where the photospheric magnetic polarity reverses, let us call this the inversion line, in an active region or very near.
- 2) The phenomenon proper is preceded by a preflare phase during which the energy to be liberated into *radiated* forms is stored in the region. This build up phase does not need to last more than some hours.
- 3) An active region filament is often present, which maps almost exactly the inversion line. Prominences, or filaments (Fig. 9) are an important object of the solar corona which I have not yet had the opportunity to describe. It is so to speak cloud like matter at chromospheric conditions hanging up high in the corona and certainly prevented from just free falling by Lorentz forces. Filaments may exist outside active regions hanging at heights of 40 000 km above the surface (they are called quiescent prominences) as well as inside active regions ; in the latter case their height does not exceed some 7 000 km. The object has the form of a thin thing hanging vertically over a height much larger than the scale height of a 10^4 K plasma (which would be very small). This means that the filament must be supported at each point in its body by Lorentz forces if it is a structure in magnetohydrostatic equilibrium which it seems to be. No really satisfactory model of filament equi-

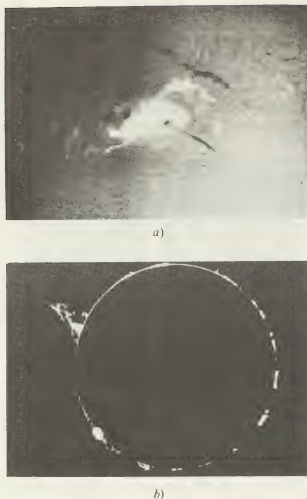


Fig. 9. — a) A flare is shown here together with several active region filaments (dark ribbons) ($H\alpha$ photograph). b) A quiescent prominence is shown here suffering an upward motion, and will soon disappear (upper left). This is a coronagraph $H\alpha$ photograph in which the bright sun is artificially hidden.

librium and energy balance exist at present, though on a global scale the problem may be looked at as a 2D MHD equilibrium problem which I shall describe below. It has been established at Meudon Observatory (Martes *et al.*) by a confrontation of magnetic map and velocity map that the flare are most likely to occur in cases when a shear flow exist on the photosphere in the vicinity of the magnetic inversion line. This has been interpreted as a necessary condition for energy storage, and this idea has been substantially supported by an approximate calculation of the amount of magnetic energy stored in the corona as a result of current driven there (Tanaka, Nakagawa) by the displacement of the feet, of field lines which are obliged to follow the photospheric motions, the latter being an energy reservoir of the process. The magnetic field in the corona which is unobservable directly, had been extrapolated from photospheric data on the basis of a constant α ($\alpha = \nabla B$) force free approximation. The value of α has been chosen to match the general direction of field lines, as observed from the $H\alpha$ pictures. It has been shown that the stored magnetic energy calculated

that way increased steadily up to the moment of the flare, but was smaller just after. Moreover, the quantitative value of this decrease was found to be compatible with the sum of the observed emissions produced by the flare in various forms (light, X rays, EUV, energetic particles, mass motions). Solar physicists, are then quite confident that the liberated energy was actually stored in the form of magnetic energy in a coronal current system. Because the β of the coronal plasma is low, the magnetic structure is very likely to be force free, except perhaps in the vicinity of possibly existing current sheets, or in the filament which is so often found to underline the line of inversion of the magnetic polarity and, as we just noted, must be sustained by Lorentz forces.

The flare itself begins abruptly by an impulsive phase which may be a short as several seconds. At that time the most conspicuous phenomenon is the emission of a spiky burst of hard X rays, in the energy band between, say, 20 keV and 100 keV, radio emission of cm and m wavelengths are also observed. Almost simultaneously bright small regions (flare knots) appear in the chromosphere as seen, in particular, in the $H\alpha$ line. This illumination is due to energy precipitating in or conduced to the photosphere. It will subsequently broaden on time scale of several minutes. This is the flash phase. In flares of some importance the illumination takes the form of two parallel ribbons (Fig. 8) and it has been shown recently, thanks to soft X ray observations that these ribbons are bridged by soft X ray emitting loops. In large event a typical radio emission at meter wavelength occurs, which is the signature of a shock wave. The system of hot loops and bright $H\alpha$ ribbons then persist for some time, typically one hour, while the ribbons separation systematically and slowly increases. At a late stage of the process these loops become progressively cooler and, become eventually visible in $H\alpha$ as a system of so-called post flare loops, such as shown here on the limb $H\alpha$ picture (Fig. 10).

In a small number of cases, one has observed a gamma ray emission. Actually the γ ray emission is



Fig. 10. — Post flare loops. $H\alpha$ picture taken near the limb of the sun.

associated with very large event only and a suitable detailed spectrum has been observed in only one case; the observed spectrum consists of a continuum emission, which can be explained by bremsstrahlung from high energy electrons, and a few number of lines. The high intensity line at 2.2 MeV results from neutron capture by protons to give deuterium nuclei. In some flares expanding mass motions are observed high in the corona, in white light photographs (coronal transients), though such motions are also often associated with non flaring events. Long after the flare (due to propagation conditions in the interplanetary space), high energy electrons are observed on space crafts as well as energetic protons and cosmic ray nuclei.

The problems posed to the theorist can then be stated as follows :

- 1) To understand the preflare stable configuration and the reason of its destabilization or at least its evolution prior to flare.
- 2) To pin point the mechanism which gives rise to the impulsive liberation of energy.
- 3) To understand why this energy is so distributed in the various observable forms, in particular, how the 25-100 keV electrons which are responsible of the impulsive manifestations during the very first seconds are accelerated.
- 4) To modelize the main phase continuous dissipation process.
- 5) To explain the acceleration of higher energy electrons (1 MeV to 10 MeV) and of high energy protons and nuclei (10-100 MeV, sometimes more).

It is impossible to review in detail all these aspects; therefore we shall consider some interesting or better observed aspects and in particular problems related to build up and impulsive phase triggering. As I explained a bit earlier, the magnetic configuration in the preflare state is a current carrying plasma. Some authors have a long time advocated that the electric currents in the corona should form a large current sheet, and the flare would be due to an impulsive dynamic reconnection process in this sheet (Syrovatskii). It is difficult however to conceive how such a sheet current system could grow to such a large extent as to contain the energy for the flare without tearing quite early of suffering the interchange instability (Uchida, Sakurai). If current concentrations in a sheet-like structure occur at all, one now thinks that they would appear on a more local scale. Probably more likely is the idea that the current system is just almost everywhere present in the flare region. We can then have two different looks at it : one can consider its global arrangement, which I think is the relevant way to analyse it as far as magnetic storage and global stability is concerned, while the other way is to look at its more detailed local configuration, and fine structure a point of view which is

on the other hand of primary importance if one is interested in flare triggering.

A suitable analysis of the first problem can be done by taking advantage of the fact that, as suggested by the two ribbon structure observed in many flares and the elongated form of the filament, a 2D approximation to the global magnetic structure, ignoring variation of quantities in the direction parallel to the line of inversion of the magnetic polarity would not be too bad an approximation. In that case the magnetic configuration is well defined by the z component of the magnetic field, B say, and the z component of the vector potential, A say. Both these quantities are functions of x and y . One can write the magnetic field as :

$$\mathbf{B} = \frac{\partial A}{\partial y} \mathbf{e}_x - \frac{\partial A}{\partial x} \mathbf{e}_y + B \mathbf{e}_z.$$

In that case $A(x, y) = \text{constant}$ represents the projection on the xy plane of lines of forces

$$\mathbf{J} = \frac{1}{\mu_0} \left(\frac{\partial B}{\partial y} \mathbf{e}_x - \frac{\partial B}{\partial x} \mathbf{e}_y - \Delta A \mathbf{e}_z \right)$$

$$\mathbf{J} \wedge \mathbf{B} = \frac{-1}{\mu_0} \left(\left(B \frac{\partial B}{\partial x} + \Delta A \frac{\partial A}{\partial x} \right) \mathbf{e}_x + \left(B \frac{\partial B}{\partial y} + \Delta A \frac{\partial A}{\partial y} \right) \mathbf{e}_y + \left(\frac{\partial B}{\partial x} \frac{\partial A}{\partial y} - \frac{\partial B}{\partial y} \frac{\partial A}{\partial x} \right) \mathbf{e}_z \right).$$

One can easily show that the force balance equation :

$$\mathbf{j} \wedge \mathbf{B} = \nabla p + \rho g \mathbf{e}_y$$

and the 2D translational symmetry, imply that the z component of the Lorentz force vanish, which (look at his expression) mean that B is constant along a line of force, or :

$$B(x, y) = B(A(x, y)) = B(A).$$

The pressure p , which is a priori a function of (x, y) can be looked at as a function of altitude y and line of force parameter A :

$$p(x, y) = p(A(x, y), y) = p(A, y).$$

With this in mind, we can write the x and y component of force balance as an hydrostatic equation of equilibrium :

$$\frac{\partial p}{\partial y} = - \frac{\mu}{R} \frac{p}{T(A, y)}$$

which expresses equilibrium along a line of force, and we obtain also, on the other hand, an equation for the shape of lines of forces :

$$-\Delta A = \frac{\partial}{\partial A} \left(\frac{B^2(A)}{2\mu_0} + p(A, y) \right).$$

The equation for the pressure can be integrated only if we know the temperature distribution along the line of force. The latter, especially if a prominence is involved in the magnetohydrostatic equilibrium of

interest can only be obtained as a result of a very complicated energy balance which is self consistently coupled to the magnetohydrostatics problem that we try to solve by means of such effect as the pattern of mechanical energy flow in the structure, heat conduction. Up to now studies of prominence equilibrium have only used crude approximations like $T = \text{constant}$ (!) and the existence of field along the direction of symmetry has largely been ignored though observations definitely show that it is present and large.

Another interesting approximation is to take advantage of the fact that the β of the plasma is small, and to solve for the force free case, the equation :

$$-\Delta A = \frac{d}{dA} \frac{B^2(A)}{2\mu_0} = \varphi(A)$$

where now B_z is non zero.

We need however to prescribe $B^2(A)$ for this non linear elliptic equation to be written in closed form. This function, at least for those values of A taken on the boundary, in that case the X axis, may be prescribed once one knows the displacement of the footpoints of line $A(x, y) = a$ one with respect to the other. The relevant relation is

$$B(a) = I(a) \left(\int_{x(a)}^{x(a')} \frac{dx'}{(\partial A / \partial x')_{A(x', y)=a}} \right)^{-1}.$$

It seems perfectly justified to assume that the energy build up proceeds through a series of equilibria. In full, the problem is to solve the coupled set of equations above for a series of time dependent functions $I(A, t)$ where t would enter as a mere parameter. This programme has not yet been completed because of the intricate relation between $B(A)$, $I(A)$ and $A(x, y)$. Authors have preferred to take a look at a schematization of this problem in which we skip the relation which relates $B(a)$ and $I(a)$ and consider that the function $\varphi(A, t)$ is given by :

$$\varphi(A, t) = \lambda(t) F(A)$$

(Low, Jockers, Birn *et al.*, Heyvaerts *et al.*), where the stretching parameter $\lambda(t)$ varies from 0 (potential configuration) to progressively larger values of λ . One can show that, stating the problem in this form amount to prescribe the vertical current driven by the boundary (the photosphere or here the X axis) into the domain of study.

The corresponding shear $I(a)$ can be deduced afterwards if one wishes, but due to the crude simplifications exerted before, it has no reason to be a monotonous function of λ nor to be regular, as one could have wished. Nevertheless some general interesting results can be obtained. We have been able (Heyvaerts *et al.*, 1978) to prove mathematically the following results for the solution of :

$$-\Delta A = \lambda F(A)$$

in $(\mathbb{R} \times \mathbb{R}^+)$ with boundary conditions $A(x, 0) = g(x)$ on the x axis, subject to the reasonable conditions that $F(A)$ be regular and finite, vanishes except for A in a certain bounded interval, and vanishes sufficiently rapidly near $A = 0$ which is the boundary value $A(\pm \infty, 0)$. The semi infinite character of the domain mathematically acts as a singularity of the operator. It seems to be a feature of essential significance.

1) The potential configuration found for $\lambda = 0$ can be followed by continuity up to some finite value λ^* of the stretching parameter.

2) Whatever λ be, however, there exist at least one solution with an asymptotically open topology. This is schematically shown in figure 11.

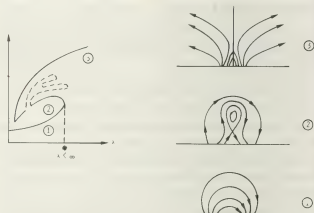


Fig. 11. — Schematic properties of the 2 dimension MHD equilibria obtained by growing the current delivered by the boundary in proportion to $\sqrt{\lambda}$ (see text).

The catastrophe behaviour of the potential like solution had been recognized earlier for special cases either by solving analytically for one case (Low, Birn *et al.*), either from semi qualitative argument and numerical study of special cases (Jockers). The universality of this behaviour is now established as well as the existence of an open topology solution, a new result, which had been suspected from earlier work, by Barnes and Sturrock.

The ideal MHD stability of the lower branch solution against 3D perturbations has been established in full generality (Birn, 1978) as well as partial results concerning dissipative stability.

Nothing general is known concerning other (intermediate solutions) which may well exist. Work is in progress on this question.

It does not seem impossible at all that the structure could be driven by continuous stretching to the catastrophe point where a dynamical evolution will necessarily take place, due to the lack of neighbouring equilibrium. A conjecture is that the structure would be blown open towards the « top » open solution; if a filament is involved in the structure this would appear as a sudden disappearance as often observed. Another conjecture would be that it jump on some intermediary equilibrium state, involving a change

of topology which could be achieved only through a dissipative process. As a phenomenological model some authors (Kopp *et al.*) propose that the trigger of the flare be actually the MHD blowing up of the global magnetic configuration, which later will reconnect to a normal, that is to a closed topology, type of configuration only then giving rise to dissipative phenomena, particle acceleration...

Although this might sometimes be so, observations also indicate that in some instances the flare is triggered by the emergence of small regions of some polarity imbedded into larger regions of the opposite polarity. Besides it is known from X ray observations that the very first soft X ray brightenings sometimes occur in tiny compact structures which look like loops. The problem of finding a *local* trigger mechanism and a way of spreading the dissipative process to the rest of the structure then arises for explaining these events. The main requirement is to get a very impulsive process, working on a time scale of a few seconds and able to produce the hard X ray emission which we observe, the latter is the hard X ray emission which we observe. The latter is the signature of the presence of fast electrons in the 100 keV range in the flaring region. The number of electrons needed to give rise to the observed radiation depends however to some extent on the conditions of production of these X rays, a problem on which we come back soon. Some models have now been examined with some detail in the literature, though it has not yet been possible, by far, to reach a definite conclusion. A large number of them have dealt with the possibility of reaching a state of microturbulence in the current carrying system, or reaching high values of the electric field, of the order of the Dreicer field (Coppi Friedland, Heyvaerts and Priest, Heyvaerts and Kuperus). All these models as well as the double layer model proposed by Alfvén face the same difficulty : it is extremely difficult to find oneself in conditions such that the necessary thresholds be reached. Reaching the Buneman threshold in a plasma with $n = 10^{11} \text{ cm}^{-3}$ and $T = 10^6 \text{ K}$ implies a current density of $64\,000 \text{ A m}^{-2}$ which corresponds to a field gradient of $1\,000 \text{ G m}^{-1}$. Sheet like current concentrations or extreme degrees of the filamentation would then be required. Observations nevertheless, as we shall see later point to extreme current densities ! I cannot enter here into the details of specific mechanisms which have been imagined to achieve this situation. In brief, I would summarize that switching the resistivity regime in a current sheet, reconnecting or not, to a microturbulent state is feasible in special conditions (Heyvaerts, Priest, Tur and Priest). A flare model based on the idea that the primary energy release is due to such a transition has been proposed. It has been shown that a small number of particles can be accelerated as a result of the sudden energy conversion that result from this change of resistivity regime. Another idea

is that the very primary release of energy be not due to micro-instabilities but instead to the rapid development of a tearing instability in some suitable structure of the region, for example a single current-carrying loop. The situation actually realized cannot be inferred from the observations because these structures should be at the limit or even smaller than the resolution of telescopes and magnetographs.

The tearing instability in a loop can only be a viable theory if the structure can be maintained stable prior to the impulsive phase while still containing an adequate amount of free energy. It should also be proved that the release time scale, once instability has started can be short enough. Concerning the first point, Spicer (1976) has established that this requirement implies that a compact low lying loop must be considered.

The time scale requirement if we take as a typical growth time the geometrical mean of Alfvén and resistive time scale :

$$\tau = \sqrt{\tau_A \tau_R}$$

has been long considered to be a fairly severe constraint. First estimations led Spicer to conclude that the mechanism was only viable if the structure contained rather concentrated current sheets with a thickness of some 80 m only. Moreover, it was known some tearing modes appear to reduce their growth at rather low levels. However, here, we should keep in mind several aspects of the question, in particular the fact that growth rates tend to be larger than those applicable to a plane sheet when other geometries are considered, that some types of tearing modes continue to exponentiate during their non linear development, and that the dependance of the growth rate on the parameter S , which may be very large, may differ substantially from the $(\tau_A \tau_R)^{1/2}$ formula. To get an idea of the importance of these effects let us consider the growth time for three different cases of tearing modes ; according to respectively :

$$\tau = (\tau_A \tau_R)^{1/2} = \tau_R S^{-1/2}$$

and the extreme cases of slow tearing modes

$$\tau_{\text{slow tearing}} = \tau_R^{3/5} \tau_A^{2/5} = \tau_R S^{-2/5}$$

and of a very fast, $m = 1$, double tearing mode, which according to Spicer (1978) has a growth time :

$$\tau_{DTM} = \tau_R^{1/4} \tau_A^{3/4} = \tau_R S^{-3/4}$$

For parameters appropriate to our problem, we have

$$\tau_R = \mu_0 \sigma a^2 = 10^6 \left(\frac{T_0}{10^6} \right)^{3/2} a_{km}^2$$

$$S = 2.18 \times 10^{10} a_{km} \left(\frac{B}{100 \text{ G}} \right) \left(\frac{T_0}{10^6} \right)^{3/2} \left(\frac{10^{16}}{n(m^{-3})} \right)^{1/2}$$

Let us consider a standard case $B = 100$ G, $T = 10^6$ K, $N = 10^{16} \text{ m}^{-3}$ but two different scales for the current carrying region, $a = 10$ km and $a = 100$ km.

	$a = 10$ km	$a = 100$ km
τ_R	10^8 s	10^{10} s
τ	$10^{2.85}$ s	$10^{4.35}$ s
τ_{STM}	$10^{3.88}$ s	$10^{5.5}$ s
τ_{DTM}	2 s	33 s

It is seen that, whereas the slow types of tearing modes are, even with these rather small characteristic sizes, far too slow as compared to the impulsive phase characteristic times, a considerable factor can be gauged if so called fast tearing modes are involved, and that non linear saturation may not be a serious limitation. It remains of course to justify that one is really in that situation. Referring to a numerical calculation by Schnack and Killeen, Spicer (1978) argues that a bit less than 5% of the total magnetic energy may be released in 14 Alfvén travel times in the form of heat, which of course represents a fairly high rate of energy release, in the case of double tearing modes and that this could rapidly raise the plasma to a very high temperature, given approximately ignoring any losses by say

$$nkT = 0.9 \times 5/100 \times B^2/2\mu_0.$$

This allows to reach 2×10^7 K for 100 G, or 2×10^9 K for a release in 1 000 G field. In the latter case the mean energy per particle is high enough to be of the order of what is required to produce the hard X rays thermally. One difficulty in the present state of this theory is of course that one does not really understand yet why the structure should wait finding itself in such a very unstable state before it starts to tear. Moreover, though the sheet thickness implied is by far not as small as the ones implied by the micro-instability phenomena it is still quite smaller than the typical size of the cross section of such a loop, which may be estimated to some thousand kilometers, so that a specific theory is also required to explain how such current concentrations may arise. An analysis of thermal instabilities applicable to a coronal plasma heated by a mechanical energy flux, as well as by Joule heating and which cools by radiation and conduction has been made in the literature (Heyvaerts, 1974; Spicer, 1976). A linear analysis indicates that currents could be concentrated as a result of what is essentially an overheating instability in certain conditions of initial temperature. However, the growth times are fairly long, of the order of several hours. This is barely compatible with the preflare time scale but this rate may be larger if an even modest factor of enhancement of the resistivity can be explained, or perhaps does this rate accelerates in the non linear stage. The degree to which currents can become concentrated is not yet precisely known.

Let us now assume that we have been able to find a mechanism which dumps the required energy at the required rate into the electrons of some finite small region in some loop. How will these particles behave, and will it then be possible to explain the observed radiations? It seems that this aspect of the question, which is a better posed problem, and which may be subject to some observational tests has met with a larger degree of success.

The point starts by a consideration of the hard X ray impulsive burst, for which it has been soon recognized that the most likely emission mechanism was bremsstrahlung. It has been first thought that the source should simply be pictured as an acceleration region high in the corona, providing fast particles travelling down and bombarding the denser parts of the solar atmosphere. However, once the required flux of electrons could be estimated from the observations (Hoyng *et al.*); it was realized that this simple model was not tenable because it would involve a flux of 10^{36} electrons s^{-1} dumped in the chromosphere, and a total number of accelerated electrons as high as 10^{37} - 10^{38} which is just the order of magnitude of the total electron content of a flaring flux tube. This directed flow of electrons constitute a beam passing through a plasma, between the acceleration region and photosphere. It will not only become unstable to plasma waves but create an enormous magnetic field. In fact the electric current represented by the downwards flowing fast particles will be compensated by a return current driven in the background plasma. This return current, if the beam is too strong, will itself turn micro-unstable and the beam will stop, because it loses all its energy driving this excessively damped current. Only ion acoustic instability has been studied up to now in this context, but I think that results concerning the electrostatic ion cyclotron instability should appear soon. The simple downward flow of energetic particles to the chromosphere may then just not be possible. Actually this is fortunate, because the embarrassingly high number of electrons required can be traced back to the fact that X ray radiative losses of these particles in a cold plasma is 10^{-5} times smaller than collisional losses on cold electrons. Bombarding a cold gas with energetic electrons is an intrinsically inefficient way of emitting X rays. A more efficient source would be one in which the electrons would be more or less thermal at temperature 15 keV say. Collision losses would be reduced to zero, but of course, one must in this case take care of conduction and expansion losses that the hot region must suffer. The conduction losses can be cut down by just the same beam return current instability mentioned above because the hot electrons which sustain the heat flow act as the beam we were speaking of before and induce also a return current. It then appears possible thanks to this process to understand the bottling up of a large part of the energetic electron population in the coronal regions, and its more

effective ability to emit X rays. However, the « corks » of turbulence are not completely opaque for the fastest electrons which leak out, driving in the exterior medium a beam-plasma instability. The beam may be strong, but according to Papadopoulos and Vlahos it can be stabilized by the transfer of waves to low phase velocities as a result of the ponderomotive force once the Langmuir turbulence has reached the threshold level for the modulational instability to set in. The resulting ion clumping according to C. Norman and B. Smith will produce a state of enhanced resistivity, which will be an ideal way of spreading of the dissipative process to a larger volume of the flaring region, while, however, the stabilized beam will be able to reach down to the chromosphere and produce there impact effects which are actually observed in the form of flare knots.

I would like now to finish this talk by explaining how a peculiarity of solar cosmic ray nuclei which has been for some time quite a puzzle finally turns out to give us interesting clues concerning the conditions in the preflare plasma.

The acceleration of high energy nuclei is an interesting aspect of the flare mechanism. This acceleration occurs only in a restricted number of flares. The proton acceleration seems well correlated with type II radio emission which is, I recall, considered to be the signature of a shock wave travelling in the corona. It is not known at present whether this shock is responsible of the particle acceleration or whether both effect are different consequences of a common cause. It seems however that nuclei and proton acceleration originate from a different, somewhat delayed, mechanism than the electrons energized in the impulsive phase (Bai, Ramaty). This point is still quite controversial, though a fair evidence of this can be obtained from a timing of γ ray line emission at 2.2 MeV.

The acceleration mechanism proposed thus far for these particles has been second order Fermi acceleration by *weak* long wave MHD turbulence (Melrose). Other processes could perhaps be operative too. It suffices for my purpose to mention that these mechanisms have an injection threshold. For 2d order Fermi acceleration, the momentum of the particle must be larger than $M_i v_A$. It has appeared rather puzzling for some time that a number of small flares, or even events not reported as qualified flares at all exhibited a strong anomaly of the isotopic abundance of helium in the accelerated ion population. Normally

$$\text{He}^3/\text{He}^4 \simeq 10^{-3} \quad \text{while} \quad \text{He}^4/\text{H} \simeq 10^{-1}.$$

Events have been reported in which the cosmic ray population exhibit :

$$\text{He}^3/\text{He}^4 \simeq 1; \quad 10^3 \text{ larger than normal!}$$

It is interesting to report that we can now reasonably think that a solution to this puzzle has been found; this explanation rests on the demonstration that in

certain conditions, the plasma which will be later exposed to the acceleration mechanism could be preheated by an electrostatic ion cyclotron turbulence in such a way that He^3 and some charge states of heavier ions be preferentially preheated. The point is as follows : assume that as a result of some unspecified conditions an electrostatic ion cyclotron instability is driven by some current. In a pure hydrogen plasma, these waves would all have frequencies above the ion gyrofrequency but if a noticeable amount of helium is present in the coronal gas they could also be excited above the ionized He^4 gyrofrequency. It is then possible, according to the excitation conditions, to have waves above $\Omega(\text{He}_i^4) = \Omega_i/2$. Now, it is remarkable that He^3 is the only neutron poor isotope susceptible to be present in reasonable amounts in the solar plasma. Its gyrofrequency lies between $\Omega(\text{He}_i^4)$ and Ω_i . Fisk, the author of this theory determined the optimal conditions for which waves in the vicinity of $\Omega(\text{He}_i^2)$ are first driven unstable. He found this to occur for :

$$\text{Te/Ti} \simeq 5 \quad \text{He/H} \sim 0.2, 0.3.$$

This is an abundance of helium larger than normal but not ruled out by any observation. It is expected, and it can be calculated that the rate of heating of He^3 exceeds in these conditions that of other abundant ions, thus making He^3 ions more likely to be injected in the acceleration mechanism, which will convert them into solar cosmic rays. Heavier ions can be also preferentially preheated by this turbulence by means of a second harmonic resonance. Of course, the ions preferentially heated are those whose second harmonic of the gyrofrequency is not much different than $\Omega(\text{He}_i^3)$. This is the case of C, O, Fe ions in the following charge states :

$$^{12}\text{C}^4, \quad ^{16}\text{O}^5, \quad ^{56}\text{Fe}^{17}.$$

It is especially significant that very recently, Gloeckler has observed that these charge states of these ions are overabundant in He^3 rich event, confirming the theory (Fisk). This success lends a great deal of support to the idea that ion cyclotron waves, are, in small flares, driven unstable somewhere. As the threshold for the instability is very high, as we remarked already earlier, the unstable current could be found in a rather thin current sheet or in the unstable return current driven in the sort of conduction front described earlier. Future observations will hopefully decide between these two possibilities by testing wherever possible whether the modest amount of electrons accelerated in these special events can or cannot drive an anomalous thermal conduction front.

As a conclusion, one can say that the solar flares encompass much of the most exciting aspects of present day plasma physics. This may be one of the reasons for which they are still ill understood, the

other being the fact that the amount of data obtained is both exceedingly abundant on some aspects but nevertheless inexistent on such crucial points as microstructures, state of turbulence... As a result theories produced up to now cannot reach the high degree of sophistication and confidence involved in

such fields as magnetospheric or laboratory physics. This review has been oriented to a presentation of the most recent trends of research, though other ideas only rapidly alluded to here may have more to do with the phenomenon than we use to believe in our present state of understanding.

References

- I) General references concerning solar physics and solar flares.
Pleins feux sur la physique solaire, 1978, Toulouse, Colloquium.
 Editions of the french C.N.R.S. Dumont, S. and Rösch, J., ed. Includes many aspects of solar physics.
 Sturrock, P. A., 1978 : Report of the NASA Skylab Workshop on solar flares.
 Švestka, Z., 1976 : *Solar flares*, Reidel pub. comp.
- II) Specific references.
- ALFVEN, H., CARLQVIST, P., *Solar Physics* **1** (1967) 220.
 BAI, T., RAMATY, R., *Solar Physics* **49** (1976) 343.
 BARNES, C. W., STURROCK, P. A., *Astrophysical Journal* **174** (1972) 659.
 BIRN, J., GOLDSTEIN, H., SCHINDLER, K., in *Pleins feux sur la physique solaire*, ed. CNRS, 1978, p. 237.
 BIRN, J., GOLDSTEIN, H., SCHINDLER, K., *Solar Physics* **57** (1978) 81.
 COPPI, B., FRIEDLAND, A., *Astrophysical Journal* **169** (1971) 379.
 COPPI, B., *Astrophysical Journal* **195** (1974) 545.
 FISK, L. A., *Astrophysical Journal* **224** (1978) 1048.
 FISK, L. A., Private communication, 1979.
 HEYVAERTS, J., *Astronomy and Astrophysics* **37** (1974) 65.
 HEYVAERTS, J., PRIEST, E., *Solar Physics* **47** (1976) 223.
 HEYVAERTS, J., PRIEST, E., RUST, D., *Astrophysical Journal* **216** (1977) 123.
 HEYVAERTS, J., KUPERUS, M., *Astronomy and Astrophysics* **64** (1978) 219.
 HEYVAERTS, J., LASRY, J. M., SCHATZMAN, M., WITOMSKI, P., JAU Coll. 44, Oslo, 1978, Jensen, Maltby, Orrall ed. Institute of Theoretical Astrophysics Blindern, Oslo, p. 174.
 HOYNG, P., BROWN, J., VAN BEEK, H., *Solar Physics* **48** (1976) 197.
 HOYNG, P., KNIGHT, J., SPICER, D., *Solar Physics* **58** (1978) 139.
 JOCKERS, K., *Solar Physics* **50** (1976) 405.
 KOPP, R., PNEUMAN, G., ŠVESTKA, Z., Private communication, 1979.
 LOW, B. C., *Astrophysical Journal* **197** (1975) 251.
 LOW, B. C., *Astrophysical Journal* **212** (1977) 234.
 MARTRES, M. J., MICHARD, R., SORU ISCOVICI, I., *Annales d'Astrophysique* **29** (1966) 245.
 MARTRES, M. J., SORU ISCOVICI, RAYROLE, J., *I.A.U. Symposium* **43** (1970), Solar Magnetic fields, Howard ed.
 MARTRES, M. J., SORU ISCOVICI, I., RAYROLE, J., *Solar Physics* **32** (1972) 365.
 MELROSE, D. B., *Solar Physics* **37** (1974) 353.
 NORMAN, C., SMITH, R. A., *Astronomy and Astrophysics* **68** (1978) 145.
 SMITH, D. F. and LILLIEQUIST, G. G., To appear in *Astrophysical Journal*, 1978.
 SPICER, D., *Naval Research Laboratory Memorandum* 8036, 1976.
 SPICER, D., *Naval Research Laboratory Memorandum* 3749, 1978.
 SYROVATSKII, S. I., *Soviet Astronomy A.J.* **10** (1966) 270.
 SYROVATSKII, S. I., *Solar Terrestrial Physics*, Vol. 1, M. Dryer ed., 1970, p. 119.
 TANAKA, K., NAKAGAWA, Y., *Solar Physics* **33**, 187.
 TANDBERG HANSEN, E., *I.A.U. Colloquium* **44**, Oslo 1978, Jensen, Maltby, Orrall ed. Institute of Theoretical Astrophysics Blindern, 1978, p. 131.
 TUR, T., PRIEST, E., *Solar Physics* **58** (1978) 181.
 VLAHOS, L., PAPADOPOULOS, K., Preprint University Maryland, 1979, AP 79-047.
 UCHIDA, Y., SAKURAI, T., *Solar Physics* **51** (1977) 413.

Contact electrode processes and microplasma diagnostics

F. Llewellyn-Jones

Department of Physics, University College of Swansea, University of Wales, Swansea, U.K.

Résumé. — Le microplasma suivant la séparation de contacts électriques, l'initiation de l'arc, ou l'émission d'ions de métaux fondus, agit avec les électrodes, même dans les conditions de tensions basses (~ 4 V). La physique de la rupture de shunt métallique fondu et du microplasma est étudiée à fond par l'utilisation des ciné-films rapides (10^4 f/s et 10^6 f/s). On a observé le spectre de recombinaison émis à partir de la vapeur métallique des électrodes en employant les mesures oscillographiques rapides du temps et un agrandisseur. Les résultats et les propriétés du microplasma, par exemple la densité des particules et la température, sont décrits et analysés.

Abstract. — In many operations such as breaking a circuit, arc initiation, ion emission from molten metals, the ensuing plasma interacts with electrodes, even in low voltage (~ 3 V) conditions. The physics of metal behaviour in such cases is discussed, and the evidence for formation of a microplasma assessed. An account is given of investigation of the plasma properties temperature, neutral metal gas density, and electron concentration obtained by time-resolved spectroscopy, and the behaviour of the microscopic molten metal bridge and the formation of a microplasma are demonstrated by high-speed cine films (10^4 f/s and 0.4×10^6 f/s).

1. Introduction. — Excepting the cases of high frequency discharges, (whether created by laser beams or by large scale E.M. fields) and plasmas maintained by external injection of charged particles, the self-maintained electrical discharge depends upon the nature and geometry of the electrodes which set up the electric field [1]. This is the case whether the discharge is in the form of a spark, glow or arc. However, the role of the electrodes is more extensive than that merely of establishing the essential electric field. In many types of discharge the electrode role is highly significant and can be a controlling, if not completely determining, factor, independent of any gas ambient. In the case of the development of the spark, or the initiation and maintenance of a cold, low current-density discharge, the electrodes play an important role in the provision of secondary emission of ions or electrons due to incidence of neutral, charged or excited atomic particles or of photons, as well as of emission due to application of high local electric fields ($\geq 10^5$ V/cm); and much work has been done investigating such processes [2, 3].

In recent years considerable interest has been directed to investigating the controlling influence of the nature of the possible electrode processes in the arc discharge in the microscopic as well as in the macroscopic state. This is especially the case when the main parameter is the local temperature and the controlling processes then are thermal in nature. This class is distinct from the class of so-called *cold arcs*, when the controlling process is primarily secondary emission due to a high local field set up over microscopically small areas by concentration of positive ions located on thin ($\sim 10^{-7}$ cm) insulating surface films. In the case of thermally controlled processes the physical properties of the electrode material in the solid, liquid and vapour states determine the behaviour of the electrode. In both micro-

scopic and in macroscopic conditions, these properties include the thermal and electrical conductivities and the thermoelectric coefficients, together with the surface tension, and their variation with temperature.

Because there is strong evidence for regarding micro-arcs as the main cause of deleterious electrode erosion in contact phenomena [4], as well as being of theoretical significance, studies of micro-arc phenomena are of considerable practical importance in all communication engineering. Investigations of cathode processes and of possible microplasma also have relevance to other discharge phenomena such as the nature and behaviour of cathode *hot-spots*, and positive ion high-field thermal emitters using liquid metals. The importance of cathode hot-spots has long been appreciated as far as the normal arc discharges are concerned, whatever the gas ambient may be, and the precise structure and their behaviour have been the subject of considerable research in recent years, particularly in connection with elucidating the processes of so-called *vacuum breakdown* [5, 6]. Further, the work at Culham [7] on positive-ion sources using pointed electrodes of liquid metals demonstrates minute but observable plasma formed at the metallic emitting tip, which influence the energies of the positive ions drawn off. All these examples of micro liquid metal surface phenomena in electrical contacts, field emitters and cathode hot-spots have a great deal of physical interest in common in that they concern processes which occur on the microscale at the interface of metal vapour and plasma with boiling metal in the presence of high local electric fields. Little is known at present about this interface, particularly in regard to changes in the solid lattice of the substrate metal in the transition through the liquid state of the vapour. The conditions may be far from those of stability and it is not clear how far macroscopic collective concepts such as

surface tension still hold. Full quantitative statement of energy balance and temperature distribution at hot-spots must depend upon accurate knowledge of the physical properties of the cathode: namely, thermal and electrical conductivities and thermo-electric coefficients and their variation with temperature up to temperatures of the boiling point of metals (~ 5000 K). However, accurate measurement of such coefficients by experiments on the macroscopic or laboratory scale is difficult and such quantitative data are scanty. Fortunately, it is precisely in this range of temperature and scale that the application of the methods and techniques of Contact Physics [4] have proved fruitful. In this way measurements of these coefficients and their temperature dependence has been made for metals in the liquid state [8] as well as at lower temperature, and also with semi-conductors, with which experiments are now also being extended to low temperatures. Even so, the properties of the initial (transient) arc formed on the explosive rupture of the molten metal bridge are important in the common method of arc initiation by first bringing together, and then separating, the two electrodes of the arc circuit.

In recent years considerable research has been directed to investigating the micro phenomena which occur when two macroscopically cold electrodes in a low voltage ($\lesssim 4$ V) circuit are separated. In high voltage power circuits the occurrence of an initial arc and subsequent heavy discharge plasma is obvious; the practical problem is usually that of extinguishing the discharge as quickly as possible. In low voltage ($\lesssim 4$ V) circuits, on the contrary, it had long been considered that no electrical discharge could occur, and, indeed, no discharge may generally be visible to the naked eye with moderate currents. On the other hand, investigation does show that complicated processes do in fact take place involving loss or dispersion of metal in apparently macroscopically cold and plasma-less conditions. These processes are of great technological importance in that they limit the lifetime of such *contacts*.

It was the suggestion of the Programme Committee of this Conference that the nature of recent investigations in this field, together with their conclusions, should be summarised in this paper. In considering usual arc plasma phenomena, it is noted that in medium voltage circuits generally used ($V \gtrsim 15$ V and greater than the ionization potential of the molecules of the ambient gas) the arc is *struck* by separating two electrodes in attempting to break the circuit. It is, however, now important to consider how the series of processes initiated by this very act can produce and control the nature of plasma subsequently formed, and this is of particular importance with microplasma. This aspect will now be discussed, mainly from fundamental physical considerations rather than from its technological significance. The subject of microplasma has been investigated for

many years at Swansea and attention has been directed to the behaviour and properties of metals in these conditions at high temperatures, and these studies required the use of techniques of high-speed cine-photography, oscillography and of time-resolved spectroscopy. As a result, the existence of transient microplasma has been established and information obtained about their duration, vapour density of ambient, electron and ion concentrations and temperature.

2. Processes at separating electrodes. — Consider the final stages of two electrodes in, say, a low voltage circuit (~ 4 V) when just about to separate, using the principles of contact physics [4].

2.1 DEVELOPMENT OF THE MICROSCOPIC MOLTEN METAL BRIDGE. — In practice the surfaces of the two electrodes of an electrical contact are not perfectly plane parallel but on the microscopic scale consist of projections and asperities $\sim 10^{-4}$ cm. Consequently, the current stream lines become concentrated at fewer and fewer points of contact until they are finally concentrated at a single microscopic area. At this stage the resistance across the contact is almost entirely *constriction* resistance given by the expression

$$R_c = \frac{1}{2} a \kappa$$

where a is the radius of the contact area (if supposed circular) and κ is the coefficient of electrical conductivity of the contact material. The contact voltage V_c is then equal to $R_c I_c$ when a current I_c passes. The local rate of generation of heat is then $R_c I_c^2$. Clearly, the contact area πa^2 depends upon the contact pressure, and to fix ideas, consider a specific example of two platinum wires in contact when a current of 1 A is passed at a voltage of 0.1 V. Thus $R_c = 0.1 \Omega$, and since the value of κ is $10^5 \Omega^{-1} \text{cm}^{-1}$, a is 5×10^{-5} cm, giving a current density $\sim 10^8 \text{A cm}^{-2}$. Such a high current density throughout the very small volume around the minute area of contact can produce a high temperature θ which it is necessary to evaluate.

This temperature θ is related to the generalised potential difference ψ between two isothermal surfaces, one in each electrode. This theorem was discovered in 1900 by Diessehorst [9], applied to contact theory by Holm [10], and shown to be independent of geometry by Davidson [11]. In a simplified form the theorem can be expressed as

$$V^2 = 8 \int_{\theta_0}^{\theta_m} (\lambda / \kappa) d\theta$$

where λ is the coefficient of thermal conductivity of the electrode, θ_0 the temperature at remote boundaries, and θ_m the maximum temperature somewhere in the system (usually within the microscopic hot-spot or

bridge). Assuming the Wiedemann-Franz law for the metals, i.e.

$$\lambda_c/k = L\theta$$

giving

$$\theta_m^2 = \theta_0^2 + V^2/4L$$

where L is the Lorenz constant. Taking $\theta_0 = 300$ K, $V = 1.5$ V, $\theta_m = 4600$ K, which is above the boiling point of platinum. Thus a low contact voltage can produce a local temperature sufficient to boil any known metal. This is the basis of an understanding of contact operation and has important practical consequences. The course of the phenomena of an opening contact can now be followed. When a current constriction first occurs, the temperature θ_m rises as the contact pressure falls, and the contact resistance R_c then increases, as does the contact voltage $V_c = I_c R_c$. The ψ , θ theorem shows that θ_m must then increase. On reaching the melting point, a sudden increase in R_c occurs giving a further increase in θ_m , thus continuing the process until θ_m reaches the boiling point. At this stage the molten volume (drawn out into a bridge or globule joining the two surfaces) must evaporate over a section and rupture the bridge connection, or even explode.

This general process involves two important problem areas. These are, firstly, the mode of formation, development and final rupture of this molten metal bridge, and secondly the consequences of the conditions thus produced in the initiation and subsequent development of any microplasma. Both these sets of phenomena have important practical consequences as far as electrode erosion and contact failure are concerned, and have distinctive properties which can influence the procedures adopted to minimise their practical ill-effects.

Investigation of the properties of these molten metal microscopic bridges has yielded interesting information on the thermal and electrical properties of metals at temperatures up to their boiling points — information in many cases which is unobtainable by other methods. It is the other field, that of the ensuing microplasma, which is the main subject of this paper.

2.2 MICROPLASMA. — **2.2.1 Initiation.** — Detailed analysis of the conditions at the fracture of the microbridge discloses the following electrical conditions :

(a) a small gap $\sim 10^{-4}$ cm is set up between the

two electrodes, (b) each surface is at a high temperature \sim its boiling point, and is then a possible thermionic emitter, (c) there is a gaseous atmosphere of the ambient gas and of metal vapour, (d) the metal vapour density may exceed atmospheric gas density, and its ionization potential may be much lower (almost one half) that of the atmosphere, and (e) the self-inductance of the local circuit can set up a voltage pulse of a value very much higher than that of the low (~ 4 V) contact circuit, and thus sufficient to produce ionization of the gas or metal vapour. For such reasons the occurrence of a micro-arc is practically a certainty in most cases of practical importance, and this can have serious consequences by producing erosion of the electrodes [4].

In practical cases when the local self-inductance is sufficient ($\geq 10^{-3}$ H), and when the circuit voltage is high (> 50 V), the presence of a post-break arc is obvious and visible, but at much lower values of inductance ($\leq 10^{-6}$ H) and of circuit voltage (~ 4 V), it has been difficult to establish the presence of significant plasma which for many years was ignored.

Further, there were strong reasons put forward for the practical significance of the behaviour and properties of the molten bridge in being the cause of a certain amount of electrode erosion. Davidson [11] had shown that the equilibrium of a liquid metal bridge would be determined by its surface tension, and that in consequence the bridge would progressively assume the geometrical symmetrical shapes of unduloid, catenoid and nodoid before rupture. If a plasma is subsequently set up it would be produced in the propitious conditions in the rupture, which itself naturally would take place at the hottest section — usually the narrowest neck of the nodoid.

Extensive static and dynamic investigation of this has been made, and the quasi-static photographs, together with a cine film at 25 frames/s illustrate the process in some detail (see Fig. 1).

However, it can be seen from the film that no definite evidence was produced at that speed to establish that an arc always, or even sometimes, occurred; and it was even thought that the film, on the contrary, provided evidence more consistent with the conclusion that any erosion, in those particular conditions, was more likely to have been produced by asymmetric rupture of the bridge. The film demonstrates the validity of the theoretical predictions of the development of the microscopic molten metal bridge through the geometrical forms

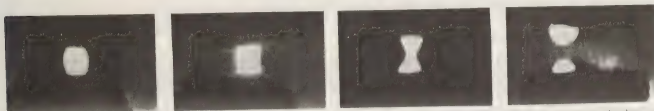


Fig. 1. Development of microscopic molten metal bridge through unduloid, catenoid and final nodoid shapes, apparently showing a clean metallic break on rupture, photographed at 25 frames/s.

of unduloid, catenoid and nodoid and the rupture at the hottest section.

A matter of some physical significance is the conclusion that surface tension processes appear to be operative right up to the stage of explosion of the molten metal. However, the film appeared to show that the bridge ruptures cleanly without the formation of a maintained arc, and so provided no evidence for the significant action of a microplasma.

2.2.2 Indirect evidence for existence of microplasma. — As a consequence, consideration of metal transfer in this regime of low voltage and self-inductance generally tended to attribute molten transfer to the properties of the molten metal bridge rather than to a plasma. On the other hand, the reasons given above in section 2.2.1 for recognising that conditions obtained at bridge rupture are precisely those which could, and probably would, lead to a micro-arc, indicate that bridge rupture must be an event which initiates a possibly complicated train of plasma events which determine the extent and characteristics of the resulting matter transfer and electrode erosion. This conclusion has been the basis of extensive research at Swansea over recent years [12, 13, 14, 15] on electrode erosion and its explanation. Clearly, it is important to establish, if at all possible, whether this conclusion, that microplasmas are set up and can account for the erosion phenomena observed is valid. The experimental methods generally employed have been based upon time-dependent techniques of increasingly high resolution, together with sensitive radiotracer methods of measuring the precise movement of matter from one electrode to the other, and not merely the net erosion or matter gain. These techniques have superseded the previous quasi-static methods of electrical measurement, arc observation and gravimetric and optical methods of surface change. The experimental investigation covered the following fields :

i) The migration of matter from one electrode to the other measured as a function of the local self-inductance down to values of 3×10^{-8} H, even for a single contact operation;

ii) Measurement of $V_c(t)$ and of $I_c(t)$ as functions of time from just prior to bridge rupture up to current extinction;

iii) High-speed cine-photography of events including formation, development and rupture of the micro-bridge, and the arc phase on a microsecond scale;

iv) Time-resolved radiation measurement using photomultipliers and high-speed oscillography, involving times down to 50×10^{-9} s, and

v) Optical and stereoscan examination of erosion patterns.

3. Investigation of microplasma. — The results of these studies provided considerable information on the physics of the bridge and on the nature of the

processes of matter transfer, and those specifically significant to the question of the existence of plasma will now be considered. These are :

a) In many cases the amount of matter transposed was greater than the total volume of the molten metal bridge contained between the two melting isothermals in the electrodes.

b) Transfer still depended upon the local self-inductance even for values as low as 3×10^{-8} H, and was never independent of inductance, as would be the case if no micro-arc occurred and if the transfer mechanism was entirely a bridge process dependent on the properties of the metals (see Fig. 2).

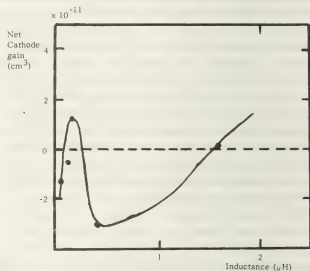


Fig. 2. — Dependence of matter transfer rate on local self-inductance as determined by radio-tracer techniques.

c) Quasi-static measurement of contact voltage V_c gave low values (1.5 V), and high-speed oscillographic methods did not disclose the high peak values that would be expected theoretically from circuit constants; the values were only about 9 to 15 V, consistent with the occurrence of strong ionization of metal vapours.

Further, the duration of the plateau of the voltage traces was equal to that calculated from the energy available in the local LC circuit for maintenance of an electrical discharge which was keeping the current flowing across the contact-gap (see Fig. 3).

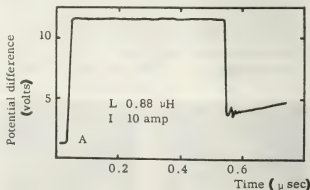


Fig. 3. — Oscillogram trace of contact voltage V_c as a function of time from bridge rupture.

d) Measurements by M. R. Hopkins *et al.* on magnetic displacement of the molten metal bridge to produce trails disclosed no asymmetry of the bridge which could produce observable transfer.

All these conclusions are consistent with the assumption that microplasma do, in fact, occur for durations determined by the local circuit parameters, and that they have significant influence on the mechanism of electrode erosion and also on the energy spread of any positive ions extracted from liquid metal emitters. It was necessary, therefore, to attempt to obtain direct specific evidence for the existence of such microplasmas, and, if successful, then to investigate their plasma properties in order to determine whether they could account for the complex erosion properties which had been established experimentally.

4. Direct visual observation of microplasma. —

Although the first cine film at 25 f. s^{-1} appeared to show a *clean metallic break* of the bridge nodoid, it was considered necessary to examine each separate frame for any further evidence, and it was eventually found that of some 20 000 frames, one actually appeared to indicate a *glow or flash*. It was possible therefore that *flashes* may have occurred between frames and so avoid record. Clearly, a faster frame rate was required, and the next attempts were made using a Fastax camera of some 10^4 f. s^{-1} .

The results obtained, as can be seen from the film shown, confirmed in considerable detail the theoretical predictions of Davidson about the equilibrium conditions of a molten metal bridge at high temperatures. In particular, the inability of surface tension forces to maintain control with pure metal without violent internal convulsions. Also that these convulsions often resulted in the emission of minute high-speed droplets which could avoid desposition on either electrode and so avoid record. This is a process of considerable practical significance, as it produces an apparent

scatter in experimental measurements of metallic transfer.

Some more evidence, albeit not yet decisive, was also obtained of a post-break flash, but clearly clouds of metallic vapour were definitely produced and it could be seen that the final rupture was not the *clean metallic break* previously thought to occur with the 25 f. s^{-1} film. The bright flash, resembling possibly a hot plasma, appeared to have a volume much greater than that of the original microscopic molten bridge. However, a higher camera speed was still required if more definite evidence was to be obtained.

Such a camera was designed and constructed at Swansea [16, 17] and with this the following conclusions were obtained (Fig. 4 and 5) :

a) Copious clouds of metallic vapour are produced around the bridge, thus indicating onset of boiling.

b) There is no *clean metallic break* of the circuit at bridge rupture, on a scale of some microseconds.

c) The molten bridge, the hottest section of it, explodes with a bright flash, resembling hot plasma; in many cases the whole bridge is involved.

d) Ejection of molten metal droplets occurred at speeds of $100\text{--}300 \text{ ms}^{-1}$.

The slides shown demonstrate the existence of the post-rupture plasma, and it now remains to investigate and, if possible, deduce the properties of the plasma which could be significant in accounting for the electrode erosion observed.

5. *Plasma properties of micro-arc.* — These results are all consistent with the conclusion that the arc takes place in the vapour supplied by the electrode metal and that the plasma and electrode processes themselves are complicated. It appears that one type of arc discharge succeeds another, and that the succession is controlled in the main by the density of metal vapour produced from the two electrodes,

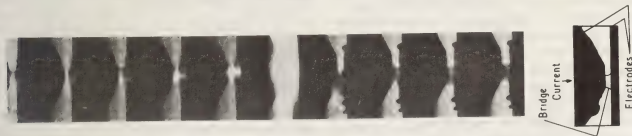


Fig. 4. — Development of microscopic metal bridge of platinum electrodes in vacuum photographed at 10^4 frames/s, showing high turbulences, ejection of metallic globules, and occurrence of transient ($< 100 \mu\text{s}$) microplasma.

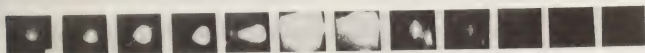


Fig. 5. — Development of microscopic bridge of platinum in vacuum photographed with Swansea high-speed camera. $I_c = 62 \text{ A}$, $L = 0.05 \mu\text{H}$, Speed 0.5×10^6 frames/s (M. C. Cowburn, Ph. D. thesis, 1969).

either by evaporation or by sputtering under electronic and ionic bombardment. Thus, the monitoring of the temporal variation of ion density in the plasma is clearly of importance and investigations of this aspect have been carried out at Swansea. The region containing the events to be analysed is not only microscopic in area but the phenomena themselves are also very transient, and significant variations can occur in times much shorter than microseconds.

5.1 PLASMA RADIATION. — Of the various methods of determining the density of the metal vapour, in the extremely small inter-electrode space between the opening contacts, that based on the spectroscopic investigation of the radiation emitted from the microplasma is probably the most convenient in the circumstances [18]. In the case of high-energy, high-density plasma such as stars, the radiation is likely to be black and forms an essential element in the plasma equilibrium equations, but in the case of these comparatively low energy contact arc discharges, on the other hand, the plasma is optically *thin*, and radiative transfer, for example, can be neglected, so that a simplified concept of radiation processes can be adopted. Radiation emitted by a plasma depends not only on the isolated radiating atomic or molecular species but also on the properties of the plasma in the neighbourhood of the radiator. For plasmas of low percentage ionization, collisional ionization and de-excitation processes are dominated by free electrons rather than by atoms or ions on account of their relatively high energy and their long-range interactions. In *thin* plasmas there cannot be complete thermodynamic equilibrium. However, when the electron-electron mean free path is small compared with plasma dimensions, plasma properties can be expressed in terms of electron mean energy (or temperature) and electron or ion densities (since the plasma is macroscopically neutral). In these conditions the electron energy distribution can be considered to be Maxwellian and *local thermodynamic equilibrium* (L.T.E.) be obtained [19]. Generally the radiation consists of two forms: one, the line spectra due to quanta emitted by transitions between quantum states of excited atoms (usually the atoms of the evaporated electrode material), and the other, mostly continuous radiation resulting from the collective action of the plasma as a whole which includes recombination spectra, Bremsstrahlung, cyclotron, Cerenkov, and black-body radiations.

In contact arc discharges, the particle energies are comparatively low ≈ 1.0 eV and the particle velocity in the plasma is far lower than that of light; consequently, Cerenkov radiation can be neglected. Similarly, the plasma being *thin*, radiation is not in equilibrium with the particles, and *black-body* radiation is negligible. Cyclotron radiation is caused by charged particles which, in the absence of collisions, orbit about the lines of force of any applied magnetic

field and consists of line spectra at frequencies which are harmonics of the cyclotron frequency. The ratio of the power loss by cyclotron radiation to Bremsstrahlung is proportional to the square root of the mean electron energy and may be neglected for mean energies $\lesssim 1$ eV.

The following are pairs of processes of importance in plasma equilibria:

- i) 3-body collisional recombination and collisional ionization;
- ii) radiative recombination and photo-ionization;
- iii) collisional de-ionization and collisional excitation; and
- iv) spontaneous and stimulated emission and photo-excitation.

In regions of L.T.E. when collisional effects dominate radiative processes, the principle of detailed balancing may be applied, and in these circumstances the equilibrium is characterised by the mean electron energy E_e since electrons dominate the collisional processes. This is the plasma model here adopted in the discussion of Bremsstrahlung and recombination. These two forms of radiation occur together because they derive from the Coulomb attraction of electrons for a positive ion. The resulting accelerated particles radiate electro-magnetic energy at rates proportional to the square of the acceleration. At high energies $\lesssim 50$ keV, plasma Bremsstrahlung is almost entirely from the electron, and the radiation is continuous and known as *free-free* when the electron is not captured; a free electron (m, e, v) may, however, be captured to a quantum level q of the attracting positive ion, and the energy lost by the electron is radiated as a photon of energy $h\nu$, where

$$h\nu = \frac{1}{2}mv^2 + E_{(z-1)}(\infty) - E_{(z-1)}(q)$$

where $E_{(z-1)}(q)$ is the energy of the quantum level q for an ion of charge z ; since v^2 may have any value, the spectrum is continuous, but there is a series limit. In hydrogenic systems

$$E_{(z-1)}(\infty) - E_{(z-1)}(q) = z^2 E_H/q^2$$

where $E_H = 2\pi^2 e^4 m/h^2$, the ionization energy of the hydrogen-like atom. At any frequency ν the lowest permissible q is given by

$$h\nu = \frac{1}{2}mv^2 + z^2 E_H/q^2 \geq z^2 E_H/q^2$$

or

$$q_{\min} > (z^2 E_H/h\nu)^{1/2}. \quad (1)$$

In accordance with the principle of microscopic reversibility the number of recombinations to the level q for a frequency interval $d\nu$ is equal to the number of photoionizations in the same frequency interval.

Precise quantum mechanical calculations can only be made for hydrogenic systems, i.e. for recombination

between an electron and bare positive ion, and only approximate treatment exists for many electron systems. This approximation will be made here. On these assumptions, Cooper [20] has shown that the total power $P^R(v) \cdot dv$ of the recombination continuum radiated in frequency interval dv for recombination to level q is given by

$$P_q^R(v) \cdot dv = \frac{n_e n_i g_{fb} K z^4}{E_e^{3/2}} \exp \left\{ -\frac{h\nu}{E_e} \right\} \times \sum_{q_{\min}}^{\infty} \exp \left\{ \frac{z^2 E_H}{q^2 E_e} \right\} \cdot \frac{dv}{q^3} \quad (2)$$

where

$$K = \frac{64 \pi^{1/2} e^4 h E_H^{3/2}}{3^{3/2} m^2 c^3}$$

and g_{fb} is the free-bound Gaunt factor ≈ 1 in the visible region, and from (1)

$$q > \left\{ \frac{z^2 E_H}{h\nu} \right\}^{1/2}$$

The summation is taken over all possible q -levels. A further simplification is made by assuming that the positive ion of the metal vapour is hydrogen-like so that E_H can be taken as the ionization energy of the metallic atom.

Unsöld [21] has given an expression for the total Bremsstrahlung radiation $P^B(v)$, where

$$P^B(v) dv = \frac{n_e n_i g_{ff} z^2 K}{2 E_H E_e^{1/2}} \cdot \exp \left\{ \frac{h\nu}{E_e} \right\} \cdot dv \quad (3)$$

where g_{ff} is the free-free Gaunt factor which is \approx unity in the visible spectrum. Comparison of (3) and (2) shows that when $E_H z^2 \gg E_e/3$, Bremsstrahlung is negligible compared with the recombination spectrum when $E_1 \lesssim 1$ eV. When $h \gg E_e$ both Bremsstrahlung and recombination spectra fall off as $\exp(-h\nu/E_1)$ when variation in Gaunt factors are small, and the free-electron velocity distribution is Maxwellian. Thus for constant E_e , the slope of the continuum power radiated vs. frequency gives the mean energy E_e .

However, in the case of extremely small contact plasma, radiation from the whole surface of the plasma falls on the detector, and the mean electron energy may vary over a cross-section. From high-speed photographs of the post-rupture contact plasma, it may be assumed, without great error, that the plasma is cylindrical (of radius r) initially of the same broad geometry as the molten metal bridge [20]. If E_{\max} , E_{\min} and $E(r)$ are the electron energies at maximum when $r = 0$, at minimum at boundary r_1 , and at the value of radius r , then (see Fig. 6),

$$E(r) = E_{\max} - (E_{\max} - E_{\min}) \frac{r^2}{r_1^2}$$

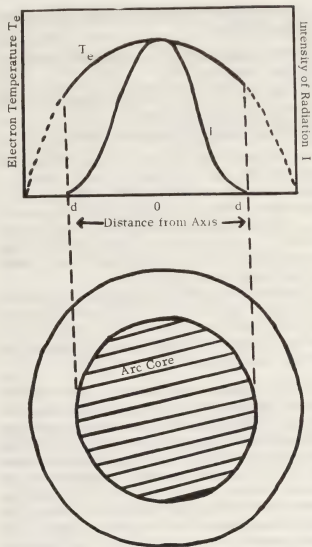


Fig. 6. — Radial variation of temperature and intensity of the continuum radiation across the arc column.

and substituting in (2) for a single level q and integrating from $r = 0$ to $r = r_1$, it follows that

$$P^R(v) = \frac{9.815 \cdot 4 \cdot 10^{-45} n_e n_i}{(h\nu - h\nu_n)^{1/2} (E_{\max} - E_{\min})} \times \left[\operatorname{erfc} \left\{ \frac{h\nu - h\nu_n}{E_{\min}} \right\}^{1/2} - \operatorname{erfc} \left\{ \frac{h\nu - h\nu_n}{E_{\max}} \right\}^{1/2} \right] \quad (4)$$

where $h\nu_n$ = series limit $= z^2 E_H/q^2$ in the spectrum of the vapour.

Further simplification follows if $E_{\min} \approx$ zero and putting $n_e = n_1 = n$, giving [22]

$$P^R(v) = \frac{9.815 \cdot 10^{-45} n_1^2}{(h\nu - h\nu_n) E_e} \cdot \operatorname{erf} \left\{ \frac{h\nu - h\nu_n}{E_e} \right\} \quad (5)$$

Thus the magnitude of the radiation recorded is a measure of the ionic density in the metal vapour in the contact gap. Data obtained from application of

eq. (5) can be used to determine, for any given contact plasma conditions :

- i) the temporal variation of radiation intensity at any given frequency ;
- ii) the estimations of plasma temperature over the whole of its duration ; and
- iii) an estimation of the plasma volume.

In the records for the mean energy E_e may vary with time [23], but in a family of such $\{P(v) \text{ vs. } v\}$ curves, definite maxima usually occur, and it is reasonable to take the value of E_e there the same as E_{\max} . This leads to a curve of $P^R(v) \text{ vs. } v$ at the same $F (= E_{\max})$. The temperature at times other than that corresponding to the maxima of the $\{P(v), t\}$ curves can be found by extrapolation.

The size of the plasma may be estimated by focussing an image of the arc on to a slit located before the radiation detector and varying the plasma current until the detector no longer records a corresponding increase in radiation.

5.2 EXPERIMENTAL PROCEDURE. — The electrode material employed was platinum of ionization potential 9 eV. The radiation detector was a high-gain, high sensitivity photo-multiplier with a spectral range of 2 300-6 000 Å, working at maximum sensitivity. Care was taken to maintain the required voltage stability at every stage. A Tektronix 555 high-speed double beam oscilloscope was used to display the time-resolved signal from the photo-multiplier, and also to monitor the contact voltage at the same time as the radiation. The recording system was triggered by externally triggering the oscilloscope from the contact voltage at a value slightly less than the rupture voltage. A block diagram of the system is illustrated in figure 7.

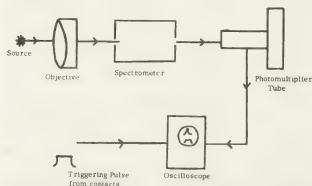


Fig. 7. — Schematic diagram of the radiation detecting system.

A number of sensitive photo-multiplier tubes were tested in attempts to record the platinum emission lines $\lambda = 3\,064\text{ Å}$ and $2\,650\text{ Å}$, but without success, but good signals of high signal to noise ratio were obtained from observation with a 100 Å bandwidth of the continuous radiation, so that the radiation

falling on the photo-multiplier was an integral of the radiation emitted from the whole arc plasma. For any given values of circuit parameters at any given value of radiation frequency, observations were recorded for 20 contact openings at any given current, and the spectrum scanned at intervals of 100 Å . The range of currents used was 5 to 15 A for values of local self-inductances from $5 \times 10^{-8}\text{ H}$ to 300 μH .

5.3 EXPERIMENTAL RESULTS. — A curve typical of the family $P^R(v), t$ is given in figure 8a and the corresponding V, t curve in figure 8b. This is interesting because (b) demonstrates the phenomenon of re-bridging after about 1 μs leading to a second arc lasting some $4/2\text{ μs}$, and that the initial sharp voltage change occurs at the same constants as the peaks in the power radiation curve.

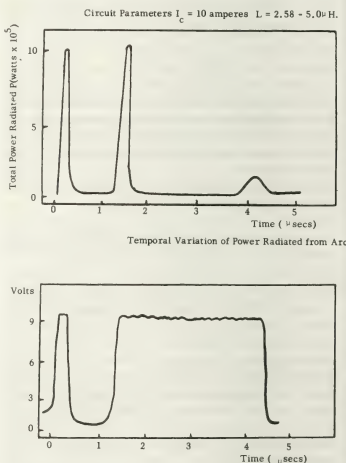


Fig. 8. — Voltage across contact.

Figure 9a, b, c gives some typical curves for high values of local inductance giving arcs lasting 9 μs when little re-bridging occurred. The second pulse of radiation is more clearly shown.

Determinations of the electron temperatures were made by the method described in the previous sections. Over the range of inductances from 0.05 μH to 5 μH and for a current range 5 to 15 A, the mean electron energy showed little variation from E_{\max} of 0.6 eV , and E_{\min} of 0.45 eV .

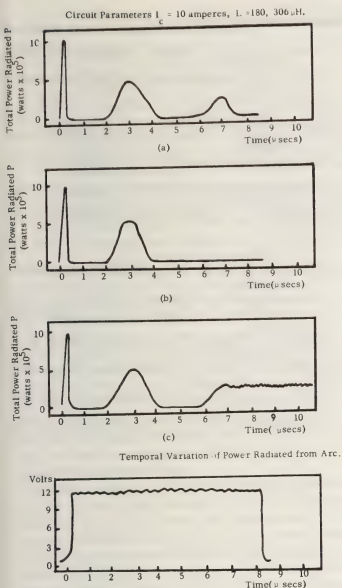


Fig. 9. — Voltage across contact.

The distribution over a cross-section was similar to that given in figure 6 and the electron temperature was about 6 900 K, the actual vapour temperature was rather less than this because of the departure from complete thermodynamic equilibrium. There were very small variations in the characteristics of the temperature-time curve. Temperature could be estimated for times greater than 20 ns after bridge rupture. Plasma dimensions were estimated by the methods described above, found to be about 6×10^{-3} cm/A. These measurements also gave a value of

$$4 \times 10^5 \text{ cm s}^{-1},$$

for the lateral growth velocity of the plasma, which is some ten times higher than that estimated by high-speed photography.

Eq. (4) can be used to estimate the particle density in the plasma together with curves similar to those of figure 8, and values $\approx 10^{16}$ – 10^{17} ions/cm³ have been found at the radiation peaks with a current of

10 A with $L = 300 \mu\text{H}$. These values occurred 10 ns after rupture. Similar values are obtained assuming that the current is carried only by electrons with drift velocity 5.10^7 cm s^{-1} . A current of 10 A gives $n_e = 10^{16} \text{ cm}^{-3}$. A temperature of 0.6 eV is consistent with these properties.

For a gas in thermal equilibrium at temperature T , the pressure p is related to the degree x of ionization by the formula

$$n_i = x \cdot N \cdot p \cdot 273/T \quad (6)$$

$$T = T_e = T_g$$

$$N = \text{Loschmidt's number}.$$

Saha's equation gives

$$\frac{px^2}{1-x^2} = 3.16 \cdot 10^{-7} T^{2.5} \exp \left[-\frac{E_i}{E_e} \right] \quad (7)$$

T in degrees Kelvin, E_e , E_i in electron-volts.

Eqs. (6) and (7) can be solved for p and x at any instant.

Curves for p , n_e , vs. t are generally similar to those of figures 8 and 9, and the values deduced show that vapour pressures of 0.5–1.0 atmospheres exist in the gap some 20 ns after rupture (Fig. 10) of the bridge during which at least 1/20th of the entire bridge is evaporated during rupture.

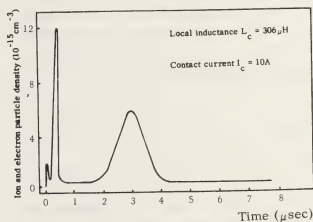


Fig. 10. — Time-resolved spectrograph of total radiation from microplasma and corresponding deduced particle density development.

These results are consistent with the occurrence after bridge rupture of a succession of types of micro-arc discharge proposed previously to account for observed complex succession erosion of the phenomena. The experimental method described has shown itself to be a useful diagnostic technique applicable to contact arcs.

Acknowledgments. — Acknowledgment and thanks are due to the Leverhulme Foundation Trustees for assistance they afforded for the preparation of this paper by the award of an Emeritus-Fellowship.

References

- [1] LLEWELLYN-JONES, F., *The Glow Discharge*, London, Methuen, 1967.
- [2] MASSEY, H. S. W. and BURHOP, E. H. S. and GILBODY, H. B., *Electronic and Ionic Impact Phenomena*, 2nd ed., Oxford, Clarendon Press, 1969.
- [3] LLEWELLYN-JONES, F., *Ionization and Breakdown in Gases*, London: Methuen, 1966.
LLEWELLYN-JONES, F., *Ionization Avalanches and Breakdown*, London: Methuen, 1967.
- [4] LLEWELLYN-JONES, F., *The Physics of Electrical Contacts*, Oxford: The Clarendon Press, 1957.
LLEWELLYN-JONES, F., *Fundamental Processes in Electrical Contact Phenomena*, London, H.M.S.O., 1953.
LLEWELLYN-JONES, F., *Materials for Electrical Contacts in Electrical Engineering*, World Electrotechnical Congress (WELK), Moscow, Paper 05.6.3B, 1977.
- [5] RAKHOVSKY, V. I., *Proc. 7th I.C.D.E.I.V.*, Novosibirsk, 1976, p. 176.
- [6] GOLDMAN, M., HAUG, R. and RAVEY, R., *ibid.*, 1976, p. 139.
- [7] CLAMPITT, R. and JEFFRIES, D. K., *Inst. Phys. Conf. Ser.* **38**, Chap. 1, 1978.
CLAMPITT, R. and JEFFRIES, D. K., *Nuclear Instruments and Methods* **149** (1978) 739.
- [8] HOPKINS, M. R., *Zeit. f. Phys.* **147** (1957) 148.
HOPKINS, M. R. (with M. Jones), *Phys. Stat. Sol. (A)*, **21** (1974) 507.
- [9] DIESELHORST, H., *Ann. Phys.* **1** (1900) 132.
- [10] HOLM, R., *Electrical Contacts*, Berlin, Springer-Verlag.
- [11] DAVIDSON, P. M., *Proc. IEE* **96** (1949) 293.
- [12] LLEWELLYN-JONES, F., *Kontakte in Electrotechnik*, Berlin, Akademie-Verlag **11**, 1965.
- [13] HOPKINS, M. R. and JONES, R. H., *Proc. VIth ICECP*, Chicago, 1972, 399.
- [14] HOPKINS, M. R., JONES, R. H. and DAVIES, A., *Proc. VIIth ICECP*, Paris, 1974, 301.
- [15] HOPKINS, M. R. and JENKINS, A. V., *Proc. Vth ICECP*, Munich, 1970, 236.
- [16] LLEWELLYN-JONES, F. and PRICE, M. J., *Nature* **207** (1969) 255.
- [16] LLEWELLYN-JONES, F. and PRICE, M. J., *Brit. J. Appl. Phys.* **2** (1969) 589.
- [17] PRICE, M. J., *Journ. Phys. E., Scientific Instruments* **3** (1970) 521.
- [18] COWBURN, M. C. and LLEWELLYN-JONES, F., *Proc. Vth ICECP*, Munich, 1970, p. 281.
- [19] GREIM, H. R., *Plasma Spectroscopy*, New York, McGraw-Hill, 1963.
GREIM, H. R., *Phys. Rev.* **131** (1963) p. 1170.
- [20] COOPER, J., *Rep. Prog. Physics* **19**, Part 1, London, 1966, p. 35-130.
- [21] UNSÖLD, A., *Physik der Sternatmosphären*, 2nd Ed. Berlin, Springer-Verlag, 1955.
- [22] LLEWELLYN-JONES, F. and COWBURN, M. C., *Proc. ICECP*, Tokyo, 1976, p. 263.
- [23] LLEWELLYN-JONES, F., *REKO Conference on Electrical Contacts*, Budapest, 1975.
LLEWELLYN-JONES, F., *Proc. IVth ICECP*, Swansea, 1968, p. 1.

Survey on actual knowledge and physical problems

K. Berger

31 Gstaadstrasse, CH 8702, Suisse

Résumé. — Résultats de la recherche moderne sur la foudre, valeurs statistiques des paramètres des impulsions du courant de la foudre, leur influence sur la protection contre la foudre.

Problèmes non résolus : coup de foudre pilote (*stepped leader*), vitesse de propagation de la foudre, temps de montée du courant de la foudre, définitions internationales des notions de la foudre.

Abstract. — Survey on results of modern lightning research, statistical values of parameters of lightning current impulses, their significance for lightning protection.

Unsolved physical problems, stepped leader, stroke velocity, rise time. International definitions.

First part : Lightning research. — How is lightning initiated ? What is reliable knowledge about it ? What phenomenon is at the base of the strong electric field which causes lightning ?

It is wellknown that during a thunderstorm a strong updraft of warm humid air causes production and separation of electric charges when passing a region with $-5 \dots -10^\circ$ freezing. Negative ions or particles remain concentrated in restricted areas or cells, light positive particles follow the wind and are deposited in higher and calmer regions. This is the case for heat thunderstorms as well as for cold or warm front thunderstorms.

Between negatively and positively charged clouds or cells an electric field has been built up which also influences the earth. Above flat countries the field is at its maximum near the negative cells. With growing space charge a downward progressing discharge will develop : The leader of a downward lightning stroke. Above steep mountains or high towers the induced electric field below the negative cloud may grow at the tower tip not only to produce corona discharges (so-called St-Elmos fires) but also to initiate real lightning discharges, so-called upward strokes or upward flashes. Like downward leaders these are relatively well conducting channels out from the cell with a speed of about $1/1\,000 \dots 1/3\,000$ of velocity of light ($100 \dots 300$ m/ms or $100 \dots 300$ km/s). Discharges which do not reach (strike) the earth are cloud-flashes ; discharges to or from the earth are earth-flashes. In multiple flashes every stroke of an earth flash is initiated by a leader stroke or shortly leader. Currents in negative downward first leaders are between less than 100 A up to several 100 kA. Currents in upward leaders below positive clouds may reach 1 000 A or even more. The relative well conducting leader channel is often on a very high potential (< 100 MV). When it approaches the earth a kind of breakdown will happen. More exactly, in most cases another leader will initiate at the earth, growing upwards and joining then the downward progressing leader. This kind of upward leader is called connecting leader (Fangentladung) (*décharge d'interception*). On tall structures (TV- or Radio-Towers) this connecting

leader may have lengths of 100 m or more. Sometimes upward and downward leaders miss themselves and a so-called loop appears in the photographs.

The observation of connecting leaders is in relation with the notion of the so-called striking distance on which there is still controversation among the physical engineers.

The highly charged leader channel, after joining the connecting leader, discharges then abruptly and initiates the return stroke. The high current impulse at its earth point is the base for disposition and dimensioning of most lightning protection devices. Velocity of progression of the return stroke is very high, about $10 \dots 60\%$ of velocity of light.

The current impulse of the return strokes is well characterized by 4 parameters :

- 1) Current amplitude \hat{i} (kA).
- 2) Rise time (μ s) or current steepness di/dt (kA/ μ s).
- 3) Electric charge $\int i \, dt$ (C).
- 4) Current square impulse $\int i^2 \, dt$ ($A^2 \cdot s$ or $kA^2 \cdot s$),
or current square integral, in USA often called action integral.

The signification of these afore-mentioned parameters regarding lightning protection is as follows :

1) The crest value of lightning current \hat{i} is responsible for ohmic voltage drops especially in the earthing ground resistance ($50 \text{ kA} \times 10 \, \Omega = 500 \text{ kV}$).

2) The steepness of lightning current di/dt determines all kind of inductive voltage drops : Voltage drop in lightning current conductors, induced voltages on magnetically coupled loops a.s.f.

$$(50 \text{ kA}/\mu\text{s} \times 10 \, \mu\text{H} = 500 \text{ kV}).$$

3) The electric charge $Q = \int i \, dt$ of lightning current is a mesure for the energy which is transmitted by the lightning arc to metallic surfaces, causing melting effects. Charge Q is responsible also for diffusion of electric fields through metallic screens (skin effect screens).

4) The *current square impulse* $\int i^2 dt$ is at the base of every mechanical effect, and for electrical impulse heating of ohmic resistors.

Some curves on frequency of occurrence of these parameters, as evaluated from the Monte San Salvatore research are given in annex 1 and will be reproduced by projection. More details are available in the Bulletin SEV 1972/1973/1978 and in the Cigré-Electra 41 (1975). Annex 2 to this Conference Paper presents a list of all principal definitions about lightning in 3 languages.

According to the available measurements from San Salvatore, some approximate values which correspond to probabilities of occurrence of a few % may be given as follows :

$$di/dt \simeq 100 \text{ kA}/\mu\text{s} \quad \text{or} \quad 10^{11} \text{ A/s},$$

$$\dot{i} \simeq 150 \text{ kA}.$$

Analog few %-values for charge and current square impulse of complete flashes are

$$\int i \cdot dt \simeq 150 \text{ Cb} \quad (\text{for negative flashes})$$

$$\int i \cdot dt \simeq 500 \text{ Cb} \quad (\text{for positive flashes})$$

$$\int i^2 \cdot dt \simeq 5 \times 10^5 \text{ A}^2 \cdot \text{s}$$

or $0.5 \text{ kA}^2 \cdot \text{s}$ for negative flashes

$$\int i^2 \cdot dt \simeq 10^7 \text{ A}^2 \cdot \text{s}$$

or $10 \text{ kA}^2 \cdot \text{s}$ for positive flashes.

For engineering purposes it is necessary to remember that positive flashes are rather seldom in the flat and warm or moderate zones, but have been observed in Sweden and Japan. There is a tendency to base usual protection on negative flashes only.

Second part : Three physical problems not yet solved sufficiently

- 1) The problem of the stepped leaders.
- 2) The problem of velocity of leader and return strokes.
- 3) The problem of current rise in first and subsequent strokes (front of current wave).

1. STEPPED LEADERS are observed in the first stroke of negative downward flashes. They do not appear in subsequent leaders if the no-current interval between strokes is less than 1 or 2 tenths of a second. They reappear with smaller steps if the no-current interval is long, say several tenths of a second. What is the reason of this stepping ?

1.1 The first stroke-leader has to open the lightning channel by ionisation (corona discharge) and to

Annex 1/1

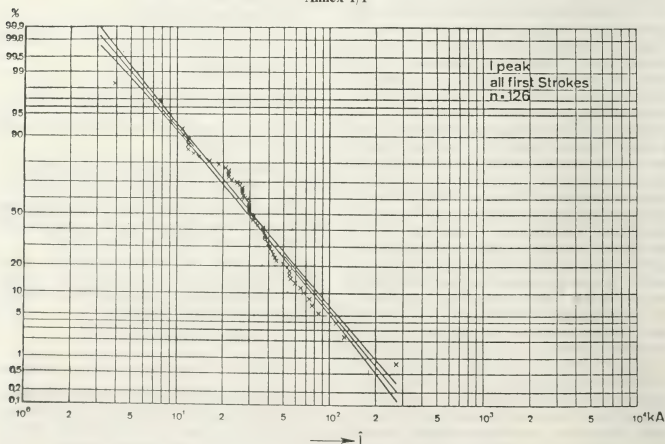


Fig. 1. — Lightning currents (first strokes).

Annex 1/2

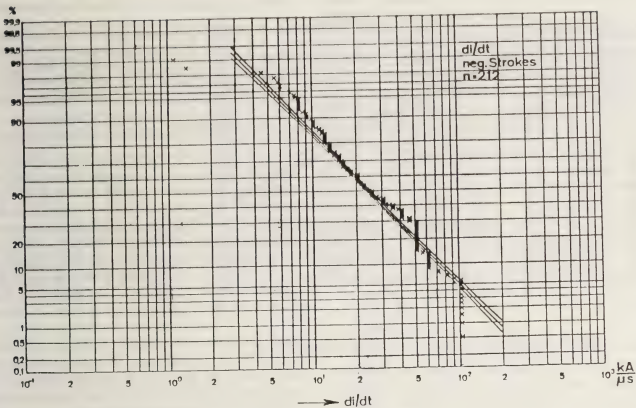


Fig. 2. — Steepness of all negative strokes in a flash dI/dt (max).

Annex 1/3

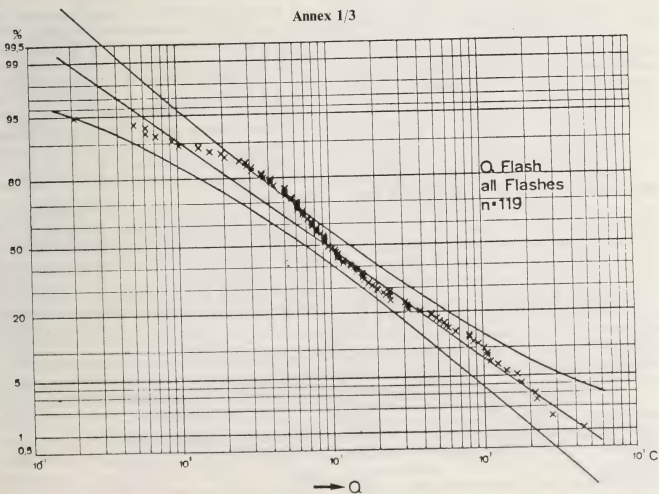


Fig. 3. — Electric charge of all positive and negative flashes.

Annex 1/4

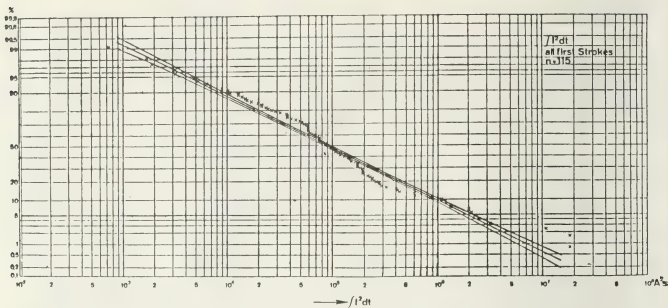


Fig. 4. — Current square impulse $\int i^2 dt$ of all positive and negative flashes.

Annex 1/5

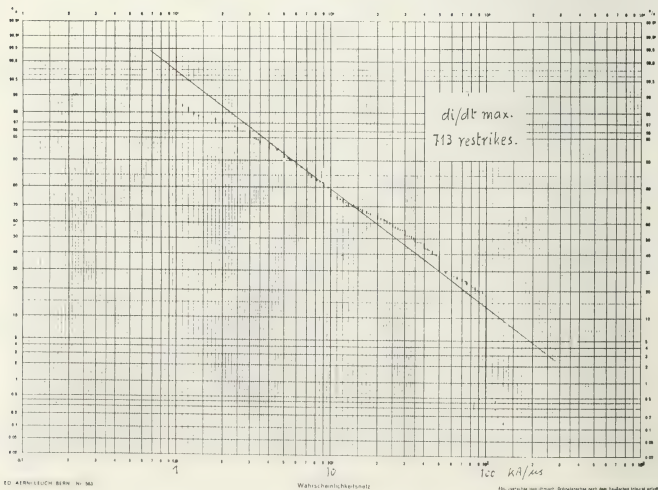


Fig. 5. — Steepness $di/dt(\max)$ of 713 negative following strokes in upward flashes.

produce a well-conducting channel (streamer or leader) with 100 or a few 100 A continuing current.

Stepping is a kind of instability in this channel progression. It may be caused :

- a) by an instability in the long feeding arc which supplies the corona-tip of the channel or
- b) by an instability during transition from corona to the streamer, before or near the tip of the channel.

Streak camera-photographs from San Salvatore show the most bright point of a new step to appear at the tip of the new step. This remembers the plasma formation by the well-known reversal of the electron avalanches, published by Meek and Raether. But there is no agreement because the steps with lightning are several m long up to more than 10 m as compared with only a few cm in the lab.

The author has the impression that in the transition process the energy transmission from *positive ions* to the gas molecules has not taken into account sufficiently until now. Indeed the ions do not ionise, but according to their mass they may transmit the whole kinetic energy they got in the electric field, to neutral molecules by central impulses. Their energy is only $4\sqrt{2}$ times smaller than that of the electrons because of their smaller free kinetic path. But their acceleration and velocities are about 10^4 times smaller than that of electrons. Transmission of energy to neutral molecules therefore is slower. May be that in the normal stepping interval of 40 ... 50 μ s transition of energy to the gas molecules i.e. *gas heating* near the avalanche is sufficient to cause an appreciable enhancement of the Townsend-Coefficient α . This initiates an instability $\alpha \rightarrow$ local gas temp. $\rightarrow \alpha$. The effect is analog to the Meek-Raether-instability but it takes more time (40 μ s ?). The author suggests an analysis of this effect of energy transmission from + ions to the gas and the enhancement of α -ionisation until the field collapses in a new step.

1.2 *Subsequent strokes* dispose of an appreciable residual charge of ions in the channel and in the surrounding corona-space charge. Furthermore temperature of the channel is still enhanced. Both effects facilitate ionisation and leader transition at a lower field intensity. This opinion is proved by the reappearance of steps if the cooling and de-ionizing time between strokes becomes longer.

2. VELOCITY OF LEADERS AND RETURN STROKES. —

A) Velocity of the first leader is determined by the stepping process. Between two steps corona progresses rel. slowly at about 100 ... 300 km/s.

B) Velocity of subsequent leaders is at least 10 times faster. A possible explanation is residual temperature and residual charge within the channel and outside in the corona shell, which could not be extracted by the preliminary stroke completely.

Mathematical treatment of these progression velocities of leaders on a physical base is extremely difficult.

C) Velocity of the return stroke, which is between 10 and 50 % that of light, has been found an experimental treatment by C. F. Wagner : He supposes the energy which is necessary to ionize and heat the channel to be able to carry the high impulse current of 10 to 200 kA to be responsible for the reduced velocity of waves when compared with the velocity of travelling waves on a metallic conductor. This energy is furnished at the front of the return stroke travelling wave, and therefore cuts permanently *slices* of charge and energy from it. Some measurements of this phenomenon were made in the high voltage laboratory with rather low impulse current values of a few kA only. An energy of 2 Ws was found to be necessary for each cm of channel and each kA of impulse current (2 Ws cm⁻¹ kA⁻¹). Velocity of return strokes is calculated on this base in function of impulse current.

A report to the 15th European Conference on Lightning Protection presented 2 weeks ago at Uppsala by R. Fieus confirms some correlation between current amplitude and progressing speed of the return stroke of triggered lightning flashes, corresponding to the theory of C. F. Wagner : Energy absorption in the front of the travelling wave. This theory should still be confirmed by direct comparison of progression velocity and return stroke measurements.

I was much interested to find in the *Journal* to this Conference an article by Mr. P. Hubert and G. Monget about measurements from St-Privat-d'Allier of return-stroke velocities in function of current (p. C7-421).

2 flashes with a total of 11 impulse currents between 3-19 kA were analysed :

the 2 first strokes present velocities of about 20 % of velocity of light,

the 9 subsequent strokes have velocities between 23 and 47 % of velocity of light,

these values seem to confirm the theoretical calculation by Lundholm and Rusk and the measurements in a laboratory by C. F. Wagner.

3. CURRENT FRONT (RISE TIME) IN FIRST AND SUBSEQUENT STROKES. — Shape of front current rise does not correspond with the double exponential curve which is generally admitted for calculations. First strokes always begin with a positive exponential rise. They present a slower current rise (less steep wave shape of current) than subsequent strokes. The difference is at least one order of magnitude (at least $10 \times$). Only first strokes have so-called *connecting leaders* (Fangentladungen) which progress from an earthed object upward towards the downcoming leader. A simple treatment of the resulting current curve bases on a *breakdown* between earth and a

metallic conductor in place of the downcoming leader, where the distance to the meeting point is treated as a simple inductivity L , and the lightning channel as a metallic conductor with surge impedance Z . A better physical treatment of this striking phenomenon with a physical explication of Z as used by C. F. Wagner is still wanted.

Subsequent strokes have no connecting leaders. Their current wave has front durations (rise times) between about 0.1 ... 1 μ s. These values do not show much difference with those of travelling waves, on transmission lines.

The difference of front duration between first and subsequent leader could possibly give a measure for the length of the connecting leader.

Regarding steepness of currents di/dt there is a very good agreement between French measurements at St-Privat-d'Allier, Italian measurements on Mte Orsa near Varese, and our 11 years statistiques from Mount San Salvatore in CH.

With these examples of still open problems I thank you for the possibility to expose our lightning problems to your international cercle of physicists.

Now some coloured pictures of lightning will be shown.

Annex 2

I. Lightning

A. Definitions. — 1. LIGHTNING. — 1.1 *Lightning flash* is an atmospheric discharge consisting of one or more lightning strokes (single stroke flash, multiple flash).

1.2 *Lightning channel* is the path of the lightning current in the atmosphere.

1.3 *Lightning stroke (stroke)* is a partial discharge in a lightning channel, led by a leader stroke.

1.4 *Leader stroke (leader)* is a pre-discharge of low light and current intensity, which produces the lightning channel of the lightning stroke.

1.5 *Return stroke (main stroke)* is the high light and current intensity discharge following the leader stroke.

1.6 *Connecting leader* is a discharge expanding towards the leader stroke of a downward flash from the earth or from earthed objects.

1.7 *Downward flash* is a lightning flash, whose first leader stroke proceeds from the cloud to the earth.

1.8 *Upward flash* is a lightning flash, whose first leader stroke extends from the earth, generally from high earthed pointed structures, towards the electrically charged cloud.

1.9 *Point of strike* is the point where the lightning stroke contacts the earth or an earthed object.

2. LIGHTNING CURRENT. — 2.1 *Lightning current* is the current flowing at the point where the lightning strikes.

2.2 *Lightning impulse current* is the high amplitude and short duration proportion of lightning current.

2.3 *Continuing current* is the current of low amplitude and long duration which follows the impulse current without interruption.

2.4 *Front* is the rising part of the lightning impulse current.

2.5 *Tail* is the falling part of the lightning impulse current.

2.6 *Rise time (front duration)* is the time from the beginning until the peak value of the lightning impulse current is reached.

2.7 *Lightning flash duration* is the time from the beginning of the first lightning stroke to the end of the last lightning stroke.

2.8 *Current peak (lightning current)* is the maximum value of the lightning impulse current i .

2.9 *Current steepness (current rise)* is the maximum value of the rise of the lightning current $di/dt(\max)$ during the rise time (steepest tangent to the current curve).

2.10 *Electric charge of a lightning flash* is the integral of the lightning current over the flash duration $\int i dt$.

2.11 *Current square impulse* is the integral from the square of the current over the time $\int i^2 dt$.

Strong turbulence and its computer simulation

Yu. S. Sigov

Keldysh Institute of Applied Mathematics, USSR Academy of Sciences, Moscow, USSR

V. E. Zakharov

Landau Institute of Theoretical Physics, USSR Academy of Sciences, Moscow, USSR

Abstract. — A short review of the results of analytical and numerical investigations of Langmuir turbulence is given. The presented theory of the strong electrostatic turbulence is based both on the concept of Langmuir collapse as a nonlinear stage of modulation instability and on the results of computer experiment which provides a continuous transition from the collapse concept (concentrated in averaged dynamical equations) to conditions of an actual experiment sufficiently well described by Vlasov equations.

The present report is a review of results of analytical investigation and computer simulation of Langmuir turbulence, which is one of the fundamental conceptions of plasma physics. The question of the nature of Langmuir turbulence is highly important both from the general theoretical and practical points of view. It is sufficient to refer to that principal part which it plays, for example, in interaction of plasma with intense electron beams and electromagnetic waves (including laser waves).

The title of the report emphasizes the fact that for an adequate understanding of Langmuir turbulence it is impossible to confine oneself by its weak turbulent description, which leads to physical paradoxes in a number of cases.

Kinetic equations for weak turbulent plasma were derived in early 1960. Later these equations were investigated in a number of papers (see, for example [1-3]). The paradoxical conclusion about unlimited accumulation of Langmuir oscillations in a small wave number region follows from these publications (if a level of turbulence is not extremely small).

Principal resolution of this paradox was given in [4], where a concept of Langmuir collapse was stated and averaged equations for dynamical description of a plasma were derived. Being relatively simple these equations were convenient for their theoretical and numerical analyses. Soon it became clear that this concept (which seemed to be very disputed) required for its testing and development a wide usage of methods of computational plasma physics.

The particle method used in the present report is based on a direct simulation of self-consistent plasma behaviour [5, 6] (so-called computer experiment) and it is free of limitations of the approximate theory. Therefore this method is an independent and rather

effective tool which provides continuous transition from collapse concept (concentrated in averaged dynamical equations) to the conditions of actual experiment sufficiently well described by Vlasov equations. In the present report the latest achievements of the computer experiments are presented.

Before the main content of the report, the brief review of the general theory of turbulence in nonlinear media is presented (§ 1). Discussion of the Langmuir turbulence theory (§§ 2-4) is based both on results of averaged theory and computer experiments. More details of the latter are presented in §§ 5-7.

1. About turbulence in physics. — The concept of turbulence arisen in hydrodynamics. During last two decades it gradually penetrated into other fields of physics, and first of all in plasma physics. At the present time it includes phenomena most of that do not resemble classical hydrodynamical turbulence. Thus it is useful to try to give a general physical definition of the turbulence which would reflect the more significant properties of the phenomenon. We shall consider only a developed turbulence, leaving aside the problems of its origin (such interesting problems as stochastic attractors including).

A developed turbulence may arise in all continuous media where dissipation processes are sufficiently small, and generally in a wide class of a Hamiltonian nonlinear dynamical systems with many degrees of freedoms.

Phenomena arising when an intense laser pulse passes through nonlinear dielectric is a fine (although unexpected) example of turbulence.

The turbulence is described statistically. But this description does not draw a theory of turbulence and statistical mechanics together. A state of a dynamical

system with a developed turbulence is rather far from a state of thermodynamical equilibrium. It is hopeless to try to describe this state using thermodynamical language, because the notion of *effective temperature of turbulence* has no physical sense. In conditions of developed turbulence some of the degrees of freedoms are excited many orders more intensively than the others. These degrees of freedoms tend to give superfluous energy (which they obtain from external source which feeds the turbulence) to the other degrees of freedoms, and the latter give this energy to an environment. Thus, studying any type of turbulence it is very important to study dissipation mechanisms by which a turbulent system loses its energy. These are those mechanisms that define qualitative character of turbulence spectrum, though in the energy containing region the dissipation is usually small. In the simplest cases the dissipation is provided by linear mechanisms. For example, in hydrodynamics, where dissipation is provided by viscosity in high wave number region. The energy flux is directed to this region from the energy containing region of the spectrum. In other more complicated cases the dissipation is provided by nonlinear mechanisms. Thus in the case of surface water waves' turbulence the energy is dissipated by

white-capping; in acoustic turbulence case — by formation of shock waves. Sometimes nonlinear dissipation mechanisms may be rather refined. The example is a collapse of Langmuir waves which provides the dissipation of Langmuir turbulence.

A principal point for the classification of different turbulent states is a division of the turbulence in a weak and a strong one. Weak turbulence is described by wave kinetic equations and it is the most simple for an analytical study. Definition of strong turbulence is purely negative — it is any turbulence which is not weak.

The important point for a study of turbulence of any type is an analysis of integrals of motion of a dynamical system with developing turbulence. Turbulence spectrum is defined by values of fluxes of these integrals of motion in high or low frequency regions.

Let's consider the main types of the weak turbulence occurring in physical problems. Let turbulence, developing in some nonlinear medium, be an excitation of one type waves with dispersion law ω_k , which permits three-wave interactions

$$\omega_k = \omega_{k_1} + \omega_{k_2}, \quad \mathbf{k} = \mathbf{k}_1 + \mathbf{k}_2. \quad (1)$$

Then the medium is described by Hamiltonian

$$H = \int \omega_k a_k a_k^* dk + \int V_{kk_1 k_2} (a_k^* a_{k_1} a_{k_2} + a_k a_{k_1}^* a_{k_2}^*) \delta(k - k_1 - k_2) dk dk_1 dk_2. \quad (2)$$

Weak turbulent description of system (2) is given by kinetic equation

$$\frac{\partial n_k}{\partial t} = St(n, n) - \gamma_k n_k + f_k. \quad (3)$$

Here $n_k = \langle |a_k|^2 \rangle$, γ_k , f_k — phenomenologically introduced damping and external force, and

$$St(n, n) = 2\pi \int |V_{kk_1 k_2}|^2 (n_{k_1} n_{k_2} - n_k n_{k_1} - n_k n_{k_2}) \delta(k - k_1 - k_2) \delta(\omega_k - \omega_{k_1} - \omega_{k_2}) dk_1 dk_2 + \\ + 4\pi \int |V_{k_1 k k_2}|^2 (n_{k_1} n_{k_2} + n_k n_{k_1} - n_k n_{k_2}) \delta(k - k_1 + k_2) \delta(\omega_k - \omega_{k_1} + \omega_{k_2}) dk_1 dk_2.$$

Criteria for application of eq. (3) are rather delicate [7]. In any case, it is necessary for it that cubic term in the Hamiltonian (2) should be considerably smaller than a quadratic one. However for the linear dispersion law $\omega_k = k$ the eq. (3) has no region of applicability at all [8].

In the isotropic case the system (2) has the single nontrivial integral H (energy); in weak turbulent approximation $H = \int \omega_k n_k dk$. Usually γ_k is high for high k , and f_k is high in the region of small k . In this case in the most of physical situations the spectrum

is controlled by the only value which is the energy flux P in the region of high k and it is of the Kolmogorov type. If dispersion law $\omega_k = k^s$, $s > 1$ is a power function and $V(ek, ek_1, ek_2) = \varepsilon^q V(k, k_1, k_2)$ is a uniform function of power q , then Kolmogorov's spectrum in inertial region of intermediate k may be found analytically.

From dimensional analysis it follows

$$\omega_k k^2 \frac{\partial n_k}{\partial t} = \frac{\partial}{\partial k} P, \quad P = \text{constant}.$$

Now it is easy to find

$$n_k \approx \frac{P^{1/2}}{k^{3+q}}. \quad (4)$$

It is notable that the spectrum (4) is the exact solution of the equation $St(n, n) = 0$ [9]. Alternative

exact solution $n_k = T/\omega_k$ (thermodynamically equilibrium Rayleigh-Jeans distribution) is physically meaningless. Now suppose that tripple processes are forbidden and only four-wave processes may occur

$$\omega_k + \omega_{k_1} = \omega_{k_2} + \omega_{k_3}, \quad \mathbf{k} + \mathbf{k}_1 = \mathbf{k}_2 + \mathbf{k}_3.$$

Then the Hamiltonian of the system has the form

$$H = \int \omega_k a_k a_k^* dk + 1/2 \int W_{kk_1k_2k_3} a_k^* a_{k_1}^* a_{k_2} a_{k_3} \delta(k + k_1 - k_2 - k_3) dk dk_1 dk_2 dk_3. \quad (5)$$

Now, together with H , wave action integral is conserved

$$I = \int |a_k|^2 dk. \quad (6)$$

In this case the collisional term in the kinetic equation has the form

$$St(n, n, n) = 2\pi \int |W_{kk_1k_2k_3}|^2 (n_{k_1} n_{k_2} n_{k_3} + n_k n_{k_2} n_{k_3} - n_k n_{k_1} n_{k_3} - n_k n_{k_1} n_{k_2}) \times \delta(k + k_1 - k_2 - k_3) \times \delta(\omega_k + \omega_{k_1} - \omega_{k_2} - \omega_{k_3}) dk_1 dk_2 dk_3. \quad (7)$$

Apart from an evident and physically absurd (in turbulent problems) spectrum

$$n_k = \frac{T}{\mu + k\zeta + \omega_k} \quad (8)$$

this expression vanishes for the uniform function

$$W(\varepsilon k, \varepsilon k_1, \varepsilon k_2, \varepsilon k_3) = \varepsilon^q W(k, k_1, k_2, k_3)$$

if we take the two power spectra [10, 11]

$$n_k = \frac{P^{1/3}}{k^{3+q}}; \quad n_k = \frac{Q^{1/3}}{k^{3+2q/3-S/3}}. \quad (9)$$

Analogous paradox arises for the third typical case of the wave turbulence. It is the case of an interaction of high frequency and low frequency waves. In such a case the Hamiltonian of the system has the form

$$H = \int \omega_k a_k a_k^* dk + \int \Omega_k b_k b_k^* dk + \int \Gamma_{kk_1k_2} (b_k a_{k_1} a_{k_2}^* + b_k^* a_{k_1}^* a_{k_2}) \times \delta(k + k_1 - k_2) dk_1 dk_2. \quad (10)$$

Here Ω_k and b_k are the dispersion law and the amplitude of low frequency waves. Kinetic equations for weak turbulence now have the form

$$\begin{aligned} \frac{\partial n_k}{\partial t} + \gamma_k n_k &= f_k + \int (T_{k_2kk_1} - T_{k_2k_1k}) dk_1 dk_2 \\ \frac{\partial N_k}{\partial t} + \gamma_k^H N_k &= - \int T_{kk_1k_2} dk_1 dk_2 \\ T_{kk_1k_2} &= 2\pi |\Gamma_{kk_1k_2}|^2 (n_k n_{k_2} - n_k N_{k_2} - n_k N_{k_1}) \delta(k - k_1 - k_2) \delta(\omega_k - \omega_{k_1} - \Omega_{k_2}). \end{aligned} \quad (11)$$

Qualitative properties of the solutions of the system (11) are similar to that of eq. (3)-(7), for in the system (10) the integral of wave action is also conserved [12].

There is a rather interesting case when a damping of low frequency waves γ_k^H is comparable to their frequency Ω_k . In such a case $N_k \ll n_k$ and the value of N_k may be expressed explicitly: δ -function is spreaded in frequency domain to width γ^H .

The equation for n_k takes the form [1, 13]

$$\frac{\partial n_k}{\partial t} + \tilde{\gamma}_k n_k = \tilde{f}_k \quad (12)$$

where

$$\begin{aligned} \tilde{\gamma}_k &= \gamma_k + \int T_{kk'} n_{k'} dk' \\ T_{kk'} &= -T_{k'k} = \int (\phi_{k_2 k k'} - \phi_{k_2 k' k}) dk_2 \\ \phi_{k_2 k k'} &= \frac{2 |\Gamma_{k_2 k k'}|^2 \gamma_{k_2}^H}{(\omega_k - \omega_{k'})^2 + (\gamma_{k_2}^H)^2} \end{aligned}$$

and the renormalized value \tilde{f}_k contains (except for f_k) cubic terms in n_k , and it is rather small for small n_k .

2. Langmuir turbulence. Averaged description.

The study of Langmuir turbulence is important from several points of view. For fast methods of plasma heating (by an electron beam or laser radiation) the energy is initially transferred to Langmuir waves, and in most cases the physics of adopting of this energy is entirely determined by developing Langmuir turbulence [14-17]. It determines such fundamental quantities as relaxation length of electron beam, laser radiation reflection coefficient and the form of

electron distribution function of heated plasma. It is probably just Langmuir turbulence which is presumably responsible in the most cases for the appearance of hot electrons (Fig. 1) that are so troublesome for a controlled thermonuclear fusion.

From the other hand, Langmuir turbulence is one of the most simple types of plasma turbulence and in general one of the most investigated examples of a turbulence, which doesn't resemble a turbulence in an incompressible fluid.

For constructing the theory of Langmuir turbulence it is convenient to use simplified plasma equations, that can be obtained by averaging of kinetic equations with respect to the fast time $1/\omega_p$ (see [4]). The main averaging parameter is the small wave number such that $(k\lambda_D)^2 \ll 1$. The other parameter is the density of the energy of oscillations

$$W/nT \approx E^2/8\pi nT.$$

If $W/nT \ll 1$ the result of averaging of Vlasov-Poisson equations for electrons leads to the linear equation

$$\Delta \left(i\Psi_t + i\tilde{\gamma}_L \Psi + \frac{3}{2} \lambda_D^2 \Delta \Psi \right) = \frac{\omega_p}{2n_0} \operatorname{div} \delta n \nabla \Psi. \quad (13)$$

Here Ψ is a complex amplitude of high frequency potential, δn is a variation of electron density in slow motions, $\tilde{\gamma}_L$ is an integral operator describing a linear (Landau and collisional) waves' damping

$$\begin{aligned} \hat{\gamma}_L \Psi &= \int \gamma_L(r - r') \Psi(r') dr' \\ \gamma_L(\xi) &= \int \gamma_L(k) \exp(-ik\xi) dk. \end{aligned} \quad (14)$$

If a plasma is stable in linear approximation relatively to excitation of Langmuir waves then $\gamma_L(k) \geq 0$. From (13) *a priori* relation follows

$$\frac{\partial}{\partial t} \int |k|^2 |\Psi_k|^2 dk + \int \gamma_k |k|^2 |\Psi_k|^2 dk = 0 \quad (15)$$

which shows that in presence of density non-homogeneities (of ion sound), the Langmuir waves cannot be excited. In particular from this fact the impossibility of excitation of Langmuir turbulence by an ion-sound one follows, though the inverse process (conversion of Langmuir waves into ion-sound waves) is, of course, possible. The eq. (13) does not contain electron nonlinearities. To estimate their role let's note [18] that the condition $(k\lambda_D)^2 \ll 1$ can be rewritten in the form

$$v_T^2 \ll \frac{\omega_p^2}{k^2}. \quad (16)$$

The accounting of electron nonlinearities leads to

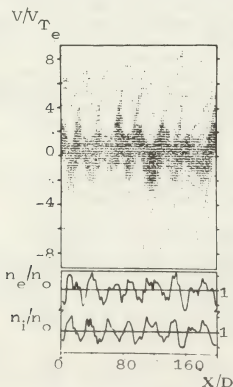


Fig. 1. — Part of the electron phase plane and electron/ion density profiles in the one-dimensional case of parametric pumping near the electron plasma frequency [14-16]. (Stage of the high energetic electron tails formation.)

adding of an oscillatory speed to a heat speed. In this case the condition (16) is replaced by

$$v_{osc}^2 \ll \frac{\omega_p^2}{k^2}$$

which is equivalent to the condition

$$\frac{W}{nT} \ll \frac{1}{(k\lambda_D)^2}.$$

Therefore the equation improving (13) contains the expansion into parameters $(k\lambda_D)^2$ and $(k\lambda_D)^2 W/nT$. The first term, nontrivial as compared to (13), has the order $(k\lambda_D)^2 W/nT$ [18, 10]. It is interesting that in a purely one dimensional problem it is identically vanished [14, 10]. If the distribution of Langmuir oscillations is quasi one-dimensional with characteristic angle $\theta \ll 1$ then the order of the first term of an electron nonlinearity is $\theta^2(k\lambda_D)^2 W/nT$. This leads to the conclusion that electron nonlinearities are usually unimportant. For closure of the eq. (13) it is necessary to have an equation for δn . Strictly speaking, it should be a kinetic equation for ions. But if the intensity of an ion sound is not too high ($\delta n/n \ll 1$) one can use the linear wave equation

$$\left(\frac{\partial^2}{\partial t^2} + 2\hat{\gamma}_s \frac{\partial}{\partial t} - c_s^2 \Delta \right) \delta n = \frac{1}{16\pi M} \Delta |\nabla \Psi|^2 \quad (17)$$

where $\hat{\gamma}_s$ is an operator of sound damping. If $\hat{\gamma}_L = 0$, the conservation law

$$\frac{\partial}{\partial t} \int |\nabla \Psi|^2 dr = 0, \quad \int |\nabla \Psi|^2 dr = I \quad (18)$$

follows from the eq. (13). If in addition $\hat{\gamma}_s = 0$, the system (13), (17) is of the Hamiltonian form. The transition to canonical variables can be performed by means of the relations

$$\Psi = \frac{8\pi e}{(2\pi)^{3/2}} \left(\frac{n_0}{2m\omega_p} \right)^{1/2} \int \frac{a_k}{k} e^{ikr} dk \quad (19)$$

$$\delta n = \frac{1}{(2\pi)^{3/2}} \int \left(\frac{n_0 k}{2Mc_s} \right)^{1/2} (b_k + b_{-k}^*) e^{ikr} dk.$$

The Hamiltonian has the form (10) and

$$\Gamma_{k_1 k_2} = \frac{1}{(2\pi)^{3/2}} \frac{\omega_p}{(2Mn_0 c_s)^{1/2}} \frac{k^{1/2}(k_1 k_2)}{|k_1| |k_2|}. \quad (20)$$

In a long wave region $k\lambda_D \ll (m/M)^{1/2}$ one can go to the static approximation

$$\delta n = -\frac{1}{16\pi M c_s^2} |\nabla \Psi|^2. \quad (21)$$

The eq. (13) is transformed to the form

$$\Delta \left(i\Psi_t + \frac{3}{2} \omega_p \lambda_D^2 \Delta \Psi \right) = -\frac{e^2}{4m\omega_p} \frac{1}{T_i + T_e} \text{div} \nabla \Psi |\nabla \Psi|^2. \quad (22)$$

The eq. (22) is of the Hamiltonian form because the changing of variables according to (19) yields the system (5) where

$$W_{kk_1 k_2 k_3} = -\frac{e^2}{8m\omega_p(T_i + T_e)} \frac{(kk_3)(k_1 k_2) + (kk_2)(k_1 k_3)}{|k| |k_1| |k_2| |k_3|}.$$

The existence of the additional integral of motion in plasma I leads to the fact that the Langmuir plasmon flux is directed into a region of small k . This flux is the main parameter of a weak turbulence spectrum. A detailed structure of the spectrum depends on the relation between electron and ion temperatures. When $T_i \sim T_e$, the turbulence is described by the kinetic eq. (12) [1-3, 18, 19]. Because of a small value of \tilde{f}_k , the stationary solutions of the eq. (12) have a rather unusual character. These solutions are singular. They are confined on *jets* in the k -space, i.e. on surfaces (two dimensional jets) or on lines (one dimensional jets) [13, 20] extending from the region of a high wave number to the region of a small one. The thickness of the jets depends on the

value of \tilde{f}_k . The characteristic time for establishing of jets' spectra is rather high [20, 21].

It is remarkable that the energy distribution on jets needn't be smooth at all. The jets may have (and they actually have) the additional fine structure — the spectrum has the form of *spots* [20] located on jets. In some cases the jets are chains of discrete peaks along which the energy transfer takes place. A plasma with a developed turbulence of this type resembles a multimode laser, more than an active turbulent fluid. The narrowness of spectral peaks may lead to its modulation instability and to further development of a phenomena like a self-focusing.

Character of a jets spectrum is illustrated in figure 2, where the result of numerical solution of

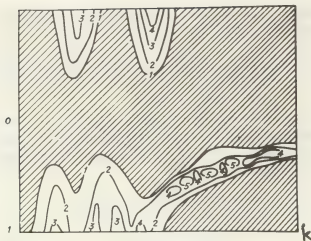


Fig. 2. — Lines of constant $\ln N(k, x)/N_0$ for the case of pumping by a relativistic electron beam [20].

the eq. (12) for the case of excitation of Langmuir oscillations by a relativistic electron beam is presented. Characteristic spectrum spots size is

$$\Delta k \lambda_D \sim (m/M)^{1/2}.$$

In a nonisothermal plasma ($T_i \ll T_e$) the picture of the spectra is more complicated. The turbulence is described by the system of eq. (11). This system may have singular as well as regular solutions. Amidst the latter are Kolmogorov's spectra (see [12]) :

$$n_k = \alpha \frac{Q^{1/2}}{k^3}, \quad N_k = \beta \frac{\omega_k}{\Omega_k} \frac{Q^{1/2}}{k^2}. \quad (23)$$

Here α and β are constants, Q is the flux of a number of Langmuir plasmons in the region of small k . The concrete selection of a solution is determined by a condition of an excitation (by an angular width of instability increment which generates the turbulence). But in all the cases the theory of a weak turbulence predicts an accumulation of plasmons in the region of small k .

3. Collapse of Langmuir waves. — In the framework of the theory of weak turbulence it is impossible to solve the paradox of an accumulation of Langmuir plasmons in the region of small wavenumbers. Until now we have not yet discussed criteria of an applicability of the weak turbulent description. These criteria are rather strict. It is necessary to satisfy the conditions [4]

$$\frac{W}{nT} < (k\lambda_D)^2 \quad \text{if} \quad (k\lambda_D)^2 < \frac{m}{M} \quad (24)$$

$$\frac{W}{nT} < k\lambda_D(m/M)^{1/2} \quad \text{if} \quad (k\lambda_D)^2 > \frac{m}{M}. \quad (25)$$

If the spectrum is narrow, one should replace

$$k\lambda_D \rightarrow \Delta k\lambda_D$$

(where Δk is the width of the spectral peak) in the relations (24) and (25).

When the Langmuir plasmons are accumulated in the region of small k the criteria (24) and (25) are violated. The fact of a modulation instability of Langmuir waves is well known [22]. A uniform (with $k = 0$) Langmuir oscillation is unstable relatively to the development of disturbances with a characteristic space size L , where $(\lambda_D/L)^2 \sim W/nT$. The growth rate of the instability has the order of $\gamma \sim \omega_p W/nT$ for $W/nT < m/M$ and $\gamma \sim \omega_p(m/M \cdot W/nT)^{1/2}$ for

$$W/nT > m/M.$$

Obviously the instability can be developed also for wave packets of a finite size only if $W/nT > (k\lambda_D)^2$.

Collapse of Langmuir waves is a nonlinear stage of a modulation instability development. In the most physical situations the inclusion of nonlinear terms stabilizes an instability development. But an opposite effect is also possible when nonlinearity accelerates the instability development and leads to *explosion effect*, i.e. to a formation of singularity during a finite time. Totality of analytical and computer investigations shows that it is true in the case of a nonlinear stage of modulation instability. As a result of its development there arise collapsing cavities in plasma, i.e. the regions of low density that are, in essence, closed resonators for Langmuir oscillations. These cavities are axisymmetrical and flattened approximately in proportion 3 : 1 [23-27]. The field in the cavity is constructed like the field in a plane condenser and in the centre of the cavity this field is directed along its short axis. The results of a numerical computation are presented in figures 3, 4. During the formation of a cavity the following stages take place.

3.1 STAGE OF SUBSONIC COLLAPSE. — This stage takes place when the initial amplitude of Langmuir wave is sufficiently small ($W/nT \ll m/M$). On this stage the cavity collapses according to the self-similar law [4, 24]

$$\frac{E^2}{8\pi nT} \sim \frac{1}{t_0 - t} \varphi\left(\frac{r}{\sqrt{t_0 - t}}\right) \quad (26)$$

and the static condition for density variations is fulfilled

$$\delta n \sim n_0 \frac{E^2}{8\pi nT} \quad (27)$$

the cavity tends to form an integrable density singularity in plasma

$$\delta n \sim n_0 \frac{\lambda_D^2}{r^2}. \quad (28)$$

The subsonic stage is over when the intensity of oscillations in the centre of cavity reaches the value

$W/nT \sim m/M$. The dimension of the central part of the cavity has the order $r_0 \sim \lambda_D(M/m)^{1/2}$. It turns out that then the energy $\varepsilon \approx (M/m)^{1/2} T \lambda_D^3$ is concentrated in the central region.

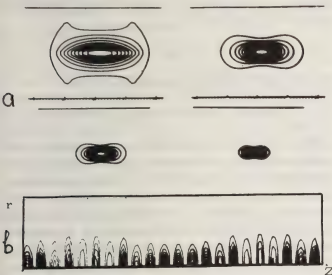


Fig. 3. — Typical collapse pictures (pattern of $E^2 = \text{constant}$) obtained by numerical solution of the averaged dynamical equations : a) single caviton [24]; b) Many cavitons of various phases in the presence of Z-oriented pump [30].

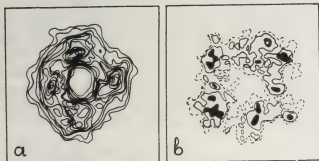


Fig. 4. — Cavitons in a turbulent cell resulting from the modulation instability of a single electrostatic wave (2D double-periodic computer simulation [25]). a) Cross-sections

$$w(X, Y) = E^2(X, Y)/8 \pi n_0 T = \text{constant};$$

b) $n(X, Y) = \text{constant}$. The distances between two neighboring lines $w = 0.05$, $n = 0.1$. The external curves correspond to $w = 0.2$, $n = 0.9$.

3.2 STAGE OF SUPERSONIC COLLAPSE. — When $W/nT > m/M$ the collapse changes into a so-called supersonic stage. On this stage the Laplacian in the wave equation can be neglected.

The cavity collapses according to the self-similar law [4, 17, 24], and the growth of density variations falls behind from the growth of Langmuir oscillations intensity [4, 16].

$$\frac{\partial n}{\partial t} \sim \frac{1}{(t_0 - t)^{4/3}} V \left(\frac{r}{(t_0 - t)^{2/3}} \right) \quad (29)$$

$$\frac{W}{nT} \sim \frac{1}{(t_0 - t)^2} R \left(\frac{r}{(t_0 - t)^{2/3}} \right). \quad (30)$$

Collapsing at the supersonic stage takes place without energy losses. Outside the cavity the divergent sound wave is formed. The supersonic stage continues until the inverse dimension of the cavity k_{max} grows so considerable that Landau damping rate becomes approximately equal to the growth rate of modulation instability which characterizes the rate of cavity contraction

$$\gamma_{\text{mod}} \sim \omega_p(mW/MnT)^{1/2}.$$

Then the dimension of the cavity does not decrease, and Langmuir oscillations in the cavity are *burnt down* [25, 29, 30]. But as ions pushed out of the cavity have a considerable inertia, the density variation in the centre of the cavity continues to increase up to the value

$$\delta n/n_0 \sim (k_{\text{max}} \lambda_D)^2.$$

Outside the cavity a divergent sound wave is formed. The energy, which is equal to the $(k_{\text{max}} \lambda_D)^2$ part of the total energy absorbed in cavity, is transmitted to this ion sound wave. This stage of collapse evolution can be called a *fly-away stage*. On the fly-away stage the collapse generates sound [25, 29]. If P is the energy flux into plasma due to collapse, the acoustic turbulence results with the intensity

$$W_s = \frac{P}{\gamma_s} (k_{\text{max}} \lambda_D)^2. \quad (31)$$

If in the beginning $W/nT > m/M$ the collapse begins immediately from the supersonic stage [23, 43].

Collapse is a very effective mechanism of absorbing of Langmuir waves. It brings the damping γ_{eff} in a wave system which can be estimated according to the relations [4, 24] :

$$\gamma_{\text{eff}} \sim \omega_p(W/nT)^{3/2} (M/m)^{1/2}, \quad W/nT < m/M \quad (32)$$

$$\gamma_{\text{eff}} \sim \omega_p(Wm/nTM)^{1/2}, \quad W/nT > m/M.$$

This damping is quite sufficient to absorb the energy flux supplied to a turbulence. The final damping mechanism is Landau damping [14-17, 30]. One can say that the cavity contraction is a process of energy transfer from the region of small wave numbers to the region of high ones.

If there is a lot of cavities, the spectrum [17, 24]

$$n_k \simeq (W_0/nT)^{1/4} (M/m)^{1/2} \omega_p P k^{-9/2} \lambda_D^{-5/2} \quad (33)$$

is formed in the region of high k , where P is the density of energy dissipated in plasma. In spite of the external similarity of this spectrum to the Kolmogorov's type of spectra, the spectrum (33) has, of course, a different physical nature.

It is necessary to stress that a collapse picture is essentially a three-dimensional one and it can not be constructed on the basis of one-dimensional theory

(like the theory of solitons and their interactions). It is also necessary to note that solitons are unstable in the relation to transverse disturbances and that the development of this instability leads to desintegration of soliton into collapsing cavities [26, 31-34]. Nevertheless, in the presence of pumping which orients the cavities' small axis along the electric field the collapse can take a quasi one-dimensional character [29-31, 35, 38, 39].

The value k_{\max} is defined by the form of the electron distribution function. In Maxwellian plasma

$$(k_{\max} \lambda_D)^{-1} \sim 2 \div 3.$$

But if there are accelerated electron tails in plasma, the value of k_{\max} decreases. Picturesquely speaking, plasma in a developed Langmuir collapse state is a stochastic linear accelerator.

Effective quasilinear equation for electrons in the presence of collapse has the form

$$\frac{\partial f}{\partial t} = \frac{1}{v^2} \frac{\partial}{\partial v} v^2 D(v) \frac{\partial f}{\partial v} + (St)_{\text{Coulomb}} \quad (34)$$

where for the subsonic collapse the relation

$$D(v) \simeq (M/m)^{1/4} (P/nT) v^2 (v/v_T)^{3/2} \quad (35)$$

for the stationary distribution function the $f \sim C/v^{5/2}$, and the number of particles diverges for the high v . Thus for a collapse damping mechanism all the energy put into plasma is spent on the acceleration of a small number of hot electrons.

Now let's consider the effect of absorption of Langmuir waves which competes with collapse. It is a conversion of Langmuir waves into ion-sound ones [37]. Conversion brings an effective damping

$$\gamma_{\text{conv}} \simeq \omega_p \frac{W_s}{nT} \frac{\gamma_k}{\omega_p (k \lambda_D)^2}.$$

Here W_s is a density of sound energy, γ_k is Landau damping for Langmuir waves of the same wave length as the sound wave. For the total energy flux into plasma P we have

$$P = P_1 + \gamma_{\text{conv}} W \quad (36)$$

where P_1 is the energy absorption in collapses.

Let us consider all the sound turbulence to be generated by collapses. Then it follows from (31) that

$$P \simeq P_1 (1 + \gamma_k W / \gamma_s nT).$$

Thus conversion competes with collapse if

$$W/nT \geq \gamma_s / \gamma_k \quad (37)$$

where $\gamma_k \simeq \omega_p (W_{\max} m/nTM)^{1/2}$ is the damping which stops the collapse. Using the self-similar relation

$$W_{\max} nT \sim (k_{\max} \lambda_D)^{3/2} (M/m)^{1/2}$$

we can rewrite the condition (37) in the form

$$W/nT > \frac{\gamma_s}{\omega_s} (m/M)^{1/4} (k_{\max} \lambda_D)^{-3/2} \quad (38)$$

where ω_s is the sound frequency. In the isothermal plasma the relation (38) gives

$$W/nT > (m/M)^{3/4} (k_{\max} \lambda_D)^{-2}.$$

For the extremely nonisothermal plasma

$$W/nT > (m/M)^{3/4} (k_{\max} \lambda_D)^{-3/2}.$$

One can see that conversion can complete with collapse only for a sufficiently high Langmuir turbulence level when accelerated electrons are absent (when $k_{\max} \lambda_D$ is not too small). An additional cause increasing γ_s and limiting the conversion is a breaking of acoustical waves and appearance of accelerated ions responsible for a sound damping (see § 7).

4. Collapse of envelopes and parametric instability.

— It is well known (see [4, 22]) that a monochromatic Langmuir wave is subjected to a modulation instability. The Langmuir collapse concept permits to understand the further development of this instability. Let E_0 be the wave intensity and k_0 be the wave number. If $E_0^2/8 \pi nT > (k_0 \lambda_D)^2$, the result of instability will be a development of collapsing cavities with the initial size of the order of magnitude k_0^{-1} , and a fast wave damping. But if $E_0^2/8 \pi nT < (k_0 \lambda_D)^2$ the result of the modulation instability will be three-dimensional self-focusing of the wave which implies the development of the density pits with the initial size

$$L \sim \lambda_D (E_0^2/8 \pi nT)^{-1/2}$$

which essentially exceeds the wave length. This phenomenon can be called a collapse of envelopes. As the collapse of envelopes develops, the wave intensity in the centre of each pit increases until of the conditions of ordinary collapse are satisfied. Under these conditions inside the initially large cavity small cavities arise with sizes of the order of magnitude of the wave length and this leads to the wave energy damping. If

$$L \sim \lambda_D (E_0^2/8 \pi nT)^{-1/2}$$

the effective collision frequency can be estimated by the formula (32).

In spite of theoretical predictions, until now the formation of a long-wave Langmuir condensate was not observed, even for small amplitudes of the excited waves [30]. This can be explained by a singular nature of weak turbulence spectra, which follows from eq. (12), and by the development of the envelope collapse.

Let's consider this phenomenon using an example of turbulence which arises due to the development of

parametric instabilities in plasma. It was a subject of numerous investigations both numerical and analytical for the reasons of the importance of this problem for the problem of controlled laser fusion (see, for example [40-42, 14-17, 29, 31, 44, 45, 49]).

Let a plasma be excited by the uniform electric field E_0 oscillating with frequency $\omega > \omega_p$ and

$$(k_0 \lambda_D)^2 \simeq (\omega - \omega_p) / \omega_p \gg m/M, \quad E_0^2 / 8 \pi n T \ll m/M$$

for an isothermal plasma. Then the weak turbulence theory can be applied (see, for instance [20]) which predicts a one-dimensional line spectrum in a form of a system of spectral lines (peaks) equidistantly located, with the distance between each other of the order of $k_d \sim (m/M)^{1/2} / \lambda_D$ and which fills a segment $(k, -k)$ of the axis parallel to E_0 . Within the weak turbulence framework the width of each peak is equal to zero, and the intensity is $W_0/nT \simeq E_0^2/8 \pi nT$.

Each of the peaks experiences the modulation instability and the result of it is an extension of the peak up to the value δk , $(\delta k \lambda_D)^2 \simeq E_0^2/8 \pi nT$, which is smaller than the distance between the peaks, so the spectrum conserves the line structure (*).

But the most important consequence of the modulation instability is a collapse of envelopes which leads to a nonlinear damping of the spectral peaks.

If one is not interested in a fine structure of the spectrum, it is possible to go to the rough *differential approximation* in eq. (12) [13, 19]. It is convenient to write down this for a nondimensional quantity

$$I_k \simeq 4 \pi k^2 \omega_p (m/M)^{1/2} n_k / n T \lambda_D$$

which is the relative energy density on a scale k_D corresponding to one of the peaks. We have

$$\frac{\partial \ln I_k}{\partial t} = \omega_p \left[(m/M)^{1/2} \frac{1}{\lambda_D} \frac{\partial}{\partial k} I_k - \alpha I_k^{3/2} (M/m)^{1/2} \right] \quad (39)$$

where α is a nondimensional constant.

Stationary solution of this equation is

$$I_k \simeq (1/\alpha^2) (m/M)^2 / \lambda_D^2 (k - k^*)^2.$$

The constant $k^* > k_0$ should be found out of the matching conditions with the first peak. This gives

$$(m/M)^2 / [\alpha^2 \lambda_D^2 (k^* - k_0)^2] \simeq E_0^2 / 8 \pi n T.$$

It can be seen that the width of the spectrum $(k^* - k_0)$ decreases with the growth of $(E_0^2/8 \pi nT)$ and the intensity at $k = 0$ tends to some limit and rather small value

$$I(0) \simeq (m/M)^2 / (k_0 \lambda_D)^2$$

which explains the absence of an observed condensate in computer experiments.

(*) It is necessary to note that as Langmuir waves' group velocity exceeds the sound speed, the modulation instability is entirely a transverse one.

For $E_0^2/8 \pi nT \sim m/M$ we have

$$\lambda_D^2 (k^* - k_0)^2 \simeq m/M$$

i.e. the spectrum consists of one or two peaks.

These peaks become wider due to this modulation instability and actually they eventually merge into a continuous spectrum. The total turbulence intensity becomes of order $E_0^2/8 \pi nT$.

Then with the further increasing of pump level, if

$$m/M < E_0^2/8 \pi nT < (k_0 \lambda_D)^2$$

the turbulence spectrum is a monochromatic wave broadened due to collapse of envelopes to the value

$$(\delta k \lambda_D)^2 \simeq E_0^2/nT.$$

The case of a high pumping

$$E_0^2/8 \pi nT > (k_0 \lambda_D)^2$$

corresponds to the fully developed strong turbulence when collapses with cavity sizes equal to the wave length as regards of order of magnitude arise everywhere with equal probability.

5. Subject of computer experiment. — Actually, computer simulations of strong turbulence processes have been carried out from early 1970. In 1970 anomalous high absorption of energy of long wave Langmuir disturbances occurred in the computer experiment [41], which was impossible to understand in the framework of weak turbulence theory. Later, high energy electron *tails* were observed in paper [42] where a parametric action on plasma was discussed. This phenomenon, together with the role and the mechanism of delivering of plasmons from a long wave part of spectrum to the short wave region, was completely explained two years later.

First observation of the density cavities' formation (as a result of action of *hf* ponderomotive force) and the usage of this fact for explanation of the mechanism of the short wave plasmon pumping and of *electron tails* generation were presented in the computer experiments [14, 15]. The obtained picture of the nonlinear self-focusing of Langmuir waves was in a complete agreement with the collapse concept [4] as a nonlinear stage of the modulation instability [22]. The latter circumstance in its turn stimulated an increasing interest in the studies of strong turbulent regimes. One may say that a number of computational papers related to this problem was mostly oriented directly to the study of specific properties of Langmuir collapse and of its role in the mechanism of an anomalous absorption of wave energy by turbulent plasma. Numerical solutions of averaged dynamical equations [23, 24] have demonstrated a general validity of the collapse concept, but at the same time these solutions show that a nonlinear self-focusing of Langmuir oscillations actually rather soon takes the solution out from the region of the validity of the

averaged description, because the parameters $(k\lambda_D)^2$ and W/nT cease being small. The necessity to study energy distribution mechanisms in cavities, i.e. the details of wave-particle interactions, also required a kinetic approach to the problem.

Thus, a construction of the closed strong turbulence theory required a creation of a bridge between the collapse concept, related to the averaged equation, and laboratory or numerical experiments, with real wave-particle interactions without any limitation of values of amplitudes, scales and the degree of non-linearity.

Below we shall show that computer simulation of a plasma by the superparticle method [5, 6] represents such a bridge. Particle methods are based on Vlasov kinetic equations for ion and electron distribution functions $f_{i,e}(\mathbf{r}, \mathbf{v}, t)$ and self-consistent electromagnetic field equations. From the latter it is sufficient to retain a single Poisson equation for scalar potential $\zeta(\mathbf{r}, t)$ for the considered electrostatic plasma:

$$\frac{\partial f_\alpha}{\partial t} + \mathbf{v} \cdot \frac{\partial f_\alpha}{\partial \mathbf{r}} - \frac{e_\alpha}{m_\alpha} \frac{\partial \zeta}{\partial \mathbf{r}} \cdot \frac{\partial f_\alpha}{\partial \mathbf{v}} = 0, \quad \alpha = i, e$$

$$\Delta \zeta = 4\pi n_0 \sum_\alpha e_\alpha f_\alpha d\mathbf{v}. \quad (40)$$

The idea of the superparticle method is extremely simple. A phase space (\mathbf{r}, \mathbf{v}) for an electron (ion) plasma component at the initial moment of time $t = 0$ is divided into N non-intersecting cells, and total charges and masses of all the real particles at the each cell are attributed to one superparticle. Solving the Vlasov equation by the method of characteristics one can step by step follow dynamical trajectories of all the superparticles in the phase space, recomputing them, using an electromagnetic field at every time step. Thus, on the one hand, it is possible to follow a self-consistent time evolution of a space electromagnetic field picture, and, on the other hand, to reproduce plasma's own charges and currents.

The presented program of computer experiments was compiled in such a way as to try to reduce the total amount of computations maximally already at the stage of the statement of the problem using analytical results of the plasma instabilities' and Langmuir collapse theories. Here the two points play a principal part:

(a) Evolution of Langmuir oscillation spectrum at the nonlinear stage of the modulation instability to the shortwave region. Thus the statement of the problem of the evolution of an isolated (periodically repeated in space) plasma region with relatively small sizes (with the scale L of the order of 45-60 Debye lengths) is physically reasonable. These regions are the so-called turbulent cells.

(b) The known analytical result [46] (confirmed later also by computer calculations [47]) on stopping of a propagating soliton or the tendency of the transformation of a propagating Langmuir wave to a

standing one with radiation of ion-sound oscillations. This permits to consider standing waves evolution as a rather general problem, when investigating collapse.

Below we mainly consider the two types of problems:

- 1) On generation of turbulence in closed systems, i.e. in the systems with the fixed total energy, where as the source of turbulence stands out the energy contained in unstable degrees of freedoms.
- 2) On plasma turbulization in open systems, for example, in parametric unstable plasma configurations with an external pumping wave of a constant intensity.

As the main purposes of kinetic computations it is naturally to list: 1) the experimental check and refinement of the main predictions of the theory based on the collapse concept; 2) the determination of applicability bounds of averaged equations; 3) the obtaining of quantitative characteristics like a caviton size, energetics and a form of electron tails, effective collision frequency and so on; 4) the discovery of new effects (for example, generation of ion-sound turbulence at the kinetic collapse stage [25, 29]) which may be important as a part of a general theory; 5) the progress in creating of hybrid models.

In the last point, we draw attention to the fact that the results and the experience of the computer simulation permit in some problems to return again to averaged equations (having knowledge about kinetic effects and dissipation mechanisms) and to enlarge considerably the region of its applicability, taking into account the damping effectively (for example as it was done in (13), (14)) and describing the ion kinetics in more details.

Because of the limited space of the present paper we give only the statement of the problem and brief comments of the main results, paying more attention to the results that were presented in the previous paragraphs more scantily.

6. Evolution of a standing monochromatic wave of a large amplitude. — Let us consider in X, Y -geometry the problem of electrostatic plasma oscillations in a cell of size $L \times L$ with periodic boundary conditions [25]. Both electrons and ions have a Maxwell velocity distribution corresponding to the temperatures T_e and T_i . At the initial moment of time $t = 0$ a one-mode disturbance is introduced in the electron distribution, as a result of which the function $f_e(\mathbf{r}, \mathbf{v}, t)$ takes the form

$$f_e(\mathbf{r}, \mathbf{v}, 0) = \frac{m}{2\pi T_{e0}} \exp \left\{ -\frac{m}{2T_{e0}} \times \right.$$

$$\left. \times \left[\left(r_x - r^0 \sin \frac{2\pi v_x}{L} \right)^2 + \left(r_y - r^0 \sin \frac{2\pi v_y}{L} \right)^2 \right] \right\}, \quad (41)$$

v is an integer.

Such a wave is modulationally unstable (§ 4) if

$$\left(\frac{2\pi v\lambda_D}{L}\right)^2 \lesssim \frac{W_{\omega}}{nT} = \frac{1}{2} \left(\frac{v_0}{v_T}\right)^2. \quad (42)$$

The development of this instability for $t > 0$ has been studied also in the one-dimensional and three-dimensional geometries [48, 43] for different values of parameters L , v_0/v_T , T_e/T_i , m/M . Let's note, that the reduced ratio $\mu = M/m$ should not qualitatively influence the dynamics of the Langmuir collapse, if the condition $\mu \gg 1$ is preserved, because the modulation growth rate $\gamma_{\text{mod}} = \omega_{pe}(mW/MnT)^{1/2}$ and the magnitude, inverse to the characteristic time of ions' delay $\tau^{-1} \approx \pi^{-1} \omega_{pi}$, are equally dependent on μ . But this, however, doesn't refer to the characteristic times of electron nonlinearities [18] :

$$\tau_{nL} \sim \left[\omega_{pe}(k\lambda_D)^2 \cdot \frac{W}{nT} \right]^{-1}$$

and therefore the dimensions of cavities and the concentration degrees of their electrostatic energies may be rather different for different values of μ .

Computer experiments of this type show that on the basis of a primary regular one-mode regime, when the condition (42) is satisfied, complicated multi-mode picture arises, as a rule, typical for a turbulence hierarchy (Fig. 5-13).

A considerable amount of energy is captured in cavities to the formation of that the enrichment of the electrostatic oscillation spectrum with high wave numbers is related. A typical pattern of constant level lines $E^2/8\pi nT$ and n_i/n_0 for one single turbulent cell (i.e. for the region $L/v \times L/v$) is shown in figure 4. The average small halfwidth of cavities (in direction of the dipole moment) is $5 \div 8 \lambda_D$.

The principal point was the discovery with the help of computer experiment of the fact that the cavity which has become empty (as a result of fast absorption of its high-frequency filling by hot electrons according to the Landau mechanism) generates a weakly dying shortwave ion sound for $T_e \gg T_i$ because of a considerable ion inertia [25] (Fig. 5, 14-16). This particular (in the case when there exists a continuous energy flux into plasma) may lead to the accumulation of the ion-sound energy and to the appearance of the mechanism of the Langmuir waves conversion in ion-sound ones, which competes with collapse (see § 3, 7).

Figure 6 shows the typical time dependence of main energetics quantities : wave energy densities and also ion and electron energies. The most part of the energy

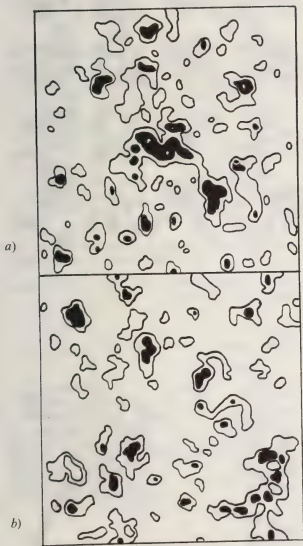


Fig. 5. — Cross sections $n_i(x, y)/n_0 = \text{constant}$ at the stage of ion sound generation [25] ($\Delta t = t_k - t_u = 2\pi/\omega_{pi}$). Black spots correspond to $n_i/n_0 \leq 0.8$ ($\Delta n_i = 0.1 n_0$, $L_x = L_y = L = 45 \lambda_D$).

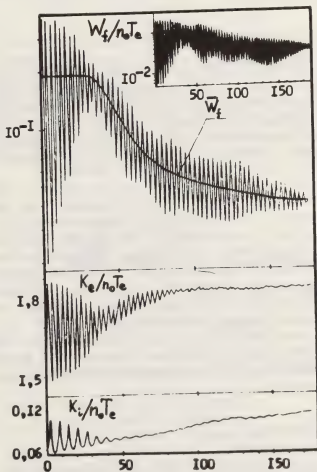


Fig. 6. — Evolution of a single wave. Energy densities in 2D (top [25]) and 3D [43] cases.

is transferred to the electron tails. The ratio of energies transferred to ions and to electrons correspondingly is $\Delta K_i/\Delta K_e \approx 0.04$. This ratio is practically independent of T_i/T_e . The value ΔK_i may contribute either to the acoustic ($T_e \gg T_i$) or to the heat ($T_e \approx T_i$) energy of ions.

It is interesting to note that in the runs with $\nu > 1$ (where the conditions of computer experiments permit a pumping of energy into the region of k , smaller than $k_0 = 2\pi\nu/L$) the energy flux through the spectrum into the region of great values of k was two orders higher (Fig. 7).

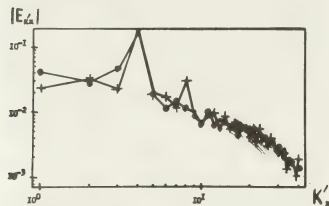


Fig. 7. — Spectrum $E_{k,x}$ vs. k'_x on the stage of cavitons' formation. $\nu = 4$, \bullet and $+$ denote cases $T_e = T_i$ and $T_e = 25 T_i$, $k = \pi k'/90 \lambda_D$.

Three-dimensional calculations with the same parameters show a complete qualitative similarity with the two-dimensional picture, but in the 3D case the collapse goes on more intensively (the comparison of focusing rates and the effective collision frequency is given in figures 6, 10). But this similarity disappears when passing from the 2D to the 1D case [48].

Let us note once more that the method of the investigation of the Langmuir turbulence via the model, in which superfluous energy is introduced artificially in a modulationally unstable mode at $t = 0$ (see (41)), is quite justified. As it can be seen from figure 13 qualitatively the same picture arises by a natural way, for example, in a problem on nonlinear development of the electron beam instability in counters treaming cold plasmas [50].

Finer effects of a convective character arise in a problem on the interaction of plasma with gentle electron beams at the expense of the correlative processes [51].

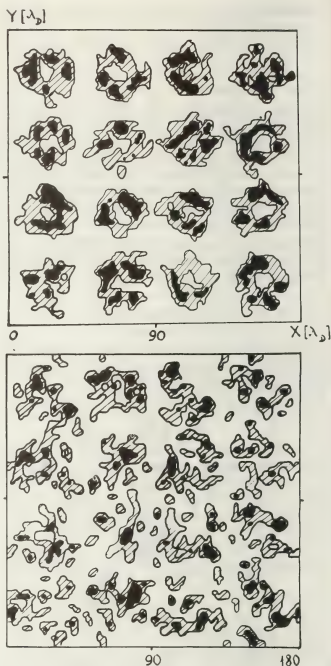


Fig. 8. — Comparison of cavity pictures $\eta(x, y) = \text{constant}$ for the cases $T_e/T_i = 25$ (top) and $T_e = T_i$; $\nu = 4$.

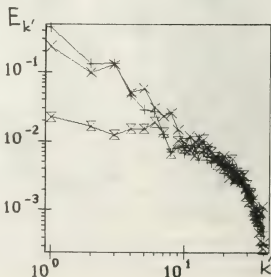


Fig. 9. — Spectrum $E_{k,x}$ in a turbulent cell resulting from the single standing wave; $\nu = 1$, $k = \pi k'/90 \lambda_D$; labels $+$, x , $*$ denote time moments of cavitons' formation, maximal self-focusing and Landau damping respectively.

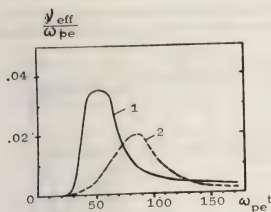


Fig. 10. — Time dependence of the effective collision frequency in the 3D (1) and 2D (2) cases [43, 25] (see Fig. 6).

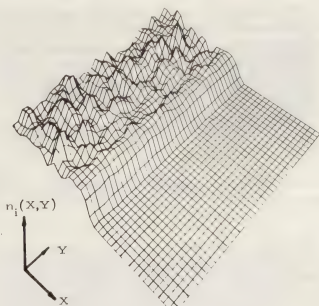


Fig. 13. — Cavities' formation in the region occupied by cold counterstreaming plasmas.

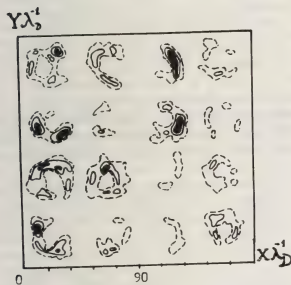


Fig. 11. — Stochastic picture of cavitons at the stage of developed turbulence in 2D-case (lines of $E^2 = \text{constant}$, $\nu = 4$).

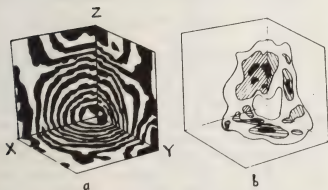


Fig. 12. — Typical pattern $\zeta(x, y, z) = \text{constant}$ (a), and $n_i(x, y, z) = \text{constant}$ (b) for the case of 3D turbulent cell [43] ($L = 45 \lambda_D$).

7. Caviton turbulence in the presence of a pump wave. — Let us consider a time evolution of a flat spatially-periodical plasma layer, $0 \leq x \leq L$, in the given external field

$$E(x) = E_0 e_x \cos \omega_0 t, \quad \omega_0 \lesssim \omega_{pe}.$$

In such a statement of the problem, where the two important points are presented together — a constant intensity of an external energy source (non closed system) and the presence of the given direction (the direction of pumping wave) — qualitative features of the turbulent regime, stipulated by the modulation instability appear even in the 1D geometry [29]. So far as in the 1D-geometry with a constant total energy

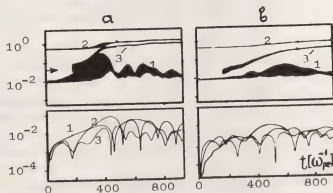


Fig. 14. — Quasicollapse in 2D-geometry [31].

1 — Electrostatic energy, 3 — electron energy.

2 — Total energy assimilated by a plasma system due to an external pump (a and b correspond to X -, Y -directions, the arrow indicates the pump level). Below-time-dependence, of the first, second and third harmonics of ion density which demonstrate an aperiodic character of the parametric instability and the ion sound excitation on the kinetic stage of the quasicollapse.

(in the absence of a pump wave) an usual collapse is forbidden by integrals of motion [4, 24], we shall call the nonlinear self-focusing of Langmuir waves in the present case as *quasicollapse* or *forced collapse*. Below we shall use the results of the computer simulation of the problem of quasicollapse both in the 1D(X) and 2D(X, Y) geometries [31].

It is interesting to consider this process for relatively weak pumpings

$$(k_0 \lambda_D)^2, \quad m/M < E_0^2/8 n T \ll 1,$$

where

$$k_0 = 2\pi/L \simeq 0.1 \lambda_D^{-1}.$$

As it can be seen from figures 14-19 a joint action of parametric and modulation instabilities leads to caviton structure of Langmuir waves excited in plasma. The maximum density of electrostatic energy averaged over the whole plasma volume considerably exceeds

(5-6 times) the energy density in pump wave. The dynamics of an isolated caviton is shown in figure 16.

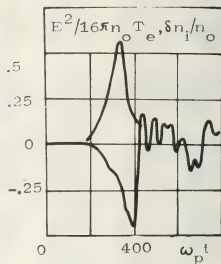


Fig. 16. — Plots of $E^2(t)$ and $n_1(t)$ for the central point of one of the 1D-cavities [29].

$$\frac{\delta n_i}{n_0} = \frac{1}{\pi_0} \left| \frac{dx}{dt} \right| \left\{ \frac{\sqrt{T_{e0}}}{m_i} \left| \frac{dx}{dt} \right| \sqrt{\frac{T_{e0}}{m_e}} \right\}$$

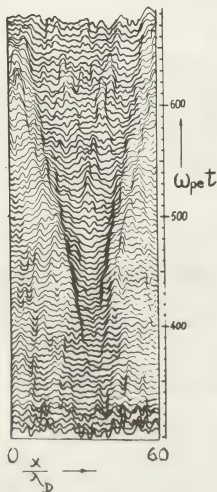


Fig. 15. — Time-evolution of the ion density profiles $n_i(x, t)$ [29].

It is interesting to note that the instability of 1D-solitons relative to transverse disturbances [32-35] shows (when quasicollapse takes place) already in the process of cavitons' formation [31] (Fig. 17, 18). The growth rate of this instability is in agreement with the growth rate of the modulation instability in such a

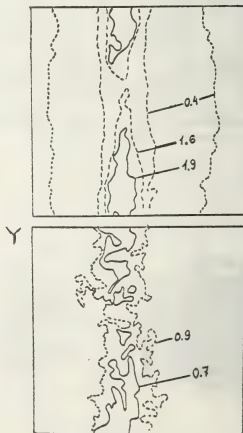


Fig. 17. — The cross-sections $E^2(x, y) = \text{constant}$ (top) and $n_i(x, y) = \text{constant}$ in a case of X-oriented pump field [31].

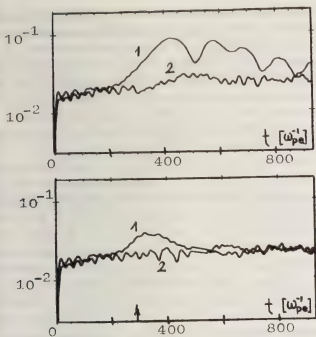


Fig. 18. — Time dependence of a space averaged density disturbance factor in X - (curve 1) and Y (curve 2)-directions, characterizing anisotropy of considered system [31]. The arrow on underlying picture denotes the moment when the pump is switched off.

way that at all the stages of the cavity growth the ratio of its dimensions is maintained and $l_x/l_y = 3 \div 4$, which is close to the anisotropy index of individual two- and three-dimensional cavities of a dipole type, which follows from calculations without pumping wave [25, 24, 43]. Thus the main cause of the stabilizing action of pumping wave (of quasi-1D picture of forced collapse) is not a damping of the transverse instability but a preferred orientation of the cavitons' electric field along E_0 . As a result, in such systems the energies transferred to electrons in X - and Y -directions are in the approximate proportion $7/2$. When switching off the pumping takes place, the isolated direction disappears and the caviton distribution in directions tends to an isotropic one (Fig. 18b).

How does Langmuir collapse proceed in real conditions? The numerical experiment confirms the decisive role of the criterion

$$E_k^2/8 \pi n T \geq \beta \cdot (k \lambda_D)^2, \quad \text{where } \beta \approx 2.$$

A nonlinear self-focusing of Langmuir waves at the supersonic stage occurs slower than if it goes according to the self-similar law (30). Here the inertial ion lagging $\Delta t \approx \pi \omega_{pi}^{-1}$ plays part, which often may be comparable with the characteristic time of collapse γ_{mod}^{-1} [25], [29] and a resonance absorption of energy of the shortest modes by electrons already in the process of caviton formation is also important. The average halfwidth of a formed cavity turns out to be of the order $10-15 \lambda_D$. According to the Landau mechanism the onset of high energetic electron tails increases the threshold of the parametric instability

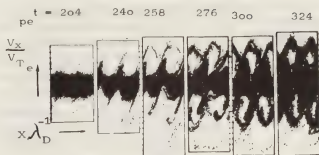


Fig. 19. — High energetic electron tail formation in the presence of a strong pump [44]. 2D-case, $E_0^2/8 \pi n T = 1/2$, $\omega_0 \lesssim \omega_p$.

(Fig. 19), and the system passes to a threshold state. After that the energy of the pump wave continues to feed plasma mainly by the shortwave conversion of the electrostatic oscillations due to the collapse-generated shortwave oscillations of ion density. A typical spectrum of spatial disturbances of the ion density at different stages of the collapse is shown in figure 20.

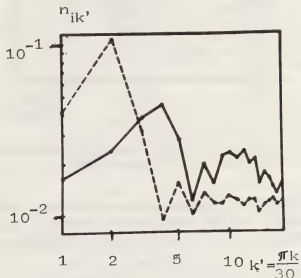


Fig. 20. — Typical spectrum of ion density disturbances before (dashed line) and after the cavity contraction [29].

Now let us try to estimate by means of the computer experiment the possibility discussed in § 3 of accumulation of an ion sound in a system with collapsing cavitons. In particular, there arises a question if the competing mechanism of conversion can suppress the forced collapse in the absence of fast electrons in the system.

The answer to this question can be obtained, for example, by exciting standing sound waves in the initial plasma state in a prescribed way, and then changing the length and amplitude of these waves. Computations show that an intense sound in the wave length band $5 \div 20 \lambda_D$ can lag a cavity formation, decreasing the growth rate in 1.5-2 times. They also show that this sound can decrease approximately at the same ratio, the value of the maximum density W_{max}

at which a saturation takes place. But we have never managed to observe a complete damping of the quasicollapse in our computer experiments. An attempt to obtain it by further increasing of the sound intensity led mostly to non-linear breaking of ion-sound oscillations. This process, accompanied by a capture and acceleration of ions, is apparently the main mechanism which limits the accumulation of the ion sound in a turbulent plasma for $T_e \gg T_i$.

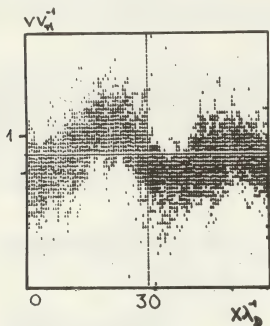


Fig. 21. — Ion wave breaking as a result of the fast absorption of hf caviton energy by the resonant electrons [29].

The capture condition permits to obtain a simple estimate for the critical amplitude of the Fourier component [52] of the ion density disturbance :

$$\frac{\delta n_{ik}}{n_0} = \frac{1}{4} \left(\frac{1}{\sqrt{1 + k^2 \lambda_D^2}} - (M/m)^{1/2} (v_i/v_{Te}) \right)^2.$$

The maximum value of δn_{ik} turns out to be rather sensitive to the value v_i characterizing an effective velocity of hot ions (for the Maxwell distribution $v_i = \sqrt{3} v_{Te}$). Let us stress that as the computer experiment shows, the first hot ions arise, as a rule, when breaking of an ion wave convergent to the centre of an empty cavity takes place, i.e. during the generation process of the considered sound oscillations.

Summing up, we may draw the conclusion that in concrete systems with a developed strong Langmuir

turbulence the final conditions for the balance between collapses that generate fast particles and conversion filling up the region of heat velocities depend on a concrete form of steady (both : electron and ion) distribution functions, i.e. these conditions have an essentially kinetic nature. It is remarkable that such a balance can be, in principle, externally affected, if one has a possibility to change a hot particle concentration of either sign in a desirable way.

The one-dimensional computer experiments [29] were repeated in the 1 + 1/2-dimensional case when a magnetized plasma is in an external magnetic field B_0 which was normal to the pump wave [53]. The case $r_{Be}^{-1} > k_0 = 0.1 \lambda_D^{-1}$ was considered. It has been shown that for a pumping frequency close to an upper hybride one, the excitation of a parametric instability takes place, on the nonlinear stage of which cavitons may arise, where the electrostatic energy is located. The main difference from the case $B_0 = 0$ is connected with a wave energy damping mechanism. Instead of the Landau damping (which is absent in the plane normal to B_0) it is a stochastic mechanism of heating (which conserves the Maxwell form of distribution function) that plays the main part.

8. Conclusion. — At the present time one can state with confidence that the results of computer simulations confirm the general concept of Langmuir collapse and permit to resolve paradoxes arising in the weak turbulence theory. One can hope that the further development of this concept together with extensive computer experiments will permit to understand (what partly has already been done) the picture of a strong plasma turbulence under conditions of different levels and methods of its excitation, both beam or parametric. The significance of a computer experiment will grow as the interest of investigators will shift to a study of the effects where the wave-particle interaction plays the principal part, i.e. when considering dissipative and strong nonlinear regimes.

After the first attack at the strong turbulence building, when first of all it was necessary to find the true qualitative regularities and a relative role of alternative nonlinear processes (and it was the aim of multidimensional kinetic calculations) we have now a good chance to start the next regular step — to create an effective and more complete theory of strong turbulence and hybrid methods of computations which would combine the good qualities of kinetic and averaged approaches.

References

- [1] KADOMTSEV, B. B., *Plasma Turbulence* (in *Voprosy Teorii Plazmy*, vol. 4, Moscow, 1964, p. 188).
- [2] SAGDEEV, R. Z. and GALEEV, A. A., *Lectures on Nonlinear Plasma Theory* (ed. by T. O'Neil, D. Book, Benjamin), New York-Amsterdam, 1969.
- [3] TSYTOVICH, V. N., *Theory of Turbulent Plasmas*, Moscow, 1971.
- [4] ZAKHAROV, V. E., *Zh. Eksp. Teor. Fiz.* **62** (1972) 1745.
- [5] *Methods in Computational Physics*, vol. 9, Plasma Physics (ed. by B. Alder, S. Fernbach, M. Rotenberg) Academic Press, N.Y.-L., 1970.
- [6] SIGOV, YU. S. and KHODYREV, YU. V., On theory of discrete plasma models, *Inst. of Appl. Math. of the USSR Acad. of Sci.*, Moscow, n° 83, 1975; *Chisl. Metody Mekh.*

Sploshn. Sredy (*), 7, no 2, 1976, 109: Two interpretation of cloud-in-cell model, *Inst. of Appl. Math. of the USSR Acad. of Sci.*, Moscow, no 10, 1976. Preprint.

- [7] ZAKHAROV, V. E., *Zh. Eksp. Teor. Fiz.* **60** (1971) 1714.
- [8] ZAKHAROV, V. E. and SAGDEEV, R. Z., *Doklady Acad. Nauk, SSSR* **15** (1970) 439.
- [9] ZAKHAROV, V. E. and FILONENKO, N. N., *Zh. Prikl. Matem. i Tech. Fiz.*, vyp. 5, 62, 1967.
- [10] ZAKHAROV, V. E., *Zh. Eksp. Teor. Fiz.* **51** (1966) 689.
- [11] ZAKHAROV, V. E. and FILONENKO, N. N., *Doklady Acad. Nauk, SSSR* **170** (1966) 1292.
- [12] ZAKHAROV, V. E. and KUZNETSOV, E. A., *Zh. Eksp. Teor. Fiz.* **75** (1978) 904.
- [13] BREIZMAN, B. N., *Zh. Eksp. Teor. Fiz.* **64** (1973) 1297.
- [14] SIGOV, Yu. S. and KHODYREV, Yu. V., Numerical simulation of high frequency heating of plasma, *Proc. 6th Europ. Conf. on Controlled Fusion and Plasma Physics*, vol. 1, Moscow, 1973, p. 579.
- [15] IVANOV, A. A., SIGOV, Yu. S., KHODYREV, Yu. V., *Doklady Acad. Nauk, SSSR* **214** (1974) 1291.
- [16] SIGOV, Yu. S., Computer Simulation of kinetic processes in plasma-laser beam interaction, *Materials of Joint Seminar on Computational Physics*, Sukhumi, 1973, p. 251-279.
- [17] SIGOV, Yu. S. and KHODYREV, Yu. V., One-dimensional experiment on parametrical plasma's heating, *Inst. of Appl. Math. of the USSR Acad. of Sci.*, Moscow, no 129, 1974.
- [18] GALEEV, A. A., SAGDEEV, R. Z., SIGOV, Yu. S., SHAPIRO, V. D., SHEVCHENKO, V. I., *Fizika Plazmy* **1**, no 1 (1975) 10.
- [19] KUZNETSOV, E. A., *Fizika Plazmy* **2** (1976) 327.
- [20] VALEO, E., OBERMAN, G., PERKINS, F. W., *Phys. Rev. Letters* **28** (1972) 340.
- [21] ZAKHAROV, V. E., *Zh. Eksp. Teor. Fiz.* **69** (1975) 155.
- [22] BREIZMAN, B. N., *Zh. Eksp. Teor. Fiz.* **70** (1975) 5.
- [23] VEDENOV, A. A. and RUDAKOV, L. I., *Doklady Acad. Nauk, SSSR* **19** (1964) 767.
- [24] ZAKHAROV, V. E., MASTRYUKOV, A. F., SYNACH, V. S., *Pisma Zh. Eksp. Teor. Fiz.* **20**, no 1, 1974; *Fizika Plazmy*, vyp. 3, 1976.
- [25] DEGTYAREV, L. M. and ZAKHAROV, V. E., *Inst. of Appl. Math. of the USSR Acad. of Sci.*, Moscow, no 106, 1974; *Pisma Zh. Eksp. Teor. Fiz.* **20**, no 6 (1974); *Pisma Zh. Eksp. Teor. Fiz.* **21**, no 9 (1975).
- [26] POLYUDOV, A. N., SAGDEEV, R. Z., SIGOV, Yu. S., Computer simulation of two dimensional Langmuir turbulence, *Inst. of Appl. Math. of the USSR Acad. of Sci.*, Moscow, no 128, 1974; *Proc. 12th Intern. Conf. on Phenomena in Ionized Gases*, Eindhoven, 1975, p. 332.
- [27] DEGTYAREV, L. M., ZAKHAROV, V. E., RUDAKOV, L. I., *Zh. Eksp. Teor. Fiz.* **68** (1975) 115; *Fizika Plazmy* **1** (1975) 6.
- [28] DENAVIT, I., PEREIRA, N. R., SUDAN, R. N., *Phys. Rev. Lett.* **33** (1974) 1435.
- [29] WONG, A. Y., *Journal de Physique* **38**, Suppl. no 12, 1977, p. 6-27.
- [30] SIGOV, Yu. S. and KHODYREV, Yu. V., One-dimensional quasi-collapse of Langmuir wave for parametric influence on plasma, *Doklady Acad. Nauk, SSSR* **229** (1976) 833; *Inst. of Appl. Math. of the USSR Acad. of Sci.*, Moscow, no 11, 1976. Preprint.
- [31] GORBUSHINA, T. A., DEGTYAREV, L. M., ZAKHAROV, V. E., RAVINSKAYA, V. N., *Inst. of Appl. Math. of the USSR Acad. of Sci.*, Moscow, no 128, 1975. Preprint.
- [32] POLYUDOV, A. N. and SIGOV, Yu. S., Parametric instability of plasma and Langmuir quasi-collapse in two-dimensional geometry, *Inst. of Appl. Math. of the USSR Acad. of Sci.*, Moscow, no 123, 1976; *Proc. XIIIth Intern. Conf. on Phenomena in Ionized Gases*, Berlin, 1977, p. 845.
- [33] POLYUDOV, A. N. and SIGOV, Yu. S., Two-dimensional kinetic models in the problem on strong Langmuir turbulence, *Proc. 3rd Intern. Congress on Waves and Instabilities in Plasmas*, Paris (Palaiseau), 1977, p. 101.
- [34] ZAKHAROV, V. E. and RUBENCHIK, A. M., *Zh. Eksp. Teor. Fiz.* **65** (1973) 997.
- [35] SHMIDT, G., *Phys. Rev. Lett.* **34** (1975) 724.
- [36] LAEDKE, E. W. and SPATCHEK, K. H., *Phys. Rev. Lett.* **41** (1978) 1798.
- [37] PEREIRA, N. R., SUDAN, R. N., DENAVIT, J., *Phys. Fluids* **20** (1977) 271; **20** (1977) 936.
- [38] GOREV, V. V., KINGSEP, A. S., RUDAKOV, L. I., *Radiofizika* **19** (1976) 691.
- [39] GALEEV, A. A., SAGDEEV, R. Z., SHAPIRO, V. D., SHEVCHENKO, V. I., *Pisma Zh. Eksp. Teor. Fiz.* **24**, vyp. 1, 1976; *Zh. Eksp. Teor. Fiz.* **73** (1977) 1352.
- [40] WONG, A. Y., CAVITONS, *Journal de Physique* **38**, Suppl. no 12, 1977.
- [41] ANTIPOV, S. V., NEZLIN, M. V., SNEJIN, E. N., TRUBNIKOV, P. M., *Pisma Zh. Eksp. Teor. Fiz.* **23** (1975) 616.
- [42] SILIN, V. P., *Parametric Effect of High Power Radiation on Plasma* (Nauka Ed.), Moscow, 1973.
- [43] KRUEER, W. L., KAW, P. K., DAWSON, J. M., OBERMAN, *Phys. Rev. Letters* **24**, no 18 (1970) 987.
- [44] KRUEER, W. L., DAWSON, J. M., *Phys. Fluids* **15** (1972) 446.
- [45] POLYUDOV, A. N., SEL'YANDIN, B. D., SIGOV, Yu. S., Three-dimensional kinetic model of nonlinear evolution of the large amplitude electrostatic plasma wave, *Keldysh Inst. of Appl. Math. of the USSR Acad. of Sci.*, Moscow, no 145, 1979; *Doklady Acad. Nauk, SSSR* **246**, no 1 (1979).
- [46] POLYUDOV, A. N. and SIGOV, Yu. S., Computer simulation of collective phenomena in plasma-laser beam interaction, *Proc. XIIth Europ. Conf. on Laser Interaction with Matter*, Moscow, 1978, p. 196.
- [47] ALTERKOP, B. A., VOLOKITIN, A. S., TARAKANOV, *Zh. Eksp. Teor. Fiz.* **71**, no 2 (1976).
- [48] RUDAKOV, L. I., *Doklady Acad. Nauk, SSSR* **207** (1972) 821.
- [49] BUCHELNIKOVA, N. S., MATOCHKIN, E. P., Instability of one-dimensional Langmuir wave, *Inst. of Nucl. Physics, Novosibirsk*, no 79-21, 1979. Preprint.
- [50] SIGOV, Yu. S. and KHODYREV, Yu. V., Numerical study of the high amplitude Langmuir oscillation, *Proc. 11th Intern. Conf. on Phenomena in Ionized Gases*, Praga, 1973, p. 333.
- [51] ANISIMOV, S. I., IVANOV, M. F., *Doklady Acad. Nauk, SSSR* **225** (1975) 280.
- [52] KOTOK, E. V. and SIGOV, Yu. S., *Report at First Kiev Conference on Plasma Theory*, Kiev, 1971.
- [53] BAKAI, A. S. and SIGOV, Yu. S., On collisionless relaxation of plasmas with unstable electron distribution function, *Inst. of Appl. Math. of the USSR Acad. of Sci.*, Moscow, no 52, 1977; *Doklady Acad. Nauk, SSSR* **237** (1977) 1326; *Proc. 3rd Intern. Congress on Waves and Instabilities in Plasmas*, Paris (Palaiseau), 1977, p. 53; On evolution of single wave intensified by gentle electron beam, *Inst. of Appl. Math. of the USSR Acad. of Sci.*, Moscow, no 34, 1978. Preprint.
- [54] FAEHL, R. J. and KRUEER, W. L., *Laser light absorption by short wavelength ion turbulence*, Preprint UCRL-71747, 1977.
- [55] BORODACHEV, L. V. and SIGOV, Yu. S., Computer experiments on parametric excitation of magnetized plasmas, *Keldysh Inst. of Appl. Math.*, Moscow, no 65, 1979. Preprint.

(*) Chislenyye Metody Mekhaniki Sploshnoj Sredy.

Particle beam interactions with plasmas and their application to inertial fusion (*)

M. J. Clauser, E. J. T. Burns, J. Chang, A. V. Farnsworth, S. A. Goldstein, D. J. Johnson, G. W. Kuswa, T. A. Mehlhorn, C. W. Mendel, L. P. Mix, J. W. Poukey, J. P. Quintenz, M. A. Sweeney, J. P. VanDevender and M. M. Widner

Sandia Laboratories, Albuquerque, New Mexico 87185, USA

Abstract. — Present day target designs indicate that particle beams with 1-10 MJ and 100-500 TW, focused to intensities around 100 TW/cm^2 will be required to ignite targets with gains of 10-100. Due to uncertainties about the symmetry and stability of the implosion, these requirements may change by as much as an order of magnitude as more is learned. The particle beams will interact with target plasmas which have temperatures of several hundred electron volts and densities up to solid density. Under these conditions the main energy-loss mechanism is collisional, however, in the case of electrons, the orbits can be substantially altered by electric and magnetic fields. Experiments with thin foils have measured energy deposition enhancement by a factor of 5-10 with foils mounted in the anode, and by a factor of 20 or more with foils mounted on a stalk extending into the diode.

Introduction. — About 1963, J. C. Martin and his colleagues in Aldermaston, England started a branch of pulse-power technology which today is capable of producing extremely powerful electrical pulses. Pulse power generators can now produce pulses with 10 TW and several hundred kilojoules. Major programs at the Kurchatov Institute in Moscow and at Sandia Laboratories, along with smaller programs at about ten other laboratories throughout the world, are investigating the application of this technology to inertial confinement fusion. Generators producing 100 TW, multimegajoule pulses are planned for the early to mid-1980's at Kurchatov and Sandia. The pulse power generators have two principle advantages over lasers : they are efficient (20 % to 50 %) and inexpensive (\$ 10/J).

The first pulse-power approach to inertial fusion used electron beams to ablate the surface of a spherically imploding target [1, 2]. More recently, the use of light ion beams to implode spherical targets [3-6] has been given serious consideration. At present, the main problem in these approaches is producing a high enough flux of energy to the surface of a target, particularly under conditions suitable for a power reactor. Beam energy fluxes of 30 TW/cm^2 with electron beams [7] and 0.2 TW/cm^2 with light ions [8] have been achieved. To obtain ignition of a target with moderate gain (≈ 30) appears to require fluxes around 100 TW/cm^2 for ion beam implosions, and several times higher for electrons with present-day target designs. With improved understanding of the twin problems of symmetry and stability of implosions, it may be possible to reduce these require-

ments by an order of magnitude [9]. To establish some of these requirements for particle beam fusion, the first section of this paper summarizes some of the basic principles of fusion target implosions, and the particle beam characteristics required to ignite the targets. The second and third sections deal with the interaction of light ion beams and of electron beams with fusion target plasmas.

Target requirements. — In its simplest form an inertial fusion target consists of three functional parts : the fuel, the pusher, and the ablator. The energy of the particle beam is deposited in the ablator, heating it to several hundred electron volts. (The momentum transfer from the particle beam to the target is generally insignificant.) The pressure produced in the ablator causes it to explode and to drive the pusher inwards. The imploding pusher compresses the fuel and consequently heats it to the ignition point. Ignition of the fuel can usually be achieved with an implosion velocity of $20 \text{ cm}/\mu\text{s}$, however, variations in target design may change this by a factor of two or more. Finally, the imploded pusher acts as a tamper, confining the fuel while it burns.

The thermonuclear reaction rate per unit mass of fuel is proportional to the density ρ , while the time for the fuel to disassemble is proportional to the fuel radius r . For unconfined fuel this is essentially an acoustic transit time, while for fuel confined by a denser pusher, the confinement time is increased in proportion to the pusher density. The quantity ρr is thus a measure of the fraction of the fuel burned [10]. Generally, a value of $\rho r \approx 1 \text{ g/cm}^2$ is required for

(*) This work was supported by the U.S. Department of Energy.

significant burnup of the fuel [11]. The range of the alpha particles produced in the DT reaction is 0.2 g/cm^2 near ignition temperature, so that the condition for further heating of the fuel by the alpha particle energy is also generally met at the same time. The ρr of spherically compressed fuel may be written $\rho r = 3 m/4 \pi r^2$. With large densities or small compressed radius, lower fuel mass is required to meet the ρr condition, and hence less energy is required to ignite the fuel.

In order to achieve high compressions, the fuel must retain some resemblance to a sphere during the implosion process. The compression is thus limited by the symmetry of energy deposition in the ablator. Generally, a greater degree of symmetry is required for higher compression ratios. A radial convergence ratio around 10, producing a volume compression ratio of 1 000 is generally considered to be achievable. The compression is also limited by the growth of hydrodynamic instabilities (e.g., Rayleigh-Taylor). Our understanding of the behavior of these instabilities and their effects on target behavior is rather incomplete. Nevertheless, a relatively simple analysis shows that the number of exponentiations of damaging instabilities during the inward acceleration of the pusher is approximately $(2r/\Delta r)^{1/2}$, where r is the initial pusher radius and Δr is its thickness around the time of peak acceleration [12]. It seems to be generally accepted that a value of $r/\Delta r < 20$ results in reasonably stable implosions, although details of target design and fabrication may change this limit up or down by a factor of several.

A variety of target designs have been published for electron [4, 12-14] and ion beams [3, 4, 12, 15, 16]. It appears that the energy and power required to drive these targets can be summarized by some relatively simple equations: The beam energy E is converted to implosion kinetic energy with an efficiency ϵ , typically of order 20%. Since the pusher is usually much more massive than the fuel, this can be written

$$E = 2 \epsilon^{-1} v^2 r^2 \Delta \rho$$

where r , Δr , and ρ are the initial radius, thickness, and density of the pusher, and v is its peak velocity. For unshaped pulses the pulse width is approximately r/v , and the beam power P is given by

$$P = 2 \pi \epsilon^{-1} v^3 r^2 \Delta \rho$$

When a shaped pulse is used, the width of the peak power pulse is somewhat shorter and the peak power somewhat higher. The flux of energy F on the target surface is just

$$F = 0.5 \epsilon^{-1} v^3 r^{-1} \Delta \rho$$

This last equation implies that flux or intensity requirements can be reduced by utilizing larger radius targets. However, this advantage is offset

by the fact that the beam energy requirement increases as r^2 or faster. The energy, power, and flux requirements can all evidently be reduced by using a lower density pusher. Such a design has been proposed [15] with reduced beam requirements, however the requirements were not reduced as much as one might expect because a higher implosion velocity and a shaped pulse were both required. The implosion velocity required for ignition can be reduced about threefold by inducing a magnetic field of 10-100 kG in the fuel region to reduce thermal conduction [15, 16, 17]. This type of target requires that the pusher ρr be higher at implosion time, which requires that $\rho \Delta r$ be initially three times higher than for corresponding non-magnetic targets. Consequently, the energy requirements are reduced about three-fold, and the power and flux requirements, about nine-fold.

Most of the target designs have a pusher diameter near 1/2 cm, for which the beam pulse length varies between 5 and 40 ns, depending on the target design. To produce gains of 10-100, these targets require ion beams of 1-10 MJ, 100-500 TW, and 10^{14} - 10^{15} W/cm^2 . The power and energy requirements for electron beam targets of similar design are typically several times higher than for ions. At the present time, the lower limit on the ion beam requirements are thus about 10^6 J , 10^{14} W , and 10^{14} W/cm^2 . As the understanding of the stability and symmetry of implosions improves, it may be possible to obtain higher compression ratios and thinner shells [18].

For effective coupling of ablation energy into implosion kinetic energy, the ablator mass should typically be several times the pusher mass. This results in an ablator thickness of 0.1-0.3 g/cm² for the target designs discussed above which in turn implies the use of 5-10 MeV protons or 1/2-1 MeV electrons. For beams of ions other than protons, the target designs and therefore the beam requirements are essentially identical provided that ions are used that have the same range in the target plasma. For target designs different than those discussed above, particles with significantly different ranges are useful.

Interaction of ion beams with target plasmas. — The ablator region of particle beam targets typically reach temperatures of several hundred electron volts and densities ranging from solid density down to a few orders of magnitude below solid density. Under these conditions, there should be no beam instabilities, and the principal energy loss mechanisms are binary coulomb collisions with the electrons and ions in the target plasma, and excitation of plasma oscillations. Coulomb scattering from the target nuclei is generally a small effect. Consequently, the ion trajectories are nearly straight, which simplifies calculations of the energy deposition in the target.

Some initial target design calculations assumed that the stopping power of the target plasma is the same as for cold, solid-density material. More recently,

the deposition models have been refined to include plasma effects which produce a weak density and temperature dependence of the stopping power [19-21]. For typical target parameters, the plasma effects reduce the range of beam particles by 10-30 % [22] and the deposition profile is altered [21] as is shown in figure 1. To compensate for this, the beam voltage can be increased by 6-20 %, with a corresponding reduction in the beam current requirements.

10 MeV Protons in Au

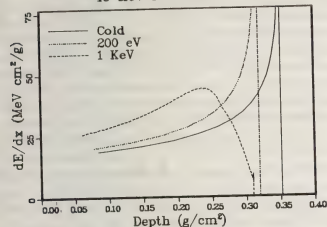


Fig. 1. — Deposition profile of 10 MeV protons in solid density gold, with the gold at various temperatures.

Interaction of electron beams with target plasmas. —

The mechanisms responsible for energy loss by the beam electrons in the target plasma are generally the same as for ion beams, binary coulomb collisions with the target electrons and ions, and excitation of plasma oscillations. In addition, some evidence of enhanced deposition due to beam-plasma instabilities has been reported [23]. Unlike ion beams, the spatial distribution of energy deposition in the target is affected by several additional factors. Electron beams produce a significant amount of bremsstrahlung, particularly in high-Z targets. This penetrates more deeply into the target, producing deleterious pre-heating of the pusher [13]. This can be offset somewhat by using lower-Z ablators [12, 14].

The rate at which a free-streaming electron beam deposits energy is $J\rho^{-1} dE/dx$, where J is the current density and $\rho^{-1} dE/dx$ is the stopping power of the target, typically 1 MeV cm²/g. Since the rate of energy deposition is proportional to the number density of beam electrons, mechanisms which increase the beam electron density by impeding or stagnating the flow of electrons can produce an enhancement of the energy deposition over the freestreaming rate. There are three principle mechanisms which are known to stagnate the electron flow by altering the trajectories of individual electrons : (1) coulomb scattering in the target material, (2) electric fields, and (3) magnetic fields. The possibility of enhancing the energy deposition by appropriate electric and magnetic fields has been a fascination from the

beginning of electron beam fusion research [2]. Enhanced deposition would generally produce higher temperatures in the deposition region, and in some cases would shorten the effective range over which energy is deposited. This would permit use of higher voltage electrons, which should be more readily focusable to high intensities.

Enhancement can be caused by fields which are either inside or outside the target. With thick targets significant enhancement can only occur when the fields are inside the target since external fields can at best cause electrons which have scattered out of the target to return to it.

One source of an internal electric field is the field established with the counterstreaming plasma current which initially neutralizes the beam current in the target [2, 24]. This return current heating may become significant at current densities around 10^9 A/cm², but not at the current densities achieved to date.

When the return current dies out, the magnetic field of the beam penetrates the target plasma and *magnetic stopping* of the beam electrons can occur [2, 25]. For magnetic stopping to be significant, the magnetic field must be large enough that the electron gyration frequency is larger than the collision frequency, and the magnetic field must have time to diffuse into the deposition region. There is concern that this may result in enhancing the deposition only in the outer, low density portion of the ablating material, which results in low ablation pressures in thick targets.

During the last few years there has been considerable interest in targets which are thin compared to the electron's collisional range. Experiments have measured several-fold deposition enhancements in two somewhat different geometries [25-29]. Rudakov and co-workers, using Triton (0.5 MV, 0.12 kA, 2 MA/cm², 30 ns), first reported a ten-fold enhancement of the energy deposited in a 10 µm platinum foil, with half of the beam energy deposited in the foil [25], heating it to 20-30 eV. The foil was mounted on the anode surface with a hole in the anode behind it as shown in figure 2. At the time of peak energy

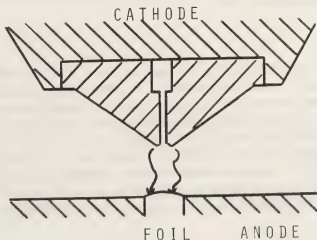


Fig. 2. — Diode used in Triton enhanced deposition experiment.

deposition, the foil had expanded to 0.5-1 mm and the magnetic field of the beam penetrates at least partially into the foil. The drift velocity of the electrons through the foil plasma is controlled principally by gradient B drift. The drift velocity can be written as $cl_A/2I$, where I_A is the Alfvén current, 17 000 $\beta\gamma$ amps, so that the deposition enhancement factor should be $2I/I_A$, in approximate agreement with the experiment [25].

More recently, similar experiments have been conducted at other laboratories, and more extensive diagnostics have been used [27, 28]. These experiments reported enhancement factors around 5. More significantly the latest experiments [28] on Proto I (1.1 MV, 0.3 MA, 7 MA/cm², 25 ns) measured the temperatures of both sides of the foil and found that while the diode side of the foil reached 20 eV, the rear surface only reached 7.6 eV. This is consistent with little or no enhancement of the rear surface deposition and is thought to be due to radial beam spreading in the foil interior where the magnetic field is weak. The rate of deposition on the front side of the foil was about 50 TW/g.

Even greater deposition enhancement has been observed when thin targets are mounted inside the diode [26, 29] rather than in the anode plane. The first such experiments [26] used small nickel spheres mounted in the focused electron beam of Hydra (0.8 MV, 0.15 MA, 0.3 MA/cm², 30 ns) as shown in figure 3. In addition to the magnetic field surrounding the target, the diode electric field is substantially altered by the presence of the target, and a potential well is formed around the sphere.

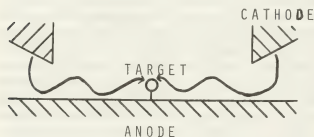


Fig. 3. — Diode and target configuration for enhanced deposition experiment on Hydra.

Electrons passing through the target are deflected back towards the target by the surrounding electric and magnetic fields, increasing the electron density and hence the energy deposition in the target. Alternatively, the electric and magnetic fields around the target may be viewed as producing an $E \times B$ drift which opposes the gradient B drift, resulting in greater stagnation of the beam and hence greater deposition enhancement than would result from the magnetic

drift alone. The deposition enhancement factor observed in these experiments was around 18. For these experiments, I/I_A was about 3.7 and the enhancement was about $5I/I_A$, or two and a half times as much enhancement as for an anode-mounted foil. Since the current density on Hydra was much lower than on Triton or Proto I, the deposition rate was lower, about 8 TW/g.

More recently, experiments have been conducted on Mite (1.8 MV, 270 kA, 40 ns) with a thin gold foil mounted on a long stalk [29]. The stalk extends across the diode into the interior of a hollow cathode as shown in figure 4. The presence of the stalk and gold foil at anode potential alters the electric fields and the electron flow even more than in the Hydra experiment. A substantial fraction of the electron current, $> 25\%$, reaches the foil as a result of both increased emission from the inside of the cathode and an $E \times B$ drift along the stalk toward the foil. In a 6 μm thick foil an energy deposition rate of 100 TW/g was observed which heated the foil to a temperature of 30-35 eV. The current density at the foil was not measured, however, it could not have been greater than 3.8 MA/cm² and was probably about 1 MA/cm². Thus a deposition enhancement by a factor of 24 or more evidently resulted from the magnetic fields and the potential well surrounding the foil.

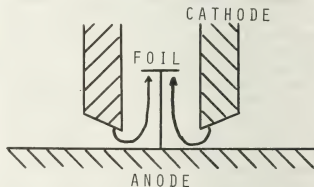


Fig. 4. — Diode with gold foil mounted on stalk extended into hollow cathode for enhanced deposition experiment on Mite.

Conclusion. — During the past few years, considerable progress has been achieved in focusing high power particle beams onto targets and understanding the interaction of the beams with the targets. Pulse power generators are under construction which are expected to be capable of producing sufficient power and energy to ignite a fusion target. The challenges of the 1980's will be to demonstrate that this power can be sufficiently concentrated in the target and that the targets perform as predicted.

References

- [1] RUDAKOV, L. I. and SAMARSKY, A. A., *Proc. 6th Europ. Conf. on Controlled Fusion and Plasma Physics*, Moscow, 1973, p. 487.
- [2] YONAS, G., POUKEY, J. W., PRESTWICH, K. R., FREEMAN, J. R., TOEPPER, A. J. and CLAUSER, M. J., *Nucl. Fusion* **14** (1974) 731.
- [3] CLAUSER, M. J., *Phys. Rev. Letters* **35** (1975) 848.
- [4] LINDL, J. D. and BANGERTER, R. O., *Proc. of Intl. Topical Conf. on Electron Beam Research and Tech.*, Albuquerque, New Mexico, USA, Nov. 3-5, 1975, p. 37.
- [5] GOLDSTEIN, SHYKE A., COOPERSTEIN, G., LEE, R., MOSHER, D. and STEPHANAKIS, S. J., *Phys. Rev. Letters* **40** (1978) 1504.
- [6] JOHNSON, D. J., KUSWA, G. W., FARNSWORTH, A. V., QUINTENZ, J. P., LEEPER, R. J., BURNS, E. J. T. and HUMPHRIES, S., *Phys. Rev. Letters* **42** (1979) 610.
- [7] GOLDSTEIN, STEVEN A., unpublished.
- [8] JOHNSON, D. J., unpublished.
- [9] YONAS, G., *3rd Intl. Topical Conf. on High Power Electron and Ion Beam Research and Technology*, Novosibirsk, USSR, July 3-6, 1979.
- [10] NUCKOLLS, J., WOOD, L., THIESSEN, A. and ZIMMERMANN, G., *Nature* **239** (1972) 139.
- [11] FRALEY, G. S., LINNEBUR, E. J., MASON, R. J. and MORSE, R. L., *Phys. Fluids* **17** (1974) 474.
- [12] CLAUSER, M. J. and SWEENEY, M. A., *Proc. of the Intl. Topical Conf. on Electron Beam Res. and Tech.*, Albuquerque, New Mexico, USA, Nov. 3-5, 1975, p. 135.
- [13] CLAUSER, M. J., *Phys. Rev. Letters* **34** (1975) 570.
- [14] SWEENEY, M. A. and CLAUSER, M. J., *Appl. Phys. Letters* **27** (1975) 483.
- [15] BANGERTER, R. O. and MEEKER, D. J., *Proc. of the 2nd Intl. Topical Conf. on High Power Electron and Ion Beam Res. and Tech.*, Ithaca, New York, USA, Oct. 3-5, 1977, p. 183.
- [16] SWEENEY, M. A. and FARNSWORTH, JR., A. V., *IEEE International Conference on Plasma Science*, Monterey, California, USA, May 15-17, 1978, Paper 4A3.
- [17] WIDNER, M. M., *Bull. Am. Phys. Soc.* **22** (1977) 1139.
- [18] AFANASIEV, YU. V. et al., *JETP Letters* **21** (1975) 68.
- [19] NARDI, E. and ZINAMON, Z., *Phys. Rev. A* **18** (1978) 1246.
- [20] BANGERTER, R. O., *Proc. 1978 Heavy Ion Fusion Workshop*, Argonne National Laboratory, Sept. 19-26, 1978.
- [21] MEHLHORN, T. A., *IEEE Intl. Conf. on Plasma Science*, Montreal, Quebec, Canada, June 4-6, 1979, paper 1Q1.
- [22] NARDI, E., PELEG, E. and ZINAMON, Z., *Phys. Fluids* **21** (1978) 574.
- [23] NAKAI, S., IMASAKI, K. and YAMANAKA, C., *Nucl. Fusion* Suppl. 1, 1977, p. 207.
- [24] MOSHER, D., *Phys. Rev. Letters* **35** (1975) 851.
- [25] BOGOLYUBSKII, S. L., GERASIMOV, B. P., LIKSONOV, V. I., POPOV, YU. P., RUDAKOV, L. I., SAMARSKII, A. A., SMIRNOV, V. P. and URUTSKOV, L. I., *JETP Lett.* **24** (1976) 178.
- [26] CLAUSER, M. J., MIX, L. P., POUKEY, J. W., QUINTENZ, J. P. and TOEPPER, A. J., *Phys. Rev. Letters* **38** (1977) 398.
- [27] GILAD, P., KAPLAN, Z., MILLER, S., NARDI, E., PELEG, E. and ZINAMON, Z., *Proc. of the 2nd Intl. Topical Conf. on High Power Electron and Ion Beam Res. and Tech.*, Ithaca, New York, USA, Oct. 3-5, 1977, p. 207.
- [28] WIDNER, M. M., GOLDSTEIN, S. A., MENDEL, C. W., BURNS, E. J. T., QUINTENZ, J. P. and FARNSWORTH, JR., A. V., *Bull. Am. Phys. Soc.* **23** (1978) 763; *Phys. Rev. Letters* (to be published 1979).
- [29] CHANG, J., VAN DEVENDER, J. P., FARNSWORTH, JR., A. V., WIDNER, M. M., BURNS, E. J. T. and QUINTENZ, J. P., *Bull. Am. Phys. Soc.* **23** (1978) 763.

Progress in toroidal magnetic confinement

G. Grieger

Max-Planck-Institut für Plasmaphysik, EURATOM Association, D-8046 Garching, F.R. Germany

Résumé. — L'objet de cet article est de discuter les propriétés de confinement des plasmas plongés dans des champs magnétiques quasi toroïdaux.

Dans de tels systèmes, le confinement est obtenu par addition de champs magnétiques toroïdaux produits, soit par des courants toroïdaux induits dans le plasma — confinement interne — soit par des courants circulant dans des conducteurs extérieurs — confinement externe.

Les principaux représentants du confinement interne et externe sont respectivement le Tokamak et le Stellarator. Cet article concerne essentiellement le Tokamak et ajoute certains commentaires quant aux différences spécifiques essentielles, s'il y a lieu.

De plus, les acquisitions actuelles sont décrites dans la perspective des impératifs d'un réacteur à fusion afin de mieux établir un bilan sur l'état de la question et les problèmes restant à résoudre.

Abstract. — This paper will discuss the confinement properties of plasma in magnetic fields which are characterized by their strong toroidal components. In such systems confinement is achieved by the addition of poloidal magnetic fields which are either produced internally by toroidal currents induced in the plasma — internal confinement — or by currents flowing in external coils — external confinement. The main representatives for internal and external confinement are the tokamak and the stellarator respectively.

This paper will mainly deal with the tokamak and add some comments on ohmically heated stellarators when there are essential differences to be reported. In addition, the present achievements will be put into perspective with fusion reactor requirements in order to allow an assessment of the state of the art and of the still open problems.

At first, the range of parameters of a fusion reactor based on the tokamak principle will be evaluated. It will turn out that the range of working conditions is very limited and that not very much freedom is offered in choosing them. This results from rather simple physical and technical considerations and does not use arguments about the ability of fusion power to be competitive. Such arguments are not within the scope of this paper although one has to keep in mind that the already large and complicated experimental devices have to be built and operated in a cost saving manner.

This paper will discuss the confinement properties of plasma in magnetic fields which are characterized by their strong toroidal components. In such systems confinement is achieved by the addition of poloidal magnetic fields which are either produced internally by toroidal currents induced in the plasma — internal confinement — or by currents flowing in external coils — external confinement. The main representatives for internal and external confinement are the tokamak and the stellarator respectively.

This paper will mainly deal with the tokamak and add some comments on ohmically heated stellarators when there are essential differences to be reported. In addition, the present achievements will be put into perspective with fusion reactor requirements in order to allow an assessment of the state of the art and of the still open problems.

Therefore, the range of parameters of a fusion reactor based on the tokamak principle will be evaluated at first. It will turn out that the range of working conditions is very limited and that not very much freedom is offered in choosing them. This results from rather simple physical and technical considerations and does not use arguments about the ability of fusion power to be competitive. Such arguments are not within the scope of this paper although one has to keep in mind that the already large and complicated experimental devices have to be built and operated in a cost saving manner.

The core of a fusion reactor based upon plasma confinement by a toroidal magnetic field is a stably burning plasma of sufficient fusion power density and of not too large unit size. In very simple terms the output power is given by

$$P = 2 \pi^2 a^2 R \bar{n}_D \bar{n}_T f(T) \quad (1)$$

for $D-T$ plasmas, where a and R are the minor and the major plasma radii, \bar{n}_D and \bar{n}_T the volume average densities of the deuterium and tritium fuel components, and $f(T)$ a description of the temperature dependent fusion cross-section.

Figure 1 shows that for not too high temperatures the fusion power density is steeply increasing with temperature [1]. But since the same is true for the plasma pressure, $3 \bar{n}_e k \bar{T}$, and since this pressure has to be balanced by the confining magnetic field,

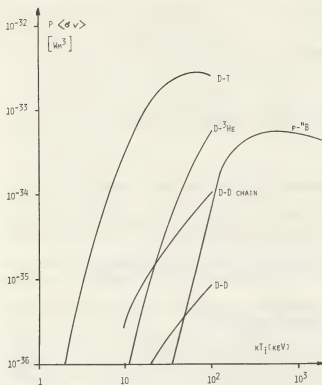


Fig. 1. — Normalized power density produced by fusion reactions. Power density: $P = \langle \sigma v \rangle \cdot n_1 \cdot n_2$, the alphas containing 1/5.

it is much more relevant to ask for, the maximum fusion power density achievable for a given confining pressure. This is answered by figure 2 where the temperature effect on pressure increase is compensated by a reduction of n_D and n_T so that the resulting pressure remains constant. It yields that optimum conditions are obtained for $n_D = n_T$ and a plasma temperature

$$(kT)_{\text{opt}} \approx 12 \text{ keV}. \quad (2)$$

This result is valid only for thermal plasmas. Systems considered to run in a non-thermal mode (e.g. hot ion mode) are not considered in this paper. A comparison between figures 1 and 2 also shows that the contributions to the generated fusion power is largest by reactions between particles of the tail of the distribution function so that their confinement properties require particular attention.

A burning plasma then requires its power losses to be balanced by the fusion power occurring with the α -particles because only these interact with the plasma particles, whereas the four times larger neutron power will be absorbed in the blanket surrounding the plasma and be converted into useful heat. Therefore, neglecting profile effects and setting $n = n_D + n_T$, the required energy confinement time is given by

$$\tau_E = \frac{E}{P_a} = \frac{3 \bar{n} k \bar{T} V}{\bar{n}^2 f(T) V}. \quad (3)$$

Since the plasma temperature has already been fixed by (2), one obtains

$$\bar{n} \tau_E = C_T \quad (4)$$

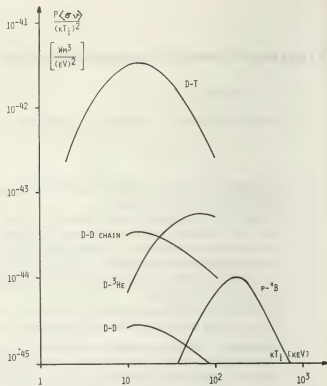


Fig. 2. — Normalized power density produced by fusion reactions for constant plasma pressure. As an example: 1 MW m⁻³ is produced for $n_D = n_T = 4.3 \times 10^{19} \text{ m}^{-3}$, $kT_1 = 13 \text{ keV}$ and $P = 5.3 \text{ bar}$.

with C_T following from figure 1

$$C_T \approx 2.2 \times 10^{20} \text{ s m}^{-3}. \quad (5)$$

Expression (4) is equivalent to the well-known Lawson criterion, but instead of considering various types of losses, like bremsstrahlung, it is based on the power production rate and an optimum plasma temperature. It is very satisfactory that the resulting value for $\bar{n} \tau_E$ is close to that of the Lawson criterion.

The tolerable range for \bar{n} will be determined by the highest acceptable values for $\bar{\beta}$ and B

$$\bar{\beta} = \frac{6 \mu_0 \bar{n} k \bar{T}}{B^2} \quad (6)$$

or

$$\bar{n} = \frac{\bar{\beta} B^2}{6 \mu_0 k \bar{T}} = C_n(\bar{\beta}, B). \quad (7)$$

Stability considerations (see later) seem to limit the achievable $\bar{\beta}$ values to 5-10%, and technical considerations make it hard to believe that B could be raised very much above 5-6 T. Therefore, as shown in figure 3, the average density of a fusion reactor will be in a rather narrow range around

$$\bar{n} = C_n \approx 2 \times 10^{20} \text{ m}^{-3}. \quad (8)$$

In addition, via eq. (4), these simple considerations also determine the required energy confinement time

$$\tau_E = \frac{C_T}{C_n} \approx 1 \text{ s}. \quad (9)$$

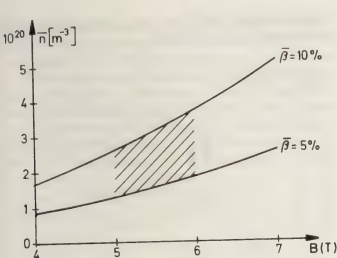


Fig. 3. — Range of \bar{n} for a fusion reactor.

It is clearly understood that the rather rough arguments given above can only yield rough results, but this may be fully sufficient for the intended reactor oriented assessment of the state of the art.

A first comparison can be made now between requirements and experimental findings. In figure 4 the gross energy confinement time vs. density is plotted for various experiments [2]. One observes that, irrespective of their other conditions, there is a linear increase of τ with n for each of the devices, only the slope being different for different machines. If one then depicts a certain density and compares (in the insert of figure 4) the resulting confinement times of the different devices, one finds that the slope is given by a^2 and that τ_E is thus best described by

$$\tau_E = C_\tau \bar{n} a^2, \quad C_\tau \approx 5 \times 10^{-21} \text{ ms} \quad (10)$$

which holds for clean ohmically heated plasmas. Obviously, this result is very general. But this is

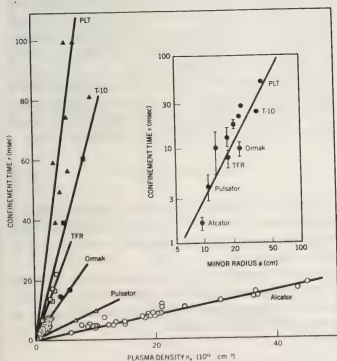


Fig. 4. — Confinement time vs. n for various devices.

striking because τ_E is found to be mainly determined by the energy losses through the electron component which however from neoclassical collisional theory would be expected to be much lower than that of the ions. There is no clear-cut theory up to now to describe these losses correctly so that extrapolations to the reactor regime are very difficult.

In order to substantiate this remark, it has to be remembered that the confining magnetic field is twisted around the magnetic axis and that therefore the magnitude of B is not constant along a magnetic line but rather varies as indicated in figure 5. This comes about by the excursion of the magnetic line in the toroidal magnetic field

$$\left(|B_\theta| \ll |B_\phi|, \quad B_\phi = \frac{R_0}{R} B_{\phi 0} \right).$$

Therefore, a particle moving around the torus experiences magnetic mirror effects which will determine its orbits; and this effect is the stronger the less collisions the particle will feel during its path.

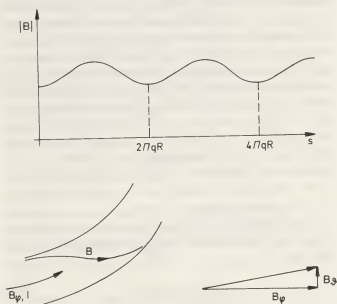


Fig. 5. — $|B|$ along a magnetic line (schematically).

Three regions have to be considered regarding their influence on particle and energy transport. They are determined by the ratio between the particle mean free path, λ , and the mirror distance, qR . In figure 6, λ vs. $(kT)^2/n$ is plotted together with two lines for $\lambda/qR = 1$ and $\lambda/qR = (R/a)^{3/2}$. These two lines separate the collisional from the collisionless regime with an intermediate one in between. $R = 5 \text{ m}$ and $a = 1 \text{ m}$ have been used in this example. Figure 6 indicates that present day experiments have hardly entered the collisionless regime, whereas the fusion reactor lies deeply within it.

It is expected that the trapped particles occurring in the collisionless regime by their interaction with the passing particles will lead to the generation of

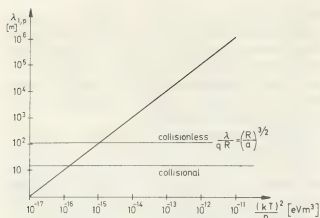


Fig. 6. — Mean free path by like particle collision for $R = 5$ m, $a = 1$ m.

trapped particle instabilities which, by their fluctuating fields, might affect both particle and energy transport. If this occurred, τ_E would have to be modified for the collisionless regime.

In this respect it was an essential result that PLT [3] with moderate plasma density and high power neutral injection could reach temperatures of about 6 keV and thus produce collisionless plasmas. Fluctuations which could be attributed to trapped particle instabilities were found indeed, but their effect on transport was obviously negligible. There was even some indication of an improvement of confinement with increasing temperature, but in this point the results are not fully conclusive yet. The experiments listed in figure 4 are not suggesting a strong temperature dependence within their range of conditions. It is conservative, therefore, to assume their validity also in the collisionless regime and to neglect potential T and q dependencies.

If one does this, one can compare the required energy confinement time (9) with the measured one (10) and obtains

$$\frac{C_T}{C_n} = C_i \bar{n} a^2 \quad (11)$$

which by using (8) results in a condition for the minor radius

$$a = \frac{1}{C_n} \sqrt{\frac{C_T}{C_i}} \approx 1 \text{ m} \quad (12)$$

which, in fact, is a very low value for a and has certainly to be increased a bit under realistic circumstances.

It has been mentioned already that in present day devices it is observed that the energy is lost preferentially via the electrons. The ion heat conduction plays only a minor role and seems to be in agreement with neoclassical theory within factors of 1 to 3. Only at high densities in small aspect ratio machines the neoclassical ion heat conduction reaches values similar to the observed electron heat conduction, and a drop of the energy confinement time was

observed indeed in ISX-A and Alcator under such circumstances (see Fig. 7) [2].

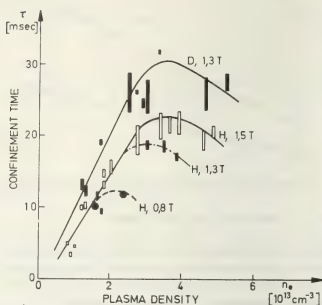


Fig. 7. — ISX-B data for high plasma densities and different values of B .

The exchange of energy between ions and electrons is rather accurately described by classical Coulomb collisions between the particles. This statement includes the interaction between beam generated particles and the bulk of the plasma. Therefore, there is little doubt at present that the same will hold also for reactor plasmas except that the fusion generated α -particles with their high energy are exceeding the Alfvén velocity and might generate some instabilities this way. One may hope, however, that this effect only leads to a faster slowing down of the α -particles and not to a serious particle and energy loss. Assuming classical energy exchange therefore would also for reactor conditions result in not more than a small difference between T_e and T_i for the bulk of the plasma.

The next question to ask is for the available means of heating these plasmas to the required temperatures. In this respect ohmic heating, though effective, is only of limited use, because the available power

$$P = 2 \pi R \int \eta^2 dA \quad (13)$$

is limited by η dropping with increasing temperature proportionally to $T^{-3/2}$, and the plasma current being determined by the magnetic configuration it has to produce.

This configuration is of helical structure and has to be stable against helical perturbations or *kinks*. They will always occur if the rotational transform $t = 1/q$ is a rational number

$$t = \frac{1}{q} = \frac{m}{n}$$

such that the field lines do not ergodically form a magnetic surface but close upon themselves after n revolutions around the machine.

These effects were discovered already very early and investigated in stellarators, in the C-stellarator for ohmically heated plasmas and in the Wendelstein W II-A stellarator for thermal plasmas. Figure 8 gives a good example [4]. Under the conditions of the W II-A stellarator, the resulting plasma density

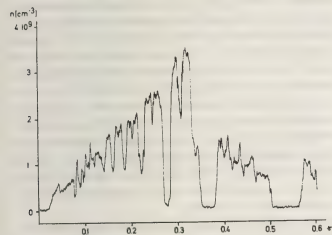


Fig. 8. — Resonances in confinement measured in the Wendelstein W II-A stellarator. n is proportional to τ under these conditions. The values of the measured iota (i) have to be reduced by 10 %.

is a direct measure of the confinement time. One observes that the confinement is reduced whenever iota passes through a rational number and that the effect is stronger the closer iota gets to unity. At $t = 1$ no confinement is possible anymore.

In a tokamak the current distribution will be determined by the loop voltage and the temperature distribution which determines the distribution of the resistivity according to $T^{-3/2}$. Since the temperature tends to be highest in the plasma center, $q=1$ will first be reached there. Further increase of the current will lead to an expansion of the $q = 1$ zone leaving a turbulent state with vanishing pressure gradients and constant current density behind and shifting the confinement regions to outer zones where $q < 1$.

This is shown schematically in figure 9. Experi-

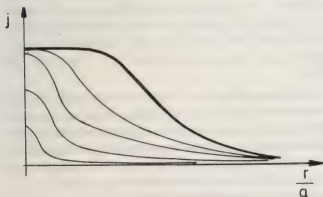


Fig. 9. — Possible cases of current distributions (schematically).

mental results show that in most cases the current can be increased until q at the plasma edge reaches values of about 3.5. Such profiles still include resonances, but if at their position the magnetic shear and ∇p could be kept at not too high levels, they are obviously not destroying the gross stability.

If the plasma current is increased further, it usually responds with a disruption, i.e. a sudden drop to zero (hard disruption). For large machines, these disruptions are extremely dangerous because by inductive coupling the plasma current is immediately transferred into the more or less conductive structure surrounding the plasma where its complicated path excites all sorts of forces and moments. Small machines are usually built disruption-proof, but whether this is also possible for very large machines is considered with some doubt.

Therefore, there is a strong incentive to aim at avoiding disruptions, or since their occurrence is of statistical nature, to reduce it to an acceptable limit which is almost zero. They are usually preceded by a growing $m = 2/n = 1$ mode and are found to be triggered by (i) impurity influx, (ii) imperfect plasma positioning, (iii) too high density, (iv) too high \dot{n} , or (v) too high I_p during plasma build-up. Some of the points could be observed by careful operation of the machine, but there seems to be a density limit above which a stable operation is no longer possible. For ohmic heating alone this limit is the Murakami limit [5]

$$n_{\text{crit}} \lesssim 1.5 \times 10^{20} \frac{B}{qRZ_{\text{eff}}} \quad (14)$$

which for reactor conditions yields about $3 \times 10^{19} \text{ m}^{-3}$. This value is almost one order of magnitude smaller than the required value of $2 \times 10^{20} \text{ m}^{-3}$, and one is relying on strong additional heating to bridge the gap.

Disruptions are completely avoided in ohmically heated stellarators if, according to present results, the contribution to the rotational transform by external fields is above $t_0 \approx 0.2$. It is conceivable that the stellarator inherent effects, namely the immediate stabilizing reactions upon any gross displacement of the plasma column are the origin of this property. The inclusion of stellarator fields in a large machine might be a difficult task, however.

In carefully performed tokamak experiments in Diva, Alcator, Pulsator, etc., it was possible to run stable discharges with q_a as small as 2.

Optimization of the stable operation of tokamaks requires the control of the plasma current distribution by properly shaping the temperature distribution. To do this with additional heating with well selected deposition profiles might be a feasible scheme for present day experiments. In reactors, however, one had to compete with the α power deposition profile so that one is probably forced to live with

the natural current profile. But one still needs strong additional heating initially for reaching ignition.

Strong heating can be achieved by the injection of intense neutral beams. It is the best heating method existing at present. It is understood and, in general, its heating effect is predictable. Only classical effects, like charge exchange and ionization, and heating via Coulomb collisions have to be considered for describing heating by neutral injection. Rather reliable high power injectors are developed for application to the present day devices, and the high temperature results by PLT, TFR, etc., were obtained with their help. If one could use neutral injection also for reactor startup, one had the advantage of even getting some additional heating by fusion reactions during the slowing down of the injected particles.

But unfortunately there are also some drawbacks connected with neutral injection. At present, neutral beams are generated by neutralization of high energy positive ion beams. This method practically limits the injection energy to 160 to 200 keV for deuterium due to the steeply decreasing neutralization efficiency for positive ions (Fig. 10). This provides no problems today, but for reactor plasmas this beam energy is too low to reach the plasma centre. In addition, these beams contain not only D^0 , but also certain fractions of D_2^0 and D_3^0 , i.e. after ionization, ions of fractional energy, the penetration depth of which is even smaller. These are heating only the plasma edge — which, in fact, needs to be cooled — and therefore represent a waste of power and, even worse, might lead to excessive sputtering of the vacuum wall.

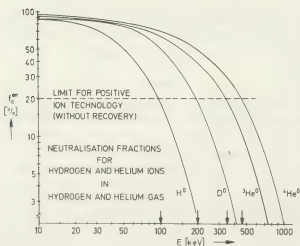


Fig. 10. — Neutralization efficiency for positive ion beams.

There is a chance to circumvent all these problems by generating neutral beams via negative ions by which way monoenergetic beams of higher energy could be established. The development of this new technology is just being started.

The alternative to neutral injection is radio-

frequency heating. There is a large variety of resonant frequencies of the plasma allowing to feed power into the plasma and, if desired, also with well determined local deposition profiles, because all of them have different properties. This is an advantage and a disadvantage at the same time. The advantage is that, in principle, one always should be able to find a frequency or a mode so that the power deposition can be tailored according to the needs. The disadvantage is that the large variety of possibilities requires a wide-spread experimental programme for testing, an essential prerequisite for application. Probably, it was this reason which led to the success of neutral injection, because there was only one choice and a straight-forward development programme could be therefore established.

Just to give an impression of the RF heating possibilities, the main representatives shall be mentioned:

Heating by transit time magnetic pumping with frequencies of about 100 kHz occurs on the ions via Landau damping. After some less successful experiments in smaller devices, the heating effect was demonstrated in Petula.

Ion cyclotron heating in the range of 100 MHz in itself offers a variety of possibilities. Perhaps the most interesting one is the heating of a minority species of the plasma to rather high energies. Heating of the bulk of the plasma would then occur in very much the same way as with high energy neutral injection via Coulomb collisions. This kind of heating would thus allow us to preserve a large part of the already proved methods. TFR, Erasmus and PLT have shown the feasibility in principle of ion cyclotron heating.

Lower hybrid heating at a few GHz could be used to heat either the ions by mode conversion or the electrons by Landau damping depending on the mode spectrum excited. The relatively high frequency allows the application of assemblies of wave guides but their required close distance to the plasma edge might be a problem. Plasma heating at the lower hybrid frequency has been demonstrated in ATC, Wega, and JFT-II.

Electron cyclotron heating occurs by direct cyclotron damping by the plasma electrons. Launching of these waves would be comparatively easy via oversized waveguides, but reliable gyatron sources for frequencies above 100 GHz and of sufficient power have still to be developed. Electron cyclotron heating has been demonstrated on Tuman-II and TM-3.

These examples show the wide variety of RF heating possibilities. But before relying on such methods for the heating of large machines, high power RF heating experiments have to be carried out successfully. There is a strong trend in this direction and, perhaps, more reliable results will soon be available.

Most of the comments made up to now are considered with the tacit assumption that the plasmas

considered are sufficiently clean, which means that the ion constituents are practically only isotopes of hydrogen. At first, experimental experience coming up during the past years showed that with decreasing amount of impurities, or with the effective charge getting closer and closer to one, there was a simultaneous transition to longer confinement times and higher temperature plasmas. This is both a direct and indirect consequence of the main effect of impurities, the much higher radiation power per atom.

It is interesting to look at the tolerable fraction of impurities for reactor plasmas. Information on this is found in figure 11 which gives, for plasmas of 10 keV, the relative concentration of impurities for all elements which just doubles the power losses (with respect to a clean plasma) by their radiation [6]. Although it restricts the fraction of light impurities, like oxygen, to only a few percent, and that of heavy impurities, like typical wall and limiter materials, to 10^{-4} or less, this concentration is probably already too high to be acceptable. These figures have to be

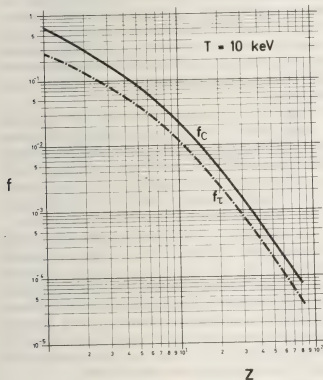


Fig. 11. — f_c : impurity concentration leading to doubling of losses via its radiation. f_r : impurity concentration requiring doubling of energy confinement time to allow for the additional radiation losses.

seen in connection with the sputtering coefficient of wall materials because these are the source of the most critical impurities. Typical values of sputtering coefficients vs. the energy of the incident particles are shown in figure 12 [7]. Unfortunately, these values are rather high already for small fractions of the plasma energy, particularly, if one includes self-sputtering. There is a tendency, therefore, to coat or

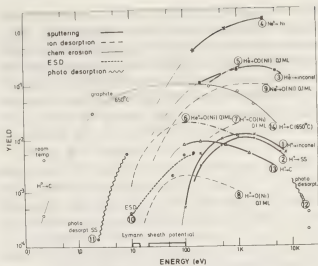


Fig. 12. — Sputtering yield vs. energy of impinging particles for various wall materials.

protect the wall with lighter elements in order to take advantage of their lower radiation power. This follows from a figure of merit which relates the tolerable fraction of impurities resulting from figure 11 to the sputtering coefficient for the same element [8]. In figure 13 this ratio is given for a number of potential wall materials, like SS, carbon, and refractory metals, as a function of the plasma edge temperature. One observes that heavier elements offer advantages only if the edge temperature is not too high. If the temperature would adjust itself to higher values, lighter elements should be preferred as wall material.

This is true in particular for limiters which, from

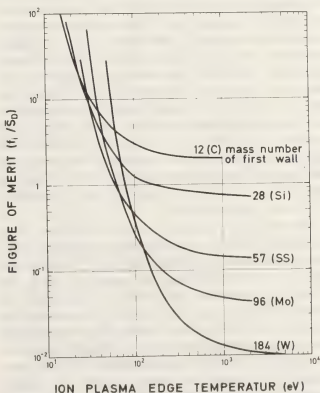


Fig. 13. — Figure of merit for different wall materials.

their very nature, are in very close contact with the plasma, and experiments have shown that upon replacing the limiter material from refractory metals to carbon the plasma temperature could be increased considerably, indeed. But, in general, the arguments are not that straightforward. They have to include particle transport within the plasma (impurities) and in the edge region, in particular. But our knowledge of particle transport is still comparatively poor.

As far as experiments are concerned, it is consistent to assume that the gross particle confinement time is about 2-4 times the energy confinement time, but the local value is not constant over the plasma cross-section. Larger machines, for which the penetration depth of neutrals originating from the wall becomes small in comparison to the plasma radius, have given some deeper insight into this problem. But it is still the outer edge, which is governed by recycling, where we need to know the details in order to formulate the full balance equations which determine the edge temperature and the sputtering in turn.

But even if one knows how many impurities are generated per unit time, one has to check how and at which rate they are penetrating deeper into the plasma. Diffusion theory predicts their accumulation in the plasma centre due to friction between light and heavy ions. Indication of such an effect was reported from Pulsator [9] for a rather collisional plasma, but no clear-cut indications about impurity accumulation are known yet for less collisional plasmas. There the best description is that the fractional impurity concentration is constant over the whole cross-section.

It would be extremely important to know if this experimental finding could still hold under reactor conditions, because even if one would succeed in reducing the impurity generation to an acceptably low value, one still has the problem of the fusion generated helium. If this would not accumulate in the centre but rather distribute itself smoothly over the cross-section, one could keep its concentration low enough by pumping at the plasma edge. If the contrary happened, the fuel would become more and more diluted so that the reactor would quench itself either, for constant pressure, due to lack of fuel, or, for constant fuel density, due to exceeding its pressure balance limit.

Also for this reason, it is very satisfactory that for experiments with high temperature plasmas impurity accumulation in the plasma centre is not found, but the even distribution of impurities over the plasma cross-section still makes it necessary to reduce their generation at the wall. This could either be done by reducing the plasma edge temperature according to the concept of a cold plasma mantle or by reducing the wall bombardment by the introduction of a divertor, or, more probably, by a combination of both. The basic principle of a divertor is the magnetic introduction of a scrape-off layer

along which most of the edge particles are carried out of the plasma chamber without too large interference with the vacuum wall. Via the pressure in the divertor chamber the pressure in the scrape-off layer could be controlled.

Although the impurity question is probably the most crucial at present, there are only very few experiments especially devoted to this problem. Dite and Diva have yielded first information on the bundle and the poloidal divertors respectively, Asdex and PDX will investigate the properties of the poloidal divertor for higher temperature plasmas and Textor will study the plasma/wall interaction. The introduction of a divertor into a tokamak machine, however, would add considerably to the technical difficulties. Therefore, one should try hard to be able to live without it. In this connection, it is surprising that there is practically no experimental programme on the concept of the cold plasma mantle although it has to be admitted that here reactor relevant experiments are difficult to perform.

A very similar situation exists with respect to β , the fraction of the magnetic field energy used for plasma confinement. In contrast to the impurity situation, however, the achievement of higher betas is not yet a vital question with the present experiments, but only comes up for the forthcoming experiments after Jet, etc., i.e. in connection with an experimental test reactor.

Theoretical investigations indicate that assuming a fixed boundary of the plasma high- n ballooning modes might allow an average β of up to a few percent. Also low- n internal modes might not become more restrictive under these conditions. A plasma cross-section slightly elongated parallel to the main axis of the torus should have a positive effect on beta.

The maximum β for low- n , free boundary kink modes depends strongly on the pressure and current profiles. If they are optimized, values for beta up to 4.5% or so can be expected from them. A conductive wall or short circuit loops around the plasma would have a stabilizing influence if their distance from the plasma edge is not larger than about 1/3 of the plasma radius. Feed-back stabilization will help to counteract the dominant modes.

Experimental results were obtained in Tosca with $\bar{\beta} = 2\%$ and in ISX-B with $\bar{\beta} = 1.8\%$ (8% on the axis). These numbers are still lower than needed in reactors, but it is essential that the poloidal beta has already exceeded one. Above this limit the pressure balance can no longer be established by the poloidal field alone, but the toroidal field has to contribute. Obviously, the transition from the paramagnetic to the diamagnetic regime occurs rather smoothly.

It would be very interesting to learn how the plasma would react when the plasma pressure gradually approaches the beta limit. If this did not result in a sudden loss of the plasma, but only in a steep increase of the losses, this would be an ideal effect for auto-

matic reactor burn control at optimum conditions. Burn control would be rather difficult to manage otherwise.

In conclusion, it is perhaps not too bold to expect the ignition of a $D-T$ plasma in the not too far future. The main obstacles still to overcome are the impurity

problem and to reach a stable plasma state at a sufficiently high beta. Certainly, this assumes that all difficulties are already known and, during the remaining step to reactor conditions, no new ones will occur. We might, however, allow ourselves this hope because of the progress made during the previous years.

References

- [1] GRIEGER, G., PALUMBO, D., Development of Pure Fusion, *Proc. 2nd UNESCO Int. Forum on Fundamental World Energy Problems*, 2nd Edition, IAEA Vienna, 1979.
- [2] MURAKAMI, M., EUBANK, H. P., Recent Progress in Tokamak Experiments, *Physics Today*, May 1979, p. 25-32.
- [3] EUBANK, H. et al., *Neutral Beam Heating Results from the Princeton Large Torus*. To be published. Private information.
- [4] GRIEGER, G., Barium-Plasma im Wendelstein Stellarator, *Mitteilungen der MPG* 1 (1970) 43-59.
- [5] MURAKAMI, M., CALLEN, J. D., BERRY, L. A., *Murakami Limit*, *Nucl. Fusion Letters* 16 (1976) 2, 347.
- [6] VERNICKEL, H., BOHDANSKY, J., A General Formula for Impurity Radiation Loss of Fusion Plasmas in Corona Equilibrium, *Nucl. Fusion (Letters)* 18 (1978) 10.
- [7] STAIB, P., STAUDENMAIER, G., Surface Effects and Impurity Production in Tokamak Machines, *J. Nucl. Materials*, 76 and 77 (1978) 78-91.
- [8] BOHDANSKY, J., ROTH, J., VERNICKEL, H., Low Energy Light Ion Sputtering and Consequences for First Wall Material Selection, *10th Symposium on Fusion Technology*, Padua, 1978.
- [9] ENGELHARDT, W., KLUBER, O., MEISEL, D., MURMANN, H., SESNIC, S., FUSSMANN, G., GLOCK, E., GOTTARDI, N., KARGER, F., LISITANO, G., MAYER, H. M., WAGNER, F., Accumulation of Impurities and Stability Behaviour in the High-Density Regime of Pulsator, *Proc. 7th Conf. on Plasma Physics and Contr. Nucl. Fusion Research I*, Innsbruck, 1978 (IAEA-CN-37/A-5), 123.

Progress of laser fusion at Lawrence Livermore Laboratory

H. G. Ahlstrom

University of California, Lawrence Livermore Laboratory, Livermore, California 94550, U.S.A.

Résumé. — Durant les années précédentes nous avons fait des progrès importants vers la compréhension des phénomènes d'interaction laser-plasma grâce à de nouveaux systèmes et techniques de diagnostics. Nous avons aussi mis en opération Shiva le plus complexe des systèmes laser du monde, et obtenu des données importantes sur le fonctionnement des cibles. Les expériences d'implosion avec le système Shiva ont produit des densités au-delà de 100 fois la densité liquide du DT. L'importance de ce résultat provient du fait que nous avons dû surmonter la nécessité d'une implosion à symétrie sphérique et le problème d'instabilités de Rayleigh-Taylor. Il n'apparaît pas que le futur nous réserve d'obstacles majeurs pour obtenir les densités nécessaires pour une réaction efficace avec des microcibles dans un réacteur à fusion. De plus, nous avons identifié un système laser qui pourrait être utilisé pour un réacteur à fusion et nous avons initié un programme très actif pour le développer. Notre « Systems Studies Program » a aussi défini une configuration qui résout la plupart des problèmes majeurs posés par des réacteurs de fusion par laser. Ce n'est pas dire que nous avons trouvé l'unique solution d'un réacteur de fusion par confinement inertiel, mais plutôt que nous proposons un système avantageux, qui peut être utilisé comme point de comparaison pour d'autres solutions dont les performances pourront être jugées par rapport à la chambre de réaction Hylife. Nous avons donc bon espoir que la fusion par confinement inertiel sera un jour une source pratique d'énergie pour le monde.

Abstract. — Inertial confinement fusion is the present and future source of energy in our universe. Derivatives, such as solar, geothermal, wind, and biomass are proposed as future substitutes for possible fuel sources. All of these possible sources of energy while they may be considered to be renewable do not fulfill the single most important criteria of being unlimited. Fuel reserves of more than 100 billion years are accepted as « unlimited ». The understanding of fusion has many « fathers », Bethe, Teller and many others, it has also had proponents (too many to list) as the world's energy supply. This author hopes that this Program's efforts will contribute positively to the advance to the time when fusion energy will positively contribute to the energy supply for mankind.

Controlled fusion is judged by us to be the world's most challenging technological problem. The potential benefit to mankind of an unlimited source of energy and thus a higher standard of living make the acceptance of this challenge worth our while. There are many dedicated scientists working on controlled fusion to make this dream a reality. Magnetic and inertial fusion are in a horse race that must not be allowed to falter or to be cancelled. Fusion is the future of the world and one of these approaches to fusion is vital to our future generations.

1. Introduction. — The basic concept of laser fusion has been describe many times in the past [1]. Here we can summarize it in a simple statement of two requirements : fuel density times radius, ρr , $\geq 1 \text{ gm/cm}^2$ and temperatures $> 5 \text{ keV}$. The intense focusing capability of the laser, 10^{14} to 10^{17} W/cm^2 is used to create a plasma at the surface of a spherical pellet, the intense heating of the plasma by the laser provides the energy required to ablate the surface of the pellet and compress the fuel to densities of a 1 000 to 10 000 \times liquid density of DT. The implosion process is tailored so that at peak compression the fuel also achieves a temperature of approximately 5 keV. At these temperatures and densities and where we have provided a sufficient large ρr , $\geq 1 \text{ g/cm}^2$ we will achieve efficient burn. As pointed out in the past, the reason for compressing the fuel is to achieve $\rho r \sim 1$ for pellet sizes which are sensible for fusion reactors. Since $\rho r \sim C^{2/3}$, where C is the compression, by compressing the fuel to 1 000 \times liquid density, we reduce the requirement on the radius of the pellet by a factor of 100. Thus the goal of the Laser Fusion

Program is to use lasers to demonstrate that these conditions can be achieved and thus prove the scientific feasibility of laser fusion.

Over the past several years, since 1974 at the Lawrence Livermore Laboratory, we have been pursuing these goals using a series of neodymium glass lasers as the driving sources. In figure 1, we summarize our results and projections for the future in a chart where we plot the results as a function of the quality of inertial confinement η which corresponds to ρr and the DT ion temperature. As seen in the figure, our experiments began with Janus using a single beam in 1974 at a power of 0.2 TW. At that time we were able to achieve an η of several times 10^{11} and approximately a 0.5 keV ion temperature. In 1975 with two beams from Janus and 0.4 TW, we were able to increase the fuel temperature to approximately 2 keV with approximately the same value of η . The major importance of the result in 1975 was that we were able to use the fusion reactions to demonstrate that the reactions produced were truly thermonuclear [2]. By 1976 we had developed Argus at 4 TW

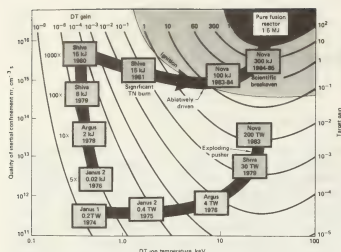


Fig. 1. — Laser fusion. Progress projections.

and had achieved ion temperatures of approximately 10 keV.

This whole series of experiments was done with a type of target which is called an exploding pusher [3]. The main idea in these experiments was to demonstrate that the laser could be used to achieve the fusion temperature conditions albeit at low fuel densities. This lower path shows that Shiva and Nova, the next laser coming on-line, could continue with this type of target and achieve higher values of η . However, this type of target with the energies available will not achieve break-even and is not a viable candidate for a fusion reactor target. In 1976 we also began our first series of experiments moving away from the exploding pusher concept in order to achieve high densities although at relatively low fuel temperatures with current laser systems [4]. By 1978 with Argus at 2 kJ, we had achieved $10 \times$ liquid density and early in 1979 with Shiva at 8 kJ we had achieved $100 \times$ liquid density. The fuel temperature in these fuel compressions are kept low at approximately a half a kilovolt to maximize the fuel compression and provide only sufficient number of thermonuclear reactions for diagnostic purposes. The achievement of $100 \times$ liquid density from significantly less than liquid density as a starting point is indeed a significant achievement. To achieve this goal, we had to provide sufficiently uniform implosion of the target and, we had to achieve a condition which alleviated the problem of the Rayleigh-Taylor instability [6].

The next step in the program to achieve greater than $1000 \times$ liquid density will also require significant developments. One is already in-hand, that is operation of Shiva at its full energy potential of 15 kJ [7]. Target designs exist which project these fuel densities; however, they require additional developments in the area of target fabrication. After once achieving $1000 \times$ liquid density, the program can then use this high density design and result to examine questions of stability through variations of the target

parameters. We also plan to trade some of the final fuel density for temperature in order to produce a significant thermonuclear burn by achieving temperatures of 2 keV at these high densities. However, 2 keV and $50 \times$ liquid density will not be sufficient to allow us to achieve self-trapping of the particles in the fuel and therefore cause the particles to raise the temperature of the burning fuel. This boundary is called the ignition boundary and is not expected to be achieved until we have at least the first phase of the Nova system. This system is presently scheduled for completion in 1983 and the full Nova system [8, 9] which is expected to produce break-even or greater will be ready in 1985.

2. Fusion laser systems at LLL. — The Laser Fusion Program at Livermore has utilized four neodymium glass laser systems for the demonstration of important milestones in laser fusion and, we are constructing the Nova system which will also be a neodymium glass laser system. The reader is referred to papers from the Livermore Solid State Program which describe our laser systems: Janus a two beam, 8.5 cm output aperture system [10], Cyclops a single beam, 20 cm output aperture system [11], Argus a two beam, 28 cm output aperture laser system [12], Shiva the twenty beam, 20 cm output aperture system [7] and Nova [8] which has not yet been frozen in a final design.

All of these systems utilize rod amplifiers and disk amplifiers, Pockel's cells, Faraday rotators, and spatial filters. The technology for these laser systems has largely been developed at the Livermore Laboratory by the Solid State Laser Program. However, the manufacturing of the parts, fabrication of the glass, the finishing of the glass, and the coatings are all done in industry primarily in the United States but also in other countries.

Shiva the system which we are now operating is a twenty beam system which has 2.5 cm and 5 cm diameter rod amplifiers; and 9 cm, 15 cm, and 20 cm diameter disk amplifiers. The system is assembled using the image relaying concept which was first put forward by John Hunt [13]. All twenty beams are fully diagnosed at the laser output to determine the energy, spatial distribution of energy, temporal profile of the output pulse, and any prepulses. The system utilizes twenty incident beam diagnostic packages, IBD, and twenty pointing focusing centering/reflected beam diagnostic packages, PFC/RBD [14]. The beams on Shiva are arrayed in two clusters of ten which approximate the focusing cone of $f/1$ lenses. The beams are arranged so that each beam has an opposite member through a diagonal in the target chamber. Thus each beam has its opposite member and the PFC/RBD system may be used for accurate alignment of the target and the focus of each one of the beams as has been done on our two beam systems,

Janus and Argus. The upper and lower clusters consist of two pentagonal arrays of beams, an inter pentagon and an outer pentagon. The inner cluster is rotated 36° with respect to the outer cluster. This arrangement of the beams on Shiva allows significant room in the equatorial region for target diagnostics. In figure 2, we show an artist's view of the Shiva target chamber showing the beams arriving at the top and the bottom of the target chamber and a number of the target diagnostic instruments that are used in the experiments.

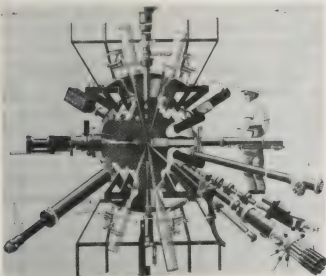


Fig. 2. — Shiva target chamber.

Three instruments that will be discussed more later in this paper are the Dante sub-kilovolt time resolved spectrometer, the FFLEX, filter fluorescer experiment, which is a time integrated, high energy X-ray spectrometer and the radiochemistry diagnostic which is used to measure the activation of various target materials. The Shiva system has 146 amplifiers, 122 relay spatial filters, and 84 optical diode gates in the laser design. There are more than 1 000 control points and more than 1 000 data records are taken on every shot. Through the use of microprocessors, fiber optic communication links, minicomputers, and a higher level supervisory computer [15], we have been able to bring this system into operation. Microprocessors are located near the control function or data taking element and are used as front-end processors. There are more than 60 LSI-11 microprocessors in the Shiva system. The LSI-11 microprocessors are connected back to a minicomputer to provide for central control and analysis of each one of the four functional blocks of the Shiva control and data system. The four functional blocks are the power conditioning which includes the charging and firing of the capacitor banks and the timing for the remainder of the system, the laser diagnostics, the alignment system, and the target diagnostics system.

The Shiva control system has been extremely

successful and has represented a very significant savings in time and money in terms of the implementation and operation of the Shiva laser target irradiation system. Shiva has attained and exceeded its design goals. The original goal was 10 kJ in 1 ns and 20 TW for pulses ≥ 100 ps. We have conducted a target campaign where we have fired a significant number of shots at 90 ps and powers of 10 to 27 TW. The 27 TW actually exceeded the damage threshold before the installation of the output spatial filters. However, now with the output spatial filters in the Shiva system, the damage threshold has been increased to 30 TW [7]. For long pulse operation, i.e. of the order of a nanosecond, we have done experiments in excess of 10 kJ and now with the output spatial filter, we can operate safely up to 15 kJ. The Nova laser system which is intended to provide more than a factor of 10 increase in both power and energy capability as compared to Shiva started out as a design study to determine what upgrade possibilities there were for the Shiva system.

Developments in the Solid State Program in terms of laser design and materials led us to the conclusion that it was possible to make a significant extension of the technology of the solid state lasers to provide a facility in the range of 0.25-0.50 MJ. The full Nova system has been proposed to Congress and the Department of Energy and at present the Congress has authorized the construction of Phase I of Nova. Phase I would consist of half of the laser building and ~ 0.4 -0.5 of the total laser capability.

Phase I of Nova will occupy a new building immediately adjacent to the present Shiva building and with the completion of Phase I it is planned to remove the Shiva target chamber from the target room and restage and rebuild the lasers in the Shiva building to conform to the Nova design in the east wing. The full system will produce of the order of 300 kJ in 3 ns and is expected to achieve target gains of break-even or greater. At scientific break-even the number of neutrons produced in a single reaction will be $> 10^{17}$. This is a number of neutrons not to be ignored. In figure 3, we show one of the conceptual designs of the Nova reaction chamber [9]. In this design, we show a double-walled vessel which uses aluminum for the inner wall, contains water between the two walls, and utilizes fiber glass as the outer wall. The materials are chosen to minimize the long term activation of materials in the target chamber and to minimize the activation of materials in the target room and the target room itself. With yields expected from the Nova system, we must begin paying serious attention to the location of diagnostic instrumentation. Although the diagnostic instrumentation is shown schematically in the target room, in actuality we expect to have the electronic instrumentation outside the target room so that the diagnostics will extend through lines of sight through the seven foot concrete wall of the Nova target room.

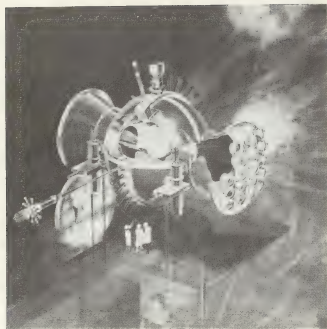


Fig. 3. Nova target chamber.

3. Target diagnostics. — In this section we will present characteristics of some of the target diagnostics which have been implemented for the Argus and Shiva experiments. As is well known by now, the X-ray spectrum from a laser irradiated target is quite complex. It consists of a thermal portion of the spectrum which contains most of the energy and generally is in the region of a 100 eV to 1.5 keV. Since targets generally contain materials with $Z > 14$, we expect line radiation in the region of 1 to several keV and above this region we expect to see the signature of the suprathermal electrons which are produced in the laser absorption process.

The two portions of the spectrum which we will be concerned with in this paper are the thermal sub-keV portion of the spectrum and the suprathermal portion of the spectrum produced by the high energy electrons. We have improved our Dante spectrometer which utilizes windowless X-ray diodes and filtering materials to produce spectral discrimination in this portion of the spectrum. The most recent implementation of this system is a ten channel spectrometer [16] designated Dante T. The aluminum photo-cathodes in combination with materials such as CH, V, Cr, Fe, Co, Ni, Cu, Zn, Ge, and Al provides spectral discrimination in this region of the spectrum. We have utilized diodes with 200 ps and 50 ps response time. Typically the Dante spectrometer is coupled with Tektronix R 7912 transient digitizers for an overall response time of the order of a 0.5 ns or to the Thompson CSF TSN 660 oscilloscope which has a band-width of 4 GHz.

For the high energy, suprathermal portion of the X-ray spectrum we have implemented what we call our filter fluorescer experiment or FFLEX [17]. In the past we have used simple K-edge filters in

combination with detectors to provide spectral discrimination. However, as the spectra have become hotter, that is more energy in the suprathermal tail, and a less rapidly falling spectrum, the contribution to a spectral channel from its response above the K-edge became significantly large and thus eliminated the spectral discrimination at the K-edge. To overcome this limitation we have gone to the addition of a fluorescer foil. The K-edge defines a region of the spectrum which is allowed to pass the first filter. This spectrum then impinges on a fluorescer foil which has its K-edge slightly below that of the prefilter. In this situation, most of the X-rays which are produced are due to X-rays between the two K-edges of the two filters. The rapidly falling cross section for the production of fluorescence radiation in the fluorescer foil by X-rays having passed through the prefilter above the K-edge produces very little response for the detector. Thus the combination of the K-edge prefilter and the fluorescer foil produces a narrow band response which can then be used to accurately define the suprathermal X-ray spectrum. In our typical filter fluorescer experiment, we utilize ten channels which provide spectral discrimination from 2 keV up to 110 keV.

As discussed earlier in the introduction, an extremely important aspect of our program is to be able to measure the density in targets with relatively high density but low temperature. One technique is by the activation of radio nuclides in the target material to determine fuel and shell densities [9, 18]. The DT fusion reaction produces the 14 MeV neutrons which then activate various materials in the target. If a seed material is placed in the fuel, then this can be activated for direct determination of the fuel ρr . An average fuel density can then be calculated. The activation of other materials provides information about the density radius product of those materials at the time of the burn of the fusion fuel.

More specifically, in figure 4 we show schematically how the neutron from the fusion reaction could be used to determine the areal density of a SiO_2 pusher.

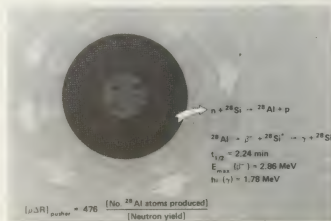


Fig. 4. — The effective $\rho \Delta R$ of the glass microsphere is determined by means of radiochemistry.

Neutrons from the fusion reaction interacting with the ^{28}Si in the pusher produce ^{28}Al which is a radioactive nuclide. It has a beta gamma decay with a half-life of 2.24 min. β 's are emitted with an energy of 2.86 MeV and the γ 's with an energy 1.78 MeV. As shown in the equation, if the neutron yield is measured independently, which is true for our experiments, then if we are able to determine the number of ^{28}Al atoms produced, we can determine the $\rho \Delta r$ of the pusher material. Knowing the $\rho \Delta r$ of the pusher material is of course very useful but we would like to also be able to relate that information to the fuel density. We can either relate the measured $\rho \Delta r$ of the pusher to the fuel density using our complex design code or we can try to find a simple way to relate these two quantities. A simple model for this target relationship assumes that the mass of the fuel and the glass pusher is conserved. We also make the assumption initially that the density of the two materials are uniform although not equal. Finally, we make the observation that the pressure and temperature at the pusher-fuel

interface must be continuous and equal and therefore, we will assume that the pressure and temperatures are uniform and equal throughout the pusher fuel regions.

Conservation of the masses of the fuel and pusher gives,

$$\frac{M_f(f)}{M_f(p)} = \frac{M_0(f)}{M_0(p)} \quad (1)$$

where the subscripts 0 and f represent the initial and final states respectively and the f and p in brackets designate the fuel and pusher. Further using the assumption of uniform densities in the fuel and the pusher, we can write,

$$\frac{\frac{4}{3} \pi r_f^3(f) \rho_f(f)}{\frac{4}{3} \pi [r_f^3(p) - r_f^3(f)] \rho_f(p)} = \frac{\frac{4}{3} \pi r_0^3(f) \rho_0(f)}{4 \pi r_0^2(p) \rho_0(p) \Delta r_0} \quad (2)$$

where we have also assumed that the initial pusher thickness $\Delta r_0 \ll r_0(f)$. Simple algebraic manipulation leads to,

$$\rho_f(f) = \rho_0(f) \left\{ \frac{\rho_f(p) \Delta r_f}{\rho_0(p) \Delta r_0} \left[1 + \frac{2}{3} \frac{\Delta r_f}{r_f(f)} + \frac{1}{3} \left(\frac{\Delta r_f}{r_f(f)} \right)^2 \right] \right\}^{3/2}. \quad (3)$$

For cases where $\Delta r_f/r_f(f) \ll 1$, we need no further assumptions.

However, this is not generally true and we make the isobaric, isothermal assumption to obtain a relationship between $\rho_f(f)$ and $\rho_f(p)$. This leads to

$$\rho(p) = \alpha \rho(f) \quad (4)$$

where α is determined by the degree of ionization of the pusher material. We can then write,

$$\rho_f(f) = [\rho_f(p) \Delta r_f]^{3/2} G[M(p), M(f), \alpha]. \quad (5)$$

In figure 5, we plot the solution for the above assumptions which is shown as the solid line relating effective SiO_2 pusher $\rho \Delta r$ to the maximum fuel density. It is interesting to note that a range of 1 D simulations essentially bounds this simple approximate solution. Another spatial distribution for the simple model is also shown. It is interesting to note that this rather extreme deviation from our simple assumption of uniform densities produces less than a factor of two difference in the inferred fuel density

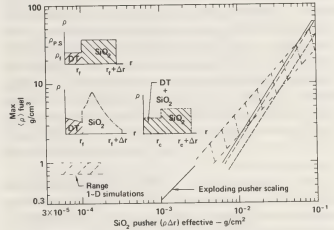


Fig. 5. — Maximum $\langle \rho \rangle$ fuel vs. effective pusher ($\rho \Delta r$).

for a given pusher $\rho \Delta r$. Finally, we show the situation for a complete mixing of the pusher into the fuel such that there are equal amounts of pusher and fuel material in the fuel region. Again, the variation from the nominal case is less than a factor of two

$$G = \left\{ \alpha \left(\frac{3}{4\pi} \right)^{1/3} \left[\left(\frac{M(p)}{\alpha} + M(f) \right)^{1/3} - M(f)^{1/3} \right] \right\}^{-3/2}.$$

The very important result from this simple study of the use of activation of radio nuclides in pusher material is that it is a very effective determinate of the

final fuel density and relatively insensitive to the distribution of fuel and pusher and even to mixing of the pusher into the fuel [19].

Now let us examine for a moment how an experiment might be performed. In the analysis of the data one must know the fraction of the target collected in any collection system. It is well known in laser interaction experiments that a simple collector does not collect the geometrical fraction of target material that it intercepts. As a result, we must have a measure of the target fraction which is collected. One approach to solving this problem is to irradiate the target in a nuclear reactor with thermal neutrons and for targets containing glass pushers the ^{23}Na in the glass can be activated to produce ^{24}Na . ^{24}Na has a half-life of 15 hrs and the target is counted before the experiment is performed. After the implosion experiment, the ^{28}Al activity can be counted for 5 min and then the remaining ^{24}Na activity can be counted for 24 hrs. The second counting of the ^{24}Na produces the target fraction which is collected allowing the determination of the ^{28}Al activity produced in the SiO_2 pusher.

In figure 6 we show schematically how this system is implemented on Shiva and we also show schematically a multiple shell target which has been irradiated. The multiple shells of course could each contain a material which could be activated by the neutrons from the fusion reaction thus providing information about the areal density of each one of the shells at the time of the fusion reaction. In this system, the collector is an Al cylinder which is lined with reactor grade Ti or Ta foils. It is important that the collector foils not contain any trace materials which could be activated by the fusion neutrons from the reaction. After the experiment has been performed, the aluminum cylinder is retracted automatically through a gate valve and then released through another valve to fall down through a plastic tube to the basement of the Shiva system where the counting system is located.

The counting system is shown schematically in figure 7 [20]. It consists of a 25.4 cm NaI crystal for measuring the gamma reactivity. It is a well detector in which we place a NE 102 fluor system which contains the Ti or Ta foils which have deposited on them the

activated material from the target. The NE 102 fluor consist of a cylinder around which the foils are wrapped and then this cylinder and the foils are placed inside another cylinder of NE 102 fluor. This combination is then placed inside the NaI fluor thus producing a system which has a 100% efficiency for counting the β ray decay and 40% efficiency for counting the γ ray decay for a combined efficiency of 40%. Because of the extreme sensitivity of the large detector system to outside radiations, we place the counting station in the basement of Shiva to provide significant concrete shielding against cosmic rays and other naturally, or artificially, occurring radiations. We also place the system inside a 10 cm thick lead chamber.

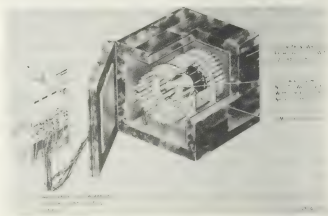


Fig. 7. — Density measurements by neutron activation.

However, even with all of these precautions, we receive significant background due to cosmic rays which enter the NaI crystal, Compton scatter and produce coincidence counts in the NaI and NE 102 fluor systems. To reduce the background due to cosmic rays, we have surrounded the counting crystals with Geiger tubes which also sense the arrival of cosmic rays and thus produce a triple coincidence in the counting system and are thus rejected. The background of this system in a five minute counting interval is two counts. Thus the utilization of this system with glass pushers has produced an extremely low threshold for determining the $\rho \Delta r$ of glass pushers.

Another technique that we have developed to determine the size of the compressed fuel region is the utilization of a spatial discriminating crystal spectrometer which is designed to look at the line emission from argon contained in the fuel [21]. A crystal spectrometer is used to provide spectral discrimination and a slit perpendicular to the direction of the spectral dispersion provides spatial discrimination in one direction. The difficulty in utilizing this type of system is that as the pusher becomes more dense, the opacity for the propagation of the seed material line radiation through the pusher

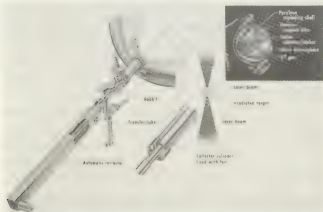


Fig. 6. — Density measurements by neutron activation.

increases thus eliminating the possibility of propagating this radiation out to the detector. Thus, as we go to pusher materials of higher density or higher opacity, we must go to seed materials with higher energy characteristic radiation thus requiring increased fuel temperature to generate the characteristic radiation.

In figure 8 we summarize the density measuring capability of a number of different techniques. We plot the density confinement radius product as a function of the DT neutron yield. The various boundaries in the figure represent the boundary of applicability of various density measuring techniques. In the past with low density targets, we have utilized imaging of the alpha particles to determine the size, shape, and distribution of the burning region of exploding pusher targets [22]. In this figure, we clearly see that this technique is limited to exploding pusher targets since the upper boundary of the density confinement radius product is 10^{-3} g/cm^2 . Thus this technique basically has no applicability for high density, intermediate yield targets. Of course, the technique can be utilized again when we can image the neutrons rather than the alpha particles [9].

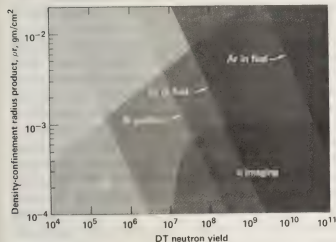


Fig. 8. — Present density diagnostic operating regimes.

The four shaded regions showing Ar, Br, Si, and Cu represent the utilization of radiochemistry either of materials in the fuel, such as Ar or Br, or materials in the pusher, such as Si or Cu. Cu appears to offer a very significant advantage in that density radius products as high as 10^{-2} g/cm^2 can be measured with neutron yields of as low as several 10^4 . The region of usefulness for the Si in the pusher is in the range of 10^6 to 10^8 neutrons. There is only a small shift over to the right for Br in the fuel and thus Br as a seed material in the fuel would be extremely useful in diagnosing the density of $100 \times$ liquid density targets. Ar requires much higher yields in the order of 10^{10} to be useful for determining fuel density. The other boundary placed in this parameter space is

the use of Ar imaging and here we show that as the neutron yield increases, basically the temperature of the fuel and pusher material are increasing thus reducing their opacity and making it possible to propagate the X-ray lines through the material surrounding the fuel. In summary, it appears that Cu is an extremely useful material in the pusher in terms of activation for density determination. The material in the fuel that would be most useful is Br; however, Si is a useful material and can provide information about fuel density for targets with glass pushers with $\rho \Delta r \approx 10^{-2} \text{ g/cm}^2$.

The final diagnostic technique which we wish to discuss in this paper is the use of an auxiliary X-ray backlighting source to provide radiographic information as to the density distribution in the target either as a function of position or as a function of time [23, 24, 25]. In considering this type of diagnostic, we must remember that the laser target itself is a very intense emitting source of X-rays. Therefore, we must provide an X-ray source which has a significantly higher spectral intensity in a spectral regime of interest in order to make radiographic measurements. As shown in figure 9, the concept is simply to use a separate laser source to irradiate an auxiliary target which emits intense line radiation which then passes through the implosion target, is spectrally discriminated by a monochromator of some type, imaged and either recorded as a function of time with a X-ray streak camera or recorded as a flash radiograph with a duration much less than the implosion time of the target. This type of diagnostic is not particularly sensitive as a density diagnostic but rather its importance is as a diagnostic which either provides information on the dynamics or in the flash radiograph mode provides significant information about symmetry of the implosion process.

With the Argus laser system, we have utilized one beam to produce the X-ray source and a static cold multi-shell target to demonstrate this technique. In the particular experiment shown in figure 10, we utilized a Sn disk as the auxiliary X-ray source which produced characteristic L line emission in the range of 3.8 to 4 keV. Actually in our study of

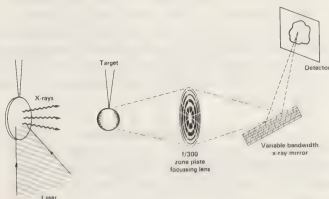


Fig. 9. — X-ray probing/backlighting.

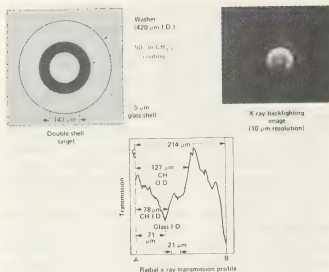


Fig. 10. — X-ray probing results (reconstructed image).

auxiliary targets for X-ray backlighting, we found that Ti, helium like lines were a much more effective source. We showed that in this case we could convert one hundredth of a per cent of the incident laser energy into the helium like lines of Ti, which occur at 4.8 keV thus providing a very intense 400 MW source of line radiation for the probing of our implosion. However, in the demonstration experiment we did utilize the Sn X-ray emission to examine the transmission through a cold static glass microshell 143 μm in diameter, 5 μm wall thickness, with 50 μm of CH plastic. In figure 10, the target is shown schematically on the left. The data from the experiment is shown on the right and the relative intensity of the X-rays transmitted through the static target are shown at the bottom of the figure. This data clearly shows that we can identify the interface between the plastic and the glass and also the interface between the glass pusher and fuel. It is important to note that this will not always be true as the pusher material becomes higher and higher Z material, even with intense sources at 5 keV, we will not be able to penetrate the pusher and accurately determine the boundary between the fuel and the pusher. However, we will still be able to determine the boundary between the pusher and the ablator and to follow its dynamics.

Thus, in summary we have developed a number of, or improved a number of, diagnostic techniques which provide us with significant new information about the plasma interaction, the density of the implosion, or the dynamics and symmetry of the implosion process.

4. Laser plasma interaction experiments. — In our experimental program we are concerned not only with implosion experiments but also with understanding the coupling of the laser energy to the fusion targets. As a result, we have spent a considerable fraction of our resources in developing diagnostic

techniques and methods to examine the interaction physics. In 1975 we first observed the effects of Brillouin scattering on small targets with short pulse lengths [26]. The observation was made by measuring the polarization dependence of the scattered 1.06 μm light. Although the effect was small at that time, it was suspected and predicted theoretically that this would become more evident and become a stronger effect for larger targets and longer pulse lengths. In May 1976 with experiments on Cyclops where larger spot sizes and longer pulses were used, the ratio of the light scattered perpendicular to the plane of polarization compared to the that in the plane of polarization grew to as large as 4 [27]. We felt at this time that this was clear evidence of the existence of Brillouin scattering. Since then we have done a considerable number of additional experiments to examine these effects. One of the clearest signatures of Brillouin scattering is a red shift in the back-scattered light. Since the incident photon is resolved into a sound wave and a backscattered photon, the photon coming back toward the laser must be red shifted. Doppler shifts tend to produce a blue shift of light due to the outward motion of the critical density surface or the surface from which the photons are scattering. Thus one way of observing the effects of Brillouin scattering is to use a spectrograph to spectrally resolve the backscattered light.

In figure 11 we show an example of the use of the spectrograph coupled to a Livermore high speed streak camera to also provide temporal resolution of the spectrally resolved backscattered light. In the experiment shown, the laser oscillator produced a 100 ps pulse which was inserted into a pulse stacker designed to produce a square pulse. Due to the instability in the pulse stacker for this particular application, a significant modulation in the output of the laser was observed. As shown on the right in the figure the output laser pulse contains four well resolved 100 ps pulses. The target was irradiated with this pulse shape and the time resolved spectrum of the backscatter is shown on the left side of the figure. It is interesting to note that the structure observed in the incident pulse is replicated in the

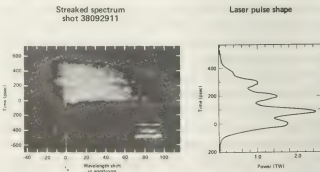


Fig. 11. — Time-resolved spectrum of the back-reflected light shows peak red shift at times of maximum laser power.

time resolved spectral shift of the backscattered light. Also, essentially all of the backscattered light is red shifted which of course does not allow for the effect of the blue shift due to the Doppler effect of the outward moving critical density surface. The amount of light back reflected through the focusing lens is typically about 8-10 %. To obtain an accurate picture of the amount of Brillouin scattering, one must also resolve the side scattered light, i.e., that light which is not back reflected through the focusing lens. For high Z targets irradiated at intensities of the order of mid 10^{14} W/cm² with pulses in the range of 0.5-1.0 ns the typical Brillouin scattering component is 25-30 % of the incident light.

Rosen and Phillion [28] have used the information from the red shift of the Brillouin scattered light to obtain information about the time history of the temperature in the corona of the target. They have shown that the mean spectral shift of the Brillouin scattered light; $\Delta\lambda \sim I_p^{0.3}$. They have also shown that they can obtain temperature information about the corona and that for disks irradiated at about 3×10^{14} W/cm² the corona temperatures are ~ 5 keV whereas for disks irradiated at 3×10^{15} W/cm² the corona temperatures are ~ 20 keV.

We have continued to measure the suprathermal X-ray spectrum from laser irradiated targets in an attempt to determine the suprathermal electron spectrum which is created by the interaction of the laser with the target. Over the years we have accumulated a significant amount of data in this area [29] and as mentioned earlier in the section on diagnostics we have recently implemented the filter fluorescer experiment in an attempt to provide accurate determination of the suprathermal X-ray spectrum. This has been a very useful instrument but unfortunately, it has not led to more repeatable data on the suprathermal X-ray spectrum. In fact with the better definition we have observed even more scatter in the data. One might imagine that there is some unstable process occurring or that there may be a possibility that the distribution of high energy X-rays is not isotropic in space. In fact, Yablonovich has shown in an experiment with a CO₂ laser that the electrons produced by resonance absorption are significantly directional. Thus one might expect that if these electrons are not scattered sufficiently in high Z target that they will produce a nonisotropic distribution of high energy X-rays. To examine this question, we fielded a number of NaI photodiode detectors filtered with Be and Cu [31]. The response function of these detectors to X-rays is effectively that of a calorimeter above 35 keV.

These detectors were utilized on Shiva. They were arrayed primarily to view the polar variation since this was the suspected direction of largest variation. However, we also arrayed several detectors at a constant polar angle in various azimuthal positions. The data from three target shots on Shiva are shown

in figure 12. The first two experiments were gold disks irradiated with the lower ten beams of Shiva. Ninety degrees in the figure represents the plane of the target. Zero° is the axis of the upper ten beams and 180° is the axis of the lower ten beams. The third experiment was a glass microshell target irradiated with all twenty beams and it produced nearly the same distribution of high energy X-rays in space. As shown in the lower part of the figure the azimuthal distribution of the X-rays at the upper peak of the polar distribution shows no variation for the three points obtained. One should also note that the Shiva beams on the gold disk or glass shell target approximate a radial distribution of polarization. Thus one would expect that whatever distribution was obtained would be axially symmetric as is the case shown by the data. The highly directional nature of the high energy X-rays on these experiments is very suggestive of a directional distribution of high energy electrons. Resonance absorption would tend to produce an oscillation of the high energy electrons into the surface of the disk. However, the angle of the lobes appears to suggest that the electrons are oscillating along the surface of the disk. This conclusion seems to be more reasonable because the energy associated with the angle of the lobes with respect to the horizontal, if the electrons are oscillating parallel to the surface of the disk, would correspond to approximately 200 keV electrons whereas if the elec-

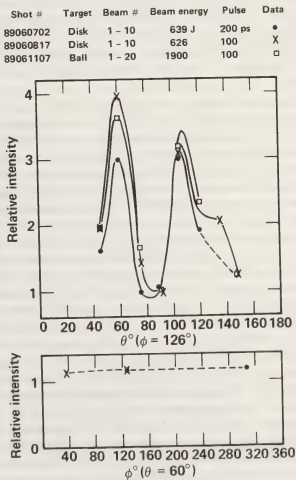


Fig. 12. — High energy X-ray angular distribution.

trons were oscillating perpendicular to the surface of the disk, the angle of the lobes would correspond to 5 keV electrons. This data certainly suggests additional experiments to determine more completely the nature of the electron spatial distribution.

We have also done a series of experiments to examine the X-ray emission from various Z disk materials. The primary purpose of this particular series was to examine the viability of various materials as X-ray backlighting sources for the diagnostic technique discussed earlier in § 3. However, in addition, using the Dante spectrometers, we obtained information about the overall emission of X-rays from these various Z disk materials [32]. As expected the fraction of X-rays emitted compared to the laser energy increased uniformly with increasing Z although appearing to saturate in the region of Au and U. Since the experiments were all done at one intensity, this is quite reasonable as one would expect that the effective Z of the plasma would not continue to increase unless the intensity were also increased. However, we also observed in one experiment where we increased the laser intensity on the target to $3 \times 10^{15} \text{ W/cm}^2$ from $5 \times 10^{14} \text{ W/cm}^2$, that there was a drastic reduction in the number of X-rays emitted by the target. This is a very interesting result and we examined the effect further by looking at the Dante signal from the 520 eV channel of the Dante spectrometer. This particular channel had the Thompson CSF TSN 660 oscilloscope connected to the detector which gave it an overall response time of 190 ps. Since the laser pulse was one nanosecond FWHM, we obtained significant information about the variation of the X-ray emission as a function of time.

Shown in figure 13 are the signals from this detector for Be, Ti, Sn, Au, and U. The interesting thing to note is the apparent broadening of the FWHM as we decrease the Z of the material. However, as we examine the various signals, we see that it is really more a distortion of the shape of the signal rather than an increase in the FWHM of a Gaussian pulse. The U signal appears to be quite Gaussian. However, the Au signal appears to have a small distortion near the peak of the pulse. The distortion is much more apparent with Sn and completely obvious with the Ti where it appears that the X-ray emission was rising normally and then was somehow clamped and not allowed to increase. Then the Be signal takes on more meaning, indicating that the clamping of the X-ray emission occurred very early in the pulse. Now with Be one would expect that the plasma is completely stripped and therefore the X-ray emission is solely from bremsstrahlung and therefore we would not expect to see the effect of stripping of the electrons during the pulse. One can interpret this data as some kind of mechanism which is inhibiting the emission of X-rays by the target as the intensity increases.

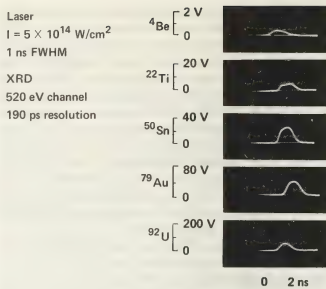


Fig. 13. — Z dependence of the time-resolved sub-keV X-ray emission from laser-produced plasmas.

The one experiment that was done with gold at the higher intensity is shown in figure 14 along with the data for the lower intensity. The appearance of an apparent inhibition mechanism is quite striking in this case. As the pulse comes up for the higher intensity, the X-ray emission is quickly clamped and we clearly see the effect of fewer X-rays being emitted at the higher intensity for this target. It should be remembered that in this case the intensity was changed simply by changing the size of the focal spot. One interpretation of these results could be to determine an intensity threshold for thermal conduction inhibition which has been observed in other experiments [26, 28]. At this point again many more experiments are suggested and this effect will be further investigated in the future.

In our program of examining the laser plasma interaction processes we continue to uncover new phenomena or if not new phenomena at least new

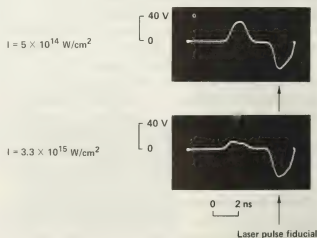


Fig. 14. — Time-resolved sub-keV X-ray emission for Au-disks at different laser intensities (XRD : 940 eV Channel, 170 ps resolution).

signatures of these phenomena. We have only brought up a few of the important salient points in the laser plasma interaction section. Clearly there are many more that are being investigated and will be investigated in the future.

5. Implosion experiments.— The experiments that were performed on Shiva as it was being brought into activation were all of the exploding pusher, low density nature. These experiments were designed to prove the quality of the laser operation. Thus these experiments were performed with single beam illumination, four beam illumination, ten beam illumination from one side, and finally with all twenty beams from both sides. After the system activation was complete, we began a series of experiments with all twenty beams to further demonstrate the performance of the system using the exploding pusher, low density targets. One of the alignment aids that has been implemented on the Shiva system is a system called Litar. This is a code which allows one to take the designated lens coordinates for a particular irradiation pattern and display the calculated absorption pattern on a color television screen. This code has proved extremely useful for the experimentalist and the target designer to arrive at an irradiation geometry. The polar microscope which is centered in the upper cluster of ten beams of the Shiva system provides X-ray spatial distributions which can be compared with the Litar predictions. This code and this diagnostic instrument have given useful information about the symmetry and the azimuthal distribution of the absorbed energy from this polar view. A four channel X-ray microscope also views the target at 90° to the center line of the beam clusters.

The typical color enhanced X-ray micrograph and the 2D computer calculation of the X-ray distribution using the two dimensional glow code are shown in figure 15. The experiment and the calculation show that most of the absorption occurred on the pole caps of the spherical microshell target and that there was significant distortion from spherical symmetry in the implosion and burn of the fuel. This was further demonstrated by data taken with the alpha zone plate camera which images the distribution of the alpha particles from the burn. This data along with

the indicated $\rho \Delta r$ measurement from the neutron activation of the SiO₂ pusher are shown in figure 16. From the alpha zone plate camera one would infer an average density of 0.1 g/cm³ or approximately 0.5 × liquid density. The radiochemistry measurement of the silicon pusher $\rho \Delta r$ gave a value of approximately 7×10^{-4} gm/cm². Using the simple theory of exploding pusher targets [33], one can calculate the target performance which gives the fuel density and the $\rho \Delta r$ of the pusher. This calculation has been made and is in reasonable agreement with the alpha zone plate image data.

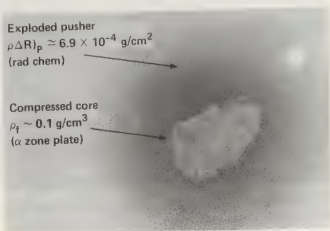


Fig. 16. — Neutron activation.

We have also utilized the argon line imaging technique with these exploding pusher targets since $\rho \Delta r < 10^{-3}$ gm/cm². A slitted spectrograph has been used to provide one dimensional spatial imaging of the emission from the fuel and corona regions. Potassium lines from the potassium trace element in the glass pusher produce images which extend out into the corona and also provide an image of the outer region of the stagnated pusher. The argon inside the glass microshell provides a spatial distribution of the helium like and the hydrogen like alpha lines. These lines are very well resolved spectrally and produce distributions which have base widths of approximately 50 μ m and 45 μ m respectively. The difference in the spatial extent of the helium like and hydrogen like lines implies either a temperature gradient across the fuel pusher interface or more likely the time integration effect due to the temperature rising as the stagnation of the pusher and the fuel occurs. As the pusher and fuel stagnate, the temperature rises rapidly and one would expect that the helium like lines would be excited before the hydrogen like lines and therefore the spatial extent of the helium like lines would be expected to be greater than that of the hydrogen like lines. The point to be made here is that any time integrated emission from the fuel region requires significant code interpretation to determine the density and is not a simple straightforward diagnostic of the final fuel density.

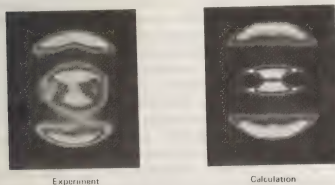


Fig. 15. — 2.0 keV X-ray photomicrograph (Shiva 88100604).

We have also implemented our zone plate camera in the coded imaging mode to image the high energy X-rays from the fuel region. Figure 17 shows one of our gold zone plates which has been implemented with a stack of films and filters to produce a large dynamic range for an individual energy and to produce images at successively higher energies through the film stack.

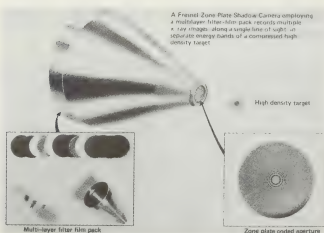


Fig. 17. — Multi-spectral X-ray imaging of compressed high density target (technique).

In figure 18 we summarize the density and neutron yield achieved for three classes of targets. The data in the lower right hand corner at neutron yields of the order of 10^{10} are from exploding pusher targets irradiated with Shiva. The density in this case is determined utilizing alpha imaging and typically we achieve approximately $0.5\text{--}1.0 \times$ liquid density where these targets typically started from densities of about $0.01 \times$ liquid density. The second class of targets typically achieved from $4\text{--}10 \times$ liquid density. As can be seen, we produced lower neutron yield for these experiments while we achieved essentially a factor of ten higher final fuel density. The last series of experiments achieved densities in the range of 40 to $150 \times$ liquid density and again we were required to

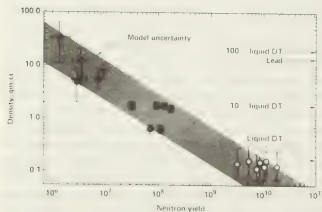


Fig. 18. — Fuel density at burn time versus neutron yield.

lower the temperature of the final fuel in order to achieve these densities.

In the coming years as we continue to push to higher and higher densities, the things that must be done are to operate Shiva at its full energy capability for long pulses and to be able to fabricate the targets which have been designed to achieve these higher densities. The success of the program in achieving these ablative driven implosions over the last year gives us a high degree of confidence in achieving the fabrication requirements, the laser irradiation requirements and the diagnostics to measure the achieved densities. The program is now well on its way towards achieving densities of interest for inertial confinement fusion reactors. In fact, the αT products are now in the range of several times 10^{14} . We have already demonstrated with low density implosion targets that we can achieve the temperatures required for ignition. So now the problem remains to achieve densities in the range of $1\,000$ to $10\,000 \times$ liquid density and at the same time drive the target to temperatures appropriate to ignition, break even and finally net energy gain.

6. Laser fusion reactor requirements and characteristics. — Our System's Studies Program has been conducting studies for a significant period of time to determine the requirements for an inertial confinement fusion reactor driver. This of course also includes studies of reactor target design by our target design group. Presently, it appears that the range of energies which may be required to produce a significant gain target to drive a fusion reactor is $0.5\text{--}3.0$ MJ. The power requirements range from 100 to 400 TW. The efficiency of the required driver is determined primarily by the target gain. Optimistic estimates of target gain are as high as $1\,000$; more pessimistic values range down to as low as 200 . With these gains, powers and energies, the repetition rate for an appropriate fusion reactor appears to lie in the range of one to ten Hertz. The requirement on pointing accuracy is tens of microradians from the final laser mirror or focusing element to the target.

The two final most important requirements are the ability to focus over large distances so as to prevent damage to the final optical element and the preheat characteristics of the driver. In a fusion reactor where a typical energy release may be in the order of the equivalent of hundreds of pounds of TNT, it is clear that the final element which focuses the beam must be a significant distance from this repetitive reaction. The two most likely candidates which satisfy this requirement are lasers and heavy ion beams which both can be focused from large distances to the appropriate target diameter of approximately 5 mm. Finally, the selection of the driver must take into account the requirements on minimizing the preheat caused in the fuel and inner pushers by high energy

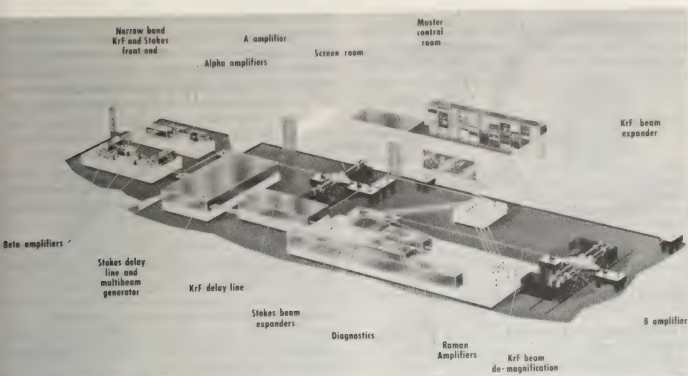


Fig. 19. — RAPIER : a laser pulse compressor testbed.

particles. It is for this reason that CO_2 lasers look less favorable than lasers operating in the 3000 \AA to $1.0 \mu\text{m}$ wavelength regime.

A laser system which looks particularly attractive from the point of view of efficiency, architecture and wavelength from the plasma physics point of view is the KrF laser [34]. It has a wavelength of 2490 \AA with a radiative life time of 6 ns. The 6 ns of course identifies it as a nonstorage medium and therefore we must find a way of efficiently pumping the medium and extracting the laser energy over times of the order of a microsecond but with pulse lengths of the order of 10 ns. The intrinsic efficiency of such a laser is 24 % and projected efficiencies for a real system are as high as 10 %. 2 % has already been demonstrated. There are two approaches to extracting the laser energy in a short time from a long pulse excitation. One is simply the reinvention of the pulse compression method which involves running short pulses through in sequence and then recombining them with mirrors to provide a single short pulse. The second is to use Raman scattering as a method of compressing the pulse in time.

In figure 19 we show schematically the test bed system which is being fabricated at the Livermore Laboratory to investigate the questions of the physics of the KrF laser, the optical properties and the problems of stacking and pulse compression by Raman means to provide the necessary short pulse. This system utilizes the double discharge configuration for the oscillator and amplifiers up to an energy of several joules and then utilizes the electron beam excitation of the gain medium for amplifiers to produce

energies of 20 and 200 J at the final output. The 200 J is provided in a long pulse and then studies will be made to determine our ability to compress this pulse by means of stacking and by Raman compression.

From the point of view of the target physics and laser physics, the KrF laser now appears to be one of the most promising concepts. However, the shortness of the wavelength is worrisome in that present experiments on damage thresholds indicate that materials will not stand more than 1 J/cm^2 as compared to damage thresholds of $4\text{--}10 \text{ J/cm}^2$ for wavelengths in the range of $0.5\text{--}1.0 \mu\text{m}$. In any case, the program is building a test bed to study these questions and to determine the viability of KrF or other rare gas halide lasers as fusion reactor drivers.

Our System Study Program has also been working diligently on reactor configurations. The most promising which we have come up with is the so-called Hylife chamber [35]. The basic concept here is to move the Li blanket from outside of the reactor vessel and place it inside in the form of jets surrounding the implosion explosion region. In figure 20 we show schematically how these jets would be arranged to allow the beams to enter the interaction regime and still provide the effective Li thickness to absorb the neutrons, reduce the power flux of neutrons on the first wall of the reactor, and radically alter their spectral distribution to that of more nearly a thermal distribution of neutrons. In table I we list the characteristics of the Hylife chamber. The major point to note is that we have reduced the first wall neutron fluence from approximately 6 MW/m^2 to 0.3 MW/m^2

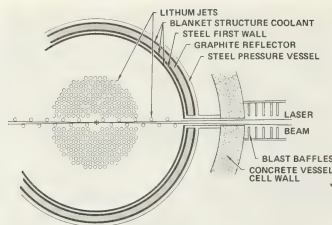


Fig. 20. — Hylife chamber cross section.

Table 1. — Hylife chamber characteristics.

Fusion energy yield per shot	2 700 MJ
Repetition rate	1 Hz
Effective lithium thickness	1 m
Lithium jet diameter at midplane	20 cm
Lithium jet velocity at inlet	4.4 m/s
Lithium pumping power	17 MW _e
Lithium temperature (ave.)	500 °C
Temperature rise in lithium per shot	11 °C
Tritium breeding ratio	1.7
First wall radius	5 m
First wall neutron fluence with lithium	0.32 MW/m ²
First wall neutron fluence without lithium	5.76 MW/m ²

for a reduction in flux of a factor of twenty. Further, the spectrum of the neutrons is significantly softer thus reducing the concern for first wall damage due to the neutron fluence. Utilizing this concept, we show in figure 21 a reactor concept. The salient features of this system are that the laser building, the building where the laser pulses are generated, is separate from the containment building where there are significant requirements on the containment of radioactive material produced in the reaction chamber and its surroundings. Thus the high technology

optical system is removed a significant distance and does not have the same containment requirements. The laser beams enter through containment release sections into the laser reactor chamber producing the reaction. Also, the electrical generating equipment, as in a fission reactor, is also separated from the stringent containment requirement building which contains the radioactive material. This Hylife concept may not be the one that is finally implemented as an inertial confinement fusion reactor but it provides a number of very useful features and characteristics against which we can judge any other reactor configuration proposal.

7. Summary. — Over the last several years we have made significant progress in the understanding of the laser plasma interaction through the use of new diagnostic instrumentation and techniques. We have also implemented the Shiva system and operated the world's most complex laser system and produced significant target data. In the implosion experiments with the Shiva system, we have achieved densities greater than $100 \times$ liquid density of DT. The significance of this result is that we have had to overcome the questions of achieving a spherically symmetric implosion and obviating the problem of Rayleigh-Taylor instability. We see no major obstacle in the future to attaining the densities appropriate to efficient burn of microfusion pellets for application to fusion reactors. Further, we have identified a laser system which may provide the architecture required for a fusion reactor driver and we have an aggressive ongoing program to investigate this option for a fusion reactor driver. In addition, our Systems Studies Program has identified a reactor configuration which solves many of the important problems associated with laser fusion reactors. This is not to say that the question of the configuration of an inertial confinement fusion reactor has been settled but rather that there is a very attractive possibility and one which can be used to judge other possibilities and grade them with respect to their performance compared to the Hylife reaction chamber.

Thus we hold great hope for the possibility of inertial confinement fusion as an eventual energy source to provide energy for the world.



Fig. 21. — Hylife fusion reactor.

Acknowledgments. — In the preparation of this paper I have drawn from LLL's total Laser Fusion Program. The Program Office provides overall Program direction, the Solid State Program is responsible for our present and future target irradiation facilities, the Advanced Quantum Electronics Program is responsible for identifying future reactor drives and our Systems Studies Group provides the reactor systems information. The major thrust of this paper has been to present the diagnostics and experimental data provided by the Fusion Experiments Program which is closely coupled to the Targets Program. These two programs encompass Code Development,

Plasma Theory, Target Design, Target Fabrication, Diagnostics Development, Diagnostics Operation, Experiments Operation and Data Management and Analysis. The outstanding accomplishments of these two programs and their groups are directly responsible for the results presented in this papers.

In addition the author thanks those physicists who provided direct assistance in the preparation of the graphics presented in this review of our program. The author especially thanks Mrs. Sanford for her efforts in the organization and preparation of this manuscript.

References

- [1] NUCKOLLS, J., WOOD, L., THIESSEN, A., ZIMMERMAN, G., *Nature* **239** (1972) 139.
- [2] SLIVINSKY, V. W., AHLSTROM, H. G., TIRSELL, K. G., LARSEN, J., GLAROS, S., ZIMMERMAN, G. and SHAY, H., Measurement of the Ion Temperature in Laser Driven Fusion, *Phys. Rev. Letts.* **35**, no 16, 20 October 1975, p. 1083-1085.
- [3] DAHLBACKA, Glen and NUCKOLLS, John, *Laser Driven Isothermal Implosions*, Lawrence Livermore Laboratory UCRL 75885, 28 October 1974.
- [4] AUERBACH, J. M. et al., Neon Spectral Line Broadening as a Diagnostic for Compressed Laser Fusion Targets, *J. of App. Phys.*, July 1979.
- [5] *LLL Laser Fusion Monthly*, MM 79 2, February 1979.
- [6] LINDL, J. D. and MEAD, W. C., Two Dimensional Simulation of Fluid Instability in Laser Fusion Pellets, *Phys. Rev. Letts.* **34**, no 20, 19 May 1975, p. 1273-1276.
- [7] SPECK, D. R. et al., Performance of the Shiva Laser Fusion Facility, *LLL UCRL 82117*, presented at the 1979 IEEE/OSA Conference on Laser Engineering and Applications, Washington, D.C., May 30-June 1, 1979.
- [8] GILMARTIN, T. J., Nova, the Laser Fusion Scientific Feasibility Experiment, *LLL UCRL 82094*, presented at the 1979 IEEE/OSA Conference on Laser Engineering and Applications, Washington, D.C. May 30-June 1, 1979.
- [9] AHLSTROM, H. G. et al., Diagnostics of Shiva Nova High Yield Thermonuclear Events, *J. Opt. Soc. Am.* **68**, no 12, December 1978, p. 1731-1741.
- [10] AUERBACH, J. M. et al., Janus Neodymium Glass Laser Operations Manual, *LLL UCID 17952*, 29 September 1978.
- [11] BLISS, E. S. et al., Cyclops Laser System, *LLL Laser Program Annual Report*, 1977, p. 69-74.
- [12] SPECK, D. R. et al., The Performance of Argus as a Laser Fusion Facility, *LLL UCRL 79816*, presented at the 11th European Conference on Laser Interaction with Matter, Oxford, England, 19 September 1977.
- [13] HUNT, J. T. et al., Improved Performance of Fusion Lasers using the Imaging Properties of Multiple Spatial Filters, *Applied Optics* **16**, no 4, April 1977, p. 779-782.
- [14] BLISS, E. S. et al., Beam Alignment, *LLL Laser Program Annual Report*, UCRL 50021-76, 1976, p. 2-141/2-145.
- [15] HOLLOWAY, F. W. et al., Alignment Control Subsystem, *LLL Laser Program Annual Report*, UCRL 50021-76, 1976, p. 2-147/2-155.
- [16] OZARSKI, R. G. et al., Beam Diagnostics, *LLL Laser Program Annual Report*, UCRL 50021-76, 1976, p. 2-155/2-169.
- [17] O'NEAL, W. C. et al., Target Chamber, *LLL Laser Program Annual Report*, UCRL 50021-76, 1976, p. 2-2-169/2-2-181.
- [18] GREENWOOD, James R. et al., Control for the Shiva Laser System, *Industrial Research*, November 1977.
- [19] TIRSELL, K. G. et al., Time Resolved, Sub-keV, X-Ray Measurements using Filtered, X-Ray Diodes, *Bull. Am. Phys. Soc.* **23**, no 7, September 1978.
- [20] KORNBLUM, H. N., Filtered Fluorescer Experiment on the Argus Laser, *Bull. Am. Phys. Soc.* **23**, no 7, September 1978.
- [21] CAMPBELL, E. M., Diagnostics of High Density Targets by Neutron Activation Techniques, *Bull. Am. Phys. Soc.* **23**, no 7, September 1978, p. 803.
- [22] CAMPBELL, E. M., Collection Fraction Determination Utilizing a Radioactive Tracer, being prepared for submission to *J. of Appl. Phys.*
- [23] CAMPBELL, E. M., *Fuel pR of ICF Targets by Neutron Activation*, being prepared for submission to *J. of App. Phys.*
- [24] ERIK, K., Storm memorandum, A Simple Way of looking at $\langle p \rangle_{fuel}$ vs. effective pusher ($p \Delta r$) for High Density Targets, *Internal memorandum LPIG-79-0534*, 22 March 1979.
- [25] CAMPBELL, E. M., *Exploding Pusher Tamper p ΔR Measurement by Neutron Activation*, being prepared for submission to *Phys. Rev. Letts.*
- [26] KOPPEL, L. N. et al., *Diagnosis of Laser Produced Implosions using Argon X-Ray Lines*, being prepared for submission to *Phys. Rev. Letts.*
- [27] CEGLIO, N. M. and COLEMAN, L. W., Spatially Resolved α Emission from Laser Fusion Targets, *Phys. Rev. Letts.* **39**, no 1, 4 July 1977, p. 20-24.
- [28] HOLZRICHTER, J. F. et al., X-Ray Point Source Projection Photography with a Laser Produced Source, *Appl. Phys. Letts.* **23**, no 12, 15 December 1973.
- [29] HAAS, R., X-Ray Schlieren and Interferometry, *LLL Laser Program Annual Report*, UCRL 50021-74, 1974, p. 329-333.
- [30] KUIZENZA, D. J., Actively Mode-Locked and Q-Switched Oscillator, *LLL Laser Program Annual Report*, LLL UCRL 50021-77, 1977, p. 2-207/2-210.
- [31] MURRAY, J. E., Regenerative Pulse Compression, *LLL Laser Program Annual Report*, LLL UCRL 50021-77, 1977, p. 2-210-2-219.
- [32] SHAY, H. et al., Interaction of 1.06 μm Laser Radiation with Variable Z Targets, *Phys. of Fluids* **21**, September 1978, p. 1634-1636.
- [33] PHILLION, D. W. et al., Evidence for Profile Steepening in Laser Irradiated Plasmas, *Phys. of Fluids* **20**, no 11, November 1977, p. 1892-1899.
- [34] ROSEN, M. D., The Interaction of 1.06 μm Laser Radiation with High Z Disk Targets, *LLL UCRL 82146* to be published in the *Phys. of Fluids*, October 1979.
- [35] MANES, K. R. et al., Light Plasma Interaction Studies with High Power Glass Lasers, *J. Opt. Soc. Am.* **67**, no 6, June 1977.
- [36] YABLONOVITCH, Eli, Plasma Resonance in the X-Ray Emission from Gaseous Laser Targets, *Phys. Rev. Letts.* **35**, no 20, 17 November 1975, p. 1346-1349.
- [37] WANG, C. L. et al., *Superthermal X-Ray Angular Distribution from Laser Produced Plasmas*, presently being prepared for presentation to the American Physical Society meeting, Boston, Mass., 12 November 1979.
- [38] MCCLELLAN, G., LEE, P. H. Y. and CAPORASO, G., *Z Dependence of Laser Intensity Threshold for Inhibited Electron Conduction*, presently being prepared for submission to *Phys. Rev. Letts.*
- [39] STORM, E. K., A Simple Model for Exploding Pusher Targets, *LLL Laser Program Annual Report*, LLL UCRL 50021-77, 1977, p. 6-38/6-46.
- [40] EWING, J. J. et al., Optical Pulse Compressor Systems for Laser Fusion, *IEEE J. Quantum Electronics*, **Qe-15**, no 5, May 1979, p. 368-379.
- [41] MONSLER, Michael J. et al., *Electric Power from Inertial Confinement Fusion. The Hylife Concept*, presented at the Heavy Ion Inertial Confinement Fusion Workshop, Argonne National Laboratory, 19-26 September 1979.

Kinetic theory of spectral line broadening in a nonequilibrium plasma

Yu. L. Klimontovich

Moscow State University, USSR

1. Introduction. — The theory of spectral line broadening has been developed for many years. On can find an account of its recent achievement in a number of monographs and reviews [1-7]. Up till now, however, most attention was focused on the problems of the radiation of ideal and equilibrium plasmas. Relatively few papers have been published, where nonideal and nonequilibrium broadening effects in plasmas were considered. Among them there are papers in which the influence of Debye screening [8, 9], of turbulence [10-13], of the nonequilibrium velocity distribution of charged particles [14] are investigated. The complexity of such problems is obvious.

No attempt is made here to give a complete survey on the recent achievements in the theory of spectral line broadening in nonideal and nonequilibrium plasmas; this is impossible in a short report.

The main purpose of this report is to show how the theory of spectral line broadening in nonequilibrium plasmas can be included into the modern kinetic theory of partly ionized plasmas.

The partly-ionized plasma is an example for a many component system with chemical reactions. Therefore the kinetic theory of this system is very complicated. We have no possibility here to discuss all processes. We shall restrict ourselves to ones which can be described by taking into account the long range interactions between the particles and the interaction with the electromagnetic field.

For this reason we shall first consider kinetic equations the corresponding cross sections of which are calculated in the polarisation approximation. This means that the cross sections are determined in the Born approximation, but with the dynamical polarization taken into account. At the end of the report we shall briefly discuss the possibility of simultaneous inclusion of both the strong interactions at small distances (to leave the Born approximation) and long range collective interactions.

The list of references contains, mainly, books and reviews, while original articles were included only where they were more or less used in the preparing this report.

2. The basic microscopic equations. — **2.1 THE FULLY IONISED PLASMA.** — In the statistical theory of a fully ionised plasma it is possible to use as the starting point the closed system of equations for the

microscopic phase densities in the sixdimensional space of each component of the plasma

$$N_a(x, t) = \sum_{1 \leq i \leq N_a} \delta(x - x_{ia}(t)), \quad x = (\mathbf{r}, \mathbf{p}) \quad (2.1)$$

and the microscopic electric and magnetic fields $\mathbf{E}^M, \mathbf{B}^M$. These equations are [15-17]

$$\frac{\partial N_a}{\partial t} + \mathbf{v} \frac{\partial N_a}{\partial \mathbf{r}} + e_a \left(\mathbf{E}^M(\mathbf{r}, t) + \frac{1}{c} [\mathbf{v} \mathbf{B}^M(\mathbf{r}, t)] \right) \times \frac{\partial N_a}{\partial \mathbf{p}} = 0,$$

$$\text{rot } \mathbf{B}^M = \frac{1}{c} \frac{\partial \mathbf{E}^M}{\partial t} + \frac{4\pi}{c} \sum_a e_a \int \mathbf{v} N_a(\mathbf{r}, \mathbf{p}, t) d\mathbf{p},$$

$$\text{rot } \mathbf{E}^M = - \frac{1}{c} \frac{\partial \mathbf{B}^M}{\partial t}, \quad (2.2)$$

$$\text{div } \mathbf{B}^M = 0,$$

$$\text{div } \mathbf{E}^M = 4\pi \sum_a e_a \int N_a(\mathbf{r}, \mathbf{p}, t) d\mathbf{p}.$$

For given experimental conditions these functions are random functions.

In the case of the Coulomb plasma the system of equations for the random functions N_a, \mathbf{E}^M is simpler, namely

$$\frac{\partial N_a}{\partial t} + \mathbf{v} \frac{\partial N_a}{\partial \mathbf{r}} + e_a \mathbf{E}^M(\mathbf{r}, t) \frac{\partial N_a}{\partial \mathbf{p}} = 0, \quad (2.3)$$

$$\text{rot } \mathbf{E}^M = 0, \quad \text{div } \mathbf{E}^M = 4\pi \sum_a e_a \int N_a(\mathbf{r}, \mathbf{p}, t) d\mathbf{p}.$$

2.2 THE MONOATOMIC GAS. — In the statistical theory of a monoatomic gas it is possible to use, as a starting point, the exact equations for the microscopic phase density

$$N(x, t) = \sum_{1 \leq i \leq N} \delta(x - x_i(t)), \quad x = (\mathbf{r}, \mathbf{p}) \quad (2.4)$$

and microscopic force $\mathbf{F}^M(\mathbf{r}, t)$

$$\frac{\partial N}{\partial t} + \mathbf{v} \frac{\partial N}{\partial \mathbf{r}} + \mathbf{F}^M(\mathbf{r}, t) \frac{\partial N}{\partial \mathbf{p}} = 0, \quad (2.5)$$

$$\mathbf{F}^M(\mathbf{r}, t) = - \text{grad} \int \phi(|\mathbf{r} - \mathbf{r}'|) N(\mathbf{r}', \mathbf{p}', t) d\mathbf{p}' d\mathbf{r}'.$$

With this method of description the statistical theory of nonequilibrium processes in plasmas can be reduced to determining the first, second and higher moments of the random functions N_a , \mathbf{E}^M , \mathbf{B}^M .

It is possible to connect these moments with the distribution functions f_1, f_2, f_3, \dots . Therefore the B-B-G-K-Y chain if equations can be obtained with the help of eq. (2.3).

2.3 THE BASIC EQUATIONS FOR A PARTLY-IONISED PLASMA [15-17]. — A fully ionised plasma and a monoatomic gas are two limiting cases of the partly-ionised plasma.

The kinetic theory of a partly-ionised plasma is much more complicated. This is due to the need to take into account intramolecular motions and ionisation and recombination processes.

In the simplest case the partly-ionized plasma consists of three components: electrons, singly-charged ions, and atoms. The first two components

will be designated by the indices $a \equiv e, b \equiv i$, and the third by the double index $ab \equiv ei$.

The charged particles of components a, b will be called *free* and those of the component ab will be called *bound*. The system as a whole is neutral, so that the total number of negatively charged particles (both free and bound) is equal the total number of positively charged particles. We denote this number by N . Here (in this respect) we restrict our discussion to the case of a Coulomb plasma.

We can use now as the starting point the equation for the microscopic phase density of pairs of charged particles in the twelvedimensional space

$$r_a p_a r_b p_b \equiv x_a x_b.$$

In the classical theory the microscopic density N_{ab} is given by definition

$$N_{ab}(x_a, x_b, t) = \sum_{1 \leq i \leq N} \delta(x_a - x_{ai}(t)) \delta(x_b - x_{bi}(t)). \quad (2.6)$$

The corresponding quantum function is the operator of the phase density. It is defined by

$$\hat{N}_{ab}(x_a, x_b, t) = \frac{N}{(2\pi)^6} \int \hat{\rho}_{ab} \left(\mathbf{r}_a \pm \frac{1}{2} \hbar \boldsymbol{\gamma}_a, \mathbf{r}_b \pm \frac{1}{2} \hbar \boldsymbol{\gamma}_b, t \right) e^{-i(\boldsymbol{\gamma}_a \mathbf{p}_a + \boldsymbol{\gamma}_b \mathbf{p}_b)} \left(\frac{2\pi\hbar}{V} \right)^2 d\boldsymbol{\gamma}_a d\boldsymbol{\gamma}_b. \quad (2.7)$$

Here $\hat{\rho}_{ab}$ is the corresponding operator density matrix.

Instead of the variables $\mathbf{r}_a, \mathbf{r}_b$, it will be more convenient to use

$$\mathbf{R} = (m_a \mathbf{r}_a + m_b \mathbf{r}_b)/M, \quad \mathbf{r} = \mathbf{r}_a - \mathbf{r}_b, \quad M = m_a + m_b. \quad (2.8)$$

The equation for the operator density matrix $\hat{\rho}_{ab}(\mathbf{R}', \mathbf{r}', \mathbf{R}'', \mathbf{r}'', t)$ takes the form

$$i\hbar \frac{\partial \hat{\rho}_{ab}}{\partial t} = - \left[\frac{\hbar^2}{2M} (\Delta_{\mathbf{R}'} - \Delta_{\mathbf{R}'}) + \frac{\hbar^2}{2\mu} (\Delta_{\mathbf{r}'} - \Delta_{\mathbf{r}'}) \right] \hat{\rho}_{ab} + \\ + [\phi_{ab}(|\mathbf{r}'|) + \hat{U}_{ab}(\mathbf{R}', \mathbf{r}', t) - (\phi_{ab}(|\mathbf{r}''|) + \hat{U}_{ab}(\mathbf{R}'', \mathbf{r}'', t))] \hat{\rho}_{ab}. \quad (2.9)$$

The operator \hat{U}_{ab} is determined by the operator of the electric potential $\hat{\phi}$ by the relation

$$\hat{U}_{ab} = e_a \hat{\phi} \left(\mathbf{R} + \frac{m_b}{M} \mathbf{r}, t \right) + e_b \hat{\phi} \left(\mathbf{R} - \frac{m_a}{M} \mathbf{r}, t \right), \quad \phi_{ab} = e_a e_b / |\mathbf{r}|. \quad (2.10)$$

The equation for the electric potential $\hat{\phi}$ can be represented in the form

$$\Delta \hat{\phi}(\mathbf{q}, t) = -4\pi \int \left[e_a \delta \left(\mathbf{q} - \left(\mathbf{R} + \frac{m_b}{M} \mathbf{r} \right) \right) + e_b \delta \left(\mathbf{q} - \left(\mathbf{R} - \frac{m_a}{M} \mathbf{r} \right) \right) \right] \hat{\rho}_{ab}(\mathbf{R}, \mathbf{R}, \mathbf{r}, t) \frac{d\mathbf{R} d\mathbf{r}}{V^2}. \quad (2.11)$$

The eqs. (2.9)-(2.11) are the basic microscopic (operator) equations for a partly-ionized plasma. It is possible to obtain with the help of this system the eq. (2.5) (for the fully ionized Coulomb plasma).

In order to separate the free and the bound states and to describe transitions between them, we shall use eigenfunctions of the energy operator of an individual atom. They are defined by the equation

$$-\frac{\hbar^2}{2\mu} (\Delta_{\mathbf{r}} + \phi_{ab}) \Psi_a(\mathbf{r}) = E_a \Psi_a, \quad -\frac{\hbar^2}{2M} \Delta_{\mathbf{R}} \Psi_{\mathbf{P}}(\mathbf{R}) = E_{\mathbf{P}} \Psi_{\mathbf{P}}. \quad (2.12)$$

We can represent now the density operator in the form

$$\hat{\rho}_{ab}(\mathbf{R}', \mathbf{r}', \mathbf{R}'', \mathbf{r}'', t) = \left(\frac{V}{(2\pi\hbar)^3} \right)^2 \sum_{\beta} \int \hat{\rho}_{\beta\beta}(\mathbf{P}', \mathbf{P}'', t) \Psi_a(\mathbf{r}') \Psi_b^*(\mathbf{r}'') \cdot \Psi_{\mathbf{P}'}(\mathbf{R}') \Psi_{\mathbf{P}''}^*(\mathbf{R}'') d\mathbf{P}' d\mathbf{P}''. \quad (2.13)$$

From (2.9)-(2.13) we obtain a system of equations for the operator $\hat{\rho}_{\alpha\beta}(\mathbf{P}', \mathbf{P}'', t)$

$$i\hbar \frac{\partial \hat{\rho}_{\alpha\beta}}{\partial t}(\mathbf{P}', \mathbf{P}'', t) = (E_\alpha + E_{\mathbf{P}'} - E_\beta - E_{\mathbf{P}''}) \hat{\rho}_{\alpha\beta}(\mathbf{P}', \mathbf{P}'', t) + \frac{V}{(2\pi\hbar)^3} \sum_{\gamma} \int [\hat{U}_{\alpha\gamma}(\mathbf{P}', \mathbf{P}, t) \hat{\rho}_{\gamma\beta}(\mathbf{P}, \mathbf{P}'', t) - \hat{\rho}_{\alpha\gamma}(\mathbf{P}', \mathbf{P}, t) \hat{U}_{\gamma\beta}(\mathbf{P}, \mathbf{P}'', t)] d\mathbf{P}. \quad (2.14)$$

The matrix element $\hat{U}_{\alpha\beta}$ is defined by the expression

$$\hat{U}_{\alpha\beta}(\mathbf{P}', \mathbf{P}'', t) = \int \Psi_{\alpha}^*(\mathbf{r}) \Psi_{\beta}(\mathbf{r}) U_{ab}(\mathbf{R}, \mathbf{r}) \Psi_{\mathbf{P}''}(\mathbf{R}) \Psi_{\mathbf{P}'}(\mathbf{r}) \frac{d\mathbf{R} d\mathbf{r}}{V^2}. \quad (2.15)$$

The values $\alpha = n, \beta = m$ correspond to the discrete spectrum, while $\alpha = \mathbf{p}', \beta = \mathbf{p}''$ correspond to the continuous spectrum.

We have thus reduced the eq. (2.9) to a system of equations for four operator density matrices

$$\hat{\rho}_{nm}(\mathbf{P}', \mathbf{P}'', t); \quad \hat{\rho}_{\mathbf{p}', \mathbf{p}''}(\mathbf{P}', \mathbf{P}'', t); \quad \rho_{\alpha\mathbf{p}'}(\mathbf{P}', \mathbf{P}'', t); \quad \rho_{\mathbf{p}''\beta}(\mathbf{P}', \mathbf{P}'', t). \quad (2.16)$$

The first two describe the bound and free states of charged particles respectively, and the last two describe transitions between the free and bound states.

3. Kinetic equations for the distribution functions of the electrons, ions and atoms. — We present the derivation of the kinetic equations in two stages. In the first we obtain kinetic equations for the distribution functions of pairs of charged particles. From this equation we obtain afterwards the equations for the distribution functions of the electrons, ions and atoms. We confine ourselves here to the case a spatially homogeneous plasma. Under this condition we have

$$\langle \hat{\rho}_{\alpha\beta}(\mathbf{P}', \mathbf{P}'', t) \rangle = \delta_{\alpha\beta} \frac{(2\pi\hbar)^3}{V} \delta(\mathbf{P}' - \mathbf{P}'') f_{\alpha}(\mathbf{P}', t); \quad \langle \hat{U} \rangle = 0. \quad (3.1)$$

Here $f_{\alpha}(\mathbf{P}', t)$ is the distribution function of pairs of free ($\alpha = \mathbf{p}'$) and bound ($\alpha = n$) charged particles,

$$\sum_{\alpha} \int f_{\alpha}(\mathbf{P}', t) \frac{V}{(2\pi\hbar)^3} d\mathbf{P}' = 1. \quad (3.2)$$

After averaging the system (2.14) we obtain under the condition (3.1) a system of two equations for the functions

$$f_{\alpha}(\mathbf{P}', t) \quad (\alpha = \mathbf{p}', n)$$

$$\frac{\partial f_{\alpha}}{\partial t}(\mathbf{P}', t) = -\frac{2}{\hbar} \sum_{\beta} \int \text{Im} \langle \delta \hat{\rho}_{\alpha\beta}(\mathbf{P}', \mathbf{P}'', t) \delta \hat{U}_{\beta\alpha}(\mathbf{P}'', \mathbf{P}', t) \rangle \cdot \frac{V}{(2\pi\hbar)^3} d\mathbf{P}'' \equiv I_{\alpha}(\mathbf{P}', t). \quad (3.3)$$

Here $I_{\alpha}(\mathbf{P}', t)$ are the corresponding collision integrals. They are determined by the correlation of the fluctuations $\delta \rho_{\alpha\beta}, \delta U_{\alpha\beta}$. It is possible to write the collision integral I_{α} in the polarization approximation in the form

$$I_{\alpha}(\mathbf{P}', t) = \frac{1}{(2\pi)^3 \hbar} \sum_{\beta} \int d\omega d\mathbf{K} d\mathbf{P}'' |P_{\alpha\beta}(\mathbf{K})|^2 \frac{1}{K^2} \delta(\hbar\mathbf{K} - (\mathbf{P}' - \mathbf{P}'')) \delta(\hbar\omega - (E_{\alpha} + E_{\mathbf{P}'} - E_{\beta} - E_{\mathbf{P}''})) \times \\ \times \left[(\delta\mathbf{E} \delta\mathbf{E})_{\omega\mathbf{K}} (f_{\beta}(\mathbf{P}'', t) - f_{\alpha}(\mathbf{P}', t)) - \frac{4\pi\hbar \text{Im} \varepsilon(\omega, \mathbf{K})}{|\varepsilon(\omega, \mathbf{K})|^2} (f_{\beta}(\mathbf{P}'', t) + f_{\alpha}(\mathbf{P}', t)) \right]. \quad (3.4)$$

The matrix elements $P_{\alpha\beta}$ are determined by the expression

$$P_{\alpha\beta}(K) = \int \left[e_a \exp\left(i \frac{m_b}{M} \mathbf{K} \mathbf{r}\right) + e_b \exp\left(-i \frac{m_a}{M} \mathbf{K} \mathbf{r}\right) \right] \Psi_{\alpha}^*(\mathbf{r}) \Psi_{\beta}(\mathbf{r}) \frac{d\mathbf{r}}{V}, \quad (3.5)$$

$\varepsilon(\omega, \mathbf{K})$ is the corresponding dielectric constant of the partly-ionized plasma. It is determined by the formula

$$\varepsilon(\omega, \mathbf{K}) = 1 + \frac{4\pi n}{K^2} \frac{V}{(2\pi\hbar)^3} \sum_{\alpha\beta} d\mathbf{P}' d\mathbf{P}'' \delta(\hbar\mathbf{K} - (\mathbf{P}' - \mathbf{P}'')) \cdot \frac{|P_{\alpha\beta}(\mathbf{K})|^2 (f_{\alpha}(\mathbf{P}', t) - f_{\beta}(\mathbf{P}'', t))}{\hbar(\omega + i\Delta) - (E_{\alpha} + E_{\mathbf{P}'} - E_{\beta} - E_{\mathbf{P}''})}. \quad (3.6)$$

The sum \sum_a in the expressions (3.2)-(3.6) has the meaning

$$\sum_a \dots = \sum_n \dots + \frac{V}{(2\pi\hbar)^3} \int d\mathbf{p}' \dots \quad (3.7)$$

It follows from (3.6), (3.7) that the polarizability of a partly-ionized plasma consists of four parts

$$\alpha(\omega, \mathbf{K}) = \alpha_{ff} + \alpha_{fb} + \alpha_{bf} + \alpha_{bb}. \quad (3.8)$$

The indices f and b denote the free and bound states.

The spectral density of the field fluctuations in the expression (3.4) is given by the formula

$$(\delta\mathbf{E} \delta\mathbf{E})_{\omega, \mathbf{K}} = \frac{2nV}{\hbar^2} \sum_{a\beta} \int d\mathbf{P}' d\mathbf{P}'' [f_a(\mathbf{P}', t) + f_\beta(\mathbf{P}'', t)] \times \\ \times \delta(\hbar\mathbf{K} - (\mathbf{P}' - \mathbf{P}'')) \delta(\hbar\omega - (E_a + E_{\mathbf{P}'} - E_\beta - E_{\mathbf{P}''})) \frac{|P_{a\beta}(\mathbf{K})|^2}{K^2 |\epsilon(\omega, \mathbf{K})|^2}. \quad (3.9)$$

The spectral density of the field fluctuations (as does the polarizability) consists of the four terms

$$(\delta\mathbf{E} \delta\mathbf{E})_{\omega, \mathbf{K}} = (\dots)_{ff} + (\dots)_{fb} + (\dots)_{bf} + (\dots)_{bb}. \quad (3.10)$$

Now we can make the second step in the derivation of the kinetic equations for the distribution functions of the electrons, ions and atoms.

The free charged particles remain most of the time at distances such that for them the eigenfunctions of the continuous spectrum can be replaced by plane waves. In this approximation the matrix element $|P_{\mathbf{p}, \mathbf{p}'}(\mathbf{K})|^2$ of the free particles is given by

$$|P_{\mathbf{p}, \mathbf{p}'}(\mathbf{K})|^2 = \frac{(2\pi\hbar)^3}{V} \left[e_a^2 \delta(\mathbf{p}' - \mathbf{p}'' - \frac{m_b}{M} \hbar\mathbf{K}) + e_b^2 \delta(\mathbf{p}' - \mathbf{p}'' + \frac{m_a}{M} \hbar\mathbf{K}) \right]. \quad (3.11)$$

To describe the motion of free particles it is more convenient to use the variables $\mathbf{p}_a, \mathbf{p}_b$. Then we have

$$f_{\mathbf{p}}(\mathbf{P}, t) \rightarrow f(\mathbf{p}_a, \mathbf{p}_b, t).$$

Note that the function $Nf(\mathbf{p}_a, \mathbf{p}_b, t)$ determines the mean number of the pairs of free charged particles with momenta \mathbf{p}_a and \mathbf{p}_b . In order to take into account the possibility of the formation of atoms from free particles of arbitrary pairs, we make the following substitutions in the collision integral term (3.4), which describe the transitions from the free states to the bound states and vice versa

$$Nf(\mathbf{p}_a, \mathbf{p}_b, t) \rightarrow Nf_a(\mathbf{p}_a, t) f_b(\mathbf{p}_b, t). \quad (3.12)$$

A similar substitution is made in expressions (3.6), (3.9).

Then, taking into account that

$$f_a = \int f_{ab}(\mathbf{p}_a, \mathbf{p}_b, t) \frac{V}{(2\pi\hbar)^3} d\mathbf{p}_b, \quad (3.13)$$

we obtain from (3.3), (3.4) the following system of the kinetic equations for the distribution functions of electrons, ions and atoms

$$\frac{\partial f_a}{\partial t}(\mathbf{p}_a, t) = \frac{V}{(2\pi\hbar)^3} \int I_{ab}(\mathbf{p}_a, \mathbf{p}_b, t) d\mathbf{p}_b \\ = I_a(\mathbf{p}_a, t), \quad a = e, i \quad (3.14)$$

$$\frac{\partial f_n}{\partial t}(\mathbf{P}, t) = I_n(\mathbf{P}, t).$$

The distribution functions of the electrons, ions and atoms are normalized in the following way

$$\frac{V}{(2\pi\hbar)^3} \int f_a(\mathbf{p}_a, t) d\mathbf{p}_a = \frac{N_a}{N} \equiv C_a, \\ \frac{V}{(2\pi\hbar)^3} \sum_n \int f_n(\mathbf{P}, t) d\mathbf{P} = \frac{N_{ab}}{N} \equiv C_{ab}. \quad (3.15)$$

Here C_a, C_{ab} are the electronic, ionic and atomic concentrations respectively. They satisfy the conditions

$$C_a + C_{ab} = 1, \quad C_a = C_b. \quad (3.16)$$

In the equilibrium state the distribution functions are given by the expressions

$$Nf_a = \exp \left[\frac{\mu_a - E_{\mathbf{p}_a}}{kT} \right]; \\ Nf_n(\mathbf{P}) = \exp \left[\frac{\mu_{ab} - E_n - E_{\mathbf{P}}}{kT} \right]. \quad (3.17)$$

Where the chemical potentials μ_a, μ_b, μ_{ab} are given by

$$\begin{aligned}\mu_a &= kT \ln \left[\frac{N_a}{V} \left(\frac{2\pi\hbar^2}{m_a kT} \right)^{3/2} \right], \\ \mu_{ab} &= kT \ln \left[\frac{N_{ab}}{V} \left(\frac{2\pi\hbar^2}{MkT} \right)^{3/2} \frac{1}{Z} \right]\end{aligned}\quad (3.18)$$

and the concentrations n_a, n_b, n_{ab} satisfy the ionization-equilibrium condition (the Saha formula)

$$I_a(p_a, t) = [I_a]_1 + [I_a]_2. \quad (3.20)$$

The first term is given by the expression

$$\begin{aligned}[I_a(p'_a, t)]_1 &= \frac{e_a^2}{(2\pi)^3 \hbar} \int d\mathbf{p}''_a d\omega d\mathbf{K} \frac{1}{K^2} \delta(\hbar\mathbf{K} - (\mathbf{p}'_a - \mathbf{p}''_a)) \delta\left(\hbar\omega - \left(\frac{\mathbf{p}_a'^2}{2m_a} - \frac{\mathbf{p}_a''^2}{2m_a}\right)\right) \times \\ &\times \left\{ (\delta\mathbf{E} \delta\mathbf{E})_{\omega\mathbf{K}} [f_a(p''_a, t) - f_a(p'_a, t)] - \frac{4\pi\hbar \operatorname{Im} \varepsilon(\omega, \mathbf{K})}{|\varepsilon(\omega, \mathbf{K})|^2} [f_a(p''_a, t) + f_a(p'_a, t)] \right\}. \quad (3.21)\end{aligned}$$

For the fully ionized plasma ($C_a = C_b = 1, C_{ab} = 0$) this term coincides with Balescu-Lenard collision integral. For the partly-ionized plasma the collision integral (3.21) consists of four parts which describe four processes

$$1. \quad p'_a + p''_{1b} \leftrightarrow p''_a + p'_{1b}$$

is the elastic scattering process.

$$2. \quad p'_a + m_1 p'_1 \leftrightarrow p''_a + p'_{1a} + p'_{1b}$$

is the (in the direction from left to right) ionization of an atom by collision with an electron ($a = e$) or ion ($a = i$).

$$3. \quad p'_a + p'_{1a} + p'_{1b} \leftrightarrow p''_a + n_1 p'_1$$

is the process inverse to « 2 ».

$$4. \quad p'_a + m_1 p'_1 \leftrightarrow p''_a + n_1 p'_1$$

is the inelastic scattering process.

In all these processes the number of the particles with momentum p_a remain unchanged. Therefore the collision integral (3.20) has the property

$$\frac{V}{(2\pi\hbar)^3} \int [I_a(p'_a, t)]_1 d\mathbf{p}'_a = 0. \quad (3.22)$$

In order to obtain an expression for the second term in (3.20) it is necessary to put in (3.4) $\alpha = n, \beta = m$ to make the substitution $\mathbf{p}', \mathbf{P}' \rightarrow \mathbf{p}'_a, \mathbf{p}'_b$ and to integrate with respect to \mathbf{p}'_b . As a result we obtain the following expression

$$\begin{aligned}[I_a(p'_a, t)]_2 &= \frac{1}{(2\pi)^3 \hbar} \frac{V}{(2\pi\hbar)^3} \sum_m \int d\mathbf{p}'_b d\mathbf{P}'' d\omega d\mathbf{K} \frac{1}{K^2} |P_{m_b \mathbf{p}_b \leftarrow m_a \mathbf{p}_a, m}(\mathbf{K})|^2 \times \\ &\times \delta(\hbar\mathbf{K} - (\mathbf{p}'_a + \mathbf{p}'_b - \mathbf{P}'')) \delta\left(\hbar\omega - \left(\frac{\mathbf{p}_a'^2}{2m_a} + \frac{\mathbf{p}_b'^2}{2m_b} - E_m - E_{\mathbf{P}''}\right)\right) \times \\ &\times \left[(\delta\mathbf{E} \delta\mathbf{E})_{\omega\mathbf{K}} (f_m(\mathbf{P}'', t) - N f_a(p'_a, t) f_b(p'_b, t)) - \frac{4\pi\hbar \operatorname{Im} \varepsilon(\omega, \mathbf{K})}{|\varepsilon(\omega, \mathbf{K})|^2} (f_m(\mathbf{P}'', t) + N f_a(p'_a, t) f_b(p'_b, t)) \right]. \quad (3.23)\end{aligned}$$

After substituting the functions $(\delta\mathbf{E} \delta\mathbf{E})_{\omega\mathbf{K}}, \varepsilon(\omega, \mathbf{K})$ this integral breaks up in turn into four parts, which describe the following processes :

$$5. \quad p'_a + p'_b + p'_{1a} \leftrightarrow m P'' + p'_{1a}.$$

$$6. \quad p'_a + p'_b + m_1 p'_1 \leftrightarrow m P'' + p'_{1a} + p'_{1b}. \quad (3.24)$$

$$7. \quad p'_a + p'_b + p'_{1a} + p'_{1b} \leftrightarrow m P'' + n_1 p'_1.$$

$$8. \quad p'_a + p'_b + m_1 p'_1 \leftrightarrow m P'' + n_1 p'_1.$$

Here the processes « 5 », « 7 », « 8 » are recombination and ionization processes which change the number of the free charged particles. The process « 6 » is the inelastic scattering process accompanied by particle exchange. In all this processes the number of particles with momentum changes. Therefore the collision integral $[I_a(p'_a, t)]_2$ has the property

$$\frac{V}{(2\pi\hbar)^3} \int [I_a(p'_a, t)]_2 d\mathbf{p}'_a \neq 0. \quad (3.25)$$

The collision integral $I_n(\mathbf{P}', t)$ in the kinetic equation for atoms also can be represented in the form of a sum of two terms

$$I_n(\mathbf{P}', t) = [I_n(\mathbf{P}', t)]_1 + [I_n(\mathbf{P}', t)]_2. \quad (3.26)$$

In the case of a zero degree of ionization, there remains in the collision integral $I_n(\mathbf{P}', t)$ only one term, describing the process

$$n\mathbf{P}' + m_1 \mathbf{P}_1'' \leftrightarrow m\mathbf{P}'' + n_1 \mathbf{P}_1'. \quad (3.27)$$

It is elastic ($n = n_1$; $m = m_1$) and inelastic scattering of the atoms.

Each term in (3.26) describes four processes. For the first term we have

$$\sum_n [I_n(\mathbf{P}', t)] \frac{V}{(2\pi\hbar)^3} d\mathbf{P} = 0, \quad (3.28)$$

$$\begin{aligned} \frac{dn_a}{dt} = & (\alpha n_a n_{ab} - \beta n_a^2 n_b) + (\alpha_1 n_{ab}^2 - \beta_1 n_a n_b n_{ab}) + (\alpha_2 n_{ab}^2 - \beta_2 n_a^2 n_b^2) + \\ & + (\alpha_3 n_a^2 n_{ab} - \beta_3 n_a^2 n_{ab}) \quad n_a + n_b = n; \quad n_a = n_b. \end{aligned} \quad (3.30)$$

Here α is the impact-ionization coefficient, β is the triple-recombination coefficient, etc. The coefficients α, β are connected by the general relation

$$\beta = (2\pi\hbar^2/\mu kT)^{3/2} Z\alpha. \quad (3.31)$$

It is possible using the developing method to obtain the kinetic equations, in which not only Coulomb interactions are taken into account, but also a transverse electromagnetic field. The kinetic equations have the form (3.14), but now the expressions for the collision integrals I_a, I_b, I_n have the additional parts. For example

$$I_a = I_a^{(\text{Coulomb})} + I_a^{(ur)} \equiv I_a^{(i)} + I_a^{(l)}. \quad (3.32)$$

The collision integral $I_a^{(ur)}$ also can be written as the sum of two terms

$$I_a^{(ur)} = [I_a^{(ur)}]_1 + [I_a^{(ur)}]_2. \quad (3.33)$$

This collision integrals take into account not only all the usual processes of photoionization, photorecombination, emission, absorption, etc., but also all so-called *anomalous* effects (Cherenkov effect, the anomalous Doppler effect, etc.).

The spectral density of the field fluctuations:

$$(\delta\mathbf{E} \delta\mathbf{E})_{\omega\mathbf{K}} = (\delta\mathbf{E}^{\parallel} \delta\mathbf{E}^{\parallel})_{\omega\mathbf{K}} + (\delta\mathbf{E}^{\perp} \delta\mathbf{E}^{\perp})_{\omega\mathbf{K}}. \quad (3.34)$$

The polarization of the plasma is defined by the two functions $\varepsilon^{\parallel}(\omega, \mathbf{K})$, $\varepsilon^{\perp}(\omega, \mathbf{K})$.

4. Kinetic theory of spectral line broadening [15].—

For the calculation of spectral line broadening it is possible to use the equation for the component of

but for the second term

$$\sum_n \int [I_n(\mathbf{P}', t)]_2 \frac{V}{(2\pi\hbar)^3} d\mathbf{P}' \neq 0. \quad (3.29)$$

The properties of collision integrals are such that they ensure conservation of the total (free and bound) number of charged particles, total momentum and energy.

Let us consider the state of a plasma in which the non-equilibrium character is due only to the fact that the concentrations n_a, n_b, n_{ab} do not satisfy the ionization equilibrium condition and the concentrations are functions only of the time.

Using the kinetic equations for the distribution functions of electrons, ions, atoms (see (3.14)) we obtain equations for the concentrations n_a, n_b, n_{ab}

polarization vector $\mathbf{P}_{nm}(\mathbf{R}, t)$ which corresponds to the $n - m$ transition. This function is connected with the off-diagonal density matrix $f_{nm}(\mathbf{R}, \mathbf{P}, t)$ by a relation:

$$\mathbf{P}_{nm}(\mathbf{R}, t) = n_{ei} \int d_{mn} f_{nm}(\mathbf{R}, \mathbf{P}, t) \frac{V}{(2\pi\hbar)^3} d\mathbf{P}. \quad (4.1)$$

Thus the task is reduced to the investigation of the kinetic equation for the function $f_{nm}(\mathbf{R}, \mathbf{P}, t)$. The density matrix is connected with operator $\hat{\rho}_{nm}$ as

$$f_{nm}(\mathbf{R}, \mathbf{P}, t) = \langle \hat{\rho}_{nm}(\mathbf{R}, \mathbf{P}, t) \rangle; \quad (4.2)$$

$$\sum_n \int f_{nm} \frac{d\mathbf{R} d\mathbf{P}}{(2\pi\hbar)^3} = C_{ei}.$$

The operator density matrix $\hat{\rho}_{nm}$ obeys the equation analogous to (2.14). With help of this equation we can obtain following kinetic equation

$$\begin{aligned} \left(\frac{\partial}{\partial t} + \mathbf{V} \frac{\partial}{\partial \mathbf{R}} + i\omega_{nm} \right) f_{nm}(\mathbf{R}, \mathbf{P}, t) - \frac{i}{\hbar} \times \\ \times \sum_{n_1} (d_{nn_1} f_{n_1 m} - f_{n_1 m} d_{n_1 m}) \mathbf{E}(\mathbf{R}, t) = I_{nm}(\mathbf{R}, \mathbf{P}, t). \end{aligned} \quad (4.3)$$

It is obvious now, that we need an expression for collision integral I_{nm} to solve the problem of spectral line broadening.

Now we present the results obtained with the following simplifying approximations.

1. Correlations of fluctuations, which determine the collision integrals are calculated, neglecting the action of the mean electromagnetic field.

2. All calculations are performed in the polarization approximation.

3. The dipole approximation is used.

The corresponding collision integral is given by expression

$$I_{nm}(\mathbf{R}, \mathbf{P}, t) = \frac{i}{\hbar} \times$$

$$\times \sum_{n_1} (\mathbf{d}_{nn_1} \langle \mathbf{d} \rho_{n,n_1} \delta \mathbf{E} \rangle - \langle \delta \rho_{nn_1} \delta \mathbf{E} \rangle \mathbf{d}_{n_1 n}) \quad (4.3 \text{ bis})$$

and can be represented in the form of a sum

$$I_{nm}(\mathbf{R}, \mathbf{P}, t) = I_{nm}^{(\text{induced})} + I_{nm}^{(\text{spontaneous})}. \quad (4.4)$$

Here we present, as an example, the expression for the induced part of the collision integral which is proportional to the spectral density of field fluctuations

$$I_{nm}^{(\text{ind})}(\omega, \mathbf{R}, \mathbf{P}) = -\frac{1}{\hbar^2} \int_0^\infty d\tau \int \frac{d\mathbf{K}}{(2\pi)^3} e^{-\Delta\tau + i(\omega - \omega_{nm} - \mathbf{K}\mathbf{V})\tau} \times \\ \times \left[\sum_{n_1} |\mathbf{d}_{nn_1}|^2 e^{i\omega_{nn_1}\tau} - (d_{nn})_i (d_{nm})_j \right] (\delta E_j \delta E_i)_{-\tau, \mathbf{K}} f_{nm}(\mathbf{R}, \mathbf{P}, \omega) + n \leftrightarrow m, *, -\omega. \quad (4.5)$$

The line width and frequency shift of the spectral line are determined from the following equation

$$I_{nm}(\omega, \mathbf{R}, \mathbf{P}) = -(\gamma_{nm}^{(\omega)} + i\Delta\omega_{nm}) f_{nm}(\mathbf{R}, \mathbf{P}, t). \quad (4.6)$$

Using (4.5), (4.6) we obtain the following expression for the spectral line width

$$\gamma_{nm}^{(\text{ind})}(\omega - \omega_{nm}) = \frac{1}{6\hbar^2} \left[\sum_{n_1 \neq n} |\mathbf{d}_{nn_1}|^2 (\delta \mathbf{E} \delta \mathbf{E})_{\omega_{nn_1}} + \sum_{n_1 \neq m} |\mathbf{d}_{n_1 m}|^2 (\delta \mathbf{E} \delta \mathbf{E})_{\omega_{n_1 m}} \right] + \\ + \frac{1}{6\hbar^2} \int (\mathbf{d}_{nn} - \mathbf{d}_{mm})^2 (\delta \mathbf{E} \delta \mathbf{E})_{\omega - \omega_{nm} - \Gamma, \mathbf{K}} \frac{d\mathbf{K}}{(2\pi)^3}. \quad (4.7)$$

The spectral density of field fluctuations is determined by expression (3.32).

Neglecting the Doppler effect and at $\omega - \omega_{nm} = 0$:

$$\gamma_{nm}^{(\text{ind})}(0) = \frac{1}{6\hbar^2} \left[\sum_{n_1 \neq n} |\mathbf{d}_{nn_1}|^2 (\delta \mathbf{E} \delta \mathbf{E})_{\omega_{nn_1}} + \sum_{n_1 \neq m} |\mathbf{d}_{n_1 m}|^2 (\delta \mathbf{E} \delta \mathbf{E})_{\omega_{n_1 m}} \right] + \frac{1}{6\hbar^2} (\mathbf{d}_{nn} - \mathbf{d}_{mm})^2 (\delta \mathbf{E} \delta \mathbf{E})_{\omega=0}. \quad (4.8)$$

We see that the γ_{nm} is determined by two different contributions. The first one is determined by the spectral density of the field fluctuations at frequencies close to the transition ones of free atoms. The second contribution is determined by the spectral density at low frequencies close to the zero.

The corresponding expression for the frequency shift $\Delta\omega_{nm}$ is given by

$$[\Delta\omega_{nm}]^{\text{ind}} = \frac{1}{3\hbar^2} \int \frac{d\mathbf{K}}{(2\pi)^3} \left\{ \sum_{n_1 \neq n} |\mathbf{d}_{nn_1}|^2 \frac{(\delta \mathbf{E} \delta \mathbf{E})_{\omega, \mathbf{K}}}{\omega_{nn_1} + \mathbf{K}\mathbf{V} - \omega} + \sum_{n_1 \neq m} |\mathbf{d}_{n_1 m}|^2 \frac{(\delta \mathbf{E} \delta \mathbf{E})_{\omega, \mathbf{K}}}{\omega_{n_1 m} + \mathbf{K}\mathbf{V} - \omega} \right\} + \\ + (\mathbf{d}_{nn} - \mathbf{d}_{mm})^2 \frac{(\delta \mathbf{E} \delta \mathbf{E})_{\omega, \mathbf{K}}}{\mathbf{K}\mathbf{V} - \omega}. \quad (4.9)$$

Neglecting the Doppler effect we can obtain the following simplified form

$$[\Delta\omega_{nm}]^{\text{ind}} = \frac{1}{3\hbar^2} \int \frac{d\omega}{2\pi} \left[\sum_{n_1 \neq n} |\mathbf{d}_{nn_1}|^2 \frac{(\delta \mathbf{E} \delta \mathbf{E})_\omega}{\omega_{nn_1} - \omega} + \sum_{n_1 \neq m} |\mathbf{d}_{n_1 m}|^2 \frac{(\delta \mathbf{E} \delta \mathbf{E})_\omega}{\omega_{n_1 m} - \omega} \right]. \quad (4.10)$$

The expression for the quadratic Stark effect in the field with spectral density $(\delta \mathbf{E} \delta \mathbf{E})_\omega$ follows from (4.10).

For the monochromatic field

$$(\delta \mathbf{E} \delta \mathbf{E})_\omega = \frac{1}{2} |\mathbf{F}_{\omega_0}|^2 2\pi(\delta(\omega - \omega_0) + \delta(\omega + \omega_0)). \quad (4.11)$$

The corresponding expression for the energy shift of the level n is

$$\Delta E_n = \frac{1}{6\hbar} \sum_{n_1 \neq n} |\mathbf{d}_{nn_1}|^2 \times \\ \times \left[\frac{1}{\omega_{nn_1} - \omega} + \frac{1}{\omega_{nn_1} + \omega} \right] |\mathbf{F}_{\omega_0}|^2. \quad (4.12)$$

Let us consider now the more general expressions for the spectral line width taking into account both the induced and spontaneous fluctuations.

5. **Broadening determined by the induced and spontaneous processes. Transition probabilities** [15]. — The integral I_n in the kinetic equation for the distribution function of atoms f_n can be represented in the form (see (3.31), (3.20))

$$I_n(\mathbf{P}, t) = I_n^{(\parallel)}(\mathbf{P}, t) + I_n^{(\perp)}(\mathbf{P}, t) \\ = \sum_m [W_{mn} f_m(\mathbf{P}, t) - W_{nm} f_n(\mathbf{P}, t)]. \quad (5.1)$$

$$W_{nm}^{\parallel} = \frac{1}{3} \frac{1}{\hbar^2} \int \frac{d\mathbf{K}}{(2\pi)^3} |\mathbf{d}_{nm}|^2 \left[(\delta\mathbf{E}^{\parallel} \delta\mathbf{E}^{\parallel})_{\omega_{nm}\mathbf{K}} + \frac{4\pi\hbar \operatorname{Im} \varepsilon^{\parallel}(\omega_{nm}, \mathbf{K})}{|\varepsilon^{\parallel}(\omega_{nm}, \mathbf{K})|^2} \right], \quad (5.3)$$

$$W_{nm}^{\perp} = \frac{1}{3} \frac{1}{\hbar^2} \int \frac{d\mathbf{K}}{(2\pi)^3} |\mathbf{d}_{nm}|^2 \left[(\delta\mathbf{E}^{\perp} \delta\mathbf{E}^{\perp})_{\omega_{nm}\mathbf{K}} + \frac{8\pi\hbar\omega_{nm}^4 \operatorname{Im} \varepsilon^{\perp}(\omega_{nm}, \mathbf{K})}{|\omega_{nm}^2 \varepsilon^{\perp}(\omega_{nm}, \mathbf{K}) - C^2 \mathbf{K}^2|^2} \right]. \quad (5.4)$$

Here the conditions $\mathbf{d}_{nn} = 0$, $\mathbf{d}_{mm} = 0$ are used. Dissipative matrix γ_{nm} which determines the spectral line broadening, is expressed in this approximation as

$$\gamma_{nm} = \frac{1}{2} \sum_{n_1} (W_{nn_1} + W_{n_1n}) \equiv \gamma_{nm}^{\parallel} + \gamma_{nm}^{\perp}. \quad (5.5)$$

We see that the transition probabilities are determined by the functions $(\delta\mathbf{E} \delta\mathbf{E})_{\omega\mathbf{K}}$, $\varepsilon(\omega, \mathbf{K})$, which have the structure (3.8), (3.10). Therefore both γ_{nm}^{\parallel} and γ_{nm}^{\perp} can be represented as a sum of the four terms.

For the radiation region

$$W_{nm}^{\perp} = \frac{|\mathbf{d}_{nm}|^2}{3\hbar^2} \times \\ \times \left[(\delta\mathbf{E}^{\perp} \delta\mathbf{E}^{\perp})_{\omega_{nm}} + \frac{2\hbar\omega_{nm}^3}{C^3} \sqrt{\operatorname{Re} \varepsilon(\omega_{nm})} \right]. \quad (5.6)$$

In the equilibrium state the right hand side of this expression can be rewritten using Einstein coefficients

$$W_{nm}^{\perp} = B_{nm}^{\perp} \rho_{\omega_{nm}}^{\perp} + A_m^{\perp}. \quad (5.7)$$

It follows from (5.5), (5.7) that the term determined by the spontaneous processes leads to the following expression for the line width :

$$\gamma_{nm}^{\perp} = \frac{1}{2} \left[\sum_{n>n_1} A_{n_1} + \sum_{m>n_1} A_{n_1}^m \right]. \quad (5.8)$$

For the partly-ionized plasma the most general transition probabilities are determined by the collision integrals $I_n(\mathbf{P}, t)$ (see eq. (3.4)). Four dissipative matrix γ_{nm} , γ_{np} , $\gamma_{p'n}$, $\gamma_{p'p}$ can be expressed via these transition probabilities.

Here the following notations for the transition probabilities are used

$$W_{nm} = W_{nm}^{(\parallel)} + W_{nm}^{(\perp)}. \quad (5.2)$$

Where the two contributions denote the transition probabilities determined by fluctuations of Coulomb (« \parallel ») and transverse (« \perp ») field respectively :

The expressions for the broadening and shift of the spectral line presented above are also valid in nonequilibrium states. In this case the functions γ_{nm} , $\Delta\omega_{nm}$ are determined by the distribution functions of electrons, ions and atoms which obey the kinetic eq. (3.14).

Therefore it is possible to determine the spectral line broadening for the nonequilibrium processes provided the solution of the kinetic equations are known. It seems natural that such a solution can be obtained practically only using the simplified (model) collision integrals.

For the radiation region the problem is reduced to the calculation of nonequilibrium spectral density of field fluctuations. This problem is related with the problem of spectral line broadening in turbulent plasma.

Let us consider now the particular applications of the general formulae.

6. **Broadening by electrons** [3-7, 15]. — We shall determine the atomic spectral line broadening with the following assumptions :

1. The concentration of atoms is small.
2. There is local equilibrium of electrons in the velocity space.
3. The dynamical polarisation is taken into account by using the effective potential.

This is equivalent to the substitution

$$\frac{4\pi}{K^2} \frac{1}{|\varepsilon(\omega, \mathbf{K})|^2} \rightarrow \frac{4\pi}{K^2} \frac{r_D^2 K^2}{1 + r_D^2 K^2}. \quad (6.1)$$

Let us divide the expression for γ_{nm} in two parts according to the structure of the general expression (4.7). The first part is determined by the high-

frequency ($\omega \approx \omega_{nm}$) field fluctuations. After some calculations one obtains

$$\gamma_{nm} = \frac{8\sqrt{2}\pi}{3} \frac{|d_{nm}|^2}{\hbar^2} \frac{e^2 n}{V_{T_e}} \ln \frac{r_{\max}}{r_{\min}}. \quad (6.2)$$

Here r_{\min} is defined as a maximum of the following three values :

$$r_{\min} = \max\left(\frac{\hbar}{mV_{T_e}}, l_A, \rho_w e\right). \quad (6.3)$$

r_{\max} is defined as a minimum of two values :

$$r_{\max} = \min\left(r_D, \frac{V_{T_e}}{\omega_{nm}}\right). \quad (6.4)$$

For the second contribution to which is determined by the low frequency field fluctuations one obtains the following expression :

$$\gamma_{nm} = \frac{4\sqrt{2}\pi}{3} \frac{(\mathbf{d}_{nn} - \mathbf{d}_{mm})^2}{\hbar^2} \frac{e^2 n}{V_{T_e}} \ln 4 \frac{r_{\max}}{r_{\min}}. \quad (6.5)$$

Where r_{\min} is determined by (6.3) and r_{\max} is defined by

$$r_{\max} = \min\left(r_D, r_A = \frac{V_{T_e}}{|\omega - \omega_{nm}|}\right), \quad (6.6)$$

r_A is Lewis parameter.

Similar calculations have been also performed for the nonequilibrium distribution functions (see for ex. [14]).

7. Resonance spectral line broadening by collision between atoms. — Let us consider another limiting case when the broadening is determined by atomic collisions.

The main contribution to the expression (4.7) can be obtained assuming that $d_{nn} = 0$, $d_{mm} = 0$ and considering only $n - m$ transitions. Then the expression for γ_{nm} can be written as

$$\gamma_{nm} = \frac{1}{3\hbar^2} |\mathbf{d}_{nm}|^2 (\delta\mathbf{E} \delta\mathbf{E})_{\omega_{nm}}. \quad (7.1)$$

Let us single out the contribution to (3.9) which corresponds to the discrete spectrum ($\alpha = n_1$, $\beta = m_1$) and put $\varepsilon(\omega, \mathbf{K}) = 1$ because the polarization effects are negligible in this approximation. Finally let us single out the contribution of the resonance levels. In order to do this it is necessary to put $n = n_1$, $m = m_1$ in the expression for the spectral density of field fluctuations.

After this we obtain the following expression for the line width (see [14]) :

$$\gamma_{nm} = \sqrt{\pi} \frac{e^2 n}{m\omega_{nm}} f_{nm}, \quad (7.2)$$

f_{nm} is oscillator strength.

This result differs from the well known one obtained by Vlasov and Fursov [18, 2] only by the numerical coefficient ($\sqrt{\pi}$ instead of $\pi/3$). In (7.2) only the long-range ($r > \rho_w$) interactions are taken into account. The inclusion of short-range interactions ($r < \rho_w$) leads to the following result [14] :

$$\gamma_{nm} = \left(\sqrt{\pi} + \frac{\pi}{2}\right) \frac{e^2 n}{m\omega_{nm}} f_{nm}. \quad (7.3)$$

The resonance spectral line broadening, caused by the resonance interaction of atoms, considered above is an inelastic process. We see that in this case the broadening is growing proportional to the gas pressure.

8. Spectral line broadening by elastic collisions [19, 4, 15]. — When the elastic collisions are taken into account the backward process is possible : the pressure growth causes narrowing of the spectral lines.

The significance of collisions in the elastic processes depends upon the relation of Doppler width KV_{T_e} , the frequency of elastic collisions ν and the line width γ_{nm} .

It was assumed above that the velocity distribution function of atoms is fixed. This is justified if two inequalities are satisfied :

$$KV_T \gg \nu \gg \gamma_{nm}. \quad (8.1)$$

It follows from (8.1) that the pressure dependence of γ_{nm} is not the only reason of the change of the spectral line profile. The change of the velocity of the atoms due to the elastic collisions is also significant.

Practically the relatively simple model of collision integrals are used when one wants to take into account the elastic collisions.

For example in the model of strong collisions [19, 4] the collision integral has the form

$$I_n(\mathbf{P}, t) = \nu f(\mathbf{P}) \int f_n(\mathbf{P}', t) \frac{V}{(2\pi\hbar)^3} d\mathbf{P}' - \nu f_n(\mathbf{P}, t). \quad (8.2)$$

Here ν is the effective frequency of collisions, $f(\mathbf{P})$ is the Maxwell distribution function.

Summarising the results of [19, 4] it is possible to conclude that the elastic collisions cause the narrowing of the Doppler width while the pressure is growing. This is reason for the narrowing of the spectral lines. The result depends also upon the function $\gamma_{nm}(p)$.

The calculations [19, 4] have shown that the qualitative results does not depend upon the particular model.

9. Prisoning of radiation. — The prisoning of radiation is significant, for example, in the theory of gas lasers.

Let us assume that «*a*» (upper level) and «*b*» are two essential levels; assume also that the transition from the upper level to the ground state «*o*» is possible. Then the effects of spontaneous emission (at *a-o* transition) and the resonance absorption (on the *o-a* transition) are possible. This process of resonance absorption prevents the radiation from leaving the active volume. Thus the prisoning of radiation takes place.

The efficiency of prisoning depends upon the concentration of atoms in the ground state. The

prisoning is complete if $l_0 \ll L$, where l_0 is the mean free path of a photon emitted at the *a-o* transition.

The theory of prisoning of radiation was first constructed on the phenomenological level [20, 21]. Recently the microscopic theory have been also developed [22-27, 15].

The collision integral $I_a^\pm(\mathbf{P}, t)$, which is determined by the transverse field fluctuations describes naturally the prisoning effect. The expression for this collision integral is given by the following form similar to (3.21):

$$I_n^\pm(\mathbf{P}, t) = \frac{1}{3(2\pi)^3 \hbar^2} \int d\omega d\mathbf{K} d\mathbf{P}' |d_{nm}|^2 \delta(\omega - \mathbf{K}\mathbf{V} - \omega_{nm}) \times \\ \times \delta(\hbar\mathbf{K} - (\mathbf{P} - \mathbf{P}')) \left[(\delta\mathbf{E}^+ \delta\mathbf{E}^\pm)_{\omega\mathbf{K}} (f_m(\mathbf{P}', t) - f_n(\mathbf{P}, t)) - \frac{8\pi\hbar\omega^4 \operatorname{Im} \varepsilon^\pm(\omega, \mathbf{K})}{|\omega^2 \varepsilon^\pm(\omega, \mathbf{K}) - C^2 K^2|^2} \right]. \quad (9.1)$$

Now we shall make the following simplifications in order to describe the prisoning of radiation with the help of the kinetic equation for the function $f_n(\mathbf{P}, t)$:

1. The equation is written for the two levels *a, b*.
2. The Doppler effect and recoil are taken into account only for the *a-o* and *b-o* transitions.
3. Only the spontaneous emission is taken into account for the transitions from the levels *a, b* to all other ones except the ground state.

Let $\gamma_{a,b}^0$ denote the corresponding dissipative constants. Then

$$\gamma_a' = \sum_{a>m>0} A_m^a; \quad \gamma_b' = \sum_{b>m>0} A_m^b. \quad (9.2)$$

4. We assume that the populations of the levels *a* and *b* are much less than that of the ground state; i.e.

$$f_a, f_b \ll f_o.$$

5. The recoil effect is neglected in the description of the spontaneous emission at the *a-o* transition. The Doppler effect can be also neglected here. For the region of radiation we obtain the following dissipative contribution:

$$- A_o^a f_a(\mathbf{P}, t). \quad (9.3)$$

Here A_o^a is the Einstein coefficient for the *a-o* transition.

6. The recoil effect is neglected in the term which describes the induced emission at the *a-o* transition. However the Doppler effect is important here.

After this simplifications the collision integral in the kinetic equation for the distribution function $f_a(\mathbf{P}, t)$ has the form

$$I_a^\pm(\mathbf{P}, t) = -\gamma_a' f_a + A_o^a \left[\frac{1}{4\pi} \int d\Omega K(\mathbf{K}_0, \mathbf{K}_0 \mathbf{V}) f_o(\mathbf{P}) - f_a(\mathbf{P}, t) \right]. \quad (9.4)$$

Here the following notation is used

$$K(\mathbf{K}_0, \mathbf{K}_0 \mathbf{V}) = \frac{\int \delta(\mathbf{K}_0 \mathbf{V} - \mathbf{K}_0 \mathbf{V}') f_a(\mathbf{P}', t) d\mathbf{P}'}{\int \delta(\mathbf{K}_0 \mathbf{V} - \mathbf{K}_0 \mathbf{V}') f_o(\mathbf{P}', t) d\mathbf{P}'} \quad (9.5)$$

where \mathbf{K}_0 is the unit vector, $d\Omega$ is the element of the spatial vector in \mathbf{K} -space.

If the velocity distribution function of atoms in the ground state is fixed, one obtains the linear integral equation for the distribution function $f_a(\mathbf{P}, t)$.

Thus the prisoning of radiation leads to the redistribution of atoms in momentum space. Finally the Maxwell distribution is established (if external sources are absent). Substituting in (9.5) the Maxwell distributions

$$\frac{N}{V} \frac{V}{(2\pi\hbar)^3} f_{a,o}(\mathbf{P}) = \frac{n_{a,o}}{(2\pi M k T)^{3/2}} \exp\left(-\frac{P^2}{2 M k T}\right) \quad (9.6)$$

one obtains

$$K = \frac{n_o}{n_a}. \quad (9.7)$$

It follows from eq. (9.4), (9.7) that the integral term equal to zero in eq. (9.4). Thus the collision integral reduces to

$$I_a(\mathbf{P}, t) = -\gamma'_a f'_a(\mathbf{P}, t). \quad (9.8)$$

We can make the conclusion that fixing of equilibrium momentum distribution for all levels corresponds to the condition of complete prisoning.

On the contrary, neglecting the prisoning one obtains the following expression for the collision integral:

$$I_a(\mathbf{P}, t) = -(\gamma'_a + A_a^a) f_a(\mathbf{P}, t) = -\sum_{a>m=0} A_m^a f_a(\mathbf{P}, t). \quad (9.9)$$

The influence of radiation prisoning on the processes in lasers was investigated in [22-27].

10. Influence of the field of ions on the spectral line profile [3-7, 15]. — The expressions of §§ 4-6 which determine the spectral line width contain the spectral densities of field fluctuations with short correlation times τ_{cor} .

This corresponding the following inequality

$$\tau_{\text{cor}} \ll \frac{1}{\gamma_{nm}}. \quad (10.1)$$

The correlation times of ions and electrons are different due to the strong difference in their masses. Introducing the notations $\tau_{e,i}$ for these correlation times one obtains

$$\tau_{e,i} \sim \frac{\rho_{W_{e,i}}}{V_{T_{e,i}}} \sim \frac{C}{V_{T_{e,i}}^2}; \quad \frac{\tau_e}{\tau_i} \sim \frac{m_e}{m_i}. \quad (10.2)$$

Here $\rho_{W_{e,i}}$ are the corresponding Weisskopf radius.

From the formula (6.5) follows that

$$\frac{1}{(\gamma_{nm})_{e,i}} \sim \frac{\tau_{e,i}}{n\rho_{W_{e,i}}^3} \frac{1}{A_{e,i}}. \quad (10.3)$$

Then the inequalities (10.1) may be satisfied simultaneously at the conditions

$$(n\rho_{W_e}^3)_{e,i} A_{e,i} \ll 1. \quad (10.4)$$

The inequalities are just only at very low pressure. More usual situation is

$$n\rho_{W_e}^3 A_e \ll 1, \quad n\rho_{W_i}^3 A_i \gg 1. \quad (10.5)$$

In this case it is possible to use quasi-static approximation for the ions. Then the shape of spectral line is defined by the formula

$$I_{nm}(\omega) = 2 \int_0^\infty \frac{\gamma_{nm}}{\left(\omega - \omega_{nm} + \frac{1}{\hbar} (d_{nn} - d_{mm}) E\right)^2 + \gamma_{nm}^2} \times \\ \times W(E) dE. \quad (10.6)$$

Here n, m are parabolic quantum numbers, $W(E)$ is the field strength distribution function of ions, γ_{nm} is the width of spectral line defined by fast fluctuations (see §§ 4-7) and the inequality (10.1).

In the zero approximation when the motion of ions are not taken into account the function $W(E)$ is the Holtsmark distribution. More general results are obtained in the papers of Kogan [28], Beranger and Mozer [1, 6], Ecker and Schumacher [8]; Kurilenkov and Filinov [9].

In the past, Stark broadening methods had most applications in equilibrium plasmas. This methods may apply also to nonequilibrium plasmas.

The influence of electric fields from plasma waves on line profiles has only recently become the subject of experimental investigations.

For strong wave excitation or turbulence the collective contribution may dominate and the shapes may be very different from line profiles calculated by formula (10.5) (see § 14).

11. Influence of the electron field on the intensity of radiation on the wings of spectral lines [7, 15]. — For investigation of the influence of the electrons on the intensity of radiation on the wings of the spectral lines, in inequality (10.1) the parameter

$$\frac{1}{|\omega - \omega_{nm}|} \ll \frac{1}{\gamma_{nm}}.$$

Then on the wings of the spectral lines when

$$|\omega - \omega_{nm}| \gg \gamma_{nm} \gg \frac{V_{T_e}}{\rho_{W_e}} \quad (11.1)$$

the fluctuations of electron field are also quasistatic.

In order to obtain more general formula giving qualitative description of the intensity of the radiation for all frequencies in the expression (10.5)

$$\gamma_{nm} \rightarrow \tilde{\gamma}_{nm} = \frac{\gamma_{nm} \gamma_{\Delta\omega_{nm}}}{\gamma_{nm} + \gamma_{\Delta\omega_{nm}}}, \quad (11.2)$$

where

$$\gamma_{\Delta\omega_{nm}} = \frac{\pi^2 n C^{3/2}}{|\omega - \omega_{nm}|^{1/2}}.$$

We see that in the case

$$|\omega - \omega_{nm}| \ll \frac{\gamma_{nm}}{n\rho_{W_e}^3} \quad \text{width} \quad \tilde{\gamma}_{nm} \approx \gamma_{nm}. \quad (11.3)$$

In opposite case when

$$|\omega - \omega_{nm}| \gg \frac{\gamma_{nm}}{n\rho_{W_e}^3} \quad \text{the width} \quad \tilde{\gamma}_{nm} \approx \gamma_{\Delta\omega_{nm}} \quad (11.4)$$

and the intensity of the radiation is described by the formula

$$I_{nm}(\omega) = 4\pi^2 n \frac{C^{3/2}}{|\omega - \omega_{nm}|^{5/2}}. \quad (11.5)$$

This is the double of the intensity of radiation defined by the ion field.

Then at the condition (11.1) influence of electron field and the ion field are equal.

More details one can find in a number of reviews [1-7].

12. Simultaneous account of strong (pair) and weak (collective) interactions. — We can discuss now the possibility of simultaneous inclusion of both the strong interactions at small distances (to leave the Born approximation) and long range collective interactions.

The Boltzmann collision integral for a plasma contains a divergence at large distances and the Balescu-Lenard integral diverges at small distances. In many papers (see § 56 in [16]) different forms of the collision integral, which simultaneously take into account binary collision processes and polarization processes, have been proposed.

The simplest form proposed is a combination of three integrals: the Boltzmann I_B , Landau I_A and Balescu-Lenard I_{B-L} integrals

$$I_a = I_a^B - I_a^L + I_a^{B-L}. \quad (12.1)$$

In this expression the integral I_a^L compensates the divergence of the Boltzmann integral at large distances and the divergence of the integral I_a^{B-L} at small distances. Such a generalisation, although

attractive because of its relative simplicity, is not completely satisfactory since this approximation leads to incorrect expressions for the thermodynamic functions for the nonideal plasma (see § 56 in [16]).

We shall consider here another model, in which the dynamical character of the plasma polarization is taken into account approximately.

The collision integral for the fully ionized plasma can be written in the form

$$I_a = \sum_b n_b \frac{\partial}{\partial p_i} \times \int K_i \phi_{ab}(K) \operatorname{Im} g_{ab}(\mathbf{K}, \mathbf{p}, \mathbf{p}', t) d\mathbf{K} d\mathbf{p}'. \quad (12.2)$$

If we substitute the solution of the equation for the correlation function g_{ab} in the polarization approximation we obtain the Balescu-Lenard expression.

The expression in the integrand in this case is proportional to the square of $\phi_{ab}(\mathbf{K})$. One of the factors (in the initial expression (12.2)) remains unchanged, while the second changes, when polarization is taken into account:

$$\phi_{ab}(\mathbf{K}) \rightarrow \phi_{ab}(\mathbf{K}) / |\varepsilon(\omega, \mathbf{K})|^2. \quad (12.3)$$

We can take the averaged effect of the dynamical polarization into account in the following way. In place of (12.3) we use following effective potential:

$$\phi_{ab}^{\text{eff}}(\mathbf{K}) = \frac{\phi_{ab}(\mathbf{K})}{\sum_d e_d^2 n_d} \int e_c^2 n_c \int \frac{f_c(\mathbf{p}, t)}{|\varepsilon(\mathbf{K}\mathbf{V}, \mathbf{K})|^2} d\mathbf{p} \equiv \frac{e_a e_b}{\sum_c e_c^2 n_c} \frac{(\delta\mathbf{E} \delta\mathbf{E})_{\mathbf{K}}}{4\pi}. \quad (12.4)$$

We use here the expression for the spectral density of the field fluctuations.

In the state of the local equilibrium

$$\phi_{ab}^{\text{eff}}(\mathbf{K}) = \frac{\phi_{ab}(\mathbf{K})}{1 + r_D^2 K^2}; \quad \phi_{ab}^{\text{eff}}(|\mathbf{r}|) = \frac{e_a e_b}{r} e^{-r/r_D}. \quad (12.5)$$

We see that in this case the effective potential coincides with the Debye potential. In same approximation the correlation function defined by expression

$$f_{ab} = 1 + g_{ab} = \exp \left[-\frac{e_a e_b}{kT r_D} e^{-r/r_D} \right]. \quad (12.6)$$

Using the effective potential we can obtain the following system of equations for the distribution functions f_a, f_b for the fully ionized plasma [16]

$$\frac{\partial f_a}{\partial t} = \sum_b n_b \int \frac{\partial \phi_{ab}}{\partial \mathbf{r}} \frac{\partial}{\partial \mathbf{p}} f_{ab} d\mathbf{r}' d\mathbf{p}' \equiv I_a(\mathbf{p}, t), \quad (12.7)$$

$$\left(\frac{\partial}{\partial t} + \mathbf{v} \frac{\partial}{\partial \mathbf{r}} + \mathbf{v}' \frac{\partial}{\partial \mathbf{r}'} - \frac{\partial \tilde{\phi}_{ab}}{\partial \mathbf{r}} \frac{\partial}{\partial \mathbf{p}} - \frac{\partial \tilde{\phi}_{ab}}{\partial \mathbf{r}'} \frac{\partial}{\partial \mathbf{p}'} \right) f_{ab} = \frac{\partial}{\partial t} (f_a(\mathbf{p}, t) f_b(\mathbf{p}', t)), \quad (12.8)$$

where $f_{ab} = f_a f_b + g_{ab}$.

Corresponding collision integral has not the divergences neither at small distances nor at large distances.

The discussed method of effective potential is used in paper [36] for the account of the spectral line broadening in the partly ionized plasma. In this paper we considered also the results of Capes, Voslamber papers [12].

$$(\delta E \delta E)_{\omega, \mathbf{K}} = \frac{(2\pi)^4}{2} [|\mathbf{E}_{\omega, \mathbf{K}_0}|^2 \delta(\omega - \omega_0) \delta(\mathbf{K} - \mathbf{K}_0) + \omega \rightarrow -\omega, \mathbf{K} \rightarrow -\mathbf{K}], \quad (13.1)$$

we can obtain the following equation for the temperature of the gas

$$n \frac{dkT}{dt} = \frac{V}{(2\pi\hbar)^3} \int d\mathbf{P} (\mathbf{K}\mathbf{V} \operatorname{Im} \alpha(\omega, \mathbf{K}, \mathbf{V})) |\mathbf{E}_{\omega, \mathbf{K}}|^2. \quad (13.2)$$

Here we use the notation for the imaginary part of the polarizability $\alpha(\omega, \mathbf{K}, \mathbf{V})$ of atoms with velocity \mathbf{V}

$$\operatorname{Im} \alpha(\omega, \mathbf{K}, \mathbf{V}) = \frac{\pi n}{3\hbar} |\mathbf{d}_{ab}|^2 \delta(\omega - \omega_{ab} - \mathbf{K}\mathbf{V}) \left[f_b \left(\mathbf{P} - \frac{1}{2} \hbar \mathbf{K} \right) - f_a \left(\mathbf{P} + \frac{1}{2} \hbar \mathbf{K} \right) \right]. \quad (13.3)$$

We see that the temperature of the gas becomes lower if $\omega - \omega_{ab} < 0$.

If the width of the resonance is not zero then in the expression (13.3)

$$\pi \delta(\omega - \omega_{ab} - \mathbf{K}\mathbf{V}) \rightarrow \frac{\gamma_{ab}}{(\omega - \omega_{ab} - \mathbf{K}\mathbf{V})^2 + \gamma_{ab}^2}. \quad (13.4)$$

(From the (13.3), (13.4) it is not difficult to find that

$$kT_{\min} \sim \hbar \gamma_{ab} \quad \text{at} \quad |\omega - \omega_{ab}| \sim \gamma_{ab}. \quad (13.5)$$

The corresponding time of cooling

$$(\Delta t)_{\min} \sim \frac{1}{\gamma_{ab}} \frac{T}{T_{\min}}. \quad (13.6)$$

The situation considered here is, of course, the simplest. For some other details it is necessary to take into account in the real situation.

14. Influence of turbulence on the broadening of spectral lines. — The investigation of the influence f of the turbulence on the radiation spectra is one of the problems of the kinetic theory of fluctuations in nonequilibrium plasmas (see [10-12] and the references quoted therein).

The kinetic fluctuations are these, the correlation time of which is larger or of the same order as the relaxation times of the kinetic equations. In other words the kinetic fluctuations are the fluctuations of

13. Narrowing of spectral lines by cooling of the gas under electromagnetic radiation. — Now we consider shortly the some results of the kinetic theory of the cooling the gas by the electromagnetic field [31-35].

We shall use again the kinetic equation for the distribution function of the atoms $f_a(\mathbf{P}, t)$ with the collision integral (9.1). Using the induced part of this integral in which the spectral density of the field fluctuation is :

the distribution functions of the electrons, ions and atoms.

In strongly nonequilibrium systems the collision integrals and consequently all kinetic characteristics are drastically changed on account of the kinetic fluctuations. This leads also to an essential change of the shape of the spectral lines. The interest in this problem is governed by the development of the experimental investigations of turbulent plasmas.

We mention here only some of the recent papers on the theory of the line broadening in turbulent plasma.

In paper [12] a method was developed for the investigation this problem, which is similar to the method of the kinetic theory of fluctuations [15-17].

In papers [10, 11] the investigation of the most specific problem is worked out. Especially the influence of the Langmuir turbulence on the Stark component is investigated. In [11] the corresponding theory is developed without application of the perturbation theory; in this way the region of applicability of theory is enlarged, and one may hope that experimental data may be explained.

15. Conclusion. — In the theory of the broadening of spectral lines there is yet a lot of unsolved problems, which are connected with the influence of collective processes in the nonequilibrium plasma.

The investigation of this problems is an actual but very difficult task, the solution of which needs collective efforts of researchers of different countries.

References

- [1] BARENGER, M., *Phys. Rev.* **111**, 481, 494; **112** (1958) 855.
- [2] BREENE, R. G., *The shift and shape of spectral lines*, Pergamon Press, 1961.
- [3] SOBELMAN, I. I., *Introduction to the theory of atomic spectra* (Fizmatgiz), 1963.
- [4] WAINSTEIN, L. A., SOBELMAN, I. I., YUKOV, A., *Atom excitation and spectral lines broadening* (Nauka) 1979.
- [5] GRIEM, H., *Plasma spectroscopy*, McGraw-Hill, 1964.
- [6] GRIEM, H., *Spectral line broadening by plasmas*, Academic Press, 1974.
- [7] LISITZA, V. S., Stark broadening of hydrogen lines in plasmas *Sov. Phys. Usp.* **122** (1977) 369.
- [8] ECKER, G., SCHUMACHER, A., *S. Naturforsch.* **30A** (1975) 413.
- [9] KURILENKOV, YU. A., FILINOV, V. S., Microfield theory in non ideal plasma, *T.V.T.* **14** (1976) 886.
- [10] OKS, YE. A., CHOLIN, G. V., *J.E.T.P. Sov. Phys. Techn. Phys.* **68** (1975) 74.
- [11] JUSANACHVILI, A. I., OKS, A. A., *J.E.T.P. Sov. Phys. Techn. Phys.* **73** (1977) 2142.
- [12] CAPEIS, H., VOSLAMBER, D., *Phys. Rev. A* **15** (1977) 1751.
- [13] KIM, S., *Nuovo Cim.* **44B** (1978) 409.
- [14] ASMARIAN, E. A., KLIMONTOVICH, YU. L., *Theory of spectral line broadening in partially ionized non equilibrium plasma* (Vestnik MGU) 1974, n° 3.
- [15] KLIMONTOVICH, YU. L., *Kinetic theory of electromagnetic processes* (Nauka) 1979.
- [16] KLIMONTOVICH, YU. L., *Kinetic theory of the nonideal gas and of the nonideal plasma*, Moscow, 1975, Pergamon Press, 1979.
- [17] KLIMONTOVICH, YU. L., Kinetic theory of fluctuations in gases and plasma; *Proc. of the 1977 International Summer School in statistical mech.*, Warszawa, 1978.
- [18] VLASOV, A. A., FURSOV, V. S., *J.E.T.P. Sov. Phys. Techn. Phys.* **6** (1936) 378, 750.
- [19] RAUTIAN, S. G., SOBELMAN, I. I., Influence of interactions on Doppler broadening of spectral lines, *Sov. Phys. Usp.* **90** (1966) 209.
- [20] HOLSTEIN, T., *Phys. Rev.* **72** (1947) 1212; **83** (1951) 750.
- [21] BIBERMAN, L. M., *Sov. Phys. Doklady.* **27** (1940) 6; *J.E.T.P. Sov. Phys. Techn. Phys.* **17** (1947) 416.
- [22] IDYAKONOV, M., PEREL, V. I., *J.E.T.P. Sov. Phys. Techn. Phys.* **47** (1967) 1483.
- [23] UDOVIN, YU. A., YERMATCHENKO, U. M., *J.E.T.P. Sov. Phys. Techn. Phys.* **54** (1968) 148.
- [24] BETEREV, I. M., MITYUGIN, YU. A., RAVTIAN, S. G., TCHEBOTAYEV, V. P., *J.E.T.P. Sov. Phys. Techn. Phys.* **58** (1970) 1943.
- [25] DYAKONOV, M. I., *J.E.T.P. Sov. Phys. Techn. Phys.* **58** (1970) 1090.
- [26] ARONOWITZ, F., *Appl. Optics* **7** (1972) 2146.
- [27] KHROMYKH, A. M., YAKUCHEV, A. I., *Kvantovaya Elektronika* **4** (1977) 27.
- [28] KOGAN, V. I., in *Plasma physics and the problems of controlled thermonuclear reactions* (M. A. Leontovich, ed.), Pergamon Press, vol. 4, 1960, p. 305.
- [29] VOSLAMBER, D., *Z. Naturforsch.* **24A** (1969) 1458.
- [30] CAPEIS, H., VOSLAMBER, D., *Phys. Rev.* **5A** (1972) 2528.
- [31] ASHKIN, A., *Phys. Rev. Lett.* **25** (1970) 1321.
- [32] HANSCH, T. W., SCHAWLOW, A. L., *Opt. Comm.* **13** (1975) 68.

Electric discharge pumping of excimer lasers (*)

W. H. Long Jr. and M. L. Bhaumik

Northrop Corporation, Northrop Research and Technology Center,
Palos Verdes Peninsula, California 90274, U.S.A.

Résumé. — Nous avons examiné le rendement et l'agrandissement à l'échelle des lasers à excimer (excités par de faisceau permet d'obtenir de haute énergie spécifique dans de grandes structures avec des courants de faisceau maintenue par faisceau électronique semble le plus prometteur pour l'obtention de grandes énergies. Les performances de ce type de laser peuvent être prédites grâce à un modèle englobant l'analyse de la cinétique des électrons, de la chimie de la décharge et le résonateur optique. Les limitations introduites par les problèmes de stabilité de décharge sont minimisées grâce à l'emploi d'un faisceau électronique uniforme. Cette bonne uniformité de faisceau permet d'obtenir de haute énergie spécifique dans de grandes structures avec des courants de faisceau électronique modérés.

Abstract. — The efficiency and scalability of excimer lasers pumped by electric discharge is examined using the KrF laser as a generic example. E-beam sustained discharges show the greatest promise for scaling to high energy. Analyses of electron kinetics, discharge chemistry, and optical resonator are incorporated into a model for predicting the performance of such lasers. Limitations imposed by discharge stability are minimized by ensuring uniform e-beam deposition. With good uniformity, high specific energy can be achieved in large devices using low beam currents.

1. Introduction. — Excimer lasers currently provide the most efficient and powerful sources of coherent radiation in the ultraviolet and visible regions. These lasers have opened up the possibility of many important applications requiring visible and shorter wavelength lasers. Although significant progress has been made in developing these lasers, some crucial problems remain to be solved before their full potential can be realized. Efficient power transfer from the primary source of excitation to the laser medium is one of these problems and constitutes the major part of the discussion presented here.

An excimer is a molecule which exists only in an excited electronic state. The ground state is either repulsive or weakly bound at room temperature. The excited state is coupled to the ground state through a radiative transition typically in the visible or ultraviolet spectral regions. Lasers based on excimer transitions are free from the bottlenecking problem common to infrared and ion lasers, since the lower laser level is naturally depopulated in a very short time. Rare gases and some metal vapors form diatomic excimers in various configurations. These include homonuclear excimers, such as Xe_2^* and Hg_2^* and heteronuclear excimers (or exciplexes) such as TlXe^* and CdHg^* . The rare gases also form excimers in association with oxygen and with the halogens.

The rare gas oxides are characterized by long radiation lifetimes ($\sim 10^{-5}$ s) and small stimulated emission cross sections ($\sim 10^{-18}$ cm²) which allow efficient excitation at low power densities; however, quenching of excited states and background absorption make the rare gas oxide lasers very inefficient. Most other excimers, however, have relatively short radiative lifetimes ($\sim 10^{-8}$ s) and large stimulated emission cross sections ($\sim 10^{16}$ cm²). As a result, they require excitation at very high power densities in order to overcome fluorescence and quenching losses. Early researchers employed high current density electron beams and fast high pressure gas discharges to study these molecules.

The rare-gas dimers were the first excimers to demonstrate laser oscillations. They operate in the vacuum ultraviolet region of the spectrum from 126 nm to 176 nm. Although the conversion of electrical energy into ions and excited states and the subsequent channeling into excimers is an extremely efficient process in the rare gases, the laser efficiency of these devices is severely limited by photoionization and electron deexcitation. The excited dimer of mercury, which was the first excimer to be observed in emission, has never been made to lase, apparently due to strong, broadband absorption from the lowest lying excited state.

The most efficient excimer lasers to date have been the rare gas halides which operate at wavelengths from 175 nm to 483 nm. Their success is due in large part to the near unity branching ratio for conversion of rare gas ions and excited states into the excimer.

(*) Work supported in part by the Advanced Research Projects Agency of the Department of Defense and monitored by the Office of Naval Research.

In addition, absorption from the lowest lying excimer states is not significant. The principal limitation comes from other absorbers present in the medium, such as diatomic rare gas ions which limit the extraction efficiency to about fifty percent. Even so, the rare gas halides have so far demonstrated the highest efficiency and energy extraction per unit volume of any other laser in the visible or ultraviolet.

A typical potential energy diagram for the rare gas halide excimer is shown in figure 1. Formation of the excimer can proceed either through a long range Coulomb attraction between the positive rare gas ion and the negative halogen ion or along a curve crossing involving charge exchange between an excited rare gas atom and the neutral halogen. These formation paths, which take place via dissociative reactions or stabilized three body collisions, are referred to as the ion and metastable channels, respectively. The initial generation of rare gas ions and metastables has traditionally been accomplished with high energy electron beams. The efficiency for this process in argon is about 75 % based on energy deposited in the gas. This number excludes energy dissipated in the pulse-forming network, the diode, and the foil and foil supports, as well as energy lost by electron transport out of the excited region. In an optimum laser mixture of argon, krypton and fluorine, roughly 80 % of the argon ions and metastables form krypton fluoride (KrF) excimers. When one accounts for the thermal energy lost in the formation process, only 20 % of the deposited energy eventually results in KrF. With a 50 % extraction efficiency limited by absorption, the laser efficiency of KrF becomes typically 10 %.

The efficiency of KrF and other rare gas halides can be improved by better electrical power condi-

tioning, higher quantum efficiency, and reduced absorption. Improvements in power conditioning efficiency may be achieved through better circuit design to reduce internal losses, optimized coupling to the load, and recycling unused energy for subsequent pulses. Improved quantum efficiency can be achieved either by altering the ratio of power transferred to metastables as compared to ions or through the use of heavier rare gases with lower excitation and ionization energies. In high pressure rare gases pumped by relativistic electron beams, more than three times as many ions are created as metastables. If the same fraction of incident energy were to go exclusively into metastable states, the quantum efficiency would be improved by about 10 %. In the electric discharge, however, more metastables are produced than ions, since excitation takes place by accelerating electrons from low energy instead of decelerating them from high energy. In addition to improving the quantum efficiency, the reduced production of ions should result in less absorption. Therefore, discharge pumping of high pressure excimers is more desirable and will be discussed in further detail. Many approaches have been taken in applying electric discharge excitation to excimer lasers. They can be divided, however, into two basic groups: self-sustained and externally-sustained. In the self-sustained glow discharge, ionization is provided by electron avalanche in an applied field. This process is difficult to control once initiated and requires extremely uniform conditions to prevent collapse into an arc. Initial uniformity is achieved by carefully shaping the electrodes to produce a constant electric field and by preionizing the gas before the field is applied. If this were not done, avalanching would proceed from localized irregularities on the electrodes, sending the discharge directly into the arc phase. In the externally-sustained discharge, ionization is controlled by an external source such as an electron beam. This has the effect of decoupling the discharge impedance from the applied voltage. In the ideal case, the impedance is determined only by the gas density and the electron beam current density. The electric field can then be varied to optimize excitation of the desired species. In practice, the process of two-step ionization can transform the externally-sustained discharge into a self-sustained one. This can be prevented only by uniform e-beam deposition and tailoring of the electric field or e-beam current density.

In the self-sustained discharge, excitation and laser energy extraction must be accomplished quickly before the discharge impedance falls to such a low value that the laser medium can no longer absorb power. During this impedance collapse, the electric field falls from a value above the breakdown field to a value where all the power dissipated in the discharge goes into gas heating. Thus, there is only a short period of time when the desired levels are

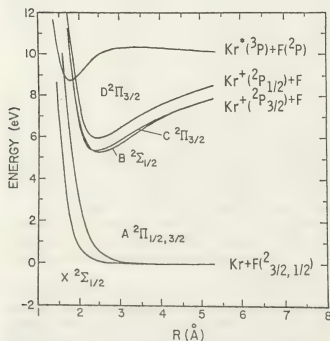


Fig. 1. — Potential energy curves for KrF.

efficiently excited. Strong coupling with the external circuit at such a low load impedance requires a low driving inductance which is difficult to achieve in large devices. An externally-sustained discharge, however, should have constant impedance as long as the external source is held constant. These devices then have the potential for long-pulse, high-energy operation. In fact, with the discharge increasing the deposited energy density, the volumetric efficiency should be much greater than with e-beam pumping alone. A KrF laser pumped by an e-beam sustained discharge has already demonstrated [1] 29 J/extracted energy from 0.12 l at 11 % intrinsic efficiency. Performance in larger devices has been much worse due to discharge instabilities caused by nonuniform e-beam deposition. These problems are discussed below using KrF as an example.

2. Electron kinetics in the KrF laser.— Since discharge pumping of the KrF laser has been demonstrated [1] to be more efficient than e-beam pumping, it is desirable to load as much energy into the discharge as possible. An analysis of the limit of energy loading and the laser efficiency requires an understanding of the electron and excited-state kinetics in the discharge. If the ratio of metastable density to ground state neutral density, m/N , is 10^{-5} or less, then electron-metastable collisions have a negligible effect on the electron energy distribution [2] and the electron kinetics can be decoupled from the excited-state chemistry model. This allows a parameter study to be made of electron transport and excitation processes in the KrF laser which can be used as input to a complete laser model including optical resonator and external circuit [3].

The following discussion will emphasize the importance of including collisions between electrons via a screened Coulomb potential in the Boltzmann analysis of the heavy rare gases. At fractional electron densities typical of e-beam sustained KrF laser discharges ($n/N = 3 \times 10^{-6} - 3 \times 10^{-5}$) these collisions appreciably alter both the electron mobility and the rate constants for excitation and ionization. Because of the sensitivity of the high energy tail of the electron energy distribution (Fig. 2), the effect of electron-electron collisions is most significant for those processes with the highest threshold energies. The reason that electron-electron collisions are not important in modeling the CO and CO₂ lasers is that the pumping occurs at much lower energies and typical values of n/N are only 10^{-7} . These collisions must be considered, however, in analyzing discharge stability because of the large effect on ionization rates.

The method employed in this study to solve the Boltzmann transport equation has been described previously [4]. The contribution to the collision term arising from Coulomb collisions between electrons is derived by Shkarofsky *et al.* [5]. The value of $\ln A$ is taken to be 10, where A is the ratio of Debye length

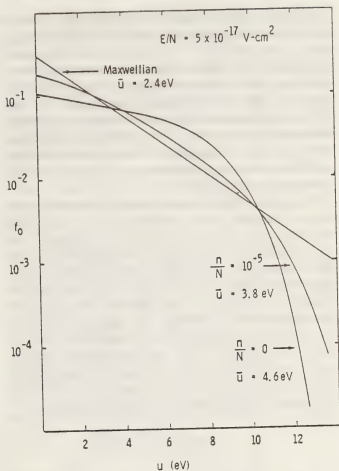


Fig. 2.— Electron energy distribution in Ar-Kr.

to the impact parameter for a 90° deflection. The momentum transfer cross sections used are those of Milloy *et al.* [6] in argon and Frost and Phelps [7] in krypton. The cross sections for electronic excitation were measured by Schaper and Scheibner [8] and the normalization checked by Jacob *et al.* [9]. The data of Rapp *et al.* [10] were used for ionization of ground state atoms.

It is assumed that the effect of fluorine on the electron energy distribution is negligible for concentrations below a few tenths of one percent. The cross sections for direct vibrational and rotational excitation are expected to be small compared to dissociation [11]. A resonant process leads to negative ion production via dissociative attachment. The cross section for attachment of electrons to F₂ has recently been measured by Chantry [12]. Using this cross section, the effect of F₂ on the electron energy distribution was found to be small, except at low values of E/N and n/N . Under normal operating conditions then, the attachment rate is proportional to the fluorine concentration and can be found from the measured cross section and the solutions of Boltzmann's equation in the rare gas mixture.

Because of the importance of electron-electron collisions, E/N is no longer the sole parameter characterizing the electron energy distribution in a given

gas mixture. The fractional ionization, n/N , must be specified as well. If the fractional metastable density, m/N , is less than 10^{-5} , it is not an important parameter. Since the largest fractional metastable density consistent with stable discharge operation is about 3×10^{-5} , the effects of superelastic collisions and metastable ionization on the electron energy distribution can be neglected. In a stable discharge, therefore, we can completely characterize the electron properties in a given gas mixture with the two parameters, E/N and n/N .

The electron drift velocity and mean energy are plotted in figure 3 as a function of E/N for typical values of n/N in a 95% Ar 5% Kr mixture. The curves labeled $n/N = 0$ apply to fractional ionizations below about 10^{-7} . The drift velocity is found to be more than a factor of two higher at typical electron densities than it is at low electron density where electron-electron collisions are unimportant. The calculated drift velocity in pure argon with $n/N = 0$ agrees within 5% with the experimental data of Pack *et al.* [13], Robertson [14] and Brambling [15] over the E/N range from 10^{-19} V cm² to 10^{-15} V cm². The power loading into the discharge is given by

$$E \cdot J = eN^2 \frac{n}{N} v_e \left(\frac{E}{N}, \frac{n}{N} \right) \frac{E}{N}.$$

As a result of the n/N dependence of v_e , this function will increase faster than linearly with n/N at constant E/N .

All the energy which goes into the discharge is converted through various channels into heat, electronic excitation, or ionization of the gas. The dominant processes include heating by momentum transfer

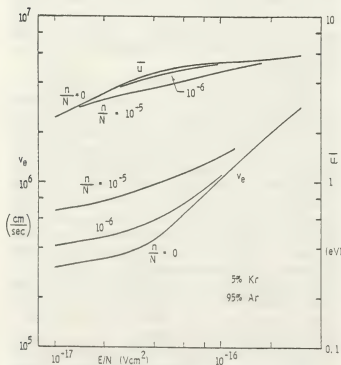


Fig. 3. — Electron drift velocity and mean energy.

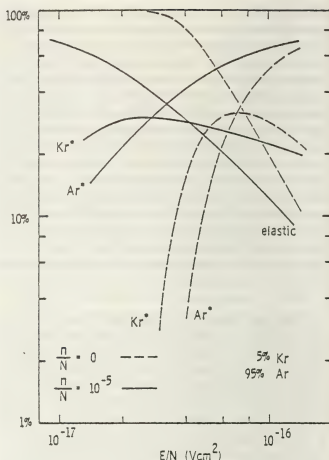


Fig. 4. — Discharge power partitioning.

in elastic collisions and excitation of various electronic states in argon and krypton. The cross sections for excitation of these electronic states are lumped together for each gas and represent an effective cross section for production of the metastable. The fractional power into each of these channels is plotted in figure 4 as a function of E/N for typical values of n/N . The power going into ionization of metastables and ground state atoms is negligible in the parameter range considered here. The effect of electron-electron collisions is dramatic in moving the range of efficient production of metastables to lower values of E/N . This has a significant impact on the predicted operating regime of the KrF laser.

The highest specific laser energy to date from an e-beam sustained discharge in Ar-Kr-F₂ was observed at an $E/N = 3 \times 10^{-17}$ V cm² [1]. The measured discharge efficiency was 20%, and yet without electron-electron collisions the theory would predict virtually no pumping of metastable states by the discharge at this E/N .

The quantum efficiency for producing KrF* can be derived from the power partitioning curves by defining

$$\eta = \frac{h\nu}{e} \left[\frac{f(\text{Ar}^*)}{11.8 \text{ eV}} + \frac{f(\text{Kr}^*)}{9.9 \text{ eV}} \right].$$

The numerator in each term is the fraction of discharge power going into the metastable and the denominator

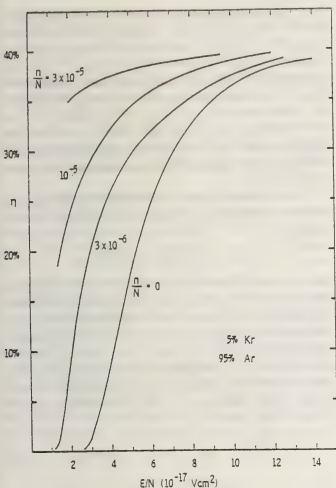


Fig. 5. — Quantum efficiency for producing KrF*.

is the energy of the metastable. This function is plotted in figure 5. At low E/N the efficiency falls off because of elastic heating and at high E/N it approaches the quantum efficiency of Ar* at 42%. The actual production efficiency will be slightly less than this because the excitation is distributed over a number of levels above the metastable. This correction will be least important at low E/N where the electrons excite preferentially those states with the lowest thresholds. Reactions which intercept the energy transfer from the metastables to KrF* will also reduce the production efficiency.

The maximum extraction efficiency for converting these upper laser levels to laser photons is given approximately by $\frac{t}{a+t}$, where t is output coupling and a is the round trip cavity absorption. For the device in reference 1 with a 50 cm cavity containing 4 torr F₂, $a \approx 20\%$. With $t = 20\%$, the maximum extraction efficiency is 50%. From figure 5 the discharge efficiency at $E/N = 3 \times 10^{-17} \text{ V cm}^2$ and $n/N = 3 \times 10^{-5}$ is 36%. The resulting net efficiency based on energy deposited in the discharge is therefore 18% in good agreement with experiment. The efficiency would appear to be a strong function of E/N and n/N . However, operating conditions in an e-beam sustained discharge are such that high electron

densities give rise to low electric field strengths and consequently the discharge efficiency is nearly constant.

In summary, a parametric study of the electron kinetics in an Ar-Kr-F₂ discharge shows that E/N and n/N are the critical parameters, while m/N and F_2/N can be neglected when they are smaller than 10^{-5} and 10^{-3} respectively. Electron-electron collisions play a significant role in increasing electron mobility and in raising the metastable production efficiency at low values of E/N . Any comprehensive model of the rare gas halide lasers must include these effects.

3. KrF kinetics. — The kinetics which lead to the population of the KrF* state in an Ar-Kr-F₂ mixture have been investigated by various laboratories. The principal channels under moderate e-beam pumping ($< 50 \text{ A/cm}^2$) proceed through the argon ion and metastable states. At high current densities, the production of Ar⁺ and Ar* under e-beam excitation is roughly 3.5 to 1 with a total efficiency of 75%. The remaining 25% of the incident energy is lost via radiation and elastic heating. At current densities less than 50 A/cm^2 the principal neutralization process is ion-ion recombination, i.e.



These reactions are responsible for populating the KrF* and ArF* states. Some of the ArF*, which is formed in the recombination of Ar⁺ and Ar₂⁺, is converted to KrF* through the displacement reaction,



The rest is lost via quenching and spontaneous emission. This loss amounts to about 10% of the Ar⁺ ions originally formed. Since it takes about 26 eV to create each Ar⁺ ion, the quantum efficiency for producing KrF* at 5 eV from Ar⁺ is 19%, and the net efficiency of the ion channel is then 17%. This, however, neglects the metastables which are also formed by e-beam excitation. The same 26 eV which produced one ion will also generate about 0.3 metastables which have a 63% chance of forming KrF*. This raises the overall efficiency for e-beam pumping to 20%. The neutral channel processes will be discussed below.

Under discharge pumping of KrF, about 80% of the input power goes into excited rare gas states Ar* and Kr*. The remaining 20% is lost in elastic scattering and dissociative attachment to F₂. The ratio of Ar* to Kr* produced is about two to one as shown in figure 4. Very few ions are generated by the discharge. There are two dominant channels for converting Ar* to KrF* (Fig. 6); one through the ArF* state and the other through the Kr* state. Typically, with a total pressure of three atmospheres and

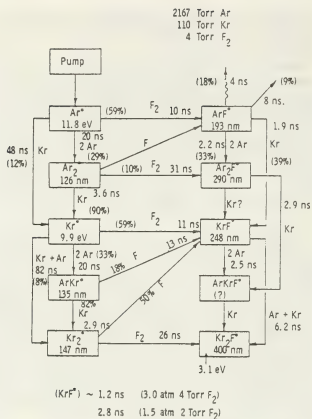
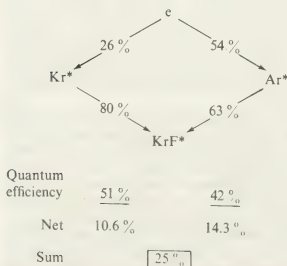


Fig. 6. — Neutral channels.

0.17% F₂, about 60% of the Ar* react with F₂ to form ArF*, which has a 55% chance of being converted to KrF*. About 37% of the Ar* undergo excitation transfer to Kr*, either directly or via Ar₂*. The remaining 3% end up as Ar₂F*. The Kr*, formed either through this channel or directly by the discharge, have a 60% chance of producing KrF*. The other 40% go into forming the rare gas dimers ArKr* and Kr₂*. It is believed that when these excited states react with F₂ about half of them produce KrF* and the rest form the ArKrF* and Kr₂F* states. The resulting discharge efficiency is summarized below:



Thus discharge pumping of KrF* is slightly more efficient than pure e-beam pumping based on energy deposited. However, wall-plug efficiency for the e-beam device will be much less due to a 50% loss in the cooled foil and foil support structure and additional losses due to scattering in the gas. The e-beam also produces molecular ions which absorb at the laser frequency. In a practical device it is therefore desirable to achieve the highest possible ratio between discharge and e-beam pumping consistent with long pulse stability.

The production rate of the KrF* state, R_p , can now be expressed as a function of the input power. Thus,

$$R_p h\nu = 0.25 P_d + 0.20 P_{eb} \quad (1)$$

where P_d and P_{eb} are the discharge and e-beam power absorbed by the gas. The loss of KrF* includes quenching by F₂, spontaneous emission and a three-body reaction leading to Kr₂F*. All of these processes will be lumped into a single decay rate, $1/\tau$. If the gain profile is homogeneously broadened, then the loss of KrF* by stimulated emission is proportional to the laser intensity, I . The continuity equation for KrF* is then

$$\frac{\partial N^*}{\partial t} = R_p - N^*/\tau - \sigma I N^*/h\nu \quad (2)$$

where σ is the cross section for stimulated emission.

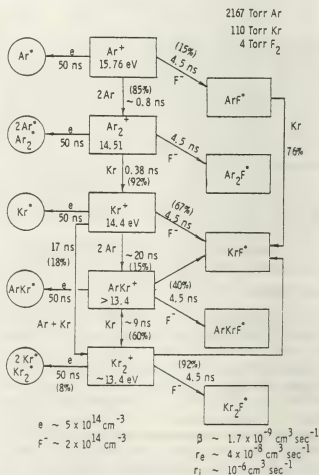


Fig. 7. — Ion channels.

The steady state population density is given by

$$N^* = R_p / (1/\tau + \sigma I / h\nu).$$

In terms of the saturated gain, $g = \sigma N^*$, and the small signal gain, $g_0 = R_p \sigma \tau$, this becomes

$$g = g_0 (1 + I/I_s).$$

The laser saturation intensity, $h\nu/\sigma\tau$, is the intensity at which stimulated emission equals quenching.

4. Optical resonator.—As discussed above, for the case of homogeneous laser transitions, the saturated gain coefficient g is related to the small signal gain coefficient g_0 by $g = g_0/(1 + \xi_+ + \xi_-)$, where ξ_+ and ξ_- are the laser intensities for the $+$ and $-x$ directions normalized to the saturation intensity. In addition to gain, the KrF laser medium contains several species which absorb at the laser frequency. This absorption is distributed throughout the cavity and may also show saturation effects. The species which exhibit gain and absorption in the KrF laser are listed in table I along with their respective saturation intensities defined as $I_s = h\nu/\sigma\tau$ where σ is the optical cross section for stimulated emission or absorption and τ is the mean lifetime of the particle.

Table I.

	σ (\AA^2)	τ (ns)	I_s (MW/cm 2)
KrF*	2	1.5	2.6
Ar $_2^+$	0.15	2.8	19
Kr $_2^+$	0.075	2.8	38
F*	0.085	2	47
F $_2$	0.00015	—	—
			3 atm 5% Kr 0.17% F $_2$ 20 A/cm 2

The growth of laser intensity in the $+$ x direction is governed by the equation,

$$\frac{1}{\xi_+} \frac{\partial \xi_+}{\partial x} = \frac{g_0}{1 + \xi_+ + \xi_-} - \sum_n \frac{\alpha_n}{1 + (\xi_+ + \xi_-) \frac{I_s}{I_n}} \quad (3)$$

where I_s is the saturation intensity for stimulated emission and I_n is the saturation intensity for the n th absorbing species. Since the gain and absorption are isotropic $\frac{1}{\xi_+} \frac{\partial \xi_+}{\partial x} = -\frac{1}{\xi_-} \frac{\partial \xi_-}{\partial x}$ and consequently

$$\xi_+ \xi_- = \text{constant} = \xi_0.$$

Using this expression to relate ξ_- to ξ_+ in eq. (3) we have, dropping the pluses,

$$\frac{1}{\xi} \frac{\partial \xi}{\partial x} = \frac{g_0}{1 + \xi + \xi_0^2/\xi} - \sum_n \frac{\alpha_n}{1 + (\xi + \xi_0^2/\xi) \frac{I_s}{I_n}} \quad (4)$$

If the cavity is defined by a perfect reflector at $x=0$ and a partial with reflectivity R at $x=L$, then

$$\xi(0) = \xi_0 \quad \text{and} \quad \xi(L) = \xi_0 / \sqrt{R}.$$

When eq. (4) is integrated from $x=0$ to $x=L$, an expression relating ξ_0 , R , g_0 , and α_n is obtained in principle. Then the laser output intensity is given by $(1-R)\xi(L) = \xi_0(1-R)/\sqrt{R}$.

In practice a simple closed-form solution to eq. (4) is only obtained if we approximate the distributed absorption as a lumped loss, a , in the output mirror. Integrating eq. (4) without the absorption term we obtain,

$$(\xi - \xi_0) + \ln(\xi/\xi_0) - \xi_0^2 \left(\frac{1}{\xi} - \frac{1}{\xi_0} \right) = g_0 x. \quad (5)$$

Evaluating this at $x=L$ with the boundary condition $\xi(L) = \xi_0/\sqrt{R}$ gives,

$$(1-R)\xi_0/\sqrt{R} = g_0 L - \frac{1}{2} \ln \frac{1}{R}. \quad (6)$$

The output intensity, defined as

$$I_{\text{out}} = (1-R-a)\xi(L)I_s,$$

is then

$$I_{\text{out}} = I_s \frac{t}{a+t} \left(g_0 L - \frac{1}{2} \ln \frac{1}{R} \right) \quad (7)$$

where $t = 1 - R - a$ is the transmissivity of the output mirror.

We now define the extraction efficiency, η_c , as the ratio of actual output intensity to the intensity which would be obtained if every KrF* generated in the cavity resulted in a photon leaving the output mirror. This maximum intensity is $I_{\text{max}} = R_p V h\nu / A = g_0 L I_s$, where R_p is the generation rate per unit volume of KrF*. The extraction efficiency from eq. (7) is then

$$\eta_c = \frac{t}{a+t} \left(1 - \frac{1}{g_0 2L} \ln \frac{1}{R} \right). \quad (8)$$

In the KrF laser, the approximation of lumped losses at the mirrors is not very good, since the round trip absorption, a , often approaches unity and the resulting transmissivity, t , may go negative. Furthermore, the threshold gain derived from eq. (8) is independent of the absorption, a result which is clearly unphysical if the absorption is distributed. For if gain equals absorption, the medium will certainly not lase even though eq. (8) says it will if we chose the right reflectivity.

An approximation which yields more viable results in the presence of large absorption losses is to assume that the intracavity intensity, $I = (\xi_+ + \xi_-) I_s$, is constant, independent of x . Eq. (4) can now be integrated readily to obtain, $\ln(\xi/\xi_0) = (g - \alpha)x$, where g and α are the saturated gain and absorption respectively. Applying the previous boundary condition at $x=L$ yields

$$\frac{1}{2L} \ln \frac{1}{R} = g - \alpha = \frac{g_0}{1 + I/I_s} - \sum_n \frac{\alpha_n}{1 + I/I_n}. \quad (9)$$

After multiplying both sides by c , this equation says that the rate at which photons are being extracted from the cavity is equal to the difference between the rate at which they are produced and the rate at which they are absorbed. The output intensity is just the product of the extraction rate and the number of photons in the cavity divided by the area of the output aperture, A , i.e.

$$I_{\text{out}} = \frac{c}{2L} \ln \frac{1}{R} \frac{IV}{ch\nu} \cdot \frac{1}{A} \cdot h\nu = \frac{I}{2} \ln \frac{1}{R}. \quad (10)$$

If $I_n \gg I_s$ (see Table 1) then $\alpha \sim \sum_n \alpha_n$ and eq. (9)

can be solved for I directly. Thus,

$$I = I_s \left(\frac{g_0}{\alpha + \frac{1}{2L} \ln \frac{1}{R}} - 1 \right) \quad (11)$$

and the output intensity is therefore,

$$I_{\text{out}} = \frac{I_s}{2} \left(\ln \frac{1}{R} \right) \left(\frac{g_0}{\alpha + \frac{1}{2L} \ln \frac{1}{R}} - 1 \right). \quad (12)$$

The extraction efficiency analogous to eq. (8) is

$$\eta_c = \frac{1}{2L} \left(\ln \frac{1}{R} \right) \left(\frac{1}{\alpha + \frac{1}{2L} \ln \frac{1}{R}} - \frac{1}{g_0} \right). \quad (13)$$

This expression has been compared with the numerical solution of eq. (4) and was found in good agreement for values of R down to 30% independent of α . In contrast to eq. (8) the threshold gain is now a function of the distributed absorption. If there is also some lumped absorption, a , in the optical components, this can be taken care of as before and the final expression for extraction efficiency becomes,

$$\eta_c = \frac{t}{a+t} \frac{1}{2L} \left(\ln \frac{1}{R} \right) \left(\frac{1}{\alpha + \frac{1}{2L} \ln \frac{1}{R}} - \frac{1}{g_0} \right). \quad (14)$$

If $a \ll t$ the optimum reflectivity is given by

$$\frac{1}{2L} \ln \frac{1}{R} = \sqrt{\alpha g_0} = \alpha \quad (15)$$

and the maximum extraction efficiency is, from eq. (14),

$$\eta_c^{\text{max}} \sim \left(1 - \sqrt{\frac{\alpha}{g_0}} \right)^2. \quad (16)$$

This function is plotted in figure 8.

In a practical device the mirrors cannot be placed directly adjacent to the gain region. Because of the electric field applied to the discharge, the mirrors must be set back a distance at least equal to the electrode separation. Alternatively, windows may be

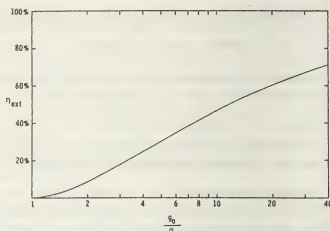


Fig. 8. — Laser extraction efficiency.

used to contain the laser gas and the mirrors mounted externally. We must then define several different lengths and modify our expression for the extraction efficiency and optimum reflectivity. Let L remain the mirror separation and define l_s as the gain length and l_n the length containing the n th absorbing species. Then eq. (14) becomes

$$\eta_c = \frac{t}{a+t} \frac{1}{2} \left(\ln \frac{1}{R} \right) \left(\frac{1}{\sum_n \alpha_n l_n + \frac{1}{2} \ln \frac{1}{R}} - \frac{1}{g_0 l_s} \right) \quad (17)$$

and the optimum reflectivity is,

$$\frac{1}{2} \ln \frac{1}{R} = \sqrt{g_0 l_s \sum_n \alpha_n l_n} = \sum_n \alpha_n l_n. \quad (18)$$

5. Discharge stability. — The glow discharge, which is an effective excitation technique for a variety of gas lasers, is unstable at high pressures unless sustained by an external ionization source. In the self-sustained mode, the initial glow collapses into a filamentary arc after a time which depends on the pressure and discharge power density. This occurrence can be prevented by keeping the discharge in a regime where the principal ionization is supplied externally.

In the e-beam sustained KrF laser, a uniform glow can be maintained for times up to a microsecond if the discharge voltage is kept below a well-defined limit. Under heavy pumping conditions, the ionization of metastable states becomes a significant source of electrons. When this two-stage ionization exceeds ionization by the e-beam, the discharge goes into a volume runaway and arcs after a few hundred nanoseconds. In order to determine the limits of the stable operating regime, a simple KrF discharge model is proposed as set forth in figure 9.

The quantities S_i and S_m are the e-beam source terms for ions and metastables respectively. The metastable ionization rate, k_m , is approximately equal to $6 \times 10^{-8} \text{ cm}^3 \text{ s}^{-1}$. β is the attachment rate

Plasma kinetics :

$$\frac{\partial n}{\partial t} = S_i + k_{mi} mn - \beta F_2 n$$

$$\frac{\partial F_-}{\partial t} = \beta F_2 n - \gamma F_-(n + F_-)$$

$$\frac{\partial m}{\partial t} = S_m + k_m Nn - k_{mi} mn - QF_2 M$$

Discharge circuit :

$$L \frac{d^2 I}{dt^2} + \frac{dV}{dt} + I/C = 0$$

$$I = eAnv_e + \frac{V}{R}$$

Fig. 9. — Simple KrF laser model.

to fluorine and γ is the ion-ion recombination rate. The continuity equations for the metastables can be lumped together with a single density, m , because the quenching rate, Q , and ionization rate, k_{mi} , are fairly independent of species. The metastable production rate, k_m , is then a weighted sum of the production rates for Ar* and Kr*. This rate is a strong function of E/N and is plotted in figure 10 for several values of fractional ionization n/N .

Since the time constant for the external circuit,

$$\sqrt{LC} \sim 200\text{-}500 \text{ ns},$$

is typically large compared to that for equilibrium of the ion and metastable species densities, the equations for the latter can be solved in the quasi-steady-state approximation. The stability of the

steady-state solution is then found by applying a small perturbation with time dependence proportional to $\exp(-i\omega t)$ and looking for positive imaginary eigenvalues of ω . When this is done for the equations in figure 9, the resulting linearized system for the perturbation on electron and metastable densities is,

$$(i\omega + k_{mi} m_0 - \beta F_2) \tilde{n} + k_{mi} n_0 \tilde{m} = 0 \quad (19)$$

$$(k_m N - k_{mi} m_0) \tilde{n} + (i\omega - k_{mi} n_0 - QF_2) \tilde{m} = 0 \quad (20)$$

The eigenvalues are then solutions of

$$\omega^2 + i\omega \left(\frac{S_i}{n_0} + QF_2 + k_{mi} n_0 \right) - \frac{S_i}{n_0} QF_2 - k_{mi} n_0 (\beta F_2 - k_m N) = 0 \quad (21)$$

Thus $2\omega = -b \pm \sqrt{b^2 - 4c}$, where b is the coefficient of ω in eq. (21) and c is the constant term. Since b is positive imaginary, ω will have a positive imaginary part only if $c > 0$. The stability requirement is then,

$$\frac{S_i}{n_0} QF_2 > k_{mi} n_0 (k_m N - F_2) \quad (22)$$

or

$$m_0 < m_p = 1/2 \left(\frac{\beta F_2}{k_{mi}} + \frac{S}{QF_2} \right), \text{ where } S = S_i + S_m.$$

In the limit of low e-beam current density, the second term in parentheses is negligible and the condition for stability reduces to that found previously [16]. In its present form the maximum metastable density is a function of e-beam source strength.

The stability criterion as presented in eq. (22) is not very useful in defining a practical operating regime since it involves the steady-state metastable density, m_0 . In order to express this in terms of experimentally definable parameters, we solve the steady-state equations for m . From figure 9,

$$n_0 = S_i / (\beta F_2 - k_{mi} m_0).$$

Using this in the equation for m , we arrive at a quadratic equation for m_0 with solutions,

$$m_0 = m_p \pm \sqrt{m_p^2 - m_c^2}, \quad (23)$$

where

$$m_c^2 = (S_m \beta F_2 + S_i k_m N) / QF_2 k_{mi}.$$

If $m_c < m_p$, then two real solutions exist, one of which, $m_0 < m_p$, is stable and the other, $m_0 > m_p$, is unstable. The stable solution is the one which is reached first as m increases from zero. Stability will be maintained as long as $m_c < m_p$ is satisfied.

A new stability criterion can now be written in

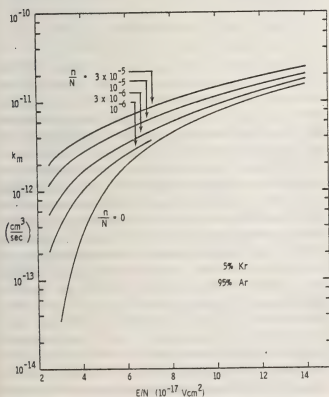


Fig. 10. — Metastable production rate.

the form of an upper limit on E/N or discharge voltage, i.e.

$$k_m \left(\frac{E}{N}, \frac{n}{N} \right) < \frac{k_{mi} Q F_2}{S_i N} \left[\frac{1}{4} \left(\frac{\beta F_2}{k_{mi}} + \frac{S}{Q F_2} \right)^2 - \frac{S_m \beta}{Q k_{mi}} \right]. \quad (24)$$

The term on the right side of the inequality is only weakly dependent on E/N . The value of n/N on the left is the steady-state fractional ionization at the point where

$$m_0 = m_p \quad \text{and} \quad n_0 = 2 S_i / (\beta F_2 - k_{mi} S / Q F_2).$$

For a given e-beam current, gas density, N , and fluorine density, F_2 , we can use figure 10 and eq. (24) to establish the critical value of E/N above which the discharge current will run away. Experimentally, with the current rise limited by circuit inductance, this runaway is seen as a drop in discharge impedance and a cessation of lasing.

In figure 11 the critical value of E/N is plotted as a function of e-beam power density for several values of total pressure and fluorine concentration. The experimental points are taken from the current and voltage waveforms obtained on the 0.1 l device described in reference [1]. The functional dependence of E/N on P_{eb} is roughly $E/N \propto P_{eb}^{-0.5}$ for the conditions indicated. The dependence of E/N on F_2 concentration is likewise $E/N \propto F_2^{1.5}$ and on total number density $E/N \propto N^{-0.5}$. These expressions are only approximately valid within the range of parameters given in figure 11.

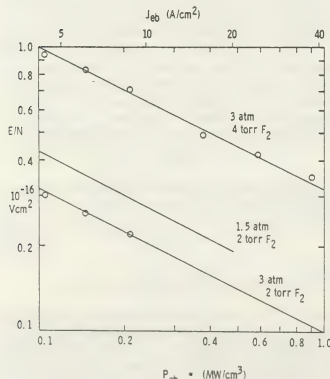


Fig. 11. — Maximum E/N vs. e-beam density.

A subsidiary criterion for stability is evident from the expression for steady-state electron density, i.e.

$$n_0 = \frac{S_i}{\beta F_2 - k_{mi} m_0}. \quad (25)$$

In order for n_0 to be positive, m_0 must be less than $\beta F_2 / k_{mi}$. If $S / Q F_2 > \beta F_2 / k_{mi}$, then eq. (25) becomes the limiting condition on E/N . However, over the range of parameters considered here, $S / Q F_2$ is always less than $\beta F_2 / k_{mi}$.

Knowing the value of E/N at which the discharge becomes unstable, we can determine the maximum discharge power loading under given operating conditions. The discharge power density is given by

$$P_d = J_e E = env_e E.$$

The electron drift velocity, v_e , was shown in figure 3 as a function of E/N and n/N . Within the range,

$$1 \text{ Td} < E/N < 10 \text{ Td} \quad \text{and} \quad 10^{-6} < n/N < 10^{-5},$$

v_e can be approximated by

$$v_e = b \left(\frac{n}{N} \right)^{0.2} \left(\frac{E}{N} \right)^{0.4}. \quad (26)$$

Then P_d is given by

$$P_d = ebN^2 \left(\frac{n}{N} \right)^{1.2} \left(\frac{E}{N} \right)^{1.4}. \quad (27)$$

For $m_0 \ll m_p$, n/N is proportional to J_{eb}/F_2 . The maximum E/N is proportional to $J_{eb}^{-0.5} F_2^{1.5} N^{-1.0}$. Therefore $P_d \propto J_{eb}^{0.5} F_2^{0.9} N^{0.6}$. Writing this in terms of the e-beam power density $P_{eb} \sim J_{eb} N$, we have

$$P_d \propto P_{eb}^{0.5} F_2^{0.9} N^{0.1}.$$

The maximum discharge power density is proportional to the square root of the e-beam power deposition. This means that the power enhancement factor, P_d/P_{eb} , is smaller at higher e-beam current densities. It is larger at higher F_2 concentrations and, in a given mixture, at higher total pressures.

For overall system efficiency, it is desirable to have P_d/P_{eb} as large as possible. In this respect then it is better to operate at low beam currents and high F_2 and total pressures. The limitation in going to low e-beam current densities is that as the total power is reduced, the ratio of small signal gain to absorption is less and extraction efficiency becomes poor, figure 8. The limitation on fluorine concentration arises from quenching of the KrF^* state and absorption by F_2 and F_{2-} . At higher pressures there is more three-body quenching of KrF^* and increased formation of the trimers, Ar_2F^* , ArKrF^* and Kr_2F^* by interception of energy channels leading to KrF^* . There is therefore an optimum choice of the parameters N , F_2 , and J_{eb} , which will give the highest overall efficiency and laser output.

6. Scaling problems of the KrF laser. — The KrF laser appears to have the greatest potential of all other candidates for scaling to very high average powers in the near ultraviolet. The highest specific energy (30 J/l) and efficiency (10 %) to date have been demonstrated in a small device (0.12 l) with an e-beam sustained discharge. In larger devices, however, discharge loading has not been nearly as effective and in most cases has been abandoned as a viable pumping technique. We believe that efficient discharge pumping in large devices can be achieved and that this represents the best alternative for a reasonably sized high average power laser.

We have undertaken a systematic study of the electron kinetics, discharge stability, e-beam deposition, and optical extraction in order to determine the scalability of the KrF laser and to assess the relative merits of e-beam *versus* discharge pumping. We find that discharge power loading is limited by the nonuniformity of e-beam deposition and by the ability of the external circuit to couple energy into a low-impedance load. If the energy deposition is made uniform through the use of opposed e-beams and the device is operated at low beam currents to maximize the discharge impedance, then an extracted laser energy of 45 J/l may be achieved with 8 % efficiency. This is about a factor of three more energy than could be extracted with an e-beam alone. The implications are that a much smaller device can be built for a given average power with all the associated savings in optics, size and gas handling equipment.

The maximum discharge power loading, P_d , consistent with stable, long-pulse operation is proportional to the square root of the e-beam power density, P_e . This relationship has been derived from a discharge stability analysis and has been confirmed experimentally. The stability criterion for discharge pumping is then,

$$P_d < \gamma P_e^{1/2}. \quad (28)$$

For the gas mixture 94.8 % Ar 5 % Kr 0.17 % F₂ at a total pressure of 3 atm, the constant, γ , is equal to 1.3 when P_d and P_e are given in MW/cm². The above condition must be satisfied at every point in the discharge or two-stage ionization will lead to volume runaway and eventual arcing.

Another condition which must be satisfied in the discharge is current continuity. Near the center of large planar electrodes, this implies constant current density along a field line, i.e.

$$J_d = env_e \left(\frac{E}{N}, \frac{n}{N} \right) = \text{constant} \quad (29)$$

where E is the electric field strength and N is the gas density. Since the electron density, n , is controlled by the e-beam deposition which varies with distance from the foil, the electric field must compensate by changing the electron drift velocity, v_e .

Using the expression for v_e from eq. (26), the current density is given by,

$$J_d = enb \left(\frac{n}{N} \right)^{1.2} \left(\frac{E}{N} \right)^{0.4} \quad (30)$$

from which it is clear that along a field line E/N must vary inversely as the cube of n/N in order to keep the current density constant.

Monte Carlo simulation studies and experimental measurements of the e-beam energy deposition in gases show that the deposition falls off more or less linearly away from the foil for the range of beam energies and foil thicknesses considered here. This spatial dependence can be written as,

$$P_d(x) = P_{e0} [1 + (r - 1)x/d] \quad (31)$$

where r is the ratio of the power density at a distance d from the foil to the power density at the foil. The source density, S , for generating electrons in the gas is related to the e-beam power density by $S = P_e/W_i$, where W_i is the energy dissipated in creating an electron-ion pair. (For argon, $W_i = 26.2$ eV.) Since the principal loss of electrons is by attachment to fluorine, the electron density is given by,

$$n = S/\beta F_2 = P_e/\beta F_2 W_i \quad (32)$$

where β is the attachment coefficient and F_2 is the fluorine density.

The discharge power density is given by,

$$P_d = NJ_d E/N \quad (33)$$

and since J_d is constant along a field line, P_d varies directly as E/N .

From eqs. (30) and (32) then, we see that P_d must vary inversely as the cube of P_e (Fig. 12), or

$$P_d(x) = c[1 + (r - 1)x/d]^{-3}. \quad (34)$$

The constant c will now be chosen so that the stability criterion, eq. (27) is satisfied throughout the discharge. It is clear from eq. (34) that the condition is most likely to be violated at $x = d$. Therefore, we set $P_d(d) = \gamma P_e^{1/2}(d)$ or $cr^{-3} = \gamma r^{1/2} P_{e0}^{1/2}$ so that c is given by $c = \gamma r^{7/2} P_{e0}^{1/2}$. The average e-beam and discharge power densities can now be found by integrating eqs. (31) and (34) over x from 0 to d . Thus,

$$\bar{P}_e = P_{e0}(1 + r)/2 \quad (35)$$

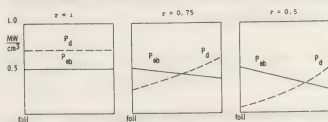


Fig. 12. — Discharge current continuity.

and

$$\bar{P}_d = \gamma P_{e0}^{1/2} r^{3/2} (1 + r)/2. \quad (36)$$

If the discharge power is supplied by a simple capacitive discharge circuit, where maximum power is reached at the end of the e-beam pulse, then the discharge power averaged over time is just half of that given in eq. (36). The total energy dissipated in the laser is then,

$$\epsilon_{in} = (\bar{P}_e + \bar{P}_d/2) \tau_p \quad (37)$$

where τ_p is the pulse length.

The quantum efficiency for converting e-beam energy into excited KrF is $h\nu(1 + \delta_e)/W_i = 25\%$, where δ_e is the fraction of excited states produced for every ion pair. (For argon $\delta_e = 0.29$.) The quantum efficiency for converting discharge energy into KrF* states is 36%. The actual conversion efficiencies are somewhat lower due to formation of trimers and the loss of ArF* to quenching and spontaneous emission. In an optimized gas mixture, conversion efficiencies of $\eta_e = 20\%$ and $\eta_d = 25\%$ can readily be achieved. These values are independent of input power density. The average production rate of KrF* per unit volume, R_p , can now be written,

$$R_p = (\eta_e P_{e0} + \eta_d \gamma P_{e0}^{1/2} r^{3/2}/2) (1 + r)/2 h\nu. \quad (38)$$

Since the ground state of KrF* is dissociative, the small-signal gain is given by $g_0 = \sigma N^* = \sigma R_p \tau$, where σ is the cross section for stimulated emission and τ is the total KrF* lifetime. Another way of writing this relation is $g_0 = R_p h\nu/I_s$, where $I_s = h\nu/\sigma\tau$ is the saturation intensity. Using a spontaneous emission lifetime of 9 ns [17], a stimulated emission cross section of 1.9 Å and the published fluorine and three-body quenching rates [18] of KrF*, the saturation intensity for the mixture 94.8% Ar 5% Kr 0.17% F₂ at 3 atm is 2.6 MW/cm². The expression for the average small-signal gain is then,

$$g_0 = (\eta_e P_{e0} + \eta_d \gamma P_{e0}^{1/2} r^{3/2}) (1 + r)/2 I_s. \quad (39)$$

Since the discharge power density is greatest where the e-beam power density is lowest, the sum of the two is fairly constant and the error in using averaged quantities is minimal.

The laser output intensity is given in terms of the small-signal gain, the gain length, l , the mirror reflectivity, R , and the absorption in the laser medium, z , by the expression,

$$I_{out} = \frac{I_s}{2} \ln \frac{1}{R} \left(\frac{g_0}{\gamma + \frac{1}{2l} \ln \frac{1}{R}} - 1 \right). \quad (40)$$

This expression has been compared with an exact numerical solution of the cavity equations, and was

found in good agreement for values of R down to 30%.

The maximum output intensity corresponding to complete extraction of all laser photons is

$$I_{max} = R_p h\nu V/A = g_0 I_s \quad (41)$$

so the extraction efficiency can be defined as,

$$\eta_{ext} = \frac{I_{out}}{I_{max}} = \frac{1}{2l} \ln \frac{1}{R} \left(\frac{1}{\gamma + \frac{1}{2l} \ln \frac{1}{R}} - \frac{1}{g_0} \right). \quad (42)$$

The optimum reflectivity is found from eq. (42) to be

$$\frac{1}{2l} \ln \frac{1}{R} = \sqrt{\alpha g_0} - \alpha \quad (43)$$

which corresponds to a maximum extraction efficiency of

$$\eta_{ext}^{max} = \left(1 - \sqrt{\frac{\alpha}{g_0}} \right)^2. \quad (44)$$

The extracted laser energy density ϵ_{out} can now be written as

$$\epsilon_{out} = \eta_{ext} R_p h\nu \tau_p. \quad (45)$$

Absorption in the laser medium is made up of two types: 1) static absorption by molecular fluorine and 2) transient absorption due to F⁻, positive molecular ions, and possibly excited electronic states. Our absorption measurements show that the dominant transient absorption is due to the ions, F⁻, Kr₂⁺ and Ar₂⁺. Since the ions are lost by recombination, their population is proportional to the square root of the e-beam power density. We can therefore write,

$$\gamma = \sqrt{c \bar{P}_e W_i} + \sigma_{F_2} [F_2] \quad (46)$$

where c is a constant determined experimentally to be 4×10^{-28} cm s and $\sigma_{F_2} = 1.5 \times 10^{-20}$ cm².

The e-beam pulse length is chosen so that

$$\tau_p J_e = 10 \mu\text{C}/\text{cm}^2.$$

This value has been found to be an upper limit for the consistent operation of a single shot e-beam device without foil damage. This limitation also points out the advantage of operating at the highest pressure consistent with good laser efficiency, since the e-beam energy deposition, $P_e \tau_p$, is now independent of the current density but proportional to gas density. We have chosen our test case at 3 atm, because this pressure has resulted in efficient laser operation in small devices. The reason that lower pressures have been found to give higher output in large devices is because of poor e-beam penetration at high pressures. The nonuniformity of e-beam

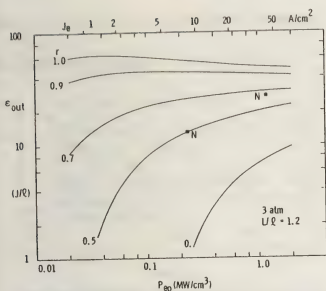


Fig. 13. — Specific energy (e-beam + discharge). (■) Experimental data obtained on two northrop devices.

deposition also limits the discharge energy loading in large devices, as we shall see below.

We now have all the information necessary to determine the extracted laser energy density from eq. (45). This is plotted as a function of P_{e0} in figure 13 for the mixture 94.8 % Ar 5 % Kr 0.17 % F_2 at 3 atm. The corresponding e-beam current density is given on the upper scale. The curves show that a high extracted laser energy is possible at low e-beam current densities if the e-beam deposition is uniform. The uniformity becomes more critical the smaller the value of P_{e0} . When $r = 0$ there is no benefit from discharge pumping at all, since the discharge is always unstable.

The small-signal gain and absorption for the same gas mixture are plotted in figure 14 as a function of e-beam power density. The horizontal line at $0.24\% \text{ cm}^{-1}$ is the absorption due to 4 torr of fluorine with the factor $L/l = 1.2$ taken into account. (L is

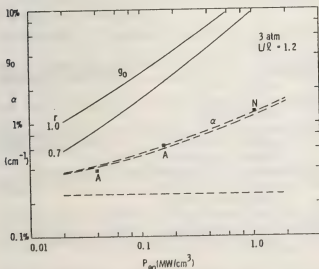


Fig. 14. — Small signal gain and absorption (e-beam + discharge).

the distance between the laser mirrors, or windows, which is filled with fluorine. The value 1.2 is required to ensure electrical isolation of the electrodes from the mirror mounts.) Most of the remaining absorption is due to the ions F^+ , Ar^+ and Kr^+ which are proportional to $P_{e0}^{1/2}$. The measurements by AVCO at the same pressure in a slightly different mix are shown for comparison. Their values, A , for the transient absorption at 1.5 and 6 A/cm² are added to our baseline at $0.24\% \text{ cm}^{-1}$. The small-signal gain is seen to increase faster than the absorption in going to harder pumping.

From eq. (43) it is seen that, for a given small-signal gain and absorption, the optimum mirror reflectivity, R , is determined by the gain length, l . As the laser is increased in length, the optimum value of R is reduced. However, there is a minimum value of R below which the mode quality of the laser suffers due to superfluorescence. The minimum reflectivity is found experimentally to be about 20 %. This condition sets a limit on the length of the laser given by.

$$l_{\max} = \frac{\ln(1/R_{\min})}{2(\sqrt{2}g_0 - \gamma)} \quad (47)$$

Thus, as the input power density increases and the small-signal gain and absorption go up, the maximum length of the device is reduced. This is an important consideration in scaling to high pulse energies.

In figure 15 the overall laser efficiency, maximum gain length and discharge enhancement factor are plotted as a function of e-beam power density. The discharge enhancement factor is defined as the ratio of energy deposited in the gas by the discharge to that deposited by the e-beam. It can be determined from eq. (35) and (36) as

$$\bar{P}_d/2\bar{P}_e = \gamma r^{3/2}/2 P_{e0}^{1/2} \quad (48)$$

The overall efficiency is an increasing function

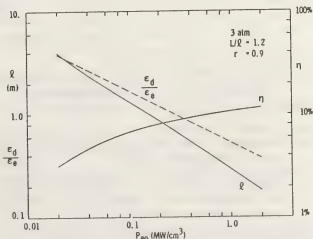


Fig. 15. Maximum gain length and efficiency (e-beam + discharge).

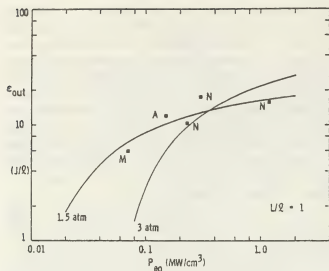


Fig. 16. — Specific energy (e-beam only). M (■) Experimental data obtained on Maxwell device.

of P_{e0} since the small signal gain is increasing faster than the absorption. From this graph we can see that there is a tradeoff to be made between the size of a device and the operating efficiency. With a one meter gain length, an extracted energy of 45 J/l can be achieved at 8 % efficiency with an e-beam current density of 6 A/cm². In contrast, a one meter laser pumped by an e-beam alone at 12 A/cm² can deliver only 11 J/l at 8 % efficiency (see Fig. 16 and 17). The difficulty comes in achieving less than 10 % variation in e-beam deposition in the field direction. We feel that the only way this can be done is with two opposed e-beams.

Some comparison runs with e-beam pumping only were made assuming uniform deposition ($r = 1$) and $L/l = 1$. The extracted energy density is plotted in figure 16 for 1.5 and 3 atm total pressure. Two conclusions may be drawn from these curves: 1) harder pumping works best at higher pressures and 2) the extracted energy always increases with pumping power. The best experimental results of Maxwell

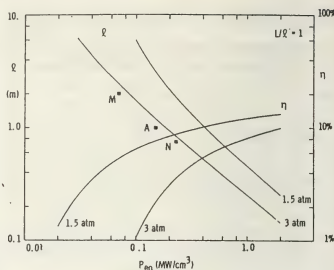


Fig. 17. — Maximum gain length and efficiency (e-beam only).

(2 atm), AVCO (1.7 atm) and Northrop are in good agreement with the predictions.

The maximum gain length and overall efficiency for an e-beam pumped KrF* laser are shown in figure 17. Again the tradeoff between device size and efficiency is clear. The lasers of Maxwell, AVCO and Northrop are seen to be very close to the limit of scalability. The only way to go to higher than 10 to 12 J/l without severely limiting the device size is through combined e-beam and discharge pumping with the uniform deposition achieved by opposing beams.

In conclusion, e-beam sustained discharge pumping seems to have some distinct advantages especially for high average power excimer lasers, even though some additional complexities are involved in discharge pumping. These complexities arise primarily due to nonuniformity of the e-beam deposition and consequent discharge instability. Solution to these problems appears to be feasible using two opposing e-beams to provide uniform ionization.

References

- [1] BRADFORD, R. S., Jr, LACINA, W. B., AULT, E. R. and BHAUMIK, M. L., *Optics Commun.* **18** (1976) 210.
- [2] JUDD, O., *J. Appl. Phys.* **47** (1976) 5297.
- [3] LACINA, W. B., Presented at Second Winter Colloquium on Laser-Induced Chemistry, Park City, Utah, 1977.
- [4] LONG, W. H., Jr, BAILEY, W. F. and GARSCHADEN, A., *Phys. Rev. A* **13** (1976) 471.
- [5] SIKAROFSKY, I. P., JOHNSON, T. W. and BACHYNSKI, M. P., *The Particle Kinetics of Plasmas* (Addison-Wesley Publishing Company, 1966), p. 283.
- [6] MILOY, H. B., CROMPTON, R. W., REES, J. A. and ROBINSON, A. G., in *Abstracts of Papers of the 9th ICPEAC*, ed. J. S. Risley and R. Geballe (University of Washington Press, Seattle, 1975), vol. 1, p. 457.
- [7] FROST, L. S. and PHELPS, A. V., *Phys. Rev.* **136** (1964) A1538.
- [8] SCHAPER, M. and SCHEIBNER, H., *Beit. Plasma Phys.* **9** (1969) 45.
- [9] JACOB, J. H. and MANGANO, J. A., *Appl. Phys. Lett.* **29** (1976) 467.
- [10] RAPP, D. and ENGLANDER-GOLDEN, P., *J. Chem. Phys.* **43** (1965) 1464.
- [11] HALL, R. J., *J. Chem. Phys.* **68** (Feb. 1978) 1803.
- [12] CHANTRY, P. J., Westinghouse Rep. 78-9C-ATACH-R1, March 1978.
- [13] PACK, J. L., VOSHALL, R. E. and PHELPS, A. V., *Phys. Rev.* **127** (1962) 2084.
- [14] ROBERTSON, A. G., in *The Diffusion and Drift of Electrons in Gases*, L. G. H. Huxley and R. W. Crompton (John Wiley and Sons, New York, 1974), p. 607.
- [15] BRAMBRING, J., *Z. Phys. (Germany)*, **179** (1964) 539.
- [16] DAUGHERTY, J. D., MANGANO, J. A. and JACOB, J. H., *Appl. Phys. Lett.* **28** (1976) 581.
- [17] BURNHAM, R. and SEARLES, S. K., *J. Chem. Phys.* **67** (1977) 5967.
- [18] NAKANO, H. H., HILL, R. M., LORENTS, D. C., HUESTIS, D. L. and MCCUSKER, M. V., SRI Report No. MP 76-99, 1976.

Optical discharges

Yu. P. Raizer

Institute for Problems in Mechanics, Moscow, USSR

Abstract. — The essential features of the processes in laser radiation are considered with demonstration of their discharge nature. Review of results is given for breakdown and maintenance of continuous equilibrium plasma by laser radiation.

1. Optical discharges and their role in comparison with other discharges. — After development of rather powerful lasers of pulsed and continuous running many effects of laser radiation on gas and laser-plasma interaction were observed and investigated. It appears at detailed consideration that there is a number of processes which correspond to the well developed branch of physics — gas discharge physics. As a matter of fact a quite new interesting and practically important part on optical discharges is included in discharge physics, and its role is the same as radio-frequency and microwave discharge physics. The aim of this lecture is to consider the essential features of the processes in laser radiation fields, to demonstrate their discharge nature and to give a review of modern results in this field.

In pre-laser époque (up to the middle of sixties) three main electromagnetic frequency ranges were investigated and used in gas discharge physics and technology :

1. Static electric field and close to it low frequency electromagnetic fields.
2. Radio-frequency — a wide range, with a megahertz as a middle of it.
3. Microwaves — frequencies of order gigahertz, wave lengths — cm, mm.

Laser technique development gave to gas discharge physics the fourth range — an optical one, which includes infrared, visible and, to some degree, ultraviolet radiation. It is curious that in pre-laser époque nobody could even imagine the possibility of gas discharge effects in optical fields — the usual non-laser light sources were too weak.

In order to make clear the role of effects of laser-plasma interaction in comparison with usual gas-discharge phenomena it is reasonable to classify these phenomena. If we bear in mind the laser radiation action which is almost free of solid surface influence we should classify these effects according to some sign which is not connected with electrode, near electrode and near wall effects. We shall distinguish three main types of volume gas discharge processes at moderate and high pressures (we consider only these pressures).

1. Gas breakdown. That is the development of ionization avalanche under action of applied external field, the conversion of initially neutral gas into plasma.

2. The maintenance of non-equilibrium plasma. In this case the temperature of electrons responsible for ionization is rather high but gas of heavy particles remains cold. Usually it is weakly ionized plasma at moderate pressures, less than hundreds of torr.

Field frequency range	Discharge plasma-type		
	Breakdown	Non-equilibrium plasma maintenance	Equilibrium plasma maintenance
Static electric field	Discharge gap breakdown	Positive column of glow discharge	Positive column of arc discharge
Radio frequencies	Rf breakdown	Radio-frequency capacity discharge at moderate pressure	Induction discharge at atmospheric pressure
Microwave frequencies	Breakdown in wave-guides and resonators	Pulse discharge in wave-guides and resonators	Microwave plasmatron
Optical radiation	Gas breakdown by laser radiation	The late stage of optical breakdown	Continuous optical discharge

3. The maintenance of equilibrium plasma by e.m. field: electron and heavy particle temperatures are almost equal, ionization degree is close to its thermodynamically equilibrium value. This is so called low temperature plasma with temperatures of order of 10 000 K of atmospheric pressures.

Each of these three processes can be realised in fields of any of four listed ranges. And, actually the most part of these phenomena was observed experimentally and investigated in detail. The following table explains the above given classification. Here, the typical conditions under which one or another process occurs are pointed out.

Considering optical discharges in more details we can see that these phenomena do not differ, in principle from corresponding discharge processes at other frequency ranges. So one can doubtless put optical discharges into above given table.

2. **Optical gas breakdown.** — This effect was discovered in 1963 [1]. The beam of *Q*-switched ruby laser was focused by lens, there was a spark in the focal region where plasma was formed. To achieve gas breakdown by light radiation one need to have high laser parameters. The atmospheric air breakdown occurs at peak power of 30 MW (pulse energy 1 J, pulse duration 30 ns) and the focal region radius 10^{-2} cm. Radiation intensity at focal region is about 10^5 MW/cm², and electric field in e.m. wave about

$$6 \times 10^6 \text{ V/cm}.$$

Breakdown threshold is very sharp, and when radiation intensity is decreased to some value the breakdown ceases to exist.

New effect is of great interest for physicists. For some years optical breakdown was investigated experimentally and theoretically in so detailed manner that now we know about it not less than we know

about its analogue — microwave breakdown — and at least more than we know about much more complicated process — breakdown in electrode gap.

The main results on optical breakdown were obtained in sixties. The theoretical explanation of this phenomenon was given at the same time. All these results are well known, they are summarized in [2]. The recent years don't add any significant results — some additional experimental values, the understanding of more fine details, more precise theoretical explanations.

The threshold fields in light wave E_i necessary for breakdown by focused radiation of ruby laser are shown at figure 1 (from [3]) for a few gases. The thresholds were measured in wide pressure intervals. The similar data on microwave breakdown is given at figure 2 (from [4]) for comparison. Note the resemblance of dependencies $E_i(p)$. As we shall see this resemblance has deep physical foundations.

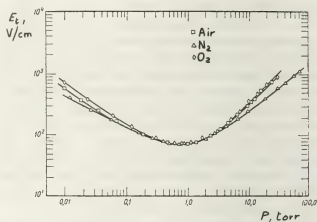


Fig. 2. — Pressure dependence of microwave breakdown field strength. Frequency 994 MHz, diffusion length 1.51 cm.

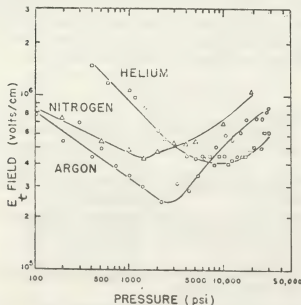


Fig. 1. — Pressure dependence of optical breakdown field strength.

The electron avalanche is developed under action of light electromagnetic field in the same manner as in other fields. The first *seed* electrons appear in the light wave field as a result of multiphoton photoelectric effect. This is different from the cases of other fields where the *seed* electrons appear by randomly chance (from cosmic radiation). In the wave field the electron acquires its energy gradually at collisions with atoms till this acquired energy would be sufficient for atom ionization and new electron appear. In such a way the electron reproduction occurs. The avalanche development is determined by the processes of electron energy increase in the electromagnetic field and electron energy losses at collisions (elastic and non-elastic ones), and also by the electron losses because of diffusion or electron attachment in electronegative gases.

The losses of electron energy and losses of electrons themselves depend weakly on the field nature and it happens more or less in the same way in any fields. Only energy increase depends on field frequency and the peculiarities of optical discharge are

connected with quantum nature of interaction between electrons and optical e.m. field. According to classical theory an electron in oscillating field oscillates and at the same time moves randomly. At every collision its average vibration energy

$$\varepsilon_{osc} = e^2 E^2 / m \omega^2$$

transforms into energy of random motion (E — mean square field, ω — frequency). The rate of energy increase from field is equal to

$$\left(\frac{d\varepsilon}{dt} \right)_E = \frac{e^2 E^2}{m(\omega^2 + \nu_m^2)} \nu_m \quad (1)$$

where ν_m effective frequency of electron-atom collisions. In the case when electron does not manage to make many oscillations during the time between collisions the energy acquired at collision is decreased in comparison with the energy ε_{osc} and we have to use $\omega^2 + \nu_m^2$ instead of ω^2 . The relation (1) is valid even in the limit of static field at $\omega \rightarrow 0$.

From (1) one can see that for any frequency at rather low pressures when $\nu_m^2 \ll \omega^2$, the law of proportionality $(d\varepsilon/dt)_E \sim E^2 \nu_m / \omega^2$ is valid. The rate of energy increase is determined by the ratio E/ω . The rate is the more the higher the pressure. To the contrary, at high pressures when $\nu_m^2 \gg \omega^2$, the rate $(d\varepsilon/dt)_E \sim E^2 / \nu_m$ is decreased with pressure and it does not depend on ω . In order an avalanche and breakdown take place it is necessary to overcome the electron and electron energy losses. That definite rates of energy increase in the field $(d\varepsilon/dt)_E$ and definite ionization frequency are required. The required ionization frequency depends on $(d\varepsilon/dt)_E$.

It follows from this fact that at $\nu_m^2 \ll \omega^2$ the threshold field is proportional to the frequency and decreases when the pressure increases. At rather high pressures when $\nu_m^2 \gg \omega^2$ the threshold field depends weakly on the frequency and, to the contrary, increases with pressure. At pressures satisfying the condition $\nu_m \approx \omega$, the function $E_t(p)$ has a minimum. The figure 2 for microwave breakdown can be explained by these considerations. In the same quality manner one can explain optical breakdown curve (Fig. 1). The relation (1) makes clear why at optical frequencies it is necessary for breakdown to have much higher fields than at microwave frequencies ($E_t \sim \omega$; threshold wave intensity $S_t \sim E_t^2 \sim \omega^2$). It is clear why minimum of $E_t(p)$ moves in the direction of very high pressure region (hundreds of atmospheres). The minimum corresponds to

$$\nu_m = \text{constant } p \approx \omega.$$

The question is how to ground the applicability of relation (1).

In one of the first papers on optical breakdown [5] the possibility to apply approximately this simple and convenient relation was shown. The quantum theory of the effect was also constructed in this paper.

In fact, in light field an electron absorbs energy quanta $\hbar\omega$, equal to 1.78 eV in the ruby laser case. It is much more than average energy of electron oscillations in the wave field $\varepsilon_{osc} = e^2 E^2 / m \omega^2$. However the analysis of kinetic equation for energy distribution function shows that formula (1) is valid not only under the condition $\hbar\omega \ll \varepsilon_{osc}$, but under weaker condition $\hbar\omega \ll \varepsilon$. In microwave region even trivial requirement $\hbar\omega \ll \varepsilon_{osc}$ is satisfied and there is no question on quantum effects. In optical range we have $\varepsilon_{osc} \sim 10^{-2}$ eV $\ll \hbar\omega \approx 1.8$ eV. But average energy of electron spectrum is of order of ionization potential, that is 10 eV, therefore one can consider the condition $\hbar\omega \ll \varepsilon$ to be satisfied.

In the case of optical fields the formula (1) is approximately valid but one has to treat it statistically. Let, for example $\varepsilon_{osc} = 0.01 \hbar\omega$. Of course an electron can not acquire 1/100 of quantum energy from field during a collision. It means roughly that it does not acquire any energy during 99 collisions and acquires an energy quanta at hundredth collision. The precise calculations of electron avalanche and breakdown threshold are made as usually on the base of kinetic equation. The calculations of paper [5] and the following ones are in agreement with experimental results.

The fact that the relation $S_t \sim \omega^2$ is satisfied for threshold radiation intensity in wide frequency range from microwave ($\omega \sim 10^{10}$ rad/s) up to optical frequencies ($\omega \sim 10^{15}$ rad/s) is a significant argument in favour of avalanche theory. The data on optical breakdown at some frequencies of visible and infrared spectrum parts (ruby, neodymium and CO₂-laser) are available. Quite recently the data on the widest range between microwave and infrared spectrum parts were obtained. The breakdown by radiation with wave length $\lambda = 0.38$ mm was investigated, the radiation source being a laser on heavy water. Figure 3

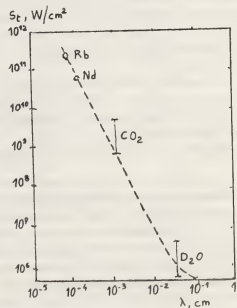


Fig. 3. — Frequency dependence of breakdown.

demonstrates the curve $S_i \sim \omega^2$. The apparent deflection in low frequency region is because of the fact that one has to put the value of $\omega^2 + v_m^2$ instead of ω^2 into formula (1). Taking into account this fact one can diminish a disagreement. The real deflection from the curve $S_i \sim \omega^2$ is observed in ultraviolet spectrum part, at breakdown by second harmonics of neodymium and ruby lasers where quantum effects are significant (second harmonics ruby quanta is very high — $\hbar\omega = 3.56$ eV).

The consideration given shows that effects of optical and microwave breakdown have much in common. There are, of course, some new details connected with quantum nature of interaction between light radiation and matter. For example the ionization of excited atoms is possible by two or three-photon effect and sometimes it is of essential influence on electron reproduction rate. But in the main, optical breakdown mechanism is not different from mechanism of volume (not streamer) breakdown in any other fields.

3. The maintenance of non-equilibrium plasma. —

This process is usual in the static field — glow discharge. But it is not typical not only for optical but even for microwave frequencies. The matter of the fact is that plasma can be a non-equilibrium one only as weakly ionized and when the pressures does not high. Energy input must be small and energy exchange between electrons and heavy particles must be very slow. Otherwise gas is quickly heated, achieves an equilibrium with electrons and ionization is a thermal one. But at very low gas densities plasma absorbs light radiation weakly, therefore steady-state non-equilibrium plasma maintenance in laser radiation field would require great laser power.

Even in microwave frequency where coefficient of electromagnetic field absorption proportional to $1/\omega^2$ is high, one can obtain a non-equilibrium plasma only in pulse fields, when high radiation intensities are possible. In steady-state microwave one can obtain only equilibrium highly ionized plasma at normal pressure conditions.

One can obtain non-equilibrium plasma at late stage of optical breakdown, but such effects did not attract attention of theoreticians and experimentators. Therefore we consider the third (according to classification adopted) type of discharge processes.

4. The maintenance of equilibrium plasma in continuous optical discharge. —

The arc-like discharges in which steady-state equilibrium plasma is maintained by e.m. field are widely applied in physical experiments and technology. The generators of dense low-temperature plasma are operating on this base. In plasmatron the cold gas flows through the region of the steady-state burning discharge. Passing the discharge region gas flows out as a continuous plasma

jet usually at normal pressure conditions. Now the e.m. fields of three frequency ranges (static, r - f and microwave) are used in industrial plasmatrons. There are arc, inductive and microwave plasmatron, respectively.

In 1970 the possibility of steady-state plasma maintenance by light radiation of continuously operating laser was grounded theoretically as well as the possibility of optical plasmatron creation [7]. In the same year continuous optical discharge (as it was called) was obtained experimentally by means of continuously operating CO₂-laser [8].

It does not differ from steady state equilibrium discharges in other fields. Plasma energy losses because of heat conductivity and thermal radiation are balanced by light wave energy absorption. Plasma achieves such a temperature (it determines the light absorption coefficient) in order to compensate exactly energy input and energy losses and secondly to stabilise stationary plasma state.

Plasma maintenance by laser radiation has its own peculiarities connected with the properties of optical frequency range of e.m. field. The main feature is the possibility of distant energy transfer. To transfer energy in any other field one requires some constructive elements: electrodes in arc discharge, solenoids — in r - f field, waveguide — in microwave but one can transfer laser beam to plasma directly through air. This makes possibly to initiate an optical discharge at unreachable places, in the free air. One can make plasma to move in space by moving light beam. It is possible to obtain optical plasmatron by gas flow through discharge.

In practice, one can obtain continuous optical discharge focusing laser beam by lens or mirror. Plasma is produced in the focal region where light intensity is high. It moves to radiations source up to light cone section where light intensity is high enough to maintain gas discharge (Fig. 4).

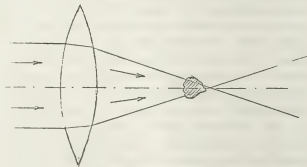


Fig. 4. — Sketch of experiment on continuous optical discharge.

In order to ignite discharge, it is necessary to create the initial plasma at the focal region by any manner. It is convenient by example, to put here the piece of metallic wire in short time.

The main problem of equilibrium discharge theory

is to determine plasma temperature as a function of applied field parameters. Generally the problem is solved on the base of equation set describing plasma-field energy balance. Let us consider a simple model. We shall simulate a focused laser beam by means of spherically convergent radiation flux with power P_0 . A fraction of radiation power P_1 is absorbed by plasma generated in central region. Plasma temperature $T(r)$ decreases monotonically from its maximal value T_k in the centre and this value $T_k = T(0)$ is plasma temperature characteristics. We neglect energy losses due to thermal radiation. Energy flux due to heat conductivity can be written in the following form

$$J = -\lambda dT/dr = -d\theta/dr, \quad \theta = \int_0^r \lambda dT \quad (2)$$

where λ heat conductivity, and θ heat flux potential.

The coefficient of light absorption by plasma μ_ω depends sharply on temperature through such kind dependence of gas ionization degree. Introduce some ionization temperature T_0 in such a way that for temperatures less than this value ionization is so weak that one can neglect light absorption. Let r_0 — is a radius of a sphere where $T = T_0$. Outside the absorbing sphere the whole heat flux through sphere surface does not depend on radius :

$$4\pi r^2 J = P_1 = \text{constant}.$$

This gives $\theta(r) = P_1/4\pi r$ and

$$P_1 = 4\pi r_0 \theta_0, \quad \theta_0 \equiv \theta(T_0). \quad (3)$$

One can approximately write the following expression for energy balance inside of absorbing sphere

$$P_1 \approx 4\pi r_0^2 \Delta\theta/r_0 = 4\pi r_0 \Delta\theta, \quad \Delta\theta = \theta_k - \theta_0 \quad (4)$$

where $\Delta\theta$ — the difference of heat flux potential between centre of sphere and plasma boundary and

$$\theta_k \equiv \theta(T_k).$$

It follows from the relations (3) and (4), that

$$\Delta\theta \approx \theta_0 \approx \frac{\theta_k}{2}. \quad (5)$$

Usually optical thickness of plasma is small. In this case the light absorption is not full and the absorbed energy is of order of $P_1 \approx \mu_\omega r_0 P_0$, where absorption coefficient corresponds to characteristic plasma temperature T_k . Combining this relation with (4) and (5) we find the relation between plasma temperature T_k and incident radiation power P_0

$$P_0 \approx \frac{2\pi\theta(T_k)}{\mu_\omega(T_k)}. \quad (6)$$

At constant pressure the function $\mu_\omega(T)$ grows very sharply, then begins to fall. Maximum $\mu_\omega(T)$

corresponds to almost full single ionization of atoms. When temperature increases farther ionization degree changes slowly till the second ionization begins, electron and ion density being decreased because of

$$p \sim nI = \text{constant}.$$

As a result the coefficient $\mu_\omega \sim n_e n_i \sim n^2$ falls. The dependence $\theta(T)$ grows monotonically therefore P_0 as a function of T_k possesses a minimum (see Fig. 5). Minimum $P_{0\min} \equiv P_t$ is in a region of maximum of $\mu_\omega(T)$, that is at temperature which corresponds to almost full single ionization of atoms.

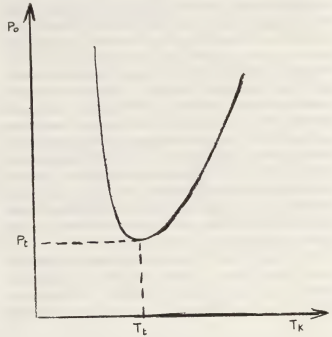


Fig. 5. — Laser power as function of plasma temperature in continuous optical discharge.

There is no steady-state regime at powers $P_0 < P_t$. The value P_t is a minimal threshold power at which continuous optical discharge is possible. The higher is gas pressure the lower is threshold power, because at high pressures light absorption coefficient is more. The threshold is lower when gas have bad heat conductivity also.

The first experiments on continuous optical discharge were made in weakly heat-conductive gas, xenon, at pressures of a few atmospheres. Low-power CO_2 -laser was required, only 150 W. In further experiments plasma was produced by means of more powerful lasers in many gases and at atmospheric pressure. In order to maintain discharge in atmospheric air the minimal radiation power of CO_2 -laser is required, $P_t \approx 2.2$ kW. Plasma temperature is $T_k = T_i = 18\,000$ K, $\theta_k \approx 0.3$ kW/cm.

$$\mu_\omega(T_k) \approx 0.85 \text{ cm}^{-1}.$$

Plasma radius r_0 is of order of 1 mm but to estimate this one need more detailed considerations [2].

When laser power increases plasma temperature grows slowly, but the region occupied by plasma grows more rapidly. This process corresponds to the right branch of curve $P_0(T_k)$ (see Fig. 5). The left branch at which $T < T_i$, corresponds to unstable states. Actually if plasma temperature randomly rises one need lower power to maintain plasma. The heating begins and representative point of gas state travels to the right branch, to the temperature point corresponding to the same power. The situation of optical discharge does not differ from the situations in other equilibrium discharges [2].

A continuous optical discharge in atmospheric air was investigated by means of 5-6 kW CO₂-lasers [9, 10] and experimental results confirmed the above given estimation of threshold power. Experimental threshold value is equal to 2 kW. The measured spatial distributions of temperature and power absorption coefficients are shown at figures 6, 7. Maximal measured parameters $T = 15\,000\text{ K}$, $\mu_\omega = 0.7\text{ cm}^{-1}$ also are in agreement with above given estimation. As it was measured [10], plasma temperature in centre of air discharge was equal to $T \approx 17\,000\text{ K}$ plasma temperature in argon discharge was equal to $23\,000\text{ K}$ at $p = 2\text{ atm}$ [11]. This heated plasma may be considered as a very high brightness light source of continuous action and this gives great possibilities for different applications.

The temperature in an optical discharge plasma is much higher than in other equilibrium discharges where it does not exceed $10\,000\text{ K}$. The reason is that in the low frequency region plasma absorbs

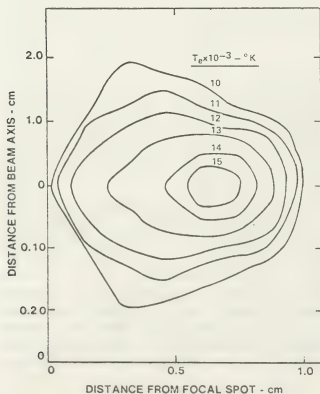


Fig. 6. — Spatial distribution of electron temperature in continuous optical discharge. Incident CO₂-laser power 3.5 kW.

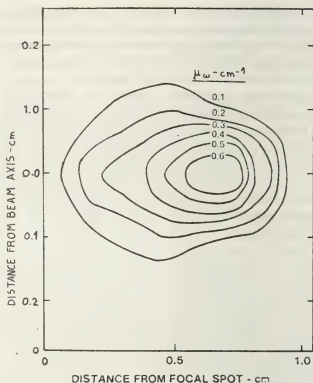


Fig. 7. — Spatial distribution of absorption coefficient. Incident CO₂-laser power 3.5 kW.

field energy even at weak ionization. Electromagnetic field cannot penetrate into highly ionized gas and this is because the condition for energy release becomes worse and plasma temperature cannot rise highly.

In optical frequency range plasma absorbs weakly because of high field frequency ($\mu_\omega \sim \omega^{-2}$). The best field dissipation occurs in fully single ionized plasma and this is why gas is so heated. The unique optical discharge property — extremely high plasma temperature.

At high pressures of order of 10 atm and higher the energy losses because of thermal radiation exceed the heat conductivity losses. As in the case of high pressure arcs, in optical discharge there is an effective conversion of laser radiation energy into the energy of thermal radiation of rather high temperature [12].

A continuous optical discharge was obtained experimentally in argon jet at atmospheric pressure [13] and it can be considered as optical plasmatron. A continuous optical discharge is sometimes generated at irradiation of metal surfaces by rather intense CO₂-laser radiation. Plasma is produced in air, in front of the surface. The surface absorbs a noticeable part of incident radiation, and as a result the surface is shielded from radiation. It makes the difficulties in the surface treatment by laser radiation.

5. Optical discharge propagation. — In any frequency region the discharges exhibit a tendency to propagate. Always there are mechanisms of energy transfer from discharge plasma to the surrounding

layers of cold gas. This makes a contribution into ionization. If just ionized layer is in external field, field energy dissipation begins. The layer is captured by discharge. The same situation is repeated the next layer and so on. Discharge boundary propagates through gas. The discharge is a static one if the walls enclosing the discharge volume prevent to its propagation or field intensity outside the discharge is not high enough to maintain plasma.

Different mechanisms are possible to transfer energy and ionization from discharge plasma to neighbour cold layers, namely, by shock waves, heat conductivity, thermal radiation. Resonance radiation diffusion, electron diffusion, also contribute into ionization process. As an example of discharge propagation one can consider a process in plasmatron, but in this case one observes reversed picture of propagation. The cold gas flows through non-moving discharge and is ionized. In the coordinate system connected with cold gas flow the discharge boundary is propagated through gas. The usual mechanism of propagation in plasmatron is the heat conductivity accompanied by thermal ionization of cold gas.

Plasma motion in the laser radiation field belongs to the phenomena of discharge propagation. It was discovered soon after the laser spark observation. Plasma boundary of optical discharge travels to the source of incident laser beam from focal point with the velocity of order of 100 km/s. In this case the

mechanism of plasma propagation is a shock wave. This effect is similar to the explosive detonation and is treated as a *light detonation*. This phenomenon was widely investigated both theoretically and experimentally (see [2]). It is interesting to note that discharge propagation by shock wave was observed only for optical frequencies, after gas breakdown by giant pulses of laser radiation. Probably the similar process is not possible in other fields at all, because very high intense fields are necessary for detonation, and in any other fields the breakdown occurs earlier than *detonation* wave.

There were many investigations of the other effect — optical discharge propagation by means of heat conductivity. This process has much in common with deflagration.

Plasma front moves to meet a laser beam and its velocity is of order of 1-10 m/s. Usually discharge propagates through plasma by means of heat conductivity, energy transfer by thermal radiation may be also of importance in propagation processes. In experiments one observes sometimes that propagation velocity is a sum of plasma front velocity relatively the gas and of gas velocity. Plasma expands and pushes cold gas — discharge front propagates in moving gas. One can find the more detailed consideration of *light deflagration* in [2]. One can also mention more recent papers [13-15].

References

- [1] MAKER, P. D., TERHUNE, R. W., SAVAGE, C. M., *III Internat. Conference on Quantum Electronics*, Paris, 1963.
- [2] RAIZER, Yu. P., *Laser-Induced Discharge Phenomena*, Consultant Bureau, New York, London, 1977.
- [3] GILL, D. H., DOUGAL, A. A., *Phys. Rev. Lett.* **15** (1965) 845.
- [4] MAC DONALD, A. D., *Microwave Breakdown in Gases*, Wiley, New York, 1966.
- [5] ZEL'DOVICH, Ya. B. and RAIZER, Yu. P., *Zh. Eksp. Teor. Fiz.* **47** (1964) 1150.
- [6] WOSKOBOINIKOW, P., MILLIGAN, W. J., PRADDAUDE, H. C., COHN, D. R., *Appl. Phys. Lett.* **32** (1978) 527.
- [7] RAIZER, Yu. P., *ZhETF Pis'ma Red* **11** (1970) 195.
- [8] GENERALOV, N. A., ZIMAKOV, V. P., KOZLOV, G. I., MASYUKOV, V. A. and RAIZER, Yu. P., *ZhETF Pis'ma Red* **11** (1970) 447.
- [9] FOWLER, M. C., SMITH, D. C., *J. Appl. Phys.* **46** (1975) 138.
- [10] KEEFER, D. R., *J. Appl. Phys.* **46** (1975) 1080.
- [11] GENERALOV, N. A., ZIMAKOV, V. P., KOZLOV, G. I., MASYUKOV, V. A. and RAIZER, Yu. P., *Zh. Eksp. Teor. Fiz.* **61** (1971) 1434.
- [12] KOZLOV, G. I., KUZNETZOV, V. A., MASYUKOV, V. A., *Zh. Eksp. Teor. Fiz.* **66** (1974) 954.
- [13] KOZLOV, G. I., *ZhETF Pis'ma Red* **4** (1978) 586.
- [14] KLOSTERMAN, E. L., BYRON, S. R., *J. Appl. Phys.* **45** (1974) 4751.
- [15] SU, F. Y., BONI, A. A., *Phys. Fluids* **19** (1976) 960.

Plasma properties and atomic processes at medium and high pressures

H. W. Drawin

Association EURATOM-CEA sur la Fusion, Département de Physique du Plasma et de la Fusion Contrôlée, Centre d'Etudes Nucléaires, B.P. 6, 92260 Fontenay-aux-Roses, France

Résumé. — Quand l'état du plasma s'écarte de l'équilibre thermodynamique local (E.T.L.), les relations d'équilibre ne sont plus valables. Les propriétés thermodynamiques doivent alors être décrites sur la base de modèles dans lesquels les propriétés atomiques individuelles et les réactions élémentaires interviennent. Dans la première partie du texte on donne une description schématique des plasmas soumis à une injection et des pertes d'énergie et qui subissent en plus des contraintes externes sous forme des conditions initiales et de limite. Les équations de bilan pour la densité des particules, la quantité de mouvement et l'énergie de systèmes ouverts sont résumées en incluant des réactions nucléaires. La seconde partie résume les progrès qui ont été faits dans la compréhension des propriétés de quelques types de plasmas en dehors de l'E.T.L. On traite, sur la base des équations de bilan, plus particulièrement la décharge lumineuse sous ses différentes formes, les plasmas d'ions négatifs (avec application à la physique des interrupteurs (SF_6) des circuits électriques), la mesure du coefficient collisionnel-radiatif de recombinaison électrons-ions et les plasmas dans les machines du type Tokamak.

Abstract. — When the state of a plasma deviates from local thermodynamic equilibrium (L.T.E.) the equilibrium relations cannot be applied. The thermodynamic properties must then be described on the basis of models in which the individual atomic properties and elementary reactions intervene. The first part of the paper gives a schematic description of a plasma suffering power input, power losses and external constraints in the form of initial and boundary conditions. The rate equations for particle density, momentum and energy of open systems are summarized, including nuclear reactions. The second part gives a review of the progress made in understanding the properties of special types of non-L.T.E. plasmas such as glow discharge plasmas, negative ion plasmas (with application to the physics of SF_6 circuit-breakers) and Tokamak plasmas on the basis of these rate equations.

1. Introduction. — We know that an ionised gas enclosed in a box with perfectly reflecting walls at plasma temperature T can at all temperatures T and pressures p thermodynamically be described by the classical equilibrium relations for *ideal* gases (Maxwell-Boltzmann distribution, Planck's law, mass action law in form of the Waage-Guldberg and Saha-Eggert relations, ...). In such a closed system, energy and entropy are state functions, the entropy has a maximum value.

Under real conditions, plasmas are never enclosed in a black-body box with the wall temperature equal to the plasma temperature T . They rather show more or less strong temperature and density gradients leading to particle, momentum, energy and entropy fluxes between different spatial regions. Photons have the largest mean free path and therefore transport momentum, energy and entropy over much larger distances than material particles. Very often the reabsorption in laboratory plasmas is so weak that most of the photon energy can freely escape. Thermodynamically speaking, under actual conditions plasmas represent *open system* which are generally far from *complete thermodynamic equilibrium* and which may even be far from *local thermodynamic equilibrium* (L.T.E.). Plasmas not obeying the classical thermodynamic equilibrium relations are termed *non-L.T.E. plasmas*.

From a general point of view, a realistic model for a non-L.T.E. plasma, which applies to both laboratory and astrophysical situations, is shown in figure 1. In order to maintain some spatial region S in an ionised state, energy must be fed into S . This energy may come from an external source (e.g. the electrical power supply G , a photon ($h\nu$) or particle (p) flux) or it may be produced by the plasma itself (chemical or nuclear reactions). In the most general case we have also to admit electric (\mathbf{E}) and magnetic (\mathbf{B}) fields. The *stationary state* in mechanical equilibrium is characterized by a *dynamic equilibrium* between all particle, momentum and energy fluxes. For instance, the ambipolar diffusion flux must be compensated by an equivalent neutral particle flux in opposite direction in order to obtain a stationary density distribution.

In the *non-stationary state* these quantities show a transient behavior. In both cases boundary conditions have an important influence on the plasma state. The external electric components (R , L , G) which close the electric current loop are part of the electrical boundary conditions (which may be time-dependent); but under special (especially astrophysical) conditions they appear sometimes not to be well-separated from the plasma proper which is investigated.

This paper reviews some aspects of the progress

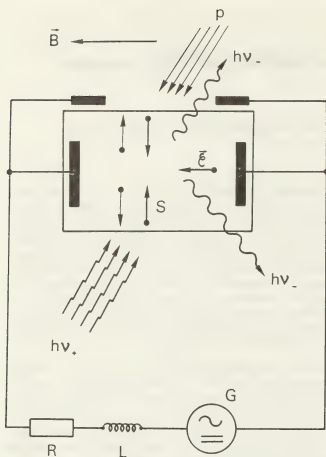


Fig. 1. — Schematic representation of a plasma suffering power input, power losses and constraints in the form of initial and boundary conditions. For further details see text.

made during the last years in describing non-equilibrium effects in laboratory plasmas at medium and high pressures. The terms *medium* and *high* pressures should in the present context only be considered as an indication that practically at all pressures of interest atomic processes in the widest sense are necessary in order to describe the plasma properties under non-L.T.E. conditions. These processes are essential when one wants to understand how a system evolves towards equilibrium. *Non-ideal* plasmas will not be treated here. (Concerning the definition and general properties of non-ideal plasmas the reader is referred to [1-4].) Also wave phenomena such as ionisation and chemical waves will be excluded from our considerations.

2. The basic equations. — Before discussing particular experimental situations and results it might be useful to summarize the basic equations by which plasmas can consistently be described. We shall adopt a more general point of view as is usually done, in agreement with the introductory remark that plasmas represent open systems, i.e. that they exchange particles, momentum and energy with the

external world. Our starting point is the kinetic collision (Boltzmann) equation

$$\frac{\partial f_s}{\partial t} + \sum_{\beta=1}^3 w_{\beta} \frac{\partial f_s}{\partial x_{\beta}} + \sum_{\beta=1}^3 \frac{I_{s,\beta}}{m_s} \frac{\partial f_s}{\partial w_{\beta}} = \left[\frac{\partial f_s}{\partial t} \right]_{\text{coll. rad.}} \quad (1)$$

and its various velocity moments. $f_s(\mathbf{r}, \mathbf{w}, t)$ is the velocity distribution function of particles of species $s = s(z, k, i)$ as a function of space point \mathbf{r} , velocity \mathbf{w} in the laboratory system and time t . $\beta = 1, 2, 3$ represents the three coordinate directions. m_s is the particle mass and $F_{s,\beta}$ represents the (external) forces \mathbf{F} exerted on s in the direction β (e.g. due to electric or magnetic fields). s stands for electrons or z -times ionised chemical species k in quantum state $|i\rangle$. The right-hand side of eq. (1) is the rate of change of f_s due to collision and radiation processes. Integration of f_s over \mathbf{w} yields the particle density of species s :

$$\iiint f_s(\mathbf{r}, \mathbf{w}, t) d\mathbf{w}_1 d\mathbf{w}_2 d\mathbf{w}_3 = n_s(\mathbf{r}, t). \quad (2)$$

Instead of \mathbf{w} we can consider f_s as a function of the momentum $m_s \mathbf{w} = \mathbf{p}$ of a particle: $f_s = f_s(\mathbf{r}, \mathbf{p}, t)$. The eq. (1) can then also be written as

$$\frac{\partial f_s}{\partial t} + \mathbf{w}_s \cdot \nabla_{\mathbf{r}} f_s + \mathbf{F}_s \cdot \nabla_{\mathbf{p}} f_s = \left[\frac{\partial f_s}{\partial t} \right]_{\text{coll. rad.}} \quad (3)$$

In this form the kinetic collision equation is also applicable to photons (massless particles): the velocity and momentum of a photon of frequency ν traveling in the direction of unit vector \mathbf{u} are (c is the velocity of light, h is Planck's constant):

$$\mathbf{w}_s = \mathbf{w}_\nu = \mathbf{u}c \quad (4)$$

$$\mathbf{p}_s = \mathbf{p}_\nu = \hbar \mathbf{u} \nu / c. \quad (5)$$

For photons, $\mathbf{F}_s = \mathbf{F}_\nu$ is in nearly all cases negligible. Thus, eq. (3) reduces to

$$\frac{\partial f_s(\mathbf{u})}{\partial t} + c \mathbf{u} \cdot \nabla_{\mathbf{r}} f_s(\mathbf{u}) = \left[\frac{\partial f_s(\mathbf{u})}{\partial t} \right]_{\text{coll. rad.}} \quad (6)$$

which represents the time-dependent radiative transport equation. $f_s(\mathbf{u}) d\mathbf{v}$ is the number of photons with frequencies between ν and $\nu + d\nu$ traveling in the direction \mathbf{u} . The specific intensity $I_s(\mathbf{u})$ and $f_s(\mathbf{u})$ are linked through the relation

$$I_s(\mathbf{u}) d\mathbf{v} = \frac{2 h \nu^3}{c^2} f_s(\mathbf{u}) d\mathbf{v}. \quad (7)$$

Integrating eq. (1) or eq. (3) over \mathbf{w} yields the rate equation for the macroscopic quantity $n_s(\mathbf{r}, t)$:

$$\frac{\partial n_s}{\partial t} + \nabla_{\mathbf{r}} \cdot (n_s \langle \mathbf{w}_s \rangle) = \left[\frac{\partial n_s}{\partial t} \right]_{\text{coll. rad.}} \quad (8)$$

where $\langle \mathbf{w}_s \rangle$ is the mean species velocity in the laboratory system. We introduce the mean mass velocity \mathbf{v}_0 of the plasma as a whole and the species peculiar ($\langle \mathbf{V}_s \rangle$) and mean diffusion velocity ($\langle \mathbf{V}_s \rangle$) by

$$\mathbf{w}_s = \mathbf{v}_0 + \mathbf{V}_s; \quad \langle \mathbf{w}_s \rangle = \mathbf{v}_0 + \langle \mathbf{V}_s \rangle. \quad (9)$$

In a coordinate system at rest with respect to the total plasma motion of velocity \mathbf{v}_0 we thus have

$$\frac{\partial n_s}{\partial t} + \nabla_r \cdot (n_s \langle \mathbf{V}_s \rangle) = \left[\frac{\partial n_s}{\partial t} \right]_{\text{coll. rad.}} \quad (10)$$

$n_s \langle \mathbf{V}_s \rangle$ can be expressed by the phenomenological relation ($q_s = e_0 z_s$ is the species electric charge)

$$\mathbf{j}_s = q_s n_s \langle \mathbf{V}_s \rangle = -\sigma_s^{dc} \mathbf{E}^0 - \sigma_s^{ac} \mathbf{E} - q_s \mathbf{D}_s \cdot \nabla_r n_s - q_s \theta_s \cdot \nabla_r T \quad (11)$$

where \mathbf{E}^0 and \mathbf{E} are the *dc* and *ac* electric fields. Further σ^{dc} and σ^{ac} are the corresponding electrical conductivities, \mathbf{D}_s and θ_s represent the particle diffusion and thermal diffusion coefficients respectively. In the most general case they represent tensors. Eq. (10) is the diffusion equation and will be discussed in connection with the glow discharge problem. The crucial point is to express the right-hand side and $\langle \mathbf{V}_s \rangle$ as a function of the atomic and nuclear reaction processes.

Summation over s of all eq. (10) yields the following rate equation for the total particle density $n = \sum n_s$:

$$\frac{\partial n}{\partial t} + \sum_s \nabla_r \cdot (n_s \langle \mathbf{V}_s \rangle) = \left[\frac{\partial n}{\partial t} \right]_{\text{coll. rad.}} \quad (12)$$

The right-hand side is not necessarily zero. For an isolated system one has

$$\left[\frac{\partial n}{\partial t} \right]_{\text{coll. rad.}} = \left[\frac{\partial n_e}{\partial t} \right]_{\text{coll. rad.}} + \left[\frac{\partial n_M}{\partial t} \right]_{\text{coll. rad.}} + \left[\frac{\partial n_{\text{nuc}}}{\partial t} \right]_{\text{coll. rad.}} \quad (13)$$

where the first term on the *r-h-s* accounts for the creation and destruction of electrons due to collisional-radiative processes, the second one takes into account the collisional-radiative formation and destruction of molecules, and the last one nuclear transformations (e.g. $\text{D} + \text{T} \rightarrow \text{He} + n$, see eq. (86)). Only in completely dissociated and ionised gases will the first two terms be zero.

The form of eq. (12) is sufficiently general to include open systems, i.e. where a plasma is submitted to a beam of particles or photons. Also nuclear reactions can be taken into account by the term on the right-hand side.

The rate equation for the total mass density $\rho = \sum n_s m_s$ is given by

$$\frac{\partial \rho}{\partial t} + \nabla_r \cdot (\rho \mathbf{v}_0) = \left[\frac{\partial \rho}{\partial t} \right]_{\text{coll. rad.}} \quad (14)$$

For an isolated system, the right-hand side is zero, since collisions alone cannot change the total density. Eq. (13) has then the form of a conservation equation. When the plasma is submitted to a stream of particles (e.g. neutral particle injection) or when nuclear reactions take place the right-hand side is different from zero (e.g. in reaction (86) one loses the neutron and mass which is transformed into kinetic energy).

Multiplication of eq. (1) by $m_s \mathbf{w}$ or $m_s \mathbf{w} \mathbf{w}$ and integration over \mathbf{w} yields respectively the rate equations for the momentum density and the pressure tensor $\mathbf{P}_s = n_s m_s \langle \mathbf{w}_s \mathbf{w}_s \rangle$ of species s . The equation for the momentum density is:

$$\frac{\partial}{\partial t} (n_s m_s \langle \mathbf{w}_s \rangle) + \nabla_r \cdot (n_s m_s \langle \mathbf{w}_s \mathbf{w}_s \rangle) - n_s \mathbf{F}_s = \left[\frac{\partial}{\partial t} n_s m_s \langle \mathbf{w}_s \rangle \right]_{\text{coll. rad.}} \quad (15)$$

Summing over all species s and substituting \mathbf{w}_s by eq. (9) yields the rate equation for the momentum density for the whole plasma as a function of \mathbf{v}_0 . Taking eq. (8) into account finally yields

$$\frac{\partial \mathbf{v}_0}{\partial t} + \mathbf{v}_0 \cdot \nabla_r \mathbf{v}_0 + \frac{1}{\rho} \nabla_r \cdot \mathbf{P} - \frac{1}{\rho} \sum_s n_s \mathbf{F}_s = \left[\frac{\partial \mathbf{v}_0}{\partial t} \right]_{\text{coll. rad.}} \quad (16)$$

where $\mathbf{P} = \sum \mathbf{P}_s$ is the total pressure tensor. The right-hand side is generally zero, since collisions between plasma particles alone cannot change \mathbf{v}_0 . Under special conditions however, it can be different from zero. This is for instance the case when a plasma is submitted to a spatially anisotropic beam of energetic particles or photons. (The observed rotation of a Tokamak plasma when it is submitted to tangential neutral particle injection belongs to such a case.) When the right-hand side of eq. (16) is put equal to zero, a corresponding contribution must formally be taken into account on the left-hand side.

The rate equation for the pressure tensor is

$$\frac{\partial}{\partial t} (n_s m_s \langle \mathbf{w}_s \mathbf{w}_s \rangle) + \nabla_r \cdot (n_s m_s \langle \mathbf{w}_s \mathbf{w}_s \mathbf{w}_s \rangle) - 2 n_s \mathbf{F}_s \cdot \langle \mathbf{w}_s \rangle = \left[\frac{\partial}{\partial t} n_s m_s \langle \mathbf{w}_s \mathbf{w}_s \rangle \right]_{\text{coll. rad.}} \quad (17)$$

Dividing this equation by two and taking the trace yields the rate equation for the kinetic energy density $(1/2) n_s m_s \langle w_s^2 \rangle$. Eq. (17) does not contain the internal energy (excitation, dissociation, ionisation energies). The rate equation for the internal energy density of species s is

$$\frac{\partial n_s E_s^{\text{int}}}{\partial t} + \nabla_r \cdot (n_s E_s^{\text{int}} \langle \mathbf{w}_s \rangle) = \left[\frac{\partial n_s E_s^{\text{int}}}{\partial t} \right]_{\text{coll. rad.}} \quad (18)$$

E_s^{int} is the internal energy per particle of species s .

Summing up the eqs. (17) and (18) over all s yields the rate equation for the energy density of the plasma as a whole. One can now express all collisional-radiative terms as a function of rate coefficients and particle densities. When one takes still into account the eqs. (9) and (12) one finally obtains the following rate equation for the thermal plus internal energy density

$$\frac{\partial}{\partial t} (U^{\text{th}} + U^{\text{int}}) + \nabla \cdot (U^{\text{th}} + U^{\text{int}}) \mathbf{v}_0 + U^{\text{th}} \nabla \cdot \mathbf{v}_0 + \nabla \cdot \mathbf{Q}^{\text{total}} + \dot{R} = \dot{\Omega} + \dot{I} + \dot{N} \quad (19)$$

where

$$U^{\text{th}} = \frac{3}{2} n_h k T_h + \frac{3}{2} n_e k T_e \quad (\text{total thermal energy density}),$$

$$U^{\text{int}} = \sum_s n_s E_s^{\text{int}} \quad (\text{total internal energy density}),$$

$$\mathbf{Q}^{\text{total}} = \mathbf{Q}^{\text{th}} + \mathbf{Q}^{\text{int}} \quad (\text{total heat flux vector}),$$

$$\dot{\Omega} = \text{ohmic (electric) power input,}$$

$$\dot{I} = \text{power input by particle injection,}$$

$$\dot{N} = \text{nuclear power heating rate,}$$

$$\dot{R} = \text{radiative loss rate.}$$

\dot{R} contains contributions from free-free ($f-f$), free-bound ($f-b$), bound-bound ($b-b$), dielectronic (di) and cyclotron (c) radiation:

$$\dot{R} = \dot{R}^{ff} + \dot{R}^{fb} + \dot{R}^{bb} + \dot{R}^{di} + \dot{R}^c. \quad (20)$$

It should be mentioned that the radiative transfer eq. (6) intervenes in the calculation of \dot{R} and that $\dot{\Omega}$, \dot{I} and \dot{N} contain contributions which are different for the electrons (e) and heavy particles (h). For instance, the 3.5 MeV α -particles created in a thermonuclear D-T plasma will preferentially heat the electrons. The ions will directly gain energy from the α -particles when most of their energy has been slowed down already. Details of this slowing-down process are described by eq. (1) in form of the Fokker-Planck equation.

The eqs. (19)–(20) will be discussed in connection with the energy loss of Tokamak plasmas.

In order to describe a plasma completely one has still to add the Maxwell equations, the charge neutrality condition and the initial and boundary conditions.

In the following we will successively treat the glow discharge plasma in molecular and atomic gases, the so-called constriction phenomenon, the recombination of SF₆ plasmas in electric circuit breakers and the problem of measuring collisional-radiative recombination coefficients in general, the dynamics of hydrogen, helium, oxygen and the problem of radiation losses in Tokamak plasmas. The latter ones must already now be considered as *high-pressure* plasmas although their density is still relatively low. Fast transient phenomena as they are encountered in laser beam-plasma interaction will only be discussed in connection with the determination of rate coefficients

from laser beam-induced fluorescence measurements of a stationary plasma.

3. The glow discharge plasma. — The plasma of a glow discharge is very far from L.T.E. Although the macroscopic properties such as the dependence of the mean electron temperature T_e and mean electron density n_e on the gas pressure p , and the dependence of the electric field strength E on the electric current I are in principal well known, finer details of these dependences related to atomic and molecular processes have still to be discovered. Especially a number of atomic and molecular processes in these discharges and their influence on the thermodynamic properties and the space-dependent values of T_e , n_e and I are still not well understood. In particular, one has not yet a satisfactory explanation of the so-called constriction phenomenon.

3.1 THE GLOW DISCHARGE; BASIC CONSIDERATIONS.

— To begin with, let us briefly recall the basic theoretical assumptions and results for the positive column of a glow discharge (for the details see [5–8]) in the frame of the Schottky theory:

- the plasma is quasi-neutral, i.e. $n_e \approx n_+$, $|n_+ - n_e| \ll n_e$;
- the electron temperature T_e is constant across the discharge;
- the electron velocity distribution is Maxwellian;
- the electron mobility is given by Langevin's equation;
- the ion-electron production rate is proportional to n_e ;
- the gas temperature is constant across the discharge and can be considered as a given quantity.

Simple considerations about the particle and energy balance lead to relations for T_e , the electron density n_e and the electric strength E as a function of given external parameters such as gas pressure p , radius R of the discharge tube, the electric (or plasma) current I and the kind of gas employed.

The balance equations for the electron and ion densities, n_e and n_+ , are (see eq. (10)):

$$\frac{\partial n_e}{\partial t} + \nabla_r (n_e \langle \mathbf{v}_e \rangle) = \left[\frac{\partial n_e}{\partial t} \right]_{\text{coll. rad.}} \quad (21a)$$

$$\frac{\partial n_+}{\partial t} + \nabla_r (n_+ \langle \mathbf{v}_+ \rangle) = \left[\frac{\partial n_+}{\partial t} \right]_{\text{coll. rad.}} \quad (21b)$$

where the right-hand sides represent the collisional-radiative source terms (sum of ionisation and recombination rates). $\langle \mathbf{v}_e \rangle$ and $\langle \mathbf{v}_+ \rangle$ are the mean diffusion velocities of electrons and ions respectively. For a cylindrical plasma column, a radial electric field is build up due to the radially diffusing electrons and ions. This field causes the electron-ion pairs to

diffuse with the same radial ambipolar diffusion velocity. The diffusion flux is described by :

$$\begin{aligned} [n_e \langle \mathbf{V}_e \rangle]_r &= [n_+ \langle \mathbf{V}_+ \rangle]_r = -D_a \nabla_r n_e \\ &= -D_a \nabla_r n_+ \end{aligned} \quad (22)$$

where D_a is the ambipolar diffusion coefficient. Further, the right-hand sides of eqs. (21a), (21b) are equal because of charge neutrality. One makes now the assumption that the collisional-radiative source term is proportional to n_e :

$$\left[\frac{\partial n_e}{\partial t} \right]_{\text{coll. rad.}} = \left[\frac{\partial n_+}{\partial t} \right]_{\text{coll. rad.}} = n_e n_0 S \quad (23)$$

where $S = \langle \sigma v \rangle$ is the ionisation coefficient for electron-neutral atom (molecule) collisions. Owing to the eqs. (22)-(23), the eqs. (21a), (21b) can be replaced by one single equation :

$$\frac{\partial n_e}{\partial t} - D_a \nabla^2 n_e = n_e n_0 S. \quad (24)$$

For a stationary cylindrical plasma column one obtains the equation :

$$D_a \frac{1}{r} \frac{\partial}{\partial r} \left(r \frac{\partial n_e}{\partial r} \right) + n_0 n_e S = 0. \quad (25)$$

Since S is assumed to be independent of n_e (which implicitly means that volume recombination is omitted), the solution of eq. (25) is for the fundamental mode

$$n_e(r) = n_e(0) J_0 \left(r \sqrt{\frac{n_0 S}{D_a}} \right) \quad (26)$$

where $n_e(0)$ is the density at the axis ($r = 0$). For $r(n_0 S/D_a)^{1/2} = 2.405$ the Bessel function is zero, $J_0 = 0$, and for larger values of $(n_0 S/D_a)^{1/2}$ one would get negative values. This would have no physical meaning. Thus, by assuming that the electron density is practically zero at the wall at $r = R$, one imposes the boundary condition :

$$R \left[\frac{n_0 S}{D_a} \right]^{1/2} = 2.405 \quad (27)$$

and obtains the following radial density distribution :

$$n_r = n_r(0) J_0 \left(2.405 \frac{r}{R} \right). \quad (28)$$

The boundary condition (27) leads to the *similarity law* for the electron temperature T_e in the following way : S is only a function of T_e and the kind of gas via the ionisation cross-section ; hence :

$$S = S(T_e, \text{kind of gas}). \quad (29)$$

Further, D_a can be expressed in terms of the individual ion diffusion coefficient D_i (see e.g. p. 143 of [8] or pp. 261-262 of [9])

$$D_a = D_i \left(1 + \frac{T_e}{T_0} \right) \quad (30)$$

where T_0 is the gas temperature (assumed to be equal to the ion temperature T_+). For D_i we can now apply the formula for the binary ion (+)-neutral (0) diffusion coefficient (see e.g. pp. 484-486, pp. 523-527 of [10], p. 345 of [11]) as given by the transport theory :

$$D_i = \frac{3}{16} \frac{1}{(n_+ + n_0) \langle \sigma \rangle_{+0}} \left[\frac{2 \pi k T_0}{\mu} \right]^{1/2} \quad (31)$$

where $\langle \sigma \rangle_{+0}$ is some average effective momentum transfer cross-section and μ the reduced mass. Since $n_+ \ll n_0$ and $m_+ = m_0$ (and thus $\mu = m_0/2$) we have :

$$\begin{aligned} D_a &= \frac{3}{8} \frac{1}{n_0 \langle \sigma \rangle_{+0}} \left[\frac{\pi k T_0}{m_0} \right]^{1/2} \left(1 + \frac{T_e}{T_0} \right) = \\ &= \frac{1}{n_0} F_a(T_e, T_0, \text{kind of gas}) \end{aligned} \quad (32)$$

where F_a depends only on T_e , T_0 and on the nature of the gas through the cross section $\langle \sigma \rangle_{+0}$ for ion-neutral collisions. Substituting in eq. (27) S and D_a by the relations (29) and (32) respectively and expressing n_0 by the gas pressure $p = n_0 k T_0$ yields the following similarity law for the electron temperature of the positive column of the glow discharge :

$$R^2 p^2 = F_1(T_e, T_0, \text{kind of gas}) \quad (33)$$

where F_1 is a function which still depends on the nature of the gas through the electronic ionisation and the ion-neutral momentum transfer cross-sections. Since one does generally not know what type of collisions (elastic ion-neutral, charge exchange, excitation transfer, ... collisions) really contribute to $\langle \sigma \rangle_{+0}$ in which proportions, one often expresses D_a in eq. (32) in terms of independently measured ion mobilities. An *analytical* expression for T_e is obtained when a suitable energy dependence of σ_1 is assumed. One generally takes the linear dependence

$$\sigma_1 = a_1(E - E_1)$$

where E_1 is the ionisation energy and a_1 a gas-dependent constant.

In the same manner one can obtain similarity laws for the electric field strength \mathcal{E} and the electron density $n_e(0)$ on the axis [5-8] :

$$\frac{\mathcal{E}}{p} = F_2(p, R, T_0, \text{kind of gas}) \quad (34)$$

$$R^2 n_e(0) = IF_3(p, R, T_0, \text{kind of gas}) \quad (35)$$

where the functions F_2 and F_3 depend on the nature of the gas through elastic and inelastic cross-sections for collisions between electrons and neutrals and on the ion-neutral momentum transfer cross-sections.

I have treated the Schottky theory of the collision-dominated glow discharge plasma in some length in order to show how many assumptions intervene in the derivation of the similarity laws and how they depend on the atomic cross-sections. It is evident that for instance the calculation of T_e can be erroneous in the case of gas mixtures containing constituents of very different ionisation energies and very different cross-sections for ion-neutral collisions which contribute to the effective $\langle \sigma \rangle_{+0}$. A classical example is the helium discharge with small admixtures of neon. The latter increase the axial field strength compared to the pure helium discharge [12]. Dote and Kaneda [13] observed by means of a double probe that also T_e increases. The effect is explained as being due to resonance excitation of neon by helium metastable atoms. This shows that still other atomic processes than those contained in the simple Schottky theory intervene and that the omission of both stepwise excitation followed by ionisation and volume recombination may represent a severe limitation to the applicability of the theory. Also radiative emission and absorption processes have to be taken into account. The influence of the ensemble of all collision and radiation processes on the electron production rate can be expressed in terms of the collisional-radiative coefficients for ionisation S and recombination α which both depend on T_e and n_e in the simplest case. Replacing in eq. (23) the collisional-radiative source term by the expression

$$\left[\frac{\partial n_e}{\partial t} \right]_{\text{coll. rad.}} = \left[\frac{\partial n_+}{\partial t} \right]_{\text{coll. rad.}} = n_e [n_0 S(n_e, T_e) - n_+ \alpha(n_e, T_e)] \quad (36)$$

leads to a non linear boundary-value problem which permits a formal analytic solution [14-16], see also [34].

In eqs. (24) (36), the function S — and thus F_1 , F_2 and F_3 — depends strongly on the exact form of the velocity distribution function $f(E)$ of the electrons which, in turn, depends in a complicated manner on all elastic, inelastic, superelastic and radiative processes. In order to avoid the calculation of $f(E)$ one sometimes replaces the Maxwell distribution by a Druyvesteyn distribution. The latter is obtained from the electron energy balance equation when one assumes that the energy which an electron gains in the electric field is only lost through elastic collisions. However, when inelastic collisions (excitation, ionisation) are added to the energy balance equation, the Druyvesteyn dependence $f(E) \propto E^{1/2} \exp(-0.55(E/\bar{E})^2)$ changes into a modified Maxwell distribution

$$f(E) \propto E^{1/2} \exp(-E/\bar{E}).$$

(For the details see e.g. pp. 548-550 of [6].) For the same mean translational energy \bar{E} the two distributions give for the reaction coefficients values which can differ by several orders of magnitude. Under real conditions, $f(E)$ has a complicated E — dependence which lies in general somewhere between a $E^{1/2} \exp(-(E/\bar{E})^2)$ and $E^{1/2} \exp(-E/\bar{E})$ dependence. The determination of the mean translational energy \bar{E} (i.e. of kT_e) of the electron gas by means of the similarity law can therefore only give an approximate value, it is not a precise method.

In most papers $f(E)$ is now directly calculated from eq. (1). The energy dependence of such calculated distribution functions depends on the individual processes and their cross-sections. It should be mentioned that most of the published results are inconsistent from the thermodynamic point of view (although they often reproduce the experimental results quite well), since they do not account for superelastic collisions. It might be that inclusion of these processes in the model together with diffusion of excited species will bring experimental and theoretical results in better agreement. It should be emphasized that the superelastic collisions play a dominant role during the recombination phase and in situations where strong resonance absorption leads to high overpopulation of the first resonance levels.

Due to the non thermal population of excited atomic (ionic) levels it is difficult to obtain reliable experimental T_e -values from the Boltzmann ratio. In general they are too low. A better method is to determine T_e from a measurement of a number of spectral line intensities without using individual Boltzmann ratios. This method applied in [17-18] to a diffusion-dominated plasma column makes use of the solutions for the excited state populations of an appropriate collisional-radiative model and their comparison with spectroscopically determined population densities. It gives reliable values provided the atomic quantities (such as transition probabilities, cross-sections, line broadening parameters, ...) are known.

Already for the obviously simplest case, namely a glow discharge plasma in hydrogen gas, many of the relevant cross-sections for collisions between hydrogen atoms and hydrogen molecules are still unknown. Therefore a sophisticated model which makes use of the collisional-radiative model will not give more reliable values than the simple Schottky theory as long as all collision processes are not well understood. New results, which have led to a better understanding of the physical processes in a glow discharge plasma in molecular gases, were recently obtained by Dubreuil and Catherinot [19] who studied the reaction kinetics of excited hydrogen atoms and excited hydrogen molecules. Since their paper touches a general aspect common to all molecular plasmas, it shall be discussed in some detail.

3.2 THE GLOW DISCHARGE IN HYDROGEN GAS. — Dubreuil and Catherinot [19] studied the emission

of both the atomic and molecular species of hydrogen by means of laser-induced fluorescence. The discharge capillary had a diameter of $2R = 4$ mm, current and pressure were varied between the following values :

$$5 \leq I(\text{mA}) \leq 40;$$

$$0.1 \leq p(\text{torr}) \leq 2.$$

For each value of I and p the mean electron density n_e was determined from the frequency shift of the resonance frequency of a r.f. cavity containing the discharge capillary. The values are given in figure 2. Also are shown the mean T_e values calculated from the similarity law (33) with two different assumptions : either pure H_2 or pure H gas. Due to the low degree

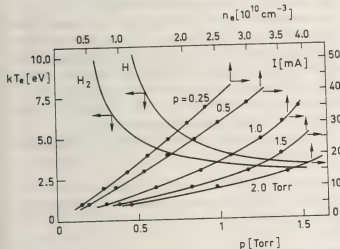


Fig. 2. — Mean electron temperature T_e as a function of pressure p for a glow discharge in pure H_2 or pure H gas, calculated from the similarity law. Also are shown the measured mean electron density n_e as a function of plasma current I at different pressures p . R is 2 mm, after [19].

of dissociation the H_2 curve is the more probable one. One further sees that the similarity law (35) with $n_e \propto I$ is approximately verified in the range of pressures employed.

By pumping successively the $n = 3, 4$ and 5 states of atomic hydrogen by means of a short laser pulse (duration ~ 4 ns) at different values of I and p and then observing the intensity decay of H_α , H_β and H_γ lines, the effective deexcitation frequencies ν_3 , ν_4 and ν_5 could be determined. Results are shown in figure 3. ν_n ($n = 1, 2, 3$) increases with p . One would also expect an increase of ν_n with I , i.e. an increase with n_e ; however, the contrary is the case. The measurements can be described by the following linear dependence :

$$\nu_n(p, I) = A_n + B_n(I)p \quad (37)$$

A_n represents the effective spontaneous deexcitation frequency of level with principal quantum number n :

$$A_n = \sum_{m < n} A_{mn} A_{mn} \quad (38)$$

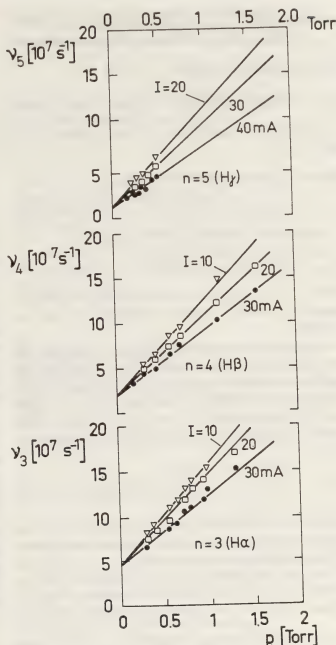


Fig. 3. — Effective de-excitation frequency ν_n of the atomic hydrogen levels $n = 3, 4$ and 5 as a function of pressure p at different plasma currents I , after [19].

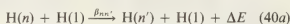
where A_{mn} are the optical escape factors. Extrapolation of the measured curves to $p = 0$ yields A_n — values consistent with the assumptions that the $\text{Ly}\alpha$ and $\text{Ly}\beta$ lines are completely reabsorbed and that only 40 % of the $\text{Ly}\delta$ intensity escapes from the plasma; the other lines being optically thin.

For ν_n we can write the following dependence (where three-body collisions are neglected due to the relatively low pressures) :

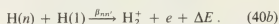
$$\nu_n(p, I) = A_n + n_{\text{H}} \sum_{n' \neq n} \beta_{nn'} + n_{\text{H}} \sum_{\zeta} \gamma_{n\zeta} + n_e \sum_{n' \neq n} v_{nn'} \quad (39)$$

where the rate coefficients $\beta_{nn'}$, $\gamma_{n\zeta}$, $v_{nn'}$ refer to the following reactions :

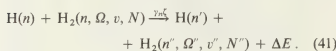
- *Excitation (de-excitation) due to atomic collisions*



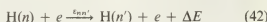
or associative ionisation



- *Excitation transfer due to atom-molecule collisions*



- *Electronic excitation (de-excitation)*



where $\zeta = (n, \Omega, v, N)$ represents the ensemble of quantum numbers which characterize an excited molecule.

The fact that induced fluorescence is only observed from the pumped levels leads to the conclusion that the processes (40a) and (42) are inefficient under the chosen experimental conditions (this was also verified experimentally). Also the reaction (40b) could be neglected. Thus, the eq. (39) can be approximated by

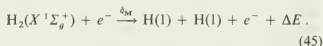
$$v_n(p, I) \approx A_n + n_{H_2}(p, T_0, I) \sum_{\zeta} \gamma_{n\zeta}(T_0) \quad (43)$$

where the reaction coefficient $\gamma_{n\zeta}$ depends only on the relative translation energy between atoms and molecules, i.e. on the gas temperature T_0 .

The gas temperature T_0 was measured with a thermo-couple ($T_0 \approx 320$ K independent of p and I). Owing to the very low degree of ionisation one has :

$$p \approx (n_{H_2} + n_H) kT_0 \quad (44)$$

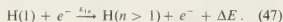
At a given pressure p , a decrease of n_{H_2} must be compensated by a corresponding increase of n_H . The decrease of v_n with increasing I (see Fig. 3) is now compatible with the relation (43) under the assumption that an increase of I , i.e. an increase of n_e (see Fig. 2) lowers the molecular density n_{H_2} due to increased dissociation according to the reaction :



The atoms are mainly formed in the ground state $n = 1$. The rate equation for the reaction (45) is

$$\frac{\partial n_1}{\partial t} = 2 \delta_M n(H_2) n_e - v_1 n_1 \quad (46)$$

where v_1 represents a loss coefficient. A second collision is necessary for excitation into the levels $n > 1$:



The rate equation for the excited hydrogen atoms $n > 1$ is given by

$$\frac{\partial n_{n>1}}{\partial t} = \epsilon_{1n} n_1 n_e - v_{n>1} n_{n>1} \quad (48)$$

For the stationary discharge ($\partial/\partial t = 0$), the number density of the excited hydrogen atoms must therefore be proportional to n_e^2 :

$$n_{n>1} = 2 \frac{\delta_M \epsilon_{1n}}{v_1 v_{n>1}} n(H_2) n_e^2 \quad (49)$$

As long as the degree of dissociation remains low ($< 5\%$) the formation of atomic hydrogen will not affect the H_2 concentration very much, whereas the atom density can strongly vary with n_e .

A measurement of the intensity of atomic and molecular lines as a function of n_e at a given pressure confirmed that the intensity of the molecular lines varies at low degrees of dissociation linearly with n_e whereas the one of the atomic lines increases with n_e^2 . It has thus been proved that the reaction (41) can explain the experimental features.

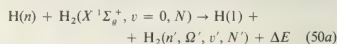
The results of the figure 3 permit to determine $\sum_{\zeta} \gamma_{n\zeta}$. Putting $\sum_{\zeta} \gamma_{n\zeta} = \langle \sigma(n) \rangle_{H-H_2} \langle v \rangle$ where $\langle v \rangle$ is the mean relative velocity between H and H_2 particles yields the mean effective cross-sections listed in table 1.

Table 1. — *Mean effective cross-section $\langle \sigma(n) \rangle_{H-H_2}$ for collisional de-excitation of excited hydrogen atoms by H_2 molecules after [19]. The values from [20] refer to a collision experiment in which H was excited by 40 keV electrons passing through H_2 gas. $\langle \sigma \rangle$ is in \AA^2 .*

	$n = 3$	$n = 4$	$n = 5$
$\langle \sigma(n) \rangle_{H-H_2} [19]$	156 ± 3	145 ± 4	146 ± 5
$\langle \sigma(n) \rangle_{H-H_2} [20]$	76 ± 3	32 ± 3	8.9 ± 0.7

The experimental values obtained from the glow discharge plasma are almost independent of n which is not the case for the collision experiment. It might be that the more abundant vibrationally-rotationally excited molecules in a discharge plasma are responsible for this discrepancy.

Dubreuil and Catherinot [19] also measured the decay of the fluorescence light of a number of molecular lines after pumping of the atomic states. The molecular fluorescence intensity is proportional to the atomic fluorescence intensity (see Fig. 4) in agreement with reaction (41). They could especially determine the reaction coefficients $\gamma_{n\zeta}$ for molecules in the electronic ground and in the excited metastable state $H_2(a^3\Sigma_g^+, v' = 0, N' = 4)$ according to :



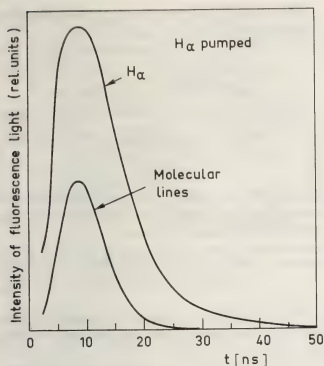
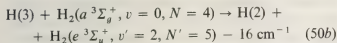
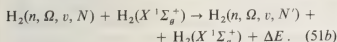
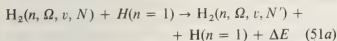


Fig. 4. — Fluorescence light of atomic and molecular lines after laser pumping of the atomic level $n = 3$ of hydrogen, after [19].



which are two special reactions of type (41). They also determined cross-sections for rotational relaxation induced by collisions with atoms and molecules according to the reactions

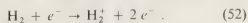


It was found that the transitions with a change of $\Delta N = \pm 1$ in the rotational quantum number were much more efficient than those with $\Delta N > 1$ indicating that Ω is not further a good quantum number for the electronic states involved. (The usual selection rule for homonuclear molecules treated in the frame of the Born-Oppenheimer method is $\Delta N = \pm 2$.)

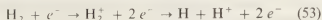
The experimental work of Dubreuil and Catherinot together with theoretical calculations by Capitelli *et al.* [21], Cacciatore *et al.* [22] and Capezzuto *et al.* [23] has led to a better comprehension of the microscopic processes which determine the properties of the hydrogen glow discharge; together with older known work the situation may be summarized as follows:

• **Formation of ion-electron pairs:** The H_2 molecules deliver the bulk of the positive ions and electrons by direct ionisation from the electronic ground level

or via a two-step process with the metastable and pseudo-metastable levels as intermediate states:

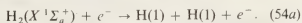


According to present knowledge the production rate of H^+ ions via the two-step process

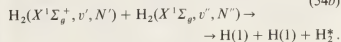
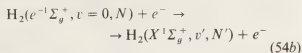


is smaller by several orders of magnitude. At higher degrees of dissociation the process $\text{H} + e^- \rightarrow \text{H}^+ + 2e^-$ may play a role (this is the process analogue to reaction (47) for the excitation of atomic levels).

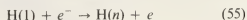
• **Dissociation:** Obviously two different processes are responsible for dissociation; first, dissociation by electron impact:



The electron rises the molecule to the first repulsive state ($^3\Sigma$), followed by dissociation; second, dissociation due to collision of two vibrotational excited molecules, the excitation arising from electronic collisions [21-23]:

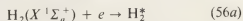


• **Formation of excited atoms** is essentially due to electronic collisions of the atom in the ground state:

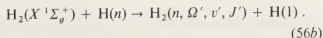


after the molecule has been dissociated.

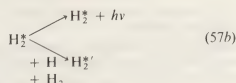
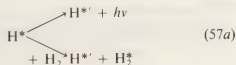
• **Formation of excited molecules:** Two processes are possible, namely direct excitation by electron collisions:



and excitation transfer due to molecule-atom collisions:



• **Destruction of excited atoms and molecules** is mainly via radiative transitions and due to collisions with atoms and molecules in the ground state:



• *Destruction of ions* (H^{2+} , H^+) is mainly due to diffusion to the walls (ambipolar diffusion) followed by recombination on the walls. This process is only dominant in a limited range of p ($\sim 10^{-1}$ to 10 torr), or R (~ 1 mm to 100 mm) and of I ($\sim 10^{-4}$ to 1 A).

The measurements showed further that the electrons contribute little to the transfer of energy between excited states (collisional excitation, de-excitation negligible).

3.3 THE GLOW DISCHARGE IN NITROGEN GAS. — An experimental study of Polak *et al.* [24] led to the result that the molecular ionisation rates for all regimes of a glow discharge in N_2 gas ($I = 5$ to 75 mA; $R = 1.6$ cm, $p = 0.6$ to 6.3 torr) must lie above the values computed under the assumption of direct ionisation by electron impact (see Fig. 5).

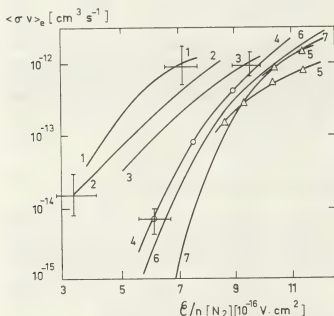
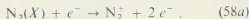


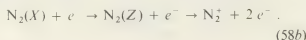
Fig. 5. — Rate coefficient $\langle \sigma v \rangle_e = S$ for volume ionisation in a glow discharge in pure N_2 gas as a function of \mathcal{E}/n . Curves 1 to 5 deduced from measurements: 1) $i = 9.5$ mA/cm²; 2) $i = 3.8$ mA/cm²; 3) $i = 1.25$ mA/cm²; 4) $i = 0.63$ mA/cm²; 5) from swarm experiments; 6) calculation for direct ionisation after reaction [40a] with $T_e = 8000$ K; 7) the same with vibrational temperature $T_e = 300$ K. After [24]. Experimental error bars are $\pm 100\%$.

Impurities could not be made responsible for the large discrepancies between theoretical and experimental values. From these and other observations the authors conclude that the ionisation mechanism under glow discharge conditions occurs via the following processes:

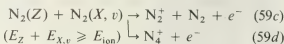
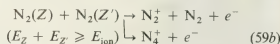
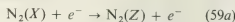
- *Direct ionisation* (X is the electronic ground state)



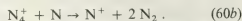
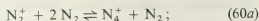
- *Stepwise electronic ionisation* (Z is an excited electronic state)



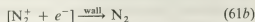
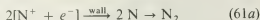
- *Electronic excitation followed by ionisation due to molecule-molecule collisions*:



where E_Z , $E_{Z'}$, $E_{X,v}$ and E_{ion} denote the excitation and ionisation energies respectively. Further the following transformations seem to be likely:



- *The destruction of the ions* is mainly due to ambipolar diffusion followed by recombination on the walls:



It has experimentally been observed that the N_4^+ concentration decreases with increasing current. This effect is interpreted as being due to a decrease of the N_2 density, because of an increase of dissociation with increasing electron density (because n_e is proportional to I) (see eq. (35)). According to the reactions (59a)-(59d) the production rate of N_4^+ should be proportional to $n_{N_2}^2 n_e^2$. This dependence has experimentally not yet been demonstrated.

In this context the theoretical work of Winkler and Pfau [26-27] on the glow discharge in N_2 gas should be mentioned. They calculated electron velocity distribution functions, collision frequencies, energy loss rates, direct ionisation frequencies and other quantities related to atomic processes. Capitelli and Dilonardo [25] (see also [22]) calculated the non-equilibrium excitation and dissociation of nitrogen molecules in electrical discharges.

The findings of Polak *et al.* [24] lead to the question if cluster ions could not play a role in glow discharge plasmas of other molecular gases?

It should finally be mentioned that Engelke [28] considered dissociating collisions in the frame of the Schottky theory.

3.4 THE GLOW DISCHARGE IN ATOMIC GASES; THE CONSTRICTION PHENOMENON. — According to the different values of p and I , a glow discharge appears visually as either a diffuse-homogeneous, a diffuse-striated, a constricted striated or a constricted-homogeneous plasma column. Figure 6 shows the existence regions of those types of discharges for neon. Similar curves for the other rare gases may be found

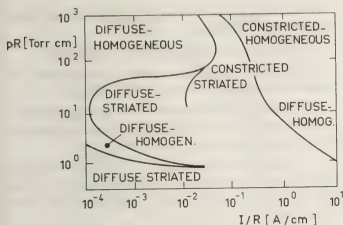


Fig. 6. — Existence diagram of the different column states in the case of a discharge in neon gas; p = filling pressure; I = discharge (plasma) current; R = tube radius; after [29, 36].

in [29]. When one goes for instance from low to higher values of I (for given values of pR) a diffuse-homogeneous discharge suddenly constricts. This constriction is accompanied by a sharp decrease of the electric field strength \mathcal{E} as shown in figure 7. If I changes from the higher to the lower values, the discharge returns to the diffuse state at a value of I slightly different from the one which was obtained for the opposite direction. One has a kind of hysteresis which increases with decreasing pressure. This constriction phenomenon has been known for a long time, however, even systematic theoretical studies have not yet led to a satisfactory description of this effect. It is interesting to see what a progress has been achieved during the last years by including various atomic and molecular processes in the theoretical model.

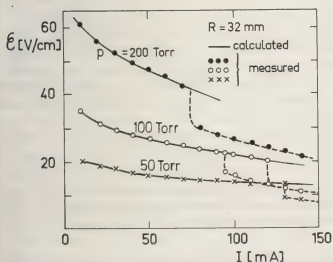


Fig. 7. — Measured electric field strength as a function of current I for a discharge in neon. $R = 32$ cm, \bullet 200 torr, \circ 100 torr, \times 50 torr, — calculations, --- constricted discharge measured. After [36].

In the following we refer first to the work of Wojacek who studied in a series of papers the constriction

by making different theoretical assumptions. In [30] the following assumptions were made :

1. The ionisation coefficient is equal to a modified Maxwell coefficient (see also eq. (23)) and has the form

$$S' = S_M \frac{b}{B} e^{-\kappa B} \quad (62)$$

where S_M refers to a Maxwell distribution. b and K are constants, B is $\sim 1/n_e$.

2. Superelastic collisions are neglected.
3. All ion-electron pairs diffuse to the walls due to ambipolar diffusion. They recombine on the walls.
4. Electron temperature T_e independent of r .
5. Gas temperature T_0 independent of r .
6. Neutral gas density constant across r .
7. Volume recombination is neglected.

The radial distribution of n_e is then described by the equation :

$$D_a \frac{1}{r} \frac{\partial}{\partial r} \left(r \frac{\partial}{\partial r} n_e \right) + S_M n_e \frac{b}{B} e^{-\kappa B} n_e = 0 \quad (63)$$

The solutions show a strong constriction with increasing values of $C_0(r=0) = KB_0$, where B_0 is the value of B on the axis. The relative distribution $n_e(r)/n_e(0)$ is shown in figure 8. The curve B represents the Bessel function. Similar curves have been obtained by Albrecht *et al.* [31].

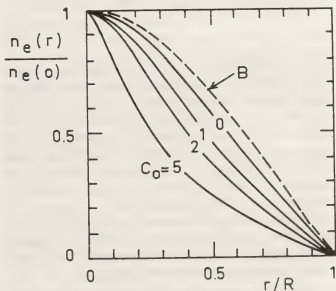


Fig. 8. — Relative radial distribution of the electron density $n_e(r)$ calculated from eq. (63), for different values of the constant C_0 on the axis. The curve B represents the Bessel function which is obtained when $b/B \exp(-KB) = 1$. After [30].

In a subsequent paper Wojacek [32] assumes instead of the condition 5 above, that the gas temperature depends on r via heat conduction. All other

assumptions remain unchanged. Now $n_e(r)$ and $T_0(r)$ are determined by the following equations:

$$\frac{1}{r} \frac{\partial}{\partial r} \left(D_a r \frac{\partial n_e}{\partial r} \right) + \frac{1}{r} \frac{\partial}{\partial r} \left(n_e D_a \frac{1}{T_0} \frac{\partial T_0}{\partial r} \right) + S_M n_0 n_e \frac{b}{B} e^{-K B(n_e)} = 0 \quad (64)$$

$$\frac{1}{r} \frac{\partial}{\partial r} \left(r \mathcal{K} \frac{\partial T_0}{\partial r} \right) - \Omega = 0 \quad (65)$$

where \mathcal{K} is the thermal heat conduction and $\dot{\Omega} = i\mathcal{E}$ is the source term (heating of the neutral gas by electron collisions). Compared to the solutions of eq. (63), the radial dependence of T_0 practically does not change the results in the range of interest.

A comparison with measurements for argon shows that the experimentally observed constriction is usually stronger than predicted by the model.

In a next paper [33] he assumed that also T_e depends on r . The solution of the corresponding differential equations leads to the conclusion that the radial dependence of T_e is of little consequence for the constricted discharge.

In a last paper [34] the calculations are based on the same assumptions 1 to 6 as in the first paper [30], however, instead of the condition 7 volume recombination is now included in the model (assumed to be independent of r). Instead of eq. (63) the following differential equation has to be solved:

$$D_a \frac{1}{r} \frac{\partial}{\partial r} \left(r \frac{\partial n_e}{\partial r} \right) + S_M n_0 n_e \frac{b}{B} e^{-K B(n_e)} - \alpha n_e^2 = 0. \quad (66)$$

The results lead with recombination to a stronger constriction of the $n_e(r)$ distribution than without recombination, but the theoretical model gives still too wide n_e —distributions compared to the experiments. Also the theoretically calculated electric field strength \mathcal{E} does not agree with the measured ones. Taking recombination into account leads to an increase of \mathcal{E} instead of a lowering as it is observed for the constricted column (see. Fig. 7).

A much more sophisticated collisional-radiative model for a glow discharge in neon and in argon has been set up and solved by Smits and Prins [35-36]. The following assumptions were made:

1. The molecular ion density (for instance $n(\text{Ne}_2^+)$) is much greater than the atomic ion density (for instance $n(\text{Ne}^+)$). The latter can therefore be neglected; the quasi-neutrality condition gives $n_e = n(\text{Ne}_2^+)$.

2. Direct ionisation is negligible with respect to stepwise ionisation. This stepwise ionisation, i.e. the ultimate formation of Ne_2^+ ions, proceeds via associative ionisation $\text{Ne}^* + 2 \text{Ne} \rightarrow \text{Ne}_2^+ + \text{Ne} + e^-$ (see Fig. 9 and ref. [37]).

3. The diffusion of the charged particles is governed by ambipolar diffusion.

4. Diffusion of excited particles is neglected.

5. Radiative transfer is taken into account by means of Holstein's radiative escape factor.

6. The radial dependence of the gas temperature is taken into account by solving the corresponding heat transfer equation for the neutral gas.

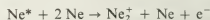
7. Volume recombination is taken into account in the form of dissociation recombination. For neon the following recombination coefficient has been chosen (see p. 2232 of [37])

$$\alpha = \frac{2.5 \times 10^{-8}}{(kT_e)^{1/2}} \left[1 - \exp\left(-\frac{900}{kT_0}\right) \right] \text{ cm}^3 \text{ s}^{-1} \quad (67)$$

where kT_0 is in eV.

8. Superelastic collisions have been neglected.

The various reaction channels which have been taken into account are shown in figure 9 for neon. The associative ionisation process



is only effective for particles belonging to the groups III and IV. The axial field strength (axially constant) and the velocity distribution function for the electrons have been calculated including elastic electron-electron, elastic electron-atom, and inelastic electron-atom collisions. The electron-electron collisions ensure

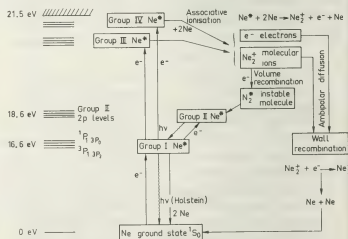


Fig. 9.—Atomic and molecular processes which have been taken into account in the collisional-radiative model of a glow discharge in neon gas, after [35, 36].

that $f(E)$ tends to a Maxwellian at high electron densities (but never reaching it). The inelastic and elastic electron-atom collisions lead to a depopulation of the tail of $f(E)$ compared to a Maxwell distribution. Figure 10 shows a calculated distribution function.

The main results of the model calculations compared to measurements are:

a) For the diffuse discharge, the calculated radial

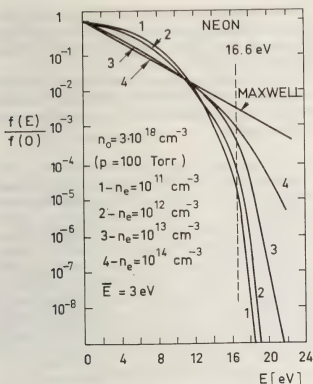


Fig. 10. — Calculated velocity distribution function $f(E)$ for electrons moving in a neon glow discharge plasma under the influence of an applied electric field at different electron densities. The mean translational energy is $\bar{E} = 3$ eV, the neutral gas density corresponds to a pressure of $p = 100$ torr. After [36].

distributions of n_e and of the excited states agree relatively well with the measurements. This is not the case for the constricted discharge.

b) For the diffuse discharge the calculated electric field strength \mathcal{E} also agrees with the measurements (see the examples given in figures 7 and 11). However, the sudden decrease of \mathcal{E} for the constricted discharge could not be reproduced.

The authors have changed several parameters and found that \mathcal{E} decreases more rapidly with current I when α is increased. Figure 11 shows an example where α was increased by a factor of three. A much better transition from the «diffuse» to the «constricted» \mathcal{E} -values could be obtained by increasing in the Boltzmann equation, which served for calculating $f(E)$ — the Coulomb terms by a factor of six. A nearly sudden transition from one regime to the other could be obtained by choosing a two-temperature model. Instead of using the calculated distribution function the authors chose a Maxwellian distribution with a bulk temperature T_0 on which another Maxwell distribution — corresponding to an electron density-dependent tail temperature T_i — was superposed. The following ratio between T_i and T_0 was assumed :

$$\frac{T_i}{T_0} = \frac{C_2 + n_e/n_0}{C_1 C_2 + n_e/n_0}. \quad (68)$$

Choosing $C_1 = 2.66$, $C_2 = 6.5 \times 10^{-7}$ the constriction phenomenon occurs at $I \approx 120$ mA as is observed experimentally (see Fig. 11).

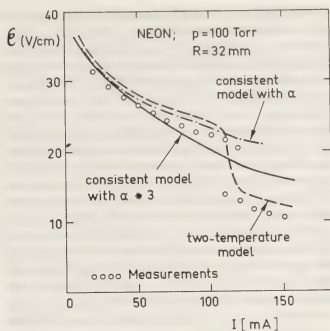


Fig. 11. — Influence of volume recombination α and of temperature model on the constriction phenomenon. —, —, — with α given by eq. (67) and consistently calculated velocity distribution function $f(E)$; — the same but with three times larger value for α ; --- two-temperature model for the electrons; $\circ \circ \circ \circ$ measured values. After [36].

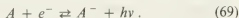
From a theoretical point of view this method is unsatisfactory. However, the fact that constriction can be obtained when a group of energetic electrons is included in the model has led the authors to propose another mechanism which might be responsible for constriction : the formation of energetic electrons caused by an ionisation instability in the form of a striations generating process.

It should be mentioned, however, that the tail of $f(E)$ can also be populated by superelastic collisions which have been neglected in the model. For instance for neon the rate of electronic deexcitation can become important due to the metastability of the first excited 3s-levels and the quasi-metastability of the 3p-levels (as a result of strong resonance reabsorption). If one includes in the model diffusion of this group of levels it might be that a kind of spatial excitation-deexcitation relaxation is build up which could be capable in producing a group of hot electrons in the tail of the velocity distribution function and which is obviously needed in order to explain the observed features. The assumption of diffusion of excited states would also be in agreement with the experimental fact that the observed line emission shows a larger radial profile than do the model calculations provided the radiating levels are sufficiently coupled to the metastable and quasi-metastable levels through collisional processes.

4. Negative ion plasmas. — 4.1 GENERAL CONSIDERATIONS. — Until now, we have only considered positive ion-electron plasmas. However, under appropriate conditions, one can produce plasmas containing

a relatively large amount of negative ions. For some gases, especially those containing halogens, a quasi-negative ion plasma can be produced, the electron density being negligible. Negative ions containing plasmas are not only of fundamental interest, they play a great role in astrophysics and are of great importance in electric circuit breakers. They may become important in the production of energetic neutral beams for plasma heating (neutral beam injection in Tokamak plasmas). Also the diffusion and wave properties of negative ion plasmas are of interest, since electron induced ambipolar fields no longer dominate the diffusion characteristics, and the shielding of low-frequency fields by electrons become increasingly inefficient with higher densities of negative ions. For a pure electronegative gas the similarity laws are different from the ones given above for pure electron-positive ion plasmas.

Negative ions can be produced in many different ways. In molecule-free plasmas, there exists only one single mechanism, that is the attachment of free electrons to neutral atoms with positive electron affinity. The energy liberated in this process is emitted in form of a photon $h\nu$ which produces the electron affinity continuum. The absorption of continuous radiation by negative ions causes photo-detachment of the bound electron. Thus,

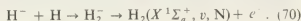


In astrophysical objects, these two reactions are of considerable interest when A represents a hydrogen, an oxygen, or a nitrogen atom. The continuum opacity of the Sun's atmosphere originates from H^- absorption, the O^- and N^- ions play a role in the sunlit ionosphere.

The electron affinity (or attachment) continua are currently observed in emission from low current arcs at atmospheric pressure and in shock-tube experiments provided the optical depth does not exceed the value one to two (for higher optical depths, the arc emits as a black-body). For further details, the reader is referred to the recent papers [39-44].

The physics of the negative ions is not yet well understood. There should exist a whole series of excited levels with energies close to those for the excited H-atom [45]. Until now, the experimental search for these states has led to negative results [46]. An exception is the experimental confirmation of the $1s\ 2p\ ^1P$ shape resonance of H^- at $\lambda = 1\ 130\ \text{\AA}$ [46-48] predicted by Macek and Burke [49], see also [50].

Recent measurements of the detachment cross-sections for the reaction $e^- + H^- \rightarrow H + 2e^-$ have led to the conclusion that the observed order of magnitude ($\sigma \lesssim 4 \cdot 10^{-15}\ \text{cm}^2$) was insufficient for the process to be important in astrophysics. It seems to be more likely that the destruction of H^- in cold stellar atmospheres is primarily due to associative detachment [51, 52]:



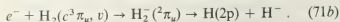
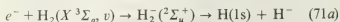
New calculations of the cross-section for reactions (70) which are capable to populate rotational-vibrational states have been published by Bieniek and Dalgarno [53].

There are also experimental indications from laboratory experiments that there might exist reaction channels for the formation of H^- which have still to be identified.

4.2 FORMATION OF H^- IN A LOW-PRESSURE PLASMA.

— Doucet and collaborators [54] produced a hydrogen plasma in a kind of cylindrical multipole and measured the negative ion density by means of an electrostatic probe (plasma volume $\sim 50\ \text{l}$, filling pressure $\sim 10^{-3}$ torr). It was found that the H^- density continuously increased with pressure, and attained values of $\sim 3 \cdot 10^9\ \text{cm}^{-3}$, that is 30% of the positive ion density. The measured values are graphically shown in figure 12. The figure also shows values calculated from the steady-state equation including the following processes with $v = 0$ in eqs. (71a, b):

• Dissociative electron attachment



• Polar dissociation

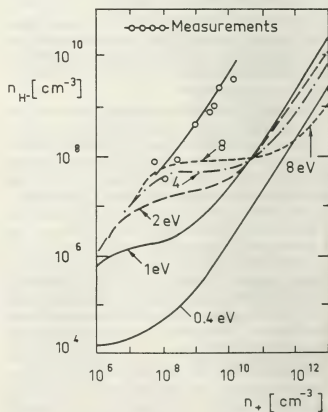
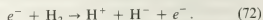
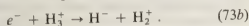
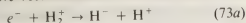
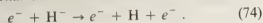


Fig. 12. — Negative ion density $n(H^-)$ as a function of positive ion density n_+ , after [54]. The electron temperature is taken as curve parameter. H^+ ions are assumed to be negligible, thus $n_+ = n(H_+)$.

- Dissociative recombination



- Collisional electron detachment



- Mutual neutralisation



and

- Diffusion

From figure 12 one sees that the measured values are 100 times higher than the calculated ones at the highest plasma density. At the present, there is no satisfactory explanation for this large discrepancy. Photodetachment measurements allowed to determine the H^- density as a function of n_e . For a plasma with the following parameters $n(H_2) \approx 2 \cdot 10^{14} \text{ cm}^{-3}$, $n_e = 1.7 \cdot 10^9$ to $1.1 \cdot 10^{10} \text{ cm}^{-3}$, $kT_e \approx 0.1 \dots 0.4 \text{ eV}$, a dependence $n(H^-) \propto n_e^3$ was found [55-56]. At maximum density, a ratio of $n(H^-)/n_e \approx 0.35$ was observed. It is assumed that one (or both) of the reactions (71a), (71b) are responsible for the H^- production. Also the process (73b) cannot completely be excluded. The reactions in H^- and D^- containing plasmas have been reviewed in [57].

4.3 ELECTRIC CIRCUIT-BREAKERS; RECOMBINATION OF SF_6 PLASMAS.—High-power electric circuit breakers are used to interrupt high currents under medium- or high-voltage conditions. Such switchgears contain sulphur hexafluoride (SF_6) gas because of its outstanding dielectric properties under high-voltage and high-temperature conditions. A circuit-breaker consists of one or two axially movable electrodes in a SF_6 containing vessel. The vessel consists of two electrode chambers connected by a channel (nozzle). During breaker operation a high pressure difference is maintained between the chambers.

In the normal position, the electrodes are in contact and the current can flow through. When the current is to be interrupted, the electrodes are separated. An arc is established which burns through the nozzle. The arc is submitted to a strong gasblast of SF_6 which cools the ionised gas. When the current goes through zero, the plasma has a temperature of approximately 10^4 K , the gas is fully dissociated and partially ionised, the thermodynamic state is close to L.T.E. The main constituents are F, S, S^+ and electrons [58-59]. Close to and at current zero, a strong ion-electron recombination begins accompanied by the formation of negative F^- ions. Also molecules are formed. When the high-voltage reappears in the next half period, the electrons must have disappeared in order to avoid re-arcing. The current interruption was successful when the gas has withstood the full voltage. The rapid formation of negative ions by electron attachment is essential for the extinguishing capability

ties of the SF_6 plasma. Industry builds current breakers which are capable to interrupt currents of the order of 75 kA per breaker unit and which can withstand voltages of the order of 70 to 100 kV. Connected in series, circuit-breakers are applied for voltages of the order of 500 kV. For further details, the reader is referred to [60-69].

The physical properties of the recombining SF_6 plasma with and without an applied electric field are not yet well understood. Both experiments and theoretical considerations have led to the conclusion that the essential reason for electrical breakdown or re-arcing of a hot SF_6 gas is the presence of negative ions of the order of 10^{13} cm^{-3} at a temperature of about 2 500 K. The dielectric properties depend on the reaction rate for electron detachment followed by electron avalanches under the influence of the applied electric field and the rate for electron attachment. The temporal evolution of the plasma composition during recombination is still unknown to a large extent.

It should in principle be possible to calculate the temporal evolution of the plasma composition from a system of coupled equations for the particle densities, momenta and energies. At constant plasma temperature, the physical situation can be described as follows: recombination will first lead to a decrease of total pressure with a rate according to (see eqs. (8) to (13))

$$\left(\frac{\partial p}{\partial t}\right)_T = \sum_s \left(\frac{\partial p_s}{\partial t}\right)_T = kT \sum_s \left[\frac{\partial n_s}{\partial t}\right]_{\text{coll. rad.}} \quad (76)$$

Thus, a pressure difference is built-up which leads to a general diffusion and mass flow of the plasma (eqs. (14) (16)) in order to re-establish the pressure. This mass motion is accompanied by a transport of energy (eq. (19)). In order to make the problem mathematically tractable many simplifying assumptions have to be made. Also the many reaction cross-sections must be known, which is not the case at present.

The physical situation becomes much simpler when a homogeneous recombining plasma volume at constant pressure is considered, which might be submitted to a simultaneous temperature variation. A simplified rate equation for the species s can then be obtained in the following way: the species s contributes to the pressure drop with a rate

$$\left(\frac{\partial p_s}{\partial t}\right)_T = \frac{n_s}{n} kT \sum_s \left[\frac{\partial n_s}{\partial t}\right]_{\text{coll. rad.}} \quad (77)$$

$$\text{hence} \quad \left(\frac{\partial n_s}{\partial t}\right)_T = \frac{n_s}{p} kT \sum_s \left[\frac{\partial n_s}{\partial t}\right]_{\text{coll. rad.}} \quad (78)$$

A temperature change at $p = \text{constant}$ leads in addition to the following rate for n_s

$$\left(\frac{\partial n_s}{\partial t}\right)_p = -\frac{n_s}{T} \left(\frac{\partial T}{\partial t}\right)_p \quad (79)$$

Thus, for the species s the following rate equation is obtained

$$\frac{\partial n_s}{\partial t} = \left[\frac{\partial n_s}{\partial t} \right]_{\text{coll. rad.}} + \frac{n_s kT}{p} \sum_s \left[\frac{\partial n_s}{\partial t} \right]_{\text{coll. rad.}} - \frac{n_s}{T} \left(\frac{\partial T}{\partial t} \right)_p \quad (80)$$

A coupled system of rate equations of type (80) has been applied by Brand and Kopainsky [70] in the frame of a simplified reaction model that takes the following chemical species into account :

F, F₂, S, S₂, SF, S⁺, S₂⁺, F⁻ and electrons.

Figure 13 shows the results of the model calculations. The initial condition is $T = 10^4$ K at $t = 0$, with the particle densities given by their equilibrium values at $p = 1$ atm. During the first 50 μ s, there is a strong electron-S⁺ ion recombination, the F⁻ density remains approximately constant. At 50 μ s begins a drastical change of the neutral particle densities. For $t > 100$ μ s, the ion density stabilizes at a value of approximately 10^{13} cm⁻³. The most abundant ions are S₂⁺ and F⁻, the electron density is negligible for $t > 100$ μ s. The formation of F⁻ and S₂⁺ ion pairs leads to a longlived negative ion plasma which determines the electrical properties of the gas and, thus, a possible dielectric failure when the voltage reappears at the electrodes.

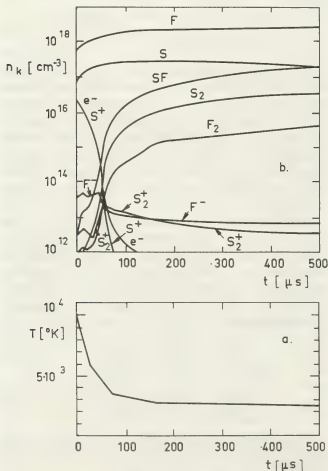


Fig. 13. — Temporal evolution of plasma composition (particle densities n_k of chemical species k) and temperature T of a recombining SF₆ plasma at a pressure of 1 atm, after [70].

5. **Collisional-radiative recombination.** — The eqs. (21a), (21b) permit to define two different collisional-radiative recombination (α) and ionisation coefficients (S) for the electrons and the ions :

$$\frac{\partial n_e}{\partial t} + \nabla_r \cdot (n_e \langle V_e \rangle) = n_d [n_0 S_e - n_s \alpha_e] \quad (81a)$$

$$\frac{\partial n_+}{\partial t} + \nabla_r \cdot (n_+ \langle V_+ \rangle) = n_d [n_0 S_+ - n_s \alpha_+] \quad (81b)$$

For negative ions, a third equation has to be added. In negative ions-free plasmas,

$$S_e = S_+ = S, \quad \alpha_e = \alpha_+ = \alpha,$$

and eq. (22) hold.

The recombination coefficient α can be determined experimentally by measuring $n_e(r, t)$ of a recombining plasma at sufficiently low temperature (in order to avoid perturbation by the term $n_e n_0 S$).

For constant volume, α is given by

$$\alpha = - \frac{1}{n_s n_e} \left[\frac{\partial n_e}{\partial t} - D_a \nabla^2 n_e \right] \quad (82)$$

The decrease of the electron density is accompanied by a decrease of total pressure with a rate

$$\left(\frac{\partial p}{\partial t} \right)_V = kT \sum_s \left[\frac{\partial n_s}{\partial t} \right]_{\text{coll. rad.}} + nk \left(\frac{\partial T}{\partial t} \right)_V \quad (83)$$

The last term accounts for a change of temperature during the recombination phase.

When the plasma recombines at constant pressure we can as a first approximation apply eq. (80) to which the ambipolar diffusion term should still be added. Putting in eq. (80) $n_s = n_e$ we obtain

$$\left[\frac{\partial n_s}{\partial t} \right]_{\text{coll. rad.}} = \left[\frac{\partial n_e}{\partial t} \right]_{\text{coll. rad.}} = - n_e n_s \alpha$$

Further, $\sum_s \left[\frac{\partial n_s}{\partial t} \right]_{\text{coll. rad.}}$ is given by eq. (13). It thus follows

$$\alpha = - \frac{1}{n_e n_s (1 + n_e kT/p)} \left[\frac{\partial n_e}{\partial t} - D_a \nabla^2 n_e - \frac{n_e kT}{p} \left[\frac{\partial n_M}{\partial t} \right]_{\text{coll. rad.}} + \frac{n_e}{T} \left(\frac{\partial T}{\partial t} \right)_p \right] \quad (84)$$

The third term — which is generally positive — accounts for the formation of neutral molecules during the recombination phase. In the denominator, the ratio of electron pressure to total pressure can in almost all cases be neglected. During recombination, T practically equals the gas temperature. When measurements of $n_e(r, t)$ and $T(t)$ are based on methods in which the length of the plasma column intervenes, corrections have eventually to be made in order to account for the contraction of the plasma column.

Substituting in eqs. (82) and (84) n_e by n_- yields the corresponding expressions for the recombination coefficient of a negative ion plasma in (which electrons are absent).

From figure 13 we can extract the order of magnitude of the recombination coefficient. One finds $\alpha \approx 10^{-8} \text{ cm}^3 \text{ s}^{-1}$ for the first 50 μs , and

$$\alpha \approx 10^{-10} \text{ cm}^3 \text{ s}^{-1}$$

for times $t > 100 \mu\text{s}$. These values differ by several orders of magnitude from those measured for the cold SF_6 gas [71] which contains mainly SF_5^+ , SF_5^- and SF_6^- ions and probably also cluster ions of the form $\text{SF}_6^- (\text{SF}_6)_x$.

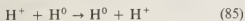
6. Atomic processes in high-temperature plasmas. —

Until now, we have dealt with relatively cool plasmas containing both atomic and molecular (neutral and ionised) species. We will now consider high-temperature plasmas. We shall limit the discussion to a selected number of atomic (ionic) processes encountered in so-called thermonuclear fusion plasmas. In the following, the word *hydrogen* is employed for either of the isotopes hydrogen, deuterium and tritium. The examples chosen apply in the first place to Tokamak plasmas.

6.1 THE DYNAMICS OF HYDROGEN ATOMS. — Apart from laser-fusion experiments, all *fusion plasmas* are submitted to strong magnetic fields in order to confine the plasma and to separate it from material walls. However, only charged particles are influenced by a magnetic field, neutrals can cross it without being affected. Owing to ion-electron recombination, the neutral particle density is not zero, but even under thermonuclear conditions can some neutral hydrogen atoms be present in the hot plasma core. One has

$$n(\text{H}^0) \approx 10^6 \dots 10^8 \text{ cm}^{-3}.$$

This follows directly from the solution of the ionisation-recombination balance for hydrogen and agrees approximately with measured values. Therefore, energetic ions $\text{H}^+ (\text{D}^+, \text{T}^+)$ can undergo charge exchange collisions with neutral atoms $\text{H}^0 (\text{D}^0, \text{T}^0)$ according to the reaction



in which the energetic ions H^+ are transformed into energetic neutral particles H^0 which can now cross the magnetic barrier. Whether these neutrals can directly reach the walls or not depends on the probability of re-ionisation, since a re-ionised particle will again be captured by the magnetic field. The ionisation probability depends on the ionisation cross-sections. In figure 14, all relevant ionisation cross-sections are compared with those for charge exchange. One sees that for kinetic energies $E \leq 60 \text{ keV}$ (that is for the whole region of thermo-nuclear interest), the charge exchange cross-sections are larger than the ionisation

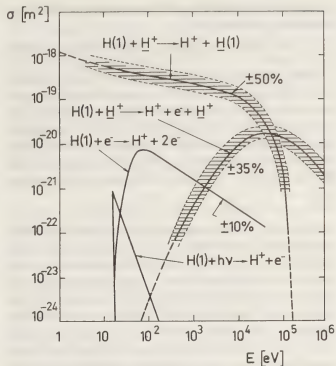


Fig. 14. — Cross-sections σ for charge exchange and ionisation of neutral hydrogen atoms (or their isotopes) in the ground state.

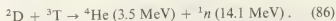
cross-sections. It follows from this that energetic neutral atoms can reach the walls where they cause sputtering of wall material [73, 74]. This represents a source of impurities.

Recent calculations [75] for the future Princeton Tokamak TFTR (now under construction) have led to the result that, due to charge exchange reactions, the flux of charge exchange neutrals will correspond to a total energy loss rate of 1 MW, that the *mean* kinetic energy of a neutral atom impinging on the wall will be 1.9 keV, and that sputtering of the stainless steel walls will result in a flux of $1.5 \cdot 10^{17}$ iron atoms/ $\text{m}^2 \text{ s}$. In one second, one will build-up a mean iron impurity concentration of approximately one percent. This can prevent thermonuclear ignition.

This example shows how important are technical solutions which minimize sputtering and avoid penetration of impurities into the plasmas. Possible solutions to this problem are the formation of cold-plasma blankets [76], mechanical divertors (scrape-off limiters) [77] or magnetic divertors [78] in connection with the development of materials having low sputtering yields.

6.2 THE DYNAMICS OF HELIUM. — The ideal fusion plasma should only contain D^+ and T^+ ions and electrons at temperatures of the order of $10^8 \text{ K} \approx 10 \text{ keV}$. In the absence of thermonuclear reactions, the only radiation processes would be electron-ion bremsstrahlung and cyclotron radiation. Both processes represent energy losses which must be compensated by some heating mechanism in order to avoid cooling of the plasma. In a continuously operated magnetically confined D – T fusion plasma (Tokamak plasma),

this heating mechanism will be provided by the thermonuclear reaction itself :



The He-ions (α particles) produced in the reaction are captured by the confining magnetic field. At $B = 4$ tesla their Larmor radius is 7 cm. The energetic α particles make collisions with the colder ion-electron gas and heat it up (so-called α -particle heating). This heating mechanism also compensates energy losses due to diffusion (charge exchange, heat conduction, ...).

The production of helium nuclei increases the ion charge state of the plasma and, thus, the bremsstrahlung losses. The plasma must therefore continuously increase its temperature in order to compensate the increasing radiation losses. The compensation is possible, since the power of the fusion reaction (86) increases exponentially with T whereas the rate of the bremsstrahlung losses increases only proportionally to $T^{1/2}$ (for the details, see e.g. [79-80].) The fusion reaction (86) leads to a kind of self-contamination. In order to avoid this effect and to keep the energy losses and temperature low, a rapid exhaust of the helium is desirable. The helium leaving the reactor is then replaced by new fuel. In a continuously operated reactor, the helium can only leave the hot reaction zone by diffusion. Both Coulomb- and atom-ion collisions can play a role.

The physical situation is shown in figure 15. Helium is assumed to be the only impurity element. He^{2+}

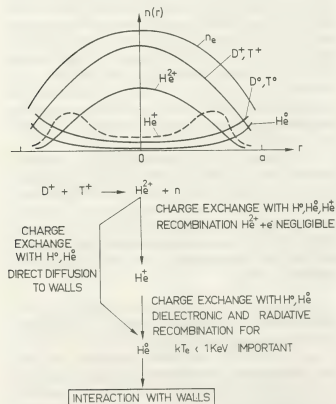
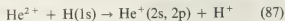


Fig. 15. — Radial distribution of helium in a hypothetical D-T fusion reactor, and possible elementary reactions which may have an influence on the exhaust of helium.

will be produced in the plasma core. The exact radial distribution of He^{2+} , He^+ and He^0 will depend on various collective processes but also on individual atomic reactions. Let us consider first the He^{2+} ions.

The He^{2+} ions can be transformed in He^+ and He^0 by different reactions. In a future reactors collisions with the neutral D^0 and T^0 atoms may become important. The density of the neutrals is not zero, but varies from approximately 10^8 cm^{-3} at the axis to 10^{10} cm^{-3} at the plasma boundary. Figure 16 shows the cross-sections for the non-symmetrical charge exchange between He^{2+} and H^0 . The reaction



has an accidental resonance leading to an especially large cross-section.

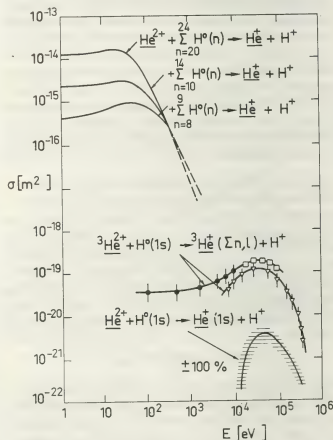


Fig. 16. — Charge exchange cross-sections for collisions between He^{2+} ions and neutral hydrogen atoms (which can be considered as representative for the isotopes D and T), after [82-84].

In a fusion plasma, there will be a relatively large number of excited D^0 and T^0 atoms (compared to those in the ground state). Owing to the extremely large charge exchange cross-sections for the excited levels, the excited particles can play a role in the transport of the helium ions. The change from He^{2+} to He^+ leads to an increase of the Larmor radius and, thus, contributes to the diffusion flux. The He^+ ions are still captured by the magnetic field.

The dynamics of the He^+ ions will now depend on whether back-ionisation into He^{2+} or further transformation into He^0 through charge exchange or

recombination occurs. Back-ionisation into He^{2+} will mainly occur through electron collisions. Figure 17 shows the relevant ionisation cross-sections.

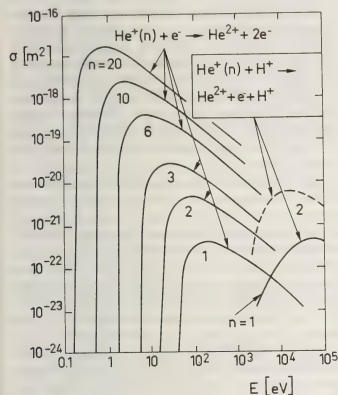


Fig. 17. — Cross-sections for ionisation of He^+ into He^{2+} , after [37], [83-85].

Also are shown the cross-sections for ionisation by proton impact. There do not exist any studies in which the relevant atomic collision processes have been taken into account. For further details concerning the exhaust problem, the reader is referred to [81].

6.3 THE DYNAMICS OF OXYGEN. — Special attention must be paid to oxygen which is found with

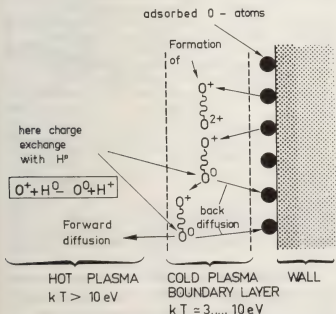
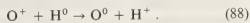
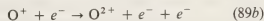
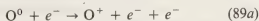


Fig. 18. — Diffusion of oxygen through a cold plasma boundary layer.

relatively high concentration (0.5 % to 5 %) in nearly all Tokamak plasmas. The physical situation is schematically shown in figure 18. Neutral oxygen atoms diffuse from the walls into the plasma-wall boundary layer where they are ionised. An ionised oxygen atom is captured by the magnetic field. Further ionisation will lead to O^{2+} ions, etc. The ions will essentially diffuse due to Coulomb collisions and eventual collective effects. However, it is also possible that the ions undergo charge exchange collisions with neutral hydrogen atoms according to the reaction



Thus, the neutral oxygen atom can again diffuse across the magnetic field. Figure 19 shows the relevant cross-sections intervening in the ionisation and charge exchange processes [82, 86]. One clearly sees that charge exchange can play a dominant role. A recent study [87] has shown that, due to the high charge exchange cross-section, up to 30 % of the oxygen atoms leaving the walls are reflected back to the walls. In this study, only the following three reactions were taken into account :



It might be that also other chemical reactions such as :

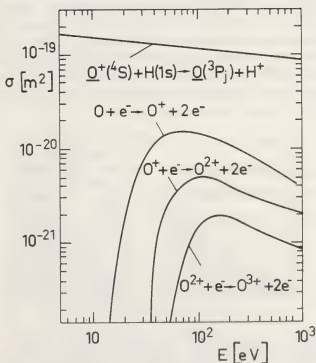
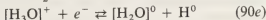
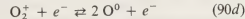
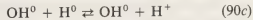
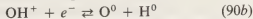
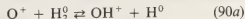


Fig. 19. — Cross-sections σ for oxygen, after [82, 85].

are of importance in the immediate vicinity of the walls. Corresponding studies are missing in the literature.

6.4 RADIATION LOSSES.—High Z-impurities—even in very small concentrations—in thermonuclear fusion plasmas can lead to high radiation losses. This can have severe consequences for the global energy balance in future thermonuclear reactors. The same problem is met in present-day fusion research machines of the Tokamak type.

Figure 20 shows how the different physical processes contribute to the power loss of the Tokamak TFR-400 [90]. The mean radius of the torus is $R = 98$ cm, the outer plasma radius is $r = 20$ cm, r being the distance from the center of the plasma. The figure shows the power which is deposited in a plasma volume defined by the value of r and the power which is lost through the surface surrounding the plasma at r . In the case of figure 20a, the plasma is only heated by the electric current circulating in the plasma (ohmic heating). The power density is $\dot{\Omega}$, see eq. (19). In the case of figure 20b, the plasma is additionally heated by an energetic neutral particle beam with power density \dot{I} . In the first case, the total power input is 570 kW, in the second case 870 kW. One sees that approximately 50% of the total energy are lost in form of radiation. The latter contributes especially in the outer zones to the energy loss.

In a pure completely ionised hydrogen (D-T) plasma the only radiation loss originates from free-free bremsstrahlung radiation and cyclotron radiation. But already small admixtures of heavy species increase the radiation loss considerably: as long as the atoms are not completely stripped, electronic excitation will cause intense bound-bound radiation; also electron-ion recombination will partly be responsible for this enhanced radiation loss (free-bound and dielectronic recombination radiation), see eq. (20). The contribution of the free-free radiation of not completely stripped atoms is small. However, for completely ionised particles the power density of the

bremsstrahlung caused by impurities can dominate the radiation loss of a plasma completely.

The radiation losses caused by impurities in Tokamaks are generally calculated in the frame of the corona model, because of the very high electron temperatures and relatively low electron densities. Figure 21 gives an example for molybdenum which has been used in Tokamaks as current-limiting diaphragm. The individual contributions to the total power loss have been typified in eq. (20). Similar calculations have been carried out in different laboratories for many other impurity species and the data are available in the literature. In more sophisticated model calculations also spatial relaxation effects due to diffusion are taken into account [92]. The application of the *corona model*—with superposed diffusion fluxes of the ground state ions—gives satisfactory results for the global radiative loss rates. However, the application of this model to the calculation of the intensity of special spectral lines may in some cases lead to erroneous results, due to strong collisional coupling between various levels compared to radiative coupling by spontaneous de-excitation. If such spectral lines are used for diagnostic purposes, their intensities should be calculated in the frame of a more general collisional-radiative model in which all important reactions are taken into account. Especially charge exchange reactions into excited levels should be taken into account. For further details see e.g. the review [88].

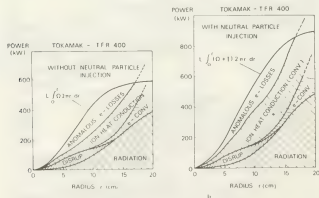


Fig. 20. — Power input into the french Tokamak TFR-400 as a function of radius, and contribution of the various processes to the power loss, after [90]. a) only ohmic heating, b) ohmic heating plus neutral particle injection heating.

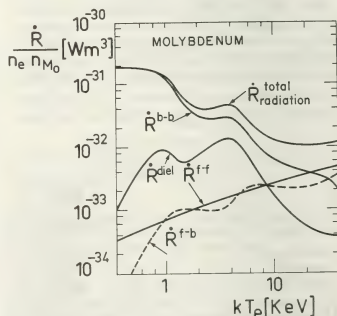


Fig. 21. — Radiation loss rate for molybdenum. $\dot{R}/n_e n_{Mo}$ is the power density radiated per electron and per molybdenum particle, after [91]. The individual contribution have been defined in eq. (20).

7. Summary and conclusion.—In order to understand the physical (and also the chemical) properties of non-L.T.E. plasmas one has to study in detail the coupled system of collisional-radiative equations for the particle densities, momenta and energies. Owing

to the complexity of the problem in general, and due to the sometimes scarce knowledge of the reaction processes in particular, many simplifying assumptions have often to be made. In this paper, three different types of non-L.T.E. plasmas have been treated: glow discharge, negative ion and Tokamak plasmas. The discussion has been restricted to stationary and quasi-stationary states and to laser-induced fluorescence. In selected examples it has been shown how the application of the rate equations permits to interpret and to calculate special plasma properties on the one hand, and how the rate equations allow to extract information about special, dominant collision pro-

cesses and to determine their rate coefficients on the other hand. In principle, quite similar problems are encountered in all other types of non-L.T.E. plasmas, fast transient plasmas included with the additional difficulty, however, that the time-dependent coupling may require the treatment of a (much) larger number of coupled rate equations compared to the stationary and quasi-stationary states. — The processes which are taken into account in the rate equations should satisfy the condition of micro-reversibility. When this condition is not fulfilled, the rate equations lead to inconsistent results from the thermodynamic point of view.

References

- [1] EBELING, W., KRAEFT, W. D., KREMP, D., Theory of Bound States and Ionization Equilibrium in Plasmas and Solids, in *Ergebnisse der Plasmaphysik und der Gaselektronik*, Bd. 5 (Ed. R. Rompe and M. Steenbeck), Akademie Verlag, Berlin, 1976.
- [2] KRAEFT, W. D., Non-ideal Plasmas, Elementary Excitations and Macroscopic Properties, in *The Physics of Ionized Gases* (Ed. R. K. Janev), The Institute of Physics, Beograd, 1978.
- [3] POPOVIĆ, M. M., Measured Properties of Non-ideal Plasmas, in *The Physics of Ionized Gases* (Ed. R. K. Janev), The Institute of Physics, Beograd, 1978.
- [4] BURGESS, D. D., Spectroscopic Effects in Dense and Ultra-dense Plasmas, in *The Physics of Ionized Gases* (Ed. R. K. Janev), The Institute of Physics, Beograd, 1978.
- [5] FRANCIS, G., The Glow Discharge at Low Pressures, in *Handbuch der Physik*, vol. XXII (Ed. S. Flügge), Springer Verlag, 1956, p. 53-208.
- [6] VON ENGEL, A., Ionization in Gases by Electrons in Electric Fields, in *Handbuch der Physik*, vol. XXI (Ed. S. Flügge), Springer Verlag, 1956, p. 504-573.
- [7] VON ENGEL, A., *Ionized Gases*, Clarendon Press, Oxford, 2nd ed., 1965, p. 238-248.
- [8] DELCROIX, J. L., *Physique des Plasmas*, tome 2, Dunod Editeur, Paris, 1966.
- [9] DRAWIN, H. W., Transport Properties of Plasmas, in *Reactions under Plasma Conditions*, vol. 1 (Ed. M. Venugopalan, Wiley-Interscience), New York, 1971.
- [10] HIRSCHFELDER, J. O., CURTIS, Ch. F., BIRD, R. B., *Molecular Theory of Gases and Liquids*, John Wiley and Sons, 1954.
- [11] FINKELNBURG, W., MAECKER, H., Elektrische Bögen und Thermisches Plasma, in *Handbuch der Physik*, vol. XXII (Ed. S. Flügge), Springer Verlag, 1956, p. 254-444.
- [12] HEADRICK, L. B., DUFFENDACK, O. S., *Phys. Rev.* **3A** (1931) 736.
- [13] DOTE, T., KANEDA, T., *Phys. Letts.* **48A** (1974) 351.
- [14] WILHELM, H. E., *J. Math. Phys.* **13** (1972) 252.
- [15] WILHELM, H. E., LIRON, N., *Phys. Fluids* **15** (1972) 1328.
- [16] WILHELM, H. E., *Canad. J. Phys.* **50** (1972) 1156.
- [17] DRAWIN, H. W., EMARD, F., KATSONIS, K., *Z. Naturforsch.* **28a** (1973) 1422.
- [18] DRAWIN, H. W., EMARD, F., DUBREUIL, B., CHAPPELLE, J., *Beiträge aus der Plasmaphysik* **14** (1974) 103.
- [19] DUBREUIL, B., CATHERINOT, A., *J. de Physique* **39** (1978) 1071.
- [20] LEWIS, J. W., WILLIAMS, W. D., *J. Quant. Spectr. Radiative Transfer* **16** (1976) 939.
- [21] CAPITELLI, M., DILONARDO, M., MOLINARI, E., *Chem. Physics* **20** (1977) 417.
- [22] CACCIATORE, M., CAPITELLI, M., DILONARDO, M., *Chem. Physics* **34** (1978) 193.
- [23] CAPEZZUTO, P., CRAMAROSSA, F., D'AGOSTINO, R., MOLINARI, E., *J. Phys. Chem.* **79** (1975) 1487; **80** (1976) 882.
- [24] POLAK, L. S., SERGEEV, P. A., SLOVETSKII, D. I., *High Temperature* **15** (1977) 13.
- [25] CAPITELLI, M., DILONARDO, M., *Rev. de Physique Appl.* **13** (1978) 115.
- [26] WINKLER, R., PFAU, S., *Beiträge aus der Plasmaphysik* **13** (1973) 273; **14** (1974) 167.
- [27] PFAU, S., WINKLER, R., *Beiträge aus der Plasmaphysik* **18** (1978) 113.
- [28] ENGELKE, B.-E., *Z. Physik* **158** (1960) 422.
- [29] PFAU, S., RUTSCHER, A., *Beiträge aus der Plasmaphysik* **8** (1968) 73.
- [30] WOJACZEK, K., *Beiträge aus der Plasmaphysik* **6** (1966) 211.
- [31] ALBRECHT, G., ECKER, G., MÜLLER, K. G., *Z. Naturforsch.* **17a** (1962) 854.
- [32] WOJACZEK, K., *Beiträge aus der Plasmaphysik* **7** (1967) 149.
- [33] WOJACZEK, K., *Beiträge aus der Plasmaphysik* **8** (1968) 109.
- [34] WOJACZEK, K., *Beiträge aus der Plasmaphysik* **9** (1969) 243.
- [35] SMITS, R. M. M., PRINS, M., *Physica* **96C** (1979) 243.
- [36] SMITS, R. M. M., PRINS, M., *Physica* **96C** (1979) 262.
- [37] MASSEY, H. S. W., GILBODY, H. B., *Electronic and Ionic Impact Phenomena*, vol. 4, Clarendon Press, Oxford, 1974.
- [38] LORENTS, D. C., The Physics of Electron Beam Excited Rare Gases at High Densities, in *Proc. 11th Intern. Cong. on Phenomena in Ionized Gases*, Eindhoven, 1975, part 2, invited papers (Eds. J. G. A. Holscher and D. C. Schram), North Holland, Amsterdam, 1976. See also *Physica* **82C** (1976) 19.
- [39] NEIGER, M., *Z. Naturforsch.* **30a** (1975) 474.
- [40] POPP, H.-P., *Vacuum* **24** (1974) 551.
- [41] POPP, H.-P., KRUSE, S., *J. Quant. Spectr. Radiat. Transfer* **16** (1976) 683.
- [42] BEHRINGER, K., THOMA, P., *Physical Rev.* **17** (1978) 1408.
- [43] HOFFMANN, H., *J. Quant. Spectr. Radiat. Transfer* **21** (1979) 163.
- [44] D'YACHKOV, L. G., KOBZEV, G. A., *High Temperature* **14** (1976) 607.
- [45] RISLEY, J. S., EDWARDS, A. K., GEBALLE, R., *Phys. Rev. A* **9** (1974) 1115.
- [46] RISLEY, J. S., DE HEER, F. J., KERKDIJK, C. B., *J. Phys. B (Atom. Molec. Phys.)* **11** (1978) 1783.
- [47] WILLIAMS, F., WILLIS, B. A., *J. Phys. B (Atom. and Molecular Physics)* **7** (1974) L61.
- [48] BEHRINGER, K., THOMA, P., *Phys. Rev. A* **17** (1978) 1408.
- [49] MACEK, J. H., BURKE, P. G., *Proc. Phys. Soc.* **92** (1967) 351.
- [50] BROAD, J. T., REINHARDT, W. P., *Phys. Rev. A* **14** (1976) 2159.
- [51] SCHMELTEKOPF, A. L., FEHSENFELD, F. C., FERGUSON, E. E., *Astrophys. J. (Letters)* **148** (1967) L155.
- [52] SCHMELTEKOPF, A. L., FEHSENFELD, F. C., FERGUSON, E. E., *Astrophys. J. (Letters)* **148** (1967) L155.
- [53] BIENIEK, R. J., DALGARNO, A., *Astrophys. J.* **228** (1979) 635.
- [54] NICOLOPOULOU, E., BACAL, M., DOUCET, H. J., *J. de Physique* **38** (1977) 1399.

- [55] BACAL, M., HAMILTON, G. W., *Phys. Rev. Letts.* **42** (1979) 1538.
- [56] BACAL, M., HAMILTON, G. W., BRUNETEAU, A. M., TAILLET, J., *Rev. Sci. Instr.* **50** (1979) 719.
- [57] HISKES, J. R., BACAL, M., HAMILTON, G. W., *Atomic Reactions in H⁺ and D⁺ Plasmas*, Report UCID-18031, Lawrence Livermore Laboratory, 1979.
- [58] FRIE, W., *Z. Physik* **201** (1967) 269.
- [59] LIEBERMANN, R. W., LOWKE, J. J., *J. Quant. Spectros. Radiat. Transfer* **16** (1976) 253.
- [60] RAGALLER, K., *Physics of Arcs in Circuit Breakers*, p. 251-268, in *Proc. (invited lectures) 13th Intern. Conf. on Phenomena in Ionized Gases*, September 12-17, 1977, Berlin; Editor Physical Society of the German Democratic Republic, 1977.
- [61] JACOB, T., SCHADE, E., SCHAUMANN, R., *Self-blasting, a new switching principle for economical SF₆ Circuit Breakers*, C.I.R.E.D., London 1977, I.E.E. Conf. paper No. 2.4, p. 63-66.
- [62] BRINKHOFF, R., BECKER, H., HÖGG, H., SCHMIDT, K. D., SCHMIDT, W., SONDEREGGER, G., *Auslegung und Prüfung der metallgekapelten SF₆-isolierten 420 kV-Schaltanlage Frankfurt/Südwest*; *Elektrizitätswirtschaft* **2** (1977) 21.
- [63] KRENICKY, A., SCHADE, E., *Recent Investigations on Arcs in SF₆ Gas-blast Breakers and Application of the Results to the Development of H-V. Switchgear*, paper No. 74, Section 2, *World Electrotechnical Congress*, June 21-25, Moscow, 1977.
- [64] HERTZ, W., MENTEL, J., TIEMANN, W., *Siemens Forsch. und Entwickl. Ber.* **3** (1974) 5.
- [65] HERTZ, W., MENTEL, J., STROH, J., TIEMANN, W., *Siemens Forsch. und Entwickl. Ber.* **4** (1975) 281.
- [66] HERMAN, W., RAGALLER, K., *IEEE Transact. on Power Apparatus and Systems*, **PAS-96** (1977) 1546.
- [67] HERMAN, W., KOEGLSCHATZ, V., NIEMEYER, L., RAGALLER, K., SCHADE, E., *IEEE Transact. on Power Apparatus and Systems*, **PAS-95** (1976) 1165.
- [68] RAGALLER, K., REICHERT, K., in *Current Interruption in High-Voltage Network* (K. Ragaller, ed.), Plenum Press, New York 1978, p. 1-28.
- [69] KOPAINSKY, J., in *Current Interruption in High-Voltage Networks* (K. Ragaller, ed.), Plenum Press, New York 1978, p. 329-354.
- [70] BRAND, K. P., KOPAINSKY, J., *Appl. Phys.* **16** (1978) 425.
- [71] SCHMIDT, W. F., JUNGBLUT, H., *J. Phys. D (Appl. Phys.)* **12** (1979) L 67.
- [72] DRAWIN, H. W., EMARD, F., *Physica* **94C** (1978) 134.
- [73] VERNICKEL, H., *Kerntechnik* **19** (1977) 279.
- [74] TELLER, E., *Peaceful Uses of Fusion*, in *Proc. Second United Nations Int. Conf. on Peaceful Use of Atomic Energy*, Geneva, Sept. 1958, printed by The United Nations, Geneva, 1958, p. 27-33.
- [75] GALLIGAN, J. G., GRALNIK, S. L., PRICE, W. G., JR., KAMMASH, T., *Nuclear Fusion* **18** (1978) 63.
- [76] ENGELMANN, F., GOEDHER, W. J., NOCENTINI, A., SCHÜLLER, F. C., *Plasmas with Cold Blankets*, in *Proc. Int. Symp. on Plasma-wall Interaction*, 18-22 Oct. 1976, Jülich, Editor: Kernforschungsanlage Jülich, Pergamon Press, Oxford 1977, p. 627-646.
- [77] BIEGER, W., DIPPEL, K. H., FUCHS, G., WOLF, H., *On Mechanical Divertors (Scrape-off Limiters)*, in *Proc. Int. Symp. on Plasma-Wall Interaction*, 18-22 Oct. 1976, Editor Kernforschungsanlage Jülich, Pergamon Press, Oxford 1977, p. 609-618.
- [78] KEILHACKER, M., *Magnetic Divertors*, in *Proc. Int. Symp. on Tokamak Reactors for Breakeven*, 21 Sept.-1 Oct. 1976, Erice (Ed. H. Knoepfel), Pergamon Press, Oxford 1977, p. 171-197.
- [79] DRAWIN, H. W., *J. de Physique, Colloque C1 40* (1979) 73-90.
- [80] DRAWIN, H. W., *Atomkernenergie* **33** (1979) 182.
- [81] HARBOUR, P. J., HARRISON, M. F. A., *Nuclear Fusion* **19** (1979) 695.
- [82] FITE, W. L., SMITH, A. C. H., STEBBING, R. F., *Proc. Roy. Soc. (London)* **268** (1962) 527.
- [83] SHAH, M. B., GILDOBY, H. B., *J. Phys. B (Atom. and Molec. Phys.)* **11** (1978) 121.
- [84] BURNIAUX, M., BROUILLARD, F., JOGNAUX, A., GOVERS, T. R., SZUCS, S., *J. Phys. B (Atom. and Molec. Phys.)* **10** (1971) 2421.
- [85] DRAWIN, H. W., *Z. Physik* **164** (1961) 513; Report EUR-CEA-FC-383, Fontenay-aux-Roses, 1966/67.
- [86] HAMDAN, M., BIRKINSHAW, K., HASTED, J. B., *J. Phys. B (Atom. and Molec. Physics)* **11** (1978) 331.
- [87] COHEN, S. A., DYLLA, H. F., *Nuclear Fusion* **18** (1978) 5.
- [88] DRAWIN, H. W., *Physics Reports* **37** (1978) 125-163.
- [89] DRAWIN, H. W., *Atomic and Molecular Structure and Collision Data with Application to Fusion Research*, in *The Physics of Ionized Gases* (R. K. Janev, ed.), The Institute of Physics, Beograd, 1978.
- [90] Equipe TRF, *Nuclear Fusion* **18** (1978) 1271.
- [91] BRETON, C., DE MICHELIS, C., MATTOI, M., *J. Quantitative Spectrosc. Radiative Transfer* **19** (1978) 367.
- [92] BOUJOT, J. P., MERCIER, C., WERKOFF, F., Report CISI-EUR-CEA, Makokot code d'évolution, Fontenay-aux-Roses, 1977.

Theoretical description of collisions in plasma : classical methods

M. Gryziński

Institute of Nuclear Research, Otwock-Świerk, Poland

Abstract. — In the paper a general idea of deterministic (classical) approach to atomic collision phenomena is presented. The key points of the theory, which has the concept of a point electron carrying a point mass and a point charge as a basis, are briefly explained. The binary encounter approximation (b.e.a.) and the unperturbed collective field approximation (u.c.f.a.), the two fundamental ways of approximate analysis of the many body atomic collision problem are described and application of the both to calculation elementary processes in a plasma is shown. Possibility of precise estimation the value of the Coulomb logarithm is analysed and new point of view on the concept of the screening radius is presented. Perspectives of the deterministic approach are discussed.

1. Introduction. — The huge variety of phenomena that are observed in ionized gases has the origin in a relatively small number of atomic processes. The collisional ionization, which is the main source of free charges in a plasma, is one of the most important among them. Slowing down of charged particles is the other important process, which along with the collisional ionization plays the decisive role in electrical break-downs. Current flow and heat transport are almost in whole determined by electron scattering properties of atoms and molecules. Atomic scattering cross section is involved in any calculation considering the transport properties of ionized gases. Capture and excitation are the other two quantities which must be taken into account in most of the plasma calculations.

These and many other processes can be relatively easily described on the grounds of the assumption that the atom can be considered as a collection of point particles, the behaviour of which is in the first instance governed by the Newtonian dynamics and the Coulomb interaction.

Here the main points of the theory which has the above assumptions as a basis, and in fact was initiated at the beginning of the twentieth century with a famous work of Rutherford [1] and with eliminated by quantum mechanics works of Thomson [2], Thomas [3] and Williams [4], will be briefly described and applicability of the theory to analysis of processes in ionized gases will be discussed.

2. Mathematical formulation of the atomic collision problem. — With the assumption that electrons and nuclei can be considered as point particles carrying a point charge (q) and a point mass (m) the whole collision problem becomes reduced to analysis of the following set of equations

$$m_i \frac{d^2 \mathbf{r}_i}{dt^2} + \sum_{j \neq i}^n q_i q_j \nabla_i \left(\frac{1}{r_{ij}} \right) = 0 \quad i = 1, 2, \dots, n,$$

where the number of equations is equal to the total number of particles involved in the collision. For solving the problem $2n$ constants defining initial conditions must be specified. In atomic collision problem those are : two sets of constants C_i^A and C_i^B describing the internal motion of electrons in isolated atoms, A and B , and data describing the initial motion of the whole atoms in space. Among the latter are : the relative velocity of atoms — v_{rel} , and two coordinates, the impact parameter D and the angle Θ , which in the plane perpendicular to the vector of relative velocity localise initial atomic trajectories in space (see Fig. 1). All C_i , which describe the behaviour of all electrons of the colliding atoms before collision, change in result of collision to C_i' . The all C_i' become known with solving the whole system of eq. (1). If relations between C_i and C_i' are known, that is the following relation is known

$$C_i' = f_i(D, \Theta; C_1, C_2, \dots, C_{2n-2}), \quad (2)$$

the cross section, which determines probability of definite change in C_i ($C_i \rightarrow C_i'$) that is the probability of definite change in the state of colliding atoms can be

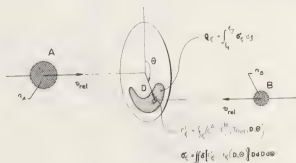


Fig. 1. — The collision between two sets of charged particles A and B is defined by internal motion of their components (by n_A and n_B constants C_i^A and C_i^B), the initial relative velocity v_{rel} , the impact parameter D and the azimuthal orientation of the shot line Θ . Cross section represents the sum of surface elements $D dD d\Theta$ for which the considered change ξ in the motion of the whole system or its components is observed.

calculated. Cross section which is formally defined in the following way [5]

$$\sigma_{\xi} = \int_0^{2\pi} \int_0^{\infty} \delta[C'_{\xi} - f_{\xi}(D, \Theta)] D \, dD \, d\Theta, \quad (3)$$

represents thus the sum of surface elements $D \, dD \, d\Theta$ for which relation (2) is fulfilled (see Fig. 1).

This formally trivial problem encounters great mathematical difficulties [6, 7]. Isolated collision between two elementary particles, that is the binary encounter, is the only case for which the exact analytical solution is known. Collisions in which three elementary particles are involved represents in fact the limit of exact numerical analysis. Practically, the only way of describing the collision processes which in ionized gases play the important role are approximate methods.

The well known binary encounter approximation (b.e.a.) is one of them [5-10]. In this approximation the collision between two systems of charged particles (atoms, molecules) is considered as a sum of independent binary collisions between the components of the both systems. In such a case, which in general is valid at large relative velocities of the systems, the cross section has the form :

$$\sigma = \sum_{i=1}^{N_A} \sum_{j=1}^{N_B} \iint f_A(\mathbf{v}_i^A) f_B(\mathbf{v}_j^B) \sigma^{b.c.}(\mathbf{v}_i^A, \mathbf{v}_j^B) d\mathbf{v}_i^A d\mathbf{v}_j^B, \quad (4)$$

where $f_A(\mathbf{v}_i^A)$ and $f_B(\mathbf{v}_j^B)$, being called the velocity distribution functions, describe in a probabilistic way the motion of individual particles in isolated systems, A and B , and $\sigma^{b.c.}(\mathbf{v}_i^A, \mathbf{v}_j^B)$ is the binary encounter cross section.

The other completely different approach, valid in general at weak interaction between systems, at large distances between systems, deals with the interaction

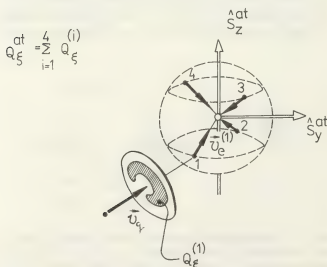


Fig. 2. — In the binary encounter approximation (b.e.a.) atomic cross sections is the sum of cross sections for collisions with atomic components (usually with atomic electrons).

of the whole systems through unperturbed collective fields [11]. Formally, this is again the two body problem, however now with very complicated interaction. To reduce mathematical difficulties and to enable physical interpretation, the atomic potential is usually expanded in series and a few of the first terms of the expansion are used in calculations. Experience show that in many cases it is sufficient to operate with the two first terms of the expansion only — the one which describes the static part of the field and the second which describes time variations of the field. Interaction between atoms can therefore be reduced to the atomic potential function of the following form :

$$\phi^{at}(\mathbf{r}, t) \approx \frac{C_n^{\omega}(\tilde{r})}{r^{n+1}} \sin(\omega t) + \frac{C_m(\tilde{r})}{r^{m+1}}, \quad (5)$$

where coefficients C_n^{ω} and C_m represent the main electric multipoles and their Fourier components. If all coefficients describing the atomic field, that is n, m, C_n^{ω}, C_m and ω , are known trajectories of colliding atoms can be determined, and cross section describing some sort of phenomena, elastic collisions for instance, can be calculated.

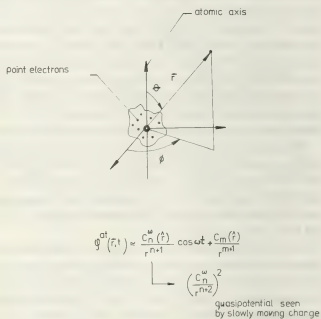


Fig. 3. — Atomic potential at large distances from the atom can be reduced to the two terms of the series expansion — the static and dynamic (oscillatory) multipole.

3. Initial conditions for the atomic collision problem.

— To carry out concrete collisional calculations some at least informations about the colliding atoms (molecules) must be known. To derive the ionization cross section for instance, one must know how the electrons in the atom (molecule) are grouped, what are the binding energies of electrons and roughly what their motion is. Let us denote the number of electrons in the s shell by N_s , the ionization potential by I_s^i

and the atomic velocity distribution function, which describes the motion of electrons in the respective shell of the atom, by $p^3(v_e/\bar{v}_e^3)$. Then in the binary encounter approximation the ionization cross section formula, has the form :

$$\sigma_i = \sum_s N_s \int_0^\infty \sigma_i^{h.e.}(u_i^s, v_e) \cdot p^3\left(\frac{v_e}{\bar{v}_e^3}\right) d\left(\frac{v_e}{\bar{v}_e}\right), \quad (6)$$

where the sum is taken for all shells of the atom and $\sigma_i^{h.e.}$ is the binary encounter ionization cross section. Distribution of electrons and binding energies, until we are not concerned with complicated molecules, are known sufficiently well. It is not in the case of the velocity distribution. The knowledge of the velocity distribution function which is in fact equivalent to the knowledge of the all details of the electron motion in the atom, is at the moment very unsatisfactory. In some calculations, however, the details of the electron motion play a secondary role and the knowledge of the mean electron velocity \bar{v}_e in the shell can be quite satisfactory. The electron ionization cross section for instance can be calculated with a relatively high degree of accuracy from the following simplified relation :

$$\sigma_i \simeq \sum_s N_s \sigma_i^{h.e.}(u_i^s, \bar{v}_e^s). \quad (7)$$

This is a sufficiently good procedure in the case of ionization by fast heavy charged particles too, but it yields completely wrong results in the case of ionization by slow heavy particles [8, 12-14] (if velocities of the latter are distinctly smaller than \bar{v}_e). This follows from the fact that the greatest amount of energy which can be transferred to the light electron from the heavy projectile depends upon the velocity of the previous

$$\Delta E_{\max} \simeq 2 m_e v_q (v_q + v_e). \quad (8)$$

Ionization can exist until $\Delta E_{\max} < U_i$, that is until the projectile velocity is high enough — higher than the threshold velocity v_q^{thr} , which at $v_e \gg v_q$ is

$$v_q^{\text{thr}} \simeq U_i / 2 m_e v_e. \quad (9)$$

It follows from the above, that nontrivial threshold (at $E_q > U_i$) disappears with the electron velocity approaching infinity. Since the threshold is not experimentally observed the following conclusion can be drawn : electron velocities in the atom are unlimited. The only possibility of satisfying the above conclusion is synchronic zero angular momentum motion of all atomic shell electrons [15-17]. This is the motion which in the early twenties was considered by Bohr and Sommerfeld and was rejected on the basis of arguments which in view of the later discovered properties of the electron appeared to be invalid [16].

In the case of a free-fall atomic model, with zero

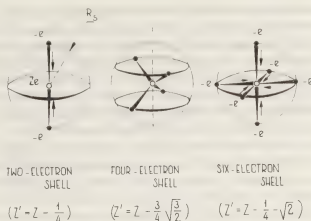


Fig. 4. — Free-fall atomic model — the first step towards the precise description of the atom.

angular momentum exactly radial electron orbits, the electron velocity distribution function has the form :

$$p\left(\frac{v_e}{\bar{v}_e}\right) = \frac{4}{\pi} \frac{1}{[1 + (v_e/\bar{v}_e)^2]^2}. \quad (10)$$

With the free-fall velocity distribution as given above many calculations were carried out and good agreement with experimental data was obtained [13, 14, 18].

Within the unperturbed collective fields approximation effective calculations are possible if at least first multipoles of the atomic field expansion in series are known. Unfortunately the knowledge of the latter, because of inquisitorial attitude of the quantum-mechanics ideology towards the classical concepts of atomic physics [16-20] is almost none. At the moment only very rough atomic model do exist (free-fall atomic model) and the rich experimental material of atomic collision physics and spectroscopy, which implicitly contains valuable informations about the atomic field, needs reinterpretation in the spirit of the

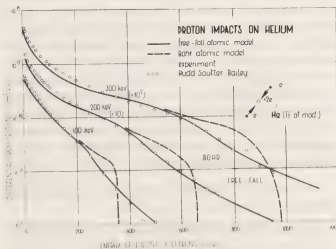


Fig. 5. — Ejection of electrons from helium atom by protons — one of many experiments investigated on the grounds of classical collision theory. Free-fall atomic model yields results which are in excellent agreement with the experimental data.

deterministic concepts outlined above (in quantum-mechanical approach atomic interaction appears as a result of polarization of initially exactly spherical distribution of a static electron cloud while in the Newton-Coulomb approximation the interaction is determined by the time dependent and aspherical from the very beginning potential of the collection of point charges being in dynamic equilibrium).

In result of reinterpretation of the low energy electron-atom and atom-atom scattering data [11] the two leading terms of the atomic field of noble atoms were deciphered. Those, excluding two-electron Helium atom, are : dynamic quadrupole and static octupole. In spherical coordinates the atomic potential of the noble atom has, therefore, the form :

$$\varphi(r, t) \approx A \frac{3 \cos^2 \theta - 1}{r^3} \sin \omega t + B \frac{\sin^3 \theta \cos^3 \phi}{r^4}, \quad (11)$$

and the only difference between different noble atoms is in the value of coefficients A and B , and ω .

In the same way it has been found that dynamic octupole is the first term of the series expansion of the field of the hydrocarbon molecules $C_n H_{n+2}$ and dynamic dipole is characteristic for the chemical π -bond [11].

Investigation of atomic energy level shifts [21], which are directly related to the deviation of the atomic core potential from the Coulomb potential, leads to the similar conclusions. Analysis of energy level shifts of alkalic metals, which have the noble-atom like atomic core, shows again that the octupole is a leading term of a static part of the atomic field of the noble atoms.

4. Present possibilities of the classical collision theory. — Effective application of the classical collision theory to analysis of elementary processes in ionized gases encounters two series of difficulties : mathematical, as we are concerned with the many body problem, and physical, as the knowledge of atomic systems specifying initial conditions of the collision problem is at the moment only fragmentary.

Nevertheless, at the present knowledge of atomic systems, and with the two approximate methods of analysis described above that is with the b.e.a. and with the u.c.f.a. some processes can be with accuracy satisfactory for plasma investigations effectively calculated. Among others are :

- ionization (including inner shell ionization and multiply ionization),
- excitation (including some $n'l - n'l'$ transitions),
- slowing down,
- scattering of electrons from atoms and molecules,
- atom-atom interactions.

The first three are those which can be effectively described with the b.e.a. and the other two with the u.c.f.a.

In the binary encounter approach, energy exchange cross section $\sigma_{\Delta E}$, which describes transfers of energy in a collision between two charged particles, forms the basis for almost all basic inelastic collision calculations. In result of appropriate integrations over ΔE one obtains :

- ionization cross section

$$Q_i = \int_{u_i}^{\Delta E_{\max}} \sigma_{\Delta E} d(\Delta E), \quad (12)$$

- excitation cross section

$$Q_{\text{exc}}^n = \int_{u_n}^{u_{n+1}} \sigma_{\Delta E} d(\Delta E), \quad (13)$$

- stopping power

$$S = \int_{\Delta E_{\min}}^{\Delta E_{\max}} \Delta E \cdot \sigma_{\Delta E} d(\Delta E), \quad (14)$$

where the symbols U_i , U_n , ΔE_{\max}^- and ΔE_{\max}^+ stand respectively for : ionization potential, excitation potential, and for the maximum gain and loss of energy in the individual binary collision.

Since b.e. cross sections depends upon velocities of colliding particles averaging over v_e and v_q must be carried out to obtain experimentally observed cross sections. Usually averaging over relative orientation of velocity vectors is the first step of calculations

$$\sigma(v_e, v_q) = \frac{1}{2} \int_{-1}^{+1} \sigma(v_e, v_q; \hat{v}_e, \hat{v}_q) f(\hat{v}_e, \hat{v}_q) d(\hat{v}_e, \hat{v}_q), \quad (15)$$

while averaging over the atomic electron velocity is the next step of calculations

$$\sigma^{at}(v_q) = \int \sigma(v_e, v_q) f^{at}(v_e) dv_e. \quad (16)$$

This is the final formula of atomic collision physics. In plasma physics and in the physics of ionized gases averaging over v_q that is over velocity of plasma particles must be yet carried out :

$$\sigma^{pl} = \int \sigma^{at}(v_q) f^{pl}(v_q) dv_q. \quad (17)$$

The two important distribution functions describing some idealistic situations in a plasma are :

- Maxwell distribution function (describing the velocity distribution in a thermal equilibrium plasma).
- Druyvestein distribution function (describing the velocity distribution of electrons in the gas at presence of electric field).

The other velocity distribution function derived recently during the analysis of magnetically insulated discharges, which play the fundamental role in ion beam fusion investigations, is the electron velocity distribution function for collisionless plasma at presence of crossed electric and magnetic fields. At negligibly small electron temperature the distribution has the form :

$$f_{(u)}^{\mathbf{E} \times \mathbf{H}} = \frac{1}{8\pi} \frac{1}{u^2} \frac{1}{\sqrt{1-u^2}}, \quad (18)$$

where u is the dimensionless electron velocity

$$u = \frac{v_e}{\sqrt{2} \frac{E}{H}}. \quad (19)$$

With the present computer technique all the cross sections listed above can be relatively easily calculated (see for instance Freeman and Jones [22]).

Analysis of processes within u.c.f.a. is a little bit more difficult, as one must usually start with numerical calculation of the individual particle orbit. Possibilities of deriving the cross sections in analytical form are almost none. In u.c.f.a. the latter can be obtained in very specific situations only. Collisions at large impact parameters in one of them, as the relation between the scattering angle θ , which is very small then, and the impact parameter D can be obtained in analytical form. If moreover the relation $\theta = f(D)$ can be explicitly solved with respect to D the scattering cross section in explicit form can be determined. It is for instance possible when the atomic field description can be reduced to the one term of the series expansion. The scattering cross section has then the form :

a) if the leading term of atomic field expansion is a static multipole [23]

$$Q(\theta) \simeq \pi \left(\frac{C}{E \cdot \theta} \right)^{2/(n+1)}, \quad (20)$$

b) if the leading term of atomic field expansion is a dynamic multipole [11]

$$Q(\theta) \simeq \begin{cases} \pi \left(\frac{C}{E \cdot \theta} \right)^{2/(n+1)} & \text{for large velocities,} \\ \pi \left(\frac{v}{\omega} \right)^2 \ln^2 \left(\frac{2}{\theta} \right) & \text{for small velocities,} \end{cases} \quad (21)$$

where E is the energy of scattered particle.

Excluding the above and few other specific cases, numerical analysis is the only possibility of effective calculations of concrete plasma collision problems in unperturbed collective field approximation.

5. Coulomb logarithm and the screening radius. —

The energy loss function — S plays a fundamental role in analysis of transport properties of a plasma. It determines for instance extremely important in plasma research — the relaxation rates ; the precise knowledge of S is necessary in analysis of penetration the charged particles in different targets, particularly for calculation of deposits of energy in solid or gaseous pellets in ion beam fusion. Unfortunately the logarithmic term appearing in the binary encounter formula :

$$S \propto \ln \frac{m_e v_q^2 D_{\max}}{Z_q \cdot e^2}, \quad (22)$$

contains not well specified the impact parameter D_{\max} . Usually, in plasma calculations D_{\max} is assumed to be equal to the Debye radius ; in atomic stopping power calculations one assumes, following Bethe, that e^2/D_{\max} is equal to the mean ionization potential of the atom. The argument of the logarithm in the first case is usually a large number and the whole term, called the Coulomb logarithm, is in plasma calculations considered a constant quantity with the value somewhere between 10 and 20.

Intuitive, not exactly equivalent in the both cases, physical reasoning was the only justification for estimation of D_{\max} [24]. The problem has however a more rigorous solution. The latter can be achieved by applying the appropriate method of mathematical analysis. This is the method of perturbation calculus developed by Gauss for analysis of evolution of planet any orbits. Simple analysis shows that the energy which can be transferred to the electron bound in the Coulomb field of nucleus from the charged particle moving at a distance D from the atom, at distances much larger than the distance between the nucleus and the electron, is

$$\Delta E \simeq 2 \frac{Z_q^2 \cdot e^4}{D^2 m_e v_q^2} e^{-\omega D/v_q}, \quad (23)$$

where ω is the angular frequency of the orbital motion of the electron, v_q is the velocity of the projectile and $Z_q \cdot e$ is its charge. Until D is smaller than v_q/ω the interaction between the bound electron and projectile can be considered as the isolated binary collision. When the impact parameter becomes larger than v_q/ω , the interaction between the electron and the nucleus becomes dominant and a rapid decrease in energy transfer is observed. It is evident from the above that :

$$D_{\max} = v_q/\omega. \quad (24)$$

The result will be exactly the same if one assumes that the electron is not exactly free but is bound around some fixed point of space with a small but the finite force proportional to the displacement

$$\delta f \simeq -k \Delta \mathbf{r}.$$

The result again has the form of eq. (23), where now

$$\omega = \sqrt{k/m_e}. \quad (25)$$

In the case of plasma electrons, which are bound with heavy ions through collective fields, the binary encounter limit is determined by the plasma frequency

$$\omega_{pl} = (4\pi n_e e^2/m_e)^{1/2}. \quad (26)$$

In the particular case of the heavy particle moving in a plasma with a thermal velocity, eq. (24) and (26) yield the following formula:

$$D_{\max}/\omega = \omega_{pl}, \quad v_q = \bar{v}_q^{\text{thermal}} = (kT/4\pi n_e e^2)^{1/2}, \quad (27)$$

which represents nothing else than Debye radius.

In general however D_{\max} is different from the Debye radius and the formula (24) should be used. The correct expression for the Coulomb logarithm, therefore, is:

$$\ln A = \ln \left(\frac{m_e v_q^2}{Z_q e^2 \omega} \right), \quad (28)$$

where ω implicitly represents the interaction of electrons with heavy components of the matter (with positively charged nuclei).

6. Other possibilities of the theory. — Although b.e.a. and u.c.f.a. play the decisive role in analysis of atomic collisions, there are some processes which need for interpretation other or more precise mathematical treatment, or which within the Coulomb interaction law and newtonian dynamics can not be interpreted at all.

The capture of electrons by protons, for instance, represents the first case. It is a typical three body problem, which only numerically can be accurately solved. One can try to find of course the appropriate approximate methods — the concept of the switched binary encounter collision is one known possibility [4, 25] and two-fixed center problem is another [26].

The excitation and ionization through cumulation small amounts of energy is a process which in some cases may be extremely important. The process can be very effectively investigated with the mentioned above the perturbation method of Gauss [27]. Analysis of ionization in many electron atom collisions requires inclusion of statistics to binary encounter calculations [28, 29].

Some important features of the small angle scattering can be found on the grounds of the second order perturbation calculus [30]. It has been found for instance that quasipotential of the dynamic multipole, including the second order term, has the form

$$\varphi \approx \frac{e^{-\omega r/v}}{r^{n+1}} + \varepsilon \left(\frac{1}{r^{n+1}} \right)^2,$$

where ε is much smaller than unity (in result quasipotential of the noble atom as seen by slowly moving charge has the form shown in figure 6).

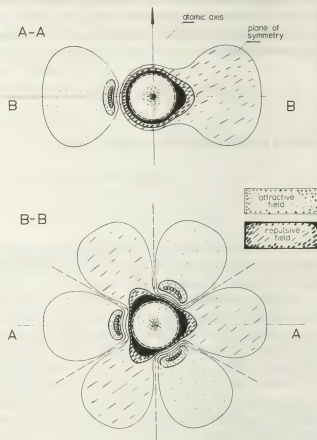


Fig. 6. — Quasipotential of the noble atom, as seen by slowly moving electron.

The problems which remain outside the scope of the Coulomb-Newton approximation are of course radiation phenomena — which as it has been shown previously are related with the gyromagnetic properties of the electron [31-33]. Gyromagnetic properties of the electron play an important role in orientation of atoms in external fields, what in some particular collision problems may be important. The other process which cannot be investigated with spin properties of the electron being neglected are polarization effects.

At the moment, however, the main limitations in application of the classical collision theory to practical problems arise from the lack of information about the electron orbits in atomic systems. Further possibilities of effective description of processes in ionized gases of practical interest depend, therefore, mostly on further progress in deciphering of the electronic structure of atomic systems. Atomic collision physics may help much in solving this problem as investigation of atomic systems can be carried out with properly designed atomic collision experiments.

References

- [1] RUTHERFORD, E., *Phil. Mag.* **71** (1911) 669.
- [2] THOMSON, J. J., *Phil. Mag.* **73** (1912) 449.
- [3] THOMAS, L. H., *Proc. Camb. Phil. Soc.* **73** (1927) 713.
- [4] WILLIAMS, E. J., *Nature* **119** (1927) 483.
- [5] GRYZIŃSKI, M., *Phys. Rev.* **115** (1959) 374.
- [6] BURGESS, A. and PERCIVAL, J. C., *Adv. Atom. Mol. Phys.* **4** (1968) 109.
- [7] BATES, D. R. and KINGSTON, A. E., *Adv. Atom. Mol. Phys.* **6** (1970) 269.
- [8] GRYZIŃSKI, M., *Phys. Rev.* **138** (1965) A 305, A 327, A 336.
- [9] GERJUOV, E., *Phys. Rev.* **148** (1966) 54.
- [10] VRIENS, L., *Proc. Phys. Soc. (London)* **30** (1967) 935.
- [11] GRYZIŃSKI, M., *J. Chem. Phys.* **62** (1975) 2610, 2620, 2629.
- [12] GARCIA, J. D., *Phys. Rev. A* **1** (1970) 280.
- [13] GRYZIŃSKI, M. and OKOPINSKA, A., *Abstr. of VIII ICPEAC*, vol. II, Beograd 1973, p. 635.
- [14] GRYZIŃSKI, M. and KUNC, J., *Abstr. of IX ICPEAC*, vol. I, Seattle 1975, p. 509.
- [15] GRYZIŃSKI, M., *Phys. Rev. Lett.* **14** (1965) 1059.
- [16] GRYZIŃSKI, M., *Phys. Lett.* **41A** (1972) 69.
- [17] GRYZIŃSKI, M., *Phys. Lett.* **44A** (1973) 131.
- [18] GRYZIŃSKI, M., KUNC, J. and ZGORZELSKI, M., *J. Phys.* **B 6** (1973) 2292.
- [19] BUNGE, M., *Quantum Theory and Reality*, Berlin-Heidelberg-New York-Springer-Verlag, 1967.
- [20] BATES, D. R., *Phys. Reports* **35** (1978) 307.
- [21] GRYZIŃSKI, M., *Phys. Lett.* **56A** (1976) 180.
- [22] FREEMAN, R. L. and JONES, E. M., Culham report CLM-R137.
- [23] MASSEY, H. S. W., *Electronic and Ionic Impact Phenomena*, vol. III, Oxford 1971, p. 1309.
- [24] GINZBURG, V. L., *Electromagnetic waves in a plasma*, Moscow 1960.
- [25] BATES, D. R., MAPLETON, R. A., *Proc. Phys. Soc. (London)* **85** (1965) 605.
- [26] GRYZIŃSKI, M., *Phys. Lett.* **46A** (1973) 5.
- [27] PERCIVAL, J. C., RICHARDS, D., *Proc. Phys. Soc. (London)* **92** (1967) 311.
- [28] RUSSEK, A. and THOMAS, M. T., *Phys. Rev.* **109** (1955) 2015.
- [29] FIRSOV, O. B., *Sov. Phys. JETP* **36** (1959) 1076.
- [30] GRYZIŃSKI, M., KIRAGA, A. and KLOS, Z., *Abstr. of VIII ICPEAC*, Beograd 1973, p. 310.
- [31] GRYZIŃSKI, M., INR report 641/XVIII/PP, Warsaw-Świerk 1965.
- [32] GRYZIŃSKI, M., INR report 908/XVIII/PP, Warsaw-Świerk 1968.
- [33] GRYZIŃSKI, M., INR report 909/XVIII/PP, Warsaw-Świerk 1968.

Formation of hydrogen negative ions by surface and volume processes with application to negative ion sources

J. R. Hiskes

Lawrence Livermore Laboratory, University of California Livermore, California 94550, U.S.A.

Abstract. — Three methods for the formation of negative ions are reviewed : double charge-exchange, whereby low-energy positive ions are converted to negative ions by two sequential electron captures in a vapor target; electron-volume-processes wherein low-energy electrons lead to negative-ion formation by dissociative attachment or dissociative recombination by collisions with hydrogen molecules or hydrogen molecular ions and, surface processes leading to negative ions by backscattering or desorption induced by energetic particle bombardment. The application of these method to the development of hydrogen-negative-ion sources is discussed.

During the last few decades interest in negative-hydrogen ion sources has been directed mainly toward synchrotron and other particle accelerator applications, with emphasis on high current densities delivered for short pulses. But within the last several years there has been an awareness in the magnetic fusion program of the future need for negative ions as a means for generating high energy neutral beams, beams with energies above a few hundred keV. Negative ions seem to be the only effective intermediary for efficiently producing such beams. Although methods for generating negative ion beams have relied upon synchrotron concepts, the requirements for fusion are very different : here one is interested in more moderate current densities, up to 100 mA cm^{-2} , but with continuous operation. Proposed source modules would accelerate of the order of 10 A of beam current and deliver several megawatts of beam power. Both H^- and D^- beams are being considered for application in different reactor systems.

The conceptualization of negative ion sources is now in a very volatile stage. But of the great variety of proposals that have been offered to date [1-4], three general areas appear ready for development. These are : first, the double charge exchange method for converting a positive ion beam into a negative ion beam ; second, electron-volume processes wherein low energy electrons interacting with molecular species lead to negative ion products via dissociative attachment or recombination ; and third, generation of negative ions in surface interactions, principally via desorption and backscattering. Both our qualitative and our quantitative understanding of these processes diminishes as one proceeds from the first through the third. In this paper we shall consider the physics of these three methods in increasing detail.

1. Charge exchange processes. — Figure 1 shows a summary of equilibrium fractions of negative ions

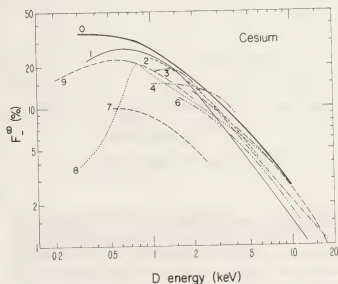


Fig. 1. — Equilibrium fraction of negative ions per incident deuteron.

for protons passing through cesium vapor [5-14]. The problem has obviously received considerable attention but with a wide disparity of results, particularly at the lower energies. The large differences are now attributed to the problem of collection of particles scattered through large angles, nevertheless the two modern experiments, numbers 0 and 9 (Refs. [5] and [14]), continue to show a relatively large discrepancy.

Although these large equilibrium yields in cesium are attractive to the ion source designer, their utilization carries with them the disadvantage of space-charge problems in the low energy positive ion beam. There has been a continuing search for a more useful neutralizer than cesium, one that would produce large equilibrium yields at higher energies.

It was hoped that the alkaline-earth would provide attractive vapor targets. The first to be studied expe-

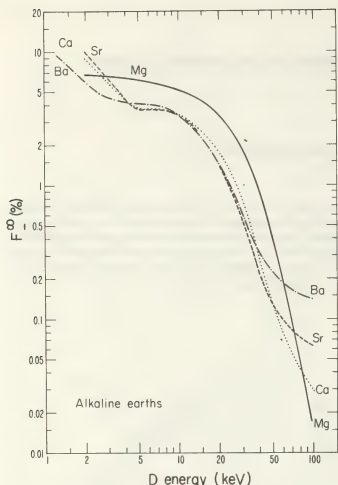


Fig. 2. — Equilibrium fractions for the alkaline-earths.

perimentally was magnesium [15-18], followed by strontium [19] and finally the entire alkaline-earth series by the group at Wesleyan University [20]. Their data is shown in figure 2. Excepting for Dyachkov's low energy equilibrium yields in magnesium, there is general agreement among the different experimental groups as regards the magnesium and strontium yields. Unfortunately, the alkaline-earth vapor targets,

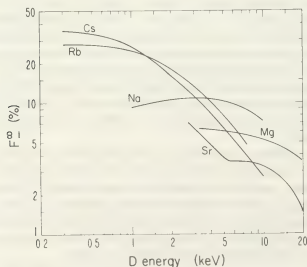


Fig. 3. — Equilibrium fractions for optimum vapor targets.

taken as a group, do not show yields as large as those for the alkalis, at least not for energies above 1 keV.

Figure 3 shows a comparison of the equilibrium yields for the more attractive alkalis and alkaline earths [21]. For the source designer, sodium offers the best prospect of reducing space charge effects by allowing operation at higher beam energies, but at the price of reduced yields. Here in Grenoble and at the Lawrence Livermore Laboratories cesium based negative ion systems are being developed [22, 23]; sodium vapor based systems are being developed both at the Kurchatov Institute [24] and at the Lawrence Berkeley Laboratory [25].

The theory of charge exchange processes in these sophisticated vapor targets is still in a developing stage. At the low energies appropriate to alkali charge exchange the relative interaction potentials are the alkali-hydride molecular potentials. Considerable care must be taken to insure the use of precise electronic energy levels, and recourse must be made to sophisticated Hartree-Fock molecular orbital methods and codes [26-28].

The equilibrium fraction of negative ions is a function of six capture and loss cross sections, but in practice the ratio is dominated by only two,

$$F_{-} \approx \sigma_{0-1} / \sigma_{-10} \quad (1)$$

The capture and loss cross sections for cesium have been discussed in a few theoretical papers [27, 29, 30]. Figure 4 shows a comparison of the calculated capture cross sections with the experimental values [31, 32]. Much theoretical work remains to be done before the alkali capture and loss cross sections are fully clarified.

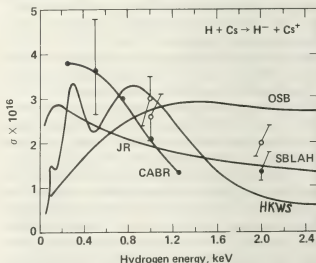


Fig. 4. — Comparison of experimental and theoretical capture cross sections.

Molecular ion beams of H_2^+ , H_3^+ offer the prospect of more negative ions per unit positive current than do H^+ beams. The necessary fragmentation of the molecular ions in the vapor cell before electron

capture can occur imposes the disadvantage of requiring a greater cell line density. The use of the H_3^+ ion introduces some further subtleties with additional reaction channels, and with consequences for the angular distribution of the product negative ions [33].

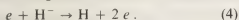
2. Electron volume processes. — Turning our attention to electron-molecule collisions, we come upon the first of many surprises. The study of hydrogen discharges is well established, but until an effort was made to diagnose the negative ion density several important electron collision processes were not appreciated. In the initial experiments at the Ecole Polytechnique, plasma probes indicated an anomalously high negative ion density [34]. This has subsequently been confirmed by photodetachment of the H^- ions and observing the rise in electron density [35]. Additional confirmation has been achieved by direct extraction of an H^- beam with a current density of the order of 1 mA cm^{-2} . The parameters of the discharge are given in table I.

Table I.

H_2 density	$2 \times 10^{14} \text{ cm}^{-3}$
Positive ion density	$2 \times 10^{10} \text{ cm}^{-3}$
H_3^+ fraction	92 %
H_2^+ fraction	5 %
H^+ fraction	3 %
Electron temperature	$0.1 \rightarrow 0.4 \text{ eV}$
Fast electron density (120 eV)	$2 \times 10^7 \text{ cm}^{-3}$
Ion temperature (uncertain)	0.1 eV

As shown in figure 5, the negative ion density increases with the third power of the electron density. There is no indication of a significant isotope dependence.

The initial interpretation of the negative ion density took into account the following well known processes :



Using the density and temperature values shown in table I, the observed density was found to be approximately two orders of magnitude larger than one would calculate using reactions (2), (3), and (4).

Three processes have been proposed [34] as possible explanations of the large negative ion density :

A) $e + H_2(c^3\Pi_u) \rightarrow H^- + H$. The cross section for dissociative attachment to this long lived [36] electronically excited state of hydrogen is estimated by Buckley and Bottcher [37] to be in the range 10^{-18} to $2 \times 10^{-17} \text{ cm}^2$. The density of these excited electronic states are limited by electron collisions to the neighboring $a^3\Sigma_g$ electronic state which in turn is subject to rapid radiative decay. The ratio of the density of the excited molecules to the density of

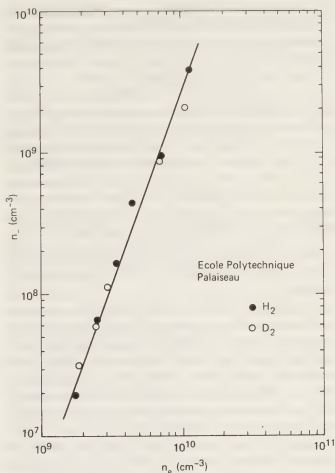


Fig. 5. — Negative ion density versus electron density.

ground state molecules is estimated to be no larger than about 10^{-5} , too small a fraction to account for the observed negative ion density [38].

The second process proposed was the dissociative attachment of H_3^+ ions :

B) $e + H_3^+ \rightarrow H^- + \dots$. This reaction cross section has recently been measured by Peart, Forrest, and Dolder [39]. As seen in figure 6, the cross section has a maximum value of $1.8 \times 10^{-18} \text{ cm}^2$ for a 6 eV electron energy. The magnitude of this cross section

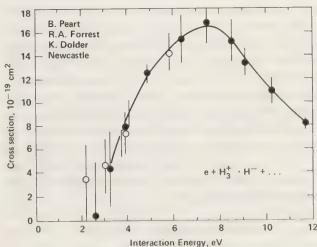
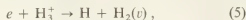


Fig. 6. — Dissociative recombination leading to negative ions.

is at least an order-of-magnitude too small to explain the observed negative ion density.

The dissociative recombination leading to neutral products

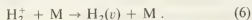


is known to have a large cross section, of order 10^{-15} cm^2 [40]. The resonance state of H_3 leading to reaction (5) and the product states on the right side of the reaction have been studied by Kulander and Guest [41]. They conclude the H_2 molecules are formed with a substantial population in the higher vibrational states. This conclusion is consistent with the experimental observations of Vogler [42].

The third and most probable process of importance is the dissociative attachment to vibrationally excited molecules :

(C) $e + H_2(v \geq 6) \rightarrow H_2^- \rightarrow H^- + H$. In a recent experiment by Allan and Wong [43], this cross section is shown to increase by approximately an order-of-magnitude for successive vibrational excitation through the lowest four levels. In the theoretical analysis of this reaction by Wadehra and Bardsley [44], these cross sections continue to increase through $v = 6$, and reach a value of $3.4 \times 10^{-16} \text{ cm}^2$ for the upper levels through $v = 9$. For the case of $D_2(v)$ the rate of increase is even more dramatic, rising from a value of $2 \times 10^{-24} \text{ cm}^2$ for $v = 0$ to greater than $2 \times 10^{-16} \text{ cm}^2$ for levels $v = 9-13$. For both $H_2(v)$ and $D_2(v)$ the dissociative attachment cross sections are greater than $2 \times 10^{-16} \text{ cm}^2$ for vibrational levels with thresholds below 1 eV. As a consequence, the very pronounced isotope effect that is so well known for the ground vibrational levels is almost non-existent for the upper levels.

The question then arises as to the origin of the vibrationally excited molecules, $H_2(v)$. Two processes appear probable : the dissociative recombination of H_3^+ illustrated in reaction (5), and the Auger neutralization of H_2^+ ions in wall collisions :



Using the Frank-Condon factors between H_2^+ and H_2 [45] and the population distributions for H_2^+ vibrational levels [46], one estimates the process (6) may yield populations for levels $v \geq 6$ which are greater than 30% of the total $H_2(v)$ distribution.

But even granted such large populations and/or the large cross section for reaction (5), the parameters listed in table I cannot be used to explain the observed negative ion yields. In order for the density of $H_2(v \geq 6)$ to rise to a sufficiently high level, the $H_2(v)$ must survive several wall collisions against vibrational de-excitation :



At least 10 but no more than 100 wall collisions are

required, on average, before de-excitation of type (7) are allowed.

In conclusion, a complete interpretation of the negative ion density is not yet possible, but the following tentative scenario is offered :

- (1) $e + H_2(v = 0) \rightarrow H_2^+(v) + 2e$
- (2) $H_2^+(v) + H_2(v = 0) \rightarrow H_3^+(v) + H$
- (3a) $H_2^+(v) + M \rightarrow H_2(v \geq 6) + M$
- (3b) $e + H_3^+(v) \rightarrow H_2(v \geq 6) + H$
- (4) $H_2(v \geq 6) + M \rightarrow H_2(v \geq 6) + M$
- (5) $e + H_2(v \geq 6) \rightarrow H_2^- \rightarrow H^- + H.$

3. **Surface formation processes.** — Among the most striking developments in negative ion research in recent years has been the generation of negative ions by particle bombardment of alkali-coated metal surfaces. First developed by the Novosibirsk group for synchrotron applications, the early technology was subsequently adopted at Brookhaven for both synchrotron and possible fusion applications, with the BNL group successfully extending the pulse length into the millisecond range. A summary account of this early work on surface production is given in the Proceedings of the 1974 Berkeley Symposium [47, 48].

From the point of view of the physical processes involved, the problem at hand is in many ways analogous to the situation in electron-volume-processes : namely, what is the principal mechanism leading to the production of negative ions. In their original papers, the Novosibirsk group interpreted the operation of their source as based on the desorption of negative ions by energetic primaries striking the cathode [47, 49].

Subsequently, they were to observe hydrogen-negative-ion secondary-emission desorption yields near unity for 2-10 keV Cs^+ ions bombarding alkali-coated surfaces in a hydrogen atmosphere [50]. More recently, Seidl [2] has reported desorption yields of H^- for Cs^+ and Na^+ ions incident upon CsH with energies up to 20 keV ; the Cs^+ secondary emission coefficients found by Seidl are similar to those reported in reference [50]. M. Yu has observed the desorption of H^- ions from cesium-coated surfaces bombarded with 150 eV Ne^+ ions [51]. His data illustrates very clearly the sensitive dependence of the negative ion yield as a function of surface work function, but he does not report the magnitude of the secondary emission coefficient. Further, Wiesemann has interpreted the negative ion yields from surface-plasma and duoplasmatron sources as due principally to surface desorption [52].

Following the Berkeley Symposium in 1974, an alternative to the desorption process was proposed whereby the energetic hydrogen primaries backscatter from the cathode substrate, and, retaining an appreciable fraction of their incident energy as they are

emitted from the cathode, capture electrons to form negative ions in a region several angstroms in front of the surface [53]. This model has been developed further in successive papers [54, 55].

The Berkeley group has bombarded alkali-coated, surfaces with D_2^+ and D_3^+ ions with energies of from 100 eV to a few keV per nucleon, and have interpreted their data as backscattering yields [56].

In a more recent experiment W. Graham has directed a thermal beam of hydrogen atoms emitted from an oven maintained at 3 000 K onto a cesium coated surface [57]. The negative ion flux observed is interpreted as resulting from the backscattering of those atoms in the tail of the incident thermal distribution with energies above about one electron-volt.

In their 1977 Brookhaven paper [58], the Novosibirsk group consider both desorption and backscattering processes, but draw no conclusions as to the relative ion yields resulting from these two mechanisms. Unfortunately, there does not exist an experiment in which the desorption and backscattering yields can be monitored simultaneously although the possibility for such an experiment has been discussed [59]. In consideration of the disparity of views that have been expressed concerning these processes, it seems appropriate to estimate the desorption yield for hydrogen particles adsorbed on the surface, and to compare the particle desorption yields with the particle backscattering yields.

3.1 SURFACE DESORPTION. — The cross sections for desorption can be estimated using the differential cross sections for electron scattering on chemisorbed hydrogen [60]. In reference [60] the jellium model is employed to account for the electron shielding of protons embedded in the surface of tungsten. Since the crystal structure and lattice spacing of tungsten and molybdenum are virtually identical, and the number of 5s and 4d valence electrons in Mo are equal to the number 6s and 5d electrons in W, the jellium model differential scattering cross sections for Mo and W should be similar. At large scattering angles these differential cross sections go over to the Rutherford cross section, but remain finite at small scattering angles. Bearing in mind that the Rutherford cross section is a function only of c.m. energy and is independent of mass, the 50 and 100 eV electron scattering cross sections given in reference [60] can be used for interpreting proton collisions where the proton energies in the laboratory system are 100 and 200 eV, respectively.

Another basis for estimating the desorption cross section can be obtained using the computer studies of hydrogen sputtering by hydrogen incident upon TiH_2 , FeH, and FeH_2 [61]. In reference [61] it is found that the essential mechanism for light-particle sputtering is the two-body collision of the backscattered light particle with the atoms near the surface. Using this observation as the basis for a desorption

model, one can use the differential scattering cross sections mentioned above, together with an expression for energy transfer in two-particle collisions, to calculate the cross section for an energetic hydrogen particle emerging from the surface to dislodge another hydrogen particle bound to the surface with energy E_a . If E_0 is the initial energy of a particle scattered through an angle θ_0 in the laboratory system that transfers an amount of energy E_2 to a particle of equal mass, the ratio of energies is

$$E_2/E_0 = 1 - \frac{1}{2}(1 + \cos 2\theta_0). \quad (8)$$

The adsorption energy of hydrogen, E_a , is approximately 2 eV. A hydrogen atom is presumed to be desorbed if it receives an amount of kinetic energy greater than 2 eV directed normally outward from the surface. The computer-calculations described below show that the backscattered particles emerge from the surface with a cosine angular distribution; it follows that the mean kinetic energy directed perpendicular to the surface is equal to one half the total kinetic energy. The minimum angle θ_0 leading to desorption is the angle for which $E_2 = 4$ eV, and the desorption cross section is the integral over the differential cross section ranging from this angle up to 90° in the lab system. The values obtained are shown in table II, including those derived from the sputtering calculations of reference [61].

Table II. — Desorption cross sections.

Backscattered energy		100 eV H sputtering		
100 eV	200 eV	TiH_2	FeH	FeH_2
0.52 \AA^2	0.27 \AA^2	0.50 \AA^2	0.82 \AA^2	0.52 \AA^2

If the angular effects are ignored and only a minimum of 2 eV energy transfer is assumed, the cross sections are increased approximately 20%. The sputtering cross sections shown in the table are not strictly comparable because the backscattered particles in this latter case are distributed in energy up to 100 eV, nevertheless the comparisons are plausible.

It is interesting to consider the magnitude of the desorption yield in the surface-plasma-source that is implied by these cross sections. Previously [53] the surface hydrogen coverage under source conditions had been estimated to be about 2×10^{14} atoms cm^{-2} , from which one would infer a hydrogen atom desorption yield of about 1%. For surfaces near room temperature, however, adsorbed hydrogen atom coverages can be as large as 10^{15} atoms cm^{-2} , implying desorption yields up to several percent.

The energy spectrum of the desorbed particles can be calculated from the differential cross sections and eq. (8). Histograms of the desorbed energy distribution have been constructed with widths corresponding to the maximum and average minimum desorption energy for a range $\Delta\theta_0 = 5^\circ$; these

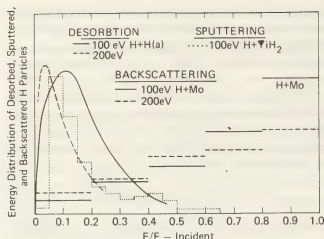


Fig. 7. — Energy distributions versus incident energy.

histograms have been summed to give the energy distribution shown in figure 7. For comparison we have included the histogram of the H sputtering yield [61] for 100 eV hydrogen incident upon TiH_2 .

Also shown in the figure is the histogram of backscattered H particles for 100 or 200 eV hydrogen atoms incident upon molybdenum. These distributions were calculated using the Marlowe [61] code discussed below. Qualitatively, the desorption and backscattering distributions are distinct: the desorption maxima occurring at lower energies, the backscattering maxima occurring near the incident energy. This distinction is expected to be generally true, but may be less distinct for low- Z substrates.

The cross sections shown in table II and the energy distributions shown in the figure refer to the total number of particles backscattered. Only a fraction of this total is converted into negative ions at the surface. The calculation of this negative ion production probability will be discussed in a later section.

3.2 BACKSCATTERING YIELDS. — Experimental data on backscattering yields are for the most part limited to incident energies above 1 keV [62-65]. The principal source of theoretical backscattering data is the Marlowe Monte Carlo code developed at Oak Ridge by Robinson and Torrens [66] and by Oen and Robinson [67]. The experimental data has been compared with the results from the Marlowe code for both backscattering and sputtering. The Marlowe code is believed to contain the proper physics for incident energies as low as 10 eV. Since the principal backscattering processes of interest in negative ion research are below 1 keV, one must rely almost entirely upon Marlowe for the relevant data. The Oak Ridge group has made available to Livermore the Marlowe code for negative ion studies. The next few figures summarize the relevant backscattering data.

Figure 8 shows the particle reflected fractions, i.e., backscattering fractions, for hydrogen incident upon

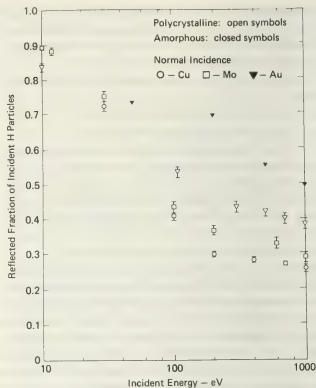


Fig. 8. — Backscattered fractions versus incident hydrogen energy.

polycrystalline Cu, Mo, and Au at normal incidence. The reflection coefficients for amorphous Cu and Au are taken from reference [67]. All of these fractions show an increase at lower energies; this is due to the larger scattering probability at low energies, causing reflection to occur nearer the surface. At a given energy, the fractions increase with the Z of target material for similar reasons. The amorphous backscattering exceeds the polycrystalline scattering presumably because of reduced channeling.

In the next figure is shown the data for the alkali polycrystalline targets. The trends are similar to those for the transition elements.

Of considerable importance for interpretation of negative ion yields is the angular and energy distribu-

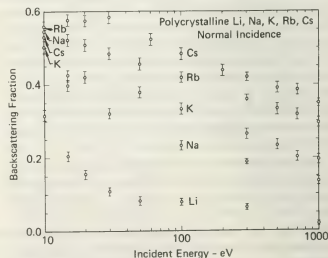


Fig. 9. — Alkali backscattered fractions for incident hydrogen.

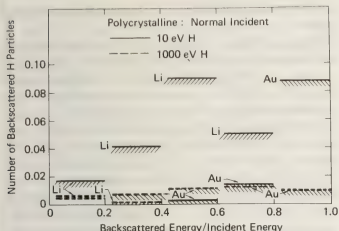


Fig. 10. — Energy distribution histograms for back scattered hydrogen.

tions of the backscattered particles. At energies above 100 eV the angular distribution fits a cosine distribution, as was found earlier for the amorphous targets [67] and with some tendency to be more peaked toward zero degrees at lower energies. The energy distributions, on the other hand, show a sensitive dependence to incident energy and target charge. In figure 10 is shown energy-distribution histograms for 10 eV and 1 000 eV hydrogen particles normally incident upon Li and Au targets. For Li, even the 10 eV particles penetrate sufficiently that there is appreciable energy degradation of the backscattered particles. In the case of 10 eV hydrogen incident upon gold, the first collision is so near the outer surface that very little energy degradation can occur. At 1 000 eV incident, virtually the entire distribution of backscattered particles undergoes a large number of collisions in diffusing backward toward the surface, and the energy distribution is necessarily very broad. In the examples shown in these figures each data point represents at least 1 000 initial trajectories, with as many as 4 000 trajectories in the case of Na.

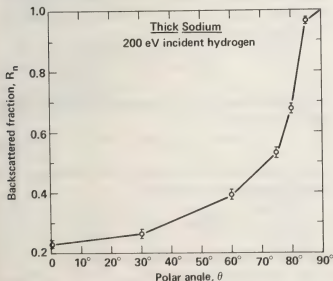


Fig. 11. — Backscattered fraction versus polar angle measured from normal.

The reflected fraction also varies markedly with the polar angle if incidence. In figure 11 is shown this dependence for hydrogen particles incident upon polycrystalline sodium targets at 200 eV. As the polar angle is varied 70° away from normal incidence, the backscattered yield is doubled. These reflected fractions show trends similar to those for hydrogen incident upon amorphous Cu at varying angles of incidence [67].

3.3 NEGATIVE ION PRODUCTION PROBABILITY. —

Given the desorption and backscattering particle yields, it remains to consider the processes leading to negative ion production for particles in transition from the bulk crystal into the vacuum. The negative ion production is a reasonably sensitive function of the surface work function. In figure 12 is shown M. Yu's data illustrating the variation of the work function and the negative ion yield with increasing cesium adsorbate coverage [51]. The negative ion yield is a maximum near the minimum of the work function, and varies in an inverse way with changes in work functions.

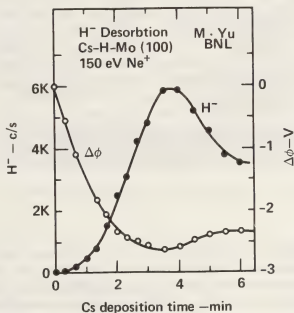


Fig. 12. — Work function and H^- production versus cesium coverage.

A similar variation is seen in the backscattering data taken from the thesis of Peter Schneider, and shown in figure 13. As Schneider has emphasized, the combination of particle backscattering and work function dependence allows for several distinct regimes. These are illustrated in the next figure.

The first case shown in figure 14 corresponds to an energetic particle backscattering from a bare substrate material with the negative ion production dependent upon the substrate work function. In the second case a partial layer of alkali substrate provides for an optimum work function, but backscattering is domi-

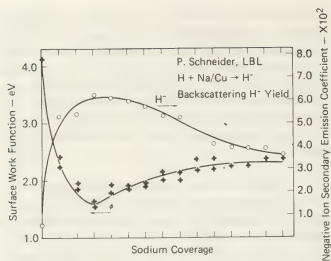


Fig. 13. — Work function and H^- backscattering yield versus sodium coverage.

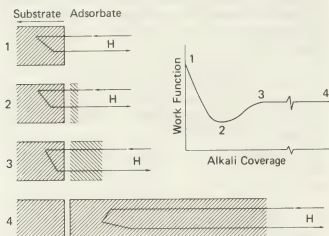


Fig. 14. — The four distinct backscattering configurations.

nated by the substrate. In the third illustration the adsorbate is a few layers thick, exhibiting the bulk alkali work function, but the adsorbate is still sufficiently thin that it does not contribute appreciably to the backscattering. Finally, the last case corresponds to a thick adsorbate where both backscattering and work function are determined by the adsorbate properties alone. A theory of negative-ion-secondary-emission by backscattered particles must account for all these possibilities.

The resonant capture and loss of electrons between the outgoing atom and the surface is the underlying basis for the sensitivity to the work function. For a proper solution to the ion production problem one requires the potential function experienced by the active electron in the surface region. The solution for the surface potential function continues to be an outstanding problem in surface physics. Some progress towards a complete solution will come by way of *ab initio* calculations of metal clusters, and clusters supporting adsorbate atoms [69]. The solution appro-

priate to alkali adsorbate coverages is still some years away.

Experiments on resonant electron scattering from surfaces indicate the electron potential in the surface region can be approximated by a truncated image potential. This view is substantiated in the jellium model calculations [60]. For our purposes the significant feature of these jellium results is that they show us where the image plane is located, and how close to the image plane the image potential is valid.

The negative-ion-production-probability can be factored into the product of a formation probability and a survival fraction. As the atom emerges from the surface, there is some distance over which it moves wherein electron capture takes place by a resonant energy transfer. At the far end of this region there is a certain probability that the negative ion has been formed. Beyond this point the energy level of the negative ion system lies above the fermi level of the solid, and resonant loss of the electron back to the vacant states of the metal will occur. Only a fraction of the negative ions formed in the first region will survive to large distances.

In his original discussions of this problem, Kishinevsky [71, 72] assumed a formation probability equal to unity and calculated the survival fraction by taking the electron energy level equal to the sum of the image energy minus the negative ion affinity, 0.75 eV. For a surface work function in the vicinity of 1.5 eV, this model yields a production-probability near unity for particles with energies above about 100 eV leaving normal to the surface. Kishinevsky calculated the survival fractions for surface work functions ranging from 1.2 eV to 1.7 eV, values that range about the minimum work function for a partial layer of cesium on a Mo or W substrate.

For an atom moving normal to the surface with velocity v_{\perp} but moving sufficiently slowly that the electrons can adjust adiabatically, the transition rate for electron transfer at any point z is $\tilde{F}(z)$. Provided the change in velocity of the atom is small as it leaves the surface, the rate of formation of negative ions from hydrogen atoms is

$$\frac{dH^-}{dz} = \frac{H^- \tilde{F}(z)}{v_{\perp}} \quad (9)$$

The general form of the formation probability must then be equal to

$$1 - e^{-\alpha/v_{\perp}} \quad (10)$$

In the loss region the loss rate is $\tilde{L}(z)$, and the rate of loss of negative ions is equal to

$$\frac{dH^-}{dz} = -\frac{H^- \tilde{L}(z)}{v_{\perp}} \quad (11)$$

The survival fraction will have the general form $e^{-\beta/v_{\perp}}$, and the product of these two probabilities

$$[1 - e^{-\alpha/v_{\perp}}] e^{-\beta/v_{\perp}} \quad (12)$$

is the production probability for a particle emitted from the surface with normal component v_{\perp} . The values for α and β must be derived from specific models for the surface potential, and contain the dependence on the surface work function.

An accurate calculation of α is quite difficult, α being sensitive to details of the surface potential in a region where the potential is least well known. Provided the ratio α/v_{\perp} is sufficiently large however, the formation probability is close to unity and the overall production probability is not too uncertain. A rough estimate for α is made in references [54] and [55], wherein is derived a formation probability near fifty percent for hydrogen emitted with normal energy component, E_{\perp} , equal to one hundred eV.

The calculation for β can be less uncertain. This is because β is dependent upon details of the surface potential at great distances from the surface where surface models are more reliable. In consideration of the calculation of α and β it is worthwhile first to digress and review qualitatively the main features of alkali adsorbates.

The valence level of an alkali atom is raised and broadened as the atom approaches a metal surface [73]. In consequence the atom loses its electron to unoccupied states in the metal, polarizes the surface, and is bound to the surface with an ionic bond. The energy level of the ion-surface systems is illustrated

in the accompanying figure. As more ions accumulate on the surface an electric dipole layer develops lowering the surface work function. The electronic level on the outside of the dipole layer is necessarily lowered. This continues until near the minimum of the work function the broadened level is lowered to a point where it now spans the fermi level. At this coverage the adsorbed ions share electrons with the metal and are only partially ionic. Semiclassical models for this configuration have been derived by Rasor and Warner [74] and by Levine and Gyftopoulos [75]. To understand the properties of the surface in the presence of an outgoing hydrogen atom, however, it is necessary to go one step further. The interaction of a hydrogen atom and a cesium atom lowers the total electronic energy of an isolated diatomic system to form a stable CsH molecule [53]. One would expect then that the perturbation of the atom near the surface will further lower the electronic level in that region, causing the cesium to be in an essentially atomic configuration.

The geometry of the surface region is shown in figure 16. Following Kishinevsky, the electronic energy level of the system is again taken to be equal to the image potential minus the affinity, but now the affinity is the affinity of the CsH molecule, not the affinity of the hydrogen atom. In consequence, the affinity will vary as the hydrogen atom moves away from the surface [54]. As can be seen from the figure, for differing trajectories 1 and 2, the image and affinity will combine to give an electronic energy level whose magnitude depends upon the particular trajectory. In figure 17 the energy level of the active electron is summarized.

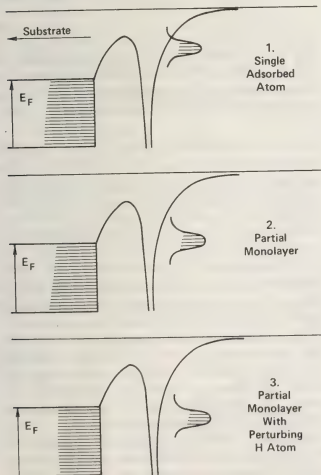


Fig. 15. — The energy level of the active electron. After Gadzuk, reference [73].

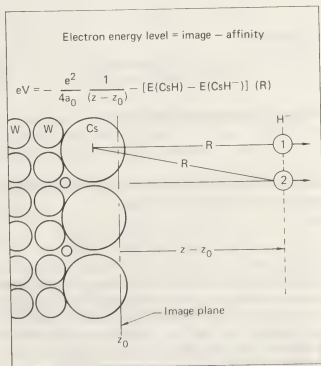


Fig. 16. — Surface geometry with adsorbate cesium.

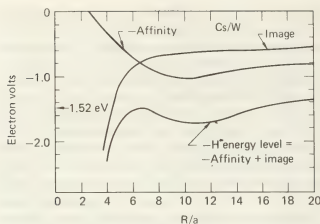


Fig. 17. — The image, affinity, and active electron energy levels.

The affinity is zero for close separations and increases to reach a maximum greater than one electron-volt near $R = 10\text{--}12 a_0$, then falls to an asymptotic value equal to the H^- affinity. The electron energy level exhibits a distinct minimum. The fermi level for a partial monolayer of cesium is near 1.52 eV. Resonant electron capture to form H^- can occur over the range from $R = 6$ to $16 a_0$. If the affinity were taken equal to a constant value of 0.75 eV, resonant electron capture would occur at separations $R < 9 a_0$. M. Yu concluded in his analysis of the Ne^+ desorption data that negative ions were formed far from the surface, at distances of from 14.3 to $15.5 a_0$ [51].

For the calculation of β recourse has been made to the method of complex eigenvalues [54, 55]. The Schroedinger equation for the active electron is taken to be

$$-\frac{\hbar}{i} \frac{\partial \Psi}{\partial t} = \left\{ -\frac{\hbar^2}{2m} \nabla^2 + V(r) \right\} \Psi, \quad (13)$$

with solution

$$\Psi = \chi(r) \exp\left(-\frac{i}{\hbar} W t\right) \quad (14)$$

taking W to be complex and equal to

$$W = E - \frac{i}{2} \Gamma, \quad (15)$$

so that at any point in space the electron density is decaying exponentially with time :

$$|\Psi^2| = |\chi(r)|^2 \exp\left(-\frac{\Gamma}{\hbar} t\right). \quad (16)$$

The solution is obtained by requiring $\chi(r)$ to have the form of an outgoing wave corresponding to the electron propagating into the bulk substrate. Janev [76] has pointed out that the problem is simplified by expressing the equation for $\chi(r)$ in parabolic coordinates :

$$\zeta = r + z, \quad \eta = r - z. \quad (17)$$

Factoring off the azimuthal part of $\chi(r)$ one obtains

$$\frac{d^2 v}{d\eta^2} + \frac{1}{4} \left\{ W + \varphi + \frac{4 Z_2}{\eta} + \frac{1}{\eta^2} + \varepsilon \eta + \frac{1}{\zeta - \eta - 2 Z_0} \right\} v = 0, \quad (18)$$

the φ is the surfacework function, Z_2 a separation constant, ε the magnitude of the electric field in the dipole layer, and z_0 the distance from the image plane. The final term in the bracket is the image term and contains the second coordinate ζ . Janev's point is that in the region where v is large, $\zeta \ll \eta$, and ζ can be ignored. The problem is then reduced to solving a one-dimensional equation. Writing $v = \mu + i\omega$, the equations for the real and imaginary parts become

$$\begin{aligned} \frac{d^2 \mu}{d\eta^2} &= -\frac{1}{4} \times \\ &\times \left\{ E + \varphi + \frac{4 z_2}{\eta} + \frac{1}{\eta^2} + \varepsilon \eta - \frac{1}{\eta + 2 z_0} \right\} \\ &\times \mu - \frac{\Gamma}{8} \omega, \end{aligned} \quad (19)$$

$$\begin{aligned} \frac{d^2 \omega}{d\eta^2} &= -\frac{1}{4} \times \\ &\times \left\{ E + \varphi + \frac{4 z_2}{\eta} + \frac{1}{\eta^2} + \varepsilon \eta - \frac{1}{\eta + 2 z_0} \right\} \\ &\times \omega + \frac{\Gamma}{8} \mu. \end{aligned} \quad (20)$$

This pair of simultaneous equations is solved for Γ, E by adjusting Γ, E until v has the form of an outgoing wave. Γ, E are evaluated for all values of z_0 , and the survival fraction is found from

$$f = \exp - \int_z^\infty \frac{\Gamma}{\hbar} \frac{dz_0}{v_\perp}. \quad (21)$$

Provided v_\perp does not change appreciably as the negative ion moves away from the surface,

$$f = \exp - \frac{1}{v_\perp} \int_z^\infty \frac{\Gamma}{\hbar} dz_0 = e^{-\beta/v_\perp}. \quad (22)$$

For a fully conducting surface the potential function employed is the truncated image potential shown in figure 18, which we have labeled Geometry A. The survival fraction has been calculated for work functions appropriate to bulk cesium or potassium, $\varphi = 1.90$ eV and $\varphi = 2.25$ eV, respectively. The results are shown in figure 19, taken from references [54, 55]. The abscissa is the perpendicular component of the backscattered energy.

For partial monolayer adsorbate coverages the adsorbate layer is not a conducting layer. The surface electric dipole layer impedes the loss of electrons from the negative ion to the underlying substrate conductor. The potential function used for partial

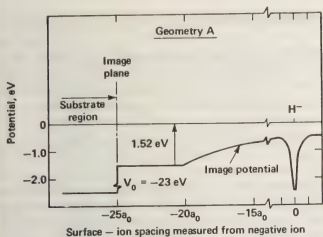


Fig. 18. — The truncated image potential.

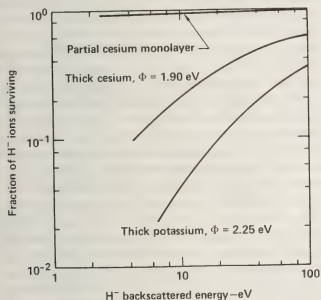


Fig. 19. — The survival fractions versus perpendicular backscattered energy.

monolayer cesium coverages is shown schematically in figure 20. The survival fraction shown in figure 18 is near unity.

We turn our attention now to the analysis of the experimental backscattering data. Peter Schneider has bombarded alkali-coated copper surfaces with H^+ , H_2^+ , H_3^+ ion beams with energies ranging from 200 eV per nucleon up to 4 keV per nucleon [68]. By heating the substrate prior to alkali deposition,

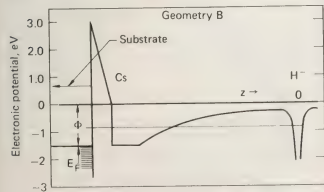


Fig. 20. — Schematic electron potential including dipole layer.

Schneider has achieved a regime in which the negative ion yields is almost entirely due to backscattered particles with only a very small desorption component. Some of his data for sodium coverages is shown in figure 21. For thick sodium coverages the surface work function is measured to be 2.3 eV; this thick sodium data corresponds to case four in figure 14. Also shown is the equivalent of case three, again with a measured work function of 2.3 eV. The energy distribution of backscattered particles from copper is more favorable for negative ion production than is the backscattered distribution from sodium. Also shown is the negative-ion-secondary-emission-coefficient (NISEC) for ions backscattered with sodium coverages near the minimum of the surface work function (see Fig. 13). Schneider has demonstrated also that for incident energies above 200 eV/nucleon, the NISEC is proportional to the number of nucleons in the molecular ion.

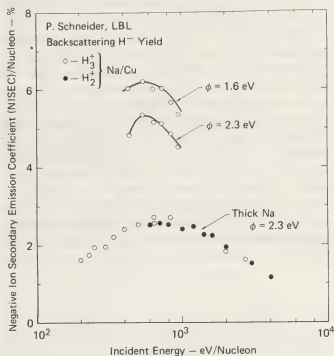


Fig. 21. — Experimental NISEC values for sodium.

For the energy range shown in the figure, the backscattered distribution of particles found in the Marlowe calculations can be factored according to

$$F(v, \theta) dv d(\cos \theta) = 2 f(v) \cos \theta dv d(\cos \theta), \quad (23)$$

with

$$R_N = \iint F(v, \theta) dv d(\cos \theta). \quad (24)$$

For any particular incident energy, E_i , the NISEC becomes

$$\begin{aligned} \text{NISEC}(E_i) = 2 \iint f_i(v) \cos \theta \times \\ \times \left[1 - \exp\left(-\frac{\alpha}{v \cos \theta}\right) \right] \exp\left(-\frac{\beta}{v \cos \theta}\right) \\ \times dv d(\cos \theta). \end{aligned} \quad (25)$$

Integrating over $\cos \theta$, this reduces to an integral over velocity, and scattering $a = \alpha/v$, $b = \beta/v$,

$$\text{NISEC}(E_i) = 2 \int f_i(v) \left\{ e^{-b} [(1-b)(1-e^{-a}) + ae^{-a}] + 0.577 \cdot 22 [(a+b)^2 - b^2] + (a+b)^2 \ln(a+b) - b^2 \ln b + \sum_{n=1}^{\infty} (-1)^n \frac{[(a+b)^{n+2} - b^{n+2}]}{n!} \right\} dv \quad (26)$$

The velocity distributions of the backscattered particles, $f_i(v)$, are calculated using Marlowe. We then attempt a least-squares fit of eq. (26) to the NISEC data treating the α and β as adjustable constants. In analogy with linear equations, we would expect to be able to determine the two parameters α and β in the polynomial, eq. (26), by fitting to the NISEC values at two energies, $E_{i,j}$. On the other hand if we attempt a fit to several data points the α and β are overdetermined. In this latter case one would not in general be able to obtain a good fit unless the $f_i(v)$'s were correct and the functional form for the formation probability and survival fraction were also correct.

In figure 22 is shown the least-squares fit to the thick sodium data at five incident energies, indicated by the + signs. Since the α and β found in this way are assumed to be functions only of the surface work function, we can use these values together with the Marlowe velocity distributions, $f_i(v)$, for backscattering from copper to predict the NISEC values of case 3, figure 14. This prediction is shown by the crosses in figure 22. These fits confirm the validity of Marlowe and the functional form of eq. (15). The application of this method to the other members of the alkali series is discussed elsewhere [77].

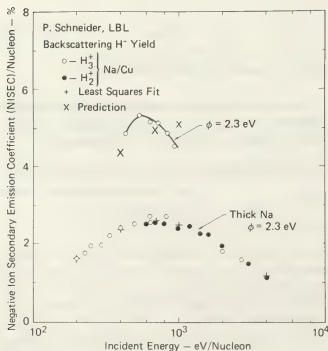


Fig. 22. — Experimental NISEC values with least squares fit.

Having obtained these semi-empirical values for α and β , the formation, survival, and production probabilities can be computed and are shown in figure 23. The probabilities are shown in double entry, corresponding to the five percent uncertainty in the experimental data points. The range shown for the production probability corresponds to using either the maximum or the minimum values of the other two probabilities, respectively. We would conclude that the optimum NISEC from thick sodium and glancing hydrogen collisions at 200 eV is approximately 15 %.

Also shown in the figure is the theoretical result for the survival probability for $\phi = 2.25$ eV, taken from figure 19. A value computed for $\phi = 2.30$ eV would lie between the theoretical and the semi-empirical curves. The formation probability found here is almost indistinguishable from that estimated in references [54, 55] for a partial monolayer of cesium.

It is interesting to ask what is the largest NISEC one would anticipate for normally incident particles. Using the particle backscattering data for hydrogen on molybdenum from figure 8, the formation and survival probabilities for partial monolayer coverages of cesium from figures 23 and 19, the predicted NISEC values are shown in the final figure. If the projection of the Marlowe backscattering yields into the lower energy range below 100 eV is valid, substan-

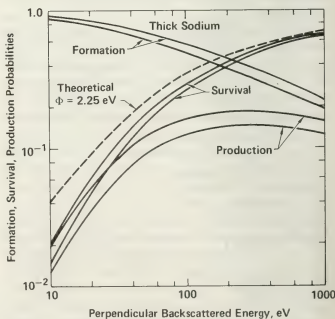


Fig. 23. — Formation, survival and production probabilities.

tial increases in the NISEC are possible at these lower energies.

In their 1977 Brookhaven paper [58], the Novosibirsk group reported the apparent NISEC values obtained by taking the ratio of negative ion current to positive ion current emitted through a small aperture in one cathode of a cesium loaded Penning source. Since there is reason to believe the optimized source operation may correspond to the optimized cesium partial-monolayer configuration, we have included their data in the figure. Their j^-/j^+ ratio shows a considerable discrepancy from the theoretical curve, although the magnitudes are similar. In view of the uncertainty in the positive ion species in the source several interpretations of the j^-/j^+ ratio are tenable. If the j^+ current were predominantly due to H^+ ions, Schneider's results would imply twice the NISEC yield compared with an H^+ ion current. Hence the j^-/j^+ ratio would of necessity be divided by two and translated to one half the incident energy, bringing the ratio into close coincidence with the theoretical curve. Alternatively, one expects a large energetic neutral flux of particles to be present in the discharge, comparable to the ion flux [53]. Including a neutral component in the denominator of the j^-/j^+ ratio would also bring it more into coincidence with the calculated curve. The Penning source data, as it stands, is not necessarily in conflict with the theoretical expectations.

This section on surface processes can be summarized in the following comments :

- (1) The usefulness of the Marlowe backscattering code has been demonstrated for incident energies down to at least 100 eV.
- (2) Marlowe together with the calculations of the survival fractions indicate the largest backscattering secondary emission yields will occur for incident particle energies between 10 and 100 eV, and for partial monolayer coverages of cesium.
- (3) Backscattering yields exceed desorption yields for incident energies below several hundred electron volts.

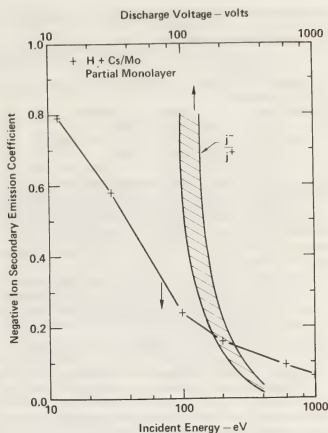


Fig. 24. — Theoretical NISEC values for partial-monolayer cesium, normal incidence. Also shown is the Penning source data from Novosibirsk.

(4) Desorption yields are large for energetic heavy particles with energies above a few keV.

(5) Backscattering yields exceed desorption yields by an order-of-magnitude or more in the optimized operation of the surface-plasma source.

Acknowledgment. — The author would like to thank those persons who permitted their data to be quoted prior to publication. The author is indebted to John Kinney for his assistance in adapting the Marlowe code to the Livermore CDC 7600.

References

- [1] The reader is referred to the *Proceedings of the Symposium on the Production and Neutralization of Negative Hydrogen Ions and Beams*, BNL-50727, K. Prelec, Editor, September, 1977.
- [2] SEIDL, M. and PARGELLIS, A. N., *Bull. Am. Phys. Soc. Series II* **23** (1978) 804.
- [3] LEUNG, K. N. and EHLERS, K. W., *Conference Abstracts of the IEEE International Conference on Plasma Science*, June 4-6, 1979, Montreal, Canada. Abstract IS5, p. 32.
- [4] DAGENHART, W. K. and STIRLING, W. L., *Montreal IEEE Conference*, Abstract IS2, p. 31.
- [5] SCHLACHTER, A. S., STALDER, K. R. and STEARNS, J. W., *Proc. X Int. Conf. on Phys. of Electronic and Atomic Collisions*, Paris, 1977, G. Watel, Editor (Commissariat à l'Energie, Paris, 1977), v. 2, p. 870.
- [6] KHIRNYI, Y. M. and KOCHEMASOVA, L. N., *Prib. Tekh. Eksp.* **3** (1970) 56. *Instr. Exp. Tech.* **3** (1970) 693.
- [7] GIRNIUS, R. J., ANDERSON, L. W. and STAAB, E., *Nucl. Instr. Methods* **143** (1977) 505.
- [8] SCHLACHTER, A. S., STEARNS, J. W., ROUSSEL, F., PRADEL, P. and SPIESS, G., *Bull. Am. Phys. Soc.* **21** (1976) 818.
- [9] BOHLEN, H., CLAUSNITZER, G. and WILSCH, H., *Z. Phys.* **708** (1968) 159.
- [10] GRUEBLER, W., SCHMELZBACH, P. A., KONIG, V. and MARMER, P., *Helv. Phys. Acta* **43** (1970) 254.
- [11] MEYER, F. W. and ANDERSON, L. W., *Phys. Lett.* **54A** (1975) 33.

- [12] CISNEROS, C., ALVAREZ, I., BARNETT, C. F. and RAY, J. A., *Phys. Rev. A* **14** (1977) 88.
- [13] AGAFONOV, Y. A., D'YACHKOV, B. A. and PAVLI, M. A., *Pisma Zh. Tekh. Fiz.* **2** (1976) 757. *Sov. Tech. Phys. Lett.* **2** (1976) 296.
- [14] MEYER, F. W., *Oak Ridge National Laboratory*, Private Communication.
- [15] D'YACHKOV, B. A., ZINENKO, V. I. and PAVLI, M. A., *Sov. Phys. Tech. Phys.* **16** (1972), 1868.
- [16] BARAGIOLA, R. A., SALVATELLI, E. R. and ALONSO, E., *Nucl. Instr. and Meth.* **110** (1973) 507.
- [17] MOSES, K. G. and FUTCHI, A. H., Jr., *Bull. Am. Phys. Soc., Ser. II*, **344** and Private Communication, 1966.
- [18] BERKNER, K. H., LEUNG, D., PYLE, R. V., SCHLACHTER, A. S. and STEARNS, J. W., *Nucl. Instr. and Meth.* **143** (1977) 157.
- [19] BERKNER, K. H., LEUNG, D., PYLE, R. V., SCHLACHTER, A. S. and STEARNS, J. W., *Phys. Letters* **64A** (1977) 217.
- [20] MORGAN, T. J., STONE, J., MAYO, M. and KUROSE, J., *Submitted to Phys. Rev. A*.
- [21] SCHLACHTER, A. S., STALDER, K. R. and STEARNS, J. W., Lawrence Berkeley Laboratory Abstract 9032, Submitted for presentation at the Eleventh International Conference on Electronic and Atomic Collision Processes, Kyoto, Japan, August, 1979.
- [22] GELLER, R., JACQUOT, C. and SERMET, P., *Brookhaven Proceedings*, 1977 (ref. [1]), p. 173.
- [23] HOOPER, E. B., Jr., ANDERSON, O. A., ORZECOWSKI, T. J. and POULSEN, P., *Brookhaven Proceedings*, 1977 (ref. [1]), p. 163.
- [24] SEMASHKO, N. N., KUSNETSOV, V. V. and KRYLOV, A. I., *Brookhaven Proceedings*, 1977 (ref. [1]), p. 170.
- [25] HOOPER, E. B., Jr. and POULSEN, P., *Conference Abstracts of the IEEE International Conference on Plasma Science*, June 4-6, 1979, Montreal, Canada. Abstract 154, p. 32.
- [26] KARO, A. M., GARDNER, M. A. and HISKES, J. R., *J. Chem. Phys.* **68** (4) (1978) 1942.
- [27] HISKES, J. R., KARO, A. M., WILLMAN, P. A. and STEVENS, W. B., *Phys. Lett.* **68A** (1978) 221.
- [28] STEVENS, W. B. and KARO, A. M., *A Pseudo-Potential Calculation of the Ground States of the Alkali Hydrides and Their Negative Ions*, Submitted for Publication.
- [29] OLSON, R. E., SHIPSEY, E. J. and BROWNE, J. C., *Phys. Rev. A* **13** (1976) 180.
- [30] JANEV, R. K. and RADULOVIC, Z. M., *Phys. Rev. A* **17** (1978) 889.
- [31] SCHLACHTER, A. S., BJORKHOLM, P. J., LOYD, D. H., ANDERSON, L. W. and HAEBERLI, W., *Phys. Rev.* **177** (1969) 184.
- [32] CISNEROS, C., ALVAREZ, I., BARNETT, C. F. and RAY, J. A., *Phys. Rev. A* **14** (1976) 76.
- [33] CISNEROS, C., ALVAREZ, I., GARCIA G., R., BARNETT, C. F., RAY, J. A. and RUSSEK, A., *Phys. Rev. A* **19** (1979) 631.
- [34] BACAL, M., NICOLOPOULOU, E. and DOUCET, H. J., *Brookhaven Proceedings*, 1977 (ref. [1]), p. 26.
- [35] BACAL, M. and HAMILTON, G. W., *Phys. Rev. Lett.* **42** (1979) 1538.
- [36] FREIS, R. P. and HISKES, J. R., *Phys. Rev. A* **2** (1970) 573.
- [37] BUCKLEY, B. D. and BOTTCHEK, C., Submitted for publication in *Journal of Physics B*, Letters, and Private Communication.
- [38] For a more detailed discussion of the atomic processes occurring in this hydrogen discharge see
HISKES, J. R., BACAL, M. and HAMILTON, G. W., Lawrence Livermore Laboratory Report UCID-18031, January 1979.
- [39] PEART, B., FORREST, R. A. and DOLDER, K., Submitted for publication in *Journal of Physics, B*, and Private Communication.
- [40] PEART, B. and DOLDER, K. T., *J. Phys. B* **7** (1974) 1948.
- [41] KULANDER, K. C. and GUEST, M. F., Submitted for publication to *Journ. of Physics, B*.
- [42] VOGLER, M., *Phys. Rev. A* **19** (1979) 1.
- [43] ALLAN, M. and WONG, S. F., *Phys. Rev. Letters* **41** (1978) 1791.
- [44] WADEHRA, J. M. and BARDLEY, J. N., *Phys. Rev. Letters* **41** (1978) 1795 and Private Communication.
- [45] FLANNERY, M. R., TAI, H. and ALBRITTON, D. L., *Atomic Data and Nuclear Data Tables* **20** (1977) 563.
- [46] VILLAREJO, D., *Journ. Chem. Phys.* **49** (1968) 2523.
- [47] BELCHENKO, Y. I., DIMOV, G. I. and DUDNIKOV, V. G., *Proceedings of the Second Symposium on Ion Sources and Formation of Ion Beams*, LBL-3399, Berkeley, California, October 1974.
- [48] SLUYTERS, T., *Proc. of Second Berkeley Symposium*, October 1974.
- [49] BELCHENKO, Y. I., DIMOV, G. I. and DUDNIKOV, V. G., *Nuclear Fusion* **14** (1974) 113.
- [50] BENDER, E. D., DIMOV, G. I. and KISHINEVSKY, M. E., Preprint IYAF 75-9, Nuclear-Physics Institute, Siberian Division, Academy of Sciences of the USSR, Novosibirsk (1975). Papers of the First All-Union Seminar on Secondary Ion-Ion Emission, Kharkov, 1975.
- [51] YU, M. L., *Proc. of Brookhaven Symposium*, 1977, p. 48. *Phys. Rev. Lett.* **40** (1978) 574.
- [52] WIESEMANN, K., *Proc. of Brookhaven Symposium*, 1977, p. 97.
- [53] HISKES, J. R., KARO, A. M. and GARDNER, M. A., *Journ. Applied Physics* **47** (1976) 3888.
- [54] HISKES, J. R. and KARO, A. M., *US-USSR Negative Ion workshop*, May-June 1977, Moscow; UCRL-79521, May 1977.
- [55] HISKES, J. R. and KARO, A. M., *Proc. of Brookhaven Symposium*, 1977, p. 42.
- [56] SCHNEIDER, P. J., BERKNER, K. H., GRAHAM, W. G., PYLE, R. V. and STEARNS, J. W., *Proc. of Brookhaven Symposium*, 1977, p. 63.
- [57] GRAHAM, W. G., *Bull. Am. Phys. Soc., Series 2* **23** (1978) 804.
- [58] BELCHENKO, Y. I., DIMOV, G. I. and DUDNIKOV, V. G., *Proc. of the Brookhaven Symposium*, 1977, p. 79.
- [59] Panel Session, *Proc. of the Brookhaven Symposium*, 1977, p. 151.
- [60] YING, S. C., SMITH, J. R. and KOHN, W., *Phys. Rev. B* **11** (1975) 1483.
- [61] OEN, O. S. and ROBINSON, M. T., *Journ. of Nucl. Materials* **76**, 77 (1978) 370.
- [62] ECKSTEIN, W. and VERBEEK, H., *Journ. of Nucl. Materials* **76**, 77 (1978) 365.
- [63] HOU, M., ECKSTEIN, W. and VERBEEK, H., *Radiation Effects* **39** (1978) 107.
- [64] BEHRISCH, R., *Surface Erosion From Plasma Materials Interaction* to be published in *Journ. of Nucl. Materials*, 1979.
- [65] TAGLAUER, E., BEITAT, U. and HEILAND, W., *Nucl. Instr. and Methods* **149** (1978) 605.
- [66] ROBINSON, M. T. and TORRENS, I. M., *Phys. Rev. B* **9** (1974) 5008.
- [67] OEN, O. S. and ROBINSON, M. T., *Nucl. Instr. and Methods* **132** (1976) 647.
- [68] SCHNEIDER, P., *Ph. d. Thesis*, Dept. of Physics, Univ. of California, Berkeley, CA, 1979.
- [69] UPTON, T. H. and GODDARD, W. A., *III Phys. Rev. Letters* **42** (1979) 472.
- [70] McRAE, E. G., *Bull. of Am. Phys. Soc., Series 2* **24** (1979) 260.
- [71] KISHINEVSKY, M. E., Preprint No. 116-73, *Inst. of Nuclear Physics*, Siberian Academy of Sciences, Novosibirsk, 1973.
- [72] KISHINEVSKY, M. E., *Journ. of Tech. Phys.* **48** (1978) 773.
- [73] GADZUK, J. W., *Surface Science* **6** (1967) 133.
- [74] RASOR, N. S. and WARNER, C., *Journ. of Appl. Phys.* **35** (1964) 2589.
- [75] LEVINE, J. D. and GYFTOPOULOS, E. P., *Surface Science* **1** (1963) 171.
- [76] JANEV, R. K., *Surface Science* **45** (1974) 609.
- [77] HISKES, J. R. and SCHNEIDER, P., To be published.

The mechanism of the long spark formation

I. Gallimberti

Dept. of Electrical Engineering, Padova University, Italy

Résumé. — L'objectif de cet article est de présenter l'état actuel des recherches sur la physique des arcs longs. La configuration de référence est un intervalle interélectrode non uniforme soumis à une impulsion de tension positive qui est la schématisation en laboratoire des conditions les plus critiques dans la conception d'un appareil UHT. Dans ces conditions la formation de l'arc s'effectue à travers diverses phases successives : l'initiation du premier phénomène d'ionisation, le développement des streamers-corona, la formation du *stem* (tronc) corona et du canal du leader, la propagation du leader, l'évolution temporelle des caractéristiques du leader, l'apparition des réilluminations du canal, le *saut final* et la transition vers le canal hautement conducteur de l'arc. Chaque phase est gouvernée par une interaction complexe de processus élémentaires électromagnétique, hydrodynamique et thermodynamique. Chaque chapitre de cet article présente à la fois les résultats expérimentaux et les modèles théoriques qui ont été obtenus pour chaque phase individuelle. Ces dernières années, un grand nombre de systèmes de mesures complexes ont été utilisés pour étudier les conditions locales des diverses phases de la décharge (distorsion de la charge d'espace, champ électrique, énergie des électrons, température et densité du gaz, etc...) : la première partie de chaque chapitre présente un sommaire de ces divers résultats expérimentaux afin de définir les conditions physiques sous lesquelles la décharge se développe et de choisir le phénomène élémentaire qui semble dominant. La seconde partie de chaque chapitre présente les divers modèles théoriques qui ont été obtenus en simplifiant les équations électromagnétiques, hydrodynamiques et thermodynamiques de base en accord avec le phénomène dominant. Le bon accord entre les résultats calculés et mesurés expérimentalement, sous une large variation de conditions de test, atteste qu'une nette étape en avant a été effectuée ces dernières années dans le domaine de la recherche sur la physique des arcs longs.

L'objectif final, à savoir, la formulation d'un modèle complet du claquage, capable de prédire les propriétés de la décharge dans toutes les configurations pratiques en partant des processus physiques élémentaires, n'est pas encore réalisé, mais cela semble être une possibilité réaliste pour le développement des recherches dans ce domaine.

Abstract. — The aim of this paper is to present the *state of the art* of the research on the physics of long sparks. The reference configuration is a non uniform long gap subjected to positive impulse voltages, which is the laboratory schematization of the most critical conditions occurring in the design of EHV apparatus. Under these conditions, the spark formation develops through different subsequent phases : the inception of the first ionization phenomena, the development of corona streamers, the formation of the corona stem and of the leader channel, the leader propagation, the time-evolution of the leader characteristics, the appearance of channel reilluminations, the final jump and the transition to the highly conductive spark channel. Each phase is governed by a complex interaction of electromagnetic, hydrodynamic and thermodynamic elementary processes. Each chapter of the paper presents both the experimental results and the theoretical models which have been obtained for each single phase. In recent years a number of sophisticated measuring systems have been used to study the local conditions of the different discharge phases (space charge distribution, electric field, electron energy, gas temperature and density, etc...) : the first part of each chapter presents a summary of these experimental results, in order to define the physical conditions under which the discharge develops, and to select the elementary phenomena which appear to be dominant. The second part of each chapter presents the different theoretical models, which have been obtained by simplifying the basic electromagnetic, hydrodynamic and thermodynamic equations, according to the dominant phenomena. The good agreement between computed and experimental results, over a large variety of test conditions, certify the large steps forward, which have been taken in the last years by the research on the physics of long sparks.

The final objective, i.e. the formulation of a complete breakdown model, able to predict the discharge features in all the possible practical configurations, starting from the physics of the elementary phenomena, is not yet realized, but it appears as a realistic possibility of the further development of the research in this area.

Introduction. — Much of the research carried out in recent years in the field of EHV and UHV power transmission dealt with the practical problems of dielectric behaviour of external insulation. The large variations of the dielectric strength of large air gaps depending on the different practical electrode configura-

tions and the various forms of voltage surges which can appear in a H.V. network, make the engineering approach of full scale tests very long and expensive. For this reason the breakdown processes have been investigated in the last ten years essentially from the point of view of the basic physical processes. The

objective is to make available a number of physical and mathematical models, able to predict the insulation behaviour under different practical conditions.

The present paper is an attempt to summarize the work which has been done in this direction in the last years; it refers essentially to rod-plane configurations subjected to positive switching surge voltages, which represent the most critical conditions. Part of the material presented is original or published work of the author; part has been derived from published work of other authors. However, the most part of this paper comes from the results of international collaborations and contacts: a great deal of the experimental work has been carried out recently by the *Les Renardières Group*; the most part of the theoretical models have been developed in permanent discussion and cooperation with E. Marode and G. Hartmann; some of the work presented makes part of a collaboration with R. Brambilla; the author is also grateful to the numerous colleagues all around the world, whose helpful discussions were essential for the development of the work: their names cover practically all the list of the references.

The main chronological sequence of events composing the positive impulse-voltage discharge in rod and sphere-plane geometry can be defined by the different elements and the subsequent phases, schematically sketched in figure 1.

Provided that the electric field strength attains sufficiently high values, the discharge commences at a time t_i after a time-lag during which a suitably placed free electron is generated.

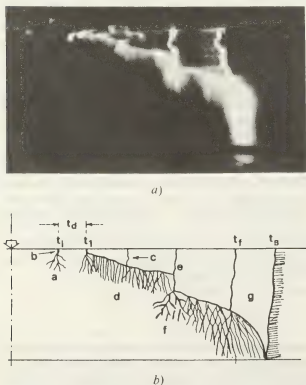


Fig. 1. — Streak Photograph (a) and schematic representation (b) of a long spark (positive point-plane gap, 10 m in length, 500/1 000 μ s wave).

The first corona represents the first observable ionization processes, which usually take the form of filamentary channels or streamers (a). The current impulse consists of a steep increase to a maximum value, followed by an exponential decay. As a result of the corona growth a net positive charge is rapidly injected into the gap. At the root of the corona streamers a short bright channel is observed (the stem, b in figure 1): from it the further development of the discharge takes origin.

This next phase is dependent upon the degree of non-uniformity of the electric field distribution in the gap. In very divergent-field configurations, the injected space charge is sufficient to reduce significantly the electric field strength. The recovery of this field will be dependent upon the rate of rise of the applied voltage and the dissipation rate of the space charge. Until this recovery occurs no ionization processes are detectable in the gap for a time duration t_d , called dark period. For more uniform configurations the dark period may be absent and a spark leader channel (c) initiates from the anode at a time t_i . In any case this leader growth is preceded by a secondary corona discharge which generally consists of a number of very fine filaments, when compared with the first corona.

The spatial characteristics of the leader channel are those of a narrow irregular path often propagating in a direction making a considerable angle to the direction of the applied field. Its velocity of propagation is dependent upon the geometry of the gap and the applied voltage. The luminosity of the leader channel is generally low except at its tip. Leader growth is continuous unless the rate of increase of applied voltage is too low or, under some conditions, sudden elongation and brightening of the channel occurs. Such phenomena are known as reilluminations or restrikes (e): these are high-velocity discontinuous increases in leader length accompanied by a large corona pulse (f), and by a brief increase of the leader luminosity and the current flow in the discharge.

The leader corona (d) is a voluminous discharge, showing some evidence of a filamentary structure, which ionizes the air ahead of the leader channel. It is the mechanism by which current flow in the developing discharge is maintained, and modifies the electric field distribution in the gap.

The final jump (g) is the last stage of leader growth prior to spark-over. Leader formation of itself is not a sufficient criterion of spark-over. Its growth may, over a wide range of voltages, terminate spontaneously. If it approaches sufficiently close to the plane, however, its velocity and the discharge current increase appreciably at time t_f , and the spark path is completed at a time t_B .

1. First corona inception. — 1.1 EXPERIMENTAL RESULTS. — When a voltage wave is applied to a long gap, the first corona starts with a time-lag which

varies from shot to shot : as a consequence the inception times t_i and voltages U_i are statistically spread on the front of the voltage impulse : in figure 2 the

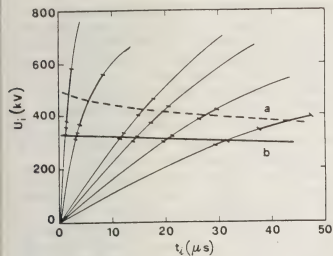


Fig. 2. — First corona inception voltage U_i versus inception time t_i , for different rates of voltage rise. The bars represent the standard deviations along the voltage wave. (4 m hemisphere-plane gap, $R = 5$ cm; (a) without UV irradiation, (b) with UV irradiation.)

average values of this distribution are given for different voltage rates of rise, together with their standard deviations. If the h.v. electrode is irradiated with a source of ultraviolet light, of sufficient intensity to produce ionization in the high field region, both the average inception times and voltages are lowered [1] and the standard deviations become negligible (Fig. 2). This indicates two important facts : first, the statistical distribution of inception time-lags should be related to the availability of initiatory electrons in an appropriate region of the gap, and the statistical fluctuations should depend on the variable rate of electron liberation; second, even if free electrons are available near the h.v. electrode at the moment of voltage application, there is a minimum voltage or field below which the corona streamers cannot form.

To compare inception fields obtained with different gaps and electrodes, the field divergence factor d_f and the equivalent curvature radius can be defined by the relation,

$$d_f = \left[-\frac{dE_g}{dz} \cdot \frac{1}{E_g} \right]_{z=0} = \frac{2}{R_{eq}}, \quad (1)$$

where E_g is the applied field; for an isolated sphere R_{eq} equals the radius of the sphere.

The minimum inception field is reported in figure 3 as a function of the divergence factor; it is the envelope of the experimental minimum values.

The experimental probability distributions of inception time lags and inception fields are reported in figure 4. As it would be expected the mean values of t_i decrease with increasing the voltage rate of rise dU/dt : on the contrary, the mean values of U_i and

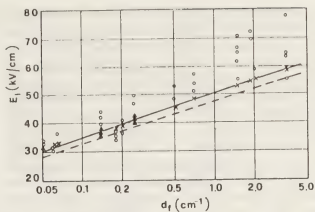


Fig. 3. — The minimum inception field as a function of the gap divergence factor; the solid and dashed lines represent theoretical calculations (see text).

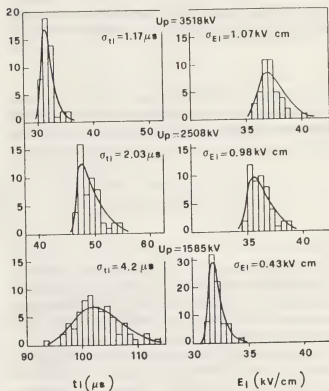


Fig. 4. — Probability distributions of inception time and field, at different crest-voltage levels (7 m hemisphere-plane gap, $R = 30$ cm, 320/10 000 μ s wave).

E_i increase. Correspondingly, the standard deviation of t_i decreases with increasing dU/dt , whereas the standard deviations of U_i and E_i increase (Fig. 5). This indicates that the statistical time-lag depends upon the volume from which an initiatory electron can develop into a corona streamer and upon the electric field within it : with a high value of dU/dt , at the minimum inception voltage, both parameters increase rapidly and the statistical time-lag is small, but with high inception fields and voltages. The same is true for the standard deviations : it has been experimentally verified [2] that the product of time and field standard deviations is roughly a constant (Fig. 5).

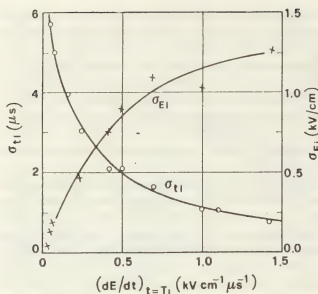


Fig. 5. — Standard deviations of inception time and field as functions of the field rate of rise, (7 m hemisphere-plane gap, $R = 30$ cm, 320/10 000 μ s wave).

1.2 MINIMUM INCEPTION FIELD. — The first step for the calculation of the minimum inception voltage is the determination of the conditions under which a

streamer can propagate at a specified value of the applied field. According to the model described in § 2, the streamer tip is represented by a sphere of radius R_s containing N_s positive ions; in air the propagation is assured by a series of new avalanches growing in the *active region*, where the total field E_t (the space charge field E_c plus the applied field E_a) is higher than 26 kV/cm; this series of avalanches is represented in the model by a single *equivalent avalanche*, which satisfies to an energy balance equation relative to the avalanche formation as equivalence condition. The head of the equivalent avalanche of radius R'_s and containing N'_s positive ions reproduces the streamer tip in a more advanced position in the gap.

As criterion for propagation it is assumed that the charge in the streamer tip ($N_s \cdot e$) must be higher than a minimum value ($N_{\text{stab}} \cdot e$) (*stability charge*): the latter is defined as the minimum charge which produces a space charge field E_s high enough to make the greatest avalanche which can develop in the active region able to reproduce the streamer tip ($N'_s = N_{\text{stab}}$, $R'_s = R_{\text{stab}}$). The stability charge depends on the applied field E_a ; its values have been calculated [3] by means of an iterative computer program, which simulates the avalanche development [4], and have been interpolated by a computer least-squares best-fit method,

$$N_{\text{stab}} = \begin{cases} 0.558 \times 10^8 - 0.231 \times 10^3 \cdot E_a & (\text{for } E_a \leq 2 \times 10^5 \text{ V/cm}) \\ 3.34 \times 10^8 \cdot \exp(-1.614 \times 10^{-5} \cdot E_a) & (\text{for } E_a \geq 2 \times 10^5 \text{ V/cm}) \end{cases} \quad (2)$$

The stability charge in a zero applied field is ($0.55 \times 10^8 \cdot e$), which is slightly lower than the value computed by Dawson and Winn [5], the discrepancy being due to the different simplifying assumptions and the computation methods used in the models.

The computation of the minimum inception voltage is based on the following criteria. Let us consider an electrode configuration with a known field distribution $E_{a1}(P)$ per unit applied voltage; at a specified voltage U it is possible to define the boundary of the *active region* (the surface over which the applied field is equal to 26 kV/cm). The more favorable avalanche for corona inception develops along the line of maximum stress starting from the boundary ($z = z_a$) of this active region. The charge (eN_s) produced by this avalanche can be computed either by simple integration of the rate equation for collisional ionization, up to the electrode surface ($z = z_0$),

$$N'_s = \exp \left[\int_{z_a}^{z_0} (\alpha - \eta) dx \right], \quad (3)$$

where α and η are the ionization and attachment coefficients; or by more sophisticated computer simulations which account also for diffusion and space charge field distortion [5, 6]. If this charge results

higher (or lower) than the stability charge corresponding to the value of the applied field on the electrode surface, the voltage U results to be higher (or lower) than the minimum inception voltage: the latter value can be calculated iteratively.

In figure 3 the computed variation of the minimum Inception field with the field divergence is reported for comparison with the corresponding experimental results: the dashed line represents the theoretical calculations, according to eq. (3); obviously they are slightly lower than those calculated with the more sophisticated avalanche simulation, because the quenching effects of electron diffusion and space charge field distortion are neglected. The experimental results are sometimes lower than the computed ones, particularly when they refer to irradiated gaps: in effect in this case the number of free electrons available to start corona avalanches can be much larger than one. It can be seen that, in the range $0.05 < d_f < 5 \text{ cm}^{-1}$, the minimum inception field increases almost logarithmically with the field divergence,

$$E_i = 6.77 \log(1.75 \times 10^3 \cdot d_f) \quad (4)$$

where E_i is expressed in kV/cm and d_f in cm^{-1} . This increase of E_i with d_f is due to the fact that the active

region and hence the avalanche path is smaller with large divergence : a higher field is therefore needed for the generation of a charge above the stability value.

1.3 INCEPTION PROBABILITY DENSITY. — In order to simulate the statistical distribution of corona inception above the minimum field, it is necessary to calculate the *critical volume* around the rod tip, in which the production of an electron leads to corona [3, 6]. First the length on the axis of the system over which a free electron gives corona must be found. This critical length is limited because if the electron is too close to the electrode it collides with it before the avalanche has produced a total number of ions larger than the critical charge. If it is too far away the field strength drops below 26 kV/cm and the avalanche cannot start. At the minimum corona inception voltage there is only one point on the gap axis where the conditions are satisfied. As the electrode voltage increases, the critical length increases, the outer boundary following the 26 kV/cm contour and the

electrons/cm³.s and is therefore far too low in the case of impulse applied voltages where the times t_i are generally lower than some hundreds of μ s. However, even if this cosmic radiation is not sufficient for the direct production of the first electron, it determines a steady state concentration of negative ions (equilibrium between production and recombination rates). The removal of an electron from the negative ions under the influence of the applied electric field, is believed to be the dominant mechanism for primary electron production [3, 6-10]. The number of electrons produced per unit volume and unit time n_-/τ_d , where n_- is the negative ion density and τ_d their mean lifetime. It can be shown in long gaps that also under the action of drift after the voltage application the negative ion concentration remains uniform in the critical volume up to time t_i [3, 10]; on the contrary τ_d depends on the electric field and varies in time and space. The total frequency of electron production p_e can be calculated by integration over the critical volume

$$p_e(t) = \int_{v_c(t)} \frac{n_-}{\tau_d(P, t)} dP. \quad (4 \text{ bis})$$

It has been shown [3] that the inception probability density $f_i(t)$, associated to the time t , has a Poisson-like distribution,

$$f_i(t) = p_e(t) \exp \left[- \int_0^t p_e(t) dt \right], \quad (5)$$

which depends essentially on the generation rate of primary electrons in the critical volume, and hence on the electrode geometry and voltage wave shape. The exponential term in eq. (5) represents the probability $F_0(t)$ that corona doesn't start before time t :

$$F_0(t) = \left[1 - \int_0^t f_i(t) dt \right] = \exp \left[- \int_0^t p_e(t) dt \right]. \quad (6)$$

Eqs. (5) and (6) can be very useful because they make possible to calculate analytically the frequency of electron generation $p_e(t)$, from best fit expressions of the experimental measurements of $f_i(t)$ (Fig. 4). In figure 7 the values of p_e are reported as a function of the applied voltage U , in a 10 m cone plane gap [8], for different values of air humidity. From this figure it is possible to see that humidity has a very large inhibitory action on the electron release in the critical volume.

1.4 PRIMARY ELECTRON PRODUCTION. — In order to explain such an effect, it is necessary to assume that humidity affects the process of electron detachment of negative ions [7, 8]. The nature of the negative ions of atmospheric interest, and the most important

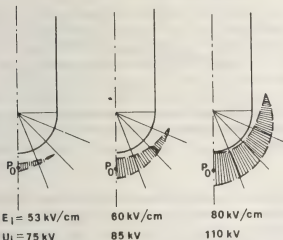


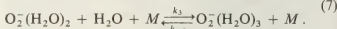
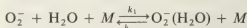
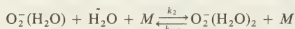
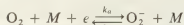
Fig. 6. — The *critical volume*, where a free electron can start corona, at different voltage levels (1.5 m hemisphere-plane gap, $R = 1$ cm).

inner boundary moving in towards the electrode. Once the minimum corona inception voltage has been exceeded it is possible for electrons in off-axis position to produce corona. The techniques used to calculate the critical length on the axis can also be used off-axis and then a critical volume v_c is defined, from which an electron can initiate corona. The volume is calculated as a function of the electrode voltage, but it can be transformed into a function of time simply from the shape of the voltage impulse.

The next step in the calculation is to convert the volume into probability distributions for the occurrence of the first corona. To do this we need to know the rate of electron production in the critical volume. The natural production rate of free electrons due to cosmic rays (or other *natural phenomena*) is around 10

conversion reactions which can change the primary ions into secondary species, have been discussed in detail by Bastien *et al.* [11] : the stable type which can

develop from the three-body attachment of the electrons produced by cosmic radiation [12] is $O_2^-(H_2O)_n$, according to the cascade clustering reactions :



Clusters larger than $n = 3$ are not probable because the production rate is very small. The best estimates of the rate constant at 300 K and zero field are reported in table I [11-14], together with the cluster dissociation energy D_0 , the effective electron detachment energy D_d , and the variation of the standard Gibbs function ΔG^0 [15].

The population repartition between the different cluster numbers depends on the equilibrium between direct and inverse reaction rates : it can be easily shown from the values reported in table I that the most probable type in air at atmospheric pressure is $O_2^-(H_2O)_3$.

While the energy D_0 for the dissociation of a water molecule decreases with the cluster number, the energy D_d necessary to detach an electron increases (see Table I). As a consequence, the direct electron detachment from the cluster ions has a very low probability; the electron production in the critical volume should preferentially follow a cascade declustering process and the detachment of the O_2^- ions which are finally formed.

When the electric field is applied in the critical volume, the negative ions are accelerated and their temperature T_- becomes larger than the gas temperature T . Consequently the rates of the clustering-declustering reactions are changed : as the clustering is an exothermic process with low activation energy, its rate is only slightly affected by the variation of the ion temperature; on the contrary, the declustering reaction is endothermic with an activation energy of

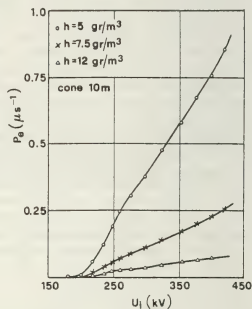


Fig. 7. — Experimental frequency of electron production inside the critical volume as a function of the applied voltage (10 m cone-plane gap).

the order of D_0 , and its rate is very sensitive to the ion temperature. The equilibrium constant K_{np} for the formation and dissociation of the n -th cluster varies with temperature according to the relation [15]

$$K_{np}(T) = N_T^0 \left(\frac{k_n}{k_{-n}} \right) = \exp \left(- \frac{\Delta G_{nT}^0}{RT} \right), \quad (8)$$

Table I. — The thermo-kinetic parameters of reactions (7).

Ion	D_0 (eV)	D_d (eV)	M	Rate constant (at 300 K)	ΔG^0 kcal/mole
O_2^-	—	0.44	O_2	$k_a = 3.0 \times 10^{-30} \text{ cm}^6 \text{ s}^{-1}$	10.13
				$k_d = 5.8 \times 10^{-19} \text{ cm}^3 \text{ s}^{-1}$	
			N_2	$k_a = 1.0 \times 10^{-31} \text{ cm}^6 \text{ s}^{-1}$	11.17
				$k_d = 1.1 \times 10^{-19} \text{ cm}^3 \text{ s}^{-1}$	
$O_2^-(H_2O)$	0.8	1.24	N_2, O_2	$k_1 = 2.0 \times 10^{-28} \text{ cm}^6 \text{ s}^{-1}$	18.44
				$k_{-1} = (2 \times 10^{-22}) \text{ cm}^3 \text{ s}^{-1}$	
$O_2^-(H_2O)_2$	0.36	1.98	N_2, O_2	$k_2 = 5.0 \times 10^{-28} \text{ cm}^6 \text{ s}^{-1}$	8.35
				$k_{-2} = 1.1 \times 10^{-14} \text{ cm}^3 \text{ s}^{-1}$	
$O_3^-(H_2O)_3$	0.23	2.65	N_2, O_2	$k_3 = 5.0 \times 10^{-29} \text{ cm}^6 \text{ s}^{-1}$	6.46
				$k_{-3} = 9.0 \times 10^{-15} \text{ cm}^3 \text{ s}^{-1}$	

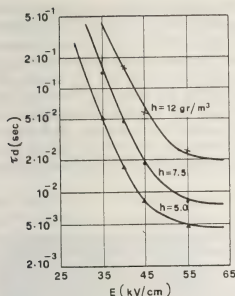


Fig. 8. — The equivalent detachment lifetime as a function of the electric field, for different humidity values. The points are experimental estimates (see text).

where N_T^0 is the gas number density at standard pressure and temperature T , and ΔG_{nT}^0 is the variation of the standard Gibbs function at temperature T . Eq. (8) has been used to calculate the values of ΔG^0 at 300 K reported in table I; it holds rigorously only in thermodynamic equilibrium; however, it has been shown by Varney [16] that it can be applied also to the case of $T_- > T$, if an adequate temperature scale is used for the negative ions as a function of the reduced applied field E/P ,

$$T_- = T + \frac{1}{g} \frac{E}{P}, \quad (9)$$

where g is a constant which depends slightly on the nature of ions and gas molecules: it is 8×10^{-2} V/cm torr K for nitrogen ions in nitrogen. For the present calculations it has been adjusted around this value to fit with eq. (8) the available experimental results on attachment and detachment rates in air as functions of E/P .

The variation of the Gibbs function ΔG_{nT}^0 has been assumed to depend essentially on the gas temperature T and not on the ion temperature T_- : as a consequence, the values reported in table I can be used in the present case for all the E/P values. The variation of the rate constant ratio with the applied field can be therefore calculated as:

$$\frac{k_n}{k_{-n}} = \frac{1}{N_T^0} \exp \left(\frac{-\Delta G_n^0}{T + \frac{1}{g} \frac{E}{P}} \right). \quad (10)$$

The equivalent time-constant of the complete cascade declustering and detachment process can be calculated from the system of rate equations for the chain of

reactions (7). For atmospheric air under normal condition it results

$$\tau_d = \frac{1 + [\text{H}_2\text{O}] \frac{k_1}{k_{-1}} \left[1 + [\text{H}_2\text{O}] \frac{k_2}{k_{-2}} \left(1 + [\text{H}_2\text{O}] \frac{k_3}{k_{-3}} \right) \right]}{k_d N_T^0} \quad (11)$$

where $[\text{H}_2\text{O}]$ is the absolute water vapour concentration. From the data in table I it is possible to see that $[\text{H}_2\text{O}] \cdot k_n/k_{-n} \gg 1$, and hence the equivalent detachment time-constant becomes

$$\tau_d = \frac{[\text{H}_2\text{O}]^3}{k_d N_T^0} \cdot \frac{k_1 k_2 k_3}{k_{-1} k_{-2} k_{-3}}, \quad (12)$$

and by use of eq. (10),

$$\tau_d = \frac{h_r^3}{k_d (N_T^0)^2} \cdot \exp \left[\frac{\sum_{n=0}^3 \Delta G_n^0}{T + \frac{1}{g} \frac{E}{P}} \right] \quad (13)$$

where $h_r = [\text{H}_2\text{O}]/N_T^0$ is the fractional concentration of water vapour. The three-body attachment rate k_a is a function of the reduced field E/p : a large amount of experimental data is available in the literature [17-20]. The computed values of τ_d are reported in figure 8 as a function of the reduced field E/p , for different values of h_r : it can be clearly seen from both figure 8 and eq. (13) the large influence of humidity on the declustering process, which is consistent with the results of figure 7.

To do better comparison between experimental and computed results the effective production rate n_-/τ_d has been calculated as a function of E/p from the experimental results of p_e in a very wide range of configurations. An analytical function has been optimized, to map the values of n_-/τ_d over the critical volume, able to fit the experimental values of p_e over the complete range of configurations and applied voltages (see Fig. 7). From the results the experimental values of τ_d can be derived (Fig. 8): the agreement is largely satisfactory. According to the theoretical lifetimes, by use of eqs. (4) and (5), the inception probability distributions have been computed for the cases of figure 4: the solid lines in the figure are the results of these calculations. It has been also demonstrated that the experimental pattern of the standard deviations σ_{ϵ_i} and σ_{ii} (Fig. 12), can be deduced in a simplified way from the outlined theory [2].

2. Streamer formation and propagation. — **2.1 EXPERIMENTAL RESULTS.** — The first corona (Fig. 9) consists of a number of narrow branched channels (streamers), which develop from a common root on the electrode surface (corona stem). It is associated to a current pulse with a short rise-time (10-50 ns)

and a longer almost exponential tail (200-500 ns), and to a sharp decrease of the electric field on the point electrode, due to the formation of a positive space charge. The streak photographs indicate that each branch is characterized by a luminous tip, which

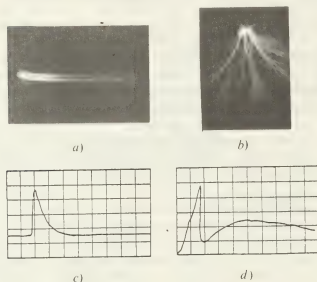


Fig. 9. — The first corona pulse; (a) and (b) streak and static photos; (c) current in the anode; (d) electric field on the anode surface.

propagates into the gap with a velocity in the range 10^8 - 10^9 cm/s. The corona size (extension, current, charge and light emission) depends essentially on the field distribution in the region where the development takes place (Fig. 10).

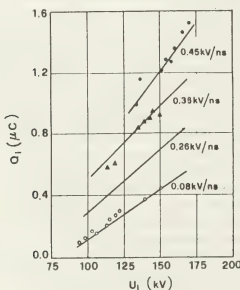


Fig. 10. — The first corona charge as a function of the inception voltage, for different rates of voltage rise. The solid lines are the theoretical calculations (see text) (1.5 m rod-plane gap; square cut end, 1 cm radius; 0.9/1 500 μ s wave).

The streamer characteristics in air at atmospheric pressure have been studied extensively in short gaps [21-28], because of the better reproducibility

of the discharge and the higher sensitivity of the measuring systems. With a detailed study of the experimental results, particularly of the displacement and conduction currents, Marode [21] has shown that the streamer is formed of two regions (Fig. 11): the streamer tip, or *active region*, where the luminous emission and the ionization processes take place, and the channel or *passive region*, where the electrons generated in the tip flow towards the point electrode and remains attached to the electronegative molecules.

2.2 THE PASSIVE REGION. — It has been shown by different experiments and theoretical simulations [22-24] that the current flowing in the passive region is essentially an electronic conduction current; after a compensation phase [22], which lasts in short gaps about 10 ns, the charge is rearranged along the channel so that a stable equilibrium is reached between the electrostatic potential distribution and the current field: the same conduction current flows in a resistive regime along all the streamer channel,

$$I = \pi a^2 \sigma E, \quad (14)$$

where a is the filament radius, σ its conductivity and E the local field; the field repartition follows the conductivity variations. The net positive charge, distributed along the channel to establish the capacitive distribution of the electrostatic potential, can be estimated according to the measurements of Suzuki [24] to correspond to an excess of 6×10^8 - 3×10^9 positive ions per cm. The electron charge per unit length is more than three order of magnitude larger (7.10^{11} - 6.10^{12} electrons/cm): the channel can be therefore assumed to be a quasi-neutral plasma filament in electrostatic equilibrium: according to the results of Marode *et al.* [25] the excess of positive ion charge is located at the external boundary of the plasma channel, and expands slowly due to ambipolar diffusion.

The radius has been estimated by Marode [21] in the range 10 to 30 μ m; the corresponding electron density can therefore vary from 5×10^{13} to 10^{15} cm^{-3} . However in long gaps the electron density can be much lower, because the attachment process reduces the number of free electrons in their flow towards the anode: obviously this will correspondingly raise the density of negative ions.

The three body and the dissociative attachment have been demonstrated to be the dominant electron collision processes in the passive region: in short gaps, Marode [22] has shown that the resistive current tail of the corona pulse (Fig. 11) varies with the partial pressure of the electronegative O_2 molecules, according to the change of the average attachment lifetime. Similarly, in long gaps the change of absolute humidity affects the almost exponential current decay of the first corona (Fig. 12): the solid lines in this figure represent the best fit exponential curves, with a decay time-constant theoretically fixed, according to the

three-body attachment rates of oxygen and water vapor molecules [17-20].

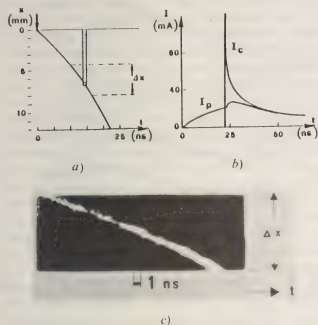


Fig. 11. — The development of positive streamers in short gaps : (a) schematic representation of the streamer advancement; (b) conduction current at the plane I_c and total current at the point I_p [22]; (c) high speed streak photo of the streamer head [25].

2.3 THE ACTIVE REGION. — When the streamer tip reaches the plane a sharp pulse of conduction current (Fig. 11) indicate the neutralization of a net concentrated positive charge. Hartmann [26-29] has done a detailed analysis of the spectra emitted by the streamer tip, and has derived the average values of the electronic, vibrational and rotational temperatures;

the average electron energy in the active region is in the range 10-15 eV, which corresponds to average fields of the order of 100-150 kV/cm [26]. Spectroscopic measurements of the light emitted by the first corona in long gaps [30, 31] have given values of the electron energies (in the range 5-7 eV) and of the average fields (45-75 kV/cm) : however the subsequent coronas developing from the leader tip present larger energies and electric fields (see 5.1). As the streamer tip propagates in external fields as low as a fraction of kV/cm, the field in the active region is essentially due to the positive space charge in the tip itself.

The rotational temperature, which can be assumed as a good estimate of the gas temperature, also under repetitive conditions [26] do not exceed 330 K : this indicate that corona streamers are *cold discharges*, i.e. they are governed essentially by gaseous electronic processes, but they do not produce significant thermal and gas-dynamic phenomena. This has been recently confirmed by Schlieren photographs [32], which do not show any appreciable change of the gas temperature and density. On the contrary the vibrational temperature is raised in the active region and in the streamer channel largely above 1 000 K : the vibrational energy is then relaxed in long times because of the long lifetimes of the vibrational states [29].

Recent measurements of the Stark broadening of H_α and H_β lines, emitted during the streamer progression in air with a small amount of hydrogen, have made possible a direct and independent estimate of both the electron density and temperature in the active region [33, 34]. The calculations account not only for the statistical effect of the ionic micro-field, but also for the effect of the applied and space charge field [33]. The average electron energy is in a good agreement with the previous spectroscopic estimates, and the density is of the order of 10^{15} cm^{-3} . From simultaneous current measurements the radius of the streamer head has been also evaluated, in the range 10 to 30 μm .

By studying the far ultraviolet radiation emitted from electron avalanches and from the streamer tip [35, 36] it has been shown that photoionization can be an efficient mechanism for the production of free electrons in the active region, particularly in air, where the N_2 molecules present a large number of excited states, whose optical transitions correspond to energies largely above the O_2 ionization threshold [37].

2.4 STREAMER STABLE PROPAGATION. — All the above reported experimental results support the original *streamer theory* proposed by Raether [38] and Loeb and Meek [39]. The streamer tip is assumed to be the front of a *space charge wave*, where positive ions and excited molecules are highly concentrated, as the result of previous ionization and excitation phenomena (Fig. 13). The decay of the excited states produces, by photoionization, a distribution of secondary electrons around the wave front. If the space

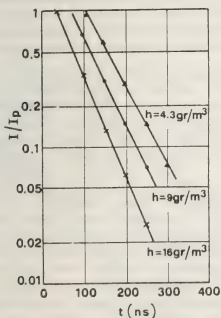


Fig. 12. — The influence of humidity on the current tail of the corona pulse; the solid lines are calculated according to the variations of the attachment coefficient (1.5 m hemisphere-plane gap, $R = 1 \text{ cm}$).

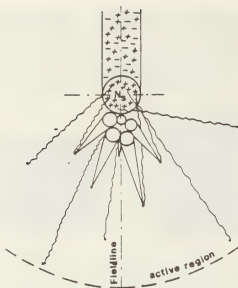


Fig. 13. — Schematic representation of the streamer active region.

charge field is high enough, these free electrons, drifting in the field direction, will produce new electrons by collisional ionization and will form electron avalanches. In air at atmospheric pressure, these avalanches can be produced only by the electrons present within an active region where the field is higher than 26 kV/cm, because only in this region the ionization probability is higher than the attachment probability. The drift of the avalanche electrons into the positive charge front causes its neutralization and the remaining avalanche ions lead to the advancement of the wave front into the gap.

As the electron multiplication in the wave front is determined by its own field, such *space charge waves*, are able to propagate in externally applied fields much lower than the minimum field required for ionization (26 kV/cm), in agreement with the experimental observations in long gaps. By studying this auto-sustained capability of propagation, Dawson and Winn [5] have shown that a spherical space charge containing 10^8 positive ions within a radius of 30 μm is able to propagate in a zero field: its advancement capability is then limited only by the energy which is lost in electron-neutral collisions in the avalanche formation and which has to be supplied at expenses of the space charge potential energy. The measurements of the life-time of positive streamers injected into zero field regions [5] are somewhat consistent with theoretical predictions, the discrepancy being probably due to an inaccurate estimation of the energy losses.

A large step forward was taken by Phelps [40-43], who designed an experiment to measure the minimum external field required to sustain an energetically stable streamer propagation. The more recent results indicate that such *stability field* E_{gs} depends on gas pressure and water vapor content (Fig. 14); the authors indicate that these results are a direct consequence of

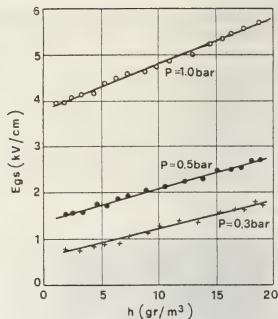


Fig. 14. — The measured variation of the stability field E_{gs} versus absolute humidity h , for three values of the pressure [42, 43].

energy and charge conservation for the streamer active region, if it is treated as an isolated space charge wave. It is interesting to note from figure 14 that the stability field varies roughly as the (5) power of air pressure, which differs considerably from what one would expect from Paschen's law or from the requirement for streamer formation in uniform gaps [44]. Furthermore, the humidity effect on E_{gs} (about 30-40% increase in going from dry to saturated conditions) is striking if compared with the relatively small variation of the net ionization coefficient with water vapor content [45]. Such an important effect has been also observed on the total corona charge, measured in long gaps under controlled humidity conditions: in figure 15 it can be seen that at the same inception voltage the corona charge can be reduced by a factor 3 if absolute humidity increases in the same proportion.

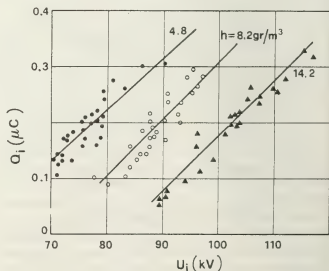


Fig. 15. — The first corona charge, as a function of the inception voltage, for different air humidities (1.5 m hemisphere-plane gap, $R = 1$ cm).

2.5 STREAMER PROPAGATION MODELS. — Two contrasting models of positive streamer characteristics have been advanced. Wright [46] and Klingbeil *et al.* [47] propose that the streamer channel is strongly conducting, with almost equal densities of positive ions and electrons, and with negligible attachment rate; the tip is maintained at nearly the anode potential and the electric field in the active region is very large due to the geometry involved, better than to the space charge at the front: the propagation is continuous, by the aid of photoionization and collisional multiplication, and the propagation characteristics are derived from self-similarity conditions. Dawson and Winn [5] and Gallimberti [23], on the other hand view the streamer as an isolated sphere of space charge that leaves behind a moderately conducting trail as it propagates. The propagation results, step by step, from avalanches that are triggered by photoionization and grow in the field produced by the pocket of space charge, with the channel playing little or no role. The above reported experimental results, and the predictions of the theoretical models, strongly support the latter interpretation.

In the step by step model, at a given instant t_n the streamer tip is represented as a spherical zone of radius R_s , containing N_s positive ions and N_e excited mole-

cules, which are the result of previous ionization and excitation phenomena. The decay of the excited states produces, by photoionization, a distribution of secondary electrons around the charged sphere. The density of secondary electrons $n_{es}(P)$ at a point P , a distance d from the tip centre, can be computed from the following relationship

$$n_{es}(P) = N_s \cdot \frac{pp_q}{p + p_a} \cdot \frac{\Psi}{d^2}, \quad (15)$$

where p and p_q are respectively the gas pressure and the quenching pressure [48] and Ψ is the ratio between the number of photoelectrons generated (per steradian, cm and Torr) and the number of ions formed in the avalanche [35, 36]; the latter is a function of the product pd .

The number of secondary electrons generated in the active region leads to the formation of a series of new avalanches. These avalanches build up a new zone containing N'_s positive ions and N'_e excited molecules in front of the streamer tip (Fig. 13). As the distribution of secondary electrons in the active region at time t_n is known (eq. (15)), the equations of continuity and Poisson can be used to follow the development of a series of avalanches until the time t_{n+1} at which they reach the streamer tip [4],

$$\left. \begin{aligned} \frac{\partial n_e}{\partial t} + v_e \cdot \nabla n_e - D \nabla^2 n_e &= (\alpha - \eta) n_e v_e \\ \frac{\partial n_-}{\partial t} &= \eta n_e v_e \\ \frac{\partial n_+}{\partial t} &= \alpha n_e v_e \\ \text{div } E &= \frac{(n_e + n_- - n_+) e}{\epsilon} \end{aligned} \right\} \text{ for } t_n \leq t \leq t_{n+1} \quad (16)$$

where ϵ is the dielectric constant of the gas, and n_e , n_- and n_+ are respectively the densities of electrons, negative and positive ions: α and η are the ionization and attachment coefficients, and D and v_e are the diffusion coefficient and the drift velocity for electrons: these parameters are nonlinear functions of the field strength E .

2.6 THE EQUIVALENT AVALANCHE MODEL. — In order to simplify the computation it is possible to represent the series of avalanches through a single *equivalent avalanche* (Fig. 16), under the condition that this equivalent avalanche produces the same space charge as the series of avalanches. The problem in such a simplified model is to determine the position of the starting point of the equivalent avalanche: it has been solved with an overall condition represented by an energy balance equation, according to the concept of energetic stability proposed by Dawson and Winn [5] and Phelps [41]. During the formation of

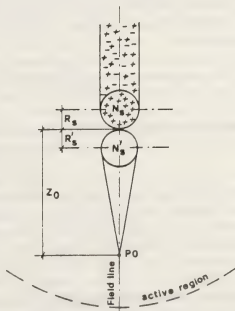


Fig. 16. — The equivalent avalanche.

the new series of avalanches, the drifting electrons lose energy in collisions with the gas molecules (ionization, excitation, attachment, scattering, etc.); this energy is supplied partly by the external circuit (through the forces of the applied field) and partly through the change in potential energy of the streamer tip (through the forces of the space-charge field). The following energy-balance equation must be satisfied,

$$W_g + \Delta W_{\text{pot}} = W_l \quad (17)$$

$$\left. \begin{aligned} W_g &= \int_{z_0}^{z_{a+1}} (e N_e E_g) dz \\ W_l &= \int_{z_0}^{z_{a+1}} \left[\alpha V_i + \eta V_a + \Sigma \delta_k V_k + \frac{f c_e}{\lambda l_e} \frac{m c_e^2}{2} + \alpha \frac{m c_e^2}{2} N_e \right] dz \\ W_{\text{pot}}(z_a) &= \frac{0.40(N_s e)^2}{4 \pi \epsilon R_s} + e N_e \int_0^{z_a} E_g dz \end{aligned} \right\} \quad (18)$$

where N_e is the integral of the electron density on a transversal plane, V_i and V_a are the ionization and resonant attachment potentials, δ_k is the excitation coefficient of the energy level V_k , c_e is the square root of the mean square velocity of electrons, and λ and f are respectively the mean free path and the fractional energy loss for elastic collisions between electrons and gas molecules. W_l takes into account the losses due to ionization, attachment, vibrational and electronic excitation (including dissociation which follows the excitation of unstable molecular states), scattering and the variations of kinetic energy along the avalanche path; W_{pot} takes into account the potential energy due both to the concentration of charges and to their position in the field.

The electric field at a point $P(z)$ in the active region is assumed to be the sum of the applied field E_g (which is practically constant over the avalanche path) plus that produced by the charge in the streamer tip (Fig. 16)

$$E(z) = E_g + \frac{e N_s}{4 \pi \epsilon (z - z_a)^2}; \quad (19)$$

the effect of the field distortion due to the charge

where ΔW_{pot} is the difference between the potential energies of the streamer tip and of the new sphere of positive ions built up by the new series of avalanches (i.e. the new streamer tip), W_g is the gain of energy due to the applied field, and W_l the total loss of energy during the formation of the new avalanches.

The terms of the energy balance have been computed according to the following relations

in the equivalent avalanche is taken into account by varying the ionization coefficient according to the number of carriers [48, 49]; with these assumptions, eqs. (16) to (18) can be integrated numerically, to obtain the number of new positive ions N'_s and the avalanche radius R'_s . It has been found [4] that, over a wide range of conditions ($N_s = 10^6$ - 10^{10} and $E_g = 0$ -500 kV/cm), the energy losses W_l are proportional to the charge N'_s produced in the avalanche, while the energy gain W_g is proportional to both the charge N'_s and the applied field E_g (Fig. 17),

$$\left. \begin{aligned} W_l &= \gamma N'_s \\ W_l &= \beta N'_s E_g \end{aligned} \right\} \quad (20)$$

where $\gamma = 7.85 \times 10^{-18}$ (49 eV) represents the average energy loss per ionizing collision and

$$\beta = 0.39 \times 10^{-24} \text{ C.m} \quad (0.243 \text{ eV cm}^{-1} \text{ kV})$$

the average energy gain in the avalanche per electron due to a unit applied field. Also the radius of the equivalent avalanche results function of N_s and E_g . By introducing eq. (20) in the energy balance condition, the latter can be written in the form

$$\frac{N'_s - N_s}{N_s} = \frac{\beta E_g - \gamma + \frac{0.40 N_s e^2}{4 \pi \epsilon_0} \frac{(R'_s - R_s)}{R_s^2} + E_g e (R'_s + R_s)}{\frac{0.40 e^2}{4 \pi \epsilon_0} \frac{2 N_s}{R_s} + e U + \gamma - \beta E_g} \quad (21)$$

which gives the variation of the charge in the streamer tip during a single step, if the initial condition N_s , R_s , E_g and the local applied potential U are known,

and the new tip radius R'_s is calculated as a function of N_s and E_g .

The elongation of the streamer channel at each step

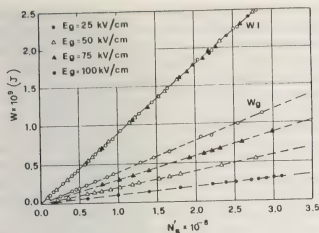


Fig. 17. — The energy gain W_g and losses W_l for an avalanche formation in the active region as a function of the number of carriers N_s , for different values of the geometric field E_g .

is computed as twice the radius R_s of the avalanche tip. The streamer propagation is followed step by step, by computing the characteristics of the successive equivalent avalanches. The propagation stops when the charge in the streamer tip has insufficient energy to produce new ion pairs; or, in other words, when it does not produce a field high enough to continue the phenomenon. This happens when the starting point of the equivalent avalanche goes outside the active region.

In this model it has been assumed that the passive region does not play any role in the streamer propagation. In order to compute the current in the external circuit, the passive region may be represented as a channel elongating behind the streamer tip, in which

the electrons are fed from the successive equivalent avalanches. Along this channel the voltage drop can be calculated from current continuity (eq. (14)); and one-dimensional continuity equations, similar to (16), may be used for electrons, positive and negative ions.

2.7 COMPUTED RESULTS. — The computed and measured curves of propagation along a field line against time are shown in figure 18, for a 150 cm gap with 125 kV corona inception voltage.

Figure 18 shows also the measured and computed current oscillograms: in both cases the time to the peak value is about 30 ns, while the time to half value is about 130 ns. The ratio between the measured and computed current values is around 150, which can be attributed both to the number of streamers developing in the experimental case and to their branched paths.

Figure 19 shows the comparison between the theoretical and the experimental values of the streamer

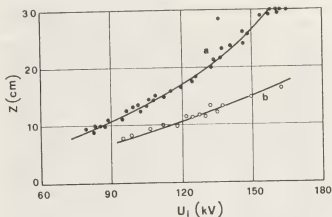


Fig. 19. — The streamer length as a function of the inception voltage for gap lengths of 30 cm (curve A) and 150 cm (curve B); the solid lines represent computed values, the points are experimental results (Square cut rod of 1 cm radius).

length as functions of the inception voltage for two gap lengths (30 and 150 cm). The variation of the streamer length is almost linear except when it becomes comparable with the gap length. It is interesting to note that the model correctly predicts this type of dependence when the influence of the earthed plane becomes important. Figure 10 shows the computed values of the corona charge (single streamer charge multiplied by the factor 150 derived from the current comparison) for different inception voltages and rates of voltage rise.

In figure 20 the number of ions in the streamer tip and the applied field distribution along the streamer path are shown as functions of the distance from the high-voltage electrode for the same conditions as figure 18. It can be seen that the charge in the streamer tip increases in the high field region, reaches a maximum in a position where the applied field is 6.8 kV cm^{-1} , and then drops again until the propagation stops. The maximum in this curve corresponds to the point where eq. (21) is reduced to zero,

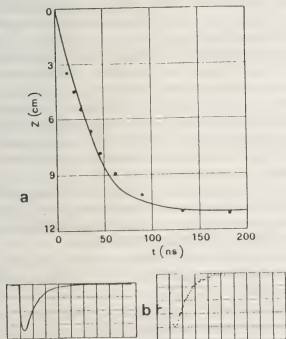


Fig. 18. — (a) The variation of the streamer length with time (the solid line represents the computed values, the points are experimental results); (b) Experimental and computed current oscillograms.

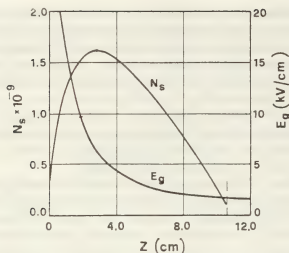


Fig. 20. — The variation of the number of positive ions in the tip N_s , and applied field distribution E_g , along the streamer path (same conditions as figure 18).

and defines the electric field for which the propagation would be energetically stable. In regions where the applied field is higher than this value the energy supplied to the new avalanches is larger than the losses in their formation, and therefore the charge in the streamer tip increases, while the opposite is true for lower field values. In the latter case the propagation occurs at the expense of the potential energy of the charge in the tip until a point where this energy is no longer sufficient for the production of new ion pairs.

With the above reported values of the parameters, and $R'_s = R_s$, the stability field results around 7 kV/cm, slightly higher than the values measured by Phelps and Griffiths (Fig. 14). The discrepancy can be due to the approximations of the model calculations, but it may also have a physical background. During the stable propagation the radius of the streamer tip can increase ($R'_s > R_s$), and part of the electrostatic potential energy of the tip charge may be available for the propagation, in addition to the energy gain due to the external field (see eq. (21)). Furthermore, the gas molecules in the active region may be preconditioned by the tip radiation or by the photoelectron drift in the outer region, where the field is too low for collisional ionization; in that case the average internal energy of the gas molecules is raised above the thermal value, and part of it can be released to the electrons in superelastic collision: this results in a further energy gain term in eq. (21) which reduces the stability field.

The latter possibility has been experimentally verified for repetitive discharges [29], where the vibrational metastable states are excited to a relatively high temperature and then relaxed on a very long time scale. The trail of preconditioned gas changes the energetic conditions of the streamer propagation, and this can explain the peculiarities of repetitive discharges (*guide effect* of previous discharges non-branching, and increase of luminous emission of the

streamer head along the whole path). In fact, the electron avalanches developing outside trail in a relatively low applied field cannot make the tip progression deviate because of the unfavourable energy balance; the metastable column extending from the tip to the plane represents a reserve of energy to be supplied to the electron avalanches, which cancels their statistical fluctuations. Furthermore, the lowering of the critical field enables the streamer tip to increase its charge (and hence the flux of photons) along the whole propagation path from the tip to the plane. Under impulse conditions in the absence of the metastable trail, the applied field becomes lower than 7 kV cm⁻¹ after the first few mm, and the charge in the streamer tip together with the luminous flux decreases during the rest of the propagation.

2.8 THE STREAMER BRANCHING. — Recently a model to simulate the branched structure of the streamers has been developed [50]: the series of avalanches is represented by two equivalent avalanches, developing towards the streamer tip along two directions symmetric with respect to the streamer axis and forming an angle ν with it. The charge repartition in the two avalanches is determined by the two starting distances; the probability of an avalanche starting at a distance d in the ν -direction is assumed to be proportional to the number of secondary electrons generated in an elementary volume at the distance d by photoionization (eq. (15)). The probabilities of the different avalanche pairs, satisfying the overall energy balance, are calculated, together with the branching probability. The streamer development is then built up step by step by a Monte Carlo method based on the following assumption:

- each branch follows the line of maximum field (the applied field plus the field due to the charge in the streamer tips);

- each branch is assumed to be energetically independent from the other ones: that means that in the energy balance equation the exchanges of potential energy between the different branches are ignored (in fact they are generally negligible, except for the first steps after a branching; in any case they don't affect the general characteristics of the propagation);

- the branching occurs on one plane of the sheaf containing the axis of the filament at the instant of the branching: the probability distribution for these planes is assumed to be isotropic;

- if the branching does not occur, the advancement of a filament is computed by a single equivalent avalanche.

The results of such a computation give a good agreement with the experimental results; as an example a two-dimensional computer picture of a corona filament is reported in figure 21.

It is interesting to compare the results of this model with those predicted by the single streamer

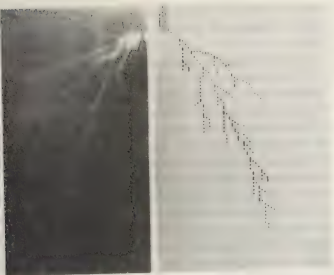


Fig. 21. — Comparison between the computed and experimental pattern of branched corona filaments (same conditions as figure 18).

model : by taking into account the branching, the total length of the filament is reduced only by about 10-15 %; this fact shows that the propagation of a streamer is not strongly affected by the repartition of the charge of its tip in different branches, but it is mainly determined by the distribution of the applied field. On the contrary, the current and the charge injected into the gap are increased by the branching process by a factor between 3 and 5.

2.9 PRESSURE AND HUMIDITY DEPENDENCE. — Let's now discuss the influence of gas pressure and humidity on the propagation characteristics and particularly on the stability field E_{gs} . If eqs. (16) to (21) are analyzed on the basis of the similitude principles it is possible to demonstrate that the electric field is scaled linearly with the gas pressure : in fact the transport parameters associated to the generation terms (ionization and attachment coefficients) vary proportionally to the pressure, while those associated to the particle motion (mobility and diffusion coefficient) are inversely proportional to the pressure; all of them are non linear function of the reduced field E/p only. As a consequence, if the time, space and charge scales are varied as the pressure inverse, similarity is maintained at constant E/p ; the velocity and energy scales are unchanged. These similarity relations are consistent with many experimental results on the streamer propagation velocity under variable pressure [51, 52].

On the contrary the large effect of humidity on corona charge (Fig. 15) do not seem to be satisfactorily explained. In the active region, the increase of humidity reduces the ultraviolet absorption length and the ionization efficiency [53]; the high electron affinity of water molecules leads to an increase of the attachment coefficient [54] : however due to the high field values in the active region the decrease of the net ionization rate is relatively small. In the passive region the increased attachment rate leads to a faster drop of

the current tail (Fig. 12). In any case, the overall effect cannot account for the variations of figure 15. The stability field E_{gs} can be calculated from eq. (21)

$$E_{gs} = \frac{\gamma}{\beta + e(R'_s + R_s)} \quad (22)$$

From eqs. (18) and (20) it appears that the loss term γ is pressure independent, while the parameter β is inversely proportional to the pressure; the same is true for the tip diffusion radii R'_s and R_s : the stability field should be therefore proportional to the gas pressure, in contradiction with the experimental evidence of figure 14. Furthermore, the only term of eq. (22) which can be significantly affected by humidity is the loss term γ : however the increase of dissociative attachment losses in going from dry to saturated conditions cannot be larger than 5-10 % of the total loss per electron. In conclusion, the equivalent avalanche model do not seem to be consistent with the measurements of Phelps and Griffiths [42, 43] on the propagation stability field.

Recently some interesting hypothesis have been suggested by these authors to explain the discrepancy and to clarify the streamer theory. If the streamer filament is assumed to play no role in the tip advancement, the field in the active region derives by the superposition of the geometric and space charge fields. However such assumption cannot hold in the filament just behind the tip; in fact in this zone the electric field should be reversed and the electrons could not be fed into the filament (Fig. 22a) : it can be therefore assumed that, due to the high electron mobility, a net positive charge appears along the filament behind the tip, which flattens the potential distribution (Fig. 22b). This charge distribution is replicated as the streamer propagates, implying a current density which decreases from A to B and an electric field in the trail interior whose value is appropriate to the electron current density and conductivity at each

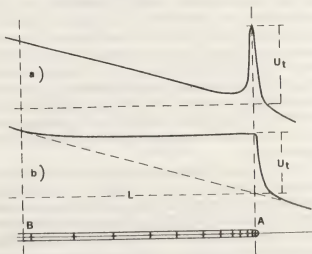


Fig. 22. — Schematic representation of the potential distribution in the active region and in the streamer trail just behind : (a) neutral trail ; (b) positively charged compensation zone.

point, it is equal to E_g at B , consistent with zero net charge density.

It is interesting to note that this distinction in the streamer channel of two regions (a space charge section with low variable field and displacement current, where charge and potential are rearranged, and a quasi-neutral plasma filament with almost constant field and conduction current under resistive regime) corresponds in a moving reference frame to the time sequence of compensation and resistive phases observed by Marode (Fig. 11).

According to the energy balance equations derived by Griffiths and Phelps [43] the stability field can be simply calculated as the ratio

$$E_{gs} = \frac{U_i}{L_c}, \quad (23)$$

of the potential drop U_i in the active region and the length L_c of the *compensation zone*. The latter should be related to the lifetime of free electrons against attachment: in fact three-body attachment is the dominant loss process in this zone and the attached electrons are not more able to move to rearranged the potential distribution. If L_c is expressed as a multiple f of the e -folding distance

$$L_c = f v_p \tau_a, \quad (24)$$

the stability field can be derived in the form,

$$E_{gs} = \frac{U_i}{f v_p} (k_1 [O_2] [N_2] + k_2 [O_2]^2 + k_3 [O_2] [H_2O]), \quad (25)$$

where v_p is the propagation velocity, $[O_2]$, $[N_2]$ and $[H_2O]$ the densities of the respective molecules, and k_1 , k_2 and k_3 the attachment reaction rates in three-body collisions of electrons with (O_2, N_2) (O_2, O_2) and (O_2, H_2O) couples of molecules. For the electron energies expected in the streamer *compensation zone*, k_3 is quite larger than k_2 and k_1 [19, 20]. This roughly explains the observed strong dependence of E_{gs} on humidity: furthermore eq. (25) suggests that such dependence should be linear (see Fig. 14). Also the large dependence of the corona charge upon humidity (Fig. 15) is qualitatively consistent with this model. According to the calculations of Griffiths and Phelps, the e -folding distance L_c is a fraction of cm, and the stability field varies as the power 1.65 of the air pressure, in a good agreement with the experimental observations.

In conclusion, the streamer head should be better represented as an isolated length of moderately conductive positive space charge, than as an isolated sphere of positive ions. The advancement mechanism is in any case associated to the electron avalanches developing from photoelectrons in the active region, and the energy balance of the streamer head reproduction governs the propagation characteristics. However, such an energy balance is not only determined by the

total net charge in the tip, but also by its repartition in the *compensation zone*.

3. Stem formation, dark period and leader inception.

— 3.1 EXPERIMENTAL RESULTS ON SECOND CORONA. — The development of the discharge after the first corona depends essentially on the electrode shape.

With electrodes of relatively large curvature radius, simultaneously with the development of the initial streamers, a luminous zone (stem) starts close to the electrode and elongates behind the streamer heads with a velocity about 10 times lower (Fig. 23). The first current peak corresponds to the start of branching in the original streamer, and the stem follows its track: the first corona streamers develop in a bunch close to the discharge axis, within a conical volume (sketched on the static photograph of figure 23). The drop in the electric field on the electrode surface indicates that a net positive charge is formed in the first corona region.

About 100-150 ns after the discharge initiation new streamers start, approximately half way of the stem path: they always propagate in the outer region (marked in figure 23), avoiding the space charge left by the first corona [1]. The current rises to a second maximum corresponding to the rapid growth of this second corona and the electric field presents a second drop; the velocity of the streamers of the first and second stage are of the same order. The subsequent leader channel develops always from the stem created by the second corona: as a consequence the time of

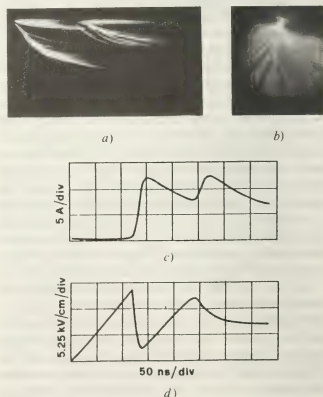


Fig. 23. — The first and second corona pulse for large curvature radii: (a) and (b) streak and static photos; (c) current in the anode; (d) electric field on the anode surface.

leader inception is assumed to coincide with the time of the second corona formation. The charge which is injected in the gap by the first corona has a double effect on the development of the second corona : first, it determines the physical processes for the stem formation, and hence the local conditions adequate for the second corona to start ; second, it produces a distortion of the electric field distribution, which is reduced near the electrode and in the space charge zone almost proportionally to the charge itself : because of this *field chocking* the second corona has to propagate in the outer region. Gallimberti and Rea [55] have put in evidence the field chocking effect of the space charge by measuring separately the first corona charge Q_1 and the total corona charge Q_t : the latter includes the first, second and eventually other subsequent corona pulses.

The regression curves (Fig. 24) have a negative slope, which shows quantitatively the space charge effect : the dashed line represents the curve for which

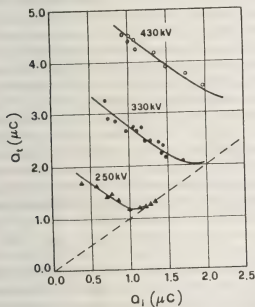


Fig. 24. — Total corona charge Q_t as a function of the first corona charge Q_1 , for different crest values of the applied voltage (1.5 m rod-plane gap; square cut rod of 1 cm radius; 0.9/1 500 μ s wave).

the subsequent corona charge is zero, when the discharge is choked by the first corona and no further development occurs. The field drop ΔE at the anode surface increases with the first corona charge, while the minimum value E_m , after the drop decreases (Fig. 25).

With electrodes of small curvature radius, the first corona streamers and the stem develop as described for large electrodes : however their extension and their current are much smaller (inspite of the higher inception fields), because of the rapid decrease of the field distribution along the gap. In this case the second corona do not appear immediately after or during the first one, but only after a relatively long dark

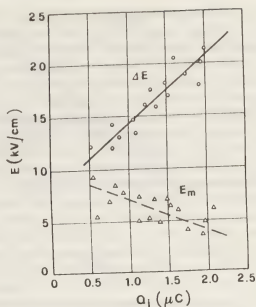


Fig. 25. — Electric field drop ΔE and minimum field E_m after the first corona, measured on the center of the rod, as functions of the first corona charge Q_1 (same conditions as figure 24).

period (10-30 μ s), during which no luminous or ionizing activity can be recorded (Fig. 26). The duration of the dark period t_d , and the corresponding growth of the applied voltage ΔU_d , increase with the

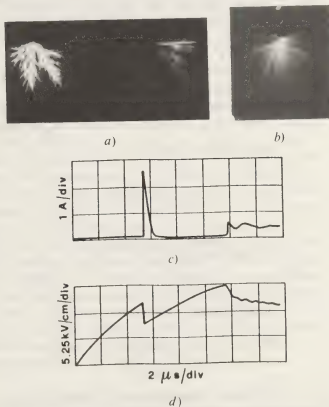


Fig. 26. — The first and second corona pulse for small curvature radii : (a) and (b) streak and static photos ; (c) current in the anode ; (d) electric field on the anode surface.

charge injected by the first corona (choking effect) and show a significant influence of the absolute humidity (Fig. 27).

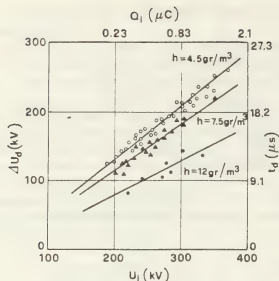


Fig. 27. — The duration of the dark period t_d and the voltage increase ΔU_0 as functions of inception voltage U_i or first corona charge Q_i , for different air humidities (10 m cone-plane gap, 500/10 000 μ s wave).

The second corona is normally followed by a continuous discharge development, corresponding to the inception and elongation of the leader channel. However, with very small curvature radii, and hence with very small corona currents, many corona may appear before the continuous leader inception.

The transition between the two leader inception processes (described respectively by Fig. 23 and 26) corresponds to the disappearance of the dark period and occurs for a critical value of the equivalent curvature radius of the high voltage electrode [56, 57] (Fig. 28). It is interesting to note that for radii smaller than the critical one the 50% breakdown voltage is constant, while the corona and leader inception

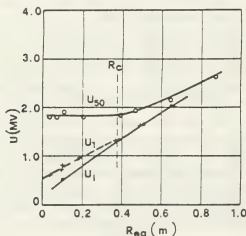


Fig. 28. — The voltages of corona inception (U_i), leader inception (U_l), and 50% breakdown (U_{50}) as functions of the equivalent curvature radius of the anode.

voltages are clearly distinct; for larger radii the 50% breakdown voltage increases with the radius itself, while leader and corona inception voltages coincide. The critical radius depends essentially on the electrode geometry and the gap length (Fig. 29).

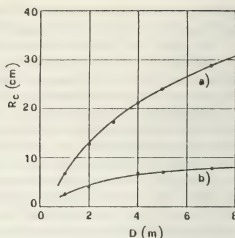


Fig. 29. — The critical radius as a function of the gap length, for anodes with spherical (a) or cylindrical (b) field distributions.

3.2 STEM FORMATION. — The physical processes which lead to the stem formation have been studied extensively in short gaps, where it has been called *secondary streamer* [21-28]. The luminous appearance and propagation velocity of the secondary streamers are very similar to those of the stem in long gaps [22, 24]: in figure 30 it can be seen that the extension of the secondary streamers depends essentially on the average current which flows to the h.v. electrode; their propagation curve presents a clear bend, when the resistive phase is established along the streamer filament (marked by the arrows) and the current flow is determined by electron attachment (see § 3). By means of a careful analysis of the relative intensities of the nitrogen bands emitted by secondary streamers, Marode [21] has derived the average electron energy ($\bar{\epsilon} = 1.4$ eV) and the reduced field

$$(E/n_e = 5.5 \times 10^{-16} \text{ V cm}^2),$$

which correspond to an ionization coefficient much lower than the attachment coefficient. Therefore, the luminosity of the secondary streamer is not related to a significant ionization rate; it is essentially due to electrons which are produced by the primary streamer, and then dragged to the anode by the field, causing mainly excitation of the molecules without any significant ionization.

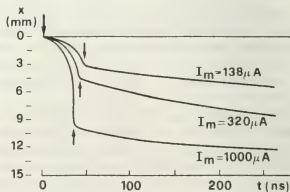


Fig. 30. — The propagation of secondary streamers for different values of the average current. The arrows indicate the end of the compensation phase [21].

Due to the characteristics of the primary streamer formation and to the high attachment rate along the filament, the electron density has to be much lower near the anode than along the rest of the streamer channel : this is confirmed by computer simulations [4, 22]. As a consequence, when the resistive phase is attained and the conduction current is uniform along all the filament, the electric field will be higher near the anode, where the conductivity is lower. The computer calculations of Marode [21, 22] indicate the formation of a field plateau, which corresponds to the extension of the secondary streamer.

When the streamers stop and the current falls down because of electron attachment, the secondary streamer development slows down and stops smoothly (Fig. 30). However, due to the non uniform field, repartition along the filament the Joule power input due to the corona current is much larger in the secondary streamer than in the rest of the channel : this can cause a temperature increase of the gas molecules, which may have a significant role in the subsequent evolution of the discharge [58-62]. Such a temperature increase has been put in evidence by Hartmann [26] through the analysis of the rotational structure of the N_2 Second Positive Bands emitted by secondary streamers. The gas and rotational temperature, which are close because of the very short relaxation time constant ($\sim 10^{-10}$ s), are in the range 1 000-1 200 K. Even larger may be the value of the vibrational temperature [28, 29].

In the case of the stem formation in long gaps, the temperature increase can be much higher than in short gaps, because of the larger corona size and current. Spectroscopic measurements of the whole corona [30], indicate the presence of spectral components which have not been observed in short gap, and which may confirm the establishment of an higher temperature in both the corona stem and the initial leader sections. Recent measurements of neutral density in the stem region with Schlieren photography [32] have shown that, particularly with negative applied voltages, the energy input and the temperature increase in the stem may be so intense and fast, to launch a spheric shock wave around the stem, similar to that of a punctual explosion.

3.3 CONDUCTIVITY TRANSITION. — From the above presented results it appears that the gas temperature in the stem and the leader channel increases largely above the ambient temperature, so that thermodynamic and hydrodynamic processes may play a determinant role in their formation and propagation. The main difficulty of the theoretical models of the stem and of the leader inception consists in the fast evolution of their internal conditions, which can not attain local thermodynamic equilibrium (LTE).

Gallimberti and Stassinopoulos [63] have shown that the start of the second corona is mainly related to the increase of the electric field in the stem region :

three different effects may play an important role in the determination of such a field : the applied voltage, the choking effect of the positive space charge and the time — dependent characteristics of the stem.

The first model for the streamer to leader transition has been proposed by Aleksandrov [64] : all the electrons flowing in the corona streamers converge in the stem, where they release their energy by elastic and inelastic collisions. If the assumption is made that the gas is heated to a sufficiently high temperature, the ionization degree in the stem may rapidly increase because of thermoionization ; by this process the first leader section is formed. The increase of conductivity enhances the electric field around the stem tip : a second corona can be therefore launched, and it may elongate the first leader section by the same mechanism. The basic idea of such a model is that a section of the leader channel is formed from the corona stem, when the conductivity of the latter is increased over a critical value. However, the reported spectroscopic measurements have shown that temperatures high enough for thermoionization are not reached in the stem : as a consequence, the mechanism which enhances the stem conductivity can not be the thermoionization of the gas molecules.

It has been shown in the previous chapter that the most part of the electrons produced in the active region are attached in the passive filament to form negative ions ; the concentration of the latter will be therefore of the same order as the density of positive ions. The stem conductivity may be expressed in the form,

$$\sigma = e(n_e \mu_e + n_- \mu_- + n_+ \mu_+) \quad (26)$$

where n_e , n_- and n_+ are the densities of electrons, negative and positive ions, and μ_e , μ_- and μ_+ their actual mobilities ; n_e should be much lower than n_- and n_+ , but the mobility μ_e is much larger than μ_- and μ_+ . As a consequence, the thermal detachment of the negative ions may lead to an important increase of the stem conductivity. Furthermore, if free electrons start to be released in the stem, they will flow to the positive electrode within a time shorter than 100 ns : the net positive charge in the stem is therefore rapidly increased. The enhancement of both the stem conductivity and the net positive charge, leads to a sharp increase of the electric field around the stem, which may cause the restart of new ionization phenomena, the inception of a second corona and the leader formation.

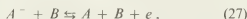
3.4 THERMAL DETACHMENT OF NEGATIVE IONS. —

The estimation of the frequency of thermal detachment as a function of the temperature is not easy : some experimental results are available in a limited temperature range for the primary ions O^- and O_2^- [65, 18]. However, the primary ions are converted into different secondary types (mainly $O_2^- | H_2O |_n$ and $O_3^- | H_2O |_n$) on a time scale which is shorter than a μs [11]. For such secondary ions some calculations of the equivalent

lifetime for declustering and detachment have been presented in § 1. The time scale of the streamer to leader transition may vary from about 100 ns to some 10 μ s : as a consequence, the nature of the ions and their detachment lifetime may change over a wide range.

In table II the lifetimes of the most probable species are reported, as functions of the ion temperature and the absolute humidity [11-14]. They represent the average times necessary for electrons and negative ions to reach their equilibrium concentrations at the ion temperature T_- . However, the effective thermalization times may be quite lower than the reported values for two reasons : first the values of table II have been calculated for a cascade declustering and detachment process, neglecting direct detachment of the cluster ions; second the fast depopulation of some species may accelerate the detachment of other species through crossed charge exchange reactions [13, 14]. In any case it can be seen that in the temperature range between 1 500 and 2 500 K all the thermalization times became shorter than the dark period duration (for radii larger than the critical one, the time scale for the second corona is so short that only the primary O^- and O_2^- ions have to be taken into account).

The equilibrium concentrations can be easily calculated for the detachment and three-body attachment reactions,



with the Saha equation for ionizational equilibrium [66],

$$\frac{n_e n_A}{n_A} = 2 \frac{g_A}{g_A} \left(\frac{2 \pi m_e k T_-}{h^2} \right)^{3/2} \exp \left[- \frac{\varepsilon_A}{k T_-} \right] \quad (28)$$

where n_e , n_A^- and n_A represent the concentration of electrons, negative ions and neutral molecules of type A , g_A and g_A the degeneracy of the ground states of molecule and ion respectively, ε_A the electron affinity of molecule A , m_e the electron mass, k and h the Boltzmann and Plank constants. The ratio n_e/n_A^- is reported in figure 31 as a function of the ion temperature : it can be seen that in the temperature range 1 500-2 500 K the detachment is practically complete for all the possible species.

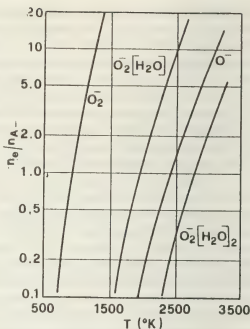


Fig. 31. — Thermal detachment degree of negative ions in air at atmospheric pressure as a function of the temperature (the ion temperature and the gas temperature are assumed in equilibrium).

The ion temperature may be assumed to be not much larger than the gas temperature. In fact, with a reduced field E/n_h and a gas temperature T_h the ion temperature is [67, 37],

$$T_- = T_h + \frac{1}{3} \frac{(m + m_i)}{k} \left(\mu_r n_0 \frac{E}{n_h} \right)^2, \quad (29)$$

where m and m_i are the molecule and ion mass respectively, μ_r the reduced mobility (under atmospheric standard conditions) n_h the gas number density and n_0 the Loschmidt number. By considering the two extreme cases of temperature increase in the stem (with constant volume or pressure), the reduced field may be estimated in the range 2×10^{-16} - 10^{-15} V cm² (see also the experimental values of § 3.2), for a gas temperature of the order of 2 000 K. This corresponds to an increase of T_- over the gas temperature in the range 15-350 K.

It is therefore possible to conclude that the negative ion detachment may be an efficient mechanism to increase the stem conductivity and to start the leader channel, if the gas temperature within the stem is

Table II. — Equivalent detachment lifetime τ_d (μ s) as a function of the ion temperature, for different absolute humidities.

T_- (K)	O^-	O_2^-	$O_2[H_2O]$		$O_2^-[H_2O]_3$	
			4 gr/m ³	8 gr/m ³	4 gr/m ³	8 gr/m ³
700	1.47	50	1.3×10^3	2.6×10^3	6×10^4	5×10^5
1 100	1.32×10^{-2}	0.70	25	50	70	6×10^2
1 500	2.1×10^{-3}	8.2×10^{-2}	3.6	7.2	6	50
1 900	4.4×10^{-4}	3.1×10^{-2}	2.9	5.8	4	30
2 300	1.96×10^{-4}	1.38×10^{-2}	2.0	4.0	2.5	20

raised above a critical value in the range 1 500–2 000 K : the lower values refer to primary ions (short time scales), the higher values to secondary ions (long time scales and high air humidity).

3.5 ENERGY INPUT. — All the electrons, which are not attached in the streamer filaments flow along the corona stem and release in collisions with gas molecules an instantaneous power $P = EI$, where I is the conduction current, which can be measured at the high voltage electrode [21, 62]. Due to the different kinds of elastic and inelastic collisions, this power is stored by the gas molecules in different forms : translational energy, rotational, vibrational and electronic excitation, dissociation and ionization energy. Only the translational and rotational component contribute to a direct increase of the gas temperature (the rotational excitation is relaxed in a few collisions). The repartition of the power input into the different forms depends essentially on the statistical electron energy distribution function and on the cross sections for the different collisions [68]. It can be calculated by solving the Boltzmann continuity equation in phase space : in the present case the numerical program developed at JILA Laboratory [37, 69, 70] has been used, which utilizes a spherical harmonics expansion arrested to the first term. The fractions of the total energy stored by the gas molecules in the different forms are reported in figure 32 as functions of the reduced field E/n_h . The most important processes for the present case ($E/n_h = 10^{-16}$ – 10^{-15} V cm²) are the vibrational and electronic excitation and the dissociation : ionization becomes important only at higher fields, while the translational and rotational fractions are negligible. However, at atmospheric pressure the electronic excitation is rapidly relaxed into translational energy by quenching collisions : the relaxation time constants are very short (10^{-10} – 10^{-6} s [71–73]) and the radiation losses are very small [26, 30, 31, 74]. As a consequence on the time scale of the corona to leader transition, the translational, rotational and electronic compo-

nents of the internal energy may be assumed to be in thermal equilibrium at the gas temperature T_g .

The dissociation power fraction may be considered a simple energy loss, if the dissociation heat is assumed to be constant with the temperature, and the thermal dissociation and recombination reactions are neglected (see next paragraph).

The vibrational excitation, on the contrary, is relaxed in relatively long times, which may be comparable with the time scale of interest. The most part of this energy is initially stored into the different vibrational levels of the N_2 ground state ($X^1\Sigma_g^{++}$) molecules, which have the largest density and cross-sections; it may then be directly relaxed into translational energy in collisions with any kind of pair particles; or transferred, with energy-exchange reactions into vibrational excitation of the ground state of different molecules. As the $CO_2(v_3)$ and $H_2O(v_2)$ vibrational states have about the same energy as the $N_2(v=1)$ level, the exchange reactions are resonant, and have a very large reaction rate. As a consequence, in spite of the small concentrations of H_2O and CO_2 in atmospheric air, a large amount of the initial energy input may be vibrationally transferred to these molecules; and the thermal relaxation may occur through different parallel channels. In figure 33 these different processes are schematically represented : the reaction rates have been reported by many authors as functions of the gas temperature [75, 76], the dashed arrows in figure 33 represent reactions with low rates, while the solid lines indicate the fast processes and represent therefore the principal channels of vibrational relaxation.

The complete relaxation process can be mathematically simulated with a complex system of rate equa-

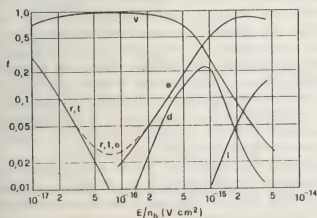


Fig. 32. — The repartition of the electron energy transferred to neutral molecules in the different forms of internal energy against the reduced field (t -translation, r -rotation, v -vibration, e -electronic excitation, d -dissociation, i -ionization).

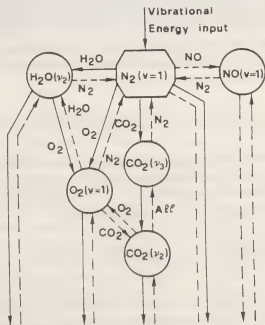


Fig. 33. — Schematic representation of the vibration-vibration and vibration-translation processes of energy transfer which can contribute to the thermal relaxation of vibrational excitation in air at atmospheric pressure.

tions : from its numerical solution an equivalent time-constant τ_{vf} has been derived (Fig. 34), which depends on both gas temperature and air humidity. In the temperature range of interest for the stem evolution, it may vary from 10^{-3} to 10^{-5} s : the vibrational energy should be therefore regarded as a reservoir, at a temperature T_v larger than the gas temperature T_h , which can be relaxed in the stem just after its formation and during the dark period.

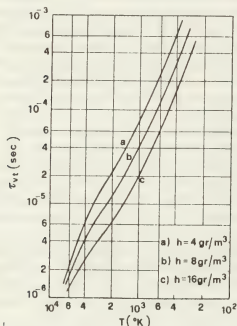


Fig. 34. — Equivalent time constant for vibrational relaxation in air at atmospheric pressure as a function of the temperature, for different values of absolute humidity.

3.6 LEADER INCEPTION MODEL. — Let's consider the stem as a cylindrical plasma channel of radius a , with uniform internal conditions : it contains $n_h \pi a^2$ molecules per unit length. The energy stored in the vibrational reservoir per unit length is [77] :

$$W_v(T_v) = n_h \pi a^2 \frac{\epsilon_v}{\exp(\epsilon_v/kT_v) - 1}, \quad (30)$$

where ϵ_v is the average vibrational excitation step : it may be assumed practically equal to the $N_2(v=1)$ energy level ($\epsilon_v = 0.28$ eV). The balance for this reservoir may be written in the form [62] :

$$\frac{dW_v(T_v)}{dt} = f_v EI - \frac{W_v(T_v) - W_v(T_h)}{\tau_{vt}}, \quad (31)$$

where the first term represents the fractional power input due to electronic collisions and the second one the power output due to relaxation in the translational form.

The energy contents of the thermal reservoir should account for translation, rotation and electronic exci-

tation, plus the expansion work. It can be therefore represented in terms of thermal enthalpy,

$$H_i(T_h) = \frac{7}{2} k n_h T_h \pi a^2, \quad (32)$$

where the electronic contribution to the internal energy is neglected, because of the relatively low temperature range (see next paragraph). The balance equation can be written in the form,

$$\frac{dH_i(T_h)}{dt} = (f_{ir} + f_e) EI + \frac{W_v(T_v) - W_v(T_h)}{\tau_{vt}}. \quad (33)$$

The equation system (30) to (33) can not be solved, if the momentum equation is not added, together with the gas state equation. However, if the conduction and radiation energy losses are small, it can be shown [78] that the mass within the plasma cylinder remains constant ($n_h \pi a^2 = \text{constant}$), whatever is the kind of expansion process (acoustic-wave under equilibrium or shock-wave with large internal overpressure). With this condition the thermal enthalpy in eq. (32) becomes only a function of the temperature T_h , and the system can be solved if the energy input is known. The initial reduced field E/n_h has been assumed according to the experimental values reported by Marode [21, 22], and the field value has been kept constant, in agreement with the constancy of the voltage distribution during the resistive phase [22, 23]. Eqs. (30) to (33) have been numerically solved for the current oscillograms of figures 23 and 26, with initial conditions $a = 0.1$ mm [32, 79] and $T = T_v = 300$ K. The results of the computation are reported in figure 35 for two different values of humidity.

It can be seen that in the case of electrodes with large curvature radius the critical temperature is reached between 100 and 150 ns independently on air humidity : the second corona can therefore start at that time, before the first one is fully developed, in good agreement with experimental results. On the contrary, in the case of electrodes with small curvature radius, the current and the power input stop before the critical temperature is reached ; however, during the dark period the energy of the vibrational reservoir is relaxed into thermal, at a rate which depends essentially on humidity. The duration of the dark period depends therefore on humidity. Since the applied impulse shape is known, the increase of voltage ΔU_d may be estimated (see the upper scale in figure 35). The computed values of both t_d and ΔU_d are in good agreement with the average experimental results reported in figure 27, for different humidities.

However the theoretical model would predict a decrease of the dark period with the increase of the first corona because of the higher rate of energy input. The discrepancy is due to the fact that the proposed model does not take into account any other effect different from the change of the internal conductivity of the stem : it neglects therefore the field increase due to the rise of the applied voltage and the chocking

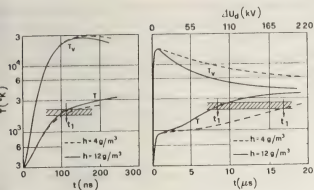


Fig. 35. — The computed temperatures T_s and T_v in the stem, for the conditions of figures 23 and 24 respectively. The dashed area represents the critical temperature range : the second corona inception time t_1 is indicated.

effect of the corona space charge. The local field around the stem comes from the combined action of all three effects : in figure 36 a schematic representation is given, where $U(t)$ represents the applied voltage, Q_- the electron charge which flows along the stem and $Q_+ = Q_-$ the net positive charge which is left in the gap. The choking effect is represented by the sharp drop of the field at the time of corona inception : the amplitude of this drop and the field E_m after the drop depend on the corona charge (Fig. 25). It is obvious that this effect is less marked on the radial field around the stem than on the longitudinal component at its tip : the second corona starts therefore preferentially in the radial direction. The field recover during the dark period is due partly to the voltage increase (dashed lines) and partly to the positive charge liberated in the stem by the detachment of negative ions (solid lines). If it is assumed that the second corona starts at an inception field E_i , it appears from figure 36 that the large recover due to a large Q_- may be masked by the larger choking effect of Q_+ (see Fig. 25), resulting in a longer dark period.

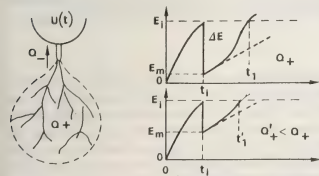


Fig. 36. — Schematic representation of the second corona inception for different charges of first corona.

The proposed model for the leader inception, indicates a physical interpretation for the critical radius ; in fact the model predicts that there is a mini-

mum corona charge (around 1 μC) necessary for the stem to be heated above the critical temperature and for the leader channel to be launched, immediately after the first corona pulse : it can be calculated by integration of eq. (33) if the vibrational relaxation is neglected, and depends slightly on the form of the current pulse. The critical radius is the minimum electrode size necessary to produce the critical corona charge.

In order to verify such an interpretation, the charge produced by a single streamer has been calculated with the theoretical model presented in § 3, for all the experimental configurations reported in figure 29 [57] : the computed charge is almost constant (in the range 20-40 nC) over the complete range of configurations, inspite of the variations of more than one order of magnitude of both gap length and critical radius.

4. Leader channel characteristics. — **4.1 EXPERIMENTAL RESULTS.** — The leader channel appears in the static photos and Image Converter frame records (Fig. 37) as a luminous thin channel, which connects the corona region to the h.v. electrode, and seems to expand in time. However, due to the low



Fig. 37. — Frame pictures of the leader channel in different stages of its development (10 m cone-plane gap, 500/10 000 μs wave).

intensity of the emitted light and to the resolution limits of the electro-optical systems, it is difficult to estimate the time-dependence of its luminous diameter. Some careful measurements, made with a photodensitometer on static photographs when breakdown does not occur [80], have shown a smooth luminous profile (Fig. 38), with average values of the final radius in the range 2-4 mm for 10 m gaps, depending essentially on the total charge flown through the leader section. For shorter gaps (1.5 m) and lower charges the luminous radius is quite smaller (0.5-1.0 mm) [81].

With time-resolved Schlieren measurements [79] the density variations in the leader region have been photographed (Fig. 39). The thermal radius of the channel in a 1.5 m gap increases from an initial value of about 0.2 mm, to 0.5-0.6 mm for a withstand and to

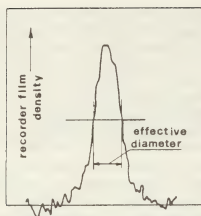


Fig. 38. — Light profile across a section of the leader channel, derived from photodensitometer measurements on static photographs when breakdown does not occur.

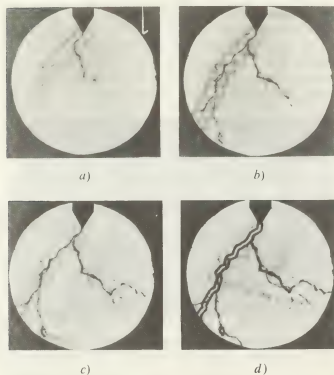


Fig. 39. — Time resolved Schlieren photographs of leader channel (1.5 m point-plane gap 30/2 500 μ s wave); (a) $t = 5.2 \mu$ s, (b) $t = 8.1 \mu$ s, (c) $t = 15.2 \mu$ s, (d) $t = 36.5 \mu$ s.

0.8-0.9 mm just before the main discharge for a breakdown. The observed rate of expansion of the column was subsonic in all cases: shock waves from leader channels are observed only after the return stroke and the formation of the main discharge. These measurements indicate a good correspondence between the luminous and the thermal diameter. Recent Schlieren photographs in longer gaps [32] have shown a similar behaviour and have given satisfactory measurements of the time-evolution of the thermal radius of the leader channel (Fig. 40).

During the discharge growth a net power is injected into the gap, which depends on the applied voltage

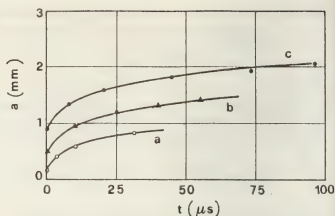


Fig. 40. — The variation of the leader thermal diameter versus time ((a) 1.5 m gap, (b) 2.5 m gap, (c) 10 m gap, extrapolated from [32, 80, 81]).

and the total current: its integral corresponds to the energy which is stored or dissipated in the gap (Fig. 41). It can be easily shown that the ionization and excitation losses in the corona region are small, compared to the total energy input, while the radiative power

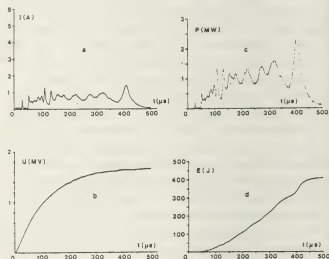


Fig. 41. — Voltage, current, power and energy input in the discharge gap (10 m cone-plane gap 500/10 000 μ s wave).

output is absolutely negligible [37, 79]. As a consequence the energy input may be stored essentially in two different forms: the electrostatic energy W_s of the positive charge distributed into the gap, and the increase of enthalpy ΔW_h of the heated parts of the discharge. Measurements of charge and field with capacitive probes and fluxometers, have given qualitative and quantitative indications on the space charge distribution during the discharge growth [82, 83]. From them W_s and ΔW_h have been separated (Fig. 42); the electrostatic component is an appreciable portion of the input energy at the shorter leader length, while the enthalpy increase becomes the most important when the leader grows more than a few

meters : from figure 42 the available energy input ΔW_h to a leader of 2 m axial length is approximately 25 J, whereas it is about 110 J at 4 m and about 210 J at 6 m. If it is assumed that this energy input balances the expansion work and the increase of internal energy

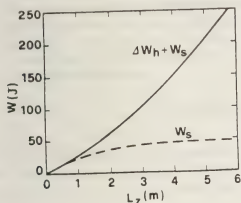


Fig. 42. — The electrostatic energy W_s and the enthalpy increase ΔW_h during the leader development as functions of its axial length L_z (10 m cone-plane gap, 500/10 000 μ s wave).

in the translational and rotational forms only (eq. (32)); the average temperature increase can be estimated around 2 200 K for a 2 m leader, around 5 500 K for 4 m and 7 000 K for 6 m (for the initial radius of figure 40). These are obviously upper-limits for the leader temperature, because of rough simplifications in the energy repartition : however they indicate that the overtemperature in the leader channel is in a range where thermal ionization and thermodynamic equilibrium can not be assumed [84].

From the same charge and field measurements, the average field along the leader channel has been estimated (Fig. 43) [82, 83]; it decreases with the leader length, which is consistent with the assumption that the local gradient is time-dependent with a decreasing characteristic : the older leader sections should have a lower gradient than the new ones. The results presented in figure 43 are also upper limits because they include any gradient between the leader

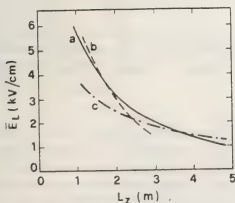


Fig. 43. — The leader average gradient \bar{E}_L as a function of the channel axial length L_z (cone-plane gap, 500/10 000 μ s wave : (a) 10 m [83], (b) 6 m, (c) 10 m [82]).

tip and the space charge boundary. For a 10 m gap, if the final value of the average leader gradient (about 1 kV/cm, see Fig. 43) are used, together with the final values of the leader radius in the case of withstand and the final peak currents (2.5 A), the average leader conductivity ($\sigma = 8.16 \times 10^{-3} \Omega^{-1} \text{ cm}^{-1}$) and the corresponding average electron density ($n_e = 2.5 \cdot 5.0 \times 10^{13} \text{ cm}^{-3}$) can be estimated.

Spectroscopic measurements of the leader emission are not very accurate, because of the low light intensity : however, the general behaviour of the spectrum indicate that the gas is essentially non dissociated : the nitrogen spectral components are all molecular, while small traces of OH, NO and O_3 systems indicate that the molecules with low dissociation energy (O_2 and H_2O) are partially dissociated. This is consistent with the low temperature range above reported. The most important band systems are located in the red region and correspond to excitation energies much lower than those observed for the corona streamers [31]. The intensity ratio of the nitrogen molecular systems allows the estimation of the average electron energy in the leader channel : it is in the range between 1 and 2.5 eV, depending essentially on the assumptions made on the form of the electron energy distribution. The corresponding values of the reduced field E/n_h will lie in the range $2.7.5 \times 10^{-16} \text{ V cm}^2$. These results are very similar to those reported in § 3 for the stem.

Current and light measurements with interference filters [74] have shown that inspite of the large fluctuations in all the records, the ratio of light to current is practically constant for any of the filters used and during all the leader development. This indicates that the excitation occurs essentially by electronic collisions, under a reduced field E/n_h which remains almost constant in time. As the leader gradient E presents a decreasing characteristic with time, the constancy of the ratio E/n_h should depend on the leader expansion, which causes a decrease of the gas number density. When strong reilluminations of the channel occur, the ratio of light to current increases, although this increase is usually not large ; since the variation of light emission with E/n_h is expected to be rapid, the increase of E/n_h during reilluminations will be small.

4.2 THE CONSERVATION EQUATIONS. — From the above presented results, the leader appears as a weakly ionized plasma channel, where the current flow and the corresponding energy input cause significant thermo-hydrodynamic processes. The mechanism of energy transfer from electrons to heavy particles and the subsequent relaxation into thermal energy should be similar to that described in the preceding chapter for the stem formation. However, the longer time-scale and the larger temperature range make the theoretical analysis more complex. In the present section a non LTE model will be presented, with simplifying assumptions which are

adequate to the internal conditions experimentally observed for the leader up to the final jump : this model will then be generalized in the next sections to represent the final stages and the leader to spark transition.

According to the discussion of the § 3, a leader section is formed when the detachment rate of negative

ions overcomes the electron attachment rate, leading to a large increase of conductivity ; as a consequence the leader plasma channel may be assumed to be composed by three kind of particles : electrons, positive ions and heavy particles. For each species the mass, momentum and energy conservation equations may be written,

$$\left. \begin{aligned} \frac{\partial n_s}{\partial t} + \nabla \cdot (n_s \bar{v}_s) &= \dot{n}_s \\ \frac{\partial}{\partial t} (m_s n_s \bar{v}_s) + \nabla \cdot (m_s n_s \bar{v}_s \bar{v}_s) + \nabla \cdot p_s &= e_s n_s \bar{E} - \sum_i \frac{m_s m_i}{m_s + m_i} n_s v_{si} (\bar{v}_s - \bar{v}_i) \\ \frac{\partial}{\partial t} \left[n_s \left(\frac{3}{2} k T_s + \varepsilon_s \right) \right] + \nabla \cdot \left[n_s \bar{v}_s \left(\frac{3}{2} k T_s + \varepsilon_s \right) \right] &+ p_s \nabla \cdot \bar{v}_s + \nabla \cdot \bar{q}_s = \bar{J}_s \cdot \bar{E} - \sum_i n_s v_{si}^* k (T_s - T_i) \end{aligned} \right\} \quad (34)$$

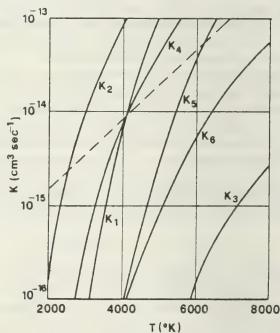
where n_s is the volume density of particles of the s -th kind, \bar{v}_s their velocity, \dot{n}_s their total generation and destruction rate by any kind of collisional processes, p_s and T_s their partial pressure and temperature ($p_s = k n_s T_s$), m_s and e_s the particle mass and charge, ε_s the average internal energy above the thermal value, \bar{J}_s and \bar{q}_s the conduction current and heat flow due the s -th species, v_{si} and v_{si}^* the effective collision frequencies for momentum transfer and energy exchange with the i -th particle species [68, 69]. The sum terms in the second and third equation represent the average momentum and energy exchanges in collisions between the particles of the s -th kind with all the other particles of the plasma. To complete system (34), the field and current density equations have to be added

$$\begin{aligned} \nabla \cdot \bar{E} &= - \frac{\sum_s e_s n_s}{\varepsilon_0} \\ \bar{J} &= \sum_s \bar{J}_s = \sum_s e_s n_s \bar{v}_s. \end{aligned} \quad (34 \text{ bis})$$

In the present case the leader channel may be assumed as a cylindrical plasma column with almost uniform longitudinal characteristics : the differential operator ∇ is then reduced only to the radial derivative.

4.3 THE OXYGEN DISSOCIATION. — When the energy conservation equation is applied to the gas molecules, the internal energy ε_s may be assumed to be a state function (i.e. to be univocally determined by the neutral temperature), only under the condition that the populations of all the possible internal energy levels are in thermodynamic equilibrium with the translational component. As it has been shown in the previous paragraph, this is not the case for the time scales of stem and leader channel in long sparks : the rotational and electronic excitation may be assumed to be in equilibrium with the gas temperature, but the vibrational reservoir has a much higher temperature, and its energy is relaxed into thermal form at a

variable rate during the discharge development. Furthermore the dissociation and recombination reactions, which have been considered in the previous section only as a component of the electron energy losses, have to be taken into account on a longer time scale and a wider temperature range. In figure 44 the reaction rates of the principal thermal dissociation reaction are reported [85, 86] ; the dashed line represents the reaction rate for dissociation corresponding to a time-constant of 100 μ s. From this



- 1) $O_2 + M \rightarrow 2O + M$
- 2) $H_2O + M \rightarrow H_2 + \frac{1}{2} O_2 + M$
- 3) $N_2 + M \rightarrow 2N + M$
- 4) $N_2 + O \rightarrow NO + N$
- 5) $NO + M \rightarrow N + O + M$
- 6) $N_2 + O_2 \rightarrow 2NO$

Fig. 44. — The rates of the principal dissociation reactions occurring in atmospheric air, as functions of the gas temperature.

Figure it appears that many dissociation reactions can be neglected, because their time-constants are much longer than the discharge time-scale; others can be neglected because the initial concentrations of the reacting molecules are small and the contribution to the energy balance is negligible. Essentially, only the O_2 dissociation and recombination can give a significant contribution to the energy exchanges in the leader channel: from the rate constants k_1 and k_{-1} [85, 86] an equivalent time constant for oxygen dissociation can be calculated.

$$\tau_{O_2} = \left[n_h \left(k_1 - k_{-1} \frac{4d^2}{1-d} n_{O_2}^0 \right) \right]^{-1}, \quad (35)$$

where n_h is the density of neutral molecules, $n_{O_2}^0$ the density of O_2 before the beginning of dissociation (in air $n_{O_2}^0 = 0.21 n_h$) and d the dissociation degree

$$d = \frac{n_{O_2}^0 - n_{O_2}}{n_{O_2}^0}. \quad (36)$$

The values of τ_{O_2} are reported in figure 45; for temperatures larger than 4 000 K the thermal dissociation of the O_2 molecules adds to the direct disso-

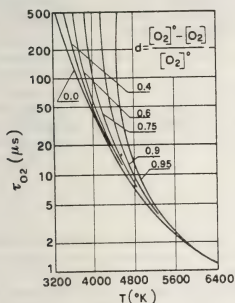


Fig. 45. — The equivalent time constant for oxygen dissociation, in atmospheric air, as a function of the gas temperature and the dissociation degree.

ciation by electron collisions; and, in the complete energy flow (Fig. 46), a third reservoir (of chemical energy) has to be considered: it has a direct input from electrons, and exchanges energy with the thermal reservoir in recombination and dissociation reactions. The energy conservation of the neutral molecules splits therefore in three equations, each one representing the balance of a single reservoir.

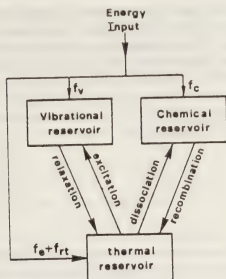


Fig. 46. — Schematic flow-chart of the energy exchanges between the different forms of internal energy, under the conditions appropriate for the leader channel.

4.4 THE HOMOGENEOUS CORE MODEL. — To simplify the system of eq. (34), according to the conclusions of Braginskii [78], the leader channel may be assumed to have a homogeneous cylindrical core of radius a , surrounded by a thin, dense shell. The pressures, temperatures and particle densities are assumed constant over the cross section of the core, the variations of these parameters to the values of the surrounding indisturbed gas being concentrated in the shell. The radial derivatives disappear from eqs. (34) inside the core, and they can be integrated from the center to the radius a . For a unit length section of such a channel the mass conservation equations become,

$$\left. \begin{aligned} \frac{dN_e}{dt} &= \frac{dN_+}{dt} = \dot{N}_e \\ \frac{dN_h}{dt} &= -\dot{N}_e + \dot{N}_d, \end{aligned} \right\} \quad (37)$$

where N_e , N_+ and N_h represent the number of electrons, positive ions and neutral molecules per unit length, \dot{N}_d and \dot{N}_e the net rates of dissociation and ionization respectively; it has been implicitly assumed that the dissociation of one molecule produces two fragments, leading to a proportional increase of the number density.

The three momentum equations can be added together, so that the collision terms vanish. Under the assumption of plasma neutrality within the core ($E_r = 0$), and identical average expansion velocity for all the particles $\langle \dot{a} \rangle$ the resultant equation becomes [87],

$$\frac{d}{dt} [(N_e m_e + N_+ m_+ + N_h m_h) \langle a \rangle] = 2 \pi a [\langle p_e \rangle - \langle p_s \rangle], \quad (38)$$

where $\langle p_e \rangle$ and $\langle p_s \rangle$ represent the average values of the pressure in the core and shell respectively.

If the ionic component of the total current I is neglected [62], the electron and ion energy conservation equations become,

$$\left. \begin{aligned} \frac{d}{dt} \left[N_e \left(\frac{3}{2} k T_e + \varepsilon_e \right) \right] + p_e \frac{d}{dt} (\pi a^2) &= EI - \dot{C}_{eh} - \dot{C}_{e+} \\ \frac{d}{dt} \left[N_+ \left(\frac{5}{2} k T_+ \right) \right] + p_+ \frac{d}{dt} (\pi a^2) &= \dot{C}_{e+} - \dot{C}_{+h} \end{aligned} \right\} \quad (39)$$

In these equations, ε_e is assumed equal to the average ionization energy of the gas molecules [66], and the vibrational and electronic components of the ion internal energy have been neglected. The second terms represent the contributions of electrons and ions to the expansion work, which are generally small at low ionization degree. The collision terms may be written in the form,

$$\left. \begin{aligned} \dot{C}_{eh} &= N_e v_{eh}^* k (T_e - T_h) \\ \dot{C}_{e+} &= N_e 3 \frac{m_e}{m_h} v_{e+} k (T_e - T_+) \\ \dot{C}_{+h} &= N_+ \frac{m_+ \cdot m_h}{(m_h + m_+)^2} v_{+h} k (T_+ - T_h) \end{aligned} \right\} \quad (40)$$

where v_{eh}^* is the effective electron-neutral energy exchange collision frequency, reported for air by Hake and Phelps [69] as a function of T_e ; v_{e+} is the effective momentum transfer collision frequency for Coulomb collisions, given by the Spitzer equation [88],

$$v_{e+} = n_+ \frac{4 \sqrt{2} \pi}{3} \left(\frac{m_e}{k T_e} \right)^{3/2} \left(\frac{e^2}{4 \pi \epsilon_0 m_e} \right)^2 \ln A, \quad (41)$$

where A is the ratio between the Debye length and the impact parameter for a 90° scattering; v_{+h} is the momentum exchange collision frequency for ion-neutral collisions, which can be simply derived from ion mobility measurements [67, 37],

$$v_{+h} = \frac{e(m_h + m_+)}{\mu_+ m_h m_+}. \quad (42)$$

In order to write the energy balance equations for the three reservoirs corresponding to the neutral molecules (Fig. 46), it has to be taken into account that the total energy transferred directly from the electrons to the molecules \dot{C}_{eh} divides in the different fractions reported in figure 30. According to these values and to eqs. (30) and (31), the balance equations can be written in the form,

$$\left. \begin{aligned} \frac{d}{dt} [N_h c_v^* T_h] + p_h \frac{d}{dt} (\pi a^2) &= (J_n + f_e) \dot{C}_{eh} + \dot{C}_{+h} + \frac{W_e(T_e) - W_e(T_h)}{\tau_{er}} - \frac{N_{O_2} D_T^0}{\tau_{O_2}} \\ \frac{d}{dt} [W_e(T_e)] &= f_e \dot{C}_{eh} - \frac{W_e(T_e) - W_e(T_h)}{\tau_{er}} \\ \frac{d}{dt} [N_{O_2} D_T] &= -f_d \dot{C}_{eh} - \frac{N_{O_2} D_T^0}{\tau_{O_2}}, \end{aligned} \right\} \quad (43)$$

where c_v^* is a partial specific heat at constant volume including only the translational, rotational and electronic components of the internal energy (Fig. 47), N_{O_2} is the total number of O_2 molecules (the opposite of its derivative corresponds to N_d in eqs. (37)) and D_T^0 is the dissociation energy at the temperature T_h (Fig. 47) it includes the formation heat and the difference of enthalpy between a couple of oxygen atoms and one molecule. In figure 47, the total specific heat c_v (at thermodynamic equilibrium and including hence also the vibrational and chemical components) is reported for comparison: it is clear that there is a large difference between c_v^* and c_v .

To complete the equation system the state and the pressure equations have to be added [87], together with the electric field equation (Poisson's equation),

$$\left. \begin{aligned} \pi a^2 p_s &= N_s k T_s \\ \pi a^2 \langle p_e \rangle &= N_e k T_e + N_+ k T_+ + N_h k T_h \\ \langle p_s \rangle &= \left[1 + \frac{2\gamma}{\gamma+1} (M^2 - 1) \right] p_0 \\ M &= \frac{\gamma+1}{4} \frac{\langle \dot{a} \rangle}{C_0} \left[1 + \sqrt{\left(\frac{4}{\gamma+1} \frac{C_0}{\langle \dot{a} \rangle} \right)^2 + 1} \right]. \end{aligned} \right\} \quad (44)$$

The last two equations represent the classical Rankine-Hugoniot formulae for shock wave [87, 89], where M represents the Mach-Number of the shock front launched by the core piston expanding with a velocity $\langle \dot{a} \rangle$; p_0 and C_0 are the pressure and the sound speed in the undisturbed gas, and γ the ratio of

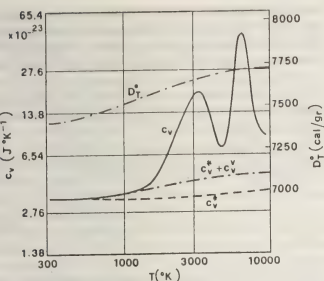


Fig. 47. — The partial specific heat at constant volume c_v^* (for translation, rotation and electronic excitation), the total specific heat c_v , and the contribution of the vibrational component c_v^v , as functions of the air temperature. D_T^0 is the dissociation heat of oxygen molecules.

the specific heats; for small values of $\langle \dot{a} \rangle$ (weak waves) M is about 1 and the shell overpressure is practically 0. This corresponds to an expansion under pressure equilibrium ($\langle p_e \rangle = \langle p_s \rangle = p_0$), where no shock waves are generated: from the above presented experimental results this seems to be the case of the leader channel, at least up to be final jump.

If it is assumed that the leader channel behaves as a resistive conductor, its conductivity (eq. (26)) may be calculated neglecting the ionic component, and the Poisson's equation may be replaced by the simple ohmic relation,

$$E = \frac{I}{e\mu_e N_e}, \quad (45)$$

where the current I has to be assumed as an external input variable, being determined by the ionizing activity in the leader corona region; the mobility μ_e , at high ionization degrees should account also for electron-ion collisions [66, 88],

$$\mu_e = \frac{e}{m_e(v_{eh} + v_{e+})}, \quad (46)$$

where v_{eh} is the effective collision frequency for momentum transfer between electrons and neutral molecules [69].

4.5 THE ELECTRON PRODUCTION RATE. — The set of eqs. (37) to (46) is complete and ready for a numerical solution for any set of initial conditions, if the net rate of electron production is defined. If the gas temperature in the leader is assumed to be relatively

low with respect to the electron temperature (see the above reported experimental results), the ionization occurs essentially by electron-neutral collisions, while the recombination occurs by three-body capture in electron-ion collisions [66].

If multistep or Penning ionization are neglected, the ionization frequency ν_i and the rate of electron production $N_e \nu_i$ can be calculated [66]:

$$\nu_i = n_h k_h^+ = n_h \int_{\epsilon_e}^{\infty} f(\epsilon) Q_h^+ \frac{8\pi}{m_e^2} \epsilon d\epsilon, \quad (47)$$

where k_h^+ and Q_h^+ are the ionization reaction rate and cross-section, ϵ_e the ionization energy and $f(\epsilon)$ the electron energy distribution function. The reduced ionization frequency ν_i/n_h has been experimentally determined as a function of T_e at low gas temperature [18, 90]: the electron energy distribution function depends strongly from the electron temperature T_e but only slightly on the gas temperature T_h , if it is rather smaller than T_e . As a consequence the experimental values of ν_i/n_h can be used over a relatively large range of T_h , and they are assumed to be appropriate for the present calculations (see the discussion in § 7).

The rate of electron destruction by recombination can be calculated

$$\pi a^2 n_e n_+ a_e = \frac{N_e N_+}{\pi a^2} a_e, \quad (48)$$

where a_e is the total electron-ion recombination coefficient [66]: the latter depends on the electron temperature T_e , but essentially on the nature of the positive ions. The primary ions, produced directly by ionization (N_2^+ and O_2^+) are rapidly converted into different secondary species by charge-transfer reactions [37]. The most important of these are listed in table 3 together with the corresponding reaction rates [12-14]. By solving the system of rate equations

Table III. — Principal positive charge-exchange reactions occurring in atmospheric air.

Reaction	Reaction rate (cm ³ /s)
$N_2^+ + O_2 \rightarrow O_2^+ + N_2$	$5 \times 10^{-11} - 5 \times 10^{-10}$
$N_2^+ + NO \rightarrow NO^+ + N_2$	4×10^{-10}
$N_2^+ + H_2O \rightarrow H_2O^+ + N_2$	2.2×10^{-9}
$H_2O^+ + H_2O \rightarrow H_3O^+ + OH$	1.7×10^{-9}
$N_2^+ + CO_2 \rightarrow CO_2^+ + N_2$	9×10^{-10}
$N_2^+ + O \rightarrow NO^+ + N$	1.4×10^{-10}
$CO_2^+ + O \rightarrow O_2^+ + CO$	2.6×10^{-10}
$CO_2^+ + O_2 \rightarrow O_2^+ + CO_2$	5×10^{-11}
$CO_2^+ + NO \rightarrow NO^+ + CO_2$	1.2×10^{-10}
$O_2^+ + NO \rightarrow NO^+ + O_2$	7×10^{-10}
$O^+ + H_2O \rightarrow H_3O^+ + O$	2.3×10^{-9}
$O^+ + CO_2 \rightarrow O_2^+ + CO$	1.1×10^{-9}
$O^+ + N_2 \rightarrow NO^+ + N$	1.2×10^{-12}

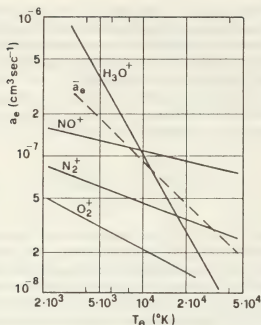


Fig. 48. — The electron-ion recombination coefficient for the principal positive ions present in the leader channel as a function of the electron temperature. The dashed line (\bar{a}_e) represents an average value, weighted on the relative concentrations.

associated to the reactions of table III, the principal species for the leader channel time-scale have been shown to be the primary ions plus NO^+ and H_3O^+ ; from their relative concentrations and from the recombination coefficients of the single species [91, 92], an average value of a_e , to be used for the present calculations, has been derived (Fig. 48) (for further discussion, see § 7).

The net electron generation rate \dot{N}_e in eq. (37) can be therefore expressed in the form :

$$\dot{N}_e = N_e v_i - N_e \frac{N_+}{\pi a^2} a_e. \quad (49)$$

4.6 COMPUTED AND EXPERIMENTAL RESULTS. —

The set of differential eq. (37) to (43) has been integrated by a conventional Runge-Kutta method. The calculated results are reported in figures 49 to 52, for an experimental current oscillogram (Fig. 49), recorded during the leader development in a 10 m cone-plane gap [93]. The initial conditions are the following :

$$\left\{ \begin{array}{l} n_e = n_+ = 2.63 \times 10^{13} \text{ cm}^{-3}; \quad n_h = 7.86 \times 10^{18} \text{ cm}^{-3} \\ T_e = 19.600 \text{ K}; \quad T_+ = 1 \text{ 150 K}; \quad T_h = T_v = 1 \text{ 000 K} \\ d = 0; \quad a = 0.1 \text{ cm}; \quad 4 = h \text{ gr/m}^3; \end{array} \right.$$

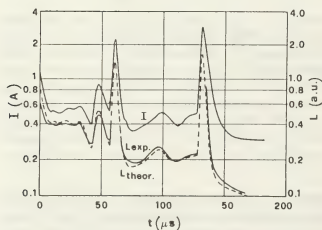


Fig. 49. — Experimental current oscillogram I (10 m cone-plane gap, 500/10 000 μs wave), and experimental and computed light emission from a section of leader channel.

the choice of these values, which at the moment may appear arbitrary, will be discussed in the next pages.

From figure 50 it can be seen that in the first 10-15 μs the vibrational temperature increases much more rapidly than the gas temperature, according to the large fraction of the energy input which feeds the vibrational reservoir; however, as the gas temperature increases the vibrational relaxation time constant

decreases rapidly : as a consequence the energy stored in the vibrational reservoir flows to the thermal one (the rate of rise of the gas temperature increases, due to the faster relaxation) and on longer times tends towards thermal equilibrium. The rate of rise of the temperature then slows down because of the decrease of the electric field and hence of the power input. When the current presents large peaks the vibrational temperature increases slightly, and the gas temperature

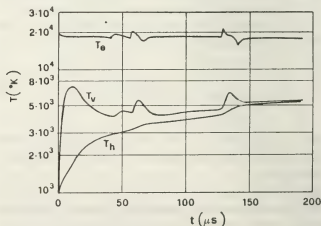


Fig. 50. — The computed variations of gas temperature T_g , vibrational temperature T_v and electron temperature T_e , for the experimental current input of figure 49.

shows only a variation of its rate of rise. The range of the gas temperature variation is in agreement with the experimental estimates. The ion temperature T_+ remains always about 100 K above the gas temperature.

In spite of the field decrease, the reduced field E/n_h and the electron temperature T_e remain about constant, having only small fluctuations in correspondence to the sharp current and power peaks. This confirms the experimental observations of the light to current ratio, which have been previously discussed. The calculated values of both E/n_h and T_e lie in the range of the experimental estimates.

The gas number density decreases with about the same pattern as the electric field, according to the constancy of E/n_h . The oxygen dissociation degree increases slightly, but it remains in any case limited (less than 20% after 200 μ s) : the most important contribution to dissociation is given by electron-neutral collisions. The electron density decreases, due to the channel expansion, but presents large peaks in correspondence with the current sharp pulses : the computed values are around 10^{13} cm^{-3} , in a quite good agreement with the experimental values. Also the field pattern of figure 51 correspond very well to the experimental measurements of figure 43.

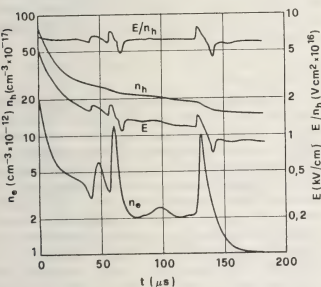


Fig. 51. — The computed variations of the gas and electron densities (n_e and n_h respectively), and of the actual and reduced electric fields (E and E/n_h respectively), for the experimental current of figure 49.

The channel expansion (Fig. 52) occurs with very small overpressure in the wave front, with a velocity which is always much smaller than the sound speed. This is consistent with the results of the Schlieren photography; the experimental diameters are in excellent agreement with the computed values. However, both the expansion velocity and the front overpressure increase rapidly with the current (see the

peaks in figure 52) : it can be therefore expected that with large overvoltages or with negative polarity (in both cases the current can reach much higher values) the energy input may be large enough to generate shock waves : they have been in fact observed in the recent experiments of the Les Renardières Group [32] on long negative sparks.

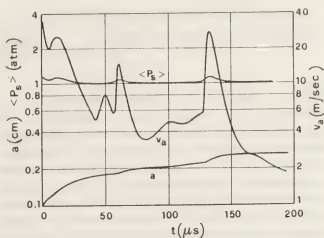


Fig. 52. — The computed variations of the channel radius a , of the shell overpressure $\langle p_s \rangle$, and of the expansion velocity v_a , for the experimental current input of figure 49.

For further comparison between experimental and computed results, the luminous emission L from the leader channel has been calculated,

$$\frac{dL}{dt} = \bar{\sigma} \bar{q} N_e \mu_e E \quad (50)$$

where $\bar{\sigma}$ and \bar{q} are the average values of the excitation coefficients and collisional quenching factors for the different band systems emitted by the nitrogen molecules (essentially the First and Second Positive Systems [30, 37]). The computed results show a very good agreement with the experimental light oscillogram recorded contemporarily to the current (Fig. 49).

4.7 QUASI-EQUILIBRIUM CONDITIONS. — The presented results indicate that in the leader evolution different quasi-equilibrium conditions are reached, which are worth of further discussion. Let's consider the electron and ion energy eqs. (39) : the output term C_{ch} (eqs. (40)) is a function of the effective energy exchange collision frequency, which is for the actual values of T_e larger than 10^8 s^{-1} [69]. As a consequence the electron energy relaxation occurs with a time constant which is much shorter than the leader time scale. Furthermore the electron and ion densities are relatively small, so that the Coulomb collision term C_{e+} is negligible, together with the partial pressures p_e and p_+ .

For these reasons the second members of eqs. (39), and hence the derivatives at the first member, are

almost zero for all the time, except in correspondence of very sharp current variations: the total power input is transferred from the electron to the neutral molecules

$$EI = N_e v_u^* k(T_e - T_h). \quad (51)$$

According to eqs. (45) and (46), the electron temperature,

$$T_e - T_h = \frac{\left(e \cdot \frac{E}{n_h}\right)^2}{m_e k \frac{v_u^*}{n_h} \cdot \frac{v_{eh}}{n_h}} \quad (52)$$

results a function of the reduced field E/n_h only. Similarly the ion temperature is in equilibrium with the local field E/n_h and can be calculated with simple formulas as eq. (29). This means that in the leader channel, inspite of the power input fluctuations, the conditions for quasi-equilibrium electron and ion swarms are realized, with almost steady-state energy distribution functions; the corresponding temperatures can be derived directly as functions of the reduced field from the results of swarm experiments.

A similar reasoning can be applied to eq. (49): the values of the reduced ionization frequency v_i/n_h and of the recombination coefficient a_e are functions of the reduced field E/n_h only; $1/v_i$ and $1/a_e n_+$ represent the ionization and recombination time constants: for the values of E/n_h and n_+ appropriate to the leader channel, they result much shorter than the time scale of the leader development. As a consequence the electron and positive ion equilibrium densities, corresponding to the balance between the ionization and recombination rates, are attained in a very short time; their evolution in the leader channel may be assumed to develop by successive quasi-equilibrium conditions,

$$n_e = n_+ = \frac{v_i}{a_e}. \quad (53)$$

According to this value of the electron density, eqs. (45) and (46) can be combined in the form

$$\frac{E}{n_h} = \frac{m_e I a_e}{e^2 N_h} \cdot \frac{v_{eh}}{v_i}. \quad (54)$$

If N_h is assumed to be practically constant (neglecting the small variations due to ionization and dissociation), eq. (54) represents an implicit function which correlates the reduced field to the leader current I ; the ratio v_{eh}/v_i and a_e are in fact dependent on E/n_h only. The values of this function are quite insensitive to the initial choice for N_h .

The values of E/n_h as functions of I are plotted in figure 53, for currents ranging from 0.1 to 100 A. The ionization degree

$$i = \frac{n_e}{n_h} = \frac{1}{a_e} \cdot \frac{v_i}{b_h} \quad (55)$$

and the leader conductivity

$$\sigma = \frac{1}{a_e} \frac{v_i}{v_{eh}} \frac{n^2}{m_e} \quad (56)$$

are also functions of the reduced field, and hence of the leader current only. Their values are reported in figure 53, together with the average electron temperature T_e , derived from eq. (52) for $T_h \ll T_e$. From this figure it can be seen that the basic electric parameters of the leader channel (conductivity, ionization degree, reduced field and electron temperature) are related only to the current which is injected into the channel by the leader corona region.

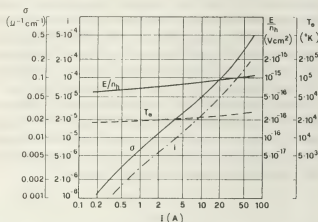


Fig. 53. — Quasi-equilibrium characteristics of the leader channel as functions of the input current ($N_h = 2.5 \times 10^{17} \text{ cm}^{-3}$).

It is interesting to note in figure 53 that the reduced field E/n_h and the electron temperature T_e vary only slightly with the leader current, while the ionization degree i and the conductivity σ are almost proportional to the current. This is due to the steep variation of the ionization frequency with the reduced field: in figure 54 a block diagram of eqs. (54) to (56) is represented: the current I and the conductivity σ determine the reduced field E/n_h ; this in turn determines the ionization degree i and the channel conductivity σ . The block diagram shows a typical feedback loop with high gain, which is given by the differential characteristics of the feedback transfer function $(v_i/a_e) \mu_e$; the output E/n_h is therefore stabilized, independently on the fluctuations of the input current.

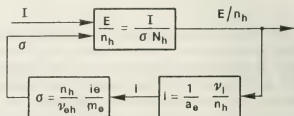


Fig. 54. — Block diagram of the relations between leader current, reduced field and conductivity.

The choice of the initial conditions for the calculations presented in figures (49) to (52) has been determined according to the initial current value and to the results of figure 53. The initial radius has been derived from the experimental results; the temperature T_h has been assumed according to the discussion on the negative ion detachment, taking into account that around the tip where the leader section is firstly formed the local field may give an important contribution to the ion temperature, so that the gas temperature may be lower (see § 5). Then, if pressure equilibrium is assumed, n_h can be calculated from the state equation and n_e , n_+ and T_e can be derived from the results of figure 53.

4.8 CRITICAL BREAKDOWN CONDITIONS. — Some consequence of practical interest can be derived from the presented leader model. As it will be seen in the next section, the leader channel propagates along its path with an almost constant velocity \bar{v}_L : it is therefore possible to change the time scale into a length scale $x_i = \bar{v}_L(t - t_1)$, and calculate the field distribution along the leader channel; by integration of this distribution the leader voltage drop can be derived at any time after its inception. In figure 55 this voltage drop is reported for the experimental case analyzed in figures 49 to 52, together with the applied voltage and the leader tip potential: it can be seen that the latter remains approximately constant during the propagation.

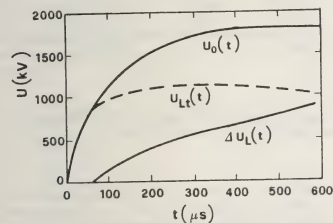


Fig. 55. — The applied voltage $U_0(t)$, the voltage drop along the leader $\Delta U_L(t)$ and the leader tip potential $\Delta U_L(t)$, in a 10 m cone-plane gap subjected to a 500/10 000 μ s voltage wave.

Due to the small radial dimension of the leader, the field distribution in the region near its tip depends mainly on the tip potential (see § 5). The leader propagation occurs therefore with almost constant field in front of it; this is consistent with the almost constant velocity and indicate that an optimum equilibrium condition is realized between the leader advancement and the voltage rate of rise in terms of a constant field on the leader tip. The time-decreasing

leader gradient makes possible that this equilibrium condition persists during the propagation even if the voltage rate of rise decreases in time.

If ψ is the distortion coefficient of the leader path (see § 5.7), the projected length on the gap axis is :

$$z_i = \frac{x_i}{\psi} = \frac{\bar{v}_L(t - t_1)}{\psi}. \quad (57)$$

In a gap of length D the average field (\bar{E}_{Lz}) in the part bridged by the leader and in the unbridged part (\bar{E}_g) are respectively :

$$\bar{E}_{Lz} = \frac{\Delta U_L(t)}{z_i} \quad \text{and} \quad \bar{E}_g = \frac{U_L(t)}{D - z_i}. \quad (58)$$

The computed values of \bar{E}_{Lz} and \bar{E}_g for a 10 m rod-plane gap are reported in figure 56 together with experimental values derived by fluxmeter measurements [82]: the \bar{E}_g values are the field values measured at the plane and they are therefore underestimated, the opposite being true for the \bar{E}_{Lz} values. For times longer than t_c the average potential which is necessary to elongate the leader channel by a unit length (\bar{E}_{Lz}) is lower than the average potential which is available per unit length on the unbridged part (\bar{E}_g): the leader propagation cannot stop anymore, and t_c represents therefore the instant when the decision whether to breakdown or not is taken. The computed values of the injected charge and of the axial and real leader length at the instant t_c are consistent with the experimental critical values [93-95], which are the limit values of charge and length above which breakdown cannot more be arrested [96]; these critical values are reached long before the final jump is launched (t_f in figure 56).

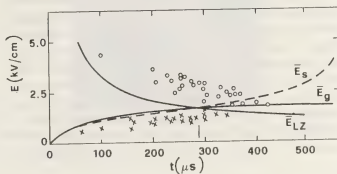


Fig. 56. — Average gradients in the gap portion bridged by the leader (\bar{E}_{Lz}), in the unbridged part (\bar{E}_g) and in the whole gap (\bar{E}_s). The points are experimental estimates derived from fluxmeter measurements.

The present results indicate that the breakdown occurs if the leader channel is not arrested (by the random fluctuations of its propagation mechanism) before it reaches the critical condition that the time decreasing average field in the bridged part \bar{E}_{Lz} becomes smaller than the average gradient in the gap

\bar{E}_g . This criterion may justify some important features of the breakdown of long gaps, such as the decrease of the average breakdown gradient as the electrode separation is increased. In fact, the longer is the gap length, the longer is the time during which the leader may propagate under optimum conditions, and the lower becomes the average gradient along the bridged part of the gap.

The proposed model, and the time-decreasing characteristics of the leader gradient which derives from it, may also explain the peculiar dependence of the breakdown voltage on the time to crest of the applied voltage : it has been experimentally observed that the 50 % flashover voltage decreases with the time to crest up to a critical value and then it increases again (U -curve). The minimum of the U -curve for a 10 m gap is around 500 μ s, and it increases with the gap length. For shorter times to crest, the leader development occurs on a faster time scale and the average gradient along the channel do not have the time to decrease enough up to the final jump : as a consequence the average breakdown voltage should be higher than that for the critical time to crest. For longer fronts, the rate of voltage rise is not enough to balance the increase of voltage drop along the channel and the leader tip potential is not maintained constant during the propagation, but it decreases in time. The leader advancement is therefore not more stable (see § 5.6) and the development becomes discontinuous ; larger voltages are therefore needed to start the discharge again and to reach complete breakdown.

5. Leader propagation. — **5.1 EXPERIMENTAL RESULTS.** — In the streak pictures the leader continuous propagation appears as the advancement of a weakly luminous front, which follows the displacement of the bright, diffuse bundle of leader corona streamers (Fig. 57a). As the leader spectral emission is mainly located in the red, while that of the streamers is almost all in the violet and near ultraviolet [31], image converter pictures taken with red filters have made possible to eliminate the corona emission (Fig. 57b) : the leader tip appears then as a sharply defined luminous point advancing into the gap with roughly uniform speed, leaving behind a

channel of much weaker luminosity. The structure of this channel is put in evidence by frame pictures, with red filter (Fig. 57c) : it looks as a tortuous thin channel, which follows the tip propagating with a sort of succession of random small steps ; the root of the corona region shows an intensification of the red emission in a small conical zone converging to the leader head. The luminous striations which appear on the channel in the streak photos do not correspond to differences of light emission, but only to horizontal bends of the tortuous path.

The leader propagation has been resolved in the details of its three dimensional time-evolution with a computer-aided analysis of streak and static photos, taken from two perpendicular directions [1, 93, 94]. The axial component of the velocity v_{Lz} shows relatively large fluctuations around its mean value : on the contrary the effective velocity v_L presents a very small dispersion (Fig. 58). Therefore the fluctuations

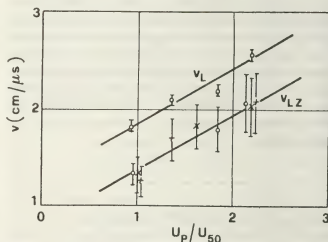


Fig. 58. — Axial and real leader velocity (v_{Lz} and v_L respectively) as functions of the overvoltage ratio U_p/U_{50} (4 to 10 m hemisphere-plane gap, $R = 30$ cm ; 320/10 000 μ s wave).

of the leader axial development towards the ground electrode depend essentially on the randomness of its path. At constant overvoltage ratio U_p/U_{50} , the velocity v_L depends on both the time to crest of the

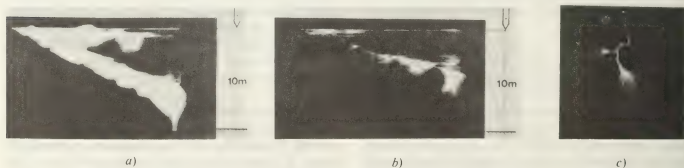


Fig. 57. — Image converter photographs of the leader advancement : streak pictures, (a) with quartz lens for total visible light ; (b) with red filter, $\lambda > 4\,000$ Å ; (c) frame picture, 2 μ s exposure, with red filter (10 m cone-plane gap, 500/10 000 μ s wave).

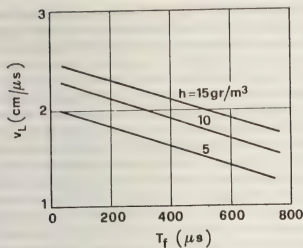


Fig. 59. — The real leader velocity v_L as a function of the time to crest T_f of the voltage wave, for different values of air humidity.

applied voltage and the absolute air humidity (Fig. 59). The front of the leader corona propagates also with approximately constant velocity (Fig. 57a) : it is roughly between 1.5 and 2 times the leader advancement velocity, and increases rapidly as the corona front approaches the plane. The current I_L measured during the propagation is proportional to the advancement velocity v_L [2, 94] (Fig. 60). The proportionality constant ($I_L = qv_L$) represents physically the charge necessary for a unit length advancement of the leader tip : it can be measured directly from current and velocity, or indirectly as the ratio of the total charge injected into the gap during leader progression to its length (Fig. 61) : it can vary from 20 to 50 $\mu\text{C}/\text{m}$ depending on time to crest and absolute humidity.

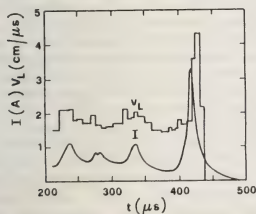


Fig. 60. — Simultaneous variations of leader current I_L and real velocity v_L (10 m cone-plane gap 500/10 000 μs wave).

Gallimberti and Rea [55] have shown that the leader coronas, which guide the leader propagation, have a much fainter and diffuse structure (Fig. 62) than the first one, which presents broad and more branched filaments. This may be probably associated

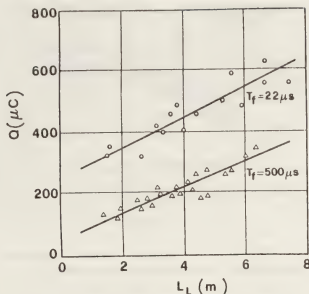


Fig. 61. — The total measured charge Q as a function of the real leader length, for different times to crest of the applied voltage (10 m cone-plane gap).



Fig. 62. — Static picture of the leader corona (1.5 m rod-plane gap, 0.9/25 μs wave).

to the significant differences of electron energies and local fields (Fig. 63), which have been observed in the corona active region by spectroscopic measurements [31]. When the first corona occurs, the field distribution is given only by the highly divergent geometrical component; the streamers cannot develop over a large distance, the charge multiplication is limited, and hence the local field and the average electron energy in the active region are relatively small; later on in the discharge, the electric field distribution becomes more uniform due to the injec-

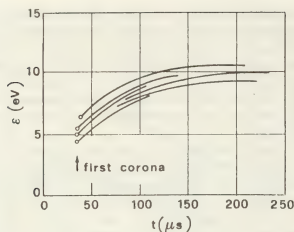


Fig. 63. — The variation of the electron energy in the active front of the leader corona, during the discharge development.

tion of positive space charge : and the charge in the streamer tip can grow, resulting in higher electric fields and electron energies in the active region. The higher streamer activity in this phase of the discharge leads to a longer extension of the leader corona streamers and a higher leader advancement velocity (Fig. 64a, b). An interesting feature of this figure is that both curves drop to zero when the electric field strength reduces to 26 kV/cm ($\bar{\epsilon} = 3.2$ eV), which is known to be the minimum field in which ionization phenomena can occur. The leader propagation can be therefore characterized by the mean electron energy and electric field in the active region of the corona at its head, which are in turn largely determined by the leader tip potential, and hence by the general leader characteristics discussed in the preceding paragraph.

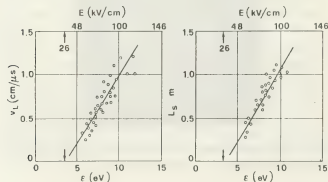


Fig. 64. — The extension of the leader corona l_L and the leader advancement velocity v_L as functions of the average electron energy ϵ in the active front.

5.2 THE LEADER STREAMER SYSTEM. — Marode [21, 22] has shown that the streamer filament in short gaps, after the tip has crossed the whole gap and the resistive phase is established, assumes characteristics very similar to the positive column of a high pressure glow : the formation of a high field cathode region, where ions are accelerated to bombard the

metal plane, and where the extracted electrons are multiplied by collisional ionization, assures the supply of electronic current to the filament. Such a similarity can be extended to the leader corona in long gaps : the role of the cathode region is played by the advancing front of the streamer active regions, where the electrons are multiplied by the avalanche mechanism ; the secondary electron production is assured not by ion bombardment but by photoionization ; the resistive phase, according to the gap dimensions, may be established in a few hundreds of nanoseconds, and the compensation zone (see § 3.8) do not extend more than a couple of cm behind the streamer heads. The rest of the filaments converging to the leader tip may be assimilated to a diffuse high pressure glow, where the electrons produced in the active region are drained towards the anode.

In this picture the leader head may be assumed as a local electrical and thermal perturbation which causes the transition from a diffuse glow to a filamentary arc (see the luminous conical zone in figure 57c) ; such instabilities in high pressure glow discharges have been experimentally observed [97, 99] : they present propagation velocities of the same order of those of the leader channel. Simplified computer simulations [58-62] have indicated that the instability may be caused by a local field intensification which concentrate in a small region a larger density of power input : the subsequent temperature rise and gas expansion lead to an increase of the reduced field E/n_h and of the local conductivity ; the current is therefore constricted over a smaller section with a further concentration of the power density. In the present case, according to the discussion presented in § 3.4, the rapid rise of conductivity may be assumed to follow the growth of the negative ion temperature (which causes electron detachment) : according to eq. (29) the latter is due to the combined effect of the increase of temperature and reduced field.

The leader-streamer system may be therefore represented as a moving diffuse glow, where a transition to filamentary arc is in course : the penetration of the leader tip potential into the gap sustains the propagation of the active region front, which in turn supplies the current necessary for the glow to arc transition to be maintained. If an equilibrium condition in this interaction is reached, the leader-streamer system can propagate with stable velocity.

5.3 THE TRANSITION REGION : CURRENT AND FIELD DISTRIBUTION. — In order to simulate theoretically the leader head region, the mass, momentum and energy conservation equations (similar to eqs. (34)) have to be written for all the particle species : in this case also the negative ions have to be considered, together with electrons, neutral molecules and positive ions. The Poisson's equation and the Ohm's law have to be added to complete the equation system. The aim of this paragraph is not to solve

such a complex equation system, but to analyze the conditions for the stable advancement of the transition region, through a simplified condition of self-similarity.

Let's consider a reference frame having a constant velocity, \bar{v}_L relative to the laboratory frame, and let's assume that there exists a steady state solution of the equation system (34), which represents the stable propagation of the transition region in the form of a non-damped wave. Let's consider the conservation equations for the charged particles. As discussed in the preceding paragraph, because of the low ionization degree and gas temperature, the energy equations may be replaced by swarm functions relating the equilibrium temperatures to the reduced field [18]; similarly the momentum equations may be replaced by simple mobility relations [59, 66]. As a consequence the complete set of electrical equations becomes

$$\left. \begin{aligned} \nabla \cdot [n_e(\bar{v}_e - \bar{v}_L)] &= \dot{n}_e \\ \nabla \cdot [n_-(\bar{v}_- - \bar{v}_L)] &= \dot{n}_- \\ \nabla \cdot [n_+(\bar{v}_+ - \bar{v}_L)] &= \dot{n}_+ \\ \nabla \cdot \bar{E} &= -e \frac{n_e + n_- - n_+}{\epsilon_0} \\ \bar{J} &= \sum_s e n_s \bar{v}_s \\ \bar{v}_s &= \mu_s \bar{E} \quad (s = e, -, +) \end{aligned} \right\} \quad (59)$$

Due to the characteristics of the glow to arc transition, the generation terms may account only for the negative ion detachment, neglecting the contributions of ionization, recombination and attachment.

Let's now assume that the negative ion detachment occurs instantaneously at a definite critical temperature T_-^c . As a consequence the conductivity transition is sharp and the leader profile can be defined as the negative-ion isothermal surface corresponding to the critical temperature T_-^c : it separates two regions of very different conductivities. The shape of this surface will be defined from both the electrical and thermodynamic conditions in the transition region: according to Kekez and Sawic [100, 101] it may be assimilated to a very slender paraboloid. In fact if the energy input at the leader tip is assumed to be high and concentrated, and to drop to much lower values in the high conductivity channel, the profile may be assimilated to the boundary of a parabolic explosion translated with a velocity \bar{v}_L [102, 103],

$$r_0 = kt^{1/2}; \quad z_0 = -\bar{v}_L t, \quad (60)$$

where the constant k depends on the gas-dynamic parameters and the rate of energy input; for the present conditions [78] it can be estimated of the order of $10^{-1} \text{ cm } \mu\text{s}^{-1/2}$. The corresponding leader profile is the paraboloid sketched in figure 65a, which has a curvature radius $\rho_c = 25 \text{ } \mu\text{m}$ at the tip. If the difference of conductivity across this surface

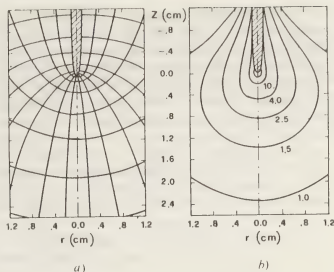


Fig. 65. — Schematic representation of the leader head transition region; (a) field and current lines; (b) lines of constant power input.

is very large, near the tip it coincides with an equipotential surface.

Under the present assumptions in the glow region, outside the leader surface, the generation terms vanish and the equation system (59) represents a steady state current field in between a paraboloid electrode and a distant plane; the equipotential and current surfaces are two sets of perpendicular confocal paraboloids (Fig. 65a). Let's introduce a frame of parabolic coordinates (φ, η) ,

$$z = \frac{1}{2}(\varphi^2 - \eta^2); \quad r = \varphi\eta, \quad (61)$$

where $\varphi = \text{constant}$ represent the equipotential surfaces and $\eta = \text{constant}$ the equiflux surfaces. The coordinate origin in both frames lies in the focus of the paraboloid set. The leader profile corresponds to the surface $\varphi^2 = \rho_c$. The potential, field and current distributions can be easily derived [104]:

$$\left. \begin{aligned} U &= U_L \frac{\lg(\varphi/\sqrt{2H})}{\lg(\sqrt{\rho_c}/\sqrt{2H})} \\ E &= \frac{-U_L}{\lg(\sqrt{\rho_c}/\sqrt{2H})} \frac{1}{\varphi \sqrt{\varphi^2 + \eta^2}} \\ J &= \sigma E \end{aligned} \right\} \quad (62)$$

where U_L is the leader tip potential (see § 4.8), ρ_c the tip curvature radius and H the height of the leader head above the ground plane. From eqs. (62) it appears that the potential, field and current distributions are only slightly affected by the distance H , if U_L and ρ_c remain approximately constant. Both field and current density increase from the outer glow to the leader surface, so that the specific power input EJ is concentrated near tip along the leader axis: figure 65b shows the lines of constant specific power input [100, 101].

5.4 THE TRANSITION REGION : THERMODYNAMIC CHARACTERISTICS. — If the neutral molecules are considered, the energy conservation equation has to be splitted into the balance between the different reservoirs of internal energy. However, due to the relatively low ionization degree and gas temperature,

the contribution of the chemical reservoir can be neglected. According to the discussion of § 4, the conservation eq. (34) may be written, with respect to the reference frame moving with constant velocity \bar{v}_L , in the form,

$$\left. \begin{aligned} \nabla \cdot [n_h (\bar{v}_h - \bar{v}_L) (\bar{v}_h - \bar{v}_L)] &= 0 \\ \nabla \cdot [m_h n_h (\bar{v}_h - \bar{v}_L) (\bar{v}_h - \bar{v}_L)] + \nabla \cdot p &= 0 \\ \nabla \cdot [n_h c_p^* T_h (\bar{v}_h - \bar{v}_L)] &= (f_n + f_e) EJ + \frac{w_v(T_v) - w_v(T_h)}{\tau_{vt}} \\ \nabla \cdot [w_v(T_v) (\bar{v}_h - \bar{v}_L)] &= f_v EJ - \frac{w_v(T_v) - w_v(T)}{\tau_{vt}} \\ p &= n_h k T_h \end{aligned} \right\} \quad (63)$$

where the partial specific heat at constant pressure c_p^* has been used at the place of c_p^* , in order to account for the total enthalpy variation of the thermal reservoir. In these equations the leader wave velocity \bar{v}_L is much larger than any possible value of the molecule displacement speed \bar{v}_h ($\bar{v}_L = 20\,000$ m/s). As a consequence, during the transit of the leader head across the transition region, the gas molecules may be assumed practically still; the temperature grows under practically constant volume and the pressure is locally raised; only after the transit of the leader head the expansion process can take place, with a rate which should be similar to a low energy punctual explosion, leading to the parabolic profile of the leader head (§ 5.3).

From the mass and momentum eqs. (63), approximate expressions can be derived for the pressure and the radial component of the expansion velocity [105]. If the two energy equations are considered and the neutral velocity is neglected with respect to the wave velocity, their integration can be carried on along the gap axis, from a point z_1 where the specific power input is negligible and the gas temperature 300 K, to the leader surface ($z = \rho_d/2$). Let's consider the last term in these two equations: its integral may be expressed in the form,

$$\int_{\rho_d/2}^{z_1} \frac{w_v(T_v) - w_v(T)}{\tau_{vt}} \frac{dz}{\bar{v}_L} = w_v \cdot \left\langle \frac{z_1/\bar{v}_L}{\tau_{vt}} \right\rangle = w_v \cdot \left\langle \frac{\tau_L}{\tau_{vt}} \right\rangle, \quad (64)$$

where w_v represents the value of the vibrational energy per unit volume at the leader surface and $\langle z_1/\bar{v}_L \cdot \tau_{vt} \rangle$ is a mean value weighted on the flux of energy from the vibrational to the thermal reservoir. It represents the fraction of the vibrational energy w_v which is relaxed into thermal in the transition region: in this sense, it may be represented as $\langle \tau_L/\tau_{vt} \rangle$, where τ_L is the equivalent *transit time* for the leader to cross the transition region. The rest of the vibra-

tional energy is relaxed later in the leader channel. The two energy eqs. of (63) can be integrated in the form

$$\left. \begin{aligned} \frac{7}{2} k n_h \Delta T_L &= (f_n + f_e) \int_{\rho_d/2}^{z_1} JE \frac{dz}{\bar{v}_L} + w_v \left\langle \frac{\tau_L}{\tau_{vt}} \right\rangle \\ w_v &= f_v \int_{\rho_d/2}^{z_1} JE \frac{dz}{\bar{v}_L} - w_v \left\langle \frac{\tau_L}{\tau_{vt}} \right\rangle \end{aligned} \right\} \quad (65)$$

where ΔT_L is the temperature increase across the transition region.

5.5 THE LEADER PROPAGATION. — If it is assumed that ΔT_L should be high enough to produce detachment of the negative ions, the leader velocity can be calculated from eqs. (65),

$$v_L = \left[f_n + f_e + f_v \frac{\langle \tau_L/\tau_{vt} \rangle}{1 + \langle \tau_L/\tau_{vt} \rangle} \right] \times \times \frac{2}{7 k n_h \Delta T_L} \cdot \int_{\rho_d/2}^{z_1} JE dz. \quad (66)$$

It represents the frame velocity which is consistent with the self-similarity of the wave during its propagation. In eq. (66) the integral of the specific power should be calculated along the axis of the glow region: J and E represent therefore the maximum values $J_\phi(\eta = 0)$ and $E_\phi(\eta = 0)$ of their distributions on the equipotential surfaces. With reference to the parabolic coordinates (61), the total current I_L can be calculated by integration of $J(\eta)$ along any equipotential surface up to the boundary of the corona glow ($\eta = \eta_0$),

$$I_L = \int_0^{\eta_0} \frac{-U_L}{\lg [\sqrt{\rho_d/2} H]} \cdot \frac{2 \pi \sigma}{\sqrt{\varphi^2 + \eta^2}} \cdot \sqrt{\varphi^2 + 4 \eta^2} \cdot \eta d\eta. \quad (67)$$

According to eqs. (62) it results :

$$J_{\phi}(\eta = 0) = \frac{I_L}{2 \eta_0^2 \pi \varphi^2} \quad (68)$$

where the denominator of the second member represents the normalized section of the corona glow (62) at the coordinate φ . By use of eq. (68) the integral of the specific power across the transition region can be calculated,

$$\int_{\rho_c/2}^{\infty} JE dz = \frac{-U_{L1} \cdot I_L}{\lg [\sqrt{\rho_c/2} H]} \cdot \frac{2}{\pi^2 \eta_0^2} \left[\frac{1}{\rho_c^2} - \frac{1}{4 z_1^2} \right]. \quad (69)$$

According to the definition of the boundary z_1 of the transition region, it appears that any value $z_1 \gg \rho_c$ do not influence the value of the power integral (69). From eqs. (66) and (69) it can be seen that the leader velocity is proportional to the total current

$$v_L = \frac{1}{q} I_L \quad (70)$$

the proportionality factor q being expressed by

$$q = - \left[f_{\pi} + f_e + f_v \frac{\langle \tau_L / \tau_{tr} \rangle}{1 + \langle \tau_L / \tau_{tr} \rangle} \right]^{-1} \times \\ \times \frac{7 k n_h \Delta T_L}{4 U_{L1}} \pi^2 \eta_0^2 \rho_c^2 \cdot \lg [\sqrt{\rho_c/2} H]. \quad (71)$$

It represents the average charge which is necessary for a unit length advancement of the leader channel. The results of eqs. (70) and (71) show some interesting features of the present model for the leader advancement. Eq. (71) states that the leader velocity cannot be calculated just on the basis of the conditions in the transition region, but it depends essentially on the ionization activity in the leader corona front, which injects the current I_L into the glow region. The velocity results proportional to the current, in good agreement with the experimental observations (Fig. 60).

The charge per unit length (eq. (71)) remains constant during the propagation, if the transition region remains self-similar : this implies only that the potential of the leader tip (and hence the field distribution in the transition region) is about constant during the propagation ; the experimental results and the theoretical calculations reported in § 4 have given strong indications for such constancy of the tip potential. Eq. (71) predicts that the charge per unit length depends essentially on humidity and on the applied voltage, because τ_{tr} is a function of the water vapour content, and the leader tip potential, the leader velocity and τ_L depend on the voltage wave. The distance H of the leader from the plane effects only slightly the values of q .

For the configuration reported in figure 65 the

values of $\langle \tau_L / \tau_{tr} \rangle$, have been calculated for a 10 m gap under the conditions of the Les Renardières experiments [1, 93, 94], with the average leader tip potentials computed in § 4.8. The theoretical values of q for different humidities and voltage waveshapes, are compared in figure 66 with the experimental results. The critical temperature which gives the best agreement with the experimental results is between 1 000 and 1 500 K, slightly lower than the values which have been used in § 3.6. This indicates that the field in the transition region is high enough to heat the negative ions to an effective temperature which is higher than the gas temperature. The value of 1 000 K has been used as initial condition for the leader channel in the model of § 4.6.

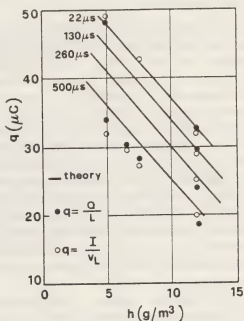


Fig. 66. — Comparison between computed and experimental values of the charge q per unit leader length, for different wavefront durations and humidities.

The good agreement between theoretical and experimental results indicates that the leader propagation is essentially governed by the energy exchanges which occur at the rooth of the corona glow : the charge which is necessary to form a unit length of leader channel is mainly determined by the fraction of vibrational energy which can be relaxed in the transition region during the leader *transit time*

$$(\langle \tau_L / \tau_{tr} \rangle).$$

Both, the increase of humidity and front duration, enhance this fraction, by decreasing τ_{tr} and increasing τ_L respectively.

5.6 THE ADVANCEMENT OF THE LEADER-STREAMER SYSTEM. — The propagation mechanism of the leader-streamer system can be illustrated with the phenomenological block diagram presented in figure 67. The field E_s in the active front of the leader corona deter-

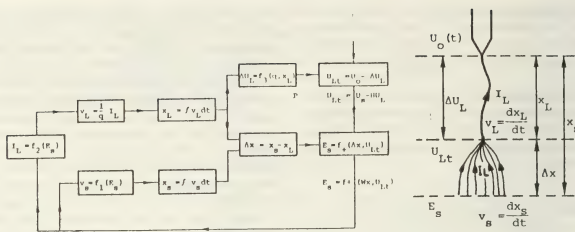


Fig. 67. — Block diagram of the relations between the parameters involved in the streamer-leader advancement.

mines the streamer activity, and hence the current I_L flowing into the glow region and the velocity v_s of advancement of the corona front. According to eq. (70) the leader velocity v_L depends on the charge per unit length and is proportional to the current I_L . Therefore the field E_s determines indirectly also the leader advancement velocity v_L . The positions z_L and z_s of the leader tip and of the streamer front (and the length of the glow region Δz) come obviously from the integration of the respective velocities. The leader length z_L and the charge per unit length q , determine the voltage drop ΔU_L along the leader channel and, together with the applied voltage $U_0(t)$, the potential of the leader tip U_L . This potential is the main parameter which influences the field E_s at the distance Δz .

The block diagram appears to be formed by a number of loops, where the only external input may be considered the applied voltage $U_0(t)$. For any voltage waveshape, there should be an equilibrium set of values for all the parameters (depending obviously on time), which corresponds to the stable propagation. Any statistical fluctuation or external perturbation will generate oscillations in the different loops (see Fig. 60), however, the propagation appears to be essentially stable because the feedback reactions have in general the effect to reconduct the different parameters to their equilibrium values. In some cases the non-linearity of the different block functions may cause large oscillations and instabilities (see next chapter).

Almost all the parameters and the functions reported in the block diagram have been theoretically estimated in §§ 4 and 5. The point which is not yet solved is the simulation of the leader corona advancement, i.e. the relationship between the field E_s and the current and velocity of the streamer front. The main difficulty is the estimation of the space charge distribution in the gap, which defines the local field and the characteristics of the charge multiplication in the active front. For simplified models and for practical purposes, the experimental correlation between

the field in the active region and the leader velocity or the corona length (Fig. 64) may be the base of a semi-empirical approach.

A different approach may be based on the estimation of the field E_s' produced in the active region by the leader tip potential, neglecting any effect of the corona space charge. Such field acts on the streamer propagation like the *applied geometrical field*, which supplies energy from the external circuit. As discussed in § 2.4, a minimum value of E_{gs} is necessary to enable an energetically stable propagation of the corona streamers. There seems to be some experimental evidence that the field E_s' is maintained around 4 kV/cm during the continuous leader propagation, in good agreement with the stability fields measured by Griffiths and Phelps [41, 43]. However, further accurate investigations are needed, before the phenomenological model of figure 67 could be quantitatively completed.

5.7 STATISTICAL CHARACTERISTICS OF LEADER PROPAGATION. — Baldo *et al.* [2] have analyzed in detail the breakdown statistics in long gaps (breakdown probabilities and time to breakdown distributions) and have shown that it depends essentially on the statistical fluctuations of the leader propagation: the statistics of the corona and leader inception, which have been discussed respectively in §§ 1 and 2, play only a minor role.

As a consequence, any non-deterministic model of the breakdown should account not only for the physical phenomena which support the leader propagation, but also for the statistical random fluctuations of its development. As experimentally observed (Fig. 58), the fluctuations of the axial velocity v_{Lz} are due to the randomness of the leader path: therefore, the statistics of its development time t_L (from the positive electrode up to the point where the final jump is launched) depends directly on the fluctuations of its geometrical pattern. The experimental histograms of t_L are reported in figure 68, for a 7 m gap with three different peak

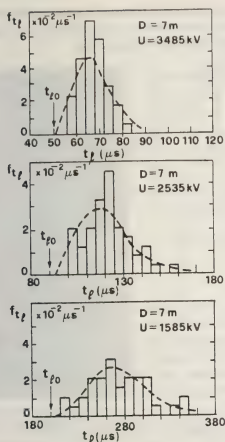


Fig. 68. — The probability distribution of the leader propagation time ($t_L = t_f - t_i$); for different peak values of the applied voltage (7 m hemisphere-plane gap, $R = 30$ cm, 320/10 000 μ s wave).

values of the applied voltage. In order to build up a simple geometrical model of the leader path, let's assume that the latter is composed by a number N of elementary steps of amplitude dx : when N tends to infinite dx is reduced to zero. Let's than assume that the single steps may be either vertical or horizontal, with elementary probabilities p and $q = (1 - p)$. The minimum number N_0 of steps necessary to reach the point of final jump will be given by a succession of identical vertical steps,

$$N_0 = \frac{D - h_f}{dx}. \quad (72)$$

The probability distribution of the excess trials $K = N - N_0$ required to get exactly N_0 successes is the Negative Binomial distribution

$$P[K] = \binom{N_0 + K - 1}{N_0 - 1} (p)^{N_0} (q)^K, \quad (73)$$

which has mean and variance

$$E[K] = \frac{N_0 q}{p}; \quad \sigma_K^2 = \frac{N_0 q}{p^2} = \frac{E[K]}{p}. \quad (74)$$

As a consequence the normalized leader propagation time

$$\tau = \frac{t_L - t_{L_0}}{t_{L_0}} = \frac{K}{N_0}; \quad t_{L_0} = \frac{N_0 dx}{v_L} = \frac{D - h_f}{v_L}, \quad (75)$$

possesses the limit distribution for $N_0 \rightarrow \infty$, with mean $E[\tau] = q/p$; t_{L_0} represents the minimum time required to cross the distance $D - h_f$ on a straight line with a velocity v_L . The values of the probabilities q and p have been derived from the experimental averages of figure 68, while t_{L_0} has been calculated from eq. (75); in all three cases $p = 0.74$ and $q = 0.36$; the computed curves are reported in figure 68 with dashed lines.

The proposed model appears quite satisfactory, particularly because it depends on a single parameter, which is not influenced by the applied voltage. However, the p value used in the calculations is an average value over the complete leader path: actually it has been experimentally observed that the differential tortuosity coefficient

$$\psi = \frac{\Delta x}{\Delta z} = 1 + \frac{K}{N_0} \quad (76)$$

varies with the leader length [2, 106], being higher for the initial part of the leader path, and dropping practically to 1 during the final jump (Fig. 69). The experimental results have been analyzed on the basis of the present model, and the p values together with the corresponding probability distributions of ψ have been derived, for different axial lengths z (Figs. 69 and 70).

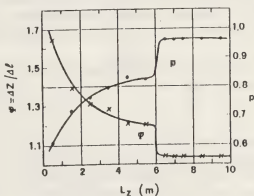


Fig. 69. — The probability of a vertical leader step and the mean value of the distortion coefficient ψ as functions of the axial leader length.

A different approach has been proposed by Hutzler [106, 107] to simulate the probabilistic structure of the leader path: an arbitrary probability distribution has been assigned for the angular deflection θ with respect to the vertical direction and the leader path is build up step by step with a Monte Carlo procedure. The present model makes possible to derive the θ probability distributions, without any arbitrary assumption: in fact it results

$$\psi = \frac{\Delta x}{\Delta z} = (\cos \theta)^{-1}$$

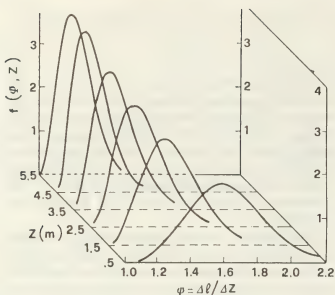


Fig. 70. — The probability density f_ψ of the distortion coefficient ψ as a function of the axial leader length.

and

$$f_\theta(\theta) = f_\psi[(\cos \theta)^{-1}] \frac{\sin \theta}{\cos^2 \theta}. \quad (77)$$

The angular probability distributions are reported in figure 71, for different axial lengths, including also the final jump (f.j.). The experimental average values of the angle θ are around 45° for $z = 2.5$ m and decrease to 30° for $z = 6$ m [93, 94], in good agreement the results of figure 71. A Monte Carlo procedure based on any of the distributions ($P[K]$, f_ψ or f_θ) makes possible to build up different examples

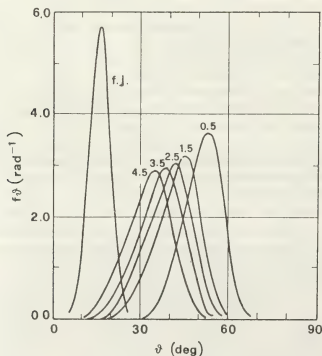


Fig. 71. — The probability density f_θ of the leader angular deflection θ from the vertical direction, at different values of the axial leader length (f.j. indicates the distribution during the final jump).

of leader path. In figure 72 some computed bidimensional projections are compared with the photo of some experimental discharges.

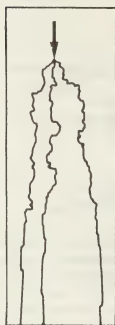


Fig. 72. — Comparison between the experimental and computed geometrical random path of the leader channel.

6. Restrikes. — 6.1 EXPERIMENTAL RESULTS. —

The leader propagation, which has been discussed in the preceding chapter, occurs under a sort of equilibrium conditions between leader and corona advancement, which produces an almost constant current and propagation velocity. Under particular conditions (long front durations or high humidity) discontinuity can appear in the leader development, which can cause rapid elongations (some tens of cm in a few microseconds) and are associated to large current pulses and sharp channel reilluminations (Fig. 73). In most cases at the tip of the leader channel in cor-

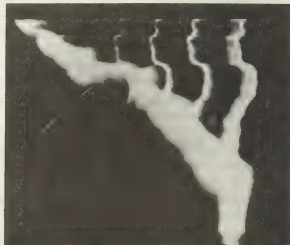


Fig. 73. — Streak photograph of a discharge with high atmospheric humidity showing a number of channel reilluminations (10 m cone-plane gap, 500/10 000 μ s wave, $h = 12.5$ gr/m³).

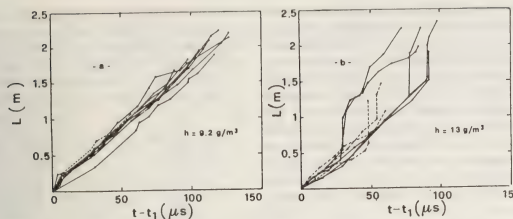


Fig. 74. — Real leader length as a function of time (4 m conductor-plane gap, 190/10 000 μ s wave). The solid lines correspond to breakdowns, the dashed ones to withstands.

response to a reillumination a large and broad corona appears, very similar to the first one.

Such discontinuities are called restrikes : the difference between these two propagation conditions (continuous uniform growth and step-wise advancement) can be clearly observed under identical experimental conditions, if humidity changes. In figure 74 the real leader length along its three-dimensional path is reported as function of the time of leader propagation t_L , for two series of shots with different air humidities. Restrikes are not observed for humidities lower than about 10 gr/m^3 : above this threshold, the total average leader velocity is largely increased by the presence of step elongations, while the continuous velocity in between restrikes increases only slightly (Fig. 75).

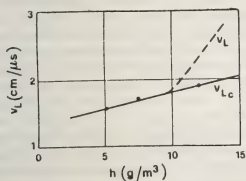


Fig. 75. — Variation of leader velocity with humidity : v_L is the total average velocity, v_{Lc} the continuous propagation velocity in between restrikes. (8 m cone-plane gap, 390/10 000 μ s wave.)

The statistical analysis of the time intervals between successive restrikes Δt_r , has suggested that they behave according to a regular statistical function, which depends on humidity [108]. The Poisson's distribution appears to be well appropriate,

$$f_r(\Delta t_r) = \lambda^2 \Delta t_r \exp(-\lambda \Delta t_r), \quad (78)$$

and with a best-fit procedure the restrike frequency λ has been derived as a function of sequence number

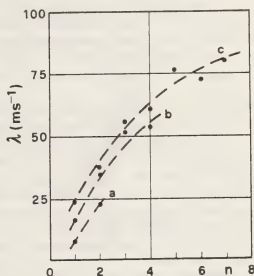


Fig. 76. — Frequency of restrikes as a function of the sequence number for different humidities : (a) $h = 10.2 \text{ gr/m}^3$, (b) $h = 14.8 \text{ gr/m}^3$, (c) $h = 16.8 \text{ gr/m}^3$ (8 m cone-plane gap, 390/10 000 μ s wave).

and humidity (Fig. 76). For the first restrike the frequency is the smallest and increases with humidity. On this basis the probability of appearance of at least one restrike during a single voltage application has been derived (Fig. 77) : it becomes very small for humidities lower than 9-10 gr/m^3 , which explains the absence of reilluminations under dry atmospheric conditions.

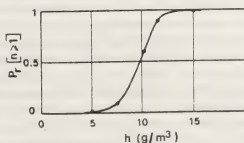


Fig. 77. — Probability of appearance of at least one restrike in a single shot as a function of humidity (8 m cone-plane gap, 390/10 000 μ s wave).

In order to understand the physical phenomena which launch the restrikes, the relationship between the continuous propagation current I_b and the peak current during the reilluminations I_p has been analysed [8]. If I_b and I_p are measured immediately before and during the restrike, their correlation curve (Fig. 78) do not depend on humidity; but the lower values of I_b (and correspondingly the higher values of I_p) are more frequent when humidity is high. This suggests that air humidity has some action enhancing the current oscillations and the instabilities in the leader advancement mechanism.

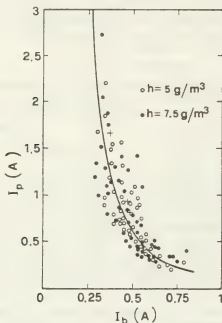


Fig. 78. — Correlation between minima I_b and maxima I_p of the current oscillations.

Let's consider the block diagram of the streamer-leader system shown in figure 67: the stable propagation corresponds to the equilibrium values imposed by the applied voltage $U_0(t)$, which represent the only external input to the system. Oscillations in the different loops may be induced by statistical fluctuations or external disturbances. With increasing humidity, the streamer activity is reduced and its stability field is increased (see § 2.8): as a consequence the velocity of the streamer front v_s is reduced, together with the current injected from the corona glow into the leader channel I_L . On the contrary the leader velocity v_L and the voltage drop ΔU_L increase because of the decrease of the charge per unit length q (see Fig. 66 and ref. [95]). Depending on the way in which the latter changes combine finally on the field E_s in the corona front, oscillations may be generated either in I_L or v_s , through the feedback loops. The smaller becomes the current I_L (which corresponds to I_b) the larger will be the system reaction and the ratio I_p/I_b . According to this model, humidity does not affect the mechanism and hence the relationship between I_p and I_b . By reducing the streamer activity,

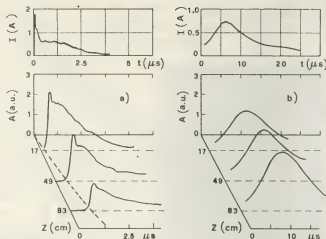


Fig. 79. — Current and light pulses propagating along the leader channel during the restrikes (4 m rod-plane, 200/2 000 μ s wave).

it produces lower values of I_b and hence larger values of I_p . At high humidity, such low values of I_b may be reached, that equilibrium is no longer possible with the external input $U_0(t)$. The streamer activity is stopped and the leader decelerates. A sharp instability might then occur, producing a new large leader corona and a sudden elongation of both x_L and x_s . Such an instability may explain the occurrence of strong reilluminations at high humidity.

The light and current pulses, associated with reilluminations, have been resolved in time [109, 110]. As represented in figure 79 two types of light and current pulses have been generally recorded. Great similarities can be noted between light output and current. The bell shaped pulse in figure 79b corresponds usually to a corona occurring at the leader tip, whereas the pulse shown in figure 79a, with shorter duration and steep rise, was always observed in the case of very long time to crest or during periodic corona occurring after the leader elongation had stopped. Additional measurements have been performed in order to resolve the direction and the velocity of propagation of the light pulse along the leader channel during a reillumination. In the case of the short risetime pulse (a), where high precision of the oscillogram interpretation could be achieved, the phenomenon is seen to propagate from the electrode tip with a velocity of the order of 10^8 cm/s [110]. In figure 80 the advancement curve of the luminous wave is reported, together with the attenuation of the light pulse amplitude during the propagation. In the case of the bell shaped pulses (b), the measurements of the propagation velocity were not possible because of the poor definition of the pulse front; in figure 79, the relatively slow variations of light seem to occur practically at the same time along the whole channel, following the current variation. The contemporary measurement of the electric field on both electrodes indicate that almost all the charge associated to this kind of restrike is located near the leader tip and is related to the leader

ongation; the voltage distribution along the channel self does not change significantly. Therefore the increase in the current should be balanced by a similar increase in the channel conductivity. Such a behaviour very similar to that described by figures 49 to 52, in correspondence to large current fluctuations.

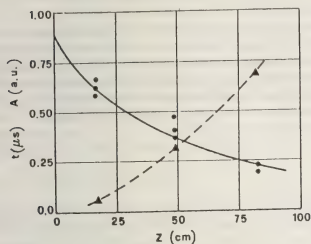


Fig. 80. — The transit time and the absolute intensity of the restrike luminous pulses, as functions of the travelled distance. Initial velocity 2.0×10^8 cm/s; Average velocity 1.0×10^8 cm/s; Attenuation factor 1.8×10^{-2} cm $^{-1}$.

6.2 THE RESTRIKE TRANSIENTS. — Restrikes in the leader channel have been observed also in all the cases when a sudden change is realized in the leader regime: when the leader is arrested by a large injection of space charge at its tip [93], when it starts again after an inactivity period, or when the applied voltage is rapidly changed [1, 94] (e.g. by triggering a parallel chopping gap which reduces the voltage to zero). Similar luminous fronts have been observed to propagate also in shorter gap along pre-discharge channels [111, 112], anytime that a sudden variation of the potential occurs in a point of the discharge circuit: this local perturbation has to be transmitted to the whole electrical system to establish a new voltage and current regime. The wave propagation may be therefore considered as the transient response of the pre-discharge channel to an electromagnetic perturbation, when the channel is assumed to be part of the complete discharge circuit; the transient behaviour of the electric field in any point of the channel may be then described by the Maxwell's equations,

$$\left. \begin{aligned} \nabla \times \vec{H} &= \vec{J} + \frac{\partial \vec{D}}{\partial t} \\ \nabla \times \vec{E} &= -\frac{\partial \vec{B}}{\partial t} \end{aligned} \right\} \quad (79)$$

where \vec{H} , \vec{B} and \vec{D} are respectively magnetic field and flux and electric flux. These equations, together

with the conservation eqs. (34) for all particles species, can describe the leader channel evolution during the reilluminations.

In the leader model presented in § 4, the channel has been assumed to be almost uniform in the longitudinal direction, and in the differential equations the longitudinal derivatives have been neglected. Furthermore, the electromagnetic field equation has been replaced by a simple ohmic relation, with the implicit assumption that the conduction current is constant along the channel and the displacement current is zero ($\partial \vec{D} / \partial t = 0$ in eqs. (79)). This leader model is therefore inadequate to represent the fast transient associated to the restrike propagation. However the results of figure 49 show a good correlation between theoretical and experimental light pulses associated to large current oscillations. This indicates that the form of the reillumination pulses is essentially related to the form of the current of the leader-streamer instability; and the increase of light follows the increase of electron density, which develops in quasi-equilibrium with the current (see § 4.7).

This suggests that it is possible to distinguish in the restrike transient to different processes: a fast transient, which appears in the form of a current and field wave [113, 114] propagating along the channel with velocities in the range 10^8 - 10^9 cm/s; the displacement current makes the conduction current different from section to section and produces the variation of the surface charges according to the potential rearrangement; and a slow transient, which appears in the form of a current oscillation with almost constant axial field and quasi-equilibrium variation of electron density; the displacement current is zero and the conduction current is longitudinally uniform. This seems to be consistent with the form of the observed light and current pulses (Fig. 79a) which present clearly the aspect of a double transient; the bell shaped pulse (Fig. 79b) is probably due to a much slower electromagnetic perturbation, associated to a fluctuation in the leader-streamer system and the intensity of the fast transient (related to the time derivatives of electric and magnetic fields) is too small to be detected.

6.3 THE WAVE PROPAGATION. — It is well known that, in the presence of a filamentary plasma support, the electromagnetic perturbation is transmitted as a wave along the filament itself the propagation characteristics depending on the initial conditions of the support medium. The solution of Maxwell's equations is in general very complex; however, in two extreme cases it can be strongly simplified, depending on the ratio ρ of the electric energy losses over the magnetic energy associated to the wave propagation per unit time and length. When the losses are negligible, the magnetic and electric field components in the propagation direction are also negligible and the

perturbation propagates without appreciable distortion as a plane transverse electromagnetic wave. When the electric losses are dominant, magnetic effects are negligible, together with the transversal component of the electric field, and the perturbation propagates with strong distortion as a spheric hypergeometric wave [115]. In both cases electric potentials can be univocally defined for any point of the channel, together with the electrical parameters of resistance, inductance and capacitance per unit length. It can be shown that under the present conditions the ratio ρ is very large [114, 116], and the spheric hypergeometric approximation is satisfactory; a scalar potential U and a capacitance per unit length C can be defined for any section of the channel and the

application of the Gauss theorem to the Maxwell's eqs. (78) [113, 114], leads to

$$\left. \begin{aligned} C \frac{\partial U}{\partial t} &= - \frac{\partial I}{\partial x} \\ I &= - \pi a^2 \sigma \frac{\partial U}{\partial x} \end{aligned} \right\} \quad (80)$$

These equations are those of the propagation of electromagnetic waves on a RC transmission line. The motion of electrons during the wave transit (the heavy particles may be assumed still) can be represented with the three conservation eqs. (34), expressed in the mono dimensional form,

$$\left. \begin{aligned} \frac{\partial n_e}{\partial t} + v_e \frac{\partial n_e}{\partial x} + n_e \frac{\partial v_e}{\partial x} &= v_i n_e \\ \frac{\partial v_e}{\partial t} + \frac{k T_e}{n_e m_e} \frac{\partial n_e}{\partial x} + v_e \frac{\partial v_e}{\partial x} + \frac{k}{m} \frac{\partial T_e}{\partial x} + \frac{e}{m} \frac{\partial U}{\partial x} &= - v_i v'_e - v_{eh} v_e \\ \frac{\partial T_e}{\partial t} + v_e \frac{\partial T_e}{\partial x} + \frac{2}{3} T_e \frac{\partial v_e}{\partial x} + \frac{2}{3} \frac{e v_e}{k} \frac{\partial U}{\partial x} &= - \frac{2}{3} v_u^* T_e - v_i \left(T_e + \frac{2}{3} \frac{\epsilon_e}{k} \right) \end{aligned} \right\} \quad (81)$$

Under the present assumptions only the electrons in the channel can contribute to the conduction current ($I = \pi a^2 n_e v_e$) and eq. (80) becomes,

$$\left. \begin{aligned} \frac{\partial U}{\partial t} + \frac{\pi a^2 e}{C} v_e \frac{\partial n_e}{\partial x} + \frac{\pi a^2 e}{C} n_e \frac{\partial v_e}{\partial x} &= 0 \\ v_e &= \mu_e \frac{\partial U}{\partial x} \end{aligned} \right\} \quad (82)$$

The second of eqs. (82) is a particular form of the Ohm's law, which defines just the value of the electron mobility, and is not essential for the solution of the equation system (81) and (82); the latter is a first order system, which can be synthetically expressed in the vector form,

$$\frac{\partial Y}{\partial t} + A(Y) \frac{\partial Y}{\partial x} + B(Y) = 0, \quad (83)$$

where

$$Y = \begin{pmatrix} n_e \\ v_e \\ T_e \\ U \end{pmatrix} \quad A(Y) = \begin{pmatrix} v_e & n_e & 0 & 0 \\ \frac{k T_e}{m_e n_e} & v_e & \frac{k}{m} & \frac{e}{m} \\ 0 & \frac{2}{3} T_e & v_e & \frac{2 e v_e}{3 k} \\ \frac{\pi a^2 e v_e}{C} & \frac{\pi a^2 e n_e}{C} & 0 & 0 \end{pmatrix} \quad B(Y) = \begin{pmatrix} - n_e v_i \\ + (v_i + v_{eh}) v_e \\ \frac{2}{3} v_u^* T_e + v_i \left(T_e + \frac{2}{3} \frac{\epsilon_e}{k} \right) \\ 0 \end{pmatrix} \quad (84)$$

The column vector Y is the vector of the variables, representing the conditions within the leader channel at any time t and position x . This vector is completely defined by the matrix eq. (83), if the initial conditions are assigned, and describes therefore the propagation of the potential perturbation along the channel. Gallimberti and Lanzaro [117] have shown that the non linear differential system (83) can be linearized around a stable solution: this corresponds to approximate in the filament region the spheric

hypergeometric wave with its tangent plane wave. In that case the wave velocity and the attenuation coefficient can be derived from a simple dispersion relation [117, 118],

$$v_f = \sqrt{\frac{2 \pi a^2 e^2 n_e \omega}{v_{eh} m_e C}}; \quad \eta = \sqrt{\frac{v_{eh} m_e C \omega}{2 \pi a^2 e^2 n_e}}; \quad (85)$$

where v_{eh} is the effective momentum-exchange collision frequency between electrons and heavy particles

and ω the angular frequency of the electromagnetic perturbation.

The most important non-linearity in eq. (83) is due to the strong dependence of the ionization frequency on the electric field : however, it can be shown [116] that, because of the short transit time of the wave, the change of the ionization degree during the fast transient can be neglected with respect to the change in the slow transient. As a consequence the electron density n_e in eqs. (85) can be assumed equal to the equilibrium density before the restrike. The average frequency ω can be estimated from the signals of figure 79 : the computed values of velocity and attenuation coefficient, for the average leader parameters of figures 49 to 52, are $v_f = 2.5 \times 10^8$ cm/s and $\eta = 2.4 \times 10^{-2}$ cm $^{-1}$; the corresponding values derived from figure 80 are respectively

$$v_f = (1.0-2.0) \cdot 10^8 \text{ cm/s} \quad \text{and} \quad \eta = 1.8 \times 10^{-2} \text{ cm}^{-1}.$$

The computer solution of eq. (83), with initial conditions appropriate for the leader channel, and for a variation of the potential U of 50 kV in 100 ns is reported in figure 81, which shows the field distribution in space and time. The results of this figure compare satisfactorily with the experimental measurements of figure 79a, except for the tail of the current and light pulses which are associated to the slow transient. Both the experimental and theoretical results show the impulse distortion during the propagation because of the higher attenuation of the high frequency components (eqs. (85)).

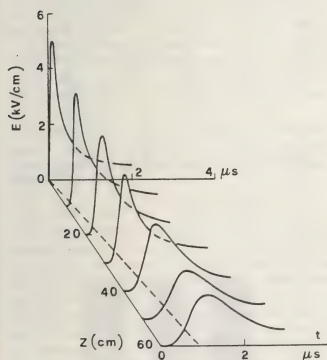
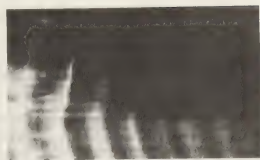
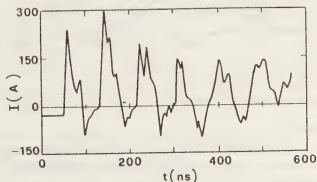


Fig. 81. — The computed field wave propagating across the leader channel for a potential linear variation of 50 kV in 100 ns. The initial conditions correspond to the average leader parameters of figures 49 to 52.



a)



b)

Fig. 82. — The streak photograph (a) of the leader reilluminations when the voltage is suddenly reduced to zero by a parallel chopping gap, and the computed current (b) for the same experimental conditions (4 m rod-plane gap, 220/2 400 μ s wave : chopping a few μ s before breakdown).

6.4 RESTRIKES WITH CHOPPED VOLTAGE. — The comparison between experimental and computed results is satisfactory. However, the overlapping of the fast and slow transients and the influence of the complete discharge circuit make an accurate check of the restrike wave model particularly difficult. A significant check has been done for chopped discharges : in that case it has been experimentally observed a rapid succession of channel reilluminations, any of which last for some 10 ns and appear with frequencies between 10 and 50 MHz (Fig. 82a). These reilluminations are clearly due to the fast transient of the chopped potential wave, propagating along the channel and reflecting up and down at any point of the discharge circuit where the impedances are not matched. For the simulation of this case, eq. (80) have been replaced by a more sophisticated computer program for transient calculations in transmission lines and electrical networks with lumped and distributed parameters variable in time (transient program BPA) [119]. In this way the complete discharge circuit has been simulated together with the leader channel [120]. The rod current is presented in figure 82b : different current waves can be seen to propagate up and down the leader channel, with frequency distributions which compare very well the experimental observations.

The potential of the leader tip U_L (Fig. 83) and the voltage drop across the leader channel ΔU_L fluctuate

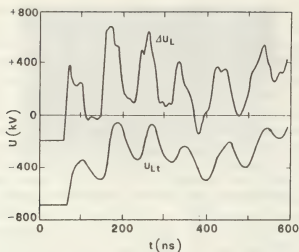


Fig. 83. — The computed leader tip potential U_{Lt} and voltage drop across the leader channel ΔU_L for the same conditions as figure 82.

in correspondence to the reflections of the potential waves in the points where the surge impedances of the different circuit elements are not matched. Figure 84 shows the electric field near the leader head and near the anode; the delay of the field establishment at the leader tip is due to the propagation time along the channel; furthermore, the high frequency components are smoothed because of the energy losses during the propagation. The general agreement with the luminous pattern of figure 81a is quite satisfactory; the simulation puts in evidence two sets of frequencies in the field and current records (short and long range reflections), which appear also in the experimental streak photos.

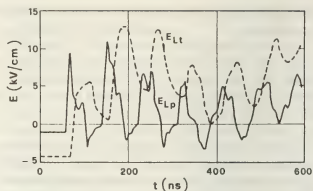


Fig. 84. — The computed field near the leader head E_{Lt} and near the anode point E_{Lp} for the same conditions as figure 82.

7. The final jump and the spark formation. —

7.1 EXPERIMENTAL RESULTS. — The final jump is the terminal stage of the leader propagation, characterized by a rapid increase of current, which leads inevitably to the short-circuit of the gap. The final jump starts when the first streamers of the leader corona reach the plane. The photographs of figure 85a to 85c show a typical case resolved in time. Figure 85a is an image converter photograph at a speed suitable for examination of the beginning of the final jump: the leader corona is recorded as a diffuse luminosity propagating across the gap. At time t_f the rate of propagation undergoes a rapid increase, accompanied by an enhanced luminosity of the leader channel. It was found that the front of the leader corona accelerates towards the plane attaining a velocity of about 10 cm/μs. In order to examine the terminal

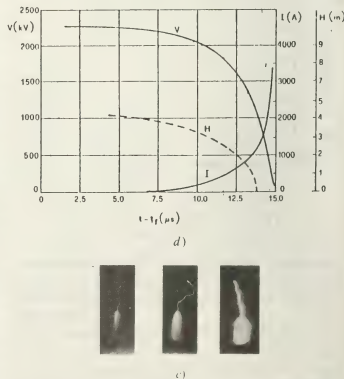
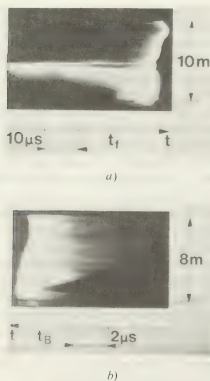


Fig. 85. — Electrical and optical measurements taken during the final jump (a) slow speed streak photo; (b) high speed streak photo; (c) framing photographs at different times before t_B ; (d) voltage and current oscillograms, together with the leader advancement curve.

stage more precisely and particularly the velocity of the leader tip, synchronized image converter records and oscillograms with high time resolution were obtained. From streak records of the type in figure 85b the progress of the leader tip during the last few microseconds before breakdown can be evaluated. When the leader tip approaches the plane the luminosity of the leader increases and at time t_b the whole gap is bridged by the leader. At times following t_b the return stroke is developed, which results in a short-circuit of the gap. The development of this terminal stage is clearly seen in the image converter frame photographs of figure 85c.

The related transient electrical records of voltage and current are shown in figure 85d. At the beginning of the final jump the axial leader velocity has an average value of about $1.4 \text{ cm}/\mu\text{s}$ and increases during the development of the final jump to a value of a few $100 \text{ cm}/\mu\text{s}$ when the leader reaches the plane. Figure 86 shows the variation of leader velocity as a function of the height H of the leader tip above the plane.

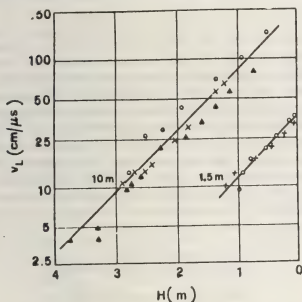


Fig. 86. — The variation of the leader velocity, as a function of the leader head above the ground electrode, for two different gap lengths.

The instantaneous voltage U_f at the beginning of the final jump is a function of h_f only (Fig. 87).

Assuming an average axial field along the leader $E_{Lz} = 1 \text{ kV/cm}$ the potential of the leader tip at the beginning of the final jump $U_{Lt}(t_f)$ can be calculated: it represents the voltage across the unbridged part of the gap, which gives the average field in the streamer glow ($3.5\text{--}4.2 \text{ kV/cm}$). These values of the field are consistent with the reported values of the average gradient along the streamers [2, 55] and with their stability propagation field [40-43]: this confirms the assumption that the final jump is launched by the arrival of the streamers at the plane.

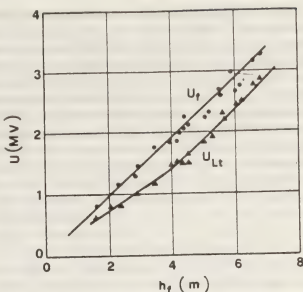


Fig. 87. — The instantaneous applied voltage U_f and the leader tip potential U_{Lt} at the beginning of the final jump, as a function of the height h_f of the final jump itself.

With high resolution electrical and optical measurements, the transition between the leader continuous progression and the final jump has been clearly observed (Fig. 88). It occurs, within 1 or $2 \mu\text{s}$ after the arrival of the streamers at the plane. This is clearly shown by charge and field oscillograms reported in figure 88; the spikes of the record of the field probe denote the neutralization at the plane of the positive charge of the streamer tip [2, 55] and the successive growth observed in the charge oscillogram indicates

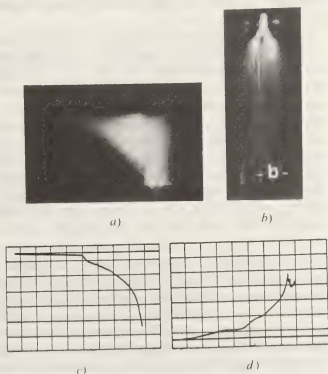


Fig. 88. — The launch of the final jump. (a) Streak photograph of the streamers arriving at the plane; (b) The corresponding frame picture ($1 \mu\text{s}$ exposure); (c) The charge measured in the anode; (d) The electric field on the cathode plane.

the onset of the final jump. From the image converter photographs, it can be seen that the streamers are strongly accelerated in their last path and seem to converge into a few thick bunches which increase their luminosity as they approach the plane and are reilluminated when they reach it. This reillumination, which appears to be stronger near the plane, climbs up towards the leader tip. Its propagation velocity could not be measured accurately because it is near the resolution power of the image converter camera: however it has been estimated to be of the order of $3 \cdot 10^8$ cm/s. This luminosity can be associated to a potential wave caused by the arrival of the streamer tips on the plane [2, 116]. As the brightness of the track decrease when it departs from the plane, it is believed that the front steepness of the potential wave and the associated electric field decrease during the propagation. This is probably due to the energy losses caused by the relatively low ionization degree in the streamer filaments.

According to the model presented in § 6, it has, been calculated that such a potential wave cannot cause a large increase of the ionization degree of the streamer filaments converging into the leader tip, because it loses its ionization capability within about 10 cm. However, following the rearrangement of the potential caused by the travelling wave, a new current regime is started, which is determined by the streamer and leader conductivities. This situation appears to be unstable, the current increases and the leader propagation is accelerated. The delay between the first arrival of the streamers on the plane and the rapid charge increase is probably due to the wave propagation and the transient required to the establish the new regime.

Spectroscopic measurements on the cathode plane, in both short and long gaps [121, 122], indicate vaporization of metal atoms into the gas: this can be associated to the formation of one or more cathodic spots, by ion bombardment, which can supply a permanent source of free electrons to the corona glow. In that case the current is not limited by the mechanism of advancement of the corona ionization front into the gap, but depends only on the applied voltage and the conductivity of the different discharge sections: the cathodic voltage drop can be obviously neglected with respect to the total applied voltage.

7.2 THE THERMALIZATION TRANSITION. — According to the current and voltage oscillograms, the instantaneous values of the power $P = UI$, of the energy $W = \int U I dt$ and of the gap impedance $R = U/I$ can be derived (Fig. 89) [123]. The initial value of the energy at time t_f has been estimated from the fluxmeter measurements, as the fraction of the energy input up to t_f which is dissipated in the leader channel (see Fig. 42). It appears from figure 89 that most of the energy input takes place in the last 4-5 μ s of the final jump. The power drops quite rapidly

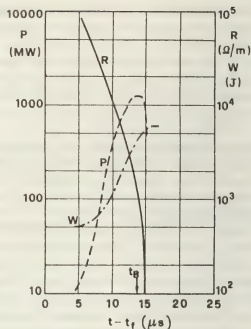


Fig. 89. — The instantaneous power P , energy W and gap impedance R during the final jump (10 m cone-plane gap, 500/10 000 μ s wave).

about 1 μ s after the return stroke, when the voltage collapses. The channel resistance drops at a rate which increases rapidly after t_B . If the channel conductance $1/R$ is plotted as a function of the injected energy (Fig. 90), two different phases can be seen; the first is during the final jump and shows a relatively slow rise of the leader conductance (slope 2.5 in the log-log plot); the second, in the spark phase shows a much higher slope (about 5-6). The transition between the two regimes occurs in less than a microsecond, in correspondence to the leader arrival at the plane and to the return stroke.

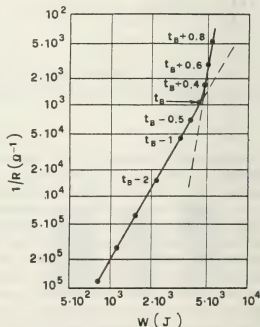


Fig. 90. — The leader conductance as a function of the input of energy (same conditions as figure 89).

The return stroke appears as a fast luminous wave which propagates along the channel at a velocity of the order of 3×10^9 cm/s : in figure 91 the geometrical pattern of the leader has been reported (dashed line) on the streak photo : it can be clearly seen the luminous wave front which climbs up along the channel leading to a strong increase of the light emission.

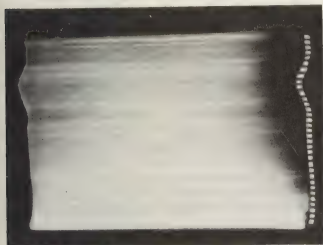


Fig. 91. — The return stroke in a high speed streak photograph (10 m cone-plane gap 500/10 000 μ s wave).

A detailed analysis of spectroscopic results [123], together with the results of figures 89 and 90, has put in evidence that the change of behaviour around the time t_B represents the transition between two different thermo-hydrodynamic regimes : an expansion under non LTE conditions and almost constant pressure during the first stages of the final jump, and a shock wave with strong channel overpressure

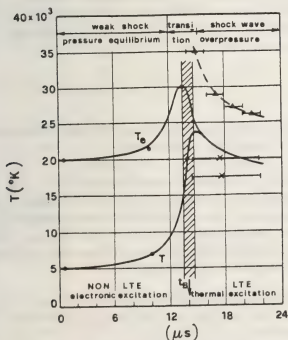


Fig. 92. — The variation of the gas and electron temperature during the final jump, estimated from electrical and spectroscopic measurements.

and complete thermalization of the plasma after the return stroke and in the spark phase. The observed spectra indicate that in the final stages of the final jump (last 5 μ s before t_B) the gas is fully dissociated and the excitation processes are essentially due to electron collisions under the field action ; after the return stroke the appearance of a continuum indicate the establishment of thermal radiation. The results on the leader internal conditions during the final jump are schematically represented in figures 92 and 93 [123-125], together with some direct experimental measurements of temperature and ionization degree in the spark phase.

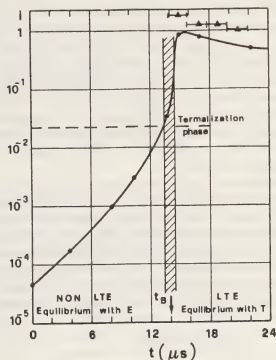


Fig. 93. — The variation of the ionization degree during the final jump, estimated from spectroscopic and electrical measurements.

From the presented experimental results, the leader channel during the final jump appears to change its internal conditions on a much shorter time scale and a wider range, than it occurs during its previous propagation. Due to the establishment of a cathodic region, which supplies a stable electron flux into the leader glow, the current can increase rapidly, together with the power input. As a consequence a number of simplifying assumptions of the model discussed in § 4 are not more valid. However, other assumptions can be made to improve the model for the simulation of the final stages and the transition to the spark phase.

It is well known [125-127], that in the spark the plasma is in local thermodynamic equilibrium : the gas molecules are fully dissociated, the different temperatures are all equal, and the ionization degree satisfies the Saha equation [66, 88].

Therefore, the final jump represents a transition phase, during which the leader conditions change

from the non-LTE characteristics discussed in § 4, to the LTE characteristics of the spark channel; as the ionization degree increases, the electron-neutral collisions become less and less important with respect to electron-ion and electron-electron collisions and the swarm conditions, controlled by the reduced field, change to the Coulomb plasma conditions, controlled by the plasma temperature. As thermodynamic equilibrium is approached, all the gaseous electronics and chemical reactions discussed in § 3 and 4 tend to be balanced by the inverse ones (due to microreversibility) and the final repartitions will then follow the Boltzmann law.

7.3 THE NITROGEN DISSOCIATION. — Let's first consider the mass conservation eq. (37) : the rate of change of particle density is essentially governed by the dissociation and ionization rates \dot{N}_d and \dot{N}_e . It is clear that eq. (43) cannot more be used for \dot{N}_d , because it does not take into account the nitrogen thermal dissociation, and neglects the dependence of the energy fraction f_d of electron collisional dissociation on the gas composition, in particular on the dissociation degree.

At relatively high temperature (5-10.10³ K) the dissociation rate of the N₂ molecules can reach significant values in the final jump timescale : in particular, the presence of the oxygen atoms and molecules can increase largely this rate, through the intermediate formation of nitric oxide. In figure 94 the more important reactions case are schematically represented : the corresponding reaction rates are reported in

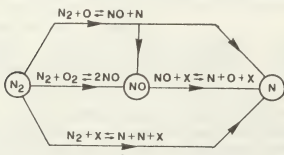


Fig. 94. — The most important reactions leading to the dissociation of nitrogen molecules in the leader channel; the reaction rates are reported in figure 44.

figure 44 [85, 86]. The equivalent time constant results essentially a function of gas temperature T_h and oxygen dissociation degree d . It has been calculated by solving the corresponding system of rate equations, and is reported in figure 95 : the dashed line τ_i represents a saturation limit, due to the fact that the overall dissociation rate is limited by the NO dissociation rate (curve τ_{NO}); τ_i is lower than τ_{NO} because of the presence of parallel direct channels. The total concentration of nitric oxide in the channel gas remains in any case very limited. The third of eq. (43) must be therefore replaced by two equations

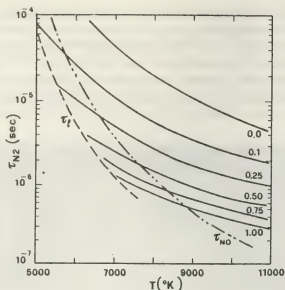


Fig. 95. — The equivalent time-constant for nitrogen dissociation as a function of the gas temperature, for different degrees of oxygen dissociation. τ_i is the saturation curve, limited by the NO dissociation (τ_{NO}).

representing respectively the dissociation of nitrogen and oxygen :

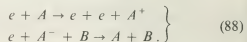
$$\left. \begin{aligned} \frac{d}{dt} [N_{N_2} D_{N_2}^N] &= -f_d^N \frac{n_{N_2}}{n_{N_2}^0} \dot{C}_{eh} - \frac{N_{N_2} D_{N_2}^N}{\tau_{N_2}} \\ \frac{d}{dt} [N_{O_2} D_{O_2}^O] &= -f_d^O \frac{n_{O_2}}{n_{O_2}^0} \dot{C}_{eh} - \frac{N_{O_2} D_{O_2}^O}{\tau_{O_2}} \end{aligned} \right\} \quad (86)$$

where the fraction of energy for direct dissociation by electron impact have been corrected for the specific molecule and for the reduction of the actual number density of undissociated molecules ($n_{O_2}^0$ and $n_{N_2}^0$ represent the corresponding values at temperature T_h without any dissociation). The total dissociation rate of eq. (37) becomes,

$$\dot{N}_d = -\frac{d}{dt} [N_{N_2} + N_{O_2}]. \quad (87)$$

Obviously all the terms of eqs. (86) and (87) are zero when dissociation is complete.

7.4 THE ELECTRON PRODUCTION RATE. — Let's now consider the net ionization rate \dot{N}_e . At relatively low temperature the ionization and recombination reactions, which have been taken into account, were essentially the electron-neutral impact ionization and the three body recombination



At high temperature and ionization degree also the inverse reactions (two-electron recombination and neutral-neutral ionization) have to be taken into

account. Furthermore, other kind of reactions may become important, like multistep ionization or dissociative recombination (and the corresponding inverse reactions). However, let's consider for simplicity the two reactions (88), which are in any case the more important for the actual conditions [66]: the rate equation for the first reaction can be written in the form

$$\frac{dn_e}{dt} = n_e n_a k_a^+ - n_e^2 n_+ k_a^+, \quad (89)$$

where k_a^+ is the direct rate defined by eq. (47) and k_a^+ is the inverse reaction rate. The equilibrium condition is represented by the Saha's equation at the electron temperature T_e ,

$$\beta_{T_e} = \frac{k_a^+}{k_a^+} = \left(\frac{n_e}{n_a} \right)_{T_e} = 2 \frac{g_+}{g_a} \left(\frac{2 \pi m_e k T_e}{h^2} \right) \exp \left[- \frac{\varepsilon_e}{k T_e} \right], \quad (90)$$

where ε_e is the ionization energy. A similar rate equation can be written for the second of reactions (88),

$$\frac{dn_e}{dt} = n_a^2 S_a^+ - n_e n_a n_+ S_a^+, \quad (91)$$

where S_a^+ and S_a^+ are the ionization and recombination rates. In this case, as the ionization occurs in a collision between two particles having an average energy $3/2 k T_h$, the equilibrium condition is expressed by the Saha's equation at the gas temperature,

$$\beta_{T_h} = \frac{S_a^+}{S_a^+} = \left(\frac{n_e}{n_a} \right)_{T_h} = 2 \frac{g_+}{g_a} \left(\frac{2 \pi m_e k T_h}{h^2} \right) \exp \left[- \frac{\varepsilon_e}{k T_h} \right]. \quad (92)$$

If charge neutrality is assumed ($n_e = n_+$), the net rate of ionization can be derived by combining eqs. (89) to (92),

$$\dot{n}_e = n_e n_a k_a^+ \left(1 - \frac{\beta}{\beta_{T_e}} \right) - n_e^2 n_a S_a^+ \left(1 - \frac{\beta_{T_h}}{\beta} \right), \quad (93)$$

where $\beta = n_e^2/n_a$ is the actual value of the density ratio in the non LTE condition. If the rates K_a^+ and S_a^+ are expressed in terms of ionization frequency ν_i and recombination coefficient a_e for the two reactions (88), the net electron production rate for the leader channel becomes,

$$\dot{N}_e = N_e \nu_i \left(1 - \frac{\beta}{\beta_{T_e}} \right) - N_e \frac{N_+}{\pi a^2} a_e \left(1 - \frac{\beta_{T_h}}{\beta} \right). \quad (94)$$

If the electron temperature is much higher than the gas temperature, the actual β value is much higher than β_{T_h} and much smaller than β_{T_e} (for $T_h = 4000$ K, $T_e = 20000$ K and the actual densities calculated in § 5.6, $\beta_{T_h}/\beta = 10^{-2}$ and $\beta/\beta_{T_e} = 10^{-10}$), and eq. (94) becomes equal to eq. (49). On the contrary,

when equilibrium conditions are approached ($T_h = T_e$) the three values become equal, the net rate N_e is reduced to zero and the electron density equals the equilibrium value of the Saha's eqs. (90) and (93). In particular, the quasi-equilibrium electron density of eq. (52) becomes

$$n_c = \frac{\nu_i}{a_e} \frac{(1 - \beta/\beta_{T_e})}{(1 - \beta_{T_h}/\beta)}. \quad (95)$$

If the gas temperature increases the β_{T_h} factor can tend to the actual value of β : in this case n_e and β are forced to follow the temperature increase in an approximate Saha's equilibrium. Physically this corresponds to a threshold where the neutral-neutral collisional ionization approximately balances the three body recombination.

This can be clearly seen if eq. (95) is solved for the ionization degree (n_e/n_h) as a function of both electron and gas temperature,

$$\left(\frac{n_e}{n_h} \right)^3 + \frac{\beta_{T_e} a_e}{\nu_i} \left(\frac{n_e}{n_h} \right)^2 - \frac{\beta_{T_e}}{n_h} \left(\frac{n_e}{n_h} \right) - \frac{\beta_{T_e} a_e}{\nu_i} \frac{\beta_{T_h}}{n_h} = 0. \quad (96)$$

This equation has two negative and one positive roots, which can be found with conventional numerical procedures as functions of T_e and T_h , according to eqs. (90) and (92). Figure 96 shows that at relatively low temperature the ionization degree depends only on the electron temperature (and is in equilibrium with the local field); on the contrary at relatively large gas temperatures the ionization degree varies in quasi-equilibrium with the Saha's equation

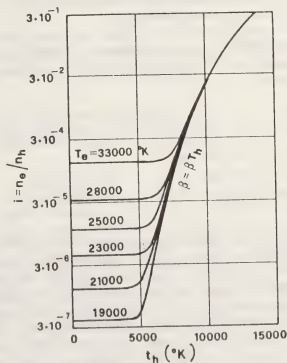


Fig. 96. — The quasi-equilibrium ionization degree in the leader channel, depending on both the electron temperature T_e and the gas temperature T_h .

at temperature T_h , even if the electron temperature is quite larger. This result is in contradiction with the assumption, which is often made in two-temperature gas discharge models, that the ionization degree can be calculated from Saha's equation at the electron temperature T_e .

7.5 COMPUTED RESULTS. — In the electron and ion energy eq. (39), the Coulomb collision term \dot{C}_{e+} increases rapidly with the ionization degree : therefore, it cannot be neglected ; for ionization degrees above 10^{-3} - 10^{-2} , \dot{C}_{e+} becomes larger than the electron-neutral term \dot{C}_{eh} : from this point the electron energy flows preferentially to the positive ions and their temperature may increase significantly above the gas temperature. Also the contributions to the expansion work eqs. (81) cannot more be neglected at large ionization degrees.

In the neutral energy equations, when the temperature increases, the repartition factors f_v and $(f_r + f_e)$ may change significantly because of the changes in the gas composition ; however, as it has been seen in the results of figure 50, the vibrational temperature T_v approaches the gas temperature T_h after about 100 μ s : therefore in the final jump the vibrational reservoir can be assumed to be in equilibrium with the thermal one, and the first two eqs. (43) can be added together. In that case the specific heat c_v^* includes also the vibrational component (see Fig. 47), and all the repartition factors are added together. At high ionization degree the ion-neutral collision term \dot{C}_{+h} becomes dominant. The first of eq. (43) has to include also the N_2 dissociation term according to eqs. (86).

With these improvements the leader model of § 4 can be applied also to represent the final jump and the leader to spark transition.

The initial conditions which have been selected correspond to the average leader conditions at the beginning of the final jump, calculated according to the results of § 4 :

$$\begin{aligned} n_e &= n_+ = 3 \times 10^{-12} \text{ cm}^{-3} & a &= 0.2 \text{ cm} \\ n_h &= 1.8 \times 10^{18} \text{ cm}^{-3} & n_{O_2} &= 5 \times 10^{15} \text{ cm}^{-3} \\ n_{N_2} &= 1.3 \times 10^{15} \text{ cm}^{-3} \\ T_e &= 19\,000 \text{ K} & T_+ &= 4\,150 \text{ K} \\ T_h &= 4\,000 \text{ K}. \end{aligned}$$

The current input is derived from the experimental oscillogram of figure 85. The results of the computation are reported in figures 97 to 100 ; different subsequent phases can be recognized in these figures, corresponding to the role played by the different physical phenomena in the evolution of the leader internal conditions. During a first phase, which lasts for about 6-7 μ s after the beginning of the final jump, the leader characteristics vary approximately in the same manner as during the continuous leader propagation discussed in § 4 : the gas number density

and the electric field decrease almost proportionally, due to the temperature increase and the channel expansion ; the internal pressure and the expansion velocity remain relatively small, increasing smoothly with the current input. Also the dissociation degree of both oxygen and nitrogen molecules increases slowly, according to the relatively low rate of electron collisional dissociation.

After about 5 μ s the temperature becomes large enough for the thermal dissociation of O_2 molecules to exceed the contribution of electron collisions : the curve of the dissociation degree (d_{O_2} in figure 98) presents a sharp bend and its values increase rapidly towards complete dissociation. A similar behaviour is shown by the nitrogen molecules at a slightly larger temperature. During the dissociation phase (7-9 μ s) a large fraction of the energy input to the thermal reservoir is absorbed by the chemical reservoir through the dissociation reactions : as a consequence the temperature rise slows down (Fig. 97) ; on the contrary, the dissociation processes increase the number of neutral particles present in the channel and the gas number density n_h stops to decrease and rises slightly up to the time when dissociation is completed (about 10 μ s). This is consistent with the spectroscopic observations, which have shown that the gas in the leader channel is completely dissociated in the last 4-5 μ s of the final jump (see § 7.2).

Around 9-10 μ s the gas temperature has reached values large enough for the electron density to be controlled essentially by the thermal ionization ($\beta = \beta_{Th}$ in eq. (94)) : the ionization degree increases rapidly, together with the channel conductivity (Figs. 98 and 99), and the electric field starts to

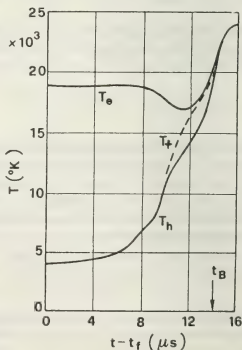


Fig. 97. — The computed temperatures of gas molecules (T_h), positive ions (T_+) and electrons (T_e), in the leader channel during the final jump : t_f = time of start t_B = time of breakdown.

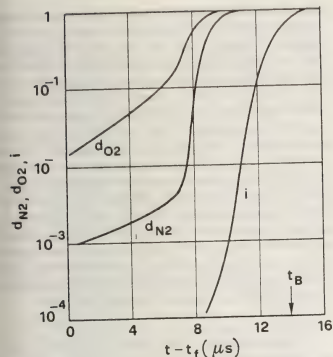


Fig. 98. — The computed dissociation degree of the O_2 and N_2 molecules (d_{O_2} and d_{N_2} , respectively) and the ionization degree (i), in the leader channel during the final jump : t_f = time of start t_B = time of breakdown.

decrease. In the mean time, a large fraction of the energy input goes into ionization losses and the rate of rise of the temperature slows down again.

When the ionization degree is around 0.5×10^{-2} the electron-neutral and electron-ion collision frequencies become approximately equal and the energy flows preferentially from electrons to the ions, better than directly to the neutral molecules. As a consequence, the overall rate of energy transfer from

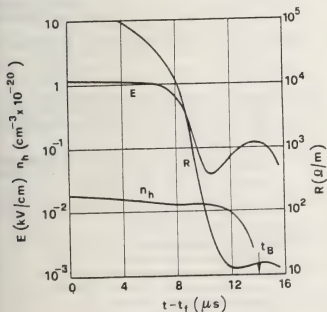


Fig. 99. — The computed electric field (E), gas number density (n_h) and resistance per unit length (R), in the leader channel during the final jump : t_f = time of start ; t_B = time of breakdown.

electrons to heavy particles is enhanced ; the electrons are cooled and the positive ions are heated. At about $14 \mu s$, which correspond approximately to the time t_B when the leader tip reaches the plane, the equilibrium between T_e , T_+ and T_h is reached and the local thermodynamic equilibrium is established.

As the ionization degree increases, together with the electron-ion collision frequency, the electron mobility is reduced (eq. (46)) and the resultant electric field (eq. (45)) is increased : the same occurs for the channel resistance (Fig. 99).

In the last microseconds before t_B , the temperature rise is very fast, leading to a rapid increase of the internal pressure of the channel and of its expansion velocity (Fig. 100). Only in this last phase the expansion velocity becomes larger than the sound speed and a shock wave is launched : this is in good agreement with the Schlieren observations and with the measurements of the channel conductance (Fig. 90).

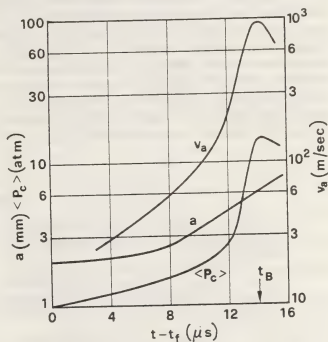


Fig. 100. — The computed radius (a), internal pressure ($\langle P_c \rangle$) and expansion velocity (v_a) of the leader channel during the final jump : t_f = time of start, t_B = time breakdown.

The general behaviour of the model calculations presented in figures 97-100, is quite consistent with the experimental results and estimates presented in §§ 7.1 and 7.2. However the model cannot account for the return stroke, as discussed in § 6 for the restrikes : in order to simulate the propagation and the affects of waves of potential gradient the Maxwell's equations have to be used at the place of the ohmic relation for the electric field (eq. (45)). The model presented in § 6 can be applied also to the conditions of the leader channel at the end of the final jump : the different parameters of eqs. (85) can be derived from the presented results, and the return stroke velocity can be calculated. It results of the order of

$2.3 \cdot 10^9$ cm/s, in satisfactory agreement with the experimental observations (Fig. 91).

According to the experimental voltage oscillogram (Fig. 85) and the computed values of the electric field along the leader channel at the moment when the leader tip reaches the plane, the potential which is short-circuited at time t_B and launches the return stroke results of some hundreds of kilovolts. The field and current waves are consequently very large and only slightly damped (almost plane waves). The plasma channel is already fully ionized, and the effect of the field and current wave is just that of rearranging the potential distribution within the gap and establishing the current regime, which corresponds to the spark phase and which is essentially determined by the characteristics of the external circuit.

Conclusions. — The different experimental results and theoretical models presented in this paper for the different phases of the long spark development testify the large steps forward which have been taken by the research on the physical processes which govern the breakdown of large air spacings. All these processes combine in a different way, depending on the gap length, the electrode geometry and the shape of the applied voltage. A complete breakdown model,

able to predict all the discharge features in all the possible practical configurations, is up to now not realistic. However, both the experimental observations and the theoretical simulations have given a physical background to semi-empirical models [57, 106, 128-134] which can predict many macroscopic breakdown parameters, useful in the design of UHV and EHV transmission lines and in the insulation coordination. Furthermore, a large amount of the knowledge gained in air breakdown can guide the research on the behaviour of the discharge in other gases of practical interest, particularly the electro-negative gases at high pressure, which present a relatively large dielectric strength. The further advancement of the research in this field may be of great help in the general approach to the economical and environmental impact of the large energy transmission systems which are foreseen for the next future.

Acknowledgments. — The author is grateful to all the colleagues and collaborators for common work and helpful discussion. Particular thanks have to be devoted to Dr. E. Marode, Prof. G. Zingales, Prof. G. Baldo, Dr. E. Poli, Dr. B. Glejeses and to all the friends, who have made possible the realization and the presentation of this work, inspite of my difficult personal situation.

References

- [1] Les Renardières Group : Positive discharge in long air gaps at Les Renardières : 1975 results and conclusions, *Electra* **53** (1977) 31-153.
- [2] BALDO, G., GALLIMBERTI, I., GARCIA, H. N., HUTZLER, B., JOUAIRE, J., SIMON, M. F., Breakdown phenomena of long gap under switching impulse conditions. Influence of distance and voltage level, *IEEE Trans. PAS* **94** (1975) 1131-1140.
- [3] BADALONI, S., GALLIMBERTI, I., *The inception mechanism of the first corona in non uniform gaps*, Padova University Report UPee 72/03, 1972.
- [4] GALLIMBERTI, I., *Mathematical model for streamer formation in non uniform gaps*, Padova University Report UPee 72/04, 1972.
- [5] DAWSON, G. A., WINN, W. P., A model for streamer propagation, *Z. Phys.* **183** (1965) 159-171.
- [6] BADALONI, S., GALLIMBERTI, I., GARY, C., HEPWORTH, J. K., KLEWE, R. C., VAREY, R. H., Analysis of first corona pulse, *Electra* **23** (1972) 105-120.
- [7] BADALONI, S., GALLIMBERTI, I., Statistical analysis of Corona inception, *Electra* **35** (1974) 77-83.
- [8] GALLIMBERTI, I., The development of long sparks and the influence of humidity, *Electra* **53** (1977) 103-113.
- [9] SOMERVILLE, I. C., TEDFORD, D. J., Time-lags to breakdown : the detachment of atmospheric negative ions, *5th Int. Conf. on Gas Discharges, IEE publ.* **165** (1978) 250-253.
- [10] SOMERVILLE, I. C., TEDFORD, D. J., The spatial and temporal variations of ion densities in non-uniform field gaps subjected to steady state or transient voltages, *ISH, Milan* 1979.
- [11] BASTIEN, F., HANG, R., LECUILLER, M., Simulation sur ordinateur de l'évolution temporelle des ions négatifs de l'air, *J. Chem. Phys.* **1** (1975) 105-112.
- [12] MC DANIEL, E. W., CERMAK, V., DALGARNO, A., FERGUSON, E. E., FRIEDMAN, L., *Ion-molecule reactions*, John Wiley, New York 1970.
- [13] FERGUSON, E. E., Rate Constants of thermal energy binary ion-molecule reactions of aeronomic interest, *Atomic Data and Nuclear Data Tables* **12** (1973) 159.
- [14] FEHSENFELD, F. C., FERGUSON, E. E., Laboratory studies of negative ion reaction with atmospheric trace constituents, *J. Chem. Phys.* **61** (1974) 3181.
- [15] BENSON, S. W., *Thermochemical Kinetics*, John Wiley, New York 1968.
- [16] VARNEY, R. N., Molecular ions, *J. Chem. Phys.* **31** (1959) 1314.
- [17] GRÜNBERG, R., Messungen des anlagerungskoeffizienten von elektronen in sauerstoff, *Z. Naturforsch.* **24A** (1969) 1039.
- [18] DUTTON, J., A survey of electron swarm data, *J. Phys. Chem. Ref. Data* **4** (1975) 577.
- [19] CHAININ, L. M., PHELPS, A. V., BIONDI, M. A., Measurement of the attachment of low-energy electrons to oxygen molecules, *Phys. Rev.* **128** (1962) 219.
- [20] PACK, J. L., PHELPS, A. V., Electron attachment and detachment. II. Mixtures of O_2 and CO_2 and of O_2 and H_2O , *J. Chem. Phys.* **45** (1966) 4316.
- [21] MARODE, E., La formation de l'arc entre une pointe positive et un plan, *Ph. D. Thesis*, Paris 1972.
- [22] MARODE, E., The mechanism of the spark breakdown in air at atmospheric pressure between a positive point and a plane. I. Experimental : nature of the streamer track. II. Theoretical : computer simulation of the streamer track, *J. Appl. Phys.* **46** (1975) 2005-2020.
- [23] GALLIMBERTI, I., A computer model for streamer propagation, *J. Phys. D. Appl. Phys.* **5** (1972) 2179-89.

- [24] SUZUKI, T., Transition from the Primary Streamer to the arc in Positive point-to-plane corona, *J. Appl. Phys.* **42** (1971) 3766-77.
- [25] MARODE, E., HILHORST, D., GALLIMBERTI, B., GALLIMBERTI, I., The radial distribution of space charge in a filamentary discharge, *Gaseous Electronic Conference*, Buffalo, New York 1978.
- [26] HARTMANN, G., Spectroscopie de la décharge couronne, *PR. D. Thesis*, Paris 1977.
- [27] HARTMANN, G., Spectres émis par des phénomènes prédisruptifs dans l'air à pression atmosphérique, *C. R. Acad. Sc. Paris B* **270** (1970) 309-12.
- [28] HARTMANN, G., Variations of the mean energy of the electrons responsible for the luminous emission from primary streamers in atmospheric air, *3rd Int. Conf. on Gas Discharges*, London, *IEE Conf. Publ.* **118** (1974).
- [29] HARTMANN, G., GALLIMBERTI, I., The influence of metastable molecules on the streamer progression, *J. Phys. D.: Appl. Phys.* **8** (1975) 670-80.
- [30] GALLIMBERTI, I., HEPWORTH, J. H., KLEWE, R. C., Spectroscopic investigation of impulse corona discharges, *J. Phys. D.: Appl. Phys.* **7** (1973) 880-98.
- [31] GALLIMBERTI, I., BADALONI, S., HARTMANN, G., KLEWE, R. C., Time resolved spectroscopic measurements of discharge phenomena, *Electra* **35** (1974) 137-147.
- [32] Les Renardières Group. 1978 Experiments, unpublished results.
- [33] BASTIEN, F., MARODE, E., Stark broadening of H α and H β in ionized gases with space charge field, *J.A.S.R.T.* **17** (1977) 453.
- [34] BASTIEN, F., MARODE, E., Mesure directe par élargissement Stark de raies de l'hydrogène de la densité de couronne dans un gaz ionisé où règne un champ macroscopique quasi uniforme, *J. Physique Appliquée* **12** (1977) 1121.
- [35] TEICH, P. H., Emission gasionisierender Strahlung aus Elektronenlawinen, *Z. Phys.* **199** (1967) 378.
- [36] PENNEY, G. W., HUMMERT, G. T., Photoionization measurements in air, oxygen and nitrogen, *J. Appl. Phys.* **41** (1970) 572.
- [37] BADALONI, S., GALLIMBERTI, I., *Basic Data of air discharges*, Padova University Report UPec 72/05, 1972.
- [38] RAETHER, H., Die Entwicklung der Elektronenlawine in den Funkenkanal, *Z. Phys.* **112** (1939) 464-89.
- [39] LOEB, L. B., MEEK, J. M., *The mechanism of the electric spark*, Stanford University Press, Stanford University, California, 1941.
- [40] PHELPS, C. T., Field enhanced propagations of corona streamers, *J. Geophys. Res.* **76** (1971) 5799-5806.
- [41] PHELPS, C. T., Positive streamer system intensification and its possible role in lightning initiation, *J. Atmos. Terr. Phys.* **36** (1974) 103-11.
- [42] GRIFFITHS, R. F., PHELPS, C. T., The effects of air pressure and water vapour content on the propagation of positive corona streamers, *Quart. J.R. Mat. Soc.* **102** (1976) 419-26.
- [43] GRIFFITHS, R. F., PHELPS, C. T., The dependence of positive corona streamer propagation on air pressure and water vapour content, private communication.
- [44] RAETHER, H., *Electron Avalanches and Breakdown in gases*, Butterworths, London, 1964.
- [45] KUFFEL, E., Electron attachment coefficients in oxygen, dry air, humid air, water vapours, *Proc. Phys. Soc.* **74** (1959) 297.
- [46] WRIGHT, J. K., A contribution to the theory of impulse corona and the long spark, *Proc. Roy. Soc. A* **280** (1964) 29-36.
- [47] KLINGBEIL, R. D., TIDMAN, A., FERNSLER, R. F., Ionizing gas breakdown waves in strong electric fields, *Phys. Fluids* **15** (1972) 1969-79.
- [48] RICHTER, K., Über die Wahrscheinlichkeit der « Kanalbildung » aus einer großen Elektronenlawine, *Z. Phys.* **158** (1960) 312.
- [49] THOLL, H., Der Übergang der Elektronenlawine in den Kanalaufbau bei hoher Überspannung in Stickstoff (mit geringem CH₄-Zusatz), *S. Natur.* **18a** (1963) 587.
- [50] BADALONI, S., GALLIMBERTI, I., Monte Carlo simulation of streamer branching, *XI Int. Conf. on Phen. in Ionized Gases*, Praha 1973.
- [51] LOEB, L. B., *Electrical Coronas*, University of California Press, Berkeley, 1965.
- [52] LOEB, L. B., Aspects of breakdown streamers, *Phys. Rev.* **94** (1954) 227.
- [53] MARR, G., *Photoionization processes in gases*, Academic Press, New York 1967.
- [54] RYZKO, H., Ionization, attachment and drift velocity of electron in Water Vapour and Dry air, *Archiv für Phys.* **32** (1966) 1.
- [55] GALLIMBERTI, I., REA, M., Development of spark discharges in long rod plane gaps under positive impulse voltages, *Alta Frequenza* **42** (1973) 264-275.
- [56] CARRARA, G., THIONE, L., Switching surge strength of large air gaps: a physical approach, *IEEE Trans. PAS* **95** (1976) 512-24.
- [57] PIGINI, A., RIZZI, G., THIONE, L., Influence of gap geometry and impulse shape on the leader characteristics, *Electra* **53** (1977) 51-61.
- [58] JAEGER, E. F., PHELPS, A. V., *Analysis of constrictions in CO₂/N₂/He and air*, private communication.
- [59] JAEGER, E. F., OSTER, L., PHELPS, A. V., Growth of thermal constrictions in a weakly ionized gas discharge in helium, *Phys. of Fluids* **19** (1976) 819-30.
- [60] MARODE, E., BASTIEN, F., BAKKER, M., A model of the streamer induced spark formation based on neutral dynamics, *J. Appl. Phys.* **50** (1979) 140.
- [61] MARODE, E., BASTIEN, F., Study of the parameter influencing gas dynamic processes allowing the current growth to spark breakdown in electro-negative gas mixture, *5th International Conference on Gas Discharge*, Liverpool 1978.
- [62] GALLIMBERTI, I., The characteristics of the leader channel in long gaps, *World Electrotech. Conf.*, Moscow 1977.
- [63] GALLIMBERTI, I., STASSINOPOULOS, C. A., Development of positive discharges in atmospheric air, *Int. Symp. H.V. Technology*, München 1972.
- [64] ALEKSANDROV, G. N., Mechanism of corona to spark transition in long air gaps, *Soviet Phys.* **10** (1966) 949.
- [65] PAEK, J. L., PHELPS, A. V., Electron attachment and detachment, *J. Chem. Phys.* **44** (1966) 1884-88.
- [66] MITCHNER, M., KRUGER, C. H., *Partially ionized gases*, John Wiley, New York 1973.
- [67] WANNIER, G. H., On the motion of Gaseous Ions in strong electric field. I. — *Phys. Rev.* **83** (1951) 281 and Motion of gaseous ions in strong electric field. II. — *Phys. Rev.* **87** (1952) 795.
- [68] GILARDINI, A., *Low energy electron collisions in gases*, John Wiley, New York 1972.
- [69] HAEKE, R. D., PHELPS, A. V., Momentum transfer and Inelastic-Collision cross sections for electrons in O₂, CO and CO₂, *Phys. Rev.* **158** (1967) 70-84.
- [70] LUFT, P. E., Description of a backward prolongation program for computing transport coefficients, *JILA Information Center Report No 14*, University of Colorado, Boulder 1975.
- [71] CALO, J. M., AXTMANN, R. C., Vibrational relaxation and electronic quenching of the C³Π_u (v* = 1) state of nitrogen, *J. Chem. Phys.* **54** (1971) 1332-41.
- [72] MITCHELL, K. B., Fluorescence efficiencies and collisional deactivation rates for N₂ and N₂⁺ bands excited by soft X rays, *J. Chem. Phys.* **53** (1970) 1795-1802.
- [73] LEGLER, W., Anregung von UV-Strahlung in Stickstoff und Wasserstoff durch einen Elektronenschwarm, *Z. Phys.* **173** (1963) 169.
- [74] ROSS, J. N., Light emitted by the discharge, *Electra* **53** (1977) 64-67.
- [75] LEWIS, P. F., TRAINOR, D. W., *Survey of vibrational relaxation data for O₂, N₂, NO, H₂, CO, HF, HCl, CO₂ and H₂O*, AMP 422, AVCO Everett Research Laboratory, Everett, Massachusetts 1974.

- [76] TAYLOR, R. L., BITTERMAN, S., *Rev. Modern Phys.* **41** (1969) 26.
- [77] MC CLELLAND, B. J., *Statistical Thermodynamics*, Chapman and Hall, London 1973.
- [78] BRAGINSKII, S. I., Theory of the development of the spark channel, *Sov. Phys. JETP* **34** (1958) 1068-74.
- [79] ROSS, J. N., The diameter of the leader channel using Schlieren photography, *Electra* **53** (1977) 71-73.
- [80] RÜHLING, F., Leader properties derived from channel diameter measurements, *Electra* **53** (1977) 67-71.
- [81] RÜHLING, F., Private communication.
- [82] WATERS, R. T., Leader and space charge characteristics derived from fluxometer results, *Electra* **35** (1974) 110-16.
- [83] WATERS, R. T., Space charge and energy storage in sphere plane gaps, *Electra* **53** (1977) 77-85.
- [84] ROSS, J. N., JONES, B., WATERS, R. T., The characteristics of the leader channel, *Electra* **53** (1977) 85-89.
- [85] Physical chemistry. An advanced treatise *Kinetics of gas reactions*, vol. VI B, Academic Press, New York, S. Francisco, London 1975.
- [86] BRADLEY, J. N., KISTIAKOWSKY, Shock waves studies by mass spectrometry. I. — *J. Chem. Phys.* **35** (1961) 256.
BRADLEY, J. N., KISTIAKOWSKY, Shock waves studies by mass spectrometry. II. — *J. Chem. Phys.* **35** (1961) 264.
- [87] BRAMBILLA, R., A numerical model for the radial expansion of high current leader channels, *5th International Conference on Gas Discharges*, Liverpool 1978.
- [88] SPITZER, L., Physics of fully ionized gases, *Interscience*, New York 1962.
- [89] PLOOSTER, M. N., Shock waves from line sources. Numerical solutions and experimental measurements, *Phys. Fluids* **13** (1970) 2665.
- [90] LABORIA, P., ROCARD, J. M., REES, J. A., *Sections efficaces électroniques, coefficients macroscopiques*, 2^e, Dunod, Paris 1971.
- [91] LEU, M. T., BIONDI, MANFRED A., JOHNSEN, R., Measurement of the recombination of electrons with H_3O^+ (H_2O)_n series ions, *Phys. Rev. A*, **7** (1973) 292.
- [92] BIONDI, MANFRED A., Atmospheric electron-ion and ion-ion recombination processes, *Canadian J. of Chem.* **47** (1969) 1711.
- [93] Les Renardières Group : Research on long air gap discharges at Les Renardières, *Electra* **23** (1972) 53-157.
- [94] Les Renardières Group : Long Air Gap discharges at Les Renardières : 1973 Results, *Electra* **35** (1974) 49-156.
- [95] GALLIMBERTI, I., A thermo-hydrodynamic model of the leader channel, *Electra* **53** (1977) 89-97.
- [96] TOZIER, B. A., The final jump, *Electra* **23** (1972) 146-50.
- [97] WESTBERG, R. G., *Ph. D. Thesis*, University of California, Berkeley 1958.
- [98] WESTBERG, R. G., Nature and role of ionizing potential space waves in glow-to-arc transitions, *Phys. Rev.* **114** (1959) 1.
- [99] WINN, W. P., *J. Appl. Phys.* **38** (1967) 783-90.
- [100] KEKEZ, U. M., SAVIC, P., An hypersonic model of the spark channel, *J. Phys. D : Appl. Phys.* **7** (1974) 620-28.
- [101] KEKEZ, U. M., SAVIC, P., Further support for the Hypersonic and Volterra models of spark channel development, *IEEE 4th Int. Conf. Gas Discharges*, Swansea 1976.
- [102] PLOOSTER, M. N., Shock waves from line sources. Numerical solution and experimental measurements, *Phys. Fluids* **13** (1970) 2665.
- [103] JOST, W., CRAFT, H. O., *Explosion and Combustion Processes in Gases*, Mc Graw Hill, New York 1946.
- [104] DURAND, E., *Electrostatique*, Masson et Cie, Paris 1966.
- [105] MIRELS, H., MULLEN, J. F., *AIAA J.* **1** (1963) 596.
- [106] HUTZLER, B., HUTZLER-BARRE, D., Grandes étincelles en polarité positive. Caractéristiques de dispersion du leader. *Int. Symp. H.V. Technology*, Zurich 1975.
- [107] HUTZLER, B., HUTZLER-BARRE, D., Leader propagation model for predetermination of switching surge flashover voltage of large air gaps, *IEEE Trans. PAS* **97** (1978) 1087-96.
- [108] BÜSCH, W., GALLIMBERTI, I., The influence of humidity on the breakdown of long air gaps, *Electra* **53** (1977) 113-20.
- [109] BALDO, G., REA, M., An investigation of leader reillumination in long gaps, *11th Int. Conf. on Phen. in Ionized gases*, Prague, 1973.
- [110] BALDO, G., REA, M., Discussion on Reilluminations, *Electra* **35** (1974) 96-100.
- [111] LOEB, L. B., Ionizing waves of potential gradient, *Science* **148** (1965) 1417.
- [112] SUZUKI, T., *J. Appl. Phys.* **44** (1973) 4534.
- [113] SUZUKI, T., Propagation of ionizing waves in glow discharge, *J. Appl. Phys.* **48** (1977) 5001-7.
- [114] GALLIMBERTI, I., LANZARO, A., LOEB, L. B., The propagation of waves of potential gradients along preionized channels, *J. Inst. Electr. Eng. Jpn.* **95** (1975) 1.
- [115] JEFFREY, A., TANIUTI, T., *Non-linear wave propagation*, Academic Press, New York 1964.
- [116] POLI, E., Simulation of the propagation of potential waves in different phases of the discharge, *Thesis*, Padova University, 1974.
- [117] GALLIMBERTI, I., LANZARO, A., *The propagation of waves of potential gradient along discharge channels*, to be published.
- [118] TANIUTI, T., YAJIMA, N., Perturbation Method for non linear wave modulation, I. — *J. Math. Phys.* **10** (1969) 1369.
II. — *J. Math. Phys.* **10** (1969) 2020.
- [119] GALLIMBERTI, I., POLI, E., To be published.
- [120] GALLIMBERTI, I., REA, M., Identificazione ed analisi di circuiti equivalenti per generatori di alte tensioni impulsive, *L'Energia Elettrica* **46** (1969) 11.
- [121] JOHNSON, R. C., BERGER, G., GOLDMAN, M., Temporal behaviour of emission from excited metal atoms in the cathode region of pulsed discharge in air, *J. Phys. D : Appl. Phys.* **10** (1977) 2245.
- [122] BERGER, G., Electrode phenomena during final jump of long sparks, *4th International Conference on Gas Discharge*, Swansea 1976.
- [123] GALLIMBERTI, I., HARTMANN, G., MARODE, E., The leader to spark transition, *Electra* **53** (1977) 123-132.
- [124] VASSY, A., NORINDER, H., VASSY, E., Etude spectrophotométrique d'étincelles de grande longueur dans l'air, *Arkiv für Fys.* **6** (1953) 497.
- [125] ORVILLE, R. E., UMAN, M. A., SLETTEN, M. A., Temperature and electron density in long air sparks, *J. Appl. Phys.* **38** (1967) 895.
- [126] UMAN, M. A., COOKSON, A. H., MORELAND, J. B., Shock wave from a 4-m spark, *J. Appl. Phys.* **41** (1970) 3148.
- [127] THOLL, H., Thermalisierung und zeitliche Entwicklung der Elektronendichte und Temperatur von Funkenkanälen in Wasserstoff, *Z. Naturforschung* **25a** (1970) 420.
- [128] ALEXANDROV, G. N., IVANOV, V. L., KIZEVETTER, V. E., *Electric Strength of external high voltage insulation* (in Russian), Editions, Energiya, Leningrad, 1969.
- [129] ALEXANDROV, G. N., GERASIMOV, YU. A., IVANOV, V. L. and REDKOV, V. P., Switching impulse strength of air gaps between conductors, *Elektricheskie Stanzij* **68** (1973).
- [130] LEMKE, E., *Durchschlagmechanismus und schlagweite-Durchschlagspannungs-Kennlinien von inhomogenen Luftfunkenstrecken bei Schaltspannungen*, Diss T.U., Dresden 1967.
- [131] LEMKE, E., Elements for the evaluation of the sparkover voltage of long air gaps (in German), *Elektr. Inform. Energietechnik*, Leipzig **3**, 4 (1973) 186.
- [132] KLEWE, R. C., WATERS, R. T., JONES, B., *Breakdown phenomena on long gaps under switching impulse conditions*, Ch. 4 Review of models of breakdown, IEEE Summer Meeting 1974, Paper 74-CH-0910-PWR.
- [133] JONES, B., Switching Surges and Air Insulation, *Phil. Trans. Roy. Soc.*, London, vol. A **275** (1973) 165.
- [134] KLINE, L. E., Corona cloud model predictions of switching surge flashover voltage VS electrode geometry, *IEEE Summer Meeting*, 1976.

Progress in the kinetic description of non-stationary behaviour of the electron ensemble in non-isothermal plasmas

J. Wilhelm and R. Winkler

Zentralinstitut für Elektronenphysik, Institutsteil V, Gasentladungsphysik « R. Seeliger », 22 Greifswald/DDR

Abstract. — The understanding of the temporal behaviour of a plasma at several time varying conditions is of great interest under general physical aspects as well as from the point of view of very different applications. After an short survey concerning the investigations related to such problems in the following we discuss some more comprehensive results which were recently obtained in the investigations of the electron ensemble both at the field free collision dominated relaxation in the afterglow during the first period of temporal decay and at the collision dominated relaxation in a plasma with additional heating by an electric field. These studies take into account all main collision processes using realistic functions for the energy dependence of the correlated collision cross sections. The results were attained by the numerical determination of the isotropic velocity distribution function of the electrons and resulting macroscopic quantities. In this way on the basis of kinetic theory a deeper insight into the temporal relaxation mechanism of the electron ensemble in weakly ionized collision dominated plasmas can be gained for many different models of the temporal behaviour of the electric field as the jump-like change and the continuous aperiodical as well as periodical alteration of the field. Thus with the developed sure and widely applicable numerical methods a firm basis has been established to perform further investigations of more general problems grouped around the relaxation models presented here.

1. Introduction. — There is a lot of problems whose solution requires a realistic description of non-stationary states of a homogeneous non-isothermal collision dominated plasma. Illustrating examples are applications of ac-discharges up to some 10 kHz for plasma light generation, the specific techniques of high frequency discharges, the afterglow behaviour with its special relations to the study of several elementary processes and so on. On the other hand there is a widespread interest in the knowledge of relaxation under the aspect of gas laser physics, optical transient processes and from the plasma chemical point of view.

For the physical understanding of the temporal behaviour of plasmas in the course of their decay or under the action of time-variable fields, or in general terms during the temporal transition between several states of the system, it is of great interest to investigate the dominant relaxation processes by which the time dependence of the macroscopic plasma properties is determined. A detailed microphysical knowledge of these processes is of general importance, and, more specifically, it makes a decision possible which degrees of freedom of the components can be treated as being in an approximate equilibrium.

In a first step a qualitative classification can be given for bounded plasmas with the aid of some basic time constants as τ_d : typical diffusion determined life times (for instance by ambipolar diffusion of charged particles and by heavy particle diffusion of the main excited atoms or molecules), τ_a : the

mean life times of the excited atoms and/or molecules (for the most important metastables and atoms in the resonant states) and τ_e : the electron relaxation times for impulse and energy transfer to the heavy particles.

The values of these time constants are especially dependent on the pressure of the heavy plasma components. If we presume a pressure of about 1 torr then the diffusion times τ_d will possess values in a range of roughly one order of magnitude around one millisecond; those of the life times τ_a of excited states have a similar variance around one hundred microseconds and those of τ_e around some tenths of microseconds.

Furthermore, if τ designates the characteristic time constant of a process which causes the temporal changing of the plasma — for example the temporal alteration of an electric field — the resulting very different situations depend primarily on the relation of τ to the other time constants mentioned before. For instance in the case of the action of a periodical electric field the resulting degree of modulation of the macroscopic quantities as the electron density, the mean electron energy, the concentration of excited atoms etc. will be very widely due to the different orders of magnitude of τ .

In this connection some additional remarks appear to be necessary : the classification scheme given is only a rough one. For the investigation of the plasma in each specific time range a further sub-classification of the basic time constants mentioned is necessary

because several processes with their own characteristic time constants are often involved. As representative examples suffice it to mention here the dissociation process via the vibrational states of molecules by eV -, VV - and VT -exchange [1, 2] and the dynamic behaviour of column plasmas as response to external disturbances [3].

Though there are still other examples, from the plasma chemical point of view the chemical relaxation time τ_c of a chemical reaction can also play an important role; its magnitude compared to the other characteristic times mentioned is essential e.g. for answering the question if the classical Arrhenius

chemistry is applicable or if the non-equilibrium kinetics has to be used [4, 5].

Next, for the energy input in the plasma by any electric field the electron component is of basic importance because the energy transfer takes place via this ensemble to the heavy components, which are the source of light or the initial material of special chemical reactions etc. From this point of view we can expect that in the first stage each relaxation response of the plasma after a perturbation in the electric field is dominantly determined by temporal changes in the electron component because of certain high speed processes resulting from the small inertia

Table I.

Problem	Authors	Method	Gas
Field free decay	Bayet, Delcroix, Denise [11]	Representation by the eigenfunctions of the collision operator	Model systems with repulsive central force law $\sim r^{-s}$ ($5 \leq s \leq \infty$) for the collision process
	Schuler a.o. [12]		
	Holway, Jr. [13]	Polynomial expansion with a Maxwellian weight factor	Model system
	Kahalas, Kashian [14]	Special case of [13]	
	Osipov [15]	Special case of [13]	
	Eaton, Holway, Jr. [16]	random-Walk analysis and collision integral expansion	Model system
	Wright [17]	Legendre polynomial expansion	Afterglow in Ar
	Stenflo [18]	Laguerre polynomial expansion	
	Ghatak a.o. [19]	Legendre polynomial expansion and additional Laguerre expansion	Response to a pulsed ac field and relaxation in model systems
	Winkler [20]	Legendre polynomial expansion	General relaxation properties
Transition to a stationary state with non-vanishing electric field	Koch [21]	Legendre polynomial expansion	Model plasma
	Shoda, Ghatak [22]	Legendre polynomial expansion	Response to a pulsed field for a model of elastic collisions (similar to Cs, He, N ₂)
	Braglia, Ferrari [23]	Representation by eigenfunctions	He, Ne, Ar, Kr, Xe
	Polman [24]	Difference-method	Model plasma
	Englert [25]	Monte Carlo	He
	Müller, Müller [26]	Monte Carlo	Relaxation times in Ar after strong increase of electric field
High frequency plasma	Carleton, Megill [27]	Approximation of first order in the electric and magnetic field	Air
	Naidis [28]	Laplace transformation	Model plasma
	Wagner a.o. [29]		Ne

of the electrons. In many cases alterations primarily connected with the greater inertia of the heavy particles will not become noticeable before this point.

The subsequent remarks are devoted to the temporal behaviour of the electron component within the discussed short first time period on the basis of the non-stationary Boltzmann equation. Some efforts were undertaken after World War II to attack pertinent problems under several points of view and with different methods.

First, we may mention here the well known work of Margenau [6], S. C. Brown [7], their coworkers and others who investigated the behaviour of high frequency discharges by means of kinetic theory and/or measurements. These investigations are dealing primarily with such specific aspects of the plasma properties in microwave fields as the electric conductivity, the break down behaviour etc. For this purpose the electron distribution function is developed not only in Legendre polynomials related to the velocity space but also in a Fourier series in time. Especially a frequency range is covered in which only a non-stationary evolution of impulse transfer and therefore also only such one of the anisotropic part of the distribution function occur whilst there is a nearly time independent energy transfer due to the collisions and as a result practically no alteration of the isotropic part during one cycle because of the high frequencies considered. Furthermore some research has also been done to describe more in detail the generation of higher harmonics of the distribution function — particularly of its anisotropic part — in wide frequency ranges of field and collisions, using the same kinetic basis [8].

Moreover, we would like to mention the research work done by Parker and Lowke, Lucas, Skullerud as well as by others [9] on the space-time development of an electron swarm based on the Boltzmann equation or Monte Carlo simulations. Finally the investigation of the time evolution of the distribution function in a beam-excited field free Xe and Ar laser discharge by Elliot and Greene [10] is worth mentioning in this context.

In the following we refer to collision dominated plasmas with low and medium degrees of ionization. In these the relaxation of the electron component is determined by energy and impulse transfer from the electrons to the atoms and/or molecules which is realized by collisions. The main processes under this aspect are the elastic and the inelastic collisions — such as excitation and dissociation — between electrons and the heavy particles. In addition, with increasing ionization degree also the Coulomb interaction, especially among the electrons, gains a remarkable influence particularly on the interchange of energy between the electrons of the different energy ranges and thus indirectly on the energy transfer from the electrons to the atoms. Furthermore, in certain gases there are also other kinds of collisions

which can win an additional influence on the relaxation processes, for example attachment in the case of electronegative gases or the recombination of electrons and ions with growing degree of ionization. Because of the numerous kinds of possible collision processes we will confine ourselves to plasmas with sufficiently low ionization degrees and therefore, besides the influence of an electric field, to the action of elastic and inelastic collisions. Also the main properties of the temporal development and the relaxation mechanism of the electron component can be understood already from studies of inert gas-plasmas.

Under these aspects those former works are of interest in which particular attention is given to the temporal energy relaxation by collisions. Special problems are the decay or in broader terms the temporal transitions between different states as well as the periodic behaviour and also its adjustment.

We may mention here a number of papers based on the kinetic approach (*), being roughly classified in the table I.

Most of the cited publications with numerical results are restricted to elastic collisions or to special models of inelastic collisions with the exception of the papers [25, 26] and [27], in which exciting collisions are also included.

In the following we will discuss some more comprehensive results which were recently obtained in the investigations both of the field free collision dominated relaxation in the afterglow during the first period of temporal decay and of the collision dominated relaxation of the electron ensemble in a plasma with additional heating by an electric field. These calculations take into account all main collision processes, using realistic functions for the energy dependence of the correlated collision cross sections. The results were attained by the determination of the isotropic velocity distribution function of the electrons and resulting macroscopic parameters. In this way a physical understanding of the macroscopic properties is attained on the basis of kinetic theory. It is also possible to gain an illustrating qualitative insight into the temporal occurrences with the aid of defined and numerically determined characteristic relaxation times, though we are not in a position here to present such a concept in detail because of the limited time.

2. The theoretical background. — Basis of the electron kinetics of a non-stationary anisothermal weakly ionized plasma under the above mentioned aspects described by a kinetic equation is the Boltzmann equation, in which we consider elastic and

(*) The papers use the Boltzmann equation or Monte Carlo methods. Besides this there are investigations applying balance equations; also relaxation processes due to Coulomb interaction only are not within the scope of our considerations.

inelastic collisions. In the Lorentz approximation the usual development of the velocity distribution func-

tion in the Legendre polynomials leads to the equation system

$$\begin{aligned} \frac{\partial}{\partial \bar{t}} f - \frac{1}{3} \frac{\bar{v}_E(U, \bar{t})}{p_0} \frac{\partial}{\partial U} (U f_A) - \frac{2}{U^{1/2}} \frac{m}{M} \frac{\partial}{\partial U} \left(U^{3/2} \frac{\bar{v}_d(U)}{p_0} f \right) + \\ + \sum_k \frac{\bar{v}_k^n(U)}{p_0} f - \sum_k \left(\frac{U + U_k}{U} \right)^{1/2} \frac{\bar{v}_k^{\text{in}}(U + U_k)}{p_0} f(U + U_k, \bar{t}) = 0, \\ \frac{\partial}{\partial \bar{t}} f_A - \frac{\bar{v}_E(U, \bar{t})}{p_0} U \frac{\partial}{\partial U} f + \frac{\bar{v}_d(U)}{p_0} f_A = 0 \end{aligned} \quad (1a, b)$$

in which the transformation to the volt equivalent of the momentary energy was performed in conformity with $e_0 U = m v^2/2$.

Here f and f_A are according to

$$\begin{aligned} f(U, \bar{t}) &= 2 \pi (2 e_0/m)^{3/2} f_0 [v(U), \bar{t}/p_0] / n_e(\bar{t}) = 0, \\ f_A(U, \bar{t}) &= 2 \pi (2 e_0/m)^{3/2} f_1 [v(U), \bar{t}/p_0] / n_e(\bar{t}) = 0 \end{aligned} \quad (2a, b)$$

the normalized isotropic and the first anisotropic part of the distribution function.

From the normalized function f the electron concentration $n_e(\bar{t})$ is determined by the expression

$$n_e(\bar{t}) = n_e(0) \int_0^\infty U^{1/2} f(U, \bar{t}) dU. \quad (3)$$

Furthermore

$$\begin{aligned} \bar{v}_E/p_0 &= (2 e_0/m)^{1/2} (E/p_0) (1/U^{1/2}), \\ \bar{v}_d/p_0 &= (2 e_0/m)^{1/2} U^{1/2} n_g Q_d(U), \quad (4a, b, c) \\ \bar{v}_k^n/p_0 &= (2 e_0/m)^{1/2} U^{1/2} n_g Q_k^n(U) \end{aligned}$$

represent the characteristic frequency for the action of the electric field and the collision frequencies for impulse transfer and for the inelastic processes respectively. Finally $E(\bar{t})$ is the homogeneous electric field, $Q_d(U)$ and $Q_k^{\text{in}}(U)$ are the total cross sections for impulse transfer and for the different inelastic collision processes, $\bar{t} = p_0 t$ the normalized time, p_0 the time-independent pressure of the neutral atoms related to 0 °C, n_g the atom concentration at 1 torr and 0 °C, U_k the threshold potentials of the several inelastic processes. Because of the special binary collision processes between electrons and atoms considered here the introduction of such normalized time scale \bar{t} becomes possible and in the same way we thus obtain normalized relaxation times.

In (1b) we have as usual neglected the unimportant terms of the inelastic collisions.

2.1 THE FIELD FREE CASE. — Under the condition $E = 0$ the eqs. (1a, b) for f and f_A are not connected with one another and can be handled separately. Eq. (1b) for the anisotropic part f_A is reduced to a simple usual differential equation of first order with the momentary energy U as parameter [30]; thus the solution can be found only if an initial function f_A at $\bar{t} = 0$ is given. On the other hand (1a) is simplified to a partial differential equation of first order for f with additional difference-terms due to the inelastic collisions. The temporal behaviour of f has a unique solution in the ranges of $\bar{t} \geq 0$ and $U \geq 0$ if an initial distribution at the moment $\bar{t} = 0$ and the boundary condition

$$\lim_{U \rightarrow \infty} f(U, \bar{t}) = 0 \quad (5)$$

for all \bar{t} are given; the latter condition follows from the fact that the distribution function can in principle be normalized. The concentration and energy balances, consistent with (1a), are obtained by integration over U from 0 to ∞ and by such integration after multiplication with U respectively in the form

$$\frac{d}{d\bar{t}} n_e(\bar{t}) = 0,$$

$$\frac{d}{d\bar{t}} \bar{U}(\bar{t}) + \bar{U}_e(\bar{t})/p_0 = 0, \quad (6a, b, c)$$

$$\bar{U}_e(\bar{t})/p_0 = \bar{U}^{\text{el}}(\bar{t})/p_0 + \sum_k \bar{U}_k^{\text{in}}(\bar{t})/p_0.$$

\bar{U} means the volt equivalent of the mean electron energy, \bar{U}^{el} and \bar{U}_k^{in} the volt equivalents for the energy losses by elastic and the different inelastic collisions normalized per one electron and time unit and accordingly \bar{U}_e designates the total energy loss by collisions.

Especially for these quantities there are the relations

$$\begin{aligned}
 \bar{U}(\bar{t}) &= \int_0^{\bar{t}} U^{3/2} f(U, \bar{t}) dU, \\
 \bar{U}^d(\bar{t})/p_0 &= 2(m/M) (2e_0/m)^{1/2} n_g \int_0^{\bar{t}} U^2 Q_d(U) f(U, \bar{t}) dU, \\
 \bar{U}_k^{in}(\bar{t})/p_0 &= U_k v_k^{in}(\bar{t})/p_0, \\
 v_k^{in}(\bar{t})/p_0 &= (2e_0/m)^{1/2} n_g \int_0^{\bar{t}} U Q_k^{in}(U) f(U, \bar{t}) dU
 \end{aligned} \tag{7a-d}$$

with v_k^{in} as the frequency for the k -th inelastic collision process.

2.2 NON-VANISHING ELECTRIC FIELD. — In this case the eqs. (1a, b) are connected with one another.

In order to solve this system of partial differential equations it is useful to estimate the rapidity of the temporal alteration of the isotropic and the anisotropic part f and f_A .

Next there are the relations

$$\begin{aligned}
 2(m/M) (\bar{v}_d/p_0) &\ll \bar{v}_d/p_0 \quad \text{for } 0 \leq U \leq (U_k)_{\min}, \\
 2(m/M) (\bar{v}_d/p_0) &\ll \sum_k v_k^{in}/p_0 \ll \bar{v}_d/p_0 \quad \text{for } U > (U_k)_{\min}
 \end{aligned} \tag{8a, b}$$

which are realized nearly for all gases. A detailed qualitative discussion of the equation system (1a, b) shows that using the supplementary condition

$$1/(E/p_0) \cdot \frac{d}{dt} (E(\bar{t})/p_0) \ll \bar{v}_d(U)/p_0 \tag{8c}$$

(i.e. the characteristic frequency for the temporal alteration of the electric field is much smaller than the frequency of impulse transfer due to elastic collisions) a rapidity of the temporal changing of the anisotropic part follows which is by some orders of magnitude greater than that of the isotropic part. Then the formal solution of (1b) is reduced under the given conditions (8) to

$$f_A(U, \bar{t}) \approx f_A(U, 0) e^{-\bar{v}_d(U)\bar{t}/p_0} + \frac{\bar{v}_E(U, \bar{t})/p_0}{\bar{v}_d(U)/p_0} U \frac{\partial}{\partial U} f(U, \bar{t}) \cdot (1 - e^{-\bar{v}_d(U)\bar{t}/p_0}) \tag{9}$$

and we can see that the adjustment of the anisotropic part proceeds exponentially with the frequency for impulse transfer to a state which is determined by the momentary electric field $E(\bar{t})$ and by the isotropic distribution $f(U, \bar{t})$. Therefore, instead of (1b) its quasi-stationary approximation can be used.

If we suppose for the further investigation that the characteristic frequency for the field alteration is always small in comparison with \bar{v}_d/p_0 , i.e. excluding ac-discharges in the range of very high frequencies, the system (1a, b) is simplified to the following parabolic partial differential equation of second order with additional difference-terms

$$\begin{aligned}
 (1, n_g) (m/2e_0)^{1/2} U^{1/2} \frac{\partial}{\partial t} f - (1/3 n_g^2) (E(\bar{t})/p_0)^2 (U/Q_d(U)) \frac{\partial^2}{\partial U^2} f - \\
 - \left[(1/3 n_g^2) (E/p_0)^2 \frac{d}{dU} (U/Q_d) + 2(m/M) U^2 Q_d \right] \frac{\partial}{\partial U} f \\
 - \left[2 \frac{m}{M} \frac{d}{dU} (U^2 Q_d) - U \sum_k Q_k^{in} \right] f - \sum_k (U + U_k) Q_k^{in} (U + U_k) f(U + U_k, \bar{t}) = 0.
 \end{aligned} \tag{10}$$

In (10) $E(\bar{t})/p_0$ is the only plasma parameter determining the temporal behaviour.

Now, in the same range $\bar{t} \geq 0$ and $U \geq 0$ the unique solution of (10) requires an additional boundary condition at $U = 0$ in relation to the field free case.

A detailed discussion suggests to apply the condition [31]

$$\lim_{U \rightarrow 0} \frac{\partial}{\partial U} f(U, \bar{t}) = 0 \quad \text{for } \bar{t} \geq 0 \tag{11}$$

i.e. that for a nearly arbitrary behaviour of Q_d for $U \rightarrow 0$ the field term does not represent a source of electrons in the concentration balance (6a).

Applying this additional boundary condition, we obtain the same concentration balance (6a) but instead of (6b) the generalized form of the energy balance

$$\frac{d}{dt} \bar{U} = \bar{U}_F p_0 - \bar{U}_c p_0. \quad (12)$$

Here

$$\bar{U}_F(\bar{t}) p_0 = p_0 b_e(E p_0)^2 \quad (13)$$

is the normalized energy input from the electric field per electron and per time unit with the electron mobility b_e due to

$$p_0 b_e(\bar{t}) = - (2 e_0/m)^{1/2} \frac{1}{3 n_g} \int_0^\infty \frac{U}{Q_d} \frac{\partial}{\partial U} f dU. \quad (14)$$

3. Review of the temporal relaxation of the electron distribution function and of characteristic macroscopic parameters. — 3.1 RELAXATION IN A TEMPORALLY DECAYING PLASMA WITHOUT FIELD HEATING. — With $E = 0$ the solution of (1b) gives

$$f_A(U, \bar{t}) = \tilde{f}_A(U) e^{-\tilde{\nu}_A \bar{t} p_0} \quad (15)$$

with $\tilde{f}_A(U)$ as an arbitrary initial distribution for the anisotropic part. We observe that the anisotropy decays exponentially with the frequency $\tilde{\nu}_A(U)/p_0$ in the normalized time \bar{t} .

Starting for instance from a stationary state in the column plasma of a usual glow discharge and assuming typical values for the diffusion cross section of 10^{-16} to 10^{-15} cm^2 , the anisotropic part f_A is markedly damped down within some 10^{-9} torr s. Because of the relation

$$f(\bar{t}) = \frac{1}{3} \left(\frac{2 e_0}{m} \right)^{1/2} \int_0^\infty U f_A(U, \bar{t}) dU \quad (16)$$

for the particle current density of the electrons practically the same short relaxation time results also for the electric current of the glow discharge plasma.

Such situation is realized for instance after a jump-like switching off of the electric field in a stationary plasma.

For the same kind of decay the temporal evolution of the isotropic part f was investigated [30, 32] in the inert gas neon and the molecular gas hydrogen in order to illustrate the general behaviour. (1a) is reduced to a partial differential equation of first order with difference terms.

As initial condition we choose the stationary isotropic distribution

$$f(U, \bar{t} = 0) = f_{st}[U, (E/p_0)_{st}]$$

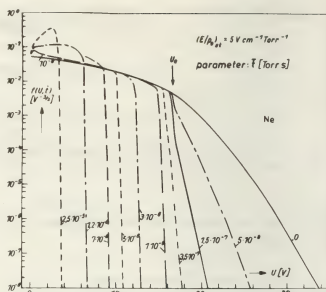


Fig. 1a.

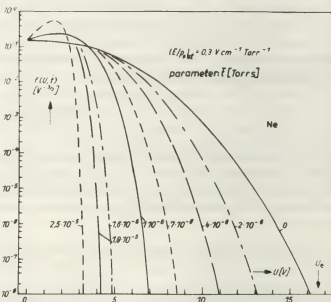


Fig. 1b.

existing at $\bar{t} = 0$ which characterizes the moment of switching off the field. The numerical solution was performed with the aid of a finite difference method using centered second-order-correct difference analogs. The concentration and energy balance (6a, b), consistent with the applied kinetic equation, were used to control the precision of the calculated isotropic distribution. Figures 1a, b show the temporal development of the isotropic distribution as function of U with \bar{t} as parameter performed for a neon plasma, where we described the exciting collisions by a lumped state with a threshold energy of $U_e = 16.6 \text{ V}$. The figures are related to the two different states determined by $(E/p_0)_{st} = 5$ and 0.3 V/(cm torr) . These initial stationary states are characterized by prevailing energy losses due to exciting or elastic collisions. It can be seen that the first part of the decay is determined first of all by the energetic situation in

the initial state where the field is switched off. If this state is dominantly determined by energy losses owing to exciting collisions (Fig. 1a) at first only a quick damping of the tail takes place during a characteristic time of $\approx 10^{-8}$ torr s for a noticeable temporal alteration. The depopulation of the high-energy range is finished within $\approx 3 \times 10^{-7}$ torr s. Then the relaxation is continued via the further thermalization of the distribution only by elastic collisions with a characteristic time of $\approx 10^{-6}$ torr s for a noticeable change. In the second case (Fig. 1b) the initial distribution is essentially restricted to the energy range where only elastic collisions occur; therefore a noticeable alteration of the distribution is found in the characteristic time $\approx 10^{-6}$ torr s because now exciting collisions are insignificant.

Because of the very different atomic data of molecular hydrogen compared to those of the inert gas neon also a very different relaxation behaviour of the distribution function in hydrogen results. In figures 2a, b the time development of this function is presented for the initial field strengths $(E/p_0)_a = 23$ and 10 V/(cm torr).

Performing the calculation, we used the main collision cross sections of vibrational excitation, of electronic excitation for singulet and triplet levels and of ionization, moreover the diffusion cross section for elastic collisions [33]. As it can be seen from figure 2a there exists a varied relaxation behaviour in the energy range from 0.5 to ≈ 9 V of marked vibrational excitation and in the range greater than ≈ 9 V of electronic excitation and ionization. Whereas the characteristic time for noticeable decay of the distribution amounts to $\approx 10^{-9}$ torr s in the latter range we find such a characteristic time of $\approx 10^{-8}$ torr s for the first

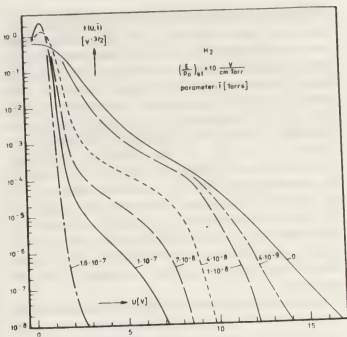


Fig. 2b.

range. This characteristic time of 10^{-8} torr s can be observed also from figure 2b where for the decay particularly the vibrational excitation is significant. Furthermore we would like to emphasize that the characteristic decay times obtained for hydrogen are shorter by orders of magnitude compared to those in the neon plasma, which is primarily due to the differences in the atomic data.

3.2 RELAXATION IN A PLASMA WITH FIELD HEATING.

— In the cases considered in the previous section the relaxation processes proceed without energy input by an electric field so that the temporal development of the isotropic distribution and thus of the macroscopic behaviour always leads to a monotonous energy loss of the electron component and therefore causes a thermalization effect. A more complicated situation will result if in addition an electric field acts on the electrons. Then the temporally successive states will be determined by two competing processes, the momentary energy input from the electric field and the energy losses by the different kinds of collisions.

From the point of view presented at the beginning of the paper there exist several problems which are of general interest; for instance the question how the transition is performed to a stationary state which is determined by a time independent value of the electric field and produced for example by a sudden jump in the field. It is further of some importance to understand the behaviour in continuous time dependent fields. In particular it is useful to explain the state behaviour in aperiodical and periodical electric fields in different situations according to diverse conditions of parameters.

Besides the practical aspects of such questions it seems of physical interest to identify the dominant

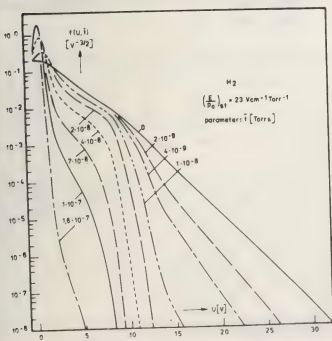


Fig. 2a.

relaxation processes under varied parameter conditions and thus to provide a detailed understanding on a kinetic basis including the different time constants which characterize them. In addition to the field free decay, where we used characteristic times for noticeably altering the distribution, now a characteristic time for the adjustment of the final state gains increasing interest, for instance the adjustment of a stationary state or of the periodical behaviour. Moreover, it is important to determine the limits of the characteristic time for noticeable alterations of the electric field at which the instationary behaviour of the electron component changes to a quasi-stationary variation in the given field or to the other extreme case of a slow time dependent behaviour of the quantities in rapidly varying fields compared to the field alteration.

Many of the questions mentioned here concerning the relaxation of the electron component in a weakly ionized plasma can already be clarified via the investigation of an inert gas plasma with its more simple structure according to the collision processes. In the last years a sure and a widely applicable method was developed [31] to obtain a very precise solution of eq. (10) as an initial-boundary value problem for different parameters. In order to perform the calculation of the isotropic distribution a generalization of the Crank-Nicolson difference-method has been used including an iterative treatment of the supplementary difference terms resulting from the inelastic collisions.

In the following sections we will discuss results obtained in solving some of the mentioned problems.

3.2.1 Relaxation after a jump-like change of the electric field. — At first we discuss some results [31, 34] concerning this case, which allows a physical understanding of the relaxation mechanism and the main reasons which determine the characteristic times for the adjustment $\bar{\tau}_r = p_0 \tau_r$ of the final new stationary

state. For this we present besides the distribution $f(U, \bar{t})$ first of all the time development of two quantities, the mean energy $\bar{U}(\bar{t})$ described by (7a), which characterizes the electrons in the bulk of their distribution and the normalized lumped frequency of exciting collisions $v_e(\bar{t})/p_0$. The latter is a special case of (7d), because we want to confine ourselves primarily to inert gas plasmas, where in certain cases we can work with such a summarized excitation level, v_e characterizing the high energy tail of the distribution. Besides this, two other quantities are very helpful for physical understanding, the energy transfer relation R_F and the energy loss quotient R_c which in conformity with (13) and (7b, c) are described by

$$R_F(\bar{t}) = \bar{U}_F / \bar{U}_c, \quad R_c(\bar{t}) = \bar{U}^{el} / (\bar{U}^{el} + \bar{U}^s). \quad (17)$$

The first term compared the energy input from the electric field with the total energy loss by collisions and is therefore, according to the energy balance (12), representative for the degree of the non-stationarity. The second quantity describes the ratio of the energy loss by elastic collisions to the total energy loss by both types of collisions.

Our investigations were performed in neon plasma using the well known data on the cross sections. We always started with the stationary distribution determined by $(E/p_0)_i$ which represents the electric field before momentary switching to the new value $(E/p_0)_f$. As representative examples we consider the transitions in table II.

Table II.

$(E/p_0)_i$ [V/(cm torr)]	$(E/p_0)_f$ [V/(cm torr)]
10 (0.092)	→ 1 (0.408)
2 (0.116)	
0.6 (0.866)	
0.3 (1.000)	

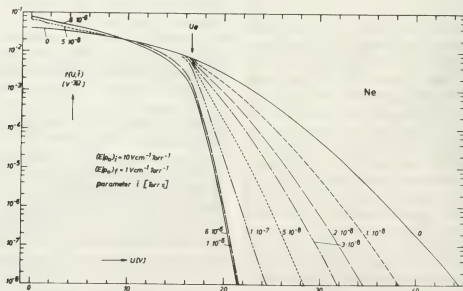


Fig. 3.

The numbers in brackets are the values of R_f for the stationary initial and final states, in each case determined by (E/p_0) . It can be seen that the initial states vary from such ones determined dominantly by energy losses due to exciting collisions to those determined by elastic losses. On the other hand the final state is characterized by nearly equal elastic and exciting energy losses.

In figure 3 we can see the time alteration of the distribution function determined by the chosen transition from $(E/p_0)_i = 10 \text{ V/(cm torr)}$ to

$$(E/p_0)_f = 1 \text{ V/(cm torr)}.$$

Due to the great field heating in the initial stationary state immediately after the jump-like decrease of the field a marked depopulation of the high energy tail takes place, noticeable already at normalized times of $\approx 10^{-8}$ torr s. This behaviour is caused mainly by the action of the exciting collisions. The whole relaxation process is finished within some 10^{-6} torr s.

Figures 4a, b show the time development of \bar{U} and v_d/p_0 and figures 5a, b that of the energy transfer relation R_F and the energy loss quotient R_C as function of the time \bar{t} . It should be emphasized that despite very diverse stationary initial distributions all transitions to the new state are realized in nearly the same time of $4-7 \cdot 10^{-6}$ torr s. Generalizing this result we have verified that, starting from different stationary initial distributions, the characteristic time for each adjustment of a new stationary state is dominantly determined by the special situation in the energy loss due the different kinds of collisions in the final state and is nearly independent of the specific initial stationary distribution.

In order to overlook the range of alterations of the adjustment times, which is rather wide due to broad changes in the parameter $(E/p_0)_f$ of the final states, we discuss some results which are presented

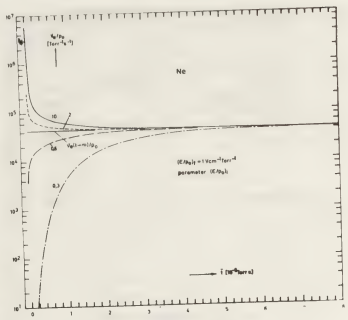


Fig. 4b.

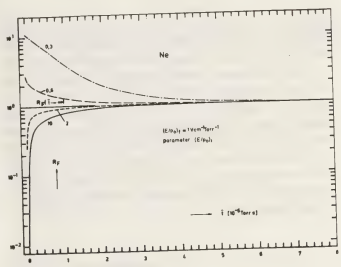


Fig. 5a.

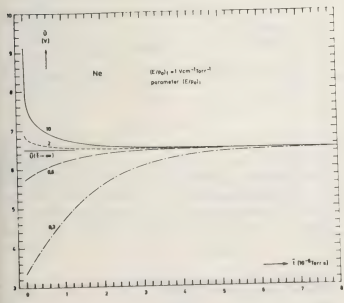


Fig. 4a.

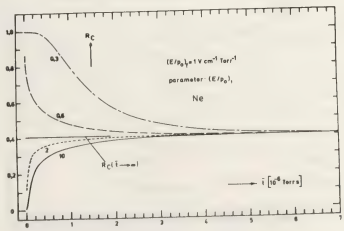


Fig. 5b.

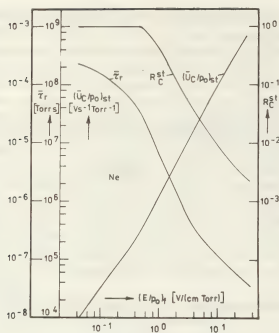


Fig. 6.

in figure 6 and describe several transitions to new stationary states. The values of $(E/p_0)_f$ used for the final states cover a range of field strengths which are of interest for many column plasmas. We can observe that the adjustment time τ_r changes by nearly four orders of magnitude due to the very different energy transfer situations in the final states caused by the collision processes. These values of τ_r can be taken for example from the adjustment of the energy transfer relation $R_f(\bar{t})$ towards the value 1 of the stationary state for the different transitions presented in the figure 7.

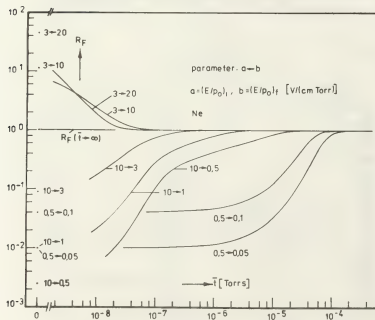


Fig. 7.

Additionally, in figure 6 the values of the total energy losses per sec $(\bar{U}_c/p_0)_{st}$ in the final stationary states are given, which illustrate that the decrease of the adjustment time is related to an increase in $(\bar{U}_c/p_0)_{st}$ of nearly the same order.

From the energy loss quotient R_c^{st} in the final state also presented in figure 6 we can see that the greatest alteration in the adjustment time takes place in the range where the transition is performed from the states dominantly determined by elastic collisions to such determined by exciting collisions. In neon this region is approximately given by

$$0.5 \text{ V/(cm torr)} \leq (E/p_0)_f \leq 3 \text{ V/(cm torr)}$$

as illustrated in figure 6 by the course of the energy loss quotient R_c^{st} in dependence of $(E/p_0)_f$. However at lower as well as higher $(E/p_0)_f$ values there are still further but smaller changes in the adjustment time. At these values the energy losses are realized almost exclusively via one kind of collision process. The strong alteration of the adjustment time can be explained qualitatively with the fact that the energy transfer per electron becomes increasingly more efficient with growing $(E/p_0)_f$. On the one hand with increasing $(E/p_0)_f$ the electrons transfer a higher amount of energy to the neutral atoms in elastic collisions. On the other hand in neon above

$$(E/p_0)_f \approx 0.5 \text{ V/(cm torr)}$$

the exciting collisions, which are much more effective than the elastic collisions because at least the threshold energy is lost per one collision, gain more and more importance. This can be distinctly recognized from figure 8, where some selected stationary distribution functions are shown which illustrate the extraordi-

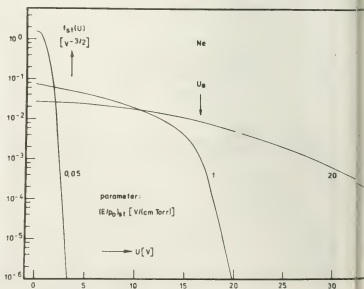


Fig. 8.

arily different population of electrons in their energy space for different electric field strengths $(E/p_0)_{st} (*)$.

The observed dependence of the adjustment time will be valid even if we do not start from stationary states correlated to $(E/p_0)_i$ but from another initial distribution according to a special physical situation [32]. To illustrate this with a representative example we applied initial distribution functions of the form

$$f_i(U) = \frac{(2n+3)^{n+(3/2)}}{\sqrt{2\pi(2n+1)}!!} \frac{U^n}{\bar{U}^{n+(3/2)}} e^{-(2n+3)U/(2\bar{U})}, \quad n \geq 0 \quad (18)$$

which becomes a Maxwellian distribution for $n=0$; for greater n more beam-like distributions around the mean energy \bar{U} result. In figure 9, besides the initial stationary distribution at

$$(E/p_0)_i = 0.5 \text{ V/(cm torr)},$$

distributions according to (18) for $n=0.3$ and 10 with the same mean energy are shown. Despite the very diverse initial distributions we found in each case nearly the same adjustment time in which the same final state was reached.

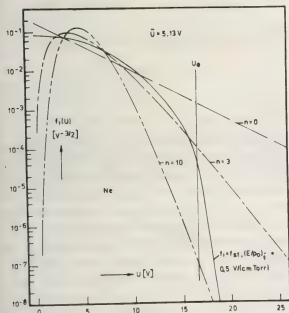


Fig. 9.

Finally, we will make a short remark concerning the dependence of the adjustment time on atomic data such as the different magnitude of cross sections and atom mass in different gas plasmas. In figures 10a,b you can see the evolution of the mean energy \bar{U} and the lumped excitation frequency ν_e/p_0 for the same transitions

(*) In [25] a similar sensitive dependence of this adjustment time on the normalized electric field strength $(E/p_0)_f$ in the final stationary state was found by Monte Carlo investigations in a He plasma.

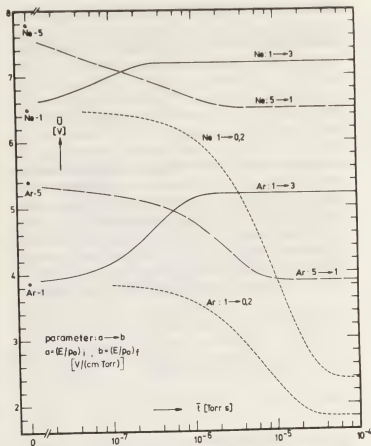


Fig. 10a.

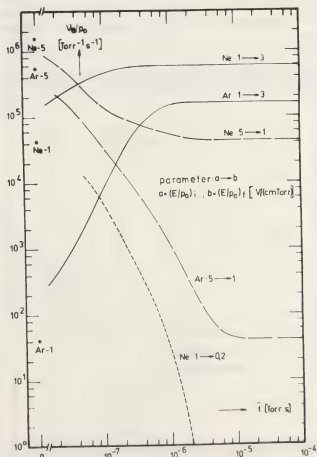


Fig. 10b.

Table III.

$(E/p_0)_i$ [V/(cm torr)]	$(E/p_0)_f$ [V/(cm torr)]
1	3
5	1
1	0.2

for Ne as well as Ar [35]. Indeed there are considerable changes in the values of the adjustment time, especially for the first two transitions where differences of about one order of magnitude for the two considered gases result. This dependence of the adjustment time can be explained first and foremost by the great differences in the energy transfer situation for the two gases at the same field strength

$$E(t)/p_0 = \begin{cases} (E/p_0)_i + \frac{1}{2}[(E/p_0)_f - (E/p_0)_i][1 + \sin \pi(\bar{t}/\bar{t}_E - \frac{1}{2})], & 0 \leq \bar{t} \leq \bar{t}_E, \\ (E/p_0)_f, & \bar{t} \geq \bar{t}_E \end{cases} \quad (19)$$

during the normalized time \bar{t}_E [36]. Next we discuss the results of the calculations performed for the parameters of the following table. In figure 11a the temporal development of the summarized frequency $\nu_{\Sigma}(t)/p_0$ for exciting collisions is presented for Ne as full lines. Curve parameter is the normalized time \bar{t}_E for adjustment of the final value of the electric field.

Table IV.

$(E/p_0)_i$ [V/(cm torr)]	$(E/p_0)_f$ [V/(cm torr)]	\bar{t}_E [torr s]
1	0.35	2×10^{-7} ; 1×10^{-6} ; 5×10^{-6} ; 1×10^{-5} ; 2.5×10^{-5} ; 5×10^{-5} ; 1×10^{-4} ; 4×10^{-4}

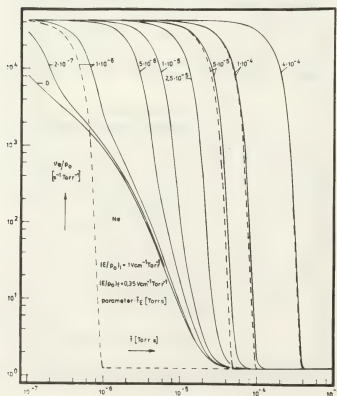


Fig. 11a.

$(E/p_0)_f$ in the final stationary state and finally by the different atomic data.

3.2.2 *Relaxation in aperiodically altering fields.* — If the electric field is acting during the relaxation process, in general a more complex situation results because of the rivalry of the continuously altering energy input by the field and the energy loss in collisions. Limiting cases are on the one hand the nearly jump-like change of the electric field — as treated above — and on the other hand the quasi-stationary change simultaneously with the field. Apart from other questions it is of interest to find relations which characterize these limiting cases. In order to investigate these questions we considered an aperiodical continuous field alteration between the initial and final values $(E/p_0)_i$ and $(E/p_0)_f$ according to the expression

In any case the dashed lines denote the alterations calculated in a quasi-stationary way whilst the curve marked with 0 is the change after jump-like switching off of the electric field. The figure clearly shows that the non-stationary time behaviour changes between these two limits, an evolution which is close to that after jump-like alteration of the electric field at sufficiently small field transition times \bar{t}_E and a behaviour at sufficiently high \bar{t}_E which coincides with the quasi-stationary course. This result is self-evident from the physical point of view. It can also be seen that the limit times are in this special case $\approx 2 \times 10^{-7}$ and

$$\approx 4 \times 10^{-4} \text{ torr s.}$$

The change of the time behaviour between these two limits will once again be demonstrated very clearly by the course of the quantity R_F in figure 11b. In the range of small field transition times \bar{t}_E we notice a strongly non-stationary behaviour — the values of R_F are far away from the stationary value 1 — which becomes smaller and smaller with increasing \bar{t}_E . The marked disturbance in the stationary state at smaller \bar{t}_E results from a quick change in the momentary energy input $\bar{U}_F(t)$ whilst the momentary energy loss $\bar{U}_L(t)$ by collisions follows this alteration much

more slowly. Thus we observe that, via the rapidity of field alteration, the time dependent electric field exerts in addition a noticeable control on the relaxation process and thus also on the adjustment time to the new stationary state or to the quasi-stationary behaviour of the electron component.

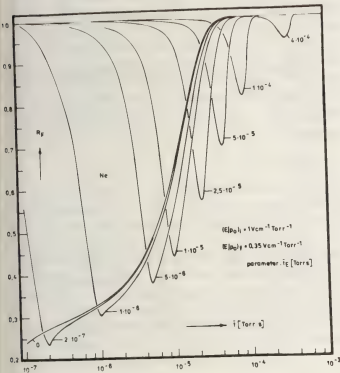


Fig. 11b.

3.2.3 The time evolution in periodical fields. — In this case also a very complex situation is to be expected which results from the competition between the momentary energy input by the electric field and

the losses by collisions. In the further statements we will give some examples which we have obtained in investigations of the temporal development of the electron ensemble in a dc-field $(E/p_0)_d$ with a superimposed ac field with the amplitude $(E/p_0)_a$. Whilst in [37] the non-stationary behaviour was investigated for small degrees of modulation in connection with the studies on the impedance, in which the linearized Boltzmann equation was used, we are now [38] in a position to examine situations with high degrees of modulation.

To calculate the periodical temporal evolution of the isotropic distribution it would be sufficient to know the real periodical state at one moment and to use it as initial state. But because such a distribution is unknown it is only possible to obtain an insight into the periodical behaviour by calculation of an adjustment process starting from a chosen initial state. Also from this point of view it is of interest not only to establish the periodical behaviour as dependent on different parameter conditions but also the adjustment to this final periodical state.

The following considerations are related to a field course

$$E(\bar{t})/p_0 = (E/p_0)_d [1 + M \sin 2\pi \bar{t}/\bar{t}_p] \quad (20)$$

with the degree of modulation

$$M = (E/p_0)_a / (E/p_0)_d \quad (21)$$

and the normalized time \bar{t}_p of a period of the electric field. As a representative example we consider the case described by the parameters given in table V for a Ne plasma.

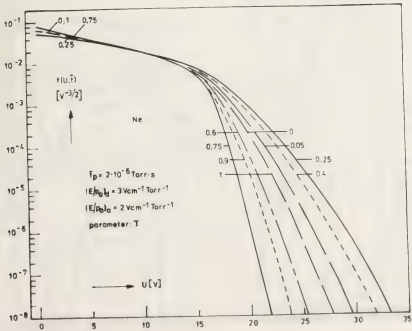


Fig. 12.

Table V.

$$(E/p_0)_d = 3 \text{ V/(cm torr)}, \quad (E/p_0)_a = 2 \text{ V/(cm torr)},$$

$$\bar{t}_p: 5 \times 10^{-6}, 2 \times 10^{-6}, 5 \times 10^{-7},$$

$$1 \times 10^{-7}, 5 \times 10^{-8}, 2 \times 10^{-8} \text{ torr s}$$

To illustrate the behaviour after adjustment to the periodical state in figure 12 the alteration of the energy distribution is exhibited over one period (here described by the parameter $\tau = t/\bar{t}_p$ counted from the start of a period after the adjustment process) with $\bar{t}_p = 2 \times 10^{-6}$ torr s. It can be noticed that the high energy tail of the distribution increases at the beginning of a period until the field has reached nearly its maximum value (which is given at $\tau = 1/4$) and then decreases until the field has almost reached its minimum. Then the distribution returns to its initial course again. In the low energy range the distribution shows a reverse behaviour and does not show such sensitive changes.

Next, let us have a look at the figures 13a, b where the temporal change of the mean energy \bar{U} and the summarized frequency ν_e/p_0 for exciting collisions is presented as full lines according to the parameters \bar{t}_p of table V. It should be pointed out that at greater \bar{t}_p -values the temporal alteration is realized in a nearly quasi-stationary way so that at each moment the non-stationary values are close to the stationary ones also presented in these figures as dashed lines which are at any moment correlated to the electric field. With decreasing time \bar{t}_p of a period the deviation from the quasi-stationary course becomes increasingly greater, an effect which is coupled with an increasing reduction of the modulation of the macroscopic quantities and a growing phase shift between the

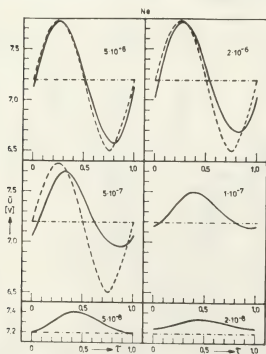


Fig. 13a.

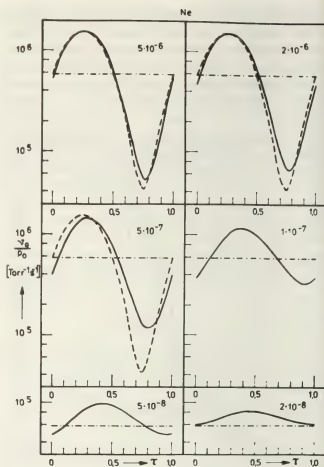


Fig. 13b.

macroscopic quantities and the electric field. The continuous transition of the temporal behaviour from a nearly quasi-stationary one to the limiting case of small amplitude modulation can be easily understood under the aspect of the energy balance (12), which is consistent with the Boltzmann equation. Figure 14 shows the non-stationary course of the

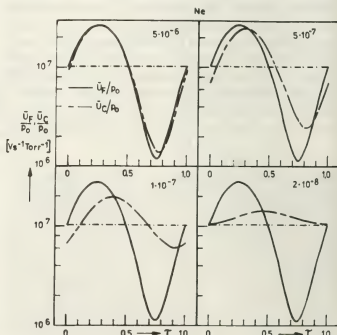


Fig. 14.

energy input \bar{U}_e/p_0 and the total loss \bar{U}_e/p_0 by collisions. There are only small differences between input and loss at the greatest chosen \bar{t}_p and thus we find disturbances of only minor importance in the stationary energy balance. With decreasing period time \bar{t}_p the deviations continue to grow. It is obvious that this is primarily caused by a change of the course of the energy losses via collisions. This latter phenomenon is combined with a continuous diminution of the modulation due to the fact that collision processes can compensate the momentary energy input less and less during larger parts of one period. Finally we would like to illustrate the adjustment behaviour using two examples which show the temporal development of the lumped collision frequency ν_e/p_0 for the two different cycle times

$$\bar{t}_p = 5 \times 10^{-7} \text{ and } \bar{t}_p = 5 \times 10^{-8} \text{ torr s,}$$

starting in each case from 3 different initial stationary distributions. The initial conditions are correlated to the zero passage of the ac-part as well as to the maximum and the minimum of the electric field. Figures 15a, b make it evident that there are very different adjustment times in which the same periodical state is reached. These are determined by the special energy transfer situations during the adjustment process and depend on the values of the electric field attained during the adjustment process and on the rapidity of the periodical field alteration.

3.2.4 An example for the comparison between calculated and experimentally determined relaxation behaviour of the electron component. — Using the above results, a special examination of the relaxation behaviour of usual column plasmas in inert gases resulting from collision processes and of the additional action of a temporal decaying electric field —

which can't be presented here in detail — shows that noticeable first alterations will occur already after very short characteristic normalized times

$$\bar{t} \approx 10^{-8} \text{ torr s}$$

if the energy transfer to the neutral atoms takes place dominantly via exciting collisions in the first period of the development. Time resolved measurements of the isotropic distribution and dependent quantities such as the mean energy, drift velocity, frequency of direct ionization, Townsend coefficient etc. are very complicated and laborious under this condition. On the other hand, when the energy transfer in the first period is realized primarily via elastic collisions, marked variations will appear in times

$$\bar{t} \approx 10^{-6} \text{ torr s,}$$

which makes possible a comparison between theoretical and experimental results. We made such a comparison for the decay of the electron-atom-Bremsstrahlung continuum. This continuum can be measured in a sufficiently short time and permits the registration of the temporal change of the isotropic distribution almost in the whole energy space via the wave length dependence of the Bremsstrahlung intensity. Therefore the time behaviour of the Bremsstrahlung in the range of 200 to 1 000 nm was calculated [39] in decaying Ne and Ar column plasmas under medium pressure conditions starting from stationary states and using decay profiles for the electric field as they are suggested by experimental measurements; on the other side time resolved decay measurements of the relative radiation intensity were performed for some ranges of the wavelength λ . To calculate the intensity it is necessary to know the volume-emission-coefficient of this radiation $\varepsilon(\lambda, \bar{t})$.

We calculated the intensity I per unit length of the column according to the relation

$$I(\lambda, \bar{t}) = 2\pi \int_0^R r \varepsilon(\lambda, t) dr = C\pi R^2 N_e N \psi^*(\lambda, \bar{t}), \quad C = \frac{4\sqrt{2}}{3\pi} \frac{e_0^{7/2}}{\varepsilon_0 m^{3/2} c^2}, \quad (22)$$

$$\psi^*(\lambda, \bar{t}) = \frac{1}{\lambda^2} \int_{hc/e_0\lambda}^{\infty} Q_d(U) U^2 \left(1 - \frac{hc}{2e_0 U \lambda}\right) \left(1 - \frac{hc}{e_0 U \lambda}\right)^{1/2} f(U, \bar{t}) dU$$

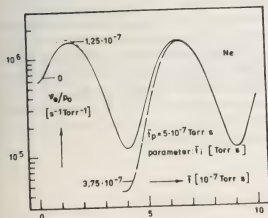


Fig. 15a.

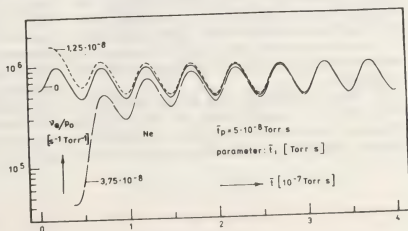


Fig. 15b.

assuming the isotropic distribution of the electrons and the atom concentration N as nearly independent of the radial coordinate r ; N_e is the electron concentration averaged over the cross section of the column and R the radius of the tube. According to (22) the time dependence of I can be realized via the distribution function and the electron concentration. Under the considered conditions the characteristic time for a noticeable onset of the relaxation process is, as mentioned already, $\approx 10^{-6}$ torr s, whilst marked alterations of the electron concentration are to be expected not before 10^{-4} – 10^{-3} torr s. Therefore down to a normalized time of $\approx 10^{-4}$ torr s the time dependence of the emission is almost exclusively determined by that of the isotropic distribution.

In order to calculate the evolution of the distribution function we must know the temporal change of the electric field. In the μ s-range time resolved direct measurements of the internal field are not easy to realize but such of the time course of the external discharge current after switch off are not so difficult. The approximate course of $E(t)/p_0$ can be obtained from the decay of the current flowing in the external circuit. Because under the considered conditions the relaxation of the anisotropic part of the distribution function and therefore also of the current occurs in an almost stationary way we can assume in a first step that the electric field is nearly proportional to the external current during the decay. As the measurements showed in the majority of cases a nearly linear decay of the discharge current in an absolute decay time t_d of some μ s, we used in the calculations also such linear field decay (the latter indicated by — — —) and additionally a parabolic decay with the same time t_d (— · — · —) and a jump-like decay (— · — · —).

The examples given in figures 16a, b are the decay of the relative intensity $I(\lambda, t)/I(\lambda, 0)$ for $\lambda = 380$ nm in neon ($p_0 = 20$ torr, $(E/p_0)_{st} = 0.42$ V/(cm torr), $t_d = 1 \times 10^{-6}$ s) and for $\lambda = 330$ nm in argon ($p_0 = 8.8$ torr, $(E/p_0)_{st} = 0.64$ V/(cm torr),

$$t_d = 2 \times 10^{-6} \text{ s});$$

that means the agreement of the measurements with the calculations for the linear and parabolic decay profiles is satisfactory. Though the real decay of the electric field in the column plasma is unknown today these and further results we obtained can nevertheless be reasonably explained by the collision dominated relaxation mechanism of the electron component applied here.

The above results show that on the basis of the kinetic theory a deeper insight into the temporal relaxation mechanism of the electron ensemble in collision dominated plasmas can be gained for many

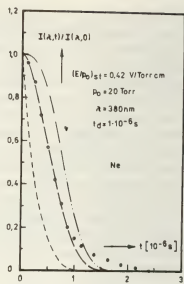


Fig. 16a.

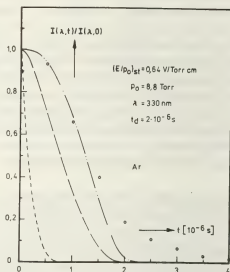


Fig. 16b.

different models of the temporal behaviour of the electric field. In addition, we investigated some more generalized relaxation models of the electron component which take into account the action of a pure high frequency field [40] as well as ionizing collisions and a particle loss term for the electrons [41], however they cannot be described here in detail. Thus a firm basis has been established to perform further investigations of more general problems grouped around the relaxation models presented here which are of interest under various aspects. Extensions of the kinetic methods to still more generalized conditions, which cover additionally also such processes as the Coulomb interaction between the electrons and the attachment of electrons, seem also promising.

References

- [1] POLAK, L. S., SERGEEV, P. A., SLOVECKI, D. I., *Ilinija Vysokih Energij* **7** (1973) 387.
- KRIZMIN, V. A., POLAK, L. S., SERGEEV, P. A., SLOVECKI, D. I., *Ilinija Vysokih Energij* **8** (1974) 129.
- [2] CAPITELLI, M., DILONARDO, M., MOLINARI, E., *Chem. Phys.* **20** (1977) 417.
- CAPITELLI, M., DILONARDO, M., *Chem. Phys.* **24** (1977) 417.
- CAPITELLI, M., DILONARDO, M., *Rev. de Physique appliquée* **13** (1978) 115.
- CACCIATORE, M., CAPITELLI, M., DILONARDO, M., *Beitr. Plasmaphys.* **18** (1978) 279.
- CRAMAROSSA, F., D'AGOSTINO, R., *Beitr. Plasmaphys.* **18** (1978) 301.
- [3] DEUTSCH, H., PFAU, S., RUTSCHER, A., *Wiss. Z. E.M. Arndt-Universität Greifswald XXIII* (1974) 9.
- [4] For instance :
SMITH, F. T., Chemical reactions in high-temperature gases as collision processes ;
LIGHT, J. C., ROSS, J., SCHULER, K. E., Rate coefficients, reaction cross sections and microscopic reversibility ; both in : Kinetic processes in gases and plasmas (Edit. by A. R. Hochstim), Academic Press 1969.
- [5] POLAK, L., *Pure App. Chem.* **39** (1975) 307.
- KOURA, K., *Journ. Chem. Phys.* **59** (1973) 691 ; **63** (1975) 3302.
- [6] MARGENAU, H., *Phys. Rev.* **69** (1946) 508 ; **73** (1948) 297.
- MARGENAU, H., HARTMANN, L. M., *Phys. Rev.* **73** (1948) 309.
- HARTMANN, L. M., *Phys. Rev.* **73** (1948) 316.
- [7] MC DONALD, A. D., BROWN, S. C., *Phys. Rev.* **76** (1969) 1634.
- VARNERIN, L. J., JR., BROWN, S. C., *Phys. Rev.* **79** (1950) 946.
- REEDER, F. H., BROWN, S. C., *Phys. Rev.* **95** (1954) 885.
- MC DONALD, A. D., BETTES, D. D., *Can. J. Phys.* **30** (1952) 565 ; **32** (1954) 812.
- BROWN, S. C., *Hdb. Phys.* (S. Flügge) bd. XXII, 2. Springer 1956, S. 531 ff.
- GOLANT, V. E., *Sh. tech. fis.* **27** (1957) 756.
- TICHOMIROV, I. A., MARUSIN, W. W., *Sh. tech. fis.* **37** (1967) 110.
- [8] For instance :
ROSEN, P., *Phys. Fluids* **4** (1961) 341.
- SODHA, M. S., KAW, P. K., *Phys. Fluids* **8** (1965) 1402.
- MURPHY, B., *Phys. Fluids* **8** (1965) 1543.
- KRENZ, J. H., *Phys. Fluids* **8** (1965) 1871.
- CHIYODA, K., *J. Phys. Soc. Japan* **20** (1965) 290.
- TANG, T. W., *Phys. Fluids* **9** (1966) 415.
- MORRONE, T., *Phys. Fluids* **10** (1967) 1507.
- STILLER, W., VOITA, G., *Z. Naturforsch.* **24a** (1969) 545, 555.
- VARNUM, W. S., DESLOGE, E. A., *Phys. Fluids* **12** (1969) 816.
- [9] For instance :
PARKER, J. H., JR., *Phys. Rev.* **139** (1965) A 1792.
- PARKER, J. H., JR., LOWKE, J. J., *Phys. Rev.* **181** (1969) 290, 302.
- HUCHITAL, D. A., HOLT, E. H., *Proc. VIIth ICIPIG, Belgrad* 1966, Contr. Pap. Vol. 2, p. 95.
- HUCHITAL, D. A., HOLLINGER, H. B., HOLT, E. H., *Phys. Fluids* **12** (1969) 1691.
- LUCAS, J., *Int. J. Electron.* **29** (1970) 465.
- LUCAS, J., SAELE, H. T., *J. Phys. D : Appl. Phys.* **8** (1975) 640.
- MCINTOSH, A. I., *Aust. J. Phys.* **27** (1974) 59.
- SKULLERUD, H. R., *Aust. J. Phys.* **27** (1974) 195.
- TAGASHIRA, H., SAKAI, Y., SAKAMOTO, S., *J. Phys. D : Appl. Phys.* **10** (1977) 1051.
- [10] ELIOT, C. J., GREENE, A. E., *J. Appl. Phys.* **47** (1976) 2946.
- [11] BAYET, M., DELCROIX, J. L., DENISSE, J. F., *Journal Phys. Rad.* **17** (1956) 923, 1005.
- ARSAC, A., BASQUIN, L., DENISSE, J. F., DELCROIX, J. L., SALMON, J., *Journal Phys. Rad.* **19** (1958) 624.
- DELCROIX, J. L., *Introduction à la théorie des gaz ionisés*, Chap. 7 (Paris 1959).
- [12] SHULER, K. E., WEISS, G. H., ANDERSON, K., *Journ. Math. Phys.* **3** (1962) 550.
- ANDERSON, K., SHULER, K. E., *Journ. Chem. Phys.* **40** (1964) 633.
- OSER, H., SHULER, K. E., WEISS, G. H., *Journ. Chem. Phys.* **41** (1964) 2661.
- [13] HOLWAY, L. H., JR., *Phys. Fluids* **10** (1967) 35.
- [14] KAHALAS, S. L., KASHAN, H. C., *Phys. Fluids* **2** (1959) 100.
- Confer also :
HANSEN, L. K., *Phys. Fluids* **9** (1966) 1618.
- [15] OSIPOV, O. I., *Bull. Moscow Univ., Ser. III* **1** (1961) 13.
- [16] EATON, C. F., HOLWAY, L. H., JR., *Phys. Rev.* **143** (1966) 48.
- [17] WRIGHT, B. L., *Quart. Rep. Res. Lab. of Electronics M.I.T.* **86** (1967) 134.
- [18] STENFLO, L., *Ark. Fys.* **38** (1968) 267.
- [19] GHATAK, A. K., *Z. Phys.* **226** (1969) 454.
- GHATAK, A. K., KAMAL, J., *Z. Phys.* **236** (1970) 245.
- GHATAK, A. K., CHAKRAVARTI, A. K., RAITAN, I., *Journ. Phys.* **D 3** (1970) L 30.
- [20] WINKLER, R., *Ann. Phys. Lpz.* (7) **31** (1974) 293.
- [21] KOCH, E., *Beitr. Plasmaphys.* **9** (1969) 267.
- [22] SODHA, M. S., GHATAK, A. K., *J. Appl. Phys.* **43** (1972) 1529.
- [23] BRAGLIA, G. L., *Nuovo Cimento* **58B** (1968) 352.
- BRAGLIA, G. L., FERRARI, L., *Nuovo Cimento* **67B** (1970) 167 ; **2B** (1971) 254 ; **4B** (1971) 245, 262.
- [24] POLMAN, J., *Physica* **54** (1971) 305.
- [25] ENGLERT, G. W., *Z. Naturforsch.* **26a** (1971) 836.
- [26] MÜLLER, K. G., MÜLLER, W. O., *Z. Naturforsch.* **30a** (1975) 1553.
- [27] CARLETON, N. P., MEGILL, L. R., *Phys. Rev.* **126** (1962) 2089.
- [28] NAIDES, G. V., *Proc. XIIIth ICIPIG, Berlin 1977*, Contr. Pap., p. 741.
- [29] WAGNER, S. D., IGNATYEV, B. K., TSENDIN, L. D., *Proc. XIIIth ICIPIG, Berlin 1977*, Contr. Pap., p. 333.
- [30] WILHELM, J., WINKLER, R., *Ann. Phys. Lpz.* (7) **34** (1977) 385.
- [31] WILHELM, J., WINKLER, R., *Beitr. Plasmaphys.* **16** (1976) 287.
- [32] In *Beitr. Plasmaphys.* **20** (1980).
- [33] MICHEL, P., WINKLER, R., *Beitr. Plasmaphys.* **16** (1976) 233.
- [34] WILHELM, J., WINKLER, R., *Ann. Phys. Lpz.* (7) **34** (1977) 119.
- [35] WILHELM, J., WINKLER, R., *Ann. Phys. Lpz.* (7) **34** (1977) 369.
- [36] WILHELM, J., WINKLER, R., *Beitr. Plasmaphys.* **17** (1977) 369.
- [37] PFAU, S., WINKLER, R., *Beitr. Plasmaphys.* **13** (1973) 297.
- WINKLER, R., PFAU, S., *Beitr. Plasmaphys.* **13** (1973) 315.
- [38] WINKLER, R., WILHELM, J., *Proc. XIIIth ICIPIG, Berlin 1977*, Contr. Pap., p. 743.
- WILHELM, J., WINKLER, R., *Ann. Phys. Lpz.* (7) **35** (1978) 321.
- WILHELM, J., WINKLER, R., *Beitr. Plasmaphys.* **18** (1978) 317.
- [39] MICHEL, P., WINKLER, R., WILHELM, J., *Proc. XIIIth ICIPIG, Berlin 1977*, Contr. Pap., p. 47.
- WINKLER, R., MICHEL, P., WILHELM, J., *Beitr. Plasmaphys.* **18** (1978) 31.
- [40] WILHELM, J., WINKLER, R., *Ann. Phys. Lpz.* (7) **36** (1979) 103.
- [41] WILHELM, J., WINKLER, R., *Ann. Phys. Lpz.* (7) (1979), in print.

Anomalous transport from plasma waves

W. M. Manheimer

Plasma Physics Division, Naval Research Laboratory, Washington DC 20315, U.S.A.

Abstract. — One of the principle manifestations of instability in plasma is the presence of anomalous transport. The problem then is how to describe and/or predict plasma behavior when the transport is dominated by unstable plasma waves. This paper describes a systematic approach to this problem and examines what knowledge of the instability is needed. Depending on the situation, the necessary information can be as little as the stability threshold, or as much as a full nonlinear description of the turbulent spectrum, with several intermediate possibilities.

In all cases, this description of the instability is used to derive a set of anomalous transport coefficients for use in a fluid formulation. Description of the plasma then comes from a numerical solution of these fluid equations. Scaling laws can often be derived from these numerical solutions, however in general, scaling laws cannot be simply derived from first principles.

Can one derive, from first principles, simple scaling laws for complicated plasma devices like a tokamak? For instance the current vogue is to scale confinement in tokamaks linearly with density; so clearly one would like a thermal conduction coefficient scaling as n^{-1} . The problem is that this thermal conduction must be derived from the quasi-linear and nonlinear theory of very esoteric instabilities. Even if someone could take these instabilities and derive a transport coefficient which had all the right magnitudes and scalings, would anyone else either understand it or believe it?

My own opinion is that one cannot derive simple scaling laws in an understandable, believable way. How then does one explain or predict the behavior of complicated plasma devices which are dominated by anomalous transport? One possibility of course is to use phenomenological transport coefficients, and this may in fact work well. It is certainly likely that current devices could be extrapolated a factor of two in every parameter this way. However this is somewhat unsatisfying, one would somehow like to relate performance to fundamental processes, if only for fundamental scientific reasons. That will be the focus of the remainder of this paper.

Let us look at what is needed to describe a plasma whose transport is dominated by instability. As we will see, there is what might be called a hierarchy of necessary information starting with the simplest questions of stability threshold and proceeding to the most complicated nonlinear theory. How high one has to proceed in this hierarchy is then an indication of how easy and/or how reliable the theory is.

Take for instance a temperature profile in a tokamak plasma, and look at some radius r_0 . The most fundamental question is whether or not the plasma is unstable at this point. If the plasma is stable here,

clearly one uses classical transport. If it is unstable anomalous transport should be involved. Thus the first necessary piece of information is the stability threshold. As we will see, there are some circumstances where this is all that is needed to describe the system. Since this description only utilizes the first step in the aforementioned hierarchy, it will surely be the simplest and most reliable theory of anomalous transport. This is the marginal stability theory which we [1-4] and others [5-7] have previously discussed.

The idea behind the marginal stability theory is the following. Imagine a plasma which is stable, but which is forced by some external mechanism to an unstable state. As a concrete example let us consider an ohmically heated tokamak. The current heats the central region and since the edge is cool, an electron temperature gradient is forced upon the system. Let us now postulate that when the electron temperature gradient

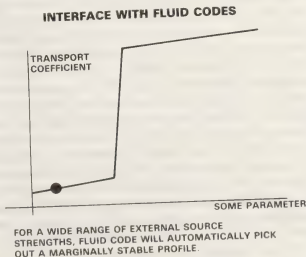


Fig. 1. — A possible plot of transport coefficient versus some relevant parameter.

exceeds some critical value, the plasma becomes unstable. Then at this point, an anomalously large thermal conduction is generated by the instability. A possible functional dependence of K_e on temperature gradient is shown in figure 1. This large K_e will cool, the plasma, the instability will shut off and K_e will go to its classical value. However once the plasma becomes stable, the ohmic heating will increase its temperature and it will again be driven unstable. Clearly then there is a dynamic balance between heating and anomalous thermal conduction with the plasma sitting at (or perhaps oscillating about) the marginal stability point. The fundamental quantity to determine then is not the turbulent spectrum, but the plasma profile. Once we have the profile, we can calculate the thermal conduction because we know the profile and input power. Once we have K_e , simple quasi-linear theory gives us the fluctuation level. Thus the logic of a marginal stability calculation is just the reverse of a conventional nonlinear calculation, as shown in figure 2.

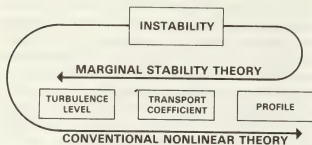


Fig. 2. — Logic of a marginal stability calculation contrasted to the logic of a conventional non-linear calculation.

Now examine the second complication in our hierarchy. Let us say that the marginal stability hypothesis is valid, but there is not one anomalous transport effect but many. To continue with our example of the tokamak, it is known that both electron temperature gradient, and density gradient contribute to instability, and that not only is there anomalous thermal conduction, but also anomalous diffusion. In this case marginal stability does not imply only particular temperature gradient but rather some relation between temperature and density gradient. Then the stability threshold is not sufficient information to determine the profile. One must also know the relation between K_e and D . If one knows the spectrum, and if quasi-linear theory is valid, then one can determine this relation. However now more information is needed than just stability threshold; correspondingly the theory is on somewhat shakier ground than it is if there is only a single anomalous effect.

Let us illustrate how a marginal stability works in a one or two parameter space. First imagine that only temperature gradient drives instability and

thermal conduction is the only anomalous process. Then the steady state equations are heat balance

$$0 = \frac{\partial}{\partial x} K \frac{\partial T}{\partial x} + S_i \quad (1)$$

and marginal stability,

$$\alpha \frac{\partial T}{\partial x} - P = 0 \quad (2)$$

where S_i denote the energy sources. In eq. (2), $\alpha \frac{\partial T}{\partial x}$ is the growth rate which is driven by temperature gradient and P denotes the damping from all sources, for instance shear, ion-ion collisions, etc. The marginal stability approach then consists of using eq. (2) instead of eq. (1) as an equation for temperature. Eq. (1) is used instead as an equation for K , and it reduces to

$$\frac{d}{dx} K \frac{P}{\alpha} = -S_i \quad (3)$$

Now imagine that there are two variables instead of one. For instance for the tokamak, say that both density and temperature gradients drive instability and that there is both anomalous diffusion and anomalous thermal conduction. Then the equations which describe the system are heat and particle balance

$$0 = \frac{\partial}{\partial x} K \frac{\partial T}{\partial x} + S_i \quad (4)$$

$$0 = \frac{\partial}{\partial x} D \frac{\partial n}{\partial x} + S_n \quad (5)$$

marginal stability

$$\alpha \frac{\partial T}{\partial x} + \beta \frac{\partial n}{\partial x} = P \quad (6)$$

and some relation between D and K

$$D = \zeta K, \quad (7)$$

which might come from for instance quasi-linear theory. Also we assume $\zeta > 0$. These equations can be solved for K as follows. Integrate eq. (4) from zero to r assuming $\partial T / \partial x = 0$ at $r = 0$ to get

$$K \frac{\partial T}{\partial x} = \int_0^r S_i dx \quad (8)$$

Then solve for D and $\partial n / \partial x$ from eqs. (6) and (7), insert in eq. (5) and integrate from 0 to r .

The result is

$$K = -\frac{\alpha}{P} \int_0^r S_i dx - \frac{\beta}{P \zeta} \int_0^r S_n dx \quad (9)$$

Then once eq. (9) is solved for K , we can solve eq. (4) for T in the standard way.

Let us now examine the conditions under which a solution to eqs. (4)-(7) can be formed. In the normal tokamak configuration where the electrons are in the plateau or banana regime negative $\partial n/\partial x$ and $\partial T/\partial x$ both drive instability. Therefore α and β have the same sign and both have opposite sign to P . Since, S_T , S_n and ζ are all positive, K is greater than zero so that an a solution exists. Now imagine that say the temperature gradient is stabilizing rather than destabilizing, that is α and P now have the same sign. Then, in order to have $K > 0$,

$$\left| \frac{\beta}{P\zeta} \int_0^x S_n dx \right| > \left| \frac{\alpha}{P} \int_0^x S_T dx \right|. \quad (10)$$

If inequality (10) is violated in some regions of x , the plasma will be stable and a marginally stable solution does not exist there. In these regions classical transport will apply.

Of course rather than solving equations like (5)-(7), a more practical procedure is usually to use a numerical transport code in which transport coefficients jump to some large value at the stability threshold, and in which the proper relation between the different transport coefficients is also used. As long as these jumps in transport coefficients are handled in a way which is numerically stable, the code will automatically handle the transition not only between stable and unstable plasma, but also between different instabilities.

For the next stage of the hierarchy one must know the nonlinear limit to the fluctuation level. However let us assume that once the fluctuation level is known, the transport coefficients can all be calculated, for instance via quasi-linear theory. Actually this is not as unreasonable as it sounds. Say that the instability is driven by electrons and is stabilized by some nonlinear effect on ions. Then quasi-linear transport coefficients for the electrons should be valid. If this be the case, at least some of the ion transport coefficients can usually be calculated by invoking global conservation relations (for instance energy or momentum conservation, pressure balance, etc.). Thus the third level of our hierarchy assumes that transport coefficients can all be calculated in terms of a fluctuation level which is specified by invoking non-linear theory, and/or experiment, and/or numerical simulation of the instability. There are at least two reasons why the fluctuation level might be required. First, the system may be so strongly driven that nonlinear effects limit the fluctuations to a value smaller than that required to maintain a marginally stable profile. Second, there may be so many anomalous transport effects that there is no simple external mechanism driving the plasma toward instability and no simple relaxation to a stable state because of the instability.

This is the approach recently used at the Naval Research Laboratory to describe anomalous absorption and flux limitation in a laser produced plasma [9].

Earlier calculations like this also examined hydrodynamic flow in an ionosphere which has been violently perturbed [10], and the implosion and post implosion phase of theta pinches [11, 12]. Since these results all require a fluctuation level which is the result of a nonlinear calculation they are less reliable than results obtained via calculations on the two lower levels of the hierarchy which we have been describing.

The fourth level of the hierarchy, and the last one which we will describe, is that where both the nonlinear fluctuation level and the transport coefficient are the results of nonlinear calculations. Needless to see results on this level are still more speculative than those on the three lower levels. We will now describe three calculations done at the Naval Research Laboratory which illustrate the three levels. They are calculations of electron and ion temperature profiles in tokamaks [4], calculation of the structure of transverse resistive shocks [3], and calculations of anomalous absorption and thermal energy flux limitation in a laser produced plasma [9].

In a tokamak, the electron temperature is limited by some anomalous process, generally thought to be instabilities. We have attempted to study this with the use of a simple transport code [4]. Specifically our code solves the equations

$$\frac{3}{2} n \frac{\partial T_e}{\partial t} = \frac{1}{r} \frac{\partial}{\partial r} R(K_{ce} + K_{an}) \frac{\partial T_e}{\partial r} + E \cdot J - 3 v_e \frac{m}{M} \times n(T_e - T_i) \quad (11)$$

$$\frac{3}{2} n \frac{\partial T_i}{\partial t} = \frac{1}{r} \frac{\partial}{\partial r} r K_{ci} \frac{\partial T_i}{\partial r} + 3 v_e \frac{m}{M} n(T_e - T_i) \quad (12)$$

$$E = J/\sigma \quad (13)$$

where $T_{e(i)}$ are the electron (ion) temperature, J is the current density, E is the toroidal electric field, assumed to be independent of radius, σ is the electrical conductivity.

The current density is assumed to always be at its steady state value, so magnetic diffusion is neglected. Eqs. (11)-(13) are solved subject to boundary conditions that $T_e = T_i = 10$ eV at the limiter, and that the total current is specified. Every term in eqs. (11)-(13) is given by neoclassical theory except for one, the anomalous electron thermal conduction K_{an} . If the plasma is unstable, K_{an} is taken as the Bohm diffusion coefficient K_B . In our study the plasma is subject to one of two instabilities, the internal kink-tearing mode whenever $q = rB_z/RB_\theta$ is less than unity, and the universal drift wave-trapped electron mode whenever the shear strength θ_{cr} is below a critical value θ_c . The value of θ_{cr} comes from the linear theory of the mode. We will not elaborate here, but a full discussion can be found in reference [4]. Thus the functional form for K_{an} is

$$K_{an} = K_B \left[\frac{q^{-n}}{1 + q^{-n}} + \frac{(\theta/\theta_{cr})^n}{1 + (\theta/\theta_{cr})^{-n}} \right] \quad (14)$$

where n^1 and n are large integers, so that K_{an} turns on abruptly as the plasma becomes unstable. Since the quantities in the brackets change abruptly from zero to one, we have called them thermostat functions. Let us now re-emphasize that the nonlinear theory of the instability plays no role in the analysis. The only thing needed to solve eqs. (11)–(13) is the instability condition which comes only from linear theory.

Now, knowing the profile, one can utilize quasi-linear theory to calculate both the anomalous thermal conduction, fluctuation wave number and fluctuation amplitude. However, even if the behavior is governed by nonlinear theory, the only thing which will be wrong is the calculation of fluctuation level, not the profile.

We will now show some results of the calculation. Since there was not much available data from PLT at the time, we did only one run. The parameters are $B = 35$ kG, $Z_{ef} = 4$, a central density of

$$n_0 = 4.2 \times 10^{13}$$

and a hydrogen plasma. The electron and ion temperature, q , and thermostat functions for q and Θ are given in figure 3. Clearly the plasma is in a marginally stable state for internal kink-tearing modes for $0 < r/a < 0.4$, and to trapped electron modes for $0.4 < r/a < 0.9$. The outer region is classical.

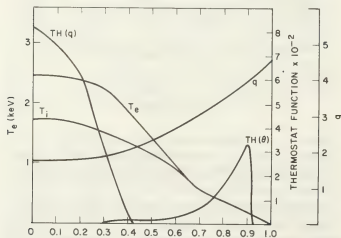


Fig. 3. — PLT electron and ion temperature profiles showing regions of fluid and micro instability.

Another tokamak which we have simulated is TFR. In TFR more than half of the input power is generally radiated away by impurity radiation [13]. However, as is clearly indicated in reference [13], most of this is oxygen line radiation arising from the plasma edge where the temperature is low enough that the plasma is stable. Thus the question is how does the energy get from the center to the edge. Reference [13] also shows that destruction of magnetic surfaces due to internal kink and tearing modes is insufficient to account for this energy transport. Here we examine whether drift and trapped particle instabilities can provide the remainder of the energy transport.

One very interesting experimental result for TFR is that the temperature half width $\Delta r(T)$ depends on only a single parameter, $q(a)$, even though two parameters, B and I are independently varied. Our calculation basically confirms this result. In figure 4 is shown (solid line) the predictions by our code for $\Delta r(T)$ as a function of $q^{-1}(a)$.

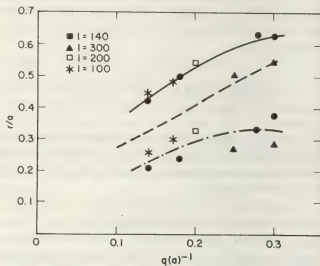


Fig. 4. — Temperature half-width and width of the $q(r) = 1$ region in TFR as a function of $q(a)^{-1}$. The solid and dash-dot line are approximate fits to the numerically obtained data points. The dashed line is the experimentally observed temperature half-width.

Here we have assumed $Z_{ef} = 3$ and $n_0 = 6 \times 10^{13}$. Various dots shown the calculated points. Although there is some scatter to the points, $\Delta r(T)$ basically does depend on the single parameter $q(a)$. The dashed line shows the experimental result from TFR.

Another interesting result from the TFR experiment is that the position of the $q = 1$ surface, as defined by the radial position of the node in the saw tooth oscillations in the soft x-ray signal, also depends only on the single parameter $q(a)$. In figure 4 the dash dot line shows that the predicted value for the $q = 1$ surface, as defined by the radial position where the q thermostat function drops to half its maximum

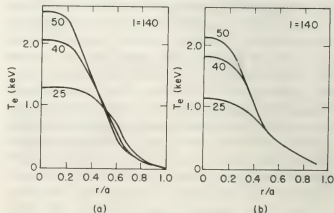


Fig. 5. — Electron temperature profiles in TFR. (a) Numerically obtained; (b) Experimentally obtained.

value, also depends principally on this single parameter.

In figures 5a and b are predictions of the code for electron temperature compared to experiment, for three discharges having $I = 140$ kA, and $B = 25$, 40 and 50 kG. Notice that the code does give good agreement with experiment as regards temperature profile. In figure 6 are plotted the radial dependence of T_e , T_i , q , for the run with $B = 50$ kG, $I = 140$ kA.

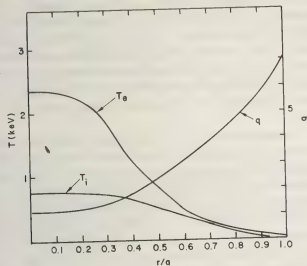


Fig. 6. — TFR electron and ion temperature profiles.

Other quantities of interest are the k_{pi} of the fluctuation and predicted values of $e\varphi/T_e$ as a function of radius. These are shown in figure 7 for a discharge with 60 kV, 300 kA. The fluctuation level seems to be comparable to that recently reported [14]

$$e\varphi/T_e \approx (3.4) \times 10^{-3}.$$

In addition to calculating the temperature profile for TFR, numerous calculations were also done for Alcator. Perhaps the most striking experimental result for Alcator is the increase of energy confinement time with density [15]. Our theory does predict this basic dependence. In figure 8 is shown the calculated dependence of energy confinement time on central density for three choices of field and current, $B = 50$ kG, $I = 100$ kA; $B = 75$ kG, $I = 100$ kA; and $B = 75$ kG, $I = 150$ kA. In all cases, $Z_{ef} = 1$ and we used a hydrogen plasma. Notice that for central densities less than about $2 \times 10^{14} \text{ cm}^{-3}$, the confinement time increases roughly linearly with density. For larger n_0 the confinement time begins to decrease again.

When the density is sufficiently high however, the plasma is in the Pfirsch Schluter regime, and there is no trapped particle instability. Then the energy confinement time begins to decrease with density. For all three choices of current and field the points with $n_0 = 5 \times 10^{14}$ were completely stable. Not only are there no trapped particle instabilities in the region of maximum gradient, q was everywhere larger than

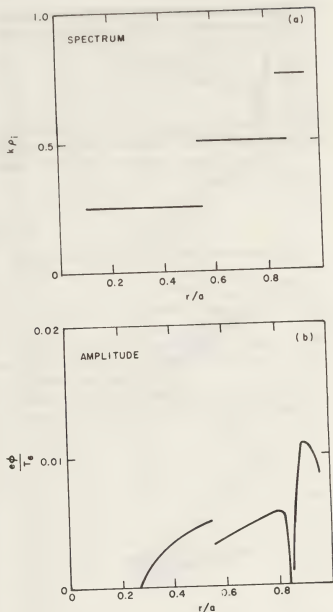


Fig. 7. — (a) The most unstable mode in TFR as a function of r/a , and (b) the fluctuation level implied by the numerically determined anomalous transport.

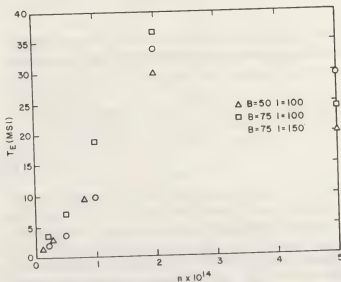


Fig. 8. — Energy confinement time versus central density in Alcator.

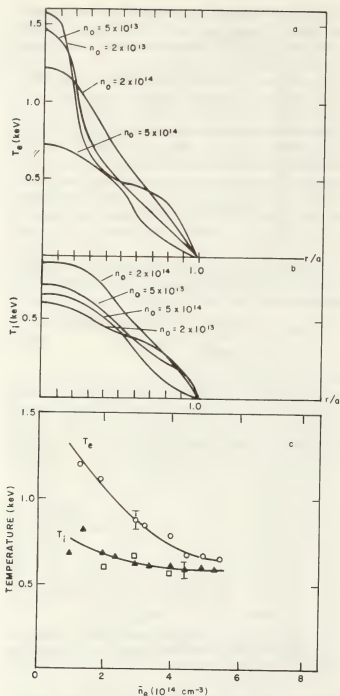


Fig. 9. — Calculated electron (a) and ion (b) temperature profiles at different densities. Also, a plot (c) of measured central electron and ion temperatures vs. density.

on the transition from anomalous to classical thermal conduction. The highest electron temperature however are in the régime of anomalous thermal conduction and low confinement time. In figures 9a and b are plotted the radial dependence of T_e and T_i for different densities for the case $B = 75$ kG, $I = 100$ kA. Notice that at low density, where the thermal conduction is anomalous, the temperature profiles are quite peaked. At higher density, where the thermal conduction is classical, the temperature profiles are quite broad.

To summarize, our calculations of tokamak temperature profiles do give qualitative and even some quantitative agreement with measured tokamak temperature profiles. The theory is simple in that non-linear theory of the instability never enters in. However there are no simple scaling laws which explain tokamak behavior; instead the temperature profiles result only from a numerical solution of the electron and ion energy equations with the appropriate anomalous electron thermal conductivity.

Now we consider a different plasma configuration, a cross field collisionless resistive shock. Here, as we will see, marginal stability appears to be a viable concept, but two transport processes, electron and ion heating play important roles. In a shock, fluid convection (that is the $V \frac{dv}{dx}$ term in the momentum equation) tends to steepen the density profile. Since the magnetic field is frozen into the flow it also steepens and the current thereby increases. However at some point, the current becomes so great that ion acoustic waves are driven unstable. These waves then grow, the anomalous resistivity increases, and the shock profile will then tend to broaden. The shock profile will then be determined by the condition that ion acoustic waves are everywhere marginally stable, that is [3]

$$\frac{c}{4\pi ne} \frac{dB}{dx} = \left(\frac{T_e}{2M} \right)^{1/2} \left[1 + \left(1 + 12 \frac{T_e}{T_i} \right)^{1/2} \right]^{1/2} \times \left(1 + \frac{M}{m} \left(\frac{T_e}{T_i} \right)^{3/2} \exp \left\{ - \frac{4 T_e}{T_i} \left[1 + \left(12 \frac{T_e}{T_i} \right)^{1/2} \right] \right\} \right) \quad (15)$$

From the Rankine-Hugoniot relations, the magnetic field, density and temperature are known are all known upstream and downstream. Thus, once we know T_i/T_e , the ion to electron temperature ratio, we can estimate $dB/dx \approx [B(\text{upstream}) - B(\text{downstream})]/L_s$ and thereby estimate the shock width L_s .

The problem now is to estimate the ion to electron temperature ratio. For an ion acoustic wave at marginal stability, this can be done by comparing the heating rates of ions and electrons. Say that the ion wave transfers momentum from ions to electrons at a rate P . Then it can be shown, from resonant quasi-

linear theory, that in the reference frame in which the ions are at rest, energy is transferred from electrons to ions at a rate $(\omega/k) \dot{P}$, where (ω/k) is the phase velocity of the ion acoustic wave. If the electron drift velocity is denoted u , then momentum and energy conservation equations for electrons and ions read

$$nm\dot{u} = -\dot{P} \quad (16a)$$

$$nm\dot{u} + 3/2 n\dot{T}_e = -\frac{\omega}{k} \dot{P} = -\frac{3}{2} n\dot{T}_i. \quad (16b)$$

From eqs. (16a) and (16b), it is a simple matter to solve for the ratio of heating rates,

$$\frac{\dot{T}_e}{\dot{T}_i} = \frac{(u - \omega/k)}{(\omega/k)}. \quad (17)$$

If both electrons and ions are substantially heated by the shock, the temperature ratio should be roughly equal to the ratio of heating rates, or

$$\frac{u - \omega/k}{\omega/k} \approx \frac{1}{\sqrt{2}} \left[1 + \left(1 + 12 \frac{T_e}{T_i} \right)^{1/2} \right]^{1/2} \left(1 + \frac{M}{m} \left(\frac{T_e}{T_i} \right)^{3/2} \exp \left\{ -\frac{T_e}{T_i} \left[1 + \left(1 + 12 \frac{T_i}{T_e} \right)^{1/2} \right] \right\} \right) - 1 \approx \frac{T_e}{T_i}. \quad (18)$$

Eq. (18) is a transcendental equation for T_e/T_i . For a hydrogen plasma, we find $T_e/T_i \sim 7.5$.

Then knowing T_i/T_e , eq. (15) gives a simple estimate for shock width. For

$$\frac{\omega_{pe}}{\omega_{ce}} \approx 70, \quad \frac{c}{4\pi ne} \frac{\Delta B}{L_s} \approx 7.5 \sqrt{\frac{T_e}{M}} \frac{4\pi nT}{B^2} \approx 0.01, \quad (19)$$

and a Mach two shock, this gives the result

$$L_s \sim 10 c/\omega_{pe}$$

which is consistent with the transverse shock experiments done at Culham laboratory [16]. From this estimate of shock width, one can calculate a resistivity and from the resistivity, a fluctuation level. This works out to be about

$$\left(\frac{e\phi}{T_e} \right)^2 \sim 5 \times 10^{-3}. \quad (20)$$

Let us re-emphasize that at *no* point in this calculation was an estimate of $e\phi/T_e$ from nonlinear theory ever required.

Actually, one can do much better than estimate these quantities. In reference [3], fluid equations for n , T_e , T_i and B , coupled to wave equations for (16) (or 64) ion acoustic fluctuations (at different wave vector) are numerically integrated from upstream to downstream. The waves are assumed to grow or damp at the local linear growth or damping rate, and quasi-linear theory is used to calculate resistivity as well as electron and ion heating rate. It was found that the shock profile did in fact remain at a marginally stable current for nearly the entire shock profile. Results of such a calculation are shown in figure 10 where spatial profiles of n , B , T_e , T_i and $(e\phi/T_e)^2$ are shown. To summarize, the structure of transverse resistive shocks in hydrogen seems to be consistent with ion acoustic waves being at marginal stability everywhere in the

profile. Estimates and calculations of shock width and fluctuation level are in good quantitative agreement with experiments.

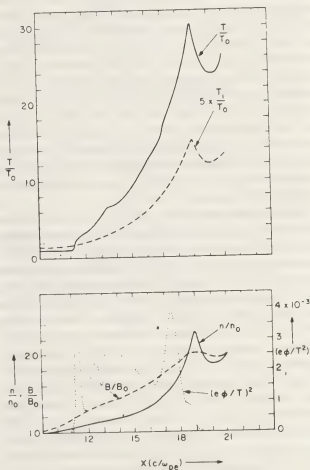


Fig. 10. — Plots of density, temperature, magnetic field and turbulence level versus distance for a resistive Mach 2 shock.

As a final example, we consider the absorption of laser light in a laser produced plasma. This is discussed much more fully in reference [9] and the description here will be very brief. The idea is to use a numerical

solution of the fluid and wave equations with anomalous transport. There are two instabilities which provide this anomalous transport. First, there is Brillouin backscatter, where in the laser light decays into a reflected wave and an ion acoustic wave; and second, there is an ion acoustic instability generated by the return current.

For Brillouin backscatter, if the growth rate in homogeneous media is γ_0 , then the spatial amplification in inhomogeneous for either an undamped [17], or strongly damped [18] ion acoustic wave, is

$$\exp \frac{2 \pi \gamma_0^2 L_{ph}^2}{\sqrt{\frac{T_e}{M}} c}$$

where L_{ph} is the size of the region of phase coherence between incident, reflected, and ion acoustic wave. This amplification turns out to be so large that any theory based upon it will give nearly total backscatter in virtually any circumstance. However when examining the amplitude of the ion acoustic wave generated, one sees that it is very large, so large that any ion trapping should be very important and linear theory of the instability invalid. Thus a description of the process has to be based on a nonlinear description of the instability. Earlier theory [19, 20] has shown that if trapping is important one way the instability can be modeled is by reducing the growth rate γ_0 by a factor of between about five and ten. We have adopted such an approach to model the effect of Brillouin backscatter. Thus we need not only a nonlinear theory of the fluctuation amplitude, but also a nonlinear reduction in the reflection due to stimulated Brillouin backscatter.

The second instability which we consider is the ion acoustic instability driven by a return current. If electrons conduct heat but carry no current, a flux of energetic particles in one direction is balanced by a flux of low velocity particles going the other way. This return current can drive ion acoustic waves unstable. There are three principle effects of this instability; first the electron thermal conductivity is reduced; second, there is an electron ion energy exchange; and third, there is anomalous absorption of laser light resulting from the scattering of laser light on the ion density fluctuations. A linear and quasi-linear theory of this instability has been published recently [21], and a self consistent steady state treatment of the coupling of anomalous absorption and flux limitation has also been presented [22]. Here, a fluctuation level is required, but then with this fluctuation level, the transport coefficients are related by quasi-linear theory.

The approach in reference [9] is to numerically solve the fluid equations where anomalous transport and backscatter results from these two instabilities. We have simulated three types of Nd laser pulses. First single short (70 ps) pulses on a target which has

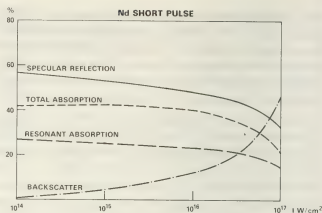


Fig. 11. — Calculated laser light absorption, resonant absorption, backscatter and specular reflection versus irradiance for a Nd laser plasma with a pulse of 70 ps fwhm.

an initial density gradient scale length of 10μ . This simulates many of the short pulse experiments, especially on slab targets. We find that the absorption is principally resonant absorption, but it gets a strong boost from return current driven turbulence. From irradiances of 10^{14} W/cm^2 to $3 \times 10^{16} \text{ W/cm}^2$ the absorption is about 40%, with about 25% resonant absorption (also shown in figure 11 is backscatter and specular reflection vs. irradiance). This is in reasonable agreement with data taken from many laboratories. In figure 12 are shown expansion velocity, electron temperature and flux limit, Q/nmV_e^3 , as a function of irradiance. The points are measured electron temperatures from the NRL experiment [23].

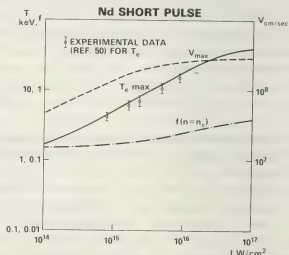


Fig. 12. — Calculations of electron temperature, blowoff velocity and flux limit for the laser pulse of figure 11.

A second simulation is of a double structured pulse. Recent experiments at NRL have shown that if the main laser pulse illuminates a prepulse formed plasma, very strong backscatter results [24]. We model this by assuming a 100μ scale length for $n < 0.1 n_{cr}$ and a 30μ scale length for $N > N_{cr}$ and illuminate with a single 70 ps pulse. Shown in figure 13

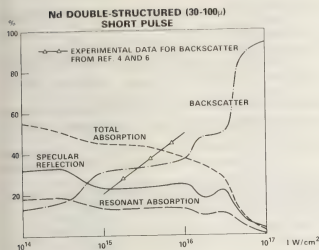


Fig. 13. — Calculated absorption, backscatter, resonant absorption and specular reflection for a double structured *Nd* laser pulse.

is absorption, backscatter, resonant absorption and specular reflection as a function of irradiance. Also shown are experimental measurements of backscatter as a function of irradiance. Clearly there is good qualitative agreement between theory and experiment here.

Finally we have simulated long pulse experiments also. Here we assume a gradient scale length of $100\ \mu$ and take a pulse which rises up to a final steady irradiance and then remains constant. In figures 14 and 15 are shown plots of absorption, backscatter and specular reflection *versus* irradiance; and then plots of electron temperature, expansion velocity and flux limit *versus* irradiance. The points on the figures are experimental measures of absorption [25, 26] for long pulse experiments. To summarize, the fluid simulation with anomalous transport seems to provide qualitative and even fair quantitative agreement with experiments on laser produced plasmas for a variety of laser pulse shapes and over nearly five orders of magnitude in irradiance.

Now what about our initial question concerning whether simple scaling laws can be derived from first

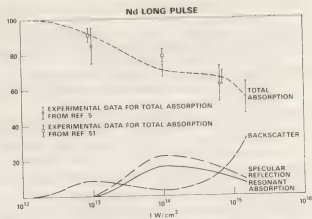


Fig. 14. — As in figure 11 for a *Nd* laser, long pulse.

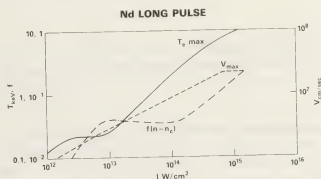


Fig. 15. — As in figure 12 for a *Nd* laser long pulse.

principles? The entire thrust of this paper is that they really cannot. However this does not mean that no progress can be made; on the contrary it seems that one can go far with fluid simulations with the instability entering via anomalous transport. In some cases, all that is needed for good modeling is the linear stability threshold. In other cases non-linear theory and/or relation between different transport coefficients is needed. However in all cases, the scaling comes from a numerical solution of the fluid equations, not from a simple scaling law.

References

- [1] MANHEIMER, W. M. and BORIS, J. P., *Comments on Plasma Physics* 3 (1977) 15.
- [2] MANHEIMER, W. M., CHU, K. R., OTT, E. and BORIS, J. P., *Phys. Rev. Lett.* 37 (1976) 286.
- [3] MANHEIMER, W. M. and BORIS, J. P., *Phys. Rev. Lett.* 28 (1972) 659.
- [4] MANHEIMER, W. M. and ANTONSEN, T. M., *Phys. Fluids*, May 1979.
- [5] KENNEL, C. F. and PETCHEK, H. E., *J. Geophysical Res.* 71 (1966) 1.
- [6] CHRISTIANSEN, J. P. and ROBERTS, K. V., *Nucl. Fusion* 18 (1978) 181.
- [7] BERK, H. L. and STEWART, J. J., *Phys. Fluids* 20 (1977) 1080.
- [8] MANHEIMER, W. M., *An Introduction to Trapped Particle Instability in Tokamaks*, Chapter II, ERDA Critical Review Series.
- [9] COLOMBANT, D. G. and MANHEIMER, W. M., *Phys. Fluids* to be published.
- [10] LAMPE, M., MANHEIMER, W. M. and PAPADOPOULOS, K., *NRL Memo. Report* 3076, June 1975.

- [11] HUI, B., DAVIDSON, R. C. and HAMASAKI, S., *Nucl. Fusion* **16** (1976) 73.
- [12] HAMASAKI, S. and KRALL, N. A., *Phys. Fluids* **20** (1977) 229.
- [13] Equipe TFR, IAEA Conference, Berchtesgaden, W. Germany, October 1976, paper IAEA CN-35/A3.
- [14] TFR Group (presented by F. Koechlin) 8th European Conference on Controlled Fusion and Plasma Physics, Prague, September 1977.
- [15] APGAR, E., COPPI, B., GONDHALEKAR, A., HELAVA, H., KOMM, D., MARTIN, F., MONTGOMERY, B., PAPPAS, D., PARKER, R. and OVERSKEL, D., *IAEA Conference*, Berchtesgaden, W. Germany, October 1976, Paper IAEA 35/A6.
- [16] PAUL, J. W. M., DAUGHNEY, C. C. and HOLMES, L. S., *Phys. Rev. Lett.* **25** (1970) 497.
- [17] ROSENBLUTH, M. N., *Phys. Rev. Lett.* **565** (1972) 29.
- [18] NISHAKAWA in *Advances in Plasma Physics*, vol. 6, A. Simon and W. Thompson, editors.
- [19] MANHEIMER, W. M. and FLYNN, R., *Phys. Fluids* **17** (1974) 409.
- [20] MANHEIMER, W. M. and KLEIN, H. H., *Phys. Fluids* **17** (1974) 1889.
- [21] MANHEIMER, W. M., *Phys. Fluids* **20** (1977) 265.
- [22] MANHEIMER, W. M., COLOMBANT, D. G. and RIPIN, B. H., *Phys. Rev. Lett.* **28** (1977) 1135.
- [23] YOUNG, F. C. and RIPIN, B. H., *Bull. Am. Phys. Soc.* **22** (1977) 1112.
- [24] RIPIN, B. H., YOUNG, F. C., STAMPER, J. A., ARMSTRONG, C. M., DECOSTE, R., MCLEANS, E. A. and BODNER, S. E., *Phys. Rev. Lett.* **39** (1977) 611.
- [25] RIPIN, B. H., WHITLOCK, R. R., YOUNG, F. C., OBENSCHAIN, S. P., MCLEAN, E. A., DECOSTE, R., NRL Memo. Report 3965 (1979).
- [26] ANTHER, J. P., PALMER, M. A., GUSINOW, M. A. and MATZEN, M. K., *Bull. Am. Phys. Soc.* **23** (1978) 777.

X-ray plasma diagnostics

L. P. Presnyakov and A. M. Urnov

P. N. Lebedev Physical Institute, USSR Academy of Sciences, Moscow, USSR

Abstract. — Results and methods are given for the investigation of hot laboratory and astrophysical plasmas parameters in a soft X-ray region $\lambda = 1-40 \text{ \AA}$. Line spectra of multiply charged ions are usually studied experimentally, and relative intensities of spectral lines are measured. Achievements of modern physics of electron-ion collisions and theoretical spectroscopy make it possible to obtain for transient plasma the electronic temperature, density, ionization stage, and to investigate time and spatial distributions of these parameters.

Introduction. — X-ray spectroscopy of high temperature plasmas, as a new direction in plasma physics, has been developed recently by efforts of many scientists in different laboratories. This field deals mainly with line spectra of multiply charged ions in the spectrum region $1-40 \text{ \AA}$, and more hard adjacent continuous component is of interest. From physical point of view the X-ray plasma spectroscopy has the following background. In a case of ions with a high charge $Z \gg 1$ any excitation decays mainly due to radiation. Other channels, both collisions and autoionization exist being well controlled corrections in comparison with radiative one. It leads to simple and understandable connections between spectral line intensities and mechanism of spectra formation. Modern physics of electronic and atomic collisions provides sufficient and accurate methods for calculations of cross sections and rate coefficients involving multiply charged ions. Theoretical spectroscopy has also reliable methods for classification and calculations of spectral lines in the X-ray region. Simultaneously, experimental technique has been developed with appropriate spectral, time and spatial resolution. It is worth noting that in the most of important cases low density astrophysical plasmas (electron density $N_e \lesssim 10^{14} \text{ cm}^{-3}$) and laboratory plasmas ($N_e \lesssim 10^{20}-10^{23} \text{ cm}^{-3}$) are optically thin for the X-ray radiation. It helps much for interpretation of experimental results, and theoretical analysis.

Therefore, the X-ray plasma spectroscopy contains three important parts: new sources and measurement methods of highly charged ion spectral data + physics of electronic and atomic collisions + theoretical spectroscopy of ions. For plasma physics the X-ray spectroscopy provides new and effective methods of contactless plasma diagnostics. It is essential that X-ray spectroscopy methods are equally valid for investigation both of astrophysical (active regions and Solar flares) and laboratory plasmas. At the present time this field has many hundreds of original

papers and just few review publications. Among the latter papers [1-6] contain some systematization and extended list of references to earlier works.

1. Plasma parameters obtained from X-ray spectra.

— Multiply charged heavy ions are small impurities (much less than 1%) in astrophysical plasmas and in stationary laboratory sources (*Tokamak*, *Stellarator*, etc.). Inertial plasmas produced by laser or electronic beams, plasmas of exploding wires and low-inductance sparks may be chemically homogeneous or consist of few heavy elements. X-ray spectroscopy provides universal diagnostic methods valid for all the cases mentioned. It is important to underline that plasma parameters can be obtained with the help of relative intensities of spectral lines, and one can avoid absolute flux calibration. Still absolute measurements provide the additional information (emission measure, etc.). Plasma parameters and types of spectral line used for the determination of them are listed in table I.

Table I.

Plasma parameter	Relative intensities
Electronic temperature T	$I_e^d = \frac{I_e^d}{I_R} = f_1(T)$, all ions
Ionization stage; effective ionization temperature T_i	$I_i^{\text{ion}} = \frac{I_i^{\text{ion}}}{I_R} = f_2(T_i)$, all ions
	$I_R[\text{H}]/I_R[\text{He}] = f_2'(T_i)$, H-like and He-like ions
Electronic density N_e	$\alpha = G^{-1} = \frac{I_R}{I_i} = f_3(N_e)$, He-like ions
	$\chi = I_e(I)/I_e(II) = f_4(N_e)$, all ions
	$\beta = \frac{I(2p_{1/2} \rightarrow 1s_{1/2})}{I(2p_{3/2} \rightarrow 1s_{1/2})} = f_5(N_e)$, H-like ions
Energy distribution of electrons;	$I_{K\alpha}/I_R$
Presence of electronic beams	$I_{K\beta}/I_R$ H- and He-like ions

Here I_R are the intensities of the resonance lines, and I_T are the intensities of the intercombination lines in He-like ions. For the satellite line intensities I_s^d and I_s^{in} mean satellites produced by the dielectronic recombination and the direct electron impact inner shell excitation respectively. The lines, K_α and K_β , are usual characteristic lines produced by ions with K-shell vacancies. Determination of T_i with the help of the Doppler shift is well known in classical spectroscopy (spectroscopy of low-temperature plasmas). Some methods of density diagnostics, for example, intercombination-to-resonance line ratio for He-like ions, α , take also their origin in classical spectroscopy. All other have been developed during the last decade simultaneously with the development of the X-ray spectroscopy.

2. Satellites of spectral lines. — General spectral structure of a multiply charged ion resembles a spectrum of a neutral atom of the same isoelectronic series. Ions with a charge $Z \gg 1$ contain bright satellite lines which arise due to radiative decay of doubly-excited autoionization states of ions. Consider usual (one-electron) radiative transition, $\gamma_1 \rightarrow \gamma_0$, in an ion with a charge Z , where γ_1 denotes the set of quantum number of excited states. Radiative decay of autoionizing state $\gamma_1 nl$ (nl are the additional electron quantum numbers) in an ion with charge $Z-1$, $\gamma_1 nl \rightarrow \gamma_0 nl$, gives a satellite line to the transition $\gamma_1 \rightarrow \gamma_0$. For large Z the wavelength difference between the parent line and its satellite is very small

$$\left| \frac{\lambda(\gamma_1 \rightarrow \gamma_0) - \lambda(\gamma_1 nl \rightarrow \gamma_0 nl)}{\lambda(\gamma_1 \rightarrow \gamma_0)} \right| \ll 1.$$

Radiative transitions from doubly-excited states in He-like ions, $2pnl \rightarrow 1snl$, give satellites to the resonance line of H-like ion, $2p \rightarrow 1s$. The resonance line of He-like ion, $1s 2p(^1P) \rightarrow 1s^2(^1S)$, has satellites from Li-like ions (transitions $1s 2pnl \rightarrow 1s^2 nl$), Be-like ions, B-like ions and so on. One may consider the K_α -lines as satellites to the resonance lines of He-like ions radiated from ions with filled L-shells. With $n = 2$ for the additional electron the satellites are well separated from the parent line and have red shift; $n = 3$ satellites are much closer and may be located on both red and blue sides of the parent line. Satellites with $n \geq 4$ are usually located within the Doppler width of the parent line. The first observations and interpretation of weak satellite lines have been published by Edlén and Tyren in 1939 [7] for the case of ions with small charge (see also [8]). Modern development of X-ray spectroscopy and diagnostics has begun about 10 years ago when hot plasma sources (both laboratory and astrophysical) became a subject of investigation [9-17]. For highly charged ions with $Z > 10$ satellite lines have intensities comparable with the resonance line intensity.

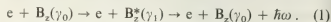
Diagnosics requires good spectral resolution

$$\lambda/\Delta\lambda \approx 10^4 \quad \text{for } \lambda = 1 - 10 \text{ \AA}.$$

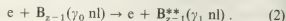
At present we have theoretical calculations [2, 18-22, 24] and experimental measurements [3, 23, 24], which are in reasonable agreement [2, 23-24] with them.

3. Mechanisms of spectra excitation. — Ionic X-ray spectral lines are formed mainly due to electron-ion collisions. In hot plasmas collisions between ions are less important because of the Coulomb repulsion. They give some contribution to collisional transitions within limited groups of neighbouring ionic levels. At present time the influence of charge transfer process is studied insufficiently, although under certain circumstances they may be important for excitation of lines belonging to higher members of the resonance series [25]. Binary electron-ion collisions lead to the following processes: i) impact excitation and ionization, ii) dielectronic recombination, iii) radiative recombination. Three-body collisions give smaller contribution to X-ray spectra excitation even in the case of superdense laser-produced plasmas.

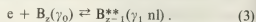
i) Direct impact excitation of an outer ionic shell produce usual (one-electron) excited states:



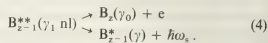
Here $\hbar\omega$ is the energy of a quantum after radiative decay. Impact ionization of the K-shell in Li-like ions leads to excited He-like ions. Impact inner shell excitation gives autoionization states of ions B_{z-1}^{**} with two (or more) excited electrons:



ii) Dielectronic recombination is the inverse process of autoionization:

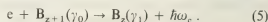


The intensity of the satellite line depends on the branching ratio for the decay of B_{z-1}^{**} by radiation (rate, A) and autoionization (rate, F)



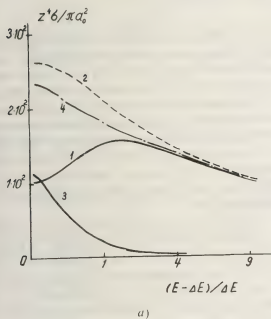
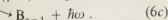
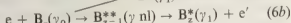
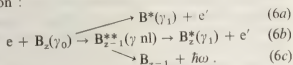
As a rule, $A \ll F$ for $Z < 15$ and $A \gtrsim F$ for $Z > 15$.

iii) Radiative recombination leads to population of usual states (ground and excited) of ions and gives some contribution to continuous spectrum

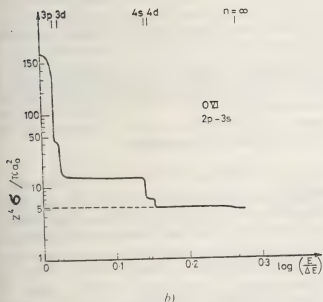


The major part of information on excitation and decay rate coefficients is provided by theoretical calculations. The experimental data, with very few exceptions, are not available now, whereas the theoretical methods are developed with sufficient accuracy. In a case of highly charged ion, $Z \gg 1$, we have the natural small parameter, Z^{-1} , which gives a tool for estimation of calculation accuracy.

Consider a physical picture of an electron-ion collision :



a)



b)

Fig. 1. — Excitation cross sections for electron-ion collisions. a) Transitions $1s^2 \rightarrow 1s2p$ in O VII ion [27] : 1) for 2^1P level with exchange; 2) the same without exchange; 3) for 2^3P level with exchange; 4) the sum of cross sections 1 and 3. b) Transition $1s^2 2p \rightarrow 1s^2 3s$ in O VI ion [26] : dashed curve is the potential excitation, solid curve is the total (potential + resonance) cross section.

The process (6a) means potential (direct and exchange) excitation; (6b) denotes resonance excitation : electron capture into doubly excited states with the principal quantum number $n \gg 1$ and autoionization decay; (6c) represents radiative decay of the resonances (radiative capture). For $Z \gg 1$ the complicated collision problem can be solved in an explicit analytic form [2, 26]. The results show that the resonance excitation is important when the excitation threshold has a value few times less than the one electron ionization threshold. In this case the effect of the electron exchange has small influence to the potential part of a cross section (for example, excitation of Li- and Be-like ions from the ground state). If the excitation threshold is comparable with the ionization one the exchange effect is important [27], and resonance excitation is small. Influence of both effects is shown in figure 1. In the case of electric dipole transitions with small energy difference ΔE , between the initial and final levels these effects do not contribute to excitation rates if $\Delta E \ll kT$, where T is the electron temperature. For this specific case simplified calculations can be done in a pure analytic form (see, for example, [6] and [28]). Extended calculations for the wavelengths λ , and for the rate coefficients (radiation A, autoionization Γ , and excitation $C = \langle v\sigma \rangle$) are given in papers [2, 6, 18-22, 24, 28].

4. Physical principles of transient plasma X-ray diagnostics. — We start our analysis with the Maxwell distribution for plasma electrons and the effective electron temperature T . If electrons have some noticeable deviation from Maxwell distribution (for example, electronic beams) it can be also noticed and investigated using spectroscopic methods. In transient plasmas the ionization stage (distribution of ions over different ionic charges) is determined by the electron temperature, electron density N_e , and the initial/boundary conditions. The ionization stage can be obtained from the ratio (N_{z-1}/N_z) , where N_z is the ion concentration with the charge Z . Following to Gabriel [18] we use the ionization parameter T_z :

$$\frac{N_{z-1}}{N_z} = f(T_z) \quad (7)$$

defined as the steady-state temperature for the given (experimentally observed) ratio (N_{z-1}/N_z) . Then, $T_z = T$ corresponds to the steady state, $T_z < T$ means supercooled plasma, and $T_z > T$ overheated. If the electron temperature remains constant, T_z goes to T , which means recombination of overheated plasmas and ionization of supercooled plasmas.

Strictly speaking, all the line intensities depend on T , N_e , and T_z . The problem lies in the selection of the spectral lines which are the most sensitive to one of the chosen plasma parameters. The great part of

diagnostics based on relative intensity measurements requires the knowledge of the excitation and relaxation rate coefficients.

4.1 ELECTRON TEMPERATURE T_e . — The resonance line intensity of the ion with the charge Z is equal to

$$I_R = N_z N_e \frac{C_R}{A_R + Q_R} A_R [\text{photon} \cdot \text{cm}^{-3} \cdot \text{s}^{-1}] \quad (8)$$

where N_z and N_e are the ion and electron densities, C_R is the effective excitation rate for the resonance line, A_R is the radiative decay probability, Q_R is the collision relaxation rate. Since in all the cases $A_R \gg Q_R$,

$$I_R = N_z N_e C_R \cdot \frac{C_R \cdot A_R}{A_R + Q_R} \approx C_R \cdot \quad (9)$$

If a doubly excited state of the ion B_{z-1} is populated by the dielectronic recombination (3) exclusively the related satellite line intensity is equal to

$$I_s^d = N_z N_e 4 \pi^{3/2} a_0^3 \frac{g_s}{g_0} \left(\frac{R_y}{kT} \right)^{3/2} \frac{A \cdot \Gamma}{\Gamma + \Sigma A} e^{-E_s/kT} \quad (10)$$

where a_0 is the Bohr radius, g_0 and g_s are the statistical weights of the ground state of B_z , γ_0 , and of the autoionization level in B_{z-1} , γ_1 nl, respectively, and $E_s = E(\gamma \text{ nl}) - E(\gamma_0)$.

The relative satellite intensity has well-defined temperature dependence

$$i_s^d = \frac{I_s^d}{I_R} = \text{constant} \frac{A \cdot \Gamma}{\Gamma + \Sigma A} \times \frac{(kT/R_y)^{-3/2} e^{-E_s/kT}}{C_R(T)} = f_1(T) \quad (11)$$

In practice the effective excitation rate, $C_R(T)$, has also some dependence of the electron density N_e , due to cascading processes, which is usually taken into consideration. For more details see, for example, [2, 6, 18-19, 28].

4.2 IONIZATION STAGE T_z . — Inner shell excitation (3) leads to the satellite intensity

$$I_s^{\text{inn}} = N_{z-1} \cdot N_e \cdot C_s \cdot \frac{A}{\Gamma + \Sigma A} [\text{photon} \cdot \text{cm}^{-3} \cdot \text{s}^{-1}] \quad (12)$$

where C_s is the inner shell electron excitation rate. Since the ratio (C_s/C_R) practically does not depend on the electron temperature, the relative intensity

$$i_s^{\text{inn}} = \frac{I_s^{\text{inn}}}{I_R} = \frac{N_{z-1}}{N_z} \cdot \frac{C_s}{C_R} \cdot \frac{A}{\Gamma + \Sigma A} = \text{constant} \frac{N_{z-1}}{N_z} = f_2(T_z) \quad (13)$$

can be used for the measurements of the ionization parameter T_z [2, 18-19].

For the same purpose can be used the resonance line intensity ratio for the He-like ions and H-like ions

$$\frac{I_R[\text{He}]_{z-1}}{I_R[\text{H}]_z} = f_2(T_z) \quad (14)$$

It is worth noting that some satellites can be mainly excited by dielectronic recombination, and the others by inner shell excitation. For the most of them the both processes lead to comparable contributions. Relevant selection rules are given in [2, 19, 21, 24]. For this reason determination of T and T_e has to be done simultaneously.

4.3 ELECTRON DENSITY N_e . — In the limiting cases of both the coronal model and Boltzmann equilibrium relative line intensities do not depend on the electron temperature. For electron density measurements one has to choose the spectral lines sensitive to the density, to solve relevant balance equations, and to compare experimental results with the calculations. This program has its origin in the classical spectroscopy. New element consists in using the satellite lines. *He-like ions*. The resonance and intercombination lines.

For He-like ions the probability of the radiative decay of the $1s2p(^3P_1)$ level is several orders of magnitude less than the decay probability of the $1s2p(^1P_1)$ level, whereas their excitation cross-sections have the same order of magnitude (Fig. 1a). As was pointed out by Edlén [29] the intensity ratio of the resonance line to the intercombination line

$$\alpha = \frac{I_R(2^1P_1 \rightarrow 1^1S_0)}{I_T(2^3P_1 \rightarrow 1^1S_0)} = f_3(N_e) \quad (15)$$

is a function of a plasma electron density, which is quite useful in its determination [30]. Recent calculations (see Fig. 2) [5, 6, 27, 28, 31] show that in the region of $N_e \ll 10^{10} \text{ cm}^{-3}$, α is independent of the N_e (coronal model). In the region

$$10^{11} \text{ cm}^{-3} \ll N_e \ll 10^{16} \text{ cm}^{-3},$$

collision relaxation of all the 2^3L_j levels leads to their radiative decay via the 2^3P_1 level, and α goes down. For $10^{16} < N_e < 10^{19} \text{ cm}^{-3}$ the ratio α is determined by the ratio of the total excitation rates of the singlet to triplet groups of the $n = 2$ levels, and α is close to 1. In the region $N_e > 10^{19} \text{ cm}^{-3}$ radiative decay of triplets is suppressed by collisions, and α increases proportionally to N_e , which is convenient for density diagnostics of superdense plasmas (Fig. 2). Calculations and comparison with the experimental results [32] are given assuming $T_z \approx T$. Results for supercooled and over-heated plasmas [31] (with $T_z \neq T$) give some corrections for the ratio α within 25%.

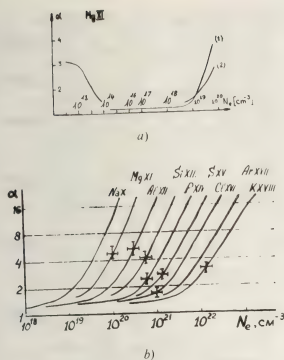


Fig. 2. — a) The dependence $\alpha(N_e)$ for Mg XI [5, 33]. b) The dependence $\alpha(N_e)$ in dense plasmas. Solid curves: calculations [28]. Crosses: experimental data [32].

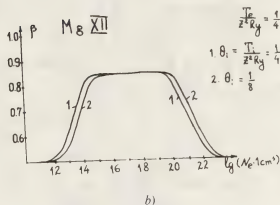
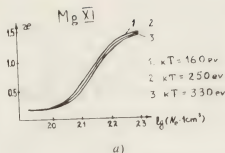


Fig. 3. — a) The dependence $\alpha(N_e)$ for Mg XI [5]. b) The dependence $\beta(N_e)$ for Mg XII [28].

H-like ions. The resonance line and related satellites.

The resonance line has two groups of density sensitive satellites

$$(I) 2s 2p \ ^3P_{0,1,2} \rightarrow 1s 2s \ ^3S_1,$$

$$(II) 2p^2 \ ^3P_2 \rightarrow 1s 2p \ ^3P_{1,2}, \ 2p^2 \ ^3P_1 \rightarrow 1s 2p \ ^3P_{0,1},$$

which are useful for diagnostic purposes [28, 33]. In the coronal limit the $2s 2p$ configuration is populated by the dielectronic recombination, whereas the population of the $2p^2$ configuration is small. With density increasing the collisions lead to the Boltzmann distribution within the triplet system, and the ratio of the line intensities of groups (I) and (II),

$$\alpha = \frac{I_s(I)}{I_s(II)} = f_4(N_e) \quad (16)$$

increases as it is shown in figure 3a. It is worth noting that the distribution between the triplet and singlet level systems remains still close to the coronal distribution in the region of electron densities

$$N_e = 10^{20} - 10^{23} \text{ cm}^{-3} \quad \text{for } Z = 10 - 15.$$

Similar situation takes place for the ratio of intensities of the fine structure components of the Lyman doublet of H-like ions [28],

$$\beta = \frac{I(2p_{1/2} \rightarrow 1s_{1/2})}{I(2p_{3/2} \rightarrow 1s_{1/2})} = f_5(N_e). \quad (17)$$

Results of calculation are shown in figure 3b. Addi-

tional aspects of the density dependence are given in the Appendix.

The methods discussed here provide possibilities for simultaneous measurements of the parameters T , T_z and N_e using the lines with small wavelength differences. All the lines belong to the ions with the charge Z and $Z \pm 1$, i.e. to the ions which can be excited under similar conditions. It helps much for the better understanding of spatial (and time) plasma properties.

5. Interpretation of experimental data. — The methods presented here are widely used for the X-ray diagnostics of hot laboratory and astrophysical plasmas. Some results are given in this section. The continuous curve is the observed spectrum while the straight vertical lines represent wavelength and intensities of the computed lines. The He-like spectra are shown by broken lines. For the satellites, the dielectronic recombination contribution is shown by solid lines while the inner-shell excitation contribution is shown by dotted lines. The lines are denoted according to Gabriel [18] (see also Appendix).

5.1 SOLAR FLARE SPECTRA. — The H-like and He-like ion spectra and associated satellites are only emitted during X-ray solar flares. Although they have been observed by several workers, by far the best spectra are those obtained by Lebedev Physical Institute experiment from the Intercosmos IV orbiting platform [15-17, 34-36]. Figure 4 shows the spectra of the initial, maximum and final phases for the

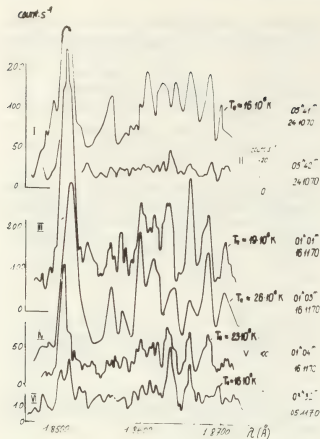


Fig. 4. — Highly charged iron ion spectra obtained by the Intercomcos IV experiment [34-35].

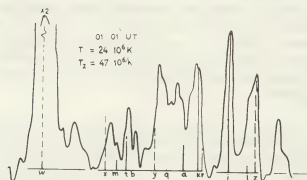


Fig. 5. — Fe XXV spectra and associated satellites recorded at two times [17] and compared with calculations [19].

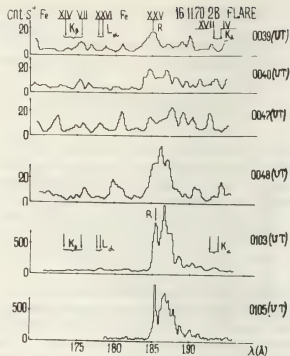


Fig. 6. — K_{α} -lines in iron ion spectra [36].

X-ray flares with good spectral resolution. By way of an example, the theoretical calculations for two of these spectra in comparison with observations are given in figure 5. The results show that the electron temperature was the same for both scans, and the ionization balance was one of recombination during the first scan ($T_e > T_x$) but reached steady state during the second ($T_e = T_x$).

Another example is given in figure 6. Presence of the K_{α} and L_{α} lines shows effective K-shell ionization of the iron ions with $Z = 7-17$ at the initial (cool) stage of the flare. The interpretation includes appearance of electron beams [36] and detailed calculations are in good agreement with the results of simultaneous observations of radiation polarization and the absolute X-ray flux measurements.

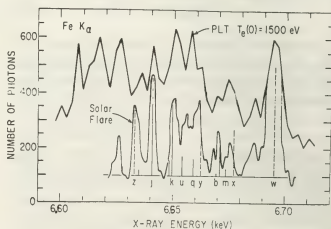


Fig. 7. — Fe XXV-Fe XXIV ion spectra of the PLT Tokamak [37] in comparison with the Intercomcos IV [17].

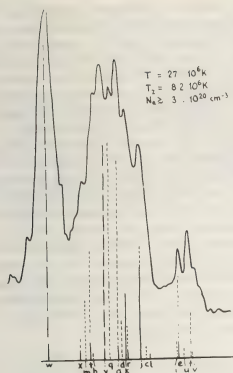


Fig. 8. — Fe XXV-Fe XXIV ion spectrum of a low-inductance vacuum spark [23] in comparison with calculations [19].

5.2 LABORATORY PLASMAS. — Non-time-resolved spectrograms of laboratory plasmas are given in figures 7, 8 and 9. An analysis of plasma conditions in tokamaks, vacuum sparks and laser plasmas shows that the values of $N_e \tau$ are close to $10^{12} \text{ cm}^{-3} \text{ s}$ (or even less). This suggests a non-steady-state conditions in the cases of highest ionization stages observed for heavy elements ($T_z < T$ for $Z > 15$).

Time-resolved spectra of some H- and He-like ion resonance lines [38] and associated satellites have been recently obtained at Lebedev Physical Institute (Fig. 10-12). With the Nd-laser pulse duration about 5 ns, the time resolution of the spectra obtained

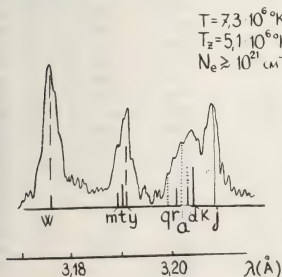


Fig. 9. — Ca XIX-Ca XVIII ion spectrum of a laser produced plasma [3] in comparison with calculations [2].

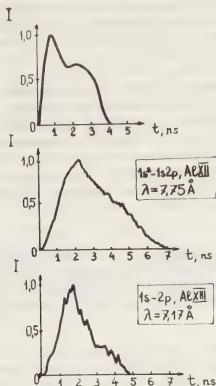


Fig. 10. — Time dependence of the Al XIII and Al XII resonance lines observed in a laser plasma [38]. The upper curve represents a laser pulse.

was about 1.5 ns. The time dependences of N_e and T have been obtained from the relative intensities of dielectronic satellites (H-like and He-like ions) and of intercombination line (He-like ions) to the resonance line [38].

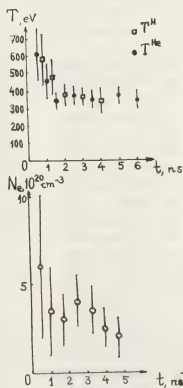


Fig. 11. — Experimental values of electron temperature T and density N_e as a function of time [38].

Further investigations of time-resolved spectra are extremely useful for better understanding of plasma dynamics.

Conclusions. — The results and methods discussed here show that the line spectra of highly charged ions provide a great deal of information on the properties of hot plasmas. The X-ray spectroscopy is of special importance for all cases where the application of contact methods for diagnostics is practically impossible (solar flares, laboratory plasmas with large electron densities and short lifetime).

Acknowledgments. — The authors would like to thank V. A. Boiko, M. A. Mazing, L. A. Vainshtein, A. V. Vinogradov, E. A. Yukov and I. A. Zhitnik of Lebedev Physical Institute for the useful discussions.

Appendix. — All diagnostics methods based on the satellite lines suggest the coronal model conditions, which are valid for rather high electron densities up to $N_1 \approx 10^{20-22} \text{ cm}^{-3}$ for $Z = 15-25$. At higher densities $N_e > N_1$ the collisional mixing between excited levels due to electron impact becomes important. The satellite relative intensity occurs sensitive to the electron density and therefore provide fairly good method of density diagnostics for superdense

plasma until the Boltzmann equilibrium between excited levels will happen. The latter case is realized at the densities $N_e \gg N_2$, where characteristic density N_2 is of order $10^{24-26} \text{ cm}^{-3}$ for the same $Z = 15-25$. The populations of all doubly-excited levels are proportional to their statistical weight when $N_e \gg N_2$, and intensities of satellite lines are proportional to the probability of radiative decay.

It happens so that all upper levels which give arise to satellite lines may be divided into two groups with different total spin, S . These states are, for example, singlet and triplet states of He-like system (satellites to the H-like resonance line) and doublet and quadruplet states for Li-like one. Taking into account only the most effective dipole transitions it is possible to derive equations for the states with definite total spin S which belongs to one configuration only (for example for levels: q, r, s, t of the $1s 2s 2p$ configuration for Li-like ions). These equations may be written in the form:

$$N_s(A_s + N_e C_s) = Q_s + a_s + \sum_{s'} N_{s'} b_{ss'} \quad (\text{A.1})$$

where

$$A_s = \sum_{s'} A_{ss'} + \Gamma_s$$

$$Q_s = N_{s+1} N_e C_{s0s}^d + N_s N_e C_{s0s}^{\text{lin}} \quad (\text{A.2})$$

$$\chi_s = \sum_{\gamma} C_{s\beta} \quad (\text{A.3})$$

Table II. — Relative satellite line intensities (in % to the total sum over all satellite lines) in respect to electron density N_e . H-like ions.

N	Transition	Key	$N_e \ll N_1$		$N_1 \ll N_e \ll N_2$		$N_e \gg N_2$	
			Mg	Fe	Mg	Fe	Mg	Fe
1	$2p^2(^3P_2)-1s 2p(^3P_2)$	A	3.2	12.7	5.9	3.4	19.3	12.0
2	$2p^2(^3P_2)-1s 2p(^3P_1)$	B	1.1	4.0	2.0	2.1	6.4	7.5
3	$2p^2(^3P_1)-1s 2p(^3P_2)$	C	—	—	2.0	1.7	6.4	6.0
4	$2p^2(^3P_1)-1s 2p(^3P_1)$	D	—	—	1.2	0.9	0.4	3.4
5	$2p^2(^3P_1)-1s 2p(^3P_0)$	E	—	—	1.6	1.35	5.2	4.7
6	$2p^2(^3P_1)-1s 2p(^3P_1)$	F	0.06	0.18	1.6	1.2	5.2	4.4
7	$2p^2(^3P_2)-1s 2p(^1P_1)$	G	—	4.5	—	1.2	—	4.2
8	$2p^2(^3P_1)-1s 2p(^1P_1)$	H	—	—	—	0.09	—	0.3
9	$2p^2(^3P_0)-1s 2p(^1P_1)$	I	—	—	—	0.02	—	0.08
10	$2p^2(^1D_2)-1s 2p(^1P_1)$	J	49.1	33.3	53.4	40.7	25.8	17.9
11	$2p^2(^1D_2)-1s 2p(^3P_2)$	K	0.2	10.7	7.2	13.4	1.3	6.0
12	$2p^2(^1D_2)-1s 2p(^3P_1)$	L	—	0.05	—	0.06	—	0.03
13	$2p^2(^1S_0)-1s 2p(^1P_1)$	M	4.0	1.7	0.9	9.4	0.6	4.2
14	$2p^2(^1S_0)-1s 2p(^3P_1)$	N	—	—	—	—	—	—
15	$2s^2(^1S_0)-1s 2p(^1P_1)$	O	2.2	2.2	2.2	1.1	1.0	0.4
16	$2s^2(^1S_0)-1s 2p(^3P_1)$	P	—	1.8	—	0.9	—	0.4
17	$2s 2p(^3P_2)-1s 2p(^3S_1)$	Q	13.8	3.26	4.0	3.4	12.9	12.0
18	$2s 2p(^3P_1)-1s 2p(^3S_1)$	R	8.3	2.9	2.4	1.95	6.4	6.8
19	$2s 2p(^3P_0)-1s 2p(^3S_1)$	S	2.8	0.65	10.1	0.7	2.6	2.3
20	$2s 2p(^1P_1)-1s 2p(^3S_0)$	T	15.3	17.3	5.5	15.7	6.4	7.0
21	$2s 2p(^3P_1)-1s 2p(^1S_0)$	U	—	0.07	—	0.08	—	0.3
22	$2s 2p(^1P_1)-2s 2p(^3S_1)$	V	—	0.7	—	0.6	—	0.3

$$a_{\alpha} = N_e \sum \frac{Q_{\beta} C_{\gamma\beta}}{\Delta_{\beta} + N_e C_{\beta}} \quad (\text{A.4})$$

$$b_{\gamma\gamma'} = N_e^2 \sum_{\beta} \frac{C_{\gamma\beta} C_{\beta\gamma'}}{(\Delta_{\beta} + N_e C_{\beta})}. \quad (\text{A.5})$$

Here $C_{\alpha\beta}$ is the rate of optically allowed collisional mixing between two levels α, β , belonging to different configurations (for instance, $1s\ 2s\ 2p$ and $2s\ 2p^2$ in the case considered above); $C_{\alpha\alpha'}$ is the rate of pumping of the level α due to radiative capture (dielectronic recombination) and/or direct electron impact. At low densities

$$N_e \ll N_1 = \min \left\{ \frac{\Delta_{\gamma}}{C_{\gamma\beta}} \right\},$$

and we get the coronal equilibrium; the population in this case is equal to :

$$N_{\alpha} = \frac{Q_{\alpha}}{A_{\alpha} + G_{\alpha}}. \quad (\text{A.6})$$

In the opposite case, $N_e \gg N_1$, when all the terms in (A.1) proportional to N_e are important, the Boltzmann equilibrium between all levels of choosed group occurs and populations become proportional to the statistical weight of the level :

$$N_{\gamma} = g_{\gamma} \cdot \frac{\sum_{\gamma'} g_{\gamma'} Q_{\gamma'}}{\sum_{\gamma'} g_{\gamma'}}. \quad (\text{A.7})$$

Here the sum is carried out over all coupled states γ (both configurations in the case afore mentioned).

In the intermediate case the relative satellite intensities depend on N_e until the quasi-coronal, quasi-Boltzmann equilibrium will be achieved when all levels within one group (doublet or quadruplet for Li-like ions) are in Boltzmann equilibrium in accordance with (A.7), and levels from different group are in coronal conditions. When density becomes so high as

$$N_e \gtrsim N_2 = \max \left\{ \frac{\Delta_{\gamma}}{C_{\gamma\beta}^{\text{int}}} \right\},$$

where $C_{\alpha\beta}^{\text{int}}$ is the rate of intercombination transition, the Boltzmann conditions for all the states are valid. Since the $C_{\alpha\beta}^{\text{int}}$ is of about two order of magnitude less compare to $C_{\alpha\beta}$ without changing of spin ($\Delta S = 0$), the N_2 value is at least two order of magnitude higher than N_1 .

The ratio

$$\delta = \frac{I_s}{\sum_s I_s}, \quad (\text{A.8})$$

where I_s is the intensity of a given satellite, can be used as a good indicator of the electron density region. Tables II and III show the δ -values for three limiting cases considered above. Calculations have been done for the temperature at which the resonance lines have their maximum intensity.

Table III. — Relative satellite line intensities (in % to the total sum over all satellite lines) in respect to electron density N_e . He-like ions.

N	Transition	Key	$N_e \ll N_1$		$N_1 \ll N_e \ll N'$		$N_e \gg N''$	
			Mg	Fe	Mg	Fe	Mg	Fe
1	$1s\ 2p^2(^2P_{3/2})-1s^2\ 2p(^2P_{3/2})$	a	8.1	10.7	24.8	23.9	24	23.6
2	$1s\ 2p^2(^2P_{3/2})-1s^2\ 2p(^2P)$	b	1.1	0.15	3.5	0.3	3.5	0.3
3	$1s\ 2p^2(^2P_{1/2})-1s^2\ 2p(^2P)$	c	0.94	0.03	4.5	3.1	4.4	3.1
4	$1s\ 2p^2(^2P_{1/2})-1s^2\ 2p(^2P)$	d	1.9	0.1	9.6	10.5	9.4	10.3
5	$1s\ 2p^2(^4P_{5/2})-1s^2\ 2p(^2P)$	e	0.3	1.8	—	1.2	0.9	2.0
6	$1s\ 2p^2(^4P_{3/2})-1s^2\ 2p(^2P)$	f	—	0.25	—	0.2	—	0.4
7	$1s\ 2p^2(^4P_{3/2})-1s^2\ 2p(^2P)$	g	—	—	—	—	—	—
8	$1s\ 2p^2(^4P_{1/2})-1s^2\ 2p(^2P)$	h	—	—	—	0.001	—	0.002
9	$1s\ 2p^2(^4P_{1/2})-1s^2\ 2p(^2P)$	i	0.4	—	—	0.2	—	0.4
10	$1s\ 2p^2(^2D_{5/2})-1s^2\ 2p(^2P)$	j	32.7	37.2	14.8	12.4	14.4	12.3
11	$1s\ 2p^2(^2D_{3/2})-1s^2\ 2p(^2P)$	k	20.7	27.0	9.0	12.6	9.0	12.4
12	$1s\ 2p^2(^2D_{3/2})-1s^2\ 2p(^2P)$	l	1.5	1.6	0.6	1.5	0.6	1.5
13	$1s\ 2p^2(^2S_{1/2})-1s^2\ 2p(^2P)$	m	5.6	2.6	3.2	4.7	3.0	4.6
14	$1s\ 2p^2(^2S_{1/2})-1s^2\ 2p(^2P)$	n	2.2	0.1	1.3	0.2	1.2	0.2
15	$1s\ 2s^2(^2S_{1/2})-1s^2\ 2p(^2P)$	o	0.7	1.7	—	0.2	0.3	0.2
16	$1s\ 2s^2(^2S_{1/2})-1s^2\ 2p(^2P)$	p	0.3	2.1	—	0.2	0.2	0.2
17	$1s\ 2s\ 2p(^2P_{3/2})-1s^2\ 2s(^2S_{1/2})$	q	10.6	0.1	18	18.7	17.8	18.5
18	$1s\ 2s\ 2p(^2P_{1/2})-1s^2\ 2s(^2S_{1/2})$	r	7.1	5.0	8.7	6.2	8.5	6.1
19	$1s\ 2s\ 2p(^2P_{3/2})-1s^2\ 2s(^2S_{1/2})$	s	3.5	0.2	1.6	0.03	1.5	0.03
20	$1s\ 2s\ 2p(^2P_{1/2})-1s^2\ 2s(^2S_{1/2})$	t	2.6	7.9	0.1	3.4	1.1	3.4
21	$1s\ 2s\ 2p(^4P_{3/2})-1s^2\ 2s(^2S_{1/2})$	u	—	0.1	—	0.4	—	0.6
22	$1s\ 2s\ 2p(^4P_{1/2})-1s^2\ 2s(^2S_{1/2})$	v	—	0.07	—	0.06	—	0.1

References

- [1] GABRIEL, A. H., in : *Highlights of Astronomy* (ed. C. de Jager), D. Reidel Publ. Comp. Co., Dordrecht-Holland, 1971, p. 486-494.
- [2] PRESNYAKOV, L. P., *Usp. Fiz. Nauk* **119** (1976) 49 (Translation : Sov. Phys. Uspekhi **19** No 5 (1976) 387).
- [3] BOIKO, V. A., FAENOV, A. Ya., PIKUS, S. A., *J. Quant. Spectrosc. Radiat. Transfer* **19** (1978) 11.
- [4] PEACOCK, N. J., in : *Proc. XIII ICPiG Invited Lectures*, Berlin, Physical Soc. of GDR, 1977, p. 383.
- [5] SOBELMAN, I. I., VINOGRADOV, A. V., YUKOV, E. A., in : *X ICPEAC Invited Papers and Progress Reports*, Paris (Ed. G. Watel, North-Holland) 1978, p. 421.
- [6] VINOGRADOV, A. V., SKOBELEV, I. Yu., YUKOV, E. A., *Usp. Fiz. Nauk* (Translation : Sov. Phys. Uspekhi) 1979 (in press).
- [7] EDLÉN, B., TYREN, F., *Nature* **143** (1939) 940.
- [8] FLEMBERG, H., *Ark. Mat. Astr. Fys.* **A 28** (18), 1, 1942.
- [9] GABRIEL, A. H., JORDAN, C., *Nature* **221** (1969) 947.
- [10] PEACOCK, N. I., SPEER, R. J., HOBBY, M. G., *J. Phys.* **B 2** (1969) 798.
- [11] PARKINSON, J. H., *Nature* **233** (1971) 44.
- [12] WALKER, A. B. C., RUGGE, H. R., *Astrophys. J.* **164** (1971) 181.
- [13] MEEKINS, J. F., DOSCHKE, G. A., FRIEDMAN, H., CHUBB, T. A., KREPLIN, R. W., *Solar Phys.* **13** (1970) 198.
- [14] NEUPERT, W. M., *Solar Phys.* **18** (1971) 474.
- [15] GRINEVA, Yu. I., MANDELSTAM, S. L., ZHITNIK, I. A. *et al.*, in : *Proc. 16th COSPAR* (Seattle, USA), 1971, p. 243; in : *Space Research XII*, Berlin Akademie-Verlag, 1972, p. 1553.
- [16] GRINEVA, Yu. I., MANDELSTAM, S. L., ZHITNIK, I. A. *et al.*, *Solar Phys.* **29** (1973) 441.
- [17] GRINEVA, Yu. I., MANDELSTAM, S. L., ZHITNIK, I. A. *et al.*, in : *Space Research XIV*, Berlin, Akademie-Verlag 1974, p. 453.
- [18] GABRIEL, A. H., *Mon. Not. Roy. Astr. Soc.* **160** (1972) 99.
- [19] BHALLA, C., GABRIEL, A. H., PRESNYAKOV, L. P., *ibid.* **172** (1975) 359.
- [20] BELY-DUBAU, F., GABRIEL, A. H., VOLONTE, S., *Mon. Not. R. astr. soc.* **186** (1979) 405.
- [21] VAINSHTEIN, L. A., SAFRONOVA, U. I., *Atomic data and nuclear data tables* **21** (1978) 49.
- [22] VAINSHTEIN, L. A., SAFRONOVA, U. I., in : *Spectroscopy constants of atoms* [in Russian]. Published by Spectroscopy Scientific Council of the USSR Academy of Sci. Moscow, 1977.
- [23] GOLTZ, E. Ya., ZHITNIK, I. A., KONONOV, E. Ya., MANDELSTAM, S. L., SIDELNIKOV, Yu. V., *DAN SSSR* **220** (1975) 560 (Translation : Sov. Phys. : Doklady).
- [24] BOIKO, V. A., CHUGUNOV, A. Yu., IVANOVA, T. G., FAENOV, A. Ya., HOLIN, I. V., PIKUZ, S. A., URNOV, A. M., VAINSHTEIN, L. A., *U.I. Safronova. Mon. Not. Roy. Astr. Soc.* **185** (1978) 305.
- [25] PRESNYAKOV, L. P., in : *X ICPEAC Invited Papers and Progress Reports*, Paris (Ed. G. Watel, North-Holland) 1978, p. 409.
- [26] PRESNYAKOV, L. P., URNOV, A. M., *J. Phys.* **B 8** (1975) 1280.
- [27] VAINSHTEIN, L. A., in : *X ICPEAC Invited Papers and Progress Reports*, Paris (Ed. G. Watel, North-Holland) 1978, p. 393.
- [28] SKOBELEV, I. Yu., VINOGRADOV, A. V., YUKOV, E. A., *Phys. Scripta* **17** (1978) 29.
- [29] EDLÉN, B., *Ark. Fys.* **4** (1952) 441.
- [30] GABRIEL, A. H., JORDAN, G., *Mont. Not. Roy. Astr. Soc.* **145** (1971) 241.
- [31] BOIKO, V. A., CHUGUNOV, A. Yu., FAENOV, A. Ya., PIKUZ, S. A., SKOBELEV, I. Yu., VINOGRADOV, A. V. and YUKOV, E. A., *J. Phys.* **B 12** No 2, 1979, 213.
- [32] BOIKO, V. A., PIKUZ, S. A., FAENOV, A. Ya., *J. Phys. B. Atomic and Molec. Phys.* (1979, in press).
- [33] VINOGRADOV, A. V., SKOBELEV, I. Yu., YUKOV, E. A., *Zh. Eksp. Teor. Fiz.* **72** (1977) 1762 (Translation : Sov. Phys. JETP).
- [34] KORNEEV, V. V., KONONOV, E. Ya., KRUTOV, V. V., MANDELSTAM, S. L., SYLWESTER, B., SYLWESTER, I., URNOV, A. M., ZHITNIK, I. A., *Solar Phys.*, 1979 (in press).
- [35] GOLTS, E. Ya., KONONOV, A. Ya., KORNEEV, V. V., KRUTOV, V. V., MANDELSTAM, S., SIDELNIKOV, Y. V., URNOV, A. M., ZHITNIK, I. A., *Solar Phys.*, 1979 (in press).
- [36] KORNEEV, V. V., KRUTOV, V. V., MANDELSTAM, S. L., SYLWESTER, B., TINDO, I. P., URNOV, A. M., VALNICEK, B., TZHITNIK, I. A., *Preprint N 76 of the Lebedev Physical Institute* (to be published in Solar Phys.) 1979.
- [37] HILL, K. W., VON GOELER, S., BITTER, H., CAMPBELL, L., COWAN, R. D., FRANKEL, D., GEENBERZER, A., HORTON, R., HOVEY, J., RONEY, W., SANTHOFF, N., STODIEK, W., *Preprint of Plasma Physics Laboratory*, Princeton, NJ 08540.
- [38] KAS'YANOV, Yu. S., MAZING, M. A., CHEVOKIN, V. K., SHEVELKO, A. P., *Pis'ma Zh. Eksp. Teor. Fiz.* **25**, No 8 (1977) 373. (Translation Sov. Phys. : *JETP Letters* **25**, No 8 (1977) 346.

Physics on plasma chemistry

P. Fauchais and J. Rakowitz

Laboratoire de Thermodynamique, U.E.R. des Sciences, Université de Limoges, 123, rue Albert-Thomas, 87100 Limoges

Résumé. — Dans cet article après un bref historique de la chimie des plasmas et une courte description des différents types de plasmas utilisés et de leurs moyens de production, nous présentons le réacteur de chimie des plasmas avec les différents problèmes rencontrés, notamment le mélange des réactifs, la trempe des produits et la catalyse. Nous continuons alors par une discussion sur les techniques de diagnostic utilisées en chimie des plasmas tant pour le plasma lui-même : mesure spectroscopique de la température et de la population des états excités, fluorescence laser, mesure de la vitesse des gaz et spectroscopie de masse des ions, que pour les matériaux en phases condensées introduits dans le plasma : vitesse, température de surface, population et diamètre des particules.

Pour les réactions en phase homogène un bref rappel des calculs à l'équilibre et de la cinétique des réactions est suivi par des exemples d'applications de tels calculs sur des expériences réelles : synthèse des oxydes d'azote dans un générateur à arc en courant continu, synthèse de l'acétylène et de l'acide cyanhydrique dans une torche haute fréquence, synthèse de composés organiques avec le métastable moléculaire de l'oxygène $O_2^1\Delta_g$ produit dans une décharge HF à basse pression.

Pour les réactions en phase hétérogène, nous rappelons tout d'abord le calcul des propriétés thermodynamiques et de transport du plasma, puis nous considérons les problèmes de transfert de chaleur et de masse plasma-particules. Les applications illustrant ces calculs sont d'abord celles où le matériau traité subit dans le plasma uniquement un changement de structure physique : projection par plasma, sphéroidisation, vaporisation, condensation puis celles où il est le siège d'une transformation chimique.

Abstract. — In this paper, after a brief historical review of plasma chemistry, a short description of the different types of plasmas used, and of their means of production, we will present the plasma chemistry reactor with the problems of mixing the reactants with the plasma, the quenching and the catalysis. This is followed by a discussion of diagnostic techniques either on the plasma itself : spectroscopic measurement of temperature and population, laser fluorescence spectroscopy, gas velocity measurements and mass spectroscopy of ions ; or on the condensed materials injected into the plasma : velocity, surface temperature, population and diameters of the particles.

For the reactions in homogeneous phase a brief summary on equilibrium and kinetics calculations is followed by an illustration of the application of this calculations with three examples : NO synthesis in a DC plasma jet, C_2H_2 and HCN synthesis in a HF plasma torch, organic compound synthesis with the $O_2^1\Delta_g$ metastable state produced in a HF low pressure plasma.

For the reactions in heterogeneous phase, first we recall thermodynamic and transport properties of the plasma and then we deal with heat and mass transfer plasma particles. The applications described are first concerned with physical changes of solid materials in plasma : plasma spraying, spheroidisation, vaporisation, condensation and second chemical reactions.

1. Introduction. — **1.1 HISTORICAL.** — The first laboratory reaction of plasma chemistry was the synthesis of acetylene in 1797 by Henry and Dalton, although they were not aware of the fact that they were doing plasma chemistry with their capacitive discharge in methane. The first industrial plasma chemistry process was the synthesis of nitric oxide in an A.C. arc by Birkeland and Eyde [1] at the end of the nineteenth century. Unfortunately the empirical work done between 1880 and 1910 on chemical reactions in electric discharges was soon forgotten because the plasma was almost completely unknown and it was impossible to correlate any properties of the products obtained to the discharge.

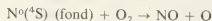
Only a few decades ago, the number of studies in

plasma chemistry increased considerably. The progress in the knowledge of plasmas allowed a better understanding of the role of the plasma components leading to a chemistry that takes into account not only neutral species and ions but also electrons, excited species (specially the metastables ones with a long life time often responsible of specific reactions) and also, if necessary, photons.

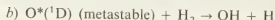
While numerous studies of elementary and simple reactions were developed under laboratory conditions with electric discharges, a large number of results is due to the research on the earth atmosphere chemistry, on the atmosphere of others planets and of the space. To illustrate this let us give some examples with the simplest molecules at 300 K.



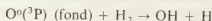
$$k \sim 10^{-11} \text{ cm}^3 \text{ molecule}^{-1} \text{ s}^{-1}$$



$$k \sim 10^{-16} \text{ cm}^3 \text{ molecule}^{-1} \text{ s}^{-1}$$



$$k \sim 3 \times 10^{-10} \text{ cm}^3 \text{ molecule}^{-1} \text{ s}^{-1}$$



$$k \sim 1.5 \times 10^{-16} \text{ cm}^3 \text{ molecule}^{-1} \text{ s}^{-1}$$

So the metastable states, even if their concentration is low must be taken into account as a distinct chemical specie.

In the seventies, with the improvement of measurement techniques, important progress have been made in the understanding of the phenomena and of the dynamics of chemical reactions in plasmas. The measurements show that, in almost all the cases, the plasmas used in plasma chemistry are out of equilibrium. Work in molecular physics allowed an understanding and modelisation of non equilibrium reactors defining the role of the kinetic, electronic, vibrational and rotational excitations and measuring the disequilibrium between these differents forms of excitation [2 to 5].

In this paper, after a short description of the plasmas used in plasma chemistry and of the means of production, we will recall the essential points of a plasma chemical reactor and the measurement techniques that can be used, either in homogeneous or in heterogeneous reactions. Then we will describe, through a few examples, how gaseous and heterogeneous reactions can be modeled mathematically with emphasis on what we know (or we believe to know) and what we would like to know better.

1.2 THE DIFFERENT TYPES OF PLASMA. — Many types of plasmas with different physical properties, usually produced by electrical discharge, have been described. Their state is characterized by the electron energy (kT_e) and electron density (n_e) figure 1 [6]. The plasmas used in plasma chemistry are high and low pressure arcs and glow discharges. In general, when the pressure is lowered the ratio T_e/T_h , the electron temperature to the heavy particles temperature, increases from about one at one atmosphere to about 100 for pressures under 1 torr. It is the same when one considers the intensity of the discharge current; more than 50 A for a ratio of about one (almost equilibrium) and less than 1 A for a ratio lower than 50. With high T_e/T_h , one has a high electron energy and a gas temperature near ambient. These plasmas are very well suited for the chemistry of materials sensitive to temperature effects (organic compounds for example), although electric power is

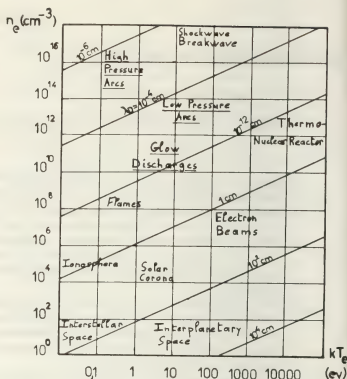


Fig. 1. — Typical plasma characterized by their electron energy and density (after [6]).

usually small and the mass treated is rather low (a few mg/s). On the contrary the plasmas near equilibrium have a rather high gas temperature (a few thousand K) and they are well suited for reactions that needs high enthalpy transfer (fusion, spheroidisation, spraying, vaporisation) or for the synthesis of inorganic materials such as ceramics, small molecules (NO , C_2H_2 , HCN , ...). The electric power is high (up to 5 MW) and the mass treated important (a few g/s to hundreds g/s). But often the temperature and density gradients are high along the radius of the plasma and it is difficult to get the same treatment for the products injected. Moreover in most cases one injects the cold reactants into the plasma jet after the electrodes and the resulting mixture is quite out of equilibrium ($T_h \sim 1\,000\text{--}2\,000\text{ K}$ and $T_e \sim 5\,000\text{--}10\,000\text{ K}$).

The plasmas mainly used in plasma chemistry are, in a stationary situation, corona discharge, glow discharge, high frequency (HF) plasma torches, microwave (MW) discharges and arcs. The electrons are the principal vector of energy. Their mean energy $\bar{\mu}$ is such that the energy losses by elastic or inelastic collisions with the heavy particles, drift and diffusion to the walls or electrodes, balance the gain of energy due to the electric field. For positive column the gain frequency of charged particles is determined by the electric field E/p (V/cm/torr) and the loss frequency by the reduced radius R_p [7]. With high fields ($E/p > 50\text{--}100$) the motion of electron is beam like, such is the case of the corona discharge. With medium ($1 < E/p < 100$) electric field, the glow, HF and MW

discharges at low pressure and low current are governed by the same energy loss of electrons (mainly inelastic collisions) as in corona discharge. On the contrary in discharges near equilibrium (high pressure HF and MW discharges and arcs) with a low electric field ($E/p < 5$) the energy loss of the electrons is due also to elastic collisions. It is then possible to define a critical value E/p above which practically the total energy delivered by the generator is fed primarily into excitation, dissociation and ionisation.

In DC and AC plasma generators the electrons reach the anode and give rise to losses and to the creation of secondary species (pollution of the plasma). On the contrary with high frequencies, the polarity of the field is reversed in such a short time compared to the transit time of the electrons that only a very low percentage of them can reach the electrodes, in that case (HF and MW discharges) the electrodes can be disposed outside of the reactor and their is no pollution or catalysis with them.

We will not describe the glow discharge now well known [8] usually used at pressures under 100 torr and with powers less than 1 kW.

The corona discharges usually with a power up to 1 kW, a voltage up to 30 kV and a frequency up to 500 kHz is now used on industrial scale for ozone synthesis [9] and for the treatment of polyethylene films [10].

The microwave discharge allows excellent concentration of the electric field inside the cavity and, due to the low value of the wave length, the diameter of the plasma may be reduced to less than one centimeter. The electric field with a frequency ω penetrates the plasma for an electron density less than that corresponding to plasma resonance [11].

Therefore the frequencies usually used are in the range 200-3 000 MHz, that plasma being produced with a resonant cavity [12]. Three years ago, a new method of microwave plasma generation was discovered and the production of long plasma columns was achieved by propagation of a surface wave [13]. For example working at 915 MHz with argon at atmospheric pressure it is possible to achieve column length of 50 cm with power of 700 W. The column diameter is about 1 mm and there is no LTE (electron density of $3 \times 10^{14}/\text{cm}^3$ and excitation temperature about 3 000 K).

The HF torches (between 1 and 20 MHz) are the most widely used with pressures between 1 torr and 5 atmosphere. With a life time of 2 300 hrs an HF plasma device can work with a power up to 1 MW, with about 40-60 % of the energy transferred to the plasma [14]. They can be used with aggressive gases such as oxygen [14], chlorine [15] or UF_6 [16]. The most often used technique of coupling is by induction. The minimum power necessary for self a sustained inductive discharge is determined by the gas nature, its pressure and the frequency of the electromagnetic field; the cost of the source is reduced as the frequency

is reduced from the MHz range to the hundreds of kHz range, unfortunately the minimum power increases from less than 10 kW to hundreds of kW unless the electrical conductivity is increased by the addition of an impurity (K, Cs, ...) which is very polluting in plasma chemistry. Capacitive coupling leads to the formation of a phase shift between the electrodes and discharge current, thus reducing the efficiency of the discharge, but the minimum power for a self sustained discharge is lower than with induction coupling (for example [14] in the range 10-20 MHz, this minimum power is 0.2 kW for air and 1.0 kW for hydrogen operation).

DC or AC arcs are used mostly at atmospheric pressure when a high energy transfer is necessary (for example with solid reactants). The energy density is much higher than in HF torches at atmospheric pressure but the mean speed of the gas is very high (hundreds of m/s) so the residence time of the reactants is short. The first design of the torch was given in 1957 by Gage [17]: the arc is struck between a cathode rod and a nozzle anode. The forced gas flow extends the arc in the nozzle anode which is strongly cooled. Various torch configurations are possible depending upon stabilisation mode: tangential gas input in the arc channel (Fig. 2a), axial gas input along the cathode (Fig. 2b), segmented anode arc (Fig. 2c), magnetic rotation of the arc root, self induced by the arc current (more than 8 000 A) or externally generated (Figs. 2d and 2e). The nozzle are generally made of copper, molybdenum or carbon and their life time is about 400 hrs (erosion between 10^{-6} - 10^{-7} g/C). The cathode

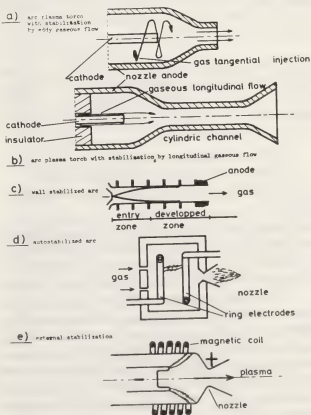


Fig. 2. — Principles of DC plasma torch stabilization.

is usually of tungsten with thorium or carbon, the erosion of a W cathode is about 10^{-9} - 10^{-10} g/C with a life time of 150 hrs approximately. Some metals like zirconium or hafnium may be used in presence of oxygen but their life time is less than 20 hrs. The thermal efficiency of such generators is up to 80 % depending on the gas nature, its flow rate and of the arc intensity and voltage. Torches up to 5 MW have been tested [18 to 34].

Some torches stabilized with liquids have been also developed, for example, the Lonza Corp [35] 250 kW torch stabilized by alcohol flow with a consumable carbon cathode.

When using AC current, in most cases the electrodes are made of copper, the arc striking between two tubes (Fig. 3) as in the design proposed by Fey [36] with power up to 1 MW. The arc rotates under the influence of a magnetic field and a tangential gas inlet. In order to avoid arc extinction a high frequency voltage is superimposed on the arc current [37, 38].

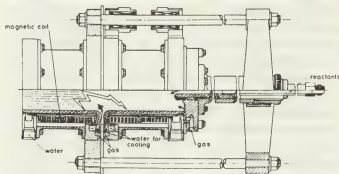


Fig. 3. — A 3.5 MW single-phase alternating-current plasma torch (after Fey [36]).

1.3 THE PLASMA CHEMISTRY REACTOR. — Generally [6] the experimental considerations in plasma chemistry may be divided into three parts (Fig. 4) corresponding as first approximation to the three stages of the reaction

- plasma generation,
- mixing of the reactants and reactions,
- quenching and recuperation of the formed products.

Unfortunately, plasma generation is not independent of the choice of the source and is of considerable importance for the others stages and the reactor must be conceived around the plasma source.

1.3.1 Mixing of the reactants with the plasma. — As we can see is figure 4 the mixing can be done before or after the plasma generation. It is much more complicated to realize the mixing at high heavy particles temperature (because of the high viscosity of the plasma) but in all cases mixing inside the plasma, or just after the plasma generation, is a difficult technological problem and many studies have been carried out to determine the optimal injection mode

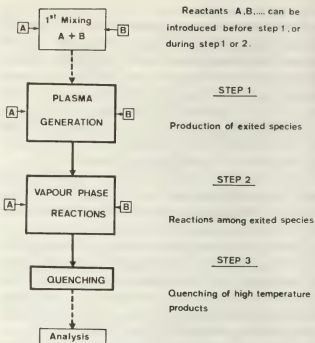
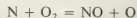


Fig. 4. — A plasma chemistry reaction.

[39 à 41]. Original systems have also been proposed such as hollow or porous cathodes [42], consumable cathodes and volatile anodes [43, 44]. Liquid injection may be realised with an ultrasonic atomizer [45] and solid particle injection is always a difficult problem.

1.3.1.1 Mixing before the generator. — In this case all the problems of mixing a cold gas with a plasma are solved but one has to be sure, as soon as the plasma is in contact with electrodes, that there is no reaction with them. For example a lot of precautions must be taken to use oxygen or chlorine in arcs, or to inject solid particles in the arcs using the Maecker effect [46].

Even if all the technical problems have been solved to inject the reactants before the plasma generation one has to think about the excitation of the reactants in the plasma because in this case there might be no selective excitation. For example if one injects oxygen and nitrogen into a HF plasma before the plasma generation the NO synthesis might be decreased because, in certain conditions the main processes are :



and it is preferable to dissociate only N_2 to get N and then to inject cold O_2 after plasma generation.

A good example of selective plasma chemistry is the use of metastable levels to transfer their energy to the required excited states, for example excitation of N_2 by Ar^m and then reaction with oxygen.

1.3.1.2 Mixing after plasma generation. — In this case there are no problems with electrodes but the

injection of a cold reactant in an extinguishing plasma is often difficult, specially if it is a hot heavy particles plasma (near ETL) and this injection modifies strongly the plasma excitations and temperatures. One has to study the heat and mass transfer and the excitation transfer that often becomes the main reaction process.

1.3.2 *Quenching*. — Quenching in plasma chemistry plays two important roles :

- To withdraw excess energy from the excited new species which are formed.
- To prevent the inverse reactions that destroy the new products.

This is obtained by :

— excess energy removal, that is to say the reduction of the kinetic temperature that governs the creation-destruction equilibriums,

— the more or less specific destruction of the electronic and vibrational excited species (walls, collisions, recombinaisons) that can induce new reactions, some time undesirable. As well in hot as in cold plasma, in most cases of plasma chemistry, quenching is the most important phenomena determining whether a new product is obtained or not.

When the reaction takes place in a hot heavy particles plasma, the speed of quenching in its classical meaning is of first importance and the quenching techniques are characterized by the quenching speed usually between 10^5 and 10^8 K/s. The techniques used are : the fast expansion of the jet in a Laval nozzle [47] ($v = 10^7$ K/s), contact with cold walls [48 to 52] ($v = 10^7$ to 10^8 K/s), liquid pulverisation [51 to 53], cold gas injection [54].

Of course the exact role of the quenching must be defined through the kinetics of the reactions if known but it is also important to emphasize that the moment of the quenching and the law of quenching ($dT/\lambda T = f(T)$) is of primary importance for the results obtained. For example Polak [55] has shown that a delay 2×10^{-3} s gives a reduction of the acetylene conversion from 15.5 % to 10 % and that a decrease of the quenching speed from 10^8 to 10^7 K/s gives a reduction of the nitrogen conversion to NO from 9.6 to 6.4 %.

1.3.3 *Catalysis*. — Very few works have been devoted to catalysis in plasma. Some work has been done in homogeneous catalysis such as O_2 dissociation with N_2 and NO [52], N_2 dissociation with O_2 and SF_6 [57] or with HCl [58] or with other gases [59]. Heterogeneous catalysis has been studied for the production of C_2H_2 and aniline in a plasma of $NH_3-C_6H_6$ with Ni [60], propane craking in an argon plasma with Fe, NH_3 decomposition or NO synthesis with Fe, Ag, Ca, Pt, Pd, Ni [61 to 67]. Unfortunately due to the complexity of the phenomena no real mechanism has been proposed. However in all cases the chemical rate of the reaction has been increased. For example Rapakoulis [68] has shown that, in a

nitrogen HF plasma where CH_4 is injected, catalysis with iron increases the conversion of C to HCN from 38 % to 60 % with a N/C ratio of 30 and Cavadias [69] has shown that with WO_2 the conversion of Nitrogen to NO increases from 9 to 18 % in a N_2-O_2 HF plasma, with an induced energy of 80 kcal/Nl. The problem is to understand what exactly happens, this results being obtained in one type of experiment and may be due to an improvement of the reactor performance in presence of metallic or oxides vapours.

1.4 MEASUREMENTS IN PLASMA CHEMISTRY. — It is of prime importance to know the gas temperatures and gas velocities, the population of the excited states, the electron density and the temperatures and velocities of the condensed materials injected. Unfortunately these measurements, with the complex molecules encountered in plasma chemistry, are rather difficult from the experimental and theoretical point of view, but the results, however approximate, are important to understand what happens during plasma treatment.

1.4.1 *Plasma diagnostic*. — 1.4.1.1 *Spectroscopic diagnostic of temperatures and population of excited levels*. — The degree of thermodynamic equilibrium has been extensively studied from a theoretical point of view by Griem [70] and Drawin [71], it has also been studied experimentally and compared with theory, for hydrogen, helium, and argon [72, 73] and recently for nitrogen [2]. The equilibrium conditions are generally stated from characteristic time and length for the process under consideration, compared to characteristic time and length of a plasma parameter. The following processes have to be studied :

- collision times between different particles [74, 75],
- Maxwellisation times [76],
- energy relaxations [77 to 81],
- kinetics of reactions [82],
- Boltzmann distribution relaxation [71],
- diffusion lengths [71, 82],
- equilibrium population of energy levels [71].

The characteristic parameters generally considered are the temperature and electron density which is of first importance under equilibrium conditions [83]. For example, with a DC plasma generator, two different zones have been pointed out in a nitrogen plasma jet at atmospheric pressure [82].

The first zone is such that $10^{15} < n_e < 10^{17} \text{ cm}^{-3}$ and $9\,000 \text{ K} < T < 15\,000 \text{ K}$, and the different criteria show that CLTE is realized. The second zone has a low electronic density $10^{12} < n_e < 10^{14} \text{ cm}^{-3}$, and a quite low temperature $3\,000 \text{ K} < T < 7\,000 \text{ K}$ and equilibrium is not realized, this is in part due to diffusion. Nevertheless in the two cases, the relaxation times of rotation-rotation, and rotation-translation

exchanges are sufficiently low to consider the rotational and the translational temperatures to be equal.

For the spectroscopic diagnostic, one must note that :

- the lines must have a high intensity compared to the continuum,
- the lines must be well separated,
- at atmospheric pressure, an Abel's inversion [84] is generally needed.

The main diagnostics used are the following :

— The continuum emission due to free-free and free-bound radiation is well suited for temperatures between 8 000 K and 14 000 K. The continuum intensity is proportional to Ne^2/\sqrt{T} , it has been studied for nitrogen [85], argon [86], helium [86], hydrogen [87] and air [88].

— The ratio of two line intensities or the Boltzmann plot [84] gives an excitation temperature [2]. Figure 5 shows for example [2] a temperature chart of a nitrogen plasma jet. These measurements have been performed spectroscopically with an automatic data acquisition system connected to a computer, which reduced the measurements time of the excitation temperature to a few hours including Abel's inversion.

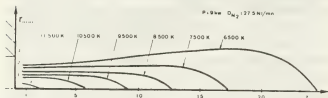


Fig. 5. — Temperature contours in a DC nitrogen plasma jet [2].

— When purely Stark, the atomic line profiles are well suited for the measurement of electron density (usually one uses Stark width of hydrogen or helium lines with either gases introduced in low quantity (less than 0.5 %) in the plasma gas) [70].

— When purely Doppler, the atomic line profile gives the neutral kinetic temperature.

— When the line profile is due to both contributions, Stark and Doppler, the respective broadening must be separated, and one needs a high resolution apparatus. The most often studied profiles are those of argon [89], helium [90] and nitrogen [2].

— When the excitation temperature is known, absolute intensity of lines can be used to measure the upper level population of the transition considered.

— When the lines are sufficiently separated molecular band spectra are used to measure the rotational temperature (equal to the translational one). But even when the lines are not separated, comparison between the experimental profile and a set of calculated profiles *versus* temperature give rather good information

especially below 6 000 K [84, 2, 91]. This method is rather useful for the measurement with complex spectra due to the emission of different molecular bands that overlap as for example in mixtures of N_2-O_2 or $SiCl_4-N_2$ or H_2 as used in plasma chemistry. For example [91], figure 6 shows the calculated NO (γ band 0-2 and 1-3) at 5 000 K and the experimental corresponding spectra.

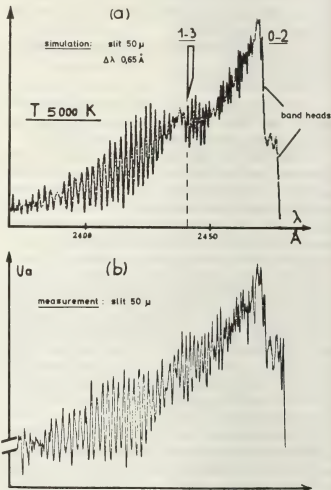


Fig. 6. — NO(γ 0-2 and γ 0-3) bands with a mean resolution (after [91]).

1.4.1.2 Laser fluorescence spectroscopy. — The development of tunable lasers with the possibility of doubling the frequency provides new possibilities to determine particle densities for a given atomic or molecular specie (in ground or excited states) or to study liquid droplets or micrometric powders.

In the last two cases, photon elastic scattering is used in Mie Scattering ($\sigma \sim 10^{-10} \text{ cm}^2$) while in the first, one uses Rayleigh ($\sigma \sim 10^{-28} \text{ cm}^2 \sim \lambda^{-4}$) and resonant scattering ($\sigma \sim 10^{-12} \text{ cm}^2, 10^{-17} \text{ cm}^2$ for atoms and molecules respectively). Fluorescence study is also used ($\sigma \sim 10^{-18} \text{ cm}^2$) and Raman scattering ($10^{-25} \text{ cm}^2 > \sigma > 10^{-29} \text{ cm}^2$). Most of the measurements performed in plasma chemistry use fluorescence. The main problem is then to get sufficiently high laser intensity to achieve saturation

and to get a fluorescence signal independent of the laser intensity and only proportional to the density of the particle in the lower state. For example a calculation made in the laboratory shows that for a laser pulse tuned to a rotational line of an electronic transition of the $\text{NO}(\gamma)$ band the energy density must be greater than 2.5 J/m^2 . But even if the pulse energy density is not sufficient to get saturation some models have been proposed to calculate the non saturation case, for example, with atomic lines [7]. In all the cases this method requires a fast electronic, due to the desexcitation time of the excited states (a few nanosecond). As it is necessary to focus the laser beam in a few hundredth of microns volume, it is possible, when observing at 90° of the laser beam, to avoid the Abel inversion to measure the local concentrations. This method is now one of the most promising one to get information on the chemical reactions between excited states and physicist began to study the kinetic constants in simple gases like nitrogen [92], helium [93, 94], argon [95] and hydrogen [96, 97].

1.4.1.3 Plasma gas velocity measurements. — Under the assumption of LTCE a rather simple method consist in measuring the dynamic pressure of the gas with a probe. But, in that case, the probe disturbs the plasma flow, so that it must be precisely profiled [98, 99]. Figure 7 shows the velocity distribution of an Ar-H_2 DC plasma jet [100].

— Another technique consists of the observation of a small electrical perturbation superimposed on the discharge [101, 102]. The use of a pulsed laser now offers new opportunities for this type of measurement.

— A third technique uses very small particles injected into the plasma. The particles velocity, supposed to be the same as that of the gas, can be measured by laser anemometry in HF or DC plasmas [103, 104, 105].

— Finally for very high velocities (higher than 2000 m/s) it is possible to utilize the Doppler shift of the lines [106].

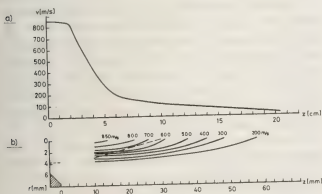


Fig. 7. — Velocity distribution in a DC plasma-jet (after [100]).

1.4.1.4 Mass spectroscopy of ions. — For low pressure plasma, by a small extraction aperture or wall probe, ions are extracted from plasma and by two

additional apertures are led to the mass-spectrometer, where an additional grid may allow an energy analysis. With such a device, used essentially for low pressure plasma, neutral as well as positive or negative ions can be analyzed by measuring current densities and energy. The main problem is the interpretation of the results because in front of the probe a sheath is formed, which changes the properties of the particles coming from the plasma to the probe. A lot of studies have been devoted to this problem and, for example, one can find a detailed analysis in [107].

1.4.2 Condensed particles injected into the plasma. — **1.4.2.1 Velocity of condensed particles.** — There are three kinds of measurement methods :

— Mechanical methods, the flow of particles is momentarily stopped with a barrier, and then one observes the rate of the flow of particles downstream. With this technique a mean velocity is obtained in a plane orthogonal to the flow direction. With two holes, in two discs it is possible to obtain more refined measurements. With this type of technique it is possible to measure velocities between 50 and 200 m/s [108].

— Optical methods have been, up to day, the most often used. An image of the jets is photographically recorded either with a rotating mirror [100, 109], or an ultra rapid camera [110]. Velocities up to 750 m/s have been measured by this technique.

— The so-called opto-electronic methods use optical detection of the particles connected to an electronic system for data treatment. This is for example the case of the *plasmacope* developed by Gold [111]; the *plasmacope* makes an analysis in space and time of the luminous perturbation of particles flowing in the plasma. A more sophisticated method is now available : Laser Döppler anemometry [112, 113]. Many techniques of this type have been developed and give fairly good results. The velocity of particles can be measured at any point in the plasma [114 to 119]. For example figure 8 from [104]

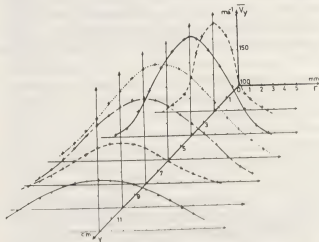


Fig. 8. — Radial particle velocity distribution along jet axis (after [104]).

shows the axial and radial velocity of alumina particles injected in a nitrogen-hydrogen plasma.

1.4.2.2 Temperature of condensed particles.

The analysis of the radiation emitted from the surface of the particles gives the radiation temperature. This method has been used by Bonet; a monochromatic photograph of the moving particles is recorded through a pyrometer which gives the reference radiation [120].

— Lesinski [121] has developed a similar method by using a photomultiplier in place of camera, the reference radiation is given by a hole travelling very rapidly in front of a reference tungsten ribbon lamp. This method has been refined by Vardelle [104], who has made a statistical treatment of the received signals. The main difficulties with this system is to know exactly the particle diameters, and their emissivities. Figure 9 shows the temperature of alumina particles along the axis of a nitrogen hydrogen plasma jet.

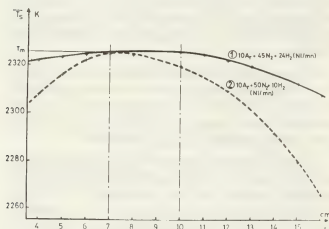


Fig. 9. — Particle temperature distribution along jet axis (after [104]).

1.4.2.3 Population and diameter of the particles.

— The population of the particles in a plasma may be measured very simply counting, during a given time, the pulses resulting of the light scattered by the particles passing through a laser beam (Ar^+ laser). Using a laser beam of 100 μm diameter and detecting

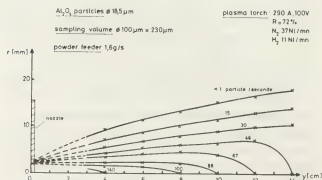


Fig. 10. — Particles ($d = 18.5 \mu\text{m}$) isoflow curves (after [104]).

the scattered light at 90° with a diaphragm of 100 μm a punctual measurement can be achieved and for example figure 10 shows the distribution of alumina particles injected in a nitrogen DC plasma jet.

— The diameter of the particles (very important for the temperature measurement) may be measured also through the scattered laser radiation. For example, Penner [122] gives the conditions to be filled and the theoretical curves needed, to define log-normal particle-size distributions from measured half widths and detectabilities of scattered laser power spectra.

2. Plasma chemical reaction in homogeneous phase.

— In this case the plasma may be considered some times as in equilibrium, but in any case the quenching of the products is always out of equilibrium.

2.1 EQUILIBRIUM CALCULATIONS. — Under ideal conditions of thermodynamic equilibrium it is possible to determine the products resulting from a given treatment but the problem is to know to which extent calculations assuming this equilibrium are applicable to real systems. For that the chemical reaction must proceed more rapidly than the physical phenomena such as relaxation of energy levels or Maxwellisation. For example with a very simple calculation one can say that on the axis of a DC plasma jet the temperature varies by 1% in $2.5 \times 10^{-3} \text{ m}$, so that at 250 m/s a variation of temperature of 1% corresponds to 10^{-7} s , so in order that thermodynamic equilibrium can be applied the reactions times must be less than 10^{-7} s . The ratio of this chemical reaction time t_c to the mechanical residence time t_m is the Damköhler parameter [123] D_i ($D_i = t_c/t_m$) and the equilibrium is obtained for $D_i \ll 1$. This kind of reactions times may be encountered if the temperature is greater than 5 000 K but in all the cases during quenching equilibrium is not possible.

The thermodynamic calculation consists in finding the chemical composition which gives the minimum Gibbs free energy [124] under the constraints of the law of conservation of matter and electrical neutrality. One gets a system of non linear equations that must be solved by use of numerical methods by computer [125, 126]. The data are sometimes limited to 6 000 K and it is necessary to carry out calculations of partition functions from spectroscopic data [127].

The results obtained must be considered very carefully but usually they give some qualitative indications about what happens. For example [91], if one consider a mixture of $\text{N}_2\text{-O}_2$ at equilibrium at atmospheric pressure, figure 11, the maximum of NO one could obtain is 6.5% at 3 500 K, but as we will see, it is possible as a function of the quenching techniques to get less or more. The calculations [128] of the system $\text{SiO}_2\text{-C}$ shows (Fig. 12) the existence of a threshold temperature in the range 2 500-3 000 K.

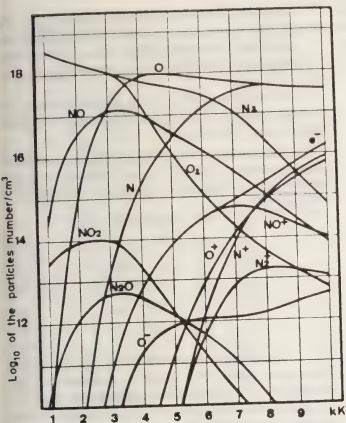


Fig. 11. — Composition of an N_2O_2 plasma at 1 atm ($N/O = 1$) (after [91]).

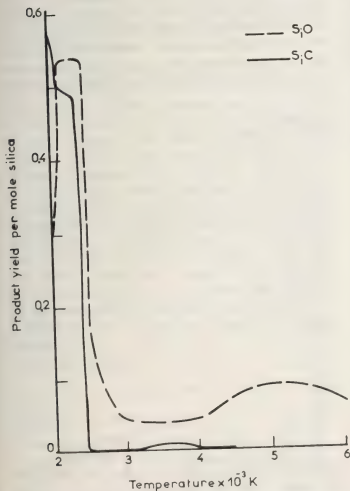


Fig. 12. — Production of SiO and SiC (at 2.0 moles of carbon) (after [128]).

On one side of this temperature the only species are SiO_2 , SiO and SiC , while there is always a low concentration of SiO above that temperature. Unfortunately thermodynamic cannot describe what happens during the cooling phase that becomes the most important to get pure Si.

2.2 KINETICS CALCULATIONS. — The kinetics models tend to predict the influence of physical conditions on the reaction rates specially when $D_i \approx 1$. In a stationary medium, the variation by unit time of the i th specie concentration C_i is given [129] by :

$$\frac{\partial C_i}{\partial t} = \nabla \cdot (D \nabla C_i) + P_i - S_i \quad (1)$$

where D is the diffusion coefficient, S_i the source term and P_i the losses term.

2.2.1 Chemical reactions at high temperature. — Disregarding the diffusion process because its contribution introduces many difficulties in the solution of (1) and because often the data are not well known [130, 131], considering a mixture of I chemical species A_i reacting in J chemical reaction with reactions rate constants k_j :

$$\sum_{j=1}^J v_{ji} A_i \xrightarrow{k_j} \sum_{j=1}^J v'_{ji} A_i$$

and assuming the thermodynamic temperature of the system is assigned to follow a law, $T = f(t)$, at constant pressure, the time dependance of the chemical composition of the system is calculated by solving the following differential system

$$\frac{dc_i}{dt} = w_i - \left(\frac{c_i}{\rho} \sum_{i=1}^I w_i + \frac{c_i}{T} \frac{dT}{dt} \right)$$

with

$$w_i = \sum_{j=1}^J k_j (v'_{ji} - v_{ji}) \prod_{l=1}^I y_l^{v_{lj}} \quad \text{and} \quad \rho = \frac{p}{kT}.$$

The solution is generally obtained by numerical integration methods, which must be highly stable one, as the problems encountered are *locally exponential* giving rise to the phenomenon called *stiffness*. Warner [130] gives a critical review of the different methods that can be used. However the main problem is due to a poor knowledge of the specific reaction rates k_j . These quantities are strongly temperature dependent and as the Arrhenius law is not sufficient in plasmas one has to take into account the potential energy of each reaction. But each chemical reaction usually consists of a set of elementary steps involving a group of molecules or atoms which gives the final reaction products after rearrangement. During an elementary step, the evolution of the system may be described by the trajectory of a representative point moving on the potential surface. In the general case the system moving on the surface must jump over a

potential barrier the height of which is equal to the activation energy E_a . The system configuration in the neighbourhood of the top of this barrier being called the *activated complex*. Unfortunately solving the quantum mechanical equations to get the potential surface configuration is very difficult [131 to 133].

In this case it is possible to write

$$k(T) = P \cdot Z_0 \cdot \exp(-E_a/kT)$$

where Z_0 is calculated through the collisional cross section (typical values are $10^{-16} \text{ cm}^3 \text{ part}^{-1} \text{ s}^{-1}$ for two bodies collisions and $10^{-32} \text{ cm}^6 \text{ part}^{-1} \text{ s}^{-1}$ for three bodies collisions), and P a *steric factor* involving the entropy variation occurring in the reaction [131 to 133] and calculated with the activated complex theory.

Finally the most difficult problem to solve is not to calculate a numerical coefficient for a given temperature, but to know what modifications of the model must be done for a very rapid and important variation of the species temperature.

2.2.2 Chemical reactions in low temperature plasma.

— In this case (low pressure plasma) one neglects the temperature variation and the processes taken into account [134, 135] are the collisions process (mainly through the electrons and the metastables states) for ionisation, recombination, excitation and desexcitation and spontaneous radiative transitions and radiative recombination. The system of eq. (1) must then be solved with some additional condition about the evolution of the electron population (generally imposed by the experimental conditions). As in the preceding case the problem is the determination of k_f . One also has to take care when neglecting the terms corresponding to small values of k (see the characteristics values of Z_0 in the preceding section) that in the equation it is the product of the population by k that is involved.

2.3 EXAMPLE : NO SYNTHESIS IN A DC PLASMA JET.

— As shown by the numerous papers presented at the last Symposium on plasma chemistry the NO synthesis in plasma is a research field actuality. In Limoges we have studied this synthesis with a DC plasma jet (up to 30 kW) [91]. The plasma gas-mixture of N_2 and O_2 is introduced along the cathode and cold oxygen is injected downstream the arc into the nozzle and thus contributes to the quenching which is completely achieved by removing the gaseous products through a water cooled probe. This device works with powers between 5 and 27 kW corresponding to specific enthalpy between 1.4 and 7.7 kWh/kg and the gas flow velocity at the nozzle exit measured without oxygen injection is between 500 and 1 000 m/s.

The experimental results [136, 137] have pointed out at atmospheric pressure that :

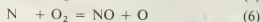
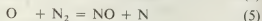
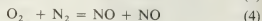
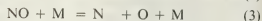
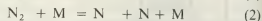
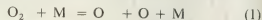
— energetic consumption is minimal with an N_2 initial molar fraction of 50 %,

— nozzle must be long enough to prevent the arc root to stay downstream the cold oxygen injection,

— cold wall quenching device allows to increase NO molar fraction and to reduce energetic consumption,

— the best results are obtained with a plasma of pure nitrogen with 25 kWh/kg of NO and a nitrogen conversion to NO of 9 %.

To explain such results (the equilibrium conditions gives a maximum of 6.5 % at 3 500 K) one has considered the following reactions for $T < 5 000 \text{ K}$



with the kinetics constants gathered by Prud'homme [138] and these recommended by Baulch [139]. The temperature evolution of the gas in the plasma has been determined by assuming a mean enthalpy temperature (homogeneous temperature in the nozzle) varying with a parabolic law for heating and quenching as represented on figure 13. At the beginning [137], as one can see on figure 14, the reaction (4) is responsible of the NO production and the NO production rate is maximum between 8 and 12 s. This simplified model gives a rather good agreement with the experimental results and it has emphasized the importance of the heating rate, which as far as we

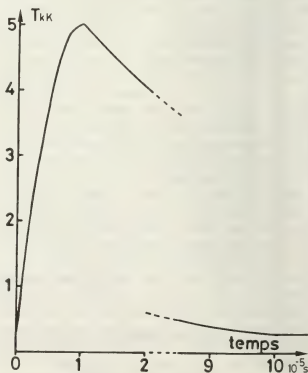


Fig. 13. — Evolution of the temperature as a function of time (after [136]).

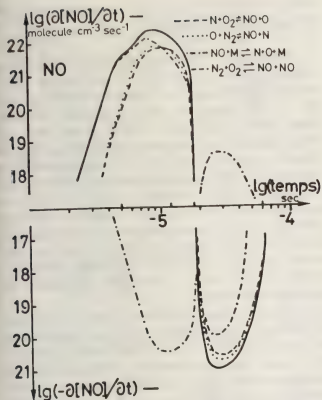


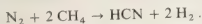
Fig. 14. — Evolution of the NO rate production as a function of time (after [136]).

know, have never been mentioned before, and also the necessity to have a high quenching rate (10^8 K/s at the beginning).

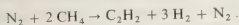
2.4 EXAMPLE : HCN AND C_2H_2 SYNTHESIS IN A HF LOW PRESSURE PLASMA. — The nitrogen plasma is created by HF inductive coupling inside a glass tube of 100 mm diameter [68] with a gas flow rate between 0.5 and 2.5 Nl/mn. The pressure is varied between 5 and 40 torrs with a power of about 2.5 kW. Cold methane is injected counter-current in the extinction plasma. In such a plasma the main mechanism is the excitation of the heavy particles by collisions with the electrons and the nitrogen plasma, studied by emission spectroscopy (1^- of N_2^+ , 1^+ and 2^+ of N_2), is such that $T_e \sim 25\,000$ K $\gg T_v$ ($\sim 5\,500$ K) $> T_r \sim T_t$ ($\sim 1\,700$ K). When the pressure is increased the electronic T_e and vibrational T_v temperatures decreases.

With N_2 and CH_4 two exchange reactions are possible :

Fixation reaction



Transfer reaction



Due to the energy requirements (neglecting the atoms because the emissions lines are very weak), the fixation reaction is postulated [68] to be more probable with the $C^3\Pi$ and $B^3\Pi$ states and the transfer

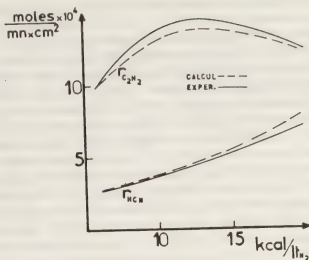


Fig. 15. — Evolution of the formation rate of C_2H_2 and HCN versus induced energy (after [68]).

reaction with $A^3\Sigma$ (metastable state). We have to mention that this hypothesis neglecting the atoms and specially the N^2D metastable state might be over simplified specially when one reminds that the dissociation of the $C^3\Pi_u$ state gives N^2D and N^4S . For a given N/C ratio the experimental results show an increase of HCN conversion and an increase followed by a decrease of C_2H_2 with the increase of the specific energy and an increase of the nitrogen flow rate. C_2H_2 conversion decreases and HCN increases with the increase of the pressure. To explain this results a simplified kinetic model (with no temperature evolution) has been proposed [68] postulating that the fixation rate is much greater than the transfer reaction rate and that the density of $A^3\Sigma$ states is greater than the density of $C^3\Pi$ states. Figure 15 shows a comparison of the evolution with the specific energy of the measured and calculated formation rates of C_2H_2 and HCN. When the influence of the pressure is considered the results are in good agreement with Polanyi's theories [140]. The energy diagram of

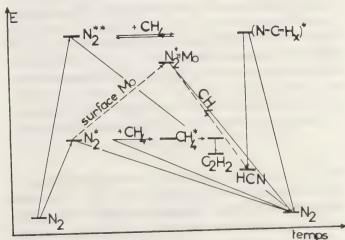


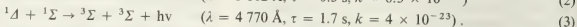
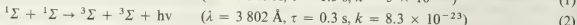
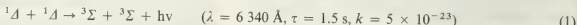
Fig. 16. — Catalysis mechanism of the reaction $N_2-C_2H_2$ (after [68]).

the reaction is represented on figure 16, where N_2^{**} corresponds to $N_2(C^3\Pi_u)$ and N_2^* to $N_2(A^3\Sigma_u)$. The fixation reaction with, as a first step, dissociation of $N_2(C^3\Pi_u)$ is favored by a high vibration energy (low pressure) but the most important step is the quenching of the highly excited formed HCN, favored by a high rotation temperature (high pressure) as indicated by the experimental results. The introduction of a molybdenum grating in the mixing area of the cold methane and nitrogen plasma was noted [68] to produce an increase in HCN conversion. This seems to be due to a catalytic effect of the grating which leads to a decrease of the excitation transfer (C_2H_2) and an increase of the fixation reaction (HCN). Neglecting a possible quenching effect on the surface of the hot metal (because a simple calculation leads to a quenching rate smaller than 10^5 K/s), the experimental results are interpreted [68] as a catalytic effect at the surface of the metal: the effect increases with the number of wires and the position of the grating is very important, the maximum of conversion being obtained right in the mixing zone. If the wires are vapourized the quantity of fixed nitrogen decreases. Figure 16 indicates the mechanism proposed by Rapakoulias [68]: a chemisorption by the metal of an excited $A^3\Sigma_u^+ N_2$ molecules breaking the N-N bonding, the nitrogen atoms reacting with CH_4 or its fragments to give an unstable molecule ($N...C...H_3$)*. By desorption of the surface, a stabilized HCN molecule is formed.

With this effect, it is possible to increase the HCN formation by as much as 50 %.

2.5 EXAMPLE : ORGANIC REACTIONS WITH METASTABLES OXYGEN MOLECULES. — The excited metastable states of atoms or molecules ionized or not, play a very important role in chemical reactions under plasma conditions. These states may act along different ways. Their high internal energy may be relaxed by collisions and help to pass the activation barrier of the reaction. In other cases it is the electronic configuration of the metastable state that gives to the reaction a stereochemistry which is different from that of the fundamental state. The exact role of the metastable states is, however, not yet well known due to the difficulty of producing them in a specific manner and to study their population (no radiative deexcitation).

One of the most extensively studied metastable state is the $O_2^1\Delta_g$ because of its interesting properties for organic reactions. The excited states $^1\Delta$ and $^1\Sigma$ have almost the same bounding length and identical potential curves as the fundamental state $^3\Sigma$. The radiative deexcitation of a $^1\Delta$ to $X^3\Sigma$ is not possible due to the selection rules but is possible with the spin orbit coupling and the life time of $^1\Delta$ is 3 900 s [141]. It is the same with $^1\Sigma$ which life time is 12 s. However, as the collisions dipole transitions between these states become more probable, the following reactions can take place :



The $O_2^1\Delta$ is mostly produced with a HF or MW discharge in pure oxygen [142 to 145] avoiding the destruction of the metastable ($^1\Delta$) with impurities and a pollution with the electrodes. For example figure 17 shows the experimental set up of Dumas [145], the power of the HF source varying from 0 to 250 W and the frequency between 55 and 70 MHz. With such discharges the states obtained are [146] :

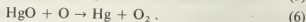
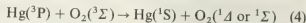
$O_2(^3\Sigma)$: 70 to 80 %, $O_2(^1\Delta)$: 5 to 20 %, ,

$O_2(^1\Sigma)$: 10^{-2} %, $O(^3P)$: 10 to 20 %, ,

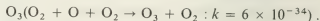
O_3 : 1 to 2 % .

The O and O_3 species are very undesirable because they deactivate very quickly the $O_2(^1\Delta)$. Also their reactivity with most organic species is much more important than the reactivity of $O_2(^1\Delta)$, so they must be eliminated to study the reactions with the singulet oxygen. That is why in its experimental set up Dumas has disposed, just before the induction

coupling, a small tank of mercury to be vaporized (R Fig. 17a). In the discharge one has the reactions :



The last two reactions ((5) and (6)) are fast enough to withdraw almost all the oxygen and to avoid the formation of



The excess of mercury is then collected in a cold trap.

The $O_2(^1\Delta)$ is analyzed through the emission of the 6 340 Å band due to the collision reaction (1) and through the calorimetric effect of the partial desexcitation of $O_2(^1\Delta)$ on a heated wire (R_0 Fig. 17a) covered with a catalyser : cobalt oxide. The maximum quantity of $O_2^1\Delta$ (rate of 12 %) is obtained for a

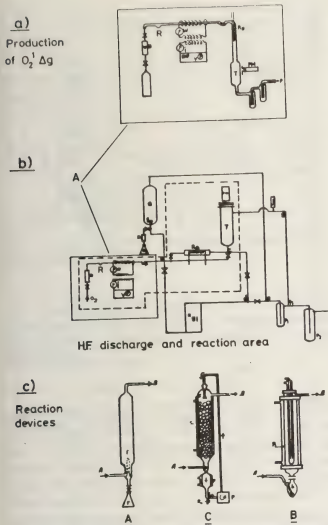
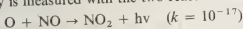
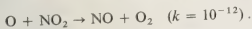


Fig. 17. — HF reactor for organic compounds (after [145]).

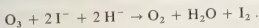
power of 30 W and a pressure of 3 torrs. The $O_2(^3P)$ density is measured with the two reactions :



and



The O_3 density is obtained by a chemical method : absorption of O_3 on silica gel at the liquid nitrogen temperature, and then reaction with iodine



The measurements show for example that at 1 torr with an oxygen flow rate of 20 Nml/min the O_3 density decreases from 4 % to 0.1 % in presence of Hg vapour.

After the discharge the desexcitation kinetic of $^1\Delta$ is given by :

$$\frac{\partial [^1\Delta]}{\partial t} = k_w[^1\Delta] + (k_{O_2}[O_2] + k_D[O] + k_{O_3}[O_3]) \times [^1\Delta] + k_c[^1\Delta]^2$$

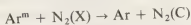
the first term corresponding to a desactivation on the wall. The calculations made by Dumas [145] shows that with a glass tube of 0.5 cm, 1 m after the discharge

zone the population of $O_2(^1\Delta)$ is only decreased of 15 to 30 %.

It is then possible to drive the $O_2(^1\Delta)$ to either tank G for a gaseous phase reaction or in a tank R where the organic product is in liquid phase (Fig. 17b). The different reactors used are represented on figure 17c. A for reactions with gas or liquid with a high vapour pressure, B for liquids with low vapour pressure and C for solids products dissolved in a convenient solvent.

Due to its analogy with the carbon-carbon bonding of an alcine one observes a specific chemical reactivity of $O_2(^1\Delta)$ as for example its fixation on a double bonding $C=C$ including a hydrogen atom in α of the bonding and in a *cis* position. If there is no H in α it is possible to get *dioxetanes* more or less stable giving a rupture of the bonding. But the most interesting case is the reaction with a double bonding in the aromatic cycle or in the heterocycle. One will find a summary of the reactions studied by Dumas [147 to 149].

3. Plasma chemistry with condensed phases. — A high temperature plasma (arc or HF at atmospheric pressure) is first a source to get high populations of excited states either by Boltzmann distribution at high temperature or by transfers with metastable (for example in an argon DC plasma jet it is possible to obtain density of the atomic metastables up to 6×10^{13} part/cm³ and if one injects cold nitrogen into such a plasma the excitation transfert



allows overpopulation factors in the range 10^{15} - 10^{20} . However when these high temperature plasmas are used for solid materials treatment they are usually considered in the first approximation as a source of energy in LTE. So using the LTE hypothesis one calculates the thermodynamic and transport properties of the plasma itself. And then one must calculates mass and heat transfert between plasma and particles or solids and study successively fusion, vaporisation, chemical changes and condensation.

3.1 THERMODYNAMIC AND TRANSPORT PROPERTIES OF THE PLASMA. — 3.1.1 Thermodynamic properties.

— For reactions in the gaseous phase we have seen that the concentration of the different species is the important parameter but for heat transfer the two important parameters are the specific heat and the enthalpy. The specific heat, is by definition,

$$C_p = \left(\frac{\partial \hat{H}}{\partial T} \right)_p$$

where \hat{H} is the mass enthalpy of the mixture. One obtains [150]

$$C_p = \frac{1}{M} \left[\sum_{i=1}^N x_i c_{pi} + \sum_{i=1}^N x_i (H_i - m_i \hat{H}_i) \left(\frac{\partial \text{Log } x_i}{\partial T} \right)_p \right]$$

where c_{pi} is the specific heat at constant pressure, x_i the mole fraction, H_i the enthalpy of the species i and M the total mass of the mixture. In this expression the first term is the frozen \bar{c}_p and the second the reaction term c_{pr} which becomes important and shows maxima each time there is dissociation, ionisation or chemical reaction. For example [150] figure 18 shows the different components of the specific heat at constant pressure for the system 1 C, 4 H, 20 and 2 Fe at atmospheric pressure. The very reactive nature of the mixture is indicated by the form of the C_p curve.

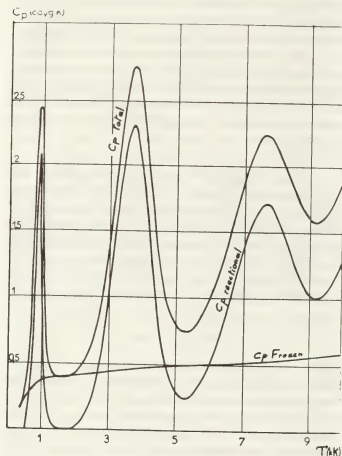


Fig. 18. — C_p versus T for the system C.H.O.F., $e^-/1.4.3.2.0$ [150].

Figure 19 shows the enthalpy of the same mixture obtained by integration of C_p .

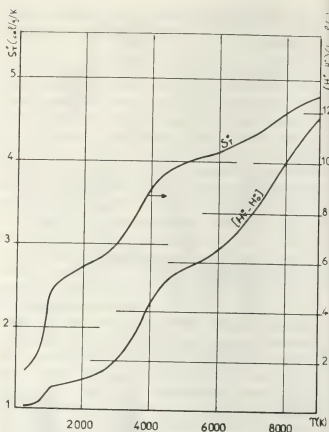


Fig. 19. — System C, 4 H, 30.2 Fe [150].

potentials to determine the collision integrals. Unfortunately there is no data for plasmas of complex mixtures (C, H, O for example), and even for these who are known there is a large uncertainty about the interaction potential. The calculation of the viscosity is made with the pressure tensor [151]. For the thermal conductivity one must take into account the reaction conductivity [159] and the internal thermal conductivity [160]. Figure 20 shows the importance of the reaction conductivity when the ionisation of argon occurs and figure 21 shows the importance of the dissociation of hydrogen in a mixture or Ar-H₂ [161].

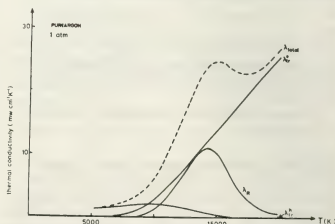


Fig. 20. — Thermal conductivity of argon versus temperature (after [161]).

3.1.2 Transport properties. — The levels of mass and heat transfer between the plasma and the introduced material are determined by the viscosity and thermal conductivity of the plasma. In the LTE hypothesis these parameters are calculated by solving the integro-differential Boltzmann equation, usually by the Enskog's method of successive approximations [151, 152]. The perturbation function is found [153] by using Sonine polynomial of order k , the problem being to find the minimum value of k that gives the best convergence of the series. For example [154 to 158] found that it is sometime necessary to carry out the calculations up to $k = 4$. In this calculations it is necessary to know the interactions

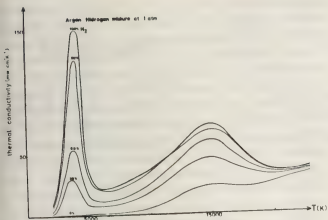


Fig. 21. — Thermal conductivity of argon-hydrogen mixtures versus T (after [161]).

3.2 HEAT AND MASS TRANSFER. — For a partially ionized gas, dimensional analysis leads to empirical correlations for heat transfer through the Nusselt number [162]

$$Nu = f(Pr, Re, Sc, \xi, \varphi)$$

where Pr , Re , Sc are respectively the Prandtl, Reynolds and Schmidt number, ξ the ionization degree and $\varphi = eV_F/kT$. The different correlations used are listed in tables I and II. Usually the plasma transport properties used to calculate the reduced numbers are integrated over the range of temperature considered (plasma temperature, particle temperature).

When the material treated is used as electrode the problem becomes very complex [163 to 166]. The heat flux going through the anode being :

$$q_a = q_c + q_r + j_e \left(\frac{5}{2} \frac{kT_e}{e} + V_a + \varphi_a \right)$$

where q_c is the conduction and convection term, q_r the radiative flux, V_a the anode fall, φ_a the work function of the anode material. T_e the electronic temperature and j_e the electron current density.

The particle trajectories are obtained by solving the *Basset-Boussinesq-Oseen* equation [167 to 171]. In this equation, the velocity variation is expressed

Table II. — Correlation in the boundary layer.

$Nu_{loc} = 0.323 Re_{loc}^{1/2} Pr^{1/3}$	$Pr > 0.7$ theoretical	[232]
$Sh_{loc} = 0.332 Re_{loc}^{1/2} Sc^{1/3}$	$Re_{loc} < 10^5$ results	
$Nu = 0.037 Re^{0.8} Pr^{1/3}$	$Pr > 0.7; Re > 10^5$	[233]
$Nu = 0.02 Re_{loc}^{0.87} Pr^{0.33}$	Hot gas striking on a wall	[234]

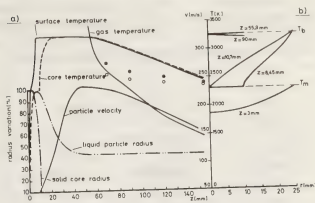


Fig. 22. — Temperature distribution for Al_2O_3 particles (after [100]).

through the drag coefficient C_D expressed as a function of the Reynolds number [167 to 171] (see Table III). For example figure 22 shows the velocity and temperature distribution of alumina $40 \mu m$ particles injected in an hydrogen plasma jet [100]. This distribution calculated from the preceeding equations (knowing plasma temperature and velocity) is in good agreement with the measurement performed on $20-28 \mu m$ particles (dark circles) and $50-63 \mu m$ particles (open circles).

For heat transfer one usually supposes that the whole energy coming from the plasma is absorbed by specific heat and lost by radiative transfer. For example figure 23 shows [170] the calculated temperatures reached by alumina particles injected into a HF argon plasma (open circles : solid particle, dark circle liquid droplet and partially shaded circle : partially melted particle). However in such a calculation an important phenomenon has been neglected, the influence of the particle thermal conductivity and for example the experimental results of Lesin-

Table I. — Correlation for Nusselt Number.

Nu	Conditions	References
$1.86 \left(Re Pr \frac{L}{D} \right) \left(\frac{\bar{u}}{u_f} \right)^{0.14}$	$Re < 200; L/D > 10$ wall with $T = \text{constant}$	[229]
$0.026 Re^{0.8} Pr^{1/3} \left(\frac{\bar{u}}{u_f} \right)^{0.14}$	$Re > 210^4; 0.6 \leq Pr < 100; L/D > 10$	[229]
$0.023 Re^{0.8} Pr^m$	$0.7 < Pr < 100; Re > 10^4; L/D > 60;$ $m = 0.3$ for cooling; $m = 0.4$ for heating	[230]
$7 + 0.025(Re Pr)^{0.8}$	$Re Pr > 100$ heat flux to the wall is constant	[231]
$5 + 0.025(Re Pr)^{0.8}$	$200 < Re Pr < 10^4 T_{wall} = \text{constant}$	

Table III. — Correlations for the drag coefficient (after [84]).

Re	Spheric particle	C_D
$Re < 0.1$	$24/Re$	Flakes : $c \cdot 0.026 D_p$
$0.1 \leq Re < 1$	$(24/Re) (1 + 3 Re/16)$	$24 S_1/Re$
$1 \leq Re < 20$	$(24/Re) (1 + 0.11 Re^{0.810})$	$(24 S_1/Re) (1 + 3 S_1 Re/16)$
$20 \leq Re < 200$	$(24/Re) (1 + 0.189 Re^{0.632})$	$(20.4/Re) (1 + 0.136 Re^{0.803})$ $(20.4/Re) (1 + 0.138 Re^{0.793})$

S_1 is a shape factor; for thin disks $S_1 = 8/3 \pi$.

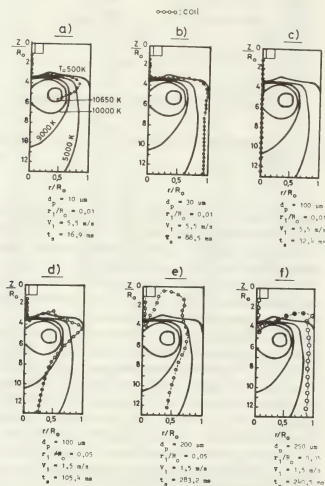


Fig. 23. — Particle trajectories (after [170]).

ski [100] shows more than 600 K of difference between the calculated and measured temperatures. This is due to the fact that for low thermal conductivity the heat flux leads to a fused zone at the surface of the particle and the vapour leaving the partially melted particle completely modifies the heat exchange [173]. Figure 24 shows the application of the calculation of the temperature history of iron particles of different diameters in a HF plasma, one has to note the change of slope near the Curie temperature due to the singular point of the thermal diffusivity. But unfortunately one has to emphasize that most of the thermal properties of the solids at high temperature are not well known.

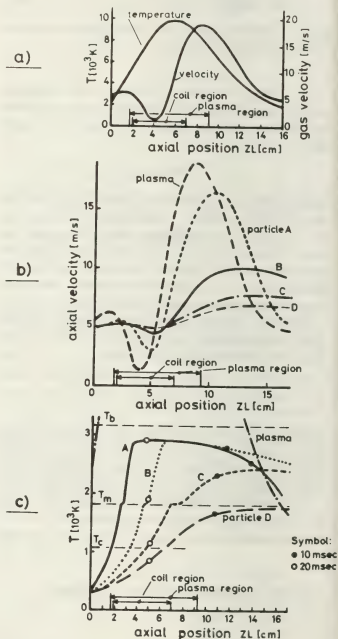


Fig. 24. — Predicted particle surface temperature and velocity (after [173]).

3.3 PHYSICAL CHANGES OF SOLID MATERIALS IN PLASMA. — 3.3.1 *Plasma spraying*. — Since 1960 DC plasma jets have been used to melt a powder feed and project the droplets at high velocity against a

material to be coated. Any material, provided a few hundred degree Celsius between its fusion temperature and its vaporization or decomposition temperature may be sprayed. We do not wish here to make a general review of the sprayed materials (see for example [174 to 176]) or of their use, but to emphasize the physical problems encountered that need to be solved. A plasma sprayed deposit consists of successive layers of material built up by the impact of molten droplets, projected at high velocity, which flatten against the substrate and solidify very rapidly. As we have seen the plasma jets are very inhomogeneous with high temperature gradients (see for example Fig. 5) corresponding to high transport properties gradient (see for example Fig. 21). The main problem is to introduce the particles inside the hot area of the plasma, which is very difficult because of its high viscosity. Measurement of the velocity of $18\text{ }\mu\text{m}$ diameter alumina particles at the end of the injector disposed orthogonally to the plasma jet [104] shows that the particles with a velocity smaller than 20 m/s could not penetrate the plasma jet and remain on the periphery and cannot be melted and on the contrary with a velocity greater than 40 m/s they just go through the jet and are not melted. Unfortunately on a commercial scale the granulometry of the particles injected is rather large and it will be possible to give the *good speed* only to the particles in the center of the distribution. To get a good plasma coating one needs to have only completely melted particles flattening on the target and to eliminate the particles travelling at the periphery of the jet at a velocity of a few m/s compared to the velocity of the particles travelling in the central zone (greater than 100 m/s see Fig. 8). Due to the difference in kinetic energy, the particles along the periphery can be eliminated by a compressed air blast normal to the plasma jet close to the substrate [177]. For particles that penetrate the plasma jet, due to the high temperature and velocity gradients of the plasma (see Fig. 5 and 7) and large size distribution, the spray stream produced will contain particles with a wide range of velocity and temperature. If they are molten they will flatten on impact with the substrate. Their degree of flattening [178, 179] (ratio of the diameter of flattened disc (D) to diameter of the initial drop (d)) is given by the following equation

$$D/d = 1.29 \left(\frac{\rho v d}{\mu} \right)^{0.2}$$

where ρ is the liquid density, μ the liquid viscosity, v the droplet impact velocity. Substituting appropriate values for Al_2O_3 in the velocity range $100/400\text{ m/s}$ gives D/d : $3\text{--}6$ which seems to be in reasonable agreement with various experimental observation [180, 181]. With such flattening, plasma spraying conditions are very similar to those occurring during splat quenching of metals. The heat transfer rate to the sub-

strate [182] may be estimated of the order of $10^5\text{ W m}^{-2}\text{ K}^{-1}$. Applying this to Al_2O_3 it gives a cooling rate of 10^7 K.s^{-1} and a freezing time of $10\text{ }\mu\text{s}$. The zone of thermal effect in the underlying material is therefore quite small and temperature gradients reach $\approx 10^5\text{ K.cm}^{-1}$. The coating has a sandwich like structure as shown in figure 25 and its properties can be regarded as resulting from the deformation and solidification processes of individual particles and their interaction on contact. The wetting and flow properties of the liquid droplets are of first importance since they will influence porosity and adhesion properties. The porosity is related to the particle temperature and velocity on impact. As shown by Vardelle [104] : the porosity decreases from 22% to 10% if the velocity is increased by 150 m/s with alumina particles. The factors controlling the adhesion are not well understood. One point of view suggests that adhesion is controlled purely by mechanical factor [183] (interlocking of the coating with the rough substrate surface) another is that chemical interaction occurs between particle and substrate [184, 175]. However, except in the case where a strong exothermic reaction occurs between two molten metals (nickel aluminide spraying [185]), it is difficult to see how an interaction layer of any significant depth can be formed. Even assuming values for diffusion coefficients (D) in the substrate of the order of that near the melting point ($10^{-9}\text{ cm}^2\text{ s}^{-1}$) the diffusion depth (x) given by $x = \sqrt{Dt}$ is of the order $10\text{ }\text{\AA}$ for a contact of $10\text{ }\mu\text{s}$. But on the contrary after grit blasting the adhesion decreases with the thickness of the oxide film formed on the substrate. Epitaxial growth and bonding occurs only when the substrate is at high temperature (greater than 1300°C for W spraying on W). So a lot of work remains to be done before the mechanism is properly understood.

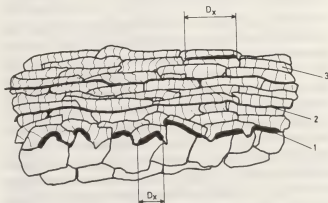


Fig. 25. — Texture of plasma sprayed coating : (1) contact surface between the coating and substrate; (2) contact surface between layers; (3) contact surface between particles. (D_x) diameter of the fused contact surface portion (after [14]).

The crystal structure of the coating is often very different from the initial material crystal structure due to extremely rapid cooling and one observes the suppression of crystallisation or the formation

of solid metastable phases [185 to 189]. Some effects of preferred orientation of the crystals relative to the surface have also been observed with hexagonal structure (coating with controlled friction coefficients) [190] but they are not clearly understood.

3.3.2 Spheroidisation. — Melting of a particle results in the formation of a spherical drop under the action of surface tension forces and this shape is usually retained by the solid particle after solidification [191, 192]. For example this treatment is used for spheroidisation of Fe_3O_4 for photocopying and UO_2 for dispersed nuclear fuels, or to get structural changes as in the dissociation of zircon to ZrO_2 and SiO_2 allowing a preferential dissolution and the preparation of ZrO_2 [193]. Spheroidisation of quartz, clays, kyanite, mullite and others aluminosilicates results [194, 195] in the formation of glasses of high melting point. The spheroidisation may also provide a purification effect by evaporation of some impurities (for example Fe, Mo, Na from Al_2O_3 [14]).

RF plasma torches are generally used for spheroidisation of particles (long residence time and no pollution by electrodes) when a high purity is required. DC or AC arc plasma jets give rise to limitations in the particle size that may be treated because of the short residence time. Plasma furnaces with fluid convective cathodes (FCC) [196 to 198] or fluidized bed [199] which give longer residence times (mean temperature 5 000 K and mean velocity a few m/s) are more suitable for large scale spheroidisation of larger particles. From a physical point of view one has to mention that the FCC uses the Maecr effect [200 to 202] that is to say magneto-hydrodynamic pumping near the cathode tip (for example at atmospheric pressure one has a reduction of the pressure of 0.02 atm at the cathode tip of an arc working in hydrogen with 500 A).

3.3.3 Vaporisation. — The vaporisation of a particle at atmospheric pressure requires a large amount of energy because, as vaporisation proceeds, the heat must be carried through the expanding vapour film on the particle surface (a silica particle of 200 μm would produce a cloud of vapour of 5 mm diameter). A number of theoretical models have been developed [203 to 205] with probably an increase of the heat transfer due to the higher temperature of electrons [203, 206], specially when the material is used as electrode. To achieve the high transfer rate one uses mostly rotating plasma furnaces [207 to 208] or arc transferred to the material being vaporized (using the material as anode see § 3.2) [209 to 210].

Experiments have been done on Mg, Zn, Fe, Sb, Al oxides [211, 212] or tin slags [213], but the most extensively treated material is silica with the aim of preparing ultrafine silica powder (used at a rate of about 10 000 t per year) [207, 208, 210, 214, 199]. In all the cases the most important physical phenomena is condensation.

3.3.4 Condensation. — We will deal only with the condensation of the vapour to obtain very small particles. This vapour is obtained either from vaporisation of solid materials or by high temperature reaction between a reactant vapour (SiCl_4 , TiCl_4 , ...) and the plasma (O_2 , CH_4 , N_2) to get for example SiO_2 , TiO_2 , TiC , SiC , TiN , Si_3N_4 , ... [14, 215, 217]. The controlling step of condensation is nucleation, which takes place when the vapour pressure exceeds the equilibrium vapour pressure of the condensed phase in the system. Often a certain degree of undercooling is necessary before nucleation occurs at a significant rate. The rate equation for nucleation is as follows :

$$I = A \exp \left(- \frac{\Delta G_c}{kT} \right)$$

the non constant preexponential term, A , is dominated by ΔG_c which depends sensitively on supersaturation ρ/ρ_0

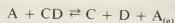
$$\Delta G_c \sim \frac{\gamma^3}{\text{Ln}(\rho/\rho_0)}$$

where γ is the interfacial energy. In plasma, nucleation occurs at a supersaturation of 2-3. The different studies specially on SiO_2 and TiO_2 [218, 219] emphasize the rapidity of nucleation and the importance of coalescence for the final particle size. However condensation of silica is a special case because liquid silica is very viscous and crystallisation does not occur on cooling, the rate of coalescence may be estimated from equation developed for sintering by viscous flow [220]. From this theory coalescence to form spherical particles would be expected to cease at temperature below approximately 2 200 °C. Condensation under this temperature, as has been observed [208], result in the formation of chains of very small particles.

For the materials which condense to liquid droplets rather than solid particles it is possible to condense two or more components to give liquid solution droplets [221] (Al_2O_3 - SiO_2 , Al_3O_4 - Cr_2O_3 , ...).

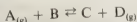
At least the solidification of liquid droplets suspended in a cooling gas stream will be different of that observed under normal conditions because they will tend to undercool well below the equilibrium melting point before crystallisation. Due to the very high cooling rate (10^4 - 10^6 K/s) both effects may result in the formation of metastable phases as discussed in detail by McPherson [221]. A number of studies have been made for Al_2O_3 , SiO_2 , TiO_2 and their mixture [222 to 226].

3.4 CHEMICAL REACTIONS. — When the plasma A is inert and just used to decompose the product :



the problems becomes essentially one heat transfer.

When the plasma A is reactive with the condensed phase B :



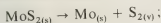
C being condensed and $D_{(g)}$ a reaction gas, one has to compare the diffusion phenomena to the heat transfer phenomena (before diffusing, the vapour must be produced by heat transfer) Bonet [227] shows that the characteristic times dt_D and dt_T are such as :

$$\frac{dt_D}{dt_T} = \frac{C_p(T_g - T_p)}{\rho_{vs} \Delta H_T}$$

where C_p is the specific heat of B, T_g the plasma temperature, T_p the particle temperature, ρ_{vs} the mass concentration of the vapour at the particle surface and ΔH_T the enthalpy flux (including the reaction enthalpy). Usually $\Delta H_T > C_p(T_g - T_p)$. So if ρ_{vs} is important then the decomposition process cannot be neglected for particle with ($\phi < 200 \mu m$).

For example the molybdenum disulfide desulfurization process is controlled by heat transfer and MoS_2 starts reacting appreciably in the solid state from 1773 K [228]. In flight (studies have been made with a FCC plasma) the moving particles go through the following phases :

- 1) $T_p = 1773 \text{ K}$: solid state (flake) : no reaction, only heating.
- 2) $1773 \text{ K} < T_p < 1923 \text{ K}$: solid state : (i) heating of $MoS_{2(s)}$; (ii) conversion of



- (iii) heating of $Mo_{(s)}$.

- 3) $T_p = 1923 \text{ K}$: melting : (i) heat for melting of $MoS_{2(s)}$; (ii) conversion of $MoS_{2(s)} \rightarrow Mo_{(s)} + S_{2(v)}$ (converted Mo stays at 1923 K).

- 4) $1923 \text{ K} < T_p < 2892 \text{ K}$: solid liquid state : (i) conversion of $MoS_{2(l)} \rightarrow Mo_{(s)} + S_{2(v)}$; (ii) heating of $MoS_{2(l)}$; (iii) heating of $Mo_{(s)}$ (continues still conversion takes place).

- 5) $T_p = 2892 \text{ K}$: melting $Mo_{(s)} \rightarrow Mo_{(l)}$.

- 6) $2892 \text{ K} < T_p < 4919 \text{ K}$: heating of liquid Mo.

- 7) $T_p = 4919 \text{ K}$: vaporizing : $Mo_{(l)} \rightarrow Mo_{(v)}$; (Mo vapour causes loss in Mo recovery).

On the contrary for the reduction of Fe_2O_3 with hydrogen or carbon in plasma furnace [229] the process seems to be controlled by diffusion. The diffusion time for $60 \mu m$ Fe_2O_3 particles is high (0.1 s) and the main problem is to use a plasma device with a long residence time to allow the chemical reaction to proceed to a significant extent. Falling film furnaces are very well suited for this; they make use of a hollow cylindrical anode into which the particles are fed in a gas vortex, melting to form a liquid falling film on the anode wall. The melted film is heated by the plasma as in others configurations but is also heated

by the Joule effect and electron condensation (anode) thus enhancing the efficiency of the heat transfer to the reactants and reducing the heat losses to the electrodes. The first furnace of this type was designed for MHD reaction [235] but the most efficient is that of Mac Rae figure 26 [236] used at a power level of 1 MW for iron ore reduction and of 400 kW for ferrovanadium preparation [237].

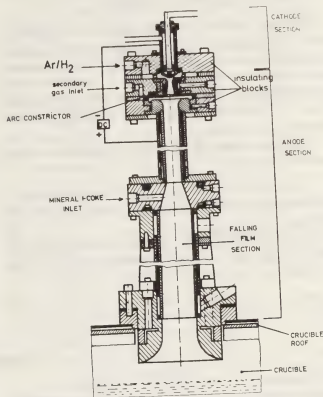


Fig. 26. — Bethlehem Steel's 1 MW falling film furnace (after US Pat 4002466 11th Jan 1970).

Conclusion. — If plasma chemistry is known since the beginning of the century, a lot of experiments (some zoological description) has been made between 1955 and 1970. However important progresses have been achieved only in the seventies with the improvement of measurement techniques. This helped to identify, in homogeneous reactions, the role of the excited states and of the kinetic, electronic, vibrational and rotational excitation and to show that the most important part of plasma chemistry is the quenching of the excited new species formed. For heterogeneous reactions the improvement of the measurement techniques allows a better understanding of the heat and mass transfer phenomena between the plasma and the particles.

Among the diagnostic techniques used one has to emphasize the use of laser diagnostic, either to determine by fluorescence the rate coefficients of reactions with excited species specially the metastable ones that may allow specific stereochemistry or to study the particles velocity and diameter.

In the future as electricity becomes the most reliable and versatile source of energy, industrial uses

of plasma chemical reactors will become increasingly attractive because :

- 1) they can be operated and stopped very quickly ;
- 2) their energy density is very high and the reaction are very fast compared to the classical reactors allowing the use of small units with a rather low investment cost ;
- 3) they are usually not polluting.

However, a lot of progress has yet to be made to further understand what happens during plasma treatment from a microscopic point of view in order to improve the conversion rates and the specific energy consumptions of the reactors. For example catalysis seems to be very promising but almost everything remains to be done.

The main areas of research in plasma chemistry seems now to be :

- research on reactions with excited states : stereochemistry with metastable states, eximers and flowing lasers...
- research on the destruction of polluting molecules (SO_2 , NO_2 , NO ...), high atmosphere and space chemistry...

- production of molecules with high added values either in organic chemistry or for ceramics with specific crystalline structure...
- production of molecules with low added values improving the conversion rates and energy consumption, in particular, due to the oil crisis, researches are developed for NO production from air, C_2H_2 and C_2H_4 from coal...
- extractive metallurgy by plasma allowing the local treatment of low grade ores and the production of high purity metals...
- production of submicronic powders or spheroidized particles for sintering...
- development of the plasma sprayed coatings for wear and corrosion protection, thermal and electrical barrier surfaces with low coefficients of friction...
- surface treatment in low pressure plasmas for electronic, optical and wear resistance applications...

Acknowledgments. — The authors are extremely grateful for the assistance given by Professor Boulos of the University of Sherbrook in preparing this lecture and for his fruitful comments.

References

- [1] EDSTROM, J. S., *Petrochem. Industr.* **2** (1904) 399.
- [2] BARONNET, J. M., *Contribution à l'étude spectroscopique des plasmas d'azote produits par un générateur à arc soufflé ; application de la chimie des plasmas : synthèse des oxydes d'azote*, Thèse de Doctorat d'Etat, Université de Limoges (1978).
- [3] CAPPEZUTO, P. et al., *J. Phys. Chem.* **60** (1976) 882.
- [4] CATHERINOT, A., SY, A., *Z. Naturforsch* **30a** (1975) 1143.
- [5] SYDUK, V. L., EREMIN, E. N., *Russ. J. Phys. Chem.* **49(4)** (1975) 917.
- [6] VENUGOPALAN, M., *Plasma Chemistry. An introduction. In : Reactions under plasma conditions*. Ch. XI. Vol. II (ed.) Venugopalan : Wiley Interscience N.Y. (1971).
- [7] MULLER, K. G., *Non equilibrium plasmas and their diagnostics*, invited paper of the Third International Symposium on Plasma Chemistry, Limoges July 13-19 1977.
- [8] LEWELLYN-JONES, F., *The glow discharge* (Ed.) : Methuen London (1966).
- [9] DAVIDSON, R. C., I.E.E.E., I.A.S. Conference on applied electrostatics, Toronto (1978).
- [10] THOMAS KITZE, P., CARLEY, J. F., *R.G.C.P.* **52** (1975) 463.
- [11] HIRSH, M., *Décharges HF et microondes*, Séminaire Chimie des Plasmas, Dourdan 20-24/02/78 (ed.) A.D.E.R.P. Orsay.
- [12] FEISENFELD, F. C., EVENSON, K. M., BROIDA, H. P., *Rev. Sci. Instrum.* **36** (1955) 294.
- [13] HUBERT, J., MOISAN, M., RICARD, A., *Spectrochimica Acta* **33** (1979) 1.
- [14] RYKALIN, N. N., *Pure and Appl. Chem.* **48** (1976) 179.
- [15] MACKINNON, I. M., REUBEN, B. G., *J. Electrochem. Soc.* **122** (1975) 806.
- [16] ROMAN, W. C., ZABIELSKI, M. F., *Spectroscopic Gas Composition Measurement of UF_6 RF plasmas*. Presented at 30th Annual Gaseous Electronics Conference, Palo Alto, CA, oct. (1977).
- [17] GAGE, R. M., *Arc Torches and process*, U.S. Patent 2 (1957) 806, 124.
- [18] BOSE, T. K., PFENDER, E., *A.I.A.A. Journal* **7** (1969) 1643.
- [19] SHIH, K. T., PFENDER, E., *A.I.A.A. Journal* **8** (1970) 211.
- [20] CAMBRAY, P., *Contribution à la mesure des flux de chaleur et de la viscosité d'écoulement du plasma dans un générateur à arc soufflé*, Thèse de 3^e cycle, Université de Poitiers, 6 avril 1971.
- [21] HASSAN, H. A., SMITH, N. S., *A.I.A.A. Journal* **8** (1970) 657.
- [22] LEONTIEV, A. J., VOLTCHKOV, E. P., *Caractéristiques électriques et thermiques d'un plasmatron de haute enthalpie in Investigations expérimentales des plasmatrons*, M. F. Joukov. Ed. Nauka Novossibirsk (1977).
- [23] KIMBLIN, S. U., *Erosion des électrodes et processus d'ionisation entre les électrodes de l'arc dans le vide et à la pression atmosphérique*, p. 226 in *Investigations expérimentales des plasmatrons*, MF Joukov ed. Nauka Novissibirsk (1977).
- [24] ROMALO, D. I., *Revue Roumaine des Sciences et Techniques, Série électrotechnique et énergétique* **13** (1968) 415.
- [25] FINKELNBURG, W., MAECKER, N., *Elektrische Bögen und thermisches Plasmas Handbuch der Physik*, Springer-Verlag, Berlin (1956).
- [26] NACHMAN, M., *Rev. Hies Temp. et Réfract.* **10** (1973) 65.
- [27] PFENDER, E., *Electric Arcs and Arc Gas Heaters, in Gaseous electronic* (ed.), M. N. Hirsh, H. J. Oskam, Acad. Press (1978).
- [28] HOYAUX, M. F., *Arc Physics* (Applied Physics and Engineering, vol. 8) Springer Verlag, Berlin (1968).
- [29] BOURDIN, E., *Calcul approximatif d'une tuyère de torche à plasma par application du modèle à propriétés constantes*, Rap. Int. Lab. Thermodynamique, avril 1978.
- [30] SCHOUMAKER, H. R. P., *Four's à chauffage plasma*, in Conference Proceedings of International Round Table on Study and Application of Transport Phenomena in Thermal Plasma, Odeillo, sept. 1975.

- [31] GEIDEMAN, W. A. V., *A general discussion of plasma generator design consideration and operating characteristics*, Plasma-dyne Corporation, PRE 107.
- [32] SCHOECK, P. A., Ph. D. Thesis Univ. Minnesota (1961).
- [33] JOUKOV, M. F., KOROTEL, OURIKOB, B. A., *Hydrodynamique appliquée des plasmas thermiques*. Rédacteur : Koutatrieladze S. S. Ed. Nauka, Novossibirsk (1975).
- [34] JOUKOV, M. F., KOUROCHKINE, POUSTOGAROV, A. V., *Etude des plasmatrone utilisant des gaz plasmagènes soufflés à travers un étage rapporté entre les électrodes*, p. 82 in *Investigation expérimentale des plasmatrone*. MF Joukov Ed. Nauka, Novossibirsk (1977).
- [35] SCHNELL, C. R., HAMBLYN, S. M. L., HENGARTNER, K. and WISSLER, M. (Lonza Ltd), The industrial application of plasma technology for the production of fumed silica, presented at the Symposium *Commercial Potential for Arc and Plasma Processes*, Atlantic City, N.J., 8-11 septembre 1974.
- [36] FEY, M. G., KEMENY, G. A., *Method of direct ore reduction using a short gap arc heater*, U.S. patent 3, 16 oct. 1973, 765, 870.
- [37] BONET, C. and al., *J. Phys. D., Appl. Phys.* **9** (1976) L 141.
- [38] SHAKOV, M. F., SMOLYAKOV, V. Ya., URGUKOV, B. A., *Electric-Arc Heaters of Gases* (ed.) Nauka, Moscow (1973).
- [39] GRIMAUD, A., Thèse 3^e cycle, U.E.R. des Sciences, Limoges (1973).
- [40] GLADISH, H., *Hydrocarbon. Process. Petrol. Refiner* **41** (1962) 159.
- [41] STOKES, C. S., KNIPE, W. W. et STRENG, J., *Electrochem. Soc.* **107** (1960) 35.
- [42] KORMAN, S., *Inter. Sci. Tech.* **30** (1964) 90.
- [43] GIBSON, J. O., WAIMAN, R., *Chem. Ing. Progr.* **9** (1963) 53.
- [44] HOLMGREN, J. D., GIBSON, J. O., SHEER, C., *J. Electrochem. Soc.* **111** (1964) 362.
- [45] KELLY, A. J., *J. Chem. Phys.* **45** (1966) 1723.
- [46] MAECKER, H., *Z. Physik* **136** (1953) 119.
- [47] MARINOWSKI, G. W., PHILLIPS, R. C., PHILLIPS, T. R., HIESTER, N. K., *Ind. Eng. Chem. Fundamentals* **1** (1962) 52.
- [48] MEUBUS, P., *J. Electrochem.* **122** (1975) 298.
- [49] BADDOUR, R. F., BLANCHET, J. L., *Ind. Ing. Chem. Process. Design. Develop.* **3** (1964) 258.
- [50] TIMMINS, R. S. et AMMAN, P. R., *A.I. Ch. E.J.* **12** (1966) 956.
- [51] ANDERSON, J. E., CASE, L. K., *Ind. Eng. Chem. Process. Design. Develop.* **1** (1962) 161.
- [52] STOKES, C. S., STRENG, L. A., *Ind. Eng. Chem. Process. Design. Dev.* **4** (1965) 36.
- [53] GLADISH, H., *Hydrocarbon. Process. Petrol. Refiner* **41** (1962) 159.
- [54] GREY, J., JACOBS, P. R., *A.I.A.A. : J. 2* (1964) 433.
- [55] POLAK, L., *Some principles of non equilibrium plasma chemical reaction kinetics*, ch. 13, p. 141, T. 2, *Plasma Chemistry* Ed. Venugopalan, Wiley-Interscience, N.Y. (1971).
- [56] KAUFMAN, F., KELS, J. R., *J. Chem. Phys.* **32** (1960) 301.
- [57] YOUNG, R. A., SHARPLESS, R. L., SRINGHAM, R., *J. Chem. Phys.* **40**(1) (1964) 117.
- [58] SAFRANY, HARTECK, REEVES, *J. Chem. Phys.* **41** (1964) 1161.
- [59] BAKER, R. R., JAKOB, A., WINKLER, C. A., *Can. J. Chem.* **49**(2) (1971) 1671.
- [60] BROOKES, B. W., SEAPORT, R. M., *J. Appl. Chem. Biotechnol.* **24** (1974) 621.
- [61] EREMIN, E. N., SYADUK, V. L., *Russ. J. Phys. Chem.* **49**(4) (1975) 587.
- [62] EREMIN, E. N., BEBESIKO, *Russ. J. Phys. Chem.* **48**(1) (1974) 50.
- [63] EREMIN, E. N., *Russ. J. Phys. Chem.* **48**(8) (1974) 1229.
- [64] EREMIN, E. N., *Russ. J. Phys. Chem.* **48**(8) (1974) 1256.
- [65] EREMIN, E. N., SYADUK, V. L., *Russ. J. Phys. Chem.* **47**(6) (1973) 864.
- [66] EREMIN, E. N., RUBATSOVA, *Russ. J. Phys. Chem.* **47**(1) (1973) 35.
- [67] EREMIN, E. N., SYADUK, V. L., *Russ. J. Phys. Chem.* **46**(11) (1972) 1644.
- [68] RAPAKOULIAS, D., *Etude des processus de fixation de l'azote dans un réacteur chimique à plasma hors équilibre*. Mise en évidence de processus catalytique, Thèse de Doctorat ès Sciences Physiques, Université de Paris VI, 11/06/1979.
- [69] CAVADIAS, S., *Synthèse directe des oxydes d'azote dans un réacteur à plasma basse pression hors équilibre*, Thèse de 3^e cycle, Université de Paris VI, 11/06/1979.
- [70] GRIEM, H. R., *Plasma Spectroscopy* (ed.) Mc Graw-Hill, N.Y. (1964).
- [71] DRAWIN, H. W., *High Pressures, High Temperatures* **2** (1970) 359.
- [72] RANSON, P., CHAPELLE, J., *J.Q.S.R.T.* **14** (1974) 1.
- [73] RANSON, P., *Thèse de Doctorat d'Etat*, Université d'Orléans (1978).
- [74] CATHERINOT, A., SY, A., *Z. Naturforsch.* **30a** (1975) 1143.
- [75] DELCROIX, J. L., *Physique des Plasmas* (ed.) Dunod, Paris (1963).
- [76] DRAWIN, H. W., *Reactions under plasma conditions* (ed.) Venugopalan, M., Wiley Interscience, N.Y. (1971).
- [77] STUPOCHENKO, Y. V., LOSEV, S. A., OSIPOV, A. J., *Relaxation in shock waves, International series applied physics and engineering*, 1 (ed.) Springer Verlag (1967).
- [78] LESKOV, L. V., SAVIN, F. A., *Soviet Physics Uspekhi* **3** (1961) 912.
- [79] LOSEV, S. A., OSIPOV, A. L., *Soviet Physics Uspekhi* **74** (1962) 525.
- [80] ZELDOVICH, B., RAISER, Y., *Physics of shock waves and high temperature hydrodynamic phenomena* (ed.) Academic Press N.Y. (1966).
- [81] ROWE, B., *Etude des réactions chimiques et ioniques dans un plasma en fort déséquilibre thermodynamique. Cas du mélange azote-argon*, Thèse de doctorat d'Etat, Université de Paris VI (1975).
- [82] CABANNES, F., *Molecular Spectroscopic Diagnostics, in Analytical Uses of Plasmas* (ed.) R. M. Barnes, John Wiley N.Y. (1978).
- [83] BOURASSEAU, D., *Contribution à l'étude de l'équilibre thermodynamique local dans les jets de plasma d'argon sous pression réduite*, Thèse de doctorat de 3^e cycle, Paris (1968).
- [84] First report on spectroscopic methods of temperature measurements, IUPAC, report of the committee on standards and measurements in plasma chemistry (ed.) P. Fauchais, Limoges University (1979).
- [85] BAYARD, S., *Contribution au calcul des fonctions de partition des plasmas azote-silicium-aluminium et détermination des températures à partir du fond continu de l'azote*. Thèse de 3^e cycle, Université de Limoges (1974).
- [86] HOFSAESS, D., *J.Q.S.R.T.* **19** (1978) 339.
- [87] FIEFFE-PREVOT, P., *Rev. de Physique Appliquée* **12** (1977) 1243.
- [88] OLSEN, H. N., BEDTAL, G., KELLY, F. L., *Development of diagnostic methods for seeded air and nitrogen plasma*, A.E.D.C.-T.R.-68-217.
- [89] RANSON, P., CHAPELLE, J., *J.Q.S.R.T.* **14** (1974) 1.
- [90] KONJEVIC, J., *J. Phys. Chem. Ref. Data* **5** (1976) 209.
- [91] COUDERT, J. F., *Contribution à l'étude de la synthèse des oxydes d'azote par chalumeau à plasma*, Thèse de 3^e cycle, Université de Limoges (1978).
- [92] CATHERINOT, A., SY, A., *Quenching of the 3p⁴S atomic nitrogen state in a low pressure nitrogen glow discharge*, *Phys. Rev. A* (à paraître).
- [93] DUBREUIL, B., CATHERINOT, A., *Physica* **93C** (1978) 408.
- [94] DUBREUIL, B., CATHERINOT, A., *J. Phys.* **D 11** (1978) 1043.
- [95] CATHERINOT, A., PLACIDET, P., DUBREUIL, B., *J. Phys.* **B 11** (1978) 3775.
- [96] CATHERINOT, A., DUBREUIL, B., GAND, M., *Phys. Rev. A* **18** (1978) 1097.
- [97] DUBREUIL, B., CATHERINOT, A., *J. de Phys.* **39** (1978) 1071.
- [98] FISZDON, J., GAUK, DANIAULT, *Rev. Int. Htes Temp. et Réfract.* **13** (1976) 11.

- [99] HARE, A. L., *Velocity measurements in plasma flows using cooled pitot tubes: an unsolved problem*, Proceedings G.3.9., 11th International Symposium on Plasma Chemistry, Limoges (1977).
- [100] FISZDON, J., LESINSKI, J., *International Round Table on Study and Application of Transport Phenomena in Thermal Plasmas*, Odeillo 12-16 sept. 1975.
- [101] CAMBRAY, P., *Contribution à la mesure des flux de chaleur et de la vitesse d'écoulement du plasma dans un générateur à arc soufflé*, Thèse de 3^e cycle, Poitiers (1971).
- [102] GUYONNET, J., BORIE, A., FAUCHAIS, P., *Projection au chalumeau à plasma de revêtements céramiques à coefficients de frottement variables*, in *Proceedings IV-5 of International Round Table on Study and Application of Transport Phenomena in Thermal Plasmas*, I.U.P.A.C., Odeillo, 12-16 sept. 1975.
- [103] GOUESBET, G., *Phénomènes de diffusion et de thermodiffusion des espèces neutres dans un plasma d'argon et d'hélium*, Thèse de Doctorat d'Etat, Université de Rouen (1977).
- [104] VARDELLE, A., *Contribution à la mesure statistique des vitesses et des températures de surface de particules injectées dans un jet de plasma d'arc*, Thèse de 3^e cycle, Université de Limoges (1979).
- [105] LESINSKI, J., LESINSKA, B., FANTON, J. C., BOULOS, M. I., L.D.A. Measurements under plasma conditions, 4th International Symposium on Plasma Chemistry, Zurich, August 27, Sept. 1st, 1979.
- [106] CAMBRAY, P., *Mesure de vitesse dans des jets de plasma comportant des gradients axiaux*, *Proceedings G.3.2.*, 3d International Symposium on Plasma Chemistry, Limoges University (1977).
- [107] LERON, H. G., MÜLLER, K. G., *Verhandlung der Deutschen Physikalischen Gesellschaft*, 1977, p. 699.
- [108] PERUGINI, G., *Analysis of dynamic fusion phenomena of ceramic and metallic powders injected into an argon plasma jet*, 3d International Meeting on Modern Ceramics Technologies, Rimini, Italy (1976).
- [109] TODOROVIC, P. S. et al., *Spectrochimica Acta* **313** (1976) 103.
- [110] ANDRÉ, M., *Les techniques de cinématographie ultra-rapide*, C.E.A., Centre de Limeil, France (1977).
- [111] GOLD, D., *J. of Physics E: Scientific Instruments* **10** (1977) 395.
- [112] DURST, F., ZARE, M., *Bibliography of laser doppler anemometry literature*, University of Karlsruhe, published by DISA Information Department.
- [113] BOUTIER, A., *Data processing in laser anemometry 3d International workshop on laser velocimetry*, Institut Franco-Allemand de Saint-Louis France (1976).
- [114] EDWARDS, R. V. et al., *J. Appl. Phys.* **42** (1971) 837.
- [115] EDWARDS, R. V. et al., *J. Appl. Phys.* **44** (1973) 1694.
- [116] CASPERSEN, C., SAUSTRAP, H., KRISTENSEN, L.D.A. *Measurements in a low-velocity wind tunnel on a thin plate model DISA information* **17** (1975).
- [117] SELF, S. A., *Laser doppler velocimetry in MHD boundary layer*, *Eng. Aspects Magnet. 14th Symp.* Tullahoma Tenn. (1974).
- [118] STEENSTRUP, F. V., *DISA Information* **18** (1975) 21.
- [119] ABBISI, J. B., *Seminar given at NATO advanced study, institute on photon correlation spectroscopy and velocimetry*, Capri (Italy), 26 july, 6 august 1976.
- [120] BONET, C., *Description d'une méthode de mesure de la température d'une particule en mouvement*, Réunion R.C.I. Gaz Ionisés Réactifs, Paris le 10/02/1978 (ed.) P. Fauchais, Limoges University.
- [121] KRUSZEWSKA, B., LESINSKI, J., *Rev. Phys. Appliquée* **12** (1977) 1209.
- [122] PENNER, S. S., CHANG, P., *J.Q.S.R.T.* **20** (1978) 447.
- [123] BARRERE, M., PRUD'HOMME, R., *Equations fondamentales de l'aérothermochimie*, Masson et Cie éditeurs, Paris (1973).
- [124] ZELENICK, F. J., GORDON, S., *Industrial Engineering Chemistry* **60** (1968) 6.
- [125] STOREY, S. H., VAN ZEGEREN, F., *The computation of chemical equilibria*, Cambridge University Press (1970).
- [126] BOURDIN, E., *Contribution à l'étude théorique et expérimentale de la synthèse de nitrures par réaction d'un jet de plasma d'azote avec des poudres d'aluminium et de silicium*, Thèse de 3^e Cycle, Université de Limoges (1976).
- [127] FAUCHAIS, P., BARONNET, J. M., BAYARD, S., *Rev. Int. Htes Temp. et Réfract.* **12** (1975) 221.
- [128] COLDWELL, D. M., *High Temperature Science* **8** (1976) 309.
- [129] FRANK-KAMENETSKII, D., *Diffusion and heat transfer in chemical kinetics*, Plenum Press, New York-London (1969).
- [130] WARNER, D. D., *The Journal of Physical Chemistry* **87** (1977) 2329.
- [131] EMANUEL, N., KNORR, D., *Cinétique chimique*, Edition Mir, Moscou (1975).
- [132] JOHNSTON, H., *Gas phase reaction rate theory*, Ronald Press company, New York (1966).
- [133] GLADSTONE, S., LAIDLIER, J. K., EYRING, H., *The theory of rate processes*, Mc Graw-Hill Book Company, Inc. New York and London (1941).
- [134] CACCIATORE, M., CAPITELLI, M., *Z. Naturforsch.* **30a** (1975) 48.
- [135] CACCIATORE, M., CAPITELLI, M., *Z. Naturforsch.* **31a** (1976) 362.
- [136] BARONNET, J. M. et al., *Journal de Chimie Physique* **75** (1978) 949.
- [137] BARONNET, J. M., COUDERT, J. F., RAKOWITZ, J., BOURDIN, E., FAUCHAIS, P., *Nitrogen oxides synthesis in a DC plasma jet*, 4th International Symposium on Plasma Chemistry, Zurich, august 27, sept. 1st, 1979.
- [138] PRUD'HOMME, R. et al., *Rapport ONERA*, Paris (1969).
- [139] BAULCH, D. L., *High Temperature Reaction Rate Data*, no 4, Leeds (1969).
- [140] POLANYI, J. C., *Chem. Phys.* **5(5)** (1972) 161.
- [141] BADGER, R. M. et al., *J. Chem. Phys.* **43** (1965) 4345.
- [142] FONER, S. N., HUDSON, R. L., *J. Chem. Phys.* **25** (1956) 601.
- [143] ARNOLD, S. J., DYRZYLO, E. A., WITZKE, H., *J. Chem. Phys.* **40** (1964) 1769.
- [145] DUMAS, J. L., GARNIER, B., *Journal de Chimie Physique* **9** (1975) 1045.
- [146] CLYNE, M., THRUSH, B., WAYNE, R., *Photochem. Photob.* **4** (1965) 957.
- [147] DUMAS, J. L., *Bulletin de la Société Chimique de France* **5-6** (1976) 658.
- [148] DUMAS, J. L., *Bulletin de la Société Chimique de France* **5-6** (1976) 661.
- [149] DUMAS, J. L., *Bulletin de la Société Chimique de France* **5-6** (1976) 665.
- [150] BOURDIN, E., AUBRETON, J., FAUCHAIS, P., *Equilibrium composition and thermodynamic properties of C-H₂, CH₄ and CH₄-H₂ plasmas, computation of their reducing action on iron oxide Fe₂O₃*, In: *11th International Symposium on plasma Chemistry*, Limoges July (1977); Proceedings III-G4-2.
- [151] DEVOTO, R. S., *Phys. of Fluids* **10** (1967) 2105.
- [152] MASON, E. A., *Kinetic processes in gases and plasma* (ed.) A. R. Hochstim Academic Press, N.Y. and London (1969).
- [153] CHAPMAN, S., COWLING, T. G., *The mathematical theory of non uniform gases* (ed.) Cambridge University Press, U.K. (1970).
- [154] ATHEY, W. F., *A critical evaluation of methods for calculating transport coefficients of partially and fully ionized gases*, NASA TN, ND-2611 (1965).
- [155] DEVOTO, R. S., *Phys. of Fluids* **9** (1966) 1230.
- [156] DEVOTO, R. S., LI, C. P., *J. Plasma Physics* **2** (1968) 17.
- [157] DEVOTO, R. S., *A.I.A.A. Journal* **7** (1969) 2.
- [158] DEVOTO, R. S., *Phys. of Fluids* **16** (1973) 616.
- [158] DEVOTO, R. S., CAPITELLI, M., *Phys. Fluids* **16** (1973) 1835.

- [159] BUTLER, J. N., BROKAW, R. S., *Journal of Chemical Physics* **26** (1957) 1636.
- [160] VANDERSLICE, J. T., WEISMAN, S., MOSON, E. A., FALLON, R. J., *Phys. of Fluids* **5** (1962) 155.
- [161] GORSE, C., Contribution au calcul des propriétés de transport des plasmas des mélanges argon-hydrogène et argon-azote. Thèse de 3^e cycle, Université de Limoges, 9 septembre 1975.
- [162] PETRIE, I. W., *The effect of ionization on heat transfer to wires immersed in an arc plasma*. Ph. D. Thesis University of Minnesota (1969).
- [163] PFENDER, E., *Pure and Appl. Chem.* **48** (1976) 199, Pergamon Press.
- [164] FINKELNBURG, W., MAECKER, H., Elektrische Bögen und Thermisches Plasma. *Encyclopedia of Physics* (ed. S. Flügge), vol. 22, p. 254, Springer, Berlin (1956).
- [165] ECKER, G., *Electrode components of the arc discharge Ergebnisse d. exakten naturwiss.*, vol. 33, p. 1, Springer, Berlin (1961).
- [166] KIMBLIN, C. W., Anode phenomena in vacuum and atmospheric pressure arcs, *I.E.E.E. Trans. plasma Sci.*, PS-2 (4), 310 (1974).
- [167] BOULOS, M. A., GAUVIN, W. H., *Can. J. Chem. Eng.* **52** (1974) 355.
- [168] BHATTACHARYA, D., GAUVIN, W. H., *A.I.Ch.E. J.* **21** (1975) 879.
- [169] LEWIS, J. A., GAUVIN, W. H., *A.I.Ch.E.J.* **19** (1973) 982.
- [170] BOULOS, M. A., *III^e Symposium International de Chimie des Plasmas : I.U.P.A.C.-S-3-2*, Limoges (1977).
- [171] TOROBIN, L. B., GAUVIN, W. H., *Can. J. Chem. Eng.* **37** (1959) 129.
- [172] BORGIANI, C., CAPITELLI, M., CRAMAROSSA, F., TRIOLO, L., MOLINARI, E., *Combust. Flame* **13**, 2 (1969) 181.
- [173] YOSHIDA, T., AKASHI, K., *Journal of Applied Physics*, **48** (1977) 2252.
- [174] RYKALIN, N. N., KUDINOV, V. V., *Pure and Appl. Chem.* **48** (1976) 229.
- [175] BESSON, J. L., BOCH, P., *Plasma Spraying of Ceramics, International Round Table Discussion on Special Ceramics for Electronics and Electrical Engineering*, Warsaw 8-11 oct. 1978.
- [176] INGHAM, H. S., SHEPARD, A. D., *Metco Flame Spray Handbook* (1965).
- [177] GUYONNET, J., Brevet C.N.R.S. 124 111 et additifs 168 044 et 7 044 678.
- [178] MADEJSKI, J., *Int. J. Heat and Mass Transfer* **19** (1976) 1009.
- [179] MADEJSKI, J., *Bull. Acad. Pol. des Sciences* **24**, n° 1 (1976).
- [180] ZOLTOWSKI, P., *Rev. Int. Htes Temp. et Réfract.* **6** (1968) 65.
- [181] MEYER, VON H., *Ber. Dtsch. Keram. Ges.* **41** (1964) 112.
- [182] JONES, H., *Rep. Prog. Phys.* **36** (1973) 1425.
- [183] DONOVAN, M., *Vrit. Weld. J.* **13** (1966) 490.
- [184] KUDINOV, V. V., KITAEV, F. I., TSIDULKO, A. G., *Parosh, Metall.* **152** (1975) 38.
- [185] MCPHERSON, R., *J. Mats. Sci.* **8** (1973) 851.
- [186] SOKOLOVA, T. V., KOZLOVA, I. R., DERKO, Kh. KIJKO, A. V., *Izv. Akad. Nauk. S.S.S.R., Neorg. Mat.* **9** (1973) 611.
- [187] EICHORN, F., METZLER, J., EYSEL, W., *Metalloberflaeche* **26** (1972) 212.
- [188] HUFFACHINE, J. B., THOMAS, A. G., *Powder. Met.* **7** (1964) 290.
- [189] THOMPSON, V. S., WHITTEMORE, O. J., *Ceram. Bull.* **47** (1968) 637.
- [190] GUYONNET, J., BORIE, A., FAUCHAIS, P., Projection au chalumeau à plasma de revêtements céramiques à coefficients de frottement variables. In *proceedings of the International Round Table on Study and Applications of Transport Phenomena in Thermal Plasmas*, Odeillo 12-16 sept. 1975.
- [191] HAMBLYN, S. M. L., *A review of application of plasma technology with particular reference to ferro-alloy production*. National Institute for Metallurgy Report n° 1895, Randburg, South Africa, 14 April 1977.
- [192] WALDIE, B., *Chem. Eng., Lond.* **262** (1972) 188.
- [193] ANON, *Chem. Eng.* **24** (1975) 56.
- [194] BONET, C., VALLBONA, G., FOEX, M., *Bull. Soc. Franc. Ceramique* **94** (1972) 27.
- [195] GANI, M. S. J., MCPHERSON, R., *J. Aust. Ceram. Soc.* (in press).
- [196] WILKS, P. H. et al., *Chem. Eng. Prog.* **68** (1972) 82.
- [197] SHEER, C., KORMAN, S., KANG, S. F., *Investigation of convective arcs for the simulation of re-entry aerodynamic heating*, AFORS-TR-74-1505, Contrat F-44 620-69-C-0104 (1974).
- [198] BAYLISS, R. K., BRYANT, J. W., SAYCE, I. G., Plasma dissociation of zircon sands, in the *proceedings (S-5-2) of the III International Symposium on Plasma Chemistry*, Limoges, France, 12-19 July 1977.
- [199] BONET, C., VALLBONA, G., FOEX, M., DAGUENET, M., DUMARGUE, P., *Rev. Int. Htes Temp. et Réfract.* **11** (1974) 11.
- [200] MAECKER, H., *Z. Physik* **136** (1953) 119.
- [201] PATEYRON, B., Interaction entre phénomènes de transport et processus de métallurgie par plasma, *Rapport Interne laboratoire de Thermodynamique de l'Université de Limoges*, juin 1978.
- [202] BHATTACHARYA, D., GAUVIN, W. H., *J. Appl. Phys.* **47** (1976) 4863.
- [203] BORGIANI, C., CAPITELLI, M., CRAMAROSSA, F., TRIOLO, L., MOLINARI, E., *Combustion and Flame* **13** (1969) 181.
- [204] JOHNSTON, P. D., *Combust. Flame* **18** (1972) 373.
- [205] BONET, C., DAGUENET, M., DUMARGUE, P., *Int. J. Heat. Mass Transfer* **17** (1974) 643.
- [206] DONG HI LEE, MCPHERSON, R., *Proc. 9st Aust. Ceramics. conf.* Melbourne (1978).
- [207] SAYCE, I. G., SELTON, B., *Special Ceramics. British Ceramics Research Association* **5** (1972) 157.
- [208] SAYCE, I. G., *Pure and Appl. Chem.* **48** (1976) 215.
- [209] BARNES, W. R., U.K. Patent 1 (1970) 211, 702.
- [210] KORMAN, S., SHEER, C., *Electrochem. Soc. Symp.*, Philadelphia (1966).
- [211] SHEER, C. et al., Arc Vaporization of refractory powders, *Proceedings of the Fine Particles Symposium*, oct. 1973. *Electrochem. Soc.*, Boston (Mass.).
- [212] HOWIE, F. H., SAYCE, I. G., *Rev. Int. Htes Temp. et Réfract.* **11** (1974) 169.
- [213] BARRETT, M. F., HOWIE, F. H., SAYCE, I. G., *Trans. Inst. Min. Metall.* **84** (1975) C 231.
- [214] BONET, C., VALLBONA, G., FOEX, M., *Bull. Soc. Fr. Ceram.* **94** (1972) 27.
- [215] ARKLESS, K., CEAVER, D., *Vrit. Patent*, 1 226 082 (1966).
- [216] DE POU, O., *Proc. 3rd Intl. Symp. Plasma Chem.*, IUPAC Université de Limoges (ed.) P. Fauchais, paper S-4-7 July 1977.
- [217] AUDSLEY, A., BAYLISS, R. K., *J. Appl. Chem.* **19** (1969) 33.
- [218] ULRICH, G., *Combust. Sci. and Technol.* **4** (1971) 47.
- [219] COZZI, C., CADORIN, D., *Combust. Sc. and Tech.* **5** (1972) 213.
- [220] MACKENZIE, J. K., SHUTTLEWORTH, R., *Proc. phys. Soc.* **B 62** (1949) 833.
- [221] MCPHERSON, R., *Proc. Intl. Round Table Study Application of Transport Phenomena in Thermal Plasmas* (ed.) C. Bonet IUPAC/CNRS Odeillo (1975).
- [222] HOLMGREN, J. D., GIBSON, J. O., SHEER, C., *Ultrafine Particles* (ed.) W. E. Kahn, Wiley, New York (1963).
- [223] MCPHERSON, R., *J. Mats. Sc.* **8** (1973) 859.
- [224] DONG HI LEE, MCPHERSON, R., *J. Mats. Sc.* (in press).
- [225] MCPHERSON, R., *J. Amer. Cer. Soc.* (in press).
- [226] DONG HI LEE, MCPHERSON, R., *Proc. 3rd Intl. Symp. Plasma Chem.*, IUPAC/Université de Limoges (ed.) P. Fauchais, paper S-4-10, July 1977.
- [227] BONET, C., Thermal Plasma Processing, *Chemical Eng. Prog. USA* **72**, 12 (1976) 63.
- [228] MUNZ, R. J., *The decomposition of Molybdenum Disulphide in an induction plasma tail flame*, Ph. D. dissertation, Mc Gill Univ. (1974).
- [229] SIEDER, E. N., TATE, G. E., *Ind. Eng. Chem.* **28** (1936) 1429-1435.

- [230] DITTUS, F. W., BOELTER, L. M. K., *University Calif. Pub. Eng.* **2** (1930) 443.
- [231] MARTINELLI, R. C., *Trans. ASME* **69** (1947) 947.
- [232] OSTRACH, S., *Nat. adv. comm. aeron.*, Tech. note 2665, Washington DC (1952).
- [233] JAKOB, M., DOW, W. M., *Trans. ASME* **68** (1946) 124.
- [234] HUANG, G. C., I. — *Heat Transfer* **85** (1963) 235.
- [235] M.H.D. Research inc., U.K. Pat. 1 (1970) 205, 676.
- [236] GOLD, R. G., SANDALL, W. R., CHEPLICK, P. G., MAC RAE, D. R., Plasma reduction of iron oxide with hydrogen and natural gas at 100 kW and 1 MW, *International Round Table on Study and Application of Transport Phenomena in Thermal Plasmas*, IUPAC Odeillo 12-16 sept. 1975.
- [237] MAC RAE, D. R. *et al.*, Ferrovandium production by plasma carbothermic reduction of vanadium oxide, T. III, *Third International Symposium on Plasma Chemistry*, IUPAC Limoges, 13-19 juillet 1977.

Surface problems in magnetic confinement systems

F. Waelbroeck, I. Ali-Khan, K. J. Dietz (*) and P. Wienhold

Institut für Plasmaphysik der Kernforschungsanlage Jülich GmbH,
Association EURATOM-KFA, 5170 Jülich, Postfach 1913, FRG

1. Introduction. — In the laboratory, plasmas originate both from gas present or introduced into the apparatus and from surrounding surfaces. In cases (material analysis) only wall particles, in others (controlled fusion) only fueled particles are desired. The latter requirement is easily satisfied in fusion schemes based on inertial confinement: the plasma pulse is shorter than the communication time to the walls. It is not stringent in magnetic mirror systems: impurities are poorly confined. But in toroidal reactors, the power producing pulses should be as long as possible and impurities are well confined (according to some theories, better than D^+ and T^+). For many materials, the release of less than 1% of a monolayer prevents D-T ignition. Thus, as experiments to achieve burning plasmas are being built and planned, plasma-wall phenomena are now studied as attentively as the closely related problems of improved heating and confinement.

The liberation of wall particles can be:

- a) thermal (evaporation, desorption);
- b) current-induced (unipolar arcs, bundles of relativistic electrons);
- c) due to energetic particles (sputtering, backscattering, ion-induced desorption, blistering), photons (photo desorption) or
- d) to a large concentration c of hydrogen dissolved in surface-near layers.

The first three topics, in particular b) and c) have been reviewed recently [1]. We concentrate on the fourth, and point out the dominant role which c plays on the:

- impurity production and release by chemical reactions between dissolved hydrogen and surface-near layers of carbides and oxides on steels,
- hydrogen exchange (recycling) between plasma and wall, and associated isotopic effects,
- tritium inventory in walls of devices which shall contain D-T plasmas,
- surface embrittlement effects.

Gaseous H_2 dissolves endothermally as interstitial atoms into SS and inconels, whereas H^0 and H^+ dis-

solve exothermally; at wall temperature $T_w \leq 600^\circ C$, evaporation as atoms is negligible.

2. Concentrations c of thermalized and c_h of non-thermal «hot» H in the wall. — In a toroidal device with a minor radius of 20 cm, a density of 10^{14} cm^{-3} and a particle confinement time of 10 ms, the flux density of atoms (including Frank-Condon from recycling) which escapes radially to the wall is $\phi_1 \approx 4 \times 10^{16} \text{ cm}^{-2} \text{ s}^{-1}$. Less than 10% of these ($\phi_h \lesssim 4 \times 10^{15} \text{ cm}^{-2} \text{ s}^{-1}$) have energies $E > 100 \text{ eV}$. A fraction α_1 of ϕ_1 penetrates into the lattice. At high [2] and low [3, 4] energies, $\alpha_1 \approx 1$; for $2 \text{ eV} < E < 200 \text{ eV}$, $1 > \alpha_1 \gtrsim 0.3$ values are expected [5]. Each second, $v_1 = \alpha_1 \phi_1$ atoms penetrate; some diffuse deeper into the wall ($v_D = -D \partial c / \partial x$), others return to the surface, recombine and are released ($v_r = 2 \sigma k_r c^2$) as H_2 molecule; σ is the ratio of the surface on which recombination occurs to the geometric surface of the wall, k_r is a phenomenological rate constant. In the quasi-stationary state, when diffusion becomes negligible, $v_1 = v_r$, i.e. (1):

$$c = (\alpha_1 \phi_1 / 2 \sigma k_r)^{1/2}. \quad (1)$$

Using the value of $\alpha_1 \phi_1$ given above and for k_r that [7] deduced from a review of available data, we find that at $40^\circ C$, c is 500 times larger than the equilibrium c in H_2 at 1 atm. High c values under atomic exposures have been reported by Kass [8] in SS and measured [4] in iron. Since the rates of many phenomena depend quadratically on c , these unexpectedly high values make it likely that, at first unsuspected effects play dominant roles in the plasma-surface interaction.

During uninterrupted plasma exposures, the thickness of the H-containing layer grows about proportionally to $t^{1/2}$. For intermittent exposures, or alternate discharges in D and H, a computer code (non-linear boundary condition) is used [9].

1 keV D^+ ions and D^0 atoms have an impact velocity of $\approx 3 \times 10^7 \text{ cm s}^{-1}$ and a range of $\lesssim 10^{-5} \text{ cm}$. They lose their kinetic energy in a time

(¹) If large amounts of H_2O , CH_4 , are produced, eq. (1) must be modified [6].

$\tau_h < 1$ ps (2) and belong thereafter (unless back-scattered) to the sea of thermalized atoms. The number of hot atoms in the wall is $\phi_h \tau_h < 4 \times 10^3$ cm $^{-2}$. Thus even if the phenomena associated with the initial energy and momentum are impressive, the importance of other effects related to c^2 should not be forgotten. Their study has formed the center of the Jülich activities in this field.

3. Chemical reactions. — Pressure measurements and gas analyses in hydrogen, using devices incorporating hot filaments are known to be delicate : some H $_2$ dissociates into atoms which stick to walls ; H $_2$ O, hydrocarbons, even CO and CO $_2$ are released from surrounding surfaces. Similar effects occur in toroidal devices under wall bombardment by atomic hydrogen : unless special measures are taken [10, 11, 12], O and C are the dominant plasma impurities and large amounts of the above-listed volatile compounds appear in the exhaust gases [13, 14].

Steel and inconel surfaces are covered by an (usually ≈ 50 Å thick) oxygen and carbon-rich layer [15, 16]. The production rates of methane v_{16} and of water v_{18} are [17] proportional to the concentration of surface carbides and oxides respectively and to c^2 , i.e., in the stationary case, to ϕ_1 (eq. (1)). Both v_{16} and v_{18} are large during plasma pulses. The gases released are dissociated and ionised by the hot plasma, converted to C and O ions which, during and at the end of the pulse, are redeposited on the wall. Plasma contamination results but little C and O are eliminated during the pulse, the pumping speed of the plasma being much larger than that of the pumps.

As shown in § 4, c does not decrease all the way down to zero at the end of the discharge : some CH $_4$ and H $_2$ O are also produced between pulses. The methane is evacuated, i.e. the carbide layer is constantly depleted. Some C reappears however on the surface by diffusion from the bulk. When walls are at room temperature the H $_2$ O produced is trapped in surface layers, probably in the form of metal hydroxides. Part of the water formed and trapped between pulses is released during the discharge, increasing the contamination rate ; furthermore only a small fraction of the water produced between discharges is eliminated via the pumping ports, limiting the clean-down rate of the system. A more detailed discussion [17, 18] shows that one method to limit the O-contamination is to decrease the concentration of surface-near metal oxides by careful prehandling of the wall : glow discharges in hydrogen [19] or dense cool tokamak discharges (to maximize ϕ_1 and minimize dissociation and ionisation of H $_2$ O) should be particularly appropriate ; high T_w 's increase v_{18} and reduce H $_2$ O-trapping effects. Measurements in

TFR 600 [12] have confirmed the rapid reduction of the oxide layer under these conditions.

Another method is to decrease c , for instance by appropriate coatings (large k_t , eq. (1)), catalysing the recombination of atomic hydrogen as it impinges onto the surface. This is probably the cause of the beneficial influence of titanium.

4. Hydrogen recycling. — A discussion of the steps involved in the hydrogen exchange at surfaces shows that the simple expressions for the rates of penetration v_1 , diffusion v_D and release v_r as defined in § 2 are applicable when surface coverage effects are negligible, provided that :

— H $_2$ physisorption and desorption is rapid and

— atomic H exchange between surface and lattice sites is fast.

The hydrogen recycling phenomenon (3) can then be described in zero'th order approximation by very simple equations [9].

During discharges, $v_1 - v_r = -D \partial c / \partial x$. In the first phase c and hence v_r are small : impinging atoms are absorbed into the wall wherein they diffuse rapidly ($\partial c / \partial x$ is very large). As the discharge proceeds, c and the recycling coefficient v_r/v_1 increase ; most impinging atoms are released back. The concentration gradient points outwards, towards the surface where c is maximum. The hydrogen which does not recombine on the surface diffuses inwards.

Between discharges, $v_1 = 0$ ($v_r = D \partial c / \partial x$) ; the concentration gradient points inwards (H diffuses towards the surface) ; the concentration at the surface ($c_0 \neq 0$) ensures the H $_2$ outgassing rate. This explains (§ 3) the production of CH $_4$ and H $_2$ O between discharges.

After a number of discharges in H $_2$, a considerable amount of H is dissolved in the wall. If a discharge in deuterium follows, the impinging D either diffuses into the bulk or recombines. Since $(c_{H^0}) \neq 0$ at the surface, both D $_2$ and HD formed. H appears into the plasma at a rate

$$v_r' = 2 \sigma k_r c_H^2 + 2 \sigma k_r' c_H c_D,$$

which is larger than expected from the outgassing rate. Many recycling events occur during one discharge so that the amount of H in the plasma at the end of the pulse is large : in Dite [20], the ratio H/(H + D) at the end of such a pulse was ≈ 65 %. The evolution of this isotopic exchange during consecutive discharges, including the effect of changing the time between

(3) We discuss recycling on deoxidized surfaces : only H $_2$ returns to the plasma. If the surface is oxidized, H $_2$ O is also released. Recycling in tokamaks is derived from the density of electrons : (not protons) : \circ atoms, source of numerous electrons, make the interpretation of recycling in poorly cleaned-down tokamaks difficult.

(2) The time during which H knows that it was initially ionic or neutral is shorter.

discharge (readjustment of the D and H profiles in the solid), is easily understood by this model.

To explain the recycling phenomenon, it has previously been postulated [1] that hydrogen *diffuses* (not recombines) out of the lattice. The concentration gradient points then inwards, even during discharges, and c at the surface remains negligible (*). The interpretation of experimental results is then intricate: trapping centers close to the surface, from which hydrogen cannot be thermally released have to be assumed, as must be an ion-induced detrapping mechanism which specifically empties hydrogen-filled trapping centers.

To check our model, and to measure σk_r , the system of equations was first extended self-consistently to the case of the solubilisation of H starting from H_2 at a pressure p_{H_2} . A fourth rate, $v_2 = 2 \sigma k_s p_{H_2}$, must be included; k_s is a second phenomenological rate constant, related to k_r and to the solubility constant K_s ($k_s = k_r K_s^2$) by equilibrium consideration. Degassing experiments, permeation experiments both stationary and nonstationary, using H_2 alone or mixtures of H_2 and H^0 upstreams, have been carried out. The parameter domain was varied from the purely diffusion-limited regime, via that where diffusion and surface effects play equivalent roles, to the one where pure surface effects dominate (see e.g. [4]). Seven independent methods of measuring σk_r resulted. Good agreement was found between them.

5. Surface embrittlement. — An internal pressure p^* within a metal exposed to atomic H particles can be defined by combining eq. (1) with the solubility law $c = K_s p^{1/2}$:

$$p^* = \alpha_1 \varphi / 2 \sigma k_r K_s^2; \quad (2)$$

p^* builds up at internal surfaces (grain boundaries, lattice defects) of the wall. For the example given, $p^* \approx 3 \times 10^5$ atm. In present-day devices, p^* is lower because of the small duty cycle ($\leq 1\%$), but still

(*) Pushing this postulate *ad absurdum* leads to positive gradients and to a negligible c value also when metals are charged with hydrogen in an H_2 atmosphere.

high enough for surface cracking and embrittlement effects to be feared. These have been observed in simulation experiments in the form of irregular gas release (bursts) [17], increase of the surface hardness of probes exposed to H-atoms, alterations of the surface topography [20, 21]. In addition, the increase of c according to eq. (1) has been directly measured [4] in our permeation experiment.

Embrittlement effects are expected to affect the contamination in two ways: the sudden localised release of H_2 at high pressure offers a favourable condition for the occurrence of unipolar arcs [22, 23, 24]. The opening of cracks is moreover probably accompanied by the ejection of metallic dust.

6. Conclusions: role of T_w and of surface layers. —

This brief discussion brings forth the following points:

— A number of impurity release mechanisms depend on c , the concentration of H dissolved into the surface layers. Of these:

— the release of H_2O , CH_4 can be controlled by appropriate surface prehandling (reduction of carbides and oxides) or by coatings (reduction of c). T_w is important (v_{18} has an activation energy of 20.3 kcal [6]).

— Surface embrittlement can be avoided by raising the wall temperatures; this increases k_r and K_s , i.e. decreases p^* (eq. (2)). Appropriate coatings catalysing the surface recombination of H, again play a beneficial role [21].

— Because they decrease c which otherwise rises to high values, thin coatings, can depress the tritium inventory in walls of devices such as JET, TFTR when they start operation with DT mixtures.

— In order to discuss quantitatively the results obtained in confinement experiments, more information should be given by the tokamak physicists on the status of the wall during the discharge: liner contamination by limiter material or vice versa, T_w , state of oxidation, of carburisation, surface roughness. These informations are of but moderate importance as long as only points a)-c) of the introduction are discussed. They become crucial when phenomena associated to point d) are envisaged.

References

- [1] MC CRACKEN, G. M. and STOTT, P. E., CLM Report p. 573, 1979, R. Behrisch, Fus. React. Mat. Conf. Miami Beach, Jan. 1979, to be publ. *J. Nucl. Mat.*, W. Bauer et al., Sand. 78-8684-Sandia Laboratories, Dec. 1978.
- [2] See e.g.: ECKSTEIN, W. et al., *J. Nucl. Mat.* **63** (1976) 199.
- [3] CLAUSING, R. E. et al., *J. Nucl. Mat.* **76** and **77** (1978) 267.
- [4] WÄELBROECK, F. et al., *Fus. React. Mat., Conf.* Miami Beach, Jan. 1979, to be publ. *J. Nucl. Mat.*
- [5] ALI-KHAN, I. et al., Jül 1597, 1979.
- [6] DIETZ, K. J. et al., IUPAC Communications, 4th Int. Symp. on Plasma Chem., Zürich, CH, Aug. 1979.
- [7] ALI-KHAN, I. et al., *J. Nucl. Mat.* **76** (1978) 138.
- [8] KASS, W. J., *Effect of Hydrogen on Behaviour of Metal*, A. W. Thomson and I. M. Bernstein ed. Metallurgical Society of AIME (1976) 327.
- [9] WIENHOLD, P. et al., *Fus. React. Mat., Conf.* Miami Beach, Jan. 1979, to be published in *J. Nucl. Mat.*

- [10] STOTT, P. E. *et al.*, *Nucl. Fus.* **15** (1975) 431.
- [11] MARMAR, E. S., *J. Nucl. Mat.* **76** and **77** (1978) 59.
- [12] TFR Group. VII. Int. Conf. on Plasma Physics and Controlled Nucl. Fus., IAEA, Innsbruck, 1978, CN-37-A-6.
- [13] TAYLOR, R. J., *J. Nucl. Mat.* **76** and **77** (1978) 41.
- [14] TFR GROUP, *Int. Symp. on Plasma-Wall Interaction*, Jülich (1976) 465.
- [15] BETZ, G. *et al.*, *J. Appl. Phys.* **45** (1974) 5312.
- [16] KIRSCHNER, J. *et al.*, *Proc. Int. Symposium on Plasma-Wall Interaction*, Garching (1976) 65.
- [17] DIETZ, K. J. and WELBROECK, F., *Proc. Int. Symp. on Plasma-Wall Interaction*, Jülich (1976) 445.
- [18] ALI-KHAN, I. *et al.*, To be published.
- [19] POSPIESZCZYK, A. *et al.*, *Proc. Int. Symp. on Plasma-Wall Interaction*, Jülich (1976).
- [20] ALI-KHAN, I. *et al.*, *J. Nucl. Mat.* **76** and **77** (1978) 337.
- [21] ALI-KHAN, I. *et al.*, *Fus. React. Mat., Conf.*, Miami Beach, Jan. 1979, to be published *J. Nucl. Mat.*
- [22] ROBSON, A. E., THONEMANN, E. C., *Proc. Phys. Soc.* **73** (959) 508.
- [23] MC CRACKEN, G. M. and GOODALL, H. J., *Nucl. Fus.* **18** (1978) 537.
- [24] MIODUSZEWSKI, P. *et al.*, *Fus. React. Mat., Conf.* Miami Beach, Jan. 1979, to be published *J. Nucl. Mat.*

Phenomena in ionized gases : some reflections on the XIVth ICPIG

F. W. Crawford (*)

Institute for Plasma Research, Stanford University, Stanford, CA 94305, USA

Abstract. — This paper reviews the scientific program of the XIVth ICPIG, held in Grenoble, 9-13 July 1979. It analyzes the distribution and contents of the roughly 425 contributed papers, and discusses the format of the program at this and previous ICPIG's.

1. Introduction. — Although an authoritative review of the 450 papers of the Conference, indicating their scientific merits, practical significance, and likely impact, would be very valuable, I shall not attempt to give one. Even if I possessed the requisite expertise in all of the fields of the Conference, I would hesitate to do so, since judgments about scientific quality and predictions of the future are notoriously difficult to make.

The further element of personal danger in singling out names for special mention is not to be disregarded lightly. Louis XIVth remarked bitterly that every time he chose someone he made *cent mécontents et un ingrat* (one hundred people discontented and one ungrateful), so I shall steer the safer course in this review of mentioning only one speaker by name.

Instead of an Olympian review, I shall examine first the areas of concentration of the roughly 425 contributed papers. This is not to confuse quantity with quality, but rather to establish the scientific topics of interest to the nearly 450 participants, and to provide food for thought as the International Scientific Committee (ISC) begins in earnest its planning for the XVth ICPIG. Second, I shall discuss the format of the scientific program, and some alternatives to it that have been used at past ICPIG's. My aim is to stimulate thought on the matter, and suggestions to the ISC.

2. Contributed papers. — Contributions were invited in fifteen categories. Counting 20 papers/star, a *Guide Michelin* to those papers accepted would give :

- *** — Waves (65 contributions).
 - High pressure discharges (64).
 - Elementary processes in gas discharges (60).
- ** — Low pressure discharges (54).
 - Diagnostic methods (45).

- * — Interaction of laser beams with plasmas (22).
- Surface phenomena (21).

Lest too much significance be attached to this list, we note that the numbers are approximate to the extent that a few authors may not have been present, or may have withdrawn their papers, and that the classification is somewhat arbitrary : some papers could be appropriately classified in more than one category. Further, as we shall see later, some other categories are close to those mentioned above, e.g. Discharges for Lasers. Nevertheless, we may conclude that three-quarters or more of the contributed papers belong to the seven categories listed.

We now examine the fifteen categories in greater detail, indicating subdivisions originally listed by the ISC, and some additional subdivisions (in parentheses) suggested by the contributions actually received.

2.1 ELEMENTARY PROCESSES IN GAS DISCHARGES (60)

- a) Excitation and ionization.
- b) Recombination, attachment and detachment.
- c) Ion-molecule and chemical reactions.
- d) [Velocity distributions, swarms, avalanches.]

About 50 papers were divided roughly equally among categories 1a)-c). The remainder concentrated on the topics of category 1d) : self-consistent calculations of velocity distributions in glows, afterglows and hollow-cathode discharges ; swarms, and avalanches.

2.2 LOW PRESSURE DISCHARGES (54)

- a) Positive columns.
- b) Ionization waves and instabilities.
- c) Negative glow, hollow cathode discharges.
- d) Radio frequency discharges.
- e) Townsend discharge, breakdown and pulse discharges.
- f) [Isotope separation.]
- g) [Sheaths.]

Many of the papers from this category could arguably have been placed in category 1 or category 10

(*) Chairman, ICPIG International Scientific Committee, 1979.

(Waves). Most of the papers fell within categories 2a)-e), with no strong themes emerging, but special mention might be made of several contributions outside these subdivisions motivated by isotope separation, and several more devoted to sheaths and double-layers.

2.3 HIGH PRESSURE DISCHARGES (64)

- a) Sparks, breakdown, corona discharge.
- b) Properties of arc plasma; arc dynamics.
- c) Plasma flows.
- d) Chemical reactors.

This category is very broad, including not only widely-differing established discharges (corona and arcs), but also the transient breakdown phase, and plasma chemistry. The principal thrusts among the contributed papers were in the directions of decaying arcs, breakdown and corona, and arcs in transverse and axial flows. These studies have particular applications to high-voltage devices and circuit-breakers.

2.4 DISCHARGES FOR LASERS (17)

- a) [Discharge characteristics.]
- b) [Basic processes.]
- c) [Waves and instabilities.]

The contributions in this category were approximately evenly divided among categories 4a)-c), and separable from categories 1, 2, and 10 primarily by their motivation, i.e. the various radiation processes and discharge instabilities likely to affect laser performance were of particular interest.

2.5 DISCHARGE AND BREAKDOWN IN VACUUM (8)

- a) [Surface phenomena.]
- b) [Effects of magnetic field.]

Two topics that have figured prominently in this small category are surface phenomena affecting breakdown, and the effects of magnetic fields in switching or extinguishing vacuum arcs.

2.6 LONG SPARKS AND LIGHTNING (6)

No special theme emerges from this small category, which might well be combined in future with categories 3a) and 5 to form a single category on spark breakdown and lightning.

2.7 SURFACE PHENOMENA (21)

- a) Electrode phenomena.
- b) Surface treatment using plasma (deposition, etching, oxidation, etc.).

This substantial category could arguably be augmented with a number of contributions dispersed through others. Those papers actually included emphasized category 7a), and included several papers on arc spots and cold cathodes; still an interesting area, even after several hundred publications.

2.8 MISCELLANEOUS DISCHARGE DEVICES (16)

- a) [Special types of discharges.]
- b) [Discharges for ion or neutral production.]
- c) [Rotating plasmas.]

This rather desperate category is intended as a catch-all for contributions on devices not fitting readily into any other category. In fact, several papers could have been placed elsewhere in the program, but a residuum remained of papers on unusual discharges, some serving special purposes such as ion or neutral production, and a few on phenomena associated with rotating plasmas.

2.9 GENERAL PLASMA THEORY (15)

- a) Transfer phenomena.
- b) Numerical methods.
- c) [Kinetic equations.]
- d) [Distribution functions and drifts.]

No contributions were received in category 9b), though papers involving sophisticated numerical methods are to be found elsewhere, for example in category 15 (Diagnostic Methods). If we consider category 9a) to refer primarily to macroscopic phenomena, then other concentrations among the papers contributed were on kinetic equations, and the velocity distribution functions and drifts predicted for various special discharges.

2.10 WAVES (65)

- a) Wave propagation.
- b) Wave-particle and wave-wave interactions.
- c) Instabilities.
- d) Strong turbulence.
- e) [Solitons.]

Although the contributions to this large category defy neat classification, certain trends are evident. Many intriguing problems in linear wave excitation, instabilities and propagation, particularly in bounded plasmas, still command attention, but the emphasis has moved towards nonlinear parametric and modulational instabilities and turbulence. Solitons, which in all fields now generate about 1 000 publications a year, have gained considerable significance in plasma physics, a fact which was reflected by several interesting papers, including experimental observations.

2.11 NON-IDEAL PLASMA (12)

- a) Theory.
- b) Experiment.

Although a cynic might be tempted to place all of the contributed papers in this category, it was intended for plasmas sufficiently dense for quantum effects to become significant. Growth of interest in this area is evidenced by the number of contributions received, several of which described experimental observations.

2.12 ASTROPHYSICAL PLASMAS (12)

- a) [Basic processes, radiation.]
- b) [Waves and instabilities.]

This category represents another growth area for the Conference. No strong theme emerges; contributions covered basic processes involving excitation and radiation, the slowing down of charged particles, wave instabilities and shocks.

2.13 INTERACTION OF LASER BEAMS WITH PLASMAS (22)

- a) Laser-induced plasmas (optical discharges).
- b) [Plasma target.]
- c) [Electrode target.]
- d) [Pellet target.]

The general category 13a) might be taken to include topics from gas breakdown by lasers to interaction with any form of plasma or solid target. In fact, most of the contributions may be classified best in categories 13b)-d), and in many cases are motivated by laser fusion.

2.14 INTERACTION OF PARTICLE BEAMS WITH PLASMAS (7)

- a) [Inertial confinement.]
- b) [Beam-plasma interaction.]
- c) [Undulator.]

Similarly, interests in beam-induced fusion with inertial confinement motivated papers in category 14a). Those in category 14b) might well have been placed in category 10c). The paper on high frequency generation by a relativistic electron beam traversing a sinuous waveguide (undulator) describes a phenomena of great interest, but which is not strictly a beam-plasma interaction.

2.15 DIAGNOSTIC METHODS (45)

- a) Probes.
- b) Spectroscopy.
- c) Miscellaneous.
- d) [Laser scattering, interferometry and holography.]
- e) [Microwaves.]

This category, which could undoubtedly be augmented with papers dispersed through many others, is always one of the most significant areas of the Conference. A natural sequence of events in the development of science is first to observe basic physical phenomena accurately, then to model and describe them precisely, and finally to use them in the form of diagnostic techniques. In that sense, the category of Diagnostic Methods illustrates a number of phenomena for which the quality of scientific description is high.

Probes now provide only a small number of contributions. A more significant number concerned various aspects of spectroscopy, including light sources and

standards. The most notable growth, however, was shown by optical techniques involving laser scattering, interferometry and holography. In contrast to many spectroscopic techniques, the discharge is actively probed with a controllable source.

A similar comment applies to the several microwave diagnostic techniques reported. A further advantage of both over invasive techniques such as probes is that they permit measurements to be made from outside the discharge.

3. Format of the scientific program. — As the Conference has evolved from its small beginnings in Oxford 26 years ago, a persistent problem for the ISC has been the choice of format for the scientific program. Many of us believe that the best conferences for developing personal contacts and exchanging information are those at which some 75-100 participants meet for a few days, preferably in a remote place, give few papers, and spend most of the time in discussion.

Larger conferences, such as the ICPIG, make it harder for groups of participants with close mutual interests to maintain contact and follow a scientific thread through parallel sessions, but can offer a much wider perspective on the field and the opportunity for more numerous personal contacts.

The ISC attempts to construct an optimal program, combining the virtues of large and small conferences, using the following elements :

- General Invited Lectures.
- Topical Invited Lectures.
- Contributed Papers.
- Oral Sessions.
- Poster Sessions.
- Rapporteur Sessions.
- Discussion Sessions.
- Post-deadline Papers.

The respective merits and defects of these elements, and the ways in which the ISC has chosen to deploy them in recent ICPIG's, are worth examining.

General invited lectures. — These are intended to be authoritative general-interest reviews of broad fields, some not otherwise emphasized at the Conference, and are given in plenary sessions. It is consequently necessary to find distinguished scientists willing and able to prepare such reviews in written form, as well as for oral presentation. They must discuss work beyond that carried out in their own groups, and since simultaneous translation facilities are not usually available must generally be prepared to do so in English.

Choosing such scientists is a difficult commission. About ten has been the recent aim, and without wishing to seem self-congratulatory, it can be said that the ISC has assembled a wide-ranging and impressive list at Grenoble, headed by Prof. Alfvén, *primus inter pares*, at the Opening Session :

Theme 1 (= Laboratory and Natural Plasmas).
Plasmas in the Laboratory and in Space
 (H. Alfvén).
Ion-Molecule Interactions in the Laboratory and in
Planetary Atmospheres (H.S.W. Massey).

Theme 2 (= Natural Plasmas).

Lightning (K. Berger).
The Solar Flare Phenomenon (J. Heyvaerts).

Theme 3 (= Laboratory Plasmas).

Contact Electrode Processes and Microplasma
Diagnostics (F. L. Jones).
Strong Turbulence and its Computer Simulation
 (V. E. Zacharov and Y. S. Sigov).
Particle Beam Interactions with Plasmas and their
Application to Inertial Fusion (M. J. Clauser).
Progress in Toroidal Magnetic Confinement
 (G. Grieger).
Progress on Laser Fusion at Lawrence Livermore
Laboratory (H. G. Ahlstrom).

Topical invited lectures. — These satisfy criteria of quality and style similar to those for General Invited Lectures, but are intended to be more specialized, and hence less appropriate for presentation in plenary sessions. They are consequently scheduled in competition with contributed papers, but not with each other. Twelve such lectures were invited by the ISC for the Grenoble Conference.

Contributed papers. — The greatest pressure on the ISC derives from the large number of contributed papers. In the past, half a dozen parallel sessions have been necessary to accommodate them all as oral presentations, or rapporteur sessions (see below) have been organized to review them in groups. There have been suggestions that the scope of the Conference should be restricted, but this militates against the aim of offering to participants a broad perspective on phenomena in ionized gases.

Rather than explicitly excluding certain areas, the ISC has chosen to solicit papers according to a list of topics which evolves following the interests shown by participants at previous conferences, and currently includes the 15 categories discussed in § 2. The result is that topics such as thermonuclear fusion, MHD energy conversion, ionospheric physics and astrophysics, which are catered for by a variety of other conferences, figure less prominently among the contributions and are typically covered by invited lectures.

At the East Berlin and Grenoble conferences, the ISC agreed to limit the oral presentation of contributed papers to two parallel sessions, so effectively limiting the numbers of oral presentations to about 75. This method of avoiding the conflicts of multiple parallel sessions has been made feasible by the organization of poster sessions running parallel to the oral sessions.

In recent years, poster sessions have become popular at many national and international conferences.

At first, some authors were apprehensive that presentations by poster constituted a second-class mode of communication. It rapidly became clear that this is not the case: they help to identify people interested in your work and engender personal contacts with them, they are a boon to inexperienced speakers, or in situations where there are language difficulties, and they are superior to brief oral presentations when large quantities of data or numerous equations are to be displayed.

As an example, we may take the Annual Meetings of the Plasma Physics Division of the American Physical Society. Opinion has swung in the last three years to the position where the majority of authors now opt for poster presentation of their work. At Grenoble, the ISC had to select about 75 out of 425 contributed papers, using as criteria the nature and scientific interest of the material, and the desirability of presenting a wide range of topics. It is possible that this process would have been unnecessary had authors been asked to state their preferences at the time of submission.

Before leaving the topic of Contributed Papers, a heavy debt of gratitude should be acknowledged to the Local Organizing Committee, and to their small army of helpers who reviewed the contributed papers. The separation into coherent sessions for oral and poster presentations and their timing on the scientific program to avoid conflicts are further onerous tasks whose outcome is never perfect. The ISC exercises final judgment and responsibility in such matters, and in the rejection of papers that are irrelevant to the Conference, of dubious scientific quality, or of impenetrable obscurity, but relies on the Local Organizing Committee for the initial groundwork, and ultimate detailed execution of its wishes.

Rapporteur sessions. — For some previous ICPIG's, rapporteurs were selected in advance to comment on groups of papers. This procedure saves time, and ideally presents a series of integrated, critical reviews of the contributed material. In practice, its aims and advantages are difficult to realize. First, the material for a rapporteur session must be sufficiently concentrated about a theme to lend itself to coherent review. Second, it is difficult to find people willing to put in the considerable time and preparation needed for successful rapporteur sessions. Third, it is sometimes difficult to supply them with the contributed papers sufficiently far in advance of the Conference for such preparation to be feasible. For these reasons, the ISC has abandoned rapporteur sessions for the present in favor of poster presentations.

Discussion sessions. — At previous ICPIG's (though not at Grenoble), discussion sessions on special topics, organized during the Conference by interested groups, have constituted a prominent feature of the scientific program. The ISC will continue to provide facilities for such meetings since they represent a valuable

means of exchanging recent information, and speculating informally on emerging topics.

Post-deadline papers. — With a similar aim in mind, the ISC has provided facilities at Grenoble for poster presentation of very recent, or highly speculative, results. They are presented at the discretion of their authors, and of course do not appear in the Conference Proceedings.

4. Future conferences. — If any justification is required for the continued existence of the ICPIG, it is provided by the large numbers of participants and presentations at Grenoble : about 450 of each. If the Conference ceased to exist, it would certainly be missed by the substantial core of participants who follow it regularly, and would probably be rapidly reinstituted in a comparable form.

It is the responsibility of the ISC to maintain the vitality of the Conference, and to be continually open to suggestions for improvement in its form and detailed organization. Work on the XVth ICPIG in Minsk, in July 1981, has already begun, so your comments and suggestions are earnestly solicited. Please write to me or any other ISC member concerning the scientific program, or to Prof. Tsytovich

concerning matters in the province of the Local Organizing Committee.

We know that there is no persistent ideal format for a conference such as the ICPIG, and that in practice its success depends on the constraints and happy accidents of time, place, organizers, scientific contributions, and participation. To that extent, *We live not as we wish to, but as we may*, as Menander remarked, and even the most heroic efforts of the ISC cannot ensure universal satisfaction.

On the other hand, the ISC has a very deep concern for the welfare of the Conference, and a wealth of experience of it (to say nothing of extraordinary modesty !). For example, although none of us can match the record of the outgoing chairman, Prof. Maecker, of having attended all fourteen ICPIG's, three of us have participated in ten, and all past ICPIG's have been attended by at least one member of the new ISC. Their experiences include memories of promising improvements in the Conference that have not succeeded, and risky experiments that have worked very well. If some of your suggestions for improvements are not adopted, it may be because of such experiences; you can be sure at least that they have not been ignored.

Author Index

Alfvén (H.). — Plasma in laboratory and space.....	C7-1	Kuswa (G. W.). — Voir Clauser (M. J.)	C7-81
Ali-Khan (I.). — Voir Waelbroeck (F.)	C7-313	Llewellyn-Jones (F.). — Contact electrode processes and microplasma diagnostics	C7-47
Berger (K.). — Survey on actual knowledge and physical problems	C7-57	Long (W. H.) Jr. and Bhaumik (M. L.). — Electric dis- charge pumping of excimer lasers	C7-127
Bhaumik (M. L.). — Voir Long (W. H.)	C7-127	Manheimer (W. M.). — Anomalous transport from plasma waves	C7-269
Burns (E. J. T.). — Voir Clauser (M. J.)	C7-81	Massey (H. S. W.). — Ionic reactions with laboratory and in planetary atmospheres	C7-21
Chang (J.). — Voir Clauser (M. J.)	C7-81	Mehlhorn (T. A.). — Voir Clauser (M. J.)	C7-81
Clauser (M. J.), Burns (E. J. T.), Chang (J.), Farns- worth (A. V.), Goldstein (S. A.), Johnson (D. J.), Kuswa (G. W.), Mehlhorn (T. A.), Mendel (C. W.), Mix (L. P.), Poukey (J. W.), Quintenz (J. P.), Sweeney (M. A.), Vandevender (J. P.) and Wid- ner (M. M.). — Particle beam interactions with plasmas and their application to inertial fusion	C7-81	Mendel (C. W.). — Voir Clauser (M. J.)	C7-81
Crawford (F. W.). — Phenomena in ionized gases : some reflections on the XIVth ICPIG	C7-317	Mix (L. P.). — Voir Clauser (M. J.)	C7-81
Dietz (K. J.). — Voir Waelbroeck (F.)	C7-313	Poukey (J. W.). — Voir Clauser (M. J.)	C7-81
Farnsworth (A. V.). — Voir Clauser (M. J.)	C7-81	Presnyakov (L. P.) and Urnov (A. M.). — X-ray plasma diagnostics	C7-279
Fauchais (P.) and Rakowitz (J.). — Physics on plasma chemistry	C7-289	Quintenz (J. P.). — Voir Clauser (M. J.)	C7-81
Goldstein (S. A.). — Voir Clauser (M. J.)	C7-81	Raizer (Yu. P.). — Optical discharges	C7-141
Grieger (G.). — Progress in toroidal magnetic confine- ment	C7-87	Rakowitz (J.). — Voir Fauchais (P.)	C7-289
Gryziński (M.). — Theoretical description of collisions in plasma : classical methods	C7-171	Sigov (Yu. S.) and Zakharov (V. E.). — Strong turbulence and its computer simulation	C7-63
Heyvaerts (J.). — Plasma and solar physics. The solar flare phenomenon	C7-37	Sweeney (M. A.). — Voir Clauser (M. J.)	C7-81
Hiskes (J. R.). — Formation of hydrogen negative ions by surface and volume processes with application to negative ion sources	C7-179	Urnov (A. M.). — Voir Presnyakov (L. P.)	C7-279
Johnson (D. J.). — Voir Clauser (M. J.)	C7-81	Vandevender (J. P.). — Voir Clauser (M. J.)	C7-81
Klimontovich (Yu. L.). — Kinetic theory of spectral line broadening in a nonequilibrium plasma	C7-113	Waelbroeck (F.), Ali-Khan (I.), Dietz (K. J.) and Wien- hold (P.). — Surface problems in magnetic confine- ment systems	C7-313
		Widner (M. M.). — Voir Clauser (M. J.)	C7-81
		Wienhold (P.). — Waelbroeck (F.)	C7-313
		Wilhelm (J.) and Winkler (R.). — Progress in the kinetic description of non-stationary behaviour of the electron ensemble in non-isothermal plasmas	C7-251
		Winkler (R.). — Voir Wilhelm (J.)	C7-251
		Zakharov (V. E.). — Voir Sigov (Yu. S.)	C7-63

Commission paritaire N° 26.741

Les Editions de Physique 1980

Directrice de la Publication : Jeanne BERGER

Imprimé en France. — Imprimerie JOUVE, 17, rue du Louvre, 75001 PARIS
Dépôt légal : 1^{er} trimestre 1980

peut être...
...
...
...
...



UNIVERSITY OF ILLINOIS-URBANA



3 0112 032097070